3rd Hand: A Device to Support Elderly and Disabled Person

Ummay Habiba[1], Shiuly Barua[2], Faisal Ahmed[3], Golap Kanti Dey[4], Kazi Tanvir Ahmmed[5]
[1,2,4,5]Department of Applied Physics, Electronics & Communication Engineering
[3]Department of Computer Science and Engineering
University of Chittagong, Chittagong-4331, Bangladesh
[1]habiba.ap16@gmail.com, [2]baruashiuly@gmail.com, [3]faisal.cse91@gmail.com, [4]d.k.golap@gmail.com, [5]tanvir@cu.ac.bd

***Abstract*— This paper represents a system "3rd HAND", that can serve a disable person or elder person to perform some of their regular tasks without any helping hand. This system helps a person to switch the regular home loads (light, fan etc.) using his voice commands and his location can be tracked when he travels outside alone with the system. In self-regulated system we used an EASY_VR voice recognition module. The recognized control commands are sent to an ARDUINO for proper program controlling and then to a Bluetooth module. After that, the commands are routed to the target device over Bluetooth network and finally carried out by the control circuit. In GPS tracking system, we used the GPS and SMS services of an android mobile phone. When a client sends a request SMS to the system to get its location, the GPS receiver of the phone calculates the location coordinates and converts it to location name using GEOCODING API. Finally the location name is sent to the client automatically. Generally it is not comfortable and secured for a disabled or elder person to switch their home loads and to travel alone. So the system "3rd hand" provides them a safety switching system and supports them to travel independently in safe.**

Keywords- self-regulated, voice recognition, wireless communication, GPS, GSM, location tracking etc.

I. INTRODUCTION

With the increasing of average age of world population as a result of advancement of medical science, the elderly population is increasing rapidly worldwide. And a statistics shows that more than 500 million people in the world are disabled as a consequence of physical, sensory, or mental impairment. It is a responsibility for the people all around the world to support this large number of population [1]. Life is very difficult for the people mentioned because they are completely dependent on others for their regular movement task. They need a constant care giver [2]. Though we can't remove the sufferings of their daily life, we can try to make their life little easier with the help of modern technologies.

Elder persons and persons with special needs are unable or face difficulties to operate their regular home loads like light, fan, AC etc. [3]. And they need a continuous attender when they travel outside. So we came up with a project that will help those persons to perform some of their daily works independently and safely. The objective of our project is to provide those persons with a system that can operate their home loads automatically with their voice commands only [4] and can detect their current location when they travel outside alone and send their location name via SMS to clients who want to monitor their current location.

The elder and disable persons face difficulties with a remote control device which controls the home appliances remotely by button press feature [5]. So we have designed and implemented this system with a feature of self-regulation controlled by voice commands instead of any button press system. In this self-regulation system, we used Easy-VR shield for voice recognition process instead of smart phones which can accept voice commands. This is because if we use smart phones for controlling home load with voice commands, we must have continuous Wi-Fi connection. But this Wi-Fi is not much available in many 3rd world countries like Bangladesh.

Voice controlled self-regulated system is based on speech recognition technology. This technology allows a CPU to recognize and analyze a set of pre-programmed voice commands produced by a person using a microphone [6]. In this voice controlled home automation system, the major challenge is to overcome the problems with distant voice command and speech recognition in the noisy environment [7].

Another feature of our project is GPS tracking. By using this feature, anyone can monitor the position of an elder or disable person when he travels outside alone. This system is based on GPS and GSM technology [8, 9]. We used android phone as target device [10]. In this system a client who is interested to monitor the position of the person mentioned carrying GPS system, sends a request message to the system. After receiving request message, the GPS system calculates the position of that person by using signals from the satellites [11, 12]. Then the system automatically sends a message containing the location name of that person to the client via GSM network.

II. DESIGN OVERVIEW

The system "3rd hand" is an integrated system to facilitate the older and disable persons with a self-regulated system that can be fully operated by voice commands and with a GPS tracking system that can detect the location of the persons mentioned when they travel alone.

In self-regulated system, there are two major parts. One is transmitter part and another is receiver part. In this section of home automation system, we used two ARDUINO mega 2560, one of which is used in transmitter part and another is used in receiver part. Here two HC-05 Bluetooth modules are used for setting up the wireless communication between the

978-1-4673-9257-0/15/$31.00 ©2015 IEEE

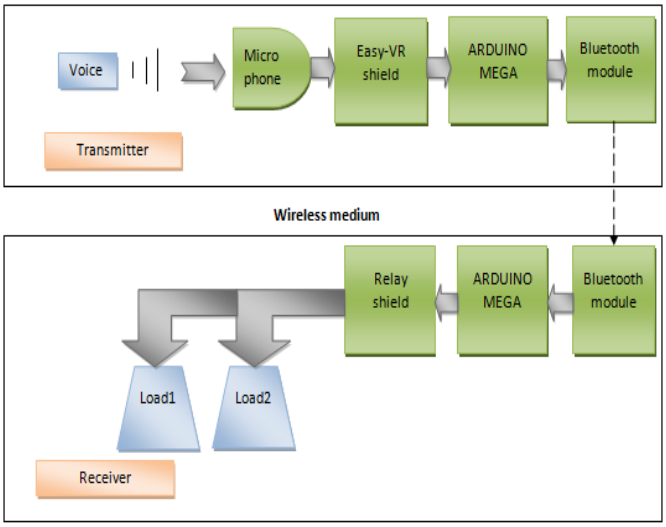

Fig. 1. Design overview of self-regulated system

transmitter part and the receiver part. One of them is interfaced with the transmitter ARDUINO and another is with receiver ARDUINO. We have used here an Easy-VR voice recognition shield. The Easy-VR shield is interfaced with the ARDUINO at the transmitter part. There is a microphone on this Easy-VR shield. The microphone receives the voice signals from a person and the Easy-VR module tries to recognize the voice commands. If the module recognizes a voice command, it sends this command to the ARDUINO. By proper program controlling the ARDUINO sends this data to the Bluetooth module. Then if the wireless communication with the Bluetooth at the receiver section is set up, the voice data is sent to the receiver portion via Bluetooth communication. Then Bluetooth module transmits this data to the ARDUINO at the receiver part. The design overview of this system is shown in fig. 1.

A 2-channel relay shield is used which is connected between the ARDUINO and the loads to be operated at the receiver part. The relay shield acts as a switch to control the ON/OFF conditions of the loads. By program controlling, the ARDUINO controls the switching mechanism of relay to operate the loads.

We implemented our GPS tracking system by using a GPS enabled Android phone and Android Application.

In this system, when a client wants to know the current location of a person who uses an android phone with this GPS tracking system, sends a request to the user's subscription number through a SMS (Short Message Service) via GSM. The SMS contains a password and the password is also stored in our system. Then the system extracts the client's IME number and password from the SMS. If it can match the password with the password stored in the system, GPS receiver of the Android phone is turned on. Then the system receives signals from the satellites and calculates the latitude and longitude of the user's location. Then the latitude and longitude are converted into human readable location name using GEO coding API (Application Programming Interface) of the android SDK (Software Development Kit).Then the

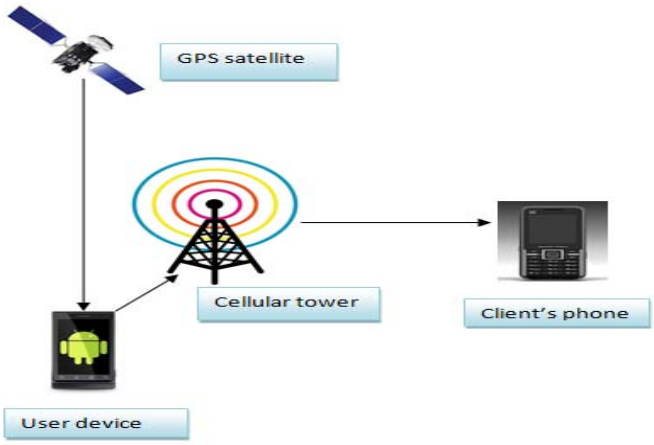

Fig. 2. Overview of GPS tracking system [13]

user location address is sent to the client automatically via GSM network. The user also gets a notification when anyone tracks his location. The overview of GPS tracking system is shown in fig. 2.

III. CONSTITUENT SUB-MODULES

A. ARDUINO MEGA 2560

The ARDUINO mega 2560 is a microcontroller board containing an ATmega2560 microcontroller. ARDUINO is a complete package that contains all the essential components to control the functions of a microcontroller. ARDUINO makes the hardware and software implementation of a system easier ARDUINO helps the microcontroller to receive instructions from the outside of the system and to run the system according to the instructions. There are 54 digital I/p pins and 16 analog input pins in this ARDUINO. ARDUINO can be interfaced with a computer via USB connection. Its operating voltage is 5v. ARDUINO can receive 5v input voltage from a pc through USB connection or from an external power source through a voltage regulator. It contains 4 UART pins for serial communications. ARDUINO contains a 16MHz crystal oscillator, a power jack and a reset button. It provides a clock speed of 16MHz. ARDUINO mega can be programmed with ARDUINO software. An ARDUINO MEGA 2560 is shown in fig. 3.

B. Easy-VR module

Easy-VR is a speech recognition module. This module is interfaced with an ARDUINO board. ARDUINO supplies 3.3v input voltage to this module. Easy-VR module communicates with the ARDUINO through serial interfaces with a default baud rate 9600. It receives data with ERX pin and transmits

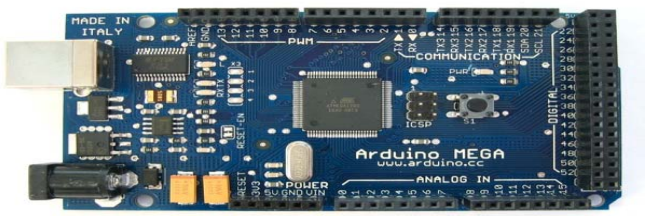

Fig. 3. ARDUINO Mega 2560 [14]

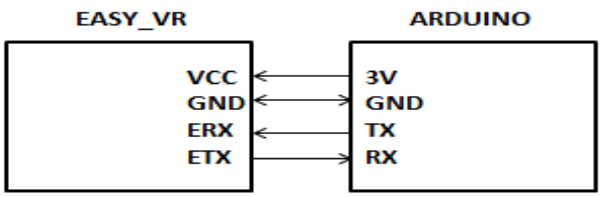

Fig. 4. Pin connections between Easy-VR and ARDUINO

data with pin ETX. Easy-VR receives voice signals with a microphone. The sensitivity of the microphone is 38dB and its frequency response is in the range of 100Hz -20KHz. Easy-VR module is trained up with the required voice commands using a software Easy-VR commander. When a command is said at the microphone, the module checks it. If it can recognize the command, it sends the command to the microcontroller to perform operation. The basic pin connection between an Easy-VR shield and an ARDUINO is shown in fig. 4.

C. *HC-05 Bluetooth module*

In our project we have used two HC-05 Bluetooth modules for wireless communication. It is very easy to interface with ARDUINO. It communicates with an ARDUINO through its serial interfaces. The sensitivity of the module to any other Bluetooth signal is about -80dB. It receives 3.3v input voltage from the ARDUINO. It transfers data with a default baud rate 9600. The module can be configured using AT-commands to communicate with other desired modules wirelessly. When two Bluetooth modules are paired, both of them blink 1times/2s. And while they are not paired, they blink 2times/s. The basic pin connection between a Bluetooth module and an ARDUINO is shown in fig. 5.

D. *3-channel 5v relay*

We have used a 3 channel relay shield in this system. The shield is interfaced between ARDUINO and loads to be operated at the receiver section. The relay shield acts as a switch to control the ON/OFF conditions of the loads. In this shield, each channel is used to control a single load. Each channel contains 3 relay pins such as COM, NO and NC. Loads are connected to the relay via relay pins. The relay shield is interfaced with the ARDUINO via digital I/O pins. The basic pin connection between a relay shield and an ARDUINO is shown in fig. 6.

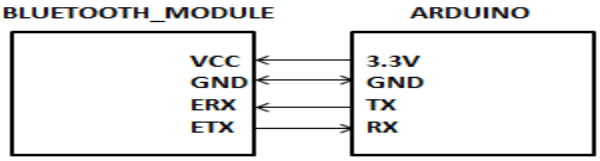

Fig. 5. Pin connections between Bluetooth and ARDUINO

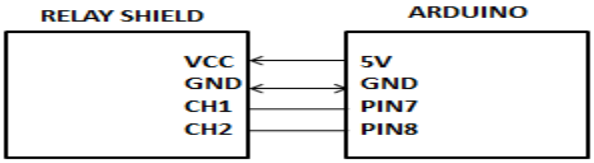

Fig. 6. Pin connections between relay and ARDUINO

E. *GPS tracking section*

1) *Hardware*

In this system, we used an android mobile phone as GPS tracking device with processor 1GHz or more and RAM 1GB or more. Client device can be any cell phone capable of send SMS.

2) *Software*

We used the OS Android 2.1.2. In this system, we used GPS and GSM technologies.

IV. SYSTEM IMPLEMENTATION

A. *Self-regulated system*

1) *Hardware implementation*

In transmitter part, the Easy-VR shield and the Bluetooth module are connected to the ARDUINO board. The ARDUINO is supplied a 5v input voltage from a laptop through USB connection. An ARDUINO supplies VCC 3.3v to the Bluetooth module and to the Easy-VR shield. The microphone is connected to the Easy-VR board. In order to transmit signal from the Bluetooth, we connected the Bluetooth TX and RX pin to the ARDUINO RX119 and TX118 pin respectively. To communicate with the ARDUINO to process voice signal, the D1 and D0 pins of Easy-VR are connected to the TXD1 and RXD0 pins of ARDUINO respectively. The total circuit diagram of the transmitter part is shown in fig. 7.

In receiver part, the Bluetooth module and the relay shield are connected on the ARDUINO board. There is no physical connection between two Bluetooth modules. The TXD and RXD pins of Bluetooth module are connected to the RX217 and TX216 pins of the ARDUINO respectively to transmit data. The Bluetooth module receives 3.3v from the ARDUINO. The total circuit diagram of the receiver section is shown in fig. 8.

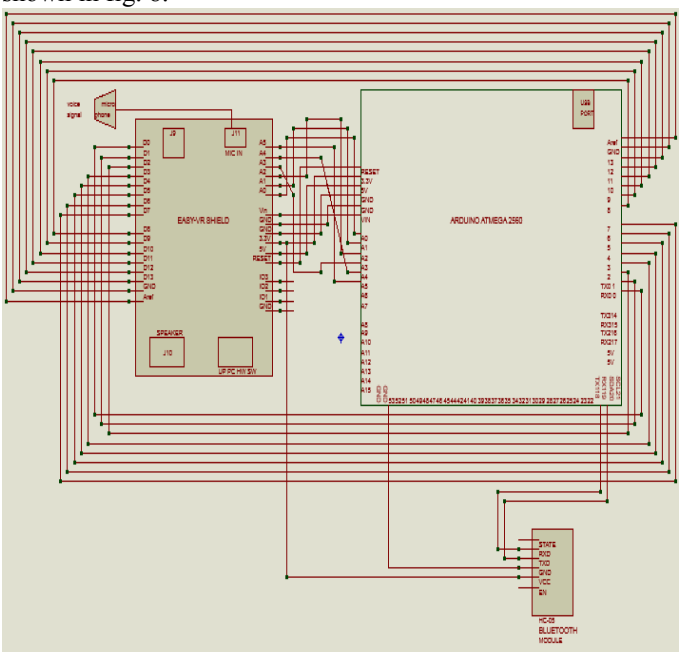

Fig. 7. Transmitter circuit

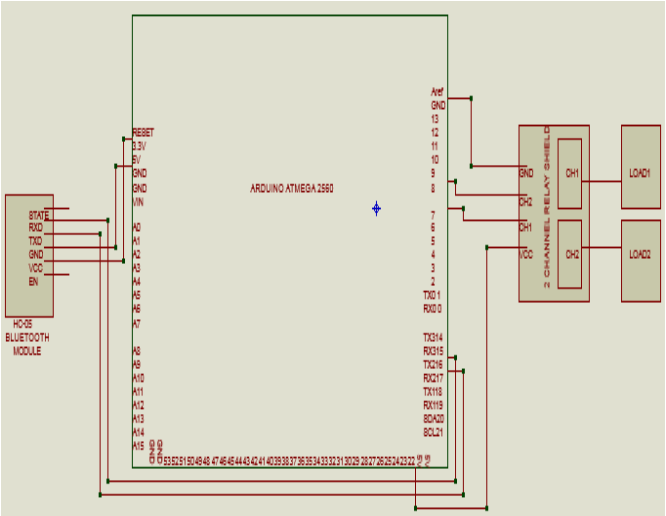

Fig. 8. Receiver part

2) Software implementation

We used the Easy-VR commander software which can record the voice command made by a user. The Easy-VR module can compare it when a command is said on the microphone of the system. To record the user's voice command, after connecting the system with the pc, the commander software is opened which is shown in fig. 9.

There are different groups of commands. We placed all the commands in a group that are needed to be used at the same time. We placed commands "LIGHT" & "FAN" in Group1, "ON" & "OFF" to switch light in Group2 and "ON" & "OFF" to switch fan in Group3. After creating a command the device should be trained twice with the user's voice. To train the device, we got the window which is shown in fig. 10 by clicking the option "Train command" in the top of the above window.

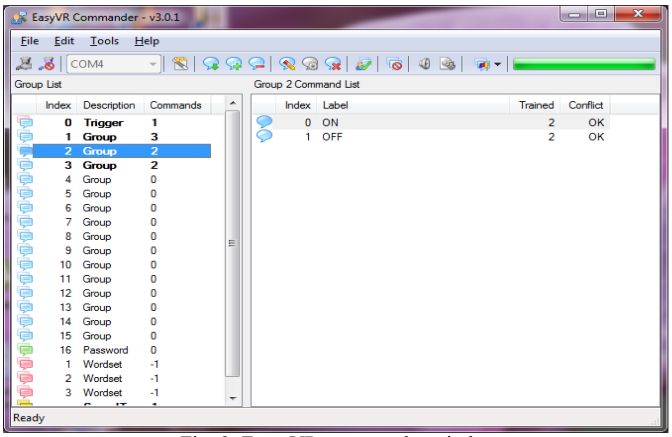

Fig. 9. Easy-VR commander window

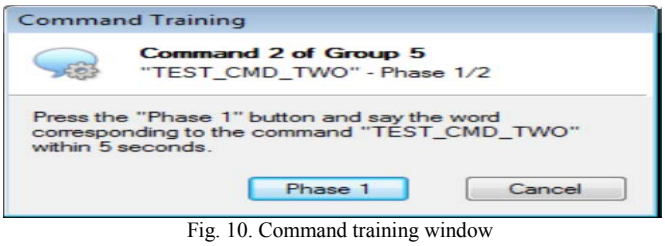

Fig. 10. Command training window

Fig. 11. Speak command window

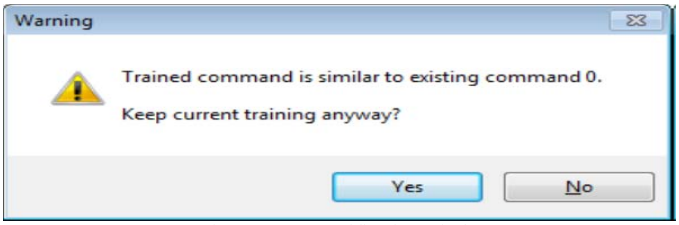

Fig. 12. Error notification window

When "phase 1" is clicked, a window is appeared which indicates to speak the command at that time. This window is shown in fig. 11.

Then this process is repeated again. If there is an error or mismatch, then a window is appeared which is shown in fig. 12.

B. GPS tracking system

Implementation of this system is divided into four different stages:

1) Listening to a location request through SMS over GSM network and authenticating it:

To listen a location request through SMS over GSM network we created a new Broadcast Receiver, extended the "BROADCAST RECEIVER()" class and override the "ON RECEIVE()" event handler. We registered this Broadcast Receiver in the application manifest using an Intent Filter that listens for the "ANDROID. PROVIDER. TELEPHONY. SMS RECEIVED" action String. We also specify the "RECEIVE SMS" manifest permission.

2) Retrieving GPS coordinates (latitude and longitude) of the device:

We used Google Play service location API to retrieve the current location of the user's device.

First of all to connect to Google Play Service API, we created an instance of the Google Play service API client using "GOOGLE APICLIENT. BUILDER()" method. Next we invoked the method "ADD API()" to specify the API we want to use. While using this method, the constant "LOCATION SERVICES. API" is defined within "GOOGLE APICLIENT" class as parameter. Before beginning a connection by calling "CONNECT()" on the "GOOGLE APICLIENT", we specified an implementation for the callback interfaces, "CONNECTION CALL BACKS" and "ON CONNECTION FAILED LISTENER". These interfaces receive callbacks in response to the asynchronous "CONNECT()" method when the connection to Google Play services succeeds, fails, or becomes suspended.

After Connecting to the Google play service location API, we create a reference to the "LOCATION REQUEST" class by invoking "LOCATION REQUEST. CREATE()".

To ask for update of the device's current location, we called the fused location provider's "REQUEST LOCATION UPDATES()". To request the last known location, we invoked the "GET LAST LOCATION()" method of the fused location provider's object. The "GET LAST LOCATION()" method returns a Location object from which we retrieved the latitude and longitude coordinates of the device location by invoking "GET LATITUDE()" and "GET LONGITUDE()" methods respectively.

3) Finding Location Address from the Coordinate:

The "GEO CODER" Class is used to convert a (latitude, longitude) coordinate into a (partial) address. The process is called reverse geocoding. We created an object of the "GEO CODER" class and invoked it's "GET FROM LOCATION()" method, passing the latitude and longitude we obtained in step 2 as parameters.

4) Transmitting the SMS over GSM network:

The SmsManager Class is used to send the SMS message directly to the client.We invoked the static method getDefault() of the SmsManager class to create an instance of the SmsManager and used the method sendTextMessage() to send SMS message to the client, a formated SMS specifying user's current location in both form(Geographical Coordinate and Address) .

Flowchart of this process is shown in fig. 13.

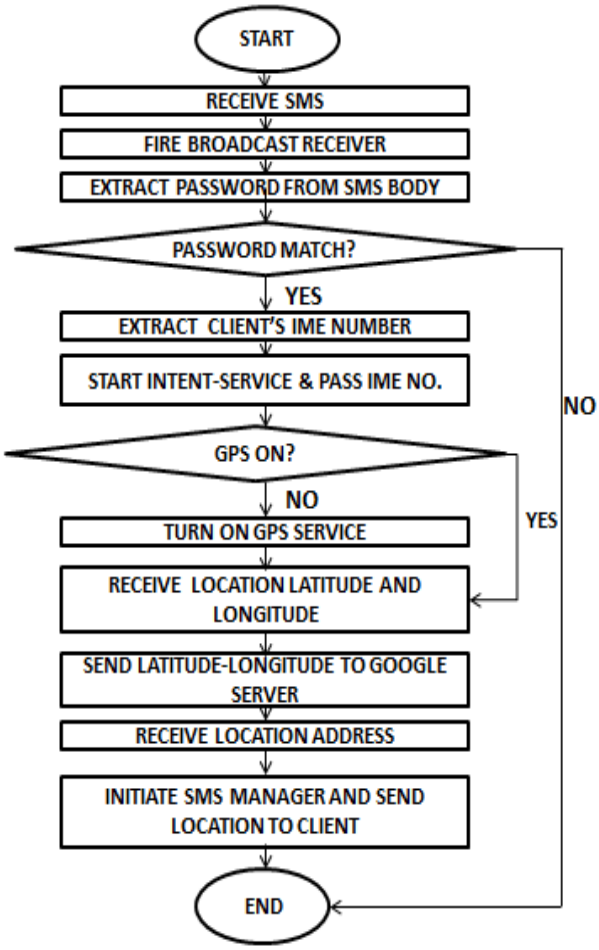

Fig. 13. GPS tracking system flowchart

V. PERFORMANCE TEST

A. *Self-regulated system*

We implemented our experiment to control two loads - fan and light. The result of our home automation section is shown in the TABLE I and the result of our home automation section while used by different person is shown in TABLE II.

By using ARDUINO software, we can observe the response of the system when a command is said. To observe the system response, the system is connected to the pc. The ARDUINO software and then the serial monitor window are opened. When commands are said on the microphone to control the ON/OFF conditions of light and fan the serial monitor responses as fig. 14.

TABLE I. RESULT OF SELF-REGULATED SYSTEM

Number	Commands	Functions
1.	Start	System gets ready
2.	Light-on	Light turns on
3.	Light-off	Light turns off
4.	Fan-on	Fan turns on
5.	Fan-off	Fan turns off

TABLE II. PRACTICAL RESULT OF SELF-REGULATED SYSTEM

Person	Commands	Responses before training	Responses after training
Elderly person Gender: Male Age: 70	Light on Light off Fan on Fan off	No response No response No response No response	Responding Responding Responding Responding
Elderly person Gender: Female Age: 60	Light on Light off Fan on Fan off	No response No response No response No response	Responding Responding Responding Responding
Physically disabled person Gender: Male Age: 34	Light on Light off Fan on Fan off	No response No response No response No response	Responding Responding Responding Responding
Child Gender: Female Age: 10	Light on Light off Fan on Fan off	No response No response No response No response	Responding Responding Responding Responding

```
Say a command in a group 0
Command: 0= start
Say a command in a group 1
Command: 0= light
Give command for light
Say a command in a group 2
Command: 0= on
Light on
Say a command in a group 1
Command: 0= light
Give command for light
Say a command in a group 2
Command: 1= off
Light off
Say a command in a group 1
Command: 1= fan
Give command for fan
Say a command in a group 3
Command: 0= on
Fan on
Say a command in a group 1
Command: 1= fan
Give command for fan
Say a command in a group 3
Command: 1= off
fan off
```

Fig. 14. Serial monitor responses

B. *GPS tracking section*

In GPS tracking system when a client sends a request to know the user's location, then the user gets the following notification on his phone screen:

"*Someone is tracking your location"*

Then the GPS system calculates the location of the user as latitude and longitude and converts it into the location name using GEO coding API of the Android phone and sends a SMS to the client. The client receives the following message:

"*Current location: (location name)"*

VI. CONCLUSION AND FUTURE WORKS

We have represented the design and implementation of a system "3rd HAND" which is targeted at elderly and disabled persons in our work. The system is very flexible. The system implements an automatic voice recognition system by using an Easy-VR module. The wireless network is implemented using Bluetooth modules. ARDUINO program controlling controls the total operation. To implement GPS tracking system, we used all built in features like GPS, GSM, and API of the android phone. This system is very secure. Anyone cannot use the home automation feature of the system. The system must be trained with one's voice and only he can use this feature. In GPS tracking system, only clients who know a pairing password, can request for tracking the current location of the person carrying the system. It is also beneficial for children. This project can be further improved by increasing the efficiency of the self-regulated system so that it can response in a noisy environment. In future, we want to implement the GPS tracking system using GPS-GSM module instead of android phone and without using data connection.

REFERENCES

[1] Humaid AlShu'eili, Gourab Sen Gupta and Subhas Mukhopadhyay, "Voice Recognition Based Wireless Home Automation System," 4th International Conference on Mechatronics (ICOM), pp. 1-6 May 2011.

[2] Dimitar H. Stefanov, Zeungnam Bien, Won-Chul Bang, "The Smart House for Older Persons and Persons With Physical Disabilities: Structure, Technology Arrangements, and Perspectives" IEEE Transactions on Neural Systems and Rehabilitation Engineering, Vol. 12, No. 2, pp. 228-250, June 2004.

[3] A.K.Gnanasekar, PJayavelu and V.Nagarajan , "Speech Recognition Based Wireless Automation Of Home Loads With Fault Identification For Physically Challenged," ICCSP-'12, pp. 128-132, April 2012.

[4] Kim Baraka, et al. "Low cost Arduino/Android-based Energy-Efficient Home Automation System with Smart Task Scheduling", Fifth International Conference on Computational Intelligence, Communication Systems and Networks, pp. 296-301, June 2013.

[5] Jieming Zhu, et al. "DEVELOPING a Voice Control System for Zigbee-based Home Automation Networks," IC-NIDC2010, pp. 737-741, September 2010.

[6] Mardiana B., et al. "Homes Appliances Controlled Using Speech Recognition in Wireless Network Environment ," International Conference on Computer Technology and Development," pp. 285-288, November 2009.

[7] Benjamin Lecouteux, Michel Vacher and François Portet, "Distant Speech Recognition for Home Automation: Preliminary Experimental Results in a Smart Home," 6th Conference on Speech Technology and Human-Computer Dialogue (SpeD), pp. 1-10 , May 2011.

[8] Pankaj Verma, J.S Bhatia, "Design and Development of GPS-GSM Based Tracking System with Google Map Based Monitoring" International Journal of Computer Science, Engineering and Applications (IJCSEA) Vol.3, No.3, pp. 33-40, June 2013.

[9] Umar Farooq, et al. "GPS-GSM Integration for Enhancing Public Transportation Management Services" Computer Engineering and Applications (ICCEA), 2010 Second International Conference (Volume:2), pp. 142-147, 19-21 March 2010.

[10] Nico Deblauwe, Peter Ruppel, "Combining GPS and GSM Cell-ID positioning for Proactive Location-based Services", Mobile and Ubiquitous Systems: Networking & Services, 2007. MobiQuitous 2007. Fourth Annual International Conference, pp. 1-7, 6-10 Aug. 2007.

[11] Youjing Cui and Shuzhi Sam Ge, "Autonomous Vehicle Positioning With GPS in Urban Canyon Environments," IEEE Transactions On Robotics And Automation, Vol. 19, NO. 1, pp. 15-25, February 2003.

[12] Tian Zhihong, Yang Jinsheng and Zhang Jianguo, "Location-based Services Applied to an Electric Wheelchair Based on the GPS and GSM Networks, " Intelligent Systems and Applications, 2009. ISA, pp. 1-4, May 2009.

[13] Al-Mazloum, E. Omer, M. F. A. Abdullah, "GPS and SMS-Based Child Tracking System Using Smart Phone," World Academy of Science, Engineering and Technology International Journal of Electrical, Computer, Electronics and Communication Engineering, Vol. 7, No. 2, pp. 171-174, 2013.

[14] http://arduino.cc/en/Main/arduinoBoardMega2560 (Accessed February 15, 2015).

Assisted Vehicle Driving Embedded with Autonomous Security System

Nur Mohammad [1], Md. Kausar Hamid Miji [1], and Prodipto Chowdhury[1,*]
[1]Chittagong University of Engineering & Technology, Bangladesh
[*] E-mail: cprodipto@gmail.com

Abstract— **The roads and highways of Bangladesh are among the most deadly roads in the world due to the movement of capacity crossing huge traffic. Yet the safety system is not very high. Hence accidents and traffic jam is very common. Still now, no collision avoiding system is used to prevent accidents. In this paper, Autonomous Embedded Vehicle Security System especially with Obstacle Collision Avoidance system has been developed. The embedded sensors of the prototyped vehicle provide related versatile information. These can be used in detecting obstacles in the vehicle trajectory and provide an alarming signals to the vehicle driver to avoid collisions. In this proposed system, a gas-sensing module has been used for the detection the potential of combustible gas. The temperature sensor has been installed in order to read the system temperature continuously. An alarm circuit has been added to the system to warn the driver about the vehicle in-front obstacle and the potential of LPG gas. The presence of LPG gas can also be determined from the indication lamp of the voltage comparator. An initial application was implemented in order to test the detection of vehicle in-front obstacle and for the measurement of the distance between the vehicle and obstacle. The LCD display indicates the distance of the obstacle and turns on the alarm to warn the driver to avoid the collision.**

Keywords— Embedded System, Gas Sensing Module, Temperature Sensing Module, Ultrasonic Sensors, Motor driver

I. INTRODUCTION

Over the past few years, road accidents, especially highway accidents have been rising alarmingly in Bangladesh [1]. According to a study conducted by the Accident Research Centre (ARC) of BUET, road accident kills on average 12,000 lives annually and causes 35,000 injuries [1]. According to World Bank Statistics, annual fatality rate from road accident is found to be 85.6 fatalities per 10,000 vehicles [1]. Maniruzzaman and Raktim Mitra, in their study claimed that 'the number of accidents has increased by 43 per cent between 1982 and 2000 while the number of fatalities has increased by around 400 per cent within the same period' [2]. The fatality rate in Bangladesh is 35 times higher than US and 50 times higher than UK [3]. Hence it is clear that roads in Bangladesh have become deadly. Besides, accidents also cause an enormous financial loss. According to World Health Organization (WHO), road traffic injuries cause a loss of about 2% of GDP in Bangladesh, or about £1.2bn annually [4].

Bangladesh is trying to develop its road network, but the attempts cannot keep pace with population and commerce, and accordingly, roads are being turned into death traps devoid of safety measures [4]. Therefore, we have identified the necessity of a system that will efficiently reduce the road accident at low cost in roads and highways.

One of the crucial causes of road accidents is alcoholism. Driving while intoxicated or drunk is dangerous and drivers with high blood alcohol content or concentration are at greatly increased risk of vehicle accidents, highway injuries and vehicular death. In our country most accidents are occurring by the drunken truck drivers.

Another type of accident we often notice is the leakage of gas from containers. However, almost all the accidents caused by collision, alcoholism, and gas-leakage are completely avoidable. So, we need an effective system to detect vehicle in-front obstacle and check out the alcohol or presence of LPG gas inside the cabin of the vehicle.

Our proposed system is composed of an obstacle sensing module, a motor driving unit, a gas sensing module, an alarm circuit, and a temperature sensor. The system detects any obstacle static or dynamic in-front of the vehicle and the gas sensing module will recognize the potential of LPG gas and alcohol.

A method to implement vehicle safety systems with one or two channels and using single transceiver, micro-controller 89C51 is used as main driver [5]**.** A remote monitoring system had been developed [6] which have focused on the GSM, because the wireless remote monitoring system has more and more application. A low cost automotive localization system had been developed using GPS and GSM-SMS services [7]. The system permits localization of the automobile and transmitting the position to the owner on his mobile phone as a short message (SMS) at his request. There is Collision Warning System (CWS), Collision Mitigation System (CMS) [8], RFID Technology [9], Cruise Control (CC), Adaptive Cruise Control (ACC) [10] [11] etc. to prevent accidents. These systems are not very cost effective that a country like Bangladesh can afford them. So to provide safety and security of the vehicle at minimum cost is our main motto.

The paper is organized as follows. Sections II and III present the sensor elements considered in the system and its programming and simulation. Section IV presents the hardware implementation, which is followed by section V that presents the result and discussion.

Copyright Notice: 978-1-4673-9257-0/15/$31.00 ©2015 IEEE

II. CONSIDERED SENSOR ELEMENTS

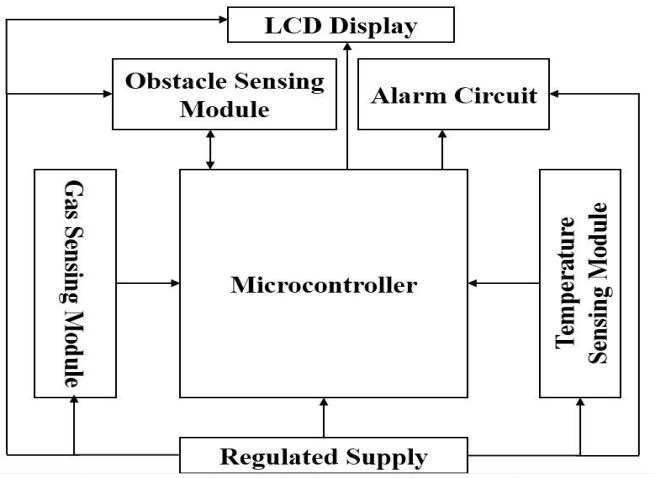

Figure 1. Complete Block Diagram of the Proposed System

A sonar based obstacle sensing module is used to measure the distance between vehicle and in-front obstacle. A motor driver circuit is used to control the vehicle. If the hindrance is at a predefined distance that may cause accident, the vehicle will stop automatically. Thus accident can be prevented. Again, the leakage of LPG gas can be detected by gas sensing module. An indication lamp is used to warn the driver about the potential of gas. The alarm circuit warns about the presence of in-front obstacle and the leakage of gas. The circuit is supplied from a 5V regulated supply. The total system is represented as in Figure 1.

A. Obstacle Sensing Module

The sensor calculates the distance from an object by sending bursts of ultrasound towards it and measuring the time it takes to the waves to get back (Distance = Velocity * Time). This information is used to determine whether there's a close "obstacle" near the vehicle. The motor driving circuit is just a simple transistor switching circuit. The microcontroller feeds the transistor at base when there is no obstacle in front of the vehicle and when there is an obstacle, the microcontroller turns off the transistor. The obstacle sensing module block diagram and motor driving circuit are shown in Figure 3 and 4, respectively.

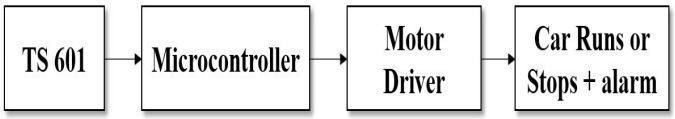

Figure 2. Functional block diagram of the Obstacle Sensing Module

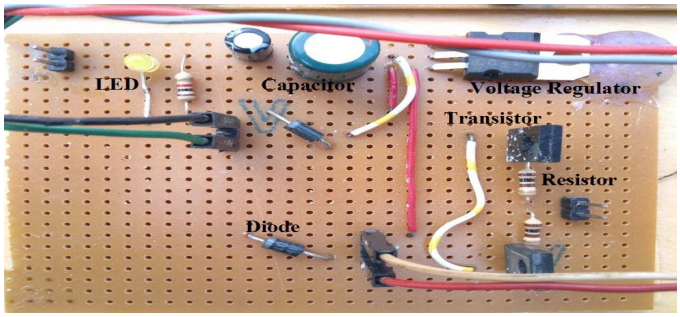

Figure 3. Motor Driver Circuit

The alarm circuit (Figure 4) is also a transistor switching circuit where a buzzer is used instead of the motor [15].

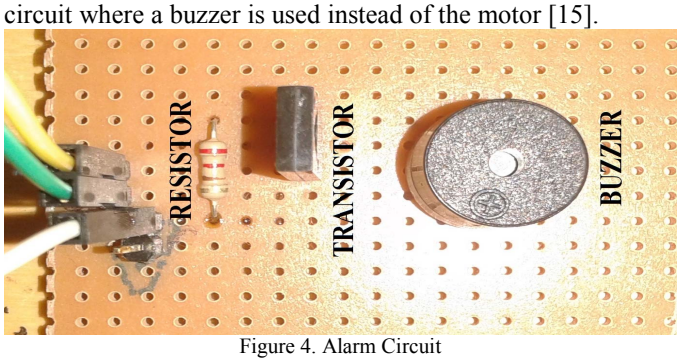

Figure 4. Alarm Circuit

B. Gas Sensing Module

MQ-5, a semiconductor sensor is used for Combustible Gas Detection. Sensitive material of MQ-5 gas sensor is SnO_2, which has lower conductivity in clean air [12]. When the target combustible gas exists, the sensor's conductivity rises. MQ-5 gas sensor has high sensitivity to Methane, Propane and Butane [12].The output voltage of the MQ-5 gas sensor is compared with the voltage comparator which is in non-inverting non-zero mode. If the output of the MQ-5 becomes equal or higher than the reference voltage, the indication lamp lit up and the alarm circuit turns on. Thus the potential of the combustible gas is detected. We used HA17339A IC as the voltage comparator circuit. The block diagram and implementation of voltage comparator and gas sensing module are shown in Figure 5, 6, and 7, respectively.

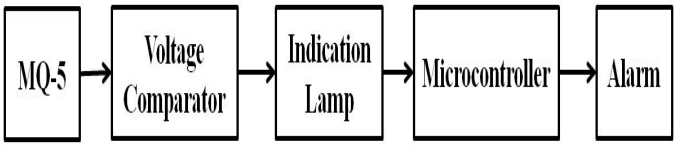

Figure 5. Functional block diagram of the Obstacle Sensing Module

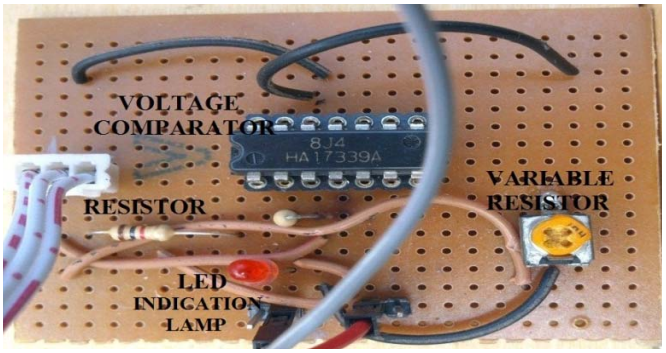

Figure 6. Voltage Comparator Circuit

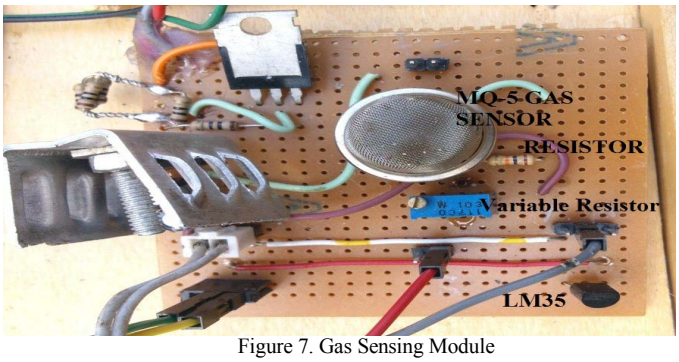

Figure 7. Gas Sensing Module

C. *Temperature Sensing Module*

Temperature is the most frequently measured environmental quantity. Most systems are affected by temperature. The performance of these systems is controlled by using proper control systems that keep temperature within specified limits[13]. Temperature sensors provide inputs to those control systems [14]. We used LM35 IC to read system temperature continuously. Figure 8 shows the temperature sensing module.

III. PROGRAMMING AND SIMULATION

For simulation and programing of the embedded system, Proteus and Mikro C were used. Algorithms were developed to interface obstacle sensing module and gas sensing module with the microcontroller.

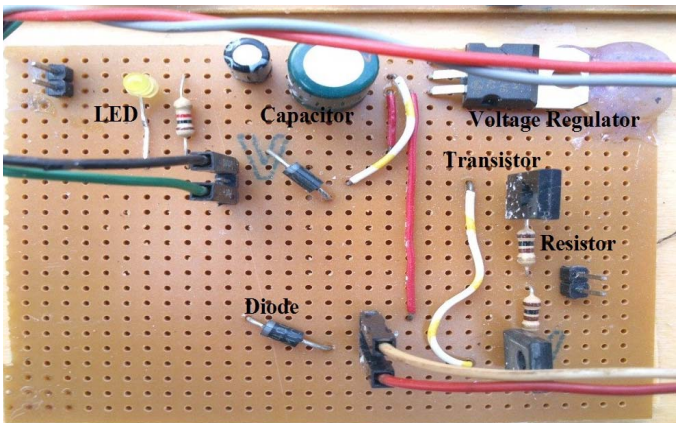

Figure 8. Temperature Sensing Module

A. *Algorithm to Interface Obstacle Sensing Module with Microcontroller*

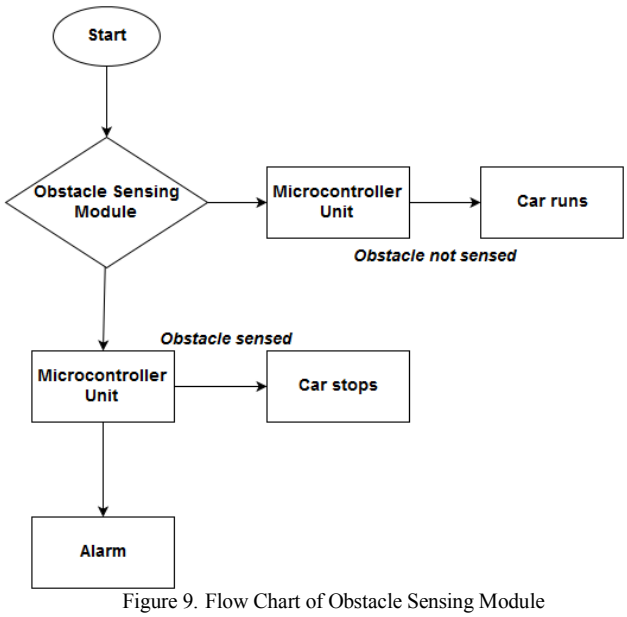

Figure 9. Flow Chart of Obstacle Sensing Module

B. *Algorithm to Interface Gas Sensing Module with Microcontroller*

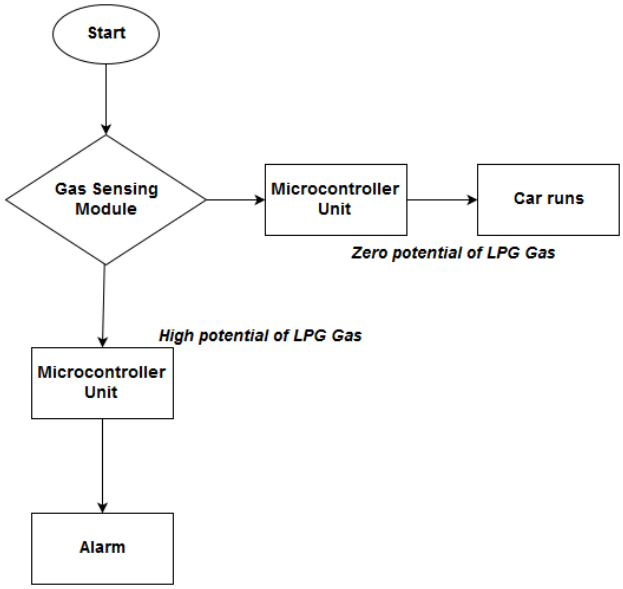

Figure 10. Flow Chart of Gas Sensing Module

IV. HARDWARE IMPLEMENTATION

The proposed system is implemented in a prototype vehicle. The prototype vehicle is designed with two gearhead motor, two wheels, a cluster wheel and mechanical body. The proposed system works properly. When there is an obstacle in-front of the vehicle, then it stops and the alarm is on. Again, when it finds any presence of LPG gas, the LED just lit up and also the alarm is switched on. The temperature sensor continuously reads the system temperature and the centigrade

value is shown in the LCD display. The entire developed system is shown in the following figure:

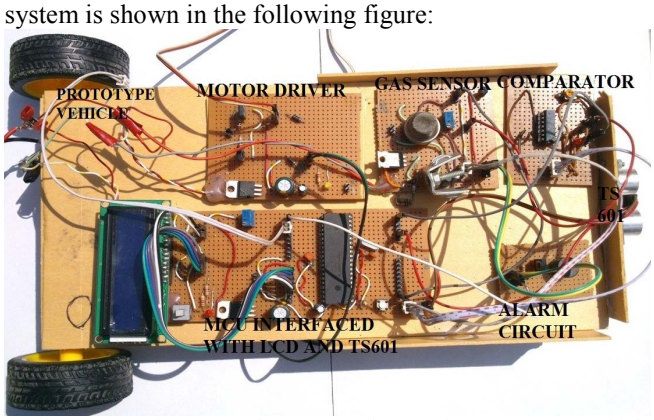

Figure 11. Entire Proposed System Implemented on a Prototype Vehicle

V. RESULT AND DISCUSSION

Each module in the system functions properly and successfully; the only minor issue is the calibration of the variable resistor of the gas sensor. Another problem is the external noise interfering with the LCD display and with the transmitter and receiver of the TS 601 obstacle sensing module. The external noise comes from a variety of sources—computers, cell phones, power supplies, etc. Other noise sources include the parts of the gas sensing module itself; these include the oscillator, battery, speaker, long wires, power on the Vero board, and the Vero board itself.

Using additional capacitors may help to filter out the noise from the power supply and to reduce board noise. Implementation on a PCB (printed circuit board) is another solution to greatly reduce noise. No extraneous wires are needed, thereby leading to cleaner and stronger signals to the components, as daisy-chaining of the power wires are eliminated. Also, implementation on a PCB makes the overall system more compact.

The circuit performance is shown in Figure 12. The performance of each module was determined by trial and error method. It can be clearly observed that the modules always did not perform successfully. For example, the gas sensor is highly sensitive to current that depends on the variable resistor .We used a battery of 12 volts as power supply, which is converted to 5 volts using a voltage regulator. The battery

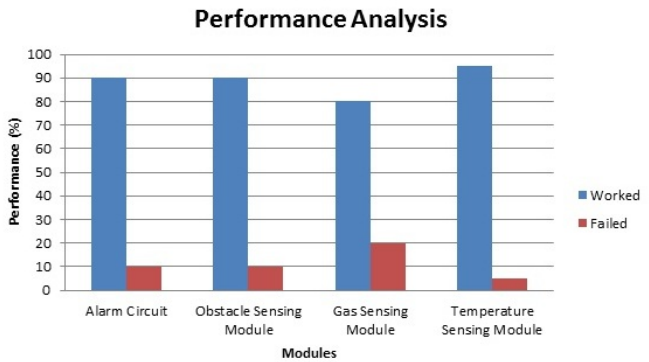

Figure 12. Performance Analysis of the Designed System

discharges rapidly during operation and is needed to charge it frequently. Again the ultrasonic sensor did not work as it is described in the data sheet. The range was lower than that is provided in the data sheet. Hence the system's modules performance was not hundred per cent. However, the total systems performance was satisfactory.

The system has been considering only the distance between the vehicle and its obstacle in front. To stop the vehicle its speed should be controlled as well. A fuzzy algorithm can be used to control the speed at different distance between the vehicle and obstacle. Again, the range of the obstacle sensing module is small. So we need to increase the range of obstacle sensation for implementing in real vehicle. It can be done using RADAR. Also a GPS tracker can be used to secure the vehicle from stealing. Although there is a vast amount of automation technology in this field, in Bangladesh, we are lagging behind, and the rate of accident is increasing day by day. So, this system can be used to reduce the rate of accident and save the life of people of Bangladesh. However, the designed system is a prototype, and not yet prepared to implement in real life. To implement it with the existing vehicles, its size should be reduced, and the best possible way to do that is to incorporate all functionalities in a single chip; which will be our future work.

This paper presents a system for automatic detection of obstacle in front of vehicle as well as potential of LPG gas inside the vehicle, and helps decrease one of the major causes of fatalities; excessive speed or potential of LPG gas. Our approach is based on a combination of three different sensor technologies: sonar based sensor to convey the information about the in-front obstacle, gas sensor to indicate the presence of LPG gas, temperature sensor to read the system temperature continuously. The proposed system is portable and suitable for use any commercial car with little modifications. The system shows promising results. Since the presence of a vehicle in front can be reliably detected in advance using sonar based technology, vehicle's behavior can be adjusted accordingly. We have testes the system in real-life conditions, and have been able to reduce the speed of the vehicle to zero at the predefined distance as a result of the detection of the obstacle. The technology developed can help drivers in avoiding collision with obstacles; consequently can reduce the fatalities of road accident, which is the main objective of this project.

REFERENCES

[1] Tashmina Rahman (2012), Road Accidents in Bangladesh: An Alarming Issue [Online]. Available: http://blogs.worldbank.org/endpovertyinsouthasia/road-accidents-bangladesh-alarming-issue

[2] KM Maniruzzaman and Raktim Mitra, "Road accidents in Bangladesh" *IATSS Research*, vol. 29, no. 2, pp. 71, May 2005

[3] FE Report (2013), Fatality rate in BD road accidents 50 times higher than in UK [Online]. Available: http://www.thefinancialexpress-bd.com/index.php?ref=MjBfMDVfMTVfMTNfMV8xOTBfMTY5NDE1

[4] Syed Zain Al-Mahmood (2012), Bangladesh's road accidents take heavy toll on poor – and on economy [Online]. Available: http://www.theguardian.com/global-

development/2012/aug/22/bangladesh-road-accidents-poor-economy.
[5] K.J. Padmini, S.S. Dorle, A.G. Keskar, Megha, and B. Chakole, "Micro-controlled based Vehicle Safety System Using Dedicated Short Range Communications (DSRC)", in *Second International Conference on Emerging Trends in Engineering and Technology*, Dec. 2009, pp. 570-575
[6] Chen Peijiang and Jiang Xuehua, "Design and Implementation of Remote monitoring system based on GSM," in *Pacific-Asia Workshop on Computational Intelligence and Industrial Application*, Dec. 2008, vol.42, pp.167-175.
[7] Ioan Lita, Ion Bogdan Cioc, and Daniel Alexandru Visan, "A New Approach of Automobile Localization System Using GPS and GSM/GPRS Transmission," in *29th International Spring Seminar on Electronics Technology*, May 2006, vol. 8, pp. 415-422
[8] OnGuard™ Collision Safety System Driver Tips, Meritor Wabco, 2009
[9] Fernando Seco, Vicente Milanés, Antonio Jiménez, Julio C. Díaz, and Teresa de Pedro, "An RFID-Based Intelligent Vehicle Speed Controller Using Active Traffic Signals", *Sensors*, vol. 10, no. 6, pp. 5872-5887, Jun. 2010
[10] Alex Forrest, Mustafa Konca, "Autonomous Cars and Society", Department of Social Science and Policy Studies Worcester Polytechnic Institute Worcester, MA 01609, Tech. Rep., 2007
[11] Raj Kamal, *Embedded Systems -Architecture, Programming and Design*, New Delhi: McGraw-Hill, 2008
[12] "MQ-5 data sheet", Henan Hanwei Electronics Co.,Ltd., Zhengzhou, China.
[13] *Temperature Sensor Handbook*, National Semiconductor, 1995.
[14] Robert F. Coughlin and Frederick F. Driscoll, *Operational Amplifiers and Linear Integrated Circuits,* Englewood Cliffs, N.J.:, Prentice Hall, 1991

A Survey on Interconnect Encoding for Reducing Power Consumption, Delay, and Crosstalk

Sujan Kumar Saha[1], Bulbul Ahmed[2], Jiangjiang Liu[3]
[1,2]Department of Electrical Engineering and [3]Department of Computer Science
Lamar University
Beaumont, USA
Email: [1]ssaha@lamar.edu, [2]bahmed@lamar.edu, and [3]jane.liu@lamar.edu

Abstract—**With the advancement of technologies, interconnect circuits are shrinking dramatically. Capacitances of interconnects are increasing due to minimized wire size and inter wire spacing. As a result, interconnect power consumption, delay, and crosstalk are increasing significantly, which is affecting overall interconnect performance. Various techniques such as buffer insertion, shielding, skewing, and encoding are used to minimize delay, crosstalk, and power consumption. This paper studies a set of encoding methods for reducing power consumption, crosstalk, and delay, and also presents a comprehensive comparison and analysis of these encoding techniques.**

Keywords—encoding, power, delay, bus invert, shielding, weighted code mapping.

I. Introduction

In Deep Sub-Micron (DSM) technology, the VLSI circuit components are now at the size of nanometer range. Along with the components, interconnects are also shrinking very quickly due to aggressive scaling down of technology. In this case, wire width is getting thinner but height is not decreasing so rapidly to keep resistance constant. As a result, the ratio of height to width is increasing prominently. Lots of research has been accomplished on low power circuit designs, focusing on the reduction of circuit component power consumption. But, now in today's Deep sub-Micron technology, interconnect energy is no longer ignorable. Due to the dense placement of interconnects, coupling capacitance is increased, which dominates the self capacitance of the wire. Consequently problems with crosstalk delay, noise and power consumption arise which affects the overall circuit performance.

Coupling capacitance contributes to extra power consumption because of the different switching pattern of the adjacent bus. Opposite transition between two adjacent buses causes worst case cross talk and produces a large delay and energy consumption in the interconnect. Different techniques have been applied to minimize crosstalk, delay, and power consumption. Some are at the circuit level and some are at the architecture level. Among these, bus encoding is a widely used method. This method is used to change the bit patterns of the data so that self-transitions, charging, discharging, and toggle transitions are reduced, which will eventually minimize power consumption, delay, and also crosstalk in some instances. In this paper, a set of encoding methods will be discussed to reduce power, and the rest of the methods are for minimizing delay and crosstalk. All methods are explained in Section II, Section III contains results reported by corresponding papers and a comprehensive comparison, followed by the conclusion in Section IV.

II. Selected Bus Encoding Methods

A. Bus Invert

Bus Invert encoding method [1] is one of the most widely used encoding methods. This encoding method is mainly focused on reducing the number of transitions. According to the method, only one control bit is needed to indicate the inversion. To implement Bus Invert encoding, first of all, we need to calculate the hamming distance between the data of two consecutive cycles. Hamming distance between the two data strings of length n is the total number of positions at which the corresponding data are different. If the hamming distance is greater than n/2 where n is the number of the bus width or length of data string, set control bit=1 and invert all the bits of next cycle original data. If the hamming distance is less than n/2, then set control=0 and keep the data value as it is in the next cycle. At the receiver side, the contents of the bus must be conditionally inverted according to the control bit.

In the example figure 1, there are 9 transitions between current cycle data and next cycle original data, which have been marked as light blue. So, hamming distance is 9. In the other 7 positions, the data is same as it is in the current cycle. As data length is 16 and hamming distance is greater than 8, control bit will be equal to 1 and all the bits of next cycle original data will be inverted. After the inversion hamming distance is 7. Thus, due to inversion of the next cycle bits, 2 self-transitions have been reduced.

As only one control bit is used to transfer the encoding information, area overhead is very small. Also this method doesn't require an extra clock cycle. Yet here, only self-transition is reduced, but crosstalk due to coupling capacitance

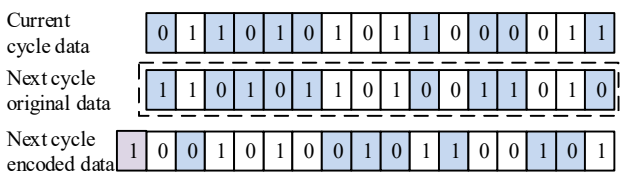

Fig.1. Bus Invert Encoding (bus width 16 bit, control bit 1)

978-1-4673-9257-0/15/$31.00 ©2015 IEEE

between adjacent wires is not considered.

B. Odd Even Invert

Odd Even Invert [2] encoding is a modified version of Bus Invert encoding. This method is also focused on reducing the number of transitions. As the number of transition is directly proportional to power, it also reduces power consumption of interconnects. The authors of this paper mentioned two encoding approaches, Simple Odd Even Invert and Calculated Odd Even Invert.

Initially there are some common features of these two encoding methods. First, we have to divide bus lines into two groups, odd lines and even lines. Bus lines are selected according to their position. Odd position lines go to the odd group and even position lines go to the even group. For this encoding method, two extra control lines are required to send the encoding information. There are four possible cases with two control lines: no bus lines are inverted (00), only odd lines are inverted (10), only even lines are inverted (01), and all lines are inverted (11). We need to transfer the bits over the invert-lines according to what we have done. This information needs to be transferred to decode the original bits. In the next subsection, two encoding approaches have been described separately.

1) Simple Odd Even Invert: To implement simple Odd-Even Bus Invert, only self transitions are considered. Coupling transition is not considered in this method. Coupling transiton is the impact of one wire due to the transition of the adjacent wire. According to this encoding, if the number of self-transitions on the odd lines is more than or equal to the half of odd lines, the odd lines are inverted, and if the number of self-transitions on the even lines is more than or equal to the half of even lines, the even lines are inverted. Following the example of figure 3 makes it easy to understand the encoding. In the example, there are 4 transitions in odd lines and 5 transitions in even lines. So all bus lines have been inverted and control bits are 11. After inversion, there are 7 transitions, which is less than the original number of transitions. Also, it should be noted that there was one toggle before inversion. After the inversion, the toggle is removed automatically. Still, if there is any toggle, then we need to apply the two phase transfer method to remove the toggle. The two Phase transfer method delays one of the two adjacent lines by a half cycle. So, this encoding method introduces some delay to eliminate toggle. The amount of delay depends on the number of toggles after inversion.

	C0	C1
No Invert	0	0
Even Invert	0	1
Odd Invert	1	0
Both Invert	1	1

Fig.2. Control Bit of Odd Even Encoding

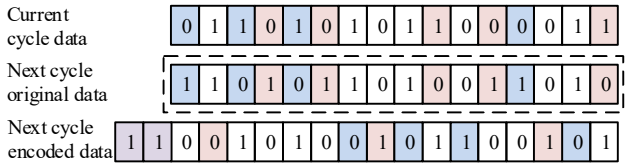

Fig.3. Simple Odd Even Invert Encoding (bus width 16 bit, control bit 2)

2) Calculated Odd Even Invert: Calculated Odd-Even Bus Invert [2] encoding is slightly different from Simple Odd-Even Bus Invert encoding. In Simple Odd Even Invert, only self transitions have been considered. Whereas in Calculated Odd Even Invert, coupling transitions are considered. According to figure 2, there can be four types of inversions. For each of the inversion types, the total number of coupling transitions (charging and discharging) [2] are calculated between current cycle data and next cycle original data. Then that inversion type is selected for encoding which has the least number of coupling transitions. For example, in figure 4, current and next cycle data are 0110101011000011 and 1101011010011010. For 00 type inversion, the total coupling transition is 20, for 01 type it's 11, for 10 type it's 15, and for 11 type it's 20. In this case it has been considered that one toggle transition is equivalent to 4 coupling transitions. As we get an 11 transition for 01 type inversion, which is smallest, it is selected as encoded data.

C. Temporal and Shielding Coding (TSC)

The encoding approach of Sainarayanan *et al*. [4] is useful for eliminating crosstalk delay. Table I shows crosstalk induced delay categorization of a wire due to two adjacent lines. In this table "↓" represents 1→0 transition, "↑" represents 0→1 transition, and "–" means there is no change of data bit. Also here, Cg is ground capacitance, R is total resistance of wire, Cc is coupling capacitance, and λ is the ratio of Cc to Cg. The encoding method is developed to eliminate crosstalk class 5 and 6. According to this approach, actual data to be transmitted is divided into groups of 3 bits. Encoded data is transmitted in the first temporal cycle and the information of encoding and shielding is transmitted in the 2nd temporal cycle. So every 3-bit real data is encoded as 2 consecutive groups of 3-bit data to be transmitted in two consecutive temporal cycles. To avoid worst-case crosstalk in boundaries of every 3-bit group, 0 is transmitted between two adjacent 3-bit groups as a shielding bit. So this approach needs an extra 1-bit line after every 3-bit group. That's 8-bit data will be encoded as 10-bit data length.

For example, a data d_{t-1} = 101 0 100 0 00 is the encoded data transmitted at time "t-1", and data d_t = 01001101 is original data to be transmitted at time "t". Before encoding

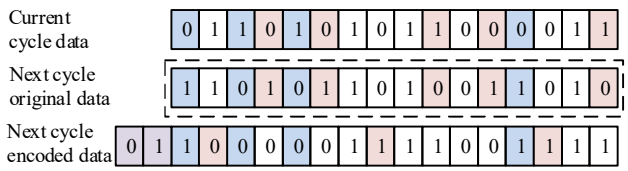

Fig.4. Calculated Odd Even Invert Encoding (bus width 16 bit)

TABLE I. CROSSTALK CATEGORIZATION

CC	Delay	Pattern of switching
1	0	−−−, −− ↑, ↑ −−, −− ↓,↓ −−, ↑ − ↑,↑ − ↓,↓ − ↑,↓ − ↓
2	C_gR	↑↑↑,↓↓↓
3	$C_gR(1+\lambda)$	− ↑↑,↑↑ −,− ↓↓,↓↓ −
4	$C_gR(1+2\lambda)$	− ↑ −,− ↓ −,↓↓↑,↑↓↓, ↑↑↓,↓↑↑
5	$C_gR(1+3\lambda)$	− ↑↓,− ↓↑,↓↑ −,↑↓ −
6	$C_gR(1+4\lambda)$	↓↑↓,↑↓↑

this, both data will be checked for crosstalk class according to the crosstalk categorization table. As in this case, the crosstalk class is greater than 1, so 3-bit groups will be inverted as the encoded data 101 0 100 0 01 and transmitted in the first temporal cycle. The 2nd temporal cycle contains the encoding and shielding information. If the data is inverted, in the 2nd temporal cycle in every 3 bit groups, 3rd bit will be set to 1; otherwise it will be 0, and the first and second bits are kept same to the 1st temporal cycle so that there is no transition. So, for the encoded data, 2nd temporal cycle data will be 101 0 101 0 01. Finally, given data d_t will be encoded as 2 consecutive temporal cycle data.

This method is further modified by adding two extra bit lines into both sides of the shielding bit. These extra bits are inserted in such a way so that the transition is same as the boundary bits of the 3-bit group. This modified approach can eliminate crosstalk class 5, 6, and also crosstalk class 4 as well as any transition pattern that is −↑−, −↓−, ↓↓↑, ↑↑↓, ↓↑↑, ↑↓↓. However these methods do not include inductance effect, increase bit lines in modified approach and eventually increase the area overhead.

D. Temporal Crosstalk Shielding(TCS)

Najeeb *et al.* [5] reduces both power and crosstalk delay by reducing bus width and using the temporal shielding approach. Original data is divided into several blocks before encoding. Then the data is encoded into two data packets and transmitted over two consecutive clock cycles. For example, the original data of n bits is divided into k bit blocks, then the number of groups are now n/k and encoded into two m bit data blocks. This is done in such a way so that n is a multiple of k and m is less than k. As the encoded bit m is less than k, active bus width is reduced. Keeping bus area constant, spacing among wires is increased so that coupling capacitance decrease. This

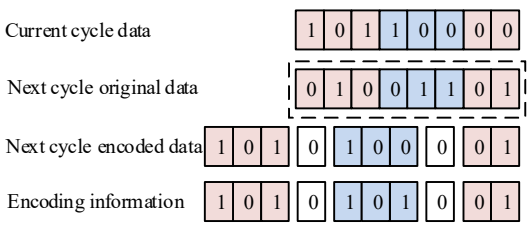

Fig.5. Temporal and Shielding Coding (bus width 8 bit, shielding bit 2)

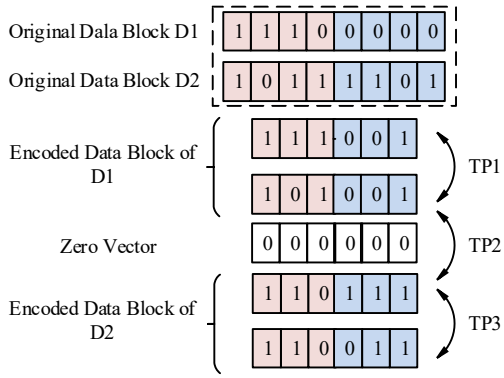

Fig.6. Temporal Crosstalk Shielding (bus width 8 bit)

method is also developed to eliminate crosstalk in class 5 and 6 of Table I.

If data D1 was transmitted at time Tt-1 and D2 is to be transmitted at Tt, D2 is encoded according to following Table II proposed by this approach. Here each 4-bit block is encoded into two 3-bit blocks. As the original data block is encoded into two data blocks, 4 cycles are needed to transmit two original data, and for these 4 transmissions, there are 3 transitions. The transition between the first transmission to the second one is named Transition Pattern 1(TP1), between 2nd and 3rd is TP2, and between 3rd and 4th is TP3. The Encoding Table is formed in such a way that there is no opposite transition between two adjacent blocks. Thus at TP1 and TP3, crosstalk class 5 and 6 are eliminated. This crosstalk may only happen at TP2. A crosstalk analyzer is used to detect crosstalk class 5 and 6; if found, then it sends a crosstalk identification vector before the next data is transmitted. To eliminate class 5 and 6 crosstalk, a Zero vector is transmitted between those affected data. At the receiver end, according to the decode bit, the decoder detects whether it receives zero vector or useful data. If zero vector is received, then it is discarded, and if it receives other than zero vector, the data is stored and using stored data and bus data, the original data is recovered. This approach is efficient for addressing bus delay reduction because there is less crosstalk and it improves power efficiency for the data bus.

E. Variable Cycle Transmission with Hybrid Spatial Temporal Redundancy (VCT_HSTR)

Zhang *et al.* [6] attempted to reduce both energy and delay. That's why the encoding method proposed in [6] combines Weighted Code Mapping (WCM) [13] with temporal redundancy. The Weighted Code Mapping focuses on reducing energy, whereas Temporal Redundancy reduces delay. The WCM algorithm relies on probability distribution of the data pattern. All patterns do not have the same probability of occurring. Suppose for the data set {00, 01, 10, 11}, the probability set is {0.1, 0.4, 0.4, 0.1}. Each value of the probability set represents the corresponding probability of the data value. So, the more probable data is mapped to a code word, which has less number of transitions among the bits. The authors also mentioned that one easy way of getting WCM code is to perform bitwise XOR operation between two consecutive cycle data.

TABLE II. TEMPORAL CROSSTALK SHIELDING ENCODING TABLE

4-bit Original data	3 bit Encoded data	4-bit Original data	3 bit Encoded data	4-bit Original data	3 bit Encoded data	4-bit Original data	3 bit Encoded data
0000	001 001	0100	011 001	1000	100 100	1100	111 001
0001	001 011	0101	011 011	1001	100 110	1101	111 011
0010	001 101	0110	011 111	1010	110 000	1110	111 101
0011	001 111	0111	100 000	1011	110 110	1111	111 111

After getting the code words, the delay between two consecutive codes are measured using the crosstalk delay types mentioned in Table I. If the delay is greater than type 4, then a temporal redundant code is inserted between the code words. Before doing this, it also checks whether the delay is type 6 or not. If the delay is type 6, then the 2nd code word is inverted; otherwise it's not. The temporal redundant code is either all zeros or all ones. It is decided based on the total delay of three consecutive codes (current code, temporal code, and next code). By using the following example of figure, it will be easy to understand the encoding method. Suppose two consecutive WCM codes are 101111000 and 010001000. As the delay between the codes is type 6, the 2nd one is inverted. So now the 2nd one is 101110111. Then the total delay of the two sets {101111000, 000000000, 101110111} and {101111000, 111111111, 101110111} is measured, where 000000000 and 111111111are temporal codes. The set which has less delay is selected as encoded data. In this example, the set {101111000, 000000000, 101110111} has less delay. So this is the encoded data.

F. *Opposite Transition Forbidden Weighted Code Mapping (OTF_WCM)*

This method [6] is a slightly modified version of WCM coding. The original WCM encoding method doesn't guarantee to eliminate crosstalk type 5 and 6. This encoding method generates a WCM codebook that doesn't have an opposite transition pattern. As a result, all crosstalk type 5 and 6 and some of type 4 are eliminated. If W denotes the set of code words of n bits, W can be represented as W ={w | w = a1a2…aiai+1….an, ai=0,1}, where i denotes the index of the opposite transition bit lines. The W will be an opposite transition forbidden (OTF) codebook if it doesn't have 2λ transitions with each other. In the original WCM coding, the codes are selected in such a way that transition energy is minimized.

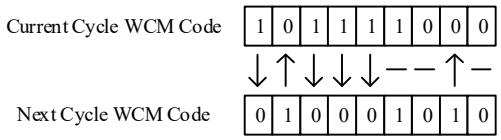

Fig. 7. Transition between two WCM code

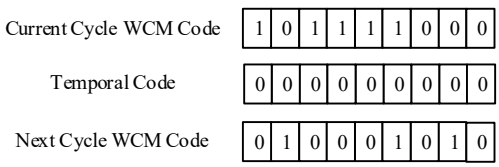

Fig. 8. VCT_HSTR Encoding (bus width 9 bit)

According to this encoding method, after selecting WCM codes, each code is checked whether it is OTF or not. If it is OTF, then it is selected as a mapping code for a particular data pattern. As the codes of OTF codebook are guaranteed not to have type 5 and 6 crosstalk delay, it can be said that this encoding method is optimized for both energy and delay.

G. *Encoding for Crosstalk*

Verma *et al.* [7] proposed an encoding method to eliminate worst-case crosstalk by reducing actual data bit lines. Required components are counter, controller, comparator, and register to design the encoder. Counter counts the number of 0s and 1s in input data lines and feeds these two inputs to the controller. Controller output follows the number, which one is higher. For example, if the number of 1s is greater than the number of 0s, controller output is set to 1 and vice versa. Then controller output is fed to the comparator and also to the decoder. Actual data lines are fed into the comparator along with the controller output. In the comparator, the controller output is compared with every bit in actual data lines to get the inverted bit positions.

For example, in the 8-bit data "10110101", the number of 1s is 5, which is greater than the number of 0s, which is 3. The controller output is set to 1 and is fed into the comparator along with original data to be compared. XOR operation between controller output and original data is performed at comparator, and the positions where controller output does not match are the inverted bit positions. In this example, inverted bit positions are 1, 3, and 7 if we set the index from LSB to MSB. So, in binary form, 001, 011, and 110 are stored in three registers and then transferred to the decoder for retrieving original data. Although this method reduces actual bus width, for the use of register, area overhead increases and to transfer register bits, an extra clock cycle is introduced.

H. *Crosstalk Quantitive Approach*

In the previous encoding methods, the inductive effect was not considered. As operating frequency is increasing in recent days, the inductance of the wires is also adding noise and

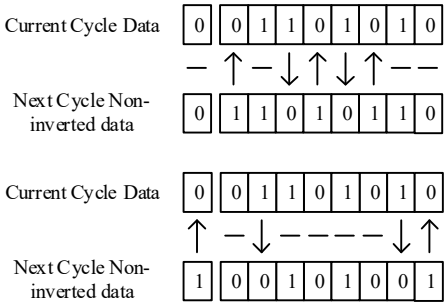

Fig.9. Crosstalk quantitative approach

delay. Ruan *et al*. [8] considered the inductance effect as well as capacitance to determine the encoded data. They used the RLC model instead of the RC model to represent bus lines. Just like the two capacitances (self and coupling), there are also two kinds of inductances, self-inductance and mutual inductance. Total inductance is the summation of self-inductance and mutual inductance between wires. But capacitance and inductance effects are not dominant at the same time. When data of two adjacent wires changes towards the opposite direction (zero to one and one to zero), the capacitance effect dominates over the inductance effect. On the other hand, when data of adjacent lines changes towards the same direction (both zero to one or one to zero) the inductance effect dominates over the capacitance effect. That's why both effects have been considered to define the cost function. The cost function is the summation of the toggle number multiplied by 2 and the maximum of switch up and switch down. Switch up means 0→1, and switch down means 1→0.

$$Cost = Toggle\# \times 2 + Max(Switchup\ \#, Switchdown\ \#) \quad (1)$$

The major components of the encoder are pattern generator, two cost estimators, one comparator, one MUX, and one Latch. Using the Latch, current cycle data is transferred to both cost estimators. On the other hand, the pattern generator generates two data for two cost estimators.

One is non-inverted next cycle data with control bit 0, and the other one is inverted next cycle data with control bit 1. These two data are transferred to the two cost estimators. Thus, using the current cycle and next cycle data, the cost estimator calculates the cost according to the above mentioned formula. The following example of 8-bit data illustrates the encoding method completely. After calculating the cost, these are transferred to the comparator to determine which one costs less between the next cycle original data and next cycle inverted data. And the lesser one is selected to transfer to the bus using the MUX. The comparator output is used as the selector of MUX. So, for the above example, inverted data will be selected as encoded data.

III. Analysis and Comparison of Encoding Methods

In the previous section, we have explained the algorithm and working principle of all the encoding methods. In this section, the important results reported by the authors and their comparison will be described. In Table III, the power, crosstalk, and delay reduction of all the methods have been presented. The area overhead, power consumption, delay, extra control line, and cycle number induced by the codec are also mentioned. From the table, we can say that, the Temporal Crosstalk Shielding and VCT_HSTR encoding approaches improve power efficiency of the bus significantly. They can reduce power consumption up to 46% and 45.47%. On the other hand, Temporal and Shielding Coding and OTF_WCM are more efficient in reducing delay. Both of the methods can reduce delay by about 49%.

Most of the methods didn't measure crosstalk separately. Only the last two methods showed crosstalk reduction. Among these, Encoding for Crosstalk can reduce crosstalk by 35% to 40% and Crosstalk Quantitative Encoding can reduce up to 14%. On the other hand, in Temporal and Shielding Coding (TSC) and Temporal Crosstalk Shielding (TCS), codec area and codec induced delay has been measured directly in μm^2 units and time units. TSC takes less area and induces less delay compared to TCS. The other two methods, VCT_HSTR and OTF_WCM measured area in terms of a NAND gate count. In Temporal and shielding coding, though power reduction was not measured, codec power consumption is 1.1mW, which is less than the other methods, and there is no need for an extra line for this encoding method. Again, Temporal Crosstalk Shielding can reduce the number of bus line by 25%. This means for each 4-bit data, the encoded data is 3-bit, but codec area and power overhead is higher than the other methods. Though the OTF_WCM can reduce delay by 48.46%, it needs an extra 7 lines for a 16-bit wide bus. Most of the encoding methods don't add extra cycles to transfer encoded data. Only in TCS, VCT_HSTR, and Encoding for Crosstalk methods, extra cycles are required to send encoded data.

TABLE III. RESULT COMPARISON OF SELECTED ENCODING METHODS

Encoding Method	Power	Crosstalk	Delay	Codec Area	Codec Power	Codec Induced Delay	Extra Control Line	Extra Cycle
Bus Invert	25%	-	-	-	-	-	1	0
Simple Odd Even Invert	32%	-	-	-	-	-	2	0
Calculated Odd Even Invert	30%	-	-	-	5%	-	2	0
Temporal & Shielding Coding	-	-	22-49%	871μm^2	1.1mW	237ps	33.3%	1
Temporal Crosstalk Shielding	46%	-	11%	2127.2μm^2	5.7mW	1.2ns	-25%	1~2
VCT Encoding with HSTR	45.47%	-	28.15%	200116	-	-	2	0~1
OTF_WCM	38.46%	-	48.46%	217147	-	-	7	0
Encoding for Crosstalk	-	35-40%	-	-	-	-	0	0~2
Crosstalk Quantitative Encoding	11-19%	11-14%	7-19%	-	1.1-8.6	-	1	0

IV. CONCLUSION

In today's deep submicron technology, a significant amount of power is consumed in interconnect due to crosstalk. In this paper, we surveyed several methods for increasing energy and delay efficiency in modern VLSI interconnects. Our study shows differences, similarities, and specific ways of reducing interconnect power consumption and delay among different research works. Based on our survey, we tried to present a comparative study of all methods. We selected some research works accomplished over the past few years. Among them, we classified 7 research works based on 8 criteria including power, crosstalk, delay, codec area, codec power, codec induced delay, extra control line, and extra clock cycle. Most of the techniques we presented focus on power consumption reduction, and the rest are based on delay reduction.

REFERENCES

[1] M.R. Stan, W.P. Burleson, "Bus-invert coding for low-power I/O," *IEEE Trans. Very Large Scale Integration (VLSI) Systems*, vol. 3, no. 1, pp. 49-58, March 1995.

[2] Z. Yan , J. Lach, K. Skadron, and M.R. Stan, "Odd/Even bus invert with two-phase transfer for buses with coupling," in *Proc. Int. Symp. On Low Power Electronics and Design*, Aug. 2002, pp.80-83.

[3] S.K. Verma, B.K. Kaushik, "Crosstalk and power reduction using bus encoding in RC coupled VLSI interconnects," in *Proc. Int. Conf. Emerging Trends in Engineering and Technology*, Nov. 2010. pp.735-740.

[4] K. S. Sainarayanan, C. Raghunandan, and M. B. Srinivas, "Bus encoding schemes for minimizing delay in VLSI interconnects," in *Proc. ACM Conference on Integrated circuits and systems design*, Sept. 2007. pp. 184-189

[5] K. Najeeb, Vishal Gupta, and V. Kamakoti, "Delay and peak power minimization for on-chip buses using temporal redundancy," in *Proc. ACM Great Lakes symposium on VLSI*, April. 2006, pp. 119-122.

[6] J. Zhang, Q. Wu, and Q. Qiu, "Bus encoding for simultaneous delay and energy optimization," in *Proc. Int. Symp. on Low Power Electronics and Design*, Aug. 2008, pp. 209-212.

[7] S. K. Verma and B. K. Kaushik, "A bus encoding method for crosstalk and power reduction in RC coupled VLSI interconnects," *International Journal of VLSI design & Communication Systems* 3, no. 2, pp. 29-39. 2012.

[8] S. J. Ruan, T. C. Kan, and J. C. Hsu, "A novel crosstalk quantitative approach for simultaneously reducing power, noise, and delay based on bus-invert encoding schemes," in *Proc. Int. Great lakes Symp. on VLSI*, May 2010, pp. 357-360.

[9] H. S. Deogun, R. R. Rao, D. Sylvester, and D. Blaauw, "Leakage-and crosstalk-aware bus encoding for total power reduction," in *Proc. Annual Design Automation Conference*, Jun. 2004, pp. 779-782.

[10] M. Cha, C. G. Lyuh, and T. Kim, "Resource-constrained low-power bus encoding with crosstalk delay elimination," in *Proc. IEEE Asia and South Pacific Design Automation Conference,* Jan. 2004, pp. 834-837.

[11] C. Duan, C. Zhu, and S. P. Khatri, "Forbidden transition free crosstalk avoidance CODEC design," in *Proc. Annual Design Automation Conference,* Jun. 2008, pp. 986-991.

[12] D. C. Suresh, B. Agrawal, J. Yang, and W. Najjar, "Energy-efficient encoding techniques for off-chip data buses," *ACM Trans. Embedded Computing Systems (TECS)*, vol. 8(2), no. 9, 2009.

Humanlike Robotic Vision System Using Artificial Neural Network

Kazi Abu Zubair*, Subha Singha, Sabrina Alam, Kazi Tanvir Ahmmed
Department of Applied Physics, Electronics and Communication Engineering
University of Chittagong, Bangladesh
*kzubair.bd@gmail.com, subha_cu10@hotmail.com, sabrina.apece@cu.ac.bd, tanvir@cu.ac.bd

Abstract— **Robotic manipulator, which is a kind of robot that interacts with its environment in order to manipulate objects, is the most extensively-employed kind of robot in practical field. Most of the robotic manipulators functioning in the industries and other fields are programmed to manipulate objects from fixed predefined points in space. However, this might create problems in real world situation where the location of the object is arbitrary and cannot be predefined. This problem can be solved if the robot is able to recognize the object by learning which one is the specific object and which one is not. The robot can then find the position where the object is located in order to drive the manipulator tool point towards that position. In this paper, an approach has been taken to design and analyze performance of a humanlike robotic vision system for robotic manipulator using artificial neural network along with image processing. Here, the robot captures image of the environment, analyzes it and determines the points in space where the object to be manipulated is locate.**

Keywords—***Robotics; Artificial Neural Network; Artificial Intilligence; Object Recognition; Image Processing***

I. INTRODUCTION

The robot vision system must be considered as part of a larger entity that interacts with the environment by analyzing images to produce descriptions of what is imaged [1]. The robot vision before the development of Artificial Neural Network relied mostly on image processing using pixel by pixel calculation. Gibson (1950) introduced first a concept on optical flow and based on his theory, mathematical models for optical flow computation on a pixel-by-pixel basis are developed [2-3]. Larry Roberts presented a research on the possibility of extracting 3D geometric information from 2D views in 1960 [4]. In such researches in [2-6] the success rate of object recognition was much less in comparison with the human brain. This is because human brain, unlike conventional robot vision mechanism, has an outstanding capability of analyzing real world non linear data. In order to be able to recognize different objects successfully in different illumination, background, view point and to some extent position of the workspace [7], the vision system of the robot should be similar to the human vision. The research on how human brain processes data using its cognitive skills and the development of such computer model which replicates the functionality of human brain is a wide research field over a few decades. Such computer model of human brain, which is known as Artificial Neural Network or ANN was first introduced by McCulloch and Pitts in 1940 [8]. In 1950's Rosenblatt developed a two layered network known as 'Perceptrons' [9]. 'Perceptrons' were capable of learning certain classifications by adjusting connection weights. These studies led to the current development of the neural network.

The practical vision technology was eagerly anticipated in industry, particularly in Japan, in the mid-1960s, typically at Hitachi's Central Research Laboratory [10]. In those attempts, the success rate was not high and the need for real AI based vision system had aroused. After the development of efficient learning algorithms like 'backpropagation' [11-13], during 1990's, machine vision starts becoming more common in manufacturing environments leading to creation of machine vision industry.

Modern-day robots can be carefully hand-programmed or "scripted" to carry out many complex manipulation tasks, ranging from using tools to assemble complex machinery, to balancing a spinning top on the edge of a sword [14-15]. But the difference between human and such robot are still apparent in because every time the robot must know the exact geometric description of the objects they are dealing with. In some recent work such as in [16-20] some robotic vision system is developed where the system tries to replicate the human vision system. In the research work [14], the goal was to make the robot grasp novel objects where the robot neither requires nor tries to build a 3D model of the object. A method is presented in [21] where the robot learns new objects from scratch, by simply observing the object in different poses and scales. The system used active tracking and depth data coming from a stereo system with 'vergence' control to segment the object from the background, and was tested with a hundred different household objects, showing around 80% recognition rate on average. The drawbacks of the system were that a certain amount of texture in the objects was required [20].

Indeed, in most cases of robotic vision, there was always an intention to analyze the geometrical shape of the object for the sake of recognition. However, the human brain, which can recognize different objects easily rely mostly on the learning process and less on geometrical description. The work presented in this paper focuses on the design and performance of a robotic vision system for manipulator arm which learns to recognize specific objects only from images of the objects, in other words, only by seeing it.

978-1-4673-9257-0/15/$31.00 ©2015 IEEE

II. METHODOLOGY

Five distinct objects, three with different colors and shapes and two with same color but different shape are taken as the test objects. The objects that the robot learned to recognize are as follows-

- Object 1; Long Blue Object
- Object 2; Circular Blue Object
- Object 3; Rectangular Orange Object
- Object 4; Trapezoidal Green Object
- Object 5; Rectangular Charleston Green Object

The images of different objects are listed in TABLE I. The workspace in this project is a white surface of 25cm by 25cm in dimension. The objects to be recognized will be placed on this workspace. The manipulator is considered to be anchored at (0, 0) position. A camera is fixed over the workspace to take images of what is placed on the workspace. Fig 1 shows the view of the system with the workspace below and a camera fixed above the workspace. Graphical User Interface in PC shows the identified objects with their respective position.

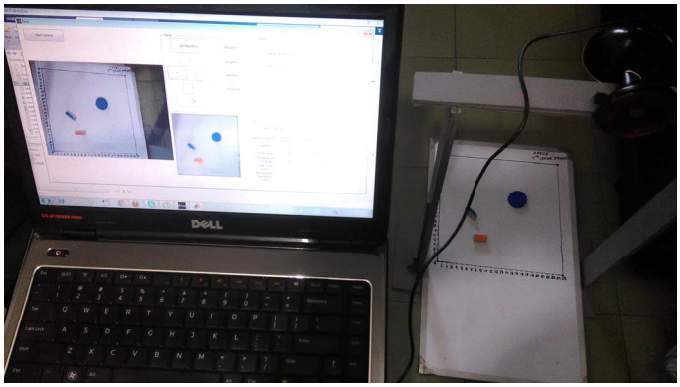

Fig. 1. The robotic vision system developed in this research work

A. *Design of the Neural Network:*

The Artificial Neural Network (Fig. 2) that has been used in this paper is a feed forward neural network with 150 hidden layers. It has 1200 input neurons and 6 output neurons. In most application of the object recognition using ANN, the RGB image is converted to Gray-Scale image and is applied at the input of the neural network. In that case, the efficiency of object recognition is reduced because the network treats the same objects with different color as identical objects.

In the system described in this paper, the approach was to make the robot recognize color objects by taking all RGB information as the input data. RGB image is a matrix of dimension m-by-n-by-3. Each color pixel contains three values for three primary colors; Red, Green and Blue. The network is designed to deal with images of 20 by 20 pixels. For that reason, the input layer must have 1200 neurons. The schematic of the neural network is shown in Fig. 2.

This is a 6-class classifier neural network. Each of last five classes corresponds to one specific object and the first class corresponds to a Non-Object class. The corresponding output class will acquire the highest value for a certain combination of the inputs. If the image given to the network has no object in it, the Non-Object class will have the highest value.

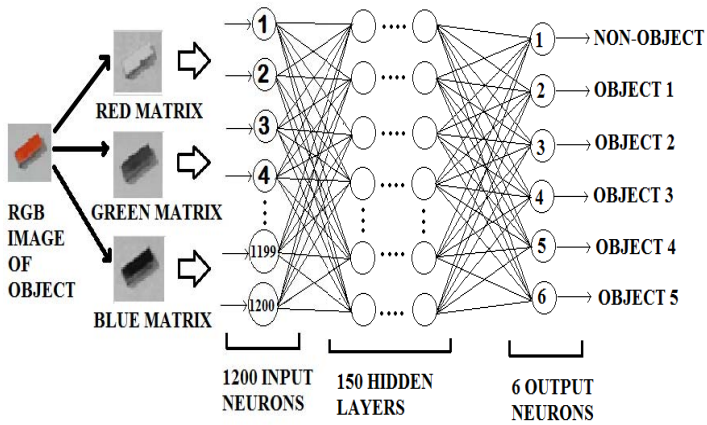

Fig. 2. Feed forward artificial neural network topology used in the vision system

B. *Data Preparation for Neural Network*

Preparing data is an important and critical step in neural network data analysis and it has an immense impact on the success of a wide variety of complex data analysis, such as data mining and knowledge discovery [22]. The main reason is that the quality of the input data into neural network models may strongly influence the results of the data analysis [23-24]. The training data that is required to perfectly train a neural network must be developed carefully for the optimum performance.

For preparing training data for the neural network in this paper, several images in different lighting conditions are taken by the webcam. Several of such images are combined and from the combined image, the some cropped images of 20x20 pixels of specific object-class and non-object class are taken as data image which are assigned with specific value.

The prepared data contains two matrixes, one for the image data and another for their corresponding class-value. In order to feed the data to the neural network, the second matrix is converted into a 6 by N matrix where N is the number of data taken. Each row of the matrix contains '0' for negative data and '1' for positive data for the corresponding class. Fig. 3 illustrates the data preparation procedure in a flow chart.

C. *Training The Neural Network*

The training data is divided into three parts before training the network with it, where-

Percentage of the total data used for training: 70%

Percentage of the total data used for validation: 15%

Percentage of the total data used for testing: 15%

The network is trained using MATLAB's Neural Network Pattern Recognition tool (nprtool). The training data prepared in the data preparation stage is corrected, extended and edited several times before feeding it to the neural network. For the ease of understanding, the whole process is divided into three approaches.

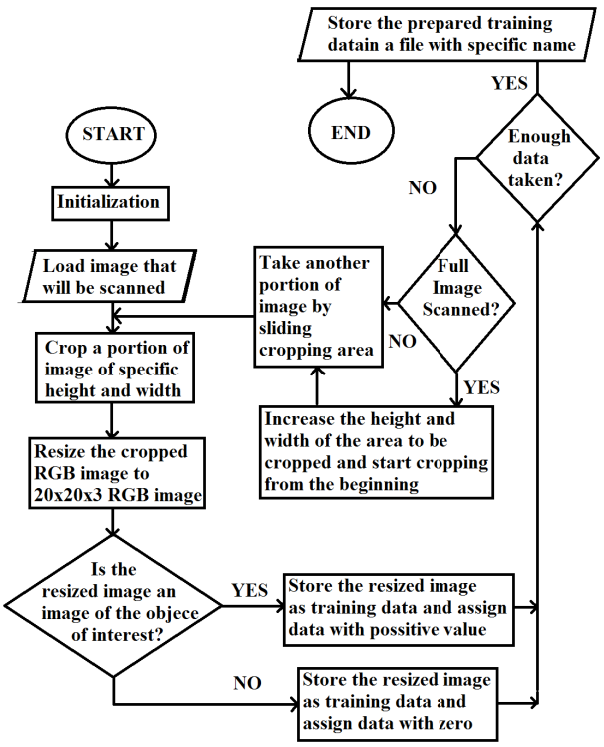

Fig. 3. Flow chart of the data preparation mechanism

1) First Approach: At first, the data taken for the ANN training contained minimum Non-Object class. The data for Object class is taken by keeping objects mostly in the center position and the Non-Object examples were taken as images of empty background image in different lighting condition.

TABLE I. DIFFERENT OBJECT AND NON OBJECT EXAMPLES IN THE FIRST APPROACH

Different data for Object class and Non-Object class in the first approach					
Object 1	*Object 2*	*Object 3*	*Object 4*	*Object 5*	*Non-Object*
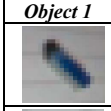					

The data taken in this step is corrected several times and finally fed to the network to observe its performance. Some examples of data taken in this approach is tabulated in TABLE I.

2) Second Approach: The number of Non-Object class data was small compared to other Object classes in the first approach and the network seemed to assume some images around the object as incorrect Object-Class data which actually falls under Non-Object class. To solve this, In second approach, the number of Non Object Class has been increased to a significant number by taking images around every object which can be considered as Non-Object image(TABLE II).

TABLE II. SOME NON-OBJECT EXAMPLES IN THE SECOND APPROACH

Some Non-Object examples taken in the second approach					
				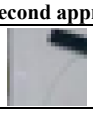	

3) Final Approach: With the progress achieved in the first and the second approach, the network was able to successfully recognize objects that are separated from other objects by a noticeable distance. But when several objects are close to each other, the network assumed the image taken between the spaces by which multiple objects are separated as wrong Object class. In order to make sure that the network predicts such space as Non-Object class, several Non-Object image data (TABLE III) are taken from the space between nearby objects.

TABLE III. SOME NON-OBJECT DATA TAKEN BETWEEN THE SPACE OF TWO OBJECTS IN THE FINAL APPROACH

Some non-object data between the spaces of different objects					
					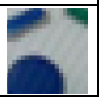

D. *Recognition of Object of Interest*

The objects are recognized by taking 20x20 pixels of the workspace and feeding the cropped image to the neural network each time to see if the image selected contains the object of the interest. Fig. 4 illustrates the block diagram of object recognition procedure.

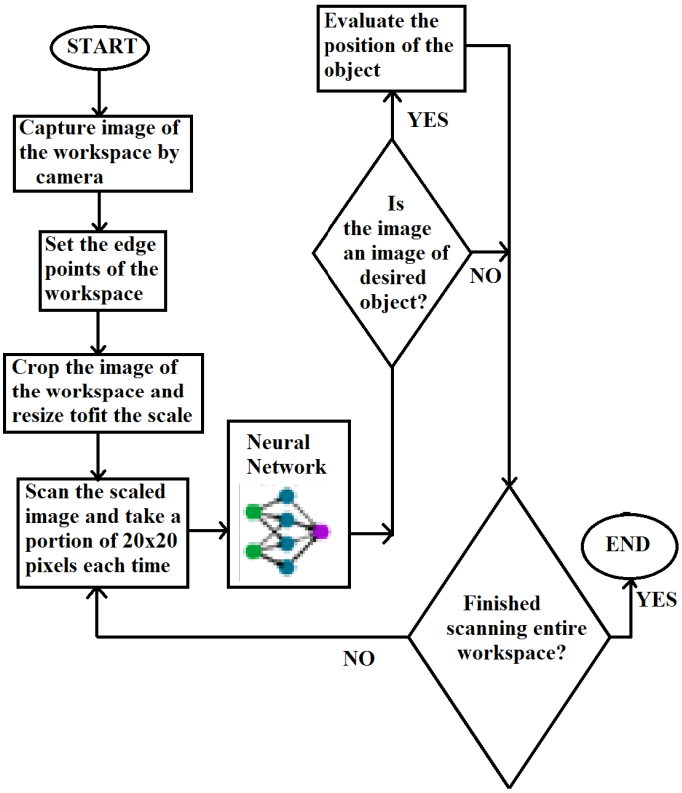

Fig. 4. Block diagram of object recognition and position evaluation

III. Performance Analysis

A. *Performance Analysis of Different Approaches:*

In the first approach, the amount of data taken was not massive. The focus of this approach was to take positive Object class data with accuracy. The performance plot of the network trained with the data taken in the first approach is shown in Fig. 5. The curve can be easily obtained using MATLAB's plotperform() function of Neural Network Toolbox. The Cross-Entropy of the best validation performance in this approach is $1.6523e^{-05}$ which is much smaller. It is clear from the plot that the network trained in this approach is much confident about the prediction. However, the characteristic of good classifier network is such that, its train, test and validation curve mostly decrease in a similar fashion. Though the cross entropy in this approach is minimum between all the approaches, it sometimes gives wrong prediction very confidently which is unacceptable.

In the second approach, an increased number of data is taken. The focus of this approach was to take more Non-Object class data to minimize the errors that occurred when the network predicted some images around one object as another object. The cross-entropy for the best validation performance in the second approach is much higher then the network trained previously in the first approach. But the network shows significant improvement as the test and validation curve mostly move in a similar fashion unlike the curves in the first approach. However, the training curve falls much rapidly compared to the test and validation curve. The performance plot of the network in the second approach is shown in Fig. 6.

In the final approach, the focus was to take more Non-Object class from the space between multiple objects. The performance plot of the final approach is shown in Fig. 7.The performance shows that the cross entropy for best validation performance is much greater than the network trained in the previous approaches, however, the three curves are now closer to each other than before and they converges to local minima with similar fashion.

The Confusion plot of the third approach is shown in Fig. 8. There is an increased number of confusions in this approach. However, in recognizing new data, the network seemed to have better performance than the previous approaches. The confusion matrix shows that only 0.7% of the data are predicted incorrectly and the rest of the 99.3% data images are correctly recognized.

B. *Testing The Network With New Data:*

After the network has been trained successfully, the network is tested with several new images captured by the camera. The TABLE IV and TABLE V show some of these images along with the prediction of the network for these images. If the network successfully identifies an image, it draws a circle at the position where the object is located. The circles are drawn as per the following rules:

- Medium green circle for Trapezoidal Green Object.
- Small blue circle for Log Blue Object.
- Large blue circle for Circular Blue Object.
- Medium orange circle for Rectangular Orange Object.
- Medium dark circle for Charleston Green Object

TABLE IV. Test Result Of Specific Object Recognition From A New Image (Sussessful Cases)

Testing the network with new image(Successful cases)		
Actual image	***Object Recognition by the network***	***Observation***
	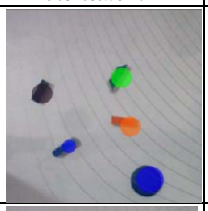	All of the five objects are identified successfully.
		All of the objects are recognized successfully
	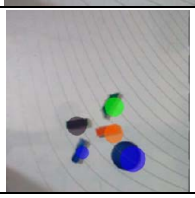	The Objects are brought closer and the network identifies each object successfully.

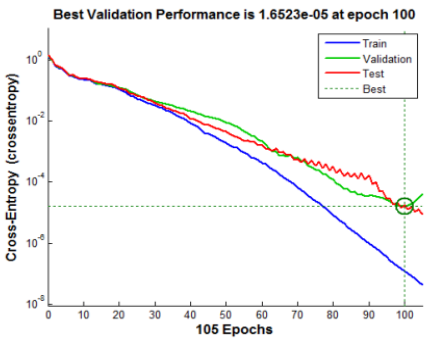

Fig. 5. Network training performance for the first approach

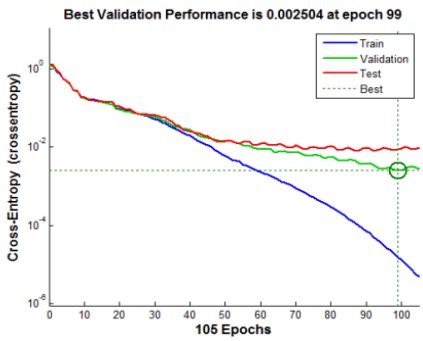

Fig. 6. Network training performance for the second approach

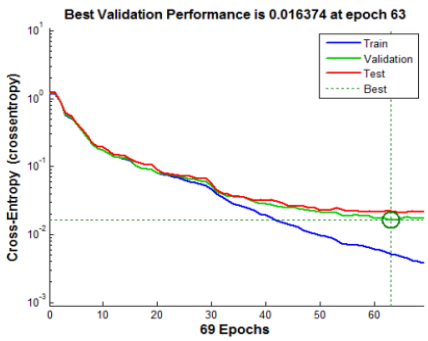

Fig. 7. Network training performance for the final approach

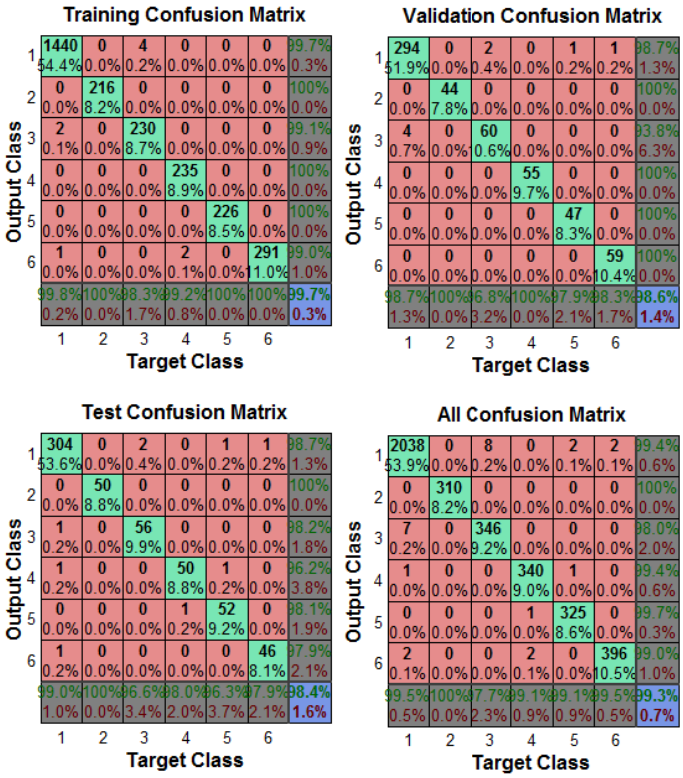

Fig. 8. Confusion matrix of the network after final approach

TABLE V. TEST RESULT OF SPECIFIC OBJECT RECOGNITION FROM A NEW IMAGE (UNSUCCESSFUL CASES)

Testing the network with new data (Unsuccessful cases)		
Image captured by camera	***Object recognitions by neural network.***	***Observation***
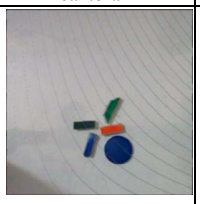	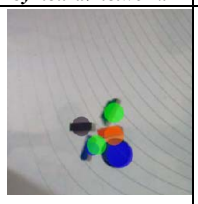	The objects are brought more close to each other and the network identifies all of them correctly, except an extra green object is predicted wrongly between two blue objects.
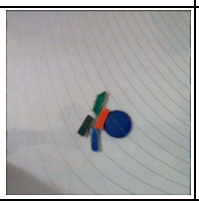	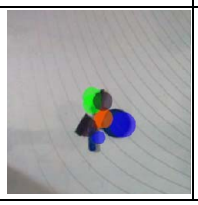	It shows the congested condition and the network now predicts an extra Charleston green object incorrectly in the vicinity of Green object.

The result shows that the network recognizes mostly all of the objects when they are placed at a significant distant apart. Some error prediction occurs when the objects are much dense and at a congested condition. This problem might be solved if smaller area of the cropped image is fed to the network, however, this would take more time to scan the full image of the workspace.

TABLE VI, tabulates some position evaluation examples using the vision system discussed in this paper.

TABLE VI. SOME POSITION EVALUATION RESULT FOR VARIOUS OBJECTS

Some example of position evaluation by the vision system		
Image of the workspace with marked object	***Position Evaluation by the vision system (snapshot from the Graphical User Interface of the system)***	***Observation***
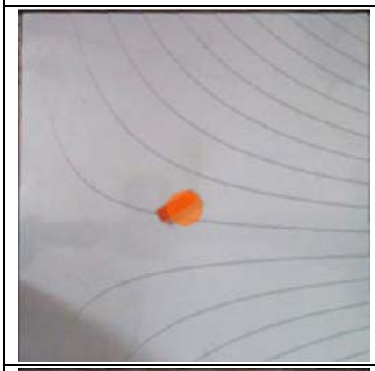	Name of object / object found? / position Long Blue: no, -- circular blue: no, -- Rectangular Orange: yes, x=11.8477, y=10.9355 Trapezoidal Green: no, -- Rectangular Charleston Green: no, --	A rectangular orange object is given and the system successfully identifies the position of the object at (11.84,10.93)
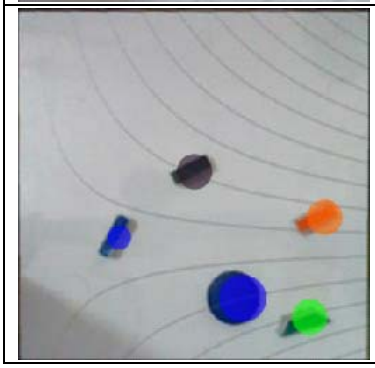	Name of object / object found? / position Long Blue: yes, x=7.2708, y=8.6667 circular blue: yes, x=16.0078, y=4.3535 Rectangular Orange: yes, x=21.8411, y=10.0827 Trapezoidal Green: yes, x=20.7083, y=3.0417 Rectangular Charleston Green: yes, x=12.5833, y=13.3542	All of the objects are given and the system successfully identifies each object at position respectively (7.2,8.6), (16.0,4.3), (21.84,10.1), (20.7,3.04) and (12.58,13.4)

The vision system in this work has a very low error or false recognition percentage. The maximum error occurs for Object 2 and is 2.2%. However, the error rate can be further reduced by careful selection of training data. Other errors are negligible. The performance of the system is tabulated in TABLE VII.

TABLE VII. RECOGNITION EFFICIENCY OF DIFFERENT OBJECT AND NON OBJECT CLASS

Recognition efficiency of different object and non-object class				
Object Class	***No. of test image***	***Successful Recognition***	***False Recognition***	***Efficiency***
Object 1	310	310	0	100%
Object 2	354	345	8	97.774%
Object 3	343	340	3	99.125%
Object 4	328	325	3	99.085%
Object 5	398	396	2	99.497%
Non-Object	2048	2038	10	99.512%
Total	3781	3755	26	99.312%

IV. CONCLUSION

In this work, a vision system for a robotic manipulator is designed so that any object of interest and its position on a scaled workspace can be recognized independently. The neural network is trained to recognize several objects and tested if the recognition system works in different lighting condition. The test result shows that the system is successful in almost all of the cases.

The robotic vision system in this paper is developed using comparatively small amount of data and the network performance is evaluated in three different approaches. In the first two approaches, the network showed minimum confusion but is comparatively inefficient in recognizing new data. However, the final approach shows the best result where it is seen to be most successful in recognizing objects from new images.

In some similar work, as in [25] the background is uniformly white by default and the target image information is passed to the neural network. This process gives high efficiency (99.99% at optimum lighting condition) for single object with uniform background according to the article [25]. However, the false recognition rate may increase if it must distinguish between several objects where one or more objects may lie in the vicinity of the target object. The work presented in this paper overcomes this problem and is 100% efficient for the recognition of one of the five test objects considered in this paper and the overall efficiency is 99.31% (Table VII).

REFERENCE

[1] B. Klaus & P. Horn, *Robot Vision*. Cambridge, MA: MIT Press, 1986.

[2] James J., Gibson, "The Perception of the Visual World," *The American Journal of Psychology,* vol. 64, no. 3, pp. 440-444, Jul. 1951.

[3] James J., Gibson, "The visual perception of objective motion and subjective movement," *Psychological Review,* vol. 101, no. 2, pp. p318-23, April 1954.

[4] L. G. Roberts, "Machine Perception of Three-Dimensional Solids," Ph. D. thesis, Massachusetts Institute of Technology. Dept. of Electrical Engineering, MA, 1963.

[5] Berthold K. P. Horn, & Brian G. Schunck "Determining optical flow," *Artificial Intelligence*, vol. 17, no. 1-3, pp. 185–203, Aug. 1981.

[6] Gordon, D. A., "Static and dynamic visual fields in humanspace perception," *Journal of the Optical Society of America*, vol. 55, no. 10, pp. 1296-1302, Oct. 1965.

[7] V. D. Hunt, *Industrial Robotics Handbook*. New York: Industrial Press Inc., 1983.

[8] W. S. McCulloch and W. Pitts , "A logical calculus of the ideas immanent in nervous activity," *The bulletin of mathematical biophysics*, vol. 5, no. 4, pp. 115–133, Dec. 1943.

[9] Rosenblatt, Frank, "The Perceptron: A Perceiving and Recognizing Automaton," Cornell Aeronautical Laboratory, New York. Rep. 85-460-1,1957.

[10] M. Ejiri, "Machine Vision in Early Days: Japan's Pioneering Contributions," in *Computer Vision – ACCV 2007 : Proceedings of the 8th Asian Conference on Computer Vision,* vol. 4843, Y. Yagi, S. B. Kang, I. S. Kweon, H. Zha, Eds. Berlin: Spinger, 2007. pp. 35-53.

[11] A. Atiya, "Learning Algorithms for Neural Networks," Ph. D. thesis, California Institute of Technology, CA, Sept. 2005.

[12] D. E. Rumelhart*, Geoffrey E. Hinton† & Ronald J. Williams*, "Learning representations by back-propagating errors," in *Nature,*vol. 323, no. 6088, pp. 533 – 536, Oct. 1986.

[13] Y. Chauvin, D. E. Rumelhart, *Backpropagation: Theory, Architectures, and Applications*. New York: Psychology Press, Feb. 1995.

[14] Ashutosh Saxena, Justin Driemeyer, Andrew Y. Ng, "Robotic Grasping of Novel Objects using Vision," in *International Journal of Robotics Research (IJRR),*vol. 27, no. 2, pp. 157-173 , Feb 2008.

[15] Torikai, Shinichi, Yasuko Sakagami en Satoshi Matsuoka, "Robots for the future," *Nipponia,*vol. 1, no. 13, pp. 12-17 ,2010.

[16] A. Teichman, J. Levinson, S. Thrun, "Towards 3D object recognition via classification of arbitrary object tracks," in *Proc. IEEE Int. Conf. on Robotics and Automation (ICRA)*, May. 2011, pp. 4034 - 4041.

[17] C. Kanan, "Fine-grained object recognition with Gnostic Fields," in *Proc. IEEE Int. Conf. on Robotics Applications of Computer Vision (WACV)*, March 2014, pp. 23 - 30.

[18] A. Teichman, "Practical object recognition in autonomous driving and beyond," *in Proc. IEEE Int. Conf. on Advanced Robotics and its Social Impacts (ARSO)*, Oct. 2011, pp. 35 – 38.

[19] T. Satonaka, T. Baba ,T. Otsuki, T. Chikamura,T. H. Meng, "Object recognition with luminance, rotation and location invariance," in *Proc. IEEE Int. Conf. on Image Processing*, Oct 1997,vol. 3, pp. 336 - 339.

[20] F. R. Aparici, A. R. Ayats, G. A. Ribas, X. T. Genis, "Object detection methods for robot grasping: Experimental assessment and tuning," in *Proc. 15th Catalan Conference on Artificial Intelligence (CCIA)*, 2012, pp. 123-132.

[21] H. Kim, "Semi-autonomous Learning of Objects," in *Proc. IEEE Int. Conf. on Computer Vision and Pattern Recognition Workshop(CVPRW)*, June 2006, pp. 145-150.

[22] X. Hu, "DB-HReduction: A data preprocessing algorithm for data mining applications," in *Applied Mathematics Letters* ,vol. 16, no. 6. Amsterdam, Netherlands : Elsevier, Aug. 2003. pp. 889–895.

[23] K. U. Sattler, E. Schallehn, "A data preparation framework based on a multidatabase language," in *Proc. IEEE Int. Symposium on Database Engineering and Applications*, Jul. 2001, pp. 219 - 228.

[24] Lean Yu, Shouyang Wang, Kin Keung Lai, "Foreign-Exchange-Rate Forecasting with Artificial Neural Networks," in *International Series in Operations Research & Management Science* ,vol. 107. Berlin: Spinger, 2007.

[25] J.P.N. Cruz, M.L. Dimaala, L.G.L. Francisco, E.J.S. Franco, A.A. Bandala, E.P. Dadios, "Object Recognition and Detection by Shape and Color Pattern Recognition utilizing Artificial Neural Network" in *IEEE International Conference of Information and Communication Technology (ICoICT),* March 2013, pp. 140-144.

Optimizing Preprocessing Method of Recursive-BKZ Lattice Reduction Algorithm

Md. Mokammel Haque,[1,*] and Josef Pieprzyk[2]
[1]Department of Computer Science and Engineering, Chittagong University of Engineering and Technology
Chittagong 4349, Bangladesh
[2]School of Electrical Engineering and Computer Science, Queensland University of Technology
Brisbane, QLD 4000, Australia
*Email: malin405@yahoo.com

***Abstract*—Lattice problems are considered as the key elements in many areas of computer science as well as in cryptography; the most important of which is the shortest vector problem (called SVP in short) and its approximate variants. Algorithms for this problem are known as lattice reduction algorithms. Currently, the most practical lattice reduction algorithm for such problems is the Block-Korkine-Zolotarev (BKZ) algorithm and its variants. Preprocessing is a technique that can be applied to certain lattice reduction algorithms (such as BKZ variants) to reduce the search time in the enumeration tree for a shortest vector. We optimize both the pruning and the preprocessing parameters of the recursive (aborted, extreme pruned) preprocessing of the BKZ lattice reduction algorithm and improve the results from Asiacrypt'11 by Chen and Nguyen.**

***Index Terms*—Cryptosystem, Algorithm, Lattice Reduction, BKZ, Optimization, Preprocessing.**

I. Introduction

The *Lattices* we are interested in are integer or point lattices; discrete subgroups of $\mathbb{R}^n$. A lattice L is defined as all integer linear combinations of some linearly independent vectors $(\mathbf{b}_1, ..., \mathbf{b}_n)$ of the form: $\sum_{i=1}^{n} x_i \cdot \mathbf{b}_i$, where $x_i \in \mathbb{Z}$ for all i. The vectors $(\mathbf{b}_1, ..., \mathbf{b}_n)$ are called a basis of the lattice. The number of vectors n is the dimension of the lattice L.

The goal of lattice reduction is to find a "good" basis for the applications which is usually the one that contains short vectors. Clearly, it is an interesting problem to find a short basis or even to try to find a shortest basis. The SVP or Shortest Vector Problem is the most common and fundamental algorithmic lattice problem on which many cryptosystems rely. It is an NP-hard problem under randomized reductions [1].

Lattice problems are considered to be building blocks in many public-key cryptographic constructions. The most significant examples of cryptographic constructions that use lattices include: public key encryption based on knapsack problem; variant of RSA and DSA signatures schemes; encryption schemes based on LWE (Learning with Error) problems [2]; fully homomorphic cryptosystems [3]; the SWIFFT hash function [4] as well as many others. If one knows how to solve lattice problems, then one can break some cryptosystems.

Lattice reduction algorithms are one of the few exciting recent techniques in cryptography. The most popular lattice reduction algorithms are the LLL (Lenstra-Lenstra-Lovász) [5] and BKZ (Block Korkine-Zolotarev) [6] algorithms and their variants. They are called *approximate algorithms*; another category is known as *exact algorithms* includes Enumeration.

In lattice reduction algorithm, preprocessing is required to give a relatively bad basis a good shape. Actually, the most classical form of preprocessing we always observe is with polynomial time LLL algorithm to work with a slow enumeration-based algorithm like BKZ. In BKZ reduction, LLL is used before the enumeration routine to produce a preprocessed basis. Then the enumeration will run more efficiently.

The aim of this paper is to describe the preprocessing method in the Recursive-BKZ (RBKZ in short) reduction. In [7], the algorithm for the RBKZ reduction is called BKZ2.0. We would like, however, to emphasize the role of preprocessing, as the preprocessing notion has not been fully explained in previous publications. We also optimize the runtime complexity of the recursive-BKZ lattice reduction based on some heuristic. Our results show better estimation of complexity than the similar results reported in [7].

II. Background Notation

Let $L = L[1, n]$ denote an n-dimensional lattice with basis $B = (\mathbf{b}_1, \ldots, \mathbf{b}_n)$. The block lattice $L_i = L[i, i+d_i-1]$ is the projection of the lattice generated by $\mathbf{b}_i, \mathbf{b}_{i+1}, \ldots, \mathbf{b}_{i+d_i-1}$ orthogonally to the space spanned by $\mathbf{b}_1, \ldots, \mathbf{b}_{k-1}$, where $d_i = k$ for $i \leq n-k+1$ and $d_i = n-i+1$ for $i > n-k+1$.

Let $B^* = (\mathbf{b}_1^*, \ldots, \mathbf{b}_n^*)$ denote the Gram-Schmidt Orthogonalization (GSO) [8] of the basis B of L, and let $\hat{\mathbf{B}}^* = (\mathbf{b}_1^*/\|\mathbf{b}_1^*\|, \ldots, \mathbf{b}_n^*/\|\mathbf{b}_n^*\|)$ denote the normalized GSO matrix. We have $B = \hat{\mathbf{B}}^* \cdot M$, where $M = (\mathbf{r}_1, \ldots, \mathbf{r}_n)$ is an upper-triangular matrix with its ith column $\mathbf{r}_i = (\mu_{i,1} \cdot \|\mathbf{b}_1^*\|, \mu_{i,2} \cdot \|\mathbf{b}_2^*\|, \ldots, \mu_{i,i} \cdot \|\mathbf{b}_i^*\|, 0, \ldots, 0)^T$ (the coordinate vector for $\mathbf{b}_i$ in the orthonormal basis $\hat{\mathbf{B}}^*$), and $\mu_{i,j} = \frac{\langle \mathbf{b}_i, \mathbf{b}_j^* \rangle}{\|\mathbf{b}_j^*\|^2}$. Let M_i denote the upper triangular $d_i \times d_i$ submatrix of M with its top-left corner at row i and column i, and a basis for block lattice L_i (represented in the orthonormal basis $\hat{\mathbf{B}}^*$).

The (aborted) BKZ-k algorithm (with pruning strategy P and the BKZ 2.0 [7] Gaussian-Heuristic-Based enumeration radius), for an input basis $B = (\mathbf{b}_1, \ldots, \mathbf{b}_n)$ of an n-dimensional lattice L, first runs the LLL reduction algorithm on B. Then it runs a $\tau(n, k) = \mathcal{P}oly(n, k)$ number of tours. In each tour, it performs a shortest-vector enumeration routine on each of n block lattices $L_i = L[i, i+d_i-1]$ for $i = 1, \ldots, n-1$ using the basis M_i, where $d_i = \min(k, n-i+1)$ is the dimension of L_i. Let $N(n, k, t, i)$ denote the number of nodes in the enumeration tree for block lattice L_i in tour t. The number $N(n, k, t, i)$ is the dominant factor in the run-time of BKZ-k for large k, since it is exponential in k. Let $B^*(n, k, t, i) = (\mathbf{b}_1^*(n, k, t, i), \ldots, \mathbf{b}_n^*(n, k, t, i))$

978-1-4673-9257-0/15/$31.00 ©2015 IEEE

denote the GSO matrix just before the enumeration of L_i. Let $D(n,k,t,i) = \det L_i = \prod_{j=i}^{i+d_i-1} \|\mathbf{b}_j^*\|$.

A shortest vector of L_i (for $i \leq n-30$) is assumed to be in a pruned subset S_P of the d_i-dimensional ball of radius

$$R(n,k,t,i) = \min\left(\|\mathbf{b}_i^*(n,k,t,i)\|, (1+\varepsilon)\cdot GH(\lambda_1(L_i))\right), \tag{1}$$

where $GH(\lambda_1(L_i)) = (D(n,k,t,i)/V_k(1))^{1/k}$ is the Gaussian Heuristic (see [8]) estimate for the length of a shortest vector of L_i, and ε is a small constant ($\varepsilon = 0.05$ in [7]). For $i > n-30$, Nguyen and Chen take $R(n,k,t,i) = \|\mathbf{b}_i^*(n,k,t,i)\|$. Here $V_k(1)$ denotes the volume of the k-dimensional ball of radius 1.

Let $N_d(n,k,t,i)$ denote the number of nodes in the enumeration tree at depth d. Then the total number of nodes,

$$N(n,k,t,i) = \sum_{d=1}^{k} N_d(n,k,t,i). \tag{2}$$

The Gaussian Heuristic says that assuming $R(n,k,t,i) = (1+\varepsilon)\cdot GH(\lambda_1(L_i))$, on average, we expect

$$\begin{aligned}\log N_d(n,k,t,i) \approx &\log(V_d(1)\cdot V_k(1)^{-d/k}\cdot(1+\varepsilon)^d)\\ &+\sum_{r=k-d+1}^{k}\left(\frac{1}{k}\log D - \log\|\mathbf{b}_{i+r-1}^*\|\right)\\ &-\log G(P,d)\end{aligned} \tag{3}$$

where $G(P,d)$ is the pruning speedup factor for level d.

The *Geometric Series Assumption* (GSA) with ratio q for a basis of L_i states that the norms $(\|\mathbf{b}_i^*\|, \|\mathbf{b}_{i+1}^*\|, \ldots, \|\mathbf{b}_{i+d_i-1}^*\|)$ form a geometric progression, so that the ratio $\|\mathbf{b}_j^*\|/\|\mathbf{b}_{j+1}^*\| = q$ for all j=$i,\ldots,i+d_i$.When blocksize k is not too small, $q(k)$ can be approximated quite accurately by the fixed point of a deterministic dynamical model as in [9], based on the Gaussian Heuristic. This approximation is:

$$q(k) \approx V_k(1)^{\frac{-2}{k\cdot(k-1)}} \tag{4}$$

For the LLL algorithm, experimental evidence shows that the GSA with ratio $q(2)$ holds approximately, with $q(2) \approx 1.04$.

If the GSA with ratio q holds (approximately) for the basis of L_i when the enumeration is performed, then the enumeration time in (3) can be approximated by

$$\begin{aligned}\log N_d(n,k,t,i) \approx &\log(V_d(1)\cdot V_k(1)^{-d/k}\cdot(1+\varepsilon)^d)\\ &+\frac{1}{2}\cdot d\cdot(k-d)\cdot\log q - \log G(P,d).\end{aligned} \tag{5}$$

The number $N_d(n,k,t,i)$ is usually maximized for $d \approx k/2$, so we get the following (usually quite tight) lower bound, under the GH and GSA with ratio q for the basis of L_i:

$$\begin{aligned}\log N(n,k,t,i) \geq &\log N_{k/2}(n,k,t,i)\\ \approx &\log(V_{k/2}(1)\cdot V_k(1)^{1/2}\cdot(1+\varepsilon)^{k/2})\\ &+\frac{k^2}{8}\cdot\log q - \log G(P,d).\end{aligned} \tag{6}$$

By Theorem 1 of [9] with $C = 1$ and assuming the GSA for the input basis with ratio $q \leq q(2)$, (see also Fig. 1 in [9]), one can get an output quality for the aborted BKZ-k satisfying the GSA with ratio close to the $q(k)$ value given in (4) if one aborts BKZ after $\tau(n,k) \approx (n/k)^2\cdot\log(n^2/50)$ tours.

A. SMA and Dynamical Model

The heuristic Sandpile Model Assumptions (SMA) with the deterministic dynamical model comes from the analysis of aborted-BKZ (or BKZ' in [9]) due to Hanrot et al. BKZ' differs from the original BKZ in such that it replaces the SVP solver in BKZ by an HKZ reduction algorithm. The purpose is to simplify the analysis of BKZ' by looking at the changes in $\mathbf{x} = \log(\|\mathbf{b}_i^*\|)_{i\leq k}$ during each tour rather than considering the whole basis after full reduction. The heuristic further allows a fixed-point dynamical model that determines $\mathbf{x}$ in each $(n-k+1)$ calls of k-dimensional HKZ-reduction by $\mathbf{x}$ only. The final fixed point of the BKZ' reduction resembles a straight line, except for the last block.

III. Extreme and Non-extreme Pruning

The idea of *extreme pruning* is to skip a large number of branches in the enumeration tree so that the time for each short-vector search reduces significantly. Unfortunately, it reduces the probability of finding a shortest vector in this process. However, the extreme pruning provides a tangible gain. The reduction of the enumeration time is significantly larger than the increase of the probability of missing shorter vectors in the solution.

Therefore, the basic extreme pruning consists of several executions of the *randomize-reduce-enumeration* loop (see Algorithm 1 in [10]) until a short vector satisfying a predefined bound is found. This multiple execution can be denoted as the branching factor. If p_{succ} is the probability of finding a short vector in each iteration of the *randomize-reduce-enumeration* loop, then the branching factor = expected number of iterations until the shortest vector is found $= \frac{1}{p_{succ}}$. The runtime T_{ext} of extreme pruning can be derived as

$$T_{ext} = \frac{T_{red} + T_{node}\cdot N_{ext}}{p_{succ}} \tag{7}$$

where T_{red} is the initial reduction or preprocessing time, T_{node} is the average time for processing a single node, p_{succ} is the success probability; N_{ext} is the total number of nodes in the pruned enumeration tree such that $N_{ext} = \sum_{k=1}^{n} H'_k$, where H'_k is the number of nodes in depth k ($1 \leq k \leq n$) of the enumeration tree. Now, the number of nodes in each level k can be heuristically estimated as $H'_k = \frac{1}{2}\cdot\frac{V_{R_1,\ldots,R_k}}{\mathrm{vol}(L_k)}$, which can be compared to that of full enumeration tree $H_k = \frac{1}{2}\cdot\frac{V_k(R)}{\mathrm{vol}(L_k)}$. Here ($\frac{1}{2}$) comes from the fact that it will be enough to search half of the tree due to the symmetry in the SVP problem; $\mathrm{vol}(L_k) = \prod_{i=n+1-k}^{n}\|\mathbf{b}_i^*\|$ is the volume of the projected lattice in level k; $V_k(R)$ is the volume of the k-dimensional ball of radius R and $V_{R_1,\ldots,R_k}$ is the volume of the cylinder intersections of radii such that $R_1 \leq \cdots \leq R_k$. In [10], two methods to compute the volume $V_{R_1,\ldots,R_k}$ are explained. The simplest one is based on Monte Carlo sampling to get an estimation. The next one, the successive integration approach, can compute this volume exactly considering certain mild constraints on radii (see Lemma 4.1 and 4.2 in [10]). The success probability p_{succ} can also be estimated using a similar approach. We use the exact computation method to derive the volume and success probability in our model implementation.

Now, the comparative speed up of extreme pruning can be computed as $G_k = S_k\cdot p_{succ}$, where $S_k = \frac{H_k}{H'_k} = \frac{V_k(R)}{V_{R_1\cdots R_k}}$ is the ratio of the number of nodes at level k of the full tree to the pruned tree.

IV. Recursive-BKZ

The preprocessing method described by Nguyen and Chen in [7] is known as the recursive preprocessing applied to the BKZ lattice reduction. In general, the case without preprocessing can be defined as follows.

Definition 1 (No Preprocessing): Given input basis B and a blocksize k, compute B' = BKZ-k(B) and return B' (note that BKZ-k internally pre-processes the input basis B by running LLL on it, so this can be more accurately described as the LLL preprocessing).

This definition can be compared to the following definition of recursive preprocessing for local block bases.

Definition 2 (RBKZ preprocessing): Let M_i be the projected block basis of index i such that $1 \leq i \leq n-1$ where n is the lattice dimension, parameter s is a step size and k_{min} is the minimum blocksize for recursion then before running enumeration on each block lattice k, run BKZ-(k-s) on the block if $k > k_{min}$ (otherwise, do as in original BKZ, i.e. only LLL preprocessing of the local block lattice).

The full RBKZ algorithm is given in Algorithm 1.

Algorithm 1 The RBKZ(n, k) basis reduction algorithm

Input: a basis $B = (\mathbf{b}_1, \ldots, \mathbf{b}_n)$ of a lattice L with blocksize $k \in (2, n)$, minimum blocksize k_{min}, step size s, the GS triangular matrix μ and a vector $\mathbf{c}$ to hold all $\|\mathbf{b}_i^*\|^2_{(1 \leq i \leq n)}$
Output: a BKZ-k reduced basis $(\mathbf{b}_1, \ldots, \mathbf{b}_n)$ with updated μ and $\mathbf{c}$

```
if k < k_min then
    return the input basis
else
    LLL(B, c, μ, δ)
    z ← 0, i ← 0
    compute τ(n, k)
    while z < τ(n, k) · (n − 1) do
        i ← i + 1, j ← min(i + k − 1, n)
        if (i = n) then
            i ← 1, j ← n
        end if
        compute the local projected block basis M_i of dim. d ← min(k, n − i + 1)
        for (1/p_succ) times do
            apply randomization on M_i        ⇒ output is a randomized basis Z_i
            n ← d, k ← (d − s)
            call RBKZ(n, k) on Z_i        ⇒ output is a preprocessed basis P_i
            apply pruned enumeration on P_i
        end for
        compute b_new as a shortest vector found among all iterations of M_i
        h = min(j + 1, n)
        B_h = (b_1, ..., b_{i−1}, b_new, b_i, ..., b_h)
        LLL(B_h, c, μ, δ); z ← z + 1
    end while
end if
```

V. Preprocessing and Pruning Variants

We consider three possibilities of optimization for our RBKZ algorithm. In the first option, we just use non-extreme (high probability) pruning at all levels, and we can afford a very good preprocessing (with a relatively small step size) because the branching factor of the recursion is small ($poly(k)$). In the second option, in order to gain extra savings of the extreme pruning at the top level, we have to pay with an exponential branching factor ($1/p_{succ}$) in the second level of recursion. To compensate, we have to lower the quality of preprocessing by increasing the step size sufficiently until the non-extreme preprocessing cost multiplied by the branching factor balances the cost of the extreme pruning at the top level. This yields an optimal step size to balance out the cost. The third option is included only for completeness, here we consider two extreme pruning levels from the top and non-extreme pruning at other lower levels. Our model implementation (see next section) is confined to the second option which gives the better results of all. This observation has been confirmed experimentally.

- Option 1 (step size s_1 and success probability p_1): Non-extreme pruning at all levels. Formally, for $r = k_{min}, ..., k, s(r) = s_1$, and $p(r) = p_1 \sim 1$ where s_1 is chosen to minimize total time.
- Option 2 (step sizes s_1, s_2 and success probabilities p_1, p_2): Extreme pruning at top level and non-extreme pruning at lower levels. Formally, for $r = k_{min}, ..., k, s(r) = s_1$ and $p(r) = p_2 = 4\alpha_1(1-\alpha_1)^{r/4}$ (asymptotically) or $p(r) = p_{succ}$ (from exact calculation) for $r > k - s_1$ and $s(r) = s_2$ and $p(r) = p_1 \sim 1$ for $r \leq k - s_1$. The step sizes s_1, s_2 and speed up parameter α_1 are chosen to minimize total runtime.
- Option 3 (step sizes s_1, s_2, s_3 and success probabilities p_1, p_2, p_3) : Extreme pruning at top two levels and non-extreme pruning at lower levels.

VI. Recursive-BKZ Model

The purpose of the RBKZ model is to simulate and test the complexity of our preprocessing variants. We write our code in C/C++ with the "RR" floating point variant of NTL [11] version 5.5.2. In particular, the model implements all theoretical formulas given in Section II of this paper including few more to estimate the runtime using SMA based GSO for HKZ and BKZ reduction. The main subroutines of the model implementation can be described as follows.

The first task is to create a subroutine for computing the SMA fixed point normalized log GSO, i.e. $\overline{x}_i = x_i - E[\mathbf{x}]$, $\forall i$, where $x_i = \log \|\mathbf{b}_i^*\|$, $E[\mathbf{x}] = \sum_{i=1}^{k} \frac{x_i}{k}$. For all $i \leq n-k$, we compute BKZ-SMA log GSO, following Lemma 4 in [9], as follows,

$$x_i = \frac{k}{2(k-1)} \cdot \log \gamma_k + \frac{1}{k-1} \cdot \sum_{j=i+1}^{i+k-1} x_j \tag{8}$$

where the Hermite constant $\gamma_k = V_k(1)^{\frac{-2}{k}}$ and $V_k(1) = \frac{\pi^{\frac{k}{2}}}{\Gamma(\frac{k}{2}+1)}$ is the volume of the k-dimensional unit ball. For the last k vectors, i.e. for all $i > n-k$, BKZ performs the HKZ reduction and we have

$$x_i = y_{i-(n-k)} \tag{9}$$

such that (following Lemma 2 in [9]), $y_j = -(k-j+1) \cdot \Psi_k(j-1) + (k-j) \cdot \Psi_k(j), \forall j < k$ and $y_k = -\Psi_k(k-1)$, where $\Psi_n(\beta) = \sum_{i=n-\beta}^{n-1} \frac{\log \gamma_{i+1}}{2i}$, $\forall\, 0 \leq \beta < n$. This eventually

TABLE I
OPTIMAL s_1 AND ENUMERATION COMPLEXITIES FOR $k = 100$ (OPTION 2) WITH PREPROCESSING OVERHEAD FOR EXTREME PRUNING.

α	s_1	s_2	$T_2(\gamma_0)$	$T_1(\gamma_0)$	$T_1(0)$	$\delta_{ov,xp}$
0.05	70	0	54.06	54.05	45.88	8.17
0.10	53	0	44.15	43.95	35.85	8.10
0.15	46	0	35.42	35.16	35.03	0.13
0.20	32	0	37.03	37.19	36.88	0.31
0.25	22	0	38.77	38.84	38.82	0.02
0.30	14	0	40.72	40.74	40.87	−0.13
0.35	07	0	43.00	42.84	42.96	−0.12
0.40	01	0	45.30	45.09	45.11	−0.02

helps in computing the complexity (number of nodes) N and the exact level for the maximum node density in the enumeration tree.

To incorporate the pruning with the complexity estimate we need to create subroutines for computing the pruning ratio S_{xp} and the success probability p_{succ} based on the successive integration method (in [10]). These subroutines will be required also to implement the variants of preprocessing/pruning options with the parameters α (speed up factor), s (step size) and p (probability of success).

Finally, the model should able to compute the log enumeration cost of blocksize r in extreme pruning: $lgTen(r) = lgNen(r) - \log(p_{succ}(r))$, where lgNen($r$) is the log enumeration cost (log number of nodes) for a dimension r and the term $p_{succ}(r)$ is due to the branching factor of extreme pruning. This is the complexity we require to compare with the numerical results in [7]. By changing the preprocessing and pruning parameters (α, s, p etc.) in different levels of the recursion we can control and thus optimize the value of lgTen(r). The model also has provision to compute the total runtime $T(n, k)$.

VII. EXPERIMENTAL RESULTS

We simulate the complexity estimates from the previous section using our RBKZ preprocessing Model. All numerical results obtained in this section are derived by running the implementation of this model. Table I shows the optimal cost of using extreme pruning for a range of pruning parameter α from the numerical model. In particular, it gives the optimal log enumeration cost of the second recursion level $T_2(\gamma_0)$, top recursion level $T_1(\gamma_0)$ and HKZ-reduced basis $T_1(0)$ for a blocksize k. We say optimal as each α entry corresponds to an optimized step size $s_1 = \gamma_0 \cdot k$ that balances the complexity of the top level and the second level. Therefore, Table I also suggests an optimal value of the pruning speed up parameter $\alpha \sim 0.15$. The last column of the table includes the preprocessing overhead ($\delta_{ov,xp}$ = $T_1(\gamma_0) - T_1(0)$ in log) due to the extreme pruning. For non-extreme pruning, the log complexity $T_1(0)$ (option 1) is approximately 41.15.

To realize the overall result, for various k we plot Figure 1 that shows three (solid line) graphs comparing the complexity of extreme pruning including preprocessing cost ($T_{xp}(\gamma_0)$, i.e. the log sum of the cost of top level, $T_1(\gamma_0)$ and second level, $T_2(\gamma_0)$), extreme pruning excluding the cost of preprocessing ($T_1(0)$, i.e. complexity of a HKZ reduced basis in dimension k at $\gamma = 0$) and non-extreme pruning ($T_1(0)$(option 1) at $\gamma = 0$). The complexity of the non-extreme case is $\approx \log N(k, 0)_{up} - (c_{S,nxp} - c_{p,nxp}) \cdot k$, where $c_{S,nxp} = \log S_{nxp}((1-\gamma)k)/((1-\gamma)k)$ and $c_{p,nxp} = \log(1/p_{succ}(k))/k \sim 0$ (we consider the success probability $p_{succ} \sim 1$ for option 1) are the non-extreme pruning constants. This is also the time to enumerate a HKZ-reduced k dimensional basis with non-extreme pruning at s_1 (or γ)= 0.

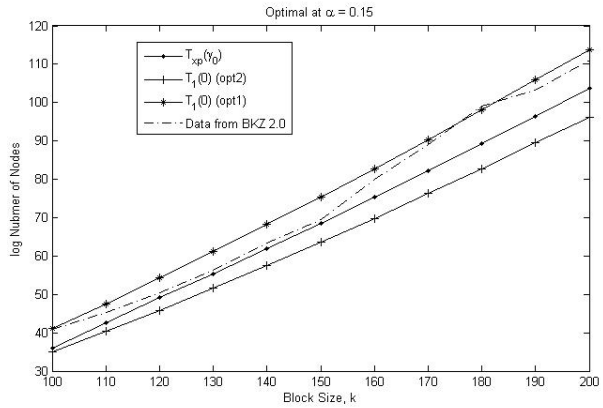

Fig. 1. Comparing extreme pruning (with and without the cost of preprocessing) and non-extreme pruning complexities with previously reported similar cost from [7].

The dotted line in Figure 1 is the Table 3 entries of [7], where one can see that the complexity we have is better than their preprocessing option (simulation of BKZ-90/100/110/120) for a range of block size k. Presumably, it is because we used an optimized preprocessing step size s_1 for those block sizes, while in [7] Chen and Nguyen used a suboptimal choice.

VIII. CONCLUSIONS

In this paper, we optimize the various parameters of the most successful practical lattice reduction algorithm known as BKZ. Thus we improve the performance of this algorithm in terms of time complexity. We also show the comparative results of the similar work reported from Chen and Nguyen's paper in Asiacrypt'11 conference.

REFERENCES

[1] M. Ajtai. *The shortest vector problem in L_2 is NP-hard for randomized reductions (extended abstract)*. In STOC'98, ACM, pp. 284-293, 1998.

[2] O. Regev. *On lattices, learning with errors, random linear codes, and cryptography*. Journal of ACM, vol 56, 2009.

[3] C. Gentry. *Fully homomorphic encryption using ideal lattices*. In STOC'09, ACM, pp. 169-178, 2009.

[4] V. Lyubashevsky, D. Micciancio, C. Peikert and A. Rosen. *SWIFFT: A Modest Proposal for FFT Hashing*. In Fast Software Encryption(FSE) 2008, LNCS, pp. 54-72. Springer-Verlag, 2008.

[5] A. K. Lenstra, H. W. Lenstra, Jr., and L. Lovász. *Factoring polynomials with rational coefficients*. Math. Ann., 261(4): 515-534, 1982.

[6] C.-P. Schnorr and M. Euchner. *Lattice basis reduction: improved practical algorithms and solving subset sum problems*. Math. Programming, 66:181-199, 1994.

[7] Y. Chen and P. Q. Nguyen. *BKZ 2.0: Better Lattice Security Estimates*. In ASIACRYPT'11, LNCS 7073, pp. 1-20, IACR, 2011.

[8] P. Q. Nguyen and V. Brigitte. *The LLL Algorithm: survey and application*. Chapter-2 (Hermite?s Constant and Lattice Algorithms). ISBN 978-3-642-02294-4, 2010.

[9] G. Hanrot, X. Pujol and D. Stehlé. *Analyzing Blockwise Lattice Algorithms using Dynamical Systems*. In CRYPTO'11. LNCS, vol. 6841, pp. 447-464. Springer, 2011.

[10] N. Gama, P. Q. Nguyen, O. Regev. *Lattice enumeration using Extreme Pruning*. In EUROCRYPT, 2010, LNCS, Springer-Verlag, 2010.

[11] V. Shoup. NTL: A library for doing number theory. Available at http://www.shoup.net/ntl/.

OPTIMAL TASK SCHEDULING IN CLOUD COMPUTING ENVIRONMENT: META HEURISTIC APPROACHES

Tripti Mandal[1], Sriyankar Acharyya[2]
[1]Computer Science and Engineering, West Bengal University of Technology, Kolkata, West Bengal, India
[2]Computer Science and Engineering, West Bengal University of Technology, Kolkata, West Bengal, India
[1]triptimandal90@gmail.com, [2]srikalpa8@gmail.com

Abstract—**Cloud computing is the latest continuation of parallel computing, distributed computing and grid computing. In this system, user can make use of different services like storage, servers and other applications. Cloud resources are not only used by numerous users but are also dynamically redistributed on demand. Requested services are delivered to user's computers and devices through the Internet. The fundamental issue in cloud computing system is related to task scheduling where a scheduler finds an optimal solution in cost-effective manner. Task scheduling issue is mainly focus on to find the best or optimal resources in order to minimize the total processing time of Virtual Machines (VMs). Cloud task scheduling is an NP-hard problem. The focus is on increasing the efficient use of the shared resources. A number of meta-heuristic algorithms have been implemented to solve this issue. In this work three meta-heuristic techniques such as Simulated Annealing, Firefly Algorithm and Cuckoo Search Algorithm have been implemented to find an optimal solution. The main goal of these algorithms is to minimize the overall processing time of the VMs which execute a set of tasks. The experimental result shows that Firefly Algorithm (FFA) performs better than Simulated Annealing and Cuckoo Search Algorithm.**

Keywords—Cloud Computing, Task Scheduling, Simulated Annealing, Firefly Algorithm, Cuckoo Search Algorithm.

I. INTRODUCTION

Cloud computing is a developing technology that provides different kind of services [1] such as infrastructure, software and different applications through network. Cloud can also be defined as a distributed computing paradigm, which is a group of interconnected and virtualized computers that are provisioned and presented dynamically [1] as unified computing resources, offered as a pay-per-use service [2]. According to the cloud definition of National Institute of Standards and Technology (NIST) [3]," Cloud computing is a model for enabling convenient, on-demand network access to a shared pool of configurable computing resources (e.g., networks, servers, storage, applications, and services) that can be rapidly provisioned and released with minimal management effort or service provider interaction". Different types of services [4] are Infrastructure as services (IaaS) where customer can initiate a new project by renting computing resources [1], Platform as services (PaaS) where platform is provided to the customer to execute any program and Software as a Service (SaaS) [1] where cloud system summarizes everything required to evaluate software life-cycle. Different kinds of requests are coming from the different part of the world. All the tasks are executed by VMs which are also known as processing element in cloud environment [5]. Before the task gets executed on the VM, it is given to the dispatcher [5]. Dispatcher or Cloud broker then assigns the tasks to appropriate cloud user. As the number of requests is more, the required number of VMs is more. As more than one task gets executed to one or more VM, so the tasks should be scheduled within the VM, such that, all the tasks must complete its processing as early as possible. This enhances the performance of cloud and makes the system more efficient and productive.

Cloud task scheduling can be described as a NP-hard optimization problem [2], [5], [6], which is best solvable using mete-heuristic algorithms [2], [10]. Different meta-heuristic methods have been applied such as Genetic algorithm (GA), Ant Colony Optimization (ACO), Simulated Annealing (SA), Particle Swarm Optimization (PSO), Max-Min Algorithm and many more to solve this task scheduling issue. Numerous research results [2], [5], [10] have been made to ensure that meta-heuristic scheduling algorithms can provide better optimal scheduling than traditional scheduling algorithms [10].

Optimal solution can be obtained by optimizing different parameters [2], [5], [6]-[9] such as makespan, processing time, execution time, communication cost, task transferring time etc. In this work processing time has been considered as a parameter to be optimized for scheduling of tasks.

To solve this scheduling issue of tasks, several works have been done. Ant Colony optimization (ACO) based task scheduling has been proposed in [7], [11]. ACO is based on the foraging behavior of ant colonies. In [7], the proposed ACO algorithm has been implemented to minimize the makespan (Total task completion time) , where as in [11] the ACO algorithm is implemented and compared with First Come First Serve and Round Robin method algorithms and showed positive result. But in both the proposed ACO, there are some problems in updating of the pheromone intensity. In

78-1-4673-9257-0/15/$31.00 ©2015 IEEE

order to let ACO get a better performance, PACO (a period based ACO) [12] has been implemented. The period based mechanism is used to improve the update pheromone strategy. PACO performs better to optimize makespan and load balance strategy. A heuristic approach, Genetic algorithm [6] has been made to optimize makespan. Each chromosome is represented by a job and every chromosome has its fitness value. Two main Disadvantages associated with this method are complexity and longtime consumption. A new evolutionary algorithm, which is based on obligate brood parasite behavior of cuckoo species [13], has been proposed. In this proposed system each cuckoo lay eggs at a time and dumps the eggs in a randomly chosen nest. Every nest has a fitness value associated with it. Considering both the cost for data transmission and computation, a PSO (Particle Swarm Optimization) algorithm [8] has been implemented to schedule the tasks. By combining the advantages of Ant Colony Optimization an Artificial bee algorithm, a hybrid task scheduling algorithm [9] has been proposed. Both the algorithms consider pheromone concentration and the edge weight but not the load on the VM. The sum of transfer time and execution time is optimized here. Multi objective particle swarm optimization (MOPSO) [14] has been applied in cloud computing to optimize task execution cost, task transferring time and task execution time.

In this paper three meta-heuristic algorithms, Simulated Annealing, Firefly Algorithm and Cuckoo Search Algorithm have been implemented to find an optimal solution of submitted tasks. From the experimental result, it has been shown that Firefly Algorithm performs better than Simulated Annealing and Cuckoo Search algorithm in finding an optimal schedule of submitted tasks in reasonable time.

The following sections are arranged as follows. In section II, Task scheduling problem has been described with mathematical model. In section III description meta-heuristic has been made. Section IV describes the result and section V concludes the paper.

II. TASK SCHEDULING PROBLEM

Task scheduling can be described as tasks or jobs that will be executed by a set of computing resources. Computing resources are known as virtual machines. For instances, given the problem that if there is a set of n tasks, $\{T_1,T_2,T_3,T_4,\ldots T_n\}$ which need to be scheduled on m identical machines $\{VM_1,VM_2,\ldots..VM_m\}$, while trying to reduce the total processing time. All the tasks are non- preemptive [5] that is processing of one task in one machine cannot be executed on another and all the resources can execute all type of tasks.

In [5], a mathematical model for scheduling has been proposed to balance the load of individual VM while trying to minimize the makespan. With the help of this model, processing time has been evaluated.

For the mathematical representation of the scheduling problem let there be a set of m virtual machines where all the tasks will be processed and n number of tasks represented as a set [5]. All the tasks in the model are non-preemptive and independent. Processing time varies from one VM to other VM based on capacity and bandwidth of the VM.

So Capacity of individual VM,

$$C_i = pe_{num,i} \times pe_{mips,i} + vm_{bw,i} \qquad (1)$$

Where number of processing element of VM is denoted by pe_{num}, pe_{mips} is the million instructions per second of all processors and vm_{bw} is the communication bandwidth ability to a VM_i.

Capacity of all VMs, $C = \sum_{i=1}^{m} C_i$ (2)

Total capacity of all the VM is known as capacity of the datacenter. Load of individual VM can be defined as the total length of tasks that are assigned to the VM.

$$L_{vmi,t} = \frac{N(T\ ,t)}{S(VM\ ,t)} \qquad (3)$$

It is calculated using number of task at time t on a service queue and divided by the service rate of individual VM at time instance t. Load of all VM is calculated as,

$$L = \sum_{i=1}^{m} L_{vmi} \qquad (4)$$

Processing time of a VM, $PT_i = \frac{L_{vmi}}{C}$ (5)

Processing time of all the VM, $PT = \frac{L}{C}$ (6)

This equation defines the total processing time of all the VM.

So the problem is to minimize,

$$PT_{max} = \sum_{i=1}^{m} PT_i \text{, where } i \in \text{VM, } i=1, 2, 3\ldots n \qquad (7)$$

And load value of a VM must be less than its capacity.

III. SOLUTION METHODS

Being the problem in NP-hard class, meta-heuristic algorithms are best suitable to solve this issue. Meta-Heuristic is a higher level heuristic methodology [10] to find optimal solution of a problem in reasonable time.

In this work each solution has been represented as a vector of n elements where n is the number of tasks to be scheduled. Vector component values are the VM's number; hence it may appear more than once because more than one task is allocated to the same VM. For an example if we consider the following example, where nine tasks get scheduled on 4 VMs.

T_1	T_2	T_3	T_4	T_5	T_6	T_7	T_8	T_9
VM_1	VM_4	VM_2	VM_1	VM_3	VM_1	VM_2	VM_3	VM_4

According to the diagram, task 1 and 4 are associated with VM_1. Tasks 3 and 7 are associated with VM_2. Tasks 5 and 8 are associated with VM_3. Tasks 2 and 9 are associated with VM_4.

A. *Simulated Annealing*

Simulated Annealing [15], [16], [17] is based on the annealing of metal. To develop a crystal, one starts by heating the raw material to a liquefied state. To get a crystalline structure, the temperature of the crystal melt is reduced. If the reduction of temperature becomes fast then irregularities get locked into the structure of crystal and the trapped energy level is much higher than in a perfectly structured crystal. In each cycle this method tries to move from the current trial solution S to a neighboring point S' in the solution space in an effort to find a better trial solution. If the problem is minimization problem and cost(S') < cost(S), S' becomes the new trial solution; the move from S to S' is then called a downhill move. If cost(S') > cost(S), S' becomes the new trial solution with probability p = exp (-Δ/temp), where temp is a parameter known as the temperature and Δ = cost(S') - cost(S). S is retained as the trial solution with probability (1- p). Thus S' can become the new trial solution even when its cost is higher. This kind of move from S to S' is called an uphill move. This ensures that the procedure does not get trapped in a local minimum.

The SA Algorithm is given below:

Step 1: Generate an initial solution S,
S* ← S
Step 2: Initialize Temperature T_0, T_0>0
T ← T_0
Step 3: Calculate Cost C
Step 4: While not frozen do the followings
4.1. Find a neighbor S'
4.2. Find Cost C' of S', ΔC=C'-C
4.3. If (ΔC<=0)
Accept solution S', S* ← S'
4.4. Else accept S' with probability $e^{-\Delta/T}$, S* ← S'
Step 5: Reduce temperature with factor r, T=T*r
Step 6: Output: the final state S*

Where the initial solution is S, the neighborhood solution is S', S* holds the current best solution. T_0 is the initial temperature. In this work, the initial solution (i.e. solution vector) has been generated randomly. Cost has been determined by its total processing time and neighborhood is selected by swapping the tasks between two randomly chosen VMs.

B. *Firefly Algorithm*

Among several swarm-intelligence algorithms, Firefly (FA) [18], [19] algorithm is one of the mostly used algorithms. This FA algorithm was illustrated by Xin-She Yang [18] in 2008 inspired by the flashing behavior of tropical fireflies. It is a population based Meta Heuristic which tries to find global optimum solution. The FA is based on two behaviors [18] of fireflies, one is to attract other fireflies with lower intensity and another is to minimize the distances between them. Fireflies are unisexual so one can be attracted to other irrespective of their sex. The attractiveness directly varies with the brightness and the brightness is inversely proportional to the distance.

The algorithm is given below:

Step 1: Initialization the population of n firefly
Step 2: Determine light intensity for each firefly
Step 3: Determine the distance between each two Fireflies
Step 4: While t< Maxgeneration (G)
for *i=1: n* for n fireflies
for *j=1: i* for n fireflies
if (I_j>I_i) move firefly i towards firefly j
Vary the attractiveness with distance r_{ij} by $exp\ [-\gamma r_{ij}]$
Evaluate new solution and update light intensity
End if
End for *j*
End for *i*
End while
Step 5: Rank the fireflies and find current global best

The attractiveness function of the firefly is established by,

$$\beta\ (r) = \beta_0\, e^{(-\gamma r^2)} \tag{8}$$

Where β_0 is the attractiveness at r=0. The movement of fireflies i attracted to another more attractive firefly (brighter) j is determined by,

$$x_i\,(t+1) = x_i\,(t) + \beta_0\, e^{(-\gamma r^2)}\,(x_i - x_j) + \alpha\varepsilon_i \tag{9}$$

The value of γ controls the scaling of intensity. For this work the initial populations of fireflies have been generated randomly in a vector with n elements, where n is the number of tasks to be scheduled. Value of the vector denotes the VM number. The fitness of the firefly is reciprocal to its processing time as this is a minimization problem.

C. *Cuckoo Search Algorithm*

Cuckoo Search Algorithm is a meta-heuristic algorithm that models natural behavior of cuckoo species [13], [20]. Each egg in the nest represents a solution. The main aim is to find better solution to change a not so better solution in the nest. At a time, each cuckoo lays one egg and dumps this egg in a nest, chosen randomly. The best nest with high quality eggs (solution) will be carried out to the next generation. The host can discover an alien egg by a probability *Pa [0, 1]*. The host bird either throws the egg away or abandons the nest to build a new nest in a new location.

The algorithm is given below:

Step 1: Objective functions $f(x)$, $x=(x_1, x_2 \ldots x_d)$
Step 2: Generate the population of n host nests x_i, $(i=1, 2 \ldots n)$
Step 3: While (t<Maxgeneration)
Get a cuckoo randomly and generate a new solution by Lévy flights
Evaluate its quality/fitness, F_i
Choose a nest among n (say j) randomly
if $(F_i > F_j)$,
Replace j with a new solution
end
Abandon a worse nest with probability (Pa)
Build new ones at new locations via Lévy flights
Keep the best solutions (with high quality)
Rank the solutions and find the current global best
End while
Step 4: Post process results and visualization.

For minimization problems, the fitness or quality function is reciprocal of objective function. A solution is represented by an egg in the nest and the cuckoo egg represents a new solution. So mainly there is no difference between an egg, a nest and solution. From x_i^t of it the next generation is calculated by,

$$X_i^{(t+1)} = X_i^{(t)} + \alpha \oplus Lévy\ (u) \quad (10)$$

And

$$Lévy\ (u) = t^{-\gamma},\ 1 < \lambda \leq 3 \quad (11)$$

Where α > 0 is the step size, depending on the scale of the given problem, ⊕ means entry-wise multiplications.

To find an optimal solution of the given problem, a solution is represented by an egg and new solution is represented by a cuckoo egg. The initial population is represented by a vector of n elements, where n represents the total number of tasks to be scheduled and vector value represents the VM number.

IV. EXPERIMENTAL RESULTS

All the three algorithms have been implemented in windows 7, 32-bit operating system and the programs are executed in GCC 32 bit compiler. All the methods are executed 100 times and the average of 100 iterations has been performed. All the methods are executed with different random solution. The C.P.U execution time is kept almost same for all the three method so that a comparison can be made.

In all the experiments, number of virtual machine is restricted to 4, while the number of tasks varies from 10 to 50 with difference of 5. All the values of data needed for virtual machine and tasks are taken from [21] where the authors have implemented an optimization techniques using Multi-Objective PSO.

TABLE I: VALUE OF PARAMETERS

Method	Parameters	Value
Simulated Annealing	Initial Temperature	100000
	Minpercent	0.01
	Tempfactor	0.85
	Sizefactor	6
	N	20
	Tcent	0.9
Firefly Algorithm	Alpha	0.2
	Beta	2.0
	Gamma	1
Cuckoo Search Algorithm	Value of alpha	2.0
	Value of P_a	0.4

Table I shows the value of all the parameters. These values have been set after running several trials. Table II shows the experimental results of the three methods. The cost refers to the total processing time of the optimal task schedule found by an algorithm. The time refers to the average execution time of the algorithm.

TABLE II: EXPERIMENTAL RESULTS

No. of task	Simulated Annealing		Firefly Algorithm		Cuckoo Search Algorithm	
	Cost	*Time(Second)*	*Cost*	*Time(Second)*	*Cost*	*Time(Second)*
10	4.35709	0.4929	2.79261	0.513	4.402067	0.525425
15	6.04389	0.59857	4.82637	0.5749	6.659729	0.566975
20	8.68716	0.7084	6.95119	0.72257	9.368409	0.717887
25	11.4436	0.82337	8.49927	0.84038	12.23402	0.792325
30	12.6499	0.93381	10.7151	0.95523	14.6173	0.994163
35	13.4607	1.07266	12.4453	1.1077	16.84712	1.06675
40	17.4611	1.12496	14.3273	1.24682	20.56502	1.169287
45	18.4573	1.21493	16.7253	1.4039	22.38663	1.186638
50	20.5931	1.26298	18.1823	1.201	23.67107	1.225288

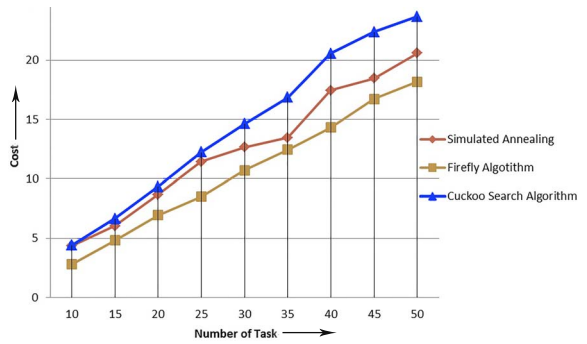

Figure 1. Comparison Graph

Graphical representation of the cost of three methods is shown in following figure 1. From figure 1, it is shown that Firefly Algorithms executes all the tasks with minimal processing time. Cuckoo Search Algorithm underperforms than Simulated Annealing and Firefly Algorithm.

V. CONCLUSION AND FUTURE WORK

In this paper we have implemented three meta-heuristics such as Simulated Annealing, Firefly Algorithm and Cuckoo Search Algorithm to find an optimal solution of the submitted tasks while trying to minimize the total processing time of

VMs. The results are taken after the average of 100 iterations. All the parameters of the three algorithms have been determined after some trials. The cost of the three methods has been calculated to make a comparison among them. The processing time is considered as the cost in these three methods. As it is a minimization problem, the less cost gives us the better solution. The average runtime of program execution for the three meta-heuristics has been kept nearest to each other so that a fair comparison can be made based on the processing time (cost). All the three methods were able to find the optimal solution for the given problem. The experimental results show that the firefly algorithm performs better in comparison with both the Simulated Annealing and Cuckoo Search Algorithm in respect of cost.

In future research, hybrid version of Firefly Algorithm will be tried to solve this problems. Other meta-heuristics like, Differential Evolution, Cat Swarm Optimization, Fish Swarm Algorithm and Bacterial Foraging Optimization will be applied to make the comparative study more judicious.

REFERENCES

[1] R. Buyya, C. S. Yeo, S. Venugopal, J. Broberg, and I. Brandic, "Cloud computing and emerging IT platforms: Vision, hype, and reality for delivering computing as the 5th utility," *Future Generation computer systems*, vol. 25, no. 6, pp.599-616, 2009.

[2] M. Tawfeek, A. El-Sisi, A. Keshk, and F. Torkey, "Cloud task scheduling based on ant colony optimization," 8th *International Conference on Computer Engineering & Systems (ICCES)*, pp. 64-69, 2013.

[3] P. Mell, and T. Grance, "The NIST definition of cloud computing," *National Institute of Standards and Technology Special Publication 800-146*, vol.53, no. 6, 2009.

[4] M. Dikaiakos, D. Katsaros, P. Mehra, G. Pallis and A. Vakali, "Cloud Computing: Distributed Internet Computing for IT and Scientific Research," *IEEE Internet Computing*, vol. 13, no. 5, pp. 10-13, 2009.

[5] D. Babu, and P. V. Krishna, "Honey bee behavior inspired load balancing of tasks in cloud computing environments," *Applied Soft Computing*, vol. 13, no. 5, pp. 2292-2303, 2013.

[6] S. H. Jang, T. Y. Kim, J. K. Kim, and J. S. Lee, "The study of genetic algorithm-based task scheduling for cloud computing." *International Journal of Control and Automation*, vol. 5, no. 4, pp.157-162, 2014.

[7] L. Wang, and L. Ai, "Task Scheduling Policy Based on Ant Colony Optimization in Cloud Computing Environment," *LISS 2012: Proceedings of 2nd International Conference on Logistics, Informatics and Service Science*, pp. 953-957, 2013.

[8] S. Pandey, L. Wu, S. Guru, and R. Buyya, "A Particle Swarm Optimization-Based Heuristic for Scheduling Workflow Applications in Cloud Computing Environments", *24th IEEE International Conference on Advanced Information Networking and Applications*, pp. 400-407, IEEE, 2010.

[9] R. Madivi, and S. Kamath, "A hybrid bio-inspired task scheduling algorithm in cloud environment," *Fifth International Conference on Computing, Communications and Networking Technologies (ICCCNT)*, pp.1-7, 2014.

[10] C. Tsai and J. Rodrigues, "Meta heuristic Scheduling for Cloud: A Survey," *IEEE Systems Journal*, vol. 8, no. 1, pp. 279-291, 2014.

[11] M. Tawfeek, A. El-Sisi, A. Keshk and F. Torkey, "Cloud task scheduling based on ant colony optimization," *8th International Conference on Computer Engineering & Systems (ICCES)*, pp. 64-69, 2013.

[12] W. Sun, N. Zhang, H. Wang, W. Yin and T. Qiu, "PACO: A Period ACO_based Scheduling Algorithm in Cloud Computing," *International Conference on Cloud Computing and Big Data*, pp.482-486, 2013.

[13] N. J. Navimipour, and F. S. Milani, "Task scheduling in the cloud computing based on the cuckoo search algorithm," *International Journal of Modeling and Optimization*, vol. 5, no. 1, pp.44-47, 2015.

[14] Q. Wang , and H. Zheng, "Optimization of task allocation and knowledge workers scheduling based-on particle swarm optimization," *International Conference on Electric Information and Control Engineering*, pp. 574-578, 2011.

[15] S. Acharyya, "The Satisfiability Problem: A Constraint Satisfaction Approach", Ph D Thesis, Computer Science & Engg., Calcutta University, 2001.

[16] S. Kirkpatrick, C.D. Geatt, and M. P. Vecchi, "Optimization by Simulated Annealing", Science, new series, vol. 220, No. 4598, pp. 671-680, 1983.

[17] M. Abdullah and M. Othman, "Simulated Annealing Approach to Cost-Based Multi-Quality of Service Job Scheduling in Cloud Computing Environment," *American Journal of Applied Sciences* ,vol. 11, no. 6, pp. 872-877, 2014.

[18] X. Yang, D. Fister, and I. Fister, "Firefly algorithm: a brief review of the expanding literature", *Cuckoo Search and Firefly Algorithm*, pp. 347-360. Springer International Publishing, 2014.

[19] A. Yousif, A. H. Abdullah, S. M. Nor, and A. A. Abdelaziz, "Scheduling jobs on grid computing using firefly algorithm.", *Journal of Theoretical and Applied Information Technology*, vol .33, no. 2,pp.155-164, 2011.

[20] E. Valian, S. Mohanna and S. Tavakoli ," Improved Cuckoo Search Algorithm for Global Optimization," *International Journal of Communications and Information Technology,* vol.1, no.1, pp.31-44, 2011.

[21] F. Ramezani, J. Lu and F. Hussain, "Task Scheduling Optimization in Cloud Computing Applying Multi-Objective Particle Swarm Optimization," *Service-Oriented Computing*, pp. 237-251, 2013.

Longest Common Subsequence using Chemical Reaction Optimization

Md. Rafiqul Islam
Computer Science and Engineering Discipline, Khulna University, Khulna - 9208, Bangladesh.
e-mail: dmri1978@gmail.com

Zarrin Tasnim Asha
Computer Science and Engineering Discipline, Khulna University, Khulna - 9208, Bangladesh.
e-mail: zarrin.ku@gmail.com

Rezoana Ahmed
Computer Science and Engineering Discipline, Khulna University, Khulna -9208, Bangladesh.
e-mail: sheme.cse@gmail.com

***Abstract*— Longest Common Subsequence (LCS) is a well-known optimization problem. It is the problem to find out a longest subsequence of each member of a given set of sequences. It is an NP-hard problem and has applications in data compression, FPGA circuit minimization and bioinformatics. Chemical Raction Optimization (CRO) is a new meta-heuristic method that is being widely used in solving optimization problem. In this paper we have proposed an efficient Chemical Reaction Optimization technique to solve Longest Common Subsequence problem. The design strategies of elementary operators and correction method are shown to solve the problem. The proposed method is compared with two other methods and the experimental results show that it takes less execution time than that of others.**

Keywords—Longest common subsequence, Chemical Reaction Optimizatio, Metaheurictic, Molecule.

I. INTRODUCTION

Longest common subsequence is an optimization problem. Longest Common Subsequence (LCS) means the longest sequence of characters that appear left-to-right in a given set of strings. But it is not necessarily that it is adjacent block of characters. LCS is essential to occupy serial positions within the original sequences or strings. The longest common subsequence is the base of data comparison programs. Many problems or applications are solved by LCS such as the applications in data compression, FPGA circuit minimization, Bioinformatics [1]. A detail of literature review related to LCS problem and its solutions can be found in [1].One of the biological applications is to compare the DNA of two or more difference organisms. DNA is sequence which consists of A (Aclenine), G (Gaunine), C (Cytosine) and T (Thymin). Thus we are given two DNA sequences and wish to find DNA sequence which is common and longest in length and such a problem is LCS problem [2]. LCS problem for two strings can be solved using Dynamic Programming (DP) [2, 3], which gives optimum results. Chemical Reaction Optimization (CRO) is a simple and powerful meta-heuristic which is showing excellent performance in solving optimization problem. CRO mimics the interactions of molecules in chemical reactions to search for the global optimum [4]. CRO was designed as an optimization framework. It has been applied to solve many practical problems, e.g. quadratic assignment problem[5], population transition problem in peer-to-peer streaming[7], network coding optimization problem[8], standard continuous benchmark function[9], cognitive radio spectrum allocation problem[10], grid scheduling problem[11][12], stock portfolio selection problem [13],artificial neural network training [14], 0-1 Knapsack problem [3] etc. In this paper we have designed an algorithm to find LCS based on the concept of CRO. The proposed method and other two dynamic programming algorithms such as dynamic programming algorithm for LCS given in [2] and fast dynamic programming method depicted in [3] have been implemented and compared the results to show the performances.

II. LONGEST COMMON SUBSEQUENCE (LCS)

Common subsequence of two given sequences is a subsequence that exits in both the sequences. However, the Longest Common Subsequence (LCS) of two given sequences is a subsequence that exits in both the sequences and have longest or maximum length. For example, we have two sequences S_1=(E,F,G,H,E,F) and S_2=(F,H,G,E,F,E), the sequence S=(F,G,F,E) is an LCS. Since the subsequence is common in both in the sequence S1 and S2 and the sub sequence S have the length, |S| = 4, which is the maximum in common sub-sequences. The problem can be formulated as follows:

Let $X = [x_1, x_2 \ldots x_n]$ be a sequence of n elements where X is a string. The elements of the string are members of a finite alphabet $\sum$, $x_n \in \sum$, $\forall i = 1, 2, 3, \ldots, n$.

A sequence $Y = [y_1, y_2, \ldots, y_m]$ is a subsequence of X if there exists an increasing sequence of indices $[i_1, i_2, \ldots, i_k]$ such that $X[i_k] = Y[j]$ holds, $\forall j = 1, 2, \ldots, k \leq n$.

978-1-4673-9257-0/15/$31.00 ©2015 IEEE

Given a finite set S of n strings $S^* = \{S_1, S_2, \ldots, S_n\}$, S is a common subsequence, if S subsequence S_i, $\forall i = 1, 2, 3, \ldots, n$.
The longest common subsequence of S* is the common subsequence of maximum length. The problem can be expressed as

$$\text{Maximize } |S|$$
$$\text{subject to } S \text{ subsequence } S_i, \forall i = 1, \ldots, n.$$

with |S| being the length of the common subsequence S. The longest common subsequences are not always unique. More than one common subsequence with maximum length can be found there.

III. Chemical Reaction Optimization (CRO)

CRO is one of the newest optimization algorithms, which is inspired by the chemical reaction process [15]. CRO has been successfully applied to many other problems. In CRO, molecule (M) is the basic operating agent which represents the solution of optimization problem. To explore solution a set of molecules are controlled and manipulated by CRO. A molecule has potential energy (PE), kinetic energy (KE), hits number, and other characteristics that represent solution. CRO simulates four types of chemical reactions. The four types of elementary reactions are on-wall ineffective collision, decomposition, inter-molecular ineffective collision and synthesis. During the process of CRO the total energy remains constant which means CRO requires conservation of energy. The CRO algorithm includes three stages: initialization, iteration and the final stage. The initialization stage generates initial population (pop) along with PopSize, KElossRate, MoleColl, buffer, InitialKE and two thresholds(α and β). In iteration stage, one elementary reaction out of four reactions takes place in each iteration. Here, we have to determine whether uni-molecular or bi-molecular reaction is taken place. The type of reaction is determined by comparing a random number t [0, 1] against MoleColl. If t > MoleColl there will be unimolecular reaction. Otherwise a bi-molecular reaction occurs. At the end of the each iteration we have to check stopping criteria. Here the potential energy value of the newly obtained molecule(s) is compared with the original molecules. The new molecules will be accepted when the new values can satisfy the energy conservation conditions. Otherwise, the new molecules are discarded**.**

The pseudo code of CRO algorithm is depicted in Algorithm 1.

Algorithm 1: CRO Algorithm

```
Input: Objective function f and the parameter values
\\ Initialization
Set PopSize, KELossRate, MoleColl, buffer, InitialKE, α, and β
Create PopSize number of molecules or solutions
\\ Iterations
while the stopping criteria not met do
Generate b ∈ [0, |S1|]
if b > MoleColl then
Randomly select one molecule or solution S'
if Decomposition criterion met then
Trigger Decompos ()
else
Trigger Onwall ()
end if
else
Randomly select two molecules or solutions S'1 and S'2
if Synthesis criterion met then
Trigger Synthesis ()
else
Trigger Intermole ()
end if
end if
Check for any new minimum solution
end while
\\ The final stage
Output the best solution found and its objective function value
```

IV. Design CRO for LCS

Here we design CRO method for two strings. In LCS problem two sequences are given for finding the longest subsequence. Suppose we have two sequences such as S_1 (first sequence) of length n and S_2 (second sequence) of length m, where $m \leq n$ and $n = |S_1|$ and $m = |S_2|$. We have to find out the longest common subsequence of S_1 and S_2.
Example 1:
S_1 = "GCCCTAGCG".
S_2 = "GGCACTA".
The output sequence, S = "GCAC".
Here we will design Chemical Reaction Optimization (CRO) algorithm for LCS problem.

S_1 :

Character	G	C	C	C	T	A	G	C	G
Index	0	1	2	3	4	5	6	7	8

S_2:

Character	G	G	C	A	C	T	A
Index	0	1	2	3	4	5	6

A. Solution Generation

To generate solution first we take an array of length $m=|S_2|$. Then we generate m random numbers from 0 to $n=|S_1|$. Next we sort the numbers to get a solution sequence. The following Fig. 1 depicts the scenario according to the example 1.

Generate $|S_2|$ random numbers $k \in [0, n]$:

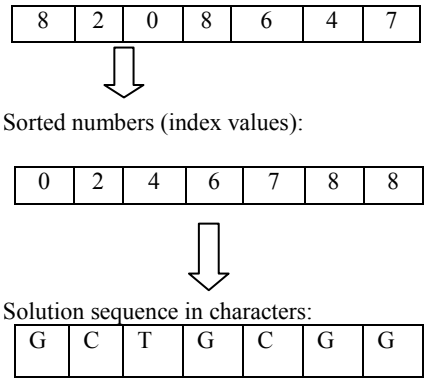

Fig. 1. Solution Representation

B. *On-wall Ineffective Collision*

This elementary reaction corresponds to the basic local search operator for CRO. It changes the solution structure of one solution. Suppose that in an on-wall ineffective collision, the solution structure S is transformed to S'. The new solution structure is generated as S' = C(S), where C(S) is a correction operator that corrects new solution structure. The detail of C (S) function is explained at the end of this section.

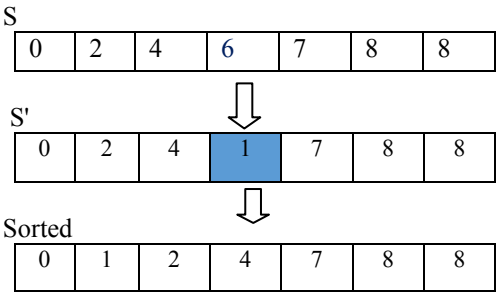

Fig. 2. Solution after On Wall Ineffective Collision

C. *Decomposition*

This elementary reaction generates two solutions from one solution. Decomposition often applies a vigorous change to the solution and the resultant solution possesses solution structures greatly different from the original one. Assume that the operator creates two solutions S'_1 and S'_2 from solution S, such as,

$$S \rightarrow S'_1 \cup S'_2$$

Firstly, S is copied to generate S'_1 and S'_2. After that, for n/2 positions in solutions S'_1 and S'_2 are changed randomly. Then we sort them. The function C (S) is invoked to make the output solution valid.

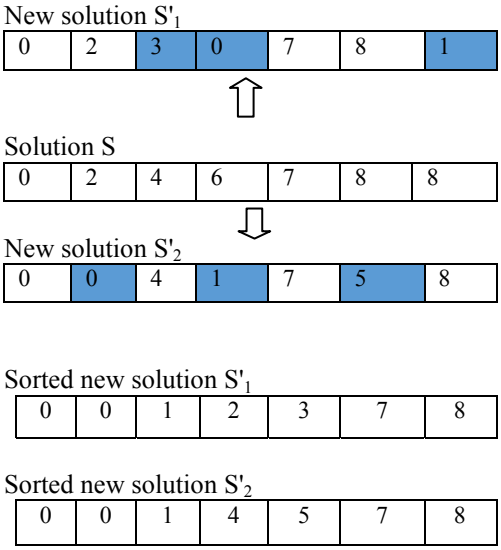

Fig. 3. Solution representation after decomposition

D. *Inter-molecular Ineffective Collision*

It changes the solution structure. The molecularity (assume two) remains unchanged before and after the process. Suppose that in an inter-molecular ineffective collision, the solution structure S_1 is transformed to S'_1 and S_2 is transformed to S'_2. It can be defined as follows:

$$S_1 \cup S_2 \rightarrow S'_1 \cup S'_2$$

Then the new solution structure is generated as S' = C (S).

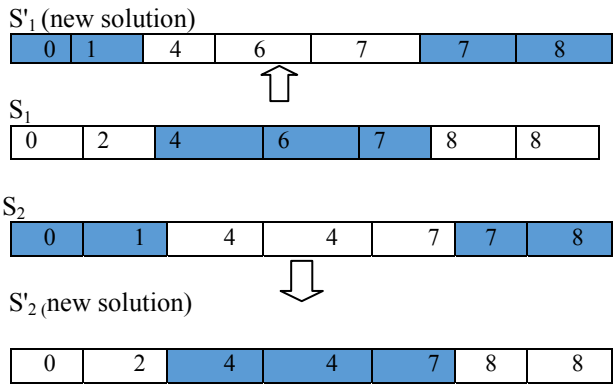

Fig. 4. Solution representation in Inter-molecular Ineffective Collision

E. *Synthesis Operator*

Synthesis takes two molecules as the inputs and combines them to generate a new molecule. In this paper we take two existing solution S'_1 and S'_2. Generate a new solution S from them. It can be represent by the following form.

$S'_1 \cup S'_2 \rightarrow S$

This new solution S is the longest common subsequence.

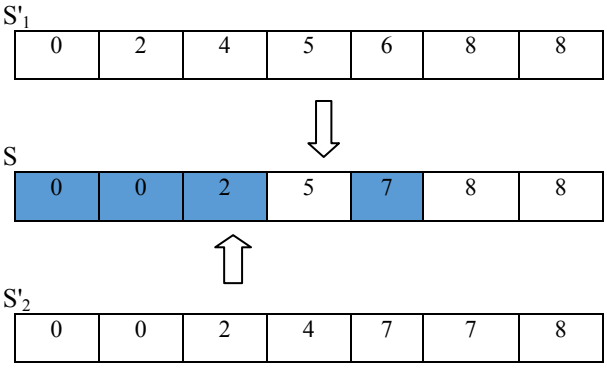

Fig. 5. Solution representation after Synthesis

F. Correction Method

In correction method, the input is solution, S. From the solution vector we get index of character in S_1. Next, we compare the character in position S[i] of S_1 with the character in position, i of S_2, where i = 0, 1…….n-1. If we find same character (character matching) in S_2 and in S_1, then we copy the value of S[i] to output vector, S'[i]. If different character is found (no character matching) then we do forward searching in S_1 starting at the position S[i] +1 to the position S[i+1]-1. If any character in position, j where j ∈ [S[i]+1 to S[i+1]-1] matches with the character in position, i of S_2, the value of j (which is the index value of S_1)is saved to S'[i]. In Fig 6, when i = 1, the character in position 1 of S_1 is C and the character in the same position of S_2 is G. So we do forward searching in S_1. Here S[i] +1 = 2 and S [i+1]-1 = 3, so we perform searching in positions 2 to 3 of S_1. In this case the character in position 3 of S_1 is G, which is same in position 1 of S_2. So we save 3 (position of S_1) to S'[1]. If character matching is not found, then backward searching is to be done in positions S[i]-1 to S [i-1] +1. In backward searching, if we find character matching in position, k of string1 where k ∈ [S [i-1] +1 to S[i]-1]. We save the value of k in S'[i]. In case, there is no character matching in forward searching and also in backward searching the value of S[i] to be copied in S'[i].

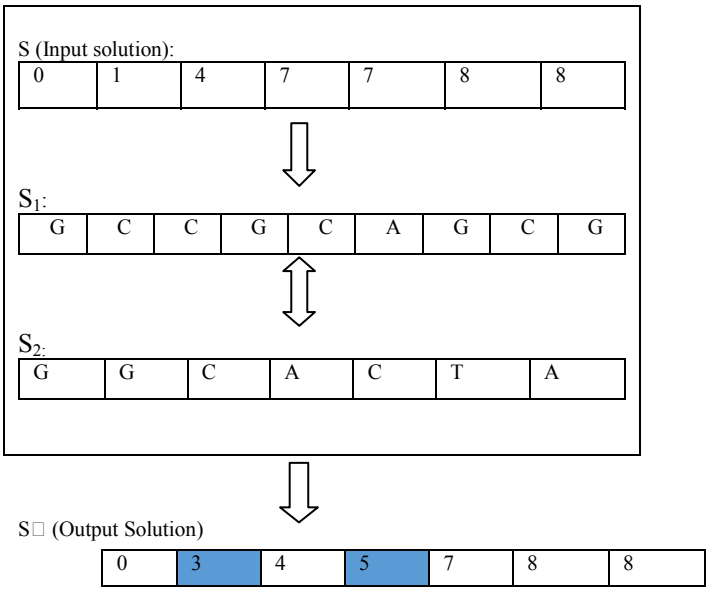

Fig. 6. Solution representation after Correction

V. Simulation Results

We compare proposed CRO method with Dynamic LCS [2] and Fast Dynamic LCS [3] algorithms to show their performances. During the experiments, we have used our own data sets in all test cases. For input string of different length generation different alphabets are used. All times the lengths of both input strings are same. As stated earlier the input sequences are generated randomly. In order to use of same input over and over, different input are used. The following alphabets: {0, 1}, {A, C, G, T} and English alphabet with 26 characters, i.e., {A….Z} or {a…z} are used in order to build input strings. Two strings of certain length are generated randomly based on certain alphabet and used those strings as an input for the algorithm. As we say in section 1(Introduction section) that DNA sequence is consists of A (Adenine), G (Guanine), C (Cytosine) and T (Thymine). For example, the DNA of any organism can be a string S=ACCTGT. So DNA can be expressed as a string that is consists of finite set {A, G, C, T}.

Two strings (S1 and S2) are generated as follows:

S_i= rand [A, G, C, T], i=1, 2, 3,……, n.

Here, rand [A, G, C, T] generates a character from {A, G, C, T} uniformly. The length of the string is n.

In CRO parameters affects its performance. For first testing we set the parameters as initialize PopSize = 10, CollisionRate = 0.2, buffer = 0, KE = 1000, lossRate = 0.1, DecompositionThreshold (α) = 15000 and SysthesisThreshold (β) =10 etc. The decomposition condition and synthesis condition respectively effect by the value of Decomposition Threshold and Systhesis Threshold. We perform 50 runs for each of the chosen values. Among the chosen values the sets of 50 runs are compared and the longest length's sequence is selected. During the experiment, we see that 50 runs for each

of the chosen values is not sufficient for longest String which length is bigger than 1000 or more. Then we need to increase the number of runs such as, 100 or more. We showed the performance of the algorithm in the table.

The test environment is set up on a personal computer with Core i5 CPU at 2.50 GHz CPU, 4G RAM, running on Windows8. Each LCS algorithm was run several times in order to obtain accurate CPU time measurements. System.currentTimeMillis() method was used for obtained the time measurement. It returns current CPU time in milliseconds. All of the algorithms are developed using Java programming language and the process of coding, Eclipse IDE is used.

TABLE I. SIMULATION RESULTS OF CRO

Case 1: Length of string 1 =180, Length of string 2 = 28 , Length of output sequence = 28				
Number of iteration	***Best case***	***Worst case***	***Average***	***Time (ms)***
50	75	57	66	1.09
100	78	50	60	1.24
150	80	48	58	1.30

TABLE II. SIMULATION RESULTS OF CRO

Case 2: Length of string 1 =270, Length of string 2 = 56 , Length of output sequence = 53				
Number of iteration	***Best case***	***Worst case***	***Average***	***Time (ms)***
50	70	58	64	6.92
100	80	50	59	6.94
150	82	40	63	7.00

TABLE III. SIMULATION RESULTS OF CRO

Case 3: Length of string 1 =360, Length of string 2 = 84 , Length of output sequence = 78				
Number of iteration	***Best case***	***Worst case***	***Average***	***Time (ms)***
50	55	53	54	13.60
100	67	48	50	13.80
150	70	30	60	14.00

TABLE IV. SIMULATION RESULTS OF CRO AND OTHER ALGORITHMS

Algorithm	***Length of string1***	***Length of string2***	***Length of output sequence***	***Time(ms)***
LCS	128	28	28	10
FLCS			28	7
CRO			28	**4.32**
LCS	270	56	53	18
FLCS			53	12
CRO			51	**6.96**
LCS	360	84	78	25
FLCS			78	21
CRO			78	**13.98**

VI. CONCLUSIONS

In this paper we have proposed an algorithm to solve longest common subsequence problem based on the concept of chemical reaction optimization. Our main target is to reduce the time complexity of LCS problem and generate an optimal solution. We have compared proposed CRO based method with Dynamic LCS [2] and Fast Dynamic LCS [3] and found that our proposed algorithm has superior performance when compared for all proposed test instances. It reduces the execution time. Here we have used two strings of different lengths. In the future, we will design a CRO algorithm to find LCS for multiple strings.

References

[1] Tabataba, Farzaneh Sadat, and Sayyed Rasoul Mousavi. "A hyper-heuristic for the Longest Common Subsequence problem." *Computational biology and chemistry* 36 (2012): 42-54.

[2] Cormen, Thomas H. *Introduction to algorithms*. MIT press, 2009.

[3] Truong, Tung Khac, Kenli Li, and Yuming Xu. "Chemical reaction optimization with greedy strategy for the 0–1 knapsack problem." *Applied Soft Computing*13.4 (2013): 1774-1780.

[4] Ossman, Mohammed, and Lamiaa Fathi Hussein. "Fast Longest Common Subsequences for Bioinformatics Dynamic Programming." *population* 5 (2012): 7.

[5] Xu, Jin, Albert YS Lam, and Victor OK Li. "Parallel chemical reaction optimization for the quadratic assignment problem." *World Congress in Computer Science, Computer Engineering, and Applied Computing*. 2010.

[6] Chaudhuri, Arindam. "A Dynamic Algorithm for the Longest Common Subsequence Problem using Ant Colony Optimization Technique." *arXiv preprint arXiv:1307.1905* (2013).

[7] Lam, Albert, Jialing Xu, and Victor OK Li. "Chemical reaction optimization for population transition in peer-to-peer live streaming." *Evolutionary Computation (CEC), 2010 IEEE Congress on*. IEEE, 2010.

[8] Pan, Bo, Albert Lam, and Victor OK Li. "Network coding optimization based on chemical reaction optimization." *Global Telecommunications Conference (GLOBECOM 2011), 2011 IEEE*. IEEE, 2011.

[9] Lam, Albert, Victor OK Li, and James JQ Yu. "Real-coded chemical reaction optimization." *Evolutionary Computation, IEEE Transactions on* 16.3 (2012): 339-353.

[10] Lam, Albert, and Victor OK Li. "Chemical reaction optimization for cognitive radio spectrum allocation." *Global Telecommunications Conference (GLOBECOM 2010), 2010 IEEE*. IEEE, 2010.

[11] Xu, Jin, Albert Lam, and Victor OK Li. "Chemical reaction optimization for the grid scheduling problem." *Communications (ICC), 2010 IEEE International Conference on*. IEEE, 2010.

[12] Xu, Jin, Albert Lam, and Victor OK Li. "Chemical reaction optimization for task scheduling in grid computing." *Parallel and Distributed Systems, IEEE Transactions on* 22.10 (2011): 1624-1631.

[13] Xu, Jin, Albert YS Lam, and Victor OK Li. "Stock portfolio selection using chemical reaction optimization." *Proceedings of the international conference on operations research and financial engineering. Paris, France*. 2011.

[14] Yu, James JQ, Albert Lam, and Victor OK Li. "Evolutionary artificial neural network based on chemical reaction optimization." *Evolutionary Computation (CEC), 2011 IEEE Congress on*. IEEE, 2011.

[15] Lam, Albert, and Victor OK Li. "Chemical-reaction-inspired metaheuristic for optimization." *Evolutionary Computation, IEEE Transactions on* 14.3 (2010): 381-399.

EaChOff: Chunk Offset Compression Scheme for High Dimensional Data based on Extendible Multidimensional Array

K. M. Azharul Hasan
Dept. of Computer Science & Engineering
Khulna University of Engineering & Technology
Khulna, Bangladesh
azhasan@gmail.com

Md. Rakibul Islam
Dept. of Computer Science & Engineering
Khulna University of Engineering & Technology
Khulna, Bangladesh
rakibislam04@gmail.com

***Abstract*—Traditional Multidimensional Array (TMA) is an essential data structure for handling large scale multidimensional dataset, but they are not extendible during run time. Another problem for representing the real life data by TMA is that it creates high degree of sparsity. Hence it is important to evolve handy scheme to compress the high dimensional data so that the maintenance becomes easier. To solve these sparsity and dynamic extension problem, we propose a novel scheme namely Extendible Multidimensional Array (EMA) based Chunk Offset Compression Scheme (*EaChOff*). The main idea of *EaChOff* scheme is to linearize each subarray of the EMA independently and break it into chunks for compressing. We evaluated our proposed schemes by comparing compression ratio and range of usability for Chunk-Offset Compression on TMA. The analysis shows that the proposed scheme is efficient if dynamic behavior of the schema is concerned for practical applications.**

Keywords— Multidimensional Array; Extendible Array; database compression; Compression ratio; Chunk offset

I. INTRODUCTION

Traditional Multidimensional Array (TMA) [1] is a superior storage for storing dense data but one main problem is that they are not dynamically extendible. To increase the length of a dimension of the TMA the total restructuring of the array is necessary. Because of sparsity problem TMA wastes huge memory. This is because a large number of array cells are empty in most of the datasets and thus are very hard to use in actual implementation [2][3]. The sparsity problem increases when the number of dimensions is higher. The number of all possible combinations of array cells exponentially increases, whereas the number of actual data values does not increase at such a rate. For Example in an international trade data set there are several dimensions such as importing country, exporting country, date-time, items, measure amount of items etc. But a small number of items are exported from any given country to other countries. The idea of extendible array solves the problem of extendibility. Extendible arrays are combination of subarrays. If the array is n dimensional then the subarrays are n-1 dimensional. Many of the compression schemes based on TMA such as Compressed Row/Column Storage (CRS/CCS) or ECRS [4][5], Chunk-offset Compression [6][7] has been proposed in the literature. One main problem of TMA based compressions schemes are that it is static in nature. This is because, if there is any extension in each dimension in TMA based compression schemes, we need to restore compressed data to its original format and perform the desired extension for the new added data sets. Then the reorganized TMA is compressed by using the compression schemes. So, efficient compression schemes are required to store dynamic sparse data for multidimensional data sets [8][9] without any reorganization and relocation. In this paper, we are going to propose and evaluate a new and efficient compression schemes based on Extendible Multidimensional Array (EMA) [10][11] to manage the problem of extendibility without reorganization of data. The scheme can be applicable to multidimensional database technology such as MOLAP [12] for multidimensional data analysis.

II. CONCEPT OF EXTENDIBLE ARRAY

Consider an n dimensional extendible array A[10][13][14]. Three kinds of auxiliary tables namely *history table* H_i, *address table* L_i, and *coefficient table* C_i are required for each extendible dimension i $(i=1,\ldots,n)$ to extend A in any dimension. See Fig. 1. History tables memorize extension history. h is the history value counter. The value of h is incremented by one for the addition of any subarray in any dimension. An n dimensional extendible array A is the combination of n-1 dimensional subarrays. If the size of A is $[d_1, d_2,\ldots, d_{n-1}, d_n]$ and the extended dimension is i, for an extension of A along dimension i, contiguous memory area that forms an n-1 dimensional subarray S of size $[d_1, d_2 ,\ldots, d_{i-1}, d_{i+1} ,\ldots, d_{n-1}, d_n]$ is dynamically allocated and added to A in dimension i. Then h is incremented by one and the value is memorized in the history table H_i, also the first address of S is held on the address table L_i. S is a usual fixed size array, and the actual data is stored in these subarrays. As is well known, an element $<i_1,i_2,\ldots,i_n>$ in an n dimensional conventional fixed size array of size $[d_1,d_2,\ldots, d_n]$ is allocated on memory using an addressing function and $<d_2d_3\ldots d_n, d_3d_4\ldots d_n,\ldots\ldots, d_n>$ is held in a coefficient table. For example, let A be a four dimensional extendible array whose current sizes are $[d_1, d_2, d_3, d_4]$. If A is extended by one along the dimension two, a three dimensional fixed array S of sizes $[d_1, d_3, d_4]$ is allocated. The addressing function to determine the address of the element $<i_1, i_2, i_3>$ is as: $d_1d_3i_1 + d_3i_2 + i_3$. Here $< d_1d_3, d_3 >$ is called a *coefficient vector*. At every extension of A, the

corresponding subarray's coefficient vector is computed and memorized in *coefficient table* of the extended dimension. In general, if *A* is an *n* dimensional extendible array where *n* is greater than two, an *n-2* dimensional coefficient vectors are required for each extendible dimension.

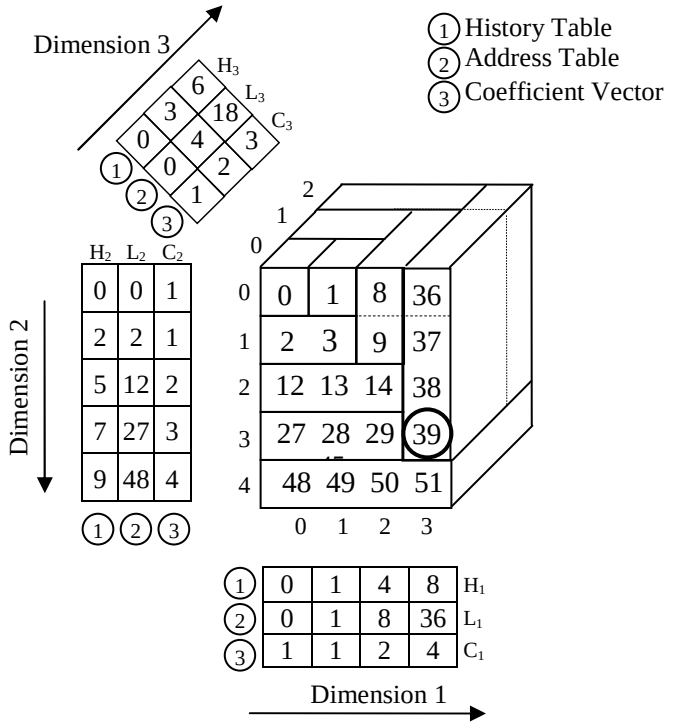

Fig. 1. The realization of extendible array.

Using the stored values of these three kinds of auxiliary tables, the address of an array element can be computed as follows. Consider the element *<3,3,0>* in Fig. 1. Compare $H_1[3] = 8$, $H_2[3] = 7$ and $H_3[0] = 0$. Since $H_1[3] > H_2[3]$, $H_1[3] > H_3[0]$, it can be proved that the element *<3,3,0>* is involved in the extended subarray *S* having history value 8 and beginning address of the corresponding subarray is 36 which is stored in $L_1[3]$. From the coefficient vector of $C_1[3] = < 4 >$, the offset of element *<3,3,0>* from the first address of *S* is computed by $4 \times 0 + 3 = 3$, the address of the element is determined as 39 (See Fig. 1).

III. The Chunk Offset Compression based on Extendible Array

The Extendible Array Based Chunk Offset Compression (*EaChOff*) scheme linearizes each subarray independently and breaks a large multi dimensional extendible array into chunks. This scheme uses one one-dimensional auxiliary table namely $ChunkNo_i$ for each dimension *i* and one one-dimensional integer array *NR*. The chunk number assigned to a subarray is held on the *ChunkNo* table. Array *NR* stores information of nonzero array elements of each subarray. If the number of subarray is *k* in an EMA then *NR* contains *k+1* elements. *NR[0]* contains 1, *NR[1]* contains the summation of the number of nonzero elements in 0th subarray and *NR[0]*. In general, *NR[i]* contains the number of nonzero elements in *(i-1)*th subarray of the EMA plus the contents of *NR[i-1]*.

The number of non zero array elements in the *i*th subarray can be obtained by subtracting the value of *NR[i]* from *NR[i+1]*. This scheme also uses one one-dimensional floating point array *data* and one dimensional integer array *OffsetInChunk* for each chunk of the EMA. Array *data* stores the values of nonzero array elements of each chunk. Array *OffsetInChunk* stores the offset in a chunk of nonzero array elements of each chunk. For each chunk, the base of these two arrays is 0. Among the three kinds of auxiliary tables (*history table, address table, coefficient table*) the *history table* H_i and *address table* L_i are required to store for each dimension. History tables are used to compute the extension dimension of the subarray and the length of other dimension to carry out the linearization computation for that subarray. Address tables are used to point the starting address of each chunk as well as the starting address of each subarray in a chunk.

A part of the *EaChOff* scheme for a three dimensional EMA of Fig. 1 is shown in Fig. 2. For convenience here we name each subarray as *SA_i_j*, where *i* indicate the extended dimension that the subarray belongs to and *j* indicates the length of that dimension. For example, *SA_1_2* is the subarray of dimension 1 of length 2. Forward mapping and backward mapping techniques for the *EaChOff* scheme are described as follows.

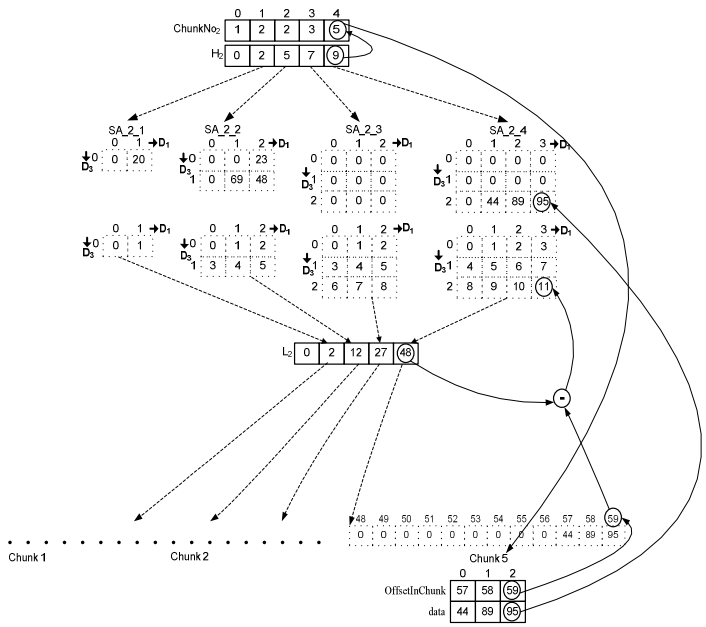

Fig. 2. *EaChOff* realization over EMA

A. Forward Mapping

Consider the element *<3,3,1>* of the EMA. Compare $H_1[3] = 8$, $H_2[3] = 7$ and $H_3[1] = 3$. Since $H_1[3] > H_2[3]$ and $H_1[3] > H_3[1]$, extended dimension is 1 and the element is involved in the subarray *SA_1_3*. $ChunkNo_1[3] = 4$ indicates that we need to access only *chunk4* for the given element. In Fig. 2, the number of nonzero elements of the 9th subarray *SA_1_3* can be found by *NR[9] – NR[8] = 7 – 1 = 6*. The

chunk offset of these 6 nonzero array elements are stored in *OffsetInChunk* array. For computing the logical position of the array element *<3,3,1>*; we consider dimension 2 as $d_1 = 4$, dimension 3 as $d_2 = 3$, second co-ordinate value of the given array element as $p_1 = 3$, third co-ordinate value of the given array element as $p_2 = 1$ and the desired logical position of the given array element can be computed as follows using the *array linearization* function $d_1 p_2 + p_1 = 4 \times 1 + 3 = 7$ (See Fig. 2) Addition of $L_1[3] = 36$ and logical position 7 give the desired chunk offset value 43 for the given array element. Binary search is performed on the *OffsetInChunk* array to find logical position 43 and it can be found that *OffsetInChunk[4]* stores the logical position 43 (since *<3,3,1>* array element is a nonzero array element). Finally the values of the nonzero array element can be found in *data[4]*.

B. Backward Mapping

Consider the physical position *<9,59>* of the physical database; where *<9>* is the history value and *<59>* is the logical index of a nonzero array element in a chunk i.e. *<59>* is the value that *OffsetInChunk* stores. We perform the binary search on the history tables to find the given history value *<9>*. Since *<9>* is stored in $H_2[4]$ (see Fig. 2), we need to access only the *OffsetInChunk* array that is stored for the subarray *SA_2_4* (i.e. subarray extended at dimension 2 at length 4). Therefore the second co-ordinate value of the desired logical array indices is *<4>* in logical database. The linearized column index of the subarray *SA_2_4* can be computed by subtracting the first address ($L_2[4] = 48$) of the subarray from the given logical chunk index i.e linearized column index = 59 – 48 = 11. For computing the first co-ordinate and third co-ordinate value of the desired logical array indices in the logical database from the given physical position *<9,59>*; we consider dimension 1 as $d_1 = 4$, dimension 3 as $d_2 = 3$, first co-ordinate value of the desired logical array indices as q_1, third co-ordinate value of the desired logical array indices as q_2, linearized column index *<11>* as *Y* and the desired logical array indices can be computed as follows using the *reverse array linearization* function

$$q_2 = Y \; mod \; d_2 = 11 \; mod \; 3 = 2$$

$$q_1 = Y/d_2 = 11/3 = 3$$

Hence the physical position *<9, 59>* of physical database is mapped to a logical position *<3,4,2>* in logical database. *EaChOff* compression scheme is mapping complete because it provides forward mapping and backward mapping.

IV. Experimental Results

The parameters are grouped as shown in Table I. Some of these parameters are provided as input, while others are derived from the input parameters. All lengths or sizes are in bytes. We have developed the detail cost model for the schemes for theoretical analysis. We present here the experimental results along with the related equations only. All the mathematical models are also validated by the experiments.

We simulate the compression ratio, retrieval cost for range key query and dynamic extension cost for *ChOff* and *EaChOff* by placing all the arrays both compressed and uncompressed in the secondary storage. The maximum range of data density up to which the compression ratio is less than 1 can be defined as Range of usability of a compression scheme. Among the three auxiliary tables of extendible array, coefficient vector and address table are void and only the history table is required for these schemes. History table acts as an index for locating the subarrays. Thus history tables are stored in main memory for fast access since the sizes of the auxiliary tables are negligible comparing to the main arrays. Table II shows the parameter values used for experimental analysis.

TABLE I. PARAMETERS CONSIDERED FOR EXPERIMENT AND ANALYSIS.

Parameters	Description
UC_{TMA}	The uncompressed size of TMA
UC_{EMA}	The uncompressed size of (EMA)
SC_{EMA}	Compressed size of EMA using the *EaChOff* scheme
SC_{TMA}	Compressed size of TMA using the *Chunk-Offset* Compression scheme
η_{ChOff}	Compression ratio for the *Chunk-Offset* Compression scheme for TMA; $\eta_{ChOff} = \frac{SC_{ChOff}}{UC_{TMA}}$
$\eta_{EaChOff}$	Compression ratio for the *Chunk-Offset* Compression scheme for EMA; $\eta_{EaChOff} = \frac{SC_{EaChOff}}{UC_{EMA}}$
n	Number of dimension of both TMA and EMA
L_i	Length of each dimension i ($0 \le i \le n$) for both the TMA and EMA
l	Length of Chunk for the TMA
ρ	Density of records both for TMA and EMA;
α	Size of subscripts for TMA and EMA
β	Size of a cell of the TMA and EMA
δ	Length extended along a dimension
$sz_i(k)$	Size of subarray k along dimension i

TABLE II. THE VALUES OF THE PARAMETERS CONSIDERED FOR EXPERIMENTAL ANALYSIS.

L	δ	ρ	α	β	n	l
10 - 40	5	0.10 ~ 0.70	4	8	5	4-16

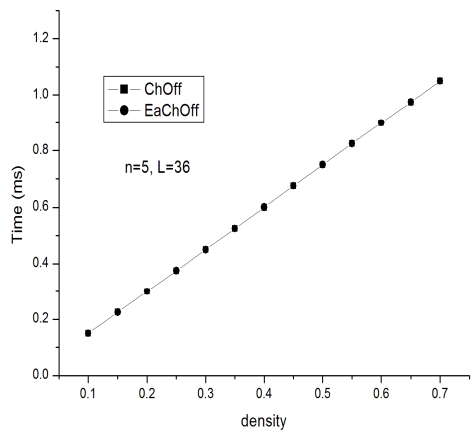

Fig. 3. Compression ratio comparison between *ChOff* and *EaChOff*.

Fig. 3 shows the compression ratio η_{ChOff} and $\eta_{EaChOff}$ having parameter values shown in Table II. It shows that the

compression ratio is almost same for both the schemes. This is because the compression ratio is characterizes as follows

$$\eta_{ChOff} = \frac{2\times\frac{L^n}{l^n}\times\alpha+\rho L^n\times\alpha+\rho L^n\beta}{L^n\times\beta} \text{ and}$$

$$\eta_{EaChOff} = \frac{[2\times\{(L-1)\times n+1\}+\left(\sum_{i=1}^{hc} sz_i(k)\times\rho\right)]\times\alpha+\left(\sum_{i=1}^{hc} sz_i(k)\times\rho\right)\times\beta}{L^n\times\beta}$$

For $\eta_{EaChOff}$, $\sum_{i=1}^{hc} sz_i = L^n$ and hence both the scheme becomes similar. The range of usability is also the same as the condition for range of usability (i.e. the compression ratio is less than 1) is $\rho < \beta/(\alpha+\beta)$ for both *ChOff* and *EaChOff*. Fig. 4 shows the retrieval comparison between EMA without comparison and *EaChOff*, *ChOff* scheme with varying ρ. The improvement with compressed form and non compressed form is huge. Hence the importance compressing sparse arrays is evident. Fig. 4 also shows the retrieval cost for both the schemes. The retrieval cost is little higher for the proposed *EaChOff* scheme than the *ChOff* and hence it is less efficient for retrieval. This is because the data stored in *ChOff* over a single stream but the data stored in *EaChOff* is in different subarrays and each subarray is necessary to search using the history values.

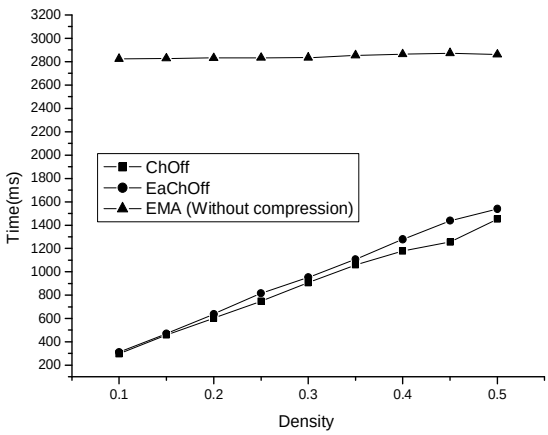

Fig. 4. Retrieval cost comparison between *ChOff* and *EaChOff*.

Fig. 5 shows the dynamic extension cost for both the systems. The *EaChOff* is very efficient than *ChOff* scheme. This is because the EMA based *EaChOff* is dynamically extendible without reorganizing the existing data but TMA is static in nature and reorganization is necessary. For extending TMA, it requires to reorganize the array and rewrite both existing and new data elements. The existing elements of the initial array need to be fetched and recalculate the new offsets due to the extension for TMA. Hence the extension cost for *ChOff* is the summation of fetched cost and reallocation cost. On the other hand the *EaChOff* is based on EMA and reallocation is not necessary and extension cost for *EaChOff* is allocation subarrays only. The extension cost is dependent on the initial volume (the volume before extension i.e., L^n) of the array. If L increases then the extension cost increases and hence the extension gain. The extension gain is defined as the difference between extension cost of *ChOff* and extension cost of *EaChOff*. The extension gain of EaChOff over *ChOff* is shown in Fig. 6. As L increases the extension gain increases. Finally we conclude that with very little retrieval penalty we can achieve huge extension gain if we use the proposed *EaChOff* scheme. The proposed scheme is efficient when dynamic nature of an array is a concern.

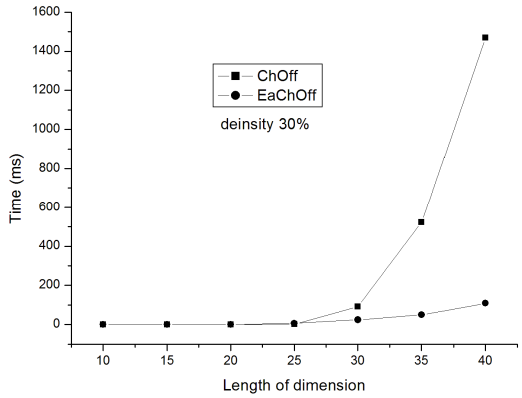

Fig. 5. Dynamic extension cost comparison between *ChOff* and *EaChOff*.

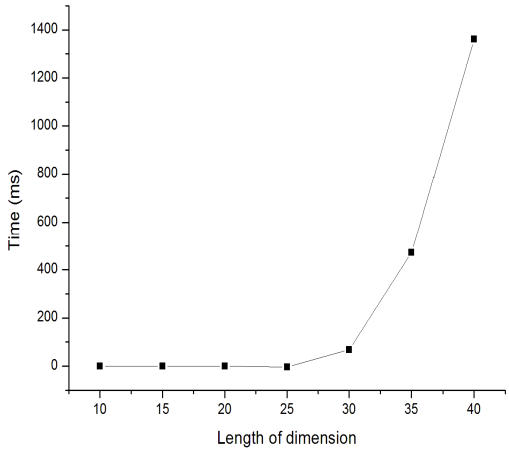

Fig. 6. Extension gain of *EaChOff* over *ChOff*.

V. RELATED WORKS

Many schemes have been proposed in the literature for storing sparse array but most of them are based on TMA [4]-[6]. The Chunk-offset compression scheme, the large multidimensional arrays are broken into chunks, is based on chunking of higher dimensional arrays [22][24] and is well addressed in the literature [6][9][12][18]. To compress the array, a pair <ChunkNumber, OffsetInChunk> is stored for each valid entry. But the main array is static in nature and dynamic reorganization is impossible. There are some compression schemes such as *EaCRS* [14], SCEKA [15], where dynamic extension possible. The *EaCRS* scheme [14] which is the dynamic version of CRS [5] supports for n dimension but it requires n one dimensional arrays to store and hence compression ratio is less for large n. SCEKA is based on EKA [11][16], a new extendible array system, but its performance degrades for large n (n>4) because EKA becomes a hierarchical structure for n>4. The history offset compression [3] [8] scheme is based on EMA. An element is specified

using the pair< history value, offset> value of the extendible array. But the offset value will be very large and will overflow the address space when the EMA is large even for 64 bit machines. The ECRS (or ECCS) [4] scheme compresses all the nonzero array elements along rows (columns for ECCS). But it is based on TMA and dynamic and dynamic extension is impossible. Hilbert curve [19] based compression scheme is proposed in [20] for TMA and dynamic extension of the dimension size is not considered.

VI. CONCLUSION

Over the years with atomization more and more systems deployed in industries are generating huge amount of data. Since they can be very large; must be stored and retrieved in an efficient way. Many scientific applications extensively use multidimensional array to represent their data for efficient processing. However in many cases the total number of data or dimension cannot be predicted beforehand. Besides this, representing the real world data in multidimensional array creates a very sparse array. Compressing the data has many advantages. In this paper, we managed both sparsity and the dynamic extension problem by presenting database compression schemes based on EMA. Since *EaChOff* scheme is based on an extendible multidimensional array system and compression scheme is applied for each subarray independently, such an array can extend its size dynamically along an arbitrary dimension without any relocation of existing data. Our evaluation shows that the proposed compression scheme has advantages when dynamic extension is important. One important application area is that the scheme can be used for big data technology. Specifically the velocity of data can be managed by the proposed *EaChOff*. One important future direction of the work is that the scheme can easily be implemented in parallel platforms. Because most of the operations described here are independent of each other, it will be very efficient to apply this scheme in parallel and multiprocessor environments.

REFERENCES

[1] S. Sarawagi and M. Stonebraker, “Efficient Organization of Large multidimensional Arrays”, in Proc. of 10th International Conference on Data Engineering, 1994, pp. 328–336.

[2] R. Acker, R. Pieringer, and R. Bayer, “Towards Truly Extensible Database Systems”, in Proc. of DEXA, LNCS, Vol. 3588, pp. 596–605, 2005

[3] K. M. Azharul Hasan, M. N. Azuma, T. Tsuji, and K. Higuchi, “An Extendible Array Based Implementation of Relational Tables for Multidimensional Databases”, in Proc. of DaWak, LNCS, Vol. 3580, pp. 233–242, 2005.

[4] Chun-Yuan Lin, Yeh-Ching Chung, Jen-Shiuh Liu, "Efficient Data Compression Methods for Multidimensional Sparse Array Operations Based on the EKMR Scheme," IEEE Transactions on Computers, Vol. 52, No. 12, pp.1640-1646, 2003.

[5] R. Barret, M. Berry, T. F. Chan, J. Dongara, V. Eljkhhout, R. Pozo, C. Romine and H. Van, “Templates for the solution of linear systems: Building blocks for the iterative methods,” second ed. SIAM, 1994.

[6] Y. Zhao, P. M. Deshpande, and J. F. Naughton, "An array based Algorithm for simultaneous multidimensional aggregates," ACM SIGMOD, pp. 159-170, 1997.

[7] K. M. Azharul Hasan, “Compression Schemes of High Dimensional Data for MOLAP”, In the Edited Book, "Evolving Application Domains of Data Warehousing and Mining: Trends and Solutions” Chapter IV, Information Science Reference, pp. 64-81, 2009.

[8] K M Azharul Hasan, Tatsuo Tsuji, Ken Higuchi “A Parallel Implementation Scheme of Relational Tables Based on Multidimensional Extendible Array” International Journal of Data warehousing and Mining, 2: 4. pp.66-85, 2006.

[9] J. Li and J. Srivastava, “Efficient Aggregation Algorithms for Compressed Data Warehouses”, IEEE Transaction on Knowledge and Data Engineering, Vol. 14, No. 3, pp. 515–529, 2002.

[10] E. J. Otoo, and T. H. Merrett, “A Storage Scheme for Extendible Arrays”, Computing, Vol. 31, pp. 1–9, 1983.

[11] Sk. Md. Masudul Ahsan, K. M. Azharul Hasan, “An Implementation Scheme for Multidimensional Extendable Array Operations and Its Evaluation”, in Proc. of ICIEIS 2011, pp. 136–150, 2013.

[12] K. M. Azharul Hasan, T. Tsuji, and K. Higuchi, “An Efficient Implementation for MOLAP Basic Data Structure and Its Evaluation”, in Proc. of DASFAA , LNCS 4443, pp. 288 – 299, 2007.

[13] E. J. Otoo, H. Wang, G. Nimako, "New Approaches to Storing and Manipulating Multi-Dimensional Sparse Arrays" , Proc. of SSDBM'l 4, pp. 2014.

[14] Md. Rakibul Islam, K M Azharul Hasan, Tsuji, Tatsuo, “LEaCRS: An Extendible Array Based Compression Scheme for High Dimensional Data using Linearization,” in Third International Conference on Advances in Computing and Communications, p. 312-315, 2013.

[15] Sk. Md. Masudul Ahsan, K. M. Azharul Hasan, "Segment Oriented Compression Scheme for MOLAP Based on Extendible Multidimensional Arrays", Journal of Computing and Information Technology(CIT), 23(2). pp. 111-121, 2015.

[16] K. M. Azharul Hasan, Kamrul Islam, Mojahidul Islam, Tatsuo Tsuji, “An Extendible Data Structure for Handling Large Multidimensional Data Sets,” in Proc. of the ICCIT 2009, pp. 669-674, 2012.

[17] Md Abu Hanif Shaikh, K M Azharul Hasan, “ Efficient Storage Scheme for n-Dimensional Sparse Array: GCRS/GCCS” in Proc. of International Conference on High Performance Computing & Simulation, pp. 137-142, 2015.

[18] Doug Burdick, Prasad M Deshpande, TS Jayram, Raghu Ramakrishnan, Shivakumar Vaithyanathan OLAP over uncertain and imprecise data, The VLDB Journal, 16 (1), pp. 123-144, 2007.

[19] J. K. Lawder, P. J. H. King, Querying multidimensional data indexed using the Hilbert spacefilling curve. *ACM SIGMOD Record*, **30**(1), pp. 19–24, Mar. 2001.

[20] T. Eavis, D. Cueva, “A Hilbert Space Compression Architecture for Data Warehouse Environments,” in *Proceedings of 9th nternational Conference on Data Warehousing and Knowledge Discovery*, pp. 1–12, 2007.

A Low Hop Distance Hierarchical Interconnection Network

Muhammad Hafiz Sohaini*, M.M. Hafizur Rahman*, Rizal Mohd Nor*, Tengku Mohd Tengku Sembok†, M. A. H. Akhand‡, and Yasushi Inoguchi‖
*Dept. of Computer Science, KICT, IIUM, Jalan Gombak, 53100, Kuala Lumpur, Malaysia
E-mail: hfzshn@gmail.com, hafizur@iium.edu.my, rizalmohdnor@iium.edu.my
†Cyber Security Center, National Defense University Malaysia, Kuala Lumpur 57000, Malaysia
E-mail: tmtsembok@gmail.com
‡Dept. of Computer Science and Engineering, KUET, Khulna - 9203, Bangladesh
E-mail: akhandkuet@yahoo.com
‖Research Center for Advanced Computing Infrastructure, JAIST, Nomi-Shi, Ishikawa 923-1292, Japan
E-mail: inoguchi@jaist.ac.jp

***Abstract*—In this paper, we have proposed a new hierarchical interconnection network called Tori-connected Flattened Butterfly Network (TFBN). It is a hierarchical interconnection network which is able to interconnect millions of nodes in the network to achieve high performance and cost-effective design for massively parallel computing system. TFBN consists of multiple basic modules of flattened butterfly network whereby the basic modules are connected using 2D-torus network. This paper focuses on the architecture of the TFBN and the evaluation of its static network performance such as degree, diameter, cost, average distance, arc connectivity, bisection width and wiring complexity. The comparison of performance shows better performance in terms of distance parameters as well as other parameters.**

Keywords*—*Massively Parallel Computer, Hierarchical Interconnection Network, TFBN, Static Network Performance.

I. Introduction

The demand of computational power will never stop. It will increase day by day. To solve the existing and forthcoming computational challenging problems we need tremendous computation power. And to meet this demand we need parallel computers consisting of millions of nodes, called massively parallel computer (MPC) systems [1]. Interconnection network to connect these huge number of nodes plays a crucial role in determining the overall performance of the MPC systems. The diameter is very large for the conventional topologies with these huge number (millions) of nodes [2], [4]. To construct MPC systems consisting of such huge nodes, Optimal Diameter-Degree (ODD) network is essential for the reliability. Hierarchical interconnection network is a plausible alternative way in which several networks can be interconnected together to have an interconnection network which gives good performance in all aspect [3].

In searching of ODD hierarchical interconnection network, we have proposed midimew connected mesh network (MMN) [5]. However, long diagonal links makes the routing algorithm complex and long length in VLSI realization [6]. It is known that the bandwidth exponentially increased in the last two decades, and the additional bandwidth can be efficiently used in high degree interconnection networks [7]. A good interconnection network is designed around the capabilities and constraints of available technology. Increasing router pin bandwidth, for example, has motivated the use of high-radix routers [8] in which the increased bandwidth is used to increase the number of ports per router, rather than maintaining a small number of ports and increasing the bandwidth per port. The Cray BlackWidow vector multiprocessor [9] is the best example of high-radix network. On the other hand, high degree network significantly increase the number of narrow links which in turns reduces the diameter of an interconnection network [10]. Thus, ODD interconnection network is achievable in this way. This is the key motivation to re-investigate our previously proposed MMN to avoid the problem of routing complexity.

With this motivation, we have replaced the 2D-mesh basic module of of a MMN by a flattened butterfly network. We have considered higher level network as 2D-torus network to reduce the number of long links. Also torus network has higher inter-node communication performance than mesh network [11]. In this paper, we proposed a new hierarchical interconnection network consisting of basic modules with the combination of flattened butterfly network and torus network. A Tori-connected Flattened Butterfly Network (TFBN) is a hierarchical interconnection network made up of multiple basic modules whereby the basic module is a flattened butterfly network and they are interconnected as torus network to form higher level interconnection in a hierarchical fashion. Analogous to the MMN, we called it **T**ori-connected **F**lattened **B**utterfly **N**etwork (**TFBN**).

The organization of the rest of this paper is as follows. In Section II, we explain the basic architecture of the TFBN. Addressing of nodes and message routing in the TFBN are discussed in Section III. The evaluation of static network performance of the TFBN is discussed in Section IV. Finally, Section V presents the conclusion of this paper.

II. Interconnection of the TFBN

A TFBN is a hierarchical interconnection network made up of multiple basic modules (BMs) where the BM is consisting of a flattened butterfly network in a 2D-grid $(2^m \times 2^m)$ of 2^{2m} nodes having 2^m rows and 2^m columns. Here m is a positive

integer. m could be any value however, the preferable one is $m = 2$ for better granularity. Therefore, considering $m = 2$, a BM of size (4×4) is portrayed in Figure 1. At the contours of the BM, there are 2^{m+2} number of free ports which are used for higher level interconnection. The free ports are used for higher level interconnection as they are defined and depicted in Figure 1. Basic module is considered as a Level-1 network.

Higher level networks are constructed by recursively interconnecting (2^{2m}) immediate lower networks as sub-net modules in a $(2^m \times 2^m)$ torus network. Considering $(m = 2)$, a Level-2 TFBN can be constructed by interconnecting $2^{2\times 2} = 16$ Level-1 TFBN, a Level-3 TFBN can be constructed by interconnecting 16 Level-2 TFBN, and so on. This phenomenon is illustrated in Figure 2. To avoid clutter, the wraparound links of the BMs are not shown. A BM uses $4 \times (2^q) = 2^{q+2}$ of its free links, $2(2^q)$ free links for vertical interconnections and $2(2^q)$ free links for horizontal interconnections. A new parameter q,$q \in \{0, 1, ..., m\}$,, is called inter-level connectivity. $q = 0$ is the minimal inter-level connectivity, while $q = m$ is the maximum inter-level connectivity. Basic modules with same co-ordinate positions are connected to form a respective higher-level network using the respective assigned free links.

Figure 2 illustrated a (4×4) basic module considering $m = 2$ and it has $2^{2+2} = 16$ free ports. Considering $q = 0$, $4(2^0) = 4$ free ports are used for every higher level interconnection, half of them (2) for horizontal and the other half (2) for vertical interconnection. One incoming and one outgoing links are tied together to form a b-direction links to connect two adjacent basic modules to for higher level networks. Vertical_in & vertical_out links are together to vertical links and horizontal_in & horizontal_out links are tied together to for horizontal links.

Considering level of hierarchy L along with m and q, TFBN is represented as $\mathrm{TFBN}(m, L, q)$. It is constructed using $2^m \times 2^m$ BMs with L levels of hierarchy and q inter-level connectivity. In this paper, we have considered $m = 2$, the best granularity. Therefore, we focus on $\mathrm{TFBN}(2, L, q)$ networks. The maximum possible level of hierarchy, L_{max}, of a TFBN can be constructed using $(2^m \times 2^m)$ BM is $L_{max} = 2^{m-q} + 1$. For example, with $q = 0$ and $m = 2$ $L_{max} = \left(2^{2-0} + 1\right) = 5$. Level-5 is the highest possible level of TFBN can be constructed using the interconnection of (4×4) BM and its associated free ports and links. The total number of nodes of a Level-L TFBN is $N = 2^{2mL}$. The largest number of nodes can be interconnected by a TFBN(m, L, q) using maximum level of hierarchy, $L_{max} = (2^{m-q} + 1)$, is $N = 2^{2m(2^{m-q}+1)}$. It means with $m = 2$ and $q = 0$ more than 1 million nodes can be interconnected together to form a massively parallel computer systems.

III. Addressing of Nodes and Routing of Messages in TFBN

A. Addressing of Nodes

As seen in Figure 1, nodes in the networks are addressed by two digits, the first representing the row index and the next representing the column index. More generally, in a Level-L TFBN, the node address is represented by:

$$\begin{aligned} A &= A^L A^{L-1} A^{L-2} \ldots \ldots \ldots A^2 A^1 \\ &= a_{n-1} a_{n-2} a_{n-3} \ldots \ldots \ldots a_2 a_1 a_0 \\ &= a_{2L-1} a_{2L-2}\ a_{2L-3} a_{2L-4} \ldots \ldots \ldots a_3 a_2\ a_1 a_0 \\ &= (a_{2L-1}\ a_{2L-2})\ (a_{2L-3}\ a_{2L-4})\ \ldots \ldots \\ &\quad \ldots \ldots \ldots (a_3\ a_2)\,(a_1\ a_0) \end{aligned} \tag{1}$$

Here, the total number of digits is $n = 2L$, where L is the level number. A^L is the address of level L and $(a_{2L-1} a_{2L-2})$ is the co-ordinate position of Level-$(L - 1)$ for Level-L network. Pairs of digits run from group number 1 for Level-1, i.e., the BM, to group number L for the L-th level. Specifically, l-th group $(a_{2l-1}\ a_{2l-2})$ indicates the location of a Level-$(l - 1)$ sub-network within the l-th group to which the node belongs; $1 \leq l \leq L$. In a two-level network the address becomes $A = (a_4\ a_3)\ (a_1\ a_0)$. The pair of digits $(a_4\ a_3)$ identifies the basic module to which the node belongs, and the pair of digits $(a_1\ a_0)$ identifies the node within that basic module.

The assignment of inter-level ports for the higher level networks has been done quite carefully so as to minimize the higher level traffic through the BM. The address of a node n^1 encompasses in BM_1 is represented as $n^1 = \left(a^1_{2L-1} a^1_{2L-2} \ldots \ldots \ldots a^1_3 a^1_2\ a^1_1 a^1_0\right)$. The address of a node n^2 encompasses in BM_2 is represented as $n^2 = \left(a^2_{2L-1} a^2_{2L-2} \ldots \ldots \ldots a^2_3 a^2_2\ a^2_1 a^2_0\right)$. The node n^1 in BM_1 and n^2 in BM_2 are connected by a link if the following condition is satisfied.

$$\begin{aligned} &\exists i \{a^1_i = (a^2_i \pm 1) \bmod 2^m \\ &\wedge \forall j (j \neq i \ \rightarrow\ a^1_j = a^2_j)\} \qquad \text{where } i, j \geq 2 \end{aligned} \tag{2}$$

B. Routing Algorithm for TFBN

The nodes communicate data and coordinate their efforts by sending and receiving messages in the supercomputer using a routing algorithm. The routing algorithm specifies how a message selects its network path to traverse from source to destination. Efficiency of message routing and simplicity of router design in crucial to the performance and acceptance of interconnection network for massively parallel computer systems.

Tori-connected Flattened Butterfly Network is a hierarchical network, hence the routing of message will take place in hierarchically in three phases, named Phase-1, Phase-2, and Phase-3. Same coordinate positions of the sub-network modules are used to form the higher level network. First of all in the Phase-1, routing will taken place in the source basic module, and the packet reach to the outlet port of the highest level network from the packet generated source node. Then routing will take place for inter-BM communication at the highest level network. After reaching the packet to its highest level sub-destination, routing continues within the sub-net modules to the next lower level sub-net destination. This process is repeated until the packet arrives at its final destination basic module [12]. This is known as Phase-2 routing. Finally in the Phase-3, the routing of packet will take place from the inlet free-port of the destination basic module to the destination itself. Actually, Phase-1 and Phase-3 routing

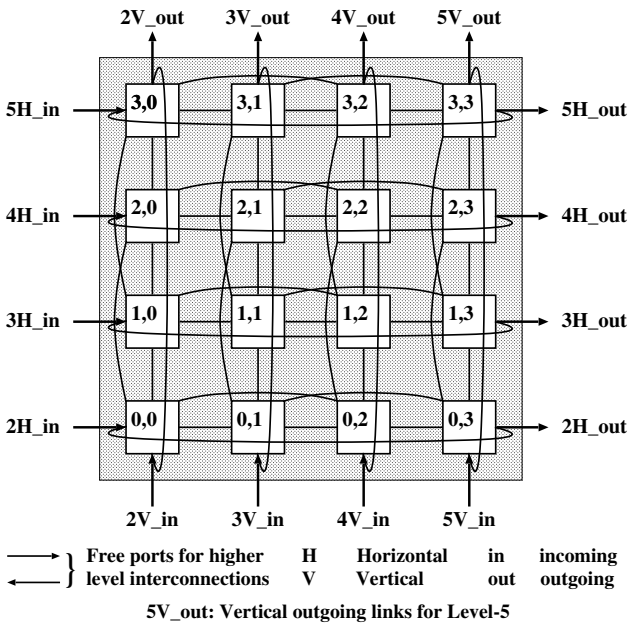

Fig. 1. Basic Module of a Tori-connected Flattened Butterfly Network

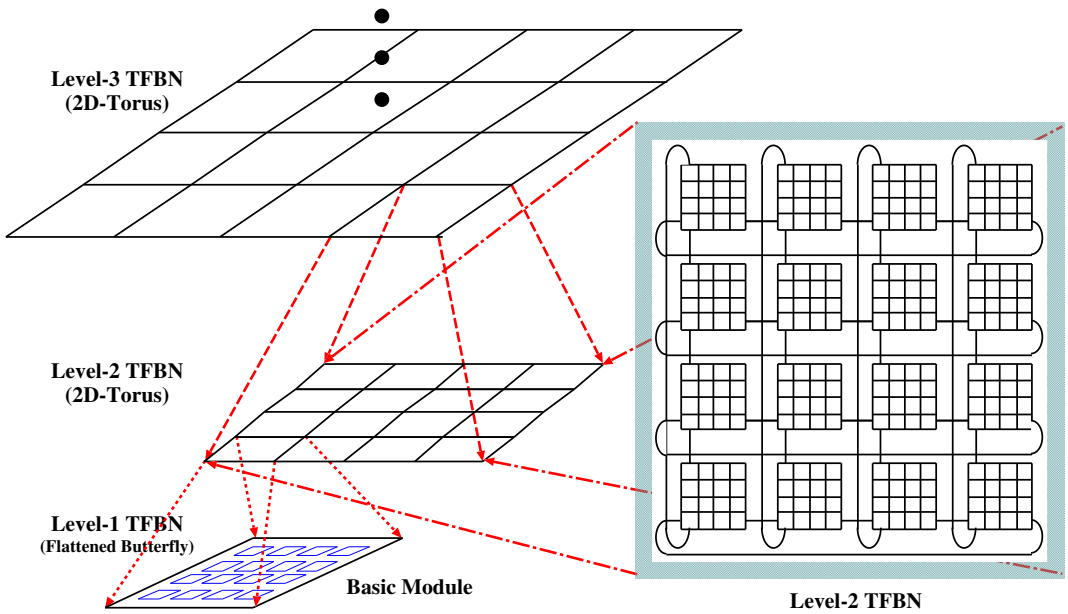

Fig. 2. Higher level network of a Tori-connected Flattened Butterfly Network

are very similar, intra-BM routing. One is in the source-BM and another one is in the destination-BM.

For the simplicity of message routing we have used simple deterministic dimension-order routing. Routing is performed first in the vertical direction and then in the horizontal direction. After generating packet in the source node, it will check its destination. If the packet's source and destination are in the same basic module then the routing is performed within the BM only. That is, only Phase-1 routing will be taken place. If the packet is destined to another basic module then the source node sends the packet to the outlet node which connects the basic module to the level at which the routing is performed. In this case all three phases of routing will be taken place.

IV. Static Network Performance

The performance of a massively parallel computer systems is crucially dependent on its underlying interconnection network. The real performance such as inter-node communication performance, fault-tolerant performance, network-on-chip realization, computational intensive application mapping, etc. depends on technology and physical implementation. However, some static parameters such as degree, diameter, average distance, arc connectivity, bisection width, and wiring complexity are used evaluate the interconnection network using technology

TABLE I. STATIC NETWORK PERFORMANCE OF DIFFERENT INTERCONNECTION NETWORKS

Network	Degree	Diameter	Average Distance	Arc Connectivity	Bisection Width	Wiring Complexity
2D-Mesh	4	30	10.67	2	16	480
2D-Torus	4	16	8.00	4	32	512
TESH(2,2,0)	4	21	10.47	2	8	416
TTN(2,2,0)	6	15	7.44	4	8	544
MMN(2,2,0)	4	17	9.07	2	8	416
TFBN(2,2,0)	8	10	5.75	4	8	800

independent graph theoretic model. These static parameters have a candid impact network actual performance. We have considered 2D-mesh, 2D-torus, TESH [13], TTN [14], MMN [6], and our proposed TFBN for the performance comparison.

A. Node Degree

In a massively parallel computer systems nodes are connected using links to form an interconnection network. Every nodes are connected to some other nodes. The number of physical links emanating from a node is called the degree of a node. The maximum degree of all nodes is called the degree of a network. Basically this maximum value is used as degree to implement the router. Here, the degree of the proposed TFBN is 8 and it is constant. For the scalability of a network constant node degree is very much needed because cost of router remains unchanged even the network scaled up.

Input-output interface cost of a node is directly related to its degree. The degree of TFBN is 8 as shown in Table I. a bit higher than that of other networks. However, it is not a problem because enormous bandwidth of a link. As mentioned earlier in the recent technology, it is desired to use high degree node and thin links for more efficient use if this bandwidth for the performance improvement.

B. Diameter

The actual distance between two nodes is the length of a link which connect themselves. However, the logical distance between them is one hop. A low hop distance is very important for the inter-node communication performance. The maximum number of hops that must be traversed to send a packet from a source to the destination among all distinct pairs of nodes along the shortest path according to the devised routing algorithm is called the diameter of an interconnection network. Static distance parameter diameter and average distance are widely used to compare the static network performance of different interconnection networks.

The latency depends upon the bandwidth, routing algorithm, and message congestion in the network. However, diameter gives an idea about the upper-bound of zero load latency of any interconnection network. In this regard, low diameter is preferable. We have evaluated the diameter of the conventional mesh and torus networks using their respective formula. Also, we have evaluated the diameter of the hierarchical TESH network, TTN, MMN, and TFBN using computer simulation. All the results are tabulated in Table I. It is clearly portrayed that the diameter of the TFBN is far lower than that of the other conventional and hierarchical networks

C. Average Distance

The average number of hops between all distinct pairs of nodes along the shortest path according to the devised routing algorithm is called the average distance of an interconnection network. It has a direct impact on the average message transfer latency. That is, low average distance indicates that the respective network will result less inter-node communication latency in terms of cycle. As like the diameter, we have calculated the average distance of conventional mesh and torus network by their respective formula and evaluated the average distance of TESH network, TTN, MMN, and TFBN by simulation. In this simulation we have evaluated the hop distance of all distinct pairs of nodes along the shortest using the routing algorithm described earlier. The maximum value and the average value are called the diameter and average distance, respectively. From the tabulated average distance for different networks in Table I, it is clearly shown that the average distance of the TFBN is far lower than that of other conventional and hierarchical networks.

D. Arc Connectivity

The resilient of an interconnection network is measured statically by the arc connectivity. The minimum number of links that must be cut to partition the network into two disjoint parts is known as arc connectivity. Though the real fault tolerance performance depends on the reconfiguration by redundant resources or routing algorithm, however, the ratio between the arc connectivity and the node degree is used to characterize the static fault tolerance performance of of an interconnection network. If the arc connectivity and node degree are same for any interconnection network, then the network will be best resilient and robust. As shown in Table I, torus is maximum fault tolerant. The static fault tolerance performance of a TFBN is equal to that of mesh, TESH, and MMN and a little bit lower than that of TTN.

E. Bisection Width

The minimum number of links that must be cut to partition the network into two exactly equal halves is called bisection width. A group of nodes in a parallel computer work together and the various data are hordes among the nodes. Small bisection width creates the congestion in the middle of the network for both uniform and non-uniform traffic patterns. on the other hand, large bisection width creates problems in the VLSI realization. Therefore moderate bisection width is preferable. As depicted in Table I, all the hierarchical interconnection network have same bisection width and it is less than that of convention mesh and torus network.

F. Wiring Complexity

The total number of links needed to connect all the nodes of an interconnection network is known as wiring complexity. It has direct impact on hardware implementation cost and complexity. A (16×16) 2D-mesh and 2D-torus networks have $\{N_x \times (N_y - 1) + (N_x - 1) \times N_y\} = 16 \times (16 - 1) + (16 - 1) \times 16 = 480$ and $(2 \times N_x \times N_y = 2 \times 16 \times 16) = 512$ links, respectively. N_i represents the number of nodes/ switches in the ith dimension. The wiring complexity of a Level-L TESH, TTN, MMN, and TFBN networks is $\left[\# \text{ of links in a BM} \times k^{2(L-1)} + \sum_{x=2}^{L} 2(2^q) \times k^{2(L-1)}\right]$. Here $k = 2^m$ is the number of nodes/sub-net modules in one direction.

Considering, $m = 2$, a basic module of a MMN and TESH network have 24 links, a TTN has 32 links, and a TFBN has 48 links. Hence, considering $q = 0$, the total number of links of a Level-2 TESH, TTN, MMN, and TFBN are 416, 544, 416, 800, respectively and these values are tabulated in Table I. Clearly, the cost in term of wire is a bit high for the TFBN. However, this extra cost of small length links in the basic module yields a promising result in the distance parameters, diameter and average distance. Even only Level-2 of hierarchy results thriving hop distance both maximum and average. We are expecting more better result in more levels of hierarchy.

V. Conclusion

A new hierarchical interconnection network, called **T**ori-connected **F**lattened **B**utterfly **N**etwork (**TFBN**), is proposed for the low hop distance MPC systems. The architectural structure, node addressing, message routing, and the evaluation of static network performance are discussed in details. From the static network performance it is seen that the diameter and average distance are quite lower than that of other network. TFBN also possesses other lucrative properties such as features moderate (neither too high nor too low) bisection width and good fault tolerance performance with the cost of some extra short length links than that of other networks. However, use of links is not a demerits for the enormous available bandwidth. Therefore TFBN is an incredible hierarchical interconnection network for the future generation massively parallel computers.

The research presented in this paper is a very first stage of this work. Issues for future work includes: (1) evaluation of static network performance of higher level TFBN [15] and (2) evaluation of dynamic communication performance of a TFBN using deadlock-free dimension order routing algorithm [16].

Acknowledgment

This research is supported by the project FRGS13-065-0306, Ministry of Education, Government of Malaysia. The authors would like to thank the anonymous reviewers for their constructive comments and suggestions on the paper which have helped to improve the quality of the paper.

References

[1] B.S.P. Mishra and S. Dehuri, Parallel Computing Environments: A Review, *IETE Technical Review*, Vol. 28, No. 3, pp. 240-247, 2011.

[2] V. Puente, J.A. Gregorio, R. Beivide and F. Vallejo, A Low Cost Fault Tolerant Packet Routing for Parallel Computers, *Proceedings of the 17th IEEE/ACM International Parallel and Distributed Processing Symposium (IPDPS)*, April, 2000.

[3] M. Abd-El-Barr and T.F. Al-Somani, Topological Properties of Hierarchical Interconnection Networks: A Review and Comparison, *Journal of Electrical and Computer Engineering*, Hindawi Publishing Corporation, Vol. 2011, 12 pages.

[4] P. Beckman, Looking Toward Exascale Computing, *Keynote Spech. International Conference on Parallel and Distributed Computing, Applications and Technologies (PDCAT08)*, Dunedin, New Zealand, December 2008.

[5] Md. Rabiul Awal, M.M. Hafizur Rahman, and M. A. H. Akhand, A New Hierarchical Interconnection Network for Future Generation Parallel Computer, *Proceedings of the 16th International Conf. on Information and Communication Technology (ICCIT)*, pp. 314-319, 2014.

[6] Md. Rabiul Awal, M. M. Hafizur Rahman and Rizal Mohd Nor, TMT Sembok, M.A.H. Akhand, Architecture and Network-on-Chip Implementation of a New Hierarchical Interconnection Network, *Journal of Circuits, Systems, and Computers*, Vol. 24, No. 2, 2015.

[7] John Kim, William J. Dally, Dennis Abts, Flattened Butterfly : A Cost-Efficient Topology for High-Radix Networks, *Proceedings of the 34th Annual International Symposium on Computer Architecture (ISCA)*, pp. 126-137, 2007.

[8] John Kim, William J. Dally, Steve Scott, Dennis Abts, Technology-Driven, Highly-Scalable Dragonfly Topology, *Proceedings of the 35th Annual International Symposium on Computer Architecture (ISCA)*, pp. 77-88, 2008.

[9] S. Scott, Dennis Abts, John Kim, and William J. Dally, The Black-Widow High-radix Clos Network, *Proceedings of the 33rd Annual International Symposium on Computer Architecture (ISCA)*, pp. 16-28, Boston, MA, USA, 2006.

[10] J. Kim, W. J. Dally, B. Towles, and A. K. Gupta, Microarchitecture of a high-radix router, *Proceedings of the 32nd Annual International Symposium on Computer Architecture (ISCA)*, pp. 420-431, Madison, WI, USA, 2005.

[11] W.J. Dally, Performance Analysis of k-ary n-cube Interconnection Networks, *IEEE Trans. on Computers*, vol. 39, no. 6, pp. 775-785, 1990.

[12] R. Holsmark, S. Kumar, M. Palesi, and A. Mekia, HiRA: A Methodology for Deadlock Free Routing in Hierarchical Networks on Chip, *Proc. of the 3rd ACM/IEEE NOCS*, pp. 2-11, 2009.

[13] V.K. Jain, T. Ghirmai, and S. Horiguchi, "TESH: A new hierarchical interconnection network for massively parallel computing", *IEICE Trans. on Inf. & Syst.*, vol.E80-D, no.9, pp.837-846, 1997.

[14] M.M. Hafizur Rahman, Yasushi Inoguchi, Y. Sato, and S. Horiguchi, TTN: A High Performance Hierarchical Interconnection Network for Massively Parallel Computers, *IEICE Transactions on Information and Systems, Japan*, Vol.E92-D, No.5, pp.1062 1078, May 2009.

[15] M.M. Hafizur Rahman, Yasushi Inoguchi, Faiz Al Faisal, and Monoz Kumar Kundu, Symmetric and Folded Tori Connected Torus Network, *Journal of Networks, Academy Publisher*, Vol. 6, No. 1, pp. 26-35, Jan. 2011.

[16] M.M. Hafizur Rahman, Y. Sato, and Yasushi Inoguchi, High Performance Hierarchical Torus Network under Adverse Traffic Patterns, *Journal of Networks, Academy Publisher*, Vol. 7, No. 3, pp. 456-467, March 2012.

Classification and pattern recognition algorithms applied to E-Nose

Md. Mizanur Rahman[1,2,*], Chalie Charoenlarpnopparut[1], Prapun Suksompong[1]
[1]Electronics and Communication Engineering (SIIT, Thammasat University, Thailand)
[2]Electronics and Communication Engineering Discipline (Khulna University, Bangladesh)
[*] E-mail: mizan.ku@gmail.com

Abstract—**Electronic noses (E-Nose) are seen to be good substitute to human or animal nose for food, and fruit quality identification. It is also used for explosive and chemical identification. We have generated typical E-Nose data to compare the existing algorithms in terms of training, and testing/validation. We have observed that *k*-nearest neighbor (*k*-NN) algorithm, support vector machine (SVM) machine learning algorithms; and radial basis function (RBF), and generalized regression neural networks (GRNNs) shows good odor detection performance. In terms of speed GRNN tops compared to other methods.**

Keywords—Electronic nose, VOC, PCA, RBF, SVM, LDA.

I. INTRODUCTION

Objects emitting volatile organic compounds (VOCs) into the air can be identified by the human and animal from the past odor experiences recorded in their memory. The VOCs reach the olfactory sensory cells at the olfactory Epithelium located into the inner most part of the nose. The sensory cells triggered by the VOCs produce electric signals which are then processed by olfactory bulb located in human or animal brain. The data remain into the memory as synaptic weights for future identification of the similar VOCs and identifying the object [1]. The object can be anything that emits VOCs into the air, such as: foods, chemicals, explosive, etc. Chemicals, and explosives are not feasible to be sensed by human or animal. In addition they cannot identify the VOCs which do not emit odor molecules or when VOC concentration level is very low. Thus identification of chemicals, explosives, foods, etc., at low concentration level without any health hazard requires artificial sensory system called Electronic Nose (E-Nose). Desire for human olfactory mimicking brought the E-Nose concept into existence to use it where human or animal cannot reach, or VOC concentration level is very low or does not smell.

A design of an electronic nose consists of six steps as shown in Fig 1. Here odor source is the food or chemical or explosive etc., which we want to sense. Sensor array is a combination of sensors with sensitivity to a wide range of chemicals to produce signature pattern for different kinds of objects. Data acquisition is done by microprocessor kits (e.g. NImyRIO, NI-CRIO, Arduino, etc.) equipped with desired program. Data pre-processing means to convert the sensed signature patterns to a suitable format which can be processed by pattern recognition and classification algorithms. In decision making stage the decision is made based on the results from pattern recognition and classification stage.

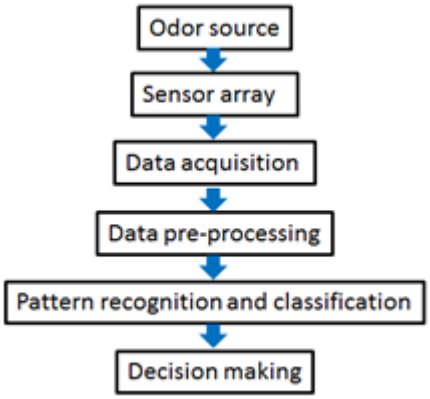

Figure 1. Electronic nose design process.

In this paper we present a review to the literature and summarize the pattern recognition and classification performances of the algorithms used in E-Nose applications. We also aim to find the optimum pattern recognition method for E-Nose system.

II. LITERATURE REVIEW

In [2] an E-Nose designed with metal oxide gas (MOG) sensors. Principal component analysis (PCA) was used to analyze quality of soft drink, olive oil, and tomato pulp. In [3] ripening shelf-life of peaches, nectarines, apples, and pears were monitored by an E-Nose designed with MOG sensors. It was shown by PCA analysis that fruit ripeness assessment by E-Nose is reliable. A MOG sensor based electronic nose was proposed in [4] where artificial neural network (ANN) was applied for classification and detection of apple ripeness. Near-infrared spectrophotometer, machine vision system, and an E-nose system were combined together in [5] and few numbers of misclassification were observed. Here the E-Nose was used to identify the rotting stage of apple based on ANN. In [6], [7] MOG sensors were used to design E-Nose. In [6] aroma of black tea was classified based on multilayer perceptron (MLP) network. In [7] concentration estimation of formaldehyde based on chaotic sequence optimized feed forward back propagation neural network (FFBPNN) was done. Basal Stem Rot disease of oil palm was identified with application of ANNs such as: FFBPNN, probabilistic neural network (PNN), radial basis function neural network (RBFNN) in [8]. In [9] an E-Nose with five semiconductor thin film sensors was

978-1-4673-9257-0/15/$31.00 ©2015 IEEE

designed. Here two groups of seven coffees' quality were analyzed by training an FFBPNN. Before feeding the data to FFBBNN, dimensions of the data were reduced by PCA. MOG sensors were used to develop an E-Nose to recognize benzene, toluene, ethyl benzene, xylene, and gasoline based on PCA, and ANN [10]. In [11] dimensionality was reduced by PCA and then a neural network was used to discriminate different types of coffee, aroma oils, perfumes and alcohol. Six clonal varieties of orthodox finished tea were classified with 100% accuracy by PCA and MLP [12]. PCA was applied to visualize data in lower dimension and PNN was applied for classification in [13]. Collected data from metal oxide semiconductor sensor based E-Nose were analyzed by FFBPNN, and support vector machine (SVM) to classify shelf-life stages of banana [14]. SVM was also applied in [15] to recognize ethanol, gasoline and acetone with good accuracy and in [16] to identify spoiled beef, and fish. Eleven different types of Spanish olive oils were classified by PCA followed to an LDA projection with 79% accuracy in [17]. A MOG sensor based E-Nose was designed in [18] with wireless connectivity where k-NN, MLP, SVM with linear and RBF kernel, PCA, and linear discriminant analysis (LDA) algorithms were used for classification. Coffee roasting degree was analyzed in [21] by applying two dimensional PCA scores to FFBPNN, and GRNN. In [22] a portable E-Nose was used to collect sensing data and pattern recognition algorithms as LDA, FFBPNN, PNN, and GRNN were used to identify adulteration of sesame oil.

III. PATTERN RECOGNITION AND CLASSIFICATION ALGORITHMS

It is seen from the E-Nose literature that pattern recognition and classification techniques that are mostly applied in E-Nose applications are: PCA, LDA, *k*-NN, ANN (FFBPNN and RBFNN, GRNN). PCA and LDA are statistical methods, while *k*-NN and ANN fall into machine learning category.

A. Statistical methods

1) Principal component analysis

PCA is a data analysis technique which finds a new set of linearly uncorrelated variables from a set of inter-correlated variables through an orthogonal transformation process. The new set of variables are known as principal components and are less than or equal to the number of original variables. The principal components are ordered in descending values of variances.

We consider a data matrix $\boldsymbol{X}$ of size $N \times D$, where N represents number of experiments and D represents number of datum (for example sensors), each row of the matrix is represented as, $x_m^{C_i} \in \Re^D$, where, $m = 1, \dots, L_{C_i}$, $i = 1, \dots, I$ is class index, I is the number of classes, C_i is the class label, and L_{C_i} is the number of observations for each sample of an object or event with known class C_i. The PCA algorithm is summarized as:

Step 1. Take the D- dimensional data matrix $\boldsymbol{X}$.

Step 2. Calculate the means for each dimension of the whole data set to generate a D-dimensional mean vector.

Step 3. Compute the scatter matrix or the covariance matrix of the data set in the data matrix $\boldsymbol{X}$.

Step 4. From the covariance or scatter matrix in step 3 calculate the eigenvectors and corresponding eigenvalues.

Step 5. Sort the eigenvectors in terms of descending eigenvalues. Form a $D \times K$ dimensional matrix $\boldsymbol{W}$ (where each column represents an eigenvector) taking K eigenvectors with the largest eigenvalues. Here, $K \leq D$.

Step 6. The whole data set in $\boldsymbol{X}$ is converted to new subspace by, $\boldsymbol{Y} = \boldsymbol{W}^{\mathrm{T}} \times \boldsymbol{X}^{\mathrm{T}}$. Here T represents transpose.

2) Linear discriminant analysis

LDA requires the measured independent variables for each observation to be continuous quantities. LDA algorithm for two classes is given below:

Step 1. Given two sets of labeled data, C_1 and C_2 whose class means μ_{C_1} and μ_{C_2} by $\mu_{C_i} = \frac{1}{L_{C_i}} \sum_{m=1}^{L_{C_i}} \boldsymbol{x}_m^{C_i}$, where, L_{C_i} is the number of examples of class C_i, $\boldsymbol{x}_m^{C_i} \in \Re^D$, where, $m = 1 \dots L_{C_i}$, and D is the number of dimensions.

Step 2. Calculate the between-class covariance matrix $\boldsymbol{S}_{between} = (\mu_{C_2} - \mu_{C_1})(\mu_{C_2} - \mu_{C_1})^{\mathrm{T}}$, and total within-class covariance matrix $\boldsymbol{S}_{Within} = \sum_{i=1,2} \sum_{m=1}^{L_{C_i}} (\boldsymbol{x}_m^{C_i} - \mu_{C_1})(\boldsymbol{x}_m^{C_i} - \mu_{C_1})^{\mathrm{T}}$.

Step 3. Calculate, $\boldsymbol{w} = S_{within}^{-1}(\mu_{C_2} - \mu_{C_1})$ which maximizes, $J(\boldsymbol{w}) = \frac{\boldsymbol{W}^T \boldsymbol{S}_{between} \boldsymbol{W}}{\boldsymbol{W}^T \boldsymbol{S}_{Within} \boldsymbol{W}}$. If within covariance of the classes are not equal calculate $\boldsymbol{w}$ by $\boldsymbol{w} = S^{-1}(\mu_{C_2} - \mu_{C_1})$, where, $S = \frac{1}{L_{C_1} + L_{C_2}}(L_{C_1} S_1 + L_{C_2} S_2)$ is a pooled covariance matrix.

Step 4. Projecting a new point onto the maximally separating direction and classify it as C_1 if, $\boldsymbol{w}^T \left(\boldsymbol{x}_m^{C_i} - \left(\frac{\mu_{C_1} + \mu_{C_2}}{2} \right) \right) > log \frac{p(C_1)}{p(C_2)}$, else classify as C_2. Here $p(C_1)$ and $p(C_2)$ are class probability of C_1 and C_2.

For multiclass LDA apply pairwise classification. Create a new classifier for each pair of classes. Total number of classifiers is $I(I-1)/2$. Produce a final classification table combining the results from individual classifiers. Apply majority voting to classify any new data.

B. Machine learning

Five machine learning techniques which got importance in E-Nose applications are: *k*-NN, SVM, FFBPNN, RBFNN, and GRNN.

1) k-Nearest Neighbor

A simple technique to predict the class of an unknown feature vector $x_m^{C_i} \in \Re^D$ is the *k*-NN method. First from the training set the k nearest vectors are found. Then the class of $x_m^{C_i} \in \Re^D$ is found using the majority class voting. Here D is the dimension of data. The *k*-NN algorithm is given below:

Step 1. Calculate the distances from each node to other nodes by the Euclidean norm of the difference of the two vectors i.e.,

$\mathrm{dist}(x_i, x_j) = \left\|x_i - x_j\right\| = \sqrt{(x_{i1} - x_{j1})^2 + (x_{i2} - x_{j2})^2 + \cdots + (x_{iD} - x_{jD})^2}$ and record all the distances in a table.

Step 2. Sort the distances in descending order.

Step 3. Compute the prediction probability by $\mathrm{p}(c_m|x, D, k) = \frac{1}{k}\sum_{i\in\{N_k(x,D)\}} \mathbb{I}(t_i = C_m)$, where, $\{N_k(x, X)\}$ is the set of k nearest points in X from $\boldsymbol{x}$, t_i are class labels of each data point in $\{N_k(x, X)\}$, C_m is the class for which the new data $\boldsymbol{x}$ is being tested, m is class index and $\mathbb{I}(\mathrm{e})$ is the indicator function defined as,

$$\mathbb{I}(\mathrm{e}) = \begin{cases} 1 & \text{if e is true} \\ 0 & \text{if e is false} \end{cases}.$$

As we assume N data with D -dimension the straight forward implementation of finding k-NN takes $\mathrm{O}(\mathrm{N}\times\mathrm{D})$ time.

2) Support Vector Machine (SVM)

The goal of the SVM is to find the hyperplane that provides largest margin betwixt two classes and has no interior data points. Data points from the two classes which lie on the boundary of the slab are called support vectors.

For two class SVM we label the data of class C_1 and C_2 as, $t_i = -1$ and $+1$ accordingly. We need to find the optimal hyperplane $g(\boldsymbol{x}) = \boldsymbol{w}^{\mathrm{T}}\boldsymbol{x} + b$, which maximizes the class separation. We consider the training data of the form, $\{x_m^{C_i}, t_m^{C_i}\}$, where, $t_m^{C_i} \in \{-1, 1\}$, $m = 1, \ldots, L_{C_i}$, $i = \{1, 2\}$, C_i is the class label, and L_{C_i} is the number of observations with known class C_i.

Step 1. By Quadratic programing find the value of α_i which maximize, $\mathrm{Q}(\alpha) \equiv \sum_{n=1}^{N} \alpha_n - \frac{1}{2}\sum_{j=1}^{N} \alpha_n\alpha_j t_n t_j x_i^{\mathrm{T}} x_j$, subject to $\alpha_i \geq 0$, $\forall i$ and $\sum_{i=1}^{N} \alpha_i y_i = 0$. Here α are Lagrange multipliers.

Step 2. Calculate $\boldsymbol{w}_0$ using α_i found in step 1 into, $w_0 = \sum_{n=1}^{N} \alpha_n t_n \boldsymbol{x}_n$.

Step 3. Put the value of w_0 into the *Karush–Kuhn–Tucker condition* [19], $\alpha_n[d_n(w_0^T x_n - b_0) - 1] = 0$ and solve for b_0.

Multiclass SVM is a combination of several binary SVM classifiers. A new data is classified based on majority votes from all binary classifiers. In Matlab this is defined as error-correcting output code multiclass model (ECOC). ECOC classification requires a coding design, and a decoding scheme. Coding design includes several binary learners formed by taking two classes at a time. The decoding scheme decides the rules of aggregating the binary classifiers' results.

We apply one-versus-one coding design, where two classes of data are taken at a time; one class is assigned to positive class and another to negative class. More combination of coding designs can be found in Matlab documentation.

3) Artificial Neural Network

A neural network resembles the brain in two respects:

- through a learning process the neural network gathers knowledge, and
- synaptic weights, i.e. calculated weights of inter-neuron connections during learning process are used to store the knowledge.

An ANN learns in any of the three techniques: supervised, unsupervised, and reinforcement learning. Reinforcement learning is rarely used in ANN applications. E-Nose data are usually organized as input-target pairs making supervised learning more common compared to unsupervised learning algorithms. FFBPNN, RBFNN, and GRNN apply supervised learning technique. The supervised learning requires a training set defined as $\{\boldsymbol{x}_m^{C_i}, t_m^{C_i}\}$, $\mathrm{m} = 1, \ldots, L_{C_i}$, $i = 1, \ldots, I$, where $\boldsymbol{x}_m^{C_i}$ is an input to the network and $t_m^{C_i}$ is the corresponding target output. On receiving each input an ANN computes the output and compares them to the corresponding targets. According to the learning rule the weights and biases of the network is updated until the error reach to a predefined limit and the network outputs move closer to the targets.

a) Feedforward backpropagation neural network

A common training method for FFBPNN is back propagation also known as error back propagation. In this method the outputs are compared to the targets to calculate the errors. The synaptic weights and threshold values are then adjusted to minimize the error contributed by each neuron next time.

Given, the topology of a neural network, the activation function for each neuron in the network A_i; training data: pairs of sets of inputs and outputs $\mathrm{T} = \{(\boldsymbol{x}_1, t_1), (\boldsymbol{x}_2, t_2), \cdots, (\boldsymbol{x}_N, t_N)\}$, where, each $\boldsymbol{x}_i$ denotes the input to all input neurons and each t_i is the desired output of the neural network after running the inputs in $\boldsymbol{x}_i$; a learning rate r having a continuous value between 0 and 1 ; the FFBPNN algorithm can be summarized as:

Step 1. Choose random values for weights and biases.

Step 2. Calculate outputs of each neuron using an activation function A_i as transfer function. Typical activation functions are sigmoid, tanh, step, etc.

Step 3. Considering the training data T compute the sum of squares error (SSE) of the network by, $\mathrm{SSE}(\mathrm{T}) = \sum_{i=1}^{N}((y_i - t_i)^2)$, where y_i is the set of outputs of the neural network for the set of inputs $\boldsymbol{x}_i$.

Step 4. Update the weights of edges and biases of neurons at a rate based on learning rate. The update is done by gradient descent minimization.

Step 5. Back to step 2 until error limit reached in step 3.

b) Radial basis function neural networks

Radial basis function networks are of two kinds: exact, and approximate. In exact RBFNN the numbers of neurons at each layer are equal to the number of samples. RBFNNs are trained in two stages. The parameters governing the basis functions are determined by unsupervised methods in the first stage. In the

second stage of training the final-layer weights are determined. A block diagram of RBFNN is shown in Fig. 2.

Every input vector is mapped exactly onto the corresponding target vector in exact RBFNN. Let's consider a D-dimensional input space X is mapped to a one-dimensional target space t, the data set $\{x_m^{C_i}, t_m^{C_i}\}$, where $x_m^{C_i}$ is an input to the network and $t_m^{C_i}$ is the corresponding correct (target) output, $m = 1, \dots, L_{C_i}$, $i = 1, \dots, I$, consists of $L_{C_1} + L_{C_2} + \cdots + L_{C_I} = N$ input vectors. The goal is to find a function $\mathrm{h}(x)$ such that $\mathrm{h}(x_m^{C_i}) = t_m^{C_i}$, $m = 1, \dots, L_{C_i}$, $i = 1 \dots I$.

The N basis functions of the form $\varphi(||\boldsymbol{x} - \boldsymbol{x}_m^{C_i}||)$ are linearly combined to produce the output of the mapping. The output is given by, $\mathrm{h}(\boldsymbol{x}) = \sum_{m,C_i} \boldsymbol{w}_m^{C_i} \varphi(-\gamma||\boldsymbol{x} - \boldsymbol{x}_m^{C_i}||)$, where, γ is a constant, the distances $||\boldsymbol{x} - \boldsymbol{x}_m^{C_i}||$ usually taken to be Euclidean, and $\phi(z) = \exp(-z)$. In matrix form the problem can be presented as, $\boldsymbol{\Phi w} = \boldsymbol{t}$, where, w is $N \times 1$ vector, t is a $N \times 1$ vector, and $\boldsymbol{\Phi}$ is a N × N matrix given as follows:

$$\boldsymbol{\Phi} = \begin{bmatrix} exp\left(-\gamma \left|\left|\boldsymbol{x}_1^{C_1} - \boldsymbol{x}_1^{C_1}\right|\right|^2\right) & \dots & exp\left(-\gamma \left|\left|\boldsymbol{x}_1^{C_1} - \boldsymbol{x}_{L_{C_I}}^{C_I}\right|\right|^2\right) \\ exp\left(-\gamma \left|\left|\boldsymbol{x}_2^{C_1} - \boldsymbol{x}_1^{C_1}\right|\right|^2\right) & \dots & exp\left(-\gamma \left|\left|\boldsymbol{x}_2^{C_1} - \boldsymbol{x}_{L_{C_I}}^{C_I}\right|\right|^2\right) \\ \vdots & \vdots & \vdots \\ exp\left(-\gamma \left|\left|\boldsymbol{x}_{L_{C_I}}^{C_I} - \boldsymbol{x}_1^{C_1}\right|\right|^2\right) & \dots & exp\left(-\gamma \left|\left|\boldsymbol{x}_{L_{C_I}}^{C_I} - \boldsymbol{x}_{L_{C_I}}^{C_I}\right|\right|^2\right) \end{bmatrix}$$

RBF exact interpolation algorithm is given below,

Step 1. Choose a value for γ ranging from 0 to 1 randomly.
Step 2. Choose random weights for vector w.
Step 3. Compute the elements, $\varphi(||\boldsymbol{x} - \boldsymbol{x}_m^{C_i}||)$ of the $\boldsymbol{\Phi}$ matrix.
Step 4. Evaluate, vector $\mathbf{w}$ from, $\boldsymbol{w} = \boldsymbol{\Phi}^{-1}\boldsymbol{t}$.
Step 5. Evaluate, output vector, y from, $\boldsymbol{y} = \boldsymbol{w\Phi}$.
Step 6. Evaluate, squared error, $E = \frac{1}{2}\sum_{n=1}^{N}\sum_{k=1}^{N}\{y_k - t_k^n\}^2$ from $\boldsymbol{y}$ and $\boldsymbol{t}$.
Step 7. If $E > E_{threshold}$, change γ and continue to step 3 else exit.

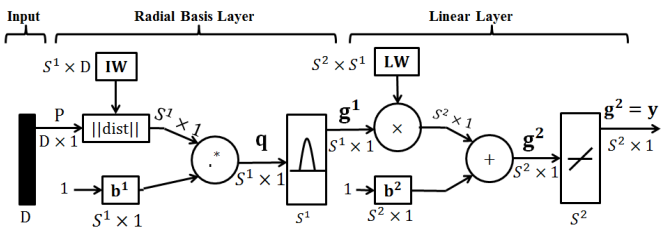

Figure 2. Radial basis function neural network. The first layer i.e. the radial basis layer has S^1 basis functions, and the second layer i.e. linear layer has S^2 pure linear functions. S^1, and S^2 are the number of neurons in the radial basis layer and linear layer accordingly; P is a D × 1 input vector, D is the number of input variables; g^1, and g^2 are the output vectors from layer 1 and layer 2 accordingly; IW, and LW are input and output weight matrices accordingly, for exact radial basis function network IW holds all the training data points, and LW is updated by training; b^1, and b^2 are the bias vectors of layer 1 and layer 2 accordingly. [20]

c) Generalized regression neural network

GRNN has two differences to exact RBFNN in Fig. 2. The LW weight matrix in the second layer in Fig. 2 is set to target vector and the summation block in the second layer is replaced by a normalized product block. Thus the GRNN network virtually does not require training and therefore is fast. During training period the weights IW and LW are initialized to the data matrix **X** and target values in vector **t**.

IV. Results and Discussion

Three classes of typical E-Nose data have been considered with each class having 100 samples. Fig. 3 shows a principal component analysis where x and y axes represent the principal components 1 and 2 respectively. Fig. 4 shows that the first two principal components hold approximately 95% variance of all the data. Thus the principal component analysis is a very useful tool to reduce the dimensionality of multidimensional data.

Classification by LDA, *k*-NN, multi class SVM, FFBPNN, RBFNN, and GRNN have been done. For these methods 70% of the data from each class were randomly chosen for training and remaining 30% were taken for testing/validation. Simulation results for LDA, *k*-NN, multi class SVM, FFBPNN, RBFNN, and GRNN are summarized in Table I. Training duration, testing/validation duration, and number of testing/validation error are also listed in Table I. It is seen that training duration for *k*-NN was minimum followed by GRNN, SVM, RBF, LDA, and FFBPNN accordingly. Whereas testing/validation duration for GRNN is minimum, followed by SVM, FFBPNN, *k*-NN, LDA, and RBF accordingly. Testing error of *k*-NN, SVM, FFBPNN, RBF, GRNN are 0% and that of LDA is 3.33%. It is seen that *k*-NN, SVM, RBF, and GRNN has good speed of training and testing speed of GRNN is the highest.

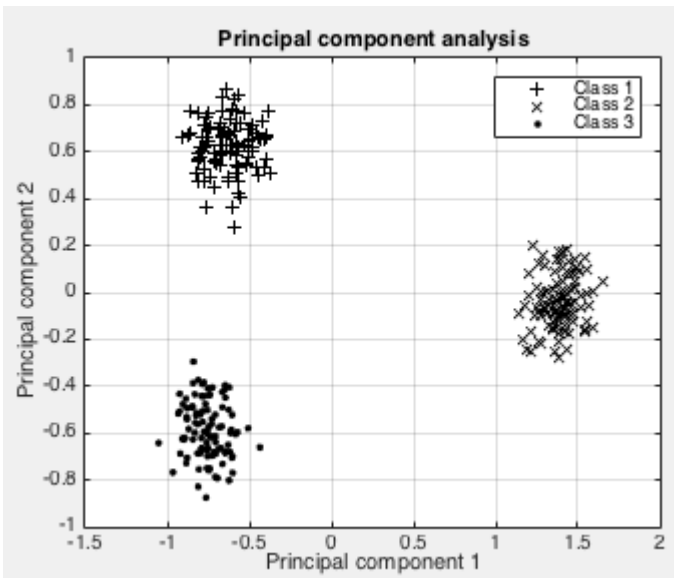

Figure 3. Three classes of data, each class having 100 samples with dimension reduced to two by PCA.

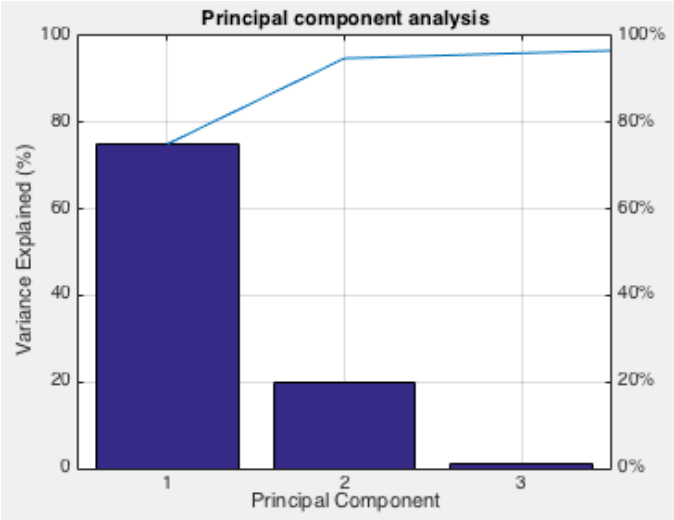

Figure 4. Variance explained of PCA analysis.

TABLE I. TRAINING DURATION, DETECTION DURATION, AND DETECTION ERROR

	Training duration	Detection time	Testing error
LDA	0.4761	0.0320	3.33%
k-NN	0.0298	0.0298	0%
SVM	0.0703	0.0183	0%
FFBPNN	0.5817	0.0243	0%
RBFNN	0.1680	0.0466	0%
GRNN	0.0546	0.0139	0%

V. CONCLUSION

In this paper data analysis methods for E-Nose applications are discussed. We find that k-NN, SVM, RBFNN, and GRNN are good methods for E-Nose data classification and pattern recognition in terms of new data classification speed, and testing error. GRNN shows best performances for the data set that we have considered. We are designing an E-Nose in our laboratory for toxic and explosive gas detection at present.

ACKNOWLEDGMENT

We thank Thammasat University research fund for supporting this research.

REFERENCES

[1] S. Firestein, "How the olfactory system makes sense of scents," *Nature*, vol. 413, pp. 211–218, Sep. 2001.

[2] I. Concina, M. Falasconi, and V. Sberveglieri, "Electronic noses as flexible tools to assess food quality and safety: should we trust them?," *IEEE Sensors Journal*, vol. 12, no. 11, pp. 3232–3237, Nov. 2012.

[3] J. Brezmes, et al., "Evaluation of an electronic nose to assess fruit ripeness," *IEEE Sensors Journal*, vol. 5, No. 1, pp. 97–108, Feb. 2005.

[4] E. L. Hines, E. Llobet, and J. W. Gardner, "Neural network based electronic nose for apple ripeness determination," *Electronic Letters*, vol. 35, no. 10, pp. 821–823, May 1999.

[5] Z. Xiaobo, and Z. Jiewen, "Apple quality assessment by fusion three sensors," in *Proc. 2005 IEEE Sensors*, Oct. 30 – Nov. 3 2005, pp. 389–392.

[6] S. S. Chowdhury, B. Tudu, R. Bandyopadhyay, and N. Bhattacharyya, "Portable electronic nose system for aroma classification of black tea," in *Proc. IEEE Region 10 and the Third Int. Conf. on Industrial and Information Systems*, Dec. 2008, pp. 1 –5.

[7] L. Zhang, and F. Tian, "A novel chaotic sequence optimization neural network for concentration estimation of formaldehyde by an electronic nose," in *Proc. Fourth Int. Conf. on Computational Intelligence and Communication Networks*, pp. 856 – 859, Nov. 2012.

[8] A. H. Abdullah et al., "Application specific electronic nose (ASEN) for ganoderma boninense detection using artificial neural network," in *Proc. 2nd Int. Conf. on Electronic Design (ICED)*, Aug. 2014, pp. 148–152.

[9] M. Pardo, G. Faglia, G. Sberveglieri, and L. Quercia, " Electronic nose for coffee quality control," in *IEEE Instrumentation and Measurement Technology Conf.*, May 2001, pp. 123–127.

[10] P. U. Kurup, and M. A. Lowell, "An electronic nose for detection hazardous chemicals and explosives," in *Proc. of IEEE Conf. on Technologies for Homeland Security*, May 2008, pp. 144–149.

[11] R. Singh, "An intelligent system for odour discrimination," in *Proc. of the first IEEE Int. workshop on Electronic Design, Test and Applications (DELTA'02)*, 2002. pp. 1–3.

[12] N. Bhattacharyya, B. Tudu, R. Bandyopadhyay, M. Bhuyan, and R. Mudi, "Aroma characterization of orthodox black tea with electronic nose," in *Proc. TENCON IEEE Region 10 Conf.*, Nov. 2004, pp. 427–430.

[13] A. G. -Cortes, J. Marti, I. Sayago, J. P. Santos, J. Gutierrez, and M. C. Horrillo, "Detection of stress through sweat analysis with an electronic nose," in *Proc. Spanish conf. on electronic devices*, Feb. 2009, pp. 338–341.

[14] A. Sanaeifar, S. S. Mohtasebi, M. G. -Varnamkhasti, and M. Siadat, "Application of an electronic nose system coupled with artificial neural network for classification of banana samples during shelf-life process," in *Proc. Int. Conf. on Control, Decision and Information Technologies (CoDIT)*, Nov. 2014, pp. 753 – 757.

[15] X. -D. Wang, H. -R. Zhang, and C. -J. Zhang, "Signals recognition of electronic nose based on support vector machines," in *Proc. of the Fourth Int. conf. on Machine Learning and Cybernetics*, Aug. 2005, pp. 3394-3398.

[16] N. ul Hasan, N. Ejaz, W Ejaz, and H. S. Kim1, "Malicious odor item identification using an electronic nose based on support vector machine classification," in *Proc. IEEE 1st Global Conf. on Consumer Electronics (GCCE)*, Oct. 2012, pp. 399–400.

[17] A. Perera, A. G. -Baena, T. Sundic, T. Pardo, and S. Marco, "Machine olfaction: pattern recognition for the identification of aromas," in *Proc. 16th Int. Conf. on Pattern Recognition*, 2002, pp. 410–413.

[18] M. Hassan and A. Bermak, "Threshold detection of carcinogenic odor of formaldehyde with wireless electronic nose," in *Proc. 2014 IEEE Sensors*, Nov. 2014, pp. 1368–1371.2014 IEEE.

[19] H. W. Kuhn, and A. W. Tucker, "Nonlinear programming," in *Proc. Second Berkeley Symposium on Mathematical Statistics and Probability*, 1951, pp. 481–492.

[20] M. T. Hagan, H. B. Demuth, M. Beale, *Neural Network Design*, , Thomson Asia Pte. Ltd. and China Machine Press and CITIC Publishing House, China, 1996.

[21] S. Romani, C. Cevoli, A. Fabbri, L. Alessandrini, and M. Dalla Rosa, "Evaluation of coffee roasting degree by using electronic nose and artificial neural network for off-line quality control," *Journal of Food Science*, vol. 77, no. 9, pp. 960–965, Jun. 2012.

[22] Zheng Hai, Jun Wang, "Electronic nose and data analysis for detection of maize oil adulteration in sesame oil," *Sensors and Actuators B*, vol. 119, no. 2, pp. 449–455, Jan. 2006.

A Novel Trust Measurement System for Cloud-based Marketplace

Sudipta Singha Roy, Tamjid Haque Sarker, and M. M. A. Hashem
Department of Computer Science and Engineering
Khulna University of Engineering and Technology
Khulna-9203, Bangladesh
E-mail: sudipta.singha.roy@outlook.com, oleevecse_47@yahoo.com, mma.hashem@outlook.com

Abstract—**Cloud Computing is an enormously growing phenomenon in the present days enabling IT related services to run in a more dynamic and scalable way than the previous days and cloud marketplace is becoming more competitive with the entrance of new cloud service providers (CSP) offering similar functionalities. The basic obstacles in the way of success of cloud marketplace are the numerous shortcomings in reliable monitoring and identifying reliable cloud service provider based on consumers' preferred services. In this paper, a multi-faceted Entrusted Trust Management (ETM) system architecture is introduced that can support the customers in reliably choosing the trustworthy cloud service provider (CSP) as well as properly weight the information sources that provide feedbacks about the quality of services (QoS) of the CSPs. This ETM system works on several issues to measure the trust value of the providers on specific domain and overall trust value. Firstly, measurement of the trust value of the specific domain of provider on the basis of certainty and uncertainty. Secondly, measurement of overall trust value of the provider from these domain specific trust values. Thirdly, measurement of "Degree of Conflict" between the rating/feedback of consumers and experts. And finally, measurement of trustworthiness of the information sources which provide the rating of the provider on the basis of the SLA between the provider and the consumer. At last, our proposed system is experimented using real datasets.**

Keywords—***Cloud computing, Cloud Service Provider, Trust Models, Trust Management, CAIQ, Self-Assessment.***

I. Introduction

Nowadays, cloud computing is becoming one of the most demanding part of human life as it offers dynamic, scalable and shared resources with more flexibility, disaster recovery plan, automatic software updates, increased collaboration and document control. But the highly distributed and nontransparent nature of cloud computing are considerable obstacles for the market success of the cloud services, as consumers of these services often feel that they lose their control over their data. A survey conducted by Fujitsu Research Institute among more than 3000 consumers of cloud services from 6 different countries shows that, about 84% of the consumers are concerned about data storage location, 88% of the consumers are worried about who has access to their data [1] and 93% consumers distrusts the security facilities of their cloud services against the facilities they were offered [2,3]. Moreover, because of massive diversity in the available cloud services, it has become challenging for the customers to select whose services they should use based on their preferred choice of services and requirements.

Consumer concerns can be redressed by implementing adequate preventive measures for privacy and security. Cloud providers show the evidence of their preventive measures by including related description in the service level agreements (SLAs). But, a survey [4] shows that, 46.6% of the cloud users think, the legal contents of the SLAs are unclear. SLAs with such obscure clauses and fuzzy technical specifications make them unreliable as standalone basis for the consumers to identify trustworthy providers.

As the cloud market is growing rapidly and new cloud service providers are entering the market, this marketplace is becoming more competitive day by day. Different cloud providers compete for customers by providing services with similar functionalities. However, there remains huge differences in terms of meeting the Quality of Service (QoS) ensured to the consumers as well as capabilities of the cloud service providers. Moreover, cloud brokers and resellers promise to provide add-on services on behalf of cloud providers with the same level of competencies and capabilities. So, consumers badly need to reliably assess the trustworthiness of the service providers offering services of good quality.

Numerous electronic marketplaces like: eBay, Amazon and app market have already utilized trust and reputation (TR) systems [5] successfully. Nowadays, cloud marketplace also needs similar approaches to support the customers in selecting trustworthy cloud service provider based on their desired services. Existing TR systems doesn't solely depends on the customer feedback. They also consider property certificates, compliance with audit standards as well as provider statements as the source of information. But, these TR systems give same preferences to all information sources and feedbacks neglecting the issue that, all the information sources may not be equally standard and trustworthy. So, it would be more reliable to the customers if these feedbacks (ratings) from different information sources are properly weighted. Hence, we feel strong requirement of a TR system in which every

978-1-4673-9257-0/15/$31.00 ©2015 IEEE

feedback from different information sources are properly entrusted (weighted). Our objective is to maintain a smooth trust in the cloud marketplace and provide them a tool that can verify and rank the cloud service providers based on the customers' desired services.

This paper provides the realization of our proposed Entrusted Trust Management (ETM) system for cloud computing marketplace which aims to reflect the multifaceted nature of trust evaluation by considering multiple attributes, entrusted sources and roots of trust as well as support the customers in selecting trustworthy service providers. As user feedback is the main source of trust evaluation, we have tried to weight their opinions and determine whether the consumer who is providing the feedback is trustworthy or not. In this paper, we implement the Entrusted Trust Management (ETM) system using the CAIQ as one of the trust information sources that extracts trust information from the CAIQs completed by cloud providers. We also contribute to determine the trustworthiness of the information sources (how much trustworthy that information source is) and weight every information sources accordingly. Finally, our ETM system is validated by experimental evaluation based on the completed CAIQs stored in the public registry (i.e. CSA STAR [6]).

The rest of the paper is organize as follows: Section 2 discusses the related work, Section 3 discusses the procedural and architectural details of the proposed ETM system based on the CSA CAIQ framework, Section 4 shows how the system is validated by experimental evaluation and finally Section 5 provides our concluding remarks.

II. Related Works

The current trust establishment trends and approaches are classified into two categories: 1) applied technologies and 2) research trends [3]. Applied technologies show various technologies available in competitive cloud marketplace for establishing trust on cloud providers. SLA validation [7] and monitoring [8] are ways to establish trust on cloud providers. But the compensation clauses written in SLAs for stakeholders in the cloud marketplace are written by the cloud providers in such a way that the customers merely get the compensations in case of not meeting the Quality of Services (QoS) as assured by the cloud providers. To reassure users about different services and platforms, cloud providers use various audit standards (e.g. SAS 70 II, FISMA etc.). They, however, cover only the operational performances and are not sufficient in abating (lessening) the users' security concerns. Recently, some cloud marketplace (e.g. SpotCloud) were launched to support the customers in selecting dependable cloud providers where cloud providers' ratings are given in an Amazon-like 'star' interface with no technical documentation on how the ratings are computed.

Research trends show some research-driven approaches regarding trust establishment in cloud environment. Trust and reputation (TR) models (e.g. KeyNote [9], REFEREE [10]) have been adapted and proven useful in cloud computing environment. But, these approaches for decision making in cloud environment usually don't take multiple attributes and assume trust relationships are monotonic. Moreover, these approaches don't address the concept of uncertainty in trust establishment where, modeling and representing uncertainty is important when trust is assessed between a provider and customer based on information that is incomplete or insufficient or derived from unreliable sources. Habib et al. [11] proposed a TM system that aggregates trust related information from different sources as well as take uncertainty into account while measuring trust value. It implemented the Cloud Control Assessment (CCA) tool based on the CSA CAIQ. But, it can't calculate/measure the weight of different information sources and consumers have to assume weight for different information sources by themselves.

Our proposed ETM system aims to measure weight of different information sources and then aggregate trust related information from those information sources e.g. user ratings, provider statements, user statements, expert assessment, property certificates.

III. Conceptual Model for Entrusted Trust Management System

This section discusses the solutions that are essential in developing an ETM system for cloud marketplace. An overview of the ETM system architecture as well as description of its internal components are also provided in this section.

A. Modeling Trustworthiness in Cloud Computing-based Market Place

Modelling the trustworthiness of a cloud provider requires statements on the expected behavior of the offered services or systems from different information sources. At the same time the trustworthiness of the information sources are also needed to be measured. These statements are required to be given in the form of propositions (e.g. Security: "Cloud provider A keeps my data confidential." Availability: "Cloud provider A provides 95% uptime in a year."). These propositions refer to different attributes. Using the operators (AND, W.FUSION) proposed in [3, 11] those propositions become the combined statements in the form of Propositional Logic Terms (PLTs).

When modeling trust, the Trust Management (TM) system has to consider trust relevant information, how a trust value derived that information are subject to uncertainty along with how much trustworthy that information source is. Thus, we propose an ETM system that aims to model trust as a subjective probability, which follows the definition of trust provided in [12].

B. Modeling Trust Metrices in Cloud Computing-based Market Place

We use CertainTrust [13] and CertainLogic [14] as the basis for a trust metric in designing the architecture of the ETM system for the idea of modelling trust as a subjective probability. In the following we discuss a brief description to the trust representation and computation that we need to support.

In CertainTrust [13] opinions are the basis of measuring trustworthiness of certain cloud provider. Opinions express one's belief whether a certain proposition (or a combination of propositions) is true or false. Each opinion is a triple of values, $o = (t, c, f) \in \{[0,1] \times [0,1] \times [0,1]\}$ where t denotes the average rating, c represents certainty associated with the average rating and f denotes the initial expectation assigned to the truth of the statement [3, 13]. In [3] each opinion is associated with an expectation value, $E(t, c, f)$ *where*:

$$E(t, c, f) = t * c + (1 - c) * f \qquad (1)$$

The consensus and discounting operators proposed in CertainTrust and CertainLogic provides means for aggregating opinions on the same statement from different information sources and weighting those opinions based on the trustworthiness of those sources respectively. In this paper we use the W.FUSION operator proposed by Habib et al. in [11] for aggregating opinions derived from the CAIQ. W.FUSION operator is defined in Table I.

C. ETM System Architecture

In this section, we propose a novel architecture of a ETM system for cloud marketplace. Fig. 1 gives a visual description of the architecture of this system. A brief description of the ETM system's internal components are as follows:

Registration Manager (RM): Cloud providers register through the RM. RM enables providers to as sellers in cloud marketplace. They provide system and service specifications related to the services they offer to the consumers and fill the CAIQ. The RM forwards the answers of the CAIQ to the CAIQ Engine and Trust Information (TI).

Consensus Assessments Initiative Questionnaire (CAIQ) Engine: The CAIQ Engine provides an interface for the cloud providers to fill in the questionnaires through the RM. The CAIQs help cloud providers to represent their competencies to thee consumers with respect to different attributes. All the questions are answered to be "yes", "no", "unknown" and "N/A (not applicable)". All these answers of CAIQs are passed to and stored in TI for further processing.

Trust Manager (TMg): The TMg allows the cloud users to customize their requirements before assessing the trustworthiness of the providers in the cloud marketplace. Based on the customized requirements of the consumer, it provides the trust value of the cloud providers.

Trust Semantics Engine (TSE): The TSE models the configuration of the PLTs customized by the consumers. A default configuration is based on the CAIQ answers stored in TI. It also converts all trust information into PLTs. TSE sends the customized PLTs to the Trust Computation Engine (TCE) for computing customized trust value.

Trust Computation Engine (TCE): The TCE contains operational information related to the operators proposed in CertainTrust [13] and CertainLogic [14] and uses the PLTs to compute the customized trust value.

Weight Measurement Engine (WME): The WME gathers opinions from each information sources regarding the trustworthiness of the cloud provider. Then measuring the

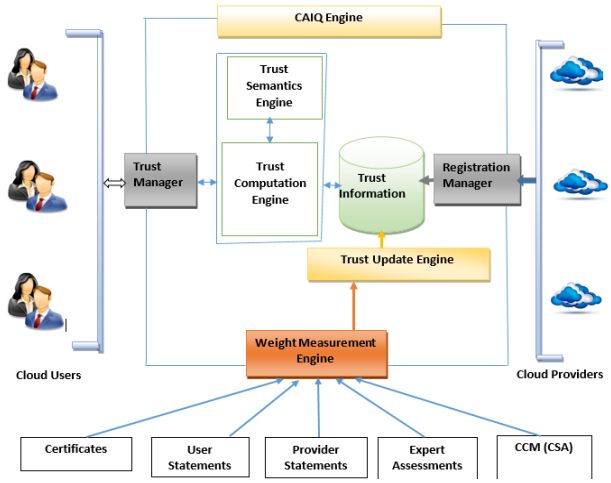

Figure 1. Architecture Overview

Degree of Conflict (DoC) of those opinions of a certain information source for a certain cloud provider from the recent opinions (opinions gathered within 2/3 months) about the service of that provider gathered from the other information sources it determines how much trustworthy that certain information source is and measure it's weight. It passes the opinions from different information sources as well as their proper weight to the Trust Update Engine.

Trust Update Engine (TUE): The TUE is responsible for the collection of opinions from different information sources regarding the trustworthiness of the providers in the cloud marketplace. Moreover, the information sources should be authorized and properly weighted before they provide opinions about the Quality of Services (QoS) of any cloud provider. The TUE combines all opinions regarding the providers and updates their trust value.

IV. CAIQ Based Entrusted Trust Management System

The CAIQ (Version 3.0.1) includes in total, 133 controls (e.g. Application Security (AS), Information System Regulatory Mapping (ISRM)) under 16 domains (e.g. Application and Interface Security (AIS), Audit Assurance & Compliance (AAC)) which are aligned with the CSA principle [15] for moving IT resources to the cloud. Each control contains one or more questions for querying the competencies and capabilities of the cloud provider. Consensus Assessments Initiative Questionnaire v3.0.1 provides 295 CAIQs under these 133 controls to support customers in identifying the trustworthy cloud provider in the marketplace.

A. Assumptions

In this conceptual model, several assumptions should be considered as follow:

- Cloud providers submit one set of legally or officially acceptable answers to the CAIQ for each of the services they offer to the consumers.
- These valid answers are stored in the TI.

TABLE I. DEFINITION OF W.FUSION OPERATOR

Operator	Functionality
W.FUSION	$t_{\widehat{\oplus}_w(A_1,A_2,\cdots,A_n)} = \begin{cases} \frac{\sum_{i=1}^{n} w_i t_{A_i}}{\sum_{i=1}^{n} w_i} & if\ c_{A_1} = c_{A_2} = \cdots = c_{A_n} = 1 \\ 0.5 & if\ c_{A_1} = c_{A_2} = \cdots = c_{A_n} = 0 \\ \frac{\sum_{i=1}^{n}\left(t_{A_i} c_{A_i} w_i \prod_{j=1,j\neq i}^{n}\left(1-c_{A_j}\right)\right)}{\sum_{i=1}^{n}\left(c_{A_i} w_i \prod_{j=1,j\neq i}^{n}\left(1-c_{A_j}\right)\right)} & if\ \left\{c_{A_i}, c_{A_j}\right\} \neq 1 \end{cases}$ $c_{\widehat{\oplus}_w(A_1,A_2,\cdots,A_n)} = \begin{cases} 1 & if\ c_{A_1} = c_{A_2} = \cdots = c_{A_n} = 1 \\ \frac{\sum_{i=1}^{n}\left(c_{A_i} w_i \prod_{j=1,j\neq i}^{n}\left(1-c_{A_j}\right)\right)}{\sum_{i=1}^{n}\left(w_i \prod_{j=1,j\neq i}^{n}\left(1-c_{A_j}\right)\right)} & if\ \left\{c_{A_i}, c_{A_j}\right\} \neq 1 \end{cases}$ $f_{\widehat{\oplus}_w(A_1,A_2,\cdots,A_n)} = \frac{\sum_{i=1}^{n} w_i f_{A_i}}{\sum_{i=1}^{n} w_i}$

- The CSA checks and validates the authenticities and accuracy of the answers regularly and some experts submit another report over the cloud providers competencies and abilities [16].
- Consumers are not bound to answer all the CAIQ questions while providing feedback about the cloud providers Quality of Services (QoS) with respect to the offered services.

B. *Conceptual Model of ETM Sysyem*

We propose a 3 step approach for assessing the CAIQ and measure the trustworthiness of the cloud providers as well as information. These steps are detailed as follows:

Firstly, the TSE shapes the PLTs based on the 16 CAIQ domains. So, PLT contains 16 operands combined with 15 W.FUSION ($\widehat{\oplus}_w$) operators.

Secondly, the opinions from different information sources based on the self-assessment according to the guidance (i.e., CAIQ) of CSA are modeled in the evidence space and we use the mapping as Habib et al. proposed in [17]. The mapping is as follows:

$$t = \begin{cases} 0 & if\ r+s=0 \\ \frac{r}{r+s} & else \end{cases}$$
$$c = \frac{N.(r+s)}{2.(N\ \ (r+s)) + N.(r+s)} \qquad (2)$$
$$f = 0.99$$

Here, t denotes the average rating, which is calculated based on the number of positive assertions. c denotes the certainty and is calculated based on the total number of questions, N and the total number of positive and negative assessments under all 16 domains. N is defined under 2 circumstances: 1) Questions not answered for 'unknown' by the cloud provider. For the first case, N is defined as, $N = r + s + u$. Here u denotes the 'unknown' marked questions. For the second case, N is defined as, $N = (r + s + u) - NA$. Here, NA denotes the 'Not Applicable' marked answers. f denotes the initial expectation and is set as high for each domain that the cloud provider release their control information regarding different domains. Finally, the weight of the information source is updated as it submit its assessment about the QoS of the cloud provider. Initially we assume all the users have weight 1. Then depending on behavior of the user the corresponding weight is updated. Here Degree of Conflict (DoC) is the basis to measure the behavior of the user. We can measure the DoC of a single opinion about a provider from the overall trust value of that provider using the following equation:

$$DoC_{A_i,A_j} = \left|\left(t_{A_i} - t_{A_j}\right)\right| * c_{A_i} * c_{A_j} * \left(1 - \left|\frac{w_i - w_j}{w_i + w_j}\right|\right) \qquad (3)$$

DoC_{avg} (Average Degree of Conflict) represents how any information source's feedback differs with the recent feedbacks from other information sources which can be calculated from the equation below:

$$\mathrm{DoC}_{avg} = \frac{\sum_{i=1}^{n}\sum_{j=1,j\neq i}^{n} DoC_{A_i,A_j}}{n} \qquad (4)$$

How much one information source's weight can be differed after contributing (i+1)th feedback can be measured from the below equation:

$$diff_{i+1} = \begin{cases} p{DoC_{avg}}^2 + qDoC_{avg} + r & if\ DoC_{avg} > .05 \\ 0 & else \end{cases} \qquad (5)$$

Here a, b, c are three constants with value,$p = 0.022$, $q = 1.023$ and $r = -0.0289$. Here $diff_{i+1}$ is the relative weight difference after contributing an opinion. The vale of p, q, r depends on the data pattern. We have found this equation by plotting the values found from our survey and using regression. The updated weight of an information source after providing (i+1) feedbacks can be measured from the following equation:

$$w_{i+1} = w_i + \alpha(diff_i - diff_{i+1}) \qquad (6)$$

Where α is the dumping factor ($\alpha > 0$) and very small which typically decreases as number of feedback from the information source increases). This learning rate α can be determined from the following equation:

$$\alpha = e^{-(i+1)} \qquad (7)$$

V. EXPERIMENTAL EVALUATION

Evaluation of our proposed ETM system is represented in sections: 1) Weight variation of the information sources with their provided feedback and 2) Trust value measurement using

TABLE III. WEIGHT UPDATE PROCESS FOR INFORMATION SOURCE 'X'

		Assessment about QoS of:			
		Cloud Provider A	***Cloud Provider B***	***Cloud Provider C***	***Cloud Provider D***
Assessment Value	***Overall***	(0.528,0.99,0.885)	(0.634,0.97,0.96)	(0.594,0.98,0.99)	(0.724,0.97,0.99)
	X's feedback	(0.34,0.77,0.99)	(0.534,0.88,0.99)	(0.594,0.77,0.99)	(0.824,0.77,0.99)
X's Weight	***Initial***	1	0.956	0.952	0.998
	After providing feedback	0.956	0.952	0.998	0.989

practical cases. We consider the following scenario to evaluate weight variation of the information sources.

Consider a scenario of a cloud market place. 'A' is cloud-based service provider. Cloud provider 'A' fills up the CAIQs and its final assessments are $o(t,c,f) = (0.5386,0.99,0.8753)$ and $E = 0.541967$. Experts from CSA's final assessments about the QoS of cloud provider 'A' are $o(t,c,f) = (0.5186,0.9945,0.8953)$ and $E = 0.5207$. So, both filled up CAIQs of cloud provider 'A' and expert's assessments are information sources here. Consider both information sources weight are 1. Another information source (i.e. consumer) 'X' provides a feedback about the cloud provider 'A''s QoS against the offered services and its final assessments are $o(t,c,f) = (0.34,0.77,0.99)$ and $E = 0.4895$. Initially, information source 'X' has weight (w_0) 1. DoC between information source 'X' and experts' and cloud provider 'A' assessments are:

$$DoC_{A_{Expert},A_X} = \left|\left(t_{A_{Expert}} - t_{A_X}\right)\right| * c_{A_{Expert}} * c_{A_X} * \left(1 - \left|\frac{w_{Expert} - w_X}{w_{Expert} + w_X}\right|\right) = 0.1368$$

$$DoC_{A_A,A_X} = \left|\left(t_{A_A} - t_{A_X}\right)\right| * c_{A_A} * c_{A_X} * \left(1 - \left|\frac{w_A - w_X}{w_A + w_X}\right|\right) = 0.1513$$

So, the average DoC for information source 'X' is $\mathrm{DoC}_{avg} = 0.144$ and its weight difference after contributing 1st feedback is:

$$diff_{i+1} = p(0.144)^2 + q * 0.144 + r = 0.1189$$

So, after submitting 1st feedback information source 'X''s weight is updated to:

$$w_1 = w_0 + \alpha(diff_i - diff_{i+1}) = 0.956$$

Table II shows how information source 'X''s weight is updated after providing each opinion. Consider all information sources except 'X' has weight 1. For cloud provider 'A' , 'B' and 'D' information source 'X''s feedback differs a lot from the recent feedbacks from other information sources about those providers. That's why X's weight decreased. But for a good feedback about cloud provider 'C', its weight raised.

We have evaluated our ETM system by filling out the CAIQ. In the real-world case, we use assessments from the cloud service providers published in the STAR hosted by CSA. The STAR repository stores the sets of completed CAIQ questionnaires from different cloud providers. We choose two sets of feedbacks (CAIQs) by two different information sources 'P' and 'Q' about QoS of cloud-based service provider 'A'. Table III presents a summary of the aggregation of assessments from two different information source with different weight.

TABLE II. Trust value measurement: Practical case

Input Opinions		**Resulting Opinions**
o_{A_P}	o_{A_Q}	$o_{A_P} \widehat{\oplus}_w o_{A_Q}$ $W_P = 1; W_Q = 2$
(0.3,0.833,0.5)	(0.9,0.5,0.5)	(0.4717,0.6996,0.5)

Although, our system reliably evaluates the trustworthiness of the cloud providers as well as information sources in the cloud marketplace there are some limitations that need to be mentioned. Our system can translate trust information from the CAIQs and measure the trust value from them. But our system is still unable to evaluate trust value from user comments. Moreover, the cloud providers' completed CAIQs are not classified according to the types of services.

VI. CONCLUSION

The cloud marketplace is rapidly increasing with new cloud providers entering the competitive market with huge investments and massive services and supports. The reason behind cloud computing's being such demanding issue are its high dynamic, scalable, flexible nature. But consumers often faces dilemma in choosing the proper cloud provider among the service providers based on their service-specific attributes. Because of being a competitive marketplace feedbacks about different cloud providers can be manipulated. Therefore, we propose an architecture of the Entrusted TM system for cloud marketplaces to measure the weight of the information sources along with the trustworthiness of the cloud providers. In order to support the consumers as well as cloud providers we proposed the Entrusted Trust Management (ETM) system that not only measures the trust value of the providers available in the cloud marketplace but also measures how trustworthy an information source is. At the same time it allows the cloud providers to represent their competencies and capabilities. In this paper, we identify and highlight the necessity of measuring the weight of the information sources and introduce a procedure to measure it. We believe that our proposed system will make the cloud marketplace more reliable for the consumers as well as more supportive for the cloud providers at the same time.

ACKNOWLEDGMENT

The authors would like to thank the anonymous reviewers for their feedbacks and suggestions to enhance the quality of this manuscript. In particular, the authors would like to acknowledge Sheikh Mahbub Habib, Mahtab Ahmed for comments and suggestions during the development of ETM system.

REFERENCES

[1] Fujitsu Research Institute. (2010). Personal data in the cloud: A global survey of consumer attitudes 2010. Updated Aug. 2010. Available from http://www.fujitsu.com/downloads/SOL/fai/reports/fujitsu_personal-data-in-the-cloud.pdf, accessed on 02 Sep. 2015.

[2] Fujitsu Research Institute. (2010). Personal data in the cloud: The importance of trust 2010. Updated Aug. 2010. Available from http://www.fujitsu.com/global/Images/FSL-0016_A4_TrustReport_online-final.pdf, accessed on 02 Sep. 2015.

[3] S. M. Habib, S. Ries, M. Mühlhäuser, P. Varikkattu, "Towards a Trust Management System for Cloud Computing Marketplaces: using CAIQ as a trust information source," Security and Communication Networks Journal, John Wiley & Sons, vol. 7, no. 11, pp. 2185-2200, Jan. 2013.

[4] F. Dickmann, M. Brodhun, J. Falkner, T. Knoch, and U. Sax. "Technology transfer of dynamic it outsourcing requires security measures in slas," Proc. *Economics of Grids, Clouds, Systems, and Services,* vol. 6296, pp. 1–15, 2010.

[5] A Jøsang, R Ismail and C Boyd. "A survey of trust and reputation systems for online service provision," Decision Support Systems, vol. 43, no. 2, pp. 618-644, Mar. 2007.

[6] CSA. (2011) Security, Assurance & Trust Registry (STAR). Updated 23 August 2011. Available from https://cloudsecurityalliance.org/research/initiatives/star-registry/ , accessed on 02 Sep. 2015.

[7] I.U. Haq, I. Brandic and E. Schikuta. "*Sla validation in layered cloud infrastructures*," Proc. Springer Lecture Notes in Computer Science, vol. 6296, pp. 153-164, 2010.

[8] CIO. Cloud Provider 3Tera Announces 'five Nines' SLA. Updated March 2009. Available from http://www.cio.com/article/2429967/infrastructure/cloud-provider-3tera-announces--five-nines--sla.html, accessed on 01 Sep. 2015.

[9] M. Blaze, J. Feigenbaum and A. D. Keromytis. "*Keynote: Trust management for public-key infrastructures,"* Proc. Lecture Notes in Computer Science, vol. 1550, pp. 59-63, 1998.

[10] Y. H. Chu, J. Feigenbaum, B. LaMacchia, P. Resnick and M. Strauss, "Referee: trust management for web applications," *Computer Networks and ISDN Systems,* vol. 2, no. 3, pp. 127-139, 1997.

[11] S . M. Habib, S. Ries, S. Hauke and M. Mühlhäuser. "Fusion of Opinions under Uncertainty and Conflict -- Application to Trust Assessment for Cloud Marketplaces," Proc. *Trust, Security and Privacy in Computing and Communications (TrustCom),* pp. 109-118, Jun. 2012.

[12] D. Gambetta**. "**Can we trust trust?,**"** Proc. *Trust: Making and Breaking Cooperative Relations*, pp. 213-237, 1988.

[13] S. Ries. "Extending bayesian trust models regarding context-dependence and user friendly representation," Proc. *SAC '09 Proceedings of the 2009 ACM symposium on Applied Computing, New York, NY, USA,* pp. 1294-1301, 2009.

[14] S Ries, S. M. Habib, M Mühlhäuser and V. Varadharajan. "Certainlogic: A logic for modeling trust and uncertainty," Technische Universität Darmstadt, Darmstadt, Germany, Technical Report TUD-CS-2011-0104, 2011.

[15] CSA. Security guidance for critical areas of focus in cloud computing v3.0. Updated 2011. Available from https://downloads.cloudsecurityalliance.org/initiatives/guidance/csaguide.v3.0.pdf , accessed on 30 Aug. 2015.

[16] CSA. Security, Assurance & Trust Registry (STAR) FAQ. Updated 2011. Available from https:// cloudsecurityalliance.org/star/faq, accessed on 30 Aug. 2015.

[17] S. Ries. "Trust in ubiquitous computing," Ph.D. dissertation, Dept. of Computer Science, Technische Universität Darmstadt, Darmstadt, Germany, 2009.

Toward Number Recognition System : A Non-stationary Signal Analyzing Approach through SVM Algorithm

Debarati Nath[1] and Mohiuddin Ahmad[1,2]
[1]Department of Electrical and Electronic Engineering,
[2]HEQEP Sub-Project, UGC, CP#3472, Dept. of Biomedical Engineering,
[1,2]Khulna University of Engineering & Technology (KUET), Khulna – 9203, Bangladesh
E-mail: debarati10kuet@yahoo.com, mohiuddin.ahmad@gmail.com

Abstract—**Non-stationary signal analysis based on visual stimulation has drawn extensive attention in BCI system to provide the promising services. The main task of this paper tries to evaluate specific pattern of each decimal number created in human brain using the specific features of EEG. For differentiating among the decimal numbers, salient features are extracted using time, frequency and time-frequency domain analysis and SVM classifiers are used to demonstrate the primitive features. It is observed that sigmoid kernel provides the highest accuracy than the other used classifiers and numbers are differentiated clearly by the best distinguishable features of PSD analysis.**

Keywords—Number recognition; BCI; SVM; Non-stationary signal; PSD.

I. INTRODUCTION

The human computer interaction (HCI) has become a vital research topic after the invention of the computer. The past two decades have seen an explosion of scientific interest in a completely different and novel approach of interacting with a computer via signals generated by the brain itself [1]. Brain computer interface (BCI) is a revolutionary communication channel that recognizes user's command only from his brainwaves and reacts according to his command. It creates a new dimension in the field of human computer interface and provides a new, common, non-muscular communication and control channel to the disabled persons with variety of impairments, ever those who are locked in [2, 3].

There are some available technologies to serve BCIs such as electro / magneto-encephalography (EEG / MEG), positron emission tomography (PET), functional magnetic resonance imaging (fMRI), and optical imaging [4]. Among all of them, the electroencephalogram (EEG) is an imperfect and distorted indicator of brain's electrical activity recorded directly from the scalp after being picked up by metal electrodes and conductive media. As the human brain is one of the most complex systems in the universe, it is a useful tool for analyzing the functional state of brain and diagnosing certain disorders [5].

Due to the difficulties in obtaining the high classification accuracy various classification algorithms have been provided to improve the EEG based BCI performances [6]. A multitude of linear and non-linear classification algorithms have been used to discriminate among the EEG signals of patients with varying degree of cognitive impairment [7].

Linear discrimination analysis (LDA) and quadratic discriminant analysis (QDA) have been used to classify cognitive impairment [8]. Although LDA has a very low computational requirement, it is not suitable for solving non-linear problems [9]. Artificial Neural Network that is based on the simulation the human cognitive process can make the classification task more suitable. Although ANN provides the ability to reproduce arbitrary non-linear functions of input, it requires a large number of training data and is also sensitive to over-fitting.

Support vector machine (SVM) uses linear and non-linear mapping applied for various purposes such as the EEG signals classification based on the neuronal activity of the brain, cancer identification, bioinformatics, seizure prediction, face recognition and speech disorder. SVM provides good performance in many applications, especially for solving problem with high dimension, nonlinearity and small dataset [10]. Polynomial kernel, radial basis function kernel and wavelet kernel function have been used for classification and the classification test performance of the LS-SVM classifier has been determined by the computation of sensitivity, specificity and accuracy [11]. The MKL-SVM algorithm has been explored for the classifications of mental tasks and working memory tasks with WPE and Granger causality features and 99.20% average accuracy for 2-class classification and above 75% for multiclass classification have been achieved [12]. In SVM, kernel function is a major element which maps samples in one feature space to another feature space. It is really a difficult task to find out the suitable kernel function.

An EEG based number recognition technique is proposed in which the efficiency of the extracted features is compared for differentiating among the decimal numbers. It is really a challenging work based on the idea of BCI system that helps paralyzed people for compensating their lost abilities, remembering their passwords and communicates with the outside world.

978-1-4673-9257-0/15/$31.00 ©2015 IEEE

II. MATERIALS AND METHODS

Non-invasive BCI technique is used for this research work. Fig. 1 is represented the main components of the proposed BCI

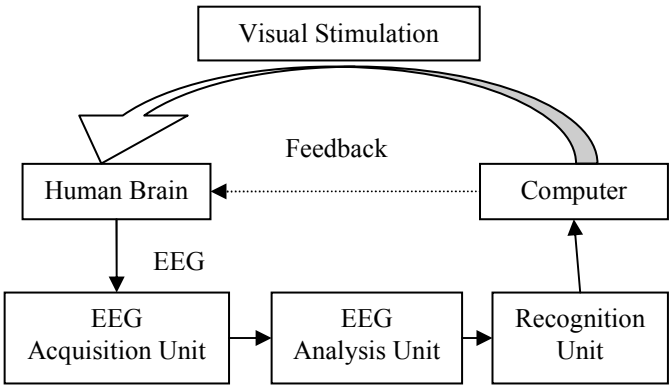

Figure 1. Block diagram of standard EEG-based BCI system.

system. Non-invasive BCI system is the communication pathway between the brain and the external device through hardware and / or software called interpreter which transforms brain wave to control signals using signal processing algorithm. It is flexible and easiest technique.

A. EEG Acquisition Unit

For the measurement of EEG data Biopac student lab hardware and software with cable and power, Biopac electrode lead set, and Biopac disposable vinyl electrodes. For EEG recoding, standard EEG measurement technique was used [13] as shown in Fig. 2. In this technique, the red electrode was placed on the occipital lobe, the white electrode was placed behind ear and the ground black lead was placed on ear lobe. The third electrode is the ground electrode. Subject selection and EEG signal recording techniques were described in [14]. Recorded EEG signal with its different bands for decimal number 1 was shown in Fig. 3.

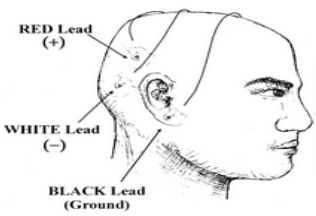

Figure 2. Standard electrode position for EEG measurement.

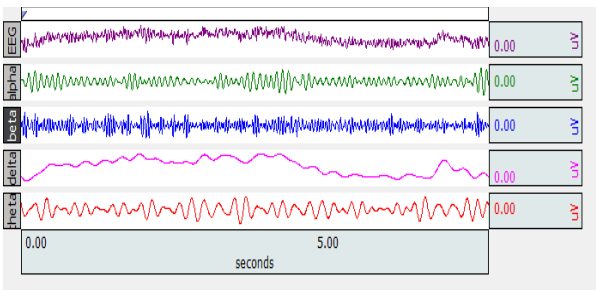

Figure 3. Raw EEG signal for decimal number 1.

B. EEG Analysis Unit

The raw EEG signal of each individual decimal number is analyzed for extracting the basic characteristics of them which is called features. Statistical analysis, frequency domain, and time-frequency domain analysis were used for best feature extraction. These features were used as the inputs of the next recognition unit for differentiating among the decimal numbers. Statistical methods are required to ensure that data are interpreted correctly and that apparent relationships are meaningful. This analysis provides ways to objectively report on how unusual an event is based on historical data. The inherent characteristics of the statistical measured on time domain signal is that they will vary in magnitude but without losing the essential element of homogeneity. Some specific features of the time domain EEG signals such as extrema, peak to peak value, mean, median, standard deviation, skew and kurtosis are extracted for recognizing the decimal numbers. The extreme point (maxima and minima) shows the maximum and minimum amplitude of the collected EEG data samples and the peak to peak value shows the difference between the maximum and minimum amplitude value of the selected area of the EEG data samples [15].

Mean computes the average value of the collected samples and this computation is achieved by Eq. (1).

$$Mean,\ \bar{m} = \frac{1}{N}\sum_{j=n_s}^{N}\left(x_{Sample\ Data}\right) \tag{1}$$

Here, $N=n_e-n_s$. n_e is the last point, and n_s is the starting point of the selected area. N is the total number of samples. j represents the values of points at horizontal axis and $x_{\text{Sample Data}}$ is the input value.

Median is a value at which the selected EEG data is divided into two regions with equal amplitude. Eq. (2) is used to extract the median value of EEG signal.

$$Median,\ m = \begin{cases} x_{\frac{N+1}{2}} & if\ N\ is\ odd \\ \frac{x_{N/2}+x_{(N/2)+1}}{2} & if\ N\ is\ even \end{cases} \tag{2}$$

Standard deviation measures the amount of variation or dispersion from the average of the selected EEG data and is defined by Eq. (3).

$$Stddev,\ s = \sqrt{\frac{1}{N-1}\sum_{j=n_s}^{N}\left(x_{Sample\ Data} - \bar{m}\right)} \tag{3}$$

Skewness is a measure of the asymmetry of a probability distribution of the selected data set. Skew normal distribution is a continuous probability distribution that generalizes the normal distribution to allow for non-zero skewness. Eq. (4) is used for extracting the skew for EEG signal.

$$\text{Sk} = \frac{\sum_{j=n_s}^{n_e}\left(x_{\text{Sample Data}}-\bar{m}\right)^3}{N} \Big/ \left(\sqrt{\frac{\sum_{j=n_s}^{n_e}\left(x_{\text{Sample Data}}-\bar{m}\right)^2}{N}}\right)^3 \tag{4}$$

Kurtosis is a measure of whether the EEG data are peaked or flat relative to a normal distribution. The formula of kurtosis is shown in Eq. (5).

$$Kurtosis = \frac{\frac{\sum_{j=n_s}^{n_e}\left(x_{Sample\ Data}-\overline{m}\right)^4}{N}}{\left(\sqrt{\frac{\sum_{j=n_s}^{n_e}(x_{Sample\ Data}-\overline{m})^2}{N}}\right)^2} \quad (5)$$

The time domain EEG signal is then converted to frequency domain using FFT for extracted the desired feature. Fast Fourier transform (FFT) is a frequency based analysis to compute the frequency component of the non-stationary signal. Features such as peak magnitude and frequency at peak magnitude were computed by using FFT which rapidly computes such transformations by factorizing the discrete Fourier transform (DFT) matrix into a product of sparse (mostly zero) factors. The DFT is generally defined by the formula in Eq. (6).

$$X_k = \sum_{j=n_s}^{n_e-1} x(j)e^{-i2\pi\frac{jk}{N}} \quad (6)$$

Power spectrum density (PSD) was used to extract features for finding out how the power of the time series data is distributed with frequency. The expression of PSD can be obtained directly as a function of frequency from the time series EEG data $x_{Sample\ Data}$ by using Eq. (7).

$$P(f) = \frac{1}{T_s}\left|T_s \sum_{q=0}^{N} x_{Sample\ Data}(q)e^{-i2\pi f q T_s}\right|^2 \quad (7)$$

Finally, discrete wavelet transform (DWT) was used because non-stationary signal contains high frequency components with short time duration and low frequency components with long time duration. It analyzes the signal at different frequency bands by decomposing of signal into a coarse approximation and detail information as shown in Fig. 4. The extracted wavelet coefficients provide compact representation that shows all the physical parameters of the EEG signal in different frequency bands. In order to reduce the increased dimensionality of the extracted features, some statistics such as maximum, minimum value, standard deviation, mean, median, skew and kurtosis over the set of the wavelet coefficients are applied.

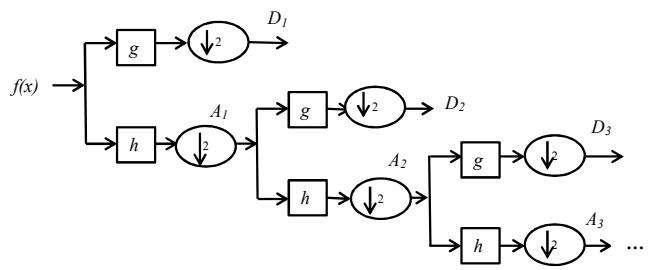

Figure 4. Sub-band decomposition of a signal by using DWT.

C. Recognition Unit

For the purpose of differentiating among the decimal numbers SVM technique is used in which the classifier operates in a higher dimensional space and attempts to label the given vectors using a dividing hyper plane [16]. The supervised learning method takes a set of training data and constructs a model that is able to label unknown test data. Given a training set of instance label pairs (x_i, y_i), $i=1, l$ where $x_i \in R^n$ and $y \in \{-1,1\}^l$ the support vector machines require the solution of the following optimization problem in Eq. (8).

$$\min_{w,b,\xi} \frac{1}{2} w^T w + C \sum_{i=1}^{l} \xi_i \quad (8)$$

$$\text{Subject to } y_i(w^T\phi(x_i) + b) \geq 1 - \xi_i,$$

$$\xi_i \geq 0.$$

Here training vectors x_i are mapped into a higher (maybe infinite) dimensional space by the function. SVM finds a linear separating hyper plane with the maximal margin in this higher dimensional space. $C>0$ is the penalty parameter of the error term. The kernel function is shown in Eq. (9).

$$K(x_i, y_j) \equiv \phi(x_i)^T\phi(x_j) \quad (9)$$

The following four kernel functions were used to find recognition rate.

- Linear : $K(x_i, x_j) = x_i^T x_j$.
- Polynomial : $K(x_i, x_j) = (\gamma x_i^T, x_j)^d, \gamma > 0$.
- RBF : $K(x_i, x_j) = \exp\left(-\gamma\|x_i - x_j\|^2\right), \gamma > 0$.
- Sigmoid : $K(x_i, x_j) = \tanh(\gamma x_i^T x_j + r)$.

Here γ, *r*, and d are kernel parameters.

For finding the higher recognition rate and best classifier for number recognition *C–SVC* and *υ– SVC* were also used. Through LIBSVM 3.12 best classifier is tried to find out and effective features for recognition is selected by the classifier. The process of number recognition by using SVM algorithm is shown in Fig. 5 by a simplified block diagram representation.

III. Features Extraction for Number Recognition

Various temporal and spatial approaches have been applied to extract features which can map the EEG data for getting higher recognition rate. From the features of beta rhythmic time domain EEG signal, it was observed that these values are almost same for same number for different peoples. The deviations in different numbers for a particular subject and different subjects are specified respectively in Fig. 6.

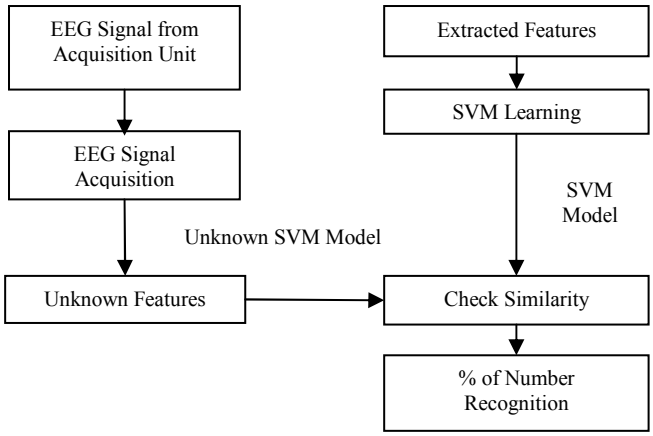

Figure 5. Block Diagram of % of Number Recognition Using Salient Features.

6. The skewness of EEG signals determines the peakedness in state of visual stimulation of different number. Again the kurtosis compares the range of the dispersion in the mental states for several subjects. It can be seen that kurtosis can differentiate the different number clearly than other features.

In case of EEG signal analysis the most distinguished information is hidden in frequency content of the signal as the frequency contents of the biomedical signals change rapidly with time. So, it can be said that frequency domain analysis provides better result than time domain analysis in case of EEG based number recognition. PSD analysis describes the

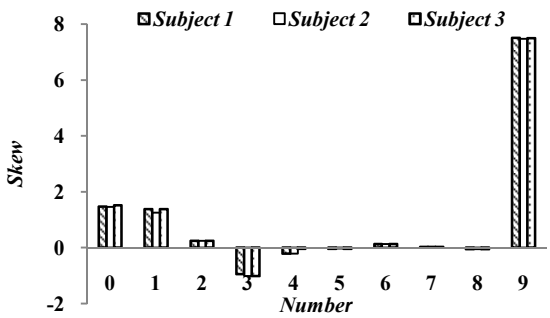

(a)

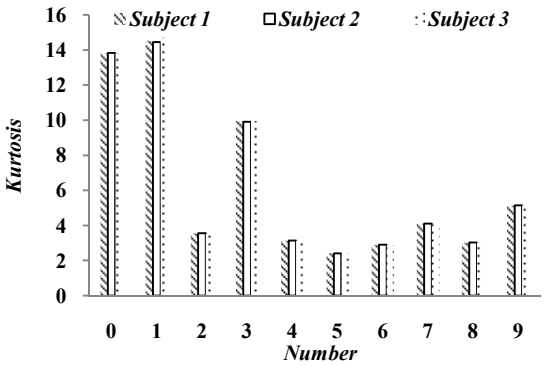

(b)

Figure 6. (a) Skew and (b) Kurtosis for 3 differet subjects.

density of power on the frequency domain and this power distribution changes according to the physiological and psychological states of the subject. Peaked power and frequency at peaked power for each number were extracted using PSD. The wavelet approach decomposes the EEG signal into its frequency components according to its range while maintaining the time resolution. Features were also extracted from DWT analysis in case of differentiating among the numbers. Fig. 7 represents the FFT and PSD for beta rhythmic EEG signal for number 0.

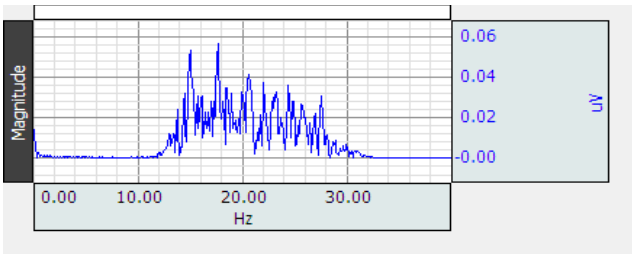

(a)

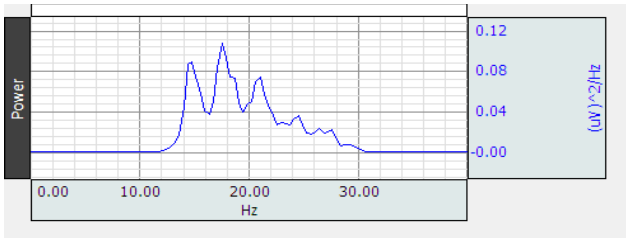

(b)

Figure 7. (a) FFT and (b) PSD of beta rhythm for number 0.

IV. Number Recognition Based on SVM

After feature extraction using time domain, frequency domain, and time-frequency domain from the beta rhythmic EEG signal, feature matrix is normalized in order to have features in a same range (-1 to 1 range has been used for number recognition). In applying SVM, the decimal numbers are classified into the defined classes. The learning and classification component consists of a training module and a classification module for different numbers. The training data of the defined features of all numbers are separated into defined classes manually. We label the train data of each action manually by an integer number. For example, Number 0=0, Number 1=1, Number 3=3, Number 4=4, Number 5=5, Number 6=6, Number 7=7, Number 8=8, and Number 9=9. The SVM classifier predicts the class label information for an arbitrary action. The SVM classifier has been trained by the training samples and then used for classifying the test data. In order to perform a more reliable classification process, three stages are implemented. Firstly, the EEG data are prepared in the specified format and scaling is performed if necessary for each subject. Secondly, the data are trained to create a model. Finally, the new input data are predicted/classified using the model. For trying to high degree of accuracy, kernel parameters are defined as that value which provides the best classification accuracy. For polynomial kernel, 3 (three) have been used for parameter "degree, d". On the other hand, 1 (one) is provided for parameter "gamma" and coef0 has been set as

0. Then, to get higher classification, the parameter *C* of *C-SVC* has been set as 1 and 0.5 has been used for the parameter *υ* of *υ-SVC*.

A. Comparison among Different Classifiers

A perfect comparison has been found among different classifiers in this section. The framework is proceeding by determining the best performance model in case of computation of classification accuracy. The classification accuracy is defined as number of correct decisions divided by the total number of cases [17].

$$Acc = \frac{TP+TN}{TP+TN+FP+FN} \times 100 \quad (10)$$

Here, TP and TN represent the total number of correctly detected true positive events and true negative events respectively. The FP and FN represent the total number of erroneously positive events and erroneously negative events, respectively. Table I shows the classification performance of the different SVM classifiers using salient features as input to the classifiers. From this table, it is seen that non-linear classification algorithm provides better result than linear classification in case of same types of attributes. Overall accuracies for features extracted from statistical, FFT, DWT, and PSD are greater in sigmoid kernel than other kernels individually and they are 76.92%, 81.82%, 93.75%, and 89.47% respectively. Although RBK provides higher accuracy than linear and polynomial kernels, it cannot provide perfect classification than sigmoid for differentiating among decimal numbers.

Two types of multiclass SVM are also considered for determining classification accuracy. It can be said that both multi-classifiers provide better recognition than linear and polynomial kernels and υ-SVC gives better accuracy than C-SVC. Overall accuracies for υ-SVC are 76%, 80%, 90.91%, and 87.5% respectively in case of features extracted from time, frequency, and time-frequency domain analysis. It is more clear from the Fig. 8 that sigmoid classifier is best than other all classifiers for EEG based number recognition because of higher accuracy. Sigmoid seems to be very efficient classifier because of leading us to get higher accuracy than the previous work of number recognition system [18] although overall accuracy of this classifier is very nearer to that of RBK.

TABLE I. OVERALL ACCURACY OF SVM CLASSIFIERS FOR CLASSIFICATION AMONG DECIMAL NUMBERS

Serial No.	Classifiers	Methods of Feature Extraction			
		Statistical	*FFT*	*PSD*	*DWT*
01.	***Linear Kernel***	70%	71.43%	84.62%	80%
02.	***Polynomial Kernel***	72.73%	75%	88.24%	83.33%
03.	***Multiclass (C - SVC)***	74%	78.57%	90%	86.67%
04.	***Multiclass (υ - SVC)***	76%	80%	90.91%	87.5%
05.	***RBK***	76.47%	80%	92.86%	88.89%
06.	***Sigmoid Kernel***	76.92%	81.82%	93.75%	89.47%

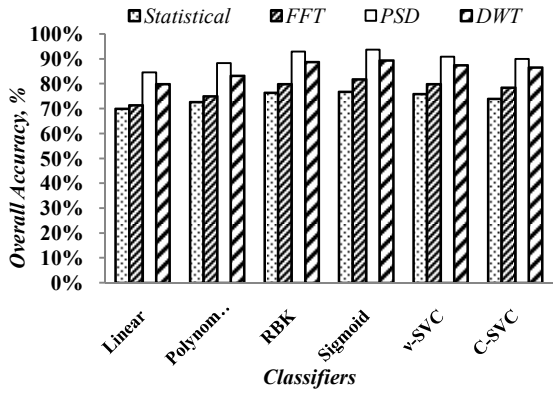

Figure 8. Overall accuracies of different features for all used classifiers.

TABLE II. COMPARISON BETWEEN PREVIOUS AND OUR WORKS BASED ON STATISTICAL ANALYSIS

Previous Work [18]	Proposed Work			
	Linear	***Polynomial***	***RBK***	***Sigmoid***
68.33%	70%	72.73%	76.47%	76.92%

The overall accuracy obtained from number recognition system based on beta rhythmic EEG in the previous work was 68.33% and this accuracy was obtained from the features of time domain analysis by LDA which is lower than our used classifiers (shown in Table II).

B. Comparison among Extracted Features

In case of EEG signal analysis the most distinguished information is hidden in frequency content of the signal as the frequency contents of the signal change rapidly with time. The frequency spectrum of the EEG signal shows the deviations in maximum amplitude and frequency in different decimal numbers for a particular subject. All classifiers provide higher accuracy in case of FFT than statistical analysis. For sigmoid classifier, the overall accuracy increases evidently from 76.92% to 81.82% when input features are transferred from statistical to FFT. The classification performance using wavelet features improves better than frequency domain features for classifying individual emotions and the obtained accuracy is 89.47%. But features based on PSD provides higher rate of classification than wavelet analysis. It is true for all used classifiers. The classification rate for all classifiers (linear, polynomial, sigmoid, RBK, C-SVC, and υ-SVC) are 80%, 83.33%, 93.75%, 92.86%, 90%, and 90.91% respectively in case of attributes of PSD. Finally, it can be said that the combination of PSD features have proved the better consideration for number recognition.

C. Individual Decimal Number Recognition

Although in case of electrical brainwave activity based on visual stimulation, the recorded by EEG is not typically expected to be the same for different subjects even under the same mental conditions, the numbers can be recognized by sigmoid kernel with salient features of PSD with higher degree of accuracy. This EEG number recognition system has shown promising result than the previous work. In case of statistical analysis, the recognition rates of all numbers were found in the range of 50% to 79% except number two which is 41.6% for

TABLE III. INDIVIDUAL RECOGNITION RATE FOR DECIMAL NUMBERS

Decimal Number	Accuracy of Previous Work (%)	Accuracy of Our Proposed Method (%)			
		Statistical	*FFT*	*DWT*	*PSD*
0	64.1	75	78.57	80	80.65
1	41.6	70.59	72.73	72.73	79.31
2	51.64	62.5	70	66.67	73.33
3	81.7	71.42	69.23	71.43	72.41
4	74.6	77.78	77.27	72.73	81.25
5	77.9	83.33	85.71	83.33	83.33
6	73.1	75	76.92	76.92	74.07
7	78.9	85.71	81.82	83.87	85.71
8	67.8	70	70	68.97	72.73
9	72	76.47	81.82	82.76	82.76

previous work. But in our proposed classifier the recognition rates varies from 70% to 85.71%. Individual accuracy is found for a specific number which provided that unique pattern for individual number is recovered by visual stimulation based EEG data analysis. Taking all time, frequency and time-frequency domain features for classification it is noticed that the performance has degraded than the individual ones. The recognition rate of individual number increases because of PSD analysis. The accuracy varies from 72.41% to 86.67% for individual number. Table III provides the individual recognition rate for number recognition using sigmoid kernel.

From this table, it is observed that the higher recognition rate is found for number 7 in case of statistical analysis and it is 85.71%. On the other hand, number 8 provides lower recognition rate and it is 62.5%. For FFT analysis, number 5 gives better recognition rate and number 3 provides lower classification rate. They are 85.71% and 69.23%. In case of DWT analysis, number 2 and 7 provide lower and higher accuracy respectively and they are 66.67% and 83.87%. In case of PSD, the individual recognition rate increases and lower value of recognition rate also increases than that of other method. The lower recognition rate in case of PSD is 72.41% and number 3 provides the accuracy.

V. CONCLUSION

BCI technology is an important building block which provides the promise of nature and intuitive human-computer interaction. This work described a framework based on the features of EEG signal in order to perform the differentiation among decimal number. In order to classify EEG signal the selection of feature extraction method and classifier becomes the major problem. For this purpose, this work evaluated the best feature extraction method for differentiating among the decimal numbers and also demonstrated the best classifier because of getting higher recognition rate. Actually EEG based decimal number recognition system tries to implement direct impacts to compensate the lost abilities of disorder person as well as their use in robotics. From this work, it is determined that frequency domain analysis provides higher recognition rate than time domain analysis and PSD analysis of beta rhythm is more suitable than FFT to produce unique patterns for number recognition with higher accuracy. It is also seen that sigmoid kernel provides higher recognition rate than the other used classifiers and it gives 93.75% accuracy for PSD analysis which is higher than the accuracy for DWT analysis. Finally, it can be said that attributes extracted from beta rhythmic EEG using PSD analysis can provide better unique pattern for a specific number and differentiate them clearly with high degree of recognition rate.

ACKNOWLEDGMENT

This work was supported by Higher Education Quality Enhancement Project (HEQEP), UGC, Bangladesh under Subproject "Postgraduate Research in BME", CP#3472, KUET.

REFERENCES

[1] R. C. Smith, "Electroencephalogram based brain computer interfaces," MEngSc thesis, University College Dublin, Dublin, Ireland, Feb. 2004.

[2] J. R. Wolpawet. al., "Brain-computer interface technology: A review of the first international meeting," *IEEE Trans. Rehab. Eng.*, vol. 8, pp. 164-173, 2000.

[3] S. J. Roberts, and W. D. Penny, "Real-time brain-computer interfacing: A preliminary study using Bayesian learning," *Med. Biol. Eng. Computing.*, vol. 38, pp. 56-61, 2000.

[4] K. An, J. Kim, W. Song, and I. Lee, "Development of an emergency call system using a brain computer interface (BCI),"in *Proc. IEEE Int. Conf. on Biomed. Rob. and Biomech.* Sep. 2010, pp. 918–923.

[5] S. Gurumurthy, V. S. Mahit, and R. Ghosh, "Analysis and simulation of brain signal data by EEG signal processing technique using Matlab," *Int. J. of Eng. And Tech. (IJET)*, vol. 5, no. 3, Jun.-Jul. 2013.

[6] R. Palaniaappan, "Brain computer interface design using band powers extracted during mental tasks," in *Proc. Of 2nd Int.Conf. on Neur. Eng.*, pp. 321-324, USA, Mar. 2005.

[7] C. Lehmann et. al., "Application and comparison of classification algorithms for recognition of Alzheimer's disease in electrical brain activity (EEG)," *J. Neurosci. Methods*, pp. 342-350, 2007.

[8] J. Dauwelset. al., "EEG synchrony analysis for early diagnosis of Alzheimer's disease: a study with several synchrony measures and EEG data sets," in *Proc. of the 31st Ann. Int. Conf. of the IEEE EMBS*, pp. 2224-2227, USA, Sep. 2009.

[9] E. Ianezet. al., "LDA-based classifiers for a mental taks-based brain-computer interference," in *Proc. Pf IEEE Int. Conf. on System, Man and Cybernetics*, South Korea, pp. 546-551, Oct. 2012.

[10] M. J. Abdin, S. M. Hosseini, and M. Rezghi, "A novel weighted support vector machine based on particle swarm optimization for gene selection and tumor classification," *Comput. Math. Method*, Article ID 320698, 2012.

[11] V. Bajaj, and R. B. Pachori, "Classification seizure and nonseizure EEG signals using empirical mode decomposition," *IEEE Trans. Inf. Technol. Biomed.*, vol. 16, no. 6, pp. 1135-1141, Nov. 2012.

[12] Xiaoou Li et. al., "Classification of EEG signals using a Multiple Kernel Learning Support Vector Machine," *Sensors*, Jul. 2014.

[13] K. Bynum, *Experimental laboratory physiology BIOPAC lab exercises*, University of North Carolina-Chapel Hill, USA, 2004.

[14] D. Nath, Md. B. Uddin, M. M. Rana, P. C. Biswas, S. Wahed, and M. Ahmad, "Number recognition using salient features of beta rhythmic EEG signal," *2nd Int. Con. On Electrical Engineering and Information & Communication Technology*(*iCEEiCT*), 21-23 May, 2015.

[15] M. Islam, T. Ahmed, S. S. Mostofa, M. S. U. Yusuf, M. Ahmad, "Human emotion recognition using frequency and statistical measures of EEG signal," *Int. Conf. on Informatics, Electronics & Vision*, May 2013, IEEE Xplore, doi: 10.1109/ICIEV. 2013.6572658.

[16] C. W. Hsu, C. C. Chang, and C. J. Lin, *A practical guide to support vector classification*, 15 April, 2010.

[17] L. Guo, D. Rivero, J. A. Seoane, and A. Pazos, "Classification of EEG signals relative wavelet energy and artificial neural networks," *GEC*, Shanghai, China, 12-14 June, 2009.

[18] S. Raoet. al., "Number recognition system using Electroencephalogram (EEG) signals," *Advanced in Computational Research*, vol. 4, no. 1, pp. 66-68, 2012.

Soft Error Tolerance Using Horizontal-Vertical-Diagonal-Blocks

Md. Shamimur Rahman
Sakib Ahammed
Dept. of Computer Science and Engineering
Khulna University of Engineering & Technology
Bangladesh
e-mail: shamimur052@gmail.com, sakib.kuet10@gmail.com

Muhammad sheikh Sadi
Dept. of Computer Science and Engineering
Khulna University of Engineering & Technology
Bangladesh
e-mail: sheikhsadi@gmail.com

Abstract—**Soft error tolerance is a matter of concern for system reliability nowadays. The likelihood of soft errors increase with system complexity, reduction in operational voltages, exponential growth in transistors per chip, increases in clock frequencies and device shrinking. As the memory bit-cell area is condensed, single event upset that would have formerly despoiled only a single bit-cell are now proficient of upsetting multiple contiguous memory bit-cells per particle strike. While these error types are beyond the error handling capabilities of the frequently used error correction codes (ECCs) for single bit, the overhead associated with moving to more sophisticated codes for multi-bit errors is considered to be too costly. To address this issue, this paper presents a new approach to detect and correct multi-bit soft error by using Horizontal-Vertical-Diagonal Blocks (HVDB) parity bits with a higher reliability.**

Keywords—Soft Error Tolerance, Horizontal Parity, Vertical Parity, Left Diagonal Parity, Right Diagonal Parity.

I. INTRODUCTION

The advent of new technologies for implementation, along with non-functional constraints (dependability, timeliness, power, cost and time-to-market), has seen the design of embedded systems become more challenging and complex [1]. The complexity of such systems is growing at a high pace through the integration of mixed-criticality applications (both safety-critical and non-safety-critical), through the high interaction of distributed application. Embedded systems engineering has evolved from designing single CPU systems (System-on-a-Chip (SoC) concept) to concurrent computing structures (Multi-Processor-System-on-a-Chip (MPSoC) and Network-on-a-Chip (NoC) concepts) often in the form of a distributed network [2], [3]. When designing high availability systems that are used in electronic-hostile environment, errors are a matter of great concern. Space programs, patient condition monitoring system in ICU where a system cannot afford a malfunction, are vulnerable to soft errors [4]. Nuclear power monitoring systems, where a single failure may cause severe destruction and real-time systems, where a missed deadline can constitute an erroneous action and a possible system failure, are a few other examples where soft error is a critical issue [5], [6], [7].

The impact of soft errors is such that action is needed to increase a system's tolerance or to lower the risk of soft errors in the system. Prior research into soft errors has focused primarily on circuit level solutions, logic level solutions, spatial redundancy and temporal redundancy [8]. However, in all cases, the system is vulnerable to soft error problems in key areas. Further, in software-based approaches, the complex use of threads presents a difficult programming model. Hardware and software duplication suffers not only from overheads due to synchronizing duplicate threads, but also from inherent performance overheads due to additional hardware. Hardware-based protection techniques based on duplication often suffers from high area, time and power overheads [9], [10], [11].

Various types of error detection and correction codes are used in computers. For example, for satellite applications, Hamming code [12] and different types of parity codes are used to protect memory devices. Complex codes are not applied due to time constraints and limited resources on board [13]. There are other methods for error detection and correction such as parity codes, rectangular parity codes, BCH codes [14], N-Dimensional parity code [15], and Golay codes [16] whose error detection and correction rate varies from method to method. In our previous paper, we used HVDD [22] i.e. Double Diagonal parity along with Horizontal, Vertical, and Diagonal parity. However, using that method we could correct up to 3 bit errors only. For this reason, there is a great need of further research to increase the error detection and correction rate with maximum reliability.

In this paper, a high-level error detection and correction method to protect against soft errors is proposed. This method is based on parities for each row, column and diagonal parity in forward and backward slash directions. The HVDB method provides high error detection and correction rate that can correct up to 12 bit upsets with high reliability in a data block.

The rest of this paper is organized as follows. We provide some related work in Section II. The proposed methodology is presented in Section III. We give an example in Section IV. In Section V, Experimental analysis is shown. Conclusions are drawn in Section VI.

II. RELATED WORK

The Several approaches are made to increase error detection and correction rate.

Pflanz et al. [17] proposed a method which can detect and correct 5 bit error using 3 dimensional parity codes. This

method cannot detect and correct all combination of 5 bit error in the data bits and it ignored the possibility of error occurrence in parity bits.

Sharma and Vijayakumar [18] proposed a method which utilizes horizontal, vertical and diagonal parity to detect and correct soft error in semiconductor memories. Here, authors described that their proposed system can detect and correct up to 5 bit errors. But Kishani et al. [13] proved that maximum 3 bit of any combination in any position can be detected and corrected by this method.

Anne et al. [19] introduces a method where data bits are arranged in different layers one over another to obtain a cube. The outer surfaces are made of the parity bits. This method forms a three dimensional structure of bits. It can detect 7 bit errors and correct 2 bit error. Anne et al. [15] described some undetectable error pattern such as 6 bit hexagonal shaped error pattern.

Aflakian et al. [20] proposed two methods for error detection and correction. In the first schema authors used horizontal, vertical and diagonal parity in both directions. This scheme can detect 7 bit errors and correct up to 4 bit errors. In the second scheme, cube of data bits are formed. Though this scheme can detect up to 15 bit errors and correct 4 bit errors, the complexity of this method is higher than existing methods.

Kishani et al. [13] corrected 3 bit errors in any combination in any position where 60 redundant bits are required for 64 data bits and can detect 100% multiple bit errors. The authors used diagonal parity in both directions along with row and column parity to detect and correct error. For this reason, their bit overhead is 73.12% which is very high. The method proposed by Kishani et al. [13] is shown in Fig. 1.

However, our correction method uses four directions same as Kishani et al. [13]. But it can detect 100% errors in any combination and correct up to twelve bit errors for almost all combinations. The correction rate of our approach is much higher than that of Kishani et al. [13].

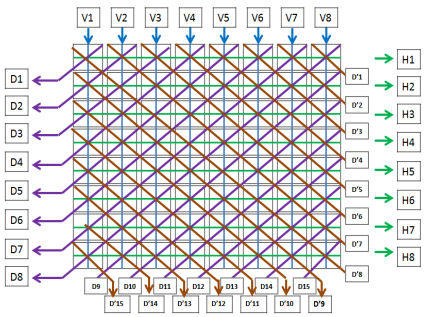

Fig. 1. The structure of the proposed method by Kishani et al. [13]

So the main differences between the proposed method and that of Kishani et al. [13] are:

1) The proposed method is relatively less complex than that of Kishani et al. [13] since it uses 100 bits for parity bits generations whereas Kishani et al. [13] uses 64bits for parity bits generations.

2) The proposed method detect and correct up to 12 bits error than that of Kishani et al. [13] which detect and correct up to 3 bits error.

III. THE PROPOSED METHODOLOGY TO DETECT AND CORRECT ERROR

The proposed method detects and corrects the soft error by using the check bits that are smeared on the Blocking (B) along with horizontal (H), vertical (V) parity and Diagonal (D) in forward and backward direction.

A. Detection Algorithm

We take a datablock of 100 bits and in a format of 10*10 array and divide them four parts of 5*5 array for calculating parity bits. In order to detect bit upsets in the codeword, all parity bits in the receiver side should be calculated again. All the menioned parity bits can be calculated independently in parallel i.e., while computing the horizontal parity bits, vertical parity bits can be computed simultaneously. This property is very operational in real-time and relatively high speed applications. After detecting the misapprehend between the received parity bits and the calculated ones, the detection algorithm will be stopped. Along with horizontal, vertical and diagonal dimensions both left and right, another four parity bits(C1, C2, C3 & C4) are calculated which is shown in the following Fig. 2 and Fig. 3.

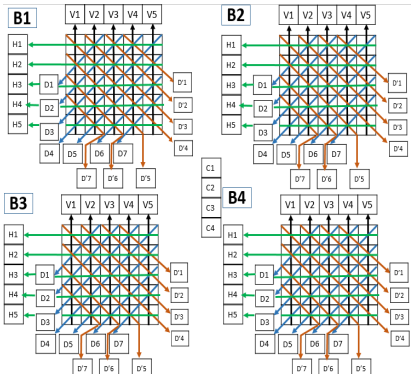

Fig. 2. The structure of the proposed method (after dividing 10*10 data block).

B. Correction Algorithm

Any difference in parity bits in horizontal, vertical and diagonal and C1, C2, C3 & C4 directions will set the corresponding syndrome bit to one. Syndrome bit is a special kind of bit which is determined by comparing sent parity and received parity. We need five arrays which clutch horizontal, vertical, left diagonal, right diagonal and C1, C2, C3 & C4 parity bits and syndrome bits respectively. Among the arrays, two are chosen and all ordered pairs of them are produced. Through every ordered pair, there may be found maximum one candidate bits. It is also mentioned that no candidate bit may be determined from some case of the ordered pair. These status are shown in Fig. 4. In the case of Fig. 4(b), two parity bits are erroneous. So, the horizontal and diagonal bits are not intersected and there is no candidate bit.

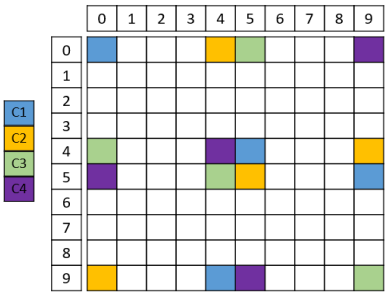

Fig. 3. Calculation of C1, C2, C3 & C4.

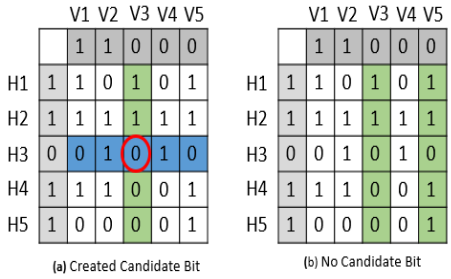

Fig. 4. The created candidate bit and no candidate bit of the intersection

According to Kishani et al. [13], all of the factual bit upsets are included in candidate bits and if a candidate bit is alone in one row of horizontal or column of vertical or diagonal dimension or C1, C2, C3 & C4 (i.e. there is not any other candidate bit in the same row of horizontal or column of vertical or diagonal dimension or C1, C2, C3 & C4) and if there is a syndrome bit which is set to one in a row or column or diagonal, the candidate bit is faulty and must be corrected. There is always a candidate bit that can be selected to be eliminated [13].

C. *HVDB Implementation*

The proposed implementation of HVDB coding arrangement is shown in Fig. 2. The figure shows 200 bit codeword consists of 100 data bits and 100 check bits. Note that, the overhead of a codeword depends on the number of additional bits compared to the whole memory block size. The memory segregated into appropriate number of slice and the codeword is calculated for the slice.

IV. AN EXAMPLE OF ERROR DETECTION AND CORRECTION

In this section, we consider 10 errors occurrence in a codeword and show how the proposed methodology corrects it. The code word architecture with errors (the red (dark) squares) is shown in Fig. 6. The detection and correction methods of HVDB are shown as follows.

Now the 10*10 bits pattern is divided by four 5*5 bits blocks as shown in Fig. 7. So, the next operation are same for all 5*5 blocks.

A. *Mark Candidate Bits*

Each parity bit has a corresponding line of codeword bits that generate it. Lines of each mistaken parity bit are considered. If there is an intersection between two lines then it is a candidate bit. Candidate bit represents the mismatched parity positions. After finding candidate bits, we need to store the address of each bit in an array. The candidate bits are marked in Fig. 9.

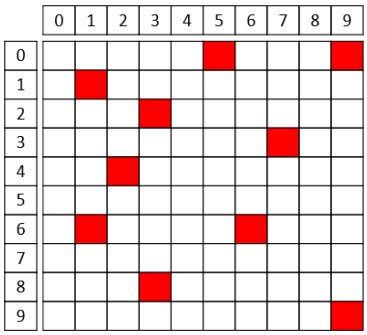

Fig. 6. Erroneous bits in 100 bits datablock.

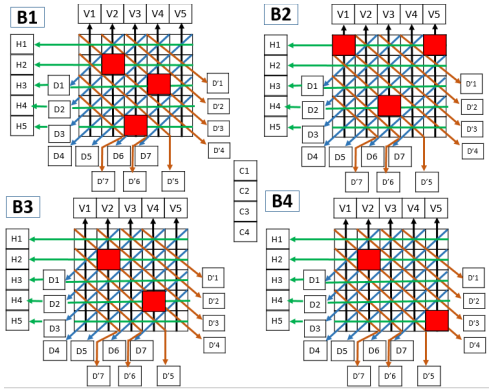

Fig. 7. Divide 100 bits datablock into four blocks with errorneous bits.

B. *Refine Candidate Bits To Find Error*

All the candidate bits are not erroneous but all erroneous bits are candidate bits. To refine candidate bits, we use the condition: in any direction (i.e. row or column or diagonal or C1, C2, C3 & C4), if there is any candidate bit found already but the corresponding syndrome bit is not set then that candidate bit is eliminated. If there is a syndrome bit which is set to one in a row or column or diagonal or C1, C2, C3 & C4, the candidate bit is erroneous and must be corrected.

For example from Fig. 9, in block-1(B1) candidate 1, 6, 7, 15 & 17 which are the only candidate bits in D1, D'1, V1, D'7 & D7 and the corresponding syndrome bits aren't set. So, these candidate bits are not erroneous and must be removed. Similarly in block-2(B2) candidate 3, 4, 5, 6, 7, 9, 10, 11 & 12 bits are eliminate and in block-3(B3) candidate 1, 2, 3 & 4 are the only candidate bits of D1, D'2, D'6 & D6. The syndrome bits for D'2 & D'6 are not set that's why candidate 2 & 3 are not erroneous and must be removed. But the syndrome bits for D2 & D6 are set. So, candidate 1 & 4 are erroneous and must be corrected. In block-4(B4), candidate 1, 2, 3 & 4 are only

candidate bits in D2, D'1, and V1 & D' 7. The syndrome bit for D2 is set i.e. candidate 1 is erroneous and must be corrected. Other candidate bits are eliminated. After this step the architecture is shown in Fig. 10.

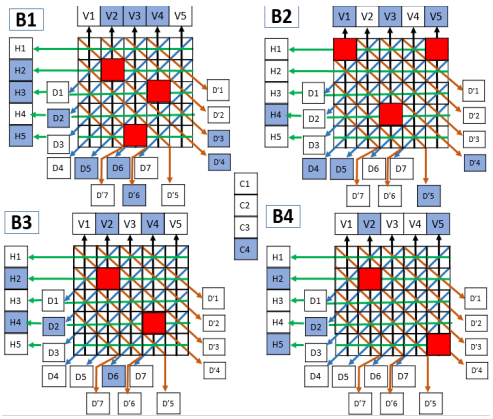

Fig. 8. Code word with parity codes.

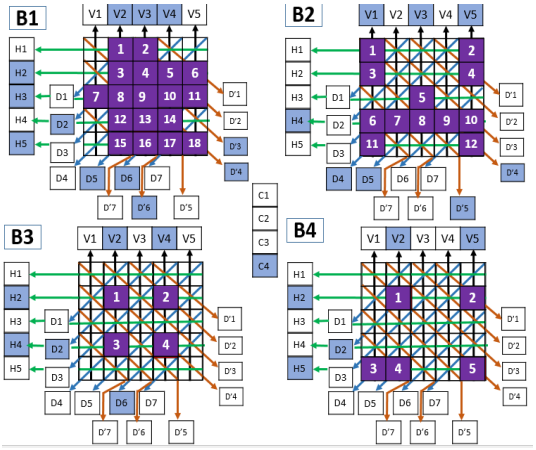

Fig. 9.Candidate bits.

For example from Fig. 9, in block-1(B1) candidate 1, 6, 7, 15 & 17 which are the only candidate bits in D1, D'1, V1, D'7 & D7 and the corresponding syndrome bits aren't set. So, these candidate bits are not erroneous and must be removed. Similarly in block-2(B2) candidate 3, 4, 5, 6, 7, 9, 10, 11 & 12 bits are eliminate and in block-3(B3) candidate 1, 2, 3 & 4 are the only candidate bits of D1, D'2, D'6 & D6. The syndrome bits for D'2 & D'6 are not set that's why candidate 2 & 3 are not erroneous and must be removed. But the syndrome bits for D2 & D6 are set. So, candidate 1 & 4 are erroneous and must be corrected. In block-4(B4), candidate 1, 2, 3 & 4 are only candidate bits in D2, D'1, and V1 & D' 7. The syndrome bit for D2 is set i.e. candidate 1 is erroneous and must be corrected. Other candidate bits are eliminated. After this step the architecture is shown in Fig. 10.

Consider candidate 2 in block-1(B1) from Fig.10 which is the only candidate bit in H1 direction but the corresponding syndrome bit is not set. So candidate 2 is removed. In block-2(B2) candidate 1 is the only bit in V1 & D'4 direction and corresponding syndrome bits are set. So candidate 1 is erroneous and must be corrected. Similarly candidate 2 and 8 are only bit in V5, D4 and V3, H4, D5, D'5 and corresponding syndrome bits are set. So these candidates are erroneous and should be corrected. In block-3(B3) all the candidate bits are evaluated. In block-4(B4) candidate 5 is only bit of V5 & H5 direction and the syndrome bits of these direction are set. So, this bit is erroneous and must be corrected. After this step the architecture is shown in Fig. 11.

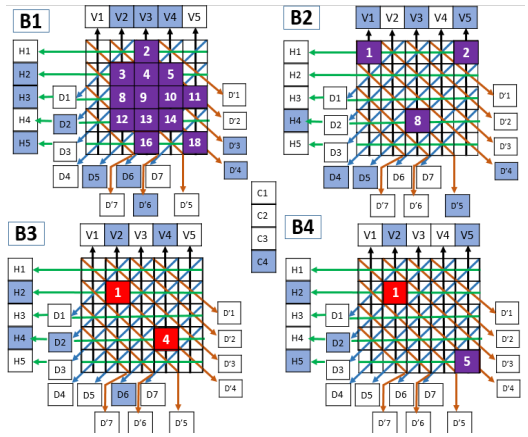

Fig. 10. Refining candidate bits: First Step.

Consider candidate 2 in block-1(B1) from Fig.10 which is the only candidate bit in H1 direction but the corresponding syndrome bit is not set. So candidate 2 is removed. In block-2(B2) candidate 1 is the only bit in V1 & D'4 direction and corresponding syndrome bits are set. So candidate 1 is erroneous and must be corrected. Similarly candidate 2 and 8 are only bit in V5, D4 and V3, H4, D5, D'5 and corresponding syndrome bits are set. So these candidates are erroneous and should be corrected. In block-3(B3) all the candidate bits are evaluated. In block-4(B4) candidate 5 is only bit of V5 & H5 direction and the syndrome bits of these direction are set. So, this bit is erroneous and must be corrected. After this step the architecture is shown in Fig. 11.

In third step, candidate 3 in block-1(B1)(Fig.11) is the only bit in D2 direction and corresponding bit is set that's why this candidate 3 is erroneous and should be corrected. Now consider candidate 18 which is the only candidate bit is C4 direction and corresponding syndrome bit is set. But there is another erroneous bit already detected in C4 direction. That's why candidate 18 is not erroneous and removed. There are no candidate bits of other block. So, these blocks are now out of consideration. After this step the architecture shown in Fig.12.

Again consider from Fig.12 in block-1(B1) candidate 11 and 16 are the only candidate bits in V5 and H5 direction. The corresponding syndrome bit of V5 is not set but H5 is set. For that candidate 11 is not erroneous but candidate 16 is erroneous bit and must be corrected. After fourth step the architecture is shown in Fig.13.

Consider candidate 5, 12, 14 in block-1(B1) from Fig.13 which are the only candidate in D'2, D'6 and D6 direction.

The syndrome bit of D'2 direction is not set that's why candidate 5 is eliminated. But the syndrome bits of D'6 and D6 direction is set and there are already an error occurred of that direction. For that, candidate 12 and 14 are not erroneous and should be removed. After this step the architecture is shown in Fig. 14.

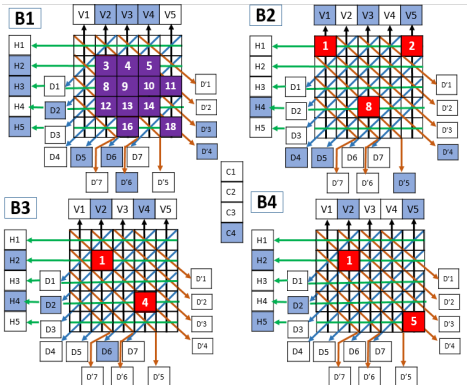

Fig. 11. Refining candidate bits: Second Step.

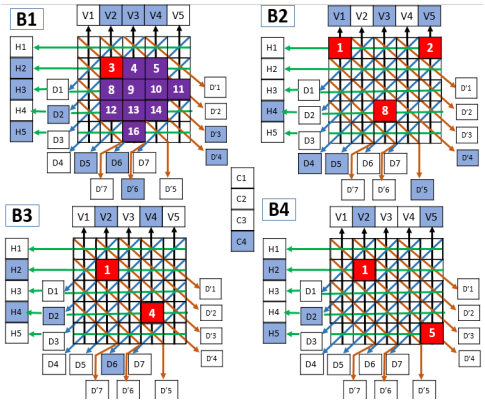

Fig. 12. Refining candidate bits: Third Step.

Now the final step, consider candidate 4, 8, 9, 10, 13 in block-1(B) from Fig.14 which are only candidate in H2, V2, D4, V4 and H4 direction. The syndrome bits of D4 and H4 are not set. So, candidate 9 and 13 are eliminated. The corresponding syndrome bits of H2, V2 and V4 are set. Candidate 4 and 8 are eliminated because in H2 and V2 direction there is already an error occurred and candidate 10 is erroneous and must be corrected. After that all candidate bits are evaluated and find the erroneous bits. The final step architecture is shown in Fig.15.

V. EXPERIMENTAL ANALYSIS

The proposed HVDB can detect all combinations of errors and correct up to 12 bit errors. Table 1 compares the HVDB method with existing dominant methods. This comparison is based on detection and correction rate.

As shown in Table 1, HVDB performs better than Golay[14], BCH[16], and HVD[13] with respect to correction rate. The first column of Table. 1 shows several dominant methods including the proposed one, second and third columns show the dataword sizes and corresponding parity bits. The fourth column presents the codeword sizes which are the summation of datawords and parity bits.

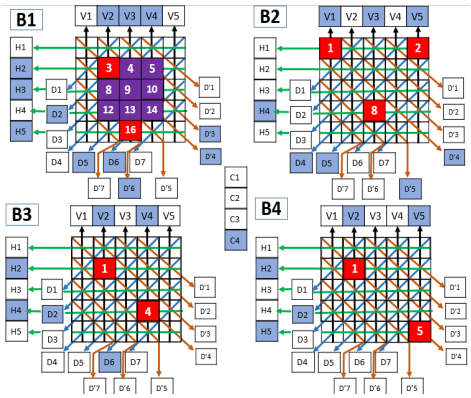

Fig. 13. Refining candidate bits: Fourth Step.

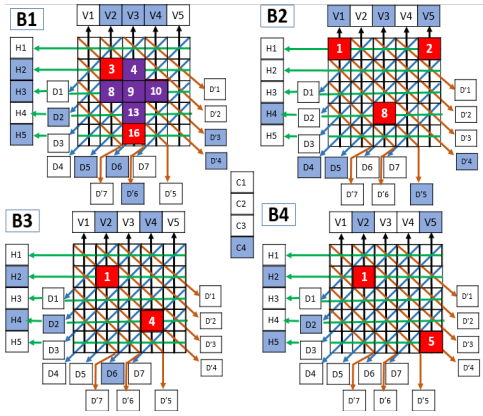

Fig. 14. Refining candidate bits: Fifth Step.

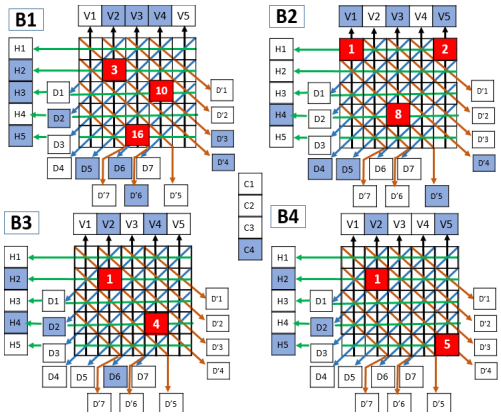

Fig. 15. Refining candidate bits: Final Step.

The fifth column shows the number of bit corrected by each method. In the first column, 'Golay(23,12,7)' represents that in the method proposed by Golay[14], they used the examples which have the codeword of size 23 bits, parity bits of size 12 bits and hamming distance of 7 and can correct only 3 bits error. BCH (31, 16, 7) represents same meaning as Golay(23,12,7). HVD (64) represent the dataword sizes of 64

bits. In HVD [13], there are 60 parity bits for 64 bits data block and correct only 3 bits error pattern whereas the proposed method working with 100 bits and correct up to 12 bits error pattern. So, the correction rate is higher than HVD [13]. HVDD (64) represents same meaning as HVD (64). The fifth and sixth column show the bit overhead and code rate of the proposed method using the following rules

$$\text{Bit Overhead} = \frac{\text{Number of Parity Bits}}{\text{Number of Data Bits}} = \frac{100}{100} = 100\% \quad (1)$$

$$\text{Code Rate} = \frac{\text{Number of Data Bits}}{\text{Number of Codeword Bits}} = \frac{100}{200} = 50\% \quad (2)$$

TABLE1. Comparison of mult bit error correcting codes

Error Correcting Method	# of Data Bits	# of parity bits	#of code word bits	# of bits corrected	Bit Overhead (%)	Code rate (%)
Golay(23,12,7)	11	12	23	3	91.67	52.17
BCH(31,16,7)	15	16	31	3	93.75	51.61
HVD(64)	64	60	124	3	78.12	56.14
HVDD(64)	64	27	91	3	42.19	70.33
HVDB(100)	100	100	200	12	100	50

From the experimental analysis it can be observed that the proposed method can detect and correct up to twelve bits errors in any combinations. To detect candidate bits, we take cross- section of two directions among the five. This method can't detect any intersection where four bits errors are in close rectangle pattern. We solved this problem in this particular situation that may rarely happen by using our previous method as shown in Sadi et al. [21].

VI. CONCLUSION

This paper proposes a high-level error detection and correction method to protect against soft errors. This method is based on parities for each row, column, diagonal (in forward and backward) and C1, C2, C3 and C4 directions. The HVDB provides error detection capabilities for all possible errors and can correct up to 12 bit errors in a data word. Though it faces problem to detect a particular error pattern and it has higher bit overhead, it has a significant contribution in increasing information correction rate than existing dominant methods. Reducing the information overhead can be captured as an extension of the current research.

REFERENCES

[1] Manoochehri,Annavaram, Dubois, "Extremely Low Cost Error Protection with Correctable Parity Protected Cache,"Computers, IEEE Transactions on (Volume:63, Issue: 10), pp. 2431-2444, September 2014.

[2] Sanchez-Macian,Reviriego, Maestro, "Hamming SEC-DAED and Extended Hamming SEC-DED-TAED CodesThroughSelective Shortening and Bit Placement,"Device and Materials Reliability, IEEE Transactions on (Volume:14, Issue: 1), pp. 574-576, March 2014

[3] Reviriego, Flanagan, Pontarelli, Maestro, "An Efficient Technique to Protect Serial Shift Registers Against Soft Errors,"Circuits and Systems ll: Express Briefs. IEEE Transactions on(Volume:60, Issue: 8), pp. 512-516, August 2013.

[4] Neale, Sachdev, "A New SEC-DED Error Correction Code Subclass for Adjacent MBU Tolerance in Embedded Memory,"Device and Materials Reliability, IEEE Transactions on (Volume:13, Issue: 1),pp. 223 – 230, March 2013

[5] Muhammad Sheikh Sadi, MizanurRahman Khan, NazimUddin, and Jan Jürjens, "An Efficient Approach towards Mitigating Soft Errors Risks," Signal& Image Processing: An International Journal (SIPIJ),vol. 2, No. 3, September 2011.

[6] Ne'amHashemIbraheem "Error-Detecting and Error-Correcting Using Hamming and Cyclic Codes," IEEE Transactions on Information Theory, vol. 51, no. 9, pp. 3347–3353, September 2005.

[7] Ferreyra PA, Marques CA, Ferreyra RT, Gaspar JP,"Failure map functions and accelerated meantime to failure tests: new approaches for improving the reliability estimation in systems exposed to single event upsets," IEEE Trans NuclSci 52(1), pp. 494–500

[8] ArgyridesC, Zarandi HR, Pradhan DK "Multiple upsets tolerance in SRAM memory," International symposium on circuits and system, New Orleans, LA, May 2007

[9] A. A. Jerraya, "Long term trends for embedded system design," Digital System Design,Euromicro Symposium on, 2004, pp. 20-26

[10] Hyun Yoon D, Erez M (2009) "Memory mapped ECC: low-cost error protection for last level caches," ACM SIGARCHComputArchit News 37(3):116–127

[11] M. S. Sadi, D. G. Myers, C. O. Sanchez, "A Design Approach for Soft Error Protection in Real-Time Embedded Systems," 19th Australian Conference on Software Engineering, ASWEC 2008, pp. 639-643

[12] Hentschke R, Marques R, Lima F, Carro L, Susin A, Reis R, "Analyzing area and performancepenalty of protecting different digital modules with hamming code and triple modular redundancy," International symposium on integrated circuits and systems design,pp. 95–100

[13] Mostafa Kishani, Hamid R. Zarandi, HosseinPedram, AlirezaTajary, Mohsen Raji, BehnamGhavami "HVD: horizontal-vertical-diagonal error detecting and correcting code to protect against with soft errors" Des Autom Embed Syst (2011) 15:289–310DOI 10.1007/s10617-011-9078-2

[14] Muhammad Imran, Zaid Al-Ars, Georgi N. Gaydadjiev, "Improving Soft Error Correction Capability of 4-D Parity Codes," 14th IEEE European Test Symposium, May 2009

[15] Rubinoff M "N-dimensional codes for detecting and correcting multiple errors,"ComunACM 545–551

[16] http://mathworld.wolfram.com/GolayCode.html

[17] M. Pflanz et al.,"On-Line Techniques for Error Detection and Correction in Processor Registers with Cross-Parity Check," Journal of Electronic Testing, October 2003, Volume 19, Issue 5, pp. 501-510

[18] Shalini Sharma, Vijayakumar P. "An HVD Based Error Detection and Correction of Soft Errors in Semiconductor Memories Used for Space Applications," International Conference on Devices, Circuits and Systems (ICDCS), 2012.pp. 563 - 567

[19] NaveenBabu Anne, UtthamanThirunavukkarasu, Dr. ShahramLatifi "Three and Four-dimensional Parity-check Codes for Correction and Detection of Multiple Errors," Proceedings of the International Conference on Information Technology: Coding and Computing (ITCC'04), pp. 267-282, 2004.

[20] DanialAflakian, Dr.TamannaSiddiqui, Najeeb Ahmad Khan, DavoudAflakian "Error Detection and Correction over Two-Dimensional and Two-Diagonal Model and Five-Dimensional Model," (IJACSA) International Journal of Advanced Computer Science and Applications, Vol. 2, No. 7, 2011

[21] M.S. Sadi, M.S. Rahman, K.M. ImrulKayesSikdar, "Error detection & correction using horizontal-vertical-diagonal-shift method," Electrical Engineering and Information & Communication Technology (ICEEICT), 2014 International Conference on, pp. 1-7 , April 2014

[22] Md. Shamimur Rahman, Muhammad Sheikh Sadi, Sakib Ahammed, and Jan Jurjens, "Soft Error Tolerance using Horizontal-Vertical-Double-Bit Diagonal Parity Method," International Conference on Electrical Engineering and Information Communication Technology (ICEEICT 2015)

Towards Tolerating Soft Errors in Memory Applications

Muhammad Sheikh Sadi, Musaddique Billah Talha, Swadin Saha, Golam Mezbah Uddin, Kazi Md. Bodrul Kabir
Department of Computer Science and Engineering
Khulna University of Engineering & Technology (KUET)
Khulna 9203, Bangladesh
sheikhsadi@gmail.com, mbtalha3110@gmail.com, rahul4kuet@hotmail.com, mezbah.isti@yahoo.com, kazi.sazid@gmail.com

Abstract— **These days' memory elements in digital systems have become more prone to soft errors or transient errors due to integration in circuits, smaller size of transistors and capacitors, combining with cosmic ray effects and many more reasons. Soft errors in memory elements have been a greater concern than soft errors in logic circuits since memories are used to hold the largest numbers and bits susceptible to particle strikes. This paper introduces a high level error detection and correction method to provide more immunity to memory elements. This paper introduces an algorithm which can decide if there is a single bit error or double bit error. If a single bit is erroneous then it determines which portion (among information bits or check bits) of the code word contains the error and then performs operation to detect and correct the error. And in case of two erroneous bits, it performs the detection and correction operation for the whole code word. The proposed approach can correct up to 2 bit upsets in a 15 bit data block within lesser computation cycles compared to existing dominant approach.**

Keywords—***Soft errors, Memory Applications, Majority logic Decodale (MLD), Shift Cycles, Error Correction Code.***

I. INTRODUCTION

All electronic storage devices have the potential to incorrectly return information different than what was originally stored. Reliability in memory applications has always been a great ask. But the newly introduced technologies in these days focus more on smaller dimensions and low operating voltages. That's why embedded memories like DRAM, SRAM, ROM, flash memory have become more susceptible to memory failures or errors [1]. For instance, a momentary failure in banking transactions may cause a huge difference in balances. These are errors in processor execution that are due to electrical noise or external radiation rather than design or manufacturing defects. So considering the consequences of it, several error techniques like Hamming codes; Triple Modular Redundancy (TMR); Error Correcting Codes(ECC) ; fault tolerant encoder/decoder [2] are already in practice. Triple Modular Redundancy hardware is faster than Hamming error correction software. Space satellite systems often use TMR, although satellite RAM usually uses Hamming error correction. But TMR has the disadvantage of large area and complexity overhead. Error Correcting Codes (ECC) [3], [4] are more preferable to mitigate soft errors in memory than TMR or Hamming codes. Advanced ECCs like Double Error Correction Codes (DEC) are already introduced but they suffer from noticeable power consumption. Multi error correction methods like Reed-Solomon (RS) and Bose Chaudhuri–Hocquenghem (BCH) are available but they follow complex decoding algorithm. Among the ECCs, cyclic block codes are most suitable because of its high error correction capability and less complex decoding algorithm and they are majority logic (ML) decodable.

This paper proposed a new algorithm which is primarily based on Majority Logic Detector/Decoder (MLDD) [5] circuit but considers three possible cases and performs separate operations on the code word according to those cases in order to lessen the error detection and correction time. The proposed method can correct up to two erroneous bits among a 15 bit code word. When the size of the code word increases, the possibility of bit flip also increases. So, when dealing with a code word of 15 bits' size, it is not feasible to test all possible conditions. Hence, dividing the combinations into possible cases improves its time efficiency.

This paper introduces a method which can correct up to two erroneous bits among a 15 bit code word. When the size of the code word increases, the possibility of bit flip also increases. So when dealing with a code word of size 15 bit, it is not feasible to test all possible conditions hence dividing the combinations into possible cases. The paper proposed a new algorithm which is based on majority logic detector/decoder (MLDD) circuit. This method calculates the parity check-sums using an encoder circuit [1]. It detects either one or two bit errors by calculating the majority of the code word using a one-step majority logic circuit [6]. The algorithm considers three possible cases and perform separate operations on the code word according to those cases. Also the method uses a cyclic shift register and majority calculation to detect and correct the erroneous bits while decoding. Determination of whether the code word is erroneous or not is done in three cycles which is quite similar to other methods. But the method provides great efficiency when it comes to one bit of error. The algorithm needs 11 cycles to correct 1 bit of error which is a great advance in performance compared to other existing methods. The remainder of the paper is organized as follows:

Section II provides an overview of existing error detection and correction method. Section III presents our proposed method for error detection and correction. Section IV discusses the results obtained with respect to speedup, delay and power consumption. Finally, Section V draws the conclusions.

II. Related Work

MLD is based on a number of parity check equations. The majority result of these parity check equations decide the correctness of the current bit under decoding.ML decoder is a simple detector, capable of detecting multiple random bit-flips depending on the number of parity check equations [7], [8]. It consists of four parts: i) a cyclic shift register; ii) an XOR matrix; iii) a majority gate; and iv) an XOR gate for correcting the codeword bit under decoding. The input signal is initially stored into the cyclic shift register and shifted through all the taps. The algorithm needs as many cycles as the number of bits in the input signal, which is also the number of taps, to detect error. This is a big impact on the performance of the system, depending on the size of the code. For example, for a codeword of N bits, the decoding would take N cycles, which would be excessive for most applications. Also the MLD technique requires equal decoding time for error and error free code words.

Majority Logic Detector/Decoder (MLDD) which is an extension from the plain MLD discussed earlier. This MLDD technique is based on Euclidian Geometry Low Density Parity Codes (EG-LDPC) [9], [6] which uses one step majority logic circuit. This technique reduces the time needed to detect errors to a great extent, i.e. the method requires only three cycles to detect errors. But this method proposed by Jayarani et. al [2] noticeably failed to provide greater performance[10] when correcting the error bits. The method requires 18 cycles to correct one or two bit errors

III. The Proposed Methodology to Detect & Correct Error

This paper proposed a new algorithm which is primarily based on Majority Logic Detector/Decoder (MLDD) circuit which has been implemented by using the Euclidean geometry low-density parity check (EG-LDPC) codes. The EG-LDPC codes [9] are based on the structure of Euclidean geometries over a Galois field. The details of encoder and corrector circuits that are used at the beginning of the proposed method are outlined shortly as follows.

A. Design Structure of Encoder of EG-LDPC

The systematic generator matrix to generate (15, 7, 5) EG-LDPC code is shown in Figure 1, which has been captured from the paper presented by Liu et al. [6]. The encoded vector mainly consists of two parts, the first part consist of information bits and second part is of check bits, where each check bit is simply an inner product of information vector and a column of X , from the generator matrix G=[I:X]. The encoder circuit [6] to compute the parity bits of the (15, 7, 5) EG-LDPC code is shown in Figure 2. In this figure, the information vectors are (i0,..,i6) and will be copied to (c0,..,c6) bits of the encoded vector, c. The rest of encoded vector (c7,……,c14), that is the parity bits are the linear sums (XOR) of the information bits.

B. Design Structure of Corrector EG-LDPC

One-step majority-logic correction is a fast and relatively compact error-correcting technique. There is a limited class of ECCs that are one-step-majority correctable which include type-I two-dimensional EG-LDPC. In this section we show the one-step majority-logic corrector [5] for EG-LDPC codes.

$$
\begin{array}{c|ccccccccccccccc}
 & c_0 & c_1 & c_2 & c_3 & c_4 & c_5 & c_6 & c_7 & c_8 & c_9 & c_{10} & c_{11} & c_{12} & c_{13} & c_{14} \\
\hline
i_0 & 1 & 0 & 0 & 0 & 0 & 0 & 0 & 1 & 0 & 0 & 1 & 1 & 1 & 0 & 1 \\
i_1 & 0 & 1 & 0 & 0 & 0 & 0 & 0 & 1 & 1 & 0 & 0 & 1 & 1 & 1 & 0 \\
i_2 & 0 & 0 & 1 & 0 & 0 & 0 & 0 & 0 & 1 & 1 & 1 & 0 & 0 & 0 & 1 \\
i_3 & 0 & 0 & 0 & 1 & 0 & 0 & 0 & 1 & 0 & 1 & 1 & 1 & 0 & 0 & 0 \\
i_4 & 0 & 0 & 0 & 0 & 1 & 0 & 0 & 0 & 1 & 0 & 1 & 1 & 1 & 0 & 0 \\
i_5 & 0 & 0 & 0 & 0 & 0 & 1 & 0 & 0 & 0 & 1 & 0 & 1 & 1 & 1 & 0 \\
i_6 & 0 & 0 & 0 & 0 & 0 & 0 & 1 & 0 & 0 & 0 & 1 & 0 & 1 & 1 & 1
\end{array}
$$

$$\underbrace{\qquad\qquad}_{I}\qquad\underbrace{\qquad\qquad\qquad}_{X}$$

Figure 1: Generator matrix of (15,7, 5) EG-LDPC code.

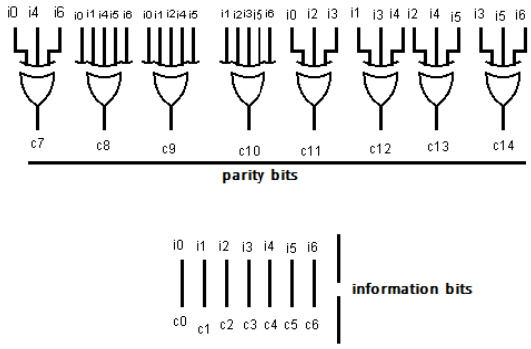

Figure 2: Structure of an encoder circuit for the (15, 7, 5) EG-LDPC code [1]

A linear sum of the received encoded vector bits can be formed by computing the inner product of the received vector and a row of a parity-check matrix. This sum is called Parity-Checksum. The core of the one-step majority-logic corrector is generating α parity-check sum from the appropriate rows of the parity-check matrix. The majority logic error correction, which corrects a potential error in one code bit, is outlined shortly using the following steps.

Step 1. Generate γ parity-check sums by computing the inner product of the received vector and the appropriate rows of parity-check matrix.

Step 2. The γ check sums are fed into a majority gate. The output of the majority gate corrects the bit cn-1 by inverting the value of cn-1 if the output of majority gate is '1'.

The circuit implementing a serial one-step majority logic corrector for (15, 7, 5) EG-LDPC code is shown in Figure 3. This circuit generates γ parity-check sums with γ XOR gates and then computes the majority value of the parity-check sums. Since each parity-check sum is computed using a row of the parity check matrix and the row density of EG-LDPC codes are ρ, each XOR gate that computes the linear sum has ρ inputs. The single XOR gate corrects the code bit cn-1 using the output of the majority gate. Once the code bit cn-1 is corrected, the codeword is cyclic shifted and code bit c_{n-2} is placed at c_{n-1} position and will be corrected. The whole codeword can be corrected in n rounds.

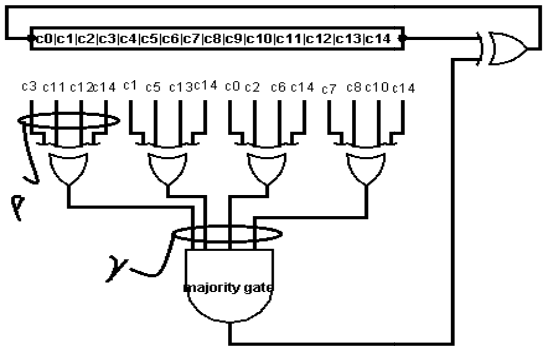

Figure 3: Serial one-step majority logic corrector structure to correct last bit (bit 14th) of 15-bit (15, 7, 5) EG-LDPC code [1].

C. The Proposed Algorithm

In general, the proposed version uses Majority Logic Detector/Decoder (MLDD) circuit [1], [2] but considers three possible cases and executes separate operations on the code word for fault detection and correction. If there is 1 bit error then it calculates the parity of information bits and check bits separately for both of the sent and received codeword. The XOR matrix is estimated for the first three cycles of the decoding process, and when all the outputs {Bj} is "0", the code word is determined to be error-free and enhanced directly to the output. Moreover, it considers three possible cases to lessen the time requirement for fault detection and correction. These cases are as follows.

1. Parity of information bits of sending code word is equal to parity of information bits of receiving codeword.
2. Parity of check bits of sending code word is equal to parity of check bits of receiving codeword.
3. Both case 1 and case 2 is not equal.

For case-1, when parity of information bits of sending and receiving end is equal then the codeword is passed to a cyclic shift register and their majority value is calculated. If the majority variable is greater than 2 that is if the majority is 1 then the bit under decoding is erroneous and hence corrected otherwise performing the cyclic shift operation for 7 times (Figure 4).

For Case-1:
Let,
The Sending Codeword : 1 1 1 0 1 1 1 0 1 0 0 0 1 1 1
And the Receiving Codeword: 1 1 0 0 1 1 1 0 1 0 0 0 1 1 1

For Sending Codeword:
Parity of information bits: 0
Parity of check bits: 0
For Receiving Codeword:
Parity of information bits: 1
Parity of check bits: 0

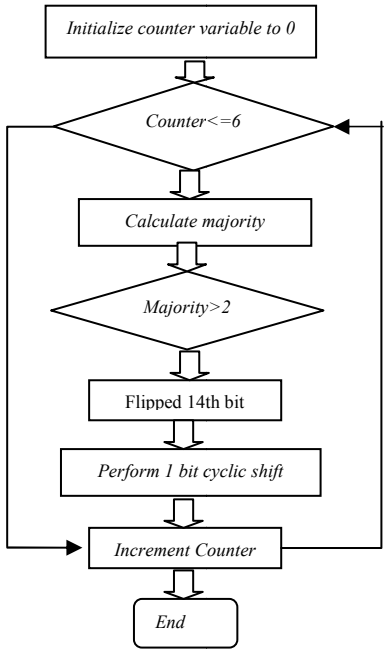

Figure 4: The Flowchart for Case-1.

For cycle 1:	1 1 0 0 1 1 1 0 1 0 0 0 1 1 1	Majority: 0
For cycle 2:	1 0 0 1 1 1 0 1 0 0 0 1 1 1 1	Majority: 0
For cycle 3:	0 0 1 1 1 0 1 0 0 0 1 1 1 1 1	Majority: 1
Inverse:	0 1 1 1 0 1 0 0 0 1 1 1 1 1 1	
For cycle 4:	0 1 1 1 0 1 0 0 0 1 1 1 1 1 1	Majority: 0
For cycle 5:	1 1 1 0 1 0 0 0 1 1 1 1 1 1 0	Majority: 0
For cycle 6:	1 1 0 1 0 0 0 1 1 1 1 1 1 0 1	Majority: 0
For cycle 7:	1 0 1 0 0 0 1 1 1 1 1 1 0 1 1	Majority: 0

The correct codeword is: 1 1 1 0 1 1 1 0 1 0 0 0 1 1 1
The error is in 3rd position.

Similarly for case-2 if the parity of check bit of sending end is equal to that of receiving side then the cyclic shift operation is performed for 8 times which is the no. of total check bits in the code word. Likewise case 1 if the majority variable is

greater than 2 then the bit under decoding is erroneous and then corrected (Figure 5).

For Case-2:
Let,
The Sending Codeword : 1 1 1 0 1 1 1 0 1 0 0 0 1 1 1
Receiving Codeword: 1 1 1 0 1 1 1 0 1 0 1 0 1 1 1
For Sending Codeword:
Parity of information bits: 0
Parity of check bits: 0
For Receiving Codeword:
Parity of information bits: 0
Parity of check bits: 1

For cycle 1: 1 1 1 0 1 1 1 0 1 0 1 0 1 1 1 Majority: 0
For cycle 2: 1 1 1 1 0 1 1 1 0 1 0 1 0 1 1 Majority: 0
For cycle 3: 1 1 1 1 1 0 1 1 1 0 1 0 1 0 1 Majority: 0
For cycle 4: 1 1 1 1 1 1 0 1 1 1 0 1 0 1 0 Majority: 0
For cycle 5: 0 1 1 1 1 1 1 0 1 1 1 0 1 0 1 Majority: 1
Inverse: 0 1 1 1 1 1 1 0 1 1 1 0 1 0 0
For cycle 6: 0 0 1 1 1 1 1 1 0 1 1 1 0 1 0 Majority: 0
For cycle 7: 0 0 0 1 1 1 1 1 1 0 1 1 1 0 1 Majority: 0
For cycle 8: 1 0 0 0 1 1 1 1 1 1 0 1 1 1 0 Majority: 0

The correct codeword: 1 1 1 1 0 1 1 1 0 1 0 0 0 1 1
The error is in 11th position.

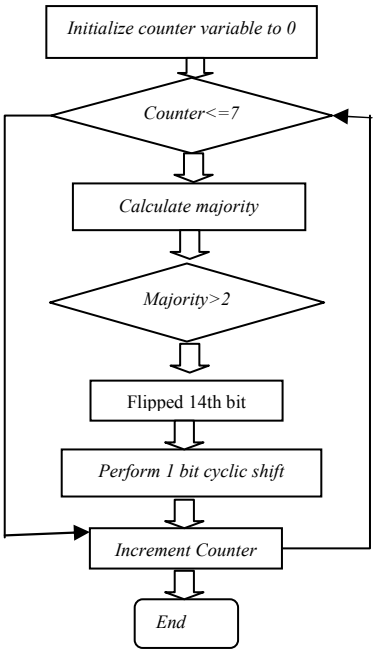

Figure 5: The Flowchart for Case-2.

And when the condition for case-3 arises, the cyclic shift operation is performed for 15 times equal to the size of code word. The erroneous bit position is detected and then corrected using majority variable like it was done for the previous cases (Figure 6).

For Case-3:
Let
The Sending Codeword : 1 1 1 0 1 1 1 0 1 0 0 0 1 1 1
Receiving Codeword: 1 1 0 0 1 1 1 0 1 0 0 0 1 0 1
For Sending Codeword:
Parity of information bits: 0
Parity of check bits: 0
For Receiving Codeword:
Parity of information bits: 1
Parity of check bits: 1

For cycle 1: 1 1 0 0 1 1 1 0 1 0 0 0 1 0 1 Majority: 0
For cycle 2: 1 1 1 0 0 1 1 1 0 1 0 0 0 1 0 Majority: 1
Inverse: 1 1 1 0 0 1 1 1 0 1 0 0 0 1 1
For cycle 3: 1 1 1 1 0 0 1 1 1 0 1 0 0 0 1 Majority: 0
For cycle 4: 1 1 1 1 1 0 0 1 1 1 0 1 0 0 0 Majority: 0
For cycle 5: 0 1 1 1 1 1 0 0 1 1 1 0 1 0 0 Majority: 0
For cycle 6: 0 0 1 1 1 1 1 0 0 1 1 1 0 1 0 Majority: 0
For cycle 7: 0 0 0 1 1 1 1 1 0 0 1 1 1 0 1 Majority: 0
For cycle 8: 1 0 0 0 1 1 1 1 1 0 0 1 1 1 0 Majority: 0
For cycle 9: 0 1 0 0 0 1 1 1 1 1 0 0 1 1 1 Majority: 0
For cycle 10: 1 0 1 0 0 0 1 1 1 1 1 0 0 1 1 Majority: 0
For cycle 11: 1 1 0 1 0 0 0 1 1 1 1 1 0 0 1 Majority: 0
For cycle 12: 1 1 1 0 1 0 0 0 1 1 1 1 1 0 0 Majority: 0
For cycle 13: 0 1 1 1 0 1 0 0 0 1 1 1 1 1 0 Majority: 1
Inverse: 0 1 1 1 0 1 0 0 0 1 1 1 1 1 1
For cycle 14: 1 0 1 1 1 0 1 0 0 0 1 1 1 1 1 Majority: 0
For cycle 15: 1 1 0 1 1 1 0 1 0 0 0 1 1 1 1 Majority: 0

The correct codeword is: 1 1 1 0 1 1 1 0 1 0 0 0 1 1 1
The error is in 3rd and 14th position.

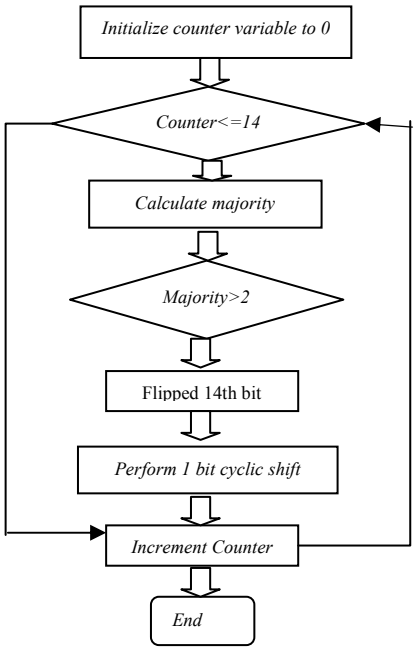

Figure 6: The Flowchart for Case-3.

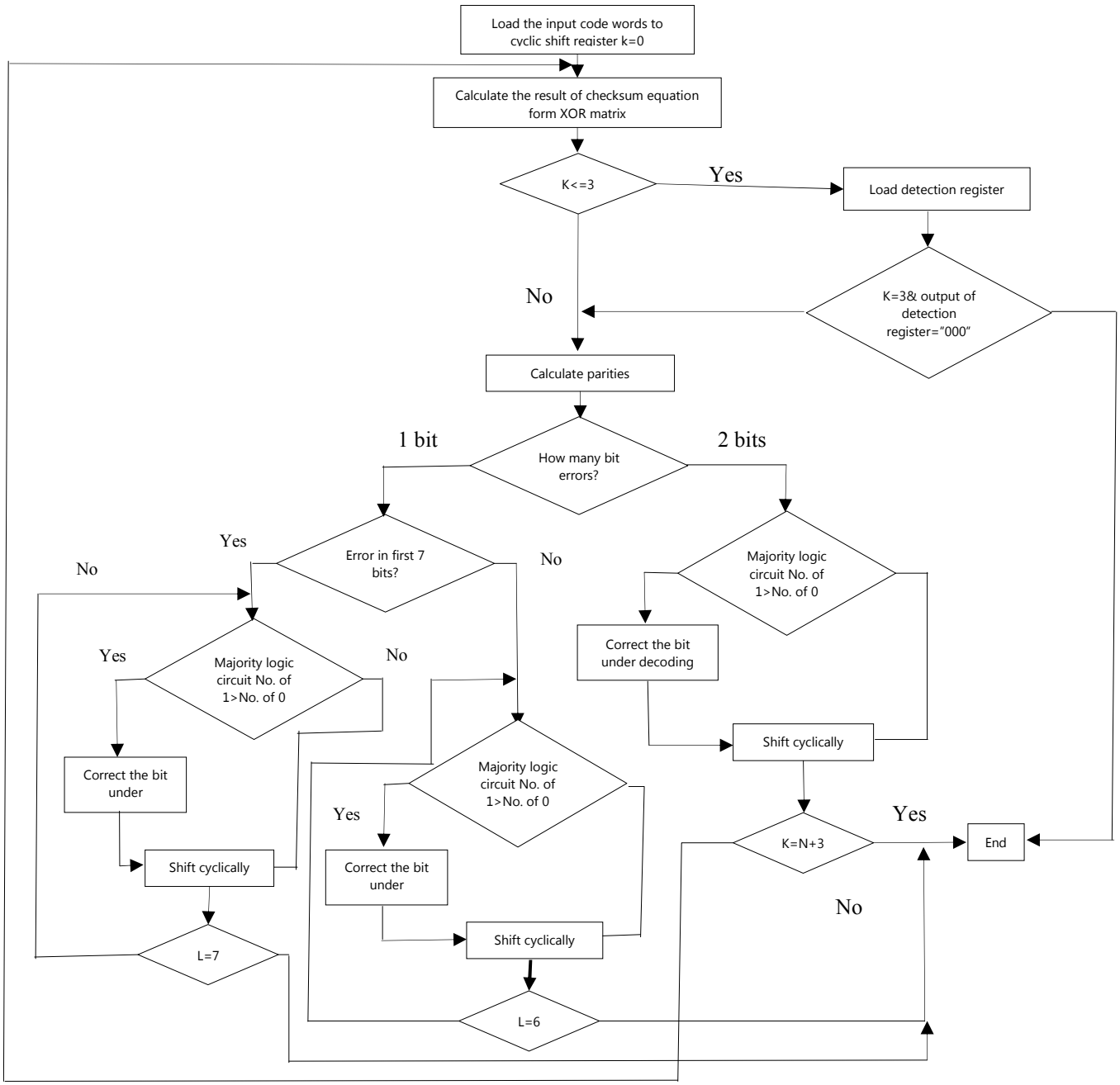

Figure 7: The Flow Diagram of the Proposed Method

Combining all the cases of above mentioned three possible conditions, the details of the proposed method is illustrated in Figure 7. The flow diagram shows the total workflow of how the erroneous bits can be detected and corrected either in the information bits or in the check bits by using majority calculation.

IV. EXPERIMENTAL ANALYSIS

The methodology is experimented through a multi-phase simulation process. The simulation process mainly envolves 'error-detection' phase and 'error-correction' phase. The experimental setup, results are outlined simulation to evaluate the proposed method shortly as follows.

A. *Experimental setup*

To work with the proposed method a machine with following configuration are used.

- Intel(R) Core i3 CPU M 350 @ 2.27 GHz
- CPU RAM 4GB
- Language C++(GNU 11)
- IDE CodeBlocks 10.05

- Input for testing erroneous dataset 120

B. Results Analysis

To validate the effectiveness of the proposed method, it is compared with the existing dominant methods. Figure 8 shows the comparison among the required cycles [11], to detect error of Plain MLD [5], the method proposed by Jayarani et. al [2], and the proposed method. The plain MLD [5] needs 15 cycles to detect any number of errors in the code word of 15 bits' size. The method proposed by Jayarani et. al [2] requires only three cycles to detect any error in that case. The proposed method also requires three cycles to detect any error.

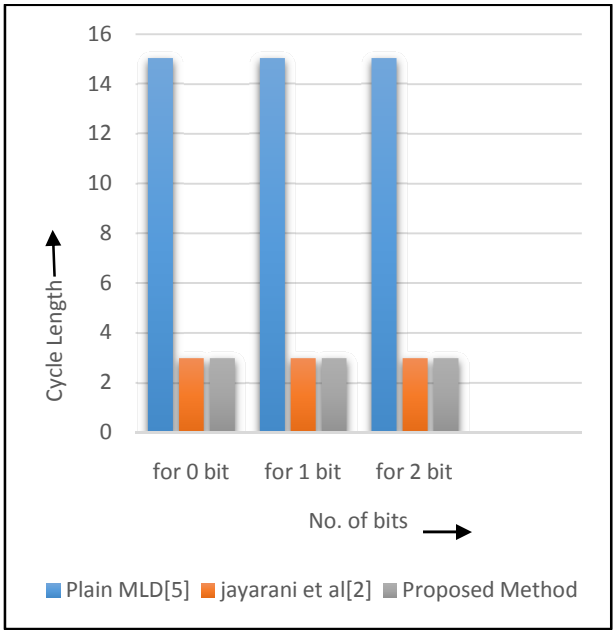

Figure 8: The Comparison among Plain MLD [5], the Method Proposed by Jayarani et. al [2], and the Proposed Method for error Detection

After the detection of errors, the proposed method performs the correction process. Figure 9 shows the comparison among the required cycles, to correct error, of Plain MLD [5], the method proposed by Jayarani et. al [2], and the proposed method. The plain MLD requires 15 cycles for the correction of one or two bits of errors. But the method proposed by Jayarani et. al [2] requires 18 cycles for one or 2 bit of errors. Whereas, the proposed method requires only 11 cycles to correct one bit of error, which is a major advancement in terms of computation
cycles' requirement. However, for two bits error correction, our proposed method requires 18 cycles which is equal to the method proposed by Jayarani et. al [2].
The proposed method has only a negligible impact on performance due to its little additional case selection, but it provides significant savings in area when code size increases.

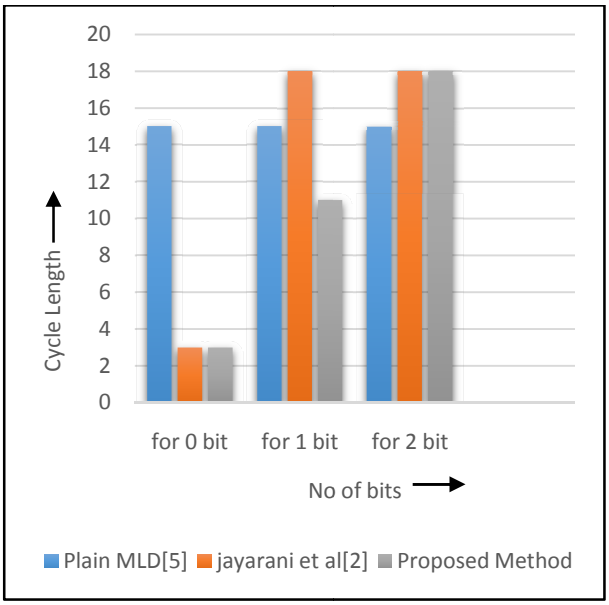

Figure 9: The Comparison among Plain MLD [5], the Method Proposed by Jayarani et. al [2], and the Proposed Method for error correction

V. Conclusions

This paper focuses on the design of a new algorithm which is primarily based on Majority Logic Detector/Decoder (MLDD) circuit but considers three possible cases and executes separate operations on the code word for fault detection and correction. The technique is independent of codeword size which decreases area overhead from other existing techniques. Though the proposed method require same time, for two bit errors detection and correction, as the method proposed by Jayarani et. al [2], in case of one bit error, it is more suitable for memory applications, where time becomes a matter of concern. Further studies can be adopted in order to find a methodology to lessen the detection and correction time requirement for two and/or more bit errors.

References

[1] Shih-Fu Liu, Pedro Reviriego, Member, IEEE, and Juan Antonio Maestro, Member, IEEE Efficient Majority Logic Fault Detection With Difference-Set Codes for Memory Applications .*IEEE transactions on very large scale integration (vlsi) systems, vol. 20, no. 1, january 2012.*

[2] JayaraniM.A , M. jagadeeswariphD .A Robust and Efficient Method For Error Detection And Correction In Memories. International Journal of Computer Applications (0975 – 8887) Volume 63– No.16, February 2013.

[3] R. J. McEliece, *The Theory of Information and Coding*. Cambridge,U.K.: Cambridge University Press, 2002.

[4] Y Kato and T. Morita, "Error correction circuit using difference-set cyclic code," *in Proc. ASP-DAC, 2003, pp. 585-586.*

[5] H. Naeimi and A. DeHon, "Fault secure encoder and decoder for NanoMemory applications," *IEEE Trans. Very Large Scale Integr.(VLSI) Syst., vol. 17, no. 4, pp. 473–486, Apr. 2009.*

[6] Pedro Reviriego,Juan A. Maestro, and Mark F. Flanagan, "Error Detection in Majority Logic Decoding of Euclidean Geometry Low

Density Parity Check (EG-LDPC) Codes," *IEEE Transactions On Very Large Scale Integration (VlSI) Systems* 1.

[7] Vasic and S. K. Chilappagari, "An information theoretical frame work for analysis and design of nanoscale fault-tolerant memories based on low-density parity-check codes," *IEEE Trans. Circuits Syst. I, Reg. Papers*, vol. 54, no. 11, pp. 2438–2446, Nov. 2007.

[8] Y. Kou, S. Lin, and M. P. C. Fossorier, "Low-density parity-check codes based on finite geometries: A rediscovery and new results," *IEEETrans. Inf. Theory*, vol. 47, no. 7, pp. 2711–2736, Jul. 2001..

[9] S.Abinaya, Mr.M.Yuvaraja "Reduction of Delay and Power by Using MLDDTechnique in Error Correction."*InternationalConferenceOn Global Innovations In Computing Technology (ICGICT'14).*

[10] R.C.Baumann,"Radiation-induced soft errors in advanced semiconductor technologies*," IEEE Trans. Device Mater. Reliabil., vol. 5, no.3, pp. 301–316, Sep. 2005*

[11] S.Abinaya, Mr.M.Yuvaraja "Reduction of Delay and Power by Using MLDDTechnique in Error Correction."*InternationalConferenceOn Global Innovations In Computing Technology (ICGICT'14).*

GSM and GPS Based Intelligent Method to Track Movement and Detect Collision and Rollover of Wheelchairs

Hasan U. Zaman, Anika Zaman, A S M Faruk Abdullah and Tamina Islam Khan
Department of Electrical and Computer Engineering, North South University, Dhaka, Bangladesh
hasan.zaman@northsouth.edu, mridulaa9@gmail.com, faruabd@gmail.com, nsu_tama@gmail.com

Abstract—**Patients such as paraplegic and most elderly people cannot move around without the help of other people. Such patients are immobile and need assistance of wheelchair for their movements. Most of these people cannot communicate with their caretaking personnel through complex cellular communications for emergency help. This paper describes the development of a portable device that can be attached to wheelchairs, which solves the problem of disabled persons in need of emergency help. This prototype has a drive system consisting of embedded microcontroller, Bluetooth, GSM (Global System for Mobile communication), GPS (Global Positioning System), and gyroscope. The system detects any accident or emergency help needed by the patient, generate a signal through embedded microcontroller to the GSM or GPS, to seek attention.**

Keywords—Paraplegic, embedded microcontroller, bluetooth, GSM, GPS, gyroscope.

I. INTRODUCTION

Developing a secured human machine interface for immobile person is a challenging issue to be solved in our society. Most of the elderly people suffer from spinal cord problem. Few even endure spinal cord injuries at a very young age. It is estimated that 52% of spinal cord injured individuals are considered paraplegic [1] [2]. As a transportation device for these patients, wheelchair is used extensively.

Over the last few decades, researchers have worked on wheelchair dependent patients, to ease their mobility. Various technologies were implemented to support the mobility of Blind or Partially Blind [3], voice recognition system were used to give required output signals from a given voice as input signal [4] [5], and image processing method were applied to detect various expressions of face of patient[6] [7].

Walking support system [8] was also introduced for paraplegic patients, which is very complex and expensive. Technology used in [9] has similar security concern about paraplegic patient, having limitations like it works only in indoors with a complex system interface, thus limiting the mobility to indoor only.The designed system prototype solves the problem of both indoor and outdoor hazards with less complexity and more user friendly interfaces and alert system.

The prototype is able to solve problems such as,

1. If the patient cannot get assistance while in emergency, the prototype will send signal to the nurse for urgent help.
2. The patient may face any unexpected accident, resulting in an injury in absence of a nurse. This calamity is detected and generates signals in terms of mobile text message to the nurse.
3. The patient may be left unattended by the nurse by any unethical means that can be monitored by local guardian. Based on an embedded microcontroller and using a common GPS antenna, this system allows patient to be located at any place by his/her nurse or any person responsible of the patient. The prototype system is hidden on the wheelchair in a strategic position. This allows maintaining a perfect coordinate positioning of wheelchair.

TABLE I. OPERATING SYSTEM OF WHEELCHAIR

DIFFERENT MODES OF WHEELCHAIR PROTOTYPE
Connectivity between patient and caretaking personals (Both indoor & outdoor)
Avoidance of rollover of wheelchair (Both indoor & outdoor)
Panic Push Button
Automatic SMS generation
Navigation of the patient

II. THEORITICAL FRAMEWORK

System implies certain technology, user efficiency and performance for each mode, recombining them to form a prototype. Each module of the prototype serves individual purpose of security.

A. Connectivity between Patient and Caretaking Personals

For connectivity within a medium range, the system uses globally available license-free 2.4 GHz ISM Band Bluetooth Device. The module uses free frequency that makes the system cheaper to use. Also, for medium range distance, HC-06 module of Bluetooth is used which covers 33 feet (10 meters) between the patient and caretaking personnel. Fig. 1

978-1-4673-9257-0/15/$31.00 ©2015 IEEE

applies both indoor and outdoor use of Bluetooth. The square box inside the Bluetooth covering range represents average area of home premise. For outdoor use, 33 feet is the maximum boundary distance, which a nurse can be further from patient. The module is also chosen for it is being a slave device, controlled and paired by master device which is present in the mobile phone of the nurse.

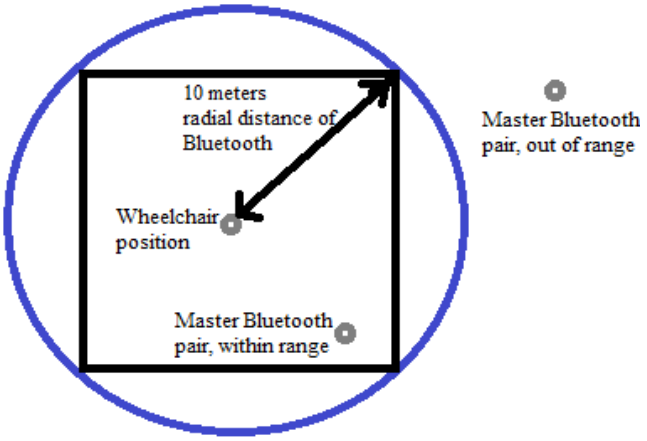

Fig. 1 Master-Slave Bluetooth impairment range

B. Avoidence of rollover of wheelchair

For avoidance of rollover, 3-axis MEMS silicon gyroscope is used. Gyroscope measures angular rate, which is the rate of rotation per unit of time in three-dimension axis. This new vibration is used to calculate the angular rate. The Coriolis force is a physical quantity first proposed by 19th century French physicist Gaspard-Gustave de Coriolis that indicates inertia at work on a rotating coordinate system.

Calculating Coriolis force on a mass with velocity (Inertia seen on a rotating coordinate system) :

$$F_c = 2mV \times \Omega \qquad (1)$$

where, F_c: $Coriolisforce$
m: $mass$
V: $velocity$
Ω: $angularrate$

C. Use of GSM for SMS generation

The minimization of the distance between patient and guardian is the main theme for our prototype. Since Bluetooth covers only few meters, for higher distance connections use of purchased frequency of GSM becomes necessary. From Fig.2 one can imagine that how signals can travel longer distances when the patient in need of emergency help. Such emergency help or interrupt handled by GSM are discussed in brief.

1. When patient pushes the panic button, it automatically generates signal through AT Command to embedded microcontroller which activates the modem to send text message to the nurse. This interface of GSM work in both indoor and outdoor cases.
2. When Bluetooth module gets disconnected, it generates message to the guardian that the patient is unattended by the nurse. When patient face any accident, message is sent to the guardian that patient has fallen down from wheelchair.
3. Gyroscope measures the inappropriate coordinate of the wheelchair, when patient faces accident. All the interfaces are programmed with AT command within the Embedded Microcontroller.

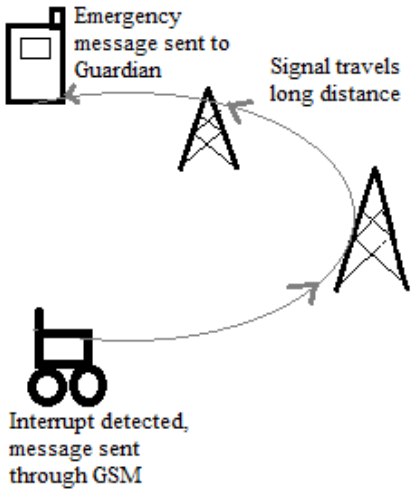

Fig. 2 Signal Transmission through GSM modem

D. Navigation

GPS works at each interrupt, when any violation occurs. It then searches GPS location every time before sending a text message and executes according to Fig. 3.Whenever the patient remains outside home, it sends URL coordinate link to the guardian that connects with the Google Map to know the position of patient.

```
if (interrupt 1 or interrupt 2 or interrupt 3){
    if (gps_available)
        sendsms with gps location();
    else
        sendsms without gps location();
}
```

Fig. 3 Algorithm for GPS Navigation

III. METHODOLOGY

The prototype is designed with a microcontroller based embedded system, interfaced with mainly GSM, GPS, Bluetooth, and Gyroscope. It has wireless communication with Bluetooth and the mobile number of guardian and nurse of the disabled patient. The switch mode of the prototype serves as a 'panic push button' for the patient.

GSM used is SIM 908 with baud rate of 19200 bps. This works with strings of AT Command, which generates unique text message to either nurse or guardian for particular use.

Module used for Bluetooth is LT108. The device is paired with mobile application of nurse, to ensure continuous monitoring of the patient as well as the nurse.

Gyroscope is programmed and interfaced with embedded microcontroller to detect the fall down of patient using a calculated boundary of three dimensional axes.

SIM 908 module also serves as GPS module. Along with a suitable GPS antenna, the system is able to generate GPS link within the text message that allows the guardian to navigate from long distance.

Apart from the module itself, the system is made 'portable', for which, rechargeable battery package installed with other modules as power source. It is then packaged, and installed at the back of the wheelchair, to generate different security concerned text message needed for the user.

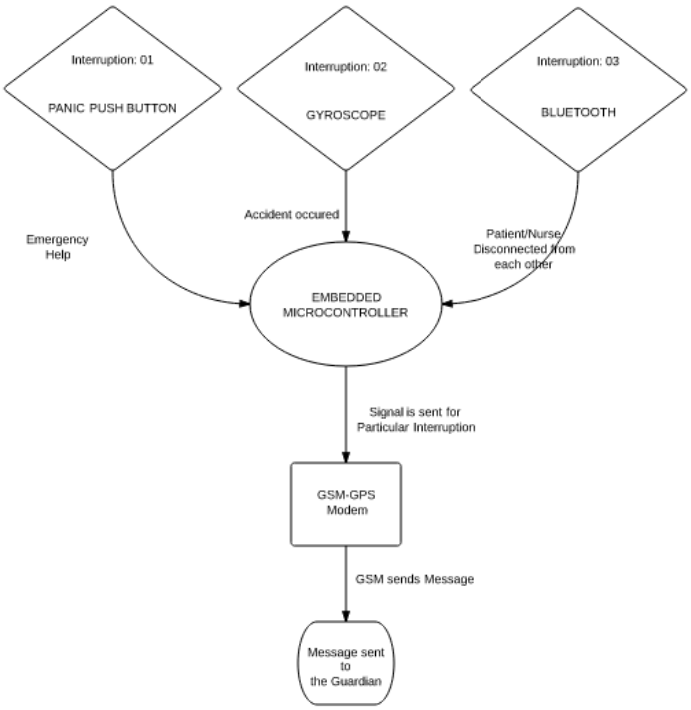

Fig. 4 Methodology Flow Chart of the prototype

In terms of engineering perspective shown in Fig. 4, the main idea is to convert the emergency help of the patient to electrical impulse, process it by embedded microcontroller Arduino, and interface with other modules to generate alarm when interruption occurs.

IV. User Interface

As shown in Fig. 5, the architecture of the system mainly consist eight module parts – six parts of inputs two outputs processed by Arduino microcontroller.

Arduino Mega and Arduino Uno are used to send AT commands to GSM_GPS modem SIM908 and check all information coming from other modules such as Bluetooth, Gyroscope, Panic Button, and PIR sensor. The system uses 'free frequency' by Bluetooth to connectivity at lower ranging distance, and uses 'purchased frequency' of GSM system to send alarms, where distance is higher.

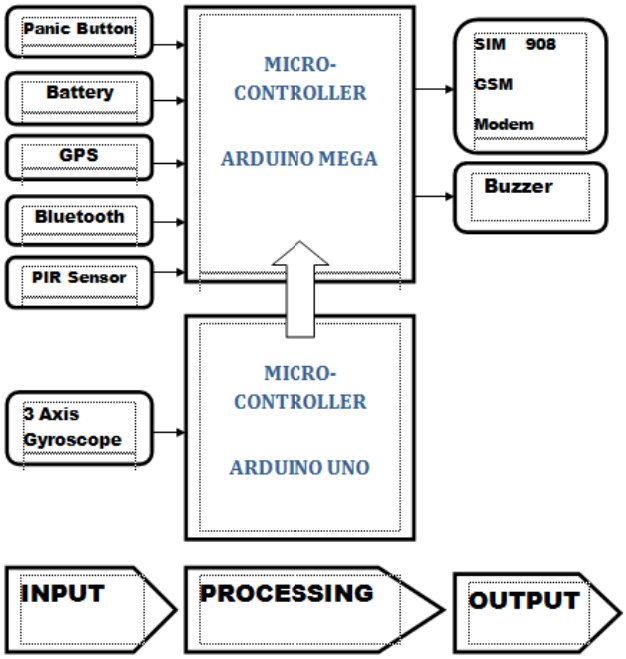

Fig. 5 Block Diagram

V. System Approach

The system consists of three input components namely, gyroscope, panic push button, and bluetooth. The standard state is the state, where all the three input devices hold the following conditions.

A. Gyroscope

Gyroscope "standardization" initially holds the pitch value > 20°, and rolling value not exceeding from -45° to 45°. If violation of the state is occurred, the system responds to the embedded microcontroller about the occurrence.

B. Panic Push button

When untouched is the normal state of the system. The violation of the system means the panic button is pressed for emergency.

C. Bluetooth

Desirable state of Bluetooth device is paired with the phone of the attendant. When the violation of this state is occurred, the system responds.

To the view point of the system, any violation is counted as "interrupt". Interrupt makes the system ready to respond. The response of the system is the GSM text message generation. So the total system can be analyzed in following pattern,

- Human and accidental Interrupt- Panic Push Button and Gyroscope.
- Distance Interrupt-Bluetooth.

The distance interrupt holds a special characteristic such that, other two input state devices need some "occurrence",

but Bluetooth in the system is Autonomous. When the system operated or powered, it search for the pair. To avoid this misleading phenomenon, the system has developed a condition of the Bluetooth connection, which ensures that no misleading response occurred by the system. The Bluetooth pair connection is guarded by the condition named "armed".

VI. Durability

The prototype currently needs 350-400mA of current as power source. Since our device is portable, we have used three cells Li-Po batteries connected in parallel to give a total 12V, 4A power supply. According to the calculation shown below,

$$\text{Battery lasting (in hours)} = 4000mA/400mA \text{ per hour} = 10 \text{ hours.}$$

This result shows that the battery lasts for 10 hours.

VII. Future Work

Our project is in prototype stage, for which upcoming design for the completion of the project is important issue. Most of the modules such as GPS, GSM, embedded Microcontroller, Gyroscope, and Bluetooth work with their individual interfaces, which serves enough to secure a disabled or paraplegic patient. Further works have to be done to make the project more feasible and user friendly for the nurse or guardian of the patient.

New modules can be added to meet the goal of the project. Buzzer will be installed for emergency purpose. For the detection of presence of the patient in the wheelchair, we need to use PIR (passive infrared) sensor to determine whether the patient is sitting on wheelchair or not. To make it more user friendly, display for battery charge has to be interfaced with battery to avoid unusual turnoff of device.

The prototype, Fig. 6, has some issues to be taken care of before packaging and installing at the back of wheelchair. First, it should be placed in upright fixed position, which cannot be twisted or tilted due to presence of Gyroscope. Secondly, both GPS and GSM antennas need to be positioned in open space, while the modules will be given insulated covering for safety.

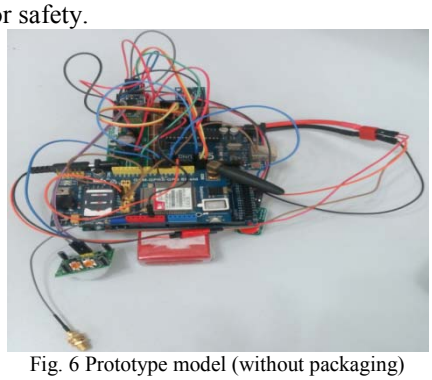

Fig. 6 Prototype model (without packaging)

Our research is only considering paraplegic patient. The system can be made more feasible for other kind of disabled people by introducing voice integrated module, which will generate certain emergency text messages by using voice recognition system.

VIII. Conclusion

Our prototype lessens the concern of insecurity of the patient as the guardian does not need to know every time that whether the patient is in safe position or not. According to research, many have worked with wheelchair related projects for disabled people with complex interfaces. But for patients with such immobility in nature, they must have security concern as their first priority. The prototype could be installed in any kind of wheel chair, because of its portability. The project has mainly targeted the metropolitan citizen group, where no family member can afford time to attend patient in his/her working hour. This device will be also helpful in hospitals and Old-aged Homes, where most of the interfaces will be very helpful to disabled or elderly patients. The patient immobility might be permanent or temporary, where this user friendly technology can be applied. Some of the issues with the current design which that have been discovered within the system are discussed briefly.

- Once the mobile numbers of the guardian and the nurse is installed within the device, it cannot be changed without the help of technicians.
- The device battery needs to be charged each day, and the SIM that is placed within the device should have enough balance to send emergency text messages.

Apart from such issues, we can conclude that the device will be able to ease the problems of disabled people by providing firm security.

References

[1] Spinal Cord Injury Facts and Statistics. [Online]. Available: http://www.sci-info-pages.com/facts.html

[2] Spinal Cord Injury. [Online]. Available: http://stephenslegal.com/practice-areas/spinal-injury

[3] Abdel IlahNourAlshbatat, "Automated Mobility and Orientation System for Blind or Partially Sighted People," International Journal on Smart And Intelligent Systems, vol. 6, no. 2, pp. 568-582, April. 2013

[4] Aakash. A. Hongunti, Mayuri. Deulkar, Varsha .Sable, "Voice Operated Wheelchair," International Journal of Advanced Research in Computer Science and Software Engineering, AISSMS, Institute of Information and Technology, vol. 4, pp. 1133-1139, April. 2014

[5] D. K Prabitha, Chidananda Murthy. M. V, and M. Z. Kurian. "Speech Recognizing Powered Wheelchair for Disabled" International Conference on Electrical Engineering and Computer Science (ICEECS-2012). May 12th, 2012, ISBN Number : 978-93-81693-58-2

[6] Lai Wei, Huosheng Hu, "A multi-modal human machine interface for controlling an intelligent wheelchair using face movement," IEEE, vol. 11, pp. 2850-2855, Dec. 2011

[7] Javier Varona, Cristina Manresa-Yee, and Francisco J. Perales, "Hands-free vision interface for computer accessibility," ScienceDirect, pp. 357-374, March. 2008.

[8] Suzuki K, Kawamura Y, Hayashi T, Sakurai T, Hasegawa Y, and Sankai Y, "Intention-Based Walking Support for Paraplegia Patient," in System, Man and Cybernetics, IEEE International Conference, vol. 3, pp. 2707-2713, Oct. 2005.

[9] RuquiaMirza, Ayesha Tehsin, and Joshi Kumar, "An Indoor Approach to Aid the Physically Disabled People," International Conference on Computing, Electronics and Electrical Technologies [ICCEET], pp. 979-983, 2012.

A Rule Based Approach for NLP Based Query Processing

Tanzim Mahmud, K. M. Azharul Hasan, Mahtab Ahmed, Thwoi Hla Ching Chak
Department of Computer Science and Engineering
Khulna University of Engineering & Technology (KUET)
Khulna – 9203, Bangladesh

Abstract— **Information is playing an important role in our lives. One of the major sources of information is databases. Databases and database technology are having major impact on the growing use of computers. In order to retrieve information from a database, one needs to formulate a query in such way that the computer will understand and produce the desired output. Generally, query processing is handled by the Structured Query Language (SQL). But the non IT people cannot be able to write SQL queries as they may not be aware of the SQL as well as structure of the database. So there is a need for non-expert users to query the databases in their natural language instead of working with the values of the attributes. This paper proposes an approach for accessing the database easily using natural language without having any knowledge about the query language. The approach is a rule based approach. The obvious advantage is that it makes a great promise for computer interfaces easier for the use of general people. Because of this, people will be able to communicate to the computer in their own language instead of learning a specialized language or commands. In order to test our approach in an actual computerenvironment, we have developed a prototype system. We obtained promising results using our system.**

Keywords— NLID, Query processing, Structured Query Language, Relational Database, Natural Language Processing.

I. INTRODUCTION

Natural language interface to database presents an interface for non-expert users to interact with the system and database[1]. To design models for automatically mapping natural language semantics into programming languages is always been a major and interesting challenge in Computer Science. For example, accessing a database requires the knowledge of structured query language (SQL) and machine-readable instructions that common users are not supposed to know. Ideally, they should only ask questions in natural language without knowing either the underlying database schema or any complex machine language. The development of Natural Language Interfaces to Database (NLIDBs) that translate the human intent into database instructions is indeed a classic problem[2]. There are many attempts[3][4] made in the past thirty years, current solutions are still not applicable in real scenarios. A huge variety of systems has been proposed, with increasing performance, but the task is still challenging.

NLIDB system has two components. One of them is Linguistic Component which is responsible for translating natural language input into a formal query and generating a natural language response based on the results from the database search. Another one is database component which performs traditional database management functions. Syntactic knowledge usually resides in the syntax analyzer whereas knowledge about the actual database resides to some extent in the semantic data model used. Questions entered in natural language form are translated into a statement in a formal query language. Once the statement is formed, the query is processed by the DBMS in order to produce the required data. Databases are the common entities that are processed by experts and non-experts with different levels of knowledge. Databases respond only to standard SQL queries which based on the relational algebra. It is nearly impossible for a general person to be well versed in SQL querying as they may be unaware of the structure of the database namely tables, their corresponding fields and types, primary keys and so on. More over the knowledge on relational algebra and its operation is also impossible except for the IT people. Natural Language Interfaces to Databases (NLIDBs) was proposed as a solution to the problem of accessing information in a simple way, allowing ideally any type of users, specially inexperienced ones to retrieve information from a database (DB) using natural language [5][6]. With the growth of technologies (for example computers, laptops, cellular phones, and Internet) information can be accessed from almost anywhere, at any time, by anybody, including general people who do not have computer background. The common and easy way for people to obtain information is by asking questions in their natural language specially mother language. But, without any proper way, computers cannot understand this language, as it merely represents a sequence of meaningless characters.

II. RELATED WORKS

[5] proposed system namely LUNAR having good performance; But it is subject to intensive use due to the limitation of its linguistic capabilities. [6] designed a system namely LADDER which was used as a natural language interface to a database of information about US Navy ships system. The LADDER based on distributed database system which uses semantic grammar to parse questions to find the result of a query in distributed database. One important difference is that the system uses semantic grammar technique that helps syntactic and semantic processing. [7] developed a system named Word Alignment-based Semantic Parsing (WASP) that address the broader goal of constructing "a complete, formal, symbolic, meaningful representation of a natural language sentence", that can be applied to the NLIDB

domain. [8] proposes NaLIX, a generic interactive natural language query interface based on XML database. The system can accept an arbitrary English language sentence as query input incorporating aggregation, nesting, and value joins etc. After reformulation, this query is then translated into an XQuery expression that can be evaluated for an XML database. The translation is done through mapping grammatical proximity of natural language parsed tokens to proximity of corresponding elements in the result XML. [9] proposes an approach to build the NLIDB based on Computational Paninian Grammar (CPG). It employs two distinct stages for processing such as syntactic processing then semantic processing. An NLID system namely D-HIRD specific for Hindi language independent of domain is proposed in [10]. A morphological analyzer based query processor is proposed in [13] based on the keyword and group of words which is used to find the type of extracted keyword using pattern matching technique. In this paper we propose an NLID using rule based system which takes questions from the users in the form of natural language. Then it processes that natural language to obtain regular SQL query. A data dictionary is used to process the natural language where all possible word related to our system is included. A Context Free Grammar (CFG) is used to determine the required attributes and SQL elements to construct the query. Finally it run the query on the database to fetch the result and show that to the user.

III. A NATURAL LANGUAGE INTERFACE FOR DATABASE

This section gives a detail overview of the proposed system. The system is based on designing Context Free Grammar (CFG). At first the NLIDB system and its sub-components are described and then the basic elements with working procedure of our proposed model are presented. We used an alumni database system as a case study. Fig. 1 shows the block diagram of the system.

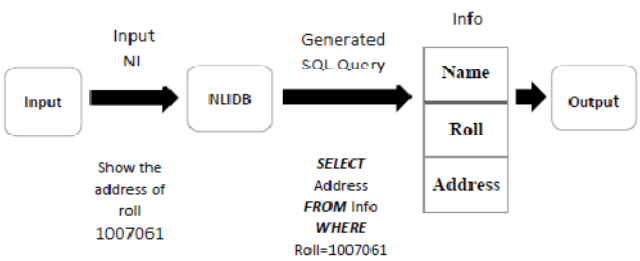

Fig. 1: Overview of Natural Language Interface of Database

One of most wide and interesting area of Natural Language Processing (NLP) is the development of a natural language interface to database systems (NLIDB). In the last few decades many NLIDB systems have been developed through which users can interact with database in a more convenient and flexible way. Fig. 1 shows the basic architecture of our NLIDB system. After taking the input from the user in the natural language form, the system converts this input into SQL query form which it mainly used for accessing database for reading and writing. The user does not have to have any kind of knowledge about SQL query and its format. Because of this application NLP is very widely used today. Natural Language Interface has been a very interesting area of research since past times. The aim of Natural language Interface to Database is to provide an interface where user can interact with database more easily using their natural language and at the same time access or retrieve their information. Generally NLIDB system converts the query in native language into SQL and vice-versa.

The proposed system is basically a translator from natural language to standard SQL. So it has some phases like compilers. We design context free grammars. When any input symbol of appropriate terminals is found then it is replaced by the corresponding attribute in the relational table or appropriate operators of SQL. The proposed system consists of the some phases namely user interface, word check, removing excess words, tokenization and mapping to CFG rules :

The user asks question or make a query. He/she generally prefers to ask that in a natural language. This module allows the user to enter the question in a natural language. After getting a natural language query, the system must identify the valid words and values required to build a standard SQL query. This process checks all the words in the user question against the data dictionary for its existence. The words which are not legitimate or required to build the SQL statement have to be removed to lessen the complexity. This process removes excessive words from the question string and blanks the positions of the words. After getting the valid sub-string from the given string, it should be split into tokens. With the help of tokens, we can identify the column and respective table name required to build the SQL query. A context-free grammar (CFG) is a set of recursive rewriting rules (or productions) used to generate patterns of strings. Using this idea we developed some string pattern matching rules where all capital letter words denote the non-terminals and small letter words denote terminals. We used the rules to detect the required column, given values and corresponding column names and valid operators assigned to those values. Fig. 2 and Fig. 3 show some of the rules for detecting the column name and their values given the natural language query.

According to the retrieved column name and values, the required SQL elements (SELECT, WHERE, JOIN, AND, OR etc.) are identified. After getting the valid columns, values and corresponding operators, SQL generation process constructs a query in SQL. When the Query is generated, it is passed to the back-end database and which runs it. Finally, data collection process collects the data retrieved from the database and show it to the user as a result. Fig. 4 shows the logical operators for SQL translation.

The mapping is done by matching the terminals and then returning its corresponding non terminals. Then non terminals are used for SELECT and FROM clause. The formation of SQL queries from the natural language query and tested the results based on their accuracy. The formation of the SQL query requires us to deal with the generation of 3 well known clauses of SQL which together construe the SQL query. The 3 clauses are as follows: SELCT clause, FROM clause, WHERE clause. The input string is used to construct the SELECT clause and FROM clause and the WHERE clause. In SELECT clause, we put the required column names i.e, the information to be extracted and in the FROM clause, we put the

corresponding table names from where the information to be extracted. To construct the SELECT clause and FROM clause we used the rules showed in the Table 1. Initially, all the rules are sorted in a decreasing order according to their length. Then the system selects the sub-string which has the highest length in the rules tables and start to check against the input string. If it finds exact match, it will return the column name directed by that sub-string showed in those rules tables and from the column name, we get the corresponding table name.

PERSONAL-INFO	→	*ROLL_ | FULL_NAME | F_NAME | BTCH | B_DATE | BLD_GRP | SPOUSE_NAME | NO_OF_CHILDREN | FLD_OF_INTEREST | JOB_TITLE | COMPANY_NAME | JOB_EXP*
CONTACT-INFO	→	*ID | CONTACT_NO | EMAIL_ID | FAX_NO | WEBSITE_INFO | CURR_ADDRESS*
*ROLL_*	→	*roll number | roll no*
FULL_NAME	→	*who is | name | name of the student | student name | student's name*
F_NAME	→	*father | father's name | dad*
BTCH	→	*Batch*
B_DATE	→	*birthday | birth date | date of birth*
BLD_GRP	→	*blood group*
SPOUSE_NAME	→	*spouse name | husband | wife | name of husband | husband's name | name of wife | wife's name*

Fig. 2: Context Free Grammar for SELECT and FROM clause

If a natural language query is of the form "Show the student's name and contact no whose blood group is A+ and B+ and lives in "Khulna" then the sub-strings "student's name", "contact no", "blood group" and "lives in" match with the sub-string in the rules tables in Fig. 2. If we order these sub-strings according to their length, "student's name" comes first. Then "blood group", "contact no" and finally "lives in" is found. Then the corresponding terminal of the CFG is returned and stored. All these sub-strings direct to their corresponding column name and thus table names. In WHERE clause, the values given for columns and corresponding column names are used to establish a relationship via an appropriate operator. The CFG shown in Fig. 3 is used for detecting appropriate column names whereas Fig. 4 is used for assigning appropriate operator. Like the process described for constructing the SELECT clause and FROM clause, the values, corresponding column name and tables name is detected. Here, the values "A+", "B+" and "Khulna" are detected. As there is no sub-string matched between "A+" and "B+", these two values will belongs to same column. Now to detect the column names, the sub-string "blood group is" and "lives in" are the exact match with the rules in Fig. 2. These two sub-string direct to the columns "bld_grp" and "curr_address".

FULL_NAME	→	*name is "| roll of "| roll number of " | roll no of " | father of " | father's name of "| dad of "|batch of "| birth date of " |birthday of "| date of birth of "| blood group of "| spouse name of "| husband of " | wife of " | name of husband of "| husband's name of " | name of wife of " | wife's name of "| children's number of "| number of children of " | children's no of " | no of children of " | field of interest of" | interested field of " | expert field of " | working field of " | job of " |job title of " | current job of " | current job title of " | current company of " | company name of " | working place of " | working company of " | experience of " | job experience of " | contact no of " | contact number of " | phone no of " | phone number of " | mobile number of " | mobile no of " | email of " | email id of " | mail of " | mail id of " | email address of " | mail address of " | fax number of " | fax no of " | fax of " | website of " | website name of " | name of website of " | name of the website of " | home of " | location of " | address of " | current address of "| current location of " | home address of "*
*ROLL_*	→	*roll is | roll number is | roll no is | of roll | of roll number | of roll no*
F_NAME	→	*child of | son of | daughter of*
BTCH	→	*batch is*
B_DATE	→	*birth date Is | birthday is | date of birth is*
BLD_GRP	→	*blood group is*

Fig. 3: Context Free Grammar for NLID with appropriate attribute to database.

Operator	→	= |< |> |<= |>=|!=
=	→	*equal*
<	→	*less than |fewer than*
>	→	*greater than |more than*
<=	→	*less than or equal |fewer than or equal*
>=	→	*greater than equal |more than or equal*
!=	→	*not equal*

Fig. 4: Context Free Grammar for operators of SQL

IV. EXPERIMENTAL RESULTS AND STUDIES

We create a prototype system and executed on our sample database named ALUMNI where the real values of an alumnae of an university was stored. From the experiments and derived results are shown in this Section. Three types of queries are employed namely

- The queries that have only SELECT and FROM clause but there is no where clause. In this case we put WHERE 1. Table 1 shows some queries of such case.

- The queries that have SELECT and FROM clause with some condition that needs to employ WHERE clause. Table 2 shows some results of such case.
- The queries that have SELECT, FROM and WHERE clause and it needs the join operation to conduct the query. Table 2 shows some results of such case.

TABLE 1: GENERATED QUERY WITHOUT CONDITION

User query	Desired SQL	Generated SQL
Tell me name of the students	*SELECT* `full_name` *FROM* `personal_info`;	*SELECT* `full_name` *FROM* `personal-info` *WHERE* 1;
Give me name of the company of the students	*SELECT* `company` *FROM* `personal-info`;	*SELECT* `company` , `full_name` *FROM* `personal-info` *WHERE* 1 ;

We executed the system for some random natural language query and collect the results. We categorize the result into three categories- Good, Fair, Bad.

- Good: The queries that the system returned correct SQL statements and the desired results from database are found are marked as "Good" output.
- Fair : The queries that system returned SQL statements which are syntactically correct but the desired result was not found are marked as "Fair" output.
- Bad: The queries that the system failed to generate any query are marked as "Bad" output.

TABLE 2: GENERATED QUERY WITH CONDITION

User query	Desired SQL	Generated SQL
get me roll of the students whose blood group is "A+"	*SELECT* `roll_` *FROM* `personal-info` *WHERE* `bld_grp`="a+";	*SELECT* `bld_grp` , `roll_` *FROM* `personal-info` *WHERE* `bld_grp` = "a+" ;
Tell me name of the students with blood group "AB+"	*SELECT* `full_name` *FROM* `personal-info` *WHERE* `bld_grp`="ab+";	*SELECT* `full_name`, `bld_grp` *FROM* `personal-info` *WHERE* `bld_grp` = "ab+";
Tell me name of the students with "AB+" blood group	*SELECT* `full_name` *FROM* `personal-info` *WHERE* `bld_grp`="ab+";	**Failed to generate**

Table 4 shows queries with Good, Fair and Bad marked. We simulated the system with varying number of queries with our system. The accuracy of queries is shown in Table 5. Although, the accuracy is not promising at this stage, but the accuracy can be improved by adding the production terms in the CFG. The accuracy is dependent on number entry on the dictionary as well.

TABLE 3: GENERATED QUERY CONDITION JOINING MULTIPLE TABLES

User query	Desired SQL	Generated SQL
Show the name and contact number who lives in "dhaka"	*SELECT* `full_name`, `contact_no` *FROM* `personal-info` *JOIN* `contact-info` *ON* `roll_` = `id` *WHERE* `curr_address` = "dhaka" ;	*SELECT* `full_name`, `contact_no` , `curr_address` *FROM* `personal-info` *JOIN* `contact-info` *ON* `roll_`=`id` *WHERE* `curr_address` = "dhaka" ;
Show the name and contact number who lives in "dhaka" and blood group is "AB+"	*SELECT* `full_name`, `contact_no` *FROM* `personal-info` *JOIN* `contact-info` *ON* `roll_` = `id` *WHERE* `curr_address` = "dhaka" and `bld_grp` = "ab+" ;	*SELECT* `bld_grp`, `full_name`, `contact_no` , `curr_address` *FROM* `personal-info` *JOIN* `contact-info` *ON* `roll_` = `id` *WHERE* `curr_address` = "dhaka" and `bld_grp` = "ab+" ;
Give me name and contact no who works at "reve system"	*SELECT* `full_name`, `contact_no` *FROM* `personal-info` *JOIN* `contact-info` *ON* roll_` = `id` *WHERE* `company` = "reve system" ;	*SELECT* `full_name`, `contact_no` *FROM* `personal-info` *JOIN* `contact-info` *ON* roll_` = `id` *WHERE* `company` = "reve system" ;

TABLE 4: GENERATED QUERY WITH GOOD, FAIR AND BAD MARKED

Natural Language Queries	Generated Queries	Comment
Give me name of the student who lives in "dhaka"	select `full_name`, `curr_address` FROM `personal-info` JOIN `contact-info` ON`roll_` = `id` WHERE (`curr_address` = "dhaka") ;	Good
Give me name of the students who works at "reve"	select `full_name` FROM `personal-info` WHERE (`company_name` = "reve") ;	Good
What is roll and contact info of the students whose roll is "0007004"	select `roll_` FROM `personal-info` WHERE (`full_name` LIKE "%0007004%") ;	Fair
What is roll and contact info of the students having roll "0007004"	select `roll_` FROM `personal-info` WHERE (`full_name` LIKE "%0007004%") ;	Fair
show all the information of "kawser"	Failed To Generate	Bad
show all the information of roll "0007005"	select `roll_` FROM `personal-info` WHERE (`roll_` = "0007005") ;	Fair

TABLE 5: ACCURY PERFORMANCE OF THE QUERIES GOOD, FAIR AND BAD

Query Category	Accuracy
Good	47%
Fair	35%
Bad	18%

The computational time of any NLP based algorithm is naturally little bit high as compared to the hardware based computations. The time complexity of our scheme depends on the number of production terms in the CFG. If the number of

production terms increase then the time computational time increases. On the other hand, the accuracy of the system depends on the number of production terms in the CFG. If the number of production terms increase then the accuracy of the system increases and vice versa

V. CONCLUSION

Natural Language Processing can bring powerful enhancements to virtually any computer program, because human language is so natural and easy to use for humans. We provide a system which is capable of handling English query to access relational database instead of structured query language. The proposed NLID provides a convenient as well as reliable means of querying access, hence, a realistic potential for bridging the gap between computer and the casual end users. The system employs CFG based system which makes it easy search the terminals. As the target terminals become separated to many nonterminals. To get the maximum performance, the data dictionary of the system will have to be regularly updated with words that are specific to the particular system. The NLID is a relatively recent area of research as compared to other fields of information technology, there have been sufficient successes to date that suggest that NLP-based information access technologies will continue to be a major area of research and development in information systems now and far into the future. The system we developed is a specific problem based system and currently can handle standard join conditions.

REFERENCES

[1] N. Nihalani, M. Motwani and S. Silakari, "Natural Language Interface to Database using Semantic Matching" *International Journal of Computer Applications*, vol. 31, no.11,pp. 0975 – 8887, Oct 2011S.

[2] A. Popescu, O. Etzioni, and H. Kautz, "Towards a Theory of Natural Language Interfaces to Databases", *Intelligent User Interfaces,* pp.149–157, 2003.

[3] P. A.Dhomne et. al., "Accessing Database using NLP", IJRET: *International Journal of Research in Engineering and Technology (IJRET)*, vol. 02, Dcec 2013.

[4] W. Woods, R. Kaplan and B. Webber, "The Lunar Sciences Natural Language Information System,*Bolt Beranek and Newman Inc., Cambridge, Massachusetts Final Report*, report no. 2378, 1972.

[5] W. Woods,"An experimental parsing system for transition network grammars",*In Natural language Processing, R. Rustin, Ed.,Algorithmic Press, New York*,1973.

[6] G. Hendrix et. al., "Developing a natural language interface to complex data",*ACMTransactions on Database Systems*, vol. 3, no. 2, pp. 105 – 147, 1978.

[7] Y. W. Wong, "Learning for Semantic Parsing Using Statistical Machine TranslationTechniques", *Technical Report UT-AI-05-323,University of Texas at Austin, Artificial Intelligence Lab,* Oct 2005.

[8] Y. Li, H. Yang and H. V. Jagadish, "NaLIX: an interactive natural language interface for querying XML", *Proceedings of the 2005 ACM SIGMOD international conference on Management of data*, pp 900-902,2005.

[9] Abhijeet Gupta, Arjun Akula, Deepak Malladi, Puneeth Kukkadapu, Vinay Ainavolu, Rajeev Sangal, A Novel Approach Towards Building a Portable NLIDB System Using the Computational Paninian Grammar Framework, 2012 International Conference on Asian Language Processing, pp. 93-96, 2012

[10] Rajender Kumal1, Mohit Dul2, Shivani Jinda D-HIRD: Domain-Independent Hindi Language Interface to Relational Database, 2014 interna nonal conference on computa non of power, energy, informa non and communica non (ICCPEIC), pp- 81-86.

[11] Filbert Reinaldha, Tricya E. Widagdo, Natural Language Interfaces to Database (NLIDB): Question Handling and Unit Conversion,

[12] Axita Shah, Jyoti Pareek, Hemal Patel, Namrata Panchal NLKBIDB - Natural Language and Keyword Based Interface to Database

[13] Rajender Kumar, Mohit Dua "Translating Controlled Natural Language Query into SQL Query using Pattern Matching Technique", International Conference for Convergence of Technology – 2014, pp. 1-5.

[14] Xuan Xuan, Liu Jianbo, Yang Jin, Research on the natural language querying for remote sensing databases, 2012 International Conference on Computer Science and Service System, pp. 228-231, 2012.

Multi Objective Non-dominated Sorting Genetic Algorithm (NSGA-II) for Optimizing Fuzzy Rule Base System

Mehnuma Tabassum Omar[1,*], Monika Gope[2], Ariful Islam Khandaker [3] and Pintu Chandra Shill [1,2]
Department of Computer Science and Engineering
Khulna University of Engineering & Technology (KUET)
Khulna 9203, Bangladesh
[*]E-mail: misty2409@gmail.com

Abstract—**Multi-objective designs are genuine models for intricate combinatorial optimization problems. This paper presents a fast elitist non-dominated sorting multi objective genetic algorithm to develop smartly tuned fuzzy logic controllers with a finer trade-off between interpretability and exactitude in linguistic fuzzy modeling problems. The multi-objective genetic algorithm produces a group of non-dominated solutions defined FLCs for multi objective problem with satisfying objective at acceptance level without dominating to any other solution. In MO-GA, an integer encoding is used to indicate the linguistic level of fuzzy rule. Here, multi-objectives are transformed to a fitness function in order to initiate the NSGA-II, i.e. selection, crossover, and mutation. The intended approach generates an efficient and reliable fuzzy logic control system through the effective searching and self-learning adaptability of the NSGA-II. The simulation results based on multi-objective exhibits better performance than single objective while controlling car like robot.**

Keywords— Fuzzy rule base system, NSGA-II, Multi-objective Optimization, Pareto-Optimal Solution.

I. INTRODUCTION

Multi-objective approaches are applied on several composite engineering optimization problems as well as on realistic paradigms where beyond one objective are necessary to be fulfilled to reach desired goal. In a multi-objective decision making scheme, multiple criteria is considered that needed to be optimized within more than one objective function together [1], [2].

Genetic Algorithms (GAs) stand for stochastic search scheme motivated by the conception of evolution and natural selection of species. Originally, GAs was drawn-out in order to answer optimization problems with multiple objectives [1]. Adapted Genetic Algorithms have been validated to be predominantly operative to govern tremendous keys to explore a set of solutions all of which contents the objective's unsatisfactory grade without being dominated by whichever solutions in further [3].

The NSGA-II algorithm has been renowned [4] as the first evolutionary multi-objective optimization (EMO) algorithms that seek the solution domain to discover Pareto-optimal solutions within a multi-objective centered scheme [5]. In a solution domain a solution is Pareto-optimal if it denies domination from other solutions [6].

Fuzzy logic control is a significant zone in real-world paradigm [7] comprising control [8], [9], decision making [4]-[7], prediction [8], classification [9], inference [10] etc. In fuzzy logic system (FLS) a crisp input vector is mapped with a crisp scalar output where a linguistic rule base is appreciated as nonlinear function [11].

Hybrid techniques have increased significant consideration in the field of Computational Intelligence. The hybridization of Fuzzy Logic and GA is the most common method that points to genetic fuzzy systems (GFSs). Basically a GFS is an enhanced fuzzy method where GAs, genetic programming and evolutionary policies are comprised through an iterative learning procedure educed as of evolutionary computation and Genetic Algorithm [12].

However, the key question in the FLC scheme is to determine the membership function's types and parameters, and to produce the rules of fuzzy system. This optimization is done for a better design in which some research has been involved for partial optimization, not for complete process. For instance, some deals with membership functions parameters where as others addresses the fuzzy rules. Based on control operators or person's experience or automatically generated experience, the parameters of membership functions are chosen. To improve the behavior of the optimization problem, several methods alike GA, can be used [13].

A non-dominated sorting centered multi-objective evolutionary algorithm (MOEA), NSGA-II is capable for seeking a great coverage of solutions and improved convergence close to the accurate Pareto-Optimal front [4].

In this research work, a multi-objective evolutionary algorithm, NSGA-II (MO-NSGA-II) has been deployed for delivering and optimizing fuzzy logic controllers along with enhancing precise objectives and contenting enforced constraints at the same time.

The association of this paper is as follows: Related researches are mentioned in section, II. In Section III, multi-objective optimization definition has been demonstrated.

978-1-4673-9257-0/15/$31.00 ©2015 IEEE

Section IV defines the underlying control problem. In Section V, the proposed algorithm of MO-NSGA-II Fuzzy Rule base system has been presented. In Section VI, the simulation result of the proposed architecture has been depicted. Finally section VII outlines the conclusion of this paper.

II. Related Work

In the method of fuzzy logic, self-learning and generalization of rules are not possible. For real-time problems where genetic fuzzy policy has been successfully applied by means of scholarly information are very efficient [12]. To explain optimization technique, different EAs were proposed **[4].** Multi Objective GA and Fuzzy procedure are used for rule optimization in [14] where [15], [16] worked on Fuzzy set theory, association rule mining with GA. However, Fonseca and Fleming's MOGA [1], Srinivas and Deb's NSGA [2], and Horn et al.'s NPGA [13] were appreciated than others. These processes explained the required methodologies for translating an EA to a MOEA [4]. NSGA-II is MOEA but it is superior throughout latter generations, ignoring the level of noise exists in the problem [17]. To achieve a proper initial fuzzy structure iteratively, [18] proposed various Pareto-optimal fuzzy schemes based on NSGA-II. To increase quality and performance of task scheduling in the market-based grid setting, [5] used NSGA-II using fuzzy operators.

In this exploration, a hybridization of NSGA-II and Fuzzy Controller has been presented where the fitness functions are optimized to get the best optimized rules for a control problem. However, to load a truck to its destination, [19] presents a model of the fuzzy control system which is comprised with hybrid clustering method and neural network. But high computational demand in truck loading is the main disadvantage to put on their algorithm to a real-time problem. On the other hand, NSGA-II is a computationally fast and elitist MOEA where non-dominated sorting approach is applied [4]. Thus, the projected NSGA-II centered fuzzy system overcomes the weaknesses of building the structure of the unidentified system and aggregates the assistances of these two control structures.

III. Multi-Objective Optimization

A multi-objective decision paradigm in general can be conveyed as a vector function '$\boldsymbol{f}$' such as

$$f: m \rightarrow n \tag{1}$$

where $\boldsymbol{m}$ is the decision variable parameters and $\boldsymbol{n}$ is the objective .

Generally:

minimize/maximize,

$$y = f(x) = (f_1(x), f_2(x), \dots, f_n(x))$$

subject to $x = (x_1, x_2, \dots . x_m) \in X$,

$$y = (y_1, y_2, \dots . y_n) \in Y \tag{2}$$

where $\boldsymbol{x}$ is called decision vector and $\boldsymbol{y}$ objective vector

The solution sets of a multi-objective optimization problem are Pareto Optimal which is not dominated by any other solutions. The collection of non-dominating feasible solutions in solution domain is stated as the Pareto Optimal Set. The Pareto Optimal solution contains each of those decision vectors that are unable to be improved within any objective without being degraded within other objectives [1], [2], [20]. Pareto front is the value of an objective function in the objective space corresponding to a given Pareto Optimal set. The ultimate aim of a multi-objective optimization algorithm is to explore a set of solutions which will substantially signify the Pareto optimal set [6]. Subsequently, the best acceptable solution can be elected by manipulating a precedence benchmark. To cope with it, the evolutionary algorithms have united new tactics to manage the constraints preferred and verified to resolve constrained multi-objective optimization models as [3].

The NSGA-II (Non-Dominated Sorting Genetic Algorithm-II) algorithm examines the solution domain to discover Pareto-optimal solutions in a sphere of multi objective optimization assembly [5]. NSGA-II practices the elitist standard and an obvious diversity conserving tool. Besides, it also underlines non-dominated solutions and characterizes the Pareto front through Pareto-optimal solutions [5]. NSGA-II practices a categorical diversity-conservation or niching policy to consign a diversity rank to entire individuals' having identical non-dominated front [4]. The participants consuming the smallest crowded region inside each non-dominated front are dispensed through a higher rank. Due to the disposition of the prototypes of the multi-objective optimization schemes, NSGA-II can be applied for discovering the non-dominant optimal solutions. Dominance and correctness of any solution above the other solutions rests on a number of factors such as user's adoption and problem circumstances. Hence, the NSGA-II governs a collection of dominant solution and subsequently Pareto front is attained [11], [21].

IV. Problem Specification

In this work, an independent truck has been simulated by the MO-NSGA-II which is incorporated with fuzzy logic controller. Fig. 1 depicts the object of the problem where the primary position of the objective truck is symbolized with x, φ and y.

Here, φ is the angle of the object regarding the horizontal line in the problem space. The point$(\boldsymbol{x}, \boldsymbol{y})$ identifies the back center location of the object truck in the problem space. The steering angle θ is a measure between the object truck and the front wheel. The object truck is simulated in order to be loaded at a position $(\boldsymbol{x_f}, \boldsymbol{y_f})$ and angle $\boldsymbol{\varphi_f} = \mathbf{90^0}$. The truck is capable of backing its position only.

From any initial location $(\boldsymbol{x_0}, \boldsymbol{y_0})$ with any initial angle $\boldsymbol{\varphi_0}$, the regulator must generate the suitable steering angle $\boldsymbol{\theta}$ at each phase to cause the truck of being loaded to a chosen location.

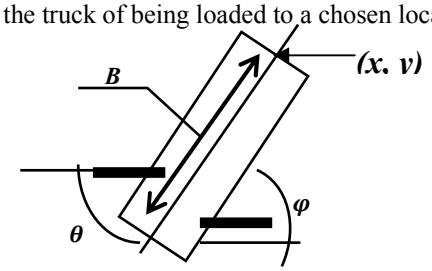

Figure 1. Illustration of a Truck Model

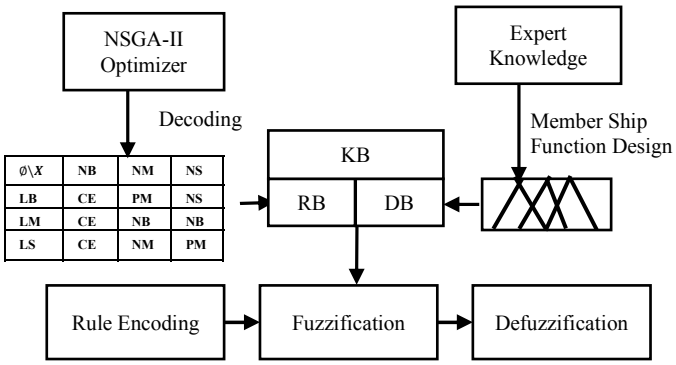

$\emptyset\backslash X$	NB	NM	NS
LB	CE	PM	NS
LM	CE	NB	NB
LS	CE	NM	PM

Figure 2. The Model of MO-NSGA-II Based Fuzzy System

The following equations have been used to find the next position of the truck to convey it to desired dock:

$$x(n+1) = x(n) - \cos((\varphi(n) + \theta(n)) - \sin(\theta(n))\sin(\varphi(n)) \quad (3)$$

$$y(n+1) = y(n) - \sin((\varphi(n) + \theta(n)) + \cos(\theta(n))\cos(\varphi(n)) \quad (4)$$

$$\varphi(n+1) = \varphi(n) - \arcsin\left(\frac{2\sin(\theta(n))}{B}\right) \quad (5)$$

V. MO-NSGA-II BASED FUZZY RULE BASE SYSTEM

Fuzzy system constitutes a Knowledge Base (KB) which contains a Rule Base (RB) and Database (DB). The Database procures membership function from the expertise. The NSGA-II algorithm operates as an optimizer providing rule to the Rule Base. The Knowledge Base then provides his acquaintance to the FLC and commences the evolution process. Fig. 2 defines the model of the projected MO NSGA-II Based Fuzzy System. The complete architecture works as follows:

A. Proposed Algorithm

The proposed NSGA-II based fuzzy rule base system (FRBS) has the succeeding stages:

1) Partition of the Input and Output Universe of Discourses: Partition the variables into several fuzzy regions (fuzzy sets) separetely and assign fuzzy MF i.e., linguistic identity of the respective sections. The system takes the position of x and alignment angle φ as input and produces steering angle θ as system output. The ranges are taken in the simulation with φ [-92, 270], X[-20, 20] and θ [-40, 40]. The MFs are manipulated with 50% overlap as a sample shown in Fig.3.

2) Chromosome Encoding: The linguistic label for x is specified by NB, NM, NS, ZE, PS, PM and PB. For φ, the linguistic label is specified by LB, LM, LS, CE, RS, RM, and RB. The linguistic label of θ is specified by NB, NM, NS, CE, PS, PM and PB. The sample database for the input data of x, phi and theta are given in Table.1. The linguistic lebels are further encoded using real integer 1 to 7 espectiely shown in Table.2

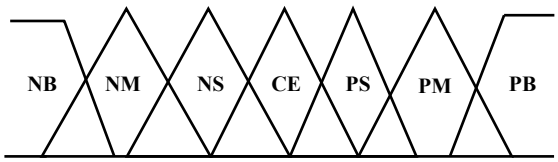

Figure 3. Fuzzy membership function details of θ

Table 1. Input partitions along with linguistic label

Input X(c, w)			Input φ(c, w)			Input θ(c, w)		
NB	-14.35	11.3	LB	-43	98	NB	-29	22
NM	-8.67	11.35	LM	6	98	NM	-18	22
NS	-3	6	LS	55	72	NS	-7	14
ZE	0	6	CE	91	72	CE	0	14
PS	3	6	RS	127	72	PS	7	14
PM	8.67	11.35	RM	174.67	95.35	PM	18	22
PB	14.35	11.3	RB	222.35	95.3	PB	29	22

3) Chromosome Generation: Use self-learning capabile scheme, NSGA-II to initiate a random chromosome of a desired population size. Here a chromosome consists of 49 genes (x×φ or 7×7). Fig.4 examplifies a FAM(Fuzzy Associative Memory). From Fig. 4 it can be found that if x = 1(NB) and φ = 1(LB) then the corresponding θ = 7(PB).

4) Chromosome Decoding: Now, the given chromosome is transfered into a collection of center and width combination for each of the x, φ and θ maintaining the input partitions given in Table.1 in order to map the corresponding θ to identify the degree of membership. Hence, the size of the chromosome becomes 49×6=(7×7×3×2), where 3 is for three variables (x, φ, θ)and 2 is for center and width for each variable. The decoding process and the decoded chromosome is shwon in Fig. 5

5) Calculate Fitness Function and Ranking the Chromosome.: Calculate the fitness of a chromosome using objective function. Usually, the objective function desires to optimize several objectives and there should be a relation between the objectives, where progress in one objective can be attained without damaging the other. The three fitness objectives to minimize the error and mature. The solution used in this algorithm are given below:

Objective 1 - Trajectory Error (TE): The trajectory orientation tracking objective will inspect the orientation of the simulation as shown below-

$$TE = \frac{\text{Length of truck trajectory}}{\text{distance(initial pos,final pos)}} \quad (6)$$

Objective 2 -Docking Error (DE): Euclidean distance is known as docking error where distance between the actual final position (φ, x, y) and the desired final position (φ_f, x_f, y_f) is being measured -

$$DE = \sqrt{(\varphi_f - \varphi)^2 + (x_f - x)^2 + (y_f - y)^2} \quad (7)$$

Objective 3 - Execution time (N): For carrying out the docking maneuver, the desired time (cycles) is stated as

Table 2. Input partitions along with linguistic label

Real INT	X	φ	θ
1	NB	LB	NB
2	NM	LM	NM
3	NS	LS	NS
4	CE	CE	CE
5	PS	RS	PS
6	PM	RM	PM
7	PB	RB	PB

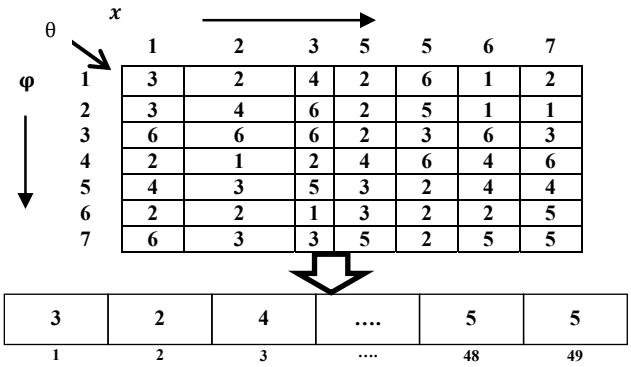

Figure 4. Fuzzy Associative Memory

Execution time. Here in the simulation Execution time is calculated by the difference of starting time of initial position and the loading time when the truck reached the destination.

6) Evaluate Chromosome: Rank the chromosome based on their fitness value. As it is a minimization problem, hence the minimum fitness will be ranked one. Then perform selection, crossover and mutation to generate next population. If the stopping criterion does not meet then repeat the steps from step 4.

B. Evulotionay Process

A new factor alongside with fitness value is known as crowding distance for every distinct value of population which is measured after the non-dominated sort. However, crowding distance is a degree of adjacent of an individual from its neighbors. Parents are selected from binary tournament

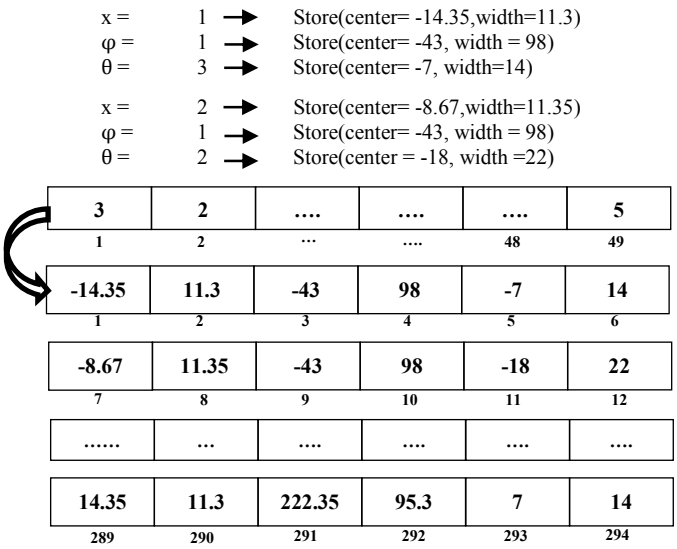

Figure 5. Chromosome Decoding

which is prepared from rank and crowding distance. The offsprings are produced by the chosen population through crossover and mutation operation [23], [24], [25]. Fig. 6 describes the control flow of the proposed model. The NSGA-II algorithm considers a set composed of several operators usually used in multi-objective optimization heuristics such as: simulated binary crossover (SBX), differential evolution operator (variation operator), polynomial mutation etc. [22]. The NSGA-II algorithm comprises of the following perimeters:

Selection: The crowded-comparison-operator ($\prec_n$) is utilized to accomplish the selection operation maintaining the following constraints:

(1) In front F_i for all entities the Non-domination rank, $p_{rank} = i$.

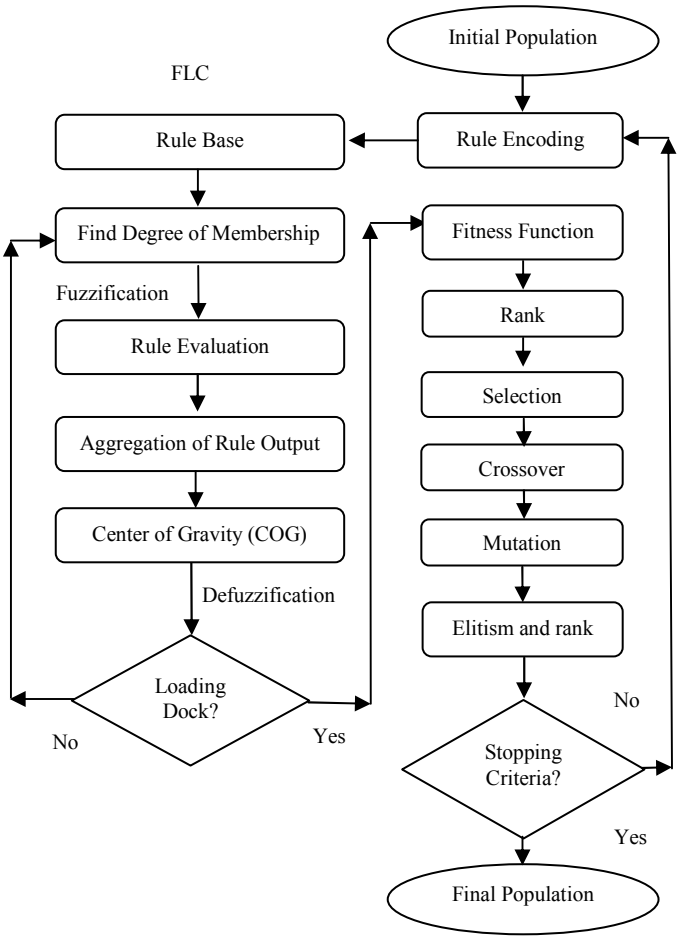

Figure 6. The Flow Chart of MO-NSGA-II based FRBS Model

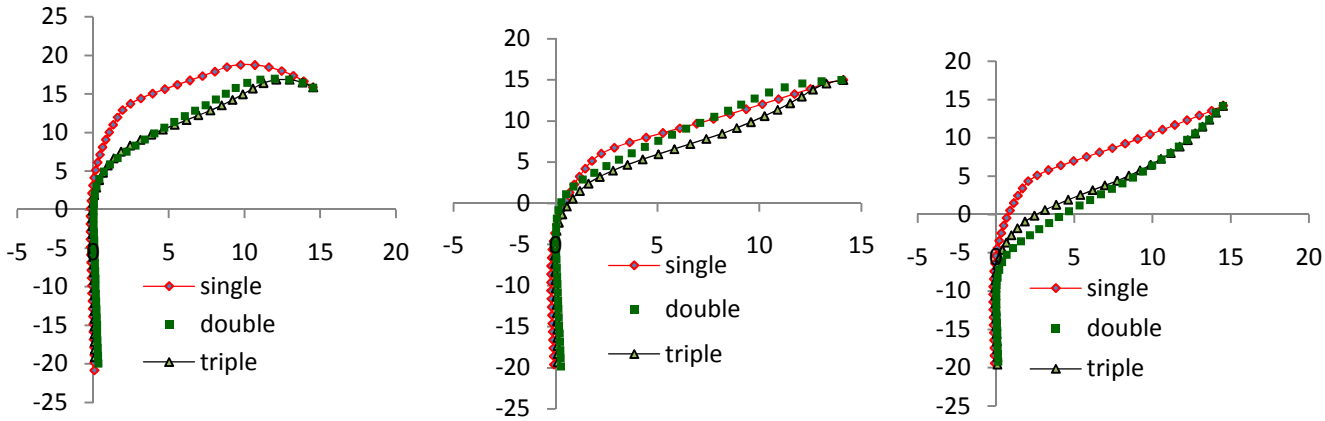

(a): Case 1 states (x, φ, y) = (15,-60, 15) (b): Case 2 states (x, φ, y) = (15, 0, 15) (c): Case 3 states (x, φ, y) = (15, 60, 15)

Figure 7. Comparisons of the result of single and MO-NSGA-II based FRBS Model

(2) Crowding distance $F_i(d_i)$

$p \prec_n q$ if

a) $p_{rank} < q_{rank}$

b) or if p and q are in the identical front F_i then $F_i(d_p) > F_i(d_q)$

With this operator the individuals are nominated through a binary tournament selection [23], [24], [25].

Genetic Operators: For crossover and polynomial mutation Genetic Algorithms apply Simulated Binary Crossover (SBX) operator [24].

Simulated Binary Crossover: Simulation perceived by the operator is given as below.

$$C_{1,k} = \frac{1}{2}[(1 - \beta_k)p_{1,k} + (1 + \beta_k)p_{2,k}] \quad (8)$$

$$C_{2,k} = \frac{1}{2}[(1 + \beta_k)p_{1,k} + (1 - \beta_k)p_{2,k}] \quad (9)$$

Where $C_{i,k}$ is the ith child, with k^{th} element, $p_{i,k}$ is the nominated parent and β_k (≥ 0) is a example as of a random number produced with density

$$\rho(\beta) = \frac{1}{2}(\eta_c + 1)\,\beta^{\eta c}, \text{if } 0 \leq \beta \leq 1 \quad (10)$$

$$\rho(\beta) = \frac{1}{2}(\eta_c + 1)\frac{1}{\beta^{\eta c}}, \text{if } \beta > 1 \quad (11)$$

From a uniformly sampled random number r among (0, 1) the distribution is achieved where $\boldsymbol{\eta_c}$ means distribution index for crossover [23], [24], [25].

To be exact,

$$\beta(r) = (2r)^{\frac{1}{(\eta+1)}} \quad (12)$$

$$\beta(r) = \frac{1}{[2(1-r)]^{\frac{1}{(\eta+1)}}} \quad (13)$$

Polynomial Mutation:

$$c_k = p_k + (p_k^u - p_k^l)\delta_k \quad (14)$$

Here, c_k is a child entity and p_k is a parent entity, p_k^u is the upper limit and p_k^l is the lower limit where δ_k is a minor difference that is measured by a polynomial distribution as follows:

$$\delta_k = 2r_k^{\frac{1}{\eta_{m+1}}} - 1, if\ r_k < .05 \quad (15)$$

$$\delta_k = 1 - [2(1 - r_k)]^{\frac{1}{\eta_{m+1}}}, if\ r_k \geq .05 \quad (16)$$

Where r_k is a random number between (0; 1) and η_m is mutation distribution index [23], [24], [25].

Recombination and Selection: The offspring population and the present population are combined. Afterwards the selection is performed in oder to get the individuals of subsequent generation where elitism is confirmed. If the addition of all the individuals in front F_j exceeds N then individuals in front F_j are selected until the population size N. The same procedure is repeated so that the following generations can be produced [23], [24], [25].

VI. Experimental Setup and Simulation Result

The experimental result is presented to show the strength of the offered method and compare the performance with the different fitness function. The experiments are peformed using real-coded rigid variables. Some essential parameters projected in the systems are presented in Table.3. Three cases as Case 1: (15, - 60, 15), Case 2: (15, 0, 15) and case 3: (15, 60, 15) are considered with initial states (x, φ, y) where the final or docking position (x_f, φ_f, y_f) is $(0, 90^0, 0)$. These cases are manipulated by three environments. The first environment is depicted by single in the graph. It considers the Objective-I which is the trajectory error. The second environment reflects the Objective-I and Objective-II which are the trajectory error and docking error pointed by double in the graph. And the last environment indicated by triple in the graph, deliberates three objectives which are the Objective-I (trajectory error), Objective-II (trajectory and docking error) and Objective-III (trajectory and docking error and execution time). Case-1, Case-2 and Case-3 are presented in Fig. 7(a), 7(b) and 7(c) respectively.

Table 3. Assumed Parameters for Constructed Prototypes

Cross-over Probability	1
Mutation Probability	0.02
Distribution Index for Crossover	100
Distribution Index for Mutation	500
Seed	1
Generation	100
Population	600

From the simulation graph it can be seen that in every environment for different starting position the truck can be loaded with desired loading angle (90^0) along with the docking position (0, 0). In the ultimate trajectory the truck first passages beside the objective link or overlaps through the objective link and then drive nearby y-axis towards the goal.

VII. CONCLUSION

In this article, Multi-objective FRBS has been developed using NSGA-II and the FRBS for intelligent control of car like robot system. The optimizations used in NSGA-II are: trajectory error, docking error and time. The rule base of the proposed FRBS MO-NSGA-II is tuned for optimal control performance by simultaneously optimizing the multiple objective functions. The instantaneous optimization of these objectives enhances the performance of the control algorithm. Simulation results demonstrate the performance advantage and quality solutions of multi-objective approach. Furthermore, in general the multi-objective based control algorithm requires high computation. Therefore, the paradigm is not apposite in applications demanding high constraints regarding time or memory.

REFERENCES

[1] Carlos M. Fonseca and Peter J. Fleming, "An Overview Of Evolutionary Algorithms In Multiobjective Optimization", Evolutionary Computation archive Volume 3, Issue 1 , MIT Press Cambridge, MA, USA, Pages 1-16, Spring 1995

[2] N. Srinivas and Kalyanmoy Deb, "Muiltiobjective Optimization Using Nondominated Sorting in Genetic Algorithms", Massachusetts Institute of Technology, Volume. 2, Issue 3, Pages 221-1994, Fall 1994

[3] J.M. Lucas, H. Martinez, and F. Jimenez, "Multi-objective Machine Learning Application: Fuzzy Tuning for the Docking Maneuver Controller of an Automated Guided Vehicle", Studies in Computational Intelligence, Volume 16, Pages 585-600, 2006

[4] K. Deb, S. Agrawal, A. Pratap, and T. Meyarivan, "A Fast And Elitist Multi-Objective Genetic Algorithm: NSGA-II", Evolutionary Computation, IEEE Transactions, Volume 6 , Issue 2, Pages 182–197, 2002

[5] Reza Salimi, Navid Bazrkar, and Mostafa Nemati, "Task Scheduling for Computational Grids Using NSGA II with Fuzzy Variance Based Crossover", Advances in Computing, Vol. 3 No. 2, pp. 22-29, 2013

[6] Abdullah Konaka ,David W. Coitb, Alice E. Smithc, "Multi-objective optimization using genetic algorithms: A tutorial", Reliability Engineering & System Safety ,Volume 91, Issue 9, Pages 992–1007, September 2006

[7] F. J. Cabrerizo, J. Lopez-gijon and A. A. Ruizo, "A Model Based On Fuzzy Linguistic Information To Evaluate The Quality Of Digital Libraries", Int. Journal of Information Technology & Decision Making, Volume 9, Issue 3, Pages 455–472, May 2010

[8] A. Daftaribesheli, M. Ataei, and F. Sereshki, "Assessment Of Rock Slope Stability Using The Fuzzy Slope Mass Rating (FSMR) System", Applied Soft Computing, Volume 11, Issue 8, Pages 4465–4473, December 2011

[9] S. E. Oltean,"Swing-up and Stabilization of the Rotational Inverted Pendulum Using PD and Fuzzy-PD Controllers", Procedia Technology, Volume 12 , Pages 57–64 , 2014

[10] C. S. Chen, Y. D. Jhong, T. Y. Wu, and S.-T. Chen, "Typhoon Event-Based Evolutionary Fuzzy Inference Model For Flood Stage Forecasting", Journal of Hydrology, Volume 490, Pages 134–143, 20 May 2013

[11] Shill P.C., Maeda Y, Murase, "Optimization of Fuzzy Logic Controllers with Rule Base Size Reduction Using Genetic Algorithms", Computational Intelligence in Control and Automation (CICA), 2013 IEEE Symposium, Pages 57 – 64, April 2013

[12] B. Dennis and S. Muthukrishnan "AGFS: Adaptive Genetic Fuzzy System for medical data classification", Applied Soft Computing, Volume 25, Pages 242–252 25, December 2014

[13] Shill, P.C., Pal K.K., Amin M.F.,Murase K.," Genetic Algorithm Based Fully Automated and Adaptive Fuzzy Logic Controller", Fuzzy Systems (FUZZ), 2011 IEEE International Conference , Pages 1572 – 1579, June 2011

[14] H. Wang, S. Kwong, Y. Jin, W. Wei, K.F. Man," Multi-Objective Hierarchical Genetic Algorithm For Interpretable Fuzzy Rule-Based Knowledge Extraction", Fuzzy Sets and Systems ,Volume 149, Issue 1, Pages 149–186, January 2005

[15] Alcala-Fdez J., Alcala R., Herrera F. "A Fuzzy Association Rule-Based Classification Model for High-Dimensional Problems With Genetic Rule Selection and Lateral Tuning", Fuzzy Systems, IEEE Transactions ,Volume 19 , Issue 5, Pages 857 – 872, April 2011

[16] C.H. Tan, K.S. Yap, H.J. Yap, "Application Of Genetic Algorithm For Fuzzy Rules Optimization On Semi Expert Judgment Automation Using Pittsburg Approach", Applied Soft Computing, Volume 12, Issue 8, Pages 2168–2177, August 2012

[17] Lam T. Bui, Daryl Essam, Hussein A. Abbass, and David Green. "Performance Analysis Of Evolutionary Multi-Objective Optimization Methods In Noisy Environments", 8th Asia Pacific Symposium on Intelligent and Evolutionary Systems, Pages 29-39, 2004.

[18] Xing Zong-yi, Zhang Yong , Hou Yuan-long , Cai Guo-Qiang "Multi-Objective Fuzzy Modeling Using NSGA-II", Cybernetics and Intelligent Systems, 2008 IEEE Conference, Pages 119 – 124, Sept. 2008

[19] Ying Li, Yuanchun Li," Neural-Fuzzy Control Of Truck Backer-Upper System Using A Clustering Method", Neurocomputing, Volume 70, Issues 4–6, Pages 680–688, January 2007

[20] Zitzler, E and Lothar Thiele, "An Evolutionary Algorithm For Multiobjective Optimization The Strength Pareto Approach", Evolutionary Computation, IEEE Transactions, Volume 3, Issue 4, Pages 257 – 271, Nov 1999.

[21] S. Padhee, N. Nayak, S.K. Panda, and S.S. Mahapatra, "Multi-Objective Parametric Optimization Of Powder Mixed Electro-Discharge Machining Using Response Surface Methodology And Non-Dominated Sorting Genetic Algorithm", Indian Academy of Sciences, Sadhana, Volume. 37, Issue 2, Pages 223–240, April 2012.

[22] Antonio J. Nebro, Juan J. Durillo, Mirialys Machın, Carlos A. Coello Coello, and Bernab´e Dorronsoro, "A Study of the Combination of Variation Operators in the NSGA-II Algorithm", 15th Conference of the Spanish Association for Artificial Intelligence, CAEPIA 2013, Pages 269–278, September 2013

[23] Hans-Georg Beyer and Kalyanmoy Deb "On Self-Adaptive Features In Real-Parameter Evolutionary Algorithms", Evolutionary Computation, IEEE Transactions Volume 5, Issue 3, Pages 250 - 270, June 2001.

[24] Kalyanmoy Deb and R. B. Agarwal. "Simulated Binary Crossover for Continuous Search Space" ,Complex Systems, Volume 9, Issue 2 Pages 115 -148, April 1995

[25] M. M. Raghuwanshi and O. G. Kakde. "Survey On Multiobjective Evolutionary And Real Coded Genetic Algorithms", 8th Asia Pacific Symposium on Intelligent and Evolutionary Systems, Pages 150 -161, 2004

A Multi-Objective Genetic Algorithm with Fuzzy Relational Clustering for Automatic Data Clustering

Animesh Kundu, Animesh Kumar Paul[1], Pintu Chandra Shill
Department of Computer Science and Engineering
Khulna University of Engineering and Technology
Khulna, Bangladesh
[1]animesh10kuet@gmail.com

Kazuyuki Murase
Department of System Design Engineering
University of Fukui,
Japan
murase@u-fukui.ac.jp

Abstract—**A multi-objective genetic algorithm based fuzzy relational eigen vector centrality based clustering algorithm (FRECCA) called FRECCA-NSGA-II is proposed for automatic data clustering in this paper. A given dataset is spontaneously promoted into an optimal number of groups in a precise fuzzy partitions through the fuzzy clustering algorithm called FRECCA. This FRECCA algorithm operates on a similarity square matrix which is generated by comparing the pair wise similarities between data points. In most of the cases, fuzzy clustering methods cannot differentiate the geometric structures of clusters due to the cohesion and separation measures of fuzzy partition and using only centroid information for clustering. NSGA-II algorithm is therefore convenient to search for uniform fuzzy partitions for different cluster shapes. The two well-known cluster validity indices, cohesion and separation, are optimized concurrently through multi-objective NSGA-II. Binary encoding is used for chromosomes, here encode the centers as well as variable length numbers of clusters. Experimental results on benchmark data sets are given to demonstrate that the FRECCA-NSGA-II is capable of determining well-separated, hyper-spherical and overlapping clusters. The superiority of the propose FRECCA-NSGA-II over the existing clustering algorithm is thoroughly elucidated for real-life benchmark data sets.**

Keywords—Fuzzy Relational Clustering (FRECCA), Multi-Objective Optimization, Non-dominated Sorting Genetic Algorithm (NSGA-II), Pareto Optimal Solution.

I. INTRODUCTION

Clustering works as a unsupervised method which classified patterns (data points or observations or feature vectors) into community or clusters, such that extracted patterns in the same community are similar to each other while extracted patterns in different communities are dissimilar [1]. Clustering methods which helps to find the underlying structures in data and this advantages are used in a wide distinction of applications, including classification, image processing, pattern recognition, document retrieval, biology, modeling and identification. These fields deploy multi-dimensional data and hence it is problematic to perceive information and clustering in high dimensional space [2]. A sustainable number of methods such as k-means [3], fuzzy c-means (FCM) [4] have been proposed to solve these clustering problems. These methods [3-4] are centroid based and the number of clusters is predefined.

In k-means clustering algorithm, *d*-dimensional space for data, a set of *n* data points and an integer *k*, representing the number of cluster are given as an input and the problem is to determine a set of *k* centers in *d*, which helps to represent the whole dataset. After assigning the all objects, it recalculate the positions of the *k* centers. These steps are repeated until the centers no longer move. For this reason, this problem can't be solved by any exactly known polynomial-time algorithms.

Fuzzy c-means (FCM) algorithm performs soft partitioning since it groups a dataset into *n* clusters. In the process, each data points in the dataset associates to every cluster to a certain degree. FCM clustering is a serviceable algorithm, but the random selection in center points and number of clusters leads to iterative process and it has a probability that the solution will easily get stuck into the local optimum. Another problem in FCM is to choose the fuzziness parameter m. Generally, m=2 is used but it is not appropriate for some datasets and optimal m value varies from one dataset to another. On the other hand, FCM cannot provide satisfactory clustering in case of noisy data [5]. In most of the cases, number of cluster is not known before and some works have suggested to handle such situation by running the algorithm several times for different values of *k* along with varying initialization [6] but this technique is not suited for large datasets since it fails to find global optimum.

In order to surpass the above problems, genetic computation have been introduced for inferring the optimal cluster's numbers to make the clustering process more efficient. In our study, to resolve the disadvantages of fuzzy clustering we have to make a hybrid genetic algorithm with fuzzy clustering.

Many real-life problems involve performance measurement or objectives that optimize all objectives simultaneously. Multi-objective genetic algorithms (MOGAs) provide better performance over single-objective clustering algorithms [7] for the complex datasets where the partitioned clusters have different sizes or different geometric shapes. In order to obtain appropriate partitioning of complex data sets consisting of different shaped clusters, the chosen objective functions should treat compactness of clusters along with the ability to deal with overlapping clusters. In such situations MOGAs provide better result than those using single objective function by incorporating two or more objective functions [7]- [8].

978-1-4673-9257-0/15/$31.00 ©2015 IEEE

In this paper, we bring up a new multi-objective evolutionary approach to evolve optimal data clustering without requiring predicting the number of clusters. This method optimizes two objectives simultaneously, fuzzy J_m index [4] and overlap-separation measure [9]-[10]. This approach called FRECCA-NSGA-II used the non-dominated sorting genetic algorithm-II (NSGA-II) [11] for multi-objective optimization whereas the FRECCA algorithm is used to generate fuzzy clusters from data points.

The basic association of the paper is given as follows: Section 2 focuses on related works of this proposed method. Section 3 briefly describes our proposed fuzzy relational clustering algorithm called FRECCA-NSGA-II. This section providing details of FRECCA algorithm, describes the evolutionary process of NSGA-II algorithm and mention the process how to integrate NSGA-II with FRECCA also. Applied data sets in our model are detailed in Section 4. Section 4 represents the analysis results of FRECCA-NSGA-II compared with other approaches and finally, a conclusion of the paper is drawn into section 5.

II. Review of Related Works

This section describes the related methods of the fuzzy clustering with genetic algorithms from the different literature particularly, in the standard journals. From the analysis of the related literature, fuzzy clustering method's deficiency can be overcome by means of the genetic algorithm. So, the considerable drawbacks of fuzzy clustering of a problem can be solved using the multi objective genetic algorithm.

To surpass the drawbacks of FCM, a PSO based fuzzy clustering algorithm is introduced in [12]. Here, it uses the PSO algorithm's receptivity of global search.

Gan *et al.*, introduced a method for clustering the categorical data sets using the genetic fuzzy *K*–modes algorithm. For finding the global optimal solution of this optimization problem, they used genetic algorithm. In the crossover process, here applied the one-step fuzzy *K*–modes instead of the traditional crossover operator.

Yang *et al.*, brought forward a hybrid data clustering algorithm based on PSO and *K*-Harmonic Means [14] in which the KHM clustering doesn't fall into local optima and helps to surpass the incompleteness of the PSO algorithm's slow convergence characteristics.

Genetic algorithms have shown to facilitate in automatically determining the number of clusters by employing varying string length [15]-[17]. GA has been used in clustering the digital data sets [15]. As it is mentioned in [15] this type of algorithms is strong to recognize the clusters of any shape, but it fails to recognize the patterns for a small spatial separation between the clusters.

III. Proposed Hybrid FRECCA-NSGA Algorithm

This section introduces the working principle of proposed multi-objective genetic algorithm (NSGA-II) based FRECCA algorithm. This section also introduces FRECCA algorithm and objective functions.

A. Multi-Objective NSGA-II based FRECCA

In this study, we design a hybrid clustering algorithm called FRECCA–NSGA-II by combined FRECCA algorithm with NSGA-II algorithm in which it sustains the goodness of both FRECCA and NSGA-II algorithms.

FRECCA–NSGA-II algorithm executes FRECCA algorithm for the solutions (chromosomes) in every number of iterations/ generations such that each solution's fitness is improved. For solving the fuzzy clustering problem, the FRECCA–NSGA-II algorithm can be explained as follows:

Algorithm: FRECCA-NSGA-II for fuzzy clustering
Step-1: Initialize the parameters of FRECCA and MO-NSGA-II containing Number of clusters *C*, population size P, Cluster membership values for each data point on each cluster { p_i^m | i = 1,....,*N*, m = 1,....,*C* }, pairwise similarity values *S* = { s_{ij} | i = 1,....,*N*, j = 1,....,*N* } where s_{ij} is the similarity between data point i and j
Step-2: Create initial generation with P chromosomes
Step-3: Multi-Objective NSGA-II algorithm:
3.1. Calculate the number of clusters for each chromosome.
3.2. Multiple objective's value is calculated for each chromosome using Eq. (3) and Eq. (4).
3.3. Selection, crossover and mutation operations are acted on parent population to produce offspring population.
3.4. Offspring population are combined with parent population.
3.5. Fast non-dominated sorting performed on combined population to place individuals in their respective front.
3.6. Using nitching strategy, preference distance of individuals is calculated.
3.7. Better front and the least preference distance contained individuals are selected for to make new parent population.
3.8. If Multi-objective NSGA-II's execution finishing condition is not accomplished, go to step 4.
Step-4: FRECCA algorithm
4.1 Initialize and normalize membership values
4.2 Weighted affinity matrix create for cluster m
4.3 PageRank scores calculate for cluster m
4.4 Assign PageRank scores to likelihoods
4.5 Calculate new cluster membership values
4.6 Update mixing coefficients
4.7 Go back to step 4.2 if FRECCA algorithm's execution finishing condition is not satisfied.

Step-5: if FRECCA-NSGA-II algorithm's execution finishing condition is not accomplished, go to step 3.

B. Fuzzy Relational Clustering Algorithm (FRECCA)

In this study, data clustering is performed using Fuzzy Relational Eigenvector Centrality-based Clustering Algorithm (FRECCA) which uses graph representation in which objects are indicated using nodes, and similarity between objects is indicated using weighted edges. This algorithm employed the modified PageRank algorithm to each cluster. Measurement of centrality of a node within a given graph is done by using Page Rank algorithm and here, it assigns a Page Rank Score to every node in graph and here page rank score is given in numerical score from 0 to 1. In this case, the Page-Rank score of a data point within some cluster is interpreted as likelihood and then determination of cluster membership values and mixing coefficients [18] is performed using Expectation-Maximization (EM) framework.

The modified PageRank algorithm to work with weighted undirected edges of a graph representing objects with nodes V.

$$PR(V_i) = (1-d) + d \times \sum_{j=1}^{N} \left(w_{ji} \quad \frac{PR(V_j)}{\sum_{k=1}^{N} w_{jk}} \right) \tag{1}$$

978-1-4673-9257-0/15/$31.00 ©2015 IEEE

where w_{ji} is the similarity between V_j and V_i, and it is assumed that matrix contains these weights $W = \{w_{ij}\}$, which is referred to as the "affinity matrix".

1) Expectation Step

This first step, using the cluster membership values and scaling the similarities, the affinity matrix weights wij are calculated. i.e.

$$w_{ij}^m = s_{ij} \times p_i^m \times p_j^m \quad (2)$$

where w_{ij}^m is the weight between objects i and j in cluster m, s_{ij} is the similarity between objects i and j, and p_i^m and p_j^m are the membership values of objects i and j to cluster m. Then, for each cluster, it calculate the PageRank values according to eqn (1). Then PageRank scores are treated as probabilities and cluster membership values are calculated by PageRank.

2) Maximization Step

In maximization step updating of mixing coefficients is performed based on the Expectation step's calculated membership values of cluster. We get cluster membership values as an output.

C. NSGA-II Optimizaion Process

In order to solve real world complex optimization problems, multiple objectives need to be optimized at one time for many problems. Clustering algorithms try to optimize the multiple validity measures such as compactness, separation among clusters simultaneously. In our work, to handle this situation on clustering algorithm, FRECCA we have joined the multi-objective genetic algorithm (NSGA-II) with FRECCA. In the present section, NSGA-II optimization process is described whose goal is to assign the appropriate number of cluster and optimize multiple clustering validity measures.

The NSGA-II, proposed in [19] is an exoteric non-domination based genetic algorithm for optimizing multi-objectives. NSGA-II main objective is using a set of objective functions to improve the candidate solution's adaptive fitness of a population to a Pareto front constrained.

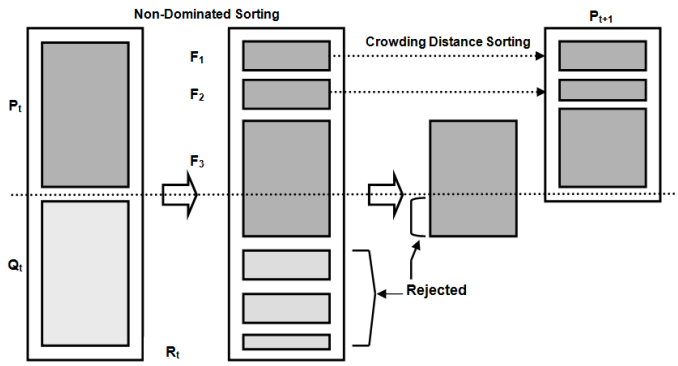

Fig. 1. NSGA-II Working Procedure

The NSGA-II working procedure is given in Fig. 1. The individuals with lower rank or larger crowding distance are selected as parents by binary tournament selection. Using crossover and mutation operations, selected population generates offspring and again select only the best N individuals as parents for the next iteration based on crowding distance on the last front and on rank from the current population and generated offspring by sorting based on non-domination.

1) Fast Nondominated Sorting

In NSGA-II, fitness assignment is done by non-dominated sorting. Front number 1 is assign to individuals which are not dominated by any other individuals and Front 2 is assign to those individuals which are only dominated by individuals whose front number are 1 and so on. Hence, two entities are calculated for each solution: a) domination count n_p, where p solution is dominated by n_p number of solutions b) S_p, solution set dominated by solution p.

Assume $n_p = 0$ for all solutions of first nondominated front. For each solution p with $n_p = 0$, each member (q) of its set S_p is visited and its n_p is reduced by one. As a result, if for any member q, the n_p becomes zero, it is dropped in a separate list Q. The second non-dominated front contains these members. Until all fronts are identified, this process continues with each member of Q and the identified third front.

2) Crowding Distance

The crowding-distance computation is part of density estimation of solutions surrounding an individual solution [20]. For density estimation, here with each of the objectives, it calculates the average distance of two points on either side of this point. This measure ($i_{distance}$), called crowding distance. By using the nearest neighbors consider as the vertices, $i_{distance}$ is treated as perimeter of the cuboid formed. The crowding-distance process includes the following steps:

a) For each given objective function m

- An infinite distance value is employed to boundary solutions.
- A distance value is assigned to other intermediate solution and here the assigned value is equal to the absolute normalized difference in the function values of two contiguous solutions.

b) Total crowding-distance value = For each objective, the total sum of individual distance values.

D. Objective Functions

In this study, we consider two objective functions fuzzy compactness and fuzzy overlap-separation. Let $X = \{x_1, x_2, \ldots, x_k\}$ be data points of M patterns, where on the n-dimensional space, each pattern x_k is a vector of features in R^n, C denotes the total number of clusters.

Minimize: Fuzzy Compactness,

$$J_m(U, V) = \sum_{k=1}^{M} \sum_{i=1}^{C} (u_{ik})^m \, d_{ik}^2 \quad (3)$$

Where, for n-dimensional space, d_{ik}^2 is the calculated squared euclidean distance.

The second objective functions is combination of l-order overlap and inter cluster separation both of which are measure for cluster validity. These are based on aggregation of membership values. The aggregation is composed of standard t-norm function $\top$ and t-conorm function $\perp$ with operator properties a $\top$ b = min (a, b) and a $\perp$ b = max (a, b).

For a data point x_k the overall inter-cluster overlap [9]-[10] is computed using fuzzy degrees by

Maximize: Inter-cluster Separation,

$$O \perp (u_k(x_k), C) = \underset{l=2,C}{\overset{1}{\perp}} \left(\underset{i=1,C}{\overset{l}{\perp}} u_{ik} \right) \quad (4)$$

978-1-4673-9257-0/15/$31.00 ©2015 IEEE

where membership vector for x_k is $u_k(x_k) = (u_{1k}, \ldots, u_{ck})$.

For x_k each u_k is associated with a single value $\perp^{l}(u_k) \epsilon$ [0, 1] by l-order fuzzy-OR operator (f OR-l) which is aggregation of t-norms and is given by

$$\underset{i=1,C}{\overset{l}{\perp}} u_{ik} = \underset{A\epsilon P_{l-1}}{\overset{\top}{}} \left(\underset{j\epsilon C\setminus A}{\perp} u_j \right) \tag{5}$$

where P denotes the power set of C= $\{1,2,\ldots,c\}$ and $P_l = \{ A\epsilon P: \ |A| = l \}$, where $|A|$ denotes the subset A's cardinality.

The separation measure is determined by highest degree of $\max_{i=1,C} u_{ik}$. The total Overlap separation (OS) calculation for M patterns is given by

$$OS = \frac{1}{M} \sum_{k=1}^{M} \frac{O\perp(u_k(x_k),C)}{max_{i=1,c} u_{ik}} \tag{6}$$

IV. Simulation Results and Discussion

In this section, data sets and simulation outputs are presented in order to interpret the effectiveness of our proposed fuzzy relational clustering algorithm called FRECCA based on multi-objective NSGA-II algorithm.

A. Data Sets

Real life data sets Iris, Glass, Wine and Liver Disorders are found from the UCI Machine Learning Repository [21]. The artificial datasets are AD_5_2 [22], AD_10_2 [23], Square-1, Square-2, Long-1. Table I shows the brief description of data sets, where D is the number of features, K is the number of clusters, M is sample size, and M_i is the number of members in cluster i.

Table I. Summary of Data Sets

Data Sets	D	K	M	M_i
AD_5_2	2	5	250	5×50
AD_10_2	2	10	500	10×50
Square-1	2	4	1000	4×250
Square-2	2	4	1000	4×250
Long-1	2	2	1000	2×500
Glass	9	6	214	70, 76, 17, 13, 9, 29
Wine	13	3	178	59, 71, 48
Iris	4	3	150	50, 50, 50
Liver-Disorders	6	2	341	142, 199

The data sets have the following features:

- AD_5_2 data set contains five classes. Each cluster has 50 points with highly overlapped 250 data point and each data point has two attributes.
- AD_10_2 data set contains ten classes with two attributes of 500 data points.
- Square-1 data set contains four classes with two attributes of 1000 data points. It is generated by normal distributions with a standard deviation of two in both dimensions.
- Square-2 data set contains four classes with two attributes of 1000 data poitns. It is generated by normal distributions with a standard deviation of two in both dimensions.
- Long-1 dataset contains two long shaped clusters with 1000 instances.
- Iris data set composed of three classes where each class consists of 50 instances. Each instance is described by four physical attributes which are length and width of sapals and petals.
- Wine consists of thirteen chemical attributes for 178 instances and divided into three classes.
- Liver-Disorders data set contains two classes with six attributes of 341 data points.

B. Experimental Results

We examine our proposed model on nine well known datasets describe in the previous section and compared with other existing algorithms. We take five artificial data sets and four real data sets for examining our proposed model.

Analyzing the result of different multi-objective techniques, FRECCA-NSGA-II provides better accuracy which is maintained by MS value and the number of clusters than other technique as shown in table-II and Fig.2, Fig. 3 and Fig. 4. Here, MS is used to obtain the best solution from the non-dominated set.

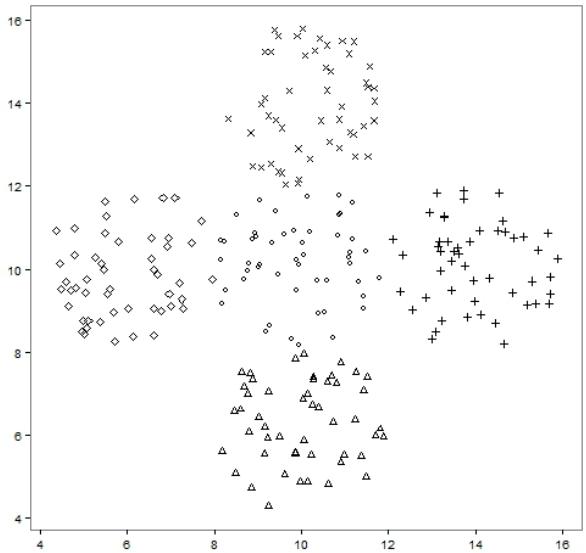

(a)

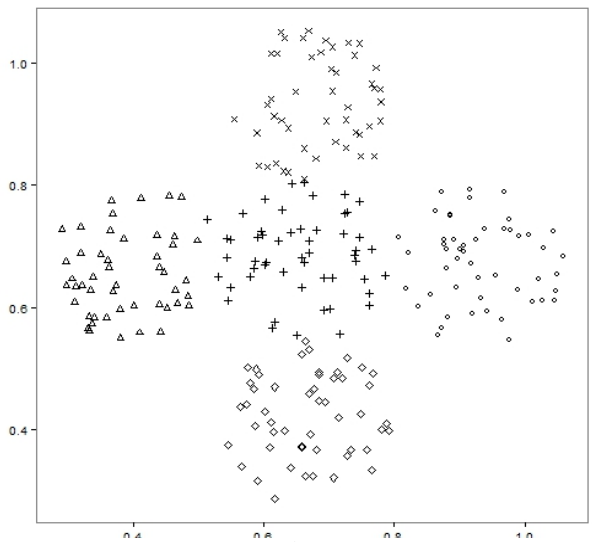

(b)

Fig. 2. (a) Original/True solution and (b) Clustering using FRECCA-NSGA-II (MS = 0.28) for the data set AD_5_2 (K = 5)

978-1-4673-9257-0/15/$31.00 ©2015 IEEE

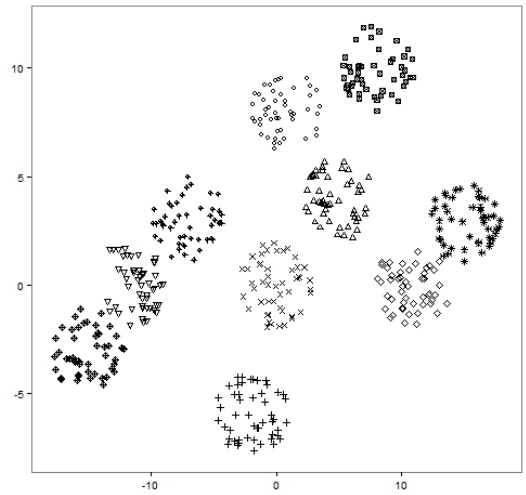

(a)

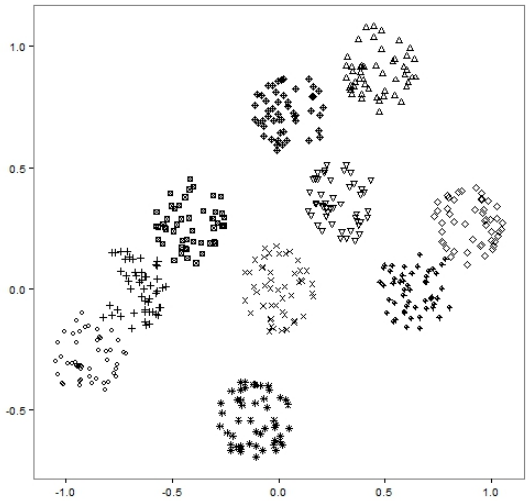

(b)

Fig. 3. (a) Original/True solution and (b) Clustering using FRECCA-NSGA-II (MS = 0.12) for the data set AD_10_2 (K = 10)

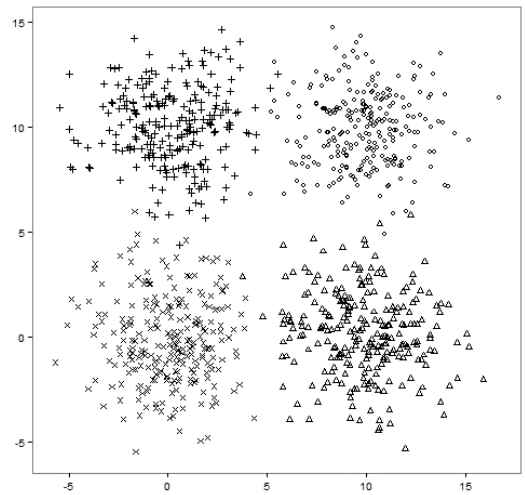

(a)

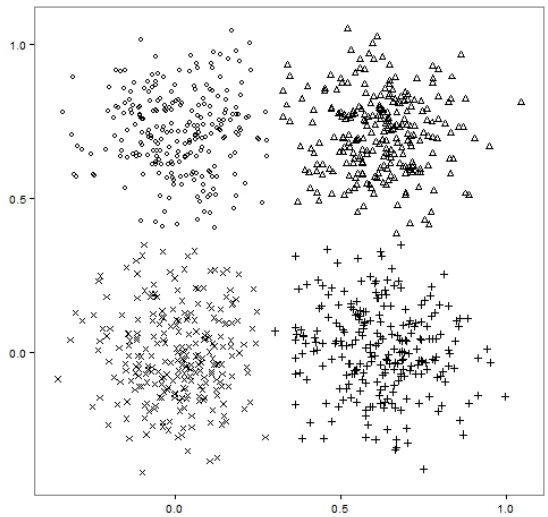

(b)

Fig. 4. (a) Original/True solution and (b) Clustering using FRECCA-NSGA-II (MS = 0.12) for the data set Square-1 (K = 4)

Figs. 2–4 compare the results of data partitioning by FRECCA-NSGA-II with the original data partitioning for three data sets. FRECCA-NSGA-II shows the better performance on separation, compactness and overlapping clusters for data sets as shown in Table-II. FRECCA-NSGA-II works effectively for the well-separated data points of AD_10_2 and Square-1 as shown in Fig. 3 and Fig. 4. Misclassification of data points can be caused by overlapping where borderline between clusters contain the data points.

In order to validate our proposed fuzzy relational clustering technique, FRECCA-NSGA-II is compared with other existing multi-objective methods like VAMOSA [7], MOCK [24], and FCM-NSGA [26] and with VGAPS [25], which is a single-objective clustering method. The comparison is made by the number of cluster and MS value as given in Table 2, where the results of VGAPS, MOCK and VAMOSA are obtained from [7] and FCM_NSGA is obtained from [26]. From the Table II, we have seen that our proposed model gives minimum MS value for most of the datasets with comparison to other approaches and it performs superior to others approaches for Wine, Iris datasets.

Table II. Comparative Analysis of FRECCA-MONSGA-II with other existing methods

DataSet	Actual K	Freeca-NSGA		FCM-NSGA		VAMOSA		MOCK		VGAPS	
		K	MS	K	MS	K	MS	K	MS	K	MS
AD_5_2	5	5	0.28	5	0.29	5	0.25	6	0.39	5	0.25
AD_10_2	10	10	**0.12**	10	0.13	10	0.43	6	1.01	7	0.84
Square-1	4	4	**0.18**	4	0.18	4	0.19	4	0.19	4	0.20
Square-4	4	4	0.50	4	0.49	4	0.51	4	0.60	5	0.52
Long-1	2	2	**0.0**	2	0.0	2	0.68	2	0.0	3	1.00
Glass	6	6	0.97	6	0.79	6	1.33	6	1.34	6	1.11
Wine	3	3	**0.52**	3	0.93	3	0.97	3	0.90	6	0.97
Iris	3	3	**0.38**	3	0.57	2	0.80	2	0.82	3	0.62
LiverDisorders	2	2	0.98	2	0.98	2	0.98	3	0.98	2	0.98

978-1-4673-9257-0/15/$31.00 ©2015 IEEE

C. Results of Non-dominated Solutions

The non-dominated solution is acquired by FRECCA-NSGA-II using artificial datasets and real-life datasets. Fig 5(a)-(b) shows non-dominated solution for Iris and Wine datasets.

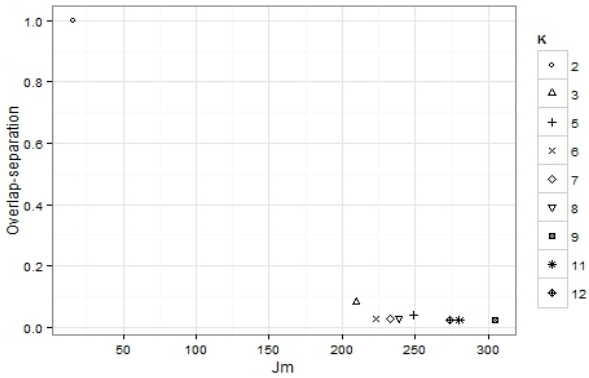

(a)

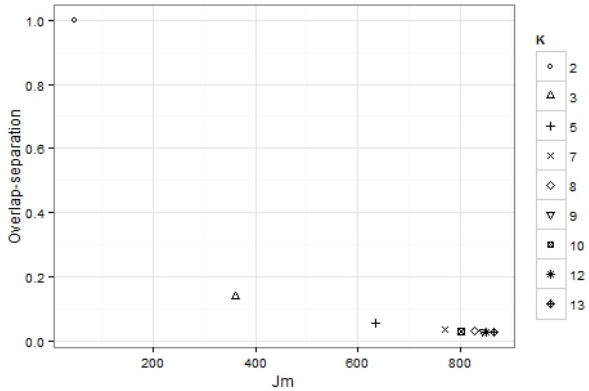

(b)

Fig.5. Non-dominated solution found while applying FRECCA-NSGA-II (a) Iris and (b) Wine dataset

V. CONCLUSIONS

This paper explorers the task of data clustering with multi-objective enabled by combination of multi-objective non-dominated sorting (NSGA-II) and fuzzy relational clustering algorithm (FRECCA). This hybrid technique is capable to partition the given data set into groups satisfying two objective functions, compactness and overlap-separation. The incorporation of fuzzy relational clustering algorithm has been an added advantage to work with real life complex data sets requiring higher clustering accuracy. The simulation results illustrate the superior capability of this propose hybrid technique in handling overlapped clusters than other single and multi-objective approaches.

REFERENCES

[1] A. K. Jain, M. N. Murty, and P. J. Flynn, "Data clustering: A review,"*ACM Comp. Surv.*, vol. 31, pp. 264–323, 1999.

[2] Kevin Beyer, Jonathan Goldstein, Raghu Ramakrishnan, and Uri Shaft, "When is nearest neighbors meaningful," in *Proc. of the International Conference of Database Theories*, 1999, pp. 217–235.

[3] J.B. MacQueen, "Some methods for classification and analysis of multivariate observations," in *Proc. of the Fifth Berkeley Symposium on Mathematical Statistics and Probability*, vol. 1, University of California Press, 1967, pp. 281–297.

[4] J.C. Bezdek, R. Ehrlich and W. Full, "FCM: the fuzzy c-means clustering algorithm," *Comp. Geosci*. Vol. 10 pp. 191–203, 1984.

[5] X.L. Yang, Q. Song and Y.L. Wu, "A robust deterministic annealing algorithm for data clustering," *Data & Knowledge Engineering,* Vol. 62 issue 1, pp. 84–100, Jul. 2007.

[6] E.R. Hruschka, R.J.G.B. Campello, A.A. Freitas and P. Leon, "A survey of evolutionary algorithms for clustering," *IEEE Trans. Systems, Man and Cybernatics- Part C: Aplications and Reviews,* vol. 39, pp. 133–155, 2009.

[7] S. Saha and S. Bandyopadhyay, "A symmetry based multiobjective clusteringtechnique for automatic evolution of clusters," *Pattern Recognit*. Vol. 43, pp.738–751, 2010.

[8] D. Karaboga and C. Ozturk, "A novel clustering approach: Artificial Bee Colony (ABC) algorithm," *Applied Soft Computing,* vol. 11, pp. 652–657, 2011.

[9] H.L. Capitaine and C. Frélicot, "A family of cluster validity indexes based on a l-order fuzzy or operator," *Lect. Notes Comp. Sci.,* pp. 622–631, 2008.

[10] H.L. Capitaine and C. Frélicot, "A cluster-validity index combining an overlap measure and a separation measure based on fuzzy-aggregation operators," *IEEE Trans. Fuzzy Syst.* Vol. 19, pp. 580–588, 2011.

[11] K. Deb, A. Pratap, S. Agarwal and T. Meyariva, "A fast elitist non-dominated sorting genetic algorithm for multi-objective," *IEEE Trans. Evol. Comp.* vol. 6 pp. 182–197, 2002.

[12] Li, L., Liu, X., and Xu, M. (2007). "A novel fuzzy clustering based on particle swarm optimization," *In First IEEE international symposium on information technologies and applications in education,* 2007*,* pp. 88–90.

[13] G. Gan, J. Wu and Z. Yang, "A genetic fuzzy k-modes algorithm for clustering categorical data," *Expert Systems with Applicationss,* Vol. (36), pp. 1615–1620, 2009.

[14] Yang, F., Sun, T. and Zhang, C., "An efficient hybrid data clustering method based on K-harmonic means, and particle swarm optimization," *Expert Systems with Applications,* Vol. 36, pp. 9847–9852, 2009.

[15] G. Garai and B.B. Chaudhuri, "A novel genetic algorithm for automatic clustering," *Pattern Recognit. Lett*. Vol. 25 pp.173–187, Jan. 2004.

[16] U. Maulik andS. Bandyopadhyay, "Genetic algorithm-based clustering technique," *Pattern Recognit.,* Vol. 33, pp. 1455–1465, Sep.2000.

[17] D.-X. Chang and X.-D. Zhang, C.-W. Zheng, "A genetic algorithm with gene rearrangement for k-means clustering," *Pattern Recognit.,* Vol. 42, pp. 1210–1222, Jul. 2009.

[18] Andrew Skabar and Khaled Abdalgader, "Clustering Sentence-Level Text Using a Novel Fuzzy Relational Clustering Algorithm," *IEEE Trans. Knowledge and Data Eng.,* vol. 25, pp. 1138-1150, Jan. 2013.

[19] N. Srinivas and K. Deb, "Multiobjective optimization using nondominated sorting ingenetic algorithms," *Evol. Comp.*, Vol. 2, no. 3, pp. 221–248, 1994.

[20] K. Deb, A. Pratap, S. Agarwal and T. Meyariva, "A fast elitist non-dominated sorting genetic algorithm for multi-objective optimization," *IEEE Trans. Evol. Comp.,* Vol. 6, pp. 182–197, 2002.

[21] A. Frank, A. Asuncion, UCI Machine Learning Repository, 2010.

[22] S. Bandyopadhyay and U. Maulik, "Genetic clustering for automatic evolution of clusters and application to image classification," *Pattern Recognition.*, vol. 35, pp. 1197–1208, 2002.

[23] S. Bandyopadhyay and S. Pal, "Classification and Learning Using Genetic Algorithms," *Applications in Bioinformatics and Web Intelligence*, Springer, pp.196-204, 2007.

[24] J. Handl, and J. Knowles, *"*An evolutionary approach to multi-objective clustering," *IEEE Trans. Evol. Comp.*, vol. 11, pp.56–76, 2007.

[25] S. Bandyopadhyay and S. Saha, "A point symmetry based clustering technique for automatic evolution of clusters," *IEEE Trans. Knowl. Data Eng.*, vol. 20, pp.1–17, 2008.

[26] Siripen Wikaisuksakul, "A multi-objective genetic algorithm with fuzzy c-means for automatic data clustering", Applied Soft Computing 24, pp.679- 691, 2014

978-1-4673-9257-0/15/$31.00 ©2015 IEEE

Modified Bus Invert Encoding to Reduce Capacitive Crosstalk, Power and Inductive Noise

Bulbul Ahmed[1], Sujan Kumar Saha[2], Jiangjiang Liu[3]
[1,2]Department of Electrical Engineering and [3]Department of Computer Science
Lamar University
Beaumont, USA
Email: [1]bahmed@lamar.edu, [2]ssaha@lamar.edu, [3]jane.liu@lamar.edu

Abstract— **As Very Large Scale Integrated (VLSI) circuits are shrinking aggressively, interconnect length is becoming longer. So interconnect power consumption due to capacitive coupling is increasing. Again, as operating frequency is increasing and rising time is very short, the inductance effect between interconnects can no longer be ignored. So, capacitive coupling and inductive coupling are both power and performance bottlenecks of modern interconnect design. In our paper, we have proposed an encoding method of data based on odd and even inverts of encoding. Our simulation results show that peak power is due to capacitive coupling and can be reduced up to 43.64%. Average power consumption decreases by 17.38%. Inductive ringing can be minimized up to 83.33% at logic high level and up to 30% at logic low level.**

Keywords— encoding, power, noise, bus invert, inductance, coupling capacitance

I. INTRODUCTION

With the improvement of Deep Sub Micron technology, chip components are getting smaller and smaller. Previous Complementary Metal Oxide Semiconductor (CMOS) transistors of micrometer range are now at the nanometer range in size. Not only the transistors, but also on-chip interconnects are shrinking aggressively. Interconnect width is scaled down with the technology, but its height can't be scaled down so aggressively to keep resistance constant. As a result, the height to width ratio (aspect ratio) of interconnects is increasing. The negative impact of this increasing aspect ratio is capacitive and inductive coupling between interconnects. Before, when operating frequency of a circuit was at the MHz range, inductive coupling was not significant enough to consider. Now, as circuit frequency is moving up to the GHz range, inductive coupling is also contributing to crosstalk noise.

In VLSI circuits, there are three major kinds of power consumption: dynamic power, leakage power, and short circuit power [1]. When a transistor switches from logic zero to logic one or logic one to logic zero, it consumes dynamic power. Leakage power is consumed in a static state. When there is a short circuit path between V_{dd} to ground due to an on-state of transistors, short circuit power is consumed. But in interconnects, only dynamic power is consumed due to capacitive coupling. As interconnects are responsible for a large portion of total power consumption of a chip, interconnect power is a major area of concern. Crosstalk delay due to capacitive coupling is another performance bottleneck. There have been several research projects on encoding methods of data to minimize power and crosstalk delay of interconnects. However, less research has been conducted into minimizing noise due to inductive coupling. Our proposed encoding method addresses both dynamic power and the inductive noise of interconnects to ensure a more reliable and lower power interconnect design.

The organization of the paper is as follows: the related work is in Section II. Section III states effects of switching patterns on capacitive and inductive coupling. Our proposed encoding method is described in Section IV. Section V contains simulation setup and results. Finally, we conclude in Section VI.

II. RELATED WORK

There has been an abundant amount of research on bus encoding methods. Among these, bus invert is one of the most widely used encoding methods [2]. Stan et al. proposed this encoding approach to reduce power consumption of I/O of a CMOS Integrated Circuit. According to the bus invert encoding, depending on the number of transitions, either inverted or non-inverted data is transferred to bus. Lin et al. suggested a caching technique named "Hierarchical Value Caching Encoding" to minimize power consumption of off-chip data buses [3]. In paper [4] and [5], frequent value encoding has been used to reduce energy of off chip buses. These four encoding methods have been proposed for power reduction of off-chip buses.

Yan et al. suggested odd-even bus invert encoding in [6] to minimize on-chip bus energy. In bus invert encoding, only self-transition is considered, whereas in odd-even bus inverts, self-transition as well as coupling transition have been considered. According to this approach, bus lines are divided into two groups: odd lines and even lines. Then, depending on the number of transitions, either odd lines are inverted or even lines are inverted. Also, in this paper, the authors mentioned a two-phase transferred method, which eliminates toggles completely. Brahmbhat et al. proposed window-based adaptive bus encoding that uses weighted code mapping to develop a new low power bus encoding [7]. Siegmund et al. mentioned adaptive partial bus inverts, and Saini et al. suggested conditionally coded block encoding in [8] and [9], respectively. A low overhead auto optimizing encoding has been used by

978-1-4673-9257-0/15/$31.00 ©2015 IEEE

TABLE I CROSSTALK CATEGORIZATION

CC	Delay	Pattern of switching
1	0	−−−, −− ↑, ↑ −−, −− ↓,↓ −−, ↑ − ↑,↑ − ↓,↓ − ↑,↓ − ↓
2	C_gR	↑↑↑,↓↓↓
3	$C_gR(1+\lambda)$	− ↑↑,↑↑ −,− ↓↓,↓↓ −
4	$C_gR(1+2\lambda)$	− ↑ −,− ↓ −,↓↓↑,↑↓↓, ↑↑↓,↓↑↑
5	$C_gR(1+3\lambda)$	− ↑↓,− ↓↑,↓↑ −,↑↓ −
6	$C_gR(1+4\lambda)$	↓↑↓,↑↓↑

Kretzschmar et al. in [10]. But, all of these encodings are inclined toward only reducing the power consumption of interconnects.

On the other hand, Sainarayan et al. proposed temporal and shielding coding to minimize the delay of interconnects [11]. According to this method, two temporal cycles are used and the shielding bit is inserted after every three bits to eliminate worst-case crosstalk scenarios. In the first temporal cycle, inverted data is transferred, and in the second temporal cycle, encoding information is passed. As a result, delays due to crosstalk are minimized. Cha et al. proposed a resource constrained bus encoding to minimize crosstalk delay [12]. Also Duan et al. and Victor et al. mentioned bus encoding methods to reduce crosstalk delay in their research, [13] and [14], respectively. Here, all these methods are focused on reducing only the delay of interconnects.

Najeeb et al. suggested temporal crosstalk shielding in [15] to reduce both the power consumption and delay of interconnects. This method also uses two temporal cycles to send encoded data and encoding information. In paper [16], Zang et al. mentioned two encoding methods: Variable Cycle Transmission with Hybrid Spatial Temporal Redundancy and Opposite Transition Forbidden Weighted Code Mapping. Madhu Mutyam proposed selective shielding in [18]. These methods are also apt to minimize power and delay of interconnects. Verma et al. also proposed a bus encoding technique to reduce crosstalk by reducing the number of bits or bus width [17]. But, all these encoding methods mentioned so far consider only the capacitive coupling of interconnects.

As the operating frequency of circuits increase, inductive coupling is a major issue to consider. LaMeres et al. proposed an encoding based minimization of inductive crosstalk for off-chip data buses [19]. Ruan et al. mentioned a crosstalk quantitative approach to minimize power, noise, and delay considering both capacitive and inductive effects [20]. A modified bus invert encoding has been proposed by Lampropoulos et al. to reduce the inductive noise of buses [22]. Our proposed encoding method also considers both capacitive and inductive coupling and delivers a solution to obtain a better encoded data to minimize power consumption and reduce crosstalk noise.

Fig. 1 Effect of Inductive Coupling for switching pattern "↑↑↑↑-↑↑↑"

III. EFFECT OF SWITCHING PATTERN ON INDUCTIVE AND CAPACITIVE COUPLING

In this section, we will discuss how inductive and capacitive coupling react according to switching patterns in bus lines. First, we will define some terms that will be used frequently. When two adjacent lines switch in opposite directions, this is known as Toggle. If any bus line switches from one logic state to another, this is known as self-transition. Charging-discharging occurs when one bus line switches and another adjacent one remains the same. The last one is stable. If a bus line does not switch or remains stuck to the same logic state, this is defined as stable. Switching from logic 0 to logic 1 and from logic 1 to logic 0 will be represented as '↑' and '↓' respectively and '-' denotes a stable position.

When signals switch in opposite directions, coupling capacitance causes signals in adjacent lines to be pulled up or down depending on the switching pattern. Thus glitches are produced in victim signals, and coupling capacitance becomes twice more than the capacitance introduced when switching in

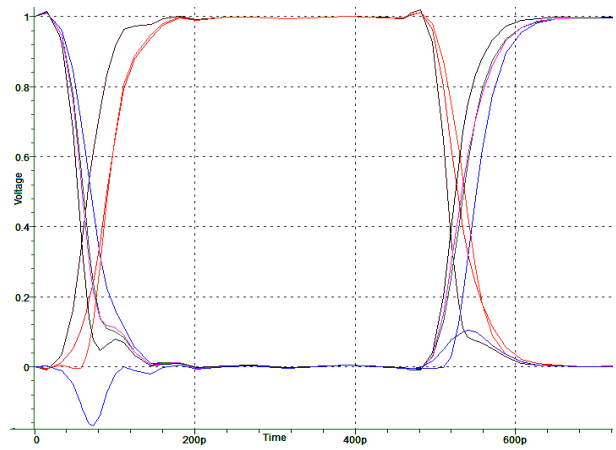

Fig. 2 Effect of Inductive Coupling for switching pattern "↑↓↑↓-↓↑↓"

the same direction. This is the worst situation for capacitive coupling.

For inductive coupling, when signals switch in the same direction, the equivalent inductance becomes the summation of self-inductance and mutual inductance [26]. This leads the signals to develop a large noise due to the ringing effect in the bus lines. Switching in the same direction causes an additive magnetic field, and that results in a ringing effect. We performed an HSPICE simulation of an 8-bit bus to observe the ringing effect due to inductive coupling. We set V_{dd} to 1V and the frequency to 1 GHz. Simulation results are shown in Figure 1 and Figure 2. In Figure 1, bus 5 remains stuck to logic 0 and all other bus lines switch in the same direction from logic 0 to logic 1.

In our simulation, inductive ringing is introduced in the waveform with a maximum peak value of almost 1.2V, and stable bus line 5 experiences a spike with a maximum value of almost .3V. On the other hand, in Figure 2, bus line 5 remains stable at logic 0 and all other bus lines switch in opposite directions. Switching in opposite direction causes magnetic field of the wires to cancel each other rather being additive when switch in the same direction. As a result, the inductive effect is greatly minimized and hence the ringing effect is also reduced.

IV. PROPOSED METHOD

In the previous section, we observed inductive and capacitive coupling effects depending on the switching patterns in bus lines. However, the best pattern for capacitive coupling appears to be the worst pattern for inductive coupling. In the best case of inductive coupling, noise will be minimized but large power consumption will occur in the chip. In the best case of capacitive coupling, a large noise will be induced in the signal while reducing power consumption. Considering both of these cases, we made a compromise between them in our proposed method. This method mainly aims to remove toggle and switching in the same direction between adjacent bus lines. Hence, power consumption and inductive noise are reduced. We used a temporal cycle to pass encoding information after the encoded data had been transmitted over the bus lines. The basic idea is to cause bus lines to stick in the same logic state for every other bus line so that switching in opposite and same direction between adjacent bus lines is completely removed. This approach is applied on half of the bus lines, and the idea of bus invert encoding [2] is used for the other half of the bus lines. However, using the bus invert approach leads the architecture to use an extra control line to carry the signal whether the data is inverted or not. This information will be used in decoder to retrieve the original signal. So, if the original data is of n bit, then according to our proposed method, the bus width will be n+1.

Figure 3 illustrates a schematic diagram of our proposed encoding architecture. The encoder consists of Odd encoding and Even encoding sections, Charging-Discharging estimators, Comparators, and a MUX. The original data and current value on bus lines sent back from bus lines are fed to the both Odd and Even encoding section. Odd and Even encoding will be described into two subsections later. Output of these two

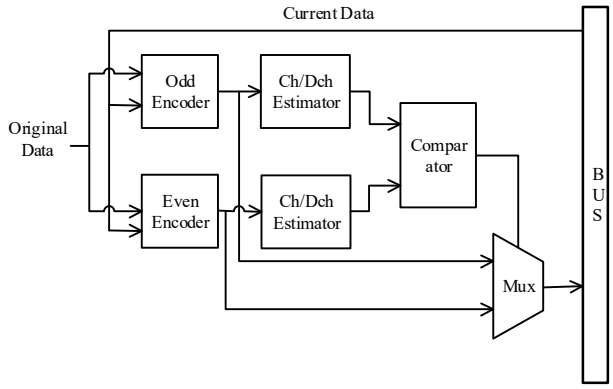

Fig. 3 Block Diagram of Proposed Encoding Method

sections is sent as the input to the Charging-Discharging estimator. At the same time, these two outputs are fed to the MUX. The Charging-Discharging estimator counts the total number of charging-discharging in the encoded data including encoding information, and it also checks whether encoded data and encoding information contain the exact same bits in every position. If in either of these two encoding circumstances, the encoded data and encoding information have the same bits, then MUX lets the odd encoding be transmitted; otherwise these two encoding outputs are fed to the comparator. The comparator determines which encoded data contains less Charging-Discharging. Based on the comparator output, MUX lets the encoded data that has a lower number of Charging-Discharging be transmitted over the bus lines. As our proposed method completely eliminates toggle in encoded data, we are concerned only with Charging-Discharging.

A. Odd and Even Encoding

With odd encoding, at first, we make the odd position bits stable in encoded data with respect to the current bus data so that we don't get any toggle and transition in the same direction between adjacent bus lines. For example, if the 8-bit original data to be transmitted over the bus at time T_t is 01110110, and the previous cycle data 10101101 has already been transmitted at time T_{t-1}, then the current value of the bus lines is 10101101. The switching between these two data, based on self-transition, toggle, charging-discharging, and stable position is shown in Figure 4.

Current Cycle Bus Data	1	0	1	0	1	1	0	1
	↓	↑	—	↑	↓	—	↑	↓
Next Cycle Original Data	0	1	1	1	0	1	1	0

Fig. 4 Transition between Current Data and Next Cycle Original data

Current Cycle Bus Data	1		1		1		0	
	—		—		—		—	
Next Cycle Original Data	1		1		1		0	

Fig. 5 Stabilization of Odd Position Bits

Current Cycle Bus Data	1	0	1	0	1	1	0	1
	—	—	—	—	—	↓	—	—
Next Cycle Encoded Data	1	0	1	0	1	0	0	1

Fig. 6 Transition between Current Data and Next Cycle Encoded data

Current Cycle Bus Data	1	0	1	0	1	1	0	1	
Transition	↓	↑	—	↑	↓	—	↑	↓	
Next Cycle Original Data	0	1	1	1	0	1	1	0	
Next Cycle Encoded Data	1	0	1	0	1	0	0	1	1
Encoding Information	1	0	0	0	1	0	0	1	1

Fig. 7 Encoded Data with Encoding Information

Here, we get 3 toggles between 1st and 2nd, 4th and 5th, and between the 7th and 8th positions. We get 4 charging-discharging at the 2nd-3rd-4th and 5th-6th-7th positions. And we get 2 stable positions at the 3rd and 6th positions, and 6 self-transitions at the 1st, 2nd, 4th, 5th, 7th and 8th positions.

In Figure 5, we made the 1st, 3rd, 5th, and 7th positions of encoded data stable with respect to the current cycle bus data. Now we will work on the even positions of original data. Here, we will follow the concept of the bus invert method only for bits of even positions. From Figure 4, it is evident that there are 4 even positions, and 3 self-transitions occur at the 2nd, 4th, and 8th position.

Based on the bus invert encoding, if the transition number is greater than half of the total number of bits, the original data will be inverted to get encoded data. In our example, there are 4 even positions, and it is obvious that transition number 3 is greater than half of 4. So, all the even position bits of the original data will be inverted to get the even position bits of encoded data. The control line will carry a logic 1 if the bits are inverted; otherwise logic 0 will be transmitted. This control bit will be used in the decoder to retrieve the original data at the receiving end. The current bus data, encoded data, and switching between these two data are represented in Figure 6.

In Figure 6, toggles are completely eliminated, 4 charging-discharging is decreased to 2 at the 5th-6th-7th position, and 6 self-transition is reduced to only 1 at the 6th position in encoded data. Evidently there is no switching in the same direction between adjacent bus lines.

The second case is known as Even encoding, and we perform the same procedure but in different bit positions. In the first case, we made all the bits in odd positions stable and applied the bus invert approach to even positions. In even encoding, we will make all bits in even positions stable, and the bus invert approach will be applied to odd positions. Then encoded data that has a lower number of Charging-Discharging will be transmitted over bus lines.

B. Encoding Information

Encoding information contains a bit pattern based on the changes we made in original data to get an encoded data. This information is transmitted at the next cycle after the encoded data has been sent, and bit width is exactly the same as encoded data.

For Odd encoding, odd positions of the original data are modified to get encoded data. This modification is performed in such a way that there is no transition between current bus data and encoded data in odd positions. In some positions, we have to change the original bits to make it stable, and we call this case "forced stable". On the other hand, in some positions, there are no transitions between current bus data and original data. In these positions, we do not make any change and leave these bits as they are to get encoded data, and we call this case "normally stable". In those odd positions where a "normally stable" case occurs, we send inverted bits of encoded data in those same positions to get encoding information. On the other hand for forced stable positions we send same bits as encoded bits in those same positions. For all even positions the bits in encoding information are exactly the same as they are in encoded data. Control line carries a signal to indicate whether the even positions are inverted or not.

Figure 7 shows current bus data, original data, and transitions between current and original data, encoded data, and encoding information. This is odd encoding. Only in the 3rd position, there is a normally stable state between current bus data and original data. In all other odd positions, there are transitions, and we had to make it forced stable to build encoded data. With the rule of building encoding information discussed above, the 3rd bit of encoding information is an inverted bit of the 3rd bit in encoded data. Here 3rd bit of encoded data is logic 1. Evidently encoding information got logic 0 for the 3rd bit. Being forced stable positions, the 1st, 5th, and 7th bits in encoding information are the same as they are in encoded data. Even positions are the same as encoded data bits. As even position bits of original data are inverted to get encoded data, control line carries logic 1.

For even encoding, the same procedure is followed to build encoding information. Here the even positions which are normally stable, those bits of encoded data are inverted to get the bits of the same positions in encoding information. All bits in odd positions are the same as they are in encoded data. Control line carries logic 1 if bits of odd positions are inverted; otherwise, logic 0 is sent over control line.

C. Decoding

Original data is transmitted in the form of encoded data over bus lines to reduce power and inductive noise. The decoder at the receiving end receives this encoded data and decodes it to retrieve the original signal based on encoding information and control line value. To retrieve the original data, the decoder needs to know whether the encoded data is odd encoded or even encoded. At first, the decoder checks if the encoded data and encoding information contain the exact same bits in the same positions or not. If so, then it takes the data as odd encoded data. Because in encoder, at the transmitting end for same bits in encoded data and encoding

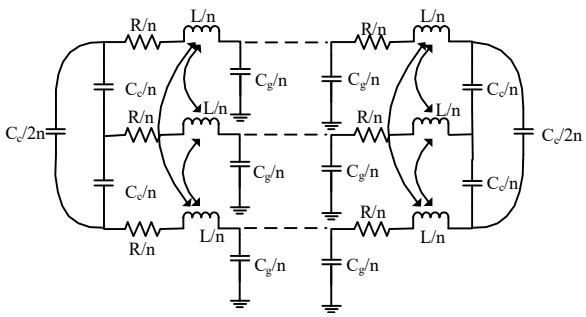

Fig. 8 Distributed RLC Model of Interconnects

information, we sent odd encoded data to be transmitted. Now if bits are different in these two data, the decoder checks which bits between all odd and even positions are stable with respect to the data that has already been transmitted in the previous cycle. If all odd bits are stable, then the decoder detects the received data as odd encoded data, and if all even bits are stable, then the data is considered even encoded data. Once encoding mode is detected based on encoding information and control line bit, the decoder easily retrieves the original data. For odd encoding, the odd positions of encoding information, for which bits are not the same as those of encoded data, in the original data, bits will be the same as encoded data in those positions; otherwise, original bits will be the inverted of those bits in encoded data. Logic 1 in control line indicates the encoded bits in even positions are already inverted. So to retrieve the original bits, the decoder needs to invert those bits again. Otherwise for logic 0 in control line, the decoder will leave even bits as they are for odd encoding. For bits in even encoded data, the retrieving procedure is exactly same. The only difference is the positions of bits.

V. Simulation Setup and Result

The simulation setup and interconnect model for our experiment and results are described in this section. Figure 8 shows the distributed RLC model [23] used in our simulation. The technology used in our experiment is 90 nm. To increase accuracy, we segmented the RLC circuit into 4 sections. The spacing, width, thickness, height, dielectric strength, and length of 90nm global interconnects were extracted from Predictive Technology Model (PTM) [25], and these values are .50um, .50um, 1.2um, .30um, 2.8, and 2000um respectively. These

TABLE III ENERGY RESULTS

Data Count (Kb)	Savings of Energy (%)
100	17.29
300	17.33
700	17.30
1000	17.23
1500	17.34

Fig. 9 Inductive Noise for Original Data/Bus Invert Encoded Data

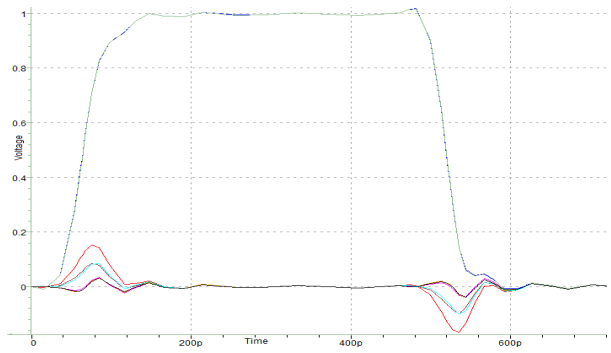

Fig. 10 Minimization of Inductive Noise for Proposed Encoding

values were used to extract self-inductance, self-capacitance, mutual inductance, coupling capacitance, and resistance from PTM [25]. Drivers and receivers are assumed to have the same size. V_{dd} was set to 1 V and frequency at 1 GHz. Power was measured in JAVA, and HSPICE simulation was performed to evaluate inductive noise. The following equation has been used to measure power consumption [24].

$$E = 0.5 * C_s * V^2 * [N_s + (N_{c+d} + 4 * N_t)(C_c/C_s)]$$

We took different sizes of data as input to simulate our encoding approach for measuring power consumption and inductive noise. We also looked at all the possible sequences for 8-bit input to increase the accuracy of our simulation. The simulation result is listed in Table III. Figure 9 and 10 show inductive noise for the original data and how this noise is minimized for encoded data. Table IV shows the significant improvement of power consumption for encoded data. A 17.38% reduction of power is observed, and Figure 10 shows a reduction of noise up to 83.33 % at logic high level and up to 30% at logic low level. Peak power is reduced up to 43.64%. This is mainly because our encoding approach eliminates all the possible toggles, which are responsible for large power consumption due to worst-case capacitive coupling. Also switching in the same direction between adjacent bus lines is completely removed in our scheme. Thus inductive ringing is largely minimized for encoded data.

We compared our encoding approach with Bus Invert Encoding [2] on the same simulation platform with same

technology. This made the comparison more fair and accurate. The bus invert method represents better area overhead because of simple logic and one extra control line. However, in terms of inductive ringing and worst-case crosstalk, coupling the performance of our encoding approach is better than bus invert encoding. Figure 9 and 10 show the comparison between Bus invert and our encoding scheme in terms of inductive ringing. We presented the noise simulation for non-encoded and encoded data for both Bus Invert encoding and our encoding approach for a specific switching pattern (↑ ↑ ↑ ↑ - - - -). In this case, the Bus invert method does not take the switching pattern into account and leaves the non-encoded data as it is. Hence, inductive ringing is not minimized. However, in our encoding method, inductive ringing is reduced by 83.33% and 30% at logic high and logic low level respectively.

VI. CONCLUSION

The goal of this research is to minimize interconnect power consumption due to capacitive coupling and to reduce the interconnect noise due to inductive coupling. Our proposed encoding method ensures that there will be no transition in opposite direction (0→1 and 1→0) and also no transition in same direction (0→0 and 1→1) between two adjacent lines by stabilizing odd/even position bits. As a result, toggle is removed, which is responsible for the highest power consumption, and also inductive noise is minimized at both logic levels. Our simulation results show that on average, 17.38% of power consumption is reduced, and a reduction in inductive noise up to 83.33% is possible at logic high level and reductions as much as 30% at logic low level. Though one extra bit and one extra cycle is needed to send the encoding information to retrieve the original data, area and delay overhead is not too much. Also, to send encoding information with encoded data, the total number of bits increases compared to the original un-encoded data, but the number of transition will be reduced. Hence, reduced power consumption is achieved. In the future, detail hardware design of the encoding approach will be studied, and hence the area, delay, and power consumption of the encoder-decoder will be measured.

REFERENCES

[1] https://www.academia.edu/4625045/POWER_REDUCTION_IN_MODERN_VLSI_CIRCUITS_A_REVIEW

[2] M.R. Stan, W.P. Burleson, "Bus-invert coding for low-power I/O," *IEEE Trans. Very Large Scale Integration (VLSI) Systems*, vol. 3, no. 1, pp. 49-58, March 1995.

[3] C. H. Lin, C. L. Yang, & K. J. King, "Hierarchical value cache encoding for off-chip data bus." in Proc. Int. Symp. On Low Power Electronics and Design, Oct. 2006, pp. 143-146.

[4] D. C. Suresh, B. Agrawal, J. Yang, W. Najjar, & L. Bhuyan, "Power efficient encoding techniques for off-chip data buses." in Proc. Int. conference on Compilers, architecture and synthesis for embedded systems, Oct. 2003, pp. 267-275.

[5] J. Yang, R. Gupta, & C. Zhang, "Frequent value encoding for low power data buses." ACM Trans. on Design Automation of Electronic Systems, 9(3), 354-384, 2004.

[6] Z. Yan , J. Lach, K. Skadron, and M.R. Stan, "Odd/Even bus invert with two-phase transfer for buses with coupling," in Proc. Int. Symp. On Low Power Electronics and Design, Aug. 2002, pp.80-83.

[7] A. R. Brahmbhatt, J. Zhang, Q. Wu, & Q. Qiu, "Low-power bus encoding using an adaptive hybrid algorithm." In Proc. of the 43rd annual Design Automation Conference, July 2006, pp. 987-990.

[8] R. Siegmund, C. Kretzschmar, & D. Müller, "Adaptive Partial Businvert encoding for power efficient data transfer over wide system buses." in Proc. 13th Symp. On Integrated Circuits and Systems Design, 2000, pp. 371-376.

[9] S. Saini, & S. B. Mandalika, "A new bus coding technique to minimize crosstalk in VLSI bus." in Proc. Int. Conference on Electronics Computer Technology, Apr. 2011,Vol. 1, pp. 424-428.

[10] C. Kretzschmar, R. Siegmund, & D. Müller, "A low overhead auto-optimizing bus encoding scheme for low power data transmission." in Integrated Circuit Design. Power and Timing Modeling, Optimization and Simulation, 2002, pp. 342-352.

[11] K. S. Sainarayanan, C. Raghunandan, and M. B. Srinivas, "Bus encoding schemes for minimizing delay in VLSI interconnects," in Proc. ACM Conference on Integrated circuits and systems design, Sept. 2007. pp. 184-189

[12] M. Cha, C. G. Lyuh, & T. Kim, "Resource-constrained low-power bus encoding with crosstalk delay elimination." in Proc. Asia and South Pacific Design Automation Conference, Jan. 2004. pp. 834-837

[13] C. Duan, & S. P. Khatri, "Exploiting crosstalk to speed up on-chip buses." in Proc. Design, Automation and Test in Europe Conference and Exhibition, Feb. 2004, Vol. 2, pp. 778-783.

[14] B. Victor, & K. Keutzer, "Bus encoding to prevent crosstalk delay." in Proc. IEEE/ACM international conference on Computer-aided design, Nov. 2001, pp. 57-63.

[15] K. Najeeb, V. Gupta, and V. Kamakoti, "Delay and peak power minimization for on-chip buses using temporal redundancy," in Proc. ACM Great Lakes symposium on VLSI, April. 2006, pp. 119-122.

[16] J. Zhang, Q. Wu, and Q. Qiu, "Bus encoding for simultaneous delay and energy optimization," in Proc. Int. Symp. on Low Power Electronics and Design, Aug. 2008, pp. 209-212.

[17] S. K. Verma and B. K. Kaushik, "A bus encoding method for crosstalk and power reduction in RC coupled VLSI interconnects," International Journal of VLSI design & Communication Systems 3, no. 2, pp. 29-39. 2012.

[18] M. Mutyam, "Selective shielding: a crosstalk-free bus encoding technique." in Proc. IEEE/ACM international conference on Computer-aided design, Nov. 2007, pp. 618-621.

[19] B. J. LaMeres, & S. P. Khatri, "Encoding-based minimization of inductive cross-talk for off-chip data transmission." in Proc. IEEE Design, Automation and Test in Europe, Mar. 2005, pp. 1318-1323.

[20] S. J. Ruan, T. C. Kan, and J. C. Hsu, "A novel crosstalk quantitative approach for simultaneously reducing power, noise, and delay based on bus-invert encoding schemes," in Proc. Int. Great lakes Symp. on VLSI, May 2010, pp. 357-360.

[21] S. K. Verma, B. K. Kaushik, "Crosstalk and power reduction using bus encoding in RC coupled VLSI interconnects," in Proc. Int. Conf. Emerging Trends in Engineering and Technology, Nov. 2010. pp.735-740.

[22] M. Lampropoulos, B. M. Al-Hashimi, & P. Rosinger, "Minimization of Crosstalk Noise, Delay and Power Using a Modi. ed Bus Invert Technique." in Proc. IEEE conference on Design, automation and test in Europe, Feb. 2004, Volume 2, p. 21372.

[23] D. D. Antono, (2003). *Modeling of Inductive Interconnect Responses and Coupling Effects in Deep-Submicron VLSI* (Doctoral dissertation, Master Thesis, Department of Electronic Engineering Graduate School of Engineering The University of Tokyo).

[24] S. Jayaprakash & N. R. Mahapatra, "Partitioned Hybrid Encoding to Minimize On-Chip Energy Dissipation ofWide Microprocessor Buses." in Proc. IEEE Int. Conference on VLSI Design, Jan. 2007, pp. 127-134.

[25] Predictive Technology Model http://www.eas.asu.edu/~ptm/

[26] Y. Ogasahara, M. Hashimoto, & T. Onoye, "Measurement and analysis of inductive coupling noise in 90 nm global interconnects." *IEEE Journal of Solid-State Circuits,* Vol. 3, No. 43, pp. 718-728. 2008

Efficient Index Computation for Array Based Structured Data

Md Abu Hanif Shaikh, Mehnuma Tabassum Omar, K.M. Azharul Hasan
Department of Computer Science and Engineering, Khulna University of Engineering & Technology
E-mail: hanif@kuet.ac.bd, misty2409@gmail.com, azhasan@cse.kuet.ac.bd

Abstract— **Traditional computing techniques widely vary over large scale computing. Some techniques are useful for structured data while some other techniques are useful for non-structured data. To store and operation on the structured data, multidimensional array is widely used as basic data structure. But the performance of multidimensional array is very poor when the number of dimension is very high i.e. 32-dimension. Data scientist suggests linearization of dimensions for higher dimensional data. But linearized data are highly compute intensive for retrieving into original data format as well as operations are very expensive on that data. It suffers from the higher index computational cost and lower data locality. In this paper, we propose an index computation algorithm based on generalized two-dimensional structure. We showed that the accessing cost of array elements is higher for traditional multidimensional array over generalized two-dimensional representation. Though the most sequential access of main memory is itself very simple for any compiler yet experimental results showed a better performance. Both theoretical analysis and experiment are done to show its' effectiveness of the proposed algorithm.**

Keywords—Higher dimensional array, Array Index, Structured data, Data locality, Array linearization, HPC.

I. INTRODUCTION

Big data is often used to describe the scale of data generated across multiple disciplines, including sensors used to gather climate information data, digital pictures and videos, purchase transaction records, and cell phone GPS signals [4]. It also includes massive volumes of marketing, spanning search, social, local and mobile analytics data across every geographical location. The generated data is categorized as structured, semi-structured and un-structured. Structured data is information with a high degree of organization found in databases, data warehouses and enterprise solutions. Internet applications extracted raw data is un-structured and social media data or location type data and user-generated data are semi-structured. Modeling and analyzing such phenomena strongly requires handling large scale of data. Traditionally the data has very high number of dimensions. Handling and operating on this higher dimensional data is still a challenge [6][12] for data scientists. The multidimensional array is the dominating structure for handling such data [14][15]. If the number of dimension is high then the cost of index computation increases and the cache miss rate also increases due to the data locality problem [3][13]. That's why very few commercial compilers eventually support large number of dimensions. Traditional algorithms and computing techniques is difficult to apply on higher dimensional data models such as the data of data-warehouse or MOLAP[10]. Most compilers have limitations over multi-dimensional array. Thus the traditional indexing for structured big data is not efficient. That's why, data scientists are arduous for new index structure [7]. Most data scientists suggest linearization of higher dimensional data. It is good enough to implement in secondary memory. But operation cost and accessing time for secondary memory data is too high as well as parallelization is seldom possible for linearized data. So, the new index structure which support parallelism, lower index computation cost, lower operation cost and higher data locality is a cramming needs for present data scientists. In this paper, we propose Generalized Two-Dimensional Array[5] based index computing algorithm for accessing structured big data. G2A converts n-dimensional array into a two dimensional array. Our goal is to lower the index computational cost and higher data locality using our proposed index structure for structured big data. The later part of this paper is decorated as section II compares some related works, Section III shows an overview of G2A (Generalized two-dimensional representation of higher dimensional Array) , the algorithms for initializing both G2A and TMA are shown in section IV. Section V shows some theoretical analysis then the experimental results are shown in section VI and finally Section VII outlines some conclusion.

II. RELATED WORKS

Many techniques have been proposed in literature for improving the cost of index computation for higher dimensional structured data [3]-[9]. Some techniques suggest linearization over higher dimensions[7]-[10]. Their argument is that the compiler allocates memory sequentially in all cases of memory allocation. EKMR scheme[3] is very effective but it is limited to four dimensions only. When the number of dimension is greater than four then it requires an abstract pointer array. Even there is no generalized indexing till four dimensional. Tamara G. Golda et.al [1][2] proposed an indexing scheme for two dimensional generalization. Though it is very effective for operation on generalized data but requires huge storage. Steve Carr [13] presents compiler optimizations to improve data locality but the scheme is based on the Traditional Multidimensional Array. It reorganizes the loops only for compiler optimization. A new storage manager for complex, parallel array processing namely the ArrayStore is proposed in [12] in the area of multidimensional data storage. The main issue handled is the way to find for parallel processing. The SciDB[14][15] proposed an array based DB model. EJ Otoo[11] introduce new storage schemes for multi-dimensional sparse arrays that handle the sparsity of the array but the array is not n dimensional. Ddynamic array structure

namely EKA[8][10] becomes an hierarchical structure when n>4. Y. Zhao *et. al.*[9] introduced the chunking of arrays but linearization of n dimensional array is required. The simplified representation of higher dimensional array suggest two-dimensional representation scheme in [5][6]. This representation highly affects for main memory computing saving huge cache locality. This two dimensional representation scheme is cost effective in terms of index computation specially when n is large.

III. GERNERALIZED TWO-DIMENSIONAL ARRAY: G2A

The ***Generalized Two-dimensional Array*** (G2A) represents an algorithm to represent an n dimensional (nD) array by a 2 dimensional (2D) array. The nD array is converted to a 2D array. Hence the indexes of the nD array are also converted to 2D array. ⌊ n/2 ⌋ columns contribute to row direction and the rest n/2 columns to column direction. Hence a nD array can be drawn in a 2D plane to visualize the data.

Let A[l_1] [l_2]… [l_n] be a TMA(n) of size [l_1, l_2,…,l_n] and <x_1, x_2,…,x_n> be a tuple of an element of the array A; where l_1, l_2,…, l_n is the length of each dimension d_1, d_2,…, d_n and x_i = 0,1,2,3, …, (l_i-1) ($1 \le i \le n$). We convert TMA(n) A of size [l_1, l_2,…,l_n] into a G2A $A'[l'_1][l'_2]$ of size $[l'_1, l'_2]$ and a tuple $< x'_1, x'_2 >$ where l'_1 and l'_2 are the length of each dimension d'_1 and d'_2 ; $x'_1 = 0,1,\dots,(l'_1 - 1)$ and $x'_2 = 0,1,\dots,(l'_2 - 1)$. In the following we will first show the 3 and 4 dimension array converting to G2A and then we will generalize to n dimensions.

Example 1: Let A[l_1][l_2][l_3] be a TMA(3) of size [2,3,4]. A multidimensional array is linearized when stored on the memory. Programming languages map the array index into the linearized memory address. Therefore a location of tuple <x_1, x_2, x_3> A[l_1][l_2][l_3] can be linearized and identified by

$$f(x_1, x_2, x_3) = x_1 l_2 l_3 + x_2 l_3 + x_3$$
$$= x_1 \times 3 \times 4 + x_2 \times 4 + x_3$$

when row major order is considered and

$$f(x_1, x_2, x_3) = x_1 l_2 l_3 + x_3 l_2 + x_2$$
$$= x_1 \times 3 \times 4 + x_3 \times 3 + x_2$$

when column major order is considered

In G2A, the 3 dimensions d_1, d_2, d_3 are converted to 2 dimensions where d_1, d_3 are for row and d_2 are for the column. Fig-1 shows the G2A $A'[l'_1][l'_2]$ for a TMA(3) A[2][3][4] where $l'_1 = l_1 \times l_3 = 8$ and $l'_2 = l_2 = 3$.

For example an element A[1][1][2] of TMA(3) is equivalent G2A is $A'[x'_1][x'_2]$ where $x'_1 = x_1 l_3 + x_3 = 1 \times 4 + 2 = 6$ and $x'_2 = x_2 = 1$. (See Fig. 1).

For backward mapping, if an element in G2A is $A'[x'_1][x'_2]$ is known then it's equivalent TMA(3) becomes A[x_1][x_2][x_3] where $x_3 = x'_1 \% l_3 = 6 \% 4 = 2$, $x_1 = \frac{x'_1}{l_3} = 6/4 = 1$ and $x_2 = x'_2 = 1$. For example, A′[6][1] is equivalent to A[1][1][2]. Here % indicates the 'modulus' operation and / indicates 'division' operation.

The generalization of the TMA(n) A[l_1][l_2] … [l_n] to G2A $A'[l'_1][l'_2]$ is as follows :

$$l'_1 = \begin{cases} l_1 \times l_3 \times \dots \times l_{n-1}, & if\ n\ is\ even \\ l_1 \times l_3 \times \dots \times l_n, & if\ n\ is\ odd \end{cases}$$

$$l'_2 = \begin{cases} l_2 \times l_4 \times \dots \times l_n, & if\ n\ is\ even \\ l_2 \times l_4 \times \dots \times l_{n-1}, & if\ n\ is\ odd \end{cases}$$

An element A[x_1][x_2]…[x_n] in TMA(n) is equivalent to $A'[x'_1][x'_2]$ where

$$x'_1 = \begin{cases} x_1 l_3 l_5 \dots l_{n-3} l_{n-1} + \dots + x_{n-3} l_{n-1} + x_{n-1}, & if\ n\ is\ even \\ x_1 l_3 l_5 \dots l_{n-2} l_n + \dots + x_{n-2} l_n + x_n, & if\ n\ is\ odd \end{cases}$$

$$x'_2 = \begin{cases} x_2 l_4 l_6 \dots l_{n-3} l_{n-1} + \dots + x_{n-3} l_{n-1} + x_{n-1}, & if\ n\ is\ odd \\ x_2 l_4 l_6 \dots l_{n-2} l_n + \dots + x_{n-2} l_n + x_n, & if\ n\ is\ even \end{cases}$$

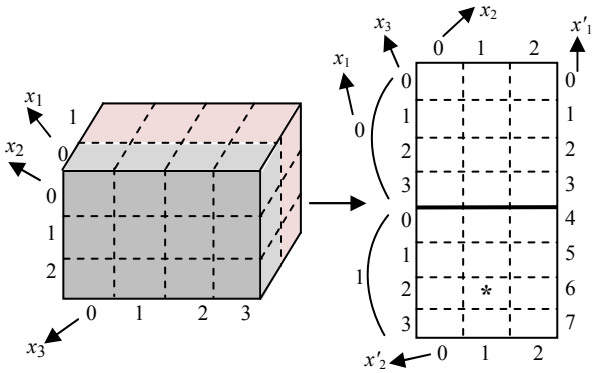

Figure 1. TMA(3) and it's equivalent G2A

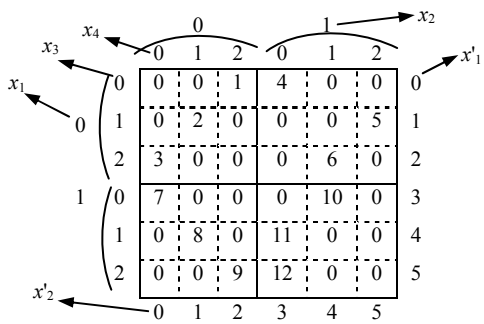

Figure 2. G2A, equivalent to TMA(4) of size (2×2×3×3)

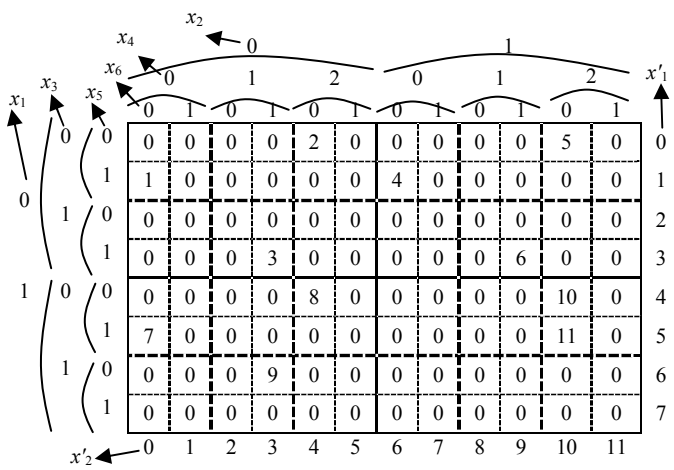

Figure 3. G2A, equivalent to TMA(6) of (2×2×2×3×2×2)

Fig. 2 and Fig. 3 shows the G2A for equivalent TMA(4) and TMA(6). For backward mapping, if an element in $A'[x'_1][x'_2]$ is known then it's equivalent $A[x_1][x_2][x_3] \ldots [x_n]$ is as follows:

When n is even then

$$x_n = x'_2 \% \, l_n$$
$$x_i = ((\ldots(x'_2 / l_n) \ldots / l_{i+2}) \% l_i, \qquad i = 4,6,\ldots,n-2$$
$$x_2 = ((\ldots(x'_2 / l_n) / l_{n-2}) \ldots) / l_6) / l_4$$

$$x_{n-1} = x'_1 \% \, l_{n-1}$$
$$x_j = ((\ldots(x'_1 / l_{n-1}) \ldots / l_{j+2}) \% l_j, \qquad j = 3,5,\ldots,n-3$$
$$x_1 = ((\ldots(x'_1 / l_{n-1}) / l_{n-3}) \ldots) / l_5) / l_3$$

And when n is odd then

$$x_n = x'_1 \% \, l_n$$
$$x_i = ((\ldots(x'_1 / l_n) \ldots / l_{i+2}) \% l_i, \quad i = 3,5,\ldots,n-2$$
$$x_1 = ((\ldots(x'_1 / l_n) / l_{n-2}) \ldots) / l_5) / l_3$$

$$x_{n-1} = x'_2 \% \, l_{n-1}$$
$$x_j = ((\ldots(x'_2 / l_{n-1}) \ldots / l_{j+2}) \% l_j, \qquad j = 4,6,\ldots,n-3$$
$$x_2 = ((\ldots(x'_2 / l_{n-1}) / l_{n-3}) \ldots) / l_6) / l_4$$

IV. Algoritms for Index Computation

For initialization of TMA, it requires n number of nested loops. But G2A requires only two loops as well as (n-2) number of multiplication operation. *Algorithm* 1 shows a TMA of n-dimension which represents n number of nested loops. As example, it requires three nested loops to initialize a TMA of 3-dimensions. Equivalent G2A of this TMA requires two nested loops and an additional multiplication operation as shown in *Algorithm* 2. Similarly, TMA(4) needs four nested loops and equivalent G2A needs two nested loops as well as two multiplication operation for deriving l'_1 and l'_2 as shown in *Algorithm* 3. G2A generalization supporting any number of dimensions is show in *Algorithm* 4. If n=100, then it requires 100-2=98 multiplications with constant two nested loops.

Algorithm 1*:* Indexing Scheme for TMA(n):(x_1-x_n, l_1- l_n)

1. *for* i_1 := 1 to l_1
2. *for* i_2 := 1 to l_2
3. *for* i_2 := 1 to l_2
4. .
5. .
6. .
n. *for* i_n := 1 to l_n
n+1. TMA[i_1] [i_2]… [i_n]=0;

Algorithm 2*:* finding G2A indexes from TMA(3) indexes:
G2A-forward_mapping (i'_1-i'_2, l'_1- l'_2, i_1- i_3, l_1- l_3)

1. $l'_1 = l_1 \times l_3$, $l'_2 = l_2$
2. *for* i'_1 := 1 to l'_1
3. *for* i'_2 := 1 to l'_2
4. G2A[i'_1][i'_2]=0;

Algorithm 3*:* finding G2A indexes from TMA(4) indexes:
G2A-forward_mapping (i'_1-i'_2, l'_1- l'_2, i_1- i_4, l_1- l_4)

1. $l'_1 = l_1 \times l_3$, $l'_2 = l_2 \times l_4$
2. *for* i'_1 := 1 to l'_1
3. *for* i'_2 := 1 to l'_2
4. G2A[i'_1][i'_2]=0;

Algorithm 4*:* finding G2A indexes from TMA(n) indexes:
G2A-forward_mapping (i'_1-i'_2, l'_1- l'_2, i_1- i_n, l_1- l_n)

1. $l'_1 = l_1 \times l_3 \times \ldots \times l_{n-1}$, $l'_2 = l_2 \times l_4 \times \ldots \times l_n$ (n is even)
   or $l'_1 = l_1 \times l_3 \times \ldots \times l_n$, $l'_2 = l_2 \times l_4 \times \ldots \times l_{n-1}$ (n is odd)
2. *for* i'_1 := 1 to l'_1
3. *for* i'_2 := 1 to l'_2
4. G2A[i'_1][i'_2]=0;

V. Memory Management by G2A

In the following, we analyze the performance of index computation shown in Section III and IV. Total cost for TMA and G2A are the cost of addition/multiplication operators for index computations of array elements. The parameters are grouped as shown in table I. Some of these parameters are provided as input, while others are derived from the input parameters. All lengths or sizes are in bytes.

TABLE I. Parameters for Indexing Scheme

Parameter	Description
n	Number of dimension
l_i	Length of dimension i ($2 \le i \le n$)for TMA. We consider $l_1 = l_2 = l_3 = \ldots = l_n = l$ for all i. Hence total array elements becomes l^n.
l'_1	Length of row for G2A; i.e. $l'_1 = l^{\lceil n/2 \rceil}$
l'_2	Length of column for G2A; i.e. $l'_2 = l^{\lceil n/2 \rceil}$
α	Cost of Multiplication operation
β	Cost of Addition/Subtraction operation
η	Improve Rate of improvement; $\eta = \left(1 - \frac{Cost\ of\ G2A}{Cost\ of\ TMA}\right) \times 100\%$

Indexing function for TMA(3) is $f(x_1, x_2, x_3; l, l, l) = x_1 \times l \times l + x_2 \times l + x_3$. So, we need three multiplications and two additions operation for each element, thus the total cost is $(3\alpha+2\beta)l^3$. Equivalent G2A has $l'_1 = l_1 \times l_3$, $l'_2 = l_2$ and $f(x'_1, x'_2; l'_1, l'_2) = x'_1 \times l'_2 + x'_2$. Thus the total cost for G2A index computation is $(\alpha+\beta)l^3 + \alpha$. So, the improvement, η is

$$\eta = [1 - \{(\alpha+\beta)l^3 + \alpha\} / (3\alpha+2\beta)l^3] \times 100\%$$

For TMA(4); $f(x_1, x_2, x_3, x_4; l, l, l, l) = x_1 \times l \times l \times l + x_2 \times l \times l + x_3 \times l + x_4$. So, the total cost for TMA is $(6\alpha+3\beta)l^3$ and the G2A is $(\alpha+\beta)l^3 + 2\alpha$. The improvement, η of G2A over TMA(4) is

$$\eta = [1 - \{(\alpha+\beta)l^3 + 2\alpha\} / (6\alpha+3\beta)l^3] \times 100\%$$

Generalizing the cost over n-dimension, TMA(n), the total cost is $\{n(n-1)/2 + n-1\}l^n$. Similarly the total cost of G2A is $(\alpha+\beta)l^n + (n-2)\alpha$. So, the improvement is

$$\eta = [1 - \{(\alpha+\beta)l^n + (n-2)\alpha\} / \{n(n-1)\alpha/2 + (n-1)\beta\}l^n] \times 100\%$$

It is well know that the cost of multiplication is very very higher than the cost of addition/subtraction. Thus we can neglect β to simplify the improvement rate equation.

$$\eta = 1 - \{(\alpha l^n + (n-2)\alpha\} / \{n(n-1)\alpha l^n/2\}$$
$$= 1 - 2(l^n + n-2) / \{n(n-1)l^n\}$$

From the above equation, improvement rate depends on both length of each dimension, l and the number of dimension, n. We can conclude that for any positive value of l and n (>2), η will be positive. Thus the performance of our proposed G2A is always better than that of traditional multidimensional array.

VI. EXPERIMENTAL RESULTS

To evaluate the performance of our proposed indexing scheme for structured data, we constructed a prototype system in Intel(R) Xeon(R) E5620 @ 2.40GHz processor having 8(eight) processors, 32 GB RAM and 1406 MB cache memory. Program is written in C and compiled in gcc compiler with –o option on debian squeeze 6.0.5 operating system. The number of dimensions is set as even numbers between 4 to 30. For simplification, we are considering equal length for each dimension. Figure 4 shows the initialization time for a four dimensional TMA and its' equivalent G2A. With the increase of each dimension length, initialization time increases exponentially as that of number of total elements. Figurate 5, Figure 6 and Figure 7 show the initialization time for 6, 8 and 10 dimensional array respectfully. Due to hardware limitation, we are limiting the length of each dimension till 230, 38, 15 and 8 for 4, 6, 8 and 10 dimensional data respectfully.

Table III shows the G2A and TMA initialization time for different number of dimensions. It is clear that we have values for limited number of lengths for each dimension greater than 10. For showing the performance at a glance, we derive the average initialization time for each element for a specific dimensional data. This is done in two steps. First find the average initialization time by diving initialization time with total number of array elements for each specific dimension and specific length. Then aggregate the derived each element initialization time over each dimension. Figure 8 shows the average initialization per element for different dimensions. Performance improvement is clearly visible. As stated in our theoretical analysis, the performance is improved with the increase of the number of dimensions.

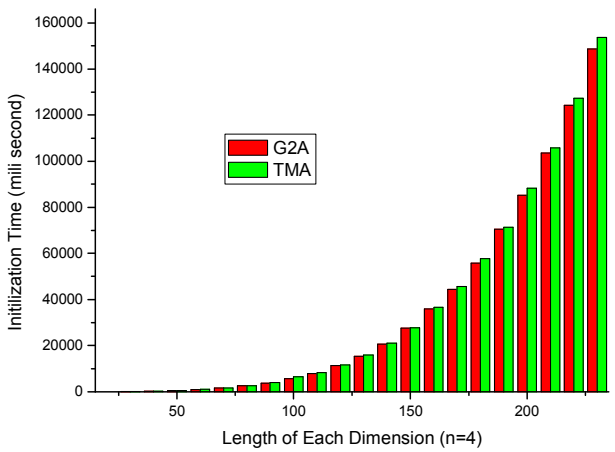

Figure 4. Execution time for TMA(4) and equivalent G2A

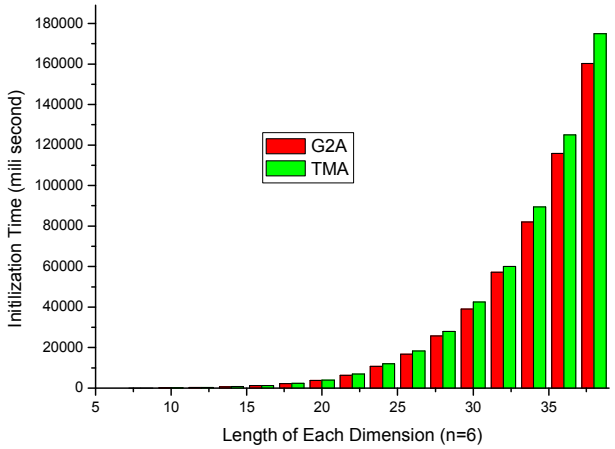

Figure 5. Execution time for TMA(6) and equivalent G2A

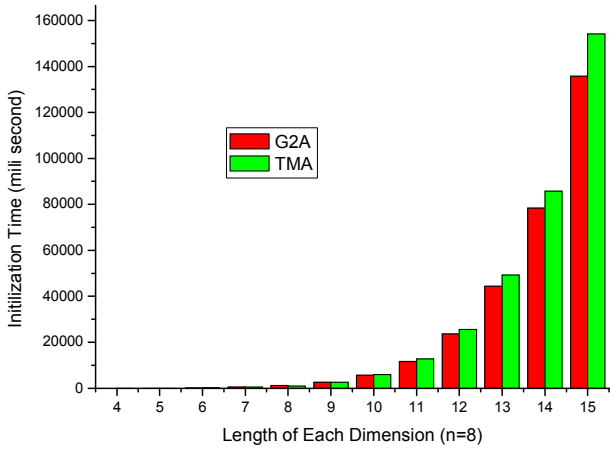

Figure 6. Execution time for TMA(8) and equivalent G2A

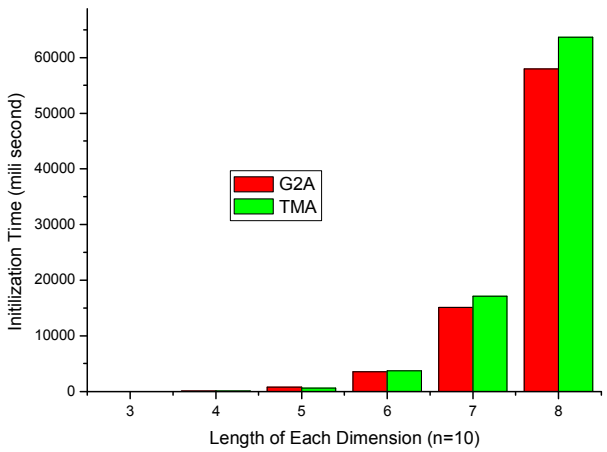

Figure 7. Execution time for TMA(10) and equivalent G2A

TABLE II. EXPERIMENTAL RESULT OVER 10-DIMENSIONAL DATA

Dimensions (n)	Length (*l*)	Initialization Time(mS)	
		G2A	TMA
12	3	40	50
12	4	1080	1290
12	5	13280	15670
12	6	115640	139390
14	3	410	520
14	4	14460	17740
16	3	2520	3270
18	2	10	20
18	3	21060	28580
20	2	80	120
22	2	350	540
24	2	1170	1570
26	2	3780	5890
28	2	14550	24360
30	2	57100	95480

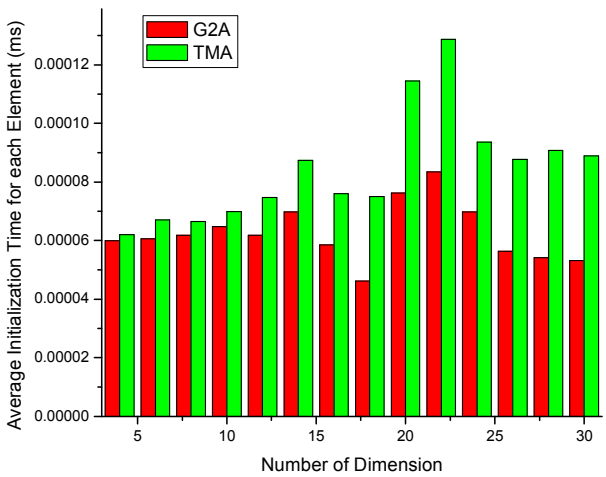

Figure 8. Average Initialization Time for each element for different number of dimesion

VII. CONCLUSION

In this paper, we proposed an index scheme for structured big data. The number of data dimension is a crucial issue for big data computation as most of the traditional compiler has limitation over higher dimensional data. Our focus was on the supporting over higher dimensional data. We have shown better indexing with our generalized two dimensional array scheme. We have experimental results relevant to the theoretical analysis described in this paper. The proposed indexing scheme gives better improvement rate with the increase of data dimensions. One important future direction is that the scheme can easily implemented in parallel environment for parallel applications.

REFERENCES

[1] Tamara G. Kolda, Brett W. Bader, *Tensor Decompositions and Applications*, SIAM Review 51(3), Page:455-500, 2009.

[2] Brett W. Bader, Tamara G. Kolda, *Efficient MATLAB computations with sparse and factored tensors*, SIAM Journal on Scientific Computing, 2007.

[3] Chun-Yuan Lin, Jen-Shiuh Liu, and Yeh-Ching Chung, *Efficient Representation Scheme for Multidimensional Array Operations*, IEEE Transactions on Computers, 51(3), pp.327-345, 2002.

[4] Kostas Zoumpatianos, Stratos Idreos, Themis Palpanas, *Indexing for Interactive Exploration of Big Data Series*, SIGMOD'14, June 22–27, 2014, Snowbird, UT, USA.

[5] K. M. Azharul Hasan, Md Abu Hanif Shaikh, *Representing Higher Dimensional Arrays into Generalized Two- dimensional Array: G2A*, 16th International Conference on Parallel and Distributed Computing, Applications and Technologies (PDCAT 2015), Published by Springer LNEE, Jeju, South Korea.

[6] Md Abu Hanif Shaikh, K.M. Azharul Hasan, *Efficient Storage Scheme for n-Dimensional Sparse Array: GCRS/GCCS*, 13th International Conference on High Performance Computing & Simulation (HPCS 2015), Page (137-142), Published by IEEE, Amsterdam, Netherlands.

[7] B. Christian, M. Urs, "Multidimensional Index Structures in Relational Databases", Intelligent Information Systems, 15, pp. 51–70, 2000

[8] Sk Md Masudul Ahsan, K M Azharul Hasan "An Implementation Scheme for Multidimensional Extendable Array Operations and Its Evaluation", ICIEIS, Part III, CCIS 253, pp. 136–150, 2011.

[9] Y. Zhao, P. M. Deshpande, and J. F. Naughton, "An array based Algorithm for simultaneous multidimensional aggregates", ACM SIGMOD, pp. 159–170, 1997.

[10] K M Azharul Hasan, Tatsuo Tsuji, Ken Higuchi "An Efficient MOLAP Basic Data structure and Its Evaluation", Proc. of DASFAA, pp. 288-299, LNCS 4443, 2011.

[11] EJ Otoo, H Wang, G Nimako, "New Approaches to Storing and Manipulating Multi-Dimensional Sparse Arrays" , Proc. of SSDBM'14, pp. 2014.

[12] Emad Soroush and Magdalena Balazinska "ArrayStore: A Storage Manager for Complex Parallel Array Processing" In Proc. of ACM SIGMOD International Conference on Management of data, pp. 253-264, 2011.

[13] Steve Carr , Kathryn S. McKinley , Chau-Wen Tseng "Compiler optimizations for improving data locality", In Proc. of the sixth international conference on Architectural support for programming languages and operating systems, p.252-262, 1994.

[14] Michael Stonebraker, David Dewitt Requirements for Science Data Bases and SciDB, CIDR Perspectives 2009

[15] SciDB: an open-source, array-oriented database management system http://database.cs.brown.edu/projects/scidb/

Orchestration Algorithms for Network-assisted Virtual Machine Migrations using OpenDayLight Controller

Shamim Ahmed[1], Barbara Martini[2], Molka Gharbaoui[3], Andrea Sgambelluri[3], SK. Shariful Alam[4]

[1]University of Trento, Trento, Italy
shamim.ahmed@unitn.it
[2]CNIT, Pisa, Italy
barbara.martini@cnit.it
[3]Scuola Superiore Sant' Anna, Pisa, Italy
m.gharbaoui@sssup.it, a.sgambelluri@sssup.it
[4]Khulna University of Engineering and Technology, Khulna, Bangladesh
ssa1996@gmail.com

***Abstract*— In the last years, prominent advances in software virtualization (e.g., Hypervisor) have enabled the agile deployment of cloud services and, at the same time, server consolidation operations through agile Virtual Machine (VM) operations (e.g., start-up, snapshot, cloning, and migrations) across Data Center (DC) servers. On the other hand, such advances pose new challenges in the overall management of the DC infrastructure since VM operations may occur much more frequently in virtualized than in legacy DCs and produce not only a computational load on the involved servers, but also a network load on all the switches connecting the servers. In this context, the Software-Defined Network (SDN) paradigm opens up new opportunities to design convergent resource management systems which is able to address the provisioning of cloud services while meeting adequate network performance during VM provisioning and migrations.**

In this paper, a promising advanced monitoring and resource allocation function for SDN-based DC networks has been proposed aiming at reporting possible suitable paths connecting specified servers that can be exploited for VM migrations. In such a way, network-assisted migrations can be triggered that assure adequate VM migration delays according to specified requirements (e.g., minimum delay for live VM migration) while addressing different management targets (e.g., network load balancing, minimization of energy consumption).

***Index Terms*—Cloud, Data Centre, OpenFlow, Software-Defined Networking, VM migration, Orchestration**

I. Introduction

CLOUD computing has emerged as a new paradigm that delivers software and hardware resources as services to the general people. Cloud computing services generally leverage virtualization of physical resources collected in large DCs (i.e., Cloud DCs). Thanks to virtualization software technologies, i.e., VM deployment, cloud service consumers may be offered a subscription-based access to infrastructures, platforms or applications, referred to as IaaS, PaaS or SaaS, respectively [1]. Virtualization technologies allow cloud service providers to apply consolidation procedures within Cloud DCs and, consequently, to achieve a more efficient use of physical servers. In contrast, new challenges arise in the management of the DC infrastructure, especially as regards VMs provisioning and interaction. In fact, thanks to the availability of more agile procedures for the set-up of new applications (i.e., snapshot, cloning of VMs), provisioning or reconfiguration operations which occur much more frequently in Cloud DCs than in legacy DCs. Moreover, from the networking perspective, the DC infrastructure is a really challenging environment due to several aspects. As previously highlighted, in Cloud DCs, services are provided according to different delivery paradigms (e.g., IaaS, PaaS, SaaS) and each of them is characterized by a specific communication model (one-to-one, one-to-many, many-to many) among VMs, that may involve hosts located inside or outside the DC. Therefore, to satisfy performance requirements of Cloud services, VM placement must take into account network link status. Definitely, the high volatility of VMs in Cloud DC requires that the intra-DC network infrastructure should be more flexible, agile and integrated with the IT (computing and storage resources) infrastructure with computing, storage and network resources acting as a unified pool of virtual resources jointly orchestrated to offer improved user experience while optimizing their usage [2]. In this context, SDN and, in particular, Openflow (OF) protocol [3] can play a key role due to their distinguished features that well adapt to virtualized environments, i.e., flow-based network resource control capabilities, combined with high programmability of routing or switching functionalities, that allow for a software-based enforcement of per-flow routing strategies.

In this paper, we present orchestration algorithms for addressing network-assisted virtual machine migrations enabling the coordinated control of IT and network resources in Cloud DCs. Indeed, the proposed algorithms can be used in the context of VM migration workflows to decide the proper servers to host VMs also taking into account the current traffic load over network links by means of OF statistics. As a result, both the migration of the VM to the selected host and the set-up of a delivery path can be addressed while assuring improved data delivery performance. The selection of network resources (i.e., switch and links to be traversed) leverages

978-1-4673-9257-0/15/$31.00 ©2015 IEEE

flow-based statistics (e.g., switch/link loads) provided by OF. More specifically, traffic statistics available from OF-based switches at per-port level have been exploited for selecting the best path towards the required server to host the VM. Accordingly, the routing table of OF-based switches is updated according to the selected best path for flow provision. When deploying an enhanced IaaS paradigm, this approach allows addressing fluid data delivery while avoiding possible congestions due to the over-subscription of network links and thus minimizing the network latency in VM migrations.

II. SDN IN DATA CENTERS FOR ORCHESTRATION AND COMPARISON WITH RELATED WORKS

SDN [1] is a paradigm that was developed with the view of managing networking elements through software running from an external server. It is an emerging architecture intending to be dynamic, manageable, cost effective, and adaptable so that seeking to be suitable for high bandwidth according to today's applications. The core part of SDN is its controller according to a new paradigm which divides the networks in two parts: forwarding and switching systems on the one side and a controlling element on the other side. Indeed, the intelligence of the network is moved to a centralized software-based controller that programmatically adds, modifies, and deletes the flow entries on network switches or routers thereby affecting their forwarding actions. While the SDN is a paradigm, the most common implementation is through OF that is the communication protocol used for the controller to enforce forwarding rules and to ask for statistics data to switches. Commercial of the self (COTS) devices are becoming much popular to the data center providers for lower costs. As like COTS servers, lower cost layer-2 switches are becoming more feasible for hundreds of ports rather than using high cost layer-3 switches. This trend emphasizes a suitable use case of SDN with OF enabled switches in data centers.

The usability of OF for virtual machines scheduling and migration within DCs is a pretty unexplored research area. To the best of our knowledge, just a couple of recent works argue on the use of OF in DC. Specifically, the authors in [5] aim at reducing the congestions by reconfiguring the routing within the network using OF controllers for addressing a fine grained traffic engineering leveraging short term predictability of traffic demands. The authors have evaluated the performance of OF in a DC environment using DC traffic models gathered from real DC measurements in [6]. However, none of the above research works consider the use of OF in the context of a VM migration process as this work actually does.

Considering the complex, heterogeneous and highly dynamic scenario of cloud DCs, a novel functionality that enables the unified and orchestrated control of IT and network resources in Cloud DC becomes a higher priority issue [7]. A number of research efforts focused on effective VM deployments across DC servers with bandwidth constraints on virtual network embedding in DCs [8][9]. However, neither VM migration cases are considered nor experimental validation are provided, in line with guidelines dictated by recent research directions [10] and emerging industry trends for DC management [11]. In [12], the design, development and deployment of a new virtualization-aware networking architecture whose advanced traffic-engineering capabilities are enabled by OpenFlow-based Virtualization-aware Networking (OFVN) systems have been described. The OFVN architecture is designed with scalability challenges, so as to guarantee performance requirements concerning communication among the servers even though the Data Center continues to grow in size. In [13] an orchestration system is presented that for dynamic computing and communication resources chaining, able to assure better than best effort VMs data exchanges across Cloud DCs. In this paper we generalize such approach to the case of VM migrations. There are many open source controllers available which support SDN such as NOX, POX, FloodLight, Beacon, Trema, Ryu and OpenDayLight (ODL) etc. For this research activity, ODL [14] is used as OF controller with additional software modules devoted to enable combined, i.e., orchestrated, resource management at computing and networking level.

III. MININET ENVIRONMENT WITH OPENDAYLIGHT CONTROLLER

ODL [14] is an open platform for network programmability to enable SDN and Network function virtualization (NFV). It is an open source project with a modular, pluggable, and flexible controller at its core. The controller is implemented in software and is contained within its own Java Virtual Machine. ODL (Hydrogen version) [15] uses some supporting software tools or paradigms such as: Maven, OSGI, Java Interfaces. One of the advantages of ODL controller is its web interface. By using web User Interface (UI), users can log in to the web portal and can access the network devices through the controller. Fig. 1 shows the graphical view of the developed network in ODL UI.

Mininet [16] is a network emulator which can be used for creating networks of virtual controllers, switches and hosts. Mininet hosts run on standard Linux network software. As its switches support OF, it is possible to make test bed network for highly flexible custom routing and SDN. Mininet networks run real code including standard Unix/Linux network applications as well as the real Linux kernel and network stack. As a result, the code developed and tested on Mininet, for an OF controller, modified switch, or hosts, can be moved to a real system with minimal changes, for real world testing, performance evaluation, and deployment.

This research has been carried out in Mininet simulation environment within a work station that has the following properties: Ubuntu version 12.10, OpenDalylight controller (updated on 10th June 2013), Mininet version 2.0.0, Eclipse 3.8 (OpenDayLight Controller, compiled through Maven).

There are many types of topologies available in literature (e.g., FatTree, BCube, DCell, FiConn, and VL2) to define a DC network. However, there is nothing to define which one is better than other. Operators are choosing the topology based on the geographical location, business requirement etc. For this research activity we have chosen FatTree topology which is widely used in many data centers around the world.

According to our proposed topology, we have created a FatTree DC network of 10 switches (Fig. 1) with 16 host servers. We consider each host as the server end for hosting

VMs, consolidating VMs as well as placing new VMs. ODL has been implemented and connected with this DC network. The existing modules from ODL that were used in this work are the following:

- switchManager: This module holds the details of the network elements. It is mainly used for discovering the network switches and routers.
- statisticsManager: It holds the statistic information of each port of the switches in the network. It is responsible for giving such information on demand.
- HostTracker: This one tracks the information of the connected hosts within the network.

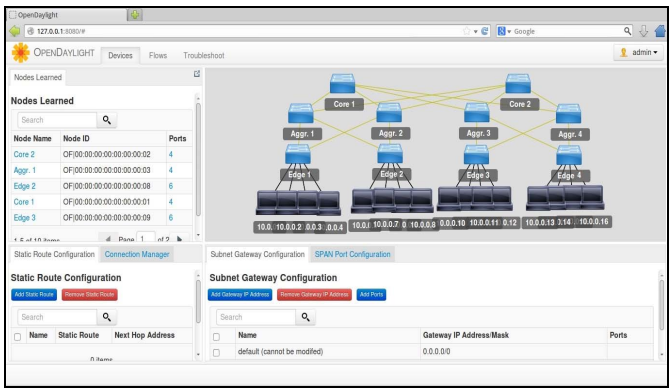

Fig. 1. Data Center implementation through ODL interface

IV. VMMIGRATION MODULE: SOFTWARE DESIGN

In this research we have introduced VMMigration module as a network control application of the ODL controller aiming at assisting VM migration with network load information in cloud DCs thereby orchestrating computing and network resources. The VMMigration module is divided in different sub modules that are useful for performing the VM migrations efficiently taking into consideration the current status of the network (Fig. 2).

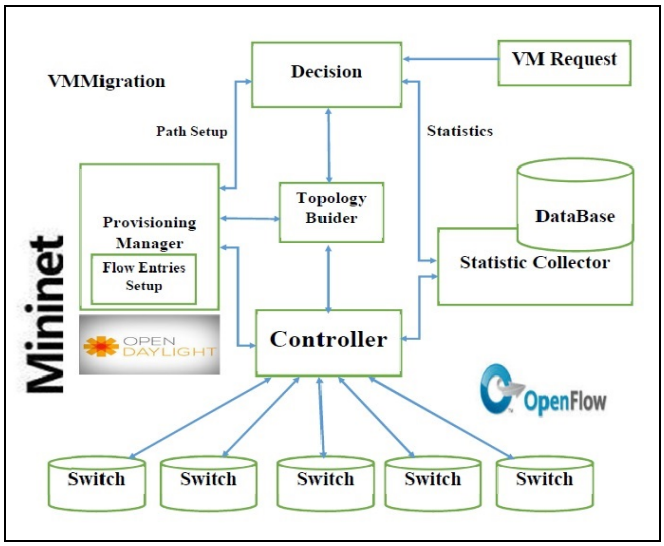

Fig. 2. OpendayLight Controller with VMMigration module

A. Statistics Collector

The Statistics Collector module is developed to periodically collect the statistics of the switches in the DC network and store them in the **Database**. At the end of each polling interval (by default equal to 30 seconds), we collect the instantaneous utilized bandwidth of each port or link of each switch. Then, by using the maximum allowable bandwidth (by default the virtual switches (OVS) that we have considered support a maximum of 10Gb) we can retrieve the available bandwidth (i.e., unused bandwidth). It is worth highlighting that Mininet (version 2.0.0) can support a maximum bandwidth equal to 1Gb for each link. For this reason, we have scaled down the switches capacities to 1Gb to make the experiment compatible with Mininet.

The Database is utilized for storing the information related to the VM migrations such as statistics of the switches and hosts information. It is refreshed after the acceptance of every migration request thus maintaining up-to-date the status of the network.

B. Topology Builder

The Topology Builder module is developed to retrieve the network topology as well as the host's information. In fact, though the topology information regarding the switches can be invoked through the SwitchManager module, it is not possible to track the host's information since they are not directly connected to the controller. For this reason, it is necessary to make each host communicate with the others (by introducing traffic flows through the network) so that the controller can be informed about their presence in the network. In such a case, the Database can be populated with the host's position, various connections between the hosts and switches, etc.

C. VM Request

This module is used to deal with the VM migration requests. As soon as a new request arrives, the controller forwards the information to the Decision component. The VM migration request can be defined manually from an external server or automatically (pre assigned). A request must contain the following parameters:

- Server source address
- Server destination address
- Bandwidth requirement B for migration.

D. Provisioning Manager

The Provisioning Manager module is developed for managing the flow entries in the switches at the DC network. In fact, it is responsible for the flow entries creation and manipulation inside the switches. Specifically, the Provisioning Manager relies on the best path, selected according to a specific algorithm, between the server source and server destination (specified in the VM migration request) to set-up the flow entries in the involved switches.

E. Decision

The Decision module is developed to take the appropriate decisions for the VM migrations. It works in collaboration with the VM Request module which sends the VM migration requests. Then, the Decision module runs the appropriate

algorithms to get the available best path between the source and destination servers specified in the requests. Once a best path is found, it is provided to the Provisioning Manager Module.

V. ALGORITHMS FOR VMMIGRATION MODULE

A. Path_Selection

The *Path Selection* algorithm is triggered by the Decision module upon reception of a VM migration request from the server source. On basis of this request all available paths from the server source to the server destination are exploited and stored in Database. Specifically, the Decision module handles the VM migration request, looking at the pool of servers that are available by querying the Topology Builder module. Once the position of the servers source (S_source) and destination (S_dest) are defined, the edge switches source (Edge_source) and destination (Edge_dest) directly connected to the servers are also determined. Then, the links from the Edge_source and Edge_dest switches are used for knowing the j-th aggregation source (Agg_source) and destination (Agg_dest) switches, respectively. This process will continue until fulfilling a direct path between S_source and S_dest. All retrieved available paths (Path[N]) are then stored in Database.

Algorithm.1 represents the description of the *Path Selection* algorithm. We denote:

S = a pool of available servers.
L = link of the corresponding unit.
Edge[k] = the k-th edge switch (k=1, 2…)
Agg[l] = the l-th aggregation switch (l=1, 2….)
Core[m] = the m-th core switch (m=1, 2…)

Algorithm 1. *Path_Selection algorithm* (Upon VM migration request)

```
// This algorithm provides a set of N available paths (Path[N]) between a
couple of servers source and destination upon a VM migration request is
received by the controller.

INPUTS:
  S_source
  S_dest
OUTPUTS:
  P[N]   N=1, 2 …..

    if S_source ∈ S && S_dest ∈ S then
      // get the set of edge switches linked to the source/dest server
      Edge_source = Edge[S_source]
      Edge_dest = Edge[S_dest]
      //get the aggregation switches linked to the edge_source/dest switches
      Agg_source = Agg[Edge_source]
      Agg_dest = Agg[Edge_dest]
      if L(Agg_source[l]) = L(Agg_dest[l]) then
        //find an available path up to the aggregation level
        P[i] = Find_Path_i(S_source, Edge_source, Agg_source[l],
                           Agg_dest[l], Edge_dest, S_dest) i=1, 2..
        //find an available path up to the core level
        P[j] = Find_Path_i(S_source, Edge_source, Agg_source[l],
                           Core_source[m], Agg_dest[l], Edge_dest,
                           S_dest)  //j=i+1…
        P[N] = P   N=1, 2,…, i+j
      else
      P[N] = Find_Path_n(S_source, Edge_source, Agg_source[l],
                         Core_source[m], Agg_dest[l], Edge_dest, S_dest)
        L = L(P[N])
      end if
    end if
```

B. Best_Path

The *Best_Path* algorithm finds the best path from all the available paths determined by the *Path_Selection* algorithm for a couple of given source (S_source) and destination servers (S_dest). For this purpose, a set of policies might be applied such as first fit, best fit and worst fit. In this paper, the scope of the VM migration process is to minimize the maximum utilization of the network links. For this reason, we consider the most unloaded links for the resources allocation which corresponds to the worst fit policy. Once Path[N] is available, we check if all the links of each path have enough bandwidth with respect to requested bandwidth B, then we apply the Worst Fit policy. We start by selecting the source server link L_{S_source} by fulfilling B requirement. Then maximum available link bandwidth L_{edge_source} is selected towards the agg_source according to Path[N]. Then most unloaded link from L(agg_source [l]) is chosen for selecting the next link L_{agg_source}. While agg_source and agg_dest are connected by the same L_{agg_source}, maximum available bandwidth link L_{agg_dest} from Agg_dest toward the Edge_dest is selected with L_{S_dest} from destination server. Hence, best path is selected without traversing the core switch. Otherwise L_{agg_source} will select the corresponding core switch Core[m] and the process continues until selecting the best path P_{best} . In this way only one possible best path is selected from Path[N] by the Best_Path algorithm.

Algorithm 2 describes the *Best Path algorithm*. We denote:

$L_e[e]$ = The e-th link of edge switch. $L_e[e] \in L$
$L_a[a]$ = The a-th link of aggregation switch. $L_a[a] \in L$
$L_c[c]$ = The c-th link of edge switch. $L_c[c] \in L$

Algorithm 2. *Best_Path algorithm* (From all the available paths from server source to server destination)

```
// This algorithm provides the best path P_best from a set of N available paths
P[N] between source and destination servers according to the bandwidth B .

INPUTS:
  P[N]
  B
OUTPUTS:
  P_best
 if P[N] ≠ null then
    //if enough bandwidth is available on the link
    if L(S_source) > B then
      L_S_source = L(S_source)
    end if
    if L(Edge_source[e]) > B then
      //Find the link which has the maximum available free bandwidth at
      //the edge and aggregation level
      L_edge_source = arg max_{L(edge_source[e])∈L} L(edge_source[e])
    end if
  if L(agg_source[l]) = L(agg_dest[l]) && L(agg_dest[l]) > B then
    L_agg_source = L(agg_source[l]) = L(agg_dest[l])= L_agg_dest
      //if a path towards the server destination is found then consider it as
      // best path
    if L(S_dest) > B then
      L_S_dest = L(S_dest)
```

P_{best} =P[N] P[N] ∈ Path[L_{S_source} L_{edge_source} L_{agg_source} L_{edge_dest} L_{S_dest}]
end if
else
if L(agg_source [l]) > B **then**
L_{agg_source} = arg max $_{L(agg_source\ [l]) \in L}$ L(agg_source [l])
end if
if L(core [m])= L_{agg_source}
L_{core_source} = L(core [m])
end if
if L(core [m]) = L(agg_dest [l]) && L(agg_dest [l]) > B **then**
L_{core_dest} = L(agg_dest [l]) = $_{\text{arg max } L(core\ [m]) \in L}$ L(core [m])
end if
if L(agg_dest [l])= L(edge_dest [k]) && L(agg_dest [l]) > B **then**
L_{agg_dest} = L(agg_dest [l])= L(edge_dest [k])
end if
if L(edge_dest[k])=L(S_dest) && L(S_dest) > B **then**
$L_{S\ dest}$ = L(S_dest)
P_{best} =P[N] P[N] ∈ Path[L_{S_source} L_{edge_source} L_{agg_source} L_{core_source} L_{core_dest} L_{agg_dest} L_{S_dest}]
end if
end if
end if

VI. PERFORMANCE EVALUATION VIA SIMULATIONS

According to our developed test-bed set up, 10 OF enabled switches are connected with each other following a Fat-tree topology with an OF controller. Each edge switch is connected with four servers. We have implemented BaseLine algorithm [17] that is compatible with our developed VMMigration module. According to the BaseLine algorithm, the selection of switches between source and destination is done by a pre-configured flow table (forwarding path). This pre-configured forwarding path goes along the same specified links without using alternative paths provided by topology redundancy. It is a static approach which can be considered an acceptable approximation for routing practices in legacy DC networks.
While a VM request is arrived for selecting a migration path from source to destination, both the baseline algorithm and Best Path (worst fit) algorithm are used. For comparison purpose we have also included bandwidth constrains with baseline algorithm so that to choose the next link from one switch to other from source to destination, there should be enough bandwidth available according to the migration request. If the available link bandwidth cannot satisfy bandwidth requirement, the request will be rejected.

The simulations ensure the ability of VMs migration by generating traffic throughout the DC network. As simulations can take large time and large amount of traffic, there are some design considerations which should be followed. Due to the scalability issues for sending traffic through Mininet, maximum acceptable bandwidth for each port of each switch has been scaled down from 1Gb to 40Mb. In this case a VM request is generated from 1 random source server and 4 probable destinations. Best path algorithm is executed for 4 best paths from one source to 4 destination servers. It is possible that there will be 4 best paths for 4 destinations, or less, or no best path. It depends on the network load and available switch ports bandwidth through which those best paths traverse. During best path generation the lowest available bandwidth along a best path is retrieved. This retrieval information is used to find the final best path among those 4 best paths. In this case maximum available bandwidth from those 4 available lowest bandwidths is selected for the final best path. Hence, the destination server along final best path is selected for final destination server for VM migration. Unlike previous case, for each VM migration request only one best path is generated.
Each VM request contains a VM with 1GByte. To pass a VM with 1GByte, using 10Mbps data rate, it is required 800s to migrate the full VM. As a result, the system can dynamically generate the VM request, allocate resources (unloaded links), migrate the VM and finalize migration after the required time. The simulations have been carried out according to the details given in Table I.

TABLE I. SIMULATIONS PARAMETERS

Parameters	Values
Statistic interval	30s
Link bandwidth	40Mb
Request bandwidth (VM migration)	10 Mb
Number of migration request	1000
VM request inter-arrival time	10s, 30s
Simulation duration	10000s

VII. EVALUATION PERFORMANCE

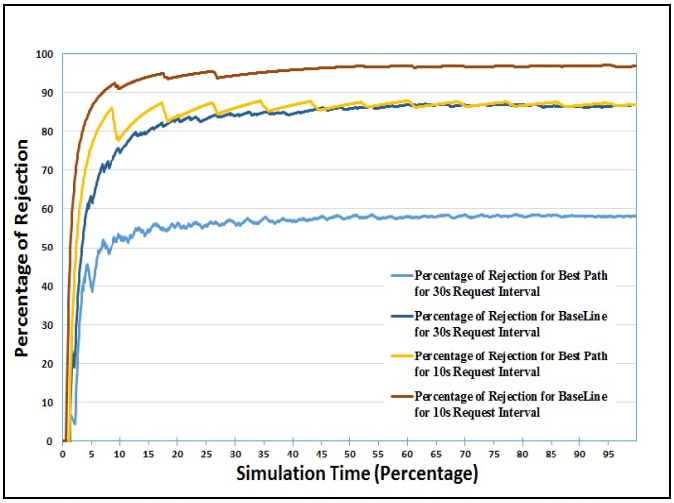

Fig. 3. Rejection percentage in time for variable inter-arrival times

Fig. 3 plots the rejection rate for both the best path algorithm and the baseline while the requested bandwidth B is fixed to 10Mb and the inter-arrival time (IAT) of the migration requests is equal to 10s and 30s. When IAT is low the requests generation rate is high and more rejection can occur since the network is overloaded. In such a case, the blocking keeps increasing until the network is unloaded again thanks to the end of the current migrations. Moreover, in both situations (10s and 30s interval) the rejection rate is lower for best path than baseline. In fact, once the preconfigured paths are saturated, no more requests can be accepted, unlike the best path algorithm which takes advantage from the redundant links in the topology to accept more requests.

Fig. 4 show the behavior of the DC network in terms of request rejection for both the Best Path and the BaseLine algorithms, while varying the statistics update interval (pooling time). When the statistics update interval is low, OF controller can provide recent network status in terms of available bandwidth for each port of each switch. As we have fixed our request interval time to 10s, the controller can process at least 6 requests between two consecutive statistics update (for 60s update interval). For example if the network can take one request (according to recent statistic update), it can accept up to 6 requests within next 60s. Therefore, request acceptance rate becomes higher for higher statistic information collection time. Though the acceptance rate for higher pooling time is higher (around 5%), it is not beneficial for the VM migration. In fact, it saturates the links of the network and the links are then unable to flow data. Finally, as previously explained, the Best_Path algorithm shows better performance in terms of request rejection than the Baseline algorithm.

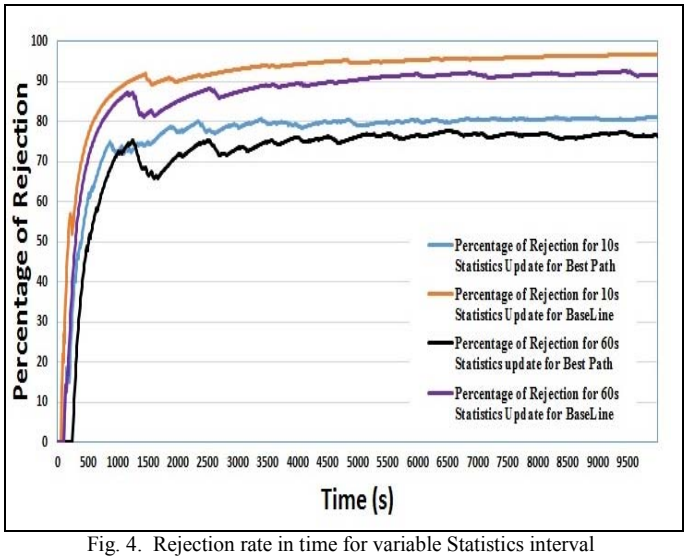

Fig. 4. Rejection rate in time for variable Statistics interval

VIII. Conclusion

DC network can be more dynamic in terms of control and management through implementing SDN. In this research work, it is demonstrated that future DCs can be more dynamic for selecting required destination server for migrating VM from probable source server. This approach has demonstrated not only the availability of the destination servers, but also has explored the selection of the best destination on the basis of network loads. In such way, the proposed solution can balance the network load. This scheme can also avoid the saturation of the link for overloading states and can distribute network loads towards available unloaded links. While the DC network has been overloaded by traversing data traffic, new requests have been rejected instead of further processing. This is also convincing that by implementing different load factors we can keep the network unsaturated for maximum number of flows that are traversing throughout the network. Moreover, the proposed dynamic solution shows a good choice for minimizing delays as well as energy consumption for VM migration. These behaviors make an orchestrated DC network for maximum resource utilization and assure adequate delays for VM migration. The effectiveness of the proposed algorithms have been evaluated in terms of the acceptance rate of VM migration requests through a significant set of simulations. Results show that our Best_Path algorithm outperforms the BaseLine, presenting a lower blocking probability and a better utilization of network links. Such load balancing has a positive impact on the quality of service perceived by the user since less links are saturated. Such improvement depends on the settings of the system parameters such as the inter-arrival time between two consecutive VM migration requests, the pooling time for the retrieval of the network statistics, etc. As future work, we will consider the effect of queuing and rescheduling the rejected requests in order to serve them once the links are unloaded. Other parameters might also be evaluated such as the number of available servers, the requested bandwidth, etc.

References

[1] G. Karagiannis C. N. Hfer, “Cloud computing services: taxonomy and comparison”, Journal of Internet Services and Applications, 2(2):81- 94, Jun 2011.

[2] Yueping Zhang; Ao-Jan Su; Guofei Jiang, “Evaluating the impact of data center net-work architectures on application performance in virtualized environments”. Quality of Service (IWQoS), 18th International Workshop, pages 1 -5, June 2010.

[3] Openflow. [Online] http://www.openflow.org.

[4] SDN–Definition [Online] https://www.opennetworking.org/sdn-resources/sdn-definition

[5] Theophilus Benson, Ashok Anand, Aditya Akella and Ming Zhang “MicroTE: Fine grained Traffic Engineering for Data Centers”, CoNEXT 2011, Tokyo, Japan

[6] Rastin Pries, Michael Jarschel, Sebastian Goll, “On the Usability of OpenFlow in Data Center Environments”, Workshop on Clouds, Networks and Data Centers collocated with the IEEE International Conference on Communications (ICC 2012), Ottawa, Canada, June 2012

[7] W. Cerroni, M.Gharbaoui, B.Martini, A. Campi, P. Castoldi, F. Callegati, Cross-layer resource orchestration for cloud service delivery: A seamless SDN approach, Computer Networks, Volume 87, 20 July 2015, Pages 16-32

[8] Rabbani, Md G., Pereira Esteves, R., Podlesny, M., Simon, G.; Granville, Zambenedetti, L., Boutaba, R., "On tackling virtual data center embedding problem" 2013 IFIP/IEEE IM 2013, May 2013

[9] Meng, X., Pappas, V., Zhang, L., "Improving the Scalability of Data Center Networks with Traffic-aware Virtual Machine Placement", IEEE INFOCOM 2010, 14-19 March 2010

[10] Chappel, C., “Unlocking Network Value: Service Innovation in the Era of SDN”, HeavyReading, white paper, June 2013

[11] “Implementing SDN and NFV with Intel Architecture”, White paper. Intel Architecture Processors. 2013

[12] Molka Gharbaoui; Piero Castoldi; Gianni Antichi; Stefano Giordano; Davide Adami, “Effective resource control strategies using openow in cloud data center”, IFIP/IEEE International Symposium on Integrated Network Management, (IM 2013), pages 568-574, May 2013.

[13] B. Martini, D. Adami, A. Sgambelluri, M. Gharbaoui, L. Donatini, S. Giordano and P. Castoldi, “An SDN Orchestrator for Resources Chaining in Cloud Data Centers”, in Proc. of EUCN 2014, Bologna, Italy, June 2014.

[14] Opendaylight tutorial. [Online] http://archive.openflow.org/wk/?title=OpenDayLight_Tutorial

[15] OpenDaylight Hydrogen release. https://wiki.opendaylight.org/view/Release/Hydrogen [online]

[16] Mininet overview [Online]. http://mininet.org/overview

[17] D. Adami G. Antichi S. Giordano M. Gharbaoui, B. Martini and P. Castoldi. (2014, May), On virtualization-aware traffic engineering in openflow data centers networks.to be published. Network Operations and Management Symposium (NOMS), 2014 IEEE.

Solving Capacitated Vehicle Routing Problem with Route Optimization using Swarm Intelligence

M. A. H. Akhand, Jaharul Jannat, Tanzima Diba and Al-Mahmud
Dept. of Computer Science and Engineering
Khulna University of Enginnering & Technology
Khulna-9203, Bangladesh

***Abstract*—**Capacitated Vehicle Routing Problem (CVRP) is a real life constrain satisfaction problem in which customers are optimally assign to individual vehicles (considering their capacity) to keep total travel distance of the vehicles as minimum as possible while serving customers. Various methods are investigated to solve CVRP in last few decades, the most popular way of solving CVRP is splitting the task into two different phases: firstly, assigning customers under different vehicles and secondly, finding optimal route of each vehicle. Sweep clustering algorithm is well studied for clustering nodes. On the other hand, route optimization is simply a traveling salesman problem (TSP) and a number of TSP optimization methods are investigated for this purpose. This study investigates a variant of Sweep algorithm for clustering nodes and different SI based methods for route generation to get optimal CVRP solution. In conventional Sweep algorithm, cluster formation starts from 0^0 and consequently advance toward 360^0 to consider all the nodes. In this study, Sweep cluster are considered from different starting angle. On the other hand, two well-known Swarm Intelligence (SI) methods (i.e., Ant Colony Optimization and Particle Swarm Optimization (PSO)) and two recent SI based algorithms (i.e., Producer-Scrounger Method and Velocity Tentative PSO) are considered for route optimization. We have compared the performance of these methods to solve CVRP. The experimental results on a large number of benchmark CVRP reveal that different starting angle has positive effect on Sweep clustering and finally, VTPSO is able to produce better solution than other methods.

Keywords - *Capacitated Vehicle Routing Problem, Sweep Clustering, Genetic Algorithm, Ant Colony Optimization, Particle Swarm Optimization (PSO), Producer-Scrounger Method and Velocity Tentative PSO.*

I. INTRODUCTION

Vehicle Routing Problem (VRP) means determining routes for several vehicles from a depot to a number of customers and then returning to the depot. Customers with known demands are visited by a homogeneous fleet of vehicles with limited capacity. VRP is a hard optimization task to minimize total travelled distance of all the vehicles to serve all the customers. The general constrains of VRP are each customer is serviced exactly once (by a single vehicle) and total load on any vehicle associated with a given route does not exceed its capacity. Since capacity constraint of vehicles is the most important the problem is alternatively called Capacitated VRP (CVRP). In general, a CVRP considers equal capacities for all vehicles; although in real life vehicle fleet with different capacities can be used to solve the delivery problem [1]. A number of variations of CVRP are also available: considers multiple depot instead of one and considers time window constraint defining time frames when a customer can be serviced. The simplest form of CVRP considering one depot and several vehicles with equal capacity is the most studied problem.

In CVRP, all customers have known demands and known locations for the delivery. The delivery for a customer cannot be split. In other words, the demand of a customer must be satisfied via only one visit. All vehicles are assumed to have the same loading capacity. They depart from a single depot at the beginning and return to the depot at the end. The service or unloading time at each customer may or may not be considered. The objective is to minimize the total travelling distance or time for all vehicles to serve all customers. Mathematically, a CVRP is defined as

$$\text{Minimize} \sum_{i\in N}\sum_{j\in N}\sum_{v\in V} C_{ij} X_{ij}^{v} \tag{1}$$

$$\text{Subject to} \sum_{v\in V} y_i^v = 1 \quad \text{for } i \in N \tag{2}$$

$$\sum_{i\in N} x_{ij}^v = y_j^v \text{ for } j \in N \text{ and } v \in V \tag{3}$$

$$\sum_{j\in N} x_{ij}^v = y_i^v \text{ for } i \in N \text{ and } v \in V \tag{4}$$

$$\sum_{i\in N} d_i y_i^v \le Q \text{ for } v \in V \tag{5}$$

$$\sum_{i\in N} x_{i1}^v \le 1 \text{ for } v \in V \tag{6}$$

$$\sum_{j\in N} x_{1j}^v \le 1 \text{ for } v \in V \tag{7}$$

In this formulation, the objective function is expressed by Eq. (1) which states that the total travelling distance of all vehicles is to be minimized. Eq. (2) represents the constraint that each customer must be visited once by one vehicle, where y_i^v=1 if vehicle v visits customer i, and 0 otherwise. It is guaranteed in Eq. (3) and Eq. (4) that each customer is visited and left with the same vehicle, where $x_{ij}^v = 1$ if vehicle v travels from customer i to customer j, and 0 otherwise. A constraint in Eq. (5) ensures that the total delivery demands of vehicle v do not exceed the vehicle capacity. Eq. (6) and Eq. (7) express that vehicle availability should not be exceeded.

CVRP is a real life constrain satisfaction problem in which customers are optimally assign to individual vehicles (considering their capacity) to keep total travel distance of the vehicles as minimum as possible. Various methods are investigated to solve CVRP in last few decades. A number of methods available that optimizes node assignment under vehicles and route of vehicles together. On the other hand, the most popular way of solving CVRP is splitting the task into two different phases: firstly, assigning customers under different vehicles and secondly, finding optimal route of each vehicle. Among several ways for customer assignment, Sweep clustering algorithm is well studied due to its simplicity. The algorithm calculates polar angles of all the nodes and then assign nodes into different clusters according to their angles. On the other hand, route optimization is simply a traveling salesman problem (TSP) and a number of TSP optimization methods are investigated for this purpose.

The capability of Sweep in solving the VRP for public transport is investigated in [2]. Here clustering is performed by joining their angles in ascending order. A node with smallest angle is joined with one with second smallest and then third smallest and so forth until the capacity constraint is satisfied. After clustering the nodes in each cluster are linked based on their distance. Then route generation is accomplished through TSP. A hybrid heuristic approach has been used in [3]. In the paper GA has been combined with Sweep algorithm to optimize routes and succeeded to produce better result.

A Sweep heuristic method with 2-opt exchange and TSP tours has been used in [4]. The method also used an integer programming model for split delivery VRP model to select the best route to pick up and delivery customers. A centroid-based heuristic algorithm to solve the capacitated VRP has been proposed in [5].The proposed algorithm consists of three phases: cluster construction, cluster adjustment, and route establishment. They compared their result with sweep algorithm and showed that 3-phase approach can result in smaller distances than the Sweep algorithm in more cases. Route establishment was also performed through TSP.

The modified Sweep algorithm was used to solve morning newspaper delivery problem through VRP in [6]. This modified algorithm optimized the total cost without violating the capacity and time window constraints. A hybrid two-phase algorithm called Sweep algorithm and ant colony system (ACS) for the classical VRP has been proposed in [7]. At the first stage, the VRP was solved by the Sweep, and at the second stage, the ACS and 3-opt local search were used for improving the solutions. Use of ACS to solve the CVRP associated with collection of recycling waste from households has been demonstrated in [8].

Recently, the outcome of Sweep algorithm has been used for clustering customers and route is optimizes using Particle Swarm Optimization (PSO), the well-known swam intelligence method, in [9]. Performance of sweep algorithm has also been compared with savings method in [10].

This study investigates a variant of Sweep algorithm for clustering nodes and different SI based methods to optimize the routes of individual vehicles. In conventional Sweep algorithm, cluster formation starts from 0^0 and consequently advance toward 360^0 to consider all the nodes. In this study, Sweep cluster are considered from different starting angle. On the other hands, two well-known SI methods (i.e., ACO and PSO) and two recent SI based algorithms (i.e., PSM and VTPSO) are considered for route optimization. The outline of the paper is as follows. Section II explains variant Sweep algorithm and GA, ACO, PSO, PSM and VTPSO methods briefly. Section III is for experimental studies which presents as well as compares the outcomes of the methods for a suite of benchmark CVRPs. At last, Section IV gives a brief conclusion of the paper.

II. Solving CVRP with Sweep Clustering and Route Optimization using Swarm Intelligence Methods

The aim of this study is to identify the effective CVRP method considering Sweep algorithm to cluster the nodes and several prominent SI based methods to optimize the routes for Sweep clusters. A variant version of Sweep is considered in this study for better outcome. This section gives description of Sweep and optimization methods.

A. Sweep Clustering with Different Starting Angles

Sweep algorithm was firstly introduced in [11] as a heuristic algorithm that have been developed for solving vehicle dispatch problems with load constraint for each vehicle. At first polar angle of each nodes are calculated and order the nodes according to polar angle. General formula for calculating polar angle is

$$\theta = \tan^{-1}(y/x) \tag{8}$$

where Θ is the angular value of a node in degree (customer location). Finally, nodes are clusters according to the polar angles. The first cluster considers the nodes from the beginning until capacity of a vehicle does not exceed. Similar way all the nodes are clustered into different vehicles.

Figure 2 shows the graphical representation of cluster formation in Sweep algorithm. The black dots represent the nodes and the straight lines represent the Sweep hand that moves anti-clockwise. Clustering is performed by joining nodes beginning from the closest node to any node that is chosen to be the first node. The closest node is one which has smallest

angle. This process is repeated by joining the second closest, the third, and so forth until it satisfies the constraint.

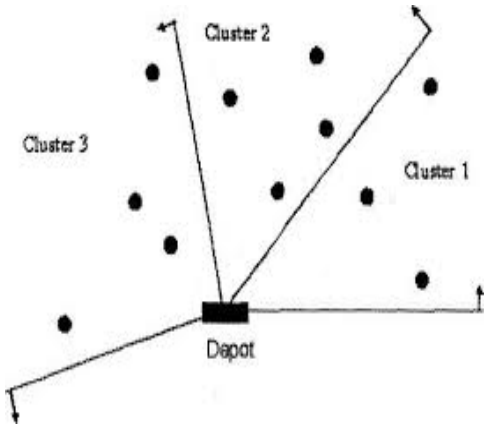

Fig. 2: Formation of cluster using Sweep algorithm.

In general, Sweep considers depot located at (0, 0) co-ordinate in two dimensional plane and cluster construction starts from the node having lowest polar angle. It is worth mentionable that starting from different angles may give different clusters and explore chance to get better CVRP solution after route optimization. Therefore, this study considers a variant of Sweep which take starting angle as user define parameter and the steps of it are as follows:

Variant Sweep Algorithm:

Initialization:

1. Update coordinates of the nodes considering depot as (0, 0) in the two-dimensional plane.
2. Compute the polar angle of each node.
3. Order the nodes according to polar angle, *ONL*
4. Take Starting Angle, Θ_s
5. Cluster C=1

Clustering:

1. Identify position of Θ_s in *ONL*.
2. Sweeping nodes to current cluster C by increasing polar angle.
3. Stop when adding the next node would exceed vehicle capacity.
4. Create a new cluster $C+1$ by resuming the sweep where the last one left off.
5. Repeat steps 2–4, until all customers have been included in a cluster

Outcome:

All the nodes are assigned into C clusters.

B. Vehicle Route Generation from Sweep Cluster Nodes

The route generation stage is aimed to optimize searching method to find the optimal solution that represents the shortest path between all nodes in each cluster generated by Sweep algorithm. In this stage each cluster is an individual traveling salesman problem (TSP). In this study four SI based method are considered for route optimization. Among the methods, Ant Colony Optimization (ACO) and Particle Swarm Optimization (PSO) very popular well-known SI methods; and Producer-Scrounger Method (PSM) and Velocity Tentative PSO (VTPSO) are two very recent methods. GA is also considered along with SI methods for optimization as it is a prominent and pioneer optimization method. Brief description of the methods to optimize route (i.e., to solve TSP) are given to make the paper self-contained.

a. Genetic Algorithm (GA)

GA is inspired by biological systems' fitness improvement through evolution and is the pioneer and widely used to solve many scientific and engineering problems. Common features of GA are: populations of chromosomes (i.e., solutions), selection according to fitness, crossover to produce new offspring, and random mutation of new offspring. To produce new tour from existing tours, Enhanced Edge Recombination cross over method [12] is used in this study. The positions of two nodes are interchanged for mutation operation.

b. Ant Colony Optimization (ACO)

ACO is inspired from ants' foraging behavior and is the prominent method for solving TSP. ACO is the first algorithm aiming to search for an optimal path in a graph, based on the behavior of ants seeking a path between their colony and a source of food. It considers population size as the number cities in a given problem and starts placing different ants in different cities. A particular ant consider next city to visit based on the visibility heuristic (i.e., inverse of distance) and intensity of the pheromone on the path. After the completion of a tour, each ant lays some pheromone on the path. Before pheromone deposit, pheromone evaporation of real ant is adopted by reducing pheromone of all the links by a fixed percentage. This behavior allows the artificial ants to forget bad choices made in the past. Finally, all the ants follow the same route after certain iteration. The detail description of ACO available in [13].

c. Particle Swarm Optimization (PSO)

PSO is a popular optimization method on metaphor of social behavior of flocks of birds or schools of fishes. PSO is a simple model of social learning whose emergent behavior has been found popularity in solving difficult optimization problems. In PSO, each particle represents a potential solution and moves to a new position (i.e., search a new point) at every iteration based on the calculated velocity. The processes of iteration continue until the stopping criterion is reached. PSO was proposed for continuous problems (e.g., function optimization) and has been proven to solve such problems effectively [14]. In function optimization domain, a particle represents a position in the multidimensional search space. At every step, each particle changes position based on its velocity depending on its previous best position and the best position particles ever visited.

PSO has also been found as an efficient method to solve combinatorial problems such as TSP. To solve TSP with PSO, each particle represents a complete tour as a feasible solution

and velocity is a measure to update the tour for better solution. Among many methods of PSO, study of [15] is the pioneer method to solve TSP that considers each particle as a complete tour and uses Swap Sequence (SS) [15] as velocity to get a new tour applying on a tour. A SS is a collection of several Swap Operators (SOs) and each one indicates two positions in a tour those might be swapped. All SOs of a SS are applied on a particle's tour maintaining order and hence implication of the SS transforms the TSP tour into a new one. The detail description of solving TSP with SS based velocity operation is available in [15, 17].

d. Producer-Scrounger Method (PSM)

PSM [16] is a new technique to solve TSP inspiring from the animal group living behavior. It models roles and interactions of three types of animal group members: producer, scrounger and dispersed. PSM considers a producer having the best tour, few dispersed members having worse tours and scroungers. In each iteration, the producer scans for better tour, scroungers explore new tours while moving toward producer's tour; and dispersed members randomly checks new tours. For producer's scanning, PSM randomly selects a city from the producer's tour and rearranges its connection with several near cities for better tours. Swap operator and swap sequence based operation is employed in PSM to update a scrounger towards the producer. Finally, producer is consider as the solution of a given problem. The description of this method is available in [16].

e. Velocity Tentative PSO (VTPSO)

VTPSO [17] is the most recent SI based method extending PSO to solve TSP. It calculates velocity SS similar to existing method [15] but apply the SS in a different and optimal way. In VTPSO, the new tour of TSP is considered after applying all the SOs of a SS and no intermediate measure is considered. VTPSO conceives a measure called partial search (PS) to apply calculated SS to update particle's position (i.e., TSP tour). On the other hand, VTPSO considers the calculated velocity SS as tentative velocity and conceives a measure called partial search (PS) to apply calculated SS to update particle's position (i.e., TSP tour). VTPSO measures tours with portions of SS and conceive comparatively better new tour with a portion or full tentative SS. The method is shown to perform well when tested on a suite of benchmark TSPs. The algorithm is described in [17].

III. Experimental Studies

This section describes the benchmark problems and experimental setup for conducting the experiment and then represents experimental results and analysis.

A. Benchmark Problems and Experimental Setup

In this study, a suite of 20 benchmark problems from [18]; Table 1 shows the brief description of the problems. In the problems, number of customer varied from 200 to 483 and vehicle capacity varied in different problems from 200 to 1000. A customer is represented as a coordinate in a problem.

Table 1: CVRP benchmark problems.

Sl.	Problem Name	Total Nodes	Total Demand	Individual Vehicle Capacity
1	kelly01	240	4800	550
2	kelly02	320	6400	700
3	kelly03	400	8000	900
4	kelly04	480	9600	1000
5	kelly05	200	4000	900
6	kelly06	280	5600	900
7	kelly07	360	7200	900
8	kelly08	440	8800	900
9	kelly09	255	13429	1000
10	kelly10	323	15195	1000
11	kelly11	399	16980	1000
12	kelly12	483	18701	1000
13	kelly13	252	25136	1000
14	kelly14	320	28672	1000
15	kelly15	396	32244	1000
16	kelly16	480	35772	1000
17	kelly17	240	4320	200
18	kelly18	300	5400	200
19	kelly19	360	6480	200
20	kelly20	420	7560	200

Therefore, the cost is found after calculating distance using the coordinates.

Sweep algorithm applied on each problem for seven different starting angles (Θ_s) and those are 0^0, 45^0, 90^0, 135^0, 180^0, 225^0, and 270^0. It is notable that conventional Sweep only considers $\Theta_s = 0^0$ for clustering. In this study, selected TSP optimization methods (i.e., GA, ACO, PSO, PSM and VTPSO) are applied on the all Sweep outcomes to get final solution.

We strongly relied on an experimental methodology for configuring the route optimization algorithms. For the fair comparison, the number of iteration was set at 100 for the algorithms. The number of ants in ACO was equal to the number of cities as it desired. The population size was 50 for GA, PSM and VTPSO. In ACO, *alpha* and *beta* were set to 1 and 3, respectively. On the other hand, the *RNC* (rate of near cities consideration) for producer scanning in PSM was set to 0.1. The selected parameters are not optimal values, but considered for simplicity as well as for fairness in observation.

The algorithms are implemented on Visual C++ of Visual Studio 2013. The experiments have been done on a PC (Intel Core i5-3470 CPU @ 3.20 GHz CPU, 4GB RAM) with Windows 7 OS.

B. Experimental Results and Analysis

This section presents experimental results for the benchmark problems for Sweep clustering with different starting angles and route optimizing using GA, ACO, PSO, PSM and VTPSO. Table 2 shows the total clusters for different starting angles (Θ_s) in Sweep and optimized route cost using the TSP algorithms for kelly15 problem. The problem has 396 nodes and total demand to be served is 32244 with vehicle having capacity 1000. From the table it is observed that Sweep manages total nodes into 34 or 35 clusters i.e., required number of vehicles. The total number vehicle are 35 for Θ_s=0, 90, 180 and 270. On the other hand, number of vehicles required 34 for Θ_s= 45, 135 and 225. It is also remarkable that total travel cost for 34 clusters is lower than the case of 35 for before and after route optimization. The best travel distance for an algorithm for different Θ_s is marked as bold-faced type. For the problem the best travel cost achieved after optimizing with GA, ACO, PSO, PSM and VTPSO are 1622.01, 1648.37, 1730.33, 1615.51 and 1598.9, respectively. The best values are for 34 cluster case with different starting angles. This result clearly indicates that starting with different starting angle has a positive effect on Sweep clustering.

Table 2: Clusters for different starting angle (Θ_s) and total travel distance after route optimizing using GA, ACO, PSO, PSM and VTPSO for kelly15 problem.

Θ_s	Clus-ters	Before Route Optimizing	Travel Cost after Optimizing with				
			GA	ACO	PSO	PSM	VTPSO
0	35	3141.25	1657.12	1687.07	1780.59	1649.93	1634.59
45	34	3119.7	1626.41	**1648.37**	1737.89	1617.14	1599.13
90	35	3141.25	1670.38	1690.54	1777.55	1650.5	1634.4
135	34	3119.7	1628.19	1649.08	1755.26	1620.42	**1598.9**
180	35	3141.25	1657.76	1686.07	1765.76	1653.92	1635.98
225	34	**3119.7**	**1622.01**	1650.24	**1730.33**	**1615.51**	1599.06
270	35	3141.25	1650.16	1685.65	1771.07	1646.35	1635.23

Table 3 compares travel distance for route optimizing using GA, ACO, PSO, PSM and VTPSO. The result presented for an algorithm is the best result from seven different starting angles in Sweep clustering. The best one (i.e., smallest value) among the five algorithms is shown in bold-face type. Pair wise Win/Draw/Loss summary is presented below the table for better understanding.

Among conventional methods ACO is shown to outperform both GA and PSO most of the cases. ACO is found better than GA for 12 cases out of 20 cases. For other eight cases GA was better than ACO. On the other hand, ACO outperformed PSO for 15 cases. On the basis of average travel distance over 20 problems, ACO is the best conventional method and PSO is the worst. ACO achieved average travel cost over 20 cases 4978.59; on the other hand, GA and PSO achieved travel cost 7576.93 and 12041.94, respectively. ACO is the well-known method for TSP and its performance solving route optimization (e. g., TSP) is well studied.

Although PSO is found inferior to other conventional methods (i.e., GA and ACO), VTPSO, the updated version of PSO, is found as the best method among the five algorithms. VTPSO calculates velocity SS similar to PSO but apply the SS in a different and optimal way. The partial search mechanism in velocity implementation ensures to get combatively better new tour with respect to traditional PSO. Therefore, outperformance of VTPSO with respect to others is logical as it was found better for TSP [14]. On the other hand, PSM, another recent SI method, also used SS operation to update its members and found better than GA and PSO but competitive to ACO. PSM is found better than ACO for eight cases out of 20 cases and VTPSO outperformed ACO for all 20 cases. The average travel cost achieved by PSM and VTPSO are 5586.71 and 4755.49, respectively.

Table 3: Benchmark CVRP travel distance cost comparison for route optimizing using GA, ACO, PSO, PSM and VTPSO.

SI.	Problem	GA	ACO	PSO	PSM	VTPSO
1	kelly01	7311.31	6066.12	11314.07	6560.02	**5748.11**
2	kelly02	12870.36	9374.67	20252.39	9816.54	**8811.22**
3	kelly03	19735.81	11972.23	33009.25	13897.76	**11371.37**
4	kelly04	28006.34	15140.39	46507.72	18264.81	**14462.41**
5	kelly05	12247.99	7286.99	19879.25	8512.03	**7115.05**
6	kelly06	15160.58	9240.71	24813.42	11092.49	**8853.34**
7	kelly07	18298.84	11069.09	30381.33	12717.64	**10790.89**
8	kelly08	21325.69	12963.9	34727.21	14839.42	**12193.8**
9	kelly09	753.92	711.72	1065.13	716.5	**703.36**
10	kelly10	1003.33	921.34	1513.61	930.95	**899.32**
11	kelly11	1311.47	1163.56	2109.82	1185.38	**1128.32**
12	kelly12	1667.13	1356.69	2735.99	1406.53	**1315.36**
13	kelly13	1018.7	1039.79	1037.28	1013.97	**1012.33**
14	kelly14	1281.81	1313.47	1333.42	1278.07	**1270.19**
15	kelly15	1622.01	1648.37	1730.33	1615.51	**1598.9**
16	kelly16	1993.42	2024.29	2185.83	1985.63	**1967.66**
17	kelly17	773.36	837.9	813.84	768.08	**763.9**
18	kelly18	1143.75	1215.41	1200.82	1134.91	**1128.13**
19	kelly19	1660.27	1757.52	1739.24	1646.47	**1639.58**
20	kelly20	2352.49	2467.71	2488.91	2351.56	**2336.6**
	Average	**7576.93**	**4978.59**	**12041.94**	**5586.71**	**4755.49**
		Pairwise Win/Draw/Loss Summary				
		GA	ACO	PSO	PSM	VTPSO
	GA	-	12/0/8	0/0/20	20/0/0	20/0/0
	ACO		-	5/0/15	8/0/12	20/0/0
	PSO			-	20/0/0	20/0/0
	PSM				-	20/0/0

Finally, the effect of population size on route optimizing has been investigated for kelly15 problem with sweep starting angle Θ_s=225. Population size was varied from 10 to 150 for GA, PSO, PSM and VTPSO; whereas, the number of ants in ACO was equal to the number of cities as it desired. Fig. 1 shows CVRP travel distance (i.e., travel cost) for fixed 100 iteration only varying population size for fair comparison. For the methods, number of clusters were same (i.e., 34) with travel cost of 3080 without route optimization. From the figure it is observed that travel cost is invariant for ACO because population variation was not employed for it. Performance of GA and PSO is highly dependent on population size; for smaller population size (e.g., less than 50) the methods showed very high travel cost. On the other hand, PSM and VTPSO are found to work well with smaller population size. At a glance VTPSO is shown to outperform any other method for any population size.

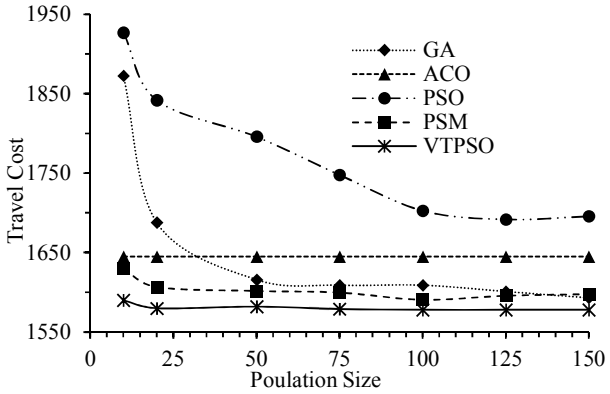

Fig. 3: Effect of population size on route optimizing for kelly15 problem with clustering Θ_s=225.

IV. CONCLUSION

CVRP is a popular combinatorial optimization problem and interest grows in recent years to solve it new ways. A popular way of solving CVRP is cluster the nodes according to vehicles using Sweep algorithm first and then generate route for each vehicle with TSP algorithm. In general, Sweep cluster construction starts from the node having lowest polar angle. This study considers a variant of Sweep which takes starting angle as a user define parameter and produces different clusters for a given problem. Finally, GA, ACO, PSO, PSM and VTPSO are applied to generate optimal route with Sweep outcome. The experimental result on the benchmark problems revealed that different starting angle have positive effect on Sweep clustering and VTPSO is better than other optimization methods to solve CVRP.

REFERENCES

[1] G. Vaira, "Genetic Algorithm for Vehicle Routing Problem," PhD. Thesis, Vilnius University, Italy, 2014.

[2] G. W. Nurcahyo, R. A. Alias, S. M. Shamsuddin and M. N. Md. Sap, "Sweep Algorithm in vehicle routing problem for public Transport," *Journal Antarabangsa (Teknologi Maklumat)*, vol. 2, pp. 51-64, 2002.

[3] S. Han and Y. Tabata, "A Hybrid Genetic Algorithm for the Vehicle Routing Problem with Controlling Lethal Gene," *Asia Pacific Management Review*, vol. 7, no. 3, pp. 405-426, 2002.

[4] N. Suthikarnnarunai, "A Sweep Algorithm for the Mix Fleet Vehicle Routing Problem," *in Proc. of the International Multi Conference of Engineers and Computer Scientists*, vol. 2, March 19-21, Hong Kong, 2008.

[5] K. Shin, "A Centroid-Based Heuristic Algorithm for the Capacitated Vehicle Routing Problem," *Computing and Informatics*, vol. 30, pp. 721–732, 2011.

[6] A. Boonkleaw, N. Suthikarnnarunai and R. Srinon, "Strategic Planning and Vehicle Routing Algorithm for Newspaper Delivery Problem: Case study of Morning Newspaper, Bangkok, Thailand," *in Proc. of the World Congress on Engineering and Computer Science 2009*, vol. 2, October 20-22, 2009.

[7] M. Yousefikhoshbakht and E. Khorram, "Solving the vehicle routing problem by a hybrid meta-heuristic algorithm," *Journal of Industrial Engineering International*, vol. 8(11), 2011.

[8] M. Reed, A. Yiannakou and R. Evering, "An ant colony algorithm for the multi-compartment vehicle routing problem," *Applied Soft Computing*, vol. 15, pp. 169-176, 2014.

[9] S. R. Venkatesan, D. Logendran, and D. Chandramohan, "Optimization of Capacitated Vehicle Routing Problem using PSO", *International Journal of Engineering Science and Technology (IJEST)*, vol. 3, pp. 7469-7477, 2011.

[10] G. K. Rand, "The life and times of the Savings Method for Vehicle Routing Problems," *Journal of the Operations Research Society of South Africa (ORSSA)*, vol. 25, no. 2, pp. 125-145, 2009.

[11] M. M. A. Aziz, H. A. El-Ghareeb and M. S. M. Ksasy, "Hybrid Heuristic Algorithm for solving Capacitated Vehicle Routing Problem," *International Journal of Computers & Technology*, vol 12, no.9, pp. 3845-3851, 2014.

[12] D. E. Goldberg, 'Genetic Algorithm in Search, Optimization and Machine Learning', New York: Addison – Wesley, 1989.

[13] T. Stutzle and M. Dorigo, "The Ant Colony Optimization Metaheuristic: Algorithms, Applications, and Advances," *International Series in Operations Research and Management Science*, Kluwer, 2001

[14] Y. F. Liao, D. H. Yau and C. L. Chen, "Evolutionary algorithm to traveling salesman problems," *Computers & Mathematics with Applications,* vol. 64, no. 5, pp. 788–797, 2012.

[15] K. P. Wang, L. Huang, C. G. Zhou and W. Pang, "Particle swarm optimization for traveling salesman problem," in *Proc. International Conference on Machine Learning and Cybernetics*, November 2003, pp. 1583–1585.

[16] M. A. H. Akhand, P. C. Shill, Md. Forhad Hossain, A. B. M. Junaed, and K. Murase, "Producer-Scrounger Method to Solve Traveling Salesman Problem", *I. J. Intelligent Systems and Applications*, vol. 7, no. 3, pp. 29-36, 2015.

[17] M. A. H. Akhand, S. Akter, M. A. Rashid and S. B. Yaakob, "Velocity Tentative PSO: An Optimal Velocity Implementation based Particle Swarm Optimization to Solve Traveling Salesman Problem," IAENG International Journal of Computer Science, vol. 42, no.3, pp 221-232, 2015.

[18] Large Capacitated Vehicle Routing Problem Instances. Available: http://neo.lcc.uma.es/vrp/vrp-instances/

Computing a Longest Common Subsequence for Multiple Sequences

Chinmay Bepery[1,*], Sk. Abdullah-Al-Mamun[2], and M. Sohel Rahman[3]
[1]Affiliation (Department of CIT, PSTU, Bangladesh)
[2]Affiliation (PSTU, Bangladesh)
[3]Affiliation (Department of CSE, BUET, Bangladesh)
[*]E-mail: chinmay.cse@pstu.ac.bd

Abstract—**The longest common subsequence problem is a classical string problem that aims at computing a common subsequence having the highest possible length from a given set of strings. This problem is one of the most studied computational problems in bioinformatics and computational biology. The problem is NP-hard for more than two input strings and the existing exact solutions are impractical for large input size. In this paper, we propose a new nondeterministic algorithm based on stochastic and dynamic programming method. In our algorithm, we have employed a heuristic that is inspired by the pheromone update strategy of the ant colony system. We have also integrated a local search technique in our algorithm to improve our results. The proposed algorithm is compared with the state-of-the-art algorithms over several standard benchmarks including simulated and real biological sequences. Experimental results show that the proposed algorithm can provide high quality solutions within a reasonable amount of time.**

Keywords—Dynamic programming, LCS, heuristics, pheromone.

I. INTRODUCTION

Given a string *s* over an alphabet $\sum$, a subsequence of it can be obtained by deleting some characters from *s*. Given a problem instance *(S,* $\sum$*),* where $S = \{s_1, s_2, \dots \dots, s_n\}$ is a set of *n* strings over a finite alphabet $\sum$, the LCS problem seeks to find the longest string t^* that is a subsequence of all the strings in *S*. Such a string t^* is called an LCS of the strings in *S*. This problem has diverse applications in areas like data compression [1], file comparison [2], text editing [3], query optimization in databases [4], clustering web users [5], circuit minimization in field programmable gate arrays (FPGAs) [6] etc. Perhaps the most important application of this problem can be found in molecular biology to compare DNA or RNA sequences and to determine homology in macromolecules [3], [7], [8],[9].

The LCS problem is NP-hard [10] for an arbitrary number (say, *n*) of input strings. The problem is polynomially solvable by dynamic programming [11] for fixed *n*. For two input strings, LCS (referred to as 2-LCS henceforth) can be efficiently solved using dynamic programming in $O(m_1.m_2)$ time, where m_1 and m_2 are the lengths of the input strings. Standard dynamic programming approaches for *n* strings require $O(m^n)$ time and space, where *m* is the length of the longest input string [12], [13]. Clearly, dynamic programming becomes quickly impractical as *n* grows. Since, the problem is NP-hard in general [14], [10], any optimal algorithm proposed for the problem has to be of exponential worst-case time complexity unless P=NP.

Existing exact algorithms for LCS include those based on dynamic programming, tree search, and integer programming. Several improvements over the dynamic programming algorithms of [12], [13] were achieved in [15], [12], [16], [13] to reduce the time complexity to $O(m^{(n-1)})$. A recent dynamic programming algorithm based on a divide-and-conquer technique to construct dominant points was proposed in [17]. Singireddy devised an integer programming formulation for the LCS problem in [18] having a time complexity of $O(m^n)$. A tree search algorithm was proposed by Hsu and Du in [19] based on backtracking. This was further enhanced by Easton and Singireddy in [20] where a selection heuristic and two new types of branch and bound pruning were adopted. The resulting algorithm, called Specialized Branching (SB), is exponential in the length of the LCS. Also, some parallel algorithms were proposed to run exact LCS solvers on multiple processors [21], [22], [23].

Due to exponential time complexity, the exact algorithms are impractical for large input sizes. Hence the use of algorithms producing near-optimal solutions (i.e., inexact algorithms) as opposed to the optimal solutions (i.e., exact algorithms) are inevitable. Extensive research has in fact been conducted in the literature to devise inexact algorithms for the LCS problem, that aim at finding good, but not necessarily optimal, solutions within an affordable amount of time. In general, inexact algorithms can be classified into two broad categories, namely, the approximation and heuristic algorithms.

The first approximation algorithm proposed for the LCS problem was *Long Run* (LR) algorithm with an approximation ratio of $|\sum|$ [24],[25]. LR simply constructs a string as its output using only a single character in $\sum$. However, it does not usually give an impressive solution. Another approximation algorithm called Expansion was introduced by Bonizzoni, Vedova and Mauri in [26] which is of the same approximation ratio of $|\sum|$ but without the single-character restriction of LR. The time complexity of Expansion was $O(nl^4 \log l)$ which was further improved by Tsai and Hsu in [27] using minimum spanning trees. Another two approximation algorithms called Best Next for Maximal Available Symbols (BNMAS) and Enhanced Long Run (ELR) were proposed by Huang, Yang and Tseng in [28]. The time complexity of BANMAS is $O(|\sum|^2 nl + |\sum|^3 m)$ and that of ELR is $O(|\sum| nm)$. Shyu and Tsai compared

BNMAS with Expansion in [29] and showed that BNMAS is more accurate and faster than Expansion especially when the size of the alphabet is small and the number of the strings is large.

The other types of inexact algorithms are heuristic algorithms that do not normally provide a performance guarantee or approximation ratio. The term 'heuristic' here is used in a general sense and includes meta-heuristics [30] and hyper- heuristics [31] as well. The Best-Next heuristic was proposed in [32] and [33] as a simple heuristic method with the time complexity of $O(|\sum|nm)$. This algorithm was shown to be superior to the approximation algorithm LR on real datasets. A linear-time dynamic programming heuristic (DPH) algorithm was devised by Guenoche and Vitte in [34], which was further improved by Guenoche in [35]. Easton and Singireddy proposed the Time Horizon Specialized Branching (THSB) heuristic based on a large neighborhood search paradigm in [36], and showed that its performance is better than DPH. Ant colony optimization (ACO) was used to solve the LCS problem in [29] by Shyu and Tsai. The resulting algorithm was compared with Expansion and BNMAS on random and biological datasets obtained from NCBI, with positive results. A constructive Beam Search algorithm, called BS, for the LCS problem was proposed by Blum, Blesa and Ibanez in [37]. In their algorithm, two different greedy functions were used to evaluate and compare candidate solutions. BS algorithm is an extension of a former approach introduced by Blum and Blesa in [38], where they considered two configurations: one called low time was a fast version of the algorithm aimed at producing quick solutions and the other called high quality was intended for obtaining high quality solutions at the cost of extra computation. Blum, Blesa and Ibanez [37] compared BS algorithm with Expansion, Best-Next, DPH, THSB and ACO algorithms on extensive datasets that were previously used in [38], [36], [29] and exhibited that BS algorithm is superior to its predecessors in terms of both the solution quality and the running-time, proving it as the state-of-the-art. Subsequently, three algorithms were proposed based on BS algorithm: Deposition and Extention (DEA) in [39] by Ning, which is based on a post-process technique; MLCS-APP in [40] by Wang, Pan, Shang and Korkin, which is based on A^* search but with a limited number of leaves in the corresponding search tree; and IBS-LCS in [41] by Mousavi and Tabataba. Notably, although IBS-LCS was inspired by BS, it used a different heuristic function. Neither IBS-LCS nor MLCS-APP, as reported in [41], [40], could outperform BS algorithm over all the benchmarks used in [37], though they did so for some of the cases. In particular, IBS-LCS could not out-perform BS over the so-called BB benchmark [38], but it obtained better average results on the other benchmarks used in [37]. MLCS-APP was compared with BS on only the rat benchmark. DEA was only shown to be better than three primitive algorithms, namely LR, Expansion, and THSB; DEA was not compared with BS at all!

One of the most recent successful heuristic methods proposed for the problem is a hyper-heuristic algorithm (HH-LCS) proposed by Tabataba and Mousavi in [42]. HH-LCS is based on two heuristics functions, one of which was previously used in [41]. HH-LCS is compared with all the three algorithms BS, IBS-LCS, and MLCS-APP on all the benchmarks used in [37], [40] and two benchmarks used in [39] for fair comparisons. The HH-LCS algorithm outperforms all the other algorithms on all the benchmarks.

In this paper, we propose two heuristic based algorithms that repeatedly use dynamic programming to compute intermediate solutions. The two algorithms differ in the heuristics applied. We call these two algorithms RepeDPH andMRepeDPH[1]. We also incorporate a local search technique in our algorithms which is inspired by the ACO algorithm of Shyu and Tsai in [29]. Hence, we get two new versions of our algorithms, namely, RepeDPH-Local-Search and MRepeDPH-Local-Search. Our proposed algorithms are compared with HH-LCS [42], BS-high-quality [38], [37] and IBS-LCS [41] algorithms on extensive datasets, namely, the BB benchmark, ACO-random benchmark, ACO-rat benchmark and ACO-virus benchmark previously introduced and used in [38] and [29]. From the experimental results we find that RepeDPH and MRepeDPH show competitive performance and are able to provide a few better results than the current state-of-the-art. On the other hand, the proposed RepeDPH-Local-Search and MRepeDPH-Local-Search algorithms outperform the state-of-the-art algorithms on all benchmark datasets. We discussed the results in detail in Section VI.

II. Basic Notations

Let, s be a string of length m i.e., $|s|=m$. We use $s[j]$ to denote the jth character of s, where $1 \leq j \leq |s|$. We say that s' is a subsequence of s, denoted by $s' \prec s$, if we get s' by deleting zero or more symbols from s. The null string, i.e., the string of zero length is considered to be a subsequence of any string. Suppose, x is a string and $S = \{s_1, s_2, \ldots \ldots, s_n\}$ is a set of n strings over a finite alphabet Σ. We write $x \prec S$ if and only if $x \prec s_i$, for all $1 \leq i \leq n$. Given a set S as defined above as the input, the Longest Common Subsequence (LCS) problem aims to compute a sequence x of maximum length such that $x \prec S$. Sometimes we abuse the notation a bit and use $S[i]$ to denote s_i, in the set S. If all the input strings, i.e., $s_i \in S$, $1 \leq i \leq n$ are of the same length, we use m to denote their length; otherwise we define $m = max\{|s_1|, |s_2|, \ldots, |s_n|\}$. We further use s_{small} to denote smallest string of S.

III. Our First Algorithm: RepeDPH

We use standard dynamic programming solution for 2-LCS for determining LCS between two strings. The main idea builds up on a simple stochastic strategy as follows: we first compute an LCS $\mathcal{L}_1$ of two randomly chosen strings; then we compute an LCS $\mathcal{L}_2$ of $\mathcal{L}_1$ and a third string from S again chosen at random; and we continue until all the strings have considered. In what follows, we will be referring back to this algorithm as the base algorithm. In fact, this particular strategy can be used in different flavours with different and perhaps better results if we can propose a particular ordering of the strings to consider (rather than a random order). Now, the main task of our

[1]RepeDP stands for *Repeated Dynamic Programming*; H stands for *heuristics*; M stands for *Modified*.

algorithm is to employ an intelligent and useful heuristic to find an ordering in which the strings of S should be considered, rather than using a pure random strategy.

In what follows we will generally follow the following convention. We will use $LCS(s_1, s_2)$ to denote the length of an LCS of s_1 and s_2 and we will use the boldfaced version, i.e., $\mathbf{LCS}(s_1, s_2)$ to denote an actual LCS (i.e., not the length). This convention will be applied on similar notations unless otherwise specified. In our algorithm we introduce a stochastic element as follows. We define, $lcs_k = LCS(s_i, \mathbf{lcs}_{(k-1)})$, where i is a randomly selected integer in the range $1.....n$ without replacement and $1 < k \leq n$. For $k = 1$, we define, $lcs_1 = LCS(s_i, s_{small})$. Note that following our convention, we will use $lcs_k = \mathbf{LCS}(s_i, \mathbf{lcs}_{(k-1)})$, to denote the actual sequence and $lcs_k = LCS(s_i, \mathbf{lcs}_{(k-1)})$, to denote its length. We further define another term $lcs_{(j,k,i)}$ for $1 < k \leq n$ as follows:

$$lcs_{(j,k,i)} = LCS(s_i, \mathbf{lcs}_{(j,k-1,i)}) \qquad (1)$$

For k = 1, we have:

$$lcs_{(j,1,i)} = LCS(s_i, s_{small}) \qquad (2)$$

Notably, although the notation suggest a three dimensional table for $lcs_{(j,k,i)}$, as will be clear later, the computation actually requires a 2-D loop. We construct a matrix called lcs_{weight} of size $n \times (\beta + 1)$, where β is a pre-defined parameter of our algorithm. The matrix lcs_{weight} is computed according to the equation below:

$$lcs_{weight}(j,i) = \begin{cases} 0 & ; \text{if } j = 0 \\ lcs_{weight}(j-1,i) + \dfrac{lcs_{(j,k,i)}}{|S[i]|} & ; \text{Otherwise} \end{cases} \qquad (3)$$

The algorithm proceeds to fill in the matrix lcs_{weight} column by column as follows. It first identifies s_{small} from S. It runs a loop of j from 0 to β. For each value of j it runs another loop of k from 1 to n to fill up the column of lcs_{weight} for a particular value of j. The first column, i.e., $j = 0$, is initialized to zero. Then, for $j = 1$ to β, we do the following. We first choose a random i for this iteration. During this iteration, s_i will be the main player. When $k = 1$ (otherwise), we compute the LCS between s_i and s_{small} ~ $lcs_{(j,k-1,i)}$ and store it in $lcs_{(j,k,i)}$. Once $lcs_{(j,k,i)}$ is computed, we update the heuristic value in the lcs_{weight} matrix according to (3). Clearly, as soon as the loop for j (with the inner loop of k) ends, we get a filled up lcs_{weight} matrix. At this point we use $lcs_{weight}(\beta, i)$, $1 \leq i \leq n$ to be the heuristic value of a string s_i and this heuristic value is referred to as $sequence_weight(i)$. The rest of the algorithm is straightforward. We rearrange S as an ordered list by sorting the strings in S according to sequence_weight computed above and apply the base algorithm using this ordering.

IV. MREPEDPH: A MODIFICATION TO REPEDPH

In this section we discuss a modification of RepeDPH and propose a modified version of the algorithm that we call MRepeDPH. Inspired by the Ant Colony Optimization technique, we here introduce the concept of pheromone. We use the lcs_{weight} matrix of RepeDPH in conjunction with a newly introduced pheromone matrix of dimension $|S| \times (\beta + 1)$ as follows. We slightly change the definition of the lcs_{weight} matrix according to the following equation:

$$lcs_{weight}(j,i) = \begin{cases} lcs_{(j,k,i)} & ; if\ lcs_{(j,k,i)} \geq lcs_{weight}(j-1,i) \\ 0 & ; if\ j = 0 \\ lcs_{weight}(j-1,i) & ; Otherwise \end{cases} \qquad (4)$$

The pheoromone matrix is updated according to the following equation:

$$pheromone(j,i) = \begin{cases} pheromone(j-1,i) + 1 & ; if\ lcs_{(j,k,i)} \geq lcs_{weight}(j-1,i) \\ 0 & ; if\ j = 0 \\ pheromone(j-1,i) & ; Otherwise \end{cases} \qquad (5)$$

MRepeDPH algorithm proceeds almost exactly like RepeDPH algorithm as described above. However, Equation (4) is used in MRepeDHP instead of (3) for computing lcs_{matrix} and while computing $lcs_{matrix}(j,i)$ it also computes pheromone(j, i) using (5). Therefore, both lcs_{matrix} and pheromone tables are computed in the same loop simultaneously. Once the computation of lcs_{matrix} and pheromone are done, we compute the sequence_weight of each string in the set according to the following equation:

$$sequence_weight(i) = lcs_{weight}(\beta, i) \times pheromone(\beta, i) \qquad (6)$$

The rest of the algorithm is identical to RepeDPH: we rearrange S as an ordered list by sorting the strings in S according to sequence_weight computed above and apply the **base algorithm** using this ordering.

V. LOCAL SEARCH

In order to improve the solutions obtained by RepeDPH and MRepeDPH, we employ a local search procedure inspired by the algorithm of Shyu and Tsai in [29]. Here we briefly describe the main idea of the local search procedure. We first need to introduce the following notations. Suppose L is a solution return by our algorithm (RepeDPH or MRepeDPH) and according to our convention we say $L = |\mathbf{L}|$, i.e, the length of this solution is L. Now, we use L vectors LOC^l, $1 \leq l \leq L$. In each vector LOC^l we keep record of the index of the common character $\mathbf{L}[l]$ in each string s_i □ S. So, $LOC^l = \{ loc_1^l, loc_2^l, \ldots\ldots, loc_n^l \}$ where $s_i[loc_i^l] = L[l]$ and $s_i[loc_i^l]$ corresponds to the *l-th* common character of $\mathbf{L}$. For a string s_i, we also refer to the range $[loc_i^{l-1} \ldots loc_i^l - 1]$ as the *l-th* interval with respect to $\mathbf{L}$. To handle the boundary conditions, we conveniently assume that $\mathbf{L}[0]$ and $\mathbf{L}[L + 1]$ exist and are null characters.

Now we randomly select a string $s_i \in S$ and for all $1 \leq l \leq L + 1$ we do the following procedure. We discuss this focusing on the *l-th* interval of s_i with respect to **L**. Now suppose that the size of the *l-th* interval is h and the characters within this interval are $\alpha_i^1, \alpha_i^2, \ldots. \alpha_i^h$ in the original order. Now these h letters are the set of candidates in our local search procedure. Each of these characters, say α_i^u will be inserted into **L** between $\mathbf{L}[l-1]$ and $\mathbf{L}[l]$ only if the following two conditions hold for $1 \leq k \neq i \leq n$:

1. There exists position x_k in s_k such that $s_k[x_k] = \alpha_i^u$ subject to $s_k[x_k'] \neq \alpha_i^u$ for $loc_k^{(l-1)} < x_k' < x_k \leq loc_k^{(l-1)} + \delta$, where $\delta = \frac{|s_i|}{L}$
2. $\mathbf{L}[1 \ldots L] \prec s_k[x_k + 1 \ldots |s_k|]$

By incorporating this local search to RepeDPH and MRepeDPH, we get two new algorithms; we call these RepeDPH-Local-Search and MRepeDPH-Local-Search respectively.

VI. Experimental results and discussions

In this section, we present an experimental comparison of our proposed algorithms (RepeDPH, RepeDPH-Local-Search, MRepeDPH and MRepeDPH-Local-Search) with the best algorithms in the literature, namely, BS-high-quality [37], IBS-LCS [41], and HH-LCS [42]. We have run our algorithms on a personal computer running 32-bit Windows 7 with a Core(TM) i3-2310M CPU @ 2.10GHz having 2.00GB (1.81GB usable) RAM and 3MB L2 cache. We implemented our algorithm in C++ using CodeBlocks platform. In our experiments we have used four datasets used in [37],[41],[42], namely BB^2, ACO-random, ACO-rat and ACO-virus[3]. BB benchmark was first introduced in [38], and the other three datasets were previously used in [29]. For space constraints here we only report the result of the BB benchmark. The results of the other datasets are reported in the Appendix.

In our algorithms, β is used to denote the number of random orders of n sequences of S from $n!$ orders. It is computationally impractical to consider all $n!$ orders for large n. The value of n is varied in different experiments. For this, we have set $\beta = 10$ for all experiments. From above discussion, each value of β provides an approximate solution. We have picked the best solution from 10 independent runs, because our algorithms are stochastic. We also have shown the worst and average solution for each experiment. Table I compares the results of our algorithm with those reported in [37], [41] and [42] for the BB benchmark. The first two columns in the Table I show the alphabet size and the number of strings and the length of the input strings (all the strings of an instance are of the same length). The next six columns (third to eight) report the results for BS-high-quality as specified in [37], IBS-LCS in [41] and HH-LCS in [42]. The third, fifth and seventh columns show the average length of the returned LCS and the fourth, sixth and eighth columns show the average run time for BB benchmark. The next 24 columns show the respective values for our algorithms. The worst and average solution of our experiment is not as good as current state-of-the-art. For this, we focus only the best solution. The thirteenth and twenty-fifth columns show the length (average of best outcomes for BB benchmark) of the returned LCS of our proposed RepeDPH and MRepeDPH algorithms and fourteen and twenty-six columns show the run time. The nineteenth and thirty-one columns show LCS length after local search integration within RepeDPH and MRepeDPH algorithms and twentieth and thirty-two columns show the run time. The records in Table I are rounded up to one decimal digit. It can be seen Table I (column nineteen) that in 5 out of the 8 cases RepeDPH-Local-Search provides solutions of higher quality than HH-LCS and in 6 out of the 8 cases MRepeDPH-Local-Search (column thirty-one) provides solutions of higher quality than HH-LCS. In all the 8 cases RepeDPH-Local-Search and MRepeDPH-Local-Search provides solutions of higher quality than those of the BS-high-quality and IBS-LCS. In 2 out of 8 cases RepeDPH and MRepeDPH provides solutions of higher quality than HH-LCS and IBS-LCS and in 3 out of 8 cases RepeDPH and MRepeDPH provides solutions of higher quality than BS-high-quality. Our RepeDPH and MRepeDPH provide solution closer with HH-LCS, IBS-LCS and BS-high-quality. But they fail to provide average improvement in solution quality compared to these algorithms. In 8 out of 8 cases, RepeDPH-Local-Search and MRepeDPH-Local-Search provide higher quality solution than BS-high-quality and IBS-LCS. In 6 out of 8 cases MRepeDPH-Local-Search and also 5 out of 8 cases RepeDPH-Local-Search provide higher quality solution than HH-LCS. On average, our MRepeDPH-Local-Search algorithm achieves about 1.59% improvement in solution quality compared to HH- LCS, 4.89% improvement in solution quality compared to IBS-LCS, 3.49% improvement in solution quality compared to BS-high-quality. Similarly, our RepeDPH-Local-Search algorithm achieves about 1.37% average improvement in solution quality compared to HH-LCS, 5.15% average improvement in solution quality compared to IBS-LCS, 3.27% average improvement in solution quality compared to BS-high-quality.

[2]Received from S.R. Mousavi and originally used in Blum and Blesa (2007)

[3]Received from S.R. Mousavi; available on NCBI using the accession numbers specified at http://pstu.ac.bd/teacher/cse/chinmay/resources

TABLE I: Comparison the Longest Common Subsequence over BB dataset produced by RepeDPH, RepeDPH-Local-Search, MRepeDPH and MRepeDPH-Local-Search with BS-high-time, IBS-LCS and HH-LCS.

M	N	BS-high-quality		IBS-LCS		HH-LCS		RepeDPH						RepeDPH-Local-Search						MRepeDPH						MRepeDPH-Local-Search					
								Worst		Average		Best		Worst		Average		Best		Worst		Average		Best		Worst		Average		Best	
|Σ|=2																															
10	1000	648	13.6	672.1	1.1	672	1.0	640	1.0	648.1	1.0	659.7	1.0	646.8	1.5	661.4	1.5	673.1	1.5	637.7	0.9	646.1	0.9	658.3	0.9	648	2.9	660.0	1.4	673.7	2.8
100	1000	541	72.5	554.2	2.4	555.9	2.5	520	7.5	528.3	7.5	535.4	7.5	525.4	11.2	541.5	11.2	555.7	11.3	523.6	6.4	530.2	6.4	539.0	6.4	525.1	11.1	539.8	10.9	556.4	11.1
|Σ|=4																															
10	1000	534.7	18.1	543.7	1.5	543.2	1.4	510.9	1.0	521.2	1.0	534.1	1.0	524.8	1.5	535.9	1.5	547.9	1.5	512.8	0.8	519.6	0.8	529.9	0.8	522.9	1.5	534.7	1.5	547.5	1.5
100	1000	369.3	121.6	361.7	2.8	381.2	3.0	327	5.9	335.1	5.9	343.8	5.9	334.7	9.3	355.9	9.3	375.3	9.4	328.3	5.1	337.7	5.0	350.3	5.1	332.8	9.1	351.3	9.2	373.1	9.1
|Σ|=8																															
10	1000	462.3	21.2	461.9	2.2	462.4	2.1	443.3	0.9	454.5	0.9	464.6	0.9	452.7	1.4	466.7	1.4	479.4	1.4	446.1	0.8	456.1	0.7	467.6	0.7	456.8	1.4	465.0	1.4	475.7	1.4
100	1000	258.7	154.7	240.9	3.5	267.4	3.8	206.3	4.3	215.7	4.3	233.3	4.3	221.7	6.6	241.1	6.6	261.1	6.7	215.3	3.9	225.3	3.9	239.4	3.8	217.1	6.7	240.4	6.6	263.3	6.5
|Σ|=24																															
10	1000	385.6	37.4	385.6	4.4	385.6	4.4	396.2	0.9	407.3	0.9	417.8	0.8	403.1	1.3	414.7	1.3	424.8	1.3	395.2	0.7	406.9	0.7	418.8	0.7	402.9	1.3	413.9	1.3	425.9	1.3
100	1000	147.7	268.3	130.5	4.9	148.6	5.3	98	2.7	107.9	2.7	121.1	2.7	110.6	4.2	127.1	4.2	148.7	4.2	101.7	2.5	112.7	2.5	130.0	2.5	121.1	4.0	136.1	4.0	151.5	4.0
Quality improvement with respect to BS-high-quality												-3.15%						3.27%						-1.81%						3.49%	
Quality improvement with respect to IBS-LCS												-1.67%						5.16%						-0.21%						4.89%	
Quality improvement with respect to HH-LCS												-4.93%						1.38%						-3.72%						1.59%	

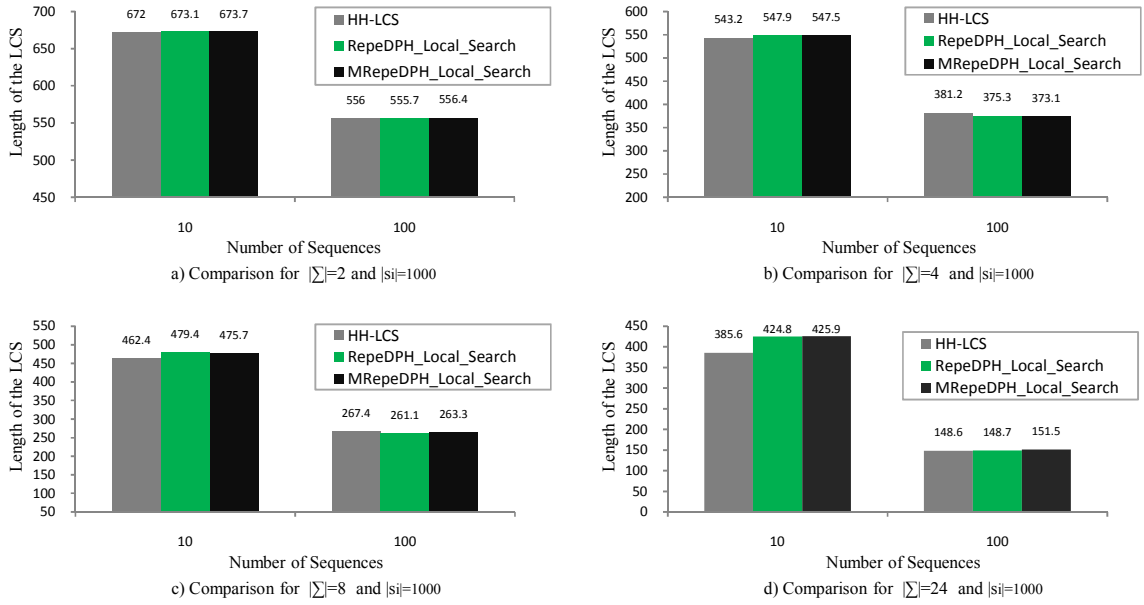

a) Comparison for |∑|=2 and |si|=1000

b) Comparison for |∑|=4 and |si|=1000

c) Comparison for |∑|=8 and |si|=1000

d) Comparison for |∑|=24 and |si|=1000

Figure 1. Comparison among HH-LCS, RepeDPH-Local-Search and MRepeDPH-Local-Search for BB dataset.

VII. CONCLUSION

In this paper, we have presented heuristic algorithms for the longest common subsequence problem for multiple sequences. The algorithms use dynamic programming (repeated) based on some heuristic functions. We also have incorporated local search to improve solutions. The proposed algorithm was compared with the state-of-the-art algorithms in the literature over several benchmarks and the results are found to be excellent.

REFERENCES

[1] Storer J. *Data compression: methods and theory*. Maryland: Computer Science Press, 1988.

[2] Aho A., Hopcroft J., Ullman J. *Data structure and algorithms*. Reading, MA: Addison-Wesley, 1983.

[3] Sankoff D., Kruskal J.B. *Time warps, string edits, and macromolecules: the theory and practice of sequence-comparison*. Reading, UK: Addison-Wesley, 1983.

[4] Sellis T. Multiple query optimization. *ACM Transactions on Database Systems*, 13(1):23–52, 1988.

[5] Banerjee A., Ghosh J. Clickstream clustering using weighted longest common subsequences. *In: Proceedings of the Web Mining Workshop at the 1st SIAM Conference on Data Mining*, pages 33–40, 2001.

[6] Brisk P., Sarrafzadeh M., Kaplan A. Area-efficient instruction set synthesis for reconfigurable system-on-chip design. *In: Proceedings of the 41st design automation conference. IEEE Press*, pages 395–400, 2004.

[7] Smith T.F., Waterman M.S. Identification of common molecular subsequences. *Journal of Molecular Biology*, 147:195–197, 1981.

[8] Jiang T., Lin G., Zhang K., Ma B. A general edit distance between RNA structures. *Journal of Computational Biology*, 9(2):371–388, 2002.

[9] Bafna V., Ravi R., Muthukrishnan S. Computing similarity between rna strings. *In: Proceedings of the sixth annual symposium on combinatorial pattern matching. Espoo, Finland*, pages 1–16, 1995.

[10] Maier D. The complexity of some problems on sub- sequences and supersequences. *Journal of the ACM*, 25:322–36, 1978.

[11] Gusfield D. Algorithms on strings, trees, and sequences. *Computer science and computational biology. Cambridge: Cambridge University Press*, 25, 1997.

[12] Hakata K., Imai H. The longest common subsequence problem for small alphabet size between many strings. *Lecture notes in computer science*, 650:469–78, 1992.

[13] Irving R.W., Fraser C.B. Two algorithms for the longest common subsequence of three (or more) strings. *Lecture notes in computer science*, 644:214–29, 1992.

[14] Garey M.R., Johnson D.S. *Computers and Intractability; A Guide to the Theory of NP-Completeness*. W. H. Freeman & Co. New York, NY, USA, 1990.

[15] Eppstein D., Galil Z., Italiano Giancarlo R. Sparse dynamic programming. ii. convex and concave cost functions. *Journal of the Association for Computing Machinery*, 39(3):546–67, 1992.

[16] Hirschberg D.S. A linear space algorithm for computing maximal common subsequences. *Communication of the Association for Computing Machinery*, 18(6):341–43, 1975.

[17] Wang Q., Korikin D., Shang Y. A fast multiple longest common subsequence (mlcs) algorithm. *IEEE Transactions on Knowledge and Data Engineering*, 2010.

[18] Singireddy A. Solving the longest common subsequence problem in bioinformatics. *Master, Kansas State University, KS, Manhattan.*, 2003.

[19] Hsu W.J., Du M.W. Computing a longest common subsequence for a set of strings. *BIT Numerical Mathematics*, 24(1):45–59, 1984.

[20] Easton T., Singireddy A. A specialized branching and fathoming technique for the longest common subsequence problem. *International Journal of Operations Research*, 4:98–104, 2007.

[21] Chen Y., Wan A., Liu W. A fast parallel algorithm for finding the longest common sequence of multiple biosequences. *BMC Bioinformatics*, 7(s4), 2006.

[22] Korkin D., Wang Q., Shang Y. An efficient parallel algorithm for the multiple longest common subsequence (MLCS) problem. *In: International Conference on Parallel Processing (ICPP)*, pages 354–363, 2008.

[23] Wang Q., Korkin D., Shang Y. Efficient dominant point algorithms for the multiple longest common subsequence (mlcs) problem. *In: International Joint Conference on Artificial Intelligence (IJCAI), Pasadena, CA, USA,*, pages 1494–1500, 2009.

[24] Chin F., Poon C. Performance analysis of some simple heuristics for computing longest common subsequences. *Algorithmica*, 12:293–311, 1994.

[25] Jiang T., Li M. On the approximation of shortestcom-monsupersequences and longest common subsequences. *SIAM Journal on Computing*, 24:1122–1139, 1995.

[26] Bonizzoni P., Vedova G.D., Mauri G. Experimenting an approximation algorithm for the lcs. *Discrete Applied Mathematics*, 110:13–24, 2001.

[27] Tsai Y.T., Hsu J.T. An approximation algorithm for multiple longest common subsequence problems. *In: Proceedings of the sixth world multi conference on systemics, cybernetics and informatics, SCI*, pages 456–60, 2002.

[28] Huang K.S., Yang C.B., Tseng K.T. Fast algorithms for finding the common subsequence of multiple sequences. *In: Proceedings of International Computer Symposium*, pages 90–95, 2004.

[29] Shyu S.J., Tsai C-Y. Finding the longest common subsequence for multiple biological sequences by ant colony optimization. *Computers and Operations Re- search*, 36:73–91, 2009.

[30] Blum C., Roli A. Metaheuristics in combinatorial optimization: Overview and conceptual comparison. *ACM*, 35:268–308, 2003.

[31] Burke E., Kendall G., Newall J., Hart E., Ross P., Schulenburg S. Hyperheuristics: an emerging direction in modern search technology. *In: Hillier, F.S.(Ed.), Handbook of Metaheuristics*, 57:457–474, 2003.

[32] Fraser C.B. Subsequences and supersequences of strings. *PhD thesis, University of Glasgow*, 1995.

[33] Johetla T. Smed J., Hakonen H., Raita T. An efficient heuristic for the lcs problem. *In: Third South American Workshop on String Processing, WSP96*, pages 126–140.

[34] Guenoche A., Vitte P. Longest common subsequence with many strings: exact and approximate methods. *Technique et Science Informatiques*, 14(7):897–915., 1995.

[35] Guenoche A. Supersequence of masks for oligo-chips. *Journal of Bioinformatics and Computational Biology*, 2(3):459–69, 2004.

[36] Easton T., Singireddy A. A large neighborhood search heuristic for the longest common subsequence problem. *Journal of Heuristics*, 14(3):271–83, 2008.

[37] Blum C., Blesa M.J., Ibanez M. Beam search for the longest common subsequence problem. *Computers and Operations Research*, 36(12):3178–86, 2009.

[38] Blum C., Blesa M. Probabilistic beam search for the longest common subsequence problem. *In: Stutzle T, Birattari M, Hoos HH, editors. Proceedings of SLS 2007engineering stochastic local search algorithms. Lecture notes in computer science*, 4638(12):150–61, 2007.

[39] Ning K. Deposition and extension approach to find longest common subsequence for thousands of long sequences. *Computational Biology and Chemistry*, 34(12):149–157, 2010.

[40] Wang Q. Pan M., Shang Y., Korkin D. A fast heuristic search algorithm for finding the longest common subsequence of multiple strings. *In: Conference on Artificial Intelligence (AAAI), Atlanta, GA, USA,*, pages 1287– 1292, 2010.

[41] Mousavi S.R., Tabataba F. An improved algorithm for the longest common subsequence problem. *Computers and Operations Research*, 39:512–520, 2012.

[42] Tabataba F., Mousavi S.R. A hyper-heuristic for the longest common subsequence problem. *Computational Biology and Chemistry*, 36:42–54, 2012.

APPENDIX

The results of our algorithms on the ACO-random, ACO-rat, and ACO-virus datasets are presented and compared with the

state-of-the-art in tables I to IV respectively. The definitions for the columns of these tables are the same as those of Table I. It can be seen from best column in Table II, in none of the 20 cases, RepeDPH and MRepeDPH provide higher quality solution than BS-high-quality, IBS-LCS, HH-LCS but provide very closer result to current state-of-the-art. MRepeDPH-Local-Search provides higher quality solution in 20 cases for BS-high-quality, 16 cases for IBS-LCS and 15 cases for HH-LCS out of 20 cases. On the other hand, RepeDPH-Local-Search provides higher quality solution in 18 cases for BS-high-quality, 16 cases for IBS-LCS and 15 cases for HH-LCS out of 20 cases. MRepeDPH-Local-Search algorithm achieves average improvement about 2.40% than BS-high-quality, 0.24% than IBS-LCS and 0.15% than HH-LCS. And RepeDPH-Local-Search algorithm achieves average improvement about 2.77% than BS-high-quality, 0.62% than IBS-LCS and 0.52% than HH-LCS. It can be seen in Table III, RepeDPH and MRepeDPH provide very closer result to current state-of-the-art. In 18 out of 20 cases and 16 out of 20 cases the MRepeDPH-Local-Search and RepeDPH-Local-Search provide better result respectively than current state-of-the-art. RepeDPH-Local-Search algorithm achieves average improvement about 3.80% than Bs-high-quality, 2.44% than IBS-LCS and 1.14% than HH-LCS. And MRepeDPH-Local-Search algorithm achieves average improvement about 4.55% than BS-high-quality, 2.93% than IBS-LCS and 1.89% than HH-LCS.

From Table IV, RepeDPH-Local-Search provides better result than BS-high-quality, IBS-LCS and HH-LCS for 18 cases, 17 cases and 16 cases out of 20 cases respectively. And in 20 out of 20 cases, MRepeDPH-Local-Search provides better result than BS-high-quality, IBS-LCS and HH-LCS. MRepeDPH-Local-Search algorithm achieves average improvement about 5.13% than BS-high-quality, 1.56% than IBS-LCS and 1.67% than HH-LCS. RepeDPH-Local-Search algorithm achieves average improvement about 4.00% than Bs- high-quality, 0.53% than IBS-LCS and 0.59% than HH-LCS.

In summary, there are 68 individual cases in tables I to IV. In cumulative (both RepeDPH-Local-Search and MRepeDPH-Local-Search) result analysis, our proposed algorithms provide better result in 6 out of 8 cases for BB benchmarks, in 19 out of 20 cases for ACO-random, in 19 out of 20 cases for ACO-rat and in 20 out of 20 cases for ACO-virus. In aggregation, in 94.12% cases out of 68 cases our proposed algorithms provide better result than current state-of-the-art. From above experiments, it reveals that the required computation time of our algorithms is based on not only string length but also intermediate LCS length. There might be produced shorter intermediate LCS, and any short length intermediate LCS shrink the dynamic programming domain. From tables II to IV, it reveals that our algorithms require comparatively low time for protein sequence because the instances of protein sequences produce small LCS.

TABLE II: Comparison the Longest Common Subsequence over ACO-random produced by RepeDPH, RepeDPH-Local-Search, MRepeDPH and MRepeDPH-Local-Search with BS-high-time, IBS-LCS and HH-LCS.

M	N	BS-high-quality		IBS-LCS		HH-LCS		RepeDPH						RepeDPH-Local-Search						MRepeDPH						MRepeDPH-Local-Search					
								Worst		Average		Best		Worst		Average		Best		Worst		Average		Best		Worst		Average		Best	
|Σ|=4																															
10	600	211	9.8	218	0.4	221	0.5	185	0.3	194.3	0.3	207	0.3	191	0.4	206.4	0.4	221	0.4	186	0.3	194.2	0.3	201	0.2	189	0.4	204.1	0.4	222	0.4
15	600	194	13.2	203	0.5	202	0.4	169	0.4	174.2	0.4	186	0.4	172	0.6	187.2	0.6	203	0.6	169	0.3	175.2	0.3	184	0.3	173	0.6	188.2	0.6	200	0.6
20	600	184	14.9	191	0.5	191	0.5	161	0.5	163.9	0.5	167	0.5	166	0.7	178.7	0.7	189	0.7	161	0.4	165.8	0.4	175	0.4	163	0.7	175.7	0.7	191	0.7
25	600	179	15.8	185	0.5	185	0.5	157	0.7	160	0.7	165	0.6	162	0.8	175.2	0.8	184	0.8	156	0.5	164.4	0.5	177	0.4	162	0.8	172.8	0.8	184	0.8
40	600	167	21	172	0.7	172	0.7	149	0.8	151.8	0.8	159	0.8	152	1.2	162.3	1.2	170	1.1	149	0.6	152.4	0.6	159	0.6	152	1.2	163	1.2	174	1.2
60	600	161	27.6	165	0.8	165	0.9	143	1.0	145.4	1.0	149	1.0	147	1.6	156.5	1.6	165	1.6	143	0.9	146	0.9	152	0.9	146	1. 6	153.5	1.6	166	1.6
80	600	156	33.5	161	1.0	161	1.0	139	1.3	142.9	1.3	145	1.3	148	2.1	155.5	2.1	163	2.1	142	1.1	143.8	1.1	149	1.2	141	2.1	150.7	2.0	159	2.1
100	600	154	40.3	158	1.2	158	1.2	138	1.6	140.3	1.6	142	1.6	142	2.5	151	2.5	159	2.5	138	1.4	142.4	1.4	149	1.4	140	2.4	149.5	2.4	158	2.4
150	600	148	56.4	151	1.5	151	1.7	136	2.3	137	2.2	139	2.2	135	3.5	146.8	3.5	152	3.5	135	1.9	137.1	1.9	140	1.9	137	3.4	144.6	3.4	151	3.4
200	600	146	74.3	150	2.1	150	2.0	134	2.9	136.7	2.9	139	2.9	138	4.4	146.5	4.4	151	4.4	134	2.5	137.1	2.5	142	2.5	137	4.4	144.6	4.5	150	4.5
|Σ|=20																															
10	600	61	33.3	61	0.5	61	0.5	44	0.2	46.8	0.2	49	0.2	48	0.3	52.9	0.2	59	0.2	44	0.1	49.2	0.1	56	0.1	45	0.2	53.9	0.2	63	0.2
15	600	51	37.6	51	0.4	52	0.5	36	0.1	37.5	0.1	39	0.1	38	0.2	43.3	0.2	49	0.2	35	0.1	36.7	0.1	39	0.1	38	0.3	42.7	0.3	52	0.3
20	600	47	39.5	47	0.5	47	0.5	31	0.2	33.5	0.2	36	0.2	34	0.3	40.2	0.3	48	0.3	32	0.1	34.1	0.1	38	0.1	35	0.3	39.3	0.3	47	0.2
25	600	43	39.5	44	0.5	44	0.5	31	0.2	32.3	0.2	35	0.2	32	0.3	37.5	0.3	45	0.3	30	0.2	32.7	0.2	36	0.1	31	0.3	36.7	0.3	45	0.3
40	600	37	43.2	38	0.6	38	0.6	26	0.3	28.2	0.3	30	0.2	30	0.3	34.1	0.3	38	0.3	27	0.2	29.2	0.2	32	0.2	29	0.3	31.9	0.3	37	0.3
60	600	34	46.5	35	0.8	35	0.8	26	0.3	27	0.3	29	0.3	27	0.4	31.3	0.4	35	0.4	26	0.2	27.7	0.2	30	0.2	28	0.4	30.8	0.4	35	0.4
80	600	32	53.2	32	1.0	33	0.9	25	0.3	25.9	0.3	27	0.3	27	0.5	29.8	0.5	33	0.6	23	0.3	25.1	0.3	28	0.3	26	0.5	28.1	0.5	32	0.5
100	600	31	59.2	31	1.2	31	1.2	24	0.5	25.1	0.4	26	0.4	26	0.6	29.1	0.6	32	0.6	24	0.3	25.6	0.3	28	0.3	27	0.6	28.5	0.6	31	0.6
150	600	29	75.6	29	1.5	29	1.4	23	0.6	23.8	0.6	25	0.6	25	0.8	28.5	0.8	30	0.8	23	0.4	24.6	0.4	27	0.4	24	0.8	26.5	0.8	29	0.8
200	600	27	98	28	1.9	27	1.8	22	0.6	23.5	0.6	25	0.6	24	1.2	27	1.1	29	1.1	22	0.5	23.2	0.5	24	0.5	24	1.0	26	1.0	28	1.0
Quality improvement with respect to BS-high-quality												-11.64%						2.77%						-8.74%						2.4%	
Quality improvement with respect to IBS-LCS												-13.55%						0.62%						-10.88%						0.24%	
Quality improvement with respect to HH-LCS												-13.62%						0.52%						-11.0%						0.15%	

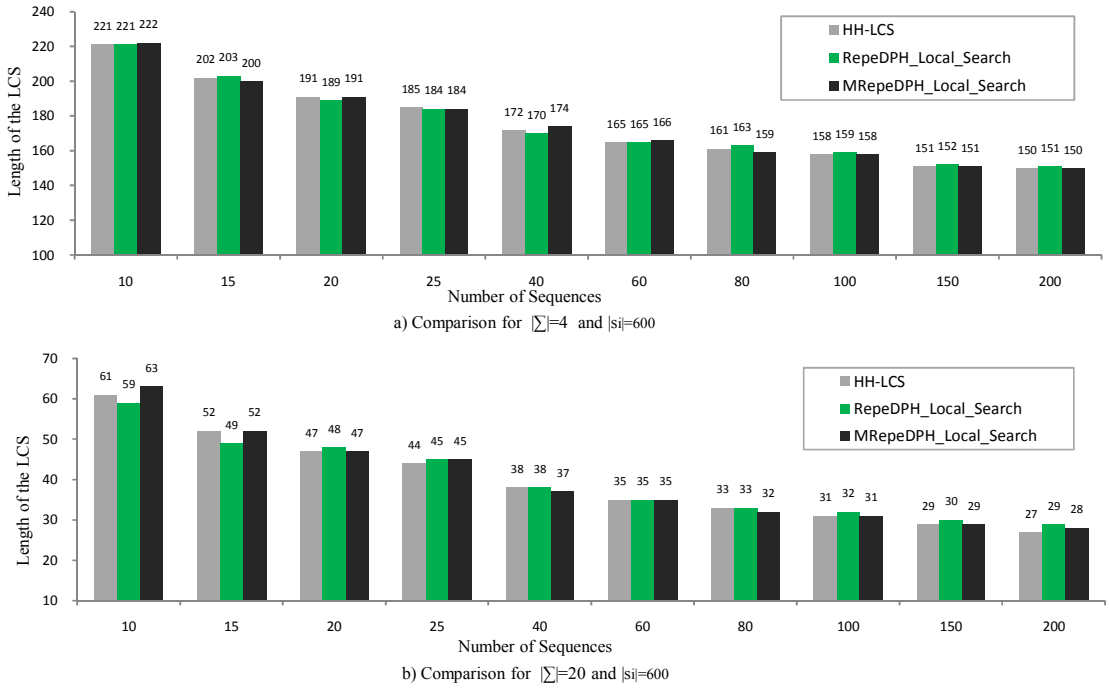

Figure 2. Comparison among HH-LCS, RepeDPH-Local-Search and MRepeDPH-Local-Search for ACO-random dataset.

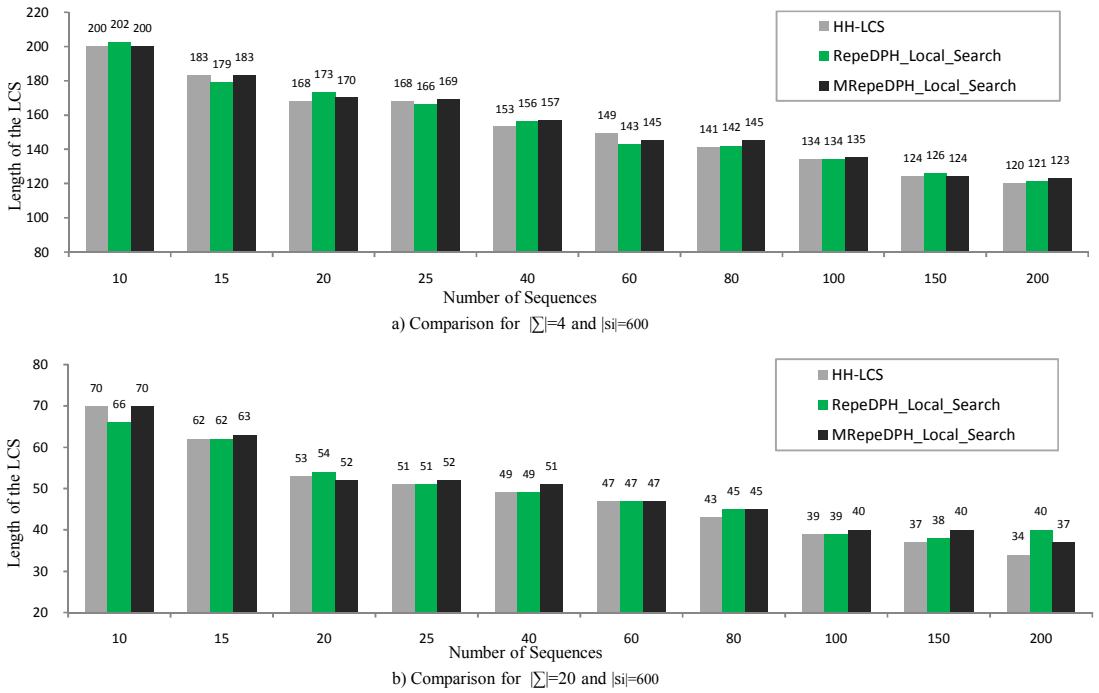

Figure 3. Comparison among HH-LCS, RepeDPH-Local-Search and MRepeDPH-Local-Search for ACO-rat dataset.

TABLE III: Comparison the Longest Common Subsequence over ACO-rat produced by RepeDPH, RepeDPH-Local-Search, MRepeDPH and MRepeDPH-Local-Search with BS-high-time, IBS-LCS and HH-LCS.

M	N	BS-high-quality		IBS-LCS		HH-LCS		RepeDPH						RepeDPH-Local-Search						MRepeDPH						MRepeDPH-Local-Search					
								Worst		Average		Best		Worst		Average		Best		Worst		Average		Best		Worst		Average		Best	
|Σ|=4																															
10	600	191	9.7	199	0.4	200	0.4	172	0.3	179	0.3	194	0.3	177	0.5	188.4	0.5	202	0.5	172	0.3	177.7	0.3	195	0.3	179	0.4	189.3	0.4	200	0.4
15	600	173	12.3	182	0.4	183	0.4	153	0.5	158.4	0.5	162	0.4	164	0.5	169	0.6	179	0.5	156	0.3	161.8	0.3	170	0.3	161	0.5	171.2	0.5	183	0.5
20	600	163	12.6	168	0.4	168	0.4	155	0.4	157.9	0.4	162	0.4	156	0.7	164.8	0.7	173	0.6	150	0.4	156.5	0.4	166	0.4	154	0.6	161.5	0.6	170	0.6
25	600	162	15.8	166	0.4	168	0.5	146	0.6	148.8	0.6	154	0.6	149	0.8	158.2	0.8	166	0.8	144	0.4	148	0.4	151	0.4	149	0.8	157.8	0.8	169	0.8
40	600	146	19.4	146	0.5	153	0.5	134	0.7	139	0.7	146	0.7	143	1.1	149.8	1.1	156	1.1	133	0.6	139.5	0.6	144	0.6	142	1. 1	148.6	1.1	157	1.1
60	600	144	26.7	147	0.7	149	0.7	129	1.0	131.6	1.0	134	0.9	132	1.5	137	1.5	143	1.4	127	0.8	130.4	0.8	134	0.8	125	1.5	134.8	1.5	145	1.5
80	600	135	31.8	141	0.9	141	0.9	122	1.3	126	1.2	131	1.2	133	2.0	136.1	1.9	142	2.0	121	1.0	124.7	1.0	127	0.9	126	1.9	133.3	1.9	145	1.9
100	600	132	38.5	132	1.0	134	1.0	115	1.4	120.9	1.4	125	1.4	120	2.3	127	2.2	134	2.1	117	1.4	120.3	1.3	123	1.3	120	2.2	127	2.2	135	2.2
150	600	121	51.1	124	1.3	124	1.4	113	1.9	118.6	1.9	122	1.9	118	3.0	122.4	3.0	126	3.1	112	1.7	117	1.7	124	1.6	114	2.9	119.5	2.9	124	2.8
200	600	121	69.1	120	1.6	120	1.7	107	2.4	114.8	2.4	120	2.4	108	3.6	116.4	3.7	121	3.8	109	2.1	114.4	2.2	120	2.2	110	3.8	117.4	3.9	123	3.9
|Σ|=20																															
10	600	69	27.4	70	0.5	70	0.7	51	0.1	55.2	0.1	61	0.1	55	0.2	59	0.2	66	0.2	52	0.1	57.7	0.1	66	0.1	54	0.3	63.5	0.3	70	0.3
15	600	60	36.7	61	0.5	62	0.5	45	0.2	48.5	0.2	51	0.2	49	0.2	53.8	0.2	62	0.2	47	0.1	49.8	0.1	55	0.1	49	0.3	55.9	0.3	63	0.3
20	600	51	34.4	53	0.5	53	0.5	36	0.3	41.2	0.3	45	0.3	41	0.3	47.9	0.3	54	0.3	38	0.2	41.3	0.1	48	0.2	43	0.3	46.4	0.3	52	0.3
25	600	51	39	50	0.5	51	0.5	36	0.3	40	0.3	43	0.3	40	0.3	43.9	0.3	51	0.3	35	0.2	38.8	0.2	41	0.2	43	0.3	46.2	0.3	52	0.3
40	600	49	47.4	49	0.6	49	0.6	34	0.3	39	0.3	42	0.3	36	0.4	41.9	0.4	49	0.4	36	0.2	38.2	0.2	40	0.2	39	0.4	45.6	0.4	51	0.4
60	600	46	60.3	46	0.8	47	0.8	33	0.4	38.2	0.3	42	0.3	33	0.5	41.1	0.5	47	0.5	34	0.3	36.8	0.3	40	0.3	37	0.6	42.5	0.6	47	0.6
80	600	43	64.4	43	1.0	43	1.1	36	0.4	39.6	0.5	45	0.5	39	0.7	42.1	0.7	45	0.7	37	0.4	40.5	0.4	44	0.4	33	0.6	39.4	0.6	45	0.6
100	600	38	64.8	39	1.1	39	1.0	29	0.5	32.3	0.5	35	0.5	29	0.7	33.6	0.7	39	0.7	23	0.4	31.4	0.4	37	0.4	28	0.8	34.2	0.8	40	0.7
150	600	36	77.8	36	1.3	37	1.3	26	0.6	31.1	0.6	35	0.6	28	1.0	34.4	1.0	38	1.0	23	0.5	30.1	0.5	35	0.5	28	1.0	32.3	1.0	40	1.0
200	600	33	101	32	1.7	34	1.7	27	0. 8	30.5	0.8	35	0.8	30	1.4	35.6	1.4	40	1.3	29	0.7	32.8	0.7	36	0.7	31	1.4	34.4	1.4	37	1.5
Quality improvement with respect to BS-high-quality												-5.13%						3.8%						-4.38%						4.55%	
Quality improvement with respect to IBS-LCS												-6.37%						2.44%						-5.77%						2.93%	
Quality improvement with respect to HH-LCS												-7.54%						1.14%						-7.0%						1.89%	

TABLE IV: Comparison the Longest Common Subsequence over ACO-virus produced by RepeDPH, RepeDPH-Local-Search, MRepeDPH and MRepeDPH-Local-Search with BS-high-time, IBS-LCS and HH-LCS.

M	N	BS-high-quality		IBS-LCS		HH-LCS		RepeDPH						RepeDPH-Local-Search						MRepeDPH						MRepeDPH-Local-Search					
								Worst		Average		Best		Worst		Average		Best		Worst		Average		Best		Worst		Average		Best	
|Σ|=4																															
10	600	212	11.6	225	0.5	225	0.5	196	0.3	203.1	0.3	212	0.3	198	0.5	213	0.5	226	0.5	195	0.2	204.9	0.3	217	0.2	206	0.5	219.9	0.4	231	0.4
15	600	193	15.4	203	0.5	202	0.4	174	0.4	177.1	0.4	182	0.4	177	0.6	184.5	0.6	200	0.6	172	0.3	179.2	0.3	192	0.3	177	0.6	186.5	0.6	203	0.6
20	600	181	17.2	189	0.5	189	0.5	162	0.5	170.7	0.5	177	0.5	177	0.7	182.7	0.7	189	0.7	162	0.5	170.7	0.5	187	0.5	171	0.8	181.3	0.8	193	0.8
25	600	185	17.9	193	0.5	193	0.6	168	0.6	172.3	0.6	181	0.6	171	0.8	181.3	0.8	193	0.8	164	0.4	172.2	0.4	187	0.5	171	0.8	181.3	0.8	193	0.8
40	600	162	21.9	168	0.6	165	0.6	147	0.8	156.7	0.8	166	0.8	156	1.2	163.3	1.2	170	1.2	150	0.6	157	0.6	166	0.6	150	1.2	160.9	1.2	171	1.2
60	600	158	29.1	165	0.8	164	0.8	143	1.0	150.3	1.1	159	1.1	153	1.5	158	1.5	166	1.5	145	0.9	149.6	0.9	156	0.9	148	1.7	157.4	1.6	165	1.7
80	600	153	36	158	0.9	158	1.0	135	1.3	144.6	1.3	150	1.3	146	2.1	154.6	2.1	163	2.1	140	1.2	146	1.4	157	1.9	146	2.9	154.9	2.5	161	2.1
100	600	150	43.9	158	1.2	158	1.2	135	1.6	144.2	1.6	151	1.6	144	2.4	152.9	2.4	164	2.5	144	1.3	149.8	1.3	158	1.3	142	2.4	154	2.5	163	2.5
150	600	148	64.5	156	1.7	156	1.7	135	2.2	138.5	2.3	144	2.3	136	3.4	143.4	3.4	153	3.4	131	2.0	137	1.9	148	2.0	137	3.4	146.5	3.4	156	3.3
200	600	145	84.5	154	2.1	154	2.1	134	2.9	136.7	2.9	141	2.9	137	4.5	143.9	4.5	154	4.5	132	2.6	137.5	2.5	145	2.5	142	4.5	149.4	4.4	157	4.4
|Σ|=20																															
10	600	75	27.2	75	0.5	75	0.6	56	0.1	58.9	0.2	65	0.1	65	0.2	69.3	0.2	75	0.2	57	0.1	61	0.1	69	0.1	65	0.2	69.3	0.2	75	0.2
15	600	63	38.6	63	0.5	63	0.5	46	0.2	49.3	0.2	51	0.2	49	0.3	54.3	0.3	63	0.3	47	0.2	50.1	0.2	58	0.1	49	0.2	57	0.2	64	0.2
20	600	57	40.3	60	0.5	60	0.5	41	0.2	43.7	0.3	47	0.2	45	0.3	50.7	0.3	59	0.3	41	0.1	45.7	0.2	54	0.1	45	0.3	51.4	0.3	60	0.3
25	600	53	38.9	54	0.5	55	0.5	39	0.2	41.1	0.2	43	0.2	42	0.4	46.5	0.3	54	0.3	39	0.2	41.1	0.2	49	0.2	40	0.3	47	0.3	55	0.3
40	600	49	48.4	49	0.7	49	0.7	34	0.3	37.2	0.3	39	0.3	37	0.5	43.6	0.5	50	0.5	36	0.2	38.5	0.2	46	0.2	39	0.4	43.5	0.4	50	0.4
60	600	45	56.1	47	1.0	47	1.0	33	0.4	35.7	0.4	38	0.4	35	0.5	40.8	0.5	48	0.5	34	0.3	37.1	0.4	45	0.3	36	0.5	41.7	0.5	50	0.5
80	600	44	67.4	45	1.1	46	1.2	31	0.4	33.4	0.4	40	0.4	34	0.6	38.4	0.6	46	0.6	31	0.4	35.7	0.4	42	0.4	35	0.6	39.5	0.5	46	0.6
100	600	43	74.2	44	1.5	44	1.3	30	0.5	32.7	0.5	35	0.5	31	0.7	35.9	0.7	44	0.7	32	0.3	36.9	0.4	43	0.3	33	0.7	38.7	94.1	44	0.7
150	600	44	108	45	1.8	45	1.9	28	0.7	32.9	0.7	35	0.7	29	1.1	36.9	1.1	45	1.1	30	0.4	37	0.4	43	0.4	34	2.0	39.8	2.0	46	2.0
200	600	43	140	44	2.2	43	2.1	28	0.9	32.5	0.9	36	0.9	29	1.5	36.5	1.4	44	1.4	27	0.4	35. 7	0.4	44	0.4	32	2.5	39.8	2.6	45	2.7
Quality improvement with respect to BS-high-quality												-9.15 %						4 %						-1.2 %						5.13 %	
Quality improvement with respect to IBS-LCS												-12.25 %						0.53 %						-4.66 %						1.56 %	
Quality improvement with respect to HH-LCS												-12.19 %						0.59 %						-4.6 %						1.67 %	

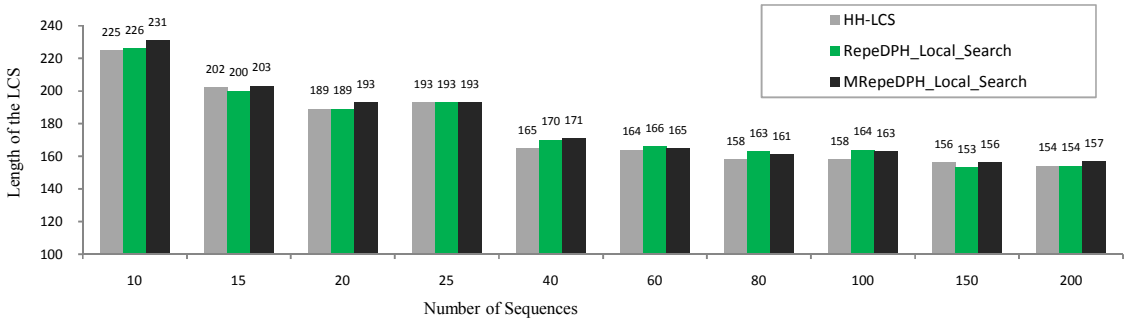

a) Comparison for |∑|=4 and |si|=600

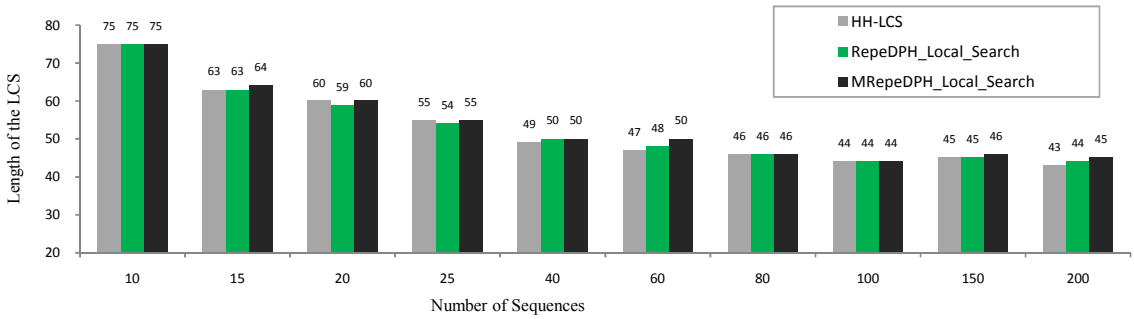

b) Comparison for |∑|=20 and |si|=600

Figure 4. Comparison among HH-LCS, RepeDPH-Local-Search and MRepeDPH-Local-Search for ACO-virus dataset.

An Efficient Approach for Designing FIR Low-pass Filter and Its Application

Hrishi Rakshit
Electrical and Electronics Engineering
Chittagong University of Engineering & Technology
Chittagong, Bangladesh
rishirok@gmail.com

Muhammad Ahsan Ullah
Electrical and Electronics Engineering
Chittagong University of Engineering & Technology
Chittagong, Bangladesh
ahsan_cuet@yahoo.com

***Abstract*—In this paper, an adjustable window function, based on combination of tangent hyperbolic function and a weighted cosine series, is proposed to design an FIR filter. The proposed window has only one adjustable parameter "r". By varying this parameter, it is possible to change the spectral characteristics of the filter. The performance of the proposed window is compared with Gaussian and Kaiser windows. The proposed window has slightly larger main–lobe width compare to the commonly used Gaussian and Kaiser windows, while featuring 19.71 dB and 8.29 dB smaller ripple ratios respectively. Moreover the side-lobe roll-off ratio of the proposed window is almost 115.03 dB and 14.95 dB better than the Gaussian and Kaiser windows respectively. Simulation results show that the filter designed by the proposed window yields 34.39 dB smaller ripple ratio than Kaiser window. Further, the low-pass filter, designed by the proposed method results 7.3766 times and 3.65 times better side-lobe roll-off ratios than those of Gaussian and Kaiser windows respectively. This paper also highlights an application of the proposed method in the area of eliminating noise from corrupted Audio signal.**

***Index Terms*— Gaussian Window, Kaiser Window, Main-lobe Width, Ripple Ratio and Side-lobe Roll-off Ratio.**

I. Introduction

The impulse response of an ideal filter is infinitely long. The most straight forward way to make the response finite, is to truncate the ideal response. If $h_d(n)$ is the response of an ideal filter, the simplest way to obtain a causal finite impulse response is to multiply the $h_d(n)$ with a finite window function w(n). In engineering term, a window is a finite array, consists of coefficients to satisfy the desirable requirements [1]. In general, the window function can be defined as

$$w[n] = \begin{cases} f(n), & 0 \le n \le N \\ 0, & otherwise \end{cases} \quad (1)$$

and the impulse response of the system is given by

$$h[n] = h_d[n]w[n] \quad (2)$$

Therefore the Fourier transform h[n], denoted by $H(e^{j\omega})$, is the periodic convolution of the $H_d(e^{j\omega})$, with the Fourier transform of w[n], denoted by $W(e^{j\omega})$. The important spectral characteristics of a window function are i) main-lobe width ii) ripple ratio and iii) its side-lobe roll-off ratio. There are two desirable specifications for any window function. They are smaller main-lobe width and the smaller ripple ratio. However these two requirements are contradictory [2]. The simplest window is the rectangular window [2].It has a very sharp transition band. However its ripple ratio is highest among the all commonly used windows. Gaussian and Kaiser windows are the adjustable functions. So by changing the adjustable parameter, one can trade-off between the main-lobe width and the ripple ratio. In many applications like FIR filters, FFT, signal processing and measurements, we are required -45 dB or less side lobe peaks [3]. Kaiser window has the computational complexity due to the calculation of Bessel functions [4]. So there has been a great interest to design a new window to meet the desire specifications for different applications.

In this paper, a novel adjustable window is proposed which has only two parameters (one is length of the window and another is the additional parameter "r") that control the spectral characteristics of the window. The proposed window is very simple as it does not involve any Bessel function like the Kaiser window. The proposed window yields better spectral characteristics than Gaussian window. The ripple ratio and the side-lobe roll-off ratio of the proposed window are respectively 19.71 dB and 115.03 dB better than Gaussian window. Our simulation result shows that the ripple ratio and the side-lobe rill-off ratio of the proposed window are 8.29 dB and 14.95 dB better respectively than what can be obtained using Kaiser window. Filter designed using the proposed window results 34.39 dB better ripple ratio than Kaiser window. Moreover, the side-lobe roll-off ratio of the proposed window based FIR low-pass filter is 7.3766 times and 3.65 times greater than the above named windows based filters respectively. The filter designed by the proposed method has been used to remove noise from corrupted audio signal. The experimental results ensure that the proposed filter performs better performance than Kaiser filter to eliminate noise from audio signal.

978-1-4673-9257-0/15/$31.00 ©2015 IEEE

Section II defines the three major spectral characteristics of a window function. Section III introduces the new window and also explains its spectral behaviors under various conditions. Section IV compares the performances of the proposed window with Gaussian and Kaiser windows. Section V describes the performance analysis of a FIR low-pass filter using the proposed windowing method. Section VI represents the efficiency of the proposed FIR low-pass filter in eliminating noise from the corrupted audio signal. Section VII shows the normalized frequency response of the filtered audio signal. Section VIII provides concluding remarks.

II. Spectral properties of Windows

A window, w(nT), with a length of N is a time domain function which is nonzero co-efficient for n<=|(N-1)/2| and zero for otherwise. A typical window has a normalized amplitude spectrum in dB as shown in Figure 1.

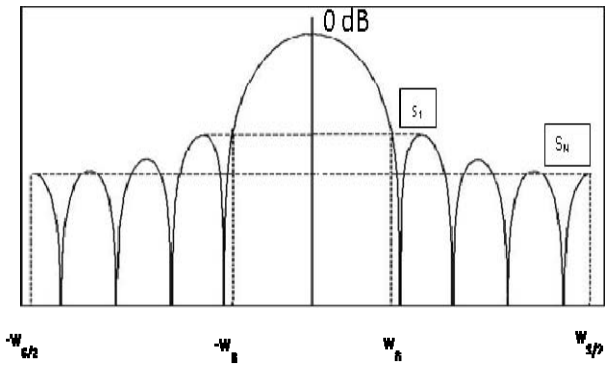

Fig 1: A typical window's normalized amplitude spectrum

Normalized spectrum in Fig 1 is obtained by following equation

$$\left|W_n(e^{j\omega T})\right| = 20\log_{10}(\left|A(w)\right|/\left|A(w)\right|_{\max}) \quad (3)$$

The spectral characteristics which determine the windows performance are the main-lobe width(w_M), the ripple ratio (R) and the side-lobe roll-off ratio(S). From the Fig 1, these parameters can be defined as

W_M= Two times half of the main-lobe width=$2w_R$.

R= (Maximum side-lobe amplitude in dB) – (Main-lobe amplitude in dB) = S_1.

S= (Maximum side-lobe amplitude in dB) – (Minimum side-lobe amplitude in dB) = S_1-S_N.

III. Proposed Window

The new proposed window is a combination of tan hyperbolic function and a weighted cosine series. The tan hyperbolic function is given by the following equation

$$y_1 = \left[\tanh\left\{\frac{n-\frac{(N-1)}{2}+\cosh^2(\alpha)}{B}\right\} - \tanh\left\{\frac{n-\frac{(N-1)}{2}-\cosh^2(\alpha)}{B}\right\}\right] \quad (4)$$

The weighted cosine function is expressed as follows

$$y_2 = 0.375 - 0.5\cos\left\{\frac{2\pi l}{N-1}\right\} + 0.125\cos\left\{\frac{4\pi l}{N-1}\right\} \quad (5)$$

Where N is the length of the window, α and B are the constants. Here n is the number of samples. Here the symbol l =0,1,2,3,……(N-1).

These two equations are combined in the following way.

$$w(n) = (y_1 * y_2)^{\gamma}, \quad where, \gamma = r^{(\frac{1}{5})} \quad (6)$$

and "*" means multiplication.

Here r is a variable which controls the shape and frequency response of the window. So "r" can be named as controlling or adjustable parameter of the window. In mathematical term, the window can be expressed as

$$w(n) = \begin{cases} (y_1 * y_2)^{\gamma}, & n \le 0 \le N \\ 0, & otherwise \end{cases} \quad (7)$$

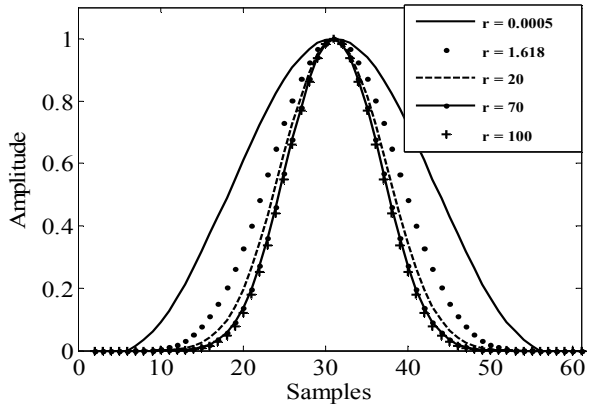

Fig 2: Shapes of the proposed windows with different values of r.

From the Fig 2 is has been seen that the shape of the window varies as the value of the adjusting parameter r changes. When r=0.0005 and r =100, the shape of the window is the widest and the narrowest respectively among the other values of r shown in the Fig 2. The width of the window gets narrower as the value of the controlling parameter "r" gets bigger.

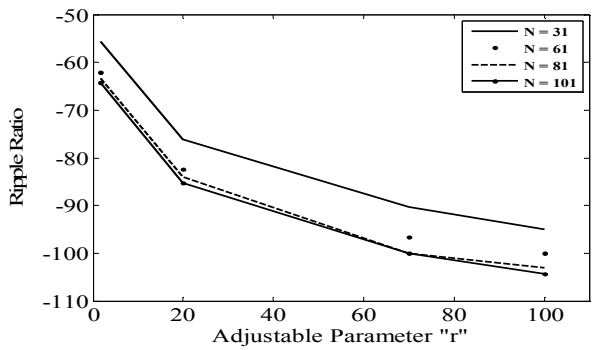

Fig 3 : Adjustable parameter "r" Vs Ripple ratio curve in different window lengths

The curve N=31 describes the ripple ratios of different values of "r" when the window length is fixed at 31. In the same way , N=61, N=81 and N=101 curves have been drawn. From the Fig 3, it has been observed that if we increase the value of "r", the ripple ratio decreases when the window length is fixed. Now if we fix "r" and increase the window length, the ripple ratio decreases. For example, let us measure the values of ripple ratio at "r=20". So what we get from the Fig 3 is that, the lowest value of R is obtained for N=101when r is fixed at r = 20. The following table

summarizes the Fig 3.

TABLE I: ADJUSTABLE PARAMETER "R" VS RIPPLE RATIO AT VARIOUS WINDOW LENGTH N.

"r"	N=31	N=61	N=81	N=101
0.0005	-25.7	-33.2	-31.84	-33.36
1.618	-55.68	-62.1	-63.31	-64.27
20	-76.16	-82.47	-84.1	-85.28
70	-90.28	-96.58	-100	-100
100	-94.92	-100	-103.1	-104.4

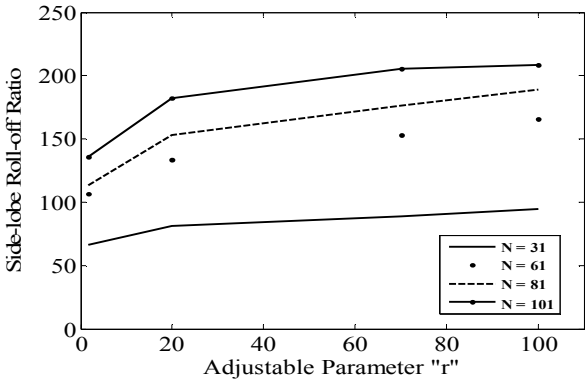

Fig 4 : Adjustable parameter "r" Vs Side-lobe roll-off ratio curve in different window lengths.

From the Fig 4 it has been seen that all the curves are increasing with the increment of their adjustable parameter "r". So we can say, the side-lobe roll-off ratio of the proposed window increases with the raise of the value of "r" when the window length is fixed. Let us consider the curve N=101. Here N is the window length. Compare to the curve N=31, N=61 and N=81 the curve N=101 remains on the higher position. The following table summarized the Fig 4.

TABLE II: ADJUSTABLE PARAMETER "R" VS SIDE-LOBE ROLL-OFF RTIO RATIO AT VARIOUS WINDOW LENGTHS

"r"	N=31	N=61	N=81	N=101
0.0005	27.09	38.54	40.39	80.64
1.618	66.42	106.9	113.29	135.73
20	81.44	133.33	152.7	182.32
70	88.52	153.42	176.3	205.4
100	94.78	166.1	189.3	208.5

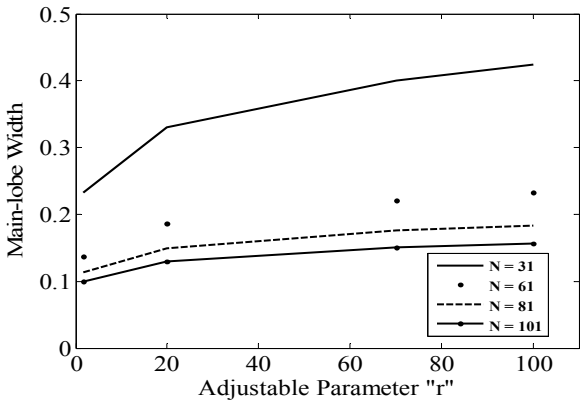

Fig 5 : Adjustable parameter "r" Vs Main-lobe width curve in different window lengths.

Fig 5 shows that as the controlling parameter of the proposed window "r" increases the main-lobe width of the proposed window also raises when the window length is fixed. Let us consider about the curve N=61. Here N is length of the proposed window. From Fig 5 we have, the curve N=61 moderately increases as the value of "r" increases with a fix window length. The following table gives the actual scenario of Fig 5.

TABLE III: ADJUSTABLE PARAMETER "R" VS MAIN-LOBE WIDTH CALCULATION AT VARIOUS WINDOW LENGTHS

"r"	N=31	N=61	N=81	N=101
0.0005	0.1096	0.07632	0.06654	0.06262
1.618	0.2329	0.137	0.1135	0.1
20	0.3307	0.1869	0.1487	0.1292
70	0.4	0.2211	0.1761	0.1507
100	0.4247	0.2329	0.184	0.1566

IV. PERFORMANCE ANALYSIS

In this section, we compare the shape and the spectral characteristics of the proposed window with several commonly used windows.

A. Gaussian Window:

The coefficients of the Gaussian window function are computed using the following equation.

$$w(n) = e^{\frac{1}{2}(\alpha \frac{n}{N/2})^2} \tag{8}$$

where α is inversely proportional to the standard deviation of a Gaussian random variable. The width of the window is inversely related to the value of α. A larger value of α produces a narrower window.[5][6]

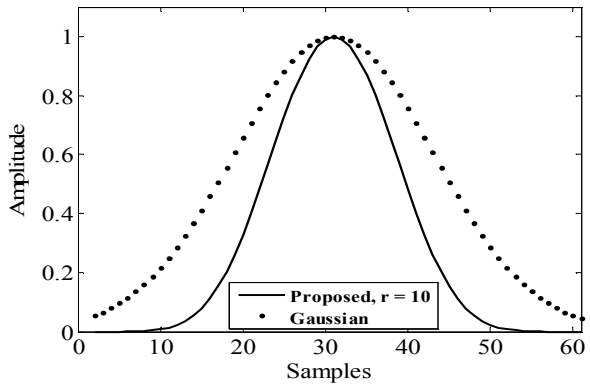

Fig 6: Time domain representation of Gaussian and the Proposed windows

From the Fig 6 it has been seen that the time domain representation of the proposed window with r =10, is narrower than the Gaussian window. Moreover the proposed window touches the X-axis while all the coefficients of the Gaussian window remain above the X-axis. Both of them are symmetric windows. None of them have any negative co-efficient. Some of the coefficients of the proposed window are zero at the beginning and at the ending edges of the window.

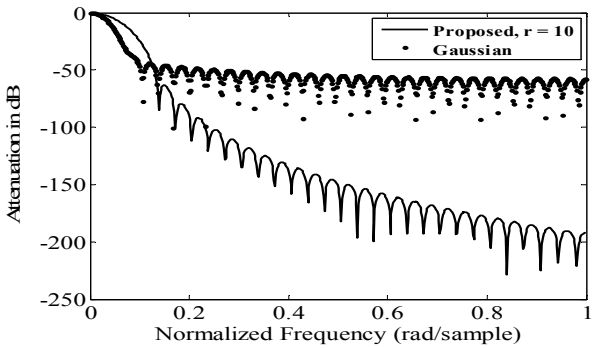

Fig7: Normalized frequency response comparison of Gaussian and the Proposed windows.

Fig 7 shows that the main lobe width of Gaussian and the

proposed windows are 2π × 0.1055 rad/sample and 2π × 0.1387 rad/sample respectively. So the main-lobe width of Gaussian window is 0.0332 rad/sample smaller than the proposed window. On the contrary, the ripple ratios of Gaussian and the proposed windows are about -44.16 dB and -63.83 dB respectively. Hence the ripple ratio of the proposed window is approximately 19.67 dB smaller. Moreover the side-lobe roll-off ratio of the proposed window is almost 115.03 dB better than Gaussian window.

TABLE IV: SPECTRAL PARAMETERS OF GAUSSIAN AND THE PROPOSED WINDOWS.

Window	Main-lobe Width (rad/sample)	Ripple Ratio (dB)	Side-lobe Roll-off Ratio(dB)
Proposed, r =10	2π × 0.1387	-63.83	128.47
Gaussian	2π×0.1055	-44.12	13.44

B. *Kaiser window:*

The Kaiser window is also known as Kaiser-Bessel window function. The Kaiser window function can be expressed as follows [7][8].

$$w(n) = \frac{I_0(\pi\alpha\sqrt{1-(\frac{2n}{N-1}-1)^2})}{I_0(\pi\alpha)} \; where, 0 \le n \le N \quad (9)$$

where I_0 is the zero-th order modified Bessel function of the first kind [8]. Kaiser window is another very popular adjustable window. The variable parameter α determines the tradeoff between the main-lobe width and the side lobe attenuation.

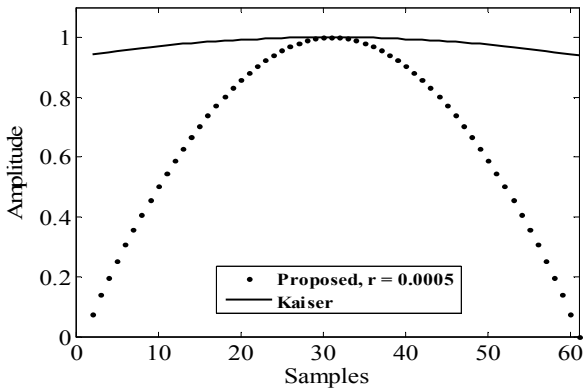

Fig 8 : Time domain representation of Kaiser and the Proposed windows

From the Fig 8 it has been seen that Kaiser window with its adjustable parameter α = 0.5 is almost like rectangular shape. On the contrary, the proposed window is almost like bell shape with its adjustable parameter r= 0.0005.

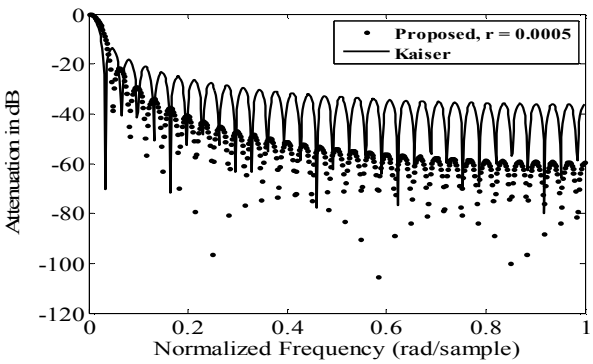

Fig 9: Normalized frequency response comparison of Kaiser and the Proposed windows.

Fig 9 shows the normalized frequency response of Kaiser and the proposed windows. It has been observed that Kaiser window has the main-lobe width of 2π×0.0332 rad/sample while the proposed window has 2π×0.0469 rad/sample. So Kaiser window is slightly better than the proposed window in main-lobe width calculation. Kaiser window has the ripple ratio of -13.63 dB and the proposed window has the ripple ratio of -21.92 dB. Hence the proposed window yields 8.29 dB better ripple ratio. Fig 9 illustrates that the first side-lobe peak of Kaiser window is -13.63 dB and the last one is -36.07dB. So the side-lobe roll-off ratio of Kaiser window is 22.44 dB. In the same way the first side-lobe peak of the proposed window is -21.92 dB and the last one is -59.31 dB. Hence the side-lobe roll-off ratio of the proposed window is 37.39 dB which is 14.95 dB better than Kaiser window.

TABLE V: SPECTRAL PARAMETERS OF KAISER AND THE PROPOSED WINDOWS.

Window	Main-lobe Width (rad/sample)	Ripple Ratio (dB)	Side-lobe Roll-off Ratio(dB)
Proposed, r =10	2π × 0.0469	-21.92	37.39
Kaiser	2π×0.0332	-13.63	22.44

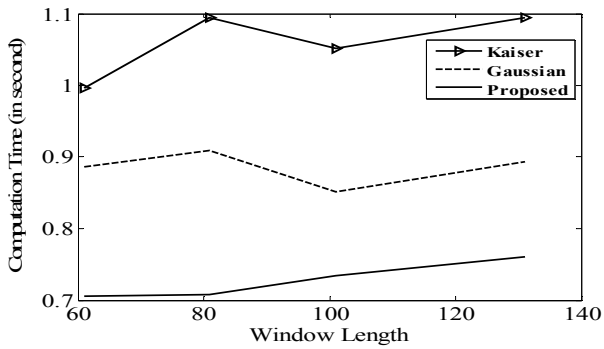

Fig 10:Computation time comparison among Kiser, gaussian and the proposed window in various window length

Fig 10 shows the computational time required for Kaiser, Gaussian and the proposed window with different window length. The elapsed time is minimum for the proposed window than the Kaiser and the Gaussian windows.

V. FIR FILTER DESIGN

In this section we will discuss how the proposed window helps us to design FIR low pass filter and also compare the simulation result with the most popular adjustable windows.

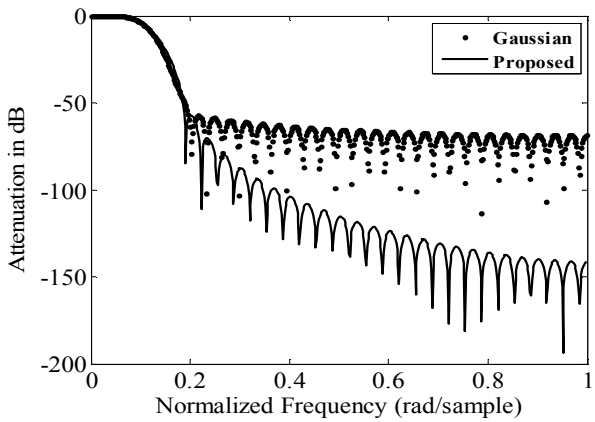

Fig 11 (a) : Normalized frequency response of FIR low pass filters designed by the proposed and Gaussian windows.

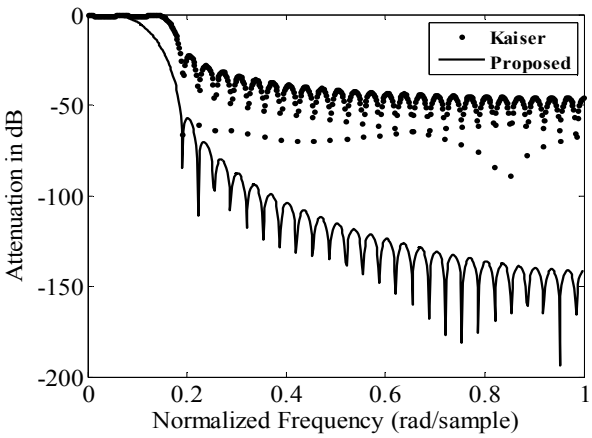

Fig 11 (b) : Normalized frequency response of FIR low pass filters designed by the proposed and Kaiser windows.

Having a cut off frequency of ω_c, the impulse response of an ideal low pass filter is given by

$$h_{LP,ideal}[n] = \frac{\sin(\omega_c n)}{\pi n} \tag{10}$$

By windowing this IIR filter with the windows discussed in this paper, different FIR filter can be achieved. For $\omega_c = 0.2\pi$ figures 11(a)-11(b) show the normalized frequency response of the FIR filters designed by applying different windows of length 61. Fig 11(a) shows the comparison of FIR low-pass filters designed by the proposed and Gaussian windows respectively. From the Fig 11 (a) it has been seen that the main-lobe width of the proposed window is slightly narrower than Gaussian window based FIR low-pass filter. Simulation result shows that the filters achieved by the proposed window and Gaussian window have the same ripple ratios. We also observe that the side-lobe roll-off ratio of the filter designed by the proposed window is near about 72.63 dB better than what can be achieved by Gaussian window. In the same way, the fig 11(b) demonstrates that the filter obtained by the proposed window results 34.39 dB better ripple ratio and approximately 60.98 dB greater side-lobe roll-off ratio than what can be obtained by using Kaiser window.

TABLE VI: DATA ANALYSIS OF FIR FILTER OBTAINED BY WINDOWING WITH DIFFERENT WINDOWS

Comparing Windows	Main-lobe Width (rad/sample)	Ripple Ratio (dB)	Side-lobe Roll-off Ratio (dB)
Proposed Vs Gaussian	2π×0.1914	-57.08	84.02
	2π×0.2031	-57.08	11.39
Proposed Vs Kaiser	2π×0.1914	-57.08	84.02
	2π×0.1933	-22.69	23.04

VI. NOISE ELIMINATION FROM AUDIO SIGNAL

Human auditory system is able to process the complex sound mixture reaching our ears [9]. The human auditory system is responsive to sounds in the frequency range of 20Hz to 20 KHz [9]. When this audio signal is passed through a communication channel or communication system, it may corrupted by Additive White Gaussian Noise. The adjective 'White' is used in the sense that white light contains equal amount of all frequencies within the visible limit of all electromagnetic radiation [10]. For testing the proposed filter, we first generate an audio signal. This audio signal is sampled at 44.1KHz. Then additive white Gaussian noise is added with the audio signal. The noise corrupted audio signal is passed through the different types of FIR low-pass filters.

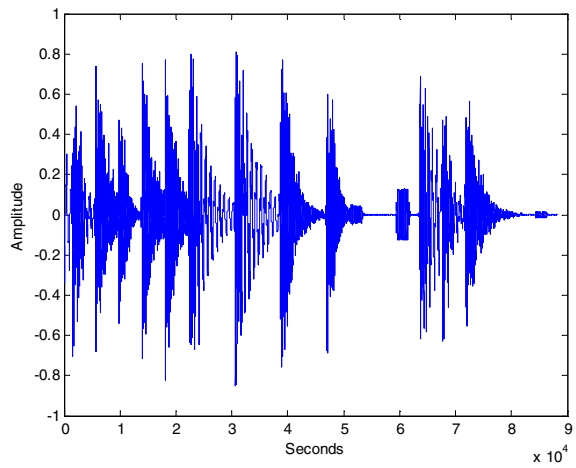

Fig 12: An audio signal without noise

When AWGN is added with the audio signal then the signal becomes as follows.

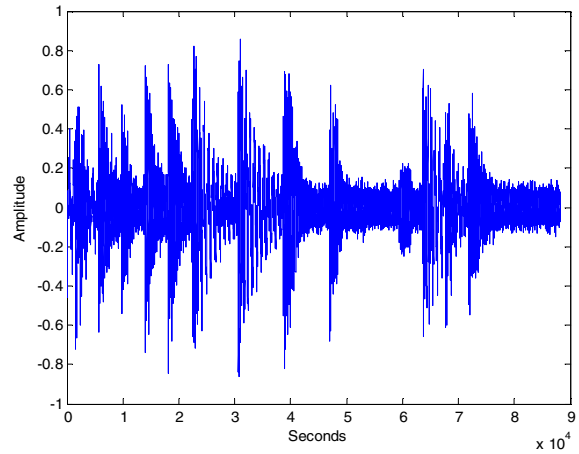

Fig 13: Audio signal corrupted by additive white Gaussian noise.

Now this noise corrupted audio signal is passed through a Kaiser window based FIR low-pass filter and the output is shown in the Fig 14.

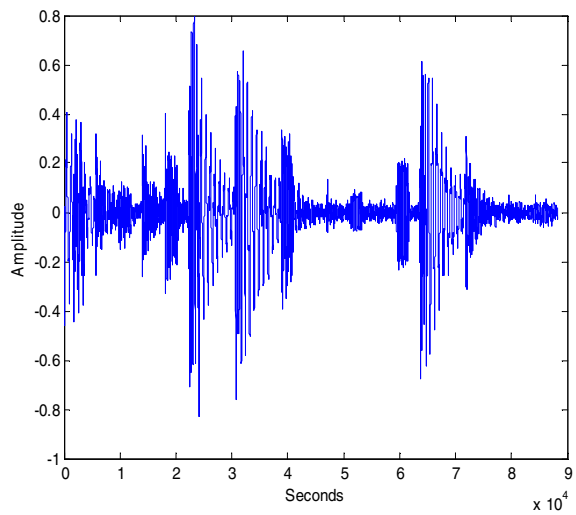

Fig 14: Filtered audio signal using Kaiser window based FIR filter

Again the same corrupted audio signal is passed through the proposed window based FIR low-pass filter and the output is represented in the Fig 15.

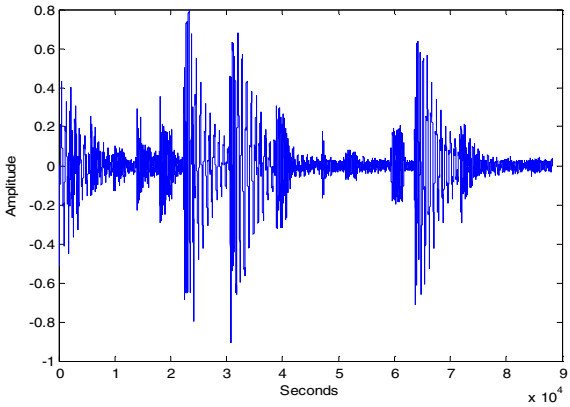

Fig 15 : Filtered audio signal using the proposed window based FIR filter.

It has been seen form the Fig 14 and Fig 15 that the proposed window based FIR low-pass filter more precisely eliminates Noise form the audio signal than Kaiser window based FIR low-pass filter. It will be more clear in the next section when we calculate the normalized frequency responses of the filtered audio signal.

VII. Normalized Frequency Response of the Filtered Audio Signal

After obtaining the filtered version of the audio signal using Kaiser and the proposed windows based FIR low-pass filters, their respective normalized frequency response has been analyzed. Fig 16 and Fig 17 show the normalized frequency response of the filtered audio signal using Kaiser and the proposed windows based FIR filters respectively.

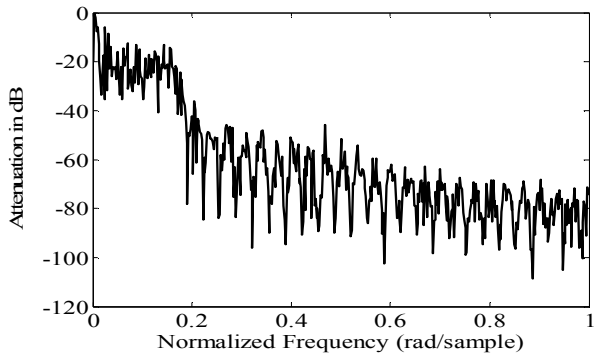

Fig 16: Normalized frequency response of the filtered audio signal using Kaiser window based FIR low-pass filter.

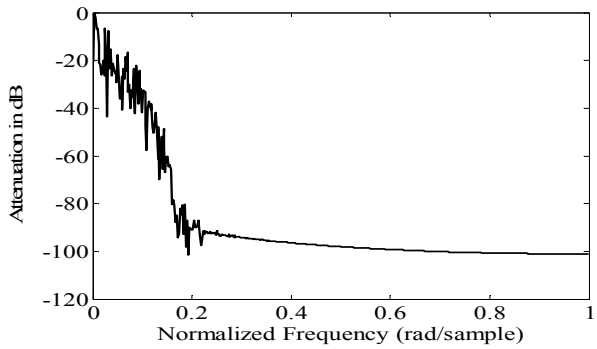

Fig 17: Normalized frequency response of the filtered audio signal using proposed window based FIR low-pass filter

From the Fig 16 it has been observed that the ripple ratio of the audio signal filtered by Kaiser window based low-pass filter is about -50.44 dB. On the contrary, the ripple ratio of the audio signal filtered by the proposed window based low-pass filter is approximately -80.72 dB which is 30.28 dB better. The following table summarized the Fig 16 and Fig 17.

Table VII: Performance Analysis of Kaiser and the Proposed Windows.

Window	Ripple Ration (dB)	Remarks
Kaiser	-50.44	The proposed window based FIR low-pass filter is 30.28 dB better.
Proposed, r=0.0005	-80.72	

VIII. Conclusion

The proposed window is symmetric one and it has only one adjustable parameter "r". So it is a very simple window. The proposed window yields 19.71 dB and 8.29 dB smaller ripple ratios than Gaussian and Kaiser windows respectively. Moreover the side-lobe roll-off ratio of the proposed window is almost 115.03 dB and 14.95 dB better than the above named windows. The performance of the FIR low pass filter, designed by the proposed window, is compared with Gaussian and Kaiser windows. Experimental results show that the filter designed by the proposed window yields better spectral characteristics than those of Gaussian and Kaiser windows respectively. The paper has also shown that the proposed filtering method can be used to achieve 30.28 dB improved ripple ratio compared to Kaiser filtering method to eliminate noise from audio signal.

References

[1] Hrishi Rakshit and Muhammad Ahsan Ullah "A Comparative Study on Window Functions for Designing Efficient FIR Filter". In Proceedings of the IEEE 9th International Forum on Strategic Technology (IFOST), ISBN: 978-1-4799-6060-6 DOI: 10.1109/IFOST.2014.6991079 pp 91-96.

[2] Oppenheim, A.V., and R.W. Schafer. Discrete-Time Signal Processing. Upper Saddle River, NJ: Prentice-Hall, 1999, pp. 468-471..

[3] Md abdus Samad "A Novel Window Function Yielding Suppressed Main-lobe Width and Minimum Side-lobe Peak" International Journal of Computer Science, Engineering and Information technology (IJCSEIT), Vol 2, No 2, April 2012.

[4] Emmanuel C. Ifeacher and Barrie W. Jervis "Digital Signal Processing" second edition, Pearson Education 2008.

[5] Roberts, Richard A., and C.T. Mullis. Digital Signal Processing. Reading, MA: Addison-Wesley, 1987, pp. 135-136.

[6] Harris, F.J. "On the Use of Windows for Harmonic Analysis with the Discrete Fourier Transform." Proceedings of the IEEE. Vol. 66, No. 1 (January 1978).

[7] Kaiser, J.; Schafer, R. (1980). "On the use of the I0-sinh window for spectrum analysis". IEEE Transactions on Acoustics, Speech, and Signal Processing 28: 105.

[8] Selected Papers in Digital Signal Processing II, IEEE Press, New York, 1975.

[9] P. Rao, Audio Signal Processing, Chapter in Speech, Audio, Image and Bio-medical Signal Processing using Neural Network, (Eds.)Bhanu Prasad and S.R. Mahadeva Prasanna, Springer –Verlag, 2007.

[10] Md. Sipon Miah, M. Mahbubur Rahman, T.K. Godder, Bikash Chandra Singh and M. Tania Parvin, 'Performance Comparisons of AWGN Flat Fading and Frequency Selective Fading for Wireless Communication System using 4QPSK',International Journal of Computer and Information Technology (IJCIT), ISSN 2078-5828(PRINT), ISSN 2218-5224(ONLINE),Vol.01, Issue 02.

Independent Component Analysis for EOG artifacts minimization of EEG signals using kurtosis as a threshold

Kazi Aminul Islam
Department of Electrical Engineering
Lamar University
Beaumont, TX, USA
russelkazi@yahoo.com

Gleb V. Tcheslavski
Department of Electrical Engineering
Lamar University
Beaumont, TX, USA
gt.lamar@gmail.com

***Abstract*—Brain electrical activity commonly represented by the Electroencephalogram (EEG), due to its miniscule amplitude (on the order of a hundred microvolts), is often contaminated with various artifacts. Independent Component Analysis (ICA) may be a useful technique to minimize the artifacts prior analyzing the original neural signal. In this paper, we used kurtosis to determine the threshold to separate the artifacts-affected ICA components from the unaffected components. Kurtosis may represent how peaked or how flat the artifacts that affect a signal are compared to the normal behavior of the original signal. To select the threshold value of the kurtosis, two statistical principles have been used: namely, the Z-score and the confidence interval. Our intention was to avoid a manual technique to determine the affected ICA components and, instead, to explore an automatic method based on the kurtosis value. Based on the observed results, we may conclude that the present technique may be used for EOG artifacts minimization.**

Keywords— EEG, Independent Component Analysis, Kurtosis, EOG

I. INTRODUCTION

Electroencephalogram (EEG) signals represent neural activities of human brain. EEG is important for many medical applications, such as in studies of epilepsy, trauma, and biofeedback. EEG signal is sensitive to different artifacts, such as ocular, cardiac, muscle, electrode, power line noise, and external device artifacts. To extract the original neural signal, these artifacts should be minimized significantly. Independent Component Analysis (ICA) may be an important tool to do so. Our goal is to consider the most damaging artifacts - the ocular artifacts originating from the muscular activity of eyes. The simplest and widely used method to minimize them is discarding the portions of EEG recording deemed as artifacts, based on exceeding a pre-determined threshold [1].

The EEG data can be viewed as a set of signals at the electrode sites that are mixtures of brain and artifact information. Blind separation methods (BSS) reduce mixture of neural and non-neural variables to components such that they are in some way independent of each other [2].

Independent Component Analysis (ICA) may work better than other methods available for separating the independent components. In many practical uncorrelated situations the signals would not be independent and easy to separate. So, the uncorrelated property is not enough to separate artifacts. This is the reason that principal component analysis (PCA) or factor analysis cannot separate such signals. On the other hand, the Independent Component Analysis (ICA) provides a method for artifacts removal where an accurate model of the process that generates the artifacts is not needed. That is why ICA is a promising technique for artifact identification and removal. The artifacts are usually independent from the rest of the signal, and this requirement of the model is reasonably well fulfilled [1].

Kurtosis is simple and important in ICA and blind source separation. The fourth order statistics called the kurtosis is usually employed, due to its useful properties not shared by the fourth central moment. Kurtosis is often used as a quantitative measure of the non-Gaussianity of a random signal. It can be used as a simple measure of non-Gaussianity if the signals to be compared are of the same type, either sub-Gaussian or super-Gaussian [1].

Joyce, Gorodnitsky and Kutas proposed a method where the artifact components have to identify manually to flag for rejection [2]. Javidi and Mandic proposed a model to identify the artifactual component with the kurtosis value as a threshold [3]. In this paper, an automatic procedure to identify and mitigate the artifact components will be attempted.

II. EEG RECORDING AND PREPROCESSING

EEG signal data used in this paper were recorded in Advanced DSP laboratory of Electrical Engineering department of Lamar University. Recording were performed and pre-processed using Advanced Neuro Technology's (ANT, Netherlands) EEG acquisition system. A 32-channel recording EEG device was used in which 32 electrodes were situated according to the International 10-20 System.

Due to their subtle amplitude, EEG data are often contaminated by different noise sources. This is the primary reason for preprocessing the EEG signals first. DC offsets are often present in EEG signals. To minimize such offset a built-in Matlab 'detrend' function was used in this research. Spatial filtering is a technique that decreases surface currents of the recorded EEG signal generated by neighboring channels.

978-1-4673-9257-0/15/$31.00 ©2015 IEEE

Common Average Reference (CAR) spatial filter for each electrode was applied by subtracting the average value of all electrode signals from the current electrode signal at every time instance. After that, Independent Component Analysis algorithm is applied.

The aim of present report is to reduce EOG signal in EEG. Eye-blink artifacts affect – to some extend – most of EEG channels. However, frontal channels are most influenced by EOG; therefore, EEG recordings at the Fp_2 channel were selected for illustration.

III. Methods

A. Independent Component Analysis (ICA)

Independent component analysis (ICA) is a method that determines primary factors or components from the multivariate or multidimensional statistical data [1]. Let assume that the source signal $S_i(t)$ contains m variables and T observations. The observed signal $Y_i(t)$ is a linear combination of the source signal and a mixing matrix W [1]:

$$Y_i(t) = \sum_j W_{ij} * S_i(t) \tag{1}$$

Un-mixing EEG data into components can be achieved through the following linear rotation [2]:

$$S = W^{-1} * X \tag{2}$$

Equation (2) indicates that the EEG data X is rotated by the un-mixing matrix W^{-1} to arrive at the components of S. We observe that all quantities in (2) are matrices [2]. Here, 'fastica' matlab toolbox will be used to identify the independent components.

B. Kurtosis

Kurtosis is defined as the standardized fourth central moment [4]:

$$k = \frac{E\left\{(x-m)^4\right\}}{E\left\{(x-m)^2\right\}^2} = \frac{\mu_4}{\sigma^4} \tag{3}$$

Here, E is the expectation operator, m is the mean, and σ is standard deviation [4].

For the normal distribution, EEG signal has a kurtosis value of 3. That is why k-3 [4] is often used so that reference normal distribution has a kurtosis of zero. Kurtosis is defined in the zero-mean case by the equation [1]:

$$kurt(x) = E\{x^4\} - 3[E\{x^2\}]^2 \tag{4}$$

The normalized kurtosis is [1]:

$$\bar{k}(x) = \frac{E\{x^4\}}{[E\{x^2\}]^2} - 3 \tag{5}$$

Built in Matlab function 'Kurtosis' will be used to determine the kurtosis value.

C. Z-scores

Standard deviation of a set of data expresses the dispersion of the scores around their mean. Assume that we consider a set of N scores, each denoted as Y_n, whose mean equals M and with a standard deviation $\hat{S}$ that can be evaluated as [5]:

$$\hat{S} = \sqrt{\frac{\sum (Y_n - M)^2}{N-1}} \tag{6}$$

To normalize a set of data using the standard deviation, each data entry is divided by the standard deviation of this set. The mean of the scores is subtracted from each score prior to dividing by the standard deviation. This normalization is known as Z-scores. Formally, a set of N scores, each of which denoted as Y_n, and with the mean M and standard deviation $\hat{S}$, can be transformed in Z-scores as [5]:

$$Z_n = \frac{Y_n - M}{\hat{S}} \tag{7}$$

It can be shown that a set of Z-score has a mean of zero and a standard deviation of one. Therefore, Z-scores constitute a unit-free measure that can be used to compare observations of different units [5].

D. Confidence Interval

A confidence interval is estimated from a given set of sample data. Confidence interval gives an estimated range of values that may include an unknown population parameter. The confidence interval (CI) is expressed as two numbers known as the confidence limits with the range in between. This range carries value of the measured variable in the population with a certain level of confidence. In medical research the confidence level is usually set to 95%. As a result it is named as "95% confidence interval". Thus, the 95% Confidence Interval is defined as a range of values for a variable of interest constructed so that this range may have a 95% probability of including the true value of the variable. It can be also expressed as it may be 95% certain that the value is somewhere inside a 95% confidence interval [6].

For N observations, Confidence can be estimated from the following equations:

For $N \leq 30$, Confidence interval (C.I.) will be [8]:

$$C.I. = \bar{x} \pm \frac{s}{\sqrt{N}} \times t_{N-1} \tag{8}$$

For $N > 30$, Confidence interval (C.I.) will be [8]:

$$C.I. = \bar{x} \pm \frac{s}{\sqrt{N}} \times Z_{N-1} \tag{9}$$

Here $\bar{x}$ is the sample mean, s is the sample standard deviation, and (N-1) is the number of degrees of freedom. At

95% significance level, t_{N-1} = 2.201 for $N \leq 30$. At 95% significance level, Z_{N-1} = 1.96 for N>30.

IV. METHOD FOR ARTIFACTUAL COMPONENT DETECTION

ICA algorithm separates the EEG signals into its original sources as independent components (ICs). After that artifact sources are identified and removed. In semi-automatic and automatic artifact removal methodologies, several classifications (markers) based on the statistical characteristics of the ICs are considered that allow for the detection of artifacts in the contaminated EEG. Then these are compared against threshold values that determine the rejection of particular components. In these methods, the IC kurtosis has been utilized to identify and minimize those artifacts. Artifact-free EEG typically have a near-zero kurtosis value, which indicates a possible Gaussian distribution. With artifacts, such as EOG, EEG exhibits a peaked distribution with a highly positive kurtosis value. This method has been used as the main concept in defining classifications based on the fourth order moment. Using this method, we aim to extract artifacts as independent sources from the recorded EEG mixture [3].

To detect the Threshold value for kurtosis, two methods have been used.

A. Using Z-scores to determine the threshold of kurtosis value

Kurtosis is positive for peaked activity distributions that may represent EOG artifacts. Kurtosis is negative for 'flat' activity distributions. It may appear that this feature is typical for noise. For finding artifactual ICs (outlier components), these EEG distributions have been normalized with respect to all ICs to zero-mean and unit standard deviation (z-score). To do so, thresholds in terms of number of standard deviations from the mean were applied (usually, thresholds are set at 1.64 according to Barbati et al [7]) If a certain percentage of segments exceeded rejection thresholds the corresponding IC was marked for rejection of the component [7].

B. Using Confidence Interval to determine the threshold of kurtosis value

Kurtosis is used to determine eye blink activity distributions in the IC signal. Kurtosis is zero for Gaussian distribution, positive for the peaked activities (which represents eye blink signals) and negative for the flat distributions. So, the upper bound of the 95% CI of the mean is used as the threshold. All the ICs having Kurtosis higher than the upper limit of CI are supposed to be blink artifacts and are marked for de-noising [8].

After evaluating confidence interval of the kurtosis of IC components, the upper limit of confidence interval has been selected as the threshold value. Therefore, any value exceeding the upper limit of confidence interval is marked as a threshold for artifactual components. Next, the identified artifactual components were removed by setting them to zero. After that, signals were reconstructed by multiplying with the mixing matrix W [2].

V. RESULTS

Table 1 illustrates Z-scores of kurtosis value for different ICs for sample EEG. If any component Z-score exceeds 1.64 on magnitude (the threshold), we consider that component as representing an EOG artifact and indicate for rejection.

Table 1 Z-score of kurtosis value for different Independent Components for sample EEG data

Independent Components	**Independent Components Properties**		
	Kurtosis Value	***Z-Score***	***Comments***
IC-1	10.4612	0.851	
IC-2	14.985	2.231	EOG effects
IC-3	11.2541	1.093	
IC-4	16.097	2.571	EOG effects
IC-5	9.0375	0.417	
IC-6	10.0066	0.712	
IC-7	8.6133	0.287	
IC-8	8.981	0.399	
IC-9	9.9804	0.704	
IC-10	12.1592	1.369	
IC-11	8.7642	0.333	
IC-12	8.8146	0.349	
IC-13	7.3491	-0.099	
IC-14	6.6133	-0.323	
IC-15	5.9161	-0.536	
IC-16	6.8611	-0.247	
IC-17	10.4211	0.839	
IC-18	8.8412	0.357	
IC-19	7.0169	-0.1999	
IC-20	5.5034	-0.662	
IC-21	5.7182	-0.596	
IC-22	5.4632	-0.674	
IC-23	6.7481	-0.282	
IC-24	4.8235	-0.869	
IC-25	4.6006	-0.937	
IC-26	4.4669	-0.978	
IC-27	4.601	-0.937	
IC-28	3.848	-1.167	
IC-29	4.2358	-1.049	
IC-30	2.6864	-1.521	
IC-31	2.9654	-1.436	

We observe in Table 1 that the second and fourth independent components z-score value are 2.231 and 2.571. So, we assume that this component may contain large EOG artifacts and, therefore, is a candidate for removal.

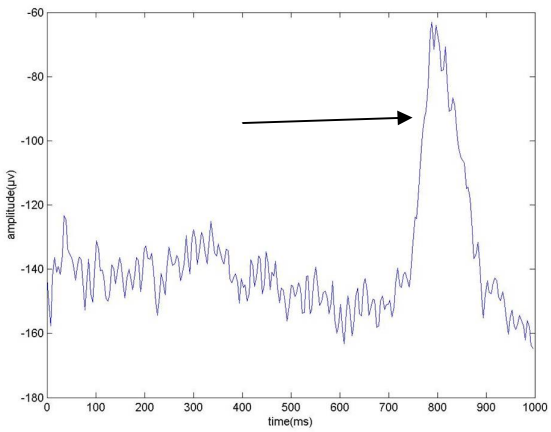

Figure 1: EEG signal of channel Fp_2before removing eye blinks; the arrow indicates the location of eye blink.

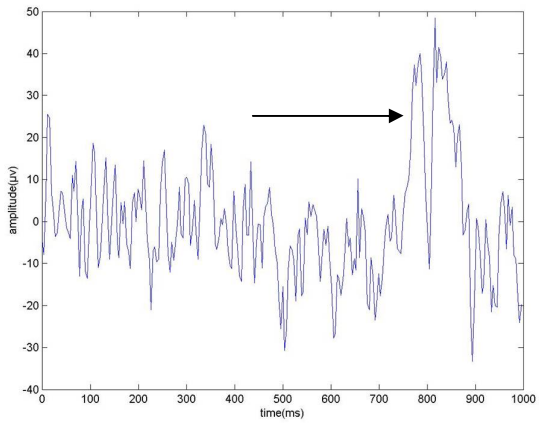

Figure 2: EEG signal of channel Fp_2 after removing eye blinks using Z-score; the arrow indicates the location of eye blink.

An eye blink artifact is evident (indicated by an arrow) in Figure 1 around 700 ms to 900 ms. On the other hand, after canceling the artifactual component (the arrow in Figure 2), it can be seen that EOG artifact was minimized. Perhaps, the actual EEG signals between 0 ms and 700 ms may be analyzed more easily after cancelling the eye blink.

Confidence interval calculation:
From the present EEG data, the following quantities were evaluated:
Sample mean = 7.672;
Standard deviation = 3.277;
The confidence interval: 7.672± 1.153;
Upper confidence level: 8.83;
Lower confidence level: 6.52;
The threshold = 8.83.

Table 2 illustrates different ICs kurtosis values with the upper limit of confidence interval to determine the EOG components. If the kurtosis value exceeds 8.83, the corresponding component is considered as an EOG component.

Table 2 Results of analyzing of kurtosis value to determine the artifact components for different Independent Components for sample EEG data.

Independent Components	**Independent Components Properties**		
	Kurtosis Value	***Artifact Detection (C.I.>8.83)***	***Comments***
IC-1	10.4612	>8.83	EOG effect
IC-2	14.985	>8.83	EOG effect
IC-3	11.2541	>8.83	EOG effect
IC-4	16.097	>8.83	EOG effect
IC-5	9.0375	>8.83	EOG effect
IC-6	10.0066	>8.83	EOG effect
IC-7	8.6133		
IC-8	8.981	>8.83	EOG effect
IC-9	9.9804	>8.83	EOG effect
IC-10	12.1592	>8.83	EOG effect
IC-11	8.7642		
IC-12	8.8146		
IC-13	7.3491		
IC-14	6.6133		
IC-15	5.9161		
IC-16	6.8611		
IC-17	10.4211	>8.83	EOG effect
IC-18	8.8412	>8.83	EOG effect
IC-19	7.0169		
IC-20	5.5034		
IC-21	5.7182		
IC-22	5.4632		
IC-23	6.7481		
IC-24	4.8235		
IC-25	4.6006		
IC-26	4.4669		
IC-27	4.601		
IC-28	3.848		
IC-29	4.2358		
IC-30	2.6864		
IC-31	2.9654		

Based on the upper limit of the confidence interval, the threshold value selected for EOG artifacts is 8.83. If any component's kurtosis value is greater than the threshold, it is marked as an artifact component. We observe in Table 2 that components 1-6, 8-10, 17 and 18 have kurtosis value exceeding the upper limit of the confidence interval that is 8.83. Therefore, these components may be contaminated with EOG artifacts and are candidates for removal.

Figure 3 illustrate the outcome of the artifact detection method using confidence interval.

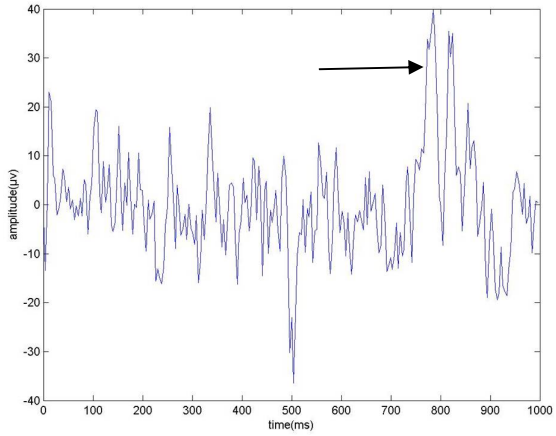

Figure 3: EEG signal of channel Fp_2 after removing eye blinks using confidence interval; the arrow indicates the location of eye blink.

We observe in Figure 1 an EOG artifact indicated by the arrow. It is seen in Figure 3 that after cancelling the artifactual components, EOG signal was considerably reduced and the source EEG was recovered.

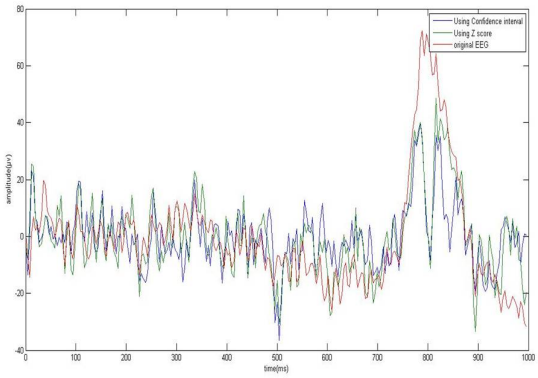

Figure 4: Comparison of EEG signal of channel Fp_2 before removing eye blinks and after removing eye blinks using Z-score and Confidence Interval.

For the comparison, Figure 4 illustrates EEG fragments for Fp_2 before and after EOG removal using Z-score and Confidence interval. We observe that only the artifact was affected by the proposed technique. This observation verifies the validity of the proposed technique.

VI. Discussion

In this paper, an automatic EOG artifact minimization technique was discussed. First the EEG signals were preprocessed. Next, each component of EEG signal was separated using the ICA algorithm. Then, using the z-score and confidence interval methods, kurtosis thresholds were determined. After that, EOG artifact components were detected and cancelled.

These EOG artifacts reduction methods – with an automatic kurtosis threshold detection based on Z-score and confident interval - were both sufficiently effective. The sample EEG signal originally contained a large eye blink artifact, as may be observed in Figure 1. The recovered signals, as might be seen, this EOG artifact was considerably reduced using the techniques. We also may conclude that more ICs were associated to EOG artifacts, while using the confidence interval method.

The traditional approach of manual inspection of each independent component to identify the artifacts is time consuming. Using the automated procedures to identify the artifactual components evaluated in the present report may lead to a considerable time saving and improved accuracy while analyzing EEG.

VII. Conclusion and Future Works

In this paper, two robust and automated methods to detect artifactual components based on kurtosis threshold value were evaluated. However, this method utilized cancelling of the entire independent component that was deemed as artifactual. As a result, some important information may be compromised while minimizing the EOG artifacts. In future, we should consider the part of IC to be modified or cancelled to remove the artifact rather than cancelling the entire component.

References

[1] Aapo Hyvärinen , Juha Karhunen and Erkki Oja *Independent Component Analysis,* John Wiley & Sons, Incorporation , 2001.

[2] Carrie A. Joyce, Irina F. Gorodnitsky, and Marta Kutas "Automatic removal of eye movement and blink artifacts from EEG data using blind component separation" *Society for Psychophysiological Research* P 313–325, 2004.

[3] Soroush Javidi and Danilo P. Mandic "Kurtosis based blind source Extraction of complex noncircular signals with application in EEG artifact removal" Technical Report: TR-ICU-BSE-1337/09-10 Updated: 26 September 2010.

[4] Lawrence T. Decarlo "On the meaning and use of Kurtosis "*The American Psychological Association, Inc.* p-292-307 1997.

[5] Herv´e Abdi *Normalizing data: Encyclopedia of Research Design,* In Neil Salkind (Ed.), Thousand Oaks, CA: Sage. 2010.

[6] M.D. Abdelhamid Attia "Why should researchers report the confidence interval in modern research?" *Middle East Fertility Society Journal* Vol. 10, No. 1, 2005.

[7] Giulia Barbati, Camillo Porcaro, Filippo Zappasodi, Paolo Maria Rossini and Franca Tecchio, "Optimization of an independent component analysis approach for artifact identification and removal in magneto-

encephalographic signals" *Clinical Neurophysiology* 115 (2004) 1220–1232 Accepted 15 December 2003.

[8] Ruhi Mahajan and Bashir I. Morshed "Unsupervised eye blink artifact denoising of EEG data with modified Multiscale Sample Entropy, Kurtosis, and Wavelet ICA" *IEEE journal of Biomedical and Health Informatics*, Vol. 19, No. 1, P 158-165, January 2015.

Automatic Detection of Optic Disc in Fundus Images by Curve Operator

M. Nahid Reza
Department of Electrical and Electronic Engineering
Hamdard University Bangladesh
Narayanganj, Bangladesh
E-mail: nahidreza2k9eee@gmail.com

Mohiuddin Ahmad
Department of Electrical and Electronic Engineering
Khulna University of Engineering & Technology
Khulna, Bangladesh
E-mail: mohiuddin.ahmad@gmail.com

***Abstract*—This paper proposes a method to detect optic disk (OD) automatically in fundus image of retina without using background mask and blood vessels. Based on the properties of OD, an idea of curve operator is presented here. This method has been implemented on three public databases and the promising results are obtained. The experimental results indicate that this proposed method of automatic OD detection has good accuracy and is also computationally efficient.**

***Keywords*—Biomedical imaging, retinal image processing, optic disk detection, bilateral filtering, curve operator.**

I. Introduction

In modern ophthalmology, detection of optic disk is a very important step for retinal image analysis and one of the main feature of extracting the anatomical structure of the retina as illustrated in Fig. 1(a). Optic disk can be defined as the circular brighter region in retinal fundus image where blood vessels converge and optic nerve is formed. OD detection is very indispensable for the computer aided diagnosis of different eye diseases such as glaucoma detection and diabetic retinopathy [1]. Fig. 1(b) represents the fundus image with retinal lesion.

Many optic disc detection methods have been proposed earlier. In [2]–[4], image brightness based methods are proposed. In these methods it is expected that the OD usually resembles according to the brightest pixels within fundus images. In [5] and [6], image variation based methods are proposed based on the statement that the OD has a high image variation due to the retinal blood vessels. But the sensitivity of these two types of methods is highly dependent on retinal lesion, illumination and exudates. Furthermore the vasculature geometry based methods [7]–[9] are more accepting to retinal lesion and imaging artifacts. But in this technique, retinal blood vessels are needed to be extracted initially which is a nontrivial task and requires long processing time. From [5], [10] the dependency between detection accuracy and processing time can be referred. In [11] OD detection is done as a part of the whole work and adaptive morphological filtering method is considered. Also in this work average computational cost is analyzed. But the work presented in this paper is the inspiration of the work [12] where a line operator with 21 orientation is used to detect OD in fundus image. Also in [12] image background segmentation mask is consumed and image intensity variation is analyzed.

978-1-4673-9257-0/15/$31.00 ©2015 IEEE

This paper proposes a method named as curve operator that is used to detect the optic disk in fundus image automatically. Curve operator is divided in two segments i.e. line and curve segment. This operator is also oriented with specific angles and pixel length. With the analysis of pixel intensity variation four points are predicted and furthermore validated to detect OD region. No background segmentation is used in this technique. Color fundus images are used from three public databases.

The rest of the paper is organized as follows. In section II, idea of curve orientation with image prepossessing and OD detection method are explained. Image database description and experimental results are exposed as well as discussed in section III. Finally the work is concluded in section IV.

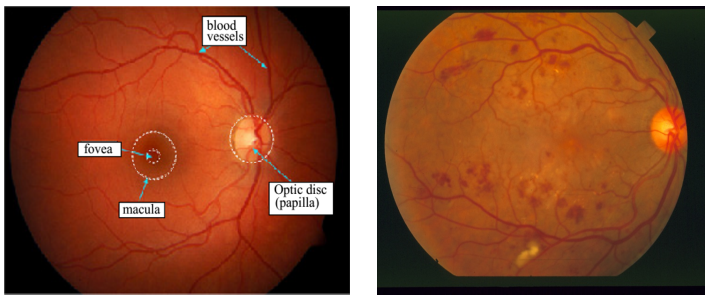

(a) Healthy fundus image with structural element (Obtained from [13])

(b) Fundus image with retinal lesion (Obtained from STARE database)

Fig. 1. Illustration of retinal fundus images.

II. Proposed Method

A. Fundus Image Preprocessing

In proposed method, the circular brightness structure of fundus image is considered and LAB color scape gives the best result for OD detection [14]. So source image color space is converted in LAB color space and only lightness channel is considered. Smoothing of converted color spaced retinal image is performed to enhance the circular brightness structure which is linked with the OD region. So for enhancement, bilateral smoothing filter [15] is used because it has the advantage of combining geometric closeness and photometric similarity as shown in (1). Also in (1), the normalization factor $k(x)$ can be expressed as (2).

$$h(x) = k^{-1}(x) \int_{-\infty}^{\infty} \int_{-\infty}^{\infty} f(\zeta) c(\zeta, x) s(f(\zeta); f(x)) d\zeta \quad (1)$$

$$k(x) = \int_{-\infty}^{\infty} \int_{-\infty}^{\infty} c(\zeta, x) s(f(\zeta); f(x)) d\zeta \quad (2)$$

Furthermore in (1) and (2), $f(x)$ indicates the converted color spaced retinal image. $c(\zeta, x)$ means the geometric closeness and $s(f(\zeta); f(x))$ measures the photometric similarity among the neighborhood pixel ζ and the center of neighborhood x . Both $c(\zeta, x)$ and $s(f(\zeta); f(x))$ are set by Gaussian functions. As conferring in [15], from the two Gaussian functions the geometric spread σ_d and the photometric spread σ_r are set at 10 and 1 . But in this work, they are set as 10 and 100 respectively. Also the number of neighbors pixel is taken 10 pixels for moderate filtered image. Considering the fundus image represented in Fig. 1(b), Fig. 2(a) shows LAB color space with only the lightness channel and Fig. 2(b) shows the corresponding filtered image.

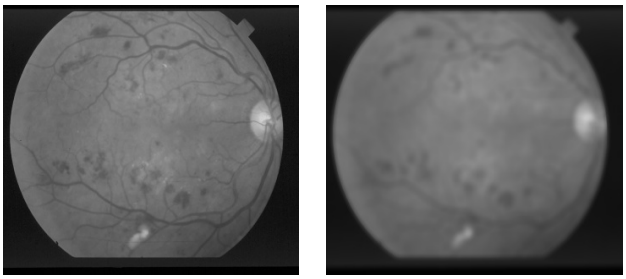

(a) Converted retinal image in LAB color space with lightness channel only

(b) Bilateral filtered image

Fig. 2. Fundus image preprocessing

B. Curve Operator Method

The optic disk region has similar brightness in the fundus image. This brightness has also gradient color from edge to center of fundus image. According to this characteristics a curve operator is proposed as shown in Fig. 3. For a pixel $P(x, y)$, the curve operator first determines line segments, $L_i = \{L_1, L_2, ..., L_l\}$ with specific length, l (i.e. number of pixels) with n orientation centered at $P(x, y)$. Curve segment, $C_j = \{C_1, C_2, ..., C_{r/2}\}$ is determined next as tangent to the orthogonal of the line segment and represented in (3). Here r is the radius of optic disk in retinal image.

$$C_{j_y} = y + \sqrt{(L_{l_x} - x)^2 + (L_{l_y} - y)^2 - (C_{j_x} - x)^2} \quad (3)$$

where $x - (r/2) \leq C_{j_x} \leq x + (r/2)$.

Chord of the curve is taken as 50% of radius of optic disk (i.e. $r/2$) with center at the middle of line segment i.e. $l/2$. Finally curve operator can be expressed as set of point of line and curve segment i.e. $COP_n = \{L_i, C_j\}$, where n is the operator orientation. A vector of intensity of each pixel, is obtained using this curve operator with n orientation. Average value is calculated with each element of vector at specified orientation which represents the curve operated pixel and is expressed as (4).

$$I_n(x, y) = (\sum_{i=1,j=1}^{i=l,j=r/2} COP_n(i, j))/(l + \frac{r}{2}) \quad (4)$$

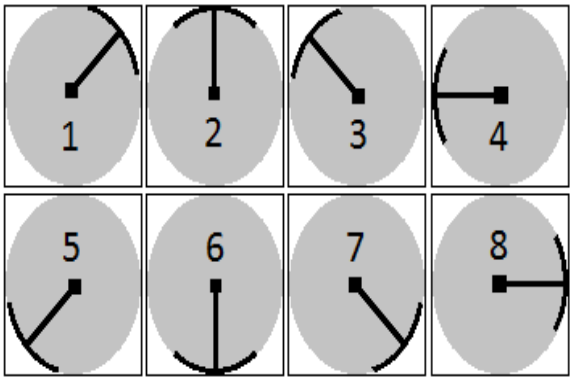

Fig. 3. Illustration of proposed curve operator in 8 orientation.

C. Optic Disk Detection

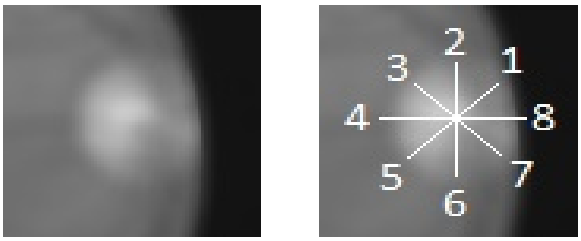

(a) (b)

Fig. 4. (a) Filtered optic disk. (b) Representation of line orientation.

From the Fig. 2(b) and Fig. 4(a) it can be seen that, inside optic disk region color intensity is not constant but it has gradient property. Color intensity is reduced from left edge (near to retinal image center) to right edge of OD or vice versa. In this paper 8 orientation of curve operator as shown in Fig. 4(b) is considered. Because curve operator with more orientation has less effect on the gradient property of OD. The length of line segment is used as $l = r/5$ as referred to [16]. According to the proposed method, 8 operated pixel intensities $(I_n(x, y); n = 1, 2, ..., 8)$ are calculated for a pixel $P(x, y)$. Oriented pixel intensity has a specific pattern with upward and downward variation. This pattern can be used to detect OD. The orientation with the upward or downward variation is generally indiscriminate for the pixels which are far away from OD in retinal image. But for those pixels which are around the OD, the image variation has upward or downward characteristics with highest and lowest intensity value. The variation of oriented pixel intensity is shown in Fig. 5. Characteristics of the curve as shown in Fig. 5(b) are defined as upward and in Fig. 5(d) as downward variation.

Two oriented images are created according to upward and downward variation and shown in Fig. 6(a) and Fig. 6(b) respectively. In case of upward variation two points are

(a) Fundus image with pixel marker

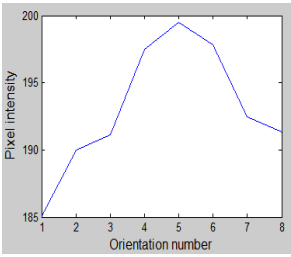

(b) Upward variation of selected pixel

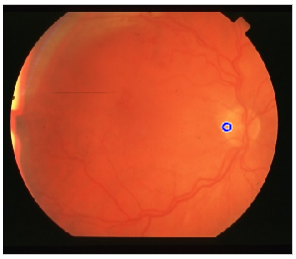

(c) Fundus image with pixel marker

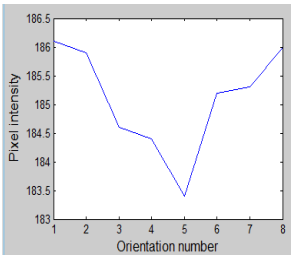

(d) Downward variation of selected pixel

Fig. 5. Representation of intensity variation for the marked pixel.

located considering highest and lowest pixel value respectively. Similarly two points are located for downward variation. These four points are predicted points for OD region and shown in Fig. 7(a). In Fig. 7(a) blue point is the highest and red point is the lowest value for upward variation as well as green point is the highest and white point is the lowest value for downward variation respectively.

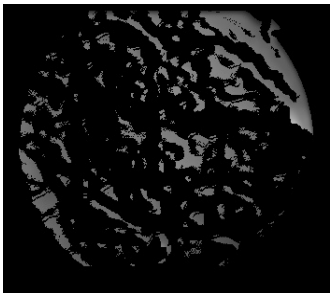

(a) Created image considering upward variation

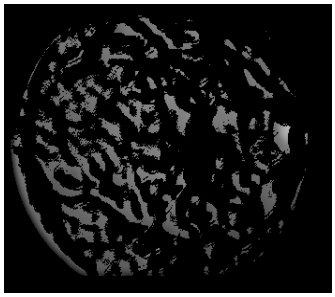

(b) Created image considering downward variation

Fig. 6. Image representation of variation in curve orientation.

To validate these points, four regions of interest (ROI) centering the four predicted points are cropped as shown in Fig. 7(b). After that correlation is calculated between cropped oriented images and correlation mask using (5), where R denotes resultant image, M mask and I cropped oriented image.

$$R(x,y) = \sum_{x',y'} (M(x',y') \cdot I(x+x',y+y')) \qquad (5)$$

Also the correlation mask is shown at inset in Fig. 8(a) on left top corner. Among these four correlation values, the point corresponds to maximum value is validated as the pixel in OD region. In this figure final detected point is shown as the small circle and the larger circle symbolizes the entire OD region. Finally Fig. 8(b) shows the result as well as the selection of point for OD region.

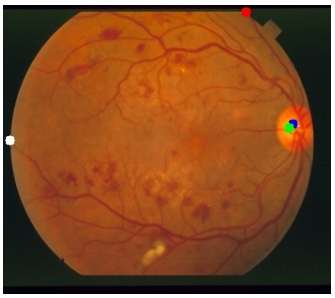

(a) Four predicted points

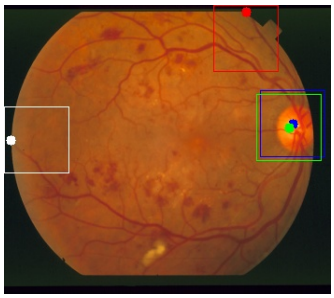

(b) Cropping region selection based on four predicted points

Fig. 7. Prediction and cropping region selection

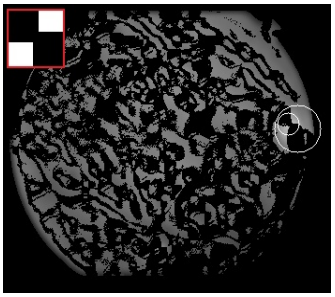

(a) Point verification using correlation mask

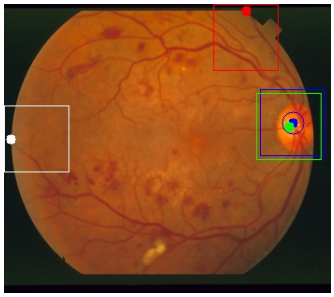

(b) Final point setection

Fig. 8. Verification and finalization of OD region

III. Results & Discussion

A. Fundus Image Database Acquisition

In this paper, three public fundus image databases are used for evaluating the proposed method. Among them DIARETDB0 [13] and DIARETDB1 [17] are created for the diagnosis of type 1 diabetes. DIARETDB0 database contains 130 color fundus images among them there are 20 images of healthy retina and 110 contain the signs of diabetic retinopathy. Also the DIARETDB1 database is being made up of 89 color fundus images in which 84 images are compromised with mild non proliferative signs of the diabetic retinopathy and 5 are considered as normal which do not contain any signs of the diabetic retinopathy. Referring from [13] and [17], the size of each image of both databases is 1500×1152 and were captured at few 50 degree field of view (FOV) with digital fundus cameras with unknown camera settings (flash intensity, shutter speed, aperture, gain). Also these images contain an unknown amount of imaging noise and optical aberrations (dispersion, transverse and lateral chromatic, spherical, field curvature, coma, astigmatism, distortion), and unknown accuracy of photometric information (color or intensity).

The third database is STARE (Structured Analysis of the Retina) project's dataset [9], [18]. In this database the number

of normal retinal image is 31 and that of pathological retina is 50. It was formed for benchmarking OD detection and is much more challenging compared with the other two databases.

B. Experimental Results

For each retinal fundus image within the three databases, firstly boundary pixels are manually labeled with a circle. The OD region is estimated as located correctly, if the validated point lies within the fitted boundary circle. Proposed method explained in this paper is implemented individually on the three public databases as mentioned before. Some examples of OD detection using the proposed curve operator technique is presented in Fig. 9. The set of six figures is separately acquired from three mentioned databases. Among them some image as 2nd in Fig. 9(a) has retinal lesion. Some as corresponds to healthy retina as 4th of Fig. 9(b). 5th in Fig. 9(c) shows retinal exudate. The significance of each color is described in subsection II-C. The circle represents the final validated point as well as the optic disk detection.

TABLE I. PERFORMANCE COMPARISON OF THE OD DETECTION METHODS ON DIARETDB1 DATABASE

Methods	Accuracy
Walter et al. [5]	92.13%
Lupascu et al. [19]	86.51%
Welfer et al. [11]	97.7%
Kande et al. [10]	88.76%
Proposed method	**94.38%**

TABLE II. PERFORMANCE COMPARISON OF THE OD DETECTION METHODS ON STARE DATABASE

Methods	Accuracy
Sinthanayothina et al. [6]	42.00%
Walter et al. [3]	58.00%
Zhu et al. [20]	93.80%
Lu et al. [12]	96.30%
Hoover et al. [9]	89.00%
Proposed method	**87.65%**

TABLE III. AVERAGE PROCESSING TIME PER IMAGE FOR DIARETDB1 DATABASE

Methods	Time (Sec.)
Welfer et al. [11]	7.89
Kande et al. [10]	72.84
Walter et al. [5]	117.63
Proposed method	**6.13**

OD detection accuracy is calculated as the ratio of number of successful OD detection image and total number of fundus image. According to the experimental results, the accuracy outcomes of STARE, DIARETDB0 and DIARETDB1 are 87.65%, 95.38% and 94.38% respectively. Performance comparison of the proposed method with some earlier reported methods is demonstrated in Table I and Table II for DIARETDB1 and STARE database respectively. In Table II, the value of accuracy for [6] is taken from [12].

Besides OD detection accuracy processing time is also deliberated as the performance parameter for the proposed method. For a single color fundus image, total processing time is calculated from the inception of reading image to optic disk detection. Then average time per image is calculated by dividing total processing time with total number of image for individual database. With the curve operator method average time per image is measured as 10.79 sec., 6.13 sec. and 8.39 sec. for DIARETDB0, DIARETDB1 and STARE database respectively. Also the average processing time to detect OD au-

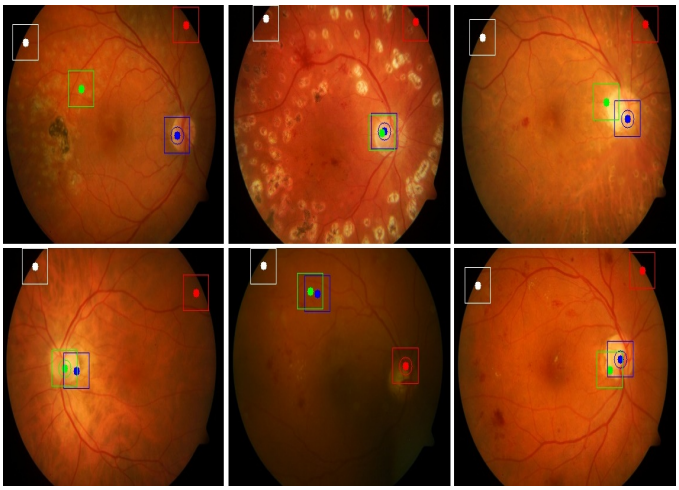

(a) Acquired images from DIARETDB0 databases

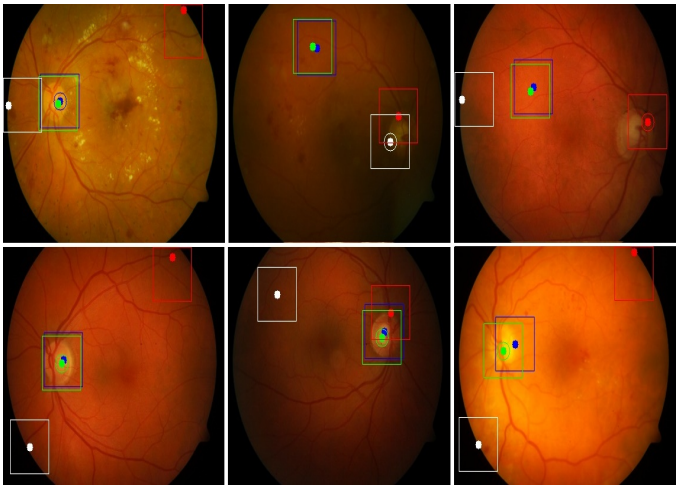

(b) Acquired images from DIARETDB1 databases

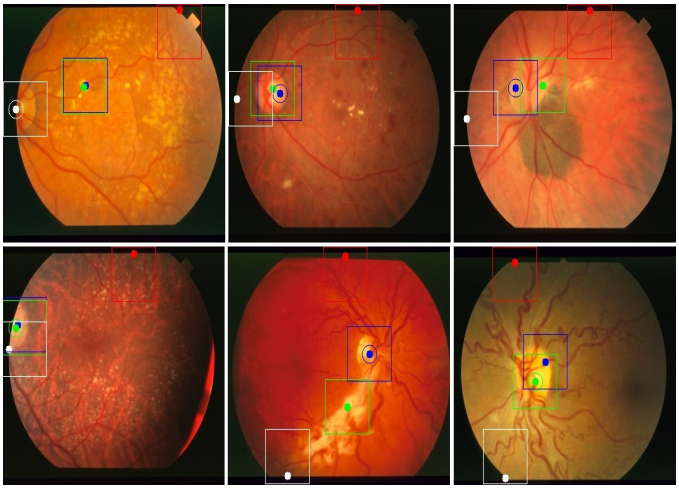

(c) Acquired images from STARE databases

Fig. 9. Illustration of experimental results of OD detection in fundus images using proposed method.

tomatically is compared with other methods for DIARETDB1 database and illustrated in Table III. Here the value of time for [5], [10] is taken from [11].

C. Discussions

From the results it is seen that the proposed method using curve operator gives promising outcomes. It is simple and performs with color fundus image with moderate lesion. From Fig. 9 it is seen that the optic disk is detected accurately though there are a level of noise, retinal lesion and imaging artifacts. This method is autonomous and other algorithms like blood vessel or background segmentation are not necessary which are very time consuming. These algorithms give high accuracy but consume long processing time. But the proposed method gives a balanced result between accuracy and processing time. In [12], 21 orientations are used but in proposed method only 8 orientations are required. Because the use of more than 8 orientations has the same result. Also this low number of orientation contributes on short processing time. Examining Table I and Table III it is seen that the proposed technique has low processing time with moderate OD detection accuracy.

The proposed method has some limitations. In particular, this method evaluates the optic disc in fundus image considering the perception that the optic disc is typically brighter or darker than the surrounding background. So it fails for those images which have a brighter or darker lesion or exudates than the OD region. Also the processing time will be reduced proportionally with image size. Also in experimental results no performance is compared for DIARETDB0 databases for the lack of other accuracy data. To perform overall processing "Intel Duel Core, 2.6 GHz" processor with 2 GB RAM is used as personal computer configuration. Also this work has been implemented in Microsoft visual studio 2010 environment with the help of Intels OpenCV library.

IV. Conclusion

A new method is proposed in this paper to detect the optic disk automatically and correctly in the color fundus images. This method takes the advantages over blood vessels segmentation and image background masking. It is important to notice that the accuracy of OD detection have to cost processing time and the proposed method gives the effective results. In this paper the importance is emphasized on the balance between detection accuracy and processing time. In this work all pixels are considered which degrade OD detection. In future works, concentration will be emphasized on macula detection with improving the accuracy using some filtering methods.

References

[1] K. W. Tobin, E. Chaum, V. P. Govindasamy, and T. P. Karnowski, "Detection of anatomic structures in human retinal imagery," *IEEE Trans. Med. Imag.*, vol. 26, p. 17291739, 2007.

[2] H. Li and O. Chutatape, "Automated feature extraction in color retinal images by a model based approach," *IEEE Trans. Biomed. Eng.*, vol. 51, p. 246254, 2004.

[3] T. Walter and J. C. Klein, "Segmentation of color fundus images of the human retina: Detection of the optic disc and the vascular tree using morphological techniques," in *Proc. Int. Symp. Med. Data Anal.*, 2001, pp. 282–287.

[4] A. Aquino, M. Gegundez-Arias, and D. Marin, "Detecting the optic disc boundary in digital fundus images using morphological, edge detection, and feature extraction techniques," *IEEE Trans. Med. Imag.*, vol. 29, no. 11, pp. 1860–1869, Nov 2010.

[5] T. Walter, J. C. Klein, P. Massin, and A. Erginay, "A contribution of image processing to the diagnosis of diabetic retinopathy - detection of exudates in color fundus images of the human retina," *IEEE Trans. Med. Imag.*, vol. 21, no. 10, pp. 1236–1243, 2002.

[6] C. Sinthanayothina, J. F. Boycea, H. L. Cookb, and T. H. Williamsonb, "Automated localisation of the optic disc, fovea, and retinal blood vessels from digital colour fundus images," *Br. J. Ophthalmol.*, vol. 83, pp. 902–910, 1999.

[7] A. A. H. Abdel-Razik Youssif, A. Z. Ghalwash, and A. A. S. Abdel-Rahman Ghoneim, "Optic disc detection from normalized digital fundus images by means of a vessels' direction matched filter," *IEEE Trans. Med. Imag.*, vol. 27, no. 1, pp. 11–18, Jan 2008.

[8] M. Foracchia, E. Grisan, and A. Ruggeri, "Detection of optic disc in retinal images by means of a geometrical model of vessel structure," *IEEE Trans. Med. Imag.*, vol. 23, no. 10, pp. 1189–1195, Oct 2004.

[9] A. Hoover and M. Goldbaum, "Locating the optic nerve in a retinal image using the fuzzy convergence of the blood vessels," *IEEE Trans. Med. Imag.*, vol. 22, no. 8, pp. 951–958, Aug 2003.

[10] G. B. Kande, P. V. Subbaiah, and T. S. Savithri, "Segmentation of exudates and optic disk in retinal images," in *Proc. Sixth Indian Conf. on Comput. Vision, Graph. Image Process. ICVGIP*, Dec 2008, pp. 535–542.

[11] D. Welfer, J. Scharcanski, C. M. Kitamura, M. M. D. Pizzol, L. W. B. Ludwig, and D. R. Marinho, "Segmentation of the optic disk in color eye fundus images using an adaptive morphological approach," *Computers in Biology and Medicine*, vol. 40, no. 2, pp. 124–137, 2010.

[12] S. Lu and J. H. Lim, "Automatic optic disc detection from retinal images by a line operator," *IEEE Trans. Biomed. Eng.*, vol. 58, no. 1, pp. 88–94, Jan 2011.

[13] T. Kauppi, V. Kalesnykiene, J. K. Kamarainen, L. Lensu, I. Sorri, H. Uusitalo, H. Klviinen, and J. Pietil, "Diaretdb0: Evaluation database and methodology for diabetic retinopathy algorithms," Lappeenranta Univ. Technol., Lappeenranta, Finland, Tech. Rep., 2006.

[14] A. Osareh, M. Mirmehdi, B. Thomas, and R. Markham, "Comparison of colour spaces for optic disc localisation in retinal images," in *Proc. Int. Conf. Pattern Recognit.*, 2002, pp. 743–746.

[15] C. Tomasi and R. Manduchi, "Bilateral filtering for gray and color images," in *Proc. IEEE Int. Conf. Comp. Vis.*, Jan 1998, pp. 839–846.

[16] W. Tasman and E. A. Jaeger, *Duanes ophthalmology*, 15th ed. Baltimore, MD: Lippincott Williams & Wilkins, 2009.

[17] T. Kauppi, V. Kalesnykiene, J. K. Kamarainen, L. Lensu, I. Sorri, H. Uusitalo, H. Klviinen, and J. Pietil, "Diaretdb1: Evaluation database and methodology for diabetic retinopathy algorithms," Lappeenranta Univ. Technol., Lappeenranta, Finland, Tech. Rep., 2007.

[18] (2003, July) Stare project website. [Online]. Available: http://www.ces.clemson.edu/~ahoover/stare

[19] C. A. Lupascu, D. Tegolo, and L. Di Rosa, "Automated detection of optic disc location in retinal images," in *Proc. 21st IEEE Int. Symp. on Comput.-Based Med. Syst. CBMS '08.*, June 2008, pp. 17–22.

[20] X. Zhu and R. Rangayyan, "Detection of the optic disc in images of the retina using the hough transform," in *Proc. 30th Annu. Int. Conf. of the IEEE Eng. in Medicine and Biology Soc. EMBS*, Vancouver, British Columbia, Canada, Aug 2008, pp. 3546–3549.

Alpha Band Dependency of EEG Signal on Different Stimulation of Brain for Human Computer Interaction

Md. Kamrul Hasan*, Nahid Al Mahmud, Md. Shazzad Hossain, and Mohiuddin Ahmad
Department of Electrical and Electronic Engineering (EEE)
Khulna University of Engineering & Technology (KUET)
Khulna-9203, Bangladesh
*E-mail: m.k.hasan@eee.kuet.ac.bd

Abstract—**Brain–computer Interfaces (BCIs) are the communicating bridges between the human brain and a computer which may be implemented on the basis of Steady-state Visual Evoked Potentials (SSVEPs). It is mandatory to improve the stimulation for the betterment of the accuracy of modern BCIs, higher Information Transfer Rate (ITR), desired bandwidth (BW), and Signal to Noise Ratio (SNR) of BCIs. The performance of stimulator depends on many factors such as size and shape of stimulator, frequency of stimulation, luminance, color, and subject attention. Information Transfer Rate (ITR) varies with the change of frequency and size of the visual stimuli. In our research, a Circular Repetitive Visual Stimulator (CRVS) of different diameters (2", 2.5"and 3"), colors (RGB), frequencies (10, 15 and 20 Hz) was used. The raw EEG signal is processed for finding the effect of diverse stimulation on alpha band of EEG signal at diverse condition. From the analysis it is found that, when the size of the stimulator changes from 2" to 2.5", resultant increase in alpha wave is 58.18%. But for a further increase in size from 2.5" to 3", there is a resultant decrease in alpha wave of 45%. Similar result is found for the changes in frequencies and colors.**

Keywords— Electroencephalogram (EEG), Brain-computer Interface (BCI), Steady-state Visual Evoked Potential (SSVEP), Circular Repetitive Visual Stimulator (CRVS), Signal power, Signal energy.

I. INTRODUCTION

In accordance with the concept of modern biomedical engineering, brain–computer interface (BCI) is a direct communication pathway between the brain and an external devices. BCIs are also called mind-machine interface (MMI), direct neural interface (DNI), synthetic telepathy interface (STI) or brain–machine interface (BMI). BCIs are often directed at assisting, augmenting, or repairing human cognitive or sensory-motor functions.

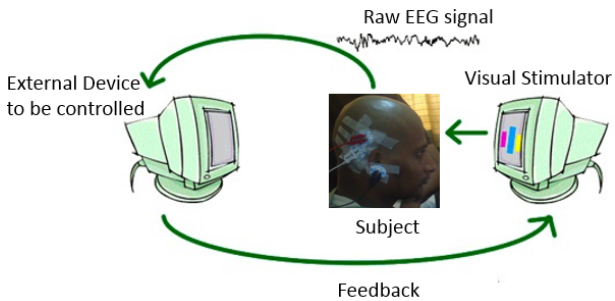

Figure 1. BCI system to communicate with external devices.

A typical BCI system is shown in Figure 1. Various techniques are now available to monitor brain function, e.g., electroencephalography (EEG), magneto-encephalography (ME), functional magnetic resonance imaging (f-MRI), and positron emission tomography (PET). The latter three techniques are technically demanding and expensive. At present, EEG is the optimal choice for BCI implementation [1]-[2]. In comparison with other systems, the VEP-based BCI is considered as a dependent BCI because the generation of the VEP depends on the control of eye movements via the output pathways of cranial nerves and extra-ocular muscles. The EEG reflects the electrical activity of the brain, which can be recorded directly from the scalp in non-invasive way using surface electrodes [3]. EEG measures the electrical potentials generated to the excitatory and inhibitory post-synaptic potentials developed by cell bodies and dendrites of pyramidal neurons [4]-[6] as shown in Figure 2. EEG signals, as one of the biological signals, are in μV range (0.5 to ~ 100μV) at low frequency (0.5 to 30 ~ 40Hz). They are usually referred to as rhythms and are classified into five frequency bands [1] shown in Table I.

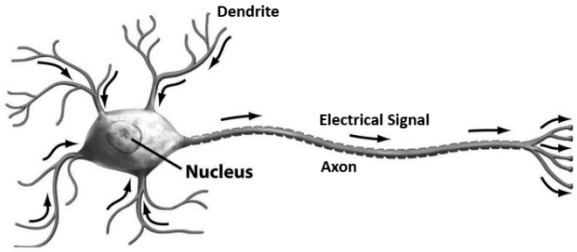

Figure 2. Neuron general structure and generation of electrical signal (EEG Signal) due to external stimulation.

The electrical activity of brain due to visual stimulation is known as the Visual evoked potential (VEP) which may be measured from the scalp of human the brain. The frequency of stimulation of steady-state VEP (SSVEP) and VEP is different in magnitude. For VEP approximately 2 Hz for the stimulator is most commonly used whereas about 6Hz stimuli are used for SSVEP which produce a periodic response called SSVEP. In modern BCI system, SSVEP are most commonly used due to its short-term identification, high SNR for data transmission for wireless BCI [7]-[8]. The extracted EEG signal contains five frequency bands in which Delta waves lie within the range of 1–4 Hz. These waves are prominent during conditions of deep sleep. Theta waves lie within the range of 4–8 Hz. They appear between the states

978-1-4673-9257-0/15/$31.00 ©2015 IEEE

of consciousness and drowsiness. Theta waves have been associated with creative inspiration and deep meditation. Alpha waves lie within the range of 8–13 Hz. These waves indicate both a relaxed awareness state without any attention. A beta wave is the EEG signal with a frequency range of 13–30 Hz. Beta waves are associated with active thinking, active attention, focus on a particular thing, or during solving concrete problems. High-level beta wave resembles a panic state. The frequencies above 30 Hz (mainly 36-44 Hz) correspond to the gamma range. These low amplitude and rarely found waves are used to detect certain brain diseases. They also indicate event-related synchronization (ERS) of the brain [9]-[11]. The bit rates, comfort and safety of SSVEP based BCI depends on the nature, size, shape, frequency and color of CRVS. The selection of SSVEP for the stimulation of brain, it is advisable to consider these essential element of SSVEP-based BCIs [12]. Existing papers focus on general VEP-based BCIs [13] and signal processing algorithms applied to BCIs [12], [14]. This paper contributes to select proper CRVS for the stimuli that have been used for SSVEP-based BCIs.

TABLE I. FREQUENCY BAND, PATTERN AND AMPLITUDE OF EEG SIGNAL

Brain Waves	Pattern of Waves	Voltage and Freq. Range	Subject Condition
Delta (Δ)		10mV, 1-4 Hz	Profound sleep
Theta (θ)		10μV, 4-8 Hz	Light sleep
Alpha (α)		10μV, 8-13 Hz	Relax state
Beta (β)		10-20μV, 13-30 Hz	Activity or thinking state
Gamma (γ)		5-10μV, 36-44 Hz	Abnormal condition

II. PROPOSED ARCHITECTURE

The proposed architecture of this research is described in three blocks as follows in Figure. 3.

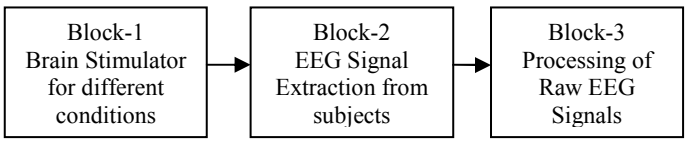

Figure 3. Overall block representation of proposed work.

A. Block-1

In Figure. 4 a typical block diagram of a stimulator is shown in which MUX block is used to select any item among three. Then three MUXed outputs are ANDed to visually stimulate the human brain for the raw EEG extraction. In this stimulation the color, frequency and diameter of a circular repetitive visual stimulator (CRVS) is varied to change the stimulation pattern.

B. Block-2

In this block as shown in Figure.5, raw EEG signal is extracted from the brain using various stimulation patterns as described in block-1. EEG signal for different stimulation patterns in visual stimulator is recorded by the acquisition unit (MP-36) which is further processed in Block-3.

C. Block-3

The raw EEG signals from Block-2 are processed using various software (MATLAB, BIOPAC, and ACQKNOWLEDGE) in accordance with Block-3 as shown in Figure 6. The raw EEG signal is filtered by band pass filter (BPF) to obtain desired EEG wave namely alpha. Energy and power of this wave are calculated using MATLAB (R2012b). Some features are also extracted from the raw EEG signal for proper classification. These features along with the energy and power calculated from the alpha wave are further analyzed to verify the hypothesis made in this manuscript.

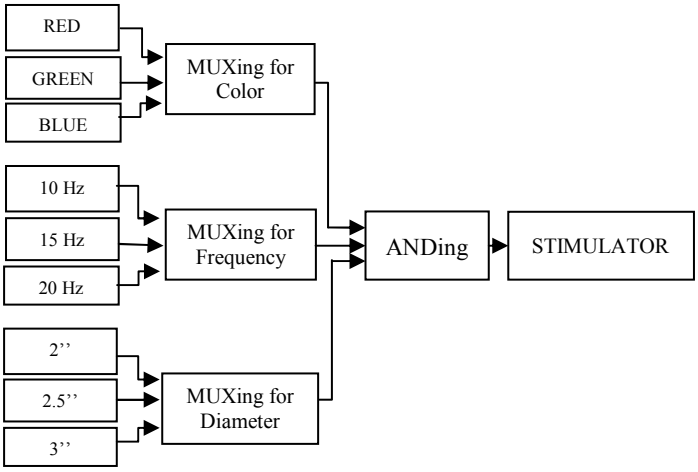

Figure 4. Visual stimulator with color, frequency and diameter variation arrangement.

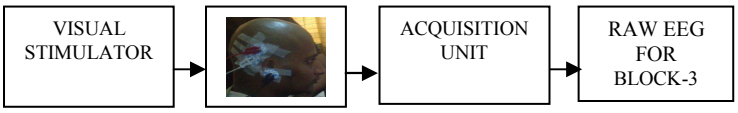

Figure 5. Raw EEG signal acquisition block.

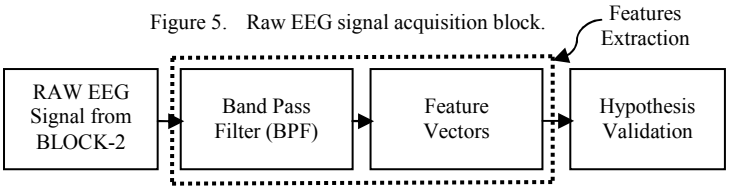

Figure 6. Feature extraction and analysis block.

III. DESIGNED STIMULATOR

To stimulate the brain visually, a stimulator is designed using JAVA script. In the Figure 7 (a) and 7 (b), the typical screen shots of this stimulator are shown. The characteristics of extracted signal depends on the configuration of laptop used for the visual stimulation. The configuration used for our stimulation was Intel (R) core (TM) 2 Duo CPU T6600 @2.20 GHz, 4 GB RAM (Installed memory) and 32-bit OS. The refresh rate of the display was 60 Hz.

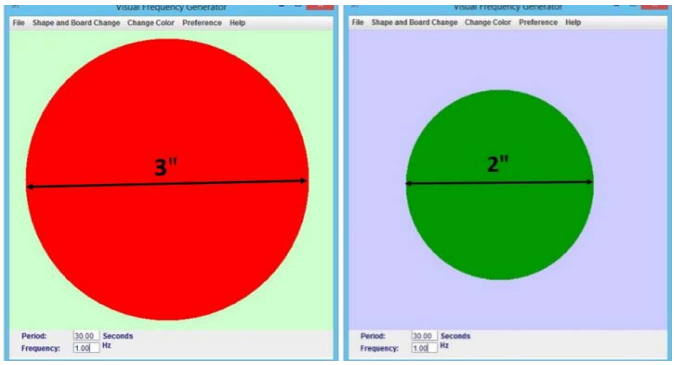

(a) (b)

Figure 7. Screenshot of the visual stimulator for two different size and color a) for red color of diameter 3" b) for green color of diameter 2".

IV. Graphical Analysis

Figure 8 shows the typical EEG signals for different conditions (green, 10 Hz and 3" dia. & green, 20 Hz and 2.5" dia.). Their corresponding Alpha waves are also shown which are obtained by filtering the raw EEG signals according to Figure 6.

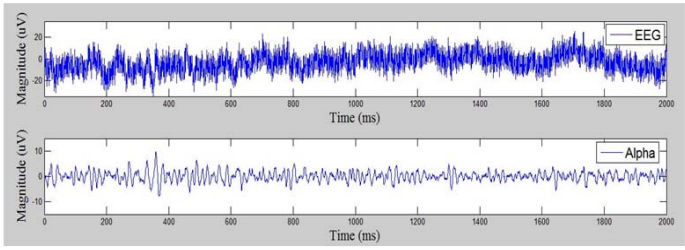

(a)

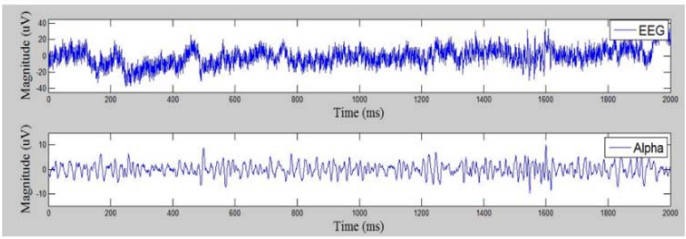

(b)

Figure 8. Typical EEG signal and their Alpha bands a) for green, 10 Hz and 3" dia. b) for green, 20 Hz and 2.5" dia. Stimulator.

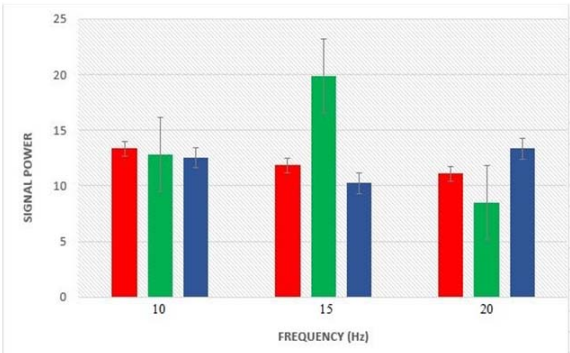

(a)

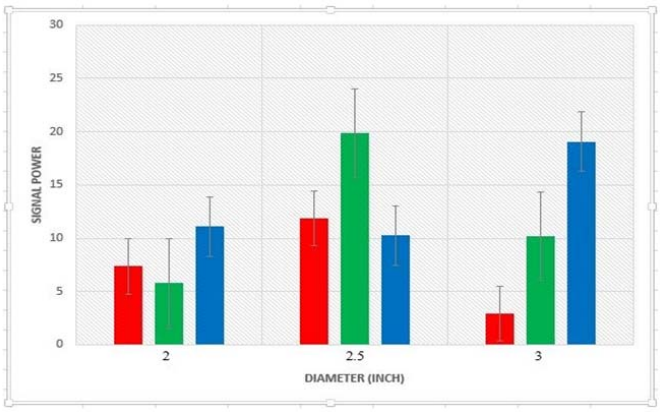

(b)

Figure 9. Variation of power of Alpha wave with variation of a) frequency as well as b) size.

Figure 9 (a) and 9 (b) represent a power variation with different frequencies and sizes for alpha (α) wave. Maximum power can be obtained at a frequency of 15 Hz for Green colored stimulation. Similar results are found when size of the stimulator is varied. Maximum power can be obtained at 2.5 inch diameter of the stimulator for Green color stimulator.

V. Tabular Analysis

TABLE II. Power and Energy Representation of Alpha Wave of EEG Bands

Size	Color	Frequency	Power	Energy($\times 10^4$)
Dia. 2"	Red	10	08.4456	3.9138
		15	07.3631	3.2265
		20	06.7715	3.0418
	Green	10	10.9952	4.9126
		15	05.7648	2.5982
		20	12.4226	5.36.3
	Blue	10	09.9841	4.7426
		15	11.0890	4.7393
		20	09.9060	4.2328
Dia. 2.5"	Red	10	13.3596	5.6791
		15	11.8485	5.1375
		20	11.0775	4.6603
	Green	10	12.8196	5.5701
		15	19.8871	8.9572
		20	08.5000	3.8207
	Blue	10	12.5278	5.4308
		15	10.2475	4.3726
		20	13.3325	5.6596
Dia. 3"	Red	10	07.2947	3.2600
		15	02.9098	1.6441
		20	16.5685	7.0714
	Green	10	11.9091	5.0781
		15	10.1972	4.4531
		20	12.8156	5.1326
	Blue	10	14.0363	6.0032
		15	19.0413	8.0821
		20	12.2827	5.2447

VI. CONCLUSION

Brain-computer Interfaces (BCIs) based on the SSVEP permit the communication with the physical world after paying attention to the visual stimulator. In this research, one of the vital factors of all stimuli in BCIs viz circular shape with different sizes, colors and frequencies is briefly analyzed. In our manuscript, the effect of size, frequency and color of a circular stimuli on the power and energy of EEG signal has been also analyzed. The number of target detection also depends on the refresh rate of the monitor and the number of stable timers supported by the system. This research helps to choose perfect stimuli which may outfit the performance of SSVEP based BCIs and safety of BCIs. Perfection to stimuli can enhance the SSVEP Signal to Noise Ratio (SNR), reduce the complexity of extracted signal processing, increase the target detection, help subjects to pay attention and allow independent BCI operation. We have designed the software for investigating the effect of frequency, color and different sizes of circular stimulator on the performance (power, energy and ITR). The major outcome of our research has been found that for a required power or energy, the size, shape, color and stimulation frequency of the brain stimulator can be chosen with the help of the Table II.

REFERENCES

[1] M. K. Hasan, R. Z. Rusho, and M. Ahmad, "A Direct Noninvasive Brain Interface with Computer Based On Steady-State Visual-Evoked Potential (SSVEP) With High Transfer Rates", International Conference on Advances in Electrical Engineering (ICAEE) (ISBN: 978-1-4799-2463-9), 2013, Dkaka, Bangladesh. DOI: 10.1109/ICAEE.2013.6750360.

[2] M. K. Hasan, T. M. Hossain, A. K. Faisal, and M. Ahmad, "Effect of Diverse Stimulations of Brain on EEG Signal for SSVEP Based Brain Computer Interface", Proc. of 2nd International Conference on Electrical Engineering and Information & Communication Technology (iCEEiCT 2015), IEEE, Jahangirnagar University (JU), Dhaka, May 2015.

[3] M. K. Hasan, R. Z. Rusho, T. M. Hossain, T. K. Ghosh, and M. Ahmad, "Design and Simulation of Cost Effective Wireless EEG Acquisition System for Patient Monitoring", International Conference on Informatics, Electronics and Vission (ICIEV) (ISBN: 978-1-4799-5179-6), 2014, Dhaka, Bangladesh. DOI: 10.1109/ICIEV.2014.6850797.

[4] H. Saadi, M. Ferroukhi and M. Attari "Development of wireless high immunity EEG recording system", 2011 International Conference on Electronic Devices, Systems and Applications (ICEDSA). (2002). DOI: 10.1109/ICEDSA.2011.5959060.

[5] C. Moulin "Contribution à l'étude et à la réalisation d'unsystème électronique de mesure et excitation de tissue nerveux à matrices microélectrodes", Thèse de doctorat, Lyon, 2006.

[6] Neuron structure. Available at: www.google.com/search?q=neuron+structure&source=lnms&tbm=isch&sa=X&ved=0CAcQ_AUoAWoVChMIocGK3ueHyQIVQU-OCh3Ndgkh&biw=1200&bih=600

[7] M. Cheng, X. Gao, S. Gao, D. Xu, "Multiple Color Stimulus Induced Steady State Visual Evoked Potentials", 23rd Annual International Conference of the IEEE Engineering in Medicine and Biology Society, 2001. Vol: 2, DOI: 10.1109/IEMBS.2001.1020359.

[8] T. F. Collura, "Real-time filtering for the estimation of steady-state visual evoked brain potentials", IEEE Trans. Biomed. Eng., vol. BME-37, pp. 650-652, June 1990.

[9] M. Salehuddin, Suprijanto, F. I. Muchtadi, "Prototype Design of Low Cost Four Channels Digital Electroecephalograph for Sleep Monitoring", 2nd International Conference on Instrumentation Control and Automation, 17-17 November 2011, bandung, Indonesia. DOI: 10.1109/ICA.2011.6130154

[10] J. r. Cameron dan J. G. Skfronik, "Medical Physics", Singapore: Jhon Wiley and Sons. 1987.

[11] D. Zhu, J. Bieger, G. G. Molina, R. M. Aarts, "A Survey of Stimulation Methods Used in SSVEP-Based BCIs", Hindawi Publishing Corporation Computational Intelligence and Neuroscience, Vol. 2010, Article ID 702357, 12 pages. DOI:10.1155/2010/702357.

[12] Y. Wang, X. Gao, B. Hong, C. Jia, and S. Gao, "Brain-computer interfaces based on visual evoked potentials: feasibility of practical system designs,"IEEE Engineering in Medicine and Biology Magazine, vol. 27, no. 5, pp. 64–71, 2008.

[13] A. Bashashati, M. Fatourechi, R. K. Ward, and G. E. Birch, "A survey of signal processing algorithms in brain-computer interfaces based on electrical brain signals," Journal of Neural Engineering, vol. 4, no. 2, pp. R32–R57, 2007.

[14] M. K. Hasan, M. S. Hossain, T. K. Ghosh, and M. Ahmad, "A SSVEP Based EEG Signal Analysis to Discriminate the Effects of Music Levels on Executional Attention", American Journal of Bioscience and Bioengineering, Science Publishing Group , vol. Vol. 3, issue 3-1, pp. 27-33, May, 2015.

An Approach to Estimate Cognitive State with the Impact of Listening Music on Brain Activity

Monira Islam, Mohiuddin Ahmad, and Md. Salah Uddin Yusuf
Department of Electrical and Electronic Engineering
Khulna University of Engineering & Technology (KUET), Khulna-9203, Bangladesh
E-mail: monira_kuet08@yahoo.com, mohiuddin.ahmad@gmail.com, ymdsalahu2@gmail.com

***Abstract*—This paper presents an approach to estimate the cognitive states depending on the variations of different effective frequency bands of EEG signal with listening music. In this work, EEG signals are collected for different types of songs to analyze the musical activity on human brain. Spatial and temporal analysis are applied to the brain signals to extract the salient features to estimate the human cognitive state. The classification accuracy of different frequency bands indicates the larger alpha or beta activity on human brain for the selected songs. The highest classification accuracy for soft song was found for θ-band which indicates the state of catnap. For medium and fast song the effectiveness of α band and β band are noteworthy, which indicate the state of relax and stress respectively. Therefore, our proposed approach is innovative and efficient to determine the human cognitive states.**

Keywords—EEG; cognitive state; brain activity; frequency band; music signal.

I. INTRODUCTION

Cognitive state comprises the functional activity of brain and subjective experience, expressions and biological stimulation for specific person in different environmental conditions. The basic socio-cognitive domain of human life is music. Listening music helps to keep the neurons and synapses more active and which varies the effective frequency bands of brain signal which is named as electroencephalogram (EEG). When sound waves are listened or pronounced, they have an impact in neurological (brain and nerve) system work in human body [1]. When neurons are activated, local current flows and generate electrical activity which is recordable on the head surface [2]. This electrical activity is termed as EEG signal which activates different parts of the brain during listening music [3]. It also indicates the cognitive states with the variations of functional activities of brain which are more influenced by exposure to music.

Fig. 1 shows the proposed way which indicates the variation of EEG signal with audio stimulation. Each of the music or song has specific frequency and bits according to which the brain activity and the effective frequency band of EEG signal may vary and the cognitive activities also change according to the frequency bands. The assignment of different cognitive states with their effective frequency band is shown in Table I.

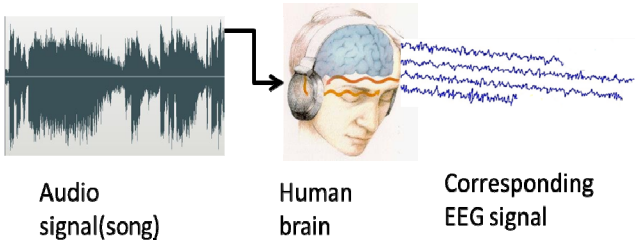

Fig. 1. Brain stimulation while listening audio signal (songs) and correponding EEG signal.

Our objective is to detect human's mental state according to the influence of different types of songs. In Table II the soft music is selected which composes a softer, more toned-down sound putting more emphasis on melody and vocal harmonies. The medium and fast music are selected according to the tempo of music i.e. rate of speed or number of beats per minutes.

While listening different types of songs such as loud or soft, high pitch or low pitch, audible or inaudible etc., our brain responses differently. Low frequency indicates the state of relax while high frequency indicates the state of stress [4]. The human brain produces different electrical activity due to the different levels of music [5]. Each type of music or songs has its own frequency. While listening music the frequency of the music can be either resonate or in conflict with the body's rhythms (heart rate) and also with the frequency bands of EEG rhythm which authorizes specific functions of brain [6].

TABLE I. FREQUENCY BAND REGION OF EEG SIGNAL

EEG wave	Frequency band region	Cognitive states
Delta (δ) wave	(0.4-4) Hz	Unconsciousness (Associated with deep sleep)
Theta (θ) wave	(4-8) Hz	Catnap (Associated with drowsiness)
Alpha (α) wave	(8-14) Hz	Relax (Associated with relaxed, alert state of consciousness)
Beta (β) wave	(14-35) Hz	Stress/Tension (Associated with active, busy or anxious thinking)

978-1-4673-9257-0/15/$31.00 ©2015 IEEE

TABLE II. CATEGORY OF SONGS SELECTED FOR COGNITIVE STATE ESTIMATION

Song type	Soft song	Medium fast song	Fast song
Bangla	Rabindra sangeet	Adhunik sangeet	Hard Rock
Hindi	Carnatic	Patriotic song	Pop
English	Melody	Folk song	Hard Rock

The categorization of selected songs for cognitive state estimation is shown in Table II. So, music can be used as a tool to estimate the cognitive states such as tension/ stress, solitude, relax and these changes are reflected clearly in physiological system for human body [7]. The major concern of this research are: (i) to propose a technique for extracting some salient statistical and time-frequency analysis based features according to the variation of effective frequency band due to different types of music and (ii) to evaluate the efficiency of the extracted features for different EEG bands to detect the cognitive states using support vector machine. The main steps of the proposed method are shown in Fig. 2. In this research, the BIOPAC data acquisition unit MP36, C++ source code and AcqKnowledge® 4.1 software are used for data acquisition, analysis, storage, and retrieval [8].

A lot of works have been carried out for addressing the problem of musical influences on the functional responses of human brain. Gerra et al. found that while listening music the corresponding changes will be induced in neurotransmitters, peptides and hormonal reactions [9]. In [10-12], Authors shows the variations of functional activities of different frequency band relating the cognitive activity with music levels. They found that beta activity relates to increased alertness and cognitive processes [10] and unpleasant music produces decrease in alpha power at the right frontal lobe [11]. Authors in [12] showed when subjects listen to the pleasant music the changes were reflected in the EEG and there was an increase in frontal midline (Fm) theta power. Authors in [13] showed the dependence of EEG spectral power on the intensity and style of music. The effect of Indian classical music and rock music on brain activity was studied using Detrended fluctuation analysis (DFA) algorithm, and Multi-scale entropy (MSE) method [14]. The brain wave variation was monitored in reference [15] by changing the music type (techno and classical) and the results showed that when the music was switched from classical to techno, there was a significant plunge of alpha band and from techno music to classical there was an increase in beta activity. Authors in [2] presented a brief study of various effects of sound on the human brain activity employing the time-frequency analysis technique. R.S. Schaefer et al. showed a difference in alpha power in different directions to indicate that both the tasks and the stimuli modulate an attentional network, which may relate to the inhibition of non-task relevant cortical areas, as well as engagement with the music [16]. In this work, a new approach is proposed to identify the cognitive states from the variation of effective EEG band. Different statistical, frequency and time-frequency analysis i.e. temporal and spectral analysis (T & S analysis) are done to extract the effective features to estimate the cognitive states.

The rest of the paper is organized as follows: Section II describes the EEG signal recordings. Section III describes the signal analysis and features extraction procedure. Section IV illustrates the cognitive state estimation by using SVM technique. Section V discusses the results of estimated cognitive sates while listening music. Finally, Section VI concludes the result.

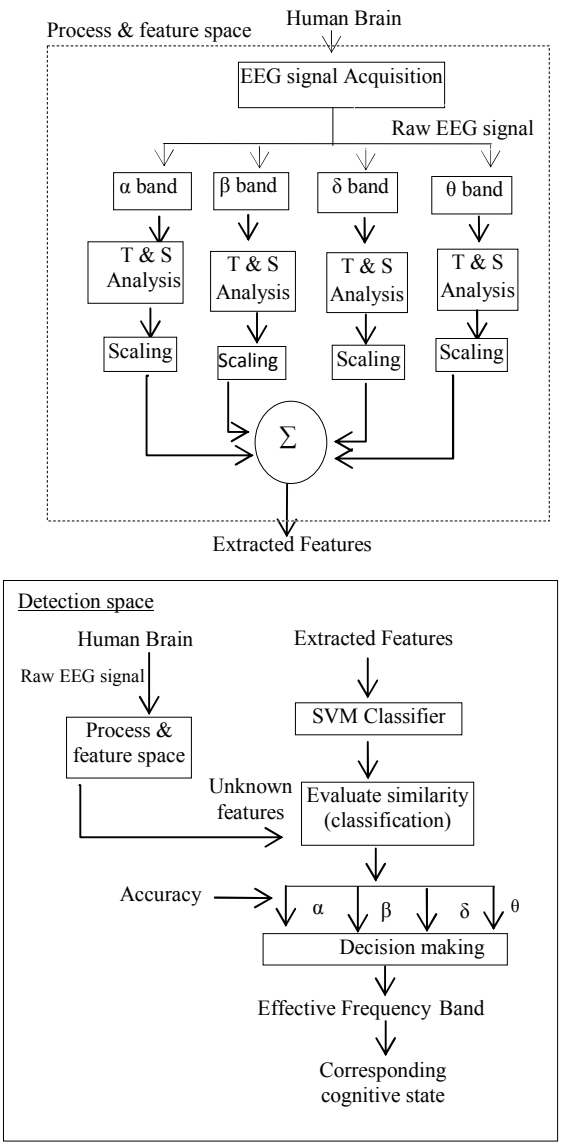

Fig. 2. Proposed approach for cognitive state estimation.

II. EEG SIGNAL RECORDING

In case of mental state evaluation brain signal is most essential so EEG data acquisition plays a significant role in this research. The electrical activity of human brain gets affected at the time of listening music. The electrical activity is measured at the scalp through a set of electrodes which are rich in information about the cognitive activity at different frequency bands of EEG signal.

A. *Music Selection for Cognitive State Estimation*

A lot of works have shown that different music has different physiological effect on human body rhythms and brain. The effect of music on brain functions rate based on subject's choice of like music (slow, medium and fast song) at different languages such that Bangla, English, Hindi. The selected songs have different spectral stimuli depending on their number of bits per second and affect separately on the EEG band waves and changes the signal characteristics. According to the selected salient features it is determined that which state is more affected with the effective frequency band influenced by the different types of selected songs.

Figs. 3(a), 4(a) and 5(a) show the frequency spectrum of soft, medium and fast song and Figs. 3(b), 4(b) and 5(b) show the corresponding brain signals respectively. In this work the Bangla, English and Hindi slow, medium fast and fast songs were played one after another taking a proper interval to evaluate the effect of cognitive activities of brain influenced by these songs. It is observed that the spectral components are higher for fast song than medium and slow depending which the effect of frequency bands for brain signal varies with the cognitive activities of brain.

B. *Subject Selection and Data Acquisition*

The EEG signals were collected in biomedical signal processing laboratory, KUET. The experimental data were collected from 48 numbers of subjects and the subjects were male, and were in good physical and mental conditions and able to react with different types of songs. Their average age was 23 years so that they are sensitive to all the mental activities.

The room was air conditioned and approximately noise free. In Fig. 6 the position of electrode on the scalp is shown for EEG data acquisition in the period of listening music.

III. Signal Analysis and Feature Extraction

The extracted EEG features are considered as the ideal characteristics to identify the variation of brain activities and represent the non-stationary characteristics of EEG signal which are particularly effective for recognition of human cognitive activities while listening different types of music.

A. *Time Domain Feature*

The most effective property of the statistical measures on time domain signal is that they will vary in magnitude with the variations of brain signal but maintains essential element of homogeneity. In this work, six different kinds of time-domain feature such as mean amplitude, median, standard deviation, variance, skewness, and kurtosis have been considered to show the influence of listening music on human brain. The expressions for different statistical features were briefly discussed in [18].

B. *Frequency Domain Feature*

The frequency-domain features used in this paper are based on the power spectrum of each 256 point of EEG samples. Each epoch of the EEG data is processed with Hamming window by zero padding for 256 points of FFT.

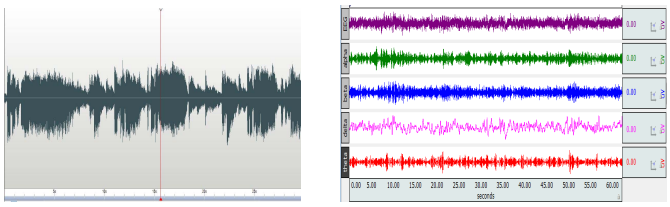

(a) (b)

Fig. 3. (a) Frequency spectrum of English soft song; (b) Corresponding EEG signal for soft song.

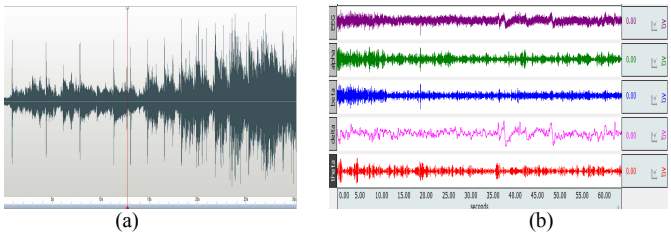

(a) (b)

Fig. 4. (a) Frequency spectrum of English medium song; (b) Corresponding EEG signal for medium song.

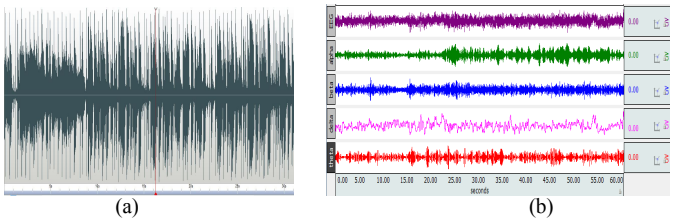

(a) (b)

Fig. 5. (a) Frequency spectrum of English fast song; (b) Corresponding EEG signal for fast song.

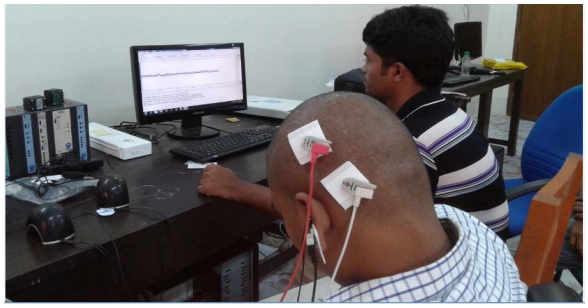

Fig. 6. Signal acquisition at the time of listening different types of music.

The power spectrum of all the sub-epochs is averaged to minimize the artifacts of the collected EEG signals in all sub-windows. Finally, EEG power spectrum is extracted in different channels such as Alpha, Beta, Delta and Theta. Different features for FFT analysis are obtained at alpha, beta, delta and theta component of EEG signal individually to determine the cognitive states influenced by different types of music is given by Eq. (1).

$$X(k)_l = \{X(0), X(1), \ldots X(n-1)\} \tag{1}$$

In Eq. (1), n represents the total number of frequency amplitude components; k represents the harmonic number of frequency components, and l represents alpha or beta or theta or delta. The real value, imaginary value, magnitude, phase angle and power spectral density are the effective features in this analysis.

It is integrated over its entire one-sided frequency domain (0, F) according to FFT analysis:

$$\int_0^F PSD(k)dk = \int_0^F 2\left|X(k)_l\right|^2 /(t_2 - t_1)dk \tag{2}$$

Equation (2) represents the expression of power spectral density in frequency domain where the average power of the signal is in the time range (t_1, t_2).

C. Temporal-Frequency Domain Feature

The discrete wavelet transform (DWT) analyzes the signal at different frequency bands to extract effective energy component by decomposing the signal into a coarse approximation and detail information [16]. In the present paper, the Daubechies4 wavelet function ("db4") is used for extracting features from the EEG signal in time frequency domain because it decomposes the high and low frequency components of EEG signal.

IV. Cognitive State Estimation using Support Vector Machine

In this work, temporal and spectral analysis based selection of effective frequency band of EEG signal for cognitive state estimation is proposed. In our proposed approach statistical and frequency based salient feature extraction are devised in to different EEG bands under the influence of different types of songs for selection of brain activities according to the classification rate of efficient frequency bands and their power spectrum analysis. The steps in effective band selection for the proposed method are given below:

i. The raw EEG signals from several subjects during hearing of different types of music are collected using three electrodes in BIOPAC data acquisition unit which are placed on the scalp.
ii. This preprocessed signal is divided into different EEG frequency bands such as Alpha, Beta, Delta and Theta and the salient global features are extracted from the specific frequency bands.
iii. From the classification rate of effective frequency band wave the pre-specified cognitive states can be determined.

For the evaluation of performance of cognitive states estimation, classification rate of different bands is achieved by using multiclass support vector machine. The human mental states are classified into the defined classes. For example, α = 1, β = 2, δ = 3, θ = 4. In order to perform a more reliable classification process, three stages are implemented. Firstly, The EEG data are prepared in the specified format and scaling is performed if necessary for each subject. Secondly, the data are trained to create a model. Finally, the new input data of another subject are predicted/classified using the model. In case of classifying mental states through SVM, the radial basis function kernel is used and the scaling range was taken -1~3 for statistical features, 0~15 for FFT and -1~1 for DWT.

The MCSVMs require the solution of the following optimization problem: minimize

$$\phi(\omega,\xi) = \frac{1}{2}\sum_{m=1}^{k}\omega_m.\omega_m + C\sum_{i=1}^{l}\sum_{m\neq y}\xi_i^m \tag{3}$$

With constraints

$$(\omega_{y_i}.x_i) + b_{y_i} \geq (\omega_m.x_i) + b_m + 2 - \xi_i^m,$$
$$\xi_i^m \geq 0, i = \{1,2,...,l\}, m \in \{1,...,k\} \mid y_i \tag{4}$$

Where C is the penalty parameter, l is the number of training data, k is the number of classes, y_i is the class of the ith training data ω points perpendicular to the separating hyperplane, b is the offset parameter to increase the margin, \ is set minus which is defined as ($m \in \{1,\ldots, k\}\backslash m \notin y_i$), and ξ is the degree of misclassification of the datum x_i. This gives the decision function:

$$f(x) = arg \max_{m=1,...,k}\left[\omega_m.x + b_m\right] \tag{5}$$

This optimization problem for a dual variable is solved by finding the saddle point of the Lagrangian [17].

$$\begin{aligned} L(\omega,b,\xi,\alpha,\beta) &= \frac{1}{2}\sum_{m=1}^{k}\omega_m.\omega_m + C\sum_{i=1}^{l}\sum_{m=1}^{k}\xi_i^m \\ &- \sum_{i=1}^{l}\sum_{m=1}^{k}\alpha_i^m\left[\left((\omega_{y_i} - \omega_m).x_i\right) + b_{y_i} - b_m - 2 + \xi_i^m\right] - \sum_{i=1}^{l}\sum_{m=1}^{k}\beta_i^m\xi_i^m \end{aligned} \tag{6}$$

With the dummy variables $\alpha_i^{y_i} = 0, \xi_i^{y_i} = 2, \beta_i^{y_i} = 0, i = 1,2,...,l$ and constraints $\beta_i^m \geq 0; \xi_i^m \geq 0; i = 1,2,....,l$

Where, $m \in \{1,2,\ldots, k\}\backslash y_i$ has to be maximized with respect to α and β, and minimized with respect to ω and ξ. Thus the decision function is obtained [8]. In this work the classification rate of different frequency band is obtained by using SVM under the variation of music or sound from which the specified cognitive states effective for the specific frequency bands are determined.

V. Result and Discussion

In this paper, the variations of different frequency bands are determined under the influence of different types of song on brain activity to estimate the cognitive states. The analyzed features and signal characteristics are changed according to the variation of song and their frequency spectrum. For EEG signal, the amplitude of alpha wave changes with the subject's attention to mental task performed.

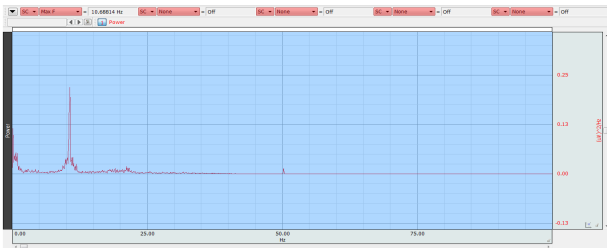

Fig. 7. Power spectral density of EEG signal when subjected to Bangla medium song.

TABLE III. CLASSIFICATION ACCURACY AT DIFFERENT EFFECTIVE BANDS USING SVM FOR BANGLA SONG

Song type	EEG frequency band	Train dataset for SVM	Test dataset for SVM	Classification accuracy
Bangla soft song	Alpha(α)	58	36	64.28%
	Beta(β)	58	35	20%
	Delta(δ)	58	36	36.11%
	Theta(θ)	58	37	86.5%
Bangla medium song	Alpha(α)	62	35	71.18%
	Beta(β)	62	36	3.61%
	Delta(δ)	62	37	23.35%
	Theta(θ)	62	35	23.1%
Bangla fast song	Alpha(α)	56	32	2.5%
	Beta(β)	56	33	97%
	Delta(δ)	56	32	65.68%
	Theta(θ)	56	34	39.47%

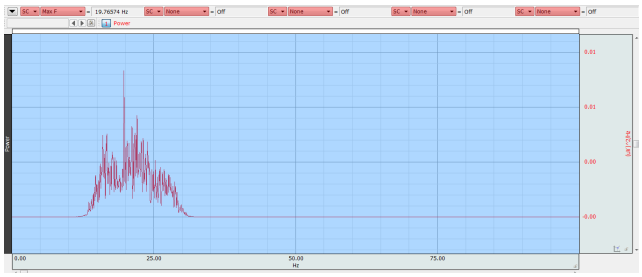

Fig. 8. Power spectral density of EEG signal when subjected to English fast song.

TABLE IV. CLASSIFICATION ACCURACY AT DIFFERENT EFFECTIVE BANDS USING SVM FOR ENGLISH SONG

Song type	EEG frequency band	Train dataset for SVM	Test dataset for SVM	Classification accuracy
English soft song	Alpha(α)	51	36	41%
	Beta(β)	51	35	31.76%
	Delta(δ)	51	36	44.44%
	Theta(θ)	51	37	84.85%
English medium song	Alpha(α)	49	35	85.7%
	Beta(β)	49	36	43.53%
	Delta(δ)	49	37	45.75%
	Theta(θ)	49	35	11.43%
English fast song	Alpha(α)	47	32	5%
	Beta(β)	47	33	88.57%
	Delta(δ)	47	32	54.54%
	Theta(θ)	47	34	31.81%

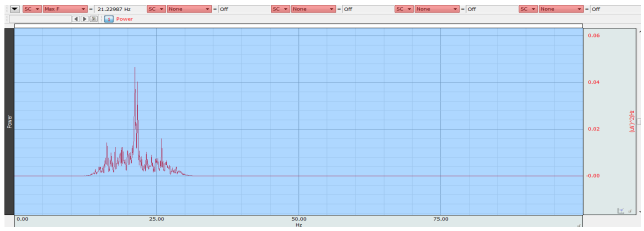

Fig. 9. Power spectral density of EEG signal when subjected to Hindi fast song.

The alpha activity is inversely proportional to concentration of mental activities. The value of alpha is the maximum for relax state and it decreases for the mental task or at stress. Fig. 7 shows the power spectral density of EEG brain wave when listening Bangla medium song. The maximum power occurs at 10.68 Hz which lies within the alpha frequency band. So, alpha band is more effective for medium type of song.

TABLE V. CLASSIFICATION ACCURACY AT DIFFERENT EFFECTIVE BANDS USING SVM FOR HINDI SONG

Song type	EEG frequency band	Train dataset for SVM	Test dataset for SVM	Classification accuracy
Hindi slow song	Alpha(α)	46	36	85.6%
	Beta(β)	46	35	65.1%
	Delta(δ)	46	36	31.25%
	Theta(θ)	46	37	96.37%
Hindi medium fast song	Alpha(α)	63	35	90.32%
	Beta(β)	63	36	3.12%
	Delta(δ)	63	37	53.12%
	Theta(θ)	63	35	80%
Hindi fast song	Alpha(α)	56	32	35.29%
	Beta(β)	56	33	94.11%
	Delta(δ)	56	32	17.14%
	Theta(θ)	56	34	54.11%

Table III shows the train and test dataset for SVM and the classification accuracy of the frequency bands for Bangla song which can detect the effective cognitive states. The classification rate of theta band is higher for Bangla soft song and alpha band is more effective for Bangla medium and fast song and they are 86.5%, 71.18%, and 97% respectively. When human brain is subjected to Bangla soft song the cognitive state was drowsiness or may be called catnap and when medium and fast Bangla song was played the cognitive states indicate relax and tension respectively.

The power spectral density when subjected to English fast song as shown in Fig. 8. It indicates that the maximum power occurs at frequency 19.76 Hz. So in case of English fast song the beta activity is prominent which indicate stress or tension for the subject.

Table IV and Table V shows the classification accuracy of the different effective frequency bands for English song and Hindi song which can detect the effective cognitive states when respective songs were played. In case of English fast, medium and soft song the higher accuracy is found at beta and alpha and theta band which indicate the stress, relax and catnap state respectively. Table V shows that theta and alpha band are more effective for Hindi slow song and medium song and they were

found 96.37% and 90.32% respectively. Hindi fast song shows the effectiveness of beta band which was 94.11%. So from this analysis it is observed that slow song detects the catnap state and medium fast song shows the relax state whereas fast shows the state at stress. So the cognitive state can be evaluated from the larger activity of alpha or beta or theta band.

The maximum power is occurred at frequency 21.22 Hz for Hindi fast song which indicates the beta frequency band as shown in Fig.9. So, the beta activity is more effective for fast song and the high frequency spectrum with fast bit of music leads human mind to stress.

VI. CONCLUSION

This work proposed a framework of cognitive state estimation based on the variations of brain activity with different types of music. The effective time domain and frequency domain features were extracted from spatial and temporal analysis. From the analysis, it was shown that θ-band is more effective for soft song whereas the α-band is effective for medium song and the β-band activity is prominent for Bangla, Hindi and English fast song. The highest classification accuracy for soft song was 96.37% for θ band. For medium and fast song they were 90.32% and 94.11% for α-band and β-band respectively. The α-band activity indicates the positive emotion pleasant or the reduction of mental stress whereas β-band activity shows the effect of mental stress. From this work, it can be concluded that the cognitive states depend on the functional activity of frequency bands while listening different types of songs. In future, cognitive state will be modeled for different types of music.

REFERENCES

[1] B. Geethanjali, K. Adalarasu, and R. Rajsekaran, "Impact of music on brain function during mental task using electroencephalography," *World Academy of Science, Engineering and Technology*, pp. 883-887, 2012.

[2] R. Bhoria, S. Gupta, "A Study of the effect of sound on EEG," *International Journal of Electronics and Computer Science Engineering,* IJECSE, vol. 2, no. 1, pp. 88-99, Dec. 14, 2012.

[3] EG. Schellenberg, T. Nakata, PG. Hunter, S. Tamoto, "Exposure to music and cognitive performance: Tests of children and adults," *Psychology of Music* , vol.35, pp. 5 – 19, 2007.

[4] J. Tanaka, M. Kimura, N. Hosaka, H. Sawaji, K. Sakakura, K. Magatani, "Development of the EEG measurement technique under exercising," *Proceedings of the IEEE Engineering in Medicine and Biology 27th Annual Conference Shanghai*, China, Sept. 2005, pp.1-4.

[5] R. Bhoria, P. Singal, D. Verma, "Analysis of effect of sound levels on EEG," *International Journal of Advanced Technology & Engineering Research (IJATER)*, vol. 2, no. 2, pp. 121-124, March 2012.

[6] H. Asada, Y. Fukuda, S. Tsunoda, M. Yamaguchi, M. Tonoike, "Frontal midline theta rhythms reflect alternative activation of prefrontal cortex and anterior cingulated cortex in humans," *Journal of Neurophysiology*, vol.50, pp. 324 – 328, Oct.1999.

[7] A. J. Lonsdale, AC. North, "Why do we listen to music? A uses and gratifications analysis," *British journal of psychology London England 1953,* vol.1, pp. 108-13, Feb. 2011.

[8] T. Ahmed, M. Islam, and M. Ahmad, "Human emotion modeling based on salient global features of EEG signal," *International Conference on in Advances in Electrical Engineering (ICAEE)*, 2013, pp. 246-251.

[9] G. Gerra, A. Zaimovic, D. Franchini, M. Palladino, G. Giucastro, N. Reali, D. Maestri, R. Caccavari, R. Delsignore, F. Brambilla, "Neuroendocrine responses of healthy volunteers to 'techno-music': relationships with personality traits and emotional state," *International Journal of Psychophysiology*, vol.28, pp. 99-111, Oct.1999.

[10] M. Steriade, "Cellular substrates of brain rhythms," In E. Niedermeyer & F. H. Lopes da Silva (Eds.), Electroencephalography Basic principles, clinical applications, and related fields, 4th Edition, Baltimore: Williams & Wilkins, pp. 28 – 75, 1999.

[11] C. D. Tsang, L. J. Trainor, D. L. Santesso, S. L. Tasker, L. A. Schmidt,"Frontal EEG responses as a function of affective musical features," *Annals of the New York Academy of Sciences*, vol.930, pp. 439 – 442, 2001.

[12] D. Sammler, M. Grigutsch, T. Fritz, S. Koelsch, "Music and emotion: Electrophysiological correlates of the processing of pleasant and unpleasant music," *Journal of Psychophysiology*, vol. 44, no. 2, pp. 293 – 304, 2007.

[13] R. A. Pavlygina, D. S. Sakharov, V. I. Davydov, "Spectral analysis of the human EEG during listening to musical compositions," *Journal of Human Physiology*,vol.30, no.1, pp. 54 – 60, 2004.

[14] N. G. Karthick, A. V. I. Thajudin, P. K. Joseph, "Music and the EEG: A study using nonlinear methods," *International Conference on Biomedical and Pharmaceutical Engineering*, 2006, pp. 424 – 427.

[15] Y. C. Chen, K. W. Wong, D.C. Kuo, T.Y. Liao, D.M. Ke, "Wavelet real time monitoring system: A case study of the musical influence on Electroencephalography," *WSEAS Transactions on Systems*, vol. 7, pp. 56 – 62, 2008.

[16] Schaefer, S. Rebecca, J. V. Rutger, P. Desain, "Music perception and imagery in EEG: Alpha band effects of task and stimulus,"*International Journal of Psychophysiology*, vol. 82, no. 3, pp. 254-259, 2011.

[17] M. Islam, T. Ahmed, M. S. U. Yusuf, and M. Ahmad, "Cognitive state estimation by effective feature extraction and proper channel selection of EEG signal," *Journal of Circuits, Systems, and Computers, World Scientific Publishing Company*, vol. 24, no. 2, pp. 1-24, Feb. 2015.

[18] M. Islam, T. Ahmed, S. S. Mostafa, M. S. U. Yusuf, and M. Ahmad, "Human emotion recognition using frequency & statistical measures of EEG signal," *International Conference on Informatics, Electronics & Vision*, May 2013 pp.1-6.

A Simple and Improved Eye Movement Features Detection Process from Saccadic Samples of Electrooculographic Data

Md. Shazzad Hossain*, Kristie Huda, Sourav Roy, Mohiuddin Ahmad
Department of Electrical and Electronic Engineering (EEE)
Khulna University of Engineering & Technology (KUET)
Khulna-9203, Bangladesh
*E-mail: shazzad2k905@gmail.com

Masud Rana
Department of Electrical and Electronic Engineering (EEE)
Dhaka University of Engineering & Technology (DUET)
Gazipur-1700, Bangladesh

Abstract—**In this manuscript a simple and improved eye movement features detection process is described. As most of human activities involve eyes, eye movement features detection is very important, particularly in ubiquitous computing and smart human computer interfaces. We all are familiar with Eye movement features detection techniques that involves image or video processing. But in this work we concentrated on a relatively new eye movement features detection technique that uses electrostatic potential from eyes, also known as Electrooculography signal. The work includes the detailed signal processing steps necessary to detect the various eye movement features from the raw Electrooculography signal. The detection process is simple and improved compared to previous counterparts. The detection process is user independent and thus free of any calibration problems.**

Keywords—electrooculography, human computer interface, baseline drift removal, eye movement features, automatic threshold determination.

I. INTRODUCTION

Most of the Human Computer Interface (HCI) systems used for rehabilitation purposes today function via bio signals, mostly electrical signals generated from human body referred to as Bio potentials. Bio potentials between any two points in living cell or organism is the result of relative change of concentration of sodium (Na+) and potassium (K+) ions [1]. Bio-potentials like Electromyography (EMG) Electroencephalography (EEG), Electrooculography (EOG) etc. are hot topics in HCI applications in recent years. But bio potentials like Electroencephalogram (EEG) or Electromyogram (EMG) needs complex signal processing and acquiring Electrocardiogram (ECG) 24×7 is not possible always. On the contrary systems based on Electrooculography are fairly easy to design and construct using surface electrodes placed around the eyes realizing EOG a preference over other bio potentials [2].

Apart from its clinical use EOG in recent years have been used in diverse applications. It is used to control devices e.g. computer [3], home appliances [4], wheelchair navigation [5] and to develop gaming consoles [7], [6]. It is also used in applications like activity recognition, analysis of human cognition etc. [5], [8], [9].

Human eye is involved in almost everything he does in his day to day life. So eye can be a potential interfacing component in HCI applications involving eye tracking and eye movement features detection. Eye movement features like eye movement patterns may provide essential cognitive cues which can be detected by analyzing eye movements [9]. There are few methods to track the movements of eye such as Scleral search coil method, Infrared-occulography (IROG), Electro-occulography (EOG), Video-occulography (VOG) etc. [10]. But in recent times EOG based method is becoming the center of eye-based HCI research due to its accuracy, ease of use and economy. This necessitates the need for simple and improved tools for EOG signal processing. This work at hand provides an edge in that regard.

II. BACKGROUNDS

A. The Resting Potential in the Human Eye

Every living cells have potentials across their plasma membranes called a membrane potential. The cytoplasm is charged negative compared to the fluid outside the cell. This discrepancy results from the fact that the distribution of anions and cations on opposite membrane sides is uneven. The membrane potential, varies from about -50 to -200 milli volts (the inside of the cell is charged negative with respect to the outside part. This is indicated by the minus sign.).

When the membrane potential of a cell goes for a long period of time without changing significantly, it is referred to as a resting potential as shown in Fig. 1 [11], [22]. The membrane potential is similar to a power source that controls the flow of all ions across the membrane. As the cell is charged more negatively in the inner part from the outer part, cations flow into the cell and anions out of the cell. This difference in ionic concentration that exists between the inside and outside of this membrane can be related to the diffusion potential – also known as the Nernst Potential. The magnitude of this Nernst potential is determined from the equation [20] below using the ratio of the concentrations of ion on opposite sides of the membrane.

978-1-4673-9257-0/15/$31.00 ©2015

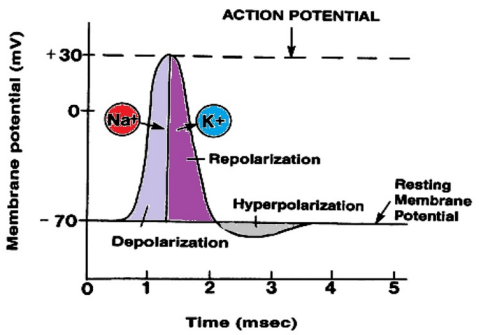

Fig. 1. Resting membrane potential.

$$E_{eq.K^+} = \frac{RT}{zF} ln \frac{[K^+]_{out}}{[K^+]_{in}} \quad (1)$$

Where: $E_{eq.K^+}$ is the equilibrium potential for potassium, R is the universal gas constant, T is the absolute temperature, z is the number of charged ions, F is the Faraday constant, $[K^+]_{out}$ is the concentration of potassium outside the cell, $[K^+]_{in}$ is the concentration of potassium inside the cell.

The eye ball can be regarded as a source of such resting potential, most of which has been attributed to the retina although some research has been done which proves the lens and maybe the cornea also play important roles. This potential known as corneo-retinal potential (CRP) is approximately lined up with the optic axis. Hence it varies with the variation of gaze. As the eyeball changes position the potential at the skin surface around the eye socket also changes. This potential difference can be measured by using surface electrodes placed on the skin around the eyes.

B. Electrooculography

The eye can be modeled as a dipole with cornea as positive pole and retina as negative pole. So the eye can be treated as a constant source of stable cornea-retinal electrostatic potential due to the potential difference between cornea and retina. This difference is attributed to the large presence of charged nerves in the retina with respect to the cornea [12]. The process of measuring the changes in this potential is called Electrooculography. A changing potential due to eye movement can be measured by using bipolar electrodes at opposite sides and a reference electrode. The electrodes are generally placed on the ends of the forehead as shown in Fig. 2 [13]. When the eye moves, the cornea approaches one electrode while the retina approaches the opposite one. Two signal components: EOG_h and EOG_v corresponding to horizontal and vertical movements can be measured [11]. Analyzing the change in these signals the eye movements can be tracked. The EOG signal amplitude varies from 50 to 3500 µV with a frequency range of about DC-100 Hz. Its behavior is practically linear for gaze angles of ±30º and changes approximately 20 µV for each degree of eye movement [7], [14]. EOG signal originates from the resting potential in the human eye.

Fig. 2. Placement of electrodes (Yellow=vertical electrode, Red=horizontal electrode, Black=reference electrode).

III. Eye Movement Features

The eye movement features that are the main concerns in this manuscript are a) Saccades, b) Fixations and c) Blinks.

A. Saccades

Saccades are swift, ballistic eye movements that abruptly change the fixation point. They range in amplitude from the small movements to the larger gaze movements. Saccades can be voluntary, but also can be reflexive whenever the eyes are open, even when fixated on an object. The duration of a saccade is governed by the angular distance the eyes travel during this movement. Typical saccade duration is 0.02 to 0.1 seconds and amplitude of 20 degrees [8], [15].

B. Fixations

Fixations are the rest state of eye between two consecutive saccades when the gaze is held constant on a specific location of the visual scene. The average fixation duration lies between 100 ms and 200 ms [15].

C. Blinks

This is subsequent closing and opening of eyelids. Blinks are of two types: a) reflex blink (in response to something invading in the eye and also as part of scared response) b) involuntary blinks (spontaneous blink controlled by brains blink generator) and b) voluntary blinks (controlled blink) [16]. A typical blink has amplitude of 100 to 400 µV and has duration of about 0.2 to 0.4 seconds. The primary functions of the blinks are to keep the corneal surface from getting dry and to protect the eyes from dirt or other possible damage. This is accomplished by three different kinds of blinks. One is voluntary and two are involuntary. The voluntary blinks are logically the result of the decision to shortly close the eyes. The involuntary blinks are divided in two sub groups. The first contains blink reflexes to protect the eyes from any possible harm and the second contains reflexes to maintain corneal moisture [17]. Fig. 3 shows the various eye movements in the EOG signal.

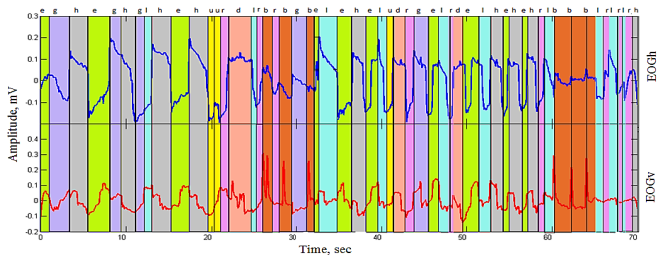

Fig. 3. Various eye movements in EOG signal: ‘r’=right, ‘l’=left, ‘u’=up, ‘d’=down, ‘e’=right-up, ‘f’=right-down, ‘g’=left-up, ‘h’=left-down, ‘b’=blink.

IV. General Detection Process

The general block diagram of the eye movement feature detection process is given below:

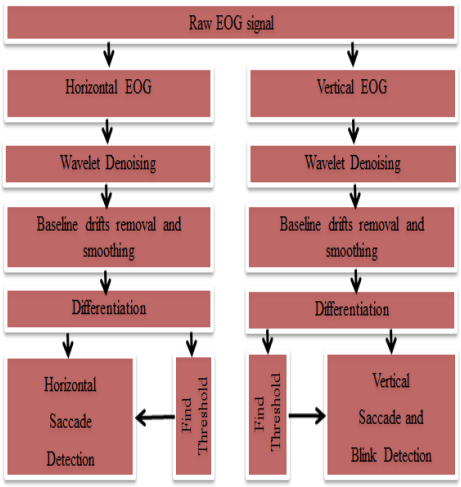

Fig. 4. General block diagram of the detection process.

V. Detailed Detection Process

A. Wavelet Denoising

To remove noise using wavelet thresholds, the wavelet coefficients are thresholded. This removes high frequency components, generally noise. This method does not require any particular assumptions about the bahaviour of the signal, can handle discontinuities and spatial variation in the signal.

In this work signal denoising is accomplished by using universal thresholding method on the wavelet coefficients. The wavelet decomposition of the signal is first found by performing a six level wavelet decomposition on the signal. The wavelet used for this purpose is db4. The denoised signal is found by thresholding the wavelet coefficients. The equation [20] of the wavelet function is given by

$$C[i] = g_0 s[2i] + g_1 s[2i+1] + g_2 s[2i+2] + g_3 s[2i+3] \quad (2)$$

Where $g_0 = h_3$, $g_1 = -h_2$, $g_2 = h_1$, $g_3 = -h_0$ and

$$h_0 = \frac{1+\sqrt{3}}{4\sqrt{2}}, h_1 = \frac{3+\sqrt{3}}{4\sqrt{2}}, h_2 = \frac{3-\sqrt{3}}{4\sqrt{2}}, h_3 = \frac{1-\sqrt{3}}{4\sqrt{2}}$$

The threshold value for the universal threshold method is given by $\sigma=\sqrt{2\log n}$; where n is the number of samples in the signal.

B. Baseline Drift Removal

User concentration is required while using eye movements to control graphical interfaces. Signal extraction for a long time may make the users tired and so it becomes more difficult for users to perform eye movements, this phenomenon is known as 'jitter' [14]. For this reason, users' capacity to control their ocular motor system decreases inversely proportional to tiredness. This event shows drift of signal from baseline. This is called baseline drift defined as the deviation of the signal baseline from a straight line. The drift of the signal from the baseline is modeled by a high degree polynomial which is then subtracted from the original signal to remove the baseline drift. A higher-order Polynomial increases the likelihood of producing an accurate baseline estimate [18]. A polynomial of degree 20 is chosen which models the baseline of the signal most accurately. Much lower and higher degree polynomials give poor results [19].

The polynomial curve fitting method used here uses a kth degree polynomial to model the signal [21]. Suppose the kth degree polynomial is

$$y = a_0 + a_1 x + a_2 x^2 + a_3 x^3 + \cdots + a_k x^k \quad (3)$$

The residual is given by,

$$R^2 = \sum_{i=1}^{n} [y_i - (a_0 + a_1 x_i + a_2 {x_i}^2 + \cdots + a_k {x_i}^k)]^2 \quad (4)$$

should be minimum to obtain least square error.

To obtain the least square error, the unknown coefficients $a_0, a_1, a_2,.., a_k$ must yield zero first derivatives. i.e

$$\frac{\partial R^2}{\partial a_0} = -2\sum_{i=1}^{n}[y - (a_0 + a_1 x + a_2 x^2 + +a_k x^k)] = 0$$

$$\frac{\partial R^2}{\partial a_1} = -2\sum_{i=1}^{n}[y - (a_0 + a_1 x + a_2 x^2 + +a_k x^k)]x = 0$$

$$\vdots$$

$$\frac{\partial R^2}{\partial a_k} = -2\sum_{i=1}^{n}[y - (a_0 + a_1 x + a_2 x^2 + +a_k x^k)]x_k = 0$$

Expanding the above equation we have,

$$\sum_{i=1}^{n} y_i = a_0 \sum_{i=1}^{n} 1 + a_1 \sum_{i=1}^{n} x_i + a_2 \sum_{i=1}^{n} x_i^2 \ldots + a_k \sum_{i=1}^{n} x_i^k$$

$$\sum_{i=1}^{n} x_i y_i = a_0 \sum_{i=1}^{n} x_i + a_1 \sum_{i=1}^{n} x_i^2 + \cdots + a_k \sum_{i=1}^{n} x_i^{k+1}$$

$$\vdots$$

$$\sum_{i=1}^{n} x_i^2 y_i = a_0 \sum_{i=1}^{n} x_i^2 + a_1 \sum_{i=1}^{n} x_i^3 + \cdots + a_k \sum_{i=1}^{n} x_i^{k+2}$$

Solution of these equations gives the value of the coefficients $a_0, a_1, a_2, \ldots, a_k$.

C. Smoothing

The EOG Signal is smoothened by using Savitzky-Golay filter. It is a digital filter which fits a polynomial to the data points according to least square fit and the central point of the fitted polynomial is taken as the new smoothed data point.

For $2M+1$ input sample and N order of polynomial, $\tilde{p}(n)$ is the impulse response design polynomial which can be obtained by following equation [23]

$$\tilde{p}(n) = \sum_{k=0}^{N} \tilde{a}_k n^k - M \le n \le M. \quad (5)$$

Where $\tilde{a}$ is the impulse input, $\tilde{a} = (A^T A)^{-1} A^T d$.

Here $d = [0,0,\ldots.,0,1,0,\ldots,0,0]^T$ is $(2M+1)\times 1$ column vector impulse and A^T is $(N+1)\times(2M+1)$ matrix.

$$A^T = \begin{bmatrix} (-M)^0 \ldots (-1)^0 & 1 & 1^0 \ldots M^0 \\ (-M)^1 \ldots (-1)^1 & 0 & 1^1 \ldots M^1 \\ (-M)^2 \ldots (-1)^2 & 0 & 1^2 \ldots M^2 \\ \vdots \quad\quad \vdots & \vdots & \vdots \quad \vdots \\ (-M)^N \ldots (-1)^N & 0 & 1^N \ldots M^N \end{bmatrix}$$

So, the impulse response of S-G filter is

$$h[-n] = h_{0,n} = \tilde{p}(n). \quad (6)$$

Finally the signal is thresholded to remove high amplitude noise components and very small saccades.

D. Feature Detection

1) Automatic threshold determination

An automatic threshold determination algorithm is adopted which eliminates the need for calibration and thus provides subject independent analysis. The algorithm first finds the local maximas of the derivative of EOG horizontal and vertical components and sorts them in ascending order. Noise usually possesses high amplitude peaks. Large noise peaks are removed by eliminating peaks (starting from high end going towards the low end) above the points where the difference between sequential peaks is less than 0.035mv. This value differentiates the noise peaks from the signal peak. From these peaks the appropriate peaks are selected (depending on the feature being desired) using a universal threshold process. The universal threshold process divides the peaks corresponding to saccades from that of the blinks. Thus blink and saccade thresholds were determined corresponding to EOGh and EOGv. Fig. 5 shows noise peak removal in automatic threshold determination method.

2) Blink detection

Blink features are detected from the vertical EOG signal (EOG_v) where it is characterized by sharp high amplitude peaks of short duration as shown in Fig. 6(a). Blinks are detected from the derivative of EOG_v which characterizes the blinks as a distinct signal feature having two peaks, one positive and one negative with a zero crossing between them as shown in Fig. 6(b). Involuntary eye blinks are eliminated by thresholding the detected blink amplitudes with the blink threshold determined earlier from the automatic threshold determination algorithm. Involuntary eye blinks has smaller amplitudes and smaller duration than voluntary eye blinks which differentiates the intentional blinks from the unintentional ones.

3) Saccade Detection

Saccades corresponding to horizontal and vertical eye movements are detected from the derivative of EOG_h and EOG_v respectively. From the EOG signal characteristics it can be concluded that when the signal amplitude increases then the corresponding eye movement is towards the rightward direction for EOG_h or towards the upward direction for EOG_v. Similarly decreasing amplitude indicates eye movement in opposite directions. So saccades can be detected by simply observing the change in amplitude i.e. by observing the derivative of the signals. The saccadic peaks for horizontal saccades are shown in Fig. 7.

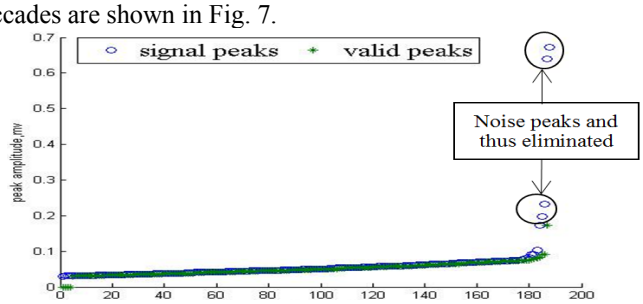

Fig. 5. Noise peak removal in automatic threshold determination.

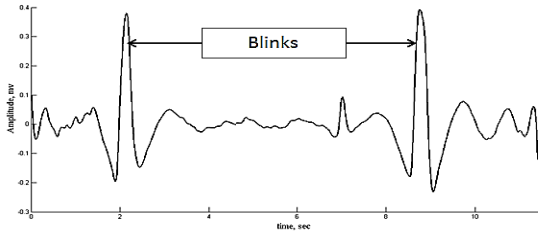

(a)

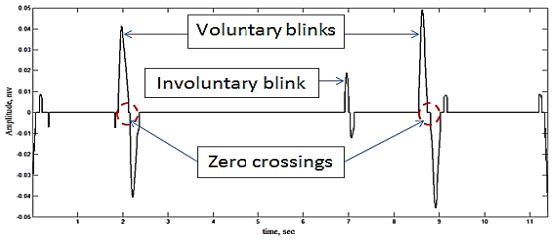

(b)

Fig. 6. (a) Blinks in EOG_v and (b) Voluntary and involuntary blinks.

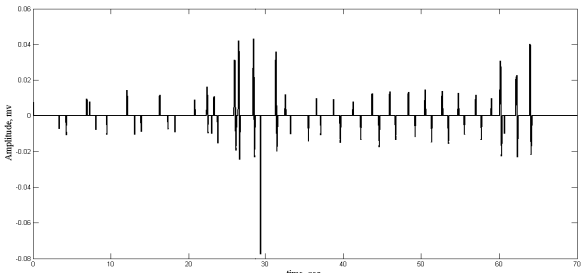

Fig. 7. Saccadic peaks for horizontal saccades.

4) Feature classification

After the features of interest are extracted from both the horizontal and vertical signals, they are classified to find out the unidirectional and oblique saccades and voluntary blinks. Horizontal and vertical saccades are extracted from the derivative of EOG_h and EOG_v respectively. An oblique saccade is found when a horizontal and a vertical saccade occur simultaneously. The blinks are found from the derivative of the EOG_v signal using the zero crossing detection algorithms.

VI. Results

A. Data Acquisition

EOG data were collected in in biomedical signal processing laboratory, Department of BME of EEE Faculty, Khulna University of Engineering & Technology (KUET), Bangladesh. The data acquisition and extracted EOG data for subject S2 is shown in Fig. 8.

The various steps of signal processing are described below for the data from subject S2.

B. Preprocessing of Raw EOG Signal

The raw EOG signal is preprocessed for denoising, baseline drift removal and smoothing to make the signal appropriate for further processing for feature extraction. Fig. 9 shows wavelet denoised EOG signal along with the Raw EOG signal for both the channels.

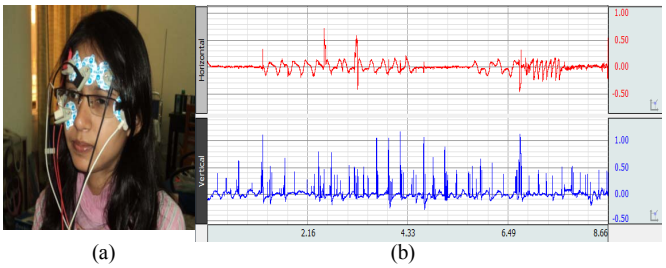

(a) (b)

Fig. 8. (a) Pictorial view of EOG measurement and (b) Measured EOG data for subject S2.

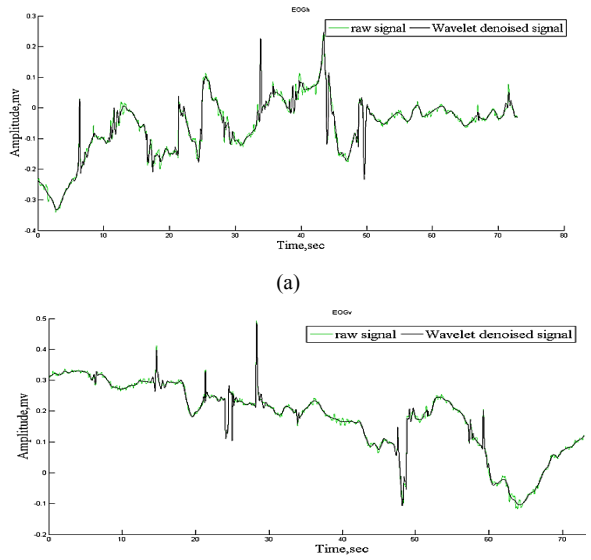

(a)

(b)

Fig. 9. Wavelet denoised EOG signal along with raw EOG signal (a) EOG_h and (b) EOG_v.

The denoised EOG signal is then processed to remove baseline drift using polynomial curve fitting. A polynomial of degree 20 is chosen. The calculated coefficients of the polynomial for the two channels for a particular set of data are given in Table I. The baseline drift removed signal for both channels are shown in Fig. 10.

TABLE I. CALCULATED COEFFICIENTS FOR THE POLYNOMIAL CURVE FITTING FOR BASELINE DRIFT REMOVAL

Signal	Value of Coefficients		
EOG_h	a_0 to a_{18}=0.00	a_{19}= 0.0023	a_{20}=-0.2821
EOG_v	a_0 to a_{18}=0.00	a_{19}= 0.0004	a_{20}=0.3057

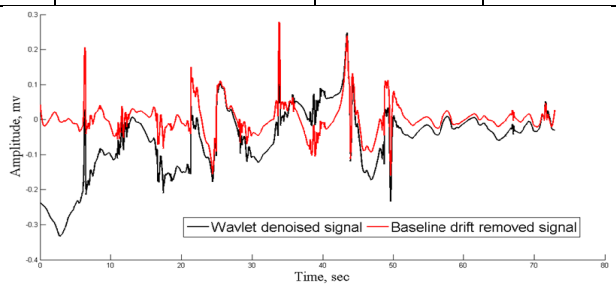

(a)

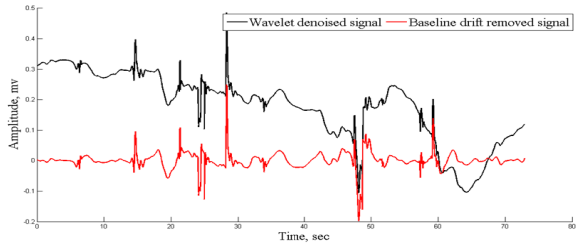

(b)

Fig. 10. Baseline drift removed EOG signal along with wavelet denoised EOG signal (a) EOG_h and (b) EOG_v.

The baseline drift removed signal is then further smoothened by using Savitzky-Golay filter as shown in Fig. 11. The filter uses a fourth degree polynomial with a frame size of 441. The degree and frame size is so chosen by inspection as it gives better results. The thresholds which separate blinks from saccades are calculated from the derivative of EOG signal.

Horizontal threshold=0.031mV; Vertical threshold=0.001 mV

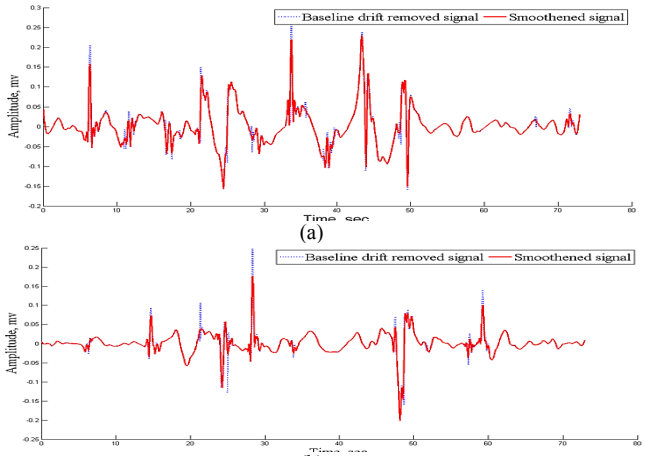

(a)

(b)

Fig. 11. Smoothened EOG signal along with Baseline drift removed EOG signal (a) EOG_h and (b) EOG_v.

C. Extracted Features

Total five eye movement features were extracted namely: Left, Right, Up, Down and Blink. From these the oblique saccades were then found. The detected eye movement features are shown in Fig. 11. The extracted features from a 200 seconds recording for three subjects are shown in Table: II.

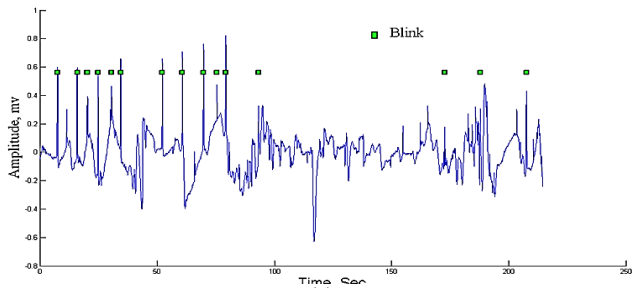

(a)

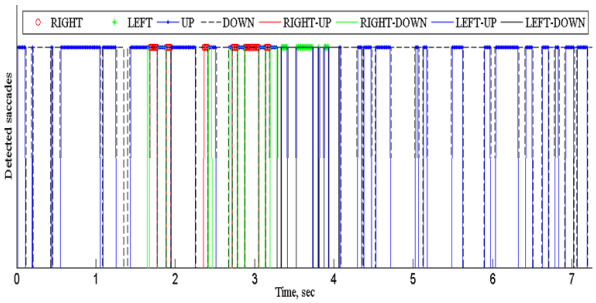

(a)

Fig. 12. Detected eye movement features (a) Blinks and (b) Saccades.

TABLE II. TABLECALCULATED COEFFICIENTS FOR THE POLYNOMIAL CURVE FITTING FOR BASELINE DRIFT REMOVAL

Subjects	Eye Movement Features (Directional movements and blinks)								
	Right	**left**	**Up**	**Down**	**Right-up**	**Right-down**	**Left-up**	**Left-down**	**blinks**
1	32	46	41	33	9	8	15	15	36
2	90	87	88	100	17	22	16	20	12
3	100	90	52	52	21	24	24	22	15

VII. CONCLUSION

In this work a simple and improved EOG signal processing is proposed. The feature detection accuracy of the proposed system in case of blinks and unidirectional saccades was found almost 100% but for oblique saccades accuracy faltered a little bit. The proposed method can be used in practically implementable real-time EOG based applications such as eye based human computer interfaces, human activity recognition, cognitive context measurement and so on.

REFERENCES

[1] N. V. Thakor, "Biopotentials and electrophysiology measurement": the measurement, instrumentation and sensors handbook, Boca Raton, CRC press, 1999.

[2] A. Banerjee, S. Chakraborty, P. Das, S. Datta, A. Konar, D. N. Tibarewala, R. Janarthanan "Single Channel Electrooculogram (EOG) based Interface for Mobility Aid": IEEE Proceedings of 4th International Conference on Intelligent Human Computer Interaction, Kharagpur, India, December 27-29, 2012.

[3] M. S. Hossain, K. Huda, M. Ahmad, "Command the computer with your eye - An electrooculography based approach" 8th International Conference on Software, Knowledge, Information Management and Applications (SKIMA), Dhaka, 18-20 Dec, 2014.

[4] H. Harun, W. Mansor," EOG Signal Detection for Home Appliances Activation ":5th International Colloquium on Signal Processing & Its Applications (CSPA), 2009.

[5] A. A. Haddad, R. Sudirman, C. Omar," Gaze At Desired Destination, and Wheelchair Will Navigate Towards It. New Technique to Guide Wheelchair Motion Based on EOG Signals": First International Conference on Informatics and Computational Intelligence, 2011.

[6] M. R. Kim, G. Yoon," Control Signal from EOG Analysis and Its Application": World Academy of Science, Engineering and Technology, International Journal of Electrical, Electronic Science and Engineering Vol: 7, No: 10, 2013.

[7] A. Bulling, D. Roggen, "Recognition of Visual Memory Recall Processes using Eye Movement Analysis", Proceedings of the 13th international conference on Ubiquitous computing (ubicomp'11), September 17–21, Beijing, China, 2011.

[8] A. Bulling, J. A. Ward, H. Gellersen, G. Tröster,"Eye Movement Analysis for Activity Recognition Using Electrooculography": IEEE transactions on pattern analysis and machine intelligence, vol. 33, no. 4, April 2011.

[9] A. Bulling, C. Weichsel, H. Gellersen," EyeContext: Recognition of High-level Contextual Cues from Human Visual Behaviour": CHI 2013, April 27–May 2, 2013, Paris, France.

[10] H. Singh, J. Singh," Human eye tracking and related issues: a review" International Journal Of Scientific Research (IJSR), 2012.

[11] H. Davison," Physiology of the eye": New York: Pergamon Press, 1990.

[12] Z. Lv, X. Wu, M. Li, C. Zhang, "Implementation of the EOG-based Human Computer Interface System", 2nd International Conference on Bioinformatics and Biomedical Engineering (ICBBE) 2008, Page.2188 – 2191, Shanghai.

[13] W. M. Bukhari W. Daud, Rubita Sudirman, "Time Frequency Analysis of Electrooculograph (EOG) Signal of Eye Movement Potentials Based on Wavelet Energy Distribution": Fifth Asia Modelling Symposium, Kuala Lumpur, 2011.

[14] R. Barea, L. Boquete, S. Ortega, E. López, J.M. Rodríguez-Ascariz,"EOG-based eye movements codification for human computer interaction": Expert Systems with Applications 39 (2012) 2677–2683.

[15] K. G. Rottach, V. E. Das, W. Wohlgemuth, A. Z. Zivotofsky., R. J. Leigh." Properties of Horizontal Saccades Accompanied by Blinks": Neurophysiology, vol.79, page.2985-2902June 1, 1998.

[16] H. Singh, J. Singh,"A review on electrooculography": International Journal of Advanced Engineering Technology (IJAET), Vol:3, Issue:4, Oct-Dec.'2012, pg:115-122.

[17] J. L. Andreassi, "Human Behavior & Physiological Response": Publisher: New York,Lawrence Erlbaum Associates, 5th edition, Published on 31 oct 2006.

[18] M. Kaur, B. Singh, Seema ,"Comparisons of Different Approaches for Removal of Baseline Wander from ECG Signal": 2nd International Conference and workshop on Emerging Trends in Technology (ICWET) 2011.

[19] K. Pettersson, S. Jagadeesan, K. Lukander, A. Henelius, E. Hæggström, K. Müller,"Algorithm for automatic analysis of electro-oculographic data": BioMedical Engineering OnLine 2013, 12:110.

[20] Wikipedia, The Free Encyclopedia. https://en.wikipedia.org/

[21] MATLAB, http://www.mathworks.com/help/

[22] http://sdsu-physics.org/physics180/physics180B/

[23] R. W. Schafer "What Is a Savitzky-Golay Filter?" IEEE Signal Processing Magazine. 07/2011; vol: 28(4), pg: 111-117.

Effects of Elevated Sleeping Postures on Cardiac Functions Analyzing Electrical Bio-impedance and Skin Blood Perfusion

Md. Bashir Uddin
Department of Biomedical Engineering
Khulna University of Engineering & Technology
Khulna-9203, Bangladesh
bas.u.kuet@gmail.com

Shabaz Khan and Mohiuddin Ahmad
Department of Electrical and Electronic Engineering
Khulna University of Engineering & Technology
Khulna-9203, Bangladesh
mohiuddin.ahmad@gmail.com

***Abstract*—This study investigated the effects of elevated sleeping postures on cardiac functions by analyzing electrical bio-impedance and skin blood perfusion in case of normal human subjects. Using different data acquisition units, the electrical bio-impedance based stroke volume and cardiac output were calculated in different elevated sleeping postures. Skin blood perfusion was measured also by laser Doppler flowmetry technique in all elevations to evaluate cardiac activity using frequency domain analysis. At first, data recordings were performed in supine sleeping (0° elevation) then sleeping elevations were changed sequentially from 0° to 15°, 15° to 30° and 30° to 45°. Data were recorded in all mentioned sleeping elevations for every subject. In most of the subjects, the parameters of cardiac functions were found highest in supine sleeping. When sleeping elevations were changed the cardiac functions were also changed in some significant level. Among all elevations except 0°, most significant improvements in cardiac functions were observed in 30° elevation only. It was highly recommended to sleep with an elevation around 30° to get best cardiac functions for those subjects only who prefer to sleep in elevation rather than supine posture.**

Keywords—sleep; elevated sleeping posture; cardiac function; electrical bio-impedance; skin blood perfusion

I. INTRODUCTION

A natural state characterized by the absence consciousness, nearly inactive sensory system of the body, and inhibition of the muscular functions in the body. The sleeping posture is the body configuration assumed by a person during sleep. There are four main sleeping postures with variables of each: left, right, supine and freefall. Some elevated postures are also seen where people prefer to sleep with head or upper body elevated to some angles. These elevated postures aren't commonly seen in our daily life that's why people are not so much aware about these. Many variations are found in sleeping on one's side, some of which are effective in helping to alleviate many sleep disorders such as insomnia and chronic sleep deprivation. The knees slightly upwards towards the chest area are considered as the most comfortable posture of sleep. Some studies have shown the cardiac output to be higher in the supine than in the right or left lateral postures in case of non-pregnant human beings [1]-[2]. Some studies have shown that cardiac output is higher in the left lateral than in the supine or right lateral postures [3], whereas others have concluded no difference in output among these various postures [4]. Cardiac output is higher in the left and right lateral postures than when the animals are in supine posture, shown by some recent studies [5].

Elevated sleeping posture may be considered as an effective way to treat some sleep disorder, although there are limited researches regarding this theme. A study claimed that the elevation resulted in less collapsible airway compared with the supine and the lateral sleeping postures [6] and concluded that in severely affected obstructive sleep apnea (OSA) patients upper body elevation, and to a lesser extent lateral posturing, improved upper airway stability significantly during sleep. In this study, upper airway stability was analyzed for OSA patients but cardiac functions have not been investigated with varying elevation that requires further exploration. Another study performed all-night polysomnography (PSG) while subject lying supine or sitting at a 60-degree angle and found that in the upright position, the frequency of OSA events decreased and gas exchange improved [7]. The above papers have addressed the effects of elevated sleeping for OSA patients only.

Many researchers have done their work on cardiac functions and elevated sleeping postures and the results are conflicting. Most of the research shows that the cardiac output is higher at 30° sleeping angle than other angles but some other research show deviations in results. No research has been conducted to evaluate cardiac functions in different elevated sleeping posture using spectral analysis. Frequency domain analysis hasn't been done to investigate the effects of elevated sleeping on normal human participants. The main goal of this study is to investigate the effects of different elevated sleeping posture (upper body elevated by 0°, 15°, 30°, and 45°) on cardiac functions (cardiac output and cardiac activity). Cardiac output and cardiac activity will be evaluated by analyzing stroke volume and blood perfusion respectively. It is hypothesized that different elevation in sleeping would have different effects on cardiac function and hence affect sleep quality.

978-1-4673-9257-0/15/$31.00 ©2015 IEEE

II. CARDIAC FUNCTIONS

A. Cardiac Output

Cardiac output (CO) is an important parameter to investigate cardiac functions. Cardiac output (CO), the amount of blood pumped by the heart per minute is the multiplication of stroke volume (SV) and heart rate (HR). SV is the amount of blood ejected by the right or left ventricle during a single cardiac cycle. CO can be determined non-invasively by employing electrical bio-impedance measurement techniques. Electrical bio-impedance is simply defined as the characteristic impedance of a volume of tissue and fluid. In case of CO measurement, the corresponding tissue includes the heart and the immediate surrounding volume of the thorax. Blood is the relevant fluid. If the electrical bio-impedance of a volume of tissue and fluid is Z_o (ohms), systolic ejection time is T (seconds), magnitude of the highest impedance change during systole is dZ/dt (ohms/sec) then the expression of SV is noted in (1) where SV is the stroke volume in ml, R is the resistivity of blood in ohms.cm and L is the distance between inner band electrodes in cm. Multiplication of SV and HR is called CO as noted in (2) where CO is the cardiac output in ml/minute and HR is the heart rate in BPM (bits per minute).

$$SV = R \times (L^2/Z_o^2) \times T \times dZ/dt_{(max)} \quad (1)$$

$$CO = SV \times HR \quad (2)$$

B. Cardiac Activity

Cardiac activity is another valuable investigation to find out cardiac functions. Cardiac activity can be demonstrated by Laser Doppler Flowmetry (LDF) and its frequency domain (spectral) analysis. An established and reliable method is LDF for the measurement of blood perfusion. Periodic oscillations in microvascular level are detected by the noninvasive technique of LDF. Five characteristic frequencies have been revealed from human forearm skin using the spectral analysis of LDF signal [8]. In addition to the cardiac and respiratory rhythms around 1 and 0.3 Hz, respectively [9], three frequencies have been detected in the regions around 0.1, 0.04, and 0.01 Hz in human skin [10]. LDF is an inexpensive, noninvasive method of measuring blood perfusion that is the continuous flow of circulating blood on a microscopic level. The working of LDF is the reading of frequency oscillation resulted by Doppler frequency shift of the red blood cells in a peripheral tissue and converts the frequency to an intensity oscillation. The LDF apparatus is composed of a low powered laser light and probe that collects readings and transmits results to an analyzer section. The emitted and reflected light is applied through optical fibers to the recorder of analyzer section. The output of the LDF recording is the flow of red blood cells, defined as the quantity of red blood cells times their velocity, which determines blood perfusion.

Frequency domain analysis of LDF signal is an established way to evaluate cardiac activity [8]-[10]. Fast Fourier transform (FFT) is a frequency based analysis to compute the frequency component of the non-stationary signal. The discrete Fourier transform of the discrete time signal *x(j)* is noted in (3) where, *k* is the harmonic number of frequency components of signal and X_k is the discrete frequency domain at different frequency. The output of a FFT will appear in the graph with magnitude plotted against frequencies. The power spectral density (PSD) is the description of power of the time series data with respect to the corresponding frequency. The expression of PSD can be obtained directly as a function of frequency from the time series data $x_{Sample\ Data}$ as noted in (4) where, *P(f)* has units of power/Hz and T_s is the sampling time period. The output of a PSD will appear in the graph with power plotted against frequencies.

$$X_k = \sum_{j=n_s}^{n_e-1} x(j) e^{-i2\pi\frac{jk}{N}} \quad (3)$$

$$P(f) = \frac{1}{T_s}\left|T_s \sum_{q=0}^{N} x_{Sample\ Data}(q) e^{-i2\pi f q T_s}\right|^2 \quad (4)$$

III. MATERIALS AND METHODS

A. Subject Selection

Several healthy young male subjects were enrolled in this study. All the subjects did not take any medication during the week prior to the study. All the subjects were free from smoking and drinking of alcohol and caffeine containing drinks at least 4 hour prior to the study. No subject was affected by cardiovascular disease or other physiological illness. After being informed about the study design, all the subjects gave their written consent. All the subjects had an initial visit to the experimental laboratory for different required assessments. The age, weight, height, body mass index (BMI) of all subjects is listed in Table I.

B. Experimental Setup and Data Acquisition

The experiment was completed in a silent laboratory room with keeping the temperature nearly constant. Four disposable strip electrodes, lead wire, and CO amplifier were used to record electrical bio-impedance and its derivatives as shown in Fig. 1. The lead was connected to non-invasive CO amplifier through data acquisition unit. Skin blood perfusion measurement on the tip of index finger was performed with fiber-optic based probes connected to LDF amplifier as shown in Fig. 2. Electrocardiogram (ECG) recoding was performed also by using disposable vinyl electrode electrodes, lead set, electrode gel, and data acquisition unit. ECG recording was used find out left ventricular ejection time (T). About 10 minutes were distributed for acclimatization before the data recordings. Data was taken sequentially with 0°, 15°, 30°, and 45° elevation. There was at least 15 minutes time gap between recordings of two successive postures. Electrical bio-impedance and its derivative, blood perfusion, and ECG signal recording for 30° elevated posture is shown in Fig. 3.

C. Processing of Recorded Signal

The recorded signals contained several noises such as 50Hz frequency component. By filtering, this high frequency component was removed. Smoothing technique was also used to find smoothed signal. Mean value smoothing was done here as noted in (5), where "*q*" is the number of points in the window and "*p*" is the sample number [11].

$$x_{Sample\ Data} = \sum_{h=p-q/2}^{h=p-(q-1)/2} x_{Measured\ Data}(h)/q \quad (5)$$

TABLE I. SUBJECT'S SPECIFICATIONS

Parameters	Value (N=4)*
Age (yr)	22±0.0
Weight(Kg)	70.5±2.06
Height (cm)	173.99±1.27
BMI (kg/m^2)	23.41±0.3122

*Values are Mean±Standard Deviation

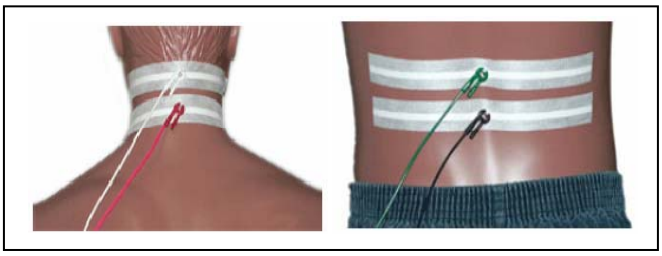

Fig. 1. Pictorial view of electrode placement and lead connection.

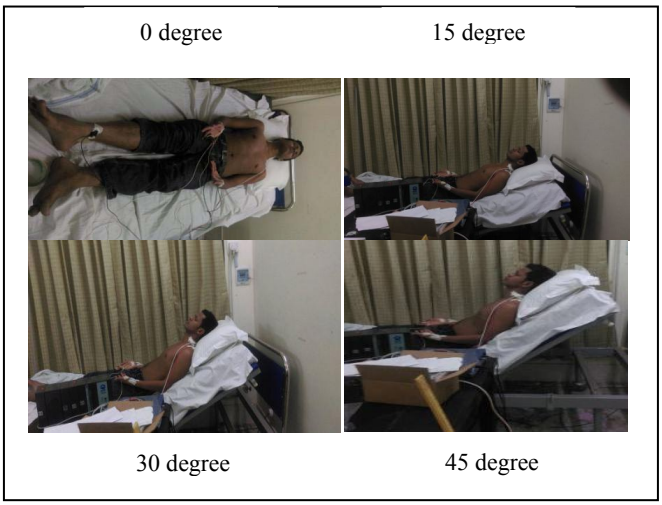

Fig. 2. Pictorial view of different elevated sleeping postures with complete data acquisition setup.

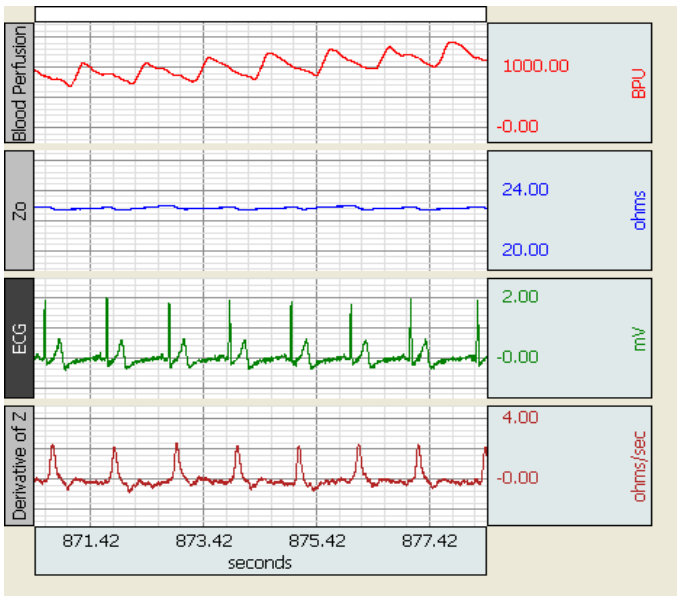

Fig. 3. Recorded signals for 30° sleeping angle.

IV. DATA ANALYSIS

A. Determination of Cardiac Output

The variations in electrical bio-impedance and its derivative, left ventricular ejection time (T), and HR with elevated sleeping postures are listed in Table II for subject 4. These variations are applied to determine SV and CO using (1) and (2) respectively for all sleeping angles. In this calculation, the resistivity of blood (R) is 147 ohms.cm and the length between inner band electrodes (L) is 28cm.

B. Frequency Spectrum Analysis

Cardiac activity can be effectively evaluated by spectral analysis of skin blood perfusion signal within the frequency range 0.6-1.6 Hz. The fast Fourier transform (FFT) and power spectral density (PSD) of skin blood perfusion signal for subject 3 are shown in Fig. 4 and Fig. 5 respectively. The peak magnitude and peak power of FFT and PSD analysis respectively within the frequency range for different sleeping elevations are noted in Table III for subject 2.

C. Statistical Analysis

The statistical analysis of stroke volume and cardiac output for all subjects with different sleeping elevations are shown in Fig. 6 and Fig. 7 respectively. The statistical analysis of spectral components of cardiac activity for all subjects with different sleeping elevations is indicated in Fig. 8 and Fig. 9.

TABLE II. VARIATIONS IN CARDIAC OUTPUT WITH SLEEPING ANGLES

Sleeping Angles	Z_o (ohm)	$dZ/dt_{(max)}$ (ohm/sec)	T (sec)	SV (ml)	HR (bpm)	CO (L/min)
0°	20.24	1.990	.265	148.3	62	9.19
15°	19.52	2.014	.263	160.2	59	9.45
30°	19.02	1.893	.268	161.5	60	9.69
45°	18.61	1.744	.252	146.2	61	8.92

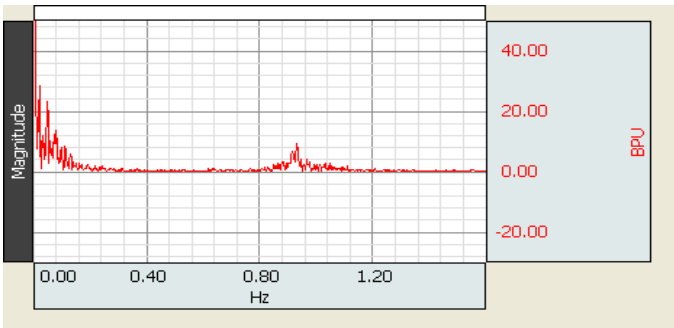

Fig. 4. Fast Fourier transform of skin blood perfusion signal for 30° elevation.

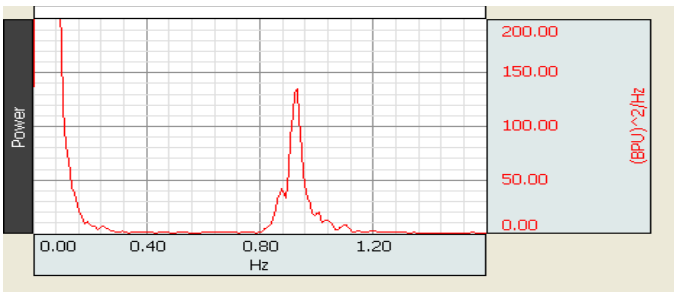

Fig. 5. Power spectral density of skin blood perfusion signal for 30° elevation.

TABLE III. VARIATIONS IN SPECTRAL COMPONENTS OF CARDIAC ACTIVITY

Sleeping Angles	FFT Analysis		PSD Analysis	
	Peak magnitude (BPU)	*f at peak magnitude (Hz)*	*Peak power $(BPU)^2/Hz$*	*f at peak power (Hz)*
0^0	7.236	1.072	81.848	1.076
15^0	4.754	1.029	63.087	1.022
30^0	4.504	1.122	30.090	1.121
45^0	5.054	1.074	31.958	1.106

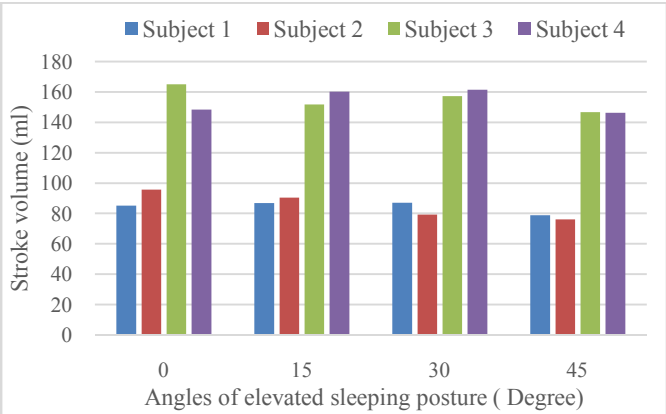

Fig. 6. Variations in SV with sleeping angles.

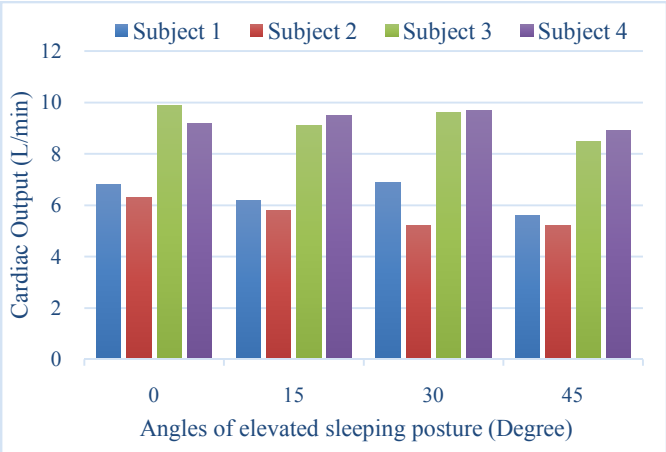

Fig. 7. Variations in CO with sleeping angles.

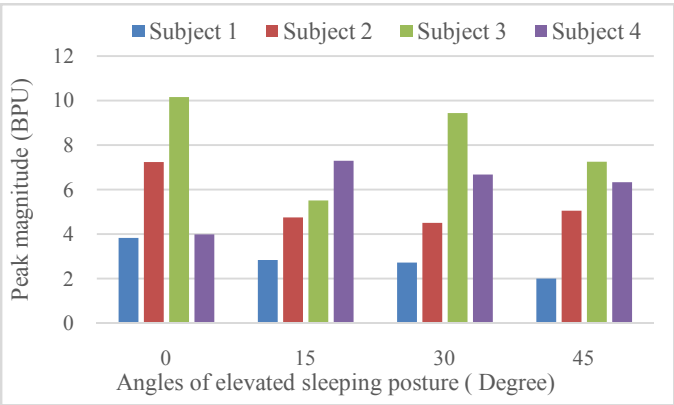

Fig. 8. Variations in peak magnitude of cardiac activity with sleeping angles.

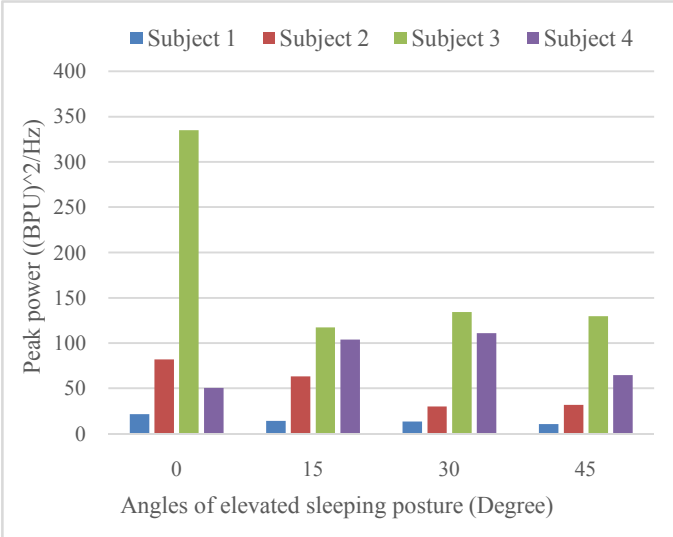

Fig 9. Variations in peak power of cardiac activity with sleeping angles.

V. RESULTS AND DISCUSSIONS

The effects of elevated sleeping postures on cardiac functions can be discussed in two sections- effects on cardiac output and effects on cardiac activity due to elevated postures, as explained below:

Effects of elevated postures on cardiac output: Stroke volume and cardiac output are totally different for different elevated sleeping postures. The highest stroke volume is found 161.5 ml at 30° sleeping angle and the lowest stroke volume is found 146.2 ml at 45° sleeping angle for subject 4. The highest cardiac output is found 9.69 L/min at 30° sleeping angle and the lowest cardiac output is found 8.92 L/min at 45° sleeping angle for the same subject. It is also seen that the highest stroke volume is found at 30° sleeping angle for subject 1 & subject 4 and subject 2 & subject 3 show highest stroke volumes at 0° sleeping angle. Similarly, the highest cardiac output is also found at 30° degree sleeping angle for subject 1 & subject 4 and subject 2 & subject 3 show highest cardiac outputs at 0° sleeping angle.

Effects of elevated postures on cardiac activity: It is found that the peak magnitude of FFT analysis is highest (7.236 BPU) at 1.072 Hz for 0° sleeping angle and lowest (4.504 BPU) at 1.122 Hz for 30° sleeping angle for subject 2. Similarly the peak power of PSD analysis is found highest (81.848 $(BPU)^2/Hz$)) at 1.076 Hz for 0° sleeping angle and lowest (30.090 $(BPU)^2/Hz$)) at 1.121 Hz for 30° sleeping angle for subject 2. The peak magnitude of FFT is found highest for most of the subjects at 0° sleeping angle. Also the peak power of PSD is found highest for most of the subjects at 0° sleeping angle. The significant increment in spectral components of cardiac activity is found at 30° sleeping angle for most of the subjects. The overall result is found by analyzing cardiac parameters such as stroke volume, cardiac output, and spectral components of cardiac activity. The results indicate highest cardiac functions at 0° (supine) sleeping angle. Besides, 30° sleeping angle also results significant increment in cardiac functions.

VI. Conclusions

The effects of different elevated sleeping postures on cardiac functions were investigated in this study by analyzing electrical bio-impedance and skin blood perfusion. Stroke volume, cardiac output and spectral components were analyzed as cardiac functions. Highest cardiac functions were found in supine sleeping (0° elevation) in most of the subjects. More significant increment in cardiac functions was observed in 30° elevation only except 0° elevation. To get best cardiac functions it was recommended to sleep with around 30° elevation in case of elevated sleeping only.

Acknowledgment

This work was partially supported by Higher Education Quality Enhancement Project (HEQEP), UGC, Bangladesh under Sub-project "Postgraduate Research in BME", CP#3472, Department of Biomedical Engineering (BME), Khulna University of Engineering & Technology (KUET), Bangladesh.

References

[1] A. J. Atkins, J. M. Watt, P. Milan, P. Davies, and J. S. Crawford, "The influence of posture upon cardiovascular dynamics throughout pregnancy," Eur J Obstet Gynecol Reprod Biol., vol.12, no. 6, pp. 357-772, December 1981.

[2] B. Newman, C. Derrington, and C. Dore, "Cardiac output and the recumbent position in late pregnancy," Anaesthesia, vol. 38, no. 4, pp. 332-335, April 1983.

[3] G. R. Whitman, D. L. Howaniak, T. S. Verga, "Comparison of cardiac output measurements in 20-degree supine and 20-degree right and left lateral recumbent positions," Heart Lung, vol. 11, pp. 256-257, 1982.

[4] K. Ueland, M. J. Novy, E. N. Peterson, and J. Metcalfe, "Maternal cardiovascular dynamics. IV. The influence of gestational age on the maternal cardiovascular response to posture and exercise," Am J Obstet Gynecol., vol. 104, no. 6, pp. 856-864, July 1969.

[5] S. Nakao, P. C. Come, M. J. Miller, S. Momomura, P. Sahagian, B. J. Ransil, and W. Grossman, "Effects of supine and lateral positions on cardiac output and intracardiac pressures: an experimental study," Circulation, vol. 73 no. 3, pp. 579-585, March 1986.

[6] A. M. Neill, S. M. Angus, D. Sajkov, and R. D. McEvoy, "Effects of sleep posture on upper airway stability in patients with obstructive sleep apnea," Am J Respir Crit Care Med, vol. 155, no. 1, pp. 199-204, 1997.

[7] R. D. McEvoy, D. J. Sharp, and A. T. Thornton, "The effects of posture on obstructive sleep apnea," Am Rev Respir Dis, vol. 133, no. 4, pp. 662-666, 1986.

[8] M. Bracic and A. Stefanovska, "Wavelet based analysis of human blood flow dynamics," Bulletin of Mathematical Biology, vol. 60, pp. 417-433, 1998.

[9] A. Stefanovska, "Self-organization of biological systems influenced by electrical current," Thesis, Faculty of Electrical Engineering, University of Ljubljana, Slovenia, 1992.

[10] A. Stefanovska and P. Kroselj, "Correlation integral and frequency analysis of cardiovascular functions," Open systems & information dynamics, vol. 4, pp. 457-478, 1997.

[11] M. Ahmad, A. Islam, T. T. Khan Munia, M. A. Rashid, and T. M. N. Tunku Mansur, "Physiological signal analysis for cognitive state estimation," Biomedical Engineering: Applications, Basis and Communication, vol. 24, no. 1, pp. 57-69, 2012.

A Novel Dual Purpose Spatial Domain Algorithm for Digital Image Watermarking and Cryptography Using Extended Hamming Code

Sudip Ghosh, Sayandip De
School of VLSI Technology
IIEST, Shibpur
Howrah-711103, India
sudipghosh2005@gmail.com, desayandip@gmail.com

Santi Prasad Maity, Hafizur Rahaman
Department of Information Technology
IIEST, Shibpur
Howrah-711103, India
spmaity@yahoo.com, rahaman_h@yahoo.co.in

Abstract—**The tremendous growth of internet in the recent years has made possible easier copying, manipulation and redistribution of digital media. As a result, the problem of security and copyright violation has greatly increased. To combat this problem, mechanisms like watermarking and cryptography are required. In this paper we have proposed a dual purpose spatial domain robust algorithm for both image cryptography and digital image watermarking where a key is generated using 'Extended Hamming Code' to make the code self-correcting. A comparative study of the proposed algorithm with other spatial domain algorithms in terms of Peak Signal to Noise Ratio (PSNR) and Normalized Correlation (NC) claims better performance in terms of robustness and imperceptibility. Cryptographic performance analysis shows that the algorithm is secure, consistent and fast to perform transmission of binary messages.**

Keywords— Digital Image Watermarking, Cryptography, Extended Hamming Code, Spatial Domain, Binary Watermark.

I. INTRODUCTION

In recent years the tremendous growth of internet has increased illegal transfer, copy, manipulation and redistribution of digital media, thus increasing the problem of copyright violation of digital media like images, audio clips, videos etc. This has highlighted the need for mechanisms like cryptography, steganography and digital watermarking [1].

Cryptography is the process of data hiding in which the contents of the message are protected from the attacker but the existence of the message is known to the attacker [2]. Steganography is the hiding of a message within the communicating data such that the attacker is unaware of the existence of the message. The original purpose of steganographic mechanisms is information hiding without concerning about the robustness.

Digital watermarking is one of the most popular methods to communicate data or message secretly in a host such as an image, audio or video in robust manner [3]. There are two domains of embedding the secret message or watermark into the host: spatial and transform domain. In spatial domain watermarking schemes, watermarks are directly applied by manipulation of intensity values of the pixels. In transform domain watermarking frequency components are manipulated to embed the watermark. Transform domain techniques like DCT, DFT etc. are more robust to attacks compared to spatial domain techniques. Easier implementation, reduced computational complexity and higher capacity has made us adopt the spatial domain watermarking scheme for our algorithm.

This paper proposes a spatial domain dual purpose blind algorithm for cryptography and digital watermarking where the watermark and the cover image are chosen to be binary and grayscale, respectively. The paper is organized with section I as introduction followed by related works in section II. Then the proposed algorithm for watermarking and cryptography has been explained in section III and IV respectively followed by performance analysis and results in section V. Conclusions are given in section VI followed by references.

II. RELATED WORK

A numerous publication exists in the field of security & copyright protection, so all of them cannot be covered in a single survey. So only a few of the popular cryptographic & spatial domain image watermarking methods has been discussed in this review.

Houtan Haddad Larijani et al. [4] presented a new algorithm called "Save Algorithm". Sakthivel. S. M. et al. [3] presented a modification of [4] which is called "PVSA (Pixel Value Search Algorithm)". Both these algorithms perform a pixel by pixel comparison between the host image and watermark and storing the host pixel location in a key in case of a match. Both [4] and [3] achieve high level of imperceptibility as they do not make any change in the host image.

Ben Wang et al. [13] presented a watermarking algorithm based on DWT (Discrete Wavelet Transform), DCT (Discrete Cosine Transform) and SVD (Singular Value Decomposition) which is robust and performs faster embedding and extraction.

Li et al. [7] proposed a robust adaptive blind watermarking scheme with the watermarks encrypted by Fresnel transform and utilizing fuzzy c- means clustering (FCM) technique.

Swaleha Saeed et al. [14] presented an encryption technique using Fisher- Yates Chaotic Shuffling which is consistent, secure and efficient for transmitting grayscale images over insecure networks.

Even though the above algorithms have already been proposed but creating a robust watermarking algorithm with

978-1-4673-9257-0/15/$31.00 ©2015 IEEE

high level of imperceptibility is still a challenging problem. However, our proposed algorithm provides high level of robustness to geometrical, noising, de-noising and image processing attacks along with better PSNR (Peak Signal to Noise Ratio) compared to the above algorithms, thus proving its imperceptibility.

III. Proposed Watermarking Algorithm

The proposed algorithm is a "self-correcting" spatial domain blind algorithm for digital watermarking where corresponding to each watermarked pixel a key is generated as per Extended Hamming Code [6] helping in self-correction. First of all, a grayscale image of size (m x n) is chosen as the host image and a binary image of size (r x c) is chosen as the secret message or watermark such that $m \geq n$. An EX-OR operation is performed between the watermark bit and the 2nd LSB of the host pixel. The result is embedded into the 1st LSB of the host pixel. Corresponding to this modified 1st LSB and the 2nd LSB of the host pixel four parity bits are generated as per Extended Hamming Code [6] (explained in section A). These four parity bits taken together form a 4-bit parity code which is converted to a decimal and stored in a key. The detailed embedding procedure is explained in section B.

A. Extended Hamming Code

Hamming codes are binary linear codes. A (n, k) Hamming code consists of a block length $n=2^r-1$ and a message length of $k=2^r-r-1$ [6] where r is an integer such that $r \geq 2$. Hamming codes can only detect and correct single bit errors. However, Extended Hamming codes are single error correcting and double error detecting (SECDED) codes which are obtained from Hamming codes by adjoining an overall parity check-bit. An (m, k) Extended Hamming code consists of a block length $m=2^r$ and a message length of $k=2^r-r-1$ where $r \geq 2$.

H0	H1	H2	H3	H4	H5	H6	H7
P1	P2	P3	M1	P4	M2	M3	M4

Figure 1. Extended Hamming Code (8,4)

Consider an (8, 4) Extended Hamming code (r = 3) given by H= (H0 H1 H2 H3 H4 H5 H6 H7) which consists of four message bits M= (M1 M2 M3 M4) and four parity bits P= (P1 P2 P3 P4). The arrangement of message and parity bits in Extended Hamming Code is shown in Fig. 1. Usually, a four-bit message code M= (M1 M2 M3 M4) is converted into an (8, 4) Extended Hamming Code by inserting parity bits P= (P1 P2 P3 P4) which are generated as follows:

$$P2= M1 \oplus M2 \oplus M4 \quad (1)$$
$$P3= M1 \oplus M3 \oplus M4 \quad (2)$$
$$P4= M2 \oplus M3 \oplus M4 \quad (3)$$
$$P1= P2 \oplus P3 \oplus M1 \oplus P4 \oplus M2 \oplus M3 \oplus M4 \quad (4)$$

Error Detection and Correction

For error detection and correction, a three-bit error code E= (E1 E2 E3) is generated from the Extended Hamming Code H as follows:

$$E1= H4 \oplus H5 \oplus H6 \oplus H7 \quad (5)$$
$$E2 = H2 \oplus H3 \oplus H6 \oplus H7 \quad (6)$$
$$E3 = H1 \oplus H3 \oplus H5 \oplus H7 \quad (7)$$

The value of E in decimal is obtained and the Eth bit location in H is complemented. If the decimal equivalent of E is 6, then H6 is complemented i.e. H6'= not (H6) to obtain modified H= (H0 H1 H2 H3 H4 H5 H6' H7). All the bits of the newly modified H are EX-ORed to obtain K.

$$K= H0 \oplus H1 \oplus H2 \oplus H3 \oplus H4 \oplus H5 \oplus H6' \oplus H7 \quad (8)$$

Case 1. If K = 0: This means single bit error is present and the error has been corrected by complementing H6.

Case 2. If K=1: This means double bit error is present and the error cannot be corrected.

B. Watermark Embedding

Input: (a) A grayscale image of size (m x n) as the host/cover image. (b) A binary image of size (r x c) is chosen as the watermark. **Output**: (a)A grayscale watermarked image of size (m x n). (b)A key of size (1 x N) where N= r x c.

Step 1. Read the cover image and the watermark image with their corresponding sizes.

$$I= \{x (i, j) \mid 0\leq i \leq m, 0\leq j \leq n, x (i, j) \in \{0, 1, \ldots, 255\}\}. \quad (9)$$
$$W= \{w (u, v) \mid 0\leq u \leq r, 0\leq v \leq c, w (u, v) \in \{0, 1\}\}. \quad (10)$$

Step 2. A key of size (1 x N) is chosen where N= r x c (r denotes row and c denotes column of the watermark image). The size of the watermark image is stored in the first two locations of the key such that key (1 x 1) = r and key (1 x 2) = c.

Step 3. A threshold value is chosen as the visual perception factor of a pixel in such a way that the threshold value and the pixel value are perceptually insignificant. Let the value of the threshold be 200.

Step 4. Count the number of cover pixels having value greater than or equal to threshold.

Step 5. Start with the first pixel of the cover image.

Step 6. Search for a cover image pixel having value greater than or equal to the threshold. Once search is completed store the current pixel location.

Step 7. Convert the obtained cover image pixel into 8-bit binary value. Replace the LSB of the cover image pixel using the following operation.

$$LSB1= LSB2 \oplus w (u, v) \quad (11)$$

where LSB1= LSB in the first bit plane position
LSB2= LSB in the second bit plane position
w (u, v) = watermark pixel

Step 8. With the help of LSB1 and LSB2 form a four-bit message code by padding two zeros in the front such that M= (M1 M2 M3 M4) = (0 0 LSB2 LSB1). As explained in section 3.1.1, obtain the Parity Code P and the Extended Hamming Code H for the message code M. Covert the Parity Code P to decimal and store in the key.

Step 9. Reconvert the modified cover image pixel from binary to decimal and pass the pixel.

Step 10. Recover the stored pixel location as stated in step 6.

Step 11. Repeat steps 6 to 10 for all pixels of the watermark image.

Lemma 1. Watermarking is possible only if N= r x c is less than the count obtained in step 4.

C. Watermark Extraction

Input: (a)A grayscale watermarked image. (b) A key of size (1 x N) where N= r x c where r x c is the dimension of the watermark. **Output**: Binary watermark of size r x c.

In the watermark extraction algorithm, the original cover image or the original watermark is not required. So, the proposed method is blind. However, the key generated during embedding is required to be known for watermark extraction.

Step 1. Read the watermarked image and the key.
Step 2. Read the first two locations of the key to obtain the dimensions of the watermark.
Step 3. Start with the first pixel of the watermarked image.
Step 4. Search for watermarked image pixel having value greater than threshold value and store the corresponding pixel location.
Step 5. Convert the corresponding pixel into 8-bit binary value and extract LSB1 and LSB2. Form a four-bit message code M= (0 0 LSB2 LSB1).
Step 6. Obtain the decimal equivalent of the parity code P from the key. Convert it into four-bit binary value to obtain P= (P1 P2 P3 P4). Combining P and M obtain the Extended Hamming Code H.
Step 7. As explained in section A, check whether single or double bit errors exist in M i.e. in LSB1 and LSB2 and correct them.
Step 8. After correction, the watermark is obtained by the following operation.

$$w(u, v) = LSB1 \oplus LSB2 \qquad (12)$$

Step 9. Extract the stored pixel location (step 4).
Step10. Repeat steps 4 to 9 for the entire dimension of the watermark obtained in step 2.

Lemma 2. The watermark can be extracted only if the key is known.

Lemma 3. This is a self-error correcting algorithm as we are only concerned of errors in LSB1 and LSB2 of watermarked image pixel. So, if by applying Extended Hamming Code, double bit error is detected in M= (0 0 LSB2 LSB1), then both LSB1 and LSB2 are complemented (other 2 bits are always 0, no errors are possible in them). In case of single bit error, Extended Hamming Code will give us the bit position of the erroneous bit and we can easily determine whether error is in LSB1 or LSB2.

IV. PROPOSED CRYPTOGRAPHIC ALGORITHM

Proposed cryptographic algorithm is applicable for symmetric-key systems where a single key or password is known only to the sender and receiver. Encryption and decryption is possible only if the key is known [2]. The message to be encrypted is a binary image of size (r x c) and the key is chosen to be a grayscale image of size equal to that of the binary image i.e. (r x c). The Symmetric-key Cryptographic Model with respect to our proposed algorithm is depicted in Fig. 2.

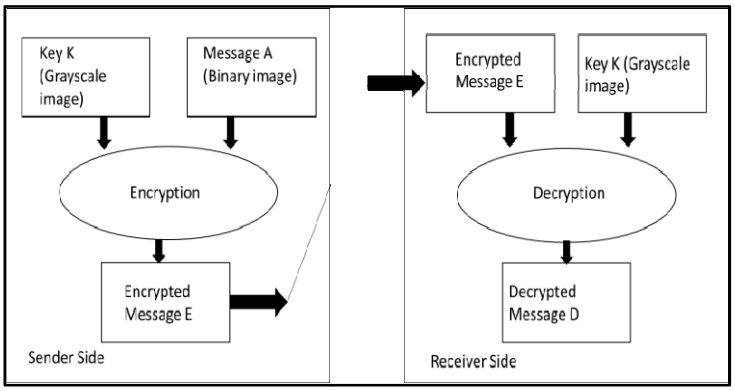

Figure 2. Symmetric-Key Cryptographic Model

D. Encryption

Input: (a) A binary image of size r x c as message A. (b) A grayscale image of size r x c as key K. **Output**: A grayscale encrypted image of size r x c as encrypted message E.

Step 1. Read the message A and the key K. Initialize two matrices B and E each of them having size equal to the message A i.e. r x c.
Step 2. Choose a pixel of the key K, say K (i, j), pixel at ith row and jth column. Convert it into 8-bit binary value. Extract the LSB in the first bit plane position (LSB1) and the LSB in the second bit plane position (LSB2).
Step 3. Choose a pixel of the message A, say A (i, j), pixel at ith row and jth column.
Step 4. Choose a four-bit code M= (M1 M2 M3 M4) such that M1=0, M2=0, M3= LSB2 and M4 = LSB2 $\oplus$ A (i, j).
Step 5. As explained in section A, obtain the Parity Code P and the Extended Hamming Code H for the four-bit code M. Covert the Parity Code P to decimal and store as a modified message pixel in B i.e. B (i, j).
Step 6. Repeat steps 2 to 5 for every set of pixels i and j in the message A and key K. Thus, we get a modified message B.
Step 7. After obtaining B, the final encrypted message E is obtained by performing bitwise EX-OR operation between each pair of pixels in B and K. The operation is shown as follows:

$$E(i, j) = \text{Bitwise EX-OR}(K(i, j), B(i, j)) \qquad (13)$$

where E (i, j) = Pixel in the ith row and jth column of E.
B (i, j) = Pixel in the ith row and jth column of B.
K (i, j) = Pixel in the ith row and jth column of K.

E. Decryption

Input: (a) A grayscale image of size r x c as encrypted message E. (b) A grayscale image of size r x c as key K. **Output**: A binary image of size r x c as decrypted message D.

Step 1. Read the encrypted message E and the key K. Initialize two matrices C and D each of them having size equal to the encrypted message E i.e. r x c.
Step 2. A partially decrypted message C is obtained by performing bitwise EX-OR operation between each pair of

pixels in encrypted message E and Key K. The operation is shown as follows:

$$C(i, j) = \text{Bitwise EX-OR}(K(i, j), E(i, j)) \quad (14)$$

where C (i, j) = Pixel in the ith row and jth column of C.
K (i, j) = Pixel in the ith row and jth column of K.
E (i, j) = Pixel in the ith row and jth column of E.

Step 3. Choose a pixel of the key K, say K (i, j), pixel at ith row and jth column. Convert it into 8-bit binary value. Extract the LSB in the first bit plane position (LSB1) and the LSB in the second bit plane position (LSB2).

Step 4. Choose a pixel of the partially decrypted message C, say C (i, j), pixel at ith row and jth column.

Step 5. Choose a four-bit code M= (M1 M2 M3 M4) such that M1=0, M2=0, M3= LSB2 and M4 = LSB1.

Step 6. Obtain the Parity Code P= (P1 P2 P3 P4) from the last four bits of the partially decrypted message pixel i.e. C (i, j). The Extended Hamming Code H is obtained by combining the four-bit code M and Parity Code P.

Step 7. As explained in section A, check for single bit error that is supposed to exist in M i.e. in LSB1 and LSB2 and correct it.

Step 8. After correction the final decrypted message pixel D (i, j) is obtained by performing EX_OR operation between M3 and M4. The operation is shown as follows:

$$D(i, j) = M3 \oplus M4 \quad (15)$$

where D (i, j) = Pixel in the ith row and jth column of D.
M3= Second LSB in M.
M4= First LSB in M.

Step 9. Repeat steps 3 to 8 for every set of pixels in the partially decrypted message C and the Key K to obtain the final decrypted message D.

Lemma 4. This is a symmetric-key cryptographic system, so the encrypted message can be decrypted only if the key K is known to the receiver.

V. Analysis and Experimental Results

F. For Watermarking Algorithm

The performance of the proposed watermarking algorithm is evaluated by using MATLAB (R2011a) in terms of five metrics- PSNR (Peak Signal to Noise Ratio), MAE (Mean Absolute Error), SSIM (Structural Similarity Index), Quality Index (Q) and Normalized Correlation (NC). Peak Signal to Noise Ratio (PSNR) is the ratio of the maximum signal power to the corrupting noise power. Structural Similarity Index (SSIM) [8] and Normalized Correlation (NC) are the parameters for measuring similarity between two images. Quality Index (Q) [9] measures the distortion of the received image compared to the original image. Mean Absolute Error (MAE) compares two images by providing a qualitative score that describes the degree of fidelity or level of distortion between them [5]. The formula of these metrics is given in Table I. For analysing the effectiveness of our proposed algorithm, we have chosen a variety of grayscale cover images and binary watermarks of different sizes as shown in Fig 3. The imperceptibility of the algorithm is analyzed in Table II by choosing cover images and watermarks of variable sizes. As the size of the watermark increases, the level of imperceptibilty decreases as can be seen in Table II.

TABLE I. Image Performance Metrics

	Formula	Description
PSNR	$MSE = \frac{\sum_{M,N}[I_1(m,n) - I_2(m,n)]^2}{M \times N}$ $PSNR = 10\log_{10}(\frac{255^2}{MSE})$	MSE= Mean Square Error I_1, I_2= The two images under consideration m, n= Rows, Columns of input images. M, N= Size of input images
NC	$NC = \frac{\sum_1^M \sum_1^N I'_{ij} I_{ij}}{\sum_1^M \sum_1^N (I_{ij})^2}$	I= Original Image I'= Extracted Image
MAE	$MAE = \frac{\sum_1^M \sum_1^N \lvert I'_{ij} - I_{ij} \rvert}{M \times N}$	I= Original Image I'= Extracted Image
MSSIM	$MSSIM = \frac{1}{M}\sum_{j=1}^{M} SSIM(x_j, y_j)$ $SSIM = \frac{(\mu_x\mu_y + C_1)(2\sigma_{xy} + C_2)}{(\mu_x^2\mu_y^2 + C_1)(\sigma_x^2 + \sigma_y^2 + C_2)}$	X= Reference Image Y= Distorted Image x_j, y_j= Image contents at jth local window M= No. of local windows
Q	$Q = \frac{4\sigma_{xy}\mu_x\mu_y}{(\sigma_x^2 + \sigma_y^2)(\mu_x^2 + \mu_y^2)}$	x_j, y_j= Image contents at jth local window μ_x, μ_y= Mean Intensity σ_x, σ_y= Standard Deviation

Various kinds of attacks are implemented on the embedded image to check the robustness of the proposed algorithm. The detailed performance of the algorithm to these attacks is shown in Table III. Figure 4 shows the cover image and the watermark chosen for the analysis of robustness.

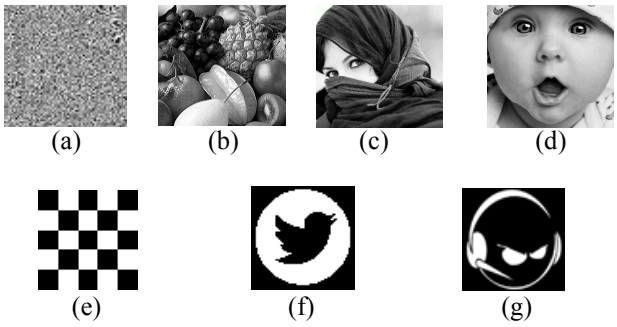

Figure 3. Grayscale Cover Images : (a) Noise (64 x 64) (b) Fruit (128 x 128) (c) Girl (256 x 256) (d) Baby (512 x 512) and Binary Watermark Images : (e) Checkerboard (16 x 16) (f) Bird (32 x 32) (g) Cartoon (64 x 64)

TABLE II. Performance Analysis of Embedded Image with Cover Image

Water mark	Cover Image	PSNR	MSSIM	Q	NC	MAE
Check-erboard	Noise	63.016	0.9999	1.00	0.9999	0.0190
	Fruit	69.668	0.9999	1.00	0.9999	0.0041
	Girl	75.257	0.9998	1.00	1.00	0.0011
	Baby	81.785	1.00	1.00	1.00	0.0002
Bird	Noise	Embedding Not Possible (Lemma 1)				
	Fruit	63.311	0.9999	1.00	0.9999	0.0153
	Girl	69.565	0.9986	1.00	0.9999	0.0039

	Baby	75.335	0.9999	1.00	1.00	0.0012
Carto-on	Noise	Embedding Not Possible (Lemma 1)				
	Fruit	Embedding Not Possible (Lemma 1)				
	Girl	63.549	0.9938	1.00	0.9999	0.0137
	Baby	69.239	0.9997	1.00	0.9999	0.0047

Figure 4. A Particular Case: (a) Chosen Cover Image (256 x 256) (b) Watermarked Image (256 x 256) (c) Chosen Watermark (32 x 32) (c) Extracted Watermarked (32 x 32)

TABLE III. PERFORMANCE ANALYSIS OF EXTRACTED WATERMARK WITH ORIGINAL WATERMARK WHERE CHOSEN WATERMARK IS BIRD IMAGE OF SIZE 32 X 32 AND CHOSEN COVER IMAGE IS GIRL IMAGE OF SIZE 256 X 256

Watermark Attacks	PSNR	MSSIM	Q	NC	MAE
Without Attack	Infinity	1.00	1.00	1.00	0.00
Gaussian Noise	Infinity	1.00	1.00	1.00	0.00
Salt & Pepper Noise	Infinity	1.00	1.00	1.00	0.00
Speckle Noise	Infinity	1.00	1.00	1.00	0.00
Poisson Noise	Infinity	1.00	1.00	1.00	0.00
Blur	Infinity	1.00	1.00	1.00	0.00
Motion Blur	Infinity	1.00	1.00	1.00	0.00
Sharpen	Infinity	1.00	1.00	1.00	0.00
Histogram Equalize	Infinity	1.00	1.00	1.00	0.00
Adaptive Histogram Equalize	Infinity	1.00	1.00	1.00	0.00
Contrast Adjusting	Infinity	1.00	1.00	1.00	0.00
Gamma Correction	Infinity	1.00	1.00	1.00	0.00
Gaussian Filter	Infinity	1.00	1.00	1.00	0.00
Median Filter	Infinity	1.00	1.00	1.00	0.00
Crop (25 %)	Infinity	1.00	1.00	1.00	0.00
Crop (50 %)	Infinity	1.00	1.00	1.00	0.00
Crop (75 %)	55.423	0.5895	0.5746	0.6698	0.1865
Crop (80 %)	52.983	0.2278	0.2698	0.4392	0.3271
Rotation (5°)	Infinity	1.00	1.00	1.00	0.00
Rotation (35°)	Infinity	1.00	1.00	1.00	0.00
Rotation (55°)	Infinity	1.00	1.00	1.00	0.00
Rotation (90°)	Infinity	1.00	1.00	1.00	0.00
Resize (2)	Infinity	1.00	1.00	1.00	0.00
Resize (0.5)	Infinity	1.00	1.00	1.00	0.00
Resize (0.2)	Infinity	1.00	1.00	1.00	0.00
Resize (0.1)	Infinity	1.00	1.00	1.00	0.00
JPEG 10	Infinity	1.00	1.00	1.00	0.00
JPEG 50	Infinity	1.00	1.00	1.00	0.00
JPEG 80	Infinity	1.00	1.00	1.00	0.00

TABLE IV. PARAMETRIC COMPARISION FOR PROPOSED ALGORITHM AND EXISTING ALGORITHMS

Author	Q	PSNR, dB	MSSIM	NC	Capacity* (bits/pixel^2)	MAE
Proposed Algorithm	1.0	81.78	1.0	1.0	$\frac{16 \times 16}{256 \times 256}$	0.0002
Y.-T.Lin et al. [10]	DNS	48.52	DNS*	DNS	$\frac{128}{256 \times 256}$	DNS
Dong Zheng et al. [11]	DNS	42	DNS	DNS	$\frac{8}{512 \times 512}$	DNS
Shijun Xiang et al. [12]	DNS	44.58	DNS	DNS	$\frac{25}{512 \times 512}$	DNS
Ben Wang et al. [13]	DNS	78.23	DNS	DNS	$\frac{32 \times 32}{512 \times 512 \times 8}$	DNS

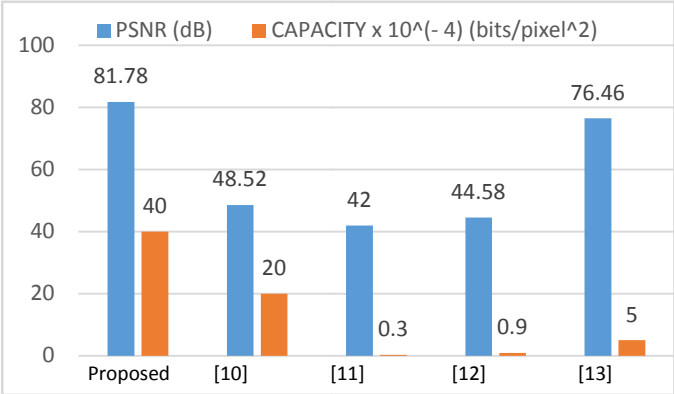

Figure 5. Comparison Statistics for various PSNR and Capacity Value (*capacity is the no. of watermark bits embedded divided by the total no. of pixels in the cover image and *DNS is Data Not Specified)

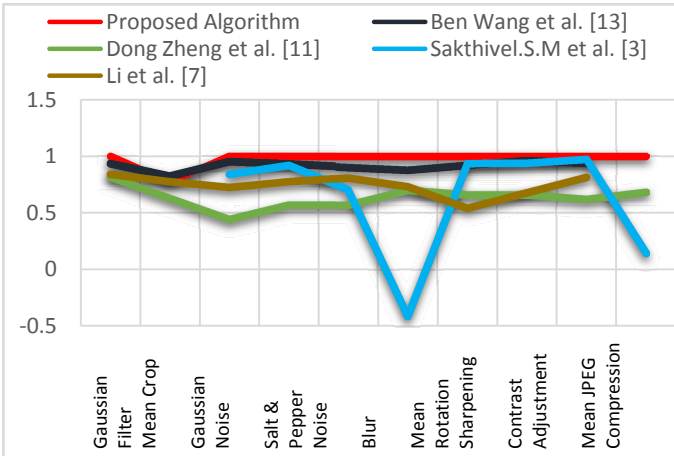

Figure 6. Comparative study of robustness of proposed algorithm with existing algorithms in terms of Normalized Correlation (NC)

A comparative study is done to prove the effectiveness of the proposed algorithm. Table IV and Fig. 5 shows that our algorithm gives a higher degree of imperceptibility by giving the highest PSNR among some of the existing schemes. Also, from Fig. 6 we can conclude that our algorithm is more robust to noise, geometrical, filtering and image processing attacks compared to the schemes proposed by Li et al. [7], Dong Zheng et al. [11], Ben Wang et al. [13] and Sakthivel. S. M et al. [3].

G. For Cryptographic Algorithm

The performance of the proposed cryptographic algorithm is evaluated by using MATLAB (R2014a) and has been implemented on Intel i5 CPU@ 3.20 GHz and 4 GB RAM memory. The grayscale key, original message, obtained encrypted and decrypted message are shown in Table V for two different cases along with the effectiveness in the algorithm for changes in the original key. The performance analysis in terms of various cryptographic parameters like encryption, decryption time [14], Encryption Ratio (*percentage of data that is encrypted with respect to total data) etc. is done in Table VI.

TABLE V. CRYPTOGRAPHIC CASE STUDY SHOWING CHOSEN GRAYSCALE KEY, ORIGINAL MESSAGE, ENCRYPTED MESSAGE AND DECRYPTED MESSAGE

Key Original	Message	Encrypted Message	Decrypted Message with correct key
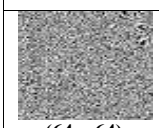 (64 x 64)	(64 x 64)	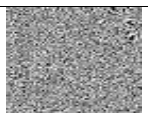 (64 x 64)	(64 x 64)
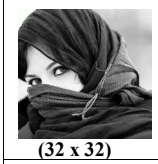 (32 x 32)	(32 x 32)	(32 x 32)	(32 x 32)
Key Original	**Message**	**Decrypted Message with incorrect key (1 pixel modified)**	**Decrypted Message with incorrect key (1 and more than 1 percent of pixels modified)**
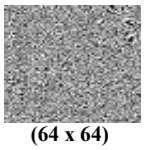 (64 x 64)	(64 x 64)	(64 x 64)	(64 x 64)
(32 x 32)	(32 x 32)	(32 x 32)	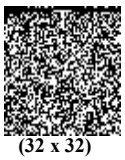 (32 x 32)

TABLE VI. CRYPTOGRAPHIC PERFORMANCE ANALYSIS

Cryptographic Parameters	Case 1 (64x 64) Key	Case 1 (64x 64) Message	Case 2(32 x 32) Key	Case 2(32 x 32) Message	Case 3(16 x 16) Key	Case 3(16 x 16) Message
	Noise	Cartoon	Girl	Bird	Fruit	Checkerboard
Encryption time	1.803 sec		0.4759 sec		0.144 sec	
Decryption time	1.920 sec		0.511 sec		0.158 sec	
Average time	1.861 sec		0.4936 sec		0.151 sec	
Bytes Processed	4608 bytes		1152 bytes		288 bytes	
Data rate	2.42 KB/sec		2.28 KB/sec		1.86 KB/sec	
Encryption Ratio*	100%		100%		100%	
Visual Degradation	PSNR = 4.34 NC = - 0.002 (Lower value preferable)		PSNR = 6.60 NC = - 0.01 (Lower value preferable)		PSNR = 6.42 NC = 0.045 (Lower value preferable)	
Decryption Quality	PSNR = Infinity NC = 1.00		PSNR = Infinity NC = 1.00		PSNR = Infinity NC = 1.00	

VI. CONCLUSION AND FUTURE WORKS

In this paper we have proposed a dual purpose robust algorithm in spatial domain for both digital watermarking and image cryptography. In case of digital watermarking the watermark can be extracted blindly using the watermarked image and the key, hence it finds applications in security and copyrighting purposes. The algorithm gives a higher degree of imperceptibility without sacrificing the robustness. The same algorithm can be used to design a symmetric-key cryptographic system having applications in secure information transferring systems. The hardware implementation of the proposed algorithm will be done in the future.

REFERENCES

[1] W. Bender, D. Gruhl, N. Morimoto and A. Lu, "Techniques for data hiding", *IBM systems Journal*, vol. 35, no 3.4, pp. 313-335,1996.

[2] W. Diffie and S. Landau, *Cryptography*, MIT Press, Edition 1, ISBN 9780262256018, 2007.

[3] J. Sakthivel. S.M. and Dr. Ravi Sankar. A, "A real time watermarking of grayscale images without altering it's content", *International Conference on VLSI-SATA*, Jan 2015, pp. 1 – 6.

[4] R Houtan Haddad Larijani and Gholamali Rezai Rad, " A new spatial domain algorithm for grayscale images watermarking", in *Proceedings of the International Conference on Computer and Communication Engineering*, May 13-15, 2008, pp. 157-161.

[5] Sudip Ghosh, Somsubhra Talapatra, Navonil Chatterjee, Santi P Maity and Hafizur Rahaman, "FPGA based implementation of embedding and decoding architecture for binary watermark by spread spectrum scheme in spatial domain", *Bonfring International Journal of Advances in Image Processing*, vol. 2, no. 4, December 2012.

[6] D. K. Bhattacharrya, S. Nandi' "An efficient class of SEC-DED-AUED codes", *ISPAN '97*, pp. 410-415. doi: 10.1109/ISPAN.1997.645128.

[7] Jianzhong Li, Xiangsu Zhang, Shou Liu, Xuechang Ren, "An adaptive secure watermarking scheme for images in spatial domain using fresnel transform", 1st *IEEE International Conference on Information Science and Engineering* , Dec 2009, pp. 1630- 1633.

[8] Z. Wang, A. C. Bovik, H. R. Sheikh and E. P. Simoncelli, "Image quality assessment: From error measurement to structural similarity" *IEEE Transactions on Image Processing*, vol. 13, no. 1, pp. 600– 612, Jan 2004.

[9] Zhou Wang and Alan C. Bovik, "A Universal Image Quality Index", *IEEE Signal Processing Letters*, vol 9, no. 3, pp. 81- 84, March 2002.

[10] Y.-T. Lin, C.-Y. Huang and G.C. Lee, "Rotation, scaling, and translation resilient watermarking for images", *Image Processing, IET*, vol. 5, no. 4, pp. 328- 340, June 2011.

[11] Dong Zheng, Sha Wang and Jiying Zhao, "RST Invariant Image Watermarking Algorithm with Mathematical Modeling and Analysis of the Watermarking Processes", *IEEE Transactions on Image Processing,* vol. 18, no. 5, pp. 1055- 1068, March 2009.

[12] Shijun Xiang, Hyoung Joong Kim and Jiwu Huang, "Invariant Image Watermarking Based on Statistical Features in the Low-Frequency Domain", *IEEE Transactions on Circuits and Systems for Video Technology,* vol.18, no. 6, pp. 777- 790, June 2008.

[13] Ben Wang, Jinkou Ding, Qiaoyan Wen, Xin Liao and Cuixiang Liu, " An image watermarking algorithm based on DWT DCT and SVD", *IEEE International Conference on IC-NIDC*, November 2009, pp. 1034- 1038.

[14] S. Saeed, M.S. Umar, M.A. Ali, M. Ahmad, " A Gray-Scale Image Encryption Using Fisher-Yates Chaotic Shuffling in Wavelet Domain", *Recent Advances and Innovations in Engineering (ICRAIE)*, May 2014, pp.1-5.

Role of Clinical Engineering to Reduce Patient's Risk Factors in Life Support Ventilator

Md. Anwar Hossain[1], A. K. M. Rahman[2], Md. Rezanur Rahman[3], Md. Rafiqul Islam[4], and Mohiuddin Ahmad[5]
[1]Department of Biomedical Engineering, Khulna University of Engineering & Technology (KUET), Khulna-9203, Bangladesh
[2]Ministry of Fisheries, Government of Bangladesh
[3]Ministry of Health & Family Welfare, Government of Bangladesh
[4, 5]Department of Electrical & Electronic Engineering, KUET, Khulna-9203, Bangladesh
E-mail: anwar.bme@gmail.com, joardrre@gmail.com, mraman@itc.nl, islambit@yahoo.com, mohiuddin.ahmad@gmail.com

Abstract— **The patients who are unable to take breathe normally is taken into life support ventilator, which without clinical engineering professional (CEP) interaction, cannot be kept in safe and functional. The operational characteristics of life support ventilator used in ICU have various risk factors such as, invasively or noninvasively perform diagnostic, therapeutic, corrective or monitoring intervention of the patients. Here we have presented an approach to develop a standard of risk factor management incorporating the role of CEP to mitigate the risks in real-time. For clinical setting and safe operation of ventilator devices, calibration must be ensured in the standard. Development of correlation among doctor, clinical engineer, and nurse is required for proper functioning of the ventilator. A comparison of risk factors is shown with and without CEP and found that the risk factor can be reduced significantly in developed countries with respect to developing countries like Bangladesh. In this study, mathematical model of risk factor reduction is also proposed.**

Keywords—Clinical Engineers, Risk factor, Intensive care, Life support ventillator, Hospital

I. INTRODUCTION

A. The Conceptual Background of the Study

A life support ventilator is an invention of modern medical technology and which is used for the patients who are unable to take breath normally but it has been observed that without clinical engineering interaction, this device could not keep in safe functional mode. An intensive care ventilator is a costly and life support medical device which is used for therapeutic and monitoring purpose of intensive care unit (ICU) patients of hospital.

Medical devices in the hospital such as mechanical ventilators and anesthesia machines have been managed by doctors and nurses throughout the world [1]. In Japan, doctors and nurses have performed the maintenance of mechanical ventilators in the past [2]. With the rapid growth of medical technology, the configuration of ventilator becomes complex due to integration of electrical, electronic and computation technologies. Due to submerge the multi-technology in ICU ventilator, doctors and nurse have felt risky of the use and maintenance of the ventilator in the hospitals [3].

B. Historical Background

The aim of this research is to investigate the effectiveness of maintaining mechanical ventilators by clinical engineers (CEs) using a specialized calibrator in hospitals. It is important to ensure appropriate quality control of mechanical ventilator support. Usually, faulty mechanical ventilators were repaired by the distributor. However, since the late 1990s, clinical engineers (CEs) who have a certificate of completion and have completed established course requirements now perform the maintenance of mechanical ventilators in hospitals. During the 1980s, general-purpose-type mechanical ventilators were in use [4]. Their operating principle was simple, and mechanical ventilators at that time had few circuit boards and/or sensors [5]. These mechanical ventilators were rugged and did not break down easily. Operator error accounted for most of the sudden malfunctions of mechanical ventilators [6, 7].

However, over the last two decades, technological developments have led to significant improvements in the performance of mechanical ventilators [8–11]. Modern critical care mechanical ventilators have circuit structures with numerous CPU boards and sensors [12]. Therefore, these mechanical ventilators have more failure points that increase the likelihood of failure. Blanch reported that spending an immense amount of time and cost could secure the reliability of an apparatus, but it was hard to anticipate the deterioration of mechanical ventilators; their safety and reliability will change significantly as ventilators are used or age [13]. The use of the PTS-2000 calibration analyzer has contributed to the discovery of previously undetected malfunctions in the new generation of high-performance mechanical ventilators. In this way, evaluating ventilation and carrying out in-house repairs has proved to be effective for obviating the chance of renting faulty units. Clinical engineering has decreased medical device failure which exposes patients to potentially harmful risks through proper use of health care technology. The current status of the clinical engineers in Bangladesh is illustrated in [14].

Thus, developed countries have reduced risk factor of ICU patients from ICU ventilators by interfacing the in-house clinical engineering professionals in their hospitals whereas, most of the developing countries such as Bangladesh, Bhutan,

978-1-4673-9257-0/15/$31.00 ©2015 IEEE

Nepal, Myanmar and so many have been maintaining the ICU ventilators through the conventionally short train electrical/mechanical trade diploma engineers on call basis. Instant failure of ventilators could not be repaired by vendor's engineers/ technicians. As a result, harmful situation is continuing for the ICU patients for the developing countries like Bangladesh in the world. From the past and present records, we have been observed that the performance of the use, calibration, software upgrades, preventive maintenance, overhaul of ventilators are very inferior and unsafe for the ICU patients of the developing countries like Bangladesh. Considering the real fact, we have taken it ethically and submit a proposal to reduce the risk factor of the ICU patients of developing countries. We firmly, believe that our research results and recommendations will be able to reduce the present uncountable risk factor of ICU patients from the ventilators. For the convenient of optimum research results, we have selected Bangladesh among the developing countries for a cause study. This research will be helpful for developing countries in world which are similar to Bangladesh.

This paper is organized as follows: Section II discusses the problem concerns. Section III illustrates the proposed methodology. Section IV gives the results and discussions. Recommendations for solving the problem are discussed in section V. Finally, section VI concludes the paper.

II. PROBLEMS CONCERNS

A lot of problems may occur in ICU unit if it is operated without interaction of CEP. Some of the major problems are given below:

- Clinical engineering is a new concept for health care planers of developing countries like Bangladesh although a huge number of medical equipments are being used by the health care services of Bangladesh.
- Health care planers completely could not add this important clinical engineering professionals (CEPs) due lack of their awareness as well as less attention.
- There is no research center /department to catch up the problems.
- Current electro-medical medical engineering department is not updated; as a result, the performance of this department is only 0.34% out of 70%.
- ICU patients are not risk free from life support ventilator as it is not operated following the standard method.

Figures 1(a) and 1(b) show the standard clinical engineering interaction with life support ventilator in ICUs of developed countries like Japan, Germany, etc. In Figure 1(a) shows the procedure of confirming the functionalities of ICU ventilator before it is applied on ICU patients. It is required to check every parameter such as hardware, software, clinical settings before handover the ICUV to the users (ICU doctor, clinical engineering technologists and nurses). Figure 1 (b) shows the activities of a doctor and clinical engineering technologist in ICU.

(a). Examination of ICUV by CEs before use (b). Practical utilization of ICUV in presence of a CE and Doctor

Figure 1. Standard clinical engineering interaction with life support ventilator in ICU.

Figure 2. ICU ventilator without any CE in developing countries.

CEs in developed countries ensure safety and risk of sophisticated modern medical equipments such as ICU ventilators, heart lung machine and so on before using. However, in developing country like Bangladesh has no in-house clinical engineer in any ICU that represents the substandard clinical engineering interaction with life support ventilator. Therefore, ICU patients of developing countries like Bangladesh is not risk free from life support ventilators. We have visited NICVDH, SSMCH and DMCH and not found CEs or CE technologists for ensuring the risk management. Normally ICU specialists and ICU nurses operate the ICU ventilator, however, they do not have enough knowledge about risk management such as low battery level alarm, lees tidal volume alert, leakage current, room temperature , humidity control, wall out let oxygen pressure, leakage of wall out let connectors, ventilator mode change such as CMV,SIMV and spontaneous mode, tidal volume, minute volume, humidity control of Oxygen by humidifier, temperature of humidifier, water changing frequency etc. In this connection, we discuss with ICU doctors, Anesthesiologists, cardiologists and nurses but they are not able to answer according to our queries. We have observed the situations about 7 days and found red alarm in ICU ventilators. The causes which are identified: loose wall out connector, incorrect setting of berating rate alarm, low battery level, patient circuit leakage, low level water in humidity fires, disconnection of humidifier heater, the ratio of inspiration and expiration is not sleeted according to patient weight.

III. PROPOSED METHODOLODY

A. Research Goal

The aim of the research is to reduce the risk factor of the ICU patients from the life support ventilator through the developing inter -professional skilled clinical engineers.

B. Research Design

- Past and presents trends of the failure of ventilator during use for ICU patients.
- Causes of the failures of ventilators.
- Standard operating procedure of ICU ventilators.
- Current operating procedure of ICU ventilator.
- Performance evaluation ICU ventilator with CE and without CEs
- Find out the risk factor of the use, calibration and maintenance of ventilator for ICU patients.

C. *Risk factor reducing method*

Modern medical devices are used in ICU ventilators in which combined knowledge of medical science, mechanical, electrical, electronic and computer are integrated. So, clinical engineering inputs are mandatory for the ICU patients to reduce the risk factor and it is globally recognized. It is therefore very much important to buildup strong correlation among the ICU doctors, CEs and nurses. The risk factor of ICU patients from the ICU ventilators may have a relation and can be expressed as follows:

Suppose the risk factor of ICU patients from the ventilators of hospitals without and with CEs is y_1 and y_2 respectively. If x_1, x_2, and x_3 represent the technical knowledge of skilled medical doctors, nurses, and CEs, then we can express,

$$y_1 = x_1 + x_2 \tag{1}$$

$$y_2 = (x_1 + x_2) + x_3 \tag{2}$$

The parameters x1, x2, and x3 indicate academic and practical score point and denoted in terms of percentage. It is found [14] that for any medical devices the score of CEs=52%= x3, medical doctors= 20% =x1, and Nurses=10% =x2, BMETs=18%=x4. The total score is 100%. Here, we consider only three indicators such as x_1, x_2 & x_3 and total score of the said indicators is 82%.

If R_f denotes the reduce of risk factor, then

$$R_f = y_2 - y_1 \tag{3}$$

Let y_1 is constant for all hospitals and standard and from Eqs. (2) and (3), we can define that $R_f = x_3$.

Values of R_f will reduce the risk factor of ICU patients from ventilators. We will need to reduce value of R_f through introducing CEPs in ICU. We have examined that for 8 bed standard ICU 4 numbers of CEs are mandatory to give the 52% technical input to cover the 24 hours roster duty and remaining 30% technical input will come from ICU doctors and Nurses. So R_f is proportional to x_3 that is CEs. Most of the developing countries like Bangladesh have no in-house clinical engineering department. But only, on call basis vendors or government conventional diploma technicians are maintaining only brake down maintenance. This performance is only average 2% of total 70 % standard requirements.

D. Sample data collection

For data collection and data analysis, we have taken data from developed and developing countries. In this connection, we have reviewed literatures in these fields and we have observed the present trends of Bangladesh.

TABLE I. TABLE FAILURE OF ICU VENTILATOR WITH AND WITOUT CEs IN HOSPITALS OF BANGADESH

Measurement components	A comparison of risk factor due failure of ventilator with respect to standard			
	Standard in developed countries 100 ventilators with CEP [15]	Developing counties like Bangladesh 100 ventilators without CEPs	Responded time in hours	
			Standard In developed countries	Sub-standard in developing countries like Bangladesh
Sensor failure	5	70	2	72
Battery Failure replacement	2	35	1	72
Musk displacement adjustement	1	95	1	2
Humidifer failure recover	2	75	1	8
Valve faileures recover	2	65	1	48
Avearge result	**2.4**	**68**	**1.2**	**40.40**

We have taken data from different hospitals of Bangladesh. We considered 100 ICU ventilators. Accordingly, we have reflected data in Table I and risk factors results are shown in Figure I. From Table I, we have found that the risk factor of ICU patients from ventilators are Bangladesh is very high and more over the responding time to run the ICU ventilators is average very higher than of developed countries. Due to absence of CEPs in hospitals such worth situation has been raised. From Table I, the performance of the ICU ventilators has been calculated. The risk factor of ICU patients from ventilators with and without CEPs for a standard developed country and a developing country like Bangladesh is shown in Fig. 3.

From Fig. 3, we have found that the rsik factors of the ICU ventilatiors are very high due to absence of CEPs. The average value of risk factor of ICU ventilators is about 65% higer in a developing contry than that of a developed country.

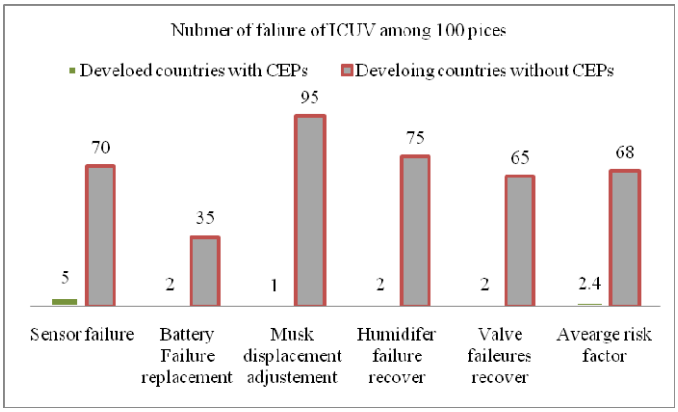

Figure 3. Risk factor of ICU patients from venticular with and without CEPs in developed and developing countries like Bangladesh.

IV. Results and Disscusion

For each ventilator, we evaluated the following parameters: (i) inspiratory flow, (ii) tidal volume, (iii) oxygen concentration, (iv) peak inspiratory pressure (P_{IP}), (v) positive end-expiratory pressure (PEEP), (vi) respiratory rate, and (vii) inspiratory time. ICU ventilators that were out of the acceptable ranges were classified as faulty. Faulty mechanical ventilators were repaired by calibration and replacing sensors and/or circuit boards. The standard parameters said in this section are depend on the category of the patients. In some models compile as machine default settings and some are needed to fix as customize. Here we have shown some data in the below Table II.

TABLE II. PARAMETERS OF ICUV

Parameters of ICU ventilators	**During checking**	**After repair and calibrations**
Inspiratory flow	Abnormal	Normal
tidal volume	Abnormal	Normal
oxygen concentration	Was too high	Normal
Peak inspiratory pressure (P_{IP})	Higher than normal value	Normal
Positive end-expiratory pressure (PEEP)	Was low	Normal
Respiratory rate	30	Normal and set at 16
Inspiratory time	Higher	Normal

We systematically checked mechanical ventilators about 570 times using a PTS-2000 calibrator during the period from January 2007 to December 2014, and there were a total of 100 cases of suspected mechanical ventilator failure. The number of faulty ventilators was 90 for ventilator volume, 39 for oxygen concentration, and 22 for malfunctions. The faulty ventilators needing valve and/or sensor replacement were repaired in-house by CEs. The rare, seriously malfunctioning ventilators (there were a total of 12 cases of circuit board failure) were sent to the distributor for repairing. Regarding response times for valve and/or sensor replacement, in-house repairs were completed immediately. However, if a machine is needed to repair to the distributor, it will take from average 8 hours to 72 hrs but more than 7 days. No ventilators could be run by local vendors within 7 days and charges were found very high which one kind of burden for the patients.

The most important item should be the checking of mechanical ventilators by CEs. CEs are certainly specialists in medical devices, and their involvement in maintaining mechanical ventilators is logical for the hospital, prompt, and most importantly safe. CEs fill an essential role for the safe operation of mechanical ventilators, and, more importantly, the CEs technology provides safe maintenance for many hospitals. From Eqs. (1), (2) and (3), the value of risk factor is found which is R_f = (68–2.4/%) = 65.6%. It means that the ICU patients from ventilators are always carrying about 65.6% risk factor. This is a moral and an emergency issue to reduce the risk factor. Without In-house clinical engineering support, risk factor should not be reduced by current ICU team such as doctors and nurses. To reduce the risk factor of ICU patents from ventilators, some recommendations have been submitted. Subject to the implementation of proposed recommendation, the risk factor will be minimized.

V. Recomedentions

The following standard operating procedure is shown in Table II for reducing the risk factor.

TABLE III. STANDARD OPERATING PROCEDURE TO REDUCE THE RESIK FACTOR

Cause of Risk Factor	Risk Factor Score	Guideline to reduce of risk factor	Responsibility
Product selection	100%	Need based technology selection according to country context	CE, Intensive care unit (ICUN) and ICUIST
Procurement terms	100%	Require consumables for ten years	Quantity depends on patients and hence for ten years a frame work consumables supply contact terms with prices should be determinate by the ICUIST, ICUN.
Oxygen disconcertion	100%	Should be ensured by ICUN.	CE will check
Calibration test	100%	Tools require PST-2000	In-house CE will checked it before use
Distill Water level for humidity and temperature control	100%	Every day ICUN check it according Manuals.	Hospital in House Clinical Engineer (HIHCE)
Oxygen sensor failure	100%	Routine check.	HIHCE
Valves failure	70%	Routine check	HIHCE
Batteries failure	50%	Periodical and predictive.	HIHCE & Vendor Engineers
Air inlet failure	60%	Routine check	HIHCE

Bactria filters	60%	Periodical and predictive.	HIHCE & Vendor Engineers
Electronic boards failure	50%	Preventive and breakdown	HIHCE & Vendor Engineers
Mechanical part failure	35%	Preventive and breakdown	HIHCE & Vendor Engineers.
Patients circuit leakage	58%	Regular check	HICEH and ICUN.

The following recommendations are submitted to reduce the risk factors of ICU patients from ventilator's support during therapeutic.

- It is urgent need to introduced skilled clinical engineers as in-house team for the safety operation, regular calibration, planned preventive maintenance of ICU ventilators in hospitals where ICU supports are available for the patient therapeutic.
- A framework maintenance contract management should be made between local vendors and hospitals to ensure the supply and services within 6 hours for any types of failure or breakdown maintenance. This contract must be made during procurement for the ten years or lifetime of ventilators.
- In-service training for the ICUN, ICUIST should be continue for ensuring better practice of operation and maintenance.
- Continuous monitoring, three-shift CEs are engaged for the safety of patients.
- Equipment enclosure or leakage current must be checked regularly.
- Ventilators self-test should confirm by the qualified CE before and after use of the ventilators.
- Operational software must be customized according to patient's criteria.

VI. CONCLUSION

From the data and results, we have found that the risk factor of ICU patients is very high in hospitals of Bangladesh due lack of proper educated and trained clinical engineers, ICUN and ICUIST. More revenue has been draining out for the new procurement of ICU ventilator since these equipments could not use properly in any hospitals of Bangladesh. As a result, ICU patients are not getting real service. Moreover, due to high risk factors from ICU ventilators, patient's death rate is found high. So ethically and economically, an in-house clinical engineering team is recommended for ensuring the safety aspects from ICU ventilators in the hospitals of Bangladesh as well as developing countries like Bangladesh. We conclude that present risk factor of ICU patents from ventilators could minimize or reduce subject to implementation of our submitted recommendations and proposals.

ACKNOWLEDGMENT

We acknowledged this research work to Ministry of Health & Family Welfare, Government of Bangladesh; Dept. of BME, KUET; NEMEMW & TC, Ministry of Health & Family Welfare, Dhaka, Bangladesh; UGC, HEQEP, CP#3472, KUET; MCH and SPH of Bangladesh.

REFERENCES

[1] S. Chapkowski, N. P. Pucilo, R. D. Cane, B. A. Shapiro, "Impact on ventilator-check time of an in-circuit computerized respiratory monitoring system," Respir Care, vol. 29, pp.144–146, 1984.

[2] A. Hartle, E. Anderson, V. Bythell, L. Gemmell, H. Jones, D. McIvor, A. Pattinson, P. Sim, I. Walke, Association of Anesthetists of Great Britain and Ireland (AAGBI) Checking anaesthetic equipment 2012: Association of Anesthetists of Great Britain and Ireland. Anaesthesia, vol. 67, pp. 660–668, 2012.

[3] J. L. Bourgain, P. Baguenard, J. M. Puizillout, J. C. Ankri, E. Damia, V. Billard, "The breakdown of anesthesia equipment survey," Ann Fr Anesth Reanim, vol. 18, pp. 303–308, 1999.

[4] M. Kawamata, T. Mayumi, M. Miyabe, A. Namiki, "An unusual cause of anesthetic ventilator malfunction," Masui, vol. 41, pp. 1994–1997, 1992.

[5] J. C. M. Richard, R. M. Kacmarek, "ICU mechanical ventilators, technological advances vs. user friendliness: the right picture is worth a thousand numbers," Intensive Care Med, vol. 35, pp. 1662–1663, 2009.

[6] P. B. Blanch, "Mechanical ventilator malfunctions: a descriptive and comparative study of 6 common ventilator brands," Respir Care, vol. 44, pp.1183–1192, 1999.

[7] L. Vignaux, D. Tassaux, P. Jolliet, "Evaluation of the user-friendliness of seven new generation intensive care ventilators, "Intensive Care Med., vol. 35, pp. 1687–1691, 2009.

[8] J. C. Richard, A. Carlucci, L. Breton, N. Langlais, S. Jaber, S. Maggiore, S. Fougère, A. Harf, L. Brochard, "Bench testing of pressure support ventilation with three different generations of ventilators," Intensive Care Med., vol. 28, pp. 1049–1057, 2002.

[9] D. Tassaux, J. B. Michotte, M. Gainnier, P. Gratadour, S. Fonseca, P. Jolliet, "Expiratory trigger setting in pressure support ventilation: from mathematical model to bedside," Crit Care Med., vol. 32, pp. 1844–1850, 2004.

[10] A. W. Thille, A. Lyazidi, J. C. Richard, F. Galia, L. Brochard. A bench study of intensive-care-unit ventilators: new versus old and turbine-based versus compressed gas-based ventilators," Intensive Care Med., vol. 35, pp. 1368–1376, 2009.

[11] A. D. Marchese, D. Chipman, P. de la Oliva, R. M. Kacmarek, "Adult ICU ventilators to provide neonatal ventilation: a lung simulator study," Intensive Care Med., vol. 35, pp. 631–638, 2009.

[12] R. L. Chatburn, "Computer control of mechanical ventilation," Respir Care, vol. 49, pp. 507–517, 2004.

[13] P. B. Blanch, "An evaluation of ventilator reliability: a multivariate, failure time analysis of 5 common ventilator brands," Respir Care, vol. 46, pp. 789–797, 2001.

[14] M. A. Hossain, M. A. Rashid, M. R. Islam, and M. Ahmad, "Current status of skilled clinical engineering in developing countries," Procedia - Social and Behavioral Sciences. vol. 195(2015), pp. 1688-1693, July 2015.

[15] M. A. Hossain, M. R. Rahman, A.K.M. Rahman, M. S. Islam, Azman Hamid, M.A. Rashid, M. H. Rahman Chowdory, B. Gangoloy, M. R. Islam, and M. Ahmad, "Necessity to Produce Clinical Engineering Professional for the Improvement of Present Health Care Management in Developing Countries," ICEHTMC 2015, pp. 173-177, October 21-22, HangZhou, China.

A Mathematical Approach to Determine the Work-done from EMG Analysis

Farzana Khanam[1], Md. Asadur Rahman[2]
[1,2]Department of Biomedical Engineering
Khulna University of Engineering & Technology (KUET)
Khulna-9203, Bangladesh.
farzana0703047@gmail.com[1], bmeasadur@gmail.com[2]

Mohiuddin Ahmad[3]
[3]Department of Electrical and Electronic Engineering
Khulna University of Engineering & Technology (KUET)
Khulna-9203, Bangladesh.
mohiuddin.ahmad@gmail.com[3]

***Abstract*—Electromyography (EMG) measures cumulative action potential by means of voltage from our muscles which means, it is related to work done. As far as we know, there is no exact technique to estimate the mathematical relation between work done and EMG value. In this work, we propose a mathematical relation between work done and EMG signal with proper curve fitting and constant parameter correction. For this purpose, different subjects are chosen for determining work done by lifting different known weight to a defined height and corresponding EMG voltage is measured. Biceps Brachii and Flexor Carpi Radialis muscles are selected for taking EMG values in millivolts. We have considered the mean value from collected sEMG (Surface Electromyography) results for final analysis. From the results, it is observed that EMG voltage maintain almost parabolic relationship with work done. In addition, with that, considering the relationship as exact linear and parabolic, the errors from the measured values are also calculated. The accuracy of our proposed mathematical model is shown numerically.**

Keywords— Surface Electromyography; cumulative action potential; work done; mathematical model; Biceps Brachii.

I. INTRODUCTION

Any human movement is produced by muscular and skeletal systems controlled by the nervous system. Many biomechanical researches have revealed mechanism of the human body dynamics. Some musculoskeletal models of whole body have been developed and reported in a number of investigations [1]. In skeletal muscle, contraction is stimulated by electrical impulses transmitted by the nerves, the motor-neurons (motor nerves) in particular. The electrical potential generated by muscle cells is detected by electromyography (EMG), when these cells are electrically or neurologically activated. EMG is an electro diagnostic medicine technique for evaluating and recording the electrical activity produced by skeletal muscles which allows the measurement of the change in the membrane potential which is transmitted along the fiber [2]. An EMG is the summation of action potentials from the muscle fibers under the electrodes placed on the skin.

Action potential is a short-lasting event in which the electrical membrane potential of a cell rapidly rises and falls. When an action potential is triggered, the membrane potential abruptly shoots upward, often reaching as high as +100 mV. Due to muscle contractions, action potentials are generated which we can measure through EMG analysis. Surface electromyography (sEMG) is a non-invasive technique for measuring the electrical activity of muscle that occurs during muscle contraction and relaxation cycles [3]. Total voltage induction process of action potential analyzed by EMG analysis is given in Fig. 1.

By sEMG analysis, there are a large number of investigations [4]-[7] by several authors. A relation between muscle force and joint moment is analyzed in [5]. Authors in [6], studied the muscle force with EMG and in [7], authors studied muscle force and sEMG where normalized EMG strength versus increment rate of force carried by muscle was calculated. Through sEMG, joint torque estimating model was proposed in [8]. From these research articles, we do not get any information about the relation between work done and cumulative muscle potential. But it is very necessary information to estimate the total work done from a sEMG signal, however as we know so far, there is no such a model to estimate the total work done from the recorded sEMG.

In this paper, we have proposed such an efficient expression that is properly able to estimate the work done or how much calorie burn to complete the work from the sEMG signal. In this proposal, at first we have collected a number of data of known work done and corresponding cumulative sEMG signal in mV. After recording the data, the mean sEMG signal in mV are calculated.

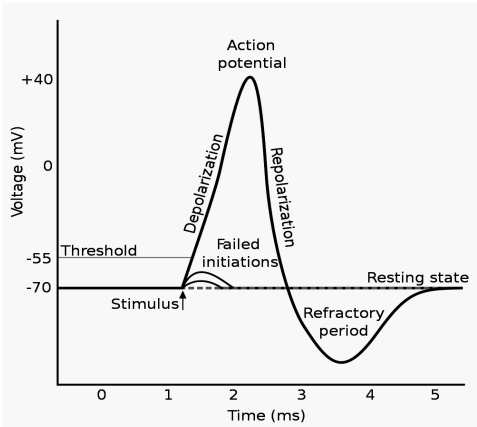

Fig. 1. Voltage induction process in muscle by Action potential.

By this result, we have shown that the cumulative action potential and the corresponding work done obey a linear or a non-linear relationship. By applying linear or parabolic regression, the relationships are established. Furthermore, the procedure to estimate the work done for a specific work from recorded EMG voltage is also presented by mathematical equation.

Amount of work cannot be easily measured in vivo. Therefore, the work done from muscles must be assessed, calculated or mathematically modeled during various amount of work done. By this mathematical modeling, we can differentiate as well as compare various kind of work output in terms of calorie or joule which helps to determine muscle fatigue, muscle work done, identify exercise which burnt calorie more or less to keep our human body fit and sound.

This paper is organized as follows: Section II described the proposed methodology of mathematical analysis and calculation procedure. The total experimental procedure is discussed in section III. Experimental results and respective discussion is presented in section IV. Our total work is concluded in section V.

II. Proposed Methodology

A. Physical Procedure of the Method

The maximum force that a limb is able to apply externally varies with angular position. This is because the geometrical arrangement determines the degree of mechanical advantage. We have chosen two muscles Biceps Brachii (BB) and Flexor Carpi Radialis (FCR) from upper limb of human body. Because, when a weight is lifted by hand; then these two muscles are activated simultaneously which helps to acquire data and electrode placement. In this work, BB was upheld alongside of FCR with angular position 90° approximately as in Fig. 2.

B. Work Done Calculation

There are three key ingredients to work, those are force, displacement, and cause. If the work done is due to force F, the displacement is S and the angular movement with the direction of force is θ, then the amount of work done, W can be equated as,

$$W = F \times S \times \cos\theta \tag{1}$$

According to this proposed procedure, we have done the work by lifting a weight of m kg against gravity from 0 to h meter, then the equation become as,

$$W = m \times g \times h \tag{2}$$

Where, g is the gravitational constant of value $9.81 ms^{-2}$ on earth.

C. Procedure of Acquiring EMG Signal

For the data acquisition of the corresponding study several steps are followed properly. Every step for this study is related to the data acquisition mentioned which is shown in Fig. 3.

Fig. 2. 90^0 angular position between BB and FCR.

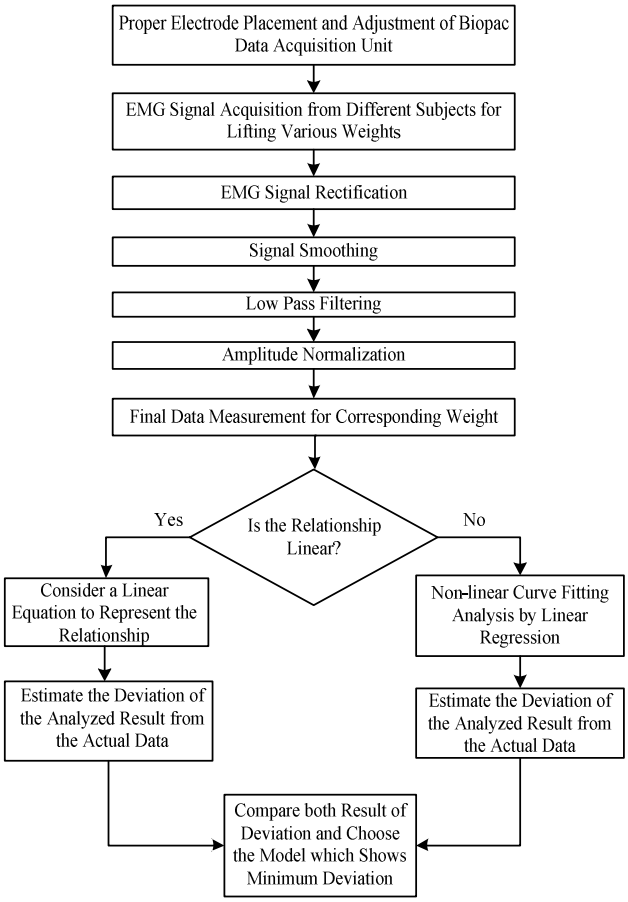

Fig. 3. Flow chart of the proposed data acquisition procedure.

D. Curve Fitting of the Results

If any set of data is nonlinear and can be considered as parabolic, then in generally the set of data can be represented by (3), where the value of the coefficients a, b, and c depends on the shape of the curve.

$$y = a + bx + cx^2 \tag{3}$$

According to least-square fitting, we have to fitted the parabola to the given points (x_1, y_1), (x_2, y_2), …, (x_n, y_n). If the error for the estimated value and measured value is e, then summation of error is $S=\sum e_i^2=(y_i - a - bx_i - cx_i^2)^2$.

By the principle of least square, the value of S is minimum; therefore,

$$\frac{\partial S}{\partial a}=0,\quad \frac{\partial S}{\partial b}=0,\quad \frac{\partial S}{\partial c}=0 \tag{4}$$

By solving (3) and dropping suffix, we have

$$\begin{cases} \sum y = na + b\sum x + c\sum x^2 \\ \sum xy = a\sum x + b\sum x^2 + c\sum x^3 \\ \sum x^2 y = a\sum x^2 + b\sum x^3 + c\sum x^4 \end{cases} \tag{5}$$

Equation (5) is known as normal equations. We can get the values of a, b, and c by solving (5). Putting the value of a, b, and c in (3), we can get the equation of the parabola for best fit [9].

III. Experimental Procedure

A. Data Acquisition Method

As we know, the muscle movement of our body creates action potential. Therefore, different work done produces different action potential according to the amount of work done. There is no direct procedure to estimate such potential to work done relationship. An indirect procedure can be established for estimating this relationship. For example, by performing a known amount of work done we can collect the cumulative action potential or EMG data. To do this, we demonstrate a procedure through some practical step in our laboratory which can be described by the following steps:

Step 1: First of all, we select a height where lifting a weight maintain 90 degree angle between the Biceps Brachii (BB) and Flexor Carpi Radialis (FCR), while the Biceps Brachii will be at the parallel of the body as shown in Fig. 2.

Step 2: We choose some weights to lift which were available in our laboratory. The weights were 0.25, 0.5, 1, 1.5, 2 and 2.5 kg which we can easily lift in the height level from floor to 0.50 meter.

Step 3: The EMG data have been collected from the subjects performing to lift different weights from floor= 0 m to 0.50 meter. In this case, we selected Biceps Brachii muscle of right hand to lift the weights.

Step 4: After collecting the EMG data which resembles the action potential of the BB, we have plotted different curves weight (kg) versus action potential (mV) for male and female subjects respectively.

Step 5: These curves show approximate non-linear parabolic relationship between weight load and EMG data i.e. action potentials. On the basis of the non-linearity, we executed interpolation and extrapolation.

B. Subjects Selection and Laboratory Specifications

The experimental data for this study were collected from 10 subjects among them five are male and five are female subjects (age: 23 ± 5 years, weight: 55±5 kg) with no medical problems. The total experiment is performed in Biomedical Signal Processing Laboratory, Department of BME, Khulna University of Engineering & Technology (KUET), Bangladesh.

C. Apparatus Specification

During data acquisition protocol, the skin was cleaned with abrasive pad and alcohol prep, Lycra swim cap initially. BIOPAC disposable vinyl electrodes (EL503) together with BIOPAC electrode lead set (SS2L) were attached on Biceps Brachii. To press electrodes, 3M Coban Self-adhering Support Wrap were applied against head for improving contact. The electrodes were associated to an EMG data collection system (Biopac Student Lab 3.7 and BIOPAC data acquisition unit) (MP36). For analysing the collected data, Acqknowledge 4.1 software was used. Electrode placement and arrangement along Biceps Brachii of subjects are shown in Fig. 4.

IV. Experimental Results and Discussions

In our work, we have chosen six types of mass such as, 0.25kg, 0.50 kg, 1 kg, 1.5 kg, 2 kg and 2.5 kg. The height is selected as 0.50 meter and it is well known to all that the standard of gravity, g =9.81 ms^{-2}. Therefore, for lifting m kg mass, the amount of work will be W= ($m\times 9.81\times 0.50$) joule or $W/4.2$ calorie (cal) [4.2 joule = 1 calorie]. The EMG signals of some weight lifting from our experiment are shown in Fig. 5. During lifting weights, incrementing weight over 2 kg undergoes in saturated EMG potential. It resembles the fatigue point of that muscle as the experiment is based on BB muscle. In addition, the various weight and corresponding work done is tabulated in Table I.

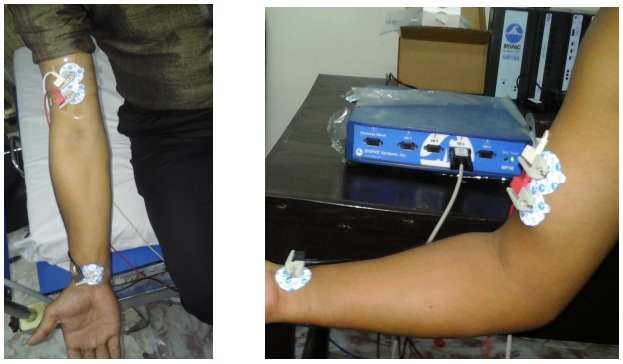

Fig. 4. Electrode placement and lead setting arrangement along Biceps Brachii of subjects.

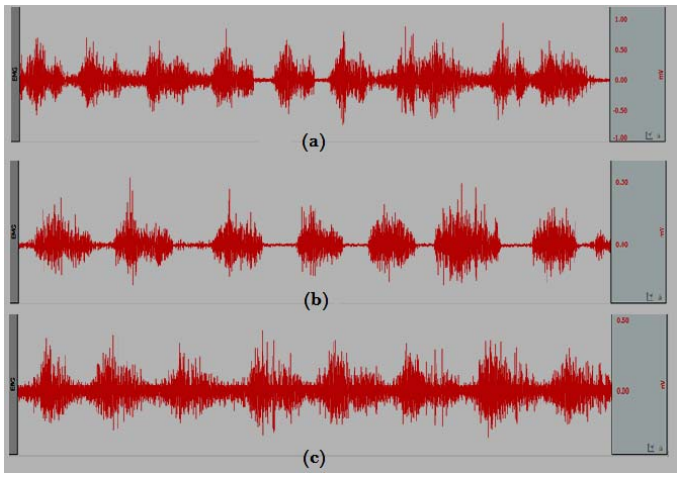

Fig. 5. Sample EMG signal in Acqknowledge 4.1 software- for (a) 2.5 kg, (b) 2 kg, and (c) 1 kg weight lifting.

TABLE I. WORK DONE AND CALORIE BURN FOR DIFFERENT WEIGHTS

SL#	Weight in Kg	Work Done (J)	Calorie (Cal)
1	0.25	1.22625	0.2919
2	0.50	2.4525	0.58392
3	1.00	4.905	1.16785
4	1.50	7.3575	1.751
5	2.00	9.81	2.335
6	2.50	12.2625	2.919

TABLE II. MEASURED ACTION POTENTIAL VALUE FOR DIFFERENT WEIGHTS (MALE)

SL#	Wt. (Kg)	S1 (mV)	S2 (mV)	S3 (mV)	Mean (mV)	St. Dev (mV)
1	0	0.22807	0.20498	0.21182	0.214957	0.011860
2	0.25	0.25574	0.26347	0.24607	0.255093	0.008718
3	0.50	0.37129	0.36925	0.36233	0.367623	0.004696
4	1.0	0.58430	0.57751	0.56895	0.57692	0.007692
5	1.5	0.69906	0.70258	0.68294	0.69486	0.010472
6	2.0	0.78043	0.76568	0.76201	0.769373	0.009750
7	2.5	0.90514	0.88703	0.86878	0.886983	0.018180
Mean Standard Deviation=0.010195 mV						

TABLE III. MEASURED ACTION POTENTIAL VALUE FOR DIFFERENT WEIGHTS (FEMALE)

SL#	Wt. (Kg)	S1 (mV)	S2 (mV)	S3 (mV)	Mean (mV)	St. Dev (mV)
1	0	0.20902	0.21417	0.22402	0.2157367	0.0076217
2	0.25	0.25021	0.26112	0.26951	0.26028	0.0096774
3	0.50	0.37672	0.36931	0.37258	0.37287	0.0037135
4	1.0	0.56912	0.58483	0.57388	0.5759433	0.0080557
5	1.5	0.69112	0.68135	0.68013	0.6842	0.0060239
6	2.0	0.76844	0.77474	0.78018	0.7744533	0.0058752
7	2.5	0.90262	0.89214	0.93426	0.9096733	0.0219280
Mean Standard Deviation=0.008985054 mV						

As shown in Fig. 5, by the use of Acqknowledge software the mean EMG voltage for every subject is acquired and among them; data of 3 male and 3 female are given by Table II and Table III. In these tables, mean and standard deviation of the data are also determined and tabularized. From the data tables, we can observe that an approximately linear relationship exists between work done and action potential or EMG voltage. From this result, we took the mean voltage value from all subject and plot it against work done and shown in Fig. 6.

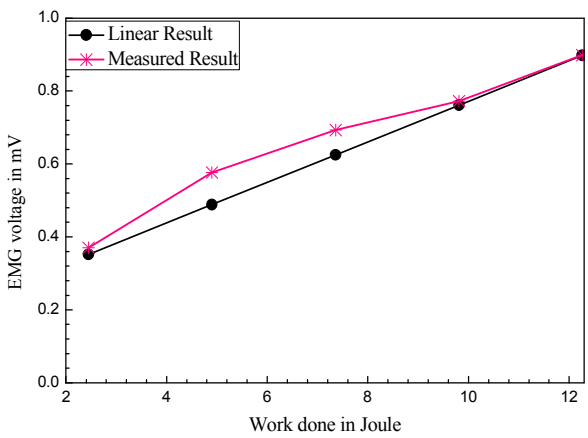

Fig. 6. Deviation of measured and conceptual relationship.

From linear regression analysis the relationship between weight-EMG is given in (6),

$$y_{line} = 0.2111 + 0.05569x \tag{6}$$

From Fig. 6, it is observed that the results, we got through our experiment is not exactly linear. The relation can be considered as approximately parabolic.

Basically, this apparently linear consideration is not correct at all. Therefore to reach the more accuracy of the measure result a nonlinear curve fitting is performed on the measured data. By nonlinear curve fitting the mathematical relationship we get, is given in (7).

$$y = 0.2111 + 0.3842x - 0.0455x^2 \tag{7}$$

The EMG voltage can be evaluated by (7) when the independent variable 'x' is considered as weight. From (7), it is also mentionable that when we consider the lifting weight is zero, then the EMG voltage will be 0.2111 which is exactly as our experimental value. It means that, without lifting any weight, according to our working procedure muscle extract EMG voltage is 0.2111mV. Nevertheless, our target is to relate EMG with work done. Therefore, another mathematical relation is also depicted to relate EMG voltage and work done which is given in (8),

$$Y_2 = 0.2111 + 0.0783i - 0.0019i^2 \tag{8}$$

As a result the actual relationship between work done and EMG voltage can be evaluated from (8) when the independent variable 'i' is considered as the work done in Joule. Furthermore, the EMG voltage from (7) and (8) will be in mV unit. From (7), we have calculated the voltage level of the given work done and their result and error is given in Table IV.

Eventually to prove the accuracy of our result we choose two different weight (0.75 kg and 1.75 kg) and evaluate their corresponding EMG voltage from the Fig. 7 by interpolation. After that, we invite two different subject for the study of the mentioned weight i.e. 0.75 and 1.75 kg from each. The result of the study is given in Table V where it is found that very low level of error exists between our proposed mathematical model and measured result. As the result we get successfully provide strong evidence of the accuracy of our proposed hypothesis on the relation between work done and cumulative action potential (EMG voltage).

TABLE IV. ERROR MEASUREMENT AFTER CONSTANT CORRECTION

SL#	Work done, J	Measured voltage in mV, M	Estimated value in mV, E	Error, |M-E|
1	0	0.21534	0.2111	0.00424
2	2.4525	0.3702465	0.3917	0.02145
3	4.905	0.57643165	0.5494	0.02703
4	7.3575	0.68953	0.6843	0.00523
5	9.81	0.77191315	0.7964	0.02448
6	12.2625	0.89832815	0.8856	0.01272

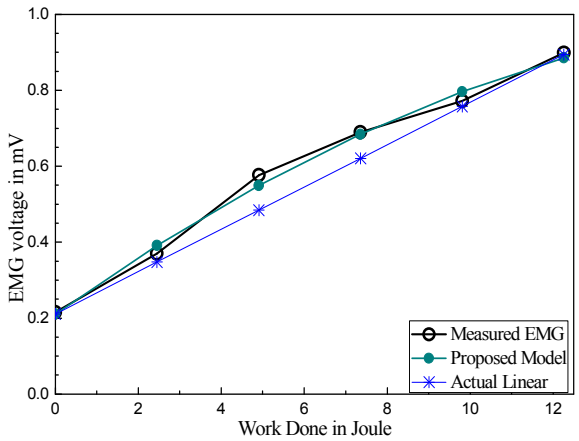

Fig. 7. Impact of proposed mathematical model in error declination.

TABLE V. ACCURACY TESTING OF THE PROPOSED HYPOTHESIS

SL#	Work done in Joule	Measured voltage in mV (Subject 1)	Measured voltage in mV (Subject 2)	EMG voltage from graph	Error
1	3.67875	0.4725	0.4674	0.4734	0.00345
2	8.58375	0.7428	0.7314	0.7432	0.00611

V. CONCLUSIONS

The contribution of this paper is to introduce and develop a new mathematical relationship between performed work and consequent EMG results. In this work, we have explored the cumulative action potential value extracted from EMG signals. All sEMG signals were collected from different male and female healthy subjects through BIOPAC acquisition unit maintaining appropriate experimental protocol. The process of calibration and standardization of EMG signals have been conducted. Then, we have plotted a curve among mean EMG value corresponding weight versus work done deviated from exact parabolic curve. To reduce this difference, we have approached a mathematical model considering all the facts of errors. We have also ensured the accuracy of this equation by putting two random weights with unknown EMG values. The calculated results show negligible errors comparing with measured values. The comparison between measured value and proposed model value will help researchers encounter the perfect method for analyzing EMG signals. Our goal was quite complex to convert a numerical methodology into a direct mathematical relation.

Since, the experiment provides very positive results which encourage us to work to research about the intended combined movements in our future work.

ACKNOWLEDGMENT

This work was supported by Higher Education Quality Enhancement Project (HEQEP), UGC, Bangladesh under Subproject "Postgraduate Research in BME", CP#3472, KUET. This work was also supported by Information and Communication Technology (ICT) Division, Ministry of Post, Telecommunications and Information Technology, Government Peoples Republic of Bangladesh.

REFERENCES

[1] S. L. Delp, F. C. Anderson, P. Loan, A. Habib, C. T. John, E. Guendelman, and D. G. Thelen "Open-source software to create and analyze dynamic simulations of movement," IEEE Trans. on Biomedical Engineeiring, vol. 54, no. 11, pp. 1940-1950, November 2007.

[2] W. C. Mackenzie, The action of muscles: including muscle rest and muscle re-education, New York P.B. Hoeber, 1921 Forgotten Books, 2013.

[3] F. Khanam, S. Islam, M. A. Rahman, and M. Ahmad, "Muscle activity estimation through surface EMG analysis during salat," 2nd International Conf. on Electrical Engineering and Information Communication Technology (ICEEICT), Bangladesh, pp. 1-6, 2015, May 21-23.

[4] M. K. M. Safee, W. A. B. Wan Abas, F. Ibrahim, N. A. Abu Osman, and M. H. R. Salahuddin, "Electromyographic Activity of the Lower Limb Muscles during Salat and Specific Exercises," Journal of Physical Therapy Science, vol. 24, pp. 549-552, July 2012.

[5] T. S. Buchanan, D. G. Lloyd, K. Manal, and T. F. Besier, "Estimation of muscle forces and joint moments using a forward-inverse dynamics model,"Journal of the American College of Sports Medicine, vol. 37, no. 11, pp. 1911–1916, November 2005.

[6] H. U. Kuriki, F. Mí. Azevedo, L. S. Takahashi, E. M. Mello, R. F. N. Filho, and N. Alves, "The relationship between electromyography and muscle force: EMG methods for evaluating muscle and nerve function," Intech Publisher, January, 2012.

[7] G. C. Ray and S. K. Guha, "Relationship between the surface emg and muscular force," Medical & Biological Engineering & Computing, vol. 21, no.5, pp. 576-586, September 1983.

[8] M. H. Jali, T. A. Izzuddin, Z. H. Bohari, H. Sarkawi, M. F. Sulaima, M. F. Baharom, and W. M. Bukhari, "Joint torque estimation model of semg signal forarm rehabilitation device using artificial neural network techniques,"ARPN Journal of Engineering and Applied Sciences, vol. 9, no. 7, July 2014.

[9] P. S. Das, A Textbook Of Engineering Mathematics - III : Transforms and Partial Differential Equations, 5th Edition, India, 2013.

Continuous Heart Rate and Body Temperature Monitoring System using Arduino UNO and Android Device

Md. Asaduzzaman Miah, Mir Hussain Kabir, Md. Siddiqur Rahman Tanveer and M. A. H. Akhand
Dept. of Computer Science and Engineering
Khulna University of Enginnering & Technology
Khulna-9203, Bangladesh

Abstract—**An integrated portable device for continuous heart rate and body temperature monitoring system development is presented in this paper. Heart related diseases are increasing day by day; therefore, an accurate, affordable and portable heart rate and body temperature measuring device is essential for taking action in proper time. Such a device is more essential in a situation where there is no doctor or clinic nearby (e.g., rural area) and patients are unable not recognize their actual condition. The developed system of this study consists of Arduino UNO microcontroller system, transmission system and Android based application. The system gives information of heart rate and body temperature simultaneously acquired on the portable device in real time and shows it through the connected Android application instantly. The developed system is more affordable with low price compared to other developed devices due to use of easy available Arduino UNO and smart phone as Android device. The developed device is shown acceptable outcomes when compared with other measuring devices.**

Keywords—*Arduino UNO, Heart Rate, Body Tempareture, Pulse Detection, Pulse Amplification, Signal Extraction.*

I. INTRODUCTION

Heart rate simply indicates the soundness of our heart. It helps assessing the condition of cardiovascular system [1]. Human's heart pounds to pump oxygen-rich blood to muscles. It carries cell waste products away from tissues [2]. Heart rate varies according to the demand of muscles to absorb oxygen and excrete carbon dioxide changes such thing happen during exercise or sleep [3]-[5]. Normally the heart rate which is calculated for a resting person is about to 70 bpm for adult males and 75 bpm for adult females. A heart rate monitor is simply a device that takes a sample of heartbeats and calculates the heart beats per minute and the information can easily track the current heart condition [6].

On the other hand, body temperature is also a general indication of body condition. Normal human body temperature is (98.6 ° F ± 0.7°F) and it varies activity of the person as well as place of measurement. When a person is too hot, the blood vessels in his/her skin expand to carry the excess heat to his/her skin's surface. And for this reason the person begins to sweat. Then the sweat evaporates and this process helps to cool his/her body. When a person is too cold, his/her blood vessels narrow so that blood flow to his/her skin gets reduced to conserve body heat. As a result he/she starts shivering and it is an involuntary, rapid contraction of the muscles.

Timely measurement of heart rate and body temperature is important for better treatment. In this era of polluted environment, concern regarding human health is top priority than ever before. Everything gets meaningless if one is sick or dead. Now a days, people spend a lot of money to keep sound health. Unfortunately, most of the cases it is found that it is too late to receive proper medical treatment and things are non-invertible. So that unexpected incident happens for being delayed treatment. Since heart rate and body temperature are the most vital notable indexes of the human health, an affordable device to measure such indexes will be helpful for human health. In general, medical equipment is expensive. Moreover, some devices can provide raw medical calculation of data to patients and doctors, but the patients can't always interpret the medical measurement into meaningful diagnosis as they have simple/no medical background. In emergency situation, time should not be wasted. Sometimes continuous assessment is also necessary. Therefore, an automated system for continuous measuring of heart rate and body temperature is very much essential.

In this study, an android assistive integrated heart rate and body temperature measuring embedded system is developed. Since the system provides the information about both heart rate and body temperature through android application, anyone can monitor physical status easily. Moreover, the system may be useful for monitoring condition of vary seek patents from remote place. Rest of the paper explains existing approaches, our system model, system development and finally system performance measurement.

II. EXISTING APPROACHES

There are some existing approaches designed and developed for measuring heart rate. At present, the recent technologies for measuring heart rate are consist of several methods using optical and electrical methods. Casually electrical method provides a bulky strap around one's chest [7]. But the optical method requires no such strap and it can be used more effectively. Low cost heart rate measuring devices were developed using optical technology. In optical method powerful LED and Light Dependent Resister (LDR) are used to sense pulses [8]. The pulse signals are then amplified by an amplifier circuit and filtered through a band pass filter. The amplified and

filtered pulse signals are sent to the microcontroller. The microcontroller checks the analog signals whether they are valid or not comparing with a standard voltage. Microcontroller counts the heart rate and displays the result in a LCD display. There exists another approach where infrared Tx and Rx are used. In that system it senses pulses, amplifies the pulses and filters pulses by a low pass filter. Finally, the pulse signal is sent to a microcontroller [9], [10]. The microcontroller also give output comparing with a reference voltage. Both the approaches give inaccurate result in many cases because analog signal of pulse varies from person to person and the approaches fail to calibrate analog signal of pulses for each person.

M. M. A Hashem *et al.* [8] developed a device which uses infrared technology to measure heart rate and use analog temperature sensor to measure body temperature. This approach can calibrate analog signal of pulses for each person. It uses wireless terminal to send data and wireless receiver to receive the data. The data are then sent to the computer using serial port. Data is then sent to the web server using the internet and can be viewed from anywhere in the web browser. The main drawback of this approach is that it needs a computer to send data to the web server through the internet.

A telemedicine system is presented by N. Navale *et al.* in [11]. In the system, the user carries a hardware device connected with an android application through Bluetooth connection. The device continuously measures the heart rate and body temperature and sends these information to the android application. Android application sends the information to the server and if the user has any problem like heart attack then it sends an emergency message to the patient's doctor and guardians containing the current location of the patient. N. Indumathy, and K. K. Patil [12] developed an android based patient health care monitoring system using several sensors like temperature, heart rate measuring sensor, eye blink detection sensors to detect the current condition of the patient. The system is developed such a way that if patients can't speak or move his hand or body then just blink his/her eyes 5 times then a message send to the caretaker about the current situation of the patient and continuously send the information about heartbeat and body temperature to the server. An android application running in the caretaker phone receive the message and generates voice sound so that caretaker can recognizes the patient's current situation. At the same time, doctor can realize the current situation of the patient accessing the server.

The aim of our study is to develop a device which is interfaced with an Android application so that the heart rate and body temperature are monitored easily. The exiting remote health monitoring system described above are fully dependent on proper communication between the server and client. So it may arise severe condition that server connection gets congested and patient's situation is serious then it creates a problem to recognize the present situation of the patient. For this reason the goal of our project is to design a portable Android assistant heart rate and body temperature monitoring device which is affordable and user friendly, at the same time inexpensive, accurate, and durable.

III. Heart Rate and Body Temperature Monitoring System using Arduino UNO and Android Device

To construct an efficient and affordable device for measuring heart rate and temperature, an infrared Tx and Rx have been used to measure the pulse by measuring the change in blood flow through one of the fingers. A noise filter has been designed to filter out any unwanted noise and interference, due to small movement of finger causes excess noise. A temperature sensor has been used to measure body temperature. The microcontroller of the Arduino UNO board is programmed to count the pulse rate and to measure the body temperature and to send the information to the developed "Heartmate" android application via Bluetooth module. Fig. 1 shows the working diagram of the system and the Fig. 2 represents the functional block diagram of the system. The following sections briefly explains of the system.

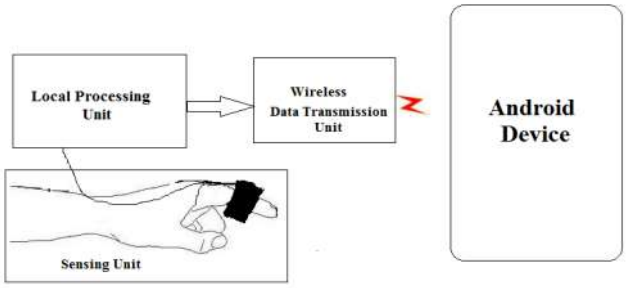

Figure 1. System diagram of the proposed system.

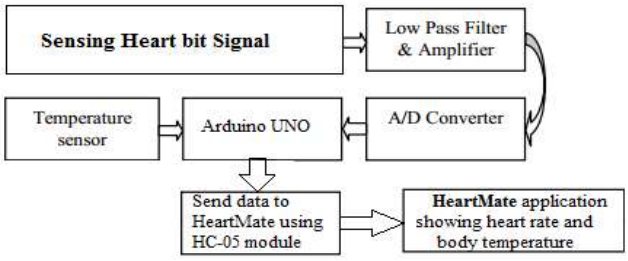

Figure 2. Functional block diagram of the system.

A. Heart Rate and Body Temperature Sensing

With a view to measuring the alteration in blood volume at fingertip with each heartbeat optical sensor has been used to perform this task. The sensor unit consists of an IRTx and IRRx, placed side by side. An infrared light is transmitted by IRTx into the fingertip, and the IRRX senses the portion of the light which is reflected back. The intensity of the reflected light depends upon the blood volume inside the fingertip. As a result each heartbeat slightly alters the amount of reflected infrared light that can be detected by IRRx. Through proper signal conditioning this little change in the amplitude of the reflected light is converted into pulse. The sensor used in this project is TCRT5000 which is a reflective optical sensor that contains both the infrared light emitter and phototransistor placed side by side. They are enclosed inside a leaded package as a result the effect of surrounding visible light is minimum. Connecting the Enable pin to 5V of Arduino will turn the IR emitter LED on and activate the sensor. A fingertip placed over the sensor will act as

a reflector of the incident light. The amount of light reflected back from the fingertip is monitored by the photo transistor. The output (VSENSOR) shows in Fig. 3 from the sensor is a periodic physiological waveform attributed to small variations in the reflected IR light and it is caused by the pulsating tissue blood volume inside the finger.

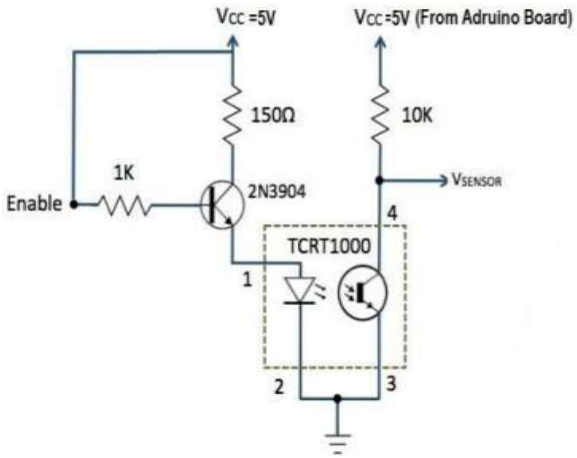

Figure 3. Pulse Detection Circuit

The waveform is synchronous with the heartbeat. This weak signal contains a lot of noise superimposed on the AC signal which is then filtered through a series of signal processing circuits via a Quad OP-AMP LM324N. To get rid of the DC component the signal is first passed through a RC high-pass filter (HPF) showed in Fig. 4. The cut-off frequency of the HPF is set to 0.7 Hz. An active low-pass filter (LPF) which is made of an Op-Amp circuit is on the next stage. The gain and the cut-off frequency of the LPF are set to 101 and 2.34 Hz respectively. As a result the combination of both HPF and LPF helps to remove unnecessary DC signal and high frequency noise which includes 50 Hz mains interference, while amplifying the low amplitude pulse signal (AC component) 101 times. In Fig. 5 shows the further filtering and amplification of the output from the first signal conditioning stage goes to a similar HPF/LPF combination. For this reason the total voltage gain achieved from the two cascaded stages is 101*101 = 10201. The two stages of filtering and amplification converts the input signals to near Transistor–Transistor Logic (TTL) pulses which are synchronous with the heartbeat. A 10K

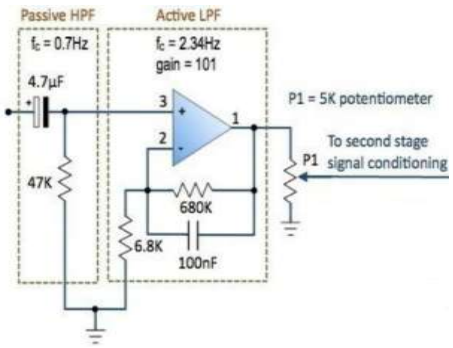

Figure 4. First Stage Signal Conditioning Circuit

potentiometer is placed at the output of the first signal conditioning stage in case the total gain of the two stages is required to be less than 10201. If a heartbeat is detected then an LED connected to the output of the second stage of signal conditioning will blink. The final stage a simple non-inverting buffer is implemented so that output impedance will be lower. While reading the amplified PPG signal through the ADC channel of a microcontroller is used to then it helps much. After that the output is connected to the Digital Pin 8 of Arduino UNO. The diagram shows the configuration of the IR emitter and IR receiver in relation to the finger. They are placed in such a way that the infrared light reflects from the finger to the to the IR receiver.

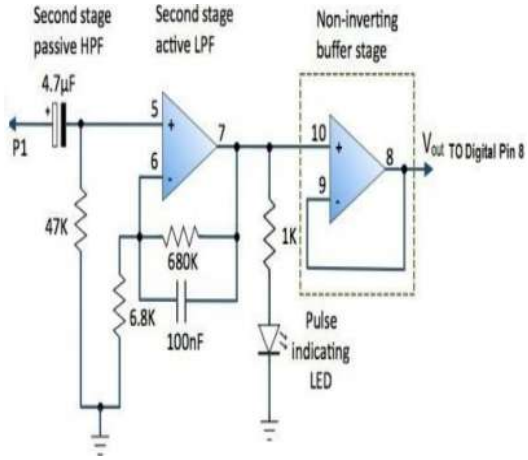

Figure 5. Second Stage Signal Conditioning Circuit

A high frequency noise is caused due to a small movement of finger. For this concern the pulse rate signal filtering is important to block any higher frequency noises present in the signal. Using a low pass filter the desired signal can be extracted from the noisy signal. The equation for cut-off frequency of the low pass filter is represented through eqn. 1.

$$\text{Cut-off Freq.} = 1 / (2\pi\ RC) \quad (1)$$

2.34 Hz is the cut off frequency of the filter which is designed for our system. If it is not amplified then the signal found from the filter circuit which amplitude is in mV level. With a view to understanding and counting pulse rate by the microcontroller it is must to amplify the signal. For this purpose a two stage signal filter and amplifier circuit using LM354 OpAmp is designed. This OpAmp is operated through 5 volts. Gain of each stage of the low pass filter is represented through the eqn. 2.

$$\text{Gain at each stage} = 1 + (R_f / C_f) \quad (2)$$

In the circuit, total gain is 10201. Values of R_f and R_i are 680 KΩ and 6.8 KΩ respectively. The 4.7uF capacitors are connected in series to the inputs of each filter blocks and they must be able to stand some reverse bias. For this purpose they should be non-polarized.

LM35 sensor has been used for measuring body temperature. According to body temperature the sensor outputs an analogue voltage. To reduce output drift due to noise in input voltage a 1uF capacitor is connected across the V_{in} and ground of the sensor. The temperature sensor circuit diagram is shown in Fig. 6.

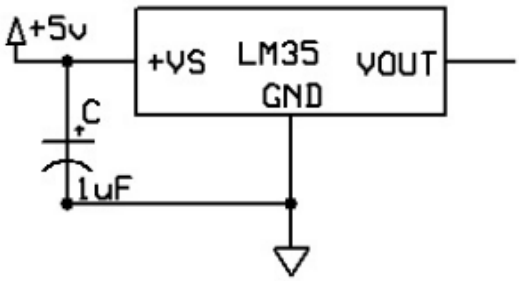

Figure 6. Temperature Sensing Circuit

For basic Centigrade temperature sensor whose rating is (+2˚Cto +150˚C). And its temperature vs. voltage relation is in represented throuh eqn. 3.

$$V_{out} = 0 \text{ mV} + 10.0\text{mV/}^{\circ}\text{C} \quad (3)$$

B. Data Processing through Arduino UNO

In this project we used the Arduino UNO development board which contains ATmega328 microcontroller and the microcontroller is used to calculate the number of heart beats per minute. It also measures the body temperature and sends the calculated values to the android application via HC-05 Bluetooth module. A thread continuously takes the analogue signal of heart condition and body temperature and sends the values to the android application. If the signal voltage is above the threshold voltage, then it is considered as a heartbeat as detected and counts up to 30 beats. A timer counts the time (t30) for 30 beats and calculates heart rate using eqn. 4.The program

$$\text{Beats per minute (BPM)} = 30\times f \quad (4)$$

also takes the analogue voltage output (Vout) of the temperature sensor and measures the body temperature by the following eqn 5 and 6.

$$\text{temp} = \text{temp} \times 0.48828125 \quad (5)$$

$$\text{tempf} = (\text{temp}\times 1.8) + 32 \quad (6)$$

C. Android Application Development to Store and Display

In our system, development of android application, called "Heartmate", is a vital portion. We monitor the heart rate and body temperature through this application. When the heartbeat and body temperature are measured the microcontroller sends the result to the application through the HC-05 Bluetooth module. Instantly the current condition of the patient is displayed in the application interface. So that anyone can easily understand the present situation of the patient and can take immediate action.

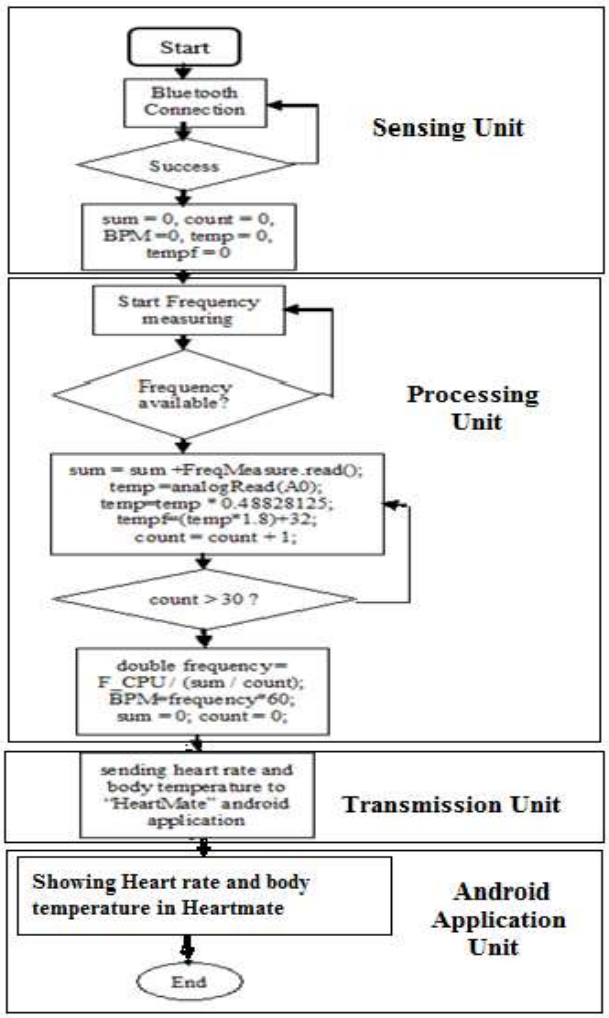

Figure 7. Algorithm for Measuring Heart rate and Body Temperatur

D. System Overview

Fig. 7 shows the system flow chart. At first the system checks the bluetooth connection between the processing unit and microcontroller and the Android device. If the connection is ok then placing the finger in the infrared sensor the microcontroller gets the some analog frequency for corresponding blood flow. Placing the finger infront of the infrared sensor an the receiver gets the transmitted signal from transmitter. After that, using both high pass filter, low pass filter and amplifier circuit shown in Fig. 3 and Fig. 4 the signal is made computable by the microcontroller used in Arduino UNO. The temperature sensor also outputs an analog signal in parallel while the heart beat signal is captured is shown in Fig. 5. For getting good performance 30 values are taken then the average values is considered the appropriate ones. When the signals are digitized by the microcontroller sends the heart rate and body temperature to the android "Heartmate" application through HC-05 Bluetooth module. Through this approach it is now become very easy for continuous heart rate and body temperature monitoring

E. *Significance of the System*

In this system we have tried to implement a low cost heart rate and body temperature monitoring system. We have implemented the system in Android platform since Android devices are available in cheap price. The device is portable and light weight so that it can be carried easily anywhere. Through this system it is possible to monitor the heart rate and body temperature continuously. As a result for those patients for whom it is must to monitor the heart rate and body temperature continuously then in that condition the system can be adopted easily. The system can provide much support to know the present condition of the patient if there is no doctor or clinic nearby.

IV. PERFORMANCE MEASUREMENT

Fig. 8 represents the bread board implementation of heart rate and body temperature measuring hardware module unit of our implemented system. In our implemented system the user has to start the hardware module first then run the *Heartmate* android application. The IR transmitter and receiver are

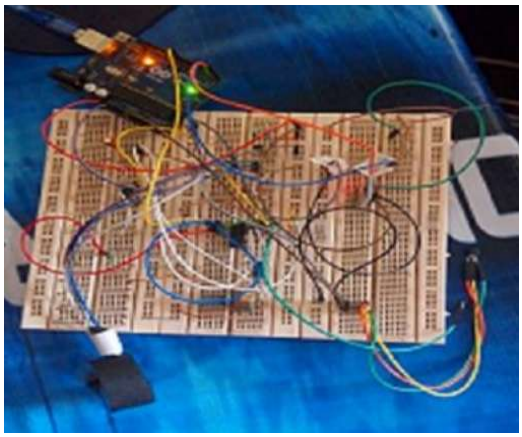

Figure 8. Heart rate and body temperature measuring device bread board implementation.

mounted in a finger ring. Then touching the temperature sensor the module begin to measure both heart rate and body temperature. Fig. 9 shows the measured result in "Heartmate" application.

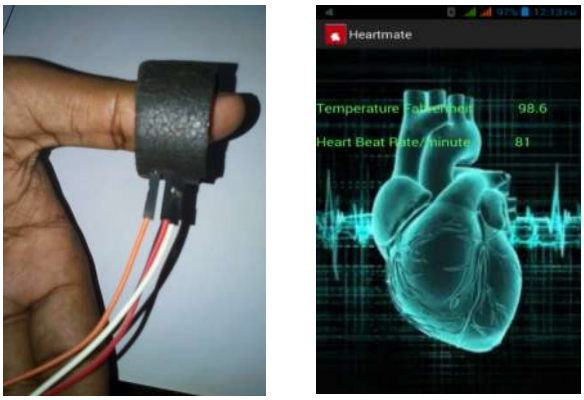

Figure 9. Measuring Heart Rate and Body Tempearture

For performance checking of our system, we measured the heart rate for a person for 20 minutes and the result is shown in the Fig. 10. In this process we measured the heartbeat through Sphygmomanometer which represents the actual measurd heart rate in the Fig. 10. At the same time we measured the heart rate placing our device in the left thumb of the person. Since a little movement of the fingure while measuring heart rate through our system the the analog value for corresponding blood flow is affected by noise. As a result we got some errors in our experimental results. For this reason we got appropriate value at beginning of our experiment then after passing several minutes the result deviated much from the original value. While measuring body temperature we measurd the actual temperature through clinical Thermometer. And along with this we also measured the body temperature with our device. Fig. 11 shows the actual and measured body temperature. We got some varriance in the measured value.

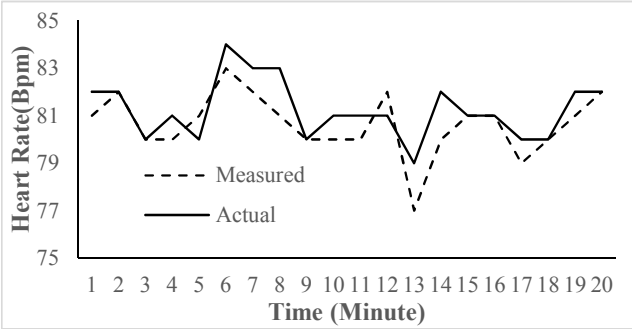

Figure 10. Actual vs. Measured Heart rate measured for 20 minutes

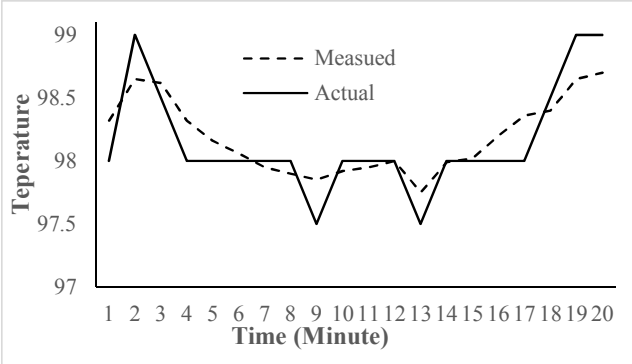

Figure 11. Actual vs. Measured Body Temperature for 20 minutes

V. CONCLUSION

In this paper, we have shown a design of a heart rate and body temperature measuring embedded system. The final outcome of our approach is an android based portable heart rate and body temperature measurement system with a suitable architecture which can be applicable in medical and home appliances in patient health monitoring system. The system has been tested for some valid signal such as heart rate and body temperature. The system gives comparatively better performance than old hand measuring system.

REFERENCES

[1] R. G. Landaeta, O. Casas, and R.P. Areny, "Heart rate detection from plantar bioimpedance measurements", *28th IEEE EMBS Annual International Conference*, USA, 2006, pp. 5113-5116.

[2] How the Heart Works, August 24, 2015 http://www.webmd.com/heart-disease/guide/how-heart-works

[3] Heart Rate During Exercise, August 24, 2015 http://btc.montana.edu/olympics/physiology/cf02.html

[4] Heart Rate Variability During Sleep, August 24, 2015 http://www.livestrong.com/article/134189heart-ratevariability-during-sleep/

[5] Heart Rate Should Slow During Sleep, July 15, 2015 http://www.healthandage.com/your-heart-rate-shouldslow-during-sleep

[6] Heart Rate Monitors, July 17, 2015 http://www.walmart.com/browser/sportsoutdoors/heartmonitors/412541341078104107814 5

[7] Determining Heart Rate from the Electrocardiogram, August 24, 2015 http://www.cvphysiology.com/Arrhythmias/A020.htm

[8] M. M. A. Hashem, R. Shams, Md. A. Kader and A. Sayed, "Design and development of a heart rate measuring device using fingertip," 3rd IEEE International Conference on Computer and Communication Engineering (ICCCE'10), Kuala Lumpur, Malaysia, May 11-12, 2010.

[9] Heart rate measurement from fingertip, August 24, 2015 http://embeddd-lab.com/blog/?p=1671

[10] Wireless Human Health Online Monitor, March 20, 2015 http://people.ece.cornell.edu/land/courses/ece4760/FinalProjects/s2011/xy222_yw437_ha245/xy222_yw437_ha245/index.html

[11] M. Navale, S. Damare, R. Chavan, R. Dube, and S. Patil "Android Based Heart Monitoring and Reporting System", International Journal of Advanced Research in Computer and Communication Engineering Vol. 3, Issue5, May 2014

[12] N. Indumathy and K. K. Patil "Medical Alert System for Remote Health Monitoring Using Sensors and Cloud Computing" International Journal of Research in Engineering and Technology, vol. 3, no. 04, pp. 884-888, 2014.

[13] Pulse oximetry explained, August 24, 2015 http://www.howequipmentworks.com/physics/respi_measurements/oxygen/oximeter/pulse_oximeter.html

A New Approach to Extract Features from ECG Signals

Muhammad Sheikh Sadi, G.M. Mahmudur Rahman, Subroto Debnath, Fahim Feroje Al Jami
Department of Computer Science and Engineering
Khulna University of Engineering & Technology (KUET)
Khulna 9203, Bangladesh
sheikhsadi@gmail.com, dtuhin28@yahoo.com, subroto16.debnath@gmail.com, fahimaljami@gmail.com

Abstract— **Electrocardiogram (ECG) is the record of electrical and muscular movement of the heart over a period of time which is useful for diagnosing many cardiac diseases. Due to the increase in mortality rate associated with cardiac diseases, automatic detection of these diseases is highly required. Hence, feature extraction and de-noising of ECG signals are highly useful in cardiology. This paper describes a novel approach for feature extraction in order to recognize trusty heart rhythm. This method consists of two components: data preprocessing and feature extraction. At pre-processing stage, baseline wander removal and power line inference have been used for removing baseline wander and de-noising the signal respectively. At the second stage, R wave is detected and then Q, S, T and P waves are extracted based on R wave. In this paper, Wavelet transformation is used for power line inference. The experimental studies show that the proposed method provides 96.79% accuracy and 5 features recognition with reduced computational complexity.**

Keywords— ECG, QRS Complex, R Wave, Baseline Wander, De-noising.

I. INTRODUCTION

Elderly population and incessant incidence of Cardio-vascular Diseases (CVD) have put present healthcare methods global under severe strain in terms of the excellence of maintenance supply and its related price [1], [2]. Appropriate disease supervision through uninterrupted monitoring and information fusion of elementary biological signals in lasting CVD patients is observed as the significant mechanism for the fundamental decrease of the cost of CVD care delivery, the improvement of the quality of care/life and the major drop in hospitalizations. The Electrocardiogram (ECG) signal - the key element of a remote CVD observation system - is the process of recording electrical variation of heartbeats of human. These signals can be used to attain clinical diagnosis. The heart's electrical activity can be measured by electrodes which are placed on the patient's limbs and on the surface of the chest. Physicians monitor this activity and its features. The parameters of this feature are: the height and interval of the waves. These parameters are collected from PP interval, RR interval, ST segment, QRS complex, QT segment etc. as shown in Figure 1. This figure presents the simple contour of a fit ECG heartbeat signal with P, Q, R, S, J, T and U.

The features, collected from ECG signals, provide clinical diagnosis of heart rate, rhythm and heart abnormalities. Various diseases like Tachycardia, Bradycardia and abnormal heartbeats etc. can be measured by examining these features of ECG signals.

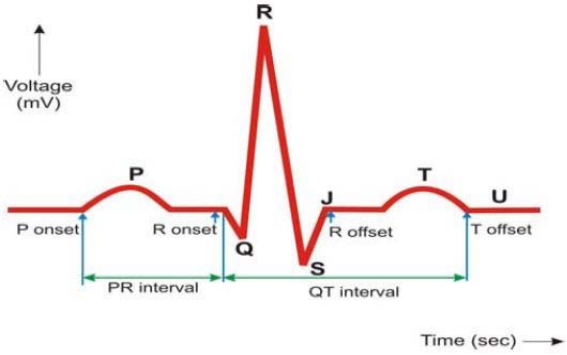

. Figure 1: An ECG Waveform [3]

In general, physicians detect diseases by interpreting those shapes of waves manually. However, this tedious job takes time and may incur additional cost. Also with the change of the parameter's value the diagnosis of disease may change. It is a tough job for a physician to memorize the names of diseases according to the parameters' value. So an automatic artificial intelligence based ECG feature detection and disease detection system is a must to reduce the complexity of interpreting ECG signal.

There are several studies proposed for the analysis of the ECG beats. P.SASIKALA1 and Dr. R.S.D [3] presented retrieval of P wave and T wave in Electrocardiogram by means of Wavelet Transform. *MATLAB* implementation of ECG signal processing was presented by V.Viknesh and P. Ram Prashanth [4]. Gradient-based algorithm and time domain morphology was presented by E.B. Mazomenos et al. [5]. Wavelet transform finds application in ECG beat detection and feature extraction as reported by S.C. Saxena et al. [6]. A wavelet-based ECG delineation was presented by P. Martinez et al. [7]. Also Mahesh used wavelet and Pan- Tompkins algorithm to extract time-frequency features for ECG beat detection system [8]. However, extracting significant and useful features from ECG signal characteristics is still a great

978-1-4673-9257-0/15/$31.00 ©2015 IEEE

challenge for successful implementation of these devices since they need to be fast, simple and computationally efficient.

Motivated by this point, this paper proposes a different computerized ECG feature extraction algorithm that is precisely designed to be effective from a computational view. It entails simpler processing and calculations to extract the features from ECG signals that are to be further used to diagnose the diseases.

The rest of the paper is organized as follows: after reviewing related work in Section II, we describe our algorithm in Section III. Section IV is devoted for the justification of the algorithm, whereas conclusions are drawn in Section V.

II. Related Work

Abdullahi Karaye et al. [2] proposed a robust ECG feature extraction technique suitable for mobile devices. Their technique was to extract samples, between R-R intervals as equivalent R-T interval, using Pan Tompkins algorithm. R-T interval samples were calculated by using discrete wavelet transform. The mean, median, standard deviation, maximum, and minimum coefficient of wavelet were used as a time-frequency domain feature.

Viknesh et al. [4] discussed about MATLAB implementation of ECG signal processing. In their paper they worked on noise filtering and detection of QRS complex using wavelet transform. Their main objective was to reduce noise from an ECG signal and data compression. But they didn't detect other features of ECG Signals.

Mukesh Tiwari et al. [9] proposed a system Feature Extraction of ECG Signal by HHT Algorithm. The HHT algorithm is useful to analyze any nonlinear signal because minor frequency attribute of any signal is produced by HHT algorithm. They used wavelet transform and Huang Hilbert Transform to retrieve the features of ECG signal in regular and irregular condition.

V.K.Srivastava et al. [10], in their paper, used discrete wavelet transform to extract features from ECG signal. They used neuro-fuzzy based approach which was a combined approach of artificial neural networks and fuzzy logic. This approach was used to classify and analyze data. Their accuracy was more than 90% but sensitivity was 60% to 70%.

Coast Doughlas et al. [11] described a method to cardiac arrhythmia investigation by Hidden Markov Models. The Hidden Markov modeling method combines structural and statistical knowledge of the ECG signal in a single parametric model. This technique was also able to detect QRS complex as well as R-R intervals to determine ventricular arrhythmias. The accuracy of the proposed system was 50% to 80%.

Franc Jager [12] developed a new approach to extract which is Kahunen Lo□eve Transform (KLT). It was a powerful approach to the feature extraction. It could provide the clarification if the probability densities of pattern vectors population of a problem domain were unknown. But it was sensitive to noisy pattern of an ECG signal and only gave 80% accuracy.

Naveen Ku. Dewangan et al. [13] made a survey on ECG Signal Feature Extraction and Analysis Techniques. This survey discussed various techniques and transformations of proposed systems for feature extraction and analysis of ECG signals and made a comparison among them.

Zhao et al. [14] offered a feature extraction way by wavelet transform and support vector machines. The proposed system was comprised of three components including data pre-processing, feature extraction and grouping of ECG signals. Wavelet transform was used to determine the coefficients of the transform and autoregressive modeling (AR) was also used to acquire the temporal configurations of ECG waveforms. The support vector machine (SVM) with Gaussian kernel was used to categorize diverse ECG heart regularity. The proposed system gave accuracy of 99.68%, high simplicity and high predictivity.

III. The Proposed Methodology To Extract Features From ECG Signals

With the purpose of extracting information from the ECG signal, the raw ECG signal should be processed. Preprocessing and Feature Extraction as shown in Figure 2.

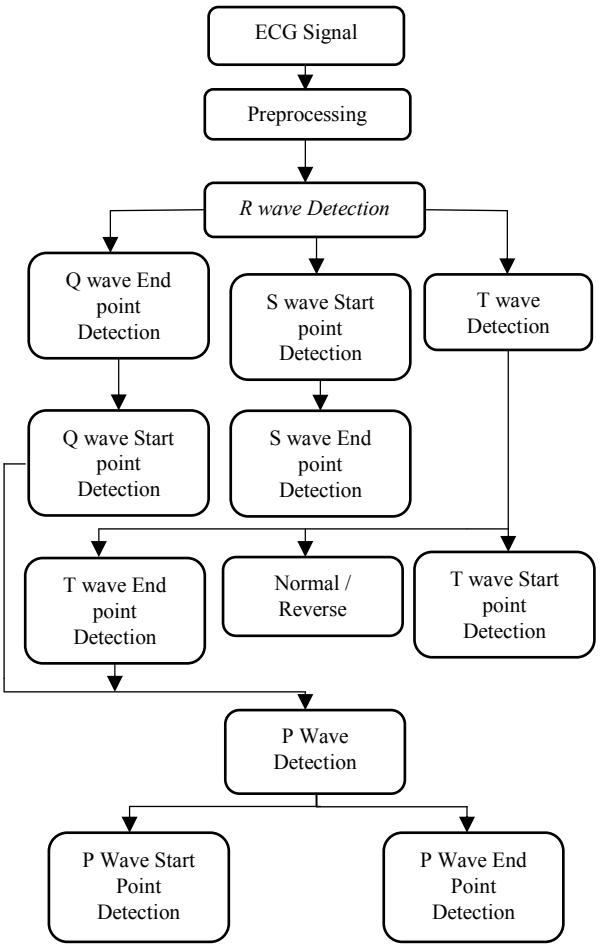

Figure 2: Workflow of ECG Feature Extraction

In our proposed method, the process of ECG signal analysis can be sub-divided into seven sub-processes. These sub-processes are as follows.

1. Data Acquisition
2. Pre-processing
3. R Wave detection
4. Detection of starting point of Q wave and S wave & ending point of S wave
5. T wave Detection
6. P Wave Detection
7. Calculation of Intervals

A. *Data Acquisition*

The heartbeats are recorded simultaneously from patients. For collection of data, we used *BIOPAC Student Inc.* ECG module which can reliably record ECG signals. The *AcqKnowledge* software is used to record ECG data from the module in .acq format then saved it in .mat file format which is *MATLAB* compatible file.

B. *Pre-Processing*

ECG signal comprises of diverse forms of noises that is frequency intrusion, baseline drift, electrode interaction noise, polarization noise, muscle noise, the inner amplifier noise and motorized objects. One of the common problems in ECG signal processing is baseline wander removal and power line inference.

- *Baseline Wander*

Different types of noises are included while an Electrocardiogram signal is recorded. These situations are responsible for an ECG signal to be affected by baseline drift which is difficult to diagnose manually [15]. It is needed to get rid of noise from the signal for proper diagnose. Eliminating the baseline drift of a signal is named as de-trending [15]. According to Vanisree K and Jyothi Singaraju [15], the achieved main ECG signal decomposes into resultant approximation and detail coefficients equal to 8 levels using *Discrete Waveletet Trasformation* where *Dabachies6* (db6) is used in the decomposition as mother wavelet or basis function. The decomposed signal is then restored to obtain main ECG signal components by means of *Inverse Discrete Wavelet Transformation* (IDWT). The recreated approximation and detail coefficients of the signal are A1, A2 . . . ., A8 and D1, D2, … D8 [15]. A1 and D1 have maximum frequencies and A8 and D8 have the lowermost frequencies. As the low frequency components affect the signal for baseline fluctuating, these components must be eliminated to obtain a signal without baseline drift [15].As A8 and D8 have the low frequency components so the De-trended Signal (DS) will be the subtraction between Original Signal, and (A8+D8) [15]. The de-trended ECG signal is shown Figure 3.

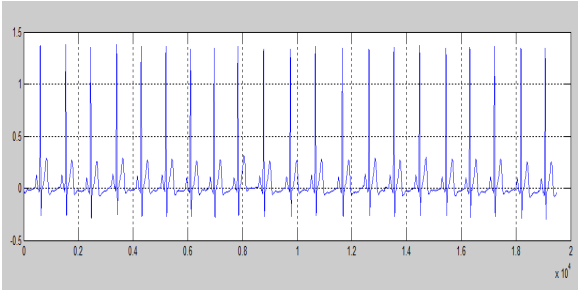

Figure 3: Waveform with Baseline Wander Removed

- *Power Line Inference*

Power line is a known noise source in ECG that is described by 50 or 60 Hz sinusoidal interference [2]. Such noise put forward the investigation and understanding of the ECG further tough, as the explanation of low-amplitude waveforms turn into unpredictable [2]. Precautions have been taken to decrease the outcome of power line inference but still certain extra types of noise may still disturb the feature extraction of ECG. To get rid of the noise, we apply Discrete Wavelet Transform 1d packet. At the beginning, it decomposes the signal into multiple sub-bands then amends each wavelet coefficient using a threshold function. Lastly it recreates the de-noised signal [9]. The signal turn into smoother and the noises vanishes when noises are noticed by high frequency components and lower details are eliminated from the main signal [9].The waveform given by these values is shown in Figure 4.

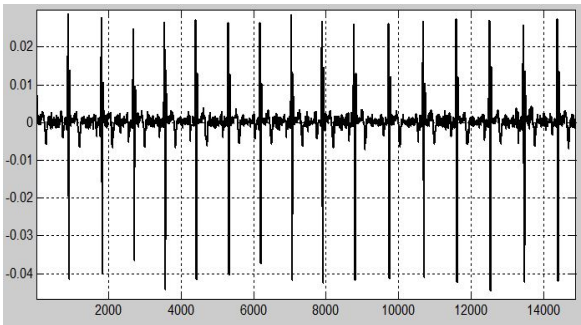

Figure 4: Waveform with Power Line Interference Removed

C. *R Wave Detection*

At first, the length of the de-noised ECG signal is determined which is found from the Wavelet Transformation. As, the height of the R wave can't go lower than the 0.6 times of the maximum height of the R wave [4], the height which is greater or equal to the 0.6 times of the maximum height of the R wave is detected. We increase the counter to 100 ms because the probability of R to R interval in 100ms range is approximately Zero. The pseudo code to detect R wave is shown in Pseudo code-1.

Pseudo code -1

```
Initialize the ECG signal as denoised
Find a=Max(denoised)
Set position counter to 0
Set height counter to 0
Set counter to 1
while counter< length (denoised)
    Set past position to 0
    Set next position to 1
    if denoised[counter]>0.60*a
      while denoised[past position] ≤ denoised[next position]
          Set past position = next position
          Increment next position by 1
      End while
      Increment position counter by 1
      Increment height counter by 1
      Set R_position[position counter]= counter + next position-1
      Set R_height[height counter]= denoised[counter + next
position-1]
      Increment counter by 100
    End if
    Increment counter to 1
End while
     Increment counter by 1
End while
```

- *Detection of start point of R wave*

  In order to determine the start point of R wave in Figure 5, we find the point which is situated before the R_position and where the height of R wave is approximately zero with respect to base line

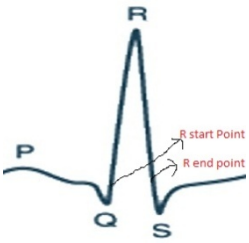

Figure 5: Start Point & End Point of R wave

The pseudo code to detect the start point of R wave is shown in Pseudo code -2.

Pseudo code -2

```
Set the position counter to 0
Set counter to 1
While counter ≤ Total number of R wave
     Set counter_r to 1
     While (height of R position-(height of (R position -
counter_r))) < height of R position
          Increment counter_r by 1
     End while
     Increment the position counter by 1
     position_R_start[position counter]=R position - counter_r
     Increment counter by 1
End while
```

D. Detection of starting point of Q wave & S wave and ending point of S wave

A similar method (pseudo code -2) is used to detect the start point of Q wave & S wave and end point of S wave with a few changes in the arithmetic operations.

E. T wave Detection

To detect T wave, the interval is taken between the end point of S wave and the starting point of next Q wave and then we find the maximum height and the minimum height. The sign of the minimum height is changed and compared with the maximum value. If maximum height is greater than the minimum height then T wave is normal. Else T wave is inverse. The pseudo code to detect of T wave is shown in Pseudo code -3.

Pseudo code -3

```
Find m=total number of R wave
Set T position counter to 0
For counter=1 to m-1
   Set max=0
   Set min=0
   For y=end point of S wave to start point of next Q wave
      Increment y by 1
      T height=denoised[y]
      If T height is greater than 0.0 and max
         max=T height
         T1 position=y
    End If
    If T height is less than 0.0 and min
       min=T height
       T2 position=y
  End For
  min=|min|
  If max>min
     T is normal
     T position[T position counter]= T1 position
  Else
     T is inverse
     T position[T position counter]= T2 position
  End If
  Increment T position counter and counter by 1
End For
```

- *Detection of starting point & ending point of T wave*

  A similar methodology (as shown in Pseudo code -2) is used to identify the starting point and end point of T wave with a few changes in the arithmetic operations.

F. Detection of P wave

In order to identify P wave, the interval is taken between the end point of T wave and the starting point of next Q wave and then we find the position where the height is maximum. A similar method (as shown in Pseudo code -3) is used to detect the position of P wave.

- *Detection of start point & end point of P wave*

A similar method (as shown in Pseudo code -2) is used to detect the starting point and end point of P wave with a few changes in the arithmetic operations.

G. *Calculation of Intervals*

At first, The average time of S wave, Q wave, T wave, QRS complex, R-R interval, Q-T interval and S-T segment are calculated and then compared with a specific S wave, Q wave, T wave, QRS complex, R-R interval, Q-T interval and S-T segment. If the difference between two intervals is greater than 10ms then the specific S wave, Q wave, T wave, QRS complex, R-R interval, Q-T interval and S-T segment are omitted and the average intervals to find the optimum result are re-calculated.

IV. EXPERIMENTAL ANALYSIS

The ECG signals necessary for analysis are gathered from Biomedical Lab, Situated in KUET, Bangladesh, using Biopac System Inc. Two types of ECG signals are used for experiment. One is .mat file and another is tracing paper from Single Channel ECG-901A developed by KADEN Yasen Medical Electronics. This experiment is done on five (Sample 1, Sample 2,…, Sample 5) different people. The samples obtained thus are shown in Figure 6.

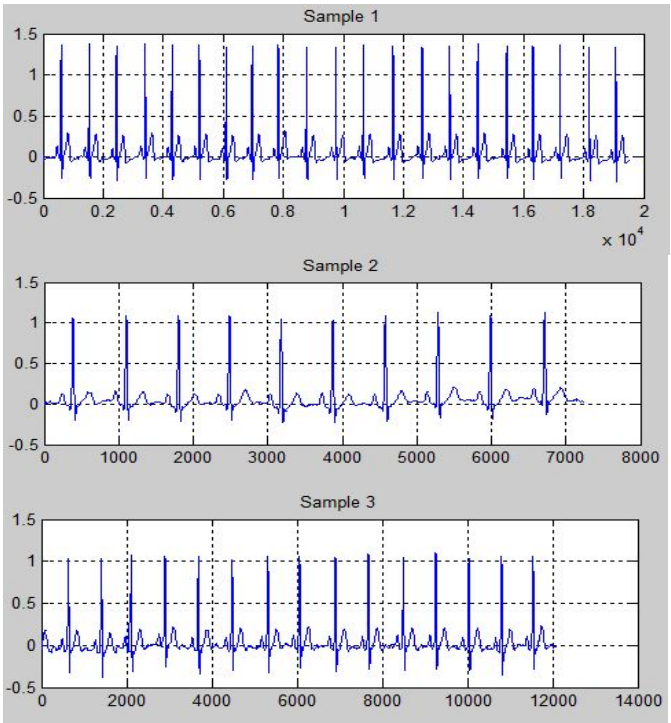

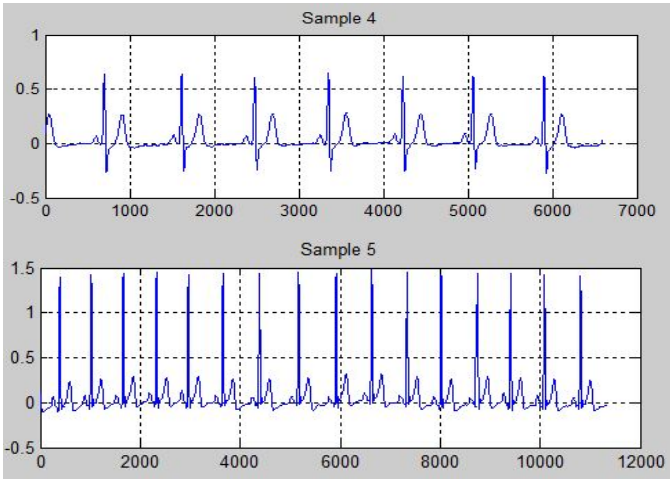

Figure 6: Five Samples from Five people

To assess and calculate the correctness of the proposed process, heart rate, PR interval, P wave, QRS complex, T wave and QT interval are used. The distance between R-R interval is extracted and heart rate is calculated established on the database standards. The info regarding the R Peak and QRS complex acquired is very valuable for ECG Classification, Investigation, Diagnosis, Verification and Documentation performance. The QRS complex is also used for beat detection and the calculation of heart rate using R-R interval estimation. The key benefit of this type of detection is a reduced amount of time consumption for long time ECG signal. The accuracy obtained for the database 96.79% which is a promising result. Table I shows the parameter calculated by using the proposed algorithm and by manually analyzing the ECG signals collected in the tracing paper.

The result of the ECG machine in tracing paper is taken as reference. The accuracy of proposed system is calculated with respect to the result of the ECG machine. The proposed method is experimented over five people. Where the sample 1 provides the accuracy level of 96.71% and the error rate is 3.29%.The proposed method provides an average accuracy level of 95%. Through a simple method we find overall good accuracy to extract the features of ECG signals.

V. CONCLUSIONS

This paper addresses one of the challenging issues in health care services especially for developing countries by proposing a novel feature extraction method. The method used ECG signal data from Biomedical Lab, Situated in KUET, Bangladesh and different filters were designed to reduce unwanted signal like baseline wander and power line interference. Then various features are detected from ECG signal. This proposed algorithm is simple to implement and may sensitive to noisy signal. Thus it is needed to de-noise the signal. Further research can be enhanced to adopt a methodology in order to de-noise the ECG signals.

TABLE I. Feature Detection Performance Comparison

ECG Record	Category	Heart Rate (BPM)	PR Interval (mS)	P Wave (mS)	QRS Complex (mS)	T wave (mS)	QT Interval (mS)	Accuracy
Sample 1	***Tracing Paper Value***	76	106	94	114	139	320	96.71%
	Proposed Algo. Value	75.4	112	98	119	143	328	
Sample 2	***Tracing Paper Value***	74	148	122	104	162	346	96.94%
	Proposed Algo. Value	75	141	119	102	153	338	
Sample 3	***Tracing Paper Value***	82	140	117	107	144	320	98.05%
	Proposed Algo. Value	82.4	138	115	103	141	313	
Sample 4	***Tracing Paper Value***	78	150	122	104	159	342	96.37%
	Proposed Algo. Value	77.4	158	127	109	168	349	
Sample 5	***Tracing Paper Value***	80	150	119	107	173	357	95.88%
	Proposed Algo. Value	80.8	143	112	102	168	348	

REFERENCES

[1] Evangelos B. Mazomenos, Dwaipayan Biswas, Amit Acharyya, Taihai Chen, Koushik Maharatna, James Rosengarten, John Morgan and Nick Curzen, "A Low-Complexity ECG Feature Extraction Algorithm for Mobile Healthcare Applications," *IEEE Journal of Biomedical and Health Informatics,* Vol. 17, No. 2, March 2013.

[2] Sani Saminu, Nalan Özkurt and Ibrahim Abdullahi Karaye, "Wavelet Feature Extraction for ECG Beat Classification," *IEEE 6th International Conference on Adaptive Science & Technology (ICAST)*, 2014.

[3] P.SASIKALA and Dr. R.S.D, "Extraction of P wave and T wave in Electrocardiogram using Wavelet Transform," (*IJCSIT) International Journal of Computer Science and Information Technologies*, Vol. 2 (1) , 489-493, 2011.

[4] V.Viknesh and P. Ram Prashanth, "Matlab implementation of ECG signal processing," *IOSR Journal of VLSI and Signal Processing (IOSR-JVSP)*, Volume 3, Issue 1 (Sep. – Oct. 2013), PP 40-47, e-ISSN: 2319 – 4200, p-ISSN No. : 2319 – 4197

[5] E.B. Mazomenos, T. Chen, A. Acharyya, A. Bhattacharya, J. Rosengarten, K. Maharatna, "A timedomain morphology and gradient based algorithm for ECG feature extraction," *Proceedings of IEEE international conference on industrial technology (ICIT)* ,pp. 117–122, 2012.

[6] S.C. Saxena, V. Kumar, S.T. Hamde, "Feature extraction from ECG signals using wavelet transforms for disease diagnosis," Int J Syst Sci. 33(13):1073–85, 2003.

[7] J.P. Martinez, R. Almeida, S. Olmos, Rocha, A.P., Laguna, P., "A wavelet-based ECG delineation: evaluation of standard databases,*" IEEE Tran Biomed Eng.* 51(4):570–81, 2004.

[8] A.N. Mahesh, "ECG feature extraction using Time-Frequency analysis," *Innovation in Computing Sciences and Software Engineering*, 2014.

[9] Neha Soorma, Jaikaran Singh and Mukesh Tiwari, "Feature Extraction of ECG Signal Using HHT Algorithm," *International Journal of Engineering Trends and Technology (IJETT)* – Volume 8 Number 8- Feb 2014.

[10] V.K.Srivastava and Dr. Devendra Prasad, "Dwt - Based Feature Extraction from ecg Signal," *American Journal of Engineering Research (AJER)*, e-ISSN: 2320-0847 p-ISSN : 2320-0936, Volume-02, Issue-03, pp-44-50.

[11] A. Coast Douglas, Rchard M. Stern, Gerald G. Cano and Stanley A. Briller, "An approach to cardiac arrhythmia analysis using hidden Markov models," IEEE Transaction on Biomed Eng., 37(9): 826-836, 1990.

[12] Franc Jager, "Feature Extraction and Shape Representation of Ambulatory Electrocardiogram Using the Karhunen-Loève Transform," Electrotechnical Review, Ljubljana, Slovenija Elektrotehniˇ ski vestnik, 69(2): 83–89, 2002.

[13] Naveen Ku. Dewangan and S. P. Shukla, "A Survey on ECG Signal Feature Extraction and Analysis Techniques," *International Journal of Innovative Research in Electrical, Electronics, Instrumentation and Control Engineering*, Vol. 3, Issue 6, June 2015.

[14] Qibin Zhao, and Liqing Zhan, "ECG Feature Extraction and Classification Using Wavelet Transform and Support Vector Machines," *International Conference on Neural Networks and Brain*, ICNN&B '05, vol. 2, pp. 1089-1092, 2005.

[15] Vanisree K and Jyothi Singaraju, "Automatic Detection of ECG R-R Interval using Discrete Wavelet Transformation," *International Journal on Computer Science and Engineering (IJCSE)*, Vol. 3 No. 4, ISSN : 0975-339, Apr 2011

Development of Low Cost Wireless Biosignal Acquisition System for ECG EMG and EOG

Md. Asif Ahamed[1*], Md. Asraf-Ul- Ahad[2], Md. Hanif Ali Sohag[1], Mohiuddin Ahmad[1]
[1]Department of Electrical and Electronic Engineering
[2]Department of Conservative Dentistry and Endodontics
[1]Khulna University of Engineering & Technology, Khulna-9203, Bangladesh
[2]Bangabandhu Sheikh Mujib Medical University, Dhaka- 1214, Bangladesh
*E-mail: asif.fx@live.com

***Abstract*— A biosignal is a human body variable that can be measured and monitored continuously and provide information about the health status. Among them well known bioelectrical signals are Electrocardiograph (ECG), Electromyography (EMG), Electroencephalogram (EEG) and Electrooculogram (EOG). Those signals are useful for different applications like disease diagnosis, human machine interface, entertainment. This paper presents a low cost, wireless biosignal acquisition system specialized for ECG, EMG and EOG. In this system, Arduino Uno in used and an application is developed for visualizing and storing the signal in real-time. This application is developed by processing. It stores the signal data in a text file, which can be used in MATLAB for analysis. In this system, biosignal is transferred by Bluetooth serial communication, which ensures safety and reduces noise interference. This system can be used either Windows, Linux, Mac OS and suitable for both laptop and desktop computer.**

Keywords—Biosignal acquisition, ECG, EMG, EOG, Powerline interference

I. INTRODUCTION

Human body generates various different signals. Biosignal can be defined as any signal in living beings that can be continually measured and monitored. It can be both electrical and non-electrical signals. Bioelectrical signals can be sensed by non-invasive method by using skin-surface transducer, which is commonly used for Electrocardiograph (ECG), Electromyography (EMG), Electroencephalogram (EEG) and electrooculogram (EOG) [1]. Both ECG and EOG signals are bipolar low-frequency signal. The normal range of ECG signal is 0.05-100Hz having its amplitude ranges from 10µV to 5mV, whose typical value is 1mV [2]. EOG signal ranges between 15 µV to 200 µV with a frequency range of about 0-30 Hz [3]. Generally the amplitude of the EMG signal ranges from 0-10mV (peak-to-peak) and its frequency ranges from 0- 500Hz [4]. The dominant energy in EMG is being in 50-150Hz [4].

The frequency information of those signal is highly useful for disease diagnosis. Among those signals ECG is very useful for diagnosis especially for heart related diseases and disorders such as, cardiovascular disease, pulmonary disease, sudden cardiac arrest, etc [5]. EMG is used clinically for diagnosis of neurological and neuromuscular problems. Another important application of EMG and EOG is human machine interface and controlling of various devices.

Our research aims to develop a low cost biosignal acquisition system which is affordable for the people of developing and under developed country. In our previous papers, we have developed an ECG data acquisition system and an ECG monitoring system [6,7]. In this research, we have modified the system for acquisition of ECG, EOG and EMG together. This paper presents a prototype biosignal acquisition system, which is portable, battery powered and it includes wireless facility. In this system biosignal is transferred by Bluetooth serial communication and it gives wireless connectivity up to 9 meter. The equipment used in this system consumes low power and this system is battery powered. For this it can be used during load shedding and on those remote areas where electricity have not reached.

This paper is organized as follows: Section II shows the architecture of the system. Section III describes the proposed methodology. Section IV explain the software implementation. Experimental results are illustrated in section V. Finally, section VI concludes the results.

II. SYSTEM ARCHITECHURE

This system consist of three electrodes. Figure 1 shows the

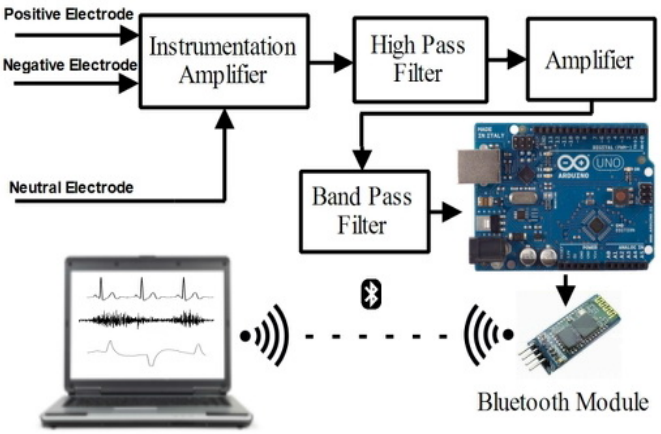

Fig. 1. System Architecture of the Biosignal acquisition system.

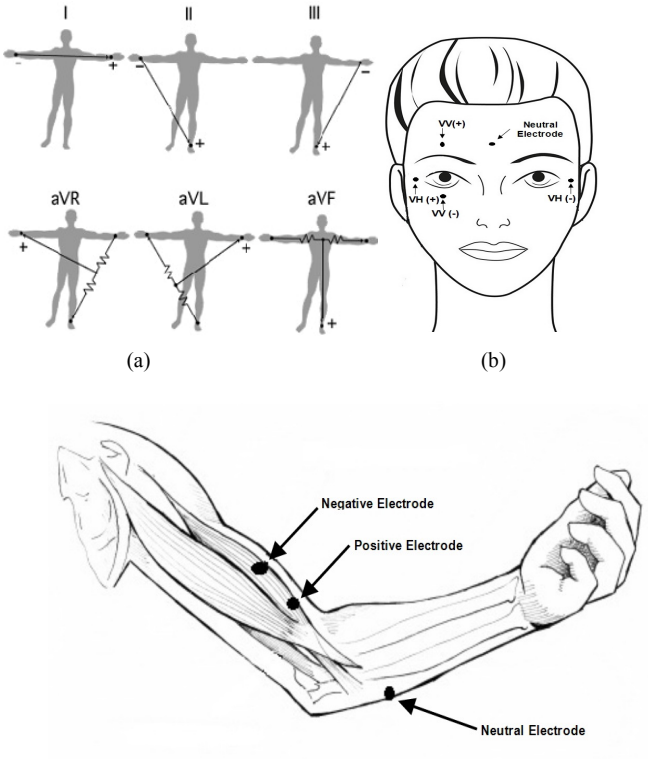

(a) (b)

(c)

Fig. 2. (a) limb leads and augmented limb leads for ECG, (b) Electrode position for horiontal and vrtical eye mvemrnt, (c) Electrode position for biceps EMG.

system architecture of this system. In this system, Arduino Uno is used for analog to digital conversion and signal transmission. By this system ECG can be taken from both limb leads and augmented limb leads. Figure 2 shows the electrode position for ECG, EOG and EMG.

III. Proposed Methodology

The proposed system consists of four units: sensor unit, signal conditioning unit, power supply unit and Microcontroller unit.

A. Sensor Unit

For sensing ECG, EMG and EOG signal, silver chloride electrodes are used. A commercially available disposable electrode named Bio Protech T716 was used, which is shown in figure 4 (b) [8].

B. Signal Conditioning Unit

Signal conditioning unit consist of instrumentation amplifier, op-amp and filter. In the top of figure 3 signal conditioning circuit is shown. In this system, a commercially available low cost instrumentation amplifier AD620 is used, which gives Common-mode rejection ratio (CMRR) greater than 100dB at nearly 1 kHz [9]. Total gain of 840 is achieved by two stage amplification. First stage amplification was done by AD620 and the gain was 13.7. Second stage amplification is done by CA3130 op-amp and the gain of second stage was 51. CA3130 was used as a non-inverting amplifier. To avoid the risk of amplifier saturation two stage amplification is done. Saturation of amplifier generally occurs due to amplification of electrode offset voltages [10]. To set the gain of AD620, a resistor R_g is used and its value was 3kΩ. The gain expression for AD 620 is given in Eq. (1).

$$\text{Gain} = \frac{49.4\ \text{k}\Omega}{R_g} + 1 \tag{1}$$

For removing the low frequency noises first a high pass filter of 0.03 Hz cut off frequency is used after first stage amplification. After second stage amplification, a band pass filter is implemented using a high pass and a low pass filter in cascade. For ECG, EOG and EMG cut off frequency of all high pass filter is 0.03 Hz. For ECG cut off frequency of the low pass filter is 159 Hz. For EMG it is 564 Hz and for EOG it is 15 Hz. Three switches S1, S2 and S3 are used for filtering path selection of the ECG, EOG and EMG signals. All those filters are passive First order filter. General expression for cut off frequency of the filter is given in Eq. (2) [11].

$$F_c = \frac{1}{2\times\pi\times R\times C} \tag{2}$$

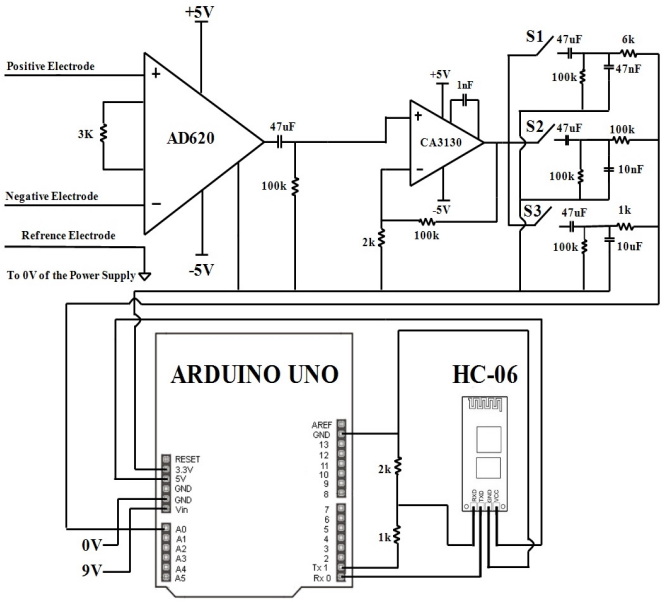

Fig. 3. Circuit diagram of the system.

C. Power Supply Unit

In this system two commercially available 9V disposable Lithium battery is used. A voltage regulator LM7805 is used for safety and short circuit protection. It gives regulated output voltage of ±5V. In this system neutral electrode must connect to the 0V of the dual supply.

D. Microcontroller Unit

This unit consists Arduino Uno board and Bluetooth module HC-06. Arduino UNO board has a 6 channel 10-bit analog to digital converter (ADC) and it returns a linear value from 0 to 1023 corresponding to 0V and +5V respectively [12]. As the ADC works between 0 to 5V, a 3.3V virtual ground is used for making the bipolar signal to unipolar. For serial transmission baud rate is taken as 38400 bps and sampling rate of 1270 samples per second is obtained. A Bluetooth module

HC-06 does signal transmission between Arduino UNO and laptop. Bluetooth module HC-06 has a default baud rate of 9600 bps, which was changed to 38400 bps by a software named putty.

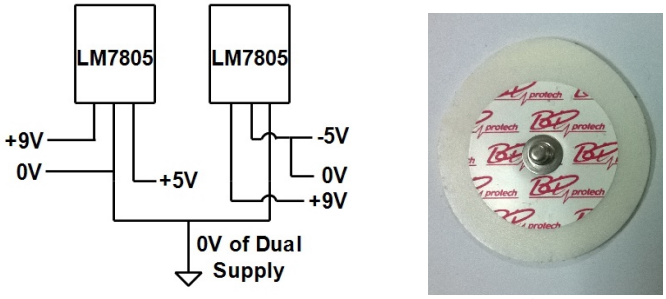

(a) (b)

Fig. 4. (a) Designed ±5V dual power supply. (b) Bio Protech T716 ECG electrode..

IV. Software Implementation

Arduino Uno board has a microcontroller named ATmega328. For programming the microcontroller, integrated development environment provided by the Arduino platform is used. For visualizing and storing the signal an application is developed by Processing. Processing is an open source programming language and integrated development environment (IDE). It builds on the Java language, but uses a simplified syntax and graphics programming model and available for Linux, Mac and Windows operating system. For receiving the signal data serial library of processing is used. In processing line() function is used for visualizing the signal and println() function is used for sorting the signal, which creates a txt file and saves the values received from Arduino ADC [13].

V. Experimental Measurements And Results

Figure 5 shows the experimental measurement performed by us for ECG signal and the prototype biosignal acquisition system.

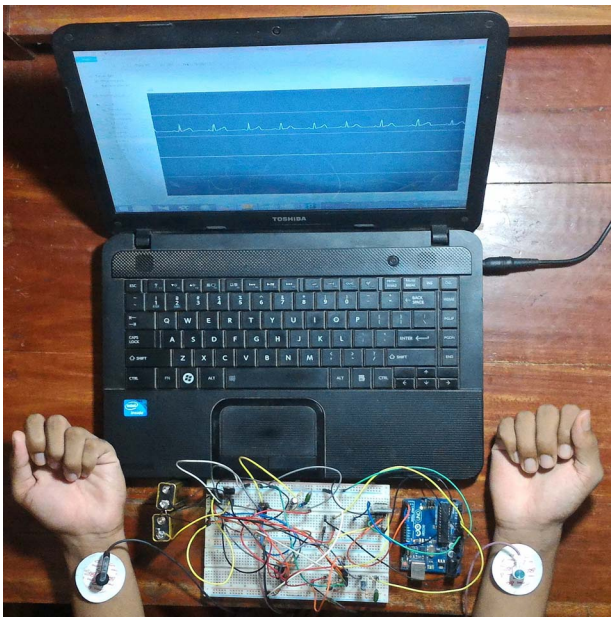

Fig. 5. Experimental measurements performed by us for ECG.

For visualizing and storing the signal a laptop running on Windows 8.1 operating system having Intel B820 processor and 4GB ram was used. ECG, EMG and EOG signals were taken from a boy of 23 years old. The ECG signal was taken in Lead I. In Figure 6, every red line indicates 1V of total 5V and both ECG and EMG signals are above 3V. This is because in this system 3.3V virtual ground is used. Stored ECG, EMG and EOG signals in text file are imported in MATLAB for analysis. MATLAB R2014a is used for analysis.

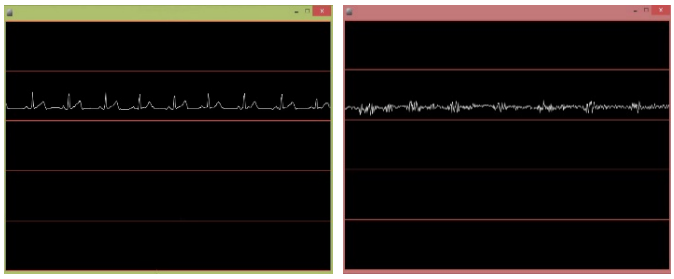

(a) (b)

Fig. 6. Output of the application for (a) ECG and (b) Biceps EMG.

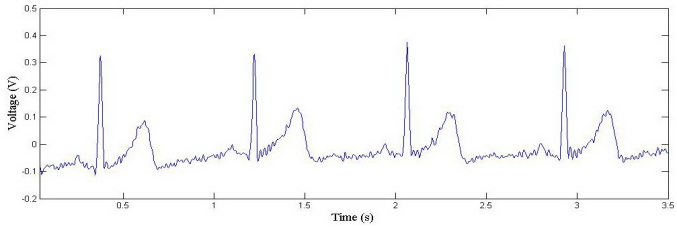

Fig. 7. ECG signal from signal conditionig circuit.

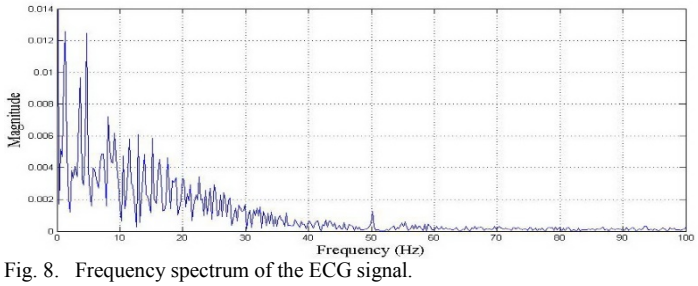

Fig. 8. Frequency spectrum of the ECG signal.

Figure 7 shows the ECG signal from signal conditioning circuit output and this signal is contaminated with power line interference (50Hz). This is because of common-mode voltage produced by the ac mains of 50 Hz frequency with line voltage 220V [14].

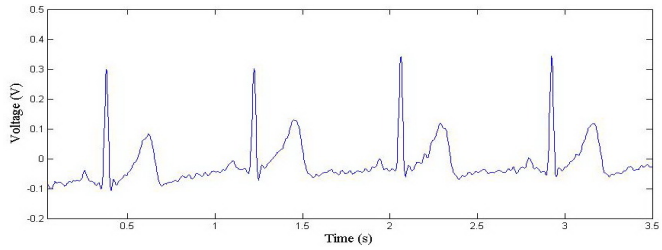

Fig. 9. ECG signal after filtering in MATLAB.

Figure 8 shows the frequency spectrum of the contaminated ECG signal. In this figure, magnitude for 50Hz is 0.001738.

Figure 9 shows the filtered ECG signal. For filtering a Butterworth band pass and an elliptic band stop filter of 50Hz was used. Lower and higher cut off frequency of Butterworth filter was .033Hz and 150 Hz.

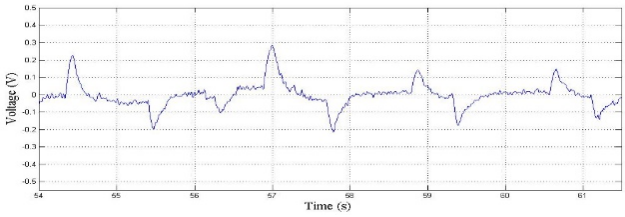

Fig. 10. EOG signal for horizontal eyemovement.

Figure 10 shows the EOG signal for horizontal eye movement. When the eye moves left, a positive peak is found and when the eye moves right, a negative peak is found. In figure 11, the frequency of the EOG signal ranges from 0-10Hz. As a low pass filter of 15 Hz is used, power line interference (50 Hz) does not exist.

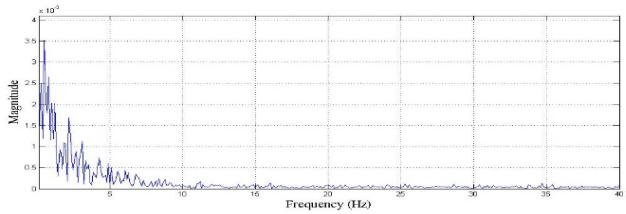

Fig. 11. Frequency spectrum of the EOG signal.

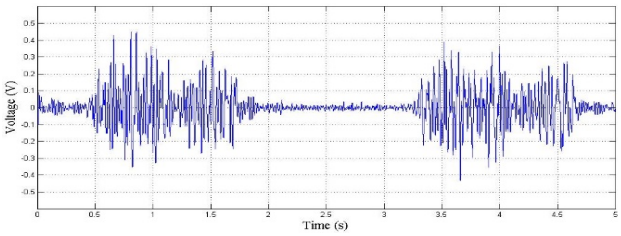

Fig. 12. Biceps EMG signal.

For Biceps EMG signal acquisition electrodes were placed according to figure 2 (c). Figure 12 shows the biceps EMG signal taken from left hand. As the force of the muscle increases the peak of the EMG signal increases. In figure 13 the frequency of the EMG signal ranges from 0-150Hz. There exists a small amount of power line interference same as the ECG signal and the magnitude of 50 Hz is found 0.0015.

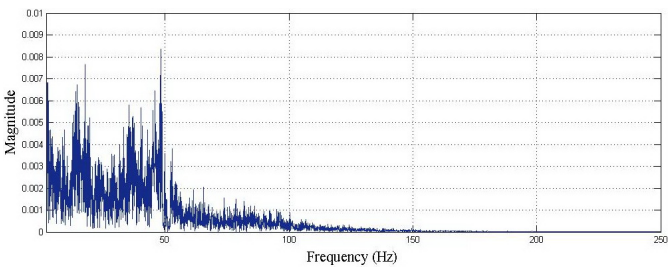

Fig. 13. Frequency spectrum of the EMG signal.

TABLE I. COMPONENT LIST FOR THIS SYSTEM

Component Name	Quantity	Unit Price (USD)	Total Cost (USD)
Arduino UNO	1	9	9
Bluetooth Dongle	1	2	2
Bluetooth Module HC-06	1	6	6
AD620 IA	1	6	6
Resistor and Capacitor	20	0.01	0.2
LM 7805	2	0.15	0.3
CA3130 op-amp	1	0.25	0.25
Electrodes	3	0.09	0.27
9V Battery	2	0.5	1
Total Cost of the system (USD)			25.02

VI. CONCLUSION

The main aim of this research has been fulfilled. We found the desired ECG, EMG and EOG signal and their frequencies in a normal range. In this system we have used simple RC filtering and we have not implemented any analog notch filter of 50Hz. But as the signal conditioning circuit is battery powered and the signal is transferred wirelessly, noise interference in reduced and there exist a very small amount of power line interference (50Hz). This is because of electric field coupling from the nearby power line to the body. The proposed hardware circuit is simple and effective for ECG, EMG and EOG data acquisition. The cost of this system is only USD 25.02. The component used for this system consumes very low power. It takes maximum current of 60mA and it can function up to 22 hours continuously by using two 9V battery.

In future, we will develop the robust biosignal acquisition system with various control supports and protection schemes.

ACKNOWLEDGMENT

This work was partially supported by Higher Education Quality Enhancement Project (HEQEP), UGC, under Sub-project "Postgraduate Research in BME", CP#3472, Bangladesh.

REFERENCES

[1] E. Kaniusas, "Biomedical signals and sensors I: Linking physiological phenomena and biosignals", Springer Science & Business Media, 2012.

[2] A. M. Al-Busaidi and L. Khriji, "Digitally Filtered ECG Signal Using Low-Cost Microcontroller," in International Conference on Control, Decision and Information Technologies (CoDIT), pp. 258-263, 2013.

[3] B. S. M Parameshwari, B. S. Madhurya, and K. U. Rao, "Preparation of papers a cost effective prototype for electrooculogram for effective eye tracking," International Journal of Innovation, Management and Technology , vol. 4, no. 5, pp.494-497, Ocotober 2013.

[4] H. Dong-Mei, Y. Yi, and W. Zheng. "Measurement System for Surface Electromyogram and Handgrip Force Based on LabVIEW", In World Congress on Medical Physics and Biomedical Engineering, Springer Berlin Heidelberg, pp. 67-70, 2009.

[5] M. K Islam, A. N. M. M Haque, G. Tangim, T. Ahammad, and M. R. H. Khondokar, "Study and Analysis of ECG Signal Using MATLAB & LABVIEW as Effective Tools, International Journal of Computer and Electrical Engineering, Vol.4, No.3, pp. 404-408, 2012.

[6] M. A. Ahamed, M. A. Ahad, M. H. A. Sohag, and M. Ahmad. "Development of Low Cost Wireless ECG Data Acquisition System," in

International Conference on Advances in Electrical Engineering (ICAEE), 2015.

[7] M. A. Ahamed, M. K. Hasan, M. S. Alam, "Design and Implementation of Low Cost ECG Monitoring System for the Patient Using Smartphone," in International Conference on Electrical & Electronic Engineering (ICEEE), 2015.

[8] Bio Protech ECG Electrode specification [Online]. Available: http://sanjayintl.com/pdf/ecg_bioprotech.pdf

[9] Datasheet of AD 620 instrumentation amplifier [Online]. Available: http://www.analog.com/media/en/technical-documentation/data-sheets/AD620.pdf

[10] D. Prutchi, M. Norris, "Design and Development of Medical Electronic Instrumentation: A Practical Perspective of the Design, Construction, and Test of Medical Devices," John Wiley & Sons, 2005.

[11] R. Raut and M. N. S. Swamy, "Modern Analog Filter Analysis and Design: A Practical Approach," John Wiley & Sons, 2011.

[12] J. Oxer and H. Blemings, "Practical Arduino: Cool Projects for Open Source Hardware," Apress, 2009.

[13] C. Reas and B. Fry,"Processing: a programming handbook for visual designers and artists", Mit Press, 2007.

[14] A. Brahme,"Comprehensive Biomedical Physics", Newnes, 2014.

An Approach to Convert Conventional Screen into Touch Screen Using Image Processing

Md. Hanif Ali Sohag[1], Mst. Mahmuda Khatun[2], and Mohiuddin Ahmad[3]
[1,3]Department of Electrical & Electronic Engineering
[1,3]Khulna University of Engineering & Technology, Khulna-9203, Bangladesh
[2]Department of English
[2]Northern University Bangladesh, Rajshahi-6204, Bangladesh
E-mail: hanifalisohag@gmail.com, mahmuda.khatun.raj@gmail.com, mohiuddin.ahmad@gmail.com

Abstract— **Touch screen are widely used in the recent electronic devices. In this paper we present a novel and cost-effective webcam based touch screen conversion system for the conventional laptop or desktop using normal LED light. This system converts the normal screen into an interactive touch screen by means of computer vision techniques. In this system the problem of ambient light has been minimized using the brighter LED light which enhances the performance in complex light environments. The position of the bright LED light is easily determined using the scene geometry and camera model. With some further processing of the LED position, the system is capable of calculating the mouse cursor coordinates in the desired laptop or desktop screen to simulate the mouse actions in real time. The user can use the on-screen keyboard for the typing purpose. The system also includes gestures based interaction for playing games and performing additional windows commands easily. The experimental results and practical applications confirmed the effectiveness of the proposed system.**

Keywords— Webcam, LED light, perspective transform, stylus, Image processing.

I. INTRODUCTION

With the growing development of technology, touch screens are becoming more popular in both commercial and personal purposes. Nowadays, Mobile phones, tablets, game machines and control panels cannot be imagined without the touch screens. The human-computer interaction involves interaction between the computer devices and human physical action. The keyboard, mouse, joystick are the main input devices for performing human-computer interaction but without the use of touch technology it is impossible to realize the broad perspective of virtual reality.

E.A. Johnson developed the first capacitive touchscreen at the Royal Radar Establishment which was published in 1965 [1]. In the conventional touch screen technology, the IR emitter and IR transmitter are arranged in such a way that it forms a matrix which indicates the coordinates by getting the block IR position of the touch point[2]. Resistive, capacitive and surface acoustic wave touchscreens are the basic touch screen systems that recognizes a person's touch. The resistive or capacitive touch screen demands the use of special materials such as indium tin oxide to be both transparent and conductive. But the formation of such materials is very expensive and so the cost of the system is gradually increased. Again the amount of material needed for the screen depends on the size of the devices.

For the last decades various types of approaches are developed to find a better solution for the difficulties associated with the resistive or capacitive touch screens. Surface acoustic wave (SAW) technology was proposed in [3] which uses ultrasonic waves. Ultrasonic waves are passed over the screen panel and at the touch point some portion of the wave is absorbed which provides the information about the position of the touch event and sent to the controller for further processing [3]. While resistive, capacitive and surface acoustic wave technology implementation requires a higher cost, optical technique may become unique since it can be used for any flat surface. J.C. Lee demonstrated of such a system using Wiimote [4]. The vision based system using camera and image processing techniques are also implemented which are considered as virtual touchscreen as they require less hardware. Han proposed of a low cost multi-touch sensing system which uses the internal reflection [5].

Another technique is used by Wilson to transform an acrylic plastic to a touchscreen [6]. However, these image processing methods require the cameras and video projector to be placed on the opposite side of the screen from the user which makes it unsuitable for desktop use. In a paper [7], an infrared glove has been used instead of a stylus to interact with the display on an interactive board for collaborative Learning. Shuai Zhang et al. in their paper [8] have presented a method to use an infrared stylus to interact with projected display, using Microsoft's Kinect. Zero-Touch [9] uses the state of art technique to provide the users with comfortable interfacing experience. Another approach is uTouch [10], uses two cameras and skin detection algorithm to get the coordinates of the touch point. But this approach fails as it cannot differ between the skin and background color similar to skin color.

This paper represents a cost-effective and novel approach to convert the normal conventional laptop or desktop screen into an interactive real time touch screen which overcomes all the shortcomings of already proposed techniques. This system is much computationally efficient and cost-effective compared to the available Kinect and Wii based hardware as it requires only an inexpensive webcam and a normal LED light. The webcam can be placed in any direction toward the screen and there is no limitation in size of the

978-1-4673-9257-0/15/$31.00 ©2015 IEEE

device screen. It requires a less amount of time to calibrate and setup is very easy.

II. System Overview

The system is developed to ensure maximum efficiency at minimum hardware requirements which makes it cost effective. It consists of only a webcam, a LED light and a battery. The system doesn't require any other equipment for the human computer interaction. It provides an efficient, natural and real time interaction between the user and normal touch screen device just like the real touch screen device. The LED light acts as a medium of interaction between the user and devices. By tracking the intensity of the LED light when it is touched on the screen the user can easily interact with the normal screen.

Figure 1. Overview of the proposed system

A. Webcam

In this system, we used a low cost webcam which feeds the capture images to the image processing software. It acts as the image source for the image processing algorithms. It captures the bright LED light spot and the software tracks the position of the spot. This system is capable of detecting the LED light in any ambient light condition so the cost of using IR webcam is reduced. With the proposed system, it doesn't require to use any kind of IR light rather the normal LED light can be tracked very efficiently.

B. Stylus

A cool stylus is designed which is used for the interaction with the screen. The stylus contains a red LED light, a push button and a battery. By pressing the push button and pointing the LED to the screen, the touch point is produced on the screen and webcam capture the spot. Then the spot is further processed by image processing algorithm to get the exact coordinate of the spot. The user can easily play interactive games and draw pictures using the stylus. The user can also type text with the stylus by touching the default on screen keyboard.

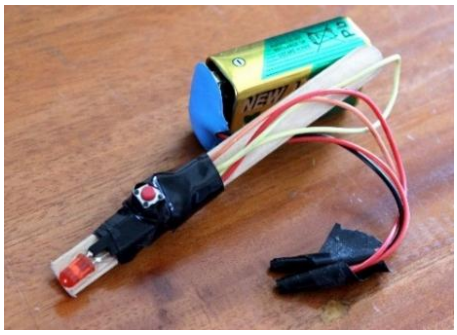

Figure 2. A stylus with normal LED light

III. System Setup And Calibration

The system requires less amount of calibration and is very easy to setup. The webcam is placed in such a position that the whole screen can easily be captured. The camera need not to be straight in front of the screen rather it can be placed at any angle provided the whole screen is visible. After placing the webcam at proper position, the software has to start. After that the calibration process starts. The user has to select the index of the webcam that is placed in front of the screen. Then the system will show the captured images from the webcam whose resolution is 640x480 @ 25fps.

The user will have to click on the four corner points of the screen that is going to be touch screen. There is no limitation of screen size as the user has to choose only the four corner points. The four corner points can be a square, a rectangular, a trapezoid or any kind of tetragonal shape. After getting the required points of the screen proper geometric transformation models are applied to the selected area which results in a desired image of the same aspect ratio of the normal screen.

IV. Proposed Methodology

The system performs the image processing algorithms when it gets the proper selected area of the screen. The area of the screen is selected by clicking the four corner points on the captured image. The overall activity diagram of the proposed system is shown in Fig. 3.

A. Selection of Screen Region

The system requires a certain area of the screen which is going to be touchscreen. So, the user has to select the required area by clicking the four corner points on the captured image from the webcam. The webcam is kept at a proper distance from where the entire screen is visible.

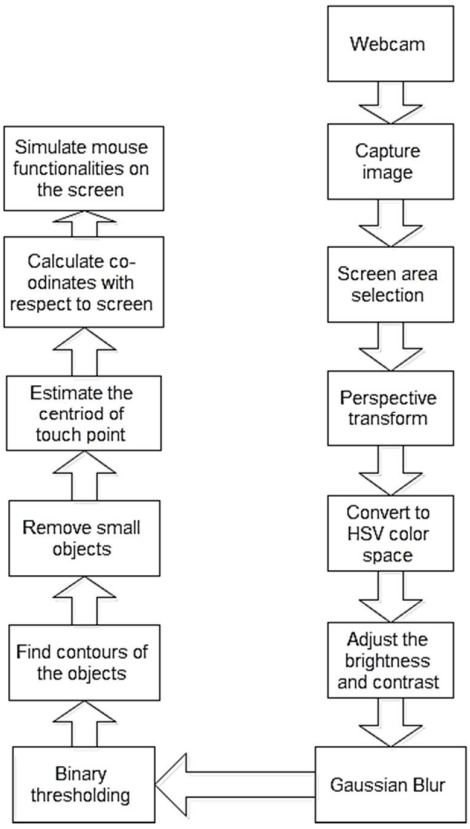

Figure 3. Block diagram of the entire system

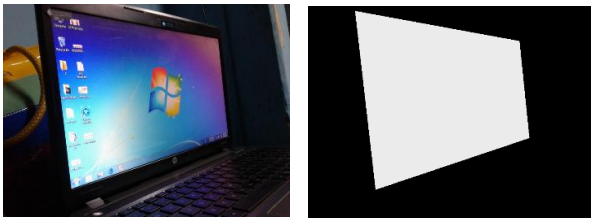

(a) (b)

Figure 4. (a) Capture image by the webcam (b) Selection of the screen region

B. *Perspective Transformation on The Selected Screen*

The selected area of the captured image is not suitable for processing as the webcam is not placed straight to the screen. So, the touch point co-ordinates is different from the real world co-ordinates for the perspective distortion of the image. But for the proper implementation of the system, it needs to establish a relationship between the pixels in the webcam and the pixels in the touch point. So perspective transform algorithm described below is applied to the selected area to overcome the problem. Projective geometry transformation relates the coordinates of a point in a scene to the coordinates of its projection onto an image plane.

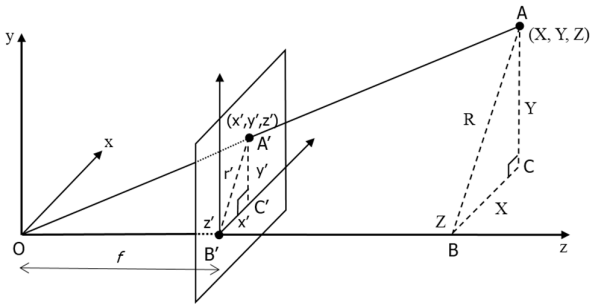

Figure 5. Perspective transformation

From $OA'B'$ and OAB triangles:

$$\frac{f}{Z} = \frac{r'}{R} \tag{1}$$

From $A'B'C'$ and ABC triangles:

$$\frac{x'}{X} = \frac{y'}{Y} = \frac{r'}{R} \tag{2}$$

So, the perspective projection equations:

$$x' = \frac{fX}{Z} \;\; ; \; y' = \frac{Yf}{Z} \;\; ; \; z' = f \tag{3}$$

Within the camera coordinate system the perspective projection of a scene point onto the image plane is described by the above equations. After performing the algorithm, a linear relation between the real screen and the virtual screen is established. The captured image and the transformed image are shown in Fig. 6.

Figure 6. After applying perspective transformation algorithm on the captured image

C. *HSV Conversion*

The captured image by the webcam is a RGB color image which takes longer time to process. As the stylus is using only bright red light as a touch point so there is no need of other color spaces. In order to extract the red light, the captured image is converted to HSV color model which defines a color space in terms of color type, color intensity and color brightness. In our proposed system, we are differentiating the bright red LED by adjusting the HSV values of the image. It provides only the area of the image which contains bright red color ignoring the other component of color.

D. Adjustment of Image and Smoothing

The brightness and contrast of the image is adjusted so that the touch point can easily be differentiated from the background image. For adjusting the contrast and brightness of the capture image the following formula is used:

$$g(x) = \alpha f(x) + \beta \tag{4}$$

The parameters $\alpha > 0$ and β are the gain and bias parameters for controlling the contrast and brightness repectively. Considering $f(x)$ as the source image pixels and $g(x)$ as the output image pixels, the formula can also be written as:

$$g(i,j) = \alpha f(i,j) + \beta \tag{5}$$

where i and j indicates that the pixel is located in the i-th row and j-th column.

E. Smoothing and Thresholding

After proper image adjustments, it is required to reduce the surrounding noises. The use of the Gaussian kernel for smoothing has become extremely popular in image processing application. So, the adjusted image is further smoothed for a better accuracy using a 3×3 Gaussian filter [11]. The Gaussian function (2D) can be expressed as the product of two one-dimensional functions in each coordinate axis.

$$g(x,y) = \frac{1}{2\pi\sigma^2} \cdot e^{-\frac{x^2+y^2}{2\sigma^2}} \tag{6}$$

where x is the distance from the origin in the horizontal axis, y is the distance from the origin in the vertical axis, and σ is the standard deviation of the Gaussian distribution.

After that adaptive threshold is applied to the binary image which provides a clear touch area for further processing.

F. Finding The Point of Touch and Mouse Functionality

The touch area by the stylus can easily be differentiated and tracked due to the fact that the LED light intensity is brighter than the background screen. The contours of the binary image are found using the contour finding algorithm of OpenCV. Around the touch point where the stylus was touched there might be some small noise areas. To eliminate the noise, only the largest contour area is considered as the touch point. The center co-ordinate is then calculated using moments calculation formula. The co-ordinate is mapped to screen co-ordinates to get the exact location of the touch co-ordinate using the following formula:

$$x = \frac{(P_x \times X)}{I_x} \tag{7}$$

$$y = \frac{(P_y \times Y)}{I_y} \tag{8}$$

where (x, y) are screen coordinates, (P_x, P_y) are the touch point coordinates on the processed image, I_x, I_y are the image resolution and X, Y are the screen resolution.

Then the corresponding co-ordinate is passed to windows default mouse events to simulate mouse actions.

Figure 7. The touch point is detected and co-ordinates are calculated

V. Experimental Results

The whole system is implemented by using only a webcam and a LED light. The system works with various ambient light conditions. We implemented the system in daylight and at dark light. But it gives higher accuracy in both conditions. Experiment is made in different ambient light conditions. The light effects are reduced by controlling the contrast and brightness of the captured image. As compared to the IR touch screen system which is affected by the sunlight, this system is more accurate and can simulate mouse events very efficiently.

The image processing is done on a laptop having Intel Core i5 processor 2.60 GHz, 4GB memory running on Windows 7 64 bit Operating system. In our experiment, the display screen of resolution 1024×768 is converted to touch screen with the captured image of resolution 640×480. The HSV values and threshold values are adjusted properly for working with all environment light condition.

We found the average pixel deviation of ± 4 pixels along x axis and deviation of ± 5 pixels along the y axis which can be consider as zero deviation with respect to the entire display screen. The processing time is found to be 19.4ms in normal lighting and 21.9ms in dark lighting as shown in Table I. We found the overall accuracy of 98% in our proposed system as shown in Table II.

TABLE I. Processing Time

Situation	LED detection	Touch Point Detection	Mouse Functionality	Total Time
Natural Lighting	12.1 ms	3.3 ms	4 ms	19.4 ms
Dark Lighting	13.3 ms	4.6 ms	4 ms	21.9 ms

TABLE II. TOUCH POINT DETECTION RESULT

Situation	Pixel Deviation along x Axis for Different Resolution			Pixel Deviation along y Axis for Different Resolution			Average Accuracy
	800×600	*1024×768*	*1366×768*	*800×600*	*1024×768*	*1366×768*	
Natural Lighting	±3	±3	±4	±3	±4	±5	98%
Dark Lighting	±4	±5	±6	±5	±5	±6	

With this system, drawing picture can easily be done shown in Fig. 8. Various kinds of interactive games can easily be played by using this system which is shown in Fig. 10. With the help of the system, typing text is also possible by using the on screen keyboard shown in Fig. 9.

Figure 8. Drawing using the stylus in microsoft paint

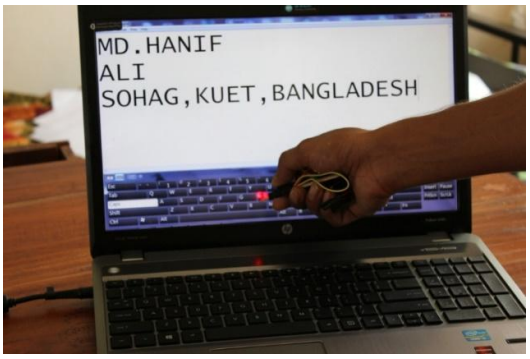

Figure 9. Typing text using input panel on screen keyboard

Figure 10. Playing Angry Birds game on PC

VI. CONCLUSION AND FUTURE WORKS

In this paper, we have designed and implemented a vision-based interactive touch screen computer interaction system using only a webcam and a stylus. The proposed system provides a natural, cost-effective and comfortable human computer interaction interface without use of any complex hardware devices. With respect to the other touch screen techniques this system does not lag efficiency in ambient light condition makes it usable at any time and at anywhere. It requires less time to setup and very easy to use. This system can be used for interactive learning, business and industrial purposes because of its high accuracy and real time response.

We are still developing the system and in our future work, we are planning to improve the feasibility of the system by including multi-touch gesture facility for zoom in, zoom out, scrolling up, scrolling down, and hand writing recognition facility which will make it more fascinating.

REFERENCES

[1] E.A. Johnson, “Touch Display – A novel input/output device for computers”, Electronics Letters, Vol. 1, No. 8, pp. 219-220, 1965.
[2] Touchscreen, http://en.wikipedia.org/wiki/Touch_screen#Infrared.
[3] How stuff works? , How do touch-screen monitors know where you're touching? , August 2011, http://computer.howstuffworks.com/question716.htm
[4] J.C. Lee, “Low-Cost Multi-point Interactive Whiteboards Using the Wiimote” http://johnnylee.net/projects/wii/, last visited Dec. 12, 2013.
[5] J. Han, “Low-cost multi-touch sensing through frustrated total internal reflection”, Proceedings of the 18th annual ACM symposium on User interface software and technology, pp. 115-118, 2005.
[6] A. Wilson, “TouchLight: An Imaging Touch Screen and Display for Gesture-Based Interaction”, 6th International Conference on Multimodal Interfaces, pp. 69-76, 2004.
[7] T. Puckdeepun, J. Jaafar, M. F. Hassan, and F. A. Hussin, “Design of Interactive Board System for Collaborative Learning”, International Symposium in Information Technology (ITSim), pp 1– 5, 2010.
[8] S.Zhang, W. He, Q. Yu, and X. Zheng, “Low-Cost Interactive Whiteboard Using the Kinect”, International Conference on Image Analysis and Signal Processing (IASP), pp. 1– 5, 2012.
[9] J. Moeller and A. Kerne, “ZeroTouch: An Optical Multi-Touch and Free-Air Interaction Architecture”, Proc. CHI, pp. 2165-2174, 2012.
[10] U. Ghufran, “uTouch: A cost effective touch screen solution for gesture based interaction”, ICCMS, 2011.
[11] R.A. Haddad and A.N. Akansu, "A Class of Fast Gaussian Binomial Filters for Speech and Image Processing," IEEE Transactions on Acoustics, Speech and Signal Processing, vol. 39, pp 723-727, March 1991.

A New Sample Preparation Technique for Linear Dilution Gradient with Minimal Sample Utilization and Waste Generation in DMFBs

[1]Pranab Roy, [2]Khokan Mondal, [3]Mayuri Kundu, [4]Hafizur Rahaman
[1,2,3,4] School of VLSI Technology, Indian Institute of Engineering Science and Technology, Shibpur, India
Email – [1]*ronmarine14@yahoo.co.in*, [2]*khokan20@gmail.com*, [3]*kundu.mayuri@gmail.com*, [4]*rahaman_h@yahoo.co.in*

Abstract – Recently, Digital Microfluidic Biochip (DMFB) is developed as a major detection mechanism for biochemical analysis. The technology aims at automation and integration of droplet based microfluidic operation within a miniaturized substrate comprised of 2D planar array of electrodes. Sample preparation remains a major issue for execution of specified bioassay protocols in DMFBs. This requires dilution of samples or formation of mixtures with different targeted concentration factors. Here, we propose new techniques for sample preparation with single source, multiple target concentration having linear dilution gradient for prespecified bioassay execution. The main objective is to i) minimize number of samples as well as reagents for obtaining targeted concentration ii) to employ minimum mixing or dilution operations and thereby optimizing the module utilization and iii) to obtain multiple copies of targeted concentration necessary for fault tolerance and parallel bioassay applications and iv) minimum generation of waste droplets to ensure optimum sample and module utilization.

Keywords: Digital Microfluidics, Bioassay protocols, sample preparation, dilution, concentration factor, module optimization, resource and waste generation

I. Introduction

Microfluidics represents the manipulation and analysis of minute volumes of fluid. Microfluidics in recent years has emerged as a powerful technology for numerous relevant applications in biomedical and biochemical analysis, diagnostics and detection. The fusion of microelectronic and bioanalytical systems has enabled the development of a new class of device known as Lab-on-Chip. Such systems are capable of shrinking an entire laboratory method within a single miniaturized device. The major advantages of such systems are i)less sample and reagent consumption, ii) enhanced heat transfer, iii)faster separation, iv)laminar flow, v)electrokinetic manipulation, vi)low power consumption, vii)parallelization and portability, viii) Improved separation efficiency. Earlier generation of microfluidic biochips were based on continuous fluid flow manipulated through a set of micrometer scale components namely channels, microvalves, micropumps, actuators, sensors and so on [1-2]. Recently, a new generation of device has been emerged as a viable alternative to this continuous flow based design. Such devices termed as Digital Microfluidic Biochip is developed as a new generation of lab-on-chip architecture based upon micro-manipulation of droplets using a programmed external electric field by an individually addressable electrode array. Actuation of droplets can occur through various mechanisms, namely electrowetting on dielectrics, dielectrophoresis, thermo capillary transport and surface acoustic wave transport [3]. Electrowetting on dielectric (EWOD) is currently used as one of the best actuation methods for droplet manipulation in digital microfluidic systems. Electrowetting is a phenomenon where an electric field modifies the wetting behavior of a polarizable or conductive liquid droplet in contact with a hydrophobic, insulated electrode. Actuation is based on the principle of modulating the interfacial tension between a liquid and an electrode coated with a dielectric layer [4]. Droplets are sandwiched between two parallel plates. The bottom plate is the chip surface, which houses the addressable electrode array, and the top is either a continuous ground plate or a passive top plate (Fig.1). The use of unit volume of droplets allows a microfluidic function to be reduced to a set of basic operations. By varying the control voltage pattern in a time-multiplexed manner, all the fluid handling operations can be accomplished at any desired location within the 2D array. Typical fluidic operations on a droplet include dispensing, transport, mixing, splitting, heating, incubation, and sensing [5-8]. DMFBs offer significant flexibility and programmability over their continuous flow counterparts while implementing various assays that mandate high-sensitivity, and low requirement of sample and reagent consumption. Automated and on-chip sample preparation has drawn significant attention in recent years [6]. In sample preparation, producing chemical and bio molecular concentration gradients is of particular interest. Dilution gradients play essential roles in in-vitro analysis of many biochemical phenomena including growth of pathogens and selection of drug concentration. Sample preparation implies formation of a sample with a single or a set of targeted dilution. Here dilution indicates the achievement of a desired concentration factor for preparing the fluid to utilize it in a specified biochemical analysis or detection process. The major step for preparation of a sample with desired concentration factor (with specified accuracy) is to formulate a sequence graph representing the necessary sequence of mixing and splitting using the set of specified samples and available buffers and reagent solutions.

Here, we propose a technique to develop a sequence graph to obtain a targeted set of samples with linear dilution gradients. The major objectives are i) to minimize the number of modules to be used for microfluidic operations namely mixing or splitting, ii) to optimize the process to have minimal number of waste droplets, iii) to use minimal number of samples and reagents and iv) to obtain a set of copies for each target concentration specifically for fault tolerance. The reason is that for obtaining a sample with specific concentration factor, the accuracy might deviate due to faulty mixing or splitting operation, which might require multiple copies of samples with same concentration for additional investigation purpose particularly in cases of preparation errors.

The rest of the work is arranged as follows. Section 2 states the prior contributions regarding sample preparation in DMFBs. Section 3 gives the basic procedures and parameters involved in sample preparation process in DMFBs. Section 4 states the motivation and objectives for the proposed method. Section 5 proposes the algorithm followed by mathematical estimation for the desired resources. Section 6 illustrates a specific example. Section 7 shows the experimental results and comparison with contemporary methods. Section 8 concludes conclusion.

II. Prior Contributions

Major assay operations performed by DMFBs include sample detection, sample pretreatment and sample preparation being integrated within the same device. Dilution is commonly used in biological studies to create a variety of concentrations of the stock solution of samples or reagents by mixing it with buffers on a microfluidic device [9]. Concentrations can be nonlinear or linear and two types of dilution methods can be employed towards generation of the targeted concentration factor, namely serial and linear dilution. In case of linear dilution, the stock solution and its diluents are mixed in different ratios and can create linearly varying concentrations of the stock solution [10]. On the contrary, in serial dilution, a common example of which is the logarithmic method, a solution is repeatedly diluted using the same mixing ratio. Recently, several methods for on chip mixing/dilution control techniques for sample or reagent preparation in DMFBs have been reported in

[11]. First, the dilution control method on DMFBs was proposed in [12], where a dilution algorithm based on binary search strategy has been proposed to determine the sequence of (1:1) mix-split steps. It deals with intermediate droplets and assumes that it is available whenever it is needed. But this technique does not address the waste droplets and storage units. In case of single target sample preparation, BS method has been proposed in [13] considering two or more fluid at any given ratio in (1:1) mixing model. It converts the target concentration into binary representation and scans the bits through right-to-left to decide the mixing and splitting steps. It takes n steps mix-split to complete dilution process with an error of at most $\frac{1}{2^{n+1}}$ in the target concentration factor (CF).

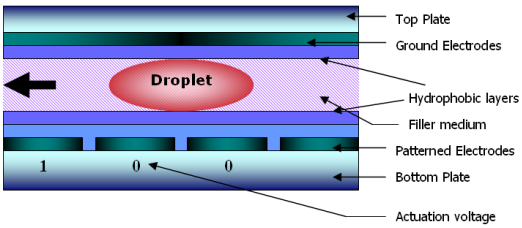

Fig 1. Biochip sectional schematic diagram with 2D array of electrodes

A binary search method has been proposed in 14] to generate a single dilution of sample and reduces the number of waste droplets significantly compared to [13], as the process reuses the intermediate droplets. A reactant minimization algorithm REMIA has been proposed in 15]. This method is based on skewed mixing tree construction. A graph-based optimal reactant minimization algorithm 'GORMA' proposed in [16] is an improved technique which concentrates on minimal reactant usage. It is important to mention that none of the mentioned techniques are capable of producing multiple target concentrations. First, reagent saving mixing algorithm for preparing multiple target concentration has been proposed in [17]. This approach makes a global view of all target concentrations and processes concurrently to generate all target concentrations for the first time.

The algorithm proposed in [15] has been extended in [18] for minimization of reactant usage. Another sample preparation technique known as RSM [19] not only minimizes the consumption of reagents, but also reduces the number of waste droplets and sample preparation time significantly. The work proposed in [16] has been further extended to a waste aware process viz. WARA [20], which states the waste recycling for producing multiple target concentrations. It takes individual mixing tree corresponding to each of multiple targets and reduces waste and increases droplet sharing by combining them. Basic idea of [20] is to mix two non-consecutive CFs that are separated by an odd number of elements of gradient sequence and to produce the median. Though, the above algorithm focuses on generation of multiple target concentration but it consumes huge number of modules. A new algorithm proposed in [21] concentrates on producing random dilutions factors with minimum wastage while it also satisfies the required accuracy in the CF. The algorithm proposed in [22] optimizes cost or increases performance when a certain concentration gradient is required. This algorithm is applied for generation of any arbitrary linear gradient with minimum wastage and also with required accuracy. Recently, a method based on binary de Brujin graph has been proposed in [23] to solve the problem by using Asymmetric travelling salesman problem to get the shortest mix–split sequence while satisfying the given upper bound in concentrations factors.

III. Sample Preparation in DMFB

The primary requirement is to prepare the sample with requisite concentration factor using minimum number of mix split operations and hence with the minimum number of module requirements.

*A. **Preliminaries:***

A few preliminary definitions regarding sample preparation are given below:

Stock solution or Sample: It is the initial sample or reagent volume dispensed into the 2D array for initiating the first step of sample preparation.

Target concentration: It is the final concentration of each stock solution which is the prerequisite to take part in the actual reaction.

Dilution: It is the process of decreasing the concentration of a solute (sample) in solution, usually simply by mixing with more solvents/diluents. The dilution of a solution means to add more solvent/diluents without the addition of more solute/sample. Dilution is commonly used in biological studies to create a variety of concentrations of the stock solution by mixing it with its diluents termed as buffer solution within a microfluidic device.

Linear dilution: The stock solution and the diluent are mixed at different ratios creating linearly varying concentration [10].

Serial dilution: Here a solution is repeatedly diluted using the same mixing ratio. For example, let the mixing ratio is 1:1.So each successive dilution reduces the concentration factor by ½. Hence for n linear dilution, the concentration factor goes down to $\frac{1}{2^n}$.

Thus, the serial dilution method creates discrete nonlinear concentration values of the stock solution [10]. However, in DMFBs, the discrete volumes of sample can only be used and hence, only serial dilution can only be employed to achieve the desired concentration level.

Interpolated Dilution: Two unit volume droplets with CF C_1 and C_2 are taken and after mix-split operation, two droplets with resultant concentration C_r, where $C_r = (C_1+C_2)/2$), are obtained. Both the dilution methods produce concentration factors whose denominators are integral power of two [21].

Concentration factor (CF): We start with a raw sample considering a 100% concentration. CF is defined as the ratio of the initial volume of the sample to the final diluted volume of the sample [14].

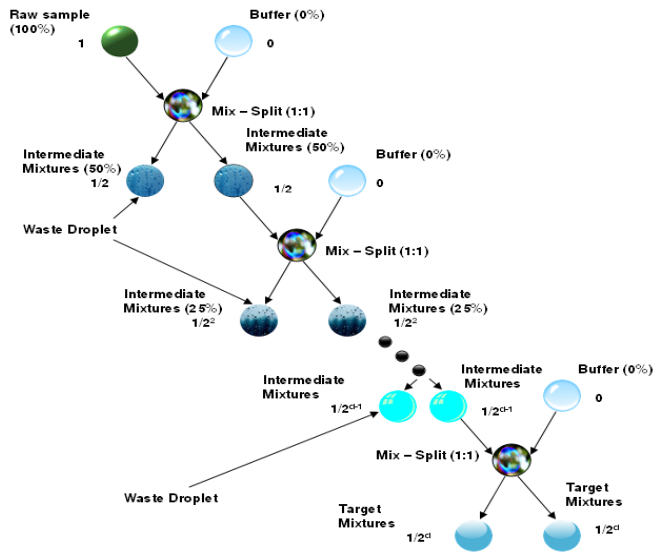

Fig. 2. A sample preparation technique using serial Dilution to achieve a target concentration of $1/2^d$

*B. **Sample preparation process**:*

We consider a preliminary sample preparation process using only serial dilution to achieve a target concentration expressed in powers of 2 as $1/2^d$. We start with a raw sample and buffer solutions together with the given target concentration C_T. Then we carry out a set of serial dilution through mix-split operation to achieve the target concentration C_T. Unlike continuous flow based biochips DMFB manipulates discrete droplets and hence only serial dilution is possible. The dilution strategy defines a mixing tree for serial

mixing that defines the steps involved in achieving the target concentration. Consider Fig. 2, where we start with a raw sample with concentration 100% denoted by '1' and a buffer solution with concentration 0% denoted by '0'. For the first level of dilution with a ratio of 1:1, two resultant mixtures each with concentration 50% denoted by ½ is obtained. Let the target concentration C_T is expressed as $1/2^d$ .This can be achieved through d number of dilution using mixing with buffer of 0% concentration at each step.
The mixing tree or dilution tree as shown in Fig. 2 represents a diagraph which displays the sequence of dilution steps to achieve the target concentration. A dilution tree is a binary tree, where each dilution step represented by a dilution (Mix-Split) node has two children. Each child represents unit volume intermediate droplet, out of which one is utilized for the next dilution step and the other is considered as waste droplet. For the leaf nodes, it is possible to achieve at least two copies of samples with target concentration. Hence, in order to achieve target concentration of $1/2^d$, we require d number of serial dilution steps and each step produces 1 waste droplet with concentration of $1/2^m$ for m^{th} dilution step.

IV. Motivation and Objectives

Biomolecular gradients strongly participate in biological phenomena including those related to cell development, cancer, inflammation, and wound healing. More specifically, the growth, differentiation, and migration of various cell types are governed by biomolecular concentration gradients in vivo [24]. There are different types of dilution profile, one of the common types used for biochemical analysis specifically for drug design is the linear concentration gradient. Here, we attempt to prepare set of sample concentrations with specified linear dilution gradient. The objective is to produce the targeted set of concentration with linear dilution gradient having minimum waste generation, minimum utilization of stock solutions or raw samples (reagents), minimal module or mix-split operation, at least one additional copy for each target concentration to handle fault tolerance and reserve storage for future extension of the specified bioassay.

V. Proposed Technique

A. Problem formulation

General dilution: Given a raw sample with 100% concentration and a buffer with concentration of 0%. A target CF of the sample is to be achieved using minimal number of sequential (m:m) mix-split operations. In our case, we always use m = 1.This is applicable directly for any single dilution gradient.
Obtaining linear dilution gradient: Given a set of linear dilution gradients $L = \left\{ \frac{a}{2^n}, \frac{a+d}{2^n}, \frac{a+2d}{2^n}, \frac{a+3d}{2^n}, \ldots\ldots, \frac{a+kd}{2^n} \right\}$
Hence $|L| = k+1$
Our objective is to obtain all $(k+1)$ number of targeted concentration with minimal number of (1:1) Mix-Split steps and minimal number of waste droplets. Unlike [21], we do not assume sufficient supply of boundary conditions. Instead, we develop a technique to use minimal number of raw samples and reagents directly to generate the sets of output with linear concentration gradient. Let there be p number of raw samples with 100% concentration gradient (denoted by 1). Let the number of Mix/split operations required is x to achieve the given set of $(k+1)$ number of concentration. Let the number of waste droplets produced in the process is w. Our aim is to produce all the $(k+1)$ number of concentration with specified linear dilution gradient such that
i) Each component of the targeted set has at least two copies.
ii) The value of p, x and w is minimal.

B. Proposed Strategy

Forming the base solutions: Let us consider two separate concentrations $\frac{1}{2^p}, \frac{1}{2^m}$ with ($m < p$) are mixed together and the resultant concentration (using interpolated dilution) is given by

$$\frac{1}{2}\left(\frac{2^{p-m}+1}{2^p}\right) = \frac{2^{p-m}+1}{2^{p+1}} = \frac{2^k}{2^{p+1}}$$

Hence any concentration represented by $\frac{x}{2^n}$ can be decomposed in the following manner.

$$\frac{x}{2^n} = \frac{1}{2}\left(\frac{2^{k1}+2^{k2}+2^{k3}+\ldots\ldots 1}{2^{n-1}}\right) \quad \text{(if x is odd)}$$

Where $([n-2]>k1>k2>k3>\ldots>1)$

Or, $\frac{x}{2^n} = \frac{1}{2}\left(\frac{2^{k1}+2^{k2}+2^{k3}+\ldots\ldots+2^{km}}{2^{n-1}}\right)$ (if x is even).

Where $([n-2]>k1>k2>k3>\ldots>km)$

Hence, it may be possible to generate a set of base solutions that can be combined to obtain the desired concentration.
Forming the target concentration: For example let us consider a target dilution for a sample is given as d=92/1024. This can be distributed as d = $\frac{1}{2}\left(\frac{2^6+2^4+2^3+2^2}{2^9}\right)$. The interpolated dilution sequence is given in Fig. 3. This requires only three mix-split operations. Fig. 3 shows a sample preparation technique using interpolated Dilution to achieve a target concentration of 92/1024. Here the base solutions required are

$$\left\langle \frac{2^6}{2^8}, \frac{2^4}{2^8}, \frac{2^3}{2^8}, \frac{2^2}{2^8} \right\rangle \Rightarrow \left\langle \frac{1}{2^2}, \frac{1}{2^4}, \frac{1}{2^5}, \frac{1}{2^6} \right\rangle$$

Each such base solution can be prepared through serial dilutions as shown in Fig.2. However, we need to estimate the number of mix-split operation necessary to achieve the target concentration for a given set of base solutions obtained earlier using serial dilution. Let us assume that m_i represent number of mixers used at stage i and x_i represent the number of intermediate or base solutions exactly taking part in mixing at $(i+1)^{th}$ level. We assume that we start at level 0 where x_0 is the number of base solutions taking part in mix-split operation at level 1. So number of level or stages the mix- splits are to be conducted is given by $l = \lceil \log_2 x_0 \rceil$. For the corresponding levels or mixers until reaching the target concentration, the following is the procedure to determine number of mixers in each level.

$m_i = \frac{x_{i-1}}{2}$ and $x_i = \frac{x_{i-1}}{2}$ if x_{i-1} is even .

Or, $m_i = \frac{x_{i-1}-1}{2}$ and $x_i = \frac{x_{i-1}-1}{2}+1$ if x_{i-1} is odd.

Thus total number of mixing modules to be used is given by

$$M = \sum_{i=1}^{l} m_i + 1 \quad ,$$

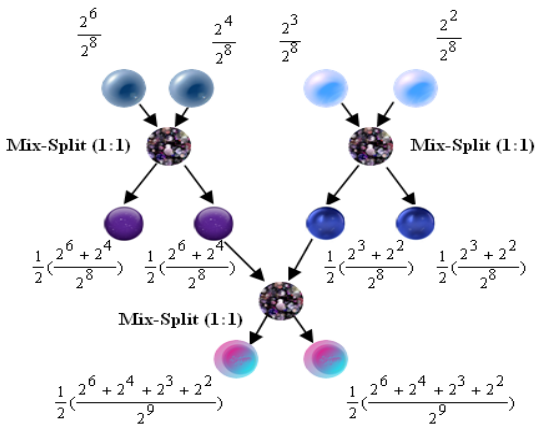

Fig.3. A sample preparation technique using interpolated Dilution

This implies that one additional mixer is used to obtain the final dilution. It has been found that for each mixing module one additional intermediate solution is obtained and is treated as waste

droplet. So for M number of mixers M numbers of waste droplets are generated. However, at level l or at the leaf node of the mixing tree, two copies of the target concentration is obtained. For a given set of base solutions where $x_0 = 10$, the mix-split sequence to reach to the target solution is shown in Fig. 4. It has been found that number of stages is found to be $l = \lceil \log_2 10 \rceil + 1 = 1 + 1 = 5$ (one additional level is necessary for final dilution with buffer solution to achieve two copies of the target solutions), number of mixers = 10, number of buffers = 1 and number of waste droplets = 9 with 2 copies of target solutions. In Fig.4, x_i represents number of base or intermediate solutions at level i, m_i represents number of mixers used at level i, w_i represents number of waste droplets at level i.

Forming the set of linear dilution gradients:

This represents a collection of linearly sequenced concentration factors. It has been found that the set of dilution gradients are arranged in Arithmetic progression. So, additional copies of few of the selected target gradients are first obtained. Thereby, these copies can be mixed together using interpolated dilution to form the arithmetic mean between any two specific target concentrations of the given set. These mean concentrations are termed as derived target concentration. This not only eliminates the effort to separately prepare the base solutions for the derived gradient but also reduces the mix-split operations for the interpolated dilution. This uses the waste droplet solutions obtained at different mixing steps to prepare the additional copies of different target solutions. A similar scheme for preparing intermediate targets is proposed in [21]. The procedure is described below:

Consider any given set of linear dilution gradients

$$L = \left\{ \frac{a}{2^n}, \frac{a+d}{2^n}, \frac{a+2d}{2^n}, \frac{a+3d}{2^n}, \ldots, \frac{a+kd}{2^n} \right\}$$

This set L is first decomposed into p number of secondary sets each containing three concentration elements where each consecutive set has an intersection of one. This implies that element m_3 of set i and element m_1 of set $i+1$ is shared.

If $|L| = k+1$ is odd , $p = (|L|-1)/2$

If $|L| = k+1$ is even, there will be $p+1$ sets where $p = (|L|-2)/2$ sets and the last set contains a single element representing the last target dilution value. We represent the collection of secondary sets as $< s_1, s_2, s_3 \ldots s_p >$, where $s_1 = \{m_{11}, m_{12}, m_{13}\}$, $s_2 = \{m_{21}, m_{22}, m_{23}\} \ldots s_p = \{m_{p1}, m_{p2}, m_{p3}\}$, and $s_i \cap s_{i+1} = m_{i3} = m_{(i+1)1}$, for $1<i<p$

and $m_{i2} = \dfrac{m_{i1} + m_{i3}}{2}$,for $1 \bullet i \bullet p$

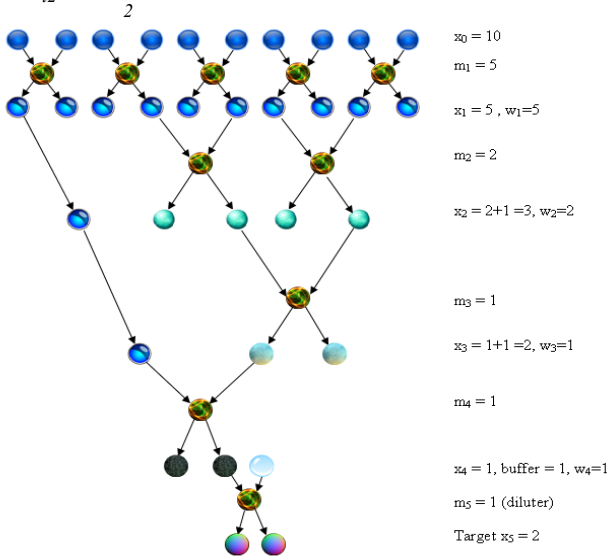

Fig.4. A interpolated dilution example showing the dilution tree starting with $x_0 = 10$ number of base solution.

Hence, for each set s_i ($1<i<p$), three copies of element m_{i3} and for set s_1 and s_p, two copies of m_{11} and m_{p3} are required to obtain the remaining sets of targeted concentrations. Fig. 5 shows the arrangement stated above for a linear dilution gradient with $k=10$. The given set of dilution gradient is

$$L = \left\{ \frac{a}{2^n}, \frac{a+d}{2^n}, \frac{a+2d}{2^n}, \frac{a+3d}{2^n}, \ldots, \frac{a+10d}{2^n} \right\} \text{ and}$$

Number of targeted concentrations $|L| = 11$, number of intersecting sets = 5, Number of initial concentrations derived using vase solutions = 6 and number of derived concentrations = 5; number of interpolated mix-split = 5; number of dilutions = 6. It has also been found that 2 separate sets of targeted concentration can be prepared with each type having two copies.

Table 1 Base solution concentration for the linear dilution gradient

Dilution Gradients	$\frac{1}{2^2}$	$\frac{1}{2^3}$	$\frac{1}{2^4}$	$\frac{1}{2^5}$	$\frac{1}{2^6}$	$\frac{1}{2^9}$
Numbers	1	1	1	2	1	6

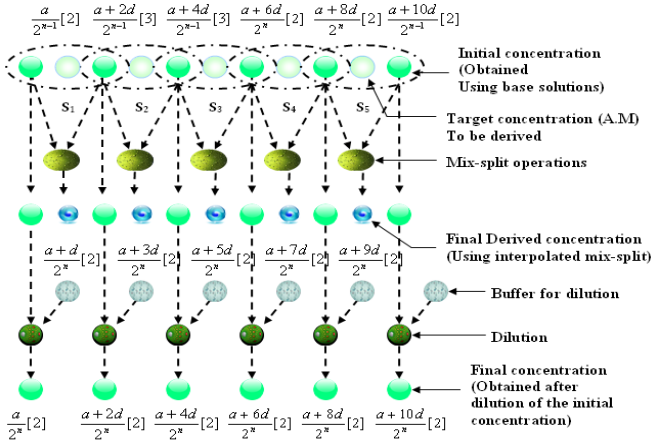

Fig. 5 A method for obtaining specified set of linear dilution gradient using Arithmetic Mean based method. Each concentration is shown with number of copies enclosed with [ ].

C. Proposed Algorithm

Algorithm 1: Linear dilution gradient preparation algorithm

Input: 1.Given set of linear dilution gradient to be obtained

$$L = \left\{ \frac{a}{2^n}, \frac{a+d}{2^n}, \frac{a+2d}{2^n}, \frac{a+3d}{2^n}, \ldots, \frac{a+kd}{2^n} \right\}$$

2. Adequate buffer solutions and estimated stock solutions

Procedure:

1. Decompose the concentration gradient set into a p number of intersecting sets each containing three elements.
2. Identify the initial concentrations to be obtained from base solutions. The number is $C_i = \dfrac{k+2}{2}$, if k is even

   And $C_i = \dfrac{k+1}{2} + 1$ if k is odd
3. Determine the number of copies required for each initial concentration using the technique stated for forming the set of linear dilution gradients in *part B* of this section.
4. Determine the base solutions necessary for each such concentration using the technique stated for *forming the target concentration* in *part B* of this section.
5. Finally prepare all the base solutions necessary as determined in step 4 using the technique stated for *forming the base solutions* (using serial dilution) in *part B* of this section.
6. While forming the base solution take stock of the waste droplets in each serial dilution step and use them for further dilution to obtain multiple copies for different base solutions.
7. Once all the copies of base solutions are obtained use interpolated dilution to prepare the selective initial target concentration(one level before the final dilution using buffer)
8. Derive the final mean derived concentration using arithmetic mean based interpolated dilution technique using reserve

copies of initial target concentrations as mentioned in *forming the linear dilution gradient* in *part B* of this section.

9. Finally the remaining copies of target concentration are subjected to next level of dilution to obtain final level concentration from the initial target concentration.
10. Count the total number of stages required for preparation of the total set and the number of mix split operations
11. Compute the number of remaining waste droplets, number of copies of each element of the target concentration obtained.
12. Compute the total number of stock solutions utilized.

Output: Final set of linear dilution gradient, number of waste droplets, number of modules used and number of stock solutions utilized.

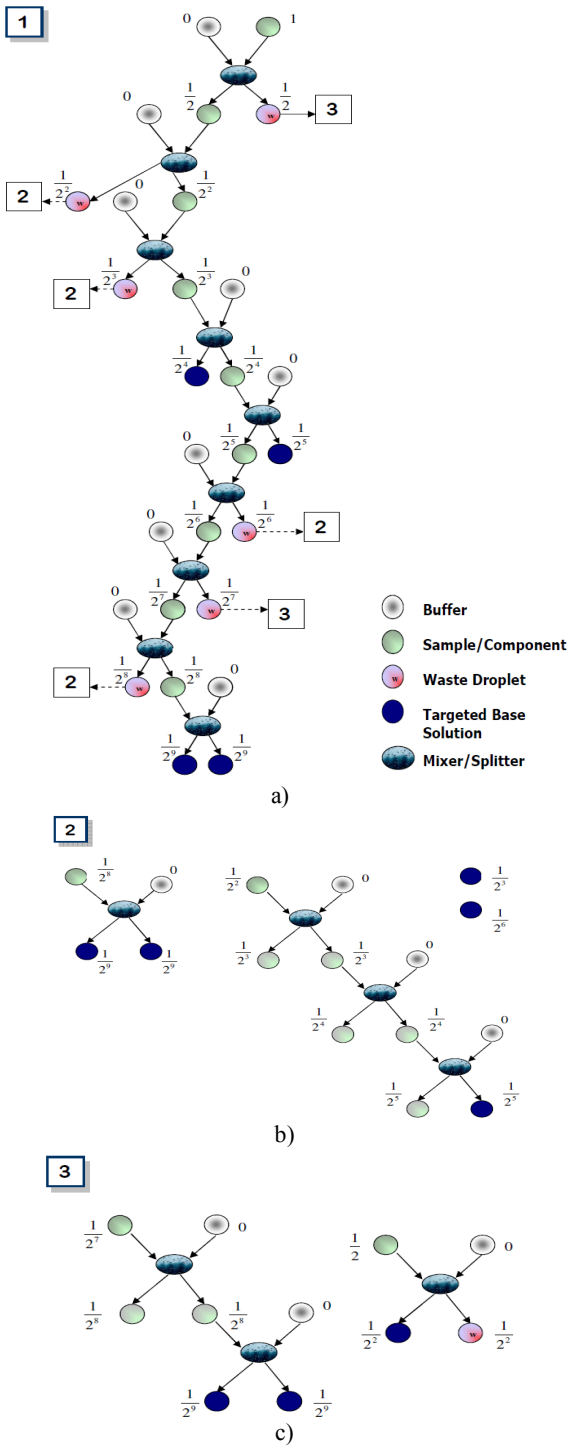

Fig.6. Three step process of preparation of base solution.

VI. Illustrative Example

We consider a set of specified linear dilution gradient (Target Set 1 [22]) given as $L = \langle \frac{50}{2^{10}}, \frac{70}{2^{10}}, \frac{90}{2^{10}}, \frac{110}{2^{10}}, \frac{130}{2^{10}} \rangle$. So initial concentration set $L_i = \langle \frac{50}{2^{10}}, \frac{90}{2^{10}}, \frac{130}{2^{10}} \rangle$, where $p = 3$. Each initial concentration is decomposed into base solutions as follows.

$$\frac{50}{2^{10}} \Rightarrow \frac{2^5+2^4+2}{2^{10}} \Rightarrow \frac{2^5+1}{2^9}, \frac{2^4+1}{2^9} \Rightarrow \frac{1}{2^4}, \frac{1}{2^9}, \frac{1}{2^5}, \frac{1}{2^9} \ldots(1)$$

$$\frac{90}{2^{10}} \Rightarrow \frac{2^6+2^4+2^3+2}{2^{10}} = \frac{2^6+1}{2^9}, \frac{2^4+1}{2^9}, \frac{2^3}{2^9} \Rightarrow \frac{1}{2^3}, \frac{1}{2^9}, \frac{1}{2^5}, \frac{1}{2^9}, \frac{1}{2^6} \ldots(2)$$

$$\frac{130}{2^{10}} \Rightarrow \frac{2^7+2}{2^{10}} \Rightarrow \frac{2^7+1}{2^9}, \frac{1}{2^9} \Rightarrow \frac{1}{2^2}, \frac{1}{2^9}, \frac{1}{2^9} \ldots(3)$$

So number of necessary base solutions for obtaining the linear dilution gradient set is given in table 1. Fig. 6 shows the serial dilution methods for obtaining base solutions necessary. We break the serial dilution methods into three steps. The waste droplets from part 1 are utilized in part 2 and part 3. In the next step, we use interpolated dilution to prepare the initial concentrations. Fig. 7 shows the interpolated dilution using the base solution to prepare initial concentration $L_i = \langle \frac{50}{2^{10}}, \frac{90}{2^{10}}, \frac{130}{2^{10}} \rangle$. Finally, Fig. 8 shows the derived arithmetic mean based interpolated dilution to prepare the derived concentrations gradients $L_d = \langle \frac{70}{2^{10}}, \frac{110}{2^{10}} \rangle$

It has been observed that multiple copies for each concentration gradient have been prepared. In section 4, we have given the detailed description of different linear dilution sets used in target set (Table 3).

VII. Experimental Results

The computed results for the linear dilution set obtained in section VI displaying the sample utilization, waste droplets, number of mix-split inclusive of the base solutions and the number of mix-split operation using only interpolated dilutions are shown in Table 2. The proposed technique is implemented on all the target sets defined in Table 3.The simulation results for all target sets are shown in Table 4. It has been observed that number of samples required while forming the linear dilution sets are reduced considerably and utilization of waste droplets are maximized. Comparison with contemporary works is shown in table 5. Detailed mixing performance for all the target sets as shown in table 4 is represented by a stacked bar graph in Fig. 9. The comparison with contemporary works in terms of number of mix-split operations used and the number of waste droplets generated is shown in Fig.10(a) and 10(b) respectively using clustered column plots.

Table 2. Dilution and mixing details for Target Set 1 [22]

Gradient	Number of Stock solutions used	modules used (additional modules for base solution)	number of copies	number of waste droplets (additional waste for base solutions)	number of base components
$\frac{50}{2^{10}}$	1	5 (+9)	3	2	4
$\frac{70}{2^{10}}$	0	2 (+0)	2	1	2
$\frac{90}{2^{10}}$	0	6 (+4)	2	2(+3)	5
$\frac{110}{2^{10}}$	0	2 (+0)	2	1	2
$\frac{130}{2^{10}}$	0	3 (+3)	2	2(+3)	3
Total	**1**	**18 (+16)**		**8(+6)**	**16**

VIII. Conclusion

In this work, we have proposed sample preparation techniques for obtaining given set of linear dilution gradients. The proposed method involves three steps namely estimation and preparation of base solution, preparation of initial set of gradients and determination of final sets of derived mean gradients. The simulation results for target set involving four sets of linear dilution gradients shows improvement in terms of sample and waste droplet utilization, number of mix-split operations involved. Further it is possible to generate more than one copy of each targeted

concentration value that facilitates verification using the reserve solution in case of faulty dilution while obtaining the targeted dilution. Here we have used linear dilution gradients arranged in arithmetic progression.

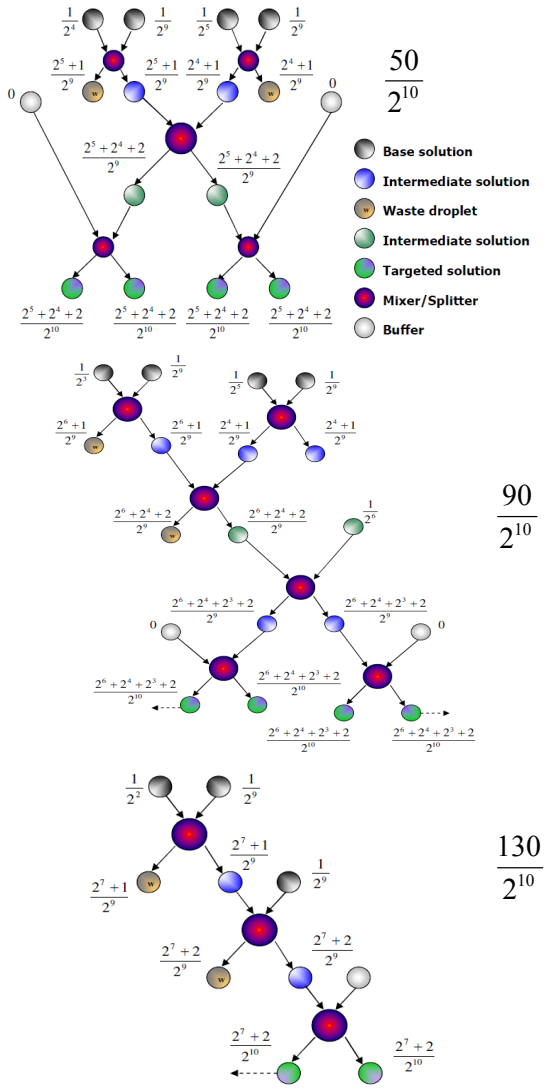

Fig. 7. The interpolated dilution method to prepare initial concentration gradients $L_i = < \frac{50}{2^{10}}, \frac{90}{2^{10}}, \frac{130}{2^{10}} >$

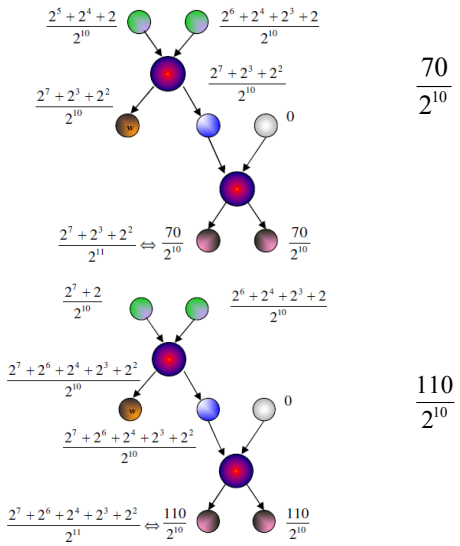

Fig. 8. Final steps using interpolated dilution method to prepare the mean derived concentrations $L_d = \langle \frac{70}{2^{10}}, \frac{110}{2^{10}} \rangle$

Table 3. Target set details [22]

TS name	TS Size	Target set details
TS_1	5	$\langle \frac{50}{2^{10}}, \frac{70}{2^{10}}, \frac{90}{2^{10}}, \frac{110}{2^{10}}, \frac{130}{2^{10}} \rangle$
TS_2	10	$\langle \frac{110}{2^{10}}, \frac{120}{2^{10}}, \frac{130}{2^{10}} \cdots\cdots \frac{200}{2^{10}} \rangle$
TS_3	17	$\langle \frac{20}{2^{10}}, \frac{70}{2^{10}}, \frac{120}{2^{10}} \cdots\cdots \frac{820}{2^{10}} \rangle$
TS_4	20	$\langle \frac{40}{2^{10}}, \frac{70}{2^{10}}, \frac{100}{2^{10}} \cdots\cdots \frac{610}{2^{10}} \rangle$

Table 4. Detailed results for all target sets mentioned in [22]

Target Samples	Mix-split	Additional Mix –split (base Soln.)	Stock samples used	Waste droplets
TS_1	18	16	1	8
TS_2	25	32	5	5
TS_3	55	48	18	7
TS_4	36	50	19	5

Table 5. Comparison of our technique with other methods

TS	Bhattacharjee et al. [22]		Mitra et al. [23]		Hsieh et al.[19]		Huang et al.[18]		Our Technique	
	Mix-Split	Waste	Mix-Split	Waste	Mix-Split	Waste	Mix-Split	Waste	Mix-Split	Waste
TS_1	24	14	33	28	37	28	32	12	18	1
TS_2	40	13	64	54	55	36	64	22	25	5
TS_3	57	12	88	71	82	50	104	39	55	7
TS_4	65	10	108	88	95	58	126	49	36	5

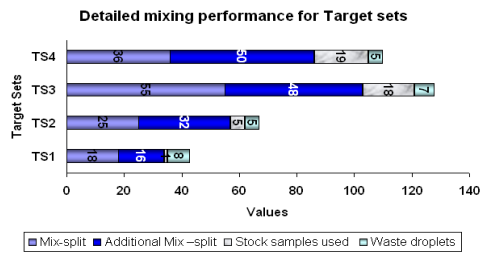

Fig. 9.Stacked bar chart representation of the detailed dilution for obtaining the linear dilution gradient

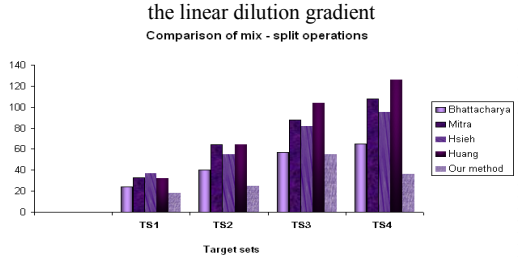

Fig. 10(a) Clustered column chart representation for the number of mix-split comparison of the proposed method to the related works

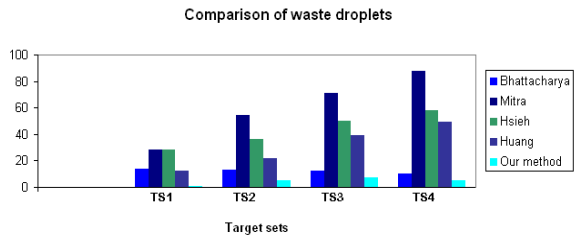

Fig.10(b). Clustered column chart representation for the number of waste droplets generated in comparison of the proposed method to the related works

References

[1] S. Mutlu, F. Svec, C. H. Mastrangelo, J. M. J. Fretcht, and Y. B Gianchandani,"Enhanced electro-osmosis pumping with liquid bridge and field effect flow rectification,"*Proc. IEEE MEMS*, pp. 850–853, Jan. 2004.

[2] T. Thorsen, S. Maerkl, and S. Quake, "Microfluidic large-scale integration," *Science*, vol. 298, no. 5593, pp. 580–584, Oct. 2002.

[3] S.-K. Cho S-K Fan H. Moon H and C-J Kim, "Towards digital microfluidic circuits: creating, transporting, cutting and merging liquid

droplets by electrowetting-based actuation," TechDig MEMS 2002 IEEE Inter Conf on Micro Electro Mechanical Systems pp. 454-61.

[4] M.G. Pollack, R.B. Fair, and A.D. Shenderov, "Electrowetting-based actuation of liquid droplets for microfluidic applications," *Appl. Phys Lett* 77,1725-1727(2000).

[5] F. Su, K. Chakrabarty, and R.B. Fair, "Microfluidics-based biochips: technology issues, implementation platforms, and design automation challenges," IEEE Trans. Computer-Aided Des. Of Integ. Cir. And Sys. 25 211-223 (2006).

[6] R. B. Fair, A. Khlystov, T. D. Tailor, V. Ivanov, R. D. Evans, V. Srinivasan, V. K. Pamula, M. G. Pollack, P. B. Griffin, and J. Zhou, "Chemical and biological applications of digital-microfluidic devices," IEEE Design & Test of Computers, vol. 24, no. 1, pp. 10–24, 2007.

[7] K. Chakrabarty and F. Su. *Digital Microfluidic Biochips - Synthesis, Testing, and Reconfiguration Techniques*. CRC Press, 2007.

[8] Y. Fouillet, D. Jary, C. Chabrol, P. Claustre, and C. Peponnet, "Digital microfluidic design and optimization of classic and new fluidic functions for lab on a chip systems," *Microfluidics and Nanofluidics 2008*, vol.4, pp.159–165.

[9] R. B. Fair, V. Srinivasan,H. Ren,P. Paik,V.K.Pamula, and M.G. Pollack, "Electrowetting-based on-chip sample processing for integrated microfluidics", *IEEE IEDM Tech. Dig.*, 2003, pp. 32.5.1–32.5.4.

[10] A. T. O'Neill and G. M. Walker, "Chapter 18: Linear dilution microfluidicdevices", *Lab-on-a-Chip Technology (Vol.1): Fabrication and Microfluidics. Norfolk, U.K.: Caister Academic Press, Aug. 2009.*

[11] H. Ren, V. Srinivasan, and R. B. Fair, "Design and testing of an interpolating mixing architecture for electrowetting-based droplet-on-chip chemical dilution", *Int. Conf. Solid-State Sensors, Actuators Microsyst. (Tranducers),* 2003, pp. 619–622.

[12] E. J. Griffith, S. Akella, and M. K. Goldberg, "Performance characterization of a reconfigurable planar-array digital microfluidic system," *IEEE TCAD*, vol. 25, no.2, pp. 345–357, Feb. 2006.

[13] W. Thies, J. P. Urbanski, T. Thorsen, and S. Amarasinghe, "Abstraction layers for scalable microfluidic biocomputing", *Nat. Comput.*, vol. 7, no. 2, pp. 255–275, 2008.

[14] S. Roy, B. B. Bhattacharya, and K. Chakrabarty, "Optimization of dilution and mixing of biochemical samples using digital microfluidic biochips" *IEEE TCAD*, vol. 29(11), pp. 1696–1708, Nov. 2010

[15] J.-D. Huang, C.-H. Liu, and T.-W. Chiang, "Reactant minimization during sample preparation on digital microfluidic biochips using skewed mixing trees", *IEEE/ACM ICCAD* 2012, pp. 377–384

[16] T.-W. Chiang, C.-H. Liu, and J.-D. Huang, "Graph-based optimal reactant minimization for sample preparation on digital microfluidic biochips", *IEEE VLSI-DAT*, Taiwan, 2013, pp. 1–4.

[17] Y.-L. Hsieh, T.-Y. Ho, and K. Chakrabarty, "On-chip biochemical sample preparation using digital microfluidics", *Int. Conf. BioCAS*, CA, USA, 2011, pp. 301–304.

[18] J.-D. Huang, C.-H. Liu, and H.-S. Lin, "Reactant and waste minimization in multitarget sample preparation on digital microfluidic biochips", *IEEE TCAD*, vol. 32(10), pp. 1484–1494, 2013.

[19] Y.-L. Hsieh, T.-Y. Ho, and K. Chakrabarty, "A reagent-saving mixing algorithm for preparing multiple-target biochemical samples using digital microfluidics", IEEE TCAD, vol.31 (11), pp. 1656–1669, 2012.

[20] S. Roy, B. B. Bhattacharya, and K. Chakrabarty, "Waste-aware dilution and mixing of biochemical samples with digital microfluidic biochips", *IEEE/ACM DATE* 2011, pp. 1059–1064.

[21] S. Bhattacharjee, A. Banerjee, and B. B. Bhattacharya, "Sample preparation with multiple dilutions on digital microfluidic biochips," *IET Comput. Digit. Tech*., vol. 8(1), pp. 49–58, Jan. 2014.

[22] S. Bhattacharjee, A. Banerjee, T-Yi Ho, K. Chakrabarty, and B. B. Bhattacharya, "Algorithms for Producing Linear Dilution Gradient with Digital Microfluidics", *Emerging Technologies (cs.ET) arXiv:1307.1251*

[23] Debasis Mitra, Sudip Roy, Sukanta Bhattacharjee, Krishnendu Chakrabarty, and Bhargab B. Bhattacharya, "On-Chip Sample Preparation for Multiple Targets Using Digital Microfluidics", *IEEE TCAD*, vol. 33(8), 2014.

[24] T. Kang, J. Han, K. S. Lee,"Concentration gradient generator using a convective diffusive balance", Lab-on-Chip 2008, vol.8, pp.1220 –1222.

Automatic Sleep Stage Classification

Ahnaf Rashik Hassan* and Mohammed Imamul Hassan Bhuiyan
Department of Electrical and Electronic Engineering
Bangladesh University of Engineering and Technology, Dhaka, Bangladesh
Email: *ahnaf.hassan0@gmail.com

***Abstract*—Automated sleep stage classification is essential for alleviating the burden of physicians since a large volume of data have to be analyzed per examination. Most of the existing works in the literature are multichannel based or yield poor classification performance. A single-channel based computerized sleep staging scheme that gives good performance is yet to emerge. In this work, we introduce a novel noise assisted decomposition scheme to perform automatic sleep stage classification from single channel EEG signals. At first, we decompose the EEG signal segments into mode functions using Complete Ensemble Empirical Mode Decomposition with Adaptive Noise (CEEMDAN). Various statistical moment based features are then computed from these mode functions. The effectiveness of statistical moment based features is validated by statistical analysis. In this work, we also introduce Adaptive Boosting for sleep stage classification. Experimental outcomes manifest that the computerized sleep staging scheme propounded herein outperforms the state-of-the-art ones in various cases of interest.**

***Index Terms*—EEG, Sleep Scoring, CEEMDAN, AdaBoost.**

I. Introduction

Sleep staging is traditionally performed by expert scorers based on visual observation of Polysomnographic (PSG) signals which is time-consuming, burdensome, error-prone, and subjective. Automated sleep staging therefore, can eradicate the burden of the physicians, expedite sleep disorder diagnosis, and benefit sleep research. Again, the push toward a wearable, portable yet low-power sleep quality monitoring device necessitates the use of minimum number of channels and reduced computational cost. Most of the existing works, on account of being multichannel or multiple physiological signal based, are unsuitable for device implementation. As a result, automatic sleep scoring based on single channel Electroencephalogram (EEG) is gaining interest in sleep research community.

Various single-channel, multichannel and multiple physiological signal based method have been proposed in the literature for automated sleep staging. Long et al. [1] computed various respiratory amplitude, depth and volume based features from respiratory effort signals and used linear discriminant classifier to perform sleep classification. Zhu et al. [2] generated difference visibility graph (VG) and horizontal VG from single channel EEG signal and extracted nine features from them to classify using support vector machine. Huang et al. [3] used two channel of forehead EEG signals, extracted spectral features by short-time Fourier transform from the signals and performed classification using relevance vector machine. Koch et al. [4] proposed a Latent Dirichlet Allocation topic model based method using four-channel multiple physiological signals (EEG and EOG) for sleep staging. Lajnef et al. [5] employed various features such as linear prediction error energy, variance, skewness, kurtosis, permutation entropy and multi-class support vector machine to perform automatic sleep scoring based on multichannel EEG, EOG and EMG signals. Kayikcioglu et al. [6] proposed an AR coefficient-based feature extraction scheme and utilized partial least squares (PLS) algorithm to classify sleep stages.

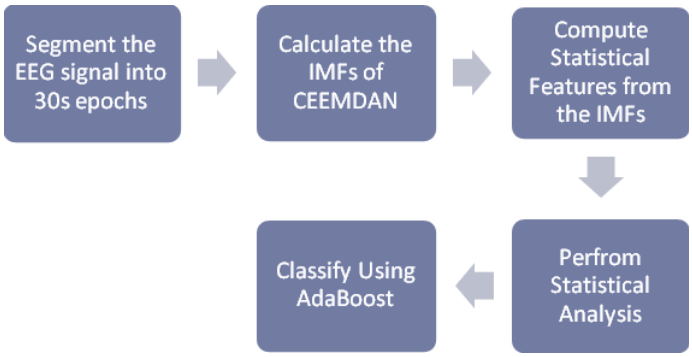

Fig. 1. A schematic outline of the proposed computerized sleep staging method.

In this work, we propound a single channel EEG based sleep scoring algorithm. The outline of our algorithm is presented in Fig. 1. After decomposing the EEG signals into 30s epochs, we further decompose the EEG signal segments into intrinsic mode functions using Complete Ensemble Empirical Mode Decomposition with Adaptive Noise (CEEMDAN). We then extract various statistical features from the intrinsic mode functions. The efficacy of the proposed feature extraction scheme is investigated using statistical analysis. Afterwards, sleep stage classification is performed using an eminent ensemble learning based classification model, namely- Adaptive Boosting (AdaBoost).

II. Materials and Methods

A. Experimental Data

The data-set used for evaluation of the proposed scheme is Physionet's Sleep-EDF data-set which is publicly available [7]. The recordings have been obtained from Caucasian males and females (21 - 35 years old) without any medication. There are eight recordings in two subsets (marked as sc^* and st^*). The first four recordings (sc4002e0, sc4012e0, sc4102e0, sc4112e0) have been acquired in 1989 from ambulatory

978-1-4673-9257-0/15/$31.00 © 2015 IEEE

healthy volunteers during 24 hours in their normal daily life. The last four data recordings (st7022j0, st7052j0, st7121j0, st7132j0) have been obtained in 1994 from subjects who had mild difficulty falling asleep but were otherwise healthy, during a night in the hospital, using a miniature telemetry system [8]. The recordings contain horizontal EOG, Fpz-Cz and Pz-Oz EEG data, each sampled at 100 Hz. It has been suggested in various studies [9] [10] [11] [2] that EEG signal from Pz-Oz channel yields better classification performance than that of the Fpz-Cz channel. So, in the present work Pz-Oz channel EEG signal is used. The sc^* recordings also contain the submental-EMG envelope, oro-nasal airflow, rectal body temperature and an event marker, all sampled at sampling rate of 1 Hz. The st^* recordings contain submental EMG sampled at sampling rate of 100 Hz and an event marker sampled at sampling rate of 1 Hz. Expert scoring of the EEG data is obtained from the same source. Each 30s of EEG data has been scored in accordance with the R&K recommendations [12]. The duration of each epoch is 30s or 3000 data points. Each epoch was scored by expert scorers in one of the eight classes: AWA, S1, S2, S3, S4, REM, MVT (Movement Time) and 'Unscored'. Table I summarizes the number of epochs of different classes that are used in this work. In total, 15,188 EEG epochs are used in this study. This study uses six sleep stages in accordance with R&K standard: AWA, S1-S4 and REM. The 5-state stages of sleep combine S3 and S4 of 6-state as Slow Wave Sleep (SWS) and the 4-state stages combine S1 and S2 of 5-state. The 3-state and 2-state stages of sleep include: AWA, NREM, REM and AWA, Sleep (S1-S4 and REM) respectively.

B. Empirical Mode Decomposition

Empirical Mode Decomposition (EMD) aims to generate highly localized time-frequency estimation of a signal in a data-driven fashion by decomposing it into a finite sum of intrinsic mode functions (IMF) or modes. Each mode must satisfy two conditions [13]:

1) The number of extrema and the number of zero crossings must be the same or differ at most by one.
2) At any point the mean value of the envelope defined by the local maxima and the envelope defined by the local minima is zero.

EMD iteratively decomposes an N-point EEG epoch X into amplitude and frequency modulated oscillatory IMFs using the following steps:

1) Set $h_1 = X$.
2) Identify the local maxima and minima of h_1.

TABLE I
DESCRIPTION OF EPOCHS OF VARIOUS SLEEP STATES USED IN OUR EXPERIMENTS

	AWA	S1	S2	S3	S4	REM	Total
Epochs	8055	604	3621	672	627	1609	15188

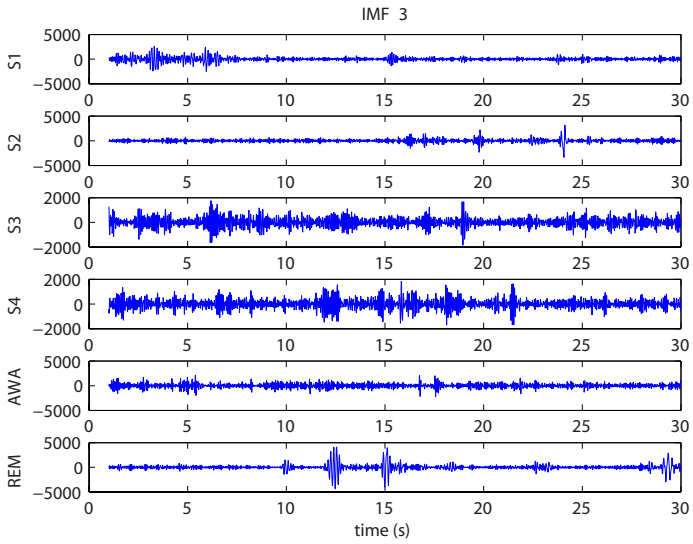

Fig. 2. $\widetilde{IMF}_3$ of CEEMDAN of various sleep stages. Note the variations of the IMFs in different sleep states.

3) Obtain the envelope of local maxima v_{max} and that of local minima v_{min} using cubic spline interpolation.
4) Generate the local mean curve m by generating the upper and lower envelopes:

$$m = \frac{v_{max} + v_{min}}{2} \tag{1}$$

5) Compute h_2 by subtracting the local mean curve from h_1:

$$h_2 = h_1 - m \tag{2}$$

6) Repeat steps 2)-5) until the difference between h_{k+1} and h_k ($SD(k)$) defined as follows reaches a predefined value ϵ.

$$SD(k) = \frac{\|h_{k+1} - h_k\|^2}{\|h_k\|^2} < \epsilon \tag{3}$$

where $\|.\|$ is the Euclidian L2-norm.
7) Set $c_1 = h_k$ as the first mode.
8) Find the residue, $r_1 = x - c_1$. Steps 1)-7) are known as sifting.
9) Substitute X in 1) with r. Repeat steps 1)-7) to find the rest of the IMFs $c_2, c_3, ..., c_L$.

Thus, the input signal can be decomposed into L IMFs until the residue becomes a monotonic function such that further extraction of an IMF is not possible. The input X can be reconstructed from all the IMFs as:

$$X = \sum_{j=1}^{L} c_j + r_L \tag{4}$$

where r_L is the residue of the L-th iteration.

C. Ensemble Empirical Mode Decomposition

A noise-assisted adaptive data analysis based extension of EMD, called EEMD has been proposed in [14] with a view

to eradicating the mode mixing problem. In EEMD, a low-level random noise is added to the input which is decomposed by EMD. The process of implementing EMD on the modified signal is referred as one trial. The trial is repeated I times to obtain the final mode. The steps of EEMD are as follows:

1) Calculate $x^i(n) = x(n) + w^i(n)$ where $w^i(n)$ with $i = 1, 2, ..., I$ represents different realizations of white Gaussian noise.
2) Compute EMD of each of the signals $x^i(n)$ and find the corresponding modes $IMF_k^i(n)$. Here, $k = 1, 2, .., K$ denotes the modes.
3) Find the modes of EEMD method, denoted by $\overline{IMF_k}(n)$ by averaging $IMF_k^i(n)$ as:

$$\overline{IMF_k}(n) = \frac{1}{I}\sum_{i=1}^{I} IMF_k^i(n) \tag{5}$$

$\overline{IMF_k}(n)$ does not necessarily obey the aforementioned conditions required to be an IMF [15].

D. Complete Ensemble Empirical Mode Decomposition with Adaptive Noise

Let us define an operator $E_j(.)$ that produces the j-th mode of EMD. If $w^i(n)$ with $i = 1, 2, ..., I$ are different realizations of white Gaussian noise with zero mean and unit variance and ϵ_0 is the standard deviation of the white Gaussian noise, the CEEMDAN algorithm can be described as follows [16].

1) Calculate $x(n) + \epsilon_0 w^i(n)$.
2) Decompose the above I signals by EMD to obtain their first modes.
3) Compute the first mode $\widetilde{IMF}_1$ of CEEMDAN as:

$$\widetilde{IMF}_1(n) = \frac{1}{I}\sum_{i=1}^{I} IMF_1^i(n) = \overline{IMF_1}(n) \tag{6}$$

4) Find the first residue as:

$$r_1(n) = x(n) - \widetilde{IMF_1}(n) \tag{7}$$

5) Decompose realizations $r_1(n) + \epsilon_1 E_1(w^i(n))$ with $i = 1, 2, ..., I$ up to their first EMD mode. ϵ_k ($k = 1$ for this stage) is the standard deviation of white Gaussian noise of the k-th stage. $\widetilde{IMF}_2(n)$ can be found as:

$$\widetilde{IMF}_2(n) = \frac{1}{I}\sum_{i=1}^{I} E_1(r_1(n) + \epsilon_1 E_1(w^i(n))) \tag{8}$$

6) Compute the k-th residue for $k = 2, 3, ..., K$ as:

$$r_k(n) = r_{k-1}(n) - \widetilde{IMF}_k(n) \tag{9}$$

7) Decompose realizations $r_1(n) + \epsilon_1 E_1(w^i(n))$ with $i = 1, 2, ..., I$ up to their first EMD mode and define the $(k+1)$-th mode as:

$$\widetilde{IMF}_{k+1}(n) = \frac{1}{I}\sum_{i=1}^{I} E_1(r_k(n) + \epsilon_k E_k(w^i(n))) \tag{10}$$

8) Go to step 6 for next k.

Steps 6 to 8 are repeated until the residue becomes a monotonic function such that further extraction of an IMF is not possible. Fig. 2 shows two such IMFs for various sleep stages. If K is the total number of modes and $r_k(n)$ is the final residue, the input $x(n)$ can be reconstructed from all the IMFs as:

$$x(n) = \sum_{k=1}^{K} \widetilde{IMF}_k(n) + r_k(n) \tag{11}$$

E. Motivation of Using CEEMDAN

The use of CEEMDAN in stead of EMD or EEMD in the algorithm propounded herein is motivated by various advantages of CEEMDAN over commonly used signal processing techniques. EMD is data-driven but it suffers from mode mixing problem which causes disparate oscillations in the same mode or similar oscillations in different modes. Despite effectively resolving the mode mixing problem, there are a number of caveats which makes EEMD unsuitable for practical implementation. Decomposing the same signal several times with EEMD can produce different number of modes [17]. If we reconstruct the signal after the application of EEMD, residual noise is obtained [17] [15]. Moreover, EEMD is also computationally expensive. CEEMDAN on the other hand, provides an exact reconstruction of the original signal and a better spectral separation of the modes [15]. The computational cost of CEEMDAN is also lower [17]. These factors motivated the use of CEEMDAN instead of EMD or EEMD in our proposed feature extraction scheme. Also, note that the traditional time-frequency transforms such as wavelet transform based methods' performance is affected by the choice of the best basis function. The best basis function is application-specific and may vary from case to case [15]. On the other hand, CEEMDAN is data-driven and does not require a prior basis function which makes it an attractive choice for processing highly nonlinear and non-stationary signals such as sleep-EEG signals.

F. Statistical Moment Based Features

The features that are used in this work are- mean, variance, skewness and kurtosis. For an N-point $\widetilde{IMF}$, $X = \{x_1, x_2, x_3, .., x_N\}$ mean (μ), variance (σ^2), Skewness (γ) and Kurtosis (κ) can be expressed mathematically as [18]:

$$\mu = \frac{1}{N}\sum_{i=1}^{N} x_i \tag{12}$$

$$\sigma^2 = \frac{1}{N}\sum_{i=1}^{N} (x_i - \mu)^2 \tag{13}$$

$$\gamma = \frac{1}{N}\sum_{i=1}^{N} \left(\frac{x_i - \mu}{\sigma}\right)^3 \tag{14}$$

$$\kappa = \frac{1}{N}\sum_{i=1}^{N} \left(\frac{x_i - \mu}{\sigma}\right)^4 \tag{15}$$

TABLE II
P-VALUES OF THE PROPOSED FEATURES

p-Values of	IMF 1	IMF 2	IMF 3	IMF 4	IMF 5	IMF 6	IMF 7
μ	2.4119e-146	3.3696e-23	7.8781e-90	2.2518e-88	4.5127e-186	8.7108e-132	4.0894e-09
σ^2	5.3247e-47	1.9888e-59	5.7717e-56	5.9530e-55	1.4858e-246	3.9000e-231	6.5459e-220
γ	3.2805e-21	2.2792e-65	9.6112e-87	7.9627e-73	1.1627e-40	4.8087e-34	4.7436e-37
κ	2.4385e-40	2.0876e-111	8.2096e-89	2.7199e-137	9.7257e-32	1.4340e-95	1.1660e-76

G. Statistical Analysis

Statistical hypothesis testing must be performed for the feature selection stage of any classification problem. This ensures that the chosen set of features has discriminatory capability among various classes [19]. Hypothesis testing also helps us ascertain whether the discriminatory capability of the selected set of features is statistically significant or not. To assess whether the values of the features in the six classes differ significantly, we perform a non-parametric Kruskal-Wallis one-way analysis of variance. Unlike its parametric equivalent which is known as one-way analysis of variance (ANOVA), Kruskal-Wallis test does not require an assumption of normal distribution of the data samples [20]. The test is carried out in MATLAB's Statistics Toolbox. The test is performed at 95% confidence level. Hence, a difference is statistically significant if $p < \alpha(= 0.05)$. Table II gives the result of the hypothesis testing and we can see that all of the IMFs features give lower p-values indicating good discriminatory capability among the six sleep states.

H. Adaptive Boosting

Boosting is one of the most eminent ensemble learning algorithms that creates an ensemble of classifiers by resampling the data in a manner such that the most informative training data is provided to each consecutive classifier [21]. Adaptive Boosting (AdaBoost) was pioneered by Freund and Schapire [22]. AdaBoost generates a set of hypotheses such that subsequent hypotheses focus on increasingly difficult instances. Afterwards, it combines them through weighted majority voting of the classes predicted by the individual hypotheses. Each of the hypothesis is generated by training a weak classifier using instances drawn from an iteratively updated distribution of the training data. This distribution update makes sure that instances misclassified by the previous classifier are more likely to be included in the training data of the next classifier. Consequently, consecutive classifiers training data are geared towards increasingly difficult-to-classify instances. This is the essence of AdaBoost learning algorithm. Freund and Schapire also propounded two extensions of AdaBoost [22], namely-AdaBoost.M1 and AdaBoost.M2. AdaBoost.M1 requires that all hypotheses generated by the weak classifiers have a weighted error no greater than 0.5. AdaBoost.M2 which is a multi-class extension of AdaBoost.M1, relaxes the weighted error restriction. Instead, it defines a pseudo-loss which itself is then required to have an error no larger than 0.5. This pseudo-loss measures the goodness of the weak hypotheses. Moreover, the probability of error for random guessing is much higher for multi-class problems ($\frac{C-1}{C}$ for C-class classification problem) than that of binary classification problems. Since the learners are weak, achieving an error of 0.5 becomes harder with the increase of classes. These two factors make AdaBoost.M2 a powerful tool for multi-class classification and motivated its use in the present study. Since, AdaBoost.M2 is a multi-class extension, for two stage classification we use AdaBoost.M1.

Algorithm 1: AdaBoost.M2

Input:

- Sequence of N instances $S = [(x_i, y_i)]$ of C classes with labels $y_i \in \omega$, $\omega = \{\omega_1, \omega_2, ..., \omega_C\}$ and $i = 1, 2, 3, ..., N$.
- Weak learning algorithm **WeakLearn**.
- Integer T specifying the number of iterations.

Let, $B = \{(i, y) : i = 1, 2, ..., N, y \neq y_i\}$

Initialize $D_1(i, y) = 1/|B| for (i, y) \in B$

for $t = 1, 2, 3, ..., T$ **do**

1. Call **WeakLearn**, providing it with distribution D_t.
2. Get back a hypothesis $h_t : X \times Y \rightarrow [0, 1]$.
3. Calculate the pseudo-error ϵ_t of h_T:

$$\epsilon_t = \frac{1}{2} \sum_{(i,y) \in B} D_t(i, y)(1 - h_t(x_i, y_i) + h_t(x_i, y))$$

4. Set $\beta_t = \epsilon_t/(1 - \epsilon_t)$.
5. Update distribution D_t:

$$D_{t+1}(i, y) = \frac{D_t(i, y)}{Z_t} \beta_t^{\frac{1}{2}(1+h_t(x_i,y_i)-h_t(x_i,y))}$$

where is a $Z_t = \sum D_t(i)$ normalization constant chosen so that D_{t+1} becomes a distribution function.

end

Output: The final hypothesis:

$$h_{final}(x) = \arg\max_{y \in Y} \sum_{t=1}^{T} (log \frac{1}{\beta_t}) \times h_t(x, y)$$

AdaBoost.M2 is expounded in Algorithm 1. In Step 1 and 2, the weak classifier denoted by **WeakLearn** is invoked with a distribution D_t and a hypothesis h_t is obtained. We use decision trees as **WeakLearn** in the proposed method. The weak learner's goal then is to minimize the pseudo-loss ϵ_t, as defined in Step 3. The distribution function is updated as shown in Step 5. For a given instance x, the final hypothesis $h_{final}(x)$ outputs the label y that maximizes a weighted average of the weak hypothesis values $h_t(x, y)$. The procedure

TABLE III
DESCRIPTION OF VARIOUS CLASSES

Class	Sleep States
6	AWA, S1, S2, S3, S4, REM
5	AWA, S1, S2, SWS (S3-S4), REM
4	AWA, S1-S2, SWS (S3-S4), REM
3	AWA, NREM (S1-S4), REM
2	AWA, Sleep (REM & NREM)

TABLE IV
PERFORMANCE COMPARISON OF VARIOUS STATE-OF-THE-ART METHODS. ONLY THE HIGHEST ACCURACY VALUES OF EACH METHOD ARE REPORTED

Authors	6-Class	5-Class	4-Class	3-Class	2-Class
Herrera et al. [23]	-	-	69.80%	-	-
Huang et al. [24]	-	-	77.12%	-	-
Berthomier et al. [9]	-	71.2%	74.5%	88.3%	95.4%
Hsu et al. [25]	-	87.20%	-	-	-
Linag et al. [10]	-	83.60%	-	-	-
Hassan et al. [26]	80.34%	82.03%	82.83%	-	-
Ronzhina et al. [11]	76.70%	-	81.42%	88.97%	96.90%
Hassan et al. [27]	85.57%	86.53%	87.49%	89.77%	95.05%
Zhu et al. [2]	**87.50**%	88.90%	89.30%	92.60%	97.90%
Proposed Method	86.89%	**89.52**%	**91.48**%	**93.18**%	**98.29**%

of AdaBoost.M1 is similar to that of Algorithm 1 except for the fact that instead of pseudo-loss, it uses a weighted error defined as:

$$\epsilon_t = \sum_{i:h_t(x_i)\neq y_i} D_t(i) \tag{16}$$

If $\epsilon_t > \frac{1}{2}$ the process halts.

III. RESULTS AND DISCUSSIONS

The configuration of the computer which has been used in our experiments is Intel(R) Core(TM) i5-3470, 3.2 GHz CPU, 4 GB of RAM. MATLAB 2013a is employed to carry out the simulations. In this paper, we consider five cases of sleep stage classification. These classes are described in Table III. The cases listed in Table III are clinically relevant and consistent with the experimental settings with contemporary works in the literature.

The performance of the proposed algorithm is evaluated against state-of-the-art sleep staging algorithms in the literature. To ensure fair comparison, Table IV compares the proposed method's performance to some contemporary works

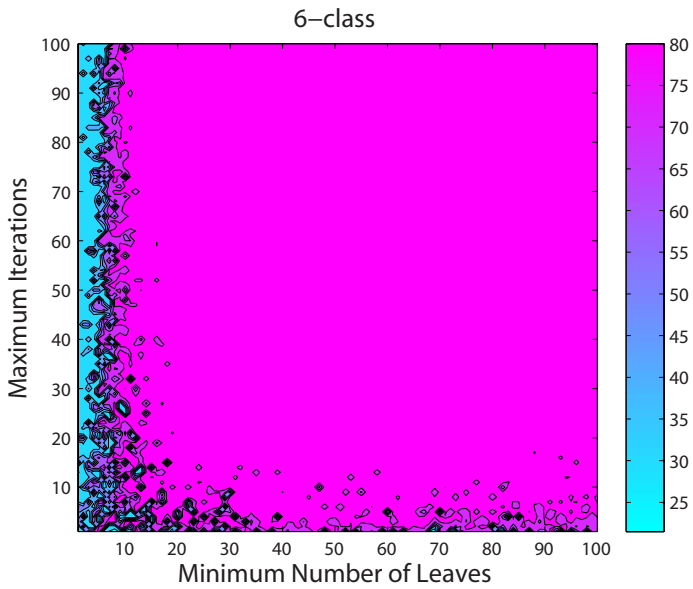

Fig. 3. Variation of accuracy with number of iterations and minimum number of leaves of decision tree. The high levels of accuracy for a wide range of value of these two parameters confirm the robustness of the proposed scheme.

in the literature based on Sleep-EDF data-set. It is evident from Table IV that the proposed method gives superior performance to prior works in the literature. Although the algorithmic performance of our method is slightly low than that of [2], in general, the performance of our method is better as Table IV evinces.

The proposed method's consistent algorithmic performance for various cases of interest already highlights its reliability. Another salient feature of the proposed scheme is that it is robust. This fact is evident from Fig. 3. Fig. 3 presents the variation of accuracy with number of iterations and minimum number of leaves of decision tree. The high levels of accuracy for a wide range of value of these two parameters confirm the robustness of the proposed scheme. In other words, the accuracy values are high not for a few sporadic values of number of decision trees merely. The proposed method's reliability and robustness suggest that this algorithm is suitable for both clinical practice and device implementation.

IV. CONCLUSIONS

In this work, we have introduced a novel signal processing technique, namely- CEEMDAN for sleep stage classification. Experimental results backed by statistical validation clearly indicates that statistical features in the CEEMDAN domain can characterize various stages of sleep quite well. AdaBoost is also implemented for computer-aided sleep scoring. Until now, this is the first time CEEMDAN in conjunction with AdaBoost is employed for sleep staging to the best of our knowledge. The proposed scheme can be extended for other physiological signal classification problems as well. In conclusion, we can anticipate that the proposed sleep staging algorithm will alleviate the onus of the clinicians, speed-up sleep disorder

diagnosis, and can be marked as an important step towards making a sleep quality evaluation device feasible.

REFERENCES

[1] X. Long, J. Foussier, P. Fonseca, R. Haakma, and R. M. Aarts, "Analyzing respiratory effort amplitude for automated sleep stage classification," *Biomedical Signal Processing and Control*, vol. 14, pp. 197 – 205, 2014.

[2] G. Zhu, Y. Li, and P. Wen, "Analysis and classification of sleep stages based on difference visibility graphs from a single channel eeg signal," *Biomedical and Health Informatics, IEEE Journal of*, vol. PP, no. 99, pp. 1–1, 2014.

[3] C.-S. Huang, C.-L. Lin, L.-W. Ko, S.-Y. Liu, T.-P. Su, and C.-T. Lin, "Knowledge-based identification of sleep stages based on two forehead electroencephalogram channels," *Frontiers in Neuroscience*, vol. 8, no. 263, 2014.

[4] H. Koch, J. A. Christensen, R. Frandsen, M. Zoetmulder, L. Arvastson, S. R. Christensen, P. Jennum, and H. B. Sorensen, "Automatic sleep classification using a data-driven topic model reveals latent sleep states," *Journal of Neuroscience Methods*, vol. 235, no. 0, pp. 130 – 137, 2014.

[5] T. Lajnef, S. Chaibi, P. Ruby, P.-E. Aguera, J.-B. Eichenlaub, M. Samet, A. Kachouri, and K. Jerbi, "Learning machines and sleeping brains: Automatic sleep stage classification using decision-tree multi-class support vector machines," *Journal of Neuroscience Methods*, no. 0, pp. –, 2015.

[6] T. Kayikcioglu, M. Maleki, and K. Eroglu, "Fast and accurate pls-based classification of eeg sleep using single channel data," *Expert Systems with Applications*, vol. 42, no. 21, pp. 7825 – 7830, 2015.

[7] B. Kemp, "The sleep-edf database online." [Online]. Available: http://www.physionet.org/physiobank/database/sleep-edf/

[8] B. Kemp, A. Zwinderman, B. Tuk, H. Kamphuisen, and J. Oberye, "Analysis of a sleep-dependent neuronal feedback loop: the slow-wave microcontinuity of the eeg," *Biomedical Engineering, IEEE Transactions on*, vol. 47, no. 9, pp. 1185–1194, Sept 2000.

[9] C. Berthomier, X. Drouot, M. Herman-Stoca, P. Berthomier, J. Prado, D. Bokar-Thire, O. Benoit, J. Mattout, and M.-P. dOrtho, "Automatic analysis of single-channel sleep eeg: Validation in healthy individuals," *Sleep*, vol. 30, no. 11, p. 15871595., Nov 2007.

[10] S.-F. Liang, C.-E. Kuo, Y.-H. Hu, Y.-H. Pan, and Y.-H. Wang, "Automatic stage scoring of single-channel sleep eeg by using multiscale entropy and autoregressive models," *Instrumentation and Measurement, IEEE Transactions on*, vol. 61, no. 6, pp. 1649–1657, June 2012.

[11] M. Ronzhina, O. Janouek, J. Kolrov, M. Novkov, P. Honzk, and I. Provaznk, "Sleep scoring using artificial neural networks," *Sleep Medicine Reviews*, vol. 16, no. 3, pp. 251 – 263, 2012.

[12] A. Rechtschaffen and A. Kales, "Manual of standardized terminology, techniques and scoring systems for sleep stages of human subjects," *U. G. P. Office, Washington DC Public Health Service*, 1968.

[13] A. R. Hassan, "Automatic screening of obstructive sleep apnea from single-lead electrocardiogram," in *Electrical Engineering and Information Communication Technology (ICEEICT), 2015 International Conference on*, May 2015, pp. 1–6.

[14] Z. Wu and N. E. Huang, "Ensemble empirical mode decomposition: a noise assisted data analysis method," *Advances in Adaptive Data Analysis*, vol. 01, no. 01, pp. 1–41, 2009.

[15] A. R. Hassan and M. I. H. Bhuiyan, "Computer-aided sleep staging using complete ensemble empirical mode decomposition with adaptive noise and bootstrap aggregating," *Biomedical Signal Processing and Control*, vol. 24, pp. 1 – 10, 2016.

[16] A. R. Hassan and M. A. Haque, "Epilepsy and seizure detection using statistical features in the complete ensemble empirical mode decomposition domain," in *TENCON 2015, 2015 IEEE Region 10 Conference*, Nov. 2015, pp. 1–6.

[17] M. Torres, M. Colominas, G. Schlotthauer, and P. Flandrin, "A complete ensemble empirical mode decomposition with adaptive noise," in *Acoustics, Speech and Signal Processing (ICASSP), 2011 IEEE International Conference on*, May 2011, pp. 4144–4147.

[18] A. R. Hassan and M. A. Haque, "Computer-aided sleep apnea diagnosis from single-lead electrocardiogram using dual tree complex wavelet transform and spectral features," in *Electrical and Electronic Engineering (ICEEE), 2015 International Conference on*, Nov. 2015, pp. 1–4.

[19] ——, "Computer-aided gastrointestinal hemorrhage detection in wireless capsule endoscopy videos," *Computer Methods and Programs in Biomedicine*, pp. –, 2015.

[20] S. Bashar, A. Hassan, and M. Bhuiyan, "Identification of motor imagery movements from eeg signals using dual tree complex wavelet transform," in *Advances in Computing, Communications and Informatics (ICACCI), 2015 International Conference on*, Aug 2015, pp. 290–296.

[21] A. R. Hassan, "A comparative study of various classifiers for automated sleep apnea screening based on single-lead electrocardiogram," in *Electrical and Electronic Engineering (ICEEE), 2015 International Conference on*, Nov. 2015, pp. 1–4.

[22] Y. Freund and R. E. Schapire, "A decision-theoretic generalization of on-line learning and an application to boosting," *Journal of Computer and System Sciences*, vol. 55, no. 1, pp. 119 – 139, 1997.

[23] L. Herrera, A. Mora, C. Fernandes, D. Migotina, A. Guillen, and A. Rosa, "Symbolic representation of the eeg for sleep stage classification," in *Intelligent Systems Design and Applications (ISDA), 2011 11th International Conference on*, Nov 2011, pp. 253–258.

[24] C.-S. Huang, C.-L. Lin, L.-W. Ko, S.-Y. Liu, T.-P. Sua, and C.-T. Lin, "A hierarchical classification system for sleep stage scoring via forehead eeg signals," in *Computational Intelligence, Cognitive Algorithms, Mind, and Brain (CCMB), 2013 IEEE Symposium on*, April 2013, pp. 1–5.

[25] Y.-L. Hsu, Y.-T. Yang, J.-S. Wang, and C.-Y. Hsu, "Automatic sleep stage recurrent neural classifier using energy features of eeg signals," *Neurocomputing*, vol. 104, no. 0, pp. 105 – 114, 2013.

[26] A. R. Hassan, S. K. Bashar, and M. I. H. Bhuiyan, "Automatic classification of sleep stages from single-channel electroencephalogram," in *India Conference (INDICON), 2015 Annual IEEE*, Dec 2015, pp. 1–6.

[27] A. Hassan, S. Bashar, and M. Bhuiyan, "On the classification of sleep states by means of statistical and spectral features from single channel electroencephalogram," in *Advances in Computing, Communications and Informatics (ICACCI), 2015 International Conference on*, Aug 2015, pp. 2238–2243.

Mitigation of Thermally Induced Crosstalk Noise by Dynamically Adjusting Driver Strength

Md M Rahman, Pankaj Bhowmik and Selahattin Sayil
Department of Electrical Engineering
Lamar University
Beaumont, USA
E-mail: mrahman5@lamar.edu, pbhowmik@lamar.edu, sayil@lamar.edu

Abstract—**The space between interconnects is shrinking and its increasing aspect ratio is causing modern VLSI circuit to be more prone to crosstalk noise. Moreover, modern high-performance CMOS circuits are more power consuming, resulting in the chip experiencing higher temperature. As a consequence of this high temperature, CMOS driver strength reduces which introduces a new reliability concern, thermally induced crosstalk noise, which is addressed in this research work for the very first time in literature. This superimposing with the normal crosstalk can cause the VLSI circuit to fail by toggling the logic or bit flipping. In this paper, our goal is to provide a solution to mitigate the thermally induced crosstalk noise by dynamically adjusting gate voltage to keep driver strength the same despite changing temperature. We propose a temperature sensor that generates the necessary voltage to the gate to keep driver strength constant. Using 10-π modelling for interconnect in 45nm technology, we explore the effect of on-chip temperature gradient on crosstalk noise. Our simulation result demonstrates that the proposed method can successfully mitigate thermally induced crosstalk noise up to 85% in the worst case temperature scenario.**

Keywords—thermally induced crosstalk noise, temperature sensor, temperature insensitivity, crosstalk noise mitigation

I. INTRODUCTION

Due to the advancement of technology and the increasing demand for miniaturizing of smart devices, the semiconductor industry has been trying to shrink the device size and the spaces between interconnects. On the other hand, the width of interconnect cannot be scaled down in similar fashion to keep interconnect resistance low, resulting in increase of its aspect ratio. This diminishing spaces between interconnects and larger aspect ratio increases coupling capacitance between adjacent interconnect lines. As reported in [1], more than 85% of the total interconnect capacitance in 90nm technology and below is due to coupling capacitance. This increasing coupling capacitance and reduced device size combined with today's multi-gigahertz signal on one interconnect adversely effects the signal integrity on the neighboring line through a mechanism called as crosstalk noise. In literature, different techniques have been proposed to reduce crosstalk noise including device sizing [2,3], repeater insertion [4] and shielding method [5,6].

On the other hand, due to the integration of hundreds of million devices in a single chip, the total power consumption and power per unit area have raised unprecedentedly. As the power consumption is converted into heat, which ultimately increases the operating temperature. This high operating temperature adversely affects the circuit performance, such as reliability and robustness. Moreover, the employment of different power management techniques and diverse activities of functional blocks cause the chip to experience non-uniform temperature throughout the whole chip area. This on-chip temperature gradient can be as high as 50°C as reported in [7]. The increased temperature affects both interconnect resistance and strength of interconnect drivers. The interconnect resistance increases as the temperature goes up, because the commonly used interconnect materials, copper and aluminum, both have a positive temperature co-efficient of 0.00401 and 0.004308[8] respectively.

However, the effect of temperature change on buffer is not straightforward, as two important device parameters, carrier mobility and threshold voltage, have conflicting effects on device drain current with the change of temperature. As temperature increases, carrier mobility decreases which causes the device current to go down. On the other hand, increased temperature reduces the device threshold voltage causing device current to increase. Depending on dominant effect in between mobility and threshold voltage, device responds accordingly. If the gate to source voltage is little higher than zero, the change of threshold voltage dominates over the change of mobility and that cause to increase the drain current with temperature rise. On the other hand, at nominal supply voltage, change in carrier mobility dominates over the change of threshold voltage which causes the device current to decrease with increased temperature. As a result of this increased interconnect resistance and decreased buffer driving strength, charge from neighboring aggressor interconnect tends to produce an extra glitch on victim line other than the normal crosstalk, this extra glitch is named as thermally induced crosstalk. Unlike other research works which were concerned with the normal crosstalk, we are first in literature to address this temperature effect on crosstalk. Superimposing this thermally induced crosstalk noise on normal crosstalk can cause the total crosstalk noise to cross the noise margin of the subsequent gate, which ultimately may generate and propagate the wrong value. If this wrong data propagates in the latching window of a storage device e.g. latch, the wrong data will be stored, eventually causing the circuit to fail.

As the thermally induced crosstalk noise results from decreased buffer strength and increased interconnect resistance, to mitigate this noise, we have proposed a buffer that keeps its driving strength constant and compensate for the increased interconnect resistance even if the temperature changes.

978-1-4673-9257-0/15/$31.00 ©2015 IEEE

Several schemes have been proposed to keep driver strength constant in changing temperature situation. In [9], the authors proposed a dynamically adaptive driver that involves designing of temperature sensor with a wave-shaping circuit. The output from the wave-shaping circuit is used to control the gate of extra pMOS and nMOS connected in series with the original buffer which dynamically adjust the buffer current as temperature changes. While this technique achieves good temperature insensitivity, designing the temperature sensor and wave-shaping circuit are complex and extra four devices in the buffer, raise area overhead. In Multi-threshold technique [10], the authors suggested that, by proper interleaving low threshold (lvt), standard threshold (stv) and high threshold (hvt) devices it is possible to achieve temperature insensitivity. As each type device (lvt,stv,hvt) has different temperature dependencies, that entails body bias for individual devices, resulting in overhead to be large. Shakeri and Meindl suggested a variable supply voltage in [11], but requirement of different voltage and routing them all over the chip is a problem. Moreover, the number of level converters required for different sections poses another design bottleneck.

In [12], Wolpert and Ampadu suggested programmable temperature compensation device (PTCD) to keep buffer current constant in variable temperature situation. They proposed an extra nMOS and pMOS device in series with original buffer transistors**.** As suggested in Section [II], both nMOS and pMOS show temperature insensitivity at particular gate voltage (V_{INS}). Wolpert and Ampadu [12] connected gates of these extra devices to V_{INS} to make the buffer strength constant. As nMOS and pMOS have different V_{INS}, two extra voltage levels have to be routed over the whole chip, which consumes costly routing resources. Furthermore, as V_{INS} is far lower than the nominal technology voltages, at this lower gate driving voltage, buffer current is much lower (~44.8% lower than nominal) resulting in degradation of overall speed performance.

In our proposed technique, instead of connecting the gates of these extra devices to a fixed voltage (V_{INS}), we connect gate of nMOS to a voltage closer to nominal voltage and sweep it up as temperature increases and for pMOS, gate is connected to a voltage closer to ground and sweep it down as temperature moves up. For setting these initial voltages and moving it up or down in response to the temperature change, we propose a simple temperature sensor which locally generates these controlling voltages preventing the routing of two voltage level.

The next sections are organized as follows: in section II, temperature dependency of device and crosstalk noise is explained, our proposed method is provided in proposed methodology, section III. Section IV is arranged by crosstalk modeling and simulation result and finally we conclude in section V.

II. TEMPERATURE EFFECT

A. Temperature Effect on Device

The dependency of device drain current (I_D) on temperature can be explained by the alpha power model for short channel MOSFET [13]. I_D mainly depends on three parameters, threshold voltage V_{th}, carrier (electron or hole) mobility μ and saturation velocity in saturation region υ_{sat} [14][15]. According to [14], these dependencies can be expressed as,

$$V_{th}(T) = V_{th}(T_0) - k(T - T_0) \quad (1)$$

$$\mu(T) = \mu(T_0)\,(T_0/T)^m \quad (2)$$

$$\upsilon_{sat}(T) = \upsilon_{sat}(T_0) - h(T - T_0) \quad (3)$$

Here T_0 is the nominal temperature, $V_{th}(T_0)$, $\mu(T_0)$ and $\upsilon_{sat}(T_0)$ are threshold voltage, mobility and the saturation velocity at the nominal temperature, k is temperature coefficient of threshold voltage (~0.8mV.K^{-1}[13]) and m and h are the technology dependent temperature coefficient (is measured as 1.5~1 and 150ms^{-1}.K^{-1} respectively [15]). All these coefficients are positive [14]. That means with the increase of temperature, threshold voltage, mobility of electrons or holes and the saturation velocity (υ_{sat}) change accordingly. The effect of μ, υ_{sat} and V_{th} on drain saturation current (I_D) of the device can be shown as follows [2]

$$I_D(T) = \upsilon_{sat}(T).W.P_s.\,[V_{GS} - V_{th}(T)]^{\alpha}(1+\lambda V_{DS}) \quad (4)$$

Where, W is the device width, Ps is the technology specified constant and λ is the channel length modulation coefficient. From the equation (4), it is evident that decreased υ_{sat} reduces $I_D(T)$ while reduced threshold voltage increases drain current. As at higher supply voltage, the change in mobility and saturation dominates over change in threshold, any increase of temperature tends to decrease I_D. On the other hand, at lower supply voltage, change in V_{th} dominates, resulting in the increase of I_D with the increase in temperature. In between these two regions, there is the supply voltage where the effects of threshold voltage and mobility on drain current are same with different temperature. So I_D will neither increase nor decrease and consequently the device will be temperature insensitive. This supply voltage is called temperature insensitive point (V_{INS}) or zero temperature coefficient (ZTC). As electron and hole have different mobility, pMOS and nMOS have different values of V_{sat} and consequently different V_{INS}. The simulation result for the pMOS and nMOS in 45nm

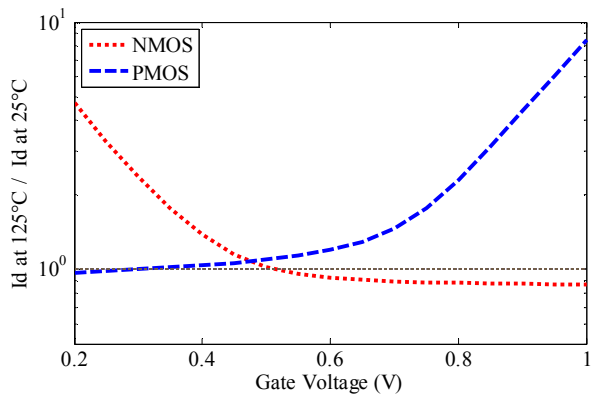

Fig. 1 Drain current dependency of temperature and gate voltage

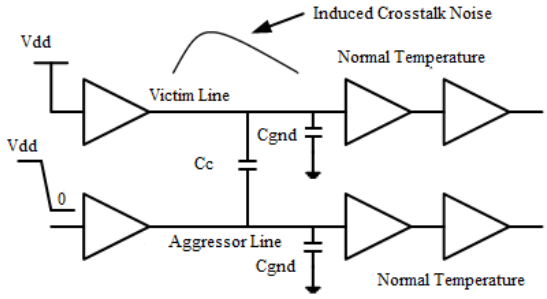

Fig. 2 Normal Crosstalk Noise

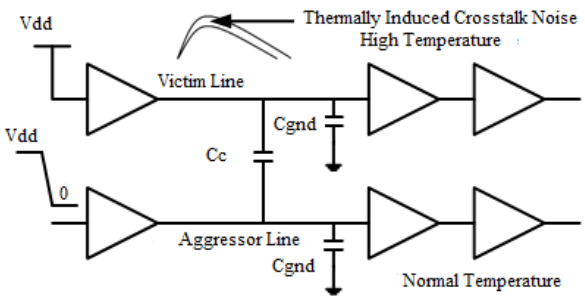

Fig. 3 Thermal Crosstalk

technology is shown in Figure 1. Where x-axis represents gate voltage and y-axis represents the ratio of drain current at 125°C and nominal temperature in logarithmic scale. In Figure 1, at lower V_{GS}, drain current ratio is more than one, indicates drain current increases with increase in temperature and this is called reverse temperature region. On the other hand, at larger V_{GS}, ratio is less than one, exhibits reverse trend in drain current, that is said to be normal temperature region. But, at V_{GS} of 0.520V for nMOS and V_{SG} of 0.680V (V_G is 0.320V) for pMOS, this ratio have a value exactly one, indicating drain current to be independent of temperature change

B. Temperature Effect on Crosstalk noise

The space between interconnect is diminishing and its width is also going down with miniaturization of CMOS circuits. But to keep interconnect resistance low, the thickness cannot be scaled down proportionately, which causes the interconnect thickness to width ratio to increase. The combination of both trends (diminishing wire spacing and increasing thickness to wire ratio) causes more parasitic.

Now, assume that aggressor is at low temperature and the victim is at higher temperature. When aggressor switches, it injects (or drain) charges to (or from) the victim which causes to generate a crosstalk induced glitch on the victim. As the victim is at higher temperature and operating at nominal voltage in Figure 3, its buffers drain current is lower than the drain current it had if it was at normal temperature. So in this case, if the aggressor switches from 0 to VDD, it injects charges to the victim and due to lower drain current victim of buffers lose its capacity to dump the excess charges, and that in turn produces an extra glitch on the victim line, generates coupling between wires. That means the switching in aggressor wire causes an undesirable glitch to its neighboring victim wire. Figure 2 illustrates how a switching aggressor causes to induce crosstalk noise to its neighboring wire (victim). When aggressor switches and victim line does not, there flows a current through the coupling capacitor due to the voltage difference between two side of the capacitor. That means aggressor injects charge to the victim when aggressor switches from Ground to VDD, which produces a positive glitch on the victim. Similarly, when aggressor switches from VDD to Ground, it drains charge from victim, producing a negative glitch. If the glitch (crosstalk noise) crosses the noise margin (VDD/2), then the subsequent logic circuit may capture a wrong value, 1 instead of 0, or 0 instead of 1, which may produce an erroneous value at the output. By increasing victim buffers size, induced crosstalk can reduce thermally induced crosstalk noise. Similarly, if the aggressor switches from VDD to 0 it drains charges from the victim and due to lower drain current of victim buffer it loses the capacity to drain charges from VDD and that in turn generates an extra temperature induced crosstalk glitch which is shown in Figure 3. And that is the reason at higher temperature the crosstalk noise boosted up by certain voltage and sometimes that is enough to cross the noise margin. That motivates us to design a temperature insensitive circuit to nullify the thermally induced crosstalk noise, which has never been noticed before.

III. PROPOSED METHODOLOGY

In this section, the technique to keep driver strength constant is explained concisely and also a new tiny temperature sensor is introduced to maintain driver strength as high as possible and also to keep the strength at constant value with temperature change.

A. Maintaining driver strength

As in (4), by controlling the gate overdrive voltage (VGS-VT) [17] transistor region of operation can be adjusted. In [12], the authors controls this gate overdrive by inserting an extra controlling device as shown in Figure 4 and adjusted its gate to tune V_{GS}. The simulation results, shown in Figure5 and Figure 6, explain how adjusting the gate voltages, temperature insensitivity can be achieved. The Y-axis of these figures represents the drain current ratio of the device at

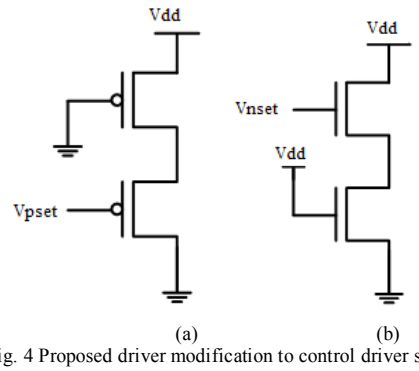

Fig. 4 Proposed driver modification to control driver strength

operating temperature to the drain current at 25°C. At V_{nset} of 1.0V and V_{pset} of 0.0V, this ratio exhibits a negative slope, indicating a decreasing trend in drain current as temperature increases. On the other hand, at V_{nset} of 0.350Vand V_{pset} of 0.700V this ratio has a positive value, which implies increased drain current at higher temperature. For V_{nset} of 0.520V and V_{pset} 0.320V this ratio shows a near zero value, indicating insensitivity to temperature change, and these values of V_{nset} and V_{pset} are referred as temperature insensitive voltage (V_{INS}). In [12], the authors use these values V_{INS} to make the buffer temperature insensitive. But as these V_{INS} are far away from the nominal supply voltage, the device drain current is lower which degrades the speed performance.

In our work, instead of connecting gate to a fixed V_{INS} as in [12], we propose to change the gate controlling voltage with change in temperature as shown in the inset figure of Figure 5 and Figure 6. Drain current decreases with increased temperature, at nominal supply voltage. Sweeping up the gate voltage of nMOS controlling device and sweeping down the gate voltage of pMOS controlling device with temperature rises, allow these devices to flow more current to compensate the reduced drain current at higher temperature. So, by setting V_{nset} at higher value than V_{nINS} and moving it up and also by setting V_{pset} at lower value than $V_{pINS,}$ and moving it down, with increase in temperature, we can make drain current constant of the device. Thus, temperature resilient buffer is achieved. For setting and sweeping the V_{nset} and V_{pset}, we propose a simple temperature sensor that dynamically adjust its generated voltage according to the requirement of controlling devices to keep its drain current constant

B. Proposed Temperature Sensor

Gate-source voltage of a diode-connected MOS transistor biased with a constant current exhibits a temperature dependency [18]. By controlling the drain current and the W/L ratio of the device, sensitivity of the generated gate-source

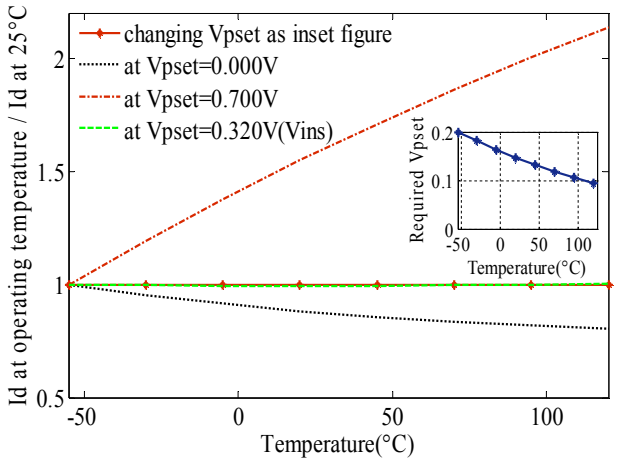

Fig. 5 Controlling temperature sensitivity for pMOS by Vpset

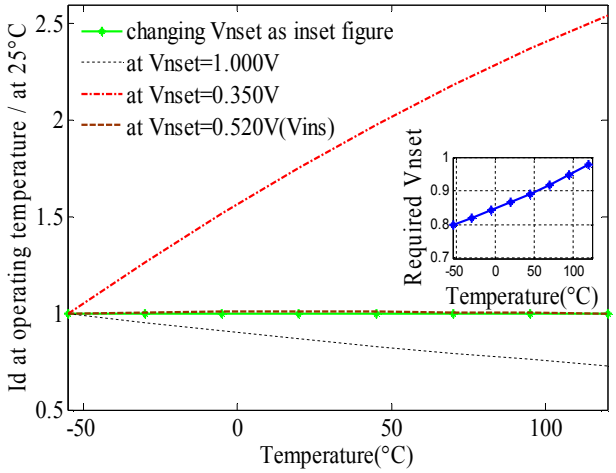

Fig. 6 Controlling temperature sensitivity for nMOS by Vnset

voltage (mV/°C) can be well controlled [17]. In our temperature sensor, resistor R1 forms the reference current and transistor M1 forms the diode connected load. The generated gate source voltage of M1, which is set to have negative sensitivity (-mV/°C), is feed to the pMOS (M2). As the pMOS(M2) drain current increases when its gate voltage is reduced. So combination of R1, M1 and M2 forms a high temperature sensitive current source.

Finally, load resistance R2 converts this current to voltage that generates the required V_{nset}. By adjusting the values of R1, R2, W/L ratio of M1, and width of M2, we set the value of V_{nset} at 25°C as 0.878V with sensitivity of 1.07mV/°C. Similarly, the values R3, R4 and W/L ratio of M3, and width of M4 is adjusted, which give V_{pset} as 0.167V at 25°C with sensitivity of -0.08mV/°C.

IV. CROSSTALK MODELLING AND SIMULATION RESULT

To analyze the temperature effect on crosstalk and to show the effectiveness of our proposed method, we consider two

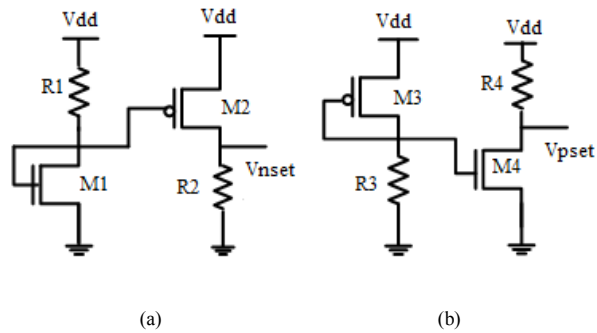

Fig. 7 Proposed temperature sensor to generate (a)Vnset (b)Vpset

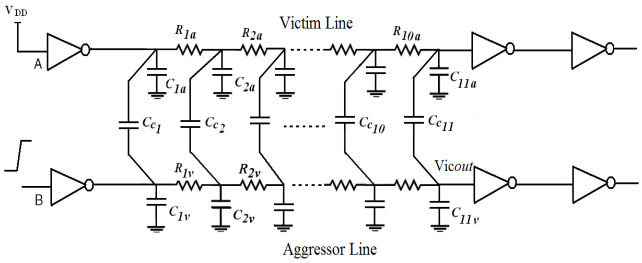

Fig. 8 Simulation setup for crosstalk noise calculation

intermediate wire in 45nm length of 500µm running parallel to each other, with dimension of width and spacing 0.14 µm, thickness is 0.35 µm [19] and modeled 10-π for interconnect [20]. For modeling the driver we have used 45nm technology model card from [19] and also performed our simulation on HSPICE. The value of interconnect resistance, capacitance and mutual capacitance is calculated from [21]. We have used V_{DD} of 1.0v, which is nominal voltage for 45nm technology. Figure 8 Shows the HSPICE implementation of our model.

A. *Crosstalk noise modelling*

To illustrate the effect of temperature on crosstalk, we have applied a step pulse at the input of aggressor buffer and victim driver input is kept at V_{DD} as shown in Figure 8. The voltage glitch that induces at the input of the second buffer in Figure 8 on the victim line, is the crosstalk noise. This crosstalk noise is measured for different driver size and also for two different temperatures (25°C and 125°C) in victim line keeping normal temperature (25°C) at aggressor and the result is shown in Figure 8, which shows that, with the gradual increase in driver size, crosstalk noise increases and also the application of high temperature (125°C) on victim line instigates the crosstalk noise. When aggressor switches, it

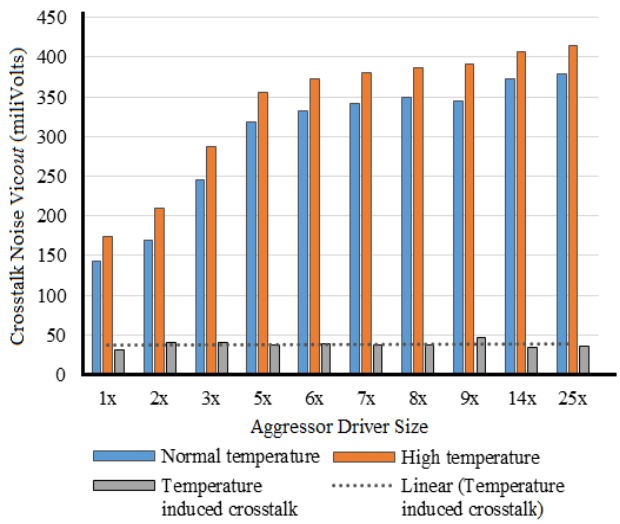

Fig. 9 Comparison of normal crosstalk noise and thermally induced crosstalk noise

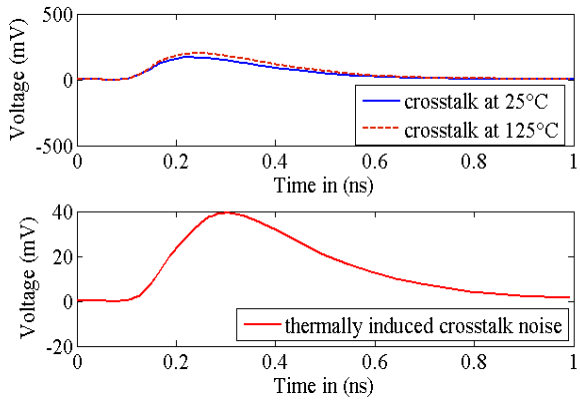

Fig. 10 High temperature and Thermal induced crosstalk at victim m node for 2x aggressor driver size

induces crosstalk noise on victim line, which complicates the normal operation of VLSI circuit. If victim line stays at higher temperature, it gets more susceptible to crosstalk due to its reduced current. As a result, more noise will be induced in high temperature. According to our simulation, thermally induced crosstalk noise remains unchanged with the change of aggressor driver sizing, which is depicted also in Figure 8. As a consequence, thermally induced crosstalk doesn't depend on driver sizing, which is treated to be the most viable approach to mitigate crosstalk noise, i.e. increasing victim driver size, it will reduce crosstalk but thermally induced crosstalk noise will remain undiminished.

B. *Mitigation of thermally Induced Crosstalk*

Figure 10, shows the simulation result for original buffer with 2X driver size for both aggressor and victim, when both the aggressor and victim are at 25°C, the crosstalk induced noise has value of 165mV, but when the victim is at higher temperature at 125°C, due to its reduced driving strength, the induce noise grows to a value of 205mV. This extra 40mV of induced noise is due to the higher temperature at victim line and that is thermally induced crosstalk noise.

Figure 11 shows the result of applying the technique proposed in this work. In our proposed method, both the aggressor and victim is first set at 25°C and V_{nset} and V_{pset} of both the aggressor and victim are connected to 878mV and 147mV respectively. As the victim temperature starts to increase, it starts to loss its capacity to mitigate the imposed extra charge due to switching aggressor. To keep its strength same at higher temperature, V_{nset} is swept up and V_{pset} is swept down. When the victim line is at 125°C, its V_{nset} is set to 985mV and V_{pset} is set to 90mV to maintain same strength as it was at 25°C. The result shows a significant reduction of thermally induced crosstalk noise. By using our technique we can limit it to 6mV whereas it was 40mV for original buffer. So our proposed method can reduce 85% thermally induced crosstalk. This success rate varies for other driver sizes because it actually depends on the temperature sensor's output. Our sensor can't

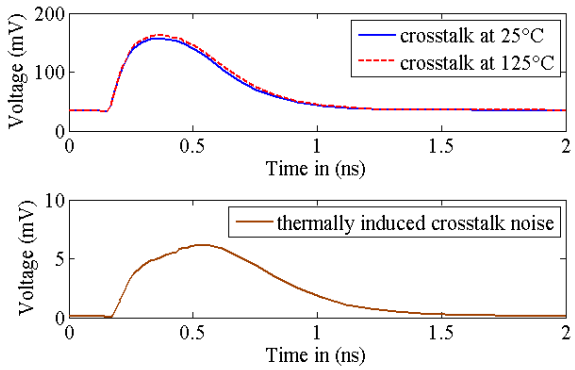

Fig. 11 Mitigation of thermally induced Crosstalk Noise

make exactly the required V_{pset} and V_{nset}. But they give an output which has 5-10% error rate. However, for instance in 3x and 4x driver size, it mitigates 86.5% and 82.9% thermal crosstalk and on an average it mitigates 85% noise successfully.

V. Conclusion

In this proposed method, the effect of on-chip temperature on crosstalk noise, has been encountered in intermediate layer of VLSI interconnect. Simulation has been made using the distributed RC model of interconnect in 45nm technology. We substantiated thermally induced crosstalk as a threat and we can tarnish this threat by controlling the gate voltage and maintaining the driver strength constant with the change of temperature profile at victim line. According to our solution, temperature sensors sense the temperature profile and give the required gate voltage for dynamically adjusting the buffer strength or drain current to a constant value. Our method demonstrates a reduction of 85% of thermally induced crosstalk noise from the victim line. In the future, this same methodology can be applied to reduce the temperature induced clock skew in clock tree for global interconnect.

References

[1] S. Dubey, and J. Jorgenson, "Crosstalk reduction using buffer insertion," in *Proc. IEEE Int. Symp. Electromagnetic compatibility*, Aug. 2002, vol. 2, pp. 639-642.

[2] S. Dubey, and J. Jorgenson, "Crosstalk reduction using buffer insertion," in *Proc. IEEE Int. Symp. Electromagnetic compatibility*, Aug. 2002, vol. 2, pp. 639-642.

[3] I. H. R Jiang, Y. W. Chang and J. Y. Jou, "Crosstalk-driven interconnect optimization by simultaneous gate and wire sizing," *IEEE Trans. Computer-Aided Design of Integrated Circuits and Syst.,* vol. 19, no. 9, pp. 999-1010, Sep. 2000.

[4] C. J. Alpert, A. Devgan, and S. T. Quay, "Buffer insertion for noise and delay optimization," *IEEE Trans. Computer -Aided Design of Integrated Circuits and Syst.*, vol. 18, no. 11, pp. 1633-1645, Nov. 1999.

[5] J. Zhang, and E. G. Friedman, "Crosstalk modeling for coupled RLC interconnects with application to shield insertion," *IEEE Trans. VLSI systems,* vol. 14, no. 6, pp. 641-646, May, 2010.

[6] G. Fattah and N. Masoumi, "Crosstalk in VLSI partially coupled interconnect structures, a comprehensive evaluation," in *Proc. 15th IEEE Workshop Signal Propagation on Interconnects,* May 2011, pp. 15-18.

[7] S. Borkar, T. Karnik, S. Narendra, J. Tschanz, A. Keshavarzi, and V. De, "Parameter variations and impact on circuits and microarchitecture," in *Proc. ACM 40th annual Design Automation Conference*. June, 2003, pp. 338-342.

[8] (2010) Fundamentals of Electrical Engineering and Electronics [Online]. Available at http://www.vias.org/feee/conduct_07.html.

[9] T. Ragheb, A. Ricketts, M. Mondal, S. Kirolos,G. M. Links, V. Narayanan, and Y. Massoud, "Design of thermally robust clock trees using dynamically adaptive clock buffers," *IEEE Trans. Circuits and Systems I,* vol. 56, no. 2, pp. 374-383, Feb. 2009.

[10] A. Calimera, E. Macii, M. Poncino, and R. I. Bahar, "Temperature insensitive synthesis using multi-vt libraries," in *Proc. 18th ACM GreatLakes Symp. VLSI*, May 2008, pp. 5–10.

[11] Q. Chen, M. Meterelliyoz, and K. Roy, "A CMOS thermal sensor and its applications in temperature adaptive design," in *Proc. Int. Symp. Qual. Electron*. Dec. 2006, pp. 243–248.

[12] D. Wolpert and P. Ampadu, "Exploiting programmable temperature compensation devices to manage temperature-induced delay uncertainty," *IEEE Trans. Circuits and Systems I,* vol. 59, no. 4, pp. 735-748, Apr. 2012.

[13] T. Sakurai, "Alpha-power law MOSFET model and its applications to CMOS inverter delay and other formulas," *IEEE Trans. Solid-State Circuits,* vol. *25*, no. 2, pp. 584-594. Apr. 1990.

[14] N. Arora, MOSFET Modeling for VLSI Simulation: Theory And Practice, Singapore: World Scientific, 2007.

[15] A. Calimera, R. Bahar, E. Macii, and M. Poncino, "Temperature-insensitive dual-synthesis for nanometer CMOS technologies under inverse temperature dependence," *IEEE Trans. VLSI,* vol. 18, no. 11, pp. 1608-1620, Oct. 2010.

[16] J. C. Ku, & Y. Ismail," On the scaling of temperature-dependent effects, Computer-Aided Design of Integrated Circuits and Systems," *IEEE Trans. Comput.-Aided Design Integr. Circuits Syst.,* vol 26, no. 10, pp. 1882-1888, Oct. 2007.

[17] R. Kumar and V. Kursun, "Reversed temperature-dependent propagation delay characteristics in nanometer CMOS circuits," *IEEE Trans. Circuits Syst. II Exp. Briefs*, vol. 53, no. 10, pp. 1078-1082, Oct. 2006.

[18] I. M. Filanovsky and S. T. Lim. "Temperature sensor applications of diode-connected MOS transistors." in *Proc. IEEE International Symp. Circuits and Syst.,* May, 2002, pp. II-149

[19] (2008) Predictive Technology Model (PTM). [Online]. Available: http://www.ptm.asu.edu/

[20] S. Sayil, V. K. Boorla and Yeddula, "Modeling Single Event Crosstalk in Nanometer Technologies" *IEEE Trans. Nuclear Science,* vol. 58, no. 5, pp. 2493-2502, Oct. 2011.

[21] K. Sundaresan, and N. R. Mahapatr, "Accurate energy dissipation and thermal modeling for nanometer-scale buses," in *Proc.11th IEEE Int. Symp. High-Performance Computer Archi*. Feb. 2005, pp. 51-60.

Implementation of Multi-Input Dual-Output DC-DC Boost Converter Using Renewable Energy for Hybrid Electric Vehicle

*Tanvir Ahmed, Tushar Kumar Kha,
S.M. Hasanuzzaman, Tafikul Islam, Al Islam
Dept. of Electrical & Electronic Engineering
Bangladesh University of Business & Technology
Dhaka, Bangladesh
*p_piash@yahoo.com

Md Aminul Hoque, Md. Abid Hossain
Dept. of Electrical & Electronic Engineering
Bangladesh University of Engineering & Technology
Dhaka, Bangladesh

Abstract— **In this paper, a systemic approach of multi-input-dual-output boost converter for any hybrid electric vehicle is proposed. This kind of multi-input-dual-output boost converter has immense application in hybridizing the electric vehicle efficiently. It also enables the scope of introducing the use of alternative natural renewable energy as well as the other electric potential energy instead of using the most familiar low efficient fuel used internal combustion engine.**

Keywords— Hybrid Electric Vehicle, Multi-Input-Dual-Output, DC-DC Boost Converter, Natural Renewable Energy, Hybrid Power System

I. INTRODUCTION

Climate change, the consequence of greenhouse effect has become one of the most sensitive issues among the climatologist in today's world. As the population is always on the rise, the uses of fuel, natural resources, and other energy resources are increasing. So the amount of these resources is decreasing in an uncontrolled rate. The main culprit of the greenhouse effect is CO_2, which is emitted from more than 50 percent from the conventional vehicles. Hybrid electric vehicle is familiarized now-a-days as an attractive solution in the traffic system to provide environmental friendly travelling with the uses of clean and renewable energy besides can bring the revolutionary change in the traffic system in modern world [2],[3]. In this kind of vehicle multi-input source is introduced to make the input system more reliable, efficient and environment-friendly. Plugin AC voltage, solar energy, environment-friendly fuel cell and some other regenerative energy sources are used as input and a battery is used bi-directionally for storing extra energy and supplying energy when other sources are not available. To provide a specific voltage level and control of power efficiently between input and output, a multi-level input and output converting system is needed [4]. So, a multi-input-dual-output DC-DC boost converter is proposed and investigated in this paper. In the multi-input process plugin AC voltage is introduced where a rectifier is used to rectify the AC sinusoidal voltage into DC voltage and a DC-DC buck converter is used to get the required voltage that is needed to charge the battery. The process of battery charging and AC-DC conversion is controlled by operational switches and manual push button switches. Then comes fuel cell, one of the modern and promising technologies that uses clean energy and can meet very efficiently the demand of future. As it is very costly, so our focus should be to use it as less as possible.

978-1-4673-9257-0/15/$31.00 ©2015 IEEE

II. WORKING PRINCIPLE

The hybrid electric vehicle is basically a modern type of electric vehicle that is more efficient in fuel consuming, environmental friendly and almost zero percent emission of toxic gas. Hybrid vehicle depends on more than one source as input to provide sufficient voltage efficiently at the output. To sustain the required high peak voltage in output with the variation of the low peak voltage in the input, a multi-input-multi-output DC-DC boost converter is already proposed [1]. In this paper, a new model of multi-level DC-DC boost converter is proposed, where total 4 types of different sources are included as input to provide voltage to the dual-output If "k" is denoted as duty cycle, "R" is denoted as load resistance of operational switch then the average output voltage and output current is given by[12],

$$V_a = \frac{Vs}{1-k} \tag{1}$$

$$\Delta I = \frac{Vsk}{fL} \tag{2}$$

Various kind of hybrid electrical vehicles are available in the market on the basis of their working purpose and they have different types of voltage shown in Table I [6]-[11].

Proposed multi-input dual-output DC-DC boost converter is made of 4 different input sources and 2 different outputs shown in Fig.1. Among them, in plugin AC voltage source AC voltage is rectified into DC voltage by a rectifier that is made of diode D1, D2, D3, and D4. Capacitor C1 reduces the ripple and output DC voltage is found across resistor R1.High peaked DC voltage is converted into 9-volt DC by buck converter made of operational switch Op_Sw1, diode D5, inductor L1, and capacitor C2 in order to charge up the 9-volt DC battery. The converted output is found across the resistor R2.The main function of plugin AC is to just charge up the battery. Then comes fuel cell, a very promising technology that supplies also 9 volts into the circuit as a second input

source. Thirdly comes battery that is charged up dually by solar cell and plugin AC voltage source and after charging up, it supplies the necessary voltage to the circuit. Diode D6 protects the circuit and other sources from the reverse current of the battery. Finally comes the solar cell which produces 9 volt, can simultaneously charge the empty 9-volt battery and also feed the necessary voltage to the running vehicle.

All the inputs need to be boosted up and hence DC-DC boost converter is introduced here [5]. The boost converter boosts to 24 voltage DC and 72 voltage DC from 9-volt DC. The boost converter for 24-volt output is made of operational switch Op_Sw2, Diode D8, Capacitor C3 and inductor L2. The capacitor C3 holds the voltage and helps to boost up the charge, the operational switch controls the duty cycle and diode D7 protects the other parts excluding the boost circuit from the reverse current of the boost converter. The boosted output is found across the resistor R3. Similarly, the boost converter for 72-volt output is made of operational switch Op_Sw3, Diode D10, Capacitor C4 and inductor L3. The capacitor C4 holds the voltage and helps to boost up the charge, the operational switch controls the duty cycle and diode D9 protects the other parts excluding the boost circuit from the reverse current of the boost converter. The boosted output is found across the resistor R4.

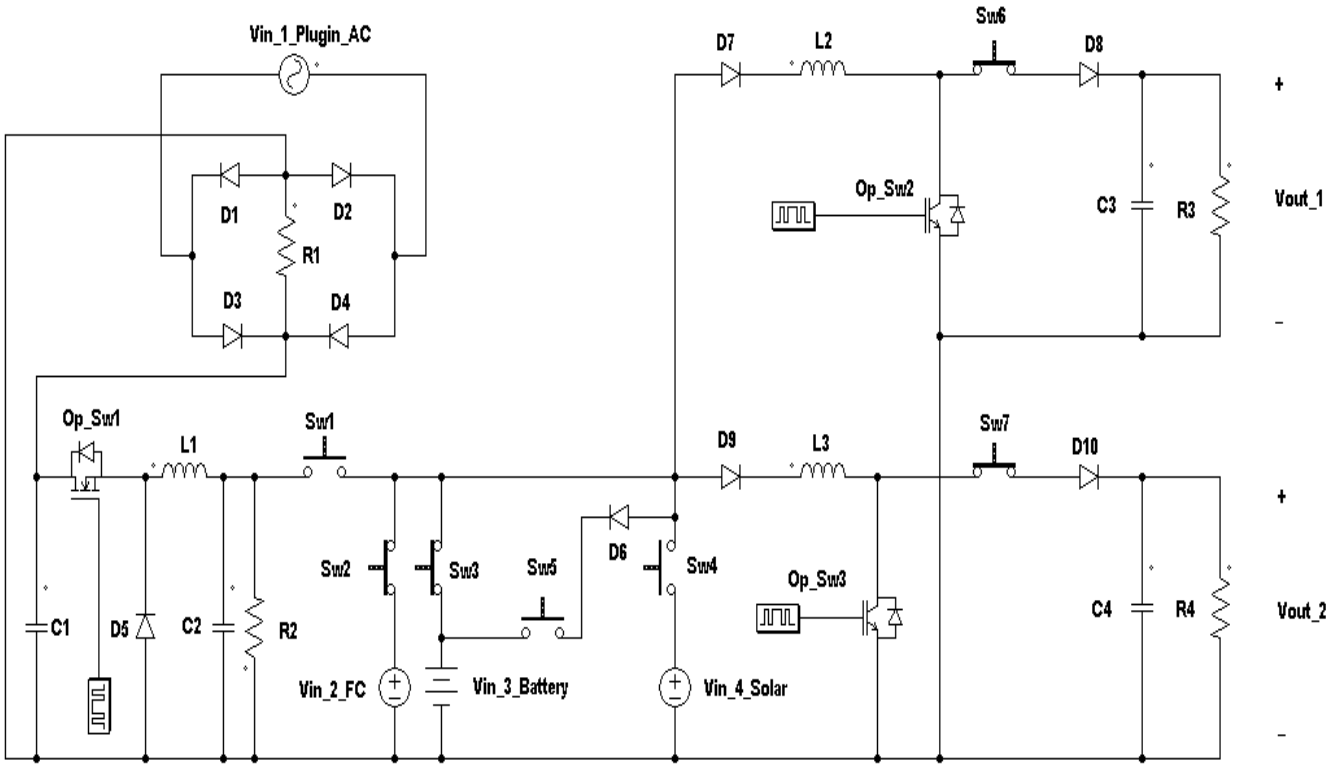

Fig. 1. Multi-input dual-output DC-DC boost converter.

TABLE I. DIFFERENT VEHICLE VOLTAGE

Sl. No	Model/Type	Battery Voltage Range (Volt)
1	Renault Twizy	12 & 400
2	Toyota Pirus PHEV	12 & 650
3	Honda Accord PHEV	12 & 320
4	Mitsubishi Outlander PHEV	12 & 300
5	Tesla Cars	250-425
6	S S Limited	12 & 48
7	Golf Car	12 & 48
8	Street Legal	12 & 48
9	People Mover	12 & 72
10	Off Road Riding or Hunting	12 & 48
11	Industrial or Commercial	12 & 72

III. Operation Mode

The modes are divided mainly into three types- full stop mode, a partial active mode where only 24 voltage is active and finally the fully active mode where both 24 and 72 voltage outputs are active. Various kinds of situations may arise with a hybrid electric vehicle in these modes. Some important situations are described here.

A. Full Stop Mode

This is also known as battery charging mode and here dual outputs are inactive through switch Sw6 and Sw7 and case wise input source switches are ON for charging the battery and also others remain OFF. Battery charging line is ON

through switch Sw5 and diode D6 protects the other elements from battery reverse current.

- Case 1: When electricity, solar and fuel cell are available then the battery is charged by electricity and solar through switch Sw1 and Sw4 and operational switch Op_Sw_1 is in operation for getting charged by electricity. Proposed circuit is shown in Fig. 2.

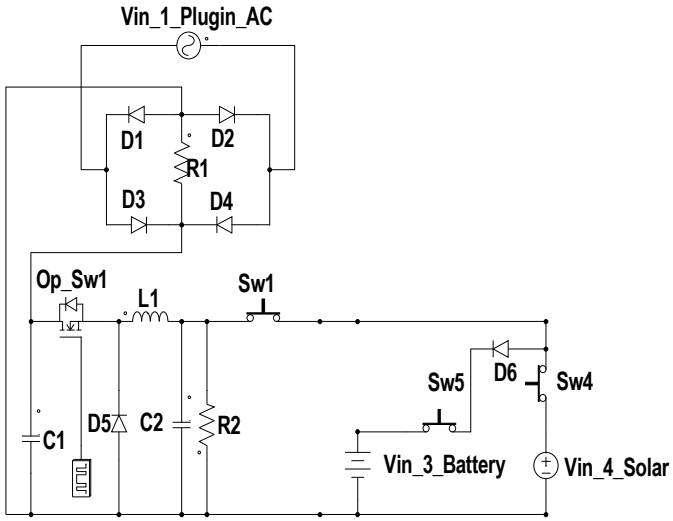

Fig. 2. The battery is getting charged by electricity and solar.

- Case 2: When electricity and fuel cell are available then the battery is just charged up by plugin AC voltage through switch Sw5. Proposed circuit is in Fig. 3.

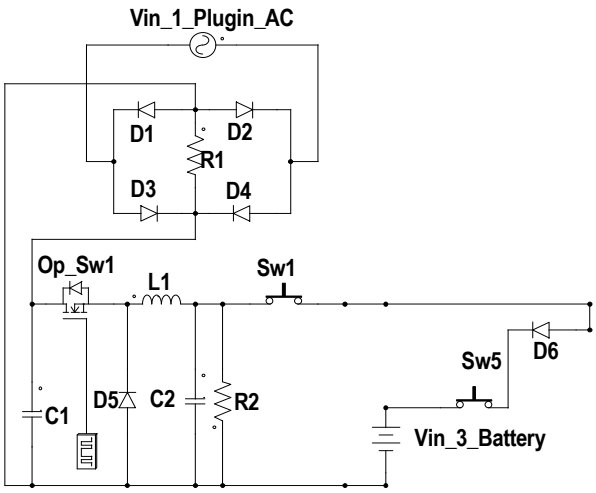

Fig. 3. Battery is charged by electricity.

B. *Partially active Mode (Only 12 V required)*

In this case, only 24-volt output is active through switch Sw6 and operational switch Op_Sw_2 is in operation. Case wise input source switches are on and others remain off. The 24-volt boost up process from 9 volt is achieved by inductor L2, diode D8, capacitor C3. Outputs are found across resistor R3 and diode D7 protect the other elements of the circuit from the reverse current.

- Case 1: When battery, electricity, solar and fuel cell are available then the output is powered by the solar cell through switch Sw4. Proposed circuit is given in Fig. 4.

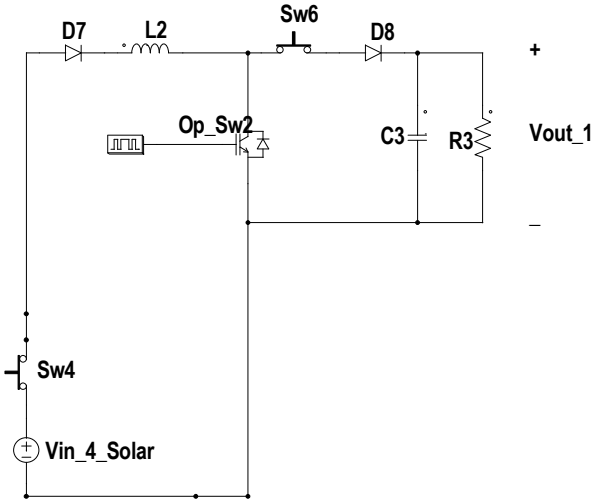

Fig. 4. Output is powered by solar cell.

- Case 2: When battery and fuel cell are available then output is powered by battery through switch Sw3. In this mode, the output 24 volt is powered by battery. Proposed circuit is given in Fig. 5.

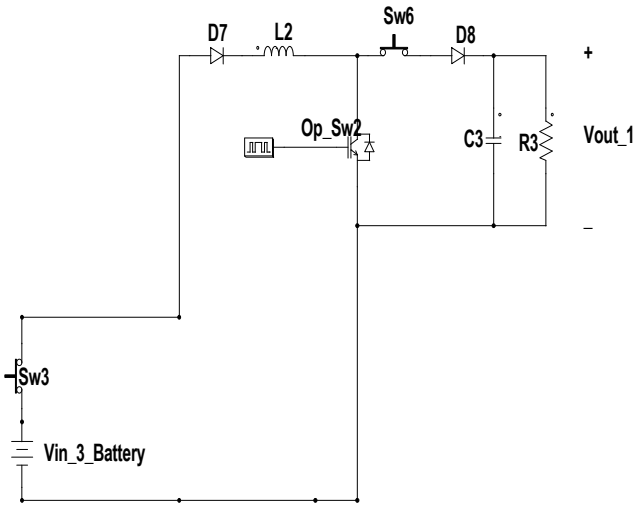

Fig. 5. Output is powered by battery

C. *Fully active Mode*

Dual outputs are active through switches Sw6 and Sw7 in this mode and operational switches Op_Sw_2 and Op_Sw_3 are active, case wise input source switches are on and others remain off. The 24-volt and 72-volt boost up process from 9-volts are achieved respectively by inductor L2, diode D8, capacitor C3 and inductor L3, diode D10, capacitor C4.

Outputs are found across resistor R3 and resistor R4. Diode D7 and diode D8 protect the other elements of the circuit from the reverse current.

- Case 1: When battery, solar and fuel cell are available outputs are powered by solar cell through switch Sw_4. Proposed circuit is given in Fig. 6.

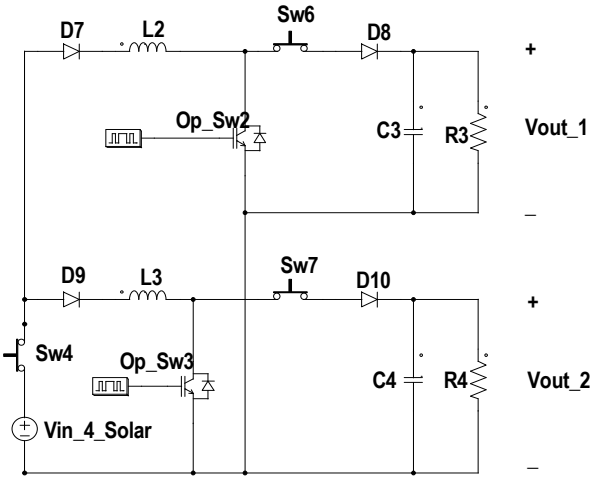

Fig. 6. Outputs are powered by solar cell.

- Case 2: When solar and fuel cell are available and the battery is empty then outputs are powered and battery is charged by the solar cell through switches Sw4 and Sw5. Battery switch Sw5 is off after charging and outputs are powers by solar cell through switch Sw4. Proposed circuit is given in Fig. 7.

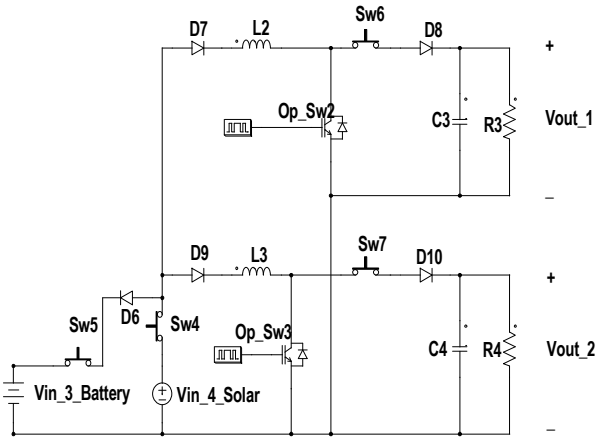

Fig. 7. Outputs and battery are powered by the solar cell.

IV. PERFORMANCE PARAMETER

In order to verify the performance of the proposed converter simulation have been done for the fully active mode with the battery is fully charged and solar and fuel cells are available by PSIM software. The input solar voltage is considered as 9 volt and outputs are desired to be 24 volt and 48 volt. Switches Sw4, Sw6 and Sw7 are active besides operational switches Op_Sw_2 and Op_Sw_3 are in operation mode. The output voltage and current curves are shown in Fig. 8 and data of the performance parameters of both outputs are given in Table II.

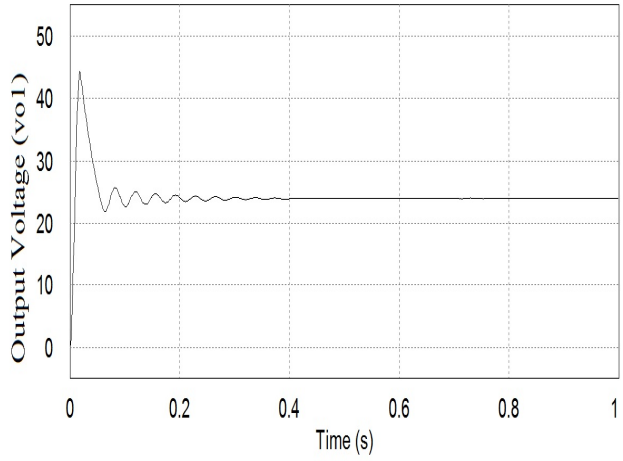

(a)

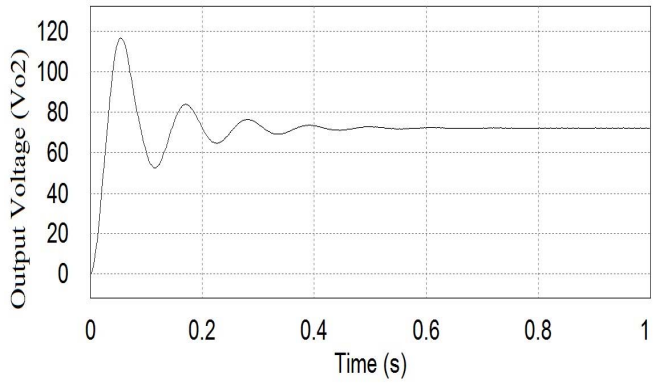

(b)

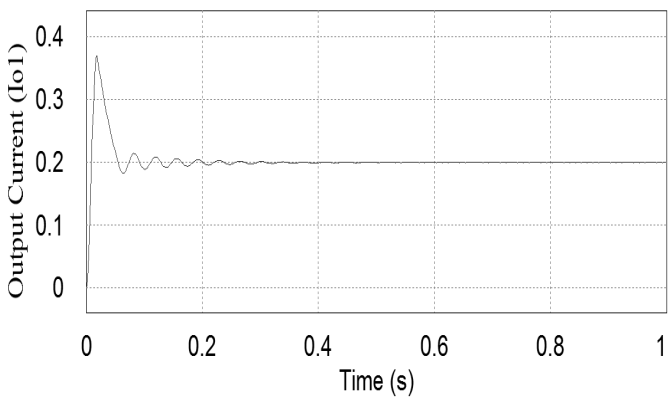

(c)

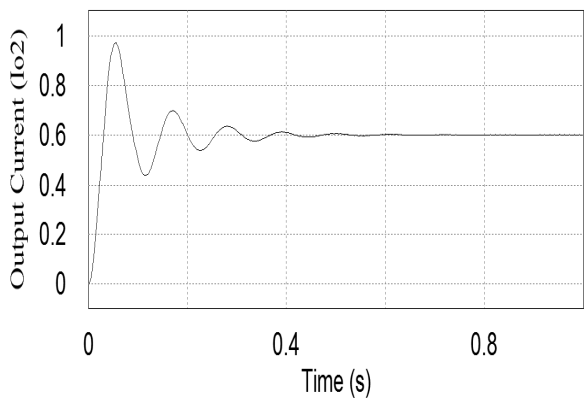

(d)

Fig. 8. Output voltage of converter (a) Vo1 (b) Vo2 and Output Current of the converter (c) Io1 (d) Io2

TABLE II PERFORMANCE PARAMETERS FOR BOTH OUTPUTS.

Performance Parameters	Vo1 (24 Volt)	Vo2 (72 Volt)
Delay time, t_d	6.67 ms	19 ms
Rise time, t_r (10% to 90%of its final value)	6.05 ms	19.85 ms
Peak time, t_p	18 ms	54.89 ms
Settling time, t_s	209 ms	440 ms
Percentage of overshoot, PO%	83.33 %	61.8 %

The transient performance can be significantly improved if concepts of control theory can be applied. For instance, an appropriate PID controller can be designed to decrease the percentage of overshoot as well as other parameters such as rise time, settling time, delay time etc. As far as the final value is concern, the system makes almost zero steady state error.

V. Research Limitation

The improvement of HEV design over conventional vehicle is largely on converter efficiency. To verify the optimal design of vehicle converter circuit, validation using costly prototype is expensive and sometimes impractical. PSIM simulation is a method for fast and systematic investigation of different design options and configurations, including the choice of various types of battery, transmission, fuel cells, renewable fuel sources, etc. as well as their parameters. Therefore, simulation based analysis on vehicle performance is both useful and crucial to the development of new hybrid vehicles. At present, the available vehicle simulation tools cannot support the modeling and analysis of all vehicle design options, rather than focusing on very specific applications. Considerable work is needed to introduce more capable and reliable converter modeling and simulation tools to guide new hybrid vehicle design.

VI. Future Prospects

The research forms the foundation for further studies on the modeling and analysis of advanced hybrid vehicle converter configurations using advanced modeling and simulation tools. The preliminary studies on renewable hybrid power system for elevating power backup system; the three mode hybrid vehicle converter configuration; and the use of PSIM to model complex hybrid vehicle converter design and thus provide promising research directions that deserve further study.

VII. Conclusion

A multi-input-dual-output DC-DC boost converter is proposed for hybridizing the input power source and furthermore can be used in transferring energy between different energy resources such as electricity, fuel cell, solar and energy storage system such as battery in this paper. Battery is used power source and energy storage system dually. This converter also can be used as single input single output converter as well as the multi-input-multi-output DC-DC boost converter. The converter have three main operation mode, full stop mode, partial active mode where 24 voltage is active and fully active mode where both 24 and 72 voltage are active. It is seen that under different conditions when the resources are not available to feed the sufficient voltage in the input, a microcontroller sensor is used and applied here that senses the instant intensity and availability of resources and changes the duty cycle of the operational switches that is made of IGBT to sustain the fixed level output voltage. It could be practically verified but shortage of resources and software older version, it has not possible yet. As it emphasizes the use renewable energy, the proposed circuit can be thought to be more efficient than others in the sense.

VIII. References

[1] Nahavandi A., Hagh M.T., Sharifian M.B.B., Danyali S., "A Nonisolated Multiinput Multioutput DC–DC Boost Converter for Electric Vehicle Applications" Power Electronics, IEEE Transactions vol. 30,Issue no. 4, pp. 1818 - 1835, May.2014

[2] X. Zhang, C. Mi, "Vehicle Power Management", springer, 2011.

[3] M. Ehsani, Y. Gao, A. Emadi, "Modern Electric, Hibrid electric and Fuel Cell vehicle Fundamentals, Theory and Design", second edition, CRC Press, New York, 2010.

[4] T. Bhattacharya, V. S. Giri, K. Mathew and L. Umanand, " Multiphase Bidirectional Flyback Converter Topology for Hybrid Electric Vehicle" IEEE Trans. Industrial Electron, vol. 56, no. 1, pp. 78-83, January. 2009.

[5] Hasaneen, B.M. and Mohammed, A.A.E.; "Design and simulation of DC/DC boost converter", Power System Conference, 2008. MEPCON 2008. 12th International Middle-East

[6] Renault Twizy Electric Vehicle. Available at: http://www.sevcon.com/renault-selects-sevcon-to-provide-controllers-for-twizy.aspx

[7] Toyota Pirus Hybrid Vehicle Dismantling Manual , Available: https://techinfo.toyota.com/techInfoPortal/staticcontent/en/techinfo/html/prelogin/docs/priusphvdisman.pdf

[8] Emergency Response Guide of Honda Accord, Available: https://techinfo.honda.com/rjanisis/logon.asp

[9] Mitsubishi Outlander PHEV 2013 New York International Auto Show, Available:http://media.mitsubishicars.com/releases/b3d9a889-c5c2-4f5b-abca-32c6babfe042

[10] Tesla Motors, Power Control, Available: http://my.teslamotors.com/roadster/technology/power-electronics-module

[11] Star electric Vehicle Website , Available at: http://www.starev.com

[12] Muhammad H. Rashid, "Power Electronics: Circuits Devices and Applications." 3rd edition, Pearson Education, 2007, Chapter 5.

Artificial Neural Network based Soft-Starter for Induction Motor

Tuton Chandra Mallick, Sharith Dhar
Department of Electrical & Electronic Engineering
Premier University
Chittagong, Bangladesh

Jubaer Khan
Department of Electrical & Electronic Engineering
Chittagong University of Engineering & Technology
Chittagong, Bangladesh

Abstract— **the necessity of soft-starter is increasing day by day to reduce the starting current & to maintain the torque smoothly according to the load requirement. Now intelligent soft-starter is developed to improve the performance of conventional starter. This paper focused on the designing of an artificial neural network controlled soft-starter. Back-propagation algorithm is used as learning algorithm in the artificial neural network. Error correcting capability of this learning algorithm makes it more suitable to use in neural network. For comparative performance analysis two different types of back propagation algorithms are used in the neural network learning process. According to condition of learning rate parameter gradient descent with momentum back-propagation algorithm provide better response. A comparative study between conventional starting method (Direct on Line) and proposed soft-starter. Artificial Neural Network controlled soft-starter is able to reduce starting current compared with DOL method & able to accelerate the load at starting period efficiently compared with star-delta starting method.**

Keywords—ANN, Soft-starter, back-propagation etc.

I. INTRODUCTION

In recent years with the development of the industrialization and the need of electrical system for manufacturing processing of the goods are taking more attention for use of efficient & easy controllable equipment. Electrical machine are one of the most common in industries. Induction motor (IM) is replacing the traditional motor like DC or Synchronous motor due to their features like low cost, rigid construction & easy control mechanism in the industrial processing. Controlling their speed, torque & current are taking much more attention in the research and development. Today's Induction motor starting is the most challenging task. The starting process of induction motor effects on the entire power system adversely. Due to the rapid technological progression the application of the power electronic devices & AC drives are increasing day by day. To maintain the power system quality, appropriate starting technique should be used otherwise electrical network fluctuation may be occurred which affects the all running electrical & electronic devices that are connected to the victim power system. During the choice of starting methods some factors need to be considered which are inrush current, torque, voltage dip, acceleration time, frequency dip, robustness, cost, reactive power & starting power factor [1]. There are different types of starting techniques such as Primary resistor, Star-delta, Auto transformer etc. [1]. These starting techniques are not enough to reduce the inrush current [6]. To overcome this problem soft starter becomes useful to start up the motor smoothly. The torque can be adjusted according to the condition of loading [5]. Today it is needed to start motor more smoothly according to the variation of the load in order to avoid unwanted situation. Although soft starter performs better than conventional starting systems to start motor smoothly, it has also some drawbacks that makes it imperfect to the application where smooth starting with different loads is the big concern. To overcome the problems of conventional soft- starter, intelligent soft-starter is being used. The intelligent soft-starter should have the ability to adapt to a new environment & to changes in the current environment, the ability to acquire knowledge from the environment, capacity for reason & abstract thought, ability to evaluate & judge [7]. The features mentioned above makes the soft-starter intelligent to start motor so smoothly with variation of loads that desired response can be achieved without any mechanical hazards.

The big revolution in the control scheme comes with the application of intelligent algorithms in the control system. Soft-starter of an Induction Motor (IM) using Neural Network (NN) based Feedback Estimator can control the inrush current & adjust the firing angle of thyristor for a specified load. This ANN based controller have two inputs (torque & speed) & single output (firing angle) [3]. Soft starting of an induction motor using adaptive neuro-fuzzy inference system reduces the inrush current & vibrations in the output torque. This controller uses artificial neural networks (ANN) & adaptive neuro-fuzzy inference system (ANFIS) based intelligent techniques for the selection of the firing angle of the thyristor of the voltage controller fed induction motor and moreover the speed characteristics is not good enough compare to reference speed [2]. Soft-starting of induction motors using ANN & adaptive neuro-fuzzy inference system uses ANN estimator to adjust the firing angle of thyristors of AC voltage controller under different loading conditions. This soft-starting system eliminates pulsations in the developed torque & controlled inrush current significantly [4].

978-1-4673-9257-0/15/$31.00 ©2015 IEEE

II. NN BASED INTELLIGENT SOFT-STARTER

Our developed system composed of five main parts which are supply unit, thyristor unit, synchronizationunit, syncronized pulse generator & artificial neural network controller. Fig.-1 shows the design flowchart. Six back to back thyristors are fired by a pulse generator. The thyristor unit is placed between the supply and Induction Motor. A synchronization unit gives the information about the supply voltage's phase and frequency according to which thyristors gets fired. The Artificial Neural Network (ANN) Controller gives the gate delay to pulse generator. According to the control signal the power flow to the motor is controlled hence the starting current is reduced. We used artificial neural network based controller that makes the soft-starter intelligent.

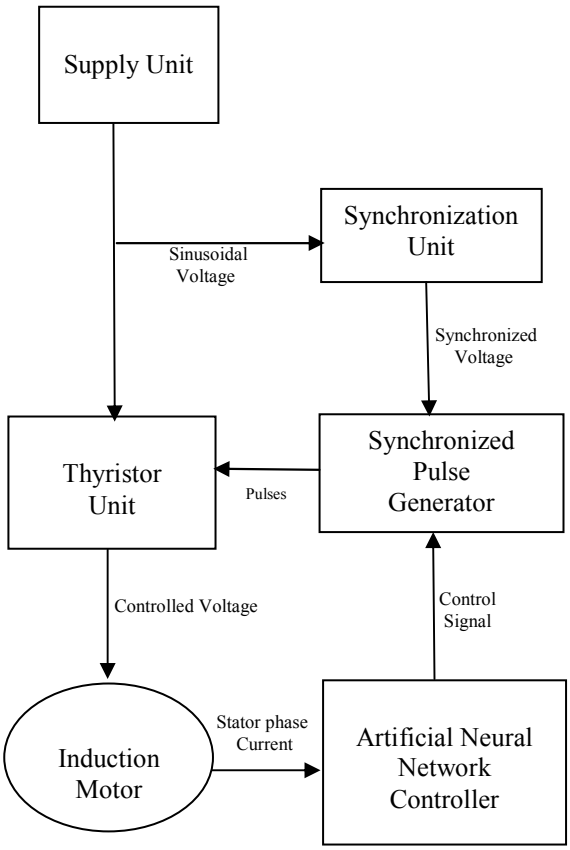

Fig. 1. Functional Representation of the control process.

A. Supply Unit

We used three AC voltage source for three phase supply each have 330V peak amplitude that provide 233V r.m.s phase to neutral voltage. The three phase supply unit is given in figure-2.

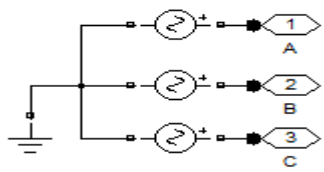

Fig. 2. Simulation model of three phase supply unit.

B. Synchronization Unit

The function of synchronization unit is to provide three line to line synchronization voltages for synchronized pulse generator. These synchronization voltages are made from supply end by building delta loop with using voltage measurement blocks. The output voltages of the

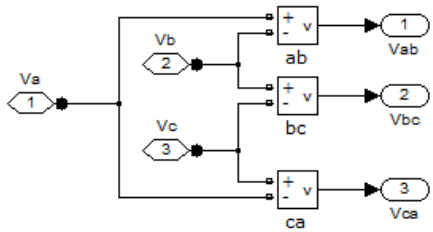

synchronization unit are connected to the six synchronized pulse generator. The simulation model of synchronization unit is shown in figure-3

Fig. 3. Simulation model of synchronization unit

C. Synchronized Pulse Generator

The synchronized pulse generator produces gate pulses for thyristor unit; pulses are generated alpha degree (delay angle) after the increasing zero crossing of the thyristors commutation voltages. The thyristor unit consists of six back to back thyristors shown in Fig.4. We configured our pulse generator to function in double pulsing mode & 60 degrees pulse width. In double pulsing mode, two pulses are provided for each thyristor; after reaching delay angle (alpha degree) the first pulse is sent, then 60 degree later the second pulse is sent.

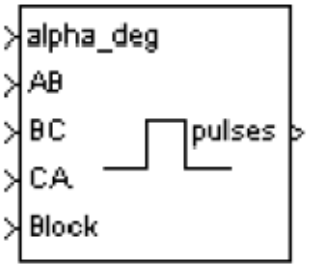

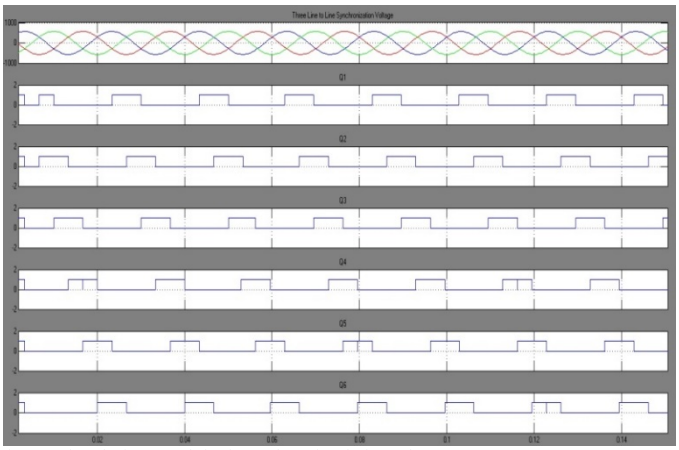

Fig. 4. Simulation model of synchronized six pulse generator
Fig. 5. Generated six gate pulses for 'traingda' training function by the synchronized 6 pulse generator.

It is important to note that, the delay angle (alpha degree) of the pulse generator is supplied from the intelligent controller. The intelligent controller controls the starting voltage & current by providing appropriate delay angle. The simulation model of the six pulse generator is shown in figure-4. Figure-5 shows Generated six gate pulses for 'traingda' training function by the synchronized 6 pulse generator.

D. Thyristors Unit

This unit consists of three pairs of back to back thyristors. Each pair of back to back thyristor is connected in series with single phase supply; other end of back to back thyristor connection is connected in series with motor terminal.

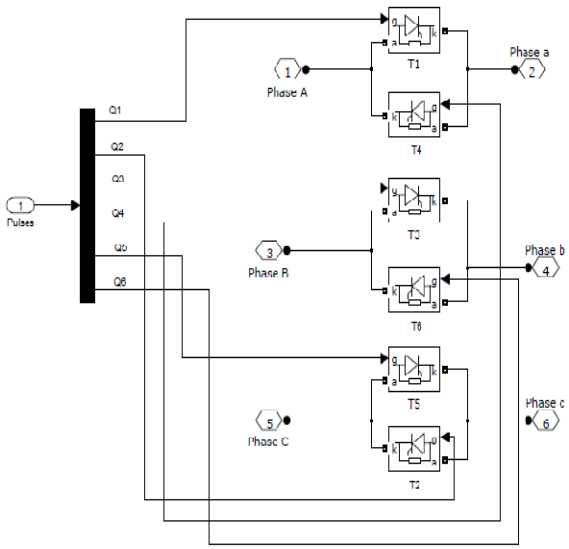

Fig. 6. Simulation model of three pairs of back to back thyristors

Figure-6 shows the back to back connection of six thyristors. The gate pulses of the thyristors are provided by synchronized six pulse generator that describes previous section. The thyristor is a semiconductor (power electronics) device that can be turned on via a gate signal (gate pulses). The series snubber circuit is connected in parallel with each thyristor. The value of snubber resistance (Rs) is set to 500ohm & snubber capacitance (Cs) is set to 250e-9F. Snubber circuit has been used to give a dv/dt protection.

E. Nerural Network Controller

During starting period, intelligent controller provides delay angle of α = 30.06 degree; pulses are generated after zero crossing of the line to line voltages. This delay angle (α = 30.06) is constant for 0 to 0.05 second, then from 0.05 to 0.1 second the delay angle α = 22.35 degree remains constant, α = 21.11 degree is constant for time 0.1 to 0.15 second; α = 25.31 degree is constant for 0.15 to 0.2 second & so on. According to these delay angles, the gate pulses are shifted & according to these gate pulses the thyristors are fired. Figure-7 shows the control signal (delay angel) generated by ANN controller.

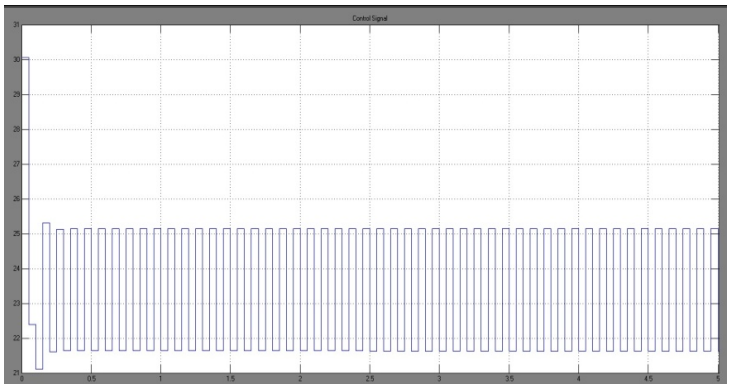

Fig. 7. Control signal (delay angle) generated by NN controller.

III. ARTIFICIAL NEURAL NETWORK

Artificial neural network' formed in a manner based on biological neural network. Basically the artificial neural network is the mathematical model or the computational model consists of artificial neurons where neurons are interconnected in a group. Biological neural network consists of real biological neurons which are connected according to the information supplied through in the nervous system; in the area of neuroscience they are formed groups that perform a particular physiological task. On the other hand, artificial neural network made up of interconnecting artificial neurons which have the properties of biological neurons. In the artificial neural network, information processing is done by the connectionist that approach to computation. Artificial neural network may change its construction external or internal way that flow through the network during learning period. We used 'model reference control' neural network

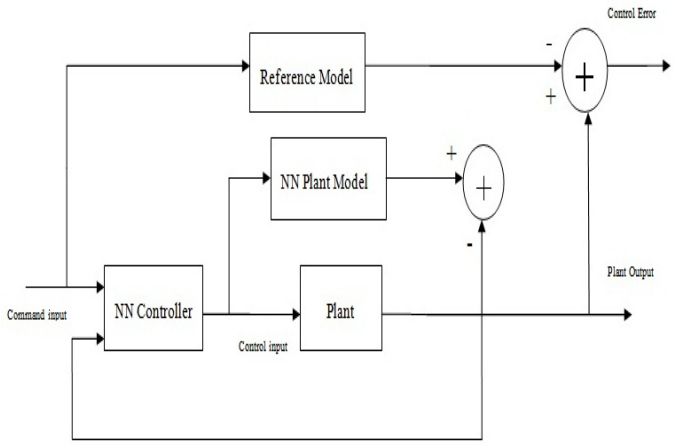

toolbox from MATLAB which act as an artificial neural

Fig. 8. Internal connection between NN controller network & plant model network.

network based controller. The controller structure uses two neural networks one is controller network & other is plant model network. Figure-8 indicates the internal connection between two networks. At first, plant models is identified. Neural network plant model is created on the basis of plant model's input-output characteristics then NN plant model is trained so that it can predict future plant output. In the NN controller, a set of output data is generated for reference model After that the controller is trained such a way that the plant output follows the reference model. On the basis of following characteristic, the NN controller generate control signal which is connected to the soft-starter as 'delay angle'. The NN plant model & NN controller both have three layers; one of them is input layer and other two are hidden layer & output layer. There is an option to select number of neuron to use in the hidden layers. For training artificial neural network plant model, a training function named 'traingda' has been used which is a gradient descent with adaptive learning rate back propagation algorithm that updates weights & bias values according to the gradient descent with adaptive learning rate [8]. For training the controller we used training function 'trainbfgc' (BFGS quasi-Newton back propagation). It is a network training function that updates weight and bias values according to the BFGS quasi-Newton method [8].

IV. SIMULATION

A MATLAB based simulation model has designed to simulate the ANN controlled soft-starter. In this simulation model we used three phase squirrel cage motor; the stator & rotor winding of the motor are connected in wye connection to an internal neutral point. The rating & internal specifications of the induction motor are given below:

Rated voltage	= 230V
Frequency	= 50Hz
Rated speed	= 1430rpm
Rated power	= 4KW
Mechanical Input (Load)	= 10 Nm
Stator resistance	= 1.405 ohm
Stator inductance	= 0.005839H
Rotor resistance	= 1.395 ohm
Rotor inductance	= 0.005839H
Mutual inductance	= 0.1722H
Inertia	= 0.0131 Kg.m²
Pole pairs	= 2

Figure-9 represents simulation model of soft starting method with artificial intelligent controller. Simulation model consists of Synchronization unit provides three line to line synchronization voltages for synchronized pulse generator. These synchronization voltages are made from supply end by building delta loop with using voltage measurement blocks. The output voltages of the synchronization unit are connected to the synchronized pulse generator. The artificial neural network controller provides control signal (delay angle) for the pulse generator. The reference input of the artificial neural network controller is stator phase current of the induction motor. The starting current of the induction motor basically controlled by control signal that produced from artificial neural network controller. Thyristor unit controlled the stator phase voltages according to the gate pulses generated by synchronized pulse generator. The gate pulses are connected to the gate inputs of the corresponding thyristors.

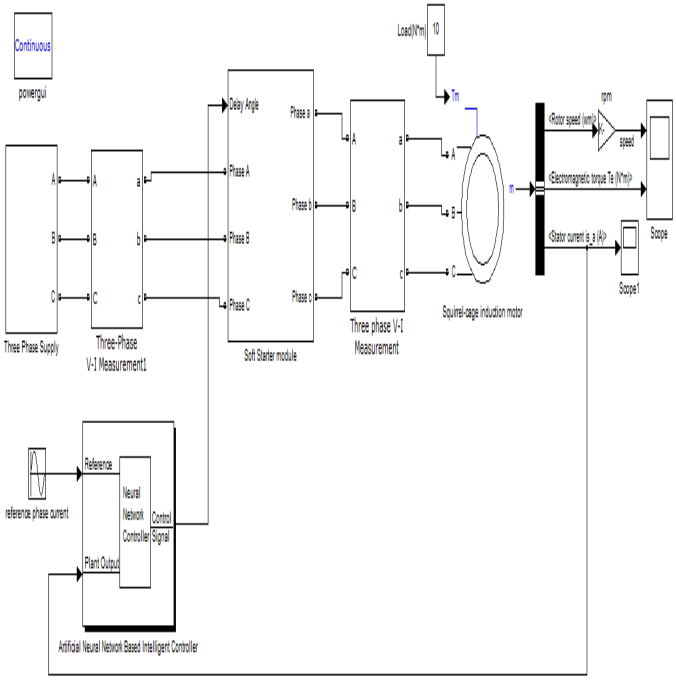

Fig. 9. Simulation model of the soft starting method with artificial neural network controller

V. RESULT & ANALYSIS

For 10 Nm load, the stator phase current of the direct on line (D.O.L) method are shown in fig-10. Fig.10 shows the starting current of DOL method is 81.66A (Peak) & after 0.08 sec. This current reduces to 6.82A (Peak) at running condition. For 'traingda' training function, starting current of soft-starting method is 73.8A (peak) shown in fig-11; that means 7.86A (peak) current is reduced from D.O.L starting current. The current during running condition is 6.8A (peak). The accelerate torque is 124.4 Nm that is enough to accelerate the load during starting condition; the rated speed is reached after 0.15 sec which have been shown in fig-12 and fig-13.

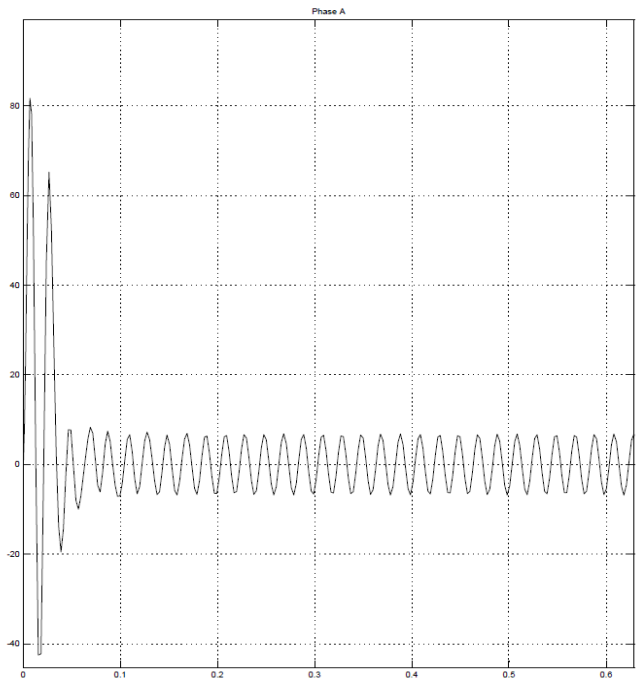

Fig. 10. Stator phase current of direct on line method

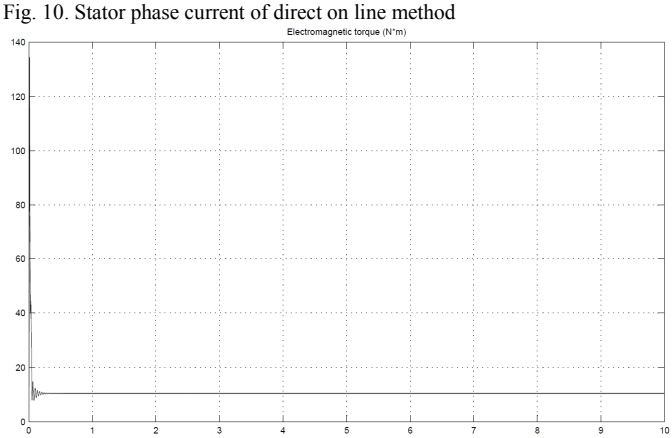

Fig. 12. torque characteristics of intelligent soft-starting method using 'traingda' training function

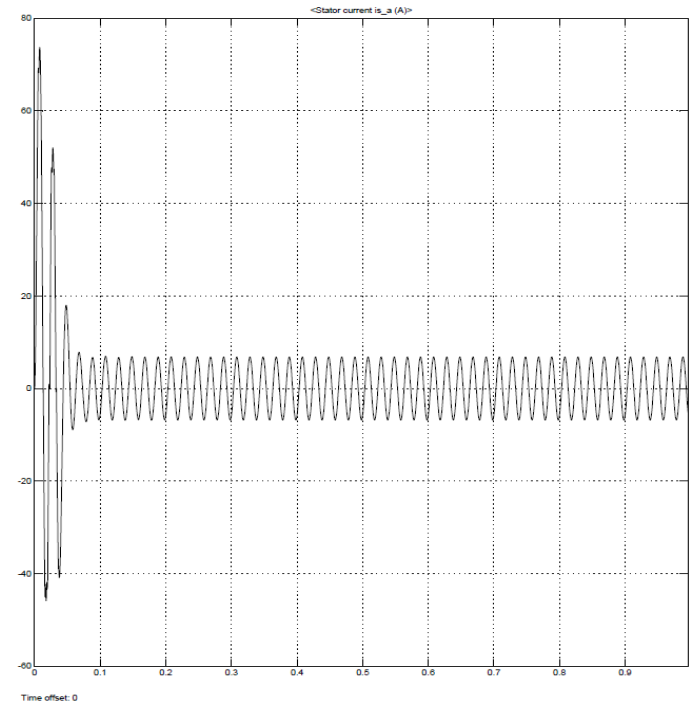

Fig. 11. Stator phase current of intelligent soft-starting method using'traingda' training function

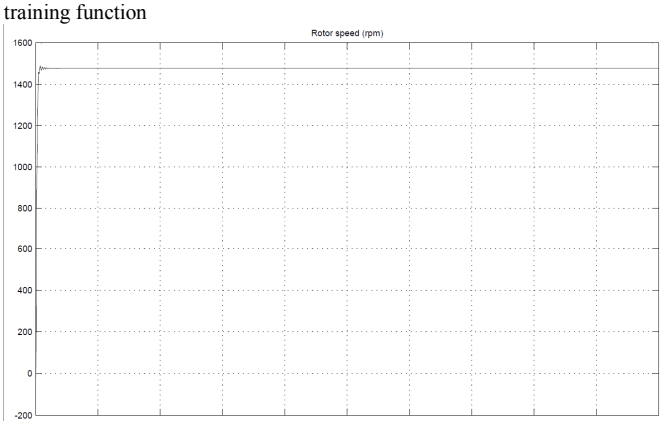

Fig. 13. Speed characteristics of intelligent soft-starting method using 'traingda' training function

.

VI. CONCLUSION

A neural network based soft-starter has been shown in this paper. An improved result has been achieved compare to conventional DOL starter and also with the improved new less starting current an adequate speed-torque goal has been achieved. Here on the simulation only one phase has counted for the simplicity.

REFERENCES

[1] Adam John Wigington, "A Comparison of Induction Motor Starting Methods Being Powered by a Diesel-Generator Set," M.S. thesis, University of Nebraska, Lincoln, Nebraska, July. 2010.

[2] A.R. Kashif and M.A. Saqib, "Soft starting of an Induction Motor Using Neuro-Fuzzy Inference system*" in Proc. IEEE Int. Conf. Electrical Eng. 2007 ,pp.1-5*

[3] M.A. Saqib, A.R. Kashif and Tehzeeb-ul-Hassan, "Soft Starter of an Induction Motor using Neural Network Based Feedback Estimator," *in Proc. IEEE Int. Conf. power Eng., Dec. 2007, pp. 1–5.*

[4] Syed Abdul Rahman Kashif and Muhammad Asghar Saqib, " Soft Starting of Induction Motors using Neuro Fuzzy and Soft Computing*" in Proc. IEEE Int. Conf. Electrical Eng., March. 2008,pp.1-7*

[5] *Soft starter Hand book*, ABB, 2003.

[6] Yuan Youxin Xia Zezhong Wang Yalan Yuan Peigang Peng Wanquan, " A Soft starter of Three Phase Asynchronous Motor *" in Proc. IEEE Int. Conf. power Electronics specialists, 2007,pp.563-567*

[7] Simon Haykin*, Neural Network: A comprehensive foundation*, Pearson Education, 1999

[8] http://www.mathworks.com/

Analysis of Common-Mode Rejection Ratio of a CMOS Differential Amplifier Considering All the Non-idealities

[1]Madiha Amina, [2]Protik Biswas, [3]Aman Ullah, [4]Md. Iqbal Bahar Chowdhury
Department of Electrical and Electronic Engineering
United International University
Dhaka, Bangladesh.
[1]opsara@ymail.com, [2]protik_biswas@yahoo.com, [3]amanullah.en@gmail.com, [4]ibchy@eee.uiu.ac.bd

***Abstract*—This paper attempts an analytical approach to accurately determine common-mode rejection ratio (CMRR) considering the effects of various non-idealities such as the presence of channel length modulation, body effect, finite resistance of the current source, mismatches in transconductances and drain resistances between the two driver MOSFETS of a common source CMOS differential amplifier. This analysis brings to light the hitherto unforeseen dire impacts of these non-idealities put together on CMRR, and hence strongly suggests that these effects should not be, in any ways, ignored from theoretical calculations for CMRR. Moreover, the work would be helpful for researchers in this field to have a better insight on the differential amplifier circuits.**

***Index Terms*—Common-Mode Rejection Ratio, Common Source CMOS Amplifier, Differential Amplifier, Non-idealities.**

LIST OF SYMBOLS

$CMRR$ = Common Mode Rejection Ratio
$A_{V,DM}$ = Differential-mode gain of the differential pair
$A_{V,CM-DM}$ = Common-mode gain of the differential pair
M_1 = 1st one of the two n-channel MOSFETs (on the left hand side of the differential pair)
M_2 = 2nd one of the two n-channel MOSFETs (on the right hand side of the differential pair)
g_{m1} = Transconductance of M_1
g_{m2} = Transconductance of M_2
CLM = Channel Length Modulation
g_{mb1} = Transconductance of M_1 due to body effect
g_{mb2} = Transconductance of M_2 due to body effect
V_{bs1} = Body-to-source voltage in M_1
V_{bs2} = Body-to-source voltage in M_2
R_{D1} = Drain resistance of M_1
R_{D2} = Drain resistance of M_2
r_{01} = Channel resistance of M_1
r_{02} = Channel resistance of M_2
V_{DD} = Supply DC Voltage
V_{in1} = Small AC signal applied to the gate of M_1
V_{in2} = Small AC signal applied to the gate of M_2
V_x = Drain voltage of M_1
V_y = Drain voltage of M_2
V_p = Voltage at the common source of M_1 and M_2
V_{bs1} = Body to source voltage of M_1
V_{bs2} = Body to source voltage of M_2
I_{ss} = Current through the current source
I_x = Current through R_{D1}
I_y = Current through R_{D2}
R_{ss} = Resistance of the current source

I. INTRODUCTION

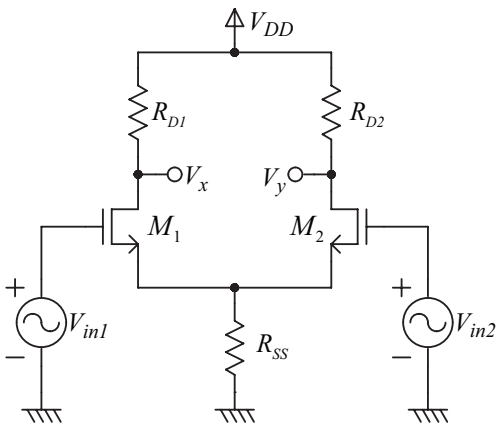

Fig. 1. A common source CMOS differential amplifier made of two similar n-channel MOSFETS

The name Differential Amplifier itself well describes its functionality. The resultant output voltage is simply the difference between the amplified output drain voltages, V_x and V_y, due to the two inputs, V_{in1} and V_{in2}, as shown in Fig. (1). When a differential signal is chosen as input to the differential pair, the unexpected environmental noise, which is very obvious to appear in analog circuits, is cancelled out automatically during the operation [1]. This particular property, besides many others, makes the differential amplifier an important building block in analog circuits. The primary concern while using differential amplifiers is to get a greater

978-1-4673-9257-0/15/$31.00 © 2015 IEEE

amplification of differential-mode input voltages while suppressing the common-mode input voltages. In doing so, the effectiveness of the differential pair in rejecting common-mode interference is termed as CMRR.

A high value of CMRR is expected in regular applications, especially in electro-encephalography where the amplifier is expected to respond to two small anti phase signals. However, the signals may appear in phase with each other with a larger interfering voltage. In that case, CMRR must have a pretty high value, preferably over 90 dB [2]–[5].Until now, several works have been done to improve the performance, especially CMRR, of CMOS differential amplifiers, but comparatively very few works have been focused on the precise mathematical derivation of CMRR [2], [3], [6], [7]. Moreover, the available models do not consider all the non-idealities that affect CMRR and make its nature less deterministic [1], [8].

This work, on the other hand, includes all the non-idealities, which are: the presence of CLM and body effect, finite resistance (R_{ss}) of the current source and mismatches between transconductances (g_m) and drain resistances (R_D) in M_1 and M_2 .

II. Analysis

The following analysis is done considering all the non-idealities mentioned in the previous section, i.e., the presence of CLM for which $r_{01} \neq \infty$ and $r_{02} \neq \infty$, the presence of body effect for which $g_{mb1} \neq 0$ and $g_{mb2} \neq 0$, finite resistance of the current source ($R_{ss} \neq \infty$), mismatch between the transconductances ($g_{m1} \neq g_{m2}$) and mismatch between the drain resistances ($R_{D1} \neq R_{D2}$).

The CMRR of a common source CMOS differential amplifier can be stated as:

$$CMRR = \frac{A_{V,DM}}{A_{V,CM-DM}} \tag{1}$$

A. Differential Mode Gain

For a differential signal input, $A_{V,DM}$ of the differential pair have the following expression:

$$\begin{aligned} A_{V,DM} &= \frac{V_x - V_y}{V_{in1} - V_{in2}} = \frac{V_x - V_y}{2V_{in1}} \\ &= \frac{1}{4}\left[\left(\frac{V_x}{V_{in1}} - \frac{V_y}{V_{in1}}\right) - \left(\frac{V_x}{V_{in2}} - \frac{V_y}{V_{in2}}\right)\right] \end{aligned} \tag{2}$$

where $\frac{V_x}{V_{in1}}$ can be determined with the application of superposition theorem. When V_{in2} is considered to be zero, according to Fig. (2), the effect of V_{in1} on V_x can be shown as:

$$\frac{V_x}{V_{in1}} = -\frac{g_{m1} r_{01} R_{D1}}{(g_{m1} + g_{mb1}) R_{s1} r_{01} + R_{s1} + r_{01} + R_{D1}} \tag{3}$$

where $R_{s1} = R_{s1}\prime \parallel R_{ss}$ and

$$R_{s1}\prime = \frac{1 + \frac{R_{D2}}{r_{02}}}{g_{m2} + g_{mb2} + \frac{1}{r_{02}}}$$

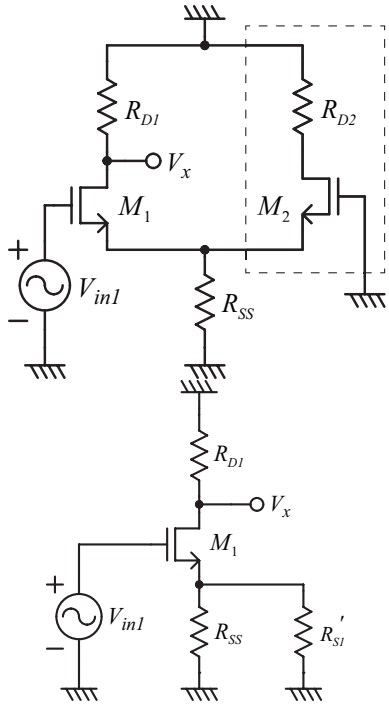

Fig. 2. AC Analysis: Effect of V_{in1} on V_x, where $V_{in2} = 0$

Similarly, the effect of V_{in2} on V_y can be expressed as:

$$\frac{V_y}{V_{in2}} = -\frac{g_{m2} r_{02} R_{D2}}{(g_{m2} + g_{mb2}) R_{s2} r_{02} + R_{s2} + r_{02} + R_{D2}} \tag{4}$$

where $R_{s2} = R_{s2}\prime \parallel R_{ss}$ and

$$R_{s2}\prime = \frac{1 + \frac{R_{D1}}{r_{01}}}{g_{m1} + g_{mb1} + \frac{1}{r_{01}}}$$

According to Fig. (3), the effect of V_{in1} on V_y becomes:

$$\frac{V_y}{V_{in1}} = \frac{V_y}{V_{th1}} \times \frac{V_{th1}}{V_{in1}} \tag{5}$$

where

$$\frac{V_y}{V_{th1}} = \frac{((g_{m2} + g_{mb2}) r_{02} + 1) R_{D2}}{(g_{m2} + g_{mb2}) r_{02} R_{th1} + R_{th1} + r_{02} + R_{D2}} \tag{6}$$

and

$$\frac{V_{th1}}{V_{in1}} = \frac{\left(\frac{1}{g_{mb1}} \parallel r_{01}\right) \parallel R_{ss}}{\frac{1}{g_{m1}} + \left(\frac{1}{g_{mb1}} \parallel r_{01}\right) \parallel R_{ss}} \tag{7}$$

In [Eqn. 6], $R_{th1} = R_{th1}\prime \parallel R_{ss}$ while

$$R_{th1}\prime = \frac{1}{g_{m1}} \parallel \left(\frac{1}{g_{mb1}} \parallel r_{01}\right)$$

In the same way, the effect of V_{in2} on V_x can be expressed as :

$$\frac{V_x}{V_{in2}} = \frac{V_x}{V_{th2}} \times \frac{V_{th2}}{V_{in2}} \tag{8}$$

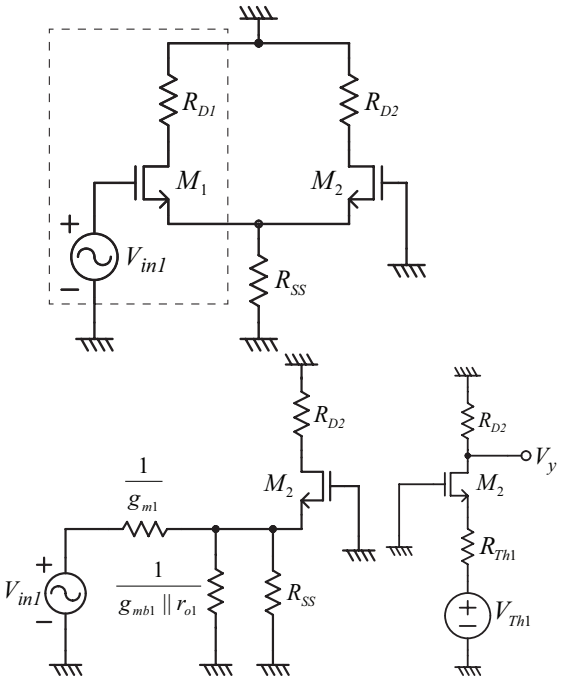

Fig. 3. AC Analysis: The effect of V_{in1} on V_y, where $V_{in2} = 0$

where

$$\frac{V_x}{V_{th2}} = \frac{((g_{m1} + g_{mb1})r_{01} + 1)R_{D1}}{(g_{m1} + g_{mb1})r_{01}R_{th2} + R_{th2} + r_{01} + R_{D1}} \tag{9}$$

and

$$\frac{V_{th2}}{V_{in2}} = \frac{\frac{1}{g_{mb2}} \parallel r_{02} \parallel R_{ss}}{\frac{1}{g_{m2}} + \frac{1}{g_{mb2}} \parallel r_{02} \parallel R_{ss}} \tag{10}$$

In [Eqn. 9], $R_{th2} = R_{th2\prime} \parallel R_{ss}$ while

$$R_{th2\prime} = \frac{1}{g_{m2}} \parallel \left(\frac{1}{g_{mb2}} \parallel r_{02}\right)$$

B. Common Mode-Differential Gain

In the following sections, the symbol δ has been used to show the small changes in the variables just next to it.

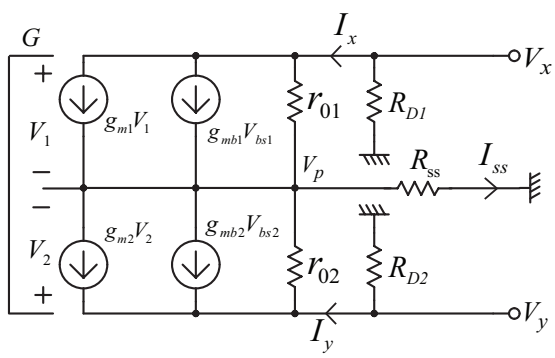

Fig. 4. Small signal equivalent circuit for common-mode input

The common-mode differential gain stated in [Eqn. 1] can be expressed as:

$$\begin{aligned} A_{V,CM-DM} &= \frac{\delta V_x - \delta V_y}{\delta V_{in,cm}} \\ &= (1 - \frac{y}{x}).p + \frac{y}{x}.q \end{aligned} \tag{11}$$

where

$$\begin{aligned} x &= \frac{1}{R_{ss}} + \left(\frac{g_{mb1}r_{01} + 1}{R_{D1} + r_{01}} + \frac{g_{mb2}r_{02} + 1}{R_{D2} + r_{02}}\right) \\ &\quad + \left(\frac{g_{m1}r_{01}}{r_{01} + R_{D1}} + \frac{g_{m2}r_{02}}{r_{02} + R_{D2}}\right) \\ y &= \frac{g_{m1}r_{01}}{r_{01} + R_{D1}} + \frac{g_{m2}r_{02}}{r_{02} + R_{D2}} \\ p &= -g_{m1}R_{D1}\frac{r_{01}}{r_{01} + R_{D1}} + g_{m2}R_{D2}\frac{r_{02}}{r_{02} + R_{D2}} \\ q &= \left(\frac{R_{D2}g_{mb2}r_{02}}{R_{D2} + r_{02}} - \frac{R_{D1}g_{mb1}r_{01}}{R_{D1} + r_{01}}\right) \\ &\quad + \left(\frac{R_{D2}}{R_{D2} + r_{02}} - \frac{R_{D1}}{R_{D1} + r_{01}}\right) \end{aligned}$$

Again, in [Eqn. 11],

$$\delta V_x - \delta V_y = -(\delta I_x R_{d1} - \delta I_y R_{D2}) \tag{12}$$

Now, by applying KCL in Fig. (4), the equation for δI_x is formed like this:

$$\begin{aligned} \delta I_x &= g_{m1}(\delta V_{in,CM} - \delta V_p) + g_{mb1}(-\delta V_p) \\ &+ \frac{\delta V_x - \delta V_p}{r_{01}} \end{aligned} \tag{13}$$

or

$$\begin{aligned} \delta I_x &= g_{m1}(\delta V_{in,CM} - \delta V_p).\frac{r_{01}}{r_{01} + R_{D1}} \\ &- \delta V_p.\frac{g_{mb1}r_{01} + 1}{R_{D1} + r_{01}} \end{aligned} \tag{14}$$

Similarly,

$$\begin{aligned} \delta I_y &= g_{m2}(\delta V_{in,CM} - \delta V_p).\frac{r_{02}}{r_{02} + R_{D2}} \\ &- \delta V_p.\frac{g_{mb2}r_{02} + 1}{R_{D2} + r_{02}} \end{aligned} \tag{15}$$

Putting the values of I_x and $I_y$in [Eqn. 12],

$$\delta V_x - \delta V_y = (\delta V_{in,cm} - \delta V_p).p - \delta V_p.q \tag{16}$$

where

$$\delta V_p = (\delta I_x + \delta I_y)R_{ss} \tag{17}$$

substituting for δI_x and δI_y in [Eqn. 17]:

$$\delta V_p = \frac{y}{x} \cdot \delta V_{in,cm} \tag{18}$$

or

$$\delta V_{in,cm} - \delta V_p = (1 - \frac{y}{x})\delta V_{in,cm} \tag{19}$$

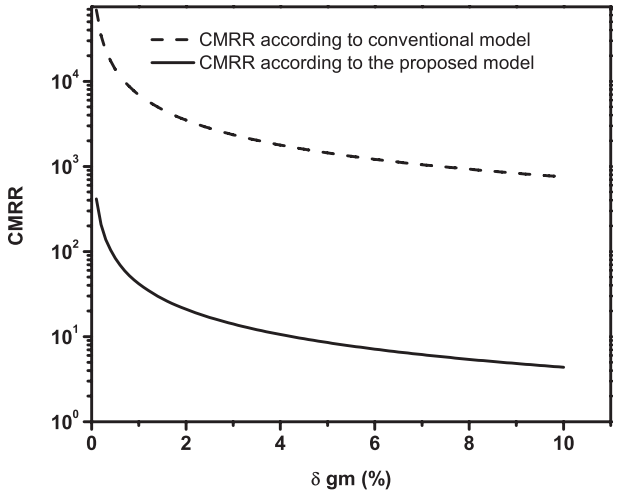

Fig. 5. Response of CMRR to various differences (0%-10%) between g_{m1} and g_{m2} (i.e., δg_m) of M_1 and M_2 respectively.

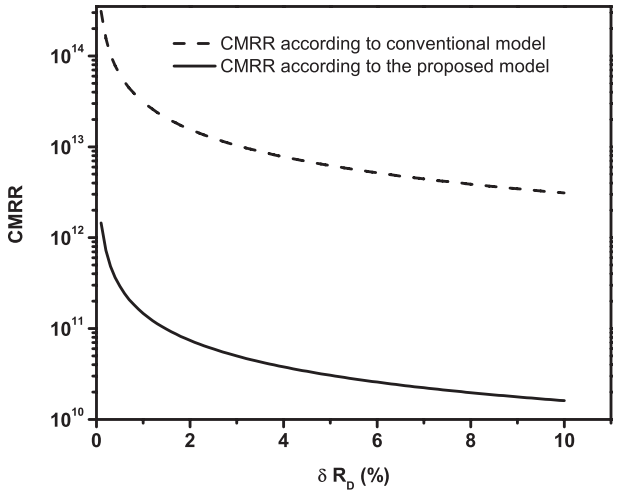

Fig. 6. Response of CMRR to various differences (0%-10%) in R_{D1} and R_{D2} (i.e., δR_D) of M_1 and M_2 respectively.

III. Results and Discussion

The simulation results, shown in Fig. (5)-(6), have been carried out considering standard 0.5μm process. In both cases, the results obtained considering all non-idealities stated here are compared with those that are obtained from equations based on conventional approaches, where the effects of some of the non-idealities have been ignored [1]. Fig. (5) shows how CMRR responds to different levels of mismatches between g_{m1} and g_{m2} (δg_m) according to both conventional (presented by dotted line) and proposed model (presented by solid line). It is clear that CMRR decays, as expected, exponentially with the increased g_m mismatches. This happens, because in common mode operation, difference in g_m causes difference in two branch currents (I_x and I_y), hence introduces difference in voltage drops against R_{D1} and R_{D2}, and finally creates difference between V_x and V_y. As a result, common-mode differential gain, which is unexpected in an ideal case, starts to rise, causing CMRR to decay. In the same way, Fig. (6) shows a similar response of CMRR to the change in δR_D, which is also varied from 0% to 10%.

In both the cases, CMRR based on the model proposed here is much less than that based on conventional model [1]. In fact, the common-mode gain increases as more and more non-idealities are added to the system. The increased common-mode gain causes the CMRR to flag drastically. This phenomenon can be realised from [Eqn. 11]. When any non-idealities such as body effect (g_{mb}), CLM (i.e., finite r_{01} and r_{02}), differences in transconductance (δg_m) and drain resistances (δR_D) are introduced, the quantity 'q' in [Eqn. 11] increases. The increased 'q' causes the common-mode gain ($A_{V,CM-DM}$) to rise and thus CMRR to fall.

IV. Conclusion

A deeper and more practical analytical model for calculating CMRR has been established here. The results are far different from those that are simulated based on conventional theoretical approaches used today. This finding indicates that the calculations for CMRR should not be done ignoring the effects of any of the non-idealities, for in that case, the experimental output would differ too much from the theoretical ones. To get closer to the experimental data, the theorists must always be concerned about the existence of all the non-idealities possible in a CMOS differential amplifier. In this paper, therefore, the authors have tried to establish an analytical model for CMRR calculations where all those non-idealities are incorporated successfully .

References

[1] B. Razavi, "Design of Analog CMOS Integrated Circuits", *McGraw-Hill, 2002.*

[2] A. K. N., S. Bose, A. Gupta, "A High Gain, High CMRR Two-Stage Fully Differential Amplifier Using g_m/I_d technique for Bio-medical Applications", *IEEE Asia Pacific Conference on Postgraduate Research in Microelectronics and Electronics (PrimeAsia)*, pp. 40-45, 2003.

[3] Y. M. Hsiao, M. S. Shiau, K. H. Li, et al., "Design a Bioamplifier with High CMRR", *VLSI Design*, vol. 2013, Article ID 210265, pp. 1-5, Apr. 2013.

[4] Nagel, J. H., "Biopotential amplifiers", *Biomedical engineering hand book, 2nd edition,* Ed. Joseph D. Bron Press LLC, 2000.

[5] K. A. Ng, and P. K. Chan, "A CMOS Analog Front-End IC for Portable EEG/ECG Monitoring Applications", *IEEE Trans. Circuits and Systems*, vol. 52, no. 11, pp. 1-12, Nov. 2005.

[6] J. I. Brown, "Differential Amplifiers That Reject Common-Mode Currents", *IEEE J. Solid-State Circuits*, vol. SC-6, no. 6, pp. 385-391, Dec. 1971.

[7] M. Brotz, and A. Kley, "The common-mode rejection of transistor differential amplifiers", *IEEE Trans. Circuits Theory*, vol. CT-13, pp. 171-175, Dec. 1966.

[8] R. Jiang, H. Tang, and K. Mayaram, "A Simple and Accurate Method for Calculating the Low Frequency Common-Mode Gain in a MOS Differential Amplifier with a Current-Mirror Load", *IEEE Trans. Education*, vol. 43, no. 3, pp. 362-364, Aug. 2000.

Implimentation And Evaluation Of An Efficient Clock Distribution Network For Deep-Submicron Technology

Md. Abdur Rahman*, Md. Mamunur Rahman, Farhadur Arifin
Department of EEE
American International University-Bangladesh
Dhaka, Bangladesh
*nayem.rahmanmdabdur@gmail.com

Abstract—**A differential clock distribution network using current mode logic (CML) buffer and RCL interconnect model for low-skew is presented in this paper. We investigate attenuation and skew of the proposed clock distribution network. An efficient differential CML buffer is used as it is capable of operating with low voltage and high frequency which makes this clock distribution network more advantageous over the conventional models. Different clock distribution networks with clock trees such as H-tree, X-tree and binary tree are designed. Those networks are analyzed by using different technological nodes, such as 22nm, 32nm, 45nm. Due to the high clock frequency, more accurate RCL interconnect model has been explored. According to the analysis, compared to other clock trees, X-tree has less skew of 179ps with large area and the binary tree has a constant delay ratio.**

Keywords—Differential clock distribution network, Differential CML Buffer, RLC interconnect, Deep-submicron technology.

I. INTRODUCTION

Latest integrated circuits are more complex with billions of transistors and run at multi-GHz frequency. Clock frequency has already exceeded 3GHz. This uprising frequency level results more power consumption. A clock distribution network approximately consumes 30%-50% of total power of processor. Besides, when VLSI technology improved and reduced under 65nm, interconnect delay gradually affects the chip performance [1]. At high frequency clocks, it is a challenge to reduce clock skew and clock jitter values. In order to cope with the progressive designs, it is important to propose a new and efficient clock distribution network for modern ICs.

A clock distribution network is a network that distributes the clock signal to the all clock element and the load inside a VLSI system. Clock tree is built with clock tree synthesis tools and it varies routing paths and placement of clock cells and clock buffers. This network is a structure that allows different loads to share the data simultaneously. Synchronous clocking is most widely used mechanism for commercial microprocessors with multi gigahertz clock pulses. The clock arrival time difference between two different levels of signal is called clock skew [2]. Networking of clock distribution system is developing continuously, such as a network with top-down flow, a network with exact equidistant trees and a presented skew balanced diagram. Later on, a model was proposed that balanced the delay using Elmore RC delay model [3]. Some buffer less resonant clock distribution network can also reduce the power consumption of the synchronous system [4].

Late clock signal, early clock signal or any kind of time related issue will limit the maximum clock frequency. Efficient clock distribution networks minimize the clock skew and jitter issue. Clock signals travel a long path operating at high frequency. These signals can be interrupted by different issues. In recent times, many signaling techniques have been proposed which have high-speed data buses with long line lengths and small power consumption [5]. One of the useful and efficient techniques is current mode logic signaling which can be used in the clock distribution network also. The transmitter-receiver pair system of current-mode clock distribution network reduces the fluctuation of delay although there are some parametric variations. In a synchronous VLSI system, clock signal drives thousands of loads. There is a hierarchy in the modeling of clock distribution network, which has three levels, namely global, regional and local as shown in fig. 1. Every level of the original clock signal is regenerated and improved by different buffer [6].

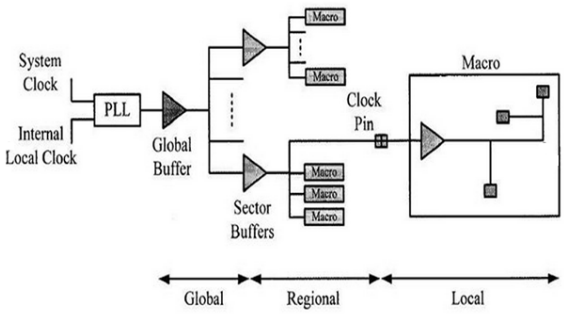

Figure 1. Hierarchy of clock distribution network for a high performance synchoronous VLSI system [6].

978-1-4673-9257-0/15/$31.00 ©2015 IEEE

In this paper, we focused on the local level of the clock distribution network where the clock pin is delivered to the load. We have implemented different clock distribution networks using different clock tree synthesis. Providing uninterrupted clock pulses from the input to the load, we used an efficient differential current mode logic (CML) buffer and a realistic interconnect equivalent model. In our proposed model, a clock pulse is provided to the network and the signal reached the load through transmission lines and buffer as shown in fig. 2 and fig. 3. The block situated at the middle represents the differential CML buffer and the other two sides of the box represent the transmission line. The differential buffer is used as a regenerator of the signal. We analyzed x-tree, H-tree & binary-tree technique and compared the resulting clock pulse on the different nodes, branches in 22nm and 45nm CMOS technologies. The realized model of X-tree has less amount of skew of 178ps which is efficient in case of using a higher number of loads as it has less number of levels.

The entire presentation is divided into four sections. In section I, the importance, present scenario and prospects of the clock distribution network is discussed. Section II discusses the CML buffer and the interconnect structure used in the proposed model. In section III, the simulation results of analysed differential networks with different trees are presented. Finally, the conclusion of this work is discussed in section IV.

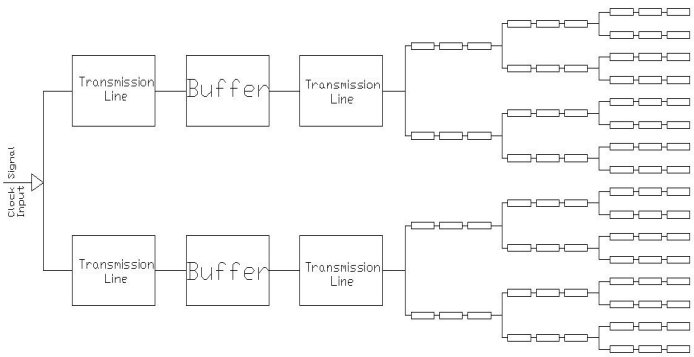

Figure 2. Distribution network with Binary tree configuration.

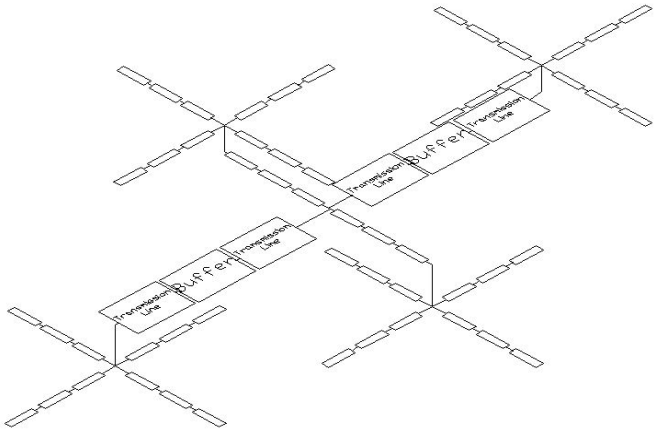

Figure 3. Distribution network with X tree configuration.

II. MODELING OF CLOCK DISTRIBUTION NETWORK

A. Differential CML buffer

As the function of the clock distribution network is to transmit a healthy clock pulse, CMOS buffer plays very important role in this system. It helps to transmit unbiased clock pulses throughout the transmission line and to achieve synchronism in the ICs. The buffer is also used to avoid the effect of load mismatch. At high speed and multi-Giga hertz transmission system, the use of conventional buffer losing advantages and exposing issues. Due to this complicated situation they cannot be used anymore. Difficulties like electromagnetic coupling of single-ended circuits, use of PMOS and its limitation of maximum operating frequency are significant [7]. Differential circuitry reduces power consumption and current mode logic is compatible with low input voltage. Current mode logic with CMOS technology is capable of working in low signal voltage, high operating frequency and low supply voltage [8].

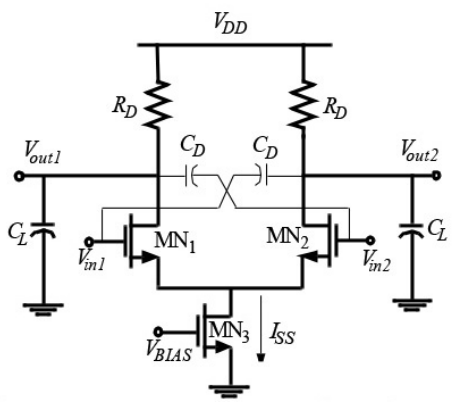

Figure 4. A current mode logic buffer [8].

Buffer is a core part of a clock distribution system. It is the part of a clock distribution system that ensures unbiased clock signal distribution. A differential buffer amplifies between its two inputs and outputs a pair of differential signal. Basic NMOS differential buffer consists of two NMOS transistors.

Variance of maximum and the minimum common mode voltage of NMOS buffer is possible when all the transistors are in the saturation region [8].

In our work we have used differential current mode logic buffer. We used only NMOS to construct the buffer due to some significant drawbacks of PMOS. Buffer parameters used as follows where operating clock frequeny is 1GHz. Table I, table II and table III represent buffer perameters that is used in this work with different technological nodes. Threshold voltage V_{th} =0.18V and V_{dd}=1V where, T_{ox}=1.1nm and R_{dsw}=155 Ω [9].

TABLE I. BUFFER PARAMETER FOR 22NM TECHNOLOGY

Tree Type	*Length (nm)*	*Width(nm)*
Binary Tree	22	33
H-Tree	22	33
X-Tree	22	33

TABLE II. BUFFER PARAMETER FOR 32NM TECHNOLOGY

Tree Type	*Length (nm)*	*Width(nm)*
Binary Tree	32	48
H-Tree	32	48
X-Tree	32	48

TABLE III. BUFFER PARAMETER FOR 45NM TECHNOLOGY

Tree Type	*Length (nm)*	*Width(nm)*
Binary Tree	45	67.5
H-Tree	45	67.5
X-Tree	45	67.5

B. Interconnects

There are some electrical properties of interconnect wires like resistance, capacitance and inductance. Some relation can be presented to drive their values and combine these properties into an electrical model and prepare an equivalent circuit of the total transmission line effect. There are different kinds of models to represent different effects and they can vary with entire circuitry, the type of conductor used in transmission line and physical or geometrical configuration of the lines, different kind of loads and technology. The internal resistance, reactance and capacitance of the wire and some mutual inductance between closely attached lines also play an important role in designing and analyzing the equivalent model [10]. The model parameters of the transmission line are mainly of two types like lumped element model of transmission line and distribution model elements of transmission line.

All wires have some value of resistance. The interconnect resistance changes proportionally with the length (L) of the wire and resistivity (ρ) and inversely with the cross sectional area (A). Resistance of a rectangular conductor can be expressed as:

$$R = (\rho . L) / A \quad (1)$$

Due to, very high frequencies, conductive materials face a phenomenon which is called the skin effect. This effect makes the resistance, frequency dependent.

In our design, we used an interconnect RCL pi model where Cu was used as a metal. The parameters were as follows in table IV [9].

TABLE IV. INTERCONNECT MODELING PARAMETERS

Dimensions	RLC	RLC (/mm)
W = 0.10 um s = 0.10 um l = 100 um t = 0.20 um h = 0.20 um K = 2.2	R = 109.999 Ohm L = 0.14 nH M12 = 0.118 nH M13 = 0.104 nH M14 = 0.096 nH (k12 = 0.842 k13 = 0.742 k14 = 0.685) C_{ground} = 1.9419 fF C_{couple} = 5.3683 fF C_{total} = 14.6204 fF	R = 1099.99 Ohm/mm L = 1.4 nH/mm C_g = 19.419 fF/mm C_c = 53.683 fF/mm C_{total} = 146.204 fF/mm

III. SIMULATION AND RESULTS

The clock pulse output of different clock distribution networks is presented using different nanometer technologies with a differential buffer and transmission line of different parameters. To show the outputs HSPICE software is used which is an analog electronic circuit simulator capable of performing transient, steady state and frequency domain analysis. To analyze the output clock pulse of 1 GHz to 5 GHz frequency level was used as input.

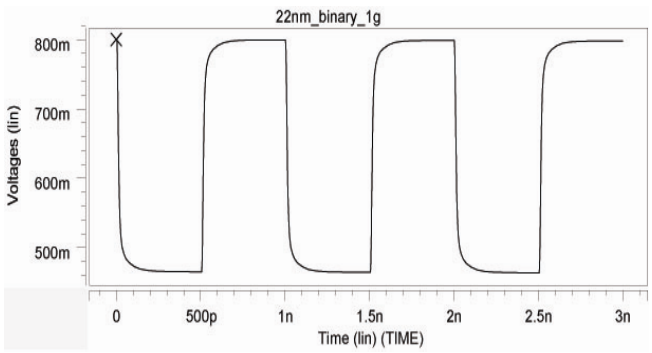

(a)

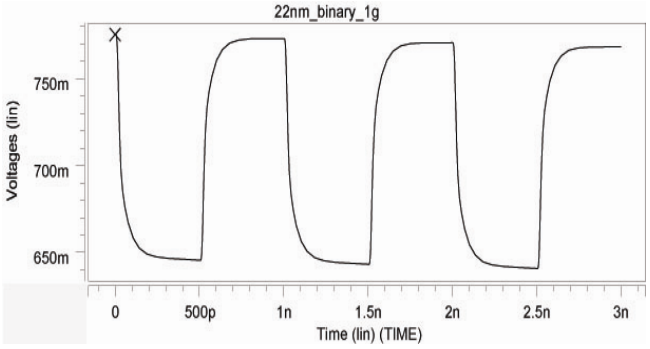

(b)

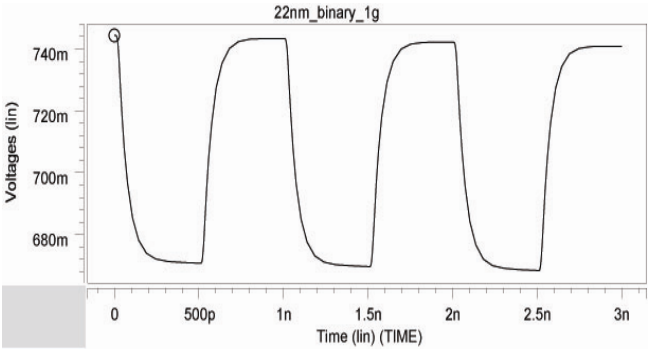

(c)

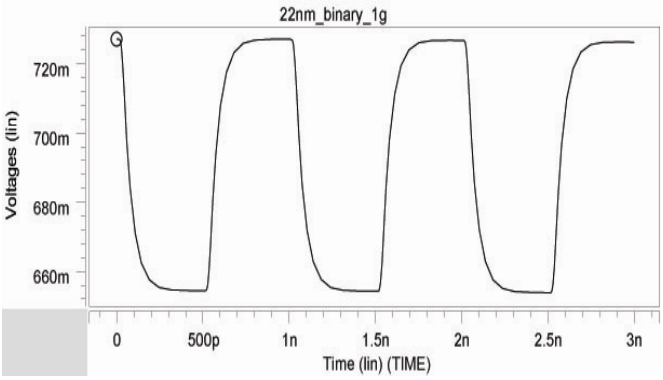

(d)

Figure 5. Waveforms of H-Tree (22nm RLC) at four consicutive levels of a, b, c and d.

Fig. 5 presents the output of H-tree 22nm technology RLC PI model. From the simulated result, it is observed that voltage level of clock pulse decreases with increasing the level. The proposed differential clock distribution network shows voltage differences in different levels of Binary tree, H-tree and X-tree. The buffer is used such that it offers low skew. The fall time and rise time is also varied with different network trees and different nanometer technologies. We measured the skew at different technology and different trees at various frequencies. Higher frequency affects the output signal of the levels. Table V analyses the skew of different levels of different nanometer technologies with different trees at 1GHz frequency.

TABLE V. SKEW AT DIFFERENT LEVELS

Level	**Binary Tree**		**H-Tree**		**X-Tree**	
	22 nm	*45 nm*	*22 nm*	*45 nm*	*22 nm*	*45 nm*
	Skew	Skew	Skew	Skew	Skew	Skew
Level 1	0.179ns	0.176 ns	0.16 ns	0.189ns	0.178ns	0.192ns
Level 2	0.238ns	0.235ns	0.242ns	0.23ns	0.224ns	0.212ns
Level 3	0.236ns	0.3ns	0.3ns	0.29ns	0.21ns	0.22ns
Level 4	0.225ns	0.312ns	0.256ns	0.312ns	0.25ns	0.231ns

IV. CONCLUSION

Different clock distribution networks in nanometer technology with less skew and power dissipation is analyzed. We designed a clock distribution network using H-tree, X-tree and Binary tree technique in this work. We used a low voltage differential CML buffer to ensure an unbiased clock pulse through the whole interconnect line. We designed and analyzed the buffer with different sub nano-CMOS technology like 22nm, 32nm, 45nm, 65nm and 90nm and implemented them in the clock distribution network. From the analysis, we found that without changing the buffer configuration, clock delay is increasing with the reduction of buffer size and technology. We improved the output by changing the buffer size and using a different model parameter. We also analyzed different clock distribution network with different buffer model with the RCL interconnect model.

According to our observation, X-tree is more effective in case of a large number of sequential loads as it has only two levels, but it has different propagation delay on different branches of the network. On the other hand, H-tree propagates the clock signal through four different levels but with almost equal propagation delay. Delay of binary-tree technique increased per branch. We used 1V and 0.8V supply voltage. As we used low power and high speed buffer, our power consumption was much less compared to other conventional design. Frequency was a very crucial element for our simulation. We used 0.5 GHz to 5 GHz clock pulse as our input signal. Our output signal was better at the 1 GHz or less frequency signal, but delay and other effects increased as we increased our clock frequency.

REFERENCES

[1] Tsai, Chia-Chun, Chung-Chieh Kuo, Feng-Tzu Hsu,Lin-Jeng Gu, and Trong-Yen Lee. "X-architecture zero-skew clock tree construction with performance and DFM considerations", 2010 International SoC Design Conference, seoul, 2010, pp. 294 – 297.

[2] Restle, Phillip J., Timothy G. McNamara, David Webber, Peter J. Camporese, Kwok F. Eng, Keith Jenkins, David H. Allen et al. "A clock distribution network for microprocessors.", Solid-State Circuits, IEEE Journal of. Vol. 36, no. 5, pp. 792-799, may, 2001.

[3] Lu, Jingwei, Wing-Kai Chow, and Chiu-Wing Sham. "Fast Power- and Slew-Aware Gated Clock Tree Synthesis", IEEE Transactions on Very Large Scale Integration (VLSI) Systems, vol. 20, no. 11, oct 2012.

[4] Xu, Yi, Shu-ming Chen, Xiang-yuan Liu, and Tao Tang. "Bufferless resonant clocking with low skew and high variation-tolerant", 2011 IEEE 54th International Midwest Symposium on Circuits and Systems (MWSCAS), pp. 1-4, Aug 2011.

[5] Kancharapu, Naveen Kumar, Marshnil Dave, Veerraju Masimukkula, Maryam Shojaei Baghini, and Dinesh Kumar Sharma. "A Low-Power Low-Skew Current-Mode Clock Distribution Network in 90nm CMOS Technology", 2011 IEEE Computer Society Annual Symposium on VLSI, Vol. 36, no. 5, pp. 792-799, 2011.

[6] Houman Zarrabi, Zeljko Zilic, Yvon Savaria and A. J. Al-Khalili. "On the Efficient Design & Synthesis of Differential Clock Distribution Networks", VLSI, Zhongfeng Wang (Ed.), 2010, available online: http://www.intechopen.com/books/vlsi/on-the-efficient-design-amp-synthesis-of-differentialclock-distribution-networks

[7] Restle,P.J; McNamara, T,G webber, D.A; Camporese , P.J; Eng,K.F;Allen, D.H;Rohin, M.J; Quaranta , M.P; Boerstler, D.W; Alpert, C.J; Carter,C.A; Bailey, R.N Petrovick, J.G. Krauter, B.L & McCredie, B.D(2001). A clock distribution network. Vol-36, pp-792-779.

[8] PayamHeydari, "Design Issues in Low-Voltage High-Speed Current-Mode Logic Buffers", IEEE Fourth International Symposium on Quality Electronic Design, 2003, P.p 293 – 298, March 24-26, 2003.

[9] Predictive Technology Model (PTM) available online: http://ptm.asu.edu/

[10] BorivojeNikolic, EE141: Digital Integrated Circuits, chapter 4, page 109, 2001.

Microcontroller Based Self Sustaining Automatic Traffic Light Control Using Speed Breaker

Mrinmoy Dey, Tawhida Akand, Sadeka Sultana and Jahedul Islam

Department of Electrical and Electronic Engineering
Chittagong University of Engineering and Technology
Chittagong-4349, Bangladesh
mrinmoycuet@gmail.com, tawhidacuet@yahoo.com, sadekazinia@yahoo.com, jahedul.islam.2014@ieee.org

Abstract—**Present development of the world is measured by the amount of energy consumption. Energy of today world is generated from conventional energy sources mostly which are decreasing day by day. Moreover, these conventional energy sources causes pollution and responsible for global warming. To solve these problems, researchers are trying frequently to explore new sources of energy which are clean, environment friendly and sustainable. This project is focused on microcontroller based auto traffic light control using energy conversion by speed breaker. In this project based research work, generated voltage depends on spring constant, displacement of rack length, gear ratio, number of gear combination and number of vehicles passing through the speed breaker. In this research work, the automatic traffic light control circuit controls the vehicle flow automatically and saves the working time which is wasted due to the traffic jam.**

Key words— **Microcontroller, Speed breaker, Traffic light.**

I. Introduction

The world is facing a problem of finishing the fuel stored in response of large demand of energy. Consequently, it has become a severe problem to fulfil energy security for next generation. According to various statistics the production of fossil fuel will start to decrease after 2015. To meet the demand of energy new sources of energy are important. So, renewable energy sources are needed to reduce the carbon dioxide emission and meet the future energy crisis. A steady increase in metro-city population, the number of automobiles and cars increases rapidly and metro traffic is growing crowded which leads to the traffic jam problem that severely affect the working time and reduce the efficiency of a person.

The control of traffic is performed by human effort at the circle of road proves to be ineffective due to the fast raise of vehicles and the complexity of road networks. Many researchers are trying to develop efficient traffic control system to reduce the traffic jam that overcomes the time waste in roadside communication. Rotake and Karmore developed an intelligent traffic signal control system using embedded system which consists of high performance, low power AVR_32 microcontroller with 32 kbytes of in-system programmable flash memory and in-built 8-channel, 10-bit ADC which is required to process the IR input from sensor network]1[. R. A. Ganiyu et. al developed a system to control roadside traffic light which was tested by constructing a prototype and showed that it can be used for real life traffic control and training kit to learn about traffic light control system [2]. A project to generate power from speed breaker through rack and ratchet mechanism implemented by A. Padma Rao et. al and tested as a power generation source for lighting the lamps near the speed breakers [3]. Md. Saiful Islam et. al designed a compact power generation unit to show how energy can be produced, stored and through the pressure of vehicles or any kind of pressure as the number of vehicles passing over the speed breaker in roads is increasing day by day [4]. Another project was done by Amanpreet Kaur et. al to harvest power using speed breaker that generated power for the various applications of street lights and traffic signal [5]. Sachin Jaiswal et. al designed intelligent traffic control using IR sensor [6].

In this research work, the proposed system designed for controlling traffic signal in an intelligent way that play vital role to avoid the traffic jam. The power generation system for controlling automatic traffic light has greater flexibility since the displacement of rack length, gear combination, rotation of dynamo, gear ratio and number of rack can be changed.

II. Methodology

A. *Block Diagram*

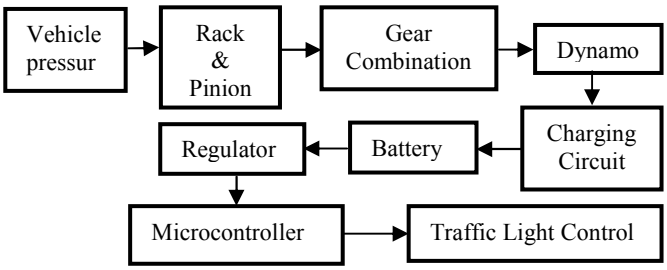

Fig.1: Block diagram

B. *Schematic Design*

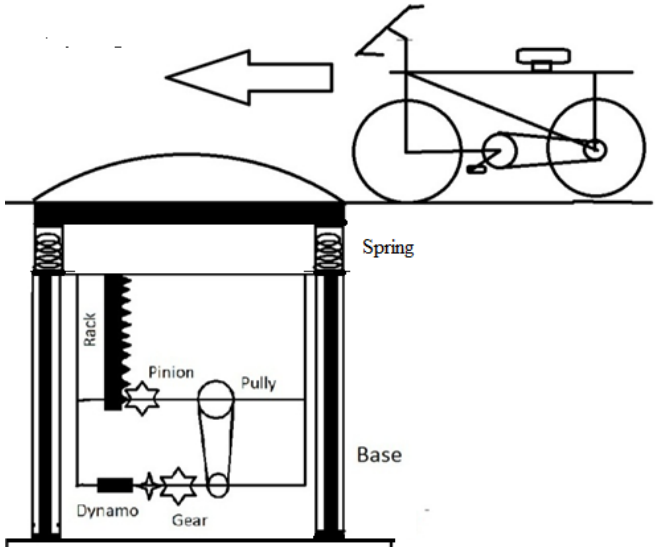

Fig. 2: Mechanical device design

978-1-4673-9257-0/15/$31.00 ©2015 IEEE

When vehicles cross across the speed breaker, it squeezes the spring and moves the rack downward which rotates the pinion, pulley and gear. Then rotary motion produces rotational energy and dynamo is used to convert it into electrical energy. The ratio of small gear and large gear diameter controls the rotation of dynamo.

The expansion of springs takes place and positioning at previous stage when the vehicles cross over the speed breaker. Movement of vehicles on the road is essential to generate continuous power supply from the implemented system. A charging circuit is to charge a 12V battery and the purpose of the regulator is to provide a fixed voltage to the microcontroller that controls the traffic light intelligently as it is programmed.

C. *Flow chart*

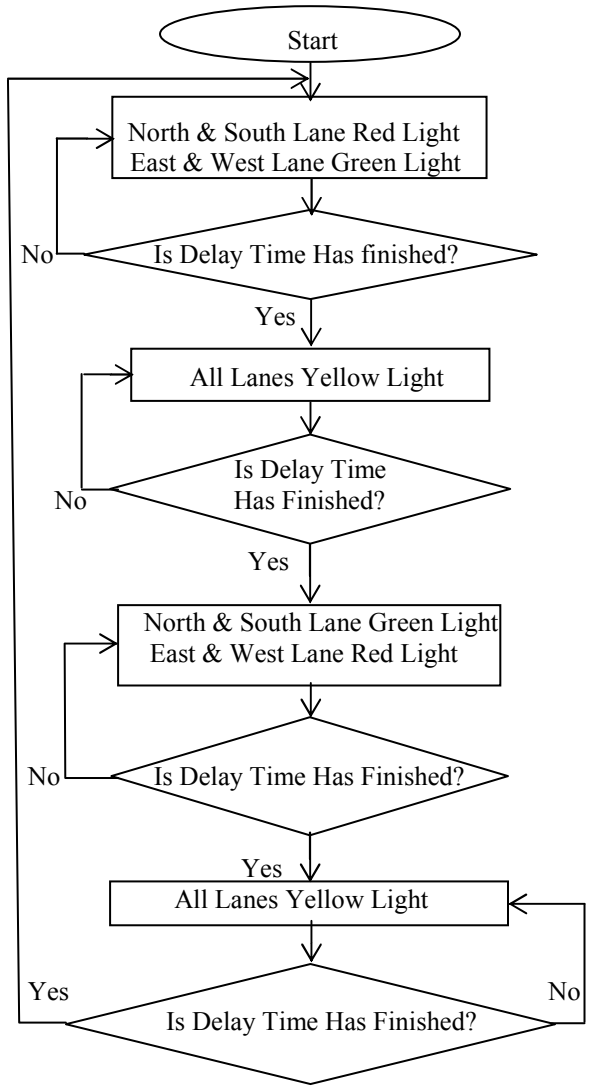

III. System Construction

The following components are used to design an automatic traffic light control system

- Speed Breaker
- Rack and Pinion
- Springs
- Gear
- Belt
- Hole
- Dynamo
- Charging Circuit
- Battery
- Regulator
- Microcontroller
- Traffic Light Control

A. *Speed Breaker*

Speed breaker is used to sustain the pressure of vehicle and event of squeeze happening when vehicle pass through it. It is mainly made of iron and physically looks like curve shaped. A certain time gap should be provided between two vehicles passing time so that the speed breaker can be restored in its original position. If speed breaker cannot restore its original place, there will be no sufficient displacement of rack that causes insufficient generated voltage.

B. *Rack and Pinion*

The circular gear is called pinion and the linear gear is called rack. Force is applied on the linear gear rack which causes pinion rotation. Thus the mechanical force is converted into rotational force. The generated voltage depends on the length of the rack displacement.

C. *Springs*

When vehicle pressurizes on speed breaker, then springs are squeezing although back into normal position on the incident of released pressure. Springs are positioned below the speed breaker.

D. *Gear*

More gear combinations are used to increase the number of rotation. Output voltage increases if gear ratio is more than unity and decreases if gear ratio is less than unity.

E. *Belt*

Belt is tied with the small gear of third gear combination to rotate the dynamo.

F. *Dynamo*

Dynamo uses rotating coils of wire and magnetic fields to convert mechanical rotation into pulsating direct electric current through Faraday's law of induction. A dynamo machine consists of a stationary structure (stator) which provides the constant magnetic field and a set of rotating windings called the armature which turns within the field. The overall mechanical setup is represented by Fig. 3.

Fig. 3: Total mechanical set up

G. *Hole*

A hole is needed to place the setup and the size of hole is same as like the mechanical set up with 4 inch clearance.

H. *Protection*

To protect the setup from extra pressure of soil, humidity, soil temperature, it is covered with polythene which is available, not erosive and cost effective. For better coverage wood box or steel box are used which can tolerate greater pressure and not erosive also.

I. *Charging Circuit*

Charging circuit is used mainly to charge the battery. In this work, lm 317 is a regulator, D1 is a 13 V zener diode and RV1 and R1 are used to set the voltage level. Green and red LED indicate the charging mode and full charged condition of the battery respectively. Red LED is lit on when voltage level is greater than 15 V. The charging circuitis shown in Fig. 6.

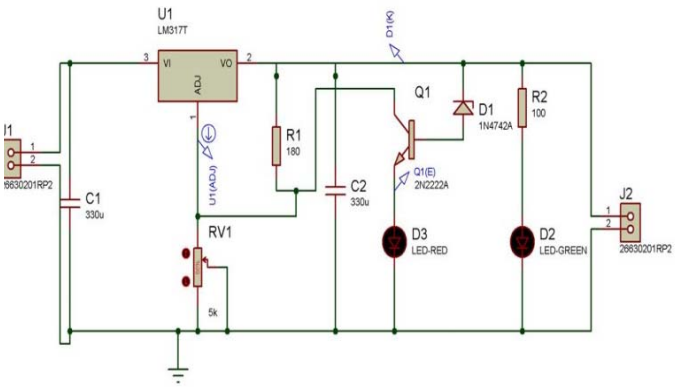

Fig. 4: Charging circuit

J. *Regulator*

A regulator of 5 V is used to power the microcontroller circuit for traffic light control system.

K. *Microcontroller Circuit*

A fixed time delay is used to control the four lane traffic signal. In this research work, microcontroller pic 16F877A is used. RB0, RB1 and RB2 are used to control the traffic signal. The control circuit is shown in Fig. 5.

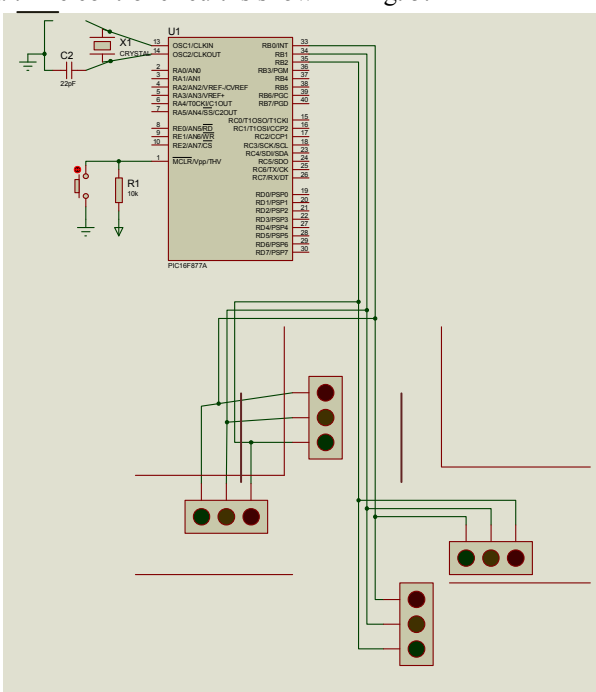

Fig. 5: Control circuit for traffic signal

IV. System Implementation

This system is implemented in Chittagong Collegiate School (CCS) situated in Ice Factory Road, Chittagong 4000, Bangladesh on 3 July, 2015. Implemented system is shown in Fig. 6.

Fig. 6: Implemented system

V. Cost Analysis

To implement the system, used essential components along with respective quantities and cost are given in Table I. The cost of these components may be varied depending on its brand, quality and place.

Equipments	No. of set	Price (BDT)
Rack	1	300
Pinion	1	400
Gear	3	1000
Dynamo	1	2000
Belt	1	60
Chain	1	100
Spring	4	200
Body	1	1000
Microcontroller	1	360
Traffic light		140
Wiring		200
Installation and maintenance cost		1000
Miscellaneous		500
Total Cost		7,260

VI. Result Analysis

A. *Theoretical Analysis:*

Pinion's rotation is expressed by

$$n = \frac{l \times N}{L} \tag{1}$$

Where, n is the number of rotation of the pinion
N is number of rotation of the pinion for total length
l is the displaced length of rack in meter
and L is the total length of rack in meter

In this system, the value of pinion's rotation,

$$n = \frac{1.2 \times 2.1}{20} = 0.1275$$

Generated voltage per rotation is expressed by

$$V_g = n \times R_G \times V_r \tag{2}$$

Where, V_g is the generated voltage per rotation in volt
n is the number of pinion's rotation
R_G is the gear ratio
and V_r is the rated voltage in volt.

The value of generated voltage per rotation

$$V_g = 0.1275 \times 7.2 \times 12 \approx 11$$

Efficiency is expressed by

$$\eta = \frac{V_g \times I}{m \times g \times l} \times 100\% \qquad (3)$$

Where, η is the efficiency of the system
I is the current through the system in mA
m is the mass of the vehicle in kg
g is the gravitational acceleration in ms^{-2}
and l is the displaced length of rack/time

Efficiency measured in this system

$$\eta = \frac{8 \times 60 \times 10^{-3}}{60 \times 9.8 \times 0.0002} \times 100\%$$
$$= 4.085\%$$

B. *Charging Time for Mechanical Device:*

Charging time is expressed by

$$t = \frac{Ah}{I} \qquad (4)$$

Where, t is the time in hour
Ah is the ampere-hour rating of the battery
I is the generated current for 10 mechanical devices

If 10 set of mechanical devices are used, then the charging time of 4.5 Ah 12 V battery is

$$t = \frac{4.5}{0.6} = 7.5 \text{ hours}$$

C. *Experimental Result*

The generated voltage and current flowing through the system are summarized in Table I.

TABLE I: RELATION AMONG VOLTAGE, CURRENT AND NUMBER OF VEHICLES

Observation No.	Number of vehicle passing	Generated Voltage, E_g (volt)	Current, I (mA)
1	1	7.19	8.09
2	1	4.48	6.52
	2	10	5.5
3	1	4.9	8.41
	2	9.07	7.4
	3	13.08	1.03
4	1	7.15	8.09
	2	9.7	3.74
	3	10.77	7.33
	4	16.48	4.8
5	1	8.9	8.04
	2	10.82	8.98
	3	15.88	1.98
	4	17 .76	5.74
	5	19.87	0.89

It is evident from Table I that generated voltage and current flowing through the system are increased with the increase of number of vehicles pass through the speed breaker. Relation between generated voltage and current flowing through the system is shown in Fig. 7.

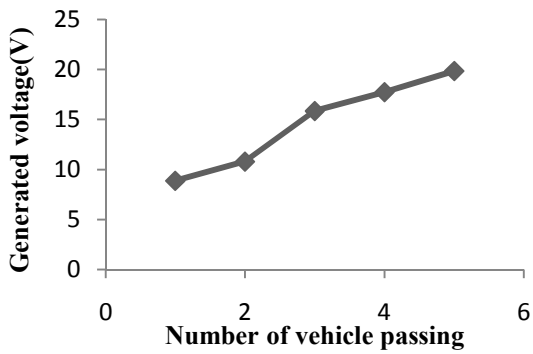

Fig. 7: Relation between generated voltage and number of vehicle passing

D. *Simulation Output*

Simulation output of traffic control system when north and south lane vehicles are stopped, all vehicles are waiting and east and west lane vehicles are stopped are shown in Fig. 8, Fig. 9 and Fig. 10 respectively.

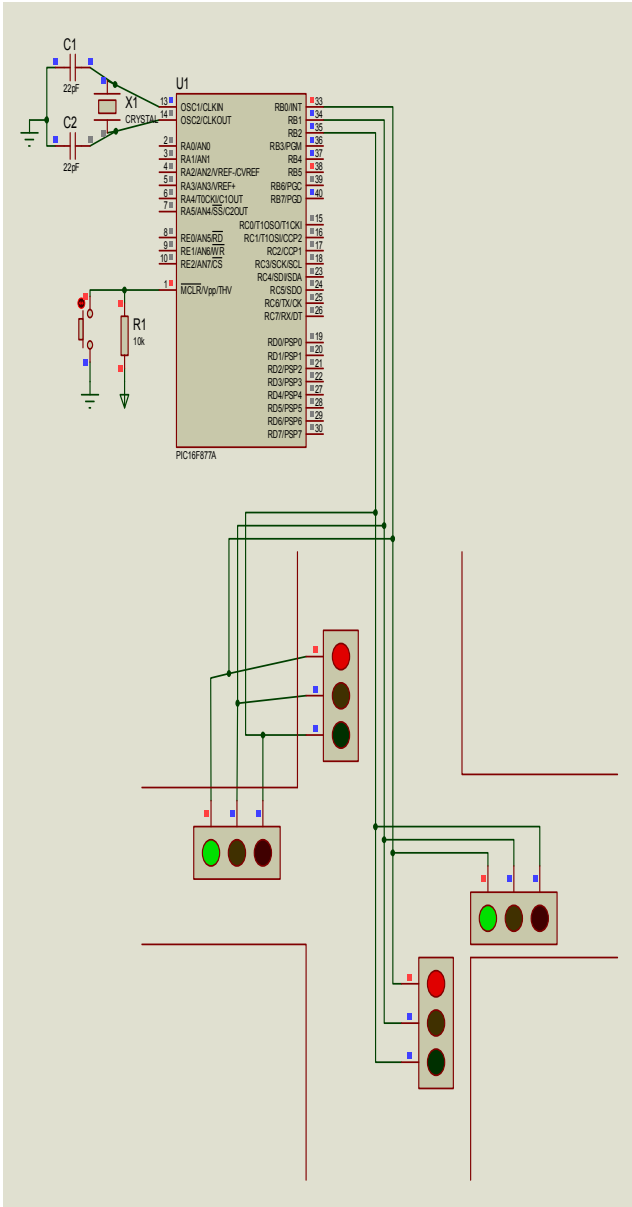

Fig. 8: North and South lane vehicles are stopped. East and west lane vehicles are running

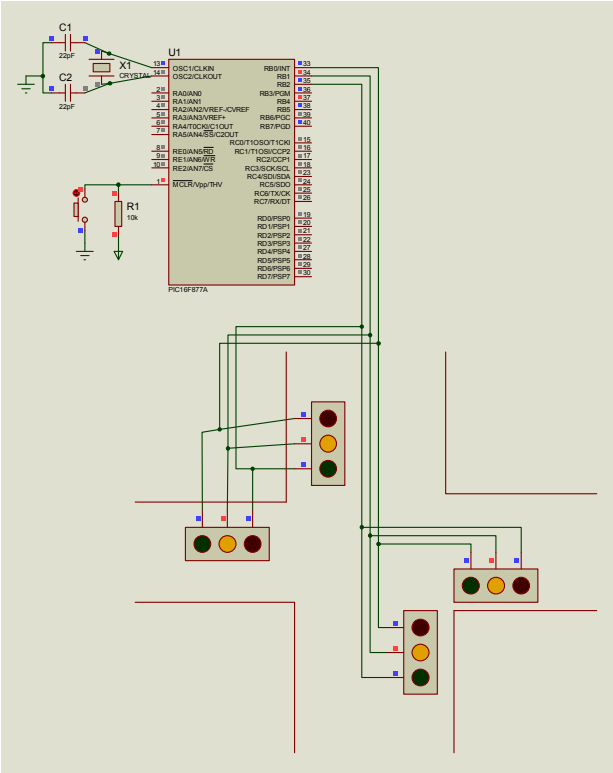

Fig. 9: All vehicles are waiting

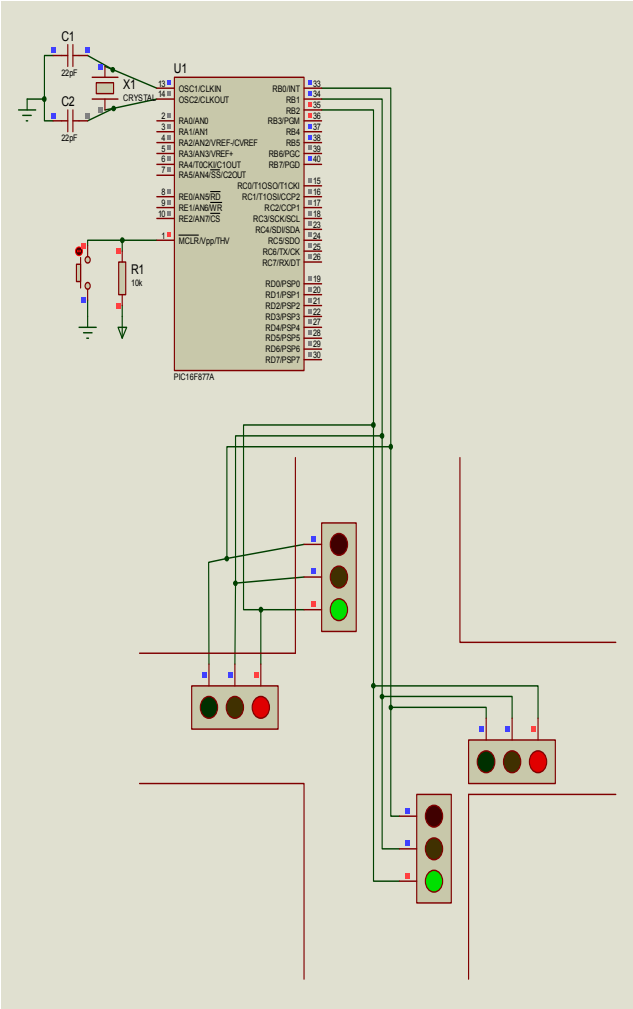

Fig. 10: North and South lane vehicles are running. East and west lane vehicles are stopped.

VII. ADVANTAGES

- Low maintenance cost
- Low installation cost
- Pollution free power generation.
- No manual work necessary during generation.
- No fuel transportation problem.
- Energy available all year round.
- Provide orderly movement of traffic
- Minimize conflicting movement
- Increase traffic handling capacity
- Simplicity

VIII. CONCLUSIONS

The power generation system for controlling automatic traffic light has greater flexibility and the power source of the implemented system is non conventional. Moreover, the way of power generation technique to control the automatic traffic light is clean, cost-effective and safe also. This system not only reduces power crisis and load shedding but also controls the vehicles flow automatically that play important role to avoid the traffic jam which wastes large man-hour in present times. The overall system is environmental friendly and sustainable development is possible by adopt this technique.

ACKNOWLEDGMENT

The authors would like to thank the Department of Electrical & Electronic Engineering (EEE) of Chittagong University of Engineering & Technology (CUET), Chittagong-4349, Bangladesh.

REFERENCES

[1] Dinesh Rotake and Prof. Swapnili Karmore, "Intelligent traffic signal control system using embedded system," *Innovative Systems Design and Engineering,* vol. 3, no. 5, 2012.

[2] R. A. Ganiyu, O. T. Arulogun and O. O. Okediran, "Development of a microcontroller-based traffic light system for road intersection Control," *International Journal of Scientific & Technology Research,* vol. 3, no. 5, May 2014.

[3] A. Padma Rao, A. Kiran Kumar and S. Suresh, "Power Generation from Speed Breaker by Rack and Ratchet Mechanism," *International Journal of Current Engineering and Technology*, sp. no. 2, February 2014.

[4] Md. Saiful Islam, Syed Khalid Rahman and Jakeya Sultana Jyoti, "Generation of Electricity Using Road Transport Pressure," *International Journal of Engineering Science and Innovative Technology (IJESIT),* vol. 2, no. 3, May 2013.

[5] Amanpreet Kaur, Shivansh Kumar Singh, Rajneesh, Parwez, and Shashank, "Power Generation Using Speed Breaker with Auto Street Light," *International Journal of Engineering Science and Innovative Technology (IJESIT),* vol. 2, no. 2, March 2013.

[6] Sachin Jaiswal, Tushar Agarwal, Akanksha Singh, and Lakshita, "Intelligent Traffic Control Unit," *International Journal of Electrical, Electronics and Computer Engineering,* vol.2, no. 2, pp. 66-72, 2013.

Password Protected Multiuser Wireless Electronic Noticing System by GSM with Robust Algorithm

Sayidul Morsalin[1], Abdur Rahman[2]
[1,2,3,4,5]Department of Electrical and Electronic Engineering
[1,2,3,4,5]Chittagong University of Engineering & Technology
Chittagong, Bangladesh
morsalinbd@yahoo.com[1], kakoncuet9@gmail.com[2]

Md Abu Bakar Siddiqe[3], Prattay Saha[4], Md. Reduanul Halim[5]
abubakar.khadachara@yahoo.com[3]
prattayeee08@gmail.com[4], mrh.eee.cuet@gmail.com[5]

Abstract—**This paper elucidates a wireless digital noticing system to provide information in an innovative and smart way. The proposed notice board is a multiuser password-protected SMS-based system fabricated with an LCD. The communication and information transfer between the authentic user and the LCD display unit is done via GSM to ensure remote display facilities, so any notice can be displayed on the electronic board from the user's mobile SMS from distant places. To ensure system flexibility, a multiuser noticing and displaying system has been implemented in the system which can display several notices simultaneously. In addition, the user also can print any notice which is of concern to them. The total system is designed with simple logic with a robust algorithm and fabricated with a PIC midrange microcontroller, LCD, GSM module and other commercially available electronic devices to ensure efficiency and reliability with less cost.**

Keywords-digital notice board; electronic notice; GSM; LCD; microcontroller

I. INTRODUCTION

A notice Board is a place where an authenticated authority can leave public messages to advertise things, announce events or provide information of general concern for any important issue [1]. Traditional analog notice boards are usually made of cork, timber or aluminium, which facilitating the addition and removal of paper messages. But some shortcomings make this analog notice board unpopular in general. Ascribed personnel are always needed to change any notice or originate a new one. Also, multiple people gather, struggle and cluster in front of a single traditional notice board for information in case of any urgent notification [1]. Sometimes malicious intentions of any persons can manipulate, remove or perish paper notices attached in a board, leaving other people uninformed. If the boards are placed in busy places, e.g. near entrances or exit points, then a busy person does not get enough time and scope to access and read all the informations posted on a notice board. It become more problematic when no digital printout is possible. One other disadvantage is that these traditional boards often get dirty, having wear and tear on notices and an unorganized pattern, which make the notice board quite inconvenient for users. There is also an unregulated display of information, difficulty in storage and no efficient reference to pass relevant information. This paper deals with an attempt to efficiently overcome the shortcomings of traditional notice boards. Here a system is developed for a modern electronic notice board using SMS-based wireless technology along with secured password protection to allow efficiently people toaccess a notice at a convenient time. With this systems high officials surely don't need to relay on the peons for the notices to hang over. Whenever or wherever the user is, they can just type what information they want to provide on a cell phone and just press the send button. The message will be sent to the board and displayed. Presently almost all electronic notice boards are designed using a wired system [2]. One of the drawbacks of the design is that the system is inflexible in terms of placement because of the messy wires [2]. Since the proposed system is wireless, this problem is alleviated. This system is user-friendly because authenticated personnel display the message at notice boards situated at different locations through a single SMS from the mobile phone. Thereby it eliminates the wastage of paper and ensures the immediate transfer of information. Information can be displayed page by page and expired notices can be stored in the database for a long time. In addition, people can print out multiple copies of any posted notices. So it can be concluded that the proposed system can used successfully in traditional Schools and Colleges, Waiting Rooms, Company Reception Areas, Factory Production Areas, Hospitals, Public Transport Timetables, Exhibition Centres, Art Galleries, Car Show Rooms, Exhibition etc. without errors and maintenance. The users can read notices posted from anywhere provided that the computer is connected through a local area network (LAN) facility.

II. SYSTEM DESCRIPTION

Figure 1 shows the overall block diagram of the system and shows how an effective and reliable communication between a mobile phone and a microcontroller is established by using a GSM modem. The system consists of two modules; transmitter and receiver. The transmitter module is accessed by a user to place a message through an input module such as a keypad or keyboard. The information then transmitted using RF technology to the receiver. It is then be decoded and displayed on an electronic notice board. The RF wireless communication system operates in the presence of a periodic noise environment, includes first and second wireless devices, each such device having, a source of power, a transceiver

coupled to the power source, and a controller/CPU for controlling the operation of the transceiver .

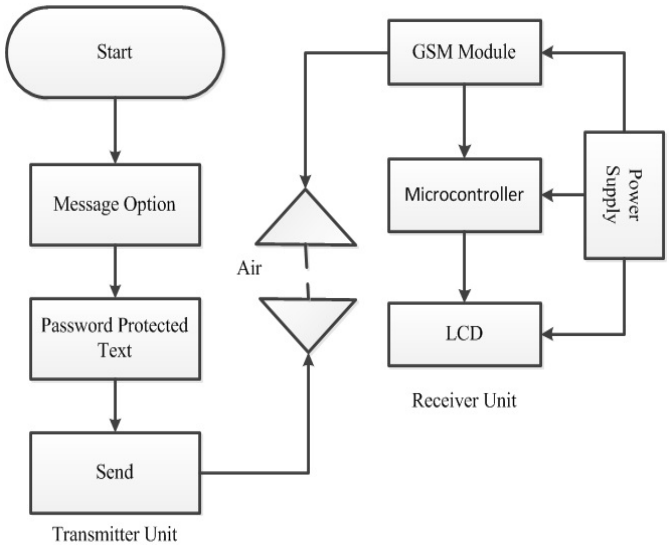

Figure 1. Block diagram of the system

A PIC microcontroller is the heart of the proposed system. The microcontroller is interfaced with GSM modem. A 20×4 Character LCD display is attached to the microcontroller to display messages as notices and notifications. The messages are displayed on the notice board until any new message comes. The new message will trash the old message automatically. Multiple users are authorized to update notices on the electronic notice board by providing password and sending an SMS from their mobile.

III. SYSTEM CIRCUIT DIAGRAM

The overall circuit diagram is depicted in Figure 2. The circuit diagram illustrates interfacing a PIC 16F73 (Peripheral Interface Controller) with GSM module Sim908c, LCD (20×4), 7805, 7812, LM317T voltage regulators, transistor BC547BP act as a power key, and another BC547BP transistor for network lighting. Sim908c is a 60-pin GSM modem; 8 pins 1, 3, 5, 7 are connected to ground and 2, 4, 6, 8 are connected to a 12 volt battery source [3]. Point 13 acts as the power key and is activated generally by a switching mechanism which is to be pressed for at least 1 second. But in our project we made the switching mechanism software based. So a transistor BC547BP along with current limiting resistors 2k, 22k, 47k has been used. When current flows through the base of the transistor then it connects the collector and emitter terminals, which powers the GSM modem [4]. The network light is a red LED, which blinks on the availability of the network. Pin 16 is connected with a voltage-divider circuit of two 47k resistors and then connected to the base of the transistor BC547BP and which turns ON so that the NET-Light blinks [5]. Whether the GSM modem is enabled or not is indicated by a green LED (whether it is on or off), passing through a resistor 47k between pins 20 and 40 of the modem. Microcontroller PIC 16F73 is the central processing unit of this system. A crystal of 20 MHz is used between pins 9 and 10. Pins 17 and 18 pins are used for the data transmit (RXD), data receive (TXD) and for interfacing the data to pins 29, 31 of the GSM module [4]. Pins 25, 26, 27, 28 are the data inputs connected to pins 12, 13 and 14 pin of the LCD display. 23, 24 are EN, RS pins connected to pins 4 and 6 of the LCD display. SIM slots are connected by pins 17, 19, 23 of the GSM modem to pins 6, 5 and 4 pin of the sim card slot. Pin 6 is used for the VDD of the sim and pins and 5 are the reset and clock pins respectively. Pin 21 is the data terminal of the GSM modem and is connected to the I/O port of the sim card and pin 3 is grounded. Pins 1, 4 and 5 are passed through 22k resistors for current limiting. A battery source of 12 volts is passed through a diode so that it gives a protection from polarity mismatch of the loads [6]. If the polarities are mismatched then the diode will not permit the flow of current, saving the instruments. The GSM modem is run by a 3.8 volt battery source and the microcontroller is powered by 5 volts. Voltage regulators 7805 and LM317T are used for this purpose. From a battery source 12 volts is passed through voltage regulator 7805 to generate 5 volts which is connected to port 1 to power up the microcontroller and to the VDD port of the LCD. LM317T gives a steady output of 3.8 volts to power the GSM modem and is connected to the 2, 4, 6, 8 ports of the GSM modem [6, 13]. 10nf and 100 microfarad capacitors are used in the battery source to make the output smooth.

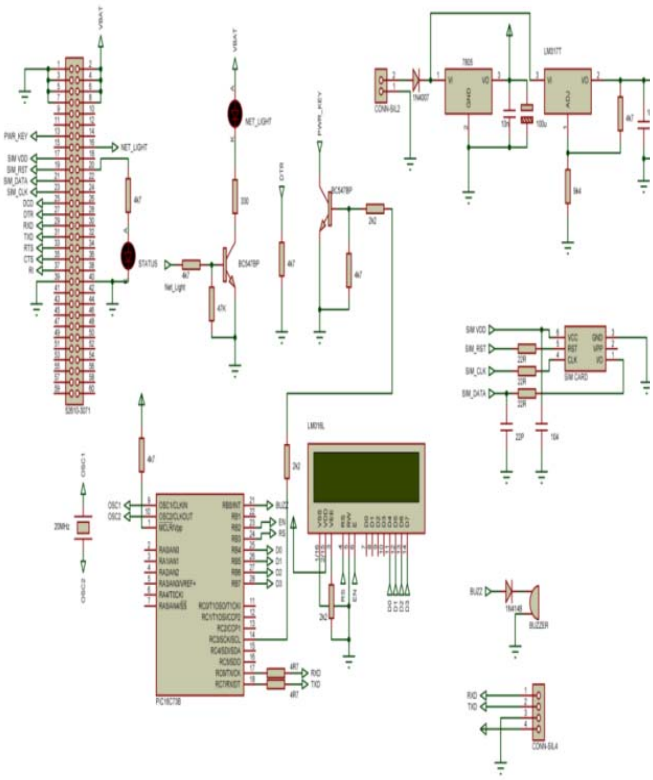

Figure 2. System circuit diagram

IV. HARDWARE DESCRIPTION

To reduce the complexityof the design process, simple algorithms and commercially available devices have been used to implement the system.

A. Central Processing Unit

A PIC 16F73 microcontroller has been chosen as the central microprocessor unit of this system. It is a 28-pin DIP IC [8-9]. It has a Program Memory of 4096 bytes (Single Word Instructions), Data SRAM of 192 bytes, 22 I/O Ports, 11 Interrupt pins, five 8-bit A/D channels, two timers 8 bit, one timer 16 bit, Operating Frequency DC - 20 MHz, FLASH Program Memory 4K (14-bit words) and instruction set of 35 instructions [8]. Basically its low cost and commercial availability make it attractive as the main processing unit. Moreover, all necessary peripherals are already built into it, saving time, space and cost. Sometimes analog circuitary with different control approach [19] can be used for the information processing, however for the simplicity microcontroller is recommended for this system [9].

B. GSM SIM908C Modem

A GSMSIM908C Modem has been used in the system to send messages from an authenticated authority to the main monitoring unit i.e. the notice board. It sends and receives data by wireless so that it can easily communicate from a distance. SIM908 is a new version of the ARM926EJ-S module and it enhances the main frequency performance compared to the previous ARM7 type. Moreover, this advanced module can save power consumption by up to 40% in sleep mode over the current industry average [11]. This modem has an internal GPS system which is integrated with the main circuit. This type of modem offers reliability, performance, efficiency, cost, and space. It occupies less space and weight: about 30*30*3.2 mm and 5.2 grams. It controls by AT commands. Its voltage range for GPRS and GPS is about 3.2- 4.8V and 3.0- 4.5 V respectively, with a very low power consumption. Its operating temperature range is 40~ 85ºC [11, 14].

C. System Power Supply Unit

The power supply of the system is designed specially. The system is run by the main power system which is placed adjacent to the digital notice board. So the system doesn't need costly battery circuitary. A rectifier converters the main supply power to the system operating level. To regulate the voltage, an IC LM 7805 voltage regulator has been used [12-14].

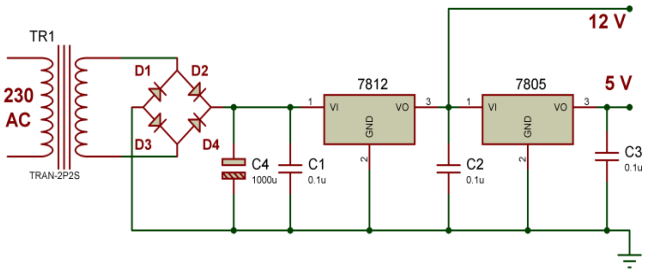

Figure 3. System power supply unit

D. AT Commands for Transmission or Reception of SMS

Basically AT commands are used as the control instructions of the modem. To control the dial-up modem or the GSM/GPRS modem several AT commands are used. The ATO command is used to return to the online data state, ATH is used for hook control, ATA is used for answer, ATD is used to dial. These commands are also supported by the mobile phones [15]. The message or information which is stored to the subscriber identity module (SIM) can be read by appropriate AT commands also. GSM/GPRS modems support some additional AT commands for same purposes side by side the standard AT commands. To read messages or information via the SIM by the computer, mobile phones or GPRS/GSM modem should support two AT commands: +CMGR (this command is used to read information or messages through the PC at a specific location of the storage) and +CMGL (This command is used to list messages, to read messages that have specific status in storage like stored unsent, stored sent, received read, received unread) [15] [18]. The +CMGL AT command is used to cover messages from the storage section. To active short message service (SMS), an authentic SIM should be used in the mobile phone or GPRS/GSM modem, and to connect to the computer [16]. Table 1 shows some AT commands which are used in the system for writing, sending, reading, status checking and others [12].

TABLE I. SOME AT COMMANDS USED IN GSM DATA TRANSFER MODULE OF THE SYSTEM

AT Command	Description
+CMGC	Sending the command
+CMGS	To send message/information
+CMMS	Additional SMS to send
+CMGW	To write message/information
+CMGD	To delete message/information
+CMSS	Send message from storage
+CMGI	Module testing

V. SOFTWARE DESCRIPTION

A flowchart for the software algorithm to implement the system is depicted in Figure 4. High-level programming language in the microcontroller has been used to implement the firmware of the system. "Proton IDE of PIC" compiler facilitate this firmware development by providing useful built-in routines and flexibility in writing code for the microcontroller [15-18]. The reason for using this software as a programmer is that this program is compiled easily and provide instant feedback on syntax errors while writing. This facility provides less hassle and uninterrupted workflow to write the code and compile using the program. This is suitable for all levels of user. The Proton Development Suite allows them to develop code in a brand-new IDE, then compile a BASIC program and view the resulting assembly language commented with its own code. Proteus software has been used for microprocessor simulation, schematic capture and printed-circuit-board (PCB) design. The suite mixes combined-mode

SPICE circuit design, microprocessors models, and animated components which is convenient in the microcontroller-based design process and simulations [16]. It simulates input/output ports, interrupts, timers, USARTs and all other peripherals present on each supported processor and allows creating clinical executable decision support guidelines with little effort. On completion, the HEX file generated from Proton IDE is loaded into the microcontroller.

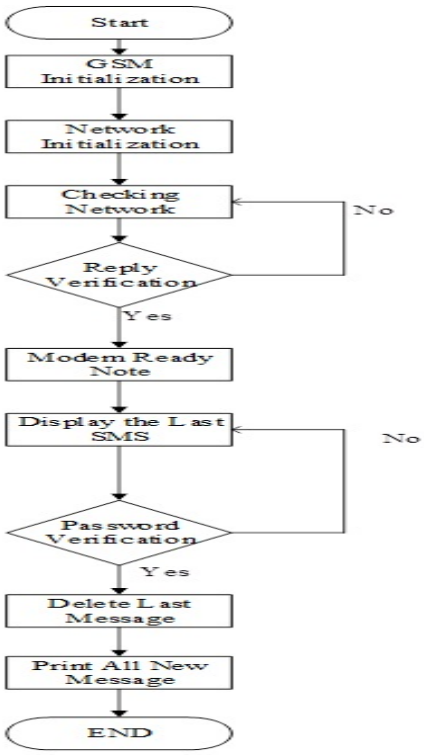

Figure 4. Flow chart of the system

VI. IMPLEMENTED SYSTEM VISUALIZATION

The implemention of the wireless noticing systems is illustrated in Figure 5.

Figure 5. Arrangement of implemented system

When an authenticated person transmits a notice, they should write the password first, then text. The receiver unit receives the SMS and match the password to see whether the person is authenticated or not. If so then there is a display 'Powering Up…. Modem Ready!!' on the LCD which is shown Figure 6.

Figure 6. Initializing the system

The notice to be displayed is always determined and maintained by the assigned authority. For this system a notice of text 'Welcome to the very new technology of messaging. This is first time in C.' is displayed on the LCD, as in Figure 7. The notice can be printed depending upon the viewer inclination.

Figure 7. Notice on LCD display

VII. CONCLUSION

The proposed system works very effectively. Due to password protection, security is maintained strictly which makes it user friendly to officials. Also the viewer can store the notice by printing if they are in hurry. Some additional features can make the system more attractive, for example interfacing an EEPROM with the system can allow it to store more messages at a time and also can give a revive facility at any hazardous condition like power failure or other power problems. The proposed implemented system's alphanumeric LCD can be replaced by a large LED display without changing the cardinal algorithm and design methodology, and can gives more space for noticing, better resolution and a more attractive display.

REFERENCES

[1] Osamor, V. C., Aloba, O. S., & Osamor, I. P., "From wooden to digital notice board (dnb): design and implementation for university administration," International Journal of Electrical & Computer Sciences, 10(2), 79-83, 2010, pp. 79-83

[2] Shruthi, K., Harsha Chawla, and Abhishek Bhaduri. "Smart notice board." Research & Technology in the Coming Decades (CRT 2013), National Conference on Challenges in. IET, 2013.

[3] Villar, N., Van Laerhoven, K., & Gellersen, H., "A physical notice board with digital logic and display." Proceedings of the 2nd European Union symposium on Ambient intelligence. ACM, 2004.

[4] Mishra, P., Pinki, S., and Shivani, G., "SMS based wireless notice board display using gsm mobile." International Journal of Advance Research in Science and Engineering (IJARSE), Vol – 2, No- 10, October, 2013

[5] Azim, M. R. S., Mahmud, K., and Das, C. K., "Automatic train track switching system with computerized control from the central monitoring unit," International Journal of u-and e-Service, Science and Technology, 7(1), 2014, pp. 201-212.

[6] Nayagi, R. P., & Seethalakshmi, R., "Design and Implementation of Digital Notice Board Using Power Line Communication." International Journal of Engineering & Technology (0975-4024) 5.2 (2013).

[7] Bhoyar, Mayur R., Suraj Chavhan, and Vaidehi Jaiswal. "Secure Method of Updating Digital Notice Board Through Sms With Pc Monitoring System."

[8] Mahmud, K., Alam, M. S., and Ghosh, R., "Design of digital thermometer based on PIC16F77A single chip microcontroller," 2013 3rd International Conference on Consumer Electronics, Communications and Networks (CECNet), 20-22 November, 2013, Xianning, China, pp. 246-249.

[9] Mahmud, K., "Neural network based PID control analysis," 2013 IEEE Global High Tech Congress on Electronics (GHTCE), 17-19 November, 2013, Shenzhen, China, pp. 141-145.

[10] Mahmud, K., Alam, M. S., and Jobayer, A., "Design and performance evaluation of PIC16F77A microcontroller based fluid velocity meter," 2013 IEEE Global High Tech Congress on Electronics (GHTCE), 17-19 November, 2013, Shenzhen, China, pp. 21-24.

[11] Gaikwad, A., Tej, K., Manan, L., and Deepak, K., "Wireless Electronic Notice Board." International Journal on Advanced Computer Theory and Engineering (IJACTE), Vol- 2, Issue- 2, 2013

[12] Zohedi, F. N., "Wireless electronic notice board." BSc. diss., Universiti Malaysia Pahang, 2007.

[13] Alam, M. S., Jamil, I. A., Mahmud, K., and Islam, N., "Design and implementation of a RF controlled robotic environmental survey assistant system," 2013 16th International Conference on Computer and Information Technology (ICCIT), 8-10 March, 2014, Khulna, Bangladesh, pp. 438-442.

[14] Morsalin, S., Mahmud, K., Halim, M. R., Saha, P., and Jamil, I. A., "Freighter fuel level detection and overload alarming system with safety notification via GSM," 2014 International Conference on Informatics, Electronics & Vision (ICIEV), 23-24 May, 2014, Dhaka, Bangladesh, pp. 1-5.

[15] Kamdar, F., Malhotra, A., and Mahadik, P., "Display message on notice board using GSM," Advance in Electronic and Electric Engineering, ISSN 2231-1297, Vol- 3, No- 7, 2013

[16] Nivetha S. R, Pujitha. R, Selvaraj, P., and Yashvanthini S. M, "SMS based wireless notice board with monitoring system," International Journal of Advanced Electrical and Electronics Engineering (IJAEEE), Vol- 2, Issue- 3, 2013

[17] Ahmed, M., Sadanand, K. M., and Nasrin, S., "Wireless Electronic Notice Board using GSM Technology." International Journal of Research in Computer Engineering & Electronics 3.6 (2015).

[18] Bashir, A., Qazi, S., Banday, S. A., Nazir, L., & Shah, B. "DTMF based smart notice board system." International Journal of Scientific and Research Publications, Volume- 3, Issue- 11, November 2013

[19] Morsalin, S., Mahmud, K., Mohiuddin, H., Halim, M.R., Saha, P.,"Induction Motor Inter-turn Fault Detection Using Heuristic Noninvasive Approach by Artificial Neural Network with Levenberg Marquardt Algorithm," 2014 International Conference on Informatics, Electronics & Vision (ICIEV), 23-24 May, 2014, Dhaka, Bangladesh, pp. 1-6.

Numerical analysis of O-PCF structure for sensing applications with high relative sensitivity

Kawsar Ahmed, Sayed Asaduzzaman and Md. Faizul Huq Arif
Department of Information and Communication Technology (ICT)
Mawlana Bhashani Science and Technology University (MBSTU)
Santosh, Tangail-1902, Bangladesh

***Abstract*— In this study, micro structured core and cladding based O-PCF has been analyzed by its propagation characteristics. The effects of pitch variation, total power consumption and effective refractive index are investigated on O-PCF. The analyzing process takes place by the full vectorial finite element method (FEM). The analysis O-PCF contains five layers of the air holes in octagonal shape which increases relative sensitivity significantly and decreases confinement loss than the prior structures. Beyond that, the analysis O-PCF can sense the three chemicals water, Ethanol and Benzene at a wide range of wavelength.**

Keywords — Chemical Sensor, Confinement Loss, Evanescent Field, Liquid Sensing, Octagonal Photonic Crystal Fiber (O-PCF) and Sensitivity

I. INTRODUCTION

In recent years, the appealing and versatile application of Photonic Crystal Fiber has aroused the attention of the pioneers and researchers. In PCF, a periodic arrangement of microscopic tiny air holes in the entire fiber contains silicon background with low and high refractive index materials which is a low loss periodic dialectric medium. Propagation of light in PCF using total internal reflection is more superior to the conventional fibers. The two main categories of PCF are index-guiding fibers and photonic band gap (Air guiding) fibers (PBF) bears the difference of effective refractive index between the core and cladding. Nonlinear generation of a UV super continuum and visible in a single transverse mode was the widespread application of PCF which enhanced the potential effectiveness on the conventional optical fiber.

A sophisticated device that converts the light rays into electrical signals which can detect the change and response of ambient condition or can measure the intensity of electromagnetic waves called an optical sensor. A photonic crystal fiber demonstrates its potentiality for sensing applications due to its unique geometrical structure. Physical and biochemical sensor based on sensor measurement parameters has been shown in [1]. PCF can be used for evanescent field sensing where core and cladding region were both microstructure [2]. The light guided in the fiber for producing evanescent field sensing with tight mode confinement possibility was shown in [3]. A Hollow core PCF (HC-PCF) was designed to detect gases as a sensor and the sensitivity was 2.27×10^{-3} dB/ppm with response time 15s [4]. Modified PCF structures with the ring defect at the core were proposed to measure toxic/ flammable gases for safety against the fire, explosion or toxic exposure. Those structures enhance the sensitivity as gas sensor to 13.23 % and reduced confinement loss to 3.77×10^{-6} [5]. W. Jin et al. [6] depict all recent micro and nano-engineered optical fibers for gas detection. Here absorption and photo acoustic spectroscopy based detection schemes were also discussed. A 2-D double hole defect PCF was designed as a refractive index sensor where sensitivity was s=500 nm/RIU [7].

A graphene based birefringent PCF had showed high amplitude sensitivity of 860 RIU^{-1} which was based on Surface Plasmon Resonance [8]. As the application field of photonic crystal fiber is increasing as sensors the PCFs are now used as bio-sensing applications [9], [10]. For sensing temperature and pressure a hollow core was proposed in [11]. In the paper, the sensitivity of the HC-PCF enhanced to 480 nm/RIU at the wavelength λ=1.55 µm. High index material based ring defect was used at the core to enhance the chemical sensing capabilities [12]. The high RIS in media with high thermo optic coefficients causes a noticeable nonlinear behavior in the temperature response of the etched Fiber Bragg Grating (FBG). Thermo optic coefficient (like water, Ethanol and other Hydro carbons) was determined in this article [13]. Fiber loop mirror (FLM) based Ethanol filled two PCF structures were proposed as a temperature sensor where refractive index changes with the applied temperature [14].

The guiding properties (relative sensitivity, confinement loss, Birefringence and dispersion) of the photonic crystal fiber depend much on its geometrical structure. Different researchers form different structures and change the existing structures to enhance the guiding properties. In [15] Y. Hou presents highly birefringent polymer terahertz (THz) fibers where cladding air holes were in honeycomb arrangement and elliptical air holes int the core region. Those structures gained high Birefringence and low confinement loss. To measure the characteristics and enhance the guiding properties different structures at the core region were applied. A THz SPSM PCF including a rectangular array of micro array air holes in the core region which could achieve the SPSM operation with a band of 320 GHz in the THz band near 1 THz at the same time the propagation loss of the guided THz wave was also relatively reduced [16]. Broader bandwidth, low loss and much more flattened dispersion were acquired by porous core photonic band gap fiber [17]. Micro structured core [18] and multicore [19] were applied to acquire the desired guiding properties. Two simple structure PCF was proposed by M. Morshed et al. [20, 21] which shows better sensitivity as gas sensors. The proposed simple structures shows higher sensitivity as a gas sensor as well as it shows lower confinement loss at the same time.

Confinement loss is an important guiding property which increases with the increase of sensitivity of PCF. As increasing the sensitivity and at the meanwhile decreasing the confinement loss is a great challenge. Many works had been performing to reduce confinement loss [22, 23].

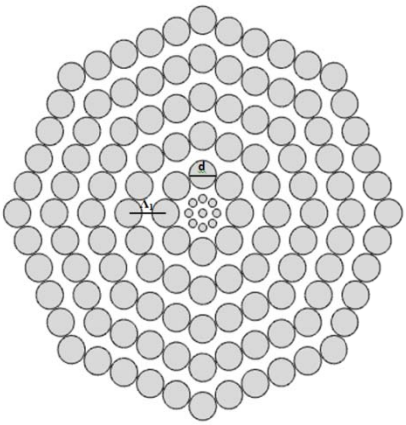

Fig. 1. Cross sectional view of O-PCF.

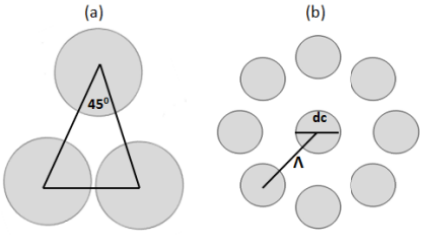

Fig. 2. (a) The unit triangle of PCF (b) The micro-core region

In this paper an octagonal photonic crystal fiber (O-PCF) has been presented which shows better sensitivity and lower confinement loss than the [24, 25]. A numerical analysis was executed on the O-PCF which was proposed [25] by K. Ahmed and M. Morshed. The maximum sensitivity and minimum confinement loss was achieved by pitch value 0.9 µm. But the article [25] did not mention the relationship between wavelength and total power as well as refractive index. This paper is also designed to show those relationships. Now fabrication is a crucial issue for microstructures PCF. Now a day's sol-gel technique has removed the complexity of fabrication of any kind of micro structured optical fiber as well as PCF [26]. So the proposed O-PCF can be easily fabricated using sol-gel technique.

II. Geometries of the Proposed O-PCF

The cross sectional view of the proposed O-PCF has been shown in the Figure 1. The figure clearly depicts the whole geometrical structure of the PCF. The proposed structure of the PCF is in octagonal in shape. So the vertices of the adjoining air holes contain 45^0 angles to form octagonal structure. The pitch between the two layers has been denoted by Λ_1=2.4 µm and the pitch between the two adjacent air holes of same layer has taken 1.80 µm. The diameters of the layers of the supplementary air holes are same for each layer and are denoted by d. The core region contains 8 holes and an air hole at the center. The diameters of the supplementary air holes at the core region is denoted by d_c and the pitch among the supplementary air holes at core is denoted by Λ. The first layer of the supplementary air holes contains 8 air holes and the other layers contain two times more air holes than the premature layer. Various analyst with refractive index like Water (n=1.33), Ethanol (n=1.354) and Benzene (n=1.366) are filled into the supplementary air holes at the core region. Fig. 2 (a) shows the unit triangles of the PCF where the angles are 45^0 and Fig. 2(b) shows the Micro-core region of the proposed O-PCF.

III. Numerical Analysis

Maxwell's equations were applied for analyzing the proposed PCF structure because of its reliability [27]. The Finite Element Method (FEM) has been utilized with a circular perfectly matched boundary layer (PML) to solve Maxwell's equations. Here we investigated and analyzed the sensitivity and the confinement loss of the proposed PCF.

Relative sensitivity coefficient is an important parameter of a PCF to quantify the efficiency of the PCF. Relative sensitivity coefficient measures the interaction between light and the analyte and it can be calculated through the following equation.

$$r = \frac{n_r}{n_{eff}} f \tag{1}$$

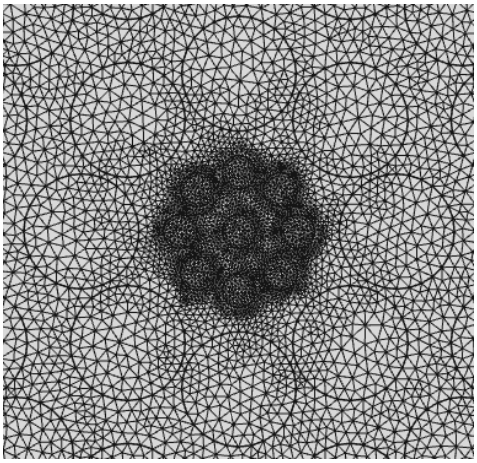

Fig. 3. Finer mesh analysis of O-PCF.

Where, n_r represents the refractive index of sensed material within the air holes and n_{eff} is the modal effective index. f is the percentage energy of holes. For particular fiber mode f can be calculated through the following equation.

$$f = \frac{\int_{sample} Re(E_x H_y - E_y H_x)\, dx\, dy}{\int_{total} Re(E_x H_y - E_y H_x)\, dx\, dy} \times 100 \tag{2}$$

Where, E_x , H_x , E_y , H_y are mode field pattern and calculated by solving Maxwell's equation using finite element method (FEM). E_x and H_x are transverse electric field and magnetic field, E_y and H_y are longitudinal electric field and magnetic field.

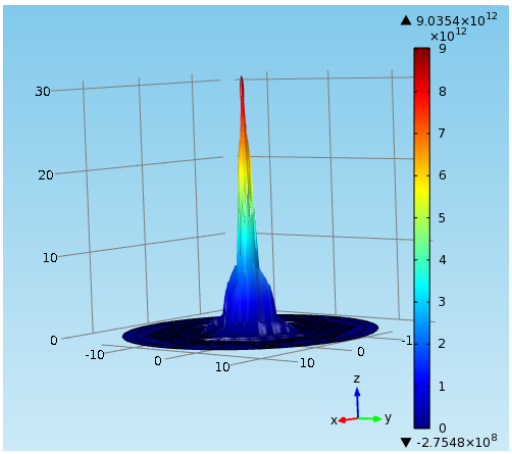

Fig. 4. 3-D view of the modal intensity distribution.

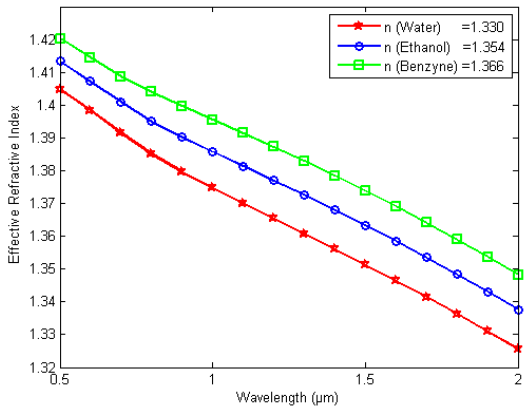

Fig. 5. Comparison of effective refractive index with the wavelength for n=1.330, n=1.354 and n=1.366

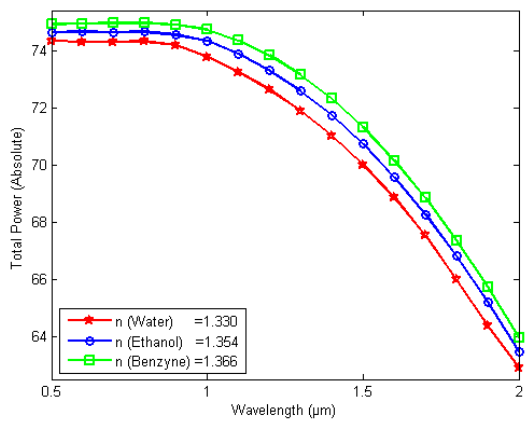

Fig. 6. Comparison of the total power for three different chemicals n= 1.330 (water), n=1.354 (Ethanol) and n=1.366 (Benzene).

A small portion of power loss happens when light energy passes through a PCF. This loss is known as confinement loss of the PCF. Confinement loss L_c (dB/m) can be calculated through the equation (3).

$$L_c = \frac{40\pi.\mathrm{Im}[n_{eff}]\times 10^6}{\lambda.ln(10)} \quad \text{(dB/m)} \qquad (3)$$

Where, $\mathrm{Im}[n_{eff}]$ is the imaginary part of the refractive index and λ is the wavelength of light.

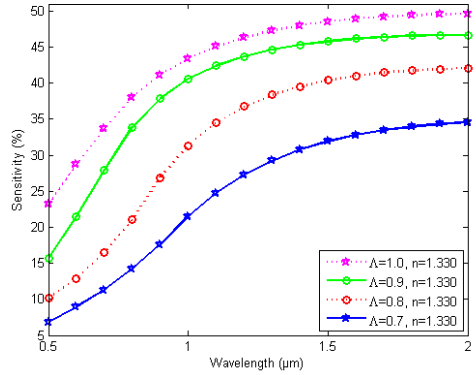

Fig. 7. Comparison of the sensitivity for Λ=1.0, Λ=0.9, Λ=0.8, Λ=0.7 when n=1.330 (water).

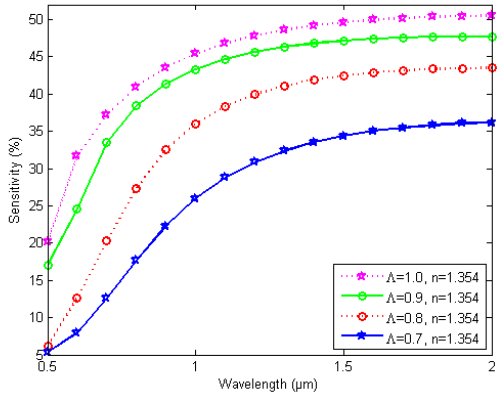

Fig. 8. Comparison of the sensitivity for Λ=1.0 μm, Λ=0.9 μm, Λ=0.8 μm, Λ=0.7 μm when n=1.354 (Ethanol).

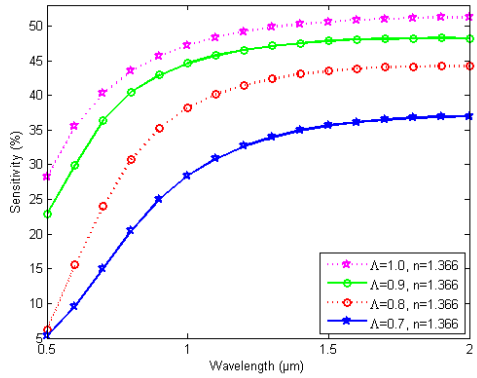

Fig. 9. Comparison of the sensitivity for Λ=1.0 μm, Λ=0.9 μm, Λ=0.8 μm, Λ=0.7 μm when n=1.366 (Benzene).

IV. Results and Analysis

In this section the field profile of fundamental mode, modal intensity distribution and comparison of the prior and proposed PCF has been shown. The comparison of relative sensitivity and confinement loss for three different chemicals

also takes place in this section. Fig. 3 illustrates that mesh analysis of O-PCF structure in finer mode.

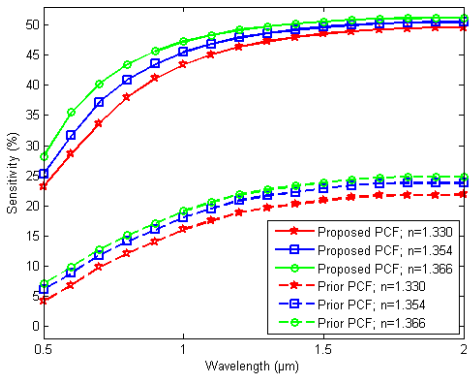

Figure 10. Comparison of the sensitivity of prior and O-PCF

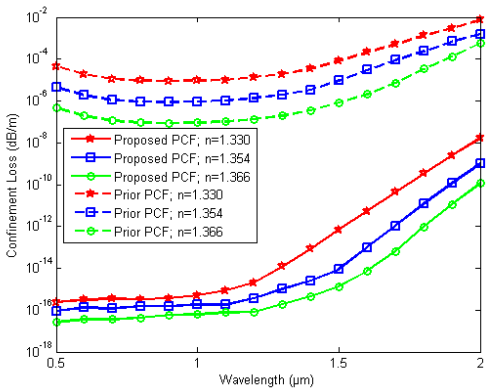

Figure 11. Comparison of the confinement loss of prior and O-PCF

Fig. 4 shows the 3-D view of the modal intensity distribution of the Proposed PCF. The mode has been tightly confined at the core region and is properly distributed along the Z-axis of the figure.

From Fig. 5 it is clear that the effective refractive index linearly decreases with the increase of the wavelength. The lower refractive index based chemical like water (n=1.330) shows higher effective refractive index and higher refractive index based chemicals like Benzene (n=1.366) shows lower effective refractive index.

The total power of a PCF means the power of the holes and the power of the total silica background with perfect matched layer (PML). From the figure it can be describe that the total power of the proposed PCF remains same for the wavelength from 0.5 μm up to 0.9 μm. Then from the wavelength 1 μm the total power decreases linearly according to the wavelength.

Fig. 7, Fig. 8 and Fig. 9 shows the comparison of the sensitivity for the different pitch values are Λ=1.0 μm, Λ=0.9 μm, Λ=0.8 μm and Λ=0.7 μm according to the three different chemicals water (n=1.330), Ethanol (n=1.354) and Benzene (n=1.366). The sensitivity increases with the wavelength and for Λ=1.0 μm the proposed O-PCF shows the higher sensitivity for water (n=1.330), Ethanol (n=1.354) and Benzene (n=1.366).

The proposed O-PCF shows the higher relative sensitivity and lower confinement loss than the previous PCF's better results for three chemicals water (n=1.330), Ethanol (n=1.354) and Benzene (n=1.366) which has been shown in Fig. 10 and Fig. 11. Here Λ_1=2.4 μm, d = 1.75 μm Λ=0.9 μm and dc= 0.514 μm of the proposed O-PCF were constant as the propagation characteristics.

V. Conclusion

In this work a micro core O-PCF has been presented for chemical sensing which shows better sensitivity along with lower confinement loss. The behavior of the proposed PCF has been investigated by changing different geometrical and optical parameters by using three different liquids water, Benzene and Ethanol as analysts. The confinement loss has been decreased and the relative sensitivity of the proposed PCF has also been enhanced almost 2.4 times than the previous PCF for the three chemicals. At the same time our proposed PCF can sense the chemical at a wide range of wavelength from 0.5 μm to 2 μm. The result is simulated using COMSOL Multiphysics 4.2 version. Due to not fabrication of proposed O-PCF the result may be little bit varied after fabrication what is the main drawback of our proposed O-PCF.

Acknowledgment

The authors are grateful who participated to this research.

References

[1] M. Pinto and M. Lopez-Amo, "Photonic crystal fibers for sensing applications," *Journal of Sensors*, vol. 2012, 2012.

[2] C. Cordeiro, M. A. Franco, G. Chesini, E. Barretto, R. Lwin, C. H. Brito Cruz, and M. C. Large, "Microstructured-core optical fibre for evanescent sensing applications," *Optics Express*, vol. 14, no. 26, pp. 13056–13066, 2006.

[3] T. M. Monro, W. Belardi, K. Furusawa, J. C. Baggett, N. G. R. Broderick, and D. J. Richardson, "Sensing with microstructured optical fibres," *Measurement Science and Technology*, vol. 12, no. 7, p. 854, 2001.

[4] X. I. N. Gui, L. Zheng-Ying, H.-H. Wang, J. I. A. He, C.-C. Hu, L.-J. Ma, and others, "Research on Distributed Gas Detection Based on Hollow-core Photonic Crystal Fiber.," *Sensors & Transducers (1726-5479)*, vol. 174, no. 7, 2014.

[5] S. Olyaee, A. Naraghi, and V. Ahmadi, "High sensitivity evanescent-field gas sensor based on modified photonic crystal fiber for gas condensate and air pollution monitoring," *Optik-International Journal for Light and Electron Optics*, vol. 125, no. 1, pp. 596–600, 2014.

[6] W. Jin, H. L. Ho, Y. C. Cao, J. Ju, and L. F. Qi, "Gas detection with micro-and nano-engineered optical fibers," *Optical Fiber Technology*, vol. 19, no. 6, pp. 741–759, 2013.

[7] L. A. Shiramin, R. Kheradmand, and A. Abbasi, "High-sensitive double-hole defect refractive index sensor based on 2-D photonic crystal," *Sensors Journal, IEEE*, vol. 13, no. 5, pp. 1483–1486, 2013.

[8] J. N. Dash and R. Jha, "Graphene-based birefringent photonic crystal fiber sensor using surface plasmon resonance," *Photonics Technology Letters, IEEE*, vol. 26, no. 11, pp. 1092–1095, 2014.

[9] U. S. Dinish, C. Y. Fu, K. S. Soh, B. Ramaswamy, A. Kumar, and M. Olivo, "Highly sensitive SERS detection of cancer proteins in low sample volume using hollow core photonic crystal fiber," *Biosensors and Bioelectronics*, vol. 33, no. 1, pp. 293–298, 2012.

[10] S. M. Shamah and B. T. Cunningham, "Label-free cell-based assays using photonic crystal optical biosensors," *Analyst*, vol. 136, no. 6, pp. 1090–1102, 2011.
[11] S. Padidar, V. Ahmadi, and M. Ebnali-Heidari, "Design of High Sensitive Pressure and Temperature Sensor Using Photonic Crystal Fiber for Downhole Application," *Photonics Journal, IEEE*, vol. 4, no. 5, pp. 1590–1599, 2012.
[12] J. Park, S. Lee, S. Kim, and K. Oh, "Enhancement of chemical sensing capability in a photonic crystal fiber with a hollow high index ring defect at the center," *Optics express*, vol. 19, no. 3, pp. 1921–1929, 2011.
[13] R. C. Kamikawachi, I. Abe, A. S. Paterno, H. J. Kalinowski, M. Muller, J. L. Pinto, and J. L. Fabris, "Determination of thermo-optic coefficient in liquids with fiber Bragg grating refractometer," *Optics Communications*, vol. 281, no. 4, pp. 621–625, 2008.
[14] D. Wu, Y. Zhao, and H. Hu, "Experimental research on FLM temperature sensor with an ethanol-filled photonic crystal fiber," *Sensors and Actuators A: Physical*, vol. 209, pp. 62–67, 2014.
[15] Y. Hou, F. Fan, Z.-W. Jiang, X.-H. Wang, and S.-J. Chang, "Highly birefringent polymer terahertz fiber with honeycomb cladding," *Optik-International Journal for Light and Electron Optics*, vol. 124, no. 17, pp. 3095–3098, 2013.
[16] H. Chen, H. Wang, H. Hou, and D. Chen, "A terahertz single-polarization single-mode photonic crystal fiber with a rectangular array of micro-holes in the core region," *Optics Communications*, vol. 285, no. 18, pp. 3726–3729, 2012.
[17] J. Liang , L. Ren , N. Chen , C. Zhou, "Broadband, low-loss, dispersion flattened porous -core photonic band gap fiber for terahertz (THz)-wav e propagation" , *Optics Communications*, vol. 295, no. 1, pp. 257–261, 2013.
[18] C. Cordeiro, M. A. Franco, G. Chesini, E. Barretto, R. Lwin, C. H. Brito Cruz, and M. C. Large, "Microstructured-core optical fibre for evanescent sensing applications," *Optics Express*, vol. 14, no. 26, pp. 13056–13066, 2006.
[19] B. Li, G. Zhou, C. Xia, H. Liu, and Z. Hou, "Analysis of supermode and structural characteristics of octagonal multicore photonic crystal fiber with large effective mode area and low confinement loss," *Optical Engineering*, vol. 53, no. 5, pp. 056114–056114, 2014.
[20] M. Morshed, M. F. H. Arif, S. Asaduzzaman, and K. Ahmed, "DESIGN AND CHARACTERIZATION OF PHOTONIC CRYSTAL FIBER FOR SENSING APPLICATIONS," *European Scientific Journal*, vol. 11, no. 12, 2015.
[21] M. Morshed, S. Asaduzzaman, M. Arif, F. Huq, and K. Ahmed, "Proposal of simple gas sensor based on micro structure optical fiber," in *Electrical Engineering and Information Communication Technology (ICEEICT), 2015 International Conference on*, 2015, pp. 1–5.
[22] T. P. White, R. C. McPhedran, C. M. de Sterke, L. C. Botten, and M. J. Steel, "Confinement losses in microstructured optical fibers," *Optics Letters*, vol. 26, no. 21, pp. 1660–1662, 2001.
[23] S. Haxha and H. Ademgil, "Novel design of photonic crystal fibres with low confinement losses, nearly zero ultra-flatted chromatic dispersion, negative chromatic dispersion and improved effective mode area," *Optics communications*, vol. 281, no. 2, pp. 278–286, 2008.
[24] H. Ademgil, "Highly sensitive octagonal photonic crystal fiber based sensor," *Optik-International Journal for Light and Electron Optics*, vol. 125, no. 20, pp. 6274–6278, 2014.
[25] K. Ahmed and M. Morshed, "Design and numerical analysis of microstructured-core octagonal photonic crystal fiber for sensing applications," *Sensing and Bio-Sensing Research*, vol. 6, 2015.
[26] R. T. Bise and D. J. Trevor, "Sol-gel derived microstructured fiber: Fabrication and characterization," in *Optical Fiber Communications Conf.(OFC)*, 2005, vol. 3.
[27] F. Brechet, J. Marcou, D. Pagnoux, and P. Roy, "Complete analysis of the characteristics of propagation into photonic crystal fibers, by the finite element method," *Optical Fiber Technology*, vol. 6, no. 2, pp. 181–191, 2000.

Free-Space Optical Communication with m-ary Pulse Position Modulation under Strong Turbulence with Different Type of Receivers

Md. Athaharul Islam* and Ashraful Bari Chowdhury
Department of EEE
Ahsanullah University of Science and Technology
Dhaka, Bangladesh.
*E-mail: a1b2i3r45@gmail.com

***Abstract*—With the exponential increase in demand for high speed precision communication system, free-space optics (FSO) has been proven to be a viable solution to this problem. This relatively new technology has gained popularity because of its wider bandwidth, comparatively greater security and relatively economical configuration. However, in FSO links, due to the atmospheric turbulence which is one of the characterizing elements in the system between the transmitter and the receiver, the magnitude of received signal intensity and also the phase of the received light signal wavers. To diminish fading in FSO systems combination of single or multiple transmitter and receiver are used. Moreover, the efficiency of the FSO systems are enhanced by utilizing the most pertinent modulation technique and channel model, making a suitable compromise between system implementation complexity and overall performance. Taking everything into account, we focus our attention in this paper on m-ary pulse position modulation (PPM) with gamma-gamma atmospheric turbulence model, under strong turbulent condition. Furthermore, APD and PIN photodiodes are used as receiver and a comparison of performance is also been made between them. The overall performance of the system are computed in the form of bit error rate (BER) and the simulation results confirm the analytical findings.**

Keywords*—avalanche photodiode (APD); free-space optics (FSO); gamma-gamma distribution model; m-ary pulse position modulation (PPM); positive intrinsic negative (PIN) photodiode; signal Intensity.

I. INTRODUCTION

Free-space optical communication (FSO) system also known as optical wireless system uses the atmosphere/space between the transmitter and receiver as the propagation medium and the line of sight as the link. It can be used between various platforms such as satellites, ships, aircrafts etc. either stationary or in motion in space and in the atmosphere. Due to its unregulated spectrum, inherent security, high data rate and wider bandwidth, FSO is considered as a supplement to radio frequency (RF) communication [1]. Despite all of its advantages over conventional communication links, because of its propagation medium which cannot be controlled or conditioned, FSO systems are subjected to the consequences of some atmospheric phenomena. The primary challenges associated with free-space optical systems are narrow beam width, transmission signal scattering and scintillation. Because of atmospheric turbulence, intensity of the received signal fluctuates which is known as scintillation [2].

Optimization of the system is achieved by minimizing transmission error rate under both weak and strong atmospheric turbulences and it is done by using combination of single or multiple transmitters and receivers [3], [4]. However, here we specifically consider single transmitter array, in combination with multiple photo detectors (PDs) as multiple receiver arrays. The transmitter and the receiver arrays are positioned in such a way that the fading phenomenon between transmitter–receiver pair is considered statistically independent. Hence, gains through diversity can be accrued from single-input and multiple-output (SIMO) system.

Due to the variable nature of the FSO channel it is very difficult to specifically design the channel with high order accuracy. Despite the difficulty and complexity, several statistical description of the atmospheric channel has been introduced. One of the most commonly used statistical model for the probability of density function (PDF) is log-normal distribution. Although, it is pertinent to the weak atmospheric turbulence [5]. Moreover, with the rise in the strength of turbulence, signal scattering intensifies and consequential aberration from log-normal distribution is manifested in the data. Hence, we consider another statistical model which is gamma-gamma distribution. It has two parameters and the basis of this distribution model is a doubly stochastic theory of scintillation and the assumption of the theory is that both small and large scale irradiance deviations of the transmitted wave are dictated by independent gamma distributions. Moreover, the validity of the gamma–gamma distribution has been proven for both weak and strong atmospheric turbulences [6].

In the receiver arrays, the positive intrinsic negative (PIN) photodiodes and the avalanche photodiodes (APDs) are the most commonly used photodiodes in FSO. PIN photodiode is widely employed because of its low-cost, high mitigation to extensive temperature fluctuations and its inherent capability to operate with cheap small-bias voltage power supply. Moreover, PIN photodiode is comparatively less sensitive than APD. In case of APD, here we use silicon (Si) APD in the system because of its ionization ratio (ς), which has a great dependency on applied electric field across the APD.

978-1-4673-9257-0/15/$31.00 ©2015 IEEE

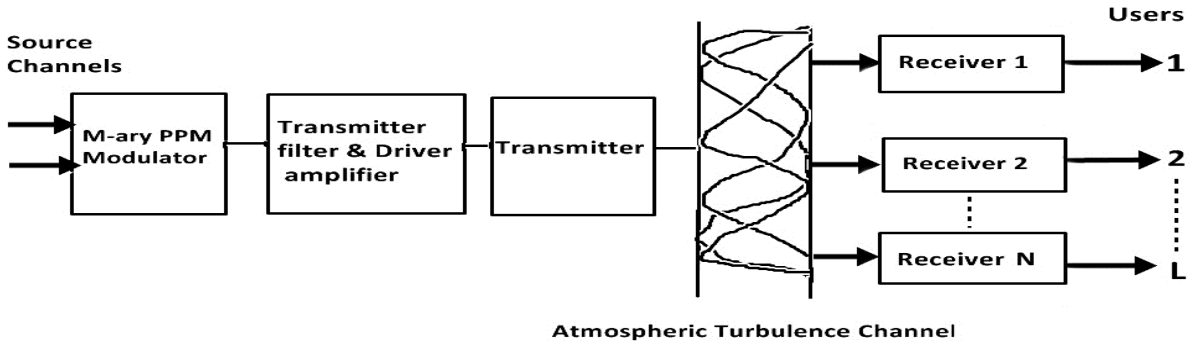

Fig. 1. FSO SIMO system with m-ary PPM under strong atmospheric turbulence.

Furthermore, at low electric fields the values of ionization ratio of APD is at its nadir (in case of Silicon). Moreover, increased power margin provides a more robust communication link than PIN receivers. This allows further reduction in transmitter power and SNR can be increased through the internal gain of APDs. However, APD is expensive and require comparatively higher voltage for operation which limits their practical usage [7], [8], [9]. Out of different modulation techniques, Pulse position modulation (PPM) is among the most commonly used modulation techniques for FSO system. In contrast to other modulation techniques such as on-off keying (OOK), PPM provides several advantages such as better power management efficiency and greater overall performance of the system at the price of a diminished efficiency of bandwidth [10]. Adopting high order m-ary PPM modulation for FSO is shown to enhance the power and bandwidth efficiencies as compared to conventional PPM technique [10], [11].

In the subsequent sections of this paper, we analyze and evaluate the performance of FSO SIMO system with m-ary PPM using two different type of receivers (APD and PIN); in order to make a comparison of performance between them. The overall system performance is computed in the form of bit error rate (BER) assuming the strong atmospheric turbulence is statistically designed with gamma-gamma distribution. The arrangement of the remainder of this paper is- System model is presented in Section II. Then, channel model is depicted in Section III followed by the theoretical analysis in Section IV. After the computation is carried out, results and discussions are carried out in Section V. Lastly, the Section VI consists of the conclusions drawn in this paper.

II. System Model

Block diagram of the model under consideration is illustrated in Fig. 1. The modulation of the source codes has been done with m-ary PPM and the encoding is done by the SIMO encoder and the laser diodes in the transmitter array are modulated by output of this encoder. Then the light passes through gamma-gamma distribution. AWGN due to shot noise and thermal noise, are added at the receiver input. As receiver, we use PIN and APD to convert the light intensity into electrical current. The information of the full channel state is considered to be available at the photo detectors. Let the gain of our considered path be A_{MN} , from M number of sources (for SIMO system, M=1) to N number of detector. In case of m-ary PPM, each transmitted data consists of m number of time slots, thereby transmitting $L=\log_2^m$ bits per data. The transmitted signals are outlined by the waveforms,

$$X = S_m(t) = \begin{cases} 1, & for\ t \in \left(\frac{(m-1)T_s}{L}, \frac{mT_s}{L}\right) \\ 0, & elsewhere \end{cases} \quad (1)$$

The received signal is directed onto the array of photodiodes. Signal at receiver is given by

$$P = P_R \times X \quad (2)$$

Here, P_R represents average power of received signal. X is defined by (1). The conversion of the optical signal to electrical signal at the photodiode is done with responsivity, R. Both shot and thermal noise are described with a zero-mean Gaussian noise. At receiver electrical signal, y is defined as-

$$y = RP + n \quad (3)$$

Here, P represents signal at the receiver and zero-mean Gaussian noise with Rytov variance σ_R^2 is represented by n. Now, the average power of optical signal at the receiver is given by [12].

$$P_R(I) = P_T \eta_T \eta_R G_T G_R \left(\frac{\lambda}{4\pi L}\right)^2 I \quad (4)$$

Here, the average transmitted power is represented by P_T; efficiency of transmitter and of receiver are respectively η_T and η_R; transmitter and receiver gains are respectively G_T and G_R; wavelength under consideration is λ; measured distance between transmitter and receiver is L; state of the channel because of turbulence is I.

III. Channel Model

The complex and variable channel can be precisely calculated if the statistical model under consideration is appropriate for the atmosphere. In order to properly model a FSO system with strong atmospheric turbulence it is essential to characterize the channel through proper probability density functions (PDFs). Several PDFs have been introduced for the intensity deviations at the photo detectors of FSO systems. From all, this paper mainly highlights on the use of gamma-gamma distribution model. This model is mathematically characterized by the Rytov variance σ_R^2.

Gamma-Gamma Distribution:

This model considers two random processes, both of which are independent and the product of them, each with a gamma PDF describes the factorization of irradiance. The probability density function of the deviation in intensity is given by [13],

$$f(I)=\frac{2(\alpha\beta)^{(\alpha+\beta)/2}}{\Gamma(\alpha)\Gamma(\beta)} I^{\frac{(\alpha-\beta)}{2}-1} K_{(\alpha-\beta)}\left(2\sqrt{\alpha\beta I}\right),\ I>0 \quad (5)$$

Here, I (w/m²) represents signal intensity, $\Gamma(.)$ represents gamma function, and $K_{(\alpha-\beta)}$ represents modified Bessel function of second kind and order $\alpha\beta$. α and β represent PDF parameters, defining scintillation and considering, zero-inner scale are defined by [13]

$$\alpha = \frac{1}{\exp\left[\frac{0.49\sigma_R^2}{\left(1+1.11\sigma_R^{12/5}\right)^{7/6}}\right]-1} \quad (6)$$

$$\beta = \frac{1}{\exp\left[\frac{0.51\sigma_R^2}{\left(1+0.69\sigma_R^{12/5}\right)^{5/6}}\right]-1} \quad (7)$$

Here, σ_R^2 is the Rytov variance, which is given by [3].

$$\sigma_R^2 = 1.23 C_n^2 K^{7/6} L^{11/6} \quad (8)$$

Here, C_n^2 represents refractive index structure parameter.

IV. Theoretical Analysis

Here, we consider two cases: m-ary PPM with APD as receiver and also with PIN photodiode as receiver. All cases are discussed for gamma-gamma distribution model. The generalized bit error rate of the system with m-ary PPM under gamma-gamma distribution, P_b^m is derived from [10]

$$P_b^m \le \frac{m}{2} W|X| \sum_{i=-N, i\neq 0}^{N} Q\left\{\frac{IX^2}{\sqrt{F\, IX^2 + K_n}}\right\} \quad (9)$$

Here, m represents level of modulation, I represents signal intensity (Irradiance), W and X respectively represent weight factors and the zeros of the Hermite polynomial, N is the receiver number, K_n represents per slot total noise and is derived from [10],

$$K_n = \frac{[\log_2(m)]2\sigma_R^2}{m(E\{g\}q)^2} + 2FK_b \quad (10)$$

Here, σ_R^2 is Rytov variance, K_b represents average background noise photons per slot, APD average gain is represented by $E\{g\}$ and q represents charge of electron. Considering statistical nature of avalanche multiplication by using McIntyre formula, excess noise factor can be defined as [14],

$$F = \varsigma E\{g\} + (1-\varsigma)\left(2 - \frac{1}{E\{g\}}\right) \quad (11)$$

Here, ς is the ionization factor. Considering $\varsigma < 0.1$ and $E\{g\} > 20$ McIntyre formula in (11) can be shortened with great accuracy and so the noise factor F of APD becomes,

$$F \approx 2 + \varsigma E\{g\} \quad (12)$$

Using the derived value of F from (12) in (9), the bit error rate is calculated for the system with APD photodector. Similarly, the bit error rate is also calculated for the system with PIN photodector by setting the value of both noise factor (F) and gain $(E\{g\})$ to unity in (11).

V. Results and Discussions

After the theoretical analysis propounded in section IV, we calculate the BER for m-ary PPM using SIMO FSO link. The simulation is completed using matlab. Different system elements used for computation are displayed in Table I [5], [10].

TABLE I. Elements Used For Computation

Element Name	Specific Value/ Range of Values
Background noise, K_b	20 photons per bit
Bit rate	2.4 Gbps
Average gain, $E\{g\}$ (for APD)	150
Average gain, $E\{g\}$ (for PIN)	1
Signal Intensity, I	0 to 3 w/m²
Ionization factor, ς	0.028
Length, L	100 m
Load resistance, R_L	50Ω
Modulation level, m	2, 8, 16
No. of receivers, N	5
Rytov variance, σ_R^2	0.7
Temperature, T	300 K
Wavelength, λ	850×10^{-9} m

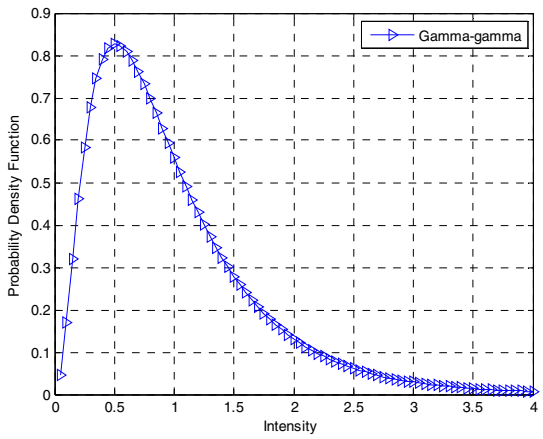

Fig. 2. Plot of PDF vs. Intensity (w/m²) for gamma-gamma distribution.

The plot of Fig. 2 depicts the PDF with respect to intensity for gamma-gamma distribution.

Fig. 3 illustrates the plots of bit error rate vs. Intensity of the system with APD as receiver; in case of m = 2, 8, 16 simultaneously.

Fig. 4 depicts the plots of bit error rate vs. Intensity of the system with PIN photodiode as receiver; in case of m = 2, 8, 16 simultaneously.

Fig. 5 provides an overall comparison of previous plots (Fig. 3 and Fig. 4). From Fig. 5, it is clear that after a certain value of Intensity ($\approx$ 0.25), differences start to emerge in the values of BER in all cases (m = 2, 8, 16) for PIN and APD. Although, regardless of the modulation level (m = 2, 8, 16), the BERs for PIN decrease slowly compared to APD. Hence, significant improvement in performance is noticed for PIN at a greater intensity; whereas in case of APD, BERs decline sharply with increasing intensity for all modulation levels (m=2, 8, 16), implying a significant improvement in performance. Conclusively, considering both APD and PIN

photodiode as receiver with m-ary PPM under strong turbulence it is clear that, APD is better as receiver than PIN photodiode, with m-ary PPM in all cases (m=2, 8, 16).

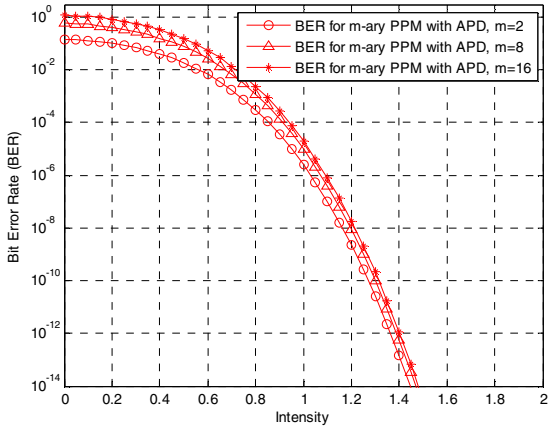

Fig. 3. Plots of BER vs. Intensity (w/m^2) for m-ary PPM with APD receiver.

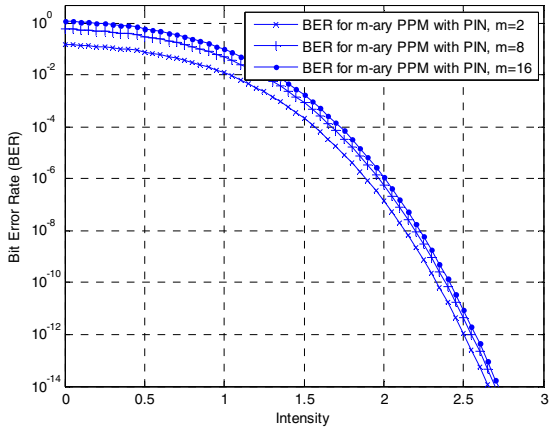

Fig. 4. Plots of BER vs. Intensity (w/m^2) for m-ary PPM with PIN receiver.

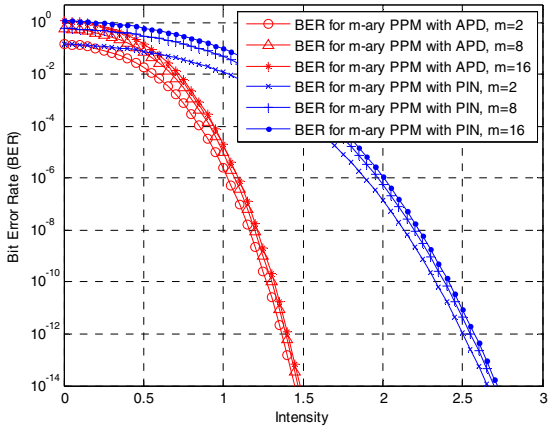

Fig. 5. Plots of BER vs. Intensity (w/m^2) for m-ary PPM with both APD and PIN receivers.

VI. Conclusions

In this paper, we have considered a FSO SIMO system modulated with m-ary PPM and with a strong atmospheric turbulence defined by gamma-gamma distribution using APD and PIN receivers separately. Then a combined comparative evaluation has been made including both cases. The correct expression of the BER is used for the system in both the cases of APD and PIN photodiode in the receiver arrays. By observing the results the following conclusions are made. APD is better than PIN photodiode as receiver with m-ary PPM in the cases of modulation levels, m=2, 8 and 16; due to a better data transmission efficiency is achieved with lower signal intensity. Moreover, due to the same reason considering practical implementations it can be said that, with m-ary pulse position modulated systems, APD is a more cost-efficient solution compared to PIN photodiode.

From the results, we have also concluded that system performance improves with increasing intensity, almost at a similar rate for the considered modulation levels, m=2, 8 and 16 in both APD and PIN photodiode receivers.

References

[1] DAS, S., HENNIGER, H., EPPLE, B., MOORE, C., RABINOVICH, W., SOVA, R., YOUNG, D. Requirements and challenges for tactical free-space lasercomm. In *IEEE Military Communications Conference.* San Diego (USA), 2008, p. 1-10.

[2] L. C. Andrews, R. L. Phillips, C. Y. Hopen, M. A. Al-Habash, "Theory of optical scintillation," J. Opt. Soc. Am. A 16, 1417–1429 (1999).

[3] Wilson S.G., Brands-Pearce M., Cao Q., and Leveque J.J.H.,III, "*Free-Space optical MIMO transmission with Q-ary PPM," IEEE Transactions on Communications,* vol. 53, pp. 1402-1412, 2005

[4] G. Ochse, Optical Detection Theory for Laser Applications. NewYork: Wiley-Interscience, 2002.

[5] Bobby Barua, Mirza Moazzem Hossain, Md. Rezwan Islam, Md. Khairul Bashar, "Performance Evaluation of Different Type of Channel Models in FSO Communication," International Journal of Science and Advanced Technology (ISSN 2221-8386), Volume 1 No 5 July 2011.

[6] M. Uysal, J. T. Li, and M. Yu, "Error rate performance analysis of coded free-space optical links over gamma-gamma atmospheric turbulence channels," *IEEE Transactions on Wireless Communications,* vol. 5, pp. 1229-1233, June 2006.

[7] H. Shaban, S. D. A. E. Aziz, and M. H. Aly, "Probability of error performance of free space optical systems in severe atmospheric turbulence channels," in *10th Mediterranean Microwave Symposium (MMS'2010),* Morphou, Cyprus, Aug. 25–27, 2010, pp. 355–359.

[8] C. Singh, J. John, Y. N. Singh, and K. K. Tripathi, "A review of indoor optical wireless systems," *IETE Technical Review*, vol. 19, no. 1-2, pp. 3–17, Jan.-Apr. 2002.

[9] K. Kiasaleh, "Performance of APD-based, PPM free-space optical communication systems in atmospheric turbulence," *IEEE Transactions on Communications,* vol. 53, no. 9, pp. 1455–1461, Sep. 2005.

[10] M. R. Abaza, N. A. Mohammed, and M. H. Aly, "BER performance of M-ary PPM free-space optical communications with channel fading," in *Proceeding of the 8th International Conference on High Capacity Optical Networks & Enabling Technologies (HONET 2011)*, Riyadh, Saudi Arabia, Dec. 19–21, 2011, pp. 111–115.

[11] J. Yan, Z. Zheng, W. Hu, and A. Xu, "Improved performance of M-ary PPM free-space optical communication systems in atmospheric turbulence due to forward error correction," in *Proceeding of the 10th International Conference on Communication Technology (ICCT)*, Guilin, China, Nov. 27–30, 2006, pp. 1–4.

[12] Hennes HENNIGER, Otakar WILFERT, "An Introduction to Free-space Optical Communications," *IEEE Transactions on RADIOENGINEERING*, vol. 19, no. 2, pp. 203–212, June 2010.

[13] M.A. Al-Habash, L.C. Andrews and R.L. Phillips, *Optical Engineering 40*, pp. 1554-1562 (2001).

[14] McIntyre, R.J., *Multiplication Noise in Uniform Avalanche Diodes, IEEE Transactions on Electron Devices*, ED-13, pp. 164-168 (1966).

Performance Analysis of Large Scale ZigBee Network Design Through Geometric Structure

MD. Jaminul Haque Biddut, Nazrul Islam, Mehedy Hasan Rafsan Jany, Asma Islam Swapna
Department of Information and Communication Technology
Mawlana Bhashani Science and Technology University
Santosh, Tangail-1902, Bangladesh
Email: biddutict@gmail.com, nazrul.islam@mbstu.ac.bd, rafsanjany@outlook.com, asma0swapna@gmail.com

***Abstract*—Wireless Sensor Network (WSN) is a group of the specialized wireless devices which forms a communication infrastructure at a diverse location. IEEE 802.15.4 standard for wireless devices like ZigBee has demonstrated its enormous application as WSN. ZigBee has got popularity for its both small range and wide range coverage. In wide range coverage, a large scale ZigBee network deployment is going ahead. Without proper network structure, a lot of sensor nodes needed for coverage. And also take down the network performance of the large-scale ZigBee network. This study, however, carries a new geometric structure to improve the formation of large scale ZigBee network and its performance. The network simulator Riverbed is used to design and implement a large ZigBee network in geometrical patterns. And also the network performance is analyzed by scrutinizing different network parameters. For real-time communication, free from network path is chosen according to the traffic inside the network. Finally, a deep analysis between two geometric structures - random and octagonal has presented with related parametric aspects. The analysis indicates the new octagonal structure shows significant performance in large scale ZigBee network deployment. This study will create a new opportunity to establish a reliable large-scale ZigBee network.**

Keywords*—WSN, ZigBee Network, Geometrical Network Structure, Performance Analysis, Riverbed.

I. Introduction

ZigBee is a standard wireless sensor device to form a perfectly interoperable sensor network. ZigBee is the standard network protocol base solely conducted under the ZigBee Alliance. IEEE 802.15.4 standard initializes the ZigBee as the standard of the wireless network. IEEE 802.15.4 defines the physical layer under network and application layer of the ZigBee network. ZigBee has superb features such as low cost, low data rate, high security, green power, low power consumption etc. That draws its global value. ZigBee is used in security, pervasive computing, indoor position monitoring, data gathering, industry, home or office automation etc. From consumer electronics to industrial PC peripherals, ZigBee has the ability to control in the various areas of use [1], [2], [3], [4].

ZigBee has three perspective nodes - Coordinator, Router and end devices [1]. Coordinator - works for network intelligence, router connects the path between selected nodes for network establishment. Hence, WSN is the potential aspect between these. Through various optimization processes in Physical and Medium Access Control (MAC) sublayer, IEEE 802.15.4 is designed to achieve an efficient and less power consuming Network [5]. ZigBee's low duty cycle is the counter parameter in the scale of efficiency. The ZigBee network layer, however, uses an altered and on demand default routing system in a large scale ZigBee network called Ad Hoc On-Demand Distance Vector (AODV) [6].

Recent studies in the field of WSN [6], [7], [8] emphasize mainly in Quality of Service (QoS) support for ZigBee network efficiency improvement. This improvement focuses on reliability and performance under heavy energy constraints of the network with respect to QoS performance in the network. Guaranteed Time Slot (GTS) allocation and scheduling algorithm with QoS support routing algorithm applied to large scale WSN [9], [10]. Moreover, Fuzzy logic based smart routing implemented in the ZigBee network [11]. In another study [12], to overcome ZigBee's delay and congestion, a Hybrid Technology Network (HTN) adopted in a large scale network. CSMA/CA mechanism, beacon enabled cluster tree structure implemented to minimize power consumption and to get adequate coverage presented in the article [6]. Furthermore, an enhanced design has adopted with an extra processor connected to the Coordinator by an RS-232 interface presented in the article [13]. Martelli et al. in [14], presented the ZigBee network with CSMA/CA model through stochastic geometry. ZigBee's wireless control system designed in the article [15].

However, all these studies describe the performance enhancement technique of the large scale ZigBee network. All these techniques applied to improve ZigBee's performance in a particular issue rather than the overall network performance. In a broad sense, there is a lacking in large-scale ZigBee network design standards and proper sensor nodes orientation pattern. A perfect network design model may improve efficiency of ZigBee network. A specific network structure analysis and performance evaluation is yet left for large-scale ZigBee network deployment. Hence, this paper emphasizes on geometric structure based network design for a large ZigBee network.

Firstly, the paper represents a performance analysis of different ZigBee network structure layout. This implies, in details, the analysis of random and a specific geometric octagonal structure is considered here, and their prospective performance comparison in terms of global MAC delay, MAC load, End to End delay, Throughput and so forth. Secondly, it accentuates the enhancement could be made in large scale ZigBee automation using the octagonal structured routing. Hence, the main purpose of this paper is to offer a real-time QoS support for a large scale ZigBee network and design it under a specific geometric structure.

The rest of the paper structured in a way where, Section II provides literature reviews with research methodology needed for network design. Section III identifies the problem, simulation study and performance evaluation of ZigBee network. Section IV presents the simulation result with the perspective parametric comparison. Section V concludes the paper with further paths derived from the research findings.

II. Methodology

A literature review has performed to devise the performance of the large-scale Zigbee network design in geometric structure. A deep study has been done to select Octagonal structure among various geometric structures and how to build this large structure with Tree routing. The Octagonal structure having great capability to form a large area coverage network and thus is chosen for constructing the large-scale ZigBee network and analyzing the QoS performance. To analyze the QoS performance of the large-scale Octagonal Zigbee network need a simulation tool which can provide sufficient parameters in different layers of Zigbee network and show precise simulation results. There is variety of simulators like Network Simulator NS-2 and NS-3 [16], OMNET++ [17], Riverbed [18], QualNet [19], Matlab [20] etc. Riverbed modeler, a simulation tool has been used to its user-friendly environment with vast parameters resources and good potential for providing precise results [21]. Riverbed has selected in this simulation study. The Riverbed has installed and configured in an Intel Core i5 based workstation for efficient analysis of ZigBee's different layers.

The different ZigBee protocol layers generate a vast variety of data after simulation. The simulated data from different layers are collected carefully. After analyzing the simulated data, different graphs are plotted. The graphs reflect the effect of ZigBee different network parameters in the large scale ZigBee network and offer competitive measurement for Octagonal versus Random structure.

III. Design and Implementation

This section presents a novel ZigBee network structure has designed with respect to Octagonal structure and randomly node distribution structure. The designed network forms a large-scale ZigBee network. The section also describes the full simulation procedure.

A. Problem Description

ZigBee network is a wireless medium with sensing capability. It constructs a sensor network field in a small area. ZigBee devices have the capability to cover 30-100 m range. ZigBee can able to construct a network with 65,535 devices [21]. The sensor ZigBee end devices are oriented randomly in the small personal area network. To build a large size network just increasing sensor nodes at the end of one sensor node's coverage range in network field [22]. Though extended end devices or routers may provide larger area coverage, it has a great problem with interference with internal and external devices [23], [24], [25]. The problem degrades ZigBee network performance. The randomly oriented sensor nodes sometimes send more application traffic to the Coordinator. Besides, more node density in one portion of the network than other portion that may effect on network performance. Moreover, in the fewer node's portion may arise also coverage problem.

In a broad sense, for setting up a large area ZigBee network to monitor or other sensing tasks in a randomly distributed manner of ZigBee nodes, some obstacles arise and network performance may be hampered.

B. ZigBee Network Planning

Extending the area of the ZigBee network in a random distribution of nodes is an ineffective procedure. To solve the above problem, a novel approach has taken. To set up a large scale ZigBee network, where a lot of ZigBee sensor nodes available and provides a long distance coverage, a geometrical structure based design would be a solution of it.

Various geometric structures exist in the field of networking. Square, Circular. Triangular, Hexagonal etc. are the most common shape in geometrical structure. These structures widely used in the field of network planning and designing context. Different networks have constructed in different shapes. These shape oriented network devices have minimum distance each other as they cover a deterministic distance as its necessity. In ZigBee, end nodes are distributed throughout the entire field.

The octagonal structure has simply eight vertices and connected edges to form an octagon shape. This octagonal structure has a great capability to form a large coverage area network. To set up a large scale ZigBee network based on above solution following sequences is implemented:-

Place all the ZigBee routers in the vertices of Octagonal structure. The ZigBee end devices have to be placed throughout the network centering at routers. All the routers maintain the equal distance from each other as per network area. Coordinator placed at the center of the network field.

Among the routers, end devices and end devices to the router always maintain a similar distance. This creates an opportunity to communicate one device to other devices via intermediary nodes like routers. This helps to Coordinator for processing. This structure runs with the Tree routing method for its high security, robust and reliable routing capability.

In the tree structure, the address of the device in a ZigBee network is assigned by its parent node. The parameter nwkmaxChildren (C_m) represents the largest number of child nodes which can associate with a router or a coordinator. The parameter nwkmaxRouters (R_m) means the number of child nodes which can be a router. The parameter nwkMaxDepth (L_m) decides the most depth in this network. And for this network, different nodes usually have the constant (C_m) and (R_m). Every potential parent is provided with a finite sub-block of the address space, which usually assigned for the network address to its children. Given nwkmaxChildren (C_m), nwkmaxDepth (L_m), and nwkmaxRouters (R_m), to compute the function C_{Skip_d} as the size of the address sub-block distributed by each parent at depth d as follows:

$$C_{Skip_d} = 0, when \;\; R_m = 0.$$

$$\mathrm{C}_{Skip_d} = \frac{1+C_m-R_m-C_m.R_m^{L_m-d-1}}{1-R_m}, when \;\; R_m > 1.$$

$$C_{Skip_d} = 1 + C_m.(L_m - d - 1), when \ \ R_m \neq 1.$$

When C_{Skip_d} of a routing node is 0, it is unable to distribute address for the child node. If C_{Skip_d} of a routing node is greater than 0, the node can accept other nodes as its child nodes and distribute network address for its child nodes. The address of a node which joins in the network firstly is one more than faster node.

Network addresses shall be assigned to the n-th router's child and 1-th end device child at depth $d+1$ in a sequential manner respectively. According to the following equations:

$$A_{d+1,rn} = A_{Parent} + C_{Skip_d}.(n-1) + 1$$

$$A_{d+1,el} = A_{Parent} + C_{Skip_d}.R_m + l$$

Where $1 \leq l \leq R_m$, and A_{Parent} represents the address of the parent. When $1 \leq l \leq (C_m - R_m)$ [26], [27].

This also increases packet delivery ratios. It decreases internal interferences. Furthermore, random orientation of ZigBee nodes and routers in the same network has low packet delivery ratio, increased packet loss etc.

C. Simulation Process

Based on the implementation procedure, popular Riverbed simulator simulates the entire network settings with the Tree routing method. Two scenarios have created as follows- one is randomly distributed nodes architecture called Random structure model (Scenario_1) as depicted in Fig. 1. And another is uniformly distributed nodes that follow the Octagonal structure in Scenario_2 as depicted in Fig. 2. The two scenarios have an equal number of end nodes, routers, and Coordinator. The Tree routing method has to set for both scenarios. Operating frequency, power, simulation time and other used simulation parameters have set for the two scenarios that shown in Table I.

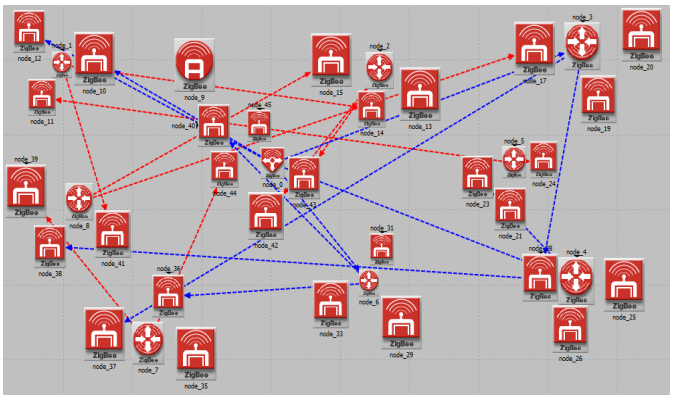

Fig. 1. Routing layout of Random structure model simulation.

IV. Results And Analysis

This section provides a competitive analysis of proposed geometric structure (Octagonal Structure Model) versus random Structure model to design a large scale ZigBee network. The results are gained from Riverbed based discrete event simulation. The graphs are plotted on the basis of analyzing ZigBees different layer parameters (e.g. the end to end delay, packet delivery ratio, MAC delay, MAC load, data dropped threshold and throughput).

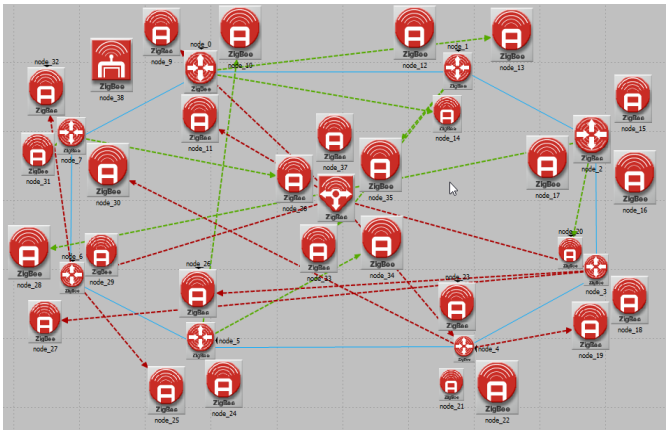

Fig. 2. Routing layout of Octagonal structure model simulation.

TABLE I. ZigBee Network Simulation Parameters Overview

Parameters	Description
ACK status	Enabled
Number of retransmission	5
Frequency Band	2.45 GHz
Data Rate	Auto Calculate
Packet Size	Constant (1024)
Packet interval time	Constant (1,0)
Packet receptionpower threshold	-85
Transmission Power	0.05
Scenario Type	Random and Octagonal
Start Time	Uniform (20,21)
Stop Time	Infinity
Traffic Dimension in Octagonal Model	Routers, End nodes and Coordinator
Traffic Destination in Random Model	Routers, End nodes and Coordinator
No. of Nodes (overall)	39
No. of Coordinator	1
No. of Routers	8
No. of End Devices	30
Network Dimension	500 m *500 m
Simulation Time	600 sec

A. End to End Delay

End-to-End delay or One-way delay is defined as the amount time a packet takes to be transmitted across a network from source to destination. Delay components:-

$$D_{end-end} = N[d_{trans} + d_{prop} + d_{proc}];$$

Where,

$$D_{end-end} = End - to - End \ \ Delay;$$

$$d_{trans} = Transmission \ \ Delay;$$

$$d_{prop} = Propagation \ \ Delay;$$

$$d_{proc} = Processing \ \ Delay;$$

$$N = Number \ \ of \ \ links \ \ (Number \ \ of \ \ routers \ \ + 1)$$

Each router will have its own d_{trans}, d_{prop}, d_{proc} hence this formula hints a rough estimate [28].

End-to-End delay for the global network in Random Structure Model is slightly higher than the Octagonal Structure Model. At the simulation start time, it is in the highest peak and after time being it gradually decreased as shown in Fig. 3.

End-to-End delay in Octagonal Structure is lower for its sequential router and other end device setup. Application traffic

from end devices at the different corner of the network travels in shortest possible time.

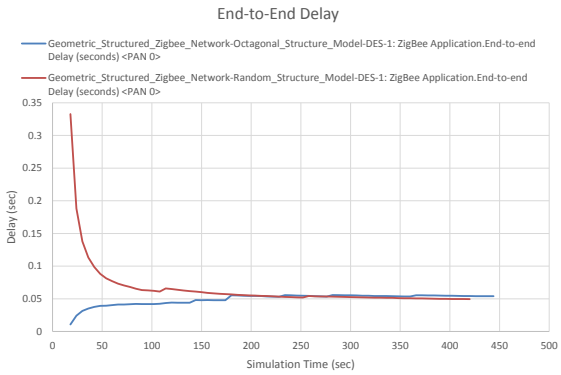

Fig. 3. End to End delay (sec) for global network.

B. Packet Delivery Ratio (PDR)

The packet delivery ratio is considered as one of the vital performance metrics in this research work. It can be calculated as the ratio between the total number of receiving data packets by the sink and the total number of data packets that are sent by all nodes in average [29]. The expression is following:

$$PDR_{avg} = P_{R_{total}} / P_{S_{total}}$$

Where,

$$PDR_{avg} = Average\ \ Packet\ \ Delivery\ \ Ratio$$

$$P_{R_{total}} = Total\ \ Packets\ \ Received\ \ by\ \ the\ \ Sink$$

$$P_{S_{total}} = Total\ \ Packets\ \ Sent\ \ by\ \ all\ \ Nodes$$

Fig. 4 illustrates PDR value for Random Structure Model (Scenario_1), is almost 0.36. In the other word, Coordinator receives in average 36% of data packets successfully.

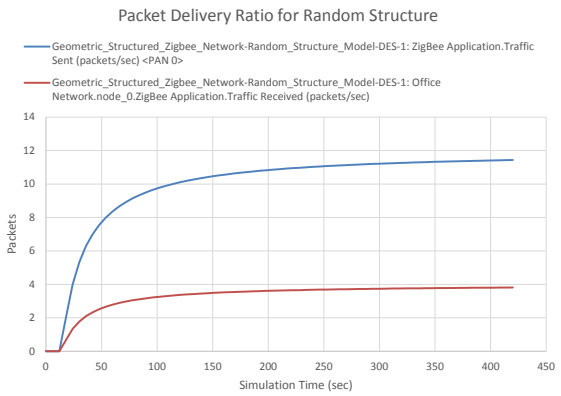

Fig. 4. PDR for Random structure model (Scenario_1).

Fig. 5 illustrates for Octagonal Structure Model (Scenario_2), PDR value is almost 0.50. This represents Coordinator receives in average 50% of data packets successfully.

It shows that in Octagonal Structure model application packets are delivered to destinations or Coordinator at the maximum rate for its end nodes and router set up.

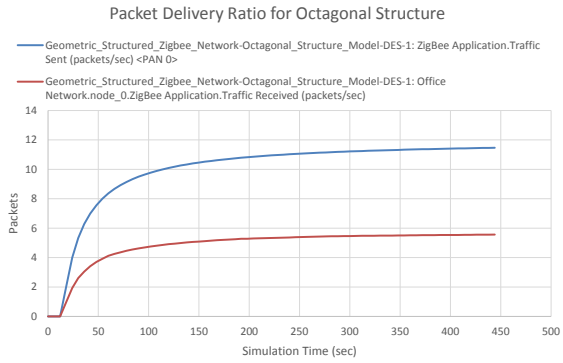

Fig. 5. PDR for Octagonal structure model (Scenario_2).

C. Global MAC Delay

MAC layer delay represents the end to end delays of all packets received through the ZigBee/802.15.4 MACs all WPAN nodes in the network and forwarded to the higher layers. The total queuing and contention delays of the data frames transmitted through all the ZigBee device's 802.15.4 MAC (Medium Access Control). For each frame, this delay is calculated as the duration from a time when it is inserted into the transmission queue, which is arrival time for higher layer data packets and creation time for all other frames types, until the time when the frame is sent to the physical layer for the first time.

Fig. 6 shows at the beginning of the simulation, Coordinator delay for Octagonal Structure Model decreases gradually from 0.09 sec to 0.025 sec. On the contrary, the Coordinator's MAC delay for Random Structure Model increases dramatically 0.01 to 0.135 sec.

MAC delay for the global network is about 2% higher in Random Structure Model than the Octagonal Structure Model.

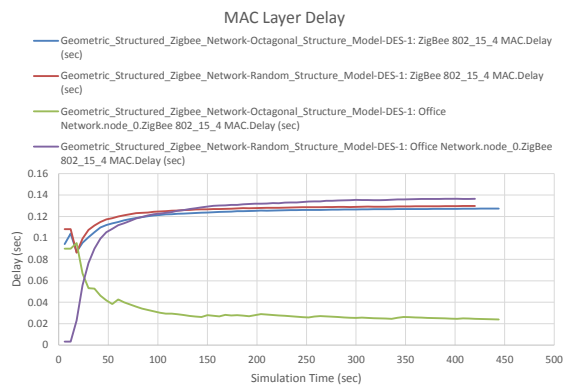

Fig. 6. MAC delay (sec) for global network and Coordinator (node_0).

All the data packets are transferred to the MAC layer for further execution. The delay affects overall network performance. In Octagonal Structure Model, the queue size is smaller and data packets spend less time in queues. Moreover, in Random Structure Model randomly many requests wait in Coordinator queue for execution. Thus, the average MAC delay is always lower in Octagonal Structure Model both for global network and Coordinator (node_0).

D. Global MAC Load

MAC layer load represents the total load (bits/sec) submitted to the ZigBee/802.15.4 MAC by all higher layers in all WPAN nodes of the network.

Fig. 7 describes MAC load for Coordinator is about 1.2% higher and 4% higher for the global network on Random Structure Model than the Octagonal Structure Model respectively.

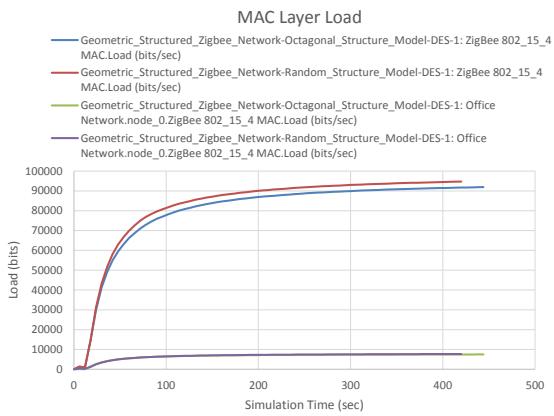

Fig. 7. MAC load (bits/sec) for global network and Coordinator (node_0).

Coordinator processes all the data request from its queue. In Random Structure Model, randomly a lot of requests come in the Coordinator queue from the different corner of the network. It increases Coordinator load as well as the overall network load. On the other hand, in Octagonal Structure Model, routers and Coordinator process request jointly. Though routers also process requests in the Random Structure Model, it is less than the Octagonal Structure Model for its random behavior.

E. Global Data Dropped Retry Threshold

Higher layer data traffic (bits/sec) dropped in the ZigBee 802.15.4 MAC due to consistently failing transmission or retransmissions. This threshold statistic reports the number of the higher layer packets that are dropped because the MAC could not receive any ACKs for the retransmissions of those packets or their fragments, and the packet retry counts reached MACs retry limit or failure to transmit a packet due to channel access failure (reaching the maximum backoff limit). The threshold statistic also reports the outstanding packets in the buffers that are dropped during roaming.

Fig. 8 describes data dropped (bits/sec) for the Coordinator in Random Structure model is increased from the start of the simulation. In Coordinator, more data drops for Random Structure model than Octagonal Structure Model. The data dropped rate is about 6.89% higher in Random Structure Model for the global network than the Octagonal Structure Model as depicted in Fig. 8.

As randomly much requests come to Coordinator queue in Random Structure Model, some data request may be lost in queuing timeout, some are lost Coordinator unavailability, some are lost internal data packet collision and some are lost for lacking coverage of intermediary nodes. Besides, routers, end devices are setup such a way that total network field gets radio coverage. In this way, data requests from the end nodes

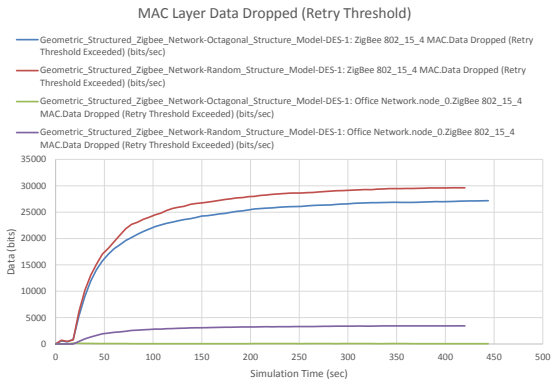

Fig. 8. Data dropped (bits/sec) for global network and Coordinator (node_0).

cannot be lost without coverage and internal interference for using the same intermediary device. Moreover, the data request process in Coordinator queue in a sequential manner and it has less time to process. Thus, data drop rate for queuing timeout has decreased as well as average data dropped rate lower in the Octagonal Structure Model.

F. Throughput

MAC layer throughput represents the total number of bits (bits/sec) forwarded from ZigBee/802.15.4 MAC to the higher layer in all WPAN of the network.

Fig. 9 illustrates MAC layer throughput for Coordinator is 30% higher in Octagonal Structure Model than Random Structure Model. Moreover, it shows that throughput for the global network is 14% higher in Random Structure Model than the Octagonal Structure Model.

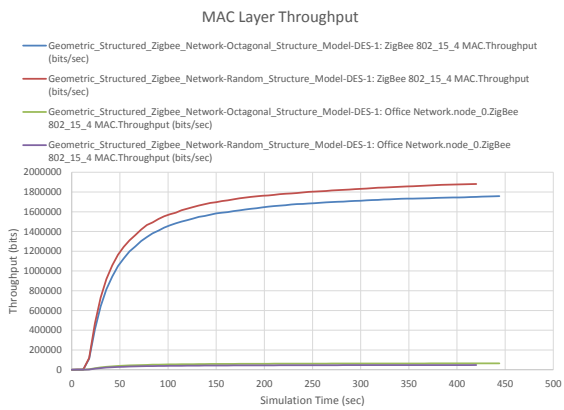

Fig. 9. Throughput (bits/sec) for global network and Coordinator (node_0).

The Coordinator has a higher throughput for Octagonal Structure model for its less data dropped and high packet delivery ratio. But average global network throughput is slightly higher in Random Structure Model for its more packet availability than the Octagonal Structure Model.

Here, different ZigBee layer parameters are analyzed on the basis of various performance measurement metrics. And also observed various characteristics of ZigBee network. To build a large-scale ZigBee network on Octagonal Structure Model shows more efficiency than random orientation. In Octagonal

Structure, all the routers and devices arranged in such a way that it looks like an octagon. This structure covers entire network field and process data request efficiently. Besides, randomly placed end devices and routers have limitations to provide maximum coverage and some routers may idle for its distinct position. That is the main potentiality of the Octagonal structure in large network formation.

V. Conclusions

This paper presents a novel study on ZigBee network design with respect to geometric structure. It deals with new Octagonal structure and Random structure. And it proposes that the newly developed Octagonal structure has higher performance for designing large scale Zigbee network than Random structure. This paper is abundantly supplied with simulation data, graphs and competitive study for corroborating the proposed structure. Almost in all the observations indicate that the Octagonal Structure network performance is going prominent than the Random Structure network. Observations show that End to End delay, MAC delay, MAC load is lower in the Octagonal structure indubitable. The study also shows that about 14% more data packets are received successfully by the coordinator and 6.89% less data dropped in Octagonal structure than Random structure. Throughput is also higher for Coordinator in the Octagonal structured network. The Octagonal Structure Model will be more suitable for large-scale automation for home, office or industry.

In the future, it would be interesting to see mobility management in large-scale for Zigbee network, performance evaluation and analysis for the mobile sensor in the large scale Zigbee network and effects on the environment.

References

[1] "Specification, ZigBee. ZigBee Alliance," http://www. Zigbee.org, [Online; Accessed: 28-Jan-2015].

[2] S.-H. Fang, C.-H. Wang, T.-Y. Huang, C.-H. Yang, and Y.-S. Chen, "An Enhanced ZigBee Indoor Positioning System with an Ensemble Approach," *IEEE Communications Letters*, vol. 16, no. 4, pp. 564–567, 2012.

[3] C. Luo, F. Wu, J. Sun, and C. W. Chen, "Compressive Data Gathering for Large-scale Wireless Sensor Networks," in *Proceedings of the 15th annual international conference on Mobile computing and networking*, Beijing, China, September 2009.

[4] W.-S. Jang, D.-E. Lee, and J.-h. Choi, "Ad-hoc Performance of Wireless Sensor Network for Large Scale Civil and Construction Engineering applications," *Automation in Construction*, vol. 26, pp. 32–45, 2012.

[5] J.-C. Cano and P. Manzoni, "A Performance Comparison of Energy Consumption for Mobile Ad-hoc Network Routing Protocols," in *Proceedings. 8th International Symposium on Modeling, Analysis and Simulation of Computer and Telecommunication Systems*, San Francisco, California, September 2000.

[6] M. Kohvakka, M. Kuorilehto, M. Hännikäinen, and T. D. Hämäläinen, "Performance Analysis of IEEE 802.15.4 and ZigBee for Large-scale Wireless Sensor Network Applications," in *Proceedings of the 3rd ACM international workshop on Performance evaluation of wireless ad hoc, sensor and ubiquitous networks*, Torremolinos, Spain, October 2006.

[7] W. Dong, Y. Liu, Y. He, T. Zhu, and C. Chen, "Measurement and Analysis on the Packet Delivery Performance in a Large-scale Sensor Network," *IEEE/ACM Transactions on Networking*, vol. 22, no. 6, pp. 1952–1963, 2014.

[8] T. R. Burchfield, S. Venkatesan, and D. Weiner, "Maximizing Throughput in ZigBee Wireless Networks through Analysis, Simulations and Implementations," in *Proc. Int. Workshop Localized Algor. Protocols WSNs*, Santa Fe, New Mexico, USA , June 2007.

[9] S. Rao, S. Keshri, D. Gangwar, P. Sundar, and V. Geetha, "A Survey and Comparison of GTS Allocation and Scheduling Algorithms in IEEE 802.15.4 Wireless Sensor Networks," in *IEEE Conference on Information & Communication Technologies (ICT)*, Tamil Nadu, India, April 2013.

[10] C. E. Perkins, E. M. Royer, S. R. Das, and M. K. Marina, "Performance Comparison of Two On-demand Routing Protocols for Ad-hoc Networks," *IEEE Personal Communications*, vol. 8, no. 1, pp. 16–28, 2001.

[11] A. M. Ortiz, T. Olivares, and L. Orozco-Barbosa, "Smart Routing Mechanism for Green ZigBee-based Wireless Sensor Networks," in *IEEE Symposium on Computers and Communications (ISCC)*, Kerkyra (Corfu), Greece, June-July 2011.

[12] P. L. Shrestha, M. Hempel, Y. Qian, H. Sharif, J. Punwani, and M. Stewart, "Performance Modeling of a Multi-tier Multi-hop Hybrid Sensor Network Protocol," in *IEEE Wireless Communications and Networking Conference (WCNC)*, Shanghai, China, April 2013.

[13] L. Yanfei, W. Cheng, Q. Xiaojun, Z. Yunhe, and Y. Chengbo, "An Improved Design of ZigBee Wireless Sensor Network," in *2nd IEEE International Conference on Computer Science and Information Technology*, Beijing, China, August 2009.

[14] F. Martelli, C. Buratti, and R. Verdone, "Modeling Query-Based Wireless CSMA Networks Through Stochastic Geometry," *IEEE Transactions on Vehicular Technology*, vol. 63, no. 6, pp. 2876–2885, 2014.

[15] M. S. Mahmoud, "Wireless Networked Control System Design: An Overview," in *IEEE 23rd International Symposium on Industrial Electronics (ISIE)*, Istanbul, Turkey, June 2014.

[16] "The Network Simulator - NS-2, NS-3," http://www.isi.edu/nsnam/ns/, [Online; Accessed: 20-Jan-2015].

[17] "OMNeT++ : Discrete Event Simulator," https://omnetpp.org/, [Online; Accessed: 15-Dec-2014].

[18] "Riverved," http://www.riverbed.com/, [Online; Accessed: 15-Feb-2015].

[19] "QualNet: Scalable Network Technologies," http://web.scalable-networks.com/content/qualnet/, [Online; Accessed: 15-Feb-2015].

[20] "MATLAB: Simulink," http://mathworks.com/, [Online; Accessed: 20-Feb-2015].

[21] N. Islam, M. J. H. Biddut, A. I. Swapna, and M. H. R. Jany, "A Study on Priority Based ZigBee Network Performance Analysis with Tree Routing Method," *Journal of Computer and Communications*, vol. 3, no. 08, pp. 1–10, 2015.

[22] A. Babaei, P. Agrawal, and B. Jabbari, "Capacity Bounds in Random Wireless Networks," *Journal of Communications and Networks*, vol. 14, no. 1, pp. 1–9, 2012.

[23] C.-J. M. Liang, N. B. Priyantha, J. Liu, and A. Terzis, "Surviving Wi-fi Interference in Low Power ZigBee Networks," in *Proceedings of the 8th ACM Conference on Embedded Networked Sensor Systems*, Zurich, Switzerland, November 2010.

[24] C. Park and T. S. Rappaport, "Short-range Wireless Communications for Next-Generation Networks: UWB, 60 GHz Millimeter-wave WPAN, and ZigBee," *IEEE Wireless Communications*, vol. 14, no. 4, pp. 70–78, 2007.

[25] P. Baronti, P. Pillai, V. W. Chook, S. Chessa, A. Gotta, and Y. F. Hu, "Wireless Sensor Networks: A Survey on the State of the Art and the 802.15.4 and ZigBee Standards," *Computer communications*, vol. 30, no. 7, pp. 1655–1695, 2007.

[26] J. Li, X. Zhu, N. Tang, and J. Sui, "Study on ZigBee Network Architecture and Routing Algorithm," in *2nd International Conference on Signal Processing Systems (ICSPS)*, Dalian, China, July 2010.

[27] T. Kim, S. H. Kim, J. Yang, S.-e. Yoo, and D. Kim, "Neighbor Table Based Shortcut Tree Routing in ZigBee Wireless Networks," *IEEE Transactions on Parallel and Distributed Systems*, vol. 25, no. 3, pp. 706–716, 2014.

[28] A. Kaur, J. Kaur, and G. Singh, "Simulation and Investigation of ZigBee Sensor Network with Mobility Support," in *IEEE International Advance Computing Conference (IACC)*, Gurgaon, India, February 2014.

[29] K. Dong, "Performance and Fairness Enhancement in ZigBee Networks," Ph.D. dissertation, TU Delft, Delft University of Technology, 2011.

A New Mu-Negative Metamaterial

S. S. Islam [1,2], M. R. I. Faruque[1]
Space Science Centre, IPI,
[1]Universiti Kebangsaan Malaysia,
Selangor, Malaysia,
[2]International Islamic University
Chittagong, Bangladesh
sikder_islam@yahoo.co.uk

M. T. Islam
Department of Electrical, Electronic
and Systems Engineering, Universiti
Kebangsaan Malaysia, Malaysia.
titareq@gmail.com

T. Alam
Dept. of CSE,
International Islamic University
Chittagong, Bangladesh
touhid13@yahoo.com

[1]***Abstract*— A new metamaterial with negative permeability is presented in this study. Negative permeability metamaterials are called mu-negative (MNG) metamaterial as well. The transmission co-efficient of this metamaterial shows resonance at a certain frequency in the C-band of microwave frequency range for the z-axis wave propagation. It also exhibits the characteristics of a mu-negative (MNG) metamaterial there. In the basic construction, the unit cell was formed by joining two metal split square resonator by a copper link on FR-4 substrate material. The measured result is presented and it shows good conformity with the simulated result.**

Keywords—C-band; MNG; Metamaterials;

I. INTRODUCTION

Recently, a new type of material usually called "metamaterial'' that are naturally unavailable and show some extraordinary electromagnetic properties. The most interesting property of this material is to exhibit negative permittivity (ε) and permeability (μ) simultaneously, which usually denoted as double negative (DNG) material or negative-refractive index material or backward wave media. A metamaterial may have either epsilon (ε) or mu (μ) negative that is denoted as 'Single Negative (SNG)' metamaterials. The epsilon (ε) negative metamaterial is called ENG. Some metamaterials have negative permeability only. This is often regarded as Mu-negative (MNG) material that has a significant effect on electomagnetic waves like the gyrotropic material. MNG material provides magneto-optic effect that alters the electromagnetic waves by its quasi-static magnetic field. In 1968, Russian scientist Victor Veselago revealed that materials with such properties. These materials' had some different properties that were not naturally found [1]. However, up to 1999 this proposal did not receive too much concern to the researcher as such material is naturally unavailable. Smith *et al.* in 2000 first showed a split ring based such material with double negative property [2].

Depending on these exceptional properties of the metamaterial, various types of designs have been proposed for numerous essential applications; for example ,designing antenna, electromagnetic cloaking, reduction of SAR etc [2-8]. Many metamaterial structure were proposed in the literature although a small number of them are appropriate for C-band (4-8 GHz) [9] microwave spectra as MNG metamaterial [10-15]. For example, Jason C. Soric *et al.* In [11], showed a metamaterial that works in the L-band and exhibit epsilon-near-zero (ENG) characteristics only. In [12], Hayet Benosman *et. al.* presented a metamaterial but it works in K_u-band only. In [13] a new SNG metamaterial was reported but it was applicable for S-band only. In [14] Evren Ekmekçi *et. al.* showed a SNG metamaterial but it works in X-band only.

In this study, we are going to present a new unit cell structure of SNG metamaterial where two split square resonators were linked by a copper strip. The resonant frequency is found for the material in the frequency of 5.13 GHz and the material displays MNG characteristics at that certain frequency.

II. STRUCTURE OF THE UNIT CELL

The Fig. 1 depicts the proposed C-band metamaterial unit cell. The unit cell was formed with two metal (copper) split square resonators. All the copper thickness was kept 0.035mm. The outer length is 10mm with 0.5mm split and the width of each resonator is 1mm. The gap between the two resonators is 1mm and they have been connected to shape an H-like structure by a 1mm wide copper stripe. The unit cell was printed over a 30×30mm^2 FR-4 substrate material having dielectric constant and loss-tangent of 4.3 and 0.025 respectively and the thickness was maintained 1.6 mm.

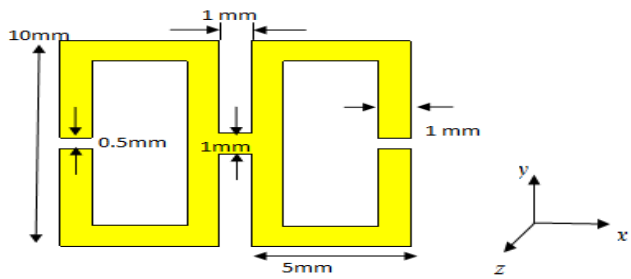

Fig. 1. The basic metamaterial cell structure

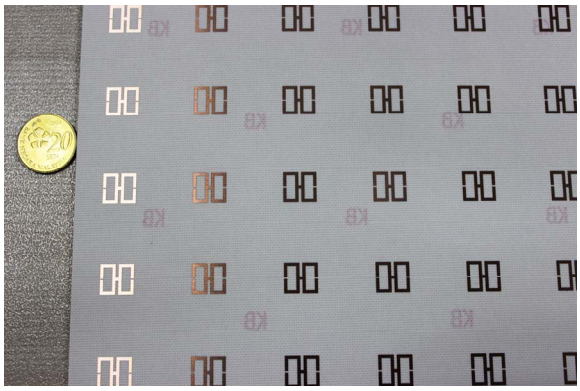

Fig. 2. Fabricated metamaterial prototype on FR-4 substrate material for measurement

III. METHODOLOGY

In this study, the well-known electromagnetic simulation software CST microwave studio was chosen for the S-parameter calculation. The unit cell was placed in such a way that electromagnetic waves pass along the Z-axis and two face-to-face waveguide ports were utilized for it. The perfect electric-magnetic conductor (PEMC) boundary conditions were applied in the consecutive X-and Y-axis. For the range of frequency 2-10 GHz, the simulation was done. The method mentioned in [16] was adopted to extract the effective medium parameters form the complex value of S_{21} and S_{11}.

$$V_1=S_{21}+S_{11} \quad (1)$$

$$V_2=S_{21}-S_{11} \quad (2)$$

$$\mu_r \approx \frac{2}{jk_0 d}\frac{1-V_2}{1+V_2} \quad (3)$$

$$\varepsilon_r \approx \frac{2}{jk_0 d}\frac{1-V_1}{1+V_1} \quad (4)$$

$$\eta = \sqrt{\varepsilon_r \mu_r} \quad (5)$$

where, ε_r is the effective permittivity, μ_r is the effective permeability, 'd' is the thickness of the substrate, k_0 is the wave number and η is the refractive index.

A 240×240 mm^2 prototype of 8×8 unit cell is fabricated for measurement, as shown in Fig. 2. The prototype is then placed between two horn antennas, which are 1.5m apart in the same plane. The vector network analyzer named 'Agilent E8363D' was taken to evaluate the S-parameters. For calibration purpose, measurement without metamaterial and with metamaterial is done. The measurement is done in a semi anechoic chamber environment. The whole measurement setup is shown in Fig. 3.

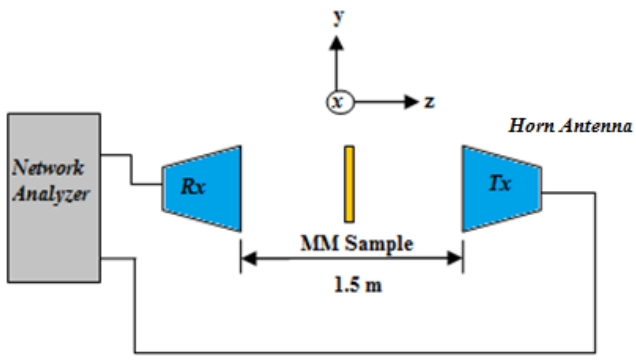

Fig. 3. Measurement set-up

IV. RESULTS AND DISCUSSION

In the Fig. 4, the transmission (S_{21}) parameters for the proposed unit cell are being displayed. It shows that the magnitude of S_{21} shows resonance in the microwave range at the frequency of 5.133 GHz. The measured transmission properties for with and without metamaterial are shown in the Fig. 5 and Fig. 6 respectively. The measured result of the transmission (S_{21}) characteristics agrees well with the simulated result.

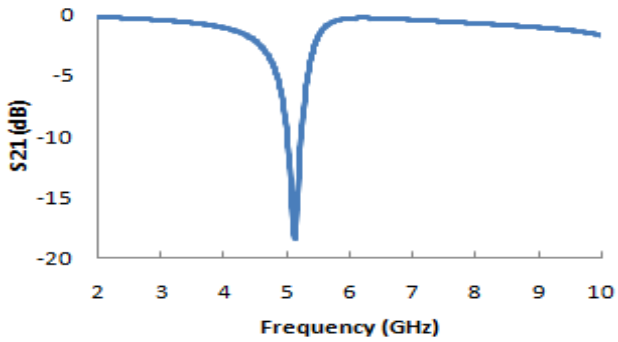

Fig. 4. Simulated magnitude of transmission parameter (S_{21}) in dB

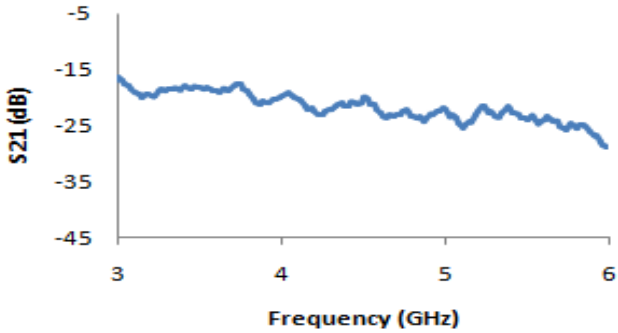

Fig. 5. Measured value of transmission parameter (S_{21}) in dB without metamaterial

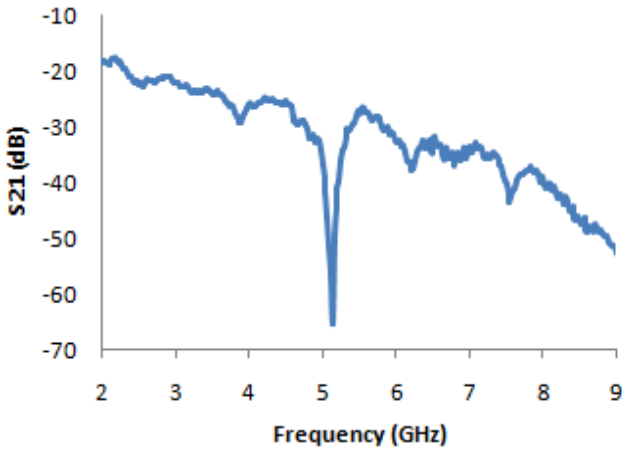

Fig. 6. Measured peak of transmission parameter (S_{21}) with metamaterial

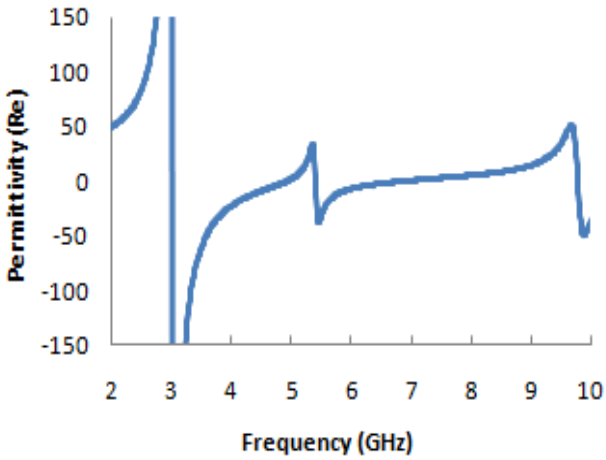

Fig. 7. Magnitude (real) of permittivity (ε)

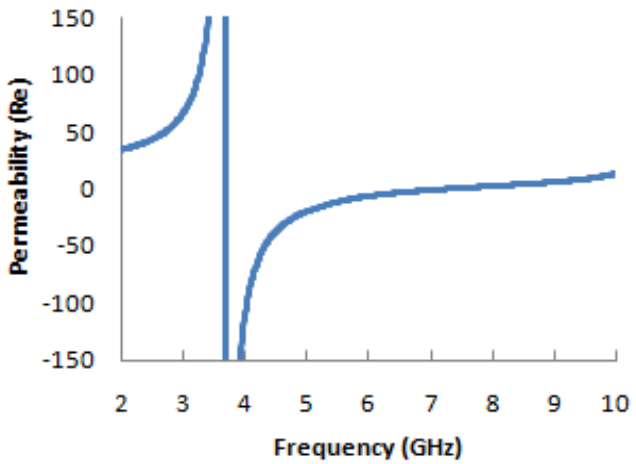

Fig. 8. Magnitude (real) permeability (μ)

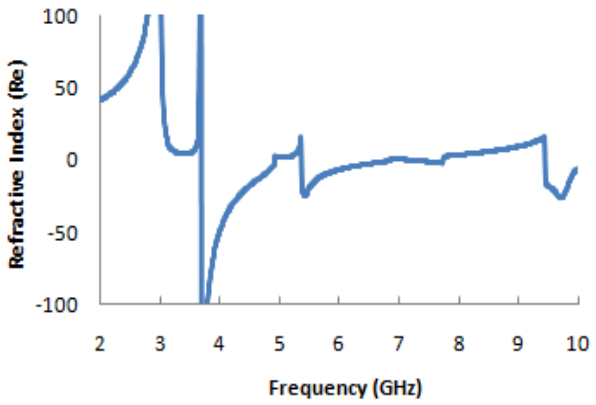

Fig. 9. Magnitude (real) of Refractive Index

The calculated permittivity (ε) as well as permeability (μ) against frequency is seen in Fig. 7 and 8 respectively. In Fig.7 it is seen that at 5.133GHz the permittivity curve displays positive real magnitude of ε = 7.80. Similarly, the Fig. 8 reveals the permeability curve where at the points of resonance frequency of 5.133GHz it has the value of μ = -17.50. Therefore the material can be characterized as a single negative (SNG) material. Here, it is seen that only permeability shows negative magnitude for the proposed structure. That is why, it can be characterized as mu-negative (MNG) metamaterial. The refractive index curve is seen in Fig. 9. It shows the positive real value of η=1.76 at the frequency of 5.133GHz.

V. Conclusion

This paper presents a MNG metamaterial, having resonance frequency at 5.133GHz of the C-Band. Usually, C-band of microwave arena is employed for remote communication like, satellite communications. Therefore, the structure has good applications in the design of antenna for satellite and other similar fields in this range. The simulated and the measured result are compared and they show good conformity as well.

References

[1] V. G. Veselago, "The electrodynamics of substances with simultaneously negative values of ε and μ," Soviet Physics Usp., vol. 10, pp.509–514, 1968.

[2] D. Schurig, J. J. Mock,1 B. J. Justice, S. A. Cummer, J. B. Pendry, A. F. Starr, D. R. Smith, Metamaterial Electromagnetic Cloak at Microwave Frequencies, *Science,* Vol. 314, pp. 977-980, 2006.

[3] M. R. I. Faruque and M. T. Islam, "Novel Design Of Triangular Metamaterial For Electromagnetic Absorption In Human Head," *Progress In Electromagnetics Research*, Vol.PIER 141, pp. 463-478, 2013.

[4] B.I. Wu, W. Wang, J. Pacheco, X. Chen, T. Grzegorczyk and J. A. Kong, A Study Of Using Metamaterials As Antenna Substrate To Enhance Gain, *Progress In Electromagnetics Research*, Vol.PIER 51, pp.295–328, 2005.

[5] S. S. Islam, M. R. I. Faruque, M. T. Islam; A Near Zero Refractive Index Metamaterial for Electromagnetic Invisibility Cloaking Operation; *Materials*, *8*, pp. 4790-4804; 2015; doi: 10.3390/ma8084790

[6] M. R. I. Faruque, M. T. Islam, N. Misran, "Electromagnetic (EM) Absorption Reduction in a Muscle Cube with Metamaterial Attachment," Medical Engineering & Physics (Elsevier), vol. 33, Issue. 5, pp. 646-652, June 2011

[7] Le-Wei Li, Ya-Nan Li,Tat Soon Yeo,Juan R. Mosig, and Olivier J. F. Martin, A broadband and high-gain metamaterial microstrip antenna, Applied Physics Letters **96**, 164101 , 2010

[8] S. S. Islam, M. R. I. Faruque and M. T. Islam; A two-component NZRI metamaterial based rectangular cloak; *AIP Advances*, Vol. 5, pp. 107116:1-9

[9] IEEE standard letter designations for Radar frequency bands, IEEE standard. 521-2002.Available at:https://standards.ieee.org/findstds/standard/521-2002.html (accessed on 22th March 2014)

[10] S. S. Islam, M. R. I. Faruque, M. T. Islam; A new double negative metamaterial for multi-band microwave applications; Applied Physics A, Volume 116, Issue 2, pp 723-733, August **2014**

[11] Jason C. Soric, N. Engheta, S. Maci, and A. Alù, 'Omnidirectional Metamaterial Antennas Based on Near-Zero Channel Matching', IEEE Transactions on Antennas and Propagation, VOL. 61, NO. 1, JANUARY 2013

[12] H. Benosman, N. B. Hacene, Design and Simulation of Double "S" ShapedMetamaterial; IJCSI International Journal of Computer Science Issues, Vol. 9, Issue 2, No 1, March 2012

[13] S. S. Islam, M. R. I. Faruque, M. T. Islam; Design of a New ENG Metamaterial for S-Band Microwave Applications; Journal of Electrical and Electronics Engineering - Vol. 7, Nr. 2, October 2014

[14] E. Ekmekci and G. Turhan-Sayan, "Investigation of effective permittivity and permeability for a novel V-shaped metamaterial using S-parameters,"proceedings od 5th International Conference on Electrical and Electronics Engineering, December 2007, Bursa, Turkey.

[15] S. S. Islam, M. R. I. Faruque, M. T. Islam; Design and Analysis of a New Double Negative Metamaterial; Informacije MIDEM; Vol. 44, No. 3, pp.218 – 223**,** 2014**.**

[16] S. S. Islam, M. R. I. Faruque and M. T. Islam; 'A New Direct Retrieval Method of Refractive Index for Metamaterials', *Current Science*, Vol. 109, No. 2, 2015

Security in Cooperative Spatial Multiplexing System with Zero-Forcing Filtering

D. K. Sarker, M. Z. I. Sarkar and M. S. Anower
Department of Electrical and Electronic Engineering
Rajshahi University of Engineering and Technology
Rajshahi-6204, Bangladesh.
Email: dks_ms@yahoo.com

***Abstract*—This paper is concerned with the analysis of secrecy capacity and secure outage performance of cooperative spatial multiplexing system with the effect of linear equalization. A confidential communication scenario is considered through Rayleigh fading channel in which a number of users communicate with a destination via multiple relays. An eavesdropper observes their communication and tries to decode the confidential information. At first, we derive the exact closed-form expression for the ergodic secrecy capacity with linear equalization in cooperative spatial multiplexing system. Then, we derive the exact closed-form expressions for the secure outage probability and the complementary cumulative distribution function (CCDF) of secrecy capacity to investigate the secure outage performance of the proposed model. Finally, we justify the validity of analytical results comparing with the Monte-Carlo simulation results.**

***Index Terms*—Ergodic secrecy capacity, secure outage probability, zero-forcing filtering.**

I. Introduction

Now a days, the security becomes an important issue in wireless communication networks due to the increase of application area and the mobility of users and network components, because of the fact that the wireless communication networks are frequently used to transmit personal and confidential information and the wireless medium is susceptible to eavesdropping and fraud. Therefore security is a challenging quality of service constraint that must be accounted for the design of wireless communication network. On the other hand, the cooperative spatial multiplexing system significantly increases the spectral efficiency compared to its cooperative diversity while the relays transmit different sub-streams to the destination simultaneously [1].

Recently, Pasolini et al. proposed an analytical framework in [2] for investigating the amount of secret information and derive the intrinsic secrecy content of wide-sense stationary wireless channels in frequency, time and spatial domains. The impact of imperfect channel state information at the transmitters (CSIT) on the achievable diversity gain in a cooperative relay channel with multiple destination antennas is investigated by X. J. Zhang in [3], considering both decode-and-forward (DF) and amplify-and-forward (AF) relaying protocols. They showed that the control of transmit power based on the imperfect CSIT significantly improves the achievable diversity gain. In [4], the performance of open-loop multi-antenna point-to-point links in ad hoc medium access control (MAC) networks is investigated considering spatial multiplexing transmission with linear maximum ratio combining and zero forcing receivers. In [5], X. Tao et al. studied cooperative techniques, such as relay, distributed antennas systems (DAS), multicell coordination, group cell, coordinated multiple point transmission and reception (CoMP), those turn the traditional cellular system into a cooperative system and proposed some joint processing policies to demonstrate the group cell (CoMP) concept. A multiple-input multiple-output (MIMO) cooperative spatial multiplexing system with distributed single antenna relay stations, operated in AF mode is proposed in [6], where the system bit error rate (BER) performance is evaluated by means of a semi-analytic bounding method. In [7], R. Bassily et al. studied the role of cooperative relays to provide and improve secure communication rates through DF and ZF strategies in a full-duplex multiple relay network with an eavesdropper.

In this paper, we analyze the secure outage performance of cooperative spatial multiplexing system over Rayleigh fading channel. At first, we define the secrecy capacity of cooperative spatial multiplexing system so that the eavesdropper is unable to decode information from the main channel (i.e., channel between users and destination) and derive the exact closed-form expressions for the ergodic secrecy capacity. Then, we find the probability density function (PDF) of secrecy capacity and use it to derive the secure outage probability and the CCDF of secrecy capacity. Finally, the analytical results are verified by comparing with Monte-Carlo simulations.

The rest of the this paper is organized as follows: The system model and problem formulation are described in Section II. Section III describes the formulation of ergodic secrecy capacity. In Section IV, the expressions for the secure outage probability and the CCDF of secrecy capacity are stated. Numerical results are shown in Section V. Finally, Section VI provides the concluding remarks of this work.

Notation: We use upper and lower case boldface letters for denoting matrices and vectors respectively. $\mathbf{I}_n$ represents the $n \times n$ identity matrix. The superscript $(\cdot)^\dagger$ stands for the complex conjugate transpose and $[\cdot]^T$ denotes the transpose operation of a vector. A complex Gaussian distribution with mean μ and variance σ^2 is denoted by $\mathcal{C}\tilde{\mathcal{N}}(\mu, \sigma^2)$. $\mathbb{E}[\cdot]$ is the expectation operator and $P_r(\cdot)$ represents the probability. $\Gamma(\cdot)$ and $2F1(\cdot)$ denote the Gamma function and the Gauss

Hypergeometric function, respectively.

II. System Model and Problem Formulation

We consider a secure cooperative spatial multiplexing system in which M sources send confidential information to the destination via K relays as shown in Fig.1. The communication between sources and destination occurs in the presence of an eavesdropper. The sources and relays are equipped with single antenna while the destination and eavesdropper are equipped with n_D and n_E antennas, respectively. All the terminals operate in half duplex mode yielding the communication occurs in a dual-hop transmission. All the propagation channels are considered to be affected by small-scale fading which is modeled as Rayleigh fading.

During the first-hop, the mth source transmits s_m, $(m = 1, \ldots, M)$ to the relays. Therefore, received signal at the kth relay is given by

$$x_k = \sum_{m=1}^{M} g_{m,k} s_m + \mu_k = \mathbf{g}_k \mathbf{s} + \mu_k, \tag{1}$$

where $g_{m,k}$ denotes the channel coefficient between mth source to kth relay and $\mathbf{g}_k = [g_{1,k}\ g_{2,k} \ldots g_{M,k}]$. $\mathbf{s} = [s_1\ s_2 \ldots s_M]^T$ and $\mu_k \sim \tilde{\mathcal{N}}\left(0, \sigma^2\right)$ denotes the background noise of kth relay with mean zero and variance σ^2. During the second hop, all the relays simultaneously transmit their own signals to the destination over the same physical channel and eavesdropper observes their transmission through another physical channel and tries to decode the information. For simplicity, we assume that the gain of each relay is unity and the kth relay transmits its own signal x_k. Let $\mathbf{y}_d$ and $\mathbf{y}_e$ denote the received signals at the destination and eavesdropper,

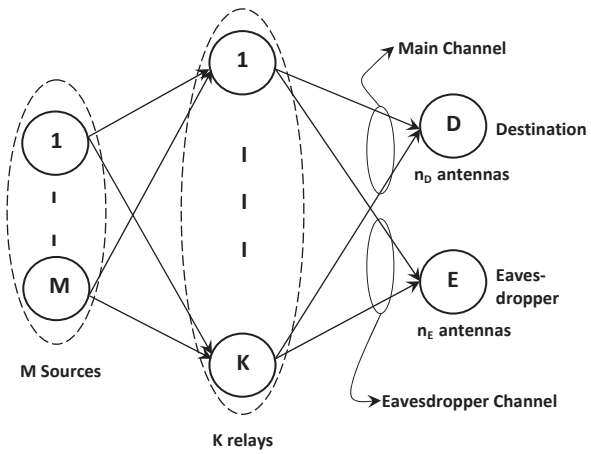

Fig. 1. A Cooperative spatial multiplexing system with M sources, K relays and a destination in the presence of an eavesdropper.

respectively. Then, we have

$$\begin{aligned}\mathbf{y}_d &= \sum_{k=1}^{K} \mathbf{h}_{dk} x_k + \mathbf{n}_d = \sum_{k=1}^{K} \mathbf{h}_{dk} \mathbf{g}_k \mathbf{s} + \sum_{k=1}^{K} \mathbf{h}_{dk} \mu_k + \mathbf{w}_d \\ &= \mathbf{H}_d \mathbf{s} + \mathbf{z}_d, \end{aligned} \tag{2}$$

$$\begin{aligned}\mathbf{y}_e &= \sum_{k=1}^{K} \mathbf{h}_{ek} x_k + \mathbf{n}_e = \sum_{k=1}^{K} \mathbf{h}_{ek} \mathbf{g}_k \mathbf{s} + \sum_{k=1}^{K} \mathbf{h}_{ek} \mu_k + \mathbf{w}_e \\ &= \mathbf{H}_e \mathbf{s} + \mathbf{z}_e, \end{aligned} \tag{3}$$

where $\mathbf{H}_d = [\mathbf{h}_{d1}\mathbf{g}_1\ \mathbf{h}_{d2}\mathbf{g}_2 \ldots \mathbf{h}_{dK}\mathbf{g}_K] \in \mathbb{C}^{n_D \times K}$ and $\mathbf{H}_e = [\mathbf{h}_{e1}\mathbf{g}_1\ \mathbf{h}_{e2}\mathbf{g}_2 \ldots \mathbf{h}_{eK}\mathbf{g}_K] \in \mathbb{C}^{n_E \times K}$ denote the channel coefficients from relays to destination and eavesdropper, respectively. The elements of $\mathbf{H}_d$ and $\mathbf{H}_e$ are the independent complex Gaussian random variables but not identically distributed (i.n.i.d.) due to the separation of relays. $\mathbf{s} \in \mathbb{C}^{K \times 1}$ denotes the transmit signal vector from the relays. $\mathbf{w}_d \sim \mathcal{C}\tilde{\mathcal{N}}\left(0, \sigma^2 \mathbf{I}_{n_D}\right)$ and $\mathbf{w}_e \sim \mathcal{C}\tilde{\mathcal{N}}\left(0, \sigma^2 \mathbf{I}_{n_e}\right)$ denote the additive white Gaussian noises imposed on the destination and eavesdropper, respectively. $\mathbf{z}_d = \sum_{k=1}^{K} \mathbf{h}_{dk}\mu_k + \mathbf{w}_d$ and $\mathbf{z}_e = \sum_{k=1}^{K} \mathbf{h}_{ek}\mu_k + \mathbf{w}_e$ are the $n_D \times 1$ and $n_E \times 1$ complex AWGN vectors which models noises at the receivers of destination and eavesdropper, respectively.

The channel mean power from the relays to destination and eavesdropper are denoted by $\alpha_{m,k,d}$ and $\alpha_{m,k,e}$, respectively. If we apply zero forcing (ZF) filtering matrix to decode the transmitted signal, then the signals can be decoded independently. The post processing SNR of x_k for the destination and eavesdropper channels are given by [1] $\gamma_{m,k,d} = \frac{\gamma_{0,d}}{\left[\left(\mathbf{H}_d^{\dagger}\mathbf{H}_d\right)^{-1}\right]_{kk}}$ and $\gamma_{m,k,e} = \frac{\gamma_{0,e}}{\left[\left(\mathbf{H}_e^{\dagger}\mathbf{H}_e\right)^{-1}\right]_{kk}}$, where $\gamma_{0,d}$ and $\gamma_{0,e}$ are the average SNR per symbol at the destination and eavesdropper channels, respectively. The probability density function (PDF) of $\gamma_{m,k,d}$ and $\gamma_{m,k,e}$ can be expressed as [1]

$$f_{\gamma_{m,k,d}}\left(\gamma_{m,k,d}\right) = \frac{e^{-\frac{\gamma_{m,k,d}}{\gamma_{0,d}\alpha_{m,k,d}}}}{\gamma_{0,d}\alpha_{m,k,d}\vartheta_d!}\left(\frac{\gamma_{m,k,d}}{\gamma_{0,d}\alpha_{m,k,d}}\right)^{\vartheta_d}, \tag{4}$$

$$f_{\gamma_{m,k,e}}\left(\gamma_{m,k,e}\right) = \frac{e^{-\frac{\gamma_{m,k,e}}{\gamma_{0,e}\alpha_{m,k,e}}}}{\gamma_{0,e}\alpha_{m,k,e}\vartheta_e!}\left(\frac{\gamma_{m,k,e}}{\gamma_{0,e}\alpha_{m,k,e}}\right)^{\vartheta_e}, \tag{5}$$

where $\vartheta_d = n_D - K$ and $\vartheta_e = n_E - K$.

III. Ergodic Secrecy Capacity

In this section, at first we deduce the expression of secrecy capacity considering the cooperative spatial multiplexing effect of relays. Then, we derive the closed-form expression for ergodic secrecy capacity.

A. Secrecy Capacity

Since each kth symbol, x_k is detected independently at the destination, capacity at the destination for M users can be expressed from (2) as

$$C_d = \frac{1}{2}\sum_{m=1}^{M}\sum_{k=1}^{K}\log_2\left(1 + \gamma_{m,k,d}\right). \tag{6}$$

Similarly, from (3), the capacity at the eavesdropper can be derived as

$$C_e = \frac{1}{2}\sum_{m=1}^{M}\sum_{k=1}^{K}\log_2\left(1+\gamma_{m,k,e}\right). \tag{7}$$

Hence, the secrecy capacity is given by

$$C_s = \max_{f(x_k)}\left(C_d - C_e\right) = \frac{1}{2}\sum_{m=1}^{M}\sum_{k=1}^{K}\log_2\left(\frac{1+\gamma_{m,k,d}}{1+\gamma_{m,k,e}}\right). \tag{8}$$

B. Ergodic Secrecy Capacity

The ergodic secrecy capacity for cooperative spatial multiplexing system over Rayleigh fading channel can be expressed as

$$\langle C_s\rangle = \frac{1}{2}\sum_{m=1}^{M}\sum_{k=1}^{K}\Big\{\mathbb{E}\left[\log_2(1+\gamma_{m,k,d})\right] - \mathbb{E}\left[\log_2(1+\gamma_{m,k,e})\right]\Big\}. \tag{9}$$

Now, we have

$$\mathbb{E}\left[\log_2(1+\gamma_{m,k,d})\right] = \int_0^\infty \log_2(1+\gamma_{m,k,d}) \times f_{\gamma_{m,k,d}}\left(\gamma_{m,k,d}\right)d\gamma_{m,k,d}. \tag{10}$$

Using (4) into (10) and by applying the result, $\int_0^\infty \ln(1+t)t^{n-1}e^{-at}dt = (n-1)!e^a\sum_i^n \frac{\Gamma(-n+i,a)}{a^i}$ from [8, Appendix B], we obtain

$$\mathbb{E}\left[\log_2(1+\gamma_{m,k,d})\right] = \frac{e^{1/\gamma_{0,d}\alpha_{m,k,d}}}{2\log_e 2} \times\sum_{l=1}^{L}\frac{\Gamma\left(-L+l,\frac{1}{\gamma_{0,d}\alpha_{m,k,d}}\right)}{\left(\gamma_{0,d}\alpha_{m,k,d}\right)^{L-l}}, \tag{11}$$

where $L = \vartheta_d + 1$. Similarly, we can express

$$\mathbb{E}\left[\log_2(1+\gamma_{m,k,e})\right] = \frac{e^{1/\gamma_{0,e}\alpha_{m,k,e}}}{2\log_e 2} \times\sum_{v=1}^{V}\frac{\Gamma\left(-V+v,\frac{1}{\gamma_{0,e}\alpha_{m,k,e}}\right)}{\left(\gamma_{0,e}\alpha_{m,k,e}\right)^{V-v}}, \tag{12}$$

where $V = \vartheta_e + 1$. Substituting (11) and (12) into (9), the closed-form expression for ergodic secrecy capacity is shown in (13) at the bottom of this page.

IV. Outage Performance Analysis

In order to analyze the secure outage performance, at first, we determine the PDF of C_s. Then, it is used to derive the closed-form expressions for the outage probability and the CCDF of secrecy multicast capacity.

A. Probability Density Function of C_s

Here, we find the PDFs of C_d and C_e from the following proposition and then use them to find the PDF of C_s.

Proposition 1: *Let the probability density function of x is denoted by $f(x)$. Then, the probability density function of $C = \log_e(1+\theta x)$ is given by*

$$q(C) = \frac{e^C}{\theta}f\left(\frac{e^C-1}{\theta}\right). \tag{14}$$

Proof: We have, $C = \log_e(1+\theta x)$. The probability density function of the capacity, C can be written as

$$q(C) = \int \delta\left(C - \log_e(1+\theta x)\right)f(x)dx. \tag{15}$$

The following mathematical facts have been used for this proof [9];
i) $\delta\left(f(x)\right) = \sum_l \frac{\delta(x-x_l)}{|\frac{df}{dx}|_{x_l}}$, where x_l are the zeros of $f(x)$, i.e. $f(x_l) = 0$;
ii) $\int_a^b \delta(x-x_1)\delta(x-x_2)dx = \delta(x_1-x_2)$ for $a < x_1, x_2 < b$; and
iii) $\int_U f(x)\delta(x-x_0)dx = \begin{cases} f(x_0), & t_0 \in U \\ 0, & \text{otherwise.}\end{cases}$
Assuming $\kappa = 1+\theta x$, we have $f(\kappa) = C - \log_e\kappa$ and $f^{'}(\kappa) = -\frac{1}{\kappa}$. Now from $f(\kappa) = 0$, $\kappa = e^C$ and $f^{'}(\kappa)|_{\kappa=e^C} = -\frac{1}{e^C}$. Using the above mathematical facts and from equation (15), we have

$$\begin{aligned} q(C) &= \int e^C\delta(1+\theta x - e^C)f(x)dx \\ &= e^C\int\delta\left(\theta\left(x-\frac{e^C-1}{\theta}\right)\right)f(x)dx \\ &= \frac{e^C}{\theta}\int\delta\left(x-\frac{e^C-1}{\theta}\right)f(x)dx \quad \text{Since, } \delta(dx) = \frac{1}{|d|}\delta(x) \\ &= \frac{e^C}{\theta}f\left(\frac{e^C-1}{\theta}\right), \end{aligned}$$

where $\delta(\cdot)$ is a delta function.

Using Proposition 1, $q(C_d)$ and $q(C_e)$ can be determined as

$$q\left(C_d\right) = \frac{e^{C_d}\rho e^{-\rho(e^{C_d}-1)}}{\vartheta_d!\left[\rho(e^{C_d}-1)\right]^{-\vartheta_d}}, \tag{16}$$

$$q\left(C_e\right) = \frac{e^{C_e}\varrho e^{-\varrho(e^{C_e}-1)}}{\vartheta_e!\left[\varrho(e^{C_e}-1)\right]^{-\vartheta_e}}, \tag{17}$$

$$\langle C_s\rangle = \frac{1}{2\log_e 2}\sum_{\eta=1}^{M}\sum_{k=1}^{K}\left[\sum_{l=1}^{L}\frac{\Gamma\left(-L+l,\frac{1}{\gamma_{0,d}\alpha_{m,k,d}}\right)}{e^{-1/\gamma_{0,d}\alpha_{m,k,d}}\left(\gamma_{0,d}\alpha_{m,k,d}\right)^{L-l}} - \sum_{v=1}^{V}\frac{\Gamma\left(-V+v,\frac{1}{\gamma_{0,e}\alpha_{m,k,e}}\right)}{e^{-1/\gamma_{0,e}\alpha_{m,k,e}}\left(\gamma_{0,e}\alpha_{m,k,e}\right)^{V-v}}\right]. \tag{13}$$

where $\rho = (1/\gamma_{0,d}\alpha_{m,k,d})$ and $\varrho = (1/\gamma_{0,e}\alpha_{m,k,e})$. The PDF of C_s can be derived as

$$q(C_s) = q(C_d) * q(C_e) = \int_{-\infty}^{\infty} q(C_s + C_e)\, q(C_e)\, dC_e. \quad (18)$$

From (16), the PDF of $(C_s + C_e)$ can be determined as

$$q(C_s + C_e) = \frac{e^{C_s+C_e}\rho e^{-\rho(e^{C_s+C_e}-1)}}{\vartheta_d!\left[\rho(e^{C_s+C_e}-1)\right]^{-\vartheta_d}}. \quad (19)$$

Substituting (17) and (19) into (18) and performing integration by changing variables and using the identity $\int_0^\infty x^n e^{-bx}dx = n!b^{-n-1}$ of [10, eq. (3.351.3)], we obtain

$$q(C_s) = \frac{\rho^L \varrho^V e^{\rho+\varrho}}{\vartheta_d!\vartheta_e!} \sum_{\kappa=0}^{\vartheta_d} \binom{\vartheta_d}{\kappa} \sum_{\upsilon=0}^{\vartheta_e} \binom{\vartheta_e}{\upsilon} \times (-1)^\nu e^{(\kappa+1)C_s} \left(\rho e^{C_s} + \varrho\right)^{-(\varphi+1)} \varphi!, \quad (20)$$

where $\varphi = (\kappa + \upsilon + 1)$ and $\nu = (\vartheta_d + \vartheta_e - \kappa - \upsilon)$.

B. Secure Outage Probability

The secure outage probability is defined as

$$P_{out}(R_s) = P_r(C_s \le R_s) = \int_0^{R_s} q(C_s)dC_s, \quad (21)$$

where R_s denotes the target secrecy rate. Now substituting (20) into (21), we have

$$P_{out}(R_s) = \frac{\rho^L \varrho^V e^{\rho+\varrho}}{\vartheta_d!\vartheta_e!} \sum_{\kappa=0}^{\vartheta_d} \binom{\vartheta_d}{\kappa} \sum_{\upsilon=0}^{\vartheta_e} \binom{\vartheta_e}{\upsilon} \times \varphi!(-1)^\nu \int_0^{R_s} e^{(\kappa+1)C_s} \left(\rho e^{C_s} + \varrho\right)^{-(\varphi+1)} dC_s. \quad (22)$$

Performing integration the closed-form expression for secure outage probability is shown in (23) at the bottom of this page.

C. CCDF of Secrecy Capacity

The CCDF of secrecy capacity C_s is defined as

$$CCDF_{C_s} = P_r(C_s > R_s) = \int_{R_s}^{\infty} q(C_s)dC_s. \quad (24)$$

Substituting (20) into (24) and performing integration, the closed-form expression for CCDF of C_s is obtained as

$$CCDF_{C_s} = \frac{\rho^L \varrho^V e^{\rho+\varrho}}{\vartheta_d!\vartheta_e!} \sum_{\kappa=0}^{\vartheta_d} \binom{\vartheta_d}{\kappa} \sum_{\upsilon=0}^{\vartheta_e} \binom{\vartheta_e}{\upsilon} \frac{(-1)^\nu \varphi!}{\rho^{(\varphi+1)}} \times \frac{2F1\left(\varphi+1, \upsilon+1, \upsilon+2, -\frac{\varrho e^{-R_s}}{\rho}\right)}{(\upsilon+1)e^{(1+\upsilon)R_s}}. \quad (25)$$

V. Numerical Results

In this section, the theoretical analysis described in sections III and IV is validated by a set of Monte-Carlo simulations. For this purpose, in the simulation environment, at first, we have generated Rayleigh fading channels $\mathbf{H}_d$ and $\mathbf{H}_e$ using Matlab code prepared by the authors using Matlab function 'random'. Secondly, 110000 realizations of the channels have been averaged before using them to calculate secrecy capacity. Thirdly, the 110000 realizations of the calculated secrecy capacity have been averaged to calculate the ergodic secrecy capacity. The similar process has been adopted to find the channels that are used to find the secure outage probability and the CCDF of secrecy capacity. Note that our work is different from [11] in the sense that it deals with the analysis of secrecy capacity and secure outage performance of cooperative spatial multiplexing system with linear equalization.

Fig.2 shows the simulation and analytical results of ergodic secrecy capacity versus average SNR with number of users $M = 2$, relays $K = 6$ and destination antennas $n_D = 7$ to investigate the effect of number of eavesdropper antennas n_E. In order to observe the effect of n_E, three curves are shown for $n_E = 5$ (dot line), $n_E = 6$ (dash-dot line) and $n_E = 7$ (dash line). We observe that, the ergodic secrecy capacity decreases with n_E.

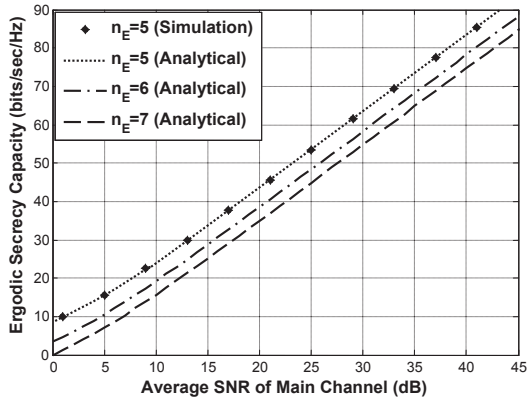

Fig. 2. The simulation and analytical results of ergodic secrecy capacity versus average SNR of main channel for selected values of n_E with $M = 2$, $K = 6$ and $n_D = 7$.

In order to investigate the effect of receive diversity provided by the destination antennas n_D and the effect of spatial multiplexing provided by the relays K, the simulation and analytical results of ergodic secrecy capacity versus average SNR are shown in Fig.3. In order to observe the effect of n_D, two curves are shown for $n_D = 4$ (dash line) and $n_D = 6$ (solid line) with $M = K = n_E = 4$. In order to see the effect of K, two curves are shown for $K = 3$ (dot line) and $K = 4$ (dash-dot line) with $M = 2$, $n_E = 4$ and $n_D = 5$. It is found

$$P_{out}(R_s) = \frac{\rho^L \varrho^V e^{\rho+\varrho}}{\vartheta_d!\vartheta_e!} \sum_{\kappa=0}^{\vartheta_d} \binom{\vartheta_d}{\kappa} \sum_{\upsilon=0}^{\vartheta_e} \binom{\vartheta_e}{\upsilon} \frac{(-1)^\nu \varphi!}{\rho^{(\varphi+1)}} \left[\frac{2F1\left(1, -\upsilon, 2+\kappa-\frac{\rho e^{R_s}}{\varrho}\right)}{e^{-(1+\kappa)R_s}\left(e^{R_s}+\frac{\varrho}{\rho}\right)^{\varphi}\frac{\varrho(1+\kappa)}{\rho}} - \frac{2F1\left(1, -\upsilon, 2+\kappa, -\frac{\rho}{\varrho}\right)}{\left(1+\frac{\varrho}{\rho}\right)^{\varphi}\frac{\varrho(1+\kappa)}{\rho}} \right]. \quad (23)$$

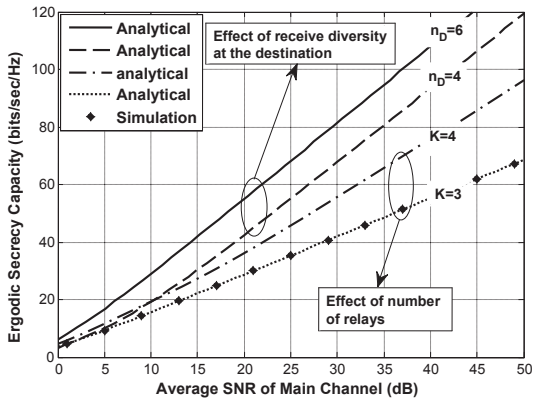

Fig. 3. The simulation and analytical results of ergodic secrecy capacity versus average SNR of main channel showing the effect of receive diversity with $M = K = n_E = 4$ and the effect of number of relays with $M = 2$, $n_E = 4$ and $n_D = 5$.

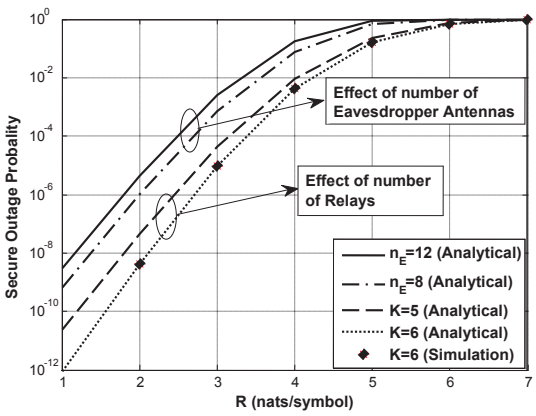

Fig. 4. The simulation and analytical results of secure outage probability versus target secrecy rate R_s showing the effect of K with $n_E = 6$ and $n_D = 12$ and the effect of n_E with $K = 5$ and $n_D = 12$.

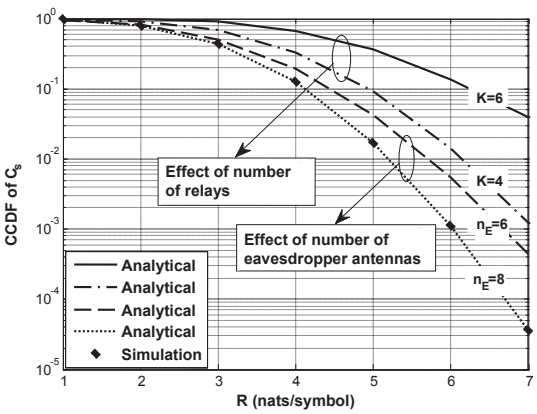

Fig. 5. The simulation and analytical results of complementary cumulative distribution function versus target secrecy rate R_s showing the effect of K with $n_E = 5$ and $n_D = 12$ and the effect of n_E with $K = 4$ and $n_D = 8$.

that, though n_D and K both are the increasing function of ergodic secrecy capacity, but with the increase in average SNR of main channel, the effect of spatial multiplexing provided by K is more significant than the effect of receive diversity provided by n_D.

Fig.4 shows the simulation and analytical results of secure outage probability as a function of target secrecy rate R_s to investigate the effect of K and n_E. In order to investigate the effect of K, two curves are shown for $K = 5$ (dash line) and $K = 6$ (dot line) with $n_E = 6$ and $n_D = 12$. We see that the secure outage probability decreases with K. To observe the effect of n_E, two curves are shown for $n_E = 8$ (dash-dot line) and $n_E = 12$ (solid line) with $K = 5$ and $n_D = 12$. We see that the secure outage probability increases with n_E.

In order to investigate the secure outage performance, we also present the simulation and analytical results of CCDF of secrecy capacity as a function of target secrecy rate R_s in Fig.5 for selected values of K and n_E. In order to observe the effect of K, two curves are shown for $K = 4$ (dash-dot line) and $K = 6$ (solid line) with $n_E = 5$ and $n_D = 12$. We see that the CCDF of secrecy capacity increases with K. To see the effect of n_E, two curves are shown for $n_E = 6$ (dash line) and $n_E = 8$ (dot line) with $K = 4$ and $n_D = 8$. We observe that the CCDF of secrecy capacity decreases with n_E. Moreover, from our observation it is clear that the effect of relays is more significant than the effect of eavesdropper antennas.

VI. Conclusion

In order to investigate the security in a cooperative spatial multiplexing system where a number of relays transmit different sub-streams to the destination antennas simultaneously, the closed-form expressions for the ergodic secrecy capacity, the secure outage probability and the CCDF of secrecy capacity using ZF filtering at the receiver terminal are derived in the Rayleigh fading environment. Based on our observations and from the numerical results, we may conclude that the cooperative spatial multiplexing provided by the relays with ZF filtering enhances spectral efficiency compared to receive diversity which causes an improvement in the ergodic secrecy capacity and decreases the secure outage probability of proposed model significantly.

Acknowledgment

This work is supported by the Research Support and Publication Division of University Grant Commission, Bangladesh.

References

[1] T. Q. Duong and H.-J. Zepernick, "On the ergodic capacity of cooperative spatial multiplexing systems in composite channels," in *Proc. IEEE Radio and Wireless Sympo. (RWS 2009), San Diego, CA*, January 2009, pp. 175–178.

[2] G. Pasolini and D. Dardari, "Secret information of wireless multidimensional Gaussian channels," *IEEE Trans. on Wireless Communications*, vol. 14, no. 6, pp. 3429–3442, February 2015.

[3] X. J. Zhang, Y. Gong, and K. Letaief, "On the diversity gain in cooperative relaying channels with imperfect csit," *IEEE Trans. on Communications*, vol. 58, no. 4, pp. 1273–1279, April 2010.

[4] H. Y. R. Louie, M. R. McKay, and I. B. Collings, "Open-loop spatial multiplexing and diversity communications in ad hoc networks," *IEEE Trans. on Information Theory*, vol. 57, no. 1, pp. 317–344, January 2011.

[5] X. Tao, X. Xu, and Q. Cui, "An overview of cooperative communications," vol. 50, no. 6, pp. 65–71, June 2012.

[6] N. Xie and A. Burr, "Cooperative spatial multiplexing with distributed amplify-and-forward relays," in *Proc. IEEE Int. Sympo. Wireless Commu. Systems (ISWCS), 2012, Paris, France*, August 2012, pp. 616–620.

[7] R. Bassily and S. Ulukus, "Secure communication in multiple relay networks through decode-and-forward strategies," *IEEE Journal of Communications and Networks*, vol. 14, no. 4, pp. 352–363, August 2012.

[8] M.-S. Alouini and A. J. Goldsmith, "Capacity of Rayleigh fading channels under different adaptive transmission and diversity-combining techniques," *IEEE Trans. on Vehicular Technology*, vol. 48, no. 4, pp. 1165–1181, July 1999.

[9] T. Ratnarajah and R. Vaillancourt, "Quadratic forms on complex random matrices and multiple-antenna systems," *IEEE Trans. on Information Theory*, vol. 51, no. 8, pp. 2976–2984, August 2005.

[10] I. S. Gradshteyn and I. M. Ryzhik, *Table of Integrals, Series, and Products*, 7th ed. San Diego, CA: Academic, 2007.

[11] S.-C. Wang and W. Liao, "Cooperative multicasting for wireless scalable video transmissions," *IEEE Trans. on Communications*, vol. 61, no. 9, pp. 3980–3989, Sept. 2013.

Evidence Theory-Based Cooperative Spectrum Sensing in Multi Antenna Cognitive Radio System

Md. Tahidul Islam
Electronic and Telecomm. Engg. Department
International Islamic University Chittagong
Chittagong, Bangladesh
Email: tahidcce@gmail.com

Muhammad Sajjad Khan
School of Electrical Engineering
University of Ulsan
Ulsan, South Korea
Email: sajjad.khan@iiu.edu.pk

Insoo Koo
School of Electrical Engineering
University of Ulsan
Ulsan, South Korea
Email: iskoo@ulsan.ac.kr

***Abstract*—Cooperative spectrum sensing has a great impact to increase the performance for detecting the Primary User (PU) signal over single node sensing. Recent developments in multiple antenna techniques adjoin a new dimension in spectrum sensing. In this paper, we have proposed a multi-antenna based signal detection for multi bands considering cooperative approach with Rayleigh fading channel. In addition to that, data fusion is considered by ordered sequential method where the sequential fusion is performed by Dempster Shafer (DS) theory-based reliability. The significance and efficiency of the proposed method is justified through analysis and simulation. The experimental results demonstrate that the proposed multi-antenna assisted DS-theory based spectrum sensing reduces sensing and reporting time significantly for the cognitive user as compared with the conventional system.**

***Keywords*—cognitive radio, evidence theory, multi-antenna, sequential fusion, spectrum sensing**

I. INTRODUCTION

Cognitive Radios (CRs) [1,2] are being considered as a promising solution that can maximize the utilization of the frequency resources by allowing Cognitive Users (CUs) to access the allocated spectrum bands, which are temporally idle. In traditional single CU, primary signal does not deal with the hidden terminal problem [3], which is occurred due to the multi-path fading and shadowing effects. An outstanding performance can be obtained by cooperative spectrum sensing over single node sensing method [4, 5]. Moreover, the concept of multiple-antenna system has drawn a lot of interest in the CR research, which can mitigate fading, and shadowing effects where multipath is effectively converted into benefit for communication system. Therefore, combination of multiple antennas with multiple user cooperation can provide outstanding performance for detecting the Primary User (PU) signal over conventional system. A number of papers have investigated the application of multiple antennas with energy detection for spectrum sensing from different point of view [6, 7, 8]. Previously, authors of [9, 10] have enlightened in the aspects of cooperative spectrum sensing and decision fusion. To implement conventional cooperative spectrum sensing, each CU makes a local decision and those decisions are reported to a fusion center to give a final decision according to some fusion rules (e.g. OR, AND, Half voting, Majority rule, etc). Unlike the conventional fusion rule, a data fusion scheme based on DS-theory of evidence was first recommend by P. Zeng et. al. where it was shown that the proposed scheme improve detection performance significantly without any prior knowledge of primary user signal [11]. N. T. Nhan et. al. proposed an enhanced DS-theory based fusion scheme for cooperative spectrum sensing [12]. Moreover, an efficient ordered sequential cooperative spectrum sensing method based on DS-theory was proposed in [13]. There are numerous works on the throughput maximization of cognitive radio communication [14-17]. Y. C. Liang et al. proposed sensing throughput tradeoff strategy for cognitive radio network [14]. Again, analysis of throughput for cooperative cognitive radio network was done by R. Muta et. al. [15]. Moreover, C. You et. al. proposed optimization of hard decision based cooperative TV spectrum sensing [16]. And throughput optimization by hard fusion based spectrum sensing was performed by [17]. However, all the papers considered conventional decision fusion rule with single antenna based sensing and yet to increase throughput significantly. In this paper, the impact of multi-antenna based spectrum sensing with energy detection for fading (Rayleigh) channel is analyzed. Moreover, instead of sensing single band, sensing and reporting accross multiple bands together are taken into account. Again, DS theory-based ordered sequential reporting methodology is applied for multiple bands. Based on the simulation result we have shown that the proposed multiple antenna and DS-theory based cooperative spectrum sensing can reduce sensing and reporting time. Moreover, reporting multiple bands in a single time slot instead of single band to FC has a significant reporting time reduction. Thus the proposed scheme has outperformed over traditional cooperative methods for shrinking sensing and reporting time.

The remainder of this paper is organized as follows. In section ii, system model is illustrated. The proposed multiple antenna and DS-theory based cooperative sensing is explained in section iii, and in section iv, proposed multiple-antenna based sensing and detection is illustrated. Moreover, the simulation result is provided in section v. and the conclusion is drawn in last section which is section vi.

II. SYSTEM MODEL

A. Spectrum Sensing

Consider a cognitive radio network with bandwidth $FHertz$ which is divided into total B disjoint small sub bands:

$$F^b = [F_b, F_{b+1}), F = \bigcup_{b=1}^{B} F^b \tag{1}$$

The received signal consists of total B sub bands with the boundaries located at $F_1 < F_2 < .... < F_B$. Therefore, total N_T CU nodes, each having M antennas is assigned to perform spectrum sensing on some sub bands. Moreover, we have considered a fusion center (FC) that has a single antenna. Signals received from the multiple antennas go through the energy detectors and the local decision is made at every CU. The received samples are represented by Y with a sample index n where and $n = 1, 2, ...N$. The local spectrum sensing problem can be formulated as binary hypothesis problem [18]:

$$Y_{i,j}(n) = \begin{cases} \eta_{i,j}(n) : H_0 \\ h_{i,j}s(n) + \eta_{i,j} : H_1 \end{cases} \tag{2}$$

where H_0 and H_1 represent signal absence and signal presence, respectively. $Y_{i,j}(n)$ is the signal from i^{th} CU with j antenna that has N samples where $i = 1, 2, ...N_T$ and $j = 1, 2, ...M$. h_{ij} is fading channel coefficient of the $i'th$ CU at antenna j. If the CU knows nothing about the waveform transmitted by the PUs in a frequency band of interest, energy detection is more suitable for detection[10] since it is only based on the measured energy of the received signal in that band.The principle of energy detection [18] is based on the difference between the energy of PU transmission signal and the noise. In the energy detection process, the energy of the received signal measured in a fixed bandwidth S over an observation time period T. The observed energy of a CU by a single antenna for a single sub-band is denoted by E and defined as: In conventional system, coarse sensing is performed with single antenna but in our proposed system it is performed by multiple antennas. Fine detector is performed with large number of samples to detect the band. In this paper, energy detection is used for fine sensing. In conventional case, fine sensing is performed by single antenna and to obtain one vacant band only. However, in proposed system, fine sensing is performed by multiple antennas and total numbers of vacant bands are dependent on number of CRU to utilize vacant band. If total vacant bands are smaller than number of required bands, the fine detector needs to seek up to last band.

$$E = \sum_{n=1}^{N} |Y(n)|^2 \tag{3}$$

The noise in each sample is a Gaussian random variable with mean zero and variance σ_η^2 and the signal variance σ_y^2. As a result, if PU is absent, $\frac{Y}{\sigma_\eta{}^2}$ follows a central chi-square distribution with N degree of freedom. Otherwise, $\frac{Y}{\sigma_\eta{}^2}$ follows a non-central chi-square distribution with N degree of freedom and a non-centrally parameter N_γ

$$\frac{Y}{\sigma_\eta{}^2} \sim \begin{cases} X_N{}^2, H_0 \\ X_N{}^2(N_\gamma), H_1 \end{cases} \tag{4}$$

where γ is the Signal to Noise Ratio (SNR). By the central limit theorem, the test statistic can be approximated as a Gaussian distribution.

$$\begin{aligned} H_0 :& E \sim Normal(N\sigma_\eta{}^2, 2N\sigma_\eta{}^4) \\ H_1 :& E \sim Normal(N(\sigma_\eta{}^2 + \sigma_y{}^2), 2N(\sigma_\eta{}^4 + \sigma_y{}^4)^2) \end{aligned} \tag{5}$$

The performance of detection is measured by two parameters P_d and P_f . The Rayleigh fading occurs when a signal experiences a Non-Line-of-Sight multipath. Due to Rayleigh fading, the signal amplitude follows a Rayleigh distribution, and the SNR of the PU signal at each CU follows an exponential distribution whose Probability Density Function is given by:

$$f_\gamma(\gamma) = \frac{1}{\gamma} e^{\frac{\gamma}{\hat{\gamma}}}, \gamma > 0 \tag{6}$$

where $\hat{\gamma}$ is the mean SNR value.

B. Frame structure for cooperative spectrum sensing

The cooperative spectrum sensing and detection is the combination of sensing and reporting period. Fig. 1 shows the time frame structure for cooperative spectrum sensing where total Q frames exist. The total frame time T of a frame is divided mainly into two parts: detection time T_d and transmission time $T - T_d$. Further, T_d is consisted of sensing time T_S and reporting time T_R.

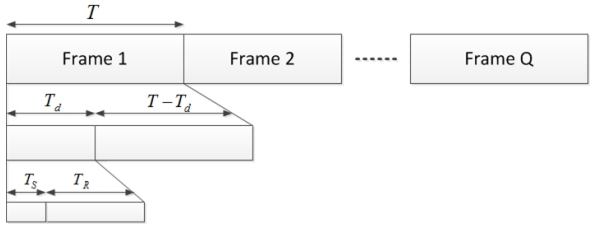

Fig. 1. The Frame structure for Cooperative Cognitive Radio

III. The Proposed Multiple Antenna and DS-Theory Based Cooperative Sensing

The overall process of the proposed scheme is shown in Fig. 2. The total spectrum sensing and decision process consists of three main parts: local sensing in CUs, data fusion to fusion center and final processing for global decision in fusion Center. In local sensing stage the sensing operation is performed by multiple antennas; and multiple sub-bands are sensed together instead of single band. The data of multiple bands are sent to FC in ordered sequential manner for making final decision. Upon obtaining the target detection and false alarm the FC manages to stop reporting for all the CUs.

The details of these operations are provided below:

A. Multiple-antenna based sensing and detection

In this paper, it is assumed that multiple antennas are uncorrelated. Energy of received signal at each antenna is calculated independently and the energy is added to perform detection. Fig. 3 shows multiple antenna signal detection and combining process for a single sub-band. For multiple bands, it is required to minimize processing complexity to reduce time and energy cost. Since the equal gain combining (EGC) method has relative lower complexity order for processing as compared to other methods complexity, in this paper EGC is utilized for signal detection. Pre-detection diversity signal output Y of a CR can be written as:

$$Y_j(n) = g_j[S_j(n) + \eta_j(n)] \tag{7}$$

Where, g_j is the weight factor from antenna $j = 1, 2, ..., M$ and $S_j = h_j s(n)$. For EGC, the branch weights are all set to unity.

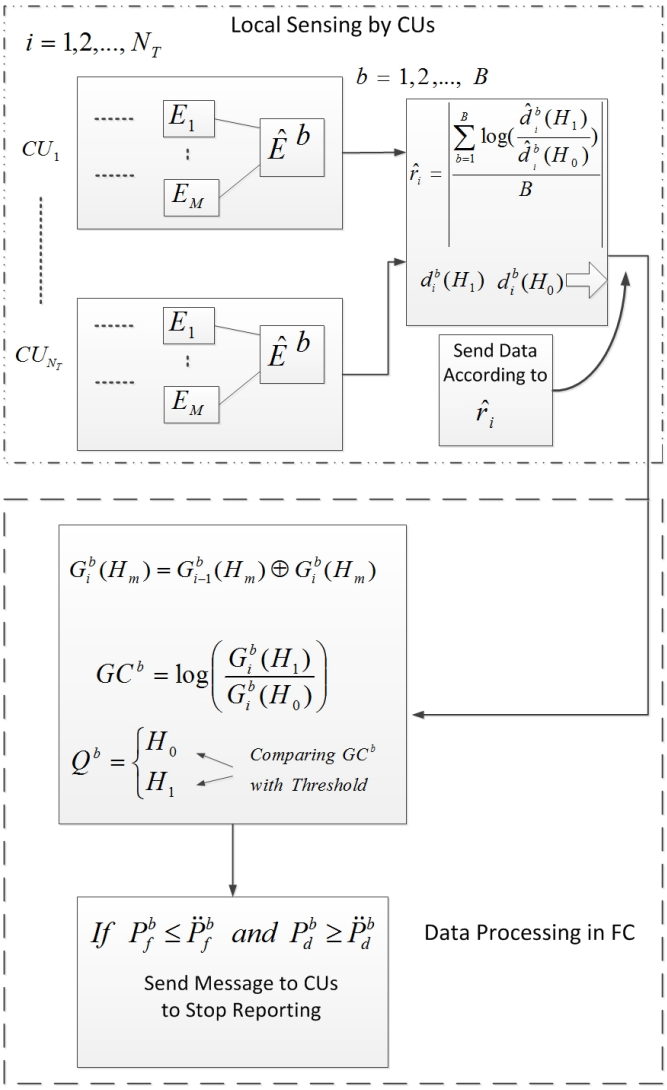

Fig. 2. Overall Structure of Multi-antenna and DS-theory Based Spectrum Sensing

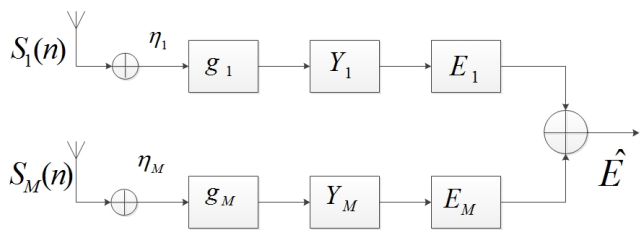

Fig. 3. Block diagram of pre-detection energy combining scheme for multiple antennas

The calculated energy for antenna j becomes:

$$E_j = \sum_{n=1}^{N} |Y_j(n)|^2 \tag{8}$$

However, the total observed energy of the CU by multiple antennas is denoted by $\hat{E}$ and defined as:

$$\hat{E} = \sum_{n=1}^{N} E_j \tag{9}$$

Therefore, for uncorrelated multiple antenna case, H_0 and H_1 hypothesis can be expressed as:

$$\begin{aligned} H_0 &: \hat{E} \sim Normal(MN{\sigma_\eta}^2, 2MN{\sigma_\eta}^4) \\ H_1 &: \hat{E} \sim Normal(MN({\sigma_\eta}^2 + {\sigma_y}^2), 2MN({\sigma_\eta}^4 + {\sigma_y}^4)^2) \end{aligned} \tag{10}$$

B. DS-theory based sequential data fusion for multiple bands

1) Local data and reliability calculation: : The D-S theory of evidence is applied to make final decision of CU's detection, the frame of discernment is defined as: $\{H_0, H_1, \zeta\}$, where ζ is ignorance hypothesis which denotes either hypothesis is true. After sensing time, each CU will estimate its self-assessed decision credibility which is equivalent to Basic Probability Assignment (BPA) for two hypotheses. The BPA function for local hypothesis measurement for every band $b(b = 1, 2, ..., B)$ can be written as a form of the cumulative density function which is found in [12] as follows:

$$\hat{d}_i^b(H_0) = \int_{\hat{E}_i}^{+\infty} exp(\frac{-(Y - \sigma_{ni})^2}{2{\sigma_{ni}}^2})dx \tag{11}$$

$$\hat{d}_i^b(H_1) = \int_{-\infty}^{\hat{E}_i} exp(\frac{-(Y - \sigma_{si})^2}{2{\sigma_{si}}^2})dx \tag{12}$$

$$\hat{d}_i^b(\zeta) = 1 - m_i(H_0) - m_i(H_1) \tag{13}$$

The sensing data reliability r_i of i'th CU for single band $(b = 1)$ can be defined as follows:

$$r_i = \frac{\hat{d}_i^b(H_1)}{\hat{d}_i^b(H_0)} \tag{14}$$

However, the reliability for multiple bands is denoted by $\hat{r_i}$ and calculated as:

$$\hat{r_i} = \frac{\sum_{b=1}^{B} log(\frac{\hat{d}_i^b(H_1)}{\hat{d}_i^b(H_0)})}{B} \tag{15}$$

Each CU transmits the data of all bands in the order of reliability $(\hat{r_i})$ of sensing result to FC where the final decision of every band is made individually based on a sequential test.

2) Reporting and global decision: : In this paper, we have considered reservation reporting method for ordered sequential reporting mechanism and followed the similar parameters of IEEE 802.11. The total reporting time consists of two main parts: reservation period and reporting period which is shown in Fig.4.

Reservation period:
In reservation period, each CU performs a reservation by utilizing a short burst signal according to a selected reservation timeslot in the common control channel. The node that has higher sensing results reliability $(\hat{r_i})$ has higher order in the reservation time and will be allowed to report in a priority

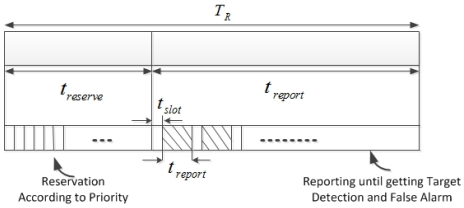

Fig. 4. Reservation reporting method

basis to FC.

Reporting period:

In reporting period, before transmitting the sensing report, the nodes have to listen to a short time for the burst signal from fusion center, which is equivalent to slot time. And a polling period is required to transmit data. Upon making final decision, the FC will perform burst to cancel reporting and decision message is sent to all CUs to stop their reporting. At FC, the BPA is sequentially combined in the order of data arrival for b^{th} band as follows:

$$G_i^b(H_m) = G_{i-1}^b(H_m) \oplus G_i^b(H_m) \tag{16}$$

$m = 0, 1$ and $G_{i-1}^b(H_m)$ and $G_i^b(H_m)$ are $(i-1)^{th}$ and i^{th} global BPA of hypothesis H_m respectively and is defined by DS theory. The global decision credibility ratio of bth band at the ith report is denoted by GC^b and is given as:

$$GC^b = log\frac{G_i^b(H_1)}{G_i^b(H_0)} \tag{17}$$

where GC^b is compared with threshold for final decision. The decision credibility ratio is justified with threshold for making final decision (Q) forbi^{th} band as follows:

$$Q^b = \begin{cases} H_0;\ if\ GC^b(H_m) < -\lambda \\ no\ decision;\ otherwise \\ H_1;\ if\ GC^b(H_m) > \lambda \end{cases} \tag{18}$$

Therefore global probability of false alarm P_f^b and detection P_d^b for the bth band is calculated as follows:

$$P_f^b = Prob(\frac{\hat{H}_1}{H_0}) \tag{19}$$

$$P_d^b = Prob(\frac{\hat{H}_1}{H_1}) \tag{20}$$

Where $\hat{H}_1$ and $\hat{H}_0$ are occupied and null hypothesis respectively detected in the fusion center.

C. Detection time and throughput

The total detection time is divided into two parts: sensing time and reporting time.

1) Sensing time: The total sensing time varies for single (multiple) antenna and bands. Sensing time for single band requires sensing only certain number of sample of a band. And single antenna does not need additional time for combining the signal. Therefore, sensing time for single band by single antenna is as follows:

$$T_S = N_S t_e \tag{21}$$

where N_S is the number of sample and t_e is the time for sensing single bit. Sensing by multiple antennas is performed in parallel way. Thus, it does not need any additional time for sensing by multiple antennas. However, after calculating energy in each antenna, all energies are combined to justify total energy. Thus for multiple antennas, it is needed a very small time for combining energies. Sensing time for single band by multiple antennas:

$$T_S = N_S t_e + t_{comb} \tag{22}$$

where t_{comb} is the time to add energy from multiple antennas. For multiple bands, each band is sensed individually to calculate energy. Therefore, it is required B times of single antenna for B bands. Sensing time for multiple bands by single antenna is:

$$T_S = \sum_{b=1}^{B} N_S t_e \tag{23}$$

Sensing time for multiple bands with multiple antennas becomes:

$$T_S = \sum_{b=1}^{B} N_S t_e + t_{comb} \tag{24}$$

2) Reporting time: All the bands of every CU are reported in a single time slot. In the first phase all the CUs perform reservation for ordered sequential reporting and the reservation time is denoted by $t_{reserve}$. And in the second phase the CU reports to the FC. For single band, every CU sends data of H_0 and H_1 hypothesis in a time slot. Total reporting time for single band with single antenna case is as follows:

$$T_R = N_{T1}(t_r + t_{slot}) + t_{reserve} \tag{25}$$

where N_{T1} is the required number of CU to obtain global target probability of detection and false alarm, t_r and t_{slot} are the reporting time and slot time respectively. For single and multiple bands, reservation time is equal. However, slot time depends on the number of CUs reporting. And since every CU sends multiple bands data of H_0 and H_1 hypothesis in a time slot, the reporting time increases. Total reporting time for multiple band with single antenna case is given by:

$$T_R = N_{T1}(\hat{t_r} + t_{slot}) + t_{reserve} \tag{26}$$

where $\hat{t_r}$ is the reporting time for multiple bands and $\hat{t_r} > t_r$. Reporting time for single band with multiple antennas is:

$$T_R = N_{T2}(t_r + t_{slot}) + t_{reserve} \tag{27}$$

where N_{T2} is the required number of CU to obtain global target probability of detection and false alarm for multiple antennas. Reporting time for multiple band with multiple antennas is given by:

$$T_R = N_{T2}(\hat{t_r} + t_{slot}) + t_{reserve} \tag{28}$$

Therefore, total detection time consists of sensing time and reporting time and can be written as:

$$T_d = T_S + T_R \tag{29}$$

IV. Simulation Result

In order to evaluate the proposed scheme for global detection, the numerical simulation results have been experienced under different conditions, which are shown in Figs.5-9. The general parameters are as following: all the simulations are conducted with the assumption that the presence and absence are equal (0.5). The Bandwidth of each sub-band is $6MHz$. Fig. 5 shows the global false alarm and miss detection for different SNRs $(-14\ to - 10dB)$. Firstly, we have considered a cognitive radio network environment with 100 nodes each of which independently senses the primary user presence and absence by energy detection. The performance shown in Fig.5 is for 10% reporting of total nodes. The comparative performance is shown by single and 4 antennas where every CU performs sensing on single and multiple bands. From the figure it is evident that the global false alarm probability is lower and detection probability is higher in the case of multiple antennas and vice versa for single antenna. Moreover, for multiple bands the probability of false alarm increases and detection decreases due to the decrement of reliability for multiple bands.

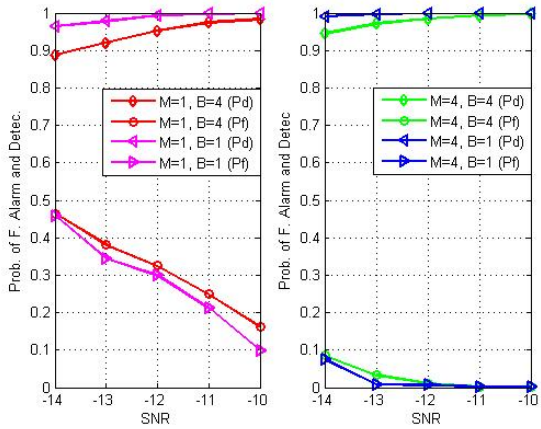

Fig. 5. ROC curve for Prob. of false alarm and detection for different SNRs

The total error probability for different percentage of reporting is plotted in Fig.6. It is assumed that every CU endures $-14\ dB\ SNR$. The total error probability is defined as a combination of the probability of miss detection and false alarm and for B bands it can be written as follows: $\epsilon_{total} = \frac{\sum_{b=1}^{B} P_f^b P(H_0) + (1-P_d^b)P(H_1)}{B}$. From Fig.6, it is observed that total error probability decreases as the number of reporting increases. In addition to that, multiple bands have higher probability of error as compared with single band. Moreover, utilizing 4 antennas has lower error probability as compared with utilizing single antenna. The Fig.7 shows total error probability for different number of samples when total 10% reporting are considered with $SNR\ -14\ dB$. Note that these samples are taken for only single band and for multiple bands the sample is multiple of the number of band. As the number of samples increases, the sensing time will increase and total error probability will be improved due to the cost of longer sensing time.

The required numbers of CUs reporting to obtain target probability of detection and false alarm for different number

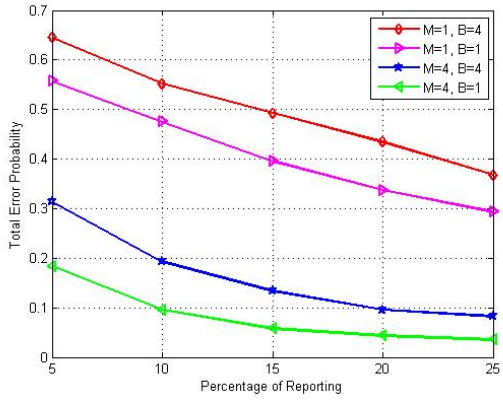

Fig. 6. Total error probability according to the percentage of reporting

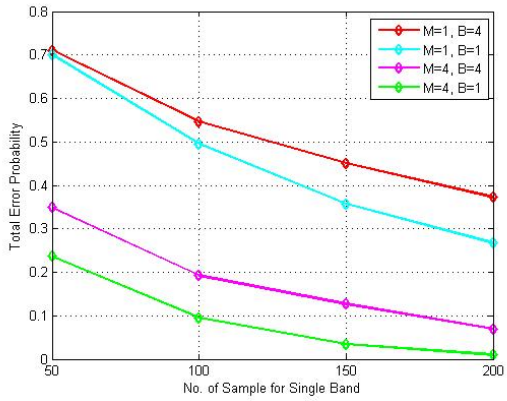

Fig. 7. Total error probability according to the number of samples for single band

of SNRs are observed in the Fig.8. The target probability of detection and false alarm are set as $P_d^b \geq 0.9$ and $P_f^b \leq 0.1$ respectively. From Fig.8, the following observations are obtained: For low SNR, the gap between single and multiple bands for single or multiple antennas are higher. As the SNR decreases, average reliability decreases and the gap becomes larger. For multiple bands $(m = 4)$, single antenna based cognitive radio needs a large number of nodes reporting, compared with CU with multiple antennas. For instance, single antenna-based sensing requires $72,\ 50\ and\ 34$ nodes reporting respectively when SNR is $-14,\ -13\ and\ -12$ respectively. On the other hand, multiple antennas-based sensing requires $12,\ 8\ and\ 4$ nodes reporting to obtain the target probability. The same phenomenon is observed in the case of single and multiple antennas for single band. Additionally, the single band case requires less number of CUs reporting than multiple bands case. Fig. 9 shows the required reporting time to obtain target probability of false alarm and detection for different values of SNRs. The simulation parameters for calculating reporting time are provided in table 1. As depicted in Fig.9, the multiple band and single antenna $(M = 1, B = 4)$ case has the highest reporting time. For single band with single antenna has second higher reporting time but CU with multiple antenna has significantly lower reporting time as compared with CU

TABLE I. THE PARAMETERS FOR CALCULATING REPORTING TIME

Parameters	Values
Slot time: t_{slot}	20 μ sec
Poll time: $t_p = 10 * (t_{slot})$	200 μ sec
Reporting slot interval for single band: $t_r = 3 * t_p$	20 mili sec
Reporting slot interval for multiple band: $t_r = 5 * t_p$	1 mili sec
Reservation time:$t_{reserve} = 5 * N_T * t_{slot}$	6 mili sec

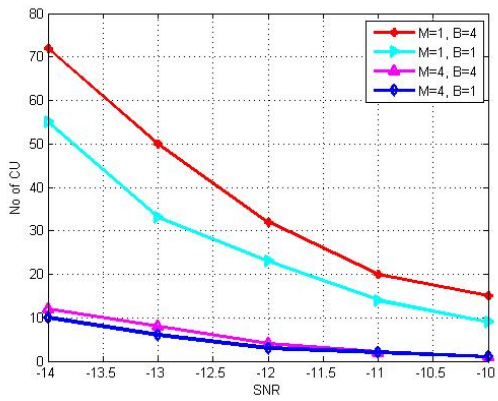

Fig. 8. The required number of CUs to obtain target probability of false alarm and detection according to SNR when 100 samples are taken for each band

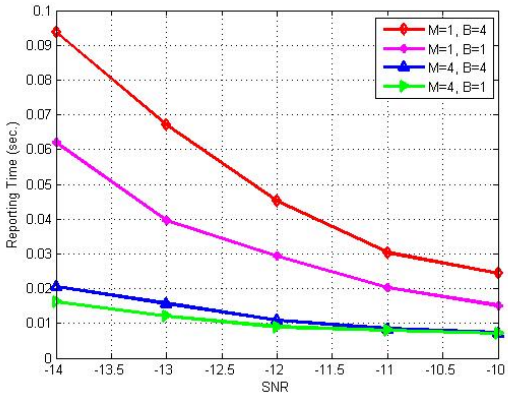

Fig. 9. The required reporting time to obtain target probability of false alarm and detection according to SNR

with single antenna. For instance, the required reporting time is 60 $milli-seconds$ when $SNR = -14dB,\ M = 1\ and\ B = 4$, and the required reporting time is 60 $milli-seconds$ when $SNR = -14dB,\ M = 1\ and\ B = 1$. These reporting times are approximately more than 100 $milli-seconds$ when 3 to 4 times higher than multiple antenna case.

V. CONCLUSION

In this paper, we have proposed a multiple antennas based multi-band cooperative spectrum sensing for cognitive radio network. The ordered sequential reporting is justified with the DS-theory based reliability. The efficiency of relative performance for global sensing is justified in terms of throughput. It has observed that the proposed multiple antennas based multi-band sensing with DS-theory based ordered sequential reporting have higher efficiency over single antenna, single band and traditional reporting method for augmenting the throughput significantly.

REFERENCES

[1] J. Mitola and G. Q. Maguire, Cognitive radios: making software radios more personal, IEEE Personal Commun., vol. 6, no. 4, pp. 13-18, 1999.

[2] S. Haykin, Cognitive radio: brain-empowered wireless communications, IEEE Trans. Commun., vol. 23, no. 2, pp. 201-220, 2005.

[3] D. Cabric, S. Mishra, and R. Brodersen, Implementation issues in spectrum sensing for cognitive radios, in Signals, Systems and Computers, 2004. Conference Record of the 38thAsilomar Conference, vol. 1, pp. 772 776, Nov. 2004.

[4] N. Nguyen-Thanh and I. Koo, An enhanced cooperative spectrum sensing scheme based on evidence theory and reliability source evaluation in cognitive radio context, Communications Letters, IEEE, vol. 13, no. 7, pp. 492 494, July 2009.

[5] G. Ganesan and Y. G. Li, Cooperative spectrum sensing in cognitive radiopart I: two user networks, IEEE Trans. Wireless Commun., vol. 6, pp. 22042213, June 2007.

[6] S. Rodriguez-Parera, V. Ramon, A. Bourdoux, et al. Spectrum Sensing over SIMO Multi-Path Fading Channels based on Energy Detection, Global Telecommunications (GLOBECOM) Conference, IEEE 2008.

[7] A.Salarvan, G.K. Kurt, Multi-Antenna Spectrum Sensing for Cognitive Radio under Rayleigh Channel, IEEE Symposium on Computers and Communications (ISCC), 2012.

[8] Sahai and D. Cabric, Spectrum sensing: fundamental limits and practical challenges," in Proc. IEEE International Symp. New Frontiers Dynamic Spectrum Access Networks (DySPAN), Baltimore, MD, Nov. 2005.

[9] Z. Wei, R.K. Mallik, and K. Ben Letaief, Cooperative spectrum sensing optimization in cognitive radio networks, in Proc. of IEEE Int. Conf. on Communications, pp. 3411-3415, May 2008.

[10] L. Chen, J. Wang, and S. Li, An adaptive cooperative spectrum sensing scheme based on the optimal data fusion rule, 4th Int. Symposium on Wireless Communication Systems, pp. 582-586, Oct. 2007.

[11] Q. Peng, K. Zeng, J. Wang ans S. Li, A distributed spectrum essnsing scheme based on credibility and evidence theory in cognitive radio context, IEEE 17th International Symposium on Personal, Indoor and Mobile Radio Communications, pp.1-5, Sept. 2006.

[12] N. T. Nhan and K. Insoo, An enhanced cooperative spectrum sensing scheme based on evidence theory and reliability source evaluation in cognitive radio, IEEE Communications Letters, vol.13, pp.492-494, 2009.

[13] N. T. Nhan and K. Insoo, An efficient ordered sequential cooperative spectrum sensing scheme based on evidence theory in Cognitive Radio, IEICE Tansactions on Communication. Vol. E93-B, No. 12 Dec 2010.

[14] Ying-Chang Liang, Yonghong Zeng, Edward C.Y. Peh, and Anh Tuan Hoang "Sensing-Throughput Tradeoff for Cognitive Radio Networks" IEEE Trans. on Wireless Communications, Vol.7, No.4 April 2008.

[15] Ryuji Muta, Ryuji Kohno, "Throughput Analysis for Cooperative Sensing in Cognitive Radio Networks" Personal, IEEE 20th International Symposium on Indoor and Mobile Radio Communications, Sept. 2009.

[16] C. You, H. Kwon, and J. Heo, Cooperative TV Spectrum Sensing in Cognitive Radio for Wi-Fi Networks, IEEE Transactions on Consumer Electronics, Vol. 57, No.1, Fe. 2011.

[17] S. Maleki. S. P. Chepuri, G. Leus, Optimization of hard fusion based spectrum sensing for energy-constrained cognitive radio networks, Physical Communication (2012), July 2012.

[18] H. Urkowitz, Energy detection of unknown deterministic signals, Proceedings of the IEEE, vol. 55, no. 4, pp. 523 531, april 1967.

A Metamaterial Based Triangular Cloak

S. S. Islam [1,2], M. R. I. Faruque[1]
Space Science Centre, IPI,
[1]Universiti Kebangsaan Malaysia,
Selangor, Malaysia; EEE,
[2]International Islamic University
Chittagong, Bangladesh
sikder_islam@yahoo.co.uk

Mohammad Tariqul Islam
Department of Electrical, Electronic
and Systems Engineering, Universiti
Kebangsaan Malaysia, Malaysia.
titareq@gmail.com

Touhidul Alam
Dept. of CSE,
International Islamic University
Chittagong, , Bangladesh.
touhid13@yahoo.com

***Abstract*— In this paper, a metamaterial based triangular shaped electromagnetic cloak is presented. The pi-shaped metamaterial shows wideband NZRI (near-zero refractive-index) characteristics in the C-band of microwave spectra. The metamaterial was then utilized in designing a triangular shaped cloak. The cloak hides a metal cylinder electromagnetically where the metamaterial shows NZRI property. At the cloaked frequency, the normalized scattering width (NSW) of the object was reduced to zero. This is a promising design for wideband NZRI characteristics and C-band electromagnetic cloaking operation.**

Keywords—Cloak; C-band; Metamaterials

I. INTRODUCTION

Advances in metamaterial have opened many opportunities to tailor the electromagnetic property of a device. Metamaterial is a naturally unavailable artificially constructed composite material that may have some extraordinary electromagnetic properties, like, negative permittivity, negative permeability, etc. Due to these existing properties, it has applications in many fields like, design of filter, antenna, cloak and so on [1-4].

In the field of invisibility cloak design, metamaterials can play an interesting role. To cloak (hide) an object, electromagnetic waves is manipulated in such a way around an object to be cloaked, that the wave will bend around the object and makes the object hidden to the outside world. For cloaking operation, near zero refractive index (NZRI) metamaterial has good prospect [5]. There are some metamaterials are found in the literature, but very few of them have NZRI property [6-9]. Among the other cloaking methods, 'scattering cancellation' is a one kind of method that had been studied in some of the literature for cloaking operation [10-13]. In this method, an object can be cloaked by reducing the scattering cross section (SCS) of the object, which can be done by metamaterial shell. To cloak an object the SCS should be kept below one [14]. However, most of the cloaking structures were cylindrical or square shape. Moreover, these cloaks were not designed for C-band.

This paper reveals a new metamaterial-based 'triangular-shape' cloak. It operates in the C-band. For numerical analysis, the finite integration technique was adopted. The metamaterial was designed first and then it was applied for building the cloak device. The measured result was presented for metamaterial that agrees well with the numerical result as well.

II. STRUCTURE OF THE UNIT CELL

The Fig.1a shows the proposed metamaterial unit cell structure. The structure has been designed with two complementary copper arms with a little split between them and all of them having a thickness of 0.035mm. The design parameters are, *d=6, g=0.33, h=6, l=8, m=1, n=1.5, p=6.27, q=1, s=0.5* all in mm unit. The design was done on the FR-4 substrate material with dielectric constant 4.2 and loss tangent 0.002 and thickness 1.6mm.

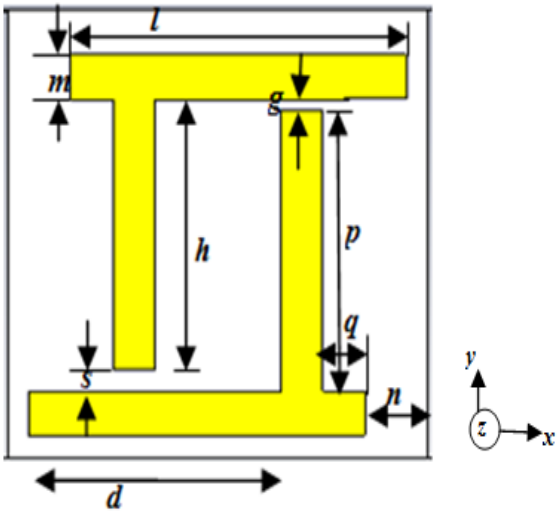

Fig. 1. The proposed unit cell structure

III. METHODOLOGY

For numerical analysis finite integration technique based, software, 'CST Microwave Studio' was adopted. Using two waveguide ports, the electromagnetic wave was propagated in the z-axis of the unit cell and the S-parameters' were calculated. The simulation was done in the frequency range of 5 GHz -9 GHz.

The NRW-method mentioned in [15] was utilized for the calculation of effective medium parameters. The simplified formulae have been given below,

$$V_1 = S_{21} + S_{11} \quad (1)$$

$$V_2 = S_{21} - S_{11} \quad (2)$$

$$\mu_r \approx \frac{2}{jk_0 d} \frac{1 - V_2}{1 + V_2} \quad (3)$$

$$\varepsilon_r \approx \frac{2}{jk_0 d} \frac{1 - V_1}{1 + V_1} \quad (4)$$

$$\eta = \sqrt{\varepsilon_r \mu_r} \quad (5)$$

Where, ε_r is the effective permittivity, μ_r is the effective permeability, 'd' is the thickness of the substrate, k_0 is the wave number and η is the refractive index.

The metamaterial was then used to design a triangular shaped cloak. A cylinder made of aluminium was chosen as object to be cloaked. The transverse electric wave was propagated parallel to the axis of the cylinder through the z-axis of the cloak structure from left to right side to observe the cloaking effect.

IV. Cloak Design

As a part of further work, the metamaterial was applied in designing a triangle-shaped cloak design. For designing the cloak, the wall composed of 2×2 unit cells of the proposed metamaterial was prepared. Three metamaterial walls were prepared and a triangular-shaped cloak was formed. The cloak structure is seen in Fig. 2.

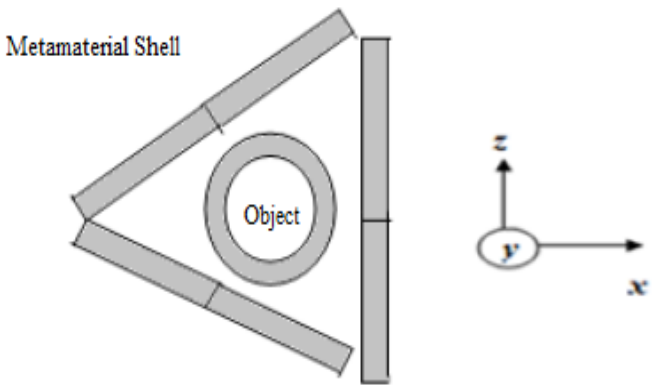

Fig. 2. The proposed cloak structure (top view)

The inner and outer radius of the object is 4mm and 5 mm respectively and the height of the object was kept 20mm.

V. Results and Discussion

The numerical results of S-parameters are presented in Fig.3 for the unit cell. The S-parameters results show one sharp resonance at 8.29 GHz.

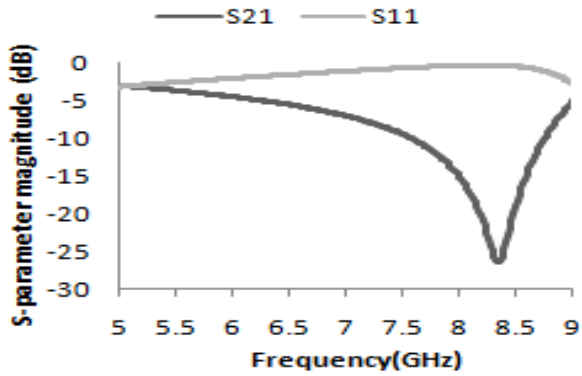

Fig. 3. S-parameter magnitude

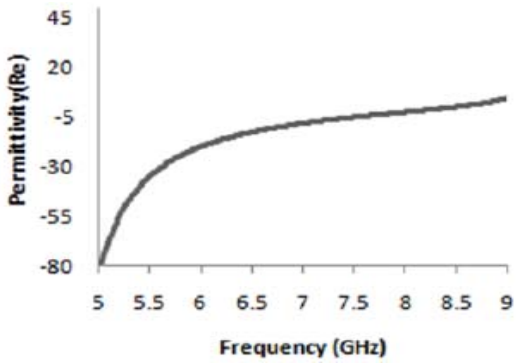

Fig. 4. Numerical real peak of permittivity (ε)

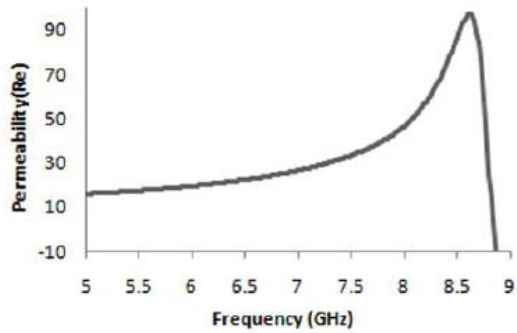

Fig. 5. Numerical real peak of permeability (μ)

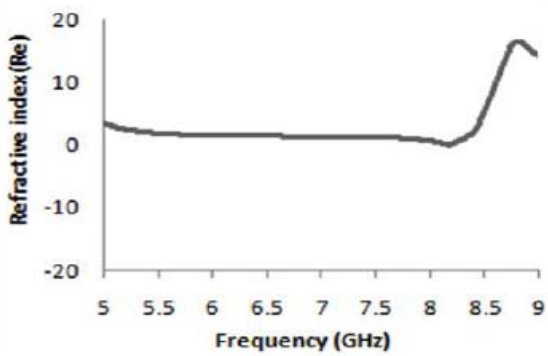

Fig. 6. Real magnitude of refractive index (η) for the unit cell

In Fig. 4 and Fig. 5 the effective permittivity and effective permeability is shown against frequency consecutively. In the Fig. 4 the permittivity curve shows negative magnitude from the 5 GHz to 8.45 GHz. However, in the Fig.5, the permeability curve displays positive peak in the same region. Moreover, at the frequency of 8.29 GHz, the permittivity curve shows negative magnitude and the permeability curve displays positive peak.

In the Fig. 6, the real magnitude of the refractive index curve is shown. It is evident that the refractive index curve displays near-zero refractive index (NZRI) region that is within the frequency range of 5 GHz to 8.40 GHz. The NZRI property has good prospects of designing an invisibility cloak.

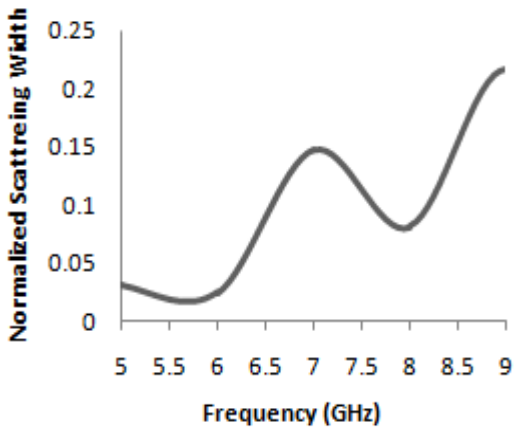

Fig. 7. Numerical value of NSW of the cloaked object

The Fig. 7 reveals the simulated outcome of the NSW of the cloaked object. Normalization of the cloaked object was done with the bare object. It is apparent from the Fig.7 that the scattering width shows the lowest value at 5.67 GHz that is very close to zero. The metamaterial also shows near zero refractive index property there. It depicts that the metallic cylinder is being cloaked at this frequency (5.67 GHz).

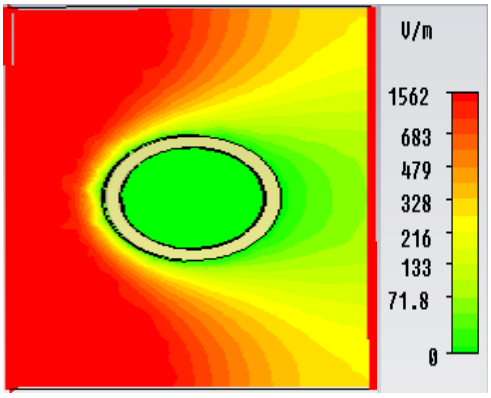

Fig. 8. E-field distribution of bare object for *x-y*-plane (mm) at 5.67 GHz

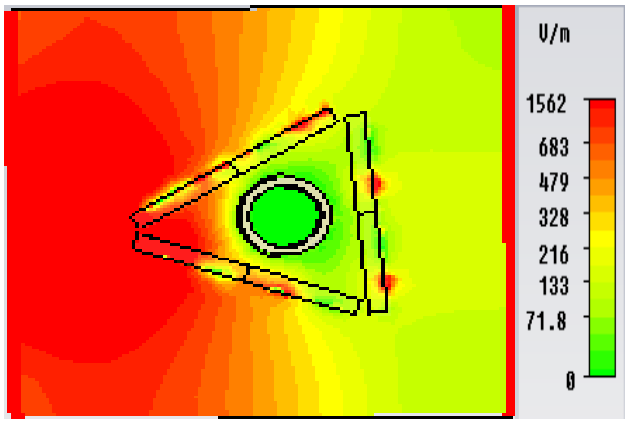

Fig. 9. E-field map in the *x-y*-plane (mm) when the object is covered with the metamaterial at the uncloaked frequency

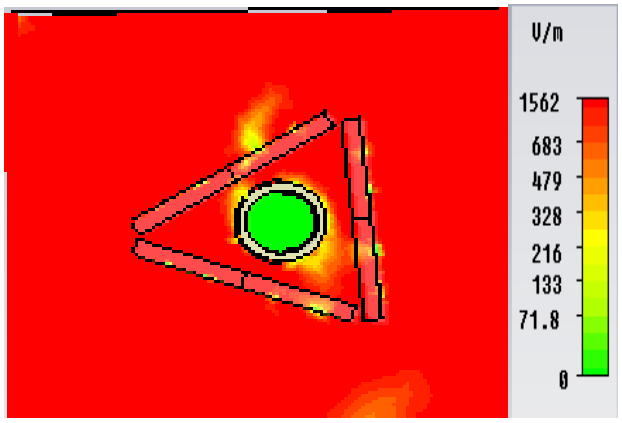

Fig. 10. E-field map in the *x-y*-plane (mm) when the object is covered with the metamaterial at the cloaked frequency (5.67 GHz).

The Fig. 8 shows the field distribution for uncloaked or bare object where some shadow in the forward direction is seen at 5.67 GHz. This shadow refers to the forward scattering of waves from the object. Fig. 9 shows the field distribution of the object at the frequency of uncloaked state. It is clear that the scattering in the forward direction is still present at the right side of the object. However, in the Fig. 10, the object inside the cloak, but at cloaked frequency is presented where the is clear that the forward scattering is completely alleviated and the scattered wave has returned to its original path. Therefore, the existence of the metal cylinder will remain completely undetected at that certain cloaked frequency.

VI. Conclusion

This paper presents a new metamaterial-based electromagnetic cloak that hides a metallic cylinder in a certain frequency of the C - band region. The metamaterial also shows more than 2 GHz NZRI property in the cloak region. Cloaking has good applications in the defense sector,

especially for stealth coating of aircraft or missile. Therefore, the this cloak can be applied in the C-band applications besides other cloaking device.

REFERENCES

[1] M. H. Ullah, M. T. Islam and M. R. I. Faruque, A Near-Zero Refractive Index Meta-Surface Structure for Antenna Performance Improvement; Materials, 6, pp.5058-5068; 2013

[2] M. M. Islam, M. T. Islam, M. Samsuzzaman, M. R. I. Faruque, N. Misran, and M. F. Mansor; A Miniaturized Antenna with Negative Index Metamaterial Based on Modified SRR and CLS Unit Cell for UWB Microwave Imaging Applications. *Materials*,8 pp. 392-407; 2015.

[3] S. S. Islam, M. R. I. Faruque, M. T. Islam; A Near Zero Refractive Index Metamaterial for Electromagnetic Invisibility Cloaking Operation; *Materials*, *8*, pp. 4790-4804; 2015; doi: 10.3390/ma8084790

[4] M. R. I. Faruque, M. T. Islam, N. Misran, "Analysis of Electromagnetic Absorption in the Mobile Phones Using Metamaterials," Electromagnetics Journal (Taylor & Francis Group), Vol. 31, Issue no. 3, pp.215-232, 2011

[5] J. Schilling, The quest for zero refractive index. *Nat. Photon.* **2011**, *5*, 449–451.

[6] S. S. Islam, M. R. I. Faruque, M. T. Islam; A new double negative metamaterial for multi-band microwave applications; Applied Physics A, Volume 116, Issue 2, pp 723-733, August **2014**

[7] S. S. Islam, M. R. I. Faruque, M. T. Islam; Design and Analysis of a New Double Negative Metamaterial; Informacije MIDEM; Vol. 44, No. 3 (2014), 218 – 223

[8] S. S. Islam, M. R. I. Faruque, M. T. Islam; Design of a New ENG Metamaterial for S-Band Microwave Applications; Journal of Electrical and Electronics Engineering - Vol. 7, Nr. 2, October 2014

[9] O. Turkmen, E. Ekmekci, G. Turhan-Sayan; Nested U-ring resonators: a novel multi-band metamaterial design in microwave region; IET Microw. Antennas Propag., Vol. 6, Iss. 10, pp. 1102–1108; 2012

[10] N. Kundtz, D. Gaultney, and D. R. Smith; Scattering cross-section of a transformation optics-based metamaterial cloak; *New Journal of Physics;* 12**;** 043039; 2010

[11] P. Alitalo and C.A. Valagiannopoulos; Demonstration of electromagnetic cloaking of conducting object by the dielectric material cover; Electronics Letters, Vol. 48 No. 17, August 2012

[12] J.C.Soric, P.Y.Chen, A. Kerkf, D.Rainwater, K.Melin, A. Alu, Demonstration of an ultralow profile cloak for scattering suppression of a finite-length rod in free space. *New J. Phys.* **2013**, *15*, 033037.

[13] R.S.Schofield, J.C.Soric, D.Rainwater, A. Kerkhoff, A. Alù, Scattering suppression and wideband tunability of a flexible mantle cloak for finite-length conducting rods. *New J. Phys.* **2014**, *16*, 063063.

[14] X.Wang, F.Chen, E. Semouchkina; Implementation of low scattering microwave cloaking by all-dielectric metamaterials. *IEEE Microw. Wirel. Comp. Lett.* **2013**, *23*, 63–65.

[15] S. S. Islam, M. R. I. Faruque and M. T. Islam; 'A New Direct Retrieval Method of Refractive Index for Metamaterials', *Current Science*, Vol. 109, No. 2, 2015

Implementation of a 1x16 Router Using 2x2 Mach-Zehnder Interferometer Electro-Optic Switch

Rabeya Khatun, Raqibul Hossen, Kazi Tanvir Ahmmed
Department of Applied Physics, Electronics & Communication Engineering
University of Chittagong, Chittagong-4331, Bangladesh
shompa.apece@gmail.com, raqib_saikat@yahoo.com, tanvir@cu.ac.bd

***Abstract*—In optical communication signal router is a novel photonic component used to ensure communication between optical networks. Signal routing has a significant commercial demand in dense wavelength division multiplexing. This paper presents the description of designing a 1x16 signal router using Mach-Zehnder electro-optic Switch operating at 1.55 µm. To design the router we used 2x2 Mach-Zehnder electro-optic switch made by titanium diffused lithium niobate (Ti:$LiNbO_3$) which is used as waveguide medium in designing the desired signal router. Enhanced performance of the switch with reduced insertion loss, excess loss and high extinction ratio was evaluated first and then the router was implemented using that optimized switch. 16 switches were required to implement the router. Optical power can be switched to each of the 16 output ports with the application of applied voltage at each central electrode of the 16 MZI switches. The results are observed using finite difference beam propagation method of OptiBPM12.2 simulation software.**

Keywords—Mach-Zehnder interferometer, Electro-optics switch, Insertion loss (IL), Extinction ratio (ER), Signal router.

I. INTRODUCTION

Mach-Zehnder interferometer is a basic component in photonic lightwave circuit (PLC). It is a classical mirror interferometer which was the most common dual-beam-interferometer for a long time and used in measuring refractive index distributions of transparent objects. It was developed by Mach and Zehnder in 1892 [1]-[2]. Now-a-days it has been used for many applications such as electro-optic switch, modulator, optical sensor, wavelength filters, multiplexers etc [3]-[7]. Directional coupler, Y-shaped splitter, multimode interference coupler etc are used as power splitter and combiner in Mach-Zehnder interferometer [8]-[10]. Electro-optic based 2x2 MZI optical switch using directional coupler requires materials with high nonlinear characteristics such as LiNbO3, KNbO3 etc [11]-[14]. LiNbO3 shows some advantages of having zero residual birefringence, less complexity, high electro-optic coefficient, high speed of operation but it is subjected to polarization sensitivity [8]. Such switches are suitable for time division signal processing and signal routing. Andy W. Brown and Min Xiao demonstrated an all-optical two-port signal router [15]. Ruiqiang Ji experimentally investigated a spatially non-blocking five-port optical router based on micro-ring resonators, which was tuned through the thermo-optics effect and 12.5 Gbps high-speed signal transmission rate was obtained [16]. S. K. Raghuwanshi analytically demonstrated a 1x4 signal router based on 2x2 electro-optic MZI switch and showed the variation in output power due to change in control signal [17]. Santosh Kumar constructed a 1x8 signal router with the application of control signal [18]. As demand for systems with higher capacity is increasing rapidly, so to adapt and to build a large optical cross-connect (OXC) for wide-area communication network and also to provide high-speed interconnections between a no of processors in a parallel, distributed computing system [19], signal router with high configuration is required. In this paper we will demonstrate a 1x16 signal router based on electro-optic effect. Section II represents basics of electro-optic switch, section III shows the construction of 1x16 signal router and section IV shows the simulation results and section V gives a conclusive study.

II. BASICS OF ELECTRO-OPTIC SWITCH

Electro-optic effect is referred to the change in the optical properties of a material with varying electric field. The term includes a number of distinct phenomena, which are, i) the change of the absorption coefficient and ii) the change of the refractive index and permittivity. Second term is referred to Pockels effect i.e. the change in the refractive index which is linearly proportional to the change in electric field. Only certain crystalline solids show the Pockels effect like $LiNbO_3$, $KNbO_3$, $NH_4H_2PO_4$, (ADP), KH_2PO_4 (KDP), $LiTaO_3$ and CdTe etc. The relation of refractive index n with applied electric field E is given below [20].

$$n(E) = n + a_1 E + \frac{1}{2} a_2 E^2 + \cdots \tag{1}$$

The change in refractive index and the resulting change is phase can be calculated by equation 2 and equation 3 [17].

$$\Delta n = (\frac{n^3}{2}) rE \tag{2}$$

$$\Delta\varphi = \frac{2\pi}{\lambda}[(\frac{n^3}{2}) rE] L. \tag{3}$$

L describes substantial length required to obtain certain phase change for directing light into desired path, which is for a 2x2 MZI electro-optic switch 10000 µm and r represents the

978-1-4673-9257-0/15/$31.00 ©2015 IEEE

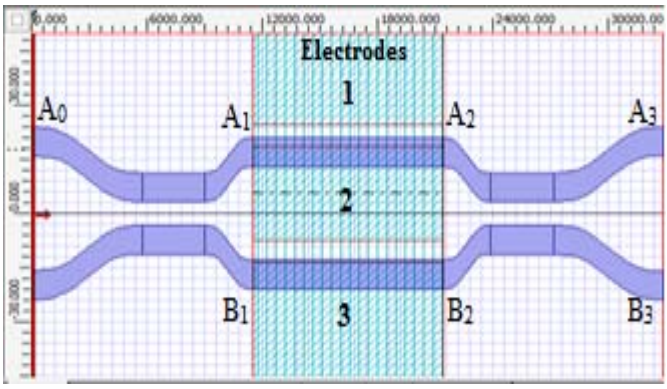

Fig. 1. 2x2 Mach-Zehnder electro-optic switch.

electro-optic coefficient and for $LiNbO_3$, it is 3.66×10^{-10} m/V. Now, if we consider that the voltage difference between two electrodes shown in Fig. 1 is V and d is the distance between the electrodes, then electric field is V/d. So, we can write

$$\Delta\varphi = \frac{2\pi}{\lambda}[(\frac{n^3}{2})\frac{V}{d}r]L. \tag{4}$$

When applied voltage is 0 V, phase change i.e Δφ become zero and with voltage V the phase change Δφ is π. This particular voltage is called V_π and is given by,

$$V_\pi = \frac{\lambda}{n^3}\frac{1}{r}\frac{d}{L}. \tag{5}$$

Now let us find power at output ports of the switch. From Fig. 1 we can see that inputs at first directional coupler i.e to the power splitter denoted as A(Z) and B(Z), which are described by the following equations [21].

$$A(\mathrm{Z}) = \{[\cos(qz) + j\frac{\delta}{q}\sin(qz)]A(0) - j\frac{k}{q}k\sin(qz)B(0)\}\exp(-j\delta_z) \tag{6}$$

$$B(\mathrm{Z}) = \{-j\frac{k}{q}\sin(qz)]A(0) + [\cos(qz) - j\frac{\delta}{q}\sin(qz)]B(0)\}\exp(j\delta_z) \tag{7}$$

Here q represents the number of local peaks of electric field propagating along the x and y-axis directions and given by

$$q = \sqrt{(k^2 + \delta^2)} \tag{8}$$

And also,

$$\delta = 2\pi\left(\frac{l_1 - l_2}{\lambda}\right) \tag{9}$$

In equation 9, l_1 represents the coupling length of the upper waveguide, where l_2 is the coupling length of the lower waveguide and k is the wave number. Let us consider that the case light is launched into the upper waveguide of a MZI. Since both arms have the same waveguide structures; so, δ=0 which results in, $A(0)=A_0$ and B(0)=0. Here the first coupler which functions as power splitter is a 3-dB coupler with kl=π/4, so the light splitting ratios can be written as,

$$A_1 = A_0\cos(kl) = \frac{A_0}{2} \tag{10}$$

$$B_1 = -jA_0\sin(kl) = -j\frac{A_0}{\sqrt{2}} \tag{11}$$

l is the coupling length. After light being traveled through the interferometer arms, the output from these arms A_2 and B_2 will be,

$$A_2 = A_1\exp(-j\beta L) = \frac{A_0}{\sqrt{2}}\exp(-j\beta L) \tag{12}$$

$$B_2 = B_1\exp(-j\beta L + J\varphi) = -j\frac{A_0}{\sqrt{2}}\exp(-j\beta L + j\varphi) \tag{13}$$

L is the length of switching region and φ represents an excess phase shift at the second arm of the interferometer. The second coupler is also a 3-dB coupler where kl=π/4. So, the outputs are given by [20],

$$|A_3|^2 = |A_0|^2.\sin^2(\frac{\varphi}{2}) \tag{14}$$

$$|B_3|^2 = |A_0|^2.\cos^2(\frac{\varphi}{2}) \tag{15}$$

If the voltage applied is 0 V, then φ = 0, the output will be switched to the lower port as $|B_3|^2 \approx |A_0|^2$. With the certain applied voltage for which φ =π, the output will be switched to the upper port as $|A_3|^2 \approx |A_0|^2$. For a 1x16 signal router the same theory is applied, only difference is that 16 control signal is to be varied to launch light to the desired port.

III. Construction of 1x16 Signal Router

To design a 1x16 signal router, 16 individual 2x2 MZI switches are required. No of switches could not be minimized, because it will either increase the width of the device or electrodes will overlap each other. The device then will not function accurately. Titanium diffused lithium niobate waveguide is used to design MZI switch. The switch is made on Z-cut wafer of lithium niobate with air surrounding. It is not more than 33000 μm long and 100 μm wide. The waveguide has a width of 8.0 μm along X-axis. In 3D wafer properties air is defined as coating material with thickness of 2.0 μm and substrate is defined as lithium niobate with a thickness of 10 μm. Three electrodes created on buffer layer with 0.3 μm thickness and refractive index of 1.47. The buffer layer has horizontal and vertical permittivity of the order of 4.

TABLE I. SIMULATION PARAMETERS.

Reference index	Modal
Wavelength	1.55 µm
Polarization	Transverse magnetic (TM)
Mesh-number of points	2000
BPM solver	Paraxial
Engine	Finite Difference
Scheme parameter	0.5
Propagation step	1.3
Boundary condition	Transparent Boundary Condition (TBC)

Thickness of each electrode is 4.0 µm. Both first and third electrodes have a width of 50 µm with zero voltage applied. The second electrode is defined with a width of 26 µm and voltage of 0 V. The separation of 1-2 and 2-3 is 6 µm. Table I shows the list of simulation parameters.

Before constructing 1x16 signal router we optimized the device parameters. Best performance was found for 0.0775 µm titanium strip thickness, 8 µm waveguide width, 9900 µm arm length, 34 µm arm gap, 14.5 µm 3dB coupler gap with outputs at 0 V, 0.000437526 mW and 0.997974 mW and at 8.8 V, 0.997974 mW and 0.000437526 mW for port 1 and 2 respectively. As a result we obtain 33.581 dB extinction ratio and 0.00881 dB insertion loss, 0.0069 dB excess loss for both cross state and bar state [22], where in reference [8] lowest insertion losses were 0.0138 dB and 0.0129 dB & maximum extinction ratios were 30 dB and 29.9 dB for cross sate and bar state respectively obtained with titanium strip thickness of 0.0825 µm. In figure 2,3,4,5,6 simulation results for optimized electro-optic 2x2 MZI switch are shown. Fig. 2 shows refractive index propagation of the optimized device.

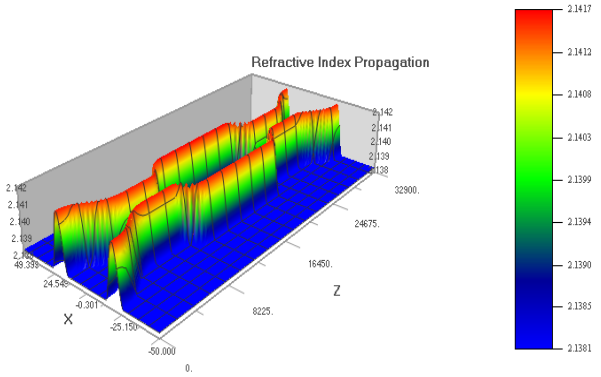

Fig. 2. Refractive index propagation of MZI switch (3D view) .

Optical field propagation for both 0V and 8.8 V are shown in Fig. 3. Fig. 4 ensures that light is switched completely from port 1 to port 2 with the application of applied voltage. It takes 11 iterations to switch light from port 1 to port 2. Fig. 5 represents power in output waveguides for a voltage range of

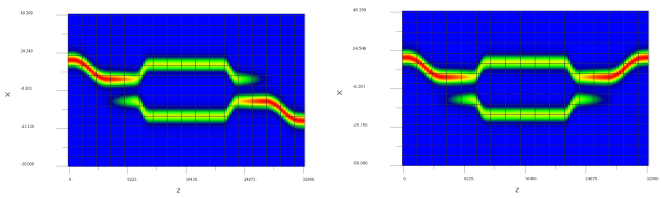

Fig. 3. Optical field propagation at 0 V and 8.8 V respectively.

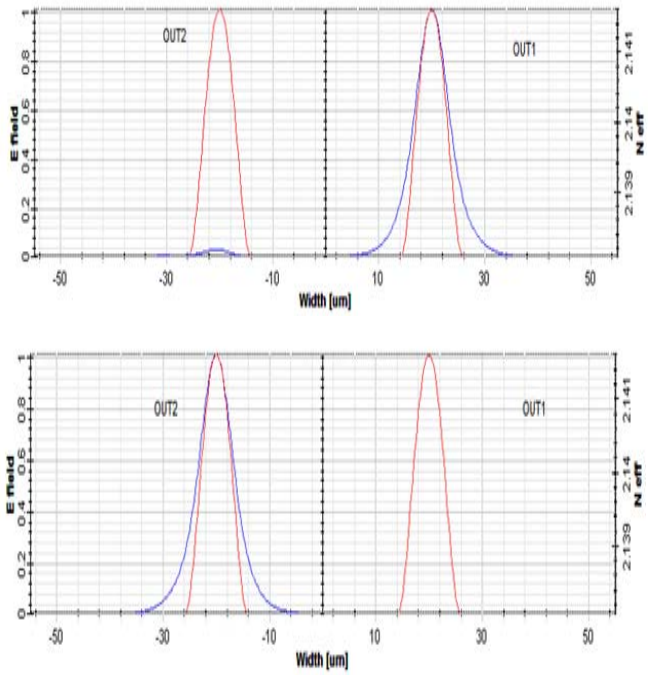

Fig. 4. Electric field at 0V and 8.8 V respectively.

0 V to 8.8 V and from Fig. 6 we can observe power overlap integral characteristics versus distance of propagation of waveguide for both low and high voltage. These results are obtained by running the following visual script,

Const NumIterations = 11

ParamMgr.SetParam “V2”, 0.0

For x= 1 to NumIterations

Param Mgr. Simulate

Param Mgr. Set Param “V2”, 0.8* x

WGMgr.Sleep (50)

Next

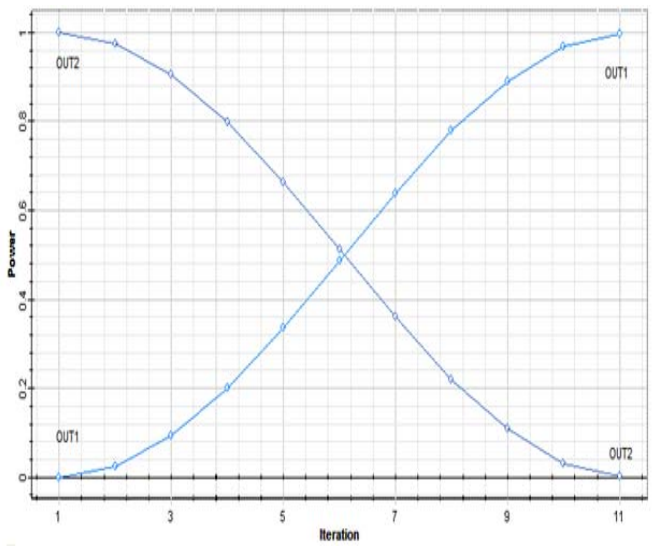

Fig. 5. Power in output waveguides.

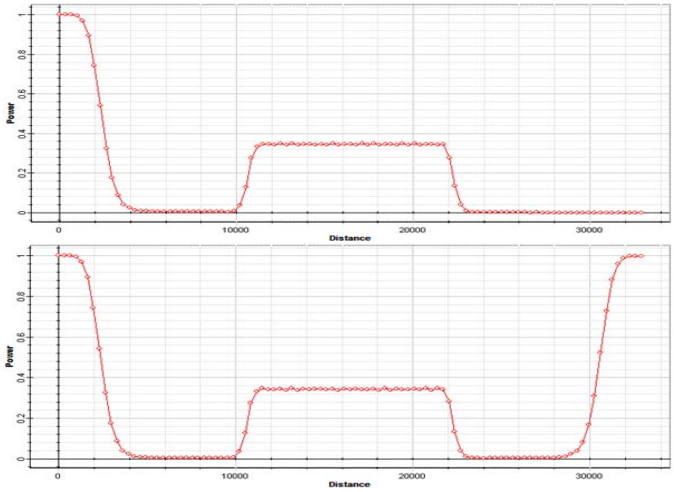

Fig. 6. Power overlap integral at 0V and 8.8 V respectively.

Fig. 7 and Fig. 8 show the layout and refractive index propagation of 1x16 signal router respectively. Central electrode of each switch was positioned 5.5 µm above from the original axis.

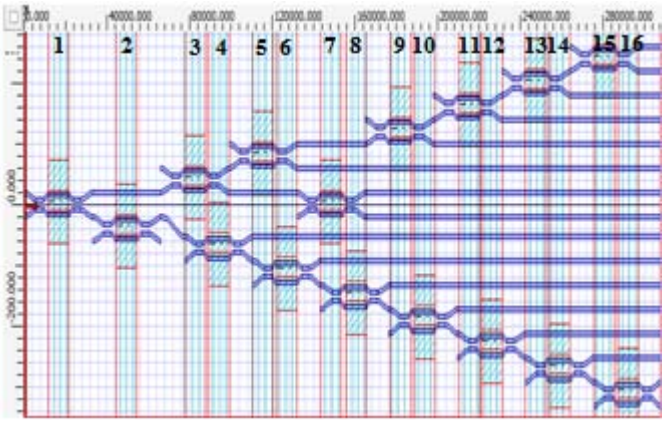

Fig. 7. Layout of 1x16 signal router.

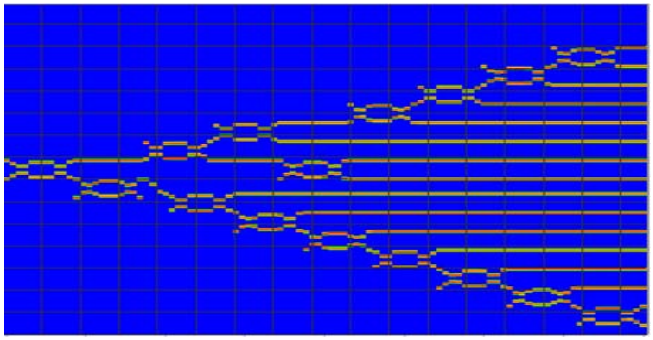

Fig. 8. Refractive index propagation of 1x16 signal router.

MZI switches are numbered as 1, 2, 3 and so on. we assumed the second electrode of each switch as control electrode and they are also numbered similarly as S_1, S_2, S_3 etc.

IV. Simulation Results

Results are observed by OptiBPM software. From Fig. 7 we can see that there are 16 output ports. To switch power into one of these ports particular combination of voltages across the central electrodes of these 16 MZI switch is required. The width of this structure is not more than 700 µm and length is not more than 307600 µm. Table II shows output power at 16 different ports on the basis of control signal S_1, S_2, S_3, S_4, S_5, S_6, S_7, S_8, S_9, S_{10}, S_{11}, S_{12}, S_{13}, S_{14}, S_{15}, S_{16} representing voltages across central electrodes of 16 switch respectively. In table II logic 0 represents 0 V and logic 1 represents 8.8 V and X represents don't care condition. S_1 is kept high to switch upper 8 output ports and with S_1 low lower 8 output ports are to be switched. When S_1 is high output goes to MZI 3, with S_3 kept at 0 V output goes to MZI 5, again with S_5 low output goes to MZI 9, with S_9 low output goes to MZI 11, consequently with S_{11}, S_{13}, S_{15} low output goes to the output port 1. Similarly for each of the combinations shown in table II we can find high output at desired output port. Fig. 9 shows the optical field propagation at different output ports.

TABLE II. Different combinations of control signal of 1x16 signal router.

Output	S_1	S_2	S_3	S_4	S_5	S_6	S_7	S_8	S_9	S_{10}	S_{11}	S_{12}	S_{13}	S_{14}	S_{15}	S_{16}
Port 1	1	X	0	X	0	X	X	X	0	X	0	X	0	X	0	X
Port 2	1	X	0	X	0	X	X	X	0	X	0	X	0	X	1	X
Port 3	1	X	0	X	0	X	X	X	0	X	0	X	1	X	X	X
Port 4	1	X	0	X	0	X	X	X	0	X	1	X	X	X	X	X
Port 5	1	X	0	X	0	X	X	X	1	X	X	X	X	X	X	X
Port 6	1	X	0	X	1	X	X	X	X	X	X	X	X	X	X	X
Port 7	1	X	1	X	X	X	1	X	X	X	X	X	X	X	X	X
Port 8	1	X	1	X	X	X	0	X	X	X	X	X	X	X	X	X
Port 9	0	1	X	1	X	X	X	X	X	X	X	X	X	X	X	X
Port 10	0	1	X	0	X	1	X	X	X	X	X	X	X	X	X	X
Port 11	0	1	X	0	X	0	X	1	X	X	X	X	X	X	X	X
Port 12	0	1	X	0	X	0	X	0	X	1	X	X	X	X	X	X
Port 13	0	1	X	0	X	0	X	0	X	0	X	1	X	X	X	X
Port 14	0	1	X	0	X	0	X	0	X	0	X	0	X	1	X	X
Port 15	0	1	X	0	X	0	X	0	X	0	X	0	X	0	X	1
Port 16	0	1	X	0	X	0	X	0	X	0	X	0	X	0	X	0

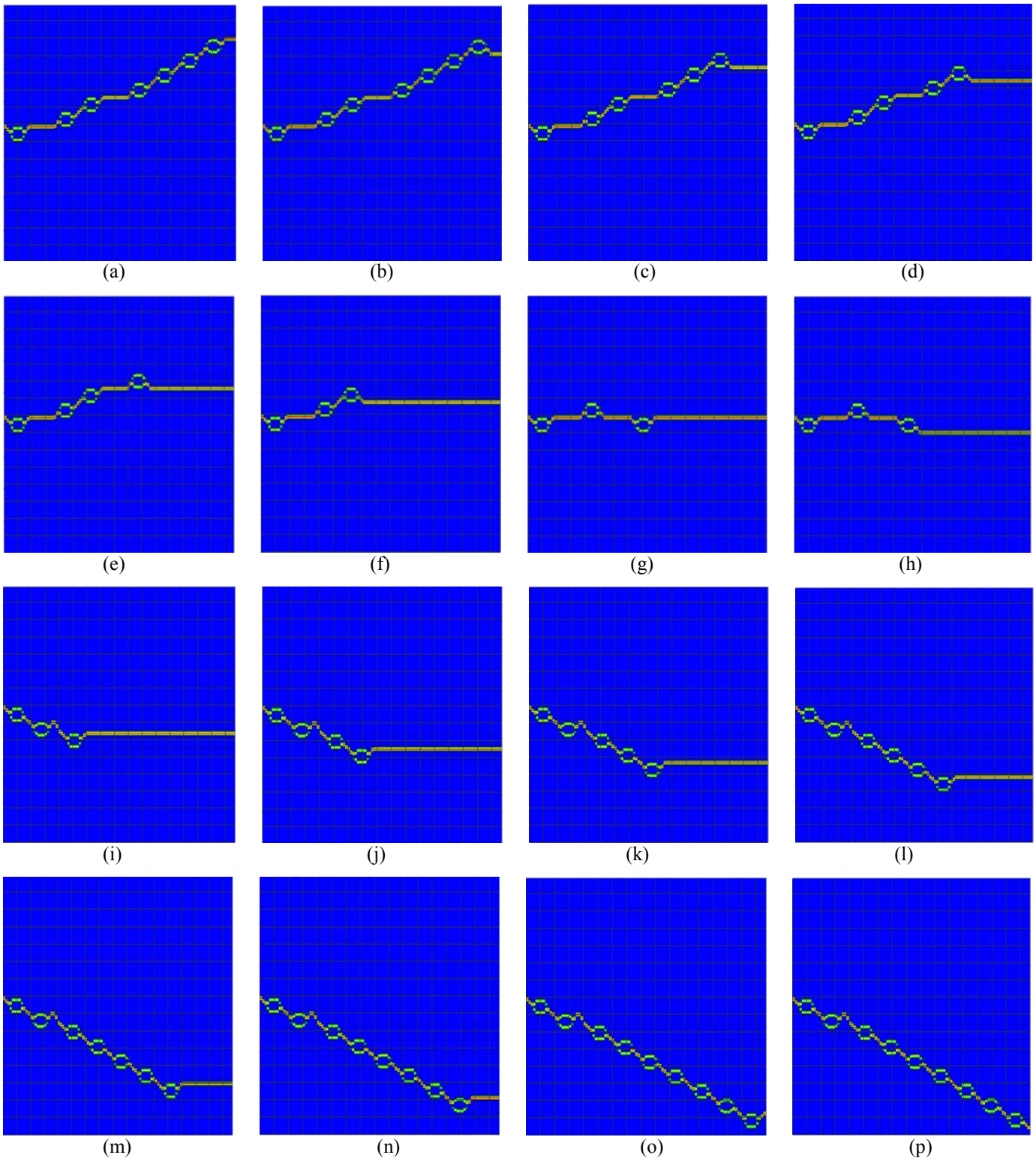

Fig. 9. Optical field propagation at (a) port 1, (b) port 2, (c) port 3, (d) port 4, (e) port 5, (f) port 6, (g) port 7, (h) port 8, (i) port 9, (j) port 10, (k) port 11, (l) port 12, (m) port 13, (n) port 14, (o) port 15, (p) port 16.

V. Conclusion

This paper gives elaborate discussion on a 1x16 signal router. 16, 2x2 electro-optic switches are used in construction, which gives the device a length of 307600 µm and width of 700 µm. At first the fundamental device i.e. MZI switch is optimized and we obtained lowest insertion loss of 0.00881 dB, excess loss of 0.0069 dB and highest extinction ratio of

33.581 dB. Then outputs for different combinations of control signals are observed and we find power being switched to each one of 16 output ports for each combination.

REFERENCES

[1] L. Mach, "Ueber einen Interferenzrefraktor," Z. Instrumentenk, Springer publication ,vol. 12, pp. 89-93, 1892.

[2] L. Zehnder, "Ein neuer Interferenzrefraktor," Z. Instrumentenk, Springer publication, vol. 11, pp. 275-285, 1891.

[3] G. Singh, "Design of 2×2 Optoelectronic Switch Based on MZI and Study the Effect of Electrode Switching Voltages," Journal of World Academy of Science, Engineering and Technology, vol. 39, pp. 401-407, 2008.

[4] D.J. Thomson, F.Y. Gardes, Sheng Liu, H. Porte, L. Zimmermann, J.M. Fedeli, Youfang Hu, M. Nedeljkovic, Xin Yang, P. Petropoulos, G.Z. Mashanovich, "High Performance Mach–Zehnder- Based Silicon Optical Modulators," IEEE Journal of Selected Topics in Quantum Electronics, vol. 19, issue. 6, pp. 85 – 94, November-December 2013.

[5] Xianxin Jiang, Yangqing Chen, Fang Yu, Longhua Tang, Mingyu Li, Jian-Jun He, "High-sensitivity optical biosensor based on cascaded Mach–Zehnder interferometer and ring resonator using Vernier effect," Opt. Lett., vol. 39, issue. 22, pp. 6363-6366, 2014.

[6] E.L. Wooten, R.L. Stone, E.W. Miles, E.M. Bradley, "Rapidly tunable narrowband wavelength filter using $LiNbO_3$ unbalanced Mach-Zehnder interferometers," Journal of Lightwave Technology, vol. 14, no. 11, pp. 2530-2536, November 1996.

[7] T. Mizuochi, T. Kitayama, K. Shimizu, K. Ito, "Interferometric crosstalk-free optical add/drop multiplexer using Mach-Zehnder-based fiber gratings," Journal of Lightwave Technology, vol. 16, issue. 2, pp. 265, 1998.

[8] Nazmi A. Mohammed, Huda S. Abo Elnasr, Moustafa H. Aly, "Performance Evaluation and Enhancement of 2×2 Ti: $LiNbO_3$ MachZehnder Interferometer Switch at 1.3 µm and 1.55 µm," The Open Electrical & Electronic Engineering Journal, vol. 6, pp. 36-49, 2012.

[9] Jing Wang, Minghao Qi, Yi Xuan, Haiyang Huang, Zhen Sheng "Ultrabroadband Silicon-on-Insulator Polarization Beam Splitter Based on Cascaded Mode-Sorting Asymmetric Y-Junctions," IEEE Photonics Journal, vol. 6, no. 6, article #. 2700608, December 2014.

[10] Shaochun Cao, Liping Sun, M. Savoie, "2×2 MMI-MZI GaAs-GaAlAs carrier-injection optical switch," Photonics Society Summer Topical Meeting Series, 2010 IEEE, pp. 207-208, 19-21 July 2010.

[11] Nazmi A. Mohammed , Huda S. Abo Elnasr , Moustafa H. Aly, "Analysis and design of an electro-optic 2 × 2 switch using Ti: $KNbO_3$ as a waveguide based on MZI at 1.3µm," Opt Quant Electron (springer journal), vol. 46, pp. 295–304, 2014.

[12] M. P. Earnshaw, " 8×8 Optical Switch Matrix Using Generalized Mach–Zehnder Interferometers," IEEE Photonics Technology Letters, vol. 15, no. 6, pp. 810-812, 2003.

[13] T. Sasaki, H. Sato, K. Nakatsuhara, T. Nakagami, "Demonstration of switching operation in a symmetric Mach-Zehnder interferometer switch using Si waveguide with a ferro-electric liquid crystal cladding," Conference on Lasers and Electro-Optics-Pacific Rim, pp. 1-2, 26-31 August 2007 .

[14] K. Suzuki, "High-Speed Optical 1×4 Switch Based on Generalized Mach–Zehnder Interferometer With Hybrid Configuration of Silica-Based PLC and Lithium Niobate Phase-Shifter Array," IEEE Photonics Technology Letters, vol. 19, no. 9, pp. 674-676, May 2007.

[15] Andy W. Brown, Min Xiao, "All-optical switching and routing based on an electromagnetically induced absorption grating," Opt. Lett., vol. 30, pp. 699-701, 2005.

[16] Ruiqiang Ji, Lin Yang, Lei Zhang, Yonghui Tian, Jianfeng Ding, Hongtao Chen, Yangyang Lu, Ping Zhou, Weiwei Zhu, "Five-port optical router for photonic networks-on-chip," Opt. Express, vol. 19, issue. 21, pp. 20258-20268, 2011.

[17] S. K. Raghuwanshi, A. Kumar, S. Kumar, "1×4 Signal Router Using 3 Mach-Zhender Interferometers," Opt. Eng., vol. 52, no. 3, pp. 035002, 2013.

[18] Santosh Kumar, Sanjeev Kumar Raghuwanshi, Ajay Kumar, "Implementation of optical switches using Mach–Zehnder interferometer," Optical Engineering, vol. 52, no. 9, pp. 097106, September 2013.

[19] Michael J. O'Mahony, "Future Optical Networks," IEEE Journal Of Lightwave Technology, vol. 24, no. 12, pp. 4684-4696, December 2006.

[20] Bahaa E. A. Saleh, Malvin Carl Teich, "Fundamentals of Photonics," Publisher: John Wiley & Sons, Inc. ISBNs: 0-471-83965-5 (Hardback), 0-471-2-1374-8 (Electronic), pp. 698, 1991.

[21] Katsunari Okamoto, "Fundamentals of Optical Waveguides," Laboratory Ltd Ibaraki: Japan, 2nd ed., pp. 195-196, 2006.

[22] Rabeya Khatun, Kazi Tanvir Ahmmed, A. Zahed Chowdhury, Raqibul Hossen, "Optimization of 2x2 MZI Electro-Optic Switch and Its Application as Logic Gate," 18th International Conference on Computer and Information Technology, 2015, in press.

Enhanced Wi-Fi Direct Power Saving with Power Control for the Mobile Phone

Nam Gon Kim[1,*], Hyun Hak Cho[1], Chang Min Eun[1], and Ok Hyun Jeong
[1]Department of Electronic Engineering, Sogang University, Seoul, Republic of Korea
[*] E-mail: kimngon88@sogang.ac.kr

Abstract— **Wi-Fi Direct, that is a peer-to-peer specification based on IEEE 802.11 standard by Wi-Fi Alliance, defines the role of power saving mechanism. However, it indicates only basic rule and does not specify effective environment and the way of configuration for each parameter. In this paper, we studied the way of the optimizing Power Save Mode (PS Mode) for Wi-Fi Direct in the mobile. To maximize efficient of the PS Mode, we dynamically controlled sleep period each fixed a beacon signal period, called Target Beacon Transmit Time (TBTT) and we adapted power control scheme based on IEEE 802.11. As a result, to schedule sleep period of NoA on the power control has a benefit for the total transmission time and power consumption.**

Keywords—Wireless LAN, Wi-Fi Direct, Power Save Mode (PS Mode), Notice of Absence(NoA) protocol.

I. INTRODUCTION

In the last decade, as a variety of mobile devices including tablet PC and mobile phone have been spread and communication technology has advanced rapidly, the data traffic has increased exponentially. Device-to-device communication, such as Wi-Fi Direct using a wireless LAN has emerged to distribute traffic based on the communication technology of at least 150Mbps speed of 4G. It was not a big issue in the past, because AP is connected to an external power source without mobility. However, recent mobile devices have a high degree of mobility and use simultaneously other wireless communication such as LTE and GPS so it increases load on the mobile phone. In other words, the continuity of battery without any external power source is arising as main issue.

For this purpose, Wi-Fi Alliance has published a new standard called Wi-Fi Direct (Wi-Fi P2P) by making up for a low-speed communication in ad-hoc network and a problem based on infrastructure in conventional wireless LAN based on IEEE 802.11 [2]-[3]. Specially, it describes efficient communication methods by concurrent operation, service discovery and power saving. We studied with a focus on PS Mode because the transfer of data payload occupies a large portion on data transmission.

Wi-Fi Direct defines two way of power saving: the Opportunistic Power Save (OppPS) and the Notice of Absence (NoA) in technical specification. OppPS Protocol is a method of determining the sleep state of Group Owner (GO) whether the clients send the data using the beacon signal. On the contrary, NoA Protocol is a method for determining a transmission timing of the client in accordance with the state of GO through the beacon signal. However, the standard defines only basic transmission Protocol. It is difficult to use the protocols of PS Mode to specify parameter configuration without describing the criteria.

Therefore, we studied how to set up efficiently the parameter of PS Mode utilizing the IEEE 802.11 network and how to optimize PS mode to avoid the ambiguity of configuration without additional overhead. Thereby, we intended to reduce the power consumption of peer-to-peer communication in the mobile environment. In this paper, we have experimented that controlling the sleep period and transmission power level of the Wi-Fi Direct using the channel information for efficient parameter setting.

We tested using the Network Simulator-3 that operates based on the C ++ in Linux OS. We tried the simplest structure with two mobile devices, each GO and Client is connected 1:1 peer-to-peer network. The simulations have been performed by modifying the number of the power level of transmission for power control and the count for NoA parameter. Namely, the simulation has been conducted by changing the sleep period and transmission level each channel state during a fixed TBTT to compare the basic operation of NoA protocol.

The paper is organized as follows. Chapter 2 reviews the background and proposal. It shows that simulation is conducted how to setup the experimental environment in chapter 3. It indicates results of implementation and analysis of performance in chapter 4. Lastly, chapter 5 sets out the conclusions of this paper.

II. BACKGROUND AND PROPOSAL

First, we discuss power save mechanism of IEEE 802.11 and Wi-Fi Direct. Then, we consider the propriety of using the power control for the power saving. Finally, we propose optimizing the Wi-Fi Direct power saving with power control scheme.

978-1-4673-9257-0/15/$31.00 ©2015 IEEE

A. Related work

As specified in the standard [3], a WLAN based on IEEE 802.11 is available a power save mechanism for the power management. It determines the AP with other station to stay in one of the states; idle, awake, or sleep. In IEEE 802.11, the AP on PSM periodically announces state to mobile stations through the Traffic Indication Map (TIM) contained in the beacon frames. The stations wake up periodically to listen to the beacon from the sleep state. Similarly, Wi-Fi Direct also defines two power management protocols [2]. The OppPS protocol is advantageous for burst data transmission when it comes to the power consumption. In contrast, the NoA protocol has profit to transmit dynamic data traffic with the Delivery Traffic Indication Map (DTIM) for power consumption [7].

Another approach about the power management is the power control. Several power/rate adaptation mechanisms have been proposed for multiple rates supported by 802.11 [13]-[14]. For example, Multi-rate adaptation algorithms were proposed to improve throughput performance in ad hoc networks. Another rate control algorithms are developed specifically to extend past algorithms with power control. However, power or rate adaptation algorithms use to minimize interference among neighboring Stations.

In Wi-Fi Direct, only channel 1, 6 and 11 are employed because they have low degree of interference. We need to shift the usage of power adaptation algorithm for its usage to only adjust the power level of RF channel.

B. Proposed method

To increase the efficiency of the NoA protocol, we applied the power control scheme to power saving mechanism. The power control scheme is an efficient scheme to reduce the channel interference caused to use adjacent channels. However, because of using less interference channel in Wi-Fi Direct, we exert the power control scheme to adjust the transmission power level for reducing power consumption. Also, we have to limit the maximum transmission level to mobile environment. The experiments have been performed with Power-controlled Auto Rate Fallback (PARF) algorithm [5] for power control as changing the two factors and optimizing the parameter.

III. Experimental Environment

A. The setup of simulator

We modified the C++ code of Wi-Fi module which had been implemented in ns-3 and we implemented a NoA protocol of Wi-Fi direct communication. Ns-3 contains various models of high-quality validated and is spread over a large community of users and developers [4]. The simulation models a wireless network interface controller based on the IEEE 802.11 standard [3]. The IEEE 802.11 MAC protocol is implemented with several C++ classes on ns-3. We have simulated based on Broadcom's BCM4335 chipset for power model of realistic environments. The results of simulation were verified transmitted packets with Wireshark [6]. Only to analysis the NoA protocol through the data transfer, we simulated without device discovery, service discovery and group formation on Wi-Fi Direct. Also, to analysis the transfer a single MPDU, we simulated an 802.11g. Table 1 indicates the configuration of the power module for Wi-Fi Direct.

For wireless systems, the radio channel is the propagation loss and propagation delay model and ignore real-world effects such as multipath fading and channel capture. First, we have to examine the effects of the number of power level of transmission and the count of NoA parameter. Then, we implemented and experimented dynamic scheduling the sleep period according to the channel state on power control scheme. The available transmission is a minimum 0 dBm and maximum 16 dBm.

TABLE I. The Configuration of Power Module in NS-3

Parameter	Value
Target Chipset	BCM4335, Broadcom
Standard	802.11g / 54Mbps (OFDM)
Input Voltage	3.6V
Sleep Current	0.1mA
Tx Current	76mA

B. The network architecture of experiment

The network structure for the experiment can be seen in Fig 1. Only for two mobile devices, GO and Client is connected 1:1 peer-to-peer network. We confirmed by transmitting a packet for 60 seconds on condition that the respective parameters of NoA were changed. During 60 seconds, the Client is moved 30 meters at the GO where is 5 meters away. It stays during every 15 seconds. After that time, it is placed a new position where is 10 meters away from previous position. In other words, the distance increases 10 meters per 15 seconds. Consequentially, the position of the Client has a different channel conditions respectively. The TBTT for NoA parameter is 10.24ms; the sleep period was a 50% duty cycle. Outputs for power consumption in the simulation showed to watt.

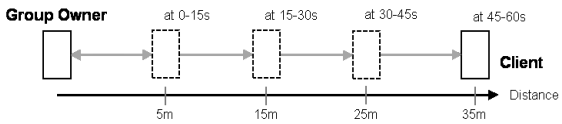

Figure 1. The network structure for the simulation

IV. Analysis of Simulation Result

A. The configuration of NoA parameter

The NoA protocol of PS Mode timing is scheduled by the values of Start time, Interval, Duration and Count. The Start time is the start time of NoA schedule. The Interval indicates the absence time. The Duration is the period of each absence. The Count is the number of absences. GO announces every beacon message to client with these four parameters. GO

978-1-4673-9257-0/15/$31.00 ©2015 IEEE

changes the state at determined time, Client keeps NoA schedule most recently received. The example of operation for P2P GO NoA protocol with power control is shown as Fig 2.

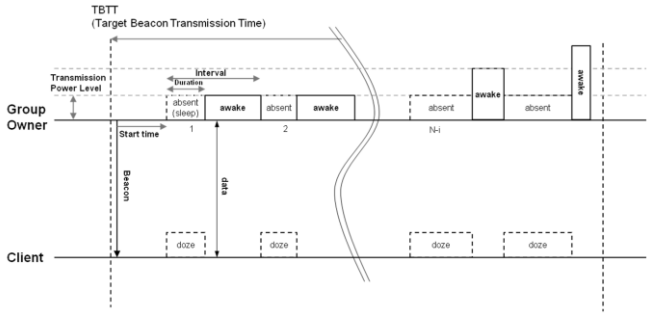

Figure 2. The example of operation for P2P GO NoA protocol with power control

1) *The number of transmission power levels*

First, we have carried out the simulation to verify the effect of power control. When the data is transmitted from WLAN devices, the maximum transmission power is typically 16~20 dBm. To use the adaptation of power control, we configured 16 dBm for maximum powers. The number of transmission power levels available between 0 dBm and 16 dBm and we turned from 4 to 16 sequencely raising 2 degrees. The Count is configured 4. At the rate of awake and sleep, that is duty cycle, is 50%.

2) *The number of count*

Next, it was set equal to a total time of transmitting the data for performance comparison of each experiment. In other words, the total processing time multiplied by the time of interval and count was configured the same one scheduling period of NoA. And by increasing the count from 4 to 12, simulation was performed with maintaining a TBTT. The setup of dividing maximum transmission level is 4. And duty cycle is fixed to 50%.

3) *The optimization of the NoA parameter*

Last, we simulated the proposed optimizing Wi-Fi Direct PS mode with power control. The simulation is conducted by scheduling sleep period and changing transmission power level according to the channel conditions. In the channel condition which is deteriorated in step 4 shown as Fig 1.; Case 1 is that sleep period is fixed the ratio of the awake and sleep time by one-to-one, the 50 percent of duty cycle. Case 2 has the time of scheduling sleep period from 87.5 to 12.5 percent per 15 seconds when the packets are transmitted. In contrast, in Case 3, the packets are transmitted with increasing the duty cycle from 12.5 to 87.5 percent. All of these cases are configured 4 as the number of transmission power level and count.

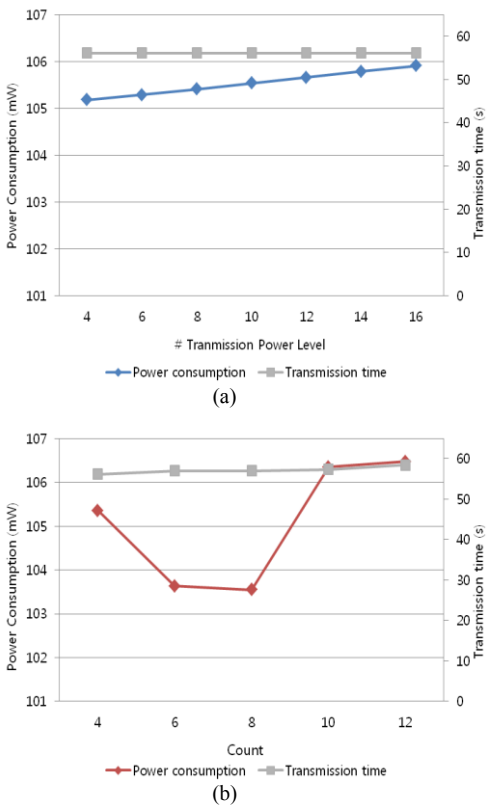

Figure 3. (a) The power consumption with the number of transmission power levels (b) The power consumption with the number of count

B. *The result of simulation*

1) *The number of transmission power levels*

We were tested by varying the number of transmission power level. In 4 to 16 levels, the power consumption was observed that the more the number of transmission power level, the more power consumption is represented. This could be the result of increasing the frequency of performing power adaptation according to the channel state for the more number of power level. The power consumption with changing the number of transmission power levels is shown in Fig 3-(a).

2) *The number of counts*

Fig 3-(b). shows power consumption with the count of NoA. The following are the results of experiments by changing the count of the NoA protocol. As the count is smaller as shown in the graph, power saving effect is larger until 8. For the total transmission time, it also completed a transmission in the first but it was little difference. While the effect of power saving is improved in infrequent scheduling and flat channel cases, it has the disadvantage that it is impossible to change flexibly the parameters due to less frequency of the scheduling in the channel which has large fluctuation. Eventually, the efficiency of NoA power saving as to the count is expected to be influence by the variation rate of channel state.

978-1-4673-9257-0/15/$31.00 ©2015 IEEE

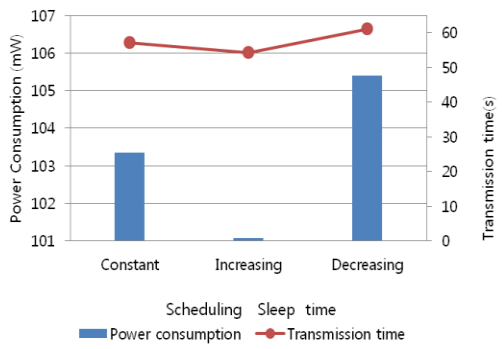

Figure 4. The power consumption in accordance with the way of dynamic scheduling.

3) *The optimization of the NoA parameter*

Finally, It is confirmed that the case 2 (Increasing sleep time) is presented the best performance in terms of the total transmission time and power consumption. Conversely, the result of case3 has the most power consumption and long transmission time. This is because the case 2 was scheduled a way to increase the capability of the transmission with NoA protocol as the transfer consumes less power when a good channel at power adaptation algorithm. As a result, it can be seen that the case 2 of performance is the best way better than 3.34% in the constant case. The power consumption in accordance with the way of dynamic scheduling is shown as Fig 4.

V. CONCLUSION

This paper has mentioned about how to use the Wi-Fi direct based on IEEE 802.11 as it is widely popular in recent years, and prepared to seek how to use a little more effective PS Mode for an increasingly important power issue. In the environment for performing power adaptation scheme according to the channel condition of the Wireless LAN, to use the NoA scheduling protocols in an efficient manner, it is good to scheduling by dividing appropriately according to the number of transmission power level in the environment and reducing the value of count in the maximum flexibility. Above all things, it is that the way to improve the power efficiency using the NoA protocol scheduling is to secure the awake time in good channel and to increase the frequency of the scheduling with the maximum flexibility in poor channel.

ACKNOWLEDGMENT

“This research was supported by the MSIP(Ministry of Science, ICT and Future Planning), Korea, under the C-ITRC(Convergence Information Technology Research Center) (IITP-2015-H8601-15-1004) supervised by the IITP(Institute for Information & communications Technology Promotion)"

REFERENCES

[1] (2015) The Wi-Fi Alliance website. [Online]. Available: http://Wi-fi.org

[2] Wi-Fi Alliance, P2P Technical Group, Wi-Fi Peer-to-Peer (P2P) Technical Specification v1.5, Wi-Fi Alliance, Aug. 2014.

[3] IEEE 802.11-2007 Standard, Wireless LAN Medium Access Control (MAC) and Physical Layer (PHY) Specifications, IEEE std. 802.11, 2012

[4] (2015) The ns-3 simulator website. [Online]. Available: http://www.nsnam.org.

[5] Aditya Akella, Glenn Judd, Srinivasan Seshan, and Peter Steenkiste, “Self-management in chaotic wireless deployments,” in *ACM Int. Conf. Mobicom.*, Jun. 2005, pp. 737–755.

[6] (2015) Wireshark: A Network Protocol Analyzer website. [Online]. Available: http://www.wireshark.org/

[7] D. Camps-Mur, A. Garcia-Saavedra, and P. Serrano, “Device-to-Device Communications with Wi-Fi Direct: Overview and Experimentation,” *IEEE Wireless Communications, vol. 20, no. 3*, pp. 96-104, Jun 2013.

[8] D. Camps-Mur, X. Perez-Costa, S. Sallent-Ribes, “Designing energy efficient access points with Wi-Fi Direct,” *ACM Computer Networks: The International Journal of Computer and Telecommunications Networking, vol. 55*, pp. 2838-2855, Sep 2011.

[9] Shojiro Takeuchi, Kosuke Yamazaki, Kaoru Sezaki, and Yasuhiko Yasuda “An Improved Power Saving Mechanism for MAC Protocol in Ad Hoc Networks,” in *Proc. IEEE int. conf,* Nov 2004. pp. 2791-2796.

[10] ByungGi Lee and SungHyun Choi, *Broadband wireless access and local networks: mobile WiMax and WiFi* , Artech House, 2008

[11] Walke and Bernhard H, *IEEE 802 wireless systems : Protocols, Multi-hop Mesh/Relaying, Performance and Spectrum Coexistence*, John Wiley & Sons, 2007

[12] Perahia, Eldad, Stacey, and Robert, *Next Generation Wireless LANs Throughput, Robustness, and Reliability in 802.11n, 802.11ac*, Cambridge University Press, 2013

[13] B. Sadeghi,V. Kanodia, A. Sabharwal and E. Knightly, “Opportunistic media access for multi-rate Ad Hoc networks”, *in Proc. ACM int. Conf. MobiCom.*, Sep 2002, pp. 24–35.

[14] A. Santhanam and R. Cruz, “*Optimal routing, link scheduling and power control in multi-hop wireless networks*”, in. *Proc. IEEE Int. Conf. Infocom.*, Apr 2003, pp. 702–711.

978-1-4673-9257-0/15/$31.00 ©2015 IEEE

PAPR Reduction of OFDM System Using Condex Matrix Based SLM Method with Low Computational Overhead

Md. Moshiur Rahman*, Muhammad Sajjadur Rahim†, Md. Nur Al Safa Bhuiyan‡ and Sabbir Ahmed§
Department of Information and Communication Engineering
University of Rajshahi, Rajshahi-6205, Bangladesh
Emails:*mintu_apee@yahoo.com, †sajid_ice@ru.ac.bd, ‡safa@ru.ac.bd, §sabbir@ru.ac.bd

***Abstract*—High Peak-to-Average Power Ratio (PAPR) is one of the main drawbacks that may limit practical applications of Orthogonal Frequency Division Multiplexing (OFDM) System. Based on the well known Selective Mapping (SLM) method of PAPR reduction, in this paper, we propose a new phase sequence generation technique from Condex matrix that can achieve better PAPR reduction compared to the generally used Bauml sequence. From the simulation results, we show that our proposed phase sequence achieves 4.0 dB higher PAPR reduction compared to original SLM method and also reduces the computational overhead about 59 percent.**

***Keywords*—OFDM; PAPR; SLM; condex matrix**

I. Introduction

The concept of Orthogonal Frequency Division Multiplexing (OFDM) in terms of parallel data transmission and frequency division multiplexing was first developed in the 50s [1]. It offers a considerable high spectral efficiency, multipath delay spread tolerance, immunity to frequency selective fading and so forth [2]. At present, OFDM is considered as a strong candidate for the next generations of mobile communication systems. However, one significant problem with OFDM systems is that it can give rise to very high values of Peak-to-Average Power Ratio (PAPR). Over the last decade, various techniques to reduce PAPR have been proposed. For example, clipping and filtering, companding and coding, multiple signal representation and so forth [3–5]. The last kind includes Selected Mapping (SLM) and Partial Transmit Sequence methods (PTS) [6, 7]. Clipping and filtering is the simplest technique but it may cause in-band distortion and out-of-band radiation. In-band distortion can not be reduced by filtering and results in performance degradation, while out-of-band radiation reduces the spectral efficiency. The coding technique does not cause distortion or out-of-band radiation, but it lacks spectral efficiency. In SLM scheme, PAPR reduction is achieved by multiplying the independent phase sequences to the original input data and determining the PAPR of each phase sequence and input data combination. The combination with the lowest PAPR is transmitted. Generally Bauml sequence, based on the value set of (± 1,$\pm j$), is used in SLM. In this paper, Condex phase sequence based SLM is proposed to reduce PAPR of OFDM signal. Here, we show that Condex matrix based sequence can be used for improved PAPR reduction capability with less computational overhead.

II. Background

A. OFDM System Model

Let us consider an OFDM system consisting of N sub-carriers in the frequency domain, where vector $X = [X_0, X_1, ..., X_{N-1}]$ denotes the input data blocks. Each symbol in X is used to modulate a sub-carrier, and the input symbol vector is called the input symbol sequence. For N-th sub-carrier, let $f_k, k = 0, 1, ...N-1$. In the OFDM system as the adjacent sub-carriers are orthogonal to each other, let, $f_k = k.\Delta f$, where $\Delta f = 1/(NT)$ and T is the symbol duration. Therefore, the complex baseband representation of the transmitted OFDM signal is given by:

$$x(t) = \frac{1}{\sqrt{N}} \sum_{k=0}^{N-1} X_k e^{j2\pi k t \Delta f}, 0 \leq t \leq NT \tag{1}$$

where $j = \sqrt{-1}$, Δf is the sub-carrier spacing, and NT denotes the useful data block period. If $x = [x_0, x_1, ..., x_{N-1}]$ denotes a discrete time OFDM signal vector, then x corresponds to the Inverse Fast Fourier Transform (IFFT) of X. that is, $x = QX$, where Q is the IFFT matrix.

B. PAPR

In general, PAPR is defined as the ratio between the maximum power and the average power for the envelope of a baseband complex signal during an OFDM symbol period. The PAPR of the OFDM signal $x(t)$ can be written as follows:

$$\text{PAPR} = \frac{\max\limits_{0 \leq t \leq T} |x(t)|^2}{E(|x(t)|^2)} \tag{2}$$

where $E[.]$ is the expectation operator which denotes the average value over the time duration of OFDM symbol. The PAPR reduction techniques are concerned with reducing max $|x(t)|$. In practical situation, the discrete-time signals are mostly used.

In OFDM system, some input sequences would result in higher PAPR than others. For example, an input sequence that requires all such carriers to transmit their maximum amplitudes would certainly result in a high output PAPR. Thus, by limiting the possible input sequences to a smallest sub set, it is possible to obtain output signals with a guaranteed low output PAPR.

Some of the important performance factors that should be considered while judging the performance of a PAPR reduction technique are PAPR reduction capability, spectral spreading, bit error rate, computational complexity, loss of data rate etc. In this paper, we focus on reduction of PAPR as well as computational complexity.

III. SLM TECHNIQUE

In the SLM technique, the transmitter generates a set of sufficiently different candidate data blocks, all representing the same information as the original data block, and selects the most favorable for transmission [6, 8]. A block diagram of the SLM technique is shown in Figure 1. Each data block is multiplied by U different phase sequences, each of length N, $B^{(u)} = [b_{u,0}, b_{u,1}, ...b_{u,N-1}], u = 1, 2, ..., U$, resulting in U modified data blocks. To include the unmodified data block in the set of modified data blocks, we set $B^{(1)}$ as the all-one vector of length N.
Let us denote the modified data block for the u_{th} phase sequence $D^{(u)} = [D_0 b_{u,0}, D_1 b_{u,1}, ...D_{N-1} b_{u,N-1}], u = 1, 2, ..., U$, after applying SLM to X, the multi-carrier signal becomes

$$d_k^{(u)} = \sum_{n=0}^{N-1} D_n.b_{u,n}.exp(\frac{j2\pi kn}{N}) \;\; 0 \leq k \leq N-1. \qquad (3)$$

Among the modified data blocks $D^{(u)}$, the one with the lowest PAPR is selected for transmission. Information about the selected phase sequence need to be transmitted to the receiver as side information. At the receiver, the reverse operation is performed to recover the original data block. For implementation,the SLM technique needs U times IDFT operations, and the number of required side information bits is $log_2 U$ for each data block. This approach is applicable with all types of modulation and any number of subcarriers.

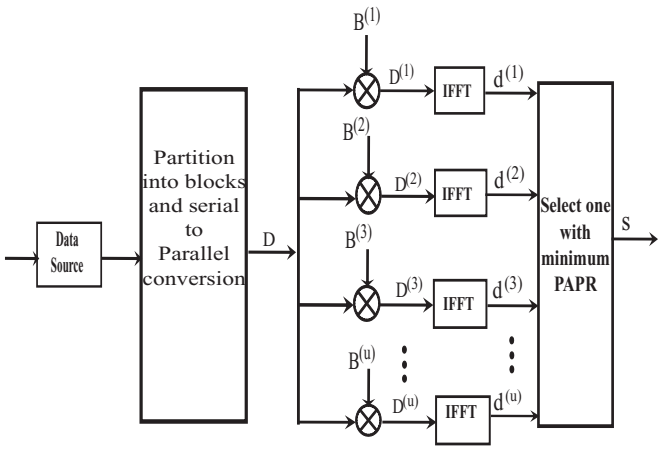

Fig. 1. Block diagram of the SLM technique with U different signal representation and phase weights to produce a minimized PAPR signal

The amount of PAPR reduction for SLM depends on the number of phase sequences U and the design of the phase sequences. There are extensions of SLM technique which does not need explicit information to be sent to the receiver. For further information see the reference [9].

IV. PHASE SEQUENCE GENERATION USING CONDEX MATRIX

PAPR of the OFDM system can be reduced by selecting appropriate phase sequences in the SLM method. In order to do so, in this paper, we have investigated a set of counter-example matrices to condition number estimators [10, 11], and practically have selected the SONEST [11] to generate proper phase sequences for the OFDM system. We term this matrix here as Condex matrix. Using the algorithm as in [11], a Condix matrix (C) of order 4 can be writhen as:

$$C = \begin{bmatrix} 1.0000 & 0.0000 & 0 & 0.0000 \\ 0.0000 & 59.7379 & -10.6796 & -48.0583 \\ 0 & -10.6796 & 2.9417 & 8.7379 \\ 0.0000 & -48.0583 & 8.7379 & 40.3204 \end{bmatrix} \qquad (4)$$

From the above equation $C^{(u)} = [C_0^{(u)}, C_1^{(u)}, .., C_{N-1}^{(u)}]$ can be defined with each row of the normalized Condex matrix C. Each input data block $D = [D_0, D_1, ...D_{N-1}]$ is multiplied with U different phase vectors $C^{(u)}, u = 1, 2, ..., U$ Then, all U subcarrier vectors are transformed into time domain to get the following:

$$d^{(u)} = IDFT\{D^{(u)}\} = IDFT\{D_{(n)}.C_n^{(u)}\} \qquad (5)$$

Finally, the one with the minimum PAPR is selected for transmission.

V. SIMULATION RESULTS

In this section, we show simulation results depicting the comparative performance of SLM technique using Condex and Bauml phase sequence. The simulation parameters are introduce in Table I. Fig. 2 shows the number of symbols that achive minimum PAPR versus Condex phase sequence

TABLE I
SIMULATION PARAMETERS

Number of Sub-carriers (N)	64
Modulation Technique	$BPSK$
Phase Sequences	$Bauml\ and\ Condex\ Matrix$
Length of Phase Sequences	64
Number of OFDM Symbols	$10,000$
Simulation Tool and Version	MATLAB [7.8.0.347 (R2009a)]

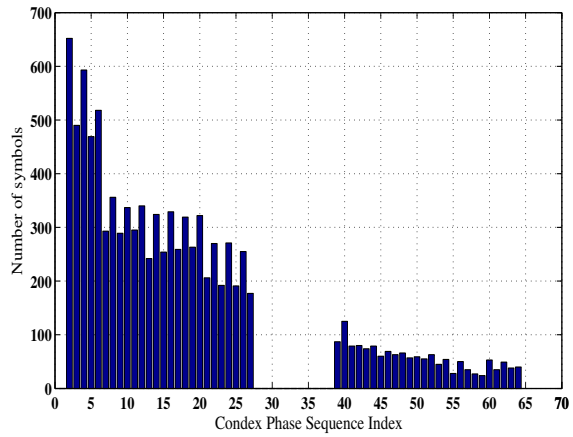

Fig. 2. Complexity diagram for SLM scheme (Condex Phase Sequence) with minimum PAPR

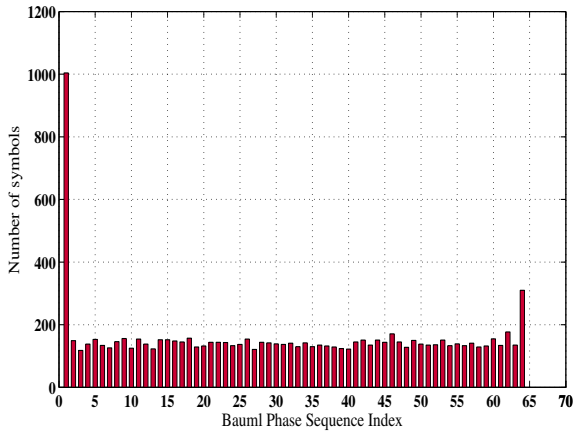

Fig. 3. Complexity diagram for SLM scheme (Bauml Phase Sequence) with minimum PAPR

index, we call this plot as the complexity diagram since it depicts the number of search operations required to achieve a certain level of PAPR. It can be observed from the figure that the highest number of symbols with minimum PAPR can be seen at the phase sequence number 2. With the increasing number of Phase sequence index from 2 to 27, it is also observed that the number of symbols is continuously decreasing. Similar decreasing phenomenon for number of symbols is also seen as we go along from phase sequence number 39 to 64. Moreover, it is observed from the figure that regarding number of symbols, even phase index showed better performance than odd one.

In Fig. 3, we show the number of OFDM symbols with minimum PAPR versus the Bauml phase sequence index. It is observed that about $1,000$ out of total $10,000$ OFDM symbols meet the minimum PAPR requirements at phase sequence index 1 while less than 200 symbols did the same

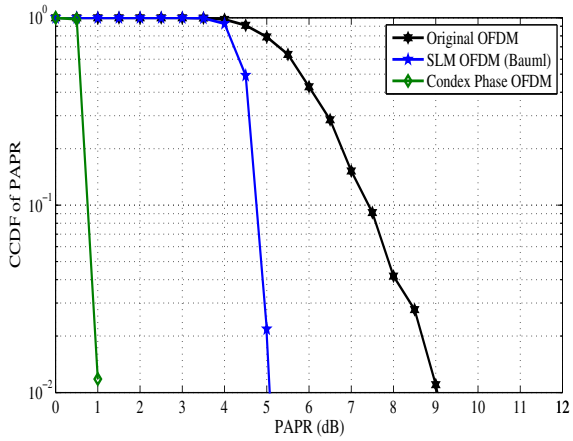

Fig. 4. CCDF vs. PAPR of OFDM Blocks

for index 2 to 63 with the exception of index 64 which has slightly higher number of such symbols.

Now the CCDFs of PAPR for Condex matrix, Bauml phase sequence and original OFDM are plotted against PAPR (dB) in Fig. 4. It shows that for a probability of 10^{-2}, the corresponding PAPRs of Condex matrix, Bauml phase sequence and original OFDM are 1dB, 5.1dB and 9.0dB, respectively.

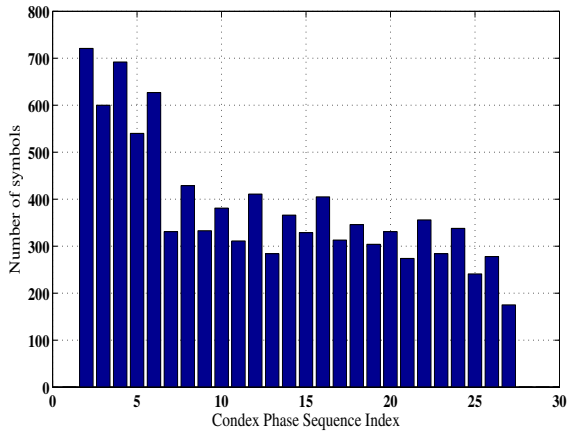

Fig. 5. Complexity diagram for SLM scheme (Condex Sequence from 2 to 27 index) with minimum PAPR

Since Fig. 2 shows that large number of OFDM symbols satisfy minimum PAPR requirement when sequence no. is between 2 to 27, we focused in this region and show the corresponding complexity diagram in Fig. 5. Since total no. of sequence are reduce from 64 to 26, it implies that only 26 numbers of iteration is required to attain almost the same level of PAPR that previously required 64 iterations. It means, a complexity reduction has been reduce by 59%.

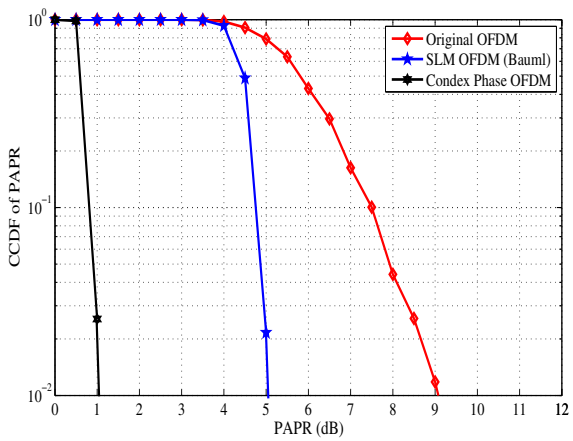

Fig. 6. CCDF vs. PAPR of OFDM Blocks Corresponding to Fig. 5

.

Figure 6 shows the comparative CCDF of PAPR for Condex and Bauml phase sequence based SLM techniques with that of original OFDM. We see for Condex sequence no. 2 to 27 that for a probability of 10^{-2}, the corresponding PAPR of Condex, Bauml and original OFDM are 1.1dB, 5.1dB and 9.0dB, respectively, which means had to sacrifice 0.1dB PAPR compared to Fig. 4.

VI. Conclusion

Large PAPR of transmitted signals may be a main cause of performance degradation of OFDM system. Several techniques have been proposed for PAPR reduction. But most of them cannot achieve simultaneously a large reduction in PAPR with high frequency efficiency, low complexity and good error correction. No specific PAPR reduction technique is the best solution for all multicarrier transmission. It is an important issue to choose the right phase sequence for original SLM method according to the above mentioned requirements. Using this techniques, we showed that it is possible to simultaneously achieve significant reduction in PAPR along with low computational overhead. The PAPR reduction capability was evaluated using MATLAB simulation tool, the results show that the proposed scheme offers better PAPR reduction than other schemes consider here. The simulation results (Figs. 5 and 6) show that the computational complexity can be reduced up to 59% if we sacrifice little 0.1 dB PAPR. In our future work, we have plans of investigating the effects of higher order modulation scheme such as 4-QAM,8-QAM using ours proposed method. This will help to make a comparative study of different modulation scheme from the perspective of PAPR performance.

References

[1] B. Saltzberg, "Performance of an efficient parallel data transmission system," *IEEE Trans. on Commun. Technology, vol. 15, no. 6, pp. 805-813, Dec. 1967.*

[2] Y. Wu and W. Y. Zou, "Orthogonal frequency division multiplexing: a multicarrier modulation scheme," *IEEE Trans. Conf. Elect., vol. 41, no. 3, pp. 392-399, Aug. 1995.*

[3] K. R. Panta and J. Armstrong, "Effect of clipping on the error performance of OFDM in frequency selective fading Channels," *IEEE Trans. Wireless Commun., vol. 3, no. 2, pp. 668-671, March 2004.*

[4] X. Wang, T. T. Tjhung, and C. S. Ng, "Reduction of peak-to-average power ratio of OFDM system using a companding technique," *IEEE Trans. on Broadcast., vol. 45, no. 3, pp. 303-307, Sept. 1999.*

[5] J. A. Davis and J. Jedwab, "Peak-to-mean power control in OFDM, Golay complementary sequence and Reed Muller codes," *IEEE Trans. on Info. Theory, vol. 45, no. 7, pp. 2397-2417, Nov. 1999.*

[6] R. W. Buml, R. F. H. Fisher, and J. B. Huber, "Reducing the peak-to-average power ratio of multicarrier modulation by selected mapping," *IEEE Elect. Letters., vol. 32, no. 22, pp. 2056-2057, Oct. 1996.*

[7] S. H. Muller and J. B. Huber, "OFDM with reduced peak-to-average power ratio by optimum combination of partial transmit sequences," *IEEE Elect. Letters, vo1. 33, no. 5, pp. 368-369, Feb. 1997.*

[8] S. H. Muller and J. B. Huber, "A comparison of peak-power reduction schemes for OFDM," *in Proc. IEEE Global Telecommu. Conference (GLOBECOM), Phoenix, AZ, vol. 1, Nov. 1997, pp. 1-5.*

[9] M. Breiling, S. H. Mller-Weinfurtner, and J. B. Huber, "SLM peak-power reduction without explicit side Information," *IEEE Commun. Letters, vol. 5, no. 6, pp. 239-241, June 2001.*

[10] A. K. Cline and R. K. Rew, "A set of counter-examples to three condition number estimators," *SIAM J. Sci. Stat. Comput., vol. 4, no. 4, pp. 602-611, Dec. 1983.*

[11] N. J. Higham, "FORTRAN codes for estimating the one-norm of a real or complex matrix, with applications to condition estimation," *ACM Trans. on Mathematical Software, vol. 14, no. 4, pp. 381-396, Dec. 1988.*

Energy-Efficient Cellular Communications Powered by Smart Grid Technology

Imtiaz Nasim, Mostafa Zaman Chowdhury, and Md. Syadus Sefat
Department of Electrical and Electronic Engineering
Khulna University of Engineering & Technology, Khulna-9203, Bangladesh
E-mail: imtiaz_nasim@hotmail.com, mzceee@yahoo.com, sefat_235711@yahoo.com

***Abstract*—The energy efficiency aspect of cellular networks is a vital topic of research over the recent days. As energy consumption is on the rise and the price of electricity is increasing very rapidly, necessity to reduce electricity usage in every aspect is becoming much more significant. The power grid infrastructure, from which the cellular networks attain the required electricity for operation is considering a significant change from the traditional electricity grid to the smart grid. The base stations, which are the main candidates for energy consumption in cellular networks, remain in operation even when there are a very few users or no user at all. In this paper, we propose an effective application scenario of the femtocell technology for power saving purpose of cellular networks. Effective deployment of femto-access-points in the required places can reduce the power usage of cellular networks by turning off the redundant base stations. Moreover, the signal to noise plus interference ratio is also enhanced in comparison to the traditional scheme. The base station turn off probability and the energy consumption in the overall network are analyzed. The comparison results show that the proposed energy efficient model can significantly reduce energy consumption and increase the service quality of the cellular users.**

Keywords*— *Smart grid, cellular network, energy consumption, QoS, and femtocell

I. Introduction

The smart grid *(SG)*, also called smart power grid, intelligent grid, intelligrid, future grid or intragrid, is an enhancement of the 20th century power grid. The traditional power grids are normally used to carry power in one way direction only. These power grids generally carry power from a few central generators to a large number of users or consumers. On the other hand, SG creates an automated and distributed advanced energy delivery network by using the two-way flow of electricity. The SG uses modern information technologies and is capable of distributing power in a more efficient way. It also emphasizes on energy saving of the different smart appliances and commodities [1].

Recently, rapidly rising energy price has led to a trend of studying the energy efficiency aspect of communication networks. The cellular operators pay a handsome amount of electricity bill which has become a significant portion of their total expenditure. The CO_2 emissions produced by wireless cellular networks all over the world are equivalent to those from more than 8 million cars. In a typical wireless cellular network, base stations (BSs) consumes 60 − 80% energy of the overall cellular network's energy consumption. Almost 120,000 new base stations are deployed throughout the world every year to provide necessary support to the cellular users [2]. Our survey works suggest that a base station consumes more than 85% of its peak energy even when there is little or no traffic. Therefore, a dynamic operation of the cellular base stations based on the traffic is very much essential for the energy efficient approach of cellular networks. The proposed model in this paper is expected to reduce the energy consumption of cellular networks to a significant level. However, this model is much more applicable for some remote areas where there are a very few cellular users and a base station remains in operation continuously to serve those few users. Using the simulation results, we show that the proposed scheme can save energy of cellular networks and improve the quality of service (QoS) to a certain level.

The rest of this paper is organized as follows. Section II shows the proposed energy efficient model. Section III shows the performance analysis of the proposed scheme. Finally, conclusions are drawn in the last section.

II. Proposed Energy Efficient Model

Suppose a cellular network is powered by smart grid where there is a flow of electricity and communication simultaneously as shown in Fig. 1.

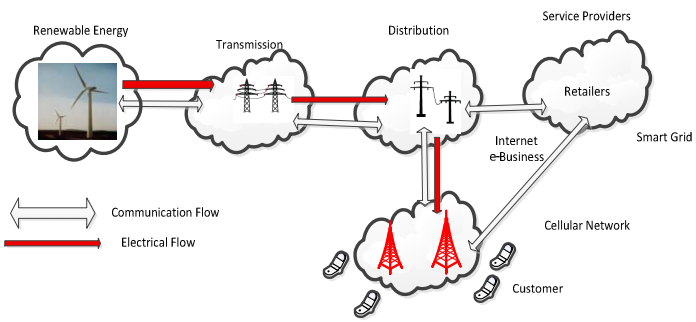

Figure 1. A cellular network powered by the smart grid [2].

978-1-4673-9257-0/15/$31.00 ©2015 IEEE

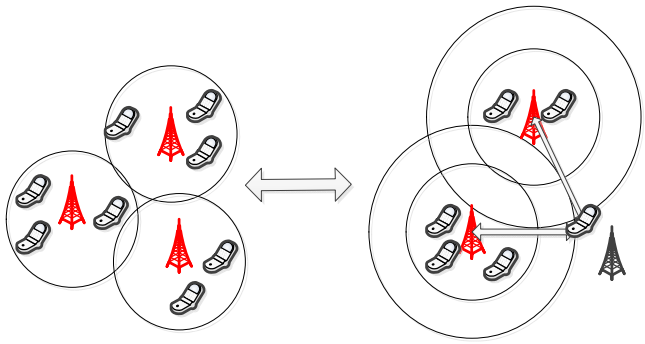

Figure 2. Coverage extension and energy saving with coordinated multipoint (CoMP) [2].

In [2], the authors proposed a model in which the redundant base station is turned off and the users of that network are served by coverage extension of the neighboring base stations using the coordinated multipoint method for energy saving purpose. This model is showed in Fig. 2.

If the redundant base station is turned off as shown in Fig. 2, a decent amount of energy can be saved if the existing user is served by the neighboring base stations. But we propose another model for saving energy of cellular networks using femtocell network which may turn out to be a very promising solution for saving more energy of cellular networks especially in remote areas.

In our proposed model, femto-access-points are installed in some places which have the most probability of carrying a mobile user in the entire cellular network served by a base station. The femto-access-points (FAPs) are low-power, small-size home-placed base stations that enhance the service quality for the indoor mobile users [3]. Fig. 3 shows an example of the proposed energy efficient model. When all the users remain inside the femtocellular coverage region, the macrocellular BS is allowed to turn off. But if any user stays outside the femtocellular coverage, the macrocellular BS must remain in operation to serve that particular user. Periodic checking of user's location and the QoS is tested by the dynamic checking application of the SG. Our purpose is not only saving energy of cellular networks but also to increase the service quality of the existing users. Femto-access-points are ideal for this case as these devices run with very low operating power and at the same time can enhance the QoS to a significant level.

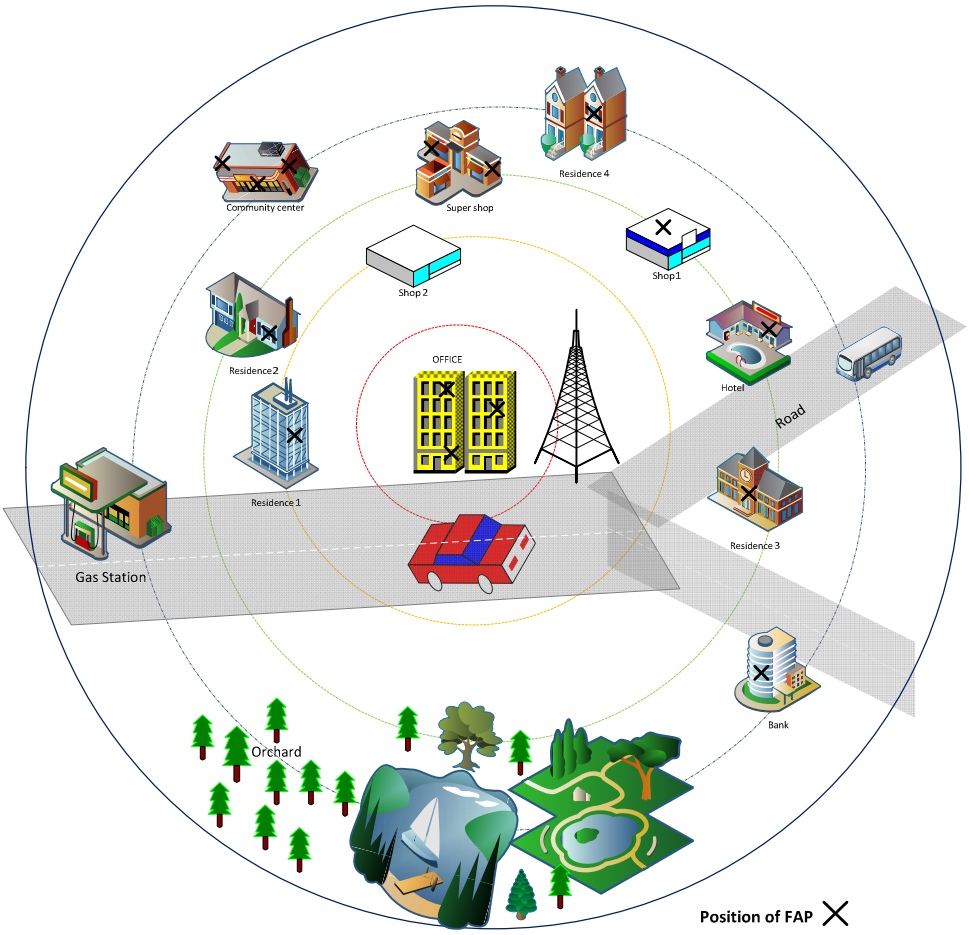

Figure 3. Proposed energy efficient model with femtocell/Macrocell integrated network.

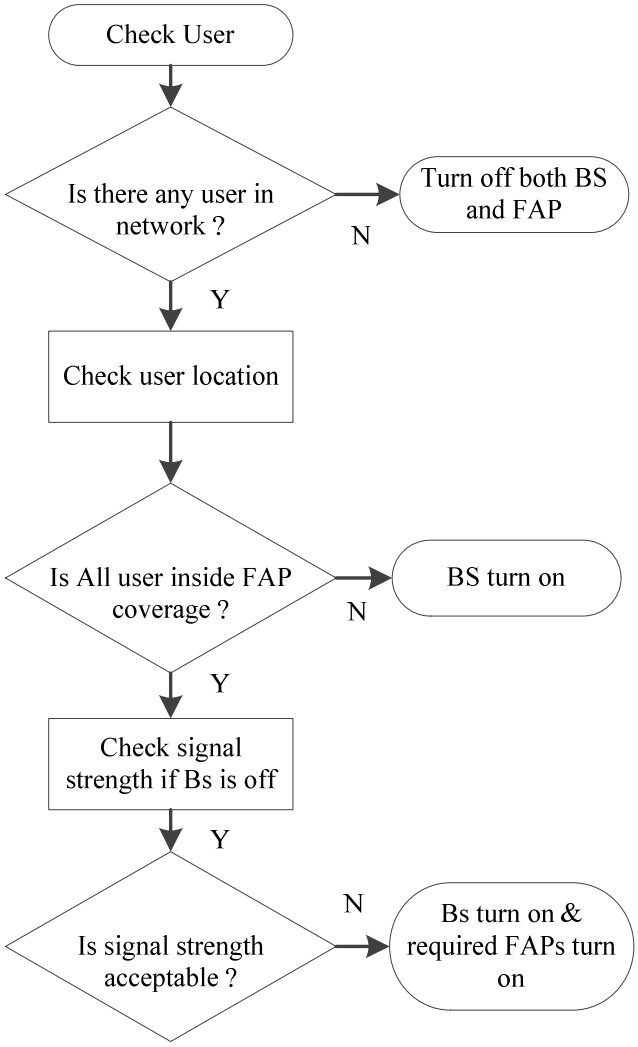

Figure 4. Flow chart showing the condition for the BS to be turned off in the proposed scheme.

Femtocells are small base stations with low transmission power, and with almost all cellular functionalities, but a limited coverage to end users in indoor environments. A femtocell allows service coverage extended to indoor environments, especially where wireless access is limited or unavailable, without expensive deployment cost.

A flow chart is shown in fig. 4 which shows the algorithms of the proposed scheme. The network will first check the existence of a user. If no user exists in the network, both the macrocellular BS and the FAPs will remain off. If any users exist, then the network will search for user's location. When any of the users remain outside the FAP coverage area, the BS will not be allowed to turn off. But, if all users exist inside the femtocellular network, then the network will check the signal strength available for the users if the BS is shut down. The BS will shut down if the signal strength is found within acceptable limit, otherwise; it will remain on in order to provide network support to the existing users. This model requires a periodic checking of the position of each user inside the network. By adopting this process, the macrocellular BS will sometimes remain turned on and sometimes remain turned off.

III. PERFORMANCE ANALYSIS

This section provides the probability analysis performance and the signal quality performance of our proposed model.

A. Probability Analysis

When a redundant BS is shut down and the users of that area are to be served using FAPs, then it is required to analyze the probability of the existence of a user under the femtocell coverage area. If all users are within the femtocell coverage area then the BS may remain shut down and service is provided to the user by the femtocell network, but if any user remains outside the femtocell coverage area, then the BS must be turned on in order to provide service to that user.

For simplicity in calculation, we have divided the total considered area into 4 sub-circles each with a fixed distance from the center point of the main circle. The coverage area of a macrocellular BS is assumed to be 500m. We performed our analysis assuming 15 FAPs in the total coverage area. All the stations considered in the coverage area have a specific factor according to the importance of that station for carrying users. The factors assumed for each station is given in Table I. The coverage area of a FAP is determined by

$$a=4\square r^2$$

where r is the radius of each FAP coverage.

If there exist stations with n number of factors then Let, A_1 is the area under user existence probability factor f_1, A_2 is the area under user existence probability factor f_2, A_3 is the area under user existence probability factor f_3, and A_n is the area under user existence probability factor f_n.

Let the remaining area where no FAPs are installed is A_M with a user existence probability factor of f_M

The probability of a user to exist in the FAP coverage area is given by

$$P=\frac{f_1\sum_{i=1}^{N_1}A_{1i}+f_2\sum_{i=1}^{N_2}A_{2i}+f_3\sum_{i=1}^{N_3}A_{3i}+.....+f_n\sum_{i=1}^{N_n}A_{ni}}{\left(f_1\sum_{i=1}^{N_1}A_{1i}+f_2\sum_{i=1}^{N_2}A_{2i}+f_3\sum_{i=1}^{N_3}A_{3i}+.....+f_n\sum_{i=1}^{N_n}A_{ni}\right)+f_mA_m} \quad (1)$$

where N_1 is the number of places under user existence probability factor f_1, N_2 is the number of places under user existence probability factor f_2, N_3 is the number of places under user existence probability factor f_3, N_n is the number of places under user existence probability factor f_n.

The probability of the BS to be turned off with the number of user can be expressed as

$$p=\left(f_p\right)^n \quad (2)$$

where f_p is the average importance factor considered for the entire region and n is the number of user.

The analysis is performed assuming only 15 FAPs in the considered total area. The performance would be better if more number of FAPs are used. However, FAPs should be installed in the places where there is a big possibility of users to exist. Unplanned deployment of FAPs in the network may result in no significant advantage for saving energy. Table II summarizes the values of the parameters that we used in our analysis.

TABLE I: SUMMARY OF NUMBER OF FAP AND DIFFERENT FACTORS USED IN ANALYSIS

Station Name	No. of FAP	Factor *(f)*
Office	3	1 (=f_1)
Super shop	2	0.8 (=f_2)
Community center	3	0.8 (=f_2)
Residence 1	1	0.7 (=f_3)
Residence 2	1	0.7 (=f_3)
Residence 3	1	0.7 (=f_3)
Residence 4	1	0.7 (=f_3)
Bank	1	1 (=f_1)
Hotel	1	0.7 (=f_3)
Shop 1	1	0.7 (=f_3)
Shop 2	0	0.3 (=f_3)
Remaining free space	0	0.01 (=f_3)

TABLE II: SUMMARY OF THE PARAMETER VALUES USED IN ANALYSIS

Parameter	Value
Carrier frequency	1800 [MHz]
Transmit signal power by the macrocellular BS	1.5 [kW]
Transmitted signal power by a FAP	15 [mW]
Power required for operation of a macrocellular BS	2 [kW]
Power required for operation of a macrocellular BS	8 [W]
Height of a macrocellular BS	100 [m]
Height of a FAP	2 [m]
Distance of the MS from reference FAP	7 [m]
Lpen	20 [dB]
Lsh	8 [dB]
Range of a macrocellular BS	500 [m]
Range of a FAP	15 [m]
Average importance factor, f_p	0.7
Total received noise	$7 * 10^{-7}$ [mW]

The probability of a macrocellular BS to be turned off increases rapidly with the increase of FAPs installed in the considered network. As FAPs are very low power consuming devices, installment of a large number of FAP in the network will still result in less energy consumption compared to that by the BS alone. Fig. 5 shows the comparison of the probability for 3 different number of users existing in the network. As the number of user increases, the probability of the BS to be turned off decreases. So, the BS needs to be turned on when the number of user is more in the network as there will be a probability of at least one user to stay outside the femtocell network region.

Fig. 6 shows the comparison between 3 different cases for BS turn off probability. The energy saving possibility is enhanced if more FAPs are used. If only 5 FAPs are used in the network, the probability of the BS to be turned off is nearly 5% when 5 users exist in the network. But if 25 FAPs are used for the same network, the probability of the BS to be turned off is more than 50% for the same number of user.

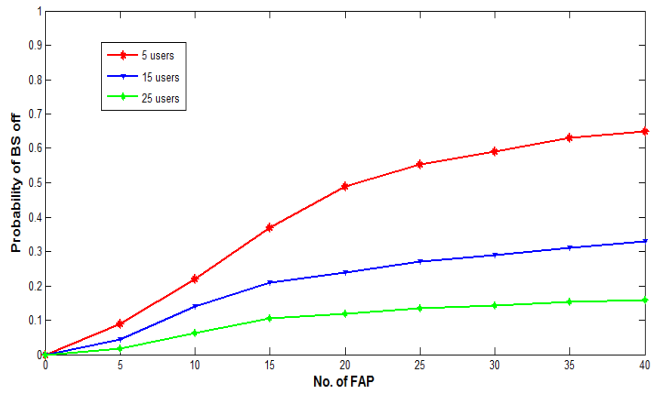

Figure 5. Probability of macrocellular BS to be turned off with increasing FAP for different number of users.

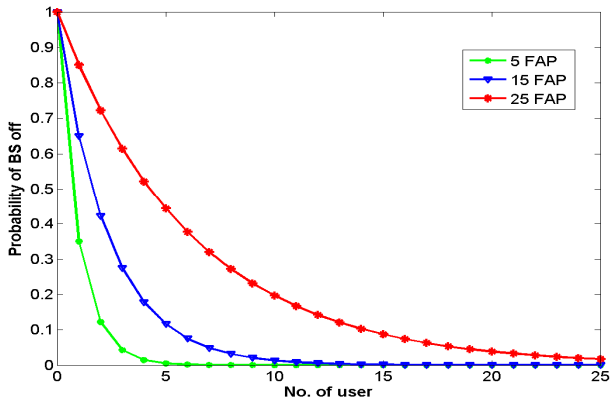

Figure 6. Comparison of macrocellular BS turn off probability with number of user for different cases.

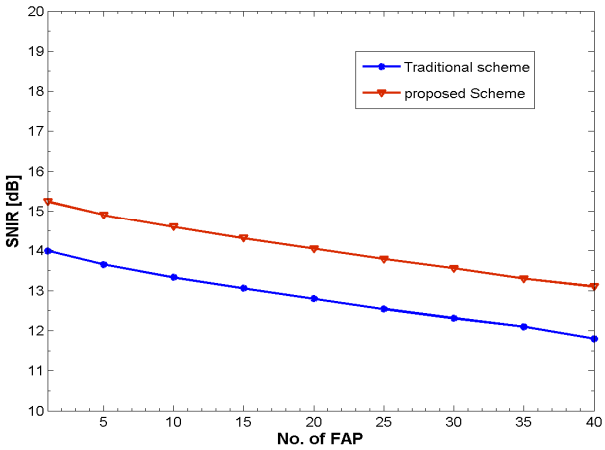

Figure 7. Comparison of *SNIR* levels between the proposed model and the traditional model

B. SNIR Analysis

The propagation model for a macrocell case can be expressed as:

$$L = 36.55 + 26.16\log_{10} f_c - 3.82\log_{10} h_b - a(h_m) + [44.9 - 6.55\log_{10} h_m] \log_{10} d + L_{sh} \quad [dB]$$

$$a(h_m) = 1.1[\log_{10} f_c - 0.7]h_m - (1.56\log_{10} f_c - 0.8) \tag{3}$$

where fc is the center frequency in MHZ, h_b is the height if the macrocellular BS in meter, h_m is the height of the MS in meter, d is the distance between the macrocellular BS and the MS in kilometer, Lsh is the shadowing standard deviation.

The propagation model for a femtocell case can be expressed as [3]:

$$L_f = 20\log_{10} f_c + N\log_{10} d_1 + 4n^2 - 28 \quad [dB] \tag{4}$$

where fc is the center frequency in MHZ of the femtocell, n is the number of walls between the MS and the FAP, and d_1 is the distance between the FAP and the MS in meter.

The received *SNIR* level of a femtocell user in a macrocell/femtocell integrated network can be expressed as:

$$SNIR = \frac{S_0}{I_m + I_f + N} \tag{5}$$

Simulation results show that the proposed model provides better signal-to-noise plus interference level. Fig. 7 demonstrates the comparison of SNIR level between traditional scheme and proposed scheme. The effect of the macrocellular BS and the number of FAPs has been considered here. As the BS will not remain turned on for all the time in the proposed model, there will be a decrease in the average noise level. Thus, the SNIR level is increased in the proposed model according to equation (5).

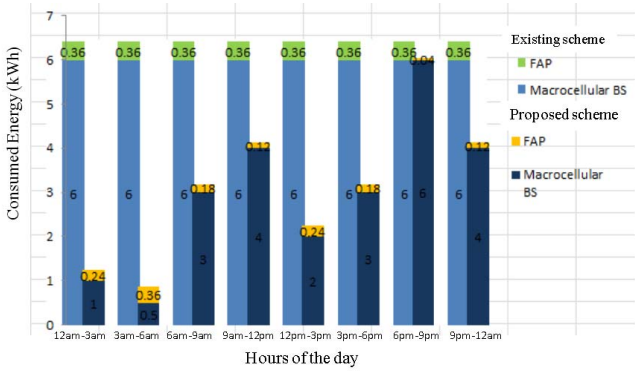

Figure 8. Comparison of energy consumption between the proposed model and traditional model

C. Comparison of Energy Consumption

In our proposed model, the macrocellular BS will only remain shut down if the existing FAP can provide proper service to all the active users. In general, the number of active user becomes low in the middle of the night. So the BS may remain shut down for most of the time during late night. Thus, a large amount of energy can be saved in that period of night. However, the BS may remain turned off even in different times of the day if the FAPs can provide proper service to the existing users in that period of time. The FAPs consume very low energy compared to the macrocellular BS. So using many FAPs can still result in significant energy saving.

If we compare the energy consumption of the cellular network for the traditional model and the proposed model, there is a large amount of energy saved in the proposed model as the main energy consuming element for cellular network i.e., the macrocellular BS remains off for a certain period of time in this model. Fig. 8 shows the comparison of energy consumed between the traditional model and the proposed model. The saving of energy can be increased further by installation of FAPs in required places where there is a great possibility of carrying mobile users. For vehicular environment, the proposed model in [4] is good enough to serve the mobile users.

IV. CONCLUSIONS

Saving of energy in cellular network communication is an important issue as energy prices are increasing day by day. Energy efficiency of the cellular network can be enhanced by the use of femto-access-points. Proper utilization of FAPs can result in improved service quality and reduction in the consumed energy of macrocellular base station. If the base station is allowed to turn off even for a small amount of time, a significant amount of energy can be saved as most of the energy required in the cellular communication is consumed by the base station. Our proposed model can be used extensively for energy saving purpose in cellular communications. Femtocells are a novel wireless networking technology that has several advantages including lower cost, better signal quality, and reduced infrastructure cost. In this paper, we

discussed the advantages of femtocellular network for saving energy of cellular communication networks. The various performance analysis and the comparison results are presented. The simulation results demonstrate that the deployment of femtocells will significantly reduce the consumption of energy of cellular networks.

REFERENCES

[1] X. Fang, S. Misra, X. Guoliang, D. Yang, "Smart Grid — The New and Improved Power Grid: A Survey," *IEEE Communications Surveys & Tutorials*, vol. 14, no. 4, pp. 944,980, Oct. 2012.

[2] B. Shengrong, F. Richard Yu, Y. Cai,and X. P. Liu, "When the Smart Grid Meets Energy-Efficient Communications: Green Wireless Cellular Networks Powered by the Smart Grid," *IEEE Transactions on Wireless Communications,* vol. 11, no. 8, pp. 3014-3017, Aug. 2012.

[3] M.Z. Chowdhury, S. H. Chae andY. M. Jang, "Group Handover Management in Mobile Femtocellular Network Deployment," *International Conference on Ubiquitous and Future Networks (ICUFN),* July 2012.

[4] M.Z. Chowdhury, S. Q. Lee, B. Han Ru, N. Park, Y. M. Jang, "Service Quality Improvement of Mobile Users in Vehicular Environment by Mobile Femtocell Network Deployment," *International Conference on ICT Convergence (ICTC)*, Sept. 2011.

Orientation Dependent Performance of 635nm Vertical Cavity Surface Emitting QW Red Laser

Muhammad Mainul Islam, Md. Shamim Sarker, Md. Mahbub Hasan, Md. Rafiqul Islam
Department of Electrical and Electronic Engineering
Khulna University of Engineering & Technology
Khulna-9203, Bangladesh
E-mail: mainul0803004@gmail.com, sarkershamimbd@gmail.com, hasanimahbub@yahoo.com, islambit@yahoo.com

Abstract— **In this paper, the crystallographic orientation-dependent performances of 635nm red quantum well (QW) laser are numerically studied. The electronic and optical characteristics of the laser are investigated by solving time independent Schrodinger equation using finite difference method. The results are obtained in (001), (101), ((111), (113), and (211) orientations and found that there is a substantial correlation of the peak gain and peak emission wavelength with crystal orientations. The maximum and minimum gains are estimated in (113) and (211) orientations and the peak emission wavelengths are found 640nm and 648nm for the crystal orientations (113) and (211). The orientation dependent energy band dispersion profiles are used to explain the results presented here.**

Keywords— VCSEL, Red laser, QW, Crystal orientation

I. INTRODUCTION

Vertical cavity surface emitting laser (VCSEL) can be used as a high power laser source in medical science, communication and industrial sectors. Red VCSEL was first demonstrated in 1992 (optical pumping) and 1993 (electrical pumping) at Sandia National Laboratories [1], [2] and Chiao Tung University in Taiwan [3]. Recent research demonstrates that lasers at 635nm wavelength are the exact vibration of a healthy living cell and is optimal for healing and most beneficial for stimulating acupuncture points [4]. Red lasers are also used in photodynamic therapy, solid state laser pumping, semiconductor surface inspection, sensor and other applications which led us to concentrate our interest in 635nm red laser [5]-[7].

Generally gallium indium phosphide ($Ga_xIn_{1-x}P$) is used in the active region of the quantum well (QW) material for red laser [8], [9]. In a QW structure energy levels are discretized due to the quantum confinement effect. Lasing occurs due to transition of electrons from the conduction band minima to different valance sub-bands. This transition plays an important role in determining the optical gain and emission wavelength of a laser. To understand the orientation dependent gain and peak emission wavelength characteristics the proposed VCSEL is modeled using time independent Schrodinger equation.

The band structures of QW strongly depend on crystal orientation [10]. Recently, some works [11]-[13] reported on orientation dependent growth techniques and laser performance. The growth of high quality epitaxial layer on (201) GaAs substrate was reported by Woolf et al. [11]. Orientation dependent growth of InGaAs/InP was noticed by Zwinge et al. [12]. Nootzel and Plog grown AlAs/GaAs multi-layered structure on (210) oriented substrate [13]. Metal Organic Chemical Vapor Deposition and Molecular Beam Epitaxy techniques are suitable for the growth of thin, uniform non-(001) crystal orientated QW structure. Although, it is possible to fabricate thin active region on non-(001) oriented substrate, it becomes very difficult to grow thick laser due to structural degradation. Wafer bonding technique is used to avoid this type of structural degradation [14], [15].

In infrared range, orientation dependent performance of InGaSb laser was reported in the past [16]. But in the visible range, orientation dependent characteristics of lasers have not been reported yet. Here, we have studied the performance of a 635nm $Ga_{0.5}In_{0.5}P/(Ga_{0.5}Al_{0.5})_{0.5}In_{0.5}P$ red laser in different crystal orientations. The orientation dependent optical gain and peak emission wavelength are investigated and their characteristics are explained by the energy separation between the conduction and valence band as well as magnitude of momentum matrix elements.

II. BAND GAP ENERGY CALCULATION

The peak emission wavelength of laser mainly depends on the band gap energy of the material used in active region. So, the selection of composition of the semiconductor material used in the active region and barrier layer is very important. In this structure GaInP is used in the active region and AlGaInP is used in the barrier of QW.

The band gap energy of $Ga_xIn_{1-x}P$ is given [17] by-

$$E_{gw}(Ga_xIn_{1-x}P) = E_g(GaP)x + E_g(InP)(1-x) - bx(1-x)$$

where, E_{gw} is the band gap energy of the material used in the QW, x is the mole fraction of Ga and b is the bowing parameter.

978-1-4673-9257-0/15/$31.00 ©2015 IEEE

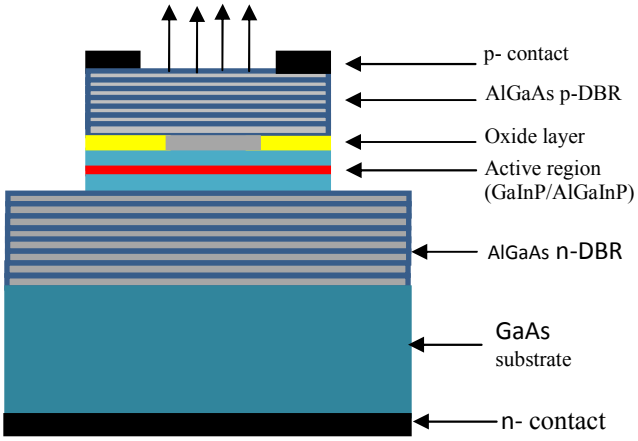

Figure 1. Structure of $Ga_{0.5}In_{0.5}P/(Ga_{0.5}Al_{0.5})_{0.5}In_{0.5}P$ red laser.

Here $(Ga_{0.5}Al_{0.5})_{0.5}In_{0.5}P$ is used in the barrier layer. The bandgap energy of the barrier material is determined using the following relationship [18]

$$E_{gb} = E_{gw}(Ga_x In_{1-x} P) + 0.36$$

III. DEVICE STRUCTURE

"Fig. 1" shows the proposed VCSEL where $Ga_{0.5}In_{0.5}P$ ternary alloy is used in the active layer and $(Ga_{0.5}Al_{0.5})_{0.5}In_{0.5}P$ quaternary alloy in the barrier layer. The QW structure is grown on n+ GaAs substrate. Above the substrate, an n-AlGaAs high reflectivity distributed bragg reflector is grown. Then the active region having a thickness of 8nm is sandwiched between two barrier layers each with a thickness of 10nm. Above the upper AlGaInP barrier layer an oxide aperture is used for current and index confinement. Highly doped contact layers are grown at the top and the bottom of the surface for the formation of ohmic contact.

III. ORIENTATION DEPENDENT GAIN

The optical gain of QW structure by considering the valence band intermixing effect can be expressed [19] by

$$g(E) = \frac{2q^2\hbar}{n\varepsilon_0 c m_0^2 LE} \sum_{n,m} \int_0^\infty \frac{k_t M_{nm}(k_t)(\Gamma/2\pi)}{(E_{cn}(k_t) - E_{kpm}(k_t) - E)^2 + (\Gamma(2\pi)^2} (f_c^n - f_v^m) dk_t \quad (1)$$

where q is the free electron charge, $\hbar$ is the reduced Planck constant, n is the refractive index, ε_0 is the free space dielectric constant, c is the speed of the light, E is the photon energy, M_{nm} is the momentum matrix, $\Gamma = 2\pi\frac{\hbar}{\tau}$ where τ is the relaxation time, f_c^n ***and*** f_v^m are the fermi functions for the conduction and valance bands, E_{cn} *is* n-th conduction subband, E_{vm} is mth valence subband, n and m denote the electron states in the conduction band and heavy/light hole states in the valence band, respectively. The momentum matrix M_{nm} is given by

$$M_{nm}(k_t) = \frac{3}{4}[<\Psi_n | g_m^{(1)}>^2 + \frac{1}{3}<\Psi_n | g_m^{(2)}>^2]M_b^2$$
$$= \frac{3}{4}[\frac{1}{3}<\Psi_n | g_m^{(3)}>^2 + <\Psi_n | g_m^{(4)}>^2]M_b^2 \quad (2)$$

where $M_b^2 = (\frac{m_0}{m_e} - 1)\frac{m_0 E_g(E_g + \Delta)}{6(E_g + (2/3)\Delta)}$ (3)

Here Ψ_n ***and*** $g_m^{(j)}$ are the conduction and valence bands wave function, M_b is the bulk average crystal momentum matrix, m_0 is the free space mass, m_e is the effective mass of electron, Eg is the band gap energy and Δ is the split off valence band energy seperation. In our calculation orientation dependent hole effective mass has not been considered.

The expression of the rotation matrix is as follows

$$O_R = \begin{pmatrix} \cos\theta\cos\phi & -\sin\phi & \sin\theta\cos\phi \\ \cos\theta\sin\phi & \cos\phi & \sin\theta\sin\phi \\ -\sin\theta & 0 & \cos\theta \end{pmatrix} \quad (4)$$

where, $\theta = \tan^{-1}(\frac{\sqrt{h^2+k^2}}{l})$ and $\phi = \tan^{-1}(k/h)$

The Hamiltonian matrix in (hkl) orientation can be calculated by the following equation [20]

$$H^{hkl} = UH^{(001)}U^* \quad (5)$$

where $U = R(\theta)R(\phi)$ (6)

Here, $R(\theta)$ and $R(\phi)$ represent the spinor rotations which transform the (001) orientated valence band Hamiltonian to arbitrary crystal orientated Hamiltonian matrix. The expressions of $R(\theta)$ and $R(\phi)$ can be given by [20]

$$R(\theta) = \begin{pmatrix} \alpha^2 & -\sqrt{3}\alpha^2\zeta & \sqrt{3}\alpha\zeta^2 & \zeta^3 \\ \sqrt{3}\alpha^2\zeta & \alpha^3 - 2\alpha\zeta^2 & -2\alpha^2\zeta + \zeta^3 & \sqrt{3}\alpha\zeta^2 \\ \sqrt{3}\alpha\zeta^2 & 2\alpha^2\zeta - \zeta^3 & \alpha^3 - 2\alpha^2\zeta & -\sqrt{3}\alpha^2\zeta \\ \zeta^3 & \sqrt{3}\alpha\zeta^2 & \sqrt{3}\alpha^2\zeta & \alpha^3 \end{pmatrix} \quad (7)$$

Here $\alpha = \cos\frac{\theta}{2}$ and $\zeta = -\sin\frac{\theta}{2}$

$$R(\phi) = \begin{pmatrix} e^{i(3/2)\phi} & 0 & 0 & 0 \\ 0 & e^{i(1/2)\phi} & 0 & 0 \\ 0 & 0 & e^{-i(1/2)\phi} & 0 \\ 0 & 0 & 0 & e^{-i(3/2)\phi} \end{pmatrix} \quad (8)$$

IV. RESULT AND DISCUSSION

Using "(1)" the gain of the laser is determined at 300k for different crystal orientations. "Fig. 2" shows the orientation dependent optical gain of the laser. It is seen that the peak gain and peak emission wavelength have crystal orientation dependence. The value of the peak gain with its emission wavelength is enlisted in Table I.

TABLE I

Orientation	Peak optical gain (cm^{-1})	Peak emission wavelength (nm)
(001)	1063	640
(101)	1017	644
(111)	1003	646
(113)	1178	642
(211)	847	648

The orientation dependent lasing characteristics of the QW VCSEL can be are described by energy dispersion profiles. To compare the energy separation characteristics, in different sub- bands the dispersion profiles are plotted in "Fig. 3" in the same scale where the valence band dispersion profiles of $Ga_{0.5}In_{0.5}P$/ $(Ga_{0.5}Al_{0.5})_{0.5}In_{0.5}P$ are presented in (001), (101), (111), (113) and (211) orientations. In this figure HH1, HH2 and HH3 indicates first, second and third heavy holes and LH1 is the first light hole bands. Lasing action occurs due to the allowed transition from conduction sub-band C1 to valence sub- bands HH1.

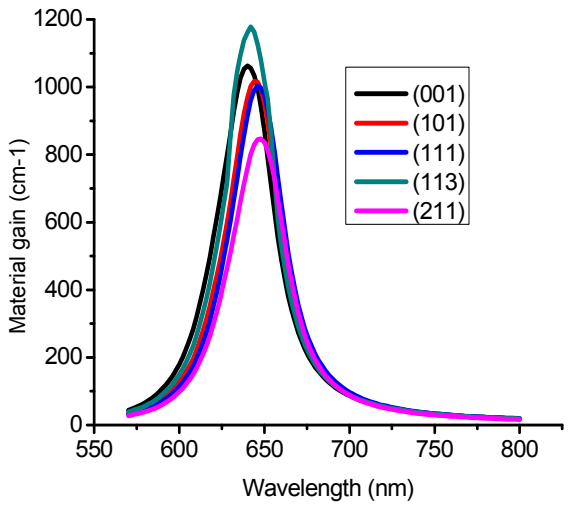

Figure 2. Optical gain spectrum of $Ga_{0.5}In_{0.5}P/(Ga_{0.5}Al_{0.5})_{0.5}In_{0.5}P$ red laser as a function of crystal orientations

Other transitions such as intra-subbands transitions are forbidden because it reduces the gain of the laser. Among the intra-subbands, transition probability is maximum between HH1 and LH1, which is reduced when the energy separation between HH1 and LH1is higher. For higher gain intra-subband transition should be reduced. For a particular orientation, the higher gain can be obtained when the energy separation between HH1 and LH1 becomes higher in the dispersion profiles. Since the energy separation between HH1 and LH1 is maximum and minimum in (113) and (211) orientation, the optical gain of the laser is found to be maximum and minimum in (113) and (211) orientations.

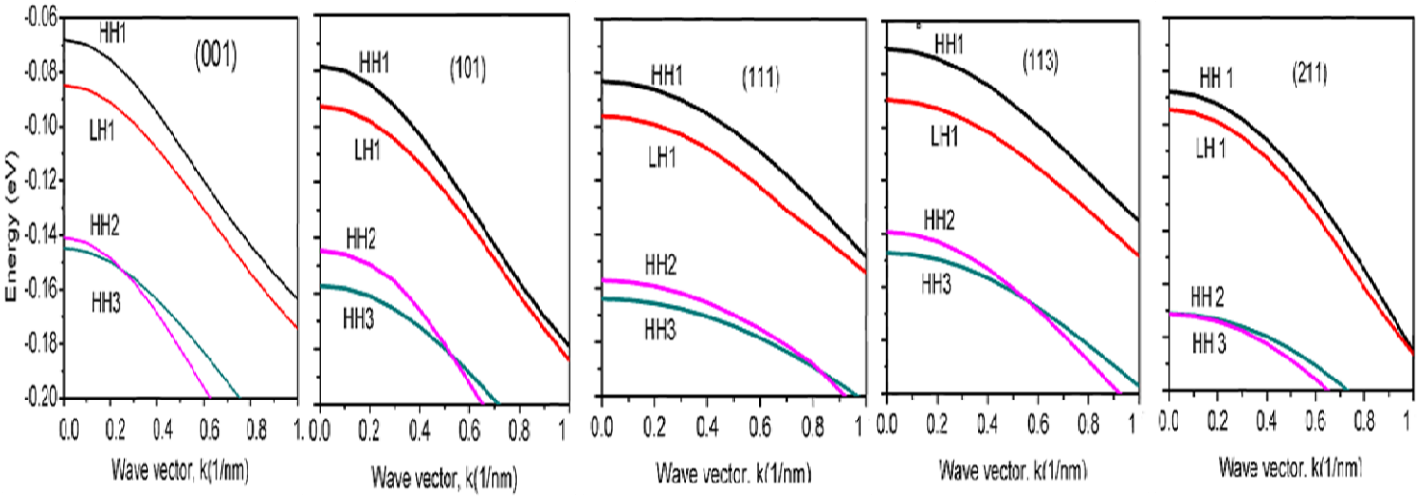

Figure 3. Valence band dispersion profile of $Ga_{0.5}In_{0.5}P$/ $(Ga_{0.5}Al_{0.5})_{0.5}In_{0.5}P$ red laser in different crystal orientation

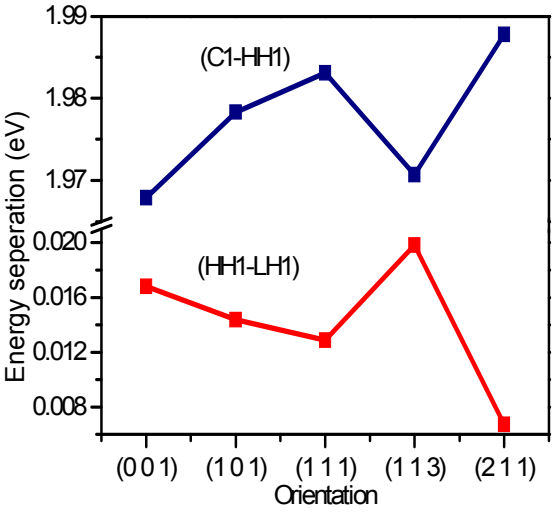

Figure 4. Orientation dependent energy separation between (C1-HH1) and (HH1-LH1)

In order to explain the wavelength dependence of peak emission wavelength the energy separation between the conduction (C1) and heavy hole (HH1) bands is estimated from the energy band dispersion profiles and plotted in "Fig. 3". It is found in Fig. 3 that the energy separation between conduction band minima and valence band maxima changes with crystal orientations. The energy separation between C1-HH1 is found to be 0.0168, 0.01438, 0.01287, 0.01983 and 0.00673 eV corresponds to the orientations (001), (101), (111), (113), and (211), respectively. This clearly explains why the peak emission wavelengths are shifted with crystal orientation. As seen in Fig. 2 the peak emission wavelength changes from 640nm to 648nm for the change in crystal orientation from (001) to (211). That is, laser with tunable characteristic can be obtained by changing the crystal orientation in the material used in active region.

To understand the orientation dependent peak gain of the laser, the energy separation between (HH1-LH1) and momentum matrix elements are further determined. The results are shown in Fig.4 and Fig. 5, respectively. The lower intra band mixing effect is observed in (131) orientation and higher in (211) orientation. Further, the orientation dependent peak gain can be explained by the momentum matrix elements, which depends on the overlapping wave functions of electrons and holes. "Fig. 5" shows that the transition probability is maximum in (113) orientation and minimum in (211) orientations. As a result, higher optical gain is estimated in (113) and lower in (211) orientation.

V. CONCLUSION

The optical gain characteristics of $Ga_{0.5}In_{0.5}P/(Ga_{0.5}Al_{0.5})_{0.5}In_{0.5}P$ 635nm red laser is investigated here in different crystal orientations. The peak gain is found to be

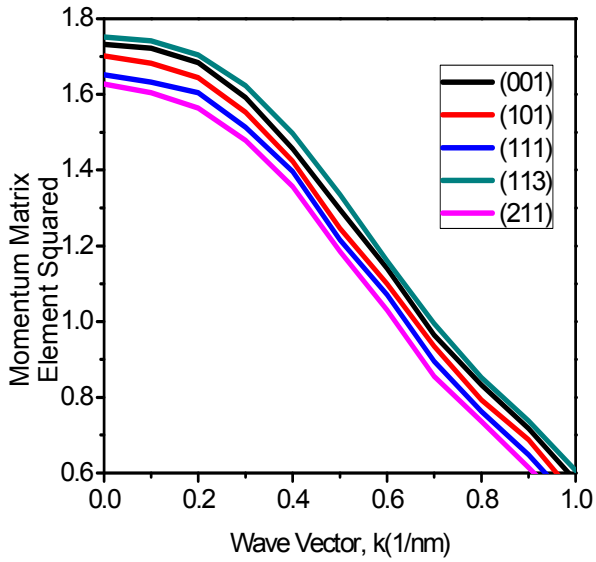

Figure 5. Crystal orientation dependent momentum matrix element squared for C1-HH1 transition

maximum in (113) orientation as the band mixing effect is minimum here. Also, the value of the momentum matrix element for the transition from C1 to HH1 and energy seperation between HH1 and LH1 is found to be higher in (113) orientation in comparison to other orientations. The peak gain is minimum in (211) orientation as the band mixing effect is maximum here. It is also seen that the peak emission wavelength varies from 640nm to 648nm when the orientation changes from (001) to (211). This demonstrates that tunable laser with various optical gains can be realized by changing crystal orientation in the active layer material.

REFERENCES

[1] R. P. Schneider, R. P. Bryan, J. A. Lott and G. R. Olbright , "Visible (657 nm) InGaP/InAlGaP strained quantum well vertical-cavity surface-emitting laser," *Applied Physics Letters*, vol. 60, no. 15, pp. 1830 – 1832, Apr. 1992

[2] R. P. Schneider and J. A. Lott, "Cavity design for improved electrical injection in InAlGaP/AlGaAs visible (639–661 nm) vertical-cavity surface-emitting laser diodes," *Applied Physics Letters*, vol. 63, no. 7, pp. 917 – 919, Sep. 1993

[3] K.F. Huang, K. Tai, C.C. Wu and J.D. Wynn, "Continuous wave visible InGaP/InGaAlP quantum-well surface-emitting laser diodes," *IEEE Trans. Electron Devices*, vol. 40, no. 11, pp. 613-614, Nov. 1993

[4] H. *Solmaz, M. Gülsoy and* Y. Ülgen***, "***635nm diode laser biostimulation on cutaneous wounds***", in*** SPIE Proceedings Vol. 9129***,*** 8 May 2014

[5] I. Charamisinau, G. S. Happawana, G. A. Evans, J. B. Kirk, D. P. Bour, A. Rosen, R. A. Hsi, "High-power semiconductor red laser arrays for use in photodynamic therapy," *IEEE Journal of Selected Topics in Quantum Electronics*, vol. 11, no. 4, pp. 881–891, Jul.-Aug. 2005.

[6] D. W. Hughes and J. R. M. Barr, "Laser diode pumped solid state lasers," *J. Phys. D: Appl. Phys.,* vol. 25, no.4, pp. 563–586, 1992.

[7] E. Alvarado-Mendez,. J. M. Estudillo-Ayala, E. Vargas-Rodriguez, M. E. Sosa-Morales, J. M. Sierra-Hernandez, D. Jauregui-Vazquez, R. Rojas-Laguna." Laser Temperature Sensor Based on a Fiber Bragg

Grating,'' *IEEE Photonics Technology Letters*, vol. 27, no. 11, pp. 1141–1144, Jun. 2015.

[8] C. Kaspari, M. Zorn, M. Weyers and G. Erbert, "Growth parameter optimization of the GaInP/AlGaInP active zone of 635 nm red laser diodes" *Journal of Crystal Growth*, vol. 310, no. 23, pp 5175–5177, Nov. 2008.

[9] C. Z. Kim, J. H. Choi, K. Song, C. S. Shin, C. G. Ko and H. Kim "Optical investigation of GaInP-AlGaInP quantum-well layers for high-power red laser diodes" *Journal of the Korean Physical Society*, Vol: 62, no: 9, pp: 1301-1306, May 2013.

[10] M. Phon, Y. Chung, W. I. Wang, ''Orientation dependence of valence-subband structures in GaAs-$Ga_{1-x}Al_xAs$ quantum-well structures,'' *J. App. Phys.*, vol. 64, no. 9, pp. 4609–4613, Nov. 1988.

[11] D. A. Woolf, J. P. Williams, D. I. Westwood, Z. Sobiesierski, J. E. Aubrey and R. H. Williams, "The homoepitaxial growth of GaAs(111)A and (111)B by molecular beam epitaxy: an investigation of the temperature dependent surface reconstructions and bulk electrical conductivity transitions," *Journal of Crystal Growth* , vol. 127, no. 1, pp. 913-917, Feb. 1993.

[12] G. Zwinge, H.-H. Wehmann, A. Schlachetzkiand and C. C. Hsu, "Orientation-dependent growth of InGaAs/InP for applications in laser-diode arrays", *Applied Physics Letters*, vol. 74, no. 9, Nov. 1993

[13] R. Notzel and K. H. Ploog, "Man-Made Low-Dimensional Solids:. New challenges in Microstructure Materials Science", *Int. J. Mod. Phys.* vol. 7, no. 15, pp. 2743-2778, Jul. 1993.

[14] Y. Okuno, "Investigation on direct bonding of III-V semiconductor wafers with lattice mismatch and orientation mismatch", *Applied Physics Letters*, vol. 68, no. 20, pp. 2855 – 2857, 1996.

[15] Y. Okuno, K. Uomi, M. Aoki, T. Tsuchiya, "Direct wafer bonding of III-V compound semiconductors for free-material and free-orientation integration",*IEEE Journal Quantum Electronics*, vol. 33, no. 6, pp. 959-969, Jun.1997

[16] M.M. Hasan, M.R. Islam, K. Teramoto, ''Crystallographic orientation dependent optical properties of GaInSb mid-infrared quantum well laser,'' *International Journal for Light and Electron Optics*, vol. 3, no. 5, pp. 1566–1575, Sep. 2004.

[17] I. Vurgaftman1, J. R. Meyer1 and L. R. Ram-Mohan, "Band parameters for III–V compound semiconductors and their alloys", *J. App. Phys.*, vol. 89, no. 11, pp. 5815–5876, Jun. 2001.

[18] Weng W. Chow, Stephan W. Koch, *Semiconductor-Laser Fundamentals Physics of the Gain Materials,* Springer-Verlag Berlin Heidelberg New York, 1999

[19] S. L. Chuang, *Physics of Optoelectronic Devices*, Wiley Series in Pure and Applied Optics, 1995

[20] T. Ohtoshi, T. Kuroda, A. Niwa, and S. Tsuji," Dependence of optical gain on crystal orientation in surface-emitting lasers with strained quantum wells", *Applied Physics Letter*, vol. 65, no.15, pp. 1886-1888, Oct.1994.

Wideband Planar Monopole Antenna for LTE, GSM, Bluetooth, WiMAX, DCS, PCS, and GPS Mobile Terminals

Rahinur Rahman, Khaled Mahbub Morshed, Sumyea Sabrin and Md Mostafizur Rahman
Department of Electronics and Communication Engineering
Khulna University of Engineering & Technology, Khulna 9203, Bangladesh
E-mail: rahinur2k11@gmail.com, khaled.morshed@ece.kuet.ac.bd, sweetykuet@gmail.com, mostafiz963@yahoo.com

Abstract—**A simple planar antenna of high gain for long term evolution (LTE), global system for mobile communications (GSM), Bluetooth, worldwide interoperability for microwave access (WiMAX), digital cellular services (DCS), personal communication services (PCS), wireless local area network (WLAN), and global positioning system (GPS) mobile terminals is presented. The antenna has wide -6 dB reflection coefficient bandwidth of 2.17 GHz (1.33 – 3.5 GHz). The antenna has a compact size of 44.9 mm ×35.5 mm × 0.87 mm placed one side of the substrate of dimension 35.5 mm × 75.5 mm. The antenna has high gain of 3.85 dBi at 2.7 GHz, maximum directivity is 5.04 dBi at 2.7 GHz and total efficiency of the antenna varies between 61% and 95% within the wide impedance bandwidth. In addition, the antenna gain and efficiency is almost constant in individual operating band of operation. Dimensions of the antenna are optimized for wide impedance band. Antenna radiation patterns are presented at 1.5, 2, 2.5, and 3 GHz.**

Keywords—Planar monopole antenna, LTE, TDD, FDD, GSM, Bluetooth, WiMAX, DCS, PCS, WLAN, and GPS.

I. INTRODUCTION

Growing demand of data rates accelerate towards next generation wireless mobile communication having wideband antenna installed within hand-held mobile devices [1] – [5] and also required added services support e.g. global positioning system (GPS), worldwide interoperability for microwave access (WiMAX), wireless local area network (WLAN), Bluetooth etc. [6] – [12]. Broadband/wideband antenna not only support these bands but also increases the channel capacity [5] – [8].

Long term evolution (LTE) bands (LTE-1 to LTE-40) can be divided into two major categories based on their dependency like time division duplex (TDD) band and frequency division duplex (FDD) band [13] – [14]. These bands cover three wide bands, lower one from 0.698 GHz to 0.966 GHz, middle band from 1.427 GHz to 2.69 GHz and the higher band from 3.4 GHz to 3.8 GHz [15] – [20]. In parallel of LTE support mobile terminals need to cover GSM bands for voice only [21] – [24].

Smartphones are attractive because of their additive services like GPS (1.559 – 1.61 GHz), Bluetooth (2.4 GHz ISM band), WiMAX in 2.3, 2.5, 3.5 GHz band, WLAN in 2.4 GHz band, digital cellular services (DCS) in the band 1.71 – 1.88 GHz, and personal communication services (PCS) in the band 1.85 – 1.99 GHz together with LTE and global system for mobile communications (GSM) support [1], [5], [34] - [36].

Several antennas has been proposed in the previous years for the use in hand held mobile devices including planar monopole [1], [6], [8], [9], planar inverted-F [5], [7], array antenna, reconfigurable antenna [2] , [3], slot antenna [10]. Also, different feeding technique e.g. multi resonance feed structure [11], hybrid feed [14], different isolation technique [24], dielectric resonator feed [19], and modified ground plane e.g. protruded [17] has been used to achieve multiband operation having limited form factor. Moreover, several antennas have been proposed for WiFi and WiMAX applications where inverted-L load [25] – [29], F-L load [30] – [32] and planar wire antenna [33], leaky wave antennas [37] [38] have been considered for gain enhancement but the size of those antennas are not feasible for hand-held mobile terminal. Most of the proposed antenna for smartphone applications comes with wideband that covers 1.6 GHz to 2.7 GHz and recently one paper has been published that support additional 3.4 – 3.8 GHz band [3].

In this paper, a technique is presented to remove notch exist in current design and using the proposed technique a simple planar wideband antenna is presented for LTE, GSM, Bluetooth, WiMAX, DCS, PCS, and GPS applications. The antenna design strategy are briefly described in Section II. Section III presents the simulation results and the paper ended with a conclusion in Section IV.

II. WIDEBAND ANTENNA DESIGN STRATEGY

The antenna is designed using low cost FR-4 substrate with dielectric constant 4.3 and loss tangent 0.025 in CST Microwave Studio. Thickness of the substrate is 0.8 mm and thickness of copper cladding is 0.035 mm. Fig. 1 shows the design steps in achieving continuous band antenna as a replacement for having a notch. Firstly, the antenna radiating legs are connected to form a loop antenna. Then, two parasitic is placed on the either side of the feeding line to form capacitive effect and finally a capacitor is placed in the right arm of the antenna, shown in Fig. 1(a), 1(b), 1(c), and 1(d), respectively.

978-1-4673-9257-0/15/$31.00 ©2015 IEEE

Fig. 2 present the top view and bottom view of the antenna. For feeding arrangement, coaxial connector is used and the antenna feeding is comes from the bottom of the antenna, shown in Fig. (2). Overall dimension of the substrate is 35.5 mm × 60.5 mm and the antenna radiator dimension is 44.9 mm × 35.5 mm. Dimension of the feeding arrangement is 10.5 mm × 31.4 mm, shown in Fig. 3, also the detailed structure of the antenna presented. Here all values are in mm. The values of the capacitor C is 2 nF and is placed by creating a gap of 1 mm. In our design we have used antenna in [1] as a reference, shown in Fig. 1(a), and we modify the structure to achieve continuous band by following aforementioned procedure/steps.

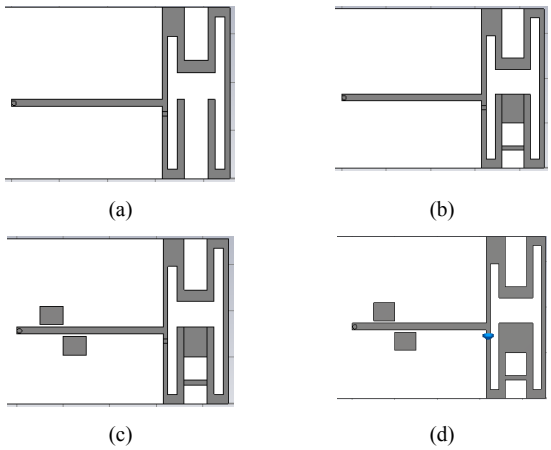

Fig. 1. Antenna design strategy for wideband operation (a) base antenna structure [1], (b) right legs are connected with two radiating elements of size 5 mm × 6.5 mm and 5 mm × 1 mm, (c) two parasitic radiator placed with a gap of 0.5 mm with the 50 Ω feeding line, and (d) final structure with addition of 2 nF capacitor on the right arm of the loop in a 1 mm space.

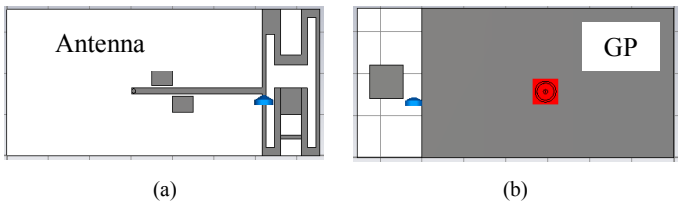

Fig. 2. Structure of the proposed monopole antenna (a) top view and (b) bottom view.

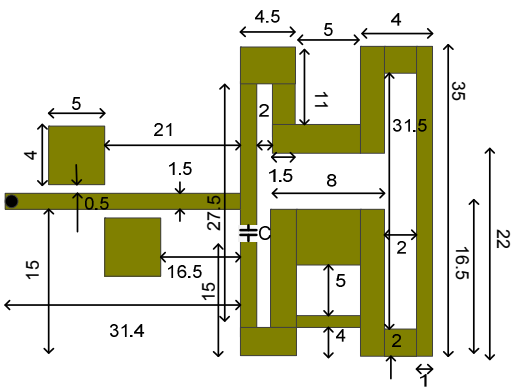

Fig. 3. Detailed geometry of the proposed antenna. Here all values/dimensions are in mm.

III. Resuls and Discussion

The antenna proposed in [1] covers 1.5 to 4.12 GHz with notches around 2.5 GHz and 3.84 GHz, shown in Fig. 4 (line AA). These two notches block the LTE 7 and radio frequency identification bands. Firstly we increase the band of the antenna by connecting two right radiator of U shape using two parallel radiator of dimension 5 mm × 6.5 mm and 5 mm × 1 mm, respectively, shown in Fig. 1(b). These two connected radiator improves the bandwidth but not reduced the notch completely, shown in Fig. 4 (line BB). After that, two parasitic patch of size 4 mm × 5mm is placed with a gap of 0.5 mm from the feeding strip shown in Fig. 1(c). This parasitic patch removes the notch slightly but has no effect on the bandwidth of the antenna, shown in Fig. 4 (line CC). To further reduce the notch at 3.84 GHz, manual impedance matching can be employed. A capacitor of size 2 nF, decided by parametric simulation studied in software, is placed on the right arm of the antenna because this arm giving resonance at that frequency, reduces the notch completely, shown in Fig. 4 (line DD). Here the positioning of the capacitor, 1 mm away from the 50 Ω feeding line.

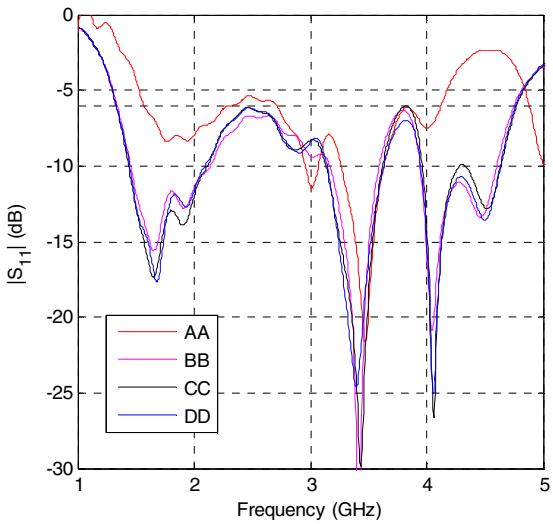

Fig. 4. Reflection coefficient of the proposed antenna for the geometry presented in Fig. (1). Here, return loss corresponds to AA, BB, CC, and DD are for the structure shown in Fig. 1(a), 1(b), 1(c) and 1(d), respectively.

After finalizing the structure, the detailed geometry are presented in Fig. 3 and the simulated reflection coefficient are shown in Fig. 5. The proposed/modified antenna has a wide impedance bandwidth of 3.43 GHz, from 1.33 GHz to 4.76 GHz, with a voltage standing wave ratio (VSWR) 3:1 (-6 dB reflection coefficient or 6 dB return loss). From the figure it can easily be observed that the proposed antenna can provide multi band operation to support GPS, DCS, PCS, WLAN, Bluetooth, WiMAX, and LTE.

Total efficiency of the antenna is varied between 61% and 95%, shown in Fig. 6. Total efficiency is minimum at 3.8 GHz and maximum at 1.6 GHz. Because of the non-symmetric structure the efficiency has significantly changes within the

978-1-4673-9257-0/15/$31.00 ©2015 IEEE

operating bandwidth which leads to the change in gain/realized gain and directivity of the antenna, shown in Fig. 7.

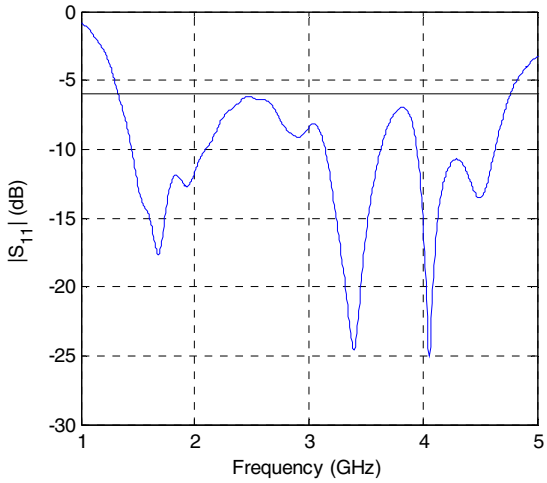

Fig. 5. Reflection coefficient vs frequency of the proposed antenna.

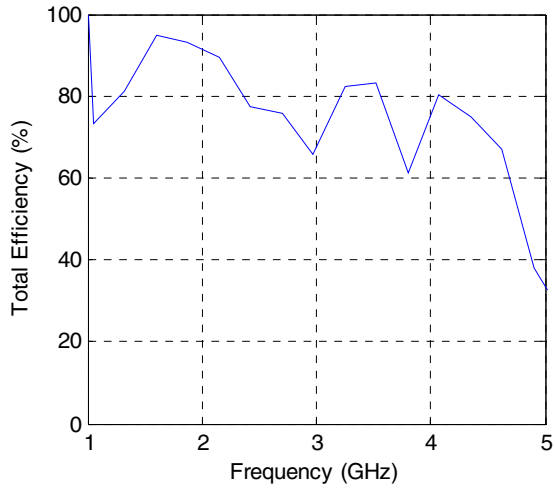

Fig. 6. Total efficiency of the proposed antenna vs frequency.

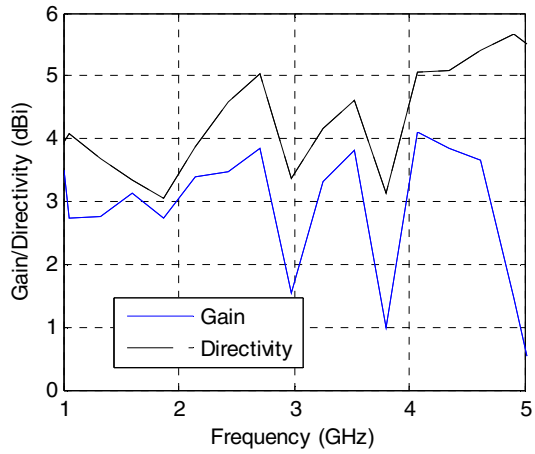

Fig. 7. Gain and directivity of the proposed antenna as a function of frequency.

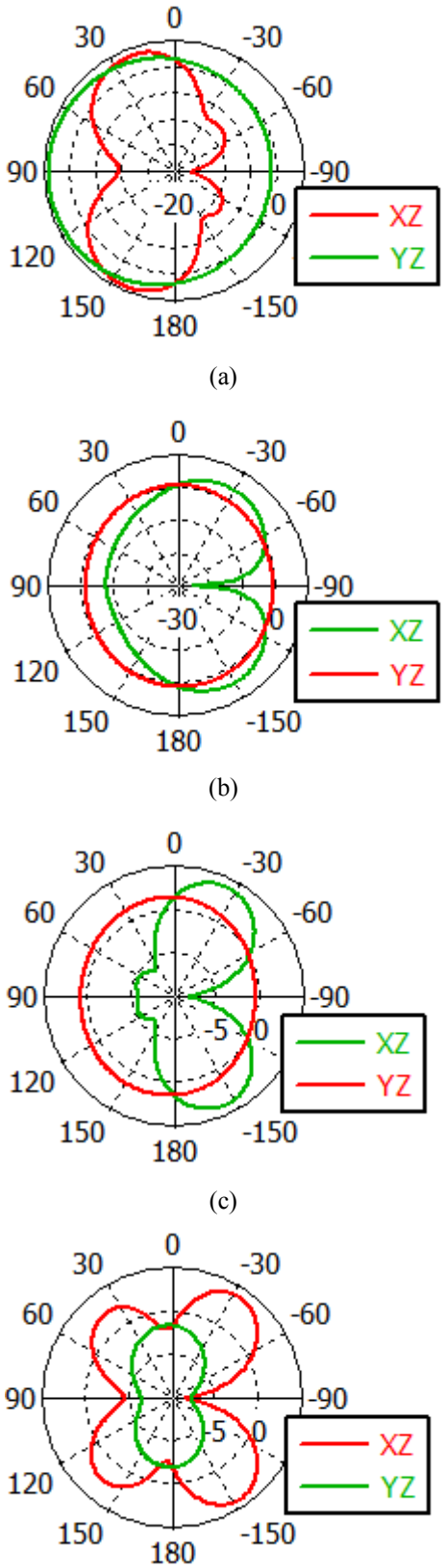

978-1-4673-9257-0/15/$31.00 ©2015 IEEE

(d)

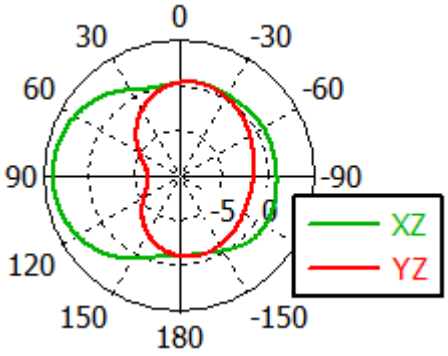

(e)

Fig. 8. Radiation patterns of the proposed antenna at (a) 1.5 GHz, (b) 2 GHz, (c) 2.5 GHz, (d) 3 GHz, and (e) 3.5 GHz.

Realized gain of the antenna is changes from 1.55 dBi (at 2.975 GHz) to 3.85 dBi (at 2.7 GHz) while the directivity of the antenna changes from 3.06 dBi (at 1.875 GHz) to 5.04 dBi (at 2.7 GHz), shown in Fig. 7. However, the gain variation within an individual band is less than 0.5 dB, e.g. < 0.5 dB at GSM 1800, <0.5 dB at ISM band. Directivity is always higher than realized gain which is expected. Realized gain is about 2.3dBi for GPS, DCS, PCS, and WiMAX band, and above 2.5dBi for WLAN, and Bluetooth. The proposed antenna has a directivity of 2.6 – 2.5 dBi for GPS, DCS, PCS band. 2.7 – 4.5 dBi directivity is achieved for WiMAX, WLAN band. The overall directivity of the antenna is above 3.06 dBi for all through the operating frequency

Radiation patterns of the antenna at 1.5, 2, 2.5, 3, and 3.5 GHz are shown in Fig. 8. At frequencies, below 3.5 GHz, this antenna radiation pattern is like planar monopole antenna having radiation almost omnidirectional shown in Fig. 8(a), 8(b), 8(c), 8(d), and 8(e). Though the antenna bandwidth covers till 4.7 6GHz but there are improvement in radiation patterns required to make this antenna useful beyond 3GHz. In obtained results, nulls have been observed on the radiation patterns and these nulls are generated because current are highly condensed along the right and left edges of the antenna loop.

IV. Conclusion

A wideband planar monopole antenna for LTE, GSM, Bluetooth, WiMAX, DCS, PCS, and GPS mobile devices/smartphones was designed. The bandwidth improvement of this antenna has been achieved through adding two parasitic element near the feeding line for capacitive effect and then adding a series capacitor in the loop monopole to maintain the impedance matching at the notch frequency. The simulated return loss, antenna efficiency, directivity and the radiation pattern suggest the potential use of this antenna for wide band operation in mobile devices.

References

[1] Y. –J. Chi, F. –C. Chen, "Compact Printed Hepta-Band Monopole Antenna for Mobile Devices," in *Asia-Pacific Microwave Conference Proceedings (APMC)*, pp.2216 – 2219, 7 – 10 Dec. 2010.

[2] Z. H. Hu, C. T. P. Song, J. Kelly, P. S. Hall, P. Gardner, "Wide Tunable Dual-Band Reconfigurable Antenna," Electronics Letters, vol.45, no.22, pp.1109-1110, Oct. 22, 2009.

[3] K. –L. Wong, Z. –G. Liao, "Passive Reconfigurable Triple-Wideband Antenna for LTE Tablet Computer," *IEEE Transactions on Antennas and Propagation*, vol.63, no.3, pp.901-908, Mar. 2015.

[4] K. –L. Wong, C. -Y. Tsai, "Low-Profile Dual-Wideband Inverted-T Open Slot Antenna for the LTE/WWAN Tablet Computer with a Metallic Frame," *IEEE Transactions on Antennas and Propagation*, vol.63, no.7, pp.2879-2886, Jul. 2015.

[5] K. R. Boyle, P. G. Steeneken, "A Five-Band Reconfigurable PIFA for Mobile Phones," *IEEE Transactions on Antennas and Propagation*, vol.55, no.11, pp.3300-3309, Nov. 2007.

[6] Y. –L. Ban, C. –L. Liu, Z. Chen, J. L. -W. Li, K. Kang, "Small-Size Multiresonant Octaband Antenna for LTE/WWAN Smartphone Applications," *IEEE Antennas and Wireless Propagation Letters*, vol.13, pp.619-622, 2014.

[7] C. –H. Chang, K. –L. Wong, "Printed-PIFA for Penta-Band WWAN Operation in the Mobile Phone," *IEEE Transactions on Antennas and Propagation*, vol.57, no.5, pp.1373-1381, May 2009.

[8] J. -H. Lu; Y. -S. Wang, "Planar Small-Size Eight-Band LTE/WWAN Monopole Antenna for Tablet Computers," *IEEE Transactions on Antennas and Propagation*, vol.62, no.8, pp.4372-4377, Aug. 2014.

[9] T. Zhang, R. L. Li, G. P. Jin, G. Wei, M. M. Tentzeris, "A Novel Multiband Planar Antenna for GSM/UMTS/LTE/Zigbee/RFID Mobile Devices," *IEEE Transactions on Antennas and Propagation*, vol.59, no.11, pp.4209-4214, Nov. 2011.

[10] Y. F. Cao, S. W. Cheung, T. I. Yuk, "A Multiband Slot Antenna for GPS/WiMAX/WLAN Systems," *IEEE Transactions on Antennas and Propagation*, vol.63, no.3, pp.952-958, Mar. 2015.

[11] J. Lee, Y. Liu, H. Kim, "Mobile Antenna Using Multi-Resonance Feed Structure for Wideband Operation," *IEEE Transactions on Antennas and Propagation*, vol.62, no.11, pp.5851-5855, Nov. 2014.

[12] J. –T. Yeh, W. –J. Liao, S. –H. Chang, "Compact Internal Antenna for Handheld Devices with Comprehensive DTV Band Coverage," *IEEE Transactions on Antennas and Propagation*, vol.62, no.8, pp.3998-4007, Aug. 2014.

[13] J. –H. Lu, J. –L. Guo, "Small-Size Octaband Monopole Antenna in an LTE/WWAN Mobile Phone," *IEEE Antennas and Wireless Propagation Letters*, vol.13, no., pp.548-551, 2014.

[14] K. –L. Wong, L. –Y. Chen, "Small-Size LTE/WWAN Tablet Device Antenna with Two Hybrid Feeds," *IEEE Transactions on Antennas and Propagation*, vol.62, no.6, pp.2926-2934, Jun. 2014.

[15] Y. –L. Ban, Y. –F. Qiang, Z. Chen, K. Kang, J. –H. Guo, "A Dual-Loop Antenna Design for Hepta-Band WWAN/LTE Metal-Rimmed Smartphone Applications," *IEEE Transactions on Antennas and Propagation*, vol.63, no.1, pp.48-58, Jan. 2015.

[16] K. –L. Wong, C. –Y. Tsai, "Small-Size Stacked Inverted-F Antenna with Two Hybrid Shorting Strips for the LTE/WWAN Tablet Device," *IEEE Transactions on Antennas and Propagation*, vol.62, no.8, pp.3962-3969, Aug. 2014.

[17] Y. –L. Ban, S. Yang, Z. Chen, K. Kang, J. L. -W. Li, "Decoupled Planar WWAN Antennas with T-Shaped Protruded Ground for Smartphone Applications," *IEEE Antennas and Wireless Propagation Letters*, vol.13, no., pp.483-486, 2014

[18] B. –Y. Park, M. –H. Jeong, S. –O. Park, "A Magneto-Dielectric Handset Antenna for LTE/WWAN/GPS Applications," *IEEE Antennas and Wireless Propagation Letters*, vol.13, no., pp.1482-1485, 2014.

[19] Y. –F. Lin, H. –M. Chen, C. –Y. Lin, Shan-Cheng Pan, "Planar Inverted-L Antenna with a Dielectric Resonator Feed in a Mobile Device," *IEEE Transactions on Antennas and Propagation*, vol.57, no.10, pp.3342-3346, Oct. 2009.

[20] Y. –L. Ban, Z. –X. Chen, Z. Chen, K. Kang, J. L. -W. Li, "Decoupled Hepta-Band Antenna Array for WWAN/LTE Smartphone Applications," *IEEE Antennas and Wireless Propagation Letters*, vol.13, pp.999-1002, 2014.

[21] Y. –L. Ban, Z. X. Chen, Z. Chen, K. Kang, J. L. –W. Li, "Reconfigurable Narrow-Frame Antenna for Heptaband WWAN/LTE

978-1-4673-9257-0/15/$31.00 ©2015 IEEE

Smartphone Applications," IEEE Antennas and Wireless Propagation Letters, vol.13, pp.1365-1368, 2014.

[22] C. –K. Hsu, S. –J. Chung, "Compact Antenna with U-Shaped Open-End Slot Structure for Multi-Band Handset Applications," *IEEE Transactions on Antennas and Propagation*, vol.62, no.2, pp.929-932, Feb. 2014.

[23] J. Lee, Y. Sung, "Heptaband Inverted-F Antenna with Independent Resonance Control for Mobile Handset Applications," *IEEE Antennas and Wireless Propagation Letters*, vol.13, pp.1267-1270, 2014

[24] A. Cihangir, F. Ferrero, G. Jacquemod, P. Brachat, C. Luxey, "Neutralized Coupling Elements for MIMO Operation in 4G Mobile Terminals," *IEEE Antennas and Wireless Propagation Letters*, vol.13, pp.141,144, 2014.

[25] K. M. Morshed, D. K. Karmokar, and M. Talukder, "Numerical and experimental analysis of impedance matched inverted-L and stair inverted-L antenna for 5 GHz WLAN operation," *Journal of Communications*, vol. 5, no. 8, pp. 612–619, Aug. 2010.

[26] K. M. Morshed, D. K. Karmokar, and A. M. Numan-Al-Mobin, "Numerical analysis of impedance matched inverted-L antennas for Wi-Fi operations," in *IEEE International Conference on Computer and Information Technology (ICCIT)*, Dhaka, Bangladesh, Dec. 2009, pp. 691–696.

[27] K. M. Morshed, D. K. Karmokar, and M. M. Rahman, "Dual band two elements inverted-L antenna for 2.3 GHz mobile WiMAX and 5.5 GHz Wi-Fi operations," in *IEEE International Conference on Computer and Information Technology (ICCIT)*, Dhaka, Bangladesh, Dec. 2011, pp. 223–228.

[28] M. A. Hossain, M. R. Basar, and K. M. Morshed, "Ultra-wideband LLI-slit slotted antenna for WLAN, bluetooth and Wi-Fi operations," in *IEEE International Conference on Computer and Information Technology (ICCIT)*, Dhaka, Bangladesh, Dec. 2011, pp. 229–233.

[29] M. R. Basar, M. A. Hossain, M. R. U. Hoque, and K. M. Morshed, "Compact dual L-slit slotted antenna for spacecraft, WLAN, Wi-Fi, and bluetooth application," in *IEEE International Conference on Electrical Computer Engineering (ICECE)*, Dhaka, Bangladesh, Dec. 2012, pp. 706–708.

[30] D. K. Karmokar, K. M. Morshed, M. S. Hossain, and M. N. Mollah, "Wideband low profile double inverted-F antenna for 5.2/5.8 GHz WLAN and 5.5 GHz WiMAX applications," *ACEEE International Journal on Communications*, vol. 2, no. 1, pp. 28–32, Mar. 2011.

[31] D. K. Karmokar, K. M. Morshed, A. M. Numan-Al-Mobin, and A. E. Kabir, "High gain multiband loaded inverted-F antennas for mobile WiMAX,Wi-Fi, bluetooth and WLAN operation," *International Journal of Engineering (IJE)*, vol. 4, no. 3, pp. 219–232, Jul. 2010.

[32] A. A. Talukder, D. K. Karmokar, K. M. Morshed, and M. N. Mollah, "Low profile inverted-F-L antenna for 5.5 GHz WiMAX applications," *ACEEE International Journal on Communications*, vol. 3, no. 1, pp. 15–19, Mar. 2012.

[33] M. J. Hossain, M. A. M. Khan, A. M. Numan-Al-Mobin, and K. M. Morshed, "A simple structured planar wire antenna for wireless communication applications," in *IEEE International Conference on Electrical Computer Engineering (ICECE)*, Dhaka, Bangladesh, Dec. 2012, pp. 709–712.

[34] J. Ilvonen, R. Valkonen, J. Holopainen, V. Viikari, "Design Strategy for 4G Handset Antennas and a Multiband Hybrid Antenna," *IEEE Transactions on Antennas and Propagation*, vol.62, no.4, pp.1918-1927, Apr. 2014.

[35] S. F. Roslan, M. R. Kamarudin, M. Khalily, M. H. Jamaluddin, "An MIMO Rectangular Dielectric Resonator Antenna for 4G Applications," *IEEE Antennas and Wireless Propagation Letters*, vol.13, pp.321-324, 2014.

[36] B. Lee, F. J. Harackiewicz, H. Wi, "Closely Mounted Mobile Handset MIMO Antenna for LTE 13 Band Application," *IEEE Antennas and Wireless Propagation Letters*, vol.13, pp.411-414, 2014.

[37] D. K. Karmokar, K. P. Esselle, "Periodic U-Slot-Loaded Dual-Band Half-Width Microstrip Leaky-Wave Antennas for Forward and Backward Beam Scanning," in *IEEE Trans. Antennas Propag.*, vol.PP, no.99, pp.1-1.

[38] D. K. Karmokar, K. P. Esselle, T. S. Bird, "An Array of Half-Width Microstrip Leaky-Wave Antennas Radiating on Boresight," in *IEEE Antennas Wireless Propag. Letters*, vol.14, no., pp.112-114, 2015.

978-1-4673-9257-0/15/$31.00 ©2015 IEEE

On the Architectures of RF Based Underwater Wireless Sensor Networks for Intruder Detection

[1]Musbiha Binte Wali and [2]Md. Farhad Hossain
Department of Electrical and Electronic Engineering
Bangladesh University of Engineering & Technology (BUET), Dhaka-1000, Bangladesh
Email: [1]musbihabintewali@yahoo.com, [2]mfarhadhossain@eee.buet.ac.bd

***Abstract*- For underwater surveillance and observations, the widely used medium is the acoustic wave based underwater wireless sensor networks (UWSNs). But acoustics in underwater environment face high challenges to meet the necessity for fast transmission rates in different newly emerging underwater operations. Then again, underwater network systems based on radio frequency (RF) have incredible potential for supporting fast information transmission. In light of this, we propose and examine two three dimensional (3D) cluster-based UWSN architectures for identifying intruders in an underwater surveillance area. The proposed architectures comprised of cluster heads (CHs) and sensor nodes (SNs) senses the presence of an intruder inside the surveillance area and then pass the real-time location of the intruder to a coastal base station (BS) via a sink situated at water surface. All the data transfers from SNs to BSs are RF based. The data of the received RF signal strength and the positions of the SNs and CHs are the information used for calculating the intruder's position. For assessing the proposed system architectures' localization capacities in a seawater circumstance, substantial simulations are carried through. Localization precision of the architectures is altogether examined in terms of inaccuracy in distance and direction estimations. Effect of different framework parameters on the performance is likewise interpretatively scrutinized exhibiting noteworthy performance discord between the architectures.**

Keywords–intruder detection; target localization; RF based UWSN; 3D sensor networks; underwater communications

I. Introduction

For enquiring into the resourceful underwater worlds, research on underwater operations conveys great significance as almost seventy five percent of the surface of the planet Earth is covered by water, most part by ocean and seas [1]. While investigating this prodigious area of underwater, UWSN systems have been approved by the analysts as an attainable, minimal effort arrangement [2] as the advances in sensor technologies have made sensor networks utilizable for any kind of circumstances. Objectives of deploying UWSNs include navigations, observation on sea boundaries, mine surveillance, trace and rescue operations, preventing cataclysms, seaward investigations, oceanography and numerous sea-going applications [1]-[2]. In most cases UWSNs use acoustics as transmission media. Notwithstanding, with the increment in the quantity of fast moving submerged vehicles and independent weapons in current times, there is a concern for speedier transmission media like optical or radio frequency (RF), particularly for detection and tracing purposes, as the transmission speed by acoustics is slower than the needed [3]. But then, optical wave is not feasible for major submerged applications as it requires line of sight (LOS) with tight arrangement and clear water in its transmission way [4]. In this way, how to utilize the RF's quick transmission capacity in underwater environment to make real-time high-throughput applications achievable is catching the attention of the related academic group. Numerous long sought aims, for example, real-time localization and transmission, resistance to acoustic clamor, turbidity and pressure slopes; diminished effect on marine life and ability of non-LOS communications can be attained utilizing RF based UWSNs which acoustic based systems cannot [5], [6].

Given this situation, this paper is meant to investigate the designs of submerged surveillance system for localizing unwelcomed objects utilizing RF as transmission coverage. Our broad survey shows that there is progressing investigation on RF communication based underwater intruder localizing systems and this field needs more efforts. Beforehand, a two dimensional (2D) submarine locating procedure utilizing a dispersed sensor system of binary-detection capacity was proposed in [7]. Furthermore, the writers in [8] introduced 2D two disseminated particle filter based object locating and tracing strategies utilizing clustered UWSNs. Then again, submerged 3D target identification and tracking strategies utilizing UWSNs were presented in [9]-[11]. The entry time of the reverberation messages originating from the object is utilized for deciding the distance from the sensor to the object in [9]. At that point trilateration is used to compute target's location. Node's position and the above speed will then be utilized for tracking the submerged target. Nonetheless, all the previously stated works are carried out in light of acoustic network systems. Provided the feasibility of diversified applications of UWSNs proven by the time, further sea trials have been carried out in [12] to introduce EM into the UWSNs with a view to undersea target detection & tracking using EM-acoustic combination.

Therefore, this paper proposes and explores two 3D UWSN architectures for identifying and locating intruders underwater. Each architecture comprises of a cluster-based UWSN formed utilizing sensor nodes (SNs) and cluster heads (CHs), a sink situated at the water surface and an inland base station (BS) with the essential mathematical models for localization. The inspiration of utilizing cluster based UWSNs originates from their powerful topology and the certainty of their inclination in extended system life through effectual energy sparing techniques [13], [14]. Every step in the communications from the SNs to the BS via CHs are proposed to be by means of RF. Intruder locations are computed utilizing the data of received RF signal strength and the positions of SNs and CHs. Performances of the presented architectures are assessed using substantial simulations.

978-1-4673-9257-0/15/$31.00 ©2015 IEEE

Localization precision is analyzed and compared in terms of inaccuracies in both distance and direction approximations. Effect of system size and signal identification threshold on the system perfection is likewise examined.

The remaining of the paper is organized as follows: Section II introduces the general outline of the proposed localization strategies. Then in Section III, Proposed architectures are illustrated in detail. Section IV characterizes new performance metrics and then the simulation results with insightful investigation in Section V. The paper concludes in Section VI by abridging the key findings.

II. Proposed Overall Localization Scheme

The general operation guideline of the proposed submerged intruder identifying and locating strategy is talked about in this segment. The network comprises of two fundamental components, SNs and CHs. Again, every SN involves low power sensor bundle and an omnidirectional RF transmitter. The sensor bundle of every SN uses distinctive standards for detecting an intruder, for example, movement sensor, pressure sensor (as a fast moving intruder will acquaint pressure amid drawing nearer to the system), metal identifier (to guarantee whether the intruder is of metal body) and passive sonar (to be sure whether the approaching intruder has a motor, particularly when submarines are to be recognized). To mention, the proposed architectures are outlined independent of the kind of detecting methods of the SNs. A CH alongside a team of SNs constructs a cluster. Every CH comprises of RF transmitter and recipient. Collecting the neighborhood data from SNs and/or different CHs and sending those to the sink are the duties of a CH.

These SNs and CHs, being organized in a specific position, construct the clusters in 3D underwater space and subsequently develop to the architectures discussed in the segment III. The working rule of the general localization strategy as appeared in Fig. 1 is as follows: Both SNs and CHs typically stay in dormant or rest mode for energy saving. Receiving RF signal strength above than a specific threshold P_{th} either from another CH or from the close-by SNs can just alter the CH's to active mode, while an SN just after sensing an intruder. When an intruder enters the reconnaissance zone, the nearby SNs sense the vicinity of the intruder and alter to active mode. Detecting the vicinity of an intruder, SN transmits its location information utilizing RF signal of power P_{SN} and frequency f_{SN}. After receiving RF signal from SNs, CHs are switched to active mode. These active CHs gather the location data of the SNs and the strength of the received RF signal from the SNs. At that point the necessary pieces of information are sent to the particular CHs of the direct upper layer using RF signal of power P_{CH} and frequency f_{CH} and so on. The data, in this manner, gets to the surface sink from the CHs of the topmost layer. The accumulated data is then transmitted to the inland BS for handling and approximating the location of the object. All the transmissions including SN-CH, CH-CH, CH-surface sink and surface sink-BS are based on RF signal.

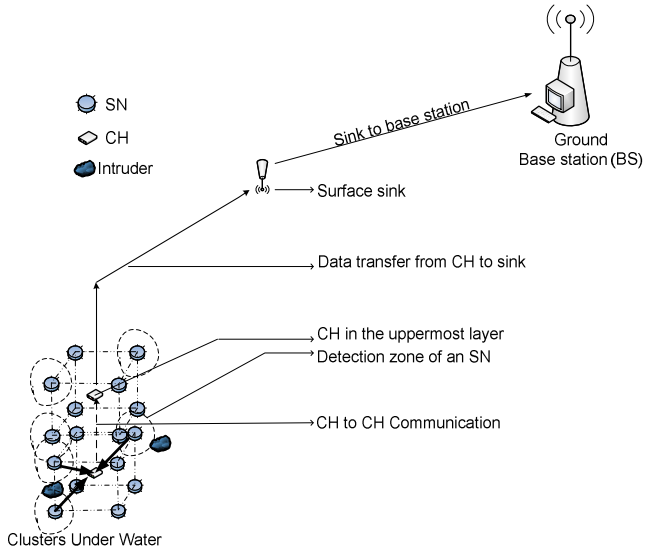

Fig. 1: Overall model of the proposed localization schemes.

III. Proposed UWSN Architectures

Proposed UWSN architectures for recognizing intruders are presented here below. We assume a plane seabed and overlook the versatility of system components. SNs and CHs are organized in 3D space constructing the basic building block as shown in Fig. 2(a). The XY plane of the arrangement is viewed as parallel to the seabed and the Z-axis is considered along the sea depth. The fundamental building block is repeated to build the UWSN covering a reconnaissance region of a cubic area $D_x \times D_y \times D_z$, where D_x, D_y, and D_z are the length of the observation region along the X-, Y-and Z-axes respectively. The evolved UWSN is shown in Fig. 2(b). Based on the localization rule, we now propose two distinct intruder detecting architectures symbolized as A_1 and A_2, which are discussed in detail in following sections.

A. Architecture A_1

In topology A_1, SNs are allocated at each of the eight vertices of a rectangular cuboid of cubic dimension $\Delta_x \times \Delta_y \times \Delta_z$ as illustrated in Fig. 2(a). In this manner, the whole UWSN is constructed by allocating SNs at each Δ_x, Δ_y and Δ_z distance along X-, Y- and Z-axis respectively. Then again, one CH is set at the focal point of every cuboid. Along these lines the distance of a CH from the SNs of its cuboid is equal to $D_{CE} = \frac{1}{2}\sqrt{\Delta_x^2 + \Delta_y^2 + \Delta_z^2}$. The UWSN, in this manner, has eight SNs encompassing every CH and vice versa.

Under A_1, we assume that each CH holds the information about its own position coordinate. As soon as an SN senses an unwelcomed approaching object, it alerts the nearby CHs around by transmitting RF signal. If a CH receives RF signal of power above P_{th} transmitted by the SN, the CH switches to active mode and sends its coordinate to the exact upper layer's

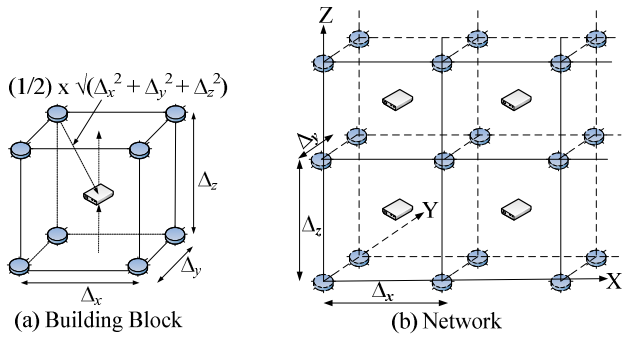

Fig. 2: Topology for architecture A_1 and A_2.

CHs through RF signal. By means of this flow of location data from CHs of one layer to those of the upper layers, the coordinates of the CHs initiating RF signal transmission is consequently known to the BS, which are also the CHs nearer to the target. If the BS receives the location data from N CHs, then the approximated coordinate (x_{est}, y_{est}, z_{est}) of the target is given by

$$x_{est} = \frac{1}{N}\sum_{i=1}^{N} x_i \tag{1}$$

$$y_{est} = \frac{1}{N}\sum_{i=1}^{N} y_i \tag{2}$$

$$z_{est} = \frac{1}{N}\sum_{i=1}^{N} z_i \tag{3}$$

where (x_i, y_i, z_i) is the coordinate of the ith active CH in 3D.

B. Architecture A_2

Architecture A_2 utilizes the same topology of A_2. However, the location approximation principle in A_2 is significantly different than that of in A_1. Architecture A_2 utilizes both the location information of the active CHs (from the CHs nearest to the target) and additionally the power of RF signal a CH received from the SNs. First, similar to A_1, an approximate location (x_{int}, y_{int}, z_{int}) of the target is calculated using (1)-(3). After that, the primarily approximated position of intruder is fine tuned to acquire a new coordinate (x_{est}, y_{est}, z_{est}) by utilizing the information of the received RF power at CHs from the SNs. The equations for this fine tuning are as below

$$x_{est} = \frac{1}{N}\sum_{i=1}^{N} \frac{(P_{max} - P_i)x_{int} - (P_{int} - P_i)x_i}{P_{max} - P_{int}} \tag{4}$$

$$y_{est} = \frac{1}{N}\sum_{i=1}^{N} \frac{(P_{max} - P_i)y_{int} - (P_{int} - P_i)y_i}{P_{max} - P_{int}} \tag{5}$$

$$z_{est} = \frac{1}{N}\sum_{i=1}^{N} \frac{(P_{max} - P_i)z_{int} - (P_{int} - P_i)z_i}{P_{max} - P_{int}} \tag{6}$$

where P_i is the true value of the strength of the RF signal that was received by the ith CH. P_{max} and P_{int} are the strength of the received RF signal at i^{th} CH if the SN were situated at the location of the CH and (x_{int}, y_{int}, z_{int}) respectively. Each of the power values utilized in (4)-(6) are expressed in dBm. Eq. (4)-(6) basically make use of the fact that the received signal strength expressed in dBm diminishes linearly with travelled distance from the transmitter, i.e., the closer the receiver's position to the transmitter, the bigger will be the value of the received power (ignoring all kind of fading).

IV. Performance Metric

For assessing the performance of the proposed intruder localization architectures, performance metrics are defined below, which calcuate the error in location approximation in terms of distance and direction. For doing this, at first the reference point is shifted to the approximated location (x_{est}, y_{est}, z_{est}) of the intruding object as demonstrated in Fig. 3. After this, the original position of an intruding object is re-calculated in spherical coordinate denoted as (r, θ, φ) with respect to the new reference.

A. Error in Distance Estimation

If (x, y, z) is the true position of the intruding object which is our target of localization, then the absolute distance r between the original and the approximated location is hereby assumed as a measure of error. The localization inaccuracy can be given by

$$r = \sqrt{(x_{est} - x)^2 + (y_{est} - y)^2 + (z_{est} - z)^2} \tag{7}$$

Then the normalized mean square error (NMSE) in location approximation defined as the mean of r^2 normalized by the square of the minimum separation between two SNs can be written as

$$NMSE_r = \frac{\sum_{i=1}^{M} r_i^2}{M\left[\min\left(\Delta_x, \Delta_y, \Delta_z\right)\right]^2} \tag{8}$$

where M is the number of Monte-Carlo simulations.

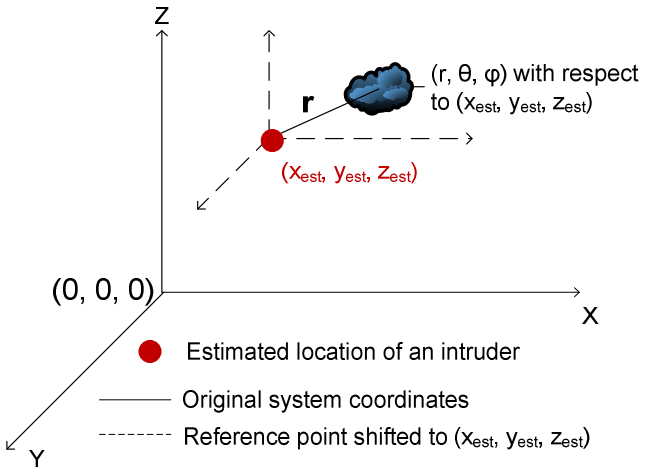

Fig. 3: Shifting of reference point for calculating the errors in localizations.

B. Error in Direction Estimation

The polar angle θ and the azimuthal angle φ of the actual location of an intruder with respect to the approximated location is considered as the measures of error in direction approximation. This can be given by

$$\theta = cos^{-1}\left(\frac{z - z_{est}}{r}\right), -90° \leq \theta \leq 90° \quad (9)$$

$$\varphi = tan^{-1}\left(\frac{y_{est} - y}{x_{est} - x}\right), -180° \leq \varphi \leq 180° \quad (10)$$

V. Simulations, Results and Discussions

A. Simulation Setup

Substantial simulations using MATLAB are implemented for assessing the performance of the proposed target localization topologies. The average results illustrated below are obtained by averaging the results over 1000 individualistic simulations. Without losing the generalized state, a 3D UWSN with measurement $D_x = D_y = D_z$ is assumed. An underwater RF propagation model with a given path-loss $20\times(\log_{10}e)\times 2\pi\times\sqrt{(\sigma \times f \times 10^{-7})}$ dB/m is used, where f is the transmission frequency in Hz and σ is the conductivity of water in S/m [5]. For fresh water, usual value is $\sigma = 0.01$ S/m, but this value is much bigger for seawater due to the increased salinity level dependent on the depth of water and temperature also [5]. Localization performance of the topologies is assessed considering salty water environment using $\sigma = 4$ S/m. Two different frequencies, $f_{SN} = 6$ kHz and $f_{CH} = 3$ kHz, and transmission power $P_{SN} = 100$ mW and $P_{CH} = 1$ W are used. If not otherwise specified, network size $D_x\times D_y\times D_z = 400\times400\times400$ m^3, $\Delta_x = \Delta_y = \Delta_z = 20$ m and the detection threshold $P_{th} = -60$ dBm are used for simulations.

B. Result Analysis

Cumulative distribution functions (CDFs) of the errors in distance and direction approximation are illustrated in Figs. 4(a)-4(c) from which, it is obvious that in spite of the use of same architecture, the better accuracy of A_2 compared to that of A_1 is directly attributed to the further fine-tuning of the initially approximated location using the information of received RF power. This additional feature however may increase the cost, computational complexity and energy consumption in CHs. On the other hand, both the polar and the azimuthal angle errors nearly follow uniform distributions over the same ranges respectively for both the architectures as seen in Figs. 4(b)-(c). The conclusion drawn from Fig. 4(a) is also corroborated by the NMSE plots in Fig. 5.

Performance of the architectures in terms of NMSE in the approximated distance normalized by 20×20 m^2 for three different detection thresholds is illustrated in Figs. 5(a)-(c). Insights identified by observing the figures: *At first*, we observe increasing trends of NMSE of both the architectures with the increase of the length of the sides of the 3D UWSNs. This increase in the length of the sides of the networks implies that keeping the relative positions as well as the number of SNs and CHs unchanged, D_x, D_y and D_z are increased in equal steps leading to increased distances among the nodes in the networks. Consequently, SNs are more distant from the target to be identified, higher distance between the SNs and the corresponding CHs which the SNs have to communicate with and CHs at a higher distance from the upper layer CH can communicate with those in the upper layer leading to decreased accuracy and increased NMSE. Besides, with the

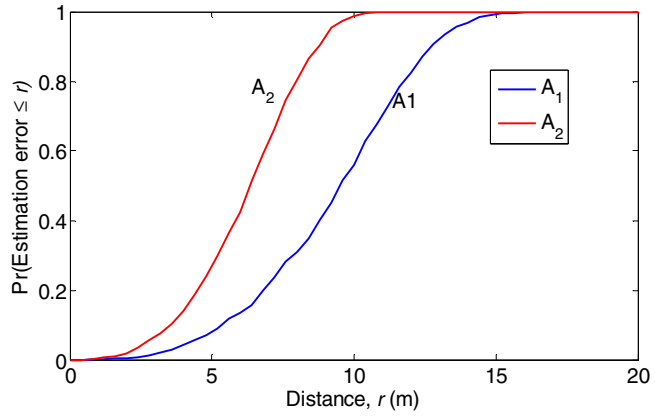

(a) Absolute distance r

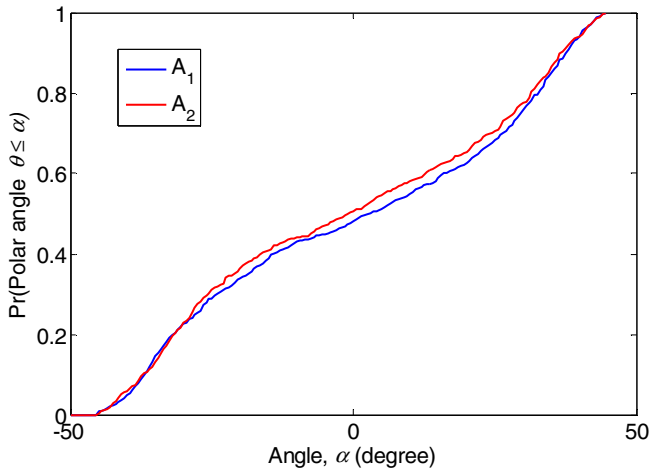

(b) Polar angle θ

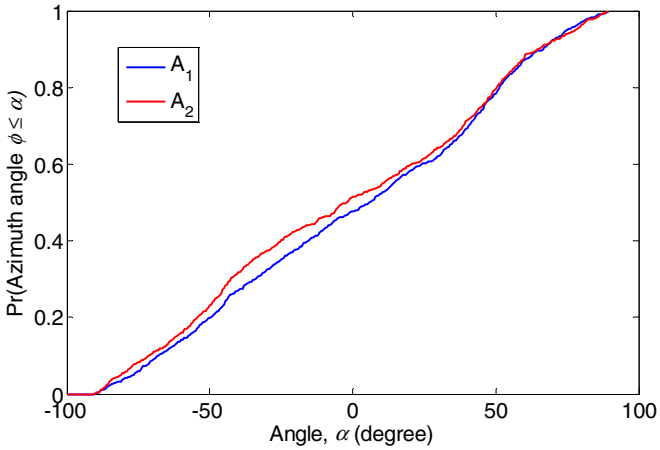

(c) Azimuthal angle φ

Fig. 4: CDF of estimation errors in distance and direction.

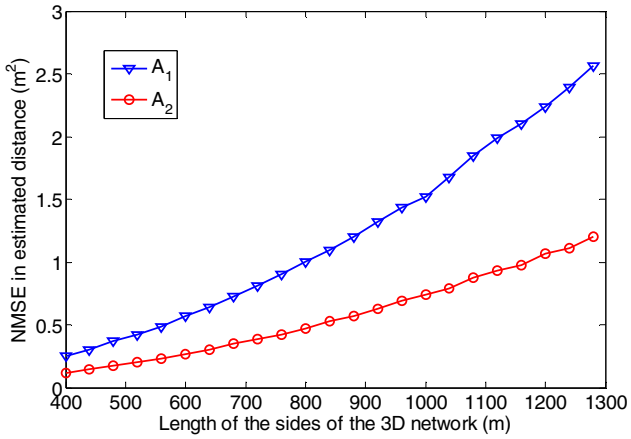

(a) P_{th} = -90 dBm

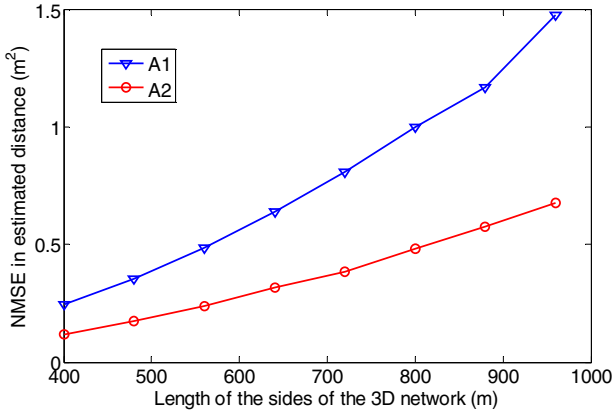

(b) P_{th} = -60 dBm

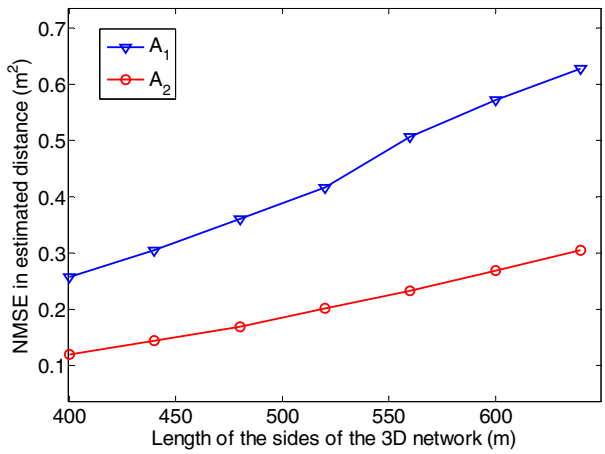

(c) P_{th} = -30 dBm

Fig. 5: NMSE in distance estimation with network length.

increase of detection threshold from -90 dBm to -30 dBm, the maximum network dimension is correspondingly reduced from 1280 m to 640 m. *Secondly*, from the better performance of A_2 compared to that of A_1, we can infer that the utilization of received power information for calculating the intruder location significantly improves the network's localization accuracy.

VI. Conclusion

The propositions of this paper include two different RF based 3D UWSNs architectures for the identification and localization of submerged intruders. The proposed architectures are both same in the topology but different in the method of estimating the location of intruding objects. Localization performance has been assessed in terms of NMSE of estimated distance as well as the polar and the azimuthal angles. Simulation results have illustrated a great effect of network's working rule on the localization performance. It has been recognized that the using of information of received RF signal strength in location approximation can essentially ameliorate the localization correctness. Furthermore, it has been identified that with the increase of the network dimension as well as the RF signal identification threshold, precision of the topologies in identifying intruding objects reduces significantly. Our future work will comprise more complicated network scenario including mobility, shadowing and multi-path fading. The localization capacity will be further upgraded by integrating further supplementary features, such as denoising filters, channel approximation mechanisms and angle-of-arrival (AoA) information.

References

[1] S. Al-Dharrab, M. Uysal and T. M. Duman, "Cooperative Underwater Acoustic Communications," *IEEE Communications Magazine*, vol. 51, no. 7, pp. 146-153, July 2013.

[2] R. Headrick and L. Freitag, "Growth of Underwater Communication Technology in the U.S. Navy," *IEEE Communications Magazine*, vol. 47, no. 1, pp. 80-82, Jan 2009.

[3] J. Partana, J. Kurosea, and B. N. Levinea, "A Survey of Practical Issues in Underwater Networks," *ACM Mobile Computing and Communications Review*, vol. 11, no. 4, pp. 23–33, 2007.

[4] S. Arnon and D. Kedar, "Non-Line-Of-Sight Underwater Optical Wireless Communication Network," *Journal of Optical Society America*, vol. 26, pp. 530–539, Mar 2009.

[5] X. Che, I. Wells, G. Dickers, P. Kear and X. Gong, "Re-evaluation of RF Electromagnetic Communication in Underwater Sensor Networks," *IEEE Communications Magazine*, vol. 48, no. 12, pp. 143-151, Dec 2010.

[6] Palmeiro, A., Martin, M., Crowther, I., Rhodes, M, "Underwater radio frequency communications," *IEEE OCEANS*, Santander, Spain, pp.1-8, June 2011.

[7] S. Zhou and P. Willett, "Submarine Location Estimation via a Network of Detection-only Sensors," *IEEE Transactions on Signal Processing*, vol. 55, no. 6, pp. 3104–3115, June 2007.

[8] Y. Huang, W. Liang, H.-B. Yu, and Y. Xiao, "Target Tracking Based on a Distributed Particle Filter," *Wireless Communications and Mobile Computing*, vol. 8, no. 8, pp. 1023–1033, Oct. 2008.

[9] G. Isbitiren and O. B. Akan, "Three-Dimensional Underwater Target Tracking with Acoustic Sensor Networks," *IEEE Transaction on Vehicular Technology*, vol. 60, no. 8, pp. 3897–3906, Oct. 2011.

[10] Z. Madadi, G. V. Anand and A. B. Premkumar, "3-D Source Localization in Shallow Ocean with Non-Gaussian Noise using a Linear Array of Acoustic Vector Sensors," *Proc. IEEE International Conference on Information Science, Signal*

Processing and their Applications (ISSPA), Montreal, QC, Canada, pp.1353-1358, July 2012.

[11] W. Cheng, A. Y. Teymorian, L. Ma, X. Cheng, X. Lu and Z. Lu, "Underwater Localization in Sparse 3D Acoustic Sensor Networks," *Proc. IEEE International Conference on Computer Communications (INFOCOM)*, Phoenix, AZ, USA, pp. 13-18, Apr 2008.

[12] Dalberg, Lauberts, Lennartsson, Levonen and Persson, "Underwater target tracking by means of acoustic and electromagnetic data fusion", *Proc. IEEE International Conference on Information Fusion*, Florence, Italy, pp.1-7, July 2006.

[13] N. M. A. Latiff, C. C. Tsimenidis and B. S. Sharif, "Energy-Aware Clustering for Wireless Sensor Networks using Particle Swarm Optimization," *Proc. IEEE International Symposium on Personal, Indoor and Mobile Radio Communications (PIMRC), pp.* 1-5, Sep 2007.

[14] M. Younis, M. Youssef, and K. Arisha, "Energy-Aware Management for Cluster-based Sensor Networks," *Computer Networks*, vol. 43, no. 5, pp. 649-668, Dec 2003.

Modelling of Highly Birefringent Dispersion Compensating Circular Photonic Crystal Fiber

Umme Ayesha Siddika[1,*], M. Shaifur Rahman[2]
[1,2]Department of Electrical and Electronic Engineering, Khulna University of Engineering & Technology, Khulna-9203
[*]E-mail: ash.kuet@gmail.com

Abstract— **This paper represents a highly birefringence circular-lattice Photonic Crystal Fiber (PCF) which compensates polarization and chromatic dispersion covering the E to U communication bands (1310–1640 nm). The finite element method (FEM) with perfectly matched layers is applied to investigate the guiding properties of the proposed PCF. From simulation, it is observed that the proposed PCF has dispersion coefficient about -220.9032 to -792.7265 (ps/nm-km) for E to U band. Particularly at the wavelength of 1550 nm the value of dispersion coefficient is found to be -678.1918 (ps/nm-km) and nonlinear coefficient is 56.41 ($W^{-1}Km^{-1}$). Besides that at that particular wavelength (1550 nm), the proposed PCF offers high birefringence which is about 0.0108 with the confinement loss of 0.0582 dB/km.**

Keywords— Chromatic dispersion, Photonic crystal fiber, Finite element method, Fiber birefringence, Confinement loss.

I. INTRODUCTION

In optical fiber communication systems, dispersion limits the maximum transmission distance and the bit rate [1]. Because the optical pulse get broadened due to dispersion while transmitting through the fiber. Thus, the dispersion must be compensated during the long distance optical data transmission system. Generally, a standard single-mode optical fiber have positive dispersion from 10 to 20 ps/(nm.km). To successfully compensate the positive dispersion of SMF over a long distance, short piece of a dispersion compensating fibers (DCFs) having large negative dispersion are widely used and commercially available [2]. Generally, conventional DCF fibers give a high negative dispersion only at a particular wavelength but not over wide band [3]. Photonic crystal fiber (PCF), known as 'holey' fiber, is a micro-structured fiber consisting of air hole arrays that run along the waveguide length of the fiber, which have unique properties that are not realized in standard optical fiber [4, 5].

The PCF is a single material optical fiber which contains microscopic air-holes in a silica background running down the length of the fiber. As a result the entire structure forms silica-air microstructure that causes lower refractive index in the cladding region and higher refractive index in the core [3]. In addition, the index-contrast between the core and cladding increases due to the silica-air microstructure in the cladding which helps to tailor the optical properties of the PCF. Modulating some parameters of the silica-air micro structure, it is possible to tune the dispersion properties of the PCF which helps to specially design the broadband dispersion compensating fiber (DCF).

Several designs of dispersion compensating PCFs (DCPCFs) have been proposed to achieve high negative dispersion as well as a suitable bandwidth for dispersion compensation in [6-16]. Silva et al. proposed a Ge-doped-core PCF using a genetic algorithm shows an average negative dispersion of −212 (ps/nm-km) [6]. But the main drawback of this structure is fabrication difficulties due to the doped core. To obtain a wide compensation bandwidth and a zero ultra-flattened dispersion coefficient, a honeycomb structure PCF has been proposed by Nghiem et al. [7]. A dual core PCF with a highly doped internal core reported by Huttunen et al. [8] which have dispersion coefficient was about −59,000 ps/(nm-km). But, these fibers exhibit more confinement loss and fabrication process more difficult. The PCFs mentioned above have not taken into account about the polarization effect and hence these are less attractive for polarization maintaining applications. To eliminate the effect of polarization mode dispersion, High birefringence property can be easily created by altering the air hole sizes near the core area [9,10] or by distorting the shape of the air holes [11,12]. Highly birefringent photonic crystal fibers are also suitable for various applications including optical device and sensing applications. Recently, Habib et al. proposed a hybrid octagonal structure with dispersion coefficient of −465.5 ps/(nm-km) and birefringence of the order 2.68 × 10−2 [13].But, Due to smaller air holes in the inner PCF, the design is more complex than the previously reported. More recently, Haque et al. proposed a hybrid circular structure with dispersion coefficient of −650 ps/(nm-km) and birefringence of the order 2.1 × 10−2[14]. In spite of attractive birefringence, this hybrid PCF is also difficult to fabricate due to its design complexity and higher no. of rings.

In this paper, we proposed a unique circular photonic crystal fiber with four air-hole rings over a widely used wavelength bands considering the polarization issue. The main advantages of the proposed structure are the design simplicity along with high negative dispersion, high birefringence and attractive nonlinear coefficient which are very crucial for high-bit rate transmission network, nonlinear optics and sensing applications. Simulation results show that it is possible to achieve large negative dispersion of about -220.90 to -792.72 ps/(nm-km) over E to U telecommunication band. At λ=1.55 μm, values of dispersion coefficient, nonlinear coefficient and birefringence are found to be -678.1918 ps/(nm-km), 56.41 (W-1km-1) and 0.0108 respectively.

978-1-4673-9257-0/15/$31.00 ©2015 IEEE

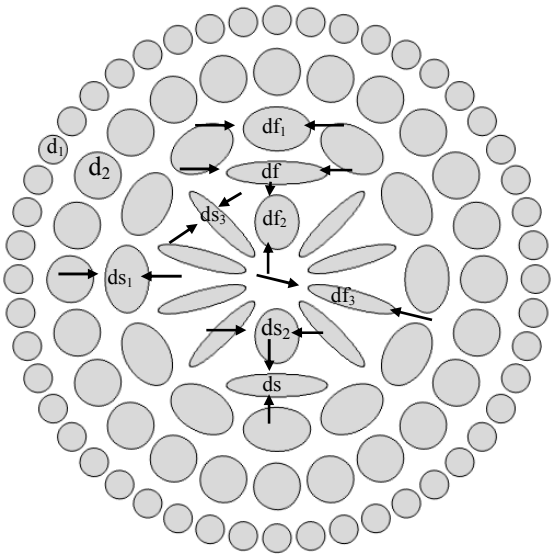

Figure 1. Air hole arrangement of the proposed DC-PCF

II. DESIGN MODEL

Fig.1 represents the air hole arrangement of proposed C-PCF. However, the construction of the CPCF for broadband dispersion compensation is mostly identical with C-PCF with these elliptical air holes which have been used to enhance the dispersion compensating capability. The proposed C-PCF contains only four air-hole rings and the material is taken to be silica which is simplest design respect to other design [6-18].

The 1st and 2nd elliptical air holes of the first ring with diameter in x direction is df and in y direction is ds which are rotated at angles 150and 450 respectively. To break symmetry of 1st ring 3rd elliptical air hole with diameter in x direction is df2 and in y direction is ds2 which is rotated 900 and just above it 4th elliptical air hole is taken which diameter in x direction is ds3 and in y direction is df3.Similarly, 5th, 6th, 7th, 8th, 11th and12th air holes of the 1st ring have diameter in x direction is df and in y direction is ds and these are rotated at angles 1350, 1650, 1950, 2250, 3150 and 3450 respectively where 9th elliptical air hole with diameter in x direction is df2 and in y direction is ds2 which is rotated 2700 and just above it 10th elliptical air hole is taken which diameter in x direction is ds3 and in y direction is df3.Diameter of second ring air holes are in x direction is ds1 and in y direction is df1 and rotated at an angle 300.The diameters of third and fourth air holes are d1 and d2 with rotation angles 150 and 7.50 respectively.

III. ANALYSIS OF MODEL AND OPTICAL CHARACTERISTICS OF PCF

The finite element method (FEM) is very suitable for handling complicated geometry structures of hollow core as well as solid Photonic Crystal Fiber. It is used to calculate chromatic dispersion, birefringence, confinement loss and effective area. The COMSOL 4.2 software is used as simulation tools.

A. Chromatic Dispersion

The performance of PCF directly effects by chromatic dispersion. Because, it affects pulse broadening, phase-matching conditions etc. It also affects to determine bandwidth and power requirements of device in which the fiber will be used. Nowadays, minimization of chromatic dispersion is one of the most challenging issues of optical fiber communication. The chromatic dispersion in ps/(nm-km) is easily calculated from the following equation[14]

$$D(\lambda) = -\frac{\lambda}{c}\frac{d^2\,\mathrm{Re}[n_{eff}]}{d\lambda^2}. \tag{1}$$

Where, $\mathrm{Re}[n_{eff}]$ is the real part of effective refractive index, λ is the wavelength, c is the velocity of light in vacuum.

B. Birefringence

In PCF, the birefringence properties are imperative for eliminating the effect of polarization mode dispersion (PMD) and in stabilizing the operation of optical devices, and can also be used in sensing applications. It can be achieved by creating asymmetric core. The birefringence is defined as a difference between effective refractive indices of two fundamental polarization modes and can be written as [14]

$$B = \left| n_x - n_y \right|. \tag{2}$$

Where, n_x and n_y are the mode indices of the two orthogonal polarization fundamental modes.

C. Confinement loss

Confinement loss is the light confinement ability within the core region. The confinement loss L_c in dB/km is then obtained from the imaginary part of $\lfloor n_{eff} \rfloor$as follows [15]:

$$L_c = \frac{\left(20\times10^6\right)}{\ln(10)} k_0\,\mathrm{Im}[n_{eff}]. \tag{3}$$

Where, $\mathrm{Im}[n_{eff}]$ represents the imaginary part of the wavelength dependent refractive index and $k_0 = 2\pi/\lambda$ is the wave number in the free space.

D. Effective Area

The effective area in μm^2 of the proposed PCF is obtained from [17] and is given by A_{eff} [14] ,

$$A_{eff} = \frac{(\iint |E|^2 dxdy)^2}{\iint |E|^4 dxdy}. \tag{4}$$

Where, E is electric field vector in the medium.

E. Nonlinear Coefficient

The nonlinear coefficient in $W^{-1}Km^{-1}$ can be obtained from the effective area [17] and is given by γ [14],

$$\gamma = \left(\frac{2\pi}{\lambda}\right)\left(\frac{n_2}{A_{eff}}\right) \quad (5)$$

IV. Simulation Result and Discussion

At operating wavelength of 1550 nm, Fig.2 represents the fundamental mode Optical Field distribution of designed C-PCF for both X and Y polarization. According to simulation, it is clearly seen that the optical field for X and Y polarization light is firmly confined into the center core region due to the relatively higher refractive index of the core as compared with the lower refractive index of the cladding region.

Fig.3. shows Chromatic dispersion at X-polarization and Y-polarization. As wavelength is increased, Chromatic dispersion coefficient increases monotonically and at 1550 nm wavelength for X and Y polarization the chromatic dispersion coefficient are found to be -678.1918 ps/(nm-km) and -607.7927 ps/(nm-km) respectively. The X-polarized mode is slightly higher in magnitude than the Y-polarized mode which represents fast axial mode. However, for optimum design parameters the designed fiber shows a very high negative dispersion coefficient of about -220.9032 to -792.7265 ps/(nm-km) over 1310 to 1640 nm bands which reduces the length of DCFs and higher cost.

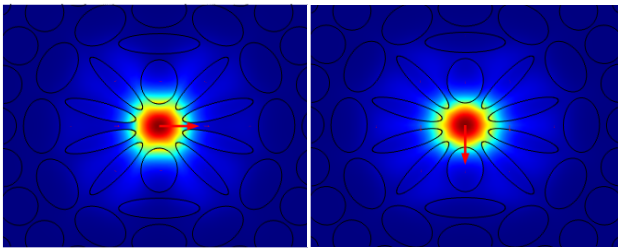

Figure 2. Optical Field distribution of fundamental mode for X and Y polarization at operating wavelength of 1550 nm.

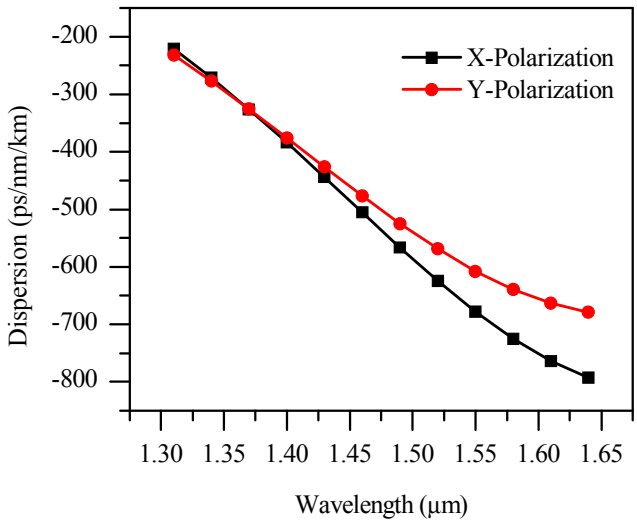

Figure 3. Chromatic dispersion properties of proposed PCF for optimum design parameters.

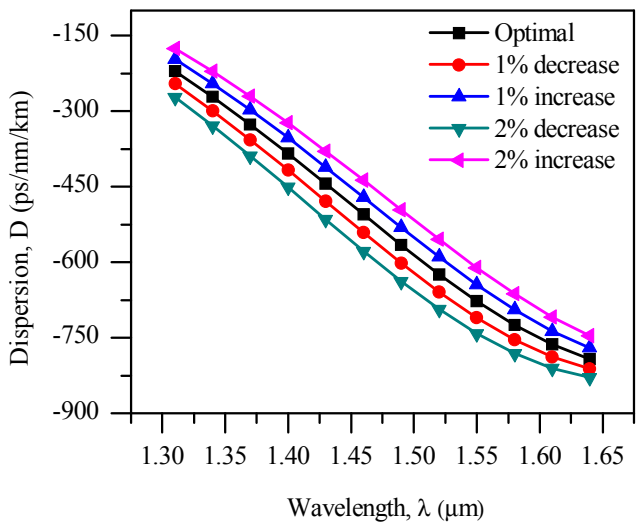

Figure 4. Chromatic dispersion properties of proposed PCF: optimum dispersion and effect of changing pitch.

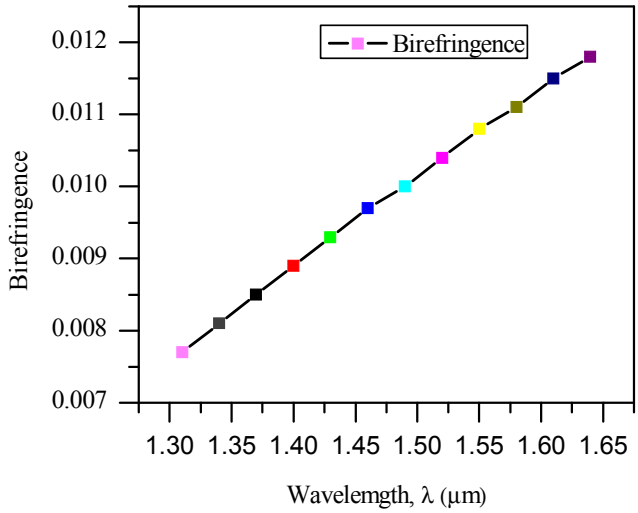

Figure 5. Birefringence properties of proposed PCF for optimum design parameters.

Fig.4 shows the effect of changing pitch on dispersion behavior whereas other parameters remain constant. For wavelength bands 1310-1640 nm, it is seen that the peak value of negative dispersion increases with the decrease of pitch due to greater index difference while the peak value decreases with the increase of pitch. From curve, it is observed that, there is an insignificant effect on dispersion behavior when pitch is varied as ±1% to ±2%.

Fig.5. shows wavelength dependent birefringence of the proposed PCF for optimum parameters. It shows a high birefringence with increase in operating wavelength and at 1550 nm wavelength, the birefringence is about 1.08×10^{-2}. Where the current conventional polarization mode fiber shows

a modal birefringence of about 5×10^{-4} which is 21.6 lower than the proposed PCF.

The effects of changing the pitch on birefringence are shown in Fig.6. Here, it is seen that the birefringence of the proposed PCF increases rapidly with decrease in pitch due to the high index difference between two orthogonal polarization axes while decreases with increase in pitch due to low index difference between the two modes. Simulation result shows that as the pitch varies from +1% to +2% birefringence decreases whereas the pitch varies from -1% to -2% birefringence increases.

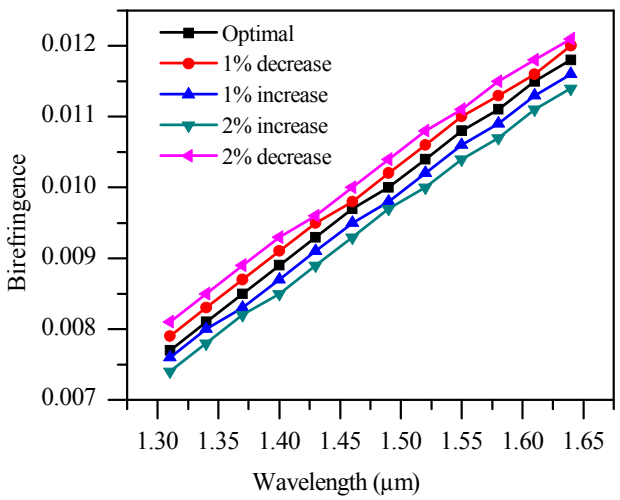

Figure 6. Birefringence of proposed PCF: optimum birefringence and effect of changing pitch

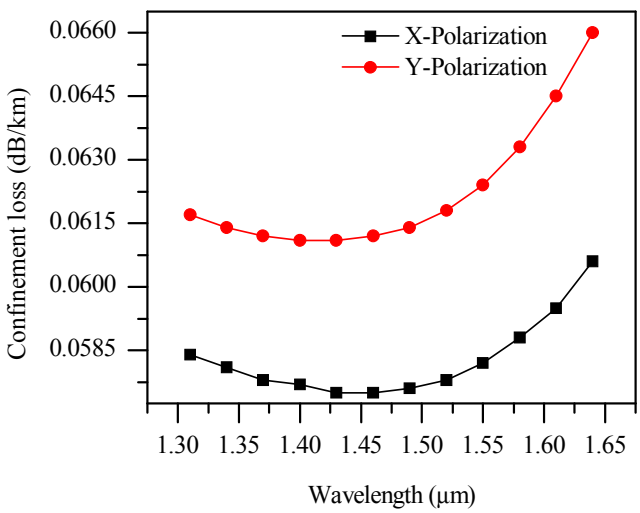

Figure 7. Confinement loss properties of proposed PCF for optimum design parameters.

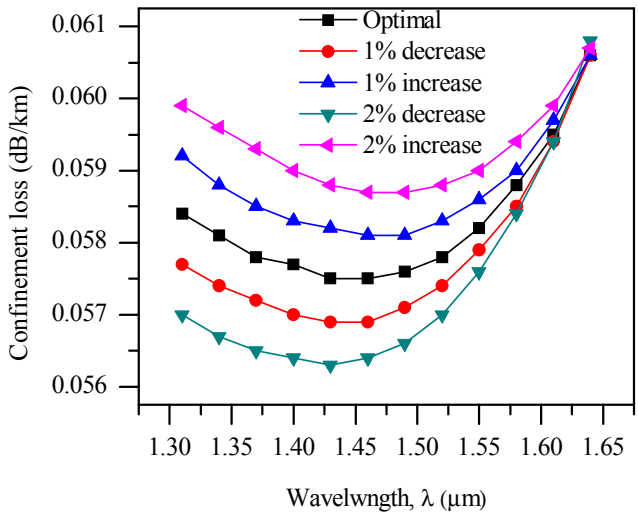

Figure 8. Confinement loss of proposed PCF: optimum confinement loss and effect of changing pitch .

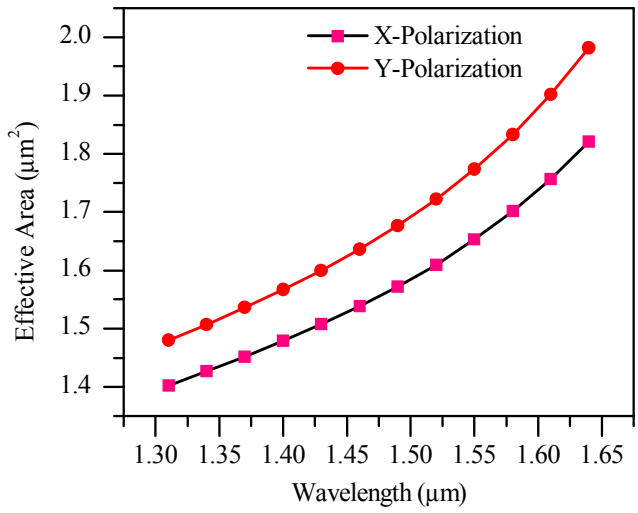

Figure 9. Effective Area of proposed PCF for optimum design parameters.

Fig.7. shows the confinement loss against wavelength for optimum design parameters. From this figure, it is observed that the confinement loss is about 0.0582 and 0.0624 for X-polarization and Y-polarization respectively. It is seen that confinement loss of Y-polarization is greater than X-polarization and increases with increase in wavelength but the value of confinement loss is in limit without causing any leakage.

The effects of changing the pitch on confinement loss are shown in Fig.8. Here, it is seen that the confinement loss of the proposed PCF increases rapidly with increase in pitch while decreases with increase in pitch.

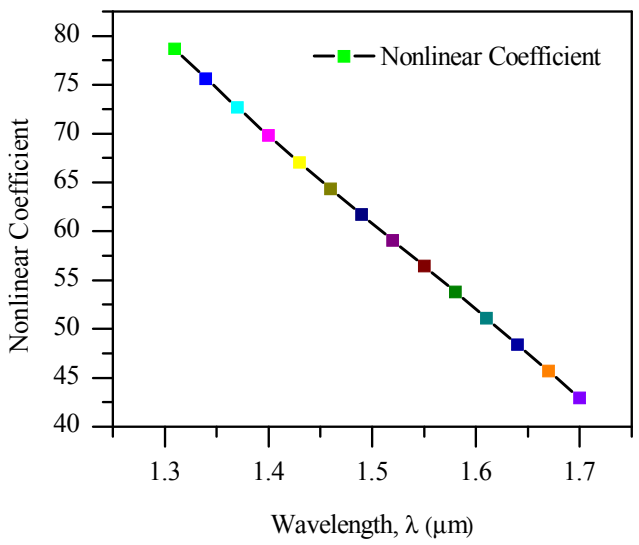

Figure 10. Nonlinear Coefficient of proposed PCF for optimum design parameters.

Simulation result shows that as the pitch varies from +1% to +2% confinement loss increases whereas the pitch varies from -1% to -2% confinement loss decreases.

Simulation result also shows that the effective area of the fiber increases with increase in wavelength as in Fig.9. At 1550 nm wavelength, the value is 1.7735 μm^2 . Due to small effective area, it is expected that the proposed PCF will be insensitive to bending and have low bending loss [15].

Fig. 10 shows nonlinear coefficient for optimum parameters. At 1550 nm, the nonlinear coefficient is found to be 56.41$W^{-1}km^{-1}$.This characteristic is suitable for dispersion compensation and effective in self-phase modulation for switching, pulse-forming, wavelength conversion applications and supercontinuum generation for frequency metrology [16].

"Table 1" shows comparison of the proposed PCF with the other existing design [14, 15]. It shows that proposed PCF is simple in design than others, because it contains only 4 air hole rings. Though, birefringence of proposed PCF is less, negative dispersion and nonlinear coefficient is higher than the other existing design [14,15].

CONCLUSION

A 4 rings Circular lattice PCF with elliptical and circular air holes has been investigated for its large negative dispersion properties as well as high birefringence and low confinement loss. It ensures large negative dispersion and high birefringence which are in the range of -220.9032 to -792.7265 (ps/nm-km) and 0.0077 to 0.0118 respectively at operating wavelengths 1310 nm to 1640 nm. It is expected that the proposed C-PCF will be applicable for broadband dispersion compensation in future optical fiber technology.

TABLE I. COMPARISON BETWEEN PROPOSED PCFS AND OTHER PCF AT 1.55 μm

PCFs	$D(\lambda)$ *ps/(nm.km)*	*Birefringence*	γ *($W^{-1}km^{-1}$)*	*No. of rings*
Ref.[13]	-491.5	3× 10-2	39.53	5
Ref.[14]	-650	2.10× 10-2	45.5	5
Proposed PCF	-678	1.08× 10-2	56.41	4

ACKNOWLEDGMENT

The authors would like to acknowledge the Information and Communication Technology (ICT) Division, Ministry of Posts, Telecommunication and IT, Government of the People's Republic of Bangladesh for their financial support.

REFERENCES

[1] K. Fukuchi, T. Kasamatsu, M. Morie, R. Ohhira, T. Ito, K. Sekiyap. Ogasawara, and T. Ono,"1092-Tb/s {273x40 Gb/s) triple-band/ultra-dense WDM optical-repeatered transmission experiment," in Proc.OFC, Anaheim, CA, Mar. 2001, pp. PD24- 1 -PD24-3.

[2] M. Samiul Habib∗, Redwan Ahmad, M. Selim Habib, S.M.A. Razzak," Design of single polarization single mode dispersion compensating photonic crystal fiber" Optik - Int. J. Light Electron Opt. vol.125, pp.4313-4318, Aug. 2014.

[3] J. Laegsgaard, S.E.Barkoulibori, K. Hougaard, J. Riished, T. T. Larsen, and T. Sorensen, "Dispersion properties of photonic crystal fibers-issues and opportunities," Mater. Res. Soc. Symp. Proc.,vol. 797, 2004.

[4] J. C. Knight, T.A. Birks, P. St. .J Russell, "All-silica single-mode optical fibre with photonic crystal cladding," Optics Letters, vol. 21, pp.1547-1549,1996.

[5] E. Yablonovitch, "Inhibited spontaneous emission in solid state physics and electronics," Phys. Rev. Lett., vol. 58, pp. 2059-2062, 1987.

[6] J. P. da Silva, D. S. Bezerra, V. F. R. Esquerre, I. E. Fonseca, and H. E. H. Figueroa, "Ge-doped defect-core micro-structured fiber design by genetic algorithm for residual dispersion compensation," IEEE Photon. Technol. Lett. 22, pp.1337–1339, 2010.

[7] Nghiem Xuan Tam, Nguyen Xuan Son, Pham Hong Thai Nguyen Hoang Hai , "New Proposal of Chromatic Dispersion Control in Honey Comb Photonic Crystal Fiber for Broadband Communication," IEEE 5th International Conference on Communications on Electronics(ICCE),July 2014, pp.34-39.

[8] A. Huttunen, P. Torma, Optimization of dual-core and microstructure fiber geometries for dispersion compensation and large mode area, Opt. Express vol.13,pp. 627–635,2005.

[9] K. Saitoh, M. Koshiba, Full-vectorial imaginary-distance beam propagation method based on a finite element scheme: application to photonic crystal fibers, IEEE J. Quant. Electron. vol.7 pp.927–933, 2002.

[10] M. A. Islam and M. S. Alam, "Design of a polarization maintaining equiangular spiral photonic crystal fiber for residual dispersion

compensation over E + S + C + L + U wavelength bands,'' IEEE Photon. Technol. Lett. vol.24, pp.930–932,2012.

[11] T. Matsui, K. Nakajima, I. Sankawa, Dispersion compensation over all the telecommunication bands with double-cladding photonic-crystal fiber, J. Light-wave Technol. vol.25 pp.757–762,2007.

[12] S. Haxha and H. Ademgil, ''Novel design of photonic crystal fibres with low confinement losses nearly zero ultra-flatted chromatic dispersion, negative chromatic dispersion and improved effective mode area,'' Optical Communications, vol. 281, no. 2, pp. 278–286, Jan. 2008.

[13] M. Samiul Habib, Redwan Ahmad, M. Selim Habib, and M. Imran Hasan, N. Ahmed, ''Residual dispersion compensation over theS+C+ L +U wavelength bands using highly birefringent octagonal photonic crystal fiber,'' APPLIED OPTICS Vol. 53, No. 14.pp.3057-3062, May 2014.

[14] M. Mejbaul Haquea, M. Shaifur Rahman, M. Selim Habib, M. Samiul Habib, ''A single mode hybrid cladding circular photonic crystal fiber dispersion compensation and sensing applications,'' Photonics and Nanostructures – Fundamentals and Applications Vol. 14, pp.63-70, April 2015.

[15] S. F. Kaijage, Y. Namihira, N. H. Hai, F. Begum, S. M. A. Razzak, T. Kinjo, K. Miayagi, and N. Zou, ''Broadband dispersion compensating octagonal photonic crystal fiber for optical communication applications,'' Japanese Journal of Applied Physics, vol.48, pp. 052401–052408, 2009.

[16] H. Ademgil, S. Haxha, F.A. Malek,''Highly nonlinear bendinginsensitive birefringent photonic crystal fibres,'' Eng. vol.2 pp.608–616, 2010.

[17] M. M. Haque, M. S. Rahman, M. Samiul Habib, M. Selim Habib, S. M. A. Razzak, ''A new circular photonic crystal fiber for effective dispersion compensation over E to L wavelength bands,'' Journal of Microwaves, Optoelectronics and Electromagnetic Applications, Vol. 12, No. 2, pp.281–291, Dec. 2013.

Design and Evaluation of a UWB Wearable Textile Antenna for Body Area Network

Kawshik Shikder*, Farhadur Arifin
Department of Electrical and Electronic Engineering (EEE)
American International University-Bangladesh
Dhaka, Bangladesh
*kawshik_pappu@yahoo.com

***Abstract*—This paper presents a novel Ultra Wide Band (UWB) wearable textile antenna for body area networks. The proposed antenna consists of a hexagonal radiating patch and a partial ground plane. The substrate of the proposed antenna is made of Dacron fabric with permittivity 3. Ultra wide bandwidth is achieved by optimizing the geometry, introducing a square notch in the partial ground plane and introducing novel slot pattern on the radiating patch of the antenna. This novel slot represents the "wireless antenna" icon. The dimension of the proposed antenna substrate is 40×34×1.7 mm^3 and the bandwidth 16.56 GHz starting from 2.6 GHz to 19.16 GHz for return loss less than -10 dB. The gain variation is from 2 dB to 6.35 dB and average total efficiency more than 83%. Maximum power of 17.39 mW may be set as input to the proposed antenna in order to guarantee compliance with the IEEE C95.1-1999 safety standard. The proposed antenna design details and simulated results are presented by Commercial electromagnetic simulation package CST Microwave Studio.**

Keywords—UWB; body area network; wearable textile antenna; patch antenna

I. INTRODUCTION

Wearable textile systems are very promising technology since their demands for navigation, tracking, portable communication, and public safety requirements are increasing rapidly. In recent years, the presence of wearable textile systems expressed the necessity for Wireless Body Area Network (WBAN) system to provide standalone outfit [1]. Antenna is the fundamental part of wearable textile system in WBAN. At present, textile antenna is one of the most impressive and cutting edge research areas of modern era. The textile antenna for wearable applications is actually the bond that integrates cloth into the communication system. These are made from textile materials and placed on body, into clothing or may be worn as a button antenna. Wearable textile antenna is mostly used microstrip patch antenna if textile fabric is used as substrate. However, the main limitation of the traditional microstrip patch antenna is limited bandwidth that restricts its applications. Due to this reason, Ultra Wide Band (UWB) technology is considered to be a favorable choice which provides wider bandwidth.

UWB is a radio technology, used for short-range communication. It occupies a bandwidth of at least 25% of the centre frequency or more than 1.5 GHz unlike the narrower frequency band of the conventional systems. UWB signal uses Orthogonal Frequency Division Multiplexing (OFDM) as the modulation technique to occupy the wide frequency band. The commercial use of frequency bands from 3.1 to 10.6 GHz for UWB systems was approved by the Federal Communications Commission (FCC) in 2002 [2]. UWB offers extremely low radiated power in low/medium data-rate applications based on narrow pulses, thus being very attractive for body worn battery operated devices in wearable computing.

Numerous papers have been published about the design, fabrication and applications of wearable antennas and systems. Previously reported works are based on single frequency band wearable antennas [3] and later dual frequency band wearable antennas [4]. In the recent researches, Wideband and UWB technology is one of the most fascinating choices for WBAN applications. Many of UWB antennas using rigid substrate material [5-6], large in size and small bandwidth [7-10][12-13] have been reported. However, it is quite difficult to obtain large bandwidth with compact size and a very low thickness in case of wearable antennas. In this paper, a novel and compact design of wearable textile antenna is proposed for WBAN applications by merging the UWB technology with wearable textile technology.

This paper is motivated from the above reported papers and presents a novel design of a wearable hexagonal UWB textile antenna. Novelty of this work is – the slotted area of hexagonal patch that represents the "wireless antenna" icon which is unique and also compact in size. The bandwidth of the proposed antenna operates in the wide range, achieving the UWB system requirements.

The outline of this paper is organized as follows. Section II represents a brief description of the wearable antennas. Design of the proposed wearable textile antenna and simulated results are illustrated in Section III & IV respectively. Finally, the conclusions of this research work are presented at the end of this paper in Section V.

II. WEARABLE ANTENNAS

Wearable textile antenna is usually consisted of three different layers which made of two types of material. A metallic conducting patch is on the top of a non-conducting dielectric substrate and a conducting ground plane is beneath the dielectric substrate.

978-1-4673-9257-0/15/$31.00 ©2015 IEEE

A. Non-conducting Material

The most important properties of textile antennas in wearable applications are flexibility to conform to the body, comfort to touch, and softness. Permittivity or Dielectric constant of the antenna substrates has a significant role in antenna designing. Different substrates having different dielectric constants affect the antenna performance in various ways. Textile substrate materials generally have a very low dielectric constant which reduces surface wave losses and improves antenna's bandwidth. Here, hypalon coated Dacron fabric textile material is used as the antenna substrate for dielectric constant is $\varepsilon_r = 3$ while the loss tangent is $\tan\delta = 0.025$. The properties of Dacron fabric include high tensile strength, high resistance to stretching, outstanding electrical property and durability.

B. Conducting Material

In order to build the communication system, an electrically conducting material is required for the radiating patches as well as for the ground plane. However, for the purposes of textile antenna designs, a conducting material needs to satisfy several requirements such as having a low and stable electrical resistance (1 ohm/square) in order to minimize losses, material must be homogeneous over the antenna area, and the variance of the resistance through the material should be small. Therefore, the conducting properties of various materials used in antenna fabrication and packaging play an important role in achieving the desired performance of antenna designs. Based on the above-mentioned facts, Perfect Electric Conductor (PEC) is used in this paper as the conducting materials for the radiating patch (front side) as well as for the ground plane (back side). A 50Ω transmission line is also made with this conducting material.

III. Antenna Design

The proposed antenna consists of a hexagonal patch with slotted area and fed by a microstrip line, and a partial ground plane. The structure of proposed antenna is shown in Fig. 1 (Front view), Fig. 2 (Cross-sectional view), Fig. 3 (Back view) and Fig. 4 (Phantom). Instead of resonance frequency or operating frequency, lower band edge frequency and entire bandwidth become the design considerations for UWB antenna. The lower band edge frequency (f_l) in GHz, has been calculated for UWB antenna according to (1) given below [11]:

$$\text{Lower band edge frequency, } f_l = \frac{c}{\lambda} = \frac{72}{(H + r + T)} \quad (1)$$

where, H is the height of the hexagonal patch in mm, r is the radius of the equivalent cylindrical monopole antenna in mm and T is the gap between ground plane and hexagonal patch in mm.

With reference to configurations in Fig. 1 with side length (L_p), the dimensions of H, r and D_p of the equivalent cylindrical monopole antenna are obtained (by equating their areas) as follows:

$$\text{Radius, } r = \frac{3L_p}{4\pi} \quad (2)$$

$$\text{Height, } H = \sqrt{3}L_p \quad (3)$$

$$\text{Diameter, } Dp = 2L_p \quad (4)$$

By selecting the value of L_p, the following parameters: r, H, D_p and f_l can be computed using (1-4). The dimensions of proposed antenna parameters are provided in Table I and computed parameters value of the proposed antenna are provided in Table II.

TABLE I. Dimensions of The Proposed Antenna Parameters

Parameters		Size (mm)
Substrate	Length	40
	Width	34
	Thickness	1.7
Ground	Length	16
	Width	34
	Thickness	0.5
Patch	Height (H)	20.551
	Side Length (L_p)	11.865
	Thickness	0.5
Feed Line	Length	18
	Width	4.6
	Thickness	0.5

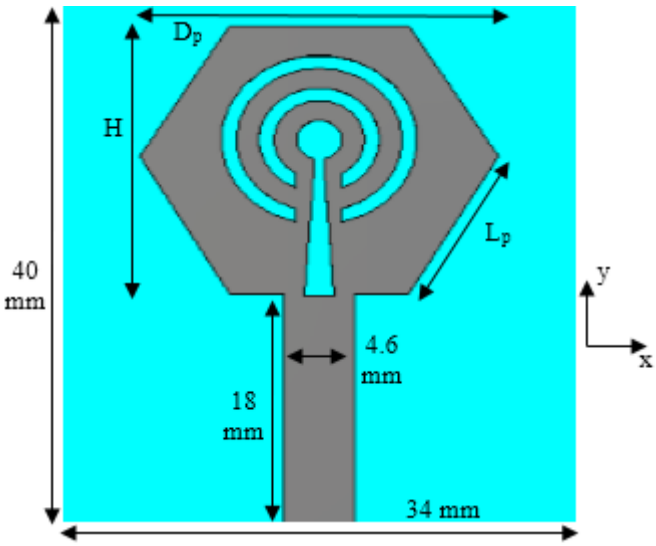

Fig. 1. Geometry of the Proposed Antenna (Front view)

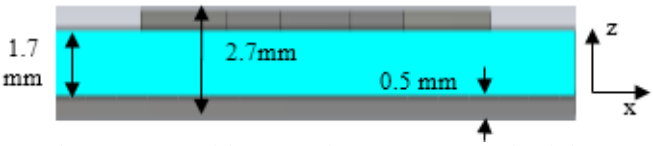

Fig. 2. Geometry of the Proposed Antenna (Cross-sectional view)

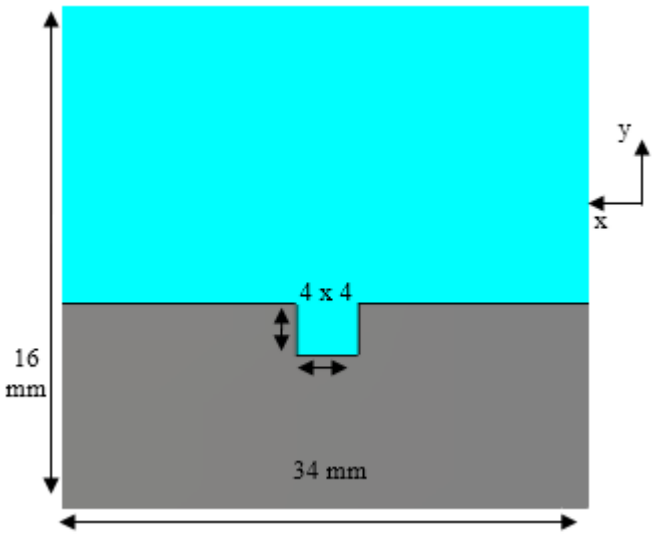

Fig. 3. Geometry of the Proposed Antenna (Back view)

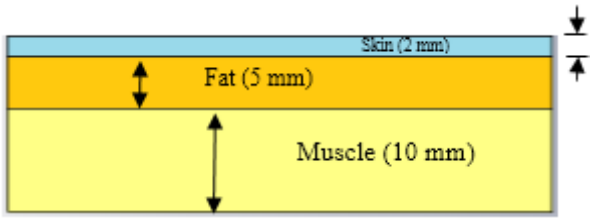

Fig. 4. Human Body Model (Phantom)

TABLE II. COMPUTED PARAMETERS VALUE FOR THE PROPOSED ANTENNA

L_p (mm)	r (mm)	H (mm)	T (mm)	D_p (mm)	f_l (GHz)
11.865	2.833	20.551	1.36	23.73	2.91

In order to enhance the bandwidth, one slotted circle along with a slotted triangle is introduced at the centre and two partial slotted rings are introduced at the top of the slotted triangle of hexagonal radiating patch.

TABLE III. OPTIMIZED VALUES FOR SLOTTED AREA OF PATCH

Parameters		Size (mm)
Radius of slotted circle at center, R_1		1.5
Triangle	Length	11
	Width (W_1, W_2)	0.5, 2
Slotted ring (Middle)	Inner radius, R_2	3
	Outer radius, R_3	4
Slotted ring (Outside)	Inner radius, R_4	5.5
	Outer radius, R_5	6.5
Distance between ring and circle, d		1.5

The overall slotted area of hexagonal patch represents the icon of "wireless antenna" shown in Fig. 1. Optimized values for slotted area of the patch are provided in Table III. Fig. 2 illustrates the cross-sectional view of the proposed antenna which indicates the thickness of different layers. A rectangular notch with size 4×4 mm^2 is also introduced on the top of partial ground plane (Fig. 3) to improve bandwidth of the presented antenna. The proposed antenna is mounted on the body phantom which model is shown in Fig. 4. The distance between antenna and phantom is 1 mm. Hence, it is explicit that the overall dimension of the antenna is quite small as compared to others. Commercial electromagnetic simulation package CST Microwave Studio is used to design the antenna.

IV. RESULTS AND DISCUSSION

This section analyzes the performances of the proposed UWB wearable textile antenna in terms of return loss (S_{11}), radiation patterns, antenna gain and efficiency over frequency, radiation effect on the body.

A. S_{11} Analysis of the Proposed Antenna

The simulated S_{11} plot over frequency of the proposed UWB wearable textile antenna is shown in Fig. 5.

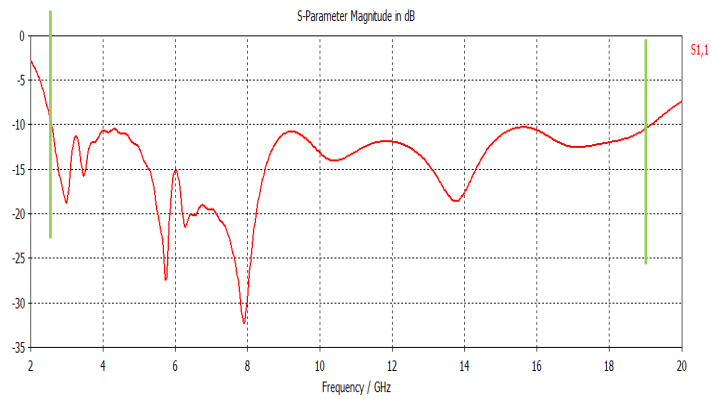

Fig. 5. Simulated S_{11} result

Fig. 5 indicates that the proposed antenna occupies a bandwidth of 16.56 GHz starting from 2.6 GHz to 19.16 GHz for S_{11} less than -10 dB. Lower edge frequency of simulated result is almost equal to the computed value. Hence, a very less number of incident waves reflect back to the source.

B. Radiation Patterns of the Proposed Antenna

The simulated azimuth and elevation radiation patterns at different frequencies of the proposed UWB wearable textile antenna are shown in Fig. 6 and Fig. 7 respectively.

The azimuth radiation patterns of the UWB wearable textile antenna at 3, 5.75, 7.9 and 13.75 GHz have been shown in Fig. 6. Theta (θ) has been set to both 0 and 90 degree for all values of phi (φ) to obtain azimuth radiation pattern. At 3 and 7.9 GHz, it exhibits almost omni-directional radiation pattern. Little deformation of radiation pattern is observed at 5.75 GHz. At 13.75 GHz, it has quite significant distortion from omni-directional pattern.

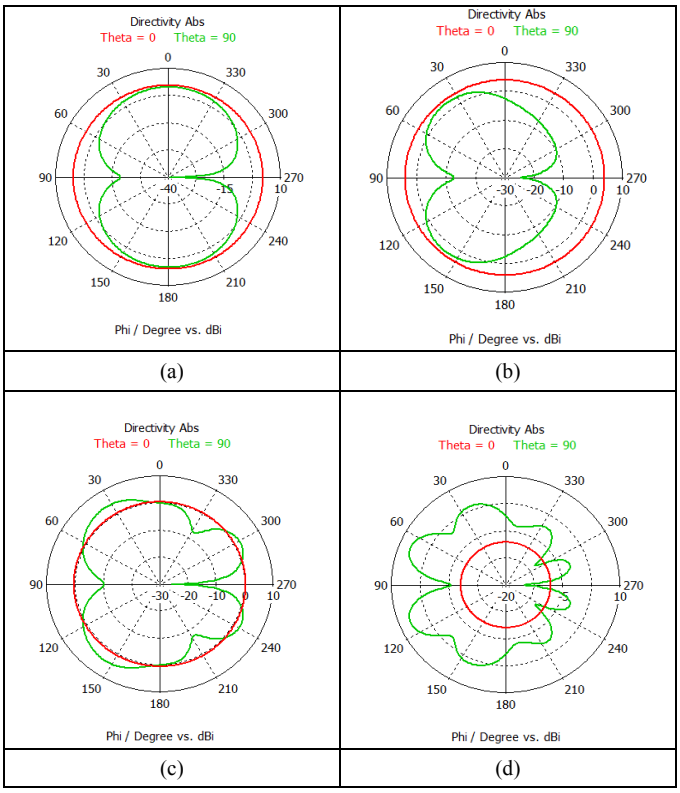

Fig. 6. Azimuth radiation patterns at (a) 3GHz, (b) 5.75 GHz, (c) 7.9 GHz and (d) 13.75 GHz

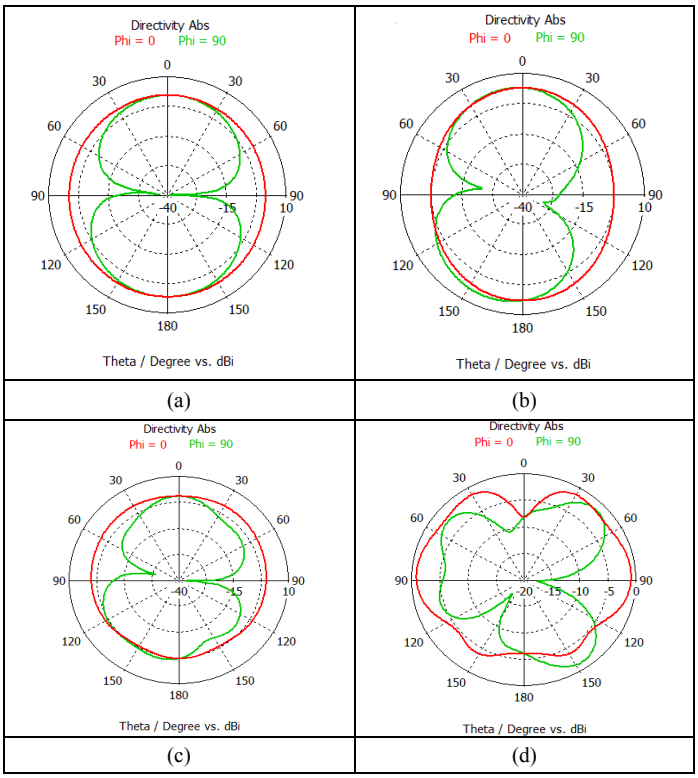

Fig. 7. Elevation radiation patterns at (a) 3GHz, (b) 5.75 GHz, (c) 7.9 GHz and (d) 13.75 GHz

Similarly for elevation pattern, phi (φ) has been set to both 0 and 90 degree for all values of theta (θ). The elevation radiation patterns of the UWB wearable textile antenna at 3, 5.75, 7.9 and 13.75 GHz have been shown in Fig. 7. At 3 and 7.9 GHz, it also exhibits almost omni-directional radiation pattern whereas little deformation of radiation pattern is observed at 5.75 GHz and quite significant distortion from omni-directional pattern observed at 13.75 GHz.

The analysis of Fig. 6 and Fig. 7 shows that the significant deviation of radiation patterns is found at higher frequencies. Furthermore, the data of radiation patterns (i.e.- main lobe magnitude, main lobe direction) of the UWB wearable textile antenna at 3, 5.75, 7.9 and 13.75 GHz have been provided in Table IV.

TABLE IV. DATA OF RADIATION PATTERNS AT DIFFERENT FREQUENCIES

Freq. [GHz]	**Main Lobe Magnitude [dBi] Direction [degree]**	**Theta (θ) [Degree]**		**Phi (φ) [Degree]**	
		0	**90**	**0**	**90**
3	Magnitude	2	1.2	2.8	2.8
	Direction	27	358	180	179
5.75	Magnitude	3.8	2.6	3.8	4.8
	Direction	86	142	180	163
7.9	Magnitude	0.2	4.1	1.2	0.2
	Direction	88	35	38	0
13.75	Magnitude	-8.2	7	-0.9	-1.5
	Direction	44	67	86	146

C. *Antenna Gain and Efficiency Results of the Proposed Antenna*

The variations of gain versus frequency and total efficiency versus frequency of the wearable textile UWB antenna designs are demonstrated in Fig. 8.

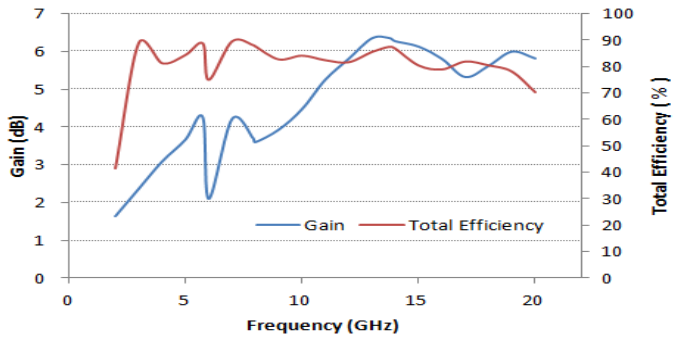

Fig. 8. Simulated Gain and Total Efficiency vs. Frequency

The highest gain and maximum total efficiency is achieved about 6.35 dB at 13.75 GHz and 90% at 7 GHz respectively

whereas the lowest gain and minimum total efficiency achieved almost 2 dB at 6 GHz and 75% at 6 GHz in the entire frequency range 2.6 ~ 19.16 GHz. From Fig. 8, the gain of the antenna varies significantly with changing frequencies while the efficiency varies slightly though it doesn't affect the overall performance. However, the gain variation is from 2 dB to 6.35 dB and average total efficiency more than 83%.

D. Specific Absorption Rate (SAR)

The SAR is a parameter to measure the power deposition in a human body when it is exposed to an electromagnetic field. For a net input power of 0.2 W at frequency 7.9 GHz incident to the antenna, the maximum 1 g averaged (1 g avg.) SAR value is found to be equal to 18.4 W/Kg. Therefore, in order to guarantee conformance with the IEEE C95.1-1999 (1 g avg. SAR ≤ 1.6 W/kg [14]) safety standard, the maximum allowed net input power has to be limited to 17.39 mW.

E. Comparison of the Proposed Antenna with Reported UWB Antennas

Table V shows the comparison of the proposed wearable UWB textile antenna with reported UWB antennas in terms of dimensions and occupied bandwidth.

TABLE V. COMPARISON WITH REPORTED UWB ANTENNAS

Ref. no.	Dimensions	Bandwidth
Proposed Antenna	34 x 40 mm^2	16.56 GHz (2.6–19.16GHz)
Ref. [7]	120 x 130 mm^2	3 GHz (1-4 GHz)
Ref. [8]	30 x 30 mm^2	10.4 GHz (3.6–14 GHz)
Ref. [10]	25 x 10 mm^2	8.2 GHz (3–11.2 GHz)
Ref. [12]	32 x 52 mm^2	10.04 GHz (3.11–13.15 GHz)
Ref. [13]	35 x 35 mm^2	9 GHz (2.8–11.8 GHz)

Comparison shown in Table V reveals the suitability for UWB applications as comparing with reference antennas. The overall performance of the proposed "wireless antenna" icon slotted hexagonal antenna on Dacron fabric material indicates that the drawbacks of reported UWB antennas have improved. Thus, the proposed antenna suits well to demonstrate the UWB characteristics.

V. CONCLUSION

In this paper, a novel UWB wearable textile antenna for body area network is presented. A novel slot pattern on hexagonal radiating patch is introduced that represents "wireless antenna" icon. A square notch in the partial ground plane is also introduced in this design. The proper selection of dimensions, square notch on the partial ground plane and positions of novel slot on the radiating patch strongly affects the antenna to achieve ultra-wide bandwidth. The proposed antenna design provides 16.56 GHz bandwidth ranges from 2.6 to 19.16 GHz with compact size on flexible substrate material. S_{11} characteristics illustrates that it has good impedance matching between antenna and transmission line with all over its occupied bandwidth. The antenna exhibits almost omni-directional radiation pattern but it has quite significant distortion from omni-directional pattern at higher frequencies. The gain of the antenna varies significantly with changing frequencies while the total efficiency varies slightly though it doesn't affect the performance. However, the gain variation of the antenna is from 2 to 6.35 dB and average total efficiency more than 83%. The IEEE C95.1-1999 standard is found to limit the aximum allowable net input power to 17.39 mW. Thereby, conclusion can be drawn that overall performance of the proposed antenna indicates that it is suitable candidate for UWB wearable textile applications. Reducing the size as well as increasing the bandwidth could be focus towards the further improvement of this design.

REFERENCES

[1] T. Zasowski, F. Althaus, M. Stäger, A. Wittneben, and G. Tröster, "UWB for noninvasive wireless body area networks: Channel measurements and results," presented at the IEEE Ultra Wideband Syst. Technol. Conf. (UWBST 2003), Reston, VA, Nov. 2003.

[2] First Report and Order, "Revision of part 15 of the commission's rule regarding ultra-wideband transmission system FCC 02-48", Federal Communications Commission, 2002.

[3] G. A. Conway and William G. Scanlon, "Antennas for over-body-surface communication at 2.45GHz," IEEE Transactions on Antennas and Propagation, vol. 57, no. 4, pp. 844-855, April 2009.

[4] S. Zhu and R. J. Langley, "Dual-Band Wearable Textile Antennas on An EBG Substrate," IEEE Transactions on Antennas and Propagation, Vol. 57, No.4, Apr 2009.

[5] Mai A. R. Osman, "The Investigation of Flannel Fabric Layers", 2010 International Symposium on Antennas and Propagations, Macao, China, 23-26 November 2010.

[6] Y. Chen, S. Yang, S. He, and Z.-P. Nie, "Design and analysis of wideband planar monopole antennas using the multilevel fast multipole algorithm," Progress In Electromagnetics Research B, Vol. 15, 95-112, 2009.

[7] Shuvashis Dey, Nandita Saha and Subrata Biswas. "Design and performance analysis of UWB circular disc monopole textile antenna and bending consequences." The 5th European Conference on Antenna and Propagation, 2011, April 2011, Rome, Italy.

[8] Mahmud MS, Jabri FJJ, Mahjabeen B. "Compact UWB Wearable antenna on leather material for wireless applications," IEEE Antennas and Propagation Society International Symposium (APSURSI). Orlando, FL; July 2013.

[9] M. Klemm and G. Troester, "Textile UWB antennas for wireless body area networks," IEEE Trans. Antennas Propag., Vol. 54, no. 11, pp. 3192-3197, Nov. 2006.

[10] Chahat N., "Design and Characterization of an UWB Wearable Antenna", 2010 Loughborough Antennas and Propagation Conference (LAPC), 2010, pp. 461-464.

[11] Ray, K. P., Tiwary, S. "Ultra Wide Band Printed Hexagonal Monopole Antennas", IET Microwaves, Antennas and Propagation, 2010, vol. 4, no. 4, p. 437-445.

[12] Mondal T, Das S. "UWB printed hexagonal monopole antennas with WLAN band rejection," IEEE Antenna Week (IAW). Kolkata, India; 2011.

[13] Lodi, G. A., R. I. Zafar, and M. Bilal. "A novel goblet shaped patch antenna for ultra wide band applications." *Communication Technology (ICCT), 2010 12th IEEE International Conference on*. IEEE, 2010.

[14] "IEEE standard for safety levels with respect to human exposure to radiofrequency electromagnetic fields, 3 kHz to 300 GHz," IEEE Standard C95.1 (1999).

Effective Modeling of Microstrip Patch Antenna with Circular EBG Structure

Md. Anwarul Quader, Minar Ashiq Tishan, Md. Masud Rana, and Reefat Inum
Department of Electrical and Electronic Engineering
Rajshahi University of Engineering and Technology
E-mail: akshuvo10@gmail.com, tishan150@gmail.com, md.masud.rana@ruet.ac.bd

***Abstract*—In this paper we have presented a rectangular microstrip patch antenna with circular Electromagnetic Band Gap (EBG) structure. The operating frequency of the patch antenna along with EBG structure is 7.3 GHz. All the simulation is done by using Computer Simulation Technology Microwave Studio (CST-MWS). In comparsion with the rectangular EBG structure, improvement has been achieved in the overall antenna return loss by 10.22% bandwidth by 8.89% and gain by 16.84%.**

Keywords— bandwidth; EBG; gain; patch antenna; return loss

I. Introduction

In recent years the microstrip patch antennas have made great progress as they offer more advantages and better prospects compared to other antennas. For example they are lighter in weight, lower in volume, lower in profile and easier to fabricate [1]. However, the main drawbacks of microstrip patch antennas are low bandwidth, low efficiency and relatively large size [2]. In case of the design of a microstrip patch antenna the most important prospect is to increase the inherent narrow bandwidth of antenna and to miniaturize the patch antenna size. The bandwidth of the antenna can be improved by increasing the substrate thickness [3]. Again, in order to minimize the other drawbacks, the substrate, ground plane and the patch of the microstrip patch antennas can be incorporated with different materials and structures. For example DGS [4], two layer Substrate [5] and metamaterials among which using metamaterials is found to be the most suitable approach [6].

Metamaterials are basically artificially engineered materials which exhibit electromagnetic properties that are not found in nature (e.g. negative refractive index and both negative permittivity and negative permeability). In 1967 Veselago discovered the concept of metamaterials [7]. He hypothesized an unknown material that possesses a negative permeability and permittivity in the same frequency range and it shows the abnormal electromagnetic properties when the uniform plane-wave propagation was studied [7]-[9]. As a result, the left-handed material (LHM) has a reverse basic feature of light, such as negative refractive index (NRI) [8]-[9]. Surprisingly, the idea got only little attention until the year 2000 when smith further studied the LHM and realized this material was a periodically-arranged conducting concrete and it shows extraordinary properties [9].

The EBG structures can be categorized as a special type of metamaterial due to their unique band gap features. This unique property has been applied to design antenna systems with better gain and efficiency, lower side-lobes and back-lobe levels by suppressing surface wave modes [2], [10]. The effect of using EBG structure is found to be the reduction of the patch resonant length and the bandwidth as a result of stronger capacitive coupling [2].

Paper [11] proposes a rectangular microstrip patch antenna along with metamaterial structure at a height of 3.2mm from the ground plane, which consists of a Split Ring Resonator (SRR). The paper focuses on increasing the bandwidth of low profile microstrip patch antenna by Double-Negative properties. The aforementioned design has increased the bandwidth by 300MHz.

Similarly paper [12] introduce a bandwidth enhancement of a narrow band rectangular microstrip antenna on square shape (EBG) patch structure. The measured results show better return loss and good impedance matching which resulted in an increase of bandwidth to more than 39.63% after the EBG structure was introduced. Both of these papers, [11] and [12], show improvement in antenna bandwidth. Considering all these articles, the novelty of our work is that we have proposed a more effective EBG structure for the patch antenna which is capable of increasing the antenna bandwidth, return loss as well as the gain of the patch antenna.

II. Design Specification

A. Patch Antenna Design

The Patch Dimension has been calculated using the following equation.

Step-1: Patch width

$$w = \frac{v_0}{2f_r}\sqrt{\frac{2}{\varepsilon_r+1}} \quad (1)$$

Where

978-1-4673-9257-0/15/$31.00 ©2015 IEEE

v_0 = The velocity of light.

ε_r = Dielectric constant of substrate.

Step-2: Effective Dielectric constant of the rectangular microstrip patch antenna.

$$\varepsilon_{eff} = \frac{\varepsilon_r+1}{2} + \frac{\varepsilon_r-1}{2}\left(\frac{1}{\sqrt{1+\frac{12h}{w}}}\right) \quad (2)$$

Step-3: Patch Length

$$L = L_{eff} - 2\Delta L \quad (3)$$

$$L_{eff} = \frac{c}{2f_r\sqrt{\varepsilon_{eff}}} \quad (4)$$

Calculation of Length Extension

$$\Delta L = 0.412h\frac{(\varepsilon_{eff}+0.3)(\frac{w}{h}+0.264)}{(\varepsilon_{eff}-0.258)(\frac{w}{h}+0.8)} \quad (5)$$

Step-4: Inset Feed

$$50 = R_{in}\,(\cos(\frac{\pi}{L}y_0))^2 \quad (6)$$

R_{in}=The input impendence at the leading radiating edge of the patch. While 50 (Ω) is the desired impendence.

Table I

Rectangular Microstrip Patch Antenna Specifications

Parameters Name		Dimensions without EBG (mm)	Optimized Dimension With Circular EBG Shape (mm)
Patch Width	W	14.53	14.53
Patch Length	L	11.53	8.95
Inset Feed	y_0	3.125	3.41
Inset Gap	g	1.901	0.38
Feed Length	L_f	13.202	11.895
Feed Width	W_f	1.901	1.9010
Substrate Width	W_S	31.02	31.0170
Substrate Length	L_S	31.68	25.92
Substrate Thickness	h	0.75	1.03
Resonant Frequency f_c		7.3 GHz	

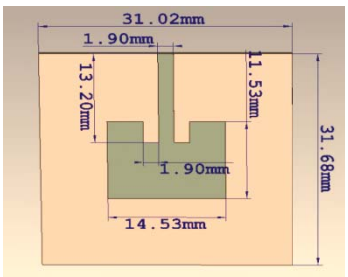

Fig. 1: Patch antenna without EBG.

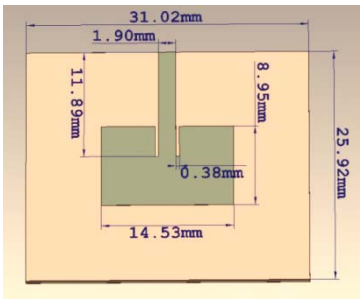

Fig. 2: Patch antenna with EBG

B. EBG Structure Design

Some equations have been adopted with a view to designing the EBG structure. The following equations are as follows for the square EBG structure,

$$L = 0.10\lambda \quad (7)$$

$$D = 0.02\lambda \quad (8)$$

and for the circular shape the radius of the circle is given by,

$$r = 0.10\lambda \quad (9)$$

Table II

DIMENSION OF EBG STRUCTURE

Parameters	Values (mm)
L	4.88
D	2.80
Radius r	2.44

The geometry of EBG structures (both rectangular and circular shapes with proper dimension) is shown in the following figure 3. Rogers R03003 has been chosen as antenna substrate due to flexibility for high frequency application compared to FR4 substrate.

Table III

ROGERS RO3003 SUBSTRATES CHARACTERISTICS

Parameters	Values
Permittivity	3
Permeability	1

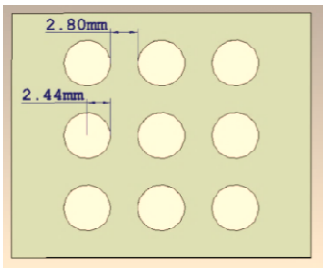

(a)

978-1-4673-9257-0/15/$31.00 ©2015 IEEE

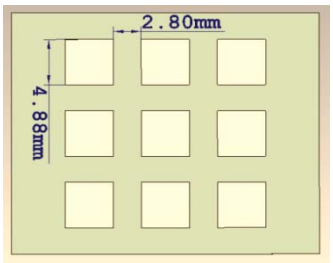

(b)

Fig. 3: (a) Circular EBG structure (b) Rectangular EBG structure.

Nicholson-Ross-Weir (NRW) technique is used as a conversion approach. Both permeability and permittivity is obtained from S-parameter using this approach [13].

III. Simulation Results

Antenna design and simulation are based on CST-MWS 2015 using frequency domain solver. From the simulation the results associated with Bandwidth, Return loss and Gain are discussed in details.

A. Return Loss and Bandwidth

Fig-4(a) shows the return loss plot of patch antenna without EBG and with rectangular EBG. From the following figure we can see that the return loss S_{11} of antenna without EBG is -17.24 dB and the return loss S_{11} of the rectangular EBG patch antenna is -47.598dB. According to fig-4(b) when we have introduced the circular shape of EBG on the ground plane of the antenna the return loss S_{11} has improved from -47.598 dB to -52.519dB.

In case of bandwidth, patch antenna without the EBG structure provides 154.27MHz, with rectangular EBG structure provides 305.48MHz, and with circular EBG structure provides 332.64 MHz.

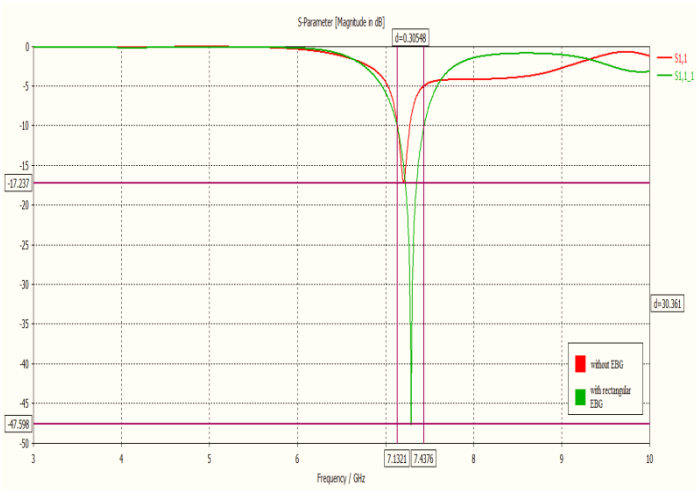

(a)

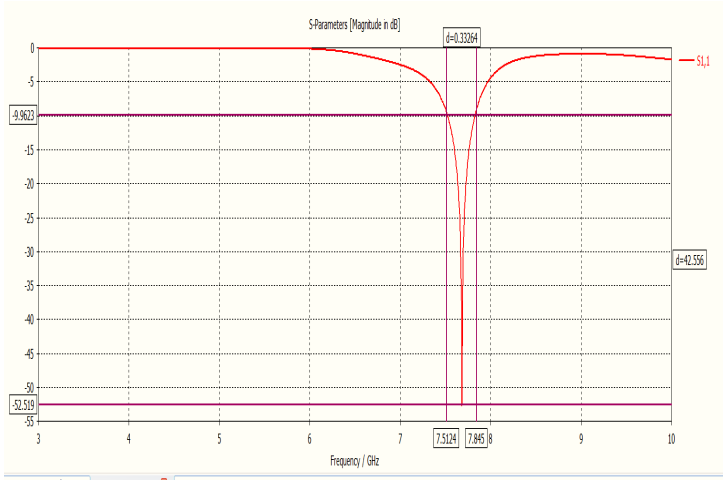

(b)

Fig. 4: (a) Return loss plot of the antenna without EBG and with rectangular EBG. (b) Return loss plot of microstrip patch antenna with Circular EBG structure.

B. Gain

Figure-5 provides 3-D plot of antenna gain for both rectangular and circular EBG structures. Normally the gain of the patch antenna without EBG structure is $7.92dB$. Patch antenna with rectangular EBG provides gain 5.94 dB . For circular EBG the gain improves from 5.94 dB to 6.94 dB.

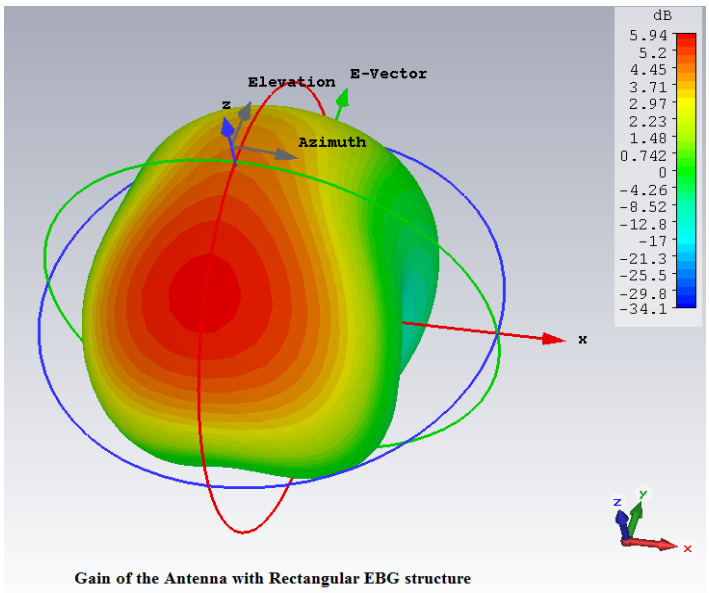

(a)

978-1-4673-9257-0/15/$31.00 ©2015 IEEE

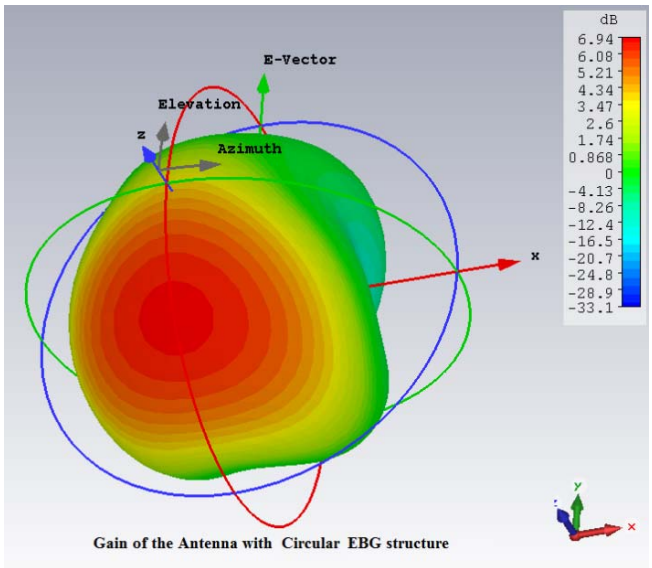

(b)

Fig. 5 (a) 3-D plot of antenna gain in dB for rectangular EBG structure (b) 3-D plot of antenna gain in dB for circular EBG structure.

Table IV
Comparison table between the simulation results

	Patch antenna without EBG	Patch antenna with Rectangular EBG	Patch antenna with Circular EBG	Improvement with respect to rectangular EBG (%)
Return loss	-17.24	-47.647	-52.519	10.22
Bandw -idth	154.27	305.49	332.64	8.89
Gain	7.92	5.94	6.94	16.84

This table represents the comparison between the simulation results in terms of Return loss, Bandwidth and Gain. It is seen that patch antenna with Circular EBG structure produced improved results.

IV. Conclusion

We have simulated the patch antenna with rectangular and circular EBG structures and after the comparison of the simulated results we have found that the EBG structure on the antenna ground plane with the circular shape provides improved results than rectangular EBG structure.

V. Future Work

Though from the simulation it is seen that the antenna bandwidth, return loss and gain have improved significantly with respect to rectangular shape of EBG but in comparison to patch antenna without EBG the gain is comparatively small. Different types of shape can be tried to improve the antenna performance

References

[1] Indrasen Sing, and Dr V. S. Tripathi, "Micro strip Patch Antenna and its Applications: a Survey," *Int. J. Comp. Tech. Appl.,* vol. 2, no. 5, pp. 1595-1599, 2011.

[2] Jing Liang, and H. Y. David Yang, "Microstrip patch antennas on tunable electromagnetic band-gap substrates," *IEEE Transactions on Antennas and Propagation.,* vol. 57, no. 6, pp. 1612-1617, June 2009.

[3] Abdelaziz, Abdelmonem Abdelaziz, "Bandwidth enhansment of microstrip antenna." *Progress In Electromagnetics Research.,* vol. 63, pp. 311-317, 2006.

[4] Amit Sing Bhadouria, Mithilesh Kumar, "Microstrip patch antenna for radiolocation using DGS with improved gain and bandwidth," *IEEE International Conference on Advances in Engineering and Technology Research (ICAETR),* 2014.

[5] Luk, K. M., et al. "Broadband microstrip patch antenna, " *Electronics Letters.,* vol. 34, no. 15, pp. 1442-1443, 1998.

[6] Bae-Ian Wu, W. Wang, J. Pacheco, X. Chen, T. Grzegorczyk, and J. A. Kong, "A study of using metamaterials as antenna substrate to enhance gain," *Progress In Electromagnetics Research,* vol. 51, pp. 295-328, 2005.

[7] M. Lapine, and S. Tretyakov, "Contemporary notes on metamaterials," *IET Microw. Antennas & Propagation.,* vol. 1, no. 1, pp. 3-11, February 2007.

[8] Nader Engheta, and Richard W. Ziolkowski, "A positive future for double-negative metamaterials," *IEEE Transactions on Microwave Theory and Techniques.,* vol. 53, no. 4, pp. 1535-1556, 2005.

[9] LI Le-Wei, YAO Hai-ying, WU Qun, and CHEN Zhi-ning, "Broad-bandwidth and low-loss metamaterials: theory, design and realization," *Journal of Zhejiang University Science A.*, vol. 7, no. 1, pp. 5-23, 2006.

[10] Abedin, M. Faisal, Mohammed Z. Azad, and Mohammod Ali, "Wideband smaller unit-cell planar EBG structures and their application," *IEEE Transactions on Antennas and Propagation,* vol. 56, no. 3, pp. 903-908, 2008.

[11] Ahmad A. Sulaiman, Ahmad S. Nasaruddin, Mohd H. Jusoh, Nor H. Baba, Rabi'atun A. Awang, and Mohd F. Ain, "Bandwidth Enhancement in patch antenna by metamaterial substrate," *European Journal of scientific research.,* vol. 44, no. 3, pp. 493-501, 2010.

[12] Nabilah Ripin, Robi'atun Adayiah Awang, Ahmad Asari Sulaiman, Noor Hasimah Baba, Suhaila Subahir, "Rectangular microstrip patch antenna with EBG structure," *2012 IEEE Student Conference on Research and Development (SCOrED)*, pp. 266-271, 2012.

[13] Kuek, C. Y. "Measurement of dielectric material properties." *Rohde & Schwarz Application Note, RAC0607-0019*, 2006.

978-1-4673-9257-0/15/$31.00 ©2015 IEEE

Observation of Low-pass Performance from Novel Trapezoidal Slotted Dumbbell Shape EBGS

S. M. Shakil Hassan
Department of Electrical and Electronic Engineering
Eastern University, EU
Dhaka, Bangladesh
shakil@easternuni.edu.bd

*Md. Nurunnabi Mollah and Khandkar Raihan Hossain
Department of Electrical and Electronic Engineering
Khulna University of Engineering and Technology, KUET
Khulna, Bangladesh
*nurunnabim12@gmail.com

***Abstract*—A novel modified dumbbell shape electromagnetic bandgap structure (EBGSs), trapezoidal slotted dumbbell shape EBGS, has been introduced. Very wide stopband and improved low-pass performances have been reported for particular designs using them. These designs are compared with conventional dumbbell shape EBGS. Trapezoidal slotted dumbbell pattern has shown very attractive performance with very sharp attenuation and significantly reduced ripple heights in insertion loss curve.**

Keywords—Dumbbel shape EBGS, Electromagnetic bandgap structure, Low-pass filter, Trapezoidal slotted EBGS.

I. INTRODUCTION

It is well known that periodic structures at the beneath of microstrip transmission line (T-line) shows very attractive band rejection property for microwave and millimeter wave frequencies [1]-[3]. Such periodic structures are called as Electromagnetic bandgap (EBG) structures or photonic bandgap (PBG) structures [4]; they are very popular in different types of microwave filter designing due to their unique behavior of rejecting certain frequencies [5]. EBG structures have found potential application in planner microwave devices such as patch antenna, phased array antenna, microwave filters, resonators [6]-[8]. Different kinds of electromagnetic bandgap structures (EBGSs) are proposed by the researchers around the world such as circular and square shapes [9], rectangular shape [10]; dumbbell shape [5], tuning fork shape [11], E-shape [8]. Periodic dumbbell shape EBGS (DS-EBGS) in the ground plane of a microstrip T-line introduces high line inductance and capacitance in microstrip line; therefore, it results wider and compact [11] stopband and low-pass [12], [13] performances. Various patterns of DS-EBGS are being studied e.g. square slotted, rectangular slotted, tapered, hybrid etc. and very promising performances are being explored by researchers [14], [15].

In this paper, we have proposed a modified dumbbell shape pattern where instead of square slots as bigger slots, trapezoids are used to give dumbbell look which is referred as trapezoidal slotted DS-EBG. Performance of this particular pattern has been compared with the same sized DS-EBGS. Another design is observed where we have noticed a wider stopband; but that performance later turned to low-pass when an increased number of EBG element are used.

This work is sponsored by Eastern University, Dhaka, Bangladesh. We are grateful to the organization for providing the financial support.

II. DUMBBELL SHAPE EBG PATTERNS

DS-EBG pattern, basically, consists of two bigger slots and a smaller slot where the smaller slot adjoins the bigger slots. Bigger slots generally are square in shape; but recently rectangular shape is taking over due to significant improvement and variation in the performance. The narrow slot is usually a rectangle. Such dumbbell like shape with square slots are, in fact, conventional DS-EBGS – formerly termed as defected ground structure (DGS) [12].

A. Rectangular Slotted DS-EBGS

In Fig. 1(a), a rectangular slotted DS-EBGS is shown. Various types of performances (i.e. wider stopband, dual-band, multi-band and LPF) of rectangular slotted DS-EBGS have been reported in [14]. In the figure, *b* and *c* are two arms of bigger slot and *g* and *h* are width and length of narrow slot respectively. It is reported that the bigger slots of dumbbell shape EBGS introduce inductance whereas the narrow slot introduces capacitance to the microstrip transmission line shown in Fig. 1(b) [12]-[13].

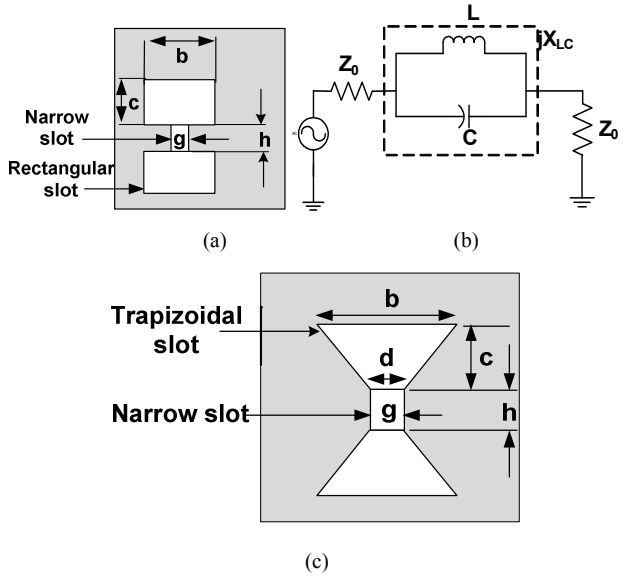

Fig. 1. (a) Conventional dumbbell shape EBGS with rectangular bigger slots, (b) equivalent circuit of conventional dumbbell shape EBGS, (c) trapizoidal slotted DS-EBGS.

978-1-4673-9257-0/15/$31.00 ©2015 IEEE

B. Trapizoidal Slotted DS-EBGS

Figure 1(c) displays a typical trapezoidal slotted DS-EBGS, where *b*, *d* and *c* are the bigger arm, smaller arm and height of the trapezoid respectively. From the figure, it can be seen that instead of square or rectangular slots two trapezoidal slots have been used at both end of the narrow slot. Height and width of the narrow slot is *h* and *g* respectively.

III. EBGS ASSISTED T-LINES

In this paper, we have designed four different designs, where in all the cases the width of the microstrip transmission line is 2.2642mm for maintaining the characteristic impedance (Z_0) 50Ω. Dielectric constant (ε_0) and thickness of the substrate are 2.45 and 31mil (0.7874mm) respectively.

A. Designs 1 : Rectangular Slotted Dumbbell Shape (b=8mm)

In this design, the width (*g*) and length (*h*) of the narrow slot are 2 mm and 1.27mm respectively; therefore, the area of the narrow slot is 2.54mm^2. The dimension of the bigger rectangular slot is b = 8mm and c = 3.987mm respectively; thus, the area of a bigger slot is 31.896 mm^2. Thus the total area (A_{EBG}) of the rectangular slotted DS-EBGS is 66.332mm^2. Inner element spacing (*a*), formally defined as center to center distance between two EBG elements, is 10.4308mm and number of EBGS elements is nine shown in Fig. 2(a).

B. Designs 2 : Trapizoidal Slotted Dumbbell Shape (b=8mm)

This pattern contain trapezoidal slot in place of rectangular slot shown in Fig. 1(c) and the size of the trapezoid is *b* = 8 mm, *d* = 2mm and *c* = 3.987mm; therefore, the area of the trapezoid is 19.94mm^2. The size of the narrow slot is *g* = 2mm and h = 1.27mm, same as the rectangular slotted dumbbell shape design. Thus the total area of an EBG element becomes 42.42mm^2, which is much less than that of design 1. Here, *a* = 10.4308mm too.

C. Designs 3&4: Trapizoidal Slotted DS-EBGS (b=4.622mm)

In this design *b* = 4.622 mm, *d* = 2 mm and *c* = 3.987 mm; the narrow slot: *g* = 2 mm and *h* = 1.27 mm. Thus the total area of an EBG element becomes 28.942 mm2, which is much less than that of design 1 and 2. We have observed the performances of this trapezoidal slotted DS-EBGS for different number of EBG elements at the beneath of T-line where a = *10.4308 mm.*

1) Designs 3 using 5 EBGSs: In this design we get five EBG elements at the beneath of T-line.

2) Designs 4 using 9 EBGSs: In this case the same size of trapezoidal slotted DS-EBGS is used; but the number of EBG element is nine.

IV. S-PARAMETER PERFORMANCES

All the simulations have been performed by using a method of moment (MOM) based software named Zeland IE3D. Simulation results obtained from this EM software have been found in good agreement with the experimented results [8], [11]. We have actually verified the simulated results with experimented results in [5]; however, in this paper we have also confirmed that the simulated result follows theoretical consideration.

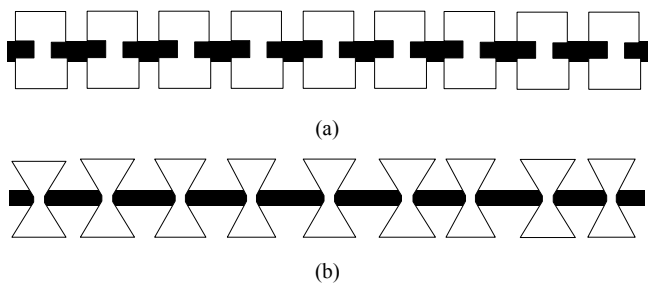

Fig. 2. EBGS assisted microstip T-line having (a) design 1: DS-EBGS with rectangular bigger slots, (b) design 2: trapizoidal slotted DS-EBGS.

In this paper, we performed all the simulations for more than 20 GHz frequency. Results have been discussed in terms of insertion loss (IL), return loss (RL), bandwidth (BW) and maximum ripple heights (RH) at passband from the Scattering parameter (S-parameter) performance of the designs. IL and RL curves are described as S_{21} and S_{11} respectively in the s-parameter performance.

A. S-parameter of rectangular DS-EBGS: Design 1

From the Fig. 3, a bigger stopband is found in Design 1. The stopband started at 4.59 GHz and ended at 17.89 GHz; therefore, the stop bandwidth is 13.3 GHz, which is quite wider than usual. However, passband width is 4.1 GHz and -3dB cut off frequency is observed at 4.13 GHz. Maximum ripple height of IL curve at the passband is -3.32dB.

B. S-parameter of trapezoidal slotted DS-EBGS: Design 2

Though the bigger arm of the trapezoid is identical to the bigger arm of the rectangular slot and height of the trapezoid is

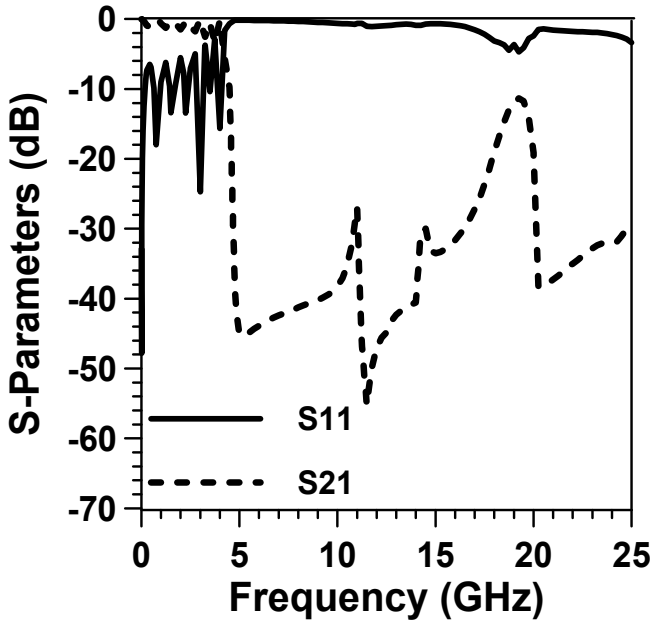

Fig. 3. S-parameter performance of rectangular slotted dumbbell shape EBGS assisted microstrip transmission line (Design 1).

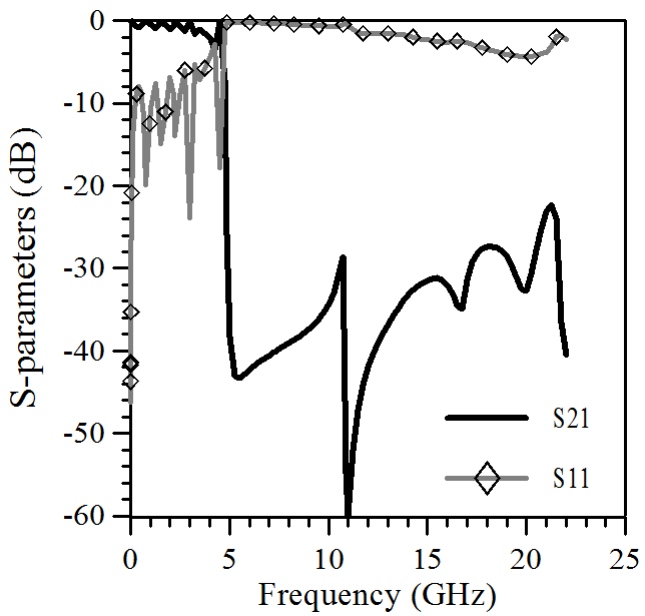

Fig. 4. S-parameter performance of trapizoidal slotted dumbbell shape EBGS assisted design of Design 2.

equal to the other arm of the rectangle, the trapezoidal slot DS-EBGS exhibits a distinguished low-pass performance up to 22 GHz simulation as showed in the Fig. 4. The stopband started from nearly 4.81 GHz. However, passband width is 4.62 GHz and -3dB cut off frequency is observed at 4.60 GHz. Maximum ripple height of IL curve at the passband is -3.33dB. Comparison with the performance of rectangular slotted DS-EBGS is shown in the Table I.

C. Performance of Design 3 & 4

T-line consisting of five trapezoidal slotted DS-EBGSs and nine EBGSs have resulted in a wider stopband and a low-pass performance respectively (shown in Fig. 5). We have observed following performances from this pattern by changing the number of EBGS only.

1) Wider Stopband performance using 5 EBGSs: Band rejection property is started at 5.68 GHz for five EBGS

TABLE I. S-PARAMETER PERFORMANCES OF ALL DESIGNS

Design Title	Different Values of S-parameter				
	Passband at -10dB (GHz)	*-3 dB cutoff frequency (GHz)*	*Stopband at -20dB*	*Max. RH (dB)*	*Total etching area (mm^2)*
Design 1	4.10	4.13	13.3	-3.32	66.332
Design 2	4.62	4.60	LPF started 4.813	-3.33	42.42
Design 3 (5 EBGs)	4.47	5.258	12.984	-1.31	28.942
Design 4 (9 EBGs)	4.20	5.058	LPF started 5.513	-1.94	28.942

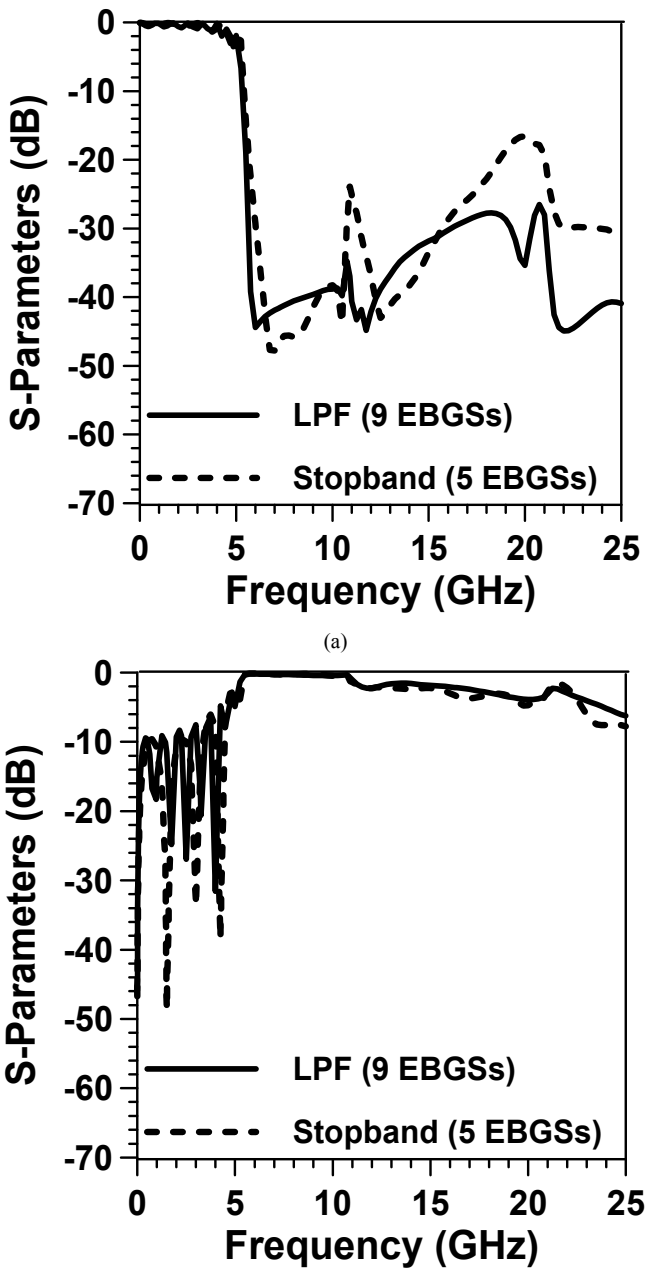

Fig. 5. (a) Insertion loss (S_{21}) curve (b) return loss (S_{11}) curve of trapizoidal slotted DS-EBGS assisted design having five and nine EBGS elements.

assisted design, the stopband width is 12.984 GHz which is larger too. Passband, -3dB cut off frequency and maximum RH at passband for this designs are 4.47 GHz, 5.258 GHz.

2) Low-pass performance utilizing 9 EBGSs: Passband, -3dB cut off frequency and maximum RH at passband for nine EBGSs assisted designs are 4.2 GHz, 5.058 GHz and -1.94 dB respectively. A prominent low-pass performance is observed from this design. Performances are compared in the Table I.

Number of EBGS, basically, has a bearing on the IL curve – the more EBGSs are used the more IL occurs [2]. However,

from the Fig. 5(a), S_{21} curve did not follow the conviction of the other frequencies except near 20 GHz. In essence, the proposed trapezoidal slotted DS-EBG structure performs better band-rejection compared to rectangular slotted DS-EBGS, although etching area is smaller. In contradiction, we know that if the etching area of EBGS (i.e. area of EBGS) is larger, more insertion loss meant to happen. From the earlier discussion, it is obvious that trapezoidal slotted DS-EBGS exhibits quite improved rejection performance.

V. Result Validation

Simulation results are obtained from Zeland IE3D usually are in good congruency with the experimented results [2], [5], [9]. However, to validate the results obtained from this simulation tool a standard 50 Ω T-line without having any EBG element etched at the ground plane has been simulated. Figure 7 shows the performance of this simulation where, it is seen that IL curve (S21) stand along the 0dB line i.e. no insertion loss is observed and return loss remained bellow -20dB; which is theoretically expected performance. Sine, the simulated result followed the theoretical realization; hence it can be considered that all the simulation results we get from the Zeland ie3d simulator will find very well agreement with experimented results.

VI. Conclusion

The design, consisting five trapezoidal slotted DS-EBGS, elements shows well formed wide stopband; in addition to that same trapezoidal slotted DS-EBGS with nine EBGS elements shows distinguished low-pass performance. While compared with rectangular slotted DS-EBGS of same bigger arm and height, it is observed that a trapezoidal slotted DS-EBG pattern has resulted very improved low-pass performance too, whereas the rectangular slotted dumbbell shape EBGS has shown a wider stopband. Therefore, band-rejection property of the proposed design is quite better than that of conventional DS-EBGS. We believe, the proposed pattern will find potential application for such low-pass filter designing soon.

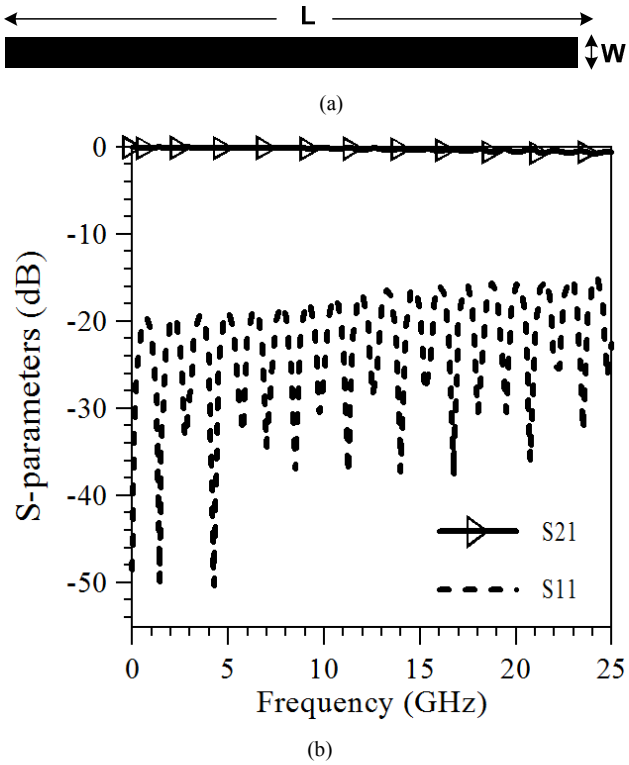

Fig. 6. (a) Standard 50Ω microstrip T-line without any EBGS (b) performance of the standard microstrip T-line.

References

[1] V. Radisic, Y. Qian, R. Coccioli, and T. Itoh, "Novel 2-D photonic bandgap structures for microstrip lines," IEEE Microwave and guided wave lett., vol. 8 no. 2, pp.69-71, Feb. 1998.

[2] Nemai C Karmaker and Mohammad N Mollah, "Potential applications of PBG engineered structures in microwave engineering - part one," Microwave Journal, vol. 47, no. 7, pp. 22-44, July 2004.

[3] S. Y. Huang, and Y. H. Lee, "Tapered dual-plane compact electromagnetic bandgap microstrip filter structures," IEEE Trans. Microw. Theory Techn., vol. 53, no. 9, pp.2656–2664, Sep. 2005.

[4] F. Falcone, T. Lopetegi, and M. Sorolla, "1-D and 2-D photonic bandgap microstrip structures," Microw. Opt. Technol. Lett., vol. 22, no. 6, pp. 411–412, Sep. 1999.

[5] S. M. S. Hassan, S. M. Anayetullah, and M. N. Mollah, "Sinusoidal appearance of nonuniform dumbbell shape EBGSs in microstrip transmission line," in 1st *Int. Conf. on Elect. Inform. and Commun. Technol.*, Khulna, Bangladesh, Feb. 2014, pp. 509-513.

[6] V. Radisic, Y. Qian, and T. Itoh, "Broad-band power amplifier using dielectric photonic bandgap structure," IEEE Microw. Guided Wave Lett., vol. 8, no. 1, pp. 13–14, Jan. 1998.

[7] M. N. Mollah, and N. C. Karmakar, "A compact photonic bandgap assisted phased array antenna," Asia-Pacific Microwave Conf., Korea, Nov. 2003.

[8] S. Y. Huang, and Y. H. Lee, "A compact E-shaped patterned ground structure and its application to tunable bandstop resonator," IEEE Trans. Microw. Theory Techn., vol. 57, no. 3, pp.657–666, Mar. 2009.

[9] N. C. Karmakar, and M. N. Mollah, "Investigation into nonuniform photonic-bandgap microstrip low-pass-filters.," IEEE Trans. Microw. Theory Techn., vol. 51, no. 2, pp.564–572, Feb. 2003.

[10] S. M. S. Hassan, S. M. Anayetullah, M. N. Mollah, K. R. Hossain, M. M. Ahmed, M. A. A. Shufian, and M. M. Hassan, "Realization of low-pass filters from arbitrarily designed nonuniform EBG structures," in 1st *Int. Conf. on Elect. Inform. and Commun. Technol.*, Khulna, Bangladesh, Feb. 2014, pp. 305-310.

[11] L. Yang, M. Fan, F. Chen, J. She, and Z. Feng, "A novel compact electromagnetic-bandgap (EBG) structure and its application for microwave circuits.," IEEE Trans. Microw. Theory Techn., vol. 53, no. 1, pp.183–190, Jan. 2005.

[12] D. Ahn, J.S. Park, C.S. Kim, J. Kim, Y. Qian and T. Itoh, "A design of the lowpass filter using the novel microstrip defected ground structure," *IEEE Trans. On Nicrowave Theory and Techniques*, vol. 49, no. 1, pp. 86-93, 2001.

[13] J. S. Lim, C. S. Kim. D. Ahn, Y. C. Jeong, and S. Nam, "Design of low-pass filters using defected ground structure.," IEEE Trans. Microw. Theory Techn., vol. 53, no. 8, pp.2539–2545, Aug. 2005.

[14] S. M. S. Hassan, M. N. Mollah, M. A. Rashid, N. H. Ramly, and M. Othman, "Dumbbell shape EBGS structure – worth to EBG assisted microwave filter designing," IEEE Asia-Pacific Conf. on Applied Electromagnetics, Malaysia, Dec. 2012.

[15] M. N. Mollah, and N. C. Karmakar, "Compact hybrid defected ground plane," Microw. Opt. Technol. Lett., vol. 44, no. 3, pp.266–270, Feb. 2005.

Receiver Initiated Multi-channel Medium Access Control Protocol for Cognitive Radio Network

Amran Hossain, Sahelee Sultana and Md. Obaidur Rahman
Department of Computer Science and Engineering , Dhaka University of Engineering & Technology(DUET), Gazipur
Gazipur-1700, Bangladesh
amran_duet38@duet.ac.bd, sahelee.cse@gmail.com, orahman@duet.ac.bd

Abstract— **At present Cognitive Radio Network (CRN) is one of the contemporary research area in order to improve efficiency as well as improve spectrum utilization factor of wireless communication. The impression of profitable CRN (i.e., simultaneous presence of primary and secondary users in licensed bands) is increasing popularity in wireless communication research. In fact fixed unlicensed band is used by wireless users in different networks to complete data communication. However, in practical number of wireless users are increasing day by day and guides this limited bandwidth to a saturation state. In CRN as at the absence of primary user, the secondary users access the channels of licensed bands; thereby the Medium Access Control (MAC) protocol for CRN faces many challenges. The challenges include throughput maximization, channel rendezvous amongst the secondary users, minimize delay, and to keep continuing data transmission without interfering the primary users. A large number of sender initiated MAC protocols have been proposed for CRN to solve these challenging issues. However we argue that efficient channel rendezvous in many scenarios still a major concern in accordance with the rest of the mentioned challenges. In this paper, we have come up with a Receiver Initiated Multi-channel (RIM) Medium Access Control (MAC) protocol named as RIM-MAC exploiting the pseudorandom number channel sequence and hopping method for multi-channel rendezvous amongst the secondary users of CRN. This protocol is efficient scheme for channel rendezvous success rate. We have analyzed and implemented our proposed RIM-MAC protocol, and found that it provides better performance in terms of throughput, rendezvous rate and delay.**

Keywords—Cognitive radio, psedurandom number channel sequence, channel rendezvous, primary user, secondary user.

I. INTRODUCTION

Cognitive Radio Network (CRN) gains popularity in the research area because it enables the current fixed spectrum channel assigned by FCC to be utilized by the new users [1]. It is noteworthy that most of the spectrums assigned to television channels, radio channels dividends a huge amount of bandwidth and are kept idle most of the time; whereas wireless network users (i.e., WLAN and Wi-fi users) share a small range of spectrum. In practical, when there are many wireless users at a time, the network gets congested because of the limited number of channels with less bandwidth. Hence, it is predictable that bandwidth would not be sufficient to provide better support for the wireless users in terms of quality of service (QoS), throughput and delay. So, the ultimate solution is to find out some alternative. CRN is one of the possible solutions to overcome this problem. Cognitive radio (CR) is an intelligent transceiver, adaptive and network technology, which can be configured with dynamism property. It has ability to automatically detect free or available channels from wireless spectrum and change its transmission parameters enabling more communications to run concurrently. In point of fact, CRN is structured with both the secondary user (SU) and primary user (PU) in which, SUs consist CR-enabled radios and the PUs whose radios need not be CR-enabled [2]. Cognitive capability means to the ability to sense opportunities in spectrum where and when channels are not employed by PUs [3].

In view of the fact that, the SUs operate separately on dissimilar channels based on availability (i.e., during the absence of primary users), channel rendezvous seems to be the most challenging issue in CRN. Fig. 1, illustrates that nodes *A* and *Y*, *W, C* and *X*, *B* and *Z*; the pairs of SUs opportunistically make channel rendezvous on channel 1, channel 3, and channel 5 respectively, where no PU exists. Note that channel 2 and 4 are occupied by the PUs. Hence, SU do not have any activity on these channels. It is observed that, there are different approaches exist for channel rendezvous between two SUs in CRN. *Firstly,* the *common control channel* (CCC) approach for channel rendezvous [4] creates bottleneck situation on the common control channel.

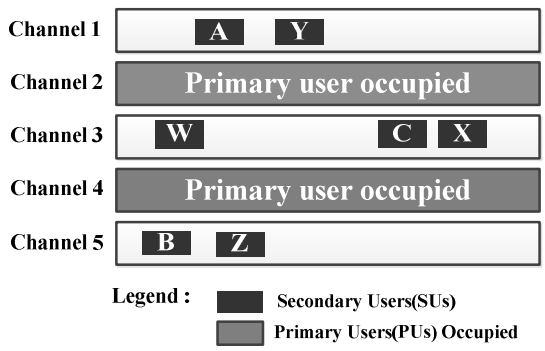

Figure 1: Basic communication manner in CRN

Furthermore, rendezvous scheduling complexity may arise. *Secondly,* the *channel hopping* approach [5-6] can be used by the SUs to discover each other on a channel while hopping different channels. This approach uses *pseudorandom sequence* according to available channel list. When PU is occupied channel(s) gradually, then decrease channel rendezvous rate as well as increase channel rendezvous delay. Conversely, if two SUs follow reciprocally exclusive sequence, still after lots of iterations, those may not succeed in

978-1-4673-9257-0/15/$31.00 ©2015 IEEE

discovering each other [7]. *Finally*, in *synchronization approach* [8], nodes are needed to be synchronized; hence synchronous overhead becomes the main concern for a large network.

Considering the above mentioned limitations on different channel rendezvous approaches, we have motivated to design an efficient channel rendezvous technique using *pseudorandom number channel sequence* for making channel rendezvous between SUs considering all channels.

The rest of the paper is organized as follows: in Section II the background study and problems domains are presented. Section III describes the proposed RIM-MAC protocol design. Analysis and performance evaluation are described in Section IV and V respectively, and Section VI concludes the paper.

II. Related Work and Problem Statement

Till date, a number of MAC protocols have been proposed for CRN to solve the channel rendezvous problem, where the protocols either use any one approach of the followings or make the combinations amongst those; such as- *common control channel approach* [9-12], *channel hopping approach* [6], and *synchronization approach* [8].

A. Common Control Channel Approach

In this approach selects one channel that serves as a rendezvous channel and all the essential control information is exchanged among the SUs on this channel [9-12]. When a SU wishes to communicate with its potential receiver (i.e., another SU), at first it switches to the CCC during *control interval* and attempts to negotiate with its potential receiver using a control packet. When negotiation is complete on CCC, the SU switches to negotiation channel [5] which is available or common to both and then data communication can be accomplished during the *data exchange interval* through available channel. In addition, bottleneck situation may occur in the CCC when multiple nodes negotiate for rendezvous in a single channel.

B. Channel Hopping Approach

In the channel hopping approach [6], each SU generates a pseudorandom sequence using its own available channels. According to predefined hopping sequence SU switches/hops from one channel to another until finds its neighbor. When two SUs meet on a channel which is common between them, they need to exchange the necessary control information as well as complete their data communication. Hence, we conclude that a large number of iterations are required for channel rendezvous using pseudorandom channel hopping sequence as well as, even after lots of iterations; neighbor discovery of SUs may not be successful if SUs follow mutually exclusive pseudorandom sequence [7].

C. Synchronization Approach

In this approach [8] time is divided into N number of equal time slots of fixed duration. Each time slot is dedicated to one channel for control signal exchange. At the end of the network initialization state, all nodes are synchronized and every node has the information about its neighbors and their respective channel sets. To exchange the control signals it chooses one of the channels common between itself and its neighbor during at the beginning of specified time slot. Therefore, nodes are needed to be synchronized; hence, synchronization overhead occurs in this approach and increase the rendezvous delay.

Considering the above mentioned limitations of different channel rendezvous approaches, in this paper we have proposed a RIM-MAC protocol for SUs. The proposed method makes a pseudorandom number channel sequence according to total number of channels for rendezvous among the SUs.

III. Proposed RIM-MAC Protocol Design

A. Protocol Overview

RIM-MAC is a multichannel asynchronous duty-cycling MAC protocol. It does not require nodes to synchronize. It also does not use common control channel behavior. In this protocol design a ***beacon packet*** (i.e., Hello Packet) is considered to exchange all the control information of a SU node. Each SU has a ***prediction state*** (i.e., *initial state*) to learn about receiver's available channel set, *beacon sending time* and *pseudorandom number channel sequence*.

In RIM-MAC protocol, a node avoids choosing channels that are occupied by PU. When a node wakes up on a channel according to pseudorandom number channel sequence to send a beacon, it uses a CCA (Clear Channel Assessment) technique to check and make sure the channel is idle/free before beginning its transmission. If the channel is idle/free, the node sends the beacon and complete data transmission with their potential sender node. If the channel is occupied by PU, the receiver node skips the channel and goes to sleep; and wait on that channel till a cycle time, denoted by T_C (i.e., mentioned later). Additionally, after waiting the nodes switch to next pseudo randomly chosen channel and repeat the CCA technique and beacon sending method.

B. Network Model

Fig. 2 is shown as simple cognitive radio network model. In this model SUs are mentioned as S (i.e., Sender Node) and R (i.e., Receiver Node). We know that in IEEE 802.11b standard protocol uses only 16 channels. SU can occupy any channel among the standard channel list of ISM band. Here, for simple explanation we have assumed only 5 channels. The PUs is mentioned as P_S in sender side and P_R in receiver side respectively.

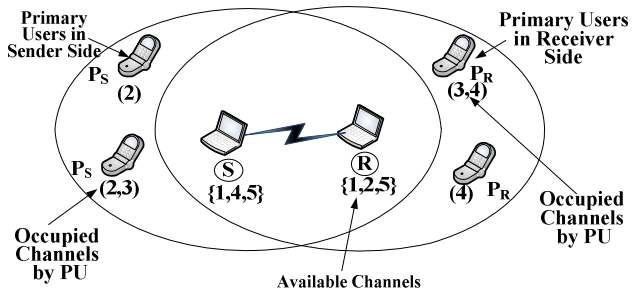

Figure 2: Simple CRN model

In sender range PUs occupied channel(s) are (2, 3) and in receiver range PUs occupied channel(s) are (3, 4). So the available channel(s) set of *S* is {1, 4, 5} and available channel(s) set of *R* is {1, 2, 5}. In the next sections we have used these available channel(s) list for explanation.

C. Protocol Operation

RIM-MAC is a multichannel asynchronous duty-cycling MAC protocol. The design of RIM-MAC is mainly encouraged by the multi-channel EM-MAC [13] protocol for WSN. RIM-MAC protocol operation is categorized into three phases such as-*Network Initialization State, Stable Phase and Adaptive Phase* which are described in the following sections.

1) Network Initialization State

Each SU node equipped with a single radio multi-channel transceiver and can act as a sender or a receiver and maintains a common communication characteristic. Initially it is considered that a node has a packet to send to a receiver but does not have the receiver's ***prediction state*** (i.e., receiver's available channel list, beacon time and pseudorandom number channel sequence). Hence, at the initialization the node having data (i.e., the sender *S*) starts sensing the first available channel of its own pseudorandom number channel sequence. *Firstly*, the sender checks that if the channel is occupied by any PU, it switches to the next channel of pseudorandom number channel sequence; otherwise, it enlists the channel in its available channel list and waits for receiver's beacon on that channel. If the sender does not receive beacon from the receiver during its waiting time interval on that channel, then the sender switch to another channel and so on. After receiving the beacon from the receiver, the sender sets a flag in the header of the data packet sent to the receiver, requesting the receiver to embed its prediction state in the following beacon. Thus, the node gets aware of the receiver's beacon time offset on respective available channels and maintains the same for future data communication. So the receiver beacon should be sufficient to ensure that the receiver will visit the channel at least once during this time. Let T_C be the cycle time interval of a node and the node wakes-up on different channels using the pseudorandom number channel sequence using the T_C cycle time interval. However, if the next channel(s) of the pseudorandom number channel sequence is occupied by the PU the node stays on its current channel and after elapsing appropriate T_C cycle time interval(s) it switches to the next available channel. It should be sufficient to ensure that receiver will visit the available channel at least once during this time. So the maximum waiting time of a sender on a channel would be

$$T_{Wait} = N_{ch} \times T_C \qquad (1)$$

Where, T_C is the cycle time, and N_{ch} is the total number of channels. Fig. 3 illustrates the initialization state of protocol. Based on the *overlapping principle* [14] it is expected that *S* would receive the beacon from *R* and subsequently sends the data packets and complete communication. If the sender does not receive a beacon from the receiver after waiting T_{Wait}, the sender switches to the next channel and repeats the waiting procedure. If the sender is unable to rendezvous with the receiver after waiting on all channels, the sender assume that

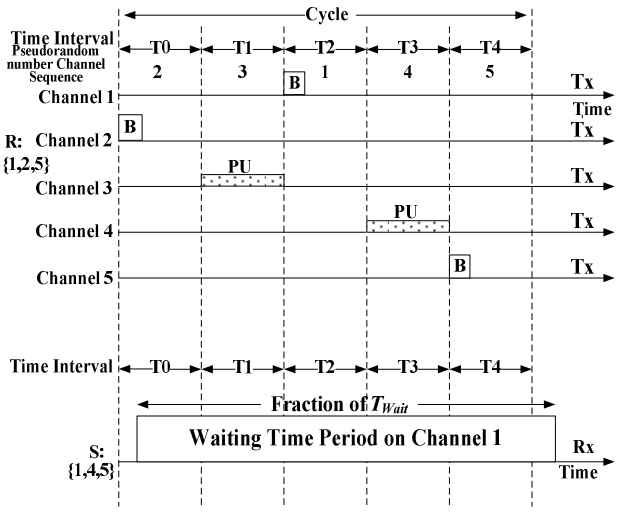

Figure 3: Network initialization state

the receiver is unreachable. In contrast, the same node, when acts as a receiver, then it sends the beacon to its potential sender(s) posterior to the waiting time *(T_{Wait})* for its own receiver's beacon.

2) Stable Phase

Every SU node independently decides and maintains its own pseudorandom number channel sequence switching behavior, wake-up offsets and available channel list. A sender rendezvous with a receiver on a particular channel by predicting the receiver's wake-up channel, wake-up offset and available channels. We denote that a SU *Sender* as node *S* and a SU *Receiver* as node *R*. Fig. 4 illustrates an example of the operation of proposed RIM-MAC, with time progressing from left to right. As RIM-MAC is a receiver initiated multichannel MAC protocol, a receiver node *R* first sends a beacon on an available channel (i.e., no primary user is on that channel) according to its generated pseudorandom number channel sequence. On the contrary, it is assumed that the sender *S* is well aware of receiver's channel sequence, available channel list and beacon time offset on different channels. Hence, the sender *S* proactively remains on the receiver's available channel to receive the beacon from node *R* and consequently sends data to *R*. As shown in Fig. 4, sender *S* has channel {1, 4, 5} as its available channel list. Now receiver *R* first scans the channels according to its pseudorandom number channel sequence. Thus, on a particular time offset/interval receiver *R* sends a beacon *B* to sender *S* and initiates a communication on available channel 2 during cycle time T_C, but on that time sender *S* is not stayed on that channel because channel 2 is occupied by PU for *S*. So *R* does not get any data from sender *S*. Now *R* switches to next channel(s) and so on. Here, channels 3 and 4 are occupied by PU so receiver skips these channels and switches to next channel. The channel 1 is available to *R,* so *R* sends a beacon to sender *S* on this channel. After receiving the beacon *B* from *R*, node *S* sends the data packet *D* to *R*. In reply, *R* sends an acknowledgement beacon *B* to *S* to acknowledge the data packet receipt. Moreover, the acknowledgement beacon *B* works as a request for another data packet to be sent to *R* by *S* or another sender. In the providing example no other data packet is available so *S* and *R*

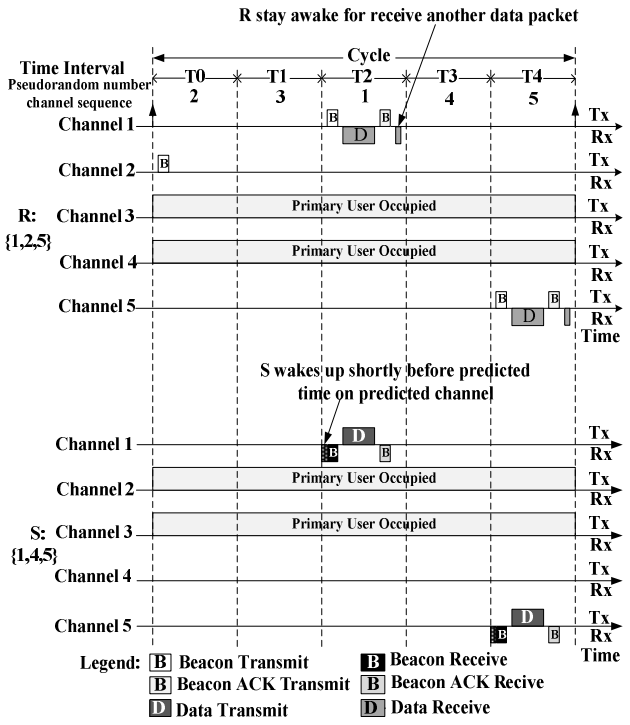

Figure 4: RIM-MAC protocol operation scenario.

quickly go back to sleep. After Cycle time T_C, R wakes up for the second time on another available channel such as 5 and complete data packet transmission with S and so on. Hence, sender S has prediction state of R, so S wakes up shortly before predicted time on predicted channel(s) before data transmission.

3) Adaptive phase

In adaptive phase, we have assumed that after sometimes or next cycle, when available channel list of R is updated with few additional channels due to non-occupation of PUs. In such case, receiver R follows its own pseudorandom number channel sequence for sending beacon in the newly added channel(s). In contrast, it is expected that S will be updated about the changes in available channel list in R through the earlier/later beacons. Thus it can perform data transmission with R in the newly added channel(s). When, available channel list of R is updated with fewer channel(s) due to channel occupation of PUs.

In such case, receiver R follows its own pseudorandom number channel sequence for sending beacon in the available channel(s) only. Here as well S will be updated or presume about the changes in available channel list in R. Thus it can perform data transmission with R in the newly added channel(s). Let, after few seconds previous sender S now acts as a new receiver R, and its available channel(s) list is {1, 4, 5} and its pseudorandom number channel sequence is 31542. Therefore, new receiver R follows its own pseudorandom number channel sequence and completes the data transmission with another sender S according to stable phase. Fig. 5 illustrates new adaptive operation in this case.

IV. Rendezvous Delay Analysis

For channel rendezvous delay analysis, we have considered three cases as follows: worst case rendezvous delay analysis, best case rendezvous delay analysis and average case rendezvous delay analysis.

Case 1: Worst case rendezvous delay analysis

If a sender S has no prediction state of R, then S first waits on an available channel until getting the receiver beacon. Let T_C be the cycle time interval of a node and the node wakes-up on different channels using the pseudorandom number channel sequence using the T_C cycle time interval. However, if the next channel(s) of the pseudorandom number sequence is occupied by the PU the S stays on its current channel and after elapsing appropriate T_C cycle time interval(s) it switches to the next available channel. It should be sufficient to ensure that receiver will visit the available channel at least once during this time. So worst case rendezvous delay would be calculated as follows:

$$T_{Wait}^{Worst} = N_{ch} \times T_C \tag{2}$$

Here, T_C = Cycle time, N_{ch} is the total number of channels.

Case 2: Best case rendezvous delay analysis

In the best case sender S would get the beacon exactly on its first available channel without wait. So the best case rendezvous delay would be calculated as follows:

$$T_{Wait}^{Best} = \delta;\ Where\ \delta \rightarrow 0 \tag{3}$$

Case 3: Average case rendezvous delay analysis

Average case rendezvous delay would be calculated as:

$$T_{Wait}^{Average} = \delta;\ where\ \delta \rightarrow \frac{N_{ch} \times T_C}{2} \tag{4}$$

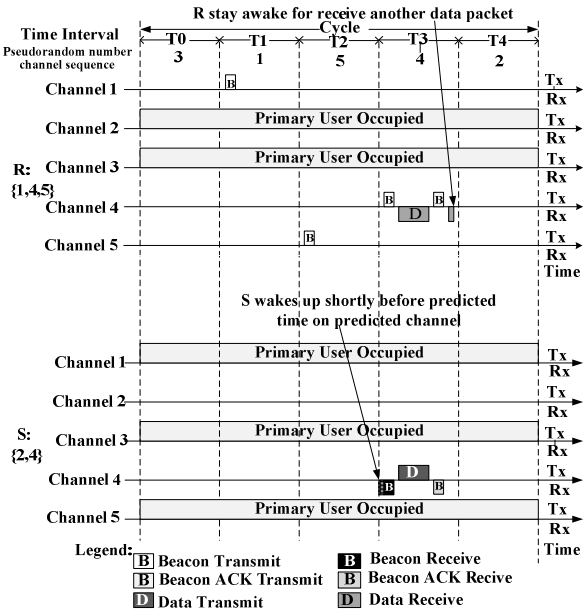

Figure 5: RIM-MAC protocol operation in adaptive phase

V. PERFORMANCE EVALUATION

We have demonstrated the performance evaluation of our proposed RIM-MAC protocol and compare the results with that of a CCC-MAC protocol and SYN-MAC protocol. We have used our own simulation model developed in Java Platform (NetBeans IDE 7.0) and we have implemented our proposed RIM-MAC, CCC-MAC and SYN-MAC protocols and compare the results with among them. In this simulation environment, 10 channels are used for modeling licensed channels for PUs and randomly some of the channels made free/unlicensed and set available to the SUs. Maximum 20 nodes are deployed in 500 x 500 m^2 area to make variation in number of PU and SU. 10 nodes are chosen randomly as the sources and the other 10 nodes as destinations. The transmission range of each node is set to 250*m*. In this simulation, 10 simulation cycles are considered, each having a cycle period of 10 seconds. Hence, total simulation time is 100 seconds. Each data packet is considered to cost 1 Joule for single transmission, which is used to calculate energy consumption of each node. In case of data packet transmission failure, 1 Unit (i.e., Second) is assumed, which is used to calculate delay of each node. In our simulation, for evaluation the performance of Proposed RIM-MAC, SYN-MAC and CCC-MAC, we have considered five performance metrics such as- *Throughput, Rendezvous Success Rate, Rendezvous Delay, Packet Transmission Success Rate,* and *Energy Consumption.*

A. *Throughput Performance*

Fig. 6 shows the aggregated throughput of proposed RIM-MAC with the SYN-MAC and CCC-MAC protocols as the network traffic is increased. The throughput of RIM-MAC is significantly higher than SYN-MAC and CCC-MAC. The main cause for this behavior is that a CCC among all the nodes is not always available and so many times a connection is not established. Hence, due to these failures the throughput is significantly lower in CCC-MAC. In SYN-MAC when nodes are increased, then synchronization overhead is increased so connection problem and problem of message collaboration among the nodes are increased. So throughput is comparatively lower than the RIM-MAC. In RIM-MAC, there is no control signal shared with among all nodes and hence, nodes are communicated any time any available channel(s). Therefore, RIM-MAC has the better throughput from the SYN-MAC and CCC-MAC protocols.

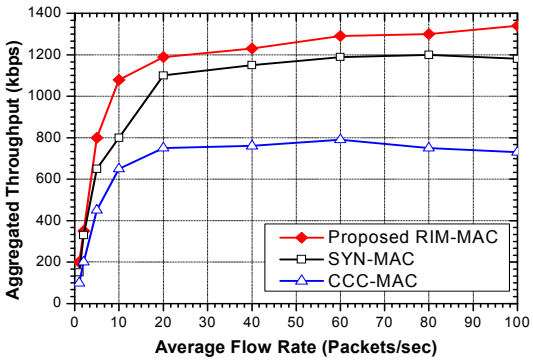

Figure 6: Average throughput Vs flow rate

B. *Rendezvous Success Rate*

Fig. 7 demonstrates the results of rendezvous success rate in percent with respect to simulation time for channel rendezvous. As shown in figure, in 1st cycle, rendezvous success rate among the SUs in RIM-MAC is 100%, in SYN-MAC is 100% and in CCC-MAC is 70%, and so on. After 10th cycle of simulation, it is observed that the rendezvous success rate in RIM-MAC is 60% and steady, and SYN-MAC and CCC-MAC are abrupt. So, it can be concluded that proposed RIM-MAC protocol provides higher rendezvous success rate than the SYN-MAC and CCC-MAC approaches.

C. *Rendezvous Delay Rate*

Fig. 8 demonstrates the outcome of rendezvous delay in second with respect to simulation time for channel rendezvous. As shown in figure, in 1st cycle, rendezvous delay among the SUs in RIM-MAC is 0 (i.e., no delay), in SYN-MAC is 1 and in CCC-MAC is 3, in 2nd cycle; rendezvous delay among the SUs in RIM-MAC is 0 in SYN-MAC is 1 and in CCC-MAC is 4 and so on. Finally at 10th cycle of simulation, it is observed that the rendezvous delay in RIM-MAC is 4 and steady, and SYN-MAC and CCC-MAC are increased. So, it can be concluded that proposed RIM-MAC protocol provides lower rendezvous delay than the SYN-MAC and CCC-MAC approaches.

D. *Packet Transmission Rate*

Fig. 9 exhibits the results of packet transmission success rate in percentage with respect to simulation time. In figure, in 1st cycle, packet transmission rate among the SUs in RIM-MAC is 100%, in SYN-MAC is 90% and in CCC-MAC is 70% and so on. It is also observed that in 10th cycle, the packet

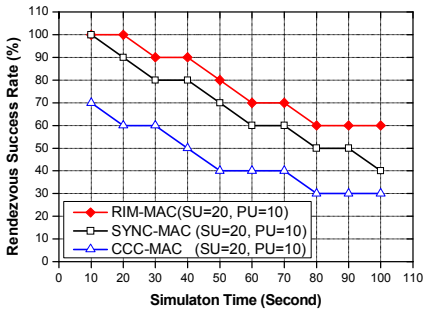

Figure 7: Rendezvous success rate with respect to simulation time

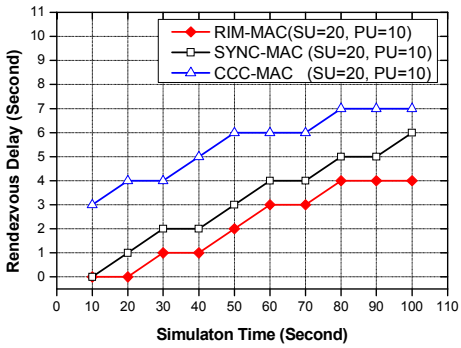

Figure 8: Rendezvous delay with respect to simulation time

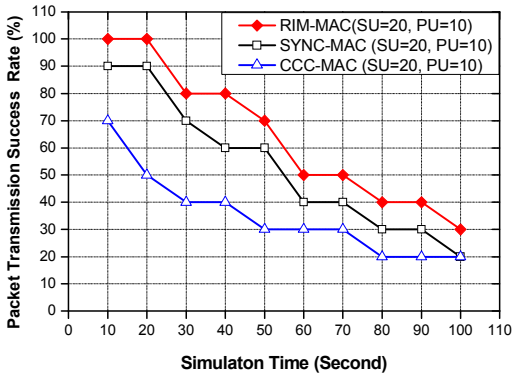

Figure 9: Packet transmission success rate with respect to simulation time

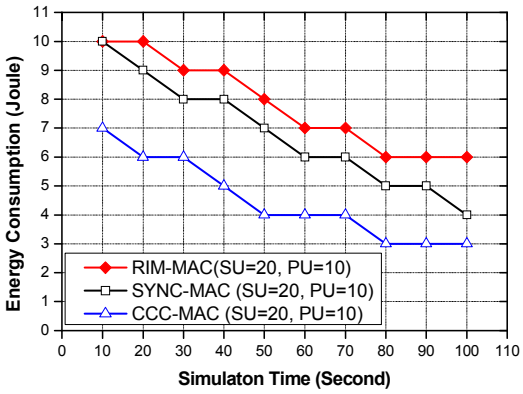

Figure 10: Energy consumption with respect to simulation time

transmission success rate in RIM-MAC is 30%, and 20% in SYN-MAC and CCC-MAC respectively. So we can say that RIM-MAC protocol provides higher packet transmission success rate than the SYN-MAC and CCC-MAC protocols

E. Energy Consumption

Fig. 10 illustrates the outcome of energy consumption in second with respect to simulation time. It is observed in RIM-MAC rendezvous success rate and packet transmission success rate is higher than the SYN-MAC and CCC-MAC which are shown in Fig. 7 and 9 respectively. So it is concluded that the energy consumption in proposed RIM-MAC is higher than the SYN-MAC and CCC-MAC.

VI. CONCLUSION

In this paper we have presented a new CRN MAC protocol and channel rendezvous scheme using pseudorandom number channel sequence based mechanism for SUs considering all the channels of the list. Proposed RIM-MAC protocol algorithm ensures that maximum number of SUs can make channel rendezvous and successfully complete their data transmission with each other. This protocol automatically eliminates the control channel saturation problem and synchronization overhead. In addition, this protocol increases throughput, maximize channel rendezvous success rate, maximize packet transmission rate and reduces delay.

ACKNOWLEDGMENT

This work is supported by the "*Research Development Fund*" of Dhaka University of Engineering & Technology (DUET), Gazipur and Dr. M. O. Rahman is the corresponding author.

REFERENCES

[1] Federal Communications Commission. (2015) The FCC website.[Online]. Available: https://apps.fcc.gov/edocs_public/ attachmatch/ FCC-03-289A1.pdf.

[2] N. Meghanathan, "A survey on the communication protocols and security in cognitive radio networks," *International Journal of Communication Networks and Information security (IJCNIS)*, vol. 5, no. 1, pp.19-38, Apr.2013.

[3] I. F. Akyildiz, W. Y. Lee, M. C. Vuran, and S. Mohanty, "Next generation dynamic spectrum access /cognitive radio wireless networks: a survey," *International Journal* of *Computer Networks (Elsevier)*, vol. 50, no.13, pp. 2127–2159, Sept. 2006.

[4] I.F. Akyildiz, W.Y, Lee, and K. R. Chowdhury, "CRAHNs: cognitive radio ad hoc networks," *International Journal of Ad Hoc Networks(Elsevier)*, vol. 7, no. 5, pp. 810-836, Jan. 2009.

[5] Z. Htike, and C.S. Hong, "Neighbor Discovery for Cognitive Radio Ad Hoc Networks," in *Proc. International conference on Ubiquitous Information Management and Communication (IMCOM),* Kota Kinabalu, Malaysia, Jan. 2013.

[6] L. DaSilva and I. Guerreiro, "Sequence-based rendezvous for dynamic spectrum access," The 3rd IEEE International Conference on New Frontiers in Dynamic Spectrum Access Networks, Chicago, IL, Oct. 2008, pp. 1-7.

[7] M. R. Islam, M.A.E. Shakib, M. A. Rahaman, M. O. Rahman, and A. S. K. Pathan, "A Neighbour Discovery Approach for Cognitive Radio Network Using Tower of Hanoi(ToH) Sequence Based Channel Rendezvous," in *Proc. The 5th International Conference on Information and Communication Technology for The Muslim World (ICT4M)*, Kuching, Nov. 2014, pp.1-6.

[8] Y. R. Kondareddy and P. Agrawal, "Synchronized MAC Protocol for Multi-hop Cognitive Radio Network," *IEEE International Conference on Communications*, May 2008, pp. 3198 - 3202.

[9] X. Zhang and H. Su, "CREAM-MAC: cognitive radio-enabled multichannel MAC protocol over dynamic spectrum access networks," *IEEE Journal of Selected Topics in Signal Processing*, vol. 5, no. 1, pp. 110 – 123, 2011.

[10] C. Cordeiro and K. Challapali, "C-MAC: A cognitive MAC protocol for multi-channel wireless networks," The 2nd *IEEE International Conference on New Frontiers in Dynamic Spectrum Access Networks, DySpan*, Dublin, Apr. 2007, pp. 147–157.

[11] B. F. Lo, "A survey of common control channel design in cognitive radio networks," *International Journal of Physical Communication (Elsevier)*, vol. 4, no. 1, pp. 26–39, Mar. 2011.

[12] K. R. Chowdhury, I. F. Akyildiz, "OFDM-Based Common Control Channel Design for Cognitive Radio Ad Hoc Networks," *IEEE International Journal of Mobile Computing*, vol.10, no.2, pp. 228-238, Feb.2011.

[13] L. Tang, Y. Sun, O. Gurewitz and D. Johnson; "EM-MAC: A Dynamic Multichannel Energy-Efficient MAC Protocol for Wireless Sensor Networks" MobiHoc '*11Proceedings of the Twelfth ACM International Symposium on Mobile Ad Hoc Networking and Computing,* Paris, France, May 2011, Article No. 23.

[14] M. O. Rahman, R. Kamal, C. S. Hong, S. Lee, Deokjai and Y.C. Bang, "A light-weight channel rendezvous Scheduling for Multi-channel Medium Access in Sensor Networks," *International Conference on ICT Convergence (ICTC),* Sept. 2011, pp. 40-45.

Opportunistic System Approach for Capacity Enhancement and Congestion Mitigation in Advanced Wireless Networks

Kazi Nawshad Azam and Mostafa Zaman Chowdhury
Department of Electrical and Electronic Engineering, Khulna University of Engineering & Technology, Bangladesh
E-mail: nawshad_kuet@yahoo.com, mzceee@yahoo.com

Abstract—**Today's technology in communicating among wireless systems are more complicated and sophisticated with more opportunities, services and facilities to its users. As wireless network technology advances so as the challenges associated with it increases to solve some basic problems such as congestion, interference, call admission and service quality control etc. In the macro integrated femtocellular or heterogeneous wireless network the system capacity enhancement in a low congestion environment is a key issue to focus on and to do so a novel approach is proposed in this paper. We propose an opportunistic system approach where intelligent resource reallocation (IRR) scheme is used to create opportunity to its user to be connected in the high capacity advanced wireless network system with reduced congestion. Performance of our proposed scheme is given in this paper where we can see that how capacity and congestion of wireless network are correlated to provide a reliable wireless system.**

Keywords— Opportunistic system, congestion, system capacity, interference, intelligent resource reallocation.

I. INTRODUCTION

Complex wireless technology is today's demand for high traffic in communication channel [1], [2]. There are different ways of resource allocation to provide better reliable network coverage to serve user's demand. In existing technology capacity of a particular communication channel is predefined that is fixed. For this predefined channel capacity user per channel is also fixed. This channel condition makes the system performance poor. System performance poor means low signal strength, high signal-to- noise plus interference ratio (SNIR), high congestion, low throughput, low quality of service for user [3]. These problems origins from different part of the system design considerations such as power control scheme, frequency allocation scheme, and interference mitigation technique etc [4]. All these problems can be reduced in a considerable limit by applying proper intelligent techniques. Cognitive or opportunistic radio system is a way where cognitive user can use dedicated channel in different way but not in the presence of dedicated user in that channel [5].

When interference is low, SNIR is high and hence increased system capacity [6]. Again when number of user is high in a system then interference may increase which in turn create possibility of reducing system capacity. Also when power control and frequency planning are not adequate in the system then it causes high interference effect [7]. Improper frequency allocations also make wastage of valuable resource. So, user suffers from congestion problem in busy areas. This congestion problem causes higher rate of call drops. To reduce call drop problem call admission control is required.

In this paper we focus on reducing congestion problem and also making system capacity dynamic of wireless network by applying intelligent resource reallocation (IRR) scheme where system capacity can be increased in some extent to support extra users according to existing user's resource utilization natures. New frequency allocation is proposed to make dynamic system capacity for both macrocell and femtocell wireless networks which is shown in Fig. 1. They are: (a) available frequency; dedicated frequency use and opportunistic frequency use (left portion of Fig. 1), and (b) reserved frequency; macrocell frequency share and femtocell frequency share (right portion of Fig. 1). To make user equipment (UE) compatible with proposed opportunistic system as shown in Fig. 2(a), existing UE should have extra mode sensing and switching mechanisms installed inside it. So, user equipments (UEs) for both macrocell and femtocell are proposed to be reconfigurable capability such as to use the above mentioned proposed frequency allocation schemes as: full mode resource utilization and reserve mode resource utilization states, respectively as shown in Fig. 2(b) [8]. Some other measurable parameters such as user's mobility/speed threshold, signal strength threshold, and decision threshold are also considered for our analysis. Here, the author's contribution is in the proposed IRR scheme, where system supports extra opportunistic user in a dedicated channel which is not fully occupied by its dedicated users at the same time seamlessly. Rest of this paper is organized as follows: section II provides our proposed opportunistic system approach; system modeling is given in section III, section IV presents the numerical results, and finally conclusions are drawn in the last section.

II. PROPOSED OPPORTUNISTIC SYSTEM APPROACH

A. Opportunity Creation in Proposed IRR Scheme

Proper resource utilization should be guaranteed in order to confirm reliable wireless communication with low cost by providing different intelligent ways which is termed as opportunity creation. Here, we provide intelligent resource reallocation (IRR) scheme which is an opportunity creative

978-1-4673-9257-0/15/$31.00 ©2015 IEEE

scheme by which overall system capacity of advanced heterogeneous wireless network can be increased along with reduced congestion problem. Congestion problem occurs when available system resource is smaller than demanded by users. For instance, let us consider a wireless system where macrocell and femtocell coexists to form advanced wireless network as shown in Fig. 3. From Fig. 3 we can see that, a channel k is allocated to j dedicated user group (UG_{dj}) where $j = 1, 2, \ldots, J$ and $l < J$ in different time slot number, N_{ts} uniformly without prior knowledge about user's actual resource demand as shown in Fig. 2(a) or actual required resource utilization as shown in Fig. 2(b). Now resource utilization occurs by different users according to their type of activities and in this case activities are not same for all users which mean different activities for each user. For this reason with existing fixed resource allocation scheme capacity of wireless network is fixed as shown in Fig. 3. With this fixed capacity of existing system users experiences more congestion problem as shown in Fig. 4, along with high rate of call drop, increased intra- and/or inter-system handover problem. To avoid these problems we proposed IRR scheme among heterogeneous system for users by considering different preliminaries and measurement of different system parameters as shown in Fig. 5.

B. *Capacity Enhancement and Congestion Reduction*

The capacity of a wireless system should be adequate to support extra users without overloading channel, increasing interference level, and higher call drop problems. Call drop rate increases with high rate of user's resource utilization in a fixed or limited capacity wireless system and also which causes high congestion problem. Fig. 6 depicts an intelligent way of resource reallocation technique to make a system with limited capacity into a dynamic capacity. Figure 6 shows that how the capacity of a particular channel in advanced macro integrated femtocellular or heterogeneous wireless network changes from fixed capacity to variable capacity according to user's activity such as actual resource demand and utilization. The natures of activities of different users are different located at the same geographic region that is under the same (only femtocell or macrocell nework) or different network (heterogeneous network) which is serving them. We can also see that each channel is reallocated at different time slots and different hypothesis are allocated for each utilization time slot for UG_{dj} such as hypotheses $H_{01,k}$ is given to first time slot (UG_{d1}), fourth time slot (UG_{d4}) and last time slot (UG_{dJ}) user group over channel k and $k = 1, 2, \ldots, K$. The hypothesis $H_{01,k}$ is indicating that among these three dedicated users group each user's resource utilization state is up to lower threshold limit ($\gamma_{low,k}$). These lower limits is less than 50% of maximum capacity of serving channel k where we can easily create opportunity for new cognitive or opportunistic user groups (UG_{cj}) where $j = 1, 2, \ldots, J$ and $l < J$ at different time slots number, N_{ts} such as UG_{c1}, UG_{c4} and UG_{cJ}. Then UG_{d1}, UG_{d4}, and UG_{dJ} and UG_{c1}, UG_{c4}, and UG_{cJ} user groups get new hypothesis notation from system as hypothesis $H_{11,kNd}$ (fully utilized channel by UG_{dj}) and hypothesis $H_{00,kNc}$ (empty channel available for UG_{cj}),

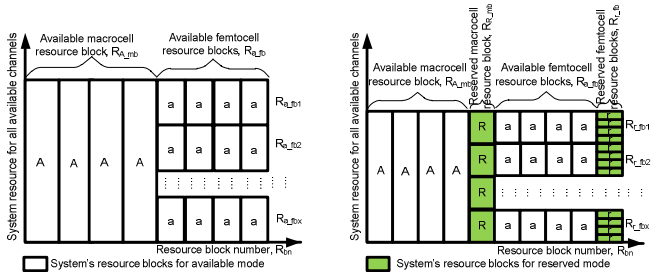

Figure 1. Allocated resource status in a channel for poposed IRR scheme in existing advanced heterogeneous wireless network.

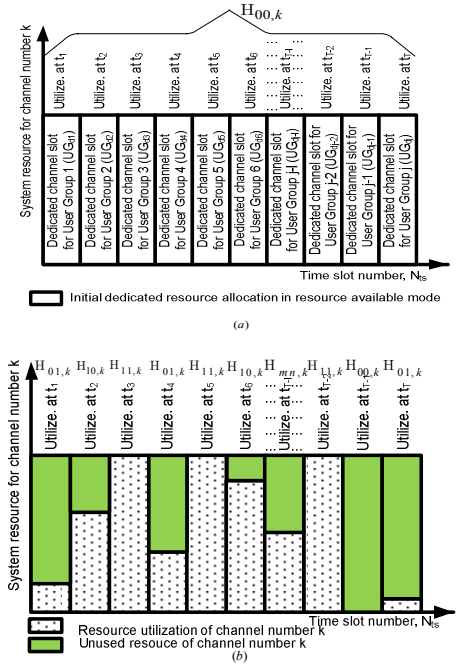

Figure 2. Allocated (a) resource status and (b) resource actual utilization status in a channel for existing advanced heterogeneous wireless network.

respectively. From hypothesis $H_{00,kNc}$, system can allow new opportunistic user to be served and hence capacity is increased. This process is done for each hypothesis except $H_{11,kN}$. Therefore, by comparing between two types of capacity such as without IRR that is fixed system capacity and with IRR that is dynamic system capacity, it is obvious that with proposed IRR scheme the dynamic system capacity serves more users than existing system having fixed capacity. The white area with dashed circle of different femto access points (FAPs) of later scenario indicates resource scarcity. With resource scarcity the new users can not be connected to the system and hence causes call drops, low signal quality and congestion problem for the existing system. With proposed IRR scheme the former scenario shows less congestion for the same number of users causing high user satisfaction in existing system. Resource is reallocated by the system in such a way that each connected users (FAPs with dotted white colored coverage area as shown in Fig. 7) can be served properly and unutilized resources are harvested to reallocate

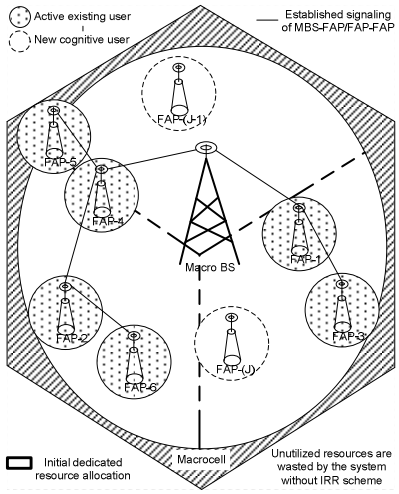

Figure 3. Scenario of capacity problem in existing advanced heterogeneous wireless network.

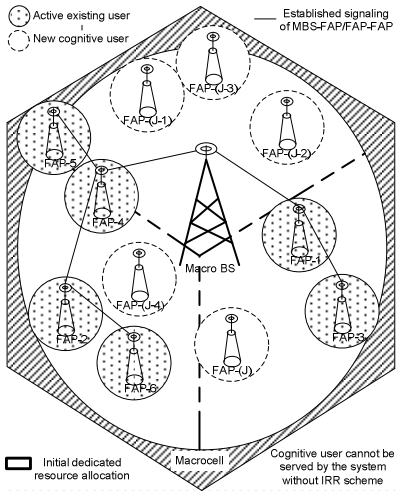

Figure 4. Scenario of congestion in existing advanced heterogeneous wireless network.

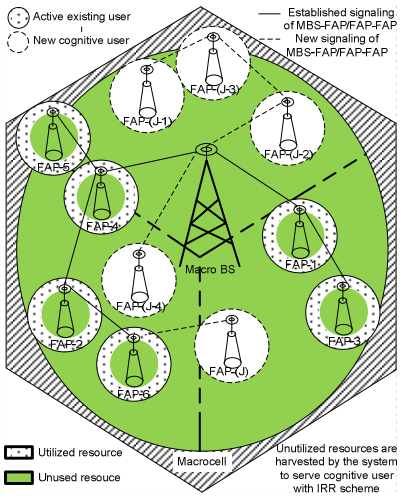

Figure 5. Scenario of resource utilization with IRR scheme in existing advanced heterogeneous wireless network.

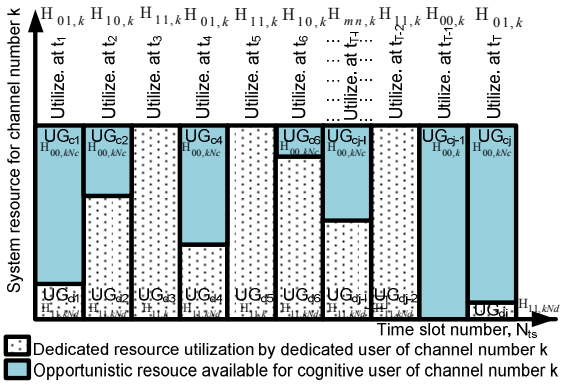

Figure 6. Allocated resource rescheduled status in a channel for poposed IRR scheme in existing advanced heterogeneous wireless network.

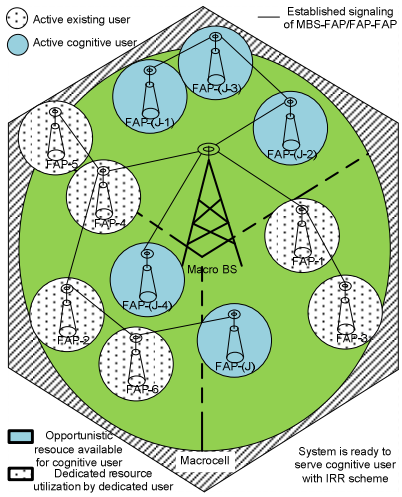

Figure 7. Scenario of IRR scheme with dynamic capacity and reduced congestion in existing advanced heterogeneous wireless network.

them to new users (FAPs with light blue colored coverage area as shown in Fig. 7). As in the network, rate of association of new users increases in a particular area causes congestion problem so, as reverse process (rate of existing user leaving the network) reduces this problem. But there is a predefined minimum resource allotment is required to allow a new user in a network which put limits to minimization of congestion. Therefore, proposed IRR scheme outperforms over existing scheme in minimizing congestion in the advanced heterogeneous wireless network. In proposed IRR scheme, when capacity increases for a certain user groups (causing congestion for existing system), causes less congestion as shown in Fig. 7 problem by opportunity creation by the system itself in an intelligent way.

III. System Modeling

In this section we provide a model of our system with k number of channels. Advanced wireless network system having macro integrated femtocellular that is heterogeneous network is modeled here and details are given in the following:

A. Hypothesis for Opportunistic System Approach

We consider four binary hypotheses to provide coordination among different allocated channels and its user's. These hypotheses are:

$$\mathrm{H}_{00,k} = (\text{"}Full\ Empty\text{"}) = Full\ Opportunity\ (FO)$$

$$\mathrm{H}_{01,k} = (\text{"}Partial\ Occupied\text{"}) = High\ Partial\ Opportunity\ (HPO)$$

$$\mathrm{H}_{10,k} = (\text{"}Partial\ Empty\text{"}) = Less\ \ Partial\ Opportunity\ (LPO)$$

$$\mathrm{H}_{11,k} = (\text{"}Full\ Occupied\text{"}) = No\ Opportunity\ (NO)$$

where 0 (channel utilization absent) and 1 (channel utilization present), respectively gives user channel utilization states over channel k and $k = 1, 2, \ldots, K$.

B. Some Decision Preliminaries

- System monitors environment continuously to identify load flow.
- If system finds any user doing real time activity then system gives this user highest priority of reliability that is not to interrupt.
- If system finds any user doing non real time activity then system gives this user lowest priority of reliability that is tries to interrupt.
- If system manages to create opportunity for new users then reallocation of resources occurs.
- System gives access to new user to avoid congestion by taking proper measurements of user's mobility, required resource demand, resource utilization type, and duration of activity etc.

C. Necessary Mathematical Relations

Decision probability of providing proper hypothesis to a channel during channel resource reallocation is

$$\Pr(\mathrm{H}_{mn,k}) = \frac{1}{4k}\Delta_k \tag{1}$$

where $\Pr(\mathrm{H}_{mn,k})$ is probability of providing proper hypothesis to a channel with subscript notation m (where $m = 0\ or\ 1$) and n (where $n = 0\ or\ 1$), and Δ_k is decision threshold over channel k and $k = 1, 2, \ldots, K$.

Channel resource utilization threshold is

$$Z_{u_j,k} = \begin{cases} \gamma_{0,k}(H_{00,k}) \\ \gamma_{low,k}(H_{01,k}) \\ \gamma_{up,k}(H_{10,k}) \\ \gamma_{max,k}(H_{11,k}) \end{cases} \quad \text{for user u_j, whwre j=1,2,} \ldots \text{,J} \tag{2}$$

where $Z_{u_j,k}$ is channel utilization threshold for user u_j, $j = 1, 2, \ldots, \mathrm{J}$ of channel k and $k = 1, 2, \ldots, K$.

Actual utilized channel capacity is

$$C_{Z,k} = \sum_{k=1}^{K} C_k Z_{u_j,k} \tag{3}$$

where $C_k = W_k \log_2(1 + SNIR_k)$ is actual capacity with channel bandwidth W_k and signal-to-noise plus interference ratio $SNIR_k$ of channel k and $k = 1, 2, \ldots, K$.

Opportunistic utilizable channel capacity is

$$C_{O_Z,k} = \sum_{k=1}^{K} C_k \Pr(\mathrm{H}_{mn,k})(1 - Z_{u_j,k}) = \frac{1}{4k}\sum_{k=1}^{K} C_k \Delta_k (1 - Z_{u_j,k}) \tag{4}$$

where $1 - Z_{u_j,k}$ is channel opportunistic utilizable spaces for user u_j, $j = 1, 2, \ldots, \mathrm{J}$ of channel k and $k = 1, 2, \ldots, K$.

User's satisfaction in resource utilization is

$$S_{u_j,k} = \begin{cases} \sum_{k=1}^{K} s_k Z_{u_j,k}, & \text{for static capacity system} \\ \sum_{k=1}^{K} s_k Z_{u_j,k} + \frac{1}{4k}\sum_{k=1}^{K} s_k \Delta_k (1 - Z_{u_j,k}), & \text{for dynamic capacity system} \end{cases} \quad \text{where } s_k = \begin{cases} 0 \\ 1 \end{cases} \tag{5}$$

where $S_{u_j,k}$ is total user's satisfaction of satisfied user, and s_k is user's level of satisfaction (0 for no satisfaction and 1 for satisfied) per channel for total user u_j, $j = 1, 2, \ldots, \mathrm{J}$ of channel k and $k = 1, 2, \ldots, K$.

Total revenue gain of operator is

$$R_k = \sum_{r=1}^{k} r_{v,k}\left(\sum_{k=1}^{K} C_k (Z_{u_j,k}) + \frac{1}{4k}\sum_{k=1}^{K} C_k \Delta_k (1 - Z_{u_j,k})\right) + r_{f,k} \tag{6}$$

where R_k is revenue earning of operator, r_{vk} rate of variable cost, and r_{fk} rate of fixed cost for contribution of user u_j, $j = 1, 2, \ldots, \mathrm{J}$ of channel k and $k = 1, 2, \ldots, K$.

D. Some Basic Observations of System

- Is it healthy (without any abnormality) system or not?
- Is it fully occupied or not?
- Is there any unused resource exists or not?
- Is there any user that demanding more or less overhead than system can provide or not (near/far-location effect)?

- Is there any user that is only connected without doing any significant activity for a long/predefined/any specified time or not?
- Is there any user that needs to use the system urgently with low/high mobility or not?
- Is there any user that is leaving the system urgently with low/high mobility or not?
- Is congestion exists or not?
- Is congestion exists due to non availability of resources or not?
- Is congestion exists due to uncontrolled traffic flow in a busy area/hot spot or not?
- Is the quality of signal adequate or not?
- Is the rate of user movement inwards or outwards of the system high/low creates congestion or not?
- Is call drop rate is high/low due to congestion or not?
- Is there any unused resource which is already allocated or not?

Finally, system search for unused resources and reallocate it again to enhance overall wireless system capacity as shown in Fig. 7.

IV. NUMERICAL RESULT

Let us, consider a system as shown in Fig. 3 where number of serving channel is k with $k = 1, 2, \ldots, K$.

A. Table and Algorithm

1) Data table for analysis: The conditional values used in the analyses are given in the following table. Different threshold values are also given in the table.

TABLE I. CONDITIONAL VALUES USED IN ANALYSES

Sl. No.	Criteria Details		
	Description	***Lower limit***	***Upper limit***
1	Full opportunity[a], $H_{00,k}$	0.76	1.00
2	High partial opportunity[a], $H_{01,k}$	0.51	0.75
3	Less partial opportunity[a], $H_{10,k}$	0.26	0.50
4	No opportunity[a], $H_{11,k}$	0.00	0.25
5	Number of femto user per FAP, u_j_f	0	5
6	Number of existing FAP, n_{fap}	1	100
7	Number of extra FAP, n_{fape}	1	20
8	Number of existing macro user, u_j_m	0	1000
9	Number of extra macro user, u_j_{me}	0	400
10	Number of channel, k	1	10
11	Decision threshold, Δ_k	0	1
12	Channel utilization threshold, $Z_{u_j,k}$	0.00	0.95

a. Hypothesis selection criteria. (For IRR scheme)

2) Algorithm for hypothesis selection: To select and reshedule the resources, proper hypotheses selection for each channel is required and is given as follows.

a) Step 1: After system power is on, system initialization and basic system parameters reading process is done.

b) Step 2: Check network environment to get information about user, network, and available resouce allocation, utilization, and management.

c) Step 3: Acoording to step 2 select proper frequency selection schem and power control scheme.

d) Step 4: System continuously monitors the network and user's activity to control traffic.

e) Step 5: At initial stage that is when full opportunity is avalable $(\gamma_{0,k})$ for all users then system selects hypothesis $H_{00,k}$ as shown in Fig. 2(a) for channel k and $k = 1, 2, \ldots, K$.

f) Step 6: When user's activity increses in each channel and in a particular channel resource allocation is utilized upto lower threshold limit $(\gamma_{low,k})$ of that channel by the user's of that particular channel then system selects hypothesis $H_{01,k}$ as shown in Fig. 2(b) for channel k and $k = 1, 2, \ldots, K$.

g) Step 7: Again user's activity increses in each channel and in a particular channel resource allocation is utilized upto upper threshold limit $(\gamma_{up,k})$ of that channel by the user's of that particular channel then system selects hypothesis $H_{10,k}$ as shown in Fig. 2(b) for channel k and $k = 1, 2, \ldots, K$.

h) Step 8: Now user's activity increses in each channel and in a particular channel resource allocation is fully utilized up to maximum limit $(\gamma_{\max,k})$ of that channel by the user's of that particular channel then system selects hypothesis $H_{11,k}$ as shown in Fig. 2(b) for channel k and $k = 1, 2, \ldots, K$.

i) Step 9: While system doing this each time, system conditions changes and step 5 to step 8 is repeated according to users activity as shown in Fig. 6. Thus, the capacity of the system changes from static to dynamic to a certain extent according to different criteria.

B. User satisfaction performance comparison

Figure 8 shows that, the capacity of a particular channel in advanced macro integrated femtocellular or heterogeneous wireless network provides better user's satisfaction. For existing system the capacity is static so number of user for a specific channel number k is fixed though that channel is not fully utilized by all the users all the time. For this reason at busy time extra user causes congestion problem. Mean while if that extra user can be served with reserved resource as shown in Fig. 1 (right portion) which is proposed in IRR scheme for the system, then user would suffer less congestion problem which ensures higher user's satisfaction.

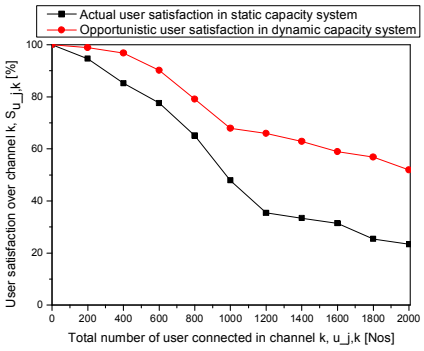

Figure 8. Performance evaluation for user satisfaction versus total number of user connected in both static and dynamic capacity system.

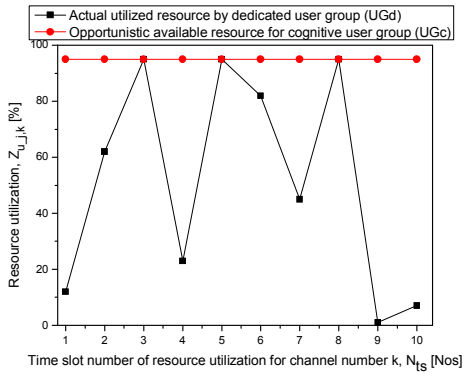

Figure 9. Performance evaluation for resource utilization versus time slot number of resource utilization for channel number k for both static and dynamic capacity system.

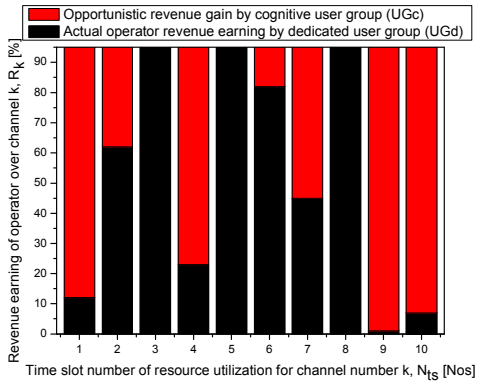

Figure 10. Performance evaluation for revenue earning of operator versus time slot number of resource utilization for channel number k for both static and dynamic capacity system.

C. *Resource utilization and revenue earning of operator performance comparison*

Figure 9 depicts efficient resource utilization for the system with less congestion with proposed IRR scheme than typical fixed resource allocation scheme. When there is less actual resource utilization in existing system then higher the opportunistic resource utilization exists in IRR scheme. We can see from Fig. 9 that for a specific channel number k when user's resource utilization is high, then low possibility of opportunity to reallocate the resource to extra users of that particular channel.

Figure 10 shows a revenue gain of operator when efficient resource utilization occurs for the system with less congestion with proposed IRR scheme than typical fixed resource allocation scheme. When there is less actual resource utilization in existing system then higher the opportunistic resource utilization exists in IRR scheme which in turn provides revenue gain opportunity to system operator. Here, when resource utilization for a specific channel number k is higher then number of user for that channel k is high and hence higher the revenue gain for system operator.

V. CONCLUSIONS

Advanced wireless network is a demanding issue for reliable and high speed communication with low power consumption, and user friendly service. For this reason user satisfaction level need to be consider as an evaluation parameter in both systems that is with existing fixed capacity and with proposed IRR scheme dynamic capacity. The user satisfaction level outperformed in proposed IRR scheme utilized system than existing typical system with increased number of users as shown in performance curve. In near future traffic will increase exponentially more than today so, channel capacity requirement would be higher than today's system. To do so with limited resources best utilization of resource is required. Along with capacity problem, dense traffic in communication channel causes significant congestion. To reduce these capacity and congestion problems together, proposed IRR scheme is a strong candidate to face the challenges associated. Performance of existing fixed capacity system in resource utilization and revenue earning of operator is poor than proposed IRR scheme performance as shown in evaluation line and bar graphs, respectively. Thus, proposed IRR scheme is promising one.

REFERENCES

[1] K. Pahlavan and P. Krishnamurthy, Principles of Wireless Networks, Prentice Hall PTR, New Jersey, 2002.

[2] J. D. Hobby and H. Claussen, "Deployment Options for Femtocells and Their Impact on Existing Macrocellular Networks," *Bell Labs Technical Journal*, vol. 13, no. 4, pp. 145-160, Feb. 2009.

[3] M. Z. Chowdhury, Y. M. Jang, and Z. J. Haas, "Network Evolution and QoS Provisioning for Integrated Femtocell/Macrocell Networks," *International Journal of Wireless & Mobile Networks (IJWMN)*, vol. 2, no. 3, pp. 1-16, Aug. 2010.

[4] Femtoforum, "OFDMA Interference Study: Evaluation Methodology Document," Nov. 2008.

[5] A. Wyglinski, M. Nekovee, and Y. Hou, Cognitive Radio Communications and Networks Principles and Practice, New York: Elsevier, 2010.

[6] K. N. Azam and M. Z. Chowdhury, "Intelligent Interference Management Based on On-Demand Service Connectivity for Femtocellular Networks" in Proceeding of *IEEE International Conference on Informatics, Electronics & Vision (ICIEV)*, May 2013.

[7] M. Z. Chowdhury, Y. M. Jang, and Z. J. Haas, "Cost-Effective Frequency Planning for Capacity Enhancement of Femtocellular Networks," *Wireless Personal Communications*, vol. 60, no.1, pp. 83-104, Sept. 2011.

[8] 3GPP TS 32.500, "Telecommunication Management; Self-Organizing Networks (SON); Concepts and Requirements," Jun. 2011.

A Comparative Analysis of the Characterization Methods for Submicron Silicon Waveguide Propagation Loss

Mohammad Istiaque Reja[1,2,3*], Jobaida Akhtar[1,2,3], Muhammad Nouman Malik[2,3], Md. Jahedul Islam[4], Md Asif Iqbal[3], Shamim Ahmed[2]

[1]Chittagong University of Engineering and Technology, Bangladesh
[2]Scuola Superiore Sant'Anna, Pisa, Italy
[3]Aston Institute of Photonic Technology, Aston University, United Kingdom
[4]University of Sydney, Australia
[*] E-mail: m.istiaquereja@master.sssup.it, rejami@aston.ac.uk

Abstract— **An important parameter in integrated optical device is the propagation loss of the waveguide. Its characterization gives the information of the fabrication quality as well as the information of other passive devices on the chip as it is the basic building block of the passive devices. Although, over the last three decades many methods have been developed, there is not a single standard present yet. This paper presents a comparative analysis of the methods existing from the past as well as methods developed very recently in order to provide a complete picture of the pros and cons of different types of methods and from this comparison the best method is suggested according to the authors opinion. To support the claim, apart from the analytical comparison, this paper also presents a comparison performed with the experimental results between the suggested best method which is recently proposed by Massachusetts Institute of Technology (MIT) researchers based on undercoupled all-pass microring structure and the popular cut-back method.**

Keywords— Integrated optics, Si photonics, waveguide propagation loss, microring reseonator.

I. INTRODUCTION

The most important feature that has made 'Silicon' the ideal and best candidate for next generation of interconnection network on chip requiring large bandwidth is the fact that it is compatible with complementary metal-oxide-semiconductor (CMOS) technology. This property has made it possible to fabricate optoelectronic chip monolithically in a cost-effective way using Silicon-on-insulator (SOI) platform [1].

A natural planar optical waveguide with a refractive index of about 3.5 for Si core and 1.46 for SiO_2 cladding at 1550 nm is provided by SOI structure. Very strong optical confinement in waveguide is possible using this high refractive index difference. This structure also allows to make waveguides with small bend radii and makes silicon the best choice for making the important photonic devices like microring having very low bend radius. Moreover this fact enables to reduce the footprint of the devices and increase the density of the integration [2].An important parameter in integrated silicon photonic devices is the propagation loss of waveguide. So to ascertain the suitability of the silicon waveguides for specific application, it is very essential to characterize the loss properly. Most of the propagation losses in Si nanowire arise mainly due to the sidewall roughness and this roughness is a result of the fabrication process, more specifically lithography and etch process [3]. Typical Roughness value is of the order of 2 nm (having a correlation length of ~40nm), which is a large value for a Si waveguide width of submicron order. So, this high roughness results to a high propagation loss of the order of 2 dB/cm [4].

Also, we know that the quality of all the passive element can be specified by knowing the quality of the silicon waveguide as it is the fundamental building block of a silicon photonic circuit. So, characterizing the waveguide loss not only help us to know the quality of the waveguide in terms of fabrication accuracy but also gives us a hint about the quality of the other passive device on the silicon chip.

There is not a single standard yet for measurement of the waveguide loss [4]. Many methods have been developed over the last three decades for measuring the loss accurately. In this paper the common loss characterization methods which are generally used will be described and their pros and cons will be presented. Also the methods, which researchers have proposed recently will be compared with the existing commonly used methods. From this comparison a conclusion will be drawn to suggest the best method according to the authors opinion. To support the claim, the suggested best method which has been reported in 2013 by the Massachusetts Institute of Technology (MIT) researchers [4] will be explained in a greater detail with some simulation results and its superiority will be assessed experimentally by comparing with an existing popular method.

II. DESCRIPTION OF DIFFERENT TYPES OF LOSS CHARACTERIZATION METHODS

A. Commonly used methods

The methods which are commonly used to measure the waveguide loss can be categorized into four types.

978-1-4673-9257-0/15/$31.00 ©2015 IEEE

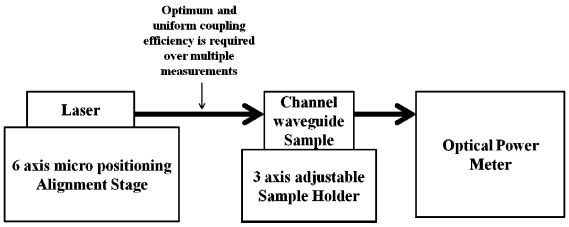

Figure 1. The measurement setup for cut-back method

These are: (i) the cut-back or paper-clip method; (ii) the Fabry-Perot resonance method; (iii) scattered light measurement method and (iv) Sliding prism method [5]. These methods are described briefly in the following subsections.

(i) Cut-back or paper-clip method

This method is based on a very simple concept. A channel waveguide sample of length l_1 is excited by a laser and then output power from the waveguide P_1 is measured. The same procedure is followed for another length l_2 and output power P_2 is measured. Therefore, we can write

$$\frac{P_1}{P_2} = exp^{-\alpha(l_1 - l_2)} \quad (1)$$

Here waveguide propagation loss (α) is in cm^{-1}. Hence, α in dB/cm

$$\alpha = 10\, log_{10}\left(\frac{1}{l_1 - l_2} ln(\frac{P_1}{P_2})\right) \quad (2)$$

However, it is not easy to make waveguides of different lengths maintaining the same quality. So, in order to change the length of the waveguide it is cut after each measurement. After cleaving the waveguide sample the edge of the waveguide facet is polished. A series of measurements are done following this procedure with different sample lengths. The output power is measured by using a optical power meter [5], [6]. The measurement setup is schematically shown in the fig. 1.

In spite of the fact that this method is very fast and simple, the accuracy of this method is poor. Because it is difficult to maintain uniform facet quality and coupling efficiency during every measurement after cutting the waveguide.

(ii) Fabry-Perot (FP) resonance method

This method is based on the concept that a waveguide can be thought of a Fabry-Perot cavity where the two facets can act as mirrors. So, the Fabry-Perot resonances can be used to measure the propagation loss [5].

The waveguide propagation loss α can be written as,

$$\alpha = -\frac{1}{L} ln\left(\frac{1}{R}\frac{\sqrt{I_{max}/I_{min}} - 1}{\sqrt{I_{max}/I_{min}} + 1}\right) \quad (3)$$

where R is the reflectivity of the facet and L is the sample length, I_{max} and I_{min} denotes the maximum and minimum transmission intensity respectively [7].

This method is more accurate than cutback method as it is more repeatable [5] and is independent of the requirement of the input coupling knowledge. But here another problem arises which is the requirement of facet reflectivity estimation and the accuracy of this method mostly depends on the knowledge of facet reflectivity [7]. Moreover, it is necessary to use a stabilized light source to maintain constant input power over Fabry-Perot fringes measurement and a source having narrow line-width.

It has been shown in [8] that, the requirement of the knowledge of facet reflectivity can be eliminated by measuring the transmission and reflection both from FP cavity. But in that case the power from the input facet need to be measured very precisely and carefully. Moreover, both from the input and output sides, similar coupling efficiencies are needed. These requirements are very complex to accomplish in the experimental setup.

So, the problem with the FP resonance method is that the experimental procedure is quite complex here.

(iii) Scattered light measurement method

This method is based on the concept that the scattered light can be measured from the top of the surface along the waveguide length in order to measure the loss [9]. It is assumed in this method that the amount of scattered light will increase with the increase of the propagated light inside the waveguide. An optical fiber can be scanned along the waveguide length in order to collect the light [5]. Though this method is independent of input coupling losses, it can be easily understood that the accuracy of this method is limited by the wafer surface quality [7].

(iv) Sliding prism method

The propagation loss can be measured by using the sliding prism method. This is also a widely used method. This method is based on the concept of measuring the guided power at varying distance from the input coupling region through the use of sliding prism placed at right-angle and thus measuring the propagation loss [10].

An experimental setup for this method is shown in fig. 2 [5]. The slab waveguide sample must be clamped very tightly under the prism. In order to couple the prism with the modes of the waveguide, either the guided mode or the substrate mode, the contact between the prism and the waveguide must be very good. Also dirt free prism must be needed [5].

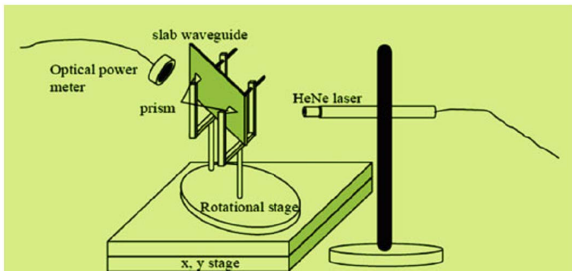

Figure 2. The measurement setup for sliding prism method [5]

The problem with this method is that the requirement of complex mechanical arrangement makes the experimental procedure difficult.

B. *Recently developed methods*

(i) Modified FP method

In conventional FP method, in order to fulfill the necessity of narrow linewidth source, external cavity tunable lasers are used. But it is not easy to stabilize it when wide wavelength region is needed. Moreover this kind of light source is also expensive. So broadband low-coherence source, which has low cost, is desirable.

It has also several other advantages over high coherence tunable lasers such as more stability in comparison to the tunable lasers and it is less prone to reflections. Also it is possible to measure over multiple wavelengths in one single measurement in contrast to the tunable laser [7].

But the issue with the broadband source such as superluminescent diode is, with the change in wavelength the input power also changes which made it difficult for the broadband source to be used in FP method. In [7], Sareh tabi *et al*. proposed a modification in conventional FP method, where they suggest a way of curve fitting in order to solve the issue of power change in broadband light source. So, in this modified method the experimental procedure has been simplified due to the use of broadband superluminescent diode.

This method also suggests a way in order to solve the reflectivity measurement issue, since for accurate measurement, the knowledge of the reflectivity is needed. They have rewritten the equation (3) as

$$-\alpha L = ln\left(\frac{1}{R}\right) + ln\left(\frac{\sqrt{I_{max}/I_{min}} - 1}{\sqrt{I_{max}/I_{min}} + 1}\right) \quad (4)$$

After that, measurement for different length waveguides are done and the value of $ln\left(\frac{\sqrt{I_{max}/I_{min}}-1}{\sqrt{I_{max}/I_{min}}+1}\right)$ is plotted with respect to length L. From this plot, the loss and the reflectivity both can be measured without assuming either of the two. Loss (α) can be found from the slope of the curve and reflectivity (R) can be measured from the intercept.

This method was proposed in 2008. Although this method is not very recent, in comparison to the other methods, proposed long ago, it can be considered as a recent method.

To summarize, this method uses curve fitting approach to solve the power consumption issue in broadband low-coherence source and eliminates the requirement of the narrow linewidth source which is very difficult to stabilize. Also, the reflectivity measurement issue is solved by taking measurement from different length waveguides. So, by solving the problems of conventional FP method, this modified FP method provides very accurate results.

(ii) Method based on undercoupled All-Pass microring structure

This is a very simple method proposed by the Massachusetts Institute of Technology (MIT) researchers in 2013 [4], which can measure the loss very accurately using simple undercoupled microring structure. The loss is measured here by way of fitting the experimental spectrum with the simulated curve generated from the developed all-pass model. The concept of this method is based on the interplay between standing wave modes and traveling ring modes which arise due to back-reflection from edge roughness.

In this method a number of microrings are coupled with a common bus waveguide with different bus to ring gap. All of the rings have radius around 10 micrometer and the radius is varied very slightly in order to have different free spectral ranges. Fig. 3 shows the schematic diagram of the structure.

In fig. 4 the five resonances corresponding to the five rings are shown. It can be seen that the first three rings which do not show any splitting in the resonances represent the overcoupled condition whereas the last two rings showing clear splitting represent undercoupled condition. The microring quality factor degrades very largely in undercoupled condition which results in a splitting in the resonance. This is because the waveguide loss effect is dominant here over the low bus to ring coupling amount. Thus, the effect of loss is very clear and explicit here. So, the ideal condition for precisely measure the waveguide loss is undercoupled condition.

In the fig. 5 the effect of loss change on the overcoupled and undercoupled resonances have been shown and it can be seen that, in the undercoupled spectrum responses are highly sensitive to α as the depth of the split resonances changes very fast with the increase of the loss.

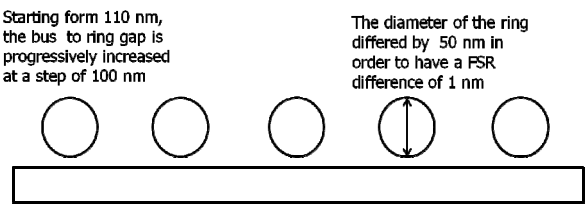

Figure 3. The schematic diagram of the all-pass architecture used in this method

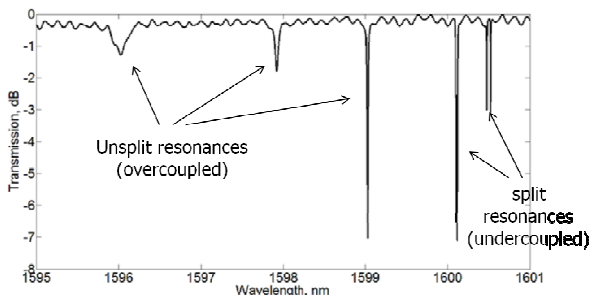

Figure 4. The spectral scan showing the five resonances for the rings having different bus to ring gap.

But, the change of loss does not have a significant effect on the response in overcoupled condition. It has been seen from the simulation results that the more we moves toward the under (over) coupled regime the more (less) sensitive the response becomes with respect to loss.

So, by way of curve fitting, this model propose to measure the waveguide propagation loss in undercoupled condition in order to see the effect of loss more clearly, thus measuring the propagation loss more accurately. Also this model is better from those models which measures the loss by assuming that critical coupling condition is met [11], because spotting the critical coupling condition is extremely difficult and it is highly intolerant [4].

Also, from the model developed it is found that in the undercoupled condition, if the reflection coefficient i.e. the amount of reflected light due to the backscattering increases the separation between the spitted peaks increases as shown in fig.6. This is because, this model considers that each scattering point leads to a backward reflection which is again reflected by the same scattering point after a round trip and thus forms a standing wave. This standing wave interacts with the radiation unaffected by scattering. In summary, the standing wave formation which is due to the intercavity scattering of light is a scenario similar to Fabry Perot (FP) cavity and the propagation of the light radiation which is unaffected by scattering is a scenario similar to travelling wave cavity. The competition between these two cavities determines the presence of the usual transmission dip [4].

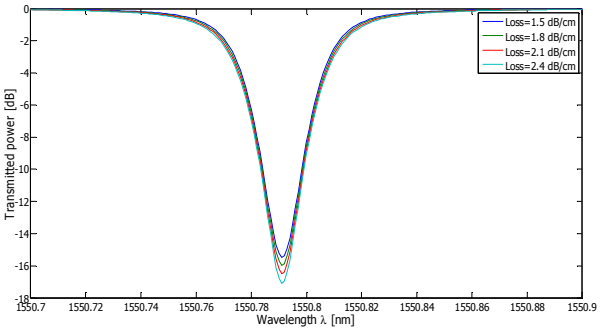

(a)

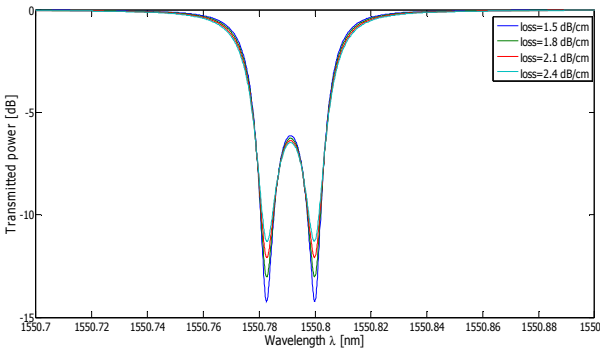

(b)

Figure 5. Effect of loss change in (a) overcoupled and (b) undercoupled condition

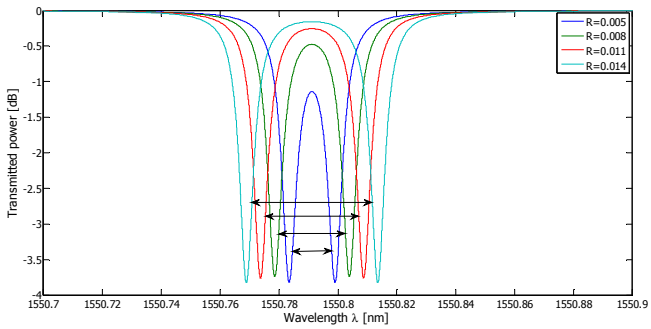

Figure 6. Effect of Reflection coefficient (R) change in undercoupled condition

So, considering all these effects, the simulated spectrum is fitted with the experimental spectrum by changing the value of loss, reflection coefficient and coupling coefficient and finally it gives the value of loss.

The fitting method based on this model is very accurate as seen from a comparison with another model reported in [12] which also assumed the backscattering as the reason for splitting in the resonances. But that model which is based on the concept of double ring filter does not lead to very good fitting in comparison to this model which is based on the competition between FP and travelling wave cavity. Indeed it has been shown in [4], the average loss measured for a number of samples using fitting of this model is 1.7 dB/cm and using the fitting of that double ring based model is 1.1 dB/cm. So, the loss is underestimated.

In summary, the advantage of this method lies on the fact that it is independent of input coupling loss and reflection which leads to very accurate measurement of propagation loss.

III. COMPARATIVE ANALYSIS OF THE METHODS

The popular cut back method, although provides very simple and direct measurement of the loss, has very poor accuracy because of various reasons. Firstly, the quality of the facet changes each time after the cutting. Secondly, The measurements must be performed under optimum input coupling efficiency. Moreover, the coupling efficiency cannot be maintained exactly same for every measurement [13].

In the conventional FP method the requirement of the exact knowledge of facet reflectivity limits the accuracy. Also the need for using stabilized narrow line width sources makes the experimental procedure very difficult.

The sliding prism technique requires extracting light with 100% efficiency. Also, the mechanical arrangement is quite complicated here. A new method, which is a modification of conventional sliding prism technique based on sliding right angle-prism (RP), is proposed in [10] in order to make the operation convenient. This method uses a RP and non sliding isosceles prism (IP) together to get accurate result. But still the method is a bit complex in comparison to other characterization methods.

TABLE I. A COMPARISON OF THE LOSS CHARACTERIZATION METHODS

Comparison parameters	Cut back	Sliding prism	Scattered light measurement	FP resonance	Modified FP	All-pass undercoupled
Input coupling loss dependency	Yes	No	No	No	No	No
Experimental Procedure / Mechanical Arrangement	Simple	Complex	Simple	Complex	Simple	Very simple
Requirement of the estimation of facet reflectivity	No	No	No	Yes	Yes (solved through curve fitting)	No
Curve fitting	No	No	No	No	Yes	Yes
Curve fitting quality	N/A	N/A	N/A	N/A	Very good	Very good
Accuracy	Poor	Poor	Poor	Poor	Good	Good
Reason for the limited accuracy	Requirement of the same facet quality and coupling efficiency over multiple measurements	Requirement of 100% light extraction efficiency	Dependency on the wafer surface quality	Requirement of facet reflectivity knowledge and narrow linewidth stable source	N/A	N/A

The accuracy of the method based on the scattered light measurement depends very strongly on the wafer surface quality.

The modified FP method seems to be very accurate as this method provides the solution of the problems of conventional FP method and may be adopted very widely for loss characterization in future. The experimental procedure has been simplified through the use of curve fitting by using the low coherence broadband source instead of high coherence tunable lasers. This method also provides a way to measure both the reflectivity and loss together without the assumption of the either.

The method based on the undercoupled all-pass microring structure seems to be the best in terms of accuracy and experimental simplicity. This method is totally independent of the input coupling loss and has tolerance to the ring to bus gap choice. This method measures the loss in undercoupled condition where the effect of loss have dominant effect over the bus to ring coupling. So, the loss effect is very explicit here which makes it possible to accurately measure the loss. Moreover, The fitting method, which is based on the concept of the competition between FP cavity and travelling wave cavity, provides very good fitting in contrast to the other fitting model based on double ring cavity.

In table 1 a comparison of different types of methods is presented and it can be said that the best method in terms of simplicity and accuracy is the method based on undercoupled all-pass microring structure.

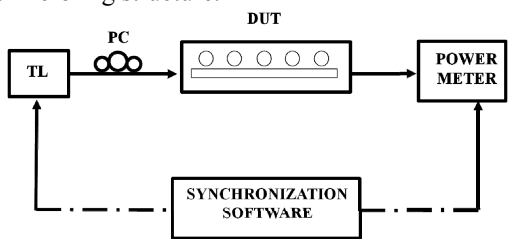

Figure 7. Experimental setup to measure the loss using the method based on all-pass structure

IV. EXPERIMENTAL COMPARISON OF COMMONLY USED 'CUT BACK METHOD' AND METHOD BASED ON 'ALL-PASS UNDERCOUPLED STRUCTURE'

The method based on all-pass undercoupled structure is used to experimentally measure the losses of ten samples. The experimental setup for spectrum measurement is shown in fig. 7. The light from a tunable laser (TL) is coupled into the device under test (DUT) through a polarization controller (PC) that maximizes the coupling efficiency between the fiber and the input grating coupler of the device under test. Then with a synchronized power meter the output spectrum is collected from the 'through' port grating coupler.

By way of fitting the undercoupled resonances taken from all the spectra with the simulated curve, the average loss has been measured as 2.14 dB/cm. The measured loss from the cutback PCM structure is 1.98 dB/cm. So, the loss in the cutback method is underestimated because of its limited accuracy.

V. CONCLUSION

As characterization of loss is an important step to know the quality of the fabrication process many loss measurements methods have been proposed over the last three decades. But still there is not a single standard for this loss characterization. This paper presents a comparative analysis of all types of loss characterization methods in order to provide a complete picture of the advantages and disadvantages of the methods. Widely used loss characterization methods from past are compared with two recently developed methods. From the comparison, the recent method based on undercoupled all-pass microring structure is suggested to be best in terms of simplicity and accuracy. To support this claim an experimental comparison between this method with the popular cut-back method is shown and it is found that the loss is underestimated in cut-back method due to its limited accuracy.

ACKNOWLEDGMENT

The authors would like to thank Scuola Superiore Sant'Anna, Pisa (SSSUP), Italy for providing the laboratory

facility for this work. The authors would also like to acknowledge the support of Institute of Microelectronics (IME), Singapore for the fabrication of PICs that have been used for the loss measurements.

REFERENCES

[1] J. K. Doylend, A. P. Knights, "The evolution of silicon photonics as an enabling technology for optical interconnection," *Laser Photonics Rev*, vol. 6, pp. 504–525, 2012.

[2] T. Hu *et al.,* "Silicon photonic network-on-chip and enabling components," *Science China Technological Sciences*, vol. 56, no. 3, pp. 543-553, March 2013.

[3] M. Williamson and A. Neureuther, "Enhanced, quantitative analysis of resist image contrast upon line edge roughness (LER)" *in Proc. SPIE 5039*, pp. 423–432, 2003.

[4] M. Moresco *et al.,* "Method for characterization of Si waveguide propagation loss" *Optics Express*, vol. 21, no. 5, pp. 5391-5400, 2013.

[5] Tong, Xingcun Colin, *Advanced Materials for Integrated Optical Waveguides*, Springer Series in Advanced Microelectronics, Springer International Publishing Switzerland, 2014, vol. 46.

[6] A. Rickman, G. T. Reed, B. L. Weiss, and F. Namavar, "Low-Loss Planar Optical Waveguides Fabricated in SIMOX Material", *IEEE photonics technology letters,* vol. 4, no. 6, June 1992.

[7] S. Taebi, M. Khorasaninejad, and S. S. Saini, "Modified Fabry-Perot interferometric method for waveguide loss measurement," *Appl. Opt.* vol. 47 no. 35, pp. 6625–6630, 2008.

[8] K. H. Park *et al.*, "Non destructive propagation loss and facet reflectance measurements of GaAs/AlGaAs strip-loaded waveguides" *J. Appl. Phys*., vol. 78, pp.6318–6320, 1995.

[9] Y. Okamura, S. Yoshinaka, and S. Yamamoto, "Measuring mode propagation losses of integrated optical waveguides: a simple method," *Appl. Opt*. vol. 22, pp. 3892–3894, 1983.

[10] J. Wei *et al.*, "Improved method for loss measurements in planar waveguides," *Elsevier Optics and Lasers in Engineering* vol. 45, pp. 419–422, 2007.

[11] T. R. Bourk, M. M. Z. Kharadly, and J. E. Lewis, "Measurement of waveguide attenuation by resonance methods," *Electron. Lett.* Vol. 4, no. 13, pp. 267–268, 1968.

[12] Z. Zhang, M. Dainese, L. Wosinski, and M. Qiu, "Resonance-splitting and enhanced notch depth in SOI ring resonators with mutual mode coupling," *Opt. Express*, vol. 16, no. 7, pp. 4621–4630, 2008.

[13] S. Chen, Q. Yan, Q. Xu, Z. Fan, J. Liu, "Optical waveguide propagation loss measurement using multiple reflections method," *Elsevier Optics Communications*, vol. 256, no.1–3, pp. 68–72, December 2005.

Effect of Complementary Triangular Split Ring Resonator on Microstrip Patch Antenna

Sunanda Roy[1,#], Swadesh Podder[2,*], M. Abdus Samad[1,+]
[1]Khulna University of Engineering & Technology, Bangladesh
[2] Banglalink digital communication ltd, Bangladesh
[#]sunandaroy75@gmail.com, [*]swadesh_ku@live.com, [+]prof.m.a.samad01@gmail.com

Abstract—**In this paper, a new complementary triangular split ring resonator (CTSRR) is proposed and the impact of CTSRR on conventional patch antenna is investigated at 2.44 GHz for WLAN applications. The electromagnetic behavior of CTSRR, as well as their equivalent circuit is developed and explained. The demonstrated theoretical approaches result in a meaningful improvement than in comparison to conventional patch antenna. The parametric studies are completed in this work with the different orientation pattern of CTSRR structure. This is exposed that with the increment of CTSRR on patch, antenna performances improve, but resonance frequency shifts toward lower frequency region.**

Keywords—Complementary triangular split ring resonator (CTSRR), gain, directivity, microstrip patch antenna (MPA), wireless local area network (WLAN).

I. INTRODUCTION

During modern centuries, there is immense evolution in wireless local area network (WLAN) applications. Providing of a quality service for the recently increased demand in WLAN is a core level concern as usually for antenna and communication devices. The WLAN is used in our everyday life applications such as notebooks, mobile phones, routers etc. To meet the daily increasing needs, antennas used in WLAN applications are noteworthy factor. With respect to performance, a low cost feed network with miniaturization in size is also very important to carry out in terms of antenna design. Therefore, microstrip patch antenna (MPA) with compactness, low cost and ease of fabrication is effective for WLAN applications and these are widely presented in books and papers in the last decade [1-3].

The standard microstrip patch antenna has a very low gain, low efficiency, low power handling capacity, narrow bandwidth, simple, and inexpensive to manufacture using modern printed–circuit technology [1]. Many researchers have amended the parameters and modified geometry to produce better performance of the patch antenna considering required applications. These improvements cover several shapes of antennas, addition of special structures, and attachment of RF components or integrated circuits into the patch antenna [2].

Now a day's split ring resonator (SRR) is used to produce the desired magnetic response which influences the applied EM field. Several theoretical and experimental works have been studied by researchers on SRR and their potential applications [4-5].There are many types of split ring resonator design such as edge coupled SRR (EC-SRR) [6],broadside-couple SRR (BC-SRR) [7], nonbianisotropic SRR (NB-SRR) [8] and etc. However, there is a very few work on resonator based patch antenna with conventional substrates. Therefore, proper background understanding of resonator and possible impacts on conventional MPA are indispensable. In this work, a complementary triangular split ring resonator (CTSRR) has been proposed on conventional inset feed patch antenna and effect of the CTSRR on regular MPA has been analyzed from various viewing platform.

II. GEOMETRIC VIEW OF CTSRR

The geometric view of the single unit of complementary triangular split ring resonator is shown in Fig. 1.The outer and inner length of the CTSRR structure is L_{out}= 4.25mm and L_{in}= 3.25mm respectively. The dimension of the resonator gap W_s =0.98mm and the thickness of the triangle T_r =1mm. The distance between two TSRR is 0.66 mm and each dimension is similar to the single unit of CTSRR structure.

For a given resonance frequency (f_r), dielectric constant (ε_r), the design equations for calculating patch width (W) and length (L) of our conventional inset feed rectangular microstrip patch antenna (RMPA) are [9]

$$W=\frac{1}{2f_r\sqrt{\mu_0\varepsilon_0}}\sqrt{\frac{2}{\varepsilon_r+1}}=\frac{c}{2f_r}\sqrt{\frac{2}{\varepsilon_r+1}} \qquad (1)$$

Where, C = free space velocity of light, ε_r =Dielectric constant of substrate, f_r = Resonance Frequency. This width, W makes equal to about half a wavelength. It leads to good radiation efficiencies and acceptable dimensions.

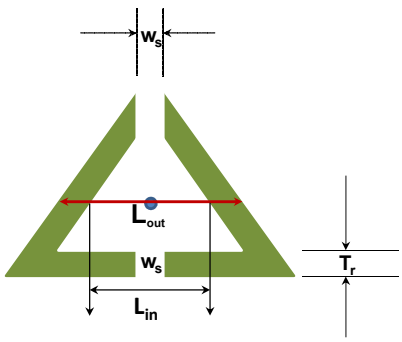

Figure 1. Top view of CTSRR Structure

978-1-4673-9257-0/15/$31.00 ©2015 IEEE

In order to account for the fringing and the wave propagation in the line [10] an effective dielectric constant (ε_{reff}) must be obtained.

$$L_{eff} = \frac{c}{2f_r\sqrt{\varepsilon_{reff}}} \qquad (2)$$

$L_{eff} > L$ .Thus, the resonance condition is

$\beta^{(n)}L_{eff} = n.\frac{\pi}{2}, n = 1, 2, ...$ which depends on L_{eff} , not L.

The effective patch length

$$\frac{\Delta L}{h} = 0.412\frac{(\varepsilon_{erff} + 0.3)(\frac{W}{h} + 0.264)}{(\varepsilon_{erff} - 0.258)(\frac{W}{h} + 0.8)} \qquad (3)$$

Equation (3) shows that the extension of the length ΔL is a function of the ratio $\frac{W}{h}$ and ε_{erff} .

To calculate the effective length, it has been added the length *L* to the extension of the length ΔL.

$$L_{eff} = L + 2\Delta L \qquad (4)$$

The length and width of ground plane L_g and W_g are given as

$$L_g = 6h + L \qquad (5)$$

$$W_g = 6h + L \qquad (6)$$

Where h = substrate height

Substrate height *h* is chosen considering surface wave & spurious radiation minimization for a given dielectric constant such that

$$h \le \frac{c}{4f_r\sqrt{\varepsilon_r - 1}} \qquad (7)$$

After calculating all the data, optimized values (ε_r=2.2, substrate height *h*= 1.5 mm) for patch width and length are *W*= 49.4 mm and *L*= 40 mm. For impedance matching, edge impedance of 50 ohm has been used for all cases and simulation has been done by CST microwave studio.

III. Equivalent Circuit Model: CTSRR Geometry

In Fig. 2(a), the geometrical view of a CTSRR and other dimensions are indicated. The modified structure of CTSRR is newly designed with strip width *c* and spacing g_1 and g_2 between the divided parts of triangle. The equivalent circuit model of the TSRR is presented in Fig. 2(b), which behaves as a resonant cavity modeled by an *LC* circuit. The inductance is due to the gap between the two halves of CTSRR and the capacitance is due to the gaps in the rings itself. The divided pure copper part of triangle contributes a total inductance *L* and C_{g1}, C_{g2} are the gap capacitances due to the triangular splits within the upper and the bottom part respectively. Here, magnetic field H, perpendicular to the plane, allows the creation of gaps capacitance at the opening of the ring.

The electromagnetic properties of CTSRRs have been already analyzed in [11] and [12]. This analysis shows that CTSRRs behave as an *LC* resonator that can be excited by an external magnetic flux and exhibits a strong diamagnetism above their first resonance. CTSRRs also exhibit cross-polarization effects (magneto electric coupling) [12] so that excitation by a properly polarized time-varying external electric field is also possible. This resonant behavior is due to capacitive elements such as gaps and splits, and in turn results in very high positive and negative values of permeability close to f_0 .Therefore, the orientation of the TSRR structure with respect to an electric field may affect the strength of the resonance.

CTSRR can be mainly considered as a resonant magnetic dipole that can be excited by an axial magnetic field [11]. In a more rigorous analysis, the cross-polarization effects in the SRR [11], thus, this element will also exhibit a resonant magnetic polarizability along its y-axis (see Fig. 2 (a)) and, therefore, its main resonance can also be excited by an external magnetic field applied along this direction [13].These features do not affect the intrinsic circuit model of the elements, although they may affect its excitation model.

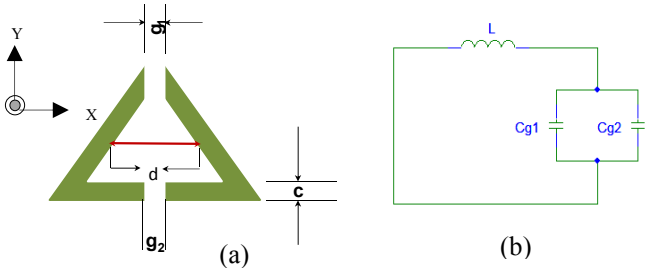

Figure 2. (a) Geometric view of CTSRR, (b) Equivalent circuit of CTSRR

IV. Antenna Design with Complementary Triangular SRR Design

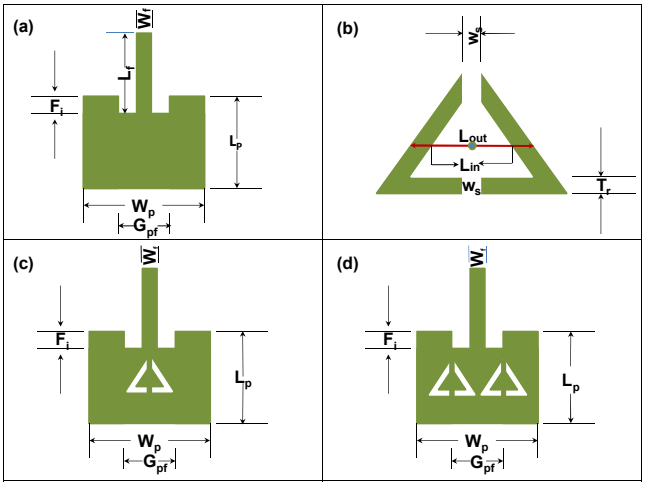

Figure 3. Schematic diagram of (a) Conventional patch antenna, (b) Top view of CTSRR, (c) Antenna with CTSRR, and (d) Antenna with dual CTSRR.

This design is simulated in CST Microwave Studio using a commercially available Roger RT/Duroid 5880 material as substrate with dielectric constant ε_r =2.2 and dielectric loss tangent δ=0.0002. The dimension of the substrate is 50 mm width x 51 mm length. The ground plane is printed in the back side of the substrate with same dimension. A 50Ω port is used to feed power into the radiator. The length of the inset feed (L_f) and the width of the feed line (W_f) for all antennas have been adjusted considering impedance matching. Fig.4 shows the geometrical top view of inset feed patch with different structures. The dimension parameters are shown in following TABLE I.

TABLE I. DIMENSION OF ANTENNA & PROPOSED CTSRR

Geometric Name	Symbol	Dimension (mm)
Resonator outer width	L_{out}	4.25
Resonator inner width	L_{in}	3.25
Thickness of TCR	T_r	1.00
Resonator gap	W_s	0.98
Patch length	L_p	40
Patch wide	W_p	49.4
Substrate length	L_s	52.7
Substrate wide	W_{sb}	50
Feed length	L_f	25.5
Feed wide	W_f	4.85
Slot or Gap of Feed line	G_{pf}	3.5
Substrate height	H	1.5

V. RESULT AND DISCUSSION

In this comparative study it has been studied on the analysis of CTSRR structure on patch antenna design, increment of the number of CTSRR on patch and various orientations of CTSRR structures. The key performance analysis results have been investigated.

The return loss (RL) is a ratio between reflected and transmitted waves at the input of an antenna. In the impedance matching network, better RL is desirable for lower insertion loss, surface wave loss, and spurious radiation loss. From TABLE II, we find that at resonance frequency (f_r), 2.400 GHz, RL of -30.835 dB is obtained for conventional patch antenna and -28.64 dB and -33.39 dB is achieved at f_r of 2.422 GHz and 2.440 GHz for CTSRR and DCTSRR respectively. The RL of patch antennas with various structures are described in Fig. 5. The f_r has been shifted because of fringing effect on MPA due to inclusion of CTSRR. Intersecting point of return loss at - 10 dB line of this design has been evaluated for bandwidth (BW) calculation and for all three antennas obtained BW is almost equal.

For WLAN antenna design the gain and directivity are some other important features need to consider achieving good signal strength for end point user. For conventional antenna gain and directivity of 7.72 dB and 8.09 dBi has been obtained, respectively. Here, proposed resonator structure contains split gaps in opposite ends which store charges and influences radiation pattern on *Z* direction. For 1 CTSRR, gain, and directivity of 7.85 dB, and 8.15 dBi and for 2 TSRR, 7.75 dB and 8.11 dBi has been obtained, individually.

TABLE II. SIMULATED PERFORMANCE OF THE CONVENTIONAL PATCH AND THE OPTIMIZATION DIMENSION OF PATCH ANTENNA

Antenna	Resonance Frequency (f_r) (GHz)	Return Loss(dB)	Gain (dB)	Directivity (dBi)
Normal	2.400	- 30.835	7.72	8.09
1 TSRR	2.422	- 28.864	7.85	8.15
2 TSRR	2.440	- 33.392	7.75	8.11

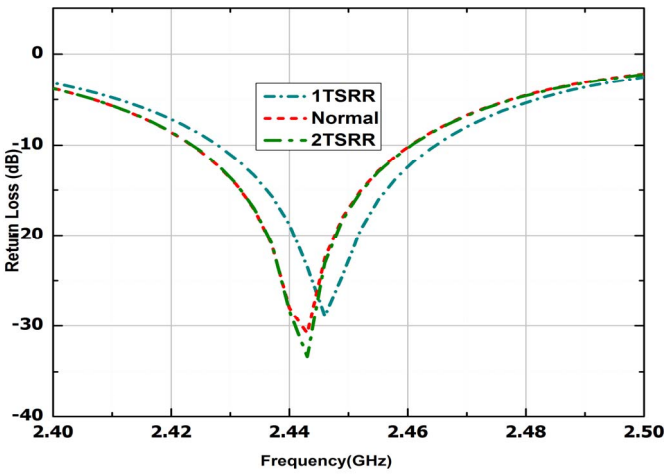

Figure 4. Return loss of normal patch antenna, TSRR & proposed DTSRR.

The radiation pattern is a graphical representation of the relative field strength transmitted from or received by the Antenna, Simply it can be said that the power radiated or received by the Antenna is the function of angular position and radial distribution from the Antenna. In Fig. 6 radiation pattern of the proposed Antenna is revealed. The directivity has been improved by 0.02dBi and radiation efficiency of antenna increase from 91.76% to 94.49%.

From above analysis, we found better RL, optimized gain and directivity for dual CTSRR. So orientation of CTSRR and increment of CTSRR unit cell on conventional patch antenna may have some influence. In this phase of optimization process, antenna performance has been measured with respect to unit cell orientation keeping internal distance equal for all case studies. Fig.7 shows the various orientation of resonant cut triangle of proposed antenna which has been denoted from A to J. All oriented dual CTSRR pattern perform on nearly same resonant frequency. The comparison of return loss among various orientationsis represented in TABLE III and IV. After extensive analysis of data and simulated results among ten oriented patterns from A to J, optimum performance has been obtained by pattern A with 7.75 dB gain and -33.391 dB of return loss while others are inferior than A. These intensive analyses prove that antenna performance also varies with orientation of recommended CTSRR.

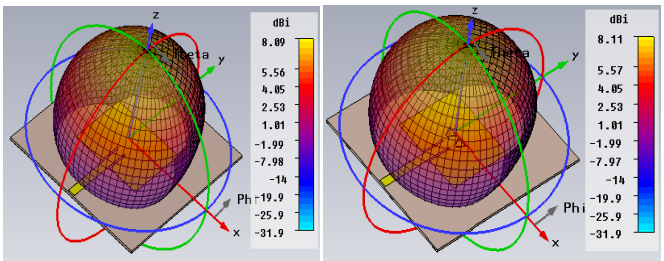

Figure 5. Farfield directivity of Normal and CTSRR Antenna.

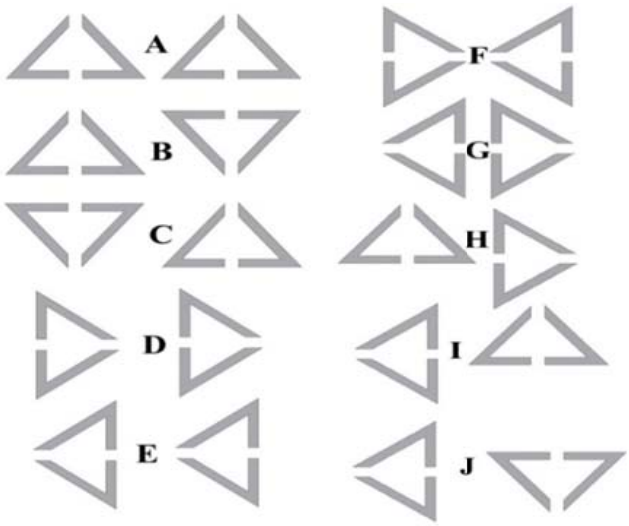

Figure 6. Orientation of dual TSRR Pattern A, B, C, D, E, F, G, H, I and J.

TABLE III. THE RETURN LOSS OF PATCH ANTENNA FOR DIFFERENT DETSRR PATTERN A TO PATTERN E

TSRR Orientation	Resonant frequency, f_r (GHz)	Return loss (dB)	Gain (dB)	Directivity(dBi)
A	2.443	- 33.391	7.75	8.11
B	2.443	- 28.245	7.73	8.10
C	2.443	- 28.175	7.73	8.21
D	2.428	- 23.968	7.39	8.29
E	2.428	-24.727	7.40	8.16

TABLE IV. THE RETURN LOSS OF PATCH ANTENNA FOR DIFFERENT DETSRR PATTERN F TO PATTERN J

TSRR Orientation	Resonant frequency, f_r (GHz)	Return loss (dB)	Gain (dB)	Directivity(dBi)
F	2.428	- 25.449	7.39	8.16
G	2.428	- 24.790	7.41	8.25
H	2.434	- 32.747	7.56	8.27
I	2.437	- 31.636	7.57	8.29
J	2.434	-34.127	7.56	8.28

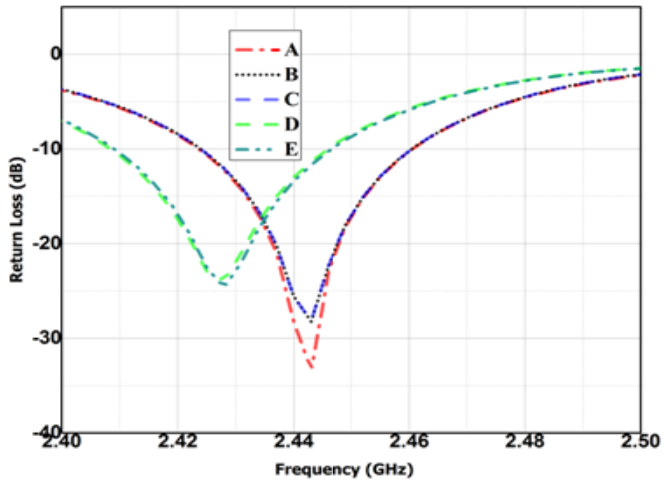

Figure 7. The return loss of patch antenna A to pattern E and pattern F to pattern J.

The directivity is alternative noticeable feature need to consider on WLAN antenna design. The directivity is the capability of an antenna to concentrate energy in a particular direction when transmitting or receiving energy in a specific course. The gain can be linked with directivity using a factor named antenna efficiency. Therefore, the design of MPA with high-directivity is not only essential but also a puzzling assignment. In Fig.10, (a) and (b) represent the Far field gain in polar form and (c) and (d) denotes the Far field directivity pattern from A to J.

In this phase of research our goal is to analysis the performance measurement of WLAN antenna with respect to the increment of CTSRR unit cell. The number of CTSRR addition has been aligned various ways on the patch antenna. TABLE V describes the various antenna parameters with respect to the number of triangular resonators. The variation of return loss in patch antenna with respect to increment of TSRR is expressed in Fig.11.This may be due to addition of capacitive charge concentration across width of MPA. So, incorporation of CTSRR on MPA can be utilized as frequency shifter.

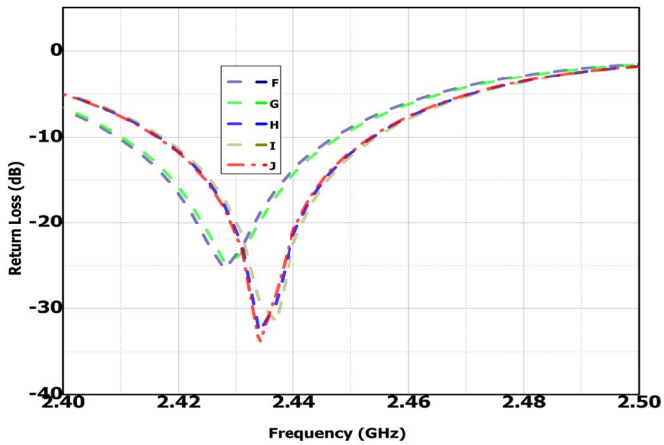

Figure 8. The return loss of patch antenna pattern F to pattern J.

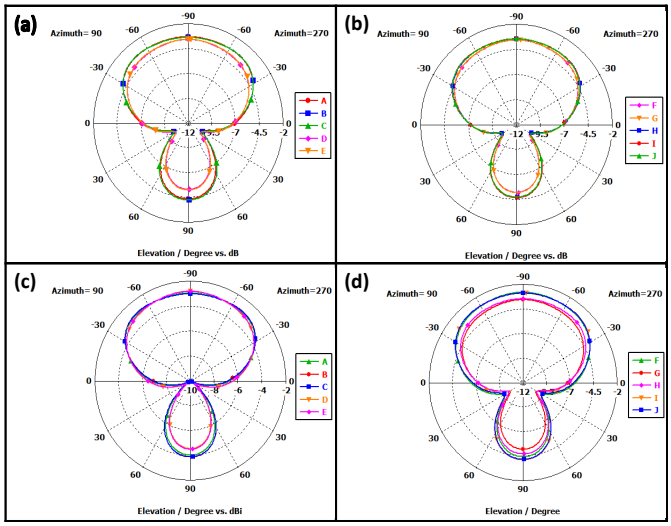

Figure 9. (a) Far field gain from orientation A to pattern E(b) Far field gain from orientation F to pattern J (c) Far field directivity from orientation A to pattern E (d) Far field directivity from orientation F to pattern J.

TABLE V. RETURN LOSS OF PATCH ANTENNA WITH INCREMENT NUMBER OF TSRR ROW WISE ALIGNMENT

Antenna	Resonant frequency, f_r (GHz)	Return loss (dB)	Gain (dB)	Directivity(dBi)
One CTSRR	2.446	- 28.864	7.85	8.29
Two CTSRR	2.443	- 33.391	7.75	8.25
Three CTSRR	2.437	- 36.114	7.31	8.21
Four CTSRR	2.434	- 41.765	7.34	8.30
Five CTSRR	2.434	-35.824	7.33	8.31
Six CTSRR	2.434	-45.386	7.29	8.24

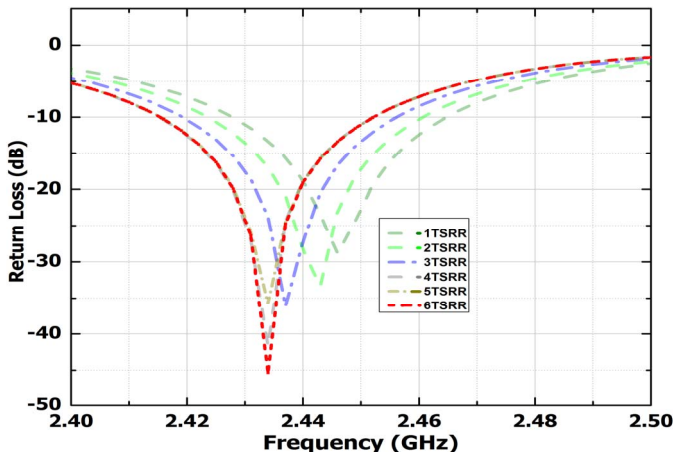

Figure 10. Return loss of patch antenna with respect to increment of TSRR.

From TABLE V, and figure 10, we observe that highest gain is achieved on antenna with one CTSRR and most directivity is achieved on antenna with five CTSRR. But on the other hand, return loss improves with respect to increment of CTSRR on patch and interestingly this shifts to lower frequency region. This may be due to concentration of electron and its impact on electromagnetic field distribution. Therefore, this finding can be indispensable for frequency tunable solution.

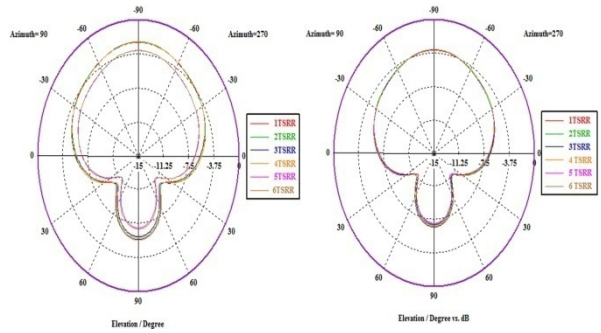

Figure 11. Fairfield gain and directivity of patch antenna with respect to increment of TSRR .

TABLE VI. COMPARISON OF DIFFERENT ANTENNA PARAMETERS WITH RECENT RELATED WORKS

Research, year	SRR structure type	Application SRR	Size (mm)	Frequency (GHz)	Return loss (dB)	Gain (dBi)
Huda, 2008[14]	Square edge-couple SRR with 2 ring gap	Microstrip antenna	9.1 x 9.1	2.4	- 18	7.47
Rahim, 2009[15]	Square edge-couple SRR with 2 ring gap	Microstrip antenna	49 x 17 2	2.7	> - 10	11.08
Jiun-Peng, 2011 [16]	Edge-coupled SRR S	Slot dipole antenna	6 x 6 2	2.49	> - 25 4	4.71
Xiaoyu, 2011[17]	Complementary rectangular edge couple SRR	Folded patch antenna	15 x 7.3	2.36	- 18.4	0.1
Norikman 2013[18]	Rombic Split Ring Resonator	Microstrip antenna	3.93x3.93	2.40	-24.029	6.37

VI. CONCLUSION

The impact of CTSRR on the performance of microstrip patch antenna is theoretically investigated. For various orientation of CTSRR and increment of CTSRR unit cell, the antenna resonates between 2.43 to 2.45 GHz bands. The antenna shows a directional radiation pattern and capacitive charge develops in gap-cut position improves gain and directivity. Numerical study of the effect and physical parameters of CTSRR on antenna has been carried out. Resonance frequency shifts toward the lower frequency region with the increment of CTSRR unit cell. So, proposed design may be helpful for frequency tunable solution. Expected improvement in bandwidth, and impact of gain and directivity with respect to addition of CTSRR on Patch has not been observed flawlessly due to patch antenna feeding technique or perfect impedance matching. Future modified feeding network or designs can be effective to overcome this problem.

REFERENCES

[1] C. A. Balanis, Antenna Theory: Analysis & Design, John Willey & Sons, Inc., 1997.

[2] Y. Qin, S. Gao, A. Sambell, E. Korolkiewicz and M. Elsdon, "Broadband patch antenna with ring slot coupling," *Electronics Letters*, Vol. 40 No. 1, January 2004.

[3] J.R. James, P.S Hall and C. Wood, "Microstrip Antenna Theory and Design",1981.

[4] WZiolkowski, R. W. and E. Heyman,"Wave propagation in mediahaving negative permittivity and permeability,"*Physical Reviewe*," Vol. 64, 56625.1-056625.15, 2001.

[5] RGundogdu, T. F., M. GÄokkavvas, K. Guven, M. Kafesaki,C. M. Soukoulis, and E. Ozbay, "Simulation and micro-fabrication of optically switchable split ring resonators," *Photonics and Nanostructures Fundamental and Applications*, Vol. 5, 106-112, 2007.

[6] TheMajid, H.A., M. Rahim and T.Masri, 2008, "Left Handed Metamaterial Design For Microstrip Antenna Application," *IEEE International RF and Microwave Conference (RFM 2008)*, Kuala Lumpur, Malaysia, pp: 218-221.

[7] Ekmekci, E. and G. Turhan-Sayan, 2011, "Metamaterial Sensor Applications Based on Broadside-couple SRR and V-Shaped Resonator Structures,"*2011 IEEE International Symposium on Antennas and Propagation (APSURI)*, Washington, USA, pp: 1170-1172.

[8] M. Marques, R., R. Medina and E. I. Raffi, 2002, "Role of Bi-anistropy in Negative Permeability and Left-handed Metamaterials," *Physical Review B*, 65(1),pp: 1-6.

[9] Constantine A. Balanis, Antenna *Theory and Design*, John Wiley & Sons, Inc., 1997.

[10] J.R James and P.S. Hall, *Handbook of Microstrip Antennas*, vol. 2, Peter Peregrinus Ltd., London, 1989.

[11] R. Marqués, F. Mesa, J. Martel, and F. Medina, "Comparative analysis of edge- and broadside coupled split ring resonators for metamaterial design Theory and experiment," *IEEE Trans. Antennas Propag.*, vol. 51, no. 10, pp. 2572–2581, Oct. 2003.

[12] R. Marqués, F. Medina, and R. Rafii-El-Idrissi,"Role of bianisotropy in negative permeability and left handed metamaterials," *Phys. Rev. B, Condens. Matter,* vol. 65, pp. 144 441(1)–144 441(6), 2002.

[13] F. Falcone, T. Lopetegi, M. A. G. Laso, J. D. Baena, J. Bonache, M.Beruete, R. Marqués, F. Martín, and M. Sorolla, "Babinet principle applied to metasurface and metamaterial design," *Phys. Rev. Lett.*, vol. 93, pp. 197 401(1)–197 401(4), 2004.

[14] M. Gil, J. Bonache, F. Martin, "Metamaterial Filters: A Review", *Metamaterial*, vol. 2, pp. 186-197, 2008.

[15] M. K. A. Rahim, H. A. Majid, T. Masri, "Microstrip Antenna Incorporated with Left-Handed Metamaterial at 2.7 GHz," *IEEE International Workshop on Antenna Technology (iWAT 2009)*, pp. 1-4, 2009.

[16] C. Jiun-Peng, H. Powen, "A Miniaturized Slot Dipole Antenna Capacitively Fed by a CPW With Split Ring Resonators," *2011 IEEE International Symposium on Antennas and Propagation (APSURSI)*, pp. 779-781, 2011.

[17] C. Xiaoyu, S. Jun, K. Cheolbok, D. E. Senior, Y. Yong-Kyu, "A Compact Self Packaged Patch Antenna with Non-Planar Complimentary Split Ring Resonator Loading," *2011 IEEE International Symposium on Antennas and Propagation (APSURSI)*, pp. 1036 – 1039, 2011.

[18] H. Nornikman, B. H. Ahmad, M. Z. A. Abd Aziz, A. R. Othman,"Effect of Single Complimentary Split Ring Resonator Structure on Microstrip Patch Antenna Design", *IEEE Symposium on Wireless Technology and Applications (ISWTA)*, pp.239-244, September 2013.

A High-Gain Slot-Loaded Microstrip Patch Antenna Fed by a Half-Width Microstrip Line for 5.5 and 5.8 GHz Wi-Fi/WiMAX Applications

Debabrata K. Karmokar*, Khaled M. Morshed†, Md. Selim Hossain*, and Md. Nurunnabi Mollah*
*Department of Electrical & Electronic Engineering
†Department of Electronics & Communication Engineering
Khulna University of Engineering & Technology, Khulna-9203, Bangladesh
E-mail: dkkarmokar@ieee.org; kmm_ece@yahoo.com; selimkueteee@yahoo.com; nurunnabim12@gmail.com

***Abstract*—A new type of antenna is presented in this paper. The main structure is a slot-loaded microstrip patch antenna fed by a half-width microstrip line. Two different types of antenna structure are combined together to make a single element antenna, and the radiation properties of both antennas are utilized in the proposed highly efficient antenna. Radiation from the antenna structure is achieved primarily from the first higher-order microstrip mode. The 10 dB return loss bandwidth of the antenna is 640 MHz (5.41 GHz to 6.05 GHz). The antenna produces a directive beam with a peak gain of 9.1 dBi, and the variation of the gain within the 640 MHz impedance bandwidth is only 1.35 dB.**

***Index Terms*—Microstrip patch antenna, leaky-wave antennas (LWAs), half-width (HW), WiMAX, Wi-Fi.**

I. Introduction

Microstrip-based antennas are attractive due to their planar low-profile configuration, fabrication simplicity, and ease of integration with microwave and millimeter-wave circuits. Low profile antennas for different wireless local area network (WLAN) systems such as wireless fidelity (Wi-Fi) and worldwide interoperability for microwave access (WiMAX) are highly desirable [1]–[3]. Wi-Fi (IEEE 802.11 standard) operates in the 2.4 GHz band (frequency range 2.4–2.5 GHz), and 5 GHz band (frequency ranges are: 5.15–5.35 GHz, 5.47–5.725 GHz, and 5.725–5.875 GHz) [1], [2]. Different standards for WiMAX have been developed by the IEEE 802.16 working group, such as 5.725–5.86 GHz [4].

Different types of antennas have been developed to meet the above mentioned requirements, most of which are patch antennas [1], [4]–[9]. Another attractive research area is microstrip leaky-wave antennas (LWAs) which usually use a microstrip line to achieve radiation. Microstrip LWAs are also planar low profile, and they have inherent beam scanning capabilities [10], [11]. The fundamental mode of a microstrip line does not radiate at lower frequencies because the electric field is strongly bound between the microstrip and the ground plane. The first higher-order mode of a microstrip line produces radiating leaky waves. Microstrip LWAs were proposed in the late 1970s with methods to excite the first higher-order microstrip mode [12]. A half-width microstrip LWA has been developed in [13] which operates in the first higher-order mode. In order to excite a microstrip line in its first higher-order mode a shorting wall was introduced along the center of the microstrip line and hence the width of the line is reduced to half of the original width. The shorting wall allows a microstrip line to excite the first higher-order mode. This antenna is called a half-width microstrip LWA (HW-MLWA). Research has been conducted on HW-MLWAs to steer the antenna beam by sweeping the frequency, or at a fixed frequency [14]–[21].

In this paper a microstrip patch antenna fed by a HW microstrip LWA is presented for 5.5 and 5.8 GHz Wi-Fi and WiMAX applications. Two different antennas, a HW-MLWA and a slot-loaded patch antenna, are cascaded to make a single directive antenna with relatively higher gain.

II. Antenna Configuration

The configuration of the antenna investigated in this paper is shown in Fig. 1. It was designed and analysed using CST Microwave Studio. The antenna is designed to be fabricated on a Rogers RT5880 substrate with a thickness (t) of 1.575 mm, dielectric constant (ε_r) of 2.2, and loss tangent (tan δ) of 0.0009. All the parameters of the antenna were optimized using parameter analysis conducted in CST. The length (L) and width (W) of the substrate and ground plane are 76.5 mm and 40 mm, respectively, i.e. the dimensions of the whole antenna are 76.5 mm $\times$ 40 mm. The complete structure can be divided into three different sections: (i) patch section, (ii) HW-MLWA section, and (iii) feed section.

A. Patch Section

The right section (Fig. 1(a)) of the antenna is the patch section which consists of a rectangular patch. The length (l_p) of the patch is 15 mm whereas the width (W) of the patch is the same as the width of the substrate i.e. 40 mm. A slot with dimensions of 5 mm $\times$ 30 mm ($w_s \times h_s$) is located at the middle of the patch.

978-1-4673-9257-0/15/$31.00 ©2015 IEEE

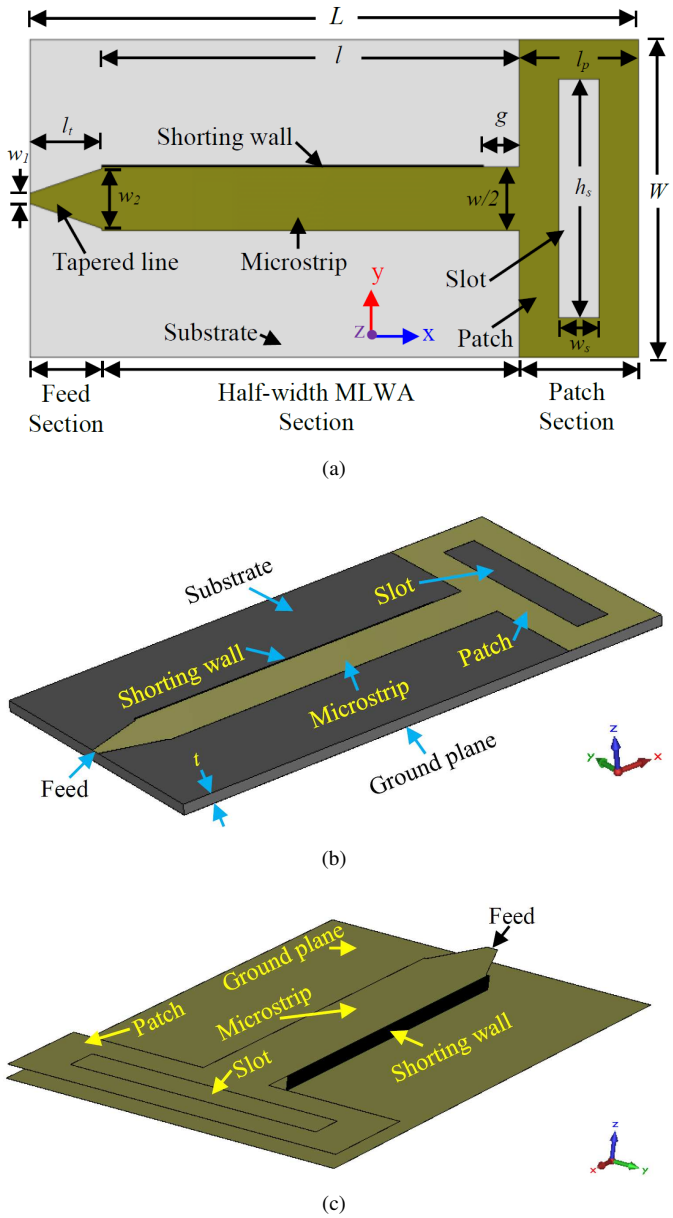

Fig. 1. Proposed microstrip antenna: (a) top view, (b) perspective view, and (c) perspective view (substrate omitted).

B. HW-MLWA Section

The middle section of the structure is the half-width microstrip LWA section, which consists of a HW-MLWA. The length (l) (along x-axis) and width ($w/2$) (along y-axis) of the microstrip line are 52.5 mm and 8 mm, respectively. As discussed earlier, in an implementation of a HW-MLWA, one edge of the microstrip is shorted to the ground plane by a shorting wall [Fig. 1(c)]. A gap (g) is introduced between the patch and the shorting wall [Fig. 1(a)]. The gap improves the impedance matching and allows the wave to propagate towards the patch. The optimum value of the gap (g) was found to be 4.5 mm, from full-wave parametric analysis conducted in CST.

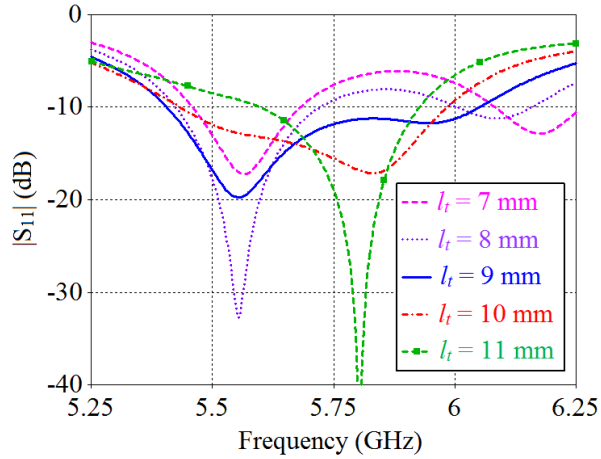

Fig. 2. Variation of reflection coefficient of the antenna in Fig. 1 with the length (l_t) of the tapered line.

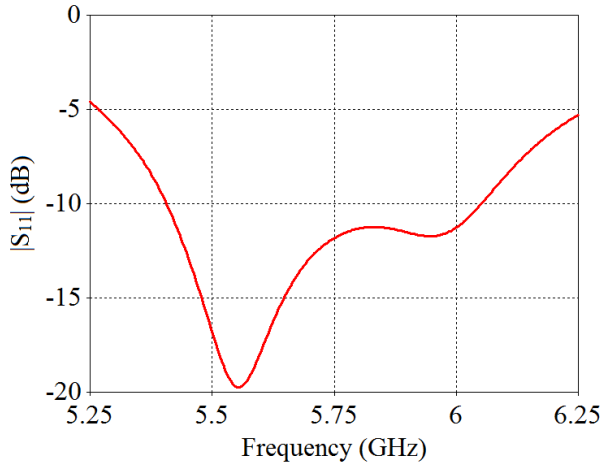

Fig. 3. Predicted $|S_{11}|$ of the antenna in Fig. 1.

C. Feed Section

The third and last section is the feed section, which is at the left side of Fig. 1(a). The antenna is fed from one end through a tapered line. To achieve good impedance matching, the dimensions of the tapered line have been optimized through some parametric studies. The effect of the tapered line length (l_t) on the return loss is depicted in Fig. 2, which shows that the best matching is achieved with l_t = 9 mm. The optimum values of the width (w_1) at the feed end and the width (w_2) at the microstrip end of the tapered line were also determined using similar parametric analysis and found to be 1.3 mm and 7.5 mm, respectively.

III. Results and Discussion

A. Reflection Coefficient

The antenna is excited from the left side by a discrete port in CST as shown in Fig. 1. Fig. 3 represents the input

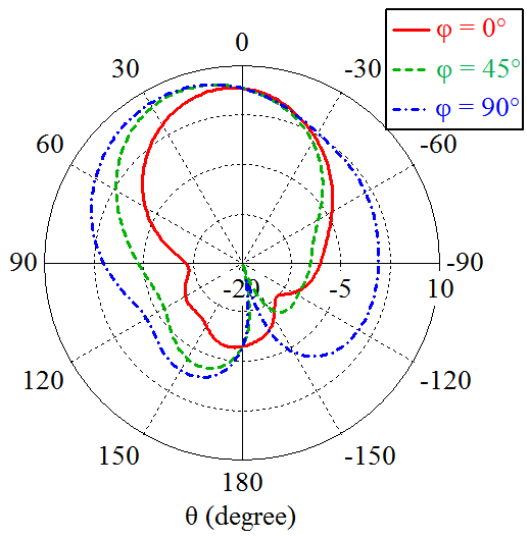

Fig. 4. Predicted radiation pattern cuts on constant-ϕ plane at 5.47 GHz.

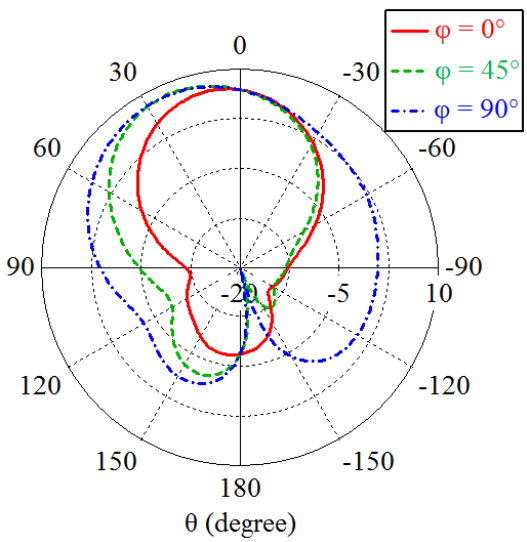

Fig. 5. Predicted radiation pattern cuts on constant-ϕ plane at 5.5 GHz.

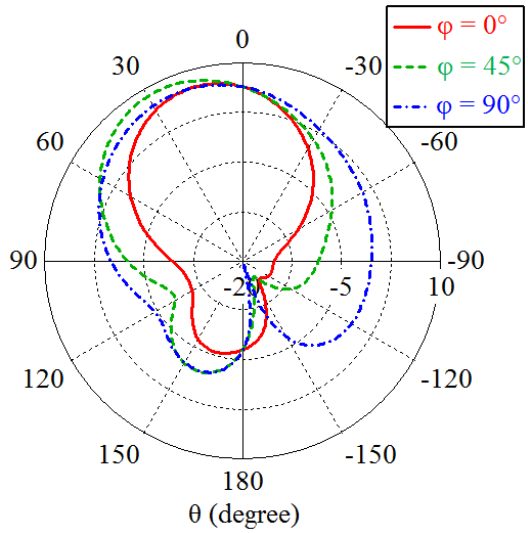

Fig. 6. Predicted radiation pattern cuts on constant-ϕ plane at 5.8 GHz.

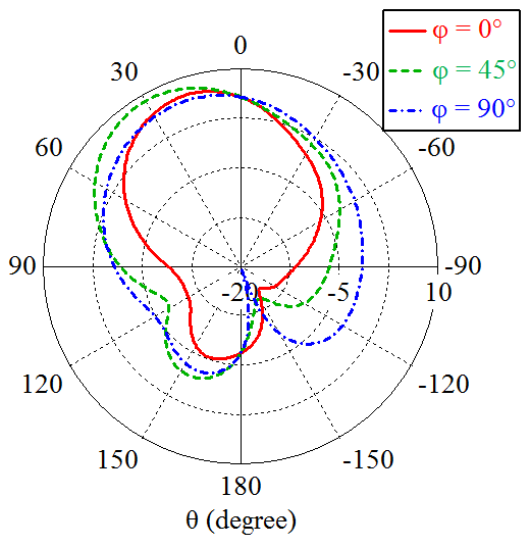

Fig. 7. Predicted radiation pattern cuts on constant-ϕ plane at 5.875 GHz.

reflection coefficient of the antenna in Fig. 1. It can be seen that the antenna has a -10 dB reflection bandwidth from 5.41 to 6.05 GHz.

B. Radiation Pattern

Figs. 4 – 7 show the radiation patterns of the antenna at four different frequencies. In order to represent the antenna beam properly the radiation pattern cuts are taken at three different constant-ϕ planes. The antenna beamwidth is narrow in the ϕ = 0° plane. However, the beamwidth is much wider in the ϕ = 90° plane. At lower frequencies the beam points closer to the boresight (Figs. 4 and 5), where, in this case, the boresight is the z-direction, perpendicular to the plane of the antenna structure. With an increase of frequency the beam in the ϕ = 0° plane shifts slightly towards the x-axis (Figs. 6 and 7). Though the beam in the ϕ = 0° plane changes slightly with frequency, the beam in the ϕ = 90° plane remains almost the same.

C. Surface Current Distribution

Fig. 8 displays the surface current distributions of the antenna at 5.5 and 5.8 GHz. It can be observed that at lower frequencies [Fig. 8(a)] most of the power radiates from a section closer to the feed and less power radiates from the patch. As the frequency increases the power travels further and more power radiates from the patch end as shown in Fig. 8(b).

D. Gain and Directivity

The variation of the directivity and gain of the antenna with frequency are shown in Fig. 9. The peak directivity of

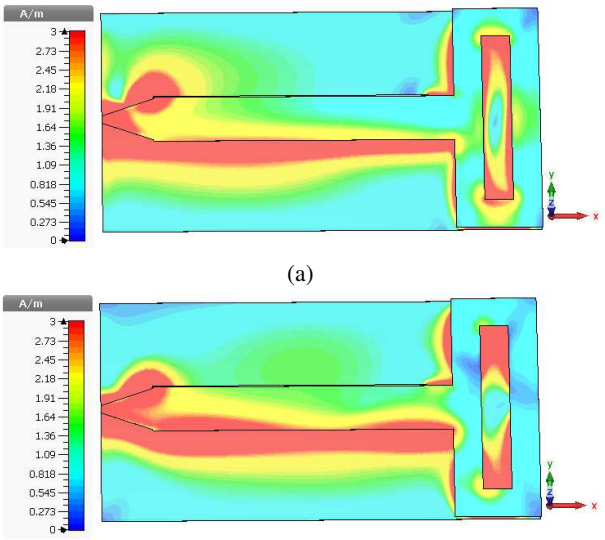

(a)

(b)

Fig. 8. Surface current distribution (amplitude) at: (a) 5.5 GHz and (b) 5.8 GHz.

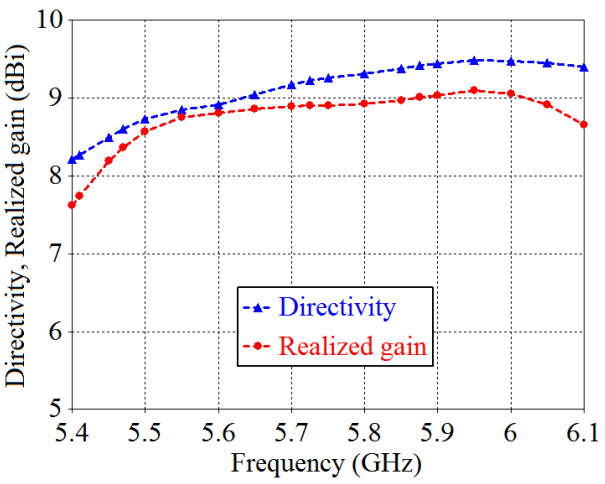

Fig. 9. Predicted directivity and gain of the antenna with frequency.

the antenna within the impedance bandwidth is 9.5 dBi at 5.95 GHz. The directivity is greater than 8.26 dBi within the impedance bandwidth. The peak gain of the antenna is 9.1 dBi at 5.95 GHz, and its variation within the impedance bandwidth is only 1.35 dB. It can be seen that the gain and directivity are low at lower frequencies and increase with frequency. This is due to the short effective aperture at lower frequencies and the long effective aperture at higher frequencies, as described in Section III-C.

E. Antenna Efficiency

Fig. 10 represents the radiation and total efficiencies of the antenna within its operating band. The radiation efficiency of the antenna is more than 98% throughout the operating band. The total efficiency of the antenna is over 84% within the impedance bandwidth and over 90% between 5.42 GHz

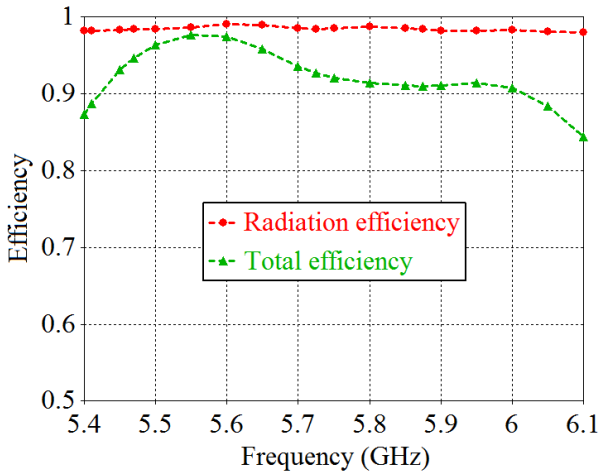

Fig. 10. Predicted radiation and total efficiencies of the antenna with frequency.

TABLE I
GAIN COMPARISON OF DIFFERENT ANTENNAS

Antenna Structure	Antenna Peak Gain
PIFA in [4]	4.4 dBi at 5.75 GHz
Self-complementary antenna in [7]	3.8 dBi in 5.8 GHz band
T-shaped monopole antenna in [8]	≈ 4 dBi in 5.8 GHz band
Printed monopole antenna in [9]	3 dBi between 5 and 6 GHz
Proposed antenna	9.1 dBi between 5.41 and 6.05 GHz

and 6.01 GHz. The total efficiency is very high from 5.47 to 5.66 GHz, almost equal to the radiation efficiencies. Since the total efficiency considers the mismatch losses, so where the return loss is high the deviation between the total and radiation efficiencies is low. For example, at 5.55 GHz the return loss is 19.7 dB ($|S_{11}|$ = -19.7 dB), the radiation efficiency is 98.6% and the total efficiency is 97.7%.

F. Comparison between the Proposed and Reference Antennas

In this subsection a comparison between the proposed and reference antennas is given in terms of antenna gain. The gains of different antennas are listed in Table I together with that of the proposed antenna. It can be seen that the proposed antenna has significantly higher gain than these reference antennas. Some of the antennas have been reported have high gain, e.g. antennas in [2], [3]. However, these antennas use a separate matching network for impedance matching.

IV. CONCLUSION

A slot-loaded patch antenna that is fed by a half-width microstrip LWA is presented in this paper. The proposed antenna is a combination of two different antennas, a LWA and a patch antenna. This antenna is able to produce a directive beam with very high gain. The Impedance bandwidth of the proposed antenna is 640 MHz and its gain is consistent within

its operating band. The predicted peak gain of the antenna is more than 9.1 dBi and its gain is above 7.75 dBi between 5.41 and 6.05 GHz. Moreover, the radiation efficiency of the antenna is above 98% and its total efficiency is over 84% throughout the operating band.

REFERENCES

[1] L. Pazin, N. Telzhensky, and Y. Leviatan, "Multiband flat-plate inverted-F antenna for Wi-Fi/WiMAX operation," *IEEE Antennas and Wireless Propag. Lett.*, vol. 7, pp. 197–200, 2008.

[2] D. K. Karmokar, M. S. Hossain, and M. N. Mollah, "Low-profile impedance matched wideband double inverted-F antenna for WiMAX/Wi-Fi operations in a laptop computer," in *Proc. Int. Conf. Devices and Communications (ICDeCom)*, Feb 2011, pp. 1–5.

[3] K. M. Morshed, D. K. Karmokar, and A. M. Numan-Al-Mobin, "Numerical analysis of impedance matched inverted-L antennas for Wi-Fi operations," in *Proc. 12th Int. Conf. on Computer and Information Tech. (ICCIT)*, 2009, pp. 691–696.

[4] S. Zuo, Y. Yin, Z. Zhang, and W. Wu, "A compact tri-band PIFA antenna for WLAN and WiMAX applications," *Microwave and Optical Technology Letters*, vol. 52, no. 4, pp. 919–922, 2010.

[5] K. M. Morshed, D. K. Karmokar, and M. Talukder, "Numerical and experimental analysis of impedance matched inverted-L and stair inverted-L antenna for 5 GHz WLAN operation," *Journal of Communications*, vol. 5, no. 8, pp. 612–619, Aug. 2010.

[6] D. K. Karmokar and K. M. Morshed, "Analysis of inverted-F and loaded inverted-F antennas for 2.4 GHz ISM band applications," *J. Elect. Eng.*, vol. EE 36, no. II, pp. 4–9, Aug. 2009.

[7] K.-L. Wong, T.-Y. Wu, S.-W. Su, and J.-W. Lai, "Broadband printed quasi-self-complementary antenna for 5.2/5.8 GHz WLAN operation," *Microwave and Optical Tech. Lett.*, vol. 39, no. 6, pp. 495–496, 2003.

[8] S.-W. Su, K.-L. Wong, and H.-T. Chen, "Broadband low-profile printed T-shaped monopole antenna for 5-GHz WLAN operation," *Microwave and Optical Tech. Lett.*, vol. 42, no. 3, pp. 243–245, 2004.

[9] W.-S. Chen, B.-Y. Lee, and P.-Y. Chang, "A compact and small printed monopole antenna for WLAN applications," *Microwave and Optical Technology Letters*, vol. 53, no. 7, pp. 1518–1522, 2011.

[10] D. K. Karmokar, K. P. Esselle, and T. S. Bird, "An array of half-width microstrip leaky-wave antennas radiating on boresight," *IEEE Antennas Wireless Propag. Lett.*, vol. 14, pp. 112–114, 2015.

[11] D. K. Karmokar, D. N. P. Thalakotuna, K. P. Esselle, and M. Heimlich, "Controlling the beam scanning limits of a microstrip leaky-wave antenna," in *Proc. IEEE APSURSI*, July 2013, pp. 1330–1331.

[12] W. Menzel, "A new travelling wave antenna in microstrip," in *Proc. 8th Eur. Microw. Conf.*, Sept. 1978, pp. 302–306.

[13] G. M. Zelinski, G. A. Thiele, M. L. Hastriter, M. J. Havrilla, and A. J. Terzuoli, "Half width leaky wave antennas," *IET Microw., Antennas Propag.*, vol. 1, no. 2, pp. 341–348, Apr. 2007.

[14] D. K. Karmokar and K. P. Esselle, "Periodic U-slot-loaded dual-band half-width microstrip leaky-wave antennas for forward and backward beam scanning," *IEEE Trans. Antennas Propag.* [Online]. Available: http://ieeexplore.ieee.org/

[15] G.-F. Cheng and C.-K. C. Tzuang, "A differentially excited coupled half-width microstrip leaky EH_1 mode antenna," *IEEE Trans. Antennas Propag.*, vol. 61, no. 12, pp. 5885–5892, Dec. 2013.

[16] D. K. Karmokar, D. N. P. Thalakotuna, K. P. Esselle, L. Matekovits, and M. Heimlich, "Reconfigurable half-width microstrip leaky-wave antenna for fixed-frequency beam scanning," in *Proc. 7th Eur. Conf. Antennas Propag.*, April 2013, pp. 1314–1317.

[17] Q. Lai, C. Fumeaux, and W. Hong, "Periodic leaky-wave antennas fed by a modified half-mode substrate integrated waveguide," *IET Microw., Antennas Propag.*, vol. 6, no. 5, pp. 594–601, Apr. 2012.

[18] D. K. Karmokar, K. P. Esselle, and S. G. Hay, "Shifting the fixed-frequency beam scanning range of a leaky-wave antenna by slot loading," in *Proc. IEEE-APS Topical Conf. Antennas and Propag. Wireless Commun.*, 2014, pp. 640–643.

[19] G.-F. Cheng and C.-K. C. Tzuang, "Guided wave structure for dual leaky-mode microstrip antenna design," in *Proc. 6th European Conf. Antennas and Propag. (EUCAP)*, Mar. 2012, pp. 2823–2826.

[20] D. K. Karmokar and K. P. Esselle, "Fixed-frequency leaky-wave antenna for simultaneous forward and backward scanning," in *Proc. IEEE Antennas and Propag. Society Int. Symp. (APSURSI)*, 2014, pp. 1794–1795.

[21] Y. Li, Q. Xue, E. K.-N. Yung, and Y. Long, "The periodic half-width microstrip leaky-wave antenna with a backward to forward scanning capability," *IEEE Trans. Antennas Propag.*, vol. 58, no. 3, pp. 963–966, Mar. 2010.

Aluminium Nitride based Parasitic Strip Patch Antenna for Multiband Wireless Applications

Swadesh Poddar[1,*], Sourav Roy[2, 3], Sunanda Roy[2], Md. Tanvir Hasan[4]
[1]Banglalink Digital Communication Ltd., Bangladesh
[2]Department of Electrical and Electronic Engineering, KUET, Khulna, Bangladesh
[3]Faculty of Electrical and Electronic Engineering, JUST, Jessore, Bangladesh
[4]Faculty of Electrical and Electronic Engineering, AIUB, Dhaka, Bangladesh
[*] E-mail: swadesh_ku@live.com

***Abstract*— A new approach with aluminum nitride (AlN) based parasitic strip wideband patch antenna has been introduced for 2.5 and 5.8 GHz wireless applications. The novelty of the proposed design is inherited in reduction of edges of patch which influences antenna performance. The impedance bandwidth of the antenna is 0.28 GHz for the first resonance, whereas 2.04 GHz for the second resonance with an antenna radiation efficiency of 89.6% and 95.32%, respectively.**

***Keywords*— Patch antenna, parasitic strip, multi-resonant, Aluminum Nitride**

I. INTRODUCTION

In this era of modern communication, prompt expansions in wireless communications have been established in order to meet the growing demand of the end terminal user. The 2.5 GHz and 5.8 GHz ISM bands are very popular for both wireless metropolitan area networks (WMAN) and wireless local area network (WLAN), respectively. Thus a multi-resonant antenna is more desirable for operations of WMAN and WLAN together. To meet the daily snowballing thirst in these operating bands, numerous antenna models with different feeding techniques have been recently anticipated for compact, efficient, and low cost design [1-4]. For an example, planar inverted-F antennas (PIFA) [5-7] are used in multiband operating at 2.5 GHz and 5.8 GHz for wireless applications. The PIFA are normally made of a large ground plane which makes the antenna bulkier. To reduce the dimension of PIFA, the feed probe point has been externally shorted. As a result, this technique leads to a decrease in the bandwidth. Besides numerous designs of fractal antennas using capacitive coupling [8], planar monopoles [4], and planar slot antenna with embedded metal strip [9] have been also suggested. In terms of design methodology, the fractal antennas are more complex, whereas the planar monopole antenna has also a large ground plane. The feeding technique of planar slot antenna is intricate to design. To overcome this problem another multi-resonant antenna, consists of bent strips printed on substrate, has been proposed [10]. However, these types of antennas are complicated in geometry and require long transmission lines [11]. Additionally, a modified feeding network is required to mitigate the difficulties like spurious feed radiation, surface wave loss, and long feed length. Therefore, it is immense important to take in account the issues such as wideband, compactness in size, and multiband for designing an antenna.

Parasitic strips for achieving resonance are well known for designing an antenna. Shorted parasitic element with monopole antenna has been employed for operation in both wideband and dual band [12-13]. Parasitic elements assure the wide banding of an antenna with many resonance frequencies which appear neighboring to the main frequency band. However, to control the resonance frequencies, details understanding of parasitic strip patch antenna are required. In this paper, a modified edge cut parasitic strip antenna for dual band operation with AlN substrate has been introduced. The antenna design; optimization and simulation have been done with Finite Element Method (FEM) based 3D full-wave electromagnetic solver HFSS v15. The antenna is comprised of modified feeding network with 50 Ω port impedance and small ground plane. The resonant frequency of the proposed antenna can be varied by tuning the length of the patch. The reflection coefficient and bandwidth are improved due to changing the width of the patch with edge cuts.

The layout of this proposal is outlined as follows: the details on Antenna evolution, design and geometry are illustrated in section 2. Results and discussions on the return loss, gain and efficiency are presented in section 3. Finally, a conclusion is depicted in section 4.

II. ANTENNA DESIGN

A. Substrate Selection

Growths in the area of III-nitride (GaN, InN, and AlN) semiconductors have been remarkable due to their inherent properties such as wide bandgap, high critical electric field, low intrinsic carrier concentration, high-electron mobility, and high-drift velocity [14]. Those parameters are very promising for high frequency, high power, and high temperature device applications. Among III-nitrides, AlN has a huge prospective to use as a substrate for a patch antenna because of wide bandgap (6.1 eV), low dielectric constant (4.84), and high critical electric field for breakdown (450 kV/cm). These suggest that AlN substrate is advantageous for wideband patch antenna.

B. Antenna Evolution

The antenna is derived and progressed from a conventional T shape parasitic strip antenna depicted in Fig. 1. The reflection coefficient has been presented for all three models.

978-1-4673-9257-0/15/$31.00 ©2015 IEEE

The antenna resonates near 2.5 GHz and 5.8 GHz for all three cases. From the Fig. 1 this is indicated that after the inclusion of edge cut on patch, antenna reflection coefficient and BW has been improved (model 3). Also the patch of proposed antenna has a 4~8% reduction in area in comparison with the patch area illustrated for model 1 and 2 in the Fig. 1. The smaller size of the proposed antenna improves dual band wireless performance. A comparative analysis is shown at table 1.

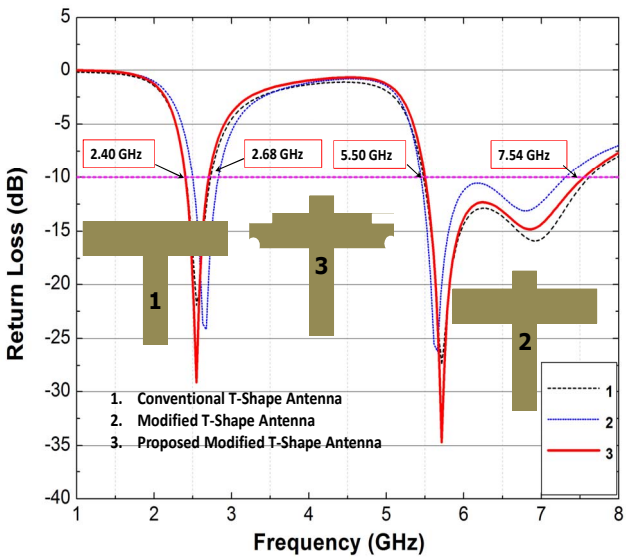

Fig 1: Antenna evolution

Table 1: Comparative analysis of conventional antenna and proposed antenna

Parameter	Conventional Patch	Proposed Antenna
Frequency(f_r)	2.5 GHz	2.5 GHz
Patch Width (W)	Patch Width $W=\frac{1}{2f_r\sqrt{\mu_0\varepsilon_0}}\sqrt{\frac{2}{\varepsilon_r+1}}=\frac{c}{2f_r}\sqrt{\frac{2}{\varepsilon_r+1}}$	
Patch Length (L)	Effective Length, $L_{eff}=\frac{c}{2f_r\sqrt{\varepsilon_{reff}}}$	
Substrate Dimension	L_s= 6h+L W_g = 6h +W	
Dimension	W = 37 mm; L = 29 mm; Height, H= 1.6 mm; L_s= 37 mm; W_s = 46 mm	W = 26.5 mm; L = 4.5 mm; H= 1.6 mm; L_s= 40 mm; W_s = 40 mm
Patch Area	1073 mm^2	156 mm^2
Substrate Area	1702 mm^2	1600 mm^2

C. Design and Geometry

Fig. 2 shows the geometry of our projected antenna. The modified patch shape with finite ground plane is printed on the same side over the AlN substrate of dielectric constant (ϵ_r) 4.84 and height of 1.6 mm. The transmission feed line of 50 Ω is printed on the back side of the substrate. The patch size occupies an overall volume of 6.28 mm^3 printed on a substrate of 40 mm * 40 mm. The physical dimension of the antenna is given in table 2.The width of the feed line W_2 and overlapping extended patch on feed line, D_2-D_1 has been kept fixed considering impedance matching. The edge cut has some advantages as these can control the surface wave loss, spurious radiation loss and reduce the patch size.

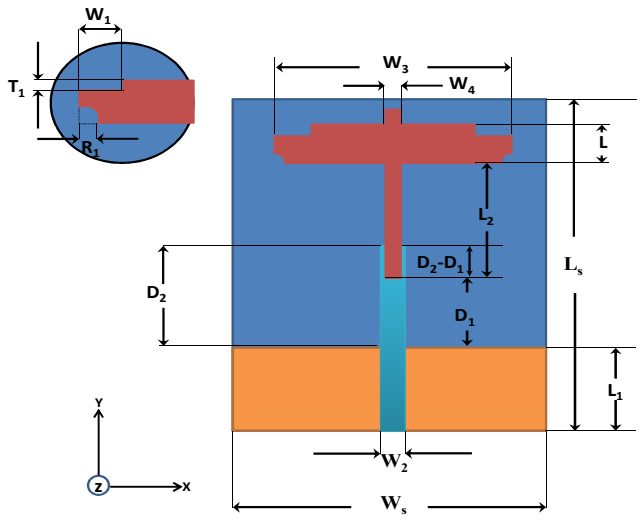

Fig 2: Geometry of the proposed antenna

Table 2: Physical Dimension of Antenna

Geometric Name	Parameter	Dimension (mm)
Substrate Length	L_s	40
Substrate Width	W_s	40
Finite Ground	L_1	12
Feed Width	W_2	3
Feed length	$D_2 + L_1$	21
Patch Length	L	4.5
Extended Patch Width	W_3	26.5
Patch Cut Width	T_1	0.6
Patch Cut Length	W_1	3
Circular Cut Radius	R_1	1.5
Patch Length	W_4	1.95

III. RESULTS AND DISCUSSIONS

A. Return Loss

The return loss (RL) is a factor that is identified as a ratio between reflected and transmitted waves at the input of an antenna. In the impedance equivalent network, improved RL is required for perfect matching. For the proposed antenna,

couple of design parameters that influences the antenna performances is the width W_3, length L, rectangular edge cut W_1, and circular edge cut R_1. The effect of these design parameters on antenna performance can be described from surface current distribution on dual resonant frequencies. In Fig. 3 and 4 the simulated RL with respect to antenna patch width (W_3) and length (L) has been represented.

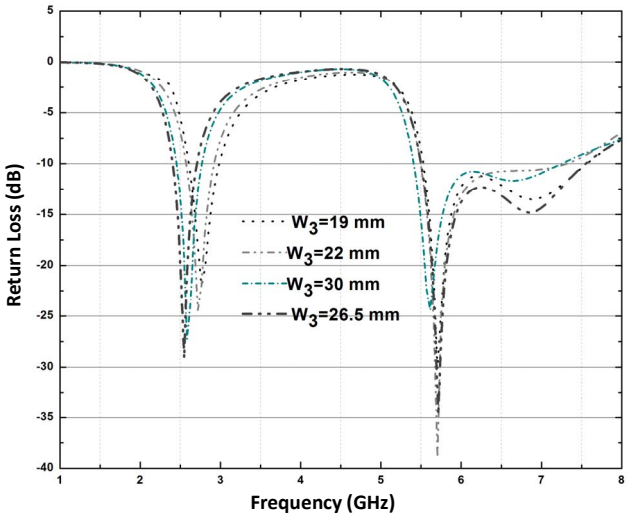

Fig 3: Return loss of antenna with variation of w_3

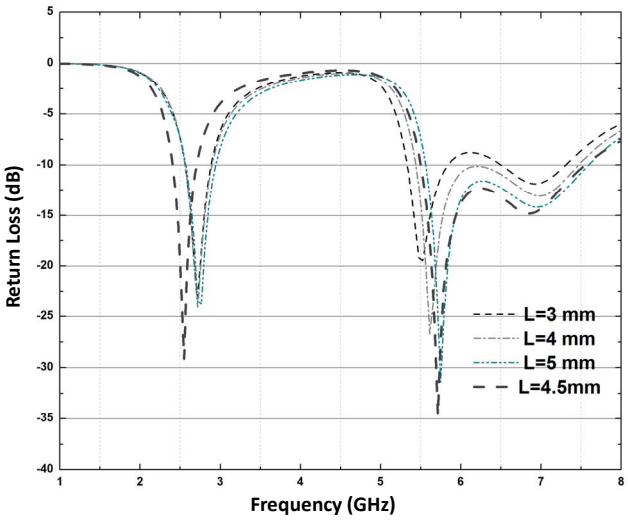

Fig 4: Return loss of antenna with variation of L (w_3=26.5mm)

B. *Electric Field, Surface Current and Polarization:*

A detailed dissemination of the excitation of the patch and the polarization of the antenna can be obtained by investigating field distribution and surface current analysis at resonance frequencies. Fig. 5(a) and 5(b) depicts the E field distribution of dual resonant frequencies near 2.5 GHz and 5.8 GHz. At the fundamental resonant frequency of 2.5 GHz and 5.8 GHz, E-field at the end of the patch is maximum and minimum at center. From Fig. 5, it is observed that E-field changes side according to instantaneous phase of the applied signal and can be denoted for multi-resonant behavior using TM_{nm} mode.

The surface current distributions of the proposed antenna in both of the bands are shown in Fig. 6(a) and 6(b). At lower resonance frequency, 2.5 GHz, the surface current along the patch are parallel with the horizontal component of the antenna whereas at lower portion on finite ground plane, surface current are vertical to horizontal component. On the other hand surface current at 5.8 GHz are parallel to horizontal component on both patch and finite ground plane. Therefore, with the increment of W_3, two resonance frequencies can shift in the lower region and by increasing L, the current path for lower region is lengthen and effects lower resonant frequency whereas higher resonant frequency remain steady. Rectangular and circular edge cut on patch may influence to minimize spurious radiation, surface wave loss, effective dielectric constant (ε_{reff}), influences radiation pattern, and enhances impedance bandwidth.

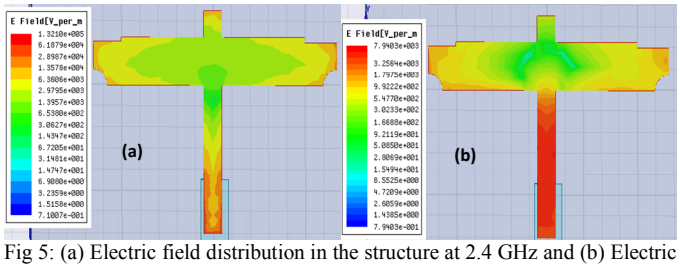

Fig 5: (a) Electric field distribution in the structure at 2.4 GHz and (b) Electric field distribution in the structure at 5.8 GHz

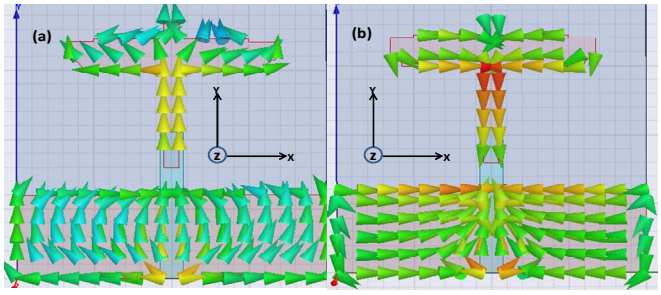

Fig 6:(a) Surface current distribution in the structure at 2.5 GHz and (b) Surface current distributions in the structure at 5.8 GHz

C. *Gain and Efficiency*

Fig. 7 depicts the 3D total gain at two resonant frequencies. The pattern is almost omnidirectional for both the bands. The last adaptive gain is 2.58 dB with peak efficiency of 89.6% at 2.5GHz and 3.69 dB with peak efficiency of 95.32% at 5.8 GHz. Fig. 8 (a) and 8 (b) depict radiation efficiency and peak gain with respect to operating bands. The return loss can be expressed in terms of voltage standing wave ratio (VSWR) which is 1.07 and 1.05 respectively for lower and higher bands. The transmitted and reflected powers are 99.90% and 99.97% for resonance frequency (f_r) of 2.52 GHz and 5.78

GHz with a mismatch loss of 0.003 dB and 0.001 dB [15].

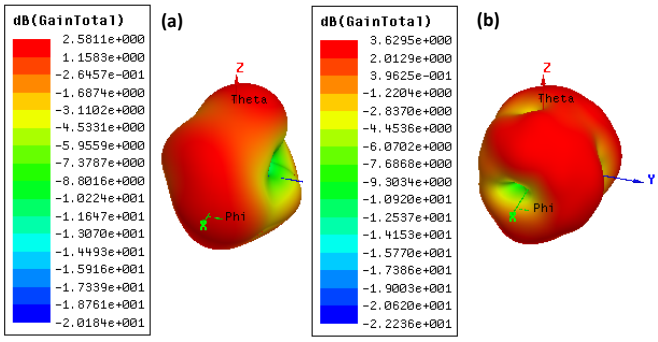

Fig 7: (a) 3D polar plot at 2.5 GHz and (b) 3D polar plot at 5.8 GHz

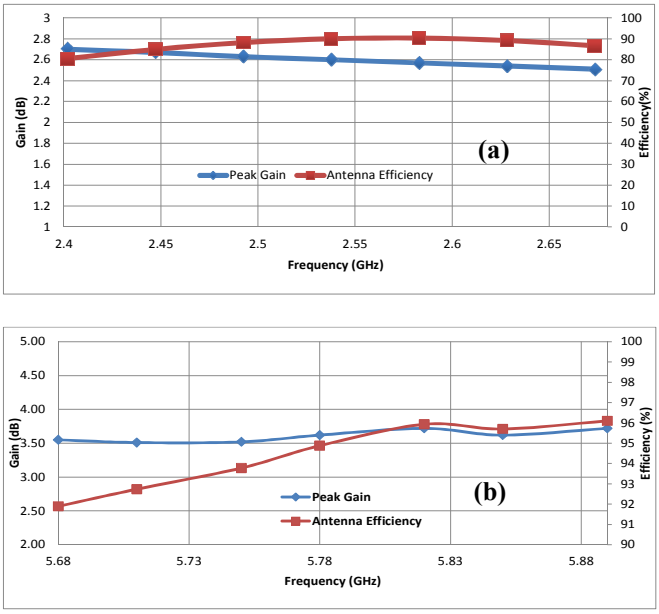

Fig 8: Simulated peak gain and efficiency of the antenna, (a) 2.5 GHz and (b) 5.8 GHz

IV. CONCLUSION

To recapitulate, the impact of modified patch shape on gain and radiation characteristics of multi-resonant wideband patch antenna with a parasitic strip are theoretically investigated to be used in wireless applications using AlN substrate. The proposed antenna model on AlN, featuring high band gap and high electron mobility may influence a significant role on fabrication of practical antenna. The exclusive reduction of ground plane and patch area in comparison with other multi-resonant antennas have been established also. From the simulation results, it has been observed that the antenna resonates at 2.52 GHz and 5.78 GHz with a bandwidth of 0.28 GHz and 2.04 GHz, separately, an impedance BW of 11.67% and 35.17%, respectively. The gain pattern of antenna is almost omnidirectional with radiation efficiency of 89.6% and 95.32% at lower and higher resonant, individually. These results regard that proposed modified patch on AlN with a parasitic strip is a highly potential structure for the wideband antenna for multi-band wireless applications.

REFERENCES

[1] Eldek, A. A., A. Z. Elsherbeni, and C. E. Smith, "Dual wideband square slot antenna with a U-shaped printed tuning stub for personal wireless communication systems," Progress In Electromagnetics Research, PIER 53, 319–333, 2005.

[2] Abdelaziz, A. A., "Bandwidth enhancement of microstrip antenna," Progress In Electromagnetics Research, PIER 63, 311–317, 2006.

[3] Zhao, G., F.-S. Zhang, Y. Song, Z.-B. Weng and Y.-C. Jiao, "Compact ring monopole antenna with double meander lines for 2.4/5 GHz dual-band operation," Progress In Electromagnetics Research, PIER 72, 187–194, 2007.

[4] Lee, E., P. Hall, and P. Gardner, "Novel compact wideband or multi-band planar monopole antenna," IEEE Antennas and Propagation Society International Symposium, 624–627, 2000.

[5] Young Jun Cho, Yong Sun Shin, and Seong-Ook Park, "An Internal PIFA for 2.4/5 GHz WLAN applications," Microwave conference proceedings, APMC, Vol. 4,Suzhou, China, 2005, pp 1-3.

[6] Wenjun Huang, Terence S. P See, Zhi Ning Chen, "2.4/5-GHz Dual-Band PIFA for Portable Devices," APSURSI, Pokane, Washington, USA, 2011, pp- 430-433.

[7] Xingyu Zhang, Jun hong Wang, "A Novel Dual-Band Planar Inverted-F Antenna for WLAN Applications," 8th International Symposium on Antennas, Propagation and EM Theory, 2008 , pp 148-151.

[8] Sindou, M., G. Ablart, and C. Sourdois, "Multiband and wideband properties of printed fractal branched antennas," Electronic Letters, Vol. 35, No. 3, 181–182, Feb. 4, 1999.

[9] Meng-Ju Chiang, Jia-Yi Sze, Guang-Fu Cheng, "A Compact Dual-Band Planar Slot Antenna Incorporating Embedded Metal Strips for WLAN Applications," EuMC, Rome, Italy, 2009, pp 221-224.

[10] Ge, Y., K. P. Esselle, and T. S. Bird, "Small quad-band WLAN antenna," IEEE Antennas and Propagation Society International Symposium, Washington D.C., USA, July 3–8, 2005.

[11] W. Qin,"A novel patch antenna with a t-shaped parasitic strip for 2.4/5.8GHz wlan applications," Journal of Electromagnetic Waves and Appl., Vol. 21, No. 15, 2311–2320, 2007.

[12] C. F. Tseng, C. L. Huang, C. H. Hsu, "Microstrip Fed Monopole Antenna With A Shorted Parasitic Element For Wideband Application," Progress in Electromagnetic Research Letters, Vol. 7, pp 115-125, 2009.

[13] C. Y. Huang, P. Y. Chiu, "Dual-band monopole antenna with shorted parasitic element," Electronics Letters, Vol. 41, No. 21, pp 1154 – 1155, 2005.

[14] Bhuiyan, Ashraful Ghani; Hashimoto, Akihiro; Yamamoto, Akio, "Indium Nitride (InN): A review on growth, characterization and properties", Journal of Applied Physics, Vol. 94, Issue 5, PP 2779-2808, 2003.

[15] Return loss to VSWR conversion table – Marki Microwave, [Online]: http://www.markimicrowave.com/Assets/data/return%20loss%20to%20vswr.pdf

The 1x1 Annular Ring: Bandwidth Enhancement of Microstrip Asymmetric Couple-Line Bandpass Filter with Superior Matching and Lower Insertion Loss

Shakhawat Parvez, * Nazmus Sakib,* Md. Nurunnabi Mollah
Department of EEE, Khulna University of Engineering & Technology
Khulna-9203, Bangladesh
*shakhawat_parvez@yahoo.com,*sakib483@yahoo.com

***Abstract*— Electromagnetic Band Gap (EBG) structures which is an exclusive innovation in modern microwave design arena by reason of their high potential and less intricacy of designing in the microwave and millimeter-wave integrated circuits. This paper examines the relationship between the filling factor (FF) of the annular ring structure on couple-line and capacitive coupling for improving the performance. A number of methods, method of moments (MOM) for numerical analysis and uniform distribution with constant aspect ratio (AR) for designing the circuit are used. In like manner, the parametric comparison has been demonstrated considering selectivity, 3-dB bandwidth (3-dB BW), insertion loss and return loss in the passband. Consequently, not only a very wide passband upto 49% increment but also a return loss upto 65 dB which illustrates great matching are achieved. Although, the insertion loss is less than 0.2 dB in the passband, but the selectivity shrinks with expanding bandwidth. In short, remodelling of the selectivity can be done by appropriately choosing the filling factor for annular ring pattern on the couple-line as well as on the transmission line.**

Keywords—3-dB Bandwidth; Aspect Ratio; Insertion Loss; Selectivity; Return Loss.

I. INTRODUCTION

Recently, Electromagnetic Band Gap structures (EBGs) which is a subset of metamaterials have grown in reputation as a result of less complexity in fabrication, superior efficiency, compact architecture and cooperative integration with microwave and millimeter-wave circuits. In brief, this metamaterials have such exclusive properties which is noteworthy for a single natural crystal [1]. However, the stopband and bandgap property of the structures can be influenced by some sophisticated design parameters. Like element spacing, number of the element on transmission line, aspect ratio and volumetric ratio of the elements, dielectric and radiation losses are the predicament for designing the EBG structures [2]. Furthermore, the efficacy of the wideband system is disturbed by the harmonics transmission which may cause increasing radiation loss. To enhance the performance of the propagation characteristics, a particular factor (namely, slow wave mode propagation) is analysed for achieving the low insertion loss [3]. On the other hand, bandpass filters having wideband, low insertion loss in the passband and wide attenuation in the stopband are the passband and wide attenuation in the stopband are appropriate for microwave system. However, by modifying the coupling coefficient of the couple-line and impedence of the transmission line, not only the pass bandwidths and transmission zeros of the filter can be regulated but also wider stopband and sharp selectivity can be achieved [4]. In addition, to increase the coupling coefficient pair of slots parallel to the microstrip line engraved on the ground plane for attaining wide bandwidth in the passband was reported in [5]. Also, the dielectric and radiation losses can be minimized without the coupling gaps. As a result, low insertion loss in the passband can be obtained with good matching. Moreover, adding two tuning stubs and dual mode characteristics, the performance of the bandpass filter in both passband and stopband can be significantly enhanced [6].

In this exposition, a lower insertion loss, better impedence matching, enhanced bandwidth and wider stopband asymmetric couple-line filter with annular ring EBG structure is proposed. In fact, annular ring structures are used in the four stage couple-line section for better optimization in the coupling coefficient. Besides, in both of the 50Ω transmission line to enhance the pass bandwidth and reduce the radiation losses in the coupled line section higher volumetric ratio element are used. In short, to enhance the 3-dB bandwidth with low insertion loss and large stopband is the individuality of this exposition.

The asymmetric couple-line bandpass filter with annular ring structures has a number of exclusive features, which includes the following:

a. The structure is compact and simple.
b. The optimization in the coupling coefficient has been made in this filter which proves the good matching.
c. The passband provides wide 3-dB bandwidth.
d. The filter has sharp rates of roll-off transfer function.
e. The insertion loss is very low with wider stopband performance.

The whole structure is simulated by method of moments (MOM) based EM software *Zeland IE3D.*

II. DESIGN THEORY

The annular ring pattern is etched on the ground plane of standard 50Ω transmission line with a period "*a*" which is a

978-1-4673-9257-0/15/$31.00 ©2015 IEEE

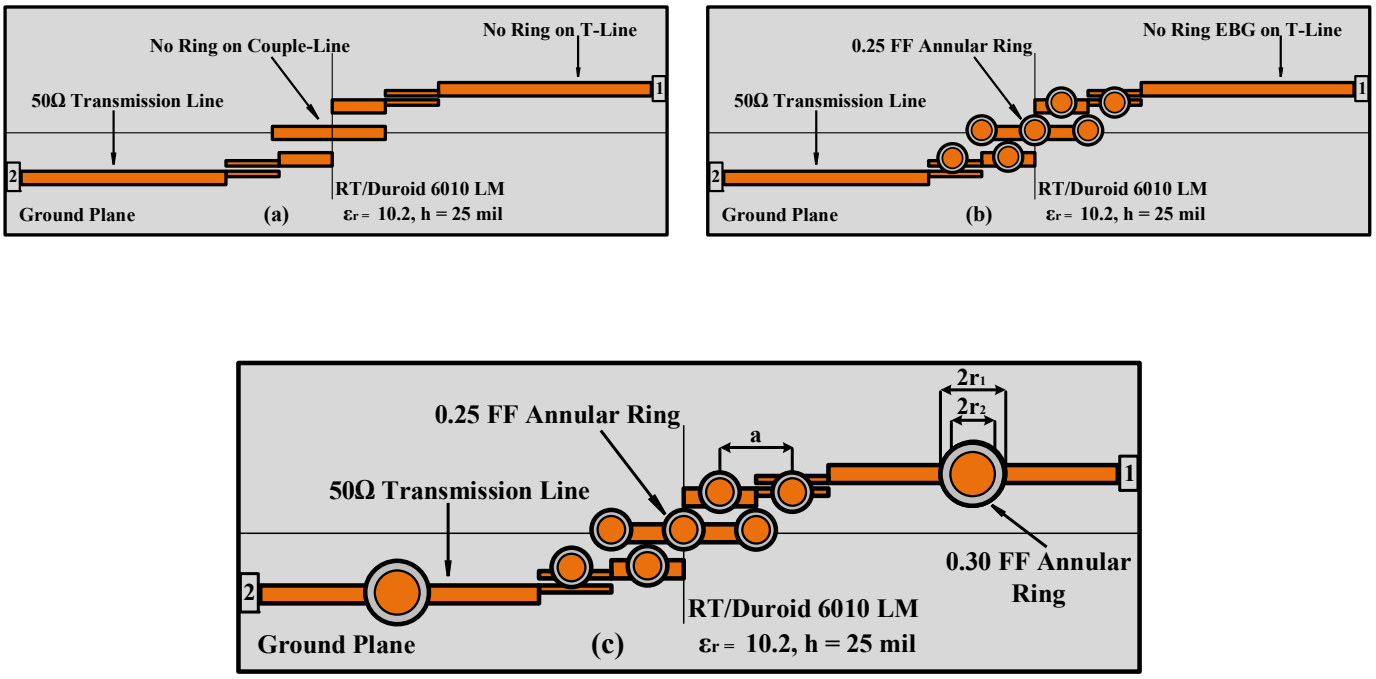

Fig. 1: Schematics of the (a) Published reference model by T. Itoh et al. [3]; (b) Proposed designed couple-line filter with 0.25 FF annular ring on four stage couple line and no EBG ring on transmission line; (c) Proposed designed couple-line filter with 0.25 FF annular ring on four stage couple line and 0.30 FF annular ring on both of the transmission line; where the AR=0.535, period, a=150 mil in 50Ω transmission line etched on the ground plane of the RT/Duroid 6010LM, h=25 mil.

crucial parameter to attain stopband characteristics. Moreover, filling factor of the annular ring patterned EBGs are drafted from the equation:

$$FF = \frac{r_1}{a} \tag{1}$$

Where, Filling Factor (*FF*), outer ring radius (r_1), spacing between two elements (*a*).

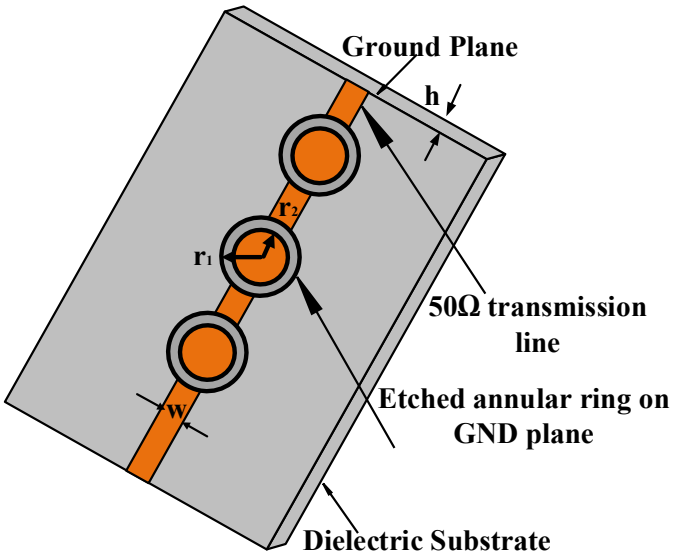

Fig. 2: Three-dimensional (3-D) view of the conventional annular ring architecture on a 50Ω transmission line.

Aspect ratio (AR) of the annular ring may be defined as the ratio of the inner ring radius (r_2) to outer ring radius (r_1) which is an exclusive feature.

$$AR = \frac{r_2}{r_1} \tag{2}$$

The center frequency of the stopband [7] can be calculated using:

$$\beta a = \pi \tag{3}$$

Where, β is the wave number of dielectric slab, *a* is the period of the annular ring pattern.

III. Proposed Structures

The proposed asymmetric couple-line filters were composed on RT/Duroid 6010 LM substrate with dielectric constant of 10.2 and thickness of 25 mil. For good tuning and simulation scope, the annular ring assisted couple-line bandpass filter is simulated by MOM based EM software Zeland IE3D. Outer ring radius r_1 can be developed from the filling factor. Likewise, inner ring radius r_2 would always be determined by aspect ratio. Nevertheless, the aspect ratio kept consistent at 0.535 while the volumetric ratio of ring structure is varied.

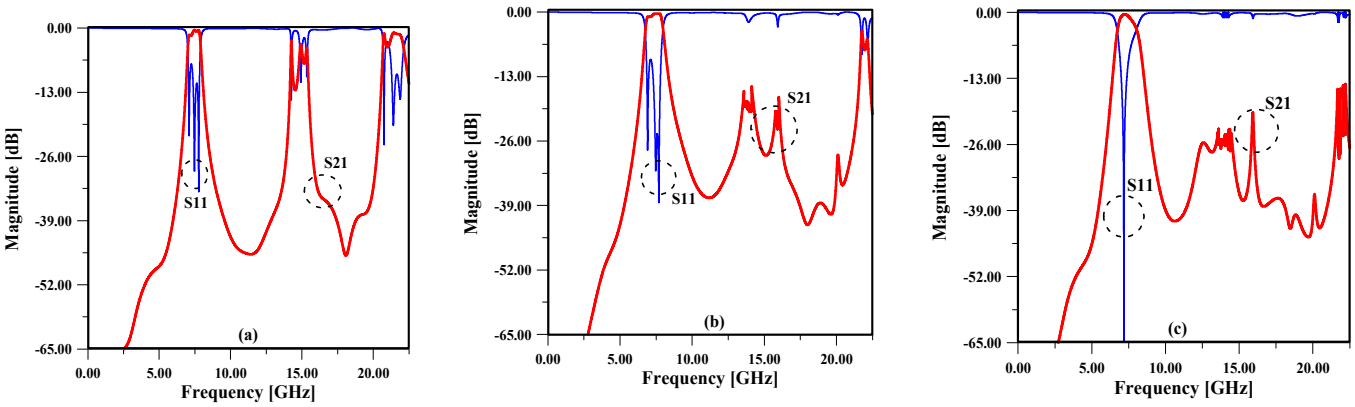

Fig. 3: Simulated frequency response of the (a) Published reference model by T. Itoh et al. [3]; (b) Proposed designed couple-line filter with 0.25 FF annular ring on four stage couple line and no EBG ring on both of the transmission line; (c) Proposed designed couple-line filter with 0.25 FF annular ring on four stage couple line and 0.30 FF annular ring on both of the transmission line; where the AR=0.535, a=150 mil in 50Ω transmission line etched on the ground plane of the RT/Duroid 6010LM, h=25 mil.

A. Design 1 :

As can be seen in Fig. 1(a), the reference asymmetric couple-line bandpass filter have four couple-line segments, lower and upper transmission line. Again, no EBG element on couple-line as well as on both of the 50Ω transmission line. This four stage coupled line filter with 0.5 dB equal ripple response where center frequency is at 7.5 GHz. In Fig. 3(a), at initial passband insertion loss starts from 120 dB. The filter has sharp selectivity of 45.95 dB/GHz and 3-dB cut-off frequency at 7.03 GHz. As the filter is tightly coupled, it results of a very narrow bandwidth. The return loss in the passband is 33.10 dB. But from Fig. 3(a), the filter is influenced by the spurious transmission in the conclusive stopband.

B. Design 2 :

Observing from Fig. 1(b), the proposed asymmetric couple-line bandpass filter have seven annular ring EBG elements with 0.25 FF on four section couple-line. But, like the Fig. 1(a), no annular ring EBG element are etched on both of the 50Ω transmission line. Consequently, for utilizing the ring element on couple line the balance between the capacitive coupling and coupling coefficient is established. In Fig. 3(b), insertion loss starts from 125 dB. As a result of balanced coupling, the 3-dB pass bandwidth has increased which is 1.17 GHz. But the matching in the Fig. 3(b) not increased significantly compare to Fig. 3(a). Likewise, no significant coupling has done as no ring EBG is etched on both of the transmission line which results no significant improve in matching in the passband. Although, the bandwidth is increased, but the selectivity is 34 dB/GHz. As seen from Fig. 3(b), not only the ripple is diminished in the passband but also the spurious transmission in conclusive stopband is also reduced. For further improvement of the overall performance (namely, coupling coefficient) of the asymmetric couple-line bandpass filter, annular ring EBG with certain FF need to be used in the both 50Ω transmission line for better coupling.

C. Design 3 :

As illustrated in Fig. 1(c), the proposed asymmetric couple-line bandpass filter have seven volumetric ratio of 0.25 annular ring EBG element on four segment couple-line like the Fig. 1(b). But, this proposed design has 0.30 FF annular ring EBG element has placed at center on both of the 50Ω transmission line. At first the coupling settled on the four stage couple-line, it also yields the mutual coupling between both of the 50Ω transmission line. Still, the signal gets weaker at the end of the port due to the dielectric and radiation losses as a result of tight coupling. Finally, with a proper volumetric ratio of 0.30 ring structure has placed on the middle for further improvement in the coupling. As seen from Fig. 3(c), insertion loss starts from 134 dB. Furthermore, not only the 3-dB pass bandwidth increased to 1.25 GHz but also the matching in the passband has significantly improved to 65 dB. But, the value of selectivity reduced to 30.81 dB/GHz which is normal compared to the bandwidth. Alternatively, the spurious transmission due to the skin effect in the conclusive stopband is also reduced significantly which results a very large stopband compared to Fig. 3(a) and Fig. 3(b).

IV. RESULTS

As illustrated in Fig. 4, Fig. 5 and Table I, a comparative study has done by virtue of their rigorous parametric analysis (namely, selectivity, return loss S_{11} in the passband, 3-dB bandwidth and percentage enhancement in the bandwidth) with respect to the volumetric ratio. In this section, overall improvement in the efficacy of the couple-line filer will be presented meticulously.

TABLE I

COMPARATIVE STUDY BETWEEN THE PERFORMANCE OF ASYMMETRIC COUPLE-LINE BANDPASS FILTER; *AR=0.535* REMAIN CONSTANT.

EBG on T-Line	Selectivity [dB/GHz]	S_{11}(Passband) [dB]	3-dB BW [GHz]	BW Enhancement [%]
Ref. [3]	45.95	33.10	0.84	N/A
No EBG	34.00	38.50	1.17	39.39
0.30 FF	30.81	65.00	1.25	48.81

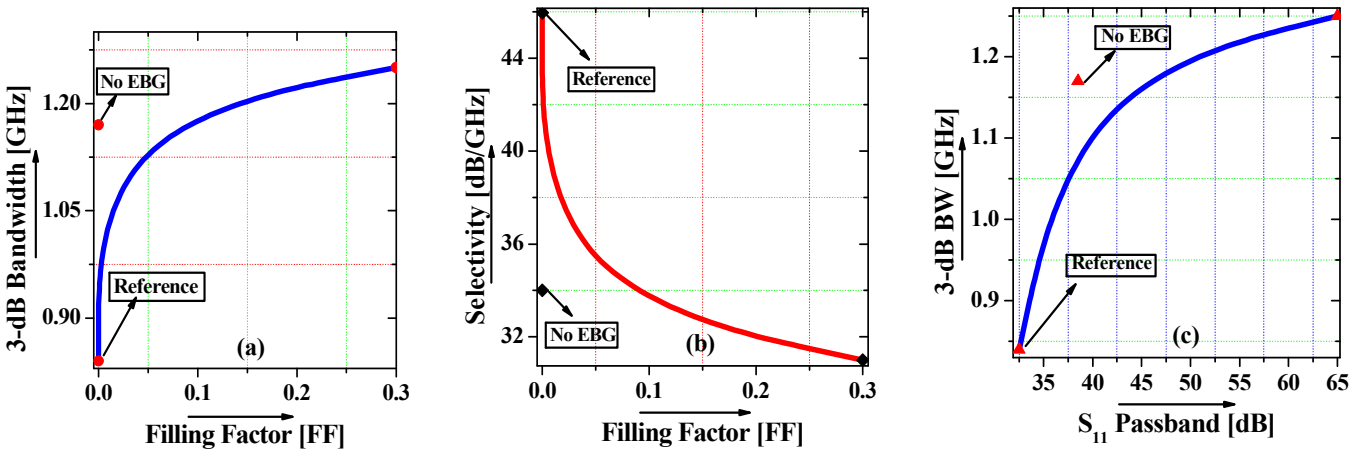

Fig. 4: Comparative study between the Published reference model by T. Itoh et al. [3], Proposed designed couple-line filter with 0.25 FF annular ring on four stage couple line and no EBG and 0.30 FF annular ring on both of the transmission line representing (a) FF vs. 3-dB BW; (b) FF vs. Selectivity; (c) return loss in the passband vs. 3-dB BW; where the AR=0.535, a=150 mil in 50Ω transmission line etched on the ground plane of the RT/Duroid 6010LM, h=25 mil.

A. Bandwidth Enhancement :

In this article, one of the most significant findings is 3-dB bandwidth enhancement with respect to the filling factor. As can be seen in Fig. 4(a) and Table I, reference filter is about less than 0.90 GHz while the proposed structure with no EBG in transmission line has 1.17 GHz and 0.30 FF EBG on transmission line has 1.25 GHz respectively. As the filter is tightly coupled, so the radiation loss due to skin effect will be more. Likewise, adding EBG on transmission line has equally distributed the capacitive coupling throughout the total transmission line. The consequence of that is, enhancement in the 3-dB bandwidth with a uniform and healthy coupling. The value of the curve increases gradually with a proper pattern. In Fig. 4(a), the curve is parabolic which shows a saturation in the coupling.

B. Shrinkage in Selectivity :

As can be seen in Fig. 4(b), the curve is decreasing exponentially which is noteworthy. The reference has the selectivity of 45.95 dB/GHz with a narrow bandwidth and no proper EBG pattern either on the couple-line or on the 50Ω transmission line. Nevertheless, involvement of the annular ring pattern on the couple-line in Fig. 1(b) and on both of the couple-line and on the T-line in Fig. 1(c), selectivity immediately falls off from 45.95 to 34 and 30.81 dB/GHz respectively. In conclusion, as the width of the passband rises, low selectivity occurs.

C. Improvement of Matching :

As illustrated in Fig. 4(c) and Table I, in the passband of the reference filter return loss is about 33.10 dB as a result of the non-uniform tight coupling between the couple-lines. At first, inclusion of the 0.25 FF ring pattern on couple-line improve the coupling balance at small-scale. Furthermore, inclusion of 0.30 FF ring with already placed 0.25 FF ring pattern on couple-line

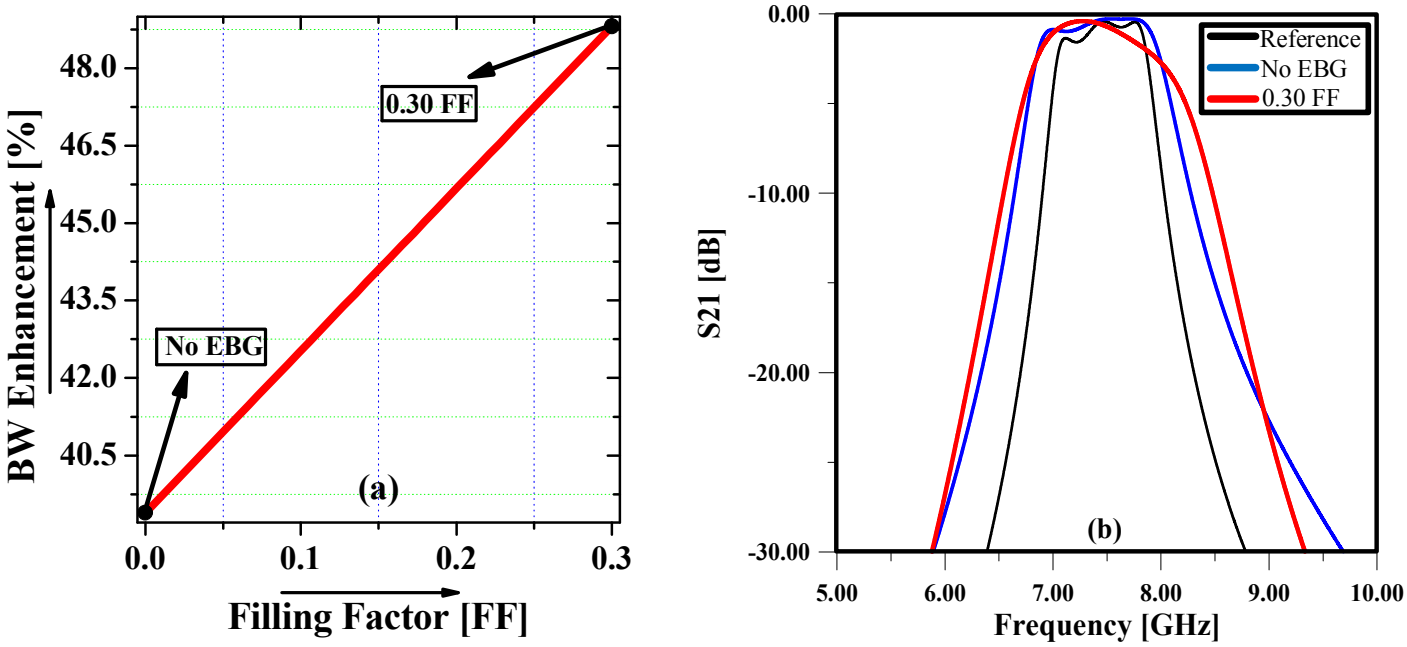

Fig. 5: Graphical representation of the (a) FF vs. percentage (%) of bandwidth enhancement; (b) frequency vs. insertion loss in the passband, black line-reference, blue line-no EBG on T-line, red line- 0.30 FF on T-Line; where the AR=0.535, a=150 mil remain constant.

a drastically improved matching in the passband of 65 dB can be observed in Fig. 4(c). From the Fig. 4(c), it can be observed that coupling is distributed consistently along the lower and upper transmission line.

D. Percentage of Bandwidth Enhancement :

As observed from Fig. 5(a) and Table I, the straight line which has very sharp tangent exhibits the percentage advancement of the bandwidth. From Fig. 5(a), the design with no EBG pattern on transmission line has increment of 39.39% and the pattern with 0.30 FF ring EBG on transmission line has 48.81%.

E. Low Insertion Loss :

Observing the Fig. 5(b), both insertion losses of the proposed circuits are improved significantly over the reference one. Furthermore, reference one bandwidth is bit narrower than both of the proposed designs. Likewise, at the tip of the passband in the reference model, ripple is present. With the increment of the filling factor, the ripple was no more with very smooth frequency response in the passband.

V. Conclusions

In this paper, the equal length asymmetric couple-line with annular ring patterns that can be utilized to effectively comprehend the bandpass filter is demonstrated. Furthermore, to certify the design method two examples of microstrip annular ring patterns on transmission line is established. In the illustrated cases, the 3-dB bandwidth increases by 39.39% and 48.81% respectively. Likewise, by properly placing the annular ring patterns on the couple-line section, sharp selectivity and more efficient passband can be obtained. On the other hand, appropriately selecting the volumetric ratio on both lower and upper transmission line, the matching and spurious transmission can be further improved. Alternatively, polynomial distribution with ring architecture can play a vital role for further improvement of overall efficacy of the couple-line filter.

References

[1] Fan Yang, Yahya Rahmat-Samii, *Electromagnetic Band Gap Structures in Antenna Engineering*. Cambridge CB2 8RU, UK: Cambridge University Press, 2009.

[2] Dal Ahn et al., "A Design of the Low-Pass Filter Using the Novel Microstrip Defected Ground Structure," in *IEEE Trans. Microwave Theory Tech,* vol. 49, no. 1, pp.86-93, Jan. 2001.

[3] F. R. Yang, K. P. Ma, Y. Qian and T. Itoh," A Uniplanar Compact Photonic-Bandgap (UC-PBG) Structure and Its Applications for Microwave Circuits," in *IEEE Trans. Microwave Theory Tech,* vol. 47, no. 8, pp.1509-1514, Aug. 1999.

[4] W. J. Feng, W. Q. Che, Y. M. Chang, S. Y. Shi and Q. Xue," High Selectivity Fifth-Order Wideband Bandpass Filters With Multiple Transmission Zeros Based on Transversal Signal-Interaction Concepts," in *IEEE Trans. Microwave Theory Tech,* vol. 61, no. 1, pp.89-97, January. 2013.

[5] M. K. Mandal, S. Sanyal," Compact Wideband Bandpass Filter," in *IEEE Microwave and Wireless Components Lett.* vol. 16, no. 1, pp.46-48, Jan. 2006.

[6] L. H. Hsieh, K. Chang," Compact, Low Insertion-Loss, Sharp-Rejection, and Wide-Band Microstrip Bandpass Filters," in *IEEE Trans. Microwave Theory Tech,* vol. 53, no. 4, pp.1241-1246, April. 2003.

[7] Nemai Chandra Karmakar, Mohammad Nurunnabi Mollah, "Investigations Into Nonuniform Photonic-Bandgap Microstripline Low-Pass Filters," IEEE Trans. Microwave Theory Tech., vol.51, no.2, pp.564-572, Feb.2003.

Dumbbell Annular Ring with Circular Patterned Microstrip Low-Pass Filter with Higher Selectivity, Wider Stopband and Lower Insertion Loss

Shakhawat Parvez, * Nazmus Sakib,* Md. Nurunnabi Mollah
Department of EEE, Khulna University of Engineering & Technology
Khulna-9203, Bangladesh
*shakhawat_parvez@yahoo.com,*sakib483@yahoo.com

***Abstract*— Electromagnetic Band Gap Structures (EBGs) have been developed to improve the efficiency of microwave and millimeter-wave devices, grown into most prominent framework by virtue of their unique electromagnetic and electrical properties. This article inspects the relationship between the operating performances of the low pass filter with the different EBG pattern. In this article, two high selectivity, wide stopband low pass filters (LPF) etched on ground plane with Tschebycheff polynomial distribution are proposed. A number of methods, method of moments (MOM) for numerical analysis and Tschebycheff polynomial distribution for designing the circuit are used. Moreover, to increase the stopband bandwidth of the new filters, a hybrid structure is used. The filter using ten dumbbell annular ring (DAR) patterns has improved selectivity of 47.19%, great matching upto 80 dB, negligible insertion loss less than 0.2 dB and two rejections in the stopband within 6.25 GHz, 12.97 GHz. In brief, this high selectivity, compact, wide stopband low pass filters were designed to alleviate the problem of low selectivity and small stopband bandwidth in microwave communication.**

Keywords—Low Pass Filters; Tschebycheff Polynomial Distribution; Selectivity; Dumbbell Annular Ring, Insertion Loss.

I. INTRODUCTION

In recent times, Electromagnetic Band Gap structures (EBGs) which is a subset of metamaterials have grown in reputation considering some periodic patterned, quite extraordinary and sophisticated properties. However, such high level properties is infrequent for a single natural material [1]. In microwave sector, EBGs display wider bandpass, steeper and deeper band rejection properties. In this present day, EBG assisted microstrip filters are frequently playing a role in modern microwave and RF engineering. To minimize the spurious transmission and register the compactness of circuits, numerous active and passive microwave and millimeter wave devices have been fabricated. However, due to the predicament of the modeling, utilizing an EBG structure for the fabrication of these components. Such as the element spacing, operating frequency, width, height of the substrate, thickness, irregularity of the surface, volumetric ratio of the EBG element, pattern of the elements which have influence on bandpass and band rejection properties. In addition, other complication in EBG circuit due to the radiation from aperiodic etching with no proper formulation as a result of the inappropriate selection of dielectric substrate [2].

978-1-4673-9257-0/15/$31.00 ©2015 IEEE

In this paper, applying Tschebycheff polynomial distribution with dumbbell annular ring (DAR) patterned EBG structures inscribe on the ground plane of a microwave transmission line is proposed. On the whole, microwave assisted low pass filter return loss, insertion loss and selectivity enhanced performance where Tschebycheff polynomial distribution are employed to fabricate the filter. Moreover, two new sharp selectivity, wide stopband low pass filter based on hybrid pattern (namely, only DAR and DAR with interleaved circular) concepts, is the novelty of the paper. Developing wider, deeper stopband and suppressing ripples in the passband are great features of the Tschebycheff polynomial. A unique measure of the Tschebycheff polynomial the side lobe level (SLL) is exploited to manage the width of stopband insertion loss, the depth of passband return loss, ripples in both passband and stopband, selectivity. Consequently, with the Tschebycheff distribution ripple, width and depth of the stop bandwidth can be mitigated with the improvement of selectivity of the transfer function at cut-off frequency [3].

The proposed low pass filter utilizing the Tschebycheff polynomial distribution with the novel Hybrid structure not only has some specific ground of originality but also has some unique features, which includes the following:

a. The stopband is greater than 12 GHz which is very wide than that of a traditional low pass filter.
b. Two architectures will be fabricated according to the Tschebycheff polynomial distribution.
c. The ripple is less than 0.2 dB and significant improvement in matching in the passband.
d. The rates of roll-off transfer function is very sharp.
e. The return loss in the stopband is negligible.

All the structures are simulated by method of moments (MOM) based EM software *Zeland IE3D*.

II. DESIGN THEORY OF STRUCTURES AND POLYNOMIAL DISTRIBUTION

Tschebycheff polynomial has a convenient characteristic of equal ripple characteristic which is observed for a selective side lobe level (SLL). The Tschebycheff excitation coefficient are determined by the SLL. The recurrence formula [4] for Tschebycheff polynomial:

$$T_m(z)=2zT_{m-1}(z)-T_{m-2}(z) \quad (1)$$

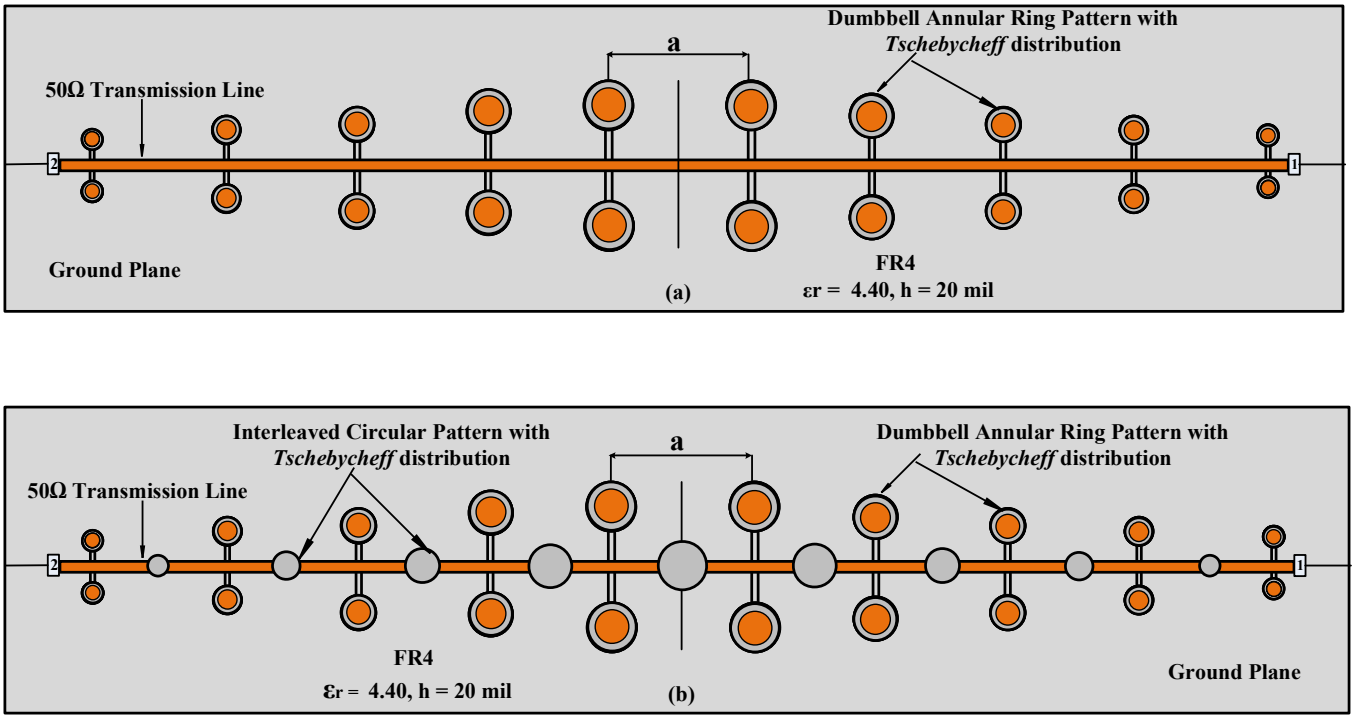

Fig. 1: Schematics of the (a) Proposed designed dumbbell annular ring assisted low pass filter on transmission line; (b) Proposed designed low pass filter with dumbbell annular ring with interleaved circular (Hybrid) pattern on the transmission line; where the AR=0.535, FF=0.25, period, a=320 mil in 50Ω transmission line etched on the ground plane of the FR4 substrate, h=20 mil.

Every polynomial can be evaluated using:

$$T_m(z)=\cos[m\cos^{-1}(z)];\ -1 \le z \le +1 \qquad (2)$$

$$T_m(z)=\cosh[m\cosh^{-1}(z)];\ z\langle -1,\ z\rangle +1 \qquad (3)$$

As major to minor lobe ratio for 25 dB, the amplitude of coefficient will be:

$$0.40\ 0.51\ 0.72\ 0.90\ 1\ 1\ 0.90\ 0.72\ 0.51\ 0.40$$

The volumetric ratio of each circular element will be:

$$FF=\frac{r}{a} \qquad (4)$$

Where, Filling Factor (*FF*), radius of each element (*r*), spacing between two elements (*a*).

On the ground plane, the ring pattern is placed into the standard 50Ω transmission line with period "*a*" which is a influential parameter for achieving sharp selectivity and wider stopband. However, the filling factor for annular ring will be:

$$FF=\frac{r_1}{a} \qquad (5)$$

Where, outer ring radius (r_1). The ratio of the inner ring radius (r_2) to outer ring radius (r_1) is called Aspect ratio (AR).

$$AR=\frac{r_2}{r_1} \qquad (6)$$

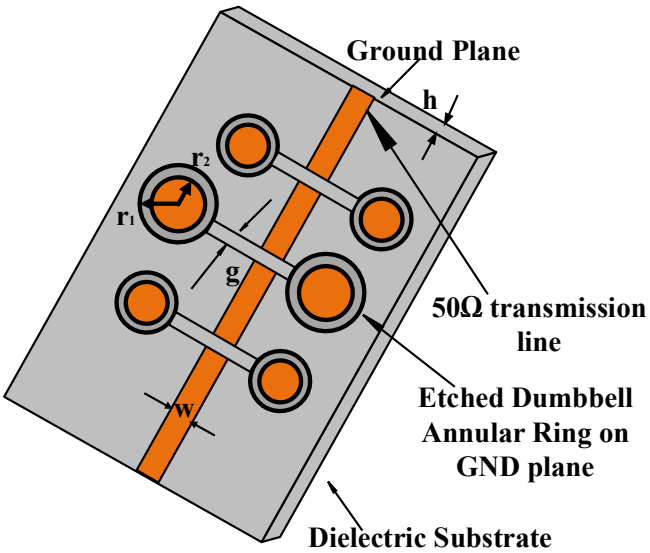

Fig. 2: Three-dimensional (3-D) view of the conventional dumbbell annular ring structure with Tschebycheff distribution etched on a ground plane on a 50Ω transmission line, grey- etched portion, colour-copper portion; where, w and g are the width of the transmission line and arm of the dumbbell annular ring respectively.

The center frequency of the stopband can be calculated using:

$$\beta a=\pi \qquad (7)$$

Where, β is the wave number of dielectric slab, a is the period of the annular ring pattern.

TABLE I

COMPARATIVE STUDY BETWEEN THE PERFORMANCE OF THE PROPOSED DUMBBELL ANNULAR RING ASSISTED LOW-PASS FILTER; *AR=0.535, FF=0.25* REMAIN CONSTANT, PERIOD, 320 MIL WILL VARY ACCORDING TO THE TSCHEBYCHEFF POLYNOMIAL.

Structures	Selectivity [dB/GHz]	Stopband isolation S_{21max} [dB]	f_0 [GHz]	20-dB IL BW [GHz]	10-dB RL BW [GHz]	3-dB Cut-Off Frequency [GHz]	Frequency Deviation %	1st Null & Peak [dB] Null	Peak
Only DAR	89.47	80.00	9.82	6.25	4.55	4.46	-1.80	59.2	17.60
DAR with Circular	130.77	78.60	9.81	12.97	4.98	4.90	-1.90	64.6	13.20

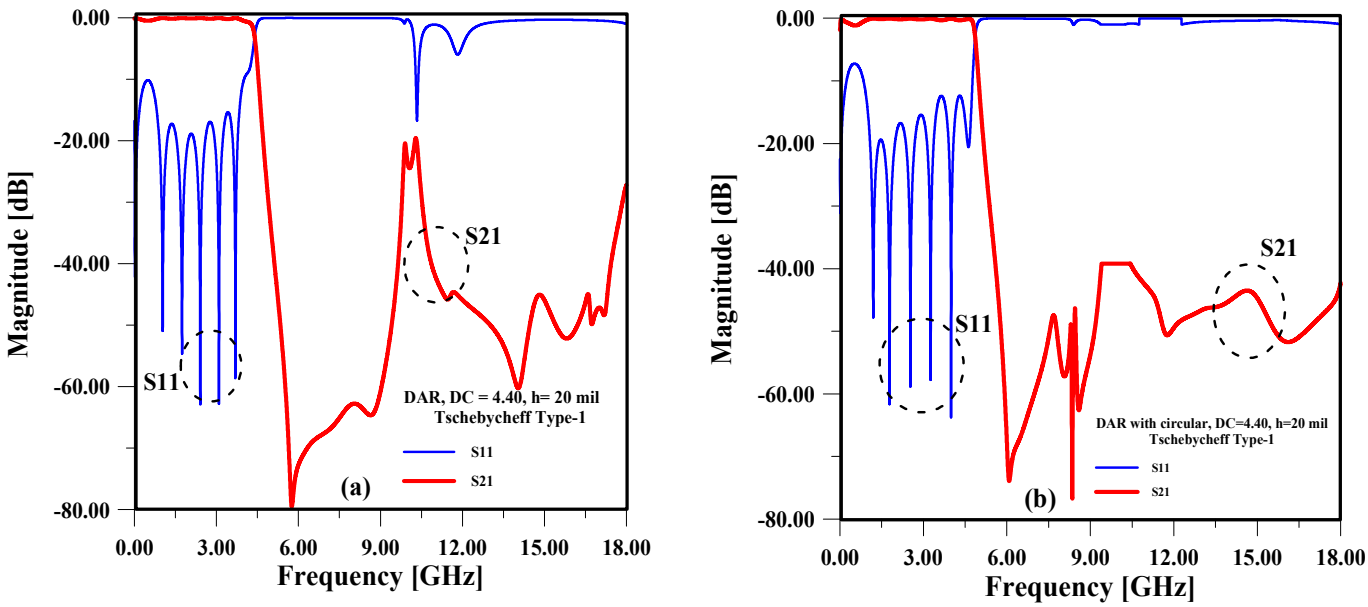

Fig. 3: Simulated frequency response of the (a) Proposed designed dumbbell annular ring assisted low pass filter on transmission line; (b) Proposed designed low pass filter with dumbbell annular ring with interleaved circular (Hybrid) pattern on the transmission line; where the AR=0.535, FF=0.25, period, a=320 mil in 50Ω transmission line etched on the ground plane of the FR4= 4.40 substrate, h=20 mil; AR = 0.535 remain constant throughout the analysis.

III. PROPOSED DESIGN STRUCTURES

The dumbbell annular ring (DAR) structured low-pass filters were constructed on FR4 substrate with dielectric constant of 4.40 and thickness of 20 mil. For simulation purpose and great tuning, the couple-line filter is simulated by EM software Zeland IE3D. Outer ring radius r_1 which derives from filling factor and inner ring radius r_2 which can be obtained from aspect ratio, this both factor are kept consistent at 0.25 and 0.535 respectively throughout the analysis. Likewise, 25-dB Side lobe level with ten amplitude coefficient will determine the dimension for each of the dumbbell annular ring (DAR) as well as the capacitive coupling between them. Besides, Tschebycheff polynomial distribution are applied with center frequency at 10GHz. Selectivity, 20-dB IL BW and 10-dB RL BW, this three significant parameters will be taken account to find out the structure for the low pass filter with the best, reliable and remarkable efficacy.

A. Only Dumbbell Annular Ring (DAR) structure on T-Line:

As can be seen from Fig. 1(a), the proposed filter have ten dumbbell annular ring (DAR) EBG elements with 0.25 FF, arm width and height of the structure are 113 and 10 mil respectively. But, like the Fig. 1(b), no other (namely, circular) pattern EBG element are etched on the 50Ω transmission line. However, by the Tschebycheff polynomial for 25-dB SLL not only the dimension of the DAR will vary but also spacing between each DAR will also fluctuate accordingly. As a result, spacing between two DAR will increase with Tschebycheff distribution However, the coupling between each element is strong which results in sharp selectivity. Although the structure is symmetric, but the capacitive coupling between each of the dumbbell annular ring are unbalanced and weak in compare with Fig. 1(b). To improve the overall coupling and bandgap properties, circular patterned EBG structures is utilized in between the DAR in Fig. 1(b).

TABLE II
PERFORMANCE COMPARISON BETWEEN DIFFERENT LPF

Filter Structures	Selectivity [dB/GHz]	Stopband isolation S_{21max} [dB]	Ripple Height [dB]
Ref. [3]	20.92	61.50	< 0.5
Ref. [5]	6.29	68.00	< 5
Ref. [6]	24.28	65.30	2
Only DAR	89.47	80.00	< 0.2
DAR with Circular	130.77	78.60	< 0.2

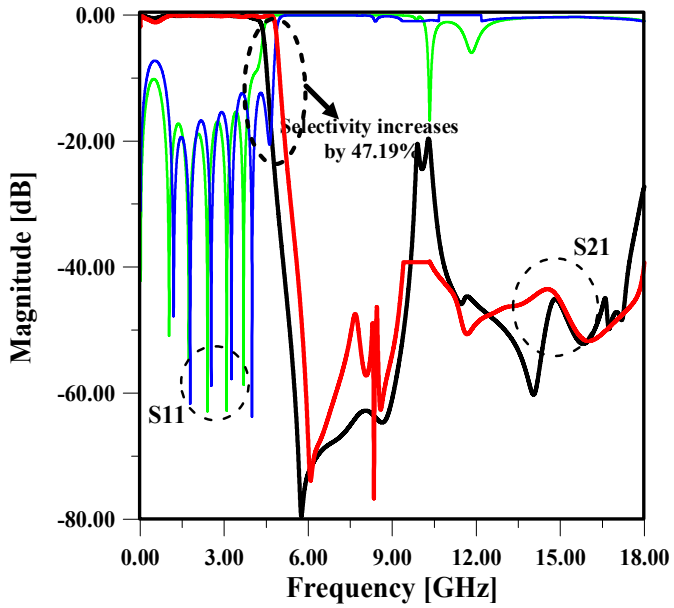

Fig. 4: Comparative study between two proposed low pass filters with Tschebycheff polynomial distribution; where, green-only DAR (S_{11}), black-only DAR(S_{21}); blue-DAR with circular (S_{11}), red- DAR with circular (S_{21}).

B. Dumbbell Annular Ring (DAR) with circular structure on T-Line:

As illustrated in Fig. 1(b), the proposed DAR assisted low pass filter have ten dumbbell annular ring EBG elements with 0.25 FF, arm width and height of the structure are 113 and 10 mil respectively. Likewise, nine circular patterns with the same volumetric ratio as annular ring, this EBG element with Tschebycheff distribution and same spacing between them like DAR are etched on the 50Ω transmission line. Moreover, in this design the dimension of DAR will also fluctuate in agreement with 25-dB SLL Tschebycheff polynomial. Consequently, the coupling between the patterns become stronger and balanced than design 1. Besides, the ripple in the stopband also diminishes with high rates of roll-off transfer function. Likewise, this hybrid design also prevails with very wide stopband with increased selectivity. In brief, DAR with circular pattern yields a unique combination, which constitutes more attractive bandgap properties in EBG structure.

IV. RESULTS

Modeling the low pass filters (LPF) by Tschebycheff polynomial distribution with hybrid patterns to realize the performance of the LPF is examined. As can be seen from Fig. 3(a), Fig. 3(b) and Table-I, it is found that, in Tschebycheff distribution with FR4 substrate for structure with only DAR and DAR with circular exhibit selectivity, 20-dB IL and 10-dB RL bandwidth of 89.47 dB/GHz, 6.25 GHz, 4.55 GHz and 130.77 dB/GHz, 12.97 GHz, 4.98 GHz respectively. However, FR4 is a lossy substrate at high frequency [7]. Nevertheless, the structure-1 displays negligible insertion loss in the passband with ripple less than 0.2 dB, great selectivity, well impedence matching upto 60 dB and very wide stop bandwidth upto 6.5 GHz. Besides, the structure-2 reveals very wide return loss bandwidth upto 5 GHz with ripple not greater than 0.2 dB, excellent matching, sharper roll-off and wider stop bandwidth upto 13 GHz. Although, in design-2, modeling is robust because of circular pattern are etched between the DAR on 50Ω transmission line. Also, the arm length of the annular ring fluctuates according to the Tschebycheff polynomial. Similarly, annular ring has a unique feature namely, aspect ratio which is equivalent of variable capacitance, so in design-2 exhibits profound performance than design-1. Observing the Table-I, design-2 has more stable passband performance with increase in 10-dB RL bandwidth as well as 3-dB cut-off frequency. At 11 GHz, design-1 exhibits poor performance in the stopband. With stronger coupling in design-2, this disturbance due to spurious transmission is alleviated. Consequently, the width and depth of the stopband increases. Besides, the maximum isolation of the stopband in design-1 is greater than design-2 with 1.75% increment. The width of the stopband has been expanded 107.52% in design-2 than design-1. As illustrated in Fig. 4, the selectivity in design-2 is sharper than design-1 with amount of 47.19%. Furthermore, from the observation of comparative study in Table II, performance of different low pass filters, it is appreciated that roll-off rates has been improved significantly with a minimum amount of 2.67 times by the proposed two structures. Moreover, the depth of the stopband is upto 80 dB and passband ripples is quite negligible. In conclusion, only DAR and DAR with circular patterns reveal more superior passband and stopband performance with Tschebycheff distribution respectively.

V. CONCLUSIONS

A new hybrid, wide stopband, low insertion loss and high selectivity microstrip low pass filter has been demonstrated. A low pass filter with hybrid structure namely, dumbbell annular ring (DAR) and circular is introduced. A new design was developed to increase not only the rate of roll-off transfer function but also the width of the stopband. However, with the hybrid design forming more stable capacitive coupling, the dielectric and radiation losses are reduced significantly. The consequence of that is, negligible

ripple in the passband with superior matching. The new low pass filters were designed to alleviate the low selectivity and small stop bandwidth in microwave communication.

REFERENCES

[1] Fan Yang, Yahya Rahmat-Samii, *Electromagnetic Band Gap Structures in Antenna Engineering*. Cambridge CB2 8RU, UK: Cambridge University Press, 2009.

[2] Dal Ahn et al., "A Design of the Low-Pass Filter Using the Novel Microstrip Defected Ground Structure," IEEE Trans. Microwave Theory Tech, vol. 49, no. 1, pp.86-93, Jan. 2001.

[3] N. C. Karmakar, M. N. Mollah, "Investigations Into Nonuniform Photonic-Bandgap Microstripline Low-Pass Filters," IEEE Trans. Microwave Theory Tech., vol.51, no.2, pp.564-572, Feb.2003.

[4] C.A. Balanis, *Antenna Theory Analysis and Design*, 2 ed. New York: Wiley, 1997.

[5] S. Parvez et al., "Investigation on EBG Structures: A Critical Analysis to optimize the performance of Asymmetric Couple-Line Bandpass Filter," in Int. Conf. on Software, Knowledge, Inform. Manage. and Applicat., Dhaka, Bangladesh, 2014, pp. 1-7.

[6] G. M. Rafiquzzaman et al., "A New to Design Microstrip Low Pass Filter Using Novel Defected Ground Structure," in Int. Conf. on Elect. and Comput. Eng., Dhaka, Bangladesh, 2014, pp. 568-571.

[7] John Conrod, "Understanding When To Use FR4 or High Frequency Laminates," Rogers Corp., Roosevelt Avenue, Chandler, AZ. Rep. 26-30, Sept. 2011.

Design & Simulation of Ultra-Flattened Dispersion Large Mode Area and Low Splice Loss Photonic Crystal Fiber

Md. Rakib Hasan
Department of Electrical and Electronic Engineering
Rajshahi University of Engineering & Technology, RUET
Rajshahi-6204, Bangladesh
sumon.ruet09@gmail.com

Md. Selim Hossain
Department of Electrical and Electronic Engineering
Rajshahi University of Engineering & Technology, RUET
Rajshahi-6204, Bangladesh
Dr.S.Hossain@ieee.org

***Abstract*— This paper presents dispersion flattened (DF) large mode area (LMA) fiber design based on single cladding structure using finite element method (FEM) with perfectly matched layer (PML) boundary. The modal properties of the PCFs are investigated due to change in cladding parameters. To improve these properties of PCF our proposed design has obtained satisfactory results especially for flattened dispersion, effective area and splice loss. It has been shown that proposed PCFs can obtain very low dispersion variation 0.3537 ps/(nm.km) along 1300nm to 1700nm wavelength, with both a large effective area more than 82 μm^2 and splice loss of 0.0040 dB in 1550nm wavelength. As the properties obtained from simulation are suitable for the C+L+U communication bands, our proposed design can be used within these bands with better performance.**

Keywords*— Photonic crystal fibers; ultra-flattened dispersion; large effective mode area; nonlinear coefficient; splice loss;

I. Introduction

Photonic crystal fiber (PCF) [1] has received increasing attention because of its novel optical characteristics [2]. Fiber-optic communication system has brought revolution in the telecommunication industry. It is advantageous in comparison with other communication system [3]. PCFs are characterized by numerous cladding air holes arranged in an orderly manner over the whole fiber length [4]. As there are several parameters to tailor in a PCF, it can be utilized to obtain very useful properties like flat negative dispersion [5], large mode effective area [6], very high or very low nonlinearity [7], splice loss [5] and low bending loss [5]. By modulating the parameters of holey cladding, the above properties can be controlled [7]. Because of high attenuation of these types of fibers, PCFs are still under investigation as high-speed optical transmission media but recently, the attenuation level has been lowered to the order 0.28 dB/km at the 1550 nm wavelength [8]. This has encouraged the researchers to rethink the applicability of PCFs in signal transmission and modern fabrication technology is giving momentum to such thinking.

Optical transmission systems require PCFs with large effective mode area is required not only to support broadband optical transmission but also to minimize the coupling losses to standard single mode fibers (SMFs) [7]. To design large mode-area (LMA) fibers, it is desired that fibers should remain single-mode (SM) to ensure the high beam quality, which is measured through beam quality factor $M2$ (<1.2) for diffraction limited operation [9]. Again, in communications systems dispersion-flattened fiber (DFF) is very effective for optical data transmission over the broadband wavelength range [10]. For example, in wavelength division multiplexing communication systems it is essential to maintain a uniform response in different wavelength channels. This is strictly achieved by ensuring ultra-flattened dispersion characteristics of fibers [7]. Splice loss and nonlinearity are other important key factors for designing PCF. When connecting two fibers using splicing technique, geometrical misalignments occurs that leads to losses known as splice loss. Controlling the splice loss of the fiber, it will be of great use in fiber to the home (FTTH) application [11]. The nonlinearity of a fiber depends on effective area and it is inversely proportional to the effective area of the fiber. There are so many literatures dealing with large mode effective area with flattened dispersion [2,7], [12-14]. Some of which even warrant low splice loss [7], [11] as well. There are only a few papers dealing with PCFs having LMA, dispersion-flattened characteristics, low splice loss and nonlinearity at the same time.

Pourmahayabadi *et al*. [13] have proposed such an LMA PCF in 2009. They have theoretically achieved dispersion variation 1.75 ps/(nm.km) in 1.53μm to 1.57 μm wavelength but their effective area is only 20.0535 μm^2. Razzak *et al*. [7] have proposed another MOF LMA PCF design in 2010. They have theoretically achieved effective area of more than 150 μm^2 with dispersion variation 0.6 ps/(nm.km) in 1.4μm to 1.7μm wavelength and a splice loss of 0.19 dB. The PCF proposed in [7] and [13] have not mentioned about nonlinearity of their designs.

In this paper, we propose a two layer cladding PCF characterized by a common pitch and three different air-hole dimensions. The whole work aims at designing and numerical simulating the large mode effective area, flattened dispersion, low splice loss and low nonlinearity photonic crystal fiber. PCFs with such novel properties are suitable for telecom applications.

II. Numerical Analysis

The key propagation properties of the PCF are evaluated using Finite Element Method (FEM). The FEM directly solves the Maxwell equations to best approximate the value of the effective refractive index [15-16]. A commercial full-vector

978-1-4673-9257-0/15/$31.00 ©2015 IEEE

finite-element software (COMSOL) has used for both the modal and loss analyses. To allow accurate evaluation of the insertion losses, anisotropic perfectly matched layer has included in the finite-element model. We have also used Sellmeier equation to evaluate the refractive index of silica. Following equations are used to evaluate dispersion D, effective area A_{eff}, nonlinear coefficient γ and splice loss L_s. The main concern of this paper is to obtain ultra flattened and low dispersion variation, large effective area, low nonlinearity and low splice loss. The dispersion D with respect to λ is given by

$$\text{Dispersion, } D(\lambda) = -\frac{\lambda}{c}\frac{d^2}{d\lambda^2} R_e[n_{eff}] \quad (1)$$

Here, $D(\lambda)$ is in ps/(nm km) and $Re[n_{eff}]$ is the real part of the effective refractive index n_{eff}. The material dispersion is directly included in the FEM calculation. The effective area A_{eff} is given by

$$\text{Effective area, } A_{eff} = \frac{\left(\int_{-\infty}^{\infty}\int_{-\infty}^{\infty}|E|^2\,dxdy\right)^2}{\int_{-\infty}^{\infty}\int_{-\infty}^{\infty}|E|^4\,dxdy} \quad (2)$$

Where, E is the electric field distribution and A_{eff} is in μm^2. The study of A_{eff} is, thus, an important starting point in understanding of the nonlinear phenomena in PCFs.

$$\text{Nonlinear coefficient, } \gamma = \left(\frac{2\pi n_2}{A_{eff}\lambda}\right)\times 10^3 \quad (3)$$

Where, n_2 is the nonlinear refractive index for silica. The nonlinear coefficient is inversely proportional to the effective mode area. The splice loss can be obtain from the following:

$$\text{Splice loss, } L_s = -20\log_{10}\frac{2w_{SMF}w_{PCF}}{w_{SMF}^2 + w_{PCF}^2} \quad (4)$$

Where, w_{SMF} and w_{PCF} are the (Mode Field Diameter) MFDs of the (Single Mode Fiber) SMFs and the PCFs, respectively.

III. Geometry of The MAC-PCF Design

We have proposed two hexagonal geometrical designed PCFs and both are arranged 8 air hole rings in the cladding region with silica background.

A. MAC-PCF-1

Fig. 1 shows our proposed MAC (Multiple Air holes Core) -PCF-1 design. The design has two layer cladding is composed of a common air-hole pitch, Λ_1. It has three different air-hole diameters d_c, d_1 and d_2, where d_c is less than d_1 and d_2 is greater than d_1. Dimension of the first ring is lowered down to flatter the dispersion characteristics and air-holes of inner rings are chosen smaller to achieve larger mode area. Moreover, five air holes having diameter d_c are placed in the core to obtain large effective area using smaller pitch. The pitch among five air holes is in the core by the relation (Λ_1*0.5). The air hole diameter of 1st four rings is d_1 and 2nd four rings are d_2.

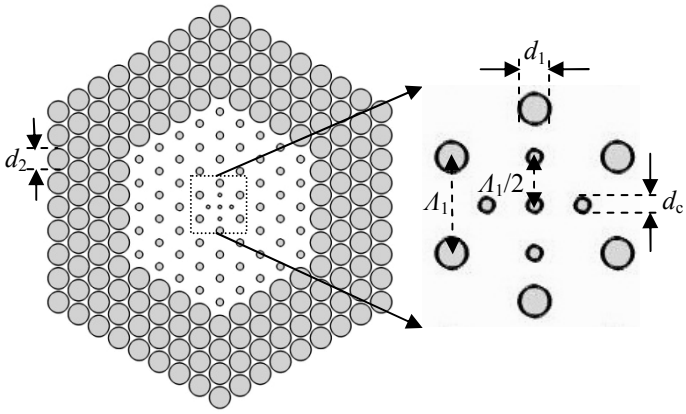

Fig. 1. Design of MAC-PCF-1.

B. MAC-PCF-2

Fig. 2 shows our another proposed MAC (Multiple Air holes core)- PCF-2 design. The design has also two layer cladding is composed of a common air-hole pitch, Λ_2. It has three different air-hole diameters d_c, d_1 and d_2, where d_c is less than d_1 and d_2 is greater than d_1. Like previous design, five air holes having diameter d_c are placed in the core to obtain large effective area using smaller pitch. The pitch among five air holes is in the core by the relation (Λ_2*0.5). In MAC-PCF-2 design diameter of all the air holes is kept d_1 except 5th ring having air hole diameter d_2 in fig. 2. As a result we have obtained almost same effective area and more flattened dispersion curve but using lower pitch in Fig. 1 than Fig. 2.

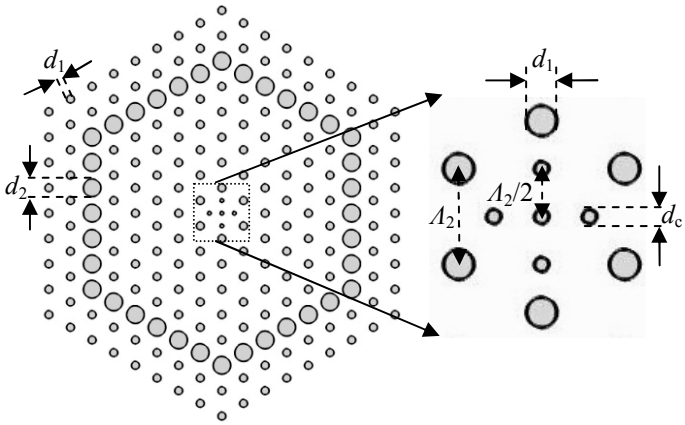

Fig. 2. Design of MAC-PCF-2.

IV. Simulation Results

Fig. 3 shows the optical field distribution for both x and y polarization at 1550 nm wavelength of MAC-PCF-1 and MAC-PCF-2. It is seen that the optical field is well confined to the outer side of the core due to the presence of air holes in the core region which increases the effective area.

Fig.4 shows the wavelength dependence of dispersion variation of the proposed two designs for y-polarized mode respectively with optimum design parameters. In MAC-PCF-1, we set pitch, Λ as 3μm, d_c=0.225 μm and d_1=0.5025 μm, d_2 = 1.35 μm. But in MAC-PCF-2, we set pitch, Λ as 2.5μm, d_c=0.1875 μm and d_1=0.39375 μm, d_2 = 0.875 μm. In Fig. 3,

MAC-PCF-1 shows almost flattened dispersion for y-polarization from 1500 nm to 1700 nm wavelength but MAC-PCF-2 shows more flattened dispersion than MAC-PCF-1 for y-polarization from 1300 nm to 1650 nm wavelength.

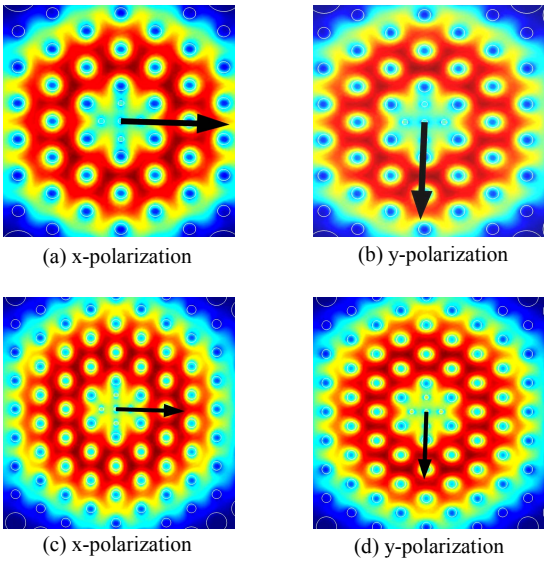

Fig. 3. Optical field distribution at 1550 nm wavelength of MAC-PCF-1 (a) &(b) and MAC-PCF-2 (c) & (d)

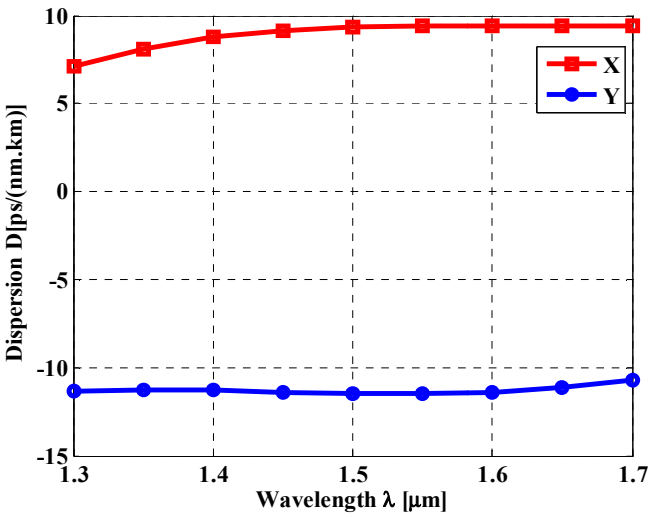

Fig. 4. Dispersion for optimum parameters of MAC-PCF-1 and MAC-PCF-2.

Fig 5(a) and 5(b) show the Effect on dispersion of pitch *Λ* variation in MAC-PCF-1 and MAC-PCF-2. The MAC-PCF-1 and MAC-PCF-2 show dispersion variation of 2.32 and 0.3537 ps/(nm.km) respectively from 1300 nm to 1650 nm wavelength.

The effective area or simply the effective area is the area where the beam intensity drops to 13.5% of the maximum value and the diameter of which is called the mode field diameter (MFD). Fig. 6 shows wavelength dependence of effective area of MAC-PCF-1 and MAC-PCF-2. We have obtained 82.88 μm^2 in MAC-PCF-1 and 83.45 μm^2 in MAC-PCF-2 at 1550 nm wavelength which is very high compared to that of conventional fiber. The PCFs with flattened dispersion and relatively high effective area would be useful to support broadband optical transmission and also in wavelength division multiplexing systems. Fig 7(a) and 7(b) also show the effect on effective area of pitch *Λ* variation in MAC-PCF-1 and MAC-PCF-2.

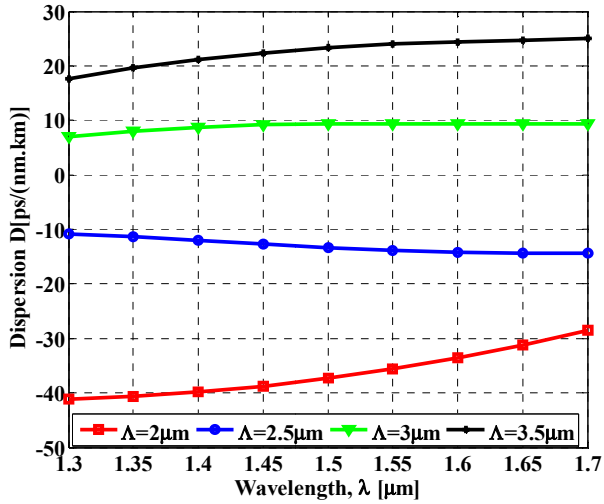

Fig. 5(a). Effect of dispersion of pitch *Λ* variation in MAC-PCF-1.

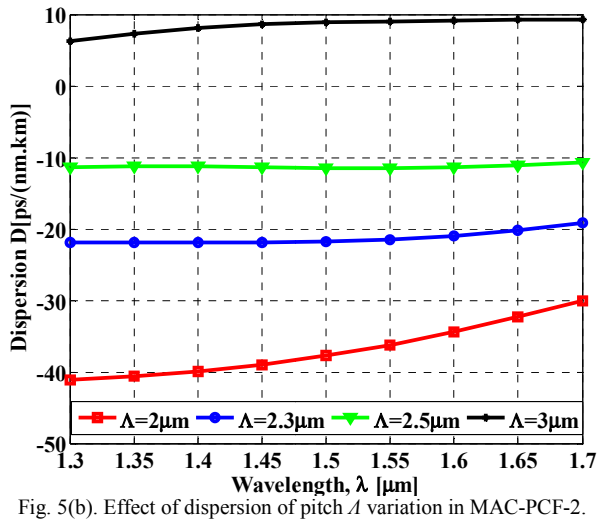

Fig. 5(b). Effect of dispersion of pitch *Λ* variation in MAC-PCF-2.

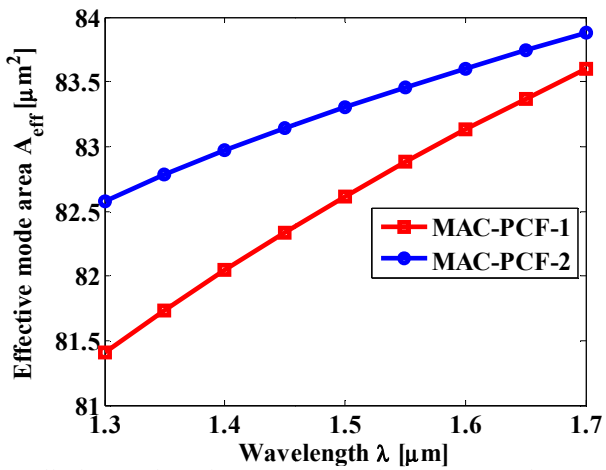

Fig. 6. Effective area for optimum parameters of MAC-PCF-1 and MAC-PCF-2.

One can observe from Fig. 5(a) & 5(b) and Fig. 7(a) & 7(b) that the flattened dispersion curve cannot be obtained for large effective area.

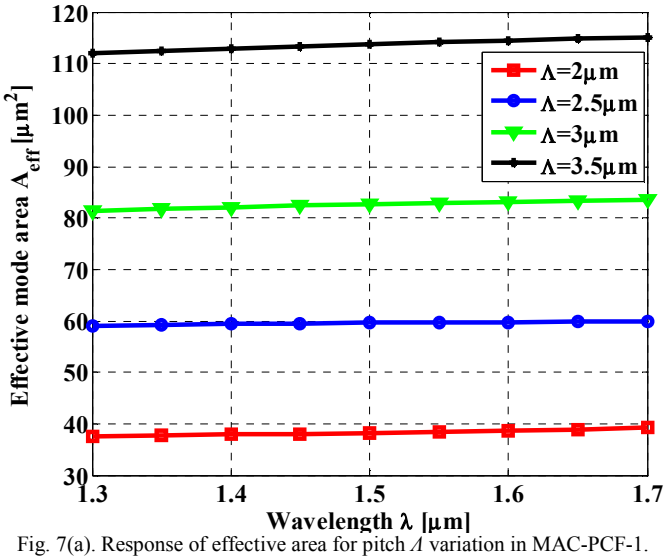

Fig. 7(a). Response of effective area for pitch *Λ* variation in MAC-PCF-1.

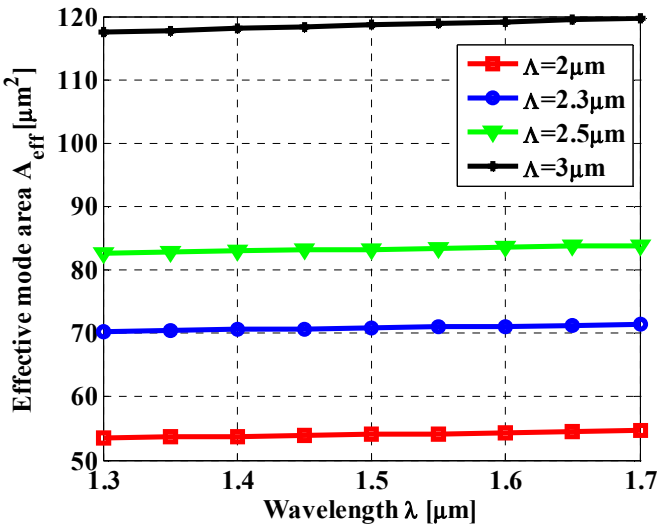

Fig. 7(b). Response of effective area for pitch *Λ* variation in MAC-PCF-2.

The nonlinear coefficient of PCFs depends on the value of the nonlinear refractive index and the effective area of the PCF. A lower value of the effective area gives a higher nonlinear coefficient and vice-versa as the value of n_2 is constant for silica PCFs. One can see from Fig.8 the MAC-PCF-2 has very low nonlinear coefficient than MAC-PCF-1. The MAC-PCF-2 design shows maximum effective area at wavelength 1550 nm than MAC-PCF-1.

The splice loss is a very important design consideration for single mode fibers. When coupling two similar fibers or a PCF with a single mode fiber (SMF) using the splicing techniques, a mismatch occurs due to the dissimilar MFD or geometrical misalignments during the fusion process that leads losses known as the splice loss. We have obtained 0.0031 dB in MAC-PCF-1 and 0.0040 dB in MAC-PCF-2 at 1550 nm wavelength in Fig. 9. By controlling the splice loss of the fiber, it will be of great use in these telecommunication applications.

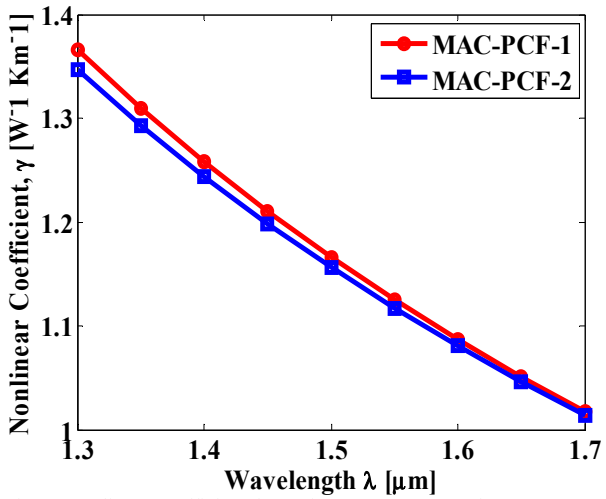

Fig. 8. Nonlinear coefficient for optimum parameters of MAC-PCF-1 and MAC-PCF-2.

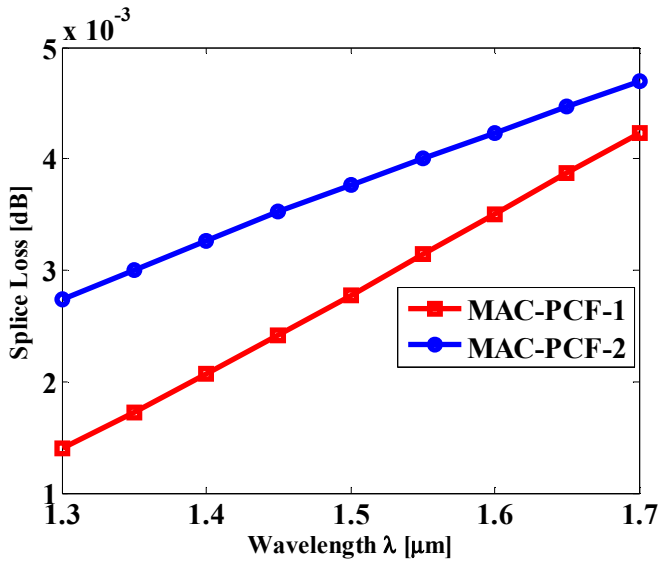

Fig.9. Splice loss for optimum parameters of MAC-PCF-1 and MAC-PCF-2.

V. COMPARATIVE STUDY

Finally a comparison is given in table I between properties of the designed PCFs and existing PCFs. It is clear from table that the four-ring photonic crystal fiber (PCF) structure addressed in [12] has low variation in dispersion curve over the telecommunication band but area is too low. Our proposed designs are better than four-ring (PCF) structure [12]. Our effective area is not so high than DF-PCF [2] but they mention about their dispersion variation only for 1.53μm to 1.57 μm and high splice loss. The large effective mode area microstructure optical fiber [7] has better effective area than ours but the splice losses of our designs are better than the microstructure optical fiber [7]. At the last though the large mode area (PCF) [13] has low dispersion variation but their area is poor and there is nothing about splice loss.

TABLE I. COMPARISON OF PROPOSED PCF DESIGN WITH THE EXISTING PCF.

PCFs	effective area in μm^2	D(Λ) ps/(nm.km)	Dispersion variation ps/(nm.km)	Splice loss dB
Ref [2]	80	4.7	<0.8 in 1.53μm to 1.57 μm	1.6
Ref [7]	122	-27.2	0.6 in 1.4μm to 1.7μm	0.19
Ref [12]	13.2	-	±0.25 in 1.295μm to 1.725 μm	-
Ref [13]	20.05	38.4	1.75 in 1.53μm to 1.57 μm	-
MAC-PCF-1	**82.88**	**9.18**	**2.32 in 1.3μm to 1.7 μm**	**0.0031**
MAC-PCF-2	**83.45**	**-11.50**	**0.3537 in 1.3μm to 1.7 μm**	**0.0040**

VI. CONCLUSION

In this paper, light guiding properties of PCF have been investigated based on FEM method with PML boundary for telecommunication and wavelength-division multiplexed (WDM) communication systems. The design of air hole(s) in the core of PCF which carrying flattened dispersion in the telecommunication band is investigated. This design offers large mode area with low splice loss. This fiber is easy to fabricate due to its hexagonal design. The proposed MAC-PCF-2 offers very low dispersion variation 0.3537 ps/(nm.km) for 1300nm to 1700nm wavelength and MAC-PCF-1 offers very low splice loss of 0.0031dB in 1550nm wavelength. So both PCFs can be used for specific applications.

REFERENCENS

[1] J. C. Knight, "Photonic crystal fibers," Nature 424, pp. 847-851, 2003.

[2] T. Matsui, J. Zhou, K. Nakajima and I. Sankawa, "Dispersion-flattened Photonic Crystal Fiber with Large Effective area and Low Confinement Loss," Journal of Lightwave Technology, Vol. 23, No. 12, pp. 4178-4183, Dec 2005.

[3] J. Broeng, D. Mogilevstev, S. E. Barkou, and A. Bjarklev, "Photonic crystal fibers: A new class of optical waveguides," Optical Fiber Technology, vol. 5, pp. 305–330, 1999.

[4] M. A. Islam, M. S. Alam, "Bend-insensitive single mode photonic crystal fiber with ultra large effective area for dual applications," Optical Engineering, Vol. 52(5), pp. 050501-1–050501-3, May 2013.

[5] P. Russell, "Photonic crystal fibers," Science 299(5605), 358 – 362(2003).

[6] M. Napierała, E. B. Pawlik, T. Nasilowski, P. Mergo, F. Berghmans, H.Thienpont, "Photonic Crystal Fiber With Large Mode Area and Characteristic Bending Properties," IEEE Photonics Technology Letters, Vol. 24, No. 16, August 15, 2012.

[7] S. M. A. Razzak, Y. Namihira, "Theoretical design of a large effective mode area microstructure optical fiber," Optica Applicata, Vol. XL, No. 3, 2010.

[8] Z. Jian, K. Tajima, K. Nakajima, K. Kurokawa, C. Fukai, T. Matsui, I. Sankawa, "Progress on low loss photonic crystal fibers," Optical Fiber Technology 11 (2), pp. 101–110, 2005.

[9] G. Thavasi Raja and S. Kumar Varshney, "Extremely Large Mode-Area Bent Hybrid Leakage Channel Fibers for Lasing Applications," IEEE Journal of selected topics in Quantum Electronics, Vol. 20, No. 5, September/October 2014.

[10] T. Okuno, H. Hatayama, K. Soma, T. Sasaki, M. Onishi, and M. Shigematsu, "Negative dispersion-flattened fiber suitable for 10 Gb/s directly-modulated signal transmission in whole telecommunication band," Electronics Letters, vol. 40, no. 12, pp. 723–724, Jun. 2004

[11] S. Priyambada, Dr. D. K. Singh, "Analysis of Effective Area and Splicing Loss Behavior of Square and Hexagonal Phtonic Crystal Fiber," International Journal of Scientific and Research Publications, Volume 3, Issue 5, May 2013

[12] T. Wu, C. Chao, "A novel ultra flattened dispersion photonic crystal fiber," IEEE Photonics Technology Letters, vol. 17, pp. 67-69, 2005.

[13] M. Pourmahayabadi and S. M. Nejad, "Design of a Large Mode Area Photonic Crystal Fiber with Flattened Dispersion and Low Confinement Loss," 17th Iranian Conference on Electrical Engineering 2009, Iran University of Science and Technology, Tehran, Iran, Electronics, vol.1, 12-14 May, 2009.

[14] S. M. A. Razzak, Y. Namihira and F. Begum, "Ultra-flattened dispersion photonic crystal fiber," Electronics Letters, Vol. 43, No. 11, 24th May 2007.

[15] M. Koshiba, "Full vector analysis of photonic crystal fibers using the finite element method," IEICE Trans. Electron, vol. E85-c, no. 4, pp. 881–888, Apr. 2002

[16] S. M. A. Razzak, Y. Namihira, M. A. G. Khan, F. Begum, and S. Kaijage, "Chromatic dispersion properties of a Decagonal Photonic crystal fiber", Information and communication Technology, pp. 159-162, 2007.

[17] G. Agrawal, Nonlinear Fiber Optics, 3rd Edition, Academic Press, 2001, pp. 5–10.

Outage Capacity Analysis of Cluster-based Forwarding Scheme for Body Area Network using Nano-electromagnetic Communication

Fariha Afsana* , M. R. Ahmed†, S. A. Mamun ‡ and M. S. Kaiser §
Institute of Information Technology*‡§
Jahangirnagar University, Dhaka-1342, Bangladesh
Military Technological College, Muscat, Oman†
Email: afsana.fariha@gmail.com*, rais80@yahoo.com†, {sam‡, kaiser§}@juniv.edu

***Abstract*—The emergence of nano-electromagnetic communication becomes appealing for potential applications in nano-scale Body Area Network (BAN). In this work a new energy aware communication model for nano-electromagnetic communication in Terahertz (THz) Band is developed based on clustering scheme for the performance improvement of BAN. The proposed conceptual network model is used to determine channel capacity. A closed-form expression for outage probability is also derived. The approach is extended to determine outage capacity for maintaining a constant rate with a specified outage probability. Simulation shows that in term of outage capacity, proposed scheme outperforms the random forwarding scheme.**

***Index Terms*—Nanotechnology, Body Area Network, Cluster, Terahertz, Outage Capacity.**

I. Introduction

Nanotechnology emerges as a promising paradigm to manupulate matter at a subatomic or nanometer level. At this level, the most basic functional unit is nano-machine which is capable of performing tasks like computing, storing, sensing or actuation. Typically such nano-machines are integrated devices around 10-100 μm^2 in size. Based on applications, multitudes of different nano-devices are used [1]. Interconnected nano-machines form nano network and execute collaborative tasks in a distributed manner. Existing electronic devices are scaled down from micro to nano domain in top-down approach. In bottom-up approach, molecular components are used to realize nano-machines. The bio-hybrid approach develops nano-machine by using biological elements as patterns to be replicated with systhesized component.

In recent years, the breadth of potential applications have been expanded tremendously with the advancement of nanotechnology. First, in the biomedical domain, nanomaterials are currently used in human body to monitor glucose, sodium and cholesterol, i.e. , in health monitoring, to support immune system, drug delivery system, to detect presence of infectious agents or to identify specific types of cancer [2]. Another domain is responsible for revealing the complexity of the induced defense signaling networks of plants by deploying molecular and genomic tools, controlling biodiversity, assisting biodegradation [3]. Again, in military and defense applications, nanotechnology can be deployed in advanced nuclear, biological and chemical (NBC) defenses and sophisticated damage detection systems for surveillance etc. Finally, in industrial domain, nanomaterials can be used for self-cleaning anti-microbial textiles, manufacturing processes and quality control procedures [1][4].

To be used in multiple nano-scenarios, classical communication paradigms need to undergo a profound revision. Based on the used transmission medium, different communication techniques - acoustic, nanomechanical, molecular and electromagnetic (EM) communication paradigms are proposed in literature [5]. At nano level, acoustic communication implies the integration of ultra-sonic transducers in nanomachines and transmission of information through acoustic energy such as pressure variations [1]. Nanomechanical communication is modeled by transmitting information through hard junctions between transmitter and receiver. In molecular communication, molecules with encoded information move as carriers from transmitter nanomachine to receiver nanomachine in a bio-inspired fashion. In EM communication, novel nanomaterial based components are used to modulate and demodulate electromagnetic waves. In acoustic communication, radio frequency transceivers and acoustic transducers represent a major barrier in integration at nanoscale because of their size. The nanomechanical communication holds the drawback by requiring physical direct contact between transmitter and receiver nanomachines. Most promising approaches for nanotechnology are therefore molecular and EM communication.

Recent advancements in Terahertz (0.06 - 10 THz) Band communication has opened the door to a new generation of nano-electromagnetic communication. Network, operating in THz Band promises new solutions for vast areas of applications such as health monitoring, military biochemical weapons monitoring, agricultural plant monitoring etc. As many molecules have resonance frequencies within the THz band, THz radiation may exploit the advantage of penetration of many opaque materials and the high selectivity, enabling their detection when they are present [6].

Health care is one of the fundamental right and thus it gets more attention for the researchers to developed energy efficient, low cost, simple, scalable e-Health solution. Espe-

978-1-4673-9257-0/15/$31.00©2015 IEEE

cially due to population aging, health care has to be made affordable in the future.With the increasing demands in body-area applications, current candidate systems have difficulties in performing consumer electronic device functions and health care application at the same time. Personal health monitoring is increasingly important to detail changes of our health status. A new emerging paradigm is the use of body area network of nano sensors based on THz Band in health care application. It is important to understand the limits of EM power exposure that human body can sustain without any crucial biological damages.

An energy efficient forwarding scheme at nano level is proposed in this paper to improve the performance of body area network so that it can facilitate e-Health application. The remainder of the paper is organized as follows. Related works on existing scheme is presented in section II. System model is presented in section III. Section IV and V includes channel behaviour model and simulation results respectively. And finally the work is concluded in section VI.

II. Literature Review

It is imperative to develop new and efficient communication and networking techniques to overcome unique challenges and requirements of nanonetworks.

Interconnecting nanoscale communication networks to the wider internet extends the Internet of Things to the Internet of Nano Things (IoNT). A reference architecture of IoNT was introduced in [7]. THz Band was considered for nano electromagnetic communication. Again, major research challenges in terms of channel modeling, information modulation and protocols for nanonetworks were highlighted from the communication and information theoretic perspective. For intrabody disease detection, a wireless nanosensor network at nanoscale was proposed in [8] as an application of IoNT. From the energy efficient point of view, proposed hexagonal cell based nanosensor network was analyzed for data transmission efficiency exploiting the hybrid, direct and multi-hop methods. A new energy efficient clustering of sensor nodes in ad hoc sensor networks was presented in [9] which guaranteed the fairly uniform cluster head distribution across the network.

Electromagnetic (EM) communications among nano-devices over the THz Band was focused in [10] with a view to developing a physical channel model. Developed propagation model was used to investigate signal path loss, molecular absorption noise and channel capacity of EM network.

In [11], Wireless Nano Sensor Network (WNSN) based on electromagnetic communication in THz Band was used to develop a new routing algorithm along with an efficient MAC protocol for communication. Focusing the attention on a WNSN operating in a health monitoring scenario, network behaviour was investigated. [12] is another approach where a new communication scheme for electromagnetic WNSNs was presented to evaluate the performance in terms of information capacity for single user case as well as aggregated network capacity for multi user case. In [13], performance of multi-hop links were analyzed and SER and outage probability were approximated based on end-to-end signal-to-noise ratio (SNR).

To better characterize the performance of channel, [14] is another approach where outage capacity was maximized over cut-off fading states for wireless channels. Authors assumed that both transmitter and receiver had full channel state information (CSI).

III. System Model

A. Assumptions and network Modeling

We assume that a network of nano sensor nodes are implanted on human body to construct a body area network. We assume that all nodes are constrained in energy. The proposed system architecture is shown in fig. 1.

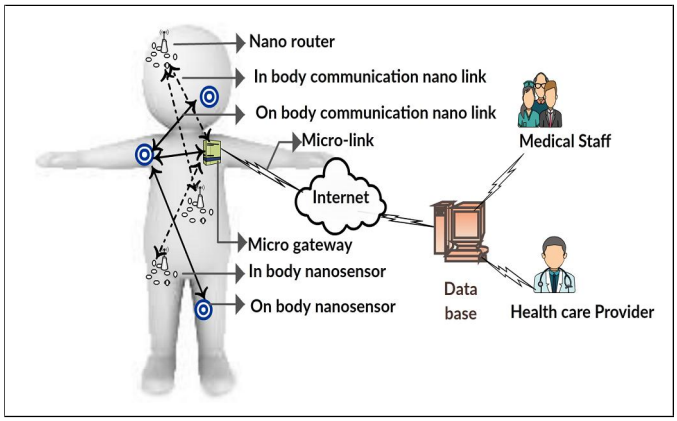

Fig. 1. A possible Scenario

The communication is considered to take place from inside of the body to the outside of the body through nano sensor nodes. Nano routers deployed in in-body communication to aggregate information coming from in-body nano sensors. Micro-gateway a wireless interface connection nano sensors to internet is used to collect data and forward them to the health care provider and medical staff.

B. Cluster Composition:

Clusters are formed to maintain efficient connectivity among deployed nano sensors. The proposed technique uses residual energy, denoted by $E_{residual}$, and packet forward ratio, denoted by PFR, to choose the cluster coordinator, CC. At first $E_{residual}$ of n nano sensors will be checked and among them m nodes having greater $E_{residual}$ from a certain threshold value will be selected as participants in cluster constellation. From m nano sensors the node with X_{max} will be selected as CC, where

$$X_i = \frac{1}{2}\left\{\frac{PFR_i}{PFR_{max}} + \frac{E_{residual_i}}{E_{max}}\right\} \qquad i = 1, 2, \cdots m. \quad (1)$$

Elected CC will broadcast short range advertisement message to remaining $(m-1)$ nano nodes. Active nano sensors having higher $RSSI$ will send join request to elected CC and register them as cluster member, CM. Similar process will be continued among rest of the nodes to form clusters. Re-clustering will be done periodically for distributing load

uniformly among all nodes. Fig. 2 is the cluster-based scenario of our proposed scheme.

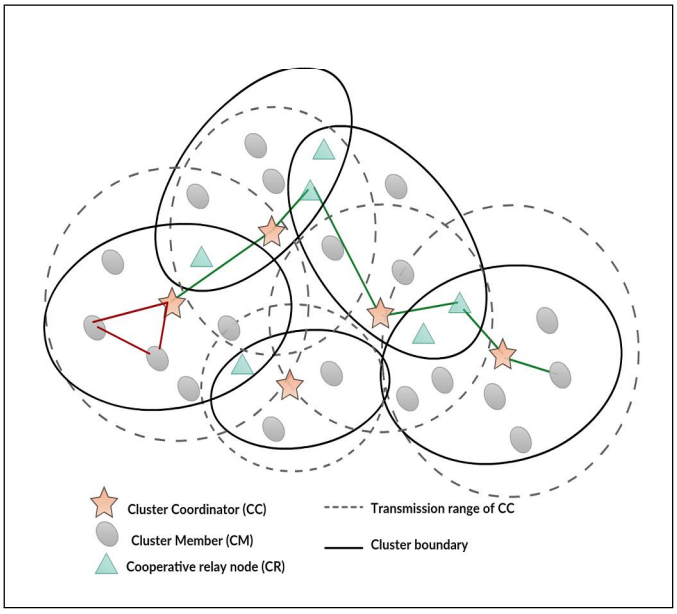

Fig. 2. A possible cluster-based Scenario

C. Communication Framework:

Communication framework is consisting of intra-cluster and inter cluster communication. Intra-cluster communication involves CC and CMs in communication. Energy efficiency is taken as a measure of extent to conduct communication. We assume that $E(d_{ik})$, $E(d_{ij})$ and $E(d_{jk})$ denote energy bit consumption through direct link ik, via link ij and jk respectively(figure 2). If equation (2) is satisfied, then data will transmitted directly to CC. Otherwise CM will use single-hop to reach CC.

$$\exists(d_{ij}, d_{jk})\{E(d_{ij}) + E(d_{jk})\} > E(d_{ik}), \tag{2}$$

where d_{ij} is distance between node i and j.

Cluster coordinators of different clusters conduct inter cluster communication. Cooperative relay nodes (CR) act as cluster gateways to conduct communication when CCs are out of transmission range of one another and operate under decode-and-forward (DF) cooperative strategy [15]. Flow chart of communication framework is depicted in fig. 3.

IV. Channel behavior Model

Nano-electromagnetic communication through human tissue suffers from frequency selective path loss and several attenuation due to shadowing and molecular absorption.

The absorption loss, A_m, is attenuation due to the molecular absorption. The type of molecular composition of the medium and concentration make it vary from medium to medium. A_m can be derived from Beer-Lambert law as [10]:

$$A_m(f, d_{i,j}) = \frac{1}{\tau} = e^{K(f)d_{i,j}}. \tag{3}$$

Here $K(f)$ stands for molecular absorption coefficient, f is frequency, τ is the transmittance of medium and $d_{i,j}$ is the distance between nanosensor i and j.

As our considered medium human body, the value of $K(f)$ for human body,$K(f)_{HB}$ is calculated as weighted average of different absorption coefficients of water molecules spreading over it in [16].

While propagating through human tissues, the expanded wave experiences attenuation named spreading loss, denoted by A_s [17].

$$A_s(f, d_{i,j}) = \left(\frac{4\pi f d_{i,j}}{c}\right)^2. \tag{4}$$

Here, c stands for speed of light in vacuum.

In THz band, transmission range of nano devices is limited due to large spreading loss. Shadowing occurs during transmission of signal between transmitter and receiver. Considering transmitted power, P_t from source, the received power, P_r at destination due to shadowing can be written as,

$$P_r(i,j) = P_t(i) G d_{i,j}^{-\eta} X_{i,j}, \tag{5}$$

where,

$X_{i,j}$	=	$10^{\frac{\xi_{i,j}}{10}}$ which represents log-normal random process representing the effect of shadowing,
$\xi_{i,j}$	=	Normal distributed random variable with zero mean and standard deviation σ
G	=	Constant representing the mean value of received power at distance $d_{i,j}$ from transmitter
η	=	Path loss exponent

Total received power in dB at destination due to molecular absorption, spreading and shadowing can be written as,

$$P_{total}(i,j) = P_r(i,j) - A_m(f, d_{i,j}) - A_s(f, d_{i,j}) \tag{6}$$

The interference power, P_I, can be expressed as,

$$P_I(k,j) = \sum_{k\epsilon(n:n\backslash i)} P_r(k,j) - A_m(f, d_{k,j}) - A_s(f, d_{k,j}) \tag{7}$$

If Signal to interference plus noise ration (SINR) of j hops are denoted by $\gamma_1, \gamma_2, \cdots, \gamma_j$ respectively, then γ_j can be computed from (8).

$$\gamma_j = \frac{P_{total}(i,j)}{P_I(k,j) + N(f, d_{k,j})}. \tag{8}$$

Here $N(f, d_{k,j})$ is Additive White Gaussian Noise.

Path loss due to shadowing in molecular level follows log-normal distribution. So, γ_j follows log-normal distribution under log normal shadowing .The probability density function (PDF) of γ_j is then given by

$$f_{\gamma_j}(\gamma) = \frac{1}{\gamma_j}\frac{\varepsilon}{\sigma\sqrt{2\pi}} exp - \left[\frac{(10\log_{10} - \mu)^2}{2\sigma^2}\right]. \tag{9}$$

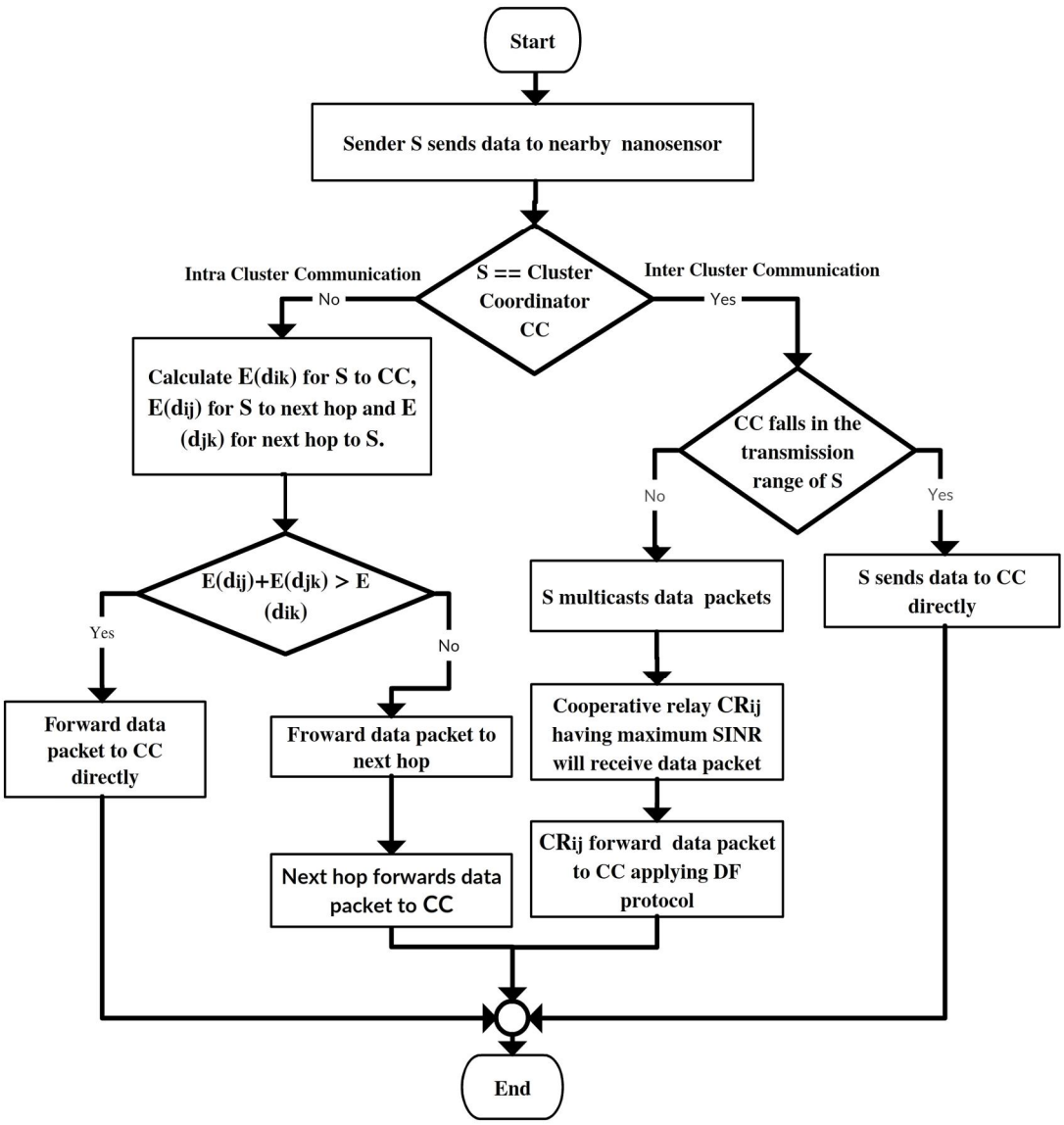

Fig. 3. A flow chart of Communication Framework

The probability that system can be in outage, denoted by P_{out}, is designed based on a certain specified threshold γ_{th} and can be expressed as [18]:

$$\begin{aligned} P_{out} &= Pr(\gamma_j < \gamma_{th}) \\ &= \int_0^{\gamma_{th}} f_{\gamma_j}(\gamma) d\gamma_j \\ &= \int_0^{\gamma_{th}} \left[\frac{1}{\gamma_j} \frac{\varepsilon}{\sigma\sqrt{2\pi}} exp - \frac{(10\log_{10}\gamma_j - \mu)^2}{2\sigma^2} \right] d\gamma_j \\ &= \int_0^{\gamma_{th}} \left[\frac{1}{\gamma_j} \frac{\varepsilon}{\sigma\sqrt{2\pi}} exp - \frac{1}{2}\Big(\frac{10\log_{10}\gamma_j - \mu}{\sigma}\Big)^2 \right] d\gamma_j \\ &= \frac{a\varepsilon}{\sigma} \times \left[1 - \frac{1}{2} erfc\Big(\frac{a\ln\gamma_{th} - b}{\sqrt{2}}\Big) \right] \end{aligned}$$

$$\text{where, } a = \frac{10\log_{10} e}{\sigma} \quad \text{and} \quad b = \frac{\mu}{\sigma}.$$

Here, (10) characterises cumulative density function (CDF) of γ_j.

It is shown in [10] that, a summation of capacity of each narrow sub-channel states THz channel capacity. Given PDF, $f_{\gamma_j}(\gamma)$, of γ_j, the capacity of channel, denoted by C, can be obtained from

$$C = \int_0^{\infty} B\log_2(1+\gamma_j) f_{\gamma_j}(\gamma) d\gamma_j \quad b/s. \tag{10}$$

Where, B is the bandwidth of each sub-channel.

Outage capacity determines the constant data rate in non-outage fading states subject to a given P_{out} and it can be

defined as:

$$C(P_{out}) = B\log_2(1+\gamma_j)(1-P_{out}). \quad (11)$$

V. Simulation Results

The performance evaluation of proposed cluster based forwarding scheme for Body Area Network using nano-electromagnetic communication is investigated in this section. The joint effects of path loss and shadowing have been considered for the simulation. In this paper, the Monte Carlo simulations have been performed for outage capacity analysis. Fig. 4 shows the BPSK and QPSK constrained outage capacity

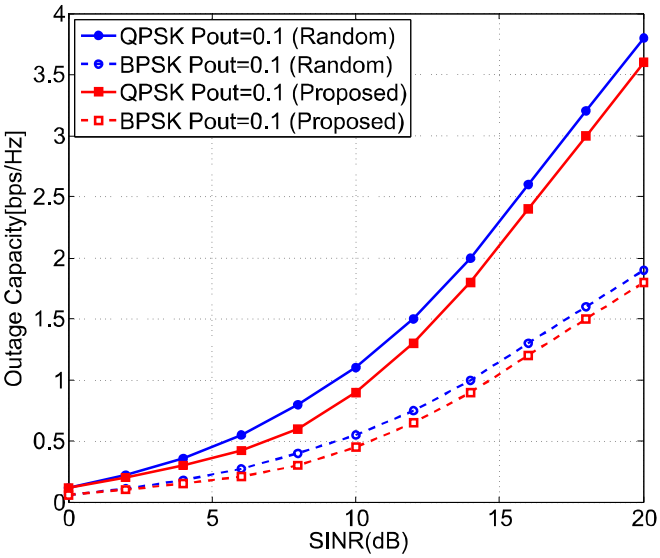

Fig. 4. Outage capacities for BPSK and QPSK

as a function of SINR in dB with 10% outage probability. For the given P_{out}, fig. 4 shows that, with BPSK values $C_{(p_{out})}$ is approximately $1.9bps/Hz$ and for QPSK it increases to $4bps/Hz$. In both cases, the proposed scheme outperforms random scheme.

Fig. 5 shows the performance comparison of outage capacity values obtained from the proposed expression and from Monte Carlo simulation. For simulating, outage capacity is considered as a function SINR for different values of outage probability. The results show that the proposed energy efficient cluster based forwarding scheme outperforms the random forwarding scheme.

VI. Conclusion

This work has proposed an energy efficient routing scheme for THz based nano-scale communication with a view to improving the performance of BAN. Link SINR has been calculated based on joint impact of shadowing, molecular absorption attenuation and spreading loss. Outage probability and outage capacity have been considered as performance metric for proposed scheme. Simulation results show that proposed scheme outperforms random forwarding scheme.

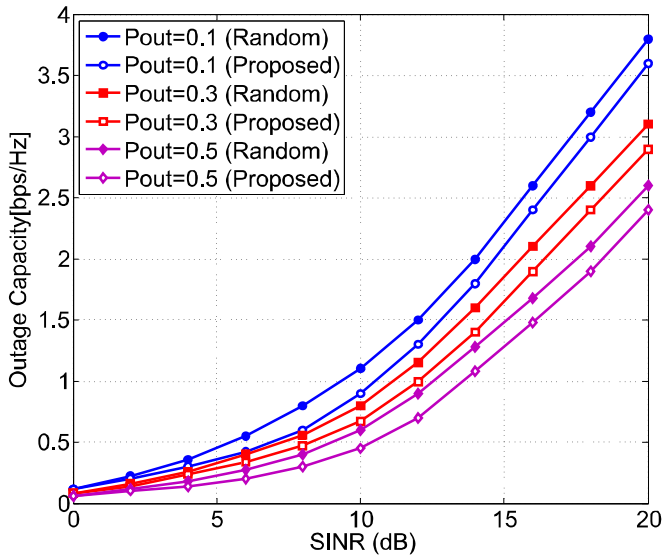

Fig. 5. Performance of random vs. proposed scheme

References

[1] I. F. Akyildiz, F. Brunetti, and C. Blázquez, "Nanonetworks: A new communication paradigm," *Comput. Netw.*, vol. 52, pp. 2260–2279, Aug. 2008.

[2] F. Dressler and F. Kargl, "Towards security in nano-communication: Challenges and opportunities," *Nano Communication Networks*, vol. 3, no. 3, pp. 151–160, 2012.

[3] S. Pudasaini, S. Shin, and K. S. Kwak, "Robust modulation technique for diffusion-based molecular communication in nanonetworks," *Computer science, Cornell University library*, pp. 1–4, Jan. 2014.

[4] N. Rikhtegar and M. Keshtgary, "Article: A brief survey on molecular and electromagnetic communications in nano-networks," *International Journal of Computer Applications*, vol. 79, pp. 16–28, October 2013.

[5] I. F. Akyildiz, J. M. Jornet, and C. Han, "Terahertz band: Next frontier for wireless communications," *Physical Communication*, vol. 12, pp. 16–32, 2014.

[6] A. Moldovan, M. Ruder, I. Akyildiz, and W. Gerstacker, "Los and nlos channel modeling for terahertz wireless communication with scattered rays," *Globecom Workshops (GC Wkshps), 2014*, pp. 388–392, Dec 2014.

[7] I. F. Akyildiz and J. M. Jornet, "The internet of nano-things," *Wireless Commun.*, vol. 17, pp. 58–63, Dec. 2010.

[8] Lee, S. Jin, et al. "Design of Wireless Nanosensor Networks for Intra-body Application," International Journal of Distributed Sensor Networks, 2015.

[9] O. Younis, S. Fahmy, "Distributed Clustering in Ad-hoc Sensor Networks: A Hybrid, Energy-Efficient Approach",Proceedings of IEEE INFOCOM, pp. 1-12, 2004.

[10] J. Jornet and I. Akyildiz, "Channel modeling and capacity analysis for electromagnetic wireless nanonetworks in the terahertz band," *Wireless Communications, IEEE Transactions on*, vol. 10, pp. 3211–3221, October 2011.

[11] G. piro, L. A. Grieco, et. al., "Nano-Sim: simulating electromagnetic-basednanonetworks in the Network Simulator 3", Proceedings of the 6th International ICST Conference on Simulation Tools and Techniques, pp. 203-210, 2013.

[12] J. M. Jornet and I. F. Akyildiz, "Information Capacity of Pulse-based Wireless Nanosensor Networks," in Proc. of the 8th Annual IEEE Communications Society Conference on Sensor, Mesh and Ad Hoc Communications and Networks (SECON), Salt Lake City, Utah, USA, June 2011.

[13] J. Cao, L. Yang, and Z. Zhong, "Performance of Multihop Wireless Links over Generalized-K Fading Channels," Vehicular Technology Conference Fall (VTC 2010-Fall), vol. 62, pp.1-5, Sept. 2010.

[14] A. Behruzifar, A. Falahati, "Maximizing Outage Capacity in Rayleigh Fading Channel ", International Journal of Computer Science and Artificial Intelligence, pp. 1-3, vol-2(1), 2012.

[15] A. Khina, Y. Kochman, G. Wornell, "Decode-and-Forward for the Gaussian Relay Channel via Standard AWGN Coding and Decoding", IEEE Information Theory Workshop, 2012.

[16] Javed, I. T., and Naqvi, I. H.," Frequency band selection and channel modeling for WNSN applications using simplenano," In Communications (ICC), 2013 IEEE International Conference , pp. 5732-5736, June 2013.

[17] K. e. e. Yang, "Terahertz communication in human skin tissues at the nano-scale for healthcare applications," *RF and Wireless Technologies for Biomedical and Healthcare Applications (IMWS-Bio), 2014 IEEE MTT-S International Microwave Workshop Series*, pp. 1–3, Dec. 2014.

[18] F. Afsana, N. Z. Zenia et al, "Multi-priority and trusted multi-path selection algorithm for ad-hoc network,"2014 International Conference on Electrical Engineering and Information & Communication Technology (ICEEICT), pp. 1-6, April 2014.

Graphene nanoribbon based Antenna For Terahertz Band Communication

Sakib Adnan[1],Md.Osman Goni[2]
Department Of Electronics & communication Engineering
Khulna University of Engineering & Technology, Khulna 9203, Bangladesh
{sakibadnan7[1], osmanhku[1]}@gmail.com

***Abstract*—Nanotechnology has enabled the use of nano-sized devices for various purposes i.e. biological, industrial, and military and especially in communication field. By using graphene the antennas can be implemented in nano scale. And the miniature antennas would work more efficiently then the conventional antennas. The miniature device can transmit data in terabyte scale. Conventional antennas would require very high frequency which is quite unfeasible. But the slower movement of electrons in graphene would enable the grapheme nano antennas to operate at a feasible frequency.[1][2].In this paper we designed, Graphene nano ribbon based antenna that would operate in terahertz band and investigatedits radiation characteristics in the 2.45-2.98 THz band. The proposed antennas are also compared with the conventional antennas operating in terahertz band. The antenna is simulated by using the finite element method based simulator -CST (computer simulation technology).**

Keywords—Nanoantennas,Graphene,nanoribbon,Terahertz band ,Patch antenna.

I. INTRODUCTION

Communication among the nano scale devices is an unsolved challenge.The main obstacle to solve this problem is that when we do the miniaturization of conventional antennas that would require very high radiating frequency. This is unfeasible because the power of the nano scale devices are very low[1].Again miniaturization process of transceiver at these very high frequencies is still an unsolved problem. Moreover, intrinsic material properties of common metals remain unknown at the nano scale [7][9]. The use of nanomaterial to fabricate miniature antennas can help to overcome these limitations[2][8]. Due to micro cracks, the metallic antennas can't transmit properly in the terhertz band. And for that reason graphenenano ribbon based antennas are more efficient than the metallic antennas in nano scale. In graphene, the carrier mobility is mainly limited by the acoustic phonon scattering of the graphene lattice and it is referred to as the intrinsic carrier mobility. Graphene offers a new approach to THz communications because of its ability to support the propagation of Surface- Plasmon Polariton (SPP) waves in the terahertz frequency band[17][18] .In this paper we discuss about the designing process of the GNR based antennas and the radiation characteristics of these antennas in terahertz band.

II. NANO ANTENNAS

Nano systems cannot be accomplished by simply decreasing the length of these metal antennas mainly because that could enforce the use of extremely high resonant frequencies within the optical array. The possibility regarding nano networks could be affected in the event that this approach ended up used because of:

• The very low limited power used in this Nano systems.

• The low electron mobility in metals where Nano scale structure are considered.

These problems occur at nano transceivers to operate at such a high frequency [4].

III. GRAPHENE BASED NANO-ANTENNA THEORY

Graphene is the building material of carbon nano tubes (1991) and grapheme nano ribbons (2004)[3].

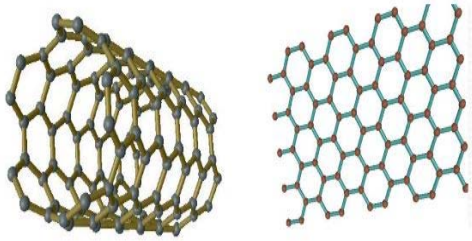

Figure 1. Carbon Nano tube (left), graphene Nano ribbon (right)

The two main important theories that are important for graphene based Nano antenna. First one is that nano patch antennas can be manufactured by graphene. And the second one is that there are several quantum effects that alter the propagation of electromagnetic waves in grapheme[3].

Initial resonant frequency along with the feedback resistance connected with graphene-based nano-patch and nano-dipole antennas acquired seeing that perform on the antenna size, edge geometry and strength[5]. Some sort of GNR can be used for any nano-patch antenna the 2-D antenna whilst CNT employed for the nano-dipole antenna virtually the 1-D antenna. New atomically accurate types will be achievable in the near future[6].

IV. ANTENNA DESIGN EQUATION AND SIMULATION TOOL

A. Microstrip Rectengular Patch antenna at 2.6 THz:

To simulate the graphene based antenna we at first design a micro strip patch antenna has resonant frequency of 2.6THz.

978-1-4673-9257-0/15/$31.00 ©2015 IEEE

The length and width of the antenna depends on the following equations [10] given below:

Antenna length and widthfor rectangular patch antenna,

$$L = \frac{c}{2f_r}\left(\frac{1}{\sqrt{\varepsilon}}\right) \quad (1)$$

Where, f_r=resonance frequency

The width of the patch antenna,

$$W = \frac{c}{2f_r}\sqrt{\frac{1}{\varepsilon+1}} \quad (2)$$

The design specification we followed to design the patch antenna is given below:

From eq. (1) and (2) by putting, frequency f_r =2.6 THz, permittivity, ε =2.3 and c=3×10^8 m/s we get, length, L= 11µm and width, W =14.76µm approximately. The rest of the measurement parameters are found from Figure.2they are given below at Table. I.

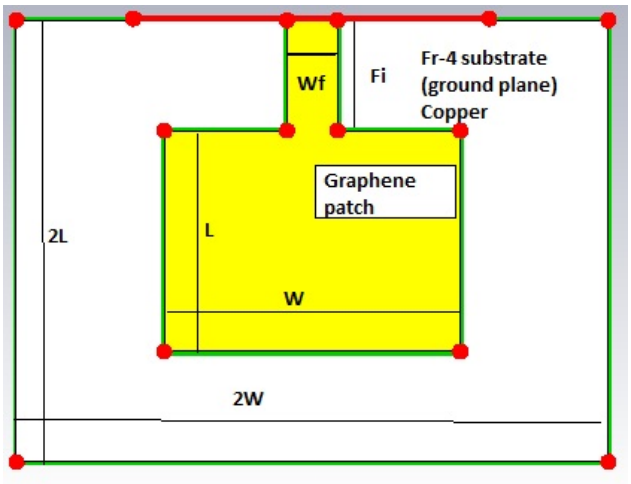

Figure 2.The model followed for designing rectangular patch antenna

B. Circular patch antenna at 2.6 THz

Circular patch antenna consists of a single circular metallic patch. But here we used graphene patch instead. The radius of the patch can be calculated from the empirical formula [10]

Patch radius

$$a = \frac{F}{\sqrt{\{1+\frac{2\times h}{\pi\varepsilon F}[\ln(\frac{\pi F}{2h})+1.7726]\}}} \quad (3)$$

Where h is the thickness, ε is the dielectric constant of the substrate material and F is related by the following equation:

$$F = \frac{8.791\times10^9}{f_r\sqrt{\varepsilon_r}} \quad (4)$$

Here a circular shapedmicro strip patch antenna is designed at resonant frequency of 2.6 THz. The proposed antenna is constructed using single circular patch of radius 11.26 □m.The proposed antenna shape is shown in Figure.3. Thesubstrate of thickness 1.305µm is used on which the structure is mounted. Dielectric constant is chosen 2.3 while the loss tangent is 0.025.The opposite side of the substrate contains the copper plate that act as the reflecting ground plane. The graphene is used as the radiating material. The thickness of both the radiator and ground plane are 0.0489 µm.The substrate we used is square of dimension 29.34 µm.Co-axial feed is used to excite the antenna.

C. Simulation tool

There are different types of simulation tool. But the most important problem is that the graphene simulator which work on mainly on the theory of Density functional theory, Classical potentials, or Extended Huckle theory they are not electromagnetic field solver. So we focus on the EM field solver tools or antenna simulation tools. These tools actually analysis high frequency devices. But the disadvantage of these types of simulator is this type of simulator does not have any model for graphene [3].

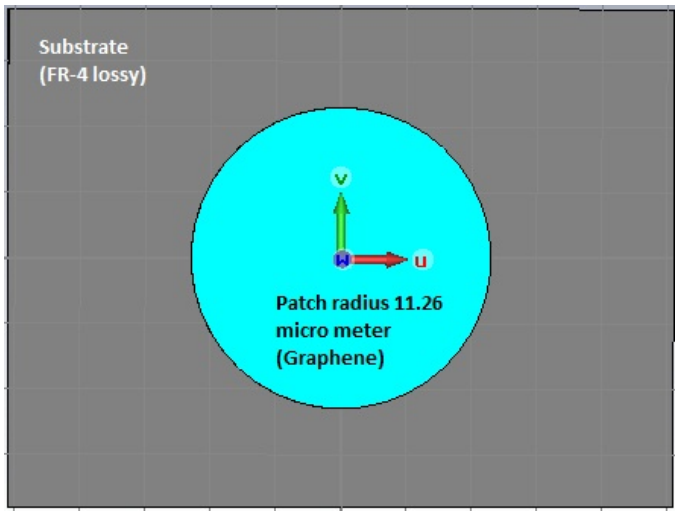

Figure 3.The model followed for designing micro strip circular patch antenna

D. Designing Graphene material for Graphene patch

Because of the absent of graphene model we followed two models to design and simulate graphene based nano antenna on this type of simulator. The models are complex permittivity model which accounts for intraband and interband transitions of electrons [11].And the second model is Drude approximation which only accounts for intraband transitions of electrons [12]. So for using graphene patch antenna we have at first designed graphene material. First, we considered the complex conductivity model by using the numerical values. CST simulates the structures which have length, width and thickness. But graphene is an one atom thick material. So for simulating graphene based antennas we make the thickness of the structures close to zero. [3].

E. Antenna design(Rectengular Patch)

The graphene nano ribbon based microstrip patch antenna is designed which has dimension in order of few micrometers. Conventionally the micro strip patch antenna consists of a

radiating patch where graphene is used as the material by editing the conductive and dispersion parameters of the drude material. The patch and the ground plane is separated by a thin dielectric substrate. We used the rectangular shape of the patch for ease in the analysis procedure. As indicated in Fig.2, the graphene nano ribbon is used as the patch where the patch thickness is much smaller than the wavelength. The radiating patch and ground plane is separated by a 1.305 µm thin substrate.

TABLE I. GNR BASED TERAHERTZ RECTANGULAR PATCH ANTENNA DESIGN PARAMETER[16]

Parameter	Description of the parameters		
	Symbol	***Value***	***Unit***
Patch length & width	L×W	11×14.76	μm^2
Resonant frequency	F	2.6	THz
Substrate length,width and thickness	2×(L×W×h)	2×(11×14.76×1.305)	μm^3
Dielectric constant	ε_r	2.3	-

The circular patch and the ground plane isalso separated by a thin dielectric substrate. We used the circular patch for comparing the performance characteristics with the rectangular patch antenna. Also the shape of the patch gives ease in the analysis procedure. As indicated in Figure. 3, the graphene nano ribbon is used as the patch where the patch thickness is much smaller than the wavelength. The radiating patch and ground plane is also separated by a 1.305 µm thin substrate.

TABLE II. GNR BASED TERAHERTZ CIRCULAR PATCH ANTENNA DESIGN PARAMETER[16]

Parameter	Description of the parameters		
	Symbol	***Value***	***Unit***
Patch area	$A=\pi r^2$	$\pi\times11.26^2$	μm^2
Resonant frequency	F	2.6	THz
Substrate length,width and thickness	2×(A×h)	$2\times\pi\times11.26^2\times1.305$)	μm^3
Dielectric constant	ε_r	2.3	-

V. SIMULATION AND EXPERIMENTAL RESULT

A. Simulation Results

The designed antenna is resonant at 2.6THz. The excitation signal is supplied by a 50Ω source. The simulation results mainly consist of the return loss, the directivity, and gain and radiation pattern of the patch antenna.

B. Return Loss,gain and Voltage standing wave ratio

The proposed rectangular patch antenna is designed and its radiation characteristics are investigated in the band of 2.45-2.98 THz, using the CST simulation tool. We have measured the return loss (S_{11}) and the voltage standing wave ratio for the patch antenna from Figure.4 & Figure5 it can be observed that the return loss at the resonant frequency is -15.179 dB and the voltage standing wave ratio at the resonant frequency is 1.421.

The proposed circular patch antenna is designed and its radiation characteristics are investigated in the band of 2.45-2.98 THz, using the CST simulation tool

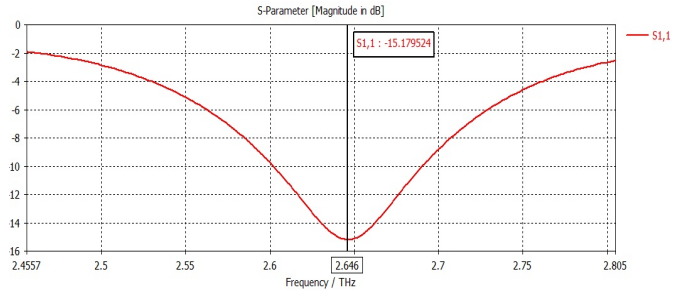

Figure 4.Return Loss for rectangular patch antenna

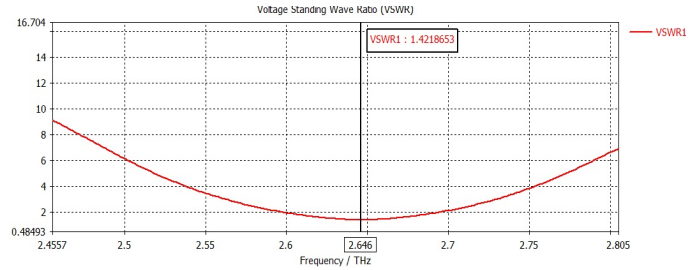

Figure 5.Voltage standing wave ratio for rectangular patch antenna

We have measured the return loss (S_{11}) and the voltage standing wave ratio for the patch antenna. From Figure.6 and Figure.7 can be observed that the return loss at the resonant frequency is -14.82 dB and the voltage standing wave ratio at the resonant frequency is 1.64.

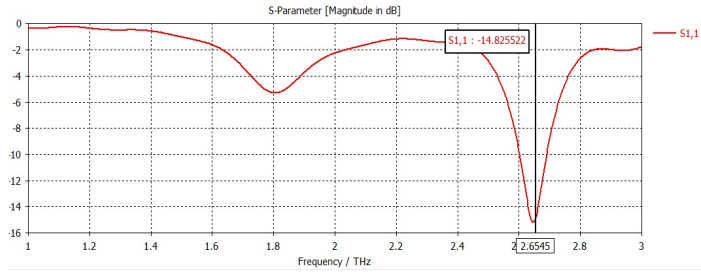

Figure 6.Return loss for circular patch antenna

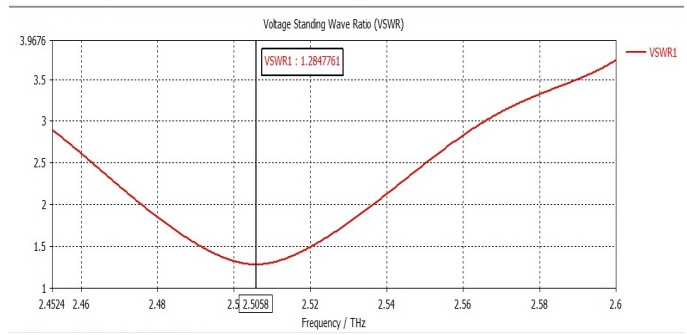

Figure 7.Voltage Standing wave ratio for circular patch antenna

The E and H planes far-field radiation patterns of the proposed rectangular and circular antennas in the range of 2.515 THz are visualized in Figure 8(a)-(b) and 9(a)-(b). The E-plane radiation plot demonstrates that the antenna has least back flap radiation in the craved band. So better front to back projection proportion is accomplished, and examined in Table III. It is seen from Figure.10, GNR based rectangular patch antenna has yielded a farfield increase of 19.8dB and the

circular patch has yielded a farfield addition of 34.3dB at 2.6 THz.

The Gain for the circular and rectangular patch antenna are shown in Figure. 10 (a)-(b) in the polar radiation pattern. For observing the gain we used linear scaling in the far field plot.

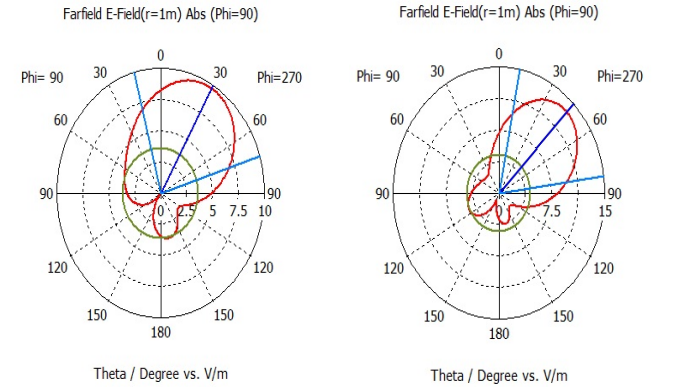

(a) (b)

Figure 8.E-plane (solid line) far field radiation patterns of the proposed antenna (a) Rectangular patch antenna (b) circular patch antenna

The visualization of far field gain as 3D radiation patterns of the proposed rectangular and circular patch antenna are shown in Figure 11(a) and 11(b) respectively.

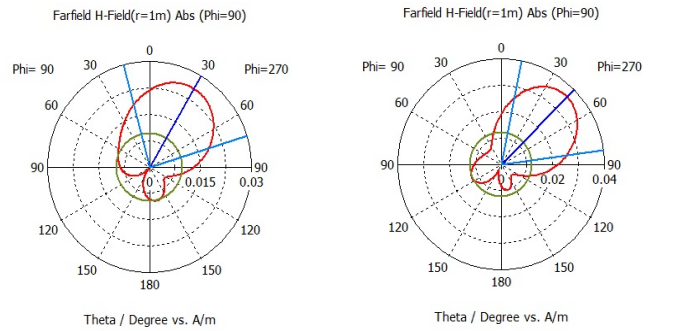

(a) (b)

Figure 9.H-plane (solid line) far field radiation patterns of the proposed antenna (a) Rectangular patch antenna (b) circular patch antenna

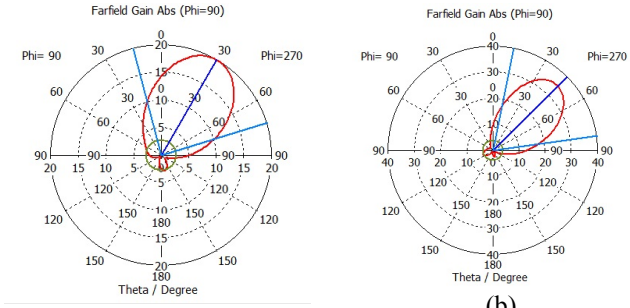

(a) (b)

Figure 10.Farfield gain (solid line) patterns of the proposed antenna (a) Rectangular patch antenna (b) circular patch antenna

The radiation qualities of the proposed antenna are contrasted and that of the already reported graphene based and ordinary antennas working in terahertz band is compressed in Table III. The proposed GNR based patch antenna is not optically transparent. So this outcome will utilize graphene based patch antenna to be utilized as a part of future THz band correspondence framework.

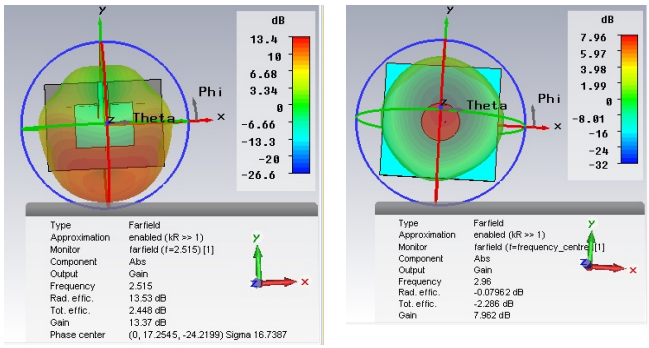

(a) (b)

Figure 11.3D radiation patterns of the proposed antenna (a) Rectangular patch antenna (b) circular patch antenna

TABLE III. PERFORMANCE COMPARISON OF THE GNR BASED ANTENNA WITH THE EXISTING ANTENNASIN THE CONTEXT OF RADIATION CHARACTERISTICS.

Parameter	GNR based antennas			Conventional antenna	
	Proposed antenna	*[16]*	*[13]*	*[14]*	*[15]*
Resonant Frequency(THz)	2.6	0.750	0.800	1.425	2.15
Gain(dB)	13.4(rectengular),7.96(circular)	5.09	-	1.65	4.97
Directivity(dB)	10.74(rectengular),9.76(circular)	5.71	0	-	-
Front To back Lobe ratio	78.3(rectangular),73.31(circular)	70.27	-	-	-

VI. CONCLUSION

In this paper, the radiation attributes of grapheme nanoribbon based nano scale strip rectangular and circular patch antenna have been explored in the 2.45-2.98 THz band. Graphene nanoribbon based terahertz patch antenna is reproduced by utilizing the finite component system based test system CST. The proposed antenna has appeared to create the top increase of 13.4dB for rectangular patch and 7.96dB for circular patch at 2.515 THz .The antenna has likewise the most astounding directivity in the desired band. The design parameters of the proposed rectangular and circular patch antenna is listed in Table I and Table II, and the proposed antenna is compared contrasted with the already reported graphene based antennas,

furthermore with ordinary patch antennas in Table III. It shows that although we used a higher resonant frequency for our proposed antenna, the gain, directivity and front to back lobe ratio have improved significantly.

REFERENCES

[1] I. F. Akyildiz and J. M. Jornet, “Electromagnetic wireless nanosensornetworks,” Nano Commun. Netw. (Elsevier) J., vol. 1, no. 1, pp. 3–19,Mar. 2010

[2] I. F. Akyildiz and J. M. Jornet,."Graphene-based Plasmonic Nano-Antenna for Terahertz Band Communication in Nanonetworks"IEEE journal

[3] Simulation of Graphene-based Nano-antennas,Nanonetworking center in catalunya ap@ac.upc.edu

[4] Z. L. Wang, “Towards self-powered nanosystems: From nanogenerators to nanopiezotronics,” Advanced Functional Materials, vol. 18, no. 22, pp. 3553–3567, 2008.

[5] A. Geim and K. Novoselov, “The rise of graphene,” Nature materials, vol. 6, no. 3, pp. 183–91, Mar. 2007.

[6] Ivan S. Maksymov , Arthur R. Davoyan , Andrey E. Miroshnichenko , Constantin Simovski ,Pavel Belov,Yuri S. Kivshar, "Multifrequency tapered plasmonic nanoantennas", Optics Communications 285 (2012) 821–824.

[7] S.P. Lacour, D. Chan, Y. Wagner, T. Li, Z. Suo, Mechanisms of reversible stretch-ability of thin metal films on elastomeric substrates, Appl. Phys. Lett. 88 (2006)204103)

[8] J. E. Burke, “Analytical study of tunable bilayered-graphene dipole antenna,” Army Armament Research, Development and Engineering Center, Dover, NJ, USA, Tech. Rep., Mar. 2011

[9] P. Burke, S. Li, and Z. Yu, “Quantitative theory of nanowire and nanotube antenna performance,” IEEE Trans. Nanotechnol., vol. 5, no. 4, pp. 314–334, July 2006

[10] Constantine A. Balanis; Antenna Theory, Analysis and Design, John Wiley & Sons Inc. 2ndedition. 1997.

[11] Gusynin, V. P., Sharapov, S. G., and Carbotte, J. P., “AC conductivity of graphene: from tight-binding model to 2+1-dimensional quantum electrodynamics,” International Journal of Modern Physics B, vol. 21, pp. 4611, 2007.

[12] Hanson, G., “Dyadic Green's Functions for an Anisotropic, Non-Local Model of Biased Graphene,” IEEE Transactions on Antennas and Propagation, vol. 56, pp. 747-757, 2008.

[13] M. Tamagnone, G.-D. Juan Sebastian, J.R. Mosig, P.-C. Julien, Reconfigurable ter-ahertz plasmonic antenna concept using a graphene stack, Appl. Phys. Lett. 101(2012) 214102.

[14] A.N.Z. Rashed, H.A. Sharshar, Optical microstrip patch antennas design andanalysis, Optik 124 (2013) 4331–4335.

[15] S. Anand, D. Sriram Kumar, R.J. Wu, M. Chavali, Analysis and design of opti-cally transparent antenna on photonic band gap structures, Optik 125 (2014)2835–2839.

[16] S. Ananda,D. Sriram Kumara, Ren Jang Wub, Murthy Chavalica' Graphene nanoribbon based terahertz antenna on polyimide substrate.'Optik 125 (2014) 5546–5549

[17] G. W. Hanson, Journal of Applied Physics103, 064302 (2008).

[18] .M. Jablan, H. Buljan, and M. Solja˘ci´c, Phys. Rev. B80, 245435 (2009).

Optimization of Indium Gallium Nitride Quantum Dots for Absorbing Light from Solar Spectra

Sadia Sultana
Department of APECE
University of Chittagong
Chittagong, Bangladesh
Sadiasultana012@gmail.com

Md. Shah Alam
Department of APECE
University of Chittagong
Chittagong, Bangladesh
Shah.alam@cu.ac.bd

***Abstract*— Use of renewable energy is the key to produce electricity from limited resources. Solar cells appear as promising candidates for this purpose. Research on third generation quantum dot solar cells have drawn much attention. Solar cells made of wide bandgap materials that utilize quantum dots have the potentials for being ideal solar cells of future. Quantum dots have a tunable bandgap, so they can be designed to absorb light from the entire solar spectra. Proper tuning of the quantum dots in the absorber layer is the key factor for absorbing solar photons. Here we have optimized Indium Gallium Nitride quantum dots for absorbing photons from most of the solar spectra. It covers the entire range of visible light along with a significant portion from ultraviolet (UV) and Infrared (IR) light . In this theoretical approach, the bandgap of Indium Gallium Nitride and the radii of the quantum dots were varied throughout the simulation. At an optimal mole fraction of Indium & Gallium, we tuned the quantum dots to absorb wavelengths from 142 nm to 1565 nm.**

Keywords—Quantum dots; tuning; intermediate band solar cells; solar spectra; Brus Equation.

I. INTRODUCTION

In solar cells, atomic level conversion of light into electricity takes place in two steps- 1) Atoms of solar cells get hit by the photons and absorb the energy transferred from the photon 2) This absorbed energy is used to free electrons. These free electrons produce electric current when they are driven in an orderly way. Light is absorbed by a semiconductor material producing an electron-hole pair known as exciton. This pair is separated by an internal electric field. It results in flow of electrons and holes. This is how and electric current is produced. In case of conventional silicon based solar cells the efficiency is limited to 30%. They have limited operation range because they can work within a limited range of solar spectra that includes visible light only. Photons only with energies higher than the bandgap of the material can free electrons and contribute to current. Those with lower energies cannot contribute to produce electricity [1], [2]. Solar spectra consists of 3 to 5% Ultraviolet (wavelength < 400 nm) , 42 to 43% Visible (400-700 nm) and 52 to 55% Infrared (wavelength > 700) light (Fig. 1) . So if the Infrared (IR) and Ultraviolet (UV) range are also utilized for energy harvesting, more of the solar energy will come into use. A solution to this problem is the intermediate band (IB) solar cell. Intermediate bands are formed by addition of a narrow band of states in the middle of the band gap of a photovoltaic material .

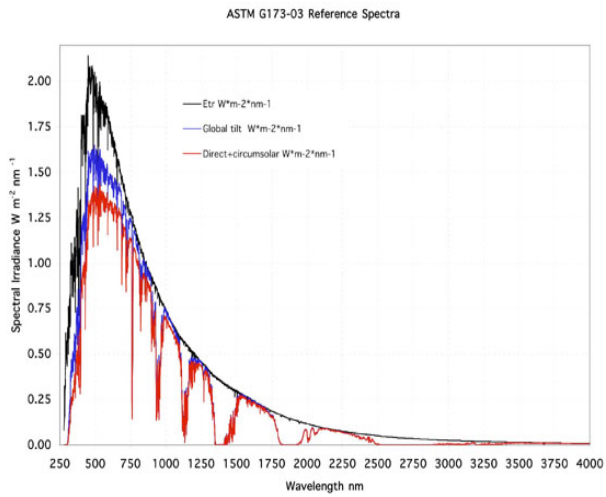

Fig. 1. AM 1.5 solar spectra [22], [23]

Electrons can jump from valence band to intermediate band being excited by a low energy photon, then jump to conduction band by another low energy photon. Thus photons with lower energies are also utilized. This can be achieved by insertion of Quantum dots as the absorbing material into the bulk semiconductor. These are nano sized particles where carriers in the semiconductor are confined by potential barriers . Quantum dot solar cells promise conversion efficiency upto 86% by using multiple junctions . Quantum dots have a tunable bandgap depending on their size. So QD (Quantum Dot) solar cells can be designed to work in any part of the solar spectra. This lets the whole spectra to be utilized [3]-[10] . Gallium Nitride (GaN) based solar cells with Indium Gallium Nitride (InGaN) quantum dots are promising candidates for ideal wide spectrum solar cells. Indium Gallium Nitride itself has a tunable bandgap which is determined by the mole fraction of Indium and Gallium present in the alloy. It can be varied from 0.7 eV to 3.42 eV corresponding to a wide range in solar spectra. This feature of InGaN along with flexible bandgap of

978-1-4673-9257-0/15/$31.00 ©2015 IEEE

quantum dots provide an excellent scope for tuning InGaN quantum dots to any desired wavelength region [11]-[14]. At a particular mole fraction of constituent elements, the radii of the embedded quantum dots in the different layers of the intrinsic region can be varied in such a way that dots in different layers absorb different wavelengths (Fig. 2).

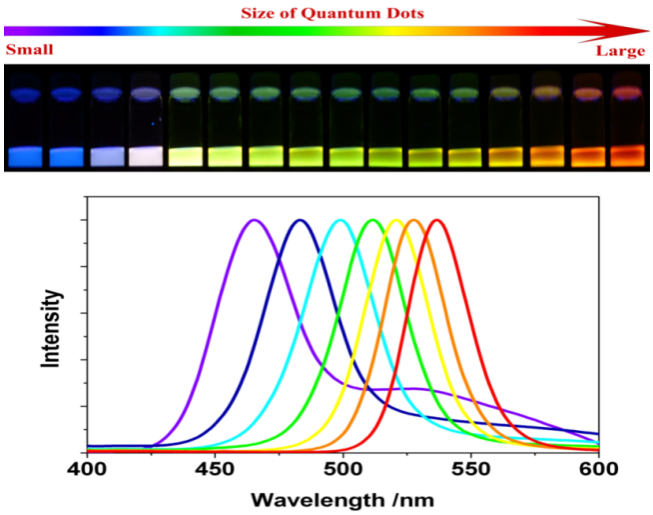

Fig. 2. Change in wavelength of quantum dots with change in size [24]

In that case, photons with energies corresponding to the quantum dots' bandgap energies will be absorbed by that layer. For designing such an efficient wide spectrum QD solar cell, the optimum bandgap of the dot material and also the required confinement radii must be known. This needs specific study on these criteria. Researchers have varied the size of Zinc Oxide (ZnO), Cadmium Selenide (CdSe), Zinc Sulphide (ZnS) and Gallium Arsenide (GaAs) QDs and calculated the resulting bandgap, emitted wavelength etc. using Brus equation which match pretty well with experimental data [15]-[18] . But no specific study on optimizing InGaN quantum dots to match the solar spectra has been reported in literature. We have varied the mole fraction of Indium (In) and Gallium (Ga) and calculated the effective bandgap of Indium Gallium Nitride. Then using the Brus equation and we have varied the size of QDs at an optimal mole fraction to absorb specific wavelength from 142 nm to 1565 nm. It covers the range of existing wavelengths of solar spectra starting from 280 nm to 1565 nm. This covers the whole range of UV and visible light from AM 1.5 solar spectra and a significant portion of IR region [23].

II. Theoretical Framework

Being a ternary compound, the bandgap of InGaN depends on the mole fractions of the constituent elements. Bandgap energy of the quantum dots depends on the effective mass of excited electrons and holes as well as the size of the dot. Absorbed wavelength can be found from the relationship between energy and wavelength (i.e. E=hc/λ). So a number of factors need to be considered to reach the optimum condition.

A. Bandgap of InGaN as a function of mole fraction

The bandgap of InGaN varies with the mole fraction of Indium (In) and Gallium (Ga) in the alloy as well as temperature. If X be the In doping relative to Ga, E_{InN} is the bandgap of Indium Nitride (InN), E_{GaN} is the bandgap of Gallium Nitride (GaN) , b is the bowing parameter of $In_xGa_{1-x}N$, then the bandgap of the alloy is given as-

$$E_{g,InGaN}(X) = XE_{InN} + (1-X)E_{GaN} - bX(1-X) \qquad (1)$$

By varying X in (1), the bandgap of InGaN can be adjusted to any desired value within 0.7 to 3.42 eV [19].

B. Brus Equation

L. E. Brus in 1984 first developed an equation for size dependence of lowest excited electronic state in case of small semiconductor crystallites [15] . With some moderations, the equation named after him is written as-

$$E(QD) = E_g(bulk) + \frac{h^2}{8R^2}\left(\frac{1}{m_e^*} + \frac{1}{m_h^*}\right) - \frac{1.786e^2}{4\pi\varepsilon_0\varepsilon_r R^2} \qquad (2)$$

Where E(QD) is the bandgap energy of quantum dot, the first term in right hand side of the equation represents the bandgap energy of bulk semiconductor, ε_0 is the permittivity of vacuum, ε_r is the relative permittivity of the semiconductor, m_e^* is the effective mass of excited electron, m_h^* is the effective mass of excited hole, R is the radius of spherical quantum dot. The second additive term in the right hand side, is dependent on inverse of square of the radius. It accounts for the additive energy due to quantum confinement. The third term in the right hand side is due to the coulombic interaction energy of exciton and is negligible for materials with high dielectric constants [16], [17]. So the overall Brus Equation to be used in this work is-

$$E(QD) = E_g(bulk) + \frac{h^2}{8R^2}\left(\frac{1}{m_e^*} + \frac{1}{m_h^*}\right) \qquad (3)$$

Varying R in (3) at a certain mole fraction, quantum dots can be tuned to absorb any specific wavelength. Quantum dot confinement region must be smaller than or comparable to their De Broglie wavelength or to the Bohr radius of excitons .

C. Calculation of electron and hole effective mass

As can be seen from (3), electron effective mass m_e^* plays an important role in determining the bandgap of the QD. It changes with varying mole fraction. Effective mass of electron in *InGaN* can be calculated using the following equation which utilizes the interpolation formula[20] , [21] –

$$m_{e,InGaN} = m_{e,GaN} + X(m_{e,InN} - m_{e,GaN}) \qquad (4)$$

The value of hole effective mass can be calculated in same way using the equation below-

$$m_{h,InGaN} = m_{h,GaN} + X(m_{h,InN} - m_{h,GaN}) \quad (5)$$

D. Condition for varying Quantum dot radius:

For the confinement effects to be prominent, the radius of the quantum dot must be kept less than the exciton Bohr radius of the quantum dot material [3]. The exciton Bohr radius of a semiconductor material can be calculated as-

$$a_B = \frac{4\pi\varepsilon_0\varepsilon_R\hbar^2}{m_{eff}q^2} \quad (6)$$

Where m_{eff} is the effective mass of the electron-hole pair, q is the charge of a carrier. If the radius of the dots exceed the exciton Bohr radius of the material, the quantum confinement effects will not hold any more and Bandgap energy of the quantum dots will not practically resemble the Brus equation. Exciton Bohr radius for InGaN is very small, it can be as small as 3 nm for less indium concentration [25] . If indium content is increased in the alloy, the exciton Bohr radius increases like 7 nm for indium concentration, X=0.75 [26]

III. PARAMETERS AND SIMULATION

Value of InN, GaN bandgap, bowing parameter of InGaN have been adapted from [12] . Interpolation formula has been used where necessary. The values of the basic parameters used in the simulation have been listed in Table I. Here, m_0 is the rest mass of an electron.

TABLE I. PARAMETER VALUES

Parameter name	Value
Bandgap of InN at 300K	0.7 eV
Bandgap of GaN (wurtzite) at 300K	3.42 eV
Bowing parameter for InGaN alloy	1.43
Electron effective mass of GaN, $m_{e,GaN}$	0.2 m_0
Hole effective mass of GaN, $m_{h,GaN}$	1.25 m_0
Electron effective mass of InN, $m_{e,InN}$	0.05 m_0
Hole effective mass of InN, $m_{h,InN}$	0.6 m_0

MATLAB version 7.10.0499 (R2010a) has been used as the simulation software throughout this work.

IV. RESULTS AND DISCUSSIONS

At first, the possible bandgaps for InGaN were calculated by varying the mole fraction of Indium, X . As can be seen from Fig. 3., it could be tuned from 3.37 eV for X = 0.01 to 0.713 eV for X = 0.99. As the mole fraction of Indium increases, the bandgap of InGaN tends to decrease because of low bandgap of InN [19].

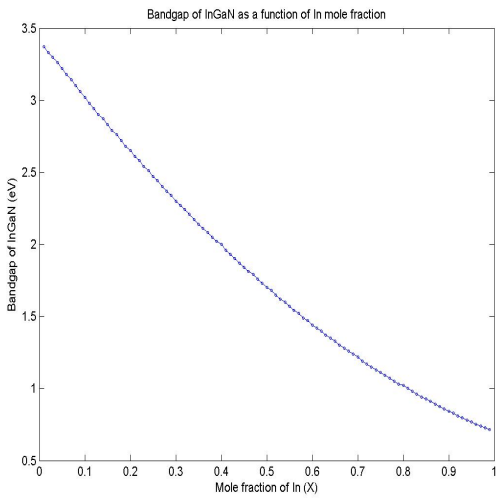

Fig. 3. Bandgap of InGaN with changing mole fraction of In

By calculating the exciton Bohr radius for various mole fraction of the constituents, it was found that as the Indium concentration in the alloy increases, exciton Bohr radius of InGan alloy increases too. Fig. 4 shows that, for X = 0.01, calculated exciton Bohr radius was 2.77 nm. The exciton Bohr radius reached its highest value of 10.75 nm for X = 0.99. This is the optimal mole fraction where the radius of the quantum dots can be varied over a wide range to cover the whole spectra. With this value of X, calculated bandgap of InGaN alloy was 0.713 eV.

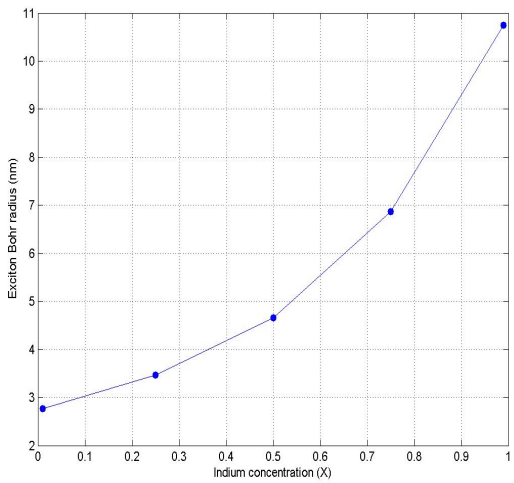

Fig. 4. Exciton Bohr radius of InGaN alloy at different In concentration

The optimum bandgap is chosen such that varying the dot size only gives an absorption range that covers as much portion as possible from UV, visible and Infrared region . For tuning the dots to absorb UV light with Indium composition X = 0.99, radius of the dots were varied from 1 nm to 1.83 nm. It gave an absorption range starting from 142 nm wavelength to 400 nm as shown in Fig. 5.

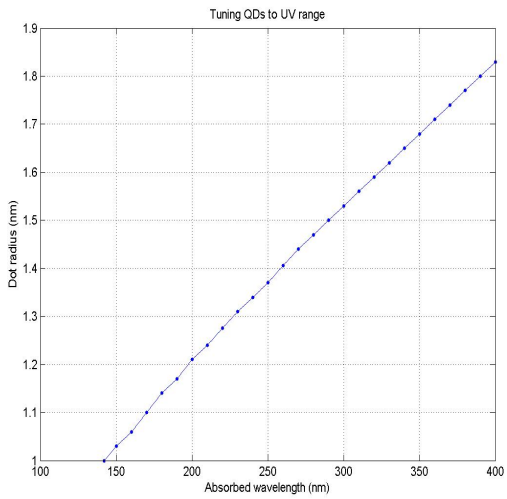

Fig. 5. Dot radius versus absorbed wavelength plot for UV region

By varying the dot radius from 1.83 nm to 2.75 nm, wavelengths from 400 to 700 nm can be absorbed which covers the whole visible range. This is shown in Fig. 6. If the dot radii are further increased, and varied from 2.75 nm to 10.05 nm, it gives an absorption range from 700 nm to 1565 nm in the Infrared region as shown in Fig. 7. Observations show that as the In mole fraction in the alloy is increased, the bandgap of the alloy gets lower. To design quantum dots for absorbing higher energy photons Indium concentration in the alloy must be reduced .

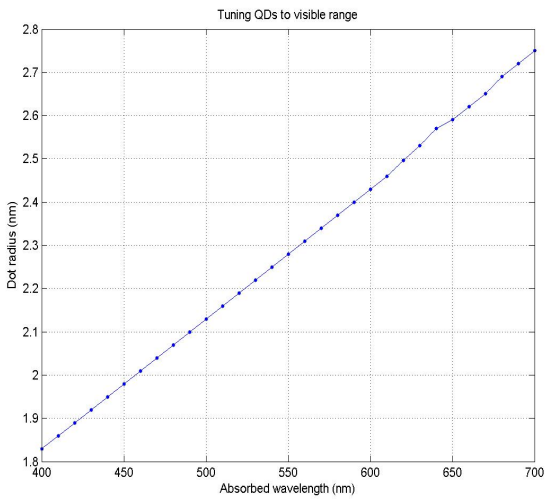

Fig. 6. Dot radius versus absorbed wavelength plot for visible region

Another thing apparent from the observation is that, smaller quantum dots with greater energy gap are able to absorb shorter wavelength photons which contain much energy. As the quantum dot radius is increased and their size gets bigger, the confinement strength gets reduced. That is why larger quantum dots have smaller bandgap energies. These quantum dots absorb photons with larger wavelengths and less energy.

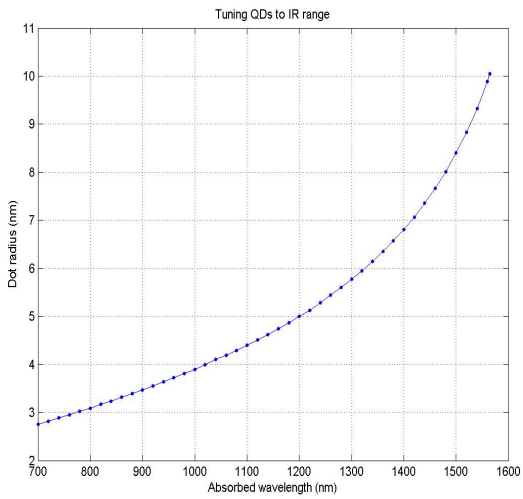

Fig. 7. Dot radius versus absorbed wavelength plot for IR region

The optimum bandgap for tuning InGaN quantum dots was found to be 0.713 eV with Indium composition X = 0.99. If the dot radius is varied from 1 nm to 10.05 nm, they can absorb wavelengths starting from 142 nm to 1565 nm which covers the whole UV and visible range along with significant portion of Infrared region of AM 1.5 solar spectra as can be seen from Fig. 8.

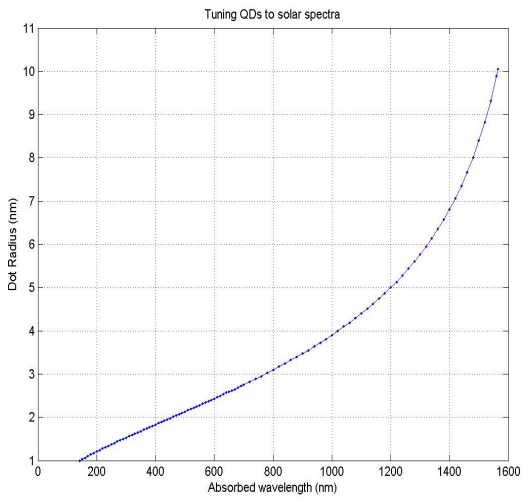

Fig. 8. Dot radius and absorption range with X = 0.99

V. CONCLUSION

InGaN quantum dots have a wide range of tunable bandgap and absorption spectra. This feature can be used to absorb almost any wavelength within the AM 1.5 solar spectra. InGaN quantum dots can be used to design an efficient wide spectrum solar cell. Solar photons over a wide range of wavelengths will be absorbed and utilized. Future work may include the investigation of the confinement effects for different shapes of InGaN quantum dots like pyramid, hexagonal, cubic etc. Effects of changing shape on the absorption spectra should also be studied.

ACKNOWLEDGMENT

We gratefully acknowledge support for this work provided by ICT Fellowship 2014-2015 under the Information and Communication Technology Division, Government of the People's Republic of Bangladesh.

REFERENCES

[1] Geoffrey A. Landis , Philip Jenkins, David Scheiman, Rayan Rafaelle, "Extended temperature solar cell technology development," in *Proc. AIAA 2nd International Energy Conversion Engineering Conference*, 2004, pp. 1-7 .

[2] International Renewable Energy Agency (irena) white paper on "Solar Photovoltaics," volume 1: power sector, 2012, pp. 1-45.

[3] Charles P. Poole Jr. and Frank J. owens, "*Introduction to nanotechnology*," Published by John Wiley & Sons, Inc., Hoboken, New Jersey (2003), pp. 226-234.

[4] A.J. Nozik, "Quantum dot solar cells," *Physica E* 14 (2002) , pp. 115-120.

[5] Dr. Dennis J. Flood, "Solar cells and quantum dots – a white paper," Natcore Technology Inc.

[6] Mohammad A. Halim, "Harnessing sun's energy with Quantum dots based next generation solar cells," in journal *Nanomaterials*, 2013, 3, issn: 2079-4991 , pp. 22-47.

[7] Brown A., Green M. , "Detailed balance limit for the series constrained two terminal tandem solar cell," *Physica E* 14 (2002), pg. : 96-100.

[8] A Luque, A Marti, A Nozik, "Solar cells based on quantum dots," *MRS bulletin*, 2007, 32:236-241.

[9] Ayman Rizk, Kazi Islam and Ammar Nayfeh , "Modeling of InAs/GaAs Quantum Dot Solar Cells," in *Proc.* 2013 *European Modelling Symposium,* 2013 issn : 978-1-4799-2578-0/13 , pp. 677-680.

[10] Boqun Dong, Christopher G. Bailey, Andrei Afanasev, Mona Zaghloul, "Modeling and Simulation of InAs/GaAs Quantum Dot Solar Cells In SILVACO TCAD," in *Proc. 40th IEEE Photovoltaic Specialists Conf.* , 2014, issn: 978-1-4799-4398-2/14 , pp. 476-478.

[11] Joshua J. Williams, April M. Jeffries, Laura Ding, Srikanth Gangam, Kunal Ghosh, Todd L. Williamson, Mariana I. Bertoni and Christiana B. Honsberg,"Structural and Optical Investigations of GaN-Si Interface for a Heterojunction Solar Cell," in *Proc. 40th IEEE Photovoltaic Specialists Conf.* , 2014, issn: 978-1-4799-4398-2/14, pp. 841-843.

[12] G.F. Brown, J.W.AgerIII, W.Walukiewicz, J. Wu, "Finite element simulations of compositionally graded InGaN solar cells," in Solar Energy Materials & SolarCells 94(2010) , Elsevier, doi:10.1016/j.solmat.2009.11.010, pp. 478-483.

[13] Nicolas Cavassilas, Fabienne Michelini and Marc Bescond, "Transport modeling of InGaN/GaN multiple quantum well solar cells," in *Proc. 40th IEEE Photovoltaic Specialists Conf.* , 2014, issn: 978-1-4799-4398-2/14, pp. 2875 – 2877.

[14] Kuang-Chung Wang, and Yuh-Renn Wu, "Transition Rate in the InGaN Quantum Dot Intermediate-Band Solar Cell," in *Proc. 38th IEEE Photovoltaic Specialists Conf.* , *2012*, issn: 978-1-4673-0066-7/12, pp. 822-825.

[15] L. E. Brus, "Electron-electron and electron-hole interactions in small semiconductor crystallites: The size dependence of the lowest excited electronic state," *J. Chem, Phys.* 80 (9), 1 May 1984, under copyright of AIP, pp. 4403-4409.

[16] Chukwuocha, E.O, Onyeaju, M.C, "Effect of Quantum Confinement on The Wavelength of CdSe, ZnS And GaAs Quantum Dots (Qds)," *International Journal of Scientific & Technology Research*, issue 7 , August 2012, issn: 2277-8616, pp. 21-24.

[17] Changiz Vatankhah, Ali Ebadi, "Quantum Size Effects on Effective Mass and Band gap of Semiconductor Quantum Dots," *Research Journal of Recent Sciences*, issn: 2277-2502 , Vol. 2(1), January (2013), pp. 21-24.

[18] Anusorn Kongkanand, Kevin Tvrdy, Kensuke Takechi, Masaru Kuno, and Prashant V. Kamat, "Quantum Dot Solar Cells. Tuning Photoresponse through Size and Shape Control of CdSe−TiO2 Architecture," *Journal of the American Chemical Society*, 2008, 130 (12), 4007-4015 DOI: 10.1021/ja0782706, pp. 908-918.

[19] R. R. Pelá et al. , "Accurate band gaps of AlGaN, InGaN, and AlInN alloys calculations based on LDA-1/2 approach", *Applied Physics Letters*, 98, 151907 (2011).

[20] Jasdeep Anand, Alexander Buccheri, Michael Gorley, Iain Weaver, "P2_12 InGaN quantum-well width w.r.t λ", *Journal of Special Topics*, Vol. 8, no 1, November 16, 2009.

[21] Ursula M. E. Christmas, A. D. Andreev, and D. A. Faux, "Calculation of electric field and optical transitions in InGaN/GaN quantum wells," *Journal of Applied Physics*, **98**, pp. 073522-1 – 073522-12. (2005)

[22] *American Society for Testing and Materials (ASTM) Terrestrial Reference Spectra for Photovoltaic Performance Evaluation*, ASTM G-173-03.

[23] Reference Solar Spectral Irradiance: Air Mass 1.5 [Online]. Available: http://rredc.nrel.gov/solar/spectra/am1.5/ (date accessed : 27-8-2015)

[24] Debasis Bera , Lei Qian, Teng-Kuan Tseng and Paul H. Holloway, "Quantum Dots and Their Multimodal Applications: A Review," in journal *Materials,* 3, pp. 2260-2345; doi:10.3390/ma3042260, 2010 .

[25] S. Amloy et al. , "Dynamic Characteristics of the exciton and the biexciton in a single InGaN quantum dot," in *Applied Physics Letters*, 101, 061910 (2012).

[26] Giovanni Giannoccaro, T. Muciaccia, Vittorio M N Passaro. "Evaluation of the Absorption Spectrum in Quantum Dots for Efficient Solar Cells," in *Proc. Fotonica AEIT Italian conference on Photonics Technologies*, 2014, pp. 1-4.

Analysis of Carrier Injection and Recombination in Modified ITO Based Organic Light Emitting Diode Using Numerical Simulation

Riku Chowdhury
Electrical & Electronic Engineering
FSET, USTC
Chittagong, Bangladesh
eeeriku@gmail.com

Md. Rashedul Haq
Electrical & Electronic Engineering
FSET, USTC
Chittagong, Bangladesh
rasahaq_17@yahoo.com

Md. Sarwar Uddin Chowdhury
Electrical & Electronic Engineering
CUET,
Chittagong, Bangladesh
sarwarcuet@gmail.com

Sukanta Paul
Computer Science & Engineering
CUET,
Chittagong, Bangladesh
skpaulustc@gmail.com

***Abstract*— Using numerical simulation, the performance of organic light emitting diode (OLED) based on modified indium tin oxide (ITO) has been investigated. The effects of ITO surface modification in energy barrier reduction at anode side which increase charge carrier injection, transport and recombination have been explained quantitatively. Calculated current balance factor from simulation results also confirmed the efficiency enhancement of bilayer OLED by the ITO work function modification technique.**

Keywords*— *indium tin oxide (ITO); hole current density; numerical simulation; current balance factor; carrier recombination

I. INTRODUCTION

As an optoelectronic device, OLED has been covered most of the area in the field of lighting and displays technologies over other existing lighting sources like light emitting diodes (LEDs) and liquid crystal displays (LCDs) because of their low turn on voltage, low input power, fast turn on response time, wide viewing angle (~180^0), thin and light weight, low cost, non-toxic materials and emitting light spectrum near to sun [1, 2]. After the demonstration of first bi-layer OLED by C. W. Tang and S. A. Vanslyke group in 1987 [3], the research on modification of OLED structures has been expanded dramatically. As a result, graded and mixed host based devices have been modeled and fabricated to improve the OLED lifetime and efficiency limitations [2, 4, 5]. However, these structures based devices increased complexity during fabrication. To overcome device fabrication complexity and increase charge injection rate into the device for improve device performance, ITO work function modification by O_2 and Cl_2 plasma treatment [6], post annealing treatments, adding buffer layer [7, 8] and UV-ozone treatments [9] are the most efficient and effective processes. Since, ITO commonly used as anode in most optoelectronic devices especially in OLEDs, hence device performance can be enhanced significantly using these ITO surface modification process which reduce the energy barrier for carriers to cross the ITO/organic interface [8].

H.-W. Lu, C.-W. Huang, P.-C. Kao, S.-Y. Chu, and Y.-D. Juang. [7] recently reported a work function modification technique of ITO by soaking in 1 wt%, 5 wt% and 10 wt% concentration of caesium fluoride (CsF) solution where the work function of ITO modified from normal work function of 4.78 eV to 4.95 eV, 5.01 eV and 5.11 eV correspondingly. They tried to explain the effects of ITO surface modification on the ITO/CsF/NPB/Alq_3/LiF/Al based bilayer OLED performance by analysis the current density- luminance - voltage (J-L-V) characteristic curves and surface morphology. However, that works unable to explain how ITO surface modification effects on the internal carrier distribution, electric field and recombination of device those are key factors for device modeling.

Motivating from this point, the effects of ITO surface modification on device J-L-V and efficiency have been explained through this numerical simulation in terms of charge carrier distribution, hole current density and carriers recombination. Moreover, the calculation of current balance factor which is proportional to the experimental quantum efficiency, able to justify this modified ITO based OLED performance. By the systematic study of the device performance of OLED, it is possible to explain some effects qualitatively. But, without numerical simulation, it is difficult to explain these effects quantitatively [10]. Numerical simulation is more viable to get any analytical results directly from the OLEDs where complicated working process and several interfaces are involved [11]. Therefore, this work led by numerical simulation which treated as powerful method to retrieve detailed information such as the charge carrier injection, distribution of electric field and recombination those are difficult to measure directly through experiments, investigate the underlying device mechanism and their amplitude which can affect the device performance.

II. ELECTRICAL MODEL

To analysis the effect of ITO work function modification on the underlying physics and performance of bi-layer OLED,

drift-diffusion electrical model has been implemented using a numerical simulator called 'SETFOS' (Semiconducting Thin Film Optics Simulation Software). Poisson equations and continuity equations as presented in "(1)," and "(2)," correspondingly considered in that electrical model to solve the electric field distribution and time evaluation of the system.

$$\frac{dE}{dx} = \frac{q}{\varepsilon\varepsilon_0}(p-n) \tag{1}$$

$$\frac{dn}{dt} = \frac{dJ_n}{qdx} - R - T \tag{2}$$

where, E is the electric field inside the OLED, q the elementary charge, □ the dielectric permittivity of the organic materials, □$_0$ the dielectric constant, p and n are the hole density and the electron density respectively, J_n the electron current density, R the recombination rate and T the trapping rate for free carriers. The carrier density distribution can be obtained by solving the drift and diffusion equation based on the Langevin recombination (R) process those are calculated using "(3)," and "(4)," respectively. The conventional electric filed dependent 'Poole-Frenkel mobility (PFM)' model as expressed in "(5)," applied for carrier mobility calculation in the device. The current balance factor (b) in "(6)," used to measure the device quantum efficiency [12] which is defined as the recombination current with the total current density.

$$J_n = qp\mu_n E + qD_n \frac{dn}{dx} \tag{3}$$

$$R = \frac{q}{\varepsilon\varepsilon_0}(\mu_p + \mu_n) \tag{4}$$

$$\mu(E) = \mu_0 \exp(\gamma * \sqrt{E}) \tag{5}$$

$$b = \frac{\int_0^L qR(x)dx}{J_T} \tag{6}$$

Here, μ_p and μ_n are the hole and electron mobility respectively, D_n the diffusion constant, $\mu(E)$ is the charge carrier mobility under electric field (E), μ_0 is the mobility under zero electric field, γ is the Poole-Frenkel field dependent factor, J_T is the total current density and L is the total device thickness.

III. Device Structure And Input Prameters For Simulation

The OLED structure as shown in "Fig. 1," used for simulation where the HOMO and LUMO levels of NPB (Alq_3) are 5.4 eV (5.7 eV) and 2.3 eV (3.0 eV) and the work function of LiF/Al is 3.0 eV [4, 7]. Before, surface modification, the usual work function of ITO is 4.78 eV which is modified after soaking in different concentration of CsF solution. The work functions of modified ITO become 4.95 eV (1 wt% CsF solution), 5.01 eV (5 wt% CsF solution) and 5.11 eV (10 wt% CsF solution). The work functions of ITO and organic materials parameters obtained from the UV- photoelectron spectrometer [7] and time of flight (TOF) measurement [13, 14] correspondingly, used as input during simulation. Considering the normal work function based ITO as reference, the effects of modified ITO work function using different concentrations of CsF solutions on hole injection efficiency, carrier recombination rates and current balance factor have been analyzed in the next section.

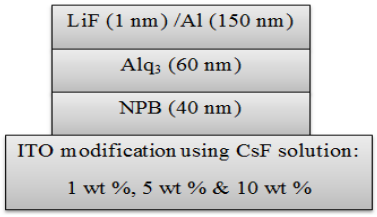

Fig. 1. Modified ITO based OLED Structure

IV. Results and Discussions

A. J-L-V Characteristics and Efficiencies

Figure 2 shows the current density-voltage (J-V) and the luminance-voltage (L-V) characteristics curves of four OLEDs where one OLED based on unmodified ITO as reference and others OLEDs based on modified ITO by CsF solution. 1 wt%, 5 wt% and 10 wt% solutions of CsF improved the work function of ITO from normal value of 4.78 eV to 4.95 eV, 5.01 eV and 5.11 eV respectively. These work function improvement of ITO increased the hole injection rate by which the J-L-V curves influenced significantly. At a constant operating voltage of 6 V (Fig. 2(a)), the current density of OLEDs based on reference, 1 wt%, 5 wt% and 10 wt% CsF solutions are 46 mA/cm^2, 356 mA/cm^2, 751 mA/cm^2 and 928 mA/cm^2. On the other side, at 500 cd/m^2 (Fig. 2(b)), the operation voltage of reference, 1 wt%, 5 wt% and 10 wt% CsF solutions based OLEDs are 6.9 V, 4.7 V, 3.7 V and 3.3 V correspondingly. 10 wt% CsF solution based OLED shows the highest current density and luminance due to higher hole injection rate which also result of higher efficiency as evidence as presented in Fig 2(c). The improved values of electroluminescence (EL.) efficiency, γ (power efficiency, η) of modified ITO based OLEDs by 1 wt%, 5 wt% and 10 wt% CsF solutions are 4.79 cd/A (4.68 lm/W), 5.28 cd/A (5.38 lm/W) and 5.39 cd/A (5.89 lm/W) over without ITO modification based OLED where the value of EL. efficiency (power efficiency) is 4.4 cd/A (4.52 lm/W). These significant performance improvements of OLEDs using ITO surface modification by CsF solutions can be visualized and explained form the carrier distribution and recombination profiles.

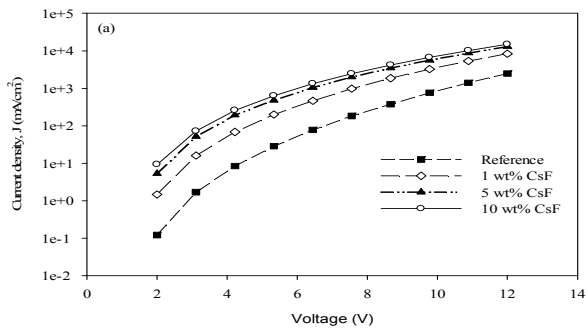

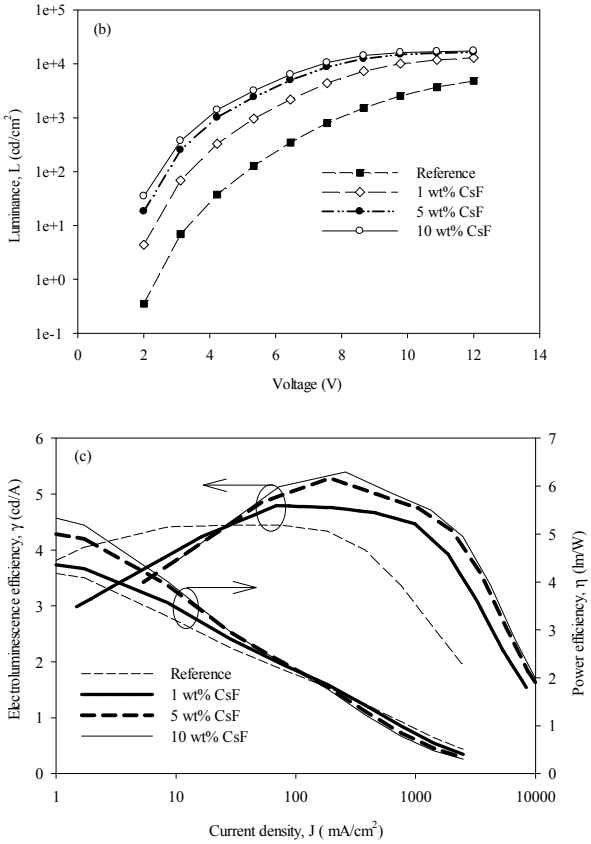

Fig. 2. Characteristics curves of OLEDs in terms of (a) Current density-Voltage, (b) Luminance-Voltage and (c) Electroluminescence and Power Efficiency-Current density

B. *Effects of ITO surface modication on current balance and recombination*

From the carrier concentration profile as shown in Fig. 3 (a), it is observed that at operation voltage of 6 V, the hole density increased around 1, 1.7 and 2 orders due to ITO surface modification by 1 wt%, 5wt% and 10 wt% CsF solutions respectively, when the interfacial energy barrier between ITO (4.95 eV, 5.01 eV and 5.11 eV) and NPB (HUMO=5.4 eV) reduced from 0.62 eV (in unmodified condition (4.78 eV)) to 0.45 eV, 0.39 eV and 0.29 eV correspondingly. Therefore, these significant reduction of interfacial energy barrier increased the hole current density in the NPB layer (Fig. 3(b)) around 5, 9 and 11 times which linked to increase the total current density of the modified ITO based OLEDs over unmodified ITO based OLED. Moreover, the electric field distribution along the device as shown in Fig. 4(a) increased steadily from anode/NPB interface to NPB/Alq_3 interface due to this CsF solution based ITO surface modification technique which harmoniously influenced the recombination rate at that organic layers interface. The highest calculated values of current balance factor in Fig. 4(b) of modified ITO based OLEDs with 1 wt%, 5wt% and 10 wt% CsF solutions are 0.68, 0.77 and 0.90 respectively where ITO surface modification based OLEDs reached steady state position before unmodified ITO based OLED (0.61).

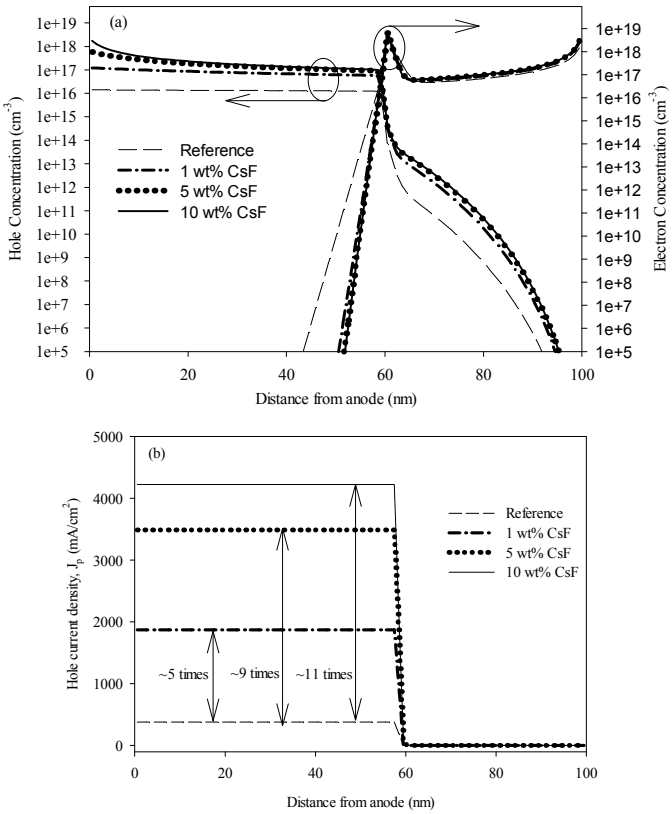

Fig. 3. (a) Carriers concentration profile and (b) Hole current density in treated and untreated ITO based OLEDs at 6V.

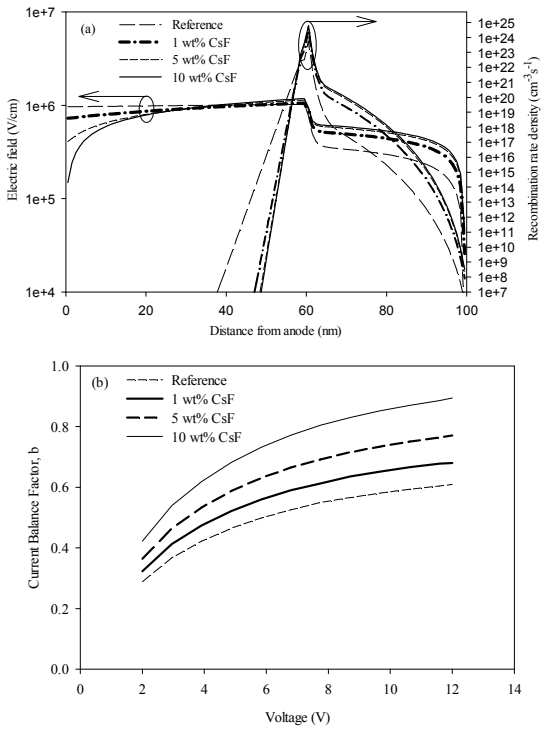

Fig. 4. (a) Distribution of Electric field and Recombination zone at 6V and (b) Current Balance Factor for treated and untreated ITO based OLED

C. Discussions

Through this numerical simulation, the influence of CsF solution on ITO work function modification and device performance have been explained from the hole current density, recombination rate and current balance factor. Due to the ITO surface modification by ITO soaking in 1 wt%, 5wt% and 10 wt% CsF solutions, the energy barrier at anode/organic interface reduced by 0.17 eV, 0.23 eV and 0.33 eV respectively from the original value (0.62 eV) and hence increased the hole injection rate. Therefore, the device EL. efficiency and power efficiency correspondingly improved by 1.08, 1.20 and 1.23 times, and 1.03, 1.19 and 1.30 times. Due to this CsF solution based ITO surface modification technique, a summary of performance improvements of all modified devices in terms of their efficiencies and CBF have been presented in TABLE I. Around 1.5 times improvement (10 wt% CsF solution) in current balance factor over normal condition also confirmed the improvement of device quantum efficiency.

TABLE I. COMPARISON OF OLEDS PERFORMANCES WITH AND WITHOUT ITO MODIFICATION.

Work function of ITO	**Simulation Results (Experimental Results [7])**					
	Max. EL. Efficiency, γ (cd/A)	***Max. Power efficiency, η (lm/W)***	**CBF**	**Improvement over unmodified ITO based OLED**		
				γ (cd/A)	**η (lm/W)**	**CBF**
4.78 eV (Reference)	*4.4 (2.81)*	*4.52 (1.47)*	*0.61*	-	-	-
4.95 eV (1 wt% CsF Sol.)	*4.79 (2.85)*	4.68 (1.51)	0.68	1.08 (1.01)	1.03 (1.02)	1.11
5.01 eV (5 wt% CsF Sol.)	*5.28 (2.62)*	5.38 (1.37)	0.77	1.2 (0.93)	1.19 (0.93)	1.26
5.11 eV (10 wt% CsF Sol.)	5.39 (3.0)	5.89 (1.58)	0.90	1.23 (1.06)	1.3 (1.08)	1.47

V. CONCLUSIONS

The effects of CsF solution based ITO surface modification technique on OLED performance have been analyzed from the 'SETFOS' based numerical simulation results. Due to ITO surface modification with 10 wt% CsF solution, the energy barrier for hole injection reduced more than 2 times (from 0.69 eV to 0.29 eV) which significantly increased hole injection rate at anode, accumulation of holes and recombination at the NPB/Alq_3 interface. Therefore, both EL. and power efficiencies increased around 1.23 and 1.30 times respectively. The value of current balance factor also improved from 0.61 to 0.90 (around 1.5 times) which is proportional to the experimental quantum efficiency. Moreover, the quantitative results of OLEDs performances by this numerical simulation comparable with experimental results [7].

REFERENCES

[1] N. C. Erickson and R. J. Holmes, "Highly efficient, single-layer organic light-emitting devices based on a graded-composition emissive layer," *Appl. Phys. Lett.*, vol. 97, no. 8, p. 083308, 2010.

[2] D. Ma, C. S. Lee, S. T. Lee, and L. S. Hung, "Improved efficiency by a graded emissive region in organic light-emitting diodes," *Appl. Phys. Lett.*, vol. 80, no. 19, p. 3641, 2002.

[3] C. W. Tang and S. a. VanSlyke, "Organic electroluminescent diodes," *Appl. Phys. Lett.*, vol. 51, no. 12, p. 913, 1987.

[4] C.-H. Hsiao, Y.-H. Chen, T.-C. Lin, C.-C. Hsiao, and J.-H. Lee, "Recombination zone in mixed-host organic light-emitting devices," *Appl. Phys. Lett.*, vol. 89, no. 16, p. 163511, 2006.

[5] C. Riku, Y. Y. Kee, T. S. Ong, S. S. Yap, and T. Y. Tou, "Simulation of mixed-host emitting layer based organic light emitting diodes," in *AIP Conference Proceding*, vol. 1657, no. 1, p. 070002, 2015.

[6] X. A. Cao and Y. Q. Zhang, "Performance enhancement of organic light-emitting diodes by chlorine plasma treatment of indium tin oxide," *Appl. Phys. Lett.*, vol. 100, no. 18, p. 183304, May 2012.

[7] H.-W. Lu, C.-W. Huang, P.-C. Kao, S.-Y. Chu, and Y.-D. Juang, "Effects of ITO Electrode Modification Using CsF Solution on Performance of Organic Light-Emitting Diodes," *ECS J. Solid State Sci. Technol.*, vol. 4, no. 3, pp. R54–R59, Jan. 2015.

[8] T. J. Whitcher, K. H. Yeoh, Y. B. C. Ng, N. A. Talik, C. L. Chua, K. L. Woon, N. Chanlek, H. Nakajima, T. Saisopa, P. Songsiriritthigul, S. Oswald, and B. K. Yap, "Enhancement of the work function of indium tin oxide by surface modification using caesium fluoride," *J. Phys. D. Appl. Phys.*, vol. 46, no. 47, p. 475102, Nov. 2013.

[9] P.-R. Huang, Y. He, C. Cao, and Z.-H. Lu, "The origin of the high work function of chlorinated indium tin oxide," *NPG Asia Mater.*, vol. 5, no. 8, p. e57, Aug. 2013.

[10] E. Knapp and B. Ruhstaller, "Numerical analysis of steady-state and transient charge transport in organic semiconductor devices," *Opt. Quantum Electron.*, vol. 42, no. 11–13, pp. 667–677, Feb. 2011.

[11] H. Wang, K. P. Klubek, and C. W. Tang, "Current efficiency in organic light-emitting diodes with a hole-injection layer," *Appl. Phys. Lett.*, vol. 93, no. 9, p. 093306, 2008.

[12] J. C. Scott, S. Karg, and S. A. Carter, "Bipolar charge and current distributions in organic light-emitting diodes," *J. Appl. Phys.*, vol. 82, no. 3, p. 1454, Aug. 1997.

[13] R. G. Kepler, P. M. Beeson, S. J. Jacobs, R. A. Anderson, M. B. Sinclair, V. S. Valencia, and P. A. Cahill, "Electron and hole mobility in tris(8-hydroxyquinolinolato-N1,O8) aluminum," *Appl. Phys. Lett.*, vol. 66, no. 26, p. 3618, Jun. 1995.

[14] S.-W. Liu, J.-H. Lee, C.-C. Lee, C.-T. Chen, and J.-K. Wang, "Charge carrier mobility of mixed-layer organic light-emitting diodes," *Appl. Phys. Lett.*, vol. 91, no. 14, p. 142106, 2007.

Study on the Prospects of Sb_2Te_3 Back Surface Field in ZnCdS/ZnCdTe Thin Film Solar Cell

Md. Muin Uddin[1], M. S. Hossain[1,3], and N. Amin[2,3]
[1]Department of Electrical & Electronic Engineering (Dhaka University of Engineering & Technology, Bangladesh)
[2]Department of Electrical, Electronic and Systems Engineering (University Kebangsaan Malaysia, Malaysia)
[3]Solar Energy Research Institute (University Kebangsaan Malaysia, Malaysia)
[*] E-mail:sharafat57@mail.com

Abstract—**This paper numerically explores the possibility of high efficiency, ultrathin and stable ZnCdTe (CZT) polycrystalline solar cell using well accepted simulator AMPS-1D. The base line structure of the ZnCdTe cell (Glass/ITO/CdS/ZnCdTe/Back Contact) was the beginning point of this work and further this base line structure was modified to achieve ultrathin, higher efficiency and stable solar cell. In modified structure, CdS window layer has been replaced by a wide band gap material $Zn_xCd_{1-x}S$ which increase the spectral response in the blue region as well as $Zn_xCd_{1-x}S$ window layer was reduced to the extreme limit with insertion of a suitable buffer layer of ZnO in between ITO and window layer to check forward leakage current of ultrathin window layer. To lessen the back surface recombination loss and barrier height at back contact another extra layer (BSF p-Sb_2Te_3) has been inserted in between p-ZnCdTe layer and back contact (BC). Then the thickness of the window layer and absorber layer of the modified structure has been optimized. The modified structure with back surface field (BSF) layer (Glass/ ITO/ZnO/$Zn_xCd_{1-x}S$/$Zn_xCd_{1-x}Te$/Sb_2Te_3/BC) shows the highest efficiency of 23.17% (*Jsc*=33.50 mA/cm^2, *FF*=0.77% and *Voc*= 0.98V). Finally the temperature effect on cell parameters was investigated and the overall temperature coefficient (TC) of the proposed cell is found to be 0.085%.**

Keywords—TFSC, CZT solar cell, ZnCdS, Photovolatic, BSF.

I. INTRODUCTION

Polycrystalline thin film solar cells such as Cu(InGa)Se_2 (CIGS), $CuInSe_2$ (CIS) and CdTe compound semiconductors are important for global application because of their high efficiency, long term stable performance and prospective for low cost production. Because of the high absorption coefficient (~10^5 cm^{-1}) a thin layer of ~2 μm is enough to absorb the useful part of the spectrum [1]. Highest recorded efficiency of 19.2% for CIGS [2] and 16.5% for CdTe [3] solar cell has been achieved. However there are rooms to improve the thin film solar cell (TFSC) performance by reformed cell design and using simple deposition technique to increase any one of cell performance parameters.

. Materials with high energy conversion efficiency have attracted substantial attention in the recent year. In this regards semiconductors having band gaps in the visible region of the electromagnetic spectrum are of commercial interest due to their valuable application in optoelectronic devices [4]. Silicon (Si) and germanium (Ge) are simplest and conventional semiconductors used in these devices but the problem with these semiconductors are their brittle nature as well as fixed and indirect band gap. CdTe is a direct band gap semiconductor with a fixed 1.45 eV band gap which is not good enough to involve wide range of energy from near infrared to near-ultraviolet. That's why the best replacement of these semiconductors in terms of efficiency and operating temperature is CZT due to its wide band gaps and high absorption rate at room temperature. In this work, a new TFSC structure is planned, where Zinc Cadmium Sulfide ($Zn_xCd_{1-x}S$) was used as window layer and Zinc Cadmium Telluride ($Zn_xCd_{1-x}Te$) was used as absorber layer with an extra benefit of variable band gap. As the spectral region sensitivity of the material depends on its band gap which depends on the controlled composition x in $Zn_xCd_{1-x}S$ and $Zn_xCd_{1-x}Te$, hence the value of x is varied symmetrically in the range $0<x<1$ to involve wide range of energy from near infrared to near ultraviolet [4]. In consideration to fabrication challenges, simulation results and resistivity of $Zn_xCd_{1-x}S$ film, in this work x=0.1 [5] is selected which showed low resistivity and high conversion efficiency in comparison to other value of x. The band gap E_g=1.57 eV is selected for ZnCdTe because it is in the range of optimum band gap. Moreover this band gap of $Zn_xCd_{1-x}Te$ can be obtained practically using the composition of x=0.1 in $Zn_xCd_{1-x}Te$ [6]. In the following text, $Zn_xCd_{1-x}S$ window layer and $Zn_xCd_{1-x}Te$ absorber layer has been written to $Zn_{0.1}Cd_{0.9}S$ and $Zn_{0.1}Cd_{0.9}Te$ respectively.

Now a day's one of the main goal of solar cell research is using a lesser amount of semiconductor material by making the cell thinner. Thinning will not only save material but also decrease layer deposition time as well as the energy requirement of production. All of these aspects will decrease the production cost of cell. In this work to reduce the cell thickness, modified cell structure (Glass/ITO/ ZnO/$Zn_xCd_{1-x}S$/$Zn_xCd_{1-x}Te$/Sb_2Te_3/BC) has been proposed and optimized the cell thickness without compromising the cell performance using Sb_2Te_3 BSF. Eventually, the modified CZT cell was investigated and achieved the maximum efficiency of 23.17% (*Jsc*=33.50 mA/cm^2, *FF*=0.77% and *Voc*= 0.98V).

978-1-4673-9257-0/15/$31.00 ©2015 IEEE

II. Device Design And Simulation

Thin film solar cell can be grown in both substrate or superstrate configuration, but the uppermost efficiency is achieved in the superstrate configuration [1]. In this work superstrate configuration is used and the usual superstrate structure of baseline CdS/ZnCdTe solar cell and modified ZnCdS/ZnCdTe solar cell is shown in Fig. 1. It is apparent from Fig. 1(a) that in the baseline structure of CZT solar cells, SnO_2 with 500 nm thickness is used as TCO or front contact, CdS with 100 nm thickness is used as window layer and ZnCdTe with 4000 nm thickness is used as absorber layer. It is also clear from Fig. 1(b) that the modified structure has an additional layer (ZnO) in the middle of TCO and n-$Zn_{0.1}Cd_{0.9}S$ layer to achieve ultrathin $Zn_{0.1}Cd_{0.9}S$ layer and another extra layer (BSF p-Sb_2Te_3) in between p-$Zn_{0.1}Cd_{0.9}Te$ layer and back contact. The key purposes of the BSF are to shrink the back surface recombination loss and to reduce the barrier height at BC. The specific BSF material selected to investigate in this work is Antimony Telluride (Sb_2Te_3).

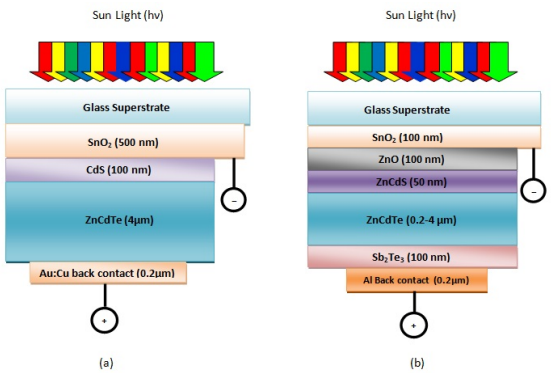

Figure 1. Schematic view of the CZT solar cell (a) baseline structure (b) proposed modified structure.

In this study, AMPS 1D [7] was used to explore the CZT baseline solar cell and modified structured solar cell for achieving ZnCdTe and ZnCdS layer with higher conversion efficiency. This simulation program has been developed to simulate faithfully the electrical characteristics of thin film heterojunction solar cell. That's why the four basic layers that have been emphasized in this modeling are the buffer layer (ZnO), n-$Zn_{0.1}Cd_{0.9}S$ window layer, p-$Zn_{0.1}Cd_{0.9}Te$ absorber layer and Sb_2Te_3 BSF layer. Table 1 displays the material parameters used in this work, which were selected based on literature values, theory or in some case, reasonable guesstimates. In this analysis, $Zn_{0.1}Cd_{0.9}Te$ absorber layer thickness has been varied from 0.2 µm to 4.0 µm and $Zn_{0.1}Cd_{0.9}S$ window layer thickness has been varied from 25 nm to 200nm by kept all other parameters at fixed value as stated in table 1 aiming to get efficient and thinner CZT solar cell.

III. Results And Discussions

A. Analysis of Baseline CZT Cell Structure

The baseline structure of CZT solar cell has shown in Fig. 1(a). The performance parameters of the baseline structure of CZT solar cell are: efficiency, η=21.63%; short circuit current density, Jsc=33.7mA/cm^2; open circuit voltage, Voc=0.96 V and fill factor, FF=0.73%. The thickness of the baseline structure cell was 4600nm. Further modifications have done to increase the cell performance as well as reduce the cell thickness to achieve an ultrathin solar cell. In the modified structure (Fig. 1(b)) of CZT cell, the window layer CdS was replaced by a wide band gap alloy ZnCdS which provide a more transparent window layer. As a result the spectral response at blue region and photocurrent generation has been increased. It is clear from the Fig. 2 that, the quantum efficiency of 50 nm thick ZnCdS shows better quantum efficiency than 100 nm thick CdS window layer. Lessening of ZnCdS thickness causes pinhole, which was reduced by insertion of 100 nm thick n-ZnO buffer layer in between TCO and n-ZnCdS window layer. Another layer has been introduced in modified structure which is called BSF to overcome rollover effect, to reduce the loss due to minority carrier recombination at back contact as well as to improve the stability of the cell at high operating temperature. All these modifications turn into increment of cell efficiency (21.63% to 23.17%). The J-V characteristics curve of the baseline structure and modified structure of CZT cell has shown in Fig. 3.

Table I. Materials properties used in AMPS-1D simulation

Typical cell properties		
Parameters	**Front contact**	**Back contact**
Φ_b [eV]	Φ_{bn} = 0.05	Φ_{bp} = 1.0 (Cu) and 0.1 (Sb_2Te_3)
S_e [cm/s]	1×10^7	1×10^7
S_h [cm/s]	1×10^7	1×10^7
R_f [I]	0.01	0.99 (Al) and 0.99 (Cu_2Te)

Layer properties				
Parameter	**ZnO**	**$Zn_xCd_{1-x}S$ (x=0.1)**	**p-$Zn_xCd_{1-x}Te$ (x=0.1)**	**p-Sb_2Te_3**
W (µm)	0.1	0.05-0.2	0.2- 4.0	0.5
$\varepsilon/\varepsilon_0$	9.0	9.3	9.5	55
μ_e (cm^2/Vs)	100	95	250	1094
μ_p (cm^2/Vs)	25	35	70	320
n, p (cm^{-3})	10^{19}	2.5×10^{16}	5×10^{14}	7.5×10^{21}
Eg (eV)	3.0	2.55	1.57	0.30
N_c (cm^{-3})	2.0×10^{18}	2.1×10^{18}	1.5×10^{17}	7.5×10^{17}
N_v (cm^{-3})	1.5×10^{19}	1.7×10^{19}	1.8×10^{19}	1.5×10^{19}
χ (eV)	4.35	4.44	4.20	4.15

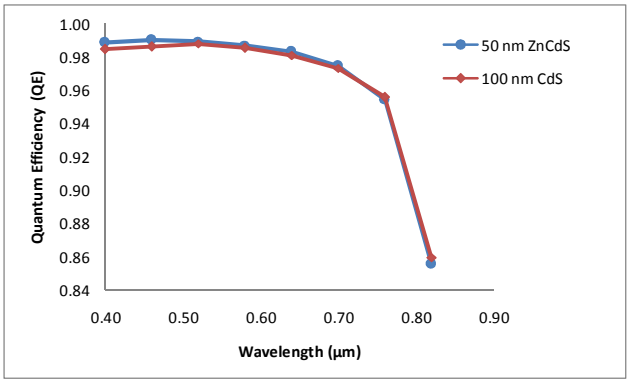

Figure 2. Spectral responses of ZnCdS and CdS window layer.

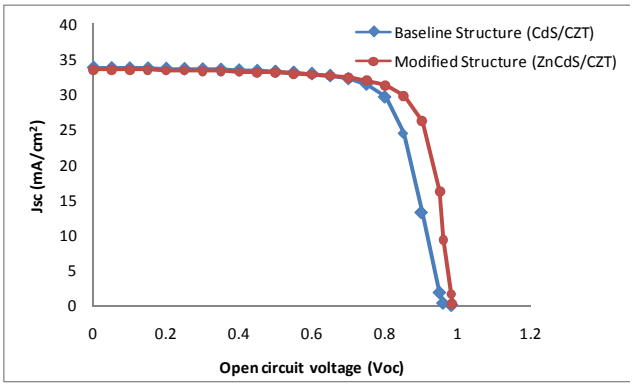

Figure 3. J-V characteristics curve of baseline and modified CZT solar cell.

Table II. Comparison of performance parameters between baseline case and modified cell

Performance parameters	Baseline case structure of CZT cell	Modified structure of CZT cell
η (%)	21.63	23.17
FF (%)	0.73	0.77
Jsc (mA/Cm^2)	33.71	33.50
Voc (V)	0.96	0.98

B. *Optimization of window and absorber layerthickness*

In this part, $Zn_{0.1}Cd_{0.9}S$ window layer thickness and $Zn_{0.1}Cd_{0.9}Te$ absorber layer thickness are optimized to form an ultrathin solar cell without affecting the cell performance. The thickness of window layer is changed from 25 nm to 200 nm.

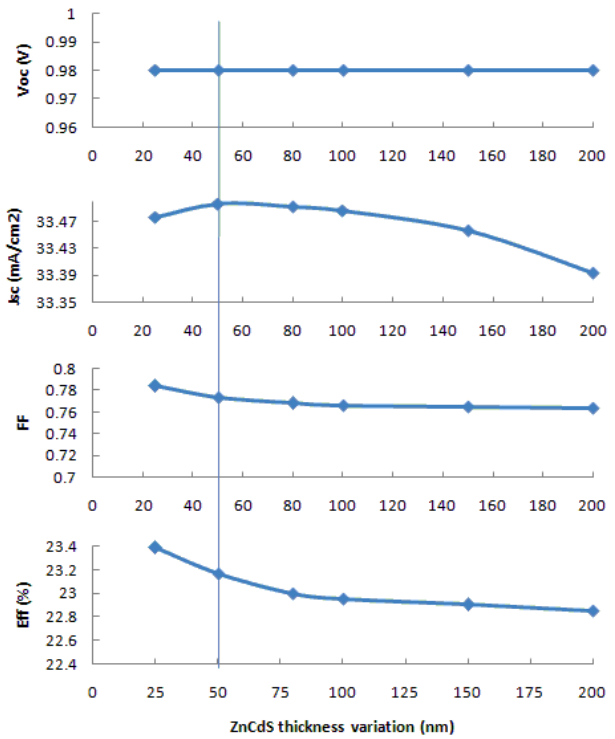

Figure 4. Effect of ZnCdS window layer thickness on cell performance parameters.

Fig. 4 shows the effect of window layer thickness variation on cell performance parameters. It is investigated that by decreasing the thickness of window layer the cell efficiency (η), current density (*Jsc)* and fill factor (*FF*) has been increased. Efficiency is increased due to increase of *Jsc* and *Jsc* is increased due to the use of wide band gap window layer as well as insertion of additional layers of ZnO and Sb_2Te_3. ZnO reduced the pinhole creation in ZnCdS layer and prevent forward leakage current. Whereas BSF layer reduced the loss due to minority carrier recombination at back contact as well as improved the stability of the cell at high operating temperature. However, by decreasing the thickness of window layer *FF* is increased a bit, because thinner window layer decreases overall cell resistance. But there is no change in *Voc* due to reduction of window layer thickness. The thickness of window layer is reduced from 200nm to 25nm and as a result the efficiency increases from 22.85% to 23.38%. Still to date it is impractical to fabricate good quality devices with ZnCdS film thickness below 50nm. Consequently the optimum thickness of window layer has been set to 50nm with conversion efficiency 23.17%.

In this work the thickness of absorber layer is varied from 0.2 µm to 4.0 µm. The effect of thickness variation of $Zn_{0.1}Cd_{0.9}Te$ absorber layer has shown in Fig. 5. It is evident from Fig. 5 that, efficiency almost follows the short circuit current trend. It can be seen that by decreasing the absorber layer thickness from 4.0 µm to 1.0µm the magnitude of *Jsc* decreases slightly. But *Jsc* decreases rapidly with the change of thickness from 1.0µm to 0.2µm. This is because of less absorption of light photon by reduced absorber layer thickness. That's why the efficiency decreases with lessening of absorber layer thickness because of the shrinking of *Jsc*. The increase of CZT layer thickness causes big area of p-n junction as the main

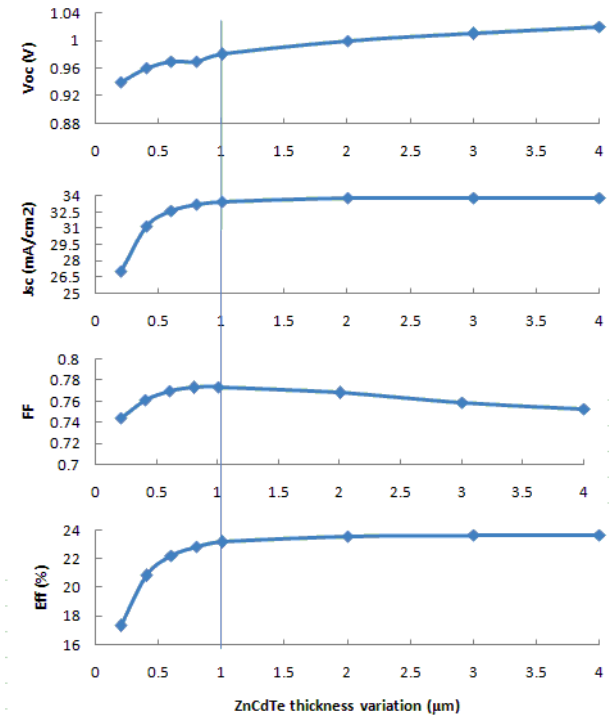

Figure 5. Effect of $Zn_{0.1}Cd_{0.9}Te$ absorber layer thickness on cell performance parameters.

part of p-n junction is formed in CZT layer. It is evident from Fig. 5 that by changing absorber layer thickness *Voc* increases gradually due to the increment of layer series resistance. On the other hand *FF* is increased with the reduction of absorber layer thickness. It is also noticed from Fig. 6 that the cell output parameters gradually decrease from 4.0µm to 1.0µm thick ZnCdTe layer. Where, all performance parameters decrease dramatically with the thinning of absorber layer thickness from 1.0µm to 0.2µm. It was also investigated that in this work the thickness of absorber layer is reduced from 4.0µm to 0.2µm and as a result the efficiency changes from 23.67% to 17.33%. Though efficiency decreases a little bit (only 0.5%) for thickness reduction from 4.0µm to 1.0µm, thus 1.0µm thick absorber layer is proposed for modified CZT cell with a little sacrifice of efficiency but grater saving of absorber layer material ($Zn_{0.1}Cd_{0.9}Te$).

C. *Effect of temperature on cell performance*

To investigate the temperature effect on cell performance of modified cell, temperature is changed from 25°C to 100°C. Temperature effect on different performance parameters has been shown in the Fig. 6. With the increment of temperature from 25°C the cell efficiency and *FF* has slightly increased up to 50°C after then it started to decrease for further temperature increment. As temperature rises, the band gap of semiconductor decreases and *Voc* decreases with a temperature dependency factor q/kT. Solar cells therefore have a negative temperature coefficient of *Voc* (β). That's why *Voc* decreases with the increase of temperature. On the other hand, as temperature rises the band gap of semiconductor shrinks meaning more incident energy is absorbed because a greater percentage of the incident light has enough energy to increase

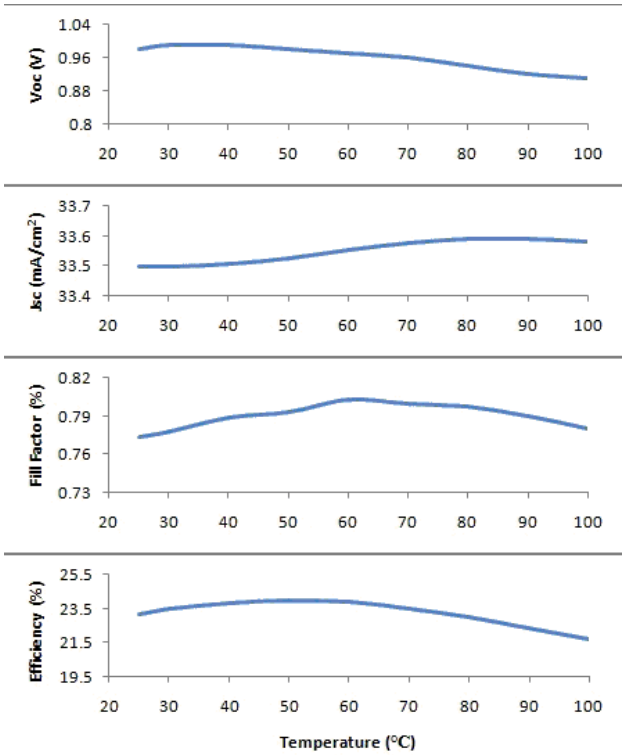

Figure 6. Effect of temperature on cell performance parameter of modified CZT cell.

charge carriers from the valance band to the conduction band. In effect, a larger photocurrent results; thus, *Isc* increases for a given insulation and solar cells have a positive temperature coefficient of *Isc* (α). Thus *Jsc* increases with the increment of temperature which is clear from the Fig. 6. The efficiency of the proposed cell at T=25°C is 23.17%, and when temperature is increased to T=50°C the efficiency become 23.83% and finally 21.68% is obtained at T=100°C. The overall temperature coefficient (TC) of the proposed cell is found 0.085% which means that this cell has good stability at higher temperature.

IV. Conclusion

From this numerical analysis it has been substantiated that the proposed modified CZT solar cell structure became thinner (1350 nm) than the reference CZT solar cell structure thickness (4600 nm) using Sb_2Te_3 BSF. It is clearly apparent that almost 70% less material will be used in this modified solar cell structure which was one of the main targets of this study. On the other hand the proposed solar cell performance has been risen (η=23.17%, *Jsc*=33.50%mA/cm^2, *Voc*=0.98V and *FF*=0.77%) due to few authentic effective modifications in the starting baseline structure. As well as the proposed cell also shows better stability (TC=0.085%) with Sb_2Te_3 BSF at high operating temperature. Thus this study clearly brings out a good prospect of the ZnCdS/ZnCdTe solar cells using Sb_2Te_3 BSF.

References

[1] A. Romeo, M. Terheggen, D. Abou-Ras, D. L. Batzner, F-J Haug, M. Kalin, D. Rudmann and A. N. Tiwari, "Development of Thin Film Cu(In,Ga)Se_2 and CdTe Solar Cell," *Progress in photovoltaics: Research and Application.*, Vol. 12, pp. 93-11, 2004.

[2] Ramanathan K, Contreras MA, Perkins CL, Asher S, Hasoon FS, Keane J, Young D, Romero M, Metzger W, Noufi R, Ward J, Duda A, "Properties of 19.% efficiency ZnO/CdS/Cu(In, Ga)Se_2 thin-film solar cell," *Progress in photovoltaics: Research and Application.*, Vol. 11, pp. 225-230, 1999.

[3] Wu X, Kane JC, Dhere RG, DeHart C, Albin DS, Duda A, Gessert TA, Asher S, Levi DH, Sheldon P, "16.5% Efficiency CdS/CdTe polycrystalline thin-film solar cell," *in Proc. 17th European Photovoltaic solar energy Conf. Munich*, 2002, pp. 995-1000.

[4] Imad Khan, H.A. Rahnamaye Aliabad, Waqar Ahmad, Zahid Ali, Iftikhar Ahmad, "First principle optoelectronic studies of visible light sensitive CZT," *Superlattices and Microstructures.*, vol. 63, pp. 91–99, Sep. 2013.

[5] M. S. Hossain, M.M Aliyu, M. A. Matin, M. A. Islam, K.Sopian, M. R. Karim and N. Amin, "prospect of $Zn_xCd_{1-x}S$ window layer in CdTe thin-film solar cell from numerical analysis ," *Int. Conf. on the development in renewable energy technology, Dhaka.*, vol. 2, pp. 04–08, Jan. 2012.

[6] T.E. Schlesinger, J. E. Toney, H. Yoon, E. Y. Lee, B. A. Brunett, L. Franks and R. B. James, "Cadmium zink telluride and its use as a numerical radiation detector materials," *Materr. Sci. Eng.* Vol. 32, no. 4-5, pp. 103-189, Apr. 2001.

[7] S. Degrave, M. Burgelman, and P. Nollet, "Modeling of polycrystalline thin-film solar cells: new feature in scaps version 2.3," *in Proc. World Conf. on Photovoltaic Energy Conversion,* May 2003, pp. 487-49

Study on Crystal Orientation-dependent Hole Effective mass in III-V Semiconductors

Sourav Roy[1, 2,*], Utpal Bhowmik[1], Md. Rafiqul Islam[1], Md. Mahbub Hasan[1]
[1]Department of Electrical and Electronic Engineering, KUET, Khulna, Bangladesh
[2]Faculty of Electrical and Electronic Engineering, JUST, Jessore, Bangladesh
[*] E-mail: souravroy2k9@gmail.com

***Abstract*— A numerical approach is presented to calculate crystal orientation-dependent effective mass of heavy hole, light hole and spin-orbit split-off hole of III-V semiconductors (GaAs, InAs, InP, GaSb, and InSb etc.) at Gamma-point by envelope approximation using *k.p* method. Unitary transformation is used to modify the wave vector and eight-band k.p Hamiltonian is applied in conventional (100) crystal orientation. The simulation is carried out for conventional crystal orientations (100), (110) and (111) as well as non-conventional orientations (113), (131) and (201). It is found that there is a substantial correlation between the effective mass and the crystal orientation. The results obtained from conventional crystal orientations are compared with that of estimated by well-established PBE, HSE and MBJLDA methods and found to have within good agreement. This indicates that the proposed technique can be applied to evaluate effective mass in arbitrary orientation of III-V semiconductors. It is also found that (113) orientation possesses lowest effective mass than other orientations. The outcome of this paper would be a boost to design high-speed optoelectronic devices with improved performance by introducing non-100 oriented epitaxial layers.**

Keywords*— *Crystal orientation, Effective mass, Tensor rotation, k.p method, III-V semiconductors

I. INTRODUCTION

The zinc-blende (ZB) III-V semiconductors have received considerable attention in the last decades due to its unique characteristics such as high electron mobility and superior carrier saturation velocity [1]. Consequently, its application scope broadens up to the operation in the active region of different optoelectronic devices [2-4]. Recently, it has become apparent that energy band dispersion profile of III-V materials is strongly co-related with crystal orientations. High performance optoelectronic devices can be realized in non-conventional orientation having favorable band structure [5-6].

Modern fabrication techniques such as molecular beam epitaxy (MBE) and metal-organic chemical vapor deposition (MOCVD) enables the growth of non-(100)-orientated crystal structure. High quality epitaxial layer on (201)-oriented GaAs substrate using MBE was cited by Woolf et al. [7]. In another research work, Nötzel and Ploog reported AlAs/GaAs multilayered structures on (210)-oriented substrate [8]. The orientation-dependent emission profile of InGaSb as well as InGaAs lasers were studied and found that non-(100) oriented laser structures show excellent performance with orientation-dependent tunable characteristics [9]. In another study, Ahmed and Debbichi showed that InAsN/GaSb quantum well laser diode in (110) and (111) orientation had better optoelectronic properties than the habitual (100) growth direction [10]. Oshima et al. reported orientation dependent features of recessed gate InGaAs/AlGaAs HEMT [11]. In a separate research, Lee and Zucca showed crystal orientation effect on planer InGaAs Schottky barrier field effect transistors [12].

To explore and explain the orientation-dependent performance of III-V semiconductor based electronic and optoelectronic devices, it is very much essential to know the orientation-dependent effective mass. Extensive researches have already been carried out experimentally and theoretically to calculate effective mass of heavy hole and light hole, paying particular attention to their fundamental properties and band topologies. The band structures and effective mass of ZB III-V semiconductor are studied using the Perdew, Burke and Ernzerhof (PBE) method, the Heyd, Scuseria, and Ernzerhof hybrid functional (HSE) method, and modified Becke-Johnson combined with the local-density approximation (MBJLDA) [13]. In these studies, the masses were evaluated numerically by fitting the calculated dispersion curves around the Γ-point along the directions (100), (110) and (111). However, these methods require an extensive fitting to experimental data, which are often scarce and possibly inaccurate. Moreover, for arbitrary crystal orientation such as, (113), (131) and (201) etc., considerable uncertainty still exists for the above mentioned methods due to unavailability of experimental effective masses [13-18].

In this paper, a general mathematical model based on tensor rotation technique is developed to determine effective mass of heavy hole (HH), light hole(LH) and spin-orbit split off hole(SH) in arbitrary (hkl) crystal orientation for ZB III-V semiconductor (GaAs, InAs, GaSb, InSb, InP) at Γ-point. The electronic band structure is calculated using an eight-band ***k.p*** Hamiltonian including spin-orbit coupling which enables us to have a good model for the non-parabolic dispersion of topmost valence band. Tensor rotation technique is used to modify wave vector and Hamiltonian for conventional (100) crystal orientation. The conduction and valence band wave functions and Eigen energies are evaluated using the finite difference method. The average heavy hole, light hole and spin-orbit split-off hole masses are obtained by exploring the orientation dependent parameters and addressing the energy separation from conduction band to heavy hole and light hole valence bands over all possible directions of wave vector. To confirm the validity of the results obtained from the proposed model, they are compared with the experimental and simulation

978-1-4673-9257-0/15/$31.00 ©2015 IEEE

results reported in previous studies for (100), (110) and (111) orientations.

The layout of this proposal is outlined as follows: the theoretical details to calculate electronic band structure and valence band effective masses of the ZB III-V semiconductor are illustrated in section 2. Results and discussions on the valence band structure in arbitrary orientation, Hole effective masses, and optical gain are presented in section 3. Finally, a conclusion is depicted in section 4.

II. THEORY

A. The k.p Method of Band-Structure Calculation near Γ-point

The electronic band structure is solved in envelope approximation using eight-band $\boldsymbol{k}\cdot\boldsymbol{p}$ Hamiltonian, H_0. The Kane's 8×8 Hamiltonian matrix can be asserted by [19]:

$$H\psi_h(z) = E\psi_h \tag{1}$$

The components of the Hamiltonian matrix are:

$$H_0=\begin{bmatrix} A & 0 & V^* & 0 & \sqrt{3}V & -\sqrt{2}U & -U & \sqrt{2}V^* \\ 0 & A & -\sqrt{2}U & -\sqrt{3}V^* & 0 & -V & \sqrt{2}V & U \\ V & -\sqrt{2}U & -P+Q & -S^* & R & 0 & \sqrt{\frac{3}{2}}S & -\sqrt{2}Q \\ 0 & -\sqrt{3}V & -S & -P-Q & 0 & R & -\sqrt{2}R & \frac{1}{\sqrt{2}}S \\ \sqrt{3}V^* & 0 & R^* & S & -P+Q & S^* & \frac{1}{\sqrt{2}}S^* & \sqrt{2}R^* \\ -\sqrt{2}U & -V^* & 0 & R^* & S & -P+Q & \sqrt{2}Q & \sqrt{\frac{3}{2}}S^* \\ -U & \sqrt{2}V^* & \sqrt{\frac{3}{2}}S^* & -\sqrt{2}R^* & \frac{1}{\sqrt{2}}S & \sqrt{2}Q & -P-\Delta & 0 \\ \sqrt{2}V & U & -\sqrt{2}Q & \frac{1}{\sqrt{2}}S^* & \sqrt{2}R & \sqrt{\frac{3}{2}}S & 0 & -P-\Delta \end{bmatrix} \tag{2}$$

The wave function $\Psi_h(z)$ can be given by:

$$\Psi_h(z) = \begin{bmatrix} \Phi_{1/2,1/2}(z) \\ \Phi_{1/2,-1/2}(z) \\ \Phi_{3/2,1/2}(z) \\ \Phi_{3/2,-1/2}(z) \\ \Phi_{3/2,3/2}(z) \\ \Phi_{3/2,-3/2}(z) \\ \Phi_{1/2,1/2}(z) \\ \Phi_{1/2,-1/2}(z) \end{bmatrix} = \begin{bmatrix} g^{(1)}(z) \\ g^{(2)}(z) \\ g^{(2)}(z) \\ g^{(4)}(z) \\ g^{(5)}(z) \\ g^{(6)}(z) \\ g^{(7)}(z) \\ g^{(8)}(z) \end{bmatrix} \tag{3}$$

where, ϕ_{j,m_j} or $g^{(j)}$ is the conduction and valence band wave function component and E is the energy of conduction band and three valence bands.

The matrix elements are [19]:

$$A=E_c-\frac{\hbar^2}{2m_0}(k_x^2+k_y^2+k_z^2) \tag{4}$$

$$P=-E_v-\gamma_1\frac{\hbar^2}{2m_0}(k_x^2+k_y^2+k_z^2) \tag{5}$$

$$Q=-\gamma_2\frac{\hbar^2}{2m_0}(k_x^2+k_y^2+k_z^2) \tag{6}$$

$$R=\sqrt{3}\frac{\hbar^2}{2m_0}[\gamma_2(k_x^2-k_y^2)-2i\gamma_3k_xk_y] \tag{7}$$

$$S=-\sqrt{3}\gamma_3\frac{\hbar^2}{2m_0}k_z(k_x-ik_y) \tag{9}$$

$$U=\frac{-i}{\sqrt{3}}p_0k_z \tag{10}$$

$$V=\frac{-i}{\sqrt{6}}P_0(k_x-ik_y) \tag{11}$$

P_0 is the coupling between the conduction and valence bands, E_c and E_v are the (unstrained) conduction and valence band energies respectively, and Δ is the spin orbit splitting. The γ_i's are modified Luttinger parameters.

The energy dispersion profile along (100) orientation is calculated as a function of k for the 8-band $\boldsymbol{k.p}$ theory by diagonalizing the Hamiltonian using finite difference scheme.

B. Crystal orientation dependent Energy Band

As the conduction band wave function does not change exclusively with crystal orientation, here we are interested about the modification in the valence band Hamiltonian matrix owing to crystal orientations. If the working region is grown on arbitrary crystal orientation, the wave vectors on (100) crystal can be attained by the subsequent formula [20]:

$$\begin{pmatrix} k_1 \\ k_2 \\ k_3 \end{pmatrix} = O_R \begin{pmatrix} k_x \\ k_y \\ k_z \end{pmatrix} \tag{12}$$

where, k_x, k_y, k_z are the wave vectors along (hkl) direction. The expression of the rotation matrix is as follows [21]:

$$O_R = \begin{pmatrix} cos\theta cos\emptyset & -sin\emptyset & sin\theta cos\emptyset \\ cos\theta sin\emptyset & cos\emptyset & sin\theta sin\emptyset \\ -sin\theta & 0 & cos\theta \end{pmatrix} \tag{13}$$

where, $\theta = \tan^{-1}\left(\frac{\sqrt{(h^2+k^2)}}{l}\right)$ and $\phi = \tan^{-1}(k/h)$

Practicing the wave vector in the (100) crystal orientation, the Hamiltonian matrix for (100) crystal orientation can be calculated using eqn. (2). Then the Hamiltonian matrix in (hkl) orientation can be obtained by [22]:

$$H^{hkl} = U H^{(100)} U^* \tag{14}$$

where, $U = R(\theta)R(\phi)$

In this equalization, $R(\theta)$ and $R(\phi)$ are symbolized as rotations which transform the (100) orientated valence band Hamiltonian to arbitrary crystal orientated Hamiltonian matrix. The argument of $R(\theta)$ and $R(\phi)$ can be defined by [21]:

$$R(\theta)=\begin{pmatrix} \alpha^2 & -\sqrt{3}\alpha^2\zeta & \sqrt{3}\alpha\zeta^2 & \zeta^3 \\ \sqrt{3}\alpha^2\zeta & \alpha^3-2\alpha\zeta^2 & -2\alpha^2\zeta+\zeta^3 & \sqrt{3}\alpha\zeta^2 \\ \sqrt{3}\alpha\zeta^2 & 2\alpha^2\zeta-\zeta^3 & \alpha^3-2\alpha^2\zeta & -\sqrt{3}\alpha^2\zeta \\ \zeta^3 & \sqrt{3}\alpha\zeta^2 & \sqrt{3}\alpha^2\zeta & \alpha^3 \end{pmatrix} \tag{15}$$

$$\alpha = \cos\frac{\theta}{2} \text{ and } \zeta = -\sin\frac{\theta}{2}$$

$$R(\phi) = \begin{pmatrix} e^{i(3/2)\phi} & 0 & 0 & 0 \\ 0 & e^{i(1/2)\phi} & 0 & 0 \\ 0 & 0 & e^{-i(1/2)\phi} & 0 \\ 0 & 0 & 0 & e^{-i(3/2)\phi} \end{pmatrix} \tag{16}$$

C. *Crystal orientation dependent Effective Mass:*

A general mathematical model based on tensor rotation technique is proposed to determine average heavy hole (m^*_{hh}), light hole (m^*_{lh}) and spin-orbit split off hole (m^*_{so}) effective masses for Zinc blende III-V semiconductors in arbitrary (*hkl*) crystal orientations over all possible directions of wave vector k considering the wrapped spheres of valence band energy surface figured out by 8×8 k.p Hamiltonian. The formulations can be given by [23]:

$$(1/m^*_{hh}) = \frac{-2A + 2B(1+ 2C^2/15B^2)}{\hbar^2} \quad (17)$$

$$(1/m^*_{lh}) = \frac{-2A - 2B(1+ 2C^2/15B^2)}{\hbar^2} \quad (18)$$

$$(1/m^*_{so}) = 1-(2/3)\left(\frac{M^2}{m_0(E_0+\Delta_0)} + \frac{2N^2}{m_0(E_0+\Delta_0)}\right) \quad (19)$$

The constants A, B, C (in units of $\hbar^2/2m$) are related to momentum matrix element between conduction band and valence band and energy band gaps and can be given by [23]:

$$\frac{2m_0}{\hbar^2}A = 1-\frac{2}{3}\left[\left(\frac{M^2}{m_0E_0}\right) + \left(\frac{2N^2}{m_0E_0'}\right)\right] \quad (20)$$

$$\frac{2m_0}{\hbar^2}B = \frac{2}{3}\left[\left(\frac{-M^2}{m_0E_0}\right) + \left(\frac{2N^2}{m_0E_0'}\right)\right] \quad (21)$$

$$\left(\frac{2m_0}{\hbar^2}C\right)^2 = \frac{16M^2N^2}{3m_0E_0m_0E_0'} \quad (22)$$

E_0= energy separation between conduction and heavy hole band
E'_0 = energy separation between conduction and light hole band
Δ_0= Spin-orbit splitting of valence band

M and N is the orientation dependent wave vector that can be given by [23]:

$$M=\left(\frac{\hbar^2\gamma_1}{2m_0}\right)(k_x^2+k_y^2+k_z^2) \quad (23)$$

$$N=\left(\frac{\hbar^2\gamma_2}{2m_0}\right)(k_x^2+k_y^2 - 2k_z^2) \quad (24)$$

Since change in crystal orientation changes the splitting between valence bands; knowing the energy separation E_0 and E'_0 and orientation dependent M and N parameters, Valence band effective masses in any arbitrary (hkl) orientation can be calculated.

III. RESULTS AND DISCUSSIONS

Following the mathematical model presented in section II, effective mass of heavy hole, light hole and spin-orbit split-off hole of ZB III-V semiconductors (GaAs, InAs, InP, GaSb, InSb etc.) at Γ-point for arbitrary (hkl) crystal orientation are determined. The simulation is carried out in MATLAB environment at room temperature. The valence band dispersion profiles of GaAs are evaluated in (100), (110), (111) and (113) orientations and shown in Fig. 1(a)-(d) respectively. To compare the orientation-dependent band dispersion profiles, the figures are plotted as a function of wave vector in the same scale. It is demonstrated that, for nonzero value of k (wave vector in the plain direction), the increasing conduction and spin-orbit split off band coupling gives rise to strong non-parabolicities in the valence band structure at (111) and (113) orientations. For (113) orientation, larger energy spacing between heavy hole and light hole is found so hole effective mass may reduce. From Fig. 1, it is demonstrated that crystal orientation exclusively changes the topmost valence band curvature which explains effective mass has an orientation-dependent characteristic.

The effective mass of heavy hole, light hole and spin-orbit split-off hole is determined from eqns. (17-19).The related parameters are extracted from the orientation-dependent band dispersion profiles. The results estimated from the proposed technique are listed in Table I for (100), (110) and (111) orientations at the Γ-point.To confirm our results; they are compared with the results obtained from the well-established

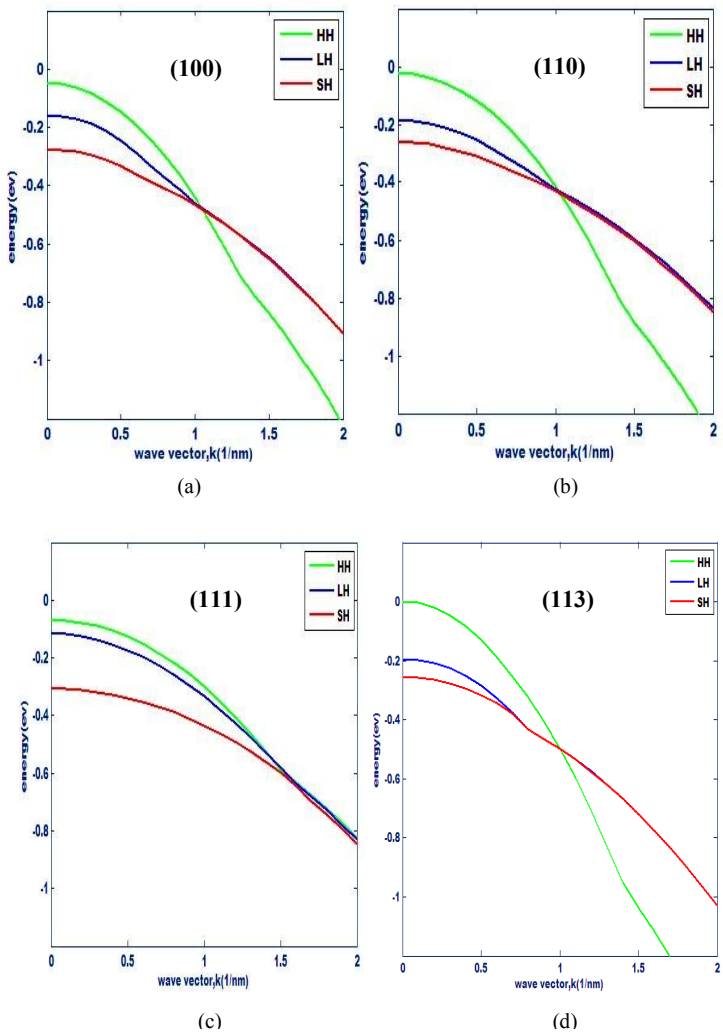

Fig. 1: Valence band dispersion profiles of (a) (100), (b) (110), (c) (111), and (d) (113) - oriented GaAs

PBE, HSE and MBJLDA methods. It is noted here that, in previous studies, the masses were evaluated numerically by fitting the calculated dispersion curves around the Γ-point for the conventional directions (100), (110), and (111) [Ref. 18]. It is seen from Table I that there is a good agreement between our results and the results obtained from the well-established methods. Fig. 2 demonstrates the correlation of heavy hole effective mass of GaAs obtained from well-established HSE, PBE, MBJLDA methods and our proposed formulations along (100), (110) and (111) orientations. It is observed that from our proposed formulations, effective mass of heavy hole of GaAs along (100), (110) and (111) orientations is found to be $0.345m_0$, $0.528\ m_0$, $0.823\ m_0$ whereas, from HSE method, they are found to be $0.3257m_0$, $0.5571\ m_0$ and $0.7299\ m_0$ which shows a reasonable agreement. From this motivation, we calculated effective mass of these materials along arbitrary (hkl) crystal orientations such as (113), (131) and (201) etc. The results are listed in Table II. From Table I and II, it can be seen that lowest heavy hole effective mass for GaAs, InAs and InSb is found in (113) orientation. So it is quite visible that the smallest effective masses in (113) orientation leads to have high performance (113)-oriented optoelectronic devices than the habitual crystal growth orientations like (100) and (111).

TABLE I: Heavy hole, light hole and split-off hole effective masses in (100), (110) and (111) orientations

Material	Method	$m^*_{heavy-hole}/m_0$			$m^*_{light-hole}/m_0$			$m^*_{split-off\ hole}/m_0$
		Crystal orientation			Crystal orientation			Crystal orientation
		(100)	(110)	(111)	(100)	(110)	(111)	(100)
InP	PBE [a]	0.4562	0.7570	0.9703	0.0723	0.0681	0.0667	0.139
	MBJLDA [a]	0.5071	0.8405	1.075	0.1410	0.1270	0.1230	0.230
	HSE [a]	0.4970	0.8032	1.0101	0.1172	0.1075	0.1047	0.212
	Expt. [a]	0.307	0.885	0.682	0.14	0.111	0.118	0.210
	Proposed model	0.425	0.853	0.754	0.118	0.108	0.105	0.200
InAs	MBJLDA[a]	0.4291	0.4494	0.9341	0.0439	0.0422	0.0416	0.133
	HSE [a]	0.3378	0.6042	0.8196	0.0332	0.0319	0.0314	0.112
	Expt. [a]	0.26	0.513	0.729	0.027	0.026	0.0259	0.140
	Proposed model	0.327	0.627	0.835	0.033	0.032	0.031	0.120
InSb	MBJLDA[a]	0.3012	0.4854	0.6097	0.0242	0.0235	0.0233	0.150
	HSE [a]	0.2590	0.4405	0.5747	0.0181	0.0176	0.0175	0.129
	Expt. [a]	0.26	0.435	0.454	0.0154	0.0148	0.014	0.110
	Proposed model	0.250	0.415	0.574	0.018	0.016	0.0175	0.130
GaAs	PBE [a]	0.3367	0.5649	0.7299	0.0362	0.0347	0.0342	0.108
	MBJLDA[a]	0.3861	0.6622	0.8695	0.1112	0.0993	0.0958	0.210
	HSE [a]	0.3257	0.5571	0.7299	0.0831	0.0756	0.0732	0.166
	Expt. [a]	0.4	0.643	0.91	0.088	0.081	0.085	0.172
	Proposed model	0.345	0.528	0.823	0.085	0.076	0.073	0.165
GaSb	MBJLDA[a]	0.2785	0.4705	0.6211	0.0536	0.0550	0.0536	0.175
	HSE [a]	0.2457	0.4184	0.5464	0.0469	0.0434	0.0424	0.143
	Expt. [a]	0.22	0.422	0.714	0.045	0.040	0.039	0.120
	Proposed model	0.234	0.209	0.526	0.047	0.022	0.042	0.150

[a]Reference 18.

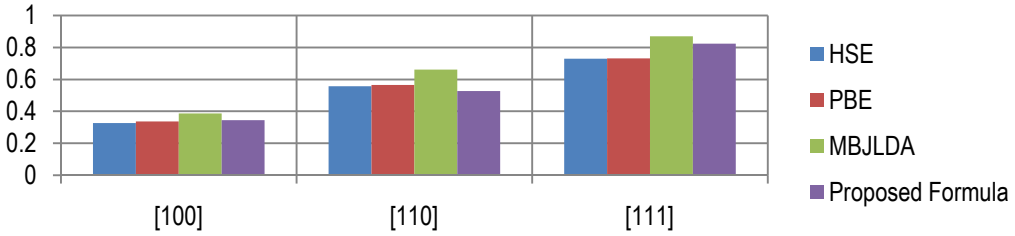

Fig. 2: Comparison between heavy hole effective mass obtained from HSE, PBE, MBJLDA methods and proposed method. The masses are calculated for GaAs along (100), (110) and (111) crystal orientations

TABLE II: Heavy hole, light hole and split-off hole effective masses evaluated by proposed method for GaAs along arbitrary (hkl) orientation

Material	Heavy hole mass(m^*_{hh}/m_0)			Light hole mass(m^*_{lh}/m_0)			Split-off hole mass(m^*_{so}/m_0)		
	(113)	(131)	(201)	(113)	(131)	(201)	(113)	(131)	(201)
GaAs	0.289	0.651	0.837	0.083	0.068	0.056	0.242	0.473	0.621
InAs	0.314	0.507	0.573	0.028	0.040	0.019	0.128	0.327	0.198
InP	0.921	0.723	0.489	0.110	0.103	0.113	0.564	0.670	0.429
GaSb	0.580	0.457	0.352	0.037	0.051	0.034	0.211	0.391	0.283
InSb	0.252	0.593	0.561	0.012	0.022	0.027	0.168	0.428	0.351

IV. CONCLUSION

A general mathematical model based on tensor rotation technique is proposed to understand the impact of crystal orientation on valence band effective masses of ZB III-V semiconductors at the Γ-point. The theoretical results depict that the curvature of topmost heavy hole and light hole bands changes exclusively with crystal orientation. Addressing the splitting between energy bands and exploring the orientation dependent parameters over all possible directions of wave vector, the average heavy hole, light hole and spin-orbit split-off hole masses are obtained which show that lowest effective masses are obtained in (113) orientation for GaAs, InAs and InSb crystals. However, this results are not consistent for GaSb and InP materials and also for light hole and split off hole masses. This simulation results demonstrate that our proposed formulations will be a boost for the fabrication of novel optoelectronic devices along other crystallographic orientations than the conventional [100] or [111] growth direction.

REFERENCES

[1] Kruse P W 1970 Semiconductors and Semimetals, vol. 5 ed. R. K Willardson and A C Bee (New York: Academic) pp. 15-70

[2] C. B. Geller, W. Wolf, S. Picozzi, A. Continenza, R. Asahi, W. Mannstadt, A. J. Freeman, and E. Wimmer, Appl. Phys. Lett. 79, 368 (2001).

[3] Brown, E R, Soderstrom J R, Parker C D, Mahoney L J,Molvar K,Mand McGill, Appl. Phys. Lett. 58, 2291(1991)

[4] S. Nakamura and G. Fasol, The Blue Laser Diode (Springer, Berlin, 1997), p. 7.

[5] H.W.A.M Rompa, M.F.H Schuurmans, and F. Williams, Phys. Rev. Lett. 52,675(1984)

[6] M. Phon, Y. Chung, W.I. Wang, Orientation dependence of valence-subband structures in GaAs–$Ga_{1-x}Al_xAs$ quantum well structures, J. Appl. Phys. 64 (1988) 4609–4613.

[7] D.A. Woolf, J.P. Williams, D.I. Westwood, Z. Sobiesierski, J.E. Aubrey, R.H. Williams, The homoepitaxial growth of non-axis GaAs(1 1 1)A, (1 1 1)B and (2 0 1) compared with GaAs(1 0 0): doping and growth temperature studies, J. Cryst. Growth 127 (2002) 913–917.

[8] R. Notzel, K.H. Ploog, Man-made low-dimensional solids: new challenges in microstructure material science, Int. J. Mod. Phys. B7 (1993) 2743–2778.

[9] M.M. Hasan, M.R. Islam, Strain-dependent optical properties of mid-infrared GaInSb/GaInAlSb quantum well laser, International Conference on Computer and Communication Engineering (ICCCE 2010), 11–13, May 2010, KualaLumpur, Malaysia, 2010, ISBN 978-1-4244-6234-6, IEEE Catalog Number:CFP10390-CDR.

[10] A ben Ahmed, S Ridne and H Bouchriha, Orientation dependence of optoelectronic properties of InAsN/GaSb quantum well laser diodes, Semicond. Sci. Technol. **28** (2013) 065006 (10pp)

[11] T. Oshima, M. Yoshida, S. Picozzi, A. Continenza, R. Asahi, W. Mannstadt, M. Tsunotani, and T. Kimura, Orientation Dependent Characteristics of Recessed-Gate InGaAs/AlGaAs HEMTs, Appl. Phys. Lett. 79, 368 (2001).

[12] P. Lee, R. Zucca, B. Welch, Orientation effect on planer InGaAs schottky barrier FET, Appl. Phys. Lett. 37, 311 (1988).

[13] J. E. Peralta, J. Heyd, G. E. Scuseria, and R. L. Martin, Phys. Rev. B 74, 073101 ,2006.

[14] J. Paier, M. Marsman, K. Hummer, G. Kresse, I. C. Gerber, and J. G. Ángán, J. Chem. Phys. 124, 154709 ,2006.

[15] J. Paier, M. Marsman, K. Hummer, G. Kresse, I. C. Gerber, and J. G. Ángán, J. Chem. Phys. 125, 249901,2006.

[16] V. Krukau, O. A. Vydrov, A. F. Izmaylov, and G. E. Scuseria, J. Chem. Phys. 125, 224106 , 2006.

[17] Dragica Vasileska, Tutorial for semiconductor band structure calculation, Arizona State University, Tempe, AZ

[18] Kim et al., Towards efficient band structure and effective mass calculations for III-V direct band-gap semiconductors, PHYSICAL REVIEW B 82, 205212 (2010)

[19] Craig Pryor, Eight-band calculations of strained InAs/GaAs quantum dots compared with one, four, and six-band approximations, Physical Review B, 03/1998

[20] T. Ohtoshi, T. Kuroda, A. Niwa, S. Tsuji, Dependence of optical gain on crystal orientation in surface-emitting lasers with strained quantum wells, Appl. Phys. Lett. 65 (1994) 1886–1889.

[21] Md. Mahbub Hasan, M.R. Islam, Crystal orientation-dependent optical properties of mid-infrared GaInSb/GaInAlSb quantum well laser, International Conference on Computer and Communication Engineering (ICCCE 10), 05/2010

[22] Semiconductors, edited by O. Madelung, M. Schilz, and H. Weiss, Landolt-B¨ornstein, Numerical Data and Functional Relations in Science and Technology Vol. 17 (Springer-Verlag, New York, 1982).

[23] I. Vurgaftman, J. R. Meyer, and L. R. Ram-Mohan, J. Appl.Phys. 89, 5815 (2001).

Realistic Edge Shape Effects on the Vibrational Properties of Graphene Nanoribbons

Md. Sherajul Islam, Ashraful G. Bhuiyan
Department of Electrical & Electronic Engineering
Khulna University of Engineering & Technology
Khulna, Bangladesh
sheraj_ruet@yahoo.com

Akihiro Hashimoto
Department of Electrical & Electronic Engineering
University of Fukui
Fukui, Japan
hasimoto@fuee.u-fukui.ac.jp

***Abstract*—Graphene nanoribbons (GNRs) are predicted to be essential components in future graphene nanoelectronics. Recent studies show that atomic scale edge structures of GNRs consist of armchair and zigzag edges with some other defects. Here we probe systematically the details of the phonon properties of GNRs with realistic edge structures combining the armchair and zigzag edges along with some vacancies using the forced vibrational method. We have calculated the phonon density of states (PDOSs) and typical mode patterns of GNRs considering the effects of the mixture of the different directional armchair edge and zigzag edge with some vacancy type defects. We find that in-plane longitudinal and transverse optical (LO) and (TO) mode phonons of realistic edge shaped GNR are non-degenerate and shifted down with the decrease of ribbon width. The PDOS at low frequency region changes significantly for the realistic edge structures. We observe a strongly localized eigenmodes of in-plane transverse optical phonon (iTO) near the armchair edges and defect sites which are conceptually very good agreement with the Raman D peak comes from the armchair edges or the defects of GNRs activated by the iTO phonons.**

Keywords—Graphene nanoribbons, realistic edge strucures, phonon density of states, vacancy defects, strong localization.

I. INTRODUCTION

High expectations are set for graphene electronics [1] due to its incomparable properties. However, the electronic applications are crippled by the absence of energy band gap in the pristine graphene. If graphene sheet is patterned into a narrow ribbon, it opens a band gap by quantum confinement [2]-[6]. It is envisaged that the large band gap opening in the nanoribbons depend on the nature of the edge structures and their orientations. The edge geometry is the preeminent parameter which determines the electronic properties of the nanoribbons. For example, localized states appear at the edge with energies close to the Fermi level [7]-[8] in the graphene nanoribbons with zigzag edges. In contrast, edge states are away for ribbons with armchair edges. It has been suggested that armchair edges give rise to intervalley backscattering, which is suppressed at zigzag edges [9]. The research of the edge dependent fundamental and application oriented properties are thus of indispensable prerequisite for tomorrow's graphene-based electronics.

Recent studies [10]-[11] on edge structures of graphene nanoribbons (GNRs) perceive that although the edge may be mainly armchair or zigzag at the microscopic scale, it is not perfect armchair or zigzag at the atomic scale, but a mix of them with some other defects. It is also believed that the armchair edge of GNRs act as a crystalline defects. As electrons and phonons are strongly coupled in graphene related materials, the electron transports of GNRs strongly depend on the nature of edge-phonon modes in addition to the roughness of the ribbon edge [12]-[13]. Because of the scattering by disorders, phonons have the finite lifetime and localization length, which is one of the main contributions to the natural line width of the Raman spectra, the widely used tool for the investigation of graphene related system. We thus require a detailed understanding of the effects of various types of edges, their orientation, and the defects on the phonon modes which noticeably change the electron transport properties.

Over the last few years, many approaches have been employed to estimate the vibrational properties of graphene nanoribbons including force constant fittings [14]-[15], density functional theory [16]-[17] and the first-principles calculations [18]-[19]. In contrast to the intensive research on the ribbons with perfect edges, there is no studies on the vibrational properties of GNRs having realistic edge structures. The disordered edges of GNRs may induce the symmetry breakdown of elemental topological arrangements [12], which generate more complex lattice structures. Therefore, the dynamical matrix technique needs enormous computational resources. These long computational times and convergence problems in the dynamical matrix calculations restrict the systems of interest to benchmark molecules. Nonetheless, a considerably larger scale model is essential for an in-depth understanding of vibrational properties of disordered atomic structures. It is thus indispensible to develop a reliable model to observe the phonon modes of GNRs with realistic edge structures directly.

In this work, we explore systematically the details of the phonon properties of GNRs consist of realistic edge structures combining the armchair and zigzag edge with some vacancy defects. We have estimated the phonon density of states (PDOSs) of GNRs considering the effects of the mixture of the various directional armchair and zigzag edges with some

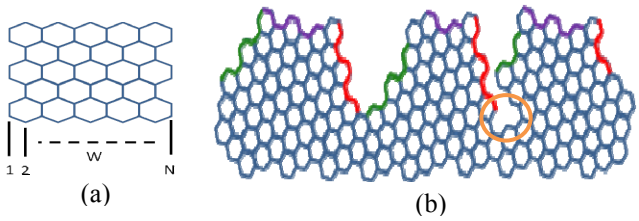

Figure 1. Graphene nanoribbons with (a) perfect armchair edge on both sides(b) realistic edge combining the armchair and ziga edges along with some point defects. The dimer and red lines indicate the ribbon width and different directional armchair edges, respectively. Orange circle shows the vacancy defects.

vacancy type defects. For all calculations, we employed the forced vibrational method [20], which is based on the mechanical resonance to extract the vibrational eigenmodes for very complex and large disordered systems by numerical simulation. Due to the defects, the phonon modes lie outside of the allowed frequency range of the pristine crystal. These are called localized modes as the mode energy is concentrated near the defect site. Since localization virtually immobilizes phonons and makes them non-conducting, these phonons lose their nature as heat carriers. In spite of graphene related systems have the excellent thermal conductance, disordered regions may interrupt the crystallinity and impede the flow of thermal energy. To study the localized eigenmodes, typical mode pattern of GNRs considering different directional real edges and defects has also been calculated. Here, we mainly concentrate on the K-point of the in-plane optical mode phonons as they have significant effects on the Raman spectra of GNRs.

II. Computational Details

All the calculations in this work were carried out using the forced vibrational (FV) method introduced by Williams and Maris [20]. The FV method is an efficient scheme for computing spectral densities, eigenvalues and eigenvectors of complex and large disordered physical systems. The algorithm utilizes a principle of Hamilton mechanics: a linear lattice dynamical system driven by a periodic external force of certain frequency will respond with large amplitudes in those eigenmodes close to this frequency. Specifically, the eigenvalue analysis is reduced to solve the time development of the equations of motion in the presence of an external periodic force. In general, the equation of motion of the system consists of N atoms which are coupled together with linear springs, with the scalar displacement of the lth mass, $u_l(t)$ is:

$$M_l \ddot{u}_l(t) + \sum_{l'} \phi_{ll'} u_{l'}(t) = 0 \qquad (1)$$

For time t > 0, a random force $F_l = F_0\sqrt{M_l}\cos(\varphi_l)\cos(\Omega t)$ is applied to each atom l at rest. Where, F_0 is a constant amplitude, the phase φ_l and Ω are a random variable with respect to the site number l and a frequency of the external force, respectively. Thus, for large times the periodic external force excites only those modes whose frequency is close to Ω. When we average all possible values of φ_l and use the orthonormality of the eigenvectors, the averaged total energy of the system after time T becomes:

$$\langle E(\Omega,T)\rangle \approx \frac{\pi t F_0^2}{8}\sum_{\lambda}\delta[(\omega_\lambda - \Omega) = \frac{\pi t F_0^2 N g(\Omega)}{8} \qquad (2)$$

where $g(\Omega)$ is the phonon density of states (PDOS). Thus:

$$g(\Omega) = \frac{8\langle E(\Omega,T)\rangle}{\pi t F_0^2 N} \qquad (3)$$

In order to obtain the PDOS, our task is to compute the averaged total energy $\langle E(\Omega,T)\rangle$. Moreover, the mode patterns can also be obtained by applying iteratively the external periodic force proportional to the displacements of atoms at each step. The calculations start with the GNRs having perfect armchair edges on both side. Following the previous convention [12]-[13], the GNRs with armchair shaped edges on both sides are classified by the number of dimer lines (N) across the ribbon width W. The structural model of GNRs with perfect armchair edge and realistic edge combining the armchair and zigzag edge along with some point defects is shown in Fig. 1a and 1b, respectively. The maximum width of up to 4 nm (~32 AGNR), while the length is about 120 nm long in the total of 17,474 atoms are considered. The simulations are performed under the free boundary conditions (FBCs). Only interactions up to the fourth nearest neighbor atoms are used and the force constant tensor between two carbon atoms is taken from Jishi et al. [21]. For atoms near an edge, only the force constant of actual atoms is included in the calculation under the FBC.

III. Results and Discussions

Fig. 2 shows the width dependent PDOSs of pure armchair GNRs in comparison with that of the GNRs consist of realistic edges combining the armchair and zigzag edges along with some vacancy type defects. There are more fine structures (peaks) in PDOS curves for the wider GNRs, and the PDOS approaches that of infinite graphene sheet with the increase of

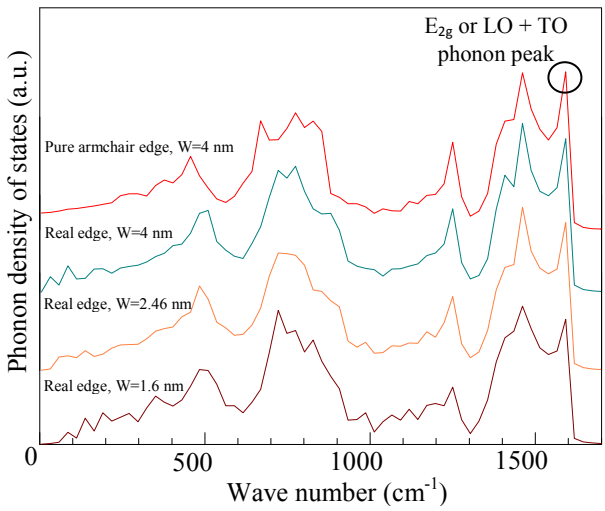

Figure 2. Width dependent phonon density of states of GNRs with realistic edge structures.

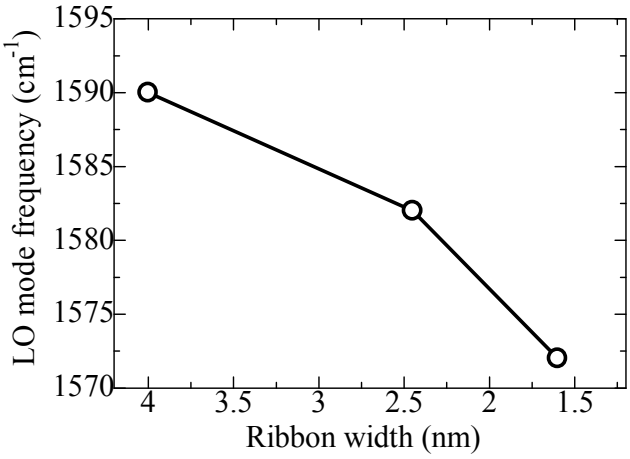

Figure 3. Longitudinal optical mode phonon as a function of ribbon width for the realistic edge structures of GNRs.

the GNR width of about 4 nm. The simulation results reveal that the PDOS of GNR with realistic edge shapes are distorted, non-degenerate and softened with the decrease of ribbon width. Generally, a group of six Γ point phonon modes are observed for GNRs. The physical origin of the G peak (around 1590 cm^{-1}) of Raman spectra comes from the scattering of a doublydegenerate longitudinal optical (LO) and transverse optical (TO) phonon at the Brillouin zone center. It is found that the Γ point of the LO and TO mode phonons of realistic edge shaped GNR are non-degenerate and shifted down with the decrease of ribbon width. The other noteworthy characteristic of the PDOS is the vanishing of fine structure (peaks) at high frequency region, while some fine peaks appear at low frequency region with the decrease of ribbon width as shown in Fig. 2. The shift of the PDOS towards the low frequency region may be induced by the increase of the numbers of the unsaturated C atom with some dangling bonds because the increase of the unsaturated C atoms in the ribbons cause to decrease of the density of high frequency modes.

In armchair graphene nanoribbons (AGNRs), only the LO phonon modes are Raman active, and the G band Raman spectra near the edge shows a down shift of the LO mode. Due to the conical shape of the energy spectrum, momentum conservation notifies that a direct electron–hole pair can couple to the Γ point LO phonon modes, thus shows a down shift of the LO mode [13]. Nevertheless, the TO phonon modes are decoupled from electron–hole pairs. Consequently, the frequency of the TO mode remains same as the original Γ point (LO and TO mode) frequencies of infinite graphene sheet [13]. These effects indicate that the LO phonon mode has the significant contribution to the electron transport in comparison with the TO phonon mode. We have extracted the LO phonon frequencies for various width of GNRs having realistic edge shapes. As can be seen from Fig. 3, the LO frequencies of the nanoribbons are shifted down. It is envisaged that the disorder edges incite the phonon non-degeneracy and move down the LO phonon frequency. The force constant tensors of carbon atoms at the disordered edges are less than that of the pure graphene nanoribbons. Therefore, the phonon frequency decreases compared with that of the ribbon with perfect edges.

The calculated typical mode pattern for the realistic edge structure of GNR is shown in Fig. 4. Here, each circle denotes an atom, and the color denotes the displacement. We mainly focus on the K point of the in plane optical modes (iTO branch) phonon of the eigenmodes due to the dominant effect of these modes on the large D band features of the Raman spectra, especially for defective states of the sample. Due to the defects, the phonons propagations are constrained into a particular region. We observe a strongly localized eigenmodes near the armchair edges and defect sites which are conceptually very good agreement with the Raman D peak comes from the armchair edges or the defects of crystals. These strongly localized states originate from the resonant vibration of the randomly arranged atoms in the disordered edges. In spite of showing the localized vibration of the mode patterns, the centers of the localized modes are not in the same places for different time development. To take out the eigenmodes, a random force has been applied to the each atom of the systems. It is thus expected that the centers of the localized modes are traveled with the each time development. However, in all time development, the centers of the localized modes stay asymmetrically near the armchair edges or the vacancies.

IV. Conclusion

In conclusions, the effect of realistic edge structures on the vibrational properties of graphene nanoribbons has been studied systematically. The forced vibrational method which is

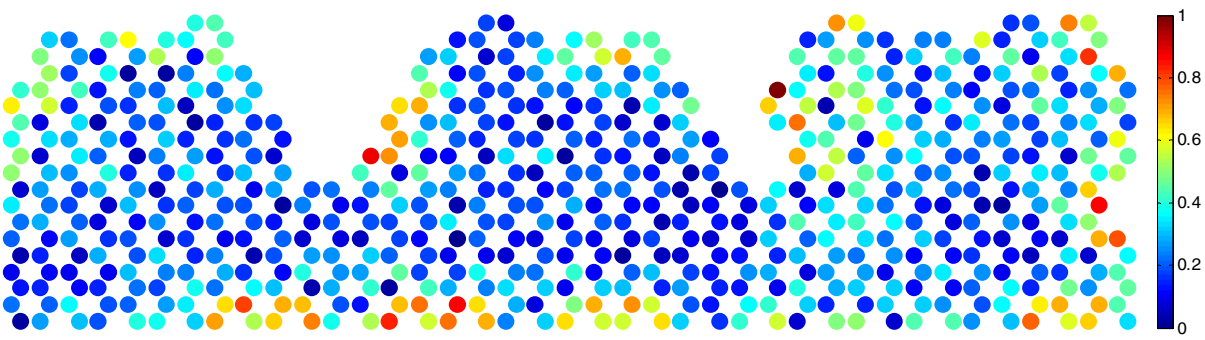

Figure 4. Typical mode pattern for in-plane transverse optical mode phonons of GNRs at 1355 cm^{-1}.

based on the mechanical response to extract the pure vibrational eigenmodes has been employed to perform the numerical experiment. We have calculated the phonon density of states (PDOSs) and typical mode patterns of GNRs considering the effects of the mixture of the different directional armchair and zigzag edges with some vacancy type defects. Our results show that the vibrational properties strongly depend on the realistic edge structures and the width of the ribbons. The PDOSs at low frequency region change significantly for the realistic edge structures. We observe a strongly localized eigenmodes of k-point iTO mode phonon near the armchair edges and defect sites which are conceptually very good agreement with the Raman D peak comes from the armchair edges or the defects of GNRs induced by the iTO mode phonon. These analyses are important not only in fundamental science, but also in advanced nanoelectronics, where the non-ideal realistic edges of GNRs affect the electronic properties significantly.

REFERENCES

[1] C. Berger, Z. Song, T. Li, X. Li, A.Y. Ogbazghi, and R. Feng et al., "Ultrathin Epitaxial Graphite: 2D Electron Gas Properties and a Route toward Graphene-based Nanoelectronics," J. Phys. Chem. B, vol. 108, pp.19912-19916, December 2004.

[2] C. Tao, L. Jiao, O.V. Yazyev, Y. Chen, J. Feng, and X. Zhang et al., "Spatially resolving edge states of chiral graphene nanoribbons," Nat. Phys., vol. 7, pp. 616-620, May 2011.

[3] Z. Chen, Y.M. Lin, M.J. Rooks, and P. Avouris, "Graphene nanoribbon electronics," Physica E, vol. 40, pp. 228-232, December 2007.

[4] M.Y. Han, B. Ozyilmaz, Y. Zhang, and P. Kim, "Energy band-gap engineering of graphene nanoribbons," Phys. Rev. Lett., vol. 98, pp. 206805, May 2007.

[5] J. Cai, P. Ruffieux, R. Jaafar, M. Bieri, T. Braun, S. Blankenburg et al., "Atomically precise bottom-up fabrication of graphene nanoribbons," Nature, vol. 466, pp. 470-473, July 2010.

[6] Y.Y. Li, M.X. Chen, M. Weinert, and L. Li, "Direct experimental determination of onset of electron-electron interactions in gap opening of zigzag graphene nanoribbons," Nat. Commun., vol. 5, pp. 4311, July 2014.

[7] M. Fujita, K. Wakabayashi, K. Nakada, and K. Kusakabe, "Peculiar Localized State at Zigzag Graphite Edge," J. Phys. Soc. Japan, vol. 65, pp. 1920-1923, July 1996.

[8] K. Wakabayashi, M. Fujita, H. Ajiki, and M. Sigrist, "Electronic and magnetic properties of nanographite ribbons," Phys. Rev. B, vol. 59, pp. 8271-8282, March 1999.

[9] L.G. Cancado, M.A. Pimenta, B.R.A. Neves, M.S.S. Dantas, and A. Jorio, "Influence of the Atomic Structure on the Raman Spectra of Graphite Edges," Phys. Rev. Lett., vol. 93, pp. 247401, December 2004.

[10] Md. Sherajul Islam, D. Tamakawa, S. Tanaka, T. Makino, and A. Hashimoto, "Polarized microscopic laser Raman scattering spectroscopy for edge structure of epitaxial graphene and localized vibrational mode," Carbon, vol. 77, pp. 1073-1081, October 2014.

[11] Md. Sherajul Islam, A.G. Bhuiyan, S. Tanaka, and A. Hashimoto, "Polarized micro Raman scattering spectroscopy for curved edges of epitaxial graphene," Appl. Phys. Lett., vol. 105, pp. 243103, December 2014.

[12] Md. Sherajul Islam, S. Tanaka, and A. Hashimoto, "Effect of vacancy defects on phonon properties of hydrogen passivated graphene nanoribbons," Carbon, vol. 80, pp. 146-154, December 2014.

[13] Md. Sherajul Islam, K. Ushida , S. Tanaka, and A. Hashimoto, "Numerical analysis on vacancy induced vibrational properties of graphene nanoribbons," Comput. Mat. Sci., vol. 79, pp. 356-361, November 2013.

[14] F. Mazzamuto, J. Saint-Martin, A. Valentin, C. Chassat, P. Dollfus, "Edge shape effect on vibrational modes in graphene nanoribbons: A numerical study," J. Appl. Phys., vol. 422, pp. 064516, March 2011.

[15] M. Xia, Y. Song, S. Zhang, "Specific heat of graphene nanoribbons," Phys. Lett. A, vol. 375, pp. 3726–3730, October 2011.

[16] Y. Yamakita, K. Ohno, "Phonon dispersion and vibronic coupling in carbon nanoribbons," J. Phys.: Conf. Ser., vol. 185, pp. 012055, October 2009.

[17] M. Vandescuren, P. Hermet, V. Meunier, L. Henrard, Ph. Lambin, "Theoretical study of the vibrational edge modes in graphene nanoribbons," Phys. Rev. B, vol. 78, pp. 195401, November 2008.

[18] R. Gillen, M. Mohr, C. Thomsen, J. Maultzsch, "Vibrational properties of graphene nanoribbons by first-principles calculations," Phys. Rev. B, vol. 80, pp. 155418, October 2009.

[19] Z.W. Tan, J.S. Wang and C.K. Gan, Nano Lett., "First-Principles Study of Heat Transport Properties of Graphene Nanoribbons," Nano Lett., vol. 11, pp. 214-219, January 2011.

[20] M.L. Williams, H.J. Maris, "Numerical study of phonon localization in disordered systems," Phys. Rev. B, vol. 31, pp. 4508-4515, April 1985.

[21] R.A. Jishi, L. Venkataraman, M.S. Dresselhaus, G. Dresselhaus, "Phonon modes in carbon nanotubules," Chem. Phys. Lett., vol. 209, pp. 77–82, January 1993.

Modeling of Crosstalk Induced Overshoot/Undershoot Effects in Multilayer Graphene Nanoribbon Interconnects

Manodipan Sahoo and Hafizur Rahaman
Department of Information Technology, Indian Institute of Engineering Science and Technology,
Shibpur, Howrah-711103, India
E-mail: manodipansahoo@gmail.com, rahaman_h@it.iiests.ac.in

***Abstract*—Crosstalk induced overshoot/undershoot effects in Multilayer Graphene Nano Ribbon interconnects (MLGNRs) are investigated using ABCD parameter matrix approach for intermediate level interconnects at 8 nm technology node. The worst case crosstalk induced peak overshoot voltage for perfectly specular doped multilayer zigzag GNR interconnects is comparable to that of copper interconnects. It is observed that the performance of neutral GNR interconnects is better than that of its doped counterpart in terms of peak crosstalk induced overshoot voltage. But from the perspective of effective electric field across the gate oxide, the multilayer doped GNR interconnects outperform neutral ones and copper interconnects for all the cases. Finally, our analysis has shown that from the gate oxide reliability perspective, the perfectly specular doped multilayer zigzag GNR interconnects are significantly advantageous to copper interconnects for future generation Integrated circuit technology.**

Keywords*—Crosstalk ; Overshoot/Undershoot ; Graphene Nano Ribbon (GNR) ; Interconnects ; ABCD parameter ; Specular ; Neutral ; Gate oxide reliability ; Integrated circuit.

I. Introduction

The ever increasing circuit complexity led by Moore's law with the continuous scaling of CMOS technology has made the role of interconnects in nanometer technology nodes very prominent. However conventional copper wires face tremendous challenges of the nanometer technology where the requirement is of reliable high speed wires with minimal crosstalk effects. Graphene has been regarded as a suitable material for nanometer technology [1], [2] because of its tolerance to higher maximum current density, lower resistivity and lower capacitive effects compared to copper at nanometer dimensions [2]. Moreover, compared to multi-walled carbon nanotubes (MWCNT), Graphene is suitable for its simpler fabrication processes, better material control and reproducibility. Recently, a CMOS Ring oscillator with graphene interconnects is fabricated to operate at a frequency of 1.3 GHz [3].

Xu et. al. have studied the performance of GNR interconnect in [5]. Naeemi and Meindl has proposed a physics based circuit model for GNR interconnect in [4]. Crosstalk effects in MLGR interconnects have been studied in [7], [8], [6]. In all these works, the crosstalk induced effects are analyzed using SPICE simulations. However Simulation tools like SPICE is computationally expensive at the full-chip level [9]. Therefore, a non-SPICE based model is necessary for analyzing crosstalk effects in dense high performance ICs. The ABCD parameter matrix based model has been proposed for analyzing crosstalk induced effects in SWCNT bundle interconnects [10], MWCNT bundle interconnects [11] and MLGNR interconnects [12]. In this work, ABCD parameter based model is used to analyze crosstalk induced overshoot/undershoot effects in multilayer neutral and doped zigzag GNR interconnects of various specularity at 8 nm technology node. The impact of overshoot/undershoot on the gate oxide reliability is also estimated. It is found that 100 μm long, doped perfectly specular MLGNR interconnects have gate oxide failure rate (AFR) of three orders lesser than copper interconnects for 8 nm technology node.

The paper is presented in the following sequence. Section II presents the equivalent RLC model for multilayer GNR interconnects. Section III discusses the proposed ABCD parameter matrix based approach in details. Section IV describes how crosstalk induced overshoot/undershoot impacts the gate oxide reliability of CMOS devices. Section V presents simulation results. Finally the conclusions are drawn in Section VI.

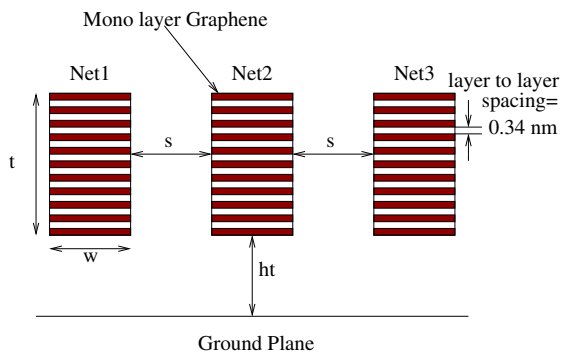

Fig. 1: Multilayer GNR structure.

II. Electrical modeling of multilayer GNR interconnects

The carbon atoms are arranged in a honeycomb structure in graphene. Graphene shhet is regarded as either armchair or

This work is partially supported by the DIT, Government of West Bengal, India under VLSI Design Project.

978-1-4673-9257-0/15/$31.00 ©2015 IEEE

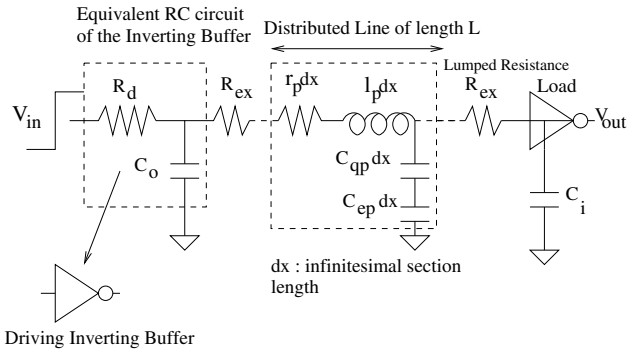

Fig. 2: Equivalent RLC model of a typical multilayer GNR interconnect system.

zigzag based on the arrangement of carbon atoms. Chirality differs the conductive property in zigzag and armchair GNR. For interconnect applications, zigzag GNR is proposed due to its metallic property. Multi-layer zigzag GNR structure is utilized in modeling the nanoscale interconnects here because of the low conductivity of the mono layer GNR interconnects. Fig. 1 shows a typical MLGNR interconnect structure [5]. The interconnect dimensions are represented as t (thickness), w(width), ht(height from ground plane), and s(spacing between the interconnects) and δ (= 0.34 nm) (spacing between each graphene layer known as the Van der Waal's gap). The interconnect dimensions have been considered according to latest ITRS-2013 data [1] as shown in Table I. The number of graphene layers is given by,

$$N_{layer} = 1 + \lfloor \frac{t}{\delta} \rfloor \tag{1}$$

Fig. 2 depicts the equivalent RLC model of a typical MLGNR interconnect system. In the figure, L is the interconnect length, R_{ex} is the lumped resistance (i.e., consists of GNR-electrode contact resistance(R_C) and quantum resistance(R_Q), $R_{ex} = (R_C + R_Q)/2$), r_p is per unit length (p.u.l) distributed resistance, l_p is p.u.l self inductance (consists of kinetic inductance, L_k and self inductance, L_s), C_{qp} is p.u.l quantum capacitance, C_{ep} is p.u.l electrostatic ground capacitance. The quantum resistance is defined as [5],

$$R_Q = \frac{\frac{h}{2q^2}}{N_{ch}N_{layer}} = \frac{12.94K\Omega}{N_{ch}N_{layer}} \tag{2}$$

where, N_{ch} is the number of conducting channels (modes) in one layer, N_{layer} is the number of GNR layers, h is the Plancks constant (=6.626×10^{-34} J.s), and q is the electronic charge (=1.6×10^{-19} C). The number of conducting channels in mono-layer graphene (i.e., N_{ch}) is given by [5],

$$N_{ch} = \sum_{j=1}^{n_C} \left[1 + e^{\frac{(E_{j,n} - E_F)}{K_B T}} \right]^{-1} + \sum_{j=1}^{n_V} \left[1 + e^{\frac{(E_{j,h} + E_F)}{K_B T}} \right]^{-1} \tag{3}$$

where, j (=1, 2, 3, ...) is a positive integer, E_F is Fermi energy, K_B is the Boltzmann constant, T is absolute temperature, and n_C and n_V are the number of conduction and valence subbands, respectively. $E_{j,n}$ and $E_{j,h}$ are the energies of electron and hole in j^{th} subband as given by [4],

$$E_j = \frac{h\nu_F}{2w} |j + \frac{1}{2}| \tag{4}$$

TABLE I: Global-level Interconnect Parameters (ITRS-2013)

Parameters \ Year	2024	2027
DRAM1/2 pitch(nm) (contacted)	11.0	8.4
MPU/ASIC Metal1 1/2 pitch(nm) (contacted)	11.3	8.0
MPU Physical gate length (nm)	7.39	5.62
No. of Metal levels	15	16
Wiring pitch (nm)	23	16
	34	24
Wiring height to width ratio	2.1	2.2
	2.34	2.4
A/R (Via)	1.9	1.9
	1.5	1.5
Effective Resistivity ($\mu\Omega$-cm)	8.75	10.81
	7.04	8.50
V_{DD} (Volt)	0.69	0.65
V_{th} (Volt)	0.233	0.265
Equivalent Oxide thickness (EOT) (nm)	0.49	0.43
Effective dielectric constant (k_{eff})	1.88-2.28	1.65-2.09
Average dielectric constant (k_{avg}) of the interlevel dielectric	2.08	1.87

TABLE II: RC parameters of the inverting buffer for various technology nodes

Parameters \ Technology node	11 nm	8 nm
R_d (in KΩ)	42.1	65.8
C_o (in fF)	0.012	0.007
C_i (in fF)	0.036	0.021

where, j(=1, 2, 3, ...) is an integer. The p.u.l resistance (r_p) of the MLGNR interconnect is calculated according to the method explained in [5].

The per unit length quantum capacitance (C_{qp}) is expressed as ,

$$C_{qp} = N_{ch}N_{layer}\frac{4q^2}{h\nu_F} = N_{ch}N_{layer} \times 193.18aF/\mu m \tag{5}$$

where, ν_F is the Fermi velocity = 8×10^5 m/s for GNR [4]. The per unit length kinetic inductance(L_k) is expressed as [5],

$$L_k = \frac{\frac{h}{4q^2\nu_F}}{N_{ch}N_{layer}} = \frac{8.0884}{N_{ch}N_{layer}} nH/\mu m \tag{6}$$

The self inductance (L_s) and electrostatic capacitance (C_{ep}) of GNR are assumed to be same as that of Cu with equal dimensions [5]. The total p.u.l inductance of the MLGNR interconnect is expressed as $l_p \approx (L_k + L_s)$. Inverting buffers are used to implement both the driver and load. The load capacitance, C_i in Fig. 2, denotes the gate capacitance of the load inverting buffer. The parameters of the buffers are R_d(equivalent switching resistance), C_o(equivalent diffusion capacitance) and C_i(equivalent gate capacitance). The RC parameters (i.e., R_d, C_o and C_i) for the driver/load buffer at 8 nm technology node are calculated from ITRS-2013 roadmap [1] as shown in Table II. The analytical equations used to calculate distributed RLC parameters of copper interconnect are taken from [13].

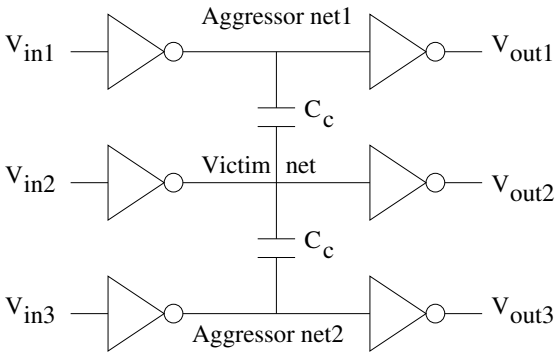

Fig. 3: How the overshoot/undershoot effects occur through coupling capacitance?

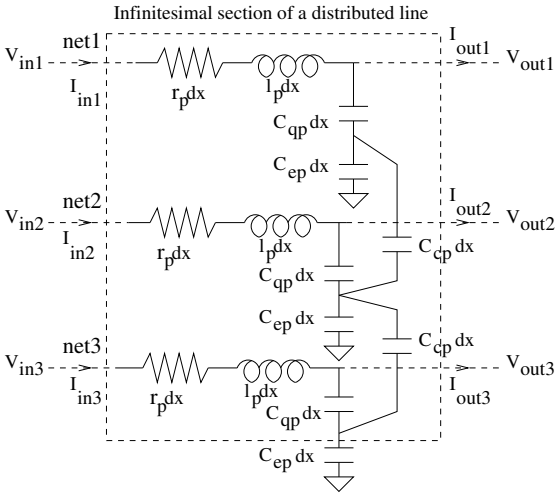

Fig. 4: Infinitesimal section of an identically coupled three conductor multilayer GNR interconnect system.

III. Modeling of Crosstalk induced overshoot/undershoot effects

Fig. 3 shows how coupling capacitance induces overshoot and undershoot in victim net. With victim net at logic high level if aggressor nets(net1 and net2) switch from logic low to high then overshoot occurs in the victim net. Whereas, for victim net kept at logic low level if both the aggressor nets switch from logic high to low then undershoot occurs.

An efficient computational model for crosstalk induced overshoot/undershoot analysis in identically coupled multilayer doped GNR interconnect systems is presented. In our proposed methodology first, we develop an analytical expression for the crosstalk induced overshoot/undershoot in Laplace domain. Then we adopt the inverse Laplace transform to find out its time-domain response. Our methodology is as accurate as SPICE but computationally much faster [10], [11]. The proposed methodology is illustrated as follows.

A. ABCD parameter based approach

An infinitesimal lumped RLC section of an identically coupled multilayer doped GNR interconnect system is shown in Fig. 4. The Kirchhoff equation for an infinitesimally small segment of these three identically coupled interconnects is given by the following equation [14],

$$\phi_{in} = P\phi_{out} \tag{7}$$

where,

$$\phi_{in} = [V_{in1}, V_{in2}, V_{in3}, I_{in1}, I_{in2}, I_{in3}]^T \tag{8}$$

$$\phi_{out} = [V_{out1}, V_{out2}, V_{out3}, I_{out1}, I_{out2}, I_{out3}]^T \tag{9}$$

and, matrix P is shown in (12). The matrix P may be diagonalized as $P = VWV^{-1}$, where,

$$V = \begin{bmatrix} Z_1 & -Z_1 & Z_2 & -Z_2 & -Z_3 & Z_3 \\ Z_1 & -Z_1 & -2Z_2 & 2Z_2 & 0 & 0 \\ Z_1 & -Z_1 & Z_2 & -Z_2 & Z_3 & -Z_3 \\ 1 & 1 & 1 & 1 & -1 & -1 \\ 1 & 1 & -2 & -2 & 0 & 0 \\ 1 & 1 & 1 & 1 & 1 & 1 \end{bmatrix} \tag{10}$$

and, W is a diagonal matrix as shown in (13). Here, dx is the length of the infinitesimal line and θ_1, θ_2 and θ_3 are the propagation constants of the decoupled interconnects. Z_1, Z_2 and Z_3 are the characteristic impedances of the decoupled interconnects. These parameters are defined as: $dx = L/n$, $\theta_1 = \sqrt{s(\alpha.C_{qp})(r_p + sl_p)}$, $\theta_2 = \sqrt{s(\beta.C_{qp})(r_p + sl_p)}$, $\theta_3 = \sqrt{s(\gamma.C_{qp})(r_p + sl_p)}$, $Z_1 = \sqrt{\frac{(r_p+sl_p)}{s(\alpha.C_{qp})}}$, $Z_2 = \sqrt{\frac{(r_p+sl_p)}{s(\beta.C_{qp})}}$ and $Z_3 = \sqrt{\frac{(r_p+sl_p)}{s(\gamma.C_{qp})}}$. Here, n is the number of infinitesimal sections. Other parameters are defined as, $\alpha = (1-2g-h)$, $\beta = (1+g-h)$ and $\gamma = (1+2f-g-h)$, where, $f = \frac{a^2}{ab^2+b^3-2a^2b}$, $g = \frac{ab}{ab^2+b^3-2a^2b}$ and $h = \frac{b^2}{ab^2+b^3-2a^2b}$ with $a = \frac{C_{cp}}{C_{qp}}$ and $b = \frac{C_{ep}+C_{qp}+C_{cp}}{C_{qp}}$. Using, $P^n = (VWV^{-1})^n = (VW^nV^{-1})$ and the identity, $\lim_{n\to+\infty}(1+\frac{x}{n})^n \to e^x$, P^n can be written as shown in (14), where, $ta = \cosh(L\theta_1)$, $tb = \cosh(L\theta_2)$, $tc = \cosh(L\theta_3)$, $td = \sinh(L\theta_1)$, $te = \sinh(L\theta_2)$,and $tf = \sinh(L\theta_3)$. Here, P_{dr} and P_{dc} are the ABCD matrices of the driving buffer, P_{Rf} is the ABCD matrix representation of the lumped resistance R_{ex} and P_{load} is that of the capacitive load. The final Kirchoff equation for the coupled interconnects can be written as,

$$\Phi_i = P_{dr}P_{dc}P_{R_{ex}}P^nP_{R_{ex}}P_{load}\Phi_o \tag{11}$$

By solving (11), the final output voltages V_{o1}(s), V_{o2}(s) and V_{o3}(s) can be represented in terms of the inputs V_{i1}(s), V_{i2}(s) and V_{i3}(s) in matrix form as shown in (15). The exact expressions of H_1(s), H_2(s) and H_3(s) in (15) are shown in (16), (17) and (18) respectively where, $A = (1 + sR_dC_o)$ and, $B = (R_d + AR_{ex})$. H_1(s), H_2(s) and H_3(s) are the transfer functions of the decoupled interconnects. Here, The transfer function for the crosstalk induced overshoot/undershoot evaluation in the victim net will be denoted as H(s) throughout the paper. H(s) can be derived from (15) for different evaluation conditions (i.e., crosstalk induced overshoot/undershoot). We consider a fifth-order Padé expansion for approximating hyperbolic functions in (16), (17) and (18) with high degree of accuracy [15]. So the transfer function H(s) will be of the form as follows [given in (19)] after the Padé expansion.

$$H(s) = \frac{1}{1 + sb_1 + s^2b_2 + s^3b_3 + s^4b_4 + s^5b_5 + s^5b_5 + s^6b_6 + s^7b_7} \tag{19}$$

where, the coefficients are shown below,

$$b_1 = \frac{L^2r_pC}{2} + R_d(C_o + C_i) + 2R_{ex}C_i + (R_d + R_{ex})LC + LC_ir_p \tag{20}$$

$$\begin{aligned} b_2 = {} & 2R_{ex}R_dC_oC_i + \frac{L^2l_pC}{2} + C_iLl_p + \frac{C_iL^3r_p^2C}{6} + \frac{L^4r_p^2C^2}{24} \\ & \frac{L^2r_pC(R_dC_o + R_dC_i + 2R_{ex}C_i)}{2} + \frac{(R_d + R_{ex})r_pL^3C^2}{6} + \\ & LR_{ex}C(R_dC_o + R_dC_i + 2R_{ex}C_i) + LC_iR_dC_or_p \end{aligned} \tag{21}$$

$$P = \begin{bmatrix} 1 & 0 & 0 & (r_p + sl_p)dx & 0 & 0 \\ 0 & 1 & 0 & 0 & (r_p + sl_p)dx & 0 \\ 0 & 0 & 1 & 0 & 0 & (r_p + sl_p)dx \\ sC_{qp}(1-(g+h-f))dx & -sC_{qp}.g.dx & -sC_{qp}.f.dx & 1 & 0 & 0 \\ -sC_{qp}.g.dx & sC_{qp}(1-h)dx & -sC_{qp}.g.dx & 0 & 1 & 0 \\ -sC_{qp}.f.dx & -sC_{qp}.g.dx & sC_{qp}(1-(g+h-f))dx & 0 & 0 & 1 \end{bmatrix} \tag{12}$$

$$W = \begin{bmatrix} (1+\theta_1 dx) & 0 & 0 & 0 & 0 & 0 \\ 0 & (1-\theta_1 dx) & 0 & 0 & 0 & 0 \\ 0 & 0 & (1+\theta_2 dx) & 0 & 0 & 0 \\ 0 & 0 & 0 & (1-\theta_2 dx) & 0 & 0 \\ 0 & 0 & 0 & 0 & (1+\theta_3 dx) & 0 \\ 0 & 0 & 0 & 0 & 0 & (1-\theta_3 dx) \end{bmatrix} \tag{13}$$

$$P^n = \begin{bmatrix} (\frac{ta}{3}+\frac{tb}{6}+\frac{tc}{2}) & (\frac{ta}{3}-\frac{tb}{3}) & (\frac{ta}{3}+\frac{tb}{6}-\frac{tc}{2}) & (\frac{td.Z1}{3}+\frac{te.Z2}{6}+\frac{tf.Z3}{2}) & (\frac{td.Z1}{3}-\frac{te.Z2}{3}) & (\frac{td.Z1}{3}+\frac{te.Z2}{6}-\frac{tf.Z3}{2}) \\ (\frac{ta}{3}-\frac{tb}{3}) & (\frac{ta}{3}+\frac{2tb}{3}) & (\frac{ta}{3}-\frac{tb}{3}) & (\frac{td.Z1}{3}-\frac{te.Z2}{6}) & (\frac{td.Z1}{3}+\frac{2te.Z2}{3}) & (\frac{td.Z1}{3}-\frac{te.Z2}{3}) \\ (\frac{ta}{3}+\frac{tb}{6}-\frac{tc}{2}) & (\frac{ta}{3}-\frac{tb}{3}) & (\frac{ta}{3}+\frac{tb}{6}+\frac{tc}{2}) & (\frac{td.Z1}{3}+\frac{te.Z2}{6}-\frac{tf.Z3}{2}) & (\frac{td.Z1}{3}-\frac{te.Z2}{3}) & (\frac{td.Z1}{3}+\frac{te.Z2}{6}+\frac{tf.Z3}{2}) \\ (\frac{td}{3Z1}+\frac{te}{6Z2}+\frac{tf}{2Z3}) & (\frac{td}{3Z1}-\frac{te}{3Z2}) & (\frac{td}{3Z1}+\frac{te}{6Z2}-\frac{tf}{2Z3}) & (\frac{ta}{3}+\frac{tb}{6}+\frac{tc}{2}) & (\frac{ta}{3}-\frac{tb}{3}) & (\frac{ta}{3}+\frac{tb}{6}-\frac{tc}{2}) \\ (\frac{td}{3Z1}-\frac{te}{3Z2}) & (\frac{td}{3Z1}+\frac{2te}{3Z2}) & (\frac{td}{3Z1}-\frac{te}{3Z2}) & (\frac{ta}{3}-\frac{tb}{3}) & (\frac{ta}{3}+\frac{2tb}{3}) & (\frac{ta}{3}-\frac{tb}{3}) \\ (\frac{td}{3Z1}+\frac{te}{6Z2}-\frac{tf}{2Z3}) & (\frac{td}{3Z1}-\frac{te}{3Z2}) & (\frac{td}{3Z1}+\frac{te}{6Z2}+\frac{tf}{2Z3}) & (\frac{ta}{3}+\frac{tb}{6}-\frac{tc}{2}) & (\frac{ta}{3}-\frac{tb}{3}) & (\frac{ta}{3}+\frac{tb}{6}+\frac{tc}{2}) \end{bmatrix} \tag{14}$$

$$\begin{bmatrix} V_{o1}(s) \\ V_{o2}(s) \\ V_{o3}(s) \end{bmatrix} = \begin{bmatrix} (\frac{1}{3}H_1(s)+\frac{1}{6}H_2(s)+\frac{1}{2}H_3(s)) & \frac{1}{3}(H_1(s)-H_2(s)) & (\frac{1}{3}H_1(s)+\frac{1}{6}H_2(s)-\frac{1}{2}H_3(s)) \\ \frac{1}{3}(H_1(s)-H_2(s)) & (\frac{1}{3}H_1(s)+\frac{2}{3}H_2(s)) & \frac{1}{3}(H_1(s)-H_2(s)) \\ (\frac{1}{3}H_1(s)+\frac{1}{6}H_2(s)-\frac{1}{2}H_3(s)) & \frac{1}{3}(H_1(s)-H_2(s)) & (\frac{1}{3}H_1(s)+\frac{1}{6}H_2(s)+\frac{1}{2}H_3(s)) \end{bmatrix} \begin{bmatrix} V_{i1}(s) \\ V_{i2}(s) \\ V_{i3}(s) \end{bmatrix} \tag{15}$$

$$H_1(s) = \frac{1}{(A(1+sC_iR_{ex})+sC_iB)\cosh(\theta_1 L)+(\frac{B}{Z_1}(1+sC_iR_{ex})+AsC_iZ_1)\sinh(\theta_1 L)} \tag{16}$$

$$H_2(s) = \frac{1}{(A(1+sC_iR_{ex})+sC_iB)\cosh(\theta_2 L)+(\frac{B}{Z_2}(1+sC_iR_{ex})+AsC_iZ_2)\sinh(\theta_2 L)} \tag{17}$$

$$H_3(s) = \frac{1}{(A(1+sC_iR_{ex})+sC_iB)\cosh(\theta_3 L)+(\frac{B}{Z_3}(1+sC_iR_{ex})+AsC_iZ_3)\sinh(\theta_3 L)} \tag{18}$$

$$\begin{aligned} b_3 = {} & \frac{L^2 l_p C(R_dC_o+R_dC_i+2R_{ex}C_i)}{2} + Cr_pL^2R_dR_{ex}C_oC_i + \\ & \frac{C^2r_pl_pL^4}{12} + l_pLC_iR_dC_o + \frac{C^2r_p^2L^4(R_dC_o+R_dC_i+2R_{ex}C_i)}{24} \\ & + CLC_iR_{ex}^2R_dC_o + \frac{C^2r_pL^3R_{ex}(R_dC_o+R_dC_i+R_{ex}C_i)}{6} + \\ & \frac{Cr_p^2L^3R_{ex}C_iC_o}{6} + \frac{Cr_pl_pC_iL^3}{6} + \Big(\frac{Cl_pL^3}{6}+\frac{C^2r_p^2L^5}{120}\Big) \\ & (C(R_d+R_{ex})+r_pC_i) \end{aligned} \tag{22}$$

$$\begin{aligned} b_4 = {} & Cl_pL^2R_dR_{ex}C_oC_i + \frac{C^2l_p^2L^4}{24} + \frac{C^2r_p^2L^4(R_dC_oR_{ex}C_i)}{12} + \\ & \frac{C^2r_pl_pL^4(R_dC_o+R_dC_i+2R_{ex}C_i)}{12} + \frac{Cr_pl_pC_iL^3R_dC_o}{6} + \\ & \frac{C^2r_pC_iL^3(R_dC_oR_{ex}^2)}{6} + \frac{C^2r_pl_pL^5}{60}(C(R_d+R_{ex})+rC_i) + \\ & \Big(\frac{Cl_pL^3}{6}+\frac{C^2r_p^2L^5}{120}\Big)(CR_{ex}R_dC_o+CR_{ex}C_i(R_d+R_{ex})+ \\ & r_pC_iR_dC_o+l_pC_i) \end{aligned} \tag{23}$$

$$\begin{aligned} b_5 = {} & \frac{C^2l_p^2L^4}{24}(R_dC_o+R_dC_i+2R_{ex}C_i) + \Big(\frac{Cl_pL^3}{6}+\frac{C^2r_p^2L^5}{120}\Big) \\ & (CR_{ex}^2C_iR_dC_o+l_pC_iR_dC_o) + \frac{C^2l_p^2L^5}{120}(C(R_d+R_{ex})+rC_i) + \\ & \frac{C^2r_pl_pL^4(R_dC_oR_{ex}C_i)}{6}(CR_{ex}R_dC_o+CR_{ex}C_i(R_d+R_{ex})+ \\ & r_pC_iR_dC_o+l_pC_i) + \frac{C^2r_pl_pL^5}{60} \end{aligned} \tag{24}$$

$$\begin{aligned} b_6 = {} & \frac{C^2l_p^2L^4(R_dC_oR_{ex}C_i)}{12} + \frac{C^2r_pl_pL^5}{60}(CR_{ex}^2C_iR_dC_o+ \\ & l_pC_iR_dC_o) + \frac{C^2l_p^2L^5}{120}(CR_{ex}R_dC_o+CR_{ex}C_i(R_d+R_{ex})+ \\ & r_pC_iR_dC_o+l_pC_i) \end{aligned} \tag{25}$$

$$b_7 = \frac{C^2l_p^2L^5}{120}(CR_{ex}^2C_iR_dC_o+l_pC_iR_dC_o) \tag{26}$$

Similarly, H_2(s) and H_3(s) can be represented in a form as given in (19). The parameter C in the coefficients b_1 to b_7 varies according to the transfer function of the decoupled interconnect and it is represented as αC_{qp}, βC_{qp} and γC_{qp} in $H_1(s)$, $H_2(s)$ and $H_3(s)$ respectively. The other parameters correspond to the distributed parameters of the copper interconnect, length of the interconnect, driver and load RC parameters.

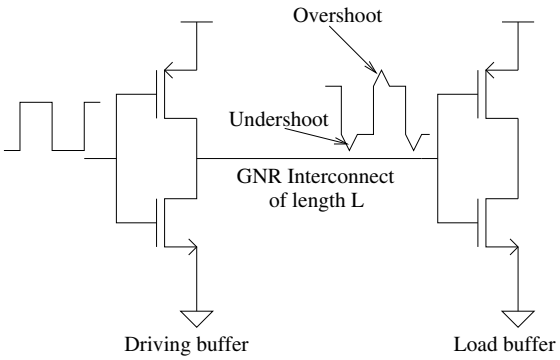

Fig. 5: Crosstalk induced overshoot/undershoot effects.

IV. Gate oxide reliability of CMOS devices

Fig. 5 depicts how overshoot stresses the NMOS gate oxide and undershoot stresses the PMOS gate oxide. As understood from the figure that, gate oxides of MOS transistors are operated under pulsed conditions. Thus the gate oxide faces an ac electric field. However, to estimate the impact of this electric stress on the oxide, an effective electric field is defined as follows [16],

$$E_{avg} = \frac{1}{\psi}\ln\Big[\frac{1}{T}\int_0^T e^{\psi E_{ins}(t)}dt\Big] \tag{27}$$

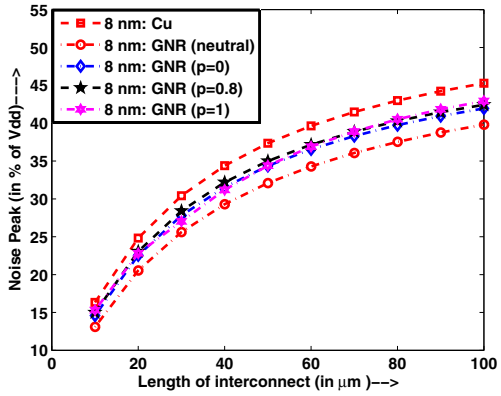

Fig. 6: Comparison of crosstalk induced peak overshoot voltage at 8 nm node

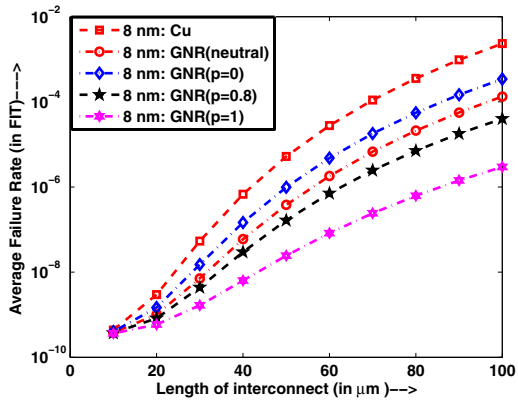

Fig. 8: Comparison of average failure rate of MOS gate oxide at 8 nm node.

where, ψ is the field acceleration factor. In [17], it is shown that the impact of the overshoot/undershoot induced electric field can be estimated by calculating the average failure rate (AFR) of the MOS gate oxides. Information about failure rates of gate oxides is already gathered under various electric stress conditions (i.e., varying oxide thickness, applied gate voltage etc.) using a reference oxide area and reference temperature. The AFR [16] of a MOS device having gate oxide area A is then expressed as below,

$$AFR = \frac{AFR_{const}}{A_{const}} A e^{\psi W_S (E_{avg} - E_{const})} \tag{28}$$

where, AFR_{const} is the reference failure rate, A_{const} is the reference area of the sample used for calculating reference failure rate, W_S is the Weibull slope, E_{avg} is the effective electric field across the gate oxide, and E_{const} is the reference electric field. Using (28), we calculate the AFR of the MOS devices. For this purpose, we consider parameters such that the failure rate of a chip operating at nominal voltage is 10 FIT, assuming one billion transistors in a chip.

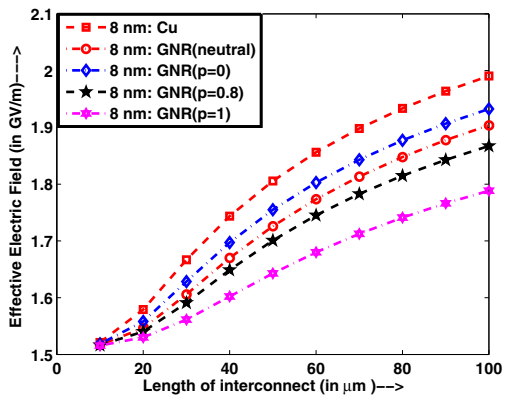

Fig. 7: Comparison of effective electric field across the gate oxide at 8 nm node.

V. Simulation Results

The proposed analytical model is implemented in MATLAB 7.1 running on standard desktop with 1.6 GHz Intel Core 2 Duo processor with 2.5 GB memory. The crosstalk induced overshoot values are calculated for different RLC values of the intermediate level multilayer GNR interconnect at 8 nm technology node with length ranging from 10 μm to 100 μm. Driving and load inverter buffer sizes are chosen as 50 times the minimum sized buffer. The individual GNR layer-electrode contact resistance is considered as 100 KΩ. Fermi levels are set as 0 eV and 0.3 eV respectively for neutral and doped GNR interconnects [5]. Perfectly specular (i.e., $p = 1.0$) GNR edges are assumed for neutral zz-GNR, whereas specularity index (i.e., p) is varied from completely diffusive edges ($p = 0.0$) to completely specular edges ($p = 1.0$) for AsF_5 intercalation doped zz-GNR interconnects [5]. Further Mean free path (i.e., λ) is considered here as 419 nm and 1.03 μm for neutral and AsF_5 doped MLGNR interconnects respectively [5].

A. Analysis of crosstalk induced overshoot effects

Fig. 6 delineates the worst case peak crosstalk induced overshoot for copper and GNR interconnects of various specularity viz. $p = 0.0, 0.8$ and 1.0 for both the technology nodes. It is a fact that the peak crosstalk induced overshoot voltage depends upon the coupling ratio (C.R.) where, C.R.=$\frac{C_{cp}L}{SC_i + C_{cp}L + C_{ep}L}$. At smaller interconnect lengths, due to smaller coupling ratio, peak overshoot is dependent upon the time constant of the interconnect system. Copper interconnects induce the maximum overshoot amongst all. While the perfectly specular GNR interconnects induce the maximum overshoot amongst the GNR counterparts (i.e., of various specularity) due to its least time constant. Being of larger time constant, the neutral GNR interconnect induces the least amount of overshoot.

B. Analysis of gate oxide reliability

Fig. 7 depicts the effective electric field produced because of this excess electric field over the gate oxide. As observed from the figure, copper interconnect again is the victim of producing maximum electric field across the gate oxide irrespective of technology nodes. Interestingly though doped perfectly specular MLGNR interconnect induces higher overshoot but produces the least effective electric field in both the technology nodes with others producing electric field in between. The reason behind this is that because of its least

time constant amongst all, it induces least amount of overshoot area (i.e., $\frac{1}{2} \times overshoot\ peak \times overshoot\ width$). Finally, Average failure rate (AFR) is plotted in Fig. 8. As observed from (28) that effective electric field is the marker for how reliable will be the interconnect and this is quantified through Average failure rate (AFR). It is seen that 100 μm long, doped perfectly specular MLGNR interconnects have an AFR of three orders smaller than copper interconnects for 8 nm technology node respectively. Further it is inferred from the figure that with higher interconnect length AFR increases, which can also be intuitively understood.

VI. Conclusions

In this work, an ABCD parameter matrix based model for crosstalk induced overshoot/undershoot has been proposed for multilayer Graphene Nano Ribbon interconnects for intermediate level interconnects at 8 nm node. The worst case crosstalk induced peak overshoot/undershoot voltages have been derived for both neutral and doped zigzag MLGNR interconnects and compared to those of conventional copper interconnects. The worst case crosstalk induced peak overshoot voltage for near specular, doped multilayer zigzag GNR interconnects is comparable to that of copper interconnects. It has been observed that the performance of neutral MLGNR interconnects is better than that of its doped counterpart with respect to peak crosstalk induced overshoot, but from the perspective of effective electric field across the gate oxide, doped MLGNR interconnects outperform neutral ones and copper interconnects for all the cases. Finally, our analysis has shown that from the gate oxide reliability perspective, perfectly specular, doped multilayer zigzag GNR interconnects are significantly advantagious compared to copper interconnects for future IC technology generations.

References

[1] International Technology Roadmap for Semiconductors (ITRS-2013) Reports, [Online]. Available: http://www.itrs.net/reports.html.

[2] A. Naeemi and J.D. Meindl., "Performance Benchmarking for Graphene Nanoribbon, Carbon Nanotube, and Cu Interconnects", *IITC 2008*, pp. 183–185.

[3] X. Chen et. al., "High-speed Graphene Interconnects Monolithically Integrated with CMOS Ring Oscillators Operating at 1.3 GHz", *IEEE IEDM*, 2009, pp. 1-4.

[4] A. Naeemi and, J. D. Meindl, "Compact Physics- Based Circuit Models for Graphene Nanoribbon Interconnects," *IEEE Trans. on Electron Devices*, vol. 56, no. 9, pp. 1822-1833, Sep. 2009.

[5] C. Xu, H. Li and, K. Banerjee, "Modeling, Analysis, and Design of Graphene Nano-Ribbon Interconnects," *IEEE Trans. on Electron Devices*, vol. 56, no. 8, pp. 1567-1578, Aug. 2009.

[6] D. Das and, H. Rahaman, "Crosstalk and Gate Oxide Reliability Analysis in Graphene Nanoribbon Interconnects", 2nd *International Symposium on Electronic System Design (ISED)*, Dec. 2011, pp. 182-187.

[7] W.-S. Zhao and, W.-Y. Yin, "Signal Integrity Analysis of Graphene Nano-Ribbon (GNR) Interconnects", *IEEE Electrical Design of Advanced Packaging and Systems Symposium (EDAPS)*, pp. 227–230, 2012.

[8] W. -S. Zhao and W. -Y. Yin, "Comparative Study on Multilayer Graphene Nanoribbon (MLGNR) Interconnects", *IEEE Trans. on Electromagnetic Compatibility*, vol. 56, no. 3, pp. 638–645, June 2014.

[9] Y. Eo et. al., "Generalized travelingwave- based waveform approximation technique for the efficient signal integrity verification technique of multicoupled transmission lines," *IEEE TCAD*, vol. 21, no. 12, pp. 1489-1497, Dec. 2002.

[10] M. Sahoo, P. Ghosal and, H. Rahaman, "An ABCD parameter based Modeling and Analysis of Crosstalk Induced Effects in Single-Walled Carbon Nanotube Bundle Interconnects", *IEEE ASQED*, Aug. 2013, pp. 264–273.

[11] M. Sahoo, P. Ghosal and, H. Rahaman, "An ABCD Parameter Based Modeling and Analysis of Crosstalk Induced Effects in Multiwalled Carbon Nanotube Bundle Interconnects", *IEEE* 27th *International Conference on VLSI Design*, pp. 433–438, Jan. 2014, .

[12] M. Sahoo and H. Rahaman, "An ABCD Parameter Based Modeling and Analysis of Crosstalk Induced Effects in Multilayer Graphene Nano Ribbon Interconnects", *IEEE ISCAS*, pp. 1138–1142, June 2014,.

[13] Predictive Technology Model [Online]. Available: http://ptm.asu.edu/.

[14] J. Zhang and E. G. Friedman, "Decoupling Technique and Crosstalk Analysis for Coupled RLC Interconnects",*IEEE ISCAS*, pp. 521–524, 2004.

[15] K. Banerjee and A. Mehrotra, "Analysis of On-Chip Inductance Effects for Distributed RLC Interconnects", *IEEE TCAD*, vol. 21, pp. 904-915, Aug. 2002.

[16] W. R. Hunter, "The statistical dependence of oxide failure rates on Vdd and, tox variations, with applications to process design, circuit design, and end use," *Proc. IEEE* 37th *Annu. Int. Rel. Phys. Symp.*, 1999, pp. 72-81.

[17] N. S. Nagaraj, W. R. Hunter, P. Balsara, and C. Cantrell, "The impact of inductance on transients affecting gate oxide reliability," *Proc.* 18th *Int. Conf. VLSI Design*, pp. 709-713, Jan. 2005.

Analytical Drain Current Model for Graphene Metal-Oxide semiconductor Field-Effect Transistor

Sudipta Bardhan
School of VLSI Technology
IIEST
Howrah, India
sudipta.bardhan15@gmail.com

Manodipan Sahoo and Hafizur Rahaman
dept. of Information Technology
IIEST
Howrah, India
manodipansahoo@gmail.com
rahaman_h@yahoo.co.in

***Abstract*— A physics based analytical model for double gate metal oxide semiconductor graphene field effect transistor (GFET) has been presented. We have derived the expression of drain to source current using the general physics of conventional silicon MOSFET. The explicit expression of drain current is very simple and few fitting parameters have been considered to obtain the I-V characteristics. This model is also applicable for top gated GFET. Results using our analytical model show very good agreement with the experimental results and result using NANOHUB tool. This model can be integrated in circuit simulation tools.**

Keywords-graphene, field effect transistor, model, fitting parameters.

I. INTRODUCTION

GRAPHENE is a promising material for high performance RF and analog electronics [1]-[3] for next generation. It has got excellent electrical properties such as high carrier mobility (2×10^5 cm^2/V.s) at room temperature [4] and high saturation velocity (6.3×10^7 cm/s) which is six times higher than silicon [5]. Due to absence of bandgap, the ON/OFF current ratio is very small, so there are certain limitations for digital application but for analog or RF application, researchers have focused on zero bandgap graphene material where high ON/OFF current ratio is not required. Device designers have shown the figure of merit of RF devices in Gigahertz range for gapless large area graphene channel MOSFET. The cutoff frequencies as high as 427 GHz have been presented in [6].

The schematic of the GFET structure is shown in Fig. 1. The double gate transistor is considered here, where top gate oxide is hafnium oxide and back gate oxide is silicon oxide. The back gate oxide has been deposited on doped silicon. Thus device models need to be developed to gauge the applicability of G-FETs for various applications as sensors, VLSI interconnects or devices.

978-1-4673-9257-0/15/$31.00©2015 IEEE

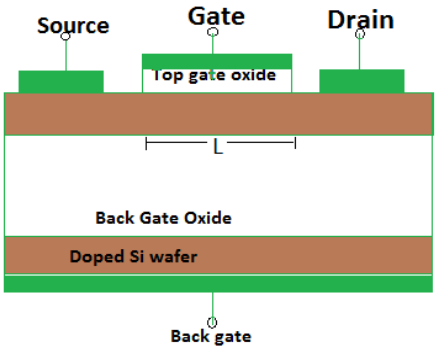

Figure 1. Schematic of GFET

Different types of models may be categorized either as physical model or empirical model. Physical model of GFET has already been developed previously [7-10] based on device physics. Empirical or semi empirical models are mostly acceptable for implementation on standard EDA tools because they achieve moderate accuracy with far lesser computational burden than very accurate physical centric models. Most of the physical models focus on the first principle based calculation of band structure, tunneling effect and carrier transport. GFETs with gapless, large area graphene channel are modeled using a quasi analytical approach in [11]. Another compact physical model for GFET has been presented in [12],[18]. Conventional MOSFET models [13]-[15] form the basis of this model. The models are only validated with experimental data for long channel GFETs ($L_G > 1\mu$m) [18]. Drift diffusion based model [16] has been used here to obtain explicit drain current model. Virtual source model [17] has been utilized for obtaining the I-V characteristics. In previously developed models, the expression of drain to source current is a function of channel potential making it more complicated than our model where, drain current expression is directly related to front gate, back gate & drain bias with few fitting parameters. The model I-V behaviors show very good agreement with experimental and simulation results.

The drain to source current expression is valid for both double and single gate technology. For positive or negative gate biases the drain current can be determined very easily, so this model is highly applicable for circuit simulation using standard EDA tools.

The paper is organized as follows. Section II discusses, about the model description of GFET. Section III discusses establishment of the drain to source current equation with the fitting parameters. The analytical results of I-V characteristics of model have been compared with the experimental and simulation results, for the same GFET configuration, and values of fitting parameters have been discussed in section IV. Finally the conclusions are drawn in section V.

II. GFET MODEL

The large area graphene channel [18] has been deposited on a thick SiO_2 layer that is grown on a heavily doped silicon wafer. The source and drain electrodes are contacting the graphene channel. The SiO_2 layer forms back gate oxide capacitance and silicon acts as a back gate. The conductivity type of the channel can be changed by applying constant back gate voltage. The top gate oxide is HfO_2 form top gate capacitance which controls the carrier charge density.

The drain current I_D of a conventional field effect transistor can be expressed as

$$I_{DS} = -q\rho_{CH}(x)v(x).W$$
$$= -q\rho_{CH}[V(x)]v[V(x)].W \quad (1)$$

where q = charge of electron.

$\rho_{CH}(x)$ = carrier density in the channel at position x

$v(x)$ = carrier drift velocity.

W = gate width

Channel sheet density and saturation velocity is function of x. The local potential $V(x)$ exist across the channel from source to drain so right hand side of equation is substituted by $V(x)$ at the position of x. Now channel sheet density and saturation velocity is function of $V(x)$.

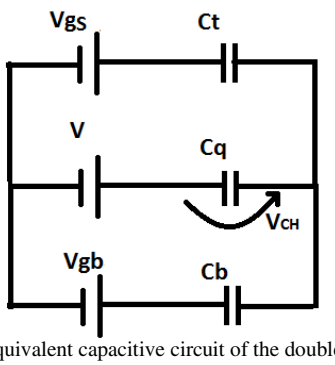

Figure 2. Equivalent capacitive circuit of the double gate GFET.

The concept of the electrostatic of dual gate GFET can be understood from equivalent capacitive circuit from figure.2. The top gate oxide and bottom oxide capacitance are Ct and Cb respectively and the quantum capacitance is Cq. The channel potential V_{CH} is the voltage drop across quantum capacitace Cq.

Here, we have considered the quantum capacitance directly depends on gate bias and drain bias. The expression of quantum capacitance is [19].

$$Cq = \left(e^2/\sqrt{\pi}v_F\hbar\right)\begin{pmatrix}\rho_{CH0}{}^2 + ([Cb(Vgb - Vgb0) + \\ Ct(Vgs - Vgs0)]/q)^2\end{pmatrix}^{1/4} \quad (2)$$

where v_F = Fermi velocity

ρ_{CH0} = residual carrier sheet density

Here, Ct=top gate capacitance, Cb= back gate capacitance. Vgs and Vgb are top gate and back gate bias respectively. Vgs0 and Vbs0 are top gate voltage and back gate voltage at Dirac point. In Dirac point the charge carrier density is minimum. This is similar to the flat band voltages in conventional silicon MOSFET.

Applying Kirchhoff's circuit law in fig.2 we get the following relation

$$V_{CH} = (Vgs - V(x))\alpha + (Vgb - V(x))\beta \quad (3)$$

where $Vgs = Vgstop - Vgs0$

$Vgb = Vgback - Vgb0$

$$\alpha = \frac{Ct}{Ct + Cb + \frac{1}{2}Cq} \quad \text{and} \quad \beta = \frac{Cb}{Ct + Cb + \frac{1}{2}Cq}$$

The α and β is treated as fitting parameter depends on top gate, back gate, and quantum capacitances used to adjust the channel potential. The voltage drop across the graphene channel is $V(x)$ which is zero at source end at x=0 and equal to drain source voltage Vds at the drain end at x=L.

The calculation of the approximate value of graphene sheet charge carrier density is defined as the [11], [20]

$$Q_{CH} = q\rho_{CH} = -\int CqV_{CH} = -\frac{1}{2}CqV_{CH} \quad (4)$$

As we consider here parallel plate capacitor, so Q_{CH} not equal not equal to $-CqV_{CH}$ but half of it. From equation (4) we get the carrier sheet density as

$$q\rho_{CH} = \theta V_{CH} \quad (5)$$

where $\theta = -(Cq/2)$

Here, θ is considered as fitting parameter, used to control the carrier sheet density in the channel region.

III. DRAIN CURRENT MODEL

The carrier velocity v=$v(x)$ has been defined in (1) is important parameter to derive the drain current expression. The steady state velocity field characteristics of graphene have been shown by Monte carlo simulations which is a soft saturation [20] that can be approximated by the expression,

$$v = \frac{\mu E}{1 + \mu E/v_{sat}} \quad (6)$$

where E = electric field

μ = low field carrier density

v_{sat} = saturation velocity

Remote interfacial phonon scattering [21] is important phenomena and the saturation velocity is affected by this

scattering. Two surface optical phonons of SiO_2 are involved in this process. With considerable accuracy, the process can be described by only one phonon with an effective energy $\hbar$. Saturation velocity depends on the effective energy and also on sheet carrier density(ρ_{CH}) and the expression is given below,

$$v_{sat} = \frac{\phi}{\sqrt{\pi \rho_{CH}}} \tag{7}$$

where, ϕ=phonon energy

Applying $E = -\frac{dV(x)}{dx}$ and combining (6) & (7) the drain current becomes,

$$Id = -q\rho_{CH} \frac{\mu\left(-\frac{dV}{dx}\right)}{1+\mu\frac{(-dV/dx)}{v_{sat}}} W \tag{8}$$

The left hand side of (8) is integrated w.r.t device length using boundary conditions x=0 to x=L and right hand side w.r.t V from V=0 at x=0 to V=V_{DS} at x=L. The resulting expression for drain current is,

$$Id = \frac{q\mu W \int_0^{Vds} \rho_{CH}\, dV}{L - \mu \int_0^{Vds} \frac{1}{v_{sat}} dV} \tag{9}$$

Integrating (9) using V as a integral variable, the explicit expression for Ids can be finally obtained,

$$Ids = \frac{\mu W \theta}{Leff}[(\alpha Vgs - \beta Vgb)Vds - (\alpha+\beta)(Vds^2/2)] \tag{10}$$

where,

$$Leff = L - \left(\frac{2}{3}\sqrt{\frac{\pi}{q}}\right)\cdot\left(\frac{\mu\sqrt{\theta}}{(\alpha+\beta)\,\phi}\right)\left[\begin{array}{l}((\alpha Vgs - \beta Vgb) - (\alpha+\beta)Vds)^{3/2} \\ -(\alpha Vgs - \beta Vgb)^{3/2}\end{array}\right]$$

IV. Result And Discussion

To compare with the experimental I/V characteristics, the voltage drop at source and drain region has to be considered. The relationship between external drain voltage $Vdsext$ and the internal drain voltage Vds is given by the corresponding equation,

$$Vds = Vdsext\left(1 - \frac{Ids}{\zeta}\right) \tag{11}$$

where $Vdsext$=External applied drain voltage

$$\zeta = \frac{Vdsext}{(Rs + R_D)}$$

Rs = Source resistance

and R_D = Drain resistance

The parameter ζ is treated as a fitting parameter which depends on external applied drain voltage and source and drain resistance.

To verify the model validity, we have benchmarked the resulting current voltage characteristics with experimental results. The model has been tested against two different experimental environments. First test (TEST A in Table I) parameters have been extracted from Meric et.al [18] and second and third test (TEST B and TEST C in Table I) parameters from Kedzierski et. al [19].

Fig. 3 shows the plot of I-V characteristics of GFET (TEST A parameters are considered) . The experimental [18] value of mobility(μ) is 550 $cm^2/V.s$, source and drain resistance value is Rs=700Ω and R_D=700Ω respectively. A good agreement between experiment and our model (as expressed in (10)) is obtained with μ=600 $cm^2/V.s$, Rs=800Ω and R_D=800Ω. So for best fit, the mobility value of 9%, source and drain resistance of 14% higher than experimental value have been chosen. The fitting parameters have been used to derive the final expression of drain current in our model. The values of the parameters are, α=0.2, β=0.004, θ= - 0.02, and ζ=-0.0025.

In the second experiment [19], the design of GFET is different, only top gate technology has been used. Fig. 4 (TEST B parameters are considered) displays the plot of output characteristics. For the best fit with the experiment, the mobility of holes and electrons agree with experiment, only resistance values Rs=400Ω and R_D=400Ω, have been considered which is 33% higher than measured value. The fitting parameters are, α=0.3, β=0,θ= - 0.01, and ζ= - 0.003.

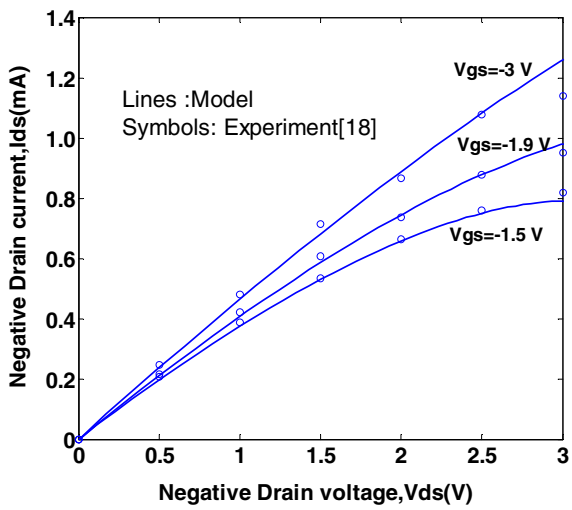

Fig. 3. Drain current as a function of drain source voltage for Vgs =-1.5V,-1.9V, and -3V, (from bottom to top) with α=0.2, β=0.004, θ= - 0.02, and ζ=-0.0025.

TABLE I. DIMENSIONS AND PARAMETERS OF THE MODELED GFET

MODEL PARAMETERS	TEST A	TEST B	TEST C	TEST D	TEST E
Channel Length, L (μm)	1	10	10	1	0.6/2
Channel Width, W (μm)	2.1	5	5	1	1
Top gate oxide Thickness, $t_{ox\text{-}top}$ (nm)	15	40	40	8/12	8
Back gate Oxide Thickness, $t_{ox\text{-}back}$ (nm)	285	…	…	300	300
Flat band voltage at top gate,Vgs0 (V)	1.45	0.85	0.65	0	0
Flat band voltage at back gate,Vbs0 (V)	2.7	…	…	…	…
Residual charge density, ρ_{CH0} (cm^{-2})	5×10^{12}	1×10^{12}	1×10^{12}	0	0
Source Resistance , Rs (Ω)	800	400	400	1	1
Drain Resistance , R_D (Ω)	800	400	400	1	1
Electron Mobility, μ_n (cm^2/V.s)	600	6500	1500	3000	3000
Hole Mobility, μ_h (cm^2/V.s)	600	6500	1500	3000	3000
Phonon energy, $\hbar$ (meV)	55	99	99	78	78
External back gate voltage (V)	-40	…	…	…	…

The plot in fig. 5 (TEST C parameters are considered) shows the transfer characteristics for two different drain biases *Vdsext*=0.1*V*, and *Vdsext*=1*V* respectively. The graph matches with the experiment taking all previously values for output characteristics, only *Vgs0*=0.65*V* have taken for final tuning with the fitting parameters α=0.2, β=0, θ= - 0.01, and ζ=-0.002.

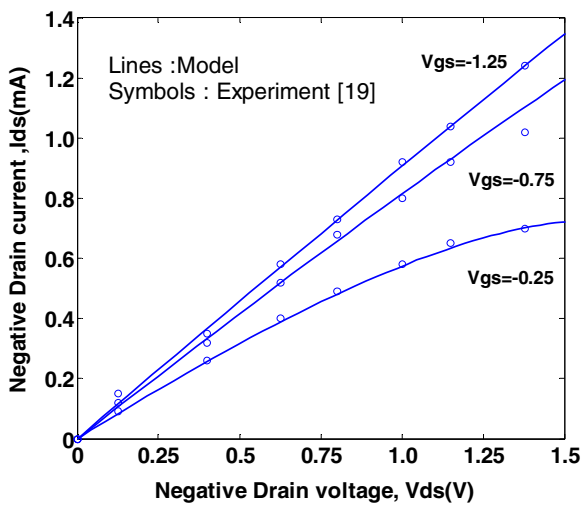

Fig. 4. Drain current as a function of drain source voltage for Vgs =-0.25V, -0.75V, and -1.25V (from bottom to top) with α=0.3, β=0,θ= - 0.01, and ζ= - 0.003.

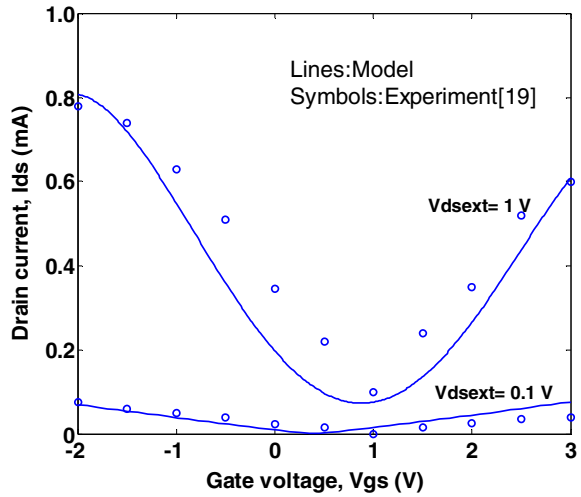

Fig. 5. Drain current as a function of gate source voltage for Vdsext= 0.1V and Vdsext= 1V with α=0.2, β=0, θ= - 0.01, and ζ=-0.002.

Finally, we have verified our model, against a known simulation tool, GFET tool from nanoHUB. In this simulation tool, the drift diffusion transport mechanism has been used to obtain the output characteristics. The dielectric material is silicon dioxide for both top gate and back gate oxide. Graphene mobility is characterized as a function of carrier density at temperature from 300 K to 500 K.

The model has been tested in two different conditions. For the first test (TEST D in Table I), channel length and width are kept fixed and top gate oxide thickness is varied. The parameters used in simulation are mentioned in Table I. Fig. 6 shows the output characteristics with this test setup.

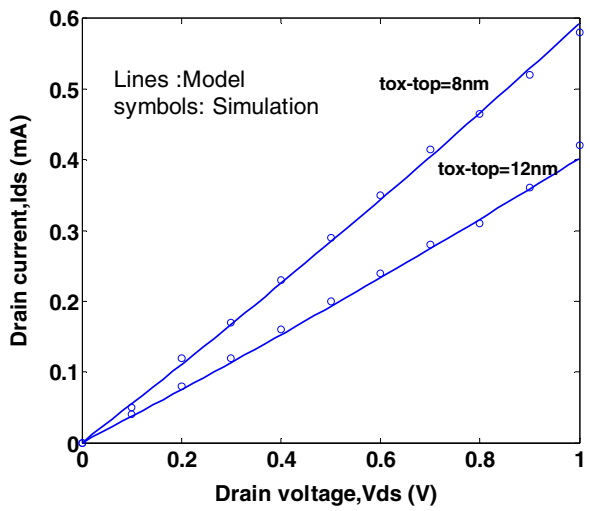

Fig. 6. Drain current of the GFETs with different top gate oxide thickness, tox-top =8nm with α=0.08, β=0,θ= - 0.02, and ζ= - 0.50 and tox-top =8nm with α=0.07, β=0,θ= - 0.01, and ζ= - 0.50 for Vgs = 0.6 V.

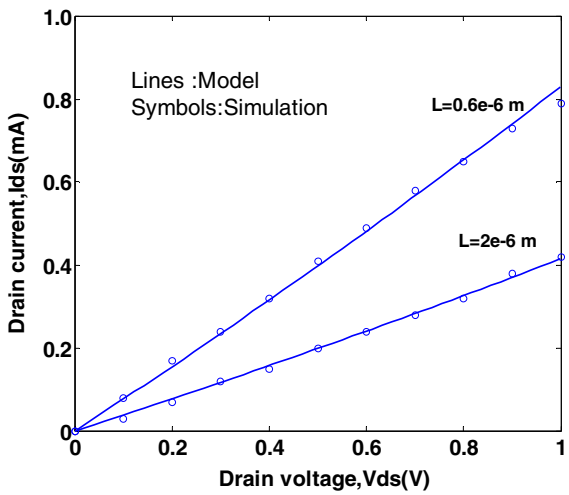

Fig. 7. Drain current of the GFETs with different channel length, L =0.6μm with α=0.08, β=0, θ= - 0.02, and ζ= - 0.50 and L =2μm with α=0.07, β=0,θ= - 0.01, and ζ= - 0.5 for Vgs = 0.6 V.

In the second test (TEST E in Table I), the channel length of GFET has been varied, for fixed channel width and top gate oxide thickness. Simulation parameters are shown in Table I. Fig. 7 shows the output characteristics with this test setup.

V. Conclusion

We have presented a compact drain current model of GFET, based on conventional transport equation for large channel area GFET, with double gate bias configuration. From saturation velocity and channel carrier density, we have determined the explicit closed form expression of drain current, using few fitting parameters. The analytical expression of drain to source current is very simple. Results using our model match very well for both experimental and simulation results and also it is valid from long channel regime (L=10μm) to short channel (L=600nm) regime. The circuit design engineers use the drain current and drain voltage characteristics to simulate different circuits. The GFET model in this paper is suitable for circuit simulation tools.

References

[1] L. Liao and X. Duan, "Graphene for radio frequency electronics," Mater.Today, vol. 15, pp. 328–338, Oct. 2012.

[2] F. Schwierz, "Graphene transistors: Status, prospects, and problems," *Proc. IEEE*, vol. 101, no. 7, pp. 1567–1584, Jul. 2013.

[3] K. S. Novoselov, V. I. Fal'ko, L. Colombo, P. R. Gellert, M. G. Schwab, and K. Kim, "A roadmap for graphene," Nature, vol. 490, no. 7419, pp. 192–200, Oct. 2012.

[4] A. S. Mayorov, R. V. Gorbachev, S. V. Morozov, L. Britnell, R. Jalil, L. A. Ponomarenko, P. Blake, K. S. Novoselov, A. K. Geim, and F. Guinea,"Micrometer-scale ballistic transport in encapsulated grapheme at Room temperature," *Nano. Lett.*, vol. 11, pp. 2396–2399, May 2011.

[5] V. E. Dorgan, M.-H. Bae, and E. Pop, "Mobility and saturation velocity in graphene on SiO2 ," *Appl. Phys. Lett.*, vol. 97, no. 8, pp. 082112-1–082112-3, Aug. 2010.

[6] R. Cheng, J. Bai, L. Liao, H. Zhou, Y. Chen, L. Liu, Y.-C. Lin, S. Jiang, Y. Huang, and X. Duan, "High-frequency self-aligned grapheme transistors with transferred gate stacks," *Proc. Nat. Acad. Sci. U.S.A.*, vol. 109,no. 29, pp. 11 588–11 592, Jun. 2012.

[7] M. Cheli, G. Fiori, and G. Iannaccone, "A semianalytical model of bilayer graphene field effect transistor," *IEEE Trans. Electron Devices*, vol. 56,no. 12, pp. 2979–2986, Dec. 2009.

[8] S. Thiele and F. Schwierz, "Modeling of the steady state characteristics of large-area graphene field-effect transistors," *J. Appl. Phys.*, vol. 110, no. 3, pp. 034506-1–034506-7, Aug. 2011.

[9] J. G. Champlain, "A first principles theoretical examination of graphene- based field effect transistors," *J. Appl. Phys.*, vol. 109, no. 8, pp. 084515-1–084515-19, Apr. 2011.

[10] S. O. Koswatta, A. Valdes-Garcia, M. B. Steiner, L. Yu-Ming Lin, and P. Avouris, "Ultimate RF performance potential of carbon electronics," *IEEE Trans. Microw. Theory Tech.*, vol. 59, no. 10, pp. 2739–2750, Oct.2011

[11] S. A. Thiele, J. A. Schaefer, and F. Schwierz, "Modeling of graphene metal–oxide–semiconductor field-effect transistors with gapless large area graphene channels," *J. Appl. Phys.*, vol. 107, no. 9, pp. 094505-1–094505-8, May 2010.

[12] K. L. Shepard, I. Meric, and P. Kim, "Characterization and modeling of graphene field-effect devices," in *Proc. IEEE/ACM ICCAD*, 2008, pp. 406–411.

[13] J. Brews, "A charge-sheet model of the MOSFET," *Solid State Electron.*,vol. 21, no. 2, pp. 345–355, Feb. 1978.

[14] A. B. Bhattacharyya, *Compact MOSFET Models for VLSI Design*. Piscataway, NJ: Wiley-IEEE Press, 2009.

[15] S. M. Sze and K. K. Ng, *Physics of Semiconductor Devices*, 3rd ed. Hoboken, NJ: Wiley, 2009, ch. 6.

[16] D. Jiménez and O. Moldovan, "Explicit drain-current model of

graphene field-effect transistors targeting analog and radio-frequency applications," *IEEE Trans. Electron Devices*, vol. 58, no. 11, pp. 4049–4052,Nov. 2011.

[17] H. Wang, A. Hsu, J. Kong, D. A. Antoniadis, and T. Palacios, "Compact virtual-source current-voltage model for top- and back-gated graphene field-effect transistors," *IEEE Trans. Electron Devices*, vol. 58, no. 5,pp. 1523–1533, May 2011.

[18] I. Meric, "Current saturation in zero-bandgap, top-gated graphene Field effect transistors," *Nature Nanotechnol.*, vol. 3, pp. 654–659, Nov. 2008.

[19] J. Kedzierski, P.-L. Hsu, A. Reina, J. Kong, P. Healey, P. Wyatt, and C. Keast, "Graphene-on-insulator transistors made using C on Ni chemical-vapor deposition," *IEEE Electron Device Lett.*, vol. 30, no. 7, pp. 745–747, Jul. 2009.

[20] T. Fang, A. Konar, H. Xing, and D. Jena, Appl. Phys. Lett. **91**, 092109 (2007).

[21] J.-H. Chen, C. Jang, S. Xiao, M. Ishigami, and M. S. Fuhrer, Nat. Nanotechnol.**3**, 206 (2008).

An Approach to Determine Bandgap Energy in Graphene under Shear Strain Condition

Md. Delwar Hossain*, Abu Bakkar Siddiq+, Md.Shamim Sarker$, Muhammad Mainul Islam&, Md. Rafiqul Islam#
Department of Electrical and Electronic Engineering,
Khulna University of Engineering & Technology,
Khulna-9203, Bangladesh
E-mail: *delwarhossain3035@gmail.com, + eeealin@gmail.com, $sarkershamimbd@gmail.com, &mainul0803004@gmail.com
mri@eee.kuet.ac.bd

Abstract— **A simple analytical approach is presented to investigate the energy band structure of graphene under the application of shear strain. The strain-induced deformation in the unit cell in terms of the angle between two unit vectors is taken into consideration in the framework of nearest neighbor tight binding model. The proposed approach is applied to evaluate the energy band gap in graphene structure under shear strained condition. The results obtained from the proposed approach are compared with those of reported by DFT calculation and they are found to be in good agreement. This demonstrates that the proposed approach can be applied to calculate the band gap energy in shear strained graphene.**

Keywords— Graphene, shear strain, tight binding model, analytical approach, band structure.

I. INTRODUCTION

Graphene [1] is a name given to a flat single layer of carbon atoms tightly bonded into a two dimensional (2D) honeycomb lattice and is a fundamental building block for graphitic materials of all other dimensionalities [2]. Graphene is considered to be the strongest material ever [3]. As the graphene has excellent electronic structure [4]-[6] and transport property [7], researchers are having great interest in graphene. Since graphene is very thin having excellent electronic properties, it may be used in future logic devices to face the challenge of Gordon Moore's law, that is, the number of logic components per integrated circuit would double every 2 years. But the main problem with graphene is its zero band gap[1,8], which reveals that it cannot be used in logic circuits as well as other electronic applications. Scientists are working to find out the way to open the energy gap in graphene. Different methods have been proposed to create band gap in graphene, such as using quantum confinement effect in graphene nanoribbon (GNR) [9]-[11], applying external electric fields, introducing symmetry breaking of regular hexagonal structure[13],[14], by the process of doping [15]-[17], and by the process of external strain [18],[19]. To calculate the band gap in strained graphene, several techniques were applied [18-20] such as first principal calculation, tight binding model, K.P method, density function theory (DFT) etc. Most of them are performed by numerical simulation techniques which have huge computational complexity and hence needs high capacity super computer [18]. Some analytical works have also been done on strained graphene and GNR using tight binding approximation which mainly focuses on the strength of strain and spin polarization interaction [19]. In a recent study [20], we have reported an analytical approach to calculate strain-dependent energy band gap in uniaxially strained graphene. In this study a simple analytical approach is presented to determine the energy dispersion of graphene under the application of shear strain. In the proposed technique strain-induced unit cell deformation is incorporated in the framework of tight binding model. Using the proposed approach the band gap is determined for different values of shear strains. The results obtained from the proposed technique are compared with the results published by the DFT [19] and found to be in good agreement.

II.PROPOSED APPROACH

In symmetrically strained graphene, the band structure remained unchanged just like unstrained graphene. To introduce band gap in graphene structure asymmetrical strain (shear /uniaxial) could be applied that breaks the symmetry in the lattice structure. This leads to localize the delocalized electron and hence to create band gap in the graphene. The strain-induced lattice structure deformation under the application of shear strain along with unstrained lattice structure is shown in Fig. 1.

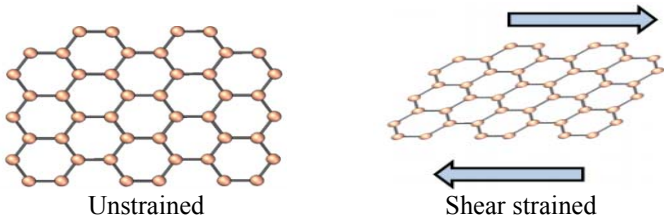

Figure 1. Unstrained and shear strained graphene structure [21].

978-1-4673-9257-0/15/$31.00 ©2015 IEEE

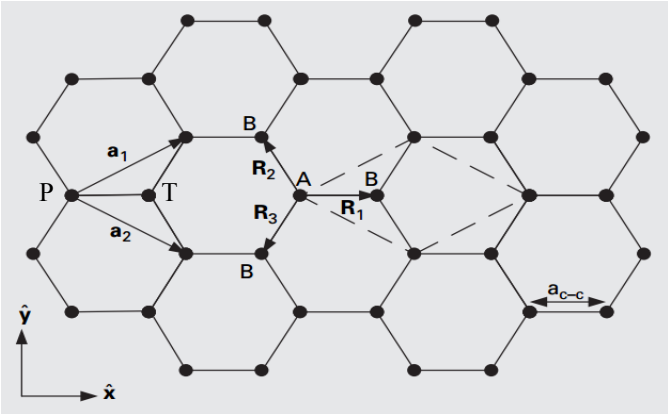

Figure 2. The honeycomb lattice of graphene. The primitive unit cell is the equilateral parallelogram (dashed lines) with a basis of two atoms denoted by A and B.

In our study, we have used the nearest neighbor tight binding model. Here the type-A atom in the graphene lattice is bonded with three of its nearest neighbors of type-B atoms as shown in fig. 2, where the primitive unit cell is also shown by dashed line. In unstrained graphene the angle between the unit vectors $\mathbf{a_1}$ and $\mathbf{a_2}$ is 60^0, which with respect to a unit vector and the reference line PT is 30^0. However, under the application of shear strain the unit cell will be deformed. As a result, the angle between the unit vectors $\mathbf{a_1}$ and $\mathbf{a_2}$ will be changed. A typical deformation of unit cell due to shear strain is shown in Fig. 3, where α and β are the angles between the line PT and unit vectors $\mathbf{a_1}$ and $\mathbf{a_2}$, respectively.

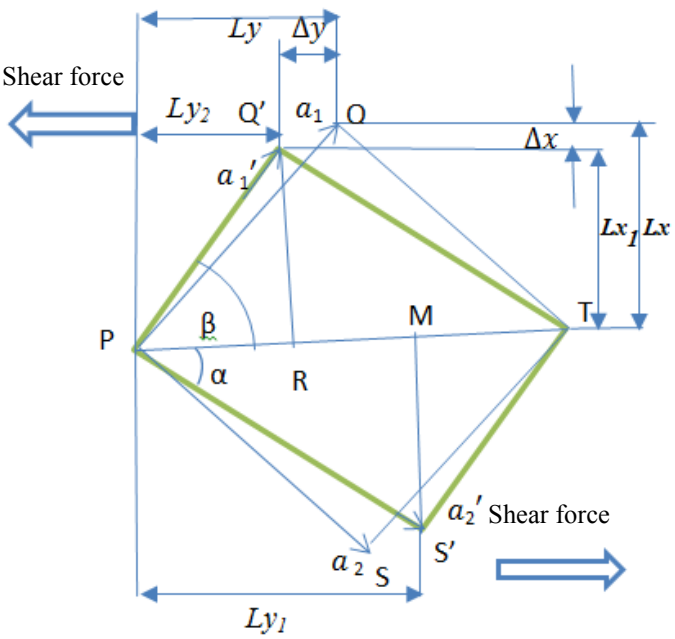

Figure 3. The un-deformed and shear strain-induced deformed primitive unit cells with their primitive unit vectors.

When shear strain is applied the points Q and S is shifted to points Q' and S' due to unit cell deformation, assuming that the points P and T are fixed as seen in Fig. 3. Using trigonometric relationship in $\Delta PQ'R$ the angle β can be expressed by

$$\beta=\tan^{-1}\frac{L_{x1}}{L_{y2}}=\tan^{-1}\frac{L_x-\Delta x}{L_y-\Delta y} \quad (1)$$

where $\Delta x = L_x - L_{x1}$ and $\Delta y = L_y - L_{y2}$. Δx and Δy represent the deformation in the primitive unit vectors due to shear strain.

Similarly from $\Delta PMS'$,

$$\alpha=\tan^{-1}\frac{L_{x1}}{L_{y1}}=\tan^{-1}\frac{L_x-\Delta x}{L_y+\Delta y} \quad (2)$$

Due to the strain-induced deformation of primitive unit cell the vectors $\boldsymbol{a_1}'$ and $\boldsymbol{a_2}'$ become

$$\boldsymbol{a_1}' = [a_1'\cos(\beta), a_1'\sin(\beta)],$$
$$\boldsymbol{a_2}' = [a_2'\cos(\alpha), -a_2'\sin(\alpha)] \quad (3)$$

Here a_1' and a_2' represent magnitude of the vectors. It is found in "Fig. 2" that there are three nearest neighboring atoms. The separation of these atoms can be represented by three vectors $\boldsymbol{R_1}$, $\boldsymbol{R_2}$, and $\boldsymbol{R_3}$.

$$\boldsymbol{R_1} = (\tfrac{2}{3}a_1'\cos\beta, 0) = \tfrac{2}{3}a_1'\cos\beta\,\mathbf{x} \quad (4)$$

$$\boldsymbol{R_2} = -\boldsymbol{a_2}' + \boldsymbol{R_1} = \left(\tfrac{2}{3}a_1'\cos\beta - a_2'\cos\alpha\right)\mathbf{x} + a_2'\sin\alpha\,\mathbf{y} \quad (5)$$

and $\boldsymbol{R_3} = -\boldsymbol{a_1}' + \boldsymbol{R_2}$

$$\boldsymbol{R_3} = \left(-\frac{1}{3}a_1'\cos\beta - a_2'\cos\alpha\right)\mathbf{x} + (a_2'\sin\alpha - a_1'\sin\beta)\,\mathbf{y} \quad (6)$$

From tight-binding energy dispersion model the formula of energy dispersion can be given by

$$E(k) = \pm\sqrt{H_{AB}(k)H_{AB}^*(k)} \quad (7)$$

where $H_{AB}(k)$ is the Hamiltonian matrix. For unstrained graphene the Hamiltonian matrix element reduces to a sum of three terms:

$$H_{AB(k)} = \gamma e^{-ikR_1} + \gamma e^{-ikR_2} + \gamma e^{-ikR_3} \quad (8)$$

When shear strain is applied " (8)" becomes

$$H_{AB(k)} = \gamma_1 e^{-ikR_1} + \gamma_2 e^{-ikR_2} + \gamma_3 e^{-ikR_3} \quad (9)$$

and its conjugate is

$$H^*_{AB(k)} = \gamma_1 e^{ikR_1} + \gamma_2 e^{ikR_2} + \gamma_3 e^{ikR_3} \quad (10)$$

Here γ is a fitting parameter which is often called the nearest neighbor overlap energy. In unstrained graphene, $\gamma_1 = \gamma_2 = \gamma_3 = \gamma = -2.8\, eV$[22]. When shear strain is applied, the change of three bond length with three nearest neighbor become different. As a result, the values of γ_1, γ_2, and γ_3 become different [22]. Now

$$H_{AB}(k)H^*_{AB}(k) = (\gamma_1 e^{-ikR_1} + \gamma_2 e^{-ikR_2} + \gamma_3 e^{-ikR_3}) * (\gamma_1 e^{ikR_1} + \gamma_2 e^{ikR_2} + \gamma_3 e^{ikR_3}) \quad (11)$$

Putting the value of $\boldsymbol{R_1}$, $\boldsymbol{R_2}$, $\boldsymbol{R_3}$ and $\boldsymbol{K} = k_x\boldsymbol{x} + k_y\boldsymbol{y}$ and after some mathematical manipulation we get

$$\mathrm{H}_{AB}(k)H^*_{AB}(k) = \gamma_1^2 + \gamma_2^2 + \gamma_3^2 + 2\gamma_1\gamma_2 c_1 + 2\gamma_2\gamma_3 c_2 + 2\gamma_3\gamma_1 c_3 \quad (12)$$

where $c_1 = \cos[-a_2^{'}\cos\alpha k_x + a_2^{'}\sin\alpha k_y]$

$$c_2 = \cos[-\, a_1^{'}\cos\beta\, \mathrm{k_x} - a_1^{'}\sin\beta\, \mathrm{k_y}] \quad (13)$$

$$c_3 = \cos[(a_1^{'}\cos\beta + a_2^{'}\cos\alpha)\mathrm{k_x} + (a_1^{'}\sin\beta - a_2^{'}\sin\alpha)k_y)]$$

Substituting "(12)" into "(7)" we have

$$E(k) = \pm\sqrt{\gamma_1^2 + \gamma_2^2 + \gamma_3^2 + 2\gamma_1\gamma_2 c_1 + 2\gamma_2\gamma_3 c_2 + 2\gamma_3\gamma_1 c_3} \quad (14)$$

This is the generalized equation for the energy dispersion relation of graphene under shear strain condition.

III.RESULTS AND DISCUSSION

We have studied the electronic band structure of shear strained graphene. Application of shear strain leads to create bandgap. The strain-induced deformation of unit cell causes change in angles (α and β) between vectors ($a_1^{'}$ and $a_2^{'}$) and reference line PT asymmetrically. These angular changes are taken as parameters to calculate the band structure of graphene under shear strained condition. Using "(1)" and "(2)" values of α and β are evaluated 29.66^0, 29.01^0, 27.75^0, 26.93^0 and 30.29^0, 30.99^0, 32.25^0, and 33.07^0 respectively, for the change in strain values 0.48% , 1.86% , 4.17%, and 5.58%. Using "(13)" the band gap energies are estimated

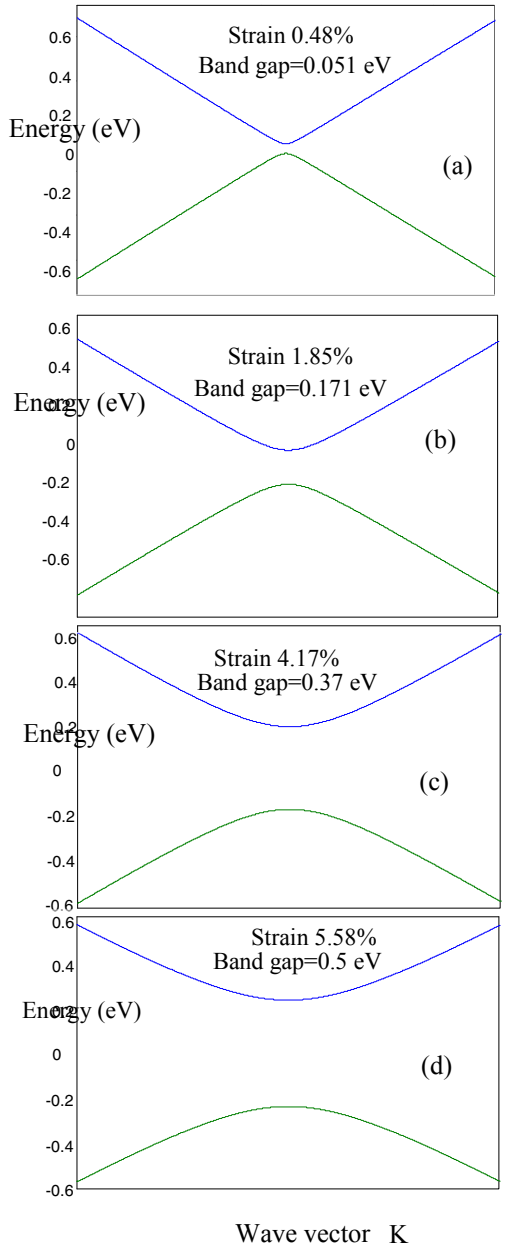

Figure 4. Bandgap opening under the application of shear strain (a) 0.48 % (b) 1.85 %(c) 4.17 %, and (d) 5.58% strain

and are found to be 0.051, 0.171, 0.37 and 0.50 eV for the corresponding percentage of strain. Due to the application of shear strain the symmetry of the regular hexagonal structure is broken, as a result, energy bangap created in shear strained graphene. The results are shown in Fig. 4 (a), (b), (c), and (d). To observe the results clearly, the dispersion profiles are extended near the K-point of the Brillouin zone.

IV. CONFIRMATION OF THE PROPOSED TECHNIQUE

In order to confirm the proposed analytical approach, the results obtained from the present study is compared with the previously published results. A comparison is shown in Table 1. It is found that the results obtained from the proposed technique agree with the results evaluated from DFT calculation, upto the 5.6 percents of applied strain [19]. This demonstrates that the proposed technique can be applied to determine the bandgap in shear strained graphene structure.

TABLE I. COMPARISON OF SHEAR STRAIN-DEPENDENT ENERGY GAPS OBTAINED FROM THE PROPOSED TECHNIQUE AND DFT CALVULATION [19]

L_{x1} (nm)	L_{y1} (nm)	L_{y2} (nm)	DFT (eV)	Proposed approach (eV)
0.12397	0.21769	0.21219	0.0489	0.051
0.12559	0.22650	0.20902	0.196	0.171
0.12673	0.23340	0.20680	0.287	0.252
0.12803	0.24029	0.20489	0.401	0.321
0.12845	0.24414	0.20359	0.435	0.37
0.13045	0.25680	0.20034	0.583	0.5

V. CONCLUSION

In this study, a simple analytical approach is proposed to evaluate the energy dispersion in shear strained graphene on the basis of nearest neighbor tight binding model. The strain-dependent change in the angle between the two primitive vectors of a unit cell of graphene is taken into consideration. It is found that the angles between two primitive vectors with respect to a reference change asymmetrically due to shear strain. It is found that with the increase in strain the energy band gap increases and it is evaluated to be 0.5 eV for the value of strain 5.58%. Finally, to confirm the proposed technique our results are compared with those of reported by DFT calculation and found to be in good agreement.

REFERENCES

[1] K.S. Novoselov, A.K. Geim, S.V. Morozov, D. Jiang, Y. Zhang, S.V. Dubonos, I.V. Grigorieva and A.A. Firsov ‘’electric field effect in atomically thin carbon film’’, Science 306, 666 (2004).

[2] H.-S. Philip Wong and Deji Akinwande,’’Carbon Nanotube and Graphene Device Physics’’, (pub: 2011).

[3] C. Lee, X. Wei, J. W. Kysar, and J.Hone, Science.321, 385(2008).

[4] M. Y. Han, B. zyilmaz, Y. B. Zhang, and P. Kim, Phys. Rev. Lett.98,206805 (2007).

[5] L. Yang, C. H. Park, Y. W. Son, M. L. Cohen, and S. G.Louie, Phys. Rev. Lett. 99, 186801 (2007).

[6] P. Shemella, Y. Zhang, M.Mailman, P. M. Ajayan, and S.K. Nayak, Appl. Phys. Lett.91, 042101(2007).

[7] Z.Y. Li, H.Y. Qian, J. Wu, B. L. Gu, and W. Duan, Phys. Rev. Lett. 100,206802 (2008).

[8] K.S. Novoselov, D. Jiang, F.Schedin, T.J. Bhoot, V.V. Khot-kevich, S.V. Morozov and A.K Geim, Proc.Natl.Acad. Sci. U.S.A. 102,10451 (2005)

[9] M.Y. Han, B. Ozylmaz, Y. Zhang, and P. Kim, “Energy band gap engineering of grapheme nanoribbons,” Phys. Rev. Lett. ,vol. 98, no. 20, P. 206805, May 2007.

[10] Y. W. Son, M. L. Cohen, and S. G. Louie, “Energy gaps in graphene nanoribbons,” Phys. Rev. Lett., vol. 97, no. 21, p. 216803, Nov. 2006.

[11] JIANG Lianjun, XIONG Cuixiu , HUANG Li , ZHOU Guanghui , “ The Gap Opening and Threshold of Graphene by Shear Strain “, Journal of Materials and Applications (2013)

[12] T. Ohta, A. Bostwick, T. Seyller, K. Horn, and E. Rotenberg, “Controlling the electronic structure of bilayer graphene,” Science, vol. 313, no. 5789, pp. 951–954, Aug. 2006.

[13] Y. Zhang, T.-T. Tang, C. Girit, Z. Hao, M. C. Martin, A. Zettl, M. F. Crommie, Y. R. Shen, and F. Wang, “Direct observation of a widely tunable bandgap in bilayer graphene,” Nature, vol. 459, no. 7248, pp.820–823, Jun. 2009.

[14] Jun Ito, Jun Nakamura, and Akiko Natori, “Semiconducting nature of the oxygen-adsorbed graphene sheet,” Journal of applied phys. 103,113712 (2008).

[15] Paolo Marconcini, Gianluca Fiori, Alessandro Ferretti, Giuseppe Iannaccone, and Massimo Macucci,“Numerical analysis of transport properties ofboron-doped graphene FETs”.

[16] Zhipping Xu and Kun Xue,“Engeneering graphene by oxidation: a first principle study,” Nanotechnology21 (2010) 045704

[17] Gui Gui, Jin Li, and Jianxin Zhong ‘Band structure engineering of graphene by strain: First-principles calculations’, PHYSICAL REVIEWB 78, 075435 2008.

[18] V.J. Surya, K. Iyakutti, H. Mizuseki, and Y. Kawazoe, “Tuning electronic structure of Graphene: A first-principle calculation,” IEEE Trans. Nanotechnology, vol.11, No.3,pp.534-541, May 2012.

[19] Yang Li, Xiaowei Jiang, Zhongfan Liu, Zhirong Liu, “Strain Effects in Graphene and Graphene Nanoribbon: The underlying mechanism,”Nano Res (2010) 3: 545–556.

[20] M. S. Sarker , M. M Islam, Md. R Islam, ‘’An Analytical Approach to Study Energy Band Structure in Strained Graphene’’,2013.

[21] Anderson Smith, Dr. Max Lemme, Prof. Mikael Östling, “Strain Effects on Electrical Properties of Suspended Graphene” October, 2010.

[22] JIANG Lianjun, XIONG Cuixiu, HUANG Li, ZHOU Guanghui, “The Gap Opening and Threshold of Graphene by Shear Strain” Journal of Materials and Applications 2:1 (2013).Trans. Nanotechnology, vol.11, No.3,pp.534-541, May 2012

Modeling and Performance Analysis of Multilayer Zigzag Graphene Nanoribbon (zz-MLGNR) Interconnect for VLSI Application

Monjurul Feeroz Meem*, Abdullah Ash-Saki and Dr. A. B. M Harun-Ur Rashid
Department of Electrical and Electronic Engineering, Bangladesh University of Engineering and Technology, Dhaka, Bangladesh
* E-mail: monjurul_bueteee@yahoo.com

***Abstract*—Based on equivalent single conductor (ESC) model, an appropriate RLC equivalent circuit model for multi layer zigzag graphene nanoribbon (zz-MLGNR) interconnect is presented. The values of different circuit parameters (i.e resistance, inductance and capacitance) are calculated. The impact of various interconnect parameters (e.g., dimension of interconnect, number of GNR layers, Fermi energy) on the circuit parameters are discussed. The per unit length resistance of zz-MLGNR interconnect is compared with other interconnect materials [e.g., copper (Cu), tungsten (W) and carbon nanotubes (CNTs)]. The analysis revealed that zz-MLGNR can offer lower resistance than Cu, W and even single-walled carbon nanotubes (SWCNs). Time delay of zz-MLGNR interconnect is analyzed using the RLC equivalent circuit model and it is shown that intercalation-doped zz-MLGNR can outperform Cu.**

Keywords—GNR interconnect, multilayer graphene nanoribbon (MLGNR), interconnect delay.

I. INTRODUCTION

To keep up with the Moore's law both transistor and interconnect dimensions are scaled down rapidly. The continuing exponential reduction in feature size on electronic chips, leads to ever larger number of faster devices at lower cost per device. The decrease in minimum feature size of devices has led to a proportional decrease in interconnect cross-sectional area and pitch, as a consequence the delay associated with the transistors, gate delay, has continuously decreased with decrease in minimum feature size, while the delay associated with interconnect, the parasitic resistance, capacitance and inductance delay has increased significantly. International Technology Roadmap for Semiconductors (ITRS) [1] has pointed out that, due to this scaling down, traditional semiconductor material, silicon (Si) and interconnect material, copper (Cu) are reaching their threshold limit, so the industry is in search for viable alternatives; and carbon based materials are the protagonist in this endeavour.

Graphene, an atomic layer of carbon atoms arranged in a two dimensional (2D) honeycomb lattice, has recently emerged as a potential candidate for nanoelectronics due to its promising electronic properties [2]. The high mobility and carrier velocity in graphene promises ballistic devices with high switching speeds. The fabrication of the first field-effect graphene-based transistor [3], led to an explosion of interest in the electronic properties of graphene. Nowadays, graphene is considered to be a viable alternative to Si and Cu [4]. If graphene sheet is patterned into narrow strips then it is called graphene nano-ribbon (GNR). GNR can conduct much larger current densities than Cu, due to its strong sp^2 hybridize bonds and absence of severe reliability problems that plague Cu, particularly for future interconnect geometries [3, 5-8]. Thermal conductivity of GNR is much larger than Cu [9-11]. Moreover, compared to Cu, GNR has larger carrier mean free path (MFP), which leads to larger electrical conductance [12-14]. Physically graphene can be metallic or semiconducting according to its chirality. For example zigzag edge GNR (zz-GNR) is always metallic, while armchair-GNR (ac-GNR) can exhibit both semiconducting and metallic behaviour depending on the number of carbon atom along its width [15]. The potential performance of GNR transistors has been studied in several publications, and it has been projected that such transistors can potentially outperform Silicon transistors because of the large carrier mobility and the better electrostatic control of gate on channel [16, 17]. GNR interconnects can potentially be used as intracell interconnects linking GNR transistors in a seamless fashion [3, 18, 19] or in a multilevel interconnect network like conventional interconnects [20]. The former would reduce the number of metal-to-graphene connections and, therefore, would improve the circuit performance by eliminating some contact and quantum resistances. Although the maximum current-carrying density up to *108 A/cm*^{2} (*~100* times of Cu) was reported, current density of SLGNR is limited by its 2D atomically-thin geometry, sensitivity to ambient, poor noise tolerance, and conductance degradation due to edge-related effects [21, 22]. 3D nano-carbon, or vertically stacked multilayer graphene (MLGNR), can potentially be employed to address this challenge, yielding an ultra conductive material system as shown in Fig. 1. Multilayer graphene has received significant amount of theoretical and experimental attentions in recent years [23]. The in-plane conductivity of graphite can be several tens of magnitude by intercalation doping, which involves an insertion of one dopent layer between each pair of graphene layers [24]. Intercalation doping can increase the carrier density due to increased layer spacing [25].

In this paper we have presented a RLC equivalent circuit model for multi layer zigzag graphene nano-ribbon (zz-MLGNR) based on equivalent single conductor (ESC) model [26]. Per unit length resistance, capacitance and inductance of zz-MLGNR are calculated using the proposed model. The effect of interconnect width, number of layers and Fermi energ-

978-1-4673-9257-0/15/$31.00 ©2015 IEEE

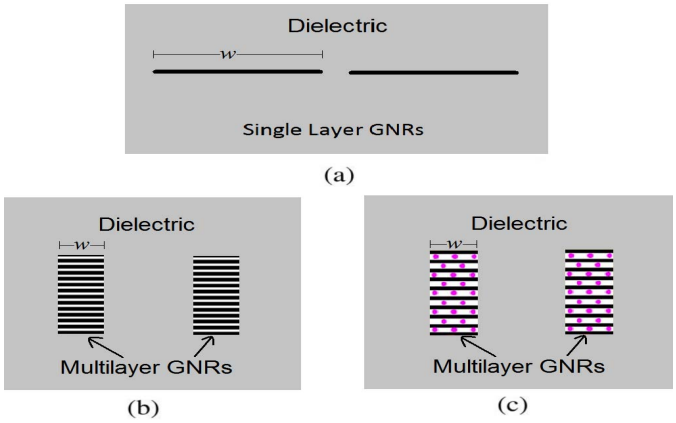

Figure 1. Schematic view of (a) monolayer GNR, (b) neutral multi layer GNR, (c) intercalation-doped multilayer GNR.

y on different parameters are discussed. Resistance of zz-MLGNR is benchmarked against other traditional interconnect materials. Finally 50 percent delay of zz-MLGNR interconnect is calculated and benchmarked against Cu.

II. CIRCUIT MODELING

Let's consider a N layer zz-MLGNR interconnect of length L, width w ($w << L$), thickness t as shown in Fig. 2(a). The per unit length equivalent circuit of zz-SLGNR is shown in Fig. 2(a). In Fig. 2(a), R_Q is the quantum resistance which is expressed as [27]

$$R_Q = h/2e^2 N_{ch} \approx 12.9\ k\Omega/N_{ch} \quad (1)$$

Where h is Plank's constant and N_{ch} is the number of conduction channel, which is a function of GNR width w, chirality, temperature and Fermi energy. N_{ch} is calculated by [28]

$$N_{ch} = \Sigma 1/[1+exp((E-E_F)/k_BT)] + \Sigma 1-1/[1+exp((E-E_F)/k_BT)] \quad (2)$$

Magnetic inductance (L_M) and electrostatic capacitance (C_E) are determined by the geometry and the materials surrounding the interconnects. Kinetic inductance (L_K) represents the kinetic energy of the electrons and because of small density of states in GNR, its value is substantially larger than the magnetic inductance [29]. Unlike magnetic inductance, kinetic inductance has no mutual component and its value decreases linearly with increase in N_{ch} ($8\ nH/\mu m/N_{ch}$) [30]. Quantum capacitance is also the consequence of small density of states and increases linearly with N_{ch} ($200\ N_{ch}\ aF\ /\mu m$). The scattering resistance per unit length is represented by r which can be expressed as $r = R_Q / l_D$. Here l_D the mean free path which is around $1\mu m$ in graphene [31]. zz-MLGNR can be considered as a arrangement of N zz-SLGNR, Fig. 2(b) shows the per unit length equivalent circuit of MLGNR, and the multiconductor transmission line (MTL) representation of it is shown in Fig. 2(c), here R_c is terminal contact resistance, L_m is magnetic inductance and C_m is mutual capacitance. In order to reduce the computational effort of the complex MTL approach, zz-MLGNR can be analyzed using an equivalent single conductor (ESC) model [32]. The ESC model is represented in Fig. 3(a). R_{ESC} can be calculated by,

$$R_{ESC} = h/2e^2\ N_{ch}\ N\ l_D \quad (3)$$

L_{ESC} and C_{ESC} are calculated from Fig. 3(b) and Fig. 3(c) respectively.

III. RESULTS AND DISCUSSIONS

In the process of modelling zz-MGNR interconnect various physical properties were investigated. Fig. 2(a) shows the schemata of the considered structure. The number of conduction channel (N_{ch}) is obtained using closed from expression Eq. 1 and plotted versus width for different Fermi energy in Fig. 4. Increasing width and Fermi energy populates more subbands and therefore, increases the number of conduction channel. Knowing the number of conduction channel the per unit length resistance of zz-MLGNR are calculated from ESC model and plotted versus width for different number of layers and Fermi energy in Fig. 5. For reference, the per unit length resistance of Cu and W wires with unity aspect ratio and monolayer single walled nanotube (SWCNT) interconnect with random chiralitiy are also plotted. The analysis reveals that the per unit length resistance of neut-

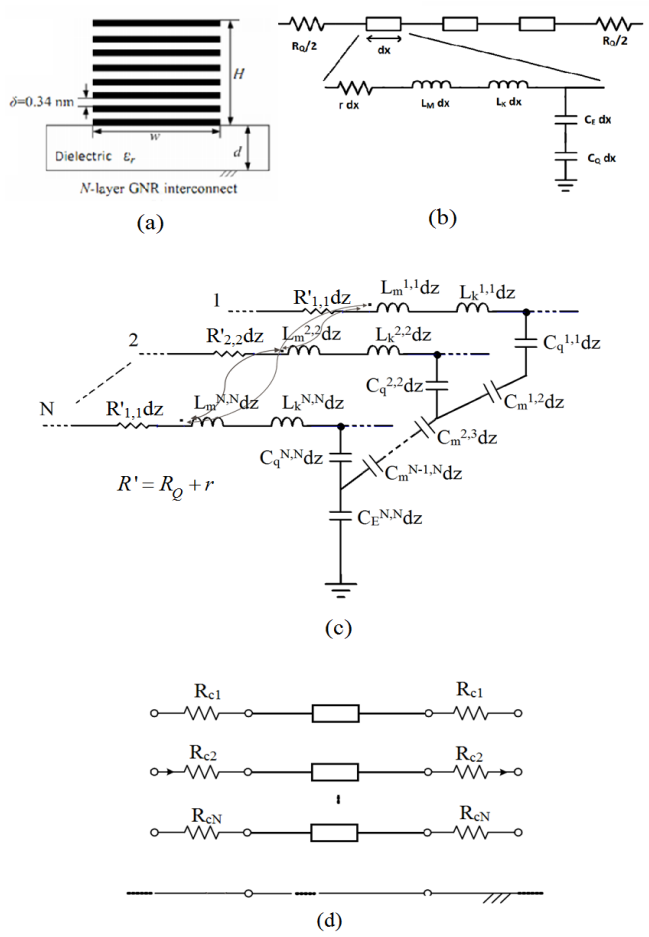

Figure 2. (a) Geometry of a N layer zz-MLGNR along with, (b) per unit length equivalent circuit model of zz-SLGNR, (c) per unit length equivalent circuit model of zz-MLGNR and (d) multiconductor representation of zz-MLGNR including terminal resistance.

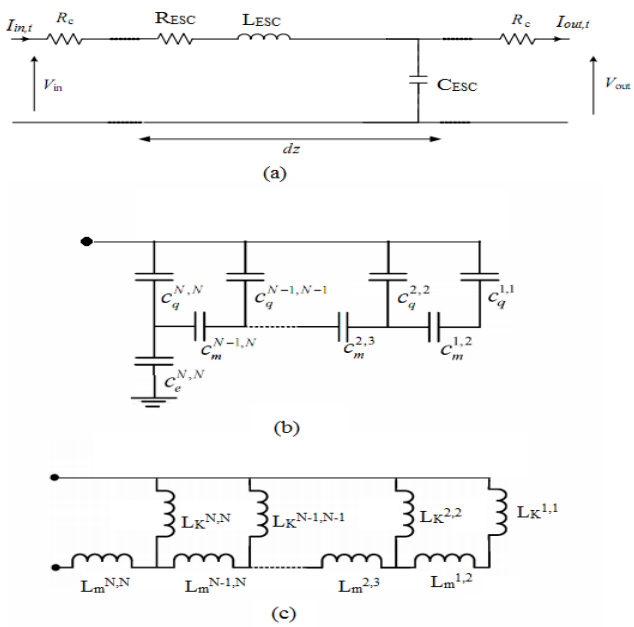

Figure 3. (a) ESC circuit of an MLGNR interconnect and per unit length equivalent network for (b) capacitance; (c) inductance.

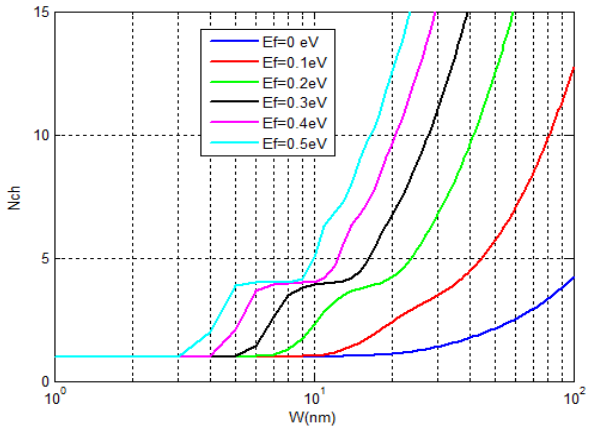

Figure 4. Number of conduction channel (N_{ch}) versus width for different Fermi energy is shown.

ral (E_F = 0) zz-MLGNR is higher that Cu and SWCNT. But at higher Fermi energy it can offer significantly less per unit length resistance than both Cu and SWCNT. The per unit length capacitance of zz-MLGNR is calculated using the ESC model and plotted. Fig. 6 (a) shows the per unit length capacitance as a function of width and Fig. 6 (b) shows the per unit length capacitance as a function of layer number for both *14nm* and *22nm* technology nodes. Fig. 6 reveals that, capacitance increases with increase in width but shows little variation due to change in Fermi energy or number of GNR layers. This is because, all the components of C_{ESC} i.e C_Q, C_m and C_E increases with width but among them only C_Q changes with Fermi energy and whose value is much-much larger than C_m or C_E.

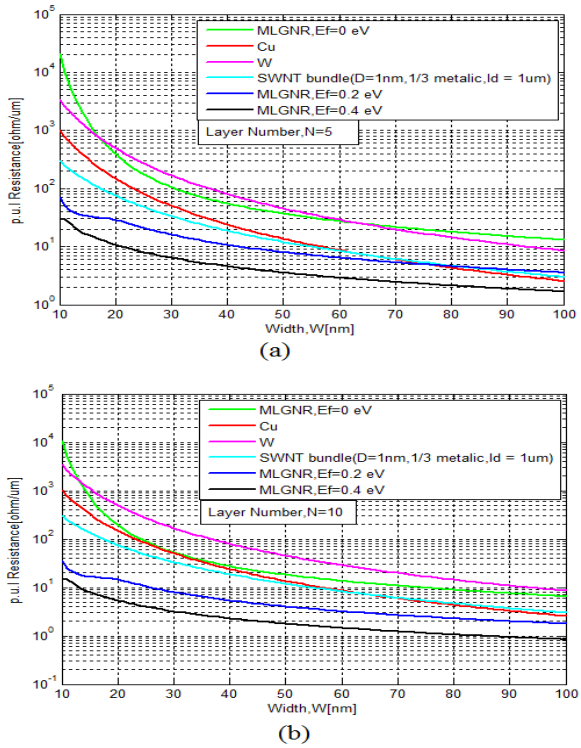

Figure 5. Per unit length resistance of zz-MLGNR shown for (a) 5 layers and, (b) 10 layers. Per unit length resistance of Cu, Wires with unit aspect ratio and monolayer SWNT (D = 1nm) with random chirality is also shown for comparison.

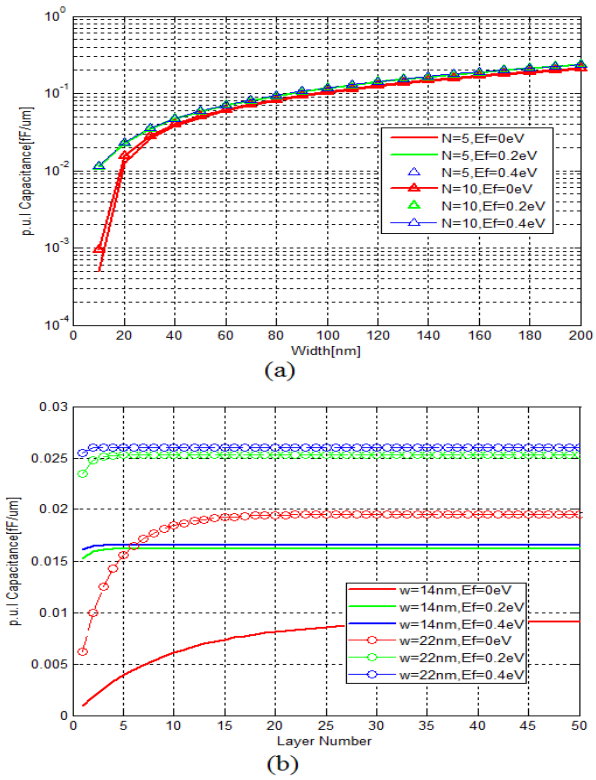

Figure 6. Per unit length capacitance of zz-MLGNR as (a) function of width (b) function of number of GNR layer.

Fig. 7 shows the per unit length inductance as a function of width and number of GNR layer . L_k decreases with increase in width, Fermi energy and number of GNR layer and L_m decreases with increase in GNR width, so the total inductance decreases with increase in width, Fermi energy and number of layers.

For delay calculation a driver-GNR interconnect as shown in Fig. 8 is studied. Based on the proposed RLC model, simulations were implemented using HSPICE. The driver equivalent resistance and capacitance are obtained from the ITRS [1]. Fig. 9 shows the 50% delay of zz-MLGNR of width *14nm* consisting of 10 layers with respect to Cu interconnect of same dimension. It is evident from Fig. 9 that the performance of neutral zz-MLGNR is much worse than Cu but it can outperform Cu when its Fermi energy is raised at 0.6 eV, which can be achieved by intercalation doping [33].

IV. Conclusion

We have developed an RLC equivalent circuit for zz-MLGNR based on ESC model. We have investigated all the lumped elements in zz-MLGNR based on the proposed model and compared with that of Cu, W and SWCNT interconnect. The analysis revealed that, zz-MLGNR can provide lower per unit length resistance than Cu, W and SWCNT it also offers lower per unit length capacitance but in the expense of higher inductance. We have analyzed interconnect delay of zz-MLGNR using the proposed RLC equivalent circuit. It is concluded that the performance of zz-MLGNR can match or become better than Cu only if it is intercalation doped.

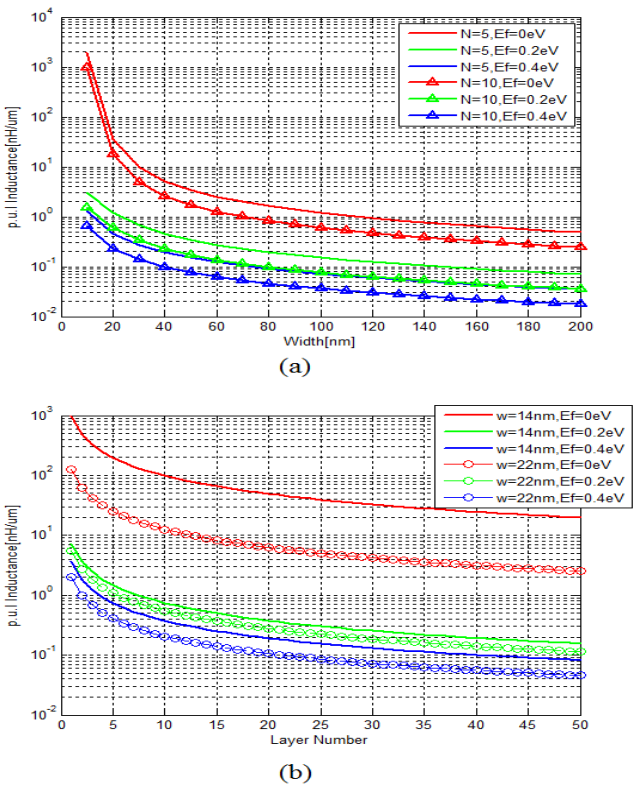

Figure 7. Per unit length inductance of zz-MLGNR as (a) function of width and, (b) as a function of number of GNR layer.

Figure 8. Configuration of the driver-GNR interconnect-load system.

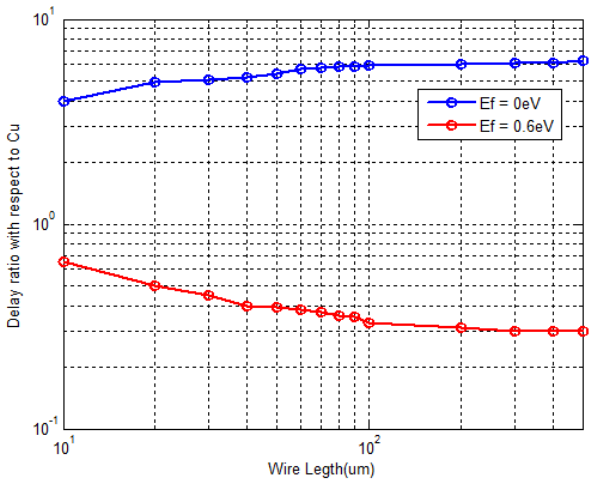

Figure 9. 50% Time delay of zz-MLGNR(layer number, $N = 10$) for 14 nm technology node with respect to the Cu interconnect delay of same dimension is shown.

References

[1] [Online]. Available: http://www.itrs.net/

[2] A. H. Castro Neto, F. Guinea, N.R. Peres, K.S. Novoselov, A.K. Geim, "The electronic properties of graphene", *Rev. Mod. Phys.*, vol. 81, pp.109-162, 2009.

[3] K. S. Novoselov *et. al.*, "Electric Field-Effect in atomically thin carbon films", *Science* vol. 306, pp. 666-669, 2004.

[4] F. Schwierz, "Graphene transistors", *Nat. Nanotechnol.*, vol. 5, pp. 487- 496, 2010.

[5] N. Srivastava and K. Banerjee, "Interconnect challenges for nanoscale electronic circuits," *TMS J. Mater.*, vol. 56, no. 10, pp. 30–31, Oct. 2004.

[6] N. Srivastava, H. Li, F. Kreupl, and K. Banerjee, "On the applicability of single-walled carbon nanotubes as VLSI interconnects," *IEEE Trans. Nanotechnol.*, vol. 8, no. 7, 2009.

[7] M. Radosavljević, J. Lefebvre, and A. T. Johnson, "High-field electrical transport and breakdown in bundles of single-wall carbon nanotubes," *Phys. Rev. B, Condens. Matter*, vol. 64, no. 24, p. 241 307, Dec. 2001.

[8] B. Q. Wei, R. Vajtai, and P. M. Ajayan, "Reliability and current carrying capacity of carbon nanotubes," *Appl. Phys. Lett.*, vol. 79, no. 8, pp. 1172–1174, Aug. 2001.

[9] J. Hone, M. Whitney, C. Piskoti, and A. Zettl, "Thermal conductivity of single-walled carbon nanotubes," *Phys. Rev. B, Condens. Matter*, vol. 59, no. 4, pp. R2 514–R2 516, Jan. 1999.

[10] P. Kim, L. Shi, A. Majumdar, and P. L. McEuen, "Thermal transport measurements of individual multiwalled carbon nanotubes," *Phys. Rev. Lett.*, vol. 87, no. 21, p. 215 502, Oct. 2001.

[11] A. A. Balandin, S. Ghosh, W. Bao, I. Calizo, D. Teweldebrhan, F. Miao, and C. N. Lau, "Superior thermal conductivity of single-layer graphene," *Nano Lett.*, vol. 8, no. 3, pp. 902–907, Mar. 2008.

[12] P. L. McEuen, M. S. Fuhrer, and H. Park, "Single-walled carbon nan-otube electronics," *IEEE Trans. Nanotechnol.*, vol. 1, no. 1, pp. 78–85, Mar. 2002.

[13] H. J. Li,W. G. Lu, J. J. Li, X. D. Bai, and C. Z. Gu, "Multichannel ballistic transport in multiwall carbon nanotubes," *Phys. Rev. Lett*., vol. 95, no. 8, p. 086 601, Aug. 2005.

[14] K. I. Bolotin, K. J. Sikes, J. Hone, H. L. Stormer, and P. Kim, "Temperature dependent transport in suspended graphene," *Phys. Rev. Lett*., vol. 101, no. 9, p. 096 802, Aug. 2008.

[15] D. A. Areshkin, D. Gunlycke, and C. T. White, "Ballistic transport in graphene nanostrips in the presence of disorder: Importance of edge effects," *Nano Lett*., vol. 7, no. 1, pp. 204–210, Jan. 2007.

[16] Y. Ouyang, Y. Yoon, J. K. Fodor, and J. Guo, "Comparison of performance limits for carbon nanoribbon and carbon nanotube transistors," *Applied Physics Letters*, vol. 89, no. 20, pp. −, 2006. [Online]. Available: http://scitation.aip.org/content/aip/journal/apl/89/20/10.1063/1.2387876

[17] G. Liang, N. Neophytou, D. Nikonov, and M. LUNDSTROM, "Performance projections for ballistic graphene nanoribbon field-effect transistors," *Electron Devices, IEEE Transactions on*, vol. 54, no. 4, pp. 677−682, April 2007

[18] R. Van Noorden, "Moving towards a graphene world," *Nature*, vol. 442, no.7100, pp. 228−229, 2006.

[19] C. Berger, Z. Song, X. Li, X. Wu, N. Brown, C. Naud, D. Mayou, T. Li, J. Hass, A. N. Marchenkov *et al*., "Electronic confinement and coherence in patterned epitaxial graphene," *Science*, vol. 312, no. 5777, pp. 1191−1196,2006.

[20] A. Naeemi and J. Meindl, "Performance benchmarking for graphene nanoribbon, carbon nanotube, and cu interconnects," in *Interconnect Technology Conference, 2008. IITC 2008. International*, June 2008, pp. 183−185.

[21] T. Yu, E.-K. Lee, B. Briggs, B. Nagabhirava, and B. Yu, "Bilayer graphene system: current-induced reliability limit," Electron Device Letters, IEEE, vol. 31, no. 10, pp. 1155−1157, 2010.

[22] R. Murali, Y. Yang, K. Brenner, T. Beck, and J. D. Meindl, "Breakdown current density of graphene nanoribbons," *Applied Physics Letters*, vol. 94, no. 24, p. 243114, 2009.

[23] Y. Sui and J. Appenzeller, "Screening and interlayer coupling in multilayer graphene field-effect transistors," *Nano letters*, vol. 9, no. 8, pp. 2973−2977,2009.

[24] M. S. Dresselhaus and G. Dresselhaus, "Intercalation compounds of graphite," *Adv. Phys*., vol. 51, no. 1, pp. 1–186, Jan. 2002.

[25] J. E. Fischer and T. E. Thompson, "Graphite intercalation compounds," *Phys. Today*, vol. 31, no. 7, pp. 36−45, Jul. 1978.

[26] M, S, Sarto and A. Tamburrano, "Comparative analysis of TL models for multilayer graphene nanoribbon and multi wall carbon nanotube interconnects," *int, Symp. EMC*, 2010, pp, 212−217.

[27] S. Datta, *Quantum transport: atom to transistor*. Cambridge University Press, 2005.

[28] D. K. Ferry and S. M. Goodnick, *Transport in Nanostructures*. Cambridge, U.K.: Cambridge Univ. Press, 1997.

[29] P. J. Burke, "Luttinger liquid theory as a model of the gigahertz electrical properties of carbon nanotubes," *IEEE Trans. Nanotechnol*., vol. 1, no. 3, pp. 129–144, Sep. 2002.

[30] A. Naeemi and J. D. Meindl, "Design and performance modeling for single-walled carbon nanotubes as local, semiglobal, and global inter connects in gigascale integrated systems," *IEEE Trans. Electron Devices*, vol. 54, no. 1, pp. 26–37, Jan. 2007.

[31] C. Berger, Z. Song, T. Li, X. Li, A. Y. Ogbazghi, R. Feng, Z. Dai, A. N. Marchenkov, E. H. Conrad, P. N. First, and W. A. de Heer, "Ultrathin epitaxial graphite: 2D electron gas properties and a route to- ward graphene-based nanoelectronics," *J. Phys. Chem. B*, vol. 108, no. 52, pp. 19 912–19 916, Dec. 2004.

[32] M. S. Sarto and A. Tamburrano, "Electromagnetic analysis of radio-frequency signal propagation along SWCN bundles", *Int. Symp. IEEE-NANO 2006*, Cincinnati, USA, July 2006.

[33] J. Shioya, H. Matsubara, and S. Murakami, "Properties of AsF_5-intercalated vapor-grown graphite," *Synth. Met*., vol. 14, no. 1/2, pp. 113–123, Mar. 1986.

Study of the Variation of Resistivity, Permeability and Curie Temperature of Rare Earth Metal Yttrium (Y) Substitution on $Ni_{0.60}Zn_{0.40-x}Y_x Fe_2O_4$ (x=0.05, 0.10, 0.15) Ferrites

M. A. Hossain
Department of Physics
Khulna University of Engineering & Technology (KUET), Khulna-9203, Bangladesh
E-mail :litonalam.bd@gmail.com
M. N. I. Khan
Materials Science Division
Atomic Energy Center
Dhaka-1000, Bangladesh
S. S. Sikder
Khulna University of Engineering & Technology (KUET), Khulna-9203, Bangladesh

***Abstract*—**In this research work, ferrites with compositions of $Ni_{0.60}Zn_{0.40-x}Re_xFe2O4$ where x=0.05, 0.10, 0.15 were prepared by double sintering ceramic technique. The samples were pre sintered at 1000^0 C for 4 hours in air and sintered at 1250^0 C for 3 hours. The influence of Yttrium (Y) substitution on various properties of Ni-Zn ferrites have been studied in this work. Investigations were carried out by the measurements of AC resistivity, Permeability and Curie temperature of the sample. AC resistivity shows the nature of the semiconductor of the samples. The initial magnetic permeability remains constant from low frequency to 10 MHz thenceforth sharply fall to very low values at higher frequencies and again remain constant onward to Zn deficient of Ni -Zn ferrites with substituting of Y. At T = T_c the sharp directress of permeability indicates the samples are good homogeneity.

Keywords— Permeability, Curie temperature, Rare Earth metal and Sintering etc.

Introduction

Iron and its alloys were used as magnetic materials in order to serve the need of the electrical industry at the beginning of the industrialization. With the advent of higher frequencies, the standard techniques of reducing eddy current losses, using lamination or iron powder cores, were no longer efficient or cost effective. S. Hilpert in Germany in 1909, first reported this realization stimulated a renewed interest in "Magnetic Insulators". By 1945 Snoek had laid down the basic fundamentals of the physics and technology of practical ferrite materials [1]. In 1948, the Neel theory of ferromagnetic provided the theoretical understanding of this type of magnetic material. Soft ferrites polycrystalline prepared from metal oxides are magnetic semi conductors and have made important role, both technological and theoretical to the development of electronics. These soft ferrites still remain the best magnetic materials and cannot replaced by any other magnetic materials with respect to their very high frequency application because they are inexpensive, more stable, easily manufactured [2].The most important progress were made in ferromagnetism in the field of magnetic oxides (ferromagnetic). The progress of high frequency ferrites was initiated by the work done by J. L. Snoek [3], who found that connected with excellent properties in the high frequency range, Mn-Zn and Ni-Zn ferrites provide a family of magnetic materials helpful for radio and TV sets as well carrier telephony as cores of inductors transformer and so forth. The most well-liked combination are Ni-Zn [4], Ni-Cu-Zn [5-7], Mg-Zn [8] and Mg-Cu-Zn [9] a ferrites. Ferrite crystallizes with two magnetic sub-lattices i.e. tetrahedral (A) site and Octahedral (B) site based on Neel's model. Magnetic and electrical properties of ferrites are strongly dependant on distribution of cation in A and B sites and their valance state [10]. The properties of Ni-Zn ferrites can be modified by substitutions them with different metals ions such as Co^{2+},Mg^{2+},Mn^{2+},Cu^{2+}etc. The addition of rare earth metal in Ni-Zn ferrite composition is known to play a crucial role in increasing the sintering density and lowering the sintering temperature. Various additives such as V_2O_5, Bi_2O_3, PbO, MoO_3, WO_3, E_2O_3 P_2O_5, La_2O_3, W_2O_3, LiO etc. having low melting point, facilitated to reduce the sintering temperature of these oxides materials due to liquid phase either due to the melting of the additives or due to the eutectic liquid phase formation between the additives and the ferrite. Amount of liquid phase increase with increasing amount of sintering aids which results in increased densification. However excessive amount of sintering additives' will deteriorate electromagnetic properties of the ferrite. So, optimum content of sintering aids is necessary to achieve good sinter ability as well as better electromagnetic properties. Till now researches have not yet been able to formulate a rigid set of rules for ferrites about a single property. Among these La_2O_3,Y_2O_3 and E_2O_3 were the most effective sintering for Ni-Zn ferrite the systematic research is still necessary for effects has been under taken to prepare Ni-Zn ferrite doped with La_2O_3,Y_2O_3 and Eu_2O_3. Scientists still continue their efforts to find out optimum parameters of ferrites, like high saturation magnetization, high permeability, high resistivity, etc. In the present research work we prepared $Ni_{0.60}Zn_{0.40-x}Y_x$ Fe_2O_4 (x=0.05, 0.10, 0.15) Ferrites. We studied the variation of electrical resistivity and magnetic permeability in both temperature and frequency dependent cases.

EXPERIMENTAL

Double Sintering Ceramic Technique: In this method, the required composition is usually prepared form the appropriate amount of raw mineral oxides or carbonates by crushing, grinding and milling. The most common type of grind is the ball grind but instead of ball grind we performed it by hand grind. Grind can be carried out in a wet medium to increase the degree of mixing. The solid state inter-diffusion between

the raw materials play crucial role in this method. Normally, solids do not react at room temperature over normal time scales. Hence it is necessary to heat them at higher temperatures for the diffusion length $(2Dt)^{1/2}$ to exceed the particle size, where t is the firing time , and D is the diffusion constant for the fast-diffusing species. At temperature above 1000^0C, the grind powders are then calcined in air or oxygen. For some time, this process is continued until the mixture is converted into the correct crystalline phase. These powders are again crushed into fine powders. Using hydrostatic pressure the tablet and ring shaped samples are prepared from these fine powders. Pre sintering is carried out at temperature 1000^0C for (3) three hours and sintering at the temperature 1250^0 C for (4) four hours. The general solid state reaction leading to a ferrite MFe_2O_4 may be represented as

$$MO + Fe_2O_3 \rightarrow MeFe_2O_4$$ where M is the divalent ions.

Table of 20 gm compositional details of $Ni_{0.6}Zn_{0.4-x}La_xFe_2O_4$ [x = 0.05, 0.10, 0.15] ferrites

Content,x	NiO	ZnO	La_2O_3	Fe_2O_4
0.05	3.756	2.387	0.473	13.384
0.10	3.731	2.033	0.940	13.296
0.15	3.707	1.683	1.401	13.209

A flow chart of preparation of sample is presented below

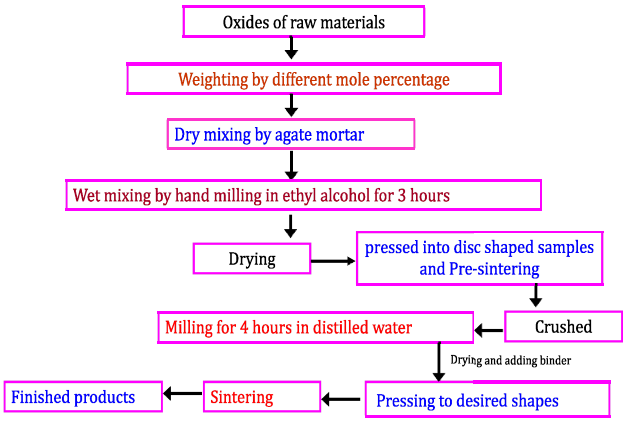

As a whole the preparation procedure generally represents:

- A mixture of materials was prepared with the cations in the ratio corresponding to that in the final product.
- Pre sintering the mixture at temperature 1000^0C to form ferrite.
- Converting the raw ferrite into powder and pressing the powder using hydrostatic pressure into the required shapes.
- Sintering at 1250^0C to produce a highly densified product.

Results and discussion

Table-1 Resistivity at room temperature of Ni0.60 $Zn_{0.40-x}$ $La_xFe_2O_4$ ferrites

Content,x	Resistivity at room temperature(30^0C)
0.05	7.562
0.10	13.112
0.15	129.08

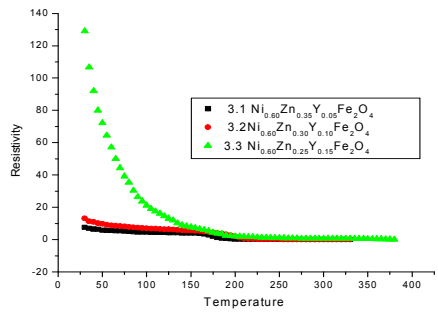

Figure-1: Temperature dependence of resistivity, as a function of Temperature of $Ni_{0.60}$ $Zn_{0.35}$ $Y_{0.05}$ Fe_2 O_4, $Ni_{0.60}$ $Zn_{0.30}$ $Y_{0.10}$ Fe_2 O_4, and $Ni_{0.60}$ $Zn_{0.25}$ $Y_{0.15}$ Fe_2 O_4, sintered at 1250^0C

In figure -1 the rectangular black sign indicates the sample $Ni_{0.60}$ $Zn_{0.35}$ $Y_{0.05}$ Fe_2 O_4.The curve of sample $Ni_{0.60}$ $Zn_{0.35}$ $Y_{0.05}$ Fe_2 O_4 shows that with increasing the temperature from room temperature the resistivity decreasing up to 180^0C. After that with increasing the temperature the resistivity becomes constant and almost temperature independent. In figure-1 the circle shaped red sign indicates $Ni_{0.60}$ $Zn_{0.30}$ $Y_{0.10}$ Fe_2 O_4 which indicates that with increasing the temperature the resistivity decreasing up to 185^0 C and becomes constant and almost temperature independent onward. In figure-1 triangular green sign indicates sample $Ni_{0.60}$ $Zn_{0.25}$ $Y_{0.15}$ Fe_2 O_4 which shows that with increasing temperature the resistivity decreasing gradually and after 190^0C becomes almost temperature independent. All the samples show the nature of the semiconductor.

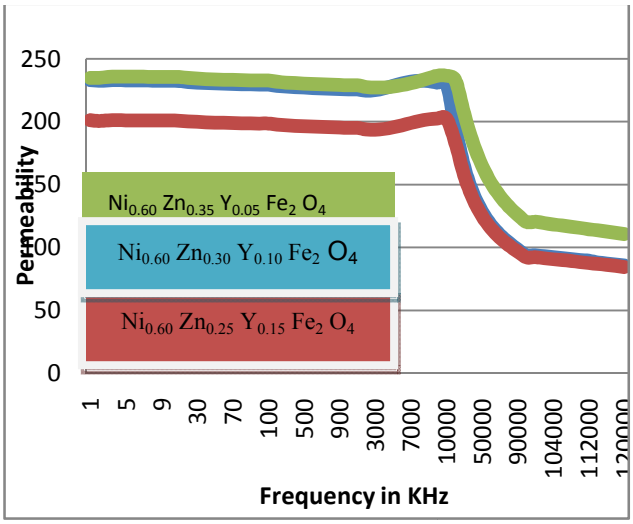

Figure-2: The real part of the permeability dependant on frequency of $Ni_{0.60}$ $Zn_{0.35}$ $Y_{0.05}$ Fe_2 O_4, $Ni_{0.60}$ $Zn_{0.30}$ $Y_{0.10}$ Fe_2 O_4, and $Ni_{0.60}$ $Zn_{0.25}$ $Y_{0.15}$ Fe_2 O_4, sintered at 1250^0C

Figure-2 describes the change of permeability with the change of frequency. For sample $Ni_{0.60}$ $Zn_{0.35}$ $Y_{0.05}$ Fe_2 O_4, $Ni_{0.60}$ $Zn_{0.30}$ $Y_{0.10}$ Fe_2 O_4, and $Ni_{0.60}$ $Zn_{0.25}$ $Y_{0.15}$ Fe_2 $O_4Ni_{0.60}Zn_{0.35}La_{0.05}Fe_2O_4$ it is seen that the initial permeability is as same as up to a very high frequency 10 MHz i.e., initial permeability is constant up to 10 MHz thenceforth the initial permeability sharply decreases up to 100MHz after that it remains constant on wards. At high frequency greater than 100 M the permeability becomes frequency independent.

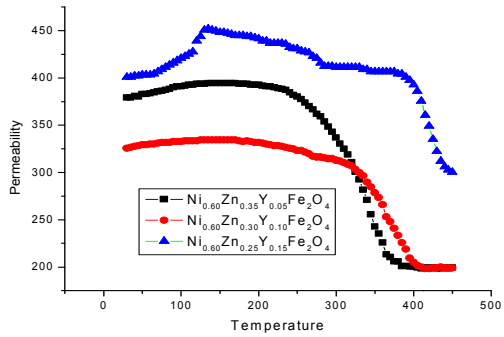

Figure-3: The real part of the permeability dependant on temperature of $Ni_{0.60}$ $Zn_{0.35}$ $Y_{0.05}$ Fe_2 O_4, $Ni_{0.60}$ $Zn_{0.30}$ $Y_{0.10}$ Fe_2 O_4, and $Ni_{0.60}$ $Zn_{0.25}$ $Y_{0.15}$ Fe_2 O_4, sintered at 1250^0C

Table-1 Data of Curie temperature (T_C) ($Ni_{0.60}$ $Zn_{0.40-x}$ $Y_xFe_2O_4$)

Zn- deficient content , x	$T_s = 1250^0$C
	T_c^{0C}
2.1 $Ni_{0.60}Zn_{0.35}Y_{0.05}Fe_2O_4$	340
2.2 $Ni_{0.60}Zn_{0.30}Y_{0.010}$ Fe_2O_4	355
2.3 $Ni_{0.60}Zn_{0.25}Y_{0.15}Fe_2O_4$	395

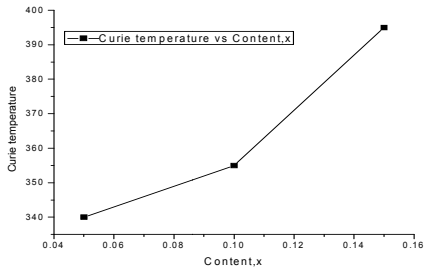

Figure-4: Curie temperature dependence of the content, as a function of Temperature of $Ni_{0.60}$ $Zn_{0.35}$ $Y_{0.05}$ Fe_2 O_4, $Ni_{0.60}$ $Zn_{0.30}$ $Y_{0.10}$ Fe_2 O_4, and $Ni_{0.60}$ $Zn_{0.25}$ $Y_{0.15}$ Fe_2 O_4, sintered at 1250^0C

Figure-4 shows the variation of Curie temperature, T_c with contents. Curie temperature gradually increases with increasing the contents mainly depends upon the strength of A-B exchange interaction.

Conclusion

Effect of electrical and magnetic properties of $Ni_{0.60}Zn_{0.40-x}Y_x$ Fe_2O_4 has studied thoroughly on the Yttrium (Y) substitution where x = 0.05, 0.10, 0.15. Temperature dependence resistivity was measured to identify the nature of the samples. Initially resistivity decreases gradually at lower temperature region and with further increasing the resistivity decreases sharply and at higher temperatures region it becomes almost independent of temperature. Initial permeability dependant on frequency was studied to fathom the frequency response initial permeability. Temperature dependence permeability has been used to measure the Curie temperature of $Ni_{0.60}Zn_{0.40-x}$ Y_x Fe_2 O_4 (x=0.05, 0.10, 0.15) Ferrites. Curie temperature of Ni-Zn ferrite increases with the decrease in Zn-content. There is much scope for further research in controlling the magnetic characteristics by changing composition and heat treatment certain important parameters like temperature dependence magnetization, anisotropy and magnetostriction can be study in detail for a better understanding of micro structure properties of the samples.

Acknowledgements

One of the authors (M. A. Hossain) is thankful to Khulna University of Engineering & Technology (KUET), Khulna, Bangladesh for the financial support. The authors are also grateful to the Materials Science Division of Atomic Energy Centre, Dhaka (AECD), Bangladesh. for allowing their facilities to prepare the samples and to utilize the laboratory facilities for various measurements. Financial support from International Program in Physical Science (IPPS), Uppsala University, Sweden for this work is highly acknowledged.

REFERENCES

[1] R. F. louh, T.G. Reynolds and R.C. Buchanan," Ceramic Materials for Electronics", 3rd edition, edited by R.C. Buchanan, Marcel Dekker Inc. 2004

[2] J. Kulikowski;1"Soft magnetic ferrites development of stagnation"; J. Magn. Magn. Matter; Vol. 41 p.56-62, 1984

[3] J. L. Snoek; "New development of Ferromagnetic Materials"; Elsevier Publ. Co. N.Y. 1984

[4] T. T. Ahmed, I. Z Rahman and S. A. M. Tofial; " Effect of Copper in distribution on the magnetization of nano scaled Ni-Zn ferrites". J. Magn. Magn. Matter; Vol. 272-276, pp. 2250-

2252, 2004
[5] Z. H. Khan, M. Mahbubur Rahman, S. S. Sikder, M. A. Hakim, D. K. Saha; "Complex Permeability of Fe deficient Ni-Cu-Zn ferrites"; Journal of Alloys and Compounds, 584, 208-215, 2013
[6] S. H. Seo and J. H. Oh; " Effect of MoO3 Addition of Sinterial behaviors and Magnetic properties of Ni-Cu-Zn Ferrite for Multilayer Chip inductors"; IEE Transctions on Magnetics, Vol. 35, No.5, 1999
[7] Kin O. Low, Frank R. Sale; " Electromagnetic properties of gel-derived Ni-Cu-Zn ferrites"; J. Magn. Magn. Mater. 246, pp.30-35, 2002
[8] M.A Hakim, M. Manjurul Haque, M. Huq, Sk. Manjura Hoque and P. Norbblad; "Reentrant Spin Glass Behavior of Diluted Mg-Zn Ferrites"; CP 1003, Magnetic Materials International Conference on Magnetic Materials, AIP. P-295, ICMM-2007
[9] M. Manjurul Huq and M. Huq and M.A. Hakim ;" Thermal hysteresis of Permeability and Transport properties of Mn Substituted Mg-Cu-Zn ferrites"; Journal of Physics D: Applied Physics, Vol.41, 055007, pp.1-10, 2008
[10] M. Manjurul Haque, M. Huq and M.A. Hakim; "Influence of CuO and Sintering Temperature on the microstructure and magnetic properties of Mg-Cu-Zn ferrites"; J. Magn. Magn. Mater . Vol. 320, pp.2792-2799, 2008.

Large Signal Performance of Graphene-FET Considering Contact Resistance

Md. Askarul Haque*; Md. Rasidul Islam; Md. Nur Kutubul Alam; Md. Rafiqul Islam;
Department of Electrical and Electronic Engineering
Khulna University of Engineering & Technology, Khulna-9203, Bangladesh
Email: shajibeeekuet@gmail.com*, ronyrasidul@gmail.com

Abstract—**Effect of source/drain contact resistance on the DC characteristics of large area Graphene Field Effect Transistor (GFET) is reported here. As graphene has been identified as a potential candidate for replacing silicon based devices, their performance has been thoroughly investigated. In practical devices, the contact resistance at the interface of channel and Source/Drain (S/D) contact is inevitable; therefore a compact model is proposed taking them into account. In the simulation, Ti, Au, Pt and Ni are considered as contact metals. The result shows the DC characteristics of GFET greatly depends on the contact resistance. Drain current reduces with increasing contact resistance and saturation in the current voltage characteristics disappears at high value of the contact resistance.**

Keywords- Graphene; GFET; Contact Resistance; DC characteristics; Compact modeling

I. INTRODUCTION

In order to sustain Moore's law, the size of silicon (Si) based field effect a transistor has been being reduced for last four decades. As they reached at 22 nm node, they are almost at their physical limit [1, 2]. Enhanced short channel effects (SCEs) as well as diminutive control of gate over the channel leads severe performance variation from the intended design [3]. To solve this problem, Si needs to be replaced from the channel with some material having superior transport properties. One of the most promising materials is graphene mainly due to its wide spread availability as well as low cost along with its excellent physical and electronic transport properties. The sp^2 bonded carbon atoms organized in hexagonal lattice format makes graphene 200 times stronger than steel. The enhanced elastic constant further leads to better thermal conductivity. For electron transport, graphene offers carrier mobility at the range of 3000 cm²/Vs to 27000cm²/Vs [4] [5]. However, the only problem is the semi-metal band structure, i.e. graphene possesses no band gap that forbids its application in logic devices. Nevertheless, its outstanding transport properties have led to many comprehensive studies on the applicability in various fields such as nanoelectronics and high frequency electronics [6], energy storage and conversion [7], field emission display [8], transparent conductors [9] and so on.

However, most of the studies are done for ideal graphene based devices. In real devices, when a channel material is connected with contact, it forms an inherent resistance at the channel-contact interface. In this study, we report the large signal model of GFET and a simple mathematical expressions to analysis the DC characteristics in presence of contact resistance. The basic model given in [10] is modified under the postulates given in [11]. And they are done by adding the effect of contact resistance (R_C) of graphene-metal contact. The values of R_C vary from a few hundred to a few thousand Ω-μm, and depends on the metal used, fabrication procedure, gate bias and measurement conditions [12]. A gate-dependent nickel-graphene contact resistance of 500 Ω μm has been reported at 300 K [13]. For a titanium–graphene system, an R_C of less than 250 Ω μm has been reported at liquid helium temperatures, and an R_C of greater than 1,000 Ω μm at 300 K [13]. These experimental values are used in the elucidation of our proposed model.

II. LARGE SIGNAL MODEL NEGLECTING R_C

Large signal model of graphene FET (GFET) is shown in Fig. 1. It consists of drain, source, graphene channel and an insulated top gate. The effect of R_C between drain/source and graphene has been neglected in this section.

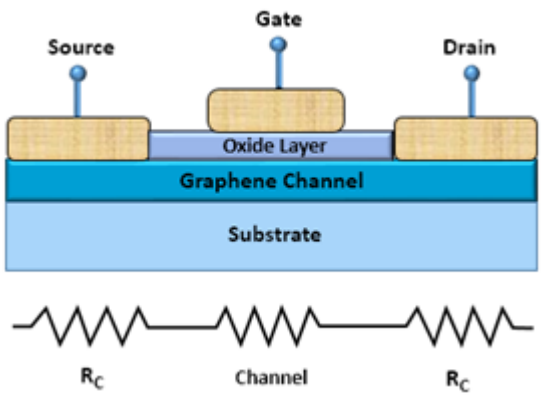

Fig. 1: Schematic diagram of graphene field effect transistor (GFET), and equivalent circuit including the contact resistance.

978-1-4673-9257-0/15/$31.00 ©2015 IEEE

A. Drain Current Modeling

The expression of drain current of top gated GFET is [10, 11]-

$$I_D = \mu W \frac{\int_0^{V_D}(|Q_{net}| + n_{puddle})dV}{L + \mu|\int_0^{V_D}\frac{1}{v_{SAT}}dV|} \quad (1)$$

Where μ is the carrier mobility, W is the width of the graphene sheet, L is the channel length, and V_{SAT} is the saturation velocity in the graphene layer, Q_{net} is the net mobile charge, e is electron charge and n_{puddle} is the residual carrier density which is induced by spatial in homogeneity within the graphene layer. It is given as [14]-

$$n_{puddle} = \frac{\Delta^2}{\pi\hbar^2 v_f^2}$$

Δ represents the spatial in homogeneity of the electrostatic potential, $\hbar$ is the reduced Planck constant, and v_f is the Fermi velocity. Equation (1) can be written as:

$$I_D = \frac{Num_1 + Num_2}{Den} \quad (2)$$

where,

$$Num_1 = \frac{\mu W}{4\beta}\int_0^{V_D}\left[-C_T + \sqrt{C_T^2 + 4\beta|C_T(V_{eff} - V) + eN_f|}\right]^2 dV \quad (3)$$

Here the factor $\beta = \frac{e^3}{\pi\hbar^2 v_f^2}$. C_T is the top oxide capacitance, V is the potential variation along the channel due to drain voltage V_D and N_f is a term that accounts for the net acceptor/donor concentration. The effective gate-source overdrive voltage, $V_{eff} = V_G + V_{TH,0}$. Where V_G is top gate voltage and $V_{TH,0} = eN_f/C_T$ is zero bias threshold voltage for GFET devices. Equation (3) contains integration of absolute function. It can be expanded as followed:

$$Num_{1\,(V_{eff} \geq V_D)} = -\frac{\mu W}{\beta^2 C_T}\left[\frac{-\beta C_T^3 V_D}{2} + \frac{\beta^2 C_T^2}{2}\left\{(V_{eff} - V_D)^2 - V_{eff}^2\right\} + \frac{C_T}{12}(C_T^2 + 4\beta C_T V_{eff})^{3/2} - \frac{C_T}{12}\left(C_T^2 + 4\beta C_T(V_{eff} - V_D)\right)^{3/2}\right] \quad (4)$$

$$Num_{1\,(V_{eff} < V_D)} = -\frac{\mu W}{\beta^2 C_T}\left[\frac{\beta C_T^3 V_D}{2} - \frac{\beta^2 C_T^2}{2}\left\{(V_{eff} - V_D)^2 + V_{eff}^2\right\} + \frac{C_T}{12}(C_T^2 + 4\beta C_T V_{eff})^{3/2} + \frac{C_T}{12}\left(C_T^2 - 4\beta C_T(V_{eff} - V_D)\right)^{3/2}\right]$$

The second term of numerator is given by:

$$Num_2 = \mu W \int_0^{V_D} en_{puddle} dV = \mu W e n_{puddle} V_D \quad (5)$$

The denominator in equation (2) can be expressed as:

$$Den = L + \mu\left|\int_0^{V_D}\frac{1}{v_{SAT}}dV\right| \quad (6)$$

This can be simplified assuming an average V_{SAT} given by [10]:

$$v_{SAT,AV} = \frac{\omega}{\sqrt{\pi\frac{|Q_{net,AV}|}{e} + n_{puddle}}} \quad (7)$$

Where ω is obtained from the surface phonon energy of the substrate ħω and $Q_{net,AV}$ is the average charge [10] given by:

$$Q_{net,AV} = \frac{1}{4\beta}\left[-C_T + \sqrt{C_T^2 + 4\beta\left|C_T\left(V_G - \frac{V_D}{2}\right)\right|}\right]^2 \quad (8)$$

The model is simulated in MATLAB using numerical parameters given in table-1. Fig. 2 shows the simulated I_d-V_D characteristics considering no contact resistance.

TABLE I

Symbol	Description	Value
μ	Mobility	$7000\ cm^2V^{-1}s^{-1}$
C_{TOP}	Top oxide capacitance	$3.6 \times 10^{-3}\ \mu Fcm^{-2}$
Δ	Spatial inhomogeneity	8.65×10^{-21}meV
e	Charge of electron	1.6×10^{-19}C
$\hbar$	Reduced plank constant	1.055×10^{-34}J/s
ω	Angular frequency	$8.5 \times 10^{13}\ s^{-1}$
L	Channel length	1μm
v_f	Fermi velocity	$960000\ cm^{-1}$
W	Channel width	$1\ \mu$m

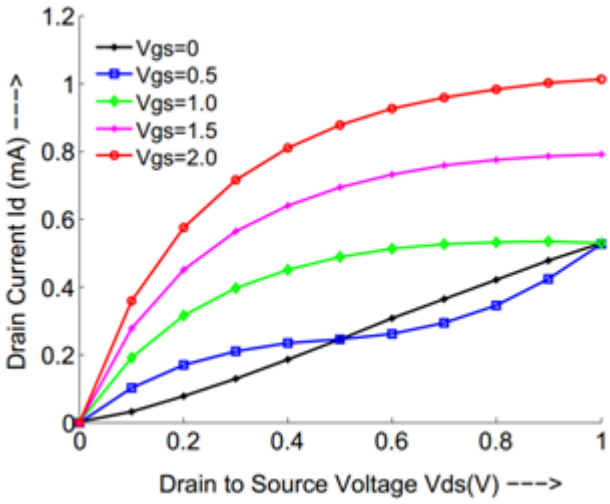

Fig. 2: I_D-V_D characteristics of large area GFET when no contact resistance is taken into account.

B. Transfer Characteristics

The voltage in gate terminal creates electric field in graphene channel that changes or controls the conductivity of the graphene channel. It also controls the number of electrons that can pass through the channel. From the equation (1), it is clear that the I_D is proportional to the polynomial of gate voltage V_G. It is seen in the I_D-V_G characteristics in Fig. 3 that both for positive and negative gate bias, the drain current is positive. Also note that drain current of GFET never goes to zero, it becomes minimum at certain gate bias called the "Dirac point". Left to the Dirac point, current is carried by hole and right to that point, it is carried by electron. That also means the Dirac point distinguishes the point of bipolar conduction.

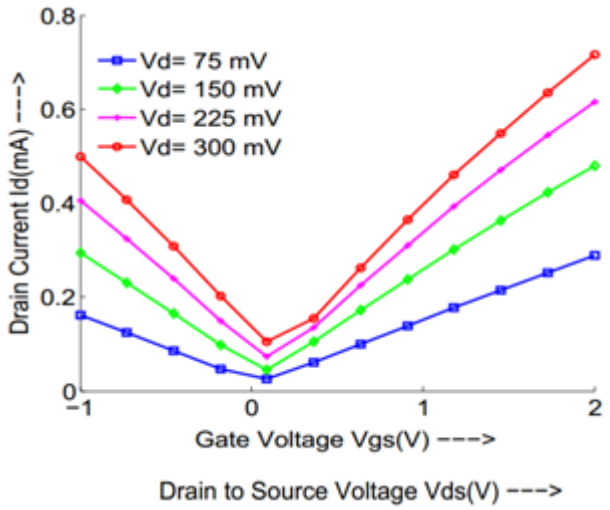

Fig. 3: I_D-V_G characteristics of large area GFET when no contact resistance is taken into account.

III. GFET MODEL CONSIDERING R_C

For a complete model of GFET, the contact resistances R_C cannot be neglected where R_C is in the order of few hundred ohms. The contact length of 0.5 μm is considered. The complete model is shown in Fig. 4.

A. Effect of R_C on Drain Current

When voltage is applied between drain to source (V_D), a portion of it drops across each R_C. In that case, the V_D is given as-

$$V_D = V_{Ch} + 2I_D R_c \qquad (9)$$

The limit used in the integrals in equation (1) is the potential extremes at the channel region. That is why when contact resistance is added, they must be modified as follows:

$$I_D = \mu W \frac{\int_{I_D R_C}^{V_D - I_D R_C} (|Q_{net}| + n_{puddle}) dV}{L + \mu \left| \int_{I_D R_C}^{V_D - I_D R_C} \frac{1}{v_{SAT}} dV \right|} \qquad (10)$$

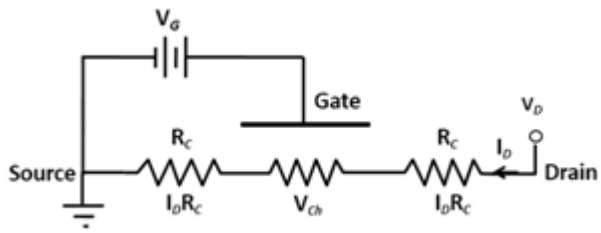

Fig. 4: The complete GFET model with the voltage drops in channel and in contact resistances.

The further calculations are same as described in section II. The equation (10) is a polynomial of drain current I_D and it cannot be solved directly. That is why it is solved by numerical root finding methods. From several available techniques, Bisection method is used here.

The simulation results of $I_D - V_D$ characteristics for different R_C are shown in Fig. 5. It is observed that the I_D decreases with the increase of R_C. Also the saturation regions of $I_D - V_D$ characteristics disappears for the higher values of R_C.

B. Effect of R_C on Transfer Characteristics

The transfer characteristics with the contact resistance can be simulated in the same way explained in preceding section, and are shown in Fig. 6. It is observed that at zero contact resistance (R_C=0), the I_D–V_G curves are linear before and after Dirac point. This linearity disappears and I_D–V_G curves get saturated for higher values R_C. However, no change in position of Dirac points is observed.

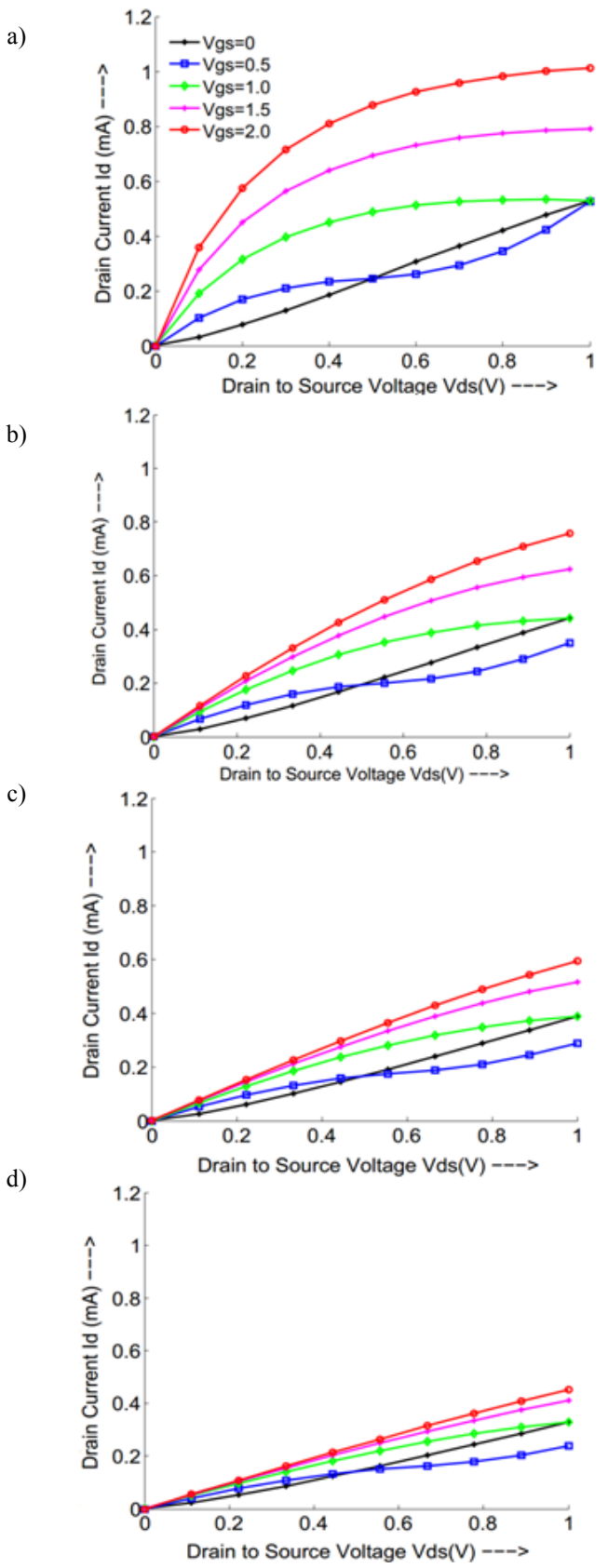

Fig. 5. The effect contact resistance R_C on I_D–V_D characteristics of GFET. (a) without R_C; (b) with R_C = 300 Ω; (c) with R_C = 600 Ω; (d) with R_C = 900 Ω

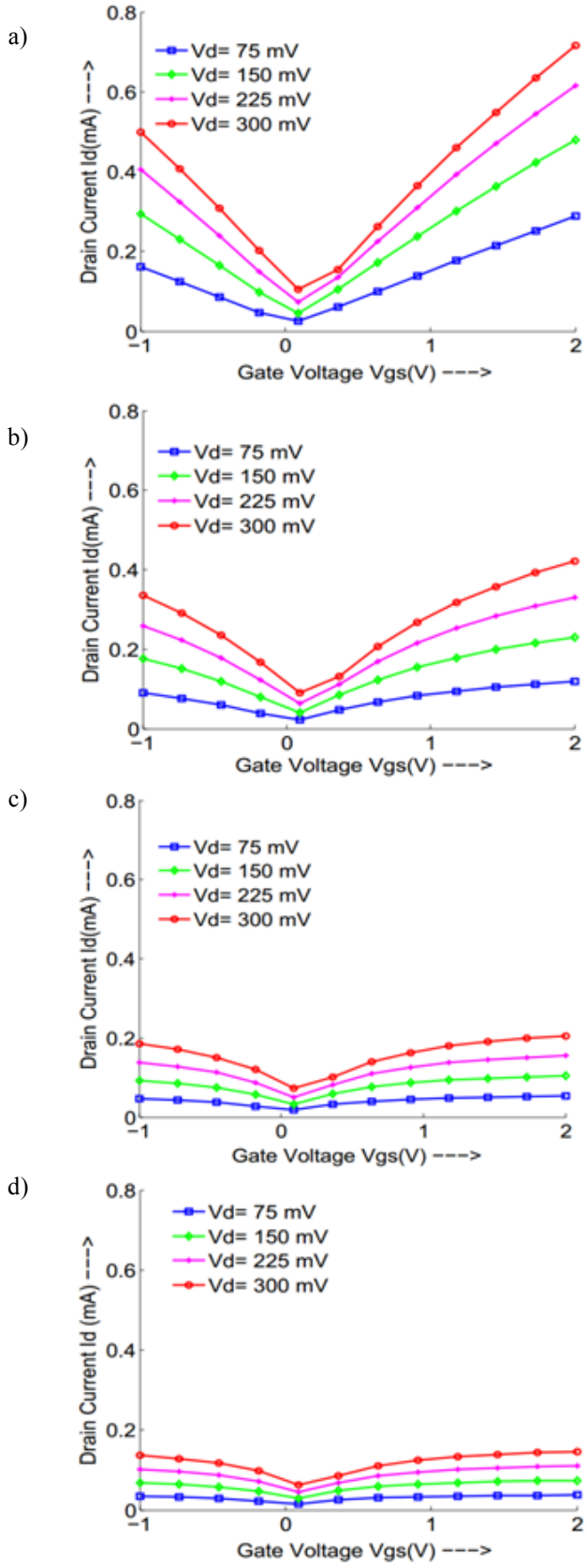

Fig. 6. The effect contact resistance R_C on I_D–V_G characteristics of GFET. (a) without R_C; (b) with R_C = 300 Ω; (c) with R_C = 600 Ω; (d) with R_C = 900 Ω

IV. CONCLUSION

In this research, we present a compact model for large signal characteristics for top-gated graphene FET with no band-gap engineering of the graphene channel. Because of zero band-gap, GFET cannot be used as logic device, but it can be used in RF (Radio Frequency) applications. Taking into account the contact resistance, an analytical expression is provided for the drain current I_D which is a polynomial function of all relevant parameters. Simulation result shows that the contact resistance has a significant effect on the $I_D - V_D$ and transfer characteristics. When contact resistance is neglected, the saturation region $I_D - V_D$ is flat enough to make the device compatible for analogue application. However, with increasing resistance, I_D decreases significantly and When R_C increases, the voltage drops in drain and source terminals increases. So for a fixed value of drain voltageV_D, the channel potential decreases. The expression of I_D is a very complex function of V_D, V_G and R_C. So it is difficult to explain the disappearance of saturation region.

References:

[1] Isabelle Ferain, Cynthia A. Colinge, and Jean-Pierre, "Multigate transistors as the future of classical metal-oxide-semiconductor field-effect transistors," Nature, vol. 479, pp. 310-316, November 2011.

[2] Farzin Assad, Zhibin Ren, Dragcia Vasileska, Supriyo Datta, and Mark Lundstrom, "On the Performance Limit for Si MOSFETs: A Theoretical Study," IEEE Trans. Electron Devices, vol. 47, no. 1, pp. 232-240, January 2000.

[3] Honghui SUN, Liang FANG, Yao WANG, Yaqing CHI, Rulin LIU "A Low Contact Resistance Graphene Field Effect Transistor with Single-Layer-Channel and Multi-Layer-Contact" Nanoscale Architectures (NANOARCH), 2014 IEEE/ACM International Symposium on, pp. 139 144,2014.

[4] K. S. Novoselov, A. K. Geim, S. V. Morozov, D. Jiang, Y. Zhang, S. V. Dubonos, I. V. Grigorieva, andA. A. Firsov, "Electric Field Effect in Atomically Thin Carbon Films", Science, Vol. 306, pp. 666-669,October 2004.

[5] C.Berger, Z. Song, X. Li, X. Wu, N. Brown, C. Naud, D. Mayou, T. Li, J. Hass, A. N. Marchenkov, E. H. Conrad, P. N. First, and W. A. de Heer, "Electronic Confinement and Coherence in Patterned Epitaxial Graphene", Science, vol. 312, pp. 1191-1196, April 2006.

[6] Yanqing Wu, Keith A. Jenkins, Alberto Valdes-Garcia, Damon B. Farmer, Yu Zhu, Ageeth A. Bol, Christos Dimitrakopoulos, Wenjuan Zhu, Fengnian Xia, Phaedon Avouris*, and Yu-Ming Lin, "State-of-the-Art Graphene High-Frequency Electronics", Nano Letters, Vol. 12 No. 6, pp 3062–3067, 2012.

[7] Rinaldo Raccichini et. al. "The role of graphene for electrochemical energy storage", Nature Materials, Vol. 14, pp. 271-279, 2015.

[8] Cheng-Kuang Huang et. al. "Well-aligned graphene arrays for field emission displays", Applied Physics Letters, Vol. 98, pp. 3104-3, 2011.

[9] Jonathan K. Wassei, Richard B. Kaner, "Graphene, a promising transparent conductor", Materialstoday, Vol. 13, issue 3, pp. 52-59, 2010.

[10] S. Fregonese, M. Magallo, C. Maneux, H. Happy, and T. Zimmer,"Scalable Electrical Compact Modelling for Graphene FET Transistors,"IEEE Trans. on Nanotechnology, vol. 12, no. 4, pp. 539–546, 2013.

[11] Rodriguez, Saul, Sam Vaziri, Anderson Smith, Sebastien Fregonese, Mikael Ostling, Max C. Lemme, and Ana Rusu. "A comprehensive graphene FET model for circuit design." arXiv preprint arXiv:1310.1940 (2013)

[12] Fengnian Xia, Vasili Perebeinos, Yu-ming Lin, Yanqing Wu and Phaedon Avouris, "The origins and limits of metal–graphene junction resistance", Nature Nanotechnology, Vol. 6, pp. 179-184, 2011.

[13] Nagashio, K., Nishimura, T., Kita, K. & Toriumi, A. Metal/graphene contact as aperformance killer of ultra-high mobility graphene—analysis of intrinsicmobility and contact resistance. IEEE International Electron Devices MeetingIEDM.2009.5424297, Baltimore, Maryland (2009).

[14] W. Zhu, V. Perebeinos, M. Freitag, et P. Avouris, "Carrier scattering, motilities, and electrostatic potential in monolayer, bi-layer, and tri-layer graphene," *Physical Review B*, vol. 80, p. 235402, Dec. 2009.

Efficient design of thermal management by graphene heat spreader in embedded system

S.M.Rafi-Ul-Islam
Department of Electrical and Electronic Engineering
Bangladesh University of Engineering and Technology
Dhaka, Bangladesh
E-mail:rafiulislam89@gmail.com

Samia Subrina
Department of Electrical and Electronic Engineering
Bangladesh University of Engineering and Technology
Dhaka, Bangladesh
E-mail:ssubrina@gmail.com

***Abstract*— In this paper, a thermal model of an embedded system consisting of MOSFET, MESFET and HFET is presented in nano-electronic system by using FEM (Finite Element Method) . This model is used to analyze the thermal effects of an embedded system and to solve the associated thermal problems by using graphene heat spreader on different positions of the embedded system. This paper also suggests the best position of graphene heat spreader to ensure maximum reduction of temperature of the electronic devices. As high temperature sets a limit to the reliability of the devices, such modeling is very useful for the optimization of an embedded system to guarantee a longer lifespan and a better reliability.**

Keywords*— *Graphene, Heat Spreader, Embedded System, Thermal Management.

I. INTRODUCTION

Self-heating is a severe problem for the high-power related electronic, optoelectronic and photonic embedded devices [1]–[3]. Average temperature rise and non-uniform distribution of dissipated power in embedded systems consist of MOSFETs, MESFETs and HFETs individually or combination of these transistors, leading to the emergence of hotspots nears the device channels. These hotspots bring about degradation of the drain current, gain and output power, and can cause thermal breakdown [4]–[6]. Furthermore, the down-scaling of devices and higher circuit speeds lead to further increase in heat generation, power densities and temperature rise [7-8]. Temperature rise to an abrupt level also causes an increase in gate-leakage current and results in a poor reliability [9]. Various thermal management solutions, for example, conventional heat spreaders (HS) like Copper or Aluminum results poor improvement in thermal management for FET devices. To overcome these shortcomings, a newly invented material named Graphene, the 2-D allotrope of carbon atoms arranged in hexagonal pattern with superior thermal conductivity, ranging from 3000-5300 W/m.K at room temperature can be a potential candidate. It has very high electron mobility as well as very low resistivity. It also provides lower thermal contact resistance due to its flat geometry. The heat propagates in a lateral direction within the graphene plane that increases the area of the heat dissipation, increases the removal of heat flux from hot spots, reduces temperature and thus high heat flux thermal management becomes more efficient [10] .

In this work we carry out two dimensional thermal modeling in order to study the effect of graphene heat spreaders in thermal management of an embedded system.

II. MODEL FOR HEAT CONDUCTION

To find out the best position for adding graphene heat spreader, we simulated the embedded system with Graphene heat spreader (a) at the drain region of every FET devices (b) at only two drain terminals of the whole embedded system (c) at the junction of GaAs and SiC substrate region.

The simulated embedded system consists of 5 FET devices with a separation of 5μm between two consecutive FET transistors (cf. Fig. 1).

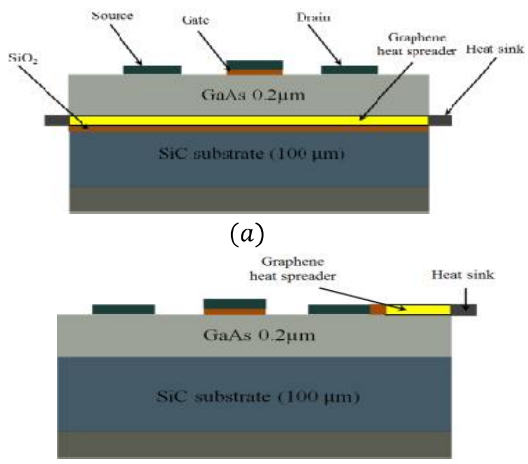

Fig. 1 Heat removal technique using graphene heat spreader (a) when graphene HS is connected to the substrate level and (b) when graphene HS is connected to the drain region. (One of the five FETs of the embedded system is shown in the figure.)

978-1-4673-9257-0/15/$31.00 ©2015 IEEE

The whole device width is 26μm. For MOSFET and MESFET, the thicknesses of SiC substrate, epitaxial GaAs film and graphene heat spreader are 100μm, and 0.2μm , and 1nm, respectively while their thermal conductivities are 490W/m.K, 46W/m.K and 2000W/m.K, respectively for different embedded systems simulated here [11-12]. A SiO_2 is used as an insulator with a thermal conductivity of 1.4 W/m.K and thickness of 10nm. For AlGaAs/GaAs HFETs, the thickness of SiC substrate, GaAs, AlGaAs and SiO_2 layers were 100μm, 192nm, 8nm and 10nm, respectively. Their corresponding thermal conductivities at the room temperature are taken from the literature to be 350W/mK, 160W/mK, 120W/mK and 1.4W/mK, respectively [13]-[15].

The whole simulation is carried out with FEM (Finite Element Method) using COMSOL software [16]. A conventional heat sink is attached to the device structure at the bottom. A graphene heat spreader, when used, is connected- at first case, at drain region of each FET devices; in the second case, at the drain region of the two terminal FET devices only; and in the third case, at GaAs and SiC layer for heat escaping. The heat spreader is insulated from the drain terminal by a thin SiO_2 layer. In our proposed device structure the size of the graphene layer is in micrometer range which is much larger than phonon mean free path of graphene (775 nm). Hence in our work, the thermal transport is considered to be diffusive and does not reveal any edge dependence[17]-[20].

In this paper, the thermal profiles have been simulated by using the Fourier's law expressed as:

$$-\nabla \cdot (k\,\nabla T) = Q \qquad (1)$$

and the Ohm's law given by:

$$J = \sigma E + J_e \qquad (2)$$

Here Q is the heat source, defined as the heat energy generated within a unit volume per unit time, T is the absolute temperature and k is the thermal conductivity of material, J is the current density, σ is electrical conductivity and E is the electric field. The operator $\nabla = \partial/\partial x + \partial/\partial y + \partial/\partial z$. The bottom surface of the substrate and the far end of the graphene heat spreader were kept at a constant temperature T = 300 K. The external boundaries were considered to be adiabatic and given by $\nabla \cdot (k\,\nabla T) = 0$ i.e. the temperature gradient across the boundary is zero. All the heat sinks were considered to be held at a constant room temperature and were described as $T = T_0$, where T_0 = 300K. The external surfaces were modeled as insulated from the environment.

III. Simulation and Results

Thermal issue is more critical in embedded systems and we get a clear picture of this phenomenon from the simulation results shown in Fig. 2. The maximum temperature in integrated chip is very high without the heat spreader. By using graphene heat spreader,maximum temperature is reduced by a significant amount.

An embedded system is energized by a drain voltage and an electric current. Maximum heat is generated in the channel region. The hot spot temperature was obtained using 2D simulation, using COMSOL multiphysics software. With the graphene heat spreader, heat generated from the hot spot can be propagated to a larger area, and dissipated by natural convection, thus a temperature drop of the embedded system's hot spot was observed. The reduced hot spot temperature suggests improved temperature uniformity across the chips and enhanced performance and lifetime for electronic devices.

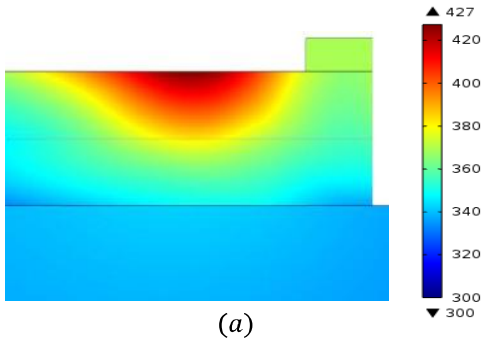

(a)

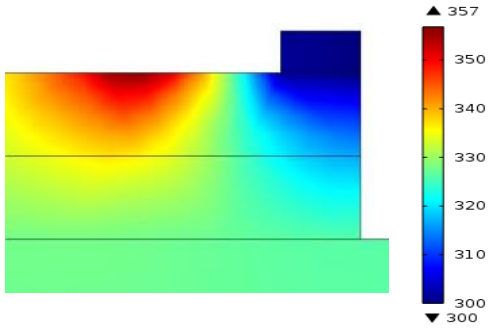

(b)

Fig.2. Temperature distribution in simulated 2-D embedded MOSFET system (a) without and (b) with graphene heat spreaders attached to the side heat sinks. (Zoomed view of one of the five MOSFETs).

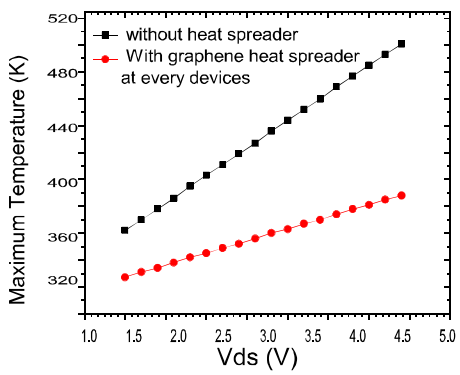

(a)

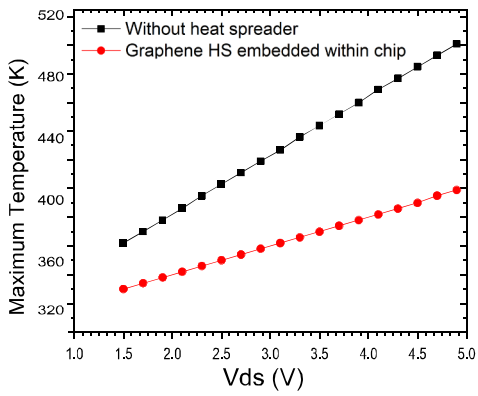

(b)

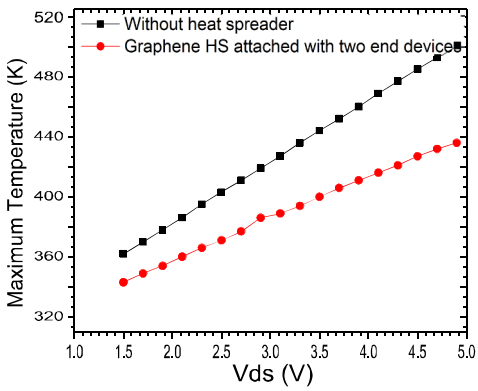

(c)

Fig.3. Temperature profile for a MOSFET embedded system with Graphene HS (red colored line) (a) at drain region of each MOSFET, (b) at SiC substrate level in another words as embedded within chip and (c) only at two MOSFETs located at the ending terminals of the embedded system. All the figures compared with respect to same system having no heat spreader (black colored line).

Fig. 3(a) represents the temperature effects on a MOSFET embedded system when no heat spreader is used (black colored line) and with graphene heat spreaders used at the end of drain terminals of each device (red colored line). We observed that graphene HS reduces temperature of the embedded system by a great extent. Fig. 3(b) and Fig. 3(c) represent the temperature effects on a MOSFET embedded system without any heat spreader and with graphene heat spreaders used at substrate levels and only at the end of two Terminal devices, respectively.

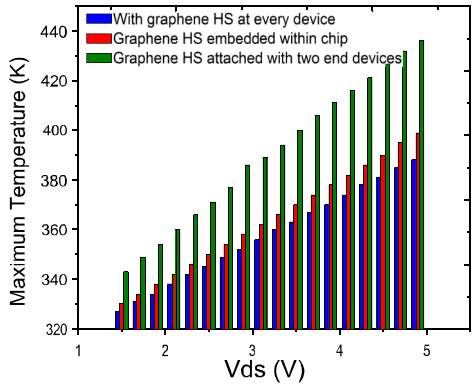

Fig.4. Comparison among three different positions of the graphene HS for the MOSFET embedded system.

Fig. 4 represents the comparison among thermal improvement of a MOSFET embedded system when graphene heat spreaders connected at different positions of the system. As it is clear from the graph that, graphene HS, if connected to each drain terminals of the system, gives the best improvement in devices; and when graphene HS is connected only at two endmost terminal devices, it gives poor result; and moderate thermal improvement occurs when graphene HS is connected at substrate level. For instance, for a given gate voltage $V_{gs} = 1.5V$ and drain voltage $V_{ds} = 3.0V$, maximum temperatures of the MOSFET embedded device are 427K, 357K, 362K and 389K in case of without heat spreader, graphene HS at every device, graphene HS at the substrate level and graphene HS at only two terminal devices, respectively.

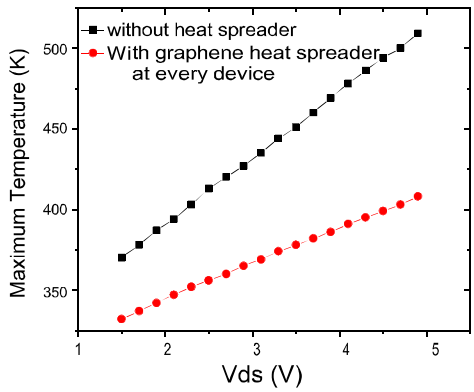

(a)

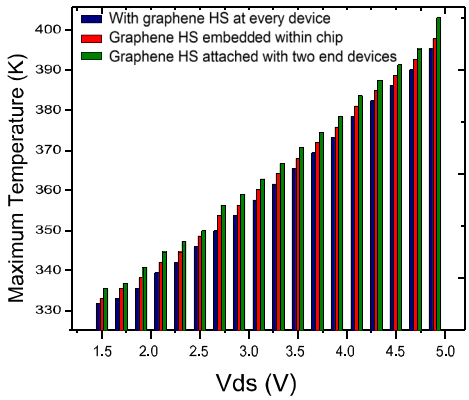

(b)

Fig.5.Temperature profile for a MESFET embedded system with graphene HS (red colored line) (a) at drain region of each MESFET, of the embedded system. The figure is compared to same system having no heat spreader. (b) Comparison among three different positions of the graphene HS.

Fig. 5(a) demonstrates the thermal improvement of a MESFET embedded system when graphene heat spreader is incorporated to device terminals with respect to without heat spreader. As it is clear form the figure that with the increment of drain to source voltage, thermal improvement is quite significant with graphene HS.

Fig. 5(b) compares the thermal improvements for different drain to source voltages for incorporation of graphene HS at different positions of the embedded system. When graphene heat spreaders are connected to the drain region of the each MESFET of the system, it gives the best result in terms of temperature reduction as well as increasing of system lifetime, while graphene HS embedded within the chip, in another words at substrate level gives a satisfactory thermal improvement and graphene HS at only terminal most two MESFET of the system gives least improvement among three possible ways of heat escaping as demonstrated here.

For a given gate voltage $V_{gs} = 1.5V$ and drain voltage $V_{ds} = 3.0V$, temperature improvements of the MESFET embedded device are 66K, 63K and 59K with respect to without HS and when graphene HS at every device, graphene HS at substrate level and HS at only two terminal devices is used to the system respectively.

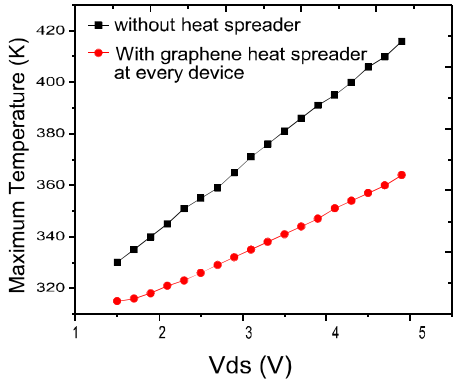

(a)

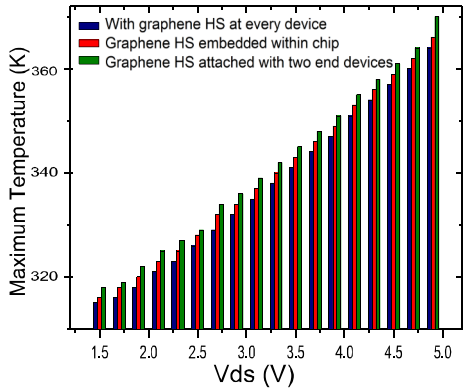

(b)

Fig.6.Temperature profile for a HFET embedded system with Graphene HS (red colored line) (a) at drain region of each HFET, of the embedded system, with the results being compared with that having no heat spreader(black colored line). (b) Comparison among three different positions of the graphene HS

As for a HFET embedded system, using of graphene heat spreader gives an outstanding thermal improvement with respect to using no heat spreader, depicted in Fig. 6(a). The maximum temperatures of the system are 371K and 335K for without heat spreader and for the case of using heat spreader respectively, at $V_{gs} = 1.5V$ and $V_{ds} = 3.0V$. Fig. 6(b) reveals the best option for incorporating of graphene heat spreader to the embedded system. It shows that graphene HS at the end of each HFET gives the best improvement and HS at only two end devices of embedded HFET system gives the least thermal improvement among three possible paths for heat escaping.

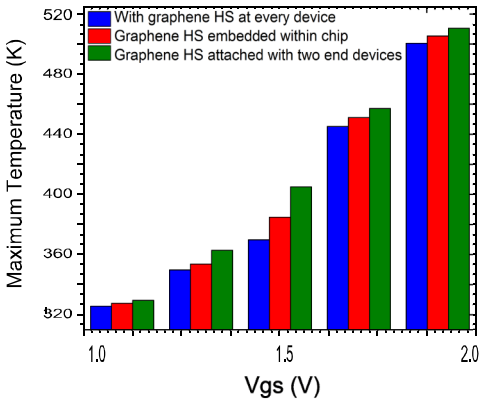

Fig.7.Temperature profile for an embedded system with Graphene HS at different positions of the MOSFET embedded system with the variation of gate to source voltage.

Fig. 7 shows the temperature variation of an embedded system with the variation of gate to source voltage. It is clear from the graph that graphene heat spreader connected at every device reduces the maximum temperature of the system to a significant amount.

IV. CONCLUSION

We carried out a feasible study of the use of graphene as the material for lateral heat spreading in embedded chips. Although our results show that the amalgamation of graphene or FLG (few layer graphene) at the drain terminal of each FET devices gives the best thermal improvement,this is a less feasible solution for fabrication perspectives. Graphene heat spreader embedded within chip,in another words graphene HS at the interface of the insulating and the substrate layer can lead to substantial reduction in temperature of the hot spots which is very close to the thermal improvement for HS connected to each device with more feasible fabrication process.Graphene HS only at the end of two endmost FET devices carried out the poorest result among these three possible positions of incorporation of graphene a HS at embedded FET devices. Hence we suggest embedded graphene heat spreader as the most pragmatic and convenient means of improving thermal issues of FET devices. The efficiency of the hot spot removal with graphene depends on the specifics of the device structure, geometry, and position of the heat spreader. The obtained results can lead to a new type of possibility of thermal management of nano-electronic circuits.

REFERENCES

[1] Trew, R. J., Green, D. S. & Shealy, J. B. AlGaN/GaN HFET reliability. *IEEE Microw. Mag.* **10,** 116–127, 2009.

[2] Kuzmik, J. *et al.* Self-heating phenomena in high-power III-N transistors and new thermal characterization methods developed within EU project TARGET. *Int. J. Microwave and Wireless Tech.* **1,** 153–160, 2009.

[3] Green, D. S. *et al.* GaN HEMT thermal behavior and implications for reliability testing and analysis. *Phys. Stat. Sol. (c)* **5,** 2026–2029, 2008.

[4] P. G. Mautry and J. Trager, "Investigation of self-heating in VLSI and ULSI MOSFET's," *Proc. 1990 IEEE Conf Microelectronic Test Structures,* 221-226, Mar. 1990.

[5] L. I. McDaid, S. Hall, W. Eccleston, and I. C. Alderman, "Monitoring the temperature rise in SOI transistors by measurement of leakage current," *Proc. 1991 IEEE Int. SOI Conf,* 28-29, Oct. 1991..

[6] L. T. Su, J. E. Chung, D. A. Antoniadis, K. E. Goodson, and M. I. Flik, "Measurement and modeling of self-heating in SOI MOSFETs," *IEEE Trans. Electron Devices,* 41, 69-75, Jan. 1994.

[7] E. Pop, S. Sinha and K. E. Goodson, "Heat generation and transport in nanometer scale transistors," *Proc. of IEEE,* 94, Aug. 2006.

[8] C. Fenigna, Y. Yang, E. Sangiorgi and A. G. O' Neill, "Analysis of self-heating effects in ultrathin-body SOI MOSFETs," *IEEE Trans. Electron Devices,* 55, 233-244, 2008.

[9] P. G. Mautry and J. Trager, "Investigation of self-heating in VLSI and ULSI MOSFET's," Proc. 1990 IEEE Conf Microelectronic Test Structures, 221-226, Mar. 1990.

[10] D. L. Nika, S. Ghosh, E. P. Pokatilov, and A. A. Balandin, "Lattice thermal conductivity of graphene flakes: Comparison with bulk graphite," *Appl. Phys. Lett.* 202-203, 2009.

[11] M. Shamsa, P. M. Solomon, K. A. Jenkins, A. A. Balandin, W. Haensch, "Investigation of thermal crosstalk between SOI FETs by the subthreshold sensing technique," *IEEE Trans. Electron Devices, 55, 1733-1740, Jul. 2008.*

[12] S.Subrina,D Kotchetkov, and A.A.Balandin, "Heat removal in Silicon-on-Insulator Integrated circuits with graphene heat spreaders,". *IEEE Elec. Dev.* 30.12.2009,pp.1281-1283.

[13] Liu, W. L. & Balandin, A. A. Thermal conduction in AlGaN alloys and thin films. *J. Appl. Phys.* **97,** 073710 , 2005.

[14] Balandin, A. A. *et al.* Low flicker-noise GaN/A1GaN heterostructure fieldeffect transistors for microwave communications. *IEEE Trans. Microwave Theory & Tech.* **47,** 1413–1417,1999.

[15] Sheppard, S. T. *et al.* High-power microwave GaN/AlGaN HEMT's on semiinsulating silicon carbide substrates. *IEEE Elec. Dev. Lett.* **20,** 161–163,1999.

[16] [Online].Available: http:// www.comsol.com

[17] W Balandin, A. A. et al. Superior thermal conductivity of single-layer grapheme. *Nano Lett.* 8, 902–907,2008.

[18] S. Ghosh, I. Calizo, D. Teweldebrhan, E. P. Pokatilov, D. L. Nika, A. A. Balandin, W. Bao, F. Miao, and C. N. Lau, "Extremely high thermal conductivity of graphene: Prospects for thermal management applications in nanoelectronics," *Appl. Phys. Lett.*, 92, 151911, Apr. 2008.

[19] D. L. Nika, E. P. Pokatilov, A. S. Askerov and A. A. Balandin, "Phonon thermal conduction in graphene: Role of Umklapp and edge roughness scattering," *Phys. Rev. B* 79, 155413, Apr. 2009.

[20] S. V. Morozov, K. S. Novoselov, M. I. Katsnelson, F. Schedin,D. C. Elias, J. A. Jaszczak, and A. K. Geim, "Giant intrinsic carrier mobilities in graphene," *Phys. Rev. Lett.*,100, 016602, Jan. 2008.

Analytical Approach of J-V Characteristics of CdTe Based Thin Film Solar Cells Including Voltage and Space Dependent Electric Field in the Absorber Layer

[1]Protik Biswas, [2]Abdullah Sakib Hasan, [3]Ashiq Been Rahim, [4]Aman Ullah, [5]Md. Iqbal Bahar Chowdhury
Department of Electrical and Electronics Engineering (EEE)
United International University
Dhaka, Bangladesh
[1]protik_biswas@yahoo.com, [2]ovi_uiu05@yahoo.com, [3]real619@hotmail.com, [4]amanullah.en@gmail.com, [5]ibchy@eee.uiu.ac.bd

***Abstract*—This work reports on development of an optimized analytical model to investigate the current-voltage (J-V) characteristics of a lightly doped CdTe-based thin film solar cell considering voltage-space dependency of electric field in the absorber region. Following the theory of perturbation, the intractable mathematical equations have been solved analytically. Finally, changes in J-V characteristics curve are observed in various conditions such as effect of stress, life time of holes and electrons and varying series resistance. The proposed model is proven to be helpful in giving better physical insight of Cds/CdTe solar cell.**

Keywords— CdS/CdTe Solar Cell, J-V Characteristics, non-uniform electric field , Perturbation Theory, stress effect.

I. INTRODUCTION

Thin-film CdS/CdTe solar cells fabricated on glass substrates have been recognised as one of the most potential candidates for the development of cost-effective and reliable solar cells in large-scale photovoltaic applications. The documented experimental efficiency of these cells is about 16%–17% and the consequent theoretical values are more than 28% [1]. The advantages of using CdTe include high absorption capability for being a direct bandgap material and the simplicity of device processing [2]. It can be deposited on glass typically a few micrometers deep as absorber layer with a very thin layer of CdS (0.1µm) in the emitter side [2], [3]. In Cds/CdTe solar cells, higher percentage of incident light is absorbed in first few micrometers of lightly doped CdTe layer. The photo-generated carriers in this region are collected by the voltage-dependent electric field [4]–[6].

A number of numerical as well as analytical models [4] – [7] have been introduced in the literature to model the current-voltage (J-V) characteristics of Cds/CdTe solar cells. All these models used a lot of fitting parameters. Anjan *et al*. [8] and Mannan *et al*. [9] developed their models with minimum number of fitting parameters. In [8] electric field is considered as uniform throughout the absorber layer, whereas the same is considered as space-dependent in [9]. Both models used the voltage-dependency of the electric field; but these models used numerical iterations to model the J_L-V_L characteristics, although they deduced the photo-generation current analytically. Later Haque *et al*. [10] derived the J_L-V_L characteristics analytically using the concept of perturbation method. But this model considered the electric field in the absorber layer as constant.

This work focuses on developing a model that removes the abovementioned limitations. In the proposed model, the electric field across absorber layer is considered nonuniform. Furthermore, the theory of perturbation has been applied in order to solve the intractable major differential equations which are proven to be more time effective and acceptable than that of typical lengthy iteration methods. The variations of J-V characteristics under different parameters, i.e., before and after stress, life time of holes and electrons and series resistance have been analysed.

II. ANALYSIS

The load current density (J_L) against the load voltage (V_L) of any solar cell including the effect of series resistance can be expressed as

$$J_L(V_L) = -J_{ph}(V_L) + J_0(V_L)(e^{\frac{V_L - J_L R_s}{nV_T}} - 1) \quad (1)$$

Where, J_{ph} is the photogenerated current density, J_0 is the dark saturation current density, n is the ideality factor and V_T is the thermal voltage. Since the band-gap of CdS (E_g = 2.42 eV) is comparatively higher than that of CdTe (E_g = 1.5 eV), the dark saturation current at the emitter region caused by diffusion is negligible and hence, is dominated by the recombination process in the absorber region. In [9], the expression for J_0 is given as

978-1-4673-9257-0/15/$31.00 ©2015 IEEE

$$J_0(V_L) = \frac{qn_iW_a}{2\sqrt{\tau_n\tau_p}} \quad (2)$$

where, q is the electronic charge, n_i is the intrinsic carrier concentration and τ_n and τ_p are the lifetimes of electron and hole respectively for CdTe, and W_a is the width of the absorber layer .

The photogenerated current can be obtained by adding the average electron current density ($J_{n,avg}$) and average hole current density ($J_{p,avg}$) in the absorber layer and can be expressed as

$$J_{ph} = J_{n,avg} + J_{p,avg} \quad (3)$$

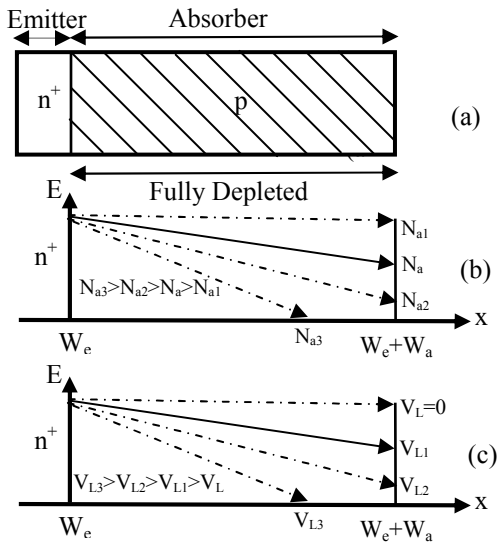

Fig. 1. Electric Field (E) Profile

where, $J_{n,avg}$ and $J_{p,avg}$ can be calculated according to [8], [9] as

$$J_{n,avg} = \frac{1}{W_a}\int_0^{W_a} J_n(x)dx \quad (4)$$

$$J_{p,avg} = \frac{1}{W_a}\int_0^{W_a} J_p(x)dx \quad (5)$$

where, $J_n(x)$ and $J_p(x)$ stands for electron current density and hole current density respectively. The basic equations needed to deduce the $J_n(x)$ and $J_p(x)$ are as follows

$$J_n(x) = qn(x)\mu_n E(x) \quad (6)$$

$$J_p(x) = qp(x)\mu_p E(x) \quad (7)$$

$$\frac{dJ_n(x)}{dx} = \frac{qn(x)}{\tau_n} - q\alpha(\lambda)G_0(\lambda)e^{-\alpha(\lambda)x} \quad (8)$$

$$\frac{dJ_p(x)}{dx} = -\frac{qp(x)}{\tau_p} + q\alpha(\lambda)G_0(\lambda)e^{-\alpha(\lambda)x} \quad (9)$$

Where, n(x) and p(x) is electron and hole density, E(x) for electric field at any point x in Fig. (1), μ_n and μ_p represents electron and hole mobility, α for wavelength-dependent absorption coefficient of the material and G_0 for the optical generation rate given by

$$G_0(\lambda) = (1 - R(\lambda))\frac{\lambda I_0(\lambda)}{hc} \quad (10)$$

Where, h is Planck's constant, c is the velocity of light, $I_0(\lambda)$ is the intensity of light, $R(\lambda)$ is the reflection coefficient and λ is the wavelength of the incident light.

In the thin film hetero-junction structure of CdS/CdTe-based solar cell deposited on the glass substrate, the base (CdTe) region is lightly doped. So, the entire absorber layer will be depleted. For intrinsic or very lightly doped absorber, the electric field can be considered as constant. Previous analysts [2-5] have used this approximation in their analytical approach; but in practical cases for a little increase in the absorber doping results in a linearly-decreasing electric field. However, the electric field in the depletion region close to the emitter side is considered negligible due to its very narrow width. If the absorber layer is fully depleted under short circuit condition, then increase in the absorber doping level [Fig. 1(b)] or in the load voltage [Fig. 1(c)] decreases the field at the right of the absorber layer. Since the electric field is linear throughout the absorber layer and non-zero at the edge, solving Poisson's Equation this field can be calculated as [9]

$$E(x) = \frac{V_{bi} - (V_L - J_L R_S)}{W_a} + \frac{qN_a}{\varepsilon}\left(x - \frac{W_a}{2}\right) \quad (11a)$$

where, ε is the permittivity of absorber material (CdTe), W_a is the absorber width which is equal to the metallurgical base width and V_{bi} is the built-in voltage across the absorber layer. However, if the absorber doping level or the load voltage is further increased, the depletion edge moves towards the left. Hence, the depletion width is no longer equal to the base width and the electric field becomes zero before the base edge. Under this situation, the expression for the electric field can be expressed as found in the standard text books [11]:

$$E(x) = \frac{qN_a}{\varepsilon}(x - W_a) \quad (11b)$$

Combining (6), (8) and (7), (9) gives the first order differential equations of n(x) and p(x) in the absorber layer as

$$\frac{dn}{dx} + \left[\frac{1}{E(x)}\frac{dE}{dx} - \frac{1}{\tau_n\mu_n E(x)}\right]n(x) = -\frac{\alpha(\lambda)G_0(\lambda)}{\mu_n E(x)}e^{-\alpha x} \quad (12)$$

$$\frac{dp}{dx}+\left[\frac{1}{E(x)}\frac{dE}{dx}+\frac{1}{\tau_p\mu_p E(x)}\right]p(x)=\frac{\alpha(\lambda)G_0(\lambda)}{\mu_p E(x)}e^{-\alpha x} \quad (13)$$

Since electrons and holes are swept out by the electric field from the absorber layer in the opposite direction, it can be assumed that $p(W_e) \approx 0$ and $n(W_e+W_a) \approx 0$. Using these boundary conditions, the solutions for the electron and hole concentration can be obtained as

$$n(x)=\frac{\alpha(\lambda)G_0(\lambda)}{\mu_n IF_n(x)}\int_{W_e+x}^{W_e+W_a} e^{-(\alpha+f_n(x))}dx \quad (14)$$

$$p(x)=\frac{\alpha(\lambda)G_0(\lambda)}{\mu_p IF_p(x)}\int_{W_e}^{W_e+x} e^{-(\alpha+f_p(x))}dx \quad (15)$$

where, $IF_n(x)=Ee^{-f_n(x)}$, $IF_p(x)=Ee^{-f_p(x)}$,

$$f_n(x)=\int\frac{dx}{\mu_n\tau_n E(x)},\ f_p(x)=\int\frac{dx}{\mu_p\tau_p E(x)}$$

Now putting the values of n(x) and p(x) from (14) and (15) to (6) and (7) gives the electron and hole current densities as

$$J_n(x)=qG_0(\lambda)\alpha(\lambda)e^{f_n(x)}\int_{W_e+x}^{W_e+W_a} e^{-(\alpha+f_n(x))}dx \quad (16)$$

$$J_p(x)=qG_0(\lambda)\alpha(\lambda)e^{f_p(x)}\int_{W_e}^{W_e+x} e^{-(\alpha+f_p(x))}dx \quad (17)$$

Putting the value of Jn(x) and Jp(x) at (4) and (5), $Jn,_{avg}$ and $Jp,_{avg}$ can be solved.

From (1) it is observed that the load current (J_L) at any load voltage (V_L) can only be determined using numerical methods due to the presence of unknown J_L on both sides. However, using the concept of the perturbation theory this J_L can be determined analytically. According to this theory, if J_L at any V_L is known then, the same at $V_L+\delta V_L$ can be determined using this value, provided that $\delta V_L \rightarrow 0$. Proceeding in the same manner, currents at $V_L+2\delta V_L$, $V_L+3\delta V_L$ …….. can be determined from the current values at $V_L+\delta V_L$, $V_L+2\delta V_L$ …… respectively. Photo-generated current calculated without considering R_s can be used as the initial guess of this process.

III. Results and Discussions

Simulation results based on the proposed model are presented and discussed in this section. The incident photon flux is the air mass (AM) 1.5 global spectrum, which is obtained from the ASTM G-173-03 standard [12]. The absorption coefficients for CdS and CdTe are obtained from the absorption curves in Ref. [13]. The thickness of CdS and CdTe layers are 0.1 and 3.5 µm respectively.

The current-voltage (J_L-V_L) characteristics curve simulated using the proposed model has been shown in Fig. (2). It is noteworthy that the open circuit voltage (0.84 v) and the short circuit current density (17.82 mA-cm^{-2}) obtained in the proposed model are in well agreement with that obtained in the work of Hegedus *et al.* (Fig. 9 of [7]), for R_s = 1.2 Ω cm^2 and n =1.7 and J_0=8×10^{-8} mA-cm^{-2}.

Fig. (3) shows the nature of J_L and V_L with respect to different values of series resistance, R_s. It is observed from the simulation result that though both J_L and V_L decrease slightly in the middle region with the increase in R_s, neither J_{sc} nor V_{oc} changes due to change in R_s.

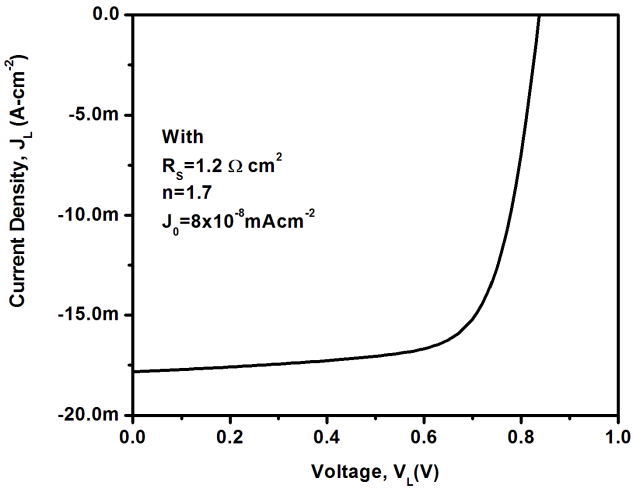

Fig. 2. J_L-V_L Characteristics of the proposed model

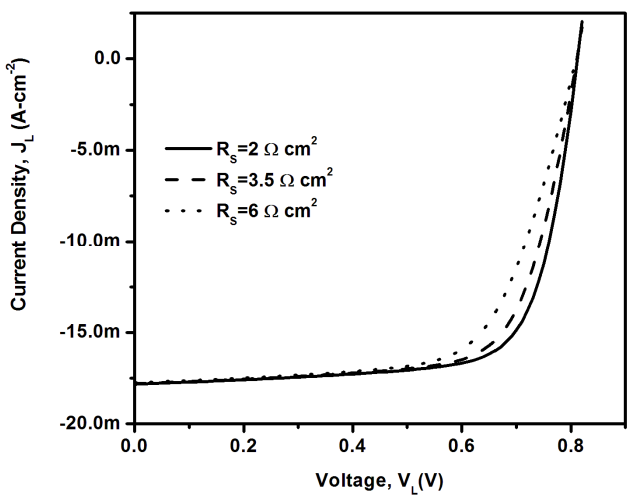

Fig. 3. J_L-V_L characteristics curve under the variation of series resistance (R_s)

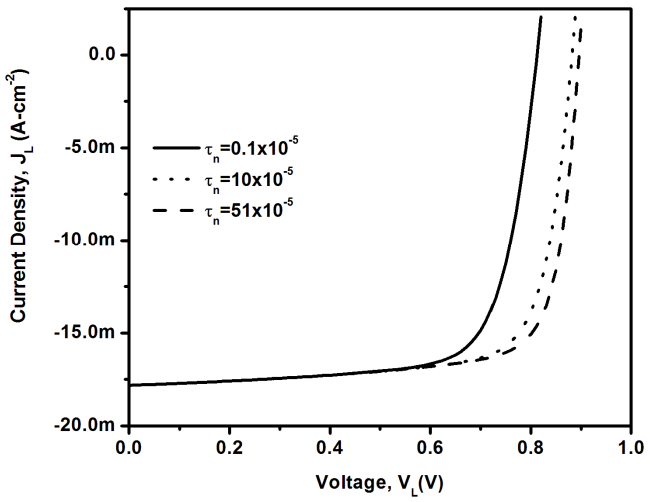

Fig. 4. J_L-V_L characteristics curve against the variation of electron lifetime (τ_n).

J_L-V_L curves have been shown for different lifetimes of electrons (τ_n) in [Fig. (4)] and of holes(τ_p) in [Fig. (5)]. It is found that J_L increases with the increase in any of τ_n or τ_p. This is quite normal, but interestingly, variation in τ_p has a noticeably greater impact on current than that in τ_n has. This phenomenon is quite logical. In fact, most of the photons are absorbed near the emitter side of the n-p junction. Since the fully depleted p-region is much longer than the n-region, it can be argued that the most of the absorption and hence the generation of electron-hole pairs is occurred in a region, which is more distant from bottom contact than from the top contact [Fig. (1)]. The built in electric field then drives the electrons towards the top and the holes towards the bottom of the cell. The holes have to travel a longer way than the electrons do before leaving the cell, holes experience more recombination than the electrons. Hence, the impact of change in τ_p is greater than that in τ_n on J_L.

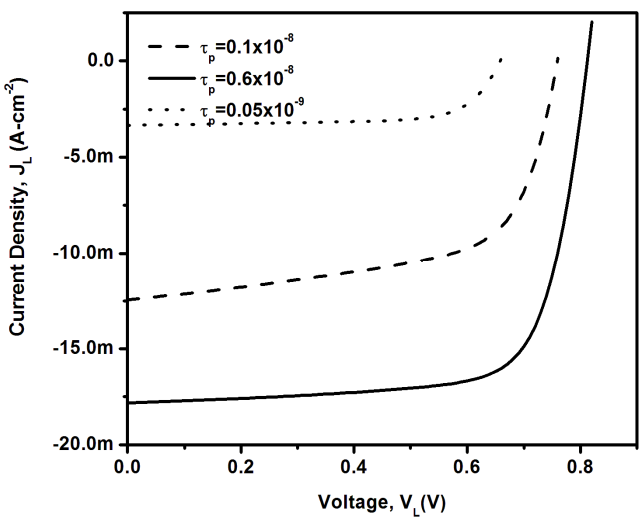

Fig. 5. J_L-V_L characteristics curve against the variation of hole lifetime (τ_p)

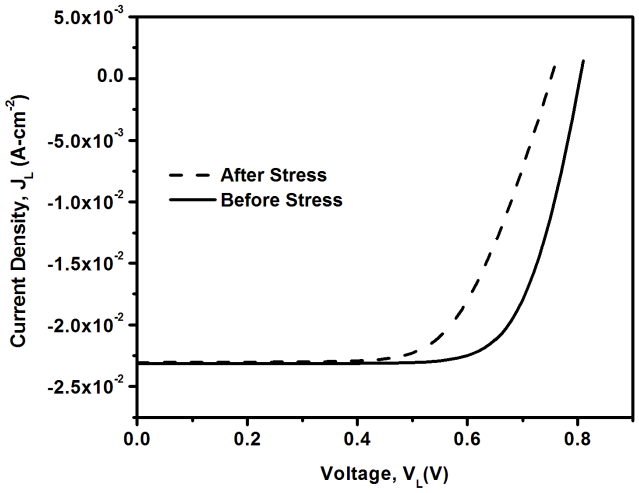

Fig. 6. J_L-V_L characteristics curve before and after applying stress.

Fig. (6) shows the behavior of J_L and V_L of CdTe based solar cell of 7 μm thick CdTe layer and with a Cu/Ni bilayer contact (15 nm/50 nm) of before and after stress, as mentioned in [6], to observe the degradation effects of contact materials over time. The cell was stressed by keeping it at 85^0 C in dry air under 100% sun illumination and open circuit condition for 15 days. Simulation has been done for n=1.66, R_s= 2.4 Ω cm^2 and J_0=1.5×10^{-10} mA cm^{-2} before stress while for n=1.58, R_s= 5.1 Ω cm^2 and J_0=2×10^{-10} mA cm^{-2} after stress. The results i.e., J_{sc} (before stress 23.16 mA cm^{-2} and after stress 23.06 mA cm^{-2}) and V_{oc} (before stress 0.8 v and after stress 0.75 v) has a good agreement with those stated in [6]. The increased value in R_s and J_0 reflects the increased recombination due to degradation, which results in a decreased value in V_{oc}.

IV. Conclusion

The current-voltage characteristics including the series resistance of a CdS/CdTe-based thin film solar cell deposited on the glass substrate have been analytically modeled and analyzed using perturbation theory. The proposed model assimilates both the voltage and the space dependency of the electric field in the absorber region. The model is able to include the stress effects due to contact, explains the more sensitivity of the solar cell to the hole transport than to the electron transport and shows the effects of series resistance. Consequently, the proposed model will be helpful for the better understanding of the physics of the thin-film solar cells.

V. References

[1] T. Aramoto, *et al*, "16.0% Efficient Thin-Film CdS/CdTe Solar Cells" *Jpn. J Appl. Phys*., vol. 36, no. 10, pp. 6304-6307, 1997.

[2] G. C. Morris and S. K. Das, "Some fabrication procedures for electrodeposited CdTe solar cells," *International Journal of Solar Energy*, vol. 12, no. 1–4, pp.95–108, 1992.

[3] S. Ikegami, "CdS/CdTe solar cells by the screen-printing-sintering technique:Fabrication, photovoltaic properties and applications," *Solar Cells*, vol. 23, no. 1-2, pp. 89–105, 1988.

[4] J. Nelson, *The Physics of Solar Cells*, Imperial College Press, Chap. 8, 2003

[5] S. Hegedus, "Current-Voltage Analysis of a-Si and a-SiGe Solar Cells including Voltage-dependent Photocurrent Collection," *Prog. in Photovoltaics: Research and Applications*, vol. 5, pp. 151–168, 1997.

[6] C. Thompson, D. Desai, and S. Hegedus, "Voltage Dependent Photocurrent Collection in CdTe/CdS Solar Cells," *Prog. in Photovoltaics: Research and Applications*, vol. 15, pp. 587–602, 2007.

[7] S. S. Hegedus and W. N. Shafarman, "Thin-Film Solar Cells: Device Measurements and Analysis," *Prog. in Photovoltaics: Research and Applications*, vol. 12, pp. 155–176, 2004.

[8] M. S. Anjan and M. Z. Kabir, "Modeling of Current-Volatge characteristics of CdS/CdTe Solar Cells," *Phys. Stat. Solidi A,* vol. 208, pp; 1813–1816, 2011.

[9] M. A. Mannan, M. S. Anjan and M. Z. Kabir, "Modeling of Current-Voltage Characteristics of Thin Film Solar Cells," *Solid-State Electron*, vol. 63, pp. 49–54, 2011.

[10] M. M. Haque, M. M. Rahman and M. I. B. Chowdhury, "Current-Voltage Characteristics of CdS/CdTe Thin Film Solar Cells: An Analytical Approach," *Proceedings of 2014 3rd International Conference on Non-Conventional Energy (ICDRET 2014)*, pp. 1-4, May 29-31, 2014, Dhaka, Bangladesh.

[11] J. Wilson and J.F.B. Hawkes, *Optoelectronics-An introduction,* 2nd ed., Englewood Cliffs, NJ, Prentice Hall, 1989, pp. 483

[12] NREL,http://rredc.nrel.gov/solarspectra/am1.5/ASTMG173/ASTMG173.html.

[13] M. Burgelman in: J. Poortmans and V. Arkhipov (Editors.), Thin film Solar Cells: Fabrication, Characterization and applications, Wiley & Sons, Chap. 7, 2006

.

Effect of Dislocation Density on the Performance of InGaN-Based MJ Solar Cell:Analytical Approach

Ibne Sabid, Md. Soyaeb Hasan, Md. Fahim-Al-Fattah and Md. Rafiqul Islam
Dept. of Electrical and Electronic Engineering (EEE)
Khulna University of Engineering & Technology (KUET),
Khulna-9203, Bangladesh
ibnesabid.10@gmail.com

Ibrahim Mustafa Mehedi
Dept. of Electrical and Computer Engineering (ECE)
King Abdulaziz University (KAU),
Jeddah, Saudi Arabia
imehedi@kau.edu.sa

***Abstract*—In this study the effect of dislocation density on the performance of InGaN based multi junction solar cell has been calculated analytically. It is found that dislocation density adversely affects the open circuit voltage, short circuit current density and conversion efficiency of a solar cell. Efficiency is found to be improved with the increase in the number of junction (24.4-43.56% for single-six junction solar cells) while considering no dislocation. Whereas it is found that the efficiency is affected when dislocation density (10^{01}-10^{13}m^{-2}) is incorporated for analyzing the performances of either single junction (24.47-8.25%) or multi junction solar cell (43.56-15.25% for six junctions). The effect of dislocation density on minority carrier life time is also been anticipated in this study.**

Keywords— Dislocation density, Multi Junction (MJ), Minority carrier diffusion length, Recombination center

I. INTRODUCTION

The ternary InGaN alloy, a direct band gap material can cover most parts of solar spectrum owing to its tunable bandgap (0.64-3.4eV) [1]. It has some unique properties such as high mobility, high absorption coefficients, and low effective mass of carriers which make it promising especially in photovoltaic (PV) applications [2]-[5]. Since single junction (SJ) InGaN solar cell is not able to convert full spectrum to electrical energy, MJ solar cell is being studied widely all over the world during the last few years. However this approach has some challenges. One of the most critical issues is the higher density of threading dislocations (TD) prevailing in III-nitrides epilayers at levels of ~1×10^{9}cm^{-2} [6]. It is found that a large lattice and thermal expansion coefficient mismatches exist between the layer and substrate. These introduce higher dislocations which lead to the degradation of material quality and consequently the performance of its constituent devices [7]–[9]. For InGaN single junction solar cell the edge, screw, and mixed type misfit dislocations are found [10]. A higher density of TDs incorporates in InGaN based MJ solar cell during hetero-epitaxial growth due to higher lattice mismatch. These dislocations emerge as scattering centers and mid bandgap states, which act as recombination centers and decrease the minority carrier lifetime.

Exploration is going on the improvement of the performances of InGaN based MJ solar cells. In available theoretical works that have been performed for analyzing InGaN solar cells, there is no such work showing the effect of dislocation density on the performances. InGaN based high efficient MJ solar cell has been projected in the literatures without considering the effect dislocation density [11]-[13]. Efficiency of InGaN-based solar cell is found to be 24.24% and 43.56% for single and six junctions respectively [11]. Theoretical investigation on InGaN/InGaN/Si three-junction tandem cell has also been performed without dislocation [13]. Moreover, literatures reviews show the discrepancy between the theoretical and practical performances of InGaN-based solar cell. In this study, dislocation density has been attributed for this disparity in projected and practical performances for InGaN-based MJ solar cell. The impacts of dislocation density, minority carrier diffusion length, and surface recombination velocity on the performance parameters of InGaN based MJ solar cells have been simulated analytically.

II. MODELING

Dislocations play a dominant role in determining the electrical and PV characteristics of thin-film InGaN based SJ and MJ solar cells acting as recombination centers. The recombination losses at dislocations which reduce short-circuit current and enhance excess leakage current is the predominant loss mechanism in thin-film InGaN solar cells. The transport of minority carrier to the dislocation can be found from one dimensional continuity equation solved by Yamaguchi and Amano [14].

$$\frac{\partial n}{\partial x} = \frac{D\partial^2 n}{\partial^2 x} \tag{1}$$

Using the following boundary conditions

$$n = 0 \text{ at } x = 0$$

$$\text{and } \frac{\partial n}{\partial x} = 0 \text{ at } x = X_c = 1/(\pi N_{dis})$$

Where n is the excess minority carrier concentration, X_c is the unit cell radius, and N_{dis} is the dislocation density. With these conditions the continuity equation can be satisfied for:

$$n = n_0 e^{-t/\tau} \sin\left(\frac{x\pi}{2x_c}\right) \tag{2}$$

978-1-4673-9257-0/15/$31.00 ©2015 IEEE

Here n_0 is the equilibrium concentration of minority carrier and τ is the minority carrier lifetime. This solution includes only the first order sine function that gives a best case result for the effective diffusion length approach. By combining (1) and (2), the minority carrier diffusion length limited by recombination at the dislocations is found to be:

$$\frac{1}{L_{dis}^2} = \frac{\pi^3 N_{dis}}{4} \tag{3}$$

With a reciprocal rule the effective minority carrier diffusion length as follows.

$$\frac{1}{L_{eff}^2} = \frac{1}{L_0^2} + \frac{1}{L_{dis}^2} \tag{4}$$

Here L_0 is the minority carrier diffusion length where dislocations are not present. The short circuit current density (J_{SC}) has been calculated from one dimensional steady state continuity equation for electron in p-type and hole in n-type semiconductor. The J_{SC} being dependent on minority carrier diffusion length has been calculated for different dislocation densities. Efficiency calculation includes the total number of photons in solar spectrum per unit area per unit time and band gap is selected in each junction so that equal number of photon can be absorbed. The bottom junction band gap energy is optimized and the other junction's band gap energy is chosen accordingly. When a light of wavelength λ is incident on semiconductor the generation rate of electron hole pairs (EHPs) at a distance x' from the semiconductor surface is given by [15]:

$$G(\lambda, x') = \alpha(\lambda) F(\lambda)[1 - R(\lambda)] e^{[-\alpha(\lambda)x']} \tag{5}$$

Where, $\alpha(\lambda)$ is the absorption coefficient, $F(\lambda)$ the number of incident photons/cm^2/s per unit bandwidth and $R(\lambda)$ is the fraction of these photons reflected from the surface.

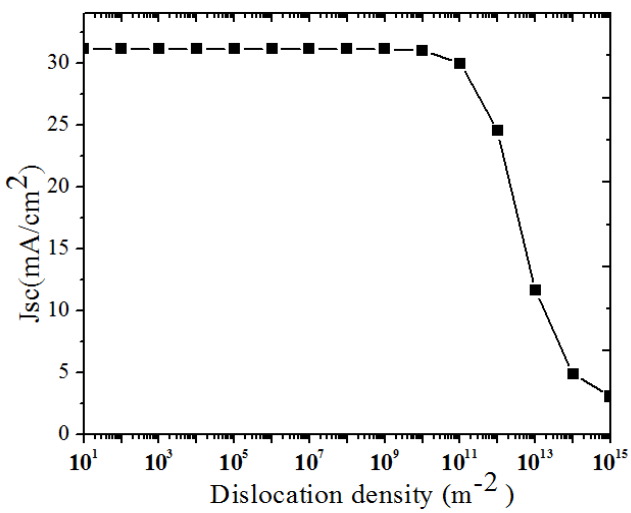

Figure 1. Dependence of short circuit current density (J_{sc}) on dislocation density.

One dimensional steady-state continuity equations for holes in n-type semiconductors under low injection condition are:

$$G_p - \frac{p_n - p_{no}}{\tau_p} + \frac{1}{q}\frac{dJ_p}{dx'} = 0 \tag{6}$$

The current density equation for hole can be expressed as:

$$J_p = q\mu_p p_n \xi - qD_p \frac{dp_n}{dx'} \tag{7}$$

Here, D_p = Diffusion coefficient for p-type. Combining the equation (5), (6) and (7) yields the expression:

$$D_p \frac{d^2 p_n}{dx'^2} + \alpha F(1-R) e^{(-\alpha x')} - \frac{p_n - p_{no}}{\tau_p} = 0 \tag{8}$$

Solving the equation (8) and using two boundary conditions at the surface, $x' = 0$ and at the edge of the depletion region $x' = x_j$ the resultant hole density can be calculated. The resultant photocurrent density due to hole collected at the depletion region, J_p has been calculated. Similarly electron photocurrent density collected at the depletion edge, J_n is evaluated. Total photocurrent density at a given wavelength:

$$J(\lambda) = J_p(\lambda) + J_n(\lambda) + J_{dr}(\lambda) \tag{9}$$

The efficiency expression is given by:

$$\eta = \frac{J_{ph} V_{oc} FF}{\Phi_0} \tag{10}$$

Finally open circuit voltage and efficiency have been calculated at a fill factor FF=0.85 and the incident irradiance Φ_0 = 96.366 mW/cm^2 [16].

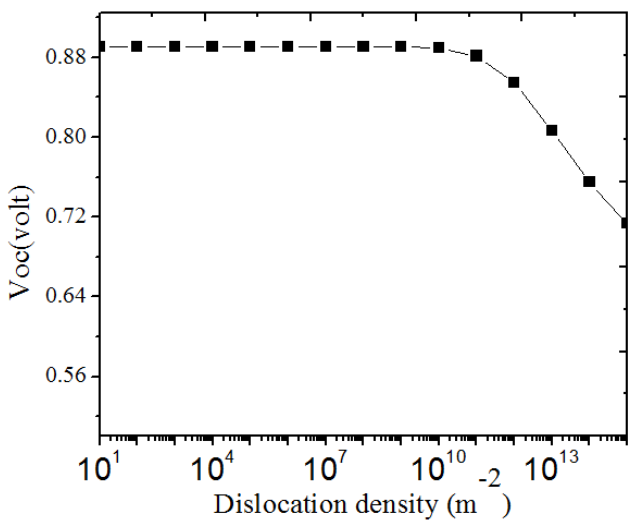

Figure 2. Dependence of open circuit voltage (V_{oc}) on dislocation density.

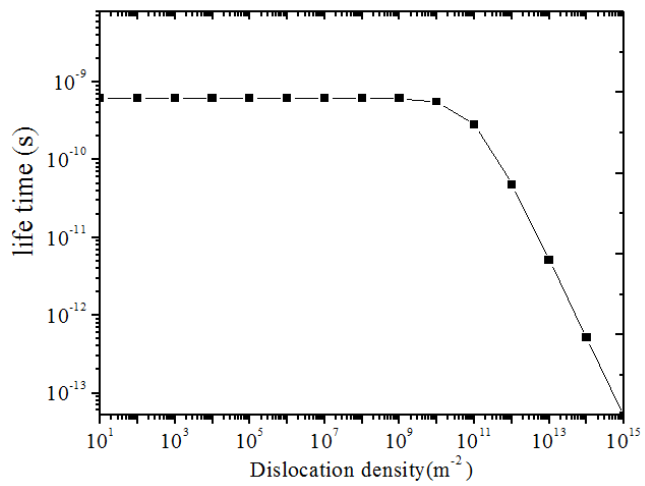

Figure 3. Change of minority carrier lifetime with the variation of dislocation density in $In_{0.51}Ga_{0.49}N$ single junction solar cell.

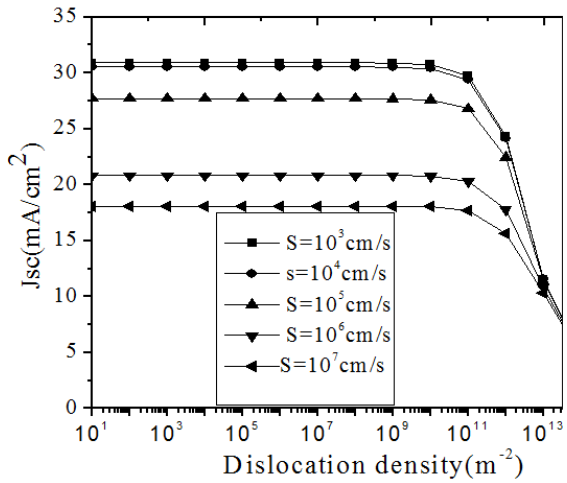

Figure 4. Variation of short circuit current density (J_{sc}) with the change of dislocation density at different values of surface recombination velocity.

III. Result and Discussion

A. Performance evaluation for Single Junction Solar Cell

Fig. 1 depicts the short circuit current density (J_{SC}) at different dislocation densities. The J_{SC} falls significantly above the dislocation density $10^{11}m^{-2}$. Fig. 2 shows that the V_{oc} decreases gradually with the increase of dislocation density above $10^{11}m^{-3}$. The V_{oc} decreases from 0.887v to 0.67v with the increase of dislocation density from 10^{01} to 10^{15} m^{-2} for a fix value of recombination velocity S=10^3cm/s in a single junction solar cell considering band gap 1.38862eV. The optimized value of band gap is 1.38862 eV when we choose x=0.514. The variation of the minority carrier lifetime with the dislocation density in above n on p-$In_xGa_{1-x}N$ solar cell is depicted in Fig. 3. The minority carrier lifetime of electrons in p-$In_{0.51}Ga_{0.49}N$ base layer is 6.25E-10s when the dislocation density is lower than 10^8 m^{-2} and starts to decrease rapidly to 10^{-13}s as the dislocation density increases above 10^9m^{-2}. Since minority carrier life time is important parameter to determine the performances of solar cell, it should be increased in order to enhance the performances. The calculated value of J_{sc} at different dislocation densities with different values of surface recombination velocity (S) are illustrated in Fig. 4. The J_{sc} decreases as the recombination velocity increases for a same set of dislocation densities. All the values of J_{sc} were plotted at finite value of S. The J_{sc} of solar cell is significantly lowered by increasing S. The S generally increases with increasing dislocation density.

The S of direct band gap semiconductor, such as GaAs, InP, GaN, InN etc. is very high. Change in efficiency is observed when the S increases at a constant dislocation density. The change in efficiency with change in S is shown in Fig. 5. A negligible variation in efficiency is observed for S when it is bellow 10^4cm/sec and efficiency falls as S increases above 10^4cm/sec. Efficiency is an important parameter to

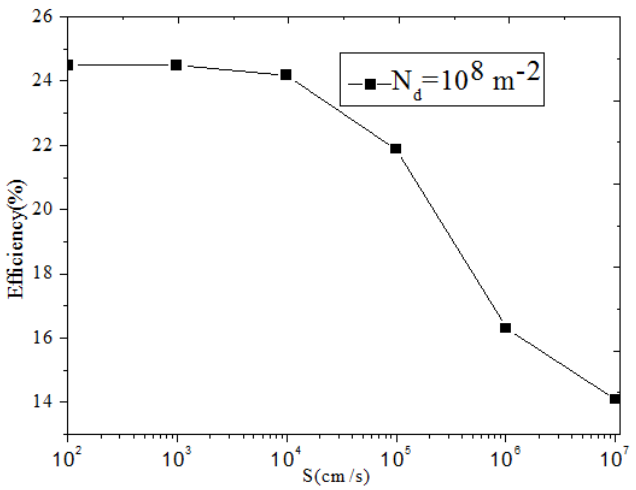

Figure 5. Dependence of efficiency on recombination velocity at a fixed value of dislocation density.

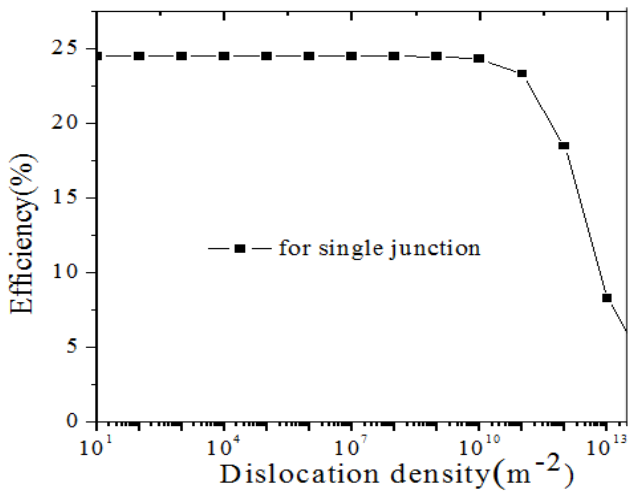

Figure 6. Dependence of efficiency on dislocation density (N_d) at a fixed value of recombination velocity, S=10^3 cm/s

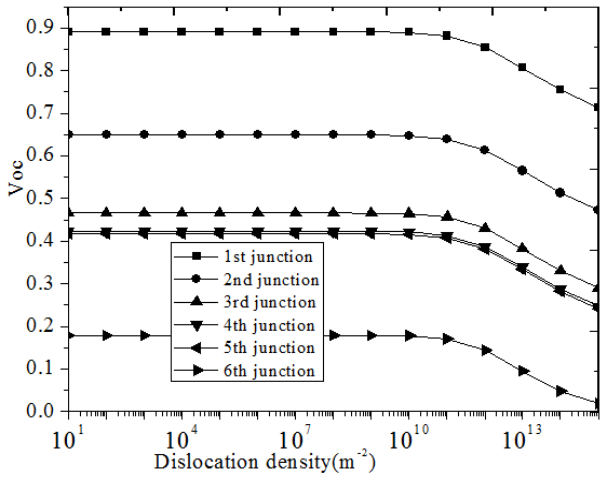

Figure 7. Change in open circuit voltage with dislocation density for individual junction.

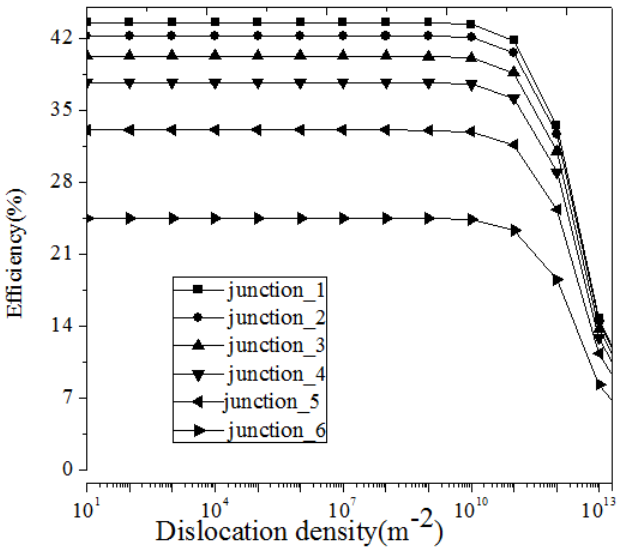

Figure 9. Dependence of Efficiency on dislocation density up to six junctions.

investigate the performances of solar cells. The efficiency of InGaN based SJ solar cell decreases as the dislocation density increases depicted in Fig. 6. There is a marginal change in cell efficiency when the dislocation density increases from 10^{10} to $10^{13}m^{-2}$ at a fixed surface recombination velocity. The efficiency remains nearly constant up to $10^{10}m^{-2}$ at a fix value of surface recombination velocity which is good agreement with [11]**.** result for SJ solar cell. There is a rapid decrease in efficiency when the dislocation density goes above $10^{10}m^{-2}$.

B. Performance evaluation for MJ

The effect of dislocation on V_{oc} for individual junction is represented in Fig. 7. The optimum band gap energies are taken as 1.381eV, 1.15eV, 0.974eV, 0.938eV, 0.938eV, 0.7eV respectively for single-to-six junctions. The open circuit voltage is found to be 0.894 V and 0.18 V, respectively for the

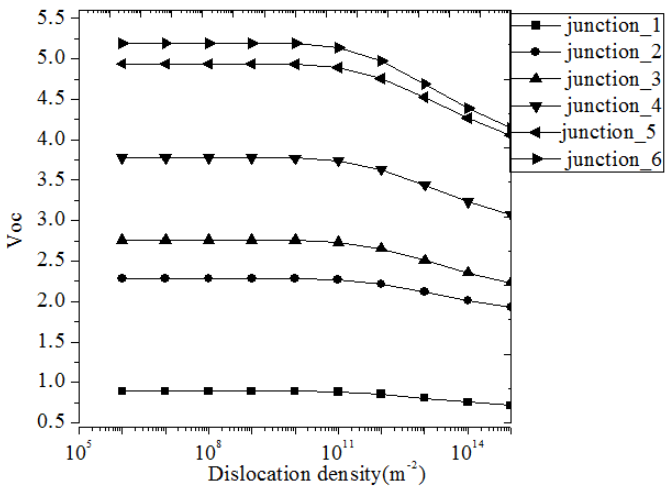

Figure 8. Open circuit voltage up to six junctions with the variation dislocation density.

1st and 6th junction individually at dislocation density below $10^{10}m^{-2}$. The variation of V_{oc} with respect to dislocation density is shown in Fig. 8. The V_{oc} is plotted as the summation of individual junction. Fig. 9 shows the efficiency of InGaN based MJ solar cell up to six junctions at different dislocation density. From the figure it is evident that the efficiency remains nearly constant up to dislocation density $10^{10}m^{-2}$. The efficiency falls dramatically above the dislocation density 10^{11} m^{-2}. The efficiency is found to be varied 24.47% to 8.25% for single junction and 43.56% to 15.25% for six junctions with the increase in dislocation density from 10^{01} to $10^{13}m^{-2}$.

It is found from the simulation results that for InGaN based MJ solar cell, the overall efficiency degradation starts to occur when dislocation density is greater than $10^{10}m^{-2}$. It is evident that the edge, screw, and mixed type misfit dislocations are found to be occurred 4.69×10^{10}, 4.53×10^{9}, and $4.03\times10^{11}cm^{-2}$ in InGaN [10], [17]. Hence, if we want fabricate InGaN-based high efficient MJ solar cell we should go through the steps that can reduce the dislocation density.

IV. CONCLUSION

The effects of dislocation density on the performance of InGaN based solar cell have been investigated analytically. It is found that higher dislocation density has negative impact on the performance of either SJ or MJ solar cells. It is seen that due to higher dislocation density, surface recombination velocity increases which results in fall in efficiency. The outcomes of our simulation depicts that the performance parameters are intensely affected when dislocation density is above $10^{11}m^{-2}$ and remains approximately persistent bellow this value. Furthermore, in comparison with previous simulation based investigations without considering the dislocation density, it is informed that the calculated efficiency is somewhat lower for each junction.

REFERENCES

[1] A. Bhuiyan, K. Sugita, A. Hashimoto, and A. Yamamoto, "InGaN Solar Cells: Present State of the Art and Important Challenges," in *Photovoltaics, IEEE Journal of* , vol.2, no.3, pp.276-293, July 2012.

[2] E. Matioli, C. Neufeld, M. Iza, S. C. Cruz, A. A. Al-heji, X. Chen, "High internal and external quantum efficiency InGaN/GaN solar cells". *Applied Physics Letters*, vol. 98, no. 2, pp. 021102-3, Jan. 2011.

[3] R. Dahal, B. Pantha, J. Li, J. Y. Lin, and H. X. Jiang. "InGaN/GaN multiple quantum well solar cells with long operating wavelengths." *Applied Physics Letters,* vol. 94, no. 6, pp. 063505-3, Feb. 2009.

[4] O. Jani, I. Ferguson, C. Honsberg, and S. Kurtz. "Design and characterization of GaN/ InGaN solar cells." *Applied Physics Letters,* vol. 91, no. 13, pp. 132117-3, Sep. 2007.

[5] Ji-Hong, Zhu, Wang Liang-Ji, Z. Shu-Ming, W. Hui, Z. De-Gang, Z. Jian-Jun, L. Zong-Shun, J. De-Sheng, and Y. Hui. "Simulation of the light extraction efficiency of nanostructure light-emitting diodes." *Chinese Physics B,* vol. 20, no. 7, pp. 077804-4, Nov. 2011.

[6] M. M. Song, Z. Wu, Y. Fang, R. Xiang, Y. Sun, H. Wang, C. Yu, H. Xiong, J. Dai, and C. Chen. "Improved photovoltaic performance of InGaN single junction solar cells by using n-on-p type device structure." *Journal of optoelectronics and advanced materials,* vol. 12, no. 7, pp. 1452 – 145, July 2010.

[7] H. K. Cho, J. Y. Lee, K. S. Kim, G.M. Yang, "Formation of misfit dislocations and stacking faults in high indium content $In_xGa_{1-x}N$ layers grown by metal organic chemical vapor deposition". *J. Korean Phys*. vol. 39, no., pp.165-169, Dec-2001.

[8] H. Wang, D. S. Jiang, U. Jahn, J. J Zhu, D.G. Zhao, Z.S. Liu, "Investigation on the strain relaxation of InGaN layer and its effects on the InGaN structural and optical properties". *Physica B: Condensed Matter*, vol. 405, no. , pp. 4668–4672, Nov. 2010

[9] H. K. Cho, G. M. Yang, "Generation of misfit dislocations in high indium content InGaN layer grown on GaN". *J. Crystal Growth,* vol. 243, no. 1, pp. 124–128, Aug. 2002.

[10] M. A. Hossain, M. R. Islam, M. K. Hossain, A. Hashimoto, and A. Yamamoto. "Dislocation reduction in heteroepitaxial $In_xGa_{1-x}N$ using step-graded interlayer for future solar cells." *Materials for Renewable and Sustainable Energy,* vol. 3, no. 1, pp. 1-14, March. 2014.

[11] M. R. Islam, M. A. Rayhan, M. E. Hossain, A. G. Bhuiyan, M. R. Islam, A. Yamamoto, "Projected Performance of $In_xGa_{1-x}N$-Based Multijunction Solar Cells," in *Electrical and Computer Engineering, 2006. ICECE '06. International Conference on* , vol., no., pp.241-244, 19-21, Dec. 2006.

[12] A. Yamamoto, M. R. Islam, T. T. Kang, and A. Hashimoto. "Recent advances in InN-based solar cells: status and challenges in InGaN and InAlN solar cells." *physica status solidi (c)* vo. 7, no. 5, pp. 1309-1316, March. 2010.

[13] L. Hsu, and W. Walukiewicz. "Modeling of InGaN/Si tandem solar cells."*Journal of Applied Physics,* vol. 104, no. 2, pp. 024507-3, Jul. 2008.

[14] M. Yamaguchi, A. Yamamoto, and Y. Itoh, "Effect of dislocations on the efficiency of thin-film GaAs solar cells on Si substrates", *J. Appl. Phys.*, vol. 59, pp. 1751-1753, Nov. 1986.

[15] Sze, Simon M., and Kwok K. Ng. *Physics of semiconductor devices*. John Wiley & Sons, 2006.

[16] U. K. Mishra, Y. F. Wu, B. P. Keller, S. Keller, and Denbaars, S. P. (1998). GaN microwave electronics. *Microwave Theory and Techniques, IEEE Transactions on*, vol. *46*, no. 6, pp. 756-761.

[17] M. R. Islam, Y. Ohmura, A. Hashimoto, A. Yamamoto, K. Kinoshita, and Y. Koji. "“Step-graded interlayers” for the improvement of MOVPE $In_xGa_{1-x}N$ (x~ 0.4) epi-layer quality." *physica status solidi (c)*, vol.7, no. 7-8, pp. 2097-2100, Nov. 2010.

Effects of Photon Recycling on the Properties of p+ n GaAs Solar Cell

Sadi Mohammad[1*], Md.Injammaul Islam Chowdhury[1], Md. Sherajul Islam[1] and Ashraful Ghani Bhuiyan[1]
[1] Khulna University of Engineering & Technology, Bangladesh
[*] E-mail: sadi_mohammad@yahoo.com
[1]

Abstract— **The main drawback of currently used photovoltaic cell is it's low conversion efficiency. Among the single junction solar cells, cells with GaAs material offers the maximum efficiency.For direct bangap material like GaAs photon recycling is an exciting approch.Benefication to solar cell properties due to photon recyling(PR) has been speculatively and carefully investigated in a p+ n structure of GaAs. In this study all the concentration has been made on the effect of PR that enhance the functioning of the cell. This study is also focused on the effect of architechtural and substantial parameters reliance on the magnitude of PR effect. For the PR effect short circuit current density, open circuit voltage of the cell is found to be increased which in turns increases the efficiency. PR is largely effected by high surface recombination velocity, emitter thickness, doping density.**

Keywords—Solar cell, Photon Recyling (PR), GaAs, p+n strcuture, Surface recombination velocity (SRV), Doping Density, Emitter thickness.

I. INTRODUCTION

Energy is major concept of economic development. World need more energy to provide the growing population with increase standard of living. Fossils fuels such as, oil, gas etc. are the major sources of energy and contribute to a bigger portion of world's energy supply. There are other source of energy, known as renewable energy source, fulfill a small portion of world's energy demand. It's importance is increasing and it is expected that it will become more important in future. The common renewable energy sources are biomass, geothermal, wind, solar etc. Among these sources solar energy is very important because it does not require any fuel cost and it is plentiful in nature. Most importantly, solar technologies are environmental friendly. Solar cell does not produce any environmental waste during it's operation and no noise is produced, if produced it is very small.

With respect to other available energy sources,the efficiency of solar cell is coparatively low. Besides the cost of solar energy is more than the conventional energy. There are many factors which affect the cost of solar energy. The cost of solar cell can be reduced by improving the performance of solar cells. Among the performance parameters, the efficiency of solar cell is very important. There are many approaches to increase the efficiency. Although most of them provide high efficiency but their fabrication process and control is much difficult and costly. An important role in the cost minimization is played by single junction cell. It's fabrication is comparatively less difficult and it provides higher efficiency with minimum cost. Among all the single junction solar cell GaAs offers maximum efficiency.

Among all the exciting approch to increase the efficieny of solar cell photon recyling is an encouraging step.The efficiency of semiconductor solar cell is dependent on minority carrier parameters.The efficiency is high if the minority carrier charge density can be increased. Minority carrier charge density is dependent on photon recycling and increased due to photon recycling in direct bandgap semiconductors.During the radiative recombination process re-absorption of photons emitted is referred to as photon recycling(PR).PR utilizes the photon emitted during the recombination of electron with hole. It minimizes the loss due to recombination. Minimization of the loss due to recombination is a contribution to the increase of efficiency. As a consequence of this process new electron–hole pairs are generated and the minority carrier charge density increases. One of the main factors that contribute to the improvement of efficiency of solar cell is short circuit current. Short circuit current increases with the increase of minority carrier charge density. So utilization of recycled photon is the best way to improve the efficiency of solar cell. As GaAs is a direct bandgap semiconductor, band-band recombination with accompanying photon emission and subsequent photon reabsorption at another location in the cell may occur [3]. Previously many scientists explored the effect of PR in the improvement of cell.Very recently Alexandre et al. has shown the current–voltage characteristics of the cells [11].This model is founded on Shockley–Read–Hall lifetimes based on internal quantum efficiency measurement.Gilt edge design of the cell has been done for the variation of base thickness and Shockley–Read–Hall lifetime using reflector. It is shown in the paper that the doping concentration is insignificant in the enhancement of open circuit voltage. Some other factors of a solar cell that have on authority in the improvement of efficiency is not considered in their model. The other factors that can grease the efficiency is considered in this paper like the surface recombination velocity, emitter thickness and the doping concentration.

978-1-4673-9257-0/15/$31. 00 ©2015 IEEE

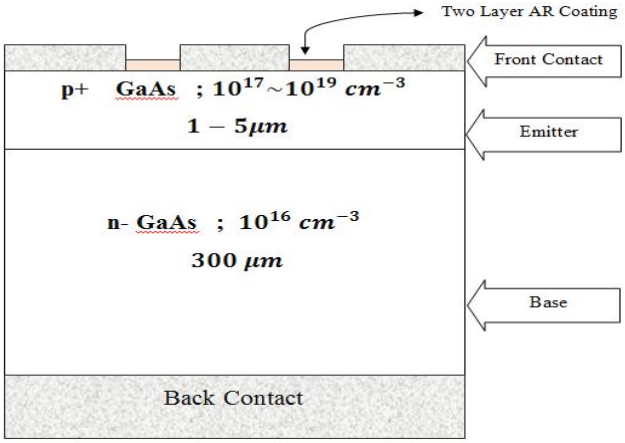

Figure 1: Structure of the p+ n solar cell used

II. MATHEMATICAL EXPRESSION FOR PHOTON RECYLING MODEL

To model PR effects, a number of different approaches have been made. Hypothesis was proposed by Asbeck regarding radiative lifetime multiplication factor to explain lifetime measurements in GaAs. Due to PR effect additional generation of minority carrier has incorporated. In order to enumerate the one dimensional photon recycling generation rate the basic formulation of Kuriyama et al. has been used in this paper. The cell model of fig.1 has been used. At first applying the boundary condition distribution of excess minority carrier density, without photon recycling is found. There will be a short circuit current density. As there are two layers in solar cell, emitter and base. Short circuit current is generated in each layer and also within the depletion region. The total short circuit current is the sum of the contribution from the emitter, base and depletion region. This will be

$$J_{sc} = J_{psc} + J_{nsc} + J_{dr} \quad \ldots\ldots\ldots\ldots\ldots\ldots\ldots\ldots\ldots\ldots\ldots\ldots(1)$$

Where,

Short circuit current due to holes collected at the depletion edge

$$J_{psc} = q(1-R_o)F\frac{\alpha_0^2 L_p^2}{\alpha_0^2 L_p^2 - 1}\left\{\frac{1+{\xi_p}/{\alpha_0 L_p}}{\cosh\left({x_j}/{L_p}\right)+\xi_p \sinh\left({x_j}/{L_p}\right)}\right\} \quad \ldots\ldots..(2)$$

Short circuit current due to electrons collected at the depletion edge

$$J_{nsc} = q(1-R_o)F\frac{\alpha_0^2 L_n^2}{\alpha_0^2 L_n^2 - 1}\left\{\frac{1+{\xi_n}/{\alpha_0 L_n}}{\cosh\left({x_j+w}/{L_p}\right)+\xi_n \sinh\left({x_j+w}/{L_n}\right)}\right\}\ldots(3)$$

Short circuit current generation takes place within the depletion region.

$$J_{dr} = qF(1-R)\exp(-\alpha x_j)\left[1-\exp(-\alpha W)\right] \quad \ldots\ldots\ldots..(4)$$

Where, τ is minority carrier lifetime, α_o is absorption coefficient of the excitation light, R_o is reflectivity, F is photon flux density, d is thickness of emitter and L is the diffusion length of minority carrier. ξ is the normalized surface recombination velocity defined by $\xi = {SL}/{D}$, S is surface recombination velocity and D is the diffusion constant. W is the width of depletion region.

Now during recombination a new photon will be emitted. From a certain point within the cell a photon will be emitted. By absorbing the photon energy a new pair of electron-hole will generate. Thus increase the minority carrier density. Including the photon recycling process the expression for short circuit current density will be:

$$J_{t,sc} = J_{pr} + J_{sc} \quad \ldots\ldots\ldots\ldots\ldots\ldots\ldots\ldots\ldots\ldots\ldots\ldots(5)$$

Where,

$$J_{pr} = J_{pr,psc} + J_{pr,nsc} + J_{dr,pr} \quad \ldots\ldots\ldots\ldots\ldots\ldots\ldots\ldots\ldots\ldots\ldots..(6)$$

From the hole density distribution the resulting hole short circuit current density due to photon recycling at the depletion edge is,

$$J_{pr,psc} = q\frac{1}{\cosh\left({x_j}/{L_p}\right)+\xi_p \sinh\left({x_j}/{L_p}\right)}\left\{\int_0^{x_j} g_{pr,k}(\xi_p)\cosh\left({\xi_p}/{L_p}\right)d\,\xi_p + \int_0^{x_j} g_{pr,k}(\xi_p)\sinh\left({\xi_p}/{L_p}\right)d\,\xi_p\right\} \quad \ldots\ldots\ldots(7)$$

The short circuit current due to electrons by photon recycling collected at the depletion edge is,

$$J_{pr,nsc} = q\frac{1}{\cosh\left({x_j+w}/{L_p}\right)+\xi_n \sinh\left({x_j+w}/{L_n}\right)}\left\{\int_0^{x_j+W} g_{pr,k}(\xi_n)\cosh\left({\xi_n}/{L_n}\right)d\,\xi_n + \int_0^{x_{j+W}} g_{pr,k}(\xi_n)\sinh\left({\xi_n}/{L_n}\right)d\,\xi_n\right\} \quad \ldots\ldots\ldots..(8)$$

The short circuit current density due to photon recycling in the depletion region is as follows:

$$J_{dr,pr} = q\int_{x_j}^{x_j+W} g_k(z)dz \ldots\ldots\ldots\ldots\ldots\ldots\ldots\ldots\ldots\ldots\ldots(9)$$

From the value of diode saturation current J_0 and short circuit current the value of open circuit voltage can be calculated. The open circuit voltage due to photon recycling, $V_{t,oc}$ will be,

$$V_{t,oc} = \frac{kT}{q}\ln\left(\frac{J_{t,sc}}{J_o}+1\right) \quad \ldots\ldots\ldots\ldots\ldots\ldots\ldots\ldots\ldots\ldots..(10)$$

In order to determine the efficiency fill factor is to be calculated. It is known that fill factor,

$$V_m J_m = FF \times V_{t,oc} \times J_{t,sc} \ldots\ldots\ldots\ldots\ldots\ldots\ldots\ldots\ldots\ldots..(11)$$

Efficiency of the cell due to photon recycling,

$$\eta = \frac{FF \times V_{t,oc} \times J_{t,sc}}{P_{in}} \quad \ldots\ldots\ldots\ldots\ldots\ldots\ldots\ldots\ldots\ldots\ldots.....(12)$$

III. SIMULATION RESULTS

Photon recycling takes place within the cell. It's performance will obviously rely on the structural and material parameter of the cell. Moreover recombination are dependent on the material of the cell, doping level and the structure. So this factor will have influence upon the magnitude of photon recycling effects. In the following section graphical representation of the dependence of photon recycling on different parameters will be shown.

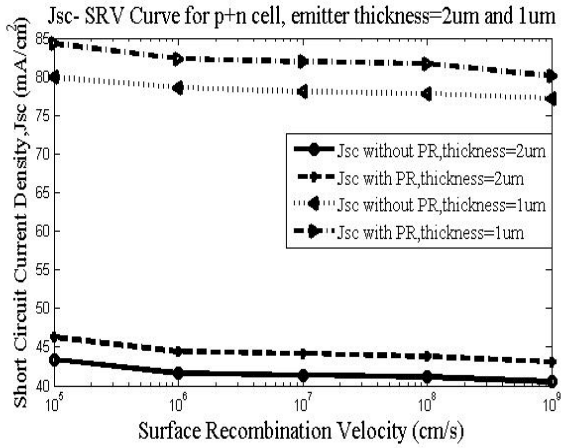

Figure 2. J_{sc}– SRV curve for p+ n cell at emitter thickness,2μm and 1μm

A. *Varying the surface recombination velocity :*

Fig 2 shows the variation of the short circuit current density with the surface recombination velocity. Two different cases has been considered. One is for emitter thickness of 1μm and the other one is for 2μm.In both the cases due to PR effect the short circuit current density has increased. But it has been found out that when the emitter thickness is reduced the PR effect increases. So one can come to conclusion that the lower the emitter thickness higher will be the PR effect. Due to increase in minority carrier density the increase in current density is observed. As the current density is increased, the open circuit voltage and the efficiency of the cell is increased in turns, shown in fig.3 and fig.4. Average increase of efficiency is 10.9% for emitter thickness of 2μm and for emitter thickness of 1μm this is 5.7%.The average increase in the two cases is different but overall increase of efficiency is higher for emitter with lower thickness. This may be due to the fact that the diffusion length of the minority carrier remain almost constant for different emitter thickness. At lower thickness the contribution of minority carrier density is more than at higher thickness.

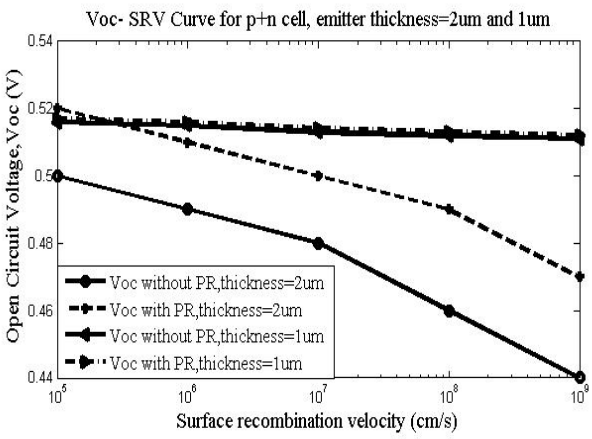

Figure 3. V_{oc}– SRV curve for p+ n cell at emitter thickness2μm and 1μm

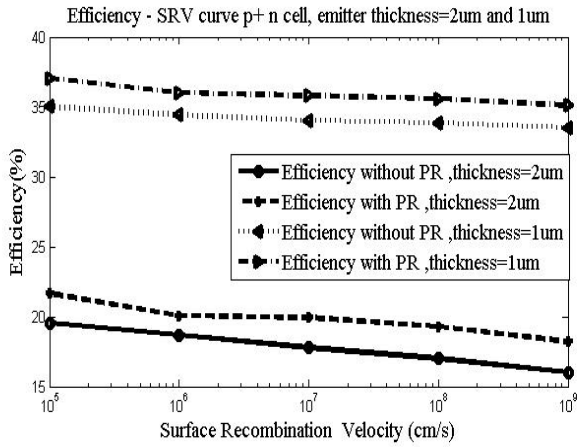

Figure 4. Efficiency– SRV curve for p+ n cell at emitter thickness 2μm and 1μm

B. *Varying the emitter thcikness :*

In the second case emitter thickness is varied taking two surface recombination velocity fixed .From fig.5 it can be easily said that the PR effect is largely dependent on the thickness of emitter. PR effect increases the short circuit current density but short circuit current density goes on decreasing with the increase of emitter thickness. At large surface recombination velocity the effect is lower. As because at higher surface recombination velocity recombination take place quickly. So the photon with minimum energy required for the generation of electron-hole pair do not emit. As the short circuit current density goes on decreasing so does the open circuit voltage and the efficiency of the cell decreases, shown in fig 6. and fig 7. The average increase of efficiency for surface recombination velocity of $10^5\ cm/s$ is 17%. On the other hand for surface recombination velocity of $10^7\ cm/s$ increase of efficiency is 15%.

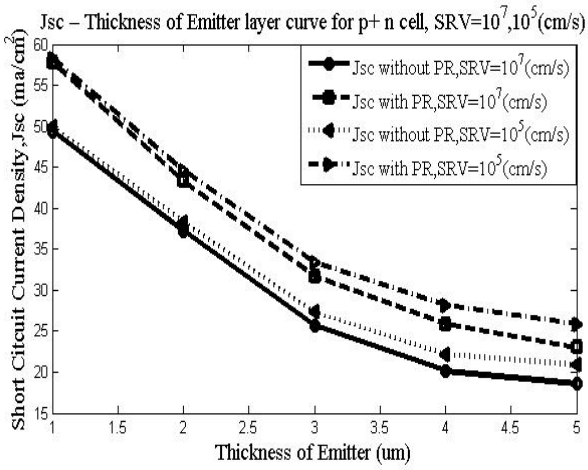

Figure 5. J_{sc}– thickness of emitter curve for p+ n cell at SRV, 10^7 cm/s and 10^5 cm/s

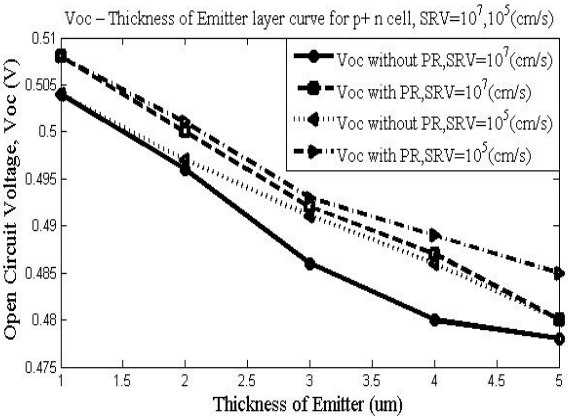

Figure 6. V_{oc}– thickness of emitter curve for p+ n cell at SRV, 10^7 cm/s and 10^5 cm/s

C. *Varying the doping density :*

In the third case keeping the surface recombination velocity and thickness of emitter constant, the doping density of the emitter is varied. From fig 8. it is clear that with the increase of doping density the short circuit density goes on decreasing. But the PR effect increases the current density for all the doping densities. As the short circuit density increases due to PR effect, the open circuit voltage and the efficiency of the cell also increases. Difference of efficiency is observed for with and without PR. At higher doping density the PR effect is more. Because the probability of radiative recombination increases with the increases of doping density .So minority carrier density in the p+ base decreases. The average increase of efficiency is 12% due to PR effect due to increase of doping density.

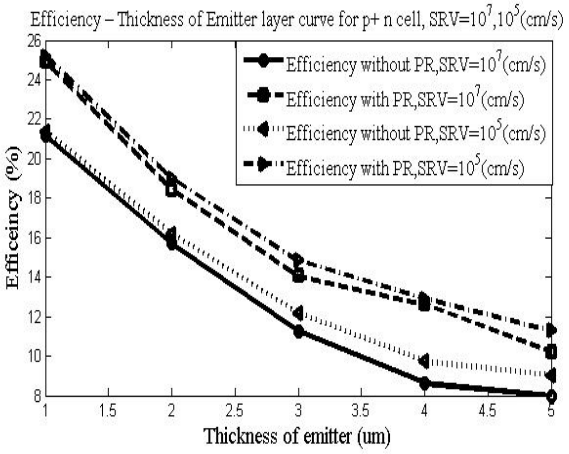

Figure 7. Efficiency– thickness of emitter curve for p+ n cell at SRV, 10^7 cm/s and 10^5 cm/s

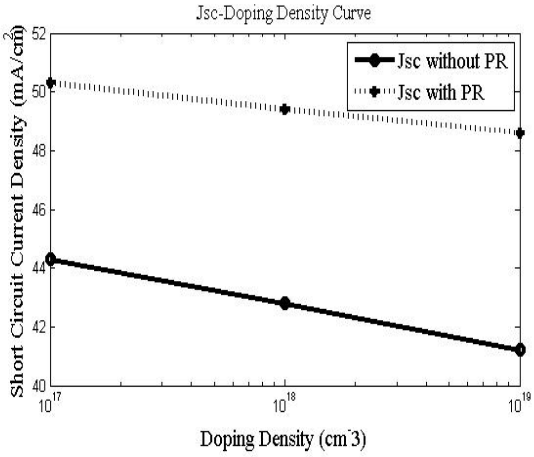

Figure 8. J_{sc}– Doping density of emitter curve

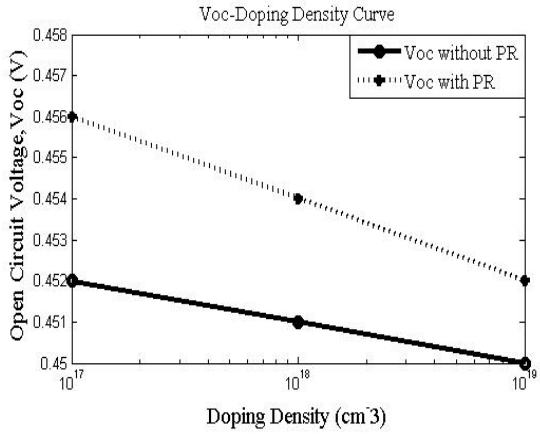

Figure 9. V_{oc}– Doping density of emitter curve for p+ n cell

IV CONCLUSION

In order to find out the prominent factors for PR in GaAS solar cell structures, research has been done on p+ n cell using the method schemed by Kuriyama et al. PR effect is actuated by thickness of emitter , surface recombination velocity and

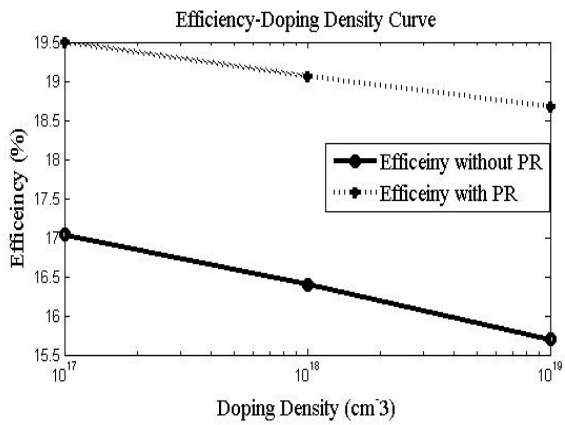

Figure 10. Efficiency– Doping density of emitter curve for p+ n cell

doping density of p+ emitter. Effect of base n-layer is negligible on PR effect. Among the three dominant factor thickness effects the PR more. The lower the thickness the better will be the efficiency of the cell. PR effect accelerate the cell performance in the positive direction. While designing a cell with PR different factors must be taken into consideration.

REFERENCES

[1] Sadao Adachi, "III-V Binary Semiconductors," in *Optical Constants of Crystalline and Amorphous Semiconductors*, Japan, Springer Science + Business Media., LLC, 1950,ch *B*, sec *B12*, pp. *213-226.*

[2] Green ,Martin A. "Efficiency Limits ,Losses and measurement," in *Solar cells*, USA, Prentice Hall, INC,1982,ch 5, pp. *85-98*.

[3] K. Ahrenkiel, S. Lundstrom, "Radiative Transitions in GaAs and Other III-V Compounds, minority carriers in III-V semiconductors physics and applications," in *Semiconductors and semimetals*, Academic Press, New York, 1993, ch *1,2*, pp. *22,119*.

[4] T. Kuriyama ,T. Kamaiya and H. Yanai, "Effect of photon recycling on Diffusion length and internal quantum efficiency of $Al_xGa_{1-x}As-GaAs$,"Japan, *J. appl. Phys* , 1977, 16,*465-477*

[5] P. Asbeck, "Self-absorption effects on the radiative lifetime in GaAs-GaAlAs double heterostructures," America, *J. appl. Phys* , 1977, 48 ,*420-822*

[6] Ph. Renaud, F. Raymond, B. Bensaïd, and C. Vèrié, "Influence of photon recycling on lifetime and diffusion coefficient in GaAs," America, *J. appl. Phys,*1992*,* 71 (4),*1907-1913*

[7] S. M. Durbin and J. L. Gray. "Numerical modeling of photon recycling in high efficiency GaAs solar cells," *Proc. 22nd IEEE Photovoltaic conf,*Las Vegas, NV. Oct. 1991. *188.*

[8] S. M. Durbin and J. L. Gray, "Numerical Modeling of Photon Recycling in Solar Cells" *IEEE Trans. on Electron Devices* , Vol. 41, No. 2, February 1994.

[9]A. Yamamoto, M. Kurizuka, Md. M. Murshid, M. Ohkubo, A. Hashimoto, "Material and structural parameter dependencies of photon recycling effects in conventional n +- p InP solar cell," *Elsevier Science B.V*, Solar Energy Materials and Solar Cells, 50, 1998,*259-264*

[10]A. Yamamoto, M. Kurizuka, Md. M. Murshid, and A. Hashimoto, "A Comparative Study on Photon Recycling effects in N+P and P+-N Inp Solar Cells with Bragg Reflector," *26th PVSC,IEEE*,1997,*903-906*

[11] Alexandre W. Walker, Oliver Hohn, Daniel Neves Micha, Benedikt Blasi, Andreas W. Bett, and Frank Dimroth, "Impact of Photon Recycling on GaAs Solar Cell Designs," *IEEE Journal of photovoltaics*, VOL. 5, NO. 6, November 2015

[12] P. Ender. "Photon recycling in double hetero structure," *Physica Status Solidi R.* 1986, vol. 1.37. p. *701*.

[13] W. P. Dumke. "Spontaneous radiative recombination in semiconductors," *Physical Rev* **,** 1957, vol. 105. p. *139*.

Studying The Impacts of Cyber-attacks On Smart Grid

Tanzim Meraj, Shaela Sharmin, Asif Mahmud

Dept. of EEE, Ahsanullah University of Science & Technology
141 & 142, Love Rd, Dhaka 1208, Bangladesh
tanzim.austianz83@gmail.com, shaela.ritu@gmail.com, asifmahmud24790@gmail.com

***Abstract*—This paper investigates the smart grid infrastructure with an upgradation of existing electricity networks and advanced information and communication technologies (ICT), intelligent devices & system. Considering the energy utilities play an increasingly important role in our daily life, smart grid technology introduces new security challenges that must be addressed. This paper has focused on the implementation of smart grid architecture to develop a real time situation and study the impacts of cyber-attacks on its communication infrastructure. A micro grid structure with particular generation and distribution specification along with its relevant communication infrastructure is designed to analyze the security challenges. The studies are performed based on a digital computer simulation approach using Power Factory 14.1. Some dynamic system events are formulated linking the change in different system parameters and effects of these changes are examined on the smart grid generation and distribution network.**

Keywords— Smart grid, communication infrastructure, microgrid, cyber attacks, generation power, power system, load demand, frequency respsonse, control center, system frequency.

I. INTRODUCTION

Smart grid is an electricity supply network which is based on a digital technology. It uses a two way digital communication to establish a communication path between the supplier and consumers. This allows the smart grid system to monitor, analysis and control the efficiency, cost, reliability and the sustainability of the production and distribution of electricity [1]. As this next generation power grid strongly depends on digital technology, it is vulnerable to different types of security issues. In recent time different research have been conducted to explore and solve the security issues and challenges of smart grid network. The concept of smart grid consists of its infrastructure, components, framework etc. The infrastructure of smart grid mainly consists of two major systems; the management system and the protection system. The management system provides advanced management and control services such as improving energy efficiency, demand profile, utility, cost and emission, based on the infrastructure by using optimization, machine learning, and game theory. The protection system provides advanced grid reliability analysis, failure protection as well as security and privacy protection services. The security of the smart grid infrastructure is very crucial to ensure uninterrupted and reliable power supply to the users during emergency situations. As this communication infrastructure highly depends on information and cyber technologies, it is highly vulnerable to cyber interruption and which can cause failure of any critical power system component and eventually lead to devastating physical impacts [2], [3]. In order to protect this infrastructure from any kind of security threats and to maintain stable and reliable power supply operations, the power grid must be modernized and incorporated with special features like advanced metering and monitoring system, advanced electricity generation and distribution, dedicated devices and software, highly secured control center etc. Another effective way of developing the security issues of smart grid is to divide a large power grid system into several microgrid structures. A microgrid system consists of interconnected set of electricity sources and loads that fall under a common control center. Microgrid system has the ability to separate and isolate itself from the utility grid manually or automatically using a switch during any kind of disturbances faultlessly with little or no disruption to the loads within the microgrid. After islanding, a microgrid remains operational in a self-directed mode and functions as an island. After the separation, a microgrid is permitted to reconnect with the utility grid only when the restoration of the main system and the microgrid is achieved. System voltages and frequencies must be either returned to normal range or maintain in a normal range for a reasonable period of time to achieve the grid restoration. The foremost objective of this paper is to identify the growing threats of cyber based attacks on nation's electrical grid and other critical infrastructure and also analyzing the changes in the real time data in different parts of the system after various faults, analyzing the fault conditions and monitors the values of these fault conditions with the help of a graph based simulation. This paper is based on a specific microgrid test system and a specific simulation tool has been used to run and analyze the test system.

II. SMART GRID COMPONENTS

A. Power System Components

Electrical power system is now one of the most effective components of the infrastructure on which modern society depends. They are used to deliver electrical energy to

978-1-4673-9257-0/15/$31.00 ©2015IEEE

industrial, residential and commercial consumers to meet the increasing demand [4]. Main components of modern electric power system are consists of: power stations, bulk generators, transformers, conductors, reactors, power utility equipments, capacitors, electronics and general load [5].

B. Communication Components

It is essential to digitize communication systems on power line in order to provide secure, profitable, reliable, proficient, environmental friendly power grid system. Communication components that are crucial for next generation power grid are: incorporated communications, measurement and sensing, advanced power devices, highly developed control methods and highly improved appliances.

C. Advanced Communication Components

The smart grid's behavior can be determined by using advanced components. These next generation power system devices will apply the latest research in materials, superconductivity, power storage, power electronics and microelectronics. Some advanced components regarding power electronics devices are dynamic volt amp reactive (DVAR), unified power flow controller (UPFC), distribution static compensator (DSTATCOM), static VAR compensator (SVC), medium voltage static voltage regulator (MV SVR), solid state transfer switch and AC/DC inverter [6].

III. CYBER SECURITY OF SMART GRID

Implementation of cyber security system and protection of a smart grid system from any sort of cyber threats or cyber intrusion has become much challenging nowadays. As the communication infrastructure of smart grid greatly depends on digital technologies, it has several vulnerabilities. These vulnerabilities can easily allow a cyber hacker to break into a network, gain access to the control center, spread malware to affect software and alter load conditions to destabilize the grid in unpredictable ways [7]. Developed cyber security strategies are required to eliminate these types of rapidly evolving threats and also to give flexibility to the manufacturers, utilities, and grid operators so that they can respond quickly and decisively during any kind of emergency situations. The basic concept of smart protection is to ensure first that the power grid has the ability to monitor, analysis, control and communication capabilities to the national electricity delivery system. Smart protection of power grid is also needed in order to maximize the output of the system and to reduce energy consumption. The reliability, security, and efficiency of the electrical grid is improved by the smart grid technologies which can be automatically adjusted by intelligent devices connected to the system and changing conditions to prevent blackouts and increase the capacity. Seven major features must be applied in a smart grid to make it self-aware and self-protective from any kind of cyber-attacks:

- Ensure customer security by protecting consumer's private information, activities and devices.
- Provide maximum security to power generation and distribution areas which may be targeted as attack entry points.
- Enable new and upgraded devices, products, technologies and services in order to fight against new types of cyber incursions.
- Maintain power quality to ensure reliable and stable electricity supply to the consumers.
- Optimize the intelligent devices which can increase the operating efficiency of the power grid.
- Implement a security system which can anticipate and respond quickly to any kind of system disturbances in a self healing manner.
- Operate resiliently against physical and kinds of natural disasters [8].

A cyber attacker can penetrate a smart grid using variety of attacks which can be classified into three categories; component wise, protocol wise and topology wise. Component wise cyber attack targets the field components and protocol wise cyber attack targets the communication protocol while topology wise cyber attack targets the topology of the smartgrid. Some other types of attacks are discussed below;

A. Spreading Malware

Malware can be developed by an attacker and spread to infect and corrupt different software which can damage smart meters or company servers. Malware can also be used to replace or add any function to a device or a system to send wrong information to the control center.

B. Exploiting The Control System Network

Activities are recorded by the control system network then mirror the logs into the business network. If the database management systems are not properly secured, a cyber hacker can easily gain access to the business database exploiting the control system network.

C. Compromising Communication Equipment

Some of the communication equipments such as multiplexers or sensors can be compromised by an attacker by injecting false information into these devices such as wrong data, false tripping information and fake emergency event causing direct damage to these devices.

D. Traffic Analysis and Network Protocol

Internet protocol (IP) and transmission control protocol (TCP)/IP stacks are used by the smart grid system which can be subjected to denial of service attacks (DoS). If these vulnerabilities are exploited by a cyber hacker then it can cause delay, block, or corruption of information transmission. A hacker can monitor the network traffic and can also obtain sensitive information by doing this.

IV. RESULTS AND ANALYSIS

A. Test System and Simulation Tool

The system shown in Fig. 1. is composed of a 13.8-kV, three-feeder distribution subsystem which is connected to a large network through a 69-kV radial line. The 13.8-kV substation busbar is radially connected to the main grid through the substation transformer and a 69-kV line. The network at the end of the 69-kV line is represented by a 69-kV, 100-MVA short-circuit capacity bus. A combination of linear and nonlinear loads of Load 1, Load 2, Load 3, Load 4 and Load 5 are supplied through three radial feeders of the subsystem. The system also includes two distributed energy resources (DER), i.e., DER1(3.5 MVA) and DER2 (3.5 MVA) on feeders F3 and F1 respectively. DER2 is a synchronous rotating machine equipped with excitation and governor control systems. DER1 utilizes a voltage-sourced converter (VSC) as the interface medium between its source and the power system. It also represents a dispatchable source with adequate capacity to meet the real/reactive power commands, within pre-specified limits. Such a dispatchable source may also include energy storage interfaced at the converter DC bus. DER1 also provides control on its output of real and reactive power components independently.

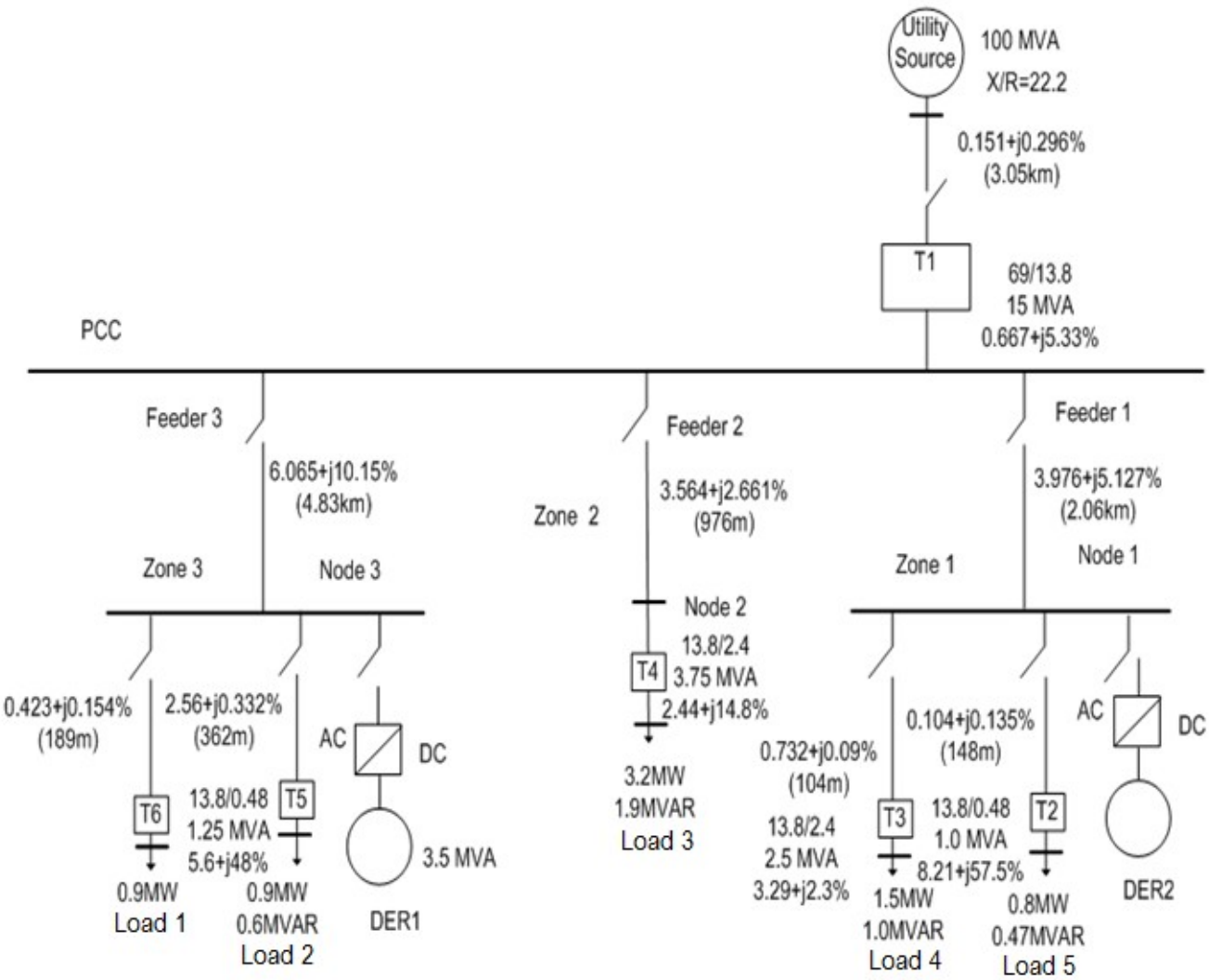

Fig. 1. Single-line diagram of the studysystem

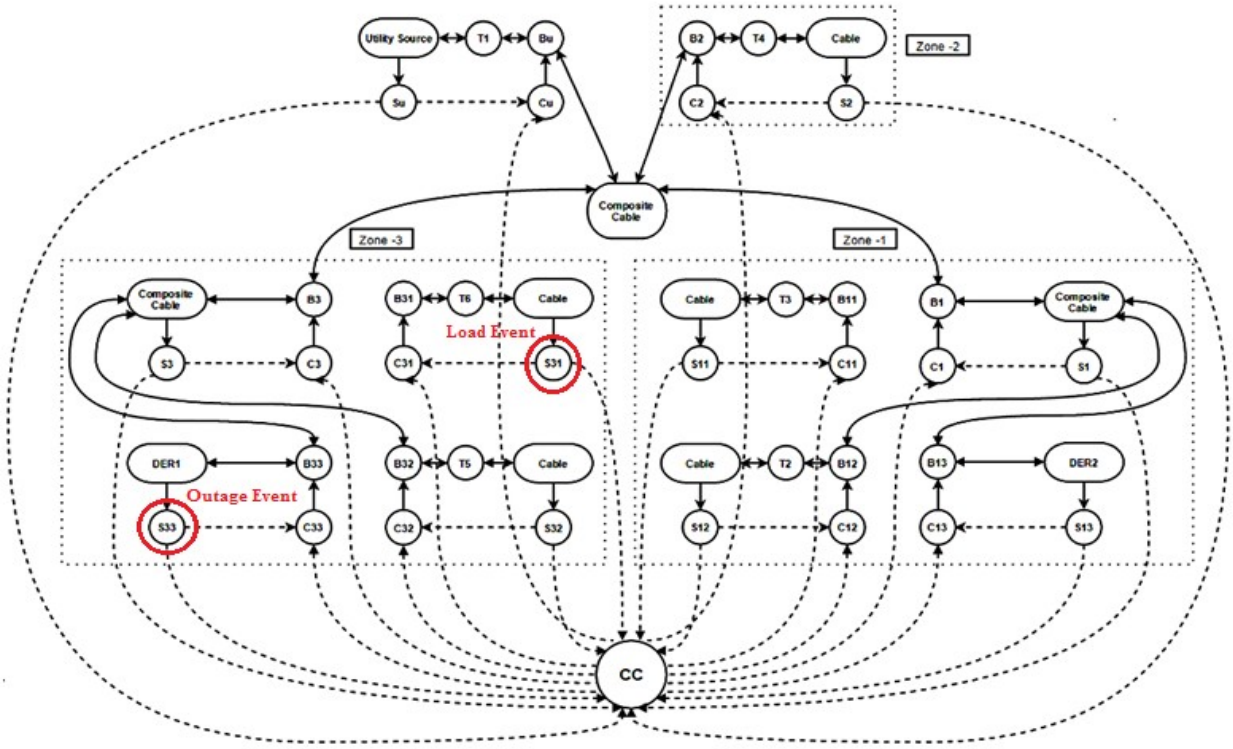

Fig. 2. Electrical and cyber graphs for system of Fig. 1. in islanding mode. Nodes are comprised of DERs, circuit breakers *Bi*, cables, transformers *T* of the electrical network and sensors *si* and actuator controls *ci* of the cyber network.

B. Simulation Results

Here the results are presented in pertaining to the graph and dynamic systems modeling of cause-effect relationships of a cyber-attack on the test system as proposed in [9]. A graph-theoretic formulation of distributed control is well-suited to this smart-grid representation. Using DigSILENT Power Factory 14.1 two types of simulation events are performed for this system; the single load event and the outage event. The utility source of this test system has a generation capacity of 3.17 MW and 3.04 MVAR. Load shedding or tripping off of generator will be occurred if an individual or the combined load demand exceeds generation. The impacts of cyber-attack on smart grid can be observed by creating events on different components of the system. The system frequency is 50Hz and the threshold value for generator under-frequency is set at 48Hz (4%); that means when the system frequency drops under 48Hz, the generator will be tripped out. Preliminary results can also be found in [9].

1) *Single Load Event*

The generator of this test system serves five general loads of different rating. If the load demand on a system suddenly increases the generation limit, this will cause frequency drop to the system and eventually the generator may trip out as the generation is not compatible with the increased demand which may apparently increase load demand on several sections of the system. Intentional load events are performed here in order to differentiate the before and after effect of increasing load demand on the system. For single load event Load 1 has been targeted where real power and reactive power are increased.

Load 1 has the rating of 0.9MW. In the simulation at 0s the load is assumed to come on along with all other loads in the system. The cyber-attack is applied at the time 1.2 sec on the sensor element by adding a load event which increases the load demand to 200% of its initial active power value and 50% of its initial reactive power value and the simulation has been performed for 400 seconds. If load demand increases suddenly, the system frequency drops from 50Hz as showed in Fig. 3. to 47.736 Hz at t=191.092 sec and after that it becomes constant as showed in Fig. 4. The under frequency relay is tripped after sensing the frequency drop in the system (at 4% mismatch of the nominal value). In normal condition when no event has taken place i.e. system is running smoothly, total generated power equals to the total load demand. If this situation remains the same, no load shedding or generator trip will take place. But the scenario changes when sudden increase on load demand takes place. This sudden change can be performed by cyber attack which has become a very common issue nowadays.

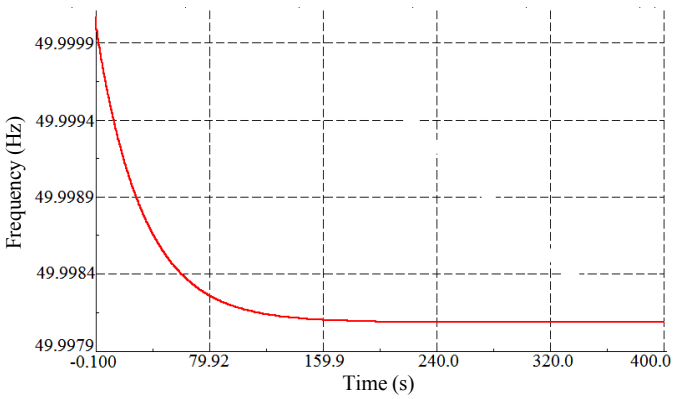

Fig. 3. The overall system frequency before any type load event taking place

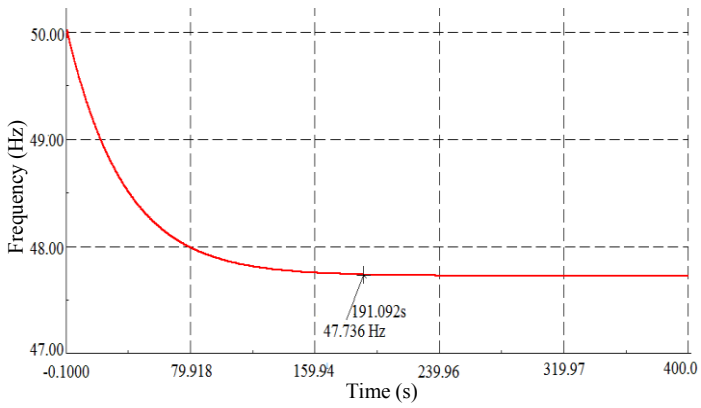

Fig. 4. Frequency plot for the sudden increase on load demand when Load 1 is increased

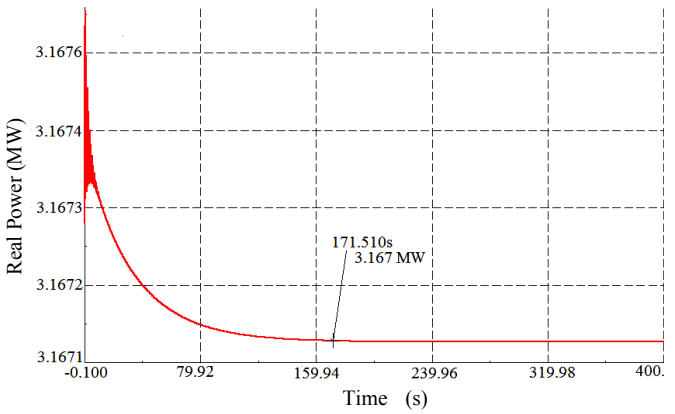

Fig. 5. Total power generation in the external grid before load event.

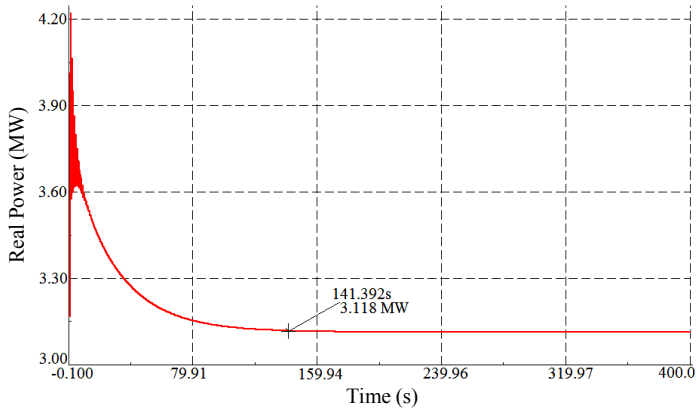

Fig. 6. The power generation at the external grid after load event takes place on Load 1

If any sensor gets wrong information due to the attacks, it may influence the control center to make a wrong decision as shown in Fig. 2 which represents an electrical cyber graph for system of Fig. 1 [6]. In case of single load event where Load 1 is suddenly increased by cyber attacks, sensor S31 is targeted. Control center, cc communicates all control signals at a particular time. For this general load, control signal C31 denotes whether a particular breaker B31 is open or close. Control center, cc collects information through sensor S31 and employs some algorithm to ideally avoid an unexpected situation if some unusual incidents occurs which make the system frequency unstable. When an attack is superimposed, sensor S31 is misinformed and this sensed information is collected by control center. It then performs necessary algorithms and makes quick decision for the whole system. If the sensed information shows that the load demand exceeds the generation power, system frequency will fall from its nominal value. An engine powered generator has a device on it named governor. In order to maintain speed it looks at the speed of the generator and controls the fuel going to the engine. The engine starts to slow down as the load increases. By increasing fuel, the governor keeps it from drifting too far out. If the requirement for electrical power is larger than what the engine can deliver, the governor can't make the engine put out more horse power that it's capable of. Then it slows down and can't maintain the frequency. If the frequency goes too slow, by using control signals the load management sheds one or more loads to avoid frequency deviation by opening their corresponding switches. In large interconnected system if this happens, sometimes we may experience cascading blackout.

2) *Outage Event*

For outage event two individual attempts have been performed, where two different system elements i.e. synchronous generator (DER1) and Load 1 of the test system have taken out of service separately in order to observe the after effect on the system frequency. For both case simulation has run for 400 seconds and elements have taken out of service from the system at t=1s. In order to take DER1 out of service, its corresponding sensor S33 becomes point to object. Fig. 7. displays the frequency response of the system after DER1 is taken out of service. This frequency plot asserts that system frequency falls from 50Hz to 43.65Hz at t=204.45s and after that it becomes constant. When DER1 is targeted by cyber-attack, corresponding sensor S33 senses the sudden change. At any time t, for a switch i, the control center, cc communicates with all control signal $C_i(t)$ where $C_i(t) = 0$ indicates open switch and $C_i(t) = 1$ indicates close switch. When sensor S33 is misinformed due to attack, corresponding

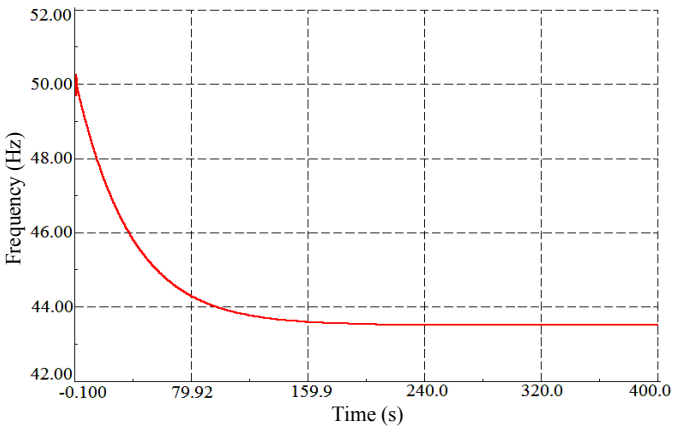

Fig. 7. Frequency plot for synchronous generator(DER1)

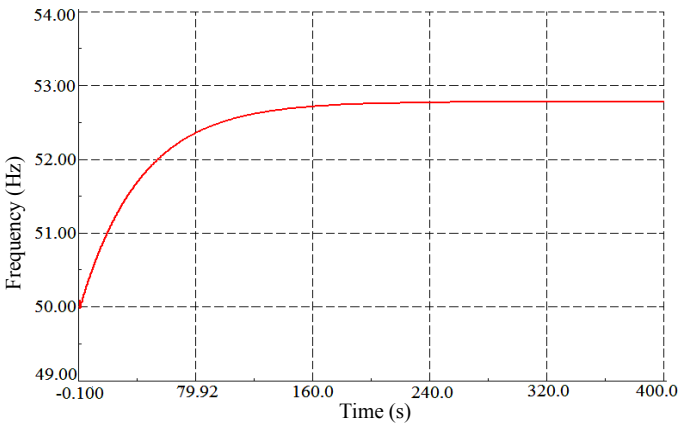

Fig. 6: Frequency plot for Load 1

control signal C33 helps control center, cc to collect this information so that it can perform necessary algorithm to make a quick decision for the whole system. DER1 is a dispatchable source of 3.5MVA rated power with adequate capacity to meet the real/reactive power demands. Due to its outage generation power will be less than total demand and consequently system frequency will fall. As the system frequency falls from its nominal value, load management sheds one or more loads by opening corresponding switches or in extreme condition it may cause system black out. Load1 has been intentionally taken out of service on the next attempt. Likely before, corresponding sensor of this load S31 is misinformed as shown in Fig. 2. This information is collected by control center, cc via control signal C31 and by performing some necessary algorithm a very fast decision is made. The frequency plot due to outage of Load 1 is shown in Fig. 8. System frequency rises from 50Hz to 52.76Hz at t= 255.41s as load demand decreases due to outage of Load 1. Studies showed that electrical equipment designed for any rated frequency may damage if they run above that rated frequency and to solve this problem some backup loads can be reserved so that system frequency remains constant.

V. CONCLUSION

A smart grid is an advanced power grid system that carries out the ever growing electricity demand in a reliable and sustainable manner. It is built on a modern communication infrastructure and adjusted to make the integration of all kinds of power utilities easier. Compared to current grid infrastructures, smart grid infrastructures adds significant complexity including security issues. As a result this increased complexity will require more effort to understand the system and will also provide numerous opportunities for the cyber hackers to exploit it. From the perspective of the defender, more complex systems require more effort to analyze and defend the system. Current approaches to secure cyber infrastructures are: techniques for key management, secure communication, secure code execution, intrusion detection systems, etc. These approaches model the malicious behaviors as components failures, fake information, false inputs and noises. Then analyzing their effects it will design counter measures to defend the attacks. However, the simulation world is modeled with estimation whereas the physical world is more complex, which can result in a deviation of any model to the reality. Therefore, theoretic approaches are mostly based on approximations compared to the physical world's unpredictability. As discussed in this paper, smart grid system demands additional security requirements, such as continuity of power delivery and accuracy of dynamic events. Such requirements are closely related to the models and states of the system, which are difficult to represent only by cyber security. Therefore, both cyber security and theory based security are essential to securing smart grid systems, offering exciting research challenges for many years to come.

ACKNOWLEDGEMENT

We would like to show our deepest gratitude to our respected and honorable supervisor Dr. Tareq Aziz, Associate Professor, Department of EEE, Ahsanullah University of Science and Technology for his unbounded guidance, encouragement, inspiration and valuable assistance in completion of this work.

REFERENCES

[1] DOE's Office of Electricity Delivery and Energy Reliability, ''The Smart Grid: An Introduction,'' 2009.

[2] Xu Li, X.Liang and X.Shen, ''Securing smart grid: cyber attacks, counter measures, and challenges,'' *IEEE Communications Society*, vol. 50, no. 8, 2012.

[3] Eric B.Rice, Anas AlMajali, ''Mitigating the risk of cyber attack on smart grid system,''*Conference on System Engineering Research*,2014.

[4] IEC-TC 57, "Communication networks and systems in substations- Part 1: Introduction and overview," *IEC Standard IEC/TR 61850-1*, 2003.

[5] Electronics lab, available at: http://www.powerelectricalblog.com

[6] Smart grid advanced components available at: https://www.smartgrid.gov/sites/default/files/pdfs/appendix_b3_advanced_components.pdf

[7] D.Wei, Y. Lu, M. Jafari, P.M. Skare, and K. Rohde, "Protecting smart grid automation systems against cyberattacks," *IEEETransactions on Smart Grid*, vol. 2, no. 4, pp. 782–795, 2011.

[8] Kundur.D., Feng.X., Mashayekh.S., Liu.S., Zourntos.T and Butler-Purry K.L, 'Towards modelling the impact of cyber attacks on a smart grid', *Int. J. Security and Networks*, Texas A&M University, USA, 2011.

[9] Tanzim Meraj, Sharmin Jahan, Shaela Sharmin, Rabeya Habiba and Asif Mahmud, ''Studying the impacts of cyber attack on a smart grid, *BSc. Thesis, Dept of EEE*, Ahsanullah University of Science and Technology, 2015.

Production of Transportation fuel from Municipal Solid waste.

Md. Alauddin[1]
Department of Mechanical Engineering
Rajshahi University of Engineering and Technology
RUET, Rajshahi, Bangladesh
alauddin102006@gmail.com

Shimul Barua[3]
Department of Mechanical Engineering
Rajshahi University of Engineering and Technology
RUET, Rajshahi, Bangladesh
shimulbarua.ruet@gmail.com

Md. Jiyaul Kabir[2]
Department of Mechanical Engineering
Rajshahi University of Engineering and Technology
RUET, Rajshahi, Bangladesh
zia.ruet10@gmail.com

Md. Abdul Mannan Akanda[4]
Department of Mechanical Engineering
Rajshahi University of Engineering and Technology
RUET, Rajshahi, Bangladesh
mannandinner@gmail.com

A.K.M. Enamul Hoque[5]
Department of Mechanical Engineering
Rajshahi University of Engineering and Technology
RUET, Rajshahi, Bangladesh
shovo.ruet102021@gmail.com

Abstract*— The energy is running out with the increase of demand of people in the world day by day. So accomplish this crisis alternative energy source can be weapon of this demand. In our project "from biogas to methane i.e. vehicle gas" can be a substitutive way to minimize this assertion. The target of this paper to produce biogas from saturated organic waste for example cow dung and pig slurries, food wastes i.e. municipal solid waste (MSW). To use as vehicle fuel, it has to be updated. In biogas contain CH_4, CO_2 and lean amount of H_2S. CO_2 is detrimental for our environment and atmosphere and H_2S have corrosive in nature. For better quality of fuel, the percentage of CH_4 have to be increased which is our main aim. By reducing CO_2 from the biogas, it is possible to increase the calorific value of the fuel and this fuel less emissive than that of fossil fuel i.e. diesel, petrol. On the other hand sources of fossil fuel are very limited in our country and it is not environmentally friendly, it causes greenhouse effect in the atmosphere. But by using biofuel, greenhouse effect is less than the fossil fuel and it is less costly and production is easy and improves local air quality compared to the other fuel. This paper is focused on preparation of available biogas production technology. This paper is going to disclose how the biogas is converted into transportation fuel to save the environment and atmosphere and to make the world green.

Keywords*— *Municipal solid waste; Biogas plant; Biogas; Impurities removals; Compress natural gas.

I. INTRODUCTION

Energy sources are decreasing gradually with the enhancement of assertion. Municipal solid waste is another form of Biomass. With fast socio economic and industrial development, the municipal solid waste increases rapidly in recent years. We have to look over alternative energy source to fulfill our challenge. Biomass is one of the major sources in present world. Every year about 140 billion metric ton of biomass is generated all over the universe [1]. Landfill gas which is produced from biomass contains about 36% to 44% carbon dioxide, 45% to 55% Methane, 17% to 19% Nitrogen, 2% or nil Oxygen, saturated with moister and H_2S is about 25ppmv to 1,000 ppmv+ [2].

Biogas is produced form biomass. Biomass recovers from residual stalks, straw, leaves, roots, husk, nut, seed shells, waste wood and animal husbandry waste. By using biofuel greenhouse effect is 21% less than the fossil fuel.

Now-a-days, Vehicle fuel is one of the important issues in present world. In this paper we are focusing about conversion

Fig. 1. Integrated Waste management of municipal solid waste

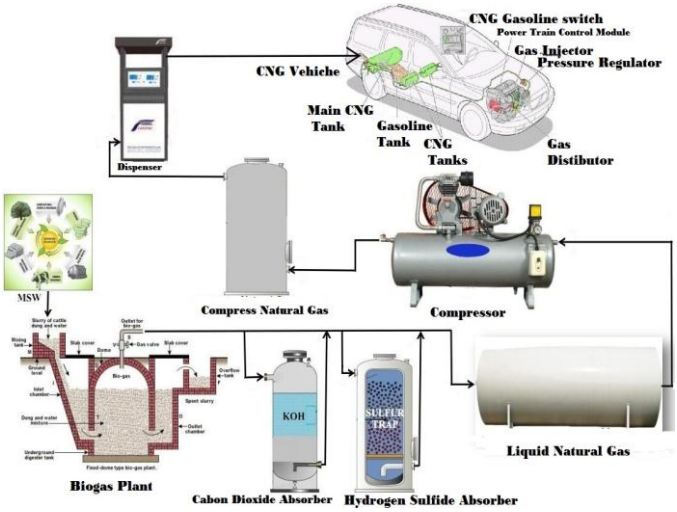

Fig. 2. Schematic view of municipal Solid waste to vehicle fuel.

from biogas to vehicle fuel. Landfill Gas can be produced from this biomass by proper utilization and it can be used in house hold works, industrial purposes. In our country, maximum vehicle are confined on fossil fuel for example Diesel, Petrol, Natural gas and Furnace oil. Diesel and Petrol is costly and not environmental friendly. It also more and emissive which is responsible for greenhouse effect and environmental pollution. Besides The Natural gas is more environmental friendly but resource of it is very limited in our country. Those resources are gradually diminished and it is a very threat full for our next generations.

By removing of carbon dioxide from landfill gas it can be used as vehicle fuel which impacts a major effect in our country. By using converted landfill gas, we can reduce extraction of natural source. After converting Landfill Gas into vehicle fuel that means it will be converted into compressed natural gas.

Volume fraction of biogas produced by controlled anaerobic digestion produces Bio-Compressed Natural Gas and there Methane (CH_4) contains 95.0% or more, Carbon dioxide (CO_2) contains 2.5% or less, Water (H_2O) contains 4 mg/ Nm^3 or less, Hydrogen sulfide (H_2S) contains 5 mg/Nm3 or less, Oxygen (O_2) contains 100 ppm or less, Hydrogen (H_2) contains 6% or less, Nitrogen (N_2) is no more [3]. This Compressed natural gas is usable for vehicle fuel.

There are different methods of managing MSW. The Integrated Waste Management (IWM) technique developed by the EPA is one such methodology in which use of different practices is made to safely and effectively handle the solid waste.

II. LITERATURE REVIEW

In ancient cities, wastes were thrown into streets and roadways, where they were left to accumulate. At that time, a system for waste removal began to evolve in Greece and in the Greek-dominated cities of the eastern Mediterranean. Disposal methods were very crude, involving open pits located just outside the city walls. As populations increased, efforts were made to transport waste farther out from the cities. In 1714 at first the city in England was found the waste management system. Toward the end of the 18th century in America, municipal collection of garbage was begun in Boston, New york city and Philadelphia [4].

The U.S Environmental Protection Agency (EPA) encourages consumers to reuse and recycle these valuable products to keep them out of the waste stream [5]. With this in mind, waste management has partnered with several companies, like LG Electronics, to recycle electronics for reprocessing [6].

There are large quantities of the biomass available in Bangladesh. Huge amount of Landfill Gas is produced from biomass by removing of CO_2 and H_2S from Landfill Gas, Landfill gas is composed of a mixture of hundreds of different gases. By volume, landfill gas typically contains 45% to 60% methane and 40% to 60% carbon dioxide. Landfill gas also includes small amounts of nitrogen, oxygen, ammonia, sulfides, hydrogen, carbon monoxide, and non-methane organic compounds (NMOCs) such as trichloroethylene, benzene, and vinyl chloride. Landfill gas produced by Bacterial decomposition, volatilization and Chemical reactions [8]. It can be easily converted into Liquid natural gas(LNG) and finally compress LNG will converted into CNG which can be used vehicle fuel.

A work on solid waste management was found that the management system and energy recovery system does not work for proper management of solid wastes because of financial resources, institutional weakness, improper selection of technology, transportation systems and disposal options, public's lack of concern towards environmental cleanliness and sanitation have made this service unsatisfactory. Wrong attitudes and perceptions of the people about sanitation issues contributed to solid waste management problems of the respective City Corporations.

III. METHODOLOGY

By bacterial decomposition of organic material contained in municipal solid waste (MSW), Landfill gas (LFG) is produced. Some factors influence the quantities of gas that a MSW landfill produces are organic compounds in the waste, and the moisture content and temperature of the waste. Temperature and moisture levels are influenced by the surrounding climate.

Landfills often accept waste over period of 20 to 30 year and large scale Landfill gas is produced by Bacterial decomposition. Natural process of bacterial decomposition of landfill waste consists of four sequential stages.

First stage: At the beginning of the first stage of decomposition, aerobic bacteria which live only in the presence of oxygen, consumes oxygen while breaking down the long molecular chains of complex carbohydrates, proteins, and lipids that comprise organic waste. The primary byproduct of this process is CO_2. In this stage, depending on the presence of oxygen, decomposition can last for days or months.

Second stage: After introducing oxygen in the landfill Gangrene starts. Bacteria is converted into compounds created by aerobic bacteria into acetic, lactic, and formic acids and alcohols such as methanol and ethanol by using an anaerobic process. The landfill becomes highly acidic. The gaseous byproducts of these processes are CO_2 and H_2.

Third stage: Initialization of decomposition depends on the consumption of organic acids produced in second stage by the certain types of anaerobic bacteria. Hence production of the landfill gas becomes more neutral environment in which methane-producing bacteria begin to establish themselves.

Fourth stage: Mortification starts in this stage, when both the production rates and the composition of landfill gas remain relatively constant. In this stage landfill gas usually contains approximately 45% to 60% CH_4 by volume, 40% to 60% CO_2 and 2% to 9% other gases for examples sulfides.

Gas is produced at a stable rate about 20 years. If greater amounts of organics are present in the waste, such as at a landfill receiving higher than average amounts of domestic animal waste [8].

The raw gas contains several impurities like water, dust, H_2S, CO_2, siloxanes, Hydrocarbons, NH_3, oxygen and several other elements that must be removed in order to reach certain standards of quality [14]. From Biogas plant firstly collect Landfill gas and burnt off in a controlled manner (flaring) in order to destroy pollutants. While flaring LFG will largely mitigate the negative effects of these emissions, the strategy can also be seen as a lost opportunity for converting the gas into a useable form of energy. LFG can be used for many energy recovery projects [7].

A. Removal of water: Possible impact of water is corrosion in compressors, gas storage, tanks and engines due to reaction with H_2S, CO_2 and NH_3 to the acid. Untreated or raw biogas is usually saturated with water and the absolute water quantity depends on the temperature (according to chemical equilibrium) and water is removed by Physical separation of condensed water or chemical drying [8].

B. Hydrogen sulfide (H_2S): It is a foul odor of rotten eggs colorless, very poisonous, flammable gas with the characteristic. It is removed by two ways [9]

i. Removal of H_2S during digestion:

$$2H_2S+O_2 \rightarrow 2S+2H_2O$$

$$2Fe^{2+}+3S^{2-} \rightarrow 2FeS+S$$

$$Fe^{2+}+S^{2-} \rightarrow FeS$$

ii. Removal of H_2S after digestion:

$$Fe_2O_3+3H_2S \rightarrow Fe_2S_3 + 3H_2O$$

$$2Fe(OH)_3+3H_2S \rightarrow Fe_2S_3 + 6H_2O$$

C. Carbon dioxide (CO_2) Removal: At the contemporary there are several alternative technologies which are adopted for CO_2 removal from gases. Many of them encouraged by the recent interests of segregation of CO_2 from power plant flue gases for the aspect of CO_2 sequestration. Various sophisticated commercial CO_2 removal technologies have been in use for several decades to produce CO_2 catherses for processed food for example soft drinks, for natural gas purification and for tertiary oil recovery. However, at the present time various researches are going on for the removal of CO_2 from gas, which is applicable to begin upgrading. CO_2 removal by using potassium carbonate solutions is now obsolete technology which were mixed with other chemicals to facilitate the process. For CO_2 catharses from the gas, recent proposed process uses refrigeration. However these process are highly sophisticated, precise researches are need to improve the process. Though there are some process of CO_2 removal, the entire world searching for "game changing" technologies for CO_2 removals from power plant and industrial emissions.

Potassium hydroxide (30 % w/v) to absorb CO_2 and cuprous chloride in hydrochloric acid to absorb CO [9]. Potassium hydroxide' solution (250g KOH in 500mL of boiled distilled water), and it absorbs only CO_2. A hydrocarbon is burnt with excess air. The Orsat analysis of the flue gas shows 10.81% CO_2, 3.78% O_2 and 85.40 N_2. Calculate the atomic ratio of C:H in the hydrocarbon and the % excess air [10].

A thin film membrane used which only allows particular molecules to pass through it and allowed molecules will affect the conductivity of the thermocouple system which send signal proportional to the chemical molecules. Based on chemical absorption principle, typical flue gas analyzers measures the quality of CO_2. On depending absorption factor of this components their bulb component, when flue gas is passed through the bulb, components are separated that helps to know the volume drop from initial flue gas volume. By absorption, water vapors in the flue gas removed on solid $CaCl_2$ and then passed a pipettes. The sequence should start from CO_2, if the reagent in the analyzer is KOH in the absorption solution. To absorb, gas then passed into KOH solution pipette to form K_2CO_3 by the following reaction.

$$2KOH+CO_2 \leftrightarrow K_2CO_3 + H_2O \text{ at ambient conditions [11]}$$

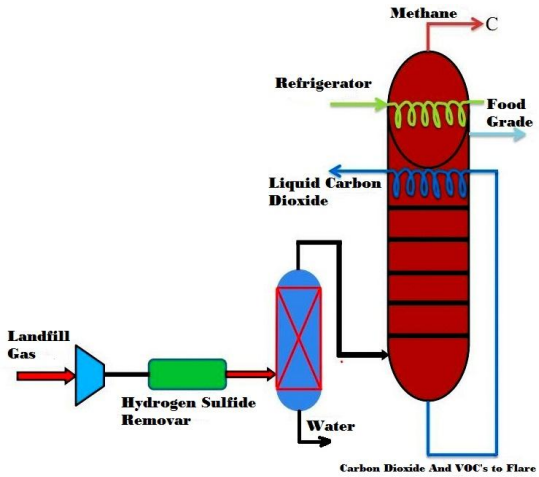

Fig. 3. Schematic view of Removal of CO2 from biogas.

TABLE. 1. TIME OF BIODEGRADABLE [12]

Item	Time to Degrade	Item	Time to Degrade
Paper towel	2-4 weeks	Normal paper	1-2 weeks
Newspaper	6 weeks	Ply wood	1-3 years
Cardboard box	2 months	Wool gloves	1 year
Apple core	2 months	Cotton gloves	1-5 months
Waxed milk carton	3 months	Photo-degradable beverage holder	6 months

TABLE 2. CONSTRUCTION COST ACCORDING TO SIZE [13].

Size (m3)	Operational hours per day	Cow dung requirement per day (kg)	Poultry litter requirement per day (kg)	Approximate construction cost (BDT)
1.6	3-4	43	23	26,000
2.0	4-5	54	28	32,000
2.4	5-6	65	34	36,000
3.2	7-8	87	45	43,000
4.8	10-12	130	68	52,000

IV. ECONOMIC ASPECTS IN BANGLADESH

The diagram depicts that, in the year of 2005, no of biogas plant was 30 and in the year of 2008 no of biogas plant was 4621. This shows within a short time establishment of biogas plant increased rapidly. In the year 2014 no of established biogas plant is 30291. From this diagram it is clear within a difference of 10 years, about 30,000 biogas plant established in Bangladesh. This also indicates that adeptness of biogas plant is increasing and it can be forecast that about 1,00000 biogas plant will be established in the next decade. Thus dependency on biomass will be increased rapidly in the upcoming decades and this introduced method will be fruitfull to compensate this energy demand specifically in transportation sector.

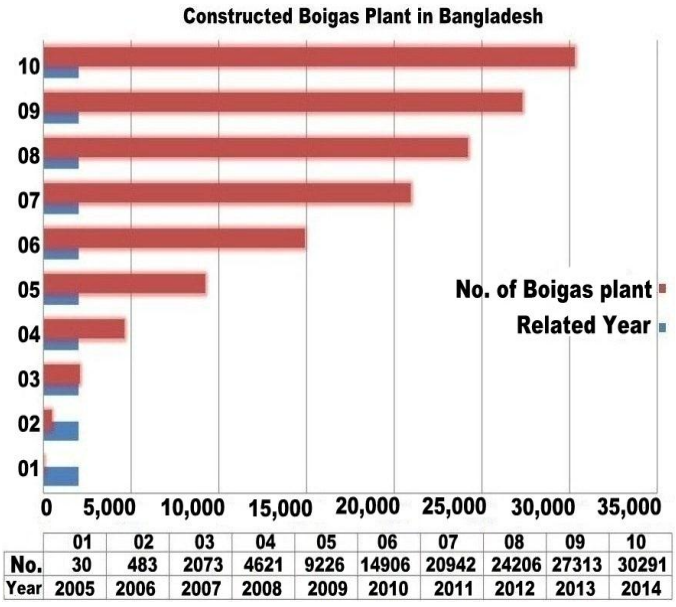

Fig. 4. Biogas plant Construction in Bangladesh previous ten years [14].

V. CONCLUSION

We are extracting energy for different purpose. Now-a-days the diesel, petrol, natural gas are used to appease our pretention. But those energy sources are tethered and diminishing day after day by the increasing amount demand. So to minimize this problem bio-fuel may be an effective source. In our under developing country bio-fuel can play a vital role in our transportation system. Because of less cost it would be popular and most useable fuel in our country. The environmental pollution occurs for food wastes, paper wastes and different organic elements. By using this pollutant elements the environment pollution is reduce considerably and by proper utilization of this toxic element bio-fuel can be produce which affix our energy source and become environmental friendly and greenhouse effect free. For under developing country, the municipal waste, food wastes is available compare to another source and it create pollution negatively. So by constructing dustbin where maximum amount of food wastes ,municipal wastes produce such as hospital where organic wastes can be found, food industry and maximum amount of biomass can be found from dairy farm, poultry farm . By using of this wastes bio-fuel can be produced that will mitigate pollution and will construct green world. If a biogas plant is set-up in every municipal area and all biomass is gathered in biogas plant. Large amount of biogas is produced form each area and it can be converted into CNG to use in vehicle. By this process we can decrease the pressure on natural gas and environment will be pollution free.

REFERENCES

[1] Converting agricultural waste into resource published by UNEP.

[2] "Landfill Gas to CNG 101 Basics of LFG Conversion to B-CNG and B-CNG Utilization" Jeffrey L. Pierce, P.E. Senior Vice President and Steve Hamilton Vice President SCS Energy Long Beach, California.

[3] World Journal of Social Sciences Vol. 2. No. 7. November 2012 Issue. Pp. 174 – 181 Biogas Technology for a Sustainable Energy: The Case of Poultry Farm in Bangladesh Rumana Rashid 1, Mohd. Hamdan Bin Ahmed2, Md. Sayem Khan 3

[4] http://www.Historical background of solid-waste management, early waste disposal, Wikipedia the encyclopedia, visits the page on 12/18/14.

[5] "Reusing and Donating Electronics". Environmental Protection Agency. In 2010-08-20.

[6] "BRIEF: Recycling at State Fair Park". TMCnet.com In 2010-08-18.It can be easily converted into Liquid natural gas(LNG) and finally compress LNG will converted into Compress natural gas which can use vehicle fuel.

[7] ATSDR - Landfill Gas Primer - Chapter 2 Landfill Gas Basics.

[8] Orsat Gas Analysis Experiment (internet source)

[9] Flue Gas Analysis by Orsat Apparatus.pdf (internet source)

[10] http://www.gshakti.org/index.php?option=com_content&view=article&id=177&Itemid=134

[11] http://www.gshakti.org/index.php?option=com_content&view=category&layout=blog&id=54& Itemid=78

[12] http://cmore.soest.hawaii.edu/cruises/super/biodegradation.htm

[13] http://www.gshakti.org/index.php?option=com_content&view=article&id=177&Itemid=134

[14] http://www.gshakti.org/index.php?option=com_content&view=category&layout=blog&id=54& Itemid=78

Simulation and Analysis of Battery Performance of a Solar Car Using a Model Implemented in SIMULINK

Abdullah Al Mahmud[1], Asif Zaman[2], Imran Bin Jafar[3], Mosaddequr Rahman[4]

School of Engineering and Computer Science, BRAC University
66 Mohakhali C/A, Dhaka-1212, Bangladesh

[1]mahmud.abdullah@bracu.ac.bd, [2]asifzaman007@gmail.com, [3]imranjafar@bracu.ac.bd, [4]mosaddeq@bracu.ac.bd

Abstract— **Battery performance of a proposed solar car has been investigated under different road conditions while the car makes a trip in one of the longest routes in Dhaka city, using a model developed in Matlab Simulink. A significant reduction in energy consumption is observed when the car runs at lower speed, which is attributed to lower air drag at lower speed. Energy consumption further reduces with the increase in number of stoppages. Thus the solar/electric car will be an ideal mode of transport for a city like Dhaka, where traffic congestion is a daily occurrence.**

Keywords— **Solar car, SIMULINK, Batteries, Battery modelling, State of charge.**

I. INTRODUCTION

In Dhaka city, a major mode of transportation for daily office commuters is fuel driven cars. However, emissions from such cars pose serious environmental and health hazards, especially during office hours when cars are caught in traffic congestion causing more and more toxic emissions. Solar powered clean cars can be of great advantage to the public and environment and can go a long way to alleviate this problem. On these premises, a solar powered light-weight economically affordable clean car for the daily office commuters of Dhaka city was proposed in [1] which is able to run on solar power alone during sunny days of summer and spring, and with complementary charging of the batteries from other sources during winter and under overcast sky.

Batteries are an indispensable and critical part of the electric drive system of a solar car. A healthy battery will ensure a longer battery life and a safe driving of the car. Further, unlike fuel driven car, there is no rapid recharging system for solar car. Therefore, it is imperative to have a prior understanding of how the battery will perform on the road under different road conditions. With this objective, this paper aims to investigate the battery performance while the car is making a trip from home to office in Dhaka city, considering one of the longest trips, Uttara to Motijheel, which is about 18 km long, under different traffic conditions.

Performance analysis is carried out using a model developed in Simulink assuming the batteries to be fully charged. The simulation has been conducted using the specifications of the solar car that is being built in the Robotics Workshop of BRAC University [2]. In this study, the discharge characteristics, mainly the variation in the state of charge (SOC) and the terminal voltage (V_t) of the battery with travel distance and time under different traffic conditions are observed and analysed. Role of the solar panels is excluded from the study as the purpose of this paper is solely to study the battery performance. Effects of temperature and aging have been ignored in the analysis. In the subsequent sections, sections II and III, models used for the battery, charge controller and the motor power are described, followed by their implementation in Simulink. Section IV provides the simulation results on the battery performance under different road conditions. Finally section V concludes the findings of this work.

II. MODELING OF SOLAR CAR

Fig. 1 shows the block diagram of the electric drive system of the solar car consisting of solar panels charging the battery through the charge controller. Charge controller also controls dissipation of energy to the motor to ensure healthy battery life. Following subsections discuss the modelling of different modules of the electric drive system, except the PV panel.

A. *Modelling of Battery*

The model used for battery is based on Thévenin battery model [3]. In Thévenin battery model (Fig. 2), the resistance R_0 and capacitance C_0 between electrodes and electrolyte of the battery is considered along with the series resistance R_S. V_{OC} is the open circuit voltage and I_L is the load current. Experiments on battery suggest that the voltage drop, V_d across R_0 or C_0 is almost constant for a particular SOC [4]. All the three parameters namely V_{OC}, R_S and V_d in Fig. 2 are functions of SOC.

The load current, I_L for a load which draws out power P can be calculated as,

$$I_L = \frac{(V_{OC} - V_d) - \sqrt{(V_{OC} - V_d)^2 - 4R_S P}}{2R_S} \quad (1)$$

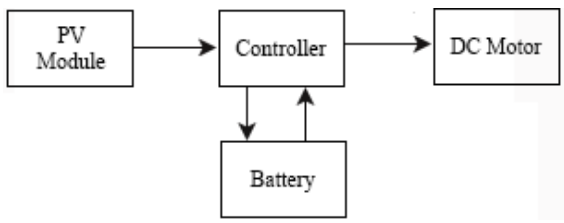

Fig. 1 Block diagram of electric drive system of solar car

978-1-4673-9257-0/15/$31.00 ©2015 IEEE

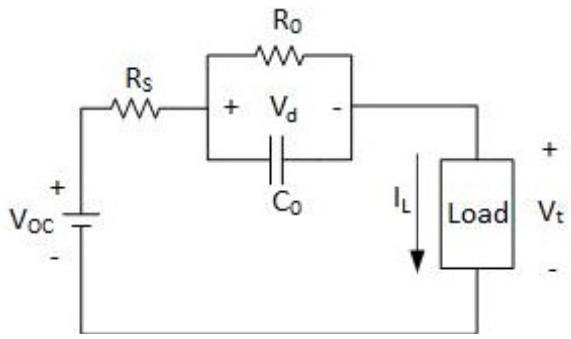

Fig. 2 Thévenin battery model

Once the current is known, the terminal voltage V_t can be determined using (2).

$$V_t = V_{OC} - I_L R_S - V_d \tag{2}$$

The total charge dissipated from battery for time t is calculated using (3).

$$Q_{dis} = I_L \mathrm{t} \tag{3}$$

In case, battery is being charged by I_{CH} current, the overall current flowing out of the battery is reduced to $(I_L - I_{CH})$.

The SOC of the battery after supplying P power for t seconds is calculated as,

$$SOC(new) = SOC(old) - \frac{Q_{dis}}{C} \tag{4}$$

where C is the capacity of the battery.

With this new SOC, V_{OC}, R_S and V_d are re-evaluated according to the following relations which were determined experimentally in [5].

$$V_{OC} = 1.4667SOC - 11.0233 \tag{5}$$

$$V_d = 0.086SOC - 0.011 \tag{6}$$

$$R_S = -0.0531SOC + 0.066 \tag{7}$$

Then the algorithm recurs with the calculation of I_L until SOC gets low enough for the process to cease.

B. *Power Calculation of DC Motor*

A motor draws out power from battery to give the solar car a driving force. The total drive force to make the vehicle move or keep it moving can be estimated by adding together individual force components that arise from different physical effects.

The major three forces are the rolling resistance force F_R, aerodynamic drag force F_D and the force of acceleration F_A. Summing up them, total driving force, F_T is obtained as [6].

$$F_T = F_R + F_D + F_A \tag{8}$$

The rolling resistance force, the frictional force that resists the motion when a vehicle rolls on a surface, is given by,

$$F_R = \mu_R mg \tag{9}$$

where μ_R is the coefficient of rolling resistance, m is the mass of the car and g is the gravitational acceleration.

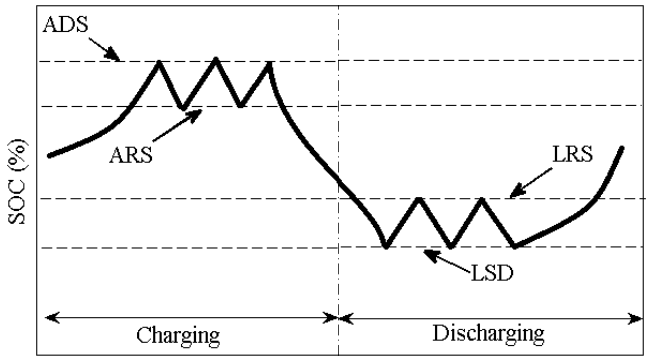

Fig. 3 Charge Controller set points

Aerodynamic drag force is the force exerted by the air against the movement of the car and is given by,

$$F_D = \frac{1}{2} C_D \rho A_{CROSS} v^2 \tag{10}$$

where ρ is the air mass density, A_{CROSS} is the cross sectional area of the car, v is the velocity of the vehicle, and C_D is the coefficient of aerodynamic drag force.

The force of acceleration is given by,

$$F_A = ma \tag{11}$$

where a is the acceleration and is accounted for when the car is accelerating. When the car moves at constant speed, the force of acceleration is zero.

If the car is running at velocity v then the power exerted by the shaft of the motor can be expressed as,

$$P_T = F_T v \tag{12}$$

If the efficiency of the motor is η_m, the power to be supplied by the battery to the motor is given by,

$$P = \frac{P_T}{\eta_m} v \tag{13}$$

C. *Mechanism of charge controller*

There are four set points in a charge controller, two to avoid overcharge and two for overdischarge as in [7]. The maximum SOC the batteries are allowed to reach and above which solar panels are disconnected from the battery is array disconnect SOC (ADS). Then the battery may discharge to a SOC level low enough to start charging again; the level is array reconnect SOC (ARS). Similarly, the load is disconnected at the minimum SOC, namely low SOC load disconnect (LSD), after which more discharging may damage the battery. Then the battery may charge for some time, the SOC rises and the load is connected again at a level of load reconnect SOC (LRS). The points are depicted in Fig. 3.

III. Implementation in Simulink

The implementation of the aforementioned models of battery, motor power and charge controller are described in the following subsections.

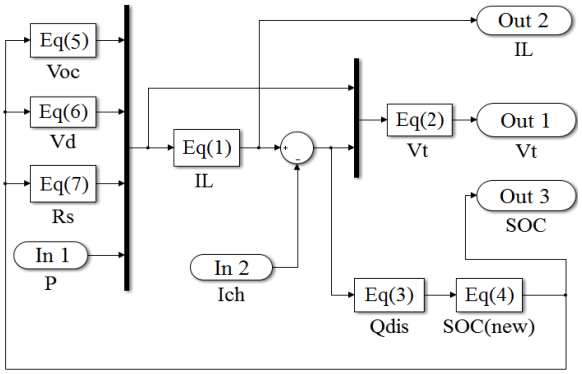

Fig. 4 Implementation of Battery model in SIMULINK

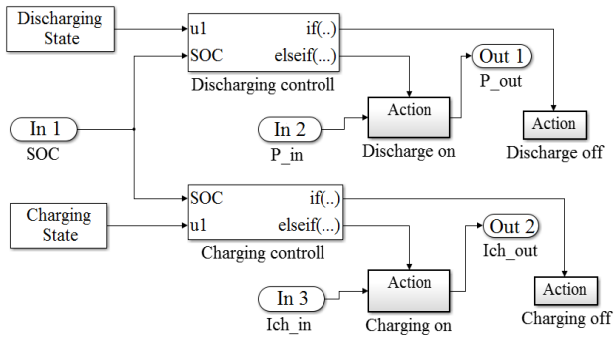

Fig. 5 Implementation of charge controller model in SIMULINK

A. *Implementation of Battery Model*

Fig. 4 shows the battery model in Simulink where the power required P and charging current I_{CH} are the inputs to battery. It calculates I_L, V_t and SOC after dissipating power for a certain time and gives out as outputs. Eq(1), Eq(2) etc. labelled in the diagram refer to the corresponding equation numbers in this paper. The time interval after which the model calculates dissipated charge and records a new SOC can be fixed by the mask parameter dialog box along with the nominal capacity of the battery, initial state of charge, temperature and number of batteries in series.

B. *Implementing Load Block in SIMULINK*

The Simulink block of Load, named 'Load' in Fig. 6, takes inputs of variable velocity on different time frames and some invariants related to the car e.g. its weight, frontal area. If the car moves at velocity v_1 kilometer per hour (kph) for t_1 minutes, comes to a halt and rests for t_1^r minutes, and then starts again at v_2 kph at which it runs for another t_2 minutes, the input format is $v = [v_1 \quad 0 \quad v_2]$ and $t = [t_1 \quad t_1^r \quad t_2]$. Time t_1 consists of the time at which the car accelerates from static position to reach v_1, the time it runs at constant v_1 kph, and fall time when the car decelerates to halt. The inputs are transferred to a MATLAB program which gives a timeseries variable P using the equations (8) to (13). The signal building block of load has some presets e.g. Busy road, Highway, Empty road etc. to select easily or the users may produce one according to their concern.

C. *Implementation of Charge Controller*

Fig. 5 implements the charge controller in SIMULINK. There are two 'if' blocks in the diagram; upper one is controlling the discharging state and lower one the charging state. If the SOC goes below the given level to turn off discharging, and the discharging process is not switched off yet, the upper if block commands the Discharge off block to disconnect the load. On the other hand, if the SOC is high enough to turn on discharging, the same if block triggers Discharge on action block to connect the load and deliver input power to the output. Same mechanism applies for the charging state controller 'if' block except, this time, the input charging current flows to output when charging is turned on.

D. *Combining the Components*

All the components portrayed in earlier sections are packed inside subsystems and combined together to build a complete model of vehicle as in Fig. 6. As mentioned earlier, the concern here studying discharging characteristics, and hence charging current is considered zero. All data found by the simulation are transfered to the MATLAB workspace to plot and analyze the results.

IV. RESULTS AND DISCUSSIONS

An itinerary is assumed for a Dhaka city dweller from his home to office, which is 18 km long. For the sake of convenience, it is assumed that the person leaves his home in the morning with his car fully charged and reaches his office by driving 10% of the distance at 10 kilometer per hour (kph) and rest of the road either 30 kph or 60 kph depending on the road condition. In the afternoon, he returns by the same route with same speed characteristics.

Fig. 7 shows the plots of power required P, SOC and V_t with respect to time as the car travels at different velocities from its origin to destination. The top most plot shows the different velocities of the car during its trip which starts with 10 kph at its origin covering 5% of the distance, goes at after that for 15% of the road, then goes at 60 kph for 60% of the road, after which it goes at 30 kph and 10 kph for the rest of

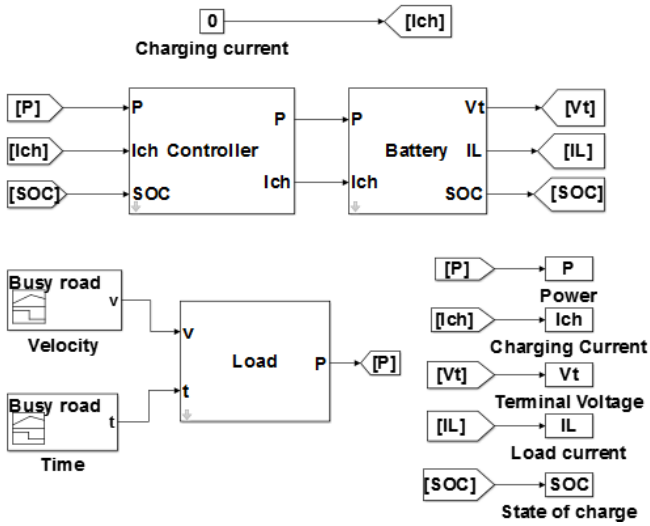

Fig. 6 The Model of the solar car combining all individual components

TABLE I
PROPERTIES OF SOLAR CAR

Components	Parameters	Value
Battery [5]	Capacity of the Battery, C (AH)	40
	Number of Batteries in Series	5
Vehicle Platform [1]	Mass of the car, m (kg)	500
	Maximum velocity, v_{max} (kph)	60
	Time to get max. velocity, t_{max} (min)	1.5
	Frontal Area, A_{CROSS} (m^2)	1.1
Environment [6]	Coeff. of Rolling Resistance, μ_R	0.01
	Coeff. of Aerodynamic drag force, C_D	0.035
	Air Density, ρ (kg/m^3)	1.2

15% and 5% of the road, respectively, before it reaches the destination. For the sake of simplicity we assumed a constant acceleration with which the car reaches the maximum speed from its rest position and a constant deceleration with which it comes to a halt from its maximum speed. For higher speed higher acceleration and deceleration are assumed than those at lower speed. The required power increases gradually with the increase in car speed as can be seen from the power plot below the velocity plot in Fig. 7. The power drops abruptly whenever the velocity reaches target speed because as the driver releases the accelerator, force of acceleration becomes zero requiring less power to drive. SOC plot shows gradual decrease in SOC with a faster drop when the car runs at the peak speed of 60 kph.

Fig. 8 shows how the SOC varies when the car travels at the top speed of 60 kph for different lengths of the road. As can be seen from this figure, SOC drops to almost 67% when the car runs 90% of the road at the top speed, indicating about 33% consumption of battery charge at this speed. However, SOC drops to only 81% when the car runs only 30% of the road at the top speed with 60% at half the top speed and the rest 10% at 10 kph, indicating more that 40% reduction in energy consumption at this slower speed. The higher energy requirement at higher speed is due to the higher aerodynamic drag force which increases as the square of the velocity according to (10). Energy requirement is further reduced if the trip is accompanied with frequent breaks (topmost plot in Fig. 8) during heavy traffic congestion which is a common phenomenon in the city of Dhaka.

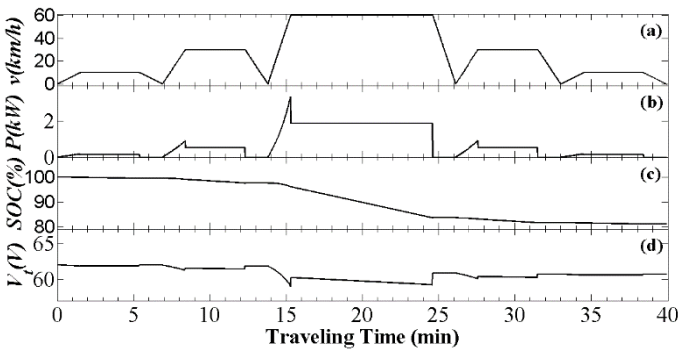

Fig. 7 Variation in (a) car speed, (b) motor power, (c) SOC, and (d) terminal voltage, V_t of the battery during one full trip as the car travels from origin to its destination.

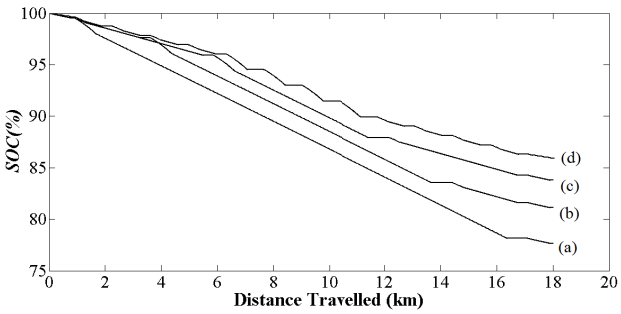

Fig. 8 Variation in SOC with the car traveling (a) 90%, (b) 60%, and (c) 30% of the road at the top speed. Plot (d) is that for 30% with 20 number of stoppages.

Consumption of less energy at slower speed will be an added advantage of the solar car over the fuel driven cars which consume more fuel at slower speed to cover the same distance due to inefficient burning of the fuel.

V. CONCLUSION

Battery performance of a propsed solar car has been investigated while the car makes a trip from home to workplace of an office commuter under different road conditions, using a model developed in Matlab Simulink. It has been observed that energy requirement decreases significantly when the car runs at a slower speed due to lower air drag force at lower velocity. Thus for a city like Dhaka, where traffic congestion is a daily occurrence, solar/electric car will be a perfect mode of transportation as it is not only emission free but also consumes less energy under heavy traffic congestion, unlike the fuel driven cars which consumes more energy and emit more toxic gases under such condition. A detailed performance study of the proposed solar car under different traffic and weather conditions that also includes the solar panels is currently under way.

REFERENCES

[1] S. Ahmed, A. H. Zenan and M. M. Rahman, "A two-seater light-weight solar powered clean car: Preliminary design and economic analysis," in *3rd Int. Conf. on the Develop. in Renewable Energy Technology (ICDRET), 2014*, May 2014.

[2] T. M. A. Khan, S. Rahman, M. K. Afgani and K. E. Fahim, Solar car, Dhaka: BRAC University, 2014 [Online]. Available:http://dspace.bracu.ac.bd/bitstream/handle/10361/3228/09221020.pdf?sequence=1

[3] H. L. Chan and D. Sutanto, "A new battery model for use with battery energy storage systems and electric vehicles power systems," *IEEE Trans. Energy Convers.,* vol. 1, pp. 470-475, January 2000.

[4] R. Carter, A. Cruden, P. J. Hall and A. S. Zaher, "An improved Lead-Acid battery pack model for use in power simulations of electric vehicles,"," *IEEE Trans. Energy Convers.,* vol. 27, no. 1, pp. 21 - 28, 2012.

[5] R. Tariq, S. Sabbir and S. Afrin, Dynamic electrical model of sealed Lead-Acid battery for EV simulation, Dhaka: BRAC University, 2014.

[6] S. Leitman and B. Brant, Build Your Own Electric Vehicle, Third Edition, McGraw Hill Professional, 2013.

[7] J. P. Dunlop, "Batteries and charge control in stand-alone photovoltaic systems fundamentals and application," Florida Solar Energy Center, Cocoa, 1997.

Enhancement of Device Performance with Optimized Absorber Layer in CIGS Solar Cell

Sharmin Aktar Chowdhury, Md. Shah Alam
Department of Applied Physics, Electronics & Communication Engineering
University of Chittagong
Chittagong-4331, Bangladesh
Sharmin_apece1291@yahoo.com, shah.alam@cu.ac.bd

***Abstract*— Numerical simulation of CIGS solar cell has been carried out in this study to investigate the performance of the solar cell with different band-gap and thickness of the absorber layer. In this paper, we also introduce the effect of Ga content on solar cell material parameters. The aim of this work is to check the device performance like open circuit voltage, short circuit current density, fill-factor and efficiency with the change of thickness and band-gap of the absorber layer. It is shown that, by optimizing the CIGS absorber layer it is possible to achieve an AM 1.5G conversion efficiency of greater than 22% which is an increased value than presently reported.**

Keywords—CIGS, band-gap, thickness, Solarcell, simulation.

I. INTRODUCTION

A solar cell is a form of photoelectric cell which generates electrical power by the photovoltaic effect. It is done by converting the sunlight into electricity directly [1]-[2]. Photovoltaic industry has grown rapidly in the last several years. Now, worldwide total installed capacity of photovoltaic reached at least 178 GW at a cost less than $1/W till date. The total output power is now greater than 200 billion kWh, which represents 1 percent demand of worldwide electricity [3]-[4]. So it is strongly desirable to raise the power conversion efficiency while reducing the costs also. It is predicted that the installation rate will grow at a double digit of 16-25 percent and in the range of 55-57 GW at the end of 2015.

Thin film PV cell is a second generation solar cell which uses <1% of the expensive raw materials compared to other wafer based solar cell. So significant price drop can be gain by per watt peak capacity. It is made on a substrate like glass, plastic or metal by depositing one or more thin layer or thin film of photovoltaic material on it [5]. Thin film solar cells are commercially used in several technologies like CdTe, CIGS, and amorphous Si etc. Thin film PV technology is for more than 90% based on silicon as source material and these are low-cost alternatives [6]. Again, CIGS is one of the most promising I-III-VI_2 chalcopyrite photovoltaic materials for thin film solar cell technology [7]. These are highly attractive because of their tunable band-gap, radiation hardness and excellent outdoor stability on the earth. Copper Indium Gallium Deselenide ($Cu(IN_{1-x}Ga_x)se_2$) based solar cell exhibits superior conductivity and higher efficiencies due to native defects [8]-[9]. Recently, CIGS solar cell efficiency has been claimed a record value of 21.7% [10]. CIGS is a compound semiconductor material which has a high absorption coefficient of more than 10^5/cm for 1.5eV band-gap. CIGS solar cell has the advantage of presenting a thin active layer due to direct band-gap of the material. Much information is available in the literature regarding single-junction CIGS solar cell. To improve the overall performance of the solar cell, increasing the open circuit voltage V_{OC} and fill-factor (FF) is highly desirable. Because increased open-circuit voltage (V_{OC}) minimizes the interconnection losses in the manufacture of cell modules. [11]. The optical band-gap of CIGS increases with the use of Gallium which finally increases the open-circuit voltage (V_{OC}) and lowers costs as compared to pure CIS. Again, Cu deficiency increases the majority carrier concentration by increasing the number of Cu vacancies. Because when the films are Cu deficient, its surface layer form an ordered defect compound (OVC) by forming a p-n homo-junction at the interface [12]. To reach the band-gap of 1.5ev which is ideal for a single junction CIGS, a [Ga/(Ga+In)] of 0.7 is optimal. But device performance drops off when the ratio exceeds 0.3 [13].

In this study, we tried to optimize the band-gap as well as the thickness of the absorber layer and enhanced the solar cell device performance.

II. SIMULATION METHODOLOGY

A. Cell Structure

The structure of the studied solar cell based on Copper Indium Gallium Deselenide (CIGS) consists of the following layers: Soda lime glass substrate (SLG) of about 1-3mm thickness which has shown a substantial increase in open-circuit voltage (V_{OC}), Molybdenum back contact generally deposited by sputtering which reflects most unabsorbed light back into the CIGS absorber, a p-type CIGS absorber layer and n-type CdS buffer layer deposited on top of the absorber layer. Next the buffer layer is overlaid with a thin, intrinsic ZnO layer (i-ZnO) which is capped by Al doped ZnO window layer. The Al doped ZnO serves as a transparent conductive oxide to collect and move electrons out of the cell [14]-[15]. The schematic diagram for a typical ZnO/CdS/CIGS solar cell structure is illustrated in Fig 1.

978-1-4673-9257-0/15/$31.00 ©2015 IEEE

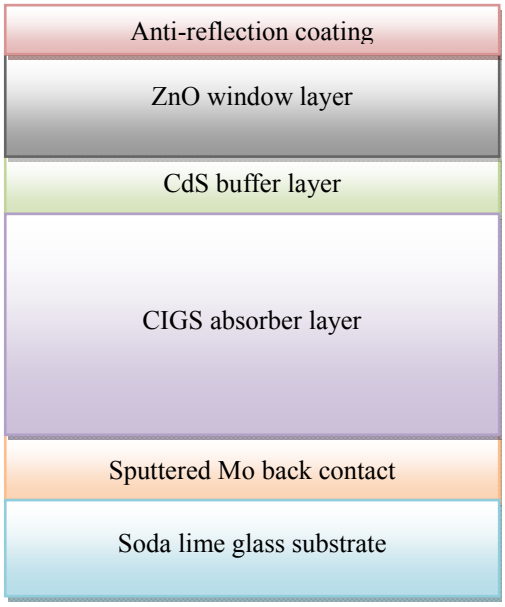

Fig. 1. CIGS solar cell structure used for the simulation

B. Numerical Simulation

In our present work, numerical simulation of CIGS thin film solar cell has been investigated by using the latest version 3.3.0.1 of SCAPS i.e. Solar Cell Capacitance Simulator. This is a 1D solar cell simulation program which developed in the University of Gent at the department of EIS, allows the definition of thin film solar cell devices stacks of layers with a large set of parameters [16]-[17]. SCAPS is originally developed for devices or the solar cell structures specially CdTe and $CuInSe_2$ family [18]. The objective of the numerical method is to test the device performance without fabrication, for analysis of the effect of material parameters variations and finally determining optimal values for the best solar cell performance. SCAPS solves the fundamental solar cell equations like Poisson's equation, the continuity equation for electrons and the continuity equation for hole in one-dimension and in steady-state condition. Generally, Poisson's equation for semiconductor device is [19]

$$\frac{\partial}{\partial x}\varepsilon(x)\frac{\partial}{\partial x}\psi(x)=q\left(p(x)-n(x)+N_D-N_A+\rho_{def}\right) \quad (1)$$

Where, n, p are the concentrations of free electrons and holes, n_t, p_t are the concentration of trapped electrons and holes, N_D, N_A are the concentrations of the ionized donors and acceptors, ε is the dielectric permittivity of semiconductor, q is the electron charge and ψ is the electrostatic potential. Here, the drift-diffusion approach is used as a function of device length, x.

Again, the continuity equation in steady state conditions for electrons and holes are:

$$\frac{1}{q}\frac{d}{dx}J_n=R_n(x)-G(x) \quad (2)$$

$$\frac{1}{q}\frac{d}{dx}J_p=G(x)-R_p(x) \quad (3)$$

Where, q is the electron charge, J_n and J_p are the electrons and holes current density, R_n and R_p are the electrons and hole recombination velocities and G is the optical generation rate.

The photocurrent which flows in opposite direction to the dark current I_D is the maximum current when the voltage across the solar cell is absolutely zero. It is caused by the generation and collection of light generated carriers. I-V characteristics of a p-n junction solar cell under illumination can be expressed as:

$$I=I_{ph}-I_{01}\left(qV/k_BT-1\right) \quad (4)$$

Where, I_{01} is the saturation current and I_{ph} is the photocurrent.

At V=0, short-circuit current is equal to the photo-generated current [20] i.e.

$$I_{sc}=I_{ph} \quad (5)$$

For removing the dependence of the solar cell area, it is usually defined short-circuit current I_{SC} as the short circuit current density J_{SC}. The equation for the short-circuit current density J_{SC} for the solar cell with perfectly passivated surface and uniform generation is as follows [21]:

$$J_{sc}=qG\left(L_n+L_p\right) \quad (6)$$

Again, open-circuit voltage V_{OC} is the maximum voltage available through the solar cell when the current is absolutely zero. Open-circuit voltage can be expressed as:

$$V_{oc}=V_T\ln\left[\frac{I_{sc}}{I_{01}}+1\right] \quad (7)$$

Where, V_T is the thermal voltage and is equal to K_BT/q. the open-circuit voltage can be increased either by increasing substrate doping density or increasing the minority carrier lifetime in the solar cell. High shot-circuit current density J_{SC} is very desirable because it can also enhance the open-circuit voltage V_{OC}, hence we can get an enhanced performance of the device. Typical values of open-circuit voltage V_{OC} ranges from 0.5 to 0.7V [20]-[21].

The fill-factor of the solar cell is the parameter in which in conjunction both the operating points corresponding to I_{SC} and V_{OC} determines the maximum power output from a solar cell. It is a measure of the squareness of the I-V characteristics and is expressed as:

$$F.F.=\frac{P_m}{V_{oc}I_{sc}} \quad (8)$$

Where, P_m is the maximum power output of the p-n junction solar cell and is equal to V_mI_m. Fill-factor depends on the series and shunt resistances and the diode ideality factors. For solar cell, fill-factor is always less than 1 [1], [20], [22].

The ratio between the output electrical power at the maximum power point on the I-V curve to the input electrical power is called the efficiency of the solar cell and is defined as:

$$\eta = \left(\frac{P_{out}(\max)}{P_{in}} \right)\% \qquad (9)$$

Where, P_{in} is the input power from the sunlight, P_{max} is the maximum power output and is equal to $V_{OC}I_{SC}FF$ and η is the solar cell efficiency [20], [21].

III. SIMULATION PARAMETERS

For the calculation of device performance, we need to know the values of the parameters. In this work, we used three layers for the simulation. These are: 1) p-type CIGS absorber layer, 2) n-type CdS buffer layer and 3) ZnO window layer. Here, the surface recombination velocities were set at 10^7 cm/s for both electrons and holes. The AM 1.5G solar spectrum is used and the temperature is set at 300k for this numerical simulation.

The CIGS absorber layer has adjustable band-gap by tuning ratio [12]. Here, band-gap of the CIGS absorber layer was varied from 1.04 to 1.69eV as the Ga content varied from x=0 to x=1, according to the equation:

$$E(x) = 1.02 + 0.67x + 0.11x(x-1) \qquad (10)$$

This band-gap alteration ability makes them perfect candidates for high performance thin film device [23]. Varying the ratio in material affects various parameters in the absorber such as band-gap, optical absorption and defect concentration which influence the solar cell performance. In our simulation, solar cell performance was examined by varying the absorber layer thickness and band-gap and keeping all other parameters at a fixed value.

TABLE I gives the summary of different layer parameters used in this paper.

TABLE I. MATERIAL PARAMETER VALUES FOR THE SIMULATION

Properties	p-CIGS	n-CdS	i-ZnO
W(μm)	variable	0.050	0.200
E_G(eV)	variable	2.4	3.3
X(eV)	4.5	4.2	4.45
Dielectric Permitivity	13.6	10	9
N_C(cm^{-3})	2.200E+18	2.200E+18	3.100E+18
N_V(cm^{-3})	1.800E+19	1.800E+19	1.800E+19
V_n(cm/s)	1.000E+7	1.000E+7	1.000E+7
V_p(cm/s)	1.000E+7	1.000E+7	1.000E+7
μ_n(cm^2/V-S)	100	100	100
μ_p(cm^2/V-S)	25	25	25

IV. RESULT AND DISCUSSION

A. *Effect of absorber layer band-gap:*

The resulting performance parameters are determined by using current-density voltage characteristics.

The simulation results of the solar performance corresponding to different band-gap of the absorber layer are given in TABLE II.

TABLE II. SIMULATED RESULT FOR VARYING BAND-GAP

Eg(eV)	V_{OC}(V)	J_{SC}(mA/cm^2)	FF(%)	η(%)
1.02	0.53	33.15	79.14	13.99
1.05	0.56	33.05	79.67	14.81
1.1	0.61	32.99	80.59	16.25
1.2	0.71	33.0	82.03	19.22
1.3	0.81	33.04	82.52	22.18
1.4	1.27	33.06	57.35	24.05
1.5	1.40	33.07	52.43	24.24
1.67	1.40	33.07	52.31	24.25

From our simulation it is originated that, the efficiency of solar cell increases with the increase of band-gap of the absorber layer. As the band-gap of CIGS absorber layer varied from 1.02 to 1.5eV, the solar cell efficiency increased from 13.99 to 24.24% and the open-circuit voltage (V_{OC}) is also increased from 0.53 to 1.40V as the recombination current falls. It is mainly depends on the saturation current I_o. Further increase in CIGS band-gap has no significant effect on these parameters. Again, it has very little effect on short-circuit current density (J_{SC}).

However, band-gap of the CIGS absorber layer affects the fill-factor of the cell. As the band-gap increased beyond 1.3eV, fill factor decreased sharply. Because increased Ga content causes higher recombination rate and lower carrier lifetime, for which recombination in SCR may overweight the recombination outside of this region. So, ideality factor in accordance with the FF will be decreased due to defect in SCR. This is a key parameter in evaluating solar cell performance. Solar cell with a high fill factor is very desirable, because small amount of the current is dissipated by internal losses [13].

Fig 2 shows the effect of band-gap variation on the performance of CIGS solar cell.

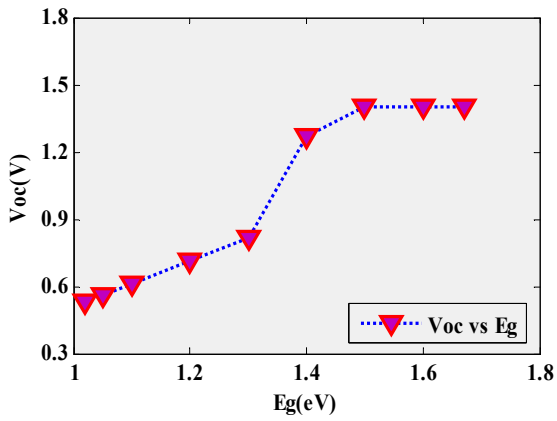

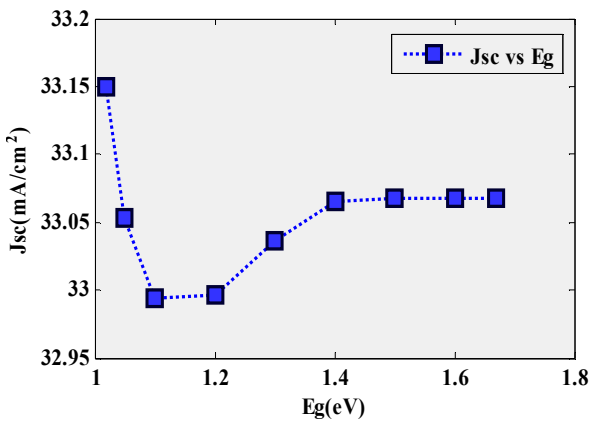

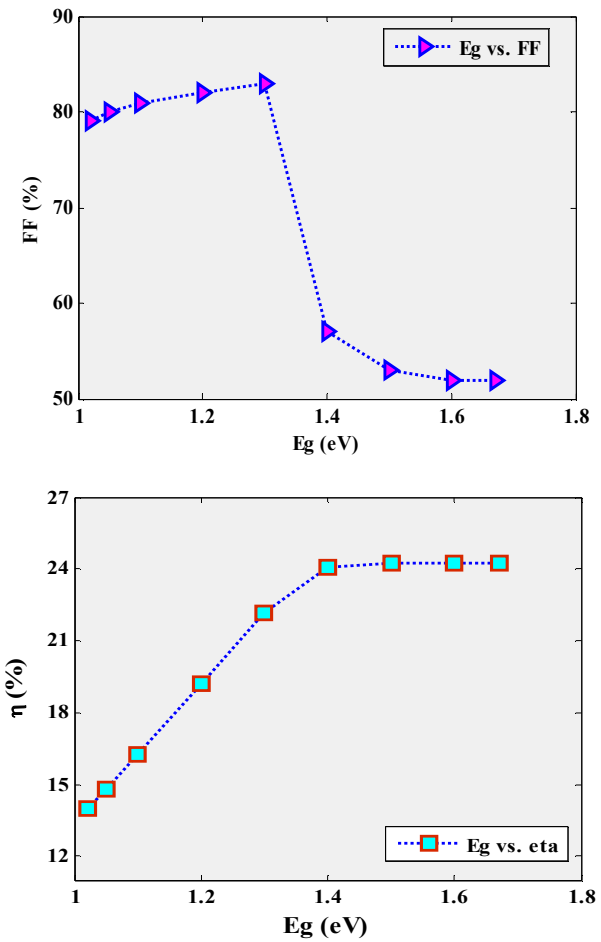

Fig. 2. Band-gap effect on solar cell performance

The trade of among these phenomena is that, an optimum band-gap of 1.3eV is proposed in which the device have a high fill factor without sacrificing its V_{OC} or J_{SC}. The result yields a maximum efficiency of 22.18%.

B. *Effect of absorber layer thickness:*

CIGS solar cell has an absorption which is more than 10 times better than for crystalline silicon. Hence, it is possible to make a solar cell which is very thin compared to well known silicon solar cell. Various researches have reported the impact of the thickness of CIGS absorber layer on solar cell performance parameters. In our simulation, CIGS layer thickness was varied from 0.3µm to 3µm, where the band-gap was kept in the optimum value at 1.3eV and all other layer parameters were kept the same as before. The simulation results for varying thickness of the absorber layer are given in TABLE III.

TABLE III. SIMULATED RESULT FOR VARYING THICKNESS

W(µm)	V_{OC}(V)	J_{SC}(mA/cm^2)	FF(%)	η(%)
0.3	0.69	26.14	69.09	12.54
0.5	0.75	27.30	77.65	15.93
0.7	0.77	28.94	79.70	17.75
0.9	0.78	30.10	80.81	18.99
1.1	0.79	30.94	81.58	19.90
1.5	0.80	32.11	82.43	21.16
2.0	0.81	33.04	82.52	22.18
2.5	0.83	33.66	82.22	22.86
3	0.84	34.10	81.80	23.35

Fig 3 shows the effect of thickness variation on the performance of solar cell.

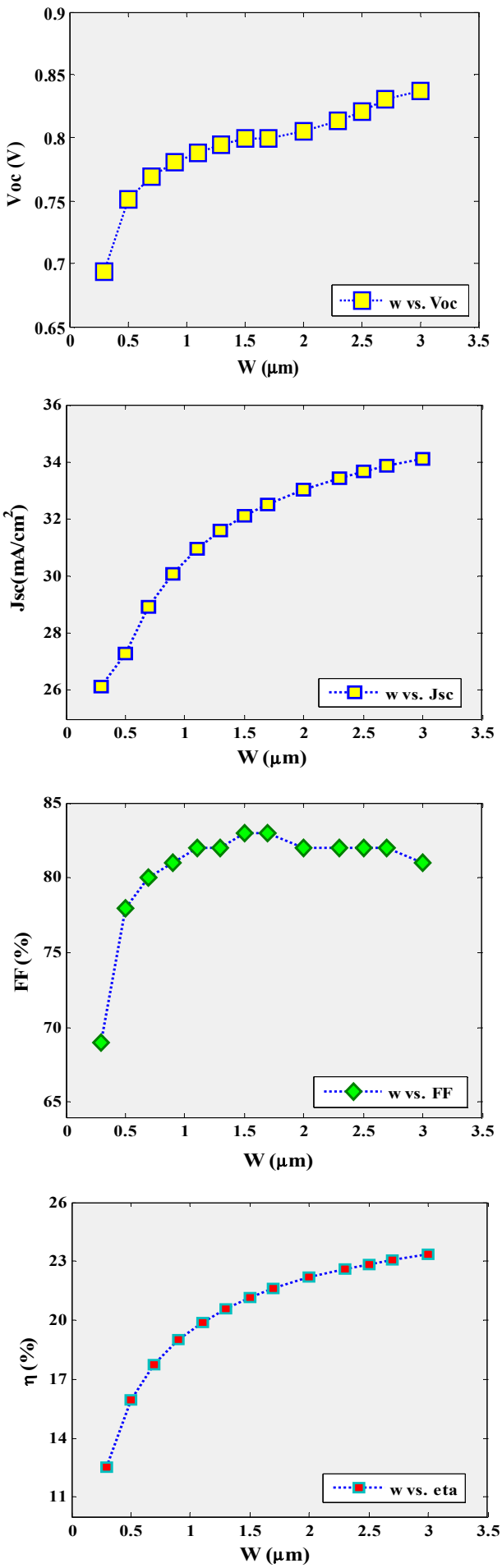

Fig. 3 Thickness effect on solar cell performance

Based on the simulated result it is seen that, device performance was considerably influenced by the absorber layer thickness. The J-V curve reveals that as the thickness of the absorber layer CIGS increases from 0.3 to 2µm, V_{OC} increases from 0.69 to 0.81V due to decreased recombination probability of photon-generated carriers. Again, when the thickness of CIGS increases beyond 2µm, V_{OC} increases very slowly.

Again, in the case of $J_{SC,}$ it follows the same trend with the increasing thickness of the absorber layer. As in fig, Fill-factor increases with the thickness from 0.3 to 2µm and after this it decreases slowly. So, we considered the optimum value of the CIGS absorber layer at 2µm in which the efficiency was 22.18%.

V. CONCLUSION

In this study, numerical optimization has been performed by adjusting parameters like thickness and band-gap of the absorber layer CIGS and it is shown that this parameters has crucial effect on solar cell performance. Simulation results exhibit that, increased solar cell efficiency is obtained by increasing the thickness and band-gap. Other performance parameters like V_{OC}, J_{SC} and FF is also enhanced by optimizing CIGS absorber layer thickness at 2µm. In the case of band-gap it is seen that, after 1.3eV fill-factor drops significantly. So we `optimized the band-gap of the absorber layer at 1.3eV and it is demonstrated that a maximum efficiency of 22.18% can be obtained by CIGS solar cell, where the presently reported best efficiency is 21.7%.

REFERENCES

[1] Antonio Luque, Steven Hegedus, "Handbook of Photovoltaic Science & Engineering," page 3, ISBN 0-471-49196-9, 2003

[2] Pearce, Joshua, "Photovoltaic - A path to Sustainable Future," Vol. 34, No. 7, pp. 663-674,2002

[3] David Feldman, Galen Barbose, Robert Margolis, Ted James, Carolyn Davidson, et al. "Photovoltaic System Pricing Trends - Historical, Recent and Near Term Projection," 2014 edition, NREL

[4] Snapshot of Global PV System 1992-2014, IEA, International Energy Agency, 2015

[5] Vincent Dusastre, Jean-Marie Tarascon, Michael Gratzel, "Materials for Sustainable Energy", ISBN-13:978-981-4317-64-1, 2011

[6] Van Swaaij, Smets, A.H.M Zeman, "Thin Film Si Technology for Highly Efficient Solar Cell," IEEE Bipolar/BiCMOSCircuits and technology meeting (BTCM) , page 1-7, ISSN: 1088-9299, 2012.

[7] Shogo Ishizuka, M. Lorelle Mansfield, Clay DeHart, et al. "Rapid Fabrication of $Cu(In,Ga)Se_2$ Thin Films by the Two-Step Selenization Process," 38th IEEE Photovoltaic specialist conference (PVSC), vol. 2, page 1-7, 2012

[8] K. Ramanathan, M. A. Contreras, C. L. Perkins, S. Asher, F. S. Hasoon, et al. "Properties of 19.2% efficiency $ZnO/CdS/CuInGaSe_2$ thin-film solar cells," Prog in Photovooltaic: Research and Application, vol.11, issue 4, 2003

[9] G F Novikov, E V Rabenok, M J Jeng, L B Chang, "The study loss kinetics of current carriers in copper-indium-gallium selenide by microwave photoconductivity method," Journal of Renewable and Sustainable Energy, vol. 4, issue 1, 2012

[10] M. A. Green, Keith Emery , Yoshihiro Hishikawa , Wilhelm Warta and D. Ewan Dunlop, "Solar Cell Efficiciency tables(version 46)", Progess in Photovoltaics: Research and Applications, Volume 23, Issue 7, June 2015

[11] Wan Fucheng, Tang Fuling, Xue Hongtao, Lu Wenjiang, Feng Yudong, et al., "Effects of defect states on the performance of CuInGaSe2 solar cells", Journal of Semiconductors, Vol. 35, No. 2, February 2014

[12] O. Lundberg, M. Edoff, and L. Stolt, "The effect of Ga-Grading in CIGS thin film solar cells," Thin Solid Films 480-481, PP. 520-525, 2004

[13] I. Repins, B. Egaas, J. Scharf, et al., "Characterization of 19.9% Efficient CIGS Absorbers," 33rd IEEE Photovoltaic Specialists Conference, 2008

[14] P. Udai Singh, Surya Patra,"Progress in Polycrystalline Thin-Film $Cu(In,Ga)Se_2$ Solar Cells" International Journal of Photoenergy, article ID 468147, 2010

[15] M. Buegelman, P. Nollet, S. Degrave, "Modelling polycrystalline semiconductor solar cell," Thin Solid films, vol. 361, pp. 527-532, 2000

[16] M. Burgelman and J. Marlein, "Analysis of graded band gap solar cells with SCAPS", Proceedings of the 23rdEuropean Photovoltaic Solar Energy Conference, p.2151-2155, 2008

[17] J. Vercharaegen, M. Burgelman, "Numerical modelling of intra-band tunneling for heterojunction dolar cell in SCAPS," Thin Solid Films 515: 6276–6279, Elsevier, 2007

[18] A. Niemegeers and M. Burgelman, "Numerical modelling of ac-characteristics of CdTe and CIS solar cells," Proc. 25nd IEEE Photovoltaic Specialists Conference, pp. 901-904, 1996

[19] S.M. Sze., K. N. G. Kwok , "Physics of semiconductor device," 3rd edition, New York: John Wiley & Sons Press, ISBN-13:978=0471-14323-9, 2007

[20] Yoshihiro Hamakawa, "Thin film Solar Cell: Next generation Photovoltaics & Its Applications," ISBN-3-540-43954-5, Springer, 2004

[21] S. Sheng Li., "Semiconductor Physical Electronics", Page 334-335, ISBN-13:978-1-4612-7635-7,1993

[22] Stephen J Fonash, "Solar Cell Device Physics", 2nd edition, ISBN 978-0-12-374774-7, Elsivier, 2012

[23] Antonino Parisi, Recardo pernice, et al., "Graded Carrier Concentration Absorber Profile for High Efficiency CIGS Solar Cells," International Journal of Photoenergy, article ID 410549, 9pages, 2015

A New Prediction Model for Solar Irradiance using Ant Colony Optimization and Neural Network

Md. Shahid Iqbal[1, *], Md. Monirul Kabir[2], H.M. Imran Hassan[3], Md. Janibul Alam Soeb[4], Md. Ataullah Mishkat[5], and Vobes Ray[6]

[1, 3, 4, 5, 6] Department of EEE, Mymensingh Engineering College, Bangladesh

[2] Department of EEE, Dhaka University of Engineering & Technology, Bangladesh

[*] Email: shahidiqbal_05@yahoo.com

Abstract—**In this paper, a new prediction model for solar irradiance has been proposed using ant colony optimization (ACO) and neural network (NN), called as ACOSIP. In ACOSIP, the most salient climatological features are selected in order to enhance the solar irradiance prediction (SIP) accuracy. To implement such idea, ACO search technique utilizes the advantages of the combined activities of the features by considering the correlation information among the features and the outcome of NN. Thus, ACOSIP introduces the wrapper and filter approaches in its feature selection process. To make an effective ACO search, two sets of new rules have been designed for pheromone update and heuristic information measurement. To evaluate the performance of ACOSIP, 12 solar irradiance data samples in between the year of 2000-2013 were collected from Bangladesh Meteorological Department (BMD). Experimental results show that ACOSIP can select six most salient features easily with increasing the prediction accuracy, which are longitude, latitude, day light hour, max temp., min temp., and humidity. In addition, the averaged prediction accuracy of ACOSIP for 35 stations of BMD in testing case is 99.74% including the MAPE of 0.26%. The proposed ACOSIP also represents high correlation of 99.93% in between the actual and forecasted data.**

Keywords—Solar radiation forecasting, Artificial neural network, Ant colony optimization and Feature selection .

I. INTRODUCTION

Solar energy research is based on solar radiation data, but is not available for most of the sites due to non-availability of solar radiation measuring equipments at the meteorological stations. Therefore, it is essential to predict solar radiation for a location using several climatic variables. Furthermore, the application of solar energy among the different types of renewable energy sources has more attentions nowadays throughout the whole world that might be increasing in the following days.

A number of works has already been published in the literature related to modeling and prediction of solar radiation for various solar energy applications [1]. Analytic formula [3], numeric simulation or statistical approaches [4] are developed two or three decades before to predict solar irradiance. But, these prediction models resulted in large errors. To overcome these limitations, NN-based models [3-9] has been introduced in the recent years for predicting the solar irradiance.

Mohandas proposed a model in [5] where solar irradiance data was collected from different 41 stations in Saudi Arabia to train the NN for finding the irradiance prediction accuracy. The incorporated input variables are latitiude, longitude, altitude and sunshine duration. The results for the testing stations are within 16.4%. In [6], NN-based model used 12 various Indian weather stations with different climatic conditions. The results of RMSE in NN model is in between 0.0486-3.562 for Indian region. On the other hand, S. Rahman's proposed model [7] used data for Abha city of Saudi Arabia in NN training where the result of MAPE is 4.49%. S. Quaiyum proposes a SIP model [8] for Bangladesh obtained the result of MSE is 0.29%. Hasni proposes a SIP model [9] for south-western region of Algeria where the MAPE obtained is 2.9971%. In [3], Kalogirou has reviewed the use of NN in the applications of renewable energy systems. In addition, Mellit [4] has shown NN for sizing of PV systems.

According to the afore-mentioned proposed models for predicting the solar irradiance, it has been observed that, NN-based models cannot perform well in predicting the solar radiation using all the available features. The reason is that, the performance of NN always degrades if some irrelevant features exist in the available feature set [10]. Therefore, selecting those irrelevant features from the original set is a crucial work in the NN-based SIP process. In this regard, Will tries in [11] to select climatic variables for 14 weather stations in North Argentina using niching genetic algorithm.

However, in this paper, an ACO-based SIP model has been proposed to select the most relevant features to increase the prediction performance of NN. ACO here incorporates two techniques in its weight update rules, which are wrapper and filter approaches.

The remainder of this paper is organized as follows. ACOSIP are broadly discussed in Section 2. Simulation results, comparison to other methods, are reported in Section 3. Short conclusions with few remarks are given in Section 4.

II. PROPOSED ACOSIP MODEL

To determine the best climatological features in increasing the solar irradiance accuracy, ACOSIP uses hybrid ACO based search technique. Furthermore, to obtain a small subset of salient features, the ants are guided at its traversal period upon the feature space. For comprehensibility, the proposed ACOSIP model can be discussed by the flowchart shown in Fig. 1, which is described as follows:

i) Let D is a given data set with n distinct features. Initialize the pheromone trails τ and the heuristic information η of all n features by giving equal values to τ and η.

ii) Measure the correlation data of individual n features using correlation measurement scheme. The reason is to select more distinct features by ants. Thus, the ants are guided to select the features which are less correlated among the original features.

iii) Motivate the ants to choose location information (i.e., latitude and longitude) at each iterations.

iv) Generate a set of artificial A ants equivalent to n, i.e. $A = n$.

v) Subset size, s is determined prior to SC for each of the A ants. By using the conventional probabilistic transition rule [13] for selecting features with which to construct the subsets as follows:

$$P_i^A(t) = \begin{cases} \dfrac{[\tau_i(t)]^\alpha [\eta_i(t)]^\beta}{\sum_{u \in j^A} [\tau_u(t)]^\alpha [\eta_u(t)]^\beta} & if \;\; i \in j^A \\ 0 & otherwise \end{cases} \quad (1)$$

where j^A is the set of effective features, τ_i and η_i are the pheromone and heuristic values for the feature i (i= 1, 2,…..,n). The relative importance of the pheromone value and heuristic information is decided by α and β. Eq. (1) shows random behavior in subset construction initially, since the initial value of τ and η for all individual features are equal.

vi) After completion of subset construction by all ants, then system move forward, on the other hand system will back to Step 4.

vii) The subsets $R^A(t)$ is evaluated and measure the performance using MAPE $M(R^A(t))$. Here, $R^A(t)$ refers to the effective sets constructed by A ants at iteration t.

Step 8) The $R^l(t)$ (local best subset) among all $R^A(t)$ and the R^g (global best subset) among all $R^l(t)$ is selected with the searching methodogy. Here, t = 1, 2,3,…….,I where I is a number of iterations.

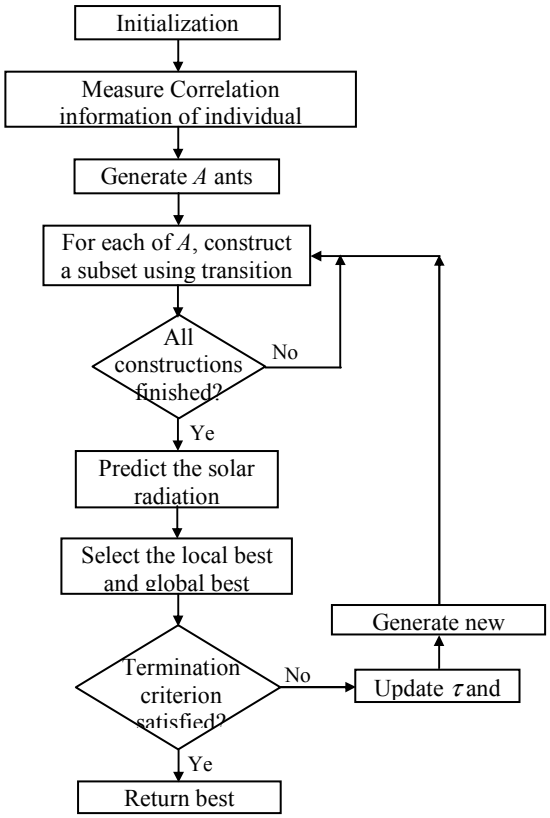

Figure 1. Flowchart of ACOSIP

Step 9) Check whether $R^l(t)$ attains a predefined SIP performance, or the algorithm execution reaches an iterative limit I_{th} and then terminate the selection process. Note that, at iteration I_{th} the model cannot find anymore variation in R^g. Otherwise continue the FS and save the evaluation results of all local best subsets, $M(R^l(t))$ for further use.

Step 10) The values of τ and η for all the features will be updated according to the rules of pheromone update and heuristic value measurement, respectively.

Step 11) A new set of artificial A ants will be generated and proceed the scheme similarly.

Clearly, the idea behind ACOSIP is straightforward, which used ACOFS algorithm to guide the ants in bounded region (between 3 to 6) of search space and providing mixed technique to the ants search. To select the distinct features which is helpful for effective learning of NN, a correlation information measurement procedure has been integrated, so performed only once throughout the FS process.

III. HYBRID SEARCH PROCESS

In ACOSIP, a hybrid search technique has been introduced that is composed by wrapper and feature approaches. These

approaches are embedded in the newly designed two sets of rules, which are pheromone update and heuristic value. Note that, these both rules are involved with correlation information measurement of individual features, which are further described as follows:

A. Pheromone Update Rule

On basis of random and probabilistic phenomena, a set of two pheromone update rules are introduced from the original one mentioned in [10] as follows:

Random case: The rule presenting in Eq. 2 is selected from [10], in which case second term is divided by f_i. The features are selected to construct subsets randomly according to their experiences. This enhances the exploration capability of ants. The rule has been accepted as follows:

$$\tau_i(t+1) = (1-\rho)\tau_i(t) + \frac{1}{f_i}\sum_{A=1}^{n}\Delta\tau_i^A(t) + e\Delta\tau_i^g(t) \tag{2}$$

$$\Delta\tau_i^A(t) = \begin{cases} M(R^A(t)) & if\ i \in R^A(t) \\ 0 & otherwise \end{cases},$$

$$\Delta\tau_i^g(t) = \begin{cases} M(R^l(t)) & if\ i \in R^l(t) \\ 0 & otherwise \end{cases}$$

Here, i refers to the number of feature (i = 1, 2,……n),and f_i is the count for the specific selected feature i in the current iteration. $\Delta\tau_i^A(t)$ is the value of pheromone taken by the local update for feature i, which is included in $R^k(t)$ at iteration t. Similarly, the global update, $\Delta\tau_i^g(t)$,is the value of pheromone for feature i that is included in $R^l(t)$. Finally, ρ and e are the pheromone decay value and elitist parameter, respectively.

Probabilistic case: Eq. (3) shows the updated pheromone rule (probabilistic case).

$$\tau_i(t+1) = (1-\rho)\tau_i(t) + \sum_{A=1}^{n}\Delta\tau_i^A(t) + e\Delta\tau_i^g(t) \tag{3}$$

$$\Delta\tau_i^A(t) = \begin{cases} M(R^k(t)) \times C_i & if\ i \in R^A(t) \\ 0 & otherwise \end{cases},$$

$$\Delta\tau_i^g(t) = \begin{cases} M(R^l(t)) \times C_i & if\ i \in R^l(t) \\ 0 & otherwise \end{cases}$$

Here, feature I is renown by the global update. The $\Delta\tau^g$ is provided only to those features that are actually efficient, because, global update has an important part in selecting the effective features in ACOSIP.

B. Heuristic Value Measurement

In this paper, we propose a set of new heuristic value estimation rule depending on two basic phenomena in SC. To describe the attractiveness for each features heuristic value, η, is important. So, to overcome the greediness η, is therefore necessary [12], and finally an effective solution may be appeared.

Random case: In the initial stage, the ants are involved to construct the feature subsets randomly, and the heuristic value of all features i can be estimated as follows:

$$\eta_i = \frac{1}{f_i}\sum_{A=1}^{n} M(R^A(t))(1+\phi e^{-\frac{|R^A(t)|}{n}})$$
$$if\ i \in R^A(t) \tag{4}$$

Probabilistic case: In the following iterations, after constructing subsets on the basis of the probabilistic behavior, the following formula is used to estimate η for all features i:

$$\eta_i = f_i\varphi_i\sum_{A=1}^{n} M_a(S^k(t))C_i(1+\phi e^{-\frac{|S^k(t)|}{n}})$$
$$if\ i \in S^k(t) \tag{5}$$

In these two rules, φ_I refer to the count of a particular selected feature I from previous iterations to the current iteration, except for the initial iteration. C_i refers to the correlation value for feature i. The aim of including C_i is based on the following two factors:(a) to select the more distinct features during SCs, and (b) enhancing the robustness of learning model. Thus, best features may be selected in the SC for different iterations, thus of course enhancing the prediction accuracy of the ACOSIP.

C. Correlation Value Measurement

In order to measure relationship between the climatological features which are used as the input pattern in ANN and to choose distinct features correlation information (CI) is important and useful statistics. To reduce the effect of features to each other and to increase the learning power of ANN we need more uncorrelated features set in training purpose. This information is providing to heuristic information measurement η of all individual features. In this work, Pearson product-moment correlation coefficient is used. The correlation coefficient, r_{ij} between two features, i and j is,

$$r_{ij} = \frac{\sum_p (x_i - \bar{x}_i)(y_j - \bar{y}_j)}{\sqrt{\sum_p (x_i - \bar{x}_i)^2}\sqrt{\sum_p (y_j - \bar{y}_j)^2}} \tag{6}$$

The correlation coefficient is computed for all possible combinations of features then ACOSIP computes the correlation of each feature. The correlation, Cor_i, of any feature i is

$$Cor_i = \frac{\sum_{j=1}^{n}|r_{ij}|}{n-1} \qquad i \neq j \tag{7}$$

where n is the number of features used. Then to find the uncorrelated features we use C_i, which is

$$C_i = 1 - Cor_i \tag{8}$$

IV. DATA COLLECTION

The significance of ACOSIP has been evaluated in this section on twelve well known climatological features as longitude (Ln), latitude (Lt), elevation (ev), year (y), month (m), station constant (sc), day light hour (DL), relative humidity(Rh), maximum temperature (Mat), minimum temperature (Mit), rainfall(Rf) and wind speed (Ws), and the solar radiation data is used as the target. These features have been used in many of solar radiation prediction models using ANN. In this study we use 14 years (2000 - 2013) monthly averaged data, for 35 stations, which are collected from Bangladesh Meteorological Department (BMD), Weather office.

V. METHODOLOGY

To verify the effectiveness of ACOSIP for FS and RP, a number of experiments have been carried out on ACOSIP. To justify the FS and RP task suitability in ACOSIP, one basic step need to be considered, namely, giving values for user-specified parameters such as $\eta, \tau, \alpha, \beta, \rho$ and ϕ, which are common for the all datasets. These parameters have been chosen after some runs. To achieve a level of balance between exploitation and exploration proper selection of the values of parameters is helpful of ants to select feasible features.

VI. EXPERIMENTAL RESULTS

The effectiveness of ACOSIP model is verified by a succession of experiments. To prove the strength of the proposed model 35 ACOSIP models have been designed for 35 stations and then results are being averaged to show the global strength of the model – shown in Table 1. As Table 1, the avg. results of PA and MAPE for 35 stations are 99.60 % (training), 99.49% (testing) and 0.42% (training), 0.49 (testing), respectively validated the ACOSIP structures for predicting solar irradiance.

TABLE I. AVERAGED PERFORMANCE RESULTS OF 35 MODEL OF ACOSIP

Local Investigated Data					
DATA	**Avg. PA (%)**	**Avg. MAPE (%)**	**Avg. RMSE (%)**	**Avg. MSE (%)**	**Avg. R (%)**
Training	99.60	0.42	0.244	0.077	99.81
Testing	99.49	0.49	0.289	0.104	99.72

TABLE II. PERFORMANCE RESULTS FOR WELL PERFORMED STATIONS

Station Names	**DATA**	**Avg. PA (%)**	**Avg. MAPE (%)**	**Avg. RMSE (%)**	**Avg. MSE (%)**
Chittagong	Training	99.79	0.21	0.0366	0.00135
	Testing	99.67	0.33	0.0576	0.00332
Dhaka	Training	99.86	0.14	0.0244	0.00059
	Testing	99.74	0.26	0.0454	0.00206
Khulna	Training	99.76	0.24	0.0419	0.00175
	Testing	99.66	0.34	0.0593	0.00352

Table 2 shows the results for different ACOSIP model of each station. The model of Dhaka region found to be best among the 35 models.

The effectiveness of FS algorithm and the prediction ability of ANN have been ascertained using the data for Dhaka region. In this respect the 15 independent runs for ACOSIP model for Dhaka have been performed and then averaged the results – shown in Table 3.

As Table 3, the PA and MAPE for training and testing case are 99.84%, 0.16% and 99.70%, 0.3%, respectively.

And as the value of R is higher (99.90%), so it can be easily understood that the ACOSIP model has stronger prediction capability.

Table 4 depicts the positive effect of feature selection strategy. PA is 99.74% with selected features.

Determination of the best solution in ACOSIP can be seen in Fig. 2, it can be showed that, the PAs varied with the size of those subsets and for the performances of the local best subsets.

The PAs were maximized in various points, but the best solution was selected (indicated by circle) by considering the reduced size subset.

How the selection of salient features in different iterations progresses in ACOSIP, Fig. 3 and Fig. 4 shows the scenario of such information for a single run.

We can see that, features 1, 2, 12, 7, 8 and 4received maximum values of τ and η so these features have a higher priority of selection.

Ultimately, a successful evaluation function NN model is used to find high- quality solutions for ACOSIP in prediction. As training process progresses and converges to a certain limit up to 40 epochs (Fig. 5(a)). However, the training is terminated, because at this instant validation error increases due to over training (Fig. 5(b)).

At the termination epoch we also observed that the number of hidden neuron is 3. Table 5 shows the correlation information that the selected features are highly uncorrelated.

TABLE III. PERFORMANCE OF ACOSIP MODEL AND RESULTS WERE AVERAGED OVER 15 INDEPENDENT RUNS.

Local Investigated Data For Dhaka Region For 15 Independent Run					
DATA	Avg. PA (%)	Avg. MAPE (%)	Avg. RMSE (%)	Avg. MSE (%)	Avg. R (%)
Training	99.84	0.16	0.027941	0.000781	99.90
Testing	99.70	0.3	0.052889	0.002745	99.82

TABLE IV. PERFORMANCE (AVERAGED) OF ACOSIP MODEL FOR FEATURE SELECTION OVER 15 INDEPENDENT RUNS.

Avg. Result for all features				Avg. Result for selected features			
N	SD	PA (%)	SD	ns	SD	PA (%)	SD
12	0.00	95.5	1.12	6.13	0.82	99.74	0.40

TABLE V. CORRELATION INFORMATION (CI) OF SELECTED FEATURES

Features	Ln.	Lt.	DL	Rh	Mat	Mit
Correlation	4.8	5.91	5.83	7.6	5.96	8.96
Less Correlated	95.2	95.09	90.17	92.4	94.04	91.04

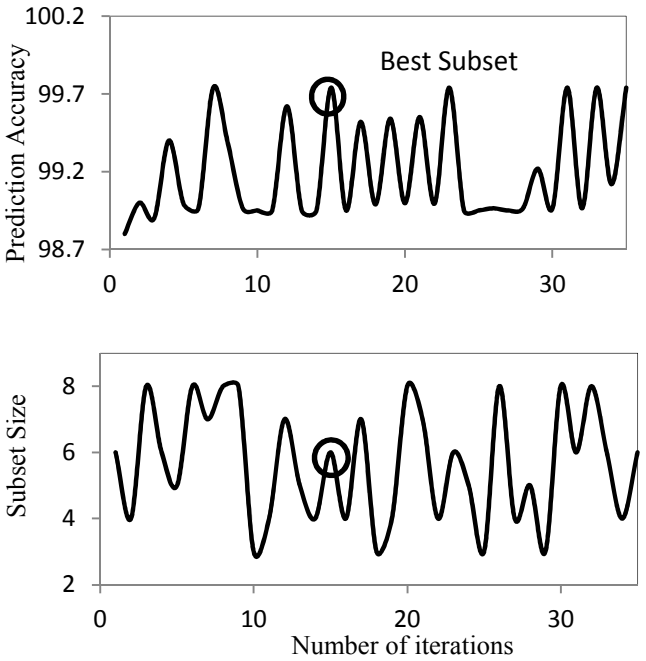

Figure 2. Finding best subset of the features for a single run.

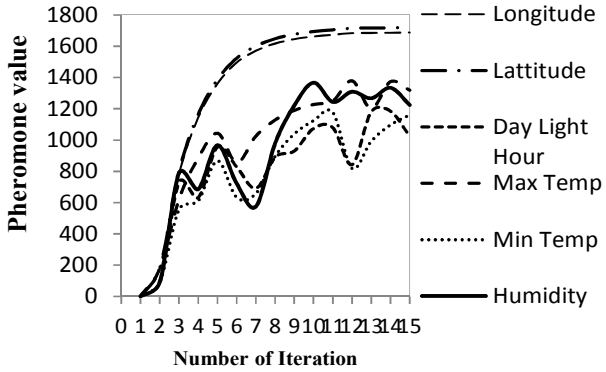

Figure 3: Distribution of pheromone level in different iterations for a single run.

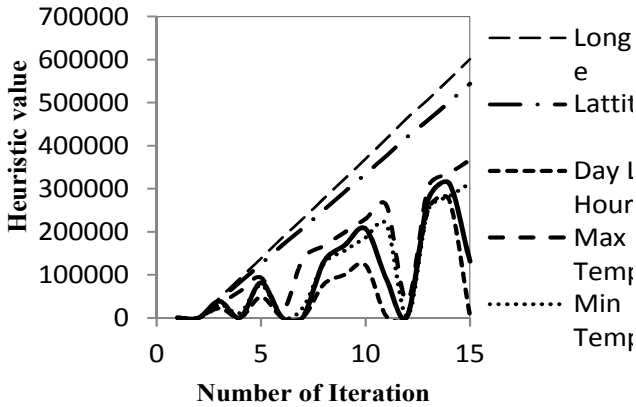

Figure 4: Distribution of heuristic level in different iterations for a single run.

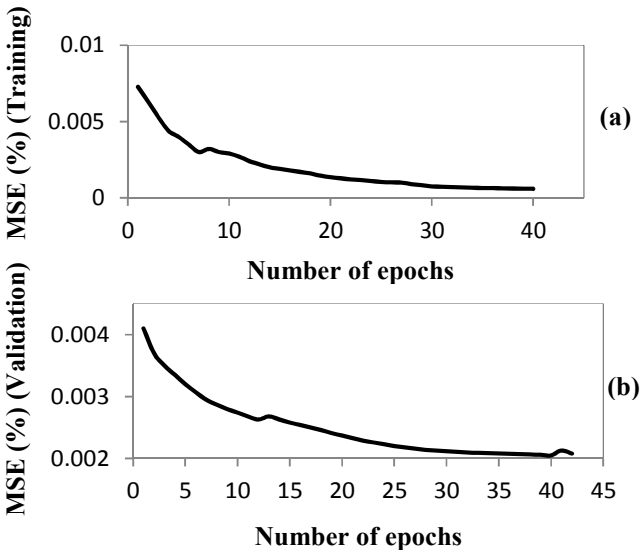

Figure 5. Training process to evaluate the constructed subsets by ants: (a) training error, (b) validation error.

It can be seen from Fig. 6 that the high correlation is present between actual and predicted data.

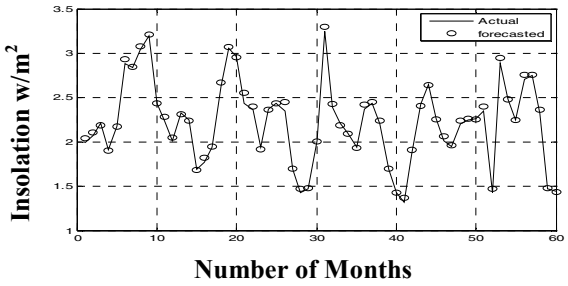

Figure 6. Actual and predicted insolation curve

VII. COMPARISON WITH OTHER WORKS.

Theoretically, a huge amount of attempts have been carried out in designing solar radiation prediction models. The proposed model is quite different from those discussed in [3 – 9], where the prediction models use the features, based on knowledge or availability with no attempts to search the best feature subset. From Table 6 it can be seen that, the proposed ACOSIP perform better with feature selection strategy.

TABLE VI. COMPARISON WITH OTHER WORKS

Name of Authors	MSE (%)	PA (%)	MAPE (%)
Proposed Model	0.000598	99.86	0.14
Amit Kumar Yadav [6]	0.0024		0.2783
Shafiqur Rahman [7]			4.49
Salman Quaiyum [8]	0.29		

VIII. CONCLUSION

This work represents a new model (ACOSIP) for predicting solar irradiance using ACO and NN. In ACOSIP, the most salient climatological features are selected in order to improve SIP accuracy. To facilitate the activity of ACOSIP, two sets of new rules have been designed for pheromone update and heuristic value measurement, where the correlation information technique and the outcome of NN are embedded. Experiment results show that, ACOSIP performs well in 12 solar radiation data samples collected from BMD, where it selected six most salient features easily with better prediction accuracy. The selected features are longitude, latitude, day light hour, max temp., min temp., and humidity. Furthermore, the averaged prediction accuracy of ACOSIP for 35 stations of BMD in testing case is 99.74% including the MAPE of 0.26% (Table 2). The proposed ACOSIP also represents high correlation of 99.93% (Table 1) in between the actual and forecasted data. On the other hand, the results of the low standard deviations of prediction accuracies exhibit the robustness of this model. Comparison results presented in Table 6 show that, ACOSIP can perform well comparing to other existing models. Thus, it can be said that, the proposed ACOSIP model may have capability to select the relevant features and to predict solar radiation at any location in the world, provided that the proper data from the locations are available.

REFERENCES

[1] EPIA Renewable Energy House, "European Photovoltaic Industry Association (EPIA): Market Report 2011," Belgium, 2012. Available online:http://www.epia.org/publications/ epiapublications.html (accessed on 22 November 2011).

[2] European Commission Joint Research Centre, "Solar Cell Production and Market Implementation of Photovoltaics: PV Status Report,"*Publications Office of the European Union*, Italy, 2011. Available online: http://ie.jrc.ec.europa.eu (accessed on 22 November 2011).

[3] S. A. Kalogirou, "Artificial neural networks in renewable energy systems applications: a review,"*Renewable and Sustainable Energy Review*, vol. 5(4), pp. 373-401, 2001.

[4] A. Mellit, S. A. Kalogirou, L. Hontoria, and S. Shaari, "Artificial intelligence techniques for sizing photovoltaic systems: a review," *Renewable and Sustainable Energy Reviews*, vol. 13, pp. 406-19, 2009.

[5] M. Mohandas, S. Rehman, and T.O. Halawani, "Estimation of global solar radiation using artificial neural networks,"*Renew Energy*, vol. 14, pp. 179-184, 1998.

[6] A.K. Yadav, S.S. Chandel, "Artificial Neural Network based Prediction of Solar Radiation for Indian Stations,"*International Journal of Computer Applications*, vol. 50, 2012.

[7] S. Rahman, M. Mohandes, "Artificial neural network estimation of global solar radiation using air temperature and relative humidity,"*Energy Policy*, vol. 36, pp. 571 – 576, 2008.

[8] S. Quaiyum, S. Rahman, "Application of Artificial Neural Network in Forecasting Solar Irradiance and Sizing of Photovoltaic Cell for Standalone Systems in Bangladesh,"*Int. Journal of Comp. App.*, vol. 32, pp. 51-56, 2011.

[9] A. Hasni, A. Sehli, B. Draoui, A. Bassou, and B. Amieur, "Estimating global solar radiation using artificial neural network and climate data in the south- western region of Algeria,"*EnergyProcedia*, vol. 18, pp. 531-7, 2012.

[10] M.M. Kabir, M. Shahjahan, and K. Murase, "A new hybrid ant colony optimization algorithm for feature selection,"*Expert Systems with Applications*, vol. 39, pp. 3747–3763, 2012.

[11] A. Will, J. Bustos, M. Bocco, J. Gotaya,andC. Lamelas,"On the use of niching genetic algorithms for variable selection in solar radiation estimation,"*Renewable Energy*, vol. 5, pp. 168-76, 2011.

[12] L. Ke, Z. Feng, and Z. Ren, "An efficient ant colony optimization approach to attribute reduction in rough set theory,"*Pattern Recognition Letters*, vol. 29, pp. 1351-1357, 2008.

[13] M. Dorigo, C. Blum, "Ant colony optimization theory: A survey,"*Theoretical Computer Science*, pp. 243-278, 2005.

[14] M.L. Gambardella, M. Dorigo, "Ant-Q: A reinforcement learning approach to the TSP,"*Proceedings of the 12th international conference on machine learning*, 1995, pp. 252-260

Power Distribution Scheme Using Smart Meter, Perspective Bangladesh

Md. Noor Hossain[1*], Jannatul Ferdous [2], Md. Farhan Fuad[3], K. M. Ahsan-uz-Zaman [4] and Abdul Wahed [5]
[1, 2, 3,4] Dept. of EEE, Mymensingh Engineering College, Mymensingh, Bangladesh
[5] Faculty, Dept. of EEE, Mymensingh Engineering College, Mymensingh, Bangladesh
[*] E-mail: noor_mec@yahoo.com

***Abstract*—Smart meter, the core part of smart grid system, is becoming an active field of research for its immense potential in efficient power distribution and load management. It is expected to have potential applications in Bangladesh as well. Efforts are already underway from distribution companies to introduce intelligence in the meter system. This paper proposes several smart meter assisted economic energy consumption schemes for consumers and power outage reduction scheme for distribution utility companies that will enhance the quality of service. Necessary analyses have been included to verify the proposed schemes. Real-life electric power demand and supply data from various substations under Dhaka Electric Supply Company (DESCO) have been used to validate the power outage reduction scheme. Results show that the schemes provide economic benefit to the consumer and an effective load management strategy for distribution companies. Operating issues related to the proposed schemes have also been detailed to highlight the practicality of the proposed schemes**

Keywords-Smart meters, power management, power outage reduction, implementation factors)

I. INTRODUCTION

Smart grid is being increasingly seen as an efficient and effective power transmission and distribution system. Smart meters at customer premises represent the core part of the intelligence and automatic control system of smart grid infrastructure [1]-[2]. Smart meters present themselves as enablers for cost-effective energy management strategies for consumers and power distribution companies [3]-[4]. An estimated 62% Bangladeshi people is connected to the electric grid. The electricity supply is not reliable and peak demand cannot be met. In the rural areas, where more than 70% of the population lives, only about 30% of them have access to electricity supply [5]. In the context of energy scenario in Bangladesh where there is a large deficit between energy generation and demand, smart meters offer the potential of providing economic usage of energy for customers and smart management of distribution system so as to minimize the impact of the energy deficit [6]. Dhaka Electric Supply Company (DESCO) in an attempt to introduce intelligent metering keeping in line with smart meter concept conducted a pilot project to introduce prepaid meters with limited feature for residential customers. Extension of such approaches will form the future of electric power distribution and consumption strategies by relying on smart meters with advanced algorithms and reliable two-way communications between the meter and the central control located at the distribution center. With increase in energy tariff coupled with energy deficit, customers will look for avenues to reduce their electricity expenses while expecting a good quality of service from the distribution companies. With a smart meter installed at the customer premise, customers can avail various options to optimize electricity usage and minimize energy expense.

This paper proposes several energy management strategies that are applicable at customer and distributor end. This includes keeping the monthly bill within a pre-set limit and being notified of tariff slabs as energy is being consumed. The proposed techniques further include energy consumption within the assigned load limit or sanctioned load. Additionally, it is possible through implementation of the proposed techniques to alleviate the existing power outage crisis and to provide uninterrupted power at a useful level. It may be worthwhile to draw differences with research that address smart meter applications at customer premises [3]-[4] and [6]. The cited research focuses on actual hardware details of a household smart meter, wider range demand side management or configuration of appliances to match the peak-hour in demand. In contrast, the research presented in this paper provides an in-depth analysis of load management scheme and addresses the practical issues that arise from such schemes. Moreover, the proposed schemes have the potential of mutually reinforcing the efficacy of load management technique. Recorded data of supply and demand over time from DESCO has been used to analyze the performance of the proposed power outage reduction scheme [7]. It is expected that the research presented in this paper will provide a practical direction for technically and economically feasible deployment.

The organization of the paper is as follows. Section II presents smart meter enabled smart electricity consumption management for customers. Section III proposes power outage reduction scheme while Section IV addresses practical issues related to the proposed management schemes. Section V touches upon the communications infrastructure to support the proposed schemes followed by concluding remarks.

II. SMART METER FOR ECONOMIC ENERGY USAGE

Consumers can regulate his/her energy usage through smart meter based usage management: (A) Fixed budget for electric bill. (B) Electricity cost management according to price slabs, and (C) Sanctioned load monitoring. These are described in details in the following subsections.

A. Fixed budget for electric bill

A smart meter can be used to help the consumer plan a monthly budget for electricity usage. The consumer will give his/her allocated budget as an input to the meter and the meter will calculate the available energy units based on the existing tariff rate. Based on the available units, the meter will calculate the daily average allowed unit. For each day, the meter will determine the consumed energy units for that day and raise an alarm if that consumed energy is higher than the average value. Thus, the consumer will be informed of his/her daily status on consumed energy units and will adjust the energy consumption for the remaining days of the month so that the total consumed energy is within the allotted budget set at the beginning of the month. An example of variation of daily consumed energy is shown in Figure 1 along with the meter computed the average daily energy unit. Here it is assumed that the allocated budget allows 570 units (i.e., kW-Hr) of energy for a given month and the resulting per day allowable energy use is about 18.8 units. Thus, whenever the consumed load exceeds the preset average value, the smart meter will raise an alarm and generate a message about exceeding the average and the remaining allowable energy units. The customer then lowers the energy consumption below the allowable daily limit.

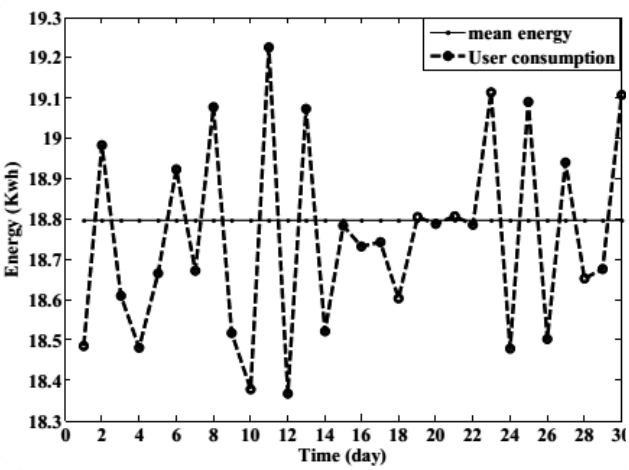

Figure 1: Energy consumption pattern following fixed budget plan.

Figure 2 shows the cumulative energy consumption from the budgeted limit (straight line representing mean energy) and from smart meter assisted user regulated scheme. The plots reveal that the proposed scheme enables the user to closely approximate the preset limit and to keep within the budget.

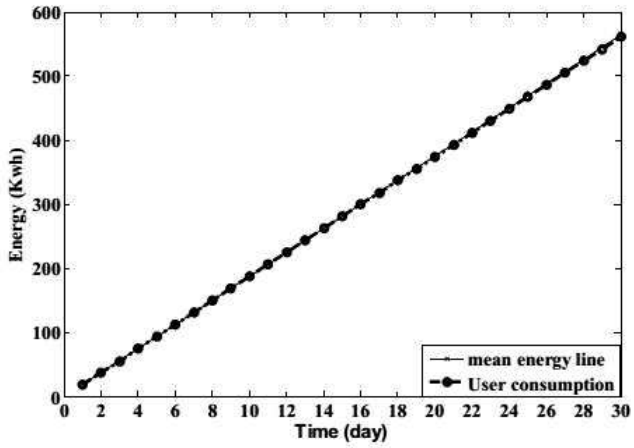

Figure 2: Allocated and daily energy consumption lines for a month.

B. Electricity cost management according to price slabs

The Dhaka electric supply company (DESCO) has implemented new tariff rates from 01 September 2012 in accordance with Bangladesh Energy Regulatory Commission (BERC) [7]. Figure 3 shows only the residential component of the tariff structure. This tariff rate is flat throughput the day irrespective of the peak demand hours.

TABLE 1: PRICE SLABS FOR RESIDENTIAL AREA IN BANGLADESH [5]

Category	Per unit Rate (BDT)
Life Line : From 1 to 50 units	3.33
First Step : From 1 to 75 units	3.53
Second Step : From 76 to 200 units	5.01
Third Step : From 201 to 300 units	5.19
Fourth Step: From 301 to 400 units	5.42
Fifth Step: From 401 to 600 units	8.51
Sixth Step: Above 600 units	9.93

As per this tariff structure, the consumer pays increasingly higher tariff as his energy consumption increases and crosses over to the higher price slabs. A smart meter can help customers become more energy-conscious as it can alert them when the energy consumption is approaching the slab with the next higher tariff rate. This will help the customers to keep the energy consumption within an affordable limit. Various algorithms can be devised to keep track of the energy consumption, the related total cost and to implement the user control (manual or automatic).

C. Sanctioned load monitoring

The customers of power distribution companies are assigned various levels of allowable sanctioned loads based on their demands whenever they subscribe to a particular company. The sanctioned load implies a tacit agreement that customer will not cross the sanctioned load. However, there is no

provision for monitoring operating customer loads and penalty for exceeding the sanctioned load. Only recently, DESCO is deploying energy meters on a small scale with instantaneous load monitoring capability and applying penalty in case of exceeding the limit. That monitoring scheme turns off the meter should there be a first-time violation of sanctioned load and the user can turn on the meter. If the violation occurs second time, the user is still allowed to turn the meter on; however, with the next violation, the meter turns off and cannot be turned on except from official intervention along with a penalty. A better and more customer-friendly approach can be adopted where the meter will alert the consumer whenever the current load limit is within a certain percentage of the sanctioned load (e.g., within 5% or if the operating load is around 950W when the sanctioned load is 1kW). Thus, with this alert in mind, the consumer will plan his energy consumption and prioritize appliances so that overall load is kept below the sanctioned load. For the case when the operating load does exceed the sanctioned limit, then the smart meter will turn off and will not turn back on until the operating load is reduced below the sanctioned load limit.

D. Operational Aspects

Hardware implementation of smart meter based energy management is an important operational aspect [8]. The proposed schemes (A-C) can be implemented through a smart meter, user interface and supporting communication system installed within consumer premises. For tracking energy consumption cost management (schemes A, B), a smart meter can be programmed to monitor daily usage and generate alert messages and alarms as needed. For implementing sanctioned load monitoring (C), the smart meter can play the role of load monitoring and generating alert messages and alarms. However, for consumer responses to the alerts and alarms, some additional features can be provided through indoor short range communication link between the smart meter and the appliances that can be controlled by the smart meter. It can be safely assumed that high-wattage appliances have major impact on operating load, pushing energy cost into higher price slabs. Thus, if the electrical outlets for these appliances are fitted with switches or relays (smart switches) controlled by smart meters through Zigbee based communication links, the operation of these devices can be controlled as per requirements from sanctioned load settings and tariff structures. For example, if the consumer would like to turn on a high-power appliance, he/she will press the smart switch and the smart switch will request the smart meter to enable it. The smart meter will monitor the parameter settings for a particular application (i.e., sanctioned load monitoring or energy cost reduction), will issue a command accordingly to the smart switch. For sanctioned load monitoring, the smart meter will not enable the smart switch till the load is reduced below the sanctioned limit. For energy cost reduction, the smart meter will disable the switch when an alert condition is encountered; however, the user can press the smart switch second time that will enable that switch and turn on the appliance.

III. POWER OUTAGE REDUCTION

There is an acute shortage of electricity production at the national level in Bangladesh and the gap between production and demand has to be compensated by power outage. In the metropolitan areas, the power outage is usually scheduled by the electricity distribution companies where an alternating hourly pattern of availability of electricity and power outage (termed load shedding) is maintained. The outage scenarios in rural areas is even worse as generated electricity is mainly channeled to city and industry areas giving less priority to rural areas. A typical hourly pattern for electricity supply, demand and the resulting amount of load shedding for a specific zone (Dhanmondi zone under DESCO) is shown in Figure 4. From the figure it can be seen that the demand is higher than the supply throughout the day with the peak demand occurring at 5 pm onwards. The peak amount of load shedding is somewhat higher than 15 MW while the peak available supply is about 22 MW.

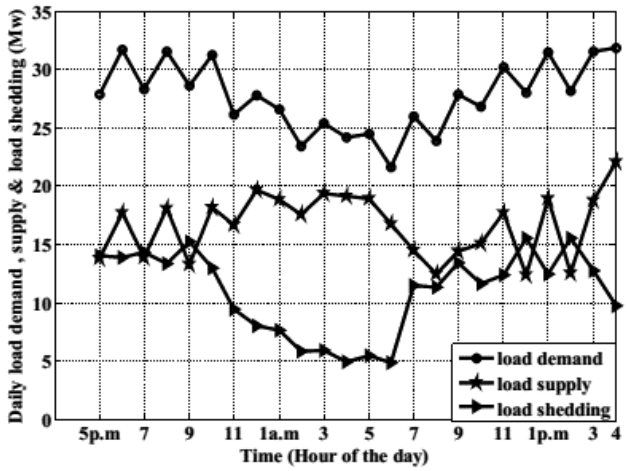

Figure 3: Load demand, supply and load shedding patterns of Dhanmondi zone in a metropolitan city Dhaka [1]

A. Proposed load management scheme

As per the current practice of load shedding, the 11 KV feeders coming out of a substation are selectively switched off in a pre-determined schedule. Thus, a group of consumers belonging to a set of feeders faces power outage in specific one hour duration while in the next hour the feeders are switched on. Thus, there is an hourly "on-off" pattern for available electricity to the consumers. The consumers usually respond to power outages by installing IPS for home use and diesel generators for high-rise residential apartments and offices and educational institutes.

Smart meters in combination with appropriate control mechanism at the distribution substation side can enable an alternative strategy where electricity can be made available to the consumers throughout the day albeit at a reduced level. The distribution companies will predict the load demand D(t) at a given time t for a given day and will

estimate a "load meet" factor *LM(t)*based on the available electricity supply S(t) allotted to it from the national grid as follows.

$$LM(t) = \frac{S(t)}{D(t)} \quad (1)$$

The central control system at the distribution substation will then relay this value to the smart meters for individual consumers and instruct the smart meters to reduce to a level as per the computed value of LM (t). A plot of LM (t) for the hourly patterns of demand and supply from figure 3 is shown in Figure 4.

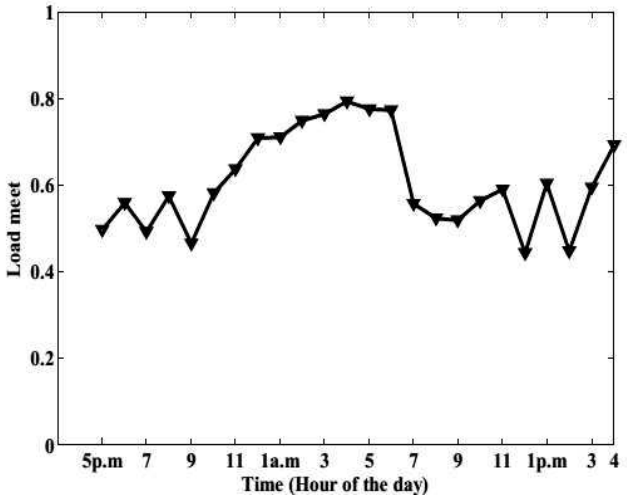

Figure 4: Variation of load meet factor with the period of time in a day.

It is instructive to compare the proposed scheme of offering energy all the time at a reduced level with the existing "on-off" hourly pattern of electricity supply.

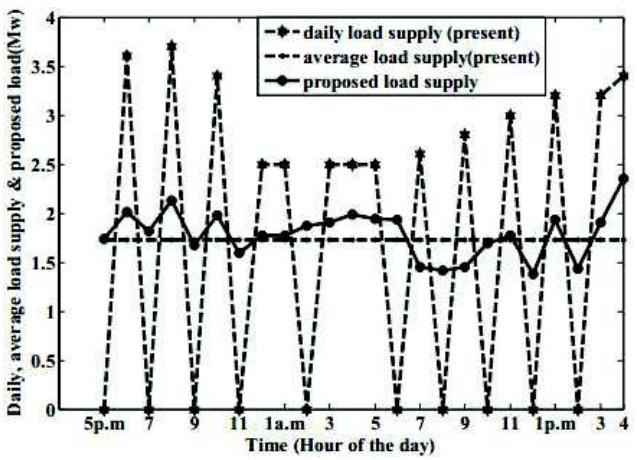

Figure 5: Existing power supply scheme and the proposed outage management scheme.

Figure 5 shows the hourly pattern of existing load shedding for a given day at a given feeder at the Dhanmondi zone for DESCO. The figure shows that except for midnight to early morning load shedding occurs regularly at alternating hours. The average available load from this load shedding approach is also shown as a straight line. The proposed load management scheme offers uninterrupted electricity supply at a reduced level of 1.5 to 2.4 MW. It can be seen that the proposed load management scheme behavior is relatively stable and is close to the average load supply from the existing load shedding technique. This shows that the proposed outage management scheme provides average energy supply to the customers that is similar to that from the present on-off scheme while maintaining continuity of service.

The different feeders of the same substation (Dhanmondi zone, DESCO) can also be studied for their allowable load variation throughout the day. The temporal patterns for the allowable load for the individual feeders for the same substation are shown in Figure 7. It can be seen that the variations are correlated depicting common residential customer energy consumption pattern. The variation in peak load supply can be attributed to individual feeder capacity.

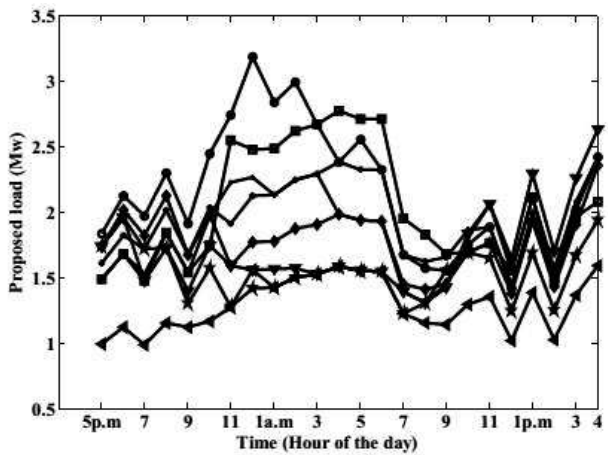

Figure 6: Variation of proposed load across different feeders of the same substation.

Let be the supplied load in a $d_1(t)$, $d_2(t)$, ⋯⋯ $d_N(t)$ substation and be the load demand of substation where N is the total number of feeders in that substation. Then total load-meet factor for a given substation can be expressed as

$$LM(t) = \frac{\sum_{n=1}^{N} P_n(t)}{\sum_{n=1}^{N} d_n(t)} \quad (2)$$

Load-meet actors for different substations (Shyamoli, Dhanmondi and Paribagh) have been computed from data available from DESCO web page. Figure 8 shows the variation of LM(t) for these substations. The plots in Figure 8 reveal that there is a strong correlation of the patterns across the substations. Thus, load distribution at different substations will follow the general pattern from applying the proposed power outage management scheme.

IV. Important Implementation Factors

The proposed load management schemes aim at more efficient and economic electricity consumption for customers. Additionally, it offers the distribution companies to provide uninterrupted electricity supply to their customers. One issue may arise and needs to be addressed is that the uninterrupted service occurs at lower load level. The main effects of that are:

- Individual consumers will need to lower their load level below the sanctioned load. Thus, the consumer needs to plan electricity appliances usage to be within the assigned load level. Thus, for a consumer with 1kW sanctioned load, he/she may be allowed minimum of 450W (45% load meet value in Figure 5) and maximum of 800W (80% load meet level in Figure 5). This can be accommodated by using more efficient electric appliances coupled with smart usage strategy implemented through smart meter.
- The availability of uninterrupted electricity will lead customers to do away with IPS and battery charging system. The charging of battery during "on" period in the current load shedding scheme can put significant burden on the available supply. Generally batteries designated for use with IPS tend to have shorter charging period by consuming higher current. For example, a 100AH battery at 12 volt can be designed to be completely charged in 3 hours; this implies that with a charging current of 100AH/3H 33 A,, the IPS system will consume 33 12 = 396 WH within the „on" time of 1 hour of the period. This can constitute a significant impact on the customer load and contribute to increase in demand during peak load.
- For high-rise apartment systems, the supply to lift/elevator and water motor can be left out of the proposed reduction scheme. Since the motors for these heavy electric devices cannot be operated at a reduced supply, the smart meters connected to these devices will be allowed to operate at their rated required capacity. This will reduce the operating expenses of the residents by excluding generators.
- Hospitals and emergency services can be left out of proposed load reduction scheme. Alternately, they can be guaranteed certain amount of supply throughout the day and difference between this supply and requirement can be compensated by installing generators.
- Since monitoring of sanctioned load does not take place currently, there is more energy consumption than the allowable limit from the consumer's side placing an increasing demand on the system. The proposed load management scheme offers monitoring of sanctioned load, and it is expected that this will bring down the demand on the distribution system with more energy aware consumers.
- These proposed load management schemes will also drive entrepreneurs to offer green energy solutions at customer premises or at the distribution centers. With additional energy from non-conventional renewable sources, the load management scheme will become more efficient and consumer friendly.

V. Communication Links for the Proposed Schemes

The proposed schemes will need a reliable two-way communications link between the smart meter and central substation [9] and between the smart meter and home appliances for automatic control. The communication link to support power outage management can be implemented via wireless or wired infrastructure. For wireless implementations, modems are needed at the smart meters to set up the link, a local concentrator to aggregate the data from multiple smart meters and relays to channelize the data to the central substation. Since the data rate is expected to low to support the scheme, the link can be designed to be small bandwidth systems. The wireless system can also be implemented through a mobile operator where data and control information can be communicated via mobile operator network so that the overall design can be made relatively simple [10]. As an alternative to the wireless systems, wired communication links can be established that will use the existing power distribution lines from the distribution substation to customer premises. This can be implemented using broadband over power lines (BPL) or power line communication (PLC) techniques [11]. Devices that are needed in this case are PLC modems at customer premises, extractor to concentrate the incoming signals, repeaters to keep the signal strength at a satisfactory level and injectors. Except for the cost of these additional devices, the PLC based implementation is expected to be economic since the existing power line network can be used as the communication infrastructure. As for energy consumption regulation at customer end (schemes A-C), customer response to smart meter alerts and alarms can be either manual or automatic. For scheme A and B, the customer can respond to alerts by planning energy consumption on his own without the need for any smart device. For scheme C, smart switches can be used for heavy load appliances to respond to alarms. In this case, low to moderate data rate links based on Zigbee systems will be sufficient for automatic control of the appliances.

VI. Conclusions

The research presented in this paper focuses on smart meter assisted energy consumption management for consumers and load management for distribution companies. Necessary analysis has been presented to verify the schemes. Analyses reveal that the proposed schemes have the potential to benefit the consumer and also assist distribution companies to provide a better quality of energy supply. The practical operational issues that can result from the proposed load outage reduction scheme have been discussed in details. The existing communications network in Bangladesh is adequate to support the proposed schemes. Thus, the proposed schemes can bring the much needed benefits and quality of electric energy supply and can be implemented through off-the-shelf components using the existing communication infrastructure.

ACKNOWLEDGMENT

The authors are grateful to Md. Faruk Hossain, Assistant Engineer, 70 MW Peaking Power plant, Bera, Pabna, for his thoughtful comment on power distribution and load shedding scheme.

REFERENCES

[1] J. Zheng ; Gao, D.W. ; Li Lin, "Smart Meters in Smart Grid: An Overview", IEEE Green Technologies Conference, 2013, Page(s): 57 – 64.

[2] Marron, L.; Osorio, X.; Llano, A. ; Arzuaga, A. ; Sendin, A., "Low voltage feeder identification for smart grids with standard narrowband PLC smart meters", 17th IEEE International Symposium on Power Line Communications and Its Applications (ISPLC), 2013, Page(s): 120 - 125.

[3] Barbato, A. ; Dipt. di Elettron. e Inf., Politec. di Milano, Milan, Italy ; Capone, A. ; Rodolfi, M. ; Tagliaferri, D., "Forecasting the usage of household appliances through power meter sensors for demand management in the smart grid"Smart Grid Communications 2011 , pp: 404 – 409

[4] Di Leo, G. ; Landi, M. ; Paciello, V. ; Pietrosanto, A. "Smart metering for demand side management", IEEE Instrumentation and Measurement Technology Conference, 2012 , pp: 1798 – 1803

[5] S. I. Khan, and Md. F. Rabbi, "An Innovative Financing Mechanism: Creating Access to Renewable Energy for Rural People of Bangladesh". Global Conference on Rural Energy Access, Addis Ababa, Ethiopia, December 4-6, 2013.

[6] GMA E. Rahman, K. I. Ahmed, R. Mostafa, and M. F. Khan,"A Novel Smart Metering System for Loss Reduction and Efficient Load Management in the Power Distribution Sector of Bangladesh,"ICAEE 2013, December 19-21, 2013

[7] https://www.desco.org.bd/index.php?page=tariff-rate

[8] M. Kuzlu, M. Pipattanasomporn, and S. Rahman, "Hardware Demonstration of a Home Energy Management System for Demand Response Applications," IEEE Tr. on Smart Grid, VOL. 3, NO. 4, DECEMBER 2012, pp. 1704-1711

[9] Y. Yan, Y. Qian, H. Sharif, and D. Tipper, "A Survey on Smart Grid Communication Infrastructures: Motivations, Requirements and Challenges" IEEE Communications Surveys and Tutorials, vol. 15, no. 1, pp. 5–20, 2012.

[10] M. M. Abdullah andB. Dwolatzky, "Smart Demand-Side Energy Management Based onCellular Technology - A way towards Smart GridTechnologies in Africa and Low Budget Economies", IEEE AFRICON 2009, 23 - 25 September 2009.

[11] S. Galli, A. Scaglione and Z. Wang, "For the Grid and Through the Grid: The Role of Power Line Communications in the Smart Grid" Proceedings of the IEEE Vol. 99, No. 6, June 2011, pp.998-1027.

Efficient PV Array Modelling by Analyzing PV System(cell/module/array) Based on MATLAB

Abu Naim Rakib Ahmed, Khalid Nowaz, Jarin Tasnim, and Nashrah Afroze
Department of Electrical and Electronic Engineering
Khulna University of Engineering & Technology (KUET), Khulna-9203, Bangladesh
E-mail: naimkuet05@gmail.com

***Abstract*—The increasing energy demand has enhanced the use of renewable energy as the source of fossil fuel cannot meet up this demand. The photovoltaic cell converts sunlight to electricity without any pollutant emission. A complete analysis on Photo Voltaic system is required to get the maximum output. But because of some external and internal factors, the generation of maximum output power is disrupted. Shading, temperature, irradiance as external factors and series and parallel resistance as internal factors change the maximum power point of a Photo Voltaic system. In this research, the generalized model for Photo Voltaic system was implemented in MATLAB interface. According to the change of the values of irradiance, shading, temperature, series and parallel resistance. The I-V and P-V characteristics are analyzed for the best case. On the basis of the analysis, effective Photo Voltaic system is built which gives approximately 5000W output by using the best values for the above mentioned factors. The proposed system is built to serve the purpose of an industry.**

Keywords—Irradiation; temperature; shading effect; bypass diode; maximum power point.

I. INTRODUCTION

The excessive demand for energy as a result of the industrial development and rapid population growth has lead to the necessity for alternative energy. The dwindling fossil fuel reserve has emphasized on this quest for alternative energy. Renewable energy is a great contribution to meet up the energy crisis. Solar energy is one of the candidates which has replaced fossil fuel by 20% to 25% over the past 20 years [1]. The use of solar power is growing at a rate of 60%. With no pollutant emission, low cost, availability, research in this topic has gained popularity. Bangladesh is also heading towards the use of solar energy in mass level in order to balance the insufficient supply of energy. In this country the duration of sunshine is 3 to 11 hours daily and the solar irradiation varies from 3.8 KWh/m^2/day to 6.4KWh/m^2/day. So there is high potential to implement solar system in the country. As a result Bangladesh Government has a target of 650 MW electricity generations by 2020. All this causes lead to the proper implementation of PV system with great performance.

The efficiency of PV system can be improved by variation of temperature, solar irradiance, shading [2, 3]. Series and parallel resistance are another factors that influence the losses.Previously some researchers gave importance on generalized PV model without considering partial shading [4].Again Partial shading [5] or MPPT [6, 5] was main focus of other authors. While the series resistance R_s and the parallel resistance R_p are discussed in others [7, 8, 9].

The focus of the paper is to develop an effective and complete PV system to manipulate important factors (shading, irradiance, temperature) and investigate a Simulink model with best values of them.

In section II, formation of a PV array is elaborated. Section III consists of the analysis of effect of irradiance, shading and temperature on cell, module and array respectively. The effect of parallel and series resistance on cell are also explained here. Section IV gives a short discussion on the analysis of section III.

II. STEP TOWARDS PV ARRAY

A. Operating Mechanism

The smallest unit of PV array is the PV cell. In a semiconductor material, electron in the valance band excites when it is irradiated and the energy of the photon exceeds the band gap energy of the material creating a hole. The n-type region gets rich of electrons and p-type region of holes because of the depletion region. This leads to a photo generated current flow if the PV cell is connected to an external circuit as shown in Fig. 1.

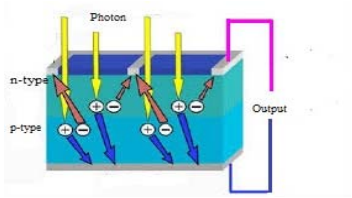

Figure 1. Process of producing photo-generated current and voltage.

B. Equivalent model of a PV cell

An equivalent model is developed to simulate a PV cell which contains a current source representing the photo generated current I_L with a diode connected in parallel can replace a PV cell. The p-n junction is represented by the diode. The external behaviour of the model is represented by a resistance in parallel named Rp and in series named Rs as shown in Fig. 2.

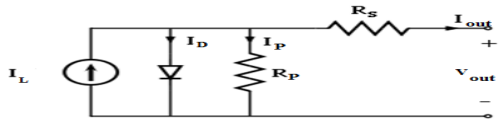

Figure 2. Equivalent model of a PV cell.

978-1-4673-9257-0/15/$31.00 ©2015 IEEE

The output voltage and current equations of a PV cell for this model are given below.

$$I_{out} = I_L - I_0(e^{\frac{qV_d}{mkT}} - 1) - \frac{V_d}{R_p} \quad (1)$$

$$V_{out} = V_d - I_{out}R_s \quad (2)$$

Here, output current is represented by (1) and output voltage by (2). In this equations above I_{out} is the output current, I_L is the photo generated current, R_s is the series resistance, R_p is the parallel resistance, I_0 is the Reverse saturation current is the electron charge (1.602 X 10^{-19}C), m is the diode ideality factor (for an ideal diode its 1), k is the Boltzmann constant (1.38 X 10^{-23}J/°K), T is the Temperature, V_d is p-n junction diode voltage. The output current is dependent on the series and parallel resistance, short circuit current and open circuit voltage, irradiation and reverse saturation current. Newton-Raphson method is very useful for solving non-linear equation which depends on numerical approximation. So V_d can be calculated by using Newton-Raphson method by using the best values of R_p and R_s randomly. The numerical process is done following the given flow chart in Fig. 3.

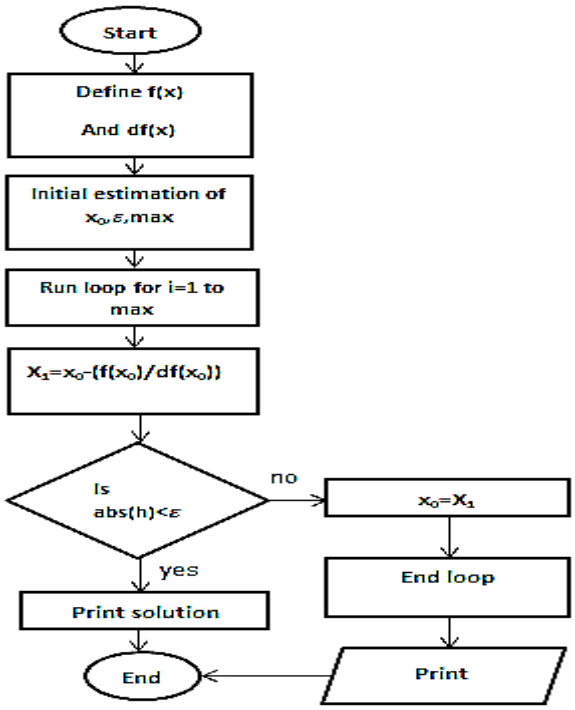

Figure 3. Algorithm of Newton-Raphson method.

C. Construction of PV module and array

To increase the total amount of voltage, PV cells are connected in series. A PV module is formed by connecting 28 to 36 PV cells as shown in Fig. 4. The total voltage is equal to the summation of the individual voltages. A PV array fulfills a desired amount of voltage as in Fig. 5 by connecting the modules in series and parallel forms. Each series branch in array is called a string.[15].

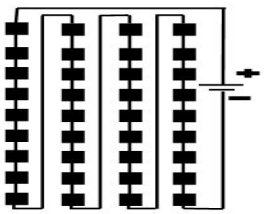

Figure 4. PV module scheme

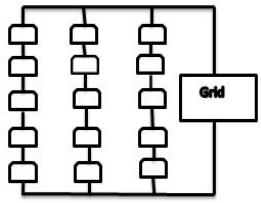

Figure 5. PV array diagram.

III. SIMULATION AND ANALYSIS

A. Cell analysis

1)Effect of series and shunt resistance on single PV cell: The performance of a cell is determined by the accuracy of series and parallel resistance. The two types of losses in the equivalent model of PV cell are leakage current loss and the losses of the semiconductor. These losses are to be minimized. Fill factor known as curve factor is the ratio of maximum power and the product of short circuit current and open circuit voltage. A large fill factor is expected.It usually ranges from 0.5 to 0.88[14-16].

$$F.F. = \frac{P_{max}}{V_{oc}.I_{sc}} = \frac{V_{max}.I_{max}}{V_{oc}.I_{sc}} \quad (3)$$

A method by which the values of R_s and R_p can be determined is using (4).

$$R_p = \frac{V_{out} + I_{out}.R_s}{I_L - I_{out} - I_0[e^{\frac{q(V_{out}+I.R_s)}{mkT}} - 1]} \quad (4)$$

Best values of R_s and R_p were assumed in order to analyze the effect of resistance. The value of V_d was estimated by using (1) and (2) on the basis of taking initial value zero. The algorithm of Newton-Raphson method used for this purpose is as Fig.3. For the required analysis, in the first case parallel resistance is taken approximately 6 Ω and series resistance is given as 0 Ω. In the second case, Rp and Rs are given as 6 Ω and 0.006 Ω respectively. In the third case, the value of R_p is made 0.06 Ω keeping R_s 0.006 Ω. The short circuit current increases but power decreases as series resistance and also parallel resistance increases as shown in Fig.6 and Fig.7. The fill factor also increases in this case.

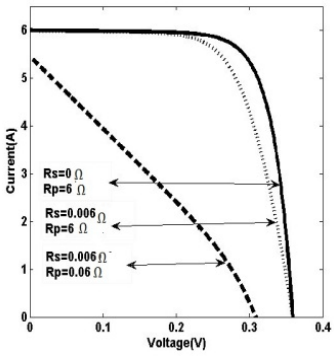

Figure 6. The influence of series and parallel resistance on I-V curve for a cell.

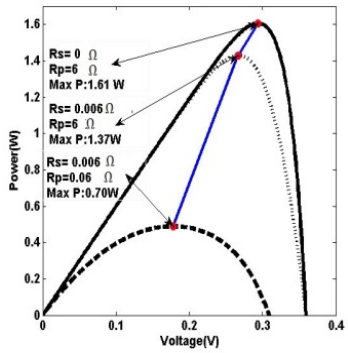

Figure 7. The influence of series and parallel resistance on P-V curve for a cell.

2)Effect of temperature on single PV cell: The reverse saturation current depends on temperature [14,15]. The performance of the PV cell is highly dependent on temperature variation. The reverse saturation current decreases with increasing temperature as from (1).

$$I_L = I_L(T_1) + K_0(T - T_1) \tag{5}$$

$$K_0 = \frac{I_{sc}(T_2) - I_{sc}(T_1)}{T_2 - T_1} \tag{6}$$

$$I_0 = I_0(T_1) \times \left(\frac{T}{T_1}\right)^{3/n} \times e^{\frac{qV_d T_1}{nk\left(\frac{1}{T} - \frac{1}{T_1}\right)}} \tag{7}$$

$$I_0(T_1) = \frac{I_{sc}(T_1)}{e^{\frac{qV_{oc}(T_1)}{nkT_1}} - 1} \tag{8}$$

The relation between photo generated current of T_1 and T can be expressed by (5). MATLAB was used to implement these equations. T is 25°C and T_1 is 75°C. The ratio of difference between short circuit current at T_1 and T_2 and the difference between the corresponding temperatures is K_0. I_0 is the reverse saturation current.

Concerning the temperature variation in Bangladesh, the variation is observed at 15°C, 25°C and 35°C and thus I-V and P-V characteristics curves are drawn as in Fig.8 and 9. These curves match with the ideal characteristics. At fixed irradiation=1000W/m^2, the reverse saturation current decreases with increasing operating temperature and so the open circuit voltage decreases but the short circuit current increases slightly.

With increasing temperature, the current increases but it cannot minimize the effect of decreasing short circuit voltage. As a result as temperature increases, MPPT seems to decrease. As shown in Fig.9, the maximum power point shifts up-ward. The MPPT was calculated 1.68W, 1.46W and 1.16W respectively at 15°C, 25°C and 35°C by MATLAB simulation. It is better to keep the temperature low. For the PV system described in this paper, temperature is chosen 25°C.

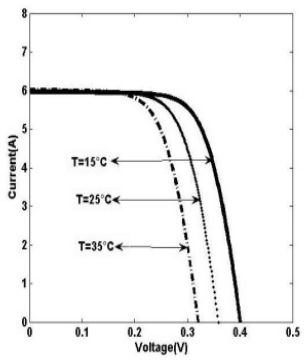

Figure 8. The influence of temperature on I-V curve for a cell.

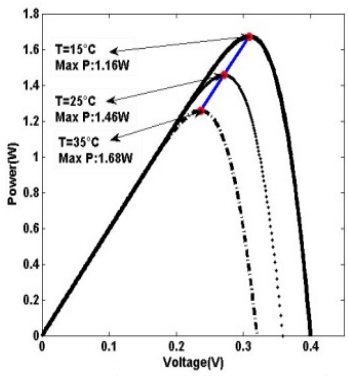

Figure 9. The influence of temperature on P-V curve for a cell.

*3)Effect of different solar irradiation on single PV cell:*Irradiation is an important effect to analyze. As it causes photo generated current to flow and at high irradiation [13, 14, 15].

$$I_L(T_1) = I_{sc}(T_1, G_{nom}) \times \frac{G}{G_{nom}} \tag{9}$$

The equation of photo generated current is given above where $I_L(T_1)$ is the photo generated current at $T_1$where T_1 is 25°C, G is the irradiance of 1000W/m^2 and G_{nom} is the irradiance which was varied. I_L is the photo generated current at 25°C and I_{sc} is the short-circuit current at 25°Cand at 1000W/m^2.

I-V and P-V curves are found by using equation (9) in MATLAB. The irradiances are taken as 1000 W/m^2, 1500 W/m^2, 2000 W/m^2. As irradiation increases, current is produced as seen in Figs. 10 and 11 which increases the open circuit voltage. This occurs because photo generated current increases at high solar irradiation. The power also increases as 0.89W, 1.38W, 1.86W shifting the maximum power point upward. So irradiance is kept at 1000 W/m^2 throughout.

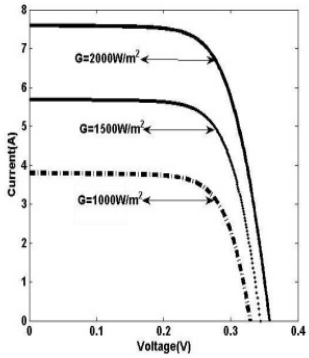

Figure 10. The influence of irradiance on I-V curve for a cell.

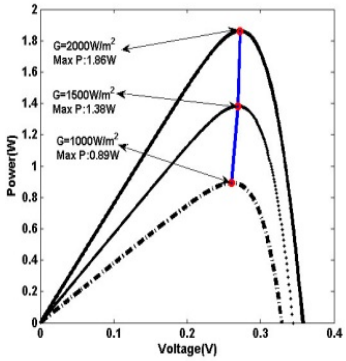

Figure 11. The influence of irradiance on P-V curve for a cell.

B. Module Analysis

By connecting 36 PV cells in series, PV module is constructed for better and accurate result. So total voltage is multiplied cell number times but the current remains constant. The cell number may be varied.

1) Effect of shading on PV module: When uneven shading is taken into account, I-V and P-V curves are slightly different. Because the heat produced by the shading effect affects the module. Shaded cells act as load. It draws current from fully illuminated cell and reduces the output power significantly. The operations are carried out on the basis of the following equations:

$$I_c = (1 - p_i)I_L - I_0\left(e^{\frac{qV_{di}}{mkT}} - 1\right) - \frac{V_{di}}{R_p} \tag{10}$$

$$V_{ci} = V_{di} - I_c.R_s \tag{11}$$

$$V_s = V_{c1} + V_{c2} + ... + V_{c(n-1)} + V_{cn} \tag{12}$$

Here, V_{di} and V_{ci} are the p-n junction diode voltages and output voltages of the *i*th PV cell, I_L is the full sun photo generated current and pi is the shading factor of the ith cell. By varying the p_i, the shading effects are taken as 0%, 40% and 80% for uneven shading.

More power is consumed and the terminal voltage is also changed when the charge carriers of the un-shaded cell flow through the shunt resistance of the shaded cell. To make the electrons flow through the shaded cells, more voltage is consumed and so the terminal voltage decreases during each kind of shading but the short circuit current remains constant. The output power decreases with the increasing shading factor because current is constant and terminal voltage decreases. During 0% shading, output power is maximum. The output maximum powers obtained are 45.68W, 50.38W and 52.54W for 80%, 40%and 0% shading respectively by simulating the equations in MATLAB. The characteristics are shown in Figs. 12 and 13.

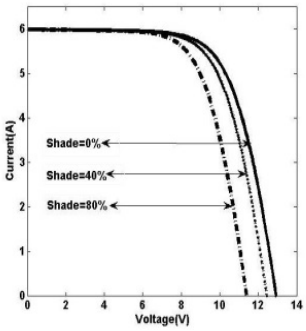

Figure 12. The influence of shading on I-V curve for a module.

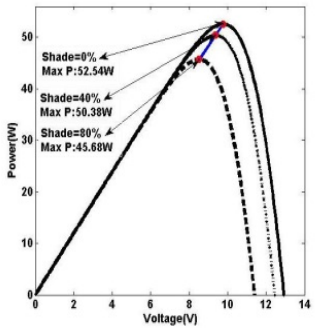

Figure 13. The influence of shading on P-V curve for a module.

2) Effect of Bypass Diode on PV Module: Bypass diode is connected in parallel with PV cells in opposite direction to reduce the impact of shading analyzed previously. Normally a bypass diode is connected in parallel with the series PV cells as in Fig**.** 14. This creates a bypass way for the current generated in the other unshaded cell [13]. The equations used for simulation are given below:

$$I_{ci} = (1 - p_{ij})I_L - I_0(e^{\frac{qV_{di}j}{mkT}} - 1) - \frac{V_{dij}}{R_p} \quad (13)$$

$$V_{pdi} = V_{ci1} + V_{ci2} + ... + V_{ci(n-1)} + V_{ciL} \quad (14)$$

$$V_{cij} = V_{dij} - I_{ci}.R_s \quad (15)$$

$$I_s = I_{ci} + I_0(e^{-qV_{pdi}/mkT} - 1) \quad (16)$$

$$V_s = V_{pd1} + V_{pd2} + ... + V_{pd(m-1)} + V_{pdM} \quad (17)$$

Here, V_{dij} and V_{cij} are p-n junction diode voltage and PV cell output voltages of the *j*th PV cell within the *i*th bypass diode group, p_{ij} stands for the shading factor relevant to the full sun condition for the *j*th PV cell within the *i*th bypass diode group, I_{ci} is the output current of the series PV cells within the *i*th bypass diode group, and V_{dpi} represents the voltage applied to the *i*th bypass diode. i is the number diode and j is the number of cell and L=N/M is the number of PV cell group where one bypass diode is connected.

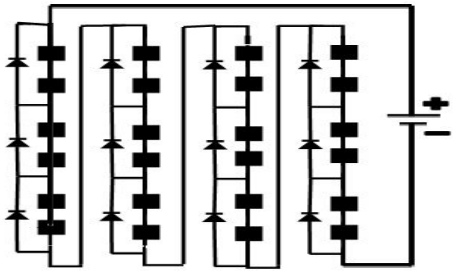

Figure 14. PV array diagram where 3 series branches, containing 6 PV modules, are connected in parallel to complete the array.

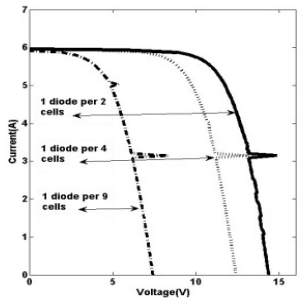

Figure 15. The influence of bypass diodes on I-V curve for a module.

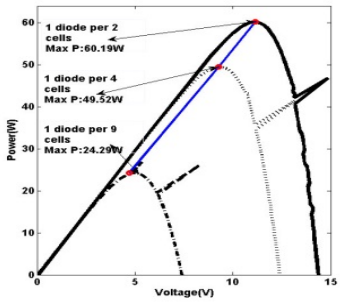

Figure 16. The influence of bypass diodes on P-V curve for a module.

From Fig**.**16**,** the less the PV cells are under one bypass diode, the less is the power consumption as seen from simulation. Because the shaded power absorption is reduced in this case and so bypass diode is added for 2, 4 and 9 PV cells respectively. The open circuit voltage increases with the maximum output power increase when less PV cells are under one bypass diode as in Fig. 15. Maximum output power obtained are 24.29 W, 49.52 W and 60.19 W when 9, 4 and 2 PV cells respectively are connected under one bypass diode. While adding one diode with each 4 PV cells maximum output power is 49.13 W. This output is increased at 60.19 W in case of reducing PV cells to 2.So better output can be produced by reducing the number of cells under one diode.

3) Effect of temperature and irradiance on PV module: The effect of temperature on the output current, voltage and power of PV module matches with that on PV cells. As voltage decreases, the power decreases with the increase of temperature. Short circuit current is constant and the simulation is done according to section III. The maximum powers are 60.33W, 52.55 W and 45.32W for the above temperatures respectively. The I-V and P-V curves with the variation of temperature are shown in Figs.17 and 18. [13,14,15] when irradiance is kept constant at 1000W/m^2.

Greater irradiance gives better results in case of PV module. This is verified by simulation as done in section III using Equation (9). The irradiance is changed as 1000W/m^2, 1500W/m^2 and 2000W/m^2 while both the short circuit current and open circuit voltage increases as in Fig. 19. The cause of increasing photogenerated current is same as explained in

section III. The maximum power point shifts upward as 32.9W, 49.91W, 66.41W.

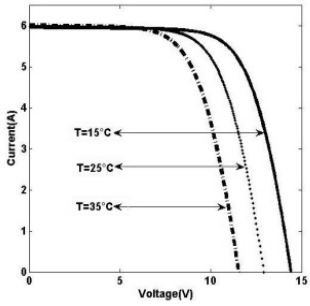

Figure 17. The influence of temperature on I-V curve for a module.

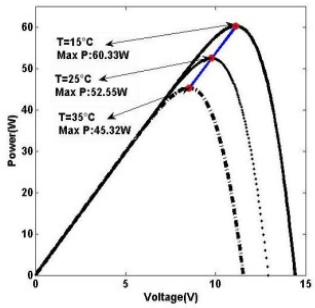

Figure 18. The influence of temperature on P-V curve for a module.

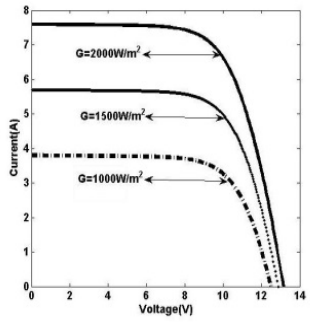

Figure 19. The influence of irradiance on I-V curve for a module.

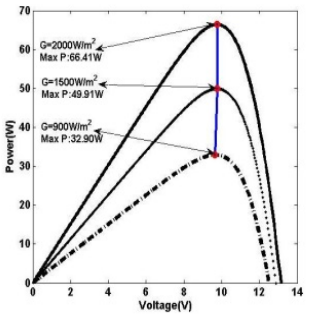

Figure 20. The influence of irradiance on P-V curve for a module.

C. Array Analysis

PV array and module shows similar characteristics.3 strings are connected in parallel consisting of 6 modules to design a 1KW PV system in the array.

*1) Effect of shading and bypass diode on PV array:*Maximum power is obtained for shading of PV array when shading is 0%. For increased shading, the output powers are 945.8 W, 906.91W and 822.24 W respectively at 0%, 40%, 80% as in Fig. 22. As seen in Fig. 21 the open circuit voltage decreases and this can be improved by using bypass diode as in Fig. 24. Power increases as 0.35 KW, 0.81 KW and 1.01 KW for 9,4 and 2 PV cells respectively under each bypass diode. By reducing the cell number by half under one bypass diode, the maximum power increases from 0.81 KW to 1.01 KW as shown in Fig. 24.

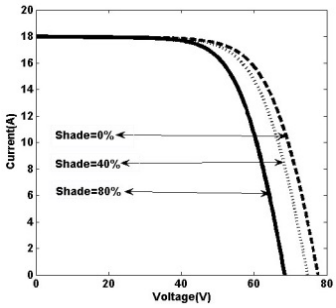

Figure 21. The influence of shading on I-V curve for an array.

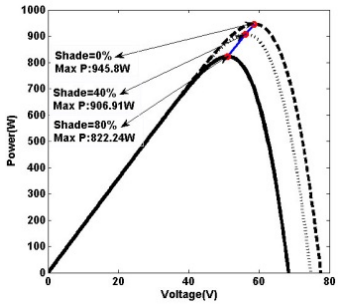

Figure 22. The influence of shading on P-V curve for an array.

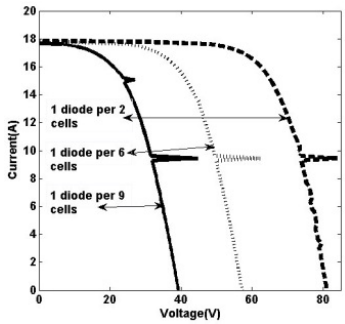

Figure 23. The influence of bypass diodes on I-V curve for an array.

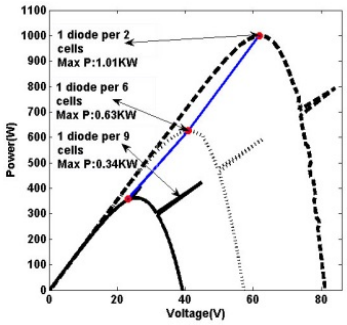

Figure 24. The influence of bypass diodes on P-V curve for an array.

*2) Effect of temperature and irradiance on PV array:*The maximum output powers are 1.09 KW, 0.95 KW and 0.82 KW for 15°C, 25°C, 35°C are obtained by simulating the equations of section III in MATLAB. This is shown in Fig. 26. With the increase in temperature, the open circuit voltage decreases as shown in Fig. 25. The theory used here matches with section III. The irradiances are considered as 2000W/m^2, 1500W/m^{2}and 1000W/m^2 for convenience and the corresponding output powers are 1.19 KW, 0.9 KW and 0.59 KW obtained from MATLAB simulation. These effects are well understood from the curves in Fig. 27 and 28.

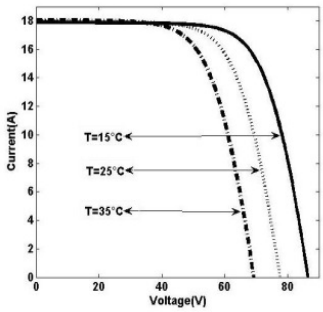

Figure 25. The influence of temperature on I-V curve for an array.

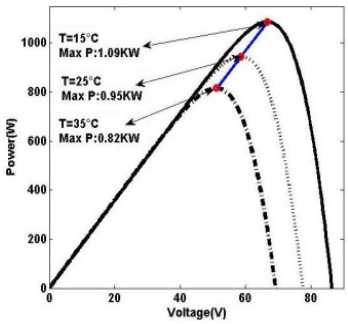

Figure 26. The influence of temperature on P-V curve for an array.

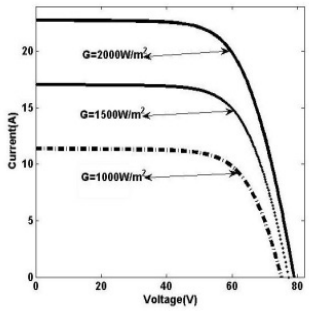

Figure 27. The influence of irradiance on I-V curve for an array.

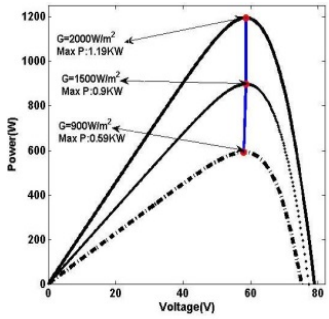

Figure 28. The influence of irradiance on P-V curve for an array.

3) Simulink Model of an array: A Simulink model is built to get around 5000 watt output power from a PV array. Built in PV cell of MATLAB was used in this purpose. A PV module of 20 PV cell is taken. It generates 250 W. And 1 string is prepared taking 4 modules in series. 2 such strings are

connected in parallel. The output is taken at solar irradiance of 1000W/m^{2}at 25°C. The Simulink model is shown in Fig.29.

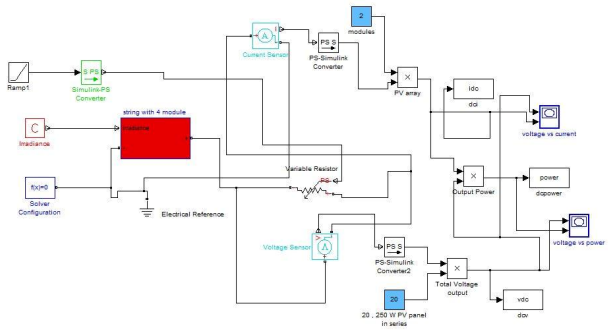

Figure 29. Simulink model for almost 1KW maximum power output.

After developing the Simulink model, the graphs are obtained as shown in Fig. 30 and Fig. 31. Analyzing the graphs it is seen that maximum output power is obtained as 5.05 KW. Under this condition V_{out} is 1129 volt and I_{out} is 5.87 Amp. R_s of 0.006Ω and R_p of 6 Ω are used. For developing the Simulink model, solar irradiation of 1000 W/m^2 and temperature of 25°c is considered.

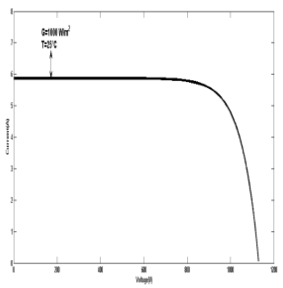

Figure 30. I-V characteristics curve for the Simulink model.

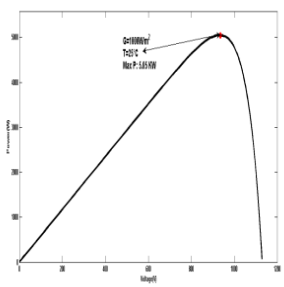

Figure 31. P-V characteristics curve for the Simulink model.

A table showing all the Electrical characteristic data of the Simulink model is as following:

TABLE I. ELETRICAL CHARACTERISTICS DATA OF THE SIMULINK MODEL

Electrical Characteristics	Values
Maximum Power	5.05 K Watt
Voltage at Maximum Power	931.2 Volt
Current at Maximum Power	5.41 Amp
Open Circuit Voltage	1129 Volt
Short Circuit Current	5.87 Amp
Series Resistance	0.006 Ω
Parallel Resistance	6 Ω
Fill Factor	0.76

IV. CONCLUSION

In the preceding sections, simulation in MATLAB was done to analyze the behavior of PV cell completely, module and array. With a view to this, different influencing factors such as temperature, irradiance, shading, series and parallel resistance are varied to observe the change in the output power. And thus the methods of improving the output performance are mentioned. All the analyses are done using the best values in MATLAB. Along with the above works, a solar panel with an output of 5 KW is designed. This work can further be used to get the maximum output from a solar panel eliminating the effects of various internal and external factors. The analyses done in the paper may be expanded in hardware side too for further study, implementation and improvements.

REFERENCES

[1] T. Salmi,M. Bouzguenda,A. Gastli,& A. Masmoudi. Matlab/simulink based modeling of photovoltaic cell. *International Journal of Renewable Energy Research (IJRER)*, *2*(2), 213-218,2012.

[2] H. Patel, V. Agarwal, MATLAB-based modeling to study the effects of partial shading on PV array characteristics, IEEE Transactions on Energy Conversion 23,302-310,2008.

[3] K. Ishaque, Z. Salam, H. Taheri, Accurate MATLAB simulink PV system simulator based on a two-diode model, Journal of Power Electronics 11, 179-187,2011.

[4] H.L. Tsai, C.S. Tu, Y.J. Su, Development of generalized photovoltaic model using MATLAB/SIMULINK, in: Proceedings of the World Congress on Engineering and Computer Science, San Francisco, USA, 2008

[5] O. Wasynczuk, Dynamic behavior of a class of photovoltaic power systems, IEEE Transactions on Power Apparatus and Systems 102 , 3031-3037,1983.

[6] C.C. Hua, C.M. Shen, Study of maximum power tracking techniques and control of dc-dc converters for photovoltaic power system, in: Proceedings of 29th Annual IEEE Power Electronics Specialists Conf., Fukuoka, 1998, pp. 86-93.

[7] Walker, Geoff. Evaluating MPPT converter topologies using a matlab PV model. Aust. J. Electr. Electron. Eng. 21,2001.

[8] A. Bouzid,R. Chenni,T. Kerbache, M. Makhlouf, A Detailed Modeling Method for Photovoltaic Cells Energy. Elsevier,2005.

[9] F. Bryan , Simulation of grid-tied building integrated photovoltaic systems. MS thesis. Solar Energy Laboratory, University of Wisconsin, Madison,1999.

[10] Townsend, T.U., Method For Estimating The Long-Term Performance Of Direct-Coupled Photovoltaic Systems. M.S. Thesis, Mechanical Engineering, U. Of Wisconsin-Madison,1989.

[11] B. Alsayid,J. Jallad. Modeling and simulation of photovoltaic cells/modules/arrays. Int. J. Res. Rev. Comput. Sci. (IJRRCS) 2 ,2001.

[12] A. Chouder,L. Rahmani,N. Sadaoui,S. Silvestre. Modeling and simulation of a grid connected PV system based on the evaluation of main PV module parameters. Simul. Model. Pract. Theory 20, 46–58,2012.

[13] H.Zheng. SOLAR PHOTOVOLTAIC ENERGY GENERATION AND CONVERSION—FROM DEVICES TO GRID INTEGRATION (Doctoral dissertation, The University of Alabama TUSCALOOSA), 2013.

[14] I. Yahyaoui,M. Ammous&F. Tadeo . Algorithm for Optimum Sizing of a Photovoltaic Water Pumping System. *International Journal of Computer Applications*, *111*(6), 21-28,2015.

[15] Elias, B. H., AlSadoon, S. H., & Abdulgafar, S. A. Modeling and Simulation of Photovoltaic Module Considering an Ideal Solar Cell.

[16] A. Blorfan, Flieller, D., Wira, P., Sturtzer, G., & Merckle, J. A new approach for modeling the Photovoltaic Cell using Orcad comparing with the Model done in Matlab. *International Review on Modelling and Simulations*, *3*(5), 948-954,2010.

Replacing Diesel Irrigation Pumps with Solar Photovoltaic Pumps for Sustainable Irrigation in Bangladesh: A Feasibility Study with HOMER

Md. Nazmul Islam Sarkar*, Anwarul Islam Sifat, Nazmul Rahim and S. M. Shamim Reza
Institute of Energy, University of Dhaka
Mokarram Hossain Bigyan Bhaban, Doel Chattar, Dhaka 1000, Bangladesh
* Corresponding author email: sarkarmni@gmail.com

***Abstract*—As a tropical country Bangladesh receives a substantial amount of solar insolation suitable for PV application. Being an agricultural economy, the irrigation need is increasing day by day. Use of diesel run pumping system is neither cost effective nor environment friendly. Even though 47.8% of the total irrigation pumps are diesel run which emits a huge amount of CO2 and other toxic gases. In this paper a typical year round irrigation load has been modelled and used to analyze the feasibility of replacing diesel irrigation pumps with solar PV powered motor-pump systems in HOMER. It was found that stand alone operation of diesel powered pumps are not at all cost effective. PV powered pumps are more feasible than a hybrid PV-Diesel Generator-Battery powered pump systems if it has a larger storage tank. If storage tank is not available then excess electricity fraction rises up to 84% which can be used in residential needs or can be used in other agricultural needs.**

***Keywords*—Feasibility of solar irrigation; Sustainable irrigation; Photovoltaic pumping; Green farming; Green energy.**

I. Introduction

Agriculture is the vital component of the economy of Bangladesh in terms of GDP share and also lifestyle. The rural economy contributes 60% of the GDP [1] which mostly comes from the agricultural sector. Irrigation is an essential component of this agriculture. Proper irrigation at proper time increases the yield of crop significantly. Due to climate change and intensive agricultural practices of changing crops and cropping patterns the demand for irrigation water increased a lot [1]. Besides this, expansion of High Yielding Variety (HYV) rice cultivation increased the need for groundwater irrigation which is 73% of the total irrigation need [2]. To lower the cost of energy (COE) and increase the renewable fraction in the energy basket we have to use renewable solutions like solar photovoltaic energy, wind energy or other type of renewable energy in the irrigation sector as well.

A design and analysis of low cost solar water pump for irrigation in rural Bangladesh was done by researchers of Bangladesh University of Engineering & Technology [16]. Some researchers have also studied the prospect of hybrid solar irrigation system in Bangladesh [17]. Practical set up of solar irrigation pump system was done by various groups from industry and local people. Direct coupling of pump with solar panel for sustainable irrigation is also investigated by Bangladesh University of Engineering & Technology [18]. Application of photovoltaic array for water pumping as an alternative to diesel engines is investigated by various researchers of the world [12-15, 19-20].

In this work, a pre-feasibility study was done to see the optimal condition to replace the diesel powered irrigation pumps with solar PV powered motor-pumps in Bangladesh.

II. Present Irrigation Scenario of Bangladesh

Presently, in 2013-14 there were around 1630866 unit irrigation pumps in operation among which 96% are Shallow Tube Well (STW) and 2% Deep Tube Wells (DTW) and 2% Low Lift Pumps (LLP) [3]. The average elevation of Bangladesh from sea level is very low and static head of surface water is less than 20-30 m in most of the places [3]. Figure 1 shows the present ground water depth in different areas of Bangladesh.

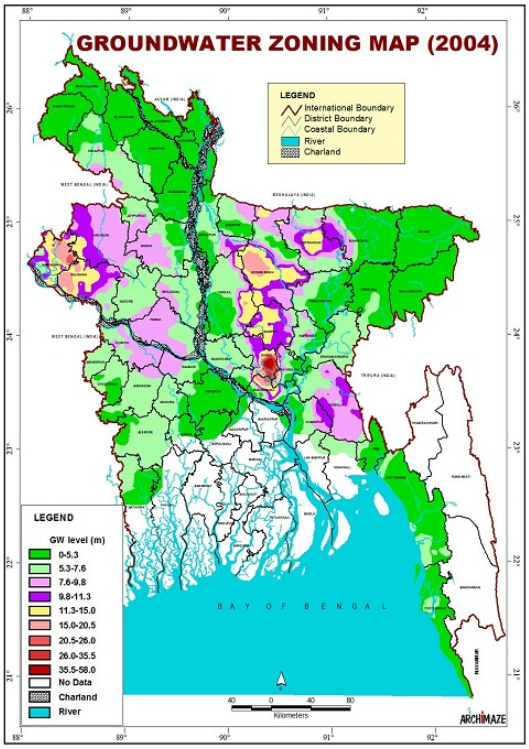

Fig. 1. Groundwater zoning map of Bangladesh [4].

978-1-4673-9257-0/15/$31.00 ©2015 IEEE

Because of this low ground water depth STWs are most popular in irrigation systems of Bangladesh. Figure 2 illustrates the irrigation pump units in 2012-13 and 2013-14 and their fuel mix. Number of irrigation pump units increased 58.8% in 2013-14 than that of 2012-13 and the number of electricity run units were very small in numbers in 2012-13 but in 2013-14 it increased 5 times. The reason behind this is governments declaration of low price of electricity for irrigation (2.51 BDT/unit) and high demand for irrigation water [5]. Whereas number of diesel run units decreased only 8% in 2013-14. From this scenario it is clear that the demand for irrigation water will increase significantly in the next upcoming years and satisfying this stepper demand with grid electricity will be quite impossible. As diesel run pumps cannot be a sustainable solution of this problem we need to find renewable sources to satisfy this demand as well as to replace the diesel run machines to ensure a sustainable irrigation system for future Bangladesh.

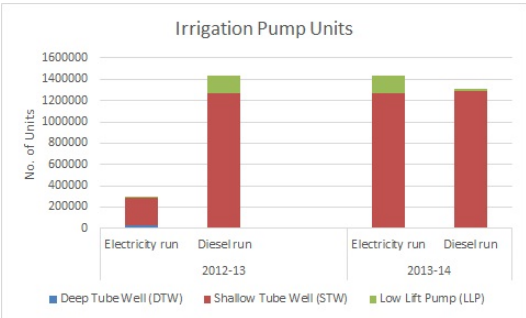

Fig. 2. Distribution of irrigation pump units according to their fuel consumption [3].

III. Characteristics of Solar PV powered motor-pumps

To calculate the working water head of the pump Koner [13] has given the following formula :

$$h = K_1(w^p)^2 - K_2(w_0 - w^p)^2 \tag{1}$$

where,
h: working water head, (m), w_p: pumping speed $(rads^{-1})$
K_1: voltage dependent water head constant, $m(rads^{-1})^{-2}$
K_2: flow rate dependent water head constant, $m(rads^{-1})^{-2}$
w_0: the speed of motor-pump system at no-flow condition, $(rads^{-1})$

The relation of water discharge to water head of the pump was given by Braunstein and Kornfield [14] as:

$$Q = K_3(h_0 - h)^{1/2} = K_3K_2^{0.5}(w_0 - w^p) \tag{2}$$

where,
Q: flow rate of a pump (ls^{-1}),
h_0: water head of a pump at no-flow condition, (m),
K_3: flow speed constant, $(ls^{-1}m^{-0.5})$
The speed-torque relationship is given as:

$$T^p = K_4(w^p)^2 \tag{3}$$

where,
T^p: pump torque, (Nm), K_4: flow-water head constant of a pump, $(ls^{-1}m^{-1/2})$
The equations for DC series motor was deduced by Hsiao and Blevins [15] as follows:

$$V^m = MI^m w^m + I^m R_t \tag{4}$$

$$T^m = M(I^m)^2 \tag{5}$$

$$M = M_0(w^m/(w_0^m)) \tag{6}$$

where,
V^m: motor terminal voltage, (V),
M_0: motor constant, (NmA^{-2})
I^m: armature current of a motor, (A)
w^m: motor shaft speed, $(rads^{-1})$
R_t: Field coil and armature resistances of motor, (ω)

Finally, the efficiency of the motor pump is given by Kolhe, Joshi, and Kothari [12] as:

$$\eta_{mp} = \frac{\rho g Q H}{VI} \tag{7}$$

and the overall efficiency as:

$$\eta = \eta_e \eta_{mp} \tag{8}$$

where,
η_e: PV array efficiency, Q: flow rate, (m^3s^{-1})
H: head of water, (m), g: constant of gravity $(9.81ms^{-2})$
ρ: density of water, (kgm^{-3})

IV. Availability of Solar Energy and Precipitation in Bangladesh

The requirement of irrigation for crops depends on mostly two factors- amount of rainfall and solar insolation. Bangladesh receives most of its rainfall (around 90%) in the monsoon from June to September [6] as shown in fig. 3. In the other months due to lack of rainfall crop production is hampered. So we need to irrigate the crops from surface water in those months.

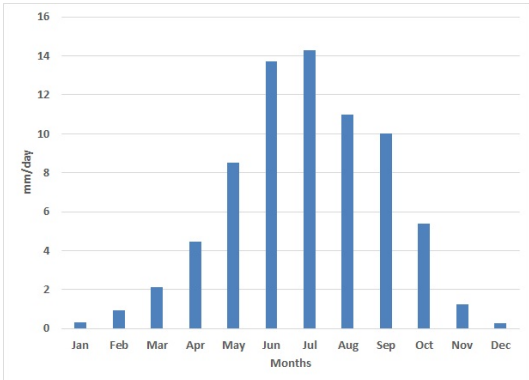

Fig. 3. Monthly Averaged Yearly Precipitation: 22 years average (1983-2005) [7].

On the other hand solar insolation level is pretty high from 4-5 kWh/day around the year [7] which ensures the potential

of solar power harvesting for irrigation in Bangladesh. In fig. 4 the 22 years average of monthly averaged daily solar insolation and clearness index is shown. The effectiveness of solar powered irrigation pump mostly depends on the solar radiation received and thus Bangladesh is a very suitable place for solar irrigation. Besides this, we can use a storage tank to harvest rain water.

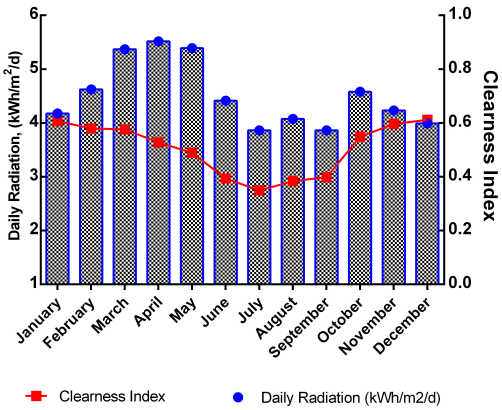

Fig. 4. Monthly averaged daily solar insolation with superimposed clearness index [7].

V. Modeling the Irrigation Pump System in HOMER

HOMER is a micropower optimization and simulation software developed by National Renewable Energy Laboratory (NREL), USA. The word HOMER came from the abbreviation of "Home Energy". It simulates the operation of a system by calculating energy balance equations for 8,760 hours in a year and compares the solutions with different possible configuration and finds the best possible and economically suitable solution [8].

As irrigation water requirement is not a primary load and can be deferred for a later time the load was modelled as a deferrable DC load in HOMER. The deferrable load, PV arrays and a battery element was connected in the DC bus, and a diesel powered AC generator was added in the AC bus coupled with a converter to power the DC bus. The schematic diagram is shown in fig. 5.

A. Modeling the deferrable load

Irrigation for crops can be delayed for 1-3 days without any disturbance in the production process [4]. Therefore we have assumed our load to be a deferrable load. A deferrable load is an electrical load that must be met within some time period, but the exact timing is not important [9]. Loads are normally classified as deferrable because they have some storage associated with them. In irrigation system we can use a storage tank, pond or canals as the storage system for the deferrable load.

Three different crops were taken to find the average water requirement per hectare land. The average water need was calculated as shown in the table 1 [10].

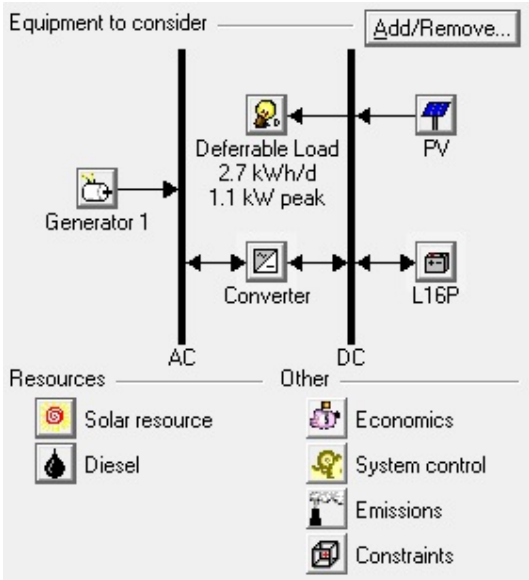

Fig. 5. Schematic diagram of the simulation in HOMER

TABLE I
Average monthly water need for crops

Name of the crops	Required Water Volume (m3/hectare)	Average (m3/hectare/year)	Average (l/hectare/month)
Rice	850		
Wheat	700	750	62500
Cotton	700		

A typical 1.1 kW solar pump has a flow rate of 55 LPM with 20m water head [11]. So, at rated power the solar pump can lift 3300 lit/hour. Ten hectares of sample land was taken to irrigate per day and therefore taking these values and the amount of precipitation approximate values of monthly averaged daily water pumping load was calculated as shown in table 2.

As the time of rainfall over the year is uncertain so 0.5 kWh/day load was added for supplementary irrigation need during May September. Figure 6 shows the daily load profile of our deferrable load.

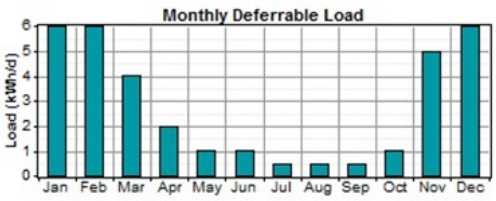

Fig. 6. Monthly average daily deferrable water pumping load modeled for HOMER.

B. Other input parameters

The present market condition was analyzed to find the current prices of PV arrays, diesel generator set, converter and batteries. Table 3 lists the other input values given in HOMER.

TABLE II
CALCULATION OF MONTHLY AVERAGED DAILY WATER NEED AND ENERGY REQUIREMENT.

Month	Average water requirement (l/hectare/month)	Rainfall (l/hectare/month)	Average irrigation requirement (l/hectare/month)	Average irrigation requirement (l/10hectare/day)	Average Energy need, kWh/day
Jan	62500	300	59500	19833.33	6.01
Feb	62500	9200	53300	17766.66	5.38
Mar	62500	21300	41200	13733.33	4.16
Apr	62500	44400	18100	603.33	0.18
May	62500	85100	-22600	-7533.33	0
Jun	62500	137000	-74500	-24833.3	0
Jul	62500	143000	-80500	-26833.3	0
Aug	62500	110000	-47500	-15833.3	0
Sep	62500	100000	-37500	-12500	0
Oct	62500	53800	8700	2900	0.87
Nov	62500	12500	50000	16666.66	5.05
Dec	62500	2800	59700	19900	6.03

TABLE III
DIFFERENT INPUT VALUES OF DIFFERENT COMPONENTS

Name of the Component	Cost ($/kW)	Replacement Cost ($/kW)	Operation & Maintenance Cost	Sizes to consider
PV array	1000	900	$ 0 (/year)	0,1-10 kW
Diesel Generator	600	500	$ 0.05 (/hr)	0,1,2,4,6,8 kW
Converter	500	400	$ 50 (/year)	0,2,4,6,8 kW
Trojan L16P Battery	300 (per piece)	200 (per piece)	$ 30 (/year)	0,2,4,6,8

C. Sensitivity Variables

A sensitivity analysis can be performed by HOMER by entering multiple values for a particular input variable. An input variable for which multiple values are specified is called a sensitivity variable [9]. HOMER repeats its optimization process for each value of that variable and lets you see how the results are affected.

As we want to see the feasibility of replacing diesel generator with PV powered motor-pump system several sensitivity variables was used to find the best possible solutions. Table 4 lists all the sensitivity variables used in HOMER.

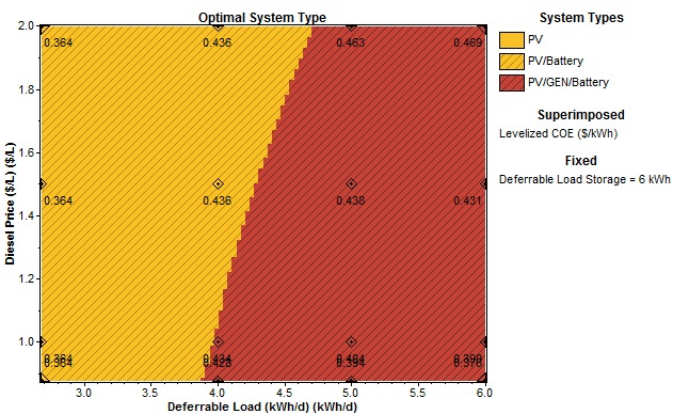

Fig. 8. Effect of diesel price.

VI. ANALYSIS AND RESULTS

After doing the analysis HOMER gives the optimal system type graph superimposed with levelized Cost of Energy (COE)

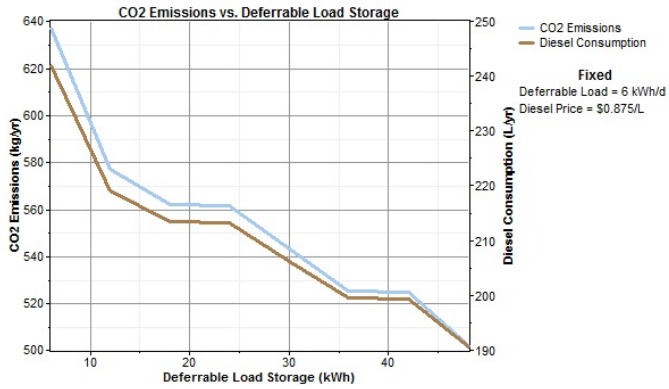

Fig. 9. CO_2 emission vs. deferrable load storage.

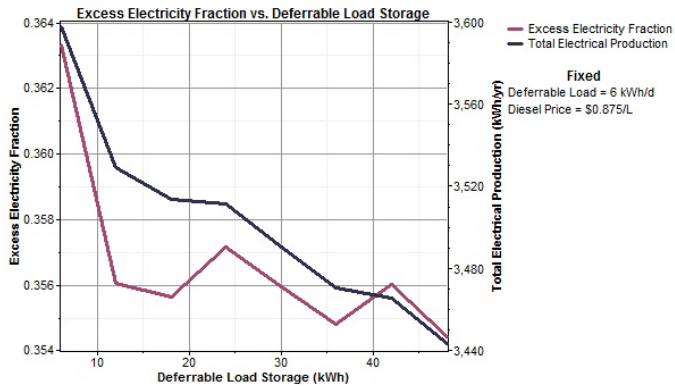

Fig. 10. Excess electricity fraction Vs. Deferrable load storage.

TABLE IV
SENSITIVITY VARIABLES

Sensitivity Variable	Input Values	Reason why this sensitivity variable was used
Deferrable Load (kWh/day)	2.67 (scaled annual average), 4, 5, 6	To find the optimum system with variable load.
Deferrable Load Storage Capacity (kW)	6, 12, 18, 24, 30, 36, 42, 48	To see how water storage capacity affects the output of the system
Diesel Price ($)	0.875 (present cost), 1, 1.5, 2	To find optimum system with a higher diesel price.

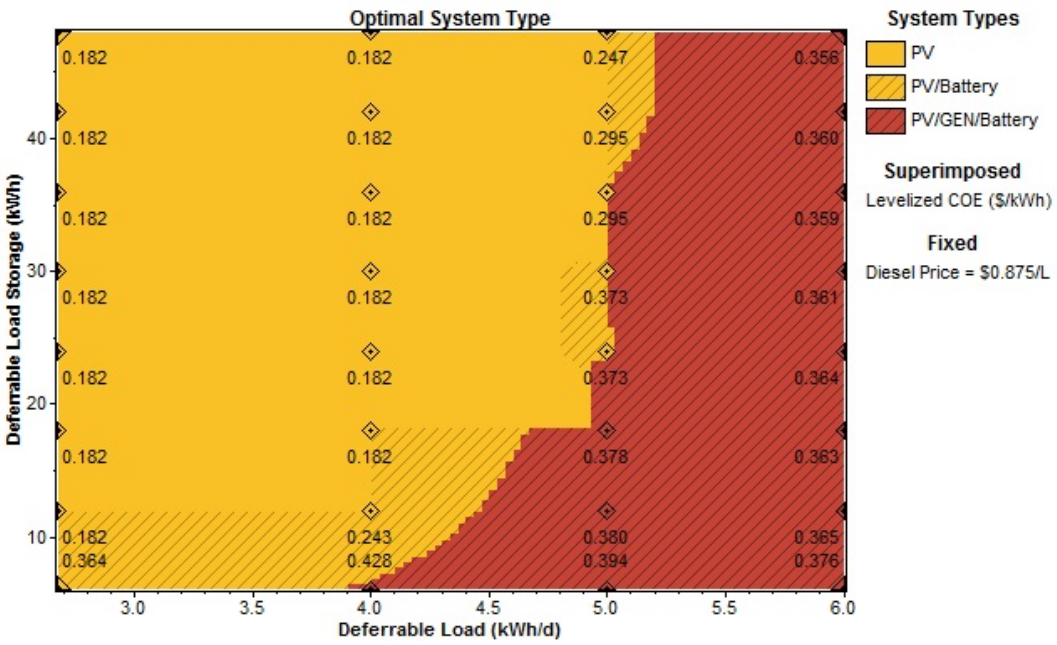

Fig. 7. Optimal system type superimposed with Levelized COE.

as shown in fig. 7. It is evident that PV has the most dominant portion in the graph. With low deferrable load storage PV needs battery backup but with high storage PV itself is sufficient. The levelized COE is as low as $0.182 with PV in operation. Interestingly using only diesel generator is not at all feasible as there is no portion of the graph with only generator shown.

By changing the axis in HOMER we can also find the graph of optimal system type with variable diesel price as shown in fig. 8. It is evident that as the diesel price increases PV becomes more feasible.

Using the line graph option fig. 9 10 shows the CO2 emissions and excess electricity fraction with the change of deferrable load storage. It is very clear from the graph that if there is low deferrable load storage which is water storage tank in our case, there will be a frequent need for diesel generator operation. PV arrays need solar insolation which is not a continuous source of energy and therefore use of a larger storage tank is important. With a larger storage tank added in the pump system will give higher system stability with lower possible COE.

Besides this, lower storage capacity will increase the excess electricity fraction significantly which can be as high as 83.2% of the total production. To lower this excess electricity fraction either we have to use larger storage tank or we can supply this excess electricity to local consumers or can run other agricultural equipment.

VII. CONCLUSIONS

From the above analysis the following conclusions can be made:

01. Stand-alone operation of diesel generator for irrigation purposes is not at all feasible in Bangladesh. So, diesel generators should be replaced with PV powered motor-pump systems as soon as possible.

02. Use of a larger water storage tank is very important. CO2 emissions and excess electricity fractions can be lowered to 0% if a larger storage tank is used.

03. If a larger storage tank is not available then the excess electricity can be supplied to the local consumers or can be used in other agricultural energy need.

ACKNOWLEDGMENT

We would like to express our gratitude to Institute of Energy, University of Dhaka for aiding with technical support. We would also like to thank Bangladesh Meteorological Department (BMD), Bangladesh Agricultural Development Corporation (BADC), Bangladesh Agricultural Research Council (BARC), and Dhaka Electric Supply Company Limited (DESCO) for their data and support.

REFERENCES

[1] M. A. H. Chowdhury, M. S. Hassan, "Handbook of Agricultural Technology", BARC, 2013.

[2] S. G. Hussain, A. Iqbal, "Research priorities in Bangladesh agriculture", BARC Feb 2011.

[3] (2015) Bangladesh Agricultural Development Corporation (BADC) website. [Online]. Available: http://www.badc.gov.bd/

[4] (2015) Bangladesh Agricultural Research Council website. [Online]. Available: http://www.barc.gov.bd/

[5] (2015) Dhaka Electric Supply Company Limited (DESCO) website. [Online]. Available: https://www.desco.org.bd/

[6] (2015) Bangladesh Meteorological Department (BMD) website.[Online]. Available: http://www.bmd.gov.bd/?/home/

[7] (2015) NASA data. [Online]. Available: http://eosweb.larc.nasa.gov/sse/

[8] T. Lambert, P. Gilman, P. Lilienthal, "Micropower system modelling with HOMER", NREL.

[9] HOMER software help index (Version 2.68beta).

[10] M. T. Khan, S. Sarkar, S. Hossain, A. U. Ahmed, and B. B. Pathik, "The Feasibility Study of Solar Irrigation: Economical Comparison between Diesel and Photovoltaic Water Pumping Systems for Different Crops", International Conference on Electrical Information and Communication Technology (EICT), 2013.

[11] (2015) Lorentz Pump System data sheet. [Online]. Available: http://www.lorentz.de/(accessed on 10 July 2015).

[12] M. Kolhe, J. C. Joshi, and D. P. Kothari, "Performance Analysis of a Directly Coupled Photovoltaic Water-Pumping System", IEEE Trans. Energy Conversion, vol. 19, no. 3, pp. 613-618, September 2004.

[13] P.K. Koner, "Optimization techniques for a photovoltaic water pumping system", Renewable Energy, Vol. 6, No. 1, pp. 53-62, 1995.

[14] A. Braunstein and A. Kornfield, "Analysis of solar powered electric water pump", Solar Energy, vol. 27, no.3, pp. 235-240, 1981.

[15] Y. R. Hsiao and B. A. Blevins, "Direct coupling of photovoltaic power source to water pumping system". Solar Energy, Vol. 32, No. 4, pp. 489-498, 1984.

[16] S. I. Khan, M. M. R. Sarkar, and M. Q. Islam, "Design and alalysis of a low cost solar water pump for irrigation in Bangladesh", Journal of Mechanical Engineering, Vol. ME 43, No. 2, December 2013.

[17] M. A. Hasnat, M. N. Hasan, and N. Hoque, "A brief study of the prospect of hybrid solar irrigation system in Bangladesh", International Conference on Mechanical, Industrial and Energy Engineering 2014, 25-26 December, 2014, Khulna, Bangladesh.

[18] S. M. S. Reza, and M. N. I. Sarkar, "Design and Performance Analysis of a Directly-Coupled Solar Photovoltaic Irrigation Pump System at Gaibandha, Bangladesh", 3rd International Conference on Green Energy & Technology (ICGET) 2015, 11-12 September, 2015, Dhaka, Bangladesh.

[19] M. Al-Smairan, "Application of photovoltaic array for pumping water as an alternative to diesel engines in Jordan Badia, Tall Hassan station: Case study", Renewable and Sustainable Energy Reviews, Vol. 16, (2012), pp. 45004507.

[20] J.K. Kaldellis, G.C. Spyropoulos, K.A. Kavadias, and I.P. Koronaki, "Experimental validation of autonomous PV-based water pumping system optimum sizing", Renewable Energy, Vol. 34, (2009), pp. 11061113.

Cost Analysis of Rural Distribution Systems with Three Phase and Single Phase Tap Lines

S. K. Roy
Department of Electrical and Electronic Engineering
Khulna University of Engineering and Technology
Khulna-9203, Bangladesh
Email: engrsanjib2010@gmail.com

N. K. Roy
Department of Electrical and Electronic Engineering
Khulna University of Engineering and Technology
Khulna-9203, Bangladesh
Email: nkroy@eee.kuet.ac.bd

***Abstract*—Rural Distribution Systems (RDSs) are expanding abruptly day by day. With this continuous expansion, the distribution loss is increasing deliberately as a coherent parameter. Constructing single phase HT (high tension) line, it becomes more alarming with respect to loss as well as system management. This paper highlights the advantages of three phase tap lines for the reduction in line loss compared to single phase. A cost analysis is carried out by designing all HT lines of RDSs with three phase taps instead of single phase taps and the obtained result is compared with the single phase tap line. Then, an optimum length of single phase tap line is determined using simplex method for linear programming considering the cost of three phase tap line as a standard. The results show that more area can be electrified using three phase tap lines compared to the single phase tap line with the same cost.**

Keywords—cost analysis; power loss; rural distribution system (RDS); single and three phase tap line; simplex method.

I. INTRODUCTION

The primary objective of a distribution power system design is to deliver reliable power to the remotest consumer with maximum efficiency and minimum cost [1]-[3]. As consumer, so load, is increasing, to meet the objective it is essential to think about the restructuring of power distribution systems [4]-[9].

Bangladesh Rural Electrification Board (BREB), among all the Electricity Distribution Utility of Bangladesh, is the largest having 2,70,000 Km of distribution line with 1,22,00,000 nos. of different category consumers purchasing 18,80,000 MWhr energy per month. The average sales per month is 16,10,000 MWhr to the consumers. Therefore, 2,70,000 MWhr of energy waste as system loss [10], which is 12.92% of the total purchased energy. This loss includes mostly technical loss, as well as minor non-technical loss. One of the important factors to increase technical loss is the design standards and considerations for the construction of HT (High Tension) and also LT (Low Tension) lines adopted so far.

As it is known that from the very beginning BREB follows the standard to construct three phase backbone distribution HT lines of 11 kV voltage with both three phase and single HT taps of 11 kV and 6.35 kV voltage, respectively and both three phase and single phase LT lines of 0.415 kV and 0.23 kV voltage, respectively. Single phase HT and LT lines are taken into consideration considering the lower construction cost for rural people. If we construct a single phase line, we do not have any option to construct other than single phase line until it is renovated or converted. When we start with a few span of single phase line, due to Area Coverage Rural Electrification (ACRE) [11], it becomes a line of fifty spans, even hundred-fifty spans, of single phase line, which ultimately creates operational problem, unbalance system and at the same time increases line loss, consequently system loss.

It is obvious that for the same load, line loss is lesser for a three phase system than that of a single phase [11]. However, the line construction and maintenance cost in a three phase system is higher than that of a single phase system. With the practical hazard for operation management, system management, and loss management, a narrow thinking was started-'Are single phase distribution lines cost effective with all respect?' To be clear from a misty thinking, this research has conducted over both single phase and three phase lines considering line loss, construction and maintenance cost for their whole life, which is normally considered as 30 years for a rural distribution line.

Traditional tapping lines of BREB are single phase which produce an unbalance system due to the loading in phases individually and it is not expected from system management and economical viewpoints. Therefore, three phase power distribution systems may be the right choice for their superior power carrying capability at a reduced cost. However, it needs a rigorous investigation before implementing three phase taps to avoid unnecessary cost.

In this paper, a RDS is designed with single phase and three phase taps for a comparative analysis. Moreover, an Excel Solver [12, 13] is used to calculate the optimum length of the single phase tap lines which determines the area coverage by tap lines in the RDS. The system is optimized using simplex algorithm for linear programming (LP). In the next of this paper, following topics are discussed: Why three phase?, losses in power distribution system, costs considered, Excel solver algorithm, case study and conclusion.

978-1-4673-9257-0/15/$31.00 ©2015 IEEE

II. WHY THREE PHASE?

A three phase line generates three individual "waves" of power which joins three alternating waves of the same frequency, each 120 degrees out of phase with each other. The power in a three phase power supply never goes down to zero, but in single-phase the power goes down to zero 3 times for every cycle as shown in Fig.1. Thus, in a three phase power supply, the power delivered is constant [14]. To fulfill the requirement of balance system and to avoid neutral **c**urrent in grounded Y-connected line, which incur additional loss, three phase lines are better choice for transmitting power.

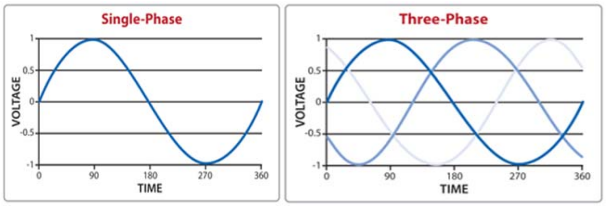

Fig.1. Single phase and three phase wave shape [14].

III. LOSSES IN POWER DISTRIBUTION SYSTEM

Losses in power distribution system is a term which may express as the difference between the total power received by a 11 kV feeder and total power delivered to the individual consumer. If P_R is the power received and P_D is the total power delivered to the consumer connected to this feeder; then power loss P_{loss} will be [11]

$$P_{loss} = P_R - P_D \quad (1)$$

A. Categorization of Losses:

The power distribution losses are commonly classified into two categories: 1) technical loss and 2) non-technical Loss.

1) Technical Losses: Technical losses are internal to the distribution power system and occur in the equipment installed in that system. In RDS, it occurs for the power dissipation in the lines (HT/LT), distribution transformers, junctions and joints, service drops, etc. [15].

2) Non-Technical Losses: Non-technical losses occur due to actions external to the power system, which includes primarily of electricity theft, not running meters and errors in accounting and record-keeping [15].

B. Mathematical Representation of Technical Losses:

In a system, technical loss means the power losses incurred by the physical properties of components connected to it. The power loss, P_{loss} (kWh) is proportional to the total line resistance (R_T) of the conductor and the square of the current (I) flows through that portion of line in Amps [11].

So, power loss is [11]

$$P_{loss} \text{ /Month} = (I^2 \text{ x } R_T \text{ x LsF x Total Hour})/1000 \text{ kWh} \quad (2)$$

where, R_T = No. of phase x R_p x line length in Km
R_p= Resistance per phase per Km of line.
Ls.F. = Loss Factor
= 0.85*(Load factor)^2+0.15*(Load factor) (3)

Load factor is defined as the ratio of average power delivered to the peak load of a certain period. The value of load factor for a 11 kV feeder of the RDS varies between 40% to 60%.

IV. COSTS CONSIDERED

Rural Distribution lines are constructed by both wooden poles and SPC (Spun Pre-stressed Concrete) poles with wooden cross-arms, GI hardware and ACSR (Aluminum Conductor Steel Reinforced) conductors. Taken geographical condition into account, the life of constructed distribution lines is considered to be almost 30 years.

In this paper, to optimize the design cost, following costs are considered [15]:

1) Cost of technical loss unit: The total cost for technical loss is calculated multiplying the technical loss unit (kWh) by per unit rate (Tk.), which occurs for whole of the life if the line is under energized condition.

2) Cost of distribition line construction: The costs for construction of distribution lines include material costs and labour costs, which occur once in its life.

3) Cost of maintenance: The maintenance cost of lines is to maintain the line in working condition which includes reparing, ROW (Right of Way) clearing, etc. This cost also occurs over whole life of the line until it becomes idle.

V. EXCEL SOLVER AS OPTIMIZATION TOOL

The Microsoft Excel Solver is very popular and the most widely used general purpose optimization tool. The Microsoft Excel Solver combines the functions of a graphical user interface (GUI), an algebraic modeling language like general algebraic modeling system (GAMS) or a mathematical programming language (AMPL), and optimizers for linear, nonlinear, and integer programs [12, 13].

The flowchart of the proposed methodology is shown in Fig. 2. The algorithm is described below.

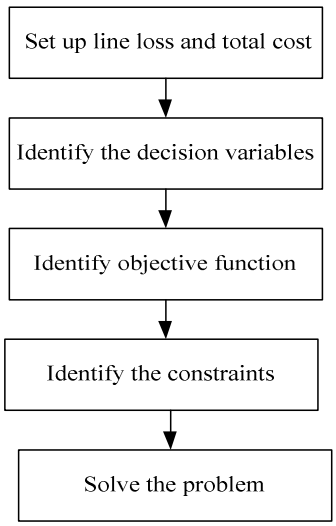

Fig. 2. Flowchart of the proposed methodology.

• *Data set up:* The first step of the proposed method is to set up distribution line loss data and total cost which includes line loss cost, construction cost and maintenance cost of the line.

• *Decision variables:* The decisions of the problem are represented as decision variables. The length of single phase tap is considered here as a decision variable.

• *Objective function:* The objective of the problem is to minimize the total cost incurred by line loss, construction and maintenance cost. For this purpose, the target value is set up which is the difference between the cost of three phase and single phase tap line.

• *Constraints:* The limitations or requirements of the problem are expressed as inequalities or equations in decision variables. The upper and lower limit of the considered tap line is specified as constraints.

The Excel Solver builds a representation of the model suitable for an optimizer by extracting the optimization problem from the spreadsheet formulas. For a linear programming (LP) problem, the focus of this model representation is the LP coefficient matrix, which in general terms, is the Jacobian matrix of partial derivatives of the problem functions (objective and constraints) with respect to the decision variables. For a linear problem, the matrix entries are constant and only need to be evaluated once at the start of the optimization [13].

The Excel Solver uses finite differences and supports all of Excel's built-in functions as well as user-written functions. In calculating finite differences, the [*i,j*]-th element of the Jacobian matrix is approximated by the formula [13].

$$\frac{|f_i(x+\delta e_j)-f_i(x)}{\delta} \quad \text{where } \delta = eps\,|1+x_j| \qquad (4)$$

The solver perform linearity test after it had obtained a solution using the simplex method. It uses these solution values x^* and the initial values x^0 for the variables, to check that the objective and each constraint function $f_i(x)$ until satisfied the following condition [13].

$$|f_i(x^*)-(f_i(x^0)+\nabla f_i(x^0)(x^*-x^0))| \le tol \qquad (5)$$

where $\nabla f_i(x^0)$ is the function gradient and ≥ is the precision value in the solver options dialog box with a default value of 10^{-6}.

The Solver results dialog box is displayed whenever the solver stops and allows the user to keep the solution or restore the original values of the variable cells to generate one or more reports.

VI. CASE STUDY

Let us consider a distribution line feeding from a sub-station, which we shall call as three phase back bone line. Line to line voltage of the backbone line is 11 kV. The line is constructed by # 4/0 ACSR conductor. The feeder backbone line distributes 1.6 MW load. We observe in the next study what will happen, what is the effect on system loss if tap lines from the backbone are constructed single phase and three phase.

A. *When All Taps are Single Phase:*

Consider 10 Km of backbone line for loss calculation. Current feeding at starting point for R-phase is 110 Amps, Y-phase is 85 Amps & B-phase is 75 Amps. For single phase tap the system is unbalance at the starting. A phase balancing is critical for this type of long and loaded single phase tap.

Here in R-phase there are two single phase tap. First tap is 5 Km and second tap is 10 Km apart from the starting point. First tap carries 30 Amps current, second tap carries 60 Amps. In Y-phase there are also two single phase tap. First tap is 3 Km and second tap is 8 Km apart from the starting point. Here, first tap carries 30 Amps current, second tap carries 45 Amps. In B-phase there are two single phase tap. First tap is 4 Km and second tap is 9 Km apart from starting point. First tap bears 30 Amps current, second tap carries 36 Amps. The connection and currents are shown in Fig. 2 given below:

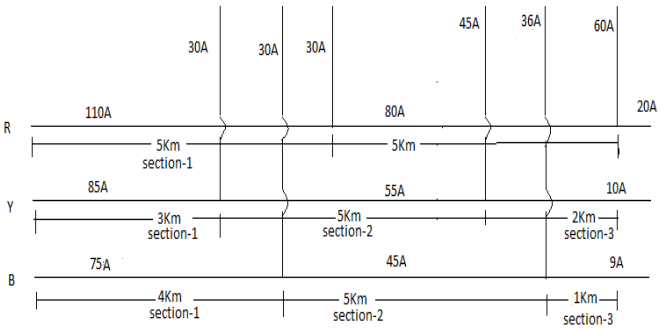

Fig. 2. Three phase system with single phase tap

For simplicity we consider load factor=0.5 for all over the line. Also, consider all tap lines (single phase & three phase) are constructed by #3 ACSR bare conductor. Resistance per Km per phase of #4/0 ACSR & #3 ACSR is R_p & R_t , value of which is 0.3522 Ohm & 1.3946 Ohm, respectively.

So, loss factor = 0.85*(Load factor)^2+0.15*(Load factor)
= 0.85*(0.5)^2+0.15*(0.5)
= 0.2875

Sample loss calculation for Section-1, Tap-1 is given below:

R-phase, Section-1:

Line Length : 5 Km
Current thru the section , I_1 : 110 Amps
Line Conductor : # 4/0

So, P_{loss} /Month = (I_1^2 x R_T x L.F x Total Hour)/1000 KWh
Here, R_T = 1 x 0.3522 x 5 Ohm=1.761 Ohm
P_{loss} /Month = [(110)^2 x 1.761 x 0.2875x720)]/1000 KWh
= 4410.77 KWh

R-phase, Tap-1:

Line Length : 5 Km
Current thru the section , I_{rt1} : 30 Amps
Line Conductor : # 3 ACSR

So, P_{loss} /Month = (I_{rt1}^2 x R_T x L.F x Total Hour)/1000 KWh
Here, R_T = 1 x 1.3946 x 5 Ohm=6.973 Ohm
P_{loss} /Month = [(30)^2 x 6.973x0.2875x720)]/1000 KWh
= 1299.07 KWh

Calculation for other sections and taps have summarized in Table I considering construction cost of three phase line of #4/0 ACSR per Km is Tk. 13,00,000, single phase line of #3 ACSR per Km is Tk. 9,00,000.

B. *When All Taps are Three Phase:*

Consider the same 10 Km of backbone line. Total load flowing through the phases was (110+85+75) = 270 Amps. So, the average load per phase is 90 amps. If all the taps or minimum the long and loaded taps are three phase, then we can get balance system, which was not easily possible for the single phase system. So, we can consider in this case, per phase current is equal and the value is 90 amps.

TABLE I. THREE PHASE LINE WITH SINGLE PHASE TAP

	A	B	C	D	E	F	G	H	I	J
1	Table 1 Three Phase Line With Single Phase Tap									
2										
3	Sl no.	Load, Amp	Resistance	Length, km	Loss per month, kwh	Loss in whole life, KWh	Loss in whole life, Tk	Cost for Line Construction/ Km, TK	Total Cost for Line Construction, TK	Maintenance cost in whole life, Tk
4	1	110	0.3522	5.00	4410.78	1587879.61	9527277.67	1300000	6500000	140000.00
5	2	30	1.3946	5.00	1299.07	467665.16	2805990.98	900000	4500000	105000.00
6	3	80	0.3522	5.00	2332.97	839870.21	5039221.25	1300000	6500000	140000.00
7	4	60	1.3946	15.00	15588.84	5611981.97	33671891.81	900000	13500000	315000.00
8	5	85	0.3522	3.00	1580.22	568880.84	3413285.02	0	0	0.00
9	6	30	1.3946	5.00	1299.07	467665.16	2805990.98	900000	4500000	105000.00
10	7	55	0.3522	5.00	1102.69	396969.90	2381819.42	0	0	0.00
11	8	45	1.3946	12.00	7014.98	2525391.89	15152351.31	900000	10800000	252000.00
12	9	10	0.3522	2.00	14.58	5249.19	31495.13	0	0	0.00
13	10	75	0.3522	4.00	1640.37	590533.74	3543202.44	0	0	0.00
14	11	30	1.3946	10.00	2598.14	935330.33	5611981.97	900000	9000000	210000.00
15	12	45	0.3522	5.00	738.17	265740.18	1594441.10	0	0	0.00
16	13	36	1.3946	7.00	2618.92	942812.97	5656877.82	900000	6300000	147000.00
17	14	9	0.3522	1.00	5.91	2125.92	12755.53	0	0	0.00
18					42244.71	15208097.07	91248582.44		61600000.00	1414000.00
19									Total cost,1-0	154262582.44

For the first, we consider the tap which was connected in Y-phase in the single phase tapping. The load was 30 amps. If the tap was constructed in three phase, we can get balanced load of 10 Amps per phase. With the same consideration, second tap which is 4 Km apart from the starting point, carries 10 Amps per phase. Thirdly, the tap is 5 km apart from starting point and carries balanced load of 10 amps per phase. Fourth tap which is 8 Km apart from starting point, carries balanced load of 15 amps per phase. For fifth and sixth tap which are apart 9 Km & 10 km from the starting point and carries balanced load of 12 Amps & 20 Amps per phase. The connection and currents are shown in Fig. 3 given next.

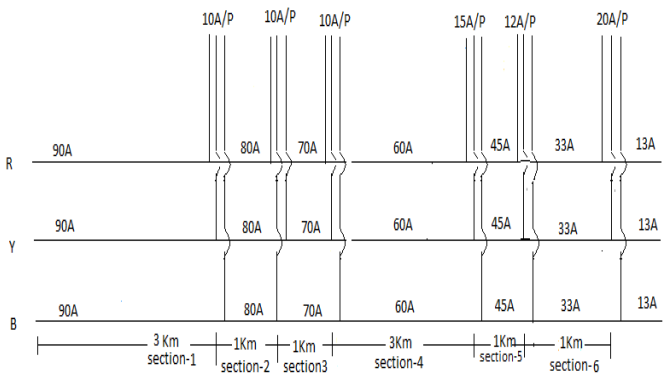

Fig. 3. Three phase system with three phase tap.

Sample loss calculation for Section-1, Tap-1 is given below:

Section-1:

Line Length : 3 Km
Current thru the section , I_{r1} : 90 Amps
Line Conductor : # 4/0

So, P_{loss} /Month = $(I_1^2 \times R_T \times L.F \times \text{Total Hour})/1000$ kWh
Here, R_T = 3 x 0.3522 x 5 Ohm=5.283 Ohm
P_{loss} /Month = $[(90)^2 \times 5.283 \times 0.2875 \times 720)]/1000$ KWh
= 5314.80 kWh

Tap-1:

Line Length : 5 Km
Current thru the section , I_{t1} : 10 Amps
Line Conductor : # 3 ACSR

So, P_{loss} /Month = $(I_{t1}^2 \times R_T \times L.F \times \text{Total Hour})/1000$ kWh
Here, R_T = 3 x 1.2673 x 5 Ohm=19.0095 Ohm
P_{loss} /Month = $[(10)^2 \times 19.0095 \times 0.2875 \times 720)]/1000$ kWh
= 393.50 kWh

Calculation for other sections and taps have summarized in Table II given below.

TABLE II. THREE PHASE LINE WITH THREE PHASE TAP

	A	B	C	D	E	F	G	H	I	J
1	Table 2 Cost for Three Phase Line with Three Phase Tap									
2										
3	Sl no.	load, amps	resistance	length, km	Loss per month, KWh	Loss in whole life, KWh	Loss in whole life, Tk	Cost for Line Construction/ Km, TK	Total Cost for Line Construction, TK	Maintenance cost in whole life, Tk
4	1	90	0.3522	3	5314.80	1913329.32	11479975.91	1300000	3900000	84000.00
5	2	10	1.2673	5	393.50	141658.79	849952.76	1200000	6000000	140000.00
6	3	80	0.3522	1	1399.78	503922.12	3023532.75	1300000	1300000	28000.00
7	4	10	1.2673	10	786.99	283317.59	1699905.53	1200000	12000000	280000.00
8	5	70	0.3522	1	1071.71	385815.38	2314892.26	1300000	1300000	28000.00
9	6	10	1.2673	5	393.50	141658.79	849952.76	1200000	6000000	140000.00
10	7	60	0.3522	3	2362.13	850368.59	5102211.51	1300000	3900000	84000.00
11	8	15	1.2673	12	2124.88	764957.49	4589744.93	1200000	14400000	336000.00
12	9	45	0.3522	1	442.90	159444.11	956664.66	1300000	1300000	28000.00
13	10	12	1.2673	7	793.29	285584.13	1713504.77	1200000	8400000	196000.00
14	11	33	0.3522	1	238.18	85745.50	514472.99	1300000	1300000	28000.00
15	12	20	1.2673	15	4721.96	1699905.53	10199433.17	1200000	18000000	420000.00
16					20043.63	7215707.33	43294244.00		77800000.00	1792000.00
17									Total cost,3-Ø	122886244.00

Analyzing two costs mentioned in Table I and Table II, it is clear that the cost for three phase line with single phase tap is higher than that of all three phase tap. However, another objective of this paper is to compare the area covered by the three phase tap and single phase tape considering the cost of Table II as standard.

If the cost of single phase line becomes same as that of three phase line i.e. cost difference reduced to '0' (zero), then that will be the optimal design with single phase. This can be done by Excel Solver Program. To obtain objective function, the target cell (J22) is set as '0' and this zero may be achieved by changing the length of single phase line i.e. cell no. D5, D7, D9, D11, D14, D16 assuming the constraints of this cell value not below zero i.e. no negative value is allowed. Maximum value is set as the exact length of single phase line. Table III shows the optimized length of single phase tap line in Column D.

TABLE III. DIFFERENCE MINIMIZES TO ZERO BY EXCEL SOLVER

	A	B	C	D	E	F	G	H	I	J
1	Table 1 Three Phase Line With Single Phase Tap									
2										
3	Sl no.	Load, Amp	Resistance	Length, km	Loss per month, kwh	Loss in whole life, KWh	Loss in whole life, Tk	Cost for Line Construction/ Km, TK	Total Cost for Line Construction, TK	Maintenance cost in whole life, Tk
4	1	110	0.3522	5.00	4410.78	1587879.61	9527277.67	1300000	6500000	140000.00
5	2	30	1.3946	3.09	803.29	289183.57	1735101.44	900000	2782602.121	64927.38
6	3	80	0.3522	5.00	2332.97	839870.21	5039221.25	1300000	6500000	140000.00
7	4	60	1.3946	10.92	11353.12	4087123.26	24522739.55	900000	9831849.835	229409.83
8	5	85	0.3522	3.00	1580.22	568880.84	3413285.02	0	0	0.00
9	6	30	1.3946	3.09	803.29	289183.57	1735101.44	900000	2782602.121	64927.38
10	7	55	0.3522	5.00	1102.69	396969.90	2381819.42	0	0	0.00
11	8	45	1.3946	9.19	5371.52	1933746.03	11602476.15	900000	8269788.62	192961.73
12	9	10	0.3522	2.00	14.58	5249.19	31495.13	0	0	0.00
13	10	75	0.3522	4.00	1640.37	590533.74	3543202.44	0	0	0.00
14	11	30	1.3946	8.09	2102.36	756848.74	4541092.42	900000	7282602.121	169927.38
15	12	45	0.3522	5.00	738.17	265740.18	1594441.10	0	0	0.00
16	13	36	1.3946	4.77	1786.06	642982.26	3857893.58	900000	4296491.865	100251.48
17	14	9	0.3522	1.00	5.91	2125.92	12755.53	0	0	0.00
18					34045.33	12256317.02	73537902.13		48245936.68	1102405.19
19									Total cost,1-Ø	122886244.00
20									Total cost,3-Ø	122886244.00
21										
22									Difference	0.00

Figure 4 shows the original and optimized lengths of the single phase tap lines from which it can be seen that lengths of all the single phase taps are reduced after optimization. These results signify that single phase taps will cover less area compared to three phase tap lines. Thus, three phase taps are cost effective for covering the whole area of the considered RDS.

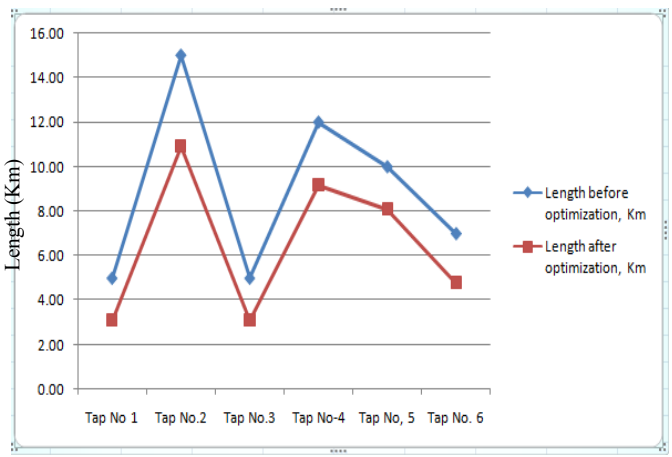

Fig. 4. Length of single phase tap before and after optimization.

VII. CONCLUSION

This paper concentrates on the analysis of the RDS with different tap lines and verifies the effectiveness of three phase tap line over single phase. An optimization model for single phase taps is developed considering the cost of all three phase taps as a standard. It is found that three phase taps provide the cost effective solution to reach all the consumers in terms of length of the considered distribution network. Therefore, to keep the door open for further expansion of reliable distribution line cost effectively, which is the main objective of the area coverage rural electrification, this paper may be an initiator of future days' design. Ultimately, this may contribute in the process of overall national development by electrifying more rural area.

REFERENCE

[1] D. Zhang, Z. Fu, and L. Zhang, "Joint optimization for power loss reduction in distribution systems," IEEE Trans. on Power Systems, vol. 23 , no. 1, pp. 161-169, 2008.

[2] T.T. Erbato and T. Hartkopf, "Smarter micro grid for energy solution to rural Ethiopia," IEEE PES Innovative Smart Grid Technologies (ISGT), pp. 1-7, 16-20 Jan. 2012.

[3] S.M. Abdelkader, "Characterization of transmission losses", IEEE Trans. on Power Systems, vol. 26, no. 1, February 2011.

[4] I. Hussain and A.K. Roy, "A new heuristic approach for optimal reconfiguration of distribution systems for improvement of power delivery efficiency through loss reduction," International Conference on Advances in Engineering, Science and Management (ICAESM), pp. 571-576, 30-31 March 2012.

[5] Joon-Ho Choi and Jae-Chul Kim, "Network reconfiguration at the power distribution system with dispersed generations for loss reduction," IEEE Power Engineering Society Winter Meeting, pp. 2363 – 2367, 23-27 Jan. 2000.

[6] R.J. Sarfi, M.M.A. Salama, and A.Y. Chikhani, "Distribution system reconfiguration for loss reduction: a new algorithm based on a set of quantified heuristic rules," Canadian Conference on Electrical and Computer Engineering, 25-28 Sep 1994.

[7] D. Shirmohammadi and H.W. Hong, "Reconfiguration of electric distribution networks for resistive losses reduction," IEEE Trans. Power Delivery, vol. 4, no. 2, pp. 1402–1498, Apr. 1989.

[8] M.W. Siti, D.V. Nicolae, A.A. Jimoh,and A. Ukil ,"Reconfiguration and load balancing in the LV and MV distribution networks for optimal performance," IEEE Trans. on Power Delivery, vol. 22, no. 4, pp. 2534 – 2540, Oct 2007.

[9] C. Cavelluccil and C. Lyra, "Minimization of energy losses in electric power distribution systems by intelligent search strategies," International Trans. in Operational Research, vol. 4, no. 1, pp. 23-33, Jan 1997.

[10] Bangladesh Rural Electrification Board, MIS Report June 2015, www.reb.gov.bd

[11] Engineering and Staking Manual, BREB Instruction No. 100-21.

[12] Frontline Systems Inc. 1994, Solver User Guide: Premium, Quadratic, and Large-Scale LP Solvers.

[13] D. Fylstra, L. Lasdon, J. Watson and A. Waren, "Design and use of the Microsoft Excel solver", INTERFACES, vol. 28, no. 5, Sept-Oct 1998, pp. 29-55.

[14] http://www.tripplite.com/products/single-vs3-phase, accessed on 3 Sept. 2015.

[15] S. Ghosh, "Loss reduction and efficiency improvement: a critical appraisal of power distribution sector in India," International Journal of Modern Engineering Research, vol. 2, no. 5, Sep-Oct. 2012, pp.3292-3297.

Investigation of THD on a 12-Pulse HVDC Transmission Network and Mitigation of Harmonic Currents Using Passive Filters

Sanjib Kumar Nandi, Ridown Rashid Riadh, Md. Siddikur Rahman

American International University-Bangladesh, Dhaka, Bangladesh

sanjib.eee.aiub@gmail.com, rashidridown@gmail.com, rahman.siddikur286@gmail.com

Abstract— **Due to the different types of conversion purposes lots of harmonic creates in DC operated power system. Our goal is to minimize the harmonics at a certain level. The main focus of this research is to explain the effects of harmonics in a 12-pulse High Voltage Direct Current (HVDC) transmission network and take corresponding steps to reduce those effects. It includes harmonic reduction technique to improve the power quality of the HVDC transmission system. This paper also explains how harmonic distortion in HVDC network is one of the important problems associated with power quality and creates several disturbances to the overall power system. In this paper, simulation results were developed on the basis of bus no 1 and 2 of an ideal HVDC transmission Link where there are a lot of harmonics created primarily both in voltage and current due to the presence of Transformer, Converter Devices and Nonlinear Loads. After using passive filter, this harmonic level will be minimized at a certain point which is explained in details on this paper with practical justification.**

Keywords—Harmonics, Total Harmonic Distortion (THD), Transmission network, HVDC Transmission, Passive Filter, Harmonic Reduction

I. INTRODUCTION

In a High voltage direct current (HVDC) system, from the transmitting station AC voltage is being converted into DC voltage with the help of a rectifier and then DC power is transmitted through the transmission line. After that at the receiving station DC power is being reconverted into AC power through an inverter and the power is supplied in the system [1]. When compared to the AC transmission, it is robust against a disturbance and improves a dynamic characteristic of AC power system and lowers the short circuit capacity as voltage, current and transmission power in the DC transmission can rapidly be controlled [1, 2]. But due to various conversion purposes and the rapid uses of nonlinear loads & power electronic devices the harmonic current distortion of the DC transmission system is a highly concerned issue.

In power system design and operation, controlling and eliminating such harmonics have been a great concern for the power engineers. Therefore, in power system planning, control, and operation the HVDC power system harmonic analysis is essential [3]. Harmonic Studies are also important in respect to avoid damages due to excessive harmonic currents in transformers and capacitor banks, to ensure that due to excessive harmonic voltage distortion sensitive electronic equipment will not malfunction and to satisfy the utility's voltage and current harmonic distortion requirements.

Previously, researches have been conducted research on load behavior and harmonic contribution in various sectors of HVDC power system. For instance Capacitor behavior on harmonic distortion is investigated [2]. HVDC Transmission Systems and HVDC Power System Harmonic Analysis were discussed in [3, 4, 5 and 6]. Harmonic characteristics of new HVDC transmission system based on new converter transformer were analyzed in [7]. Harmonic reduction methods using active filters for HVDC networks were introduced in [8, 9]. Different control topologies of the HVDC network have been further developed in [15, 16 and 17].

This paper represents the results of a simulation study of Passive filter on a 12 pulse HVDC (High Voltage Direct Current) Transmission network using a system design in SimPowerSystems tools of Matlab. The objective of the study is to investigate the performance of the system's harmonic contents with and without the presence of Passive Filters. This paper is organized as follows: Section II presents a brief overview of sources of harmonics on HVDC Transmission network and their effects on the overall Power System. A brief introduction to Passive filter technique for harmonic reduction used in this study has been presented in section III. Simulation results along with the influence in harmonic contents with the appearance of Passive filters have been discussed in section IV. Some discussions and explanations of the findings have also been provided finally in section V conclude the work highlighting the major contributions.

II. HARMONICS ON 12-PULSE HVDC TRANSMISSION NETWORK

Among all power transmission systems, HVDC utilized direct current (DC) for high voltage bulk transmission of electrical power contrary to the more common alternating current (AC) systems [3, 10]. A constitutional task occurred in an HVDC system when the conversion of electrical current from AC to DC (rectifier) and from DC to AC (inverter) at the transmitting end and the receiving end respectively.

978-1-4673-9257-0/15/$31.00 ©2015 IEEE

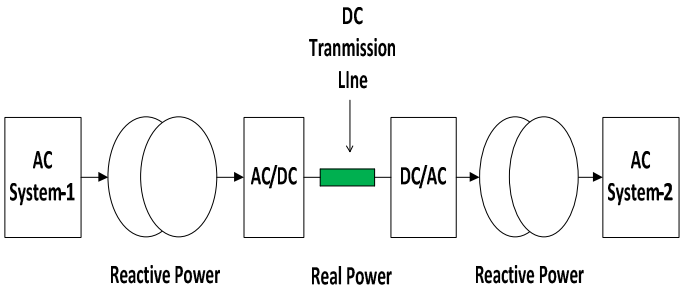

Figure.1: Simple mono polar HVDC Transmission System

HVDC transmission may be performed in two ways, mono polar and bi-polar. Mono-polar HVDC transmits power in one way whether bi-polar HVDC can transmit power in a bi - directional path.

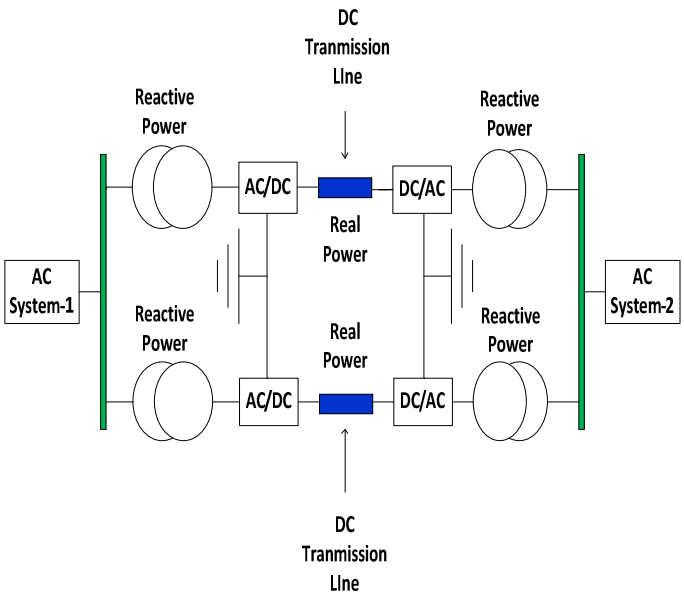

Figure.2: Bipolar HVDC Transmission system

The performance of HVDC power system is being affected by the harmonics created by the higher use of non-linear devices. Due to the presence of solid state drives or electric furnaces and capacitor banks in the HVDC power system, harmonics are generated frequently. Just as high blood pressure can cause stress and serious problems in the human body, high levels of harmonic distortion could result in problems for the utility's transmission system, the plant's distribution system, as well as the equipment under that transmission system. Most familiarize sources of HVDC harmonics and their effects are described in details below.

A. Sources of HVDC Harmonics

Since electrical signal is scrutinized, matter of harmonic is considered also. Harmonic is defined as the content of the signal whose frequency is an intrinsic multiple of the radical system frequency assembled by the generators. In HVDC power system, harmonics are assembled by some system elements which have non-linear characteristics, such as transformers, generators, power converters and electrical machines [11, 12 and 13]. Specifically, converters are the considerable sources of harmonic in an HVDC network during a steady state operation and engender harmonics on both AC and DC sides of their valve groups. The valve operation in converters of a 12 pulse HVDC link changed the original shape of voltage and current in a steady state condition, as a result of system harmonics. In HVDC power system, the interaction of primary currents and characteristic harmonic in non-linear components assembles sum as well as the difference in frequencies. The secondary voltage harmonics to the primary three phase voltage waves fetch the voltage zeros from the zeros of the primary waves unescorted and these fetches of zeros cause asymmetrical firings of the valves and non-characteristic AC harmonics are engendered.

Transformers are other acceptable source of harmonics, and this harmonics are incorporated with their design and operation. Besides, throughout the large disturbances transformers can substantially increase their contribution of harmonic and the transfer current accommodated both odd and even harmonics in an unbalanced condition. Generators such as electric machines are another acceptable source of harmonics also in HVDC power systems because of their economical as well as practical design. A machine has not operated in the saturation region if the magnetic flux of a machine has a perfectly sinusoidal distribution around the air gap. In machines, the magnetic saturation can also be contributed to the generation of harmonics like as transformers [3].

B. Effects of Harmonics

In HVDC system, harmonics reduced the efficiency of power generation and transmission. They lower the efficiency of power utilization and damage the insulation of system components also. If the system has high harmonic contents, the plant malfunction can be occurred after that the harmonics are entering the ark network and the DC line may result in the overheating of generators and capacitors, the interference with communication circuits and the instability of the system controls. The unwanted signal induced by a power system on a communication circuit degrades the transmission quality of the communication signals [11]. Harmonic resonances genesis excessive currents and over voltages which dramatically increase the losses of system devices and even can damage them. Effects of HVDC power system harmonics have been seen in rotating machines, which introduced losses [14]. The pierce of harmonics in a network cause additional network losses due to the increase of the effective values of current. Harmonic currents increased the harmonic voltage drops across circuit impedances. When the electric power is transmitted by cables, harmonic voltages increased dielectric stress in proportion to their crest voltages. The high dielectric stress shortens the useful life of the cables. The harmonics also have effects on the corona. The corona starting and extinction levels depend on peak-to-peak voltages, which are affected by

978-1-4673-9257-0/15/$31.00 ©2015 IEEE

harmonics. These types of scenario are seen in converter stations.

III. PASSIVE FILTER TECHNIQUES FOR HVDC HARMONICS REDUCTION

Due to the commutating process of the converter bridge, several characteristic and non-characteristic harmonics are generated on the 12-pulse HVDC transmission system [7].There are many ways to reduce harmonics in HVDC power system. Such as- using phase controlled thyristor rectifier, using larger DC or AC inductor, using Tuned single or multiple arm passive filter, External active filter etc. To maintain the power quality of an HVDC transmission system Active and passive filters is essential [9]. Filtering is currently the most common method used for limiting the effects of harmonics to the rest of the system [8]. Filters typically consist of Tuned Series L-C circuits and its impedance is negligible with respect to the rest of the transmission network [14].

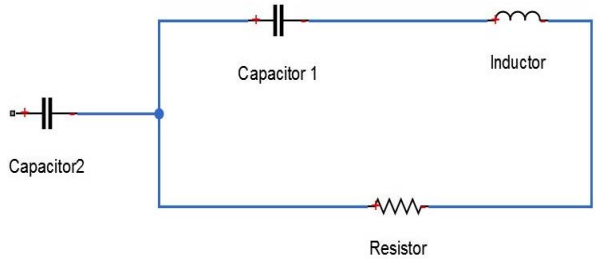

Figure.3: Basic representation of C-type high pass passive filter

Passive filters consist of resistors, inductors and capacitors. They are not expensive and are often used to restrict the harmonic currents from entering the power system thereby minimizing the effect of harmonics. Also, the passive filters are kept close to the source of harmonic generated loads. Doing so, in reducing the harmonic effect the passive filters produce better results. The passive filters create a resonance frequency in order to reduce the harmonic effect. This resonance frequency is kept away from the harmonic distortion of the nonlinear loads.

IV. DESIGN AND SIMULATION RESULTS

The peak demand of Bangladesh is of the order of 4200-5500 MW and the peak deficit is about 1000-1500 M [14]. The HVDC interconnection between the electrical grids of India and Bangladesh would facilitate transfer of 500 MW Power in either direction [14]. This section deals with the design and implementation of a Software Based system where SimPowerSystems tools of Matlab were used as the simulation tool. The proposed Simulink model consists of several parts. The block representation, including the overall system is shown in Figure 4 below.

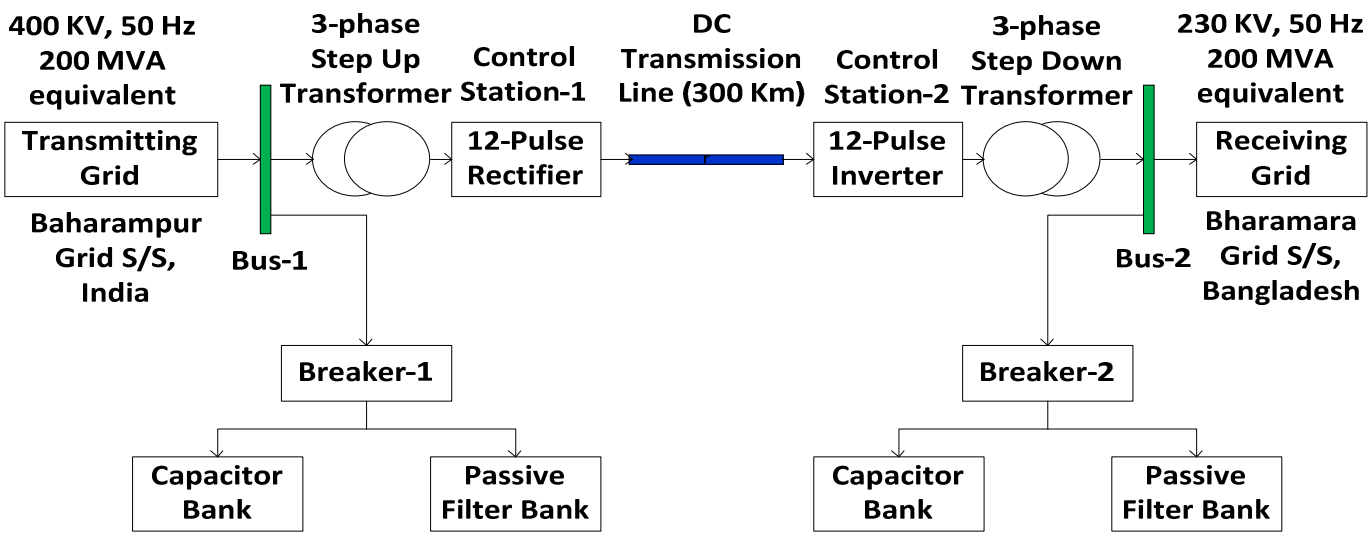

Figure.4: Test System

In the above HVDC system design in figure 4, 500 MW Power is transmitted from a 400 KV network to a 230 KV network. Both the network has a power rating of 200 MVA and frequency of 50 Hz. The converter is connected to the system with a 200 MVA Three-Phase transformer (three windings). The rectifier and the inverter are 12-pulse converters using two 6-pulse thyristor bridges, are interconnected in series through a 300 km distributed parameter line and two 30 mH smoothing reactors. Two three-phase Circuit Breakers (CB-1 & CB-2) are separately used to connect the filters set on the AC bus. The filter sets connected to Bus-1on the transmitting grid through Circuit Breaker-1 are made of the following components - one

978-1-4673-9257-0/15/$31.00 ©2015 IEEE

capacitor banks of 75 Mvar, 3x75 Mvar tuned low pass filters for removing the lower order harmonic (11th, 12th and 13th) and one 75 Mvar high pass damped filter for higher order (24th) harmonic reduction using the three-phase harmonic filter modeling. The total Mvar rating of the filter sets connected to Bus-2 is then 455 Mvar. The filter sets connected to Bus-2 on Load side through Circuit Breaker-2 are made of the following components - one capacitor banks of 91 Mvar, 3x91 Mvar tuned low pass filters for removing the lower order harmonic (11th, 12th and 13th) and one 91 Mvar high pass damped filter for higher order (24th) harmonic reduction using the three-phase harmonic filter modeling. The total Mvar rating of the filter sets connected to Bus-2 is then 455 Mvar.

From the design, four parameters Vabc_B1, Iabc_B1, Vabc_B2 and Iabc_B2 and their corresponding harmonic components (both voltage harmonics and current harmonics) has been observed for three phases. With the help of SimPowerSystems under SimScape division in Matlab results of THD have been measured for with and without passive filter connections. Simulations have been carried out with two different conditions. Condition 1 calculates the existing THD of the 12-pulse HVDC transmission network without any filter in the system. Condition 2 represents the improved THD value of the HVDC network after adding passive filters into. The results of this design and implementation considering phase sequence A are described briefly for a better comparison scenario.

Condition-1: When both the Breakers were open (Without Passive Filter)

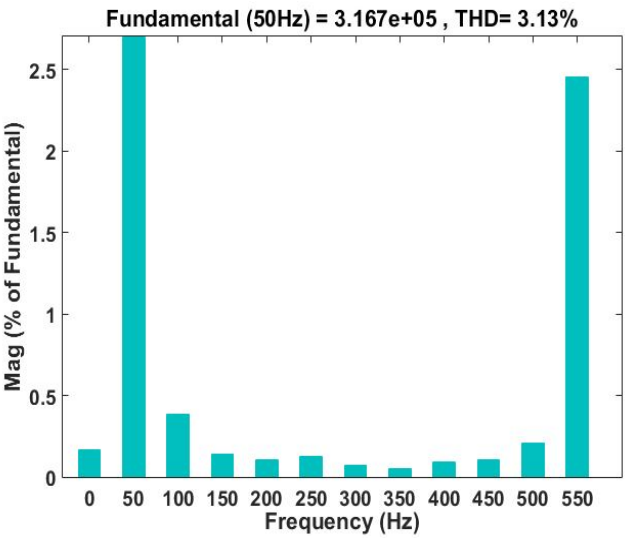

Figure.5: Voltage Harmonics (THD_V) – At Phase A of Bus 1.

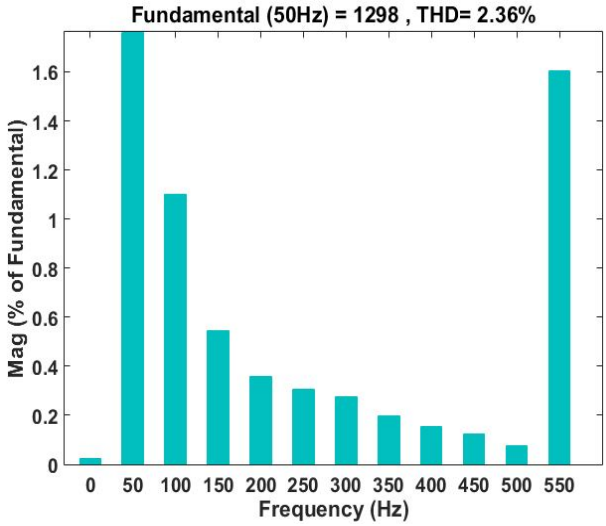

Figure.6: Current Harmonics (THD_I) – At Phase A of Bus 1.

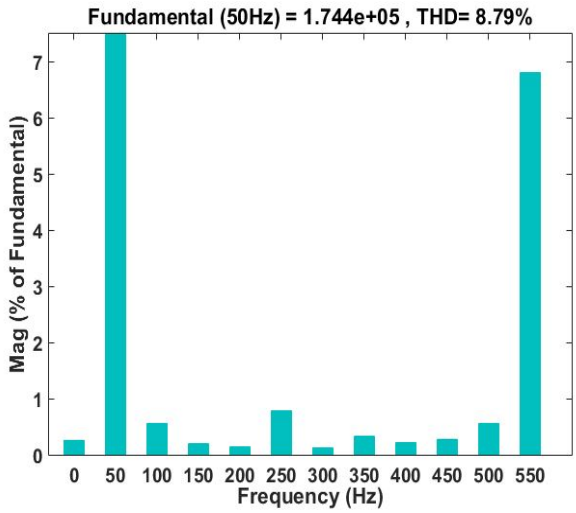

Figure.7: Voltage Harmonics (THD_V) – At Phase A of Bus 2.

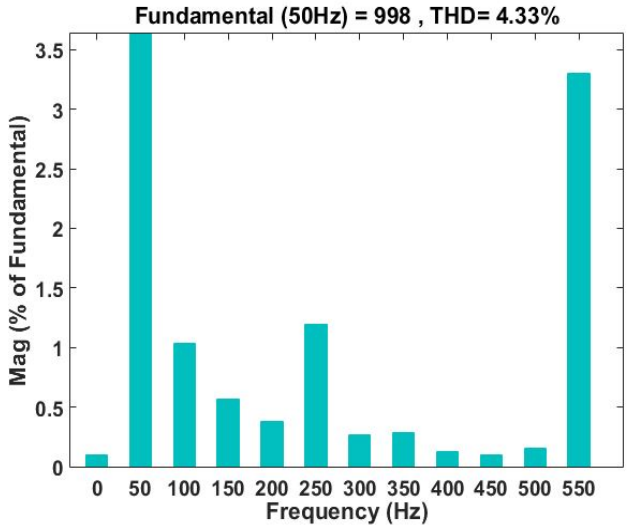

Figure.8: Current Harmonics (THD_I) –At Phase A of Bus 2.

978-1-4673-9257-0/15/$31.00 ©2015 IEEE

In the above figures (5, 6, 7, 8), THD of the system without harmonic filter has been demonstrated and found that design's THD is much higher without harmonic filter installation. At fundamental frequency, the Voltage (THD_V) & Current (THD_I) harmonic distortion level at Bus-1(phase A) are 3.13% and 2.36% respectively. And at Bus-2 (phase A), Voltage (THD_V) & Current (THD_I) harmonic distortion level are 8.79% and 4.33% respectively. That's why a second case study was performed by designing passive harmonic filter on the HVDC transmission network to examine the performance of the system and harmonic distortion level.

Condition-2: When both the Breakers were closed (With Passive Filter)

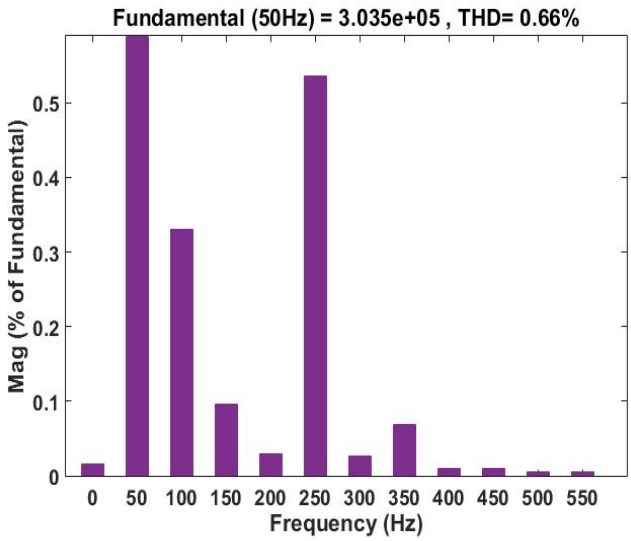

Figure.9: Voltage Harmonics (THD_V) – At Phase A of Bus 1.

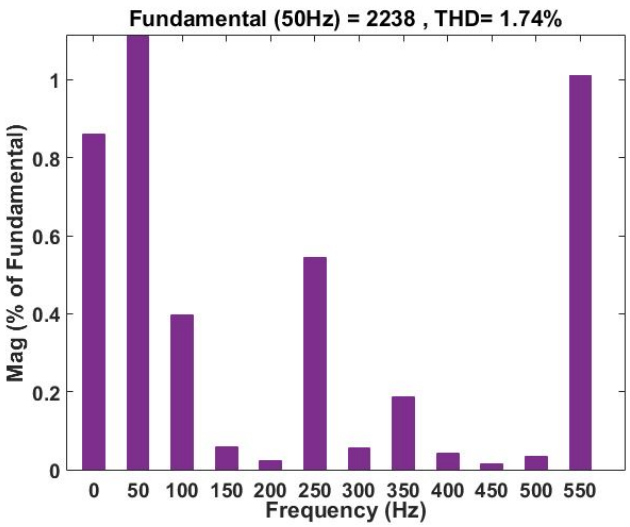

Figure.10: Current Harmonics (THD_I) – At Phase A of Bus 1.

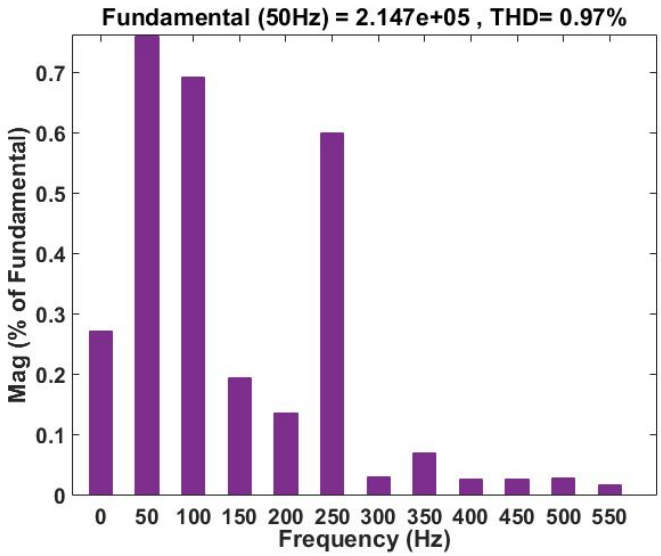

Figure.11: Voltage Harmonics (THD_V) – At Phase A of Bus 2.

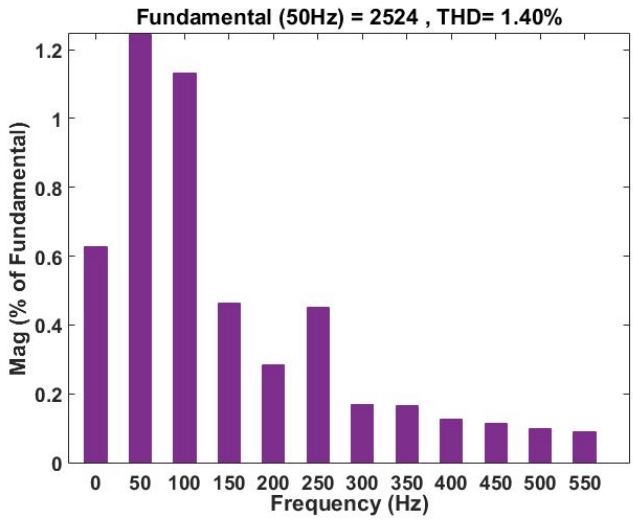

Figure.12: Current Harmonics (THD_I) – At Phase A of Bus 2.

In the above figures (9, 10, 11, 12), THD of the system with passive harmonic filter has been demonstrated. At fundamental frequency, the Voltage (THD_V) & Current (THD_I) harmonic distortion level at Bus-1(phase A), are 0.66% and 1.74% respectively. And at Bus-2 (phase A), Voltage (THD_V) & Current (THD_I) harmonic distortion level are 0.97% and 1.40% respectively. All the findings of the proposed design and simulation results of two different conditions are tabulated in Table-1.

The above results are about time domain simulation. The findings of the above discussions are demonstrated in the table below.

978-1-4673-9257-0/15/$31.00 ©2015 IEEE

Table.1: Value of THD for fundamental component of 50Hz with and without passive filter

Bus No.	Phase	THD(%) without passive filter		THD(%) with passive filter	
		Voltage	Current	Voltage	Current
1	A	3.13	2.36	0.66	1.74
2	A	8.79	4.33	0.97	1.40

From the above comparison, the harmonic limit is under the IEEE std. 519 after using the passive harmonic filter. The observation was that the harmonic filters almost eliminate the harmonics generated by the converter.

V. CONCLUSION

When large amounts of power are to be transmitted for long distances, HVDC is considered an economically beneficial because of their low electrical losses. But the impact of harmonics in HVDC network might be detrimental and redundant to both loads and grid. With the use of Passive harmonic filters are ways of mitigating the effects of such. To determine harmonic distortion levels and filtering requirements harmonic studies with passive filter on the HVDC transmission network were performed. Designing proper implementation with the help of the Simscape division of Matlab was performed with practical system and data's. This study determines if harmonic voltages and currents are at acceptable levels. An evaluation of the harmonic voltage and current limits is completed to determine the effectiveness of the proposed filter installation. The founding's of this work concludes that Harmonic analysis with passive harmonic filter is a very important discussion on the modern day's power system which reduces excessive current flow on the non-linear load. The application of Passive harmonic filters will significantly alter the frequency response of the power system. After completing the task, it will be minimize the wasteful impact of unnecessary power conversion, which saves more energy in the system. With the rapid conversion of AC to DC system more and more filters will be required to keep the harmonic limits within the acceptable range. So in future, further studies can be performed for improved implementation based on this research work.

VI. REFERENCES

[1] Ghijselen, Jozef, Wouter R. Ryckaert, and Jan Melkebeek. *"Required load behaviour for power quality improvement."* In Power Engineering Society Summer Meeting, 2002 IEEE, vol. 2, pp. 998-1003. IEEE, 2002.

[2] Herrera, Reyes S., Patricio Salmerón, and Salvador P. Litrán. *"Assessment of Harmonic Distortion Sources in Power Networks with Capacitor Banks."*

[3] Louie, K. W., P. Wilson, R. W. Wachal, A. Wang, and P. Buchanan. *"HVDC power system harmonic analysis in the time and frequency domains."* In Power System Technology, 2006. PowerCon 2006. International Conference on, pp. 1-8. IEEE, 2006.

[4] Zidi, S. A., S. Hadjeri, and M. K. Fellah. *"Regular paper Dynamic Performance of an HVDC Link."* J. Electrical Systems 1, no. 3 (2005): 15-23.

[5] Rudervall, Roberto, J. P. Charpentier, and Raghuveer Sharma. *"High voltage direct current (HVDC) transmission systems technology review paper."* Energy week 2000.

[6] Kure, Hans Magnus, Carl Olav Larsson, Tore Skottvoll Lefstad, Leif Arne Müller, and Øyvind August Rui. *"HVDC Transmission–Skagerrak 4."* Group 9: 2.

[7] Luo, Longfu, Yong Li, Kazuo Nakamura, Gerhard Krost, Ji Li, Jiazhu Xu, and Fusheng Liu. *"Harmonic characteristics of new HVDC transmission system based on new converter transformer."* In Electric Utility Deregulation and Restructuring and Power Technologies, 2008. DRPT 2008. Third International Conference on, pp. 1868-1872. IEEE, 2008.

[8] *"Harmonic reduction methods",* Eaton Corporation, Printed in USA, Publication No. AP04014001E / Z12198 April 2012, Eaton Corporation

[9] Islam, F. R., and H. R. Pota. *"Virtual active filters for HVDC networks using V2G technology."* International Journal of Electrical Power & Energy Systems54 (2014): 399-407.

[10] Arrillaga, J., and D. A. Bradley. "P S Bodger,*"Power system harmonics."* A Wiley-Interscience Publication, Norwich (1985).

[11] Louie, K. W., P. Wilson, R. A. Rivas, A. Wang, and P. Buchanan. *"Discussion on power system harmonic analysis in the frequency domain."* In Transmission & Distribution Conference and Exposition: Latin America, 2006. TDC'06. IEEE/PES, pp. 1-6. IEEE, 2006.

[12] M D Singh and K B Kanchandani, *"Power Electronics",* Second Edition, Tata McGraw Hill Education Private Limited

[13] Okba, Mohamed H., Mohamed H. Saied, M. Z. Mostafa, and T. M. Abdel-Moneim. *"Harmonics in HVDC Links, part II—Effects and reduction techniques."* In IECON 2012-38th Annual Conference on IEEE Industrial Electronics Society. 2012.

[14] Data Collected from PGCB (Power Grid Company of Bangladesh Ltd.) and POWERGRID, India.

[15] Karlsson, Per, and Jörgen Svensson. *"DC bus voltage control for a distributed power system."* Power Electronics, IEEE Transactions on 18, no. 6 (2003): 1405-1412.

[16] Roy, Rajib Baran, and Md Ruhul Amin. *"Analysis of Proposed Controlling Topology of the HVDC link between Bangladesh and India."* In Strategic Technology (IFOST), 2014 9th International Forum on, pp. 390-395. IEEE, 2014.

[17] Flourentzou, Nikolas, Vassilios G. Agelidis, and Georgios D. Demetriades. *"VSC-based HVDC power transmission systems: An overview."* Power Electronics, IEEE Transactions on 24, no. 3 (2009): 592-602.

978-1-4673-9257-0/15/$31.00 ©2015 IEEE

Harmonic Analysis on LVDC Distribution System and Passive Filter Techniques for Harmonic Reduction

Sanjib Kumar Nandi, Md. Siddikur Rahman, Ridown Rashid Riadh

American International University-Bangladesh, Dhaka, Bangladesh

sanjib.eee.aiub@gmail.com, rahman.siddikur286@gmail.com, rashidridown@gmail.com

Abstract— **Usages of DC power instead of AC power on the secondary distribution system creates a lot of harmonics. Our goal is to eliminate the harmonics onto the system and due to the limited specification of filter it has not been possible to reduce all the harmonics in the secondary distribution system. But we must be more focused to achieve this goal, because large shares of household loads are turning into DC in recent years. If this trend continues, the impact of harmonics on customer end will reach a level which might be detrimental and redundant to both loads and grid. The main objective of this research is to explain the effects of harmonics on the low voltage direct current (LVDC) distribution system and measure the harmonic content present in the network and proposed a recovery method by inserting filter. Due to additional non-linear loads on the LVDC distribution system, a sufficient amount of harmonics will be created. To solve this issue, use of passive harmonic filter is recommended for the DC operated secondary distribution system. After using a passive filter into the LVDC network, the system harmonics are being reduced into the acceptable limits and almost eliminate the harmonics generated by the converter and nonlinear loads.**

Keywords—Harmonics, Total Harmonic Distortion (THD), DC Power, LVDC Distribution System, Passive Filter, Harmonic Reduction

I. INTRODUCTION

Among all the existing network technologies, LVDC system is one of the emanating technology renovations for Smart Grid application to the distribution of electricity and a highly interesting challenge [1]. The salient purposes beyond this development of the LVDC network is to enhance the power quality and furnish security experienced by the end users of the electricity for ameliorating the distribution economy [1]. This pledge flexible and robust coupling point for small scale generation and evolve infrastructure for interactive and intelligent distribution network [1, 2]. The distribution transformer is one of the key parts of LVDC system [3]. The nonlinear nature of the load has generated harmonic currents which may cause problems in the power system and overheating transformers. Nonlinear loads have generated harmonic currents which are flown from the load towards the power source, following the least impedance paths [4].

Modern electrical system consists of a vast amount of nonlinear loads which causes disturbances in DC current. Commercial buildings often have a large amount of nonlinear electronic loads such as lighting, computers, monitors and adjustable-speed drives for air conditioning. Due to this huge presence of nonlinear loads, electromagnetic-compatibility and power quality problems may occur [5]. For which power system suffers from unfavorable consequences and may damage electrical equipment's. IEEE Standard 519-1992 specifies limits for each harmonic up to the 35th and limits the total harmonic distortion (THD) to 5% [6]. EN 50160 limits the THD to 8% and the unbalance to 2% [7].

This problem can require special consideration to serve non-linear loads with a reduce amount of harmonic distortion. Using various techniques power distribution system's Harmonic distortion might be restrained [2]. Previously, researches have been conducted on load behavior and harmonic contribution in various sectors of the power system. For instance, The LVDC power distribution network concept is presented [8]. Harmonic analysis and DC operated electrical system with distributed resources for recovery from the effects of harmonics and closely relevant criteria have been proposed in [9, 10, 11 and 12]. The LVDC distribution system concept has been developed in [13]. Passive filter installation for reducing harmonic in single phase motor, varying load has been introduced in [4].

Analysis of harmonics and measuring simulation based results is helpful for preparing data based efficient models of the LVDC distribution system. Investigation of harmonic content present in low voltage direct current (LVDC) power distribution network has been demonstrated in this article. This paper mainly focuses on the effects of the increase amount of harmonics in a LVDC distribution network and possible solution to overcome. The primary objective is to measure harmonic contents on the LVDC distribution system. And the secondary objective of this work is using an active harmonic filter to improve the system performance of the LVDC distribution system. For investigation, simulation environment at SimPowerSystems tool of Matlab Simulink is used. The organization of the paper is set as: in Section II, a brief overview of LVDC distribution network was introduced. Sources of harmonics in LVDC network and their effects in distribution feeders have been discussed in section III. A brief introduction to Passive filter technique for harmonic reduction used in this study has been presented in section IV. Simulation

978-1-4673-9257-0/15/$31.00 ©2015 IEEE

results along with the influence in harmonic contents of LVDC system with the appearance of Passive filters have been discussed in section V. Some discussions and explanations of the findings have also been provided finally in section VI conclude the work highlighting the major contributions.

II. LVDC DISTRIBUTION SYSTEM

The LVDC distribution system is an advanced revolution in the field of electricity distribution. Recently, power electronic constituents have developed in the way of economic and technological, which enabled to apply power electronics in LV network. A basic conviction of LVDC distribution system concentrated at the DC/AC interface focused on implementation of customer-end inverter [13]. The LVDC distribution system builds of power electronic converters and DC link between the converters. A LVDC distribution system can have different types of topologies that the AC/DC conversion can be placed at various locations [14].

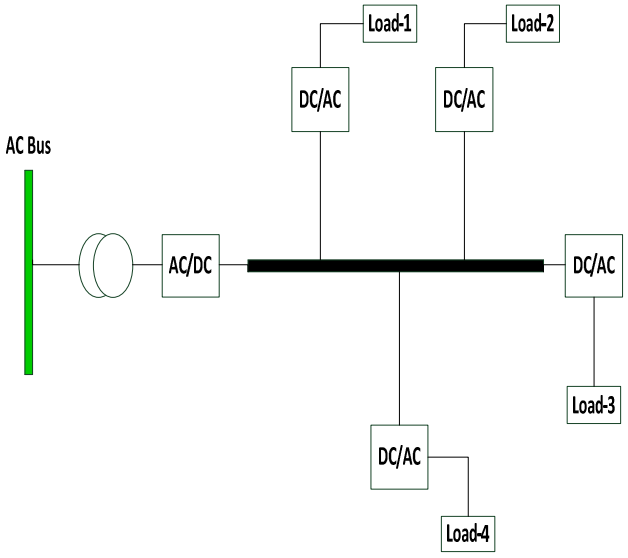

Figure.1: Simple LVDC Distribution system

LVDC system consists of a distribution transformer, a DC link, a rectifier, DC/AC inverter units, customer loads and filters [15]. In LVDC distribution system, DC connection is used to avoid the need to build a medium voltage branch line as well as traditional low voltage AC grid to furnish electricity to a group of low power customers [16, 17]. In LVDC distribution grid, DC grid is powered by a front-end rectifier. The front-end rectifier includes of two 6-pulse thyristor bridges. Thyristor bridges are powered by phase shifting transformer with two secondary windings to form a 12-pulse rectifier. The customer-end inverters loaded the DC system. The bipolar DC power distribution network serves as the power supplier of the inverters. Both single phase and three phase inverters can be used to energize the consumer end AC network. Due to high ±750 VDC voltage used in the LVDC network, inverters are generally connected in between the zero pole and plus or minus DC pole. Customer's coupling point can also be located in the DC side in some special cases [18].

III. HARMONICS ON LVDC DISTRIBUTION NETWORK

Using a DC distribution system makes it easier to incorporate more local energy storage and sources. To connect an energy source with a DC system only the voltage has to be controlled, as opposed to the AC system where voltage magnitude, frequency and phase must be matched [9]. An indispensable deliberation when estimating the smash of harmonics is their effect on power system constituent and loads [16]. Higher consumption of reactive power causes more system losses and malfunction the protection of the power system [5]. The current harmonics found in the grid components may sustain impairments in distinct devices which are fastened to the same grid [16].

The converters used in the LVDC distribution system produce flexible harmonic contents. The distortion of voltages and currents can cause extra losses in system components [17]. Generally, industrial electronic devices and nonlinear loads are the considerable source of harmonic generation. When sinusoidal voltage is applied to a nonlinear load, then the resulting current is distorted. So, non-linear loads are the leading source of harmonic distortion in power system. Modern personal computer's power supply is a familiar example of nonlinear load. It's switching action results in distortion of the current waveform [19]. With the increase use of PV grid integration also causes harmonics problem inside the power system [20].

Distribution transformer is one of the vital constituents of LVDC system. Harmonic load currents consequence heating inside and cause eddy current losses in transformer. The escalated depletions due to harmonic distortion can seed excessive depletions as well, hence the anomalous temperature rise. The assessment of iron depletions and copper depletions of transformers is the prime in particular for transformers feeding nonlinear loads [16].

Whenever there is a large number of a nonlinear load, more harmonics are observed in the LVDC distribution system. Harmonic currents which are engendered by nonlinear loads are flown from the load toward the power source, shadowed the ways of minimal impedance. Due to greater percentage of harmonics many more unnatural situation may occur such as - overheating of electrical distribution system wiring, transformer overheating which shortened transformer service life, false circuit breaker tripping, power factor correction capacitor failure etc. [21] The likelihood of experiencing problems increases with the increase of harmonic levels. In Rising temperature and creating Skin Effect harmonic is an important factor. Both the electrical distribution systems and equipment have consequences due to heating effect. Problems in neutral conductors, unpredictable operation of relays and breakers, presence of distinct magnetic fields near transformers and switchgear etc. are also the outcomes of harmonics. Harmonics may also results in electronic instrument's reading errors, false instruction, excessive line loss, thermal loading of motors, malfunction of transformers, generators, electronics equipment like computers, air conditioning systems, PLCs, remote monitoring systems etc.

978-1-4673-9257-0/15/$31.00 ©2015 IEEE

IV. HARMONICS REDUCTION BY PASSIVE FILTER

A lot of harmonics are generated on the LVDC distribution system due to different types of conversion process and nonlinear loads. There are many ways to reduce LVDC power system harmonics. Such as- using phase controlled thyristor rectifier, using larger DC or AC inductor, using Tuned single or multiple arm passive filter, External active filter etc. To maintain the power quality of an LVDC distribution system Active and passive filters is essential. Filtering is currently the most common method used for limiting the effects of harmonics to the rest of the system. Filters typically consist of Tuned Series L-C circuits and its impedance is negligible with respect to the rest of the distribution network. Passive filters are used to restrict the harmonic currents by providing a low impedance path to enter the power system. Resistors, inductors and capacitors are the main components for designing of the passive harmonic filters [22]. A basic structure of a Passive Shunt Filter with Load connection has been shown in figure.2.

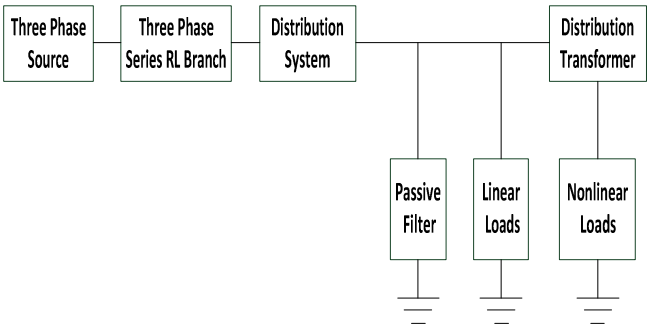

Figure.2: Passive Shunt Filter with Load connection

By using Passive filter as a harmonic reduction technique, power quality of the distribution network can be improved [4, 23]. Passive harmonic filter reduces harmonics which are existed due to nonlinear loads in the power system by injecting equal current or voltage distortion [4]. Passive filters are not expensive and often used to restrict the harmonic currents from entering the power system thereby minimizing the effect of harmonics. Also, the passive filters are kept close to the source of harmonic generated loads. Doing so, in reducing the harmonic effect the passive filters produce better results. The passive filters create a resonance frequency in order to reduce the harmonic effect [4]. This resonance frequency is kept away from the harmonic distortion of the nonlinear loads.

V. SIMULATION RESULTS

When designing a system, several things need to be addressed in order to observe the Impact of increased share of DC load. LVDC grid requires 1500 VDC Medium-voltage fretwork and 20 KV voltages have to be laid down by a transformer to low AC voltage like 1 KV in power distribution. When ripple voltage is not more than 10 % of the nominal voltage, is to be known as DC voltage, but the real scenario of the ripple voltage has considerably underneath the margin of losses in DC cables. For analyses of a bipolar LVDC network ± 750 VDC distribution systems is considered. The proposed Simulink model block diagram representation is shown in Figure 3 below that presents the overall system where a simple LVDC system is designed.

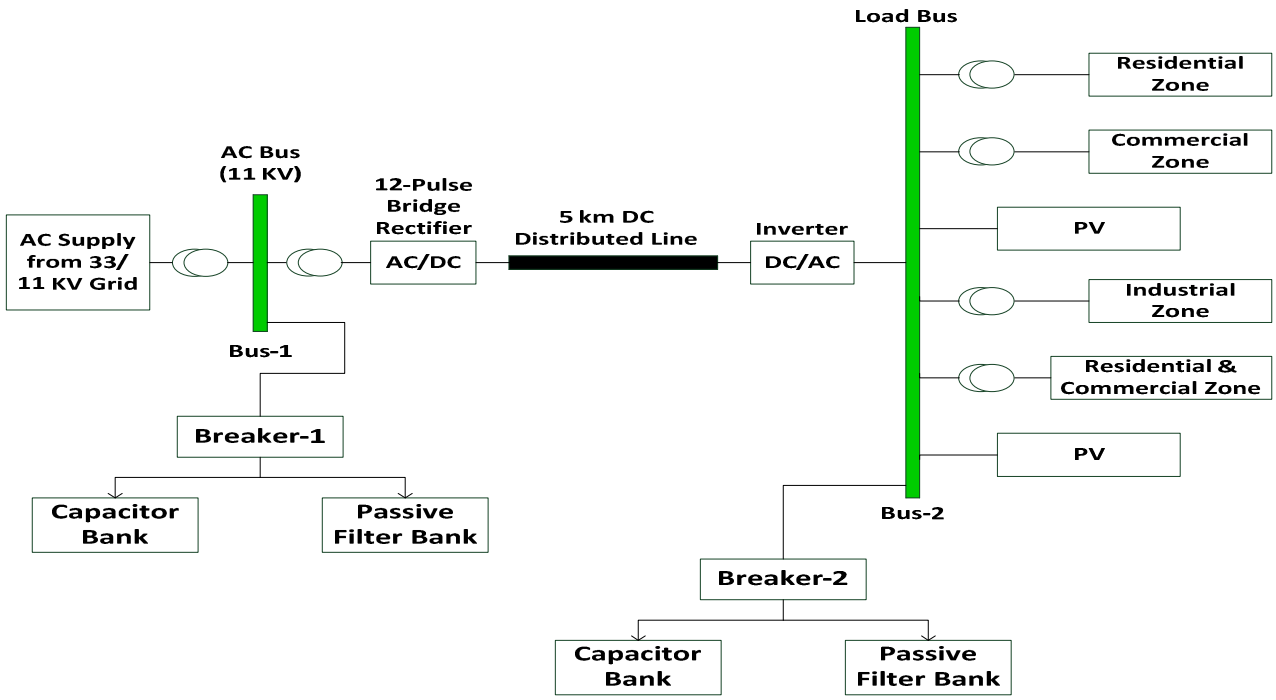

Figure.3: Test System

978-1-4673-9257-0/15/$31.00 ©2015 IEEE

The Simulink model consists of a LVDC distribution system along with Passive Harmonic Filters connected to the adjacent AC Bus. It is important to get familiarized with the components needed to observe the impact of increased share of DC loads. The components used for observing the impact of increased share of DC loads are Three-Phase Source, Series RLC Branch, Three-Phase Transformer, 12 pulse Thyristor controlled bridge rectifier, inverter, linear and nonlinear loads and Three-Phase Harmonic Filter. Designing and implementing of this Software Based system is followed by the implementation using SimPowerSystems Tool of Matlab. The Harmonic Filter uses a Phase Locked Loop to generate a reference sinusoidal source current which is in phase and has the same RMS gain as the load current.

A 5 km DC interconnection is used to transmit power from an 11 KV, 50 Hz distribution Grid to load side. The converter is connected to the system with Three-Phase transformer windings. The rectifier is a 12-pulse converter using two 6-pulse thyristor bridges. An inverter bridge is used in the load side for DC/AC conversion which is interconnected in series through a 5 km distributed parameter line. Six individual feeders carrying on different types of loads (both linear and nonlinear) are connected to Bus-2 through individual transformer. Here, along with residential, commercial and industrial loads, Photovoltaic (PV) was also inserted to have a better scenario. 8 MW load in residential feeder, 2.5 MW load in Commercial feeder, 4.5 MW load in (Residential + Commercial) feeder, 5 MW load on Industrial feeder and 2 MW load in each PV individually were considered and connected to the system. Total load connected to the LVDC network was amounted to be 24 MW. Two Passive filters were connected to Bus 1 and 2 The filter sets are made of the following four components – one capacitor banks of 91 Mvar, one C-type high-pass filter of 150 Mvar, two single-tuned filter of 2x150 Mvar for reduction of odd harmonics, one high-pass damped filter of 150 Mvar modeled using the three-phase harmonic filter. The total Mvar rating of the filters set was 455 Mvar at individual Bus. A three-phase circuit breaker was used with each filter block to connect the filters set on the AC bus separately.

The most important part of this design was to observe the impact increased share of DC load. From the design, four parameters Vabc_B1, Iabc_B1, Vabc_B2 and Iabc_B2 and their corresponding harmonic components (both voltage harmonics and current harmonics) has been observed for three phases. With the help of SimPowerSystems under SimScape division in Matlab results of THD have been measured for with and without passive filter connections. Simulations have been carried out with two different conditions. Condition 1 calculates the existing THD of the LVDC distribution network without any filter in the system. Condition 2 represents the improved THD value of the LVDC network after adding passive filters into it. The results of this design and implementation considering phase sequence C of each Bus are described briefly for a better comparison scenario.

<u>Condition-1:</u> When both the breakers were open (without Passive filter)

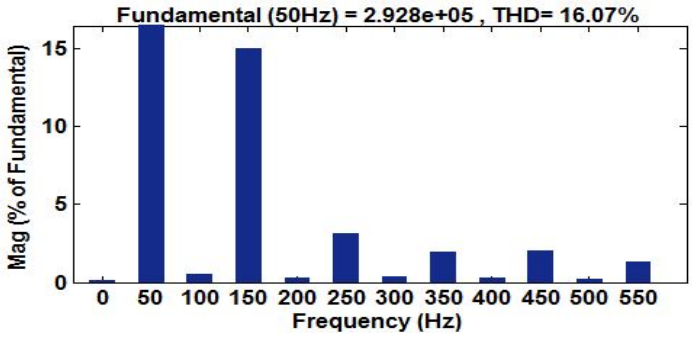

Figure.4: Voltage Harmonics (THD_V) – At Phase C of Bus 1.

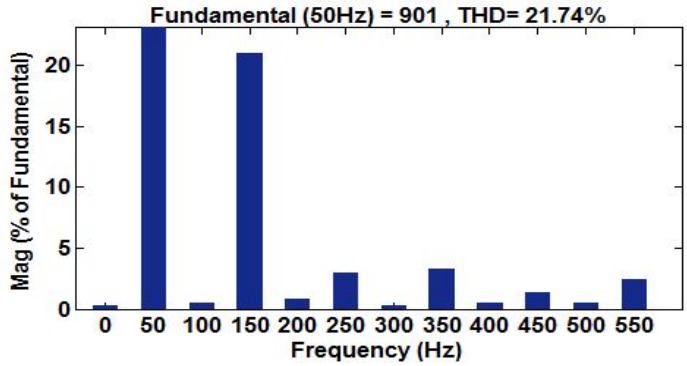

Figure.5: Current Harmonics (THD_I) – At Phase C of Bus 1.

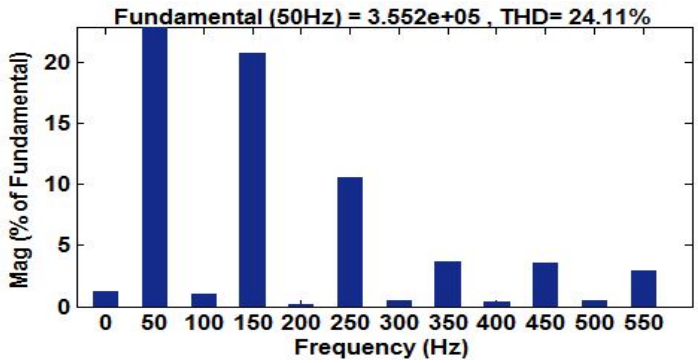

Figure.6: Voltage Harmonics (THD_V) – At Phase C of Bus 2.

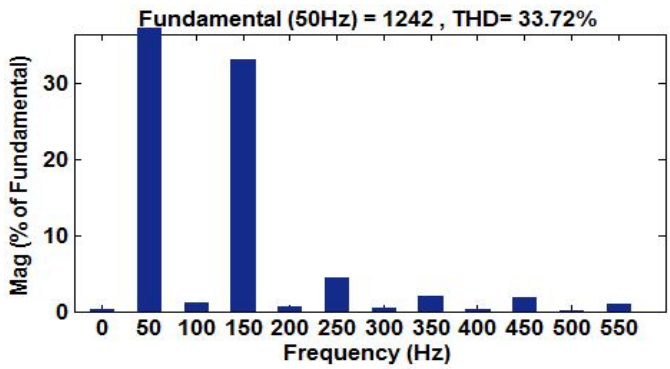

Figure.7: Current Harmonics (THD_I) –At Phase C of Bus 2.

978-1-4673-9257-0/15/$31.00 ©2015 IEEE

In the above figures (4, 5, 6, 7), THD of the system without harmonic filter has been demonstrated. It has been found that design's THD is much higher without harmonic filter installation. At fundamental frequency, the Voltage (THD_V) & Current (THD_I) harmonic distortion level at Bus-1(phase C) were 16.07% and 21.74% respectively. And at Bus-2 (phase C), Voltage (THD_V) & Current (THD_I) harmonic distortion level were 24.11% and 33.72% respectively. That's why a second case study was performed by designing passive harmonic filter on the LVDC distribution network to examine the performance of the system and harmonic distortion level.

<u>Condition-2:</u> When both the breakers were closed (with Passive filter)

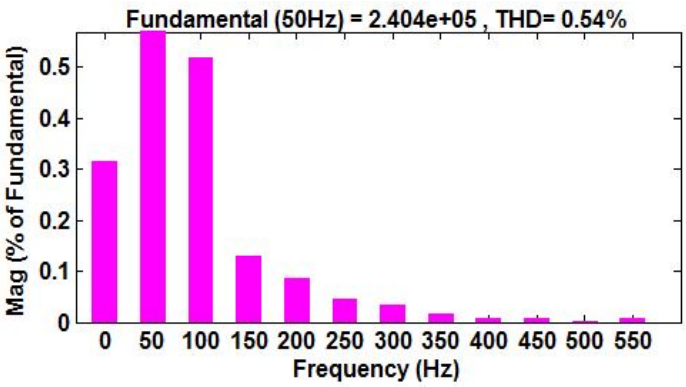

Figure.8: Voltage Harmonics (THD_V) – At Phase C of Bus 1.

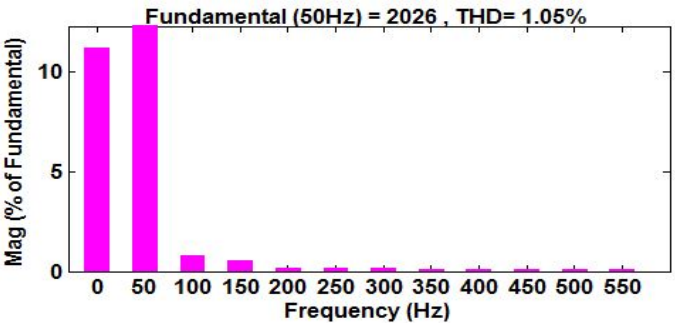

Figure.9: Current Harmonics (THD_I) – At Phase C of Bus 1.

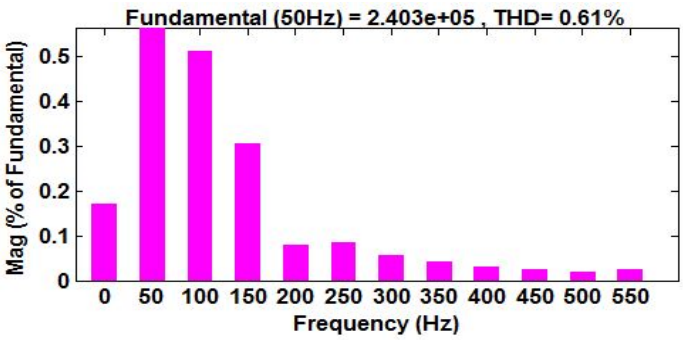

Figure.10: Voltage Harmonics (THD_V) – At Phase C of Bus 2.

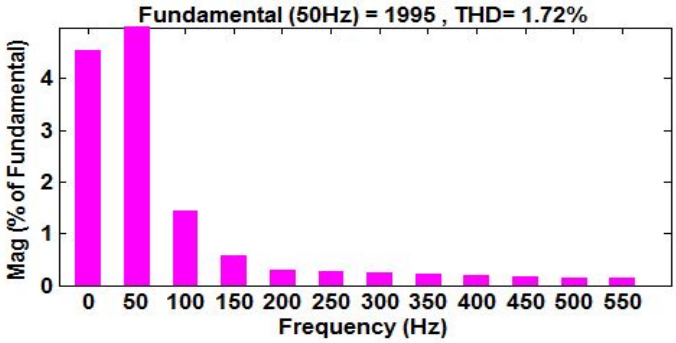

Figure.11: Current Harmonics (THD_I) – At Phase C of Bus 2.

In the above figures (8, 9, 10, 11), THD of the system with passive harmonic filter has been demonstrated. At fundamental frequency, the Voltage (THD_V) & Current (THD_I) harmonic distortion level at Bus-1 (phase C) were 0.54% and 1.05% respectively. And at Bus-2 (phase C), Voltage (THD_V) & Current (THD_I) harmonic distortion level were 0.61% and 1.72% respectively. All the findings of the proposed design and simulation results of two different conditions are tabulated in Table-1.

Table.1: Value of THD for fundamental component of 50Hz with and without passive filter

Bus No.	Phase	THD(%) without passive filter		THD(%) with passive filter	
		Voltage	Current	Voltage	Current
1	C	16.07	21.74	0.54	1.05
2	C	24.11	33.72	0.61	1.72

Analyzing from the First Furrier Transform (FFT) tool of the PowerGui the finding is that the passive harmonic filter reduces the THD of the voltage and current injected into the system.

VI. CONCLUSION

In this work, the wasteful impact of unnecessary power conversion was sought for and recognizes that negative impact of increasing the amount of nonlinear loads. It creates lots of harmonic if the DC power distribution system is used instead of an AC power distribution system. The investigation into power quality and analyzing the harmonics of a LVDC distribution system is performed using Matlab simulation environment. The simulation results are compared by verifications with measurements and practical examples. The effect of system reconfiguration on DC network and transformer harmonic content is determined. The simulated LVDC network with passive harmonic filter is meeting voltage and current harmonic distortion limits of IEEE std. 519. As the amounts of nonlinear loads are increasing day by day throughout the power system, efficient filter designing are required instantly to overcome from the effects of harmonics. The achieved models and results of this paper will be useful in the dimensioning LVDC distribution network components and system designing. This work will be highly applicable on the

978-1-4673-9257-0/15/$31.00 ©2015 IEEE

sight of rural area and different kind of office, bank and where solar panel should be used. After using the proposed filtering, it will be minimize the wasteful impact of unnecessary power conversions, which saves more energy in the system. In future work, using DC power and measurement of maximum tolerable range of DC load integration with the variation of nonlinear load up to which harmonics are tolerable in the secondary distribution system based further analysis can be developed.

VII. REFERENCES

[1] P. Nuutinen. *"Implementing a laboratory development platform for an LVDC distribution system",* 2011 IEEE International Conference on Smart Grid Communications (SmartGridComm), 10/2011

[2] Nasr, Abdulhakim. *"Harmonics analysis of a wind energy conversion system with a permanent magnet synchronous generator",* 2015.

[3] Ghijselen, Jozef, Wouter R Ryckaert, and Jan Melkebeek. *"Required load behaviour for power quality improvement."* In Power Engineering Society Summer Meeting, 2002 IEEE, vol. 2, pp. 998-1003. IEEE, 2002.

[4] Khan, M. Shuja. *"Implementation of a Passive Tune Filter to Reduce Harmonics in Single Phase Induction Motor with Varying Load",* International Journal of Engineering & Technology/20771185, 20110601

[5] Sannino, Ambra, Giovanna Postiglione, and Math HJ Bollen. *"Feasibility of a DC network for commercial facilities."* Industry Applications, IEEE Transactions on 39, no. 5 (2003): 1499-1507.

[6] Horowitz, Noah. *"Power supplies: a hidden opportunity for energy savings."* Natural Resources Defense Council, Tech. Rep (2002).

[7] IEEE Std. 519-1992, IEEE Recommended Practices and Requirements for Harmonic Control in Electrical Power Systems, New York, 1992.

[8] Kaipia, Tero, Janne Karppanen, Aleksi Mattsson, Andrey Lana, Pasi Nuutinen, Pasi Peltoniemi, Pekka Salonen et al. *"A system engineering approach to low voltage DC distribution."* (2013): 1292-1292.

[9] Rekola, Jenni. *"DC distribution and power electronics applications in smart grid."* (2012).

[10] Salomonsson, Daniel, and Ambra Sannino. *"Low-voltage DC distribution system for commercial power systems with sensitive electronic loads."* Power Delivery, IEEE Transactions on 22, no. 3 (2007): 1620-1627.

[11] Brenna, Morris, Enrico Tironi, and Giovanni Ubezio. *"Proposal of a local dc distribution network with distributed energy resources."* In Harmonics and Quality of Power, 2004. 11th International Conference on, pp. 397-402. IEEE, 2004.

[12] Karlsson, per, *"DC distributed power systems-Analysis, design and control for a renewable energy system".* Lund University, 2002.

[13] Louis Hapeshis, P. E., and D. Square. *"Power System Harmonic Mitigation for Water and Wastewater Treatment Plants."*

[14] Zavalani, Orion, Myrteza Braneshi, Aida Spahiu, and Luela Prifti. *"Potentials of power electronics in LV electricity distribution systems in Albania",* Proceedings of 14th International Power Electronics and Motion Control Conference EPE-PEMC 2010, 2010.

[15] Hur, Don, and Ross Baldick. *"An Economic Analysis of Potential Cost Savings from the Use of Low Voltage DC (LVDC) Distribution Network",* Journal of Electrical Engineering and Technology, 2014.

[16] Salonen, Pasi, Tero Kaipia, Pasi Nuutinen, Pasi Peltoniemi, and Jarmo Partanen. *"An LVDC distribution system concept."* In Nordic Workshop on Power and Industrial Electronics (NORPIE/2008), June 9-11, 2008, Espoo, Finland. Helsinki University of Technology, 2008.

[17] Kaipia, Tero, Pasi Peltoniemi, Jukka Lassila, Pasi Salonen, and Jarmo Partanen. *"Impact of low voltage DC system on reliability of electricity distribution."* In Electricity Distribution-Part 1, 2009. CIRED 2009. 20th International Conference and Exhibition on, pp. 1-4. IET, 2009.

[18] Khramov, Alexey. *"Converter supply transformer for LVDC distribution system."* (2009).

[19] M D Singh and K B Kanchandani, *"Power Electronics",* Second Edition, Tata McGraw Hill Education Private Limited

[20] Li, H., and Z. Wang. *"An Integrated Three-port Bidirectional DC-DC Converter for PV Application on DC Distribution System",* IEEE Transactions on Power Electronics, 2012.

[21] Shwehdi, M.H.. *"Harmonics Effect in Industrial and University Environments",* Power Quality Harmonics Analysis and Real Measurements Data, 2011.

[22] Kaipia, Tero, Pasi Salonen, Jukka Lassila, and Jarmo Partanen. *"Possibilities of the low voltage DC distribution systems."* In Nordac, Nordic Distribution and Asset Management Conference, pp. 1-10. 2006.

[23] Singh, S, G Bhuvaneswari, and B Singh. *"Power quality improvement in switched mode power supplies using two stage DC-DC converter",* International Journal of Engineering Science and Technology, 2012.

978-1-4673-9257-0/15/$31.00 ©2015 IEEE

An Accurate and Efficient Solar Tracking System Using Image Processing and LDR Sensor

Md. Hanif Ali Sohag[1], Md. Mahmudul Hasan[2], Mst. Mahmuda Khatun[3], and Mohiuddin Ahmad[4]
[1,2,4]Department of Electrical & Electronic Engineering
[1,2,4]Khulna University of Engineering & Technology, Khulna-9203, Bangladesh.
[3]Department of English
[3]Northern University Bangladesh, Rajshahi-6204, Bangladesh.
E-mail: hanifalisohag@gmail.com, mubin.eee.kuet@gmail.com, mahmuda.khatun.raj@gmail.com, mohiuddin.ahmad@gmail.com

Abstract— **The use of renewable energy resources is increasing for the purpose of producing electricity in modern world due to lack of non-renewable sources. As solar panels are becoming more popular day by day, it is a crying need to maximize the solar panel efficiency. The efficiency of solar panels can be increased to a great extent if the solar panels continuously rotate in the direction of sun. Microcontroller and an arrangement of LDR sensors can be used for the purpose of tracking the sun. But the system is less efficient because of the low sensitivity and disturbance of light dependent resistors. In this paper, a methodology of an automatic solar tracker is proposed by means of both sensors and image processing simultaneously. The mechanism of solar tracking was implemented by the use of an image processing software which combines the effect of sensors and processed image of sun and controls the solar panel accordingly. The methodology is a combination of hardware and software which can be used to control hundreds of solar panels in a solar power plant with more accuracy. It can be concluded that the proposed system is more accurate and efficient than the conventional solar tracking systems which can optimize the power requirement.**

Keywords—Photovoltaic cell, Solar tracker, Light dependent resistor, Microcontroller, Servomotor.

I. INTRODUCTION

While thinking about the development of a nation, the prime factor comes to mind is 'energy'. Huge amount of nonrenewable energy is extracted, distributed, converted and consumed in the global society daily. Almost 85% of energy production depends on fossil fuels. The resources of the fossil fuels are limited and their usage results in global warming because it can be a threat for human being by the emission of greenhouse gases. If we want to provide a sustainable power production and safe world to the future generation, we have to utilize the growing demand for energy from renewable sources like solar energy. Renewable energy sources are considered to be the best sources of energy which means no harm to global environment. Solar energy is a renewable resource which is clean, economical, and less polluted compared to other resources and energy [1].

Photovoltaic module is one of the efficient sources by which solar energy is converted in the form of electricity. Different semiconductor materials are used to make a solar panel. If Si is used to make solar panel, it becomes approximately 24.5% efficient [2]. Solar panel engrosses the energy from the sun and the energy can be stored in the battery which can be used for different purposes. Solar tracker is a system by which a solar panel can actually follow the sun to increase the power [3]. The main objective of this system is to develop a standard model of solar tracking system which consists of image processing using C++ programming language and sensor simultaneously. Thus it can increase the efficiency of solar panel at a great extent compared with the conventional systems.

The paper is organized as follows: Section II describes the photovoltaic technology and methods to improve efficiency of solar panel. Section III illustrates the proposed system. The hardware implementation is described in section IV. The methodology and developed prototype are briefly described in section V and VI respectively. The experimental result and discussion is described in section VII. Finally, section VIII concludes the paper.

II. PHOTOVOLTAIC TECHNOLOGY AND IMPROVING EFFICIENCY OF SOLAR PANEL

Researchers are trying to develop various methods whereby maximum power can be obtained from the solar panel. Maximum power point is the point where the maximum power from the system can be obtained by tracking that point during the sunshine hours. Fig. 1 represents the short circuit current versus voltage and power versus voltage characteristics of a photovoltaic cell [4].

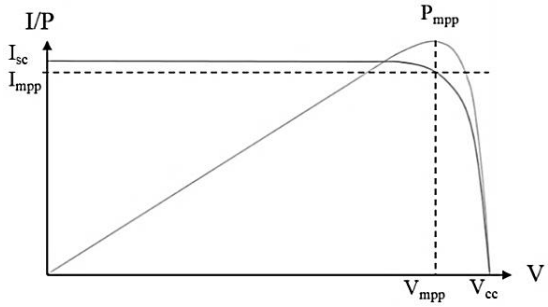

Figure 1. I_{sc}-V and P-V characteristics of solar cell

Researchers developed many Maximum power point tracking (MPPT) algorithms to maximize the output power from solar panel [5]. A solar tracker can increase the efficiency of the

978-1-4673-9257-0/15/$31.00 ©2015 IEEE

solar panel by tracking the sun. This mechanism can increase the power output of solar panel 30% to 60% than the fixed solar panel system [6]. Researchers developed different solar tracking algorithms recently [7, 9].

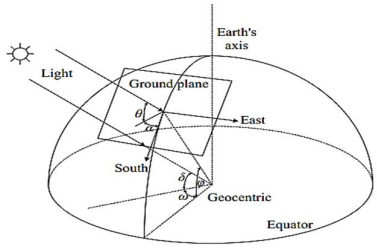

Figure 2. Geometric model of solar position

The sun trajectory tracking mode can work normally till the panel's azimuth and elevation angle change in accordance with the current solar azimuth and elevation angle [10]. From astrophysical knowledge, the solar azimuth and elevation angle at any given time can be calculated [11] [12].

The solar azimuth α and the elevation angle θ can be calculated using (1) and (2):

$$sin\theta = sin\varphi sin\delta + cos\varphi\ cos\delta\ cosw \quad (1)$$

$$sin\alpha = \frac{cos\delta\ sinw}{cos\theta} \quad (2)$$

Where, φ indicates the latitude angle, δ indicates the declination angle, ω indicates solar hour angle. The meanings of the parameters used are presented in Fig. 2 [10].

The declination angle δ and the solar hour angle ω can be calculated using (3) (Cooper Equation) and (4) [11].

$$\delta = 23.45° sin\frac{360°(284+d)}{365} \quad (3)$$

$$\omega = (h + E) \times 15 + \psi - 300° \quad (4)$$

In (3) and (4), h signifies the Beijing time, E indicates jet lag, ψ indicates the local longitude, d indicates the date, for example, d=2 stands for January 2nd, d=364 stands for December 30th [12]. Let, solar position is (α_t, θ_t) at t. Now, after interval T, the position changes to $(\alpha_{t+T}, \theta_{t+T})$. During this time, the variation of solar position can be expressed by $\Delta\alpha=\alpha_{t+T}-\alpha_t$, $\Delta\theta=\theta_{t+T}-\theta_t$.Let the panel has been aligned at t, if it is still aligned from t to T, the panel should rotate Δα in the horizontal direction and Δθ in the vertical direction respectively. In this way, sun trajectory can be explored.

III. Proposed System

The block diagram of the proposed system is presented in Fig. 3. The LDR sensor first takes the solar panel to a desired position. Then image processing is applied to track the sun coordinate. The servo motors are adjusted such that the canter of sun is always at the middle of the scaled camera window. By the iterative method it frequently checks the position of the sun and thus adjusts it to that particular position. The combined effect of LDR sensors and image processing operates simultaneously which gives better performance and efficiency.

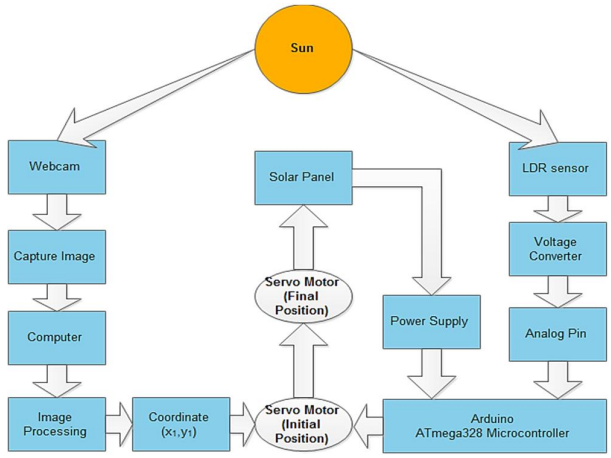

Figure 3. Block diagram of the system

IV. Hardware Design

The hardware consists of an Arduino UNO, two servo motors and four LDR sensors. The LDR sensors sense the sun light and the Arduino UNO takes decision to whether to rotate the vertical servo or horizontal servo motor. The circuit diagram of the system is shown in Fig. 4.

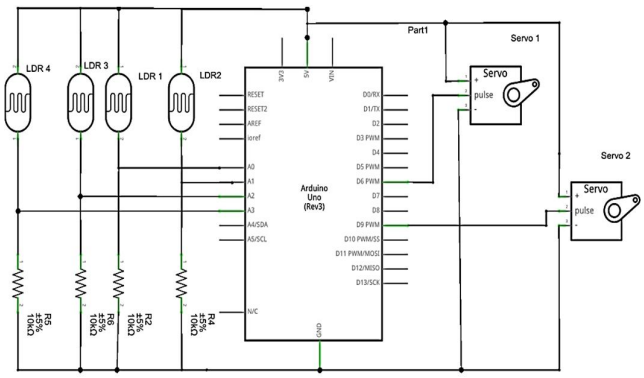

Figure 4. Circuit diagram of the system

V. Methodology

The sun is tracked in two stages- using the sensitivity of LDRs and then the adjustment of camera in new position by shifting the origin. Firstly, LDR sensors with the shadow arrangement compares the intensities fall on them and thus adjust the solar panel at an initial position. If the solar panel is out of track or in the opposite direction of sun it is adjusted towards the direction of sun. Secondly, the webcam mounted on the solar panel captures image of the sun and the computer processes the image using image processing algorithm. A new co-ordinate point is calculated by the described process and the two servo motors are controlled such that the sun remains at the center point of the captured image. The two steps occurred repeatedly and position of the sun is tracked accurately by the webcam.

A. Solar Tracking Using LDR Sensor

The resistivity of photo resistor decreases when the intensity of incident light increases. In the dark, an LDR can have a high

resistance like few mega ohms (MΩ). In the light, it can have very low resistance like a few hundred ohms. When we apply a constant voltage across the LDR and the intensity of light is increased, the current starts increasing. There are four LDRs in the proposed system as shown in Fig. 5. The resistivity of the LDRs will vary according to the intensity of light fall on them. LDR sensors are light sensitive. So, we arranged the LDRs in the proposed system in such a position that when the incident light is on the LDRs of one side (east), the LDRs of other side (west) are shaded. When it is afternoon and the sun goes towards the west, gradually the light intensity on the LDRs of the west will be high and the east LDRs will be in the shaded portion.

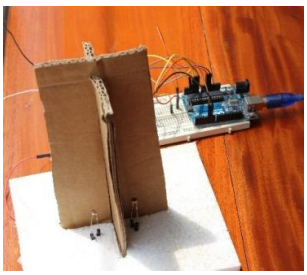

Figure 5. Shadow effect on LDRs

B. Image Processing

The proposed system represents the steps of estimating sun co-ordinates by using image processing. The steps involved in tracking the sun are given in Fig. 6.

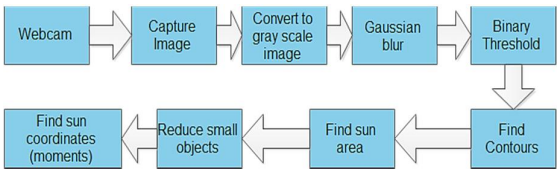

Figure 6. Image processing steps

1) Gray scale conversion and filtering: The captured image consists of the bright sun and blue sky. The processing of image is done in gray scale by extracting the luminescence plane from the RGB plane. Then Gaussian filter is used for the noise reduction of the captured image. The gray scale image is shown in Fig. 7.

Figure 7. Gray scale image with bright sun image

2) Sun detection: In order to extract the bright sun spot, binary thresholding technique is applied on the filtered image. Due to having cloud around the sun, there are some smaller objects detected in the image. Finding the largest contours, the smaller objects are removed. This situation is shown in Fig. 8 (a) and Fig. 8 (b).

(a) (b)

Figure 8. (a) After binary threshold, (b) Estimating the largest area

3) Sun tracking and co-ordinate estimation: After proper segmentation of the blob, the co-ordinates of the sun are estimated by using the centroid formula for irregular objects. The center position of the image is also calculated. Sun co-ordinate point is compared with the image center co-ordinate as shown in Fig. 9 for proper controlling of the servomotors.

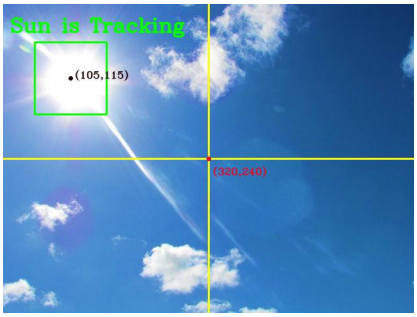

Figure 9. Sun co-ordinates calculation

C. Axis Transformation

1) Transformaton of origin with respect to change of axis: If the origin $O(x_0, y_0)$is shifted at $O'(x_1, y_1)$but the direction of axes remain unchanged, then in the transformed coordinate the origin to be shifted by $(x_1 - x_0)$distance in the x direction and $(y_1 - y_0)$distance in the y direction. The axis transformation is shown on Fig. 10.

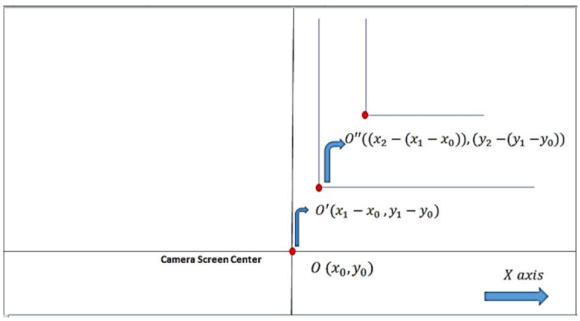

Figure 10. Transformation of origin

2) Adjustment of the solar panel position by tracking the cordinates of the sun: The webcam captures the images of the

sun and the coordinates of the sun is calculated. Now, the initial camera screen center point is adjusted such that the sun always remains at the center point which is shown in Fig. 11. Then proper transformation formulas are used to get the distance from the initial origin point to the sun coordinates. The two servo motors are controlled to get the proper position.

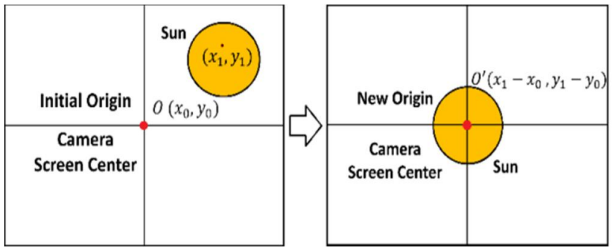

(a) (b)

Figure 11. Camera position control (a) camera detect sun at (x_1, y_1) point (b) camera screen center is shifted to that point

VI. Developed Prototype

The hardware for LDR based solar tracking system consists of an Arduino UNO, two servo motors and four LDR sensors. The LDR sensors are arranged such that the shadow effect works on them. The image processing based solar tracking system consists of a webcam and a personal computer. The system was tested on a core i5 2.60 GHz processor, 4GB memory running on Windows 7, 64-bit Operating system. The webcam installed on the solar panel had a resolution of 2 mega pixels. The developed prototype for real time sun tracking is shown in Fig. 12.

(a)

(b)

Figure 12. Developed Prototype (a) solar panel with webcam (b) LDR arrangement with Arduino and image processing using PC

VII. Experimental Results and Discussion

In this proposed system we used a mono crystalline BX-5W solar panel. The technical specifications were rated power of 5W, 17.4V rated voltage and 0.29A rated current. The open circuit voltage was V_{oc} =21.6V and short circuit current was I_{sc} =0.32A. The normal operating cell temperature of solar panel was45 ℃. The experimental data was recorded in Khulna University of Engineering & Technology (KUET) campus, Khulna-9203, Bangladesh at different times of the day. The experimental data is shown in Table 1.

While working using fixed solar panel, we found the maximum short circuit current of 0.2420A and maximum open circuit voltage of 19.170V at 1pm. Then the experiment was done using same solar panel and with the LDR based solar tracking system. In this case we found the maximum short circuit current of 0.2443A and maximum open circuit voltage of 20.016V at 12pm. Finally, the solar tracking system was implemented using both LDR arrangement and using webcam. In this case, we found the maximum short circuit current of 0.2497A at 2pm and maximum open circuit voltage of 20.456V at 11am. The short circuit current versus the day time was plotted in Fig. 13. The open circuit voltage versus the day time curve is shown in Fig. 14. The power versus the day time curve was plotted in Fig. 15.

This literature describes a novel system of solar tracking mechanism which repeatedly uses LDR sensors and image processing to track the sun. The image processing was done in C++ using OpenCV library. This mechanism is more efficient than the previous solar tracking mechanisms. From the power versus day time curve in Fig. 15, the maximum power was 4.89W at 12pm when we used only LDR sensors in the solar tracker. The maximum power was found to be of 4.96W at 12pm when we used the LDR sensors and webcam simultaneously. Of course the LDR based solar tracking system power curve was above the fixed system. So, it was better than the fixed solar panel system. But the LDR arrangement and webcam based solar tracking system was more efficient during morning and evening but it was quite difficult for the LDR arrangement alone. It was because of the low intensity of the sun light during this period. This system is much preferable compared with the conventional systems.

The sun can be tracked solely by either using Image processing of sun or using LDR sensors. When the LDR sensors are inactive or disabled or become obsolete, the solar tracker can track the sun using image processing spontaneously. On the other hand, if the webcam becomes obsolete or a fault occurs to it, the solar panel can easily operate using the sensitivity of LDRs. After the sun sets, the power supply to the system is disconnected and the system again operates in the next morning.

TABLE I. DATA OBTAINED FOR DIFFERENT SOLAR SYSTEM

Day Time	Fixed Panel			Solar Tracker using LDR			Solar Tracker using LDR and Image Processing		
	Isc (A)	*Voc (V)*	*Pout (W)*	*Isc (A)*	*Voc (V)*	*Pout (W)*	*Isc (A)*	*Voc (V)*	*Pout (W)*
7:00 AM	0.0586	15.674	0.91826	0.0718	17.113	1.229	0.0782	17.316	1.3536
8:00 AM	0.0882	15.791	1.393	0.0988	17.674	1.747	0.1228	18.861	2.316
9:00 AM	0.1167	16.341	1.908	0.1394	18.142	2.530	0.1436	19.012	2.729
10:00 AM	0.1363	18.025	2.457	0.1534	18.423	2.827	0.1725	19.889	3.430
11:00 AM	0.1616	18.342	2.965	0.1852	19.073	3.533	0.2021	20.456	4.134
12:00 PM	0.2401	19.042	4.572	0.2443	20.016	4.891	0.2460	20.161	4.962
1:00 PM	0.2420	19.170	4.642	0.2441	19.432	4.752	0.2446	19.742	4.831
2:00 PM	0.2135	18.026	3.849	0.2358	18.329	4.323	0.2497	19.021	4.753
3:00 PM	0.1724	15.977	2.754	0.1885	17.307	3.263	0.2018	18.892	3.812
4:00 PM	0.0636	15.322	0.975	0.0728	17.023	1.239	0.0934	18.723	1.748
5:00 PM	0.0542	14.136	0.766	0.0673	16.453	1.107	0.0734	17.674	1.297

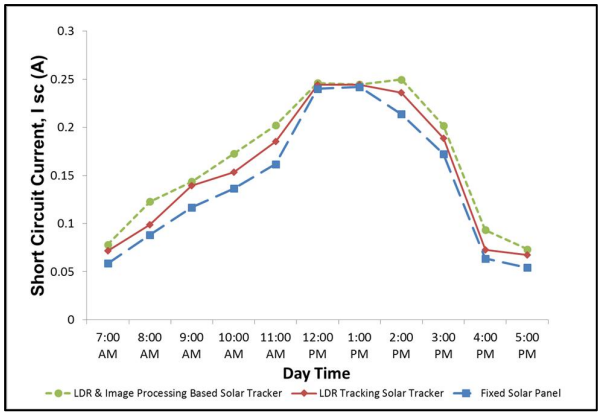

Figure 13. I_{sc}vs Day time for different solar panel system

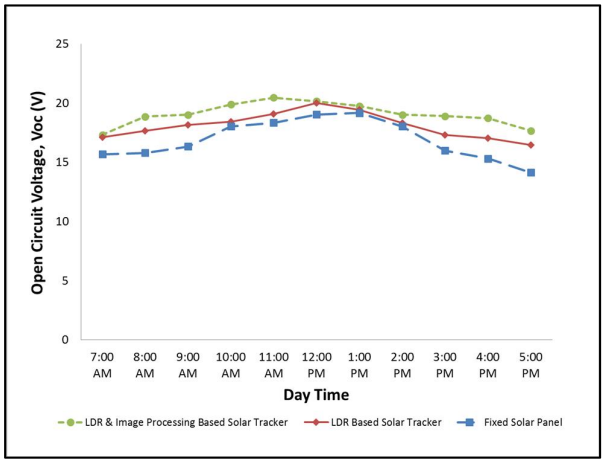

Figure 14. V_{oc} vs Day time for different solar panel system

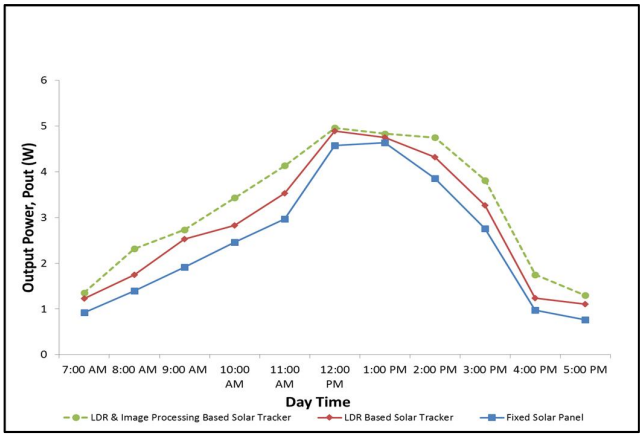

Figure 15. P_{out} vs Day time for different solar panel system

VIII. CONCLUSION

To conclude, it can be said that the proposed system increased the efficiency of the solar panel by tracking the sun in appropriate direction. The mechanism can be more effective if more LDR sensors are used and every solar panel in a particular area has a webcam. But for minimizing cost, thousands or hundreds of solar panel can track the sun using a single arrangement of LDR and a single webcam. The greater the resolution of the camera the better will be the performance of the solar tracking system. Thousands of solar panel can be operated by using this mechanism in the solar power plant. PLC can be used for the controlling purpose of thousands of solar panels. The more cameras be used; the efficiency of solar trackers will be more high. For minimizing cost, Raspberry Pi can be used instead of computer. The motors and microcontroller can be fed through the power produced by the solar panel itself. After all, we can say that the proposed system can optimize the power requirement by tracking the sun more appropriately.

REFERENCES

[1] A. Zahedi, "Energy, People, Environment, Development of an integrated renewable energy and energy storage system, an uninterruptible power supply for people and for better environment," Int'l Conf. on Systems, Man, and Cybernetics, 1994. 'Humans, Information and Technology', vol. 3, pp. 2692-2695, 1994.

[2] M. A. Green, “Clean Electricity from Photovoltaics,” Ed. Mary D. Archer and R. Hill, Series on Photo conversion of Solar Energy, vol.1, Imperial College Press, UK.
[3] D. Appleyard, “Solar Trackers: Facing the Sun,” Renewable Energy World Magazine, UK: Ralph Boon, June 1, 2009.
[4] M. T. A. Khan, S.M. S. Tanzil, R. Rahman, and S M S. Alam, “Design and Construction of an Automatic Solar Tracking System,” 6th International Conference on Electrical and Computer Engineering, Dhaka, Bangladesh, December 18-20, 2010.
[5] C. Hua and C. Shen, “Comparative study of peak power tracking techniques for solar storage system,’’ Applied Power Electronics Conference and Exposition, vol. 2, pp. 679-685, February 15-19, 1998.
[6] A. K. Saxena and V. Dutta, “A versatile microprocessor based controller for solar tracking,’’ Photovoltaic Specialists Conference, vol. 2, pp. 1105-1109, 1990.
[7] B. Koyuncu and K. Balasubramanian, “A microprocessor controlled automatic sun tracker,’’ IEEE Transactions on Consumer Electronics, vol. 37, no. 4, pp. 913-917, 1991.
[8] O. Bingol, A. Altinta, and Y. Oner, “Microcontroller based solar tracking system and its implementation,” Journal of Engineering Sciences, vol. 12, pp. 243–248, 2006.
[9] M. F. Khan and R. L. Ali, “Automatic sun tracking system,” All Pakistan Engineering Conference, Islamabad, Pakistan, 2005.
[10] H. Peng , T. Du, and W. G, “Application Design of A Sun-Tracking System,” 25th Chinese Control and Decision conference(CCDC) , 2013
[11] S. Wang, W. Gao, and S.Huang, “Research on the mixed two-axes sun tracker,” Renewable Energy Resources, vol.25, no.6, pp.10-13, 2007.
[12] J. Xiu, “GA based T-S type model of switched reluctance motor,” Micromotors, vol.42, no.3, pp.27-31, 2009.

Effect of Different Solar Radiation on the Efficiency of $GaInP_2/GaAs/Ge$ based MultiJunction Solar Cell

Syed Nazmus Sakib
Syeda Puspita Mouri
and Zannatul Ferdous
Dept. of Electrical, Electronic &
Communication Engineering
MIST, Dhaka, Bangladesh
Email:s.nazmus.sakib@ieee.org

Abu Kowsar
Institute of Fuel Research and Development
Bangladesh Council of Scientific
and Industrial Research

M. Shamim Kaiser
Institute of Information Technology
Jahangirnagar University
Savar, Bangladesh
Email:mskaiser@juniv.edu

***Abstract*—This paper represents the effect of solar radiance on the efficiency of GaInP$_2$/GaAs/Ge based multi junction solar cell. Solar radiation changes with the different wavelength and air mass. With the change in the irradiance data, the theoretical efficiency of the multi junction solar cell changes. The whole calculation is based on a modified version of spectral p-n junction solar cell model. The three sub layers are lattice matched and connected in series so that optical transparency and maximum current conductivity through the top and bottom cell can be produced. Short circuit current density, open circuit voltage, maximum current density, maximum power, fill factor and efficiency change with the variation of irradiance for the different air mass. For the simplicity of calculation, there are some assumptions which are necessary. The analysis is done under one sun condition. The J-V curves is also plotted for different layers under different air mass condition.**

***Index Terms*—multijunction solar cell, efficiency, air mass, current density, irradiance**

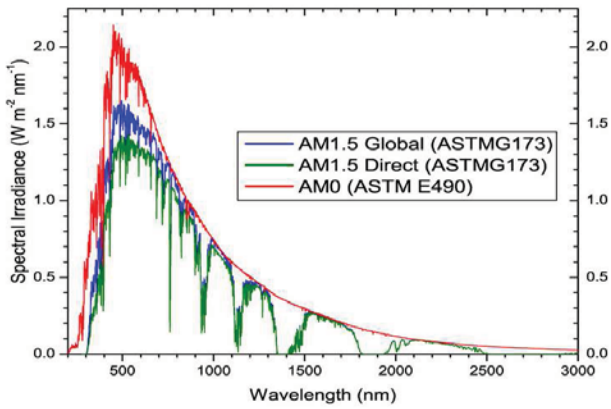

Fig. 1. Spectral irradiance for the different AM

I. Introduction

Power crisis has been one of the most significant issues all over the world. Scientists and researchers have been working relentlessly to find a solution for this problem. Most of them are doing their work on renewable energy. Because the amount of energy that can be generated from coal, gas or any other petroleum materials is limited. So scientists are more encouraged to work on the renewable energy sources for its unlimited availability. Among all the renewable energy sources, solar energy has got more popularity than all the others. Many works have been done to increase the efficiency of the solar cell.

Single junction solar cell was first introduced. But the efficiency of this solar cell is very low because the maximum efficiency depends on the incident spectrum [1]. The reason working behind that is, there is a good amount of solar spectrum remains unabsorbed due to the single junction. As the absorption is done by only one layer, the energy of the photon greater than the band gap cannot be absorbed by the single junction.

The researchers then developed an idea of converting different parts of solar spectrum that will be incident to the cell. This idea was considered since 1995 [2] [3]. So to reduce the losses and to increase the efficiency of solar cell, multi junction solar cell is introduced. With the innovation of multi junction solar cell, different solar spectrum now can be absorbed by the different layer of the multi junction solar cell. So the losses are reduced that results in increasing the efficiency.

In the figure: 1, it is clearly seen the solar spectra for different air mass [4]. From the figure it is seen that in multi junction solar cell it is possible to absorb most portions of solar radiation by choosing the band gap of different layers.

For the calculations of different parameters of solar cell, many scientists have given different models. First modern silicon solar cell with efficiency of 6 % has been developed in Bell Laboratory in 1954 [5]. In 1961,William Shockley and Hans Queisser reported the maximum theoretical efficiency of 33.7% for a single junction solar cell [6]. Spectral p-n junction model was published both for single junction cell and tandem

978-1-4673-9257-0/15/$31.00 ©2015 IEEE

cell for infinity thickness cell that is the thickness absorbed all incident irradiance equal or greater than thecorresponding band gap of the material [7]. Considering the thickness and modifying the reversesaturation current density equation, a theoretical model for tandem solar cell was reported [8].

For different value of air mass (AM) condition such as AM0,AM 1.5D and AM 1.5G the efficiency of $GaInP_2$/$GaAs$/Ge based multijunction solar cell has been calculated in this paper.

In this paper, section II depicts the discussion about solar cell and renewable energy, section III describes the multi junction solar cell model parameters, section IV gives the idea about the assumptions that are made for the calculations as well as the optoelectronic parameters of the different layer materials, section V shows the results for three air mass conditions and then the paper is concluded in the next section.

II. Solar Cell

Renewable energy is derived from naturally regenerative sources like solar, wind, geothermal or hydroelectric actions. Among these sources the demand of solar energy is increasing rapidly for its feasibility in developing countries. A solar cell is an electrical device by which light energy can be converted into electricity. The electrical characteristics of this photoelectric cell vary due to the different intensity of light [9]. There are various types of solar cells. Single crystalline i.e. monosilicon solar cell having commercial efficiency of about 22% is mostly used in integrated circuits and processing units of computers.

Thin film solar cells have semitransparent nature with lower efficiency of about 12-20%.The third generation PV cell or Organic PV cell are used for light absorption or electrical charge transport [10]. Single junction solar cells usually have lower efficiency. Increasing short circuit current density by better light trapping the efficiency can be improved for single junction solar cells [11].

III. Multijunction Solar Cell Model

Single junction solar cells have lower efficiency. Increasing the efficiency of PV cell is the main motto of current generation that is why multi junction solar cell is introduced into modern technology. Multijunction solar cells are constructed by connecting two or more p-n junction layers in series. Multijunction solar cells can generate power over a larger spectrum of sunlight having a higher efficiency than single junction solar cells. The lattice of the materials must be matched with each other to produce the same current in the different layers of multijunction solar cell. Thus the design for this kind of solar cell becomes complex with an increasing cost [12].The efficiency can be increased due to the reduction of top cell thickness. Cells with low surface recombination velocities can also help to increase open circuit voltage, resulting in higher efficiency [1]. The irradiance changes with the change in air mass coefficient. Thus the efficiency can be varied by using different air mass coefficient (AM).

The short circuit current density J_sc can be calculated by using irradiance data [13].

$$J_{sc} = eF \tag{1}$$

Where, F is the photon flux and e is the charge of an electron. Again,

$$F = \frac{\lambda I}{hc} \tag{2}$$

Where, is the wavelength, I is the irradiance, h is the Planck's constant and c is the speed of light.

The reverse saturation current density can be expressed as [1] [7] [8],

$$J_0 = e\sqrt{\frac{D_e}{\tau_e}}\frac{n_i^2}{N_A}\left(\frac{S_e\sqrt{\frac{\tau_e}{D_e}}\cosh\left(\frac{x_p}{\sqrt{D_e\tau_e}}\right)+\sinh\left(\frac{x_p}{\sqrt{D_e\tau_e}}\right)}{S_e\sqrt{\frac{\tau_e}{D_e}}\sinh\left(\frac{x_p}{\sqrt{D_e\tau_e}}\right)+\cosh\left(\frac{x_p}{\sqrt{D_e\tau_e}}\right)}\right) + e\sqrt{\frac{D_h}{\tau_h}}\frac{n_i^2}{N_D}\left(\frac{S_h\sqrt{\frac{\tau_h}{D_h}}\cosh\left(\frac{x_n}{\sqrt{D_h\tau_h}}\right)+\sinh\left(\frac{x_n}{\sqrt{D_h\tau_h}}\right)}{S_h\sqrt{\frac{\tau_h}{D_h}}\sinh\left(\frac{x_n}{\sqrt{D_h\tau_h}}\right)+\cosh\left(\frac{x_n}{\sqrt{D_h\tau_h}}\right)}\right) \tag{3}$$

Where, D_e and D_h are the diffusion current constant for electron and hole respectively. $N_A$is acceptor concentration, N_D is donor concentration, S_e and S_h are the surface recombination for electron and hole respectively, n_i is the intrinsic carrier concentration, τ_e is the minority carrier lifetime for electron and τ_h is the minority carrier lifetime for hole, x_p and x_n are the thickness of p-layer and n-layer respectively.

For the ease of calculation the above equation can be simplified as,

$$J_0 = eS_e\frac{n_i^2}{N_A} + eS_h\frac{n_i^2}{N_D} \tag{4}$$

The diffusion constants can be calculated from the Einstein Relationship,

$$D_e = kT\frac{\mu_e}{e}$$
$$D_h = kT\frac{\mu_h}{e}$$

Where, k is the Boltzmann's constant, μ_e is the electron mobility and μ_h is the hole mobility. The equation for minority carrier lifetime for electron and hole are:

$$\tau_e = \frac{1}{\frac{1}{\tau_{SRH}} + BN_D}$$
$$\tau_h = \frac{1}{\frac{1}{\tau_{SRH}} + BN_D}$$

B is the direct band-band recombination coefficient and is the Shockley-Read-Hall lifetime. The surface recombination velocities for electron and hole can be written as:

$$S_e = \sqrt{\frac{D_e}{\tau_e}}$$
$$S_h = \sqrt{\frac{D_h}{\tau_h}}$$

The intrinsic carrier concentration can be calculated from:

$$n_i^2 = 4M_cM_v\left(\frac{2\pi kT}{h^2}\right)^3 (m_e^* m_h^*)^{\frac{3}{2}} \exp\frac{-E_g}{kT}$$

Where, M_c and M_v are the densities of states in the conduction and valance band, T is the temperature, E_g is the energy gap of the material, $^*_e$ and m_h^* are the effective mass of electrons and holes respectively, M_c and M_v are the number of equivalent minima in the conduction and valance band. The open circuit voltage can be expressed as:

$$V_{oc} = \left(\frac{kT}{e}\right)\ln\left(\left(\frac{J_{sc}}{J_0}\right)+1\right) \tag{5}$$

The maximum voltage is:

$$V_m = V_{oc} - \frac{1}{\beta}\ln(1+\beta V_m)$$

Maximum current density is:

$$J_m = J_{sc}\left(1 - \frac{1}{\beta V_m}\right)$$

The final equation for the efficiency of the solar cell is:

$$\eta = \frac{V_{oc}J_{sc}F.F.}{P_{in}} \times 100\%$$

Where, P_{in} is the input power and F.F. is the fill factor

IV. ASSUMPTIONS AND PARAMETERS

The parameters that are required for calculation of different layers of the semiconductor materials are considered at the temperature of 298K. The input power densities for AM0 is 1353 W/m^2 and for AM1.5G is 1000 W/m^2 and for AM1.5D is 900 W/m^2 [14] [15] [16]. It is also assumed that there are no losses regarding reflection, grid coverage and series resistance. All the calculations are done using the modified versions of standard equations that is the modified version of spectral p-n junction model [1] [8]. The value of irradiance data is gathered from the data provided by ASTM [17].

It has been considered that, there is no carrier generation or recombination in the space charge region, neutral region operates at low injection condition and electric field in neutral region is negligible and photon recycling effects are also negligible.

The optoelectronic parameters are collected for 298K temperature [18] [19] for the different materials used for the three layers.Taking the values of different parameters from the table I, the calculations are done for the various equations that are mentioned in the previous section. The three materials that are chosen for the different layers are lattice matched.

TABLE I
OPTOELECTRONIC PARAMETERS [18] [19]

Parameter	$GaInP_2$	$GaAs$	Ge
Band Gap,(E_g) eV	1.9	1.42	0.67
wavelength,(λ) nm	654.28	875	1775
No of Equivalent Minima in Conduction Band (M_c)	1	1	1
No of Equivalent Maxima in Conduction Band (M_v)	3	1	1
electron mobility (η_e) m^2/Vs	0.4	0.2322	0.39
hole mobility (η_h) m^2/Vs	0.02	0.02	0.19
m_c^*/m_e	0.155	0.067	1.64
m_h^*/m_h	0.460	0.473	0.28
Shockley-Read-Hall Lifetime(T_{SRH}) s	10^{-5}	10^{-5}	10^{-5}
Direct band-band recombination co-efficient(B) s^1m^3	7.5×10^{-16}	7.5×10^{-16}	7.5×10^{-16}
Acceptor Concentration (N_A) m^{-3}	1×10^{23}	9×10^{23}	1×10^{23}
Donor Concentration (N_D) m^{-3}	2×10^{24}	7.8×10^{23}	2×10^{24}
Thickness of p-layer(X_p) m	1×10^{-07}	1×10^{-07}	1×10^{-07}
Thickness of n-layer(X_n) m	2.08×10^{-07}	3×10^{-07}	4×10^{-07}
Lattice constant (a) m	5.660×10^{-10}	5.659×10^{-10}	5.646×10^{-10}

Most of the parameters are dependent on the temperature. So if the temperature is changed, the values of these parameters will change. The thickness of the p layer is kept same for the each layer whereas the thickness for the m layer is different for the three layers of the multi junction solar cell.

V. RESULTS

Using the different equations mentioned in section III the following calculations are done. MATLAB is used for the calculations of the different parameters.

In table II the variations of short circuit current density and the open circuit voltage of the three layers for different air mass condition is shown.

Table III depicts the variations in overall current density, total open circuit voltage, maximum voltage, maximum current density, fill factor and efficiency of the solar cell for different solar radiation spectrum for different air mass.

The total leakage current density vs the open circuit voltage for each multi junction solar cell under different air mass solar radiation spectrum is plotted in the graph.

Figure:2 shows the J-V characteristic for solar radiation spectrum under AM0 condition, figure: 3 shows the J-V

TABLE II
COMPARISON OF DIFFERENT LAYERS

Parameters	AM0	AM 1.5 G	AM 1.5D
Top Layer $GaInP_2$			
Short circuit current density(J_{sc1}), A/m^2	828.9520	744.89	674.0564
Open circuit voltage(V_{oc1}), V	1.4387	1.4300	1.4334
Mid Layer $GaAs$			
Short circuit current density(J_{sc2}), A/m^2	658.5420	652.39	623.859
Open circuit voltage(V_{oc2}), V	1.0418	1.0415	1.0404
Bottom Layer Ge			
Short circuit current density(J_{sc3}), A/m^2	251.3022	163.9747	160.1052
Open circuit voltage(V_{oc3}), V	0.1325	0.1216	0.1210

TABLE III
COMPARISON OF THE TOTAL CELL PARAMETER

Parameters	AM0	AM 1.5 G	AM 1.5D
Short circuit current density(J_{sc}), A/m^2	251.3022	163.9747	160.1052
Total open circuit voltage(V_{oc}), V	2.6129	2.5991	2.5947
Maximum voltage (V_m), V	2.4939	2.4802	2.4759
Maximum current density (J_m), A/m^2	248.7122	162.2754	158.4431
Fill Factor (F.F.)	0.9446	0.9444	0.9443
Power input (P_{in}) , W/m^2	1353	1000	900
Efficiency (η), %	45.8441	40.2482	43.5879

characteristic for solar radiation spectrum under AM1.5D condition & figure: 4 shows the J-V characteristic for solar radiation spectrum under AM1.5G condition.

The total leakage current density is different for different layer and also for different solar radiation spectrum. The reason behind this is the short circuit density is dependent on the irradiance. The value of irradiance varies for the different wavelength. The wavelength is different for different band gap as well as for different layers for absorption. So as the value of irradiance is varying so does the total leakage current density.

For AM0 condition, the value of irradiance data [20] is higher than that of the AM1.5G and AM1.5D.because AM0 is suitable condition for space where the solar radiation is much more than the earth surface. The data that is used is generated by the American Society for Testing and materials (ASTM). It is one of the most accurate and recognized data for multi junction solar cell which is developed by counting one year average weather of United States of America [14]. Efficiency

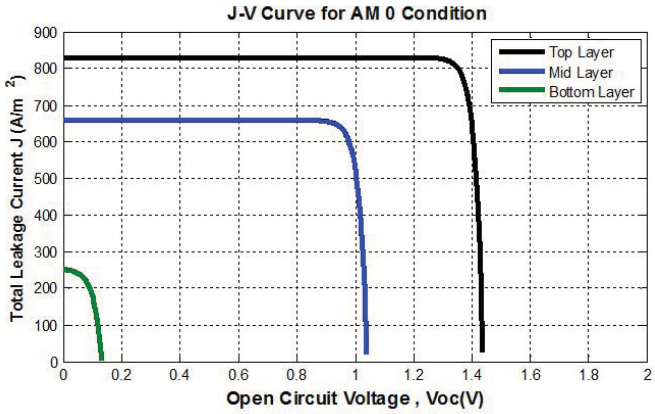

Fig. 2. J-V characteristic for AM0

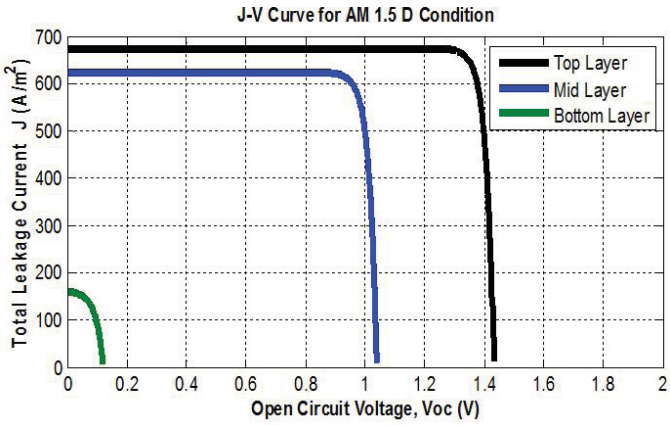

Fig. 3. J-V characteristic for AM1.5D

for AM1.5D is greater than the efficiency for AM1.5G because sunlight hit the solar cell directly in case of AM1.5D and for AM1.5G sunlight hit the solar cell after diffusion.

In the above figures, it is clearly seen that the total leakage current density remains same for a certain increment of open circuit voltage. But after a certain voltage the current density falls. By finding a maximum current and voltage and

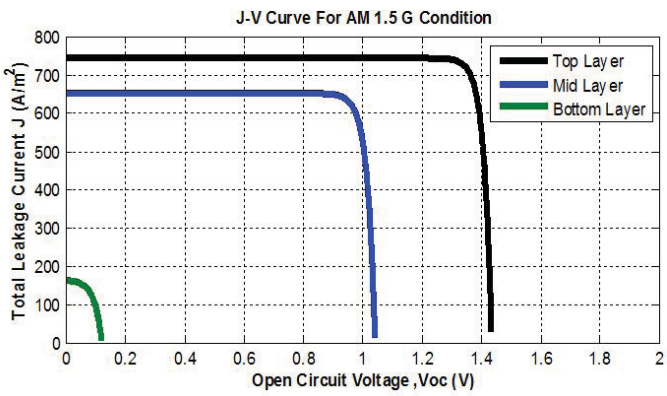

Fig. 4. J-V characteristic for AM1.5G

multiplying them maximum power can found for the solar cell.

In each solar cell, the minimum leakage current is flowing from the bottom layer. So the total cell current density will be the value of the bottom cell current density. So to increase the cell efficiency, the increase of leakage of current density in the bottom cell is necessary.

This characteristic may change in the practical scenario as there are losses. Conditions like carrier recombination in the space charge region, operating injection condition of neutral region, the amount of electric field in the neutral region, effects of photon recycling can cause decrement to the leakage current density and open circuit voltage leads to the reduction in the maximum power resulting in reducing the overall efficiency.

VI. Conclusion

The paper represents the variations in efficiency of GaInP2/GaAs/Ge based multijunction solar cell in different AM conditions such as AM0 , AM1.5D & AM 1.5G. Parameters such as short circuit current density, open circuit voltage also vary in each of the three layers considering change in AM condition. Maximum current density ,maximum voltage & total leakage current for the cell shows a significant change for diverse air mass values. For the three layer solar cell, the minimum current density is found in the bottom cell and it is the current density for the solar cell. As the junctions are connected in series, the open circuit voltage rises as the total open circuit voltage is the summation of three layers open circuit voltages.

References

[1] A. Kowsar, M. S. Islam, K. R. Mehzabeen and Z. H. Mahmood, *Study on the Efficiency of the $GaInP_2$/GaAs/Ge Multijunction Solar Cell*, Proc. of International Conference on Environmental Aspects of Bangladesh (ICEAB10), Japan, Sept. 2010

[2] D. Trivich and P. A. Flinn, *Maximum efficiency of solar energyconversion by quantum processes* , Solar Energy Research, F. Daniels, J. A. Duffie, Eds. Madison, WI: Univ. of Wisconsin Press, 1955, p. 143

[3] E. D. Jackson, Areas for improvement of the semiconductor solarenergy converter, Trans. Intern. Con. *Use of Solar EnergyThe Scientific Basis*, vol. V, p. 122, 1955.

[4] ASTM G-173-03 (International standard ISO 9845-1, 1992)

[5] D. M. Chapin, C. S. Fuller, and G. L. Pearson, *A new silicon p- n junction photocell for converting solar radiation into electricalpower*, Journal of Applied Physics, 25, 1954, 676677..

[6] William Shockley and Hans J. Queisser, *Detailed Balance Limit of Efficiency of p-n Junction Solar*, Journal of Applied Physics, 32, 1961, 510-519

[7] E. M. Nell and A. M. Barnett, *The spectral p-n junction model for tandem solar-cell design*, IEEE Transaction on Electron Devices,Ed-34, No. 2, 1987, 257-266.

[8] S. R. Kurtz, P. Faine, J. M. Olson, *Modeling of two-junction, series-connected tandem solar cells using top-cell thickness as anadjustable parameter*, Journal of Applied Physics, 68 (4), 1990, 1890 1895

[9] L.A. Coldren and S.W. Corzine, *"Diode Lasers and Photonic Integrated Circuits"* ,Wiley Interscience, 1995.

[10] F. Meillaud, A. Shah, C. Droz, E. Vallat-Sauvain, C. Miazza, *Efficiency limits for single-junction and tandem solar cells*, Institute of Microtechnology (IMT), University of Neuchtel, A.-L Breguet 2, 2000 Neuchtel, Switzerlan.

[11] *Solar Tech-USA* http://www.solartech-usa.com/types-of-solar-cells.

[12] Andrew Bates, Sherif Michael, *The Design and Optimization of an Advanced Four Junction Solar Cell*, Naval Postgraduate School, Monterey, California, 93955

[13] R. Hulstrom, R. Bird and C. Riordan, *Spectral solar irradiance datasets for selected terrestrial condition*, solar cells 15(1985) 365 391

[14] ASTM Standard G173, *Standard Tables for Reference Solar Spectral Irradiance:Direct Normal and Hemispherial on 37o Tilled Surface,* , Amer. Society for Testing Matls. West Conshochen PA, USA 2007.

[15] K. W. Mitchell, *High efficiency concentrator solar cells,*, Conf., of 15th IEEE Photovoltaic specialists con., pp . 142-146, 1981.

[16] Abu Kowsar, Abdullah Yousuf Imam, Mashudur Rahaman, Muhammad ShahriarBashar, Md. Saidul Islam, Sumona Islam, Nowrin Akter Surovi, Zahid Hasan Mahmood, *IOSR Journal of Applied Physics (IOSR-JAP)* Issue 6 Ver. IV (Nov.-Dec. 2014), PP 13-17.

[17] ASTM G173-03 Reference Spectra Derived from SMARTS v. 2.9.2

[18] Hamza Bennacer, Smail Berrah, Abdelkader Boukortt, Mohamed Issam Ziane *Electronic and optical properties of $GaInX_2$ (X= As, P) from first principles study*, Indian Journal of pure & Applied Physics, Vol. 53, March 2015, pp. 181-189.

[19] *Physics of Semicoductor Devices* 3rd Edition by S . M. Sze and Kwok K. Ng, Copyright 2007, John Wiley & Sons, Inc

[20] *Solar Spectra: Air Mass Zero* 2000 ASTM Standard Extraterrestrial Spectrum Reference E-490-00

Multi-agent System Modeling For Managing Limited Distributed Generation of Microgrid

Mirajul Islam, Abu Md. Safiul Alam and C. K. Das
Department of Electrical and Electronic Engineering
Chittagong University of Engineering and Technology
Chittagong-4349, Bangladesh
mirajul.islam075@gmail.com, foisal52cuet@yahoo.com, choton46@gmail.com

***Abstract*— This paper focuses on operation of small scale renewable plants so that the energy produced can be utilized to its highest potential. Energy crisis being one of the main problems is leading the researchers to find fossil fuel replacement which is eventually renewable energy. In most cases, renewable energy is unpredictable as they rely on the nature. Besides, in developing countries it is discouraged to install renewable technology due to their random nature. In order to design a reliable microgrid where renewable resources contribute to its grid power supply, multi-agent system has been incorporated to add intelligence to the system. The various loads to be fed are divided according to importance. The proposed concept also allows sharing of load among utility supply and renewable sources during normal operation.**

***Index Terms*—microgrid, intelligent, multi-agent system, limited renewable resource**

I. INTRODUCTION

Microgrid may be the eventual answer to the present energy crisis that is growing steadily in our world. Implementation of microgrid increases reliability in power distribution system. The utilization of renewable energy in a microgrid though may be a great challenge, this is where the assistance of another system is required which will act as the brain for the microgrid. The multi-agent system (MAS) technology is quite attractive in this respect as it provides a touch of intelligence to the system. There has been significant research on MAS technology in the recent times. MAS use multiple software agents to complete a collective task by dividing and distributing the task among the agents. Renewable energy resources like solar PV, wind turbine etc. contributes a lot to the distributed energy resources (DER) of the microgrid. These renewable energy sources being unpredictable and not always reliable, it becomes a great challenge to utilize them to their highest potential. Hence a system is needed that can adapt to the dynamic behavior of the sources.

Designing agent architecture for microgrid is a complex task. Several studies have been conducted in this field are noteworthy. The research on Intelligent Distributed Autonomous Power System (IDAPS) [1] has discussed on developing architecture for an intelligent system which works in co-ordination with different agents for managing customer owned units in the distribution network. Another research on securing critical loads in a PV-based microgrid with multi-agent system [2] was conducted which basically focused on the design and implementation of a multi-agent system through simulation. There were further discussions on securing critical loads during grid failure. Practical implementation of a multi-agent system was somewhat achieved in [3]. The research concentrated on building hardware modules for the agents. A research on optimization of solar panel output for microgrid based on multi-agent system has been conducted in [4]. Detailed research on scheduling of distributed generation is discussed in [5]. Some more application of MAS in microgrid have been deliberated in [6]-[8].

The sole purpose of this research is to develop a control mechanism for required agents so that they can respond to the changes in the scenario and act accordingly. It is also intended that the power generated from the renewable sources be wisely utilized in order to reduce power consumption from the utility grid supply. In order to make the research as reliable as possible the load profiles for the microgrid is based on the load of Chittagong University of Engineering & Technology (CUET), Chittagong, Bangladesh.

II. OVERVIEW

The first task was to analyze the electrical loading in different feeders of CUET. The microgrid was designed according to the data acquired from the analysis of the loads. The units comprising the DER of the microgrid were selected. This was followed by choosing of different agents that are responsible for managing the DER output. At last model architecture was developed using the agents.

III. LOAD ANALYSIS

A. Collection of data

The data was collected from CUET substation on an hourly basis for a month. There are in total 11 feeders in this educational facility that provides electricity to various loads.

B. Determination of peak load

The data collected was later processed to a load profile of a single day by taking into count the average loadings of working

978-1-4673-9257-0/15/$31.00 ©2015 IEEE

days in the institution. The list of feeders and their peak loads are given in table I.

TABLE I. ESTIMATED PEAK LOAD FOR EACH FEEDER

Feeders	Details	Daily power consumption (kW)	Estimated Peak loads(KW)
Feeder 0	12 floor engineering building, auditorium, Ansar camp	447	50
Feeder 1	Electrical & Mechanical Engineering building Mechanical Engineering Workshop	319	45
Feeder 2	teachers & officer's quarters	1052	70
Feeder 3	Civil & CSE building	510	50
Feeder 4	Vice Chancellor's Bungalow	172	13
Feeder 5	Sufia Kamal Hall	276	18
Feeder 6	Pump , IRP	546	40
Feeder 7	Shaheed Tareq Huda Hall, Shaheed Mohammad shah Hall and Dr. Qudrate Khuda Hall	1169	72
Feeder 8	Pre-engineering building, VC office, library	781	75
Feeder 9	Staff quarter	509	28
Feeder 10	Bangabandhu Hall, canteen, Bank, Mosque, PME Building	414	35

C. *Load curve*

Each feeder was analyzed in order to get a daily load curve that gives an idea on the load behavior of the grid. The load curve gives better prediction on what the demand will be and measures can be taken accordingly.

For simplicity the load curve of all the feeders united is shown in Fig. 1.

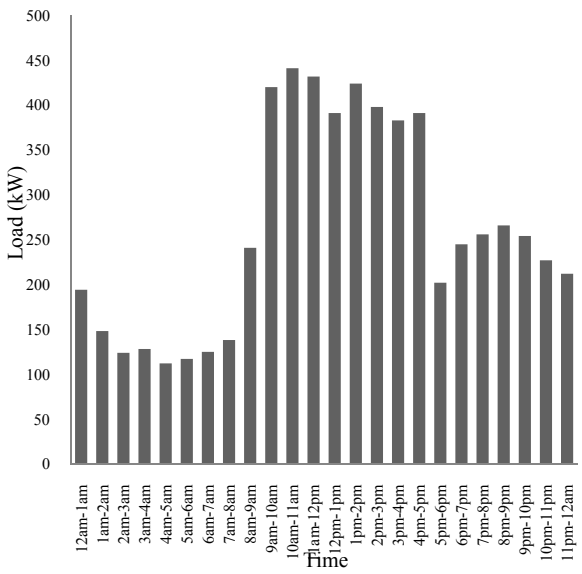

Figure 1. Load curve of the whole system for a single day

From the load curve in Fig. 1 we can observe the electrical activities for a whole day.

IV. MICROGRID MODELING

The microgrid that is intended to design has two parts, the physical part and the virtual part. The virtual part will be discussed later. The distribution system is divided into two parts, (i) utility grid and (ii) DER grid. Considering each feeder as a subsystem that consists of the load, we have 11 subsystems. These subsystems will be powered by utility grid supply and the DER sources. The DER sources include a PV panel and a diesel generator. The different parts of the microgrid are briefly discussed below.

A. *Utility Grid*

Two lines have merged, one from Madunaghat substation and the other from Chandraghona substation supplying 33kV line to the CUET substation.

B. *The subsystems*

The 33kV line is further stepped down to 11kV and then again to 380V. This line is fed to all the feeders. As mentioned earlier, different feeders are considered as subsystems that will denote the loads. The subsystems are further divided into critical and non-critical loads. The selection of critical load depends on the type of load that is to be supplied. Critical loads for residential purpose will differ from that in a class room.

C. *The DER grid*

For efficient distribution of energy, DER grid has been designed to operate isolated from the utility grid. For this research, it is vital fact as the alternative sources which we selected are not able to fully sustain all the critical loads during outage or fault.

The DER grid as mentioned earlier is powered by a PV module and a diesel generator as discussed below:

1) PV module: We assume that a 50kW solar PV panel provided with a battery is existent in our system.

2) Diesel generator: A diesel generator of 67.5kVA is being used for our model.

Each subsystem is provided supply from the DER grid. Another important fact for the diesel generator is that it will only be activated during 'emergency' protocol. The 'emergency' protocol is a manual override during which the diesel generator will be allowed to supply power. The schematic diagram of the whole system is shown in Fig. 2.

V. SELECTION OF CRITICAL LOAD

Selection of critical load is very important for our microgrid design. Critical loads may vary from subsystem to subsystem. At optimum condition, a total of 50 + 67.5 = 117.5 kW (considering power factor unity) can be generated. Owing to the fact that there are several unavoidable losses, the sum is multiplied by a factor of 0.9 which leads to getable power of 105.75kW. Hence while selecting critical loads each subsystem

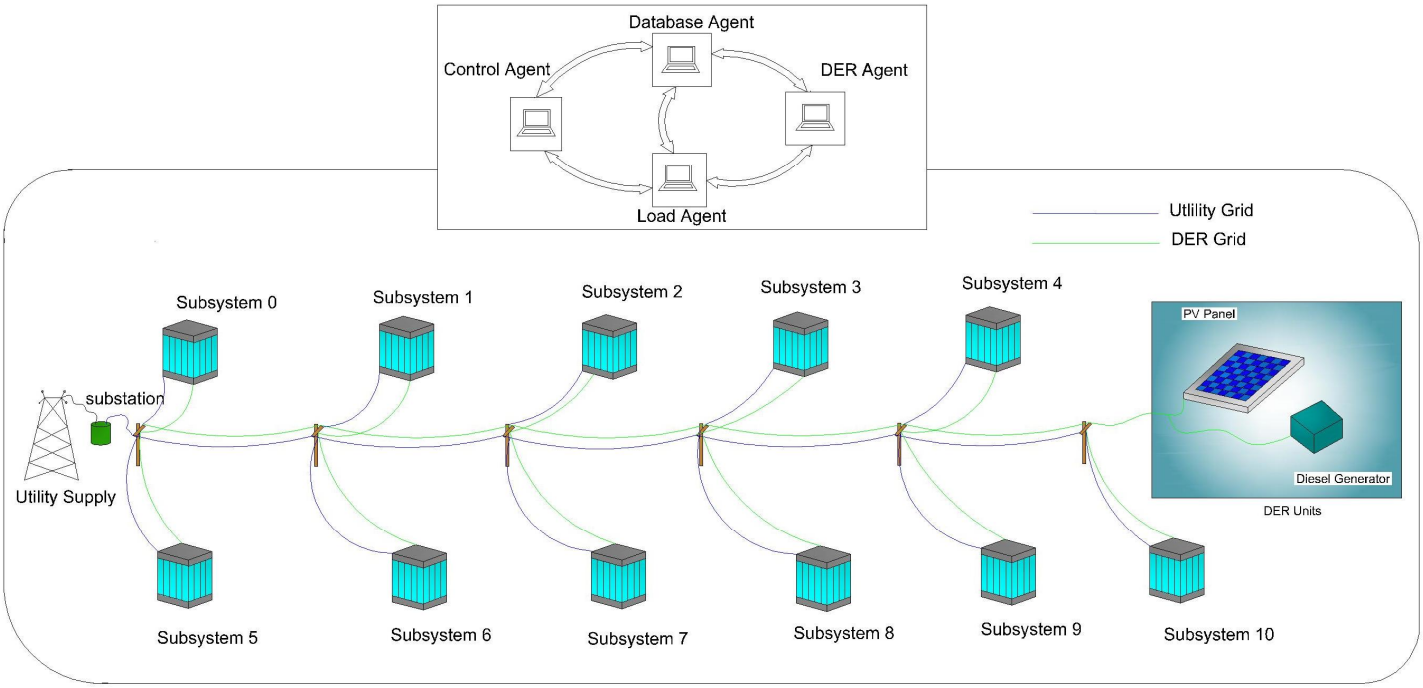

Figure 2. Schematic diagram of the Microgrid in collaboration of MAS

will be assigned a specific amount of loads to gain supply. The selection of load was done according to the need of the subsystem. The allocation of critical loads for each substation is given in table II.

TABLE II. CRITICAL LOAD ALLOCATION

Subsystem	Types of load	Allocated load in kW
0	light, fan, multimedia projectors	12.5
1	light, fan, multimedia projectors, computer	11.5
2	light, fan	18
3	light, fan, multimedia projectors, computer	13
4	light, fan	4
5	light, fan	4.5
6	pump, street lamps	10
7	light, fan	15
8	light, fan, computers	20
9	light, fan	8
10	light, fan , computers	9
	Total	**125.5**

From the table, we observe that a total of 125.5 kW load has been assigned and our total getable power is 105.75 kW. Moreover, the diesel generator is not intended to be used until dire need arises. Hence, distributing the 50 kW PV output among the loads is our main objective.

VI. MULTI-AGENT ARCHITECTURE

According to the requirements of our microgrid the agents are to be selected. The agents must be well defined in order to complete their assigned tasks.

A. Selection of agents

Four agents are required to achieve the goal that has been set. They are,

1) Control Agent: Control agent acts as the actuator of the decisions that are taken. It controls all circuit breakers (CB).

2) Load Agent: Load agent monitors the voltage and frequency of the different subsystem. It sends power request during fault or outages.

3) DER Agent: DER agent monitors the output from the various DER sources. It also checks fuel inventory for diesel generator.

4) Database Agent: Database agent stores data in the form of log.

B. Assign task to the agents

In order to function the agents properly, primarily their tasks and goals have to be set. The tasks are discussed as follows

1) Islanding: This the task performed by the database agent when fault occurs in the utility grid. The other agents are informed about the fault. During islanding the internal grid system is isolated from utility grid.

2) Load shed: This task is performed by the control agent. During islanding all the non-critical loads are shed by invoking this task

3) Emergency: The database agent responds to this task and broadcasts if emergency protocol has been activated

4) Check DER output: The DER agent performs this task by continuously monitoring the output of various DER sources.

5) Check inventory: The DER agent monitors the fuel inventory for diesel generator through this task.

6) Check demand: The load agent checks the voltage and current of various loads through this task.

7) CB open/close: This task is performed by the control agent. Through this task, command signal are sent to the circuit breakers to open or close.

8) Check priority: Priority is a floating number assigned to each subsystem from 0-1. Higher the value the greater the priority.

C. Agent Collaboration

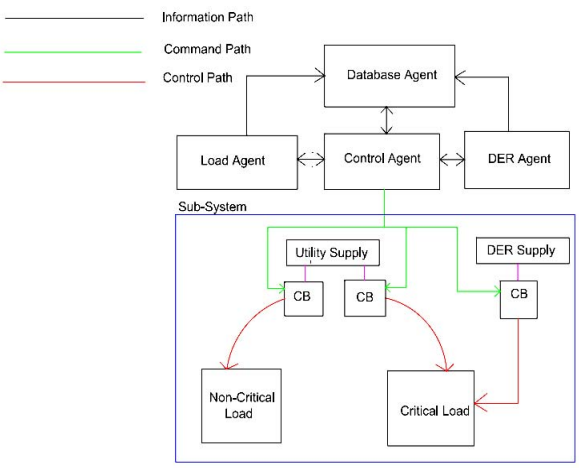

Figure 3. Agent Collaboration

Analogy of a single substation is shown in the Fig. 3. The load agent and the DER agent constantly update the database. The control agent checks for any fault or emergency and acts accordingly. Control agent also controls the circuit breakers that provide power to the loads.

D. Agent Algorithm

The main objective of the agents is to distribute the power output from the DER grid as efficiently as possible. The flow diagram of the control algorithm is shown in Fig. 4.

Suppose an outage occurs, so the grid algorithm will be objected to restore power in the DER grid. At first the subsystem with highest priority is chosen. The output power of the PV panel and the demand of the subsystem are checked. If the demand is less than or equal to the output, circuit breaker to the critical load is closed. If the demand is greater, although being of higher priority the subsystem is ignored. Then the process is repeated for the next priorities until all the subsystem are checked. The system will check if emergency protocol is activated. If not then the system remain as it is until the priority changes or PV output changes.

Next, if there is emergency then the fuel inventory are checked. If there are sufficient supplies, the generator will start. Subsystems those which were ignored will be checked again. If the demand and output match then the critical circuit breaker will close or the system will stay as it is until the priority changes or there is short of supplies.

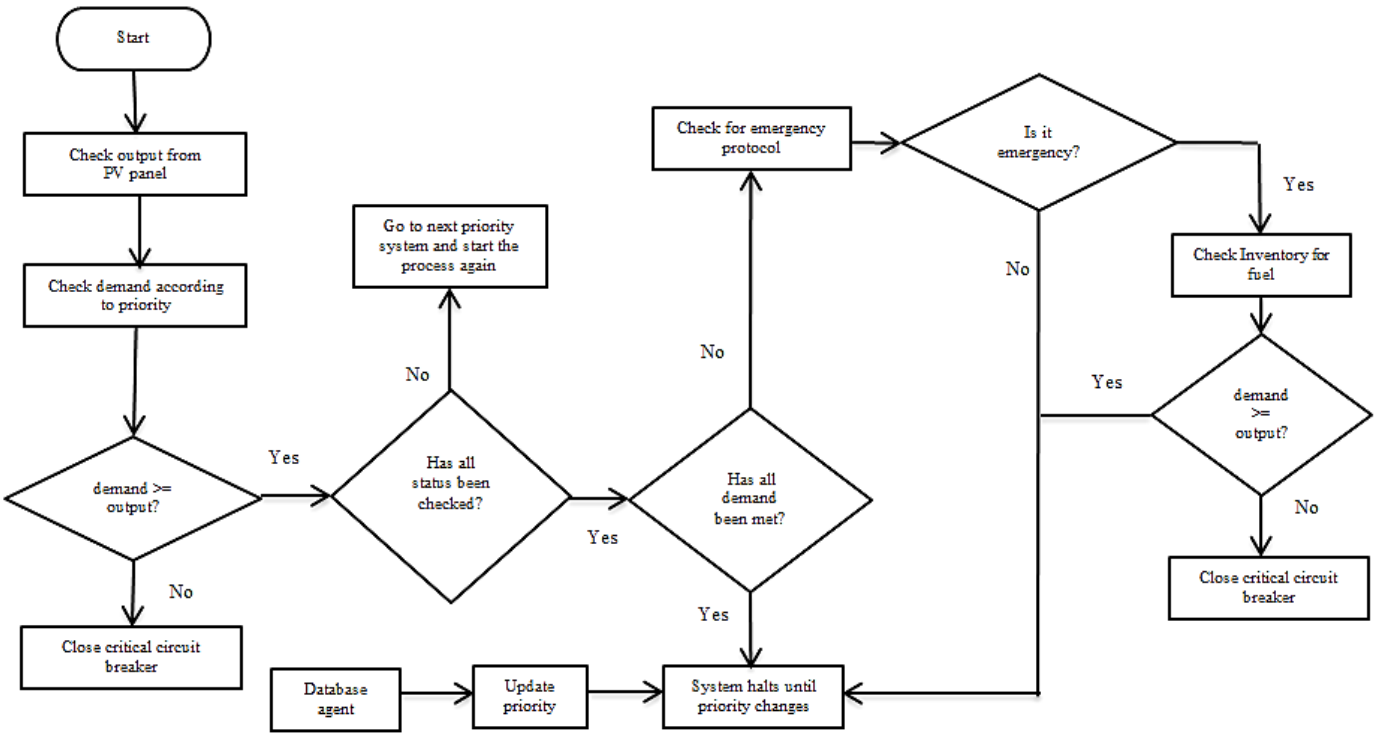

Figure 4. Control analogy for distribution of DER output during outage, fault or load sharing

VII. MICROGRID FEATURES

The designed microgrid has two noteworthy features as discussed below:

A. Islanding Mode

The islanding mode is a very important feature of the microgrid. It protects the microgrid from external fault by isolating it. This feature helps in prevention of blackout, brownout or any other utility grid faults affecting the system.

B. Load Sharing Mode

The designed microgrid not only restores power during outages but also reduces load on utility supply whenever the PV panel is producing enough. The load is at its peak during 9am to 4pm. During this time the PV panel also produces sufficient power. So the critical load which can be sustained by the PV supply are disconnected from the main grid and instead powered by the DER grid. The reduction in power consumption can be shown in Fig. 5.

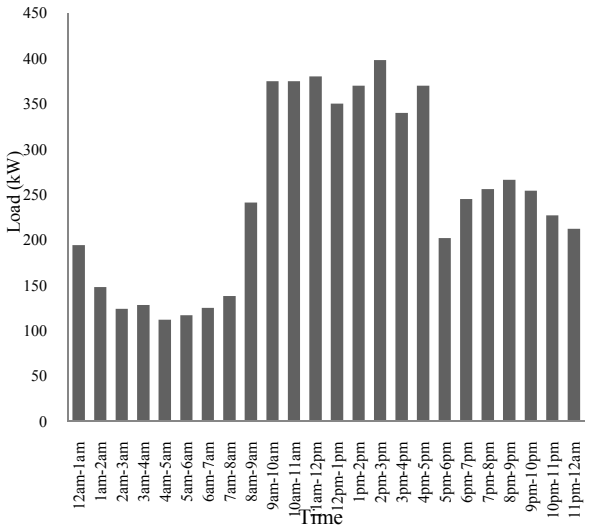

Figure 5. Load curve of the whole system while load sharing

It can be observed that the peak power demand has reduced to 360kW which was around 400kW initially.

VIII. SYSTEM REALIZATION

Multi-agent system realization has been shown in various research works. Some published researches on realization of the system have been mentioned in [9]-[12]. Although system realization is beyond the scope of this research, but a brief process is discussed as follows.

In most of the cases, the microgrid is simulated using MATLAB/Simulink. The loads, sources and other components are available in the library. The agents are developed using agent building toolkit such as JADE [13] and Zeus [14]. The physical system i.e. the microgrid developed in Simulink and the virtual system which are the agents are connected over a TCP/IP connection. The TCP/IP protocol allows computer of different sizes and operating system to communicate with each other [15]. Then a third party software [16] is used to establish the link. The agents communicate among themselves in various ways. For ZEUS based agent architecture, message is exchanged among the agents as a means of communication [2]. In case of IP based network, the agents are placed at single server [12] where they can communicate among themselves easily.

The physical system can be implemented in several ways. In this research, different grid for utility supply and DER supply has been used. The one line diagram of a single system is shown in Fig. 6. The other subsystems also have a similar arrangement. The critical load circuit breakers, non-critical load circuit breakers and the DER control circuit breakers are controlled by the agents while the LV circuit breakeris dependant on fault conditions.

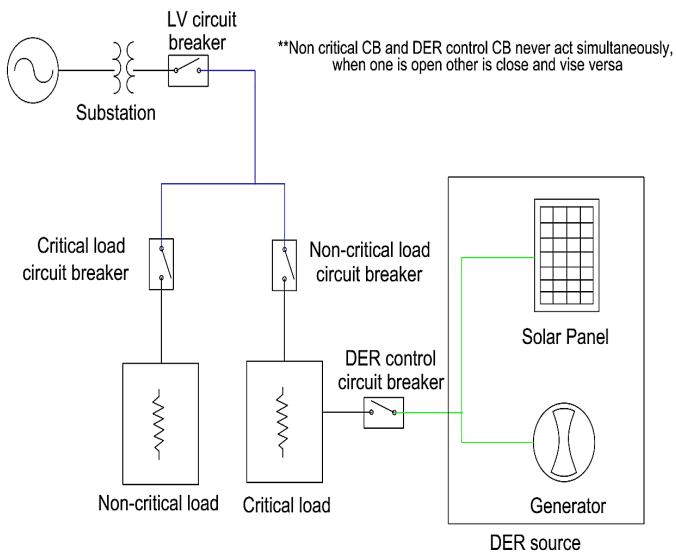

Figure 6. One line diagram of a single subsystem

IX. RESULT AND DISCUSSION

The load analysis revealed that most of the electrical activities are around 9 am to 5pm when the peak load is about 400 kW. For supplying a critical load of 125.5 kW a collective distributed generation of 105 kW is available. In order to distribute the power generated by the PV panel and the generator, the algorithm proposed earlier for scheduling the distributed generation is quite important. Some test conditions are applied to the algorithm and the results are tabulated in table III & table IV.

The four agents as defined earlier are able to function properly to achieve the goal of proper distribution of limited distributed generation. This gives a lot of option and alternative to make an efficient scheduling for distributed generation. Even when there is no sunlight the grid can be supplied by the

generator without taking the machine to overload conditions. If any unit is added or is unavailable the agents will act accordingly to maintain power supply.

Two cases have been shown for visualization of the effectiveness of the algorithm. In the first case only, a PV output of 50 kW is incorporated as shown in table III. In the second case, a combined output of which the PV output of 30 kW and the generator supply of 67.5 kW is considered. For both cases, the priority orders are set as depicted in table III and table IV.

TABLE III. SCHEDULING WHEN PV OUTPUT IS 50 KW AND GENERATOR IS OFF

Sub-system	Priority order	Critical load in kW	State of DER control CB	Power supplied by		
				Grid	PV	Gener-ator
0	1	12.5	closed		✓	
1	2	11.5	closed		✓	
2	3	18	closed		✓	
3	4	13	open	-	-	-
4	5	4	closed		✓	
5	6	4.5	open	-	-	-
6	7	10	open	-	-	-
7	8	15	open	-	-	-
8	9	20	open	-	-	-
9	10	8	open	-	-	-
10	11	9	open	-	-	-
Demand fulfilled by PV				**45.5 kW**		
Demand fulfilled by generator				**0 kW**		

TABLE IV. SCHEDULING WHEN PV OUTPUT IS 30 KW AND GENERATOR IS ON (67.5 KW)

Subs-ystem	Priority order	Critical load in kW	State of DER control CB	Power supplied by		
				Grid	PV	Gener-ator
0	1	12.5	closed		✓	
1	2	11.5	closed		✓	
2	3	18	closed			✓
3	4	13	closed			✓
4	5	4	closed		✓	
5	6	4.5	closed			✓
6	7	10	closed			✓
7	8	15	closed			✓
8	9	20	open	-	-	-
9	10	8	open	-	-	-
10	11	9	open	-	-	-
Demand fulfilled by PV				**28 kW**		
Demand fulfilled by generator				**60.5 kW**		

Power consumption can be reduced up to 10% when running on load sharing mode.

X. CONCLUSION

In this research, a microgrid model is designed for adapting to limited DER supply. The multi-agent architecture is also developed which incorporated with the microgrid helps to develop an autonomous system which is able to adapt to the dynamic behavior of the renewable energy sources. The control algorithm ensured that the system is a reliable and efficient. Successful implementation of small scale renewable power plants will encourage the initiative of making larger plants. Besides, the system is also able to deal with faults and outages and take necessary actions.

Automation of electrification in case of microgrid opens up a lot of scope in research. Meshing up two or three microgrids and sharing power among them is also possible. Hence, a market can be created where power will be the currency. Agent behavior and performance can be greatly enhanced by the use of neural network and fuzzy logic.

REFERENCES

[1] S. Rahman, M. Pipattanasomporn and Y. Teklu, "Intelligent Distributed Autonomous Power Systems (IDAPS)", in *Proc. of the IEEE PES Annual General Meeting,* Tampa, Florida, Jun. 2007, pp. 8.

[2] M. Pipattanasomporn, H. Feroze and S. Rahman, "Securing critical loads in a PV-based microgrid with a multi-agent system", in *Proc. Elsevier B.V.,Renewable Energy*, v.39, no.1,pp. 166-174, Mar. 2012

[3] Il-Yop Chung, Cheol-HeeYoo and Sang-Jin Oh, "Distributed Intelligent Microgrid Control Using Multi-Agent Systems", Engineering, vol 5, Jan. 2013, pp:1-6.

[4] L. Rajua, S. Sankar and R. S. Milton "Distributed Optimization of Solar Micro-grid using Multi Agent Reinforcement Learning*",in Proc. Elsvier B. V. Procedia Computer Science*, v 46, 2015, pp 231-239

[5] Y.S. Foo Eddy, H.B. Gooi and S.X Chen., "Multi-Agent System for Distributed Management of Microgrids", in *Proc. Power Systems, IEEE Transactions* on , vol.30, no.1, Jan. 2015, pp.24,34.

[6] P. Oliveira, T. Pinto, I. Praca, Z. Vale, and H. Morais, "Intelligent micro grid management using a multi-agent approach," in *PowerTech (POWERTECH), IEEE Grenoble*, 2013, pp. 1–6.

[7] D.H. Moore, J.M Murray, F.P. Maturana, T Wendel, "Agent-based control of a DC MicroGrid" in *2013 IEEE Energytech*, Cleveland 2013, pp. 1–6.

[8] F. Ibarra Hernandez , C. A. Canesin , R. Zamora , F. Martina , and A. K. Srivastava , " Energy management and control for islanded microgrid using multi-agents," in *North American Power Symposium (NAPS)*, 22–24 September 2013, pp. 1, 6.

[9] M. Pipattanasomporn, H. Feroze, S. Rahman, "Multi-Agent Systems in a Distributed Smart Grid: Design and Implementation," *Proc. IEEEIPES 2009 Power Systems Conference and Exposition*, Mar. 2009, pp. 1-8.

[10] T. Logenthiran, D. Srinivasan, and D. Wong, "Multi-agent coordination for DER in MicroGrid," in *Proc. IEEE Int. Conf. Sustainable Energy Technologies*, Singapore, 2008, pp. 77–82.

[11] E. Kremers, J. Gonzalez de Durana and O. Barambones "Multi-agent modeling for the simulation of a simple smart microgrid" *Energy Conversion and Management*, Nov. 2013, vol. 75, pp. 643-650.

[12] T. Li, Z. Xiao, M. Huang and J. Yu "Control System Simulation of Microgrid Based on IP and Multi-Agent*", International Conference on Information, Networking and Automation (ICINA)*, Kunming, Oct. 2010, vol. 1, pp. 235-239.

[13] Zeus agent development toolkit [Online]. Available: http://labs.bt.com/projects/agents/zeus/. (23rd Mar. 2015)

[14] JADE agent development toolkit [Online]. Available: http://jade.tilab.com. (23rd Mar. 2015)

[15] W. Richard Stevens, *TCP/IP Illustrated Volume 1*, the Protocols, pp. 15.

[16] Zimmermann W. IOlib e Hardware Input/Output Library for Matlab and Simulink [Online]. Available, http://www.it.hs-esslingen.de/wzimmerma/software/index_uk.html; April 2011. Retrieved.

Renewable Energy Based Hybrid Power System: the Best Way to Keep the World Pollution Free from GHG

Md. Nurunnabi
Department of Electrical and Electronic Engineering
Khulna University of Engineering and Technology
Khulna-9203, Bangladesh
Email: nurnabi32@yahoo.com

N. K. Roy
Department of Electrical and Electronic Engineering
Khulna University of Engineering and Technology
Khulna-9203, Bangladesh
Email: nkroy@eee.kuet.ac.bd

***Abstract*—Current power generation scenarios all over the world are not climate friendly as the generation systems are mainly dependent on fossil fuels that produce greenhouse gas (GHG) which contributes to global warming. This paper conducts a feasibility analysis to explore the potentialities of green energy at Kuakata in Bangladesh. The considered renewable energies for investigation are solar and wind. Initially, a hybrid model has been designed with varying the contribution of renewable resources for the considered coastal region of Bangladesh using Hybrid Optimization Model for Electric Renewable (HOMER) software. This model explores a suitable design for mini-grid by varying the capacity of wind and solar units. Also, a comparison has been carried out for different models on the basis of GHG emission. The simulation results show that the proposed grid-PV-wind hybrid power system model with 76% renewable fraction is most suitable, economical and eco-friendly for the considered region.**

Keywords—greenhouse gas (GHG); grid; HOMER; hybrid power system; solar; wind.

I. Introduction

Renewable energy (RE) can play an important role in reducing global warming and high cost of energy [1]. Every sector of modern civilization is dependent on energy which comes from various energy sources such as nuclear energy and fossil fuel (coal, oil and natural gas). The combustion of these energy sources emits huge amount of greenhouse gases (GHG) such as carbon dioxide, sulfur dioxide, nitrogen dioxide that harm the atmosphere and health of the population [2]. Recently, hybrid power systems using RE are becoming popular due to their potential benefits on environment [3].

Presently, the power demand of Bangladesh is about 10,000 MW and it is increasing day by day. As natural gas is used for about 80% energy generation, Bangladesh is responsible for a large amount of GHG emission [4]. Moreover, the present reserve of fuel used for power generation would be depleted by a decade [5]. Therefore, an alternative way of energy generation in Bangladesh is very urgent. RE sources are considered as the best way to meet the energy demand as they are clean and environmental friendly [6].

Although RE sources such as wind and solar have several advantages, a solar or wind generator in a stand-alone system cannot supply the load continuously due to their intermittent nature [7]. As load demands are always changing with time, the changes in solar or wind energy generation do not always match with the time distribution of load [8]. Therefore, there is a need of additional battery storage or other components for providing continuous power supply to the consumer. It has been investigated that a hybrid PV/Wind/battery system is a reliable source of electricity [9]. However, due to the high cost of battery energy storage, a stand-alone system is very expensive [10]. Therefore, it is important to find a suitable combination of different RE sources to maximize the benefit.

Therefore, the main objective of this paper is to quantify the amount of GHG gas emissions from different system models. The economic and environmental feasibility of grid connected proposed model is analyzed. The potential of PV and wind energy is also investigated in the considered region (Kuakata, Bangladesh) and finally, the contribution of renewable energy is determined to get the optimum performance.

The rest of the paper is organized as follows. Section II describes the system description. Methodology is given in Section III. Simulation models are provided in Section IV and results are evaluated in Section V. Finally, conclusions are drawn in Section VI.

II. System Description

In this paper, a number of hybrid power system models with different percentage of renewable energy contribution have been designed to evaluate and determine the cost of different models. GHG emissions from each model are also determined. The analysis is conducted using HOMER software. The HOMER simulation software needs some input data to evaluate the optimization results for different combinations which are described in the next section [11].

978-1-4673-9257-0/15/$31.00 ©2015 IEEE

A. Electricity Demand in Considered Region

The region considered in this paper is Kuakata situated in Patuakhali district in Bangladesh. In this study, after collecting data for load calculation, we assumed that 200 families consumed average 6.6 kWh/d/family, 50 shops consumed 2.5 kWh/d/shop, 15 tourist hotels that consumed 25 kWh/d/hotel, 300 battery run auto rickshaw consumed about 9.66 kWh/d/rickshaw, the total load for the whole area is 4820.87 kWh per day with a peak load of 794.66 kW. The load is grouped in two parts, one is load 1 which consists of houses, shops and hotels loads; another is load 2 which consists of battery run auto rickshaws. The daily average load profile for two types of load is shown in Fig. 1 and Fig. 2, respectively in which 17:00 to 23:00 h time period has been observed as peak demand for domestic load and 23.00 to 06.00 h for charging of the battery of auto rickshaw. The peak value of demand requirement determines the size of the system.

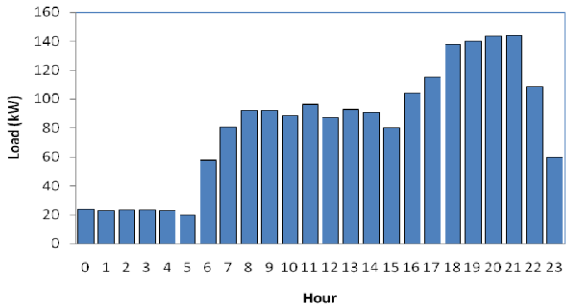

Fig. 1. Daily household load profile.

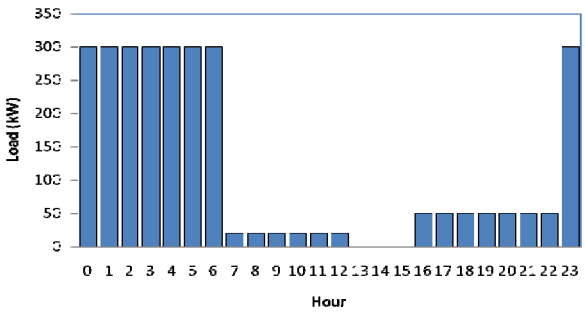

Fig. 2. Daily load profile for auto rickshaw charging.

B. Energy Sources in Kuakata

The coastal area of Bangladesh is suitable for the production of electricity as there is strong wind flow coming from Indian Ocean. This wind blows over Bangladesh form March to September. According to the meteorological department of Bangladesh, monthly average wind speed is observed 3 m/s to 8.3 m/s [12]. The wind speed is high during March to September and other months of a year (October to February) wind speed remains quite low. The peak wind speed occurs during the month of April and May [8]. Fig. 3 shows the monthly average wind speed around the year at Kuakata. Monthly average solar radiation is obtained from NASA surface meteorology and solar energy database and it is shown in Fig. 4. As used in HOMER software, the latitude and longitude of Potuakhali district are 21°49.3´N and 90°7.39´E, respectively. The annual average solar radiation is estimated to be 4.76 kWh/m^2/day [11].

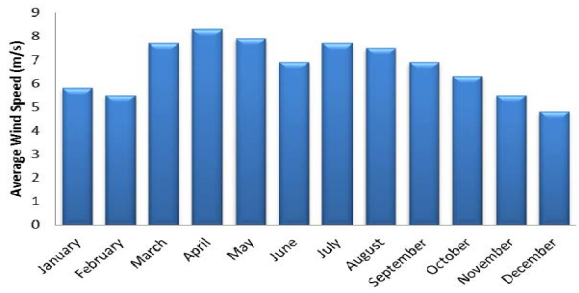

Fig. 3. Monthly average daily wind speed.

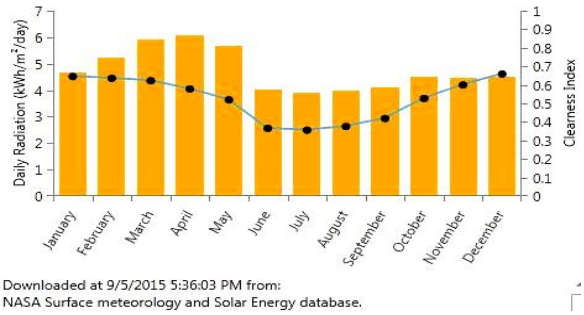

Fig. 4. Monthly average daily solar radiation and clearness index..

III. Methodology

A. HOMER Software

HOMER software is developed by the National Renewable Energy Laboratory (NREL) [13] in the United States (USA). It is generally used for the design and analysis of hybrid power system. In this paper, electrical load, solar radiation and wind speed data, and component details and cost are provided as input information to HOMER.

B. Cost Analysis Procedure by HOMER[2,11,13]

1) Net present cost (NPC): NPC means the present value of al component (operating and maintenance cost) that isinstalled in the plant, minus the present value of all the revenues that it earns over the plant life-span [2,11].

2) Total annualized cost: The total net present cost in a year is called the total annualized cost. It expressed as [2,11]:

$$C_{yr,total} = CRF\ (i, R_{plant\text{-}life}).\ C_{NPC,total}$$

where $C_{NPC,total}$, i, CRF, and $R_{plant\text{-}life}$ represents the total net present cost in dollar, the annual real interest rate, capital recovery factor and the plant life-time in year, respectively.

3) Capital recovery factor (CRF): It is a ratio which is needed to calculate the present value of a series of equal yearly cash flows. It can be expressed as [2,11]:

$$CRF(i,n) = \frac{i \times (1+i)^n}{(1+i)^{n-1}}$$

where, n = number of years and

i = the real interest rate in a year

4) Annual real interest rate: It is the discount rate which is used to convert between one-time costs and yearly costs. It is calculates as follows [2,11].

$$i = \frac{i' - F}{1+F}$$

where, i, i' and F is the real interest rate, nominal interest rate, and annual inflation rate, respectively.

5) Cost of energy (COE): It is defined as the mean value of cost per kWh of useful electrical energy produced by the plant. It is expressed as the ratio of electricity production cost in a year to the total electrical load served by the system. The electricity production cost includes plant installation cost and operation and maintenance cost. Total electrical loads are divided into AC primary load and DC primary load. It is calculated by the following equation [2,11].

$$COE = \frac{C_{yr,total}}{AC_{load} + DC_{load}}$$

where, $C_{yr,total}$ AC_{load} and DC_{load} is the total annualized cost, AC primary load and DC primary load, respectively.

IV. SYSTEM DESIGN

The components are chosen from HOMER to perform the simulation. Fig. 5 shows the grid connected hybrid power system design using HOMER which consists of PV array, wind generator, converter, load, and grid connection.

In order to estimate the system performance under different situations, HOMER simulates the result of the above two arrangements at the same area and same load based on different criteria such as the estimated installation cost, replacement cost, operation and maintenance cost, interest, and cost of energy.

The major components of the different models designed here are wind turbine, PV, battery bank, and a power converter. For economic analysis, the following values are used.

A. PV Array:

In this paper, the initial installation cost of PV arrays is assumed as $3000 per kW and the operation and maintenance cost is zero.

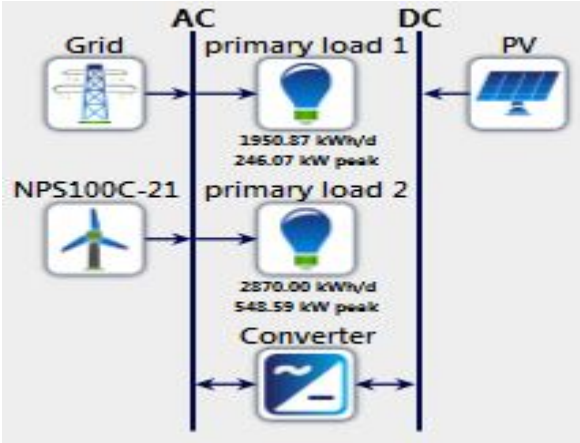

Fig. 5. Grid connected hybrid power system design using HOMER

B. Wind Turbine:

For this study, average wind velocity at 50 m height is 6.73 m/s in Kuakata. It varies from 3 to 8.3 m/s. Here, nine Northern Power NPS100C-21,100 kW wind turbines are used [11]. The wind turbine power output characteristic is shown in Fig. 6. The capital costs are $320000 and also operation and maintenance cost are $2500/yr.

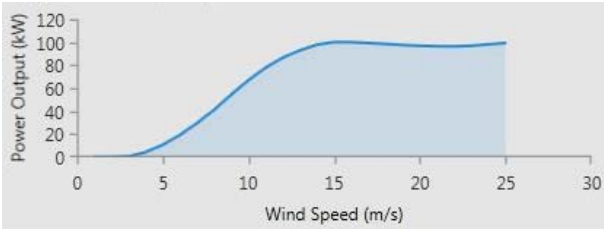

Fig. 6. Wind turbine power curve [11].

C. Power Converter:

In this paper, the capital cost for a 1 kW converter is $300, replacement cost is $300 and operation and maintenance cost practically zero.

D. Battery Bank:

The name of the battery bank is CELLCUBE®FB10-40, manufactured by Gildemeister, with a capacity of 40 kWh, life time 876000 kWh. A battery bank is only used for a stand-alone system design.

E. Grid:

In grid connected design, a grid is used as a backup power component or excess power absorber. The grid supplies power when there is not enough RE power to meet the load demand and grid consumes power when an excessive power is available.

V. SIMULATION RESULTS

The simulation results are described below.

A. Economic Impact

Table I shows the optimization results for the hybrid power system model with different share of renewable energies. For grid connected system, the minimum cost of energy (COE) obtained from the result is $0.0891 whereas for off-grid system it is $0.1588375. Figures 7 and 8 show the COE and NPC values as a function of the number of PV units. It can be observed that the COE and NPC values of the system are increased with the increase in the capacity of PV unit. Also, with the increase of PV capacity, the capital cost of the system is increased. On the other hand, figures 9 and 10 show the graphs of COE and NPC values as a function of the number of wind turbines, respectively from which it can be noticed that COE and NPC values decrease with the increase in the number of wind turbines. It can be also seen that the values of COE and NPC vary from $0.1617027/kWh to $0.0891009/kWh and 5.370379 million dollar to 3.669484 million dollar, respectively. In this paper, size of the plant is considered as 1 MW for which 76% renewable fraction gives the feasible solution. It has to be mentioned that by increasing the size of hybrid power plant the percentage of renewable share can be increased.

TABLE I. SIMULATION RESULT FOR FINDING OPTIMAL DESIGN

Type of the system	PV (kW)	No. of Wind turbine	Battery Bank	COE ($)	NPC ($ million)	Renewable Fraction (%)	CO_2 emission (Tons/yr)
Grid connected	900	1	0	0.1617027	5.370379	52%	269.0764
Grid connected	800	2	0	0.1501716	5.075439	57%	169.8644
Grid connected	700	3	0	0.1403417	4.817061	61%	85.23243
Grid connected	600	4	0	0.1306933	4.583252	65%	1.258075
Grid connected	500	5	0	0.1216871	4.367301	68%	-76.02873
Grid connected	400	6	0	0.1125443	4.16875	70%	-161.3187
Grid connected	300	7	0	0.1040462	3.985773	72%	-245.622
Grid connected	200	8	0	0.0962585	3.818419	74%	-328.4017
Grid connected	100	9	0	0.0891009	3.669484	76%	-410.4542
Off Grid	100	9	8000	0.1588375	3613144	100%	0
Only Grid	0	0	0	0.2000003	4549493	0	1112.077

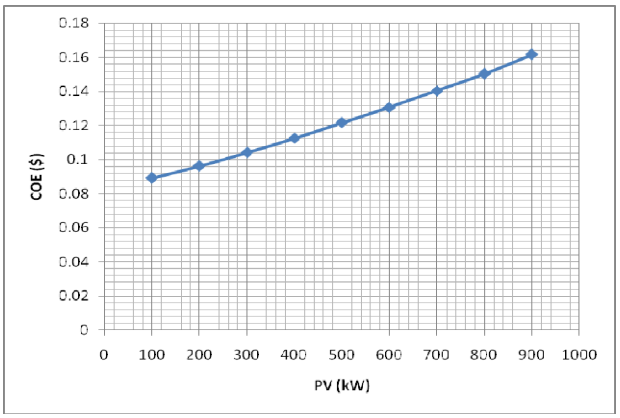

Fig. 7. The COE vs. PV capacity.

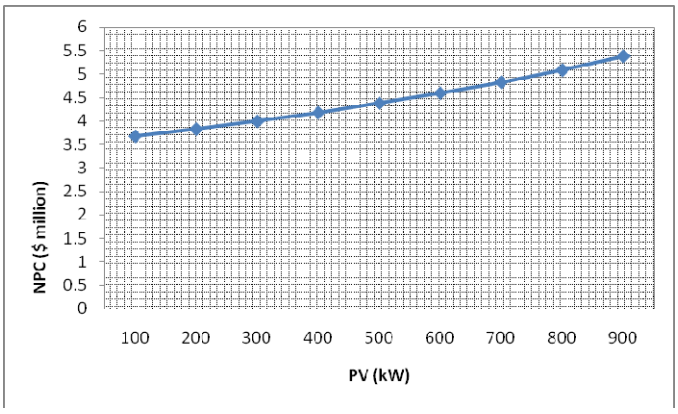

Fig. 8. The NPC vs. PV capacity.

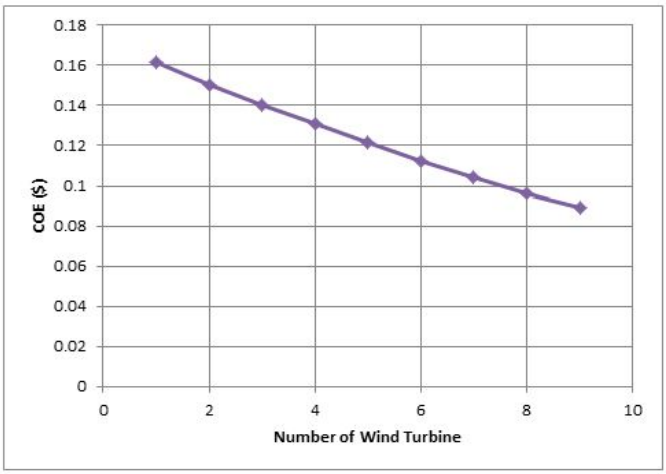

Fig. 9. The COE vs. the number of wind turbines.

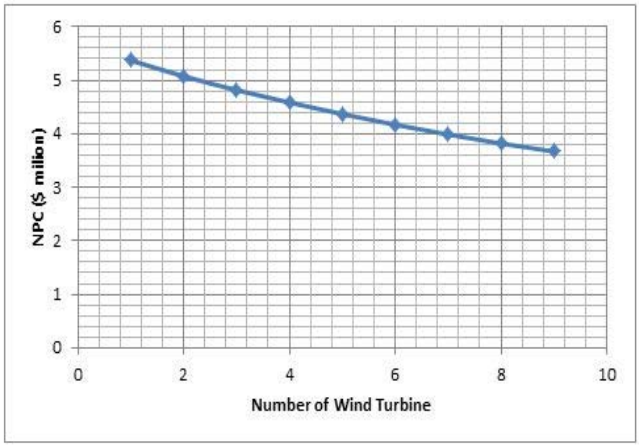

Fig. 10. The NPC vs. the number of wind turbines.

B. *Environmental Impact*

The CO_2 emission with the various contribution of renewable energy is shown in Fig. 11 from which it can be investigated that the emission decreases as the contribution from renewable energy increases. The share of renewable energy can be increased by increasing the number of wind turbines as there is an abundant of wind energy in the considered area compared to solar radiation. The result (Table I) shows that only grid-connected system emitted 11,12077 kg CO_2 per year while wind-PV-grid connected system emitted -410454.2 kg CO_2 per year. Here, the negative CO_2 emission is observed for 76% and some other renewable fraction rate because this system sells more power than it purchases from the grid as it has an excess of electricity. Figure 12 shows the monthly average electric production of various components for 76% renewable fraction rate where the major contribution is coming from wind turbine.

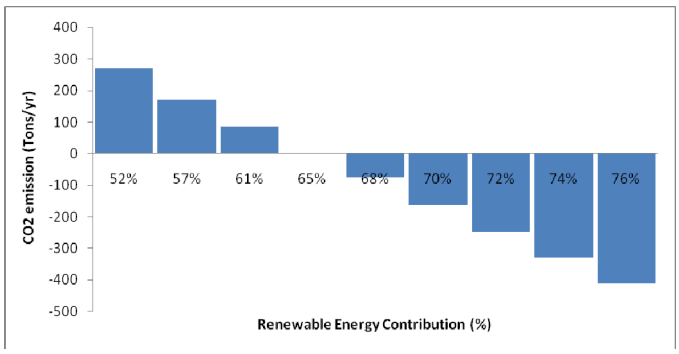

Fig. 11. The CO_2 emission against the various contribution of renewable energy.

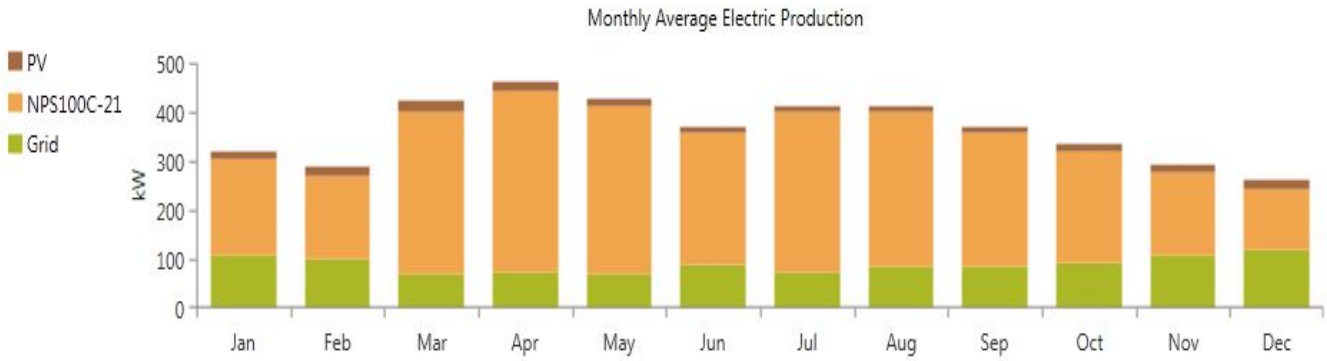

Fig. 12. Monthly average electricity production for final model (renewable fraction 76%)

VI. CONCLUSION

From the analysis it can be concluded that proper utilization of renewable energy reduces an enormous amount of GHG emission in the atmosphere. It is found that the proposed hybrid model with 76% renewable fraction is most suitable, economical and eco-friendly than the other models. It can be concluded that although hybrid model with 100% renewable fraction (off-grid) emits zero kg GHG, it is not always cost effective. The excess output power of the off-grid system goes unused. On the other hand, the proposed grid connected hybrid system does not require an extra battery bank in normal operating condition and excess power that is produced by renewable energy are added to the grid, thereby reducing the total emission.

REFERENCES

[1] A. Rohani, K. Mazlumi, and H. Kord, "Modeling of a hybrid power system for economic analysis and environmental impact in HOMER," 18th Iranian conference on Electrical Engineering (ICEE), 2010, pp.819-823, 11-13 May 2011.

[2] H. Rezzouk and A. Mellit, "Feasibility study and sensitivity analysis of a stand-alone photovoltaic–diesel–battery hybrid energy system in the north of Algeria," Renewable and Sustainable Energy Reviews, vol. 43, pp. 1134–1150, 2015.

[3] G.M Shafiullah, M.T.O Amanullah, A.B.M. Shawkat Ali, Dennis Jarvis, and Peter Wolfs, "Prospects of renewable energy - a feasibility study in the Australian context" Renewable and Sustainable Energy Reviews, vol. 39, no. 1, pp. 183-197, 2012.

[4] *http://www.bpdb.gov.bd/bpdb/index.php* (accessed on 15 July 2015)

[5] P. Mazumder, M.H. Jamil, C.K. Das, and M.A. Matin, "Hybrid energy optimization: an ultimate solution to the power crisis of St. Martin Island, Bangladesh" 9th International Forum on Strategic Technology (IFOST), pp.363-368, 21-23 Oct. 2014.

[6] M.S. Nagan and C.W. Tan, "Assessment of economic viability for PV/wind/diesel hybrid energy system in southern Peninsular Malaysia," Renewable and Sustainable Energy Reviews, vol. 16, no. 1, pp. 634–647, January 2012.

[7] S.K. Pawar, Y.V. Aaher, A.C. Chaudhari, and Y.B. Jadhav, "Modeling and simulation of hybrid solar-wind-grid power generation system for electrification," International Conference on Advances in Engineering and Technology (ICAET), pp.1-6, 2-3 May 2014.

[8] A. Zubair, A.A. Tanvir, and M. M. Hasan, "Optimal planning of standalone solar-wind-deesel hybrid energy system for a coastal area of Bangladesh," International Journal Of Electrical And Computer Engineering (IJECE), vol. 2, no. 6, pp. 731-738, 2012.

[9] S. Liu, Z. Wu, X. Dou, and B. Zhao,"Optimal configuration of hybrid solar-wind distributed generation capacity in a grid-connected microgrid" IEEE PES Innovative Smart Grid Technologies (ISGT), pp. 1-6, 24-27 Feb. 2013.

[10] B. Roy, A.K. Basu, and S. Paul, "Techno-economic feasibility analysis of a grid connected solar photovoltaic power system for a residential load" First International Conference on Automation, Control, Energy and Systems (ACES), pp. 1-5, 1-2 Feb. 2014.

[11] Getting Started Guide for HOMER Version 3.3.1; ⟨https://www.homerenergy. com⟩.

[12] *www.bmd.gov.bd* (accessed on 20 July 2015)

[13] *www.nrel.gov/homer* (accessed on 18 July 2015)

Damping of Power System Oscillations using STATCOM

Mehedi Hassan
Department of Electrical and Electronic Engineering
Jessore University of Science and Technology
Jessor-7408, Bangladesh
Email: mhj24.jsr@gmail.com

N. K. Roy
Department of Electrical and Electronic Engineering
Khulna University of Engineering and Technology
Khulna-9203, Bangladesh
Email: nkroy@eee.kuet.ac.bd

***Abstract*—This paper investigates the damping performance of power systems through eigenvalue analysis. The analysis is conducted on an IEEE 14-bus test system. The maximum loading limits of the load buses are determined using continuation power flow method and a static synchronous compensator (STATCOM) is installed as an objective to increase the system loadability. Then, the dominant modes and associated states that affect the damping of the system are identified and an oscillation damping controller is designed. The result shows that the proposed damping controller equipped with STATCOM can improve the damping performance of the system significantly.**

Keywords—damping performance; eigenvalue; synchronous generator; static voltage stability; STATCOM.

I. Introduction

Power system is a large interconnected complex network. The main challenges that power system engineers are facing around the world is related to stability [1]-[3]. Reactive power support is a vital issue to improve a power system's performance.

In order to improve the stability of power systems, a static synchronous compensator (STATCOM) is increasingly popular [4, 5]. A STATCOM can dynamically support/absorb the reactive power to/from the power network and hence improves the system voltage profile and angle stability [6]. It can also enhance the overall stability of a power system if it is equipped with some more supplementary control signals.

The effect of different loads and voltage compensation using voltage source converter based STATCOM is presented in [7] which shows that, in some cases, it is hard to maintain the load angle close to unity. Time-domain analysis of a system with and without STATCOM is investigated in [8] for different types of faults in which inadequately damped oscillations are observed under certain critical conditions.

The disturbance in power system is mainly due to the connection/disconnection of large loads, faults, and loss of excitation in the generator [9]. The occurrence of contingencies in power system can cause poorly damped or even unstable oscillations which must be damped to ensure reliable power supply.

A STATCOM is usually used for voltage regulation. However, to achieve satisfactory performance, a proper and efficient control system should be designed for this device. Therefore, the aim of this paper is to investigate the damping performance of power systems through linear and nonlinear simulations. To improve the damping of the oscillatory mode of the system a supplementary controller for STATCOM is designed.

The rest of the paper is organized as follows. The description of the system is given in Section II, static and dynamic analysis is given in Section III and conclusions are given in Section IV.

II. System Description

A single line diagram of the IEEE 14-bus test system considered in this paper is shown in Fig. 1 [10]. It consists of two synchronous generators with IEEE type-1 exciters and three synchronous compensators. All the loads are considered as constant impedance loads and mechanical inputs to the generators are assumed to be constant. A sixth order model of the synchronous generator is used for the analysis. The test system data is given in Appendix.

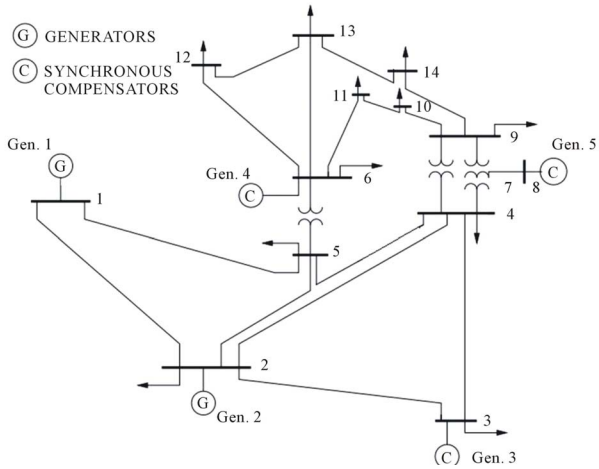

Fig. 1. IEEE 14-bus test system [10].

978-1-4673-9257-0/15/$31.00 ©2015 IEEE

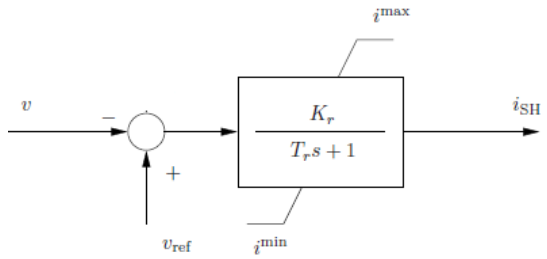

Fig. 2. Block diagram of STATCOM [10].

A STATCOM is used as a Flexible AC Transmission System (FACTS) device in this analysis. Figure 2 shows the block diagram of a STATCOM where v is the measured voltage at the connected bus, v_{ref} is the reference voltage, i^{max} and i^{min} is the maximum and minimum current, respectively, i_{SH} is the total injected current at the connected bus, K_r and T_r is the regulator gain and time constant, respectively. A STATCOM is equipped with a power oscillation damping (POD) controller as shown in Fig. 3 which contains gain, wash-out and compensator blocks.

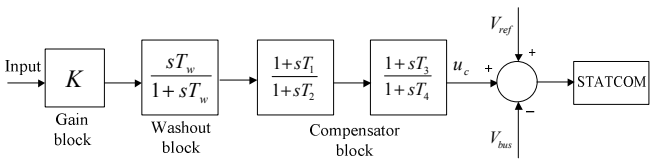

Fig. 3. STATCOM with POD controller

III. Static and Dynamic Analysis

A load flow study for the considered test system is conducted using Newton-Raphson method [11]. To analyze the static voltage stability generally real power-voltage (P-V) or reactive power-voltage (Q-V) curves are used which determine the maximum loading limit of a system [1, 12]. Here, P-V curve has been produced by using a series of power flow solutions (continuation power flow) using power system analysis toolbox (PSAT) in MATLAB environment for different load levels.

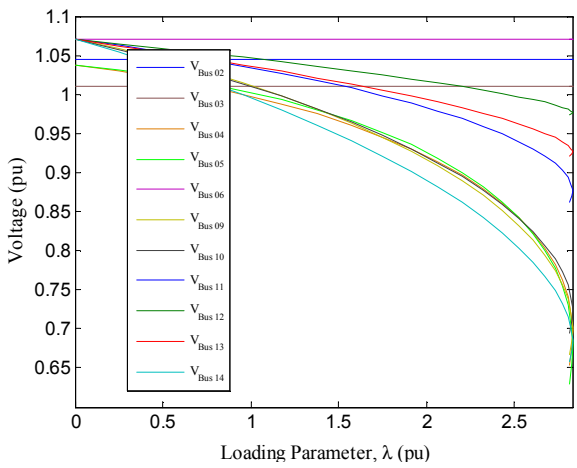

Fig. 4. Loading parameter-voltage curve under base case.

The variations in load bus voltages with the loading factor are obtained and plotted in Fig. 4 from which it can be observed that us-14 is the weakest bus of this network. In this paper, a STATCOM is installed at bus-14 to enhance the static voltage stability of the system.

Next, to understand the inherent dynamics of the system, the test system is linearized and eigenvalues are calculated without STATCOM connection. It is found that the system has a pair of eigenvalue at -0.04654±8.1151 which is the critical mode of this system. Table I shows the participation factors of the dominant states associated with this mode, where e1q_Syn_1 and vf_Exc_1 represents the quadrature axis voltage of synchronous machine 1 and voltage of the exciter 1, respectively; delta_Syn_1 and omega_Syn_1 represents the angle and speed of the generator 1, respectively. This mode has a damping ratio of 0.57%. It is known that the minimum damping requirements for reliable operation of power system is 5%.

TABLE I. Critical Mode of the Considered System

Critical mode	Dominant States and participation factor	Damping ratio (%)
-0.04654±8.1151	e1q_Syn_1=0.22377, vf_Exc_1=0.17139 delta_Syn_1=0.04332,omega_Syn_1=0.04332	0.57

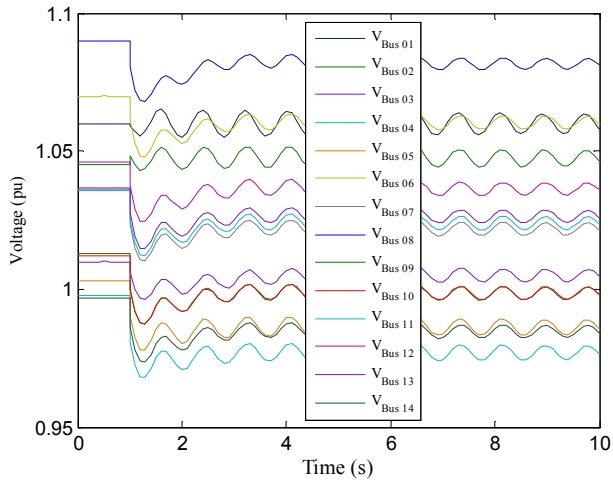

Fig. 5. Bus voltages of IEEE 14-bus test system under disturbance.

To test the dynamic performance of the system, the line between bus 2 and bus 4 is disconnected at 1s. Figure 5 shows the bus voltage profile of the system from which it can be seen that the system suffers from low frequency oscillations. The real power of the sysnchronous generator is shown in Fig. 6. In this analysis, mechanical input to the generator is kept constant. It can be seen from Fig. 6 that the system has large oscillations in its output power.

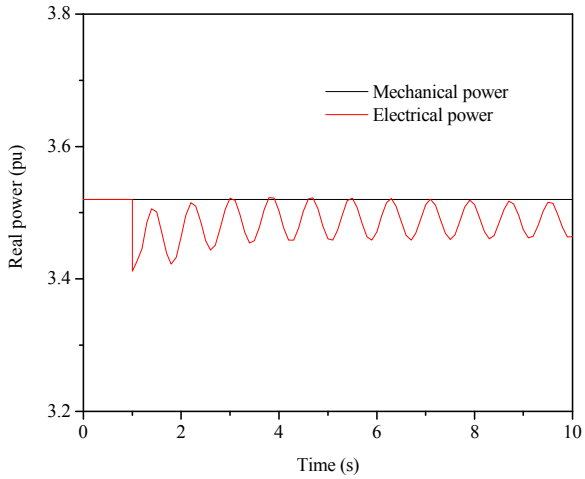

Fig. 6. Mechanical input power and electrical output power of synchronous generator 1.

To solve the above problems, a STATCOM is connected and a POD controller is equipped with it based on the line active power measurement from bus 1. The transfer function of the POD controller is given below [13].

$$H(s) = K\frac{sT_w}{sT_w+1}\left[\frac{sT_{ld}+1}{sT_{\lg}+1}\right]^{m_c} \quad (1)$$

$$\varphi_{comp} = 180^0 - \arg(R_i) \quad (2)$$

$$\alpha_c = \frac{T_{ld}}{T_{\lg}} = \frac{1-\sin(\frac{\varphi_{comp}}{m_c})}{1+\sin(\frac{\varphi_{comp}}{m_c})} \quad (3)$$

$$T_{\lg} = \frac{1}{\omega_i\sqrt{\alpha_c}}, \quad T_{ld} = \alpha_c T_{\lg} \quad (4)$$

where, the phase angle φ_{comp} shows the compensation angle needs to move the eigenvalue direct to the left parallel with the real axis. T_w, T_{ld} and $T_{\lg}$ are the time constant of the wash-out, lead and lag block, respectively, $\arg(R_i)$ is the phase angle of the residue R_i, ω_i, m_c and K is the frequency of the mode of oscillation in rad/s., number of compensation stages and the controller gain, respectively. In this paper, number of compensation stages are 2.

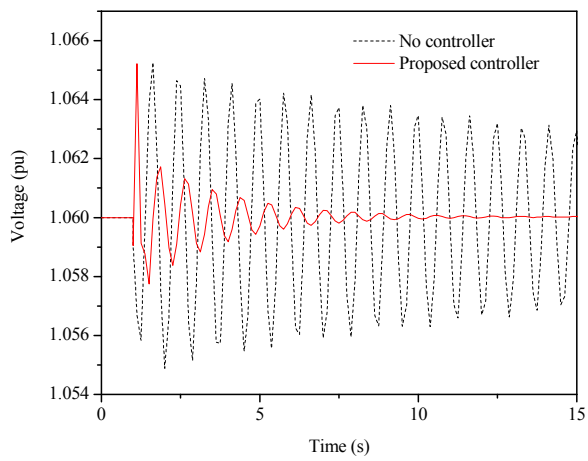

Fig. 7. Bus 1 voltage.

The voltage profile of the test system at bus 1 with and without the proposed controller is shown in Fig. 7 from which it can be clearly observed that the proposed control scheme damps the oscillations quickly. The dominant eigenvalue of the system with the proposed controller is -0.6402±7.6527 with a damping ratio 8.3% which is greater than the minimum limit (5%).

IV. Conclusion

This article investigates the stability improvement problem of a power system considering a STATCOM. The small-signal stability assessment of IEEE 14-bus test system is conducted. It is found that the system has low frequency oscillations with reduced damping. As the weakest bus requires highest reactive power, a STATCOM is connected at the weakest bus of the network. Although a STATCOM improves the static voltage stability of the system, it is not always suitable for damping the oscillatory mode of the system. Therefore, a supplementary controller is designed using the real power deviation as input signal. The result shows that the proposed controller can enhance the damping performance of the system. Thus, this paper proves that an auxiliary control law can be applied to existing devices to enhance the dynamic performance of the system. Determining the optimum size of a STATCOM through static and dynamic analysis is the future aim of this work.

APPENDIX

The line and load data of IEEE 14-bus test system is given in Table II and Table III, respectively [14].

TABLE II. LINE DATA OF IEEE 14-BUS TEST SYSTEM

From bus - To bus	Line charging (pu)	Tap ratio	Resistance, (pu)	Reactance, (pu)
1-2	0.0528	1	0.01938	0.05917
1-5	0.0492	1	0.05403	0.22304
2-3	0.0438	1	0.04699	0.19797
2-4	0.0374	1	0.05811	0.17632
2-5	0.034	1	0.05695	0.17388
3-4	0.0346	1	0.06701	0.17103
4-5	0.0128	1	0.01335	0.04211
4-7	0.00	0.978	0.00	0.20912
4-9	0.00	0.969	0.00	0.55618
5-6	0.00	0.932	0.00	0.25202
6-11	0.00	1	0.09498	0.1989
6-12	0.00	1	0.12291	0.25581
6-13	0.00	1	0.06615	0.13027
7-8	0.00	1	0.00	0.17615
7-9	0.00	1	0.00	0.11001
9-10	0.00	1	0.03181	0.08450
9-14	0.00	1	0.12711	0.27038
10-11	0.00	1	0.08205	0.19207
12-13	0.00	1	0.22092	0.19988
13-14	0.00	1	0.17093	0.34802

TABLE III. LOAD DATA OF IEEE 14-BUS TEST SYSTEM

Bus no.	P_{load} (pu)	Q_{load} (pu)
1	0.00	0.00
2	0.2170	0.1270
3	0.9420	0.1900
4	0.4780	0.00
5	0.0760	0.0160
6	0.1120	0.0750
7	0.00	0.00
8	0.00	0.00
9	0.2950	0.1660
10	0.0900	0.0580
11	0.0350	0.0180
12	0.0610	0.0160
13	0.1350	0.0580
14	0.1490	0.0500

REFERENCES

[1] P. Kundur, Power system stability and control. McGraw-Hill, New York, 1994.

[2] T. Zabaiou, L.-A. Dessaint, and I. Kamwa, “Preventive control approach for voltage stability improvement using voltage stability constrained optimal power flow based on static line voltage stability indices,” IET Generation, Transmission & Distribution, vol. 8, pp. 924 – 934, 2014.

[3] B. H. Lee and K.Y. Lee, “Dynamic and static voltage stability enhancement of power systems,” IEEE Trans. on Power Systems, vol. 8, pp. 231 – 238, 2002.

[4] P.C. Thomas, “Placement of STATCOM in a wind integrated power system with storage for improving the loadability of the system,” 7th International Conference on Intelligent Systems and Control (ISCO), pp. 31 – 35, 4-5 Jan. 2013.

[5] J. Lakkireddy, “Steady state voltage stability enhancement using shunt and series FACTS devices,” Clemson University Power Systems Conference (PSC), 10-13 March 2015.

[6] M. R. S. Tirtashi, A. Rohani, and R. Noroozian, "PSS and STATCOM controller design for damping power system oscillations using fuzzy control strategies," 18th Iranian Conference on Electrical Engineering (ICEE), pp.901-906, 11-13 May 2010.

[7] H.S. Dalvi, and V.K. Chandrakar, "Voltage improvement using STATCOM for prototype hardware model, using synchronous and induction type generator," 3rd International Conference on Emerging Trends in Engineering and Technology (ICETET), pp.413-417, 19-21 Nov. 2010.

[8] S. P. Teeuwsen, "STATCOM with optimized POD controller for efficient inter-area oscillation damping," IEEE Power and Energy Society General Meeting (PES), pp.1-5, 21-25 July 2013.

[9] S. Vishwakarma, R. K. Tripathi, "Transient energy dissipation and damping improvement using STATCOM & SSSC," International Conference on Power, Control and Embedded Systems (ICPCES), pp.1-4, Nov. 29 2010-Dec. 1 2010.

[10] F. Milano, “Power System Analysis Toolbox (PSAT) documentation” version 2.1.6.

[11] E. Balagurusamy, Numerical methods, Tata Mc-Graw-Hill, New Delhi, 1999.

[12] N.K. Roy, H.R. Pota and A. Anwar, “A new approach for wind and solar type DG placement in power distribution networks to enhance systems stability," IEEE Power Engineering and Optimization Conference (PEOCO), pp. 296-301, 6-7 June 2012.

[13] R. Sadikovic, P. Korba, and G. Andersson, "Application of FACTS devices for damping of power system oscillations," IEEE Russia Power Tech, pp.1-6, 27-30 June 2005.

[14] S.K.M. Kodsi and C.A. Cañizares, “Modeling and simulation of IEEE 14 bus system with FACTS controllers,” Technical Report no. 2003−3,https://ece.uwaterloo.ca/~ccanizar/papers/IEEEBenchmarkTFreport.pdf.

Automatic Gender Identification System for Bengali Speech

Md. Shahriar Rahman*, Md. Fasihul Kabir†, Khandaker Abdullah-Al-Mamun‡ and Mohammad Nurul Huda§
Department of Computer Science and Engineering, United International University, Dhaka, Bangladesh
*tiloknet@gmail.com, †aboutrafi@gmail.com, ‡mamun@cse.uiu.ac.bd, §mnh@cse.uiu.ac.bd

***Abstract*—This paper describes a set of features along with different classifiers for gender (male, female) identification. Gender identification is the problem to detect the gender of the speaker of the audio content. The proposed method in this study comprises three stages: i) Corpus construction, iii) Input Feature Vector Construction and iii) Identification using a classifier. In this connection, we have constructed a medium scale Bengali speech corpus from The Bengali Daily Newspaper Prothom Alo. The total number of male/female speakers and spoken sentences are eighty and eight thousand, respectively, where the training and test corpus is selected by the 10-fold cross validation. From the experiments it is observed that the accuracies using the most of the classifiers are 100% on audio content duration size 0.7 minutes to 8.4 minutes.**

***Keywords*—Gender identification; Logistic Regression; K-Nearest Neighbor; Decision Tree, Support Vector Machine; Ridge Classifier**

I. Introduction

In modern multimedia information retrieval systems, gender identification has several potential applications. It can be used in audio or video content indexing, gender based classifiers can improve the accuracy of speech recognition [1] and speech coders [2] system. Moreover it can be used in forensic investigations.

In this study, we have proposed a method for gender identification that consists of corpus construction, input feature vector construction, and identification using a classifier. Here, a medium scale Bengali speech corpus is constructed from The Bengali Daily Newspaper Prothom Alo. The originality of this research for Bengali is special features (Energy, Envelope, LPC, etc; in total we used 27 features) extraction from an input speech and use of machine learning tools for this identification. The training and test corpus is selected by the 10-fold cross validation from the eight thousand spoken sentences uttered by eighty male and female speakers. From the experiments it is observed that the accuracies using the most of the classifiers are 100%.

II. Related Works

Gender Recognition based several types of research work have been done for decades. The system described in [3] introduced a new gender identification method using Bootstrapping on audio classification. This paper shows good performance (more than 90%) for Naive Bayes, Decision Trees (C4.5), k-Nearest Neighbors, Logistic regression, Neural Network and Support Vector Machine Classifiers. Content based multimedia indexing using Piecewise Gaussian Modeling with mixture of neural networks was presented in [4]. With one second audio segments, the classification accuracy was 90% regardless of any language and channel of the speech. A system is proposed in [5] where audio classification using multimedia indexing on audio channel having more than 90% accuracy. In [6] a support vector machine (SVM) based gender identification is applied on discriminative weight training. By SVM consisting of optimally weighted mel-frequency cepstral coefficient (MFCC) which is based on minimum classification error (MCE) method, generates a gender decision rule. It outperformed another method mentioned in [7] and has the accuracy almost 100%. Gender Identification based on pitch is proposed in [8], where two stages classifier using Gaussian Mixture Model (GMM) is created to ensure low complexity and high accuracy. Following this method we can get more than 95%. Most of the above described previous works were performed using foreign language (not used Bengali Corpus). But unfortunately for Bengali language, we cannot see much example. The method described in [9] proposed a gender identification method for Bengali consisting of a front end and a back end system. Feature extraction is done using Fast Fourier Transform (FFT) in front end and in back end, a gender model is created using a classifier which produces poor performance around 80%.

III. Methodology

A. Corpus Construction

Different sentences from the Bengali newspaper Prothom Alo uttered by male and female speakers of different regions of Bangladesh are collected. All of the speakers are Bangladeshi nationals and native speakers of Bangla. The age of the speakers ranges from 20 to 40 years. We have chosen the speakers from a wide area of Bangladesh: Dhaka (central region), Comilla Noakhali (East region), Rajshahi (West region), Dinajpur Rangpur (North-West region), Khulna (South-West region), Mymensingh and Sylhet (North-East region). On the other hand, though all of them speak in standard Bangla, they are not free from their regional accent.

Recording was done in a quiet room located at United International University (UIU), Dhaka, Bangladesh. A desktop was used to record the voices using a head mounted close-talking microphone. We record the voice in a place, where ceiling fan and air conditioner were switched on and some low level street or corridor noise could be heard.

978-1-4673-9257-0/15/$31.00 ©2015 IEEE

Jet Audio 7.1.1.3101 software was used to record the voices. The speech was sampled at 16 kHz and quantized to 16 bit stereo coding without any compression and no filter is used on the recorded voice. Duration of the speech files are between 0.7 minutes and 8.4 minutes.

The development of data sets is given as follows.

Data Set-I (D1): This data set consists of 3000 sentences uttered by 30 male speakers (each speaker by 100 sentences). The data is sampled at 16 kHz.

Data Set-II (D2): This data set consists of 3000 sentences uttered by 30 female speakers (each speaker by 100 sentences). The data is sampled at 16 kHz.

Data Set-III (D3): This data set consists of 1000 sentences uttered by 10 male speakers (each speaker by 100 sentences). These sentences are different from D1 data set. The data is sampled at 16kHz.

Data Set-IV (D4): This data set consists of 1000 sentences uttered by 10 female speakers (each speaker by 100 sentences). These sentences are different from D2 data set. The data is sampled at 16 kHz

B. Input Feature Vector Construction

a feature vector is an n-dimensional vector of numerical features that represent some object. In machine learning and pattern recognition, a feature is an individual measurable property of a phenomenon being observed [10]. Choosing informative, discriminating and independent features is a crucial step for effective algorithms in pattern classification. In our experiment we used two steps to construct our feature vector. In first step, we extracted the features from the audio files and in the second step, we normalize the features using different statistical formulas.

1) Feature Extraction: Feature extraction is an essential pre-processing step to pattern recognition and machine learning problems. We extracted time, frequency, coefficient domain features using yaafe - audio features extraction [11]. Followed is the description of each of the features we extracted using the tool:

1) **Amplitude Modulation** [12] is a form of modulation used for radio transmissions for broadcasting and two way radio communication applications. We have used 200 Decimation factor to compute envelope, 32768 output frames size, 16384 steps between consecutive frames are used to calculate the Amplitude Modulation.
2) **Auto Correlation** is used to compare a signal with a time-delayed version of itself. Here, 49 auto correlation coefficients are used. To calculate it we used 1024 output frames size, 512 step between consecutive frames.
3) **Complex Domain Onset Detection** [13] is computed onset detection using a complex domain spectral flux method. Hanning method is used weighting window to apply before FFT, output frames size equals to 1024 and step between consecutive frames equals to 512 is used to calculate the value.
4) **Energy** [14] is computed as root mean square of an audio Frame. We have used output frames size equals to 1024 and step between consecutive frames equals to 512, to calculate the Energy.
5) **Envelope**, extract amplitude envelope using Hilbert transform, low-pass filtering and decimation. Decimation factor equals to 200, output frames size equals to 32768 and step between consecutive frames equals to 16384 is used to calculate the Envelope.
6) **Envelope Shape Statistics** is centroid, spread, skewness and kurtosis of each frames amplitude envelope. Same parameters in calculation of Envelope are used to calculate Envelope Shape Statistics.
7) **Frames** are segment in input signal. Same parameters in calculation of Energy are used to calculate Frames.
8) The **LPC** [15], [16] coefficients are a short-time measure of the speech signal, which describe the signal as the output of an all-pole filter. The first 2 orders of LPC parameters are chosen.
9) **Loudness** [17], [18] coefficients are the energy in each Bark band, normalized by the overall sum.
10) **MFCC** [16] calculation includes discrete Fourier transform of audio frames, followed by filtering by a triangular bandpass filter bank, logarithmic scaling and discrete cosine transform. Here, 13 MFCCs are used.
11) **Magnitude Spectrum** is computed using an analysis window (Hanning or Hamming), or not.
12) **Mel-Spectrum** [19] computes the Mel-frequencies spectrum.
13) **OBSI** [20] or Octave band signal intensity is calculated using a triangular octave filter bank.
14) **OBSIR** computes log of OBSI ratio between consecutive octaves.
15) **Perceptual Sharpness** [17] computes the sharpness of Loudness coefficients.
16) **Perceptual Spread** [17] computes the spread of Loudness coefficients.
17) **Spectral Crest Factor Per Band** computes spectral crest factor per log-spaced band of $1/4$ octave.
18) **Spectral Decrease** [17] computes spectral decrease.
19) **Spectral Flatness** computes global spectral flatness using the ratio between geometric and arithmetic mean.
20) **Spectral Flatness per Band** computes spectral flatness per log-spaced band of $1/4$ octave, as proposed in MPEG7 standard.
21) **Spectral Flux** computes flux of spectrum between consecutive frames.
22) **Spectral Roll off** [21] is the frequency so that 99% of the energy is contained below.
23) **Spectral Shape Statistics** [17] computes shape statistics of Magnitude Spectrum.
24) **Spectral Slope** [17] is computed by linear regression of the spectral amplitude.
25) **Spectral Variation** [17] is the normalized correlation of spectrum between consecutive frames.
26) **Temporal Shape Statistics** computes shape statistics of signal frames.
27) **ZCR** [16] or a zero-crossing is said to occur if successive samples have different signs. The zero-crossing ratio is the number of the time-domain zero-

crossings and total number of samples in a frame. To calculate the value we have kept Minimal distance between consecutive autocorrelation peaks equals to 5, number of autocorrelation peaks equals to 3, number of frames to integrate together equals to 60 and number of frames to skip between two integration equals to 30.

2) Feature Normalization: Feature Normalization is a method used to standardize the range of independent variables or features of data. To normalize the features data we have used mean, variance or standard deviation of the each feature data.

C. Identification Using a Classifier

In this phase we design a classifier using different machine learning approaches [22] and use that classifier to identify gender. Fig-1 describes how we design the classifier and use the classifier to identify gender using unlabeled audio content.

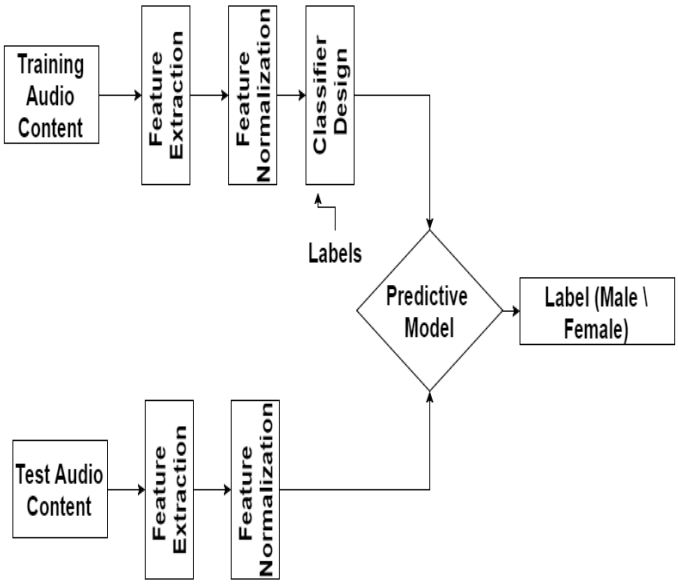

Fig. 1: Gender Identification Using Designed Classifier

Followed we describe about the experimental setup we have used to design our gender identification classifier.

- **Logistic Regression:** [23] For experiment we have used tolerance for stopping criteria=0.0001, C=1.0 and maximum number of iteration is fixed to 100. One vs Rest concept has been used for multi-class classification.
- **Decision Tree:** [24] We have used Gini impurity [25] function to measure the quality of a split, two as minimum number of samples required to split an internal node and one as minimum number of samples required to be at a leaf node.
- **K-Nearest Neighbors (KNN):** [26] For our experimental setup, we used Ball Tree [27] algorithm to compute the nearest neighbors, five as number of neighbors, leaf size = 30, Minkowski is used as the distance metric to use for the tree, where power parameter=2 is used for the Minkowski metric.
- **Ridge Regression Classifier:** [28] For our experimental setup we have used $\alpha = 1.0$ and $tol = 0.001$.
- **Support Vector Machine (SVM):** [29] For our experimental setup we have used, $C = 1.0$, $tol = 0.0001$, max iteration=1000, penalty='l2' and Linear function as kernel function. One vs rest [30] method is used to work for multi-class classification.

IV. Experimental Results

For our experiment we have used the corpus in two different manner: **CS1:** Considering eight thousand speech file and applied 10-fold cross validation and **CS2:** Considering 80 speakers and applied 10-fold cross selection. Moreover we have used three different statistical formula Mean (MN), Variance (VE) or Standard Deviation (SD) to normalize the feature obtain from the feature extraction phase. Therefore, in total we have setup six experiments in this connection: EXP-I)CS1 + MN, EXP-II)CS1 + VE, EXP-III)CS1 + SD, EXP-IV)CS2 + MN, EXP-V)CS2 + VE, EXP-VI)CS2 + SD.

To evaluate our experiments we used Precision (P), Recall (R) and F1-Score(FS) [31].

$$precision = \frac{tp}{tp + fp} \tag{1}$$

$$recall = \frac{tp}{tp + fn} \tag{2}$$

$$f1 - score = 2\frac{precision * recall}{precision + recall} \tag{3}$$

Where, tp equals to true positive, fp equals to false positive and fn equals to false negative.

Here, Table-I, Table-II, Table-III, Table-IV, Table-V and Table-VI show the results of our six experimental setups. From the tables we can observe that KNN gives the best performance for all the six experimental setup and gives a recall equals to 1.0.

Table-I shows result of experimental setup **EXP-I**, where we considered eight thousand speech files and applied 10-fold cross validation(CS1) and Mean(MN) as statistical formula to normalize the extracted features. We got the best recall value for Logistic Regression, KNN and SVM. From the table we can see that, F1-Score is almost same for every classifier.

TABLE I: Result of EXP-I

Classifier	P	R	FS
Logistic Regression	0.999	1.0	0.999
Decision Tree	0.999	0.999	0.999
KNN	0.999	1.0	0.999
Ridge	1.0	0.999	0.999
SVM	0.999	1.0	0.999

Table-II expresses data of experiment setup **EXP-II**, where we considered eight thousand speech files and applied 10-fold

cross selection (CS1). Here we use Variance (VE) as statistical formula to normalize the extracted features and got best recall value for decision tree and KNN classifier which is also same if consider Precision and F1-Score value.

TABLE II: Result of EXP-II

Classifier	P	R	FS
Logistic Regression	0.999	0.999	0.999
Decision Tree	1.0	1.0	1.0
KNN	1.0	1.0	1.0
Ridge	0.969	0.985	0.977
SVM	0.999	0.999	0.999

Table-III demonstrates the consequence of the experiment setup **EXP-III**, where we considered eight thousand speech files and applied 10-fold cross validation (CS1) and Standard Deviation (SD) statistical formula to normalize the extracted features. We got best result for Logistical Regression, Decision Tree and SVM classifier in basis of Recall values.

TABLE III: Result of EXP-III

Classifier	P	R	FS
Logistic Regression	0.999	1.0	0.999
Decision Tree	1.0	1.0	1.0
KNN	1.0	1.0	1.0
Ridge	0.999	0.998	0.999
SVM	0.999	1.0	0.999

Table-IV shows the result of experimental setup EXP-IV. In this setup we consider 80 speakers and applied 10-fold cross selection (CS2) and used Mean (MN) statistical formula to normalize the feature obtained from the feature extraction phase, we got the result that except Ridge classifier, the recall value for every classifier is 1.0.

TABLE IV: Result of EXP-IV

Classifier	P	R	FS
Logistic Regression	0.999	1.0	0.999
Decision Tree	0.999	1.0	0.999
KNN	0.999	1.0	0.999
Ridge	1.0	0.999	0.999
SVM	0.999	1.0	0.999

In Table-V, we mentioned the results of experimental setup EXP-V. Where we considered 80 speakers and applied 10-fold cross section (CS2) and to normalize the extracted feature, we have used Variance. Here we got the best recall value for Decision Tree and KNN classifier.

TABLE V: Result of EXP-V

Classifier	P	R	FS
Logistic Regression	0.999	0.999	0.999
Decision Tree	1.0	1.0	1.0
KNN	1.0	1.0	1.0
Ridge	0.965	0.983	0.973
SVM	0.999	0.997	0.998

Table-VI describes the result of the experiment step up EXP-VI, where we considered 80 speakers and applied 10-fold cross section (CS2) and to normalize the extracted features we have used Standard Deviation (SD) statistical formula. We got best recall value for Logistic Regression, Decision Tree, KNN and SVM classifier.

TABLE VI: Result of EXP-VI

Classifier	P	R	FS
Logistic Regression	0.999	1.0	0.999
Decision Tree	1.0	1.0	1.0
KNN	1.0	1.0	1.0
Ridge	0.999	0.997	0.998
SVM	0.999	1.0	0.999

V. Discussions

In this connection we setup six experiments using our media Bengali speech corpus and for each setup we incorporate five machine learning approaches. Among these experimental setups EXP-IV gives the best performance in terms of recall score and KNN gives the best result among five classification algorithms we used for all the six setups with recall score equals to 1.0.

In this experiment, we were able to produce higher accuracy rate as both the training data and test data are almost know because Data set D1 and D2 is built using the same hundred lines and on the other hand Data set D3 and D4 is built using the same hundred lines. Though we used 10-fold cross validation to split our corpus, the input sentences of audio files are nearly same. Moreover, the age range of the speakers is between 20 to 40 years which may tend to give wrong label for speaker age out of the range. In future we would like to add more speakers of different age groups and also use unique sentences to develop our corpus. In spite of this issue, our experiment is able to identify gender from noisy audio content and also from small size of audio content as we used audio content of duration from 0.7 seconds to 8.4 seconds.

In this paper, we only consider two genders male and female. Third Gender (Transgender) sample is not provided in corpus nor we test with this type of voice. In future we would like to extend our experiments with third gender.

VI. Conclusion

This study has proposed a system for gender identification. The paper concludes the following:

- This study incorporates special features with respect to [9]. These features are Energy, Envelope, LPC, etc.
- This study embeds the machine learning tools, which were not in [9].
- In our method accuracy (recall value) is approximately 100%, but corresponding value of [9] is 80% only.

The author would like to do further experiments for male, female and Trans Gender in near future. Also try to add speaker count and age identification of the speakers.

References

[1] W. Abdulla, N. Kasabov, and D.-N. Zealand, "Improving speech recognition performance through gender separation," *changes*, vol. 9, p. 10, 2001.

[2] I. Potamitis, N. Fakotakis, and G. Kokkinakis, "Gender-dependent and speaker-dependent speech enhancement," in *Acoustics, Speech, and Signal Processing (ICASSP), 2002 IEEE International Conference on*, vol. 1. IEEE, 2002, pp. I–249.

[3] G. Tzanetakis, "Audio-based gender identification using bootstrapping," in *Communications, Computers and signal Processing, 2005. PACRIM. 2005 IEEE Pacific Rim Conference on*. IEEE, 2005, pp. 432–433.

[4] H. Harb and L. Chen, "Voice-based gender identification in multimedia applications," *Journal of intelligent information systems*, vol. 24, no. 2-3, pp. 179–198, 2005.

[5] ——, "A general audio classifier based on human perception motivated model," *Multimedia Tools and Applications*, vol. 34, no. 3, pp. 375–395, 2007.

[6] S.-I. Kang and J.-H. Chang, "Discriminative weight training-based optimally weighted mfcc for gender identification," *IEICE Electronics Express*, vol. 6, no. 19, pp. 1374–1379, 2009.

[7] L. Kye-Hwan, K. Sang-Ick, K. Deok-Hwan, and J.-H. Chang, "A support vector machine-based gender identification using speech signal," *IEICE transactions on communications*, vol. 91, no. 10, pp. 3326–3329, 2008.

[8] Y. Hu, D. Wu, and A. Nucci, "Pitch-based gender identification with two-stage classification," *Security and Communication Networks*, vol. 5, no. 2, pp. 211–225, 2012.

[9] M. S. Ali, M. S. Islam, and M. A. Hossain, "Gender recognition system using speech signal."

[10] C. M. Bishop, *Pattern recognition and machine learning*. springer, 2006.

[11] B. Mathieu, S. Essid, T. Fillon, J. Prado, and G. Richard, "Yaafe, an easy to use and efficient audio feature extraction software." in *ISMIR*, 2010, pp. 441–446.

[12] A. Eronen *et al.*, "Automatic musical instrument recognition," *Mémoire de DEA, Tempere University of Technology*, p. 178, 2001.

[13] C. Duxbury, J. P. Bello, M. Davies, M. Sandler *et al.*, "Complex domain onset detection for musical signals," in *Proc. Digital Audio Effects Workshop (DAFx)*, no. 1, 2003, pp. 6–9.

[14] Y. Konig and N. Morgan, "Gdnn: a gender-dependent neural network for continuous speech recognition," in *Neural Networks, 1992. IJCNN., International Joint Conference on*, vol. 2, Jun 1992, pp. 332–337 vol.2.

[15] J. Makhoul, "Linear prediction: A tutorial review," *Proceedings of the IEEE*, vol. 63, no. 4, pp. 561–580, 1975.

[16] M. Liu, C. Wan, and L. Wang, "Content-based audio classification and retrieval using a fuzzy logic system: towards multimedia search engines," *Soft Computing*, vol. 6, no. 5, pp. 357–364, 2002.

[17] G. Peeters, "{A large set of audio features for sound description (similarity and classification) in the CUIDADO project}," 2004.

[18] B. C. Moore, B. R. Glasberg, and T. Baer, "A model for the prediction of thresholds, loudness, and partial loudness," *Journal of the Audio Engineering Society*, vol. 45, no. 4, pp. 224–240, 1997.

[19] S. B. Davis and P. Mermelstein, "Comparison of parametric representations for monosyllabic word recognition in continuously spoken sentences," in *Readings in speech recognition*. Morgan Kaufmann Publishers Inc., 1990, pp. 65–74.

[20] S. Essid, "Classification automatique des signaux audio-fréquences: reconnaissance des instruments de musique," Ph.D. dissertation, Université Pierre et Marie Curie-Paris VI, 2005.

[21] E. Scheirer and M. Slaney, "Construction and evaluation of a robust multifeature speech/music discriminator," in *Acoustics, Speech, and Signal Processing, 1997. ICASSP-97., 1997 IEEE International Conference on*, vol. 2. IEEE, 1997, pp. 1331–1334.

[22] F. Kabir, S. Siddique, M. Kotwal, and M. Huda, "Bangla text document categorization using stochastic gradient descent (sgd) classifier," in *Cognitive Computing and Information Processing (CCIP), 2015 International Conference on*, March 2015, pp. 1–4.

[23] D. G. Kleinbaum and M. Klein, *Analysis of Matched Data Using Logistic Regression*. Springer, 2010.

[24] M. A. Friedl and C. E. Brodley, "Decision tree classification of land cover from remotely sensed data," *Remote sensing of environment*, vol. 61, no. 3, pp. 399–409, 1997.

[25] L. Breiman, "Technical note: Some properties of splitting criteria," *Machine Learning*, vol. 24, no. 1, pp. 41–47, 1996.

[26] W. Henley and D. J. Hand, "A k-nearest-neighbour classifier for assessing consumer credit risk," *The Statistician*, pp. 77–95, 1996.

[27] A. M. Kibriya and E. Frank, "An empirical comparison of exact nearest neighbour algorithms," in *Knowledge Discovery in Databases: PKDD 2007*. Springer, 2007, pp. 140–151.

[28] N. R. Draper, H. Smith, and E. Pownell, *Applied regression analysis*. Wiley New York, 1966, vol. 3.

[29] N. Cristianini and J. Shawe-Taylor, *An introduction to support vector machines and other kernel-based learning methods*. Cambridge university press, 2000.

[30] J. Weston, C. Watkins *et al.*, "Support vector machines for multi-class pattern recognition." in *ESANN*, vol. 99, 1999, pp. 219–224.

[31] D. M. Powers, "Evaluation: from precision, recall and f-measure to roc, informedness, markedness and correlation," 2011.

A Support Vector Regression Model for Forecasting Rainfall

Nasimul Hasan[1], Nayan Chandra Nath[1], Risul Islam Rasel[2]
Department of Computer Science and Engineering
International Islamic University Chittagong, Bangladesh
Email: nasimul_hsn@yahoo.com[1],nayanctg143@gmail.com[1],rasel.kmutnb@gmail.com[2]

Abstract— Rainfall prediction is a very important part of weather forecasting. In countries like Bangladesh; which has several seasons a year, rainfall prediction is really a key factor for many sectors. Rainfall data is a time series data and it changes time to time as climate and season changes. Moreover, rainfall depends on several factors as flow of wind, humidity etc., it is very challenging to make a hundred percent perfect prediction. This paper exhibits a robust rainfall prediction technique in view of the recent rainfall data of Bangladesh utilizing Support Vector Regression (SVR), a relapse methodology of Support Vector Machine (SVR). The collected raw data wasn't prepared for using as input of algorithm, thus it had been pre processed manually to suit into the algorithm, then fed to the algorithm. The evaluation results of the study conducted on the data shows that the projected technique performs higher than the conventional frameworks in term of accuracy and process running time. The proposed approach yielded the utmost prediction of 99.92%

Keywords— Rainfall prediction; timeseries data; windowing operator; sliding window validation; Support Vector Regression;

I. INTRODUCTION

Weather (especially rainfall) has a great influence over cultivation, flood and some other sectors, The cultivation of corps relies mostly on rainfall here and it is important to predict how much rainfall may happen in an upcoming season. A perfect rainfall prediction can help us to take decision what to cultivate and what to not. Since many other things such as drought, tourism, transportation, construction etc. also sometimes depends on rainfall; a good prediction can help to take decisions regarding these sectors. From ancient time people are trying to find the pattern of weather and predict weather for their well-being. From the very beginning of science and technology, weather prediction is a very interesting sector of study. Forecasting rainfall is a tough task due to the complication of the physics and different variable which cause rainfall [1]. It is actually a very noisy and deterministically disordered natural event. Some very important factors as monsoon, wind, moisture, heat, rotation of earth etc. plays a very strong role on the rainfall issue.

A lot of intelligent techniques as Artificial Neural have been used to predict rainfall. Among them Artificial Neural Network (ANN) is a commonly used technique to produce a good prediction [2] [3] [4]. Frequent study shows that ANN can work way better than different regression, MA and EMA. ANN frequently displays conflicting and unpredictable execution on boisterous data [5]. Support Vector Machine (SVM) is a supervised classification and regression algorithm. An SVM model represents the samples as point spaces. It is mainly based of decision plane concept. It separates objects with different class by a visible gap as much as possible between the classes. SVM can perform both linear and non-linear classification with super efficiency. Kesheng Lu and Lingzhi Wang [6] showed in their research that Support Vector Machine can perform an efficient rainfall prediction with a low error rate. Their model can produce almost 99% accurate prediction. A. Mellit, A. Massi Pavan & M. Benghanem [7] developed a SVM model which can produce up to 99% accurate prediction for different models. At the point when utilizing SVM, the fundamental issue is defied: how to pick the appropriate kernel and how to set the best kernel function. The best possible parameters setting can enhance the SVM relapse exactness. Diverse kernel capacity and distinctive parameter settings can bring about huge contrasts in execution. However, there are no investigative strategies on the other hand solid heuristics that can direct the client in selecting a fitting part capacity and great parameter values [6].

In this study, different kernel functions of Support Vector Machine (SVM) and a data preprocessing technique windowing is combined to predict rainfall. Three different models- Total rainfall prediction, maximum rainfall prediction and average rainfall prediction with three different sub models, for 1day ahead, 7 day ahead and 10 day ahead prediction are proposed here for a better rainfall prediction technique.

II. METHODOLOGY

ε-insensitive loss function was introduced by Vapnik and then SVM was developed to solve regression problems as well. The process is known as Support Vector Regression (SVR). SVR has an excellent performance regarding the perfection of solving non-linear regression.

Support Vector Regression: Almost all principals of SVM classification are followed by Support Vector Regression (SVR). As the output is real number and there are unlimited possibilities. To handle this problem, a limitation to the tolerance (epsilon) is set to the SVM which would have effectively asked for from the problem. It minimizes $\|\omega\|^2$ to reduce the model complexity. Here ξ_i and ξ_i^* are slack variables and i= 1, …, n to calculate the difference of training data outside $\varepsilon -$ sensitive zone [8] [9].

Minimize:

978-1-4673-9257-0/15/$31.00 ©2015 IEEE

$$\frac{1}{2}\|\omega\|^2 + C\sum_{i=1}^{n}(\xi_i + \xi_i^*) \quad (1)$$

Subject to:

$$\begin{cases} y_i - f(x_{i,\omega}) \leq \in + \xi_i^* \\ f(x_{i,\omega}) - y_i \leq \in + \xi_\iota \\ \xi_\iota, \xi_i^* \geq 1, \dots, \mathrm{n} \end{cases} \quad (2)$$

The optimization problem can lead to the dual problem and the solution is:

$$f(x) = \sum_{i=1}^{n_{sv}}(\alpha_i - \alpha_i^*)K(x_i, x) \quad (3)$$

Subject to, $0 \leq \alpha_i^* \leq C, 0 \leq \alpha_i \leq C$

Here, n_{sv} denotes the number of Support Vector (SVs).

Kernel Functions:

$$K(x_i, x_j) = \begin{Bmatrix} X_i, X_j & \text{Linear} \\ (\gamma X_i \cdot X_j + C)^d & \text{Polynomial} \\ exp\left(-\gamma|X_i - X_j|^2\right) & \text{RBF} \\ \tan h\,(\gamma X_i \cdot X_j) + C & Sigmoid \end{Bmatrix} \quad (4)$$

Here, $K(X_i, X_j) = \emptyset(X_i, X_j)$ and γ is the adjustable parameter.

A. Time series data:

Rainfall data is time series data. Time series data is a set of values of something where the intervals of the value are listed in such a way that the time period between each attribute is exactly same.

B. Moving Average:

A Moving Average (rolling average or running average) is an estimation to analyze data points by making a progression of midpoints of distinctive subsets of the full data set.

$$\text{MA} = \frac{x_1 + x_2 + \cdots + x_n}{n} \quad (5)$$

Here, $x_1 + x_2 + \cdots + x_n$ are the average values of the monthly rainfall and n is the total number of observation. Moving average of 7 days was considered for all attributes taken as labels in this study

C. Windowing operator:

Windowing operator is an exclusive operator which can perform better for time series prediction. It converts series sample data into single valued data. The series data must be given as Example Set. The parameter "series representation" defines how the series data is represented by the Example Set.

III. Evaluation Process

A. RMSE

Root Mean Square Error is a well-known and commonly used evaluation process for regression models.

$$\text{RMSE} = \sqrt{\frac{\sum_{i=1}^{n}(yt - \widehat{yt})^2}{n}} \quad (6)$$

Here, yt is the original value of a point for a given time period *t*, *n* is the total number of fitted points, and $\widehat{yt}$ is the fitted forecast value for the time period *t*.

B. MAE

Mean Average Error (MAE) is an widely used evaluation formula. Mean Absolute Error (MAE) measures how far predicted values are away from observed values.

$$\text{MAE} = \frac{\sum_{i=1}^{N}|x_i - \hat{x}_j|}{N} \quad (7)$$

Here, x_i is the actual observations time series, is the estimated or forecasted time series, SAE is the sum of the absolute errors (or deviations), N is the number of non-missing data points

IV. Experiment Design

A. Research Data:

6 years Rainfall data (2008-2014) of Chittagong, Bangladesh from the Meteorological Department, Bangladesh were collected to perform experiment and evaluation this study. Here we took only the data of March to October of each year as basically in this period rainfall occurs here normally. Three different models for forecasting maximum, total r and average rainfall were built with the same data. 80% of the data were considered as training data and the rest 20% as testing data. Six attributes, Date, total, avg., max, min, MA included both the training and test data. The 'Date' attribute was selected as id for all three models and another attribute ('max' for maximum rainfall prediction, 'avg.' for average rainfall prediction and 'total' for total rainfall prediction) was chosen as label. Figure 1 shows the actual rainfall (2008-2014)

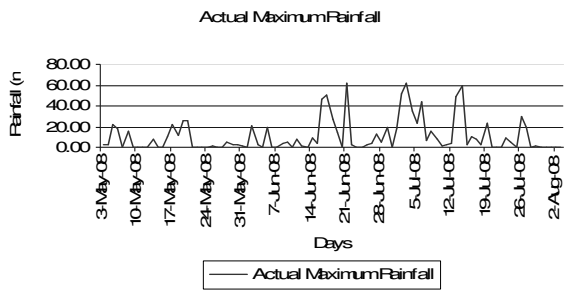

Figure1. Actual Rainfall of Chittagong (Total, 2008-2014)

B. Model construction and analysis:

This step starts with the preprocessing step of data. At the very first Moving Average (MA) technique was applied on the data set. Then windowing operator was used so that it can convert series data to universal dataset and feed the learning process [10]. As learning technique we used Support Vector Regression (SVR). The model structure includes two vital stages, training and testing. Both the stages are continuous process as the main objective of the study was to build a efficient model for rainfall forecasting.

Training and testing stages are mentioned below.

1*) Training stage:*

The training stage starts with the retrieving of data from the repository. The data were processed before entering this stage. After this, the role of the attributes in the dataset was assigned. Then one of the attributes (Date) was selected as the id and another as the label. The selection of label was different for three different models. The next step was to set the windowing operator. The parameters of windowing operator were set and then windowing was performed. A special and efficient validation 'Sliding Window Validation' was performed for validation. Afterwards, the main process was fed and the parameters of the Support Vector Regression. Then the model was set to run.

2) Testing stage:

In this phase the testing data were retrieved from the repository and the role of the attributes of the data was set and then the id and label were selected as done in the training stage. Like the training stage, the parameters of windowing operator were set and run and then the main process was fed. The performance was compared finally.

V. EXPERIMENT RESULT

A. Windowing operator analysis:

At this point we used windowing operator to the time series data to convert it into generic data. Table I shows the windowing operators parameter settings used in this study.

TABLE I. WINDOWING OPERATOR ANALYSIS

Model		Horizon	Window size	Step Size
Total	1 day	1	2	1
	7 day	7	2	1
	10 day	10	2	1
Maximum	1 day	1	3	1
	7 day	7	2	1
	10 day	10	2	1
Average	1 day	1	2	1
	7 day	7	2	1
	10 day	10	2	1

B. Support Vector kernel Analysis:

The parameters selecting of Support Vector Regression is a very crucial and important part. The perfection of prediction depends on best setting of parameters. So that, the parameters were chosen carefully and a log was kept to find the best parameter set. Table II shows the parameter settings for Support vector used in this study. Here, C is the constant of complexity and G is the value of kernel gamma.

TABLE II. SUPPORT VECTOR KERNEL ANALYSIS

Model	Days	Kernel Type	degree	C	G	∈	∈ +	∈ -
Total	1	Anova	1	2000	1	1	1	1
	7		1	1000	1	1	1	1
	10		1	1000	1	1	1	1
Max	1		1	400	1	1	1	1
	7		1	700	1	1	1	1
	10		1	1000	1	1	1	1
Average	1		1	1000	1	1	1	1
	7		1	1000	1	1	1	1
	10		1	1000	1	1	1	1

C. Sliding window validation:

As the validation process for this study sliding window validation was used. It is a special validation for series data. It takes a certain window for training and another window for testing. The window then moves to another window and determine the average of all estimation. The parameter "cumulative training" shows if every single previous sample ought to be utilized for preparing (rather than just the present window) [11]. Table III shows the parameter properties of Sliding Window validation and Table IV shows the result of the study.

TABLE III. SLIDING WINDOW VALIDATION

Model		Training Window Width	Training Window step	Test Window width	Horizon
Total	1	2	1	2	1
	7	2	1	2	7
	10	2	1	2	10
Max	1	2	1	2	1
	7	2	1	2	7
	10	2	1	2	10
Avg	1	2	1	2	1
	7	2	1	2	7
	10	2	1	2	10

TABLE IV. RESULT FOR 1 DAY AHEAD PREDICTION

	Date	Actual Rainfall	Predicted Rainfall 1 day
Total	4-Jul-12	0.1	0.19
	5-Jul-12	2.5	1.76
	6-Jul-12	0.0	0.74
	7-Jul-12	1.6	1.17

	Date	Actual Rainfall	Predicted Rainfall 1 day
Maximum	4-Jul-12	0.1	0.85
	5-Jul-12	2	1.26
	6-Jul-12	0	1.04
	7-Jul-12	1	1.11
Average	4-Jul-12	0.0125	0.76
	5-Jul-12	0.3125	0.76
	6-Jul-12	0	0.68
	7-Jul-12	0.2	0.81

TABLE V. RESULT FOR 7 DAY AHEAD PREDICTION

	Date	Actual Rainfall	Predicted Rainfall 7day
Total	10-Jul-12	6.8	1.81
	11-Jul-12	4.6	6.97
	12-Jul-12	78	107.79
	13-Jul-12	115	30.54
Maximum	10-Jul-12	6	1.47
	11-Jul-12	4.6	1.90
	12-Jul-12	53.8	5.48
	13-Jul-12	106	1.52
Average	10-Jul-12	0.85	1.17
	11-Jul-12	0.575	0.06
	12-Jul-12	9.75	14.49
	13-Jul-12	14.375	5.72

TABLE VI. RESULT FOR 10 DAY AHEAD PREDICTION

	Date	Actual Rainfall	Predicted Rainfall 10 day
Total	13-Jul-12	115	28.65
	14-Jul-12	66.2	7.83
	15-Jul-12	44.1	1.41
	16-Jul-12	5	2.41
Maximum	13-Jul-12	106	14.10
	14-Jul-12	40	0.38
	15-Jul-12	16	2.63
	16-Jul-12	4	2.91
Average	13-Jul-12	14.375	10.74
	14-Jul-12	8.275	2.93
	15-Jul-12	5.5125	0.51
	16-Jul-12	0.625	1.88

D. *Error calculation:*

The error calculated from the actual rainfall value and the predicted rainfall value from the Support Vector Regression model proposed in this study.

TABLE VII. ERROR CALCULATION

Model		RMSE	MAE
Total	1 day	18.60	0.08
	7 day	24.95	4.99
	10 day	24.97	86.35
Maximum	1 day	11.39	0.75
	7 day	15.99	4.53
	10 day	14.26	91.90
Average	1 day	2.85	0.45
	7 day	3.30	0.31
	10 day	3.54	3.63

E. *Graphical Representation of the study:*

Two different models- Maximum rainfall prediction and Total rainfall prediction are proposed here with 1 day ahead, 7 day ahead and 10 day ahead models for each. Figure 2, Figure 3, Figure 4, Figure 5, Figure 6, Figure 7, Figure 8, Figure 9 and Figure 10 shows the difference between the actual value of rainfall (mm) and the predicted value of rainfall (mm).

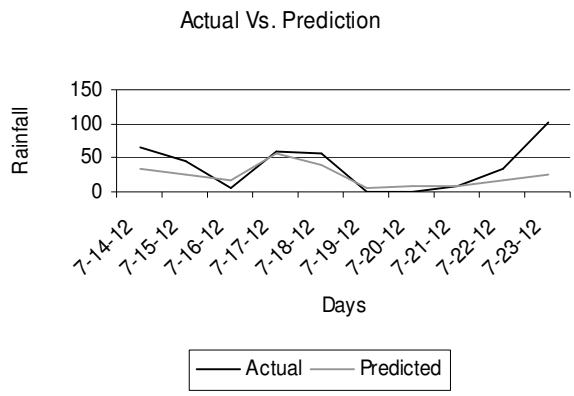

Fig 2 . Actual Vs. Prediction (Total, 1 day Ahead)

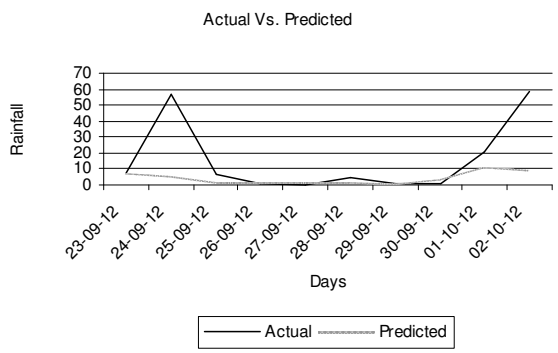

Fig 3. Actual Vs. Prediction (Total, 7 day Ahead)

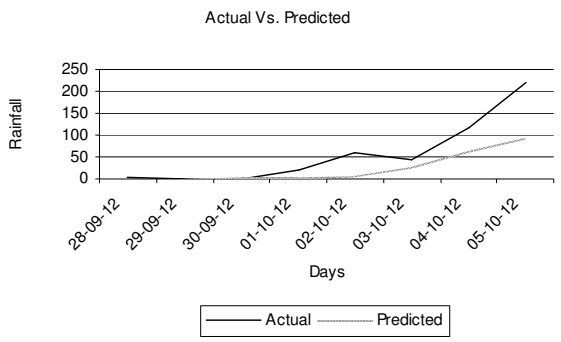

Fig 4. Actual Vs. Prediction (Total, 10 day Ahead)

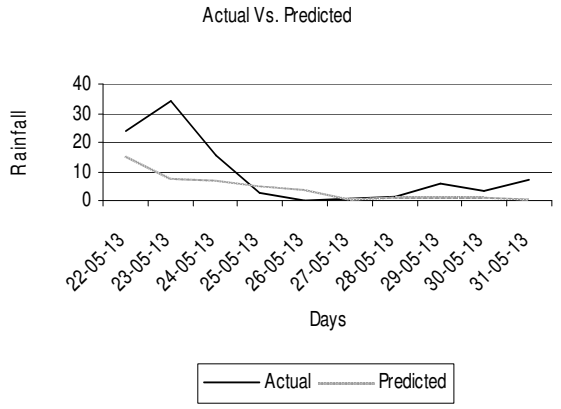

Fig 5. Actual Vs. Prediction (Max, 1 day Ahead)

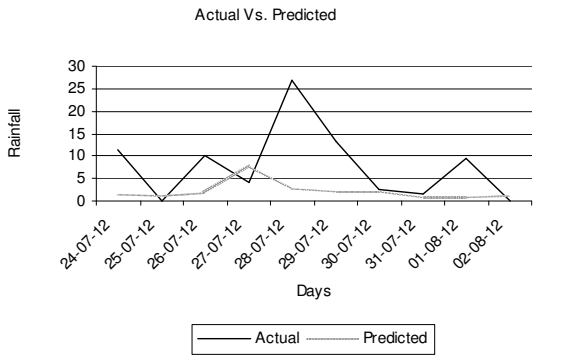

Fig 6. Actual Vs. Prediction (Max, 7 day Ahead)

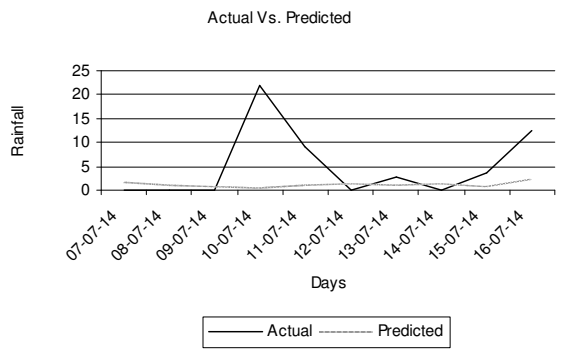

Fig 7. Actual Vs. Prediction (Max, 10 day ahead)

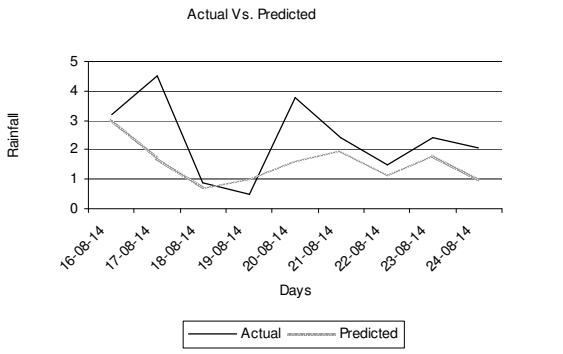

Fig 8. Actual Vs. Prediction (Average, 1 day ahead)

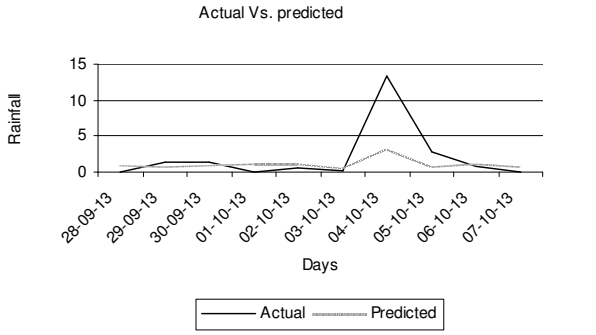

Fig 9 Actual Vs. Prediction (Average, 7 day ahead)

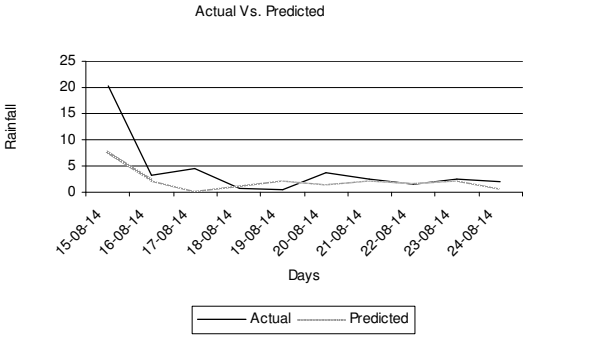

Fig 10. Actual Vs. Prediction (Average, 10 day ahead)

VI. CONCLUSION

A. Discussion

This paper presents a robust rainfall prediction technique using Support Vector Regression. The result of the experiment done with the data of Chittagong, Bangladesh shows that the proposed model can forecast more accurately in comparison with the regular technique used. The proposed model can predict better than any model before one day. The 7 days ahead model also performs very well than conventional processes.

B. Limitation and Future Work

Only Moving Average and Windowing operator were used as data preprocessing step in this study. The data was taken for only Chittagong area of Bangladesh. In future more data preprocessing steps and different algorithms will be used. Data from other stations of different countries and area will be used to get a universal model.

REFERENCES

[1] Lihua Xiong, K. M. Connor, "An empirical method to improve the prediction limits of the GLUE methodology in rainfall– runoff modeling," Journal of Hydrology, Vol. 349, pp: 115–124, 2008.

[2] Jiansheng Wu; Liangyong Huang; Xiaoming Pan, "A Novel Bayesian Additive Regression Trees Ensemble Model Based on Linear Regression and Nonlinear Regression for Torrential Rain Forecasting," in Computational Science and Optimization (CSO), 2010 Third International Joint Conference on , vol.2, no., pp.466-470, 28-31 May 2010

[3] Jiansheng Wu, "A novel nonparametric regression ensemble for rainfall forecasting using particle swarm optimization technique coupled with artificial neural network," Lecture Note Computer Science, Vol. 5553, No. 3, pp: 49–58, Springer- Verlag Berlin Heidelberg, 2009.

[4] G. F. Lin and L. H. Chen, "Application of an artificial neural network to typhoon rainfall forecasting," Hydrological Processes,Vol. 19, pp. 1825–1837, 2005.

[5] W. C. Hong, "Rainfall forecasting by technological machine learning models," Applied Mathematics and Computation, Vol. 200, pp: 41–57, 2008.

[6] Kesheng Lu; Lingzhi Wang, "A Novel Nonlinear Combination Model Based on Support Vector Machine for Rainfall Prediction," in Computational Sciences and Optimization (CSO), 2011 Fourth International Joint Conference on , vol., no., pp.1343-1346, 15-19 April 2011

[7] A. Mellit, A. Massi Pavan, M. Benghanem, "Least squares support vector machine for short-term prediction of meteorological time series" in Theoretical and Applied Climatology, Volume 111, Issue 1-2 , pp 297-307

[8] Lucas, K., Lai, C., James, N., Liu, K.: Stock Forecasting Using Support Vector Machine. In: Proceedings of the Ninth International Conference on Machine Learning and Cybernetics, pp. 1607–1614 (2010)

[9] Debasish, B., Srimanta, P., Dipak, C.P.: "Support Vector Regression. Neural Information Processing"– Letters and Reviews 11(10), 203–224 (2007)

[10] R.I.Rasel, Nasrin Sultana, P.Meesad (in press), "An Efficient Modelling Approach for Forecasting Financial Time Series Data Using Support Vector Regression and Windowing operators", In: International Journal of Computational Intelligence Studies, 2015

[11] F.R.EngLucas, K., Lai, C., James, N., Liu, K.: Stock Forecasting Using Support Vector Machine. In: Proceedings of the Ninth International Conference on Machine Learning and Cybernetics,pp. 1607–1614 (2010).

Enhancing Software Development Process Using Automated Adaptation of Object Ensembles

Md. Emran, Humaun Kabir, Ziaur Rahman, Nazrul Islam

Department of Information and Communication Technology

Mawlana Bhashani Science and Technology University

Santosh, Tangail-1902, Bangladesh

Email: emranict08@gmail.com, humaunkabirmstu10@gmail.com, zia@iut-dhaka.edu, nazrul.islam@mbstu.ac.bd

***Abstract*— Software development has been changing rapidly. This development process can be influenced through changing developer friendly approaches. We can save time consumption and accelerate the development process if we can automatically guide programmer during software development. There are some approaches that recommended relevant code snippets and API-items to the developer. Some approaches apply general code, searching techniques and some approaches use an online based repository mining strategies. But it gets quite difficult to help programmers when they need particular type conversion problems. More specifically when they want to adapt existing interfaces according to their expectation. One of the familiar triumph to guide developers in such situation is adapting collections and arrays through automated adaptation of object ensembles. But how does it help to a novice developer in real time software development that is not explicitly specified? In this paper, we have developed a system that works as a plugin-tool integrated with a particular Data Mining Integrated environment (DMIE) to recommend relevant interface while they seek for a type conversion situation. We have a mined repository of respective adapter classes and related APIs from where developer, search their query and get their result using the relevant transformer classes. The system that recommends developers titled automated objective ensembles (AOE plugin). From the investigation as we have ever made, we can see that our approach much better than some of the existing approaches.**

***Keywords*—Adaptation of Object Ensembles, Source Repository, Software Developing Process, Data Mining Integrated Environment.**

I. INTRODUCTION

The Software development process can be enriched by using many processes. Many guidelines are given which influence software development process, especially in the coding stage. Reusing previously completed software repository to enhance the development process is a common phenomenon in the field of Mining Software Repository (MSR). If developers get suggestions in e.g. API recommendations, object usage pattern, class structure or code snippets from the existing projects they might be benefited a lot what they eventually expect while coding. Some of the approaches have integrated web based code, searching in their customized tool like MAC [1] and MAPO [2] before mining the code source abstractions. Although MAC and MAPO are server dependent or online based, by which they are not flexible for a developer. Automated Adaptation of Object Ensembles (AOE) shows a process of adapting the collection frameworks and Arrays, but it is not clear view how to use it as a plug-in tool.

In software development there are different ways available to guide software developers during the development period. A programmer can use programming code in a software system easily by using an automated adaptation of object ensembles. By this process user can find out required data easily. We have used an AOE Plug-in by which a software developer can complete a code in a short time. It takes less time compared to existing approaches. The existing approaches like simply using the Integrated Development Environment (IDE) like Net Beans [3], IntellijIdea [4], and Eclipse [5], is vulnerable to flaws and it is unable to provide us the required interfaces. In essence, it consumes developers' valuable times. We have investigated between the conventional ways and our AOE plug-in approach to evaluate the efficiency of our proposed tool. The study shows that it is able to accelerate the developer's performance and facilitate less time consuming with decreasing code flaws and errors.

Although in MAC [1], MAPO [2], AOE [6]and many others code repository had several limitations such as server dependent searching, either database based or Internet based where data is not preprocessed according to rules of data mining so these are not friendly for a developer. In our methodology we try to show our repository plugin as an offline repository that is filed based instead of a database and it has special source abstraction technique. Adapter classes are the key point in our approach. In AOE the result depends on the resource of the repository of adapter classes. Recently, a number of works are available to guide developers in the field of software engineering. All we have seen is that our approach is comparatively easier to handle than other existing approaches.

The paper is so far structured in the followings: Section II background and related works of this study. Section III shows that full design and proposed approach. The detailed results and evaluation of this paper is presented in Section IV. Section V concludes with the set of observation and future work of this research.

II. BACKGROUNDS AND RELATED WORKS

As the software development process can be influenced by using many techniques, so many researchers try to provide a flexible way that can influence the software development process. Need not to say that previously completed software repository technique enhance the development process is a common framework in the field of mining software repository. The developers can be benefited by following the provided suggestions from various recommendations like API recommendations, object usage pattern, class structure or code snippets from the existing projects. Some of the approaches have integrated web based code, searching in their customized tool like MAC [1] and MAPO [2] before mining the code source abstractions.

There are some processes by which a software system is established by code reusing. But in our approach we use a repository of adapter classes and a tool which adapt this code. By using this AOE plug-in which integrates with the IDE, the user can find the required data type easily. There are some existing efforts such as adapting collection and array by using Automated Adaption of Object (AOE)[6]. Some approaches like Code reusing in MAPO [2], better user recommendation using enhancing software development repository, Scenario Based API Recommendation System [7] and others are also used to accelerate the software development process. As we have proposed that if there have been adapter tools [8] which adapt the given interfaces it will be more helpful for the programmers to find the required interfaces. Mining API Usages from Open Source Repositories (MAPO) [2], [3] was one of the first and MAC [1] was one of the updated triumphs to mine API usage pattern. Other recent works called Enhancing Software Development Process (ESDP) [9] where the developers are highly guided by recommendations from a mined repository is also one of our referral works.

One of the best concepts of test-driven reuse showed by Reiss [10] common test-cases issued as input for a component search engine in [11]. Nevertheless, there exist some problems such as license problem and dependency problem. When the user changes the parameter types, then it might need an even more propagated deep adjustment of type changes. The formal and rule-based language is proposed by Kell [12] that was named Cake for automated wrapper generations. The designing used to define interface relations; transformation object structures are possible by applying these rules. We introduced that transformation should happen automatically but it is most overhead for a developer writing mapping rules, basically for an unknown complex object. It overcame Nita and Notkin [13] by providing an approach which concerned with adapting programs to alternative APIs. When the variations among the APIs are small its schema considers not-straightforward structural respect as out of scope, which is the main challenge, is providing transformation. The work showed by Hummel [14] is depending on the Identity Map Pattern from Fowler [15] and identifies the answer about the problems of the Gang of Four adapter pattern. The approach is integrated into another work by Hummel and Atkinson [14] that supplies relaxed-signature matching for primitive data types.

Recently there have done many works to enhance the software development process. There have applied many tools such as adapter generation tool [6]. In this way a user can find the required method easily. As a result a user can save time and solve any problem easily. The software development process is an easy task for a developer.

In the approach we try to overcome the limitations of existing repository tools. We try to provide as an offline repository tool that are file based instead of a database that has special source abstraction. Adapter and transformer classes are the key point in our approach.

III. PROPOSED APPROACH

In our approach we have developed a plug-in tool that is able to guide software development through suggesting interfaces by using the respective adapter classes. The tool is completely written in java and is executable as a standalone application. It can work with IDE like Net beans [3] and Eclipse [5] as they have the software extensibility.

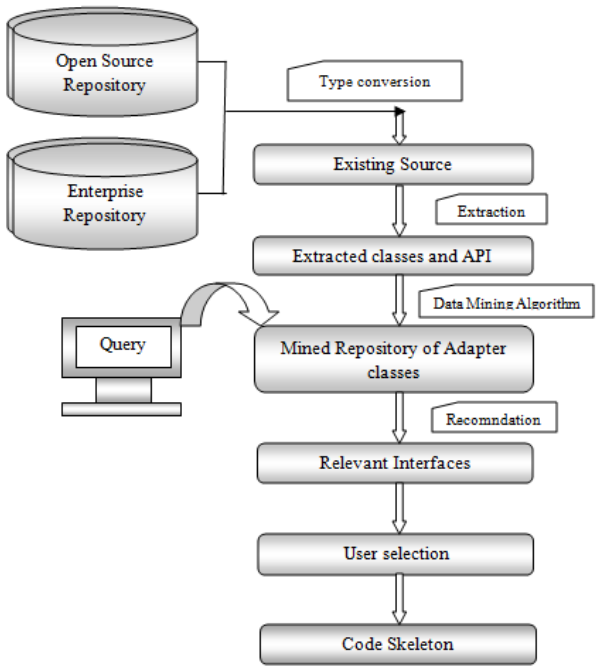

Fig. 1. Automated Object Ensembles (AOE) plugin Framework

Open Source Repository (OSR) is an online software code repository. In this repository many projects problem solving codes are stored. When a programmer stays in online and gets any programming problem, then the programmer can search in this repository for required code. OSP is an Internet based repository. In many software companies, there are stored many projects. It is called the Enterprise Repository.

In repository, there are stored a large number of programs. Many unusual code lines are staying in programs. We take the

only important line for a program. By using type conversion we build up Existing Source where projects are stored without unusual code lines. Programming code is stored in Existing Sources. We extract classes of API from these projects which exist in Existing Sources.

Data Mining Algorithm is used to build up a mined repository of Adapter classes. When a programmer searches any classes, the required classes are shown at first. Then we will find related classes. Programmers, search their needed query in the mined repository of Adapter Classes. Then we get relevant interfaces with the help of a transformer and recommendation interfaces. The user selects the required interfaces and gets code skeleton.

Now a day, there has various tools to increase the optimizing capability in software development field; adapter generation tool is one of them. To overcome mismatches on the signature level a good way is to add an adapter that controls message forwarding from one interface to the other. The adapters allow classes to work together that could not otherwise because of incompatible interfaces. It can also be familiar as a "Wrapper" which wraps the incompatible class into the adapter class, where adapter adapt any types of object, method and interface that helps in the programming fields. There exist projects available the newly integrated ability to transform arrays and collections, which can be executed for verifying the adaptation capabilities. This idea is to describe by Hummel [11], where able to generate a random Array List and a sorted Vector instance the helper class Generator is used. When a client uses an automated adapter class that depends on the interfaces that are provided by collection frameworks then the client needs help to use any plugin.

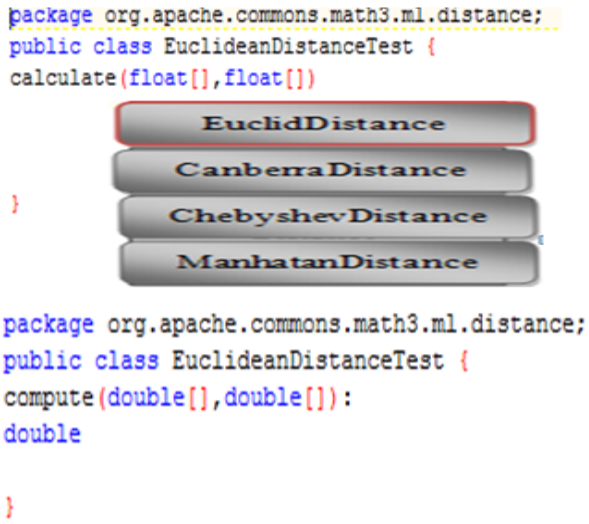

Fig. 2. Adaptation testing overview

For example, when a programmer writes their code in the IDE like as Net Beans they must write the full code to reach the required result, But when they use AOE plug-in by pressing the right button, then the programmer will be guided by the several adapter classes that are shown in the fig. 2., which is remarked by red color box is chosen. Suppose coder write ,calculate (float [], float []) then AOE plaguing suggest Euclid Distance adoptee adapt that generate in D. Seffert and O. Hummel [7] where adapter depends on transformer that transform provided instance to require instance and vice versa. Suppose a client requires a specific data types, then its search in the adapter fields after matching needed data types client can choose any of them. By finishing the process of adaptation successfully the modified test case was executed here using the final adapter instead of the adapter directly. Nevertheless, test case executed full filly the adapter's transformation capability was verified. For example, in the test case the compute method of the selected class from *org.apache.commons.math3.ml.distance* package is tested. That takes as an input two vectors, showed by an array of type double each, and calculates the distance between them. The distance should be zero, if the same vector is provided as the first and second parameter such as in this example. The public double computes (double [], double []) is the interface of the compute method.

```
package org.apache.commons.math3.ml.distance;
public class EuclideanDistanceTest {
final DistanceMeasure distance = new EuclideanDistance();
public void testZero() {
final double [] a = {0, 1, -2, 3.4, 5, -6.7, 89};
Assert.assertEquals(0, distance. compute(a, a), 0d);
```

The array of type double was replaced with a Link List<Float> after the verification of the original test case executed successfully, where the expected name of the method was changed from compute to calculate. The test case is changed to public void double calculate (Linked List<Float>) for the require interfacing. The adapter generator overcome a parameter type and the method name mismatch, namely from Linked List<Float> on double [] and calculate in a computer.

Imagine a client requires one method within two parameters, but there exist more than two parameters in a similar method in the tool then adaptation process solves this complexity. In this paper, we want to describe how easily use collection frameworks as a plug-in tool in software development fields. The collection framework refers the way of implementing interfaces with the help of several classes that are considered as a supported plaguing tool.

We have seen in the approaches [2] [MAPO] that they have used a code search engine to find the desired item following a search query given by a particular client. Like MAPO this paper also enhances the automated adaptation of object ensembles as a repository tool. In this approach the require source may online or offline repository that contain various

kinds of tools. Eventually, the approaches are not only suggesting an adapter class, but also provide its related code implementation to reach the desired goal of a software developer. It works automatically when a client type any code during programing according to their require data types or interfaces. In order to consider the existing paper [6] that shows how to generate an adapter with the help of transforms that can able to solve the matching problems of complex data types. In fig.2. There have given a snapshot of the adapter generation tool. On other existing paper there have no idea about the plugin. But in our paper, we want to use plugin for a user.

A plugin is a software component that adds a specific feature to an existing once. When an application supports plug-in, it enables customization. In our paper we want to provide an adapter plug-in by which any client can complete a task more easily than existing processes. When a client wants to find classes or interfaces, there have given some adapter class options. From these options which is chosen then it finds out the required data by using adapter plug-in.

```
package result;
import java.util.WeakHashMap;

public calss Matrix{

private adaptees Rechteck adaptee;
private static WeakHashMap<adaptees.Rechteck,Matrix>Map=

public Matrix (int param0,int param1,String param2){
    adaptee=new adaptees.Rechteck (param0,param1,param2);
    map.put(adaptee,this);
    }
private Matrix(adaptees.Rechteck adaptee){
    this.adaptee=adaptee;
    map.put(adapte,this);
        }
public adaptees Reckteck getAdaptee(){
    return adaptee;
    }
}
```

Fig. 3. A snapshot 1 of Adapter generation tool (AOE)

IV. Evaluation

There have given a guideline for a programmer to enhance the software development process. An automated adaptation of object ensembles is a process by which any software developer can find the required data easily. There have given some comparison by which we will understand which process is better than another.

a. Environmental setup

In this development process, there have used a repository of adapter classes. How much healthier this repository the development process is more easy. If our adapter class repository is enriched, a user can find the required interfaces in a short time and easily. There have given same adapter class name such as:

SL	Adapter Classes	Line of Code (LOC)
A	EuclidDistance	17
B	CanberraDistance	11
C	ChebyshevDistance	15
D	ManhattanDistance	14
E	OnewayAnova	16

There used an adapter generation tool. Some object oriented language is used. There needs an adapter by which adaptation code is plagued with user. There have given an adapter generation tool such as adaptation tool.zip [6].

b. Time complexity

Time is an important thing when a program is solved. By which a program is solved quickly this process is better than other. When a programmer solves a program in IDE (Net Beans, eclipse) there have needed some times such as 40sec.

TABLE I. TIME COMPLEXITY

Task	IDE with AOE plug-in(no of solved problem)	NetBeans(no of solved problem)
T1	60 sec	120 sec
T2	130 sec	200 sec
T3	150 sec	310 sec
T4	120 sec	360 sec
T5	140 sec	400 sec

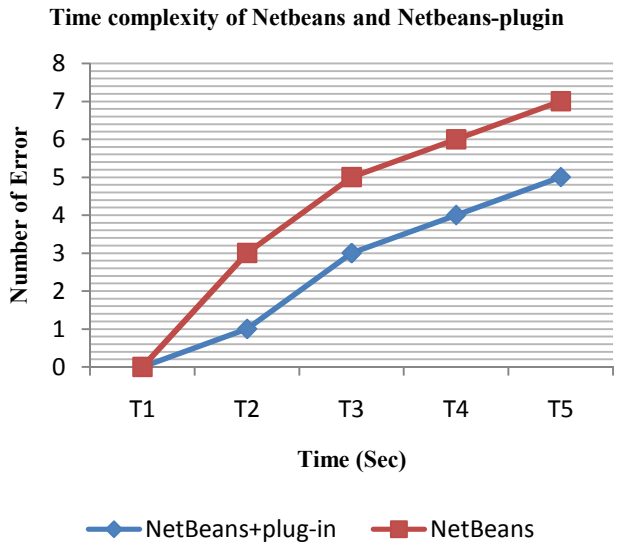

Fig. 4. Time complexity between NetBeans and NetBeans+plug-in

But the same programmer solves this same problem in net beans, but there have plugged-in AOE. As a result, we see that at this time the programmer can solve this problem in 0.20sec. When AOE is plugged-in, they have saved 20sec. There have given a table of how much program is solved without AOE plugged-in and within AOE plugged-in.

c. *Error Vulnerability*

In TABLE II we see that after the total time in IDE with plague-in there have found 13 errors, but at the same time problem solving only in IDE there have found out 21 errors.

TABLE II. Error possibility

Time	NetBeans+plug-in	NeatBeans
T1	0	0
T2	1	3
T3	3	5
T4	4	6
T5	5	7
Total error	=13	=21

As a result, we understand that when the plugin is used error rate is low. So this process is better than another.

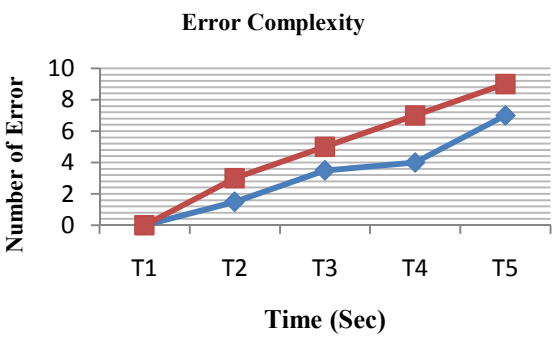

Fig. 5. Error comparison between net beans and NetBeans+plug-in

d. *Thread of the evaluation*

Everything has a limitation. There has some limitation of evaluation. This guideline for software development process is more effective. The evaluation is observed at the same time and same experiment. Such as

a. By having more AOE adapter classes in the repository a user finds more accurate data.

b. A program is evaluated by the same user.

c. It is a lengthy process to plug in a user in an adapter class repository.

d. A user cannot find the mining data.

The results observed in the empirical study may not be applicable to the programming tasks other than those considered in the study, being a threat to the external validity. If the tasks mentioned out there in the study change the results may also be changed. Before we start our evaluation the team members are well trained. The receiving capacity of team members may vary. So the learning curve of these numbers may affect the results.

Within many problems this guideline for a programmer is more effective to develop software process. By this process a user can find any data very quickly. It will keep an important role to enhance the software development process.

V. CONCLUSION

The AOE plug-in approach is more enriched than any other Existing approaches. The approach is able to find out any required data easily and there have needed less time than any other approach. A user finds a data in adapter classes than the AOE plug-in give the required data to the client. The process which we have provided in this paper is different from any other existing process. That is able to enhance the SDP recently.

This paper provided a guideline by which a user can get the required data easily and it is comfortable to use. But these data are not mined. In Future there have used data mining algorithm and find out mined data to enhance software development process.

REFERENCES

[1] Hsu, Sheng-Kuei, and Shi-Jen Lin. "MACs: Mining API code snippets for code reuse." *Expert Systems with Applications* 38.6, p. 7291-7301, 2011.

[2] Xie, Tao, and Jian Pei. "MAPO: Mining API usages from open source repositories." *Proceedings of the 2006 international workshop on Mining software repositories*. ACM, p. 54-57, 2006.

[3] NetBeans plug-in(2015),Retrieved from: https:// www.plugins.netbeans./ [Accessed June 28, 2015]

[4] Jet Brain, (2015), Retrieved from: https:// www.jetbrains.com/idea/[Accessed" June 25, 2015]

[5] Genuitec,(2015),Retrievedfrom:http://www.genuitec.com/myeclips

[6] Seiffert, Dominic, and Oliver Hummel. "Adapting Collections and Arrays: Another Step towards the Automated Adaptation of Object Ensembles." *Software Reuse for Dynamic Systems in the Cloud and Beyond.* Springer, pp. 348-363, 2014

[7] Shahnewaz, "A Scenerio based API recommendation system using syntax and semantics of client source code". Master's Thesis, Department of CSE, Islamic University of Technology, OIC, Gazipur-1704, Bangladesh. April, 2014

[8] http: // oliverhummel. com / adaptation / tool.zip [Accessed July 29, 2015]

[9] Rahman, Z., Hasan, K., "*Enhancing Software Development using Data Mining Integrated Environment*," Master's Thesis of Islamic University of Technology, Dhaka, pp. 1-75, June 2012.

[10] Reiss, S.P.: Semantics-based code search. *In: IEEE 31st International Conference on Software Engineering, ICSE* 2009, pp. 243–253 (2009)

[11] Hummel, O., Janjic, W.: Test-Driven Reuse: Key to Improving Precision of search Engins for Software Reuse. *In: Finding Source Code on the Web for Remix and Reuse*, pp. 227–250. Springer(2013)

[12] Kell, S.: Component adaptation and assembly using interface relations. *In: Proceedings of the ACM International Conference on ObjectOriented Programming Systems Languagesand Application*, OOPSLA 2010, pp. 322-340 , 2010.

[13] Nita, M., Notkin, D.: Using twinning to adapt programs to alternative apis. In: Proceedings of the *32nd ACM/IEEE International* Conference on Software Engineering, ICSE 2010, vol. 1, pp. 205–214 ,2010

[14] Hummel, O., & Atkinson, C. "Automated creation and assessment of component adapters with the test cases*" In Comonent-Based Software Engineering* (pp. 166-181). Springer Berlin Heidelberg.

[15] Janjic, W., Atkinson, C.: Leveraging software search and reuse with automated software adaptation. *In: 2012 ICSE Workshop on Search Driven Development - Users, Infrastructure, Tools and Evaluation*, pp. 23-26 , 2012

A Modified Fuzzy Relational Clustering Approach for Sentence-Level Text

Sikder Tahsin Al-Amin, Mahade Hasan, and M. M. A. Hashem
Department of Computer Science and Engineering
Khulna University of Engineering and Technology
Khulna-9203, Bangladesh
E-mail: stahsin.cse@gmail.com, mahade047@gmail.com, mma.hashem@outlook.com

Abstract— **This paper proposes a fuzzy relational clustering (FRC) to find similar sentences from a set of sentences as well as group them in clusters. For finding similar sentences here FRC used both word-to-word and order similarity. For word-to-word similarity FRC used Jiang and Conrath similarity measure (JnC) with the help of WordNet database. Order similarity is calculated from joint word set. As a sentence may relate to more than one theme so FRC used a fuzzy clustering approach. Here FRC used FRECCA algorithm for the sentence clustering purpose. The algorithm works on Expectation-Maximization where importance of a sentence is expressed by PageRank score which is treated as likelihood. The PageRank scores and mixing coefficients are initialized with Uniform Random Number generation technique. Applying this method on a quotation dataset of different classes we found that it is capable of identifying and grouping similar sentences in a cluster. FRC is also applied on a news article dataset and found admirable results.**

Keywords—Fuzzy Clustering, Sentence Similarity, Relational Data.

I. INTRODUCTION

The amount of data being generated and stored is growing exponentially which presents new opportunities and challenges for unlock the information embedded within this data. Modern field of data mining can be used to extract important knowledge from data [1]. This method only emphasizes on text data. FRC used pre-processed text data of quotes. This method can be further used on pre-processed text data from emails, newspapers, websites, online blogs etc. One of the applications is that, on a certain day many newspapers are published. There are some news articles that are printed in all or most of them but are not written in the same format or language nevertheless the idea of the news is similar. So the main objective is to find similarity between the sentences residing in the news article.

Several works have been done on fuzzy clustering. First one was Relational Fuzzy c-means by Hathaway et al [2]. Then ARCA and K-Medoids [3],[4] was also proposed. But these algorithms had some limitations. In Relational Fuzzy C-means distance between data points couldn't be measured although it could operate on relational data. If the size of data set increased by high number, it causes the ARCA algorithm to fail. K-Medoids were affected by poor initialization which is done randomly.

A sentence is likely to be related to more than one theme or topic present within a document. However, because most sentence similarity measures do not represent sentences in a common metric space, a bag-of-words [5] approach or conventional fuzzy clustering approaches based on prototypes or mixtures of Gaussians are generally not applicable to sentence clustering [6].

Hence there is a need of fuzzy clustering algorithm that operates on relational input data. Relational data are in the form of a square matrix of pairwise similarities between data objects. FRC finds similarities between sentences and puts them into a cluster by calculating the cluster membership values. As the approach is fuzzy, a sentence may reside in more than one cluster with some amount of membership value. The sum of the membership values of a sentence in all clusters is 1. A sentence is considered to be in a cluster for which the corresponding membership value is largest.

This paper has improved the 'Measuring Sentence Similarity' method. The sentence similarity method measures similarity between two sentences based on both Word-to-Word similarity and Order similarity. Word-to-Word similarity measures the similarity between two words with the help of a lexical database known as WordNet [7]. On the other hand Order similarity measures the positioning of a word in a sentence.

The proposed method Sentence-Clustering based on FRC (SBFRC) has improved the 'Initialization' step of the algorithm. The FRECCA algorithm initializes the membership values and PageRank values using simple random number generation technique. FRC implemented 'Uniform Random Number' generation technique.

The rest of the paper is organized as follows. Section 2 summarizes some related works. Section 3 describes the methodology of SBFRC. Section 4 illustrates the experimental studies. Finally Section 5 concludes the paper.

II. RELATED WORKS

Hathaway et al.'s Relational Fuzzy c-Means (RFCM) algorithm [2] is considered as the first successful fuzzy clustering algorithm. Although RFCM operates on relational

978-1-4673-9257-0/15/$31.00 ©2015 IEEE

data input, it does not the express the relation by this data to be Euclidean.

Though having success, the Euclidean requirement in RFCM was considered limited, and various alternatives have been proposed. For instance, the ARCA algorithm [8] uses an attribute-based representation. A limitation of this method is the high dimensionality. It causes by representing objects in terms of their similarity with all other objects.

K-Medoid family is popular in clustering algorithms. Fuzzy versions of k-Medoids have also been introduced. Like k-Means, k-Medoids are also highly sensitive to the initial selection of centroids which is done randomly. And often requires running the algorithm several times from different random initializations.

Many spectral clustering algorithms that can be applied to sentence clustering by Zha [9], and Wang et al. [10]. They have recently applied a closely related nonnegative matrix factorization [11] technique to sentence clustering in the context of multi-document summarization.

Our proposed approach Sentence-Clustering based on FRC (SBFRC) is based on a fuzzy relational clustering algorithm which is known as FRECCA algorithm [6]. Here, Cluster Membership values for each node represent the degree or extent to which the object or a sentence belongs to each of the respective clusters, and mixing coefficients represent the probability of an object being in a cluster [6].

III. SENTENCE-CLUSTERING BASED ON FRC (SBFRC)

To overcome the shortcomings of the above approaches, SBFRC has proposed in this paper that can group similar sentences together in a cluster. It contains several steps which are described as follows. Fig. 1 is the flowchart of the steps of SBFRC.

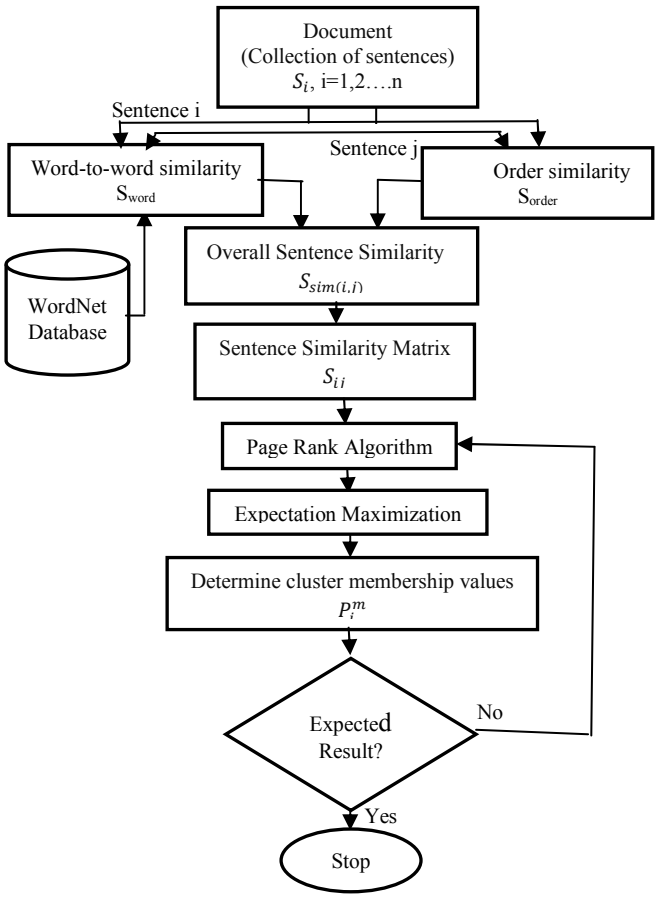

Fig. 1. Flow chart of SBFRC

Step 1: The input set is produced by pre-processing a text document. The sentences are extracted from a paragraph and the numbers of sentences are determined.

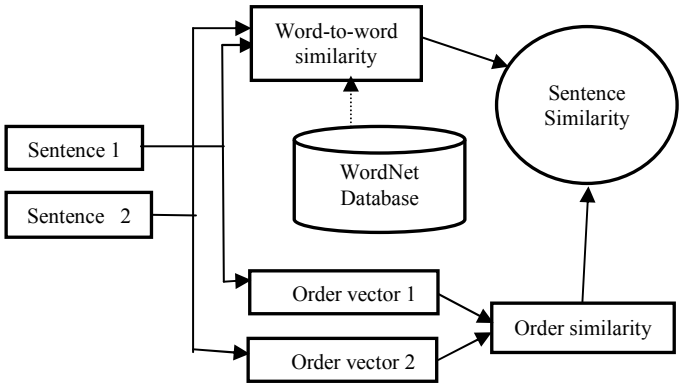

Fig. 2. Measuring Sentence Similarity

Step 2: Second step of SBFRC is to word-to-word similarity measure. Sentence similarity measures play an important role in text-related research. Existing methods for measuring sentence similarity have been adopted from approaches used for long text documents. These methods process sentences in a very high-dimensional space and are consequently inefficient and are not adaptable to some application domains. [12]

The proposed sentence similarity method derives similarity between two sentences using both word-to-word similarity and order similarity. A text is considered to be a sequence of words. The words, along with their combination structure, make a specific meaning.

Unlike existing methods, the proposed method calculates both word-to-word similarity and order similarity to compute final sentence similarity.

For word-to-word similarity the method used knowledge based measures, the WordNet [7] based measure due to Jiang and Conrath[13].

The Jiang-Conrath measure is based on the idea that the degree to which two words are similar is proportional to the amount of information they share. The similarity between words w1 and w2 is defined as equation 1:

$$Sim_{j\&c}(w1,w2) = \frac{1}{IC(w1)+IC(w2)-2*IC(LCS(w1,w2))} \quad (1)$$

Where , $LCS(w1,w2)$ is the word that is the deepest common ancestor of word w1 and w2, $IC(w)$ is the information content of word w, and defined as $IC(w) = -logP(w)$, where $logP(w)$ is the probability that word w appears in a large corpus [12].

Step 3: Third of SBFRC is to measure order similarity. For each sentence, a raw semantic vector is derived [12]. An order similarity is calculated using the two order vectors.

Step 4: The fourth step is to calculate the overall similarity as showed in Fig 2. Word-to-word similarity represents the lexical similarity. On the other hand, word order similarity provides information about the relationship between words: which words come before or after other words. Then, the overall sentence similarity is derived by combining word-to-word similarity and order similarity. And the similarity value is stored in the similarity matrix in respective position.

Overall sentence similarity is calculated using the equation 2 [12]-

$$S_{sim(s1,s2)} = r * S_{word} + (1 - r) * S_{order} \quad (2)$$

Where r <=1 decides the relative contributions of word-to-word and word order information to the overall similarity computation [12]. Since word-to-word similarity is more important and plays a vital role to overall sentence similarity, r should be a value greater than 0.5.

Step 5: Fifth step is to form the similarity matrix. The similarity method is applied between all possible pairs of sentences. After calculating similarity values between all the sentences in a document, the similarity values are stored in a matrix. If there are N sentences in a document then the matrix S_{sim} which size is NxN.

Step 6: Sixth step is to applying the PageRank algorithm [14],[15]. Unlike Gaussian mixture models, which use a likelihood function parameterized by the means and covariances of the mixture components, this method uses the PageRank score of an object within a cluster as a measure of its centrality to that cluster. These PageRank values are then treated as likelihoods. PageRank values are calculated using the equation no. 3:

$$PR_i^m = (1 - d) + d * \sum_{j=1}^{N} w_{ji}^m \left(\frac{PR_j^m}{\sum_{k=1}^{N} w_{jk}^m}\right) \quad (3)$$

Here, PR_i^m is the pagerank score of object i in cluster m. W_{ij}^m is the weight between objects i and j in cluster m calculated previously. And d is the damping factor. The damping factor d that appears in the PageRank calculation affects the fuzziness of the clustering, but generally does not affect the number of clusters, provided that the value is above approximately 0.8. In general, the higher the value of d, the harder is the clustering, with cluster membership values being close to either zero or one. We have used a value of 0.85.

After PageRank scores are calculated, these are treated as likelihoods and then they are used to calculate cluster membership values. Cluster membership values are obtained using the equation 4:

$$P_i^m = \frac{\pi_m * l_i^m}{\sum_{j=1}^{C} \pi_j * l_i^j} \quad (4)$$

Where, π_m is the mixing coefficient for cluster m. And l_i^m is the likelihoods for object i in cluster m which is obtained from the PageRank values. Membership values are normalized so that membership for an object sums to 1 for all clusters [6].

Step 7: Seventh step is the Expectation-Maximization (EM) step. Here there are two steps. The E-step calculates the membership values for each cluster. For each pair of sentences in a cluster weight is calculated using values from similarity matrix and membership values. That is –

$$W_{ij}^m = S_{ij} * P_i^m * P_j^m \quad (5)$$

In equation no. 5, W_{ij}^m is the weight between sentences i and j in cluster m. S_{ij} is the similarity between sentences i and j derived from Sentence similarity matrix. And P_i^m and P_j^m are the respective membership values of sentences i and j in cluster m [6]. With the help of this step once the PageRank scores are calculated they are treated as likelihoods and cluster membership values are calculated afterwards.

In the M-step the membership values are updated until convergence. It actually updates the mixing coefficients based on membership values. The value of mixing coefficient for each sentence in a cluster is same. As in the equation no. 6.

$$\pi_m = \frac{1}{N} \sum_{i=1}^{N} P_i^m \quad (6)$$

Where, π_m is the mixing coefficient for cluster m, P_i^m is the membership values calculated in expectation step and N is the total number of sentences.

Step 8: The eighth and last step is to find the convergence point for the clusters. The convergence is achieved when the membership of the sentences in the clusters is not updating anymore or the difference between the previous values is very little.

IV. Experimental Analysis

A. Experimental Setup

SBFRC has been development under the environment on Intel core i5-2.30 GHz processor with 4.0 GBytes of RAM running on windows 7 operating system. Here SBFRC has been developed in Java. WordNet database has been used while measuring word-to-word similarity. The quotation dataset on Table 1 [16] and news article dataset on Table 3 [6] are partial of the full dataset.

Table 1: Quotation dataset

Knowledge Class
1. Our knowledge can only be finite, while our ignorance must necessarily be infinite. 2. Everybody gets so much common information all day long that they lose their common sense. ……
Marriage Class
11. A husband is what is left of a lover, after the nerve has been extracted. 12. Marriage has many pains, but celibacy has no pleasures. ….
Nature Class
21. I have called this principle by which each slight variation if useful is preserved by the term natural selection. 22. Nature is reckless of the individual. When she has points to carry, she carries them. ….
Peace Class
31. There is no such thing as inner peace there is only nervousness and death. 32. Once you hear the details of victory, it is hard to distinguish it from a defeat. …..
Food Class
41. Food is an important part of a balanced diet. 42. To eat well in England you should have breakfast three times a day. …..

Experimental Results and Comparisons

Table 2 shows the results of applying our method, ARCA, Spectral Clustering, and k-Medoids algorithms to the quotations data set and evaluating using the external measures.

Our method requires that an initial number of clusters must be specified. This number was varied from 3 to 8, running 50 trials for each case, each trial commencing from a different random initialization of membership values. In each case the same affinity matrix was used, with pairwise similarities calculated as described before. However, only three unique clustering were found, each containing a different number of clusters, which ranged from four to seven.

Table 2: Evaluation of quotation dataset

No. of Cluster	Purity	Entropy	Rand	F-Measure
		SBFRC		
4	.350	**.550**	**.750**	**.450**
5	.400	**.500**	**.795**	.400
6	.400	**.445**	.765	**.480**
7	.400	.550	.770	.340
		ARCA		
4	.543	.646	.710	.391
5	.622	.515	.786	.459
6	.680	.451	.815	.462
7	.678	.444	.817	.427
		Spectral Clust.		
4	.641	.572	.715	.440
5	.652	.508	.785	.477
6	.690	.475	.800	.444
7	.699	.429	.809	.431
		K-Medoids		
4	.560	.605	.691	.392
5	.600	.569	.733	.433
6	.720	.457	.779	.459
7	.740	.425	.805	.461

To demonstrate how the algorithm may perform in more general use in activities related to text mining, the system is also applied to clustering sentences from a news article.
Table 3 shows the sentences from an article about President Barak Obama's presidency.

Table 3: News article dataset

News Articles
1. President Barak Obama on Tuesday championed nuclear energy expansion as the latest way that feuding parties can move beyond the broken politics …… 12. That mission however remains in doubt … 15. In Saginaw Biden insisted the stimulus is working even as he acknowledged it's going to take us a while to get us out of this ditch ….. 27. It includes more direct and rapid response to criticism more events at which the president speaks directly to the public without the filter of the media 28. The intended narrative is one in which Obama hears people's frustrations and is working directly to end them. 29. There is a little doubt the public is angry. 30. A CBS news poll in early February found eighty one percent saying it's time to elect new people to congress

The result from the news article dataset is shown below-

Table 4: Results of News Article dataset

Sentences
3,5,6,9,10,13,14,15,16,17,19,21,24
2,7,12,18,20,22,25,26,27,28,29
1,8,23,30

B. Discussions

The performance measure techniques (Purity, Entropy [17], Rand, F-measure [18]) evaluated our method. The algorithm is run 50 times for the quotation dataset and chosen the best results from it. Since the method is unsupervised, there is no fixed output. As the four performance measures are not always consistent as to which algorithm achieves best performance for a given number of clusters, boldface indication of the value corresponding to SBFRC for which the measure is a maximum. For example, for the Rand Index corresponding to Cluster No =5, our method achieves a value of 0.795, which is greater than that achieved by the other algorithms (0.786, 0.785, and 0.733), and for cluster No. = 6, the proposed method achieves the value of entropy .445 whereas other method has higher value than it (0.451, 0.475 and 0.457) hence these values are represented in boldface. It can be seen from the table that when the number of clusters is 5, the algorithm performs well than when cluster number is 5 or 6 as measured by all five external cluster evaluation criteria.
The result achieved from the news article dataset, it is observed that in 1st cluster, sentence 15 has the highest PageRank score. So the sentence 15 would go in cluster 1. The sentences 3, 5, 6, 9, 10, 13, 14, 16, 17, 19, 21, 24 are also in cluster 1. There PageRank score in close to the PageRank of sentence 15. These sentences are of similar meaning. For 2nd cluster sentence 27 has highest PageRank. Closer to this are the sentences 2, 7, 12, 18, 20, 22, 25, 26, 28, 29. And most of them are similar as they are of negative sense (criticism, angry, frustration).

V. CONCLUSION

An obvious potential application of the algorithm is to document classification and summarization. Like any other clustering algorithm, the performance of this method will ultimately depend on the quality of the input set, and as for the sentence clustering the performance can be improved with better sentence similarity measures. As the cluster number is provided initially the algorithm appears to be able to converge to an appropriate number of clusters. The idea can be expanded to the development of a hierarchical fuzzy relational clustering algorithm as well as the proposed method can also be applied to a cloud trust system to measure its performance by analyzing user feedback comments.

REFERENCES

[1] Gary M. Weiss & Brian D. Davison, "To appear in the Handbook of Technology Management", H. Bidgoli (Ed.), John Wiley and Sons, 2010.

[2] R.J. Hathaway, J.W. Devenport, and J.C. Bezdek, "Relational Dual of the C-Means Clustering Algorithms," Pattern Recognition, vol. 22, no. 2, pp. 205-212, 1989.

[3] R. Krishnapuram, A. Joshi, and Y. Liyu, "A Fuzzy Relative of the k-Medoids Algorithm with Application to Web Document and Snippet Clustering,"Proc. IEEE Fuzzy Systems Conf.,pp. 1281-1286, 1999.

[4] T. Geweniger, D. Zu¨hlke, B. Hammer, and T. Villmann, "Median Fuzzy C-Means for Clustering Dissimilarity Data,"Neurocomputing, vol. 73, nos. 7-9, pp. 1109-1116, 2010.

[5] Wikipedia: the Free Encyclopedia. Wikimedia Foundation Inc. Updated 26 August 2015. 16.19 UTC. Encyclopedia online. Available from https://en.wikipedia.org/wiki/Bag-of-words_model. Accessed on 2 September 2015.

[6] Skabar, A. and Abdalgader, K. "Clustering Sentence-Level Text Using a Novel Fuzzy Relational Clustering Algorithm", IEEE transactions on knowledge and data engineering, vol. 25, no. 1, 2013.

[7] C. Fellbaum, WordNet: An Electronic Lexical Database. MIT Press, 1998.

[8] P. Corsini, F. Lazzerini, and F. Marcelloni, "A New Fuzzy Relational Clustering Algorithm Based on the Fuzzy C-Means Algorithm," Soft Computing, vol. 9, pp. 439-447, 2005.

[9] H. Zha, "Generic Summarization and Keyphrase Extraction Using Mutual Reinforcement Principle and Sentence Clustering," Proc. 25th Ann. Int'l ACM SIGIR Conf. Research and Development in Information Retrieval, pp. 113-120, 2002.

[10] D. Wang, T. Li, S. Zhu, and C. Ding, "Multi-Document Summarization via Sentence-Level Semantic Analysis and Symmetric Matrix Factorization," Proc. 31st Ann. Int'l ACM SIGIR Conf. Research and Development in Information Retrieval, pp. 307-314, 2008.

[11] D. Lee and H. Seung, "Algorithms for Non-Negative Matrix Factorization," Advances in Neural Information Processing Systems, vol. 13, pp. 556-562, 2001.

[12] Y. Li, D. McLean, Z.A. Bandar, J.D. O'Shea, and K. Crockett, "Sentence Similarity Based on Semantic Nets and CorpusStatistics," IEEE Trans. Knowledge and Data Eng., vol. 8, no. 8, pp. 1138-1150, Aug. 2006.

[13] J.J. Jiang and D.W. Conrath, "Semantic Similarity Based on Corpus Statistics and Lexical Taxonomy,"Proc. 10th Int'l Conf. Research in Computational Linguistics,pp. 19-33, 1997.

[14] S. Brin and L. Page, "The Anatomy of a Large-Scale Hypertextual Web Search Engine," Computer Networks and ISDN Systems, vol. 30, pp. 107-117, 1998.

[15] [5] Wikipedia: the Free Encyclopedia. Wikimedia Foundation Inc. Updated 30 August 2015. 7.27 UTC. Encyclopedia online. Available from http://en.wikipedia.org/wiki/PageRank, accessed on 02 September, 2015.

[16] http://www.famousquotesandauthors.com,2012, accessed on 30 August, 2014.

[17] Wikipedia: the Free Encyclopedia. Wikimedia Foundation Inc. Updated 1 September 2015. 8.20 UTC. Encyclopedia online. Available from http://en.wikipedia.org/wiki/Entropy_(information_theory), accessed on 02 September, 2015.

[18] Wikipedia: the Free Encyclopedia. Wikimedia Foundation Inc. Updated 27 July 2015. 11.13 UTC. Encyclopedia online. Available from http://en.wikipedia.org/wiki/Precision_and_recall#F-measure, accessed on 02 September, 2015.

Performance Analysis for Detection of Breast Cancer Biomarker HER2 using a Double Gate FET Nano Biosensor

Mohsin Sajjad
Department of Electrical & Electronic Engineering
Bangladesh University of Engineering & Technology
Dhaka, Bangladesh
md.mohsinsajjad@gmail.com

Md. Raqibull Hasan and Arif Abdullah Samy
Department of Electrical & Electronic Engineering
Primeasia University
Dhaka, Bangladesh
rakib0803011@gmail.com

***Abstract*— This paper addresses the performance of a double gate field effect transistor (FET) based nano biosensor in detecting human epidermal growth factor receptor 2 (HER2) which is a key biomarker for detecting breast cancer. At first dimensions of different parameters of a double gate FET were set in order to enhance sensitivity. Then various parameters of HER2 protein were calculated. Various nano biosensor characteristics in terms of settling time, selectivity and sensitivity were simulated. The results demonstrate that the designed nano biosensor has significant prospects of detecting the target.**

Keywords*— *diffussion; hydrophobic; potentiometric; sensitivity.

I. Introduction

In the present world, breast cancer is one the most invasive cancers. It accounts for 16% of all female cancers and 22.9% of invasive cancers in women. 18.2% of all cancer deaths worldwide, including both males and females, are from breast cancer. Research suggests that breast cancers can be divided in four molecular subtypes according to hormone receptor expression (HR±) and/or epithelial cell of origin (luminal or basal). There are two HR+ breast cancers (Luminal A and Luminal B) and two HR- cancers (human epidermal growth factor receptor 2 (HER2)-enriched and basal-like) [1-2]. Gene-expression profiling is not currently standard clinical practice, but, for nearly a decade, testing for joint HR/HER2 status has been a routine part of treatment planning [3]. Breast cancers with HER2 gene amplification or HER2 protein overexpression are called HER2-positive in the pathology report. HER2-positive breast cancers tend to grow faster and are more likely to spread and come back compared to HER2-negative breast cancers [4].

The small size, improved solubility and multifunctionality of nanoelectronics have opened many new research avenues for scientists. Though a lot of research activity has been involved in developing biosensors for various purposes the time has come to bring this technology to the forefront and make it commercially available. Biological signaling mechanism categorizes the types of biosensors. These types are potentiometric detection, amperometric detection, mass detection etc. In this paper a potentiometric detection system is analyzed. Potentiometric biosensors are generally based on ion-selective electrodes (ISE) and ion-sensitive field effect transistors (ISFET) [5-6]. To detect biomolecules, however, ISFET should be immersed and operated in the electrolyte solution to immobilize biomolecules. Thus, it has been pointed out that biosensors based on ISFET showed unreliable operational behaviors, such as drift and hysteresis [7-8]. To overcome these problems a double gate FET biosensor is presented. A Si channel FET is straddled by double gates is demonstrated. The separated double gates allow independent voltage control for channel potential which allows to beat the fundamental Nernst limit and improve sensitivity [9].

II. Modeling of Biosensor

Figure 1 shows the proposed design of a Double Gate Field Effect Transistor based nano biosensor (DGFET). The channel is made of Si. The FET channel is doped with p-type material as our experimental biomarker contains positive charge when acidic solution is used [10]. The front or reference gate is submersed in the solution. It is to be noted that the electrode used in this FET must be faradic electrode. The solution (pH<7) may create an insulator on non-faradic electrode surface which will affect the charge flow.

There are two dielectrics. Top dielectric is the receptor surface. This surface needs to be hydro phobic surface. If hydro phobic surface is not used the surface will not be able to hold on the sample solution. Hydrophobic surface will create a spherical structure of the solution which will help to capture maximum target molecules. Below the drain and source there is a second dielectric whose oxide thickness is much bigger than the front oxide one in order to increase sensitivity. This phenomena will be discussed later. The response time required for minimum number of analyte molecules to be captured to activate the sensor is called the settling time. There is a fundamental limitation for settling time (t_s) for each sensor which is given by the following equation.

$$\rho_0 = N_s * t_s^{-(\frac{3-D_F}{2})} \quad (1)$$

N_s is the minimum number of analyte molecules to activate the sensor which depends on transduction process and ρ_0 is the density of analyte. D_F is the fractal dimension of the surface which is equal to 2 for this sensor.

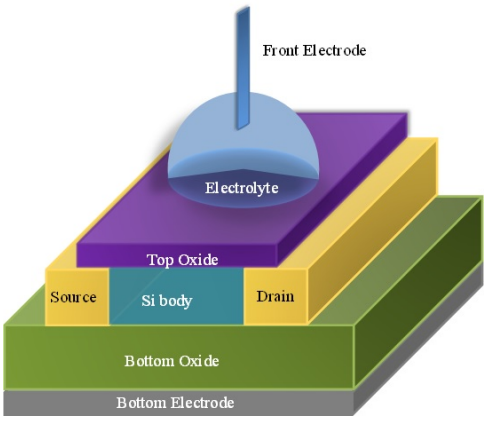

Fig. 1. Structure of DGFET biosensor.

$$N(t) = C_{D(t)}\rho_0 t \quad (2)$$

$$C_{D(t)} = \frac{D}{\sqrt{2Dt}} \quad (3)$$

The number of captured molecules ($N(t)$) in a given time can be calculated from the transient response of biosensor. $C_{D(t)}$ is the diffusion coefficient dependent capacitance. The sensitivity of the biosensor is defined by several ways. In this paper we have worked with the drain current and showed its response. The change in drain current (I_D) with respect to initial current (I_D) is normally called sensitivity (S).

$$S = \frac{\Delta I_D}{I_D} \quad (4)$$

$$S(t) = c_1 \ln(\rho_0) + c_2 \frac{(3-D_F)\ln(t)}{2} - c_3 \ln(I_0) + c_4 \quad (5)$$

c_1, c_2, c_3, c_4 are constants. Several experimental results have shown that sensitivity is non-linear, time dependent and depends on several aspects of the mechanism.

This sensitivity has logarithmic response to density of analyte. Sensitivity is further increased logarithmically with time but decreases logarithmically as we increase the buffer ion concentration. This complex response indicates that all of the parameters should be carefully chosen to design a successful biosensor [11]. One of the fundamental problems of the biosensor is the screening. For screening the salt concentration is generally about 100mM which is very high comparatively when we try to detect biomolecules at a range of µM to nM. From equation (5) we can easily understand how high salt concentration can reduce the sensitivity. There are several ways to beat the screening effect. One of the ways is amplification. This is why double gate is used. The drain current can be amplified by the bottom gate. Top gate and bottom gate produce two drain currents $I_{D,top}$ and $I_{D,bot}$ respectively.

$$I_{D,top} = \mu_1 C_{tox}(\frac{W}{L})V_{DS}V_{G,top} \quad (6)$$

$$I_{D,bot} = \mu_1 C_{box}(\frac{W}{L})V_{DS}V_{G,bot} \quad (7)$$

μ_1 is the carrier mobility, W and L are the channel width and length respectively. $V_{DS}$is the drain to source voltage. C_{tox} and C_{box} are the top and bottom dielectric capacitance respectively. $V_{G,top}$ and $V_{G,bot}$ are two gate voltages. Total drain current (I_D) is denoted by,

$$I_D = \frac{C_{tox}+C_{box}}{C_{tox}+C_{box}+C_{DL}}\nu \quad (8)$$

Q_{MOS} is the deposited charge on FET, ν is the charge velocity and Φ is the extra potential. Equation (8) shows that the total drain current (I_D) on FET operating in accumulation mode is dependent on top oxide capacitance (C_{tox}), bottom oxide capacitance (C_{box}) and capacitance associated with Debye length (C_{DL}). As capacitance is inversely proportional to thickness of oxide layer, in order to increase the sensitivity the bottom oxide thickness is made much bigger than the top oxide thickness. This phenomena helps to beat the Nernst Limit.

The biosensor needs to address two selectivity issues mainly. First one is the binding to wrong molecule. There will be a lot of parasite molecules in the analyte solution. Before the sensing process Polymerase Chain Reaction (PCR) can be used to amplify the number of target biomolecules. The second problem is binding in the empty space. The biosensor surface needs to be hydrophobic and the receptor density should be as much as possible. The signal-to-noise ratio (SNR) of the biosensor can be found by equation (11).

$$SNR = \frac{\sigma_T k_T \rho_T}{\sigma_p k_p \rho_p}\frac{r_T^2}{r_p^2}\frac{\theta}{\theta_{r,p}^{\infty}-\theta} \quad (11)$$

σ_T/σ_p denotes the signal transduction scheme. For example, it could be the ratio of electrostatic charge of the target and the parasitic molecule for electrical detection, or the ratio of the thickness of the target molecular layer to the parasitic molecule etc. k_T and k_p are the association constants of target and parasite molecules. ρ_T and ρ_p are the density of target and parasite molecules respectively. r_T and r_p are the radius surface coverage of each target and parasite molecules respectively. θ is the surface coverage for all target molecules. $\theta_{r,p}^{\infty}$ is the asymptotic surface coverage for a DRSA consisting of receptor conjugation followed by parasitic conjugation. As θ is directly proportional to the receptor density (N_0), the SNR is rapidly increased with higher receptor density [12].

III. HER2 Biomarker

HER2 overexpression and amplification has been linked to augmented cell proliferation, cell motility, tumor invasiveness, accelerated angiogenesis and reduced apoptosis. HER2 positive breast cancers are considered in the "intermediate or high histologic grade," absent of estrogen and progesterone receptors, while including positive lymph node metastases [13-14]. The structure of HER2 can be found in protein data bank. The accepted FASTA sequence of HER2 is given below [15]:

DIQMTQSPSS LSASVGDRVT ITCRASQDVN
TAVAWYQQKP GKAPKLLIYS ASFLYSGVPS
RFSGSRSGTD FTLTISSLQP EDFATYYCQQ
HYTTPPTFGQ GTKVEIKRTV AAPSVFIFPP
SDEQLKSGTA SVVCLLNNFY PREAKVQWKV
DNALQSGNSQ ESVTEQDSKD STYSLSSTLT
LSKADYEKHK VYACEVTHQG LSSPVTKSFN RGEC

The total number of sequence in 214 and the protein weighs 23.45 kilo Daltons. As the charge of the protein will be transduced into signal and the protein charge is associated with the pH of the solution. The pH vs charge relationship is

calculated using protein data bank calculator and is represented in figure 2. The isoelectric point (*pI*) is calculated using Henderson-Hasselbalch equation. The *pI* is found to be 7.70 approximately. This denotes that when pH level is below 7.70 then the protein contains positive charge and vice versa.

IV. Simulation and Results

The modelled DGFET has length and width of 1μm. The bottom oxide is taken 10 times thicker than the top oxide. The channel is a Si body having width of 40nm where the doping concentration is 1e19cm^{-2}**.** The sensor surface is assumed to be highly sticky. So the association and dissociation constant value are taken to be 3e06 and 1 respectively. The protein diffusion coefficient is associated with its size. The diffusion coefficient value for the selected protein is 1.11e06 cm^{2}s^{-1}. The experiment incubation time is set to 180min and temperature is set at 27^{0}C. The receptor density is 1e12 cm^{-2}.

The DGFET response over HER2 was simulated in online biosensor lab from nanohub.org. Figure 3 demonstrates the settling time changing with analyte concentration. The settling time is described in equation (1). It is also to be noted that the settling time increases with the minimum number of captured molecules is increased. But increment of settling time tends to saturate when higher no of molecules to be captured.

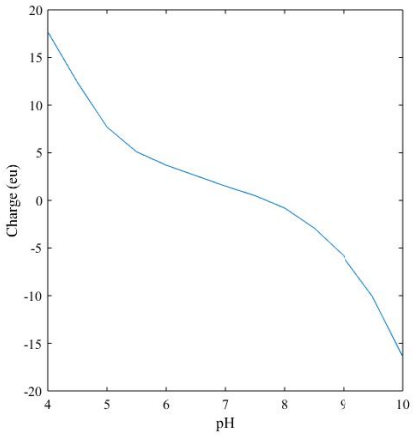

Fig. 2. HER2 charge at different pH level.

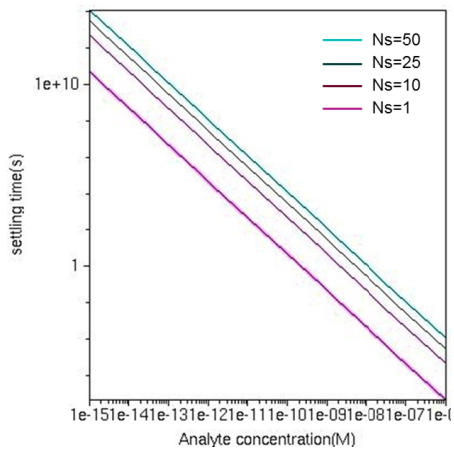

Fig. 3. Effect of analyte concentration on settling time.

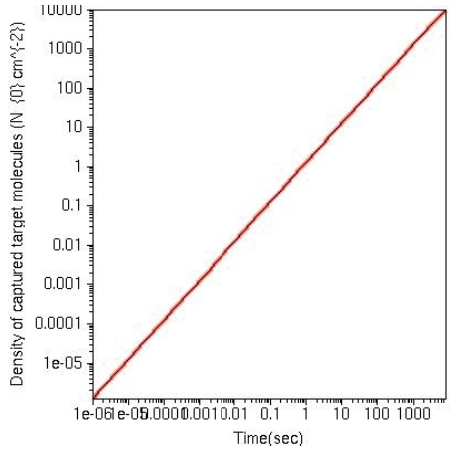

Fig. 4. Time dependency of density of captured molecules.

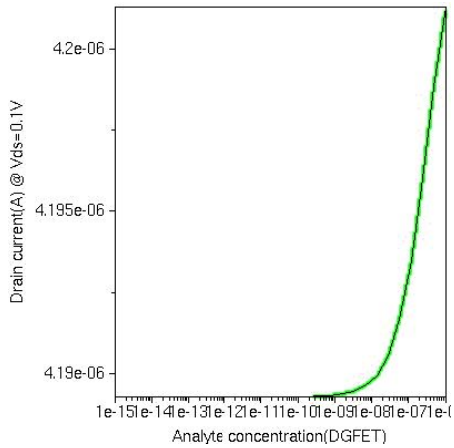

Fig. 5. Drain current response at different analyte concentrations.

The time dependent capture of target molecules is shown in figure 4. The starting time is accounted to be 1e-06sec. it is found that after 1000sec a significant density of captured molecules can be achieved. The sensitivity is assessed by the response in drain current of the FET. Figure 5 depicts the drain current response. A very insignificant response is found when analyte concentration is less than 1nM. The current increases exponentially with analyte concentration. But when the back gate voltage is introduced the response is amplified. From equation (5) we can understand that for a lower buffer ion concentration the drain current is increased with time. But at high concentration due to negative logarithmic effect the increment of current tends to saturate which is shown in figure 6. This is called the screening problem of biomolecule detection where high salt concentration is necessary. This effect can be reduced by using high frequency descreening.

The charge of the biomolecule varies with the pH. With the increase of pH the charge tend to change from positive to negative. So the drain current is also reduced for solution having high pH. Figure 7 clearly indicates that the solution should be acidic and pH level is set to 4 for the biosensor operation. For checking the selectivity it is assumed that the size of the parasite molecules is half of the target molecules. The concentration of parasite molecules is set to be 1μM which is higher than the target molecule concentration of 1nM and 1fM. The maximum surface coverage is 0.54. From figure 8 it

is indicated that SNR increases with the receptor density and if a target molecule is to be detected at 1fM range then the receptor density should be higher. But in reality it is very difficult to achieve receptor density much more than 1e12 cm^{-2}.

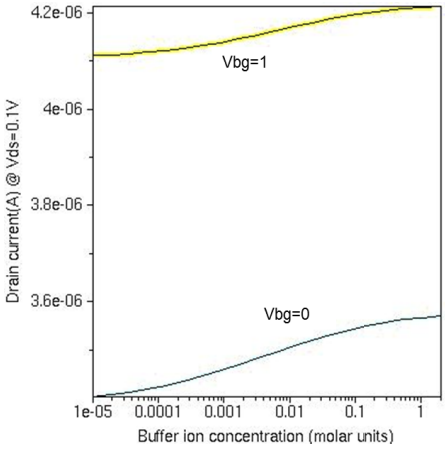

Fig. 6. The effect of buffer ion concentration on drain current.

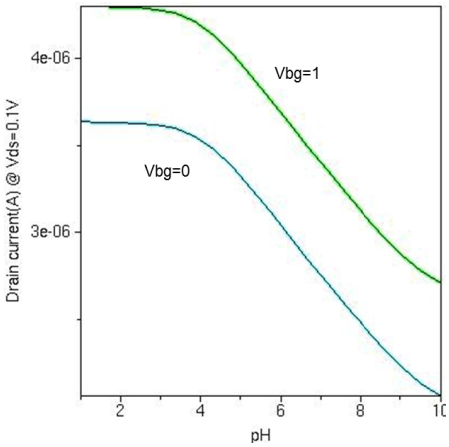

Fig. 7. The change in drain current over pH level.

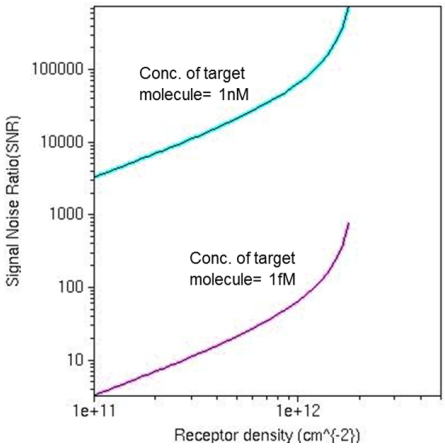

Fig. 8. SNR vs receptor density.

V. Conclusion

The simulated settling time and SNR results clearly indicate that it is possible to detect HER2 biomarker at a minimum concentration of 1nM. The biosensor sensitivity can also be enhanced by back voltage and increased buffer ion concentration. Another way of detection of target molecule can be done by varying the pH level of the solution and checking the difference in drain current. The DGFET biosensor model discussed above for detecting HER2 exhibits satisfactory performance. But several aspects like binding energy of the biomolecule or screening problem should be carefully examined in terms of fabrication of the sensor.

References

[1] W.F. Anderson, P.S. Rosenberg, A. Prat, C.M. Perou and M.E. Sherman, "How many etiological subtypes of breast cancer: two, three, four, or more?," J Natl Cancer Inst, vol. 106, August 2014.

[2] W.F. Anderson, S. Luo and N. Chatterjee, "Human epidermal growth factor receptor-2 and estrogen receptor expression, a demonstration project using the residual tissue repository of the Surveillance, Epidemiology, and End Results (SEER) program," Breast Cancer Res Treat, vol. 113, pp. 189–196, 2009.

[3] W.F. Anderson, P.S. Rosenberg and H.A. Katki, "Tracking and evaluating molecular tumor markers with cancer registry data: HER2 and breast cancer," J Natl Cancer Inst, vol. 106, May 2014.

[4] A.W. Kurian, K. Fish, S.J. Shema and C.A. Clarke, "Lifetime risks of specific breast cancer subtypes among women in four racial/ethnic groups," Breast Cancer Res., vol. 12, 2010.

[5] D.R. Thevenot, K. Toth, R.A. Durst and G.S. Wilson, "Electrochemical biosensors: recommended definitions and classification," Biosensors & Bioelectronics., vol.16, pp.121–131, 2001.

[6] J. Ding and W. Qin, "Potentiometric sensing of nuclease activities and oxidative damage of single stranded DNA using a polycation-sensitive membrane electrode," Biosensors and Bioelectronics., vol. 47, pp. 559–565, 2013.

[7] C. G. Jakobson, M. Feinsod and Y. Nemirovsky, "Low frequency noise and drift in ion sensitive field effect transistors," Sens. Actuators B Chem., vol. 68, no. 1–3, pp. 134–139, Aug. 2000.

[8] J. C. Chou and C. N. Hsiao, "The hysteresis and drift effect of hydrogenated amorphous silicon for ISFET," Sens. Actuators B Chem., vol. 66, no. 1–3, pp. 181–183, Jul. 2000.

[9] O. Knopfmacher, et al., "Nernst Limit in Dual-Gated Si-Nanowire FET Sensors,"Nano lett., vol. 10, pp. 2268–2274, 2010.

[10] Nair, R. Pradeep and A.A. Muhammad, "Design considerations of silicon nanowire biosensors." Electron Devices, IEEE Transactions, vol. 54, Issue 12, pp. 3400-3408, 2007.

[11] Baumgartner and Stefan, "Predictive simulations and optimization of nanowire field-effect PSA sensors including screening," Nanotechnology, vol. 24, no. 22, pp. 225-503, 2013.

[12] Nair, R. Pradeep and A.A. Muhammad, "Theory of"Selectivity of label-free nanobiosensors: A geometro-physical perspective." Journal of applied physics, vol. 107, no.6, pp. 064701-064701, 2010.

[13] N.E. Hynes, H.A. Lane, "ERBB receptors and cancer: The complexity of targeted inhibitors," Nat. Reviews Cancer, vol. 5, pp. 341-354, May 2005.

[14] A.W. Burgess, H.S. Cho, C. Eigenbrot, K.M. Ferguson and S. Yokoyama, "An open-and-shut case? Recent insights into the activation of EGF/ErbB receptors," Molecular cell, vol. 12, pp. 541-552, Sep. 2003.

[15] H.S. Cho, et al., "Structure of the extracellular region of HER2 alone and in complex with the Herceptin," Fab. Nature, vol. 421, pp. 256-260, 2003.

Helping Software Developers through Offline Repository Based API Searching in Data Mining Integrated Environment

Md. Ratul Uddin Ashraf[*], Anujoy Das[*], Ziaur Rahman[*], Ali Newaz Bahar[*], Husne Ara Rubaiyeat[γ]

[*] *Department of Information and Communication Technology,* [γ]*Department of Computer Science*

[*] *Mawlana Bhashani Science and Technology University, Tangail-1902,* [γ]*National University, Gazipur-1704*

Mail: ratulshourov01@gmail.com, anujoydas@gmail.com, zia@iut-dhaka.edu, bahar_mitdu@yahoo.com, rubaiyeat@yahoo.com

***Abstract*—Software development is getting changed so rapidly. It will be highly benefited if we can accelerate software development process by guiding developers. Appropriate guidelines and accurate recommendations to developers during development process can reduce software development expenses, as well as can save valuable times of developers. There are a number of approaches to speed up the software development process. It can be done through code assistance tools that help developers by recommending relevant items from searching particular repository of Application Programming Interface (API). Some approaches are based on online searching that have some drawbacks due to request and response latency as it has to deal with the extra-large files in a server. Developers generally uses previously completed resources as well as libraries or frameworks to generate relevant snippets which are supplied by the referral repository of APIs. Developers find it hard to choose the appropriate methods as there are thousands of methods in which some are not properly documented. In this paper we have proposed a concept and its respective framework to guide developers that suggests relevant API methods from an offline mined repository. From the investigation we made, we can say that our approach works much better than some of the existing approaches.**

Keywords—Application Programming Inteface (API), Offline Repository, ORBAS, Data Mining Integrated Environment (DMIE).

I. INTRODUCTION

Software development processes for a system is basically done by writing a program based on specific design specification. Nowadays it can be done by using various techniques. To do this development process developers in the software industries generally creates new methods or modifies existing ones or reuses previously defined methods. One of the processes to develop software is the reuse of existing libraries and frameworks. Developers can be highly benefited if they get appropriate guidelines and accurate recommendations. It can decrease development cost and can save valuable time. Application Programming Interface (API) is a process to search relevant items from an existing repository. This process is widely used all over the world. Some approaches of these API search processes are based on online searching. Developers usually searches for API usage pattern using online repositories provided by different tools.

General code search engines often deals with the extra-large files. These extra-large files often contain a large number of API methods. Developers find it very difficult to choose the appropriate API methods to use as there are also duplicate methods. The API methods returned by the search engines are not mined so relevant data cannot be displayed. As the database of the search engines contains a large amount of data; it takes a long time to find appropriate methods. The online search processes for API methods are fully dependent on the server; as it is fully internet based it takes more time to generate the entire API methods thus making it a time consuming process. Normal API library or framework written in object oriented languages and it contains a huge number of methods and classes. If the API methods and classes do not have the meaningful name sometimes even experienced programmers often face a lot of problems. The API methods returned by the search engines are not often well documented. Developers find it challenging to use the most effective and appropriate methods.

To solve these problems we have proposed ORBAS (Offline Repository Based API Searching) thatis an offline repository that contains various API attributes. ORBAS mines API pattern usage methods from the innovative sequences of API in source code. The mined patterns contain less redundant patterns so that the developers cannot find the similar patterns repeatedly. The high coverage usage of API methods should be returned by the patterns to ensure a beneficial achievement to the developers.

In this paper we first plan to make a query in the repository for searching methods. Then the repository returns the associated source files of the matched inquiries. After that there is a code analyzer which extracts API methods from the source files. In the paper we have propose PMD [1] source code analyzer which extracts the API methods from the source code even if the source code is not compilable. The methods are then clustered into groups for mining. Then mining is implemented on the clusters to produce frequent closed sequence. We propose the BIDE [2] algorithm for mining frequently closed API usage patterns. We have again used a clustering technique in the frequent closed sequences. Thus two-step clustering techniques are implemented before and after the BIDE algorithm to produce more accurate usage patterns. Finally the closed API usage clusters are then produced and the related API usage methods are

recommended to the developers. We have come to see that after following this approach ours are more efficient than some of the exiting approach to guide developers for getting API usage patterns.

II. Background and Related works

There exist a number of API usage pattern search theories or tools to find out useful API patterns from source code. Some of these are MAPO[3], MAC[4], ESDP[5], Hipikat[6], ParseWeb[7] etc. Often this search tools are based on online code search repositories such as Koders[8] and Google code search[9]. These code search engines generally evaluate code snippets containing keywords of API methods. Strathcoma[12] is a code snippet recommender, which finds out a set of code snippets by matching the structure of the codes. MAPO is a tool which mines API usage patterns and uses mined patterns for recommending code snippets. MAPO mines API usage pattern which have sequential information among the method calls. But the sequences patterns are not clustered in MAPO. ParseWeb accepts queries from the programmer and generates code samples based on the object type of the source and destination. UP-miner is also a mining tool for mining closed sequences returned from the API methods. It uses two-step clustering technique to find out frequently closed sequences. But it does not use a code analyzer to extract source files from the given result provided by search engines based the programmer query.

Unlike many related works, we have developed ORBAS based on the mining algorithm to mine API methods and a two-step clustering technique to produce frequently closed sequences. As our process searches an offline repository we aim to make it a time consuming procedure.

III. Framework

To mine API usage patterns from an offline based repository we have developed a framework based on the mining and clustering of frequent closed sequences acquired from the source files which are resulted from the query performed in the repository. There are five major components in the framework: an offline repository, a code analyzer, sequence miner, sequence cluster and recommender.The implementation of ORBAS framework is given here. The total procedure works as illustrated in Fig. 1.

Step-1: In the ORBAS framework there is an offline repository in which programmer performs a query.

Step-2: A set of source code is returned from which the code analyzer extracts API methods.

Step-3: A two-step clustering technique is performed before and after mining API sequences.

Step-4: The best API usage cluster is produced and the required methods are recommended to the programmers.

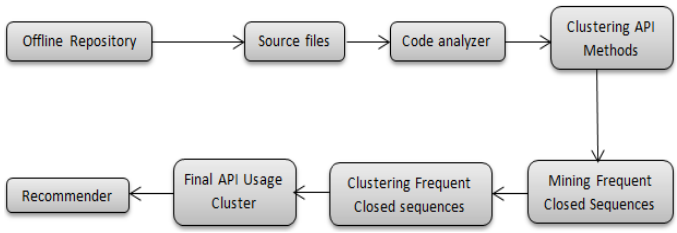

Fig. 1.An overview of ORBAS framework.

IV. Working Approach

A. *Offline repository:*

We have developed an offline repository in which different API methods are being inserted. The repository is organized by using a XML document to store API methods. The repository consists of sections such as search, update and delete. In the search section API methods can be searched by providing the method name. The update section makes necessary steps to add a new API method in the repository. It provides the insertion of methods. The delete section can remove API methods from the repository.

B. *Source files:*

As our framework is based on offline repository so the source files are collected directly from the repository based on the query implemented in the repositories. The repository provides the API methods which matches the input query. If the input method matches with the API methods stored in the repository, the complete source files of the methods are returned by the query.

C. *Code analyzer:*

Code analyzer helps us to extract the API methods from the source files. PMD [1] is a source code analyzer which does not need compilable source files for extracting API methods. PMD search outs common programming flaws like unused variables, empty catch blocks, unnecessary object creations etc. The code analyzer extracts a list of methods for each source files. This is done by collecting class name and full package name for each method. Based on the receiver object name we track the field declarations and local declarations to know the class name of the method calls. For the case of the classes which are exported in the import statement; we keep tracks of import statements to get the full package name of these classes.

D. *Clustering API methods:*

The method sequences returned by the source code analyzer can be two types. One is the frequently used API patterns which have large threshold support and another is less frequently used patterns which has minimum threshold. Clustering technique increases the chance of less frequently used sequence patterns to mine out before mining the frequently closed sequence. *SeqSim* [10] is an n-gram based technique which computes the similarity of two different sequences.

The set G(X) is defined as the n-gram set for a sequence $S(s_1 s_2 \ldots s_n)$ as a collection of unigrams, bi-grams, … , n-gram of *S*:

$(S) = \{s_1, s_2 \ldots, s_n, s_1s_2, s_2s_3 \ldots, s_{n-1}s_n, \ldots, s_1s_2..s_{n-1}, s_2s_3..s_{n-1}s_n, s_1s_2..s_{n-1}s_n\}$

Two situations are considered to evaluate a similarity between two sequences:

i) Sequences are similar if they both equally have a large number of API methods between their representative n-gram sets.

ii) Sequences are similar if they both equally have common subsequences.

If two sequences are s_1 and s_2 then the similarities are:

$$\text{SeqSim}(s_1, s_2) = \frac{\sum i \text{ Weight } (gi\cap)}{\sum i \text{ Weight } (giU)}$$

Where $g^i_\cap$ € $G_\cap = G(s_1) \cap G(s_2)$, g^i_U€ $G_U = G(s_1) \text{ U } G(s_2)$, weight $(g^i_\cap)$ is equal to the length of $g^i_\cap$.

As an example, given s_1 = abc and s_2 = cab, then we will have

$G_\cap$ = {a,b,c,ab}, G_U = {a,b,c,ab,bc,ca,abc,cab} andWeight(ab) = 1, Weight(ab) = 2, SeqSim(s_1,s_2) = 0.33 .

Based on the result of SeqSim, we cluster the API sequences. The remoteness of two clusters is considered as the highest value of remoteness between a pair of items in these two clusters.

E. Mining frequent closed sequence:

BIDE algorithm [11] is used to recognize the frequent API usages for mining frequent closed sequences. A sequence s_1 is a sub-sequence of s_2 and s_2 is a super-sequence of s_1 when s_1 is contained in s_2 and s is a frequent sequence. As there are no appropriate super sequences of s with the same support then s is a frequent sequence in a set of sequence if sup(s) ≥ min_sup. Sup(s) is called the support of sequence which is derived by the ratio of the sequences that are super sequences of s in the sequence set. Min_sup is the minimum threshold support [2].To prepare the frequent closed sequences for the cluster, BIDE algorithm is applied to each cluster originated from the procedure described in the previous section. For example, let us assume there are three sequences is a cluster which are xy, xyz, xyt. If the minimum threshold support is 0.5, BIDE algorithm gives the result of frequent closed sequences xy, where other sequence mining algorithms will provide the result x, y and xy. If xy is frequent then it can be easily noted that x and y will also be frequent. Thus x and y does not need to be enlisted. BIDE algorithm provides the sequences in which there are subsequences of similar support.

F. Clustering frequent closed sequences:

The API method sequences that are clustered using the proposed SeqSim technique in previous section; can be of two types. One is the sequences which are not similar to each other and another is the sequences which are similar. The sequences that are not similar are partitions into clusters. But the sequences that are similar can produce redundancy in the final API usage patterns. To solve this problem, another clustering is performed for the similar sequences. In this process the resulting clusters are considered as usage patterns. For example, we consider two frequent closed sequence xyz and zy which are mined from two distinct clusters. These two sequences are grouped together and shown as xyz after performing the clustering technique. The total number of superfluous sequences can also be removed using the technique. By applying the SeqSim technique; we can measure similarities between two frequent closed sequences.

G. Recommender:

After performing the clustering techniques the frequent closed sequences are produced and the results are shown to the programmers. The programmers can bypass the process of checking code sequences one by one as the recommender returns the mined patterns as an index of sequences. The best API patterns are shown on the top of the index thus providing the programmers a suggestion to select which one is to be used.

V. EVALUATION

A. Environmental Setup:

The implementation of our work requires the usage of severe environmental setups. ORBAS, MAPO and Koders are used as search engine. To produce a graph based result we have implemented our result data in MATLAB. The system platforms in which we developed our framework contain core-i5 processor (2.30 GHz), RAM of 4GB and 3G network.

B. Time Response Evaluation:

Our work in ORBAS is compared to the existing MAPO and Koders search engine for evaluating time response. For example we have consideredWebRequest.create as sequence 1, then we have considered another sequence HTTPWebRequest.getResponse as sequence 2 for both Table I and Table II and so on. By inputting these sequences we generate an output based on the time response of the search tools which is shown in Table I.

TABLE I. TIME RESPONSE EVALUATION

Squ. No.	API Name	MAPO[3]	Koders[8]	ORBAS
1	WebRequest.create	5	7	3
2	HTTPWebRequest. getResponse	7	9	2
3	HTTPWebRequest.create	6	7	4
4	SQLConnection.open	3	5	1
5	SQLDatabase.read	4	6	2
6	SQLConnection.close	2	5	1
7	SQLCommand. parametersAdd	4	8	2
8	SQLDataAdapter.Bill	5	7	1
9	HTTPResponse.setContent	6	5	3
10	HTTPResponse.write	7	5	3

Fig. 2 shows the graphical representation of the response time from the data of Table I. The graph shows result analysis of the time response evaluation of API sequences among ORBAS, MAPO and Koders. The graph is designed in MATLAB by inserting the values of Table I. From the graph it is clear that the time responses for each method are lesser in ORBAS than MAPO and Koders.

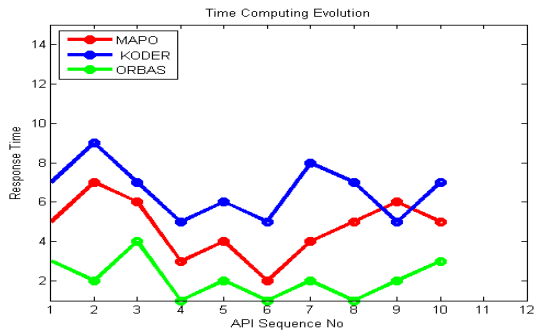

Fig. 2. Response time with different API sequences.

C. Performance Evaluation:

By inputting the sequences into different search engines we have evaluated the performance. Table II shows the performance evaluation based on the methods returned by each search tools. It is shown that ORBAS returns a few number of effective and useful methods compared to MAPO and Koders.

TABLE II. PERFORMANCE EVALUATION

Squ. no.	API Name	MAPO [3]	Koders [8]	ORBAS
1	WebRequest.create	71	110	8
2	HTTPWebRequest.Get Response	58	95	7
3	HTTPWebRequest.cre ate	22	55	4
4	SQLConnection.open	94	105	12
5	SQLDataReader.Read	67	82	10
6	SQLConnection.close	44	50	2
7	SQLCommad.paramet ersAdd	56	70	8
8	SQLDataAdapter.Bill	19	25	3
9	HTTPResponse.setcon tent	8	14	2
10	HTTPResponse.write	5	9	1

Fig. 3 shows the graphical representation of the number of methods returned by per API sequence. The graph shows the result analysis of the number of methods returned for ORBAS, MAPO and Koders. The graph is designed in MATLAB by inserting the data of Table II. It is clear from the graph that ORBAS returns a few but useful API methods than MAPO and Koders.

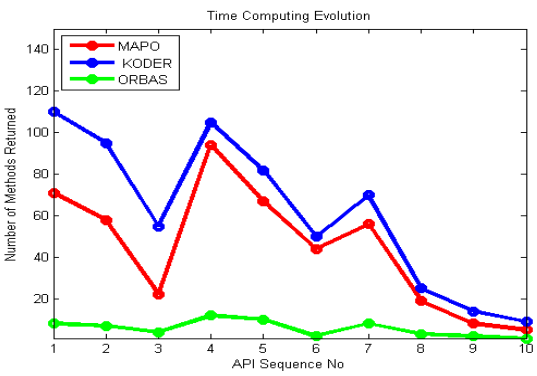

Fig. 3.Methods return from different API sequences.

VI. CONCLUSION AND FUTURE WORK

With a view to helping developers to understand API usages and client code more nicely we have developed a framework called ORBAS which is a supporting tool for mining API usages from anoffline repository. Our experimental results show that ORBAS generates useful API pattern than the existing tools. In future we will try to focus on automatic code generation based on the returned API patterns. Then these automatic generated codes can easily be inserted into developer's code. Our framework ORBAS may require some more data mining techniques. We further need to investigate to confirm whether the selected technique is the best or not. For the purpose of mining API usage patterns we plan to apply other clustering techniques such as k-means clustering. We also have a plan to apply other partial order miner in the mining stage. We plan to include other features such as class structure for clustering. We plan to find out the weights and thresholds value. We will concern other approach and technique and compare with our current process. In our working procedure we do not see the quality of the mined pattern directly. Usually most libraries do not provide usage pattern, there islacking in the field of the usage pattern. We must concern to experiment the quality of the usage pattern. Our framework approach must be applicable to many other object oriented languages. We will try to adapt our supporting tool in other large-scale databases. In our approach we have extracted API usages only for the API client code. In the future we will try to extract to the client code and the implementation code both.

REFERENCES

[1] 'PMD', GitHub. [Online]. Available: https://pmd.github.io/ [Accessed: 4-Sep-2015].

[2] J.Wang and J. Han. "BIDE: efficient mining of frequent closed sequences," In Proc. ICDE 2004, pp. 79.

[3] H. Zhong, T. Xie, L. Zhang, J. Pei, H. Mei. "MAPO: mining and recommending API usage patterns," In Proc. ECOOP 2009, pp. 318-343.

[4] SK. Hsu and SJ. Lin. "MACs: Mining API code snippets for code resuse," Elsvier 2011.

[5] Z. Rahman and K. Hasan. "Enhancing Software Development Process using Data Mining Integrated Environment," Masters Thesis of Islamic University of Technology, 16-80, 2015,

[6] A. Michail. "Data mining library reuse patterns usinggeneralized association rules," In Proc. 22nd InternationalConference on Software Engineering, pages 167–176, 2000.

[7] S.Thummalapenta, T. Xie. "PARSEWeb: a programmer assistant for reusing open source code on the web," In Proc. ASE 2007.

[8] 'Koders source code search engine', [Online]. https://www.blackducksoftware.com/news/releases/2009-09-09 [Accessed: 4-Sep-2015].

[9] 'Google code search', [Online].https://code.google.com/p/chromium/codesearch [Accessed: 4-Sep-2015].

[10] J. Wang, Y. Dang, H Zhang, K. Chen, T.Xie. "Mining Succinct and High-Coverage API Usage Patterns From Source Code," In conference on Mining-dl.acm.org, 2013.

[11] P.L. Buse and W. Weimer. "Synthesizing API Usage Examples," In Proc. ICSE, pp 782-792, 2012.

[12] R.Holmes and G. C. Murphy. "Using structural context to recommend source code examples," In Proc. ICSE, 2005.

An Experimental Study of Stylometry in Bangla Literature

Prapti Das, Rishmita Tasmim, Sabir Ismail
Department of Computer Science and Engineering
Shahjalal University of Science & Technology
Sylhet-3114, Bangladesh.
prapti.das.06@gmail.com, rishmita.sustcse015@gmail.com,sabir-cse@sust.edu

Abstract— **Every writer has a different style of writing of their own. By analyzing various kinds of features we can identify and specify some characteristics in a writer's writing which is known as stylogenetics. In this paper we gathered Bangla blogs written by four different Bangladeshi writers. Using machine learning methods we tried to identify special Stylometry features in their writing style. We analyzed various features in their writings, for example, percentage of unique words, word length, sentence length, and frequency of some parts of speech, number of suffix, frequency of first word, second word, second last word and last word of a sentence, counting average number of question marks per document, frequency of word by its position in a sentence etc. We gathered statistical data from analyzing those features and tried to find the variance among these writers using the statistical data.**

Keywords— stylogenetics, stylometry, machine learning, unique word, word length, sentence length, parts of speech

I. INTRODUCTION

Now-a-days language technology has reached to a different level of art. This enables the systematic study of the variation of linguistic properties in texts like author detection, find time period of the author, genre of writing, gender of the author etc. In short it helps to detect the characteristic and personality of the author.

Stylogenetics is clustering-based stylistic analysis of literary corpora [1]. It is a way of analyzing written texts to learn about the writer. Some features are often included unconsciously by the writer, for example gender, age, geographic location of the writer, personality characteristics, etc. A writer may use two specific consecutive words most frequently, may start and end a sentence with specific parts of speech, may write using a specific tense most of the time etc. These are some of the features that can be used to identify a writer.

Stylogenetics helps to detect who is the actual author of a specific writing and may assist in identifying fraudulent writing or in cases where multiple authors claim the ownership of a particular writing. Stylogenetics will analyze the writing and find a specific pattern or characteristic of that writing. Through which we can detect the original author.

Stylogenetics is a new area of research in the field of Bangla literature. Researchers in the past have worked with English literature, particularly with worked famous English writers like Shakespeare, Jane Austen, Charles Dickens etc.

However, there has not been any analysis on Bengali writers. There are many talented and skillful writers in our country and we often find interesting style and pattern in their writings. By analyzing their writing we can distinguish among the characteristics and features of individual writers.

Bangla is our mother tongue and Bangla literature is very rich and famous all around the world, which prompted us to initiate the first stylogenetics research in this area.

In this paper we investigated on the writings of four different Bangladeshi writers namely AH, EZ, MZI, SS (Due to Copyright Protection original name of the writers are not used in this paper).The reason behind choosing these four specific writers is the availability and popularity of their writings. We collected the blogs in a random way. A writer may write on a wide range of topics, for example, political issues, educational infrastructure, economical development, critics/novel etc. In this paper, we tried to identify the specific topic used most frequently by a writer.

Through our analysis we found some features that proved to be important to detect an author. But we did not find any absolute way of author detection. So our end-goal is to find a way which can identify an author perfectly.

The methodology we propose is to work with features like unique words used by an author, word length, sentence length which means number of words used in a sentence, number of parts of speech like conjunction and pronoun, number of question mark etc. There are several other possible features, for example, use of punctuations, use of stop words, use of simple/complex/compound sentences etc, which we plan to incorporate into our study in the future. Since in Bangla literature lexical and morphological analyzer is not rich, we could not work with some small details yet.

II. RELATED WORKS

Stylogenetics is the statistical analysis of variations in literary style between one writer or genre and another. Stylogenetics analyzes written texts to learn about the author. In various papers they worked with different features for the purpose of analysis.

Ramyaa et. al. [6] investigated some features like type-

token ratio, mean word length, mean sentence length, standard deviation of sentence length, mean paragraph length, number of commas, question marks, exclamation marks per thousand tokens.

Daelemans et. al [1] adopted a methodology from topic detection research, which included more complex features than the simple lexical features suggested by traditional approaches. They used authors or group of authors as a prediction of class, with clustering methods to indicate the differences and similarities between authors.

On the basis of the stylistic genome of authors, they tried to cluster them into closely related and meaningful groups. They also reported on experiments with a literary corpus of five million words consisting of representative samples of female and male authors.

III. OUR METHODOLOGY

We collected around 50 blogs each written by four different Bangladeshi writers for this study. The features we used and the detail experimental setup are described below.

A. Features Used :

1) Word frequency:

Word frequency means how many times a word was used in a writers writing. We counted frequency of both one word and two consecutive words. This is used as a feature to find the most frequent words used by a writer.

2) Word length:

The distributions of words of different length have been used as a feature. We calculated the frequency of words of different length.

3) Sentence length:

The number of words present in a sentence is used as a feature.

4) Type-token ratio:

The type-token ratio is *N/V*, where *V* is representing the size of the vocabulary of the sample, and *N* is representing the number of unique words. It is a measure indicating the vocabulary richness of an author.

5) Distribution of parts-of-speech:

Syntax-based features are not under the conscious control of the author and therefore it is considered as a feature. We mainly calculated the number of conjunction and pronoun in the texts.

6) Position specific word frequency:

We counted the frequency of words in first, second, last, second last and other random positions.

7) Writer specific unique words:

We created a list of words for each writer containing words which are mainly used by that particular writer. If another writer uses any of those words more than five times, then those words were not be considered as a unique word for that specific writer.

8) Previous and following words of a unique word:

We collected the previous and following words in a sentence for every unique word used by a writer.

9) Frequency of words related with "আমি", "করা","পারা" :

When we considered the word "আমি" we selected words like, আমি, আমরা, আমার, আমাদের etc. For "করা" we selected করা, করর, কররনা etc. And for "পারা" we selected পারা, পারর, পাররনা, etc.

B. Experimental Study:

1) Calculating Word Frequency:

A writer may frequently use some specific words and by calculating frequency of those words we can rank them as words most frequently used by a writer.

2) Frequency of one word:

We have implemented a program using java programming language to calculate the frequency of every word. Fig. 1 shows the words most frequently used by the four writers.

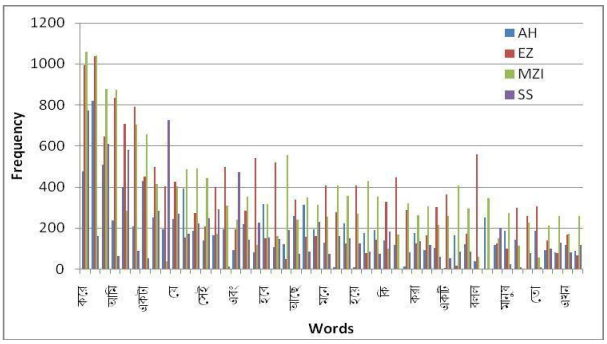

Figure 1. One word frequency of four writers.

As shown in Fig. 1 the words 'বলল' were most frequently used by EZ compared to other writers. So we can say that this can be used as a significant feature in case of EZ.

3) Frequency of two consecutive words:

Writers often use two specific words consecutively. We counted the frequency of two consecutive words using another program implemented in java similar to the program used above. Fig. 2 shows the most frequent two consecutive words used by the four writers.

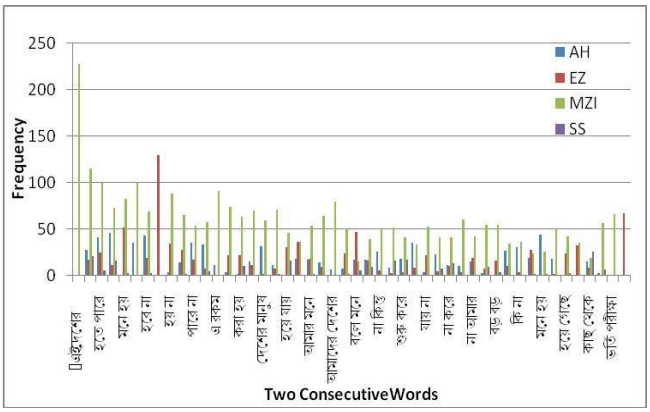

Figure 2. Two consecutive word frequency of four writers.

As shown in Fig. 2 the pair 'এই দেশের' were used in a higher

frequency by MZI than the others. The similar differences are shown in case of other writers.

4) Word Length:

Longer words are traditionally associated with more formal style, whereas shorter words are a typical feature of informal spoken language. Shorter words are also a feature of the modern day writes.

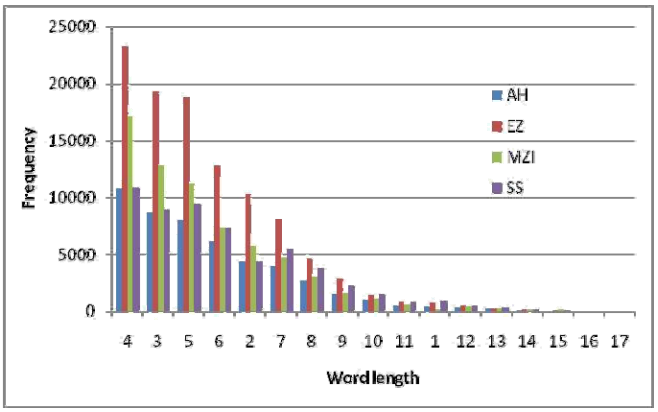

Figure 3. Frequency of words with different lengths.

As shown in Fig. 3 all the writers prefer to use shorter words more frequently than longer words most noticeably the writer EZ.

5) Sentence Length:

While shorter sentences are more indicative of spoken language, longer sentences indicate formal writing. Fig. 4 shows the usage of shorter sentences in a high frequency in case of all four writers.

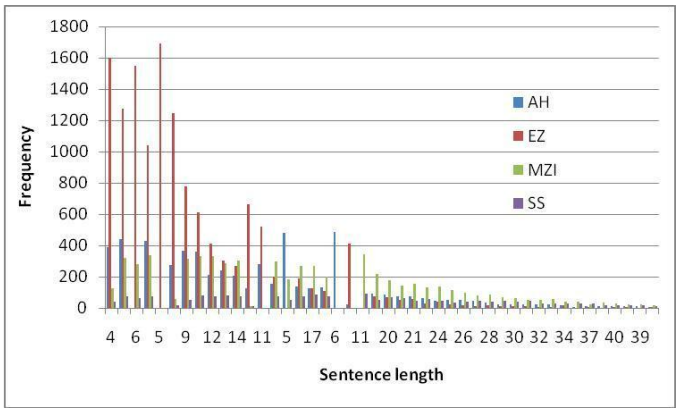

Figure 4. Frequency of sentences with different length.

As shown in Fig. 4 shorter sentences were used most frequently by EZ, while longer sentences were used in a higher frequency in case of MZI.

6) Type-token ratio**:**

The ratio of number of unique words and total number of words present in a document.

$$\text{Type-token ratio} = N/V, \qquad (1)$$

Here, N= number of unique words, V= Total words

Type-token ratio helps to find the richness of the vocabulary of a text. The writer that has the larger ratio has a richer vocabulary. Fig. 5 shows a pie-chart of the type-token ratio of all four writers.

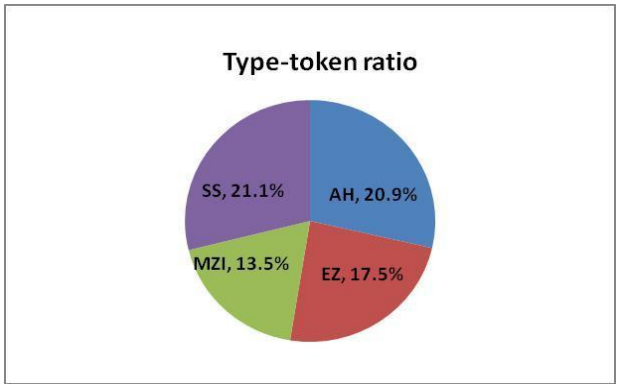

Figure 5. Type-token ratio of four writers.

The pie-chart above shows that SS and AH has higher type-token ratio compared to MZI and EZ. SS has highest type-token ratio, while MZI has the lowest ratio.

7) Distribution of parts-of-speech**:**

As part of identifying the distribution of parts-of-speech, we calculated the number of "conjunction" and "pronoun" in the documents.

Frequency of conjunction indicate continuity in someone's writing. On the other hand frequency of pronoun is indicative of particular pattern or style in writing.

Fig. 6 below shows the comparison of average number of conjunction and pronoun used per document by each writer.

It shows that average number of pronoun used by AH is higher than the others and in case of average number of conjunction is higher for EZ.

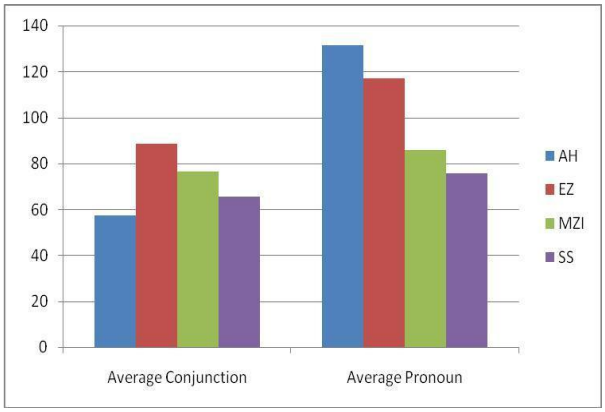

Figure 6. Average number of "Conjunction" & "Pronoun" per document.

8) Position wise word frequency:

Same words can be used in a different position in a sentence by different writers.

9) Writer wise unique words:

These words are especially used by one particular writer. These can be considered as recognizable words for a writer, which indicates the type or category of the text. In our analysis we found some recognizable words of three of the four writers.

In case of EZ, the "Recognizable words" are using different "Names."

Fig. 7 shows the frequency of recognizable words used by EZ comparing to other three writers.

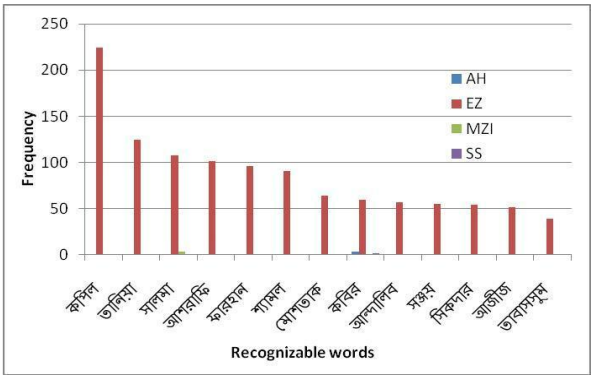

Figure 7. Comparison of "Recognizable words" used by EZ with others.

In case of MZI, the recognizable words are "Educational Words".

Fig. 8 shows the frequency of "Recognizable words" used by MZI comparing to other three writers.

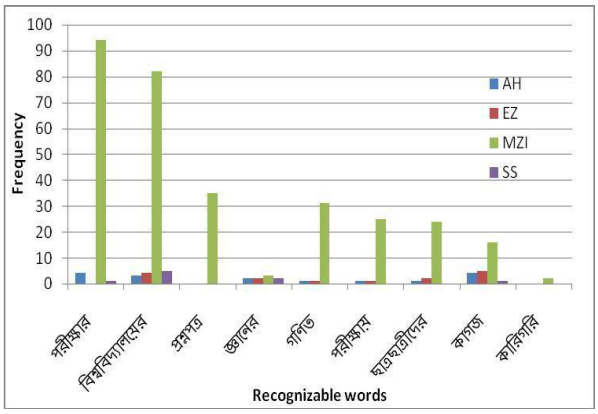

Figure 8. Comparison of "Recognizable words" used by MZI with others.

In case of SS the "Recognizable words" are "Political Words".

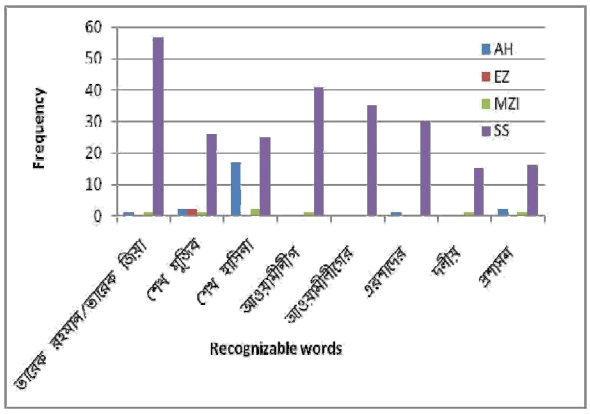

Figure 9. Comparison of "Recognizable words" used by SS with others.

10) Previous and Following words of a unique word:

There might be several words that are used frequently by all four writers. But analyzing the previous and following we can find some difference which could be an important feature.

11) Frequency of words related with "আমি", "করা", "পারা":

If the usage of words related with "আমি" is high in someone's writing, it can indicate that he is more likely to write in first person.

Fig. 10 shows the comparison of using words related with "আমি", "করা", "পারা" among four writers.

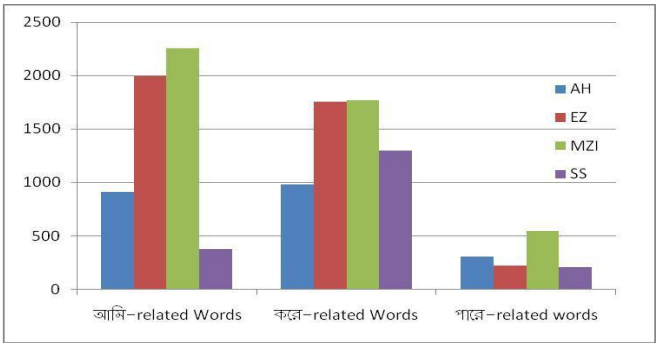

Figure 10. Usage of words related with "আমি", "করা" and "পারা".

We collected training data from these feature analysis. Then we compared the data with some random test data using statistical and machine learning approaches.

A. Standard Deviation:

It is a measure that is used to quantify the amount of variation or dispersion of a set of data values.

We counted the average number of conjunction per document for each writer from our training data. We did the same for test data. Then we calculated the standard deviation between a test data and each of the four writers' training data, e.g. we have test_data_1 and training data of four writers- AH, EZ, MZI and SS. If test_data_1 has the lowest standard deviation with training data of EZ, this indicates that test_data_1 might be the writing of EZ. Fig. 11 shows the standard deviation between test data and training data for average number of conjunction.

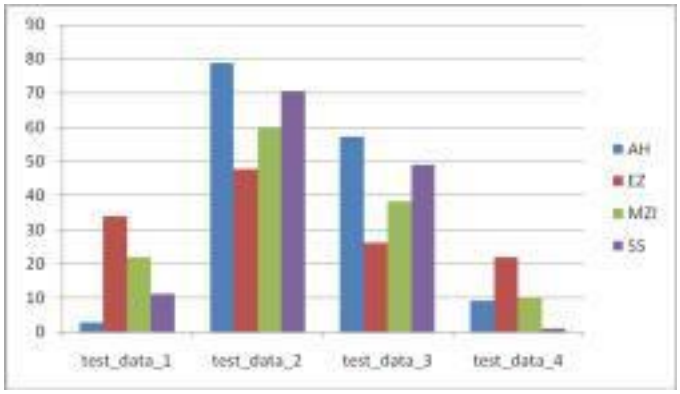

Figure 11. Standard Deviation between "Test data" & "Training data" for average number of "Conjunction".

We applied the same approach for average number of Pronoun.

Fig. 12 shows the standard deviation between test data and training data for average number of pronoun.

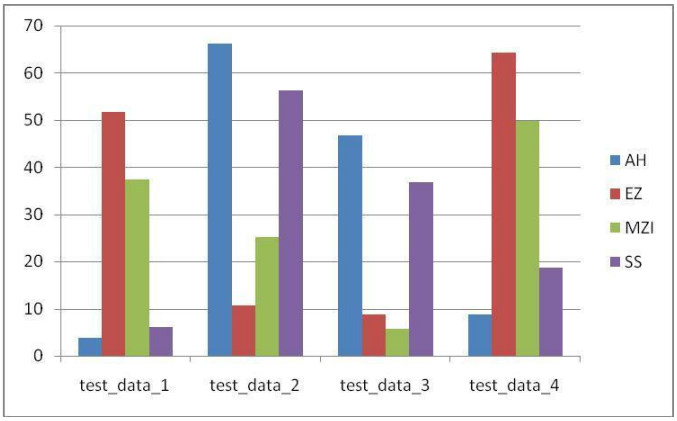

Figure 12. Standard Deviation between "Test data" & "Training data" for average number of "Pronoun".

B. Jaccard Similarity:

Jaccard Similarity is used to find similarity between two data sets. We applied this method for the feature writer wise unique word. We created a vector space model for the training data of unique words of each of the four writers and also for test data. Then we calculated the Jaccard similarity between test and training data, e.g. if test_data_1 has highest similarity value with AH, it indicates test_data_1 is most likely to be written by AH. Fig. 13 shows the Jaccard Similarity between test data and training data for writer wise unique words.

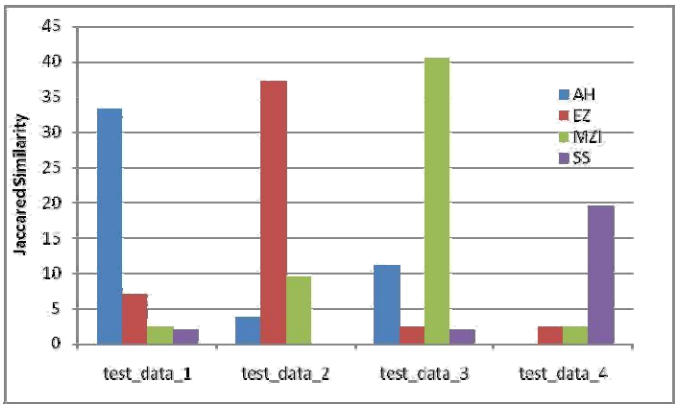

Figure 13. Jaccard Similarity between test data and training data for writer wise unique words.

IV. CONCLUSION

Stylogenetics provides an interesting venue for motivating and demonstrating many standard multivariate statistical techniques. This can be very useful for exploring and analyzing literary data. This paper attempts to recognize different authors based on their style of writing. As our first approach in this paper we analyzed twelve features according to the style of Bangla literature. Both standard deviation and Jaccard similarity can be one of the approaches to find some significant Stylometric features of a writer.

There have been no previous works on Stylometry for Bangla literature. Machine learning methods like Cosine similarity or Clustering can also be used to find some Stylometric features of a writer.

Stylogenetics is quite a new topic in the field of science and literature, especially Bangla literature. We hope our work will inspire others to work with Bangla literature in future.

REFERENCES

[1] Kim Luyckx,Walter Daelemans and Edward Vanhoutte, "Stylogenetics: Clustering-based stylistic analysis of literary corpora" , University of Antwerp Faculty of Arts Universiteitsplein 1, B-2610 Antwerp, Belgium.

[2] Roger Peng and Nicolas Hengartner, "Quantitative Analysis of Literary Styles", The American Statistician 56.3 (2002), 175-185.

[3] Michael Brennan and Rachel Greenstad," Practical Attacks Against Authorship Recognition Techniques", Dept. of Computer Science, Drexel University, 3175 JFK Blvd Room 140 Philadelphia, PA 19104.

[4] David. I. Holmes, "A Stylometric Analysis of Mormon Scripture and Related Texts", Journal of the Royal Statistical Society. Series A (Statistics in Society), Vol. 155, No. 1,(1992), 91-120.

[5] Holmes, David I, "The Analysis of Literary Style: A Review," Journal of the Royal Statistical Society, Series A (General), (1985), 328-341.

[6] Ramyaa, Congzhou He, Khaled Rasheed, "Using Machine Learning Techniques for Stylometry", Artificial Intelligence Center, Proceedings of International Conference on Machine Learning, 2004.

[7] Jan Rygl, "Automatic Adaptation of Author's Stylometric Features to Document Types", Text, Speech and Dialogue, Springer International Publishing, 2014, 53-61.

[8] Bangla Blog, http://blog.priyo.com/blogs, Last accesses: 11th May, 2015.

[9] Bangla Blog, http://www.somewhereinblog.net/blog, Last accesses: 11th May, 2015

[10] Bangla Blog, https://shadashidhekothaarchive.wordpress.com, Last accesses: 11th May, 2015.

Designing an Empirical Framework to Measure the Level of Interest of Human

Mizanur Rahman, Minakshi Debnath, ShylaSarmin, Lamia Alam, Safayet Arefin, and Mohammed Moshiul Hoque
Chittagong University of Engineering & Technology (CUET), Bangladesh
* E-mail: mmoshiulh@gmail.com

Abstract— **Human–robot interaction (HRI) is an interdisciplinary research field aimed at improving the interaction between human beings and robots. For effective and prolonged interaction, both interacting partners need to be identified the focus of attention of each other. In other words, need to tracks or determine the each other interest and their level of interest. Interaction between a human and a robot may influence by the proximity and angle between them. In this paper, we proposed a computer vision framework for robots that will determine the level of interest of its human partner in two-party setting. We have used the distance and angle parameters to determine the level of interest in several categories: high, medium, low, and so on. The level of interest information can be used as an indicator of people's willingness to engage in an interaction with a robot. The proposed framework uses depth and visual information, provided by a Kinect sensor. Experimental results show that the system is functioning quite well to measure level of interest of the human with a reasonable accuracy.**

Keywords*—— *Human robot interaction, level of interest, human detection, interest classification, evaluation.

I. INTRODUCTION

Interest may be defined as the cognitive process of selectively concentrating on one thing of the environment while ignoring or giving lower concentration to the other things. Determining someone's interest is the pre-requisite in any human-human and human-robot interactions. Determining human's interest and its level considered also as one of the important features for a social robot. Though human behavior is complex, it is need to be structured along individual and social lines [1]. In order to interact with the human in an uncontrolled environment, the robotic system should able to interpret, predict and respond to the human behaviors appropriately [2]. Thus, to behave in a socially acceptable manner, the robot should be capable of performing a lot of social and cognitive functions [3].

Due to the increased introduction of robots in the human world such as home, offices, shopping mall and so on, the robots are still stumbling to adjust with the social behavior of the human which can be solved by detection of level of interest. For example, considering the scenario of a service robot in a shopping mall where the robot needs to deal with plenty of customers. In that case, the robot needs to understand who is asking for service from it and has to be aware about who is trying to draw its attention. Again, the robot has to serve the customer on a priority basis (i.e. physical positioning of customers in the queue, who comes earlier). In different cases, the robot is required to have the ability to analyze the level of attention of human. Communication between a human and a robot may take several forms, but these forms are largely influenced by whether the human and the robot are in close proximity to each other or not. It also depends on their angular position. Thus, interest can be considered as a function of distance and angle. Depending on the functions, the level of interest varies from high to low. The level of interest can be measured in terms of physical and physiological parameters. In order to measure the level of interest, we consider two parameters: (i) distance between the human and the robot and (ii) angle between the human and the robot (with respect to the camera position of the robot and the line of sight of the human). In this work, we propose an empirical framework to measure the level of interest of human in terms of two parameters that can lead robots with the necessary capability to initiate an interaction episode in a more natural and social manners. After measuring the level of interest of the interacting human, the robot is able to display appropriate behaviors to him/her who are willing to interact with it.

II. RELATED WORK

There are lots of research activities have been conducted on designing several social capabilities of robots such as eye contact [4, 5], joint attention [6, 7], and attention control [8, 9]. However, still there are plenty issues remained unsolved related to developing the social capabilities of robots. In this paper, we focus such one of the important issue: measuring level of attention of human. Miguel et al. [10] estimated the level of attention by analyzing looking response toward the robot. Their system was able to detect the persons in its vicinity by using the stereo system and fuzzy logic is used to define a possibility of interest for the detected persons to interact with the robot. An attention system is proposed by Alcalde et al. [11] for robot-human interaction. This system uses depth and visual information, provided by a Kinect sensor to detect a user when s/he is requiring attention and predict the objects that are suitable for interaction. An approach is presented in [12] for a mobile robot to detect the level of attention of a human (i.e., null, partial, and total) in first-person interactions. Das et al. [13] proposed an attention control mechanism for social robots that attracts and controls the attention of a target person depending on his/her current attentional focus. Their system detects the interest or willingness of the target person to interact with it.

Most of the previous work used expensive color cameras and evaluated only in laboratory conditions. The proposed system uses a comparatively cheaper sensor (i.e., Kinect) that will work in non-laboratory conditions too. The IR color sensor of Kinect will produces better results. Moreover, the most of

the previous works dealt only with analytical dimensions rather than making a system. We propose an empirical framework which can estimate the level of interest of human with better accuracy.

III. PROPOSED FRAMEWORK

Although there are various parameters can be used to measure the level of interest of interacting partner, in this work, we considered two important parameters regarding the detection of human interest visually. First one is the distance between the human and the robot's camera and second one is the angle between the camera and the human. Level of interest of human can be measured by observing these parameters in real environment. We consider depth information by Kinect in this context to estimate the physical distance and angle between the human and the robot's camera.

Initial position of the human head is determined based on the depth image. Positioning is updated frame by frame according to the depth data which results in tracking the human. Distance and angle from the Kinect to the human is then measured by the system. Finally, the level of interest is determined based on the predefined rules. Fig. 1 illustrates the schematic demonstration of the proposed framework.

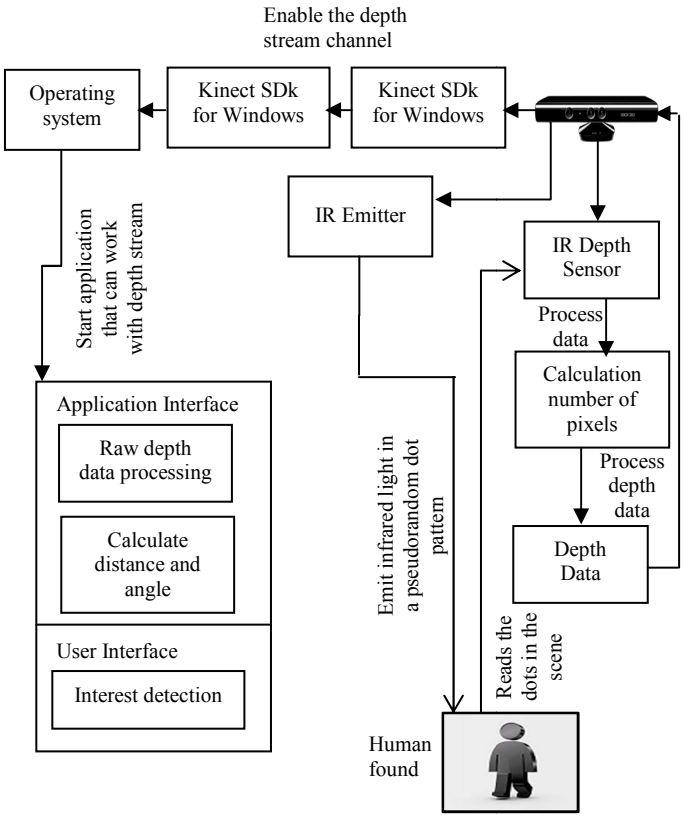

Figure.1: Proposed framework to measure the level of interest.

A. Capturing Depth Data

The infrared (IR) emitter and infrared (IR) depth sensors of Kinnect are used to capture the depth information of human. Kinnect produces a depth image of the human in front of it. The IR emitter and the IR depth sensor are used a combined function to obtain the X, Y and Z co-ordinate values on specific point of the detected human. We considered the head part of the human body to detect the human in our current implementation.

B. Identification of Human and Tracking

We use a model based method for human detection from depth images. Here, human is detected using depth information obtained by Kinect using a 2-stage head detection process, which includes a 2D edge detector and a 3D shape detector. Fig. 2 shows the overview of the human detection process.

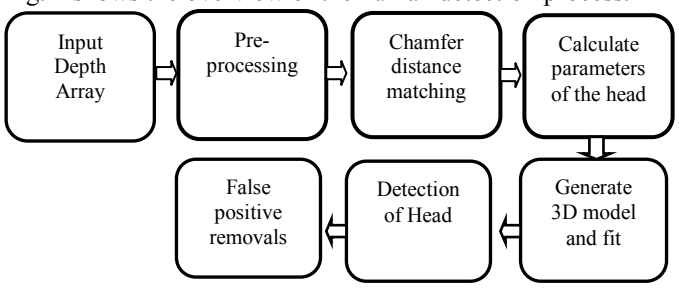

Figure 2: Overview of Human Detection Process

2D chamfer for distance matching algorithm is used. It scans across the whole image and gives the possible regions that may contain people. We examine each of these regions using a 3D head model. We extract the parameters of the head from the depth array and use the parameter to build a 3D head model. Then we match the 3D model against all the detected regions to make a final estimation. From the detection result of 2D chamfer matching, we can get the depth of the head like object from the depth array. In order to generate virtual 3D model of sphere (i.e. head), the only parameter that is required is radius of the sphere has conducted a regression test that have arrived at a cubic equation that gives the relationship between the depth value and the approximate height of head [10]. The cubic equation that fits the geometrical height of the head is computed as Eq. 1.

$$-y = -1.3835\times10^{-9}x^3 + 1.8435\times10^{-5}x^2 - 0.09140x + 189.38 \quad (1)$$

By equation Eq. (1), we calculate the standard height of the head in this depth. Then search for the head within a certain range that is defined by the standard height of the head by the Eq. (2).

$$R = 1.33\,\frac{h}{2} \quad (2)$$

Here, h is the height of the head, R is the search radius. Now, convert the height from millimeter into pixel unit as the matching works pixel by pixel.

$$Radius\ (pixel) = \left(\frac{1}{1.3}\right) \times Radius\ (\text{mm}) \quad (3)$$

Then we fit the model onto the regions detected from previous steps. We extract a circular region with radius R around the detect center and normalize its depth using Eq. (4).

$$En = \sum |\,\text{normalized_real_depth}\ (i,j) - \text{ideal_depth}\ (i,j)\,|^2 \quad (4)$$

We used a threshold value to decide the region is actually a head or not and remove the false positives. If the matching value is within the threshold, then we say the head is detected that in turns means there is a human.

Tracking algorithm is worked based on the movements of the human's head. This Kinect-based head tracking system uses user-specific 3D face template to track head pose. Head movement prediction is used to provide initialization result for ICP tracking, depending on whether or not the previous tracking results are available. The work flow of the human head tracking process is presented in a flowchart [Fig. 3].

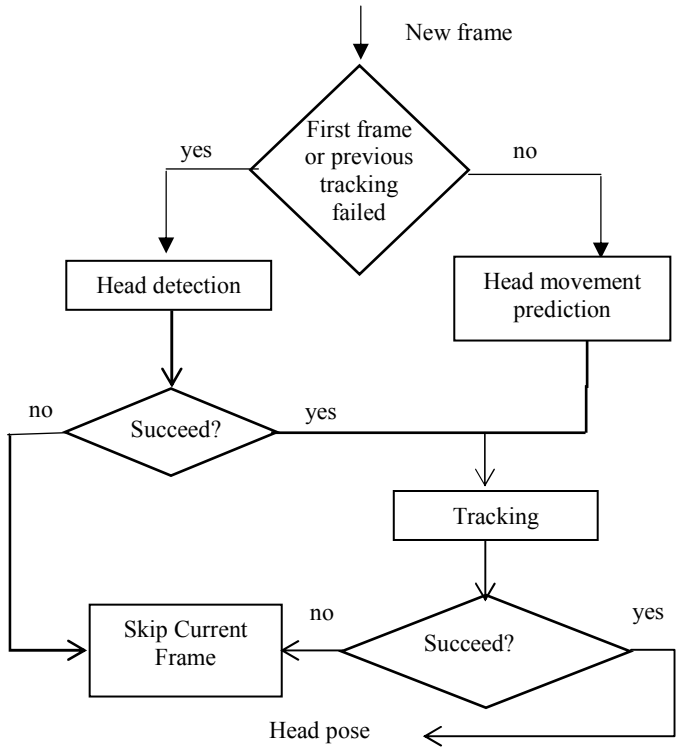

Figure 3: Workflow of the Human Head Tracking System.

Human can be detected either while s/he standing or sitting and facing the Kinect. However, sideways poses could prove to be difficult to be detected because of parts of the human are not visible to the camera.

C. Depth Information Processing

Kinect for windows device is connected to a general purpose PC with an USB cable. When there is a need to capture depth data, the Kinect is turned on and all of its sensors are initiated. Then IR emitter constantly emits infrared light in a random dot pattern over everything in front of it. IR depth sensor that reads the dots in the scene, processes the data, and sends the depth information from which they were reflected.

D. Measuring the Level of Interest Human

Interest can be considered as a function of two parameters distance (D) and angle (θ), $LI(H) = f(D,\theta)$, Where, LI (H) is the level of interest of human, D is the distance between the human and the Kinect sensor, and θ is the angle between the human and the Kinect respectively. Level of interest depends on the distance and varies inversely. Lower distance indicates the higher level of interest and vice-versa. Similarly, interest depends on the angle too. If we consider these two parameters together, then we can calculate interest from the rules below,

$$LI(H) = f(D,\theta)$$

$$LI = \frac{1}{(D+\theta)}; \quad when\ \theta > 0 \tag{5}$$

Here, D is the distance and θ is the angle between the human and Kinect. From the Eq. (5), level of interest is determined with respect to D and θ and varies inversely with them. We classify the level of interests in terms of ten categories based on the measurements of LI. The classification rules of level of interest level are illustrated in Table I.

TABLE I. CLASSIFICATION OF LEVEL OF INTEREST (LI)

Level of Interest (LI)	Classification
If (I = 0)	No Interest
If (I > 0 && I< 10)	Minimum Interest (MNI)
If (I >=10 && I< 20)	Very Low Interest (VLI)
If (I >=20 && I< 30)	Low Interest (LWI)
If (I >=30 && I< 40)	Lower Medium Interest(LMI)
If (4 >=40 && I< 50)	Medium Interest (MDI)
If (I >=50 && I< 60)	Higher Medium Interest (HMI)
If (I >=60 && I< 70)	High Interest (HGI)
If (I >=70 && I< 80)	Very High Interest (VHI)
If (I >=80 && I< 100)	Maximum Interest (MXI)

E. Measuring Parameters (D and θ):

After getting the depth stream data as a succession of the depth image frame the Kinect sensor returns raw depth with 16-bit grey scale format then we can measure distance. Behind the scenes the Kinect sensor runs a series of algorithms on the captured data to give more than an image, which tells how far each pixel in that frame is. Hence the depth pixel contains the distance between the Kinect device and the human in front of the device, in meters. Here we consider the head position of the human, so we measure the distance of the head of the human from the Kinect. The joint positions (here only head) are measured by three coordinates (X, Y, and Z). After getting these coordinate values, finally we calculate the distance between the Kinect and the detected human. The distance between two points (x_1, y_1, z_1) and (x_2, y_2, z_2) in 3-dimensional space can be determined by the Eq. 6.

$$d = \sqrt{\{(x_2 - x_1)^2 + (y_2 - y_1)^2 + (z_2 - z_1)^2\}} \tag{6}$$

Here, we assume that the sensor is in the origin point and another point is the position of the head of the detected human. Then we calculate the angle between Kinect and the human. We consider the angle to the respect of the line of sight of Kinect. In this set up line of sight is the straight line through the sensor. Here x axis is the line of sight and the negative value of θ indicates left side of the human. We use Eq. (7) to calculate the angle (θ).

$$\theta = \tan^{-1}(a/b) \tag{7}$$

Where, a indicates the value along X axis of the head position of human and b indicates the value along Z axis of the head position of the human.

IV. Evaluation Results

In order to evaluate the proposed framework, we have performed several trials in different environments. In each trails, we varied the distance as well as angle to estimate the level of interest. In one trial, a participant is asked at a time to interact with the framework and instructed to move forward and backward to change the distance. The participant also instructed to change their position for varying angle. We have calculated the level of interest of the participant in terms of distance only, angle only, and combined distance and angle respectively.

A. Output of the system

We experiment and analyze the system with different human as input in different real-world environments. We found significant results for most of the cases. We consider the level of interest in three criteria (i.e. IL against distance, angle and distance plus angle) for proper evaluation. A graphical interface is also represented to observe the variation of the interest level over time and to comprehend the significance of distance and angle both for measuring the interest level [Fig. 4].

Figure 4: Graphical User Interface of the System

In Fig. 4, a detected human is seen in the graphical interface of the application, this human stands from Kinect at 1.59 meter distance, and her angle from Kinect is -1.34 degrees. That means, from the equation (3) the level of interest of the participant with respect to distance and angle is 47.38%, which is Medium Interest (MI) according to the table 1.

B. Quantative Analysis of Level of Interest Measurement

To evaluate the level of interest, we have followed a three steps evaluation method. Firstly, we have taken the level of interest (LI) against a single parameter (i.e. distance). Secondly, the level of interest measured against another single parameter (i.e. angle). Finally, the level of interest will measured by combing distance and angles both parameters. We find significant changes among the outcomes that worked with combined parameter than that of single parameter.

Table II shows the summary of the analysis. We considered 10 interaction cases at different positions. Interest level based on single parameter and interest level based on both parameters together is compared. If we consider the first case of the table, here we can see the human in front of Kinect standing at 1.98 meter distance and her angle is 0.01 radian from the Kinect sensor. Therefore, we found that her level of interest is 30.9% which indicates category of Lower Medium. Fig. 5 illustrates this fact.

TABLE II. Measurement of Level of Interest (IL) with Distance, Angle and Combined Distance with Angle.

Case No.	Distance only (D) (m)	Level of interest	Angle only (θ) (rad)	Level of interest	Level of interest (D+θ)
1	1.98	50%	0.01	50%	30.9%
2	2.27	44%	0.07	14.28%	20.72%
3	0.97	100%	0.03	33%	100%
4	0.23	100%	0.16	6.25%	58.23%
5	1.37	73%	0.06	16.66%	9.34%
6	2.2	58%	0.21	4.76%	18.27%
7	2.43	39%	0 .45	2.22%	11.43%
8	1.73	41%	0.5	2%	38.7%
9	1.1	80%	0.04	34%	82.94%
10	4.55	Out of Social Distance	0.39	2.1%	No interest

Figure. 5: Graphical User Interface for case 1. In that case, the distance is 1.98 m, angle is 0.01 (rad), level of interest is 30.9%, and interest category is low medium.

Fig. 6 shows the graphical representation of Interest with respect to D, θ and both of them (D+θ). This Fig. indicates that the level of interest measurement varies both on the parameters D and θ. For example, if the distance is small but the angle is large (i.e., the human is attending the opposite side of the camera), the level of attention can be considered as very low. On the other hand, if the distance is large but the angle is small, then the level of interert can be consideded as the high. Thus, it is better to consider both parameters. In this work, we have proposed to combine the both distance and angle parameters for determining the level of interest of the human partner. Fig. 6 indicates that the level of interest changes

moderately while using combined distance and angle parameters than that of the individual parameter (distance or angle).

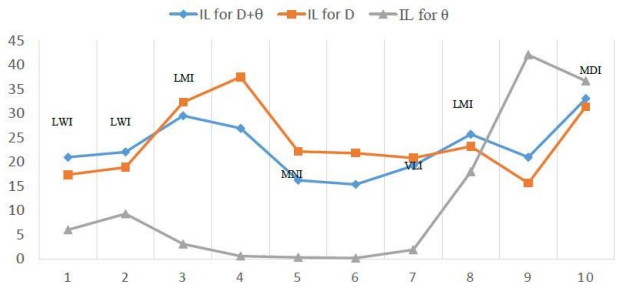

Figure. 6: Graphical representation of level of interest based on D, θ and (D+θ) parameters.

V. CONCLUSION

Measurement of level of interest of human can play a significant role in natural human-robot interaction. In this work, we presented a framework which can primarily measure the level of interest of human based on the distance between the human and camera and angle between them. The system also detects and tracks human as a pre-requisite of the interest measurement. As we worked with depth data rather than that of RGB image processing, performance is quite improved overcoming the environmental effects. Image based processing requires complex algorithm and computational costs. We used simpler algorithm for dealing with depth data. The system was evaluated in different environments with different participants and results reveal that it is able to measure the level of interest of the human with a reasonable accuracy. The proposed system is limited only two parameters. However, more parameters may include such as face area, sound source, attention span, and so on that will enhance the effectiveness of the proposed framework. The system may also extend for estimating the level of interest of multi-person scenario.

REFERENCES

[1] S. Lang, and G. Sagerer, "Multi-modal anchoring for human robot interaction", Robotics and Autonomous Systems, vol. 43, no. 2-3, pp. 133–147, 2003.

[2] B. Walker., P. Caroline, D.S. William, "Using depth information to improve face detection, Proc. of the 6th International Conference on Human-Robot Interaction; Lausanne, pp. 119-120, Switzerland, 2011.

[3] D. Das, Y. Kobayashi, and Y. Kuno, "Attracting attention and establishing a communication channel based on the level of visual focus of attention", in IEEE/RSJ International Conference on Intelligent Robots and Systems (IROS), pp. 2194-2201, Japan, 2013.

[4] D. Das, G. M. Rashed, Y. Kobayashi, and Y. Kuno "Supporting human-robot interaction based on the level of visual focus of attention", IEEE Trans. On Human Machine Systems, pp. 1-12, no. 99, 2015.

[5] D. Miyauchi, A. Nakamura and Y. Kuno, "Bidirectional eye contact for human-robot communication", IEICE Trans. Info. Syst. 88-D, pp. 2509-2516, 2005.

[6] P. Michalowski, S. Sabanovic, and R. Simmons, "A spatial model of engagement for a social robot", Proc. *IEEE International Workshop on Advanced Motion Control*, Istanbul, Turkey, pp. 762-767, 2006.

[7] K. Hosoda, H. Sumioka, A. Morita, and M. Asada. Acquisition of human-robot joint attention through real-time natural interaction. In *IEEE/RSJ International Conference on Intelligent Robots and Systems*, pp. 2867–2872, USA, 2004.

[8] M. M. Hoque, T. Onoki, Y. Kobayashi and Y. Kuno, Effect of robot's gaze behaviors for attracting and controlling human attention, Adv. Robo. vol. 27, pp. 813-829, 2013.

[9] G. S. and V. Hafner "Evaluating the effect of saliency detection and attention manipulation in human-robot interaction", in International Journal of Social Robotics, vol. 4, pp.123-139, 2012.

[10] G. Miguel and A. Gonz´alez, "A fuzzy system for visual detection of interest in human-robot interaction," [online], Available: http://www.researchgate, 2008.

[11] F. J. Alcalde, I. varea, and J. M. G´omez, "Active attention for human robot interaction using visual and depth information," Workshop of Physical Agents, 2012.

[12] L. C. Gonzalez-Garcia, L. A. Torres-Mendez, J. Martinez, J. Sattar and J. J. Little, "Are you talking to me? Detecting attention in first-person interactions, Proc. 17th International Conference on Advanced Cognitive Technologies and Applications, pp. 137-142, 2015.

[13] D. Das, M. M. Hoque, Y. Kobayashi, and Y. Kuno, Attention control sysetm considering the target person's attention level, 8th ACM/IEEE International Conference on Human Robot Interaction, pp. 111-112, 2013.

BQAS: A Bilingual Question Answering System

Sanjidul Hoque
Department of CSE,
CUET, Bangladesh
Email: sanjid133@gmail.com

Mohammad Shamsul Arefin
Department of CSE,
CUET, Bangladesh
Email: sarefin_406@yahoo.com

Mohammed Moshiul Hoque
Department of CSE,
CUET, Bangladesh
Email: moshiulh@yahoo.com

***Abstract*—In this paper, we present a bilingual question answering system, BQAS that can generate questions and provide their answers from electronic Bangla and English documents. The system first performs the analysis of the contents of the documents to generate questions based on user provided query. It then generates answers of the questions. The system has been evaluated with real documents. We have found that our system can generate questions and related answers up to a satisfactory level from the documents of two different languages as well as from the documents of the same language.**

***Index Terms*—Bilingual systems, keywords extraction, query execution, clustering.**

I. INTRODUCTION

Question Answering System is system where it produces an amount of questions from one or several documents and justifies users answer. It is one of the popular topics in natural language processing and one of the best ways to retrieve information from the documents. It is very helpful for those students who want to justify his / her learning through putting answer of generated questions.

There are many existing question answering systems. Most of them are unilingual in nature and none of them considers the generation of questions and answers considering the documents of Bangla and English. Considering this fact, in this paper, we develop a bilingual question answering system known as BQAS that can generate questions and their related answers considering the documents of Bangla and English. We implement the system considering users' provided queries and domain information. At first, the system extracts keywords from the documents those are related to the user query. Here, we consider postfix statistics to determine the root words. Then, digit and keyword based questions are generated from those documents. Our translation system then translates those generated questions and stores those questions into the database. A number of questions are shown to the user's screen in users selected language. Later on the system provides the answers of the generated questions.

Our main goal is to generate fact-based questions from the documents of Bangla and English. The importance of the generated is measured in two steps. In the first steps, we identify whether the question is asking something about the topic or something that is very closely related to the topic. For this purpose, we use Latent Dirichlet Allocation (LDA) [1] to identify the sub-topics in the given body of texts and apply the Extended String Subsequence Kernel (ESSK) [1] to calculate their similarity with the questions. In the second step, we judge the syntactic correctness of each generated question. We rank the questions by considering their topic relevance and syntactic correctness scores.The contribution of this paper can be summarized as follows:

The remainder of this paper is organized as follows. Section II provides a brief review of related work. In section III, we detail the computation framework of our proposed approach. Section IV presents the experimental results. Finally, we conclude and sketch future research directions in Section V.

II. RELATED WORK

The idea of automatically generating questions from sentences has been proposed and implemented as early as 1976. Recently question generation has got immense attention from the researchers and hence different methods have been proposed to accomplish the task in different relevant fields.

There are some question answering systems thats operate in English only. Such as, Plamondon et al. [1] developed a system where the question must be asked in English, the document collection is in English and the answer extraction is performed in English. Kaur et al. [2] described a system that first collects the corpus of data or paragraph from encyclopedia to make the questions and find the exact answer. Filho et al. [3] developed a system where they tried to classify the questions in only 4 types ("who", "where", "when" and "how many" questions). Hitomi et al. [4] concerned with a type of infant bilingualism in which children have been regularly exposed to two languages from birth as a result of each of their parent's speaking a different language. Their system produces only negative question in both Japanese and English language and judge the user's response.

Xu et al. [5] focused on the methods for question generation and answer judgement as well as the game implementation. Here they worked with Chinese and English statements. A cross-language question answering system is developed by Plamondon et al. [6]. Here they develop a system that receives questions in English language and show the answer in English for English document collection. They also transformed the system into a bilingual system to allow French speakers to ask their questions in French and get answer in French as well, but using an English document collection.

GistSumm [7] is an automatic summarizer based on a simple extractive method, called gist-based method. QUASAR [8] is

978-1-4673-9257-0/15/$31.00 ©2015 IEEE

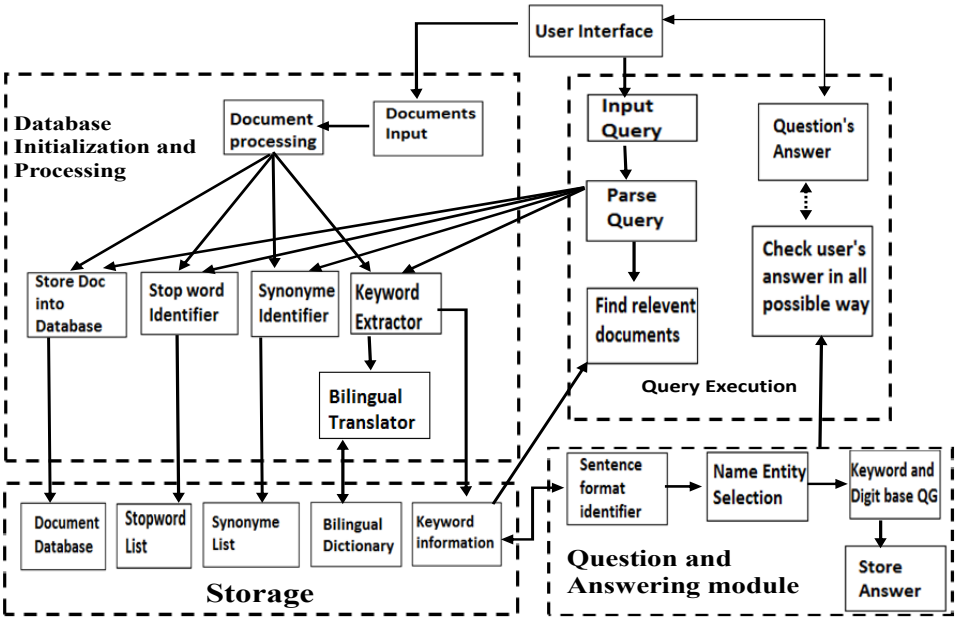

Fig. 1. System architecture of the proposed system

a QA system based on the JIRS1 Passage Retrieval engine, which has been fine-tuned for the QA task, whereas most QA systems use classical PR methods.

A few Banglaa and English question answering system also developed. Haque et al. [9] developed a question answering system based on transliteration and table look-up as an interface for the medical domain. The system is in no way a complete QA system; however, it gives a basis to implement a complete QA system for Bangla. The implementation involves questions from the medical domain only. They also consider only simple questions (wh-question).

There are about 220 million native and 250 million total Bangla language speakers. But there are a few works on Bengali language. So, working with Bangla language is most significant. Besides, Bangla and English question answering system helps students to make their learning more effective.

Considering this fact, in this paper we propose a framework for generating questions and corresponding answers considering the documents of two different languages: Bangla and English.

III. System Architecture and Design

The system architecture of Bilingual Question Answering System comprises four basic modules: Database initialization and processing module, storage module, question and answering module and query execution module. The function of database initialization and processing module is to set up the database from a set of documents for information retrieval. Storage module store all related information to the database. Question and answering module is for generating question and analyzing the answer and query execution module performs all information retrieval queries. The architecture of the proposed system is shown in shown in Fig. 1.

Algorithm: *Documents_storing*

Input: Documents

Require: Store the documents.

1. **begin**
2. create a table named document having the field DocID, Doc Title, No of word
3. Initialize the counter variable is 1
4. While the counter variable is less than the no of total document
5. Insert the file name and counter into the table
6. Increment the counter variable
7. **End**

Fig. 2. Algorithm for storing documents into database

A. Database Initialization and Processing Module

The database initialization and processing module consists of sub-modules: store documents into database, stop word identification, synonym identification, keyword extraction. The relationships among the sub-modules are also shown in the Fig. 1. The document database is created with document ID, document title and total word into the document. Algorithm for storing documents is given in Fig. 2.

There are some words which do not make any significant change in absence of them. Those words are called stop word. Our current step is to remove those words from the documents. There are a lot of stop words in English language such as: a, about, above, across, after, afterwards, again, against, all, back, be, became, because, become, becomes, becoming, been, before, by, call, can, cannot, can't, due, during, each, eg, etc. There are also a lot of stop words in Bengali as well. A list of English stopwords and Bangla stopwords are enlisted and stored into the database, which are used in the process of stopwords elimination by the system. Algorithm for stopwords removal is given in Fig.3.

```
Algorithm: Stop_word_elimination
Input: List of words.
Require: Delete the unnecessary word.
begin
for each word do
    search the stop word list
  if word is found then
      remove the word from sentence
  else
      do nothing
  end if
end for
End
```

Fig. 3. Algorithm for stopwords elimination

```
Algorithm: Keyword_Extraction
Input: sentences and list of words.
Require: Find the keyword.
begin
for each independent word do
    initialize a 2D matrix with value=0;
end for
count=0;
for each independent word do
    if word match with the sentence's word then
        count++;
    else
        Do nothing;
    put the counted value in corresponding index;
  end if
end for
Determine the maximum value
    define the keyword;
End
```

Fig. 4. Algorithm for keywords extraction

Synonym identification sub-module performs the identification of synonyms from the documents. A words having the same meaning as another in the same language is called the synonym of that word. It is very much important to manage the synonyms efficiently. Because if the synonyms having same meaning are not treated as same words, there will be a great degradation of system's accuracy.

Keywords are used for different purposes. They are used to determine those documents which are related to the domain information. Keywords are also used to generate questions. Each keyword is stored into the database by its ID and name. Keyword extractor sub-module extracts the keywords from the documents with the help of algorithm of Fig. 4.

B. Storage Module

The storage module handles the storage of the document and important information for retrieval purposes. The stop lists are stored into the database. Synonyms are stored into the database accordingly. A bilingual dictionary is also stored for translation purposes. For further calculation keywords are necessary so keywords are also stored into the database.

C. Question and Answering module

It is the main module of our system. Here questions are generated and corresponding answers are also retrieved. There are several sub-modules: Sentence format identification, Name entity identification, Keyword and Digit based question generation and the storage of answer.

1) Sentence Format Identification: It is our first step to generate questions. Fist, we have to identify the sentence structure. If the sentence is simple then it is ready to generate question. For complex and compound sentences we convert them to simple sentences for making questions generation task easier.

2) Name Entity Selection: We use our database information to determine a name entity in the document. We use some general purpose rules to create some basic questions related to name.

3) Digit and keyword based question generation: Digits in documents play significant roles for generating questions. It is easy to generate questions by replacing the digits with a question word shown in Table I. We also consider keywords to generate the questions.

TABLE I
QUESTION TEMPLATE

English Question	Bangla Question word	Arguments
Who	কে	Person
Where	কোথায়	Place
When	কখন	Time
What	কি	Object
Which	কোনটি	Object
How	কিভাবে	Process
Why	কেন	Cause

D. Query Execution

The sub-modules are: Input query, parse query, find relevant document, user's answer, and find all possible answer. At first user input a domain name on which he/she wants to generate question. After taking the domain name as input from user our system needs to parse the domain name. Then using a clustering algorithm (such as cosine similarities) our system finds the relevant documents which are used for generating question. While answering a question our system needed to check the all possible solution for that question and match with the user's answer.

E. Documents Categorization

The similarity between domain and documents can be calculated by the cosine similarity. If the the cosine similarity -1 between the vectors of two documents means that the documents are exactly opposite, 1 means exactly same, 0 usually indicates independent documents, and in-between values indicates intermediate similarity or dissimilarity. For text matching, the attribute vectors are usually the term frequency vectors of the documents. In our situation, the cosine similarity range from 0 to 1. Based on the similarity measures, we short the documents in descending order of similarity with the query information. Then, we choose the documents those have the similarity scores grater than a defined threshold for considering question generation. Fig. 5 shows the algorithm of this approach.

```
Algorithm: Document_Categorization
Input: domain name and keyword list
Require: select the desired documents.
1.  begin
2.  for each keyword do
3.      Calculate the cosine similarity.
4.  end for
5.  if similarity_ value >= threshold do
6.      select the document for generating question
7.  else
8.      do nothing;
9.  end if
10. end for
```

Fig. 5. Algorithm for documents categorization

```
Algorithm: Duplicate_question_elimination
Input: List of generated questions.
Require: Delete the duplicate questions.
1.  begin
2.  for each question do
3.      search the question database
4.      if question is found more than one then
5.          remove the duplicate question
6.      else
7.          do nothing
8.      end if
9.  end for
```

Fig. 6. Algorithm for duplicate questions elimination

F. Duplicate Question Elimination

The system may generate same question from different documents. So, we need to remove the duplicate questions. The algorithm for duplicate questions elimination is given in Fig. 6. As our system first generates question from each document separately and store them in the database, we can easily eliminate duplicate questions by searching the database. While we insert a question into our question database, we first check whether the question is already in the database or not. If any question from our database matches with our newly generated question then the system does not insert it into our question database. Otherwise, the system inserts the question into the database.

G. Bilingual Translation

Algorithm for translation is given in Fig. 7. Generally Bangla sentence structure is different from English sentence structure. A simple Bangla sentence structure is "Subject + Object + Verb" while in English it is "Subject + Verb + Object". At first using bilingual dictionary, we have to find the translated word and feature of each word. Then by using word's feature we have to determine the sentence structure. After that we have to place those translated word in corresponding sentence structure.

H. Answer Judging

When users insert the answer for each question we have to check the answer whether it is right or wrong. There are many ways to answer a question correctly. An answer to a wh-question "How many versions of the Internet Protocol (IP)?" can be "two", "2", "2 versions" etc. The system needs to accept all these possible answers, and at the same time reject incorrect answers. Algorithm in Fig. 8 is used by our system for this purpose.

```
Algorithm: Bilingual_Translation
Input: Sentence
Require: Translated sentence.
1.  begin
2.  for each word in the sentence do
3.      search the word into the dictionary
4.      if found then
5.          Store into an array
6.      else
7.          do nothing
8.      end if
9.  end for
10. for each rule do
11.     if sentence matches with a rule do
12.         Apply translation rule to translate.
13.     else
14.         do nothing;
15.     end if
16. end for
17. End
```

Fig. 7. Algorithm for bilingual translation

```
Algorithm: Answer_Judging
Input: user's answer and answer database
Require: result.
1.  begin
2.  for each word in the answer do
3.      search the word into the database
4.      if match partially then
5.          calculate the percentage of matching
6.      else
7.          do nothing
8.      end if
9.  end for
10. set correct=0;
11. set wrong=0;
12.     if matching percentage>=70% do
13.         .increment correct value'
14.     else
15.         increment wrong value;
16.     end if
17. show the result
18. End
```

Fig. 8. Algorithm for answer judging

IV. Implementations and Experiments

In this section, we provide the implementation procedure and performance analysis of our developed system.

A. Experimental Setup

The developed Bilingual Question Answering System has been implemented on a machine having the windows 7, 2.50 Core i3-4100 processor with 4GB RAM. The system has been developed in JAVA in the front end and SQLite manager is used in the back end for storing related data to complete this project. For coding we have used NetBeans IDE.

For experimental purpose, we consider total twenty three Bangla and English documents of different domains. Table II shows the document name, domain name and number of containing words on those documents.

B. Implementation

Fig. 9 shows the generated questions with user provided answers in Bangla. Fig. 10 shows the accuracy of user's answers by comparing it with system generated answers. Here,

TABLE II
LIST OF THE DOCUMENTS FOR EXPERIMENTS

Doc_name	Domain	No_of_words
bangladesh.doc	Bangladesh	227
bangladesh_english.doc	Bangladesh	319
Bangladesh_education.doc	Bangladesh	275
bangladesh_government_bangla.doc	Bangladesh	179
bangladesh_government2_bangla.doc	Bangladesh	302
Economics.doc	Bangladesh	413
computerbng2.doc	Computer	175
computeren2.doc	Computer	413
computer_bangla.doc	Computer	255
computer_english.doc	Computer	242
bangladesh_histroy2_bangla.doc	Independence day	415
bangladesh_histroy3_bangla.doc	Independence day	335
independence_bangla.doc	Independence day	687
inter_english.doc	Internet	554
interneten2.doc	Internet	253
Interneten3.doc	Internet	602
interneteng.doc	Internet	413
internet_bangla.doc	Internet	97
IP_english.doc	IP address	284
ip_english2.doc	IP address	260
Ip2bangla.doc	IP address	315
Ip3bangla.doc	IP address	497
urlbangla.doc	IP address	228

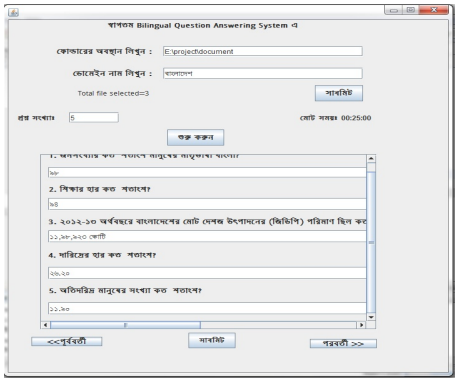

Fig. 9. Question with user's answer

for generating questions and answers for Bangladesh domain it considers eight documents out of twenty three documents.

Table III shows the number of retrieve documents considering by the system under different domains.

C. Performance Evaluation

We have evaluated the performance of our proposed system with respect to documents of Table II. For the experimental evaluation, we have generated questions and answers by our system and compared them with human generated questions and answers.

Our first experiment shows a comparison about question generation with respect to different domain information. Fig. 11 shows the result. From the graph of Fig. 11, we can find that human always generates more question than our system. This is because Human can generate a line of text in different way.

In our next experiment, we show top-10 questions generated by our system and by the human. Table IV and Table V show the results in Bangla and English, respectively. From

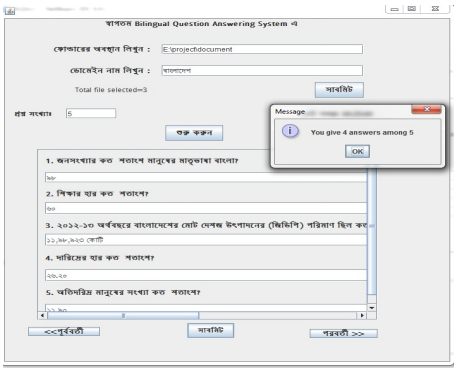

Fig. 10. User's score

TABLE III
DOMAIN SPECIFIC DOCUMENTS INFORMATION

Domain information	Total found documents	Documents
Bangladesh	8	bangladesh.doc, bangladesh_english.doc, Bangladesh_education.doc, bangladesh_government_bangla.doc, bangladesh_government2_bangla.doc, Economics.doc, bangladesh_histroy2_bangla.doc, bangladesh_histroy3_bangla.doc
Independence day	4	independence_bangla.doc, bangladesh_histroy2_bangla.doc, bangladesh_histroy3_bangla.doc, bangladesh_government_bangla.doc,
Computer	6	computer_bangla.doc, computer_english.doc, inter_english.doc, internet_bangla.doc, computerbng2.doc, computeren2.doc
Internet	7	inter_english.doc, internet_bangla.doc, IP_english.doc, ip_english2.doc, interneten2.doc, Interneten3.doc, interneteng.doc
IP address	5	IP_english.doc, ip_english2.doc, Ip2bangla.doc, Ip3bangla.doc,Urlbangla.doc

the tables, we can find that our system can generate questions almost as accurate as the human. This is due to small domain size.

Our next experiment shows the accuracy in translation. The result is shown in Table VI. From Table VI we can see that our system can perform translation of the questions in the desired language upto a satisfactory level.

For each generated question our system produce answers. When user put answer for a corresponding question our system try to check produce all sorts of possibility to check the

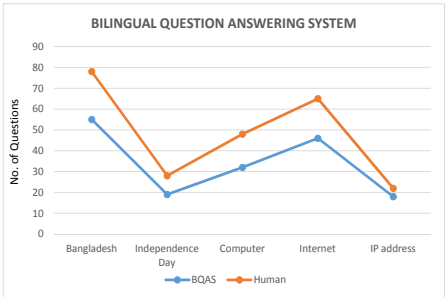

Fig. 11. Comparative question generation performance

TABLE IV
TOP 10 QUESTIONS GENERATED IN BANGLA BY HUMAN AND BQAS

Rank	Top 10 Questions generated by Human	Top 10 Questions generated by BQAS
1	আয়তন হিসেবে বাংলাদেশ বিশ্বে কত তম?	বাংলাদেশ বিশ্বে কত তম আয়তন?
2	বাংলাদেশের আয়তন কত ?	জনসংখ্যার কত শতাংশ মানুষের মাতৃভাষা বাংলা?
3	জনসংখ্যার কত শতাংশ মানুষের মাতৃভাষা বাংলা?	শিক্ষার হার কত শতাংশ?
4	২০১২-১৩ অর্থবছরে বাংলাদেশের মোট দেশজ উৎপাদনের (জিডিপি) পরিমাণ ছিল কত টাকা?	২০১২-১৩ অর্থবছরে বাংলাদেশের মোট দেশজ উৎপাদনের (জিডিপি) পরিমাণ ছিল কত টাকা?
5	শিক্ষার হার কত শতাংশ?	দারিদ্রের হার কত শতাংশ?
6	দারিদ্রের হার কত শতাংশ?	অতিদরিদ্র মানুষের সংখ্যা কত শতাংশ?
7	বাংলাদেশের সংবিধান কত খ্রিস্টাব্দে প্রণীত হয়?	বার্ষিক দারিদ্র হ্রাসের হার কত শতাংশ?
8	২০১১ খ্রিস্টাব্দ পর্যন্ত সর্বমোট কত টি সংশোধনী আনা হয়েছে?	২০১১ খ্রিস্টাব্দ পর্যন্ত সর্বমোট কত টি সংশোধনী আনা হয়েছে?
9	বার্ষিক দারিদ্র হ্রাসের হার কত শতাংশ?	মহিলাদের জন্য কত টি সংরক্ষিত আসন আছে?
10	মহিলাদের জন্য কত টি সংরক্ষিত আসন আছে?	বাংলাদেশ কত টি প্রশাসনিক বিভাগে বিভক্ত?

TABLE V
TOP 10 QUESTIONS GENERATED IN BANGLA BY HUMAN AND BQAS

Rank	Top 10 Questions generated by Human	Top 10 Questions generated by BQAS
1	What is the position of Bangladesh in the world in terms of area?	What is the position of Bangladesh in the world in terms of area?
2	what is the area of Bangladesh?	What percentage of population people mother tongue Bengali?
3	What percentage of population people's mother tongue is Bengali?	What percentage of literacy rate?
4	What is the total production amount of Bangladesh in 2012-2013 economic year?	
5	What is the percentage of literacy rate?	What percentage of poverty rate?
6	What is the percentage of poverty rate?	What percentage of extremely poor people number?
7	When did the constitution of Bangladesh applied?	What percentage of poverty reduction rate?
8	How many amendments brought in up to2011?	How many amendments brought in up to2011?
9	What percentage of poverty reduction rate?	How many reserved seat for women?
10	How many reserved seat for women?	How many administrative division separate in Bangladesh?

correctness. Table VII shows the result. From Table VII we can find that our system can judge the answers upto a satisfactory level.

V. CONCLUSION

In this paper, we provided a framework for bilingual question answering system. We have implemented the system with Bangla and English electronic documents. Form the experimental evaluation, we found that the developed system can generate questions and answers efficiently. Although in this paper, we have considered documents of two different languages, it can incorporate other language easily.

In this work, we considered an in-house database of documents and it is necessary to scan a document before it is considered in the system. In future, we hope to develop a system that can efficiently generate questions and answers from the documents of the Internet without scanning them in the system.

TABLE VI
QUESTION TRANSLATION INFORMATION

Domain name	No. of Bangla doc	No. of English doc	No. of generated question in Bangla	No. of generated question in English	Total No. of correct translated question
Bangladesh	6	2	37	18	44
Independence Day	3	1	12	7	13
Computer	4	2	21	11	19
Internet	4	3	29	17	31
IP address	3	2	11	7	11

TABLE VII
ANSWER JUDGING ACCURACY

No.	Domain Name	No. of Generated Questions	Total correct answer	Total incorrect answer	Answer not found	Correctness %
1	Bangladesh	55	48	5	2	87.24%
2	Independence day	19	14	4	1	73%
3	Computer	32	24	6	2	75%
4	Internet	46	32	10	4	69.57%
5	IP address	18	12	2	4	66.67%

REFERENCES

[1] L. Plamondon, G. Lapalme, L. Kosseim, "The QUANTUM question answering system at TREC-11", *In Proceedings of the Eleventh Text Retrieval Conference*, Gaithersburg, Maryland (2002)

[2] H. Kaur, R Kumari, "Novel scoring system for identify accurate answers for factoid questions", *In International Journal of Science and Research (IJSR)*, 2013.

[3] P.P.B. Filho, V.R. de Uzeda, T.A.S. Pardo, M.D.G.V. Nunes, "Using a text summarization system for monolingual question answering", *NcleoInterinstitucional de LingsticaComputacional (NILC)Instituto de CitnciasMatemticas e de Computao - Universidade de So Paulo*, CP 668, 13.560-970 So Carlos-SP, Brasil, 2003.

[4] N. Hitomi, "A Japanese-English bilingual child's system of answering negative questions", *In Proc. of Japan Journal of Multilingualismand Multiculturalism*, vol.1,no.1, pp. 28-37.

[5] Y. Xu, A. Goldie, S. Seneff, "Automatic question generation and answer judging: a QA game for language learning", *Spoken Language Systems Group, MIT Computer Science and Artificial Intelligence Laboratory*, United States, 2009.

[6] L. Plamondon, G. Foster, "Quantum, a French/English cross-language question answering system", *in In Proc. of Cross Language Evaluation Forum*, 2003.

[7] C. Amaral, H. Figueira, A. Martins, A. Mendes, P. Mendes, C. Pinto, "Priberams question answering system for Portuguese", CLEF 2005.

[8] J. Soriano, D. Buscaldi, E. Asensi, P. Rosso, E. Arnal, "QUASAR: The question answering system of the universidad politecnica de Valencia", LNCS 4022, pp. 439-448, CLEF 2006.

[9] N. Haque, M. Rosner, "A prototype framework for a Bangla question answering system using translation based on transliteration and table look-up as an interface for the medical domain", *Masters Thesis*, University of Malta Gertjan Van Noord, 2010.

3rd Hand: A Device to Support Elderly and Disabled Person

Ummay Habiba[1], Shiuly Barua[2], Faisal Ahmed[3], Golap Kanti Dey[4], Kazi Tanvir Ahmmed[5]
[1,2,4,5]Department of Applied Physics, Electronics & Communication Engineering
[3]Department of Computer Science and Engineering
University of Chittagong, Chittagong-4331, Bangladesh
[1]habiba.ap16@gmail.com, [2]baruashiuly@gmail.com, [3]faisal.cse91@gmail.com, [4]d.k.golap@gmail.com, [5]tanvir@cu.ac.bd

***Abstract*— This paper represents a system "3rd HAND", that can serve a disable person or elder person to perform some of their regular tasks without any helping hand. This system helps a person to switch the regular home loads (light, fan etc.) using his voice commands and his location can be tracked when he travels outside alone with the system. In self-regulated system we used an EASY_VR voice recognition module. The recognized control commands are sent to an ARDUINO for proper program controlling and then to a Bluetooth module. After that, the commands are routed to the target device over Bluetooth network and finally carried out by the control circuit. In GPS tracking system, we used the GPS and SMS services of an android mobile phone. When a client sends a request SMS to the system to get its location, the GPS receiver of the phone calculates the location coordinates and converts it to location name using GEOCODING API. Finally the location name is sent to the client automatically. Generally it is not comfortable and secured for a disabled or elder person to switch their home loads and to travel alone. So the system "3rd hand" provides them a safety switching system and supports them to travel independently in safe.**

Keywords- self-regulated, voice recognition, wireless communication, GPS, GSM, location tracking etc.

I. INTRODUCTION

With the increasing of average age of world population as a result of advancement of medical science, the elderly population is increasing rapidly worldwide. And a statistics shows that more than 500 million people in the world are disabled as a consequence of physical, sensory, or mental impairment. It is a responsibility for the people all around the world to support this large number of population [1]. Life is very difficult for the people mentioned because they are completely dependent on others for their regular movement task. They need a constant care giver [2]. Though we can't remove the sufferings of their daily life, we can try to make their life little easier with the help of modern technologies.

Elder persons and persons with special needs are unable or face difficulties to operate their regular home loads like light, fan, AC etc. [3]. And they need a continuous attender when they travel outside. So we came up with a project that will help those persons to perform some of their daily works independently and safely. The objective of our project is to provide those persons with a system that can operate their home loads automatically with their voice commands only [4] and can detect their current location when they travel outside alone and send their location name via SMS to clients who want to monitor their current location.

The elder and disable persons face difficulties with a remote control device which controls the home appliances remotely by button press feature [5]. So we have designed and implemented this system with a feature of self-regulation controlled by voice commands instead of any button press system. In this self-regulation system, we used Easy-VR shield for voice recognition process instead of smart phones which can accept voice commands. This is because if we use smart phones for controlling home load with voice commands, we must have continuous Wi-Fi connection. But this Wi-Fi is not much available in many 3rd world countries like Bangladesh.

Voice controlled self-regulated system is based on speech recognition technology. This technology allows a CPU to recognize and analyze a set of pre-programmed voice commands produced by a person using a microphone [6]. In this voice controlled home automation system, the major challenge is to overcome the problems with distant voice command and speech recognition in the noisy environment [7].

Another feature of our project is GPS tracking. By using this feature, anyone can monitor the position of an elder or disable person when he travels outside alone. This system is based on GPS and GSM technology [8, 9]. We used android phone as target device [10]. In this system a client who is interested to monitor the position of the person mentioned carrying GPS system, sends a request message to the system. After receiving request message, the GPS system calculates the position of that person by using signals from the satellites [11, 12]. Then the system automatically sends a message containing the location name of that person to the client via GSM network.

II. DESIGN OVERVIEW

The system "3rd hand" is an integrated system to facilitate the older and disable persons with a self-regulated system that can be fully operated by voice commands and with a GPS tracking system that can detect the location of the persons mentioned when they travel alone.

In self-regulated system, there are two major parts. One is transmitter part and another is receiver part. In this section of home automation system, we used two ARDUINO mega 2560, one of which is used in transmitter part and another is used in receiver part. Here two HC-05 Bluetooth modules are used for setting up the wireless communication between the

978-1-4673-9257-0/15/$31.00 ©2015 IEEE

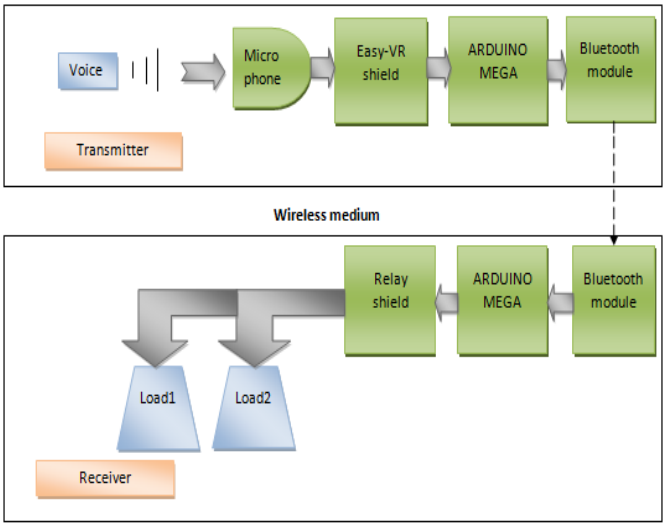

Fig. 1. Design overview of self-regulated system

transmitter part and the receiver part. One of them is interfaced with the transmitter ARDUINO and another is with receiver ARDUINO. We have used here an Easy-VR voice recognition shield. The Easy-VR shield is interfaced with the ARDUINO at the transmitter part. There is a microphone on this Easy-VR shield. The microphone receives the voice signals from a person and the Easy-VR module tries to recognize the voice commands. If the module recognizes a voice command, it sends this command to the ARDUINO. By proper program controlling the ARDUINO sends this data to the Bluetooth module. Then if the wireless communication with the Bluetooth at the receiver section is set up, the voice data is sent to the receiver portion via Bluetooth communication. Then Bluetooth module transmits this data to the ARDUINO at the receiver part. The design overview of this system is shown in fig. 1.

A 2-channel relay shield is used which is connected between the ARDUINO and the loads to be operated at the receiver part. The relay shield acts as a switch to control the ON/OFF conditions of the loads. By program controlling, the ARDUINO controls the switching mechanism of relay to operate the loads.

We implemented our GPS tracking system by using a GPS enabled Android phone and Android Application.

In this system, when a client wants to know the current location of a person who uses an android phone with this GPS tracking system, sends a request to the user's subscription number through a SMS (Short Message Service) via GSM. The SMS contains a password and the password is also stored in our system. Then the system extracts the client's IME number and password from the SMS. If it can match the password with the password stored in the system, GPS receiver of the Android phone is turned on. Then the system receives signals from the satellites and calculates the latitude and longitude of the user's location. Then the latitude and longitude are converted into human readable location name using GEO coding API (Application Programming Interface) of the android SDK (Software Development Kit).Then the

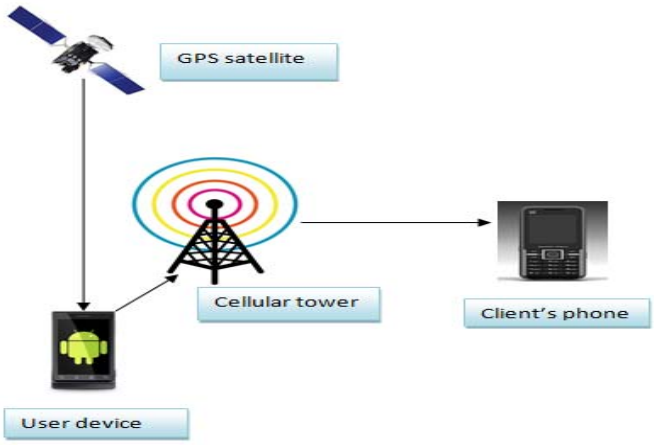

Fig. 2. Overview of GPS tracking system [13]

user location address is sent to the client automatically via GSM network. The user also gets a notification when anyone tracks his location. The overview of GPS tracking system is shown in fig. 2.

III. CONSTITUENT SUB-MODULES

A. ARDUINO MEGA 2560

The ARDUINO mega 2560 is a microcontroller board containing an ATmega2560 microcontroller. ARDUINO is a complete package that contains all the essential components to control the functions of a microcontroller. ARDUINO makes the hardware and software implementation of a system easier ARDUINO helps the microcontroller to receive instructions from the outside of the system and to run the system according to the instructions. There are 54 digital I/p pins and 16 analog input pins in this ARDUINO. ARDUINO can be interfaced with a computer via USB connection. Its operating voltage is 5v. ARDUINO can receive 5v input voltage from a pc through USB connection or from an external power source through a voltage regulator. It contains 4 UART pins for serial communications. ARDUINO contains a 16MHz crystal oscillator, a power jack and a reset button. It provides a clock speed of 16MHz. ARDUINO mega can be programmed with ARDUINO software. An ARDUINO MEGA 2560 is shown in fig. 3.

B. Easy-VR module

Easy-VR is a speech recognition module. This module is interfaced with an ARDUINO board. ARDUINO supplies 3.3v input voltage to this module. Easy-VR module communicates with the ARDUINO through serial interfaces with a default baud rate 9600. It receives data with ERX pin and transmits

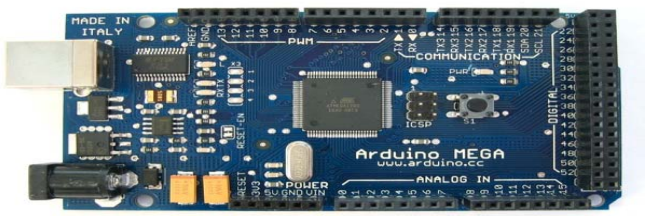

Fig. 3. ARDUINO Mega 2560 [14]

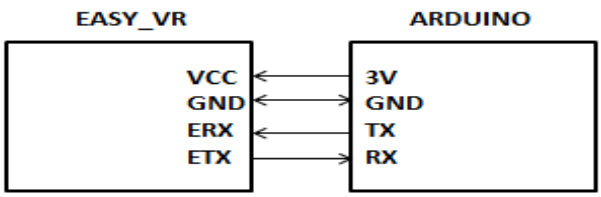

Fig. 4. Pin connections between Easy-VR and ARDUINO

data with pin ETX. Easy-VR receives voice signals with a microphone. The sensitivity of the microphone is 38dB and its frequency response is in the range of 100Hz -20KHz. Easy-VR module is trained up with the required voice commands using a software Easy-VR commander. When a command is said at the microphone, the module checks it. If it can recognize the command, it sends the command to the microcontroller to perform operation. The basic pin connection between an Easy-VR shield and an ARDUINO is shown in fig. 4.

C. *HC-05 Bluetooth module*

In our project we have used two HC-05 Bluetooth modules for wireless communication. It is very easy to interface with ARDUINO. It communicates with an ARDUINO through its serial interfaces. The sensitivity of the module to any other Bluetooth signal is about -80dB. It receives 3.3v input voltage from the ARDUINO. It transfers data with a default baud rate 9600. The module can be configured using AT-commands to communicate with other desired modules wirelessly. When two Bluetooth modules are paired, both of them blink 1times/2s. And while they are not paired, they blink 2times/s. The basic pin connection between a Bluetooth module and an ARDUINO is shown in fig. 5.

D. *3-channel 5v relay*

We have used a 3 channel relay shield in this system. The shield is interfaced between ARDUINO and loads to be operated at the receiver section. The relay shield acts as a switch to control the ON/OFF conditions of the loads. In this shield, each channel is used to control a single load. Each channel contains 3 relay pins such as COM, NO and NC. Loads are connected to the relay via relay pins. The relay shield is interfaced with the ARDUINO via digital I/O pins. The basic pin connection between a relay shield and an ARDUINO is shown in fig. 6.

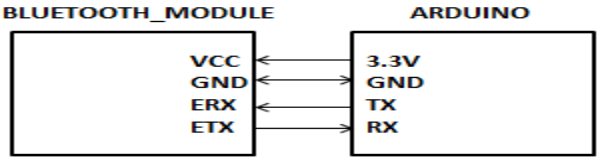

Fig. 5. Pin connections between Bluetooth and ARDUINO

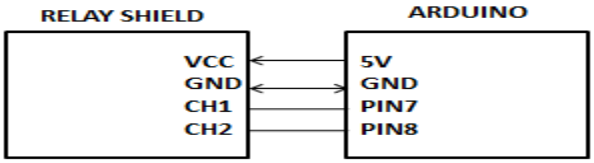

Fig. 6. Pin connections between relay and ARDUINO

E. *GPS tracking section*

1) *Hardware*

In this system, we used an android mobile phone as GPS tracking device with processor 1GHz or more and RAM 1GB or more. Client device can be any cell phone capable of send SMS.

2) *Software*

We used the OS Android 2.1.2. In this system, we used GPS and GSM technologies.

IV. SYSTEM IMPLEMENTATION

A. *Self-regulated system*

1) *Hardware implementation*

In transmitter part, the Easy-VR shield and the Bluetooth module are connected to the ARDUINO board. The ARDUINO is supplied a 5v input voltage from a laptop through USB connection. An ARDUINO supplies VCC 3.3v to the Bluetooth module and to the Easy-VR shield. The microphone is connected to the Easy-VR board. In order to transmit signal from the Bluetooth, we connected the Bluetooth TX and RX pin to the ARDUINO RX119 and TX118 pin respectively. To communicate with the ARDUINO to process voice signal, the D1 and D0 pins of Easy-VR are connected to the TXD1 and RXD0 pins of ARDUINO respectively. The total circuit diagram of the transmitter part is shown in fig. 7.

In receiver part, the Bluetooth module and the relay shield are connected on the ARDUINO board. There is no physical connection between two Bluetooth modules. The TXD and RXD pins of Bluetooth module are connected to the RX217 and TX216 pins of the ARDUINO respectively to transmit data. The Bluetooth module receives 3.3v from the ARDUINO. The total circuit diagram of the receiver section is shown in fig. 8.

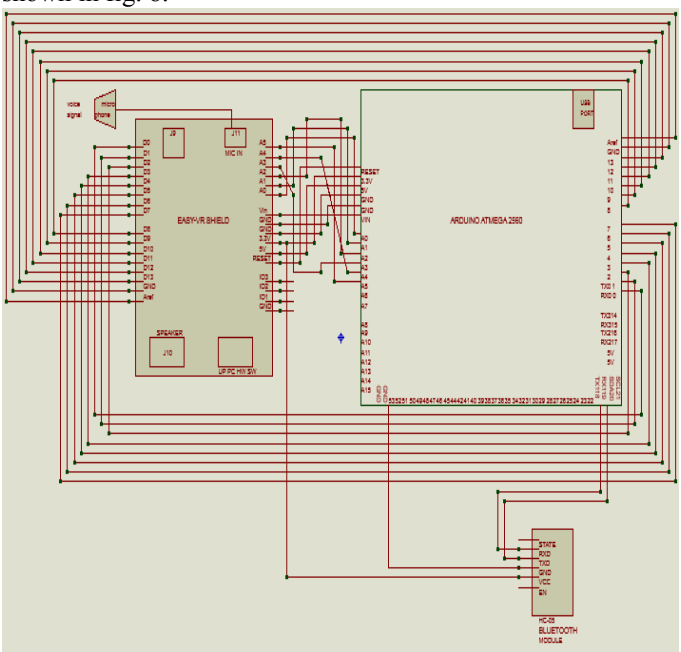

Fig. 7. Transmitter circuit

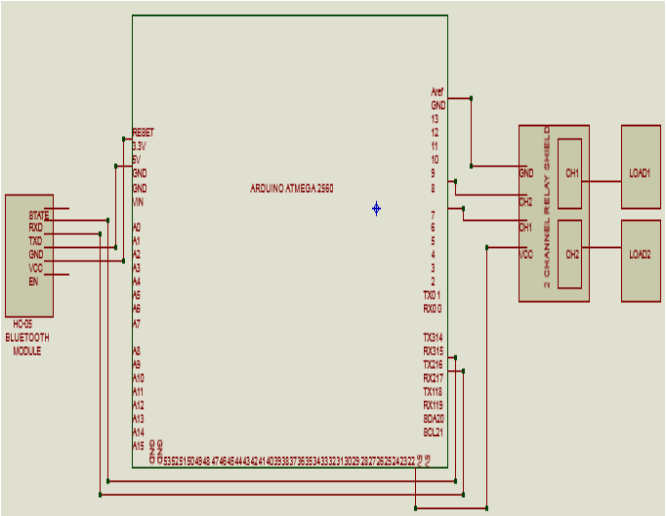

Fig. 8. Receiver part

2) Software implementation

We used the Easy-VR commander software which can record the voice command made by a user. The Easy-VR module can compare it when a command is said on the microphone of the system. To record the user's voice command, after connecting the system with the pc, the commander software is opened which is shown in fig. 9.

There are different groups of commands. We placed all the commands in a group that are needed to be used at the same time. We placed commands "LIGHT" & "FAN" in Group1, "ON" & "OFF" to switch light in Group2 and "ON" & "OFF" to switch fan in Group3. After creating a command the device should be trained twice with the user's voice. To train the device, we got the window which is shown in fig. 10 by clicking the option "Train command" in the top of the above window.

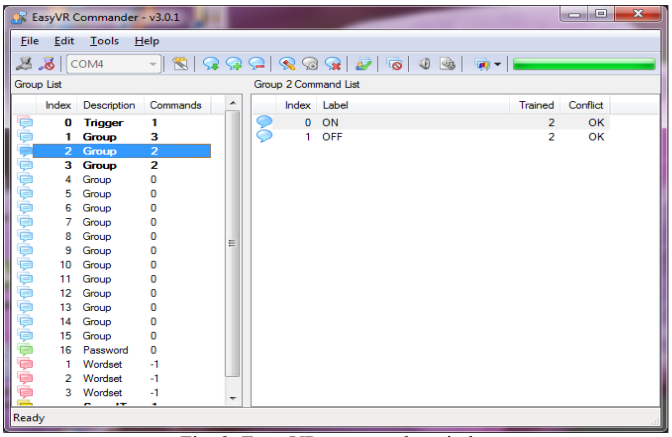

Fig. 9. Easy-VR commander window

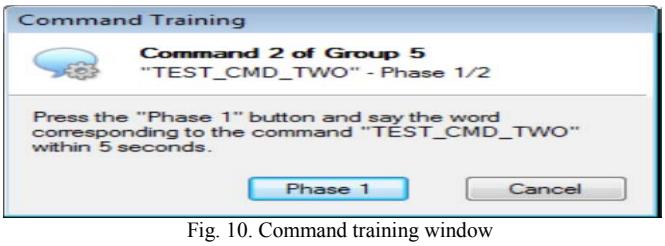

Fig. 10. Command training window

Fig. 11. Speak command window

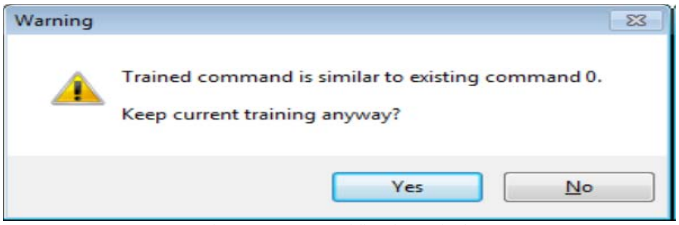

Fig. 12. Error notification window

When "phase 1" is clicked, a window is appeared which indicates to speak the command at that time. This window is shown in fig. 11.

Then this process is repeated again. If there is an error or mismatch, then a window is appeared which is shown in fig. 12.

B. GPS tracking system

Implementation of this system is divided into four different stages:

1) Listening to a location request through SMS over GSM network and authenticating it:

To listen a location request through SMS over GSM network we created a new Broadcast Receiver, extended the "BROADCAST RECEIVER()" class and override the "ON RECEIVE()" event handler. We registered this Broadcast Receiver in the application manifest using an Intent Filter that listens for the "ANDROID. PROVIDER. TELEPHONY. SMS RECEIVED" action String. We also specify the "RECEIVE SMS" manifest permission.

2) Retrieving GPS coordinates (latitude and longitude) of the device:

We used Google Play service location API to retrieve the current location of the user's device.

First of all to connect to Google Play Service API, we created an instance of the Google Play service API client using "GOOGLE APICLIENT. BUILDER()" method. Next we invoked the method "ADD API()" to specify the API we want to use. While using this method, the constant "LOCATION SERVICES. API" is defined within "GOOGLE APICLIENT" class as parameter. Before beginning a connection by calling "CONNECT()" on the "GOOGLE APICLIENT", we specified an implementation for the callback interfaces, "CONNECTION CALL BACKS" and "ON CONNECTION FAILED LISTENER". These interfaces receive callbacks in response to the asynchronous "CONNECT()" method when the connection to Google Play services succeeds, fails, or becomes suspended.

After Connecting to the Google play service location API, we create a reference to the "LOCATION REQUEST" class by invoking "LOCATION REQUEST. CREATE()".

To ask for update of the device's current location, we called the fused location provider's "REQUEST LOCATION UPDATES()". To request the last known location, we invoked the "GET LAST LOCATION()" method of the fused location provider's object. The "GET LAST LOCATION()" method returns a Location object from which we retrieved the latitude and longitude coordinates of the device location by invoking "GET LATITUDE()" and "GET LONGITUDE()" methods respectively.

3) Finding Location Address from the Coordinate:

The "GEO CODER" Class is used to convert a (latitude, longitude) coordinate into a (partial) address. The process is called reverse geocoding. We created an object of the "GEO CODER" class and invoked it's "GET FROM LOCATION()" method, passing the latitude and longitude we obtained in step 2 as parameters.

4) Transmitting the SMS over GSM network:

The SmsManager Class is used to send the SMS message directly to the client.We invoked the static method getDefault() of the SmsManager class to create an instance of the SmsManager and used the method sendTextMessage() to send SMS message to the client, a formated SMS specifying user's current location in both form(Geographical Coordinate and Address) .

Flowchart of this process is shown in fig. 13.

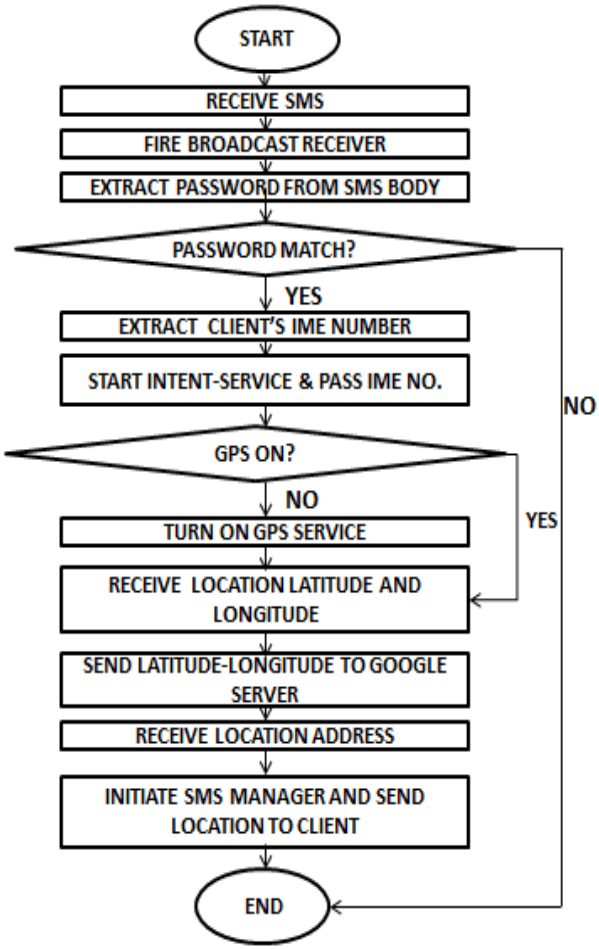

Fig. 13. GPS tracking system flowchart

V. PERFORMANCE TEST

A. *Self-regulated system*

We implemented our experiment to control two loads - fan and light. The result of our home automation section is shown in the TABLE I and the result of our home automation section while used by different person is shown in TABLE II.

By using ARDUINO software, we can observe the response of the system when a command is said. To observe the system response, the system is connected to the pc. The ARDUINO software and then the serial monitor window are opened. When commands are said on the microphone to control the ON/OFF conditions of light and fan the serial monitor responses as fig. 14.

TABLE I. RESULT OF SELF-REGULATED SYSTEM

Number	Commands	Functions
1.	Start	System gets ready
2.	Light-on	Light turns on
3.	Light-off	Light turns off
4.	Fan-on	Fan turns on
5.	Fan-off	Fan turns off

TABLE II. PRACTICAL RESULT OF SELF-REGULATED SYSTEM

Person	Commands	Responses before training	Responses after training
Elderly person Gender: Male Age: 70	Light on Light off Fan on Fan off	No response No response No response No response	Responding Responding Responding Responding
Elderly person Gender: Female Age: 60	Light on Light off Fan on Fan off	No response No response No response No response	Responding Responding Responding Responding
Physically disabled person Gender: Male Age: 34	Light on Light off Fan on Fan off	No response No response No response No response	Responding Responding Responding Responding
Child Gender: Female Age: 10	Light on Light off Fan on Fan off	No response No response No response No response	Responding Responding Responding Responding

```
Say a command in a group 0
Command: 0= start
Say a command in a group 1
Command: 0= light
Give command for light
Say a command in a group 2
Command: 0= on
Light on
Say a command in a group 1
Command: 0= light
Give command for light
Say a command in a group 2
Command: 1= off
Light off
Say a command in a group 1
Command: 1= fan
Give command for fan
Say a command in a group 3
Command: 0= on
Fan on
Say a command in a group 1
Command: 1= fan
Give command for fan
Say a command in a group 3
Command: 1= off
fan off
```

Fig. 14. Serial monitor responses

B. *GPS tracking section*

In GPS tracking system when a client sends a request to know the user's location, then the user gets the following notification on his phone screen:

"*Someone is tracking your location"*

Then the GPS system calculates the location of the user as latitude and longitude and converts it into the location name using GEO coding API of the Android phone and sends a SMS to the client. The client receives the following message:

"*Current location: (location name)"*

VI. CONCLUSION AND FUTURE WORKS

We have represented the design and implementation of a system "3rd HAND" which is targeted at elderly and disabled persons in our work. The system is very flexible. The system implements an automatic voice recognition system by using an Easy-VR module. The wireless network is implemented using Bluetooth modules. ARDUINO program controlling controls the total operation. To implement GPS tracking system, we used all built in features like GPS, GSM, and API of the android phone. This system is very secure. Anyone cannot use the home automation feature of the system. The system must be trained with one's voice and only he can use this feature. In GPS tracking system, only clients who know a pairing password, can request for tracking the current location of the person carrying the system. It is also beneficial for children. This project can be further improved by increasing the efficiency of the self-regulated system so that it can response in a noisy environment. In future, we want to implement the GPS tracking system using GPS-GSM module instead of android phone and without using data connection.

REFERENCES

[1] Humaid AlShu'eili, Gourab Sen Gupta and Subhas Mukhopadhyay, "Voice Recognition Based Wireless Home Automation System," 4th International Conference on Mechatronics (ICOM), pp. 1-6 May 2011.

[2] Dimitar H. Stefanov, Zeungnam Bien, Won-Chul Bang, "The Smart House for Older Persons and Persons With Physical Disabilities: Structure, Technology Arrangements, and Perspectives" IEEE Transactions on Neural Systems and Rehabilitation Engineering, Vol. 12, No. 2, pp. 228-250, June 2004.

[3] A.K.Gnanasekar, PJayavelu and V.Nagarajan , "Speech Recognition Based Wireless Automation Of Home Loads With Fault Identification For Physically Challenged," ICCSP-'12, pp. 128-132, April 2012.

[4] Kim Baraka, et al. "Low cost Arduino/Android-based Energy-Efficient Home Automation System with Smart Task Scheduling", Fifth International Conference on Computational Intelligence, Communication Systems and Networks, pp. 296-301, June 2013.

[5] Jieming Zhu, et al. "DEVELOPING a Voice Control System for Zigbee-based Home Automation Networks," IC-NIDC2010, pp. 737-741, September 2010.

[6] Mardiana B., et al. "Homes Appliances Controlled Using Speech Recognition in Wireless Network Environment ," International Conference on Computer Technology and Development," pp. 285-288, November 2009.

[7] Benjamin Lecouteux, Michel Vacher and François Portet, "Distant Speech Recognition for Home Automation: Preliminary Experimental Results in a Smart Home," 6th Conference on Speech Technology and Human-Computer Dialogue (SpeD), pp. 1-10 , May 2011.

[8] Pankaj Verma, J.S Bhatia, "Design and Development of GPS-GSM Based Tracking System with Google Map Based Monitoring" International Journal of Computer Science, Engineering and Applications (IJCSEA) Vol.3, No.3, pp. 33-40, June 2013.

[9] Umar Farooq, et al. "GPS-GSM Integration for Enhancing Public Transportation Management Services" Computer Engineering and Applications (ICCEA), 2010 Second International Conference (Volume:2), pp. 142-147, 19-21 March 2010.

[10] Nico Deblauwe, Peter Ruppel, "Combining GPS and GSM Cell-ID positioning for Proactive Location-based Services", Mobile and Ubiquitous Systems: Networking & Services, 2007. MobiQuitous 2007. Fourth Annual International Conference, pp. 1-7, 6-10 Aug. 2007.

[11] Youjing Cui and Shuzhi Sam Ge, "Autonomous Vehicle Positioning With GPS in Urban Canyon Environments," IEEE Transactions On Robotics And Automation, Vol. 19, NO. 1, pp. 15-25, February 2003.

[12] Tian Zhihong, Yang Jinsheng and Zhang Jianguo, "Location-based Services Applied to an Electric Wheelchair Based on the GPS and GSM Networks, " Intelligent Systems and Applications, 2009. ISA, pp. 1-4, May 2009.

[13] Al-Mazloum, E. Omer, M. F. A. Abdullah, "GPS and SMS-Based Child Tracking System Using Smart Phone," World Academy of Science, Engineering and Technology International Journal of Electrical, Computer, Electronics and Communication Engineering, Vol. 7, No. 2, pp. 171-174, 2013.

[14] http://arduino.cc/en/Main/arduinoBoardMega2560 (Accessed February 15, 2015).

Assisted Vehicle Driving Embedded with Autonomous Security System

Nur Mohammad [1], Md. Kausar Hamid Miji [1], and Prodipto Chowdhury[1,*]
[1]Chittagong University of Engineering & Technology, Bangladesh
[*] E-mail: cprodipto@gmail.com

Abstract— **The roads and highways of Bangladesh are among the most deadly roads in the world due to the movement of capacity crossing huge traffic. Yet the safety system is not very high. Hence accidents and traffic jam is very common. Still now, no collision avoiding system is used to prevent accidents. In this paper, Autonomous Embedded Vehicle Security System especially with Obstacle Collision Avoidance system has been developed. The embedded sensors of the prototyped vehicle provide related versatile information. These can be used in detecting obstacles in the vehicle trajectory and provide an alarming signals to the vehicle driver to avoid collisions. In this proposed system, a gas-sensing module has been used for the detection the potential of combustible gas. The temperature sensor has been installed in order to read the system temperature continuously. An alarm circuit has been added to the system to warn the driver about the vehicle in-front obstacle and the potential of LPG gas. The presence of LPG gas can also be determined from the indication lamp of the voltage comparator. An initial application was implemented in order to test the detection of vehicle in-front obstacle and for the measurement of the distance between the vehicle and obstacle. The LCD display indicates the distance of the obstacle and turns on the alarm to warn the driver to avoid the collision.**

Keywords— Embedded System, Gas Sensing Module, Temperature Sensing Module, Ultrasonic Sensors, Motor driver

I. INTRODUCTION

Over the past few years, road accidents, especially highway accidents have been rising alarmingly in Bangladesh [1]. According to a study conducted by the Accident Research Centre (ARC) of BUET, road accident kills on average 12,000 lives annually and causes 35,000 injuries [1]. According to World Bank Statistics, annual fatality rate from road accident is found to be 85.6 fatalities per 10,000 vehicles [1]. Maniruzzaman and Raktim Mitra, in their study claimed that 'the number of accidents has increased by 43 per cent between 1982 and 2000 while the number of fatalities has increased by around 400 per cent within the same period' [2]. The fatality rate in Bangladesh is 35 times higher than US and 50 times higher than UK [3]. Hence it is clear that roads in Bangladesh have become deadly. Besides, accidents also cause an enormous financial loss. According to World Health Organization (WHO), road traffic injuries cause a loss of about 2% of GDP in Bangladesh, or about £1.2bn annually [4].

Bangladesh is trying to develop its road network, but the attempts cannot keep pace with population and commerce, and accordingly, roads are being turned into death traps devoid of safety measures [4]. Therefore, we have identified the necessity of a system that will efficiently reduce the road accident at low cost in roads and highways.

One of the crucial causes of road accidents is alcoholism. Driving while intoxicated or drunk is dangerous and drivers with high blood alcohol content or concentration are at greatly increased risk of vehicle accidents, highway injuries and vehicular death. In our country most accidents are occurring by the drunken truck drivers.

Another type of accident we often notice is the leakage of gas from containers. However, almost all the accidents caused by collision, alcoholism, and gas-leakage are completely avoidable. So, we need an effective system to detect vehicle in-front obstacle and check out the alcohol or presence of LPG gas inside the cabin of the vehicle.

Our proposed system is composed of an obstacle sensing module, a motor driving unit, a gas sensing module, an alarm circuit, and a temperature sensor. The system detects any obstacle static or dynamic in-front of the vehicle and the gas sensing module will recognize the potential of LPG gas and alcohol.

A method to implement vehicle safety systems with one or two channels and using single transceiver, micro-controller 89C51 is used as main driver [5]**.** A remote monitoring system had been developed [6] which have focused on the GSM, because the wireless remote monitoring system has more and more application. A low cost automotive localization system had been developed using GPS and GSM-SMS services [7]. The system permits localization of the automobile and transmitting the position to the owner on his mobile phone as a short message (SMS) at his request. There is Collision Warning System (CWS), Collision Mitigation System (CMS) [8], RFID Technology [9], Cruise Control (CC), Adaptive Cruise Control (ACC) [10] [11] etc. to prevent accidents. These systems are not very cost effective that a country like Bangladesh can afford them. So to provide safety and security of the vehicle at minimum cost is our main motto.

The paper is organized as follows. Sections II and III present the sensor elements considered in the system and its programming and simulation. Section IV presents the hardware implementation, which is followed by section V that presents the result and discussion.

Copyright Notice: 978-1-4673-9257-0/15/$31.00 ©2015 IEEE

II. CONSIDERED SENSOR ELEMENTS

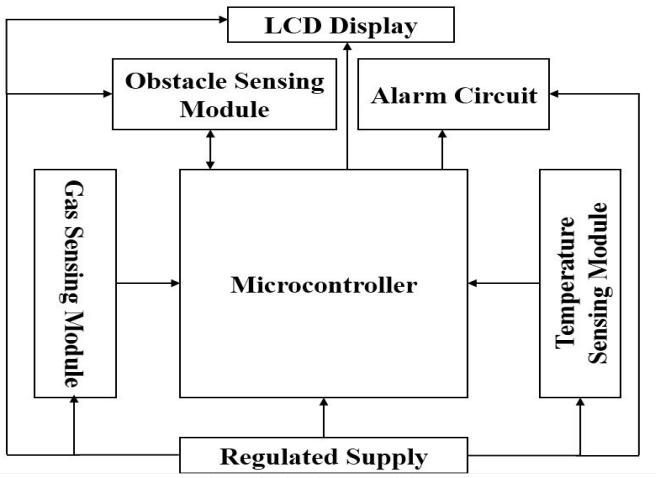

Figure 1. Complete Block Diagram of the Proposed System

A sonar based obstacle sensing module is used to measure the distance between vehicle and in-front obstacle. A motor driver circuit is used to control the vehicle. If the hindrance is at a predefined distance that may cause accident, the vehicle will stop automatically. Thus accident can be prevented. Again, the leakage of LPG gas can be detected by gas sensing module. An indication lamp is used to warn the driver about the potential of gas. The alarm circuit warns about the presence of in-front obstacle and the leakage of gas. The circuit is supplied from a 5V regulated supply. The total system is represented as in Figure 1.

A. Obstacle Sensing Module

The sensor calculates the distance from an object by sending bursts of ultrasound towards it and measuring the time it takes to the waves to get back (Distance = Velocity * Time). This information is used to determine whether there's a close "obstacle" near the vehicle. The motor driving circuit is just a simple transistor switching circuit. The microcontroller feeds the transistor at base when there is no obstacle in front of the vehicle and when there is an obstacle, the microcontroller turns off the transistor. The obstacle sensing module block diagram and motor driving circuit are shown in Figure 3 and 4, respectively.

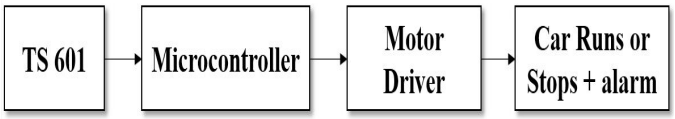

Figure 2. Functional block diagram of the Obstacle Sensing Module

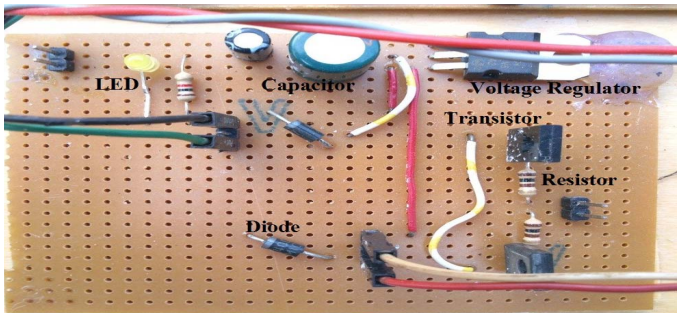

Figure 3. Motor Driver Circuit

The alarm circuit (Figure 4) is also a transistor switching circuit where a buzzer is used instead of the motor [15].

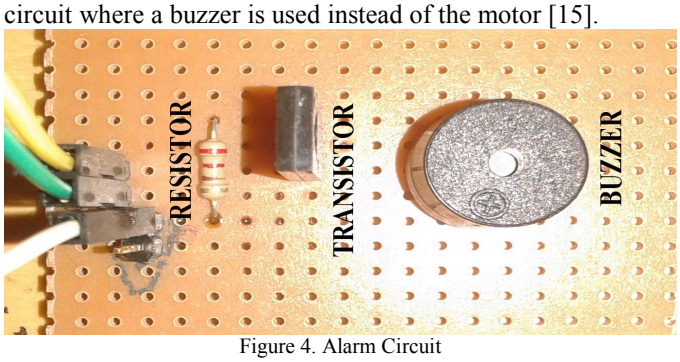

Figure 4. Alarm Circuit

B. Gas Sensing Module

MQ-5, a semiconductor sensor is used for Combustible Gas Detection. Sensitive material of MQ-5 gas sensor is SnO_2, which has lower conductivity in clean air [12]. When the target combustible gas exists, the sensor's conductivity rises. MQ-5 gas sensor has high sensitivity to Methane, Propane and Butane [12].The output voltage of the MQ-5 gas sensor is compared with the voltage comparator which is in non-inverting non-zero mode. If the output of the MQ-5 becomes equal or higher than the reference voltage, the indication lamp lit up and the alarm circuit turns on. Thus the potential of the combustible gas is detected. We used HA17339A IC as the voltage comparator circuit. The block diagram and implementation of voltage comparator and gas sensing module are shown in Figure 5, 6, and 7, respectively.

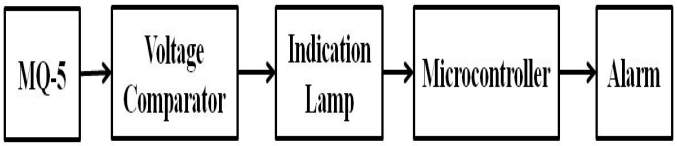

Figure 5. Functional block diagram of the Obstacle Sensing Module

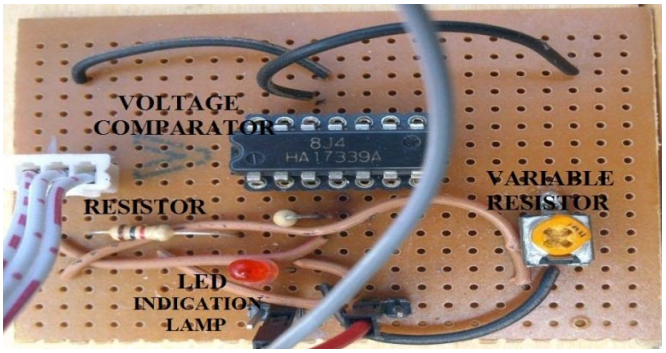

Figure 6. Voltage Comparator Circuit

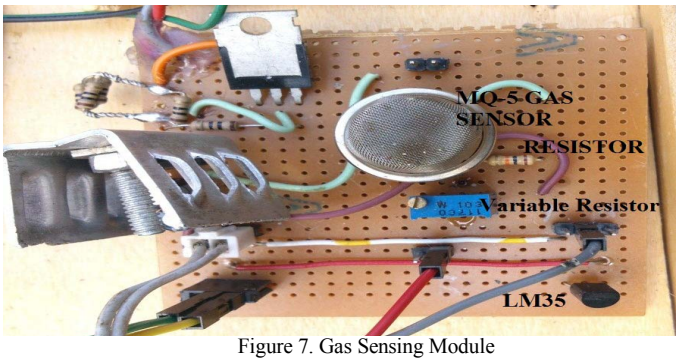

Figure 7. Gas Sensing Module

C. *Temperature Sensing Module*

Temperature is the most frequently measured environmental quantity. Most systems are affected by temperature. The performance of these systems is controlled by using proper control systems that keep temperature within specified limits[13]. Temperature sensors provide inputs to those control systems [14]. We used LM35 IC to read system temperature continuously. Figure 8 shows the temperature sensing module.

III. PROGRAMMING AND SIMULATION

For simulation and programing of the embedded system, Proteus and Mikro C were used. Algorithms were developed to interface obstacle sensing module and gas sensing module with the microcontroller.

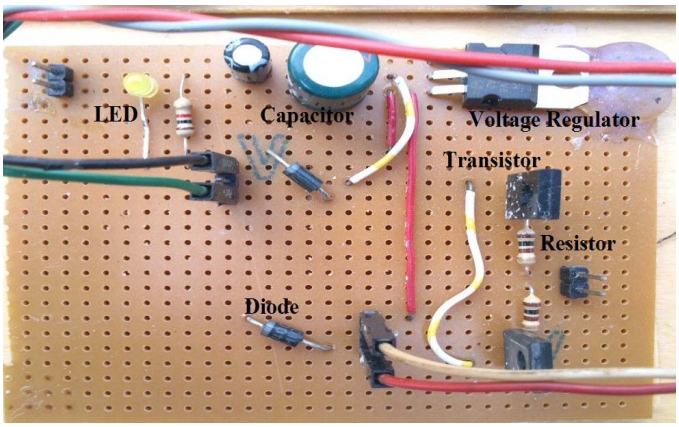

Figure 8. Temperature Sensing Module

A. *Algorithm to Interface Obstacle Sensing Module with Microcontroller*

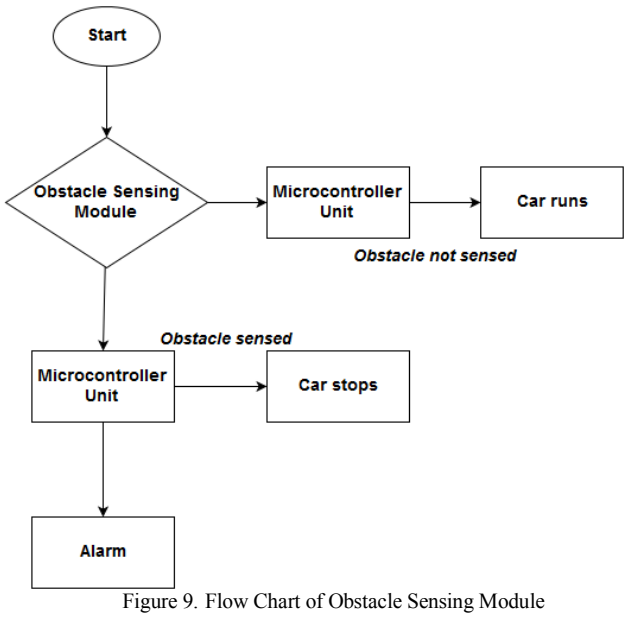

Figure 9. Flow Chart of Obstacle Sensing Module

B. *Algorithm to Interface Gas Sensing Module with Microcontroller*

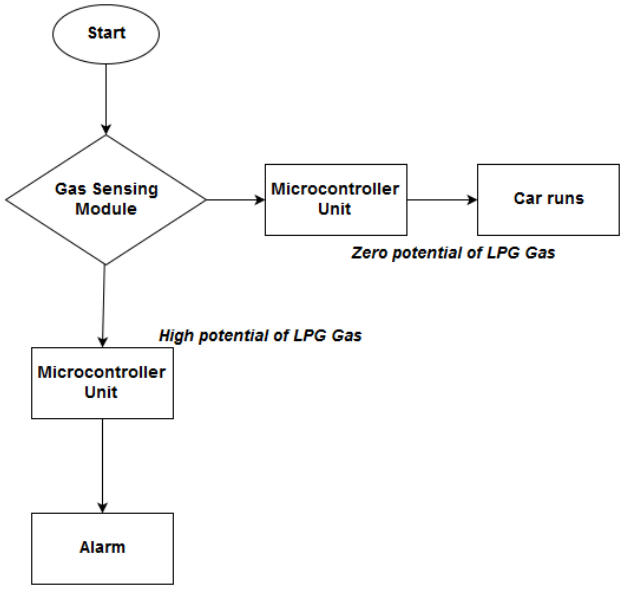

Figure 10. Flow Chart of Gas Sensing Module

IV. HARDWARE IMPLEMENTATION

The proposed system is implemented in a prototype vehicle. The prototype vehicle is designed with two gearhead motor, two wheels, a cluster wheel and mechanical body. The proposed system works properly. When there is an obstacle in-front of the vehicle, then it stops and the alarm is on. Again, when it finds any presence of LPG gas, the LED just lit up and also the alarm is switched on. The temperature sensor continuously reads the system temperature and the centigrade

value is shown in the LCD display. The entire developed system is shown in the following figure:

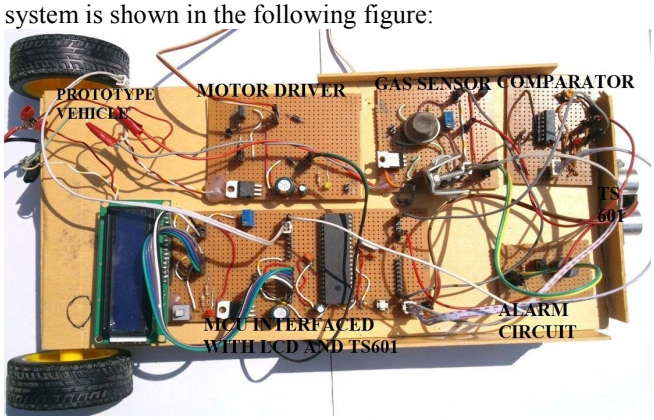

Figure 11. Entire Proposed System Implemented on a Prototype Vehicle

V. RESULT AND DISCUSSION

Each module in the system functions properly and successfully; the only minor issue is the calibration of the variable resistor of the gas sensor. Another problem is the external noise interfering with the LCD display and with the transmitter and receiver of the TS 601 obstacle sensing module. The external noise comes from a variety of sources—computers, cell phones, power supplies, etc. Other noise sources include the parts of the gas sensing module itself; these include the oscillator, battery, speaker, long wires, power on the Vero board, and the Vero board itself.

Using additional capacitors may help to filter out the noise from the power supply and to reduce board noise. Implementation on a PCB (printed circuit board) is another solution to greatly reduce noise. No extraneous wires are needed, thereby leading to cleaner and stronger signals to the components, as daisy-chaining of the power wires are eliminated. Also, implementation on a PCB makes the overall system more compact.

The circuit performance is shown in Figure 12. The performance of each module was determined by trial and error method. It can be clearly observed that the modules always did not perform successfully. For example, the gas sensor is highly sensitive to current that depends on the variable resistor .We used a battery of 12 volts as power supply, which is converted to 5 volts using a voltage regulator. The battery

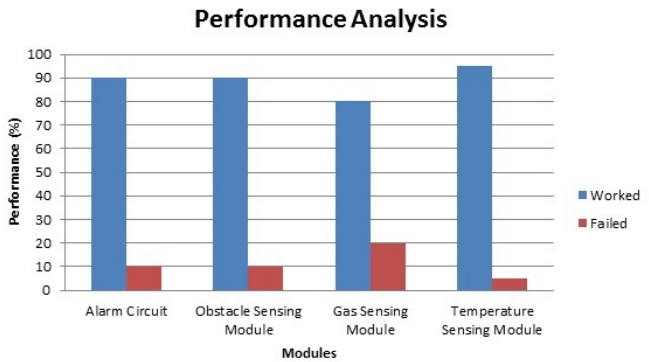

Figure 12. Performance Analysis of the Designed System

discharges rapidly during operation and is needed to charge it frequently. Again the ultrasonic sensor did not work as it is described in the data sheet. The range was lower than that is provided in the data sheet. Hence the system's modules performance was not hundred per cent. However, the total systems performance was satisfactory.

The system has been considering only the distance between the vehicle and its obstacle in front. To stop the vehicle its speed should be controlled as well. A fuzzy algorithm can be used to control the speed at different distance between the vehicle and obstacle. Again, the range of the obstacle sensing module is small. So we need to increase the range of obstacle sensation for implementing in real vehicle. It can be done using RADAR. Also a GPS tracker can be used to secure the vehicle from stealing. Although there is a vast amount of automation technology in this field, in Bangladesh, we are lagging behind, and the rate of accident is increasing day by day. So, this system can be used to reduce the rate of accident and save the life of people of Bangladesh. However, the designed system is a prototype, and not yet prepared to implement in real life. To implement it with the existing vehicles, its size should be reduced, and the best possible way to do that is to incorporate all functionalities in a single chip; which will be our future work.

This paper presents a system for automatic detection of obstacle in front of vehicle as well as potential of LPG gas inside the vehicle, and helps decrease one of the major causes of fatalities; excessive speed or potential of LPG gas. Our approach is based on a combination of three different sensor technologies: sonar based sensor to convey the information about the in-front obstacle, gas sensor to indicate the presence of LPG gas, temperature sensor to read the system temperature continuously. The proposed system is portable and suitable for use any commercial car with little modifications. The system shows promising results. Since the presence of a vehicle in front can be reliably detected in advance using sonar based technology, vehicle's behavior can be adjusted accordingly. We have testes the system in real-life conditions, and have been able to reduce the speed of the vehicle to zero at the predefined distance as a result of the detection of the obstacle. The technology developed can help drivers in avoiding collision with obstacles; consequently can reduce the fatalities of road accident, which is the main objective of this project.

REFERENCES

[1] Tashmina Rahman (2012), Road Accidents in Bangladesh: An Alarming Issue [Online]. Available: http://blogs.worldbank.org/endpovertyinsouthasia/road-accidents-bangladesh-alarming-issue

[2] KM Maniruzzaman and Raktim Mitra, "Road accidents in Bangladesh" *IATSS Research*, vol. 29, no. 2, pp. 71, May 2005

[3] FE Report (2013), Fatality rate in BD road accidents 50 times higher than in UK [Online]. Available: http://www.thefinancialexpress-bd.com/index.php?ref=MjBfMDVfMTVfMTNfMV8xOTBfMTY5NDE1

[4] Syed Zain Al-Mahmood (2012), Bangladesh's road accidents take heavy toll on poor – and on economy [Online]. Available: http://www.theguardian.com/global-

development/2012/aug/22/bangladesh-road-accidents-poor-economy.
[5] K.J. Padmini, S.S. Dorle, A.G. Keskar, Megha, and B. Chakole, "Micro-controlled based Vehicle Safety System Using Dedicated Short Range Communications (DSRC)", in *Second International Conference on Emerging Trends in Engineering and Technology*, Dec. 2009, pp. 570-575
[6] Chen Peijiang and Jiang Xuehua, "Design and Implementation of Remote monitoring system based on GSM," in *Pacific-Asia Workshop on Computational Intelligence and Industrial Application*, Dec. 2008, vol.42, pp.167-175.
[7] Ioan Lita, Ion Bogdan Cioc, and Daniel Alexandru Visan, "A New Approach of Automobile Localization System Using GPS and GSM/GPRS Transmission," in *29th International Spring Seminar on Electronics Technology*, May 2006, vol. 8, pp. 415-422
[8] OnGuard™ Collision Safety System Driver Tips, Meritor Wabco, 2009
[9] Fernando Seco, Vicente Milanés, Antonio Jiménez, Julio C. Díaz, and Teresa de Pedro, "An RFID-Based Intelligent Vehicle Speed Controller Using Active Traffic Signals", *Sensors*, vol. 10, no. 6, pp. 5872-5887, Jun. 2010
[10] Alex Forrest, Mustafa Konca, "Autonomous Cars and Society", Department of Social Science and Policy Studies Worcester Polytechnic Institute Worcester, MA 01609, Tech. Rep., 2007
[11] Raj Kamal, *Embedded Systems -Architecture, Programming and Design*, New Delhi: McGraw-Hill, 2008
[12] "MQ-5 data sheet", Henan Hanwei Electronics Co.,Ltd., Zhengzhou, China.
[13] *Temperature Sensor Handbook*, National Semiconductor, 1995.
[14] Robert F. Coughlin and Frederick F. Driscoll, *Operational Amplifiers and Linear Integrated Circuits,* Englewood Cliffs, N.J.:, Prentice Hall, 1991

A Survey on Interconnect Encoding for Reducing Power Consumption, Delay, and Crosstalk

Sujan Kumar Saha[1], Bulbul Ahmed[2], Jiangjiang Liu[3]
[1,2]Department of Electrical Engineering and [3]Department of Computer Science
Lamar University
Beaumont, USA
Email: [1]ssaha@lamar.edu, [2]bahmed@lamar.edu, and [3]jane.liu@lamar.edu

Abstract—**With the advancement of technologies, interconnect circuits are shrinking dramatically. Capacitances of interconnects are increasing due to minimized wire size and inter wire spacing. As a result, interconnect power consumption, delay, and crosstalk are increasing significantly, which is affecting overall interconnect performance. Various techniques such as buffer insertion, shielding, skewing, and encoding are used to minimize delay, crosstalk, and power consumption. This paper studies a set of encoding methods for reducing power consumption, crosstalk, and delay, and also presents a comprehensive comparison and analysis of these encoding techniques.**

Keywords—encoding, power, delay, bus invert, shielding, weighted code mapping.

I. Introduction

In Deep Sub-Micron (DSM) technology, the VLSI circuit components are now at the size of nanometer range. Along with the components, interconnects are also shrinking very quickly due to aggressive scaling down of technology. In this case, wire width is getting thinner but height is not decreasing so rapidly to keep resistance constant. As a result, the ratio of height to width is increasing prominently. Lots of research has been accomplished on low power circuit designs, focusing on the reduction of circuit component power consumption. But, now in today's Deep sub-Micron technology, interconnect energy is no longer ignorable. Due to the dense placement of interconnects, coupling capacitance is increased, which dominates the self capacitance of the wire. Consequently problems with crosstalk delay, noise and power consumption arise which affects the overall circuit performance.

Coupling capacitance contributes to extra power consumption because of the different switching pattern of the adjacent bus. Opposite transition between two adjacent buses causes worst case cross talk and produces a large delay and energy consumption in the interconnect. Different techniques have been applied to minimize crosstalk, delay, and power consumption. Some are at the circuit level and some are at the architecture level. Among these, bus encoding is a widely used method. This method is used to change the bit patterns of the data so that self-transitions, charging, discharging, and toggle transitions are reduced, which will eventually minimize power consumption, delay, and also crosstalk in some instances. In this paper, a set of encoding methods will be discussed to reduce power, and the rest of the methods are for minimizing delay and crosstalk. All methods are explained in Section II, Section III contains results reported by corresponding papers and a comprehensive comparison, followed by the conclusion in Section IV.

II. Selected Bus Encoding Methods

A. Bus Invert

Bus Invert encoding method [1] is one of the most widely used encoding methods. This encoding method is mainly focused on reducing the number of transitions. According to the method, only one control bit is needed to indicate the inversion. To implement Bus Invert encoding, first of all, we need to calculate the hamming distance between the data of two consecutive cycles. Hamming distance between the two data strings of length n is the total number of positions at which the corresponding data are different. If the hamming distance is greater than n/2 where n is the number of the bus width or length of data string, set control bit=1 and invert all the bits of next cycle original data. If the hamming distance is less than n/2, then set control=0 and keep the data value as it is in the next cycle. At the receiver side, the contents of the bus must be conditionally inverted according to the control bit.

In the example figure 1, there are 9 transitions between current cycle data and next cycle original data, which have been marked as light blue. So, hamming distance is 9. In the other 7 positions, the data is same as it is in the current cycle. As data length is 16 and hamming distance is greater than 8, control bit will be equal to 1 and all the bits of next cycle original data will be inverted. After the inversion hamming distance is 7. Thus, due to inversion of the next cycle bits, 2 self-transitions have been reduced.

As only one control bit is used to transfer the encoding information, area overhead is very small. Also this method doesn't require an extra clock cycle. Yet here, only self-transition is reduced, but crosstalk due to coupling capacitance

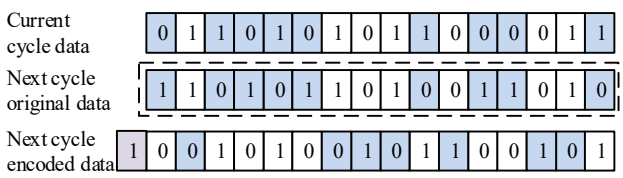

Fig.1. Bus Invert Encoding (bus width 16 bit, control bit 1)

978-1-4673-9257-0/15/$31.00 ©2015 IEEE

between adjacent wires is not considered.

B. Odd Even Invert

Odd Even Invert [2] encoding is a modified version of Bus Invert encoding. This method is also focused on reducing the number of transitions. As the number of transition is directly proportional to power, it also reduces power consumption of interconnects. The authors of this paper mentioned two encoding approaches, Simple Odd Even Invert and Calculated Odd Even Invert.

Initially there are some common features of these two encoding methods. First, we have to divide bus lines into two groups, odd lines and even lines. Bus lines are selected according to their position. Odd position lines go to the odd group and even position lines go to the even group. For this encoding method, two extra control lines are required to send the encoding information. There are four possible cases with two control lines: no bus lines are inverted (00), only odd lines are inverted (10), only even lines are inverted (01), and all lines are inverted (11). We need to transfer the bits over the invert-lines according to what we have done. This information needs to be transferred to decode the original bits. In the next subsection, two encoding approaches have been described separately.

1) Simple Odd Even Invert: To implement simple Odd-Even Bus Invert, only self transitions are considered. Coupling transition is not considered in this method. Coupling transiton is the impact of one wire due to the transition of the adjacent wire. According to this encoding, if the number of self-transitions on the odd lines is more than or equal to the half of odd lines, the odd lines are inverted, and if the number of self-transitions on the even lines is more than or equal to the half of even lines, the even lines are inverted. Following the example of figure 3 makes it easy to understand the encoding. In the example, there are 4 transitions in odd lines and 5 transitions in even lines. So all bus lines have been inverted and control bits are 11. After inversion, there are 7 transitions, which is less than the original number of transitions. Also, it should be noted that there was one toggle before inversion. After the inversion, the toggle is removed automatically. Still, if there is any toggle, then we need to apply the two phase transfer method to remove the toggle. The two Phase transfer method delays one of the two adjacent lines by a half cycle. So, this encoding method introduces some delay to eliminate toggle. The amount of delay depends on the number of toggles after inversion.

	C0	C1
No Invert	0	0
Even Invert	0	1
Odd Invert	1	0
Both Invert	1	1

Fig.2. Control Bit of Odd Even Encoding

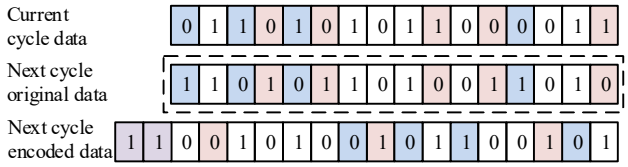

Fig.3. Simple Odd Even Invert Encoding (bus width 16 bit, control bit 2)

2) Calculated Odd Even Invert: Calculated Odd-Even Bus Invert [2] encoding is slightly different from Simple Odd-Even Bus Invert encoding. In Simple Odd Even Invert, only self transitions have been considered. Whereas in Calculated Odd Even Invert, coupling transitions are considered. According to figure 2, there can be four types of inversions. For each of the inversion types, the total number of coupling transitions (charging and discharging) [2] are calculated between current cycle data and next cycle original data. Then that inversion type is selected for encoding which has the least number of coupling transitions. For example, in figure 4, current and next cycle data are 0110101011000011 and 1101011010011010. For 00 type inversion, the total coupling transition is 20, for 01 type it's 11, for 10 type it's 15, and for 11 type it's 20. In this case it has been considered that one toggle transition is equivalent to 4 coupling transitions. As we get an 11 transition for 01 type inversion, which is smallest, it is selected as encoded data.

C. Temporal and Shielding Coding (TSC)

The encoding approach of Sainarayanan *et al*. [4] is useful for eliminating crosstalk delay. Table I shows crosstalk induced delay categorization of a wire due to two adjacent lines. In this table "↓" represents 1→0 transition, "↑" represents 0→1 transition, and "–" means there is no change of data bit. Also here, Cg is ground capacitance, R is total resistance of wire, Cc is coupling capacitance, and λ is the ratio of Cc to Cg. The encoding method is developed to eliminate crosstalk class 5 and 6. According to this approach, actual data to be transmitted is divided into groups of 3 bits. Encoded data is transmitted in the first temporal cycle and the information of encoding and shielding is transmitted in the 2nd temporal cycle. So every 3-bit real data is encoded as 2 consecutive groups of 3-bit data to be transmitted in two consecutive temporal cycles. To avoid worst-case crosstalk in boundaries of every 3-bit group, 0 is transmitted between two adjacent 3-bit groups as a shielding bit. So this approach needs an extra 1-bit line after every 3-bit group. That's 8-bit data will be encoded as 10-bit data length.

For example, a data d_{t-1} = 101 0 100 0 00 is the encoded data transmitted at time "t-1", and data d_t = 01001101 is original data to be transmitted at time "t". Before encoding

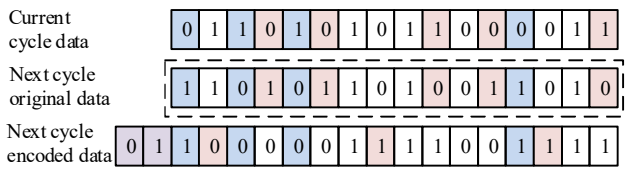

Fig.4. Calculated Odd Even Invert Encoding (bus width 16 bit)

TABLE I. CROSSTALK CATEGORIZATION

CC	Delay	Pattern of switching
1	0	−−−, −− ↑, ↑ −−, −− ↓,↓ −−, ↑ − ↑,↑ − ↓,↓ − ↑,↓ − ↓
2	C_gR	↑↑↑,↓↓↓
3	$C_gR(1+\lambda)$	− ↑↑,↑↑ −,− ↓↓,↓↓ −
4	$C_gR(1+2\lambda)$	− ↑ −,− ↓ −,↓↓↑,↑↓↓, ↑↑↓,↓↑↑
5	$C_gR(1+3\lambda)$	− ↑↓,− ↓↑,↓↑ −,↑↓ −
6	$C_gR(1+4\lambda)$	↓↑↓,↑↓↑

this, both data will be checked for crosstalk class according to the crosstalk categorization table. As in this case, the crosstalk class is greater than 1, so 3-bit groups will be inverted as the encoded data 101 0 100 0 01 and transmitted in the first temporal cycle. The 2nd temporal cycle contains the encoding and shielding information. If the data is inverted, in the 2nd temporal cycle in every 3 bit groups, 3rd bit will be set to 1; otherwise it will be 0, and the first and second bits are kept same to the 1st temporal cycle so that there is no transition. So, for the encoded data, 2nd temporal cycle data will be 101 0 101 0 01. Finally, given data d_t will be encoded as 2 consecutive temporal cycle data.

This method is further modified by adding two extra bit lines into both sides of the shielding bit. These extra bits are inserted in such a way so that the transition is same as the boundary bits of the 3-bit group. This modified approach can eliminate crosstalk class 5, 6, and also crosstalk class 4 as well as any transition pattern that is −↑−, −↓−, ↓↓↑, ↑↑↓, ↓↑↑, ↑↓↓. However these methods do not include inductance effect, increase bit lines in modified approach and eventually increase the area overhead.

D. Temporal Crosstalk Shielding(TCS)

Najeeb *et al.* [5] reduces both power and crosstalk delay by reducing bus width and using the temporal shielding approach. Original data is divided into several blocks before encoding. Then the data is encoded into two data packets and transmitted over two consecutive clock cycles. For example, the original data of n bits is divided into k bit blocks, then the number of groups are now n/k and encoded into two m bit data blocks. This is done in such a way so that n is a multiple of k and m is less than k. As the encoded bit m is less than k, active bus width is reduced. Keeping bus area constant, spacing among wires is increased so that coupling capacitance decrease. This

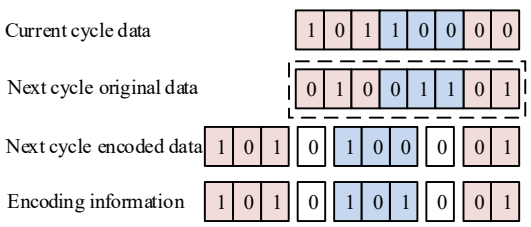

Fig.5. Temporal and Shielding Coding (bus width 8 bit, shielding bit 2)

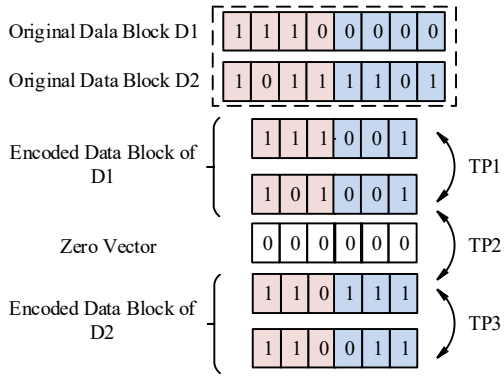

Fig.6. Temporal Crosstalk Shielding (bus width 8 bit)

method is also developed to eliminate crosstalk in class 5 and 6 of Table I.

If data D1 was transmitted at time Tt-1 and D2 is to be transmitted at Tt, D2 is encoded according to following Table II proposed by this approach. Here each 4-bit block is encoded into two 3-bit blocks. As the original data block is encoded into two data blocks, 4 cycles are needed to transmit two original data, and for these 4 transmissions, there are 3 transitions. The transition between the first transmission to the second one is named Transition Pattern 1(TP1), between 2nd and 3rd is TP2, and between 3rd and 4th is TP3. The Encoding Table is formed in such a way that there is no opposite transition between two adjacent blocks. Thus at TP1 and TP3, crosstalk class 5 and 6 are eliminated. This crosstalk may only happen at TP2. A crosstalk analyzer is used to detect crosstalk class 5 and 6; if found, then it sends a crosstalk identification vector before the next data is transmitted. To eliminate class 5 and 6 crosstalk, a Zero vector is transmitted between those affected data. At the receiver end, according to the decode bit, the decoder detects whether it receives zero vector or useful data. If zero vector is received, then it is discarded, and if it receives other than zero vector, the data is stored and using stored data and bus data, the original data is recovered. This approach is efficient for addressing bus delay reduction because there is less crosstalk and it improves power efficiency for the data bus.

E. Variable Cycle Transmission with Hybrid Spatial Temporal Redundancy (VCT_HSTR)

Zhang *et al.* [6] attempted to reduce both energy and delay. That's why the encoding method proposed in [6] combines Weighted Code Mapping (WCM) [13] with temporal redundancy. The Weighted Code Mapping focuses on reducing energy, whereas Temporal Redundancy reduces delay. The WCM algorithm relies on probability distribution of the data pattern. All patterns do not have the same probability of occurring. Suppose for the data set {00, 01, 10, 11}, the probability set is {0.1, 0.4, 0.4, 0.1}. Each value of the probability set represents the corresponding probability of the data value. So, the more probable data is mapped to a code word, which has less number of transitions among the bits. The authors also mentioned that one easy way of getting WCM code is to perform bitwise XOR operation between two consecutive cycle data.

TABLE II. TEMPORAL CROSSTALK SHIELDING ENCODING TABLE

4-bit Original data	3 bit Encoded data	4-bit Original data	3 bit Encoded data	4-bit Original data	3 bit Encoded data	4-bit Original data	3 bit Encoded data
0000	001 001	0100	011 001	1000	100 100	1100	111 001
0001	001 011	0101	011 011	1001	100 110	1101	111 011
0010	001 101	0110	011 111	1010	110 000	1110	111 101
0011	001 111	0111	100 000	1011	110 110	1111	111 111

After getting the code words, the delay between two consecutive codes are measured using the crosstalk delay types mentioned in Table I. If the delay is greater than type 4, then a temporal redundant code is inserted between the code words. Before doing this, it also checks whether the delay is type 6 or not. If the delay is type 6, then the 2nd code word is inverted; otherwise it's not. The temporal redundant code is either all zeros or all ones. It is decided based on the total delay of three consecutive codes (current code, temporal code, and next code). By using the following example of figure, it will be easy to understand the encoding method. Suppose two consecutive WCM codes are 101111000 and 010001000. As the delay between the codes is type 6, the 2nd one is inverted. So now the 2nd one is 101110111. Then the total delay of the two sets {101111000, 000000000, 101110111} and {101111000, 111111111, 101110111} is measured, where 000000000 and 111111111are temporal codes. The set which has less delay is selected as encoded data. In this example, the set {101111000, 000000000, 101110111} has less delay. So this is the encoded data.

F. *Opposite Transition Forbidden Weighted Code Mapping (OTF_WCM)*

This method [6] is a slightly modified version of WCM coding. The original WCM encoding method doesn't guarantee to eliminate crosstalk type 5 and 6. This encoding method generates a WCM codebook that doesn't have an opposite transition pattern. As a result, all crosstalk type 5 and 6 and some of type 4 are eliminated. If W denotes the set of code words of n bits, W can be represented as W ={w | w = a1a2…aiai+1….an, ai=0,1}, where i denotes the index of the opposite transition bit lines. The W will be an opposite transition forbidden (OTF) codebook if it doesn't have 2λ transitions with each other. In the original WCM coding, the codes are selected in such a way that transition energy is minimized.

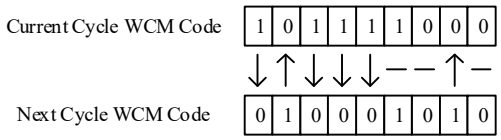

Fig. 7. Transition between two WCM code

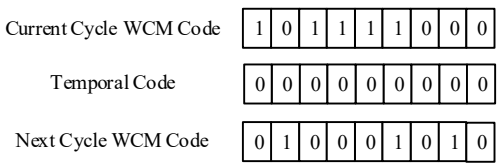

Fig. 8. VCT_HSTR Encoding (bus width 9 bit)

According to this encoding method, after selecting WCM codes, each code is checked whether it is OTF or not. If it is OTF, then it is selected as a mapping code for a particular data pattern. As the codes of OTF codebook are guaranteed not to have type 5 and 6 crosstalk delay, it can be said that this encoding method is optimized for both energy and delay.

G. *Encoding for Crosstalk*

Verma *et al.* [7] proposed an encoding method to eliminate worst-case crosstalk by reducing actual data bit lines. Required components are counter, controller, comparator, and register to design the encoder. Counter counts the number of 0s and 1s in input data lines and feeds these two inputs to the controller. Controller output follows the number, which one is higher. For example, if the number of 1s is greater than the number of 0s, controller output is set to 1 and vice versa. Then controller output is fed to the comparator and also to the decoder. Actual data lines are fed into the comparator along with the controller output. In the comparator, the controller output is compared with every bit in actual data lines to get the inverted bit positions.

For example, in the 8-bit data "10110101", the number of 1s is 5, which is greater than the number of 0s, which is 3. The controller output is set to 1 and is fed into the comparator along with original data to be compared. XOR operation between controller output and original data is performed at comparator, and the positions where controller output does not match are the inverted bit positions. In this example, inverted bit positions are 1, 3, and 7 if we set the index from LSB to MSB. So, in binary form, 001, 011, and 110 are stored in three registers and then transferred to the decoder for retrieving original data. Although this method reduces actual bus width, for the use of register, area overhead increases and to transfer register bits, an extra clock cycle is introduced.

H. *Crosstalk Quantitive Approach*

In the previous encoding methods, the inductive effect was not considered. As operating frequency is increasing in recent days, the inductance of the wires is also adding noise and

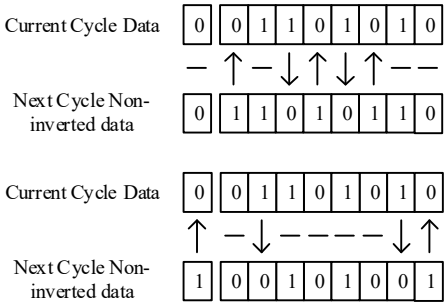

Fig.9. Crosstalk quantitative approach

delay. Ruan *et al*. [8] considered the inductance effect as well as capacitance to determine the encoded data. They used the RLC model instead of the RC model to represent bus lines. Just like the two capacitances (self and coupling), there are also two kinds of inductances, self-inductance and mutual inductance. Total inductance is the summation of self-inductance and mutual inductance between wires. But capacitance and inductance effects are not dominant at the same time. When data of two adjacent wires changes towards the opposite direction (zero to one and one to zero), the capacitance effect dominates over the inductance effect. On the other hand, when data of adjacent lines changes towards the same direction (both zero to one or one to zero) the inductance effect dominates over the capacitance effect. That's why both effects have been considered to define the cost function. The cost function is the summation of the toggle number multiplied by 2 and the maximum of switch up and switch down. Switch up means 0→1, and switch down means 1→0.

$$Cost = Toggle\# \times 2 + Max(Switchup\ \#, Switchdown\ \#) \quad (1)$$

The major components of the encoder are pattern generator, two cost estimators, one comparator, one MUX, and one Latch. Using the Latch, current cycle data is transferred to both cost estimators. On the other hand, the pattern generator generates two data for two cost estimators.

One is non-inverted next cycle data with control bit 0, and the other one is inverted next cycle data with control bit 1. These two data are transferred to the two cost estimators. Thus, using the current cycle and next cycle data, the cost estimator calculates the cost according to the above mentioned formula. The following example of 8-bit data illustrates the encoding method completely. After calculating the cost, these are transferred to the comparator to determine which one costs less between the next cycle original data and next cycle inverted data. And the lesser one is selected to transfer to the bus using the MUX. The comparator output is used as the selector of MUX. So, for the above example, inverted data will be selected as encoded data.

III. Analysis and Comparison of Encoding Methods

In the previous section, we have explained the algorithm and working principle of all the encoding methods. In this section, the important results reported by the authors and their comparison will be described. In Table III, the power, crosstalk, and delay reduction of all the methods have been presented. The area overhead, power consumption, delay, extra control line, and cycle number induced by the codec are also mentioned. From the table, we can say that, the Temporal Crosstalk Shielding and VCT_HSTR encoding approaches improve power efficiency of the bus significantly. They can reduce power consumption up to 46% and 45.47%. On the other hand, Temporal and Shielding Coding and OTF_WCM are more efficient in reducing delay. Both of the methods can reduce delay by about 49%.

Most of the methods didn't measure crosstalk separately. Only the last two methods showed crosstalk reduction. Among these, Encoding for Crosstalk can reduce crosstalk by 35% to 40% and Crosstalk Quantitative Encoding can reduce up to 14%. On the other hand, in Temporal and Shielding Coding (TSC) and Temporal Crosstalk Shielding (TCS), codec area and codec induced delay has been measured directly in μm^2 units and time units. TSC takes less area and induces less delay compared to TCS. The other two methods, VCT_HSTR and OTF_WCM measured area in terms of a NAND gate count. In Temporal and shielding coding, though power reduction was not measured, codec power consumption is 1.1mW, which is less than the other methods, and there is no need for an extra line for this encoding method. Again, Temporal Crosstalk Shielding can reduce the number of bus line by 25%. This means for each 4-bit data, the encoded data is 3-bit, but codec area and power overhead is higher than the other methods. Though the OTF_WCM can reduce delay by 48.46%, it needs an extra 7 lines for a 16-bit wide bus. Most of the encoding methods don't add extra cycles to transfer encoded data. Only in TCS, VCT_HSTR, and Encoding for Crosstalk methods, extra cycles are required to send encoded data.

TABLE III. RESULT COMPARISON OF SELECTED ENCODING METHODS

Encoding Method	Power	Crosstalk	Delay	Codec Area	Codec Power	Codec Induced Delay	Extra Control Line	Extra Cycle
Bus Invert	25%	-	-	-	-	-	1	0
Simple Odd Even Invert	32%	-	-	-	-	-	2	0
Calculated Odd Even Invert	30%	-	-	-	5%	-	2	0
Temporal & Shielding Coding	-	-	22-49%	871μm^2	1.1mW	237ps	33.3%	1
Temporal Crosstalk Shielding	46%	-	11%	2127.2μm^2	5.7mW	1.2ns	-25%	1~2
VCT Encoding with HSTR	45.47%	-	28.15%	200116	-	-	2	0~1
OTF_WCM	38.46%	-	48.46%	217147	-	-	7	0
Encoding for Crosstalk	-	35-40%	-	-	-	-	0	0~2
Crosstalk Quantitative Encoding	11-19%	11-14%	7-19%	-	1.1-8.6	-	1	0

IV. CONCLUSION

In today's deep submicron technology, a significant amount of power is consumed in interconnect due to crosstalk. In this paper, we surveyed several methods for increasing energy and delay efficiency in modern VLSI interconnects. Our study shows differences, similarities, and specific ways of reducing interconnect power consumption and delay among different research works. Based on our survey, we tried to present a comparative study of all methods. We selected some research works accomplished over the past few years. Among them, we classified 7 research works based on 8 criteria including power, crosstalk, delay, codec area, codec power, codec induced delay, extra control line, and extra clock cycle. Most of the techniques we presented focus on power consumption reduction, and the rest are based on delay reduction.

REFERENCES

[1] M.R. Stan, W.P. Burleson, "Bus-invert coding for low-power I/O," *IEEE Trans. Very Large Scale Integration (VLSI) Systems*, vol. 3, no. 1, pp. 49-58, March 1995.

[2] Z. Yan , J. Lach, K. Skadron, and M.R. Stan, "Odd/Even bus invert with two-phase transfer for buses with coupling," in *Proc. Int. Symp. On Low Power Electronics and Design*, Aug. 2002, pp.80-83.

[3] S.K. Verma, B.K. Kaushik, "Crosstalk and power reduction using bus encoding in RC coupled VLSI interconnects," in *Proc. Int. Conf. Emerging Trends in Engineering and Technology*, Nov. 2010. pp.735-740.

[4] K. S. Sainarayanan, C. Raghunandan, and M. B. Srinivas, "Bus encoding schemes for minimizing delay in VLSI interconnects," in *Proc. ACM Conference on Integrated circuits and systems design*, Sept. 2007. pp. 184-189

[5] K. Najeeb, Vishal Gupta, and V. Kamakoti, "Delay and peak power minimization for on-chip buses using temporal redundancy," in *Proc. ACM Great Lakes symposium on VLSI*, April. 2006, pp. 119-122.

[6] J. Zhang, Q. Wu, and Q. Qiu, "Bus encoding for simultaneous delay and energy optimization," in *Proc. Int. Symp. on Low Power Electronics and Design*, Aug. 2008, pp. 209-212.

[7] S. K. Verma and B. K. Kaushik, "A bus encoding method for crosstalk and power reduction in RC coupled VLSI interconnects," *International Journal of VLSI design & Communication Systems* 3, no. 2, pp. 29-39. 2012.

[8] S. J. Ruan, T. C. Kan, and J. C. Hsu, "A novel crosstalk quantitative approach for simultaneously reducing power, noise, and delay based on bus-invert encoding schemes," in *Proc. Int. Great lakes Symp. on VLSI*, May 2010, pp. 357-360.

[9] H. S. Deogun, R. R. Rao, D. Sylvester, and D. Blaauw, "Leakage-and crosstalk-aware bus encoding for total power reduction," in *Proc. Annual Design Automation Conference*, Jun. 2004, pp. 779-782.

[10] M. Cha, C. G. Lyuh, and T. Kim, "Resource-constrained low-power bus encoding with crosstalk delay elimination," in *Proc. IEEE Asia and South Pacific Design Automation Conference,* Jan. 2004, pp. 834-837.

[11] C. Duan, C. Zhu, and S. P. Khatri, "Forbidden transition free crosstalk avoidance CODEC design," in *Proc. Annual Design Automation Conference,* Jun. 2008, pp. 986-991.

[12] D. C. Suresh, B. Agrawal, J. Yang, and W. Najjar, "Energy-efficient encoding techniques for off-chip data buses," *ACM Trans. Embedded Computing Systems (TECS)*, vol. 8(2), no. 9, 2009.

Humanlike Robotic Vision System Using Artificial Neural Network

Kazi Abu Zubair*, Subha Singha, Sabrina Alam, Kazi Tanvir Ahmmed
Department of Applied Physics, Electronics and Communication Engineering
University of Chittagong, Bangladesh
*kzubair.bd@gmail.com, subha_cu10@hotmail.com, sabrina.apece@cu.ac.bd, tanvir@cu.ac.bd

Abstract— **Robotic manipulator, which is a kind of robot that interacts with its environment in order to manipulate objects, is the most extensively-employed kind of robot in practical field. Most of the robotic manipulators functioning in the industries and other fields are programmed to manipulate objects from fixed predefined points in space. However, this might create problems in real world situation where the location of the object is arbitrary and cannot be predefined. This problem can be solved if the robot is able to recognize the object by learning which one is the specific object and which one is not. The robot can then find the position where the object is located in order to drive the manipulator tool point towards that position. In this paper, an approach has been taken to design and analyze performance of a humanlike robotic vision system for robotic manipulator using artificial neural network along with image processing. Here, the robot captures image of the environment, analyzes it and determines the points in space where the object to be manipulated is locate.**

Keywords—***Robotics; Artificial Neural Network; Artificial Intilligence; Object Recognition; Image Processing***

I. INTRODUCTION

The robot vision system must be considered as part of a larger entity that interacts with the environment by analyzing images to produce descriptions of what is imaged [1]. The robot vision before the development of Artificial Neural Network relied mostly on image processing using pixel by pixel calculation. Gibson (1950) introduced first a concept on optical flow and based on his theory, mathematical models for optical flow computation on a pixel-by-pixel basis are developed [2-3]. Larry Roberts presented a research on the possibility of extracting 3D geometric information from 2D views in 1960 [4]. In such researches in [2-6] the success rate of object recognition was much less in comparison with the human brain. This is because human brain, unlike conventional robot vision mechanism, has an outstanding capability of analyzing real world non linear data. In order to be able to recognize different objects successfully in different illumination, background, view point and to some extent position of the workspace [7], the vision system of the robot should be similar to the human vision. The research on how human brain processes data using its cognitive skills and the development of such computer model which replicates the functionality of human brain is a wide research field over a few decades. Such computer model of human brain, which is known as Artificial Neural Network or ANN was first introduced by McCulloch and Pitts in 1940 [8]. In 1950's Rosenblatt developed a two layered network known as 'Perceptrons' [9]. 'Perceptrons' were capable of learning certain classifications by adjusting connection weights. These studies led to the current development of the neural network.

The practical vision technology was eagerly anticipated in industry, particularly in Japan, in the mid-1960s, typically at Hitachi's Central Research Laboratory [10]. In those attempts, the success rate was not high and the need for real AI based vision system had aroused. After the development of efficient learning algorithms like 'backpropagation' [11-13], during 1990's, machine vision starts becoming more common in manufacturing environments leading to creation of machine vision industry.

Modern-day robots can be carefully hand-programmed or "scripted" to carry out many complex manipulation tasks, ranging from using tools to assemble complex machinery, to balancing a spinning top on the edge of a sword [14-15]. But the difference between human and such robot are still apparent in because every time the robot must know the exact geometric description of the objects they are dealing with. In some recent work such as in [16-20] some robotic vision system is developed where the system tries to replicate the human vision system. In the research work [14], the goal was to make the robot grasp novel objects where the robot neither requires nor tries to build a 3D model of the object. A method is presented in [21] where the robot learns new objects from scratch, by simply observing the object in different poses and scales. The system used active tracking and depth data coming from a stereo system with 'vergence' control to segment the object from the background, and was tested with a hundred different household objects, showing around 80% recognition rate on average. The drawbacks of the system were that a certain amount of texture in the objects was required [20].

Indeed, in most cases of robotic vision, there was always an intention to analyze the geometrical shape of the object for the sake of recognition. However, the human brain, which can recognize different objects easily rely mostly on the learning process and less on geometrical description. The work presented in this paper focuses on the design and performance of a robotic vision system for manipulator arm which learns to recognize specific objects only from images of the objects, in other words, only by seeing it.

978-1-4673-9257-0/15/$31.00 ©2015 IEEE

II. METHODOLOGY

Five distinct objects, three with different colors and shapes and two with same color but different shape are taken as the test objects. The objects that the robot learned to recognize are as follows-

- Object 1; Long Blue Object
- Object 2; Circular Blue Object
- Object 3; Rectangular Orange Object
- Object 4; Trapezoidal Green Object
- Object 5; Rectangular Charleston Green Object

The images of different objects are listed in TABLE I. The workspace in this project is a white surface of 25cm by 25cm in dimension. The objects to be recognized will be placed on this workspace. The manipulator is considered to be anchored at (0, 0) position. A camera is fixed over the workspace to take images of what is placed on the workspace. Fig 1 shows the view of the system with the workspace below and a camera fixed above the workspace. Graphical User Interface in PC shows the identified objects with their respective position.

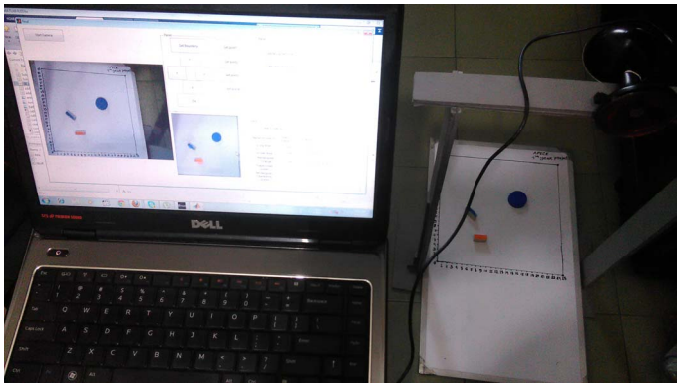

Fig. 1. The robotic vision system developed in this research work

A. *Design of the Neural Network:*

The Artificial Neural Network (Fig. 2) that has been used in this paper is a feed forward neural network with 150 hidden layers. It has 1200 input neurons and 6 output neurons. In most application of the object recognition using ANN, the RGB image is converted to Gray-Scale image and is applied at the input of the neural network. In that case, the efficiency of object recognition is reduced because the network treats the same objects with different color as identical objects.

In the system described in this paper, the approach was to make the robot recognize color objects by taking all RGB information as the input data. RGB image is a matrix of dimension m-by-n-by-3. Each color pixel contains three values for three primary colors; Red, Green and Blue. The network is designed to deal with images of 20 by 20 pixels. For that reason, the input layer must have 1200 neurons. The schematic of the neural network is shown in Fig. 2.

This is a 6-class classifier neural network. Each of last five classes corresponds to one specific object and the first class corresponds to a Non-Object class. The corresponding output class will acquire the highest value for a certain combination of the inputs. If the image given to the network has no object in it, the Non-Object class will have the highest value.

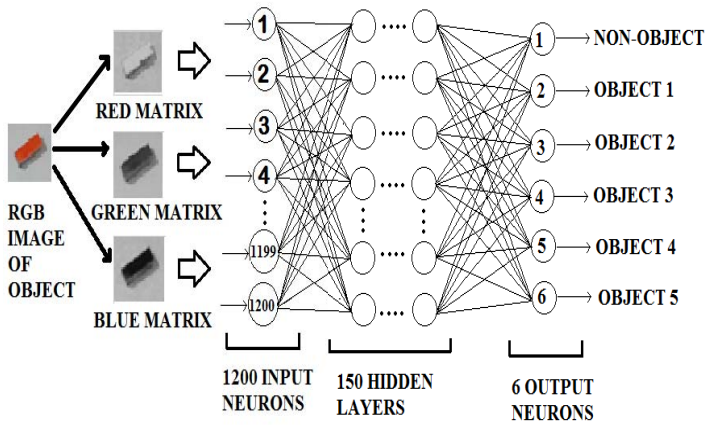

Fig. 2. Feed forward artificial neural network topology used in the vision system

B. *Data Preparation for Neural Network*

Preparing data is an important and critical step in neural network data analysis and it has an immense impact on the success of a wide variety of complex data analysis, such as data mining and knowledge discovery [22]. The main reason is that the quality of the input data into neural network models may strongly influence the results of the data analysis [23-24]. The training data that is required to perfectly train a neural network must be developed carefully for the optimum performance.

For preparing training data for the neural network in this paper, several images in different lighting conditions are taken by the webcam. Several of such images are combined and from the combined image, the some cropped images of 20x20 pixels of specific object-class and non-object class are taken as data image which are assigned with specific value.

The prepared data contains two matrixes, one for the image data and another for their corresponding class-value. In order to feed the data to the neural network, the second matrix is converted into a 6 by N matrix where N is the number of data taken. Each row of the matrix contains '0' for negative data and '1' for positive data for the corresponding class. Fig. 3 illustrates the data preparation procedure in a flow chart.

C. *Training The Neural Network*

The training data is divided into three parts before training the network with it, where-

Percentage of the total data used for training: 70%

Percentage of the total data used for validation: 15%

Percentage of the total data used for testing: 15%

The network is trained using MATLAB's Neural Network Pattern Recognition tool (nprtool). The training data prepared in the data preparation stage is corrected, extended and edited several times before feeding it to the neural network. For the ease of understanding, the whole process is divided into three approaches.

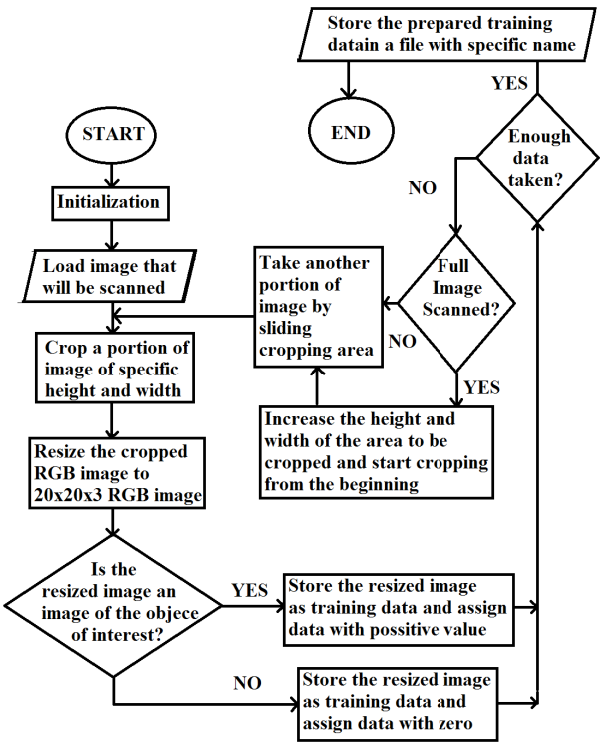

Fig. 3. Flow chart of the data preparation mechanism

1) First Approach: At first, the data taken for the ANN training contained minimum Non-Object class. The data for Object class is taken by keeping objects mostly in the center position and the Non-Object examples were taken as images of empty background image in different lighting condition.

TABLE I. DIFFERENT OBJECT AND NON OBJECT EXAMPLES IN THE FIRST APPROACH

Different data for Object class and Non-Object class in the first approach					
Object 1	*Object 2*	*Object 3*	*Object 4*	*Object 5*	*Non-Object*
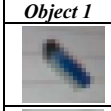					

The data taken in this step is corrected several times and finally fed to the network to observe its performance. Some examples of data taken in this approach is tabulated in TABLE I.

2) Second Approach: The number of Non-Object class data was small compared to other Object classes in the first approach and the network seemed to assume some images around the object as incorrect Object-Class data which actually falls under Non-Object class. To solve this, In second approach, the number of Non Object Class has been increased to a significant number by taking images around every object which can be considered as Non-Object image(TABLE II).

TABLE II. SOME NON-OBJECT EXAMPLES IN THE SECOND APPROACH

Some Non-Object examples taken in the second approach					
				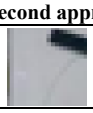	

3) Final Approach: With the progress achieved in the first and the second approach, the network was able to successfully recognize objects that are separated from other objects by a noticeable distance. But when several objects are close to each other, the network assumed the image taken between the spaces by which multiple objects are separated as wrong Object class. In order to make sure that the network predicts such space as Non-Object class, several Non-Object image data (TABLE III) are taken from the space between nearby objects.

TABLE III. SOME NON-OBJECT DATA TAKEN BETWEEN THE SPACE OF TWO OBJECTS IN THE FINAL APPROACH

Some non-object data between the spaces of different objects					
					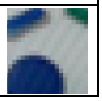

D. *Recognition of Object of Interest*

The objects are recognized by taking 20x20 pixels of the workspace and feeding the cropped image to the neural network each time to see if the image selected contains the object of the interest. Fig. 4 illustrates the block diagram of object recognition procedure.

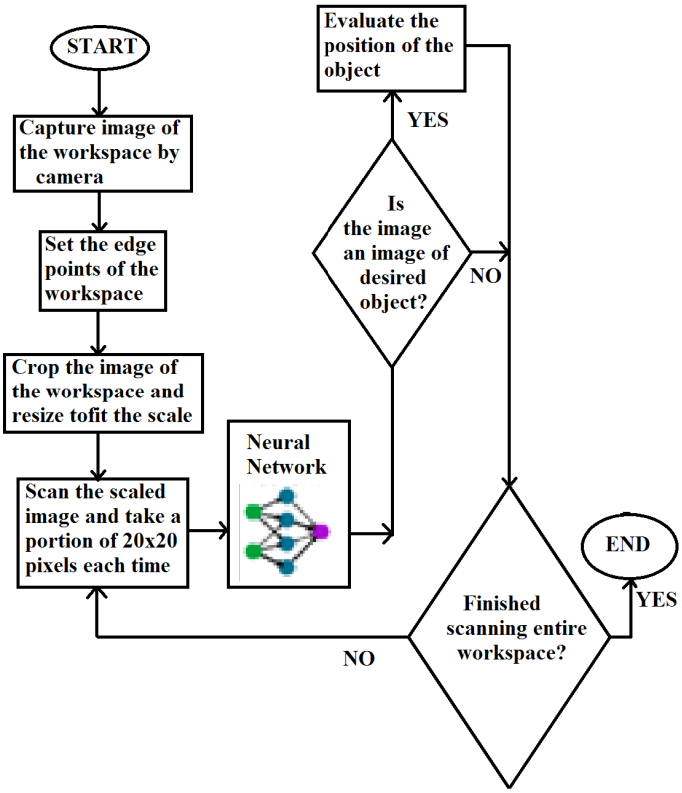

Fig. 4. Block diagram of object recognition and position evaluation

III. Performance Analysis

A. *Performance Analysis of Different Approaches:*

In the first approach, the amount of data taken was not massive. The focus of this approach was to take positive Object class data with accuracy. The performance plot of the network trained with the data taken in the first approach is shown in Fig. 5. The curve can be easily obtained using MATLAB's plotperform() function of Neural Network Toolbox. The Cross-Entropy of the best validation performance in this approach is $1.6523e^{-05}$ which is much smaller. It is clear from the plot that the network trained in this approach is much confident about the prediction. However, the characteristic of good classifier network is such that, its train, test and validation curve mostly decrease in a similar fashion. Though the cross entropy in this approach is minimum between all the approaches, it sometimes gives wrong prediction very confidently which is unacceptable.

In the second approach, an increased number of data is taken. The focus of this approach was to take more Non-Object class data to minimize the errors that occurred when the network predicted some images around one object as another object. The cross-entropy for the best validation performance in the second approach is much higher then the network trained previously in the first approach. But the network shows significant improvement as the test and validation curve mostly move in a similar fashion unlike the curves in the first approach. However, the training curve falls much rapidly compared to the test and validation curve. The performance plot of the network in the second approach is shown in Fig. 6.

In the final approach, the focus was to take more Non-Object class from the space between multiple objects. The performance plot of the final approach is shown in Fig. 7.The performance shows that the cross entropy for best validation performance is much greater than the network trained in the previous approaches, however, the three curves are now closer to each other than before and they converges to local minima with similar fashion.

The Confusion plot of the third approach is shown in Fig. 8. There is an increased number of confusions in this approach. However, in recognizing new data, the network seemed to have better performance than the previous approaches. The confusion matrix shows that only 0.7% of the data are predicted incorrectly and the rest of the 99.3% data images are correctly recognized.

B. *Testing The Network With New Data:*

After the network has been trained successfully, the network is tested with several new images captured by the camera. The TABLE IV and TABLE V show some of these images along with the prediction of the network for these images. If the network successfully identifies an image, it draws a circle at the position where the object is located. The circles are drawn as per the following rules:

- Medium green circle for Trapezoidal Green Object.
- Small blue circle for Log Blue Object.
- Large blue circle for Circular Blue Object.
- Medium orange circle for Rectangular Orange Object.
- Medium dark circle for Charleston Green Object

TABLE IV. Test Result Of Specific Object Recognition From A New Image (Sussessful Cases)

Testing the network with new image(Successful cases)		
Actual image	***Object Recognition by the network***	***Observation***
	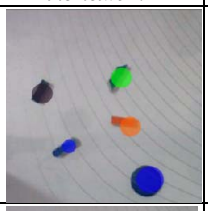	All of the five objects are identified successfully.
		All of the objects are recognized successfully
	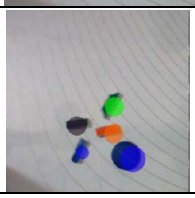	The Objects are brought closer and the network identifies each object successfully.

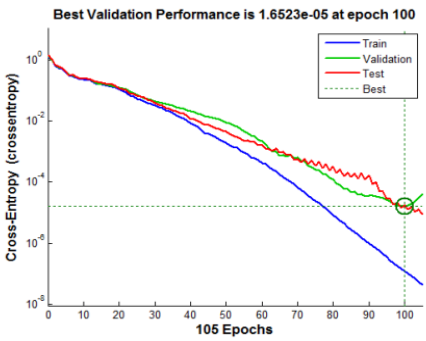

Fig. 5. Network training performance for the first approach

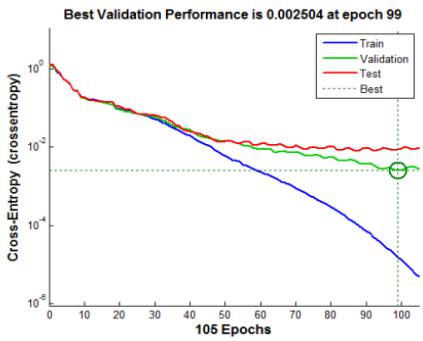

Fig. 6. Network training performance for the second approach

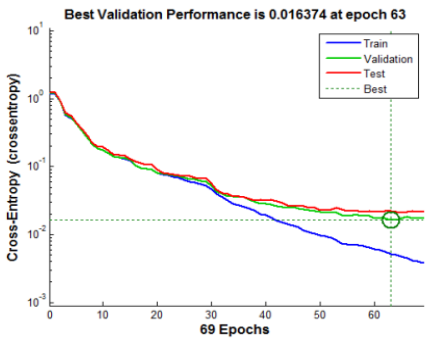

Fig. 7. Network training performance for the final approach

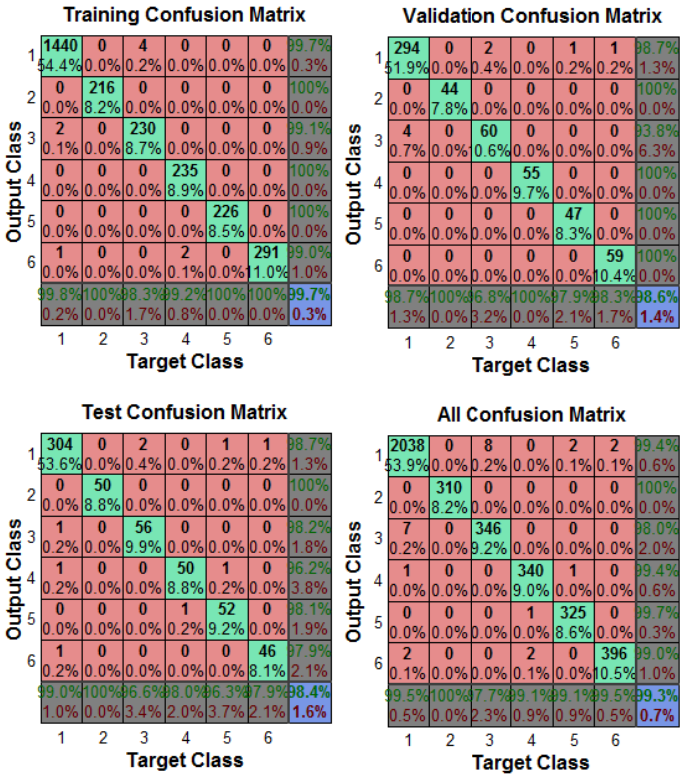

Fig. 8. Confusion matrix of the network after final approach

TABLE V. TEST RESULT OF SPECIFIC OBJECT RECOGNITION FROM A NEW IMAGE (UNSUCCESSFUL CASES)

Testing the network with new data (Unsuccessful cases)		
Image captured by camera	***Object recognitions by neural network.***	***Observation***
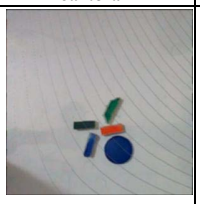	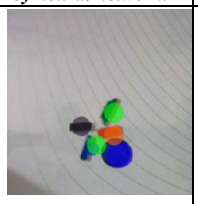	The objects are brought more close to each other and the network identifies all of them correctly, except an extra green object is predicted wrongly between two blue objects.
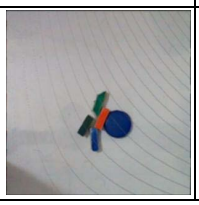	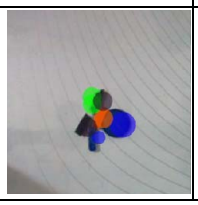	It shows the congested condition and the network now predicts an extra Charleston green object incorrectly in the vicinity of Green object.

The result shows that the network recognizes mostly all of the objects when they are placed at a significant distant apart. Some error prediction occurs when the objects are much dense and at a congested condition. This problem might be solved if smaller area of the cropped image is fed to the network, however, this would take more time to scan the full image of the workspace.

TABLE VI, tabulates some position evaluation examples using the vision system discussed in this paper.

TABLE VI. SOME POSITION EVALUATION RESULT FOR VARIOUS OBJECTS

Some example of position evaluation by the vision system		
Image of the workspace with marked object	***Position Evaluation by the vision system (snapshot from the Graphical User Interface of the system)***	***Observation***
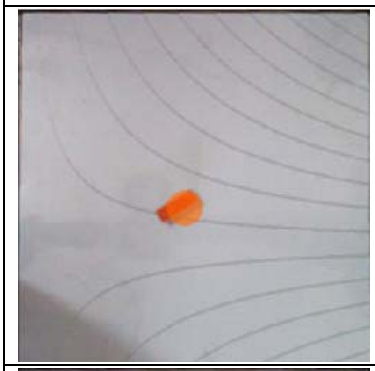	Name of object / object found? / position Long Blue: no, -- circular blue: no, -- Rectangular Orange: yes, x=11.8477, y=10.9355 Trapezoidal Green: no, -- Rectangular Charleston Green: no, --	A rectangular orange object is given and the system successfully identifies the position of the object at (11.84,10.93)
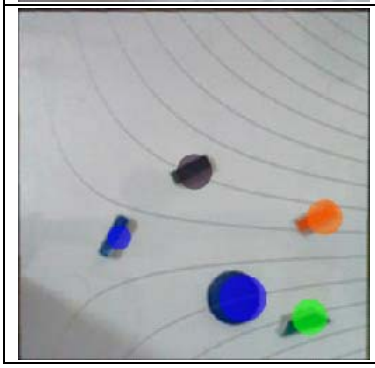	Name of object / object found? / position Long Blue: yes, x=7.2708, y=8.6667 circular blue: yes, x=16.0078, y=4.3535 Rectangular Orange: yes, x=21.8411, y=10.0827 Trapezoidal Green: yes, x=20.7083, y=3.0417 Rectangular Charleston Green: yes, x=12.5833, y=13.3542	All of the objects are given and the system successfully identifies each object at position respectively (7.2,8.6), (16.0,4.3), (21.84,10.1), (20.7,3.04) and (12.58,13.4)

The vision system in this work has a very low error or false recognition percentage. The maximum error occurs for Object 2 and is 2.2%. However, the error rate can be further reduced by careful selection of training data. Other errors are negligible. The performance of the system is tabulated in TABLE VII.

TABLE VII. RECOGNITION EFFICIENCY OF DIFFERENT OBJECT AND NON OBJECT CLASS

Recognition efficiency of different object and non-object class				
Object Class	***No. of test image***	***Successful Recognition***	***False Recognition***	***Efficiency***
Object 1	310	310	0	100%
Object 2	354	345	8	97.774%
Object 3	343	340	3	99.125%
Object 4	328	325	3	99.085%
Object 5	398	396	2	99.497%
Non-Object	2048	2038	10	99.512%
Total	3781	3755	26	99.312%

IV. CONCLUSION

In this work, a vision system for a robotic manipulator is designed so that any object of interest and its position on a scaled workspace can be recognized independently. The neural network is trained to recognize several objects and tested if the recognition system works in different lighting condition. The test result shows that the system is successful in almost all of the cases.

The robotic vision system in this paper is developed using comparatively small amount of data and the network performance is evaluated in three different approaches. In the first two approaches, the network showed minimum confusion but is comparatively inefficient in recognizing new data. However, the final approach shows the best result where it is seen to be most successful in recognizing objects from new images.

In some similar work, as in [25] the background is uniformly white by default and the target image information is passed to the neural network. This process gives high efficiency (99.99% at optimum lighting condition) for single object with uniform background according to the article [25]. However, the false recognition rate may increase if it must distinguish between several objects where one or more objects may lie in the vicinity of the target object. The work presented in this paper overcomes this problem and is 100% efficient for the recognition of one of the five test objects considered in this paper and the overall efficiency is 99.31% (Table VII).

REFERENCE

[1] B. Klaus & P. Horn, *Robot Vision*. Cambridge, MA: MIT Press, 1986.

[2] James J., Gibson, "The Perception of the Visual World," *The American Journal of Psychology,* vol. 64, no. 3, pp. 440-444, Jul. 1951.

[3] James J., Gibson, "The visual perception of objective motion and subjective movement," *Psychological Review,* vol. 101, no. 2, pp. p318-23, April 1954.

[4] L. G. Roberts, "Machine Perception of Three-Dimensional Solids," Ph. D. thesis, Massachusetts Institute of Technology. Dept. of Electrical Engineering, MA, 1963.

[5] Berthold K. P. Horn, & Brian G. Schunck "Determining optical flow," *Artificial Intelligence*, vol. 17, no. 1-3, pp. 185–203, Aug. 1981.

[6] Gordon, D. A., "Static and dynamic visual fields in humanspace perception," *Journal of the Optical Society of America*, vol. 55, no. 10, pp. 1296-1302, Oct. 1965.

[7] V. D. Hunt, *Industrial Robotics Handbook*. New York: Industrial Press Inc., 1983.

[8] W. S. McCulloch and W. Pitts , "A logical calculus of the ideas immanent in nervous activity," *The bulletin of mathematical biophysics*, vol. 5, no. 4, pp. 115–133, Dec. 1943.

[9] Rosenblatt, Frank, "The Perceptron: A Perceiving and Recognizing Automaton," Cornell Aeronautical Laboratory, New York. Rep. 85-460-1,1957.

[10] M. Ejiri, "Machine Vision in Early Days: Japan's Pioneering Contributions," in *Computer Vision – ACCV 2007 : Proceedings of the 8th Asian Conference on Computer Vision,* vol. 4843, Y. Yagi, S. B. Kang, I. S. Kweon, H. Zha, Eds. Berlin: Spinger, 2007. pp. 35-53.

[11] A. Atiya, "Learning Algorithms for Neural Networks," Ph. D. thesis, California Institute of Technology, CA, Sept. 2005.

[12] D. E. Rumelhart*, Geoffrey E. Hinton† & Ronald J. Williams*, "Learning representations by back-propagating errors," in *Nature,*vol. 323, no. 6088, pp. 533 – 536, Oct. 1986.

[13] Y. Chauvin, D. E. Rumelhart, *Backpropagation: Theory, Architectures, and Applications*. New York: Psychology Press, Feb. 1995.

[14] Ashutosh Saxena, Justin Driemeyer, Andrew Y. Ng, "Robotic Grasping of Novel Objects using Vision," in *International Journal of Robotics Research (IJRR),*vol. 27, no. 2, pp. 157-173 , Feb 2008.

[15] Torikai, Shinichi, Yasuko Sakagami en Satoshi Matsuoka, "Robots for the future," *Nipponia,*vol. 1, no. 13, pp. 12-17 ,2010.

[16] A. Teichman, J. Levinson, S. Thrun, "Towards 3D object recognition via classification of arbitrary object tracks," in *Proc. IEEE Int. Conf. on Robotics and Automation (ICRA)*, May. 2011, pp. 4034 - 4041.

[17] C. Kanan, "Fine-grained object recognition with Gnostic Fields," in *Proc. IEEE Int. Conf. on Robotics Applications of Computer Vision (WACV)*, March 2014, pp. 23 - 30.

[18] A. Teichman, "Practical object recognition in autonomous driving and beyond," *in Proc. IEEE Int. Conf. on Advanced Robotics and its Social Impacts (ARSO)*, Oct. 2011, pp. 35 – 38.

[19] T. Satonaka, T. Baba ,T. Otsuki, T. Chikamura,T. H. Meng, "Object recognition with luminance, rotation and location invariance," in *Proc. IEEE Int. Conf. on Image Processing*, Oct 1997,vol. 3, pp. 336 - 339.

[20] F. R. Aparici, A. R. Ayats, G. A. Ribas, X. T. Genis, "Object detection methods for robot grasping: Experimental assessment and tuning," in *Proc. 15th Catalan Conference on Artificial Intelligence (CCIA)*, 2012, pp. 123-132.

[21] H. Kim, "Semi-autonomous Learning of Objects," in *Proc. IEEE Int. Conf. on Computer Vision and Pattern Recognition Workshop(CVPRW)*, June 2006, pp. 145-150.

[22] X. Hu, "DB-HReduction: A data preprocessing algorithm for data mining applications," in *Applied Mathematics Letters* ,vol. 16, no. 6. Amsterdam, Netherlands : Elsevier, Aug. 2003. pp. 889–895.

[23] K. U. Sattler, E. Schallehn, "A data preparation framework based on a multidatabase language," in *Proc. IEEE Int. Symposium on Database Engineering and Applications*, Jul. 2001, pp. 219 - 228.

[24] Lean Yu, Shouyang Wang, Kin Keung Lai, "Foreign-Exchange-Rate Forecasting with Artificial Neural Networks," in *International Series in Operations Research & Management Science* ,vol. 107. Berlin: Spinger, 2007.

[25] J.P.N. Cruz, M.L. Dimaala, L.G.L. Francisco, E.J.S. Franco, A.A. Bandala, E.P. Dadios, "Object Recognition and Detection by Shape and Color Pattern Recognition utilizing Artificial Neural Network" in *IEEE International Conference of Information and Communication Technology (ICoICT),* March 2013, pp. 140-144.

Optimizing Preprocessing Method of Recursive-BKZ Lattice Reduction Algorithm

Md. Mokammel Haque,[1,*] and Josef Pieprzyk[2]
[1]Department of Computer Science and Engineering, Chittagong University of Engineering and Technology
Chittagong 4349, Bangladesh
[2]School of Electrical Engineering and Computer Science, Queensland University of Technology
Brisbane, QLD 4000, Australia
*Email: malin405@yahoo.com

***Abstract*—Lattice problems are considered as the key elements in many areas of computer science as well as in cryptography; the most important of which is the shortest vector problem (called SVP in short) and its approximate variants. Algorithms for this problem are known as lattice reduction algorithms. Currently, the most practical lattice reduction algorithm for such problems is the Block-Korkine-Zolotarev (BKZ) algorithm and its variants. Preprocessing is a technique that can be applied to certain lattice reduction algorithms (such as BKZ variants) to reduce the search time in the enumeration tree for a shortest vector. We optimize both the pruning and the preprocessing parameters of the recursive (aborted, extreme pruned) preprocessing of the BKZ lattice reduction algorithm and improve the results from Asiacrypt'11 by Chen and Nguyen.**

***Index Terms*—Cryptosystem, Algorithm, Lattice Reduction, BKZ, Optimization, Preprocessing.**

I. Introduction

The *Lattices* we are interested in are integer or point lattices; discrete subgroups of $\mathbb{R}^n$. A lattice L is defined as all integer linear combinations of some linearly independent vectors $(\mathbf{b}_1, ..., \mathbf{b}_n)$ of the form: $\sum_{i=1}^{n} x_i \cdot \mathbf{b}_i$, where $x_i \in \mathbb{Z}$ for all i. The vectors $(\mathbf{b}_1, ..., \mathbf{b}_n)$ are called a basis of the lattice. The number of vectors n is the dimension of the lattice L.

The goal of lattice reduction is to find a "good" basis for the applications which is usually the one that contains short vectors. Clearly, it is an interesting problem to find a short basis or even to try to find a shortest basis. The SVP or Shortest Vector Problem is the most common and fundamental algorithmic lattice problem on which many cryptosystems rely. It is an NP-hard problem under randomized reductions [1].

Lattice problems are considered to be building blocks in many public-key cryptographic constructions. The most significant examples of cryptographic constructions that use lattices include: public key encryption based on knapsack problem; variant of RSA and DSA signatures schemes; encryption schemes based on LWE (Learning with Error) problems [2]; fully homomorphic cryptosystems [3]; the SWIFFT hash function [4] as well as many others. If one knows how to solve lattice problems, then one can break some cryptosystems.

Lattice reduction algorithms are one of the few exciting recent techniques in cryptography. The most popular lattice reduction algorithms are the LLL (Lenstra-Lenstra-Lovász) [5] and BKZ (Block Korkine-Zolotarev) [6] algorithms and their variants. They are called *approximate algorithms*; another category is known as *exact algorithms* includes Enumeration.

In lattice reduction algorithm, preprocessing is required to give a relatively bad basis a good shape. Actually, the most classical form of preprocessing we always observe is with polynomial time LLL algorithm to work with a slow enumeration-based algorithm like BKZ. In BKZ reduction, LLL is used before the enumeration routine to produce a preprocessed basis. Then the enumeration will run more efficiently.

The aim of this paper is to describe the preprocessing method in the Recursive-BKZ (RBKZ in short) reduction. In [7], the algorithm for the RBKZ reduction is called BKZ2.0. We would like, however, to emphasize the role of preprocessing, as the preprocessing notion has not been fully explained in previous publications. We also optimize the runtime complexity of the recursive-BKZ lattice reduction based on some heuristic. Our results show better estimation of complexity than the similar results reported in [7].

II. Background Notation

Let $L = L[1, n]$ denote an n-dimensional lattice with basis $B = (\mathbf{b}_1, \ldots, \mathbf{b}_n)$. The block lattice $L_i = L[i, i+d_i-1]$ is the projection of the lattice generated by $\mathbf{b}_i, \mathbf{b}_{i+1}, \ldots, \mathbf{b}_{i+d_i-1}$ orthogonally to the space spanned by $\mathbf{b}_1, \ldots, \mathbf{b}_{k-1}$, where $d_i = k$ for $i \leq n-k+1$ and $d_i = n-i+1$ for $i > n-k+1$.

Let $B^* = (\mathbf{b}_1^*, \ldots, \mathbf{b}_n^*)$ denote the Gram-Schmidt Orthogonalization (GSO) [8] of the basis B of L, and let $\hat{\mathbf{B}}^* = (\mathbf{b}_1^*/\|\mathbf{b}_1^*\|, \ldots, \mathbf{b}_n^*/\|\mathbf{b}_n^*\|)$ denote the normalized GSO matrix. We have $B = \hat{\mathbf{B}}^* \cdot M$, where $M = (\mathbf{r}_1, \ldots, \mathbf{r}_n)$ is an upper-triangular matrix with its ith column $\mathbf{r}_i = (\mu_{i,1} \cdot \|\mathbf{b}_1^*\|, \mu_{i,2} \cdot \|\mathbf{b}_2^*\|, \ldots, \mu_{i,i} \cdot \|\mathbf{b}_i^*\|, 0, \ldots, 0)^T$ (the coordinate vector for $\mathbf{b}_i$ in the orthonormal basis $\hat{\mathbf{B}}^*$), and $\mu_{i,j} = \frac{\langle \mathbf{b}_i, \mathbf{b}_j^* \rangle}{\|\mathbf{b}_j^*\|^2}$. Let M_i denote the upper triangular $d_i \times d_i$ submatrix of M with its top-left corner at row i and column i, and a basis for block lattice L_i (represented in the orthonormal basis $\hat{\mathbf{B}}^*$).

The (aborted) BKZ-k algorithm (with pruning strategy P and the BKZ 2.0 [7] Gaussian-Heuristic-Based enumeration radius), for an input basis $B = (\mathbf{b}_1, \ldots, \mathbf{b}_n)$ of an n-dimensional lattice L, first runs the LLL reduction algorithm on B. Then it runs a $\tau(n, k) = \mathcal{P}oly(n, k)$ number of tours. In each tour, it performs a shortest-vector enumeration routine on each of n block lattices $L_i = L[i, i+d_i-1]$ for $i = 1, \ldots, n-1$ using the basis M_i, where $d_i = \min(k, n-i+1)$ is the dimension of L_i. Let $N(n, k, t, i)$ denote the number of nodes in the enumeration tree for block lattice L_i in tour t. The number $N(n, k, t, i)$ is the dominant factor in the run-time of BKZ-k for large k, since it is exponential in k. Let $B^*(n, k, t, i) = (\mathbf{b}_1^*(n, k, t, i), \ldots, \mathbf{b}_n^*(n, k, t, i))$

978-1-4673-9257-0/15/$31.00 ©2015 IEEE

denote the GSO matrix just before the enumeration of L_i. Let $D(n,k,t,i) = \det L_i = \prod_{j=i}^{i+d_i-1} \|\mathbf{b}_j^*\|$.

A shortest vector of L_i (for $i \leq n-30$) is assumed to be in a pruned subset S_P of the d_i-dimensional ball of radius

$$R(n,k,t,i) = \min\left(\|\mathbf{b}_i^*(n,k,t,i)\|, (1+\varepsilon)\cdot GH(\lambda_1(L_i))\right), \tag{1}$$

where $GH(\lambda_1(L_i)) = (D(n,k,t,i)/V_k(1))^{1/k}$ is the Gaussian Heuristic (see [8]) estimate for the length of a shortest vector of L_i, and ε is a small constant ($\varepsilon = 0.05$ in [7]). For $i > n-30$, Nguyen and Chen take $R(n,k,t,i) = \|\mathbf{b}_i^*(n,k,t,i)\|$. Here $V_k(1)$ denotes the volume of the k-dimensional ball of radius 1.

Let $N_d(n,k,t,i)$ denote the number of nodes in the enumeration tree at depth d. Then the total number of nodes,

$$N(n,k,t,i) = \sum_{d=1}^{k} N_d(n,k,t,i). \tag{2}$$

The Gaussian Heuristic says that assuming $R(n,k,t,i) = (1+\varepsilon)\cdot GH(\lambda_1(L_i))$, on average, we expect

$$\begin{aligned}\log N_d(n,k,t,i) \approx &\log(V_d(1)\cdot V_k(1)^{-d/k}\cdot(1+\varepsilon)^d)\\ &+\sum_{r=k-d+1}^{k}\left(\frac{1}{k}\log D - \log\|\mathbf{b}_{i+r-1}^*\|\right)\\ &-\log G(P,d)\end{aligned} \tag{3}$$

where $G(P,d)$ is the pruning speedup factor for level d.

The *Geometric Series Assumption* (GSA) with ratio q for a basis of L_i states that the norms $(\|\mathbf{b}_i^*\|, \|\mathbf{b}_{i+1}^*\|, \ldots, \|\mathbf{b}_{i+d_i-1}^*\|)$ form a geometric progression, so that the ratio $\|\mathbf{b}_j^*\|/\|\mathbf{b}_{j+1}^*\| = q$ for all j=$i,\ldots,i+d_i$.When blocksize k is not too small, $q(k)$ can be approximated quite accurately by the fixed point of a deterministic dynamical model as in [9], based on the Gaussian Heuristic. This approximation is:

$$q(k) \approx V_k(1)^{\frac{-2}{k\cdot(k-1)}} \tag{4}$$

For the LLL algorithm, experimental evidence shows that the GSA with ratio $q(2)$ holds approximately, with $q(2) \approx 1.04$.

If the GSA with ratio q holds (approximately) for the basis of L_i when the enumeration is performed, then the enumeration time in (3) can be approximated by

$$\begin{aligned}\log N_d(n,k,t,i) \approx &\log(V_d(1)\cdot V_k(1)^{-d/k}\cdot(1+\varepsilon)^d)\\ &+\frac{1}{2}\cdot d\cdot(k-d)\cdot\log q - \log G(P,d).\end{aligned} \tag{5}$$

The number $N_d(n,k,t,i)$ is usually maximized for $d \approx k/2$, so we get the following (usually quite tight) lower bound, under the GH and GSA with ratio q for the basis of L_i:

$$\begin{aligned}\log N(n,k,t,i) \geq &\log N_{k/2}(n,k,t,i)\\ \approx &\log(V_{k/2}(1)\cdot V_k(1)^{1/2}\cdot(1+\varepsilon)^{k/2})\\ &+\frac{k^2}{8}\cdot\log q - \log G(P,d).\end{aligned} \tag{6}$$

By Theorem 1 of [9] with $C = 1$ and assuming the GSA for the input basis with ratio $q \leq q(2)$, (see also Fig. 1 in [9]), one can get an output quality for the aborted BKZ-k satisfying the GSA with ratio close to the $q(k)$ value given in (4) if one aborts BKZ after $\tau(n,k) \approx (n/k)^2\cdot\log(n^2/50)$ tours.

A. SMA and Dynamical Model

The heuristic Sandpile Model Assumptions (SMA) with the deterministic dynamical model comes from the analysis of aborted-BKZ (or BKZ' in [9]) due to Hanrot et al. BKZ' differs from the original BKZ in such that it replaces the SVP solver in BKZ by an HKZ reduction algorithm. The purpose is to simplify the analysis of BKZ' by looking at the changes in $\mathbf{x} = \log(\|\mathbf{b}_i^*\|)_{i\leq k}$ during each tour rather than considering the whole basis after full reduction. The heuristic further allows a fixed-point dynamical model that determines $\mathbf{x}$ in each $(n-k+1)$ calls of k-dimensional HKZ-reduction by $\mathbf{x}$ only. The final fixed point of the BKZ' reduction resembles a straight line, except for the last block.

III. Extreme and Non-extreme Pruning

The idea of *extreme pruning* is to skip a large number of branches in the enumeration tree so that the time for each short-vector search reduces significantly. Unfortunately, it reduces the probability of finding a shortest vector in this process. However, the extreme pruning provides a tangible gain. The reduction of the enumeration time is significantly larger than the increase of the probability of missing shorter vectors in the solution.

Therefore, the basic extreme pruning consists of several executions of the *randomize-reduce-enumeration* loop (see Algorithm 1 in [10]) until a short vector satisfying a predefined bound is found. This multiple execution can be denoted as the branching factor. If p_{succ} is the probability of finding a short vector in each iteration of the *randomize-reduce-enumeration* loop, then the branching factor = expected number of iterations until the shortest vector is found $= \frac{1}{p_{succ}}$. The runtime T_{ext} of extreme pruning can be derived as

$$T_{ext} = \frac{T_{red} + T_{node}\cdot N_{ext}}{p_{succ}} \tag{7}$$

where T_{red} is the initial reduction or preprocessing time, T_{node} is the average time for processing a single node, p_{succ} is the success probability; N_{ext} is the total number of nodes in the pruned enumeration tree such that $N_{ext} = \sum_{k=1}^{n} H'_k$, where H'_k is the number of nodes in depth k ($1 \leq k \leq n$) of the enumeration tree. Now, the number of nodes in each level k can be heuristically estimated as $H'_k = \frac{1}{2}\cdot\frac{V_{R_1,\ldots,R_k}}{\mathrm{vol}(L_k)}$, which can be compared to that of full enumeration tree $H_k = \frac{1}{2}\cdot\frac{V_k(R)}{\mathrm{vol}(L_k)}$. Here ($\frac{1}{2}$) comes from the fact that it will be enough to search half of the tree due to the symmetry in the SVP problem; $\mathrm{vol}(L_k) = \prod_{i=n+1-k}^{n}\|\mathbf{b}_i^*\|$ is the volume of the projected lattice in level k; $V_k(R)$ is the volume of the k-dimensional ball of radius R and $V_{R_1,\ldots,R_k}$ is the volume of the cylinder intersections of radii such that $R_1 \leq \cdots \leq R_k$. In [10], two methods to compute the volume $V_{R_1,\ldots,R_k}$ are explained. The simplest one is based on Monte Carlo sampling to get an estimation. The next one, the successive integration approach, can compute this volume exactly considering certain mild constraints on radii (see Lemma 4.1 and 4.2 in [10]). The success probability p_{succ} can also be estimated using a similar approach. We use the exact computation method to derive the volume and success probability in our model implementation.

Now, the comparative speed up of extreme pruning can be computed as $G_k = S_k\cdot p_{succ}$, where $S_k = \frac{H_k}{H'_k} = \frac{V_k(R)}{V_{R_1\cdots R_k}}$ is the ratio of the number of nodes at level k of the full tree to the pruned tree.

IV. Recursive-BKZ

The preprocessing method described by Nguyen and Chen in [7] is known as the recursive preprocessing applied to the BKZ lattice reduction. In general, the case without preprocessing can be defined as follows.

Definition 1 (No Preprocessing): Given input basis B and a blocksize k, compute B' = BKZ-k(B) and return B' (note that BKZ-k internally pre-processes the input basis B by running LLL on it, so this can be more accurately described as the LLL preprocessing).

This definition can be compared to the following definition of recursive preprocessing for local block bases.

Definition 2 (RBKZ preprocessing): Let M_i be the projected block basis of index i such that $1 \leq i \leq n-1$ where n is the lattice dimension, parameter s is a step size and k_{min} is the minimum blocksize for recursion then before running enumeration on each block lattice k, run BKZ-(k-s) on the block if $k > k_{min}$ (otherwise, do as in original BKZ, i.e. only LLL preprocessing of the local block lattice).

The full RBKZ algorithm is given in Algorithm 1.

Algorithm 1 The RBKZ(n, k) basis reduction algorithm

Input: a basis $B = (\mathbf{b}_1, \ldots, \mathbf{b}_n)$ of a lattice L with blocksize $k \in (2, n)$, minimum blocksize k_{min}, step size s, the GS triangular matrix μ and a vector $\mathbf{c}$ to hold all $\|\mathbf{b}_i^*\|^2_{(1 \leq i \leq n)}$
Output: a BKZ-k reduced basis $(\mathbf{b}_1, \ldots, \mathbf{b}_n)$ with updated μ and $\mathbf{c}$

```
if k < k_min then
    return the input basis
else
    LLL(B, c, μ, δ)
    z ← 0, i ← 0
    compute τ(n, k)
    while z < τ(n, k) · (n − 1) do
        i ← i + 1, j ← min(i + k − 1, n)
        if (i = n) then
            i ← 1, j ← n
        end if
        compute the local projected block basis M_i of dim. d ← min(k, n − i + 1)
        for (1/p_succ) times do
            apply randomization on M_i        ⇒ output is a randomized basis Z_i
            n ← d, k ← (d − s)
            call RBKZ(n, k) on Z_i        ⇒ output is a preprocessed basis P_i
            apply pruned enumeration on P_i
        end for
        compute b_new as a shortest vector found among all iterations of M_i
        h = min(j + 1, n)
        B_h = (b_1, ..., b_{i−1}, b_new, b_i, ..., b_h)
        LLL(B_h, c, μ, δ); z ← z + 1
    end while
end if
```

V. Preprocessing and Pruning Variants

We consider three possibilities of optimization for our RBKZ algorithm. In the first option, we just use non-extreme (high probability) pruning at all levels, and we can afford a very good preprocessing (with a relatively small step size) because the branching factor of the recursion is small ($poly(k)$). In the second option, in order to gain extra savings of the extreme pruning at the top level, we have to pay with an exponential branching factor ($1/p_{succ}$) in the second level of recursion. To compensate, we have to lower the quality of preprocessing by increasing the step size sufficiently until the non-extreme preprocessing cost multiplied by the branching factor balances the cost of the extreme pruning at the top level. This yields an optimal step size to balance out the cost. The third option is included only for completeness, here we consider two extreme pruning levels from the top and non-extreme pruning at other lower levels. Our model implementation (see next section) is confined to the second option which gives the better results of all. This observation has been confirmed experimentally.

- Option 1 (step size s_1 and success probability p_1): Non-extreme pruning at all levels. Formally, for $r = k_{min}, ..., k, s(r) = s_1$, and $p(r) = p_1 \sim 1$ where s_1 is chosen to minimize total time.
- Option 2 (step sizes s_1, s_2 and success probabilities p_1, p_2): Extreme pruning at top level and non-extreme pruning at lower levels. Formally, for $r = k_{min}, ..., k, s(r) = s_1$ and $p(r) = p_2 = 4\alpha_1(1-\alpha_1)^{r/4}$ (asymptotically) or $p(r) = p_{succ}$ (from exact calculation) for $r > k - s_1$ and $s(r) = s_2$ and $p(r) = p_1 \sim 1$ for $r \leq k - s_1$. The step sizes s_1, s_2 and speed up parameter α_1 are chosen to minimize total runtime.
- Option 3 (step sizes s_1, s_2, s_3 and success probabilities p_1, p_2, p_3) : Extreme pruning at top two levels and non-extreme pruning at lower levels.

VI. Recursive-BKZ Model

The purpose of the RBKZ model is to simulate and test the complexity of our preprocessing variants. We write our code in C/C++ with the "RR" floating point variant of NTL [11] version 5.5.2. In particular, the model implements all theoretical formulas given in Section II of this paper including few more to estimate the runtime using SMA based GSO for HKZ and BKZ reduction. The main subroutines of the model implementation can be described as follows.

The first task is to create a subroutine for computing the SMA fixed point normalized log GSO, i.e. $\overline{x}_i = x_i - E[\mathbf{x}]$, $\forall i$, where $x_i = \log \|\mathbf{b}_i^*\|$, $E[\mathbf{x}] = \sum_{i=1}^{k} \frac{x_i}{k}$. For all $i \leq n-k$, we compute BKZ-SMA log GSO, following Lemma 4 in [9], as follows,

$$x_i = \frac{k}{2(k-1)} \cdot \log \gamma_k + \frac{1}{k-1} \cdot \sum_{j=i+1}^{i+k-1} x_j \tag{8}$$

where the Hermite constant $\gamma_k = V_k(1)^{\frac{-2}{k}}$ and $V_k(1) = \frac{\pi^{\frac{k}{2}}}{\Gamma(\frac{k}{2}+1)}$ is the volume of the k-dimensional unit ball. For the last k vectors, i.e. for all $i > n-k$, BKZ performs the HKZ reduction and we have

$$x_i = y_{i-(n-k)} \tag{9}$$

such that (following Lemma 2 in [9]), $y_j = -(k-j+1) \cdot \Psi_k(j-1) + (k-j) \cdot \Psi_k(j), \forall j < k$ and $y_k = -\Psi_k(k-1)$, where $\Psi_n(\beta) = \sum_{i=n-\beta}^{n-1} \frac{\log \gamma_{i+1}}{2i}$, $\forall\, 0 \leq \beta < n$. This eventually

TABLE I
OPTIMAL s_1 AND ENUMERATION COMPLEXITIES FOR $k = 100$ (OPTION 2) WITH PREPROCESSING OVERHEAD FOR EXTREME PRUNING.

α	s_1	s_2	$T_2(\gamma_0)$	$T_1(\gamma_0)$	$T_1(0)$	$\delta_{ov,xp}$
0.05	70	0	54.06	54.05	45.88	8.17
0.10	53	0	44.15	43.95	35.85	8.10
0.15	46	0	35.42	35.16	35.03	0.13
0.20	32	0	37.03	37.19	36.88	0.31
0.25	22	0	38.77	38.84	38.82	0.02
0.30	14	0	40.72	40.74	40.87	−0.13
0.35	07	0	43.00	42.84	42.96	−0.12
0.40	01	0	45.30	45.09	45.11	−0.02

helps in computing the complexity (number of nodes) N and the exact level for the maximum node density in the enumeration tree.

To incorporate the pruning with the complexity estimate we need to create subroutines for computing the pruning ratio S_{xp} and the success probability p_{succ} based on the successive integration method (in [10]). These subroutines will be required also to implement the variants of preprocessing/pruning options with the parameters α (speed up factor), s (step size) and p (probability of success).

Finally, the model should able to compute the log enumeration cost of blocksize r in extreme pruning: $lgTen(r) = lgNen(r) - \log(p_{succ}(r))$, where lgNen($r$) is the log enumeration cost (log number of nodes) for a dimension r and the term $p_{succ}(r)$ is due to the branching factor of extreme pruning. This is the complexity we require to compare with the numerical results in [7]. By changing the preprocessing and pruning parameters (α, s, p etc.) in different levels of the recursion we can control and thus optimize the value of lgTen(r). The model also has provision to compute the total runtime $T(n, k)$.

VII. EXPERIMENTAL RESULTS

We simulate the complexity estimates from the previous section using our RBKZ preprocessing Model. All numerical results obtained in this section are derived by running the implementation of this model. Table I shows the optimal cost of using extreme pruning for a range of pruning parameter α from the numerical model. In particular, it gives the optimal log enumeration cost of the second recursion level $T_2(\gamma_0)$, top recursion level $T_1(\gamma_0)$ and HKZ-reduced basis $T_1(0)$ for a blocksize k. We say optimal as each α entry corresponds to an optimized step size $s_1 = \gamma_0 \cdot k$ that balances the complexity of the top level and the second level. Therefore, Table I also suggests an optimal value of the pruning speed up parameter $\alpha \sim 0.15$. The last column of the table includes the preprocessing overhead ($\delta_{ov,xp}$ = $T_1(\gamma_0) - T_1(0)$ in log) due to the extreme pruning. For non-extreme pruning, the log complexity $T_1(0)$ (option 1) is approximately 41.15.

To realize the overall result, for various k we plot Figure 1 that shows three (solid line) graphs comparing the complexity of extreme pruning including preprocessing cost ($T_{xp}(\gamma_0)$, i.e. the log sum of the cost of top level, $T_1(\gamma_0)$ and second level, $T_2(\gamma_0)$), extreme pruning excluding the cost of preprocessing ($T_1(0)$, i.e. complexity of a HKZ reduced basis in dimension k at $\gamma = 0$) and non-extreme pruning ($T_1(0)$(option 1) at $\gamma = 0$). The complexity of the non-extreme case is $\approx \log N(k, 0)_{up} - (c_{S,nxp} - c_{p,nxp}) \cdot k$, where $c_{S,nxp} = \log S_{nxp}((1-\gamma)k)/((1-\gamma)k)$ and $c_{p,nxp} = \log(1/p_{succ}(k))/k \sim 0$ (we consider the success probability $p_{succ} \sim 1$ for option 1) are the non-extreme pruning constants. This is also the time to enumerate a HKZ-reduced k dimensional basis with non-extreme pruning at s_1 (or γ)= 0.

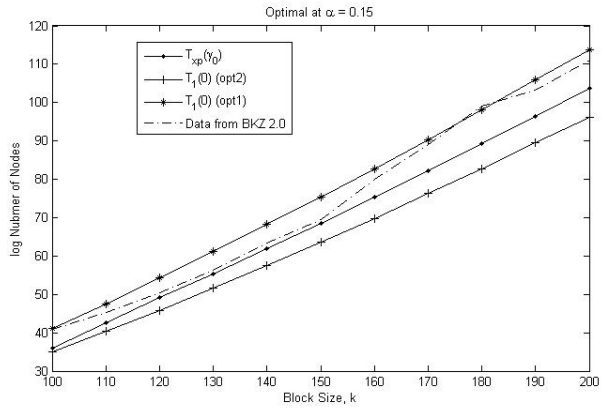

Fig. 1. Comparing extreme pruning (with and without the cost of preprocessing) and non-extreme pruning complexities with previously reported similar cost from [7].

The dotted line in Figure 1 is the Table 3 entries of [7], where one can see that the complexity we have is better than their preprocessing option (simulation of BKZ-90/100/110/120) for a range of block size k. Presumably, it is because we used an optimized preprocessing step size s_1 for those block sizes, while in [7] Chen and Nguyen used a suboptimal choice.

VIII. CONCLUSIONS

In this paper, we optimize the various parameters of the most successful practical lattice reduction algorithm known as BKZ. Thus we improve the performance of this algorithm in terms of time complexity. We also show the comparative results of the similar work reported from Chen and Nguyen's paper in Asiacrypt'11 conference.

REFERENCES

[1] M. Ajtai. *The shortest vector problem in L_2 is NP-hard for randomized reductions (extended abstract)*. In STOC'98, ACM, pp. 284-293, 1998.

[2] O. Regev. *On lattices, learning with errors, random linear codes, and cryptography*. Journal of ACM, vol 56, 2009.

[3] C. Gentry. *Fully homomorphic encryption using ideal lattices*. In STOC'09, ACM, pp. 169-178, 2009.

[4] V. Lyubashevsky, D. Micciancio, C. Peikert and A. Rosen. *SWIFFT: A Modest Proposal for FFT Hashing*. In Fast Software Encryption(FSE) 2008, LNCS, pp. 54-72. Springer-Verlag, 2008.

[5] A. K. Lenstra, H. W. Lenstra, Jr., and L. Lovász. *Factoring polynomials with rational coefficients*. Math. Ann., 261(4): 515-534, 1982.

[6] C.-P. Schnorr and M. Euchner. *Lattice basis reduction: improved practical algorithms and solving subset sum problems*. Math. Programming, 66:181-199, 1994.

[7] Y. Chen and P. Q. Nguyen. *BKZ 2.0: Better Lattice Security Estimates*. In ASIACRYPT'11, LNCS 7073, pp. 1-20, IACR, 2011.

[8] P. Q. Nguyen and V. Brigitte. *The LLL Algorithm: survey and application*. Chapter-2 (Hermite?s Constant and Lattice Algorithms). ISBN 978-3-642-02294-4, 2010.

[9] G. Hanrot, X. Pujol and D. Stehlé. *Analyzing Blockwise Lattice Algorithms using Dynamical Systems*. In CRYPTO'11. LNCS, vol. 6841, pp. 447-464. Springer, 2011.

[10] N. Gama, P. Q. Nguyen, O. Regev. *Lattice enumeration using Extreme Pruning*. In EUROCRYPT, 2010, LNCS, Springer-Verlag, 2010.

[11] V. Shoup. NTL: A library for doing number theory. Available at http://www.shoup.net/ntl/.

OPTIMAL TASK SCHEDULING IN CLOUD COMPUTING ENVIRONMENT: META HEURISTIC APPROACHES

Tripti Mandal[1], Sriyankar Acharyya[2]
[1]Computer Science and Engineering, West Bengal University of Technology, Kolkata, West Bengal, India
[2]Computer Science and Engineering, West Bengal University of Technology, Kolkata, West Bengal, India
[1]triptimandal90@gmail.com, [2]srikalpa8@gmail.com

Abstract—**Cloud computing is the latest continuation of parallel computing, distributed computing and grid computing. In this system, user can make use of different services like storage, servers and other applications. Cloud resources are not only used by numerous users but are also dynamically redistributed on demand. Requested services are delivered to user's computers and devices through the Internet. The fundamental issue in cloud computing system is related to task scheduling where a scheduler finds an optimal solution in cost-effective manner. Task scheduling issue is mainly focus on to find the best or optimal resources in order to minimize the total processing time of Virtual Machines (VMs). Cloud task scheduling is an NP-hard problem. The focus is on increasing the efficient use of the shared resources. A number of meta-heuristic algorithms have been implemented to solve this issue. In this work three meta-heuristic techniques such as Simulated Annealing, Firefly Algorithm and Cuckoo Search Algorithm have been implemented to find an optimal solution. The main goal of these algorithms is to minimize the overall processing time of the VMs which execute a set of tasks. The experimental result shows that Firefly Algorithm (FFA) performs better than Simulated Annealing and Cuckoo Search Algorithm.**

Keywords—Cloud Computing, Task Scheduling, Simulated Annealing, Firefly Algorithm, Cuckoo Search Algorithm.

I. INTRODUCTION

Cloud computing is a developing technology that provides different kind of services [1] such as infrastructure, software and different applications through network. Cloud can also be defined as a distributed computing paradigm, which is a group of interconnected and virtualized computers that are provisioned and presented dynamically [1] as unified computing resources, offered as a pay-per-use service [2]. According to the cloud definition of National Institute of Standards and Technology (NIST) [3]," Cloud computing is a model for enabling convenient, on-demand network access to a shared pool of configurable computing resources (e.g., networks, servers, storage, applications, and services) that can be rapidly provisioned and released with minimal management effort or service provider interaction". Different types of services [4] are Infrastructure as services (IaaS) where customer can initiate a new project by renting computing resources [1], Platform as services (PaaS) where platform is provided to the customer to execute any program and Software as a Service (SaaS) [1] where cloud system summarizes everything required to evaluate software life-cycle. Different kinds of requests are coming from the different part of the world. All the tasks are executed by VMs which are also known as processing element in cloud environment [5]. Before the task gets executed on the VM, it is given to the dispatcher [5]. Dispatcher or Cloud broker then assigns the tasks to appropriate cloud user. As the number of requests is more, the required number of VMs is more. As more than one task gets executed to one or more VM, so the tasks should be scheduled within the VM, such that, all the tasks must complete its processing as early as possible. This enhances the performance of cloud and makes the system more efficient and productive.

Cloud task scheduling can be described as a NP-hard optimization problem [2], [5], [6], which is best solvable using mete-heuristic algorithms [2], [10]. Different meta-heuristic methods have been applied such as Genetic algorithm (GA), Ant Colony Optimization (ACO), Simulated Annealing (SA), Particle Swarm Optimization (PSO), Max-Min Algorithm and many more to solve this task scheduling issue. Numerous research results [2], [5], [10] have been made to ensure that meta-heuristic scheduling algorithms can provide better optimal scheduling than traditional scheduling algorithms [10].

Optimal solution can be obtained by optimizing different parameters [2], [5], [6]-[9] such as makespan, processing time, execution time, communication cost, task transferring time etc. In this work processing time has been considered as a parameter to be optimized for scheduling of tasks.

To solve this scheduling issue of tasks, several works have been done. Ant Colony optimization (ACO) based task scheduling has been proposed in [7], [11]. ACO is based on the foraging behavior of ant colonies. In [7], the proposed ACO algorithm has been implemented to minimize the makespan (Total task completion time) , where as in [11] the ACO algorithm is implemented and compared with First Come First Serve and Round Robin method algorithms and showed positive result. But in both the proposed ACO, there are some problems in updating of the pheromone intensity. In

78-1-4673-9257-0/15/$31.00 ©2015 IEEE

order to let ACO get a better performance, PACO (a period based ACO) [12] has been implemented. The period based mechanism is used to improve the update pheromone strategy. PACO performs better to optimize makespan and load balance strategy. A heuristic approach, Genetic algorithm [6] has been made to optimize makespan. Each chromosome is represented by a job and every chromosome has its fitness value. Two main Disadvantages associated with this method are complexity and longtime consumption. A new evolutionary algorithm, which is based on obligate brood parasite behavior of cuckoo species [13], has been proposed. In this proposed system each cuckoo lay eggs at a time and dumps the eggs in a randomly chosen nest. Every nest has a fitness value associated with it. Considering both the cost for data transmission and computation, a PSO (Particle Swarm Optimization) algorithm [8] has been implemented to schedule the tasks. By combining the advantages of Ant Colony Optimization an Artificial bee algorithm, a hybrid task scheduling algorithm [9] has been proposed. Both the algorithms consider pheromone concentration and the edge weight but not the load on the VM. The sum of transfer time and execution time is optimized here. Multi objective particle swarm optimization (MOPSO) [14] has been applied in cloud computing to optimize task execution cost, task transferring time and task execution time.

In this paper three meta-heuristic algorithms, Simulated Annealing, Firefly Algorithm and Cuckoo Search Algorithm have been implemented to find an optimal solution of submitted tasks. From the experimental result, it has been shown that Firefly Algorithm performs better than Simulated Annealing and Cuckoo Search algorithm in finding an optimal schedule of submitted tasks in reasonable time.

The following sections are arranged as follows. In section II, Task scheduling problem has been described with mathematical model. In section III description meta-heuristic has been made. Section IV describes the result and section V concludes the paper.

II. TASK SCHEDULING PROBLEM

Task scheduling can be described as tasks or jobs that will be executed by a set of computing resources. Computing resources are known as virtual machines. For instances, given the problem that if there is a set of n tasks, $\{T_1,T_2,T_3,T_4,\ldots T_n\}$ which need to be scheduled on m identical machines $\{VM_1,VM_2,\ldots..VM_m\}$, while trying to reduce the total processing time. All the tasks are non- preemptive [5] that is processing of one task in one machine cannot be executed on another and all the resources can execute all type of tasks.

In [5], a mathematical model for scheduling has been proposed to balance the load of individual VM while trying to minimize the makespan. With the help of this model, processing time has been evaluated.

For the mathematical representation of the scheduling problem let there be a set of m virtual machines where all the tasks will be processed and n number of tasks represented as a set [5]. All the tasks in the model are non-preemptive and independent. Processing time varies from one VM to other VM based on capacity and bandwidth of the VM.

So Capacity of individual VM,

$$C_i = pe_{num,i} \times pe_{mips,i} + vm_{bw,i} \qquad (1)$$

Where number of processing element of VM is denoted by pe_{num}, pe_{mips} is the million instructions per second of all processors and vm_{bw} is the communication bandwidth ability to a VM_i.

Capacity of all VMs, $C = \sum_{i=1}^{m} C_i$ (2)

Total capacity of all the VM is known as capacity of the datacenter. Load of individual VM can be defined as the total length of tasks that are assigned to the VM.

$$L_{vmi,t} = \frac{N(T\ ,t)}{S(VM\ ,t)} \qquad (3)$$

It is calculated using number of task at time t on a service queue and divided by the service rate of individual VM at time instance t. Load of all VM is calculated as,

$$L = \sum_{i=1}^{m} L_{vmi} \qquad (4)$$

Processing time of a VM, $PT_i = \frac{L_{vmi}}{C}$ (5)

Processing time of all the VM, $PT = \frac{L}{C}$ (6)

This equation defines the total processing time of all the VM.

So the problem is to minimize,

$$PT_{max} = \sum_{i=1}^{m} PT_i \text{, where } i \in \text{VM, } i=1, 2, 3\ldots n \qquad (7)$$

And load value of a VM must be less than its capacity.

III. SOLUTION METHODS

Being the problem in NP-hard class, meta-heuristic algorithms are best suitable to solve this issue. Meta-Heuristic is a higher level heuristic methodology [10] to find optimal solution of a problem in reasonable time.

In this work each solution has been represented as a vector of n elements where n is the number of tasks to be scheduled. Vector component values are the VM's number; hence it may appear more than once because more than one task is allocated to the same VM. For an example if we consider the following example, where nine tasks get scheduled on 4 VMs.

T_1	T_2	T_3	T_4	T_5	T_6	T_7	T_8	T_9
VM_1	VM_4	VM_2	VM_1	VM_3	VM_1	VM_2	VM_3	VM_4

According to the diagram, task 1 and 4 are associated with VM_1. Tasks 3 and 7 are associated with VM_2. Tasks 5 and 8 are associated with VM_3. Tasks 2 and 9 are associated with VM_4.

A. *Simulated Annealing*

Simulated Annealing [15], [16], [17] is based on the annealing of metal. To develop a crystal, one starts by heating the raw material to a liquefied state. To get a crystalline structure, the temperature of the crystal melt is reduced. If the reduction of temperature becomes fast then irregularities get locked into the structure of crystal and the trapped energy level is much higher than in a perfectly structured crystal. In each cycle this method tries to move from the current trial solution S to a neighboring point S' in the solution space in an effort to find a better trial solution. If the problem is minimization problem and cost(S') < cost(S), S' becomes the new trial solution; the move from S to S' is then called a downhill move. If cost(S') > cost(S), S' becomes the new trial solution with probability p = exp (-Δ/temp), where temp is a parameter known as the temperature and Δ = cost(S') - cost(S). S is retained as the trial solution with probability (1- p). Thus S' can become the new trial solution even when its cost is higher. This kind of move from S to S' is called an uphill move. This ensures that the procedure does not get trapped in a local minimum.

The SA Algorithm is given below:

Step 1: Generate an initial solution S,
S* ← S
Step 2: Initialize Temperature T_0, T_0>0
T ← T_0
Step 3: Calculate Cost C
Step 4: While not frozen do the followings
4.1. Find a neighbor S'
4.2. Find Cost C' of S', ΔC=C'-C
4.3. If (ΔC<=0)
Accept solution S', S* ← S'
4.4. Else accept S' with probability $e^{-\Delta/T}$, S* ← S'
Step 5: Reduce temperature with factor r, T=T*r
Step 6: Output: the final state S*

Where the initial solution is S, the neighborhood solution is S', S* holds the current best solution. T_0 is the initial temperature. In this work, the initial solution (i.e. solution vector) has been generated randomly. Cost has been determined by its total processing time and neighborhood is selected by swapping the tasks between two randomly chosen VMs.

B. *Firefly Algorithm*

Among several swarm-intelligence algorithms, Firefly (FA) [18], [19] algorithm is one of the mostly used algorithms. This FA algorithm was illustrated by Xin-She Yang [18] in 2008 inspired by the flashing behavior of tropical fireflies. It is a population based Meta Heuristic which tries to find global optimum solution. The FA is based on two behaviors [18] of fireflies, one is to attract other fireflies with lower intensity and another is to minimize the distances between them. Fireflies are unisexual so one can be attracted to other irrespective of their sex. The attractiveness directly varies with the brightness and the brightness is inversely proportional to the distance.

The algorithm is given below:

Step 1: Initialization the population of n firefly
Step 2: Determine light intensity for each firefly
Step 3: Determine the distance between each two Fireflies
Step 4: While t< Maxgeneration (G)
for *i=1: n* for n fireflies
for *j=1: i* for n fireflies
if (I_j>I_i) move firefly i towards firefly j
Vary the attractiveness with distance r_{ij} by $exp\ [-\gamma r_{ij}]$
Evaluate new solution and update light intensity
End if
End for *j*
End for *i*
End while
Step 5: Rank the fireflies and find current global best

The attractiveness function of the firefly is established by,

$$\beta\ (r) = \beta_0\, e^{(-\gamma r^2)} \tag{8}$$

Where β_0 is the attractiveness at r=0. The movement of fireflies i attracted to another more attractive firefly (brighter) j is determined by,

$$x_i\,(t+1) = x_i\,(t) + \beta_0\, e^{(-\gamma r^2)}\,(x_i - x_j) + \alpha\varepsilon_i \tag{9}$$

The value of γ controls the scaling of intensity. For this work the initial populations of fireflies have been generated randomly in a vector with n elements, where n is the number of tasks to be scheduled. Value of the vector denotes the VM number. The fitness of the firefly is reciprocal to its processing time as this is a minimization problem.

C. *Cuckoo Search Algorithm*

Cuckoo Search Algorithm is a meta-heuristic algorithm that models natural behavior of cuckoo species [13], [20]. Each egg in the nest represents a solution. The main aim is to find better solution to change a not so better solution in the nest. At a time, each cuckoo lays one egg and dumps this egg in a nest, chosen randomly. The best nest with high quality eggs (solution) will be carried out to the next generation. The host can discover an alien egg by a probability *Pa [0, 1]*. The host bird either throws the egg away or abandons the nest to build a new nest in a new location.

The algorithm is given below:

Step 1: Objective functions $f(x)$, $x=(x_1, x_2 \ldots x_d)$
Step 2: Generate the population of n host nests x_i, $(i=1, 2 \ldots n)$
Step 3: While (t<Maxgeneration)
Get a cuckoo randomly and generate a new solution by Lévy flights
Evaluate its quality/fitness, F_i
Choose a nest among n (say j) randomly
if $(F_i > F_j)$,
Replace j with a new solution
end
Abandon a worse nest with probability (Pa)
Build new ones at new locations via Lévy flights
Keep the best solutions (with high quality)
Rank the solutions and find the current global best
End while
Step 4: Post process results and visualization.

For minimization problems, the fitness or quality function is reciprocal of objective function. A solution is represented by an egg in the nest and the cuckoo egg represents a new solution. So mainly there is no difference between an egg, a nest and solution. From x_i^t of it the next generation is calculated by,

$$X_i^{(t+1)} = X_i^{(t)} + \alpha \oplus Lévy\ (u) \quad (10)$$

And

$$Lévy\ (u) = t^{-\gamma},\ 1 < \lambda \leq 3 \quad (11)$$

Where α > 0 is the step size, depending on the scale of the given problem, ⊕ means entry-wise multiplications.

To find an optimal solution of the given problem, a solution is represented by an egg and new solution is represented by a cuckoo egg. The initial population is represented by a vector of n elements, where n represents the total number of tasks to be scheduled and vector value represents the VM number.

IV. EXPERIMENTAL RESULTS

All the three algorithms have been implemented in windows 7, 32-bit operating system and the programs are executed in GCC 32 bit compiler. All the methods are executed 100 times and the average of 100 iterations has been performed. All the methods are executed with different random solution. The C.P.U execution time is kept almost same for all the three method so that a comparison can be made.

In all the experiments, number of virtual machine is restricted to 4, while the number of tasks varies from 10 to 50 with difference of 5. All the values of data needed for virtual machine and tasks are taken from [21] where the authors have implemented an optimization techniques using Multi-Objective PSO.

TABLE I: VALUE OF PARAMETERS

Method	Parameters	Value
Simulated Annealing	Initial Temperature	100000
	Minpercent	0.01
	Tempfactor	0.85
	Sizefactor	6
	N	20
	Tcent	0.9
Firefly Algorithm	Alpha	0.2
	Beta	2.0
	Gamma	1
Cuckoo Search Algorithm	Value of alpha	2.0
	Value of P_a	0.4

Table I shows the value of all the parameters. These values have been set after running several trials. Table II shows the experimental results of the three methods. The cost refers to the total processing time of the optimal task schedule found by an algorithm. The time refers to the average execution time of the algorithm.

TABLE II: EXPERIMENTAL RESULTS

No. of task	Simulated Annealing		Firefly Algorithm		Cuckoo Search Algorithm	
	Cost	*Time(Second)*	*Cost*	*Time(Second)*	*Cost*	*Time(Second)*
10	4.35709	0.4929	2.79261	0.513	4.402067	0.525425
15	6.04389	0.59857	4.82637	0.5749	6.659729	0.566975
20	8.68716	0.7084	6.95119	0.72257	9.368409	0.717887
25	11.4436	0.82337	8.49927	0.84038	12.23402	0.792325
30	12.6499	0.93381	10.7151	0.95523	14.6173	0.994163
35	13.4607	1.07266	12.4453	1.1077	16.84712	1.06675
40	17.4611	1.12496	14.3273	1.24682	20.56502	1.169287
45	18.4573	1.21493	16.7253	1.4039	22.38663	1.186638
50	20.5931	1.26298	18.1823	1.201	23.67107	1.225288

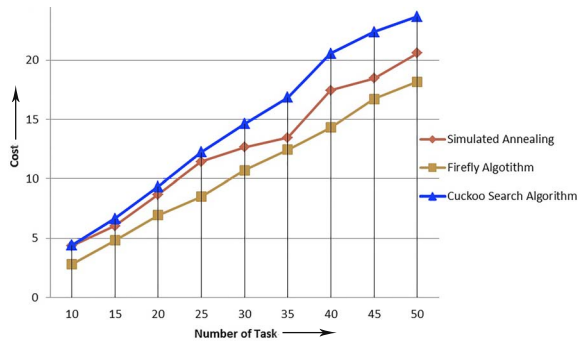

Figure 1. Comparison Graph

Graphical representation of the cost of three methods is shown in following figure 1. From figure 1, it is shown that Firefly Algorithms executes all the tasks with minimal processing time. Cuckoo Search Algorithm underperforms than Simulated Annealing and Firefly Algorithm.

V. CONCLUSION AND FUTURE WORK

In this paper we have implemented three meta-heuristics such as Simulated Annealing, Firefly Algorithm and Cuckoo Search Algorithm to find an optimal solution of the submitted tasks while trying to minimize the total processing time of

VMs. The results are taken after the average of 100 iterations. All the parameters of the three algorithms have been determined after some trials. The cost of the three methods has been calculated to make a comparison among them. The processing time is considered as the cost in these three methods. As it is a minimization problem, the less cost gives us the better solution. The average runtime of program execution for the three meta-heuristics has been kept nearest to each other so that a fair comparison can be made based on the processing time (cost). All the three methods were able to find the optimal solution for the given problem. The experimental results show that the firefly algorithm performs better in comparison with both the Simulated Annealing and Cuckoo Search Algorithm in respect of cost.

In future research, hybrid version of Firefly Algorithm will be tried to solve this problems. Other meta-heuristics like, Differential Evolution, Cat Swarm Optimization, Fish Swarm Algorithm and Bacterial Foraging Optimization will be applied to make the comparative study more judicious.

REFERENCES

[1] R. Buyya, C. S. Yeo, S. Venugopal, J. Broberg, and I. Brandic, "Cloud computing and emerging IT platforms: Vision, hype, and reality for delivering computing as the 5th utility," *Future Generation computer systems*, vol. 25, no. 6, pp.599-616, 2009.

[2] M. Tawfeek, A. El-Sisi, A. Keshk, and F. Torkey, "Cloud task scheduling based on ant colony optimization," 8th *International Conference on Computer Engineering & Systems (ICCES)*, pp. 64-69, 2013.

[3] P. Mell, and T. Grance, "The NIST definition of cloud computing," *National Institute of Standards and Technology Special Publication 800-146*, vol.53, no. 6, 2009.

[4] M. Dikaiakos, D. Katsaros, P. Mehra, G. Pallis and A. Vakali, "Cloud Computing: Distributed Internet Computing for IT and Scientific Research," *IEEE Internet Computing*, vol. 13, no. 5, pp. 10-13, 2009.

[5] D. Babu, and P. V. Krishna, "Honey bee behavior inspired load balancing of tasks in cloud computing environments," *Applied Soft Computing*, vol. 13, no. 5, pp. 2292-2303, 2013.

[6] S. H. Jang, T. Y. Kim, J. K. Kim, and J. S. Lee, "The study of genetic algorithm-based task scheduling for cloud computing." *International Journal of Control and Automation*, vol. 5, no. 4, pp.157-162, 2014.

[7] L. Wang, and L. Ai, "Task Scheduling Policy Based on Ant Colony Optimization in Cloud Computing Environment," *LISS 2012: Proceedings of 2nd International Conference on Logistics, Informatics and Service Science*, pp. 953-957, 2013.

[8] S. Pandey, L. Wu, S. Guru, and R. Buyya, "A Particle Swarm Optimization-Based Heuristic for Scheduling Workflow Applications in Cloud Computing Environments", *24th IEEE International Conference on Advanced Information Networking and Applications*, pp. 400-407, IEEE, 2010.

[9] R. Madivi, and S. Kamath, "A hybrid bio-inspired task scheduling algorithm in cloud environment," *Fifth International Conference on Computing, Communications and Networking Technologies (ICCCNT)*, pp.1-7, 2014.

[10] C. Tsai and J. Rodrigues, "Meta heuristic Scheduling for Cloud: A Survey," *IEEE Systems Journal*, vol. 8, no. 1, pp. 279-291, 2014.

[11] M. Tawfeek, A. El-Sisi, A. Keshk and F. Torkey, "Cloud task scheduling based on ant colony optimization," *8th International Conference on Computer Engineering & Systems (ICCES)*, pp. 64-69, 2013.

[12] W. Sun, N. Zhang, H. Wang, W. Yin and T. Qiu, "PACO: A Period ACO_based Scheduling Algorithm in Cloud Computing," *International Conference on Cloud Computing and Big Data*, pp.482-486, 2013.

[13] N. J. Navimipour, and F. S. Milani, "Task scheduling in the cloud computing based on the cuckoo search algorithm," *International Journal of Modeling and Optimization*, vol. 5, no. 1, pp.44-47, 2015.

[14] Q. Wang , and H. Zheng, "Optimization of task allocation and knowledge workers scheduling based-on particle swarm optimization," *International Conference on Electric Information and Control Engineering*, pp. 574-578, 2011.

[15] S. Acharyya, "The Satisfiability Problem: A Constraint Satisfaction Approach", Ph D Thesis, Computer Science & Engg., Calcutta University, 2001.

[16] S. Kirkpatrick, C.D. Geatt, and M. P. Vecchi, "Optimization by Simulated Annealing", Science, new series, vol. 220, No. 4598, pp. 671-680, 1983.

[17] M. Abdullah and M. Othman, "Simulated Annealing Approach to Cost-Based Multi-Quality of Service Job Scheduling in Cloud Computing Environment," *American Journal of Applied Sciences* ,vol. 11, no. 6, pp. 872-877, 2014.

[18] X. Yang, D. Fister, and I. Fister, "Firefly algorithm: a brief review of the expanding literature", *Cuckoo Search and Firefly Algorithm*, pp. 347-360. Springer International Publishing, 2014.

[19] A. Yousif, A. H. Abdullah, S. M. Nor, and A. A. Abdelaziz, "Scheduling jobs on grid computing using firefly algorithm.", *Journal of Theoretical and Applied Information Technology*, vol .33, no. 2,pp.155-164, 2011.

[20] E. Valian, S. Mohanna and S. Tavakoli ," Improved Cuckoo Search Algorithm for Global Optimization," *International Journal of Communications and Information Technology,* vol.1, no.1, pp.31-44, 2011.

[21] F. Ramezani, J. Lu and F. Hussain, "Task Scheduling Optimization in Cloud Computing Applying Multi-Objective Particle Swarm Optimization," *Service-Oriented Computing*, pp. 237-251, 2013.

Longest Common Subsequence using Chemical Reaction Optimization

Md. Rafiqul Islam
Computer Science and Engineering Discipline, Khulna University, Khulna - 9208, Bangladesh.
e-mail: dmri1978@gmail.com

Zarrin Tasnim Asha
Computer Science and Engineering Discipline, Khulna University, Khulna - 9208, Bangladesh.
e-mail: zarrin.ku@gmail.com

Rezoana Ahmed
Computer Science and Engineering Discipline, Khulna University, Khulna -9208, Bangladesh.
e-mail: sheme.cse@gmail.com

***Abstract*— Longest Common Subsequence (LCS) is a well-known optimization problem. It is the problem to find out a longest subsequence of each member of a given set of sequences. It is an NP-hard problem and has applications in data compression, FPGA circuit minimization and bioinformatics. Chemical Raction Optimization (CRO) is a new meta-heuristic method that is being widely used in solving optimization problem. In this paper we have proposed an efficient Chemical Reaction Optimization technique to solve Longest Common Subsequence problem. The design strategies of elementary operators and correction method are shown to solve the problem. The proposed method is compared with two other methods and the experimental results show that it takes less execution time than that of others.**

Keywords—Longest common subsequence, Chemical Reaction Optimizatio, Metaheurictic, Molecule.

I. INTRODUCTION

Longest common subsequence is an optimization problem. Longest Common Subsequence (LCS) means the longest sequence of characters that appear left-to-right in a given set of strings. But it is not necessarily that it is adjacent block of characters. LCS is essential to occupy serial positions within the original sequences or strings. The longest common subsequence is the base of data comparison programs. Many problems or applications are solved by LCS such as the applications in data compression, FPGA circuit minimization, Bioinformatics [1]. A detail of literature review related to LCS problem and its solutions can be found in [1].One of the biological applications is to compare the DNA of two or more difference organisms. DNA is sequence which consists of A (Aclenine), G (Gaunine), C (Cytosine) and T (Thymin). Thus we are given two DNA sequences and wish to find DNA sequence which is common and longest in length and such a problem is LCS problem [2]. LCS problem for two strings can be solved using Dynamic Programming (DP) [2, 3], which gives optimum results. Chemical Reaction Optimization (CRO) is a simple and powerful meta-heuristic which is showing excellent performance in solving optimization problem. CRO mimics the interactions of molecules in chemical reactions to search for the global optimum [4]. CRO was designed as an optimization framework. It has been applied to solve many practical problems, e.g. quadratic assignment problem[5], population transition problem in peer-to-peer streaming[7], network coding optimization problem[8], standard continuous benchmark function[9], cognitive radio spectrum allocation problem[10], grid scheduling problem[11][12], stock portfolio selection problem [13],artificial neural network training [14], 0-1 Knapsack problem [3] etc. In this paper we have designed an algorithm to find LCS based on the concept of CRO. The proposed method and other two dynamic programming algorithms such as dynamic programming algorithm for LCS given in [2] and fast dynamic programming method depicted in [3] have been implemented and compared the results to show the performances.

II. LONGEST COMMON SUBSEQUENCE (LCS)

Common subsequence of two given sequences is a subsequence that exits in both the sequences. However, the Longest Common Subsequence (LCS) of two given sequences is a subsequence that exits in both the sequences and have longest or maximum length. For example, we have two sequences S_1=(E,F,G,H,E,F) and S_2=(F,H,G,E,F,E), the sequence S=(F,G,F,E) is an LCS. Since the subsequence is common in both in the sequence S1 and S2 and the sub sequence S have the length, |S| = 4, which is the maximum in common sub-sequences. The problem can be formulated as follows:

Let $X = [x_1, x_2 \ldots x_n]$ be a sequence of n elements where X is a string. The elements of the string are members of a finite alphabet $\sum$, $x_n \in \sum$, $\forall i = 1, 2, 3, \ldots, n$.

A sequence $Y = [y_1, y_2, \ldots, y_m]$ is a subsequence of X if there exists an increasing sequence of indices $[i_1, i_2, \ldots, i_k]$ such that $X[i_k] = Y[j]$ holds, $\forall j = 1, 2, \ldots, k \leq n$.

978-1-4673-9257-0/15/$31.00 ©2015 IEEE

Given a finite set S of n strings $S^* = \{S_1, S_2, \ldots, S_n\}$, S is a common subsequence, if S subsequence S_i, $\forall i = 1, 2, 3, \ldots, n$.
The longest common subsequence of S* is the common subsequence of maximum length. The problem can be expressed as

$$\text{Maximize } |S|$$
$$\text{subject to } S \text{ subsequence } S_i, \forall i = 1, \ldots, n.$$

with |S| being the length of the common subsequence S. The longest common subsequences are not always unique. More than one common subsequence with maximum length can be found there.

III. Chemical Reaction Optimization (CRO)

CRO is one of the newest optimization algorithms, which is inspired by the chemical reaction process [15]. CRO has been successfully applied to many other problems. In CRO, molecule (M) is the basic operating agent which represents the solution of optimization problem. To explore solution a set of molecules are controlled and manipulated by CRO. A molecule has potential energy (PE), kinetic energy (KE), hits number, and other characteristics that represent solution. CRO simulates four types of chemical reactions. The four types of elementary reactions are on-wall ineffective collision, decomposition, inter-molecular ineffective collision and synthesis. During the process of CRO the total energy remains constant which means CRO requires conservation of energy. The CRO algorithm includes three stages: initialization, iteration and the final stage. The initialization stage generates initial population (pop) along with PopSize, KElossRate, MoleColl, buffer, InitialKE and two thresholds(α and β). In iteration stage, one elementary reaction out of four reactions takes place in each iteration. Here, we have to determine whether uni-molecular or bi-molecular reaction is taken place. The type of reaction is determined by comparing a random number t [0, 1] against MoleColl. If t > MoleColl there will be unimolecular reaction. Otherwise a bi-molecular reaction occurs. At the end of the each iteration we have to check stopping criteria. Here the potential energy value of the newly obtained molecule(s) is compared with the original molecules. The new molecules will be accepted when the new values can satisfy the energy conservation conditions. Otherwise, the new molecules are discarded**.**

The pseudo code of CRO algorithm is depicted in Algorithm 1.

Algorithm 1: CRO Algorithm

```
Input: Objective function f and the parameter values
\\ Initialization
Set PopSize, KELossRate, MoleColl, buffer, InitialKE, α, and β
Create PopSize number of molecules or solutions
\\ Iterations
while the stopping criteria not met do
Generate b ∈ [0, |S1|]
if b > MoleColl then
Randomly select one molecule or solution S'
if Decomposition criterion met then
Trigger Decompos ()
else
Trigger Onwall ()
end if
else
Randomly select two molecules or solutions S'1 and S'2
if Synthesis criterion met then
Trigger Synthesis ()
else
Trigger Intermole ()
end if
end if
Check for any new minimum solution
end while
\\ The final stage
Output the best solution found and its objective function value
```

IV. Design CRO for LCS

Here we design CRO method for two strings. In LCS problem two sequences are given for finding the longest subsequence. Suppose we have two sequences such as S_1 (first sequence) of length n and S_2 (second sequence) of length m, where $m \leq n$ and $n = |S_1|$ and $m = |S_2|$. We have to find out the longest common subsequence of S_1 and S_2.
Example 1:
S_1 = "GCCCTAGCG".
S_2 = "GGCACTA".
The output sequence, S = "GCAC".
Here we will design Chemical Reaction Optimization (CRO) algorithm for LCS problem.

S_1 :

Character	G	C	C	C	T	A	G	C	G
Index	0	1	2	3	4	5	6	7	8

S_2:

Character	G	G	C	A	C	T	A
Index	0	1	2	3	4	5	6

A. Solution Generation

To generate solution first we take an array of length $m=|S_2|$. Then we generate m random numbers from 0 to $n=|S_1|$. Next we sort the numbers to get a solution sequence. The following Fig. 1 depicts the scenario according to the example 1.

Generate $|S_2|$ random numbers $k \in [0, n]$:

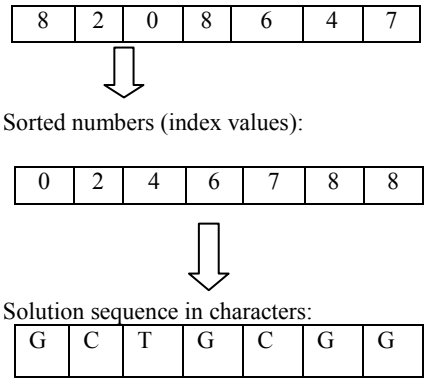

Fig. 1. Solution Representation

B. *On-wall Ineffective Collision*

This elementary reaction corresponds to the basic local search operator for CRO. It changes the solution structure of one solution. Suppose that in an on-wall ineffective collision, the solution structure S is transformed to S'. The new solution structure is generated as S' = C(S), where C(S) is a correction operator that corrects new solution structure. The detail of C (S) function is explained at the end of this section.

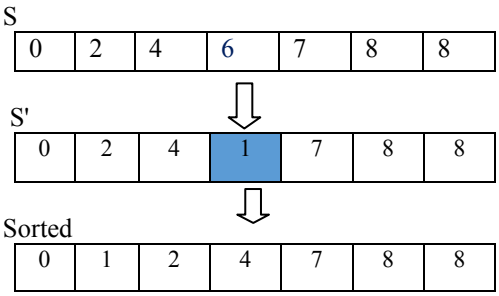

Fig. 2. Solution after On Wall Ineffective Collision

C. *Decomposition*

This elementary reaction generates two solutions from one solution. Decomposition often applies a vigorous change to the solution and the resultant solution possesses solution structures greatly different from the original one. Assume that the operator creates two solutions S'_1 and S'_2 from solution S, such as,

$$S \rightarrow S'_1 \cup S'_2$$

Firstly, S is copied to generate S'_1 and S'_2. After that, for n/2 positions in solutions S'_1 and S'_2 are changed randomly. Then we sort them. The function C (S) is invoked to make the output solution valid.

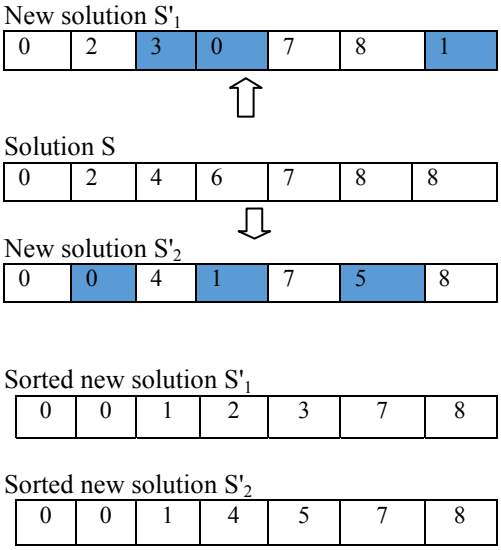

Fig. 3. Solution representation after decomposition

D. *Inter-molecular Ineffective Collision*

It changes the solution structure. The molecularity (assume two) remains unchanged before and after the process. Suppose that in an inter-molecular ineffective collision, the solution structure S_1 is transformed to S'_1 and S_2 is transformed to S'_2. It can be defined as follows:

$$S_1 \cup S_2 \rightarrow S'_1 \cup S'_2$$

Then the new solution structure is generated as S' = C (S).

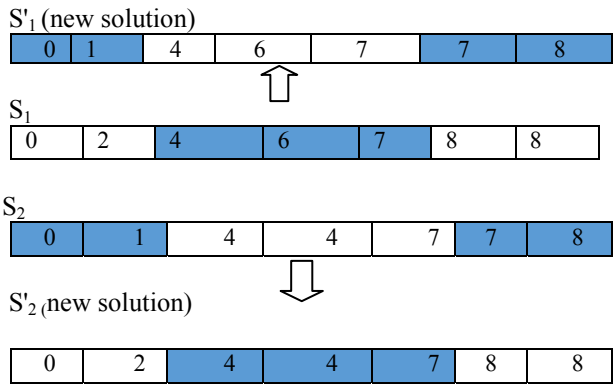

Fig. 4. Solution representation in Inter-molecular Ineffective Collision

E. *Synthesis Operator*

Synthesis takes two molecules as the inputs and combines them to generate a new molecule. In this paper we take two existing solution S'_1 and S'_2. Generate a new solution S from them. It can be represent by the following form.

$S'_1 \cup S'_2 \rightarrow S$

This new solution S is the longest common subsequence.

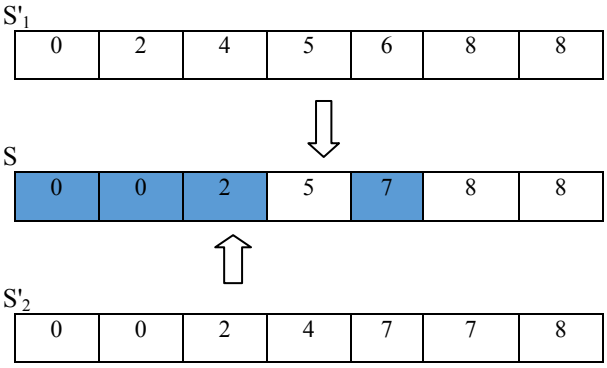

Fig. 5. Solution representation after Synthesis

F. Correction Method

In correction method, the input is solution, S. From the solution vector we get index of character in S_1. Next, we compare the character in position S[i] of S_1 with the character in position, i of S_2, where i = 0, 1…….n-1. If we find same character (character matching) in S_2 and in S_1, then we copy the value of S[i] to output vector, S'[i]. If different character is found (no character matching) then we do forward searching in S_1 starting at the position S[i] +1 to the position S[i+1]-1. If any character in position, j where j ∈ [S[i]+1 to S[i+1]-1] matches with the character in position, i of S_2, the value of j (which is the index value of S_1)is saved to S'[i]. In Fig 6, when i = 1, the character in position 1 of S_1 is C and the character in the same position of S_2 is G. So we do forward searching in S_1. Here S[i] +1 = 2 and S [i+1]-1 = 3, so we perform searching in positions 2 to 3 of S_1. In this case the character in position 3 of S_1 is G, which is same in position 1 of S_2. So we save 3 (position of S_1) to S'[1]. If character matching is not found, then backward searching is to be done in positions S[i]-1 to S [i-1] +1. In backward searching, if we find character matching in position, k of string1 where k ∈ [S [i-1] +1 to S[i]-1]. We save the value of k in S'[i]. In case, there is no character matching in forward searching and also in backward searching the value of S[i] to be copied in S'[i].

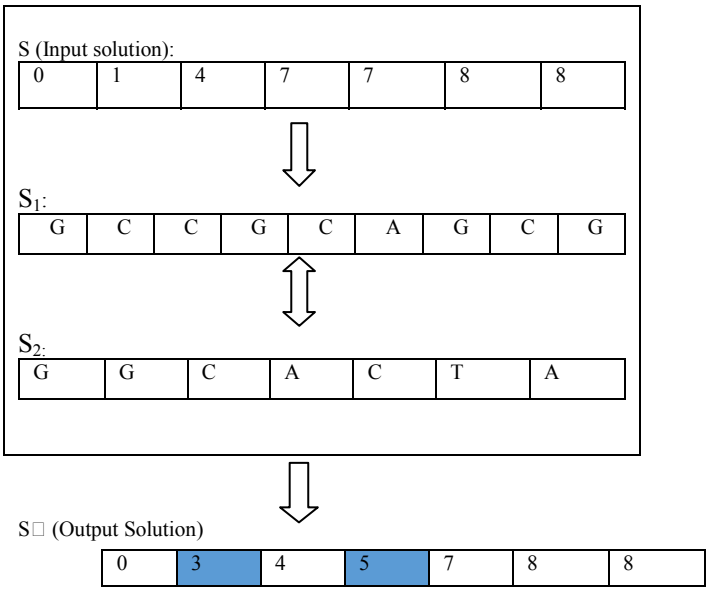

Fig. 6. Solution representation after Correction

V. Simulation Results

We compare proposed CRO method with Dynamic LCS [2] and Fast Dynamic LCS [3] algorithms to show their performances. During the experiments, we have used our own data sets in all test cases. For input string of different length generation different alphabets are used. All times the lengths of both input strings are same. As stated earlier the input sequences are generated randomly. In order to use of same input over and over, different input are used. The following alphabets: {0, 1}, {A, C, G, T} and English alphabet with 26 characters, i.e., {A….Z} or {a…z} are used in order to build input strings. Two strings of certain length are generated randomly based on certain alphabet and used those strings as an input for the algorithm. As we say in section 1(Introduction section) that DNA sequence is consists of A (Adenine), G (Guanine), C (Cytosine) and T (Thymine). For example, the DNA of any organism can be a string S=ACCTGT. So DNA can be expressed as a string that is consists of finite set {A, G, C, T}.

Two strings (S1 and S2) are generated as follows:

S_i= rand [A, G, C, T], i=1, 2, 3,……, n.

Here, rand [A, G, C, T] generates a character from {A, G, C, T} uniformly. The length of the string is n.

In CRO parameters affects its performance. For first testing we set the parameters as initialize PopSize = 10, CollisionRate = 0.2, buffer = 0, KE = 1000, lossRate = 0.1, DecompositionThreshold (α) = 15000 and SysthesisThreshold (β) =10 etc. The decomposition condition and synthesis condition respectively effect by the value of Decomposition Threshold and Systhesis Threshold. We perform 50 runs for each of the chosen values. Among the chosen values the sets of 50 runs are compared and the longest length's sequence is selected. During the experiment, we see that 50 runs for each

of the chosen values is not sufficient for longest String which length is bigger than 1000 or more. Then we need to increase the number of runs such as, 100 or more. We showed the performance of the algorithm in the table.

The test environment is set up on a personal computer with Core i5 CPU at 2.50 GHz CPU, 4G RAM, running on Windows8. Each LCS algorithm was run several times in order to obtain accurate CPU time measurements. System.currentTimeMillis() method was used for obtained the time measurement. It returns current CPU time in milliseconds. All of the algorithms are developed using Java programming language and the process of coding, Eclipse IDE is used.

TABLE I. SIMULATION RESULTS OF CRO

Case 1: Length of string 1 =180, Length of string 2 = 28 , Length of output sequence = 28				
Number of iteration	***Best case***	***Worst case***	***Average***	***Time (ms)***
50	75	57	66	1.09
100	78	50	60	1.24
150	80	48	58	1.30

TABLE II. SIMULATION RESULTS OF CRO

Case 2: Length of string 1 =270, Length of string 2 = 56 , Length of output sequence = 53				
Number of iteration	***Best case***	***Worst case***	***Average***	***Time (ms)***
50	70	58	64	6.92
100	80	50	59	6.94
150	82	40	63	7.00

TABLE III. SIMULATION RESULTS OF CRO

Case 3: Length of string 1 =360, Length of string 2 = 84 , Length of output sequence = 78				
Number of iteration	***Best case***	***Worst case***	***Average***	***Time (ms)***
50	55	53	54	13.60
100	67	48	50	13.80
150	70	30	60	14.00

TABLE IV. SIMULATION RESULTS OF CRO AND OTHER ALGORITHMS

Algorithm	***Length of string1***	***Length of string2***	***Length of output sequence***	***Time(ms)***
LCS	128	28	28	10
FLCS			28	7
CRO			28	**4.32**
LCS	270	56	53	18
FLCS			53	12
CRO			51	**6.96**
LCS	360	84	78	25
FLCS			78	21
CRO			78	**13.98**

VI. CONCLUSIONS

In this paper we have proposed an algorithm to solve longest common subsequence problem based on the concept of chemical reaction optimization. Our main target is to reduce the time complexity of LCS problem and generate an optimal solution. We have compared proposed CRO based method with Dynamic LCS [2] and Fast Dynamic LCS [3] and found that our proposed algorithm has superior performance when compared for all proposed test instances. It reduces the execution time. Here we have used two strings of different lengths. In the future, we will design a CRO algorithm to find LCS for multiple strings.

References

[1] Tabataba, Farzaneh Sadat, and Sayyed Rasoul Mousavi. "A hyper-heuristic for the Longest Common Subsequence problem." *Computational biology and chemistry* 36 (2012): 42-54.

[2] Cormen, Thomas H. *Introduction to algorithms*. MIT press, 2009.

[3] Truong, Tung Khac, Kenli Li, and Yuming Xu. "Chemical reaction optimization with greedy strategy for the 0–1 knapsack problem." *Applied Soft Computing*13.4 (2013): 1774-1780.

[4] Ossman, Mohammed, and Lamiaa Fathi Hussein. "Fast Longest Common Subsequences for Bioinformatics Dynamic Programming." *population* 5 (2012): 7.

[5] Xu, Jin, Albert YS Lam, and Victor OK Li. "Parallel chemical reaction optimization for the quadratic assignment problem." *World Congress in Computer Science, Computer Engineering, and Applied Computing*. 2010.

[6] Chaudhuri, Arindam. "A Dynamic Algorithm for the Longest Common Subsequence Problem using Ant Colony Optimization Technique." *arXiv preprint arXiv:1307.1905* (2013).

[7] Lam, Albert, Jialing Xu, and Victor OK Li. "Chemical reaction optimization for population transition in peer-to-peer live streaming." *Evolutionary Computation (CEC), 2010 IEEE Congress on*. IEEE, 2010.

[8] Pan, Bo, Albert Lam, and Victor OK Li. "Network coding optimization based on chemical reaction optimization." *Global Telecommunications Conference (GLOBECOM 2011), 2011 IEEE*. IEEE, 2011.

[9] Lam, Albert, Victor OK Li, and James JQ Yu. "Real-coded chemical reaction optimization." *Evolutionary Computation, IEEE Transactions on* 16.3 (2012): 339-353.

[10] Lam, Albert, and Victor OK Li. "Chemical reaction optimization for cognitive radio spectrum allocation." *Global Telecommunications Conference (GLOBECOM 2010), 2010 IEEE*. IEEE, 2010.

[11] Xu, Jin, Albert Lam, and Victor OK Li. "Chemical reaction optimization for the grid scheduling problem." *Communications (ICC), 2010 IEEE International Conference on*. IEEE, 2010.

[12] Xu, Jin, Albert Lam, and Victor OK Li. "Chemical reaction optimization for task scheduling in grid computing." *Parallel and Distributed Systems, IEEE Transactions on* 22.10 (2011): 1624-1631.

[13] Xu, Jin, Albert YS Lam, and Victor OK Li. "Stock portfolio selection using chemical reaction optimization." *Proceedings of the international conference on operations research and financial engineering. Paris, France*. 2011.

[14] Yu, James JQ, Albert Lam, and Victor OK Li. "Evolutionary artificial neural network based on chemical reaction optimization." *Evolutionary Computation (CEC), 2011 IEEE Congress on*. IEEE, 2011.

[15] Lam, Albert, and Victor OK Li. "Chemical-reaction-inspired metaheuristic for optimization." *Evolutionary Computation, IEEE Transactions on* 14.3 (2010): 381-399.

EaChOff: Chunk Offset Compression Scheme for High Dimensional Data based on Extendible Multidimensional Array

K. M. Azharul Hasan
Dept. of Computer Science & Engineering
Khulna University of Engineering & Technology
Khulna, Bangladesh
azhasan@gmail.com

Md. Rakibul Islam
Dept. of Computer Science & Engineering
Khulna University of Engineering & Technology
Khulna, Bangladesh
rakibislam04@gmail.com

***Abstract*—Traditional Multidimensional Array (TMA) is an essential data structure for handling large scale multidimensional dataset, but they are not extendible during run time. Another problem for representing the real life data by TMA is that it creates high degree of sparsity. Hence it is important to evolve handy scheme to compress the high dimensional data so that the maintenance becomes easier. To solve these sparsity and dynamic extension problem, we propose a novel scheme namely Extendible Multidimensional Array (EMA) based Chunk Offset Compression Scheme (*EaChOff*). The main idea of *EaChOff* scheme is to linearize each subarray of the EMA independently and break it into chunks for compressing. We evaluated our proposed schemes by comparing compression ratio and range of usability for Chunk-Offset Compression on TMA. The analysis shows that the proposed scheme is efficient if dynamic behavior of the schema is concerned for practical applications.**

Keywords— Multidimensional Array; Extendible Array; database compression; Compression ratio; Chunk offset

I. INTRODUCTION

Traditional Multidimensional Array (TMA) [1] is a superior storage for storing dense data but one main problem is that they are not dynamically extendible. To increase the length of a dimension of the TMA the total restructuring of the array is necessary. Because of sparsity problem TMA wastes huge memory. This is because a large number of array cells are empty in most of the datasets and thus are very hard to use in actual implementation [2][3]. The sparsity problem increases when the number of dimensions is higher. The number of all possible combinations of array cells exponentially increases, whereas the number of actual data values does not increase at such a rate. For Example in an international trade data set there are several dimensions such as importing country, exporting country, date-time, items, measure amount of items etc. But a small number of items are exported from any given country to other countries. The idea of extendible array solves the problem of extendibility. Extendible arrays are combination of subarrays. If the array is n dimensional then the subarrays are n-1 dimensional. Many of the compression schemes based on TMA such as Compressed Row/Column Storage (CRS/CCS) or ECRS [4][5], Chunk-offset Compression [6][7] has been proposed in the literature. One main problem of TMA based compressions schemes are that it is static in nature. This is because, if there is any extension in each dimension in TMA based compression schemes, we need to restore compressed data to its original format and perform the desired extension for the new added data sets. Then the reorganized TMA is compressed by using the compression schemes. So, efficient compression schemes are required to store dynamic sparse data for multidimensional data sets [8][9] without any reorganization and relocation. In this paper, we are going to propose and evaluate a new and efficient compression schemes based on Extendible Multidimensional Array (EMA) [10][11] to manage the problem of extendibility without reorganization of data. The scheme can be applicable to multidimensional database technology such as MOLAP [12] for multidimensional data analysis.

II. CONCEPT OF EXTENDIBLE ARRAY

Consider an n dimensional extendible array A[10][13][14]. Three kinds of auxiliary tables namely *history table* H_i, *address table* L_i, and *coefficient table* C_i are required for each extendible dimension i $(i=1,\ldots,n)$ to extend A in any dimension. See Fig. 1. History tables memorize extension history. h is the history value counter. The value of h is incremented by one for the addition of any subarray in any dimension. An n dimensional extendible array A is the combination of n-1 dimensional subarrays. If the size of A is $[d_1, d_2,\ldots, d_{n-1}, d_n]$ and the extended dimension is i, for an extension of A along dimension i, contiguous memory area that forms an n-1 dimensional subarray S of size $[d_1, d_2 ,\ldots, d_{i-1}, d_{i+1} ,\ldots, d_{n-1}, d_n]$ is dynamically allocated and added to A in dimension i. Then h is incremented by one and the value is memorized in the history table H_i, also the first address of S is held on the address table L_i. S is a usual fixed size array, and the actual data is stored in these subarrays. As is well known, an element $<i_1,i_2,\ldots,i_n>$ in an n dimensional conventional fixed size array of size $[d_1,d_2,\ldots, d_n]$ is allocated on memory using an addressing function and $<d_2d_3\ldots d_n, d_3d_4\ldots d_n,\ldots\ldots, d_n>$ is held in a coefficient table. For example, let A be a four dimensional extendible array whose current sizes are $[d_1, d_2, d_3, d_4]$. If A is extended by one along the dimension two, a three dimensional fixed array S of sizes $[d_1, d_3, d_4]$ is allocated. The addressing function to determine the address of the element $<i_1, i_2, i_3>$ is as: $d_1d_3i_1 + d_3i_2 + i_3$. Here $< d_1d_3, d_3 >$ is called a *coefficient vector*. At every extension of A, the

corresponding subarray's coefficient vector is computed and memorized in *coefficient table* of the extended dimension. In general, if *A* is an *n* dimensional extendible array where *n* is greater than two, an *n-2* dimensional coefficient vectors are required for each extendible dimension.

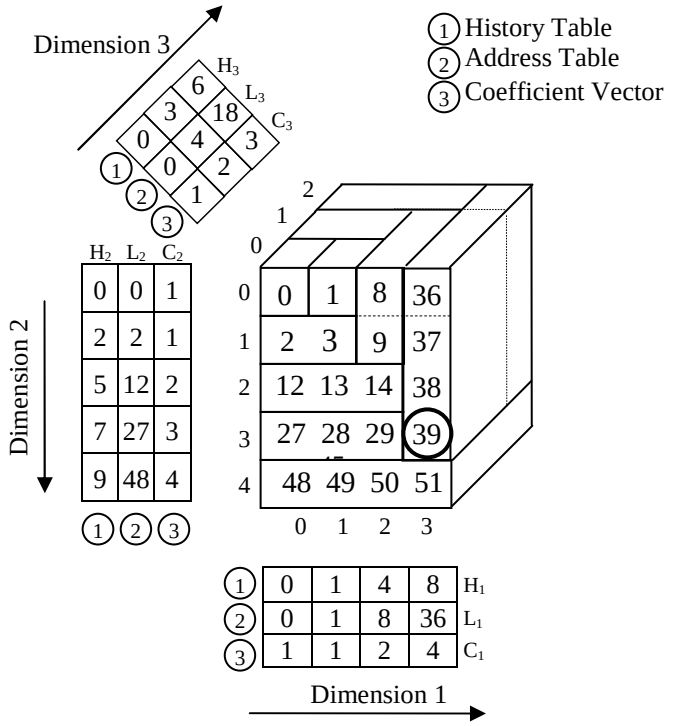

Fig. 1. The realization of extendible array.

Using the stored values of these three kinds of auxiliary tables, the address of an array element can be computed as follows. Consider the element *<3,3,0>* in Fig. 1. Compare $H_1[3] = 8$, $H_2[3] = 7$ and $H_3[0] = 0$. Since $H_1[3] > H_2[3]$, $H_1[3] > H_3[0]$, it can be proved that the element *<3,3,0>* is involved in the extended subarray *S* having history value 8 and beginning address of the corresponding subarray is 36 which is stored in $L_1[3]$. From the coefficient vector of $C_1[3] = < 4 >$, the offset of element *<3,3,0>* from the first address of *S* is computed by $4 \times 0 + 3 = 3$, the address of the element is determined as 39 (See Fig. 1).

III. The Chunk Offset Compression based on Extendible Array

The Extendible Array Based Chunk Offset Compression (*EaChOff*) scheme linearizes each subarray independently and breaks a large multi dimensional extendible array into chunks. This scheme uses one one-dimensional auxiliary table namely $ChunkNo_i$ for each dimension *i* and one one-dimensional integer array *NR*. The chunk number assigned to a subarray is held on the *ChunkNo* table. Array *NR* stores information of nonzero array elements of each subarray. If the number of subarray is *k* in an EMA then *NR* contains *k+1* elements. *NR[0]* contains 1, *NR[1]* contains the summation of the number of nonzero elements in 0th subarray and *NR[0]*. In general, *NR[i]* contains the number of nonzero elements in *(i-1)*th subarray of the EMA plus the contents of *NR[i-1]*.

The number of non zero array elements in the *i*th subarray can be obtained by subtracting the value of *NR[i]* from *NR[i+1]*. This scheme also uses one one-dimensional floating point array *data* and one dimensional integer array *OffsetInChunk* for each chunk of the EMA. Array *data* stores the values of nonzero array elements of each chunk. Array *OffsetInChunk* stores the offset in a chunk of nonzero array elements of each chunk. For each chunk, the base of these two arrays is 0. Among the three kinds of auxiliary tables (*history table, address table, coefficient table*) the *history table* H_i and *address table* L_i are required to store for each dimension. History tables are used to compute the extension dimension of the subarray and the length of other dimension to carry out the linearization computation for that subarray. Address tables are used to point the starting address of each chunk as well as the starting address of each subarray in a chunk.

A part of the *EaChOff* scheme for a three dimensional EMA of Fig. 1 is shown in Fig. 2. For convenience here we name each subarray as *SA_i_j*, where *i* indicate the extended dimension that the subarray belongs to and *j* indicates the length of that dimension. For example, *SA_1_2* is the subarray of dimension 1 of length 2. Forward mapping and backward mapping techniques for the *EaChOff* scheme are described as follows.

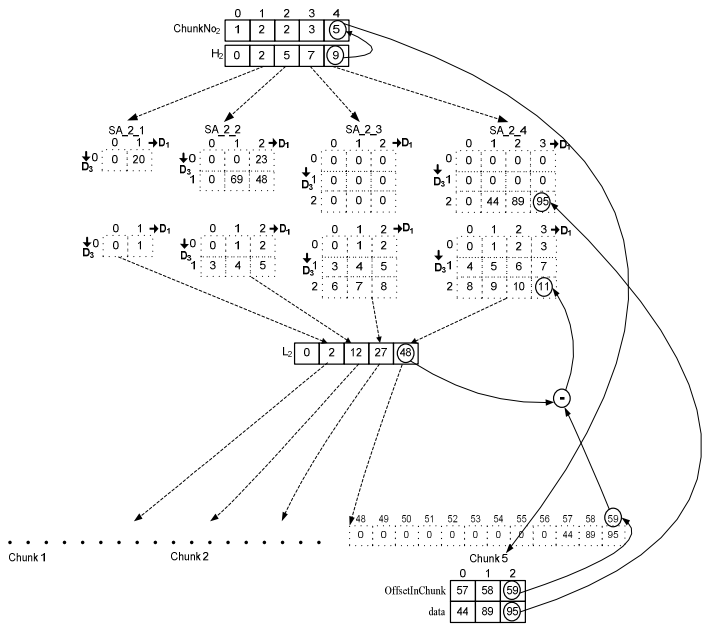

Fig. 2. *EaChOff* realization over EMA

A. Forward Mapping

Consider the element *<3,3,1>* of the EMA. Compare $H_1[3] = 8$, $H_2[3] = 7$ and $H_3[1] = 3$. Since $H_1[3] > H_2[3]$ and $H_1[3] > H_3[1]$, extended dimension is 1 and the element is involved in the subarray *SA_1_3*. $ChunkNo_1[3] = 4$ indicates that we need to access only *chunk4* for the given element. In Fig. 2, the number of nonzero elements of the 9th subarray *SA_1_3* can be found by *NR[9] – NR[8] = 7 – 1 = 6*. The

chunk offset of these 6 nonzero array elements are stored in *OffsetInChunk* array. For computing the logical position of the array element *<3,3,1>*; we consider dimension 2 as $d_1 = 4$, dimension 3 as $d_2 = 3$, second co-ordinate value of the given array element as $p_1 = 3$, third co-ordinate value of the given array element as $p_2 = 1$ and the desired logical position of the given array element can be computed as follows using the *array linearization* function $d_1 p_2 + p_1 = 4 \times 1 + 3 = 7$ (See Fig. 2) Addition of $L_1[3] = 36$ and logical position 7 give the desired chunk offset value 43 for the given array element. Binary search is performed on the *OffsetInChunk* array to find logical position 43 and it can be found that *OffsetInChunk[4]* stores the logical position 43 (since *<3,3,1>* array element is a nonzero array element). Finally the values of the nonzero array element can be found in *data[4]*.

B. Backward Mapping

Consider the physical position *<9,59>* of the physical database; where *<9>* is the history value and *<59>* is the logical index of a nonzero array element in a chunk i.e. *<59>* is the value that *OffsetInChunk* stores. We perform the binary search on the history tables to find the given history value *<9>*. Since *<9>* is stored in $H_2[4]$ (see Fig. 2), we need to access only the *OffsetInChunk* array that is stored for the subarray *SA_2_4* (i.e. subarray extended at dimension 2 at length 4). Therefore the second co-ordinate value of the desired logical array indices is *<4>* in logical database. The linearized column index of the subarray *SA_2_4* can be computed by subtracting the first address ($L_2[4] = 48$) of the subarray from the given logical chunk index i.e linearized column index = 59 – 48 = 11. For computing the first co-ordinate and third co-ordinate value of the desired logical array indices in the logical database from the given physical position *<9,59>*; we consider dimension 1 as $d_1 = 4$, dimension 3 as $d_2 = 3$, first co-ordinate value of the desired logical array indices as q_1, third co-ordinate value of the desired logical array indices as q_2, linearized column index *<11>* as *Y* and the desired logical array indices can be computed as follows using the *reverse array linearization* function

$$q_2 = Y \; mod \; d_2 = 11 \; mod \; 3 = 2$$

$$q_1 = Y/d_2 = 11/3 = 3$$

Hence the physical position *<9, 59>* of physical database is mapped to a logical position *<3,4,2>* in logical database. *EaChOff* compression scheme is mapping complete because it provides forward mapping and backward mapping.

IV. Experimental Results

The parameters are grouped as shown in Table I. Some of these parameters are provided as input, while others are derived from the input parameters. All lengths or sizes are in bytes. We have developed the detail cost model for the schemes for theoretical analysis. We present here the experimental results along with the related equations only. All the mathematical models are also validated by the experiments.

We simulate the compression ratio, retrieval cost for range key query and dynamic extension cost for *ChOff* and *EaChOff* by placing all the arrays both compressed and uncompressed in the secondary storage. The maximum range of data density up to which the compression ratio is less than 1 can be defined as Range of usability of a compression scheme. Among the three auxiliary tables of extendible array, coefficient vector and address table are void and only the history table is required for these schemes. History table acts as an index for locating the subarrays. Thus history tables are stored in main memory for fast access since the sizes of the auxiliary tables are negligible comparing to the main arrays. Table II shows the parameter values used for experimental analysis.

TABLE I. PARAMETERS CONSIDERED FOR EXPERIMENT AND ANALYSIS.

Parameters	Description
UC_{TMA}	The uncompressed size of TMA
UC_{EMA}	The uncompressed size of (EMA)
SC_{EMA}	Compressed size of EMA using the *EaChOff* scheme
SC_{TMA}	Compressed size of TMA using the *Chunk-Offset* Compression scheme
η_{ChOff}	Compression ratio for the *Chunk-Offset* Compression scheme for TMA; $\eta_{ChOff} = \frac{SC_{ChOff}}{UC_{TMA}}$
$\eta_{EaChOff}$	Compression ratio for the *Chunk-Offset* Compression scheme for EMA; $\eta_{EaChOff} = \frac{SC_{EaChOff}}{UC_{EMA}}$
n	Number of dimension of both TMA and EMA
L_i	Length of each dimension i ($0 \le i \le n$) for both the TMA and EMA
l	Length of Chunk for the TMA
ρ	Density of records both for TMA and EMA;
α	Size of subscripts for TMA and EMA
β	Size of a cell of the TMA and EMA
δ	Length extended along a dimension
$sz_i(k)$	Size of subarray k along dimension i

TABLE II. THE VALUES OF THE PARAMETERS CONSIDERED FOR EXPERIMENTAL ANALYSIS.

L	δ	ρ	α	β	n	l
10 - 40	5	0.10 ~ 0.70	4	8	5	4-16

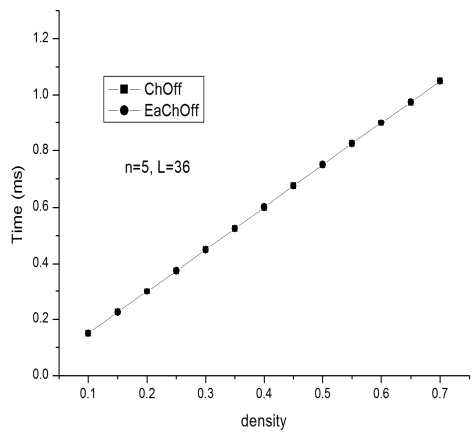

Fig. 3. Compression ratio comparison between *ChOff* and *EaChOff*.

Fig. 3 shows the compression ratio η_{ChOff} and $\eta_{EaChOff}$ having parameter values shown in Table II. It shows that the

compression ratio is almost same for both the schemes. This is because the compression ratio is characterizes as follows

$$\eta_{ChOff} = \frac{2\times\frac{L^n}{l^n}\times\alpha+\rho L^n\times\alpha+\rho L^n\beta}{L^n\times\beta} \text{ and}$$

$$\eta_{EaChOff} = \frac{[2\times\{(L-1)\times n+1\}+\left(\sum_{i=1}^{hc} sz_i(k)\times\rho\right)]\times\alpha+\left(\sum_{i=1}^{hc} sz_i(k)\times\rho\right)\times\beta}{L^n\times\beta}$$

For $\eta_{EaChOff}$, $\sum_{i=1}^{hc} sz_i = L^n$ and hence both the scheme becomes similar. The range of usability is also the same as the condition for range of usability (i.e. the compression ratio is less than 1) is $\rho < \beta/(\alpha+\beta)$ for both *ChOff* and *EaChOff*. Fig. 4 shows the retrieval comparison between EMA without comparison and *EaChOff*, *ChOff* scheme with varying ρ. The improvement with compressed form and non compressed form is huge. Hence the importance compressing sparse arrays is evident. Fig. 4 also shows the retrieval cost for both the schemes. The retrieval cost is little higher for the proposed *EaChOff* scheme than the *ChOff* and hence it is less efficient for retrieval. This is because the data stored in *ChOff* over a single stream but the data stored in *EaChOff* is in different subarrays and each subarray is necessary to search using the history values.

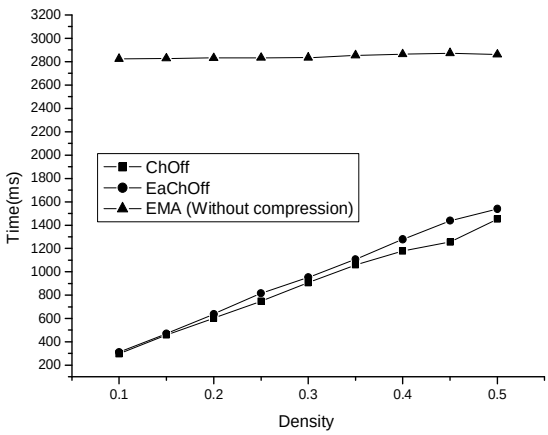

Fig. 4. Retrieval cost comparison between *ChOff* and *EaChOff*.

Fig. 5 shows the dynamic extension cost for both the systems. The *EaChOff* is very efficient than *ChOff* scheme. This is because the EMA based *EaChOff* is dynamically extendible without reorganizing the existing data but TMA is static in nature and reorganization is necessary. For extending TMA, it requires to reorganize the array and rewrite both existing and new data elements. The existing elements of the initial array need to be fetched and recalculate the new offsets due to the extension for TMA. Hence the extension cost for *ChOff* is the summation of fetched cost and reallocation cost. On the other hand the *EaChOff* is based on EMA and reallocation is not necessary and extension cost for *EaChOff* is allocation subarrays only. The extension cost is dependent on the initial volume (the volume before extension i.e., L^n) of the array. If L increases then the extension cost increases and hence the extension gain. The extension gain is defined as the difference between extension cost of *ChOff* and extension cost of *EaChOff*. The extension gain of EaChOff over *ChOff* is shown in Fig. 6. As L increases the extension gain increases. Finally we conclude that with very little retrieval penalty we can achieve huge extension gain if we use the proposed *EaChOff* scheme. The proposed scheme is efficient when dynamic nature of an array is a concern.

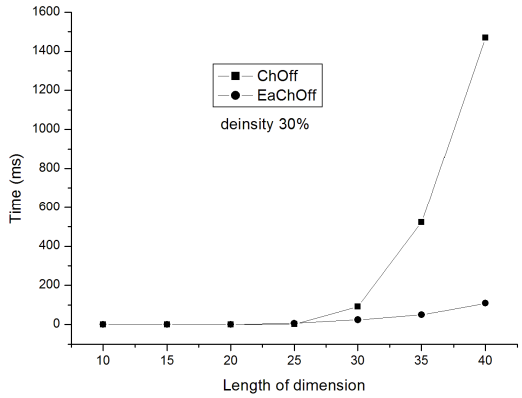

Fig. 5. Dynamic extension cost comparison between *ChOff* and *EaChOff*.

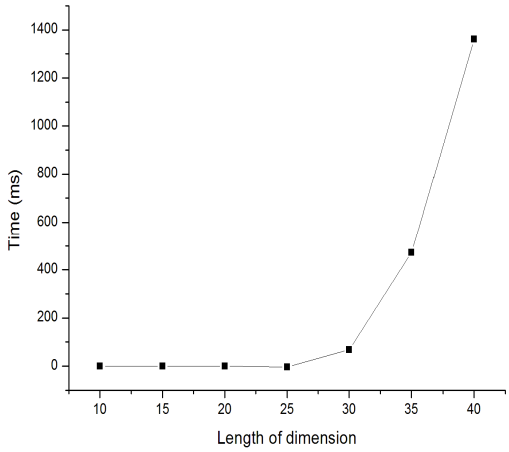

Fig. 6. Extension gain of *EaChOff* over *ChOff*.

V. RELATED WORKS

Many schemes have been proposed in the literature for storing sparse array but most of them are based on TMA [4]-[6]. The Chunk-offset compression scheme, the large multidimensional arrays are broken into chunks, is based on chunking of higher dimensional arrays [22][24] and is well addressed in the literature [6][9][12][18]. To compress the array, a pair <ChunkNumber, OffsetInChunk> is stored for each valid entry. But the main array is static in nature and dynamic reorganization is impossible. There are some compression schemes such as *EaCRS* [14], SCEKA [15], where dynamic extension possible. The *EaCRS* scheme [14] which is the dynamic version of CRS [5] supports for n dimension but it requires n one dimensional arrays to store and hence compression ratio is less for large n. SCEKA is based on EKA [11][16], a new extendible array system, but its performance degrades for large n (n>4) because EKA becomes a hierarchical structure for n>4. The history offset compression [3] [8] scheme is based on EMA. An element is specified

using the pair< history value, offset> value of the extendible array. But the offset value will be very large and will overflow the address space when the EMA is large even for 64 bit machines. The ECRS (or ECCS) [4] scheme compresses all the nonzero array elements along rows (columns for ECCS). But it is based on TMA and dynamic and dynamic extension is impossible. Hilbert curve [19] based compression scheme is proposed in [20] for TMA and dynamic extension of the dimension size is not considered.

VI. CONCLUSION

Over the years with atomization more and more systems deployed in industries are generating huge amount of data. Since they can be very large; must be stored and retrieved in an efficient way. Many scientific applications extensively use multidimensional array to represent their data for efficient processing. However in many cases the total number of data or dimension cannot be predicted beforehand. Besides this, representing the real world data in multidimensional array creates a very sparse array. Compressing the data has many advantages. In this paper, we managed both sparsity and the dynamic extension problem by presenting database compression schemes based on EMA. Since *EaChOff* scheme is based on an extendible multidimensional array system and compression scheme is applied for each subarray independently, such an array can extend its size dynamically along an arbitrary dimension without any relocation of existing data. Our evaluation shows that the proposed compression scheme has advantages when dynamic extension is important. One important application area is that the scheme can be used for big data technology. Specifically the velocity of data can be managed by the proposed *EaChOff*. One important future direction of the work is that the scheme can easily be implemented in parallel platforms. Because most of the operations described here are independent of each other, it will be very efficient to apply this scheme in parallel and multiprocessor environments.

REFERENCES

[1] S. Sarawagi and M. Stonebraker, “Efficient Organization of Large multidimensional Arrays”, in Proc. of 10th International Conference on Data Engineering, 1994, pp. 328–336.

[2] R. Acker, R. Pieringer, and R. Bayer, “Towards Truly Extensible Database Systems”, in Proc. of DEXA, LNCS, Vol. 3588, pp. 596–605, 2005

[3] K. M. Azharul Hasan, M. N. Azuma, T. Tsuji, and K. Higuchi, “An Extendible Array Based Implementation of Relational Tables for Multidimensional Databases”, in Proc. of DaWak, LNCS, Vol. 3580, pp. 233–242, 2005.

[4] Chun-Yuan Lin, Yeh-Ching Chung, Jen-Shiuh Liu, "Efficient Data Compression Methods for Multidimensional Sparse Array Operations Based on the EKMR Scheme," IEEE Transactions on Computers, Vol. 52, No. 12, pp.1640-1646, 2003.

[5] R. Barret, M. Berry, T. F. Chan, J. Dongara, V. Eljkhhout, R. Pozo, C. Romine and H. Van, “Templates for the solution of linear systems: Building blocks for the iterative methods,” second ed. SIAM, 1994.

[6] Y. Zhao, P. M. Deshpande, and J. F. Naughton, "An array based Algorithm for simultaneous multidimensional aggregates," ACM SIGMOD, pp. 159-170, 1997.

[7] K. M. Azharul Hasan, “Compression Schemes of High Dimensional Data for MOLAP”, In the Edited Book, "Evolving Application Domains of Data Warehousing and Mining: Trends and Solutions” Chapter IV, Information Science Reference, pp. 64-81, 2009.

[8] K M Azharul Hasan, Tatsuo Tsuji, Ken Higuchi “A Parallel Implementation Scheme of Relational Tables Based on Multidimensional Extendible Array” International Journal of Data warehousing and Mining, 2: 4. pp.66-85, 2006.

[9] J. Li and J. Srivastava, “Efficient Aggregation Algorithms for Compressed Data Warehouses”, IEEE Transaction on Knowledge and Data Engineering, Vol. 14, No. 3, pp. 515–529, 2002.

[10] E. J. Otoo, and T. H. Merrett, “A Storage Scheme for Extendible Arrays”, Computing, Vol. 31, pp. 1–9, 1983.

[11] Sk. Md. Masudul Ahsan, K. M. Azharul Hasan, “An Implementation Scheme for Multidimensional Extendable Array Operations and Its Evaluation”, in Proc. of ICIEIS 2011, pp. 136–150, 2013.

[12] K. M. Azharul Hasan, T. Tsuji, and K. Higuchi, “An Efficient Implementation for MOLAP Basic Data Structure and Its Evaluation”, in Proc. of DASFAA , LNCS 4443, pp. 288 – 299, 2007.

[13] E. J. Otoo, H. Wang, G. Nimako, "New Approaches to Storing and Manipulating Multi-Dimensional Sparse Arrays" , Proc. of SSDBM'l 4, pp. 2014.

[14] Md. Rakibul Islam, K M Azharul Hasan, Tsuji, Tatsuo, “LEaCRS: An Extendible Array Based Compression Scheme for High Dimensional Data using Linearization,” in Third International Conference on Advances in Computing and Communications, p. 312-315, 2013.

[15] Sk. Md. Masudul Ahsan, K. M. Azharul Hasan, "Segment Oriented Compression Scheme for MOLAP Based on Extendible Multidimensional Arrays", Journal of Computing and Information Technology(CIT), 23(2). pp. 111-121, 2015.

[16] K. M. Azharul Hasan, Kamrul Islam, Mojahidul Islam, Tatsuo Tsuji, “An Extendible Data Structure for Handling Large Multidimensional Data Sets,” in Proc. of the ICCIT 2009, pp. 669-674, 2012.

[17] Md Abu Hanif Shaikh, K M Azharul Hasan, “ Efficient Storage Scheme for n-Dimensional Sparse Array: GCRS/GCCS” in Proc. of International Conference on High Performance Computing & Simulation, pp. 137-142, 2015.

[18] Doug Burdick, Prasad M Deshpande, TS Jayram, Raghu Ramakrishnan, Shivakumar Vaithyanathan OLAP over uncertain and imprecise data, The VLDB Journal, 16 (1), pp. 123-144, 2007.

[19] J. K. Lawder, P. J. H. King, Querying multidimensional data indexed using the Hilbert spacefilling curve. *ACM SIGMOD Record*, **30**(1), pp. 19–24, Mar. 2001.

[20] T. Eavis, D. Cueva, “A Hilbert Space Compression Architecture for Data Warehouse Environments,” in *Proceedings of 9th nternational Conference on Data Warehousing and Knowledge Discovery*, pp. 1–12, 2007.

A Low Hop Distance Hierarchical Interconnection Network

Muhammad Hafiz Sohaini*, M.M. Hafizur Rahman*, Rizal Mohd Nor*, Tengku Mohd Tengku Sembok†, M. A. H. Akhand‡, and Yasushi Inoguchi‖
*Dept. of Computer Science, KICT, IIUM, Jalan Gombak, 53100, Kuala Lumpur, Malaysia
E-mail: hfzshn@gmail.com, hafizur@iium.edu.my, rizalmohdnor@iium.edu.my
†Cyber Security Center, National Defense University Malaysia, Kuala Lumpur 57000, Malaysia
E-mail: tmtsembok@gmail.com
‡Dept. of Computer Science and Engineering, KUET, Khulna - 9203, Bangladesh
E-mail: akhandkuet@yahoo.com
‖Research Center for Advanced Computing Infrastructure, JAIST, Nomi-Shi, Ishikawa 923-1292, Japan
E-mail: inoguchi@jaist.ac.jp

***Abstract*—In this paper, we have proposed a new hierarchical interconnection network called Tori-connected Flattened Butterfly Network (TFBN). It is a hierarchical interconnection network which is able to interconnect millions of nodes in the network to achieve high performance and cost-effective design for massively parallel computing system. TFBN consists of multiple basic modules of flattened butterfly network whereby the basic modules are connected using 2D-torus network. This paper focuses on the architecture of the TFBN and the evaluation of its static network performance such as degree, diameter, cost, average distance, arc connectivity, bisection width and wiring complexity. The comparison of performance shows better performance in terms of distance parameters as well as other parameters.**

Keywords*—*Massively Parallel Computer, Hierarchical Interconnection Network, TFBN, Static Network Performance.

I. Introduction

The demand of computational power will never stop. It will increase day by day. To solve the existing and forthcoming computational challenging problems we need tremendous computation power. And to meet this demand we need parallel computers consisting of millions of nodes, called massively parallel computer (MPC) systems [1]. Interconnection network to connect these huge number of nodes plays a crucial role in determining the overall performance of the MPC systems. The diameter is very large for the conventional topologies with these huge number (millions) of nodes [2], [4]. To construct MPC systems consisting of such huge nodes, Optimal Diameter-Degree (ODD) network is essential for the reliability. Hierarchical interconnection network is a plausible alternative way in which several networks can be interconnected together to have an interconnection network which gives good performance in all aspect [3].

In searching of ODD hierarchical interconnection network, we have proposed midimew connected mesh network (MMN) [5]. However, long diagonal links makes the routing algorithm complex and long length in VLSI realization [6]. It is known that the bandwidth exponentially increased in the last two decades, and the additional bandwidth can be efficiently used in high degree interconnection networks [7]. A good interconnection network is designed around the capabilities and constraints of available technology. Increasing router pin bandwidth, for example, has motivated the use of high-radix routers [8] in which the increased bandwidth is used to increase the number of ports per router, rather than maintaining a small number of ports and increasing the bandwidth per port. The Cray BlackWidow vector multiprocessor [9] is the best example of high-radix network. On the other hand, high degree network significantly increase the number of narrow links which in turns reduces the diameter of an interconnection network [10]. Thus, ODD interconnection network is achievable in this way. This is the key motivation to re-investigate our previously proposed MMN to avoid the problem of routing complexity.

With this motivation, we have replaced the 2D-mesh basic module of of a MMN by a flattened butterfly network. We have considered higher level network as 2D-torus network to reduce the number of long links. Also torus network has higher inter-node communication performance than mesh network [11]. In this paper, we proposed a new hierarchical interconnection network consisting of basic modules with the combination of flattened butterfly network and torus network. A Tori-connected Flattened Butterfly Network (TFBN) is a hierarchical interconnection network made up of multiple basic modules whereby the basic module is a flattened butterfly network and they are interconnected as torus network to form higher level interconnection in a hierarchical fashion. Analogous to the MMN, we called it **T**ori-connected **F**lattened **B**utterfly **N**etwork (**TFBN**).

The organization of the rest of this paper is as follows. In Section II, we explain the basic architecture of the TFBN. Addressing of nodes and message routing in the TFBN are discussed in Section III. The evaluation of static network performance of the TFBN is discussed in Section IV. Finally, Section V presents the conclusion of this paper.

II. Interconnection of the TFBN

A TFBN is a hierarchical interconnection network made up of multiple basic modules (BMs) where the BM is consisting of a flattened butterfly network in a 2D-grid $(2^m \times 2^m)$ of 2^{2m} nodes having 2^m rows and 2^m columns. Here m is a positive

integer. m could be any value however, the preferable one is $m = 2$ for better granularity. Therefore, considering $m = 2$, a BM of size (4×4) is portrayed in Figure 1. At the contours of the BM, there are 2^{m+2} number of free ports which are used for higher level interconnection. The free ports are used for higher level interconnection as they are defined and depicted in Figure 1. Basic module is considered as a Level-1 network.

Higher level networks are constructed by recursively interconnecting (2^{2m}) immediate lower networks as sub-net modules in a $(2^m \times 2^m)$ torus network. Considering $(m = 2)$, a Level-2 TFBN can be constructed by interconnecting $2^{2\times 2} = 16$ Level-1 TFBN, a Level-3 TFBN can be constructed by interconnecting 16 Level-2 TFBN, and so on. This phenomenon is illustrated in Figure 2. To avoid clutter, the wraparound links of the BMs are not shown. A BM uses $4 \times (2^q) = 2^{q+2}$ of its free links, $2(2^q)$ free links for vertical interconnections and $2(2^q)$ free links for horizontal interconnections. A new parameter q,$q \in \{0, 1, ..., m\}$,, is called inter-level connectivity. $q = 0$ is the minimal inter-level connectivity, while $q = m$ is the maximum inter-level connectivity. Basic modules with same co-ordinate positions are connected to form a respective higher-level network using the respective assigned free links.

Figure 2 illustrated a (4×4) basic module considering $m = 2$ and it has $2^{2+2} = 16$ free ports. Considering $q = 0$, $4(2^0) = 4$ free ports are used for every higher level interconnection, half of them (2) for horizontal and the other half (2) for vertical interconnection. One incoming and one outgoing links are tied together to form a b-direction links to connect two adjacent basic modules to for higher level networks. Vertical_in & vertical_out links are together to vertical links and horizontal_in & horizontal_out links are tied together to for horizontal links.

Considering level of hierarchy L along with m and q, TFBN is represented as $\mathrm{TFBN}(m, L, q)$. It is constructed using $2^m \times 2^m$ BMs with L levels of hierarchy and q inter-level connectivity. In this paper, we have considered $m = 2$, the best granularity. Therefore, we focus on $\mathrm{TFBN}(2, L, q)$ networks. The maximum possible level of hierarchy, L_{max}, of a TFBN can be constructed using $(2^m \times 2^m)$ BM is $L_{max} = 2^{m-q} + 1$. For example, with $q = 0$ and $m = 2$ $L_{max} = \left(2^{2-0} + 1\right) = 5$. Level-5 is the highest possible level of TFBN can be constructed using the interconnection of (4×4) BM and its associated free ports and links. The total number of nodes of a Level-L TFBN is $N = 2^{2mL}$. The largest number of nodes can be interconnected by a TFBN(m, L, q) using maximum level of hierarchy, $L_{max} = (2^{m-q} + 1)$, is $N = 2^{2m(2^{m-q}+1)}$. It means with $m = 2$ and $q = 0$ more than 1 million nodes can be interconnected together to form a massively parallel computer systems.

III. Addressing of Nodes and Routing of Messages in TFBN

A. Addressing of Nodes

As seen in Figure 1, nodes in the networks are addressed by two digits, the first representing the row index and the next representing the column index. More generally, in a Level-L TFBN, the node address is represented by:

$$\begin{aligned} A &= A^L A^{L-1} A^{L-2} \ldots \ldots \ldots A^2 A^1 \\ &= a_{n-1} a_{n-2} a_{n-3} \ldots \ldots \ldots a_2 a_1 a_0 \\ &= a_{2L-1} a_{2L-2}\ a_{2L-3} a_{2L-4} \ldots \ldots \ldots a_3 a_2\ a_1 a_0 \\ &= (a_{2L-1}\ a_{2L-2})\ (a_{2L-3}\ a_{2L-4})\ \ldots \ldots \\ &\quad \ldots \ldots \ldots (a_3\ a_2)\,(a_1\ a_0) \end{aligned} \tag{1}$$

Here, the total number of digits is $n = 2L$, where L is the level number. A^L is the address of level L and $(a_{2L-1} a_{2L-2})$ is the co-ordinate position of Level-$(L - 1)$ for Level-L network. Pairs of digits run from group number 1 for Level-1, i.e., the BM, to group number L for the L-th level. Specifically, l-th group $(a_{2l-1}\ a_{2l-2})$ indicates the location of a Level-$(l - 1)$ sub-network within the l-th group to which the node belongs; $1 \leq l \leq L$. In a two-level network the address becomes $A = (a_4\ a_3)\ (a_1\ a_0)$. The pair of digits $(a_4\ a_3)$ identifies the basic module to which the node belongs, and the pair of digits $(a_1\ a_0)$ identifies the node within that basic module.

The assignment of inter-level ports for the higher level networks has been done quite carefully so as to minimize the higher level traffic through the BM. The address of a node n^1 encompasses in BM_1 is represented as $n^1 = \left(a^1_{2L-1} a^1_{2L-2} \ldots \ldots \ldots a^1_3 a^1_2\ a^1_1 a^1_0\right)$. The address of a node n^2 encompasses in BM_2 is represented as $n^2 = \left(a^2_{2L-1} a^2_{2L-2} \ldots \ldots \ldots a^2_3 a^2_2\ a^2_1 a^2_0\right)$. The node n^1 in BM_1 and n^2 in BM_2 are connected by a link if the following condition is satisfied.

$$\begin{aligned} &\exists i \{a^1_i = (a^2_i \pm 1) \bmod 2^m \\ &\wedge \forall j (j \neq i \ \rightarrow\ a^1_j = a^2_j)\} \qquad \text{where } i, j \geq 2 \end{aligned} \tag{2}$$

B. Routing Algorithm for TFBN

The nodes communicate data and coordinate their efforts by sending and receiving messages in the supercomputer using a routing algorithm. The routing algorithm specifies how a message selects its network path to traverse from source to destination. Efficiency of message routing and simplicity of router design in crucial to the performance and acceptance of interconnection network for massively parallel computer systems.

Tori-connected Flattened Butterfly Network is a hierarchical network, hence the routing of message will take place in hierarchically in three phases, named Phase-1, Phase-2, and Phase-3. Same coordinate positions of the sub-network modules are used to form the higher level network. First of all in the Phase-1, routing will taken place in the source basic module, and the packet reach to the outlet port of the highest level network from the packet generated source node. Then routing will take place for inter-BM communication at the highest level network. After reaching the packet to its highest level sub-destination, routing continues within the sub-net modules to the next lower level sub-net destination. This process is repeated until the packet arrives at its final destination basic module [12]. This is known as Phase-2 routing. Finally in the Phase-3, the routing of packet will take place from the inlet free-port of the destination basic module to the destination itself. Actually, Phase-1 and Phase-3 routing

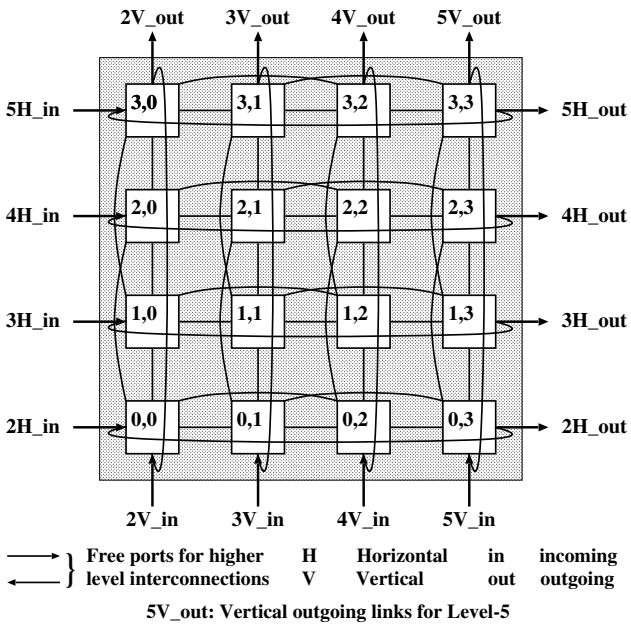

Fig. 1. Basic Module of a Tori-connected Flattened Butterfly Network

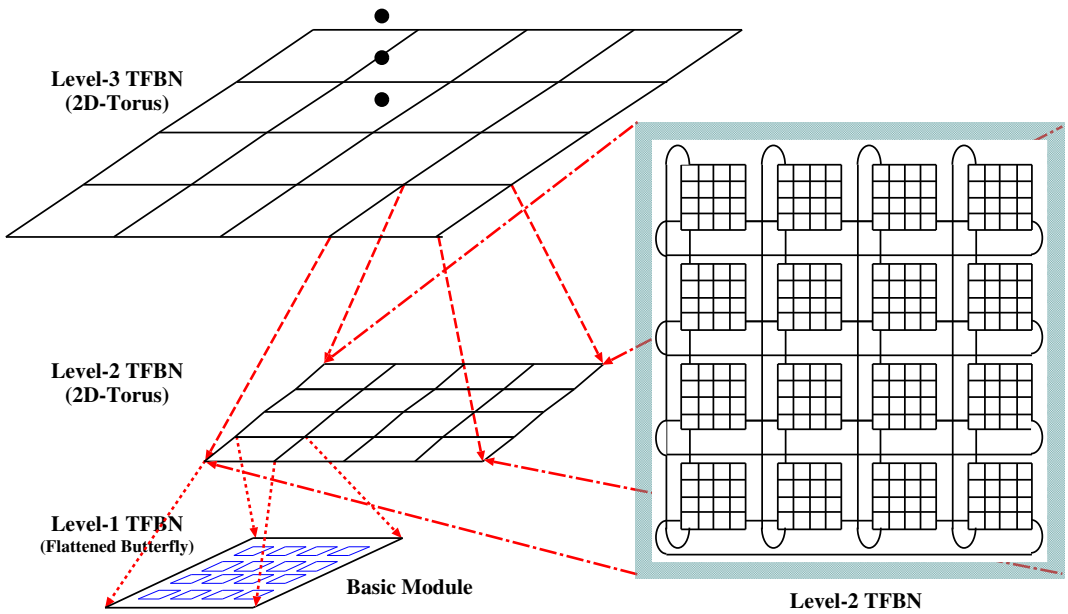

Fig. 2. Higher level network of a Tori-connected Flattened Butterfly Network

are very similar, intra-BM routing. One is in the source-BM and another one is in the destination-BM.

For the simplicity of message routing we have used simple deterministic dimension-order routing. Routing is performed first in the vertical direction and then in the horizontal direction. After generating packet in the source node, it will check its destination. If the packet's source and destination are in the same basic module then the routing is performed within the BM only. That is, only Phase-1 routing will be taken place. If the packet is destined to another basic module then the source node sends the packet to the outlet node which connects the basic module to the level at which the routing is performed. In this case all three phases of routing will be taken place.

IV. Static Network Performance

The performance of a massively parallel computer systems is crucially dependent on its underlying interconnection network. The real performance such as inter-node communication performance, fault-tolerant performance, network-on-chip realization, computational intensive application mapping, etc. depends on technology and physical implementation. However, some static parameters such as degree, diameter, average distance, arc connectivity, bisection width, and wiring complexity are used evaluate the interconnection network using technology

TABLE I. STATIC NETWORK PERFORMANCE OF DIFFERENT INTERCONNECTION NETWORKS

Network	Degree	Diameter	Average Distance	Arc Connectivity	Bisection Width	Wiring Complexity
2D-Mesh	4	30	10.67	2	16	480
2D-Torus	4	16	8.00	4	32	512
TESH(2,2,0)	4	21	10.47	2	8	416
TTN(2,2,0)	6	15	7.44	4	8	544
MMN(2,2,0)	4	17	9.07	2	8	416
TFBN(2,2,0)	8	10	5.75	4	8	800

independent graph theoretic model. These static parameters have a candid impact network actual performance. We have considered 2D-mesh, 2D-torus, TESH [13], TTN [14], MMN [6], and our proposed TFBN for the performance comparison.

A. Node Degree

In a massively parallel computer systems nodes are connected using links to form an interconnection network. Every nodes are connected to some other nodes. The number of physical links emanating from a node is called the degree of a node. The maximum degree of all nodes is called the degree of a network. Basically this maximum value is used as degree to implement the router. Here, the degree of the proposed TFBN is 8 and it is constant. For the scalability of a network constant node degree is very much needed because cost of router remains unchanged even the network scaled up.

Input-output interface cost of a node is directly related to its degree. The degree of TFBN is 8 as shown in Table I. a bit higher than that of other networks. However, it is not a problem because enormous bandwidth of a link. As mentioned earlier in the recent technology, it is desired to use high degree node and thin links for more efficient use if this bandwidth for the performance improvement.

B. Diameter

The actual distance between two nodes is the length of a link which connect themselves. However, the logical distance between them is one hop. A low hop distance is very important for the inter-node communication performance. The maximum number of hops that must be traversed to send a packet from a source to the destination among all distinct pairs of nodes along the shortest path according to the devised routing algorithm is called the diameter of an interconnection network. Static distance parameter diameter and average distance are widely used to compare the static network performance of different interconnection networks.

The latency depends upon the bandwidth, routing algorithm, and message congestion in the network. However, diameter gives an idea about the upper-bound of zero load latency of any interconnection network. In this regard, low diameter is preferable. We have evaluated the diameter of the conventional mesh and torus networks using their respective formula. Also, we have evaluated the diameter of the hierarchical TESH network, TTN, MMN, and TFBN using computer simulation. All the results are tabulated in Table I. It is clearly portrayed that the diameter of the TFBN is far lower than that of the other conventional and hierarchical networks

C. Average Distance

The average number of hops between all distinct pairs of nodes along the shortest path according to the devised routing algorithm is called the average distance of an interconnection network. It has a direct impact on the average message transfer latency. That is, low average distance indicates that the respective network will result less inter-node communication latency in terms of cycle. As like the diameter, we have calculated the average distance of conventional mesh and torus network by their respective formula and evaluated the average distance of TESH network, TTN, MMN, and TFBN by simulation. In this simulation we have evaluated the hop distance of all distinct pairs of nodes along the shortest using the routing algorithm described earlier. The maximum value and the average value are called the diameter and average distance, respectively. From the tabulated average distance for different networks in Table I, it is clearly shown that the average distance of the TFBN is far lower than that of other conventional and hierarchical networks.

D. Arc Connectivity

The resilient of an interconnection network is measured statically by the arc connectivity. The minimum number of links that must be cut to partition the network into two disjoint parts is known as arc connectivity. Though the real fault tolerance performance depends on the reconfiguration by redundant resources or routing algorithm, however, the ratio between the arc connectivity and the node degree is used to characterize the static fault tolerance performance of of an interconnection network. If the arc connectivity and node degree are same for any interconnection network, then the network will be best resilient and robust. As shown in Table I, torus is maximum fault tolerant. The static fault tolerance performance of a TFBN is equal to that of mesh, TESH, and MMN and a little bit lower than that of TTN.

E. Bisection Width

The minimum number of links that must be cut to partition the network into two exactly equal halves is called bisection width. A group of nodes in a parallel computer work together and the various data are hordes among the nodes. Small bisection width creates the congestion in the middle of the network for both uniform and non-uniform traffic patterns. on the other hand, large bisection width creates problems in the VLSI realization. Therefore moderate bisection width is preferable. As depicted in Table I, all the hierarchical interconnection network have same bisection width and it is less than that of convention mesh and torus network.

F. Wiring Complexity

The total number of links needed to connect all the nodes of an interconnection network is known as wiring complexity. It has direct impact on hardware implementation cost and complexity. A (16×16) 2D-mesh and 2D-torus networks have $\{N_x \times (N_y - 1) + (N_x - 1) \times N_y\} = 16 \times (16 - 1) + (16 - 1) \times 16 = 480$ and $(2 \times N_x \times N_y = 2 \times 16 \times 16) = 512$ links, respectively. N_i represents the number of nodes/ switches in the ith dimension. The wiring complexity of a Level-L TESH, TTN, MMN, and TFBN networks is $\left[\# \text{ of links in a BM} \times k^{2(L-1)} + \sum_{x=2}^{L} 2(2^q) \times k^{2(L-1)}\right]$. Here $k = 2^m$ is the number of nodes/sub-net modules in one direction.

Considering, $m = 2$, a basic module of a MMN and TESH network have 24 links, a TTN has 32 links, and a TFBN has 48 links. Hence, considering $q = 0$, the total number of links of a Level-2 TESH, TTN, MMN, and TFBN are 416, 544, 416, 800, respectively and these values are tabulated in Table I. Clearly, the cost in term of wire is a bit high for the TFBN. However, this extra cost of small length links in the basic module yields a promising result in the distance parameters, diameter and average distance. Even only Level-2 of hierarchy results thriving hop distance both maximum and average. We are expecting more better result in more levels of hierarchy.

V. Conclusion

A new hierarchical interconnection network, called **T**ori-connected **F**lattened **B**utterfly **N**etwork (**TFBN**), is proposed for the low hop distance MPC systems. The architectural structure, node addressing, message routing, and the evaluation of static network performance are discussed in details. From the static network performance it is seen that the diameter and average distance are quite lower than that of other network. TFBN also possesses other lucrative properties such as features moderate (neither too high nor too low) bisection width and good fault tolerance performance with the cost of some extra short length links than that of other networks. However, use of links is not a demerits for the enormous available bandwidth. Therefore TFBN is an incredible hierarchical interconnection network for the future generation massively parallel computers.

The research presented in this paper is a very first stage of this work. Issues for future work includes: (1) evaluation of static network performance of higher level TFBN [15] and (2) evaluation of dynamic communication performance of a TFBN using deadlock-free dimension order routing algorithm [16].

Acknowledgment

This research is supported by the project FRGS13-065-0306, Ministry of Education, Government of Malaysia. The authors would like to thank the anonymous reviewers for their constructive comments and suggestions on the paper which have helped to improve the quality of the paper.

References

[1] B.S.P. Mishra and S. Dehuri, Parallel Computing Environments: A Review, *IETE Technical Review*, Vol. 28, No. 3, pp. 240-247, 2011.

[2] V. Puente, J.A. Gregorio, R. Beivide and F. Vallejo, A Low Cost Fault Tolerant Packet Routing for Parallel Computers, *Proceedings of the 17th IEEE/ACM International Parallel and Distributed Processing Symposium (IPDPS)*, April, 2000.

[3] M. Abd-El-Barr and T.F. Al-Somani, Topological Properties of Hierarchical Interconnection Networks: A Review and Comparison, *Journal of Electrical and Computer Engineering*, Hindawi Publishing Corporation, Vol. 2011, 12 pages.

[4] P. Beckman, Looking Toward Exascale Computing, *Keynote Spech. International Conference on Parallel and Distributed Computing, Applications and Technologies (PDCAT08)*, Dunedin, New Zealand, December 2008.

[5] Md. Rabiul Awal, M.M. Hafizur Rahman, and M. A. H. Akhand, A New Hierarchical Interconnection Network for Future Generation Parallel Computer, *Proceedings of the 16th International Conf. on Information and Communication Technology (ICCIT)*, pp. 314-319, 2014.

[6] Md. Rabiul Awal, M. M. Hafizur Rahman and Rizal Mohd Nor, TMT Sembok, M.A.H. Akhand, Architecture and Network-on-Chip Implementation of a New Hierarchical Interconnection Network, *Journal of Circuits, Systems, and Computers*, Vol. 24, No. 2, 2015.

[7] John Kim, William J. Dally, Dennis Abts, Flattened Butterfly : A Cost-Efficient Topology for High-Radix Networks, *Proceedings of the 34th Annual International Symposium on Computer Architecture (ISCA)*, pp. 126-137, 2007.

[8] John Kim, William J. Dally, Steve Scott, Dennis Abts, Technology-Driven, Highly-Scalable Dragonfly Topology, *Proceedings of the 35th Annual International Symposium on Computer Architecture (ISCA)*, pp. 77-88, 2008.

[9] S. Scott, Dennis Abts, John Kim, and William J. Dally, The Black-Widow High-radix Clos Network, *Proceedings of the 33rd Annual International Symposium on Computer Architecture (ISCA)*, pp. 16-28, Boston, MA, USA, 2006.

[10] J. Kim, W. J. Dally, B. Towles, and A. K. Gupta, Microarchitecture of a high-radix router, *Proceedings of the 32nd Annual International Symposium on Computer Architecture (ISCA)*, pp. 420-431, Madison, WI, USA, 2005.

[11] W.J. Dally, Performance Analysis of k-ary n-cube Interconnection Networks, *IEEE Trans. on Computers*, vol. 39, no. 6, pp. 775-785, 1990.

[12] R. Holsmark, S. Kumar, M. Palesi, and A. Mekia, HiRA: A Methodology for Deadlock Free Routing in Hierarchical Networks on Chip, *Proc. of the 3rd ACM/IEEE NOCS*, pp. 2-11, 2009.

[13] V.K. Jain, T. Ghirmai, and S. Horiguchi, "TESH: A new hierarchical interconnection network for massively parallel computing", *IEICE Trans. on Inf. & Syst.*, vol.E80-D, no.9, pp.837-846, 1997.

[14] M.M. Hafizur Rahman, Yasushi Inoguchi, Y. Sato, and S. Horiguchi, TTN: A High Performance Hierarchical Interconnection Network for Massively Parallel Computers, *IEICE Transactions on Information and Systems, Japan*, Vol.E92-D, No.5, pp.1062 1078, May 2009.

[15] M.M. Hafizur Rahman, Yasushi Inoguchi, Faiz Al Faisal, and Monoz Kumar Kundu, Symmetric and Folded Tori Connected Torus Network, *Journal of Networks, Academy Publisher*, Vol. 6, No. 1, pp. 26-35, Jan. 2011.

[16] M.M. Hafizur Rahman, Y. Sato, and Yasushi Inoguchi, High Performance Hierarchical Torus Network under Adverse Traffic Patterns, *Journal of Networks, Academy Publisher*, Vol. 7, No. 3, pp. 456-467, March 2012.

Classification and pattern recognition algorithms applied to E-Nose

Md. Mizanur Rahman[1,2,*], Chalie Charoenlarpnopparut[1], Prapun Suksompong[1]
[1]Electronics and Communication Engineering (SIIT, Thammasat University, Thailand)
[2]Electronics and Communication Engineering Discipline (Khulna University, Bangladesh)
[*] E-mail: mizan.ku@gmail.com

Abstract—**Electronic noses (E-Nose) are seen to be good substitute to human or animal nose for food, and fruit quality identification. It is also used for explosive and chemical identification. We have generated typical E-Nose data to compare the existing algorithms in terms of training, and testing/validation. We have observed that *k*-nearest neighbor (*k*-NN) algorithm, support vector machine (SVM) machine learning algorithms; and radial basis function (RBF), and generalized regression neural networks (GRNNs) shows good odor detection performance. In terms of speed GRNN tops compared to other methods.**

Keywords—Electronic nose, VOC, PCA, RBF, SVM, LDA.

I. INTRODUCTION

Objects emitting volatile organic compounds (VOCs) into the air can be identified by the human and animal from the past odor experiences recorded in their memory. The VOCs reach the olfactory sensory cells at the olfactory Epithelium located into the inner most part of the nose. The sensory cells triggered by the VOCs produce electric signals which are then processed by olfactory bulb located in human or animal brain. The data remain into the memory as synaptic weights for future identification of the similar VOCs and identifying the object [1]. The object can be anything that emits VOCs into the air, such as: foods, chemicals, explosive, etc. Chemicals, and explosives are not feasible to be sensed by human or animal. In addition they cannot identify the VOCs which do not emit odor molecules or when VOC concentration level is very low. Thus identification of chemicals, explosives, foods, etc., at low concentration level without any health hazard requires artificial sensory system called Electronic Nose (E-Nose). Desire for human olfactory mimicking brought the E-Nose concept into existence to use it where human or animal cannot reach, or VOC concentration level is very low or does not smell.

A design of an electronic nose consists of six steps as shown in Fig 1. Here odor source is the food or chemical or explosive etc., which we want to sense. Sensor array is a combination of sensors with sensitivity to a wide range of chemicals to produce signature pattern for different kinds of objects. Data acquisition is done by microprocessor kits (e.g. NImyRIO, NI-CRIO, Arduino, etc.) equipped with desired program. Data pre-processing means to convert the sensed signature patterns to a suitable format which can be processed by pattern recognition and classification algorithms. In decision making stage the decision is made based on the results from pattern recognition and classification stage.

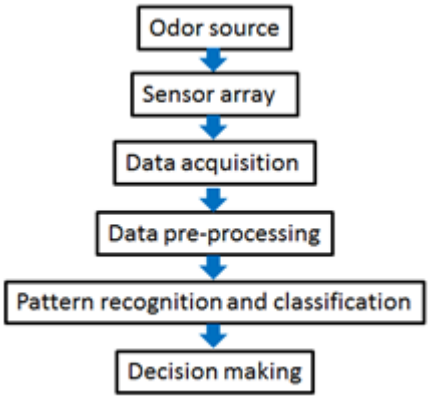

Figure 1. Electronic nose design process.

In this paper we present a review to the literature and summarize the pattern recognition and classification performances of the algorithms used in E-Nose applications. We also aim to find the optimum pattern recognition method for E-Nose system.

II. LITERATURE REVIEW

In [2] an E-Nose designed with metal oxide gas (MOG) sensors. Principal component analysis (PCA) was used to analyze quality of soft drink, olive oil, and tomato pulp. In [3] ripening shelf-life of peaches, nectarines, apples, and pears were monitored by an E-Nose designed with MOG sensors. It was shown by PCA analysis that fruit ripeness assessment by E-Nose is reliable. A MOG sensor based electronic nose was proposed in [4] where artificial neural network (ANN) was applied for classification and detection of apple ripeness. Near-infrared spectrophotometer, machine vision system, and an E-nose system were combined together in [5] and few numbers of misclassification were observed. Here the E-Nose was used to identify the rotting stage of apple based on ANN. In [6], [7] MOG sensors were used to design E-Nose. In [6] aroma of black tea was classified based on multilayer perceptron (MLP) network. In [7] concentration estimation of formaldehyde based on chaotic sequence optimized feed forward back propagation neural network (FFBPNN) was done. Basal Stem Rot disease of oil palm was identified with application of ANNs such as: FFBPNN, probabilistic neural network (PNN), radial basis function neural network (RBFNN) in [8]. In [9] an E-Nose with five semiconductor thin film sensors was

978-1-4673-9257-0/15/$31.00 ©2015 IEEE

designed. Here two groups of seven coffees' quality were analyzed by training an FFBPNN. Before feeding the data to FFBBNN, dimensions of the data were reduced by PCA. MOG sensors were used to develop an E-Nose to recognize benzene, toluene, ethyl benzene, xylene, and gasoline based on PCA, and ANN [10]. In [11] dimensionality was reduced by PCA and then a neural network was used to discriminate different types of coffee, aroma oils, perfumes and alcohol. Six clonal varieties of orthodox finished tea were classified with 100% accuracy by PCA and MLP [12]. PCA was applied to visualize data in lower dimension and PNN was applied for classification in [13]. Collected data from metal oxide semiconductor sensor based E-Nose were analyzed by FFBPNN, and support vector machine (SVM) to classify shelf-life stages of banana [14]. SVM was also applied in [15] to recognize ethanol, gasoline and acetone with good accuracy and in [16] to identify spoiled beef, and fish. Eleven different types of Spanish olive oils were classified by PCA followed to an LDA projection with 79% accuracy in [17]. A MOG sensor based E-Nose was designed in [18] with wireless connectivity where k-NN, MLP, SVM with linear and RBF kernel, PCA, and linear discriminant analysis (LDA) algorithms were used for classification. Coffee roasting degree was analyzed in [21] by applying two dimensional PCA scores to FFBPNN, and GRNN. In [22] a portable E-Nose was used to collect sensing data and pattern recognition algorithms as LDA, FFBPNN, PNN, and GRNN were used to identify adulteration of sesame oil.

III. PATTERN RECOGNITION AND CLASSIFICATION ALGORITHMS

It is seen from the E-Nose literature that pattern recognition and classification techniques that are mostly applied in E-Nose applications are: PCA, LDA, *k*-NN, ANN (FFBPNN and RBFNN, GRNN). PCA and LDA are statistical methods, while *k*-NN and ANN fall into machine learning category.

A. Statistical methods

1) Principal component analysis

PCA is a data analysis technique which finds a new set of linearly uncorrelated variables from a set of inter-correlated variables through an orthogonal transformation process. The new set of variables are known as principal components and are less than or equal to the number of original variables. The principal components are ordered in descending values of variances.

We consider a data matrix $\boldsymbol{X}$ of size $N \times D$, where N represents number of experiments and D represents number of datum (for example sensors), each row of the matrix is represented as, $x_m^{C_i} \in \Re^D$, where, $m = 1, \dots, L_{C_i}$, $i = 1, \dots, I$ is class index, I is the number of classes, C_i is the class label, and L_{C_i} is the number of observations for each sample of an object or event with known class C_i. The PCA algorithm is summarized as:

Step 1. Take the D- dimensional data matrix $\boldsymbol{X}$.

Step 2. Calculate the means for each dimension of the whole data set to generate a D-dimensional mean vector.

Step 3. Compute the scatter matrix or the covariance matrix of the data set in the data matrix $\boldsymbol{X}$.

Step 4. From the covariance or scatter matrix in step 3 calculate the eigenvectors and corresponding eigenvalues.

Step 5. Sort the eigenvectors in terms of descending eigenvalues. Form a $D \times K$ dimensional matrix $\boldsymbol{W}$ (where each column represents an eigenvector) taking K eigenvectors with the largest eigenvalues. Here, $K \leq D$.

Step 6. The whole data set in $\boldsymbol{X}$ is converted to new subspace by, $\boldsymbol{Y} = \boldsymbol{W}^{\mathrm{T}} \times \boldsymbol{X}^{\mathrm{T}}$. Here T represents transpose.

2) Linear discriminant analysis

LDA requires the measured independent variables for each observation to be continuous quantities. LDA algorithm for two classes is given below:

Step 1. Given two sets of labeled data, C_1 and C_2 whose class means μ_{C_1} and μ_{C_2} by $\mu_{C_i} = \frac{1}{L_{C_i}} \sum_{m=1}^{L_{C_i}} \boldsymbol{x}_m^{C_i}$, where, L_{C_i} is the number of examples of class C_i, $\boldsymbol{x}_m^{C_i} \in \Re^D$, where, $m = 1 \dots L_{C_i}$, and D is the number of dimensions.

Step 2. Calculate the between-class covariance matrix $\boldsymbol{S}_{between} = (\mu_{C_2} - \mu_{C_1})(\mu_{C_2} - \mu_{C_1})^{\mathrm{T}}$, and total within-class covariance matrix $\boldsymbol{S}_{Within} = \sum_{i=1,2} \sum_{m=1}^{L_{C_i}} (\boldsymbol{x}_m^{C_i} - \mu_{C_1})(\boldsymbol{x}_m^{C_i} - \mu_{C_1})^{\mathrm{T}}$.

Step 3. Calculate, $\boldsymbol{w} = S_{within}^{-1}(\mu_{C_2} - \mu_{C_1})$ which maximizes, $J(\boldsymbol{w}) = \frac{\boldsymbol{W}^T \boldsymbol{S}_{between} \boldsymbol{W}}{\boldsymbol{W}^T \boldsymbol{S}_{Within} \boldsymbol{W}}$. If within covariance of the classes are not equal calculate $\boldsymbol{w}$ by $\boldsymbol{w} = S^{-1}(\mu_{C_2} - \mu_{C_1})$, where, $S = \frac{1}{L_{C_1} + L_{C_2}}(L_{C_1} S_1 + L_{C_2} S_2)$ is a pooled covariance matrix.

Step 4. Projecting a new point onto the maximally separating direction and classify it as C_1 if, $\boldsymbol{w}^T \left(\boldsymbol{x}_m^{C_i} - \left(\frac{\mu_{C_1} + \mu_{C_2}}{2} \right) \right) > log \frac{p(C_1)}{p(C_2)}$, else classify as C_2. Here $p(C_1)$ and $p(C_2)$ are class probability of C_1 and C_2.

For multiclass LDA apply pairwise classification. Create a new classifier for each pair of classes. Total number of classifiers is $I(I-1)/2$. Produce a final classification table combining the results from individual classifiers. Apply majority voting to classify any new data.

B. Machine learning

Five machine learning techniques which got importance in E-Nose applications are: *k*-NN, SVM, FFBPNN, RBFNN, and GRNN.

1) k-Nearest Neighbor

A simple technique to predict the class of an unknown feature vector $x_m^{C_i} \in \Re^D$ is the *k*-NN method. First from the training set the k nearest vectors are found. Then the class of $x_m^{C_i} \in \Re^D$ is found using the majority class voting. Here D is the dimension of data. The *k*-NN algorithm is given below:

Step 1. Calculate the distances from each node to other nodes by the Euclidean norm of the difference of the two vectors i.e.,

$\mathrm{dist}(x_i, x_j) = \left\|x_i - x_j\right\| = \sqrt{(x_{i1} - x_{j1})^2 + (x_{i2} - x_{j2})^2 + \cdots + (x_{iD} - x_{jD})^2}$ and record all the distances in a table.

Step 2. Sort the distances in descending order.

Step 3. Compute the prediction probability by $\mathrm{p}(c_m|x, D, k) = \frac{1}{k}\sum_{i\in\{N_k(x,D)\}} \mathbb{I}(t_i = C_m)$, where, $\{N_k(x, X)\}$ is the set of k nearest points in X from $\boldsymbol{x}$, t_i are class labels of each data point in $\{N_k(x, X)\}$, C_m is the class for which the new data $\boldsymbol{x}$ is being tested, m is class index and $\mathbb{I}(\mathrm{e})$ is the indicator function defined as,

$$\mathbb{I}(\mathrm{e}) = \begin{cases} 1 & \text{if e is true} \\ 0 & \text{if e is false} \end{cases}.$$

As we assume N data with D -dimension the straight forward implementation of finding k-NN takes $\mathrm{O}(\mathrm{N}\times\mathrm{D})$ time.

2) Support Vector Machine (SVM)

The goal of the SVM is to find the hyperplane that provides largest margin betwixt two classes and has no interior data points. Data points from the two classes which lie on the boundary of the slab are called support vectors.

For two class SVM we label the data of class C_1 and C_2 as, $t_i = -1$ and $+1$ accordingly. We need to find the optimal hyperplane $g(\boldsymbol{x}) = \boldsymbol{w}^{\mathrm{T}}\boldsymbol{x} + b$, which maximizes the class separation. We consider the training data of the form, $\{x_m^{C_i}, t_m^{C_i}\}$, where, $t_m^{C_i} \in \{-1, 1\}$, $m = 1, \ldots, L_{C_i}$, $i = \{1, 2\}$, C_i is the class label, and L_{C_i} is the number of observations with known class C_i.

Step 1. By Quadratic programing find the value of α_i which maximize, $\mathrm{Q}(\alpha) \equiv \sum_{n=1}^{N} \alpha_n - \frac{1}{2}\sum_{j=1}^{N} \alpha_n\alpha_j t_n t_j x_i^{\mathrm{T}} x_j$, subject to $\alpha_i \geq 0$, $\forall i$ and $\sum_{i=1}^{N} \alpha_i y_i = 0$. Here α are Lagrange multipliers.

Step 2. Calculate $\boldsymbol{w}_0$ using α_i found in step 1 into, $w_0 = \sum_{n=1}^{N} \alpha_n t_n \boldsymbol{x}_n$.

Step 3. Put the value of w_0 into the *Karush–Kuhn–Tucker condition* [19], $\alpha_n[d_n(w_0^T x_n - b_0) - 1] = 0$ and solve for b_0.

Multiclass SVM is a combination of several binary SVM classifiers. A new data is classified based on majority votes from all binary classifiers. In Matlab this is defined as error-correcting output code multiclass model (ECOC). ECOC classification requires a coding design, and a decoding scheme. Coding design includes several binary learners formed by taking two classes at a time. The decoding scheme decides the rules of aggregating the binary classifiers' results.

We apply one-versus-one coding design, where two classes of data are taken at a time; one class is assigned to positive class and another to negative class. More combination of coding designs can be found in Matlab documentation.

3) Artificial Neural Network

A neural network resembles the brain in two respects:

- through a learning process the neural network gathers knowledge, and
- synaptic weights, i.e. calculated weights of inter-neuron connections during learning process are used to store the knowledge.

An ANN learns in any of the three techniques: supervised, unsupervised, and reinforcement learning. Reinforcement learning is rarely used in ANN applications. E-Nose data are usually organized as input-target pairs making supervised learning more common compared to unsupervised learning algorithms. FFBPNN, RBFNN, and GRNN apply supervised learning technique. The supervised learning requires a training set defined as $\{\boldsymbol{x}_m^{C_i}, t_m^{C_i}\}$, $\mathrm{m} = 1, \ldots, L_{C_i}$, $i = 1, \ldots, I$, where $\boldsymbol{x}_m^{C_i}$ is an input to the network and $t_m^{C_i}$ is the corresponding target output. On receiving each input an ANN computes the output and compares them to the corresponding targets. According to the learning rule the weights and biases of the network is updated until the error reach to a predefined limit and the network outputs move closer to the targets.

a) Feedforward backpropagation neural network

A common training method for FFBPNN is back propagation also known as error back propagation. In this method the outputs are compared to the targets to calculate the errors. The synaptic weights and threshold values are then adjusted to minimize the error contributed by each neuron next time.

Given, the topology of a neural network, the activation function for each neuron in the network A_i; training data: pairs of sets of inputs and outputs $\mathrm{T} = \{(\boldsymbol{x}_1, t_1), (\boldsymbol{x}_2, t_2), \cdots, (\boldsymbol{x}_N, t_N)\}$, where, each $\boldsymbol{x}_i$ denotes the input to all input neurons and each t_i is the desired output of the neural network after running the inputs in $\boldsymbol{x}_i$; a learning rate r having a continuous value between 0 and 1 ; the FFBPNN algorithm can be summarized as:

Step 1. Choose random values for weights and biases.

Step 2. Calculate outputs of each neuron using an activation function A_i as transfer function. Typical activation functions are sigmoid, tanh, step, etc.

Step 3. Considering the training data T compute the sum of squares error (SSE) of the network by, $\mathrm{SSE}(\mathrm{T}) = \sum_{i=1}^{N}((y_i - t_i)^2)$, where y_i is the set of outputs of the neural network for the set of inputs $\boldsymbol{x}_i$.

Step 4. Update the weights of edges and biases of neurons at a rate based on learning rate. The update is done by gradient descent minimization.

Step 5. Back to step 2 until error limit reached in step 3.

b) Radial basis function neural networks

Radial basis function networks are of two kinds: exact, and approximate. In exact RBFNN the numbers of neurons at each layer are equal to the number of samples. RBFNNs are trained in two stages. The parameters governing the basis functions are determined by unsupervised methods in the first stage. In the

second stage of training the final-layer weights are determined. A block diagram of RBFNN is shown in Fig. 2.

Every input vector is mapped exactly onto the corresponding target vector in exact RBFNN. Let's consider a D-dimensional input space X is mapped to a one-dimensional target space t, the data set $\{x_m^{C_i}, t_m^{C_i}\}$, where $x_m^{C_i}$ is an input to the network and $t_m^{C_i}$ is the corresponding correct (target) output, $m = 1, \dots, L_{C_i}$, $i = 1, \dots, I$, consists of $L_{C_1} + L_{C_2} + \cdots + L_{C_I} = N$ input vectors. The goal is to find a function $\mathrm{h}(x)$ such that $\mathrm{h}(x_m^{C_i}) = t_m^{C_i}$, $m = 1, \dots, L_{C_i}$, $i = 1 \dots I$.

The N basis functions of the form $\varphi(||\boldsymbol{x} - \boldsymbol{x}_m^{C_i}||)$ are linearly combined to produce the output of the mapping. The output is given by, $\mathrm{h}(\boldsymbol{x}) = \sum_{m,C_i} \boldsymbol{w}_m^{C_i} \varphi(-\gamma||\boldsymbol{x} - \boldsymbol{x}_m^{C_i}||)$, where, γ is a constant, the distances $||\boldsymbol{x} - \boldsymbol{x}_m^{C_i}||$ usually taken to be Euclidean, and $\phi(z) = \exp(-z)$. In matrix form the problem can be presented as, $\boldsymbol{\Phi w} = \boldsymbol{t}$, where, w is $N \times 1$ vector, t is a $N \times 1$ vector, and $\boldsymbol{\Phi}$ is a N × N matrix given as follows:

$$\boldsymbol{\Phi} = \begin{bmatrix} exp\left(-\gamma \left|\left|\boldsymbol{x}_1^{C_1} - \boldsymbol{x}_1^{C_1}\right|\right|^2\right) & \dots & exp\left(-\gamma \left|\left|\boldsymbol{x}_1^{C_1} - \boldsymbol{x}_{L_{C_I}}^{C_I}\right|\right|^2\right) \\ exp\left(-\gamma \left|\left|\boldsymbol{x}_2^{C_1} - \boldsymbol{x}_1^{C_1}\right|\right|^2\right) & \dots & exp\left(-\gamma \left|\left|\boldsymbol{x}_2^{C_1} - \boldsymbol{x}_{L_{C_I}}^{C_I}\right|\right|^2\right) \\ \vdots & \vdots & \vdots \\ exp\left(-\gamma \left|\left|\boldsymbol{x}_{L_{C_I}}^{C_I} - \boldsymbol{x}_1^{C_1}\right|\right|^2\right) & \dots & exp\left(-\gamma \left|\left|\boldsymbol{x}_{L_{C_I}}^{C_I} - \boldsymbol{x}_{L_{C_I}}^{C_I}\right|\right|^2\right) \end{bmatrix}$$

RBF exact interpolation algorithm is given below,

Step 1. Choose a value for γ ranging from 0 to 1 randomly.
Step 2. Choose random weights for vector w.
Step 3. Compute the elements, $\varphi(||\boldsymbol{x} - \boldsymbol{x}_m^{C_i}||)$ of the $\boldsymbol{\Phi}$ matrix.
Step 4. Evaluate, vector $\mathbf{w}$ from, $\boldsymbol{w} = \boldsymbol{\Phi}^{-1}\boldsymbol{t}$.
Step 5. Evaluate, output vector, y from, $\boldsymbol{y} = \boldsymbol{w\Phi}$.
Step 6. Evaluate, squared error, $E = \frac{1}{2}\sum_{n=1}^{N}\sum_{k=1}^{N}\{y_k - t_k^n\}^2$ from $\boldsymbol{y}$ and $\boldsymbol{t}$.
Step 7. If $E > E_{threshold}$, change γ and continue to step 3 else exit.

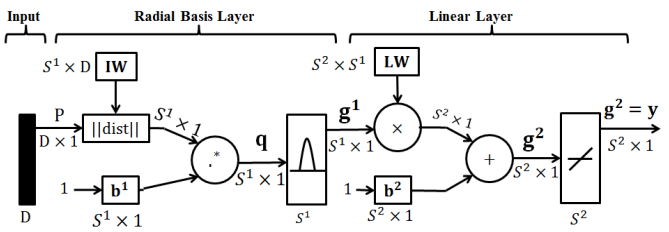

Figure 2. Radial basis function neural network. The first layer i.e. the radial basis layer has S^1 basis functions, and the second layer i.e. linear layer has S^2 pure linear functions. S^1, and S^2 are the number of neurons in the radial basis layer and linear layer accordingly; P is a D × 1 input vector, D is the number of input variables; g^1, and g^2 are the output vectors from layer 1 and layer 2 accordingly; IW, and LW are input and output weight matrices accordingly, for exact radial basis function network IW holds all the training data points, and LW is updated by training; b^1, and b^2 are the bias vectors of layer 1 and layer 2 accordingly. [20]

c) Generalized regression neural network

GRNN has two differences to exact RBFNN in Fig. 2. The LW weight matrix in the second layer in Fig. 2 is set to target vector and the summation block in the second layer is replaced by a normalized product block. Thus the GRNN network virtually does not require training and therefore is fast. During training period the weights IW and LW are initialized to the data matrix **X** and target values in vector **t**.

IV. Results and Discussion

Three classes of typical E-Nose data have been considered with each class having 100 samples. Fig. 3 shows a principal component analysis where x and y axes represent the principal components 1 and 2 respectively. Fig. 4 shows that the first two principal components hold approximately 95% variance of all the data. Thus the principal component analysis is a very useful tool to reduce the dimensionality of multidimensional data.

Classification by LDA, *k*-NN, multi class SVM, FFBPNN, RBFNN, and GRNN have been done. For these methods 70% of the data from each class were randomly chosen for training and remaining 30% were taken for testing/validation. Simulation results for LDA, *k*-NN, multi class SVM, FFBPNN, RBFNN, and GRNN are summarized in Table I. Training duration, testing/validation duration, and number of testing/validation error are also listed in Table I. It is seen that training duration for *k*-NN was minimum followed by GRNN, SVM, RBF, LDA, and FFBPNN accordingly. Whereas testing/validation duration for GRNN is minimum, followed by SVM, FFBPNN, *k*-NN, LDA, and RBF accordingly. Testing error of *k*-NN, SVM, FFBPNN, RBF, GRNN are 0% and that of LDA is 3.33%. It is seen that *k*-NN, SVM, RBF, and GRNN has good speed of training and testing speed of GRNN is the highest.

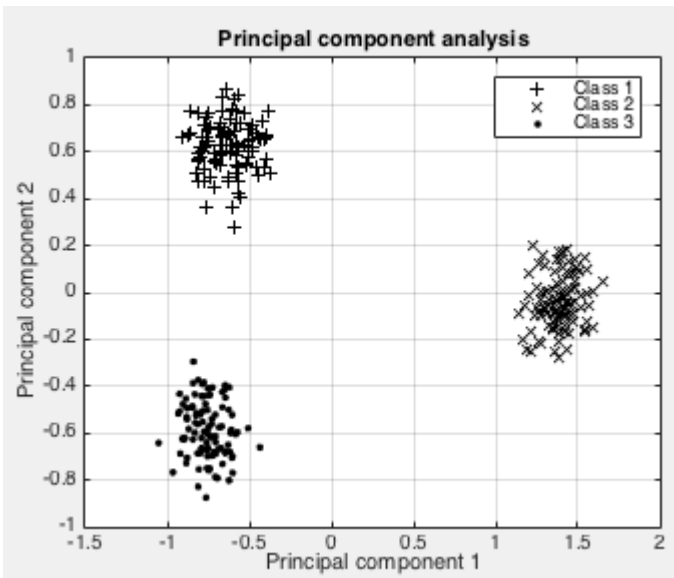

Figure 3. Three classes of data, each class having 100 samples with dimension reduced to two by PCA.

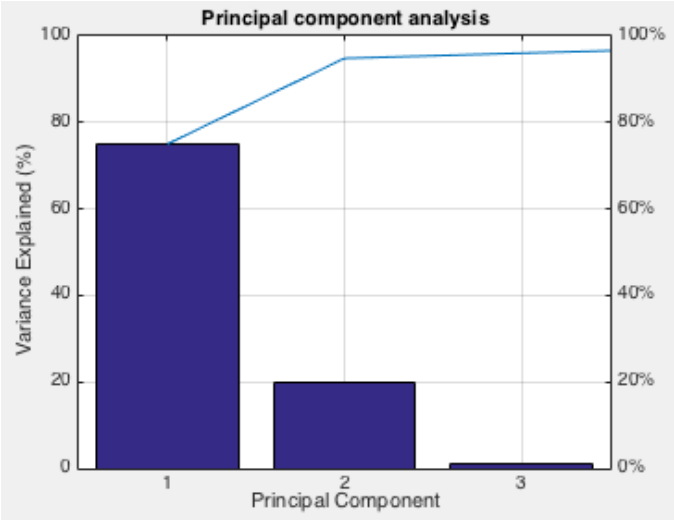

Figure 4. Variance explained of PCA analysis.

TABLE I. TRAINING DURATION, DETECTION DURATION, AND DETECTION ERROR

	Training duration	Detection time	Testing error
LDA	0.4761	0.0320	3.33%
k-NN	0.0298	0.0298	0%
SVM	0.0703	0.0183	0%
FFBPNN	0.5817	0.0243	0%
RBFNN	0.1680	0.0466	0%
GRNN	0.0546	0.0139	0%

V. CONCLUSION

In this paper data analysis methods for E-Nose applications are discussed. We find that k-NN, SVM, RBFNN, and GRNN are good methods for E-Nose data classification and pattern recognition in terms of new data classification speed, and testing error. GRNN shows best performances for the data set that we have considered. We are designing an E-Nose in our laboratory for toxic and explosive gas detection at present.

ACKNOWLEDGMENT

We thank Thammasat University research fund for supporting this research.

REFERENCES

[1] S. Firestein, "How the olfactory system makes sense of scents," *Nature*, vol. 413, pp. 211–218, Sep. 2001.

[2] I. Concina, M. Falasconi, and V. Sberveglieri, "Electronic noses as flexible tools to assess food quality and safety: should we trust them?," *IEEE Sensors Journal*, vol. 12, no. 11, pp. 3232–3237, Nov. 2012.

[3] J. Brezmes, et al., "Evaluation of an electronic nose to assess fruit ripeness," *IEEE Sensors Journal*, vol. 5, No. 1, pp. 97–108, Feb. 2005.

[4] E. L. Hines, E. Llobet, and J. W. Gardner, "Neural network based electronic nose for apple ripeness determination," *Electronic Letters*, vol. 35, no. 10, pp. 821–823, May 1999.

[5] Z. Xiaobo, and Z. Jiewen, "Apple quality assessment by fusion three sensors," in *Proc. 2005 IEEE Sensors*, Oct. 30 – Nov. 3 2005, pp. 389–392.

[6] S. S. Chowdhury, B. Tudu, R. Bandyopadhyay, and N. Bhattacharyya, "Portable electronic nose system for aroma classification of black tea," in *Proc. IEEE Region 10 and the Third Int. Conf. on Industrial and Information Systems*, Dec. 2008, pp. 1 –5.

[7] L. Zhang, and F. Tian, "A novel chaotic sequence optimization neural network for concentration estimation of formaldehyde by an electronic nose," in *Proc. Fourth Int. Conf. on Computational Intelligence and Communication Networks*, pp. 856 – 859, Nov. 2012.

[8] A. H. Abdullah et al., "Application specific electronic nose (ASEN) for ganoderma boninense detection using artificial neural network," in *Proc. 2nd Int. Conf. on Electronic Design (ICED)*, Aug. 2014, pp. 148–152.

[9] M. Pardo, G. Faglia, G. Sberveglieri, and L. Quercia, " Electronic nose for coffee quality control," in *IEEE Instrumentation and Measurement Technology Conf.*, May 2001, pp. 123–127.

[10] P. U. Kurup, and M. A. Lowell, "An electronic nose for detection hazardous chemicals and explosives," in *Proc. of IEEE Conf. on Technologies for Homeland Security*, May 2008, pp. 144–149.

[11] R. Singh, "An intelligent system for odour discrimination," in *Proc. of the first IEEE Int. workshop on Electronic Design, Test and Applications (DELTA'02)*, 2002. pp. 1–3.

[12] N. Bhattacharyya, B. Tudu, R. Bandyopadhyay, M. Bhuyan, and R. Mudi, "Aroma characterization of orthodox black tea with electronic nose," in *Proc. TENCON IEEE Region 10 Conf.*, Nov. 2004, pp. 427–430.

[13] A. G. -Cortes, J. Marti, I. Sayago, J. P. Santos, J. Gutierrez, and M. C. Horrillo, "Detection of stress through sweat analysis with an electronic nose," in *Proc. Spanish conf. on electronic devices*, Feb. 2009, pp. 338–341.

[14] A. Sanaeifar, S. S. Mohtasebi, M. G. -Varnamkhasti, and M. Siadat, "Application of an electronic nose system coupled with artificial neural network for classification of banana samples during shelf-life process," in *Proc. Int. Conf. on Control, Decision and Information Technologies (CoDIT)*, Nov. 2014, pp. 753 – 757.

[15] X. -D. Wang, H. -R. Zhang, and C. -J. Zhang, "Signals recognition of electronic nose based on support vector machines," in *Proc. of the Fourth Int. conf. on Machine Learning and Cybernetics*, Aug. 2005, pp. 3394-3398.

[16] N. ul Hasan, N. Ejaz, W Ejaz, and H. S. Kim1, "Malicious odor item identification using an electronic nose based on support vector machine classification," in *Proc. IEEE 1st Global Conf. on Consumer Electronics (GCCE)*, Oct. 2012, pp. 399–400.

[17] A. Perera, A. G. -Baena, T. Sundic, T. Pardo, and S. Marco, "Machine olfaction: pattern recognition for the identification of aromas," in *Proc. 16th Int. Conf. on Pattern Recognition*, 2002, pp. 410–413.

[18] M. Hassan and A. Bermak, "Threshold detection of carcinogenic odor of formaldehyde with wireless electronic nose," in *Proc. 2014 IEEE Sensors*, Nov. 2014, pp. 1368–1371.2014 IEEE.

[19] H. W. Kuhn, and A. W. Tucker, "Nonlinear programming," in *Proc. Second Berkeley Symposium on Mathematical Statistics and Probability*, 1951, pp. 481–492.

[20] M. T. Hagan, H. B. Demuth, M. Beale, *Neural Network Design*, , Thomson Asia Pte. Ltd. and China Machine Press and CITIC Publishing House, China, 1996.

[21] S. Romani, C. Cevoli, A. Fabbri, L. Alessandrini, and M. Dalla Rosa, "Evaluation of coffee roasting degree by using electronic nose and artificial neural network for off-line quality control," *Journal of Food Science*, vol. 77, no. 9, pp. 960–965, Jun. 2012.

[22] Zheng Hai, Jun Wang, "Electronic nose and data analysis for detection of maize oil adulteration in sesame oil," *Sensors and Actuators B*, vol. 119, no. 2, pp. 449–455, Jan. 2006.

A Novel Trust Measurement System for Cloud-based Marketplace

Sudipta Singha Roy, Tamjid Haque Sarker, and M. M. A. Hashem
Department of Computer Science and Engineering
Khulna University of Engineering and Technology
Khulna-9203, Bangladesh
E-mail: sudipta.singha.roy@outlook.com, oleevecse_47@yahoo.com, mma.hashem@outlook.com

Abstract—**Cloud Computing is an enormously growing phenomenon in the present days enabling IT related services to run in a more dynamic and scalable way than the previous days and cloud marketplace is becoming more competitive with the entrance of new cloud service providers (CSP) offering similar functionalities. The basic obstacles in the way of success of cloud marketplace are the numerous shortcomings in reliable monitoring and identifying reliable cloud service provider based on consumers' preferred services. In this paper, a multi-faceted Entrusted Trust Management (ETM) system architecture is introduced that can support the customers in reliably choosing the trustworthy cloud service provider (CSP) as well as properly weight the information sources that provide feedbacks about the quality of services (QoS) of the CSPs. This ETM system works on several issues to measure the trust value of the providers on specific domain and overall trust value. Firstly, measurement of the trust value of the specific domain of provider on the basis of certainty and uncertainty. Secondly, measurement of overall trust value of the provider from these domain specific trust values. Thirdly, measurement of "Degree of Conflict" between the rating/feedback of consumers and experts. And finally, measurement of trustworthiness of the information sources which provide the rating of the provider on the basis of the SLA between the provider and the consumer. At last, our proposed system is experimented using real datasets.**

Keywords—***Cloud computing, Cloud Service Provider, Trust Models, Trust Management, CAIQ, Self-Assessment.***

I. Introduction

Nowadays, cloud computing is becoming one of the most demanding part of human life as it offers dynamic, scalable and shared resources with more flexibility, disaster recovery plan, automatic software updates, increased collaboration and document control. But the highly distributed and nontransparent nature of cloud computing are considerable obstacles for the market success of the cloud services, as consumers of these services often feel that they lose their control over their data. A survey conducted by Fujitsu Research Institute among more than 3000 consumers of cloud services from 6 different countries shows that, about 84% of the consumers are concerned about data storage location, 88% of the consumers are worried about who has access to their data [1] and 93% consumers distrusts the security facilities of their cloud services against the facilities they were offered [2,3]. Moreover, because of massive diversity in the available cloud services, it has become challenging for the customers to select whose services they should use based on their preferred choice of services and requirements.

Consumer concerns can be redressed by implementing adequate preventive measures for privacy and security. Cloud providers show the evidence of their preventive measures by including related description in the service level agreements (SLAs). But, a survey [4] shows that, 46.6% of the cloud users think, the legal contents of the SLAs are unclear. SLAs with such obscure clauses and fuzzy technical specifications make them unreliable as standalone basis for the consumers to identify trustworthy providers.

As the cloud market is growing rapidly and new cloud service providers are entering the market, this marketplace is becoming more competitive day by day. Different cloud providers compete for customers by providing services with similar functionalities. However, there remains huge differences in terms of meeting the Quality of Service (QoS) ensured to the consumers as well as capabilities of the cloud service providers. Moreover, cloud brokers and resellers promise to provide add-on services on behalf of cloud providers with the same level of competencies and capabilities. So, consumers badly need to reliably assess the trustworthiness of the service providers offering services of good quality.

Numerous electronic marketplaces like: eBay, Amazon and app market have already utilized trust and reputation (TR) systems [5] successfully. Nowadays, cloud marketplace also needs similar approaches to support the customers in selecting trustworthy cloud service provider based on their desired services. Existing TR systems doesn't solely depends on the customer feedback. They also consider property certificates, compliance with audit standards as well as provider statements as the source of information. But, these TR systems give same preferences to all information sources and feedbacks neglecting the issue that, all the information sources may not be equally standard and trustworthy. So, it would be more reliable to the customers if these feedbacks (ratings) from different information sources are properly weighted. Hence, we feel strong requirement of a TR system in which every

978-1-4673-9257-0/15/$31.00 ©2015 IEEE

feedback from different information sources are properly entrusted (weighted). Our objective is to maintain a smooth trust in the cloud marketplace and provide them a tool that can verify and rank the cloud service providers based on the customers' desired services.

This paper provides the realization of our proposed Entrusted Trust Management (ETM) system for cloud computing marketplace which aims to reflect the multifaceted nature of trust evaluation by considering multiple attributes, entrusted sources and roots of trust as well as support the customers in selecting trustworthy service providers. As user feedback is the main source of trust evaluation, we have tried to weight their opinions and determine whether the consumer who is providing the feedback is trustworthy or not. In this paper, we implement the Entrusted Trust Management (ETM) system using the CAIQ as one of the trust information sources that extracts trust information from the CAIQs completed by cloud providers. We also contribute to determine the trustworthiness of the information sources (how much trustworthy that information source is) and weight every information sources accordingly. Finally, our ETM system is validated by experimental evaluation based on the completed CAIQs stored in the public registry (i.e. CSA STAR [6]).

The rest of the paper is organize as follows: Section 2 discusses the related work, Section 3 discusses the procedural and architectural details of the proposed ETM system based on the CSA CAIQ framework, Section 4 shows how the system is validated by experimental evaluation and finally Section 5 provides our concluding remarks.

II. Related Works

The current trust establishment trends and approaches are classified into two categories: 1) applied technologies and 2) research trends [3]. Applied technologies show various technologies available in competitive cloud marketplace for establishing trust on cloud providers. SLA validation [7] and monitoring [8] are ways to establish trust on cloud providers. But the compensation clauses written in SLAs for stakeholders in the cloud marketplace are written by the cloud providers in such a way that the customers merely get the compensations in case of not meeting the Quality of Services (QoS) as assured by the cloud providers. To reassure users about different services and platforms, cloud providers use various audit standards (e.g. SAS 70 II, FISMA etc.). They, however, cover only the operational performances and are not sufficient in abating (lessening) the users' security concerns. Recently, some cloud marketplace (e.g. SpotCloud) were launched to support the customers in selecting dependable cloud providers where cloud providers' ratings are given in an Amazon-like 'star' interface with no technical documentation on how the ratings are computed.

Research trends show some research-driven approaches regarding trust establishment in cloud environment. Trust and reputation (TR) models (e.g. KeyNote [9], REFEREE [10]) have been adapted and proven useful in cloud computing environment. But, these approaches for decision making in cloud environment usually don't take multiple attributes and assume trust relationships are monotonic. Moreover, these approaches don't address the concept of uncertainty in trust establishment where, modeling and representing uncertainty is important when trust is assessed between a provider and customer based on information that is incomplete or insufficient or derived from unreliable sources. Habib et al. [11] proposed a TM system that aggregates trust related information from different sources as well as take uncertainty into account while measuring trust value. It implemented the Cloud Control Assessment (CCA) tool based on the CSA CAIQ. But, it can't calculate/measure the weight of different information sources and consumers have to assume weight for different information sources by themselves.

Our proposed ETM system aims to measure weight of different information sources and then aggregate trust related information from those information sources e.g. user ratings, provider statements, user statements, expert assessment, property certificates.

III. Conceptual Model for Entrusted Trust Management System

This section discusses the solutions that are essential in developing an ETM system for cloud marketplace. An overview of the ETM system architecture as well as description of its internal components are also provided in this section.

A. Modeling Trustworthiness in Cloud Computing-based Market Place

Modelling the trustworthiness of a cloud provider requires statements on the expected behavior of the offered services or systems from different information sources. At the same time the trustworthiness of the information sources are also needed to be measured. These statements are required to be given in the form of propositions (e.g. Security: "Cloud provider A keeps my data confidential." Availability: "Cloud provider A provides 95% uptime in a year."). These propositions refer to different attributes. Using the operators (AND, W.FUSION) proposed in [3, 11] those propositions become the combined statements in the form of Propositional Logic Terms (PLTs).

When modeling trust, the Trust Management (TM) system has to consider trust relevant information, how a trust value derived that information are subject to uncertainty along with how much trustworthy that information source is. Thus, we propose an ETM system that aims to model trust as a subjective probability, which follows the definition of trust provided in [12].

B. Modeling Trust Metrices in Cloud Computing-based Market Place

We use CertainTrust [13] and CertainLogic [14] as the basis for a trust metric in designing the architecture of the ETM system for the idea of modelling trust as a subjective probability. In the following we discuss a brief description to the trust representation and computation that we need to support.

In CertainTrust [13] opinions are the basis of measuring trustworthiness of certain cloud provider. Opinions express one's belief whether a certain proposition (or a combination of propositions) is true or false. Each opinion is a triple of values, $o = (t, c, f) \in \{[0,1] \times [0,1] \times [0,1]\}$ where t denotes the average rating, c represents certainty associated with the average rating and f denotes the initial expectation assigned to the truth of the statement [3, 13]. In [3] each opinion is associated with an expectation value, $E(t, c, f)$ *where*:

$$E(t, c, f) = t * c + (1 - c) * f \qquad (1)$$

The consensus and discounting operators proposed in CertainTrust and CertainLogic provides means for aggregating opinions on the same statement from different information sources and weighting those opinions based on the trustworthiness of those sources respectively. In this paper we use the W.FUSION operator proposed by Habib et al. in [11] for aggregating opinions derived from the CAIQ. W.FUSION operator is defined in Table I.

C. ETM System Architecture

In this section, we propose a novel architecture of a ETM system for cloud marketplace. Fig. 1 gives a visual description of the architecture of this system. A brief description of the ETM system's internal components are as follows:

Registration Manager (RM): Cloud providers register through the RM. RM enables providers to as sellers in cloud marketplace. They provide system and service specifications related to the services they offer to the consumers and fill the CAIQ. The RM forwards the answers of the CAIQ to the CAIQ Engine and Trust Information (TI).

Consensus Assessments Initiative Questionnaire (CAIQ) Engine: The CAIQ Engine provides an interface for the cloud providers to fill in the questionnaires through the RM. The CAIQs help cloud providers to represent their competencies to thee consumers with respect to different attributes. All the questions are answered to be "yes", "no", "unknown" and "N/A (not applicable)". All these answers of CAIQs are passed to and stored in TI for further processing.

Trust Manager (TMg): The TMg allows the cloud users to customize their requirements before assessing the trustworthiness of the providers in the cloud marketplace. Based on the customized requirements of the consumer, it provides the trust value of the cloud providers.

Trust Semantics Engine (TSE): The TSE models the configuration of the PLTs customized by the consumers. A default configuration is based on the CAIQ answers stored in TI. It also converts all trust information into PLTs. TSE sends the customized PLTs to the Trust Computation Engine (TCE) for computing customized trust value.

Trust Computation Engine (TCE): The TCE contains operational information related to the operators proposed in CertainTrust [13] and CertainLogic [14] and uses the PLTs to compute the customized trust value.

Weight Measurement Engine (WME): The WME gathers opinions from each information sources regarding the trustworthiness of the cloud provider. Then measuring the

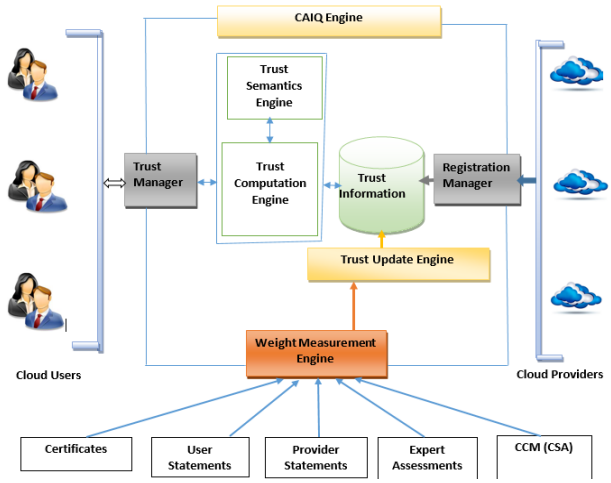

Figure 1. Architecture Overview

Degree of Conflict (DoC) of those opinions of a certain information source for a certain cloud provider from the recent opinions (opinions gathered within 2/3 months) about the service of that provider gathered from the other information sources it determines how much trustworthy that certain information source is and measure it's weight. It passes the opinions from different information sources as well as their proper weight to the Trust Update Engine.

Trust Update Engine (TUE): The TUE is responsible for the collection of opinions from different information sources regarding the trustworthiness of the providers in the cloud marketplace. Moreover, the information sources should be authorized and properly weighted before they provide opinions about the Quality of Services (QoS) of any cloud provider. The TUE combines all opinions regarding the providers and updates their trust value.

IV. CAIQ Based Entrusted Trust Management System

The CAIQ (Version 3.0.1) includes in total, 133 controls (e.g. Application Security (AS), Information System Regulatory Mapping (ISRM)) under 16 domains (e.g. Application and Interface Security (AIS), Audit Assurance & Compliance (AAC)) which are aligned with the CSA principle [15] for moving IT resources to the cloud. Each control contains one or more questions for querying the competencies and capabilities of the cloud provider. Consensus Assessments Initiative Questionnaire v3.0.1 provides 295 CAIQs under these 133 controls to support customers in identifying the trustworthy cloud provider in the marketplace.

A. Assumptions

In this conceptual model, several assumptions should be considered as follow:

- Cloud providers submit one set of legally or officially acceptable answers to the CAIQ for each of the services they offer to the consumers.
- These valid answers are stored in the TI.

TABLE I. DEFINITION OF W.FUSION OPERATOR

Operator	Functionality
W.FUSION	$t_{\widehat{\oplus}_w(A_1,A_2,\cdots,A_n)} = \begin{cases} \frac{\sum_{i=1}^{n} w_i t_{A_i}}{\sum_{i=1}^{n} w_i} & if\ c_{A_1} = c_{A_2} = \cdots = c_{A_n} = 1 \\ 0.5 & if\ c_{A_1} = c_{A_2} = \cdots = c_{A_n} = 0 \\ \frac{\sum_{i=1}^{n}\left(t_{A_i} c_{A_i} w_i \prod_{j=1,j\neq i}^{n}\left(1-c_{A_j}\right)\right)}{\sum_{i=1}^{n}\left(c_{A_i} w_i \prod_{j=1,j\neq i}^{n}\left(1-c_{A_j}\right)\right)} & if\ \left\{c_{A_i}, c_{A_j}\right\} \neq 1 \end{cases}$ $c_{\widehat{\oplus}_w(A_1,A_2,\cdots,A_n)} = \begin{cases} 1 & if\ c_{A_1} = c_{A_2} = \cdots = c_{A_n} = 1 \\ \frac{\sum_{i=1}^{n}\left(c_{A_i} w_i \prod_{j=1,j\neq i}^{n}\left(1-c_{A_j}\right)\right)}{\sum_{i=1}^{n}\left(w_i \prod_{j=1,j\neq i}^{n}\left(1-c_{A_j}\right)\right)} & if\ \left\{c_{A_i}, c_{A_j}\right\} \neq 1 \end{cases}$ $f_{\widehat{\oplus}_w(A_1,A_2,\cdots,A_n)} = \frac{\sum_{i=1}^{n} w_i f_{A_i}}{\sum_{i=1}^{n} w_i}$

- The CSA checks and validates the authenticities and accuracy of the answers regularly and some experts submit another report over the cloud providers competencies and abilities [16].
- Consumers are not bound to answer all the CAIQ questions while providing feedback about the cloud providers Quality of Services (QoS) with respect to the offered services.

B. *Conceptual Model of ETM Sysyem*

We propose a 3 step approach for assessing the CAIQ and measure the trustworthiness of the cloud providers as well as information. These steps are detailed as follows:

Firstly, the TSE shapes the PLTs based on the 16 CAIQ domains. So, PLT contains 16 operands combined with 15 W.FUSION ($\widehat{\oplus}_w$) operators.

Secondly, the opinions from different information sources based on the self-assessment according to the guidance (i.e., CAIQ) of CSA are modeled in the evidence space and we use the mapping as Habib et al. proposed in [17]. The mapping is as follows:

$$t = \begin{cases} 0 & if\ r+s=0 \\ \frac{r}{r+s} & else \end{cases}$$
$$c = \frac{N.(r+s)}{2.(N\ \ (r+s)) + N.(r+s)} \qquad (2)$$
$$f = 0.99$$

Here, t denotes the average rating, which is calculated based on the number of positive assertions. c denotes the certainty and is calculated based on the total number of questions, N and the total number of positive and negative assessments under all 16 domains. N is defined under 2 circumstances: 1) Questions not answered for 'unknown' by the cloud provider. For the first case, N is defined as, $N = r + s + u$. Here u denotes the 'unknown' marked questions. For the second case, N is defined as, $N = (r + s + u) - NA$. Here, NA denotes the 'Not Applicable' marked answers. f denotes the initial expectation and is set as high for each domain that the cloud provider release their control information regarding different domains. Finally, the weight of the information source is updated as it submit its assessment about the QoS of the cloud provider. Initially we assume all the users have weight 1. Then depending on behavior of the user the corresponding weight is updated. Here Degree of Conflict (DoC) is the basis to measure the behavior of the user. We can measure the DoC of a single opinion about a provider from the overall trust value of that provider using the following equation:

$$DoC_{A_i,A_j} = \left|\left(t_{A_i} - t_{A_j}\right)\right| * c_{A_i} * c_{A_j} * \left(1 - \left|\frac{w_i - w_j}{w_i + w_j}\right|\right) \qquad (3)$$

DoC_{avg} (Average Degree of Conflict) represents how any information source's feedback differs with the recent feedbacks from other information sources which can be calculated from the equation below:

$$\mathrm{DoC}_{avg} = \frac{\sum_{i=1}^{n}\sum_{j=1,j\neq i}^{n} DoC_{A_i,A_j}}{n} \qquad (4)$$

How much one information source's weight can be differed after contributing (i+1)th feedback can be measured from the below equation:

$$diff_{i+1} = \begin{cases} p{DoC_{avg}}^2 + qDoC_{avg} + r & if\ DoC_{avg} > .05 \\ 0 & else \end{cases} \qquad (5)$$

Here a, b, c are three constants with value,$p = 0.022$, $q = 1.023$ and $r = -0.0289$. Here $diff_{i+1}$ is the relative weight difference after contributing an opinion. The vale of p, q, r depends on the data pattern. We have found this equation by plotting the values found from our survey and using regression. The updated weight of an information source after providing (i+1) feedbacks can be measured from the following equation:

$$w_{i+1} = w_i + \alpha(diff_i - diff_{i+1}) \qquad (6)$$

Where α is the dumping factor ($\alpha > 0$) and very small which typically decreases as number of feedback from the information source increases). This learning rate α can be determined from the following equation:

$$\alpha = e^{-(i+1)} \qquad (7)$$

V. EXPERIMENTAL EVALUATION

Evaluation of our proposed ETM system is represented in sections: 1) Weight variation of the information sources with their provided feedback and 2) Trust value measurement using

TABLE III. WEIGHT UPDATE PROCESS FOR INFORMATION SOURCE 'X'

		Assessment about QoS of:			
		Cloud Provider A	***Cloud Provider B***	***Cloud Provider C***	***Cloud Provider D***
Assessment Value	***Overall***	(0.528,0.99,0.885)	(0.634,0.97,0.96)	(0.594,0.98,0.99)	(0.724,0.97,0.99)
	X's feedback	(0.34,0.77,0.99)	(0.534,0.88,0.99)	(0.594,0.77,0.99)	(0.824,0.77,0.99)
X's Weight	***Initial***	1	0.956	0.952	0.998
	After providing feedback	0.956	0.952	0.998	0.989

practical cases. We consider the following scenario to evaluate weight variation of the information sources.

Consider a scenario of a cloud market place. 'A' is cloud-based service provider. Cloud provider 'A' fills up the CAIQs and its final assessments are $o(t,c,f) = (0.5386,0.99,0.8753)$ and $E = 0.541967$. Experts from CSA's final assessments about the QoS of cloud provider 'A' are $o(t,c,f) = (0.5186,0.9945,0.8953)$ and $E = 0.5207$. So, both filled up CAIQs of cloud provider 'A' and expert's assessments are information sources here. Consider both information sources weight are 1. Another information source (i.e. consumer) 'X' provides a feedback about the cloud provider 'A''s QoS against the offered services and its final assessments are $o(t,c,f) = (0.34,0.77,0.99)$ and $E = 0.4895$. Initially, information source 'X' has weight (w_0) 1. DoC between information source 'X' and experts' and cloud provider 'A' assessments are:

$$DoC_{A_{Expert},A_X} = \left|\left(t_{A_{Expert}} - t_{A_X}\right)\right| * c_{A_{Expert}} * c_{A_X} * \left(1 - \left|\frac{w_{Expert} - w_X}{w_{Expert} + w_X}\right|\right) = 0.1368$$

$$DoC_{A_A,A_X} = \left|\left(t_{A_A} - t_{A_X}\right)\right| * c_{A_A} * c_{A_X} * \left(1 - \left|\frac{w_A - w_X}{w_A + w_X}\right|\right) = 0.1513$$

So, the average DoC for information source 'X' is $\mathrm{DoC}_{avg} = 0.144$ and its weight difference after contributing 1st feedback is:

$$diff_{i+1} = p(0.144)^2 + q * 0.144 + r = 0.1189$$

So, after submitting 1st feedback information source 'X''s weight is updated to:

$$w_1 = w_0 + \alpha(diff_i - diff_{i+1}) = 0.956$$

Table II shows how information source 'X''s weight is updated after providing each opinion. Consider all information sources except 'X' has weight 1. For cloud provider 'A' , 'B' and 'D' information source 'X''s feedback differs a lot from the recent feedbacks from other information sources about those providers. That's why X's weight decreased. But for a good feedback about cloud provider 'C', its weight raised.

We have evaluated our ETM system by filling out the CAIQ. In the real-world case, we use assessments from the cloud service providers published in the STAR hosted by CSA. The STAR repository stores the sets of completed CAIQ questionnaires from different cloud providers. We choose two sets of feedbacks (CAIQs) by two different information sources 'P' and 'Q' about QoS of cloud-based service provider 'A'. Table III presents a summary of the aggregation of assessments from two different information source with different weight.

TABLE II. Trust value measurement: Practical case

Input Opinions		**Resulting Opinions**
o_{A_P}	o_{A_Q}	$o_{A_P} \widehat{\oplus}_w o_{A_Q}$ $W_P = 1; W_Q = 2$
(0.3,0.833,0.5)	(0.9,0.5,0.5)	(0.4717,0.6996,0.5)

Although, our system reliably evaluates the trustworthiness of the cloud providers as well as information sources in the cloud marketplace there are some limitations that need to be mentioned. Our system can translate trust information from the CAIQs and measure the trust value from them. But our system is still unable to evaluate trust value from user comments. Moreover, the cloud providers' completed CAIQs are not classified according to the types of services.

VI. CONCLUSION

The cloud marketplace is rapidly increasing with new cloud providers entering the competitive market with huge investments and massive services and supports. The reason behind cloud computing's being such demanding issue are its high dynamic, scalable, flexible nature. But consumers often faces dilemma in choosing the proper cloud provider among the service providers based on their service-specific attributes. Because of being a competitive marketplace feedbacks about different cloud providers can be manipulated. Therefore, we propose an architecture of the Entrusted TM system for cloud marketplaces to measure the weight of the information sources along with the trustworthiness of the cloud providers. In order to support the consumers as well as cloud providers we proposed the Entrusted Trust Management (ETM) system that not only measures the trust value of the providers available in the cloud marketplace but also measures how trustworthy an information source is. At the same time it allows the cloud providers to represent their competencies and capabilities. In this paper, we identify and highlight the necessity of measuring the weight of the information sources and introduce a procedure to measure it. We believe that our proposed system will make the cloud marketplace more reliable for the consumers as well as more supportive for the cloud providers at the same time.

ACKNOWLEDGMENT

The authors would like to thank the anonymous reviewers for their feedbacks and suggestions to enhance the quality of this manuscript. In particular, the authors would like to acknowledge Sheikh Mahbub Habib, Mahtab Ahmed for comments and suggestions during the development of ETM system.

REFERENCES

[1] Fujitsu Research Institute. (2010). Personal data in the cloud: A global survey of consumer attitudes 2010. Updated Aug. 2010. Available from http://www.fujitsu.com/downloads/SOL/fai/reports/fujitsu_personal-data-in-the-cloud.pdf, accessed on 02 Sep. 2015.

[2] Fujitsu Research Institute. (2010). Personal data in the cloud: The importance of trust 2010. Updated Aug. 2010. Available from http://www.fujitsu.com/global/Images/FSL-0016_A4_TrustReport_online-final.pdf, accessed on 02 Sep. 2015.

[3] S. M. Habib, S. Ries, M. Mühlhäuser, P. Varikkattu, "Towards a Trust Management System for Cloud Computing Marketplaces: using CAIQ as a trust information source," Security and Communication Networks Journal, John Wiley & Sons, vol. 7, no. 11, pp. 2185-2200, Jan. 2013.

[4] F. Dickmann, M. Brodhun, J. Falkner, T. Knoch, and U. Sax. "Technology transfer of dynamic it outsourcing requires security measures in slas," Proc. *Economics of Grids, Clouds, Systems, and Services,* vol. 6296, pp. 1–15, 2010.

[5] A Jøsang, R Ismail and C Boyd. "A survey of trust and reputation systems for online service provision," Decision Support Systems, vol. 43, no. 2, pp. 618-644, Mar. 2007.

[6] CSA. (2011) Security, Assurance & Trust Registry (STAR). Updated 23 August 2011. Available from https://cloudsecurityalliance.org/research/initiatives/star-registry/ , accessed on 02 Sep. 2015.

[7] I.U. Haq, I. Brandic and E. Schikuta. "*Sla validation in layered cloud infrastructures*," Proc. Springer Lecture Notes in Computer Science, vol. 6296, pp. 153-164, 2010.

[8] CIO. Cloud Provider 3Tera Announces 'five Nines' SLA. Updated March 2009. Available from http://www.cio.com/article/2429967/infrastructure/cloud-provider-3tera-announces--five-nines--sla.html, accessed on 01 Sep. 2015.

[9] M. Blaze, J. Feigenbaum and A. D. Keromytis. "*Keynote: Trust management for public-key infrastructures,"* Proc. Lecture Notes in Computer Science, vol. 1550, pp. 59-63, 1998.

[10] Y. H. Chu, J. Feigenbaum, B. LaMacchia, P. Resnick and M. Strauss, "Referee: trust management for web applications," *Computer Networks and ISDN Systems,* vol. 2, no. 3, pp. 127-139, 1997.

[11] S . M. Habib, S. Ries, S. Hauke and M. Mühlhäuser. "Fusion of Opinions under Uncertainty and Conflict -- Application to Trust Assessment for Cloud Marketplaces," Proc. *Trust, Security and Privacy in Computing and Communications (TrustCom),* pp. 109-118, Jun. 2012.

[12] D. Gambetta**. "**Can we trust trust?,**"** Proc. *Trust: Making and Breaking Cooperative Relations*, pp. 213-237, 1988.

[13] S. Ries. "Extending bayesian trust models regarding context-dependence and user friendly representation," Proc. *SAC '09 Proceedings of the 2009 ACM symposium on Applied Computing, New York, NY, USA,* pp. 1294-1301, 2009.

[14] S Ries, S. M. Habib, M Mühlhäuser and V. Varadharajan. "Certainlogic: A logic for modeling trust and uncertainty," Technische Universität Darmstadt, Darmstadt, Germany, Technical Report TUD-CS-2011-0104, 2011.

[15] CSA. Security guidance for critical areas of focus in cloud computing v3.0. Updated 2011. Available from https://downloads.cloudsecurityalliance.org/initiatives/guidance/csaguide.v3.0.pdf , accessed on 30 Aug. 2015.

[16] CSA. Security, Assurance & Trust Registry (STAR) FAQ. Updated 2011. Available from https:// cloudsecurityalliance.org/star/faq, accessed on 30 Aug. 2015.

[17] S. Ries. "Trust in ubiquitous computing," Ph.D. dissertation, Dept. of Computer Science, Technische Universität Darmstadt, Darmstadt, Germany, 2009.

Toward Number Recognition System : A Non-stationary Signal Analyzing Approach through SVM Algorithm

Debarati Nath[1] and Mohiuddin Ahmad[1,2]
[1]Department of Electrical and Electronic Engineering,
[2]HEQEP Sub-Project, UGC, CP#3472, Dept. of Biomedical Engineering,
[1,2]Khulna University of Engineering & Technology (KUET), Khulna – 9203, Bangladesh
E-mail: debarati10kuet@yahoo.com, mohiuddin.ahmad@gmail.com

Abstract—**Non-stationary signal analysis based on visual stimulation has drawn extensive attention in BCI system to provide the promising services. The main task of this paper tries to evaluate specific pattern of each decimal number created in human brain using the specific features of EEG. For differentiating among the decimal numbers, salient features are extracted using time, frequency and time-frequency domain analysis and SVM classifiers are used to demonstrate the primitive features. It is observed that sigmoid kernel provides the highest accuracy than the other used classifiers and numbers are differentiated clearly by the best distinguishable features of PSD analysis.**

Keywords—Number recognition; BCI; SVM; Non-stationary signal; PSD.

I. INTRODUCTION

The human computer interaction (HCI) has become a vital research topic after the invention of the computer. The past two decades have seen an explosion of scientific interest in a completely different and novel approach of interacting with a computer via signals generated by the brain itself [1]. Brain computer interface (BCI) is a revolutionary communication channel that recognizes user's command only from his brainwaves and reacts according to his command. It creates a new dimension in the field of human computer interface and provides a new, common, non-muscular communication and control channel to the disabled persons with variety of impairments, ever those who are locked in [2, 3].

There are some available technologies to serve BCIs such as electro / magneto-encephalography (EEG / MEG), positron emission tomography (PET), functional magnetic resonance imaging (fMRI), and optical imaging [4]. Among all of them, the electroencephalogram (EEG) is an imperfect and distorted indicator of brain's electrical activity recorded directly from the scalp after being picked up by metal electrodes and conductive media. As the human brain is one of the most complex systems in the universe, it is a useful tool for analyzing the functional state of brain and diagnosing certain disorders [5].

Due to the difficulties in obtaining the high classification accuracy various classification algorithms have been provided to improve the EEG based BCI performances [6]. A multitude of linear and non-linear classification algorithms have been used to discriminate among the EEG signals of patients with varying degree of cognitive impairment [7].

Linear discrimination analysis (LDA) and quadratic discriminant analysis (QDA) have been used to classify cognitive impairment [8]. Although LDA has a very low computational requirement, it is not suitable for solving non-linear problems [9]. Artificial Neural Network that is based on the simulation the human cognitive process can make the classification task more suitable. Although ANN provides the ability to reproduce arbitrary non-linear functions of input, it requires a large number of training data and is also sensitive to over-fitting.

Support vector machine (SVM) uses linear and non-linear mapping applied for various purposes such as the EEG signals classification based on the neuronal activity of the brain, cancer identification, bioinformatics, seizure prediction, face recognition and speech disorder. SVM provides good performance in many applications, especially for solving problem with high dimension, nonlinearity and small dataset [10]. Polynomial kernel, radial basis function kernel and wavelet kernel function have been used for classification and the classification test performance of the LS-SVM classifier has been determined by the computation of sensitivity, specificity and accuracy [11]. The MKL-SVM algorithm has been explored for the classifications of mental tasks and working memory tasks with WPE and Granger causality features and 99.20% average accuracy for 2-class classification and above 75% for multiclass classification have been achieved [12]. In SVM, kernel function is a major element which maps samples in one feature space to another feature space. It is really a difficult task to find out the suitable kernel function.

An EEG based number recognition technique is proposed in which the efficiency of the extracted features is compared for differentiating among the decimal numbers. It is really a challenging work based on the idea of BCI system that helps paralyzed people for compensating their lost abilities, remembering their passwords and communicates with the outside world.

978-1-4673-9257-0/15/$31.00 ©2015 IEEE

II. MATERIALS AND METHODS

Non-invasive BCI technique is used for this research work. Fig. 1 is represented the main components of the proposed BCI

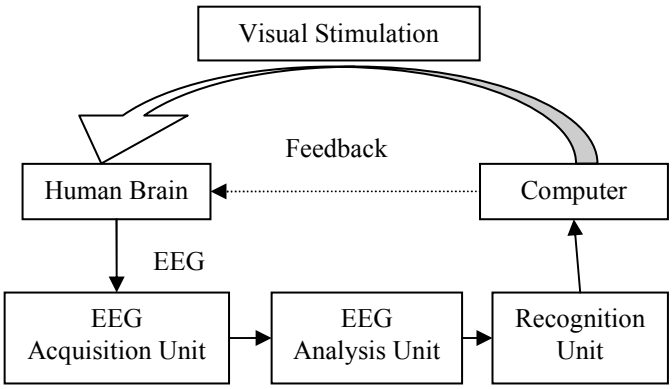

Figure 1. Block diagram of standard EEG-based BCI system.

system. Non-invasive BCI system is the communication pathway between the brain and the external device through hardware and / or software called interpreter which transforms brain wave to control signals using signal processing algorithm. It is flexible and easiest technique.

A. EEG Acquisition Unit

For the measurement of EEG data Biopac student lab hardware and software with cable and power, Biopac electrode lead set, and Biopac disposable vinyl electrodes. For EEG recoding, standard EEG measurement technique was used [13] as shown in Fig. 2. In this technique, the red electrode was placed on the occipital lobe, the white electrode was placed behind ear and the ground black lead was placed on ear lobe. The third electrode is the ground electrode. Subject selection and EEG signal recording techniques were described in [14]. Recorded EEG signal with its different bands for decimal number 1 was shown in Fig. 3.

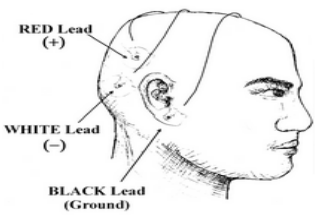

Figure 2. Standard electrode position for EEG measurement.

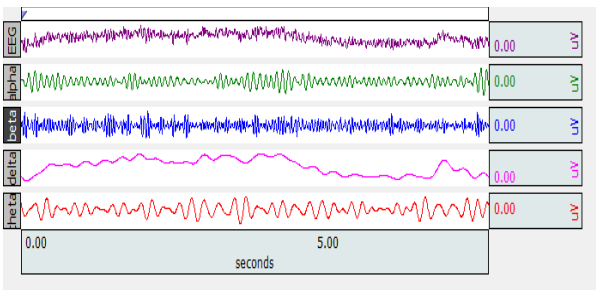

Figure 3. Raw EEG signal for decimal number 1.

B. EEG Analysis Unit

The raw EEG signal of each individual decimal number is analyzed for extracting the basic characteristics of them which is called features. Statistical analysis, frequency domain, and time-frequency domain analysis were used for best feature extraction. These features were used as the inputs of the next recognition unit for differentiating among the decimal numbers. Statistical methods are required to ensure that data are interpreted correctly and that apparent relationships are meaningful. This analysis provides ways to objectively report on how unusual an event is based on historical data. The inherent characteristics of the statistical measured on time domain signal is that they will vary in magnitude but without losing the essential element of homogeneity. Some specific features of the time domain EEG signals such as extrema, peak to peak value, mean, median, standard deviation, skew and kurtosis are extracted for recognizing the decimal numbers. The extreme point (maxima and minima) shows the maximum and minimum amplitude of the collected EEG data samples and the peak to peak value shows the difference between the maximum and minimum amplitude value of the selected area of the EEG data samples [15].

Mean computes the average value of the collected samples and this computation is achieved by Eq. (1).

$$Mean,\ \bar{m} = \frac{1}{N}\sum_{j=n_s}^{N}\left(x_{Sample\ Data}\right) \tag{1}$$

Here, $N=n_e-n_s$. n_e is the last point, and n_s is the starting point of the selected area. N is the total number of samples. j represents the values of points at horizontal axis and $x_{\text{Sample Data}}$ is the input value.

Median is a value at which the selected EEG data is divided into two regions with equal amplitude. Eq. (2) is used to extract the median value of EEG signal.

$$Median,\ m = \begin{cases} x_{\frac{N+1}{2}} & if\ N\ is\ odd \\ \frac{x_{N/2}+x_{(N/2)+1}}{2} & if\ N\ is\ even \end{cases} \tag{2}$$

Standard deviation measures the amount of variation or dispersion from the average of the selected EEG data and is defined by Eq. (3).

$$Stddev,\ s = \sqrt{\frac{1}{N-1}\sum_{j=n_s}^{N}\left(x_{Sample\ Data} - \bar{m}\right)} \tag{3}$$

Skewness is a measure of the asymmetry of a probability distribution of the selected data set. Skew normal distribution is a continuous probability distribution that generalizes the normal distribution to allow for non-zero skewness. Eq. (4) is used for extracting the skew for EEG signal.

$$\text{Sk} = \frac{\sum_{j=n_s}^{n_e}\left(x_{\text{Sample Data}}-\bar{m}\right)^3}{N} \Big/ \left(\sqrt{\frac{\sum_{j=n_s}^{n_e}\left(x_{\text{Sample Data}}-\bar{m}\right)^2}{N}}\right)^3 \tag{4}$$

Kurtosis is a measure of whether the EEG data are peaked or flat relative to a normal distribution. The formula of kurtosis is shown in Eq. (5).

$$Kurtosis = \frac{\frac{\sum_{j=n_s}^{n_e}\left(x_{Sample\ Data}-\overline{m}\right)^4}{N}}{\left(\sqrt{\frac{\sum_{j=n_s}^{n_e}(x_{Sample\ Data}-\overline{m})^2}{N}}\right)^2} \quad (5)$$

The time domain EEG signal is then converted to frequency domain using FFT for extracted the desired feature. Fast Fourier transform (FFT) is a frequency based analysis to compute the frequency component of the non-stationary signal. Features such as peak magnitude and frequency at peak magnitude were computed by using FFT which rapidly computes such transformations by factorizing the discrete Fourier transform (DFT) matrix into a product of sparse (mostly zero) factors. The DFT is generally defined by the formula in Eq. (6).

$$X_k = \sum_{j=n_s}^{n_e-1} x(j)e^{-i2\pi\frac{jk}{N}} \quad (6)$$

Power spectrum density (PSD) was used to extract features for finding out how the power of the time series data is distributed with frequency. The expression of PSD can be obtained directly as a function of frequency from the time series EEG data $x_{Sample\ Data}$ by using Eq. (7).

$$P(f) = \frac{1}{T_s}\left|T_s \sum_{q=0}^{N} x_{Sample\ Data}(q)e^{-i2\pi f q T_s}\right|^2 \quad (7)$$

Finally, discrete wavelet transform (DWT) was used because non-stationary signal contains high frequency components with short time duration and low frequency components with long time duration. It analyzes the signal at different frequency bands by decomposing of signal into a coarse approximation and detail information as shown in Fig. 4. The extracted wavelet coefficients provide compact representation that shows all the physical parameters of the EEG signal in different frequency bands. In order to reduce the increased dimensionality of the extracted features, some statistics such as maximum, minimum value, standard deviation, mean, median, skew and kurtosis over the set of the wavelet coefficients are applied.

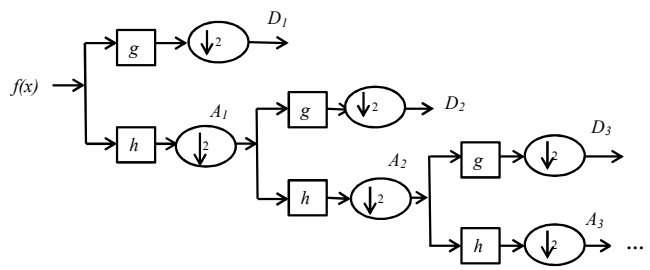

Figure 4. Sub-band decomposition of a signal by using DWT.

C. Recognition Unit

For the purpose of differentiating among the decimal numbers SVM technique is used in which the classifier operates in a higher dimensional space and attempts to label the given vectors using a dividing hyper plane [16]. The supervised learning method takes a set of training data and constructs a model that is able to label unknown test data. Given a training set of instance label pairs (x_i, y_i), $i=1, l$ where $x_i \in R^n$ and $y \in \{-1,1\}^l$ the support vector machines require the solution of the following optimization problem in Eq. (8).

$$\min_{w,b,\xi} \frac{1}{2} w^T w + C \sum_{i=1}^{l} \xi_i \quad (8)$$

$$\text{Subject to } y_i(w^T\phi(x_i) + b) \geq 1 - \xi_i,$$

$$\xi_i \geq 0.$$

Here training vectors x_i are mapped into a higher (maybe infinite) dimensional space by the function. SVM finds a linear separating hyper plane with the maximal margin in this higher dimensional space. $C>0$ is the penalty parameter of the error term. The kernel function is shown in Eq. (9).

$$K(x_i, y_j) \equiv \phi(x_i)^T\phi(x_j) \quad (9)$$

The following four kernel functions were used to find recognition rate.

- Linear : $K(x_i, x_j) = x_i^T x_j$.
- Polynomial : $K(x_i, x_j) = (\gamma x_i^T, x_j)^d, \gamma > 0$.
- RBF : $K(x_i, x_j) = \exp\left(-\gamma\|x_i - x_j\|^2\right), \gamma > 0$.
- Sigmoid : $K(x_i, x_j) = \tanh(\gamma x_i^T x_j + r)$.

Here γ, *r*, and d are kernel parameters.

For finding the higher recognition rate and best classifier for number recognition *C–SVC* and *υ– SVC* were also used. Through LIBSVM 3.12 best classifier is tried to find out and effective features for recognition is selected by the classifier. The process of number recognition by using SVM algorithm is shown in Fig. 5 by a simplified block diagram representation.

III. Features Extraction for Number Recognition

Various temporal and spatial approaches have been applied to extract features which can map the EEG data for getting higher recognition rate. From the features of beta rhythmic time domain EEG signal, it was observed that these values are almost same for same number for different peoples. The deviations in different numbers for a particular subject and different subjects are specified respectively in Fig. 6.

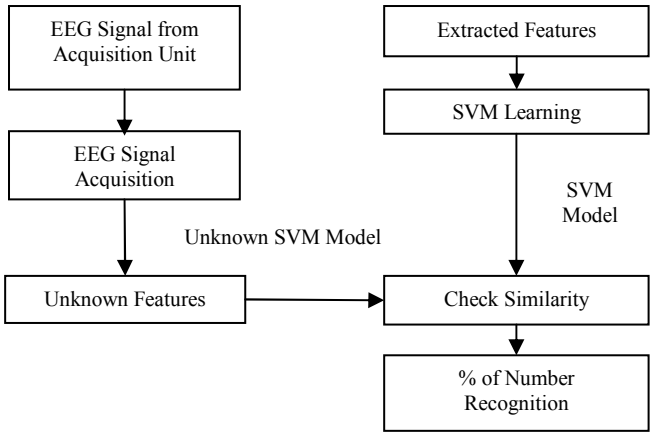

Figure 5. Block Diagram of % of Number Recognition Using Salient Features.

6. The skewness of EEG signals determines the peakedness in state of visual stimulation of different number. Again the kurtosis compares the range of the dispersion in the mental states for several subjects. It can be seen that kurtosis can differentiate the different number clearly than other features.

In case of EEG signal analysis the most distinguished information is hidden in frequency content of the signal as the frequency contents of the biomedical signals change rapidly with time. So, it can be said that frequency domain analysis provides better result than time domain analysis in case of EEG based number recognition. PSD analysis describes the

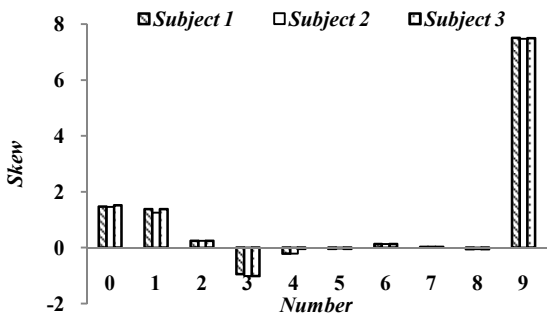

(a)

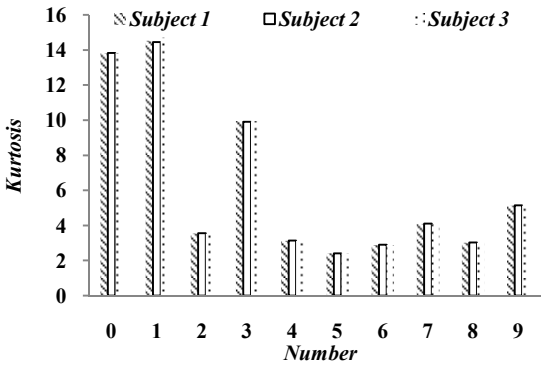

(b)

Figure 6. (a) Skew and (b) Kurtosis for 3 differet subjects.

density of power on the frequency domain and this power distribution changes according to the physiological and psychological states of the subject. Peaked power and frequency at peaked power for each number were extracted using PSD. The wavelet approach decomposes the EEG signal into its frequency components according to its range while maintaining the time resolution. Features were also extracted from DWT analysis in case of differentiating among the numbers. Fig. 7 represents the FFT and PSD for beta rhythmic EEG signal for number 0.

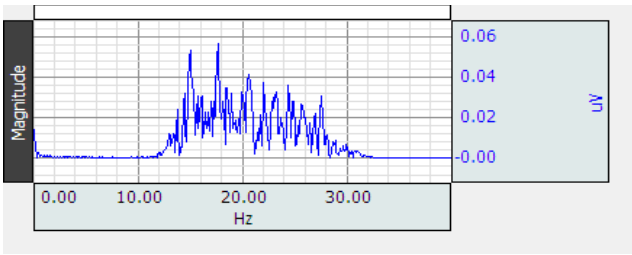

(a)

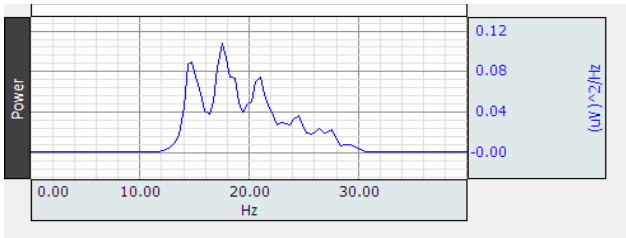

(b)

Figure 7. (a) FFT and (b) PSD of beta rhythm for number 0.

IV. Number Recognition Based on SVM

After feature extraction using time domain, frequency domain, and time-frequency domain from the beta rhythmic EEG signal, feature matrix is normalized in order to have features in a same range (-1 to 1 range has been used for number recognition). In applying SVM, the decimal numbers are classified into the defined classes. The learning and classification component consists of a training module and a classification module for different numbers. The training data of the defined features of all numbers are separated into defined classes manually. We label the train data of each action manually by an integer number. For example, Number 0=0, Number 1=1, Number 3=3, Number 4=4, Number 5=5, Number 6=6, Number 7=7, Number 8=8, and Number 9=9. The SVM classifier predicts the class label information for an arbitrary action. The SVM classifier has been trained by the training samples and then used for classifying the test data. In order to perform a more reliable classification process, three stages are implemented. Firstly, the EEG data are prepared in the specified format and scaling is performed if necessary for each subject. Secondly, the data are trained to create a model. Finally, the new input data are predicted/classified using the model. For trying to high degree of accuracy, kernel parameters are defined as that value which provides the best classification accuracy. For polynomial kernel, 3 (three) have been used for parameter "degree, d". On the other hand, 1 (one) is provided for parameter "gamma" and coef0 has been set as

0. Then, to get higher classification, the parameter *C* of *C-SVC* has been set as 1 and 0.5 has been used for the parameter *υ* of *υ-SVC*.

A. Comparison among Different Classifiers

A perfect comparison has been found among different classifiers in this section. The framework is proceeding by determining the best performance model in case of computation of classification accuracy. The classification accuracy is defined as number of correct decisions divided by the total number of cases [17].

$$Acc = \frac{TP+TN}{TP+TN+FP+FN} \times 100 \quad (10)$$

Here, TP and TN represent the total number of correctly detected true positive events and true negative events respectively. The FP and FN represent the total number of erroneously positive events and erroneously negative events, respectively. Table I shows the classification performance of the different SVM classifiers using salient features as input to the classifiers. From this table, it is seen that non-linear classification algorithm provides better result than linear classification in case of same types of attributes. Overall accuracies for features extracted from statistical, FFT, DWT, and PSD are greater in sigmoid kernel than other kernels individually and they are 76.92%, 81.82%, 93.75%, and 89.47% respectively. Although RBK provides higher accuracy than linear and polynomial kernels, it cannot provide perfect classification than sigmoid for differentiating among decimal numbers.

Two types of multiclass SVM are also considered for determining classification accuracy. It can be said that both multi-classifiers provide better recognition than linear and polynomial kernels and υ-SVC gives better accuracy than C-SVC. Overall accuracies for υ-SVC are 76%, 80%, 90.91%, and 87.5% respectively in case of features extracted from time, frequency, and time-frequency domain analysis. It is more clear from the Fig. 8 that sigmoid classifier is best than other all classifiers for EEG based number recognition because of higher accuracy. Sigmoid seems to be very efficient classifier because of leading us to get higher accuracy than the previous work of number recognition system [18] although overall accuracy of this classifier is very nearer to that of RBK.

TABLE I. OVERALL ACCURACY OF SVM CLASSIFIERS FOR CLASSIFICATION AMONG DECIMAL NUMBERS

Serial No.	Classifiers	Methods of Feature Extraction			
		Statistical	*FFT*	*PSD*	*DWT*
01.	***Linear Kernel***	70%	71.43%	84.62%	80%
02.	***Polynomial Kernel***	72.73%	75%	88.24%	83.33%
03.	***Multiclass (C - SVC)***	74%	78.57%	90%	86.67%
04.	***Multiclass (υ - SVC)***	76%	80%	90.91%	87.5%
05.	***RBK***	76.47%	80%	92.86%	88.89%
06.	***Sigmoid Kernel***	76.92%	81.82%	93.75%	89.47%

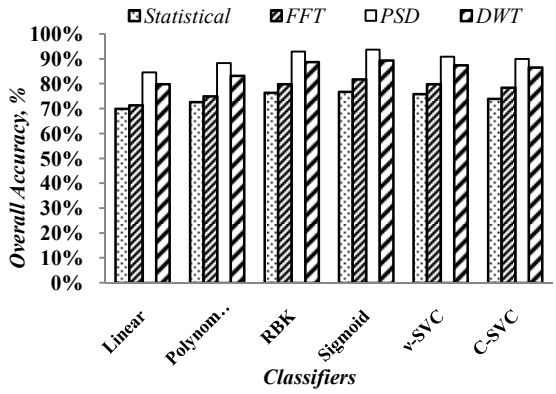

Figure 8. Overall accuracies of different features for all used classifiers.

TABLE II. COMPARISON BETWEEN PREVIOUS AND OUR WORKS BASED ON STATISTICAL ANALYSIS

Previous Work [18]	Proposed Work			
	Linear	***Polynomial***	***RBK***	***Sigmoid***
68.33%	70%	72.73%	76.47%	76.92%

The overall accuracy obtained from number recognition system based on beta rhythmic EEG in the previous work was 68.33% and this accuracy was obtained from the features of time domain analysis by LDA which is lower than our used classifiers (shown in Table II).

B. Comparison among Extracted Features

In case of EEG signal analysis the most distinguished information is hidden in frequency content of the signal as the frequency contents of the signal change rapidly with time. The frequency spectrum of the EEG signal shows the deviations in maximum amplitude and frequency in different decimal numbers for a particular subject. All classifiers provide higher accuracy in case of FFT than statistical analysis. For sigmoid classifier, the overall accuracy increases evidently from 76.92% to 81.82% when input features are transferred from statistical to FFT. The classification performance using wavelet features improves better than frequency domain features for classifying individual emotions and the obtained accuracy is 89.47%. But features based on PSD provides higher rate of classification than wavelet analysis. It is true for all used classifiers. The classification rate for all classifiers (linear, polynomial, sigmoid, RBK, C-SVC, and υ-SVC) are 80%, 83.33%, 93.75%, 92.86%, 90%, and 90.91% respectively in case of attributes of PSD. Finally, it can be said that the combination of PSD features have proved the better consideration for number recognition.

C. Individual Decimal Number Recognition

Although in case of electrical brainwave activity based on visual stimulation, the recorded by EEG is not typically expected to be the same for different subjects even under the same mental conditions, the numbers can be recognized by sigmoid kernel with salient features of PSD with higher degree of accuracy. This EEG number recognition system has shown promising result than the previous work. In case of statistical analysis, the recognition rates of all numbers were found in the range of 50% to 79% except number two which is 41.6% for

TABLE III. INDIVIDUAL RECOGNITION RATE FOR DECIMAL NUMBERS

Decimal Number	Accuracy of Previous Work (%)	Accuracy of Our Proposed Method (%)			
		Statistical	*FFT*	*DWT*	*PSD*
0	64.1	75	78.57	80	80.65
1	41.6	70.59	72.73	72.73	79.31
2	51.64	62.5	70	66.67	73.33
3	81.7	71.42	69.23	71.43	72.41
4	74.6	77.78	77.27	72.73	81.25
5	77.9	83.33	85.71	83.33	83.33
6	73.1	75	76.92	76.92	74.07
7	78.9	85.71	81.82	83.87	85.71
8	67.8	70	70	68.97	72.73
9	72	76.47	81.82	82.76	82.76

previous work. But in our proposed classifier the recognition rates varies from 70% to 85.71%. Individual accuracy is found for a specific number which provided that unique pattern for individual number is recovered by visual stimulation based EEG data analysis. Taking all time, frequency and time-frequency domain features for classification it is noticed that the performance has degraded than the individual ones. The recognition rate of individual number increases because of PSD analysis. The accuracy varies from 72.41% to 86.67% for individual number. Table III provides the individual recognition rate for number recognition using sigmoid kernel.

From this table, it is observed that the higher recognition rate is found for number 7 in case of statistical analysis and it is 85.71%. On the other hand, number 8 provides lower recognition rate and it is 62.5%. For FFT analysis, number 5 gives better recognition rate and number 3 provides lower classification rate. They are 85.71% and 69.23%. In case of DWT analysis, number 2 and 7 provide lower and higher accuracy respectively and they are 66.67% and 83.87%. In case of PSD, the individual recognition rate increases and lower value of recognition rate also increases than that of other method. The lower recognition rate in case of PSD is 72.41% and number 3 provides the accuracy.

V. CONCLUSION

BCI technology is an important building block which provides the promise of nature and intuitive human-computer interaction. This work described a framework based on the features of EEG signal in order to perform the differentiation among decimal number. In order to classify EEG signal the selection of feature extraction method and classifier becomes the major problem. For this purpose, this work evaluated the best feature extraction method for differentiating among the decimal numbers and also demonstrated the best classifier because of getting higher recognition rate. Actually EEG based decimal number recognition system tries to implement direct impacts to compensate the lost abilities of disorder person as well as their use in robotics. From this work, it is determined that frequency domain analysis provides higher recognition rate than time domain analysis and PSD analysis of beta rhythm is more suitable than FFT to produce unique patterns for number recognition with higher accuracy. It is also seen that sigmoid kernel provides higher recognition rate than the other used classifiers and it gives 93.75% accuracy for PSD analysis which is higher than the accuracy for DWT analysis. Finally, it can be said that attributes extracted from beta rhythmic EEG using PSD analysis can provide better unique pattern for a specific number and differentiate them clearly with high degree of recognition rate.

ACKNOWLEDGMENT

This work was supported by Higher Education Quality Enhancement Project (HEQEP), UGC, Bangladesh under Subproject "Postgraduate Research in BME", CP#3472, KUET.

REFERENCES

[1] R. C. Smith, "Electroencephalogram based brain computer interfaces," MEngSc thesis, University College Dublin, Dublin, Ireland, Feb. 2004.

[2] J. R. Wolpawet. al., "Brain-computer interface technology: A review of the first international meeting," *IEEE Trans. Rehab. Eng.*, vol. 8, pp. 164-173, 2000.

[3] S. J. Roberts, and W. D. Penny, "Real-time brain-computer interfacing: A preliminary study using Bayesian learning," *Med. Biol. Eng. Computing.*, vol. 38, pp. 56-61, 2000.

[4] K. An, J. Kim, W. Song, and I. Lee, "Development of an emergency call system using a brain computer interface (BCI),"in *Proc. IEEE Int. Conf. on Biomed. Rob. and Biomech.* Sep. 2010, pp. 918–923.

[5] S. Gurumurthy, V. S. Mahit, and R. Ghosh, "Analysis and simulation of brain signal data by EEG signal processing technique using Matlab," *Int. J. of Eng. And Tech. (IJET)*, vol. 5, no. 3, Jun.-Jul. 2013.

[6] R. Palaniaappan, "Brain computer interface design using band powers extracted during mental tasks," in *Proc. Of 2nd Int.Conf. on Neur. Eng.*, pp. 321-324, USA, Mar. 2005.

[7] C. Lehmann et. al., "Application and comparison of classification algorithms for recognition of Alzheimer's disease in electrical brain activity (EEG)," *J. Neurosci. Methods*, pp. 342-350, 2007.

[8] J. Dauwelset. al., "EEG synchrony analysis for early diagnosis of Alzheimer's disease: a study with several synchrony measures and EEG data sets," in *Proc. of the 31st Ann. Int. Conf. of the IEEE EMBS*, pp. 2224-2227, USA, Sep. 2009.

[9] E. Ianezet. al., "LDA-based classifiers for a mental taks-based brain-computer interference," in *Proc. Pf IEEE Int. Conf. on System, Man and Cybernetics*, South Korea, pp. 546-551, Oct. 2012.

[10] M. J. Abdin, S. M. Hosseini, and M. Rezghi, "A novel weighted support vector machine based on particle swarm optimization for gene selection and tumor classification," *Comput. Math. Method*, Article ID 320698, 2012.

[11] V. Bajaj, and R. B. Pachori, "Classification seizure and nonseizure EEG signals using empirical mode decomposition," *IEEE Trans. Inf. Technol. Biomed.*, vol. 16, no. 6, pp. 1135-1141, Nov. 2012.

[12] Xiaoou Li et. al., "Classification of EEG signals using a Multiple Kernel Learning Support Vector Machine," *Sensors*, Jul. 2014.

[13] K. Bynum, *Experimental laboratory physiology BIOPAC lab exercises*, University of North Carolina-Chapel Hill, USA, 2004.

[14] D. Nath, Md. B. Uddin, M. M. Rana, P. C. Biswas, S. Wahed, and M. Ahmad, "Number recognition using salient features of beta rhythmic EEG signal," *2nd Int. Con. On Electrical Engineering and Information & Communication Technology*(*iCEEiCT*), 21-23 May, 2015.

[15] M. Islam, T. Ahmed, S. S. Mostofa, M. S. U. Yusuf, M. Ahmad, "Human emotion recognition using frequency and statistical measures of EEG signal," *Int. Conf. on Informatics, Electronics & Vision*, May 2013, IEEE Xplore, doi: 10.1109/ICIEV. 2013.6572658.

[16] C. W. Hsu, C. C. Chang, and C. J. Lin, *A practical guide to support vector classification*, 15 April, 2010.

[17] L. Guo, D. Rivero, J. A. Seoane, and A. Pazos, "Classification of EEG signals relative wavelet energy and artificial neural networks," *GEC*, Shanghai, China, 12-14 June, 2009.

[18] S. Raoet. al., "Number recognition system using Electroencephalogram (EEG) signals," *Advanced in Computational Research*, vol. 4, no. 1, pp. 66-68, 2012.

Soft Error Tolerance Using Horizontal-Vertical-Diagonal-Blocks

Md. Shamimur Rahman
Sakib Ahammed
Dept. of Computer Science and Engineering
Khulna University of Engineering & Technology
Bangladesh
e-mail: shamimur052@gmail.com, sakib.kuet10@gmail.com

Muhammad sheikh Sadi
Dept. of Computer Science and Engineering
Khulna University of Engineering & Technology
Bangladesh
e-mail: sheikhsadi@gmail.com

Abstract—**Soft error tolerance is a matter of concern for system reliability nowadays. The likelihood of soft errors increase with system complexity, reduction in operational voltages, exponential growth in transistors per chip, increases in clock frequencies and device shrinking. As the memory bit-cell area is condensed, single event upset that would have formerly despoiled only a single bit-cell are now proficient of upsetting multiple contiguous memory bit-cells per particle strike. While these error types are beyond the error handling capabilities of the frequently used error correction codes (ECCs) for single bit, the overhead associated with moving to more sophisticated codes for multi-bit errors is considered to be too costly. To address this issue, this paper presents a new approach to detect and correct multi-bit soft error by using Horizontal-Vertical-Diagonal Blocks (HVDB) parity bits with a higher reliability.**

Keywords—Soft Error Tolerance, Horizontal Parity, Vertical Parity, Left Diagonal Parity, Right Diagonal Parity.

I. INTRODUCTION

The advent of new technologies for implementation, along with non-functional constraints (dependability, timeliness, power, cost and time-to-market), has seen the design of embedded systems become more challenging and complex [1]. The complexity of such systems is growing at a high pace through the integration of mixed-criticality applications (both safety-critical and non-safety-critical), through the high interaction of distributed application. Embedded systems engineering has evolved from designing single CPU systems (System-on-a-Chip (SoC) concept) to concurrent computing structures (Multi-Processor-System-on-a-Chip (MPSoC) and Network-on-a-Chip (NoC) concepts) often in the form of a distributed network [2], [3]. When designing high availability systems that are used in electronic-hostile environment, errors are a matter of great concern. Space programs, patient condition monitoring system in ICU where a system cannot afford a malfunction, are vulnerable to soft errors [4]. Nuclear power monitoring systems, where a single failure may cause severe destruction and real-time systems, where a missed deadline can constitute an erroneous action and a possible system failure, are a few other examples where soft error is a critical issue [5], [6], [7].

The impact of soft errors is such that action is needed to increase a system's tolerance or to lower the risk of soft errors in the system. Prior research into soft errors has focused primarily on circuit level solutions, logic level solutions, spatial redundancy and temporal redundancy [8]. However, in all cases, the system is vulnerable to soft error problems in key areas. Further, in software-based approaches, the complex use of threads presents a difficult programming model. Hardware and software duplication suffers not only from overheads due to synchronizing duplicate threads, but also from inherent performance overheads due to additional hardware. Hardware-based protection techniques based on duplication often suffers from high area, time and power overheads [9], [10], [11].

Various types of error detection and correction codes are used in computers. For example, for satellite applications, Hamming code [12] and different types of parity codes are used to protect memory devices. Complex codes are not applied due to time constraints and limited resources on board [13]. There are other methods for error detection and correction such as parity codes, rectangular parity codes, BCH codes [14], N-Dimensional parity code [15], and Golay codes [16] whose error detection and correction rate varies from method to method. In our previous paper, we used HVDD [22] i.e. Double Diagonal parity along with Horizontal, Vertical, and Diagonal parity. However, using that method we could correct up to 3 bit errors only. For this reason, there is a great need of further research to increase the error detection and correction rate with maximum reliability.

In this paper, a high-level error detection and correction method to protect against soft errors is proposed. This method is based on parities for each row, column and diagonal parity in forward and backward slash directions. The HVDB method provides high error detection and correction rate that can correct up to 12 bit upsets with high reliability in a data block.

The rest of this paper is organized as follows. We provide some related work in Section II. The proposed methodology is presented in Section III. We give an example in Section IV. In Section V, Experimental analysis is shown. Conclusions are drawn in Section VI.

II. RELATED WORK

The Several approaches are made to increase error detection and correction rate.

Pflanz et al. [17] proposed a method which can detect and correct 5 bit error using 3 dimensional parity codes. This

method cannot detect and correct all combination of 5 bit error in the data bits and it ignored the possibility of error occurrence in parity bits.

Sharma and Vijayakumar [18] proposed a method which utilizes horizontal, vertical and diagonal parity to detect and correct soft error in semiconductor memories. Here, authors described that their proposed system can detect and correct up to 5 bit errors. But Kishani et al. [13] proved that maximum 3 bit of any combination in any position can be detected and corrected by this method.

Anne et al. [19] introduces a method where data bits are arranged in different layers one over another to obtain a cube. The outer surfaces are made of the parity bits. This method forms a three dimensional structure of bits. It can detect 7 bit errors and correct 2 bit error. Anne et al. [15] described some undetectable error pattern such as 6 bit hexagonal shaped error pattern.

Aflakian et al. [20] proposed two methods for error detection and correction. In the first schema authors used horizontal, vertical and diagonal parity in both directions. This scheme can detect 7 bit errors and correct up to 4 bit errors. In the second scheme, cube of data bits are formed. Though this scheme can detect up to 15 bit errors and correct 4 bit errors, the complexity of this method is higher than existing methods.

Kishani et al. [13] corrected 3 bit errors in any combination in any position where 60 redundant bits are required for 64 data bits and can detect 100% multiple bit errors. The authors used diagonal parity in both directions along with row and column parity to detect and correct error. For this reason, their bit overhead is 73.12% which is very high. The method proposed by Kishani et al. [13] is shown in Fig. 1.

However, our correction method uses four directions same as Kishani et al. [13]. But it can detect 100% errors in any combination and correct up to twelve bit errors for almost all combinations. The correction rate of our approach is much higher than that of Kishani et al. [13].

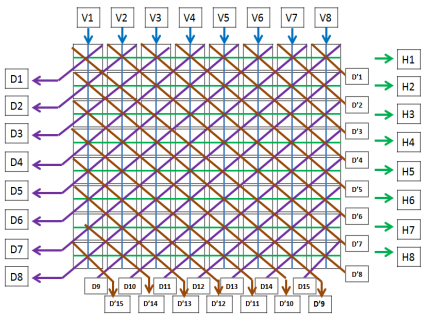

Fig. 1. The structure of the proposed method by Kishani et al. [13]

So the main differences between the proposed method and that of Kishani et al. [13] are:

1) The proposed method is relatively less complex than that of Kishani et al. [13] since it uses 100 bits for parity bits generations whereas Kishani et al. [13] uses 64bits for parity bits generations.

2) The proposed method detect and correct up to 12 bits error than that of Kishani et al. [13] which detect and correct up to 3 bits error.

III. THE PROPOSED METHODOLOGY TO DETECT AND CORRECT ERROR

The proposed method detects and corrects the soft error by using the check bits that are smeared on the Blocking (B) along with horizontal (H), vertical (V) parity and Diagonal (D) in forward and backward direction.

A. Detection Algorithm

We take a datablock of 100 bits and in a format of 10*10 array and divide them four parts of 5*5 array for calculating parity bits. In order to detect bit upsets in the codeword, all parity bits in the receiver side should be calculated again. All the menioned parity bits can be calculated independently in parallel i.e., while computing the horizontal parity bits, vertical parity bits can be computed simultaneously. This property is very operational in real-time and relatively high speed applications. After detecting the misapprehend between the received parity bits and the calculated ones, the detection algorithm will be stopped. Along with horizontal, vertical and diagonal dimensions both left and right, another four parity bits(C1, C2, C3 & C4) are calculated which is shown in the following Fig. 2 and Fig. 3.

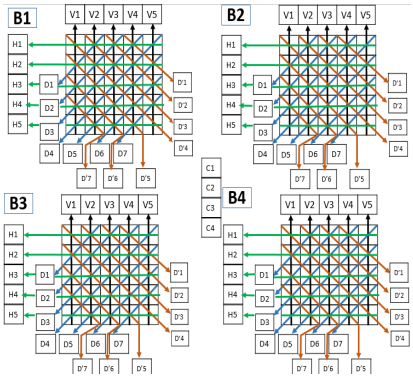

Fig. 2. The structure of the proposed method (after dividing 10*10 data block).

B. Correction Algorithm

Any difference in parity bits in horizontal, vertical and diagonal and C1, C2, C3 & C4 directions will set the corresponding syndrome bit to one. Syndrome bit is a special kind of bit which is determined by comparing sent parity and received parity. We need five arrays which clutch horizontal, vertical, left diagonal, right diagonal and C1, C2, C3 & C4 parity bits and syndrome bits respectively. Among the arrays, two are chosen and all ordered pairs of them are produced. Through every ordered pair, there may be found maximum one candidate bits. It is also mentioned that no candidate bit may be determined from some case of the ordered pair. These status are shown in Fig. 4. In the case of Fig. 4(b), two parity bits are erroneous. So, the horizontal and diagonal bits are not intersected and there is no candidate bit.

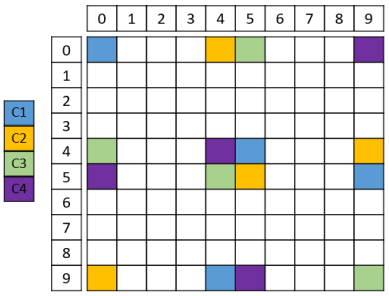

Fig. 3. Calculation of C1, C2, C3 & C4.

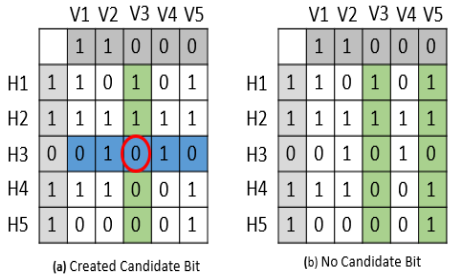

Fig. 4. The created candidate bit and no candidate bit of the intersection

According to Kishani et al. [13], all of the factual bit upsets are included in candidate bits and if a candidate bit is alone in one row of horizontal or column of vertical or diagonal dimension or C1, C2, C3 & C4 (i.e. there is not any other candidate bit in the same row of horizontal or column of vertical or diagonal dimension or C1, C2, C3 & C4) and if there is a syndrome bit which is set to one in a row or column or diagonal, the candidate bit is faulty and must be corrected. There is always a candidate bit that can be selected to be eliminated [13].

C. *HVDB Implementation*

The proposed implementation of HVDB coding arrangement is shown in Fig. 2. The figure shows 200 bit codeword consists of 100 data bits and 100 check bits. Note that, the overhead of a codeword depends on the number of additional bits compared to the whole memory block size. The memory segregated into appropriate number of slice and the codeword is calculated for the slice.

IV. AN EXAMPLE OF ERROR DETECTION AND CORRECTION

In this section, we consider 10 errors occurrence in a codeword and show how the proposed methodology corrects it. The code word architecture with errors (the red (dark) squares) is shown in Fig. 6. The detection and correction methods of HVDB are shown as follows.

Now the 10*10 bits pattern is divided by four 5*5 bits blocks as shown in Fig. 7. So, the next operation are same for all 5*5 blocks.

A. *Mark Candidate Bits*

Each parity bit has a corresponding line of codeword bits that generate it. Lines of each mistaken parity bit are considered. If there is an intersection between two lines then it is a candidate bit. Candidate bit represents the mismatched parity positions. After finding candidate bits, we need to store the address of each bit in an array. The candidate bits are marked in Fig. 9.

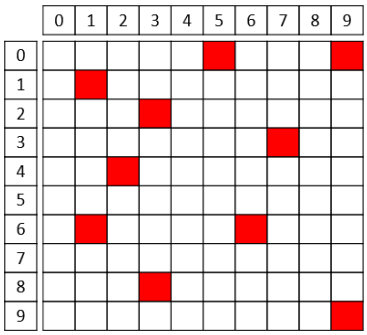

Fig. 6. Erroneous bits in 100 bits datablock.

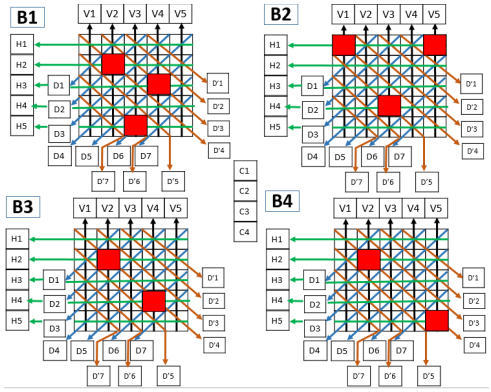

Fig. 7. Divide 100 bits datablock into four blocks with errorneous bits.

B. *Refine Candidate Bits To Find Error*

All the candidate bits are not erroneous but all erroneous bits are candidate bits. To refine candidate bits, we use the condition: in any direction (i.e. row or column or diagonal or C1, C2, C3 & C4), if there is any candidate bit found already but the corresponding syndrome bit is not set then that candidate bit is eliminated. If there is a syndrome bit which is set to one in a row or column or diagonal or C1, C2, C3 & C4, the candidate bit is erroneous and must be corrected.

For example from Fig. 9, in block-1(B1) candidate 1, 6, 7, 15 & 17 which are the only candidate bits in D1, D'1, V1, D'7 & D7 and the corresponding syndrome bits aren't set. So, these candidate bits are not erroneous and must be removed. Similarly in block-2(B2) candidate 3, 4, 5, 6, 7, 9, 10, 11 & 12 bits are eliminate and in block-3(B3) candidate 1, 2, 3 & 4 are the only candidate bits of D1, D'2, D'6 & D6. The syndrome bits for D'2 & D'6 are not set that's why candidate 2 & 3 are not erroneous and must be removed. But the syndrome bits for D2 & D6 are set. So, candidate 1 & 4 are erroneous and must be corrected. In block-4(B4), candidate 1, 2, 3 & 4 are only

candidate bits in D2, D'1, and V1 & D' 7. The syndrome bit for D2 is set i.e. candidate 1 is erroneous and must be corrected. Other candidate bits are eliminated. After this step the architecture is shown in Fig. 10.

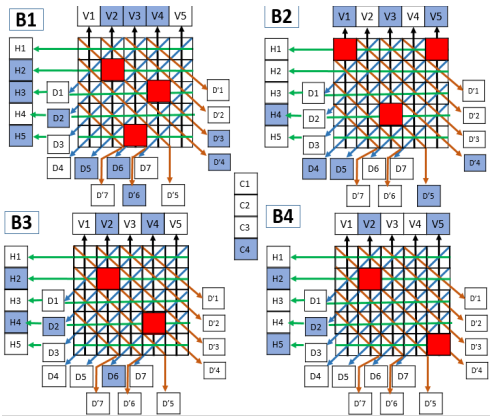

Fig. 8. Code word with parity codes.

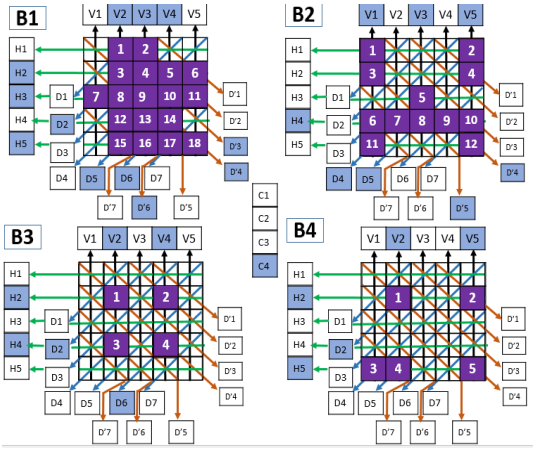

Fig. 9.Candidate bits.

For example from Fig. 9, in block-1(B1) candidate 1, 6, 7, 15 & 17 which are the only candidate bits in D1, D'1, V1, D'7 & D7 and the corresponding syndrome bits aren't set. So, these candidate bits are not erroneous and must be removed. Similarly in block-2(B2) candidate 3, 4, 5, 6, 7, 9, 10, 11 & 12 bits are eliminate and in block-3(B3) candidate 1, 2, 3 & 4 are the only candidate bits of D1, D'2, D'6 & D6. The syndrome bits for D'2 & D'6 are not set that's why candidate 2 & 3 are not erroneous and must be removed. But the syndrome bits for D2 & D6 are set. So, candidate 1 & 4 are erroneous and must be corrected. In block-4(B4), candidate 1, 2, 3 & 4 are only candidate bits in D2, D'1, and V1 & D' 7. The syndrome bit for D2 is set i.e. candidate 1 is erroneous and must be corrected. Other candidate bits are eliminated. After this step the architecture is shown in Fig. 10.

Consider candidate 2 in block-1(B1) from Fig.10 which is the only candidate bit in H1 direction but the corresponding syndrome bit is not set. So candidate 2 is removed. In block-2(B2) candidate 1 is the only bit in V1 & D'4 direction and corresponding syndrome bits are set. So candidate 1 is erroneous and must be corrected. Similarly candidate 2 and 8 are only bit in V5, D4 and V3, H4, D5, D'5 and corresponding syndrome bits are set. So these candidates are erroneous and should be corrected. In block-3(B3) all the candidate bits are evaluated. In block-4(B4) candidate 5 is only bit of V5 & H5 direction and the syndrome bits of these direction are set. So, this bit is erroneous and must be corrected. After this step the architecture is shown in Fig. 11.

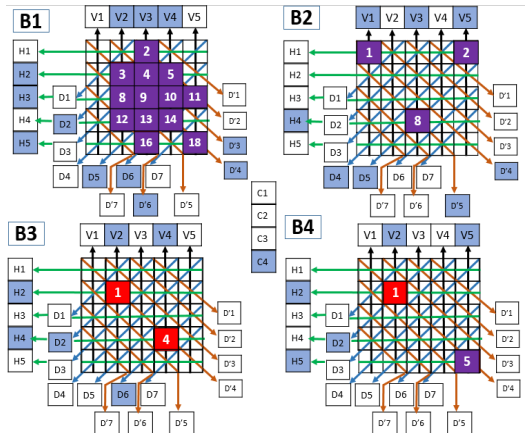

Fig. 10. Refining candidate bits: First Step.

Consider candidate 2 in block-1(B1) from Fig.10 which is the only candidate bit in H1 direction but the corresponding syndrome bit is not set. So candidate 2 is removed. In block-2(B2) candidate 1 is the only bit in V1 & D'4 direction and corresponding syndrome bits are set. So candidate 1 is erroneous and must be corrected. Similarly candidate 2 and 8 are only bit in V5, D4 and V3, H4, D5, D'5 and corresponding syndrome bits are set. So these candidates are erroneous and should be corrected. In block-3(B3) all the candidate bits are evaluated. In block-4(B4) candidate 5 is only bit of V5 & H5 direction and the syndrome bits of these direction are set. So, this bit is erroneous and must be corrected. After this step the architecture is shown in Fig. 11.

In third step, candidate 3 in block-1(B1)(Fig.11) is the only bit in D2 direction and corresponding bit is set that's why this candidate 3 is erroneous and should be corrected. Now consider candidate 18 which is the only candidate bit is C4 direction and corresponding syndrome bit is set. But there is another erroneous bit already detected in C4 direction. That's why candidate 18 is not erroneous and removed. There are no candidate bits of other block. So, these blocks are now out of consideration. After this step the architecture shown in Fig.12.

Again consider from Fig.12 in block-1(B1) candidate 11 and 16 are the only candidate bits in V5 and H5 direction. The corresponding syndrome bit of V5 is not set but H5 is set. For that candidate 11 is not erroneous but candidate 16 is erroneous bit and must be corrected. After fourth step the architecture is shown in Fig.13.

Consider candidate 5, 12, 14 in block-1(B1) from Fig.13 which are the only candidate in D'2, D'6 and D6 direction.

The syndrome bit of D'2 direction is not set that's why candidate 5 is eliminated. But the syndrome bits of D'6 and D6 direction is set and there are already an error occurred of that direction. For that, candidate 12 and 14 are not erroneous and should be removed. After this step the architecture is shown in Fig. 14.

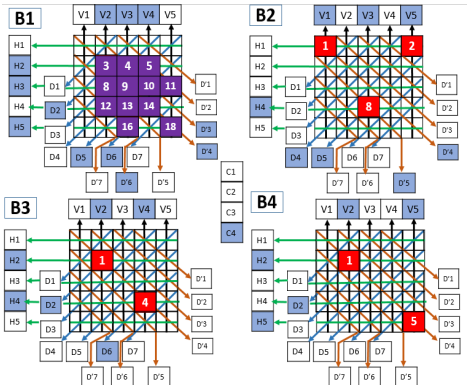

Fig. 11. Refining candidate bits: Second Step.

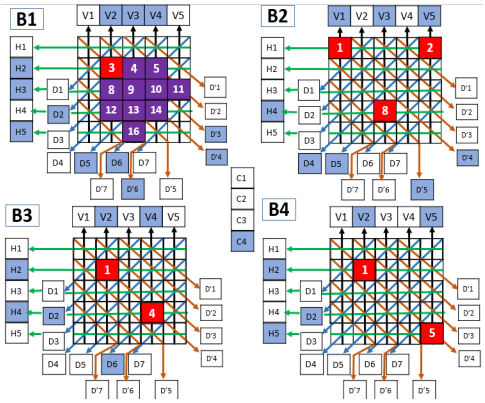

Fig. 12. Refining candidate bits: Third Step.

Now the final step, consider candidate 4, 8, 9, 10, 13 in block-1(B) from Fig.14 which are only candidate in H2, V2, D4, V4 and H4 direction. The syndrome bits of D4 and H4 are not set. So, candidate 9 and 13 are eliminated. The corresponding syndrome bits of H2, V2 and V4 are set. Candidate 4 and 8 are eliminated because in H2 and V2 direction there is already an error occurred and candidate 10 is erroneous and must be corrected. After that all candidate bits are evaluated and find the erroneous bits. The final step architecture is shown in Fig.15.

V. EXPERIMENTAL ANALYSIS

The proposed HVDB can detect all combinations of errors and correct up to 12 bit errors. Table 1 compares the HVDB method with existing dominant methods. This comparison is based on detection and correction rate.

As shown in Table 1, HVDB performs better than Golay[14], BCH[16], and HVD[13] with respect to correction rate. The first column of Table. 1 shows several dominant methods including the proposed one, second and third columns show the dataword sizes and corresponding parity bits. The fourth column presents the codeword sizes which are the summation of datawords and parity bits.

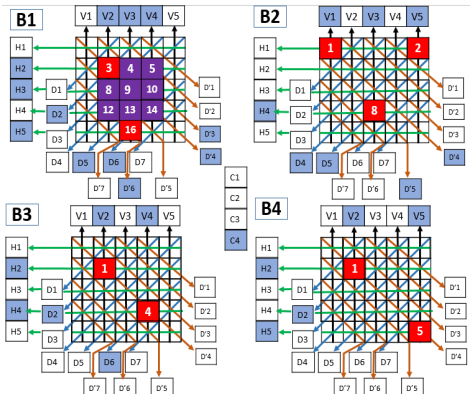

Fig. 13. Refining candidate bits: Fourth Step.

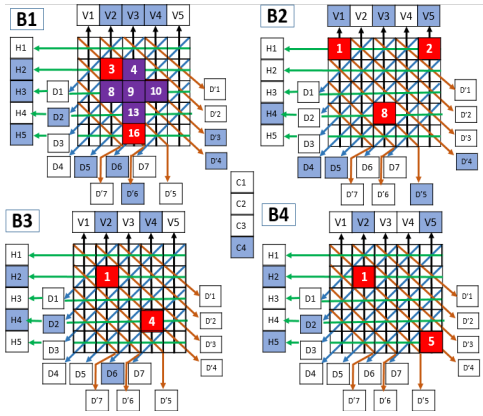

Fig. 14. Refining candidate bits: Fifth Step.

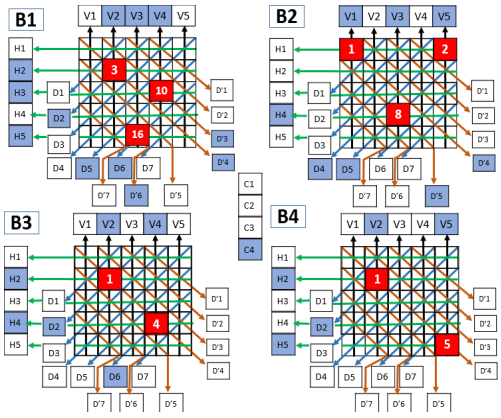

Fig. 15. Refining candidate bits: Final Step.

The fifth column shows the number of bit corrected by each method. In the first column, 'Golay(23,12,7)' represents that in the method proposed by Golay[14], they used the examples which have the codeword of size 23 bits, parity bits of size 12 bits and hamming distance of 7 and can correct only 3 bits error. BCH (31, 16, 7) represents same meaning as Golay(23,12,7). HVD (64) represent the dataword sizes of 64

bits. In HVD [13], there are 60 parity bits for 64 bits data block and correct only 3 bits error pattern whereas the proposed method working with 100 bits and correct up to 12 bits error pattern. So, the correction rate is higher than HVD [13]. HVDD (64) represents same meaning as HVD (64). The fifth and sixth column show the bit overhead and code rate of the proposed method using the following rules

$$\text{Bit Overhead} = \frac{\text{Number of Parity Bits}}{\text{Number of Data Bits}} = \frac{100}{100} = 100\% \quad (1)$$

$$\text{Code Rate} = \frac{\text{Number of Data Bits}}{\text{Number of Codeword Bits}} = \frac{100}{200} = 50\% \quad (2)$$

TABLE1. Comparison of mult bit error correcting codes

Error Correcting Method	# of Data Bits	# of parity bits	#of code word bits	# of bits corrected	Bit Overhead (%)	Code rate (%)
Golay(23,12,7)	11	12	23	3	91.67	52.17
BCH(31,16,7)	15	16	31	3	93.75	51.61
HVD(64)	64	60	124	3	78.12	56.14
HVDD(64)	64	27	91	3	42.19	70.33
HVDB(100)	100	100	200	12	100	50

From the experimental analysis it can be observed that the proposed method can detect and correct up to twelve bits errors in any combinations. To detect candidate bits, we take cross- section of two directions among the five. This method can't detect any intersection where four bits errors are in close rectangle pattern. We solved this problem in this particular situation that may rarely happen by using our previous method as shown in Sadi et al. [21].

VI. CONCLUSION

This paper proposes a high-level error detection and correction method to protect against soft errors. This method is based on parities for each row, column, diagonal (in forward and backward) and C1, C2, C3 and C4 directions. The HVDB provides error detection capabilities for all possible errors and can correct up to 12 bit errors in a data word. Though it faces problem to detect a particular error pattern and it has higher bit overhead, it has a significant contribution in increasing information correction rate than existing dominant methods. Reducing the information overhead can be captured as an extension of the current research.

REFERENCES

[1] Manoochehri,Annavaram, Dubois, "Extremely Low Cost Error Protection with Correctable Parity Protected Cache,"Computers, IEEE Transactions on (Volume:63, Issue: 10), pp. 2431-2444, September 2014.

[2] Sanchez-Macian,Reviriego, Maestro, "Hamming SEC-DAED and Extended Hamming SEC-DED-TAED CodesThroughSelective Shortening and Bit Placement,"Device and Materials Reliability, IEEE Transactions on (Volume:14, Issue: 1), pp. 574-576, March 2014

[3] Reviriego, Flanagan, Pontarelli, Maestro, "An Efficient Technique to Protect Serial Shift Registers Against Soft Errors,"Circuits and Systems ll: Express Briefs. IEEE Transactions on(Volume:60, Issue: 8), pp. 512-516, August 2013.

[4] Neale, Sachdev, "A New SEC-DED Error Correction Code Subclass for Adjacent MBU Tolerance in Embedded Memory,"Device and Materials Reliability, IEEE Transactions on (Volume:13, Issue: 1),pp. 223 – 230, March 2013

[5] Muhammad Sheikh Sadi, MizanurRahman Khan, NazimUddin, and Jan Jürjens, "An Efficient Approach towards Mitigating Soft Errors Risks," Signal& Image Processing: An International Journal (SIPIJ),vol. 2, No. 3, September 2011.

[6] Ne'amHashemIbraheem "Error-Detecting and Error-Correcting Using Hamming and Cyclic Codes," IEEE Transactions on Information Theory, vol. 51, no. 9, pp. 3347–3353, September 2005.

[7] Ferreyra PA, Marques CA, Ferreyra RT, Gaspar JP,"Failure map functions and accelerated meantime to failure tests: new approaches for improving the reliability estimation in systems exposed to single event upsets," IEEE Trans NuclSci 52(1), pp. 494–500

[8] ArgyridesC, Zarandi HR, Pradhan DK "Multiple upsets tolerance in SRAM memory," International symposium on circuits and system, New Orleans, LA, May 2007

[9] A. A. Jerraya, "Long term trends for embedded system design," Digital System Design,Euromicro Symposium on, 2004, pp. 20-26

[10] Hyun Yoon D, Erez M (2009) "Memory mapped ECC: low-cost error protection for last level caches," ACM SIGARCHComputArchit News 37(3):116–127

[11] M. S. Sadi, D. G. Myers, C. O. Sanchez, "A Design Approach for Soft Error Protection in Real-Time Embedded Systems," 19th Australian Conference on Software Engineering, ASWEC 2008, pp. 639-643

[12] Hentschke R, Marques R, Lima F, Carro L, Susin A, Reis R, "Analyzing area and performancepenalty of protecting different digital modules with hamming code and triple modular redundancy," International symposium on integrated circuits and systems design,pp. 95–100

[13] Mostafa Kishani, Hamid R. Zarandi, HosseinPedram, AlirezaTajary, Mohsen Raji, BehnamGhavami "HVD: horizontal-vertical-diagonal error detecting and correcting code to protect against with soft errors" Des Autom Embed Syst (2011) 15:289–310DOI 10.1007/s10617-011-9078-2

[14] Muhammad Imran, Zaid Al-Ars, Georgi N. Gaydadjiev, "Improving Soft Error Correction Capability of 4-D Parity Codes," 14th IEEE European Test Symposium, May 2009

[15] Rubinoff M "N-dimensional codes for detecting and correcting multiple errors,"ComunACM 545–551

[16] http://mathworld.wolfram.com/GolayCode.html

[17] M. Pflanz et al.,"On-Line Techniques for Error Detection and Correction in Processor Registers with Cross-Parity Check," Journal of Electronic Testing, October 2003, Volume 19, Issue 5, pp. 501-510

[18] Shalini Sharma, Vijayakumar P. "An HVD Based Error Detection and Correction of Soft Errors in Semiconductor Memories Used for Space Applications," International Conference on Devices, Circuits and Systems (ICDCS), 2012.pp. 563 - 567

[19] NaveenBabu Anne, UtthamanThirunavukkarasu, Dr. ShahramLatifi "Three and Four-dimensional Parity-check Codes for Correction and Detection of Multiple Errors," Proceedings of the International Conference on Information Technology: Coding and Computing (ITCC'04), pp. 267-282, 2004.

[20] DanialAflakian, Dr.TamannaSiddiqui, Najeeb Ahmad Khan, DavoudAflakian "Error Detection and Correction over Two-Dimensional and Two-Diagonal Model and Five-Dimensional Model," (IJACSA) International Journal of Advanced Computer Science and Applications, Vol. 2, No. 7, 2011

[21] M.S. Sadi, M.S. Rahman, K.M. ImrulKayesSikdar, "Error detection & correction using horizontal-vertical-diagonal-shift method," Electrical Engineering and Information & Communication Technology (ICEEICT), 2014 International Conference on, pp. 1-7 , April 2014

[22] Md. Shamimur Rahman, Muhammad Sheikh Sadi, Sakib Ahammed, and Jan Jurjens, "Soft Error Tolerance using Horizontal-Vertical-Double-Bit Diagonal Parity Method," International Conference on Electrical Engineering and Information Communication Technology (ICEEICT 2015)

Towards Tolerating Soft Errors in Memory Applications

Muhammad Sheikh Sadi, Musaddique Billah Talha, Swadin Saha, Golam Mezbah Uddin, Kazi Md. Bodrul Kabir
Department of Computer Science and Engineering
Khulna University of Engineering & Technology (KUET)
Khulna 9203, Bangladesh
sheikhsadi@gmail.com, mbtalha3110@gmail.com, rahul4kuet@hotmail.com, mezbah.isti@yahoo.com, kazi.sazid@gmail.com

Abstract— **These days' memory elements in digital systems have become more prone to soft errors or transient errors due to integration in circuits, smaller size of transistors and capacitors, combining with cosmic ray effects and many more reasons. Soft errors in memory elements have been a greater concern than soft errors in logic circuits since memories are used to hold the largest numbers and bits susceptible to particle strikes. This paper introduces a high level error detection and correction method to provide more immunity to memory elements. This paper introduces an algorithm which can decide if there is a single bit error or double bit error. If a single bit is erroneous then it determines which portion (among information bits or check bits) of the code word contains the error and then performs operation to detect and correct the error. And in case of two erroneous bits, it performs the detection and correction operation for the whole code word. The proposed approach can correct up to 2 bit upsets in a 15 bit data block within lesser computation cycles compared to existing dominant approach.**

Keywords—***Soft errors, Memory Applications, Majority logic Decodale (MLD), Shift Cycles, Error Correction Code.***

I. INTRODUCTION

All electronic storage devices have the potential to incorrectly return information different than what was originally stored. Reliability in memory applications has always been a great ask. But the newly introduced technologies in these days focus more on smaller dimensions and low operating voltages. That's why embedded memories like DRAM, SRAM, ROM, flash memory have become more susceptible to memory failures or errors [1]. For instance, a momentary failure in banking transactions may cause a huge difference in balances. These are errors in processor execution that are due to electrical noise or external radiation rather than design or manufacturing defects. So considering the consequences of it, several error techniques like Hamming codes; Triple Modular Redundancy (TMR); Error Correcting Codes(ECC) ; fault tolerant encoder/decoder [2] are already in practice. Triple Modular Redundancy hardware is faster than Hamming error correction software. Space satellite systems often use TMR, although satellite RAM usually uses Hamming error correction. But TMR has the disadvantage of large area and complexity overhead. Error Correcting Codes (ECC) [3], [4] are more preferable to mitigate soft errors in memory than TMR or Hamming codes. Advanced ECCs like Double Error Correction Codes (DEC) are already introduced but they suffer from noticeable power consumption. Multi error correction methods like Reed-Solomon (RS) and Bose Chaudhuri–Hocquenghem (BCH) are available but they follow complex decoding algorithm. Among the ECCs, cyclic block codes are most suitable because of its high error correction capability and less complex decoding algorithm and they are majority logic (ML) decodable.

This paper proposed a new algorithm which is primarily based on Majority Logic Detector/Decoder (MLDD) [5] circuit but considers three possible cases and performs separate operations on the code word according to those cases in order to lessen the error detection and correction time. The proposed method can correct up to two erroneous bits among a 15 bit code word. When the size of the code word increases, the possibility of bit flip also increases. So, when dealing with a code word of 15 bits' size, it is not feasible to test all possible conditions. Hence, dividing the combinations into possible cases improves its time efficiency.

This paper introduces a method which can correct up to two erroneous bits among a 15 bit code word. When the size of the code word increases, the possibility of bit flip also increases. So when dealing with a code word of size 15 bit, it is not feasible to test all possible conditions hence dividing the combinations into possible cases. The paper proposed a new algorithm which is based on majority logic detector/decoder (MLDD) circuit. This method calculates the parity check-sums using an encoder circuit [1]. It detects either one or two bit errors by calculating the majority of the code word using a one-step majority logic circuit [6]. The algorithm considers three possible cases and perform separate operations on the code word according to those cases. Also the method uses a cyclic shift register and majority calculation to detect and correct the erroneous bits while decoding. Determination of whether the code word is erroneous or not is done in three cycles which is quite similar to other methods. But the method provides great efficiency when it comes to one bit of error. The algorithm needs 11 cycles to correct 1 bit of error which is a great advance in performance compared to other existing methods. The remainder of the paper is organized as follows:

Section II provides an overview of existing error detection and correction method. Section III presents our proposed method for error detection and correction. Section IV discusses the results obtained with respect to speedup, delay and power consumption. Finally, Section V draws the conclusions.

II. Related Work

MLD is based on a number of parity check equations. The majority result of these parity check equations decide the correctness of the current bit under decoding.ML decoder is a simple detector, capable of detecting multiple random bit-flips depending on the number of parity check equations [7], [8]. It consists of four parts: i) a cyclic shift register; ii) an XOR matrix; iii) a majority gate; and iv) an XOR gate for correcting the codeword bit under decoding. The input signal is initially stored into the cyclic shift register and shifted through all the taps. The algorithm needs as many cycles as the number of bits in the input signal, which is also the number of taps, to detect error. This is a big impact on the performance of the system, depending on the size of the code. For example, for a codeword of N bits, the decoding would take N cycles, which would be excessive for most applications. Also the MLD technique requires equal decoding time for error and error free code words.

Majority Logic Detector/Decoder (MLDD) which is an extension from the plain MLD discussed earlier. This MLDD technique is based on Euclidian Geometry Low Density Parity Codes (EG-LDPC) [9], [6] which uses one step majority logic circuit. This technique reduces the time needed to detect errors to a great extent, i.e. the method requires only three cycles to detect errors. But this method proposed by Jayarani et. al [2] noticeably failed to provide greater performance[10] when correcting the error bits. The method requires 18 cycles to correct one or two bit errors

III. The Proposed Methodology to Detect & Correct Error

This paper proposed a new algorithm which is primarily based on Majority Logic Detector/Decoder (MLDD) circuit which has been implemented by using the Euclidean geometry low-density parity check (EG-LDPC) codes. The EG-LDPC codes [9] are based on the structure of Euclidean geometries over a Galois field. The details of encoder and corrector circuits that are used at the beginning of the proposed method are outlined shortly as follows.

A. Design Structure of Encoder of EG-LDPC

The systematic generator matrix to generate (15, 7, 5) EG-LDPC code is shown in Figure 1, which has been captured from the paper presented by Liu et al. [6]. The encoded vector mainly consists of two parts, the first part consist of information bits and second part is of check bits, where each check bit is simply an inner product of information vector and a column of X , from the generator matrix G=[I:X]. The encoder circuit [6] to compute the parity bits of the (15, 7, 5) EG-LDPC code is shown in Figure 2. In this figure, the information vectors are (i0,..,i6) and will be copied to (c0,..,c6) bits of the encoded vector, c. The rest of encoded vector (c7,……,c14), that is the parity bits are the linear sums (XOR) of the information bits.

B. Design Structure of Corrector EG-LDPC

One-step majority-logic correction is a fast and relatively compact error-correcting technique. There is a limited class of ECCs that are one-step-majority correctable which include type-I two-dimensional EG-LDPC. In this section we show the one-step majority-logic corrector [5] for EG-LDPC codes.

$$
\begin{array}{c|ccccccccccccccc}
 & c_0 & c_1 & c_2 & c_3 & c_4 & c_5 & c_6 & c_7 & c_8 & c_9 & c_{10} & c_{11} & c_{12} & c_{13} & c_{14} \\
\hline
i_0 & 1 & 0 & 0 & 0 & 0 & 0 & 0 & 1 & 0 & 0 & 1 & 1 & 1 & 0 & 1 \\
i_1 & 0 & 1 & 0 & 0 & 0 & 0 & 0 & 1 & 1 & 0 & 0 & 1 & 1 & 1 & 0 \\
i_2 & 0 & 0 & 1 & 0 & 0 & 0 & 0 & 0 & 1 & 1 & 1 & 0 & 0 & 0 & 1 \\
i_3 & 0 & 0 & 0 & 1 & 0 & 0 & 0 & 1 & 0 & 1 & 1 & 1 & 0 & 0 & 0 \\
i_4 & 0 & 0 & 0 & 0 & 1 & 0 & 0 & 0 & 1 & 0 & 1 & 1 & 1 & 0 & 0 \\
i_5 & 0 & 0 & 0 & 0 & 0 & 1 & 0 & 0 & 0 & 1 & 0 & 1 & 1 & 1 & 0 \\
i_6 & 0 & 0 & 0 & 0 & 0 & 0 & 1 & 0 & 0 & 0 & 1 & 0 & 1 & 1 & 1
\end{array}
$$

$$\underbrace{\qquad\qquad}_{I}\qquad\underbrace{\qquad\qquad\qquad}_{X}$$

Figure 1: Generator matrix of (15,7, 5) EG-LDPC code.

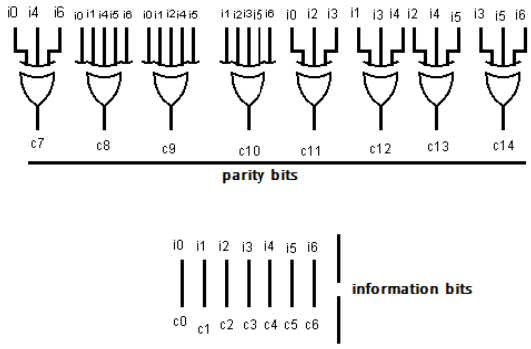

Figure 2: Structure of an encoder circuit for the (15, 7, 5) EG-LDPC code [1]

A linear sum of the received encoded vector bits can be formed by computing the inner product of the received vector and a row of a parity-check matrix. This sum is called Parity-Checksum. The core of the one-step majority-logic corrector is generating α parity-check sum from the appropriate rows of the parity-check matrix. The majority logic error correction, which corrects a potential error in one code bit, is outlined shortly using the following steps.

Step 1. Generate γ parity-check sums by computing the inner product of the received vector and the appropriate rows of parity-check matrix.

Step 2. The γ check sums are fed into a majority gate. The output of the majority gate corrects the bit cn-1 by inverting the value of cn-1 if the output of majority gate is '1'.

The circuit implementing a serial one-step majority logic corrector for (15, 7, 5) EG-LDPC code is shown in Figure 3. This circuit generates γ parity-check sums with γ XOR gates and then computes the majority value of the parity-check sums. Since each parity-check sum is computed using a row of the parity check matrix and the row density of EG-LDPC codes are ρ, each XOR gate that computes the linear sum has ρ inputs. The single XOR gate corrects the code bit cn-1 using the output of the majority gate. Once the code bit cn-1 is corrected, the codeword is cyclic shifted and code bit c_{n-2} is placed at c_{n-1} position and will be corrected. The whole codeword can be corrected in n rounds.

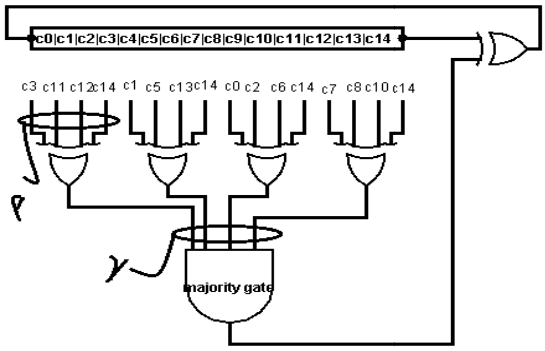

Figure 3: Serial one-step majority logic corrector structure to correct last bit (bit 14th) of 15-bit (15, 7, 5) EG-LDPC code [1].

C. The Proposed Algorithm

In general, the proposed version uses Majority Logic Detector/Decoder (MLDD) circuit [1], [2] but considers three possible cases and executes separate operations on the code word for fault detection and correction. If there is 1 bit error then it calculates the parity of information bits and check bits separately for both of the sent and received codeword. The XOR matrix is estimated for the first three cycles of the decoding process, and when all the outputs {Bj} is "0", the code word is determined to be error-free and enhanced directly to the output. Moreover, it considers three possible cases to lessen the time requirement for fault detection and correction. These cases are as follows.

1. Parity of information bits of sending code word is equal to parity of information bits of receiving codeword.
2. Parity of check bits of sending code word is equal to parity of check bits of receiving codeword.
3. Both case 1 and case 2 is not equal.

For case-1, when parity of information bits of sending and receiving end is equal then the codeword is passed to a cyclic shift register and their majority value is calculated. If the majority variable is greater than 2 that is if the majority is 1 then the bit under decoding is erroneous and hence corrected otherwise performing the cyclic shift operation for 7 times (Figure 4).

For Case-1:
Let,
The Sending Codeword : 1 1 1 0 1 1 1 0 1 0 0 0 1 1 1
And the Receiving Codeword: 1 1 0 0 1 1 1 0 1 0 0 0 1 1 1

For Sending Codeword:
Parity of information bits: 0
Parity of check bits: 0
For Receiving Codeword:
Parity of information bits: 1
Parity of check bits: 0

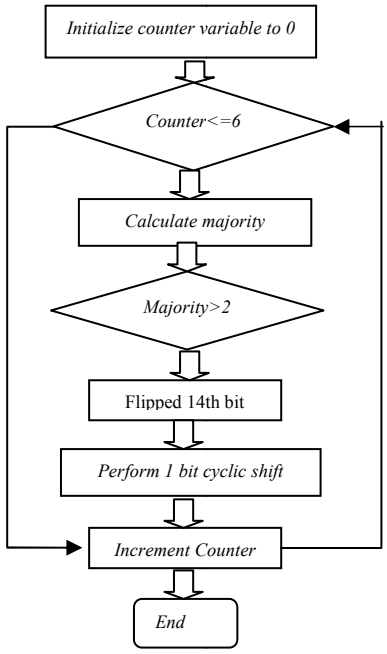

Figure 4: The Flowchart for Case-1.

For cycle 1:	1 1 0 0 1 1 1 0 1 0 0 0 1 1 1	Majority: 0
For cycle 2:	1 0 0 1 1 1 0 1 0 0 0 1 1 1 1	Majority: 0
For cycle 3:	0 0 1 1 1 0 1 0 0 0 1 1 1 1 1	Majority: 1
Inverse:	0 1 1 1 0 1 0 0 0 1 1 1 1 1 1	
For cycle 4:	0 1 1 1 0 1 0 0 0 1 1 1 1 1 1	Majority: 0
For cycle 5:	1 1 1 0 1 0 0 0 1 1 1 1 1 1 0	Majority: 0
For cycle 6:	1 1 0 1 0 0 0 1 1 1 1 1 1 0 1	Majority: 0
For cycle 7:	1 0 1 0 0 0 1 1 1 1 1 1 0 1 1	Majority: 0

The correct codeword is: 1 1 1 0 1 1 1 0 1 0 0 0 1 1 1
The error is in 3rd position.

Similarly for case-2 if the parity of check bit of sending end is equal to that of receiving side then the cyclic shift operation is performed for 8 times which is the no. of total check bits in the code word. Likewise case 1 if the majority variable is

greater than 2 then the bit under decoding is erroneous and then corrected (Figure 5).

For Case-2:
Let,
The Sending Codeword : 1 1 1 0 1 1 1 0 1 0 0 0 1 1 1
Receiving Codeword: 1 1 1 0 1 1 1 0 1 0 1 0 1 1 1
For Sending Codeword:
Parity of information bits: 0
Parity of check bits: 0
For Receiving Codeword:
Parity of information bits: 0
Parity of check bits: 1

For cycle 1: 1 1 1 0 1 1 1 0 1 0 1 0 1 1 1 Majority: 0
For cycle 2: 1 1 1 1 0 1 1 1 0 1 0 1 0 1 1 Majority: 0
For cycle 3: 1 1 1 1 1 0 1 1 1 0 1 0 1 0 1 Majority: 0
For cycle 4: 1 1 1 1 1 1 0 1 1 1 0 1 0 1 0 Majority: 0
For cycle 5: 0 1 1 1 1 1 1 0 1 1 1 0 1 0 1 Majority: 1
Inverse: 0 1 1 1 1 1 1 0 1 1 1 0 1 0 0
For cycle 6: 0 0 1 1 1 1 1 1 0 1 1 1 0 1 0 Majority: 0
For cycle 7: 0 0 0 1 1 1 1 1 1 0 1 1 1 0 1 Majority: 0
For cycle 8: 1 0 0 0 1 1 1 1 1 1 0 1 1 1 0 Majority: 0

The correct codeword: 1 1 1 1 0 1 1 1 0 1 0 0 0 1 1
The error is in 11th position.

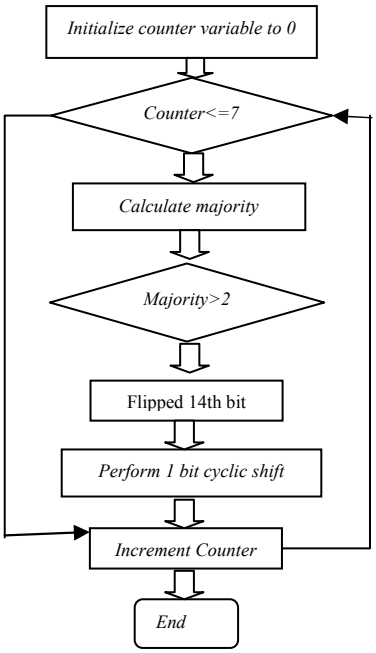

Figure 5: The Flowchart for Case-2.

And when the condition for case-3 arises, the cyclic shift operation is performed for 15 times equal to the size of code word. The erroneous bit position is detected and then corrected using majority variable like it was done for the previous cases (Figure 6).

For Case-3:
Let
The Sending Codeword : 1 1 1 0 1 1 1 0 1 0 0 0 1 1 1
Receiving Codeword: 1 1 0 0 1 1 1 0 1 0 0 0 1 0 1
For Sending Codeword:
Parity of information bits: 0
Parity of check bits: 0
For Receiving Codeword:
Parity of information bits: 1
Parity of check bits: 1

For cycle 1: 1 1 0 0 1 1 1 0 1 0 0 0 1 0 1 Majority: 0
For cycle 2: 1 1 1 0 0 1 1 1 0 1 0 0 0 1 0 Majority: 1
Inverse: 1 1 1 0 0 1 1 1 0 1 0 0 0 1 1
For cycle 3: 1 1 1 1 0 0 1 1 1 0 1 0 0 0 1 Majority: 0
For cycle 4: 1 1 1 1 1 0 0 1 1 1 0 1 0 0 0 Majority: 0
For cycle 5: 0 1 1 1 1 1 0 0 1 1 1 0 1 0 0 Majority: 0
For cycle 6: 0 0 1 1 1 1 1 0 0 1 1 1 0 1 0 Majority: 0
For cycle 7: 0 0 0 1 1 1 1 1 0 0 1 1 1 0 1 Majority: 0
For cycle 8: 1 0 0 0 1 1 1 1 1 0 0 1 1 1 0 Majority: 0
For cycle 9: 0 1 0 0 0 1 1 1 1 1 0 0 1 1 1 Majority: 0
For cycle 10: 1 0 1 0 0 0 1 1 1 1 1 0 0 1 1 Majority: 0
For cycle 11: 1 1 0 1 0 0 0 1 1 1 1 1 0 0 1 Majority: 0
For cycle 12: 1 1 1 0 1 0 0 0 1 1 1 1 1 0 0 Majority: 0
For cycle 13: 0 1 1 1 0 1 0 0 0 1 1 1 1 1 0 Majority: 1
Inverse: 0 1 1 1 0 1 0 0 0 1 1 1 1 1 1
For cycle 14: 1 0 1 1 1 0 1 0 0 0 1 1 1 1 1 Majority: 0
For cycle 15: 1 1 0 1 1 1 0 1 0 0 0 1 1 1 1 Majority: 0

The correct codeword is: 1 1 1 0 1 1 1 0 1 0 0 0 1 1 1
The error is in 3rd and 14th position.

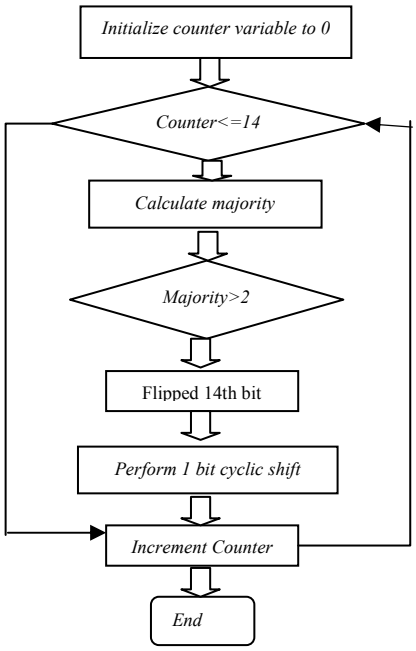

Figure 6: The Flowchart for Case-3.

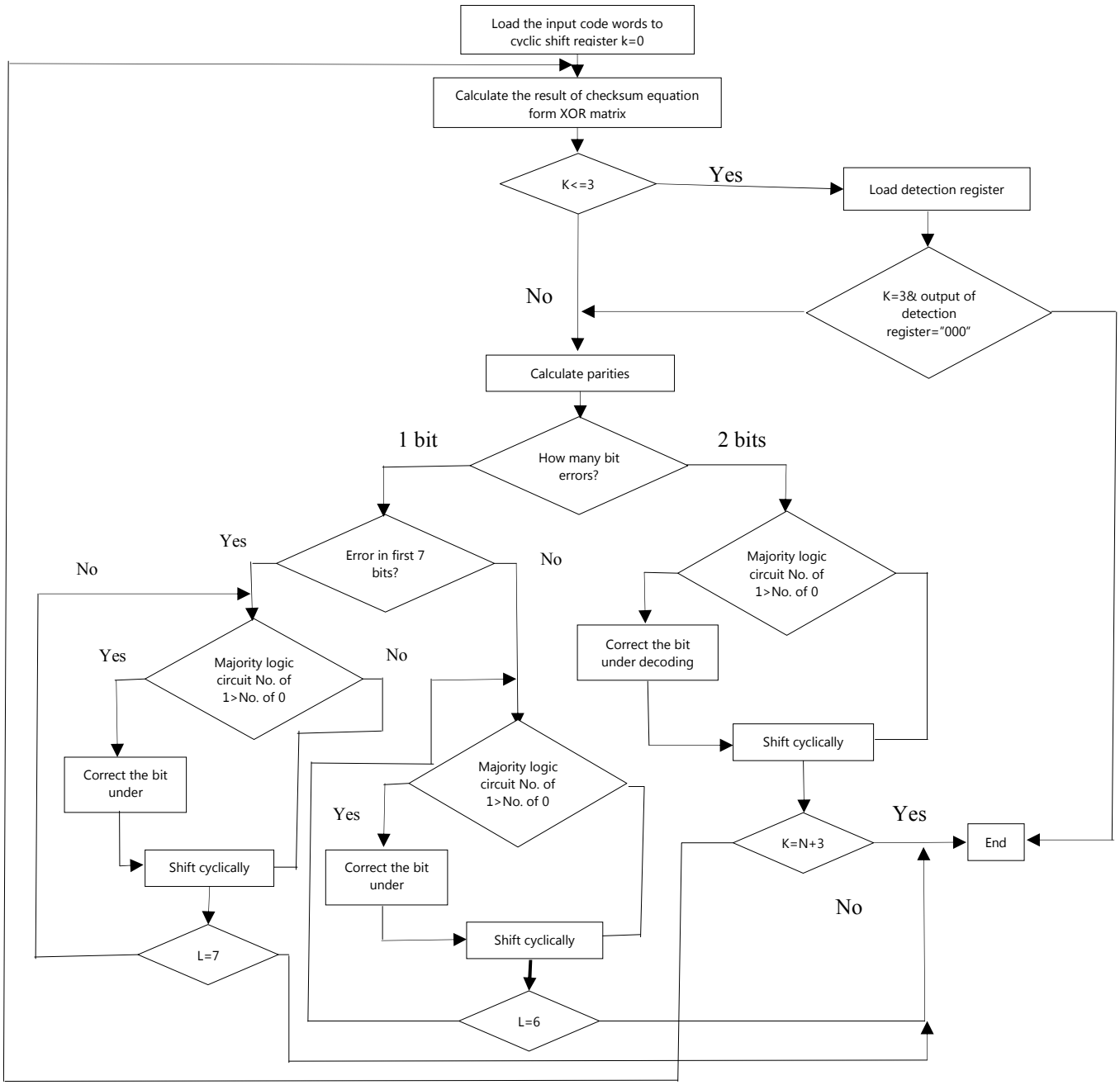

Figure 7: The Flow Diagram of the Proposed Method

Combining all the cases of above mentioned three possible conditions, the details of the proposed method is illustrated in Figure 7. The flow diagram shows the total workflow of how the erroneous bits can be detected and corrected either in the information bits or in the check bits by using majority calculation.

IV. EXPERIMENTAL ANALYSIS

The methodology is experimented through a multi-phase simulation process. The simulation process mainly envolves 'error-detection' phase and 'error-correction' phase. The experimental setup, results are outlined simulation to evaluate the proposed method shortly as follows.

A. *Experimental setup*

To work with the proposed method a machine with following configuration are used.

- Intel(R) Core i3 CPU M 350 @ 2.27 GHz
- CPU RAM 4GB
- Language C++(GNU 11)
- IDE CodeBlocks 10.05

- Input for testing erroneous dataset 120

B. Results Analysis

To validate the effectiveness of the proposed method, it is compared with the existing dominant methods. Figure 8 shows the comparison among the required cycles [11], to detect error of Plain MLD [5], the method proposed by Jayarani et. al [2], and the proposed method. The plain MLD [5] needs 15 cycles to detect any number of errors in the code word of 15 bits' size. The method proposed by Jayarani et. al [2] requires only three cycles to detect any error in that case. The proposed method also requires three cycles to detect any error.

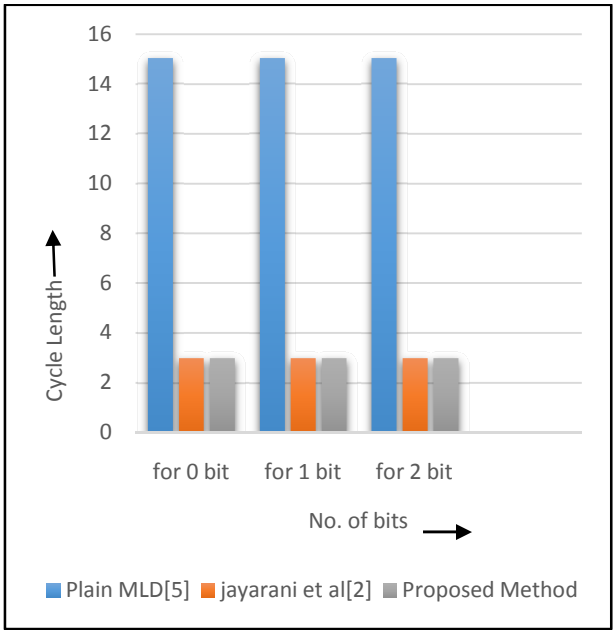

Figure 8: The Comparison among Plain MLD [5], the Method Proposed by Jayarani et. al [2], and the Proposed Method for error Detection

After the detection of errors, the proposed method performs the correction process. Figure 9 shows the comparison among the required cycles, to correct error, of Plain MLD [5], the method proposed by Jayarani et. al [2], and the proposed method. The plain MLD requires 15 cycles for the correction of one or two bits of errors. But the method proposed by Jayarani et. al [2] requires 18 cycles for one or 2 bit of errors. Whereas, the proposed method requires only 11 cycles to correct one bit of error, which is a major advancement in terms of computation
cycles' requirement. However, for two bits error correction, our proposed method requires 18 cycles which is equal to the method proposed by Jayarani et. al [2].
The proposed method has only a negligible impact on performance due to its little additional case selection, but it provides significant savings in area when code size increases.

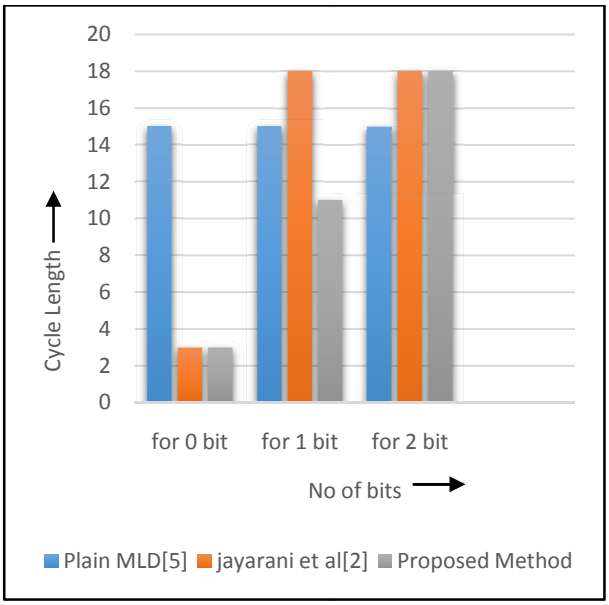

Figure 9: The Comparison among Plain MLD [5], the Method Proposed by Jayarani et. al [2], and the Proposed Method for error correction

V. Conclusions

This paper focuses on the design of a new algorithm which is primarily based on Majority Logic Detector/Decoder (MLDD) circuit but considers three possible cases and executes separate operations on the code word for fault detection and correction. The technique is independent of codeword size which decreases area overhead from other existing techniques. Though the proposed method require same time, for two bit errors detection and correction, as the method proposed by Jayarani et. al [2], in case of one bit error, it is more suitable for memory applications, where time becomes a matter of concern. Further studies can be adopted in order to find a methodology to lessen the detection and correction time requirement for two and/or more bit errors.

References

[1] Shih-Fu Liu, Pedro Reviriego, Member, IEEE, and Juan Antonio Maestro, Member, IEEE Efficient Majority Logic Fault Detection With Difference-Set Codes for Memory Applications .*IEEE transactions on very large scale integration (vlsi) systems, vol. 20, no. 1, january 2012.*

[2] JayaraniM.A , M. jagadeeswariphD .A Robust and Efficient Method For Error Detection And Correction In Memories. International Journal of Computer Applications (0975 – 8887) Volume 63– No.16, February 2013.

[3] R. J. McEliece, *The Theory of Information and Coding*. Cambridge,U.K.: Cambridge University Press, 2002.

[4] Y Kato and T. Morita, "Error correction circuit using difference-set cyclic code," *in Proc. ASP-DAC, 2003, pp. 585-586.*

[5] H. Naeimi and A. DeHon, "Fault secure encoder and decoder for NanoMemory applications," *IEEE Trans. Very Large Scale Integr.(VLSI) Syst., vol. 17, no. 4, pp. 473–486, Apr. 2009.*

[6] Pedro Reviriego,Juan A. Maestro, and Mark F. Flanagan, "Error Detection in Majority Logic Decoding of Euclidean Geometry Low

Density Parity Check (EG-LDPC) Codes," *IEEE Transactions On Very Large Scale Integration (VlSI) Systems* 1.

[7] Vasic and S. K. Chilappagari, "An information theoretical frame work for analysis and design of nanoscale fault-tolerant memories based on low-density parity-check codes," *IEEE Trans. Circuits Syst. I, Reg. Papers*, vol. 54, no. 11, pp. 2438–2446, Nov. 2007.

[8] Y. Kou, S. Lin, and M. P. C. Fossorier, "Low-density parity-check codes based on finite geometries: A rediscovery and new results," *IEEETrans. Inf. Theory*, vol. 47, no. 7, pp. 2711–2736, Jul. 2001..

[9] S.Abinaya, Mr.M.Yuvaraja "Reduction of Delay and Power by Using MLDDTechnique in Error Correction."*InternationalConferenceOn Global Innovations In Computing Technology (ICGICT'14).*

[10] R.C.Baumann,"Radiation-induced soft errors in advanced semiconductor technologies*," IEEE Trans. Device Mater. Reliabil., vol. 5, no.3, pp. 301–316, Sep. 2005*

[11] S.Abinaya, Mr.M.Yuvaraja "Reduction of Delay and Power by Using MLDDTechnique in Error Correction."*InternationalConferenceOn Global Innovations In Computing Technology (ICGICT'14).*

GSM and GPS Based Intelligent Method to Track Movement and Detect Collision and Rollover of Wheelchairs

Hasan U. Zaman, Anika Zaman, A S M Faruk Abdullah and Tamina Islam Khan
Department of Electrical and Computer Engineering, North South University, Dhaka, Bangladesh
hasan.zaman@northsouth.edu, mridulaa9@gmail.com, faruabd@gmail.com, nsu_tama@gmail.com

Abstract—**Patients such as paraplegic and most elderly people cannot move around without the help of other people. Such patients are immobile and need assistance of wheelchair for their movements. Most of these people cannot communicate with their caretaking personnel through complex cellular communications for emergency help. This paper describes the development of a portable device that can be attached to wheelchairs, which solves the problem of disabled persons in need of emergency help. This prototype has a drive system consisting of embedded microcontroller, Bluetooth, GSM (Global System for Mobile communication), GPS (Global Positioning System), and gyroscope. The system detects any accident or emergency help needed by the patient, generate a signal through embedded microcontroller to the GSM or GPS, to seek attention.**

Keywords—Paraplegic, embedded microcontroller, bluetooth, GSM, GPS, gyroscope.

I. INTRODUCTION

Developing a secured human machine interface for immobile person is a challenging issue to be solved in our society. Most of the elderly people suffer from spinal cord problem. Few even endure spinal cord injuries at a very young age. It is estimated that 52% of spinal cord injured individuals are considered paraplegic [1] [2]. As a transportation device for these patients, wheelchair is used extensively.

Over the last few decades, researchers have worked on wheelchair dependent patients, to ease their mobility. Various technologies were implemented to support the mobility of Blind or Partially Blind [3], voice recognition system were used to give required output signals from a given voice as input signal [4] [5], and image processing method were applied to detect various expressions of face of patient[6] [7].

Walking support system [8] was also introduced for paraplegic patients, which is very complex and expensive. Technology used in [9] has similar security concern about paraplegic patient, having limitations like it works only in indoors with a complex system interface, thus limiting the mobility to indoor only.The designed system prototype solves the problem of both indoor and outdoor hazards with less complexity and more user friendly interfaces and alert system.

The prototype is able to solve problems such as,

1. If the patient cannot get assistance while in emergency, the prototype will send signal to the nurse for urgent help.
2. The patient may face any unexpected accident, resulting in an injury in absence of a nurse. This calamity is detected and generates signals in terms of mobile text message to the nurse.
3. The patient may be left unattended by the nurse by any unethical means that can be monitored by local guardian. Based on an embedded microcontroller and using a common GPS antenna, this system allows patient to be located at any place by his/her nurse or any person responsible of the patient. The prototype system is hidden on the wheelchair in a strategic position. This allows maintaining a perfect coordinate positioning of wheelchair.

TABLE I. OPERATING SYSTEM OF WHEELCHAIR

DIFFERENT MODES OF WHEELCHAIR PROTOTYPE
Connectivity between patient and caretaking personals (Both indoor & outdoor)
Avoidance of rollover of wheelchair (Both indoor & outdoor)
Panic Push Button
Automatic SMS generation
Navigation of the patient

II. THEORITICAL FRAMEWORK

System implies certain technology, user efficiency and performance for each mode, recombining them to form a prototype. Each module of the prototype serves individual purpose of security.

A. Connectivity between Patient and Caretaking Personals

For connectivity within a medium range, the system uses globally available license-free 2.4 GHz ISM Band Bluetooth Device. The module uses free frequency that makes the system cheaper to use. Also, for medium range distance, HC-06 module of Bluetooth is used which covers 33 feet (10 meters) between the patient and caretaking personnel. Fig. 1

978-1-4673-9257-0/15/$31.00 ©2015 IEEE

applies both indoor and outdoor use of Bluetooth. The square box inside the Bluetooth covering range represents average area of home premise. For outdoor use, 33 feet is the maximum boundary distance, which a nurse can be further from patient. The module is also chosen for it is being a slave device, controlled and paired by master device which is present in the mobile phone of the nurse.

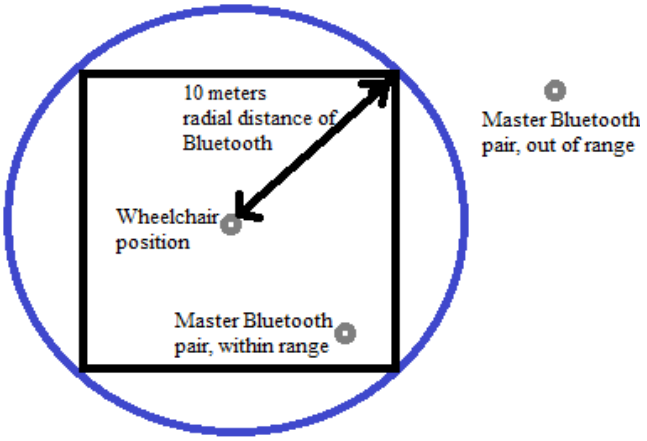

Fig. 1 Master-Slave Bluetooth impairment range

B. Avoidence of rollover of wheelchair

For avoidance of rollover, 3-axis MEMS silicon gyroscope is used. Gyroscope measures angular rate, which is the rate of rotation per unit of time in three-dimension axis. This new vibration is used to calculate the angular rate. The Coriolis force is a physical quantity first proposed by 19th century French physicist Gaspard-Gustave de Coriolis that indicates inertia at work on a rotating coordinate system.

Calculating Coriolis force on a mass with velocity (Inertia seen on a rotating coordinate system) :

$$F_c = 2mV \times \Omega \qquad (1)$$

where, F_c: $Coriolisforce$
m: $mass$
V: $velocity$
Ω: $angularrate$

C. Use of GSM for SMS generation

The minimization of the distance between patient and guardian is the main theme for our prototype. Since Bluetooth covers only few meters, for higher distance connections use of purchased frequency of GSM becomes necessary. From Fig.2 one can imagine that how signals can travel longer distances when the patient in need of emergency help. Such emergency help or interrupt handled by GSM are discussed in brief.

1. When patient pushes the panic button, it automatically generates signal through AT Command to embedded microcontroller which activates the modem to send text message to the nurse. This interface of GSM work in both indoor and outdoor cases.
2. When Bluetooth module gets disconnected, it generates message to the guardian that the patient is unattended by the nurse. When patient face any accident, message is sent to the guardian that patient has fallen down from wheelchair.
3. Gyroscope measures the inappropriate coordinate of the wheelchair, when patient faces accident. All the interfaces are programmed with AT command within the Embedded Microcontroller.

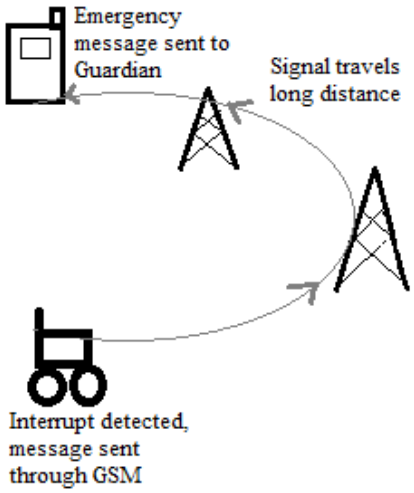

Fig. 2 Signal Transmission through GSM modem

D. Navigation

GPS works at each interrupt, when any violation occurs. It then searches GPS location every time before sending a text message and executes according to Fig. 3.Whenever the patient remains outside home, it sends URL coordinate link to the guardian that connects with the Google Map to know the position of patient.

```
if (interrupt 1 or interrupt 2 or interrupt 3){
    if (gps_available)
        sendsms with gps location();
    else
        sendsms without gps location();
}
```

Fig. 3 Algorithm for GPS Navigation

III. METHODOLOGY

The prototype is designed with a microcontroller based embedded system, interfaced with mainly GSM, GPS, Bluetooth, and Gyroscope. It has wireless communication with Bluetooth and the mobile number of guardian and nurse of the disabled patient. The switch mode of the prototype serves as a 'panic push button' for the patient.

GSM used is SIM 908 with baud rate of 19200 bps. This works with strings of AT Command, which generates unique text message to either nurse or guardian for particular use.

Module used for Bluetooth is LT108. The device is paired with mobile application of nurse, to ensure continuous monitoring of the patient as well as the nurse.

Gyroscope is programmed and interfaced with embedded microcontroller to detect the fall down of patient using a calculated boundary of three dimensional axes.

SIM 908 module also serves as GPS module. Along with a suitable GPS antenna, the system is able to generate GPS link within the text message that allows the guardian to navigate from long distance.

Apart from the module itself, the system is made 'portable', for which, rechargeable battery package installed with other modules as power source. It is then packaged, and installed at the back of the wheelchair, to generate different security concerned text message needed for the user.

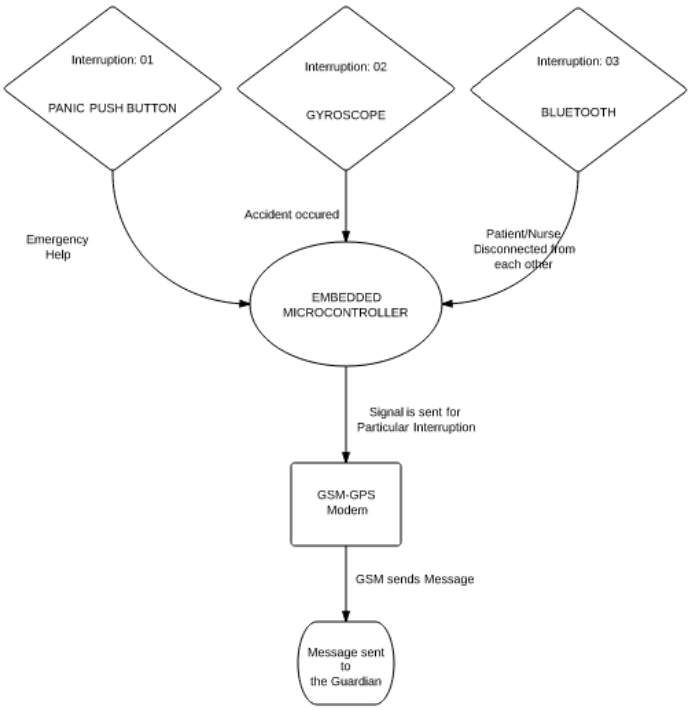

Fig. 4 Methodology Flow Chart of the prototype

In terms of engineering perspective shown in Fig. 4, the main idea is to convert the emergency help of the patient to electrical impulse, process it by embedded microcontroller Arduino, and interface with other modules to generate alarm when interruption occurs.

IV. User Interface

As shown in Fig. 5, the architecture of the system mainly consist eight module parts – six parts of inputs two outputs processed by Arduino microcontroller.

Arduino Mega and Arduino Uno are used to send AT commands to GSM_GPS modem SIM908 and check all information coming from other modules such as Bluetooth, Gyroscope, Panic Button, and PIR sensor. The system uses 'free frequency' by Bluetooth to connectivity at lower ranging distance, and uses 'purchased frequency' of GSM system to send alarms, where distance is higher.

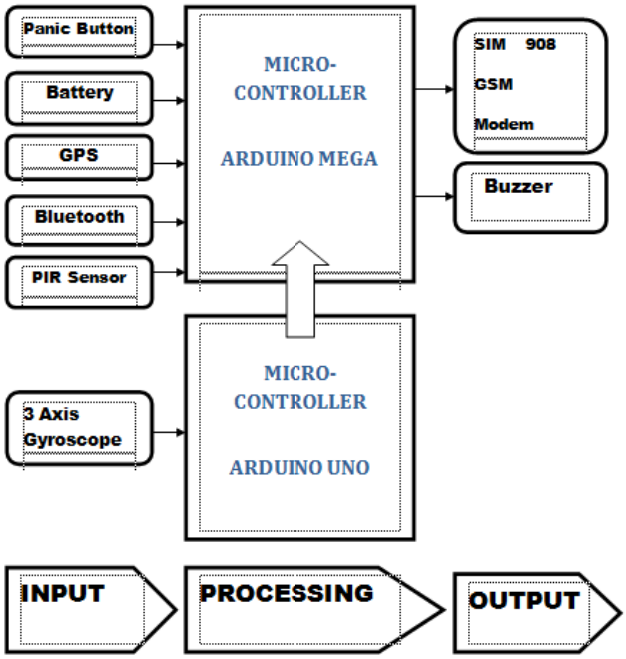

Fig. 5 Block Diagram

V. System Approach

The system consists of three input components namely, gyroscope, panic push button, and bluetooth. The standard state is the state, where all the three input devices hold the following conditions.

A. Gyroscope

Gyroscope "standardization" initially holds the pitch value > 20°, and rolling value not exceeding from -45° to 45°. If violation of the state is occurred, the system responds to the embedded microcontroller about the occurrence.

B. Panic Push button

When untouched is the normal state of the system. The violation of the system means the panic button is pressed for emergency.

C. Bluetooth

Desirable state of Bluetooth device is paired with the phone of the attendant. When the violation of this state is occurred, the system responds.

To the view point of the system, any violation is counted as "interrupt". Interrupt makes the system ready to respond. The response of the system is the GSM text message generation. So the total system can be analyzed in following pattern,

- Human and accidental Interrupt- Panic Push Button and Gyroscope.
- Distance Interrupt-Bluetooth.

The distance interrupt holds a special characteristic such that, other two input state devices need some "occurrence",

but Bluetooth in the system is Autonomous. When the system operated or powered, it search for the pair. To avoid this misleading phenomenon, the system has developed a condition of the Bluetooth connection, which ensures that no misleading response occurred by the system. The Bluetooth pair connection is guarded by the condition named "armed".

VI. Durability

The prototype currently needs 350-400mA of current as power source. Since our device is portable, we have used three cells Li-Po batteries connected in parallel to give a total 12V, 4A power supply. According to the calculation shown below,

$$\text{Battery lasting (in hours)} = 4000mA/400mA \text{ per hour} = 10 \text{ hours.}$$

This result shows that the battery lasts for 10 hours.

VII. Future Work

Our project is in prototype stage, for which upcoming design for the completion of the project is important issue. Most of the modules such as GPS, GSM, embedded Microcontroller, Gyroscope, and Bluetooth work with their individual interfaces, which serves enough to secure a disabled or paraplegic patient. Further works have to be done to make the project more feasible and user friendly for the nurse or guardian of the patient.

New modules can be added to meet the goal of the project. Buzzer will be installed for emergency purpose. For the detection of presence of the patient in the wheelchair, we need to use PIR (passive infrared) sensor to determine whether the patient is sitting on wheelchair or not. To make it more user friendly, display for battery charge has to be interfaced with battery to avoid unusual turnoff of device.

The prototype, Fig. 6, has some issues to be taken care of before packaging and installing at the back of wheelchair. First, it should be placed in upright fixed position, which cannot be twisted or tilted due to presence of Gyroscope. Secondly, both GPS and GSM antennas need to be positioned in open space, while the modules will be given insulated covering for safety.

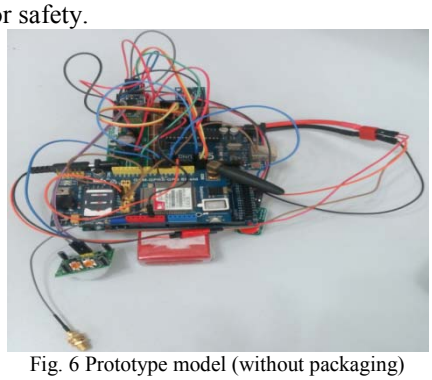

Fig. 6 Prototype model (without packaging)

Our research is only considering paraplegic patient. The system can be made more feasible for other kind of disabled people by introducing voice integrated module, which will generate certain emergency text messages by using voice recognition system.

VIII. Conclusion

Our prototype lessens the concern of insecurity of the patient as the guardian does not need to know every time that whether the patient is in safe position or not. According to research, many have worked with wheelchair related projects for disabled people with complex interfaces. But for patients with such immobility in nature, they must have security concern as their first priority. The prototype could be installed in any kind of wheel chair, because of its portability. The project has mainly targeted the metropolitan citizen group, where no family member can afford time to attend patient in his/her working hour. This device will be also helpful in hospitals and Old-aged Homes, where most of the interfaces will be very helpful to disabled or elderly patients. The patient immobility might be permanent or temporary, where this user friendly technology can be applied. Some of the issues with the current design which that have been discovered within the system are discussed briefly.

- Once the mobile numbers of the guardian and the nurse is installed within the device, it cannot be changed without the help of technicians.
- The device battery needs to be charged each day, and the SIM that is placed within the device should have enough balance to send emergency text messages.

Apart from such issues, we can conclude that the device will be able to ease the problems of disabled people by providing firm security.

References

[1] Spinal Cord Injury Facts and Statistics. [Online]. Available: http://www.sci-info-pages.com/facts.html

[2] Spinal Cord Injury. [Online]. Available: http://stephenslegal.com/practice-areas/spinal-injury

[3] Abdel IlahNourAlshbatat, "Automated Mobility and Orientation System for Blind or Partially Sighted People," International Journal on Smart And Intelligent Systems, vol. 6, no. 2, pp. 568-582, April. 2013

[4] Aakash. A. Hongunti, Mayuri. Deulkar, Varsha .Sable, "Voice Operated Wheelchair," International Journal of Advanced Research in Computer Science and Software Engineering, AISSMS, Institute of Information and Technology, vol. 4, pp. 1133-1139, April. 2014

[5] D. K Prabitha, Chidananda Murthy. M. V, and M. Z. Kurian. "Speech Recognizing Powered Wheelchair for Disabled" International Conference on Electrical Engineering and Computer Science (ICEECS-2012). May 12th, 2012, ISBN Number : 978-93-81693-58-2

[6] Lai Wei, Huosheng Hu, "A multi-modal human machine interface for controlling an intelligent wheelchair using face movement," IEEE, vol. 11, pp. 2850-2855, Dec. 2011

[7] Javier Varona, Cristina Manresa-Yee, and Francisco J. Perales, "Hands-free vision interface for computer accessibility," ScienceDirect, pp. 357-374, March. 2008.

[8] Suzuki K, Kawamura Y, Hayashi T, Sakurai T, Hasegawa Y, and Sankai Y, "Intention-Based Walking Support for Paraplegia Patient," in System, Man and Cybernetics, IEEE International Conference, vol. 3, pp. 2707-2713, Oct. 2005.

[9] RuquiaMirza, Ayesha Tehsin, and Joshi Kumar, "An Indoor Approach to Aid the Physically Disabled People," International Conference on Computing, Electronics and Electrical Technologies [ICCEET], pp. 979-983, 2012.

A Rule Based Approach for NLP Based Query Processing

Tanzim Mahmud, K. M. Azharul Hasan, Mahtab Ahmed, Thwoi Hla Ching Chak
Department of Computer Science and Engineering
Khulna University of Engineering & Technology (KUET)
Khulna – 9203, Bangladesh

Abstract— **Information is playing an important role in our lives. One of the major sources of information is databases. Databases and database technology are having major impact on the growing use of computers. In order to retrieve information from a database, one needs to formulate a query in such way that the computer will understand and produce the desired output. Generally, query processing is handled by the Structured Query Language (SQL). But the non IT people cannot be able to write SQL queries as they may not be aware of the SQL as well as structure of the database. So there is a need for non-expert users to query the databases in their natural language instead of working with the values of the attributes. This paper proposes an approach for accessing the database easily using natural language without having any knowledge about the query language. The approach is a rule based approach. The obvious advantage is that it makes a great promise for computer interfaces easier for the use of general people. Because of this, people will be able to communicate to the computer in their own language instead of learning a specialized language or commands. In order to test our approach in an actual computerenvironment, we have developed a prototype system. We obtained promising results using our system.**

Keywords— NLID, Query processing, Structured Query Language, Relational Database, Natural Language Processing.

I. INTRODUCTION

Natural language interface to database presents an interface for non-expert users to interact with the system and database[1]. To design models for automatically mapping natural language semantics into programming languages is always been a major and interesting challenge in Computer Science. For example, accessing a database requires the knowledge of structured query language (SQL) and machine-readable instructions that common users are not supposed to know. Ideally, they should only ask questions in natural language without knowing either the underlying database schema or any complex machine language. The development of Natural Language Interfaces to Database (NLIDBs) that translate the human intent into database instructions is indeed a classic problem[2]. There are many attempts[3][4] made in the past thirty years, current solutions are still not applicable in real scenarios. A huge variety of systems has been proposed, with increasing performance, but the task is still challenging.

NLIDB system has two components. One of them is Linguistic Component which is responsible for translating natural language input into a formal query and generating a natural language response based on the results from the database search. Another one is database component which performs traditional database management functions. Syntactic knowledge usually resides in the syntax analyzer whereas knowledge about the actual database resides to some extent in the semantic data model used. Questions entered in natural language form are translated into a statement in a formal query language. Once the statement is formed, the query is processed by the DBMS in order to produce the required data. Databases are the common entities that are processed by experts and non-experts with different levels of knowledge. Databases respond only to standard SQL queries which based on the relational algebra. It is nearly impossible for a general person to be well versed in SQL querying as they may be unaware of the structure of the database namely tables, their corresponding fields and types, primary keys and so on. More over the knowledge on relational algebra and its operation is also impossible except for the IT people. Natural Language Interfaces to Databases (NLIDBs) was proposed as a solution to the problem of accessing information in a simple way, allowing ideally any type of users, specially inexperienced ones to retrieve information from a database (DB) using natural language [5][6]. With the growth of technologies (for example computers, laptops, cellular phones, and Internet) information can be accessed from almost anywhere, at any time, by anybody, including general people who do not have computer background. The common and easy way for people to obtain information is by asking questions in their natural language specially mother language. But, without any proper way, computers cannot understand this language, as it merely represents a sequence of meaningless characters.

II. RELATED WORKS

[5] proposed system namely LUNAR having good performance; But it is subject to intensive use due to the limitation of its linguistic capabilities. [6] designed a system namely LADDER which was used as a natural language interface to a database of information about US Navy ships system. The LADDER based on distributed database system which uses semantic grammar to parse questions to find the result of a query in distributed database. One important difference is that the system uses semantic grammar technique that helps syntactic and semantic processing. [7] developed a system named Word Alignment-based Semantic Parsing (WASP) that address the broader goal of constructing "a complete, formal, symbolic, meaningful representation of a natural language sentence", that can be applied to the NLIDB

domain. [8] proposes NaLIX, a generic interactive natural language query interface based on XML database. The system can accept an arbitrary English language sentence as query input incorporating aggregation, nesting, and value joins etc. After reformulation, this query is then translated into an XQuery expression that can be evaluated for an XML database. The translation is done through mapping grammatical proximity of natural language parsed tokens to proximity of corresponding elements in the result XML. [9] proposes an approach to build the NLIDB based on Computational Paninian Grammar (CPG). It employs two distinct stages for processing such as syntactic processing then semantic processing. An NLID system namely D-HIRD specific for Hindi language independent of domain is proposed in [10]. A morphological analyzer based query processor is proposed in [13] based on the keyword and group of words which is used to find the type of extracted keyword using pattern matching technique. In this paper we propose an NLID using rule based system which takes questions from the users in the form of natural language. Then it processes that natural language to obtain regular SQL query. A data dictionary is used to process the natural language where all possible word related to our system is included. A Context Free Grammar (CFG) is used to determine the required attributes and SQL elements to construct the query. Finally it run the query on the database to fetch the result and show that to the user.

III. A NATURAL LANGUAGE INTERFACE FOR DATABASE

This section gives a detail overview of the proposed system. The system is based on designing Context Free Grammar (CFG). At first the NLIDB system and its sub-components are described and then the basic elements with working procedure of our proposed model are presented. We used an alumni database system as a case study. Fig. 1 shows the block diagram of the system.

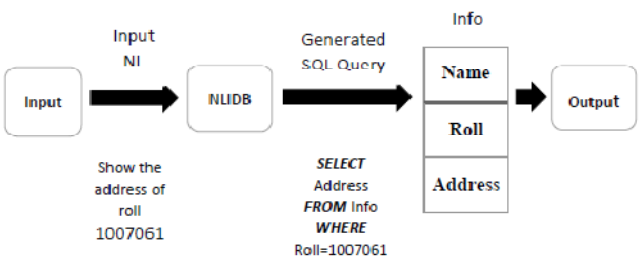

Fig. 1: Overview of Natural Language Interface of Database

One of most wide and interesting area of Natural Language Processing (NLP) is the development of a natural language interface to database systems (NLIDB). In the last few decades many NLIDB systems have been developed through which users can interact with database in a more convenient and flexible way. Fig. 1 shows the basic architecture of our NLIDB system. After taking the input from the user in the natural language form, the system converts this input into SQL query form which it mainly used for accessing database for reading and writing. The user does not have to have any kind of knowledge about SQL query and its format. Because of this application NLP is very widely used today. Natural Language Interface has been a very interesting area of research since past times. The aim of Natural language Interface to Database is to provide an interface where user can interact with database more easily using their natural language and at the same time access or retrieve their information. Generally NLIDB system converts the query in native language into SQL and vice-versa.

The proposed system is basically a translator from natural language to standard SQL. So it has some phases like compilers. We design context free grammars. When any input symbol of appropriate terminals is found then it is replaced by the corresponding attribute in the relational table or appropriate operators of SQL. The proposed system consists of the some phases namely user interface, word check, removing excess words, tokenization and mapping to CFG rules :

The user asks question or make a query. He/she generally prefers to ask that in a natural language. This module allows the user to enter the question in a natural language. After getting a natural language query, the system must identify the valid words and values required to build a standard SQL query. This process checks all the words in the user question against the data dictionary for its existence. The words which are not legitimate or required to build the SQL statement have to be removed to lessen the complexity. This process removes excessive words from the question string and blanks the positions of the words. After getting the valid sub-string from the given string, it should be split into tokens. With the help of tokens, we can identify the column and respective table name required to build the SQL query. A context-free grammar (CFG) is a set of recursive rewriting rules (or productions) used to generate patterns of strings. Using this idea we developed some string pattern matching rules where all capital letter words denote the non-terminals and small letter words denote terminals. We used the rules to detect the required column, given values and corresponding column names and valid operators assigned to those values. Fig. 2 and Fig. 3 show some of the rules for detecting the column name and their values given the natural language query.

According to the retrieved column name and values, the required SQL elements (SELECT, WHERE, JOIN, AND, OR etc.) are identified. After getting the valid columns, values and corresponding operators, SQL generation process constructs a query in SQL. When the Query is generated, it is passed to the back-end database and which runs it. Finally, data collection process collects the data retrieved from the database and show it to the user as a result. Fig. 4 shows the logical operators for SQL translation.

The mapping is done by matching the terminals and then returning its corresponding non terminals. Then non terminals are used for SELECT and FROM clause. The formation of SQL queries from the natural language query and tested the results based on their accuracy. The formation of the SQL query requires us to deal with the generation of 3 well known clauses of SQL which together construe the SQL query. The 3 clauses are as follows: SELCT clause, FROM clause, WHERE clause. The input string is used to construct the SELECT clause and FROM clause and the WHERE clause. In SELECT clause, we put the required column names i.e, the information to be extracted and in the FROM clause, we put the

corresponding table names from where the information to be extracted. To construct the SELECT clause and FROM clause we used the rules showed in the Table 1. Initially, all the rules are sorted in a decreasing order according to their length. Then the system selects the sub-string which has the highest length in the rules tables and start to check against the input string. If it finds exact match, it will return the column name directed by that sub-string showed in those rules tables and from the column name, we get the corresponding table name.

PERSONAL-INFO	→	*ROLL_ | FULL_NAME | F_NAME | BTCH | B_DATE | BLD_GRP | SPOUSE_NAME | NO_OF_CHILDREN | FLD_OF_INTEREST | JOB_TITLE | COMPANY_NAME | JOB_EXP*
CONTACT-INFO	→	*ID | CONTACT_NO | EMAIL_ID | FAX_NO | WEBSITE_INFO | CURR_ADDRESS*
*ROLL_*	→	*roll number | roll no*
FULL_NAME	→	*who is | name | name of the student | student name | student's name*
F_NAME	→	*father | father's name | dad*
BTCH	→	*Batch*
B_DATE	→	*birthday | birth date | date of birth*
BLD_GRP	→	*blood group*
SPOUSE_NAME	→	*spouse name | husband | wife | name of husband | husband's name | name of wife | wife's name*

Fig. 2: Context Free Grammar for SELECT and FROM clause

If a natural language query is of the form "Show the student's name and contact no whose blood group is A+ and B+ and lives in "Khulna" then the sub-strings "student's name", "contact no", "blood group" and "lives in" match with the sub-string in the rules tables in Fig. 2. If we order these sub-strings according to their length, "student's name" comes first. Then "blood group", "contact no" and finally "lives in" is found. Then the corresponding terminal of the CFG is returned and stored. All these sub-strings direct to their corresponding column name and thus table names. In WHERE clause, the values given for columns and corresponding column names are used to establish a relationship via an appropriate operator. The CFG shown in Fig. 3 is used for detecting appropriate column names whereas Fig. 4 is used for assigning appropriate operator. Like the process described for constructing the SELECT clause and FROM clause, the values, corresponding column name and tables name is detected. Here, the values "A+", "B+" and "Khulna" are detected. As there is no sub-string matched between "A+" and "B+", these two values will belongs to same column. Now to detect the column names, the sub-string "blood group is" and "lives in" are the exact match with the rules in Fig. 2. These two sub-string direct to the columns "bld_grp" and "curr_address".

FULL_NAME	→	*name is "| roll of "| roll number of " | roll no of " | father of " | father's name of "| dad of "|batch of "| birth date of " |birthday of "| date of birth of "| blood group of "| spouse name of "| husband of " | wife of " | name of husband of "| husband's name of " | name of wife of " | wife's name of "| children's number of "| number of children of " | children's no of " | no of children of " | field of interest of" | interested field of " | expert field of " | working field of " | job of " |job title of " | current job of " | current job title of " | current company of " | company name of " | working place of " | working company of " | experience of " | job experience of " | contact no of " | contact number of " | phone no of " | phone number of " | mobile number of " | mobile no of " | email of " | email id of " | mail of " | mail id of " | email address of " | mail address of " | fax number of " | fax no of " | fax of " | website of " | website name of " | name of website of " | name of the website of " | home of " | location of " | address of " | current address of "| current location of " | home address of "*
*ROLL_*	→	*roll is | roll number is | roll no is | of roll | of roll number | of roll no*
F_NAME	→	*child of | son of | daughter of*
BTCH	→	*batch is*
B_DATE	→	*birth date Is | birthday is | date of birth is*
BLD_GRP	→	*blood group is*

Fig. 3: Context Free Grammar for NLID with appropriate attribute to database.

Operator	→	= |< |> |<= |>=|!=
=	→	*equal*
<	→	*less than |fewer than*
>	→	*greater than |more than*
<=	→	*less than or equal |fewer than or equal*
>=	→	*greater than equal |more than or equal*
!=	→	*not equal*

Fig. 4: Context Free Grammar for operators of SQL

IV. EXPERIMENTAL RESULTS AND STUDIES

We create a prototype system and executed on our sample database named ALUMNI where the real values of an alumnae of an university was stored. From the experiments and derived results are shown in this Section. Three types of queries are employed namely

- The queries that have only SELECT and FROM clause but there is no where clause. In this case we put WHERE 1. Table 1 shows some queries of such case.

- The queries that have SELECT and FROM clause with some condition that needs to employ WHERE clause. Table 2 shows some results of such case.
- The queries that have SELECT, FROM and WHERE clause and it needs the join operation to conduct the query. Table 2 shows some results of such case.

TABLE 1: GENERATED QUERY WITHOUT CONDITION

User query	Desired SQL	Generated SQL
Tell me name of the students	*SELECT* `full_name` *FROM* `personal_info`;	*SELECT* `full_name` *FROM* `personal-info` *WHERE* 1;
Give me name of the company of the students	*SELECT* `company` *FROM* `personal-info`;	*SELECT* `company` , `full_name` *FROM* `personal-info` *WHERE* 1 ;

We executed the system for some random natural language query and collect the results. We categorize the result into three categories- Good, Fair, Bad.

- Good: The queries that the system returned correct SQL statements and the desired results from database are found are marked as "Good" output.
- Fair : The queries that system returned SQL statements which are syntactically correct but the desired result was not found are marked as "Fair" output.
- Bad: The queries that the system failed to generate any query are marked as "Bad" output.

TABLE 2: GENERATED QUERY WITH CONDITION

User query	Desired SQL	Generated SQL
get me roll of the students whose blood group is "A+"	*SELECT* `roll_` *FROM* `personal-info` *WHERE* `bld_grp`="a+";	*SELECT* `bld_grp` , `roll_` *FROM* `personal-info` *WHERE* `bld_grp` = "a+" ;
Tell me name of the students with blood group "AB+"	*SELECT* `full_name` *FROM* `personal-info` *WHERE* `bld_grp`="ab+";	*SELECT* `full_name`, `bld_grp` *FROM* `personal-info` *WHERE* `bld_grp` = "ab+";
Tell me name of the students with "AB+" blood group	*SELECT* `full_name` *FROM* `personal-info` *WHERE* `bld_grp`="ab+";	**Failed to generate**

Table 4 shows queries with Good, Fair and Bad marked. We simulated the system with varying number of queries with our system. The accuracy of queries is shown in Table 5. Although, the accuracy is not promising at this stage, but the accuracy can be improved by adding the production terms in the CFG. The accuracy is dependent on number entry on the dictionary as well.

TABLE 3: GENERATED QUERY CONDITION JOINING MULTIPLE TABLES

User query	Desired SQL	Generated SQL
Show the name and contact number who lives in "dhaka"	*SELECT* `full_name`, `contact_no` *FROM* `personal-info` *JOIN* `contact-info` *ON* `roll_` = `id` *WHERE* `curr_address` = "dhaka" ;	*SELECT* `full_name`, `contact_no` , `curr_address` *FROM* `personal-info` *JOIN* `contact-info` *ON* `roll_`=`id` *WHERE* `curr_address` = "dhaka" ;
Show the name and contact number who lives in "dhaka" and blood group is "AB+"	*SELECT* `full_name`, `contact_no` *FROM* `personal-info` *JOIN* `contact-info` *ON* `roll_` = `id` *WHERE* `curr_address` = "dhaka" and `bld_grp` = "ab+" ;	*SELECT* `bld_grp`, `full_name`, `contact_no` , `curr_address` *FROM* `personal-info` *JOIN* `contact-info` *ON* `roll_` = `id` *WHERE* `curr_address` = "dhaka" and `bld_grp` = "ab+" ;
Give me name and contact no who works at "reve system"	*SELECT* `full_name`, `contact_no` *FROM* `personal-info` *JOIN* `contact-info` *ON* roll_` = `id` *WHERE* `company` = "reve system" ;	*SELECT* `full_name`, `contact_no` *FROM* `personal-info` *JOIN* `contact-info` *ON* roll_` = `id` *WHERE* `company` = "reve system" ;

TABLE 4: GENERATED QUERY WITH GOOD, FAIR AND BAD MARKED

Natural Language Queries	Generated Queries	Comment
Give me name of the student who lives in "dhaka"	select `full_name`, `curr_address` FROM `personal-info` JOIN `contact-info` ON`roll_` = `id` WHERE (`curr_address` = "dhaka") ;	Good
Give me name of the students who works at "reve"	select `full_name` FROM `personal-info` WHERE (`company_name` = "reve") ;	Good
What is roll and contact info of the students whose roll is "0007004"	select `roll_` FROM `personal-info` WHERE (`full_name` LIKE "%0007004%") ;	Fair
What is roll and contact info of the students having roll "0007004"	select `roll_` FROM `personal-info` WHERE (`full_name` LIKE "%0007004%") ;	Fair
show all the information of "kawser"	Failed To Generate	Bad
show all the information of roll "0007005"	select `roll_` FROM `personal-info` WHERE (`roll_` = "0007005") ;	Fair

TABLE 5: ACCURY PERFORMANCE OF THE QUERIES GOOD, FAIR AND BAD

Query Category	Accuracy
Good	47%
Fair	35%
Bad	18%

The computational time of any NLP based algorithm is naturally little bit high as compared to the hardware based computations. The time complexity of our scheme depends on the number of production terms in the CFG. If the number of

production terms increase then the time computational time increases. On the other hand, the accuracy of the system depends on the number of production terms in the CFG. If the number of production terms increase then the accuracy of the system increases and vice versa

V. CONCLUSION

Natural Language Processing can bring powerful enhancements to virtually any computer program, because human language is so natural and easy to use for humans. We provide a system which is capable of handling English query to access relational database instead of structured query language. The proposed NLID provides a convenient as well as reliable means of querying access, hence, a realistic potential for bridging the gap between computer and the casual end users. The system employs CFG based system which makes it easy search the terminals. As the target terminals become separated to many nonterminals. To get the maximum performance, the data dictionary of the system will have to be regularly updated with words that are specific to the particular system. The NLID is a relatively recent area of research as compared to other fields of information technology, there have been sufficient successes to date that suggest that NLP-based information access technologies will continue to be a major area of research and development in information systems now and far into the future. The system we developed is a specific problem based system and currently can handle standard join conditions.

REFERENCES

[1] N. Nihalani, M. Motwani and S. Silakari, "Natural Language Interface to Database using Semantic Matching" *International Journal of Computer Applications*, vol. 31, no.11,pp. 0975 – 8887, Oct 2011S.

[2] A. Popescu, O. Etzioni, and H. Kautz, "Towards a Theory of Natural Language Interfaces to Databases", *Intelligent User Interfaces,* pp.149–157, 2003.

[3] P. A.Dhomne et. al., "Accessing Database using NLP", IJRET: *International Journal of Research in Engineering and Technology (IJRET)*, vol. 02, Dcec 2013.

[4] W. Woods, R. Kaplan and B. Webber, "The Lunar Sciences Natural Language Information System,*Bolt Beranek and Newman Inc., Cambridge, Massachusetts Final Report*, report no. 2378, 1972.

[5] W. Woods,"An experimental parsing system for transition network grammars",*In Natural language Processing, R. Rustin, Ed.,Algorithmic Press, New York*,1973.

[6] G. Hendrix et. al., "Developing a natural language interface to complex data",*ACMTransactions on Database Systems*, vol. 3, no. 2, pp. 105 – 147, 1978.

[7] Y. W. Wong, "Learning for Semantic Parsing Using Statistical Machine TranslationTechniques", *Technical Report UT-AI-05-323,University of Texas at Austin, Artificial Intelligence Lab,* Oct 2005.

[8] Y. Li, H. Yang and H. V. Jagadish, "NaLIX: an interactive natural language interface for querying XML", *Proceedings of the 2005 ACM SIGMOD international conference on Management of data*, pp 900-902,2005.

[9] Abhijeet Gupta, Arjun Akula, Deepak Malladi, Puneeth Kukkadapu, Vinay Ainavolu, Rajeev Sangal, A Novel Approach Towards Building a Portable NLIDB System Using the Computational Paninian Grammar Framework, 2012 International Conference on Asian Language Processing, pp. 93-96, 2012

[10] Rajender Kumal1, Mohit Dul2, Shivani Jinda D-HIRD: Domain-Independent Hindi Language Interface to Relational Database, 2014 interna nonal conference on computa non of power, energy, informa non and communica non (ICCPEIC), pp- 81-86.

[11] Filbert Reinaldha, Tricya E. Widagdo, Natural Language Interfaces to Database (NLIDB): Question Handling and Unit Conversion,

[12] Axita Shah, Jyoti Pareek, Hemal Patel, Namrata Panchal NLKBIDB - Natural Language and Keyword Based Interface to Database

[13] Rajender Kumar, Mohit Dua "Translating Controlled Natural Language Query into SQL Query using Pattern Matching Technique", International Conference for Convergence of Technology – 2014, pp. 1-5.

[14] Xuan Xuan, Liu Jianbo, Yang Jin, Research on the natural language querying for remote sensing databases, 2012 International Conference on Computer Science and Service System, pp. 228-231, 2012.

Multi Objective Non-dominated Sorting Genetic Algorithm (NSGA-II) for Optimizing Fuzzy Rule Base System

Mehnuma Tabassum Omar[1,*], Monika Gope[2], Ariful Islam Khandaker [3] and Pintu Chandra Shill [1,2]
Department of Computer Science and Engineering
Khulna University of Engineering & Technology (KUET)
Khulna 9203, Bangladesh
[*]E-mail: misty2409@gmail.com

Abstract—**Multi-objective designs are genuine models for intricate combinatorial optimization problems. This paper presents a fast elitist non-dominated sorting multi objective genetic algorithm to develop smartly tuned fuzzy logic controllers with a finer trade-off between interpretability and exactitude in linguistic fuzzy modeling problems. The multi-objective genetic algorithm produces a group of non-dominated solutions defined FLCs for multi objective problem with satisfying objective at acceptance level without dominating to any other solution. In MO-GA, an integer encoding is used to indicate the linguistic level of fuzzy rule. Here, multi-objectives are transformed to a fitness function in order to initiate the NSGA-II, i.e. selection, crossover, and mutation. The intended approach generates an efficient and reliable fuzzy logic control system through the effective searching and self-learning adaptability of the NSGA-II. The simulation results based on multi-objective exhibits better performance than single objective while controlling car like robot.**

Keywords— Fuzzy rule base system, NSGA-II, Multi-objective Optimization, Pareto-Optimal Solution.

I. INTRODUCTION

Multi-objective approaches are applied on several composite engineering optimization problems as well as on realistic paradigms where beyond one objective are necessary to be fulfilled to reach desired goal. In a multi-objective decision making scheme, multiple criteria is considered that needed to be optimized within more than one objective function together [1], [2].

Genetic Algorithms (GAs) stand for stochastic search scheme motivated by the conception of evolution and natural selection of species. Originally, GAs was drawn-out in order to answer optimization problems with multiple objectives [1]. Adapted Genetic Algorithms have been validated to be predominantly operative to govern tremendous keys to explore a set of solutions all of which contents the objective's unsatisfactory grade without being dominated by whichever solutions in further [3].

The NSGA-II algorithm has been renowned [4] as the first evolutionary multi-objective optimization (EMO) algorithms that seek the solution domain to discover Pareto-optimal solutions within a multi-objective centered scheme [5]. In a solution domain a solution is Pareto-optimal if it denies domination from other solutions [6].

Fuzzy logic control is a significant zone in real-world paradigm [7] comprising control [8], [9], decision making [4]-[7], prediction [8], classification [9], inference [10] etc. In fuzzy logic system (FLS) a crisp input vector is mapped with a crisp scalar output where a linguistic rule base is appreciated as nonlinear function [11].

Hybrid techniques have increased significant consideration in the field of Computational Intelligence. The hybridization of Fuzzy Logic and GA is the most common method that points to genetic fuzzy systems (GFSs). Basically a GFS is an enhanced fuzzy method where GAs, genetic programming and evolutionary policies are comprised through an iterative learning procedure educed as of evolutionary computation and Genetic Algorithm [12].

However, the key question in the FLC scheme is to determine the membership function's types and parameters, and to produce the rules of fuzzy system. This optimization is done for a better design in which some research has been involved for partial optimization, not for complete process. For instance, some deals with membership functions parameters where as others addresses the fuzzy rules. Based on control operators or person's experience or automatically generated experience, the parameters of membership functions are chosen. To improve the behavior of the optimization problem, several methods alike GA, can be used [13].

A non-dominated sorting centered multi-objective evolutionary algorithm (MOEA), NSGA-II is capable for seeking a great coverage of solutions and improved convergence close to the accurate Pareto-Optimal front [4].

In this research work, a multi-objective evolutionary algorithm, NSGA-II (MO-NSGA-II) has been deployed for delivering and optimizing fuzzy logic controllers along with enhancing precise objectives and contenting enforced constraints at the same time.

The association of this paper is as follows: Related researches are mentioned in section, II. In Section III, multi-objective optimization definition has been demonstrated.

978-1-4673-9257-0/15/$31.00 ©2015 IEEE

Section IV defines the underlying control problem. In Section V, the proposed algorithm of MO-NSGA-II Fuzzy Rule base system has been presented. In Section VI, the simulation result of the proposed architecture has been depicted. Finally section VII outlines the conclusion of this paper.

II. Related Work

In the method of fuzzy logic, self-learning and generalization of rules are not possible. For real-time problems where genetic fuzzy policy has been successfully applied by means of scholarly information are very efficient [12]. To explain optimization technique, different EAs were proposed **[4].** Multi Objective GA and Fuzzy procedure are used for rule optimization in [14] where [15], [16] worked on Fuzzy set theory, association rule mining with GA. However, Fonseca and Fleming's MOGA [1], Srinivas and Deb's NSGA [2], and Horn et al.'s NPGA [13] were appreciated than others. These processes explained the required methodologies for translating an EA to a MOEA [4]. NSGA-II is MOEA but it is superior throughout latter generations, ignoring the level of noise exists in the problem [17]. To achieve a proper initial fuzzy structure iteratively, [18] proposed various Pareto-optimal fuzzy schemes based on NSGA-II. To increase quality and performance of task scheduling in the market-based grid setting, [5] used NSGA-II using fuzzy operators.

In this exploration, a hybridization of NSGA-II and Fuzzy Controller has been presented where the fitness functions are optimized to get the best optimized rules for a control problem. However, to load a truck to its destination, [19] presents a model of the fuzzy control system which is comprised with hybrid clustering method and neural network. But high computational demand in truck loading is the main disadvantage to put on their algorithm to a real-time problem. On the other hand, NSGA-II is a computationally fast and elitist MOEA where non-dominated sorting approach is applied [4]. Thus, the projected NSGA-II centered fuzzy system overcomes the weaknesses of building the structure of the unidentified system and aggregates the assistances of these two control structures.

III. Multi-Objective Optimization

A multi-objective decision paradigm in general can be conveyed as a vector function '$\boldsymbol{f}$' such as

$$f: m \rightarrow n \tag{1}$$

where $\boldsymbol{m}$ is the decision variable parameters and $\boldsymbol{n}$ is the objective .

Generally:

minimize/maximize,

$$y = f(x) = (f_1(x), f_2(x), \dots, f_n(x))$$

subject to $x = (x_1, x_2, \dots . x_m) \in X$,

$$y = (y_1, y_2, \dots . y_n) \in Y \tag{2}$$

where $\boldsymbol{x}$ is called decision vector and $\boldsymbol{y}$ objective vector

The solution sets of a multi-objective optimization problem are Pareto Optimal which is not dominated by any other solutions. The collection of non-dominating feasible solutions in solution domain is stated as the Pareto Optimal Set. The Pareto Optimal solution contains each of those decision vectors that are unable to be improved within any objective without being degraded within other objectives [1], [2], [20]. Pareto front is the value of an objective function in the objective space corresponding to a given Pareto Optimal set. The ultimate aim of a multi-objective optimization algorithm is to explore a set of solutions which will substantially signify the Pareto optimal set [6]. Subsequently, the best acceptable solution can be elected by manipulating a precedence benchmark. To cope with it, the evolutionary algorithms have united new tactics to manage the constraints preferred and verified to resolve constrained multi-objective optimization models as [3].

The NSGA-II (Non-Dominated Sorting Genetic Algorithm-II) algorithm examines the solution domain to discover Pareto-optimal solutions in a sphere of multi objective optimization assembly [5]. NSGA-II practices the elitist standard and an obvious diversity conserving tool. Besides, it also underlines non-dominated solutions and characterizes the Pareto front through Pareto-optimal solutions [5]. NSGA-II practices a categorical diversity-conservation or niching policy to consign a diversity rank to entire individuals' having identical non-dominated front [4]. The participants consuming the smallest crowded region inside each non-dominated front are dispensed through a higher rank. Due to the disposition of the prototypes of the multi-objective optimization schemes, NSGA-II can be applied for discovering the non-dominant optimal solutions. Dominance and correctness of any solution above the other solutions rests on a number of factors such as user's adoption and problem circumstances. Hence, the NSGA-II governs a collection of dominant solution and subsequently Pareto front is attained [11], [21].

IV. Problem Specification

In this work, an independent truck has been simulated by the MO-NSGA-II which is incorporated with fuzzy logic controller. Fig. 1 depicts the object of the problem where the primary position of the objective truck is symbolized with x, φ and y.

Here, φ is the angle of the object regarding the horizontal line in the problem space. The point$(\boldsymbol{x}, \boldsymbol{y})$ identifies the back center location of the object truck in the problem space. The steering angle θ is a measure between the object truck and the front wheel. The object truck is simulated in order to be loaded at a position $(\boldsymbol{x_f}, \boldsymbol{y_f})$ and angle $\boldsymbol{\varphi_f} = \mathbf{90^0}$. The truck is capable of backing its position only.

From any initial location $(\boldsymbol{x_0}, \boldsymbol{y_0})$ with any initial angle $\boldsymbol{\varphi_0}$, the regulator must generate the suitable steering angle $\boldsymbol{\theta}$ at each phase to cause the truck of being loaded to a chosen location.

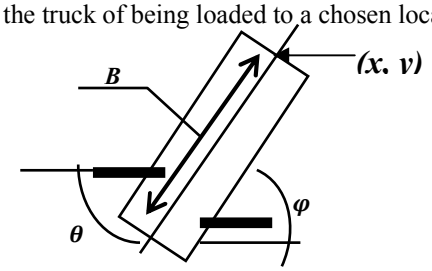

Figure 1. Illustration of a Truck Model

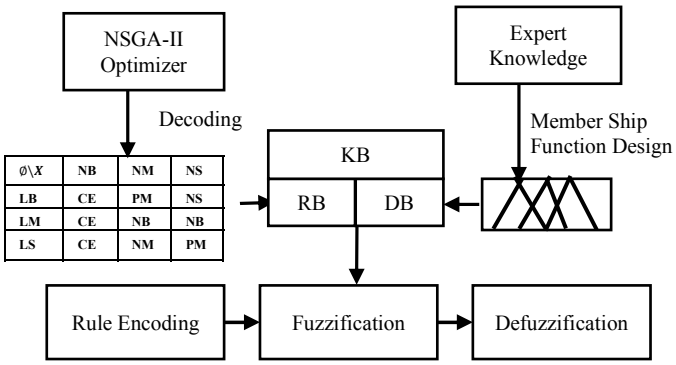

$\emptyset\backslash X$	NB	NM	NS
LB	CE	PM	NS
LM	CE	NB	NB
LS	CE	NM	PM

Figure 2. The Model of MO-NSGA-II Based Fuzzy System

The following equations have been used to find the next position of the truck to convey it to desired dock:

$$x(n+1) = x(n) - \cos((\varphi(n) + \theta(n)) - \sin(\theta(n))\sin(\varphi(n)) \quad (3)$$

$$y(n+1) = y(n) - \sin((\varphi(n) + \theta(n)) + \cos(\theta(n))\cos(\varphi(n)) \quad (4)$$

$$\varphi(n+1) = \varphi(n) - \arcsin\left(\frac{2\sin(\theta(n))}{B}\right) \quad (5)$$

V. MO-NSGA-II BASED FUZZY RULE BASE SYSTEM

Fuzzy system constitutes a Knowledge Base (KB) which contains a Rule Base (RB) and Database (DB). The Database procures membership function from the expertise. The NSGA-II algorithm operates as an optimizer providing rule to the Rule Base. The Knowledge Base then provides his acquaintance to the FLC and commences the evolution process. Fig. 2 defines the model of the projected MO NSGA-II Based Fuzzy System. The complete architecture works as follows:

A. Proposed Algorithm

The proposed NSGA-II based fuzzy rule base system (FRBS) has the succeeding stages:

1) Partition of the Input and Output Universe of Discourses: Partition the variables into several fuzzy regions (fuzzy sets) separetely and assign fuzzy MF i.e., linguistic identity of the respective sections. The system takes the position of x and alignment angle φ as input and produces steering angle θ as system output. The ranges are taken in the simulation with φ [-92, 270], X[-20, 20] and θ [-40, 40]. The MFs are manipulated with 50% overlap as a sample shown in Fig.3.

2) Chromosome Encoding: The linguistic label for x is specified by NB, NM, NS, ZE, PS, PM and PB. For φ, the linguistic label is specified by LB, LM, LS, CE, RS, RM, and RB. The linguistic label of θ is specified by NB, NM, NS, CE, PS, PM and PB. The sample database for the input data of x, phi and theta are given in Table.1. The linguistic lebels are further encoded using real integer 1 to 7 espectiely shown in Table.2

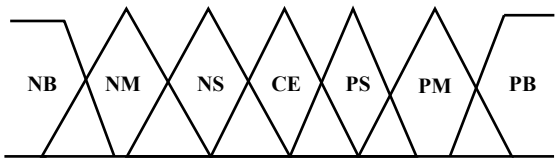

Figure 3. Fuzzy membership function details of θ

Table 1. Input partitions along with linguistic label

Input X(c, w)			Input φ(c, w)			Input θ(c, w)		
NB	-14.35	11.3	LB	-43	98	NB	-29	22
NM	-8.67	11.35	LM	6	98	NM	-18	22
NS	-3	6	LS	55	72	NS	-7	14
ZE	0	6	CE	91	72	CE	0	14
PS	3	6	RS	127	72	PS	7	14
PM	8.67	11.35	RM	174.67	95.35	PM	18	22
PB	14.35	11.3	RB	222.35	95.3	PB	29	22

3) Chromosome Generation: Use self-learning capabile scheme, NSGA-II to initiate a random chromosome of a desired population size. Here a chromosome consists of 49 genes (x×φ or 7×7). Fig.4 examplifies a FAM(Fuzzy Associative Memory). From Fig. 4 it can be found that if x = 1(NB) and φ = 1(LB) then the corresponding θ = 7(PB).

4) Chromosome Decoding: Now, the given chromosome is transfered into a collection of center and width combination for each of the x, φ and θ maintaining the input partitions given in Table.1 in order to map the corresponding θ to identify the degree of membership. Hence, the size of the chromosome becomes 49×6=(7×7×3×2), where 3 is for three variables (x, φ, θ)and 2 is for center and width for each variable. The decoding process and the decoded chromosome is shwon in Fig. 5

5) Calculate Fitness Function and Ranking the Chromosome.: Calculate the fitness of a chromosome using objective function. Usually, the objective function desires to optimize several objectives and there should be a relation between the objectives, where progress in one objective can be attained without damaging the other. The three fitness objectives to minimize the error and mature. The solution used in this algorithm are given below:

Objective 1 - Trajectory Error (TE): The trajectory orientation tracking objective will inspect the orientation of the simulation as shown below-

$$TE = \frac{\text{Length of truck trajectory}}{\text{distance(initial pos,final pos)}} \quad (6)$$

Objective 2 -Docking Error (DE): Euclidean distance is known as docking error where distance between the actual final position (φ, x, y) and the desired final position (φ_f, x_f, y_f) is being measured -

$$DE = \sqrt{(\varphi_f - \varphi)^2 + (x_f - x)^2 + (y_f - y)^2} \quad (7)$$

Objective 3 - Execution time (N): For carrying out the docking maneuver, the desired time (cycles) is stated as

Table 2. Input partitions along with linguistic label

Real INT	X	φ	θ
1	NB	LB	NB
2	NM	LM	NM
3	NS	LS	NS
4	CE	CE	CE
5	PS	RS	PS
6	PM	RM	PM
7	PB	RB	PB

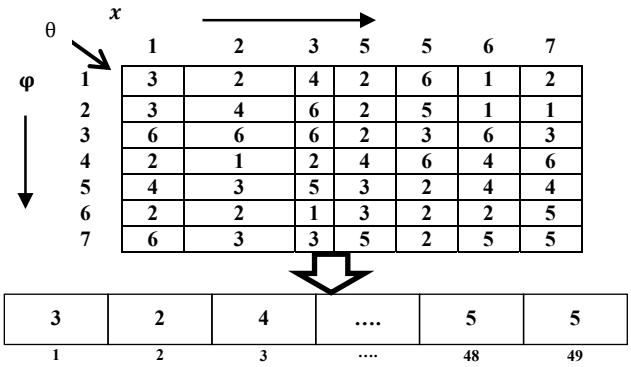

Figure 4. Fuzzy Associative Memory

Execution time. Here in the simulation Execution time is calculated by the difference of starting time of initial position and the loading time when the truck reached the destination.

6) Evaluate Chromosome: Rank the chromosome based on their fitness value. As it is a minimization problem, hence the minimum fitness will be ranked one. Then perform selection, crossover and mutation to generate next population. If the stopping criterion does not meet then repeat the steps from step 4.

B. Evulotionay Process

A new factor alongside with fitness value is known as crowding distance for every distinct value of population which is measured after the non-dominated sort. However, crowding distance is a degree of adjacent of an individual from its neighbors. Parents are selected from binary tournament

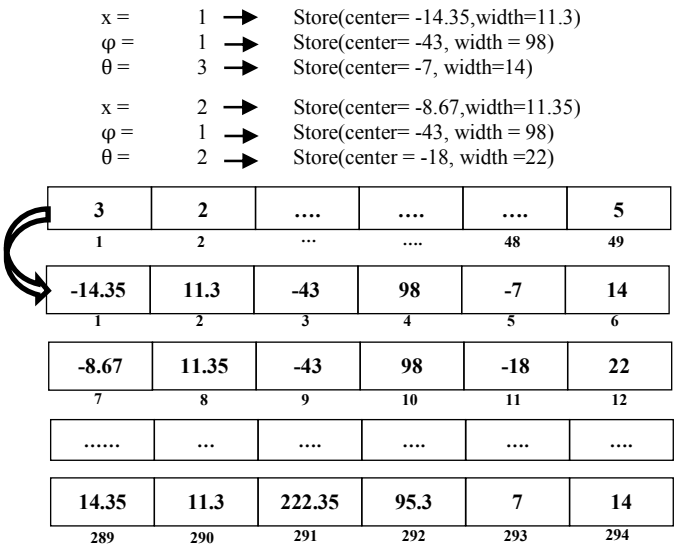

Figure 5. Chromosome Decoding

which is prepared from rank and crowding distance. The offsprings are produced by the chosen population through crossover and mutation operation [23], [24], [25]. Fig. 6 describes the control flow of the proposed model. The NSGA-II algorithm considers a set composed of several operators usually used in multi-objective optimization heuristics such as: simulated binary crossover (SBX), differential evolution operator (variation operator), polynomial mutation etc. [22]. The NSGA-II algorithm comprises of the following perimeters:

Selection: The crowded-comparison-operator ($\prec_n$) is utilized to accomplish the selection operation maintaining the following constraints:

(1) In front F_i for all entities the Non-domination rank, $p_{rank} = i$.

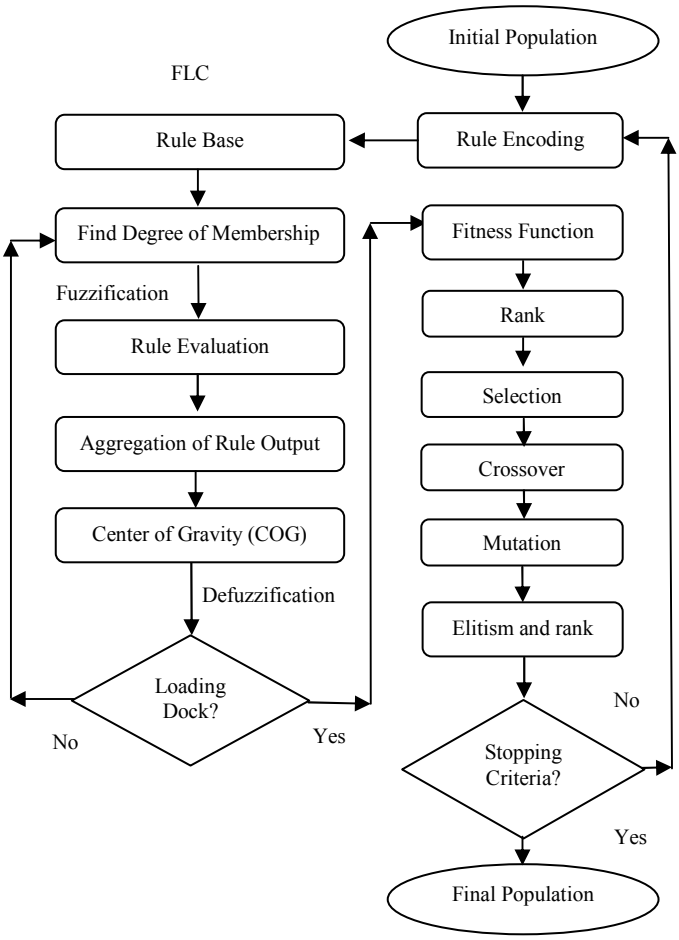

Figure 6. The Flow Chart of MO-NSGA-II based FRBS Model

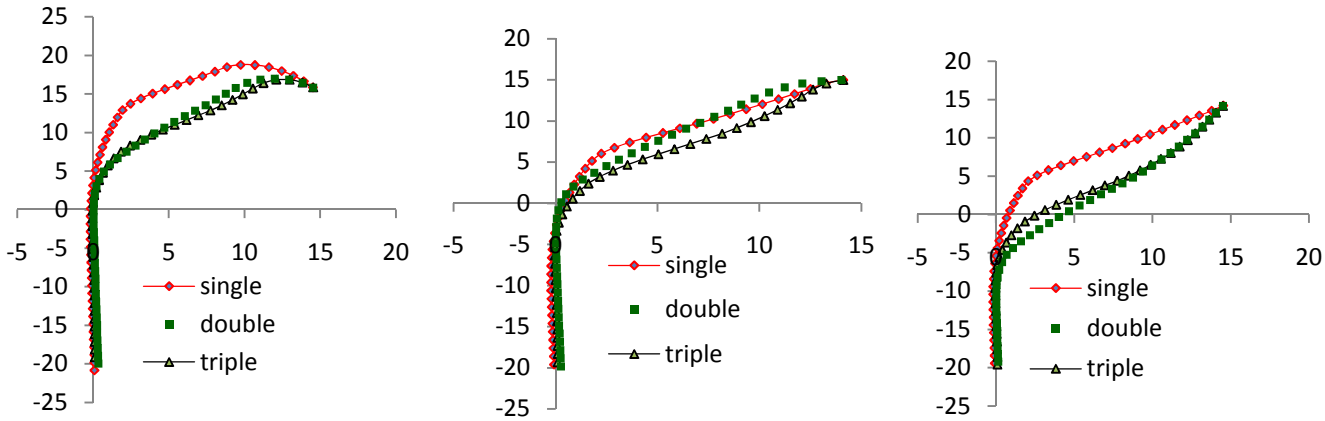

(a): Case 1 states (x, φ, y) = (15,-60, 15) (b): Case 2 states (x, φ, y) = (15, 0, 15) (c): Case 3 states (x, φ, y) = (15, 60, 15)

Figure 7. Comparisons of the result of single and MO-NSGA-II based FRBS Model

(2) Crowding distance $F_i(d_i)$

$p \prec_n q$ if

a) $p_{rank} < q_{rank}$

b) or if p and q are in the identical front F_i then $F_i(d_p) > F_i(d_q)$

With this operator the individuals are nominated through a binary tournament selection [23], [24], [25].

Genetic Operators: For crossover and polynomial mutation Genetic Algorithms apply Simulated Binary Crossover (SBX) operator [24].

Simulated Binary Crossover: Simulation perceived by the operator is given as below.

$$C_{1,k} = \frac{1}{2}[(1 - \beta_k)p_{1,k} + (1 + \beta_k)p_{2,k}] \quad (8)$$

$$C_{2,k} = \frac{1}{2}[(1 + \beta_k)p_{1,k} + (1 - \beta_k)p_{2,k}] \quad (9)$$

Where $C_{i,k}$ is the ith child, with k^{th} element, $p_{i,k}$ is the nominated parent and β_k (≥ 0) is a example as of a random number produced with density

$$\rho(\beta) = \frac{1}{2}(\eta_c + 1)\,\beta^{\eta c}, \text{if } 0 \leq \beta \leq 1 \quad (10)$$

$$\rho(\beta) = \frac{1}{2}(\eta_c + 1)\frac{1}{\beta^{\eta c}}, \text{if } \beta > 1 \quad (11)$$

From a uniformly sampled random number r among (0, 1) the distribution is achieved where $\boldsymbol{\eta_c}$ means distribution index for crossover [23], [24], [25].

To be exact,

$$\beta(r) = (2r)^{\frac{1}{(\eta+1)}} \quad (12)$$

$$\beta(r) = \frac{1}{[2(1-r)]^{\frac{1}{(\eta+1)}}} \quad (13)$$

Polynomial Mutation:

$$c_k = p_k + (p_k^u - p_k^l)\delta_k \quad (14)$$

Here, c_k is a child entity and p_k is a parent entity, p_k^u is the upper limit and p_k^l is the lower limit where δ_k is a minor difference that is measured by a polynomial distribution as follows:

$$\delta_k = 2r_k^{\frac{1}{\eta_{m+1}}} - 1, if\ r_k < .05 \quad (15)$$

$$\delta_k = 1 - [2(1 - r_k)]^{\frac{1}{\eta_{m+1}}}, if\ r_k \geq .05 \quad (16)$$

Where r_k is a random number between (0; 1) and η_m is mutation distribution index [23], [24], [25].

Recombination and Selection: The offspring population and the present population are combined. Afterwards the selection is performed in oder to get the individuals of subsequent generation where elitism is confirmed. If the addition of all the individuals in front F_j exceeds N then individuals in front F_j are selected until the population size N. The same procedure is repeated so that the following generations can be produced [23], [24], [25].

VI. Experimental Setup and Simulation Result

The experimental result is presented to show the strength of the offered method and compare the performance with the different fitness function. The experiments are peformed using real-coded rigid variables. Some essential parameters projected in the systems are presented in Table.3. Three cases as Case 1: (15, - 60, 15), Case 2: (15, 0, 15) and case 3: (15, 60, 15) are considered with initial states (x, φ, y) where the final or docking position (x_f, φ_f, y_f) is $(0, 90^0, 0)$. These cases are manipulated by three environments. The first environment is depicted by single in the graph. It considers the Objective-I which is the trajectory error. The second environment reflects the Objective-I and Objective-II which are the trajectory error and docking error pointed by double in the graph. And the last environment indicated by triple in the graph, deliberates three objectives which are the Objective-I (trajectory error), Objective-II (trajectory and docking error) and Objective-III (trajectory and docking error and execution time). Case-1, Case-2 and Case-3 are presented in Fig. 7(a), 7(b) and 7(c) respectively.

Table 3. Assumed Parameters for Constructed Prototypes

Cross-over Probability	1
Mutation Probability	0.02
Distribution Index for Crossover	100
Distribution Index for Mutation	500
Seed	1
Generation	100
Population	600

From the simulation graph it can be seen that in every environment for different starting position the truck can be loaded with desired loading angle (90^0) along with the docking position (0, 0). In the ultimate trajectory the truck first passages beside the objective link or overlaps through the objective link and then drive nearby y-axis towards the goal.

VII. CONCLUSION

In this article, Multi-objective FRBS has been developed using NSGA-II and the FRBS for intelligent control of car like robot system. The optimizations used in NSGA-II are: trajectory error, docking error and time. The rule base of the proposed FRBS MO-NSGA-II is tuned for optimal control performance by simultaneously optimizing the multiple objective functions. The instantaneous optimization of these objectives enhances the performance of the control algorithm. Simulation results demonstrate the performance advantage and quality solutions of multi-objective approach. Furthermore, in general the multi-objective based control algorithm requires high computation. Therefore, the paradigm is not apposite in applications demanding high constraints regarding time or memory.

REFERENCES

[1] Carlos M. Fonseca and Peter J. Fleming, "An Overview Of Evolutionary Algorithms In Multiobjective Optimization", Evolutionary Computation archive Volume 3, Issue 1 , MIT Press Cambridge, MA, USA, Pages 1-16, Spring 1995

[2] N. Srinivas and Kalyanmoy Deb, "Muiltiobjective Optimization Using Nondominated Sorting in Genetic Algorithms", Massachusetts Institute of Technology, Volume. 2, Issue 3, Pages 221-1994, Fall 1994

[3] J.M. Lucas, H. Martinez, and F. Jimenez, "Multi-objective Machine Learning Application: Fuzzy Tuning for the Docking Maneuver Controller of an Automated Guided Vehicle", Studies in Computational Intelligence, Volume 16, Pages 585-600, 2006

[4] K. Deb, S. Agrawal, A. Pratap, and T. Meyarivan, "A Fast And Elitist Multi-Objective Genetic Algorithm: NSGA-II", Evolutionary Computation, IEEE Transactions, Volume 6 , Issue 2, Pages 182–197, 2002

[5] Reza Salimi, Navid Bazrkar, and Mostafa Nemati, "Task Scheduling for Computational Grids Using NSGA II with Fuzzy Variance Based Crossover", Advances in Computing, Vol. 3 No. 2, pp. 22-29, 2013

[6] Abdullah Konaka ,David W. Coitb, Alice E. Smithc, "Multi-objective optimization using genetic algorithms: A tutorial", Reliability Engineering & System Safety ,Volume 91, Issue 9, Pages 992–1007, September 2006

[7] F. J. Cabrerizo, J. Lopez-gijon and A. A. Ruizo, "A Model Based On Fuzzy Linguistic Information To Evaluate The Quality Of Digital Libraries", Int. Journal of Information Technology & Decision Making, Volume 9, Issue 3, Pages 455–472, May 2010

[8] A. Daftaribesheli, M. Ataei, and F. Sereshki, "Assessment Of Rock Slope Stability Using The Fuzzy Slope Mass Rating (FSMR) System", Applied Soft Computing, Volume 11, Issue 8, Pages 4465–4473, December 2011

[9] S. E. Oltean,"Swing-up and Stabilization of the Rotational Inverted Pendulum Using PD and Fuzzy-PD Controllers", Procedia Technology, Volume 12 , Pages 57–64 , 2014

[10] C. S. Chen, Y. D. Jhong, T. Y. Wu, and S.-T. Chen, "Typhoon Event-Based Evolutionary Fuzzy Inference Model For Flood Stage Forecasting", Journal of Hydrology, Volume 490, Pages 134–143, 20 May 2013

[11] Shill P.C., Maeda Y, Murase, "Optimization of Fuzzy Logic Controllers with Rule Base Size Reduction Using Genetic Algorithms", Computational Intelligence in Control and Automation (CICA), 2013 IEEE Symposium, Pages 57 – 64, April 2013

[12] B. Dennis and S. Muthukrishnan "AGFS: Adaptive Genetic Fuzzy System for medical data classification", Applied Soft Computing, Volume 25, Pages 242–252 25, December 2014

[13] Shill, P.C., Pal K.K., Amin M.F.,Murase K.," Genetic Algorithm Based Fully Automated and Adaptive Fuzzy Logic Controller", Fuzzy Systems (FUZZ), 2011 IEEE International Conference , Pages 1572 – 1579, June 2011

[14] H. Wang, S. Kwong, Y. Jin, W. Wei, K.F. Man," Multi-Objective Hierarchical Genetic Algorithm For Interpretable Fuzzy Rule-Based Knowledge Extraction", Fuzzy Sets and Systems ,Volume 149, Issue 1, Pages 149–186, January 2005

[15] Alcala-Fdez J., Alcala R., Herrera F. "A Fuzzy Association Rule-Based Classification Model for High-Dimensional Problems With Genetic Rule Selection and Lateral Tuning", Fuzzy Systems, IEEE Transactions ,Volume 19 , Issue 5, Pages 857 – 872, April 2011

[16] C.H. Tan, K.S. Yap, H.J. Yap, "Application Of Genetic Algorithm For Fuzzy Rules Optimization On Semi Expert Judgment Automation Using Pittsburg Approach", Applied Soft Computing, Volume 12, Issue 8, Pages 2168–2177, August 2012

[17] Lam T. Bui, Daryl Essam, Hussein A. Abbass, and David Green. "Performance Analysis Of Evolutionary Multi-Objective Optimization Methods In Noisy Environments", 8th Asia Pacific Symposium on Intelligent and Evolutionary Systems, Pages 29-39, 2004.

[18] Xing Zong-yi, Zhang Yong , Hou Yuan-long , Cai Guo-Qiang "Multi-Objective Fuzzy Modeling Using NSGA-II", Cybernetics and Intelligent Systems, 2008 IEEE Conference, Pages 119 – 124, Sept. 2008

[19] Ying Li, Yuanchun Li," Neural-Fuzzy Control Of Truck Backer-Upper System Using A Clustering Method", Neurocomputing, Volume 70, Issues 4–6, Pages 680–688, January 2007

[20] Zitzler, E and Lothar Thiele, "An Evolutionary Algorithm For Multiobjective Optimization The Strength Pareto Approach", Evolutionary Computation, IEEE Transactions, Volume 3, Issue 4, Pages 257 – 271, Nov 1999.

[21] S. Padhee, N. Nayak, S.K. Panda, and S.S. Mahapatra, "Multi-Objective Parametric Optimization Of Powder Mixed Electro-Discharge Machining Using Response Surface Methodology And Non-Dominated Sorting Genetic Algorithm", Indian Academy of Sciences, Sadhana, Volume. 37, Issue 2, Pages 223–240, April 2012.

[22] Antonio J. Nebro, Juan J. Durillo, Mirialys Machın, Carlos A. Coello Coello, and Bernab´e Dorronsoro, "A Study of the Combination of Variation Operators in the NSGA-II Algorithm", 15th Conference of the Spanish Association for Artificial Intelligence, CAEPIA 2013, Pages 269–278, September 2013

[23] Hans-Georg Beyer and Kalyanmoy Deb "On Self-Adaptive Features In Real-Parameter Evolutionary Algorithms", Evolutionary Computation, IEEE Transactions Volume 5, Issue 3, Pages 250 - 270, June 2001.

[24] Kalyanmoy Deb and R. B. Agarwal. "Simulated Binary Crossover for Continuous Search Space" ,Complex Systems, Volume 9, Issue 2 Pages 115 -148, April 1995

[25] M. M. Raghuwanshi and O. G. Kakde. "Survey On Multiobjective Evolutionary And Real Coded Genetic Algorithms", 8th Asia Pacific Symposium on Intelligent and Evolutionary Systems, Pages 150 -161, 2004

A Multi-Objective Genetic Algorithm with Fuzzy Relational Clustering for Automatic Data Clustering

Animesh Kundu, Animesh Kumar Paul[1], Pintu Chandra Shill
Department of Computer Science and Engineering
Khulna University of Engineering and Technology
Khulna, Bangladesh
[1]animesh10kuet@gmail.com

Kazuyuki Murase
Department of System Design Engineering
University of Fukui,
Japan
murase@u-fukui.ac.jp

Abstract—**A multi-objective genetic algorithm based fuzzy relational eigen vector centrality based clustering algorithm (FRECCA) called FRECCA-NSGA-II is proposed for automatic data clustering in this paper. A given dataset is spontaneously promoted into an optimal number of groups in a precise fuzzy partitions through the fuzzy clustering algorithm called FRECCA. This FRECCA algorithm operates on a similarity square matrix which is generated by comparing the pair wise similarities between data points. In most of the cases, fuzzy clustering methods cannot differentiate the geometric structures of clusters due to the cohesion and separation measures of fuzzy partition and using only centroid information for clustering. NSGA-II algorithm is therefore convenient to search for uniform fuzzy partitions for different cluster shapes. The two well-known cluster validity indices, cohesion and separation, are optimized concurrently through multi-objective NSGA-II. Binary encoding is used for chromosomes, here encode the centers as well as variable length numbers of clusters. Experimental results on benchmark data sets are given to demonstrate that the FRECCA-NSGA-II is capable of determining well-separated, hyper-spherical and overlapping clusters. The superiority of the propose FRECCA-NSGA-II over the existing clustering algorithm is thoroughly elucidated for real-life benchmark data sets.**

Keywords—Fuzzy Relational Clustering (FRECCA), Multi-Objective Optimization, Non-dominated Sorting Genetic Algorithm (NSGA-II), Pareto Optimal Solution.

I. INTRODUCTION

Clustering works as a unsupervised method which classified patterns (data points or observations or feature vectors) into community or clusters, such that extracted patterns in the same community are similar to each other while extracted patterns in different communities are dissimilar [1]. Clustering methods which helps to find the underlying structures in data and this advantages are used in a wide distinction of applications, including classification, image processing, pattern recognition, document retrieval, biology, modeling and identification. These fields deploy multi-dimensional data and hence it is problematic to perceive information and clustering in high dimensional space [2]. A sustainable number of methods such as k-means [3], fuzzy c-means (FCM) [4] have been proposed to solve these clustering problems. These methods [3-4] are centroid based and the number of clusters is predefined.

In k-means clustering algorithm, *d*-dimensional space for data, a set of *n* data points and an integer *k*, representing the number of cluster are given as an input and the problem is to determine a set of *k* centers in *d*, which helps to represent the whole dataset. After assigning the all objects, it recalculate the positions of the *k* centers. These steps are repeated until the centers no longer move. For this reason, this problem can't be solved by any exactly known polynomial-time algorithms.

Fuzzy c-means (FCM) algorithm performs soft partitioning since it groups a dataset into *n* clusters. In the process, each data points in the dataset associates to every cluster to a certain degree. FCM clustering is a serviceable algorithm, but the random selection in center points and number of clusters leads to iterative process and it has a probability that the solution will easily get stuck into the local optimum. Another problem in FCM is to choose the fuzziness parameter m. Generally, m=2 is used but it is not appropriate for some datasets and optimal m value varies from one dataset to another. On the other hand, FCM cannot provide satisfactory clustering in case of noisy data [5]. In most of the cases, number of cluster is not known before and some works have suggested to handle such situation by running the algorithm several times for different values of *k* along with varying initialization [6] but this technique is not suited for large datasets since it fails to find global optimum.

In order to surpass the above problems, genetic computation have been introduced for inferring the optimal cluster's numbers to make the clustering process more efficient. In our study, to resolve the disadvantages of fuzzy clustering we have to make a hybrid genetic algorithm with fuzzy clustering.

Many real-life problems involve performance measurement or objectives that optimize all objectives simultaneously. Multi-objective genetic algorithms (MOGAs) provide better performance over single-objective clustering algorithms [7] for the complex datasets where the partitioned clusters have different sizes or different geometric shapes. In order to obtain appropriate partitioning of complex data sets consisting of different shaped clusters, the chosen objective functions should treat compactness of clusters along with the ability to deal with overlapping clusters. In such situations MOGAs provide better result than those using single objective function by incorporating two or more objective functions [7]- [8].

978-1-4673-9257-0/15/$31.00 ©2015 IEEE

In this paper, we bring up a new multi-objective evolutionary approach to evolve optimal data clustering without requiring predicting the number of clusters. This method optimizes two objectives simultaneously, fuzzy J_m index [4] and overlap-separation measure [9]-[10]. This approach called FRECCA-NSGA-II used the non-dominated sorting genetic algorithm-II (NSGA-II) [11] for multi-objective optimization whereas the FRECCA algorithm is used to generate fuzzy clusters from data points.

The basic association of the paper is given as follows: Section 2 focuses on related works of this proposed method. Section 3 briefly describes our proposed fuzzy relational clustering algorithm called FRECCA-NSGA-II. This section providing details of FRECCA algorithm, describes the evolutionary process of NSGA-II algorithm and mention the process how to integrate NSGA-II with FRECCA also. Applied data sets in our model are detailed in Section 4. Section 4 represents the analysis results of FRECCA-NSGA-II compared with other approaches and finally, a conclusion of the paper is drawn into section 5.

II. Review of Related Works

This section describes the related methods of the fuzzy clustering with genetic algorithms from the different literature particularly, in the standard journals. From the analysis of the related literature, fuzzy clustering method's deficiency can be overcome by means of the genetic algorithm. So, the considerable drawbacks of fuzzy clustering of a problem can be solved using the multi objective genetic algorithm.

To surpass the drawbacks of FCM, a PSO based fuzzy clustering algorithm is introduced in [12]. Here, it uses the PSO algorithm's receptivity of global search.

Gan *et al.*, introduced a method for clustering the categorical data sets using the genetic fuzzy *K*–modes algorithm. For finding the global optimal solution of this optimization problem, they used genetic algorithm. In the crossover process, here applied the one-step fuzzy *K*–modes instead of the traditional crossover operator.

Yang *et al.*, brought forward a hybrid data clustering algorithm based on PSO and *K*-Harmonic Means [14] in which the KHM clustering doesn't fall into local optima and helps to surpass the incompleteness of the PSO algorithm's slow convergence characteristics.

Genetic algorithms have shown to facilitate in automatically determining the number of clusters by employing varying string length [15]-[17]. GA has been used in clustering the digital data sets [15]. As it is mentioned in [15] this type of algorithms is strong to recognize the clusters of any shape, but it fails to recognize the patterns for a small spatial separation between the clusters.

III. Proposed Hybrid FRECCA-NSGA Algorithm

This section introduces the working principle of proposed multi-objective genetic algorithm (NSGA-II) based FRECCA algorithm. This section also introduces FRECCA algorithm and objective functions.

A. Multi-Objective NSGA-II based FRECCA

In this study, we design a hybrid clustering algorithm called FRECCA–NSGA-II by combined FRECCA algorithm with NSGA-II algorithm in which it sustains the goodness of both FRECCA and NSGA-II algorithms.

FRECCA–NSGA-II algorithm executes FRECCA algorithm for the solutions (chromosomes) in every number of iterations/ generations such that each solution's fitness is improved. For solving the fuzzy clustering problem, the FRECCA–NSGA-II algorithm can be explained as follows:

Algorithm: FRECCA-NSGA-II for fuzzy clustering
Step-1: Initialize the parameters of FRECCA and MO-NSGA-II containing Number of clusters *C*, population size P, Cluster membership values for each data point on each cluster { p_i^m | i = 1,....,*N*, m = 1,....,*C* }, pairwise similarity values *S* = { s_{ij} | i = 1,....,*N*, j = 1,....,*N* } where s_{ij} is the similarity between data point i and j
Step-2: Create initial generation with P chromosomes
Step-3: Multi-Objective NSGA-II algorithm:
3.1. Calculate the number of clusters for each chromosome.
3.2. Multiple objective's value is calculated for each chromosome using Eq. (3) and Eq. (4).
3.3. Selection, crossover and mutation operations are acted on parent population to produce offspring population.
3.4. Offspring population are combined with parent population.
3.5. Fast non-dominated sorting performed on combined population to place individuals in their respective front.
3.6. Using nitching strategy, preference distance of individuals is calculated.
3.7. Better front and the least preference distance contained individuals are selected for to make new parent population.
3.8. If Multi-objective NSGA-II's execution finishing condition is not accomplished, go to step 4.
Step-4: FRECCA algorithm
4.1 Initialize and normalize membership values
4.2 Weighted affinity matrix create for cluster m
4.3 PageRank scores calculate for cluster m
4.4 Assign PageRank scores to likelihoods
4.5 Calculate new cluster membership values
4.6 Update mixing coefficients
4.7 Go back to step 4.2 if FRECCA algorithm's execution finishing condition is not satisfied.

Step-5: if FRECCA-NSGA-II algorithm's execution finishing condition is not accomplished, go to step 3.

B. Fuzzy Relational Clustering Algorithm (FRECCA)

In this study, data clustering is performed using Fuzzy Relational Eigenvector Centrality-based Clustering Algorithm (FRECCA) which uses graph representation in which objects are indicated using nodes, and similarity between objects is indicated using weighted edges. This algorithm employed the modified PageRank algorithm to each cluster. Measurement of centrality of a node within a given graph is done by using Page Rank algorithm and here, it assigns a Page Rank Score to every node in graph and here page rank score is given in numerical score from 0 to 1. In this case, the Page-Rank score of a data point within some cluster is interpreted as likelihood and then determination of cluster membership values and mixing coefficients [18] is performed using Expectation-Maximization (EM) framework.

The modified PageRank algorithm to work with weighted undirected edges of a graph representing objects with nodes V.

$$PR(V_i) = (1-d) + d \times \sum_{j=1}^{N} \left(w_{ji} \quad \frac{PR(V_j)}{\sum_{k=1}^{N} w_{jk}} \right) \tag{1}$$

978-1-4673-9257-0/15/$31.00 ©2015 IEEE

where w_{ji} is the similarity between V_j and V_i, and it is assumed that matrix contains these weights $W = \{w_{ij}\}$, which is referred to as the "affinity matrix".

1) Expectation Step

This first step, using the cluster membership values and scaling the similarities, the affinity matrix weights wij are calculated. i.e.

$$w_{ij}^m = s_{ij} \times p_i^m \times p_j^m \quad (2)$$

where w_{ij}^m is the weight between objects i and j in cluster m, s_{ij} is the similarity between objects i and j, and p_i^m and p_j^m are the membership values of objects i and j to cluster m. Then, for each cluster, it calculate the PageRank values according to eqn (1). Then PageRank scores are treated as probabilities and cluster membership values are calculated by PageRank.

2) Maximization Step

In maximization step updating of mixing coefficients is performed based on the Expectation step's calculated membership values of cluster. We get cluster membership values as an output.

C. NSGA-II Optimizaion Process

In order to solve real world complex optimization problems, multiple objectives need to be optimized at one time for many problems. Clustering algorithms try to optimize the multiple validity measures such as compactness, separation among clusters simultaneously. In our work, to handle this situation on clustering algorithm, FRECCA we have joined the multi-objective genetic algorithm (NSGA-II) with FRECCA. In the present section, NSGA-II optimization process is described whose goal is to assign the appropriate number of cluster and optimize multiple clustering validity measures.

The NSGA-II, proposed in [19] is an exoteric non-domination based genetic algorithm for optimizing multi-objectives. NSGA-II main objective is using a set of objective functions to improve the candidate solution's adaptive fitness of a population to a Pareto front constrained.

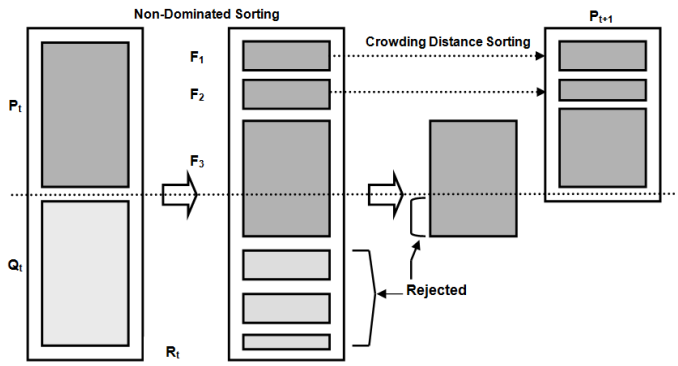

Fig. 1. NSGA-II Working Procedure

The NSGA-II working procedure is given in Fig. 1. The individuals with lower rank or larger crowding distance are selected as parents by binary tournament selection. Using crossover and mutation operations, selected population generates offspring and again select only the best N individuals as parents for the next iteration based on crowding distance on the last front and on rank from the current population and generated offspring by sorting based on non-domination.

1) Fast Nondominated Sorting

In NSGA-II, fitness assignment is done by non-dominated sorting. Front number 1 is assign to individuals which are not dominated by any other individuals and Front 2 is assign to those individuals which are only dominated by individuals whose front number are 1 and so on. Hence, two entities are calculated for each solution: a) domination count n_p, where p solution is dominated by n_p number of solutions b) S_p, solution set dominated by solution p.

Assume $n_p = 0$ for all solutions of first nondominated front. For each solution p with $n_p = 0$, each member (q) of its set S_p is visited and its n_p is reduced by one. As a result, if for any member q, the n_p becomes zero, it is dropped in a separate list Q. The second non-dominated front contains these members. Until all fronts are identified, this process continues with each member of Q and the identified third front.

2) Crowding Distance

The crowding-distance computation is part of density estimation of solutions surrounding an individual solution [20]. For density estimation, here with each of the objectives, it calculates the average distance of two points on either side of this point. This measure ($i_{distance}$), called crowding distance. By using the nearest neighbors consider as the vertices, $i_{distance}$ is treated as perimeter of the cuboid formed. The crowding-distance process includes the following steps:

a) For each given objective function m

- An infinite distance value is employed to boundary solutions.
- A distance value is assigned to other intermediate solution and here the assigned value is equal to the absolute normalized difference in the function values of two contiguous solutions.

b) Total crowding-distance value = For each objective, the total sum of individual distance values.

D. Objective Functions

In this study, we consider two objective functions fuzzy compactness and fuzzy overlap-separation. Let $X = \{x_1, x_2, \ldots, x_k\}$ be data points of M patterns, where on the n-dimensional space, each pattern x_k is a vector of features in R^n, C denotes the total number of clusters.

Minimize: Fuzzy Compactness,

$$J_m(U, V) = \sum_{k=1}^{M} \sum_{i=1}^{C} (u_{ik})^m \, d_{ik}^2 \quad (3)$$

Where, for n-dimensional space, d_{ik}^2 is the calculated squared euclidean distance.

The second objective functions is combination of l-order overlap and inter cluster separation both of which are measure for cluster validity. These are based on aggregation of membership values. The aggregation is composed of standard t-norm function $\top$ and t-conorm function $\perp$ with operator properties a $\top$ b = min (a, b) and a $\perp$ b = max (a, b).

For a data point x_k the overall inter-cluster overlap [9]-[10] is computed using fuzzy degrees by

Maximize: Inter-cluster Separation,

$$O \perp (u_k(x_k), C) = \underset{l=2,C}{\overset{1}{\perp}} \left(\underset{i=1,C}{\overset{l}{\perp}} u_{ik} \right) \quad (4)$$

978-1-4673-9257-0/15/$31.00 ©2015 IEEE

where membership vector for x_k is $u_k(x_k) = (u_{1k}, \ldots, u_{ck})$.

For x_k each u_k is associated with a single value $\perp^{l}(u_k) \epsilon$ [0, 1] by l-order fuzzy-OR operator (f OR-l) which is aggregation of t-norms and is given by

$$\underset{i=1,C}{\overset{l}{\perp}} u_{ik} = \underset{A\epsilon P_{l-1}}{\overset{\top}{}} \left(\underset{j\epsilon C\setminus A}{\perp} u_j \right) \tag{5}$$

where P denotes the power set of C= $\{1,2,\ldots,c\}$ and $P_l = \{ A\epsilon P: \ |A| = l \}$, where $|A|$ denotes the subset A's cardinality.

The separation measure is determined by highest degree of $\max_{i=1,C} u_{ik}$. The total Overlap separation (OS) calculation for M patterns is given by

$$OS = \frac{1}{M} \sum_{k=1}^{M} \frac{O\perp(u_k(x_k),C)}{max_{i=1,c} u_{ik}} \tag{6}$$

IV. Simulation Results and Discussion

In this section, data sets and simulation outputs are presented in order to interpret the effectiveness of our proposed fuzzy relational clustering algorithm called FRECCA based on multi-objective NSGA-II algorithm.

A. Data Sets

Real life data sets Iris, Glass, Wine and Liver Disorders are found from the UCI Machine Learning Repository [21]. The artificial datasets are AD_5_2 [22], AD_10_2 [23], Square-1, Square-2, Long-1. Table I shows the brief description of data sets, where D is the number of features, K is the number of clusters, M is sample size, and M_i is the number of members in cluster i.

Table I. Summary of Data Sets

Data Sets	D	K	M	M_i
AD_5_2	2	5	250	5×50
AD_10_2	2	10	500	10×50
Square-1	2	4	1000	4×250
Square-2	2	4	1000	4×250
Long-1	2	2	1000	2×500
Glass	9	6	214	70, 76, 17, 13, 9, 29
Wine	13	3	178	59, 71, 48
Iris	4	3	150	50, 50, 50
Liver-Disorders	6	2	341	142, 199

The data sets have the following features:

- AD_5_2 data set contains five classes. Each cluster has 50 points with highly overlapped 250 data point and each data point has two attributes.
- AD_10_2 data set contains ten classes with two attributes of 500 data points.
- Square-1 data set contains four classes with two attributes of 1000 data points. It is generated by normal distributions with a standard deviation of two in both dimensions.
- Square-2 data set contains four classes with two attributes of 1000 data poitns. It is generated by normal distributions with a standard deviation of two in both dimensions.
- Long-1 dataset contains two long shaped clusters with 1000 instances.
- Iris data set composed of three classes where each class consists of 50 instances. Each instance is described by four physical attributes which are length and width of sapals and petals.
- Wine consists of thirteen chemical attributes for 178 instances and divided into three classes.
- Liver-Disorders data set contains two classes with six attributes of 341 data points.

B. Experimental Results

We examine our proposed model on nine well known datasets describe in the previous section and compared with other existing algorithms. We take five artificial data sets and four real data sets for examining our proposed model.

Analyzing the result of different multi-objective techniques, FRECCA-NSGA-II provides better accuracy which is maintained by MS value and the number of clusters than other technique as shown in table-II and Fig.2, Fig. 3 and Fig. 4. Here, MS is used to obtain the best solution from the non-dominated set.

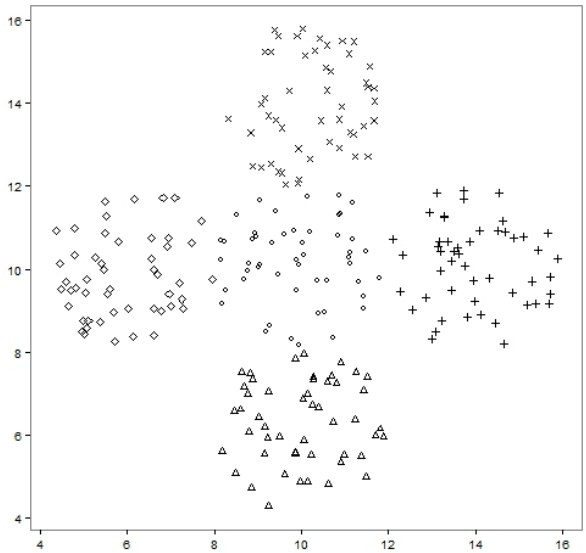

(a)

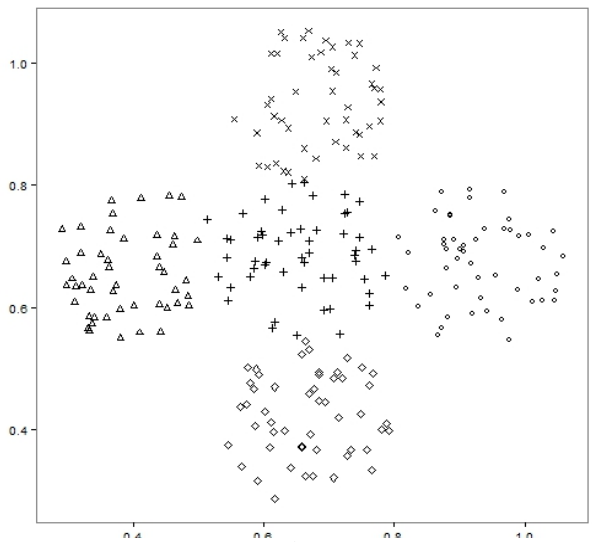

(b)

Fig. 2. (a) Original/True solution and (b) Clustering using FRECCA-NSGA-II (MS = 0.28) for the data set AD_5_2 (K = 5)

978-1-4673-9257-0/15/$31.00 ©2015 IEEE

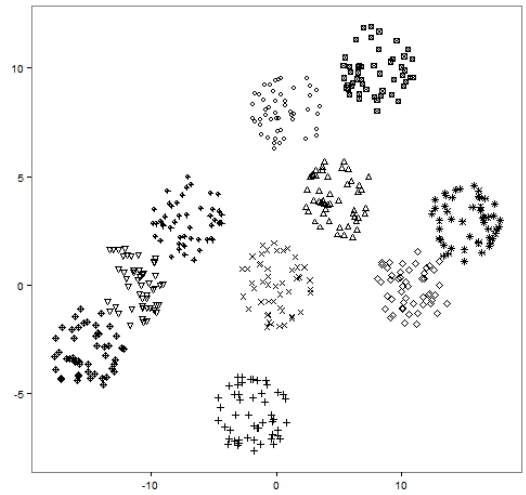

(a)

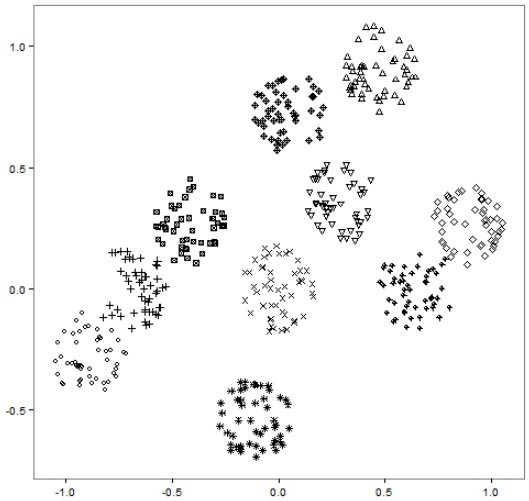

(b)

Fig. 3. (a) Original/True solution and (b) Clustering using FRECCA-NSGA-II (MS = 0.12) for the data set AD_10_2 (K = 10)

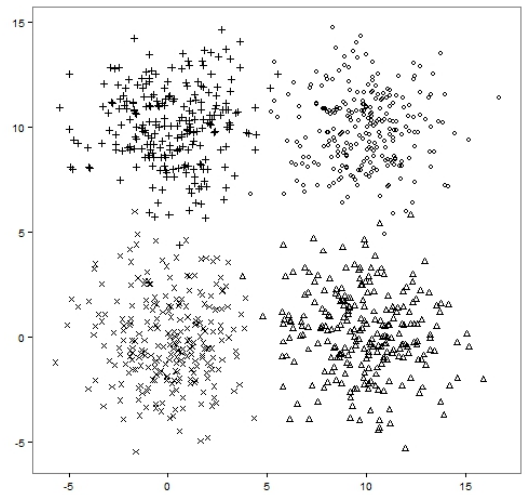

(a)

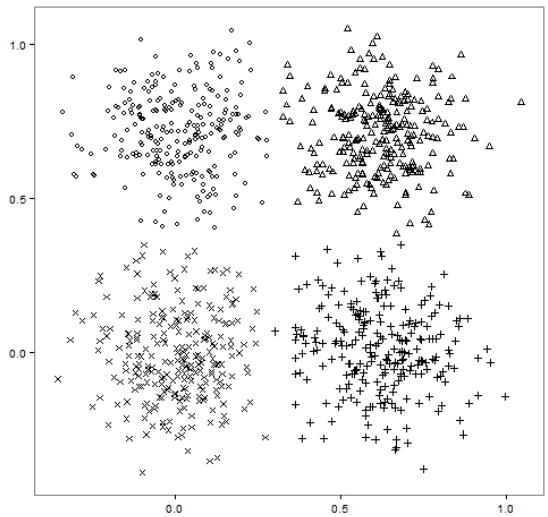

(b)

Fig. 4. (a) Original/True solution and (b) Clustering using FRECCA-NSGA-II (MS = 0.12) for the data set Square-1 (K = 4)

Figs. 2–4 compare the results of data partitioning by FRECCA-NSGA-II with the original data partitioning for three data sets. FRECCA-NSGA-II shows the better performance on separation, compactness and overlapping clusters for data sets as shown in Table-II. FRECCA-NSGA-II works effectively for the well-separated data points of AD_10_2 and Square-1 as shown in Fig. 3 and Fig. 4. Misclassification of data points can be caused by overlapping where borderline between clusters contain the data points.

In order to validate our proposed fuzzy relational clustering technique, FRECCA-NSGA-II is compared with other existing multi-objective methods like VAMOSA [7], MOCK [24], and FCM-NSGA [26] and with VGAPS [25], which is a single-objective clustering method. The comparison is made by the number of cluster and MS value as given in Table 2, where the results of VGAPS, MOCK and VAMOSA are obtained from [7] and FCM_NSGA is obtained from [26]. From the Table II, we have seen that our proposed model gives minimum MS value for most of the datasets with comparison to other approaches and it performs superior to others approaches for Wine, Iris datasets.

Table II. Comparative Analysis of FRECCA-MONSGA-II with other existing methods

DataSet	Actual K	Freeca-NSGA		FCM-NSGA		VAMOSA		MOCK		VGAPS	
		K	MS	K	MS	K	MS	K	MS	K	MS
AD_5_2	5	5	0.28	5	0.29	5	0.25	6	0.39	5	0.25
AD_10_2	10	10	**0.12**	10	0.13	10	0.43	6	1.01	7	0.84
Square-1	4	4	**0.18**	4	0.18	4	0.19	4	0.19	4	0.20
Square-4	4	4	0.50	4	0.49	4	0.51	4	0.60	5	0.52
Long-1	2	2	**0.0**	2	0.0	2	0.68	2	0.0	3	1.00
Glass	6	6	0.97	6	0.79	6	1.33	6	1.34	6	1.11
Wine	3	3	**0.52**	3	0.93	3	0.97	3	0.90	6	0.97
Iris	3	3	**0.38**	3	0.57	2	0.80	2	0.82	3	0.62
LiverDisorders	2	2	0.98	2	0.98	2	0.98	3	0.98	2	0.98

978-1-4673-9257-0/15/$31.00 ©2015 IEEE

C. Results of Non-dominated Solutions

The non-dominated solution is acquired by FRECCA-NSGA-II using artificial datasets and real-life datasets. Fig 5(a)-(b) shows non-dominated solution for Iris and Wine datasets.

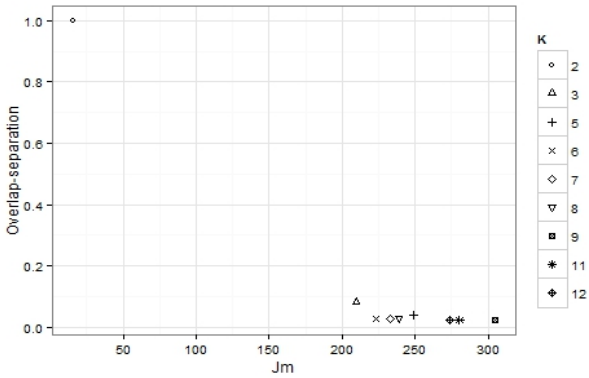

(a)

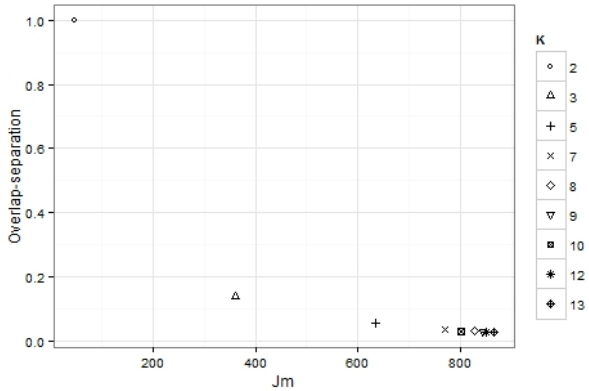

(b)

Fig.5. Non-dominated solution found while applying FRECCA-NSGA-II (a) Iris and (b) Wine dataset

V. CONCLUSIONS

This paper explorers the task of data clustering with multi-objective enabled by combination of multi-objective non-dominated sorting (NSGA-II) and fuzzy relational clustering algorithm (FRECCA). This hybrid technique is capable to partition the given data set into groups satisfying two objective functions, compactness and overlap-separation. The incorporation of fuzzy relational clustering algorithm has been an added advantage to work with real life complex data sets requiring higher clustering accuracy. The simulation results illustrate the superior capability of this propose hybrid technique in handling overlapped clusters than other single and multi-objective approaches.

REFERENCES

[1] A. K. Jain, M. N. Murty, and P. J. Flynn, "Data clustering: A review,"*ACM Comp. Surv.*, vol. 31, pp. 264–323, 1999.

[2] Kevin Beyer, Jonathan Goldstein, Raghu Ramakrishnan, and Uri Shaft, "When is nearest neighbors meaningful," in *Proc. of the International Conference of Database Theories*, 1999, pp. 217–235.

[3] J.B. MacQueen, "Some methods for classification and analysis of multivariate observations," in *Proc. of the Fifth Berkeley Symposium on Mathematical Statistics and Probability*, vol. 1, University of California Press, 1967, pp. 281–297.

[4] J.C. Bezdek, R. Ehrlich and W. Full, "FCM: the fuzzy c-means clustering algorithm," *Comp. Geosci*. Vol. 10 pp. 191–203, 1984.

[5] X.L. Yang, Q. Song and Y.L. Wu, "A robust deterministic annealing algorithm for data clustering," *Data & Knowledge Engineering,* Vol. 62 issue 1, pp. 84–100, Jul. 2007.

[6] E.R. Hruschka, R.J.G.B. Campello, A.A. Freitas and P. Leon, "A survey of evolutionary algorithms for clustering," *IEEE Trans. Systems, Man and Cybernatics- Part C: Aplications and Reviews,* vol. 39, pp. 133–155, 2009.

[7] S. Saha and S. Bandyopadhyay, "A symmetry based multiobjective clusteringtechnique for automatic evolution of clusters," *Pattern Recognit*. Vol. 43, pp.738–751, 2010.

[8] D. Karaboga and C. Ozturk, "A novel clustering approach: Artificial Bee Colony (ABC) algorithm," *Applied Soft Computing,* vol. 11, pp. 652–657, 2011.

[9] H.L. Capitaine and C. Frélicot, "A family of cluster validity indexes based on a l-order fuzzy or operator," *Lect. Notes Comp. Sci.,* pp. 622–631, 2008.

[10] H.L. Capitaine and C. Frélicot, "A cluster-validity index combining an overlap measure and a separation measure based on fuzzy-aggregation operators," *IEEE Trans. Fuzzy Syst.* Vol. 19, pp. 580–588, 2011.

[11] K. Deb, A. Pratap, S. Agarwal and T. Meyariva, "A fast elitist non-dominated sorting genetic algorithm for multi-objective," *IEEE Trans. Evol. Comp.* vol. 6 pp. 182–197, 2002.

[12] Li, L., Liu, X., and Xu, M. (2007). "A novel fuzzy clustering based on particle swarm optimization," *In First IEEE international symposium on information technologies and applications in education,* 2007*,* pp. 88–90.

[13] G. Gan, J. Wu and Z. Yang, "A genetic fuzzy k-modes algorithm for clustering categorical data," *Expert Systems with Applicationss,* Vol. (36), pp. 1615–1620, 2009.

[14] Yang, F., Sun, T. and Zhang, C., "An efficient hybrid data clustering method based on K-harmonic means, and particle swarm optimization," *Expert Systems with Applications,* Vol. 36, pp. 9847–9852, 2009.

[15] G. Garai and B.B. Chaudhuri, "A novel genetic algorithm for automatic clustering," *Pattern Recognit. Lett*. Vol. 25 pp.173–187, Jan. 2004.

[16] U. Maulik andS. Bandyopadhyay, "Genetic algorithm-based clustering technique," *Pattern Recognit.,* Vol. 33, pp. 1455–1465, Sep.2000.

[17] D.-X. Chang and X.-D. Zhang, C.-W. Zheng, "A genetic algorithm with gene rearrangement for k-means clustering," *Pattern Recognit.,* Vol. 42, pp. 1210–1222, Jul. 2009.

[18] Andrew Skabar and Khaled Abdalgader, "Clustering Sentence-Level Text Using a Novel Fuzzy Relational Clustering Algorithm," *IEEE Trans. Knowledge and Data Eng.,* vol. 25, pp. 1138-1150, Jan. 2013.

[19] N. Srinivas and K. Deb, "Multiobjective optimization using nondominated sorting ingenetic algorithms," *Evol. Comp.*, Vol. 2, no. 3, pp. 221–248, 1994.

[20] K. Deb, A. Pratap, S. Agarwal and T. Meyariva, "A fast elitist non-dominated sorting genetic algorithm for multi-objective optimization," *IEEE Trans. Evol. Comp.,* Vol. 6, pp. 182–197, 2002.

[21] A. Frank, A. Asuncion, UCI Machine Learning Repository, 2010.

[22] S. Bandyopadhyay and U. Maulik, "Genetic clustering for automatic evolution of clusters and application to image classification," *Pattern Recognition.*, vol. 35, pp. 1197–1208, 2002.

[23] S. Bandyopadhyay and S. Pal, "Classification and Learning Using Genetic Algorithms," *Applications in Bioinformatics and Web Intelligence*, Springer, pp.196-204, 2007.

[24] J. Handl, and J. Knowles, *"*An evolutionary approach to multi-objective clustering," *IEEE Trans. Evol. Comp.*, vol. 11, pp.56–76, 2007.

[25] S. Bandyopadhyay and S. Saha, "A point symmetry based clustering technique for automatic evolution of clusters," *IEEE Trans. Knowl. Data Eng.*, vol. 20, pp.1–17, 2008.

[26] Siripen Wikaisuksakul, "A multi-objective genetic algorithm with fuzzy c-means for automatic data clustering", Applied Soft Computing 24, pp.679- 691, 2014

978-1-4673-9257-0/15/$31.00 ©2015 IEEE

Modified Bus Invert Encoding to Reduce Capacitive Crosstalk, Power and Inductive Noise

Bulbul Ahmed[1], Sujan Kumar Saha[2], Jiangjiang Liu[3]
[1,2]Department of Electrical Engineering and [3]Department of Computer Science
Lamar University
Beaumont, USA
Email: [1]bahmed@lamar.edu, [2]ssaha@lamar.edu, [3]jane.liu@lamar.edu

Abstract— **As Very Large Scale Integrated (VLSI) circuits are shrinking aggressively, interconnect length is becoming longer. So interconnect power consumption due to capacitive coupling is increasing. Again, as operating frequency is increasing and rising time is very short, the inductance effect between interconnects can no longer be ignored. So, capacitive coupling and inductive coupling are both power and performance bottlenecks of modern interconnect design. In our paper, we have proposed an encoding method of data based on odd and even inverts of encoding. Our simulation results show that peak power is due to capacitive coupling and can be reduced up to 43.64%. Average power consumption decreases by 17.38%. Inductive ringing can be minimized up to 83.33% at logic high level and up to 30% at logic low level.**

Keywords— encoding, power, noise, bus invert, inductance, coupling capacitance

I. INTRODUCTION

With the improvement of Deep Sub Micron technology, chip components are getting smaller and smaller. Previous Complementary Metal Oxide Semiconductor (CMOS) transistors of micrometer range are now at the nanometer range in size. Not only the transistors, but also on-chip interconnects are shrinking aggressively. Interconnect width is scaled down with the technology, but its height can't be scaled down so aggressively to keep resistance constant. As a result, the height to width ratio (aspect ratio) of interconnects is increasing. The negative impact of this increasing aspect ratio is capacitive and inductive coupling between interconnects. Before, when operating frequency of a circuit was at the MHz range, inductive coupling was not significant enough to consider. Now, as circuit frequency is moving up to the GHz range, inductive coupling is also contributing to crosstalk noise.

In VLSI circuits, there are three major kinds of power consumption: dynamic power, leakage power, and short circuit power [1]. When a transistor switches from logic zero to logic one or logic one to logic zero, it consumes dynamic power. Leakage power is consumed in a static state. When there is a short circuit path between V_{dd} to ground due to an on-state of transistors, short circuit power is consumed. But in interconnects, only dynamic power is consumed due to capacitive coupling. As interconnects are responsible for a large portion of total power consumption of a chip, interconnect power is a major area of concern. Crosstalk delay due to capacitive coupling is another performance bottleneck. There have been several research projects on encoding methods of data to minimize power and crosstalk delay of interconnects. However, less research has been conducted into minimizing noise due to inductive coupling. Our proposed encoding method addresses both dynamic power and the inductive noise of interconnects to ensure a more reliable and lower power interconnect design.

The organization of the paper is as follows: the related work is in Section II. Section III states effects of switching patterns on capacitive and inductive coupling. Our proposed encoding method is described in Section IV. Section V contains simulation setup and results. Finally, we conclude in Section VI.

II. RELATED WORK

There has been an abundant amount of research on bus encoding methods. Among these, bus invert is one of the most widely used encoding methods [2]. Stan et al. proposed this encoding approach to reduce power consumption of I/O of a CMOS Integrated Circuit. According to the bus invert encoding, depending on the number of transitions, either inverted or non-inverted data is transferred to bus. Lin et al. suggested a caching technique named "Hierarchical Value Caching Encoding" to minimize power consumption of off-chip data buses [3]. In paper [4] and [5], frequent value encoding has been used to reduce energy of off chip buses. These four encoding methods have been proposed for power reduction of off-chip buses.

Yan et al. suggested odd-even bus invert encoding in [6] to minimize on-chip bus energy. In bus invert encoding, only self-transition is considered, whereas in odd-even bus inverts, self-transition as well as coupling transition have been considered. According to this approach, bus lines are divided into two groups: odd lines and even lines. Then, depending on the number of transitions, either odd lines are inverted or even lines are inverted. Also, in this paper, the authors mentioned a two-phase transferred method, which eliminates toggles completely. Brahmbhat et al. proposed window-based adaptive bus encoding that uses weighted code mapping to develop a new low power bus encoding [7]. Siegmund et al. mentioned adaptive partial bus inverts, and Saini et al. suggested conditionally coded block encoding in [8] and [9], respectively. A low overhead auto optimizing encoding has been used by

978-1-4673-9257-0/15/$31.00 ©2015 IEEE

TABLE I CROSSTALK CATEGORIZATION

CC	Delay	Pattern of switching
1	0	−−−, −− ↑, ↑ −−, −− ↓,↓ −−, ↑ − ↑,↑ − ↓,↓ − ↑,↓ − ↓
2	C_gR	↑↑↑,↓↓↓
3	$C_gR(1+\lambda)$	− ↑↑,↑↑ −,− ↓↓,↓↓ −
4	$C_gR(1+2\lambda)$	− ↑ −,− ↓ −,↓↓↑,↑↓↓, ↑↑↓,↓↑↑
5	$C_gR(1+3\lambda)$	− ↑↓,− ↓↑,↓↑ −,↑↓ −
6	$C_gR(1+4\lambda)$	↓↑↓,↑↓↑

Kretzschmar et al. in [10]. But, all of these encodings are inclined toward only reducing the power consumption of interconnects.

On the other hand, Sainarayan et al. proposed temporal and shielding coding to minimize the delay of interconnects [11]. According to this method, two temporal cycles are used and the shielding bit is inserted after every three bits to eliminate worst-case crosstalk scenarios. In the first temporal cycle, inverted data is transferred, and in the second temporal cycle, encoding information is passed. As a result, delays due to crosstalk are minimized. Cha et al. proposed a resource constrained bus encoding to minimize crosstalk delay [12]. Also Duan et al. and Victor et al. mentioned bus encoding methods to reduce crosstalk delay in their research, [13] and [14], respectively. Here, all these methods are focused on reducing only the delay of interconnects.

Najeeb et al. suggested temporal crosstalk shielding in [15] to reduce both the power consumption and delay of interconnects. This method also uses two temporal cycles to send encoded data and encoding information. In paper [16], Zang et al. mentioned two encoding methods: Variable Cycle Transmission with Hybrid Spatial Temporal Redundancy and Opposite Transition Forbidden Weighted Code Mapping. Madhu Mutyam proposed selective shielding in [18]. These methods are also apt to minimize power and delay of interconnects. Verma et al. also proposed a bus encoding technique to reduce crosstalk by reducing the number of bits or bus width [17]. But, all these encoding methods mentioned so far consider only the capacitive coupling of interconnects.

As the operating frequency of circuits increase, inductive coupling is a major issue to consider. LaMeres et al. proposed an encoding based minimization of inductive crosstalk for off-chip data buses [19]. Ruan et al. mentioned a crosstalk quantitative approach to minimize power, noise, and delay considering both capacitive and inductive effects [20]. A modified bus invert encoding has been proposed by Lampropoulos et al. to reduce the inductive noise of buses [22]. Our proposed encoding method also considers both capacitive and inductive coupling and delivers a solution to obtain a better encoded data to minimize power consumption and reduce crosstalk noise.

Fig. 1 Effect of Inductive Coupling for switching pattern "↑↑↑↑-↑↑↑"

III. EFFECT OF SWITCHING PATTERN ON INDUCTIVE AND CAPACITIVE COUPLING

In this section, we will discuss how inductive and capacitive coupling react according to switching patterns in bus lines. First, we will define some terms that will be used frequently. When two adjacent lines switch in opposite directions, this is known as Toggle. If any bus line switches from one logic state to another, this is known as self-transition. Charging-discharging occurs when one bus line switches and another adjacent one remains the same. The last one is stable. If a bus line does not switch or remains stuck to the same logic state, this is defined as stable. Switching from logic 0 to logic 1 and from logic 1 to logic 0 will be represented as '↑' and '↓' respectively and '-' denotes a stable position.

When signals switch in opposite directions, coupling capacitance causes signals in adjacent lines to be pulled up or down depending on the switching pattern. Thus glitches are produced in victim signals, and coupling capacitance becomes twice more than the capacitance introduced when switching in

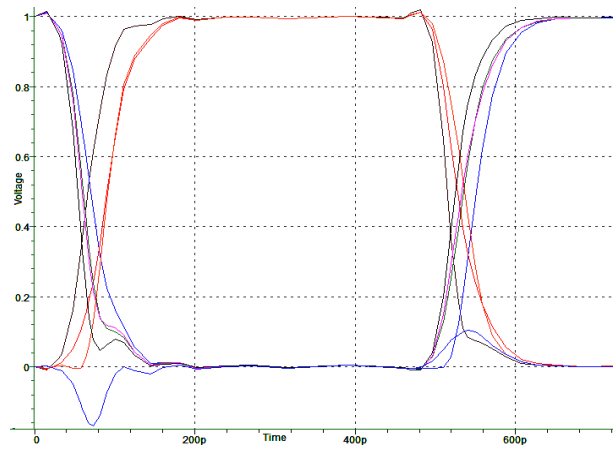

Fig. 2 Effect of Inductive Coupling for switching pattern "↑↓↑↓-↓↑↓"

the same direction. This is the worst situation for capacitive coupling.

For inductive coupling, when signals switch in the same direction, the equivalent inductance becomes the summation of self-inductance and mutual inductance [26]. This leads the signals to develop a large noise due to the ringing effect in the bus lines. Switching in the same direction causes an additive magnetic field, and that results in a ringing effect. We performed an HSPICE simulation of an 8-bit bus to observe the ringing effect due to inductive coupling. We set V_{dd} to 1V and the frequency to 1 GHz. Simulation results are shown in Figure 1 and Figure 2. In Figure 1, bus 5 remains stuck to logic 0 and all other bus lines switch in the same direction from logic 0 to logic 1.

In our simulation, inductive ringing is introduced in the waveform with a maximum peak value of almost 1.2V, and stable bus line 5 experiences a spike with a maximum value of almost .3V. On the other hand, in Figure 2, bus line 5 remains stable at logic 0 and all other bus lines switch in opposite directions. Switching in opposite direction causes magnetic field of the wires to cancel each other rather being additive when switch in the same direction. As a result, the inductive effect is greatly minimized and hence the ringing effect is also reduced.

IV. PROPOSED METHOD

In the previous section, we observed inductive and capacitive coupling effects depending on the switching patterns in bus lines. However, the best pattern for capacitive coupling appears to be the worst pattern for inductive coupling. In the best case of inductive coupling, noise will be minimized but large power consumption will occur in the chip. In the best case of capacitive coupling, a large noise will be induced in the signal while reducing power consumption. Considering both of these cases, we made a compromise between them in our proposed method. This method mainly aims to remove toggle and switching in the same direction between adjacent bus lines. Hence, power consumption and inductive noise are reduced. We used a temporal cycle to pass encoding information after the encoded data had been transmitted over the bus lines. The basic idea is to cause bus lines to stick in the same logic state for every other bus line so that switching in opposite and same direction between adjacent bus lines is completely removed. This approach is applied on half of the bus lines, and the idea of bus invert encoding [2] is used for the other half of the bus lines. However, using the bus invert approach leads the architecture to use an extra control line to carry the signal whether the data is inverted or not. This information will be used in decoder to retrieve the original signal. So, if the original data is of n bit, then according to our proposed method, the bus width will be n+1.

Figure 3 illustrates a schematic diagram of our proposed encoding architecture. The encoder consists of Odd encoding and Even encoding sections, Charging-Discharging estimators, Comparators, and a MUX. The original data and current value on bus lines sent back from bus lines are fed to the both Odd and Even encoding section. Odd and Even encoding will be described into two subsections later. Output of these two

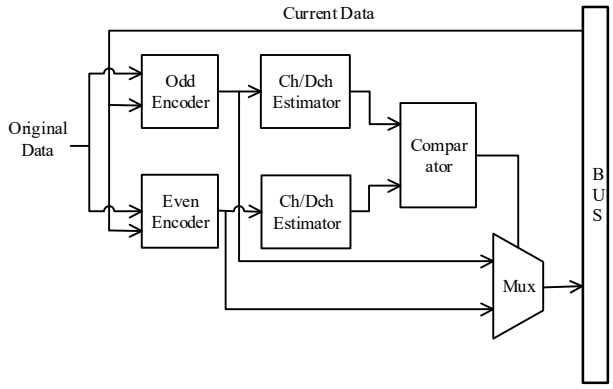

Fig. 3 Block Diagram of Proposed Encoding Method

sections is sent as the input to the Charging-Discharging estimator. At the same time, these two outputs are fed to the MUX. The Charging-Discharging estimator counts the total number of charging-discharging in the encoded data including encoding information, and it also checks whether encoded data and encoding information contain the exact same bits in every position. If in either of these two encoding circumstances, the encoded data and encoding information have the same bits, then MUX lets the odd encoding be transmitted; otherwise these two encoding outputs are fed to the comparator. The comparator determines which encoded data contains less Charging-Discharging. Based on the comparator output, MUX lets the encoded data that has a lower number of Charging-Discharging be transmitted over the bus lines. As our proposed method completely eliminates toggle in encoded data, we are concerned only with Charging-Discharging.

A. Odd and Even Encoding

With odd encoding, at first, we make the odd position bits stable in encoded data with respect to the current bus data so that we don't get any toggle and transition in the same direction between adjacent bus lines. For example, if the 8-bit original data to be transmitted over the bus at time T_t is 01110110, and the previous cycle data 10101101 has already been transmitted at time T_{t-1}, then the current value of the bus lines is 10101101. The switching between these two data, based on self-transition, toggle, charging-discharging, and stable position is shown in Figure 4.

Current Cycle Bus Data	1	0	1	0	1	1	0	1
	↓	↑	—	↑	↓	—	↑	↓
Next Cycle Original Data	0	1	1	1	0	1	1	0

Fig. 4 Transition between Current Data and Next Cycle Original data

Current Cycle Bus Data	1		1		1		0	
	—		—		—		—	
Next Cycle Original Data	1		1		1		0	

Fig. 5 Stabilization of Odd Position Bits

Current Cycle Bus Data	1	0	1	0	1	1	0	1
	—	—	—	—	—	↓	—	—
Next Cycle Encoded Data	1	0	1	0	1	0	0	1

Fig. 6 Transition between Current Data and Next Cycle Encoded data

Current Cycle Bus Data	1	0	1	0	1	1	0	1	
Transition	↓	↑	—	↑	↓	—	↑	↓	
Next Cycle Original Data	0	1	1	1	0	1	1	0	
Next Cycle Encoded Data	1	0	1	0	1	0	0	1	1
Encoding Information	1	0	0	0	1	0	0	1	1

Fig. 7 Encoded Data with Encoding Information

Here, we get 3 toggles between 1st and 2nd, 4th and 5th, and between the 7th and 8th positions. We get 4 charging-discharging at the 2nd-3rd-4th and 5th-6th-7th positions. And we get 2 stable positions at the 3rd and 6th positions, and 6 self-transitions at the 1st, 2nd, 4th, 5th, 7th and 8th positions.

In Figure 5, we made the 1st, 3rd, 5th, and 7th positions of encoded data stable with respect to the current cycle bus data. Now we will work on the even positions of original data. Here, we will follow the concept of the bus invert method only for bits of even positions. From Figure 4, it is evident that there are 4 even positions, and 3 self-transitions occur at the 2nd, 4th, and 8th position.

Based on the bus invert encoding, if the transition number is greater than half of the total number of bits, the original data will be inverted to get encoded data. In our example, there are 4 even positions, and it is obvious that transition number 3 is greater than half of 4. So, all the even position bits of the original data will be inverted to get the even position bits of encoded data. The control line will carry a logic 1 if the bits are inverted; otherwise logic 0 will be transmitted. This control bit will be used in the decoder to retrieve the original data at the receiving end. The current bus data, encoded data, and switching between these two data are represented in Figure 6.

In Figure 6, toggles are completely eliminated, 4 charging-discharging is decreased to 2 at the 5th-6th-7th position, and 6 self-transition is reduced to only 1 at the 6th position in encoded data. Evidently there is no switching in the same direction between adjacent bus lines.

The second case is known as Even encoding, and we perform the same procedure but in different bit positions. In the first case, we made all the bits in odd positions stable and applied the bus invert approach to even positions. In even encoding, we will make all bits in even positions stable, and the bus invert approach will be applied to odd positions. Then encoded data that has a lower number of Charging-Discharging will be transmitted over bus lines.

B. Encoding Information

Encoding information contains a bit pattern based on the changes we made in original data to get an encoded data. This information is transmitted at the next cycle after the encoded data has been sent, and bit width is exactly the same as encoded data.

For Odd encoding, odd positions of the original data are modified to get encoded data. This modification is performed in such a way that there is no transition between current bus data and encoded data in odd positions. In some positions, we have to change the original bits to make it stable, and we call this case "forced stable". On the other hand, in some positions, there are no transitions between current bus data and original data. In these positions, we do not make any change and leave these bits as they are to get encoded data, and we call this case "normally stable". In those odd positions where a "normally stable" case occurs, we send inverted bits of encoded data in those same positions to get encoding information. On the other hand for forced stable positions we send same bits as encoded bits in those same positions. For all even positions the bits in encoding information are exactly the same as they are in encoded data. Control line carries a signal to indicate whether the even positions are inverted or not.

Figure 7 shows current bus data, original data, and transitions between current and original data, encoded data, and encoding information. This is odd encoding. Only in the 3rd position, there is a normally stable state between current bus data and original data. In all other odd positions, there are transitions, and we had to make it forced stable to build encoded data. With the rule of building encoding information discussed above, the 3rd bit of encoding information is an inverted bit of the 3rd bit in encoded data. Here 3rd bit of encoded data is logic 1. Evidently encoding information got logic 0 for the 3rd bit. Being forced stable positions, the 1st, 5th, and 7th bits in encoding information are the same as they are in encoded data. Even positions are the same as encoded data bits. As even position bits of original data are inverted to get encoded data, control line carries logic 1.

For even encoding, the same procedure is followed to build encoding information. Here the even positions which are normally stable, those bits of encoded data are inverted to get the bits of the same positions in encoding information. All bits in odd positions are the same as they are in encoded data. Control line carries logic 1 if bits of odd positions are inverted; otherwise, logic 0 is sent over control line.

C. Decoding

Original data is transmitted in the form of encoded data over bus lines to reduce power and inductive noise. The decoder at the receiving end receives this encoded data and decodes it to retrieve the original signal based on encoding information and control line value. To retrieve the original data, the decoder needs to know whether the encoded data is odd encoded or even encoded. At first, the decoder checks if the encoded data and encoding information contain the exact same bits in the same positions or not. If so, then it takes the data as odd encoded data. Because in encoder, at the transmitting end for same bits in encoded data and encoding

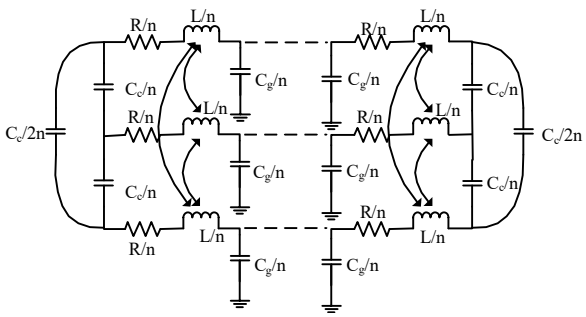

Fig. 8 Distributed RLC Model of Interconnects

information, we sent odd encoded data to be transmitted. Now if bits are different in these two data, the decoder checks which bits between all odd and even positions are stable with respect to the data that has already been transmitted in the previous cycle. If all odd bits are stable, then the decoder detects the received data as odd encoded data, and if all even bits are stable, then the data is considered even encoded data. Once encoding mode is detected based on encoding information and control line bit, the decoder easily retrieves the original data. For odd encoding, the odd positions of encoding information, for which bits are not the same as those of encoded data, in the original data, bits will be the same as encoded data in those positions; otherwise, original bits will be the inverted of those bits in encoded data. Logic 1 in control line indicates the encoded bits in even positions are already inverted. So to retrieve the original bits, the decoder needs to invert those bits again. Otherwise for logic 0 in control line, the decoder will leave even bits as they are for odd encoding. For bits in even encoded data, the retrieving procedure is exactly same. The only difference is the positions of bits.

V. Simulation Setup and Result

The simulation setup and interconnect model for our experiment and results are described in this section. Figure 8 shows the distributed RLC model [23] used in our simulation. The technology used in our experiment is 90 nm. To increase accuracy, we segmented the RLC circuit into 4 sections. The spacing, width, thickness, height, dielectric strength, and length of 90nm global interconnects were extracted from Predictive Technology Model (PTM) [25], and these values are .50um, .50um, 1.2um, .30um, 2.8, and 2000um respectively. These

TABLE III ENERGY RESULTS

Data Count (Kb)	Savings of Energy (%)
100	17.29
300	17.33
700	17.30
1000	17.23
1500	17.34

Fig. 9 Inductive Noise for Original Data/Bus Invert Encoded Data

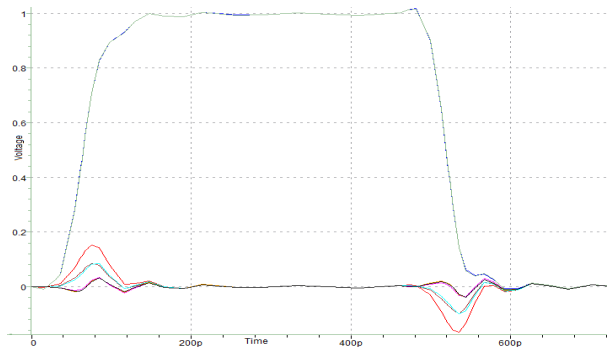

Fig. 10 Minimization of Inductive Noise for Proposed Encoding

values were used to extract self-inductance, self-capacitance, mutual inductance, coupling capacitance, and resistance from PTM [25]. Drivers and receivers are assumed to have the same size. V_{dd} was set to 1 V and frequency at 1 GHz. Power was measured in JAVA, and HSPICE simulation was performed to evaluate inductive noise. The following equation has been used to measure power consumption [24].

$$E = 0.5 * C_s * V^2 * [N_s + (N_{c+d} + 4 * N_t)(C_c/C_s)]$$

We took different sizes of data as input to simulate our encoding approach for measuring power consumption and inductive noise. We also looked at all the possible sequences for 8-bit input to increase the accuracy of our simulation. The simulation result is listed in Table III. Figure 9 and 10 show inductive noise for the original data and how this noise is minimized for encoded data. Table IV shows the significant improvement of power consumption for encoded data. A 17.38% reduction of power is observed, and Figure 10 shows a reduction of noise up to 83.33 % at logic high level and up to 30% at logic low level. Peak power is reduced up to 43.64%. This is mainly because our encoding approach eliminates all the possible toggles, which are responsible for large power consumption due to worst-case capacitive coupling. Also switching in the same direction between adjacent bus lines is completely removed in our scheme. Thus inductive ringing is largely minimized for encoded data.

We compared our encoding approach with Bus Invert Encoding [2] on the same simulation platform with same

technology. This made the comparison more fair and accurate. The bus invert method represents better area overhead because of simple logic and one extra control line. However, in terms of inductive ringing and worst-case crosstalk, coupling the performance of our encoding approach is better than bus invert encoding. Figure 9 and 10 show the comparison between Bus invert and our encoding scheme in terms of inductive ringing. We presented the noise simulation for non-encoded and encoded data for both Bus Invert encoding and our encoding approach for a specific switching pattern (↑ ↑ ↑ ↑ - - - -). In this case, the Bus invert method does not take the switching pattern into account and leaves the non-encoded data as it is. Hence, inductive ringing is not minimized. However, in our encoding method, inductive ringing is reduced by 83.33% and 30% at logic high and logic low level respectively.

VI. CONCLUSION

The goal of this research is to minimize interconnect power consumption due to capacitive coupling and to reduce the interconnect noise due to inductive coupling. Our proposed encoding method ensures that there will be no transition in opposite direction (0→1 and 1→0) and also no transition in same direction (0→0 and 1→1) between two adjacent lines by stabilizing odd/even position bits. As a result, toggle is removed, which is responsible for the highest power consumption, and also inductive noise is minimized at both logic levels. Our simulation results show that on average, 17.38% of power consumption is reduced, and a reduction in inductive noise up to 83.33% is possible at logic high level and reductions as much as 30% at logic low level. Though one extra bit and one extra cycle is needed to send the encoding information to retrieve the original data, area and delay overhead is not too much. Also, to send encoding information with encoded data, the total number of bits increases compared to the original un-encoded data, but the number of transition will be reduced. Hence, reduced power consumption is achieved. In the future, detail hardware design of the encoding approach will be studied, and hence the area, delay, and power consumption of the encoder-decoder will be measured.

REFERENCES

[1] https://www.academia.edu/4625045/POWER_REDUCTION_IN_MODERN_VLSI_CIRCUITS_A_REVIEW

[2] M.R. Stan, W.P. Burleson, "Bus-invert coding for low-power I/O," *IEEE Trans. Very Large Scale Integration (VLSI) Systems*, vol. 3, no. 1, pp. 49-58, March 1995.

[3] C. H. Lin, C. L. Yang, & K. J. King, "Hierarchical value cache encoding for off-chip data bus." in Proc. Int. Symp. On Low Power Electronics and Design, Oct. 2006, pp. 143-146.

[4] D. C. Suresh, B. Agrawal, J. Yang, W. Najjar, & L. Bhuyan, "Power efficient encoding techniques for off-chip data buses." in Proc. Int. conference on Compilers, architecture and synthesis for embedded systems, Oct. 2003, pp. 267-275.

[5] J. Yang, R. Gupta, & C. Zhang, "Frequent value encoding for low power data buses." ACM Trans. on Design Automation of Electronic Systems, 9(3), 354-384, 2004.

[6] Z. Yan , J. Lach, K. Skadron, and M.R. Stan, "Odd/Even bus invert with two-phase transfer for buses with coupling," in Proc. Int. Symp. On Low Power Electronics and Design, Aug. 2002, pp.80-83.

[7] A. R. Brahmbhatt, J. Zhang, Q. Wu, & Q. Qiu, "Low-power bus encoding using an adaptive hybrid algorithm." In Proc. of the 43rd annual Design Automation Conference, July 2006, pp. 987-990.

[8] R. Siegmund, C. Kretzschmar, & D. Müller, "Adaptive Partial Businvert encoding for power efficient data transfer over wide system buses." in Proc. 13th Symp. On Integrated Circuits and Systems Design, 2000, pp. 371-376.

[9] S. Saini, & S. B. Mandalika, "A new bus coding technique to minimize crosstalk in VLSI bus." in Proc. Int. Conference on Electronics Computer Technology, Apr. 2011,Vol. 1, pp. 424-428.

[10] C. Kretzschmar, R. Siegmund, & D. Müller, "A low overhead auto-optimizing bus encoding scheme for low power data transmission." in Integrated Circuit Design. Power and Timing Modeling, Optimization and Simulation, 2002, pp. 342-352.

[11] K. S. Sainarayanan, C. Raghunandan, and M. B. Srinivas, "Bus encoding schemes for minimizing delay in VLSI interconnects," in Proc. ACM Conference on Integrated circuits and systems design, Sept. 2007. pp. 184-189

[12] M. Cha, C. G. Lyuh, & T. Kim, "Resource-constrained low-power bus encoding with crosstalk delay elimination." in Proc. Asia and South Pacific Design Automation Conference, Jan. 2004. pp. 834-837

[13] C. Duan, & S. P. Khatri, "Exploiting crosstalk to speed up on-chip buses." in Proc. Design, Automation and Test in Europe Conference and Exhibition, Feb. 2004, Vol. 2, pp. 778-783.

[14] B. Victor, & K. Keutzer, "Bus encoding to prevent crosstalk delay." in Proc. IEEE/ACM international conference on Computer-aided design, Nov. 2001, pp. 57-63.

[15] K. Najeeb, V. Gupta, and V. Kamakoti, "Delay and peak power minimization for on-chip buses using temporal redundancy," in Proc. ACM Great Lakes symposium on VLSI, April. 2006, pp. 119-122.

[16] J. Zhang, Q. Wu, and Q. Qiu, "Bus encoding for simultaneous delay and energy optimization," in Proc. Int. Symp. on Low Power Electronics and Design, Aug. 2008, pp. 209-212.

[17] S. K. Verma and B. K. Kaushik, "A bus encoding method for crosstalk and power reduction in RC coupled VLSI interconnects," International Journal of VLSI design & Communication Systems 3, no. 2, pp. 29-39. 2012.

[18] M. Mutyam, "Selective shielding: a crosstalk-free bus encoding technique." in Proc. IEEE/ACM international conference on Computer-aided design, Nov. 2007, pp. 618-621.

[19] B. J. LaMeres, & S. P. Khatri, "Encoding-based minimization of inductive cross-talk for off-chip data transmission." in Proc. IEEE Design, Automation and Test in Europe, Mar. 2005, pp. 1318-1323.

[20] S. J. Ruan, T. C. Kan, and J. C. Hsu, "A novel crosstalk quantitative approach for simultaneously reducing power, noise, and delay based on bus-invert encoding schemes," in Proc. Int. Great lakes Symp. on VLSI, May 2010, pp. 357-360.

[21] S. K. Verma, B. K. Kaushik, "Crosstalk and power reduction using bus encoding in RC coupled VLSI interconnects," in Proc. Int. Conf. Emerging Trends in Engineering and Technology, Nov. 2010. pp.735-740.

[22] M. Lampropoulos, B. M. Al-Hashimi, & P. Rosinger, "Minimization of Crosstalk Noise, Delay and Power Using a Modi. ed Bus Invert Technique." in Proc. IEEE conference on Design, automation and test in Europe, Feb. 2004, Volume 2, p. 21372.

[23] D. D. Antono, (2003). *Modeling of Inductive Interconnect Responses and Coupling Effects in Deep-Submicron VLSI* (Doctoral dissertation, Master Thesis, Department of Electronic Engineering Graduate School of Engineering The University of Tokyo).

[24] S. Jayaprakash & N. R. Mahapatra, "Partitioned Hybrid Encoding to Minimize On-Chip Energy Dissipation ofWide Microprocessor Buses." in Proc. IEEE Int. Conference on VLSI Design, Jan. 2007, pp. 127-134.

[25] Predictive Technology Model http://www.eas.asu.edu/~ptm/

[26] Y. Ogasahara, M. Hashimoto, & T. Onoye, "Measurement and analysis of inductive coupling noise in 90 nm global interconnects." *IEEE Journal of Solid-State Circuits,* Vol. 3, No. 43, pp. 718-728. 2008

Efficient Index Computation for Array Based Structured Data

Md Abu Hanif Shaikh, Mehnuma Tabassum Omar, K.M. Azharul Hasan
Department of Computer Science and Engineering, Khulna University of Engineering & Technology
E-mail: hanif@kuet.ac.bd, misty2409@gmail.com, azhasan@cse.kuet.ac.bd

Abstract— **Traditional computing techniques widely vary over large scale computing. Some techniques are useful for structured data while some other techniques are useful for non-structured data. To store and operation on the structured data, multidimensional array is widely used as basic data structure. But the performance of multidimensional array is very poor when the number of dimension is very high i.e. 32-dimension. Data scientist suggests linearization of dimensions for higher dimensional data. But linearized data are highly compute intensive for retrieving into original data format as well as operations are very expensive on that data. It suffers from the higher index computational cost and lower data locality. In this paper, we propose an index computation algorithm based on generalized two-dimensional structure. We showed that the accessing cost of array elements is higher for traditional multidimensional array over generalized two-dimensional representation. Though the most sequential access of main memory is itself very simple for any compiler yet experimental results showed a better performance. Both theoretical analysis and experiment are done to show its' effectiveness of the proposed algorithm.**

Keywords—Higher dimensional array, Array Index, Structured data, Data locality, Array linearization, HPC.

I. INTRODUCTION

Big data is often used to describe the scale of data generated across multiple disciplines, including sensors used to gather climate information data, digital pictures and videos, purchase transaction records, and cell phone GPS signals [4]. It also includes massive volumes of marketing, spanning search, social, local and mobile analytics data across every geographical location. The generated data is categorized as structured, semi-structured and un-structured. Structured data is information with a high degree of organization found in databases, data warehouses and enterprise solutions. Internet applications extracted raw data is un-structured and social media data or location type data and user-generated data are semi-structured. Modeling and analyzing such phenomena strongly requires handling large scale of data. Traditionally the data has very high number of dimensions. Handling and operating on this higher dimensional data is still a challenge [6][12] for data scientists. The multidimensional array is the dominating structure for handling such data [14][15]. If the number of dimension is high then the cost of index computation increases and the cache miss rate also increases due to the data locality problem [3][13]. That's why very few commercial compilers eventually support large number of dimensions. Traditional algorithms and computing techniques is difficult to apply on higher dimensional data models such as the data of data-warehouse or MOLAP[10]. Most compilers have limitations over multi-dimensional array. Thus the traditional indexing for structured big data is not efficient. That's why, data scientists are arduous for new index structure [7]. Most data scientists suggest linearization of higher dimensional data. It is good enough to implement in secondary memory. But operation cost and accessing time for secondary memory data is too high as well as parallelization is seldom possible for linearized data. So, the new index structure which support parallelism, lower index computation cost, lower operation cost and higher data locality is a cramming needs for present data scientists. In this paper, we propose Generalized Two-Dimensional Array[5] based index computing algorithm for accessing structured big data. G2A converts n-dimensional array into a two dimensional array. Our goal is to lower the index computational cost and higher data locality using our proposed index structure for structured big data. The later part of this paper is decorated as section II compares some related works, Section III shows an overview of G2A (Generalized two-dimensional representation of higher dimensional Array) , the algorithms for initializing both G2A and TMA are shown in section IV. Section V shows some theoretical analysis then the experimental results are shown in section VI and finally Section VII outlines some conclusion.

II. RELATED WORKS

Many techniques have been proposed in literature for improving the cost of index computation for higher dimensional structured data [3]-[9]. Some techniques suggest linearization over higher dimensions[7]-[10]. Their argument is that the compiler allocates memory sequentially in all cases of memory allocation. EKMR scheme[3] is very effective but it is limited to four dimensions only. When the number of dimension is greater than four then it requires an abstract pointer array. Even there is no generalized indexing till four dimensional. Tamara G. Golda et.al [1][2] proposed an indexing scheme for two dimensional generalization. Though it is very effective for operation on generalized data but requires huge storage. Steve Carr [13] presents compiler optimizations to improve data locality but the scheme is based on the Traditional Multidimensional Array. It reorganizes the loops only for compiler optimization. A new storage manager for complex, parallel array processing namely the ArrayStore is proposed in [12] in the area of multidimensional data storage. The main issue handled is the way to find for parallel processing. The SciDB[14][15] proposed an array based DB model. EJ Otoo[11] introduce new storage schemes for multi-dimensional sparse arrays that handle the sparsity of the array but the array is not n dimensional. Ddynamic array structure

namely EKA[8][10] becomes an hierarchical structure when n>4. Y. Zhao *et. al.*[9] introduced the chunking of arrays but linearization of n dimensional array is required. The simplified representation of higher dimensional array suggest two-dimensional representation scheme in [5][6]. This representation highly affects for main memory computing saving huge cache locality. This two dimensional representation scheme is cost effective in terms of index computation specially when n is large.

III. GERNERALIZED TWO-DIMENSIONAL ARRAY: G2A

The ***Generalized Two-dimensional Array*** (G2A) represents an algorithm to represent an n dimensional (nD) array by a 2 dimensional (2D) array. The nD array is converted to a 2D array. Hence the indexes of the nD array are also converted to 2D array. ⌊ n/2 ⌋ columns contribute to row direction and the rest n/2 columns to column direction. Hence a nD array can be drawn in a 2D plane to visualize the data.

Let A[l_1] [l_2]… [l_n] be a TMA(n) of size [l_1, l_2,…,l_n] and <x_1, x_2,…,x_n> be a tuple of an element of the array A; where l_1, l_2,…, l_n is the length of each dimension d_1, d_2,…, d_n and x_i = 0,1,2,3, …, (l_i-1) ($1 \le i \le n$). We convert TMA(n) A of size [l_1, l_2,…,l_n] into a G2A $A'[l'_1][l'_2]$ of size $[l'_1, l'_2]$ and a tuple $< x'_1, x'_2 >$ where l'_1 and l'_2 are the length of each dimension d'_1 and d'_2 ; $x'_1 = 0,1,\dots,(l'_1 - 1)$ and $x'_2 = 0,1,\dots,(l'_2 - 1)$. In the following we will first show the 3 and 4 dimension array converting to G2A and then we will generalize to n dimensions.

Example 1: Let A[l_1][l_2][l_3] be a TMA(3) of size [2,3,4]. A multidimensional array is linearized when stored on the memory. Programming languages map the array index into the linearized memory address. Therefore a location of tuple <x_1, x_2, x_3> A[l_1][l_2][l_3] can be linearized and identified by

$$f(x_1, x_2, x_3) = x_1 l_2 l_3 + x_2 l_3 + x_3$$
$$= x_1 \times 3 \times 4 + x_2 \times 4 + x_3$$

when row major order is considered and

$$f(x_1, x_2, x_3) = x_1 l_2 l_3 + x_3 l_2 + x_2$$
$$= x_1 \times 3 \times 4 + x_3 \times 3 + x_2$$

when column major order is considered

In G2A, the 3 dimensions d_1, d_2, d_3 are converted to 2 dimensions where d_1, d_3 are for row and d_2 are for the column. Fig-1 shows the G2A $A'[l'_1][l'_2]$ for a TMA(3) A[2][3][4] where $l'_1 = l_1 \times l_3 = 8$ and $l'_2 = l_2 = 3$.

For example an element A[1][1][2] of TMA(3) is equivalent G2A is $A'[x'_1][x'_2]$ where $x'_1 = x_1 l_3 + x_3 = 1 \times 4 + 2 = 6$ and $x'_2 = x_2 = 1$. (See Fig. 1).

For backward mapping, if an element in G2A is $A'[x'_1][x'_2]$ is known then it's equivalent TMA(3) becomes A[x_1][x_2][x_3] where $x_3 = x'_1 \% l_3 = 6 \% 4 = 2$, $x_1 = \frac{x'_1}{l_3} = 6/4 = 1$ and $x_2 = x'_2 = 1$. For example, A′[6][1] is equivalent to A[1][1][2]. Here % indicates the 'modulus' operation and / indicates 'division' operation.

The generalization of the TMA(n) A[l_1][l_2] … [l_n] to G2A $A'[l'_1][l'_2]$ is as follows :

$$l'_1 = \begin{cases} l_1 \times l_3 \times \dots \times l_{n-1}, & if\ n\ is\ even \\ l_1 \times l_3 \times \dots \times l_n, & if\ n\ is\ odd \end{cases}$$

$$l'_2 = \begin{cases} l_2 \times l_4 \times \dots \times l_n, & if\ n\ is\ even \\ l_2 \times l_4 \times \dots \times l_{n-1}, & if\ n\ is\ odd \end{cases}$$

An element A[x_1][x_2]…[x_n] in TMA(n) is equivalent to $A'[x'_1][x'_2]$ where

$$x'_1 = \begin{cases} x_1 l_3 l_5 \dots l_{n-3} l_{n-1} + \dots + x_{n-3} l_{n-1} + x_{n-1}, & if\ n\ is\ even \\ x_1 l_3 l_5 \dots l_{n-2} l_n + \dots + x_{n-2} l_n + x_n, & if\ n\ is\ odd \end{cases}$$

$$x'_2 = \begin{cases} x_2 l_4 l_6 \dots l_{n-3} l_{n-1} + \dots + x_{n-3} l_{n-1} + x_{n-1}, & if\ n\ is\ odd \\ x_2 l_4 l_6 \dots l_{n-2} l_n + \dots + x_{n-2} l_n + x_n, & if\ n\ is\ even \end{cases}$$

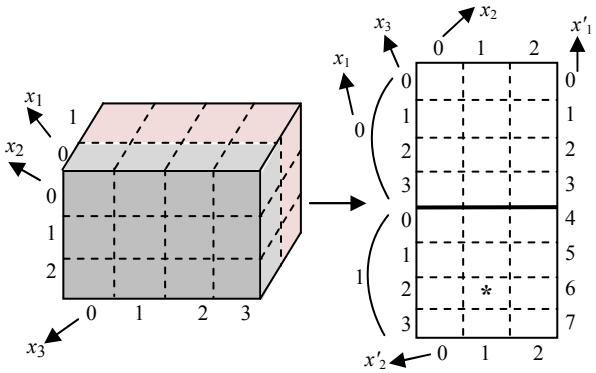

Figure 1. TMA(3) and it's equivalent G2A

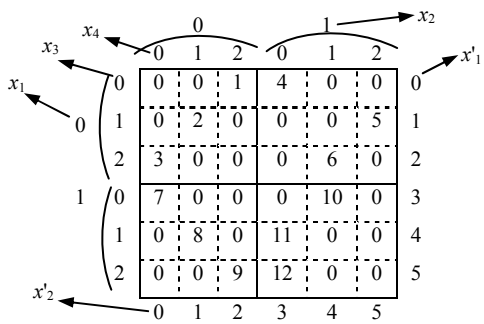

Figure 2. G2A, equivalent to TMA(4) of size (2×2×3×3)

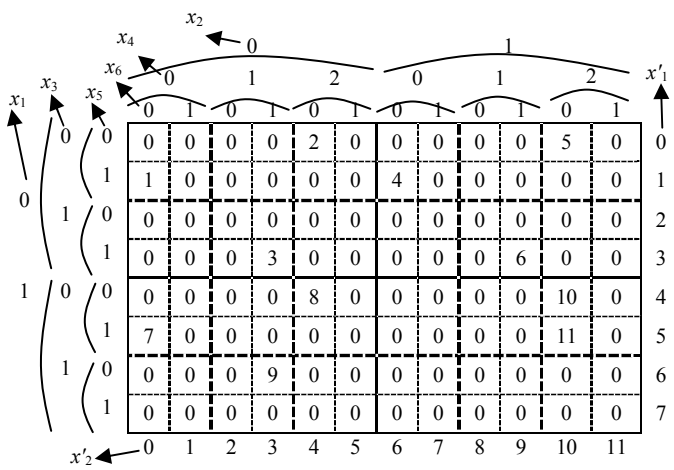

Figure 3. G2A, equivalent to TMA(6) of (2×2×2×3×2×2)

Fig. 2 and Fig. 3 shows the G2A for equivalent TMA(4) and TMA(6). For backward mapping, if an element in $A'[x'_1][x'_2]$ is known then it's equivalent $A[x_1][x_2][x_3] \ldots [x_n]$ is as follows:

When n is even then

$$x_n = x'_2 \% \, l_n$$
$$x_i = ((\ldots(x'_2 / l_n) \ldots / l_{i+2}) \% l_i, \qquad i = 4,6,\ldots,n-2$$
$$x_2 = ((\ldots(x'_2 / l_n) / l_{n-2}) \ldots) / l_6) / l_4$$

$$x_{n-1} = x'_1 \% \, l_{n-1}$$
$$x_j = ((\ldots(x'_1 / l_{n-1}) \ldots / l_{j+2}) \% l_j, \qquad j = 3,5,\ldots,n-3$$
$$x_1 = ((\ldots(x'_1 / l_{n-1}) / l_{n-3}) \ldots) / l_5) / l_3$$

And when n is odd then

$$x_n = x'_1 \% \, l_n$$
$$x_i = ((\ldots(x'_1 / l_n) \ldots / l_{i+2}) \% l_i, \quad i = 3,5,\ldots,n-2$$
$$x_1 = ((\ldots(x'_1 / l_n) / l_{n-2}) \ldots) / l_5) / l_3$$

$$x_{n-1} = x'_2 \% \, l_{n-1}$$
$$x_j = ((\ldots(x'_2 / l_{n-1}) \ldots / l_{j+2}) \% l_j, \qquad j = 4,6,\ldots,n-3$$
$$x_2 = ((\ldots(x'_2 / l_{n-1}) / l_{n-3}) \ldots) / l_6) / l_4$$

IV. Algoritms for Index Computation

For initialization of TMA, it requires n number of nested loops. But G2A requires only two loops as well as (n-2) number of multiplication operation. *Algorithm* 1 shows a TMA of n-dimension which represents n number of nested loops. As example, it requires three nested loops to initialize a TMA of 3-dimensions. Equivalent G2A of this TMA requires two nested loops and an additional multiplication operation as shown in *Algorithm* 2. Similarly, TMA(4) needs four nested loops and equivalent G2A needs two nested loops as well as two multiplication operation for deriving l'_1 and l'_2 as shown in *Algorithm* 3. G2A generalization supporting any number of dimensions is show in *Algorithm* 4. If n=100, then it requires 100-2=98 multiplications with constant two nested loops.

Algorithm 1*:* Indexing Scheme for TMA(n):(x_1-x_n, l_1- l_n)

1. *for* i_1 := 1 to l_1
2. *for* i_2 := 1 to l_2
3. *for* i_2 := 1 to l_2
4. .
5. .
6. .
n. *for* i_n := 1 to l_n
n+1. TMA[i_1] [i_2]… [i_n]=0;

Algorithm 2*:* finding G2A indexes from TMA(3) indexes:
G2A-forward_mapping (i'_1-i'_2, l'_1- l'_2, i_1- i_3, l_1- l_3)

1. $l'_1 = l_1 \times l_3$, $l'_2 = l_2$
2. *for* i'_1 := 1 to l'_1
3. *for* i'_2 := 1 to l'_2
4. G2A[i'_1][i'_2]=0;

Algorithm 3*:* finding G2A indexes from TMA(4) indexes:
G2A-forward_mapping (i'_1-i'_2, l'_1- l'_2, i_1- i_4, l_1- l_4)

1. $l'_1 = l_1 \times l_3$, $l'_2 = l_2 \times l_4$
2. *for* i'_1 := 1 to l'_1
3. *for* i'_2 := 1 to l'_2
4. G2A[i'_1][i'_2]=0;

Algorithm 4*:* finding G2A indexes from TMA(n) indexes:
G2A-forward_mapping (i'_1-i'_2, l'_1- l'_2, i_1- i_n, l_1- l_n)

1. $l'_1 = l_1 \times l_3 \times \ldots \times l_{n-1}$, $l'_2 = l_2 \times l_4 \times \ldots \times l_n$ (n is even)
   or $l'_1 = l_1 \times l_3 \times \ldots \times l_n$, $l'_2 = l_2 \times l_4 \times \ldots \times l_{n-1}$ (n is odd)
2. *for* i'_1 := 1 to l'_1
3. *for* i'_2 := 1 to l'_2
4. G2A[i'_1][i'_2]=0;

V. Memory Management by G2A

In the following, we analyze the performance of index computation shown in Section III and IV. Total cost for TMA and G2A are the cost of addition/multiplication operators for index computations of array elements. The parameters are grouped as shown in table I. Some of these parameters are provided as input, while others are derived from the input parameters. All lengths or sizes are in bytes.

TABLE I. Parameters for Indexing Scheme

Parameter	Description
n	Number of dimension
l_i	Length of dimension i ($2 \le i \le n$)for TMA. We consider $l_1 = l_2 = l_3 = \ldots = l_n = l$ for all i. Hence total array elements becomes l^n.
l'_1	Length of row for G2A; i.e. $l'_1 = l^{\lceil n/2 \rceil}$
l'_2	Length of column for G2A; i.e. $l'_2 = l^{\lceil n/2 \rceil}$
α	Cost of Multiplication operation
β	Cost of Addition/Subtraction operation
η	Improve Rate of improvement; $\eta = \left(1 - \frac{Cost\ of\ G2A}{Cost\ of\ TMA}\right) \times 100\%$

Indexing function for TMA(3) is $f(x_1, x_2, x_3; l, l, l) = x_1 \times l \times l + x_2 \times l + x_3$. So, we need three multiplications and two additions operation for each element, thus the total cost is $(3\alpha+2\beta)l^3$. Equivalent G2A has $l'_1 = l_1 \times l_3$, $l'_2 = l_2$ and $f(x'_1, x'_2; l'_1, l'_2) = x'_1 \times l'_2 + x'_2$. Thus the total cost for G2A index computation is $(\alpha+\beta)l^3 + \alpha$. So, the improvement, η is

$$\eta = [1 - \{(\alpha+\beta)l^3 + \alpha\} / (3\alpha+2\beta)l^3] \times 100\%$$

For TMA(4); $f(x_1, x_2, x_3, x_4; l, l, l, l) = x_1 \times l \times l \times l + x_2 \times l \times l + x_3 \times l + x_4$. So, the total cost for TMA is $(6\alpha+3\beta)l^3$ and the G2A is $(\alpha+\beta)l^3 + 2\alpha$. The improvement, η of G2A over TMA(4) is

$$\eta = [1 - \{(\alpha+\beta)l^3 + 2\alpha\} / (6\alpha+3\beta)l^3] \times 100\%$$

Generalizing the cost over n-dimension, TMA(n), the total cost is $\{n(n-1)/2 + n-1\}l^n$. Similarly the total cost of G2A is $(\alpha+\beta)l^n + (n-2)\alpha$. So, the improvement is

$$\eta = [1 - \{(\alpha+\beta)l^n + (n-2)\alpha\} / \{n(n-1)\alpha/2 + (n-1)\beta\}l^n] \times 100\%$$

It is well know that the cost of multiplication is very very higher than the cost of addition/subtraction. Thus we can neglect β to simplify the improvement rate equation.

$$\eta = 1 - \{(\alpha l^n + (n-2)\alpha\} / \{n(n-1)\alpha l^n/2\}$$
$$= 1 - 2(l^n + n-2) / \{n(n-1)l^n\}$$

From the above equation, improvement rate depends on both length of each dimension, l and the number of dimension, n. We can conclude that for any positive value of l and n (>2), η will be positive. Thus the performance of our proposed G2A is always better than that of traditional multidimensional array.

VI. EXPERIMENTAL RESULTS

To evaluate the performance of our proposed indexing scheme for structured data, we constructed a prototype system in Intel(R) Xeon(R) E5620 @ 2.40GHz processor having 8(eight) processors, 32 GB RAM and 1406 MB cache memory. Program is written in C and compiled in gcc compiler with –o option on debian squeeze 6.0.5 operating system. The number of dimensions is set as even numbers between 4 to 30. For simplification, we are considering equal length for each dimension. Figure 4 shows the initialization time for a four dimensional TMA and its' equivalent G2A. With the increase of each dimension length, initialization time increases exponentially as that of number of total elements. Figurate 5, Figure 6 and Figure 7 show the initialization time for 6, 8 and 10 dimensional array respectfully. Due to hardware limitation, we are limiting the length of each dimension till 230, 38, 15 and 8 for 4, 6, 8 and 10 dimensional data respectfully.

Table III shows the G2A and TMA initialization time for different number of dimensions. It is clear that we have values for limited number of lengths for each dimension greater than 10. For showing the performance at a glance, we derive the average initialization time for each element for a specific dimensional data. This is done in two steps. First find the average initialization time by diving initialization time with total number of array elements for each specific dimension and specific length. Then aggregate the derived each element initialization time over each dimension. Figure 8 shows the average initialization per element for different dimensions. Performance improvement is clearly visible. As stated in our theoretical analysis, the performance is improved with the increase of the number of dimensions.

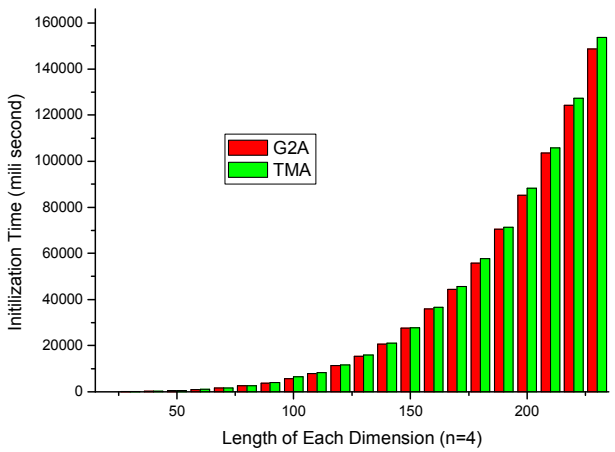

Figure 4. Execution time for TMA(4) and equivalent G2A

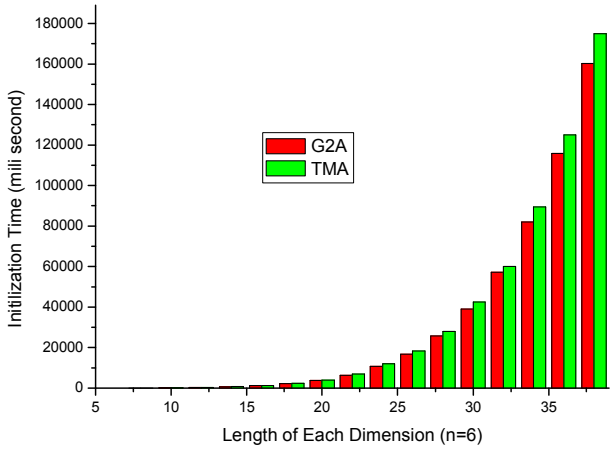

Figure 5. Execution time for TMA(6) and equivalent G2A

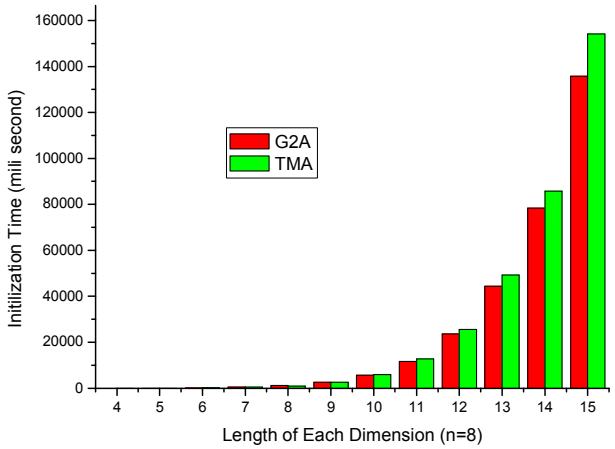

Figure 6. Execution time for TMA(8) and equivalent G2A

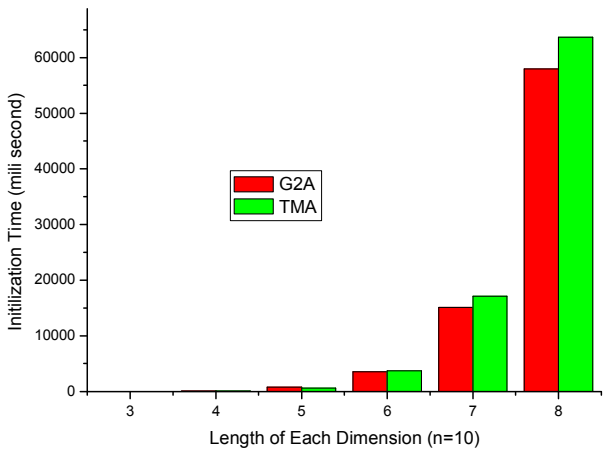

Figure 7. Execution time for TMA(10) and equivalent G2A

TABLE II. EXPERIMENTAL RESULT OVER 10-DIMENSIONAL DATA

Dimensions (n)	Length (*l*)	Initialization Time(mS)	
		G2A	TMA
12	3	40	50
12	4	1080	1290
12	5	13280	15670
12	6	115640	139390
14	3	410	520
14	4	14460	17740
16	3	2520	3270
18	2	10	20
18	3	21060	28580
20	2	80	120
22	2	350	540
24	2	1170	1570
26	2	3780	5890
28	2	14550	24360
30	2	57100	95480

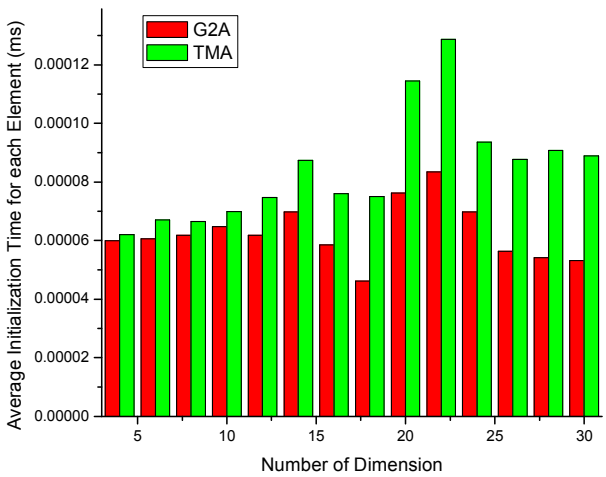

Figure 8. Average Initialization Time for each element for different number of dimesion

VII. CONCLUSION

In this paper, we proposed an index scheme for structured big data. The number of data dimension is a crucial issue for big data computation as most of the traditional compiler has limitation over higher dimensional data. Our focus was on the supporting over higher dimensional data. We have shown better indexing with our generalized two dimensional array scheme. We have experimental results relevant to the theoretical analysis described in this paper. The proposed indexing scheme gives better improvement rate with the increase of data dimensions. One important future direction is that the scheme can easily implemented in parallel environment for parallel applications.

REFERENCES

[1] Tamara G. Kolda, Brett W. Bader, *Tensor Decompositions and Applications*, SIAM Review 51(3), Page:455-500, 2009.

[2] Brett W. Bader, Tamara G. Kolda, *Efficient MATLAB computations with sparse and factored tensors*, SIAM Journal on Scientific Computing, 2007.

[3] Chun-Yuan Lin, Jen-Shiuh Liu, and Yeh-Ching Chung, *Efficient Representation Scheme for Multidimensional Array Operations*, IEEE Transactions on Computers, 51(3), pp.327-345, 2002.

[4] Kostas Zoumpatianos, Stratos Idreos, Themis Palpanas, *Indexing for Interactive Exploration of Big Data Series*, SIGMOD'14, June 22–27, 2014, Snowbird, UT, USA.

[5] K. M. Azharul Hasan, Md Abu Hanif Shaikh, *Representing Higher Dimensional Arrays into Generalized Two- dimensional Array: G2A*, 16th International Conference on Parallel and Distributed Computing, Applications and Technologies (PDCAT 2015), Published by Springer LNEE, Jeju, South Korea.

[6] Md Abu Hanif Shaikh, K.M. Azharul Hasan, *Efficient Storage Scheme for n-Dimensional Sparse Array: GCRS/GCCS*, 13th International Conference on High Performance Computing & Simulation (HPCS 2015), Page (137-142), Published by IEEE, Amsterdam, Netherlands.

[7] B. Christian, M. Urs, "Multidimensional Index Structures in Relational Databases", Intelligent Information Systems, 15, pp. 51–70, 2000

[8] Sk Md Masudul Ahsan, K M Azharul Hasan "An Implementation Scheme for Multidimensional Extendable Array Operations and Its Evaluation", ICIEIS, Part III, CCIS 253, pp. 136–150, 2011.

[9] Y. Zhao, P. M. Deshpande, and J. F. Naughton, "An array based Algorithm for simultaneous multidimensional aggregates", ACM SIGMOD, pp. 159–170, 1997.

[10] K M Azharul Hasan, Tatsuo Tsuji, Ken Higuchi "An Efficient MOLAP Basic Data structure and Its Evaluation", Proc. of DASFAA, pp. 288-299, LNCS 4443, 2011.

[11] EJ Otoo, H Wang, G Nimako, "New Approaches to Storing and Manipulating Multi-Dimensional Sparse Arrays" , Proc. of SSDBM'14, pp. 2014.

[12] Emad Soroush and Magdalena Balazinska "ArrayStore: A Storage Manager for Complex Parallel Array Processing" In Proc. of ACM SIGMOD International Conference on Management of data, pp. 253-264, 2011.

[13] Steve Carr , Kathryn S. McKinley , Chau-Wen Tseng "Compiler optimizations for improving data locality", In Proc. of the sixth international conference on Architectural support for programming languages and operating systems, p.252-262, 1994.

[14] Michael Stonebraker, David Dewitt Requirements for Science Data Bases and SciDB, CIDR Perspectives 2009

[15] SciDB: an open-source, array-oriented database management system http://database.cs.brown.edu/projects/scidb/

Orchestration Algorithms for Network-assisted Virtual Machine Migrations using OpenDayLight Controller

Shamim Ahmed[1], Barbara Martini[2], Molka Gharbaoui[3], Andrea Sgambelluri[3], SK. Shariful Alam[4]

[1]University of Trento, Trento, Italy
shamim.ahmed@unitn.it
[2]CNIT, Pisa, Italy
barbara.martini@cnit.it
[3]Scuola Superiore Sant' Anna, Pisa, Italy
m.gharbaoui@sssup.it, a.sgambelluri@sssup.it
[4]Khulna University of Engineering and Technology, Khulna, Bangladesh
ssa1996@gmail.com

***Abstract*— In the last years, prominent advances in software virtualization (e.g., Hypervisor) have enabled the agile deployment of cloud services and, at the same time, server consolidation operations through agile Virtual Machine (VM) operations (e.g., start-up, snapshot, cloning, and migrations) across Data Center (DC) servers. On the other hand, such advances pose new challenges in the overall management of the DC infrastructure since VM operations may occur much more frequently in virtualized than in legacy DCs and produce not only a computational load on the involved servers, but also a network load on all the switches connecting the servers. In this context, the Software-Defined Network (SDN) paradigm opens up new opportunities to design convergent resource management systems which is able to address the provisioning of cloud services while meeting adequate network performance during VM provisioning and migrations.**

In this paper, a promising advanced monitoring and resource allocation function for SDN-based DC networks has been proposed aiming at reporting possible suitable paths connecting specified servers that can be exploited for VM migrations. In such a way, network-assisted migrations can be triggered that assure adequate VM migration delays according to specified requirements (e.g., minimum delay for live VM migration) while addressing different management targets (e.g., network load balancing, minimization of energy consumption).

***Index Terms*—Cloud, Data Centre, OpenFlow, Software-Defined Networking, VM migration, Orchestration**

I. Introduction

CLOUD computing has emerged as a new paradigm that delivers software and hardware resources as services to the general people. Cloud computing services generally leverage virtualization of physical resources collected in large DCs (i.e., Cloud DCs). Thanks to virtualization software technologies, i.e., VM deployment, cloud service consumers may be offered a subscription-based access to infrastructures, platforms or applications, referred to as IaaS, PaaS or SaaS, respectively [1]. Virtualization technologies allow cloud service providers to apply consolidation procedures within Cloud DCs and, consequently, to achieve a more efficient use of physical servers. In contrast, new challenges arise in the management of the DC infrastructure, especially as regards VMs provisioning and interaction. In fact, thanks to the availability of more agile procedures for the set-up of new applications (i.e., snapshot, cloning of VMs), provisioning or reconfiguration operations which occur much more frequently in Cloud DCs than in legacy DCs. Moreover, from the networking perspective, the DC infrastructure is a really challenging environment due to several aspects. As previously highlighted, in Cloud DCs, services are provided according to different delivery paradigms (e.g., IaaS, PaaS, SaaS) and each of them is characterized by a specific communication model (one-to-one, one-to-many, many-to many) among VMs, that may involve hosts located inside or outside the DC. Therefore, to satisfy performance requirements of Cloud services, VM placement must take into account network link status. Definitely, the high volatility of VMs in Cloud DC requires that the intra-DC network infrastructure should be more flexible, agile and integrated with the IT (computing and storage resources) infrastructure with computing, storage and network resources acting as a unified pool of virtual resources jointly orchestrated to offer improved user experience while optimizing their usage [2]. In this context, SDN and, in particular, Openflow (OF) protocol [3] can play a key role due to their distinguished features that well adapt to virtualized environments, i.e., flow-based network resource control capabilities, combined with high programmability of routing or switching functionalities, that allow for a software-based enforcement of per-flow routing strategies.

In this paper, we present orchestration algorithms for addressing network-assisted virtual machine migrations enabling the coordinated control of IT and network resources in Cloud DCs. Indeed, the proposed algorithms can be used in the context of VM migration workflows to decide the proper servers to host VMs also taking into account the current traffic load over network links by means of OF statistics. As a result, both the migration of the VM to the selected host and the set-up of a delivery path can be addressed while assuring improved data delivery performance. The selection of network resources (i.e., switch and links to be traversed) leverages

978-1-4673-9257-0/15/$31.00 ©2015 IEEE

flow-based statistics (e.g., switch/link loads) provided by OF. More specifically, traffic statistics available from OF-based switches at per-port level have been exploited for selecting the best path towards the required server to host the VM. Accordingly, the routing table of OF-based switches is updated according to the selected best path for flow provision. When deploying an enhanced IaaS paradigm, this approach allows addressing fluid data delivery while avoiding possible congestions due to the over-subscription of network links and thus minimizing the network latency in VM migrations.

II. SDN IN DATA CENTERS FOR ORCHESTRATION AND COMPARISON WITH RELATED WORKS

SDN [1] is a paradigm that was developed with the view of managing networking elements through software running from an external server. It is an emerging architecture intending to be dynamic, manageable, cost effective, and adaptable so that seeking to be suitable for high bandwidth according to today's applications. The core part of SDN is its controller according to a new paradigm which divides the networks in two parts: forwarding and switching systems on the one side and a controlling element on the other side. Indeed, the intelligence of the network is moved to a centralized software-based controller that programmatically adds, modifies, and deletes the flow entries on network switches or routers thereby affecting their forwarding actions. While the SDN is a paradigm, the most common implementation is through OF that is the communication protocol used for the controller to enforce forwarding rules and to ask for statistics data to switches. Commercial of the self (COTS) devices are becoming much popular to the data center providers for lower costs. As like COTS servers, lower cost layer-2 switches are becoming more feasible for hundreds of ports rather than using high cost layer-3 switches. This trend emphasizes a suitable use case of SDN with OF enabled switches in data centers.

The usability of OF for virtual machines scheduling and migration within DCs is a pretty unexplored research area. To the best of our knowledge, just a couple of recent works argue on the use of OF in DC. Specifically, the authors in [5] aim at reducing the congestions by reconfiguring the routing within the network using OF controllers for addressing a fine grained traffic engineering leveraging short term predictability of traffic demands. The authors have evaluated the performance of OF in a DC environment using DC traffic models gathered from real DC measurements in [6]. However, none of the above research works consider the use of OF in the context of a VM migration process as this work actually does.

Considering the complex, heterogeneous and highly dynamic scenario of cloud DCs, a novel functionality that enables the unified and orchestrated control of IT and network resources in Cloud DC becomes a higher priority issue [7]. A number of research efforts focused on effective VM deployments across DC servers with bandwidth constraints on virtual network embedding in DCs [8][9]. However, neither VM migration cases are considered nor experimental validation are provided, in line with guidelines dictated by recent research directions [10] and emerging industry trends for DC management [11]. In [12], the design, development and deployment of a new virtualization-aware networking architecture whose advanced traffic-engineering capabilities are enabled by OpenFlow-based Virtualization-aware Networking (OFVN) systems have been described. The OFVN architecture is designed with scalability challenges, so as to guarantee performance requirements concerning communication among the servers even though the Data Center continues to grow in size. In [13] an orchestration system is presented that for dynamic computing and communication resources chaining, able to assure better than best effort VMs data exchanges across Cloud DCs. In this paper we generalize such approach to the case of VM migrations. There are many open source controllers available which support SDN such as NOX, POX, FloodLight, Beacon, Trema, Ryu and OpenDayLight (ODL) etc. For this research activity, ODL [14] is used as OF controller with additional software modules devoted to enable combined, i.e., orchestrated, resource management at computing and networking level.

III. MININET ENVIRONMENT WITH OPENDAYLIGHT CONTROLLER

ODL [14] is an open platform for network programmability to enable SDN and Network function virtualization (NFV). It is an open source project with a modular, pluggable, and flexible controller at its core. The controller is implemented in software and is contained within its own Java Virtual Machine. ODL (Hydrogen version) [15] uses some supporting software tools or paradigms such as: Maven, OSGI, Java Interfaces. One of the advantages of ODL controller is its web interface. By using web User Interface (UI), users can log in to the web portal and can access the network devices through the controller. Fig. 1 shows the graphical view of the developed network in ODL UI.

Mininet [16] is a network emulator which can be used for creating networks of virtual controllers, switches and hosts. Mininet hosts run on standard Linux network software. As its switches support OF, it is possible to make test bed network for highly flexible custom routing and SDN. Mininet networks run real code including standard Unix/Linux network applications as well as the real Linux kernel and network stack. As a result, the code developed and tested on Mininet, for an OF controller, modified switch, or hosts, can be moved to a real system with minimal changes, for real world testing, performance evaluation, and deployment.

This research has been carried out in Mininet simulation environment within a work station that has the following properties: Ubuntu version 12.10, OpenDalylight controller (updated on 10th June 2013), Mininet version 2.0.0, Eclipse 3.8 (OpenDayLight Controller, compiled through Maven).

There are many types of topologies available in literature (e.g., FatTree, BCube, DCell, FiConn, and VL2) to define a DC network. However, there is nothing to define which one is better than other. Operators are choosing the topology based on the geographical location, business requirement etc. For this research activity we have chosen FatTree topology which is widely used in many data centers around the world.

According to our proposed topology, we have created a FatTree DC network of 10 switches (Fig. 1) with 16 host servers. We consider each host as the server end for hosting

VMs, consolidating VMs as well as placing new VMs. ODL has been implemented and connected with this DC network. The existing modules from ODL that were used in this work are the following:

- switchManager: This module holds the details of the network elements. It is mainly used for discovering the network switches and routers.
- statisticsManager: It holds the statistic information of each port of the switches in the network. It is responsible for giving such information on demand.
- HostTracker: This one tracks the information of the connected hosts within the network.

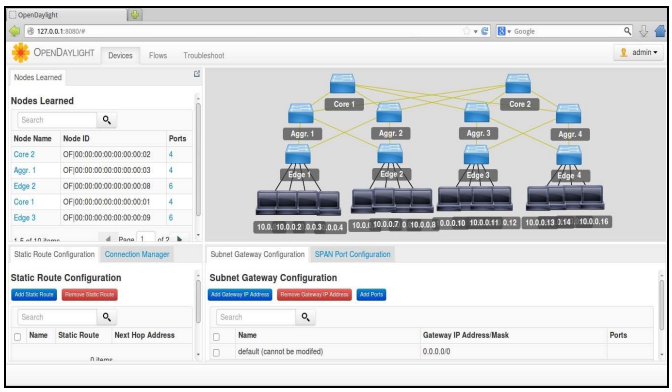

Fig. 1. Data Center implementation through ODL interface

IV. VMMIGRATION MODULE: SOFTWARE DESIGN

In this research we have introduced VMMigration module as a network control application of the ODL controller aiming at assisting VM migration with network load information in cloud DCs thereby orchestrating computing and network resources. The VMMigration module is divided in different sub modules that are useful for performing the VM migrations efficiently taking into consideration the current status of the network (Fig. 2).

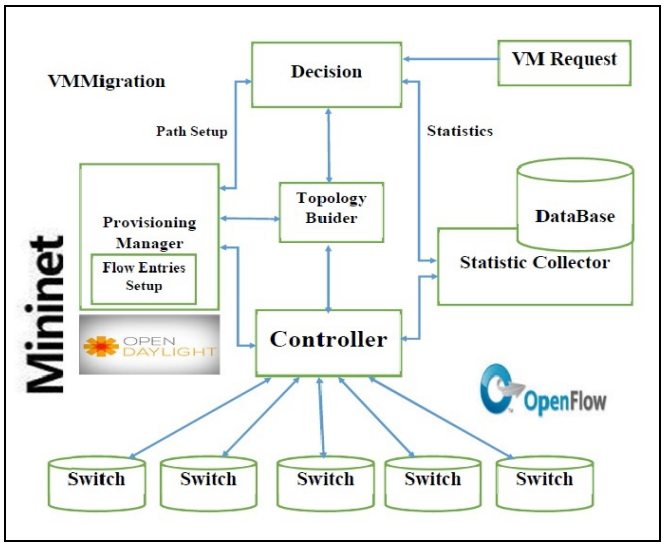

Fig. 2. OpendayLight Controller with VMMigration module

A. Statistics Collector

The Statistics Collector module is developed to periodically collect the statistics of the switches in the DC network and store them in the **Database**. At the end of each polling interval (by default equal to 30 seconds), we collect the instantaneous utilized bandwidth of each port or link of each switch. Then, by using the maximum allowable bandwidth (by default the virtual switches (OVS) that we have considered support a maximum of 10Gb) we can retrieve the available bandwidth (i.e., unused bandwidth). It is worth highlighting that Mininet (version 2.0.0) can support a maximum bandwidth equal to 1Gb for each link. For this reason, we have scaled down the switches capacities to 1Gb to make the experiment compatible with Mininet.

The Database is utilized for storing the information related to the VM migrations such as statistics of the switches and hosts information. It is refreshed after the acceptance of every migration request thus maintaining up-to-date the status of the network.

B. Topology Builder

The Topology Builder module is developed to retrieve the network topology as well as the host's information. In fact, though the topology information regarding the switches can be invoked through the SwitchManager module, it is not possible to track the host's information since they are not directly connected to the controller. For this reason, it is necessary to make each host communicate with the others (by introducing traffic flows through the network) so that the controller can be informed about their presence in the network. In such a case, the Database can be populated with the host's position, various connections between the hosts and switches, etc.

C. VM Request

This module is used to deal with the VM migration requests. As soon as a new request arrives, the controller forwards the information to the Decision component. The VM migration request can be defined manually from an external server or automatically (pre assigned). A request must contain the following parameters:

- Server source address
- Server destination address
- Bandwidth requirement B for migration.

D. Provisioning Manager

The Provisioning Manager module is developed for managing the flow entries in the switches at the DC network. In fact, it is responsible for the flow entries creation and manipulation inside the switches. Specifically, the Provisioning Manager relies on the best path, selected according to a specific algorithm, between the server source and server destination (specified in the VM migration request) to set-up the flow entries in the involved switches.

E. Decision

The Decision module is developed to take the appropriate decisions for the VM migrations. It works in collaboration with the VM Request module which sends the VM migration requests. Then, the Decision module runs the appropriate

algorithms to get the available best path between the source and destination servers specified in the requests. Once a best path is found, it is provided to the Provisioning Manager Module.

V. ALGORITHMS FOR VMMIGRATION MODULE

A. Path_Selection

The *Path Selection* algorithm is triggered by the Decision module upon reception of a VM migration request from the server source. On basis of this request all available paths from the server source to the server destination are exploited and stored in Database. Specifically, the Decision module handles the VM migration request, looking at the pool of servers that are available by querying the Topology Builder module. Once the position of the servers source (S_source) and destination (S_dest) are defined, the edge switches source (Edge_source) and destination (Edge_dest) directly connected to the servers are also determined. Then, the links from the Edge_source and Edge_dest switches are used for knowing the j-th aggregation source (Agg_source) and destination (Agg_dest) switches, respectively. This process will continue until fulfilling a direct path between S_source and S_dest. All retrieved available paths (Path[N]) are then stored in Database.

Algorithm.1 represents the description of the *Path Selection* algorithm. We denote:

S = a pool of available servers.
L = link of the corresponding unit.
Edge[k] = the k-th edge switch (k=1, 2…)
Agg[l] = the l-th aggregation switch (l=1, 2….)
Core[m] = the m-th core switch (m=1, 2…)

Algorithm 1. *Path_Selection algorithm* (Upon VM migration request)

```
// This algorithm provides a set of N available paths (Path[N]) between a
couple of servers source and destination upon a VM migration request is
received by the controller.

INPUTS:
  S_source
  S_dest
OUTPUTS:
  P[N]   N=1, 2 …..

    if S_source ∈ S && S_dest ∈ S then
      // get the set of edge switches linked to the source/dest server
      Edge_source = Edge[S_source]
      Edge_dest = Edge[S_dest]
      //get the aggregation switches linked to the edge_source/dest switches
      Agg_source = Agg[Edge_source]
      Agg_dest = Agg[Edge_dest]
      if L(Agg_source[l]) = L(Agg_dest[l]) then
        //find an available path up to the aggregation level
        P[i] = Find_Path_i(S_source, Edge_source, Agg_source[l],
                           Agg_dest[l], Edge_dest, S_dest) i=1, 2..
        //find an available path up to the core level
        P[j] = Find_Path_i(S_source, Edge_source, Agg_source[l],
                           Core_source[m], Agg_dest[l], Edge_dest,
                           S_dest)  //j=i+1…
        P[N] = P   N=1, 2,…, i+j
      else
      P[N] = Find_Path_n(S_source, Edge_source, Agg_source[l],
                         Core_source[m], Agg_dest[l], Edge_dest, S_dest)
        L = L(P[N])
      end if
    end if
```

B. Best_Path

The *Best_Path* algorithm finds the best path from all the available paths determined by the *Path_Selection* algorithm for a couple of given source (S_source) and destination servers (S_dest). For this purpose, a set of policies might be applied such as first fit, best fit and worst fit. In this paper, the scope of the VM migration process is to minimize the maximum utilization of the network links. For this reason, we consider the most unloaded links for the resources allocation which corresponds to the worst fit policy. Once Path[N] is available, we check if all the links of each path have enough bandwidth with respect to requested bandwidth B, then we apply the Worst Fit policy. We start by selecting the source server link L_{S_source} by fulfilling B requirement. Then maximum available link bandwidth L_{edge_source} is selected towards the agg_source according to Path[N]. Then most unloaded link from L(agg_source [l]) is chosen for selecting the next link L_{agg_source}. While agg_source and agg_dest are connected by the same L_{agg_source}, maximum available bandwidth link L_{agg_dest} from Agg_dest toward the Edge_dest is selected with L_{S_dest} from destination server. Hence, best path is selected without traversing the core switch. Otherwise L_{agg_source} will select the corresponding core switch Core[m] and the process continues until selecting the best path P_{best} . In this way only one possible best path is selected from Path[N] by the Best_Path algorithm.

Algorithm 2 describes the *Best Path algorithm*. We denote:

$L_e[e]$ = The e-th link of edge switch. $L_e[e] \in L$
$L_a[a]$ = The a-th link of aggregation switch. $L_a[a] \in L$
$L_c[c]$ = The c-th link of edge switch. $L_c[c] \in L$

Algorithm 2. *Best_Path algorithm* (From all the available paths from server source to server destination)

```
// This algorithm provides the best path P_best from a set of N available paths
P[N] between source and destination servers according to the bandwidth B .

INPUTS:
  P[N]
  B
OUTPUTS:
  P_best
 if P[N] ≠ null then
    //if enough bandwidth is available on the link
    if L(S_source) > B then
      L_S_source = L(S_source)
    end if
    if L(Edge_source[e]) > B then
      //Find the link which has the maximum available free bandwidth at
      //the edge and aggregation level
      L_edge_source = arg max_{L(edge_source[e])∈L} L(edge_source[e])
    end if
  if L(agg_source[l]) = L(agg_dest[l]) && L(agg_dest[l]) > B then
    L_agg_source = L(agg_source[l]) = L(agg_dest[l])= L_agg_dest
      //if a path towards the server destination is found then consider it as
      // best path
    if L(S_dest) > B then
      L_S_dest = L(S_dest)
```

P_{best} =P[N] P[N] ∈ Path[L_{S_source} L_{edge_source} L_{agg_source} L_{edge_dest} L_{S_dest}]
end if
else
if L(agg_source [l]) > B **then**
L_{agg_source} = arg max $_{L(agg_source\ [l]) \in L}$ L(agg_source [l])
end if
if L(core [m])= L_{agg_source}
L_{core_source} = L(core [m])
end if
if L(core [m]) = L(agg_dest [l]) && L(agg_dest [l]) > B **then**
L_{core_dest} = L(agg_dest [l]) = $_{\text{arg max } L(core\ [m]) \in L}$ L(core [m])
end if
if L(agg_dest [l])= L(edge_dest [k]) && L(agg_dest [l]) > B **then**
L_{agg_dest} = L(agg_dest [l])= L(edge_dest [k])
end if
if L(edge_dest[k])=L(S_dest) && L(S_dest) > B **then**
$L_{S\ dest}$ = L(S_dest)
P_{best} =P[N] P[N] ∈ Path[L_{S_source} L_{edge_source} L_{agg_source} L_{core_source} L_{core_dest} L_{agg_dest} L_{S_dest}]
end if
end if
end if

VI. PERFORMANCE EVALUATION VIA SIMULATIONS

According to our developed test-bed set up, 10 OF enabled switches are connected with each other following a Fat-tree topology with an OF controller. Each edge switch is connected with four servers. We have implemented BaseLine algorithm [17] that is compatible with our developed VMMigration module. According to the BaseLine algorithm, the selection of switches between source and destination is done by a pre-configured flow table (forwarding path). This pre-configured forwarding path goes along the same specified links without using alternative paths provided by topology redundancy. It is a static approach which can be considered an acceptable approximation for routing practices in legacy DC networks.
While a VM request is arrived for selecting a migration path from source to destination, both the baseline algorithm and Best Path (worst fit) algorithm are used. For comparison purpose we have also included bandwidth constrains with baseline algorithm so that to choose the next link from one switch to other from source to destination, there should be enough bandwidth available according to the migration request. If the available link bandwidth cannot satisfy bandwidth requirement, the request will be rejected.

The simulations ensure the ability of VMs migration by generating traffic throughout the DC network. As simulations can take large time and large amount of traffic, there are some design considerations which should be followed. Due to the scalability issues for sending traffic through Mininet, maximum acceptable bandwidth for each port of each switch has been scaled down from 1Gb to 40Mb. In this case a VM request is generated from 1 random source server and 4 probable destinations. Best path algorithm is executed for 4 best paths from one source to 4 destination servers. It is possible that there will be 4 best paths for 4 destinations, or less, or no best path. It depends on the network load and available switch ports bandwidth through which those best paths traverse. During best path generation the lowest available bandwidth along a best path is retrieved. This retrieval information is used to find the final best path among those 4 best paths. In this case maximum available bandwidth from those 4 available lowest bandwidths is selected for the final best path. Hence, the destination server along final best path is selected for final destination server for VM migration. Unlike previous case, for each VM migration request only one best path is generated.
Each VM request contains a VM with 1GByte. To pass a VM with 1GByte, using 10Mbps data rate, it is required 800s to migrate the full VM. As a result, the system can dynamically generate the VM request, allocate resources (unloaded links), migrate the VM and finalize migration after the required time. The simulations have been carried out according to the details given in Table I.

TABLE I. SIMULATIONS PARAMETERS

Parameters	Values
Statistic interval	30s
Link bandwidth	40Mb
Request bandwidth (VM migration)	10 Mb
Number of migration request	1000
VM request inter-arrival time	10s, 30s
Simulation duration	10000s

VII. EVALUATION PERFORMANCE

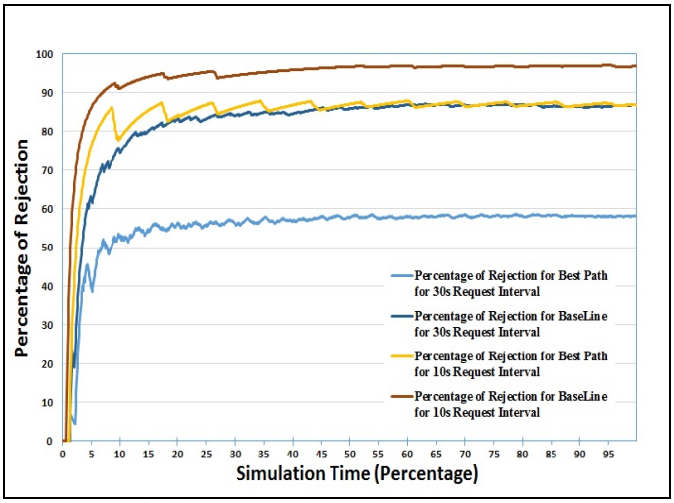

Fig. 3. Rejection percentage in time for variable inter-arrival times

Fig. 3 plots the rejection rate for both the best path algorithm and the baseline while the requested bandwidth B is fixed to 10Mb and the inter-arrival time (IAT) of the migration requests is equal to 10s and 30s. When IAT is low the requests generation rate is high and more rejection can occur since the network is overloaded. In such a case, the blocking keeps increasing until the network is unloaded again thanks to the end of the current migrations. Moreover, in both situations (10s and 30s interval) the rejection rate is lower for best path than baseline. In fact, once the preconfigured paths are saturated, no more requests can be accepted, unlike the best path algorithm which takes advantage from the redundant links in the topology to accept more requests.

Fig. 4 show the behavior of the DC network in terms of request rejection for both the Best Path and the BaseLine algorithms, while varying the statistics update interval (pooling time). When the statistics update interval is low, OF controller can provide recent network status in terms of available bandwidth for each port of each switch. As we have fixed our request interval time to 10s, the controller can process at least 6 requests between two consecutive statistics update (for 60s update interval). For example if the network can take one request (according to recent statistic update), it can accept up to 6 requests within next 60s. Therefore, request acceptance rate becomes higher for higher statistic information collection time. Though the acceptance rate for higher pooling time is higher (around 5%), it is not beneficial for the VM migration. In fact, it saturates the links of the network and the links are then unable to flow data. Finally, as previously explained, the Best_Path algorithm shows better performance in terms of request rejection than the Baseline algorithm.

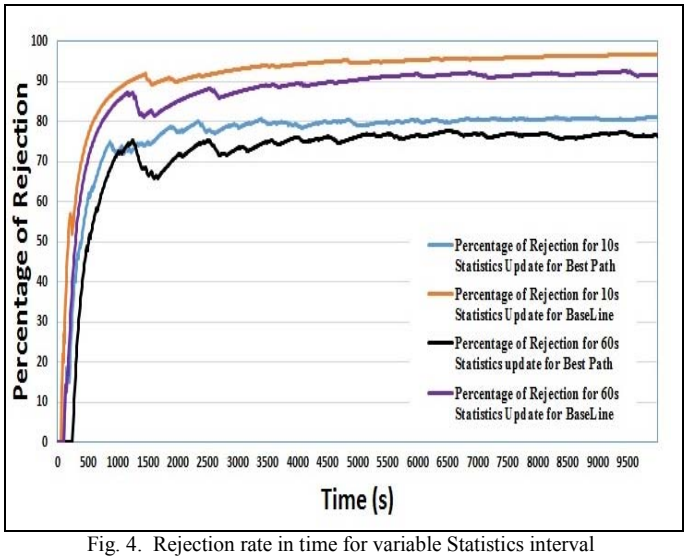

Fig. 4. Rejection rate in time for variable Statistics interval

VIII. Conclusion

DC network can be more dynamic in terms of control and management through implementing SDN. In this research work, it is demonstrated that future DCs can be more dynamic for selecting required destination server for migrating VM from probable source server. This approach has demonstrated not only the availability of the destination servers, but also has explored the selection of the best destination on the basis of network loads. In such way, the proposed solution can balance the network load. This scheme can also avoid the saturation of the link for overloading states and can distribute network loads towards available unloaded links. While the DC network has been overloaded by traversing data traffic, new requests have been rejected instead of further processing. This is also convincing that by implementing different load factors we can keep the network unsaturated for maximum number of flows that are traversing throughout the network. Moreover, the proposed dynamic solution shows a good choice for minimizing delays as well as energy consumption for VM migration. These behaviors make an orchestrated DC network for maximum resource utilization and assure adequate delays for VM migration. The effectiveness of the proposed algorithms have been evaluated in terms of the acceptance rate of VM migration requests through a significant set of simulations. Results show that our Best_Path algorithm outperforms the BaseLine, presenting a lower blocking probability and a better utilization of network links. Such load balancing has a positive impact on the quality of service perceived by the user since less links are saturated. Such improvement depends on the settings of the system parameters such as the inter-arrival time between two consecutive VM migration requests, the pooling time for the retrieval of the network statistics, etc. As future work, we will consider the effect of queuing and rescheduling the rejected requests in order to serve them once the links are unloaded. Other parameters might also be evaluated such as the number of available servers, the requested bandwidth, etc.

References

[1] G. Karagiannis C. N. Hfer, “Cloud computing services: taxonomy and comparison”, Journal of Internet Services and Applications, 2(2):81- 94, Jun 2011.

[2] Yueping Zhang; Ao-Jan Su; Guofei Jiang, “Evaluating the impact of data center net-work architectures on application performance in virtualized environments”. Quality of Service (IWQoS), 18th International Workshop, pages 1 -5, June 2010.

[3] Openflow. [Online] http://www.openflow.org.

[4] SDN–Definition [Online] https://www.opennetworking.org/sdn-resources/sdn-definition

[5] Theophilus Benson, Ashok Anand, Aditya Akella and Ming Zhang “MicroTE: Fine grained Traffic Engineering for Data Centers”, CoNEXT 2011, Tokyo, Japan

[6] Rastin Pries, Michael Jarschel, Sebastian Goll, “On the Usability of OpenFlow in Data Center Environments”, Workshop on Clouds, Networks and Data Centers collocated with the IEEE International Conference on Communications (ICC 2012), Ottawa, Canada, June 2012

[7] W. Cerroni, M.Gharbaoui, B.Martini, A. Campi, P. Castoldi, F. Callegati, Cross-layer resource orchestration for cloud service delivery: A seamless SDN approach, Computer Networks, Volume 87, 20 July 2015, Pages 16-32

[8] Rabbani, Md G., Pereira Esteves, R., Podlesny, M., Simon, G.; Granville, Zambenedetti, L., Boutaba, R., "On tackling virtual data center embedding problem" 2013 IFIP/IEEE IM 2013, May 2013

[9] Meng, X., Pappas, V., Zhang, L., "Improving the Scalability of Data Center Networks with Traffic-aware Virtual Machine Placement", IEEE INFOCOM 2010, 14-19 March 2010

[10] Chappel, C., “Unlocking Network Value: Service Innovation in the Era of SDN”, HeavyReading, white paper, June 2013

[11] “Implementing SDN and NFV with Intel Architecture”, White paper. Intel Architecture Processors. 2013

[12] Molka Gharbaoui; Piero Castoldi; Gianni Antichi; Stefano Giordano; Davide Adami, “Effective resource control strategies using openow in cloud data center”, IFIP/IEEE International Symposium on Integrated Network Management, (IM 2013), pages 568-574, May 2013.

[13] B. Martini, D. Adami, A. Sgambelluri, M. Gharbaoui, L. Donatini, S. Giordano and P. Castoldi, “An SDN Orchestrator for Resources Chaining in Cloud Data Centers”, in Proc. of EUCN 2014, Bologna, Italy, June 2014.

[14] Opendaylight tutorial. [Online] http://archive.openflow.org/wk/?title=OpenDayLight_Tutorial

[15] OpenDaylight Hydrogen release. https://wiki.opendaylight.org/view/Release/Hydrogen [online]

[16] Mininet overview [Online]. http://mininet.org/overview

[17] D. Adami G. Antichi S. Giordano M. Gharbaoui, B. Martini and P. Castoldi. (2014, May), On virtualization-aware traffic engineering in openflow data centers networks.to be published. Network Operations and Management Symposium (NOMS), 2014 IEEE.

Solving Capacitated Vehicle Routing Problem with Route Optimization using Swarm Intelligence

M. A. H. Akhand, Jaharul Jannat, Tanzima Diba and Al-Mahmud
Dept. of Computer Science and Engineering
Khulna University of Enginnering & Technology
Khulna-9203, Bangladesh

***Abstract*—**Capacitated Vehicle Routing Problem (CVRP) is a real life constrain satisfaction problem in which customers are optimally assign to individual vehicles (considering their capacity) to keep total travel distance of the vehicles as minimum as possible while serving customers. Various methods are investigated to solve CVRP in last few decades, the most popular way of solving CVRP is splitting the task into two different phases: firstly, assigning customers under different vehicles and secondly, finding optimal route of each vehicle. Sweep clustering algorithm is well studied for clustering nodes. On the other hand, route optimization is simply a traveling salesman problem (TSP) and a number of TSP optimization methods are investigated for this purpose. This study investigates a variant of Sweep algorithm for clustering nodes and different SI based methods for route generation to get optimal CVRP solution. In conventional Sweep algorithm, cluster formation starts from 0^0 and consequently advance toward 360^0 to consider all the nodes. In this study, Sweep cluster are considered from different starting angle. On the other hand, two well-known Swarm Intelligence (SI) methods (i.e., Ant Colony Optimization and Particle Swarm Optimization (PSO)) and two recent SI based algorithms (i.e., Producer-Scrounger Method and Velocity Tentative PSO) are considered for route optimization. We have compared the performance of these methods to solve CVRP. The experimental results on a large number of benchmark CVRP reveal that different starting angle has positive effect on Sweep clustering and finally, VTPSO is able to produce better solution than other methods.

Keywords - *Capacitated Vehicle Routing Problem, Sweep Clustering, Genetic Algorithm, Ant Colony Optimization, Particle Swarm Optimization (PSO), Producer-Scrounger Method and Velocity Tentative PSO.*

I. INTRODUCTION

Vehicle Routing Problem (VRP) means determining routes for several vehicles from a depot to a number of customers and then returning to the depot. Customers with known demands are visited by a homogeneous fleet of vehicles with limited capacity. VRP is a hard optimization task to minimize total travelled distance of all the vehicles to serve all the customers. The general constrains of VRP are each customer is serviced exactly once (by a single vehicle) and total load on any vehicle associated with a given route does not exceed its capacity. Since capacity constraint of vehicles is the most important the problem is alternatively called Capacitated VRP (CVRP). In general, a CVRP considers equal capacities for all vehicles; although in real life vehicle fleet with different capacities can be used to solve the delivery problem [1]. A number of variations of CVRP are also available: considers multiple depot instead of one and considers time window constraint defining time frames when a customer can be serviced. The simplest form of CVRP considering one depot and several vehicles with equal capacity is the most studied problem.

In CVRP, all customers have known demands and known locations for the delivery. The delivery for a customer cannot be split. In other words, the demand of a customer must be satisfied via only one visit. All vehicles are assumed to have the same loading capacity. They depart from a single depot at the beginning and return to the depot at the end. The service or unloading time at each customer may or may not be considered. The objective is to minimize the total travelling distance or time for all vehicles to serve all customers. Mathematically, a CVRP is defined as

$$\text{Minimize} \sum_{i\in N}\sum_{j\in N}\sum_{v\in V} C_{ij} X_{ij}^{v} \tag{1}$$

$$\text{Subject to} \sum_{v\in V} y_i^v = 1 \quad \text{for } i \in N \tag{2}$$

$$\sum_{i\in N} x_{ij}^v = y_j^v \text{ for } j \in N \text{ and } v \in V \tag{3}$$

$$\sum_{j\in N} x_{ij}^v = y_i^v \text{ for } i \in N \text{ and } v \in V \tag{4}$$

$$\sum_{i\in N} d_i y_i^v \le Q \text{ for } v \in V \tag{5}$$

$$\sum_{i\in N} x_{i1}^v \le 1 \text{ for } v \in V \tag{6}$$

$$\sum_{j\in N} x_{1j}^v \le 1 \text{ for } v \in V \tag{7}$$

In this formulation, the objective function is expressed by Eq. (1) which states that the total travelling distance of all vehicles is to be minimized. Eq. (2) represents the constraint that each customer must be visited once by one vehicle, where y_i^v=1 if vehicle v visits customer i, and 0 otherwise. It is guaranteed in Eq. (3) and Eq. (4) that each customer is visited and left with the same vehicle, where $x_{ij}^v = 1$ if vehicle v travels from customer i to customer j, and 0 otherwise. A constraint in Eq. (5) ensures that the total delivery demands of vehicle v do not exceed the vehicle capacity. Eq. (6) and Eq. (7) express that vehicle availability should not be exceeded.

CVRP is a real life constrain satisfaction problem in which customers are optimally assign to individual vehicles (considering their capacity) to keep total travel distance of the vehicles as minimum as possible. Various methods are investigated to solve CVRP in last few decades. A number of methods available that optimizes node assignment under vehicles and route of vehicles together. On the other hand, the most popular way of solving CVRP is splitting the task into two different phases: firstly, assigning customers under different vehicles and secondly, finding optimal route of each vehicle. Among several ways for customer assignment, Sweep clustering algorithm is well studied due to its simplicity. The algorithm calculates polar angles of all the nodes and then assign nodes into different clusters according to their angles. On the other hand, route optimization is simply a traveling salesman problem (TSP) and a number of TSP optimization methods are investigated for this purpose.

The capability of Sweep in solving the VRP for public transport is investigated in [2]. Here clustering is performed by joining their angles in ascending order. A node with smallest angle is joined with one with second smallest and then third smallest and so forth until the capacity constraint is satisfied. After clustering the nodes in each cluster are linked based on their distance. Then route generation is accomplished through TSP. A hybrid heuristic approach has been used in [3]. In the paper GA has been combined with Sweep algorithm to optimize routes and succeeded to produce better result.

A Sweep heuristic method with 2-opt exchange and TSP tours has been used in [4]. The method also used an integer programming model for split delivery VRP model to select the best route to pick up and delivery customers. A centroid-based heuristic algorithm to solve the capacitated VRP has been proposed in [5].The proposed algorithm consists of three phases: cluster construction, cluster adjustment, and route establishment. They compared their result with sweep algorithm and showed that 3-phase approach can result in smaller distances than the Sweep algorithm in more cases. Route establishment was also performed through TSP.

The modified Sweep algorithm was used to solve morning newspaper delivery problem through VRP in [6]. This modified algorithm optimized the total cost without violating the capacity and time window constraints. A hybrid two-phase algorithm called Sweep algorithm and ant colony system (ACS) for the classical VRP has been proposed in [7]. At the first stage, the VRP was solved by the Sweep, and at the second stage, the ACS and 3-opt local search were used for improving the solutions. Use of ACS to solve the CVRP associated with collection of recycling waste from households has been demonstrated in [8].

Recently, the outcome of Sweep algorithm has been used for clustering customers and route is optimizes using Particle Swarm Optimization (PSO), the well-known swam intelligence method, in [9]. Performance of sweep algorithm has also been compared with savings method in [10].

This study investigates a variant of Sweep algorithm for clustering nodes and different SI based methods to optimize the routes of individual vehicles. In conventional Sweep algorithm, cluster formation starts from 0^0 and consequently advance toward 360^0 to consider all the nodes. In this study, Sweep cluster are considered from different starting angle. On the other hands, two well-known SI methods (i.e., ACO and PSO) and two recent SI based algorithms (i.e., PSM and VTPSO) are considered for route optimization. The outline of the paper is as follows. Section II explains variant Sweep algorithm and GA, ACO, PSO, PSM and VTPSO methods briefly. Section III is for experimental studies which presents as well as compares the outcomes of the methods for a suite of benchmark CVRPs. At last, Section IV gives a brief conclusion of the paper.

II. Solving CVRP with Sweep Clustering and Route Optimization using Swarm Intelligence Methods

The aim of this study is to identify the effective CVRP method considering Sweep algorithm to cluster the nodes and several prominent SI based methods to optimize the routes for Sweep clusters. A variant version of Sweep is considered in this study for better outcome. This section gives description of Sweep and optimization methods.

A. Sweep Clustering with Different Starting Angles

Sweep algorithm was firstly introduced in [11] as a heuristic algorithm that have been developed for solving vehicle dispatch problems with load constraint for each vehicle. At first polar angle of each nodes are calculated and order the nodes according to polar angle. General formula for calculating polar angle is

$$\theta = \tan^{-1}(y/x) \tag{8}$$

where Θ is the angular value of a node in degree (customer location). Finally, nodes are clusters according to the polar angles. The first cluster considers the nodes from the beginning until capacity of a vehicle does not exceed. Similar way all the nodes are clustered into different vehicles.

Figure 2 shows the graphical representation of cluster formation in Sweep algorithm. The black dots represent the nodes and the straight lines represent the Sweep hand that moves anti-clockwise. Clustering is performed by joining nodes beginning from the closest node to any node that is chosen to be the first node. The closest node is one which has smallest

angle. This process is repeated by joining the second closest, the third, and so forth until it satisfies the constraint.

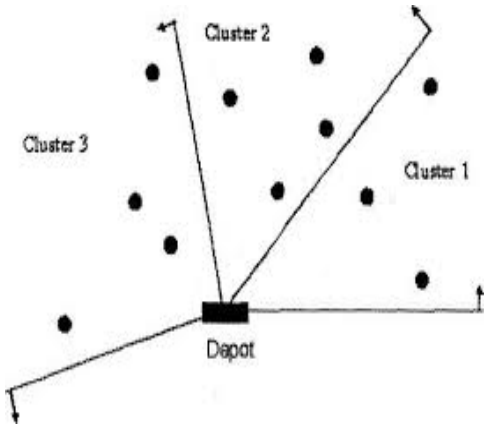

Fig. 2: Formation of cluster using Sweep algorithm.

In general, Sweep considers depot located at (0, 0) co-ordinate in two dimensional plane and cluster construction starts from the node having lowest polar angle. It is worth mentionable that starting from different angles may give different clusters and explore chance to get better CVRP solution after route optimization. Therefore, this study considers a variant of Sweep which take starting angle as user define parameter and the steps of it are as follows:

Variant Sweep Algorithm:

Initialization:

1. Update coordinates of the nodes considering depot as (0, 0) in the two-dimensional plane.
2. Compute the polar angle of each node.
3. Order the nodes according to polar angle, *ONL*
4. Take Starting Angle, Θ_s
5. Cluster C=1

Clustering:

1. Identify position of Θ_s in *ONL*.
2. Sweeping nodes to current cluster C by increasing polar angle.
3. Stop when adding the next node would exceed vehicle capacity.
4. Create a new cluster $C+1$ by resuming the sweep where the last one left off.
5. Repeat steps 2–4, until all customers have been included in a cluster

Outcome:

All the nodes are assigned into C clusters.

B. Vehicle Route Generation from Sweep Cluster Nodes

The route generation stage is aimed to optimize searching method to find the optimal solution that represents the shortest path between all nodes in each cluster generated by Sweep algorithm. In this stage each cluster is an individual traveling salesman problem (TSP). In this study four SI based method are considered for route optimization. Among the methods, Ant Colony Optimization (ACO) and Particle Swarm Optimization (PSO) very popular well-known SI methods; and Producer-Scrounger Method (PSM) and Velocity Tentative PSO (VTPSO) are two very recent methods. GA is also considered along with SI methods for optimization as it is a prominent and pioneer optimization method. Brief description of the methods to optimize route (i.e., to solve TSP) are given to make the paper self-contained.

a. Genetic Algorithm (GA)

GA is inspired by biological systems' fitness improvement through evolution and is the pioneer and widely used to solve many scientific and engineering problems. Common features of GA are: populations of chromosomes (i.e., solutions), selection according to fitness, crossover to produce new offspring, and random mutation of new offspring. To produce new tour from existing tours, Enhanced Edge Recombination cross over method [12] is used in this study. The positions of two nodes are interchanged for mutation operation.

b. Ant Colony Optimization (ACO)

ACO is inspired from ants' foraging behavior and is the prominent method for solving TSP. ACO is the first algorithm aiming to search for an optimal path in a graph, based on the behavior of ants seeking a path between their colony and a source of food. It considers population size as the number cities in a given problem and starts placing different ants in different cities. A particular ant consider next city to visit based on the visibility heuristic (i.e., inverse of distance) and intensity of the pheromone on the path. After the completion of a tour, each ant lays some pheromone on the path. Before pheromone deposit, pheromone evaporation of real ant is adopted by reducing pheromone of all the links by a fixed percentage. This behavior allows the artificial ants to forget bad choices made in the past. Finally, all the ants follow the same route after certain iteration. The detail description of ACO available in [13].

c. Particle Swarm Optimization (PSO)

PSO is a popular optimization method on metaphor of social behavior of flocks of birds or schools of fishes. PSO is a simple model of social learning whose emergent behavior has been found popularity in solving difficult optimization problems. In PSO, each particle represents a potential solution and moves to a new position (i.e., search a new point) at every iteration based on the calculated velocity. The processes of iteration continue until the stopping criterion is reached. PSO was proposed for continuous problems (e.g., function optimization) and has been proven to solve such problems effectively [14]. In function optimization domain, a particle represents a position in the multidimensional search space. At every step, each particle changes position based on its velocity depending on its previous best position and the best position particles ever visited.

PSO has also been found as an efficient method to solve combinatorial problems such as TSP. To solve TSP with PSO, each particle represents a complete tour as a feasible solution

and velocity is a measure to update the tour for better solution. Among many methods of PSO, study of [15] is the pioneer method to solve TSP that considers each particle as a complete tour and uses Swap Sequence (SS) [15] as velocity to get a new tour applying on a tour. A SS is a collection of several Swap Operators (SOs) and each one indicates two positions in a tour those might be swapped. All SOs of a SS are applied on a particle's tour maintaining order and hence implication of the SS transforms the TSP tour into a new one. The detail description of solving TSP with SS based velocity operation is available in [15, 17].

d. Producer-Scrounger Method (PSM)

PSM [16] is a new technique to solve TSP inspiring from the animal group living behavior. It models roles and interactions of three types of animal group members: producer, scrounger and dispersed. PSM considers a producer having the best tour, few dispersed members having worse tours and scroungers. In each iteration, the producer scans for better tour, scroungers explore new tours while moving toward producer's tour; and dispersed members randomly checks new tours. For producer's scanning, PSM randomly selects a city from the producer's tour and rearranges its connection with several near cities for better tours. Swap operator and swap sequence based operation is employed in PSM to update a scrounger towards the producer. Finally, producer is consider as the solution of a given problem. The description of this method is available in [16].

e. Velocity Tentative PSO (VTPSO)

VTPSO [17] is the most recent SI based method extending PSO to solve TSP. It calculates velocity SS similar to existing method [15] but apply the SS in a different and optimal way. In VTPSO, the new tour of TSP is considered after applying all the SOs of a SS and no intermediate measure is considered. VTPSO conceives a measure called partial search (PS) to apply calculated SS to update particle's position (i.e., TSP tour). On the other hand, VTPSO considers the calculated velocity SS as tentative velocity and conceives a measure called partial search (PS) to apply calculated SS to update particle's position (i.e., TSP tour). VTPSO measures tours with portions of SS and conceive comparatively better new tour with a portion or full tentative SS. The method is shown to perform well when tested on a suite of benchmark TSPs. The algorithm is described in [17].

III. Experimental Studies

This section describes the benchmark problems and experimental setup for conducting the experiment and then represents experimental results and analysis.

A. Benchmark Problems and Experimental Setup

In this study, a suite of 20 benchmark problems from [18]; Table 1 shows the brief description of the problems. In the problems, number of customer varied from 200 to 483 and vehicle capacity varied in different problems from 200 to 1000. A customer is represented as a coordinate in a problem.

Table 1: CVRP benchmark problems.

Sl.	Problem Name	Total Nodes	Total Demand	Individual Vehicle Capacity
1	kelly01	240	4800	550
2	kelly02	320	6400	700
3	kelly03	400	8000	900
4	kelly04	480	9600	1000
5	kelly05	200	4000	900
6	kelly06	280	5600	900
7	kelly07	360	7200	900
8	kelly08	440	8800	900
9	kelly09	255	13429	1000
10	kelly10	323	15195	1000
11	kelly11	399	16980	1000
12	kelly12	483	18701	1000
13	kelly13	252	25136	1000
14	kelly14	320	28672	1000
15	kelly15	396	32244	1000
16	kelly16	480	35772	1000
17	kelly17	240	4320	200
18	kelly18	300	5400	200
19	kelly19	360	6480	200
20	kelly20	420	7560	200

Therefore, the cost is found after calculating distance using the coordinates.

Sweep algorithm applied on each problem for seven different starting angles (Θ_s) and those are 0^0, 45^0, 90^0, 135^0, 180^0, 225^0, and 270^0. It is notable that conventional Sweep only considers $\Theta_s = 0^0$ for clustering. In this study, selected TSP optimization methods (i.e., GA, ACO, PSO, PSM and VTPSO) are applied on the all Sweep outcomes to get final solution.

We strongly relied on an experimental methodology for configuring the route optimization algorithms. For the fair comparison, the number of iteration was set at 100 for the algorithms. The number of ants in ACO was equal to the number of cities as it desired. The population size was 50 for GA, PSM and VTPSO. In ACO, *alpha* and *beta* were set to 1 and 3, respectively. On the other hand, the *RNC* (rate of near cities consideration) for producer scanning in PSM was set to 0.1. The selected parameters are not optimal values, but considered for simplicity as well as for fairness in observation.

The algorithms are implemented on Visual C++ of Visual Studio 2013. The experiments have been done on a PC (Intel Core i5-3470 CPU @ 3.20 GHz CPU, 4GB RAM) with Windows 7 OS.

B. Experimental Results and Analysis

This section presents experimental results for the benchmark problems for Sweep clustering with different starting angles and route optimizing using GA, ACO, PSO, PSM and VTPSO. Table 2 shows the total clusters for different starting angles (Θ_s) in Sweep and optimized route cost using the TSP algorithms for kelly15 problem. The problem has 396 nodes and total demand to be served is 32244 with vehicle having capacity 1000. From the table it is observed that Sweep manages total nodes into 34 or 35 clusters i.e., required number of vehicles. The total number vehicle are 35 for Θ_s=0, 90, 180 and 270. On the other hand, number of vehicles required 34 for Θ_s= 45, 135 and 225. It is also remarkable that total travel cost for 34 clusters is lower than the case of 35 for before and after route optimization. The best travel distance for an algorithm for different Θ_s is marked as bold-faced type. For the problem the best travel cost achieved after optimizing with GA, ACO, PSO, PSM and VTPSO are 1622.01, 1648.37, 1730.33, 1615.51 and 1598.9, respectively. The best values are for 34 cluster case with different starting angles. This result clearly indicates that starting with different starting angle has a positive effect on Sweep clustering.

Table 2: Clusters for different starting angle (Θ_s) and total travel distance after route optimizing using GA, ACO, PSO, PSM and VTPSO for kelly15 problem.

Θ_s	Clus-ters	Before Route Optimizing	Travel Cost after Optimizing with				
			GA	ACO	PSO	PSM	VTPSO
0	35	3141.25	1657.12	1687.07	1780.59	1649.93	1634.59
45	34	3119.7	1626.41	**1648.37**	1737.89	1617.14	1599.13
90	35	3141.25	1670.38	1690.54	1777.55	1650.5	1634.4
135	34	3119.7	1628.19	1649.08	1755.26	1620.42	**1598.9**
180	35	3141.25	1657.76	1686.07	1765.76	1653.92	1635.98
225	34	**3119.7**	**1622.01**	1650.24	**1730.33**	**1615.51**	1599.06
270	35	3141.25	1650.16	1685.65	1771.07	1646.35	1635.23

Table 3 compares travel distance for route optimizing using GA, ACO, PSO, PSM and VTPSO. The result presented for an algorithm is the best result from seven different starting angles in Sweep clustering. The best one (i.e., smallest value) among the five algorithms is shown in bold-face type. Pair wise Win/Draw/Loss summary is presented below the table for better understanding.

Among conventional methods ACO is shown to outperform both GA and PSO most of the cases. ACO is found better than GA for 12 cases out of 20 cases. For other eight cases GA was better than ACO. On the other hand, ACO outperformed PSO for 15 cases. On the basis of average travel distance over 20 problems, ACO is the best conventional method and PSO is the worst. ACO achieved average travel cost over 20 cases 4978.59; on the other hand, GA and PSO achieved travel cost 7576.93 and 12041.94, respectively. ACO is the well-known method for TSP and its performance solving route optimization (e. g., TSP) is well studied.

Although PSO is found inferior to other conventional methods (i.e., GA and ACO), VTPSO, the updated version of PSO, is found as the best method among the five algorithms. VTPSO calculates velocity SS similar to PSO but apply the SS in a different and optimal way. The partial search mechanism in velocity implementation ensures to get combatively better new tour with respect to traditional PSO. Therefore, outperformance of VTPSO with respect to others is logical as it was found better for TSP [14]. On the other hand, PSM, another recent SI method, also used SS operation to update its members and found better than GA and PSO but competitive to ACO. PSM is found better than ACO for eight cases out of 20 cases and VTPSO outperformed ACO for all 20 cases. The average travel cost achieved by PSM and VTPSO are 5586.71 and 4755.49, respectively.

Table 3: Benchmark CVRP travel distance cost comparison for route optimizing using GA, ACO, PSO, PSM and VTPSO.

SI.	Problem	GA	ACO	PSO	PSM	VTPSO
1	kelly01	7311.31	6066.12	11314.07	6560.02	**5748.11**
2	kelly02	12870.36	9374.67	20252.39	9816.54	**8811.22**
3	kelly03	19735.81	11972.23	33009.25	13897.76	**11371.37**
4	kelly04	28006.34	15140.39	46507.72	18264.81	**14462.41**
5	kelly05	12247.99	7286.99	19879.25	8512.03	**7115.05**
6	kelly06	15160.58	9240.71	24813.42	11092.49	**8853.34**
7	kelly07	18298.84	11069.09	30381.33	12717.64	**10790.89**
8	kelly08	21325.69	12963.9	34727.21	14839.42	**12193.8**
9	kelly09	753.92	711.72	1065.13	716.5	**703.36**
10	kelly10	1003.33	921.34	1513.61	930.95	**899.32**
11	kelly11	1311.47	1163.56	2109.82	1185.38	**1128.32**
12	kelly12	1667.13	1356.69	2735.99	1406.53	**1315.36**
13	kelly13	1018.7	1039.79	1037.28	1013.97	**1012.33**
14	kelly14	1281.81	1313.47	1333.42	1278.07	**1270.19**
15	kelly15	1622.01	1648.37	1730.33	1615.51	**1598.9**
16	kelly16	1993.42	2024.29	2185.83	1985.63	**1967.66**
17	kelly17	773.36	837.9	813.84	768.08	**763.9**
18	kelly18	1143.75	1215.41	1200.82	1134.91	**1128.13**
19	kelly19	1660.27	1757.52	1739.24	1646.47	**1639.58**
20	kelly20	2352.49	2467.71	2488.91	2351.56	**2336.6**
	Average	**7576.93**	**4978.59**	**12041.94**	**5586.71**	**4755.49**
		Pairwise Win/Draw/Loss Summary				
		GA	ACO	PSO	PSM	VTPSO
	GA	-	12/0/8	0/0/20	20/0/0	20/0/0
	ACO		-	5/0/15	8/0/12	20/0/0
	PSO			-	20/0/0	20/0/0
	PSM				-	20/0/0

Finally, the effect of population size on route optimizing has been investigated for kelly15 problem with sweep starting angle Θ_s=225. Population size was varied from 10 to 150 for GA, PSO, PSM and VTPSO; whereas, the number of ants in ACO was equal to the number of cities as it desired. Fig. 1 shows CVRP travel distance (i.e., travel cost) for fixed 100 iteration only varying population size for fair comparison. For the methods, number of clusters were same (i.e., 34) with travel cost of 3080 without route optimization. From the figure it is observed that travel cost is invariant for ACO because population variation was not employed for it. Performance of GA and PSO is highly dependent on population size; for smaller population size (e.g., less than 50) the methods showed very high travel cost. On the other hand, PSM and VTPSO are found to work well with smaller population size. At a glance VTPSO is shown to outperform any other method for any population size.

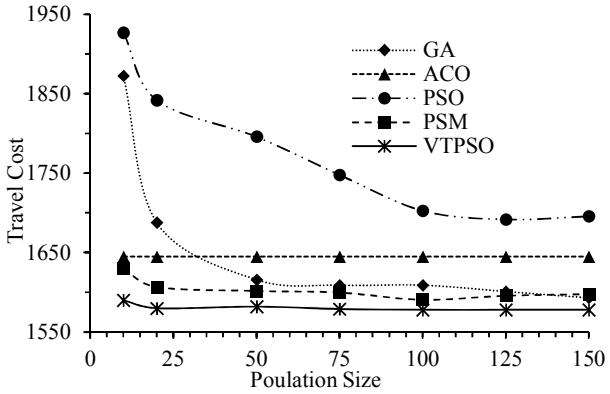

Fig. 3: Effect of population size on route optimizing for kelly15 problem with clustering Θ_s=225.

IV. CONCLUSION

CVRP is a popular combinatorial optimization problem and interest grows in recent years to solve it new ways. A popular way of solving CVRP is cluster the nodes according to vehicles using Sweep algorithm first and then generate route for each vehicle with TSP algorithm. In general, Sweep cluster construction starts from the node having lowest polar angle. This study considers a variant of Sweep which takes starting angle as a user define parameter and produces different clusters for a given problem. Finally, GA, ACO, PSO, PSM and VTPSO are applied to generate optimal route with Sweep outcome. The experimental result on the benchmark problems revealed that different starting angle have positive effect on Sweep clustering and VTPSO is better than other optimization methods to solve CVRP.

REFERENCES

[1] G. Vaira, "Genetic Algorithm for Vehicle Routing Problem," PhD. Thesis, Vilnius University, Italy, 2014.

[2] G. W. Nurcahyo, R. A. Alias, S. M. Shamsuddin and M. N. Md. Sap, "Sweep Algorithm in vehicle routing problem for public Transport," *Journal Antarabangsa (Teknologi Maklumat)*, vol. 2, pp. 51-64, 2002.

[3] S. Han and Y. Tabata, "A Hybrid Genetic Algorithm for the Vehicle Routing Problem with Controlling Lethal Gene," *Asia Pacific Management Review*, vol. 7, no. 3, pp. 405-426, 2002.

[4] N. Suthikarnnarunai, "A Sweep Algorithm for the Mix Fleet Vehicle Routing Problem," *in Proc. of the International Multi Conference of Engineers and Computer Scientists*, vol. 2, March 19-21, Hong Kong, 2008.

[5] K. Shin, "A Centroid-Based Heuristic Algorithm for the Capacitated Vehicle Routing Problem," *Computing and Informatics*, vol. 30, pp. 721–732, 2011.

[6] A. Boonkleaw, N. Suthikarnnarunai and R. Srinon, "Strategic Planning and Vehicle Routing Algorithm for Newspaper Delivery Problem: Case study of Morning Newspaper, Bangkok, Thailand," *in Proc. of the World Congress on Engineering and Computer Science 2009*, vol. 2, October 20-22, 2009.

[7] M. Yousefikhoshbakht and E. Khorram, "Solving the vehicle routing problem by a hybrid meta-heuristic algorithm," *Journal of Industrial Engineering International*, vol. 8(11), 2011.

[8] M. Reed, A. Yiannakou and R. Evering, "An ant colony algorithm for the multi-compartment vehicle routing problem," *Applied Soft Computing*, vol. 15, pp. 169-176, 2014.

[9] S. R. Venkatesan, D. Logendran, and D. Chandramohan, "Optimization of Capacitated Vehicle Routing Problem using PSO", *International Journal of Engineering Science and Technology (IJEST)*, vol. 3, pp. 7469-7477, 2011.

[10] G. K. Rand, "The life and times of the Savings Method for Vehicle Routing Problems," *Journal of the Operations Research Society of South Africa (ORSSA)*, vol. 25, no. 2, pp. 125-145, 2009.

[11] M. M. A. Aziz, H. A. El-Ghareeb and M. S. M. Ksasy, "Hybrid Heuristic Algorithm for solving Capacitated Vehicle Routing Problem," *International Journal of Computers & Technology*, vol 12, no.9, pp. 3845-3851, 2014.

[12] D. E. Goldberg, 'Genetic Algorithm in Search, Optimization and Machine Learning', New York: Addison – Wesley, 1989.

[13] T. Stutzle and M. Dorigo, "The Ant Colony Optimization Metaheuristic: Algorithms, Applications, and Advances," *International Series in Operations Research and Management Science*, Kluwer, 2001

[14] Y. F. Liao, D. H. Yau and C. L. Chen, "Evolutionary algorithm to traveling salesman problems," *Computers & Mathematics with Applications,* vol. 64, no. 5, pp. 788–797, 2012.

[15] K. P. Wang, L. Huang, C. G. Zhou and W. Pang, "Particle swarm optimization for traveling salesman problem," in *Proc. International Conference on Machine Learning and Cybernetics*, November 2003, pp. 1583–1585.

[16] M. A. H. Akhand, P. C. Shill, Md. Forhad Hossain, A. B. M. Junaed, and K. Murase, "Producer-Scrounger Method to Solve Traveling Salesman Problem", *I. J. Intelligent Systems and Applications*, vol. 7, no. 3, pp. 29-36, 2015.

[17] M. A. H. Akhand, S. Akter, M. A. Rashid and S. B. Yaakob, "Velocity Tentative PSO: An Optimal Velocity Implementation based Particle Swarm Optimization to Solve Traveling Salesman Problem," IAENG International Journal of Computer Science, vol. 42, no.3, pp 221-232, 2015.

[18] Large Capacitated Vehicle Routing Problem Instances. Available: http://neo.lcc.uma.es/vrp/vrp-instances/

Computing a Longest Common Subsequence for Multiple Sequences

Chinmay Bepery[1,*], Sk. Abdullah-Al-Mamun[2], and M. Sohel Rahman[3]
[1]Affiliation (Department of CIT, PSTU, Bangladesh)
[2]Affiliation (PSTU, Bangladesh)
[3]Affiliation (Department of CSE, BUET, Bangladesh)
[*]E-mail: chinmay.cse@pstu.ac.bd

Abstract—**The longest common subsequence problem is a classical string problem that aims at computing a common subsequence having the highest possible length from a given set of strings. This problem is one of the most studied computational problems in bioinformatics and computational biology. The problem is NP-hard for more than two input strings and the existing exact solutions are impractical for large input size. In this paper, we propose a new nondeterministic algorithm based on stochastic and dynamic programming method. In our algorithm, we have employed a heuristic that is inspired by the pheromone update strategy of the ant colony system. We have also integrated a local search technique in our algorithm to improve our results. The proposed algorithm is compared with the state-of-the-art algorithms over several standard benchmarks including simulated and real biological sequences. Experimental results show that the proposed algorithm can provide high quality solutions within a reasonable amount of time.**

Keywords—Dynamic programming, LCS, heuristics, pheromone.

I. INTRODUCTION

Given a string *s* over an alphabet $\sum$, a subsequence of it can be obtained by deleting some characters from *s*. Given a problem instance *(S,* $\sum$*),* where $S = \{s_1, s_2, \dots \dots, s_n\}$ is a set of *n* strings over a finite alphabet $\sum$, the LCS problem seeks to find the longest string t^* that is a subsequence of all the strings in *S*. Such a string t^* is called an LCS of the strings in *S*. This problem has diverse applications in areas like data compression [1], file comparison [2], text editing [3], query optimization in databases [4], clustering web users [5], circuit minimization in field programmable gate arrays (FPGAs) [6] etc. Perhaps the most important application of this problem can be found in molecular biology to compare DNA or RNA sequences and to determine homology in macromolecules [3], [7], [8],[9].

The LCS problem is NP-hard [10] for an arbitrary number (say, *n*) of input strings. The problem is polynomially solvable by dynamic programming [11] for fixed *n*. For two input strings, LCS (referred to as 2-LCS henceforth) can be efficiently solved using dynamic programming in $O(m_1.m_2)$ time, where m_1 and m_2 are the lengths of the input strings. Standard dynamic programming approaches for *n* strings require $O(m^n)$ time and space, where *m* is the length of the longest input string [12], [13]. Clearly, dynamic programming becomes quickly impractical as *n* grows. Since, the problem is NP-hard in general [14], [10], any optimal algorithm proposed for the problem has to be of exponential worst-case time complexity unless P=NP.

Existing exact algorithms for LCS include those based on dynamic programming, tree search, and integer programming. Several improvements over the dynamic programming algorithms of [12], [13] were achieved in [15], [12], [16], [13] to reduce the time complexity to $O(m^{(n-1)})$. A recent dynamic programming algorithm based on a divide-and-conquer technique to construct dominant points was proposed in [17]. Singireddy devised an integer programming formulation for the LCS problem in [18] having a time complexity of $O(m^n)$. A tree search algorithm was proposed by Hsu and Du in [19] based on backtracking. This was further enhanced by Easton and Singireddy in [20] where a selection heuristic and two new types of branch and bound pruning were adopted. The resulting algorithm, called Specialized Branching (SB), is exponential in the length of the LCS. Also, some parallel algorithms were proposed to run exact LCS solvers on multiple processors [21], [22], [23].

Due to exponential time complexity, the exact algorithms are impractical for large input sizes. Hence the use of algorithms producing near-optimal solutions (i.e., inexact algorithms) as opposed to the optimal solutions (i.e., exact algorithms) are inevitable. Extensive research has in fact been conducted in the literature to devise inexact algorithms for the LCS problem, that aim at finding good, but not necessarily optimal, solutions within an affordable amount of time. In general, inexact algorithms can be classified into two broad categories, namely, the approximation and heuristic algorithms.

The first approximation algorithm proposed for the LCS problem was *Long Run* (LR) algorithm with an approximation ratio of $|\sum|$ [24],[25]. LR simply constructs a string as its output using only a single character in $\sum$. However, it does not usually give an impressive solution. Another approximation algorithm called Expansion was introduced by Bonizzoni, Vedova and Mauri in [26] which is of the same approximation ratio of $|\sum|$ but without the single-character restriction of LR. The time complexity of Expansion was $O(nl^4 \log l)$ which was further improved by Tsai and Hsu in [27] using minimum spanning trees. Another two approximation algorithms called Best Next for Maximal Available Symbols (BNMAS) and Enhanced Long Run (ELR) were proposed by Huang, Yang and Tseng in [28]. The time complexity of BANMAS is $O(|\sum|^2 nl + |\sum|^3 m)$ and that of ELR is $O(|\sum| nm)$. Shyu and Tsai compared

BNMAS with Expansion in [29] and showed that BNMAS is more accurate and faster than Expansion especially when the size of the alphabet is small and the number of the strings is large.

The other types of inexact algorithms are heuristic algorithms that do not normally provide a performance guarantee or approximation ratio. The term 'heuristic' here is used in a general sense and includes meta-heuristics [30] and hyper- heuristics [31] as well. The Best-Next heuristic was proposed in [32] and [33] as a simple heuristic method with the time complexity of $O(|\sum|nm)$. This algorithm was shown to be superior to the approximation algorithm LR on real datasets. A linear-time dynamic programming heuristic (DPH) algorithm was devised by Guenoche and Vitte in [34], which was further improved by Guenoche in [35]. Easton and Singireddy proposed the Time Horizon Specialized Branching (THSB) heuristic based on a large neighborhood search paradigm in [36], and showed that its performance is better than DPH. Ant colony optimization (ACO) was used to solve the LCS problem in [29] by Shyu and Tsai. The resulting algorithm was compared with Expansion and BNMAS on random and biological datasets obtained from NCBI, with positive results. A constructive Beam Search algorithm, called BS, for the LCS problem was proposed by Blum, Blesa and Ibanez in [37]. In their algorithm, two different greedy functions were used to evaluate and compare candidate solutions. BS algorithm is an extension of a former approach introduced by Blum and Blesa in [38], where they considered two configurations: one called low time was a fast version of the algorithm aimed at producing quick solutions and the other called high quality was intended for obtaining high quality solutions at the cost of extra computation. Blum, Blesa and Ibanez [37] compared BS algorithm with Expansion, Best-Next, DPH, THSB and ACO algorithms on extensive datasets that were previously used in [38], [36], [29] and exhibited that BS algorithm is superior to its predecessors in terms of both the solution quality and the running-time, proving it as the state-of-the-art. Subsequently, three algorithms were proposed based on BS algorithm: Deposition and Extention (DEA) in [39] by Ning, which is based on a post-process technique; MLCS-APP in [40] by Wang, Pan, Shang and Korkin, which is based on A^* search but with a limited number of leaves in the corresponding search tree; and IBS-LCS in [41] by Mousavi and Tabataba. Notably, although IBS-LCS was inspired by BS, it used a different heuristic function. Neither IBS-LCS nor MLCS-APP, as reported in [41], [40], could outperform BS algorithm over all the benchmarks used in [37], though they did so for some of the cases. In particular, IBS-LCS could not out-perform BS over the so-called BB benchmark [38], but it obtained better average results on the other benchmarks used in [37]. MLCS-APP was compared with BS on only the rat benchmark. DEA was only shown to be better than three primitive algorithms, namely LR, Expansion, and THSB; DEA was not compared with BS at all!

One of the most recent successful heuristic methods proposed for the problem is a hyper-heuristic algorithm (HH-LCS) proposed by Tabataba and Mousavi in [42]. HH-LCS is based on two heuristics functions, one of which was previously used in [41]. HH-LCS is compared with all the three algorithms BS, IBS-LCS, and MLCS-APP on all the benchmarks used in [37], [40] and two benchmarks used in [39] for fair comparisons. The HH-LCS algorithm outperforms all the other algorithms on all the benchmarks.

In this paper, we propose two heuristic based algorithms that repeatedly use dynamic programming to compute intermediate solutions. The two algorithms differ in the heuristics applied. We call these two algorithms RepeDPH andMRepeDPH[1]. We also incorporate a local search technique in our algorithms which is inspired by the ACO algorithm of Shyu and Tsai in [29]. Hence, we get two new versions of our algorithms, namely, RepeDPH-Local-Search and MRepeDPH-Local-Search. Our proposed algorithms are compared with HH-LCS [42], BS-high-quality [38], [37] and IBS-LCS [41] algorithms on extensive datasets, namely, the BB benchmark, ACO-random benchmark, ACO-rat benchmark and ACO-virus benchmark previously introduced and used in [38] and [29]. From the experimental results we find that RepeDPH and MRepeDPH show competitive performance and are able to provide a few better results than the current state-of-the-art. On the other hand, the proposed RepeDPH-Local-Search and MRepeDPH-Local-Search algorithms outperform the state-of-the-art algorithms on all benchmark datasets. We discussed the results in detail in Section VI.

II. Basic Notations

Let, s be a string of length m i.e., $|s|=m$. We use $s[j]$ to denote the jth character of s, where $1 \leq j \leq |s|$. We say that s' is a subsequence of s, denoted by $s' \prec s$, if we get s' by deleting zero or more symbols from s. The null string, i.e., the string of zero length is considered to be a subsequence of any string. Suppose, x is a string and $S = \{s_1, s_2, \ldots \ldots, s_n\}$ is a set of n strings over a finite alphabet Σ. We write $x \prec S$ if and only if $x \prec s_i$, for all $1 \leq i \leq n$. Given a set S as defined above as the input, the Longest Common Subsequence (LCS) problem aims to compute a sequence x of maximum length such that $x \prec S$. Sometimes we abuse the notation a bit and use $S[i]$ to denote s_i, in the set S. If all the input strings, i.e., $s_i \in S$, $1 \leq i \leq n$ are of the same length, we use m to denote their length; otherwise we define $m = max\{|s_1|, |s_2|, \ldots, |s_n|\}$. We further use s_{small} to denote smallest string of S.

III. Our First Algorithm: RepeDPH

We use standard dynamic programming solution for 2-LCS for determining LCS between two strings. The main idea builds up on a simple stochastic strategy as follows: we first compute an LCS $\mathcal{L}_1$ of two randomly chosen strings; then we compute an LCS $\mathcal{L}_2$ of $\mathcal{L}_1$ and a third string from S again chosen at random; and we continue until all the strings have considered. In what follows, we will be referring back to this algorithm as the base algorithm. In fact, this particular strategy can be used in different flavours with different and perhaps better results if we can propose a particular ordering of the strings to consider (rather than a random order). Now, the main task of our

[1]RepeDP stands for *Repeated Dynamic Programming*; H stands for *heuristics*; M stands for *Modified*.

algorithm is to employ an intelligent and useful heuristic to find an ordering in which the strings of S should be considered, rather than using a pure random strategy.

In what follows we will generally follow the following convention. We will use $LCS(s_1, s_2)$ to denote the length of an LCS of s_1 and s_2 and we will use the boldfaced version, i.e., $\mathbf{LCS}(s_1, s_2)$ to denote an actual LCS (i.e., not the length). This convention will be applied on similar notations unless otherwise specified. In our algorithm we introduce a stochastic element as follows. We define, $lcs_k = LCS(s_i, \mathbf{lcs}_{(k-1)})$, where i is a randomly selected integer in the range $1.....n$ without replacement and $1 < k \leq n$. For $k = 1$, we define, $lcs_1 = LCS(s_i, s_{small})$. Note that following our convention, we will use $lcs_k = \mathbf{LCS}(s_i, \mathbf{lcs}_{(k-1)})$, to denote the actual sequence and $lcs_k = LCS(s_i, \mathbf{lcs}_{(k-1)})$, to denote its length. We further define another term $lcs_{(j,k,i)}$ for $1 < k \leq n$ as follows:

$$lcs_{(j,k,i)} = LCS(s_i, \mathbf{lcs}_{(j,k-1,i)}) \qquad (1)$$

For k = 1, we have:

$$lcs_{(j,1,i)} = LCS(s_i, s_{small}) \qquad (2)$$

Notably, although the notation suggest a three dimensional table for $lcs_{(j,k,i)}$, as will be clear later, the computation actually requires a 2-D loop. We construct a matrix called lcs_{weight} of size $n \times (\beta + 1)$, where β is a pre-defined parameter of our algorithm. The matrix lcs_{weight} is computed according to the equation below:

$$lcs_{weight}(j,i) = \begin{cases} 0 & ; \text{if } j = 0 \\ lcs_{weight}(j-1,i) + \dfrac{lcs_{(j,k,i)}}{|S[i]|} & ; \text{Otherwise} \end{cases} \qquad (3)$$

The algorithm proceeds to fill in the matrix lcs_{weight} column by column as follows. It first identifies s_{small} from S. It runs a loop of j from 0 to β. For each value of j it runs another loop of k from 1 to n to fill up the column of lcs_{weight} for a particular value of j. The first column, i.e., $j = 0$, is initialized to zero. Then, for $j = 1$ to β, we do the following. We first choose a random i for this iteration. During this iteration, s_i will be the main player. When $k = 1$ (otherwise), we compute the LCS between s_i and s_{small} ~ $lcs_{(j,k-1,i)}$ and store it in $lcs_{(j,k,i)}$. Once $lcs_{(j,k,i)}$ is computed, we update the heuristic value in the lcs_{weight} matrix according to (3). Clearly, as soon as the loop for j (with the inner loop of k) ends, we get a filled up lcs_{weight} matrix. At this point we use $lcs_{weight}(\beta, i)$, $1 \leq i \leq n$ to be the heuristic value of a string s_i and this heuristic value is referred to as $sequence_weight(i)$. The rest of the algorithm is straightforward. We rearrange S as an ordered list by sorting the strings in S according to sequence_weight computed above and apply the base algorithm using this ordering.

IV. MREPEDPH: A MODIFICATION TO REPEDPH

In this section we discuss a modification of RepeDPH and propose a modified version of the algorithm that we call MRepeDPH. Inspired by the Ant Colony Optimization technique, we here introduce the concept of pheromone. We use the lcs_{weight} matrix of RepeDPH in conjunction with a newly introduced pheromone matrix of dimension $|S| \times (\beta + 1)$ as follows. We slightly change the definition of the lcs_{weight} matrix according to the following equation:

$$lcs_{weight}(j,i) = \begin{cases} lcs_{(j,k,i)} & ; if\ lcs_{(j,k,i)} \geq lcs_{weight}(j-1,i) \\ 0 & ; if\ j = 0 \\ lcs_{weight}(j-1,i) & ; Otherwise \end{cases} \qquad (4)$$

The pheoromone matrix is updated according to the following equation:

$$pheromone(j,i) = \begin{cases} pheromone(j-1,i) + 1 & ; if\ lcs_{(j,k,i)} \geq lcs_{weight}(j-1,i) \\ 0 & ; if\ j = 0 \\ pheromone(j-1,i) & ; Otherwise \end{cases} \qquad (5)$$

MRepeDPH algorithm proceeds almost exactly like RepeDPH algorithm as described above. However, Equation (4) is used in MRepeDHP instead of (3) for computing lcs_{matrix} and while computing $lcs_{matrix}(j,i)$ it also computes pheromone(j, i) using (5). Therefore, both lcs_{matrix} and pheromone tables are computed in the same loop simultaneously. Once the computation of lcs_{matrix} and pheromone are done, we compute the sequence_weight of each string in the set according to the following equation:

$$sequence_weight(i) = lcs_{weight}(\beta, i) \times pheromone(\beta, i) \qquad (6)$$

The rest of the algorithm is identical to RepeDPH: we rearrange S as an ordered list by sorting the strings in S according to sequence_weight computed above and apply the **base algorithm** using this ordering.

V. LOCAL SEARCH

In order to improve the solutions obtained by RepeDPH and MRepeDPH, we employ a local search procedure inspired by the algorithm of Shyu and Tsai in [29]. Here we briefly describe the main idea of the local search procedure. We first need to introduce the following notations. Suppose L is a solution return by our algorithm (RepeDPH or MRepeDPH) and according to our convention we say $L = |\mathbf{L}|$, i.e, the length of this solution is L. Now, we use L vectors LOC^l, $1 \leq l \leq L$. In each vector LOC^l we keep record of the index of the common character $\mathbf{L}[l]$ in each string s_i □ S. So, $LOC^l = \{ loc_1^l, loc_2^l, \ldots\ldots, loc_n^l \}$ where $s_i[loc_i^l] = L[l]$ and $s_i[loc_i^l]$ corresponds to the *l-th* common character of $\mathbf{L}$. For a string s_i, we also refer to the range $[loc_i^{l-1} \ldots loc_i^l - 1]$ as the *l-th* interval with respect to $\mathbf{L}$. To handle the boundary conditions, we conveniently assume that $\mathbf{L}[0]$ and $\mathbf{L}[L + 1]$ exist and are null characters.

Now we randomly select a string $s_i \in S$ and for all $1 \leq l \leq L + 1$ we do the following procedure. We discuss this focusing on the *l-th* interval of s_i with respect to **L**. Now suppose that the size of the *l-th* interval is h and the characters within this interval are $\alpha_i^1, \alpha_i^2, \ldots. \alpha_i^h$ in the original order. Now these h letters are the set of candidates in our local search procedure. Each of these characters, say α_i^u will be inserted into **L** between $\mathbf{L}[l-1]$ and $\mathbf{L}[l]$ only if the following two conditions hold for $1 \leq k \neq i \leq n$:

1. There exists position x_k in s_k such that $s_k[x_k] = \alpha_i^u$ subject to $s_k[x_k'] \neq \alpha_i^u$ for $loc_k^{(l-1)} < x_k' < x_k \leq loc_k^{(l-1)} + \delta$, where $\delta = \frac{|s_i|}{L}$
2. $\mathbf{L}[1 \ldots L] \prec s_k[x_k + 1 \ldots |s_k|]$

By incorporating this local search to RepeDPH and MRepeDPH, we get two new algorithms; we call these RepeDPH-Local-Search and MRepeDPH-Local-Search respectively.

VI. Experimental results and discussions

In this section, we present an experimental comparison of our proposed algorithms (RepeDPH, RepeDPH-Local-Search, MRepeDPH and MRepeDPH-Local-Search) with the best algorithms in the literature, namely, BS-high-quality [37], IBS-LCS [41], and HH-LCS [42]. We have run our algorithms on a personal computer running 32-bit Windows 7 with a Core(TM) i3-2310M CPU @ 2.10GHz having 2.00GB (1.81GB usable) RAM and 3MB L2 cache. We implemented our algorithm in C++ using CodeBlocks platform. In our experiments we have used four datasets used in [37],[41],[42], namely BB^2, ACO-random, ACO-rat and ACO-virus[3]. BB benchmark was first introduced in [38], and the other three datasets were previously used in [29]. For space constraints here we only report the result of the BB benchmark. The results of the other datasets are reported in the Appendix.

In our algorithms, β is used to denote the number of random orders of n sequences of S from $n!$ orders. It is computationally impractical to consider all $n!$ orders for large n. The value of n is varied in different experiments. For this, we have set $\beta = 10$ for all experiments. From above discussion, each value of β provides an approximate solution. We have picked the best solution from 10 independent runs, because our algorithms are stochastic. We also have shown the worst and average solution for each experiment. Table I compares the results of our algorithm with those reported in [37], [41] and [42] for the BB benchmark. The first two columns in the Table I show the alphabet size and the number of strings and the length of the input strings (all the strings of an instance are of the same length). The next six columns (third to eight) report the results for BS-high-quality as specified in [37], IBS-LCS in [41] and HH-LCS in [42]. The third, fifth and seventh columns show the average length of the returned LCS and the fourth, sixth and eighth columns show the average run time for BB benchmark. The next 24 columns show the respective values for our algorithms. The worst and average solution of our experiment is not as good as current state-of-the-art. For this, we focus only the best solution. The thirteenth and twenty-fifth columns show the length (average of best outcomes for BB benchmark) of the returned LCS of our proposed RepeDPH and MRepeDPH algorithms and fourteen and twenty-six columns show the run time. The nineteenth and thirty-one columns show LCS length after local search integration within RepeDPH and MRepeDPH algorithms and twentieth and thirty-two columns show the run time. The records in Table I are rounded up to one decimal digit. It can be seen Table I (column nineteen) that in 5 out of the 8 cases RepeDPH-Local-Search provides solutions of higher quality than HH-LCS and in 6 out of the 8 cases MRepeDPH-Local-Search (column thirty-one) provides solutions of higher quality than HH-LCS. In all the 8 cases RepeDPH-Local-Search and MRepeDPH-Local-Search provides solutions of higher quality than those of the BS-high-quality and IBS-LCS. In 2 out of 8 cases RepeDPH and MRepeDPH provides solutions of higher quality than HH-LCS and IBS-LCS and in 3 out of 8 cases RepeDPH and MRepeDPH provides solutions of higher quality than BS-high-quality. Our RepeDPH and MRepeDPH provide solution closer with HH-LCS, IBS-LCS and BS-high-quality. But they fail to provide average improvement in solution quality compared to these algorithms. In 8 out of 8 cases, RepeDPH-Local-Search and MRepeDPH-Local-Search provide higher quality solution than BS-high-quality and IBS-LCS. In 6 out of 8 cases MRepeDPH-Local-Search and also 5 out of 8 cases RepeDPH-Local-Search provide higher quality solution than HH-LCS. On average, our MRepeDPH-Local-Search algorithm achieves about 1.59% improvement in solution quality compared to HH- LCS, 4.89% improvement in solution quality compared to IBS-LCS, 3.49% improvement in solution quality compared to BS-high-quality. Similarly, our RepeDPH-Local-Search algorithm achieves about 1.37% average improvement in solution quality compared to HH-LCS, 5.15% average improvement in solution quality compared to IBS-LCS, 3.27% average improvement in solution quality compared to BS-high-quality.

[2]Received from S.R. Mousavi and originally used in Blum and Blesa (2007)

[3]Received from S.R. Mousavi; available on NCBI using the accession numbers specified at http://pstu.ac.bd/teacher/cse/chinmay/resources

TABLE I: Comparison the Longest Common Subsequence over BB dataset produced by RepeDPH, RepeDPH-Local-Search, MRepeDPH and MRepeDPH-Local-Search with BS-high-time, IBS-LCS and HH-LCS.

M	N	BS-high-quality		IBS-LCS		HH-LCS		RepeDPH						RepeDPH-Local-Search						MRepeDPH						MRepeDPH-Local-Search					
								Worst		Average		Best		Worst		Average		Best		Worst		Average		Best		Worst		Average		Best	
|Σ|=2																															
10	1000	648	13.6	672.1	1.1	672	1.0	640	1.0	648.1	1.0	659.7	1.0	646.8	1.5	661.4	1.5	673.1	1.5	637.7	0.9	646.1	0.9	658.3	0.9	648	2.9	660.0	1.4	673.7	2.8
100	1000	541	72.5	554.2	2.4	555.9	2.5	520	7.5	528.3	7.5	535.4	7.5	525.4	11.2	541.5	11.2	555.7	11.3	523.6	6.4	530.2	6.4	539.0	6.4	525.1	11.1	539.8	10.9	556.4	11.1
|Σ|=4																															
10	1000	534.7	18.1	543.7	1.5	543.2	1.4	510.9	1.0	521.2	1.0	534.1	1.0	524.8	1.5	535.9	1.5	547.9	1.5	512.8	0.8	519.6	0.8	529.9	0.8	522.9	1.5	534.7	1.5	547.5	1.5
100	1000	369.3	121.6	361.7	2.8	381.2	3.0	327	5.9	335.1	5.9	343.8	5.9	334.7	9.3	355.9	9.3	375.3	9.4	328.3	5.1	337.7	5.0	350.3	5.1	332.8	9.1	351.3	9.2	373.1	9.1
|Σ|=8																															
10	1000	462.3	21.2	461.9	2.2	462.4	2.1	443.3	0.9	454.5	0.9	464.6	0.9	452.7	1.4	466.7	1.4	479.4	1.4	446.1	0.8	456.1	0.7	467.6	0.7	456.8	1.4	465.0	1.4	475.7	1.4
100	1000	258.7	154.7	240.9	3.5	267.4	3.8	206.3	4.3	215.7	4.3	233.3	4.3	221.7	6.6	241.1	6.6	261.1	6.7	215.3	3.9	225.3	3.9	239.4	3.8	217.1	6.7	240.4	6.6	263.3	6.5
|Σ|=24																															
10	1000	385.6	37.4	385.6	4.4	385.6	4.4	396.2	0.9	407.3	0.9	417.8	0.8	403.1	1.3	414.7	1.3	424.8	1.3	395.2	0.7	406.9	0.7	418.8	0.7	402.9	1.3	413.9	1.3	425.9	1.3
100	1000	147.7	268.3	130.5	4.9	148.6	5.3	98	2.7	107.9	2.7	121.1	2.7	110.6	4.2	127.1	4.2	148.7	4.2	101.7	2.5	112.7	2.5	130.0	2.5	121.1	4.0	136.1	4.0	151.5	4.0
Quality improvement with respect to BS-high-quality												-3.15%						3.27%						-1.81%						3.49%	
Quality improvement with respect to IBS-LCS												-1.67%						5.16%						-0.21%						4.89%	
Quality improvement with respect to HH-LCS												-4.93%						1.38%						-3.72%						1.59%	

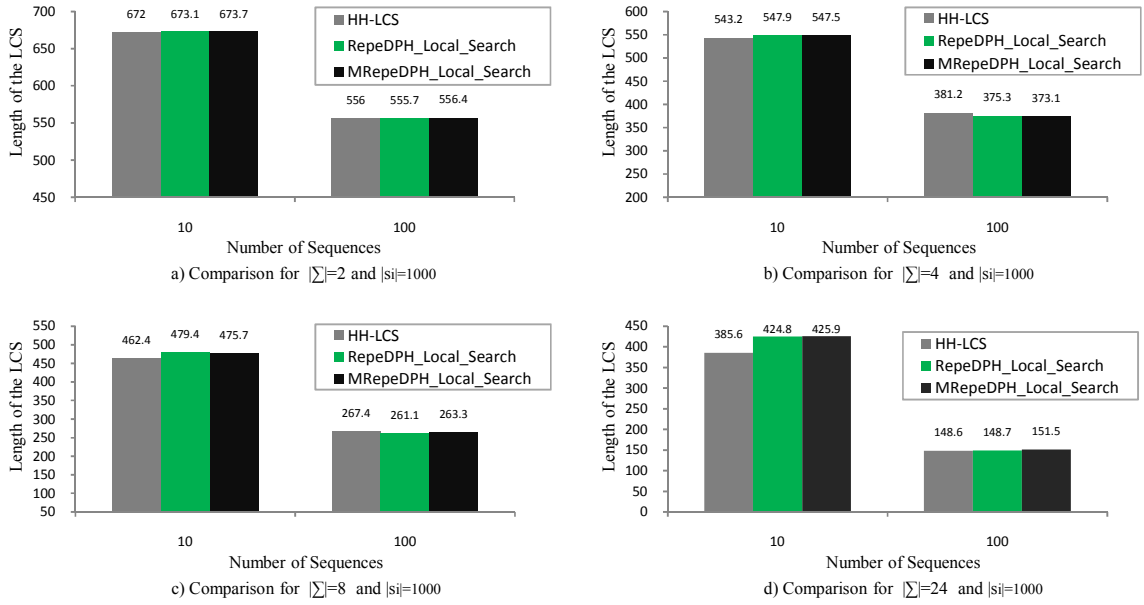

a) Comparison for |∑|=2 and |si|=1000

b) Comparison for |∑|=4 and |si|=1000

c) Comparison for |∑|=8 and |si|=1000

d) Comparison for |∑|=24 and |si|=1000

Figure 1. Comparison among HH-LCS, RepeDPH-Local-Search and MRepeDPH-Local-Search for BB dataset.

VII. CONCLUSION

In this paper, we have presented heuristic algorithms for the longest common subsequence problem for multiple sequences. The algorithms use dynamic programming (repeated) based on some heuristic functions. We also have incorporated local search to improve solutions. The proposed algorithm was compared with the state-of-the-art algorithms in the literature over several benchmarks and the results are found to be excellent.

REFERENCES

[1] Storer J. *Data compression: methods and theory*. Maryland: Computer Science Press, 1988.

[2] Aho A., Hopcroft J., Ullman J. *Data structure and algorithms*. Reading, MA: Addison-Wesley, 1983.

[3] Sankoff D., Kruskal J.B. *Time warps, string edits, and macromolecules: the theory and practice of sequence-comparison*. Reading, UK: Addison-Wesley, 1983.

[4] Sellis T. Multiple query optimization. *ACM Transactions on Database Systems*, 13(1):23–52, 1988.

[5] Banerjee A., Ghosh J. Clickstream clustering using weighted longest common subsequences. *In: Proceedings of the Web Mining Workshop at the 1st SIAM Conference on Data Mining*, pages 33–40, 2001.

[6] Brisk P., Sarrafzadeh M., Kaplan A. Area-efficient instruction set synthesis for reconfigurable system-on-chip design. *In: Proceedings of the 41st design automation conference. IEEE Press*, pages 395–400, 2004.

[7] Smith T.F., Waterman M.S. Identification of common molecular subsequences. *Journal of Molecular Biology*, 147:195–197, 1981.

[8] Jiang T., Lin G., Zhang K., Ma B. A general edit distance between RNA structures. *Journal of Computational Biology*, 9(2):371–388, 2002.

[9] Bafna V., Ravi R., Muthukrishnan S. Computing similarity between rna strings. *In: Proceedings of the sixth annual symposium on combinatorial pattern matching. Espoo, Finland*, pages 1–16, 1995.

[10] Maier D. The complexity of some problems on sub- sequences and supersequences. *Journal of the ACM*, 25:322–36, 1978.

[11] Gusfield D. Algorithms on strings, trees, and sequences. *Computer science and computational biology. Cambridge: Cambridge University Press*, 25, 1997.

[12] Hakata K., Imai H. The longest common subsequence problem for small alphabet size between many strings. *Lecture notes in computer science*, 650:469–78, 1992.

[13] Irving R.W., Fraser C.B. Two algorithms for the longest common subsequence of three (or more) strings. *Lecture notes in computer science*, 644:214–29, 1992.

[14] Garey M.R., Johnson D.S. *Computers and Intractability; A Guide to the Theory of NP-Completeness*. W. H. Freeman & Co. New York, NY, USA, 1990.

[15] Eppstein D., Galil Z., Italiano Giancarlo R. Sparse dynamic programming. ii. convex and concave cost functions. *Journal of the Association for Computing Machinery*, 39(3):546–67, 1992.

[16] Hirschberg D.S. A linear space algorithm for computing maximal common subsequences. *Communication of the Association for Computing Machinery*, 18(6):341–43, 1975.

[17] Wang Q., Korikin D., Shang Y. A fast multiple longest common subsequence (mlcs) algorithm. *IEEE Transactions on Knowledge and Data Engineering*, 2010.

[18] Singireddy A. Solving the longest common subsequence problem in bioinformatics. *Master, Kansas State University, KS, Manhattan.*, 2003.

[19] Hsu W.J., Du M.W. Computing a longest common subsequence for a set of strings. *BIT Numerical Mathematics*, 24(1):45–59, 1984.

[20] Easton T., Singireddy A. A specialized branching and fathoming technique for the longest common subsequence problem. *International Journal of Operations Research*, 4:98–104, 2007.

[21] Chen Y., Wan A., Liu W. A fast parallel algorithm for finding the longest common sequence of multiple biosequences. *BMC Bioinformatics*, 7(s4), 2006.

[22] Korkin D., Wang Q., Shang Y. An efficient parallel algorithm for the multiple longest common subsequence (MLCS) problem. *In: International Conference on Parallel Processing (ICPP)*, pages 354–363, 2008.

[23] Wang Q., Korkin D., Shang Y. Efficient dominant point algorithms for the multiple longest common subsequence (mlcs) problem. *In: International Joint Conference on Artificial Intelligence (IJCAI), Pasadena, CA, USA,*, pages 1494–1500, 2009.

[24] Chin F., Poon C. Performance analysis of some simple heuristics for computing longest common subsequences. *Algorithmica*, 12:293–311, 1994.

[25] Jiang T., Li M. On the approximation of shortestcom-monsupersequences and longest common subsequences. *SIAM Journal on Computing*, 24:1122–1139, 1995.

[26] Bonizzoni P., Vedova G.D., Mauri G. Experimenting an approximation algorithm for the lcs. *Discrete Applied Mathematics*, 110:13–24, 2001.

[27] Tsai Y.T., Hsu J.T. An approximation algorithm for multiple longest common subsequence problems. *In: Proceedings of the sixth world multi conference on systemics, cybernetics and informatics, SCI*, pages 456–60, 2002.

[28] Huang K.S., Yang C.B., Tseng K.T. Fast algorithms for finding the common subsequence of multiple sequences. *In: Proceedings of International Computer Symposium*, pages 90–95, 2004.

[29] Shyu S.J., Tsai C-Y. Finding the longest common subsequence for multiple biological sequences by ant colony optimization. *Computers and Operations Re- search*, 36:73–91, 2009.

[30] Blum C., Roli A. Metaheuristics in combinatorial optimization: Overview and conceptual comparison. *ACM*, 35:268–308, 2003.

[31] Burke E., Kendall G., Newall J., Hart E., Ross P., Schulenburg S. Hyperheuristics: an emerging direction in modern search technology. *In: Hillier, F.S.(Ed.), Handbook of Metaheuristics*, 57:457–474, 2003.

[32] Fraser C.B. Subsequences and supersequences of strings. *PhD thesis, University of Glasgow*, 1995.

[33] Johetla T. Smed J., Hakonen H., Raita T. An efficient heuristic for the lcs problem. *In: Third South American Workshop on String Processing, WSP96*, pages 126–140.

[34] Guenoche A., Vitte P. Longest common subsequence with many strings: exact and approximate methods. *Technique et Science Informatiques*, 14(7):897–915., 1995.

[35] Guenoche A. Supersequence of masks for oligo-chips. *Journal of Bioinformatics and Computational Biology*, 2(3):459–69, 2004.

[36] Easton T., Singireddy A. A large neighborhood search heuristic for the longest common subsequence problem. *Journal of Heuristics*, 14(3):271–83, 2008.

[37] Blum C., Blesa M.J., Ibanez M. Beam search for the longest common subsequence problem. *Computers and Operations Research*, 36(12):3178–86, 2009.

[38] Blum C., Blesa M. Probabilistic beam search for the longest common subsequence problem. *In: Stutzle T, Birattari M, Hoos HH, editors. Proceedings of SLS 2007engineering stochastic local search algorithms. Lecture notes in computer science*, 4638(12):150–61, 2007.

[39] Ning K. Deposition and extension approach to find longest common subsequence for thousands of long sequences. *Computational Biology and Chemistry*, 34(12):149–157, 2010.

[40] Wang Q. Pan M., Shang Y., Korkin D. A fast heuristic search algorithm for finding the longest common subsequence of multiple strings. *In: Conference on Artificial Intelligence (AAAI), Atlanta, GA, USA,*, pages 1287– 1292, 2010.

[41] Mousavi S.R., Tabataba F. An improved algorithm for the longest common subsequence problem. *Computers and Operations Research*, 39:512–520, 2012.

[42] Tabataba F., Mousavi S.R. A hyper-heuristic for the longest common subsequence problem. *Computational Biology and Chemistry*, 36:42–54, 2012.

APPENDIX

The results of our algorithms on the ACO-random, ACO-rat, and ACO-virus datasets are presented and compared with the

state-of-the-art in tables I to IV respectively. The definitions for the columns of these tables are the same as those of Table I. It can be seen from best column in Table II, in none of the 20 cases, RepeDPH and MRepeDPH provide higher quality solution than BS-high-quality, IBS-LCS, HH-LCS but provide very closer result to current state-of-the-art. MRepeDPH-Local-Search provides higher quality solution in 20 cases for BS-high-quality, 16 cases for IBS-LCS and 15 cases for HH-LCS out of 20 cases. On the other hand, RepeDPH-Local-Search provides higher quality solution in 18 cases for BS-high-quality, 16 cases for IBS-LCS and 15 cases for HH-LCS out of 20 cases. MRepeDPH-Local-Search algorithm achieves average improvement about 2.40% than BS-high-quality, 0.24% than IBS-LCS and 0.15% than HH-LCS. And RepeDPH-Local-Search algorithm achieves average improvement about 2.77% than BS-high-quality, 0.62% than IBS-LCS and 0.52% than HH-LCS. It can be seen in Table III, RepeDPH and MRepeDPH provide very closer result to current state-of-the-art. In 18 out of 20 cases and 16 out of 20 cases the MRepeDPH-Local-Search and RepeDPH-Local-Search provide better result respectively than current state-of-the-art. RepeDPH-Local-Search algorithm achieves average improvement about 3.80% than Bs-high-quality, 2.44% than IBS-LCS and 1.14% than HH-LCS. And MRepeDPH-Local-Search algorithm achieves average improvement about 4.55% than BS-high-quality, 2.93% than IBS-LCS and 1.89% than HH-LCS.

From Table IV, RepeDPH-Local-Search provides better result than BS-high-quality, IBS-LCS and HH-LCS for 18 cases, 17 cases and 16 cases out of 20 cases respectively. And in 20 out of 20 cases, MRepeDPH-Local-Search provides better result than BS-high-quality, IBS-LCS and HH-LCS. MRepeDPH-Local-Search algorithm achieves average improvement about 5.13% than BS-high-quality, 1.56% than IBS-LCS and 1.67% than HH-LCS. RepeDPH-Local-Search algorithm achieves average improvement about 4.00% than Bs- high-quality, 0.53% than IBS-LCS and 0.59% than HH-LCS.

In summary, there are 68 individual cases in tables I to IV. In cumulative (both RepeDPH-Local-Search and MRepeDPH-Local-Search) result analysis, our proposed algorithms provide better result in 6 out of 8 cases for BB benchmarks, in 19 out of 20 cases for ACO-random, in 19 out of 20 cases for ACO-rat and in 20 out of 20 cases for ACO-virus. In aggregation, in 94.12% cases out of 68 cases our proposed algorithms provide better result than current state-of-the-art. From above experiments, it reveals that the required computation time of our algorithms is based on not only string length but also intermediate LCS length. There might be produced shorter intermediate LCS, and any short length intermediate LCS shrink the dynamic programming domain. From tables II to IV, it reveals that our algorithms require comparatively low time for protein sequence because the instances of protein sequences produce small LCS.

TABLE II: Comparison the Longest Common Subsequence over ACO-random produced by RepeDPH, RepeDPH-Local-Search, MRepeDPH and MRepeDPH-Local-Search with BS-high-time, IBS-LCS and HH-LCS.

M	N	BS-high-quality		IBS-LCS		HH-LCS		RepeDPH						RepeDPH-Local-Search						MRepeDPH						MRepeDPH-Local-Search					
								Worst		Average		Best		Worst		Average		Best		Worst		Average		Best		Worst		Average		Best	
|Σ|=4																															
10	600	211	9.8	218	0.4	221	0.5	185	0.3	194.3	0.3	207	0.3	191	0.4	206.4	0.4	221	0.4	186	0.3	194.2	0.3	201	0.2	189	0.4	204.1	0.4	222	0.4
15	600	194	13.2	203	0.5	202	0.4	169	0.4	174.2	0.4	186	0.4	172	0.6	187.2	0.6	203	0.6	169	0.3	175.2	0.3	184	0.3	173	0.6	188.2	0.6	200	0.6
20	600	184	14.9	191	0.5	191	0.5	161	0.5	163.9	0.5	167	0.5	166	0.7	178.7	0.7	189	0.7	161	0.4	165.8	0.4	175	0.4	163	0.7	175.7	0.7	191	0.7
25	600	179	15.8	185	0.5	185	0.5	157	0.7	160	0.7	165	0.6	162	0.8	175.2	0.8	184	0.8	156	0.5	164.4	0.5	177	0.4	162	0.8	172.8	0.8	184	0.8
40	600	167	21	172	0.7	172	0.7	149	0.8	151.8	0.8	159	0.8	152	1.2	162.3	1.2	170	1.1	149	0.6	152.4	0.6	159	0.6	152	1.2	163	1.2	174	1.2
60	600	161	27.6	165	0.8	165	0.9	143	1.0	145.4	1.0	149	1.0	147	1.6	156.5	1.6	165	1.6	143	0.9	146	0.9	152	0.9	146	1. 6	153.5	1.6	166	1.6
80	600	156	33.5	161	1.0	161	1.0	139	1.3	142.9	1.3	145	1.3	148	2.1	155.5	2.1	163	2.1	142	1.1	143.8	1.1	149	1.2	141	2.1	150.7	2.0	159	2.1
100	600	154	40.3	158	1.2	158	1.2	138	1.6	140.3	1.6	142	1.6	142	2.5	151	2.5	159	2.5	138	1.4	142.4	1.4	149	1.4	140	2.4	149.5	2.4	158	2.4
150	600	148	56.4	151	1.5	151	1.7	136	2.3	137	2.2	139	2.2	135	3.5	146.8	3.5	152	3.5	135	1.9	137.1	1.9	140	1.9	137	3.4	144.6	3.4	151	3.4
200	600	146	74.3	150	2.1	150	2.0	134	2.9	136.7	2.9	139	2.9	138	4.4	146.5	4.4	151	4.4	134	2.5	137.1	2.5	142	2.5	137	4.4	144.6	4.5	150	4.5
|Σ|=20																															
10	600	61	33.3	61	0.5	61	0.5	44	0.2	46.8	0.2	49	0.2	48	0.3	52.9	0.2	59	0.2	44	0.1	49.2	0.1	56	0.1	45	0.2	53.9	0.2	63	0.2
15	600	51	37.6	51	0.4	52	0.5	36	0.1	37.5	0.1	39	0.1	38	0.2	43.3	0.2	49	0.2	35	0.1	36.7	0.1	39	0.1	38	0.3	42.7	0.3	52	0.3
20	600	47	39.5	47	0.5	47	0.5	31	0.2	33.5	0.2	36	0.2	34	0.3	40.2	0.3	48	0.3	32	0.1	34.1	0.1	38	0.1	35	0.3	39.3	0.3	47	0.2
25	600	43	39.5	44	0.5	44	0.5	31	0.2	32.3	0.2	35	0.2	32	0.3	37.5	0.3	45	0.3	30	0.2	32.7	0.2	36	0.1	31	0.3	36.7	0.3	45	0.3
40	600	37	43.2	38	0.6	38	0.6	26	0.3	28.2	0.3	30	0.2	30	0.3	34.1	0.3	38	0.3	27	0.2	29.2	0.2	32	0.2	29	0.3	31.9	0.3	37	0.3
60	600	34	46.5	35	0.8	35	0.8	26	0.3	27	0.3	29	0.3	27	0.4	31.3	0.4	35	0.4	26	0.2	27.7	0.2	30	0.2	28	0.4	30.8	0.4	35	0.4
80	600	32	53.2	32	1.0	33	0.9	25	0.3	25.9	0.3	27	0.3	27	0.5	29.8	0.5	33	0.6	23	0.3	25.1	0.3	28	0.3	26	0.5	28.1	0.5	32	0.5
100	600	31	59.2	31	1.2	31	1.2	24	0.5	25.1	0.4	26	0.4	26	0.6	29.1	0.6	32	0.6	24	0.3	25.6	0.3	28	0.3	27	0.6	28.5	0.6	31	0.6
150	600	29	75.6	29	1.5	29	1.4	23	0.6	23.8	0.6	25	0.6	25	0.8	28.5	0.8	30	0.8	23	0.4	24.6	0.4	27	0.4	24	0.8	26.5	0.8	29	0.8
200	600	27	98	28	1.9	27	1.8	22	0.6	23.5	0.6	25	0.6	24	1.2	27	1.1	29	1.1	22	0.5	23.2	0.5	24	0.5	24	1.0	26	1.0	28	1.0
Quality improvement with respect to BS-high-quality												-11.64%						2.77%						-8.74%						2.4%	
Quality improvement with respect to IBS-LCS												-13.55%						0.62%						-10.88%						0.24%	
Quality improvement with respect to HH-LCS												-13.62%						0.52%						-11.0%						0.15%	

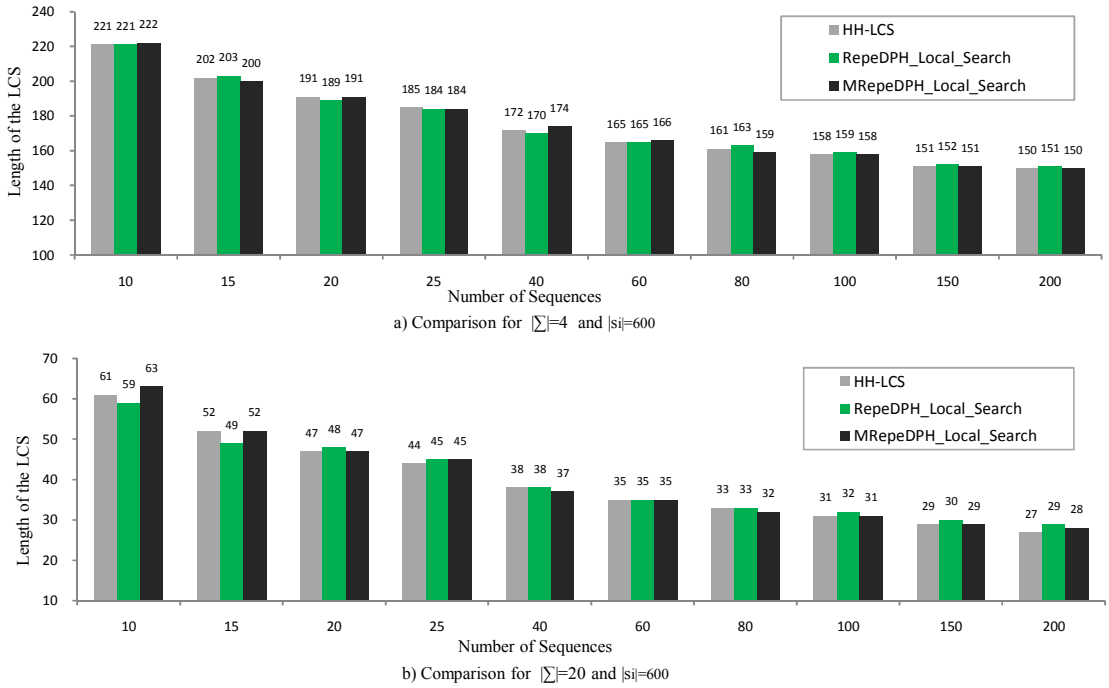

Figure 2. Comparison among HH-LCS, RepeDPH-Local-Search and MRepeDPH-Local-Search for ACO-random dataset.

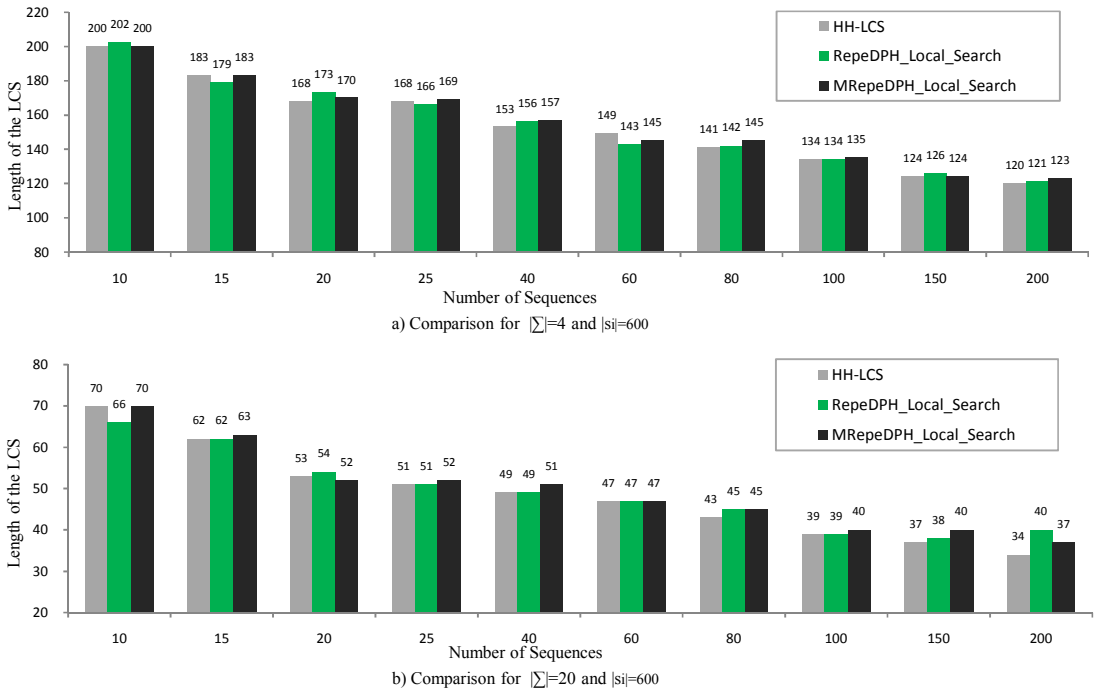

Figure 3. Comparison among HH-LCS, RepeDPH-Local-Search and MRepeDPH-Local-Search for ACO-rat dataset.

TABLE III: Comparison the Longest Common Subsequence over ACO-rat produced by RepeDPH, RepeDPH-Local-Search, MRepeDPH and MRepeDPH-Local-Search with BS-high-time, IBS-LCS and HH-LCS.

M	N	BS-high-quality		IBS-LCS		HH-LCS		RepeDPH						RepeDPH-Local-Search						MRepeDPH						MRepeDPH-Local-Search					
								Worst		Average		Best		Worst		Average		Best		Worst		Average		Best		Worst		Average		Best	
|Σ|=4																															
10	600	191	9.7	199	0.4	200	0.4	172	0.3	179	0.3	194	0.3	177	0.5	188.4	0.5	202	0.5	172	0.3	177.7	0.3	195	0.3	179	0.4	189.3	0.4	200	0.4
15	600	173	12.3	182	0.4	183	0.4	153	0.5	158.4	0.5	162	0.4	164	0.5	169	0.6	179	0.5	156	0.3	161.8	0.3	170	0.3	161	0.5	171.2	0.5	183	0.5
20	600	163	12.6	168	0.4	168	0.4	155	0.4	157.9	0.4	162	0.4	156	0.7	164.8	0.7	173	0.6	150	0.4	156.5	0.4	166	0.4	154	0.6	161.5	0.6	170	0.6
25	600	162	15.8	166	0.4	168	0.5	146	0.6	148.8	0.6	154	0.6	149	0.8	158.2	0.8	166	0.8	144	0.4	148	0.4	151	0.4	149	0.8	157.8	0.8	169	0.8
40	600	146	19.4	146	0.5	153	0.5	134	0.7	139	0.7	146	0.7	143	1.1	149.8	1.1	156	1.1	133	0.6	139.5	0.6	144	0.6	142	1. 1	148.6	1.1	157	1.1
60	600	144	26.7	147	0.7	149	0.7	129	1.0	131.6	1.0	134	0.9	132	1.5	137	1.5	143	1.4	127	0.8	130.4	0.8	134	0.8	125	1.5	134.8	1.5	145	1.5
80	600	135	31.8	141	0.9	141	0.9	122	1.3	126	1.2	131	1.2	133	2.0	136.1	1.9	142	2.0	121	1.0	124.7	1.0	127	0.9	126	1.9	133.3	1.9	145	1.9
100	600	132	38.5	132	1.0	134	1.0	115	1.4	120.9	1.4	125	1.4	120	2.3	127	2.2	134	2.1	117	1.4	120.3	1.3	123	1.3	120	2.2	127	2.2	135	2.2
150	600	121	51.1	124	1.3	124	1.4	113	1.9	118.6	1.9	122	1.9	118	3.0	122.4	3.0	126	3.1	112	1.7	117	1.7	124	1.6	114	2.9	119.5	2.9	124	2.8
200	600	121	69.1	120	1.6	120	1.7	107	2.4	114.8	2.4	120	2.4	108	3.6	116.4	3.7	121	3.8	109	2.1	114.4	2.2	120	2.2	110	3.8	117.4	3.9	123	3.9
|Σ|=20																															
10	600	69	27.4	70	0.5	70	0.7	51	0.1	55.2	0.1	61	0.1	55	0.2	59	0.2	66	0.2	52	0.1	57.7	0.1	66	0.1	54	0.3	63.5	0.3	70	0.3
15	600	60	36.7	61	0.5	62	0.5	45	0.2	48.5	0.2	51	0.2	49	0.2	53.8	0.2	62	0.2	47	0.1	49.8	0.1	55	0.1	49	0.3	55.9	0.3	63	0.3
20	600	51	34.4	53	0.5	53	0.5	36	0.3	41.2	0.3	45	0.3	41	0.3	47.9	0.3	54	0.3	38	0.2	41.3	0.1	48	0.2	43	0.3	46.4	0.3	52	0.3
25	600	51	39	50	0.5	51	0.5	36	0.3	40	0.3	43	0.3	40	0.3	43.9	0.3	51	0.3	35	0.2	38.8	0.2	41	0.2	43	0.3	46.2	0.3	52	0.3
40	600	49	47.4	49	0.6	49	0.6	34	0.3	39	0.3	42	0.3	36	0.4	41.9	0.4	49	0.4	36	0.2	38.2	0.2	40	0.2	39	0.4	45.6	0.4	51	0.4
60	600	46	60.3	46	0.8	47	0.8	33	0.4	38.2	0.3	42	0.3	33	0.5	41.1	0.5	47	0.5	34	0.3	36.8	0.3	40	0.3	37	0.6	42.5	0.6	47	0.6
80	600	43	64.4	43	1.0	43	1.1	36	0.4	39.6	0.5	45	0.5	39	0.7	42.1	0.7	45	0.7	37	0.4	40.5	0.4	44	0.4	33	0.6	39.4	0.6	45	0.6
100	600	38	64.8	39	1.1	39	1.0	29	0.5	32.3	0.5	35	0.5	29	0.7	33.6	0.7	39	0.7	23	0.4	31.4	0.4	37	0.4	28	0.8	34.2	0.8	40	0.7
150	600	36	77.8	36	1.3	37	1.3	26	0.6	31.1	0.6	35	0.6	28	1.0	34.4	1.0	38	1.0	23	0.5	30.1	0.5	35	0.5	28	1.0	32.3	1.0	40	1.0
200	600	33	101	32	1.7	34	1.7	27	0. 8	30.5	0.8	35	0.8	30	1.4	35.6	1.4	40	1.3	29	0.7	32.8	0.7	36	0.7	31	1.4	34.4	1.4	37	1.5
Quality improvement with respect to BS-high-quality												-5.13%						3.8%						-4.38%						4.55%	
Quality improvement with respect to IBS-LCS												-6.37%						2.44%						-5.77%						2.93%	
Quality improvement with respect to HH-LCS												-7.54%						1.14%						-7.0%						1.89%	

TABLE IV: Comparison the Longest Common Subsequence over ACO-virus produced by RepeDPH, RepeDPH-Local-Search, MRepeDPH and MRepeDPH-Local-Search with BS-high-time, IBS-LCS and HH-LCS.

M	N	BS-high-quality		IBS-LCS		HH-LCS		RepeDPH						RepeDPH-Local-Search						MRepeDPH						MRepeDPH-Local-Search					
								Worst		Average		Best		Worst		Average		Best		Worst		Average		Best		Worst		Average		Best	
|Σ|=4																															
10	600	212	11.6	225	0.5	225	0.5	196	0.3	203.1	0.3	212	0.3	198	0.5	213	0.5	226	0.5	195	0.2	204.9	0.3	217	0.2	206	0.5	219.9	0.4	231	0.4
15	600	193	15.4	203	0.5	202	0.4	174	0.4	177.1	0.4	182	0.4	177	0.6	184.5	0.6	200	0.6	172	0.3	179.2	0.3	192	0.3	177	0.6	186.5	0.6	203	0.6
20	600	181	17.2	189	0.5	189	0.5	162	0.5	170.7	0.5	177	0.5	177	0.7	182.7	0.7	189	0.7	162	0.5	170.7	0.5	187	0.5	171	0.8	181.3	0.8	193	0.8
25	600	185	17.9	193	0.5	193	0.6	168	0.6	172.3	0.6	181	0.6	171	0.8	181.3	0.8	193	0.8	164	0.4	172.2	0.4	187	0.5	171	0.8	181.3	0.8	193	0.8
40	600	162	21.9	168	0.6	165	0.6	147	0.8	156.7	0.8	166	0.8	156	1.2	163.3	1.2	170	1.2	150	0.6	157	0.6	166	0.6	150	1.2	160.9	1.2	171	1.2
60	600	158	29.1	165	0.8	164	0.8	143	1.0	150.3	1.1	159	1.1	153	1.5	158	1.5	166	1.5	145	0.9	149.6	0.9	156	0.9	148	1.7	157.4	1.6	165	1.7
80	600	153	36	158	0.9	158	1.0	135	1.3	144.6	1.3	150	1.3	146	2.1	154.6	2.1	163	2.1	140	1.2	146	1.4	157	1.9	146	2.9	154.9	2.5	161	2.1
100	600	150	43.9	158	1.2	158	1.2	135	1.6	144.2	1.6	151	1.6	144	2.4	152.9	2.4	164	2.5	144	1.3	149.8	1.3	158	1.3	142	2.4	154	2.5	163	2.5
150	600	148	64.5	156	1.7	156	1.7	135	2.2	138.5	2.3	144	2.3	136	3.4	143.4	3.4	153	3.4	131	2.0	137	1.9	148	2.0	137	3.4	146.5	3.4	156	3.3
200	600	145	84.5	154	2.1	154	2.1	134	2.9	136.7	2.9	141	2.9	137	4.5	143.9	4.5	154	4.5	132	2.6	137.5	2.5	145	2.5	142	4.5	149.4	4.4	157	4.4
|Σ|=20																															
10	600	75	27.2	75	0.5	75	0.6	56	0.1	58.9	0.2	65	0.1	65	0.2	69.3	0.2	75	0.2	57	0.1	61	0.1	69	0.1	65	0.2	69.3	0.2	75	0.2
15	600	63	38.6	63	0.5	63	0.5	46	0.2	49.3	0.2	51	0.2	49	0.3	54.3	0.3	63	0.3	47	0.2	50.1	0.2	58	0.1	49	0.2	57	0.2	64	0.2
20	600	57	40.3	60	0.5	60	0.5	41	0.2	43.7	0.3	47	0.2	45	0.3	50.7	0.3	59	0.3	41	0.1	45.7	0.2	54	0.1	45	0.3	51.4	0.3	60	0.3
25	600	53	38.9	54	0.5	55	0.5	39	0.2	41.1	0.2	43	0.2	42	0.4	46.5	0.3	54	0.3	39	0.2	41.1	0.2	49	0.2	40	0.3	47	0.3	55	0.3
40	600	49	48.4	49	0.7	49	0.7	34	0.3	37.2	0.3	39	0.3	37	0.5	43.6	0.5	50	0.5	36	0.2	38.5	0.2	46	0.2	39	0.4	43.5	0.4	50	0.4
60	600	45	56.1	47	1.0	47	1.0	33	0.4	35.7	0.4	38	0.4	35	0.5	40.8	0.5	48	0.5	34	0.3	37.1	0.4	45	0.3	36	0.5	41.7	0.5	50	0.5
80	600	44	67.4	45	1.1	46	1.2	31	0.4	33.4	0.4	40	0.4	34	0.6	38.4	0.6	46	0.6	31	0.4	35.7	0.4	42	0.4	35	0.6	39.5	0.5	46	0.6
100	600	43	74.2	44	1.5	44	1.3	30	0.5	32.7	0.5	35	0.5	31	0.7	35.9	0.7	44	0.7	32	0.3	36.9	0.4	43	0.3	33	0.7	38.7	94.1	44	0.7
150	600	44	108	45	1.8	45	1.9	28	0.7	32.9	0.7	35	0.7	29	1.1	36.9	1.1	45	1.1	30	0.4	37	0.4	43	0.4	34	2.0	39.8	2.0	46	2.0
200	600	43	140	44	2.2	43	2.1	28	0.9	32.5	0.9	36	0.9	29	1.5	36.5	1.4	44	1.4	27	0.4	35. 7	0.4	44	0.4	32	2.5	39.8	2.6	45	2.7
Quality improvement with respect to BS-high-quality												-9.15 %						4 %						-1.2 %						5.13 %	
Quality improvement with respect to IBS-LCS												-12.25 %						0.53 %						-4.66 %						1.56 %	
Quality improvement with respect to HH-LCS												-12.19 %						0.59 %						-4.6 %						1.67 %	

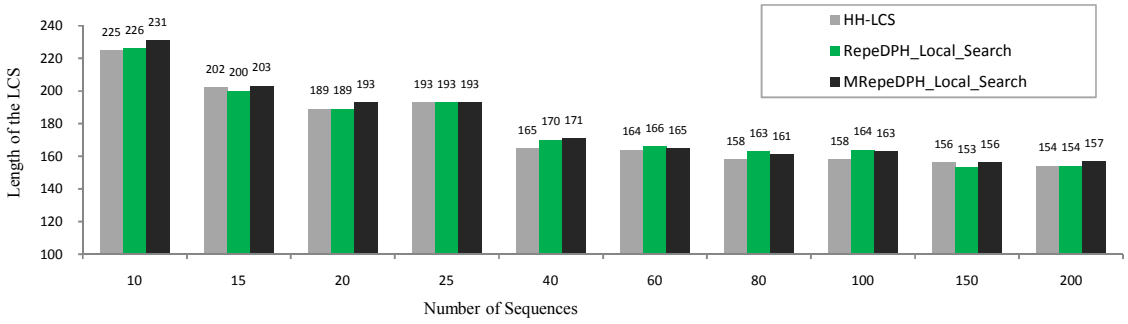

a) Comparison for |∑|=4 and |si|=600

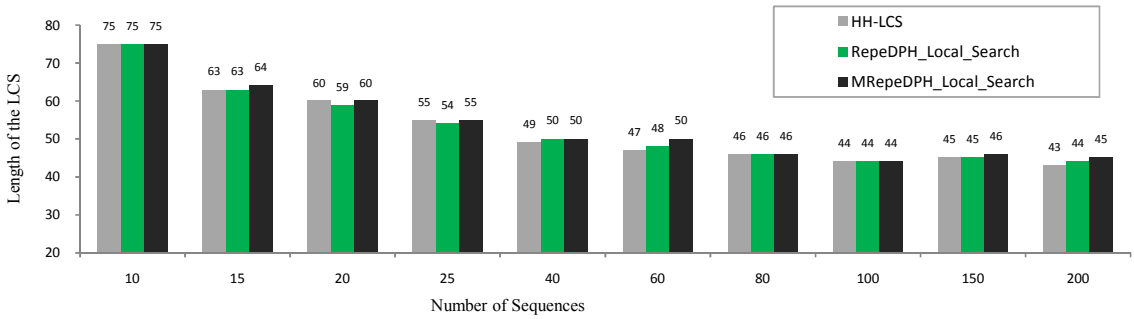

b) Comparison for |∑|=20 and |si|=600

Figure 4. Comparison among HH-LCS, RepeDPH-Local-Search and MRepeDPH-Local-Search for ACO-virus dataset.

An Efficient Approach for Designing FIR Low-pass Filter and Its Application

Hrishi Rakshit
Electrical and Electronics Engineering
Chittagong University of Engineering & Technology
Chittagong, Bangladesh
rishirok@gmail.com

Muhammad Ahsan Ullah
Electrical and Electronics Engineering
Chittagong University of Engineering & Technology
Chittagong, Bangladesh
ahsan_cuet@yahoo.com

***Abstract*—In this paper, an adjustable window function, based on combination of tangent hyperbolic function and a weighted cosine series, is proposed to design an FIR filter. The proposed window has only one adjustable parameter "r". By varying this parameter, it is possible to change the spectral characteristics of the filter. The performance of the proposed window is compared with Gaussian and Kaiser windows. The proposed window has slightly larger main–lobe width compare to the commonly used Gaussian and Kaiser windows, while featuring 19.71 dB and 8.29 dB smaller ripple ratios respectively. Moreover the side-lobe roll-off ratio of the proposed window is almost 115.03 dB and 14.95 dB better than the Gaussian and Kaiser windows respectively. Simulation results show that the filter designed by the proposed window yields 34.39 dB smaller ripple ratio than Kaiser window. Further, the low-pass filter, designed by the proposed method results 7.3766 times and 3.65 times better side-lobe roll-off ratios than those of Gaussian and Kaiser windows respectively. This paper also highlights an application of the proposed method in the area of eliminating noise from corrupted Audio signal.**

***Index Terms*— Gaussian Window, Kaiser Window, Main-lobe Width, Ripple Ratio and Side-lobe Roll-off Ratio.**

I. Introduction

The impulse response of an ideal filter is infinitely long. The most straight forward way to make the response finite, is to truncate the ideal response. If $h_d(n)$ is the response of an ideal filter, the simplest way to obtain a causal finite impulse response is to multiply the $h_d(n)$ with a finite window function w(n). In engineering term, a window is a finite array, consists of coefficients to satisfy the desirable requirements [1]. In general, the window function can be defined as

$$w[n] = \begin{cases} f(n), & 0 \le n \le N \\ 0, & otherwise \end{cases} \quad (1)$$

and the impulse response of the system is given by

$$h[n] = h_d[n]w[n] \quad (2)$$

Therefore the Fourier transform h[n], denoted by $H(e^{j\omega})$, is the periodic convolution of the $H_d(e^{j\omega})$, with the Fourier transform of w[n], denoted by $W(e^{j\omega})$. The important spectral characteristics of a window function are i) main-lobe width ii) ripple ratio and iii) its side-lobe roll-off ratio. There are two desirable specifications for any window function. They are smaller main-lobe width and the smaller ripple ratio. However these two requirements are contradictory [2]. The simplest window is the rectangular window [2].It has a very sharp transition band. However its ripple ratio is highest among the all commonly used windows. Gaussian and Kaiser windows are the adjustable functions. So by changing the adjustable parameter, one can trade-off between the main-lobe width and the ripple ratio. In many applications like FIR filters, FFT, signal processing and measurements, we are required -45 dB or less side lobe peaks [3]. Kaiser window has the computational complexity due to the calculation of Bessel functions [4]. So there has been a great interest to design a new window to meet the desire specifications for different applications.

In this paper, a novel adjustable window is proposed which has only two parameters (one is length of the window and another is the additional parameter "r") that control the spectral characteristics of the window. The proposed window is very simple as it does not involve any Bessel function like the Kaiser window. The proposed window yields better spectral characteristics than Gaussian window. The ripple ratio and the side-lobe roll-off ratio of the proposed window are respectively 19.71 dB and 115.03 dB better than Gaussian window. Our simulation result shows that the ripple ratio and the side-lobe rill-off ratio of the proposed window are 8.29 dB and 14.95 dB better respectively than what can be obtained using Kaiser window. Filter designed using the proposed window results 34.39 dB better ripple ratio than Kaiser window. Moreover, the side-lobe roll-off ratio of the proposed window based FIR low-pass filter is 7.3766 times and 3.65 times greater than the above named windows based filters respectively. The filter designed by the proposed method has been used to remove noise from corrupted audio signal. The experimental results ensure that the proposed filter performs better performance than Kaiser filter to eliminate noise from audio signal.

978-1-4673-9257-0/15/$31.00 ©2015 IEEE

Section II defines the three major spectral characteristics of a window function. Section III introduces the new window and also explains its spectral behaviors under various conditions. Section IV compares the performances of the proposed window with Gaussian and Kaiser windows. Section V describes the performance analysis of a FIR low-pass filter using the proposed windowing method. Section VI represents the efficiency of the proposed FIR low-pass filter in eliminating noise from the corrupted audio signal. Section VII shows the normalized frequency response of the filtered audio signal. Section VIII provides concluding remarks.

II. Spectral properties of Windows

A window, w(nT), with a length of N is a time domain function which is nonzero co-efficient for n<=|(N-1)/2| and zero for otherwise. A typical window has a normalized amplitude spectrum in dB as shown in Figure 1.

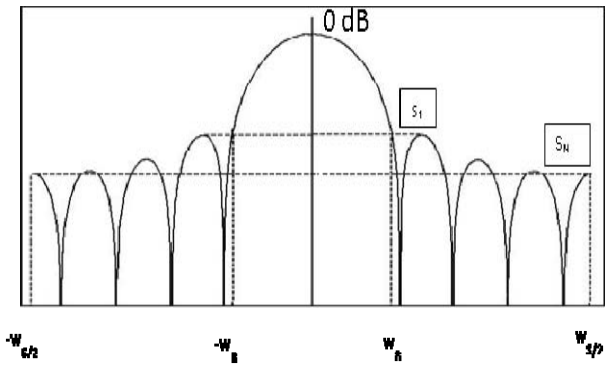

Fig 1: A typical window's normalized amplitude spectrum

Normalized spectrum in Fig 1 is obtained by following equation

$$\left|W_n(e^{j\omega T})\right| = 20\log_{10}(\left|A(w)\right|/\left|A(w)\right|_{\max}) \quad (3)$$

The spectral characteristics which determine the windows performance are the main-lobe width(w_M), the ripple ratio (R) and the side-lobe roll-off ratio(S). From the Fig 1, these parameters can be defined as

W_M= Two times half of the main-lobe width=$2w_R$.

R= (Maximum side-lobe amplitude in dB) – (Main-lobe amplitude in dB) = S_1.

S= (Maximum side-lobe amplitude in dB) – (Minimum side-lobe amplitude in dB) = S_1-S_N.

III. Proposed Window

The new proposed window is a combination of tan hyperbolic function and a weighted cosine series. The tan hyperbolic function is given by the following equation

$$y_1 = \left[\tanh\left\{\frac{n-\frac{(N-1)}{2}+\cosh^2(\alpha)}{B}\right\} - \tanh\left\{\frac{n-\frac{(N-1)}{2}-\cosh^2(\alpha)}{B}\right\}\right] \quad (4)$$

The weighted cosine function is expressed as follows

$$y_2 = 0.375 - 0.5\cos\left\{\frac{2\pi l}{N-1}\right\} + 0.125\cos\left\{\frac{4\pi l}{N-1}\right\} \quad (5)$$

Where N is the length of the window, α and B are the constants. Here n is the number of samples. Here the symbol l =0,1,2,3,……(N-1).

These two equations are combined in the following way.

$$w(n) = (y_1 * y_2)^{\gamma}, \quad where, \gamma = r^{(\frac{1}{5})} \quad (6)$$

and "*" means multiplication.

Here r is a variable which controls the shape and frequency response of the window. So "r" can be named as controlling or adjustable parameter of the window. In mathematical term, the window can be expressed as

$$w(n) = \begin{cases} (y_1 * y_2)^{\gamma}, & n \le 0 \le N \\ 0, & otherwise \end{cases} \quad (7)$$

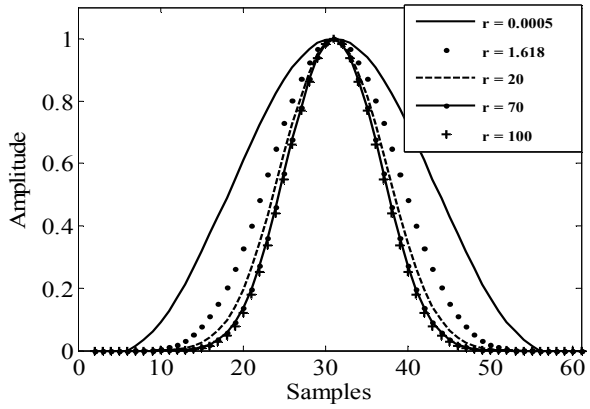

Fig 2: Shapes of the proposed windows with different values of r.

From the Fig 2 is has been seen that the shape of the window varies as the value of the adjusting parameter r changes. When r=0.0005 and r =100, the shape of the window is the widest and the narrowest respectively among the other values of r shown in the Fig 2. The width of the window gets narrower as the value of the controlling parameter "r" gets bigger.

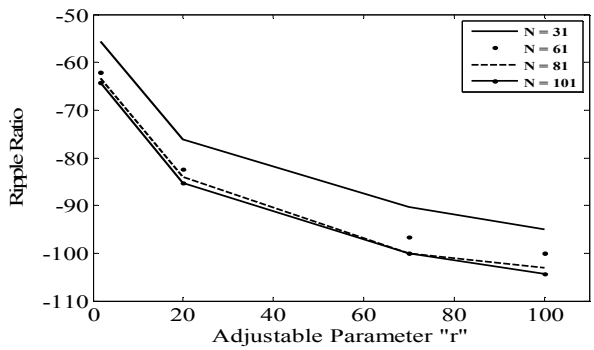

Fig 3 : Adjustable parameter "r" Vs Ripple ratio curve in different window lengths

The curve N=31 describes the ripple ratios of different values of "r" when the window length is fixed at 31. In the same way , N=61, N=81 and N=101 curves have been drawn. From the Fig 3, it has been observed that if we increase the value of "r", the ripple ratio decreases when the window length is fixed. Now if we fix "r" and increase the window length, the ripple ratio decreases. For example, let us measure the values of ripple ratio at "r=20". So what we get from the Fig 3 is that, the lowest value of R is obtained for N=101when r is fixed at r = 20. The following table

summarizes the Fig 3.

TABLE I: ADJUSTABLE PARAMETER "R" VS RIPPLE RATIO AT VARIOUS WINDOW LENGTH N.

"r"	N=31	N=61	N=81	N=101
0.0005	-25.7	-33.2	-31.84	-33.36
1.618	-55.68	-62.1	-63.31	-64.27
20	-76.16	-82.47	-84.1	-85.28
70	-90.28	-96.58	-100	-100
100	-94.92	-100	-103.1	-104.4

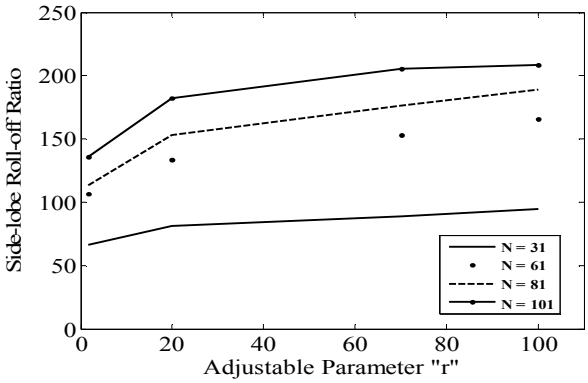

Fig 4 : Adjustable parameter "r" Vs Side-lobe roll-off ratio curve in different window lengths.

From the Fig 4 it has been seen that all the curves are increasing with the increment of their adjustable parameter "r". So we can say, the side-lobe roll-off ratio of the proposed window increases with the raise of the value of "r" when the window length is fixed. Let us consider the curve N=101. Here N is the window length. Compare to the curve N=31, N=61 and N=81 the curve N=101 remains on the higher position. The following table summarized the Fig 4.

TABLE II: ADJUSTABLE PARAMETER "R" VS SIDE-LOBE ROLL-OFF RTIO RATIO AT VARIOUS WINDOW LENGTHS

"r"	N=31	N=61	N=81	N=101
0.0005	27.09	38.54	40.39	80.64
1.618	66.42	106.9	113.29	135.73
20	81.44	133.33	152.7	182.32
70	88.52	153.42	176.3	205.4
100	94.78	166.1	189.3	208.5

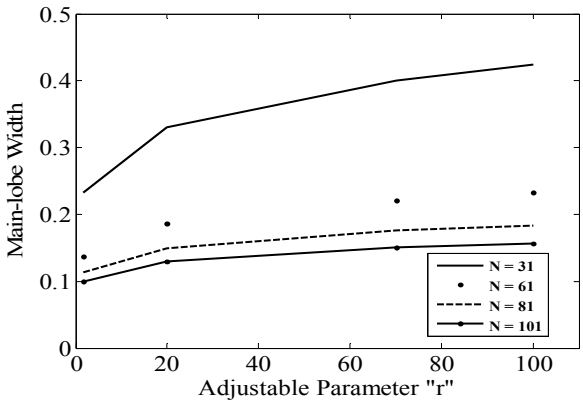

Fig 5 : Adjustable parameter "r" Vs Main-lobe width curve in different window lengths.

Fig 5 shows that as the controlling parameter of the proposed window "r" increases the main-lobe width of the proposed window also raises when the window length is fixed. Let us consider about the curve N=61. Here N is length of the proposed window. From Fig 5 we have, the curve N=61 moderately increases as the value of "r" increases with a fix window length. The following table gives the actual scenario of Fig 5.

TABLE III: ADJUSTABLE PARAMETER "R" VS MAIN-LOBE WIDTH CALCULATION AT VARIOUS WINDOW LENGTHS

"r"	N=31	N=61	N=81	N=101
0.0005	0.1096	0.07632	0.06654	0.06262
1.618	0.2329	0.137	0.1135	0.1
20	0.3307	0.1869	0.1487	0.1292
70	0.4	0.2211	0.1761	0.1507
100	0.4247	0.2329	0.184	0.1566

IV. PERFORMANCE ANALYSIS

In this section, we compare the shape and the spectral characteristics of the proposed window with several commonly used windows.

A. Gaussian Window:

The coefficients of the Gaussian window function are computed using the following equation.

$$w(n) = e^{\frac{1}{2}(\alpha \frac{n}{N/2})^2} \tag{8}$$

where α is inversely proportional to the standard deviation of a Gaussian random variable. The width of the window is inversely related to the value of α. A larger value of α produces a narrower window.[5][6]

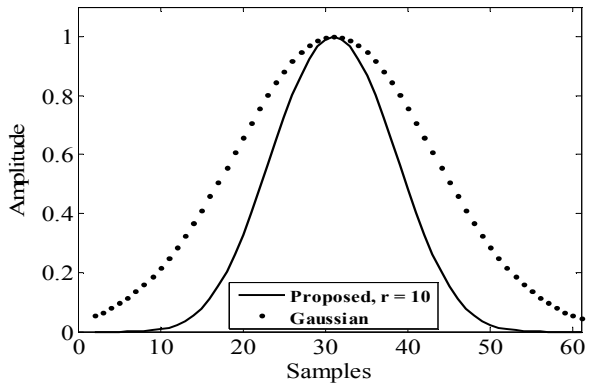

Fig 6: Time domain representation of Gaussian and the Proposed windows

From the Fig 6 it has been seen that the time domain representation of the proposed window with r =10, is narrower than the Gaussian window. Moreover the proposed window touches the X-axis while all the coefficients of the Gaussian window remain above the X-axis. Both of them are symmetric windows. None of them have any negative co-efficient. Some of the coefficients of the proposed window are zero at the beginning and at the ending edges of the window.

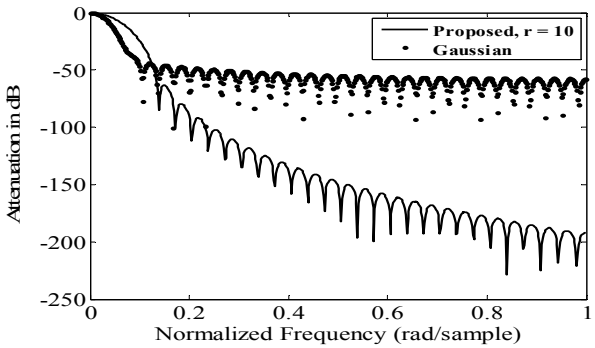

Fig7: Normalized frequency response comparison of Gaussian and the Proposed windows.

Fig 7 shows that the main lobe width of Gaussian and the

proposed windows are 2π × 0.1055 rad/sample and 2π × 0.1387 rad/sample respectively. So the main-lobe width of Gaussian window is 0.0332 rad/sample smaller than the proposed window. On the contrary, the ripple ratios of Gaussian and the proposed windows are about -44.16 dB and -63.83 dB respectively. Hence the ripple ratio of the proposed window is approximately 19.67 dB smaller. Moreover the side-lobe roll-off ratio of the proposed window is almost 115.03 dB better than Gaussian window.

TABLE IV: SPECTRAL PARAMETERS OF GAUSSIAN AND THE PROPOSED WINDOWS.

Window	Main-lobe Width (rad/sample)	Ripple Ratio (dB)	Side-lobe Roll-off Ratio(dB)
Proposed, r =10	2π × 0.1387	-63.83	128.47
Gaussian	2π×0.1055	-44.12	13.44

B. *Kaiser window:*

The Kaiser window is also known as Kaiser-Bessel window function. The Kaiser window function can be expressed as follows [7][8].

$$w(n) = \frac{I_0(\pi\alpha\sqrt{1-(\frac{2n}{N-1}-1)^2})}{I_0(\pi\alpha)} \; where, 0 \le n \le N \quad (9)$$

where I_0 is the zero-th order modified Bessel function of the first kind [8]. Kaiser window is another very popular adjustable window. The variable parameter α determines the tradeoff between the main-lobe width and the side lobe attenuation.

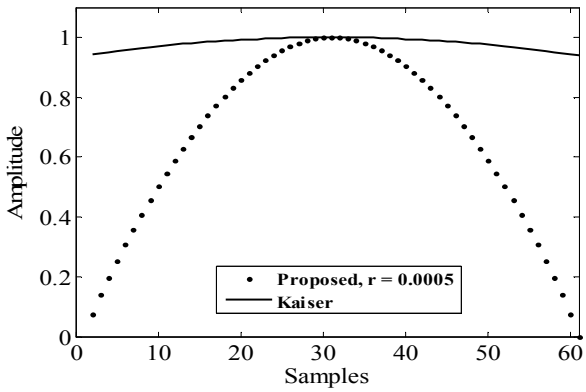

Fig 8 : Time domain representation of Kaiser and the Proposed windows

From the Fig 8 it has been seen that Kaiser window with its adjustable parameter α = 0.5 is almost like rectangular shape. On the contrary, the proposed window is almost like bell shape with its adjustable parameter r= 0.0005.

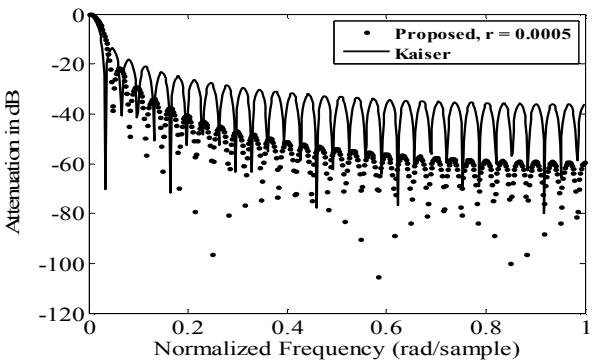

Fig 9: Normalized frequency response comparison of Kaiser and the Proposed windows.

Fig 9 shows the normalized frequency response of Kaiser and the proposed windows. It has been observed that Kaiser window has the main-lobe width of 2π×0.0332 rad/sample while the proposed window has 2π×0.0469 rad/sample. So Kaiser window is slightly better than the proposed window in main-lobe width calculation. Kaiser window has the ripple ratio of -13.63 dB and the proposed window has the ripple ratio of -21.92 dB. Hence the proposed window yields 8.29 dB better ripple ratio. Fig 9 illustrates that the first side-lobe peak of Kaiser window is -13.63 dB and the last one is -36.07dB. So the side-lobe roll-off ratio of Kaiser window is 22.44 dB. In the same way the first side-lobe peak of the proposed window is -21.92 dB and the last one is -59.31 dB. Hence the side-lobe roll-off ratio of the proposed window is 37.39 dB which is 14.95 dB better than Kaiser window.

TABLE V: SPECTRAL PARAMETERS OF KAISER AND THE PROPOSED WINDOWS.

Window	Main-lobe Width (rad/sample)	Ripple Ratio (dB)	Side-lobe Roll-off Ratio(dB)
Proposed, r =10	2π × 0.0469	-21.92	37.39
Kaiser	2π×0.0332	-13.63	22.44

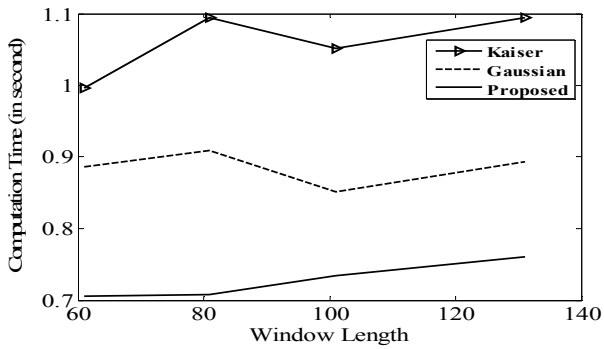

Fig 10:Computation time comparison among Kiser, gaussian and the proposed window in various window length

Fig 10 shows the computational time required for Kaiser, Gaussian and the proposed window with different window length. The elapsed time is minimum for the proposed window than the Kaiser and the Gaussian windows.

V. FIR FILTER DESIGN

In this section we will discuss how the proposed window helps us to design FIR low pass filter and also compare the simulation result with the most popular adjustable windows.

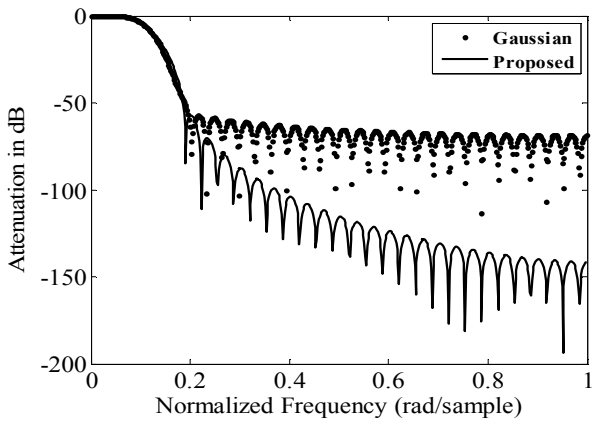

Fig 11 (a) : Normalized frequency response of FIR low pass filters designed by the proposed and Gaussian windows.

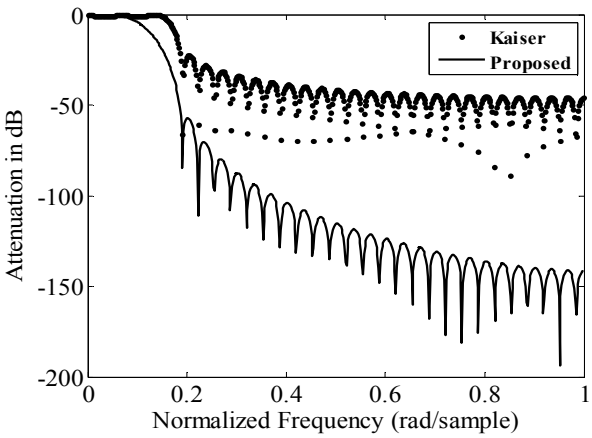

Fig 11 (b) : Normalized frequency response of FIR low pass filters designed by the proposed and Kaiser windows.

Having a cut off frequency of ω_c, the impulse response of an ideal low pass filter is given by

$$h_{LP,ideal}[n] = \frac{\sin(\omega_c n)}{\pi n} \tag{10}$$

By windowing this IIR filter with the windows discussed in this paper, different FIR filter can be achieved. For $\omega_c = 0.2\pi$ figures 11(a)-11(b) show the normalized frequency response of the FIR filters designed by applying different windows of length 61. Fig 11(a) shows the comparison of FIR low-pass filters designed by the proposed and Gaussian windows respectively. From the Fig 11 (a) it has been seen that the main-lobe width of the proposed window is slightly narrower than Gaussian window based FIR low-pass filter. Simulation result shows that the filters achieved by the proposed window and Gaussian window have the same ripple ratios. We also observe that the side-lobe roll-off ratio of the filter designed by the proposed window is near about 72.63 dB better than what can be achieved by Gaussian window. In the same way, the fig 11(b) demonstrates that the filter obtained by the proposed window results 34.39 dB better ripple ratio and approximately 60.98 dB greater side-lobe roll-off ratio than what can be obtained by using Kaiser window.

TABLE VI: DATA ANALYSIS OF FIR FILTER OBTAINED BY WINDOWING WITH DIFFERENT WINDOWS

Comparing Windows	Main-lobe Width (rad/sample)	Ripple Ratio (dB)	Side-lobe Roll-off Ratio (dB)
Proposed Vs Gaussian	2π×0.1914	-57.08	84.02
	2π×0.2031	-57.08	11.39
Proposed Vs Kaiser	2π×0.1914	-57.08	84.02
	2π×0.1933	-22.69	23.04

VI. NOISE ELIMINATION FROM AUDIO SIGNAL

Human auditory system is able to process the complex sound mixture reaching our ears [9]. The human auditory system is responsive to sounds in the frequency range of 20Hz to 20 KHz [9]. When this audio signal is passed through a communication channel or communication system, it may corrupted by Additive White Gaussian Noise. The adjective 'White' is used in the sense that white light contains equal amount of all frequencies within the visible limit of all electromagnetic radiation [10]. For testing the proposed filter, we first generate an audio signal. This audio signal is sampled at 44.1KHz. Then additive white Gaussian noise is added with the audio signal. The noise corrupted audio signal is passed through the different types of FIR low-pass filters.

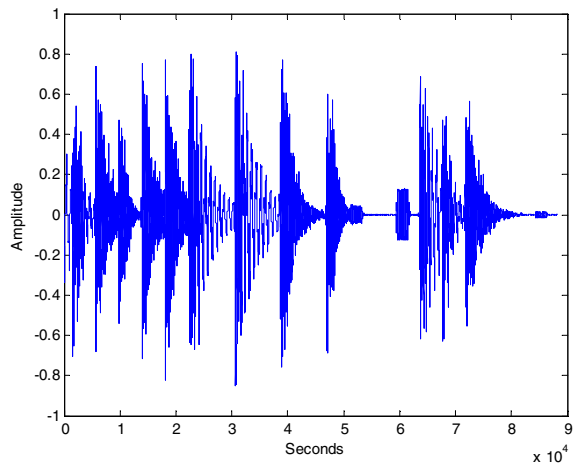

Fig 12: An audio signal without noise

When AWGN is added with the audio signal then the signal becomes as follows.

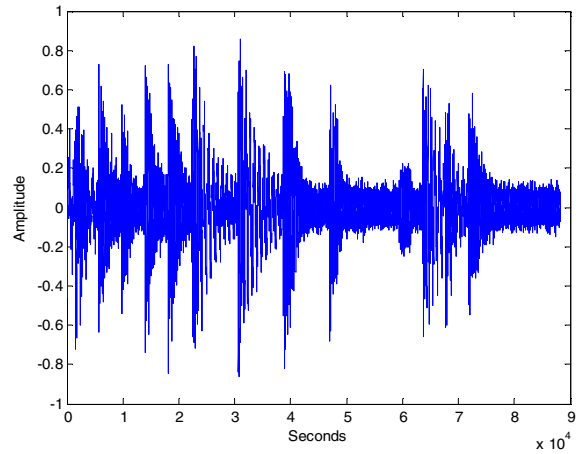

Fig 13: Audio signal corrupted by additive white Gaussian noise.

Now this noise corrupted audio signal is passed through a Kaiser window based FIR low-pass filter and the output is shown in the Fig 14.

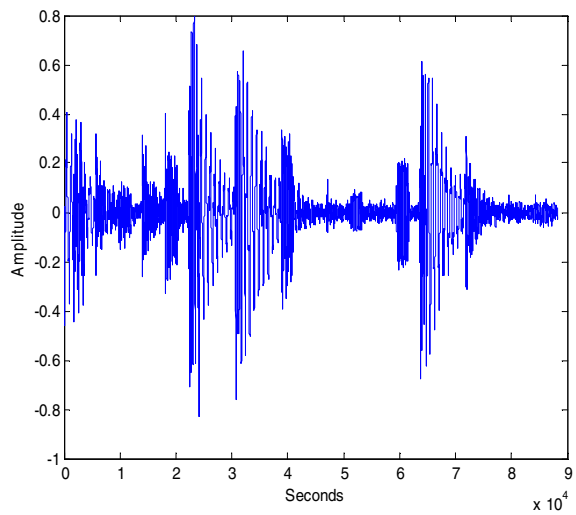

Fig 14: Filtered audio signal using Kaiser window based FIR filter

Again the same corrupted audio signal is passed through the proposed window based FIR low-pass filter and the output is represented in the Fig 15.

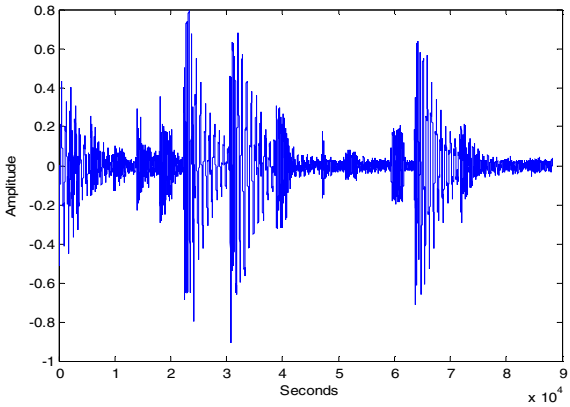

Fig 15 : Filtered audio signal using the proposed window based FIR filter.

It has been seen form the Fig 14 and Fig 15 that the proposed window based FIR low-pass filter more precisely eliminates Noise form the audio signal than Kaiser window based FIR low-pass filter. It will be more clear in the next section when we calculate the normalized frequency responses of the filtered audio signal.

VII. Normalized Frequency Response of the Filtered Audio Signal

After obtaining the filtered version of the audio signal using Kaiser and the proposed windows based FIR low-pass filters, their respective normalized frequency response has been analyzed. Fig 16 and Fig 17 show the normalized frequency response of the filtered audio signal using Kaiser and the proposed windows based FIR filters respectively.

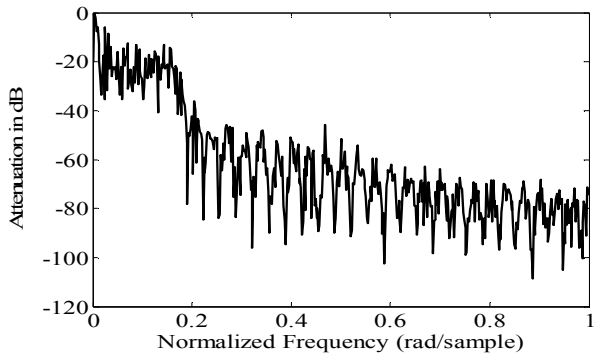

Fig 16: Normalized frequency response of the filtered audio signal using Kaiser window based FIR low-pass filter.

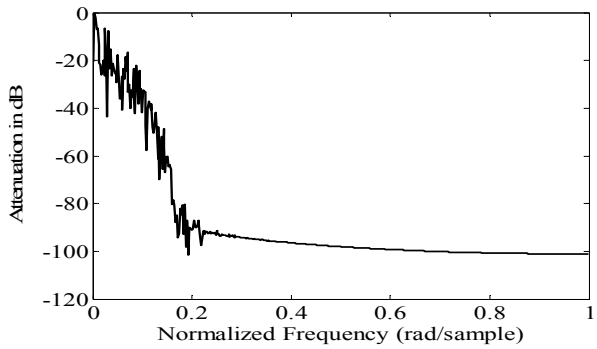

Fig 17: Normalized frequency response of the filtered audio signal using proposed window based FIR low-pass filter

From the Fig 16 it has been observed that the ripple ratio of the audio signal filtered by Kaiser window based low-pass filter is about -50.44 dB. On the contrary, the ripple ratio of the audio signal filtered by the proposed window based low-pass filter is approximately -80.72 dB which is 30.28 dB better. The following table summarized the Fig 16 and Fig 17.

Table VII: Performance Analysis of Kaiser and the Proposed Windows.

Window	Ripple Ration (dB)	Remarks
Kaiser	-50.44	The proposed window based FIR low-pass filter is 30.28 dB better.
Proposed, r=0.0005	-80.72	

VIII. Conclusion

The proposed window is symmetric one and it has only one adjustable parameter "r". So it is a very simple window. The proposed window yields 19.71 dB and 8.29 dB smaller ripple ratios than Gaussian and Kaiser windows respectively. Moreover the side-lobe roll-off ratio of the proposed window is almost 115.03 dB and 14.95 dB better than the above named windows. The performance of the FIR low pass filter, designed by the proposed window, is compared with Gaussian and Kaiser windows. Experimental results show that the filter designed by the proposed window yields better spectral characteristics than those of Gaussian and Kaiser windows respectively. The paper has also shown that the proposed filtering method can be used to achieve 30.28 dB improved ripple ratio compared to Kaiser filtering method to eliminate noise from audio signal.

References

[1] Hrishi Rakshit and Muhammad Ahsan Ullah "A Comparative Study on Window Functions for Designing Efficient FIR Filter". In Proceedings of the IEEE 9th International Forum on Strategic Technology (IFOST), ISBN: 978-1-4799-6060-6 DOI: 10.1109/IFOST.2014.6991079 pp 91-96.

[2] Oppenheim, A.V., and R.W. Schafer. Discrete-Time Signal Processing. Upper Saddle River, NJ: Prentice-Hall, 1999, pp. 468-471..

[3] Md abdus Samad "A Novel Window Function Yielding Suppressed Main-lobe Width and Minimum Side-lobe Peak" International Journal of Computer Science, Engineering and Information technology (IJCSEIT), Vol 2, No 2, April 2012.

[4] Emmanuel C. Ifeacher and Barrie W. Jervis "Digital Signal Processing" second edition, Pearson Education 2008.

[5] Roberts, Richard A., and C.T. Mullis. Digital Signal Processing. Reading, MA: Addison-Wesley, 1987, pp. 135-136.

[6] Harris, F.J. "On the Use of Windows for Harmonic Analysis with the Discrete Fourier Transform." Proceedings of the IEEE. Vol. 66, No. 1 (January 1978).

[7] Kaiser, J.; Schafer, R. (1980). "On the use of the I0-sinh window for spectrum analysis". IEEE Transactions on Acoustics, Speech, and Signal Processing 28: 105.

[8] Selected Papers in Digital Signal Processing II, IEEE Press, New York, 1975.

[9] P. Rao, Audio Signal Processing, Chapter in Speech, Audio, Image and Bio-medical Signal Processing using Neural Network, (Eds.)Bhanu Prasad and S.R. Mahadeva Prasanna, Springer –Verlag, 2007.

[10] Md. Sipon Miah, M. Mahbubur Rahman, T.K. Godder, Bikash Chandra Singh and M. Tania Parvin, 'Performance Comparisons of AWGN Flat Fading and Frequency Selective Fading for Wireless Communication System using 4QPSK',International Journal of Computer and Information Technology (IJCIT), ISSN 2078-5828(PRINT), ISSN 2218-5224(ONLINE),Vol.01, Issue 02.

Independent Component Analysis for EOG artifacts minimization of EEG signals using kurtosis as a threshold

Kazi Aminul Islam
Department of Electrical Engineering
Lamar University
Beaumont, TX, USA
russelkazi@yahoo.com

Gleb V. Tcheslavski
Department of Electrical Engineering
Lamar University
Beaumont, TX, USA
gt.lamar@gmail.com

***Abstract*—Brain electrical activity commonly represented by the Electroencephalogram (EEG), due to its miniscule amplitude (on the order of a hundred microvolts), is often contaminated with various artifacts. Independent Component Analysis (ICA) may be a useful technique to minimize the artifacts prior analyzing the original neural signal. In this paper, we used kurtosis to determine the threshold to separate the artifacts-affected ICA components from the unaffected components. Kurtosis may represent how peaked or how flat the artifacts that affect a signal are compared to the normal behavior of the original signal. To select the threshold value of the kurtosis, two statistical principles have been used: namely, the Z-score and the confidence interval. Our intention was to avoid a manual technique to determine the affected ICA components and, instead, to explore an automatic method based on the kurtosis value. Based on the observed results, we may conclude that the present technique may be used for EOG artifacts minimization.**

Keywords— EEG, Independent Component Analysis, Kurtosis, EOG

I. INTRODUCTION

Electroencephalogram (EEG) signals represent neural activities of human brain. EEG is important for many medical applications, such as in studies of epilepsy, trauma, and biofeedback. EEG signal is sensitive to different artifacts, such as ocular, cardiac, muscle, electrode, power line noise, and external device artifacts. To extract the original neural signal, these artifacts should be minimized significantly. Independent Component Analysis (ICA) may be an important tool to do so. Our goal is to consider the most damaging artifacts - the ocular artifacts originating from the muscular activity of eyes. The simplest and widely used method to minimize them is discarding the portions of EEG recording deemed as artifacts, based on exceeding a pre-determined threshold [1].

The EEG data can be viewed as a set of signals at the electrode sites that are mixtures of brain and artifact information. Blind separation methods (BSS) reduce mixture of neural and non-neural variables to components such that they are in some way independent of each other [2].

Independent Component Analysis (ICA) may work better than other methods available for separating the independent components. In many practical uncorrelated situations the signals would not be independent and easy to separate. So, the uncorrelated property is not enough to separate artifacts. This is the reason that principal component analysis (PCA) or factor analysis cannot separate such signals. On the other hand, the Independent Component Analysis (ICA) provides a method for artifacts removal where an accurate model of the process that generates the artifacts is not needed. That is why ICA is a promising technique for artifact identification and removal. The artifacts are usually independent from the rest of the signal, and this requirement of the model is reasonably well fulfilled [1].

Kurtosis is simple and important in ICA and blind source separation. The fourth order statistics called the kurtosis is usually employed, due to its useful properties not shared by the fourth central moment. Kurtosis is often used as a quantitative measure of the non-Gaussianity of a random signal. It can be used as a simple measure of non-Gaussianity if the signals to be compared are of the same type, either sub-Gaussian or super-Gaussian [1].

Joyce, Gorodnitsky and Kutas proposed a method where the artifact components have to identify manually to flag for rejection [2]. Javidi and Mandic proposed a model to identify the artifactual component with the kurtosis value as a threshold [3]. In this paper, an automatic procedure to identify and mitigate the artifact components will be attempted.

II. EEG RECORDING AND PREPROCESSING

EEG signal data used in this paper were recorded in Advanced DSP laboratory of Electrical Engineering department of Lamar University. Recording were performed and pre-processed using Advanced Neuro Technology's (ANT, Netherlands) EEG acquisition system. A 32-channel recording EEG device was used in which 32 electrodes were situated according to the International 10-20 System.

Due to their subtle amplitude, EEG data are often contaminated by different noise sources. This is the primary reason for preprocessing the EEG signals first. DC offsets are often present in EEG signals. To minimize such offset a built-in Matlab 'detrend' function was used in this research. Spatial filtering is a technique that decreases surface currents of the recorded EEG signal generated by neighboring channels.

978-1-4673-9257-0/15/$31.00 ©2015 IEEE

Common Average Reference (CAR) spatial filter for each electrode was applied by subtracting the average value of all electrode signals from the current electrode signal at every time instance. After that, Independent Component Analysis algorithm is applied.

The aim of present report is to reduce EOG signal in EEG. Eye-blink artifacts affect – to some extend – most of EEG channels. However, frontal channels are most influenced by EOG; therefore, EEG recordings at the Fp_2 channel were selected for illustration.

III. Methods

A. Independent Component Analysis (ICA)

Independent component analysis (ICA) is a method that determines primary factors or components from the multivariate or multidimensional statistical data [1]. Let assume that the source signal $S_i(t)$ contains m variables and T observations. The observed signal $Y_i(t)$ is a linear combination of the source signal and a mixing matrix W [1]:

$$Y_i(t) = \sum_j W_{ij} * S_i(t) \tag{1}$$

Un-mixing EEG data into components can be achieved through the following linear rotation [2]:

$$S = W^{-1} * X \tag{2}$$

Equation (2) indicates that the EEG data X is rotated by the un-mixing matrix W^{-1} to arrive at the components of S. We observe that all quantities in (2) are matrices [2]. Here, 'fastica' matlab toolbox will be used to identify the independent components.

B. Kurtosis

Kurtosis is defined as the standardized fourth central moment [4]:

$$k = \frac{E\left\{(x-m)^4\right\}}{E\left\{(x-m)^2\right\}^2} = \frac{\mu_4}{\sigma^4} \tag{3}$$

Here, E is the expectation operator, m is the mean, and σ is standard deviation [4].

For the normal distribution, EEG signal has a kurtosis value of 3. That is why k-3 [4] is often used so that reference normal distribution has a kurtosis of zero. Kurtosis is defined in the zero-mean case by the equation [1]:

$$kurt(x) = E\{x^4\} - 3[E\{x^2\}]^2 \tag{4}$$

The normalized kurtosis is [1]:

$$\bar{k}(x) = \frac{E\{x^4\}}{[E\{x^2\}]^2} - 3 \tag{5}$$

Built in Matlab function 'Kurtosis' will be used to determine the kurtosis value.

C. Z-scores

Standard deviation of a set of data expresses the dispersion of the scores around their mean. Assume that we consider a set of N scores, each denoted as Y_n, whose mean equals M and with a standard deviation $\hat{S}$ that can be evaluated as [5]:

$$\hat{S} = \sqrt{\frac{\sum (Y_n - M)^2}{N-1}} \tag{6}$$

To normalize a set of data using the standard deviation, each data entry is divided by the standard deviation of this set. The mean of the scores is subtracted from each score prior to dividing by the standard deviation. This normalization is known as Z-scores. Formally, a set of N scores, each of which denoted as Y_n, and with the mean M and standard deviation $\hat{S}$, can be transformed in Z-scores as [5]:

$$Z_n = \frac{Y_n - M}{\hat{S}} \tag{7}$$

It can be shown that a set of Z-score has a mean of zero and a standard deviation of one. Therefore, Z-scores constitute a unit-free measure that can be used to compare observations of different units [5].

D. Confidence Interval

A confidence interval is estimated from a given set of sample data. Confidence interval gives an estimated range of values that may include an unknown population parameter. The confidence interval (CI) is expressed as two numbers known as the confidence limits with the range in between. This range carries value of the measured variable in the population with a certain level of confidence. In medical research the confidence level is usually set to 95%. As a result it is named as "95% confidence interval". Thus, the 95% Confidence Interval is defined as a range of values for a variable of interest constructed so that this range may have a 95% probability of including the true value of the variable. It can be also expressed as it may be 95% certain that the value is somewhere inside a 95% confidence interval [6].

For N observations, Confidence can be estimated from the following equations:

For $N \leq 30$, Confidence interval (C.I.) will be [8]:

$$C.I. = \bar{x} \pm \frac{s}{\sqrt{N}} \times t_{N-1} \tag{8}$$

For $N > 30$, Confidence interval (C.I.) will be [8]:

$$C.I. = \bar{x} \pm \frac{s}{\sqrt{N}} \times Z_{N-1} \tag{9}$$

Here $\bar{x}$ is the sample mean, s is the sample standard deviation, and (N-1) is the number of degrees of freedom. At

95% significance level, t_{N-1} = 2.201 for $N \leq 30$. At 95% significance level, Z_{N-1} = 1.96 for N>30.

IV. METHOD FOR ARTIFACTUAL COMPONENT DETECTION

ICA algorithm separates the EEG signals into its original sources as independent components (ICs). After that artifact sources are identified and removed. In semi-automatic and automatic artifact removal methodologies, several classifications (markers) based on the statistical characteristics of the ICs are considered that allow for the detection of artifacts in the contaminated EEG. Then these are compared against threshold values that determine the rejection of particular components. In these methods, the IC kurtosis has been utilized to identify and minimize those artifacts. Artifact-free EEG typically have a near-zero kurtosis value, which indicates a possible Gaussian distribution. With artifacts, such as EOG, EEG exhibits a peaked distribution with a highly positive kurtosis value. This method has been used as the main concept in defining classifications based on the fourth order moment. Using this method, we aim to extract artifacts as independent sources from the recorded EEG mixture [3].

To detect the Threshold value for kurtosis, two methods have been used.

A. Using Z-scores to determine the threshold of kurtosis value

Kurtosis is positive for peaked activity distributions that may represent EOG artifacts. Kurtosis is negative for 'flat' activity distributions. It may appear that this feature is typical for noise. For finding artifactual ICs (outlier components), these EEG distributions have been normalized with respect to all ICs to zero-mean and unit standard deviation (z-score). To do so, thresholds in terms of number of standard deviations from the mean were applied (usually, thresholds are set at 1.64 according to Barbati et al [7]) If a certain percentage of segments exceeded rejection thresholds the corresponding IC was marked for rejection of the component [7].

B. Using Confidence Interval to determine the threshold of kurtosis value

Kurtosis is used to determine eye blink activity distributions in the IC signal. Kurtosis is zero for Gaussian distribution, positive for the peaked activities (which represents eye blink signals) and negative for the flat distributions. So, the upper bound of the 95% CI of the mean is used as the threshold. All the ICs having Kurtosis higher than the upper limit of CI are supposed to be blink artifacts and are marked for de-noising [8].

After evaluating confidence interval of the kurtosis of IC components, the upper limit of confidence interval has been selected as the threshold value. Therefore, any value exceeding the upper limit of confidence interval is marked as a threshold for artifactual components. Next, the identified artifactual components were removed by setting them to zero. After that, signals were reconstructed by multiplying with the mixing matrix W [2].

V. RESULTS

Table 1 illustrates Z-scores of kurtosis value for different ICs for sample EEG. If any component Z-score exceeds 1.64 on magnitude (the threshold), we consider that component as representing an EOG artifact and indicate for rejection.

Table 1 Z-score of kurtosis value for different Independent Components for sample EEG data

Independent Components	**Independent Components Properties**		
	Kurtosis Value	***Z-Score***	***Comments***
IC-1	10.4612	0.851	
IC-2	14.985	2.231	EOG effects
IC-3	11.2541	1.093	
IC-4	16.097	2.571	EOG effects
IC-5	9.0375	0.417	
IC-6	10.0066	0.712	
IC-7	8.6133	0.287	
IC-8	8.981	0.399	
IC-9	9.9804	0.704	
IC-10	12.1592	1.369	
IC-11	8.7642	0.333	
IC-12	8.8146	0.349	
IC-13	7.3491	-0.099	
IC-14	6.6133	-0.323	
IC-15	5.9161	-0.536	
IC-16	6.8611	-0.247	
IC-17	10.4211	0.839	
IC-18	8.8412	0.357	
IC-19	7.0169	-0.1999	
IC-20	5.5034	-0.662	
IC-21	5.7182	-0.596	
IC-22	5.4632	-0.674	
IC-23	6.7481	-0.282	
IC-24	4.8235	-0.869	
IC-25	4.6006	-0.937	
IC-26	4.4669	-0.978	
IC-27	4.601	-0.937	
IC-28	3.848	-1.167	
IC-29	4.2358	-1.049	
IC-30	2.6864	-1.521	
IC-31	2.9654	-1.436	

We observe in Table 1 that the second and fourth independent components z-score value are 2.231 and 2.571. So, we assume that this component may contain large EOG artifacts and, therefore, is a candidate for removal.

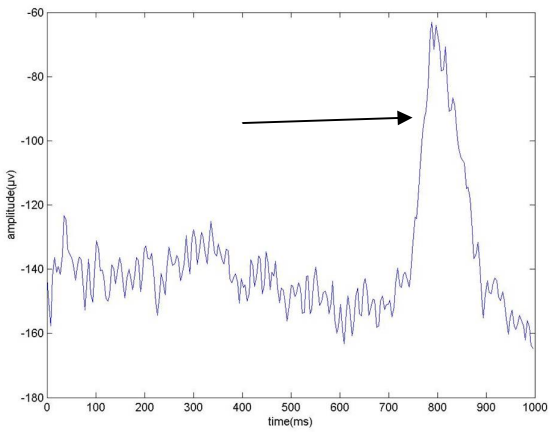

Figure 1: EEG signal of channel Fp_2before removing eye blinks; the arrow indicates the location of eye blink.

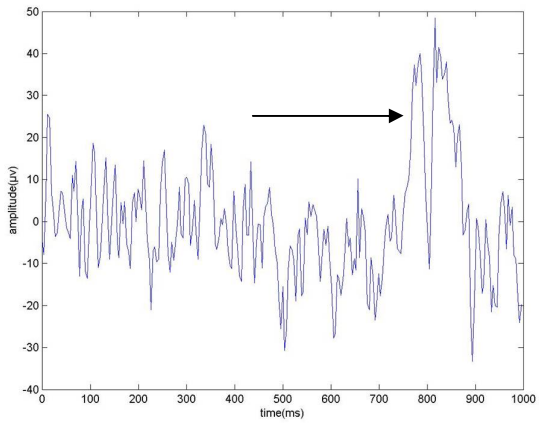

Figure 2: EEG signal of channel Fp_2 after removing eye blinks using Z-score; the arrow indicates the location of eye blink.

An eye blink artifact is evident (indicated by an arrow) in Figure 1 around 700 ms to 900 ms. On the other hand, after canceling the artifactual component (the arrow in Figure 2), it can be seen that EOG artifact was minimized. Perhaps, the actual EEG signals between 0 ms and 700 ms may be analyzed more easily after cancelling the eye blink.

Confidence interval calculation:
From the present EEG data, the following quantities were evaluated:
Sample mean = 7.672;
Standard deviation = 3.277;
The confidence interval: 7.672± 1.153;
Upper confidence level: 8.83;
Lower confidence level: 6.52;
The threshold = 8.83.

Table 2 illustrates different ICs kurtosis values with the upper limit of confidence interval to determine the EOG components. If the kurtosis value exceeds 8.83, the corresponding component is considered as an EOG component.

Table 2 Results of analyzing of kurtosis value to determine the artifact components for different Independent Components for sample EEG data.

Independent Components	**Independent Components Properties**		
	Kurtosis Value	***Artifact Detection (C.I.>8.83)***	***Comments***
IC-1	10.4612	>8.83	EOG effect
IC-2	14.985	>8.83	EOG effect
IC-3	11.2541	>8.83	EOG effect
IC-4	16.097	>8.83	EOG effect
IC-5	9.0375	>8.83	EOG effect
IC-6	10.0066	>8.83	EOG effect
IC-7	8.6133		
IC-8	8.981	>8.83	EOG effect
IC-9	9.9804	>8.83	EOG effect
IC-10	12.1592	>8.83	EOG effect
IC-11	8.7642		
IC-12	8.8146		
IC-13	7.3491		
IC-14	6.6133		
IC-15	5.9161		
IC-16	6.8611		
IC-17	10.4211	>8.83	EOG effect
IC-18	8.8412	>8.83	EOG effect
IC-19	7.0169		
IC-20	5.5034		
IC-21	5.7182		
IC-22	5.4632		
IC-23	6.7481		
IC-24	4.8235		
IC-25	4.6006		
IC-26	4.4669		
IC-27	4.601		
IC-28	3.848		
IC-29	4.2358		
IC-30	2.6864		
IC-31	2.9654		

Based on the upper limit of the confidence interval, the threshold value selected for EOG artifacts is 8.83. If any component's kurtosis value is greater than the threshold, it is marked as an artifact component. We observe in Table 2 that components 1-6, 8-10, 17 and 18 have kurtosis value exceeding the upper limit of the confidence interval that is 8.83. Therefore, these components may be contaminated with EOG artifacts and are candidates for removal.

Figure 3 illustrate the outcome of the artifact detection method using confidence interval.

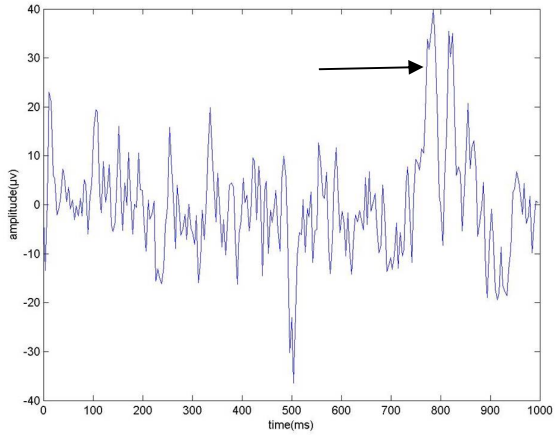

Figure 3: EEG signal of channel Fp_2 after removing eye blinks using confidence interval; the arrow indicates the location of eye blink.

We observe in Figure 1 an EOG artifact indicated by the arrow. It is seen in Figure 3 that after cancelling the artifactual components, EOG signal was considerably reduced and the source EEG was recovered.

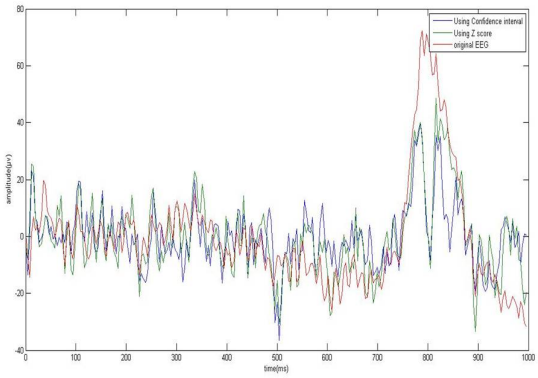

Figure 4: Comparison of EEG signal of channel Fp_2 before removing eye blinks and after removing eye blinks using Z-score and Confidence Interval.

For the comparison, Figure 4 illustrates EEG fragments for Fp_2 before and after EOG removal using Z-score and Confidence interval. We observe that only the artifact was affected by the proposed technique. This observation verifies the validity of the proposed technique.

VI. Discussion

In this paper, an automatic EOG artifact minimization technique was discussed. First the EEG signals were preprocessed. Next, each component of EEG signal was separated using the ICA algorithm. Then, using the z-score and confidence interval methods, kurtosis thresholds were determined. After that, EOG artifact components were detected and cancelled.

These EOG artifacts reduction methods – with an automatic kurtosis threshold detection based on Z-score and confident interval - were both sufficiently effective. The sample EEG signal originally contained a large eye blink artifact, as may be observed in Figure 1. The recovered signals, as might be seen, this EOG artifact was considerably reduced using the techniques. We also may conclude that more ICs were associated to EOG artifacts, while using the confidence interval method.

The traditional approach of manual inspection of each independent component to identify the artifacts is time consuming. Using the automated procedures to identify the artifactual components evaluated in the present report may lead to a considerable time saving and improved accuracy while analyzing EEG.

VII. Conclusion and Future Works

In this paper, two robust and automated methods to detect artifactual components based on kurtosis threshold value were evaluated. However, this method utilized cancelling of the entire independent component that was deemed as artifactual. As a result, some important information may be compromised while minimizing the EOG artifacts. In future, we should consider the part of IC to be modified or cancelled to remove the artifact rather than cancelling the entire component.

References

[1] Aapo Hyvärinen , Juha Karhunen and Erkki Oja *Independent Component Analysis,* John Wiley & Sons, Incorporation , 2001.

[2] Carrie A. Joyce, Irina F. Gorodnitsky, and Marta Kutas "Automatic removal of eye movement and blink artifacts from EEG data using blind component separation" *Society for Psychophysiological Research* P 313–325, 2004.

[3] Soroush Javidi and Danilo P. Mandic "Kurtosis based blind source Extraction of complex noncircular signals with application in EEG artifact removal" Technical Report: TR-ICU-BSE-1337/09-10 Updated: 26 September 2010.

[4] Lawrence T. Decarlo "On the meaning and use of Kurtosis "*The American Psychological Association, Inc.* p-292-307 1997.

[5] Herv´e Abdi *Normalizing data: Encyclopedia of Research Design,* In Neil Salkind (Ed.), Thousand Oaks, CA: Sage. 2010.

[6] M.D. Abdelhamid Attia "Why should researchers report the confidence interval in modern research?" *Middle East Fertility Society Journal* Vol. 10, No. 1, 2005.

[7] Giulia Barbati, Camillo Porcaro, Filippo Zappasodi, Paolo Maria Rossini and Franca Tecchio, "Optimization of an independent component analysis approach for artifact identification and removal in magneto-

encephalographic signals" *Clinical Neurophysiology* 115 (2004) 1220–1232 Accepted 15 December 2003.

[8] Ruhi Mahajan and Bashir I. Morshed "Unsupervised eye blink artifact denoising of EEG data with modified Multiscale Sample Entropy, Kurtosis, and Wavelet ICA" *IEEE journal of Biomedical and Health Informatics*, Vol. 19, No. 1, P 158-165, January 2015.

Automatic Detection of Optic Disc in Fundus Images by Curve Operator

M. Nahid Reza
Department of Electrical and Electronic Engineering
Hamdard University Bangladesh
Narayanganj, Bangladesh
E-mail: nahidreza2k9eee@gmail.com

Mohiuddin Ahmad
Department of Electrical and Electronic Engineering
Khulna University of Engineering & Technology
Khulna, Bangladesh
E-mail: mohiuddin.ahmad@gmail.com

***Abstract*—This paper proposes a method to detect optic disk (OD) automatically in fundus image of retina without using background mask and blood vessels. Based on the properties of OD, an idea of curve operator is presented here. This method has been implemented on three public databases and the promising results are obtained. The experimental results indicate that this proposed method of automatic OD detection has good accuracy and is also computationally efficient.**

***Keywords*—Biomedical imaging, retinal image processing, optic disk detection, bilateral filtering, curve operator.**

I. Introduction

In modern ophthalmology, detection of optic disk is a very important step for retinal image analysis and one of the main feature of extracting the anatomical structure of the retina as illustrated in Fig. 1(a). Optic disk can be defined as the circular brighter region in retinal fundus image where blood vessels converge and optic nerve is formed. OD detection is very indispensable for the computer aided diagnosis of different eye diseases such as glaucoma detection and diabetic retinopathy [1]. Fig. 1(b) represents the fundus image with retinal lesion.

Many optic disc detection methods have been proposed earlier. In [2]–[4], image brightness based methods are proposed. In these methods it is expected that the OD usually resembles according to the brightest pixels within fundus images. In [5] and [6], image variation based methods are proposed based on the statement that the OD has a high image variation due to the retinal blood vessels. But the sensitivity of these two types of methods is highly dependent on retinal lesion, illumination and exudates. Furthermore the vasculature geometry based methods [7]–[9] are more accepting to retinal lesion and imaging artifacts. But in this technique, retinal blood vessels are needed to be extracted initially which is a nontrivial task and requires long processing time. From [5], [10] the dependency between detection accuracy and processing time can be referred. In [11] OD detection is done as a part of the whole work and adaptive morphological filtering method is considered. Also in this work average computational cost is analyzed. But the work presented in this paper is the inspiration of the work [12] where a line operator with 21 orientation is used to detect OD in fundus image. Also in [12] image background segmentation mask is consumed and image intensity variation is analyzed.

978-1-4673-9257-0/15/$31.00 ©2015 IEEE

This paper proposes a method named as curve operator that is used to detect the optic disk in fundus image automatically. Curve operator is divided in two segments i.e. line and curve segment. This operator is also oriented with specific angles and pixel length. With the analysis of pixel intensity variation four points are predicted and furthermore validated to detect OD region. No background segmentation is used in this technique. Color fundus images are used from three public databases.

The rest of the paper is organized as follows. In section II, idea of curve orientation with image prepossessing and OD detection method are explained. Image database description and experimental results are exposed as well as discussed in section III. Finally the work is concluded in section IV.

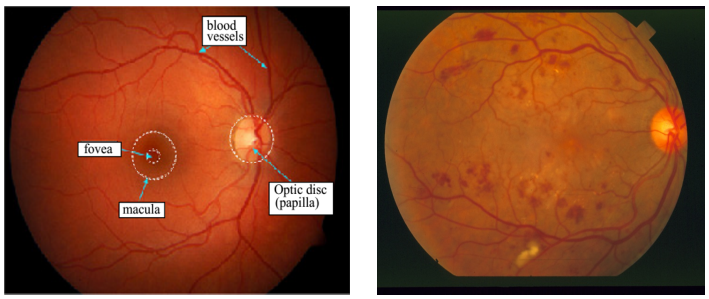

(a) Healthy fundus image with structural element (Obtained from [13])

(b) Fundus image with retinal lesion (Obtained from STARE database)

Fig. 1. Illustration of retinal fundus images.

II. Proposed Method

A. Fundus Image Preprocessing

In proposed method, the circular brightness structure of fundus image is considered and LAB color scape gives the best result for OD detection [14]. So source image color space is converted in LAB color space and only lightness channel is considered. Smoothing of converted color spaced retinal image is performed to enhance the circular brightness structure which is linked with the OD region. So for enhancement, bilateral smoothing filter [15] is used because it has the advantage of combining geometric closeness and photometric similarity as shown in (1). Also in (1), the normalization factor $k(x)$ can be expressed as (2).

$$h(x) = k^{-1}(x) \int_{-\infty}^{\infty} \int_{-\infty}^{\infty} f(\zeta) c(\zeta, x) s(f(\zeta); f(x)) d\zeta \quad (1)$$

$$k(x) = \int_{-\infty}^{\infty} \int_{-\infty}^{\infty} c(\zeta, x) s(f(\zeta); f(x)) d\zeta \quad (2)$$

Furthermore in (1) and (2), $f(x)$ indicates the converted color spaced retinal image. $c(\zeta, x)$ means the geometric closeness and $s(f(\zeta); f(x))$ measures the photometric similarity among the neighborhood pixel ζ and the center of neighborhood x . Both $c(\zeta, x)$ and $s(f(\zeta); f(x))$ are set by Gaussian functions. As conferring in [15], from the two Gaussian functions the geometric spread σ_d and the photometric spread σ_r are set at 10 and 1 . But in this work, they are set as 10 and 100 respectively. Also the number of neighbors pixel is taken 10 pixels for moderate filtered image. Considering the fundus image represented in Fig. 1(b), Fig. 2(a) shows LAB color space with only the lightness channel and Fig. 2(b) shows the corresponding filtered image.

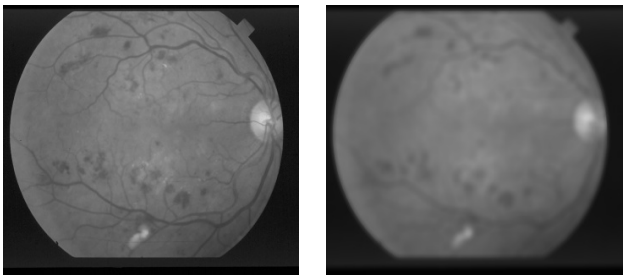

(a) Converted retinal image in LAB color space with lightness channel only

(b) Bilateral filtered image

Fig. 2. Fundus image preprocessing

B. Curve Operator Method

The optic disk region has similar brightness in the fundus image. This brightness has also gradient color from edge to center of fundus image. According to this characteristics a curve operator is proposed as shown in Fig. 3. For a pixel $P(x, y)$, the curve operator first determines line segments, $L_i = \{L_1, L_2, ..., L_l\}$ with specific length, l (i.e. number of pixels) with n orientation centered at $P(x, y)$. Curve segment, $C_j = \{C_1, C_2, ..., C_{r/2}\}$ is determined next as tangent to the orthogonal of the line segment and represented in (3). Here r is the radius of optic disk in retinal image.

$$C_{j_y} = y + \sqrt{(L_{l_x} - x)^2 + (L_{l_y} - y)^2 - (C_{j_x} - x)^2} \quad (3)$$

where $x - (r/2) \leq C_{j_x} \leq x + (r/2)$.

Chord of the curve is taken as 50% of radius of optic disk (i.e. $r/2$) with center at the middle of line segment i.e. $l/2$. Finally curve operator can be expressed as set of point of line and curve segment i.e. $COP_n = \{L_i, C_j\}$, where n is the operator orientation. A vector of intensity of each pixel, is obtained using this curve operator with n orientation. Average value is calculated with each element of vector at specified orientation which represents the curve operated pixel and is expressed as (4).

$$I_n(x, y) = (\sum_{i=1,j=1}^{i=l,j=r/2} COP_n(i, j))/(l + \frac{r}{2}) \quad (4)$$

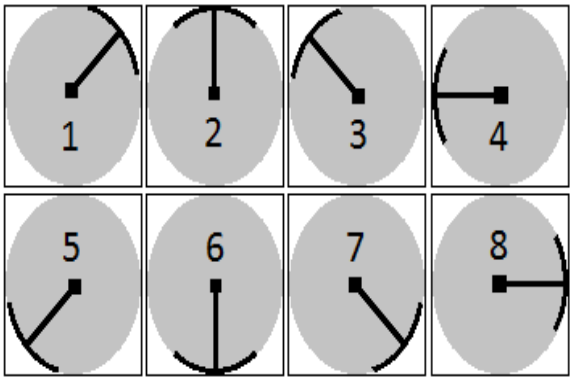

Fig. 3. Illustration of proposed curve operator in 8 orientation.

C. Optic Disk Detection

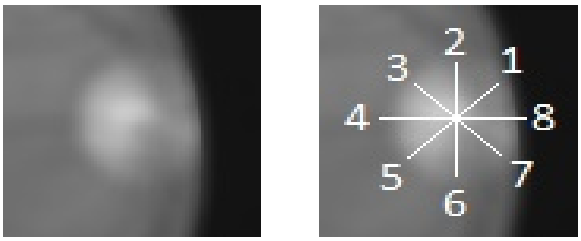

(a) (b)

Fig. 4. (a) Filtered optic disk. (b) Representation of line orientation.

From the Fig. 2(b) and Fig. 4(a) it can be seen that, inside optic disk region color intensity is not constant but it has gradient property. Color intensity is reduced from left edge (near to retinal image center) to right edge of OD or vice versa. In this paper 8 orientation of curve operator as shown in Fig. 4(b) is considered. Because curve operator with more orientation has less effect on the gradient property of OD. The length of line segment is used as $l = r/5$ as referred to [16]. According to the proposed method, 8 operated pixel intensities $(I_n(x, y); n = 1, 2, ..., 8)$ are calculated for a pixel $P(x, y)$. Oriented pixel intensity has a specific pattern with upward and downward variation. This pattern can be used to detect OD. The orientation with the upward or downward variation is generally indiscriminate for the pixels which are far away from OD in retinal image. But for those pixels which are around the OD, the image variation has upward or downward characteristics with highest and lowest intensity value. The variation of oriented pixel intensity is shown in Fig. 5. Characteristics of the curve as shown in Fig. 5(b) are defined as upward and in Fig. 5(d) as downward variation.

Two oriented images are created according to upward and downward variation and shown in Fig. 6(a) and Fig. 6(b) respectively. In case of upward variation two points are

(a) Fundus image with pixel marker

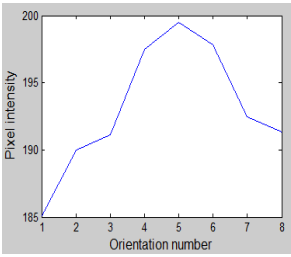

(b) Upward variation of selected pixel

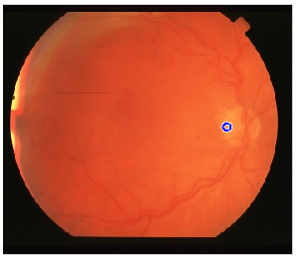

(c) Fundus image with pixel marker

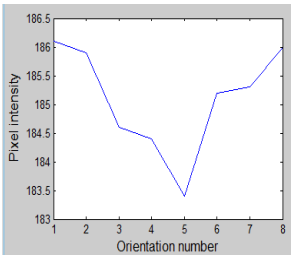

(d) Downward variation of selected pixel

Fig. 5. Representation of intensity variation for the marked pixel.

located considering highest and lowest pixel value respectively. Similarly two points are located for downward variation. These four points are predicted points for OD region and shown in Fig. 7(a). In Fig. 7(a) blue point is the highest and red point is the lowest value for upward variation as well as green point is the highest and white point is the lowest value for downward variation respectively.

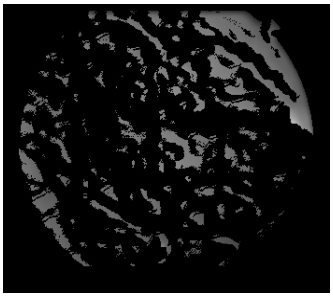

(a) Created image considering upward variation

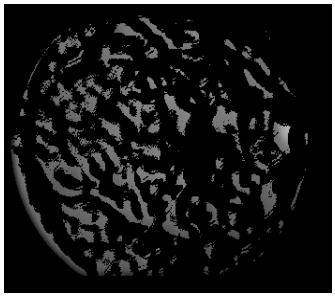

(b) Created image considering downward variation

Fig. 6. Image representation of variation in curve orientation.

To validate these points, four regions of interest (ROI) centering the four predicted points are cropped as shown in Fig. 7(b). After that correlation is calculated between cropped oriented images and correlation mask using (5), where R denotes resultant image, M mask and I cropped oriented image.

$$R(x,y) = \sum_{x',y'} (M(x',y') \cdot I(x+x',y+y')) \qquad (5)$$

Also the correlation mask is shown at inset in Fig. 8(a) on left top corner. Among these four correlation values, the point corresponds to maximum value is validated as the pixel in OD region. In this figure final detected point is shown as the small circle and the larger circle symbolizes the entire OD region. Finally Fig. 8(b) shows the result as well as the selection of point for OD region.

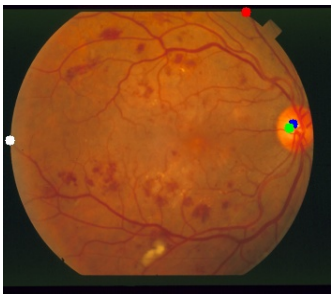

(a) Four predicted points

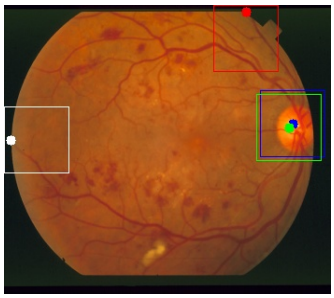

(b) Cropping region selection based on four predicted points

Fig. 7. Prediction and cropping region selection

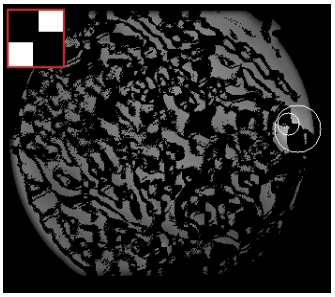

(a) Point verification using correlation mask

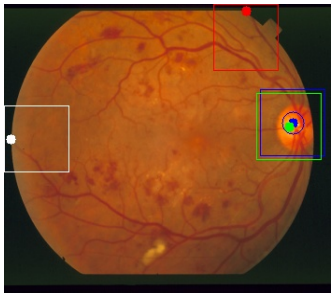

(b) Final point setection

Fig. 8. Verification and finalization of OD region

III. Results & Discussion

A. Fundus Image Database Acquisition

In this paper, three public fundus image databases are used for evaluating the proposed method. Among them DIARETDB0 [13] and DIARETDB1 [17] are created for the diagnosis of type 1 diabetes. DIARETDB0 database contains 130 color fundus images among them there are 20 images of healthy retina and 110 contain the signs of diabetic retinopathy. Also the DIARETDB1 database is being made up of 89 color fundus images in which 84 images are compromised with mild non proliferative signs of the diabetic retinopathy and 5 are considered as normal which do not contain any signs of the diabetic retinopathy. Referring from [13] and [17], the size of each image of both databases is 1500×1152 and were captured at few 50 degree field of view (FOV) with digital fundus cameras with unknown camera settings (flash intensity, shutter speed, aperture, gain). Also these images contain an unknown amount of imaging noise and optical aberrations (dispersion, transverse and lateral chromatic, spherical, field curvature, coma, astigmatism, distortion), and unknown accuracy of photometric information (color or intensity).

The third database is STARE (Structured Analysis of the Retina) project's dataset [9], [18]. In this database the number

of normal retinal image is 31 and that of pathological retina is 50. It was formed for benchmarking OD detection and is much more challenging compared with the other two databases.

B. Experimental Results

For each retinal fundus image within the three databases, firstly boundary pixels are manually labeled with a circle. The OD region is estimated as located correctly, if the validated point lies within the fitted boundary circle. Proposed method explained in this paper is implemented individually on the three public databases as mentioned before. Some examples of OD detection using the proposed curve operator technique is presented in Fig. 9. The set of six figures is separately acquired from three mentioned databases. Among them some image as 2nd in Fig. 9(a) has retinal lesion. Some as corresponds to healthy retina as 4th of Fig. 9(b). 5th in Fig. 9(c) shows retinal exudate. The significance of each color is described in subsection II-C. The circle represents the final validated point as well as the optic disk detection.

TABLE I. PERFORMANCE COMPARISON OF THE OD DETECTION METHODS ON DIARETDB1 DATABASE

Methods	Accuracy
Walter et al. [5]	92.13%
Lupascu et al. [19]	86.51%
Welfer et al. [11]	97.7%
Kande et al. [10]	88.76%
Proposed method	**94.38%**

TABLE II. PERFORMANCE COMPARISON OF THE OD DETECTION METHODS ON STARE DATABASE

Methods	Accuracy
Sinthanayothina et al. [6]	42.00%
Walter et al. [3]	58.00%
Zhu et al. [20]	93.80%
Lu et al. [12]	96.30%
Hoover et al. [9]	89.00%
Proposed method	**87.65%**

TABLE III. AVERAGE PROCESSING TIME PER IMAGE FOR DIARETDB1 DATABASE

Methods	Time (Sec.)
Welfer et al. [11]	7.89
Kande et al. [10]	72.84
Walter et al. [5]	117.63
Proposed method	**6.13**

OD detection accuracy is calculated as the ratio of number of successful OD detection image and total number of fundus image. According to the experimental results, the accuracy outcomes of STARE, DIARETDB0 and DIARETDB1 are 87.65%, 95.38% and 94.38% respectively. Performance comparison of the proposed method with some earlier reported methods is demonstrated in Table I and Table II for DIARETDB1 and STARE database respectively. In Table II, the value of accuracy for [6] is taken from [12].

Besides OD detection accuracy processing time is also deliberated as the performance parameter for the proposed method. For a single color fundus image, total processing time is calculated from the inception of reading image to optic disk detection. Then average time per image is calculated by dividing total processing time with total number of image for individual database. With the curve operator method average time per image is measured as 10.79 sec., 6.13 sec. and 8.39 sec. for DIARETDB0, DIARETDB1 and STARE database respectively. Also the average processing time to detect OD au-

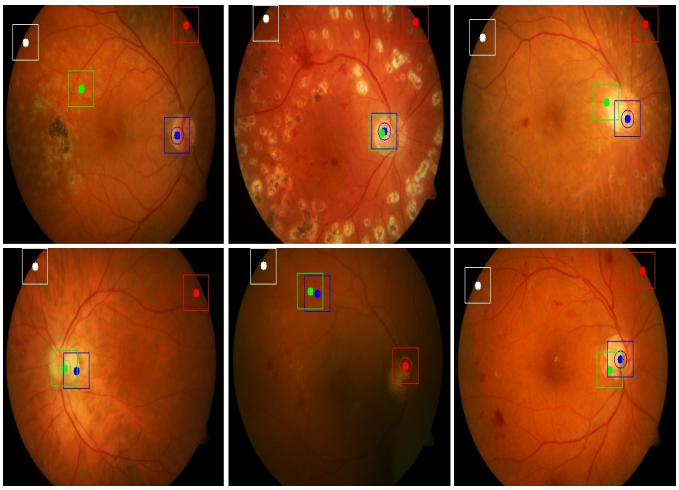

(a) Acquired images from DIARETDB0 databases

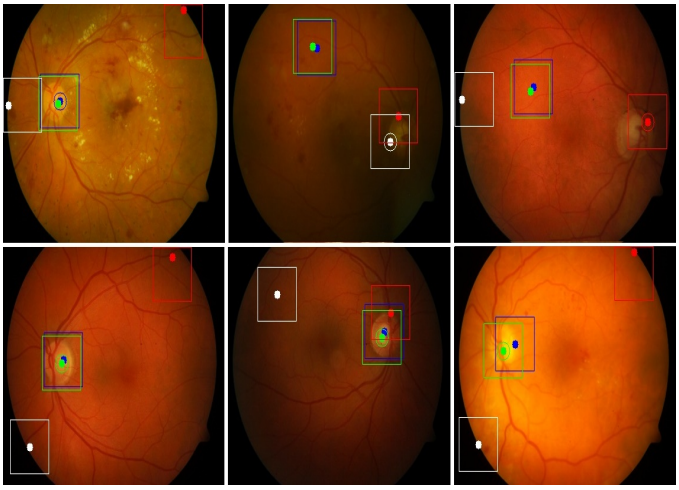

(b) Acquired images from DIARETDB1 databases

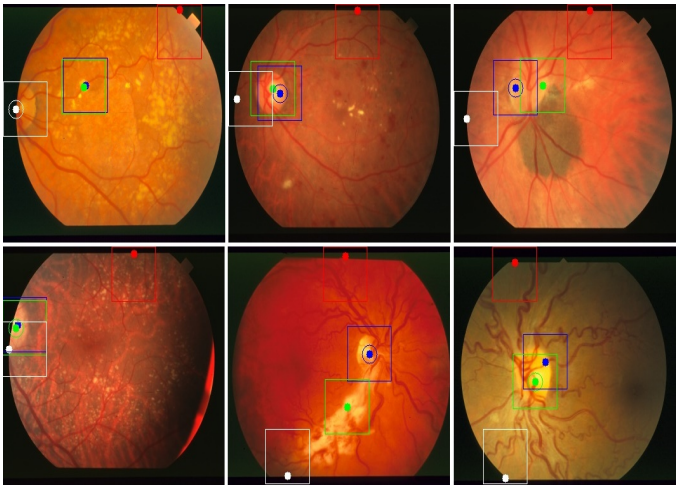

(c) Acquired images from STARE databases

Fig. 9. Illustration of experimental results of OD detection in fundus images using proposed method.

tomatically is compared with other methods for DIARETDB1 database and illustrated in Table III. Here the value of time for [5], [10] is taken from [11].

C. Discussions

From the results it is seen that the proposed method using curve operator gives promising outcomes. It is simple and performs with color fundus image with moderate lesion. From Fig. 9 it is seen that the optic disk is detected accurately though there are a level of noise, retinal lesion and imaging artifacts. This method is autonomous and other algorithms like blood vessel or background segmentation are not necessary which are very time consuming. These algorithms give high accuracy but consume long processing time. But the proposed method gives a balanced result between accuracy and processing time. In [12], 21 orientations are used but in proposed method only 8 orientations are required. Because the use of more than 8 orientations has the same result. Also this low number of orientation contributes on short processing time. Examining Table I and Table III it is seen that the proposed technique has low processing time with moderate OD detection accuracy.

The proposed method has some limitations. In particular, this method evaluates the optic disc in fundus image considering the perception that the optic disc is typically brighter or darker than the surrounding background. So it fails for those images which have a brighter or darker lesion or exudates than the OD region. Also the processing time will be reduced proportionally with image size. Also in experimental results no performance is compared for DIARETDB0 databases for the lack of other accuracy data. To perform overall processing "Intel Duel Core, 2.6 GHz" processor with 2 GB RAM is used as personal computer configuration. Also this work has been implemented in Microsoft visual studio 2010 environment with the help of Intels OpenCV library.

IV. Conclusion

A new method is proposed in this paper to detect the optic disk automatically and correctly in the color fundus images. This method takes the advantages over blood vessels segmentation and image background masking. It is important to notice that the accuracy of OD detection have to cost processing time and the proposed method gives the effective results. In this paper the importance is emphasized on the balance between detection accuracy and processing time. In this work all pixels are considered which degrade OD detection. In future works, concentration will be emphasized on macula detection with improving the accuracy using some filtering methods.

References

[1] K. W. Tobin, E. Chaum, V. P. Govindasamy, and T. P. Karnowski, "Detection of anatomic structures in human retinal imagery," *IEEE Trans. Med. Imag.*, vol. 26, p. 17291739, 2007.

[2] H. Li and O. Chutatape, "Automated feature extraction in color retinal images by a model based approach," *IEEE Trans. Biomed. Eng.*, vol. 51, p. 246254, 2004.

[3] T. Walter and J. C. Klein, "Segmentation of color fundus images of the human retina: Detection of the optic disc and the vascular tree using morphological techniques," in *Proc. Int. Symp. Med. Data Anal.*, 2001, pp. 282–287.

[4] A. Aquino, M. Gegundez-Arias, and D. Marin, "Detecting the optic disc boundary in digital fundus images using morphological, edge detection, and feature extraction techniques," *IEEE Trans. Med. Imag.*, vol. 29, no. 11, pp. 1860–1869, Nov 2010.

[5] T. Walter, J. C. Klein, P. Massin, and A. Erginay, "A contribution of image processing to the diagnosis of diabetic retinopathy - detection of exudates in color fundus images of the human retina," *IEEE Trans. Med. Imag.*, vol. 21, no. 10, pp. 1236–1243, 2002.

[6] C. Sinthanayothina, J. F. Boycea, H. L. Cookb, and T. H. Williamsonb, "Automated localisation of the optic disc, fovea, and retinal blood vessels from digital colour fundus images," *Br. J. Ophthalmol.*, vol. 83, pp. 902–910, 1999.

[7] A. A. H. Abdel-Razik Youssif, A. Z. Ghalwash, and A. A. S. Abdel-Rahman Ghoneim, "Optic disc detection from normalized digital fundus images by means of a vessels' direction matched filter," *IEEE Trans. Med. Imag.*, vol. 27, no. 1, pp. 11–18, Jan 2008.

[8] M. Foracchia, E. Grisan, and A. Ruggeri, "Detection of optic disc in retinal images by means of a geometrical model of vessel structure," *IEEE Trans. Med. Imag.*, vol. 23, no. 10, pp. 1189–1195, Oct 2004.

[9] A. Hoover and M. Goldbaum, "Locating the optic nerve in a retinal image using the fuzzy convergence of the blood vessels," *IEEE Trans. Med. Imag.*, vol. 22, no. 8, pp. 951–958, Aug 2003.

[10] G. B. Kande, P. V. Subbaiah, and T. S. Savithri, "Segmentation of exudates and optic disk in retinal images," in *Proc. Sixth Indian Conf. on Comput. Vision, Graph. Image Process. ICVGIP*, Dec 2008, pp. 535–542.

[11] D. Welfer, J. Scharcanski, C. M. Kitamura, M. M. D. Pizzol, L. W. B. Ludwig, and D. R. Marinho, "Segmentation of the optic disk in color eye fundus images using an adaptive morphological approach," *Computers in Biology and Medicine*, vol. 40, no. 2, pp. 124–137, 2010.

[12] S. Lu and J. H. Lim, "Automatic optic disc detection from retinal images by a line operator," *IEEE Trans. Biomed. Eng.*, vol. 58, no. 1, pp. 88–94, Jan 2011.

[13] T. Kauppi, V. Kalesnykiene, J. K. Kamarainen, L. Lensu, I. Sorri, H. Uusitalo, H. Klviinen, and J. Pietil, "Diaretdb0: Evaluation database and methodology for diabetic retinopathy algorithms," Lappeenranta Univ. Technol., Lappeenranta, Finland, Tech. Rep., 2006.

[14] A. Osareh, M. Mirmehdi, B. Thomas, and R. Markham, "Comparison of colour spaces for optic disc localisation in retinal images," in *Proc. Int. Conf. Pattern Recognit.*, 2002, pp. 743–746.

[15] C. Tomasi and R. Manduchi, "Bilateral filtering for gray and color images," in *Proc. IEEE Int. Conf. Comp. Vis.*, Jan 1998, pp. 839–846.

[16] W. Tasman and E. A. Jaeger, *Duanes ophthalmology*, 15th ed. Baltimore, MD: Lippincott Williams & Wilkins, 2009.

[17] T. Kauppi, V. Kalesnykiene, J. K. Kamarainen, L. Lensu, I. Sorri, H. Uusitalo, H. Klviinen, and J. Pietil, "Diaretdb1: Evaluation database and methodology for diabetic retinopathy algorithms," Lappeenranta Univ. Technol., Lappeenranta, Finland, Tech. Rep., 2007.

[18] (2003, July) Stare project website. [Online]. Available: http://www.ces.clemson.edu/~ahoover/stare

[19] C. A. Lupascu, D. Tegolo, and L. Di Rosa, "Automated detection of optic disc location in retinal images," in *Proc. 21st IEEE Int. Symp. on Comput.-Based Med. Syst. CBMS '08.*, June 2008, pp. 17–22.

[20] X. Zhu and R. Rangayyan, "Detection of the optic disc in images of the retina using the hough transform," in *Proc. 30th Annu. Int. Conf. of the IEEE Eng. in Medicine and Biology Soc. EMBS*, Vancouver, British Columbia, Canada, Aug 2008, pp. 3546–3549.

Alpha Band Dependency of EEG Signal on Different Stimulation of Brain for Human Computer Interaction

Md. Kamrul Hasan*, Nahid Al Mahmud, Md. Shazzad Hossain, and Mohiuddin Ahmad
Department of Electrical and Electronic Engineering (EEE)
Khulna University of Engineering & Technology (KUET)
Khulna-9203, Bangladesh
*E-mail: m.k.hasan@eee.kuet.ac.bd

Abstract—**Brain–computer Interfaces (BCIs) are the communicating bridges between the human brain and a computer which may be implemented on the basis of Steady-state Visual Evoked Potentials (SSVEPs). It is mandatory to improve the stimulation for the betterment of the accuracy of modern BCIs, higher Information Transfer Rate (ITR), desired bandwidth (BW), and Signal to Noise Ratio (SNR) of BCIs. The performance of stimulator depends on many factors such as size and shape of stimulator, frequency of stimulation, luminance, color, and subject attention. Information Transfer Rate (ITR) varies with the change of frequency and size of the visual stimuli. In our research, a Circular Repetitive Visual Stimulator (CRVS) of different diameters (2", 2.5"and 3"), colors (RGB), frequencies (10, 15 and 20 Hz) was used. The raw EEG signal is processed for finding the effect of diverse stimulation on alpha band of EEG signal at diverse condition. From the analysis it is found that, when the size of the stimulator changes from 2" to 2.5", resultant increase in alpha wave is 58.18%. But for a further increase in size from 2.5" to 3", there is a resultant decrease in alpha wave of 45%. Similar result is found for the changes in frequencies and colors.**

Keywords— Electroencephalogram (EEG), Brain-computer Interface (BCI), Steady-state Visual Evoked Potential (SSVEP), Circular Repetitive Visual Stimulator (CRVS), Signal power, Signal energy.

I. INTRODUCTION

In accordance with the concept of modern biomedical engineering, brain–computer interface (BCI) is a direct communication pathway between the brain and an external devices. BCIs are also called mind-machine interface (MMI), direct neural interface (DNI), synthetic telepathy interface (STI) or brain–machine interface (BMI). BCIs are often directed at assisting, augmenting, or repairing human cognitive or sensory-motor functions.

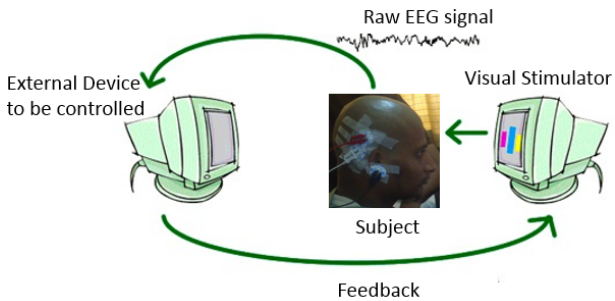

Figure 1. BCI system to communicate with external devices.

A typical BCI system is shown in Figure 1. Various techniques are now available to monitor brain function, e.g., electroencephalography (EEG), magneto-encephalography (ME), functional magnetic resonance imaging (f-MRI), and positron emission tomography (PET). The latter three techniques are technically demanding and expensive. At present, EEG is the optimal choice for BCI implementation [1]-[2]. In comparison with other systems, the VEP-based BCI is considered as a dependent BCI because the generation of the VEP depends on the control of eye movements via the output pathways of cranial nerves and extra-ocular muscles. The EEG reflects the electrical activity of the brain, which can be recorded directly from the scalp in non-invasive way using surface electrodes [3]. EEG measures the electrical potentials generated to the excitatory and inhibitory post-synaptic potentials developed by cell bodies and dendrites of pyramidal neurons [4]-[6] as shown in Figure 2. EEG signals, as one of the biological signals, are in μV range (0.5 to ~ 100μV) at low frequency (0.5 to 30 ~ 40Hz). They are usually referred to as rhythms and are classified into five frequency bands [1] shown in Table I.

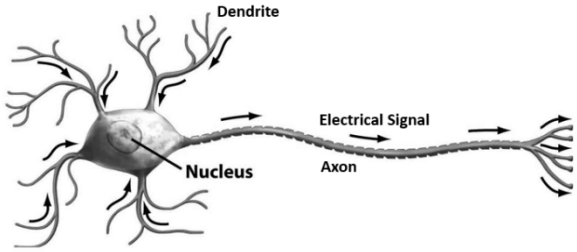

Figure 2. Neuron general structure and generation of electrical signal (EEG Signal) due to external stimulation.

The electrical activity of brain due to visual stimulation is known as the Visual evoked potential (VEP) which may be measured from the scalp of human the brain. The frequency of stimulation of steady-state VEP (SSVEP) and VEP is different in magnitude. For VEP approximately 2 Hz for the stimulator is most commonly used whereas about 6Hz stimuli are used for SSVEP which produce a periodic response called SSVEP. In modern BCI system, SSVEP are most commonly used due to its short-term identification, high SNR for data transmission for wireless BCI [7]-[8]. The extracted EEG signal contains five frequency bands in which Delta waves lie within the range of 1–4 Hz. These waves are prominent during conditions of deep sleep. Theta waves lie within the range of 4–8 Hz. They appear between the states

978-1-4673-9257-0/15/$31.00 ©2015 IEEE

of consciousness and drowsiness. Theta waves have been associated with creative inspiration and deep meditation. Alpha waves lie within the range of 8–13 Hz. These waves indicate both a relaxed awareness state without any attention. A beta wave is the EEG signal with a frequency range of 13–30 Hz. Beta waves are associated with active thinking, active attention, focus on a particular thing, or during solving concrete problems. High-level beta wave resembles a panic state. The frequencies above 30 Hz (mainly 36-44 Hz) correspond to the gamma range. These low amplitude and rarely found waves are used to detect certain brain diseases. They also indicate event-related synchronization (ERS) of the brain [9]-[11]. The bit rates, comfort and safety of SSVEP based BCI depends on the nature, size, shape, frequency and color of CRVS. The selection of SSVEP for the stimulation of brain, it is advisable to consider these essential element of SSVEP-based BCIs [12]. Existing papers focus on general VEP-based BCIs [13] and signal processing algorithms applied to BCIs [12], [14]. This paper contributes to select proper CRVS for the stimuli that have been used for SSVEP-based BCIs.

TABLE I. FREQUENCY BAND, PATTERN AND AMPLITUDE OF EEG SIGNAL

Brain Waves	Pattern of Waves	Voltage and Freq. Range	Subject Condition
Delta (Δ)		10mV, 1-4 Hz	Profound sleep
Theta (θ)		10μV, 4-8 Hz	Light sleep
Alpha (α)		10μV, 8-13 Hz	Relax state
Beta (β)		10-20μV, 13-30 Hz	Activity or thinking state
Gamma (γ)		5-10μV, 36-44 Hz	Abnormal condition

II. PROPOSED ARCHITECTURE

The proposed architecture of this research is described in three blocks as follows in Figure. 3.

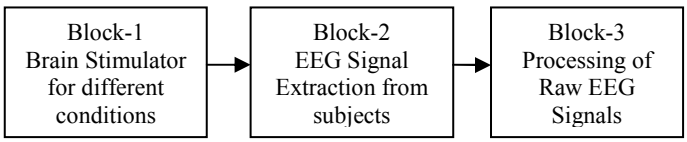

Figure 3. Overall block representation of proposed work.

A. Block-1

In Figure. 4 a typical block diagram of a stimulator is shown in which MUX block is used to select any item among three. Then three MUXed outputs are ANDed to visually stimulate the human brain for the raw EEG extraction. In this stimulation the color, frequency and diameter of a circular repetitive visual stimulator (CRVS) is varied to change the stimulation pattern.

B. Block-2

In this block as shown in Figure.5, raw EEG signal is extracted from the brain using various stimulation patterns as described in block-1. EEG signal for different stimulation patterns in visual stimulator is recorded by the acquisition unit (MP-36) which is further processed in Block-3.

C. Block-3

The raw EEG signals from Block-2 are processed using various software (MATLAB, BIOPAC, and ACQKNOWLEDGE) in accordance with Block-3 as shown in Figure 6. The raw EEG signal is filtered by band pass filter (BPF) to obtain desired EEG wave namely alpha. Energy and power of this wave are calculated using MATLAB (R2012b). Some features are also extracted from the raw EEG signal for proper classification. These features along with the energy and power calculated from the alpha wave are further analyzed to verify the hypothesis made in this manuscript.

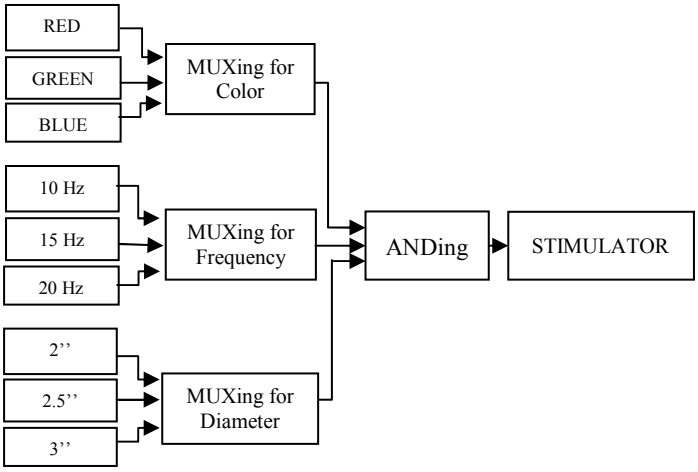

Figure 4. Visual stimulator with color, frequency and diameter variation arrangement.

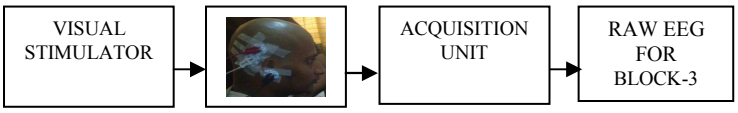

Figure 5. Raw EEG signal acquisition block.

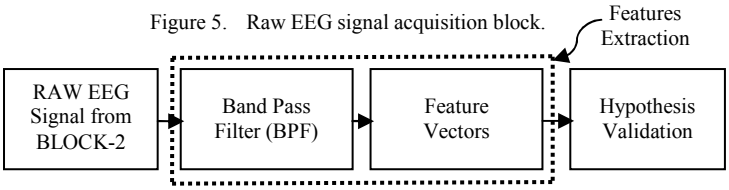

Figure 6. Feature extraction and analysis block.

III. DESIGNED STIMULATOR

To stimulate the brain visually, a stimulator is designed using JAVA script. In the Figure 7 (a) and 7 (b), the typical screen shots of this stimulator are shown. The characteristics of extracted signal depends on the configuration of laptop used for the visual stimulation. The configuration used for our stimulation was Intel (R) core (TM) 2 Duo CPU T6600 @2.20 GHz, 4 GB RAM (Installed memory) and 32-bit OS. The refresh rate of the display was 60 Hz.

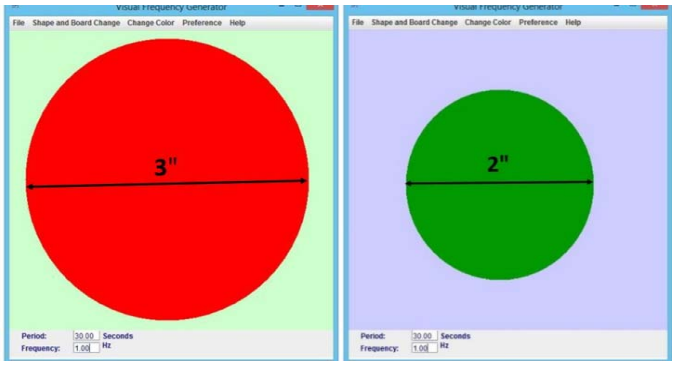

(a) (b)

Figure 7. Screenshot of the visual stimulator for two different size and color a) for red color of diameter 3" b) for green color of diameter 2".

IV. Graphical Analysis

Figure 8 shows the typical EEG signals for different conditions (green, 10 Hz and 3" dia. & green, 20 Hz and 2.5" dia.). Their corresponding Alpha waves are also shown which are obtained by filtering the raw EEG signals according to Figure 6.

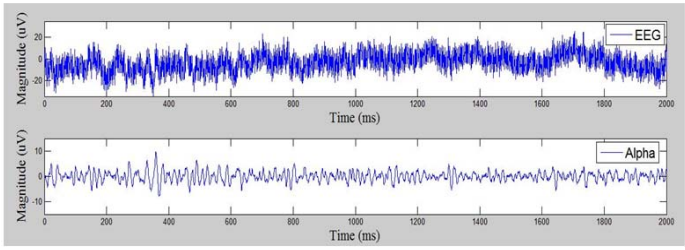

(a)

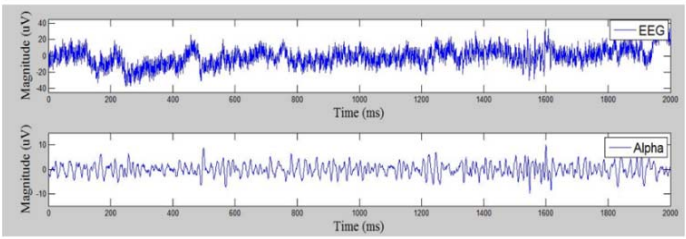

(b)

Figure 8. Typical EEG signal and their Alpha bands a) for green, 10 Hz and 3" dia. b) for green, 20 Hz and 2.5" dia. Stimulator.

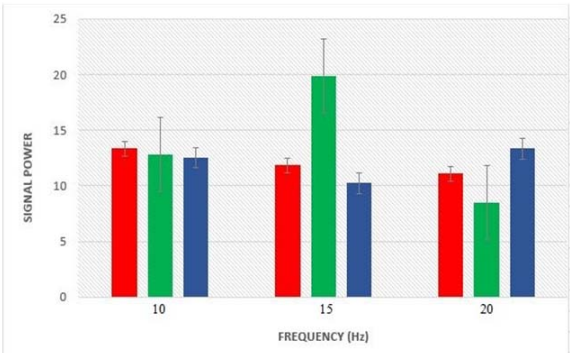

(a)

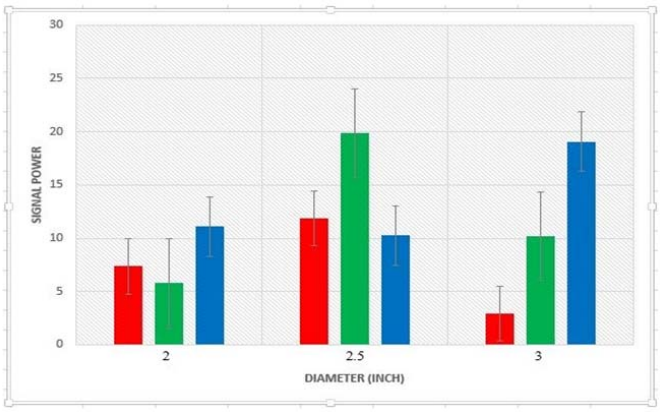

(b)

Figure 9. Variation of power of Alpha wave with variation of a) frequency as well as b) size.

Figure 9 (a) and 9 (b) represent a power variation with different frequencies and sizes for alpha (α) wave. Maximum power can be obtained at a frequency of 15 Hz for Green colored stimulation. Similar results are found when size of the stimulator is varied. Maximum power can be obtained at 2.5 inch diameter of the stimulator for Green color stimulator.

V. Tabular Analysis

TABLE II. Power and Energy Representation of Alpha Wave of EEG Bands

Size	Color	Frequency	Power	Energy($\times 10^4$)
Dia. 2"	Red	10	08.4456	3.9138
		15	07.3631	3.2265
		20	06.7715	3.0418
	Green	10	10.9952	4.9126
		15	05.7648	2.5982
		20	12.4226	5.36.3
	Blue	10	09.9841	4.7426
		15	11.0890	4.7393
		20	09.9060	4.2328
Dia. 2.5"	Red	10	13.3596	5.6791
		15	11.8485	5.1375
		20	11.0775	4.6603
	Green	10	12.8196	5.5701
		15	19.8871	8.9572
		20	08.5000	3.8207
	Blue	10	12.5278	5.4308
		15	10.2475	4.3726
		20	13.3325	5.6596
Dia. 3"	Red	10	07.2947	3.2600
		15	02.9098	1.6441
		20	16.5685	7.0714
	Green	10	11.9091	5.0781
		15	10.1972	4.4531
		20	12.8156	5.1326
	Blue	10	14.0363	6.0032
		15	19.0413	8.0821
		20	12.2827	5.2447

VI. CONCLUSION

Brain-computer Interfaces (BCIs) based on the SSVEP permit the communication with the physical world after paying attention to the visual stimulator. In this research, one of the vital factors of all stimuli in BCIs viz circular shape with different sizes, colors and frequencies is briefly analyzed. In our manuscript, the effect of size, frequency and color of a circular stimuli on the power and energy of EEG signal has been also analyzed. The number of target detection also depends on the refresh rate of the monitor and the number of stable timers supported by the system. This research helps to choose perfect stimuli which may outfit the performance of SSVEP based BCIs and safety of BCIs. Perfection to stimuli can enhance the SSVEP Signal to Noise Ratio (SNR), reduce the complexity of extracted signal processing, increase the target detection, help subjects to pay attention and allow independent BCI operation. We have designed the software for investigating the effect of frequency, color and different sizes of circular stimulator on the performance (power, energy and ITR). The major outcome of our research has been found that for a required power or energy, the size, shape, color and stimulation frequency of the brain stimulator can be chosen with the help of the Table II.

REFERENCES

[1] M. K. Hasan, R. Z. Rusho, and M. Ahmad, "A Direct Noninvasive Brain Interface with Computer Based On Steady-State Visual-Evoked Potential (SSVEP) With High Transfer Rates", International Conference on Advances in Electrical Engineering (ICAEE) (ISBN: 978-1-4799-2463-9), 2013, Dkaka, Bangladesh. DOI: 10.1109/ICAEE.2013.6750360.

[2] M. K. Hasan, T. M. Hossain, A. K. Faisal, and M. Ahmad, "Effect of Diverse Stimulations of Brain on EEG Signal for SSVEP Based Brain Computer Interface", Proc. of 2nd International Conference on Electrical Engineering and Information & Communication Technology (iCEEiCT 2015), IEEE, Jahangirnagar University (JU), Dhaka, May 2015.

[3] M. K. Hasan, R. Z. Rusho, T. M. Hossain, T. K. Ghosh, and M. Ahmad, "Design and Simulation of Cost Effective Wireless EEG Acquisition System for Patient Monitoring", International Conference on Informatics, Electronics and Vission (ICIEV) (ISBN: 978-1-4799-5179-6), 2014, Dhaka, Bangladesh. DOI: 10.1109/ICIEV.2014.6850797.

[4] H. Saadi, M. Ferroukhi and M. Attari "Development of wireless high immunity EEG recording system", 2011 International Conference on Electronic Devices, Systems and Applications (ICEDSA). (2002). DOI: 10.1109/ICEDSA.2011.5959060.

[5] C. Moulin "Contribution à l'étude et à la réalisation d'unsystème électronique de mesure et excitation de tissue nerveux à matrices microélectrodes", Thèse de doctorat, Lyon, 2006.

[6] Neuron structure. Available at: www.google.com/search?q=neuron+structure&source=lnms&tbm=isch&sa=X&ved=0CAcQ_AUoAWoVChMIocGK3ueHyQIVQU-OCh3Ndgkh&biw=1200&bih=600

[7] M. Cheng, X. Gao, S. Gao, D. Xu, "Multiple Color Stimulus Induced Steady State Visual Evoked Potentials", 23rd Annual International Conference of the IEEE Engineering in Medicine and Biology Society, 2001. Vol: 2, DOI: 10.1109/IEMBS.2001.1020359.

[8] T. F. Collura, "Real-time filtering for the estimation of steady-state visual evoked brain potentials", IEEE Trans. Biomed. Eng., vol. BME-37, pp. 650-652, June 1990.

[9] M. Salehuddin, Suprijanto, F. I. Muchtadi, "Prototype Design of Low Cost Four Channels Digital Electroecephalograph for Sleep Monitoring", 2nd International Conference on Instrumentation Control and Automation, 17-17 November 2011, bandung, Indonesia. DOI: 10.1109/ICA.2011.6130154

[10] J. r. Cameron dan J. G. Skfronik, "Medical Physics", Singapore: Jhon Wiley and Sons. 1987.

[11] D. Zhu, J. Bieger, G. G. Molina, R. M. Aarts, "A Survey of Stimulation Methods Used in SSVEP-Based BCIs", Hindawi Publishing Corporation Computational Intelligence and Neuroscience, Vol. 2010, Article ID 702357, 12 pages. DOI:10.1155/2010/702357.

[12] Y. Wang, X. Gao, B. Hong, C. Jia, and S. Gao, "Brain-computer interfaces based on visual evoked potentials: feasibility of practical system designs,"IEEE Engineering in Medicine and Biology Magazine, vol. 27, no. 5, pp. 64–71, 2008.

[13] A. Bashashati, M. Fatourechi, R. K. Ward, and G. E. Birch, "A survey of signal processing algorithms in brain-computer interfaces based on electrical brain signals," Journal of Neural Engineering, vol. 4, no. 2, pp. R32–R57, 2007.

[14] M. K. Hasan, M. S. Hossain, T. K. Ghosh, and M. Ahmad, "A SSVEP Based EEG Signal Analysis to Discriminate the Effects of Music Levels on Executional Attention", American Journal of Bioscience and Bioengineering, Science Publishing Group , vol. Vol. 3, issue 3-1, pp. 27-33, May, 2015.

An Approach to Estimate Cognitive State with the Impact of Listening Music on Brain Activity

Monira Islam, Mohiuddin Ahmad, and Md. Salah Uddin Yusuf
Department of Electrical and Electronic Engineering
Khulna University of Engineering & Technology (KUET), Khulna-9203, Bangladesh
E-mail: monira_kuet08@yahoo.com, mohiuddin.ahmad@gmail.com, ymdsalahu2@gmail.com

***Abstract*—This paper presents an approach to estimate the cognitive states depending on the variations of different effective frequency bands of EEG signal with listening music. In this work, EEG signals are collected for different types of songs to analyze the musical activity on human brain. Spatial and temporal analysis are applied to the brain signals to extract the salient features to estimate the human cognitive state. The classification accuracy of different frequency bands indicates the larger alpha or beta activity on human brain for the selected songs. The highest classification accuracy for soft song was found for θ-band which indicates the state of catnap. For medium and fast song the effectiveness of α band and β band are noteworthy, which indicate the state of relax and stress respectively. Therefore, our proposed approach is innovative and efficient to determine the human cognitive states.**

Keywords—EEG; cognitive state; brain activity; frequency band; music signal.

I. INTRODUCTION

Cognitive state comprises the functional activity of brain and subjective experience, expressions and biological stimulation for specific person in different environmental conditions. The basic socio-cognitive domain of human life is music. Listening music helps to keep the neurons and synapses more active and which varies the effective frequency bands of brain signal which is named as electroencephalogram (EEG). When sound waves are listened or pronounced, they have an impact in neurological (brain and nerve) system work in human body [1]. When neurons are activated, local current flows and generate electrical activity which is recordable on the head surface [2]. This electrical activity is termed as EEG signal which activates different parts of the brain during listening music [3]. It also indicates the cognitive states with the variations of functional activities of brain which are more influenced by exposure to music.

Fig. 1 shows the proposed way which indicates the variation of EEG signal with audio stimulation. Each of the music or song has specific frequency and bits according to which the brain activity and the effective frequency band of EEG signal may vary and the cognitive activities also change according to the frequency bands. The assignment of different cognitive states with their effective frequency band is shown in Table I.

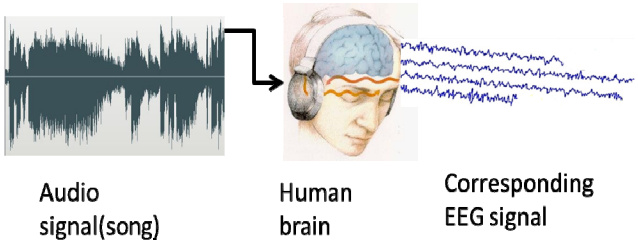

Fig. 1. Brain stimulation while listening audio signal (songs) and correponding EEG signal.

Our objective is to detect human's mental state according to the influence of different types of songs. In Table II the soft music is selected which composes a softer, more toned-down sound putting more emphasis on melody and vocal harmonies. The medium and fast music are selected according to the tempo of music i.e. rate of speed or number of beats per minutes.

While listening different types of songs such as loud or soft, high pitch or low pitch, audible or inaudible etc., our brain responses differently. Low frequency indicates the state of relax while high frequency indicates the state of stress [4]. The human brain produces different electrical activity due to the different levels of music [5]. Each type of music or songs has its own frequency. While listening music the frequency of the music can be either resonate or in conflict with the body's rhythms (heart rate) and also with the frequency bands of EEG rhythm which authorizes specific functions of brain [6].

TABLE I. FREQUENCY BAND REGION OF EEG SIGNAL

EEG wave	Frequency band region	Cognitive states
Delta (δ) wave	(0.4-4) Hz	Unconsciousness (Associated with deep sleep)
Theta (θ) wave	(4-8) Hz	Catnap (Associated with drowsiness)
Alpha (α) wave	(8-14) Hz	Relax (Associated with relaxed, alert state of consciousness)
Beta (β) wave	(14-35) Hz	Stress/Tension (Associated with active, busy or anxious thinking)

978-1-4673-9257-0/15/$31.00 ©2015 IEEE

TABLE II. CATEGORY OF SONGS SELECTED FOR COGNITIVE STATE ESTIMATION

Song type	Soft song	Medium fast song	Fast song
Bangla	Rabindra sangeet	Adhunik sangeet	Hard Rock
Hindi	Carnatic	Patriotic song	Pop
English	Melody	Folk song	Hard Rock

The categorization of selected songs for cognitive state estimation is shown in Table II. So, music can be used as a tool to estimate the cognitive states such as tension/ stress, solitude, relax and these changes are reflected clearly in physiological system for human body [7]. The major concern of this research are: (i) to propose a technique for extracting some salient statistical and time-frequency analysis based features according to the variation of effective frequency band due to different types of music and (ii) to evaluate the efficiency of the extracted features for different EEG bands to detect the cognitive states using support vector machine. The main steps of the proposed method are shown in Fig. 2. In this research, the BIOPAC data acquisition unit MP36, C++ source code and AcqKnowledge® 4.1 software are used for data acquisition, analysis, storage, and retrieval [8].

A lot of works have been carried out for addressing the problem of musical influences on the functional responses of human brain. Gerra et al. found that while listening music the corresponding changes will be induced in neurotransmitters, peptides and hormonal reactions [9]. In [10-12], Authors shows the variations of functional activities of different frequency band relating the cognitive activity with music levels. They found that beta activity relates to increased alertness and cognitive processes [10] and unpleasant music produces decrease in alpha power at the right frontal lobe [11]. Authors in [12] showed when subjects listen to the pleasant music the changes were reflected in the EEG and there was an increase in frontal midline (Fm) theta power. Authors in [13] showed the dependence of EEG spectral power on the intensity and style of music. The effect of Indian classical music and rock music on brain activity was studied using Detrended fluctuation analysis (DFA) algorithm, and Multi-scale entropy (MSE) method [14]. The brain wave variation was monitored in reference [15] by changing the music type (techno and classical) and the results showed that when the music was switched from classical to techno, there was a significant plunge of alpha band and from techno music to classical there was an increase in beta activity. Authors in [2] presented a brief study of various effects of sound on the human brain activity employing the time-frequency analysis technique. R.S. Schaefer et al. showed a difference in alpha power in different directions to indicate that both the tasks and the stimuli modulate an attentional network, which may relate to the inhibition of non-task relevant cortical areas, as well as engagement with the music [16]. In this work, a new approach is proposed to identify the cognitive states from the variation of effective EEG band. Different statistical, frequency and time-frequency analysis i.e. temporal and spectral analysis (T & S analysis) are done to extract the effective features to estimate the cognitive states.

The rest of the paper is organized as follows: Section II describes the EEG signal recordings. Section III describes the signal analysis and features extraction procedure. Section IV illustrates the cognitive state estimation by using SVM technique. Section V discusses the results of estimated cognitive sates while listening music. Finally, Section VI concludes the result.

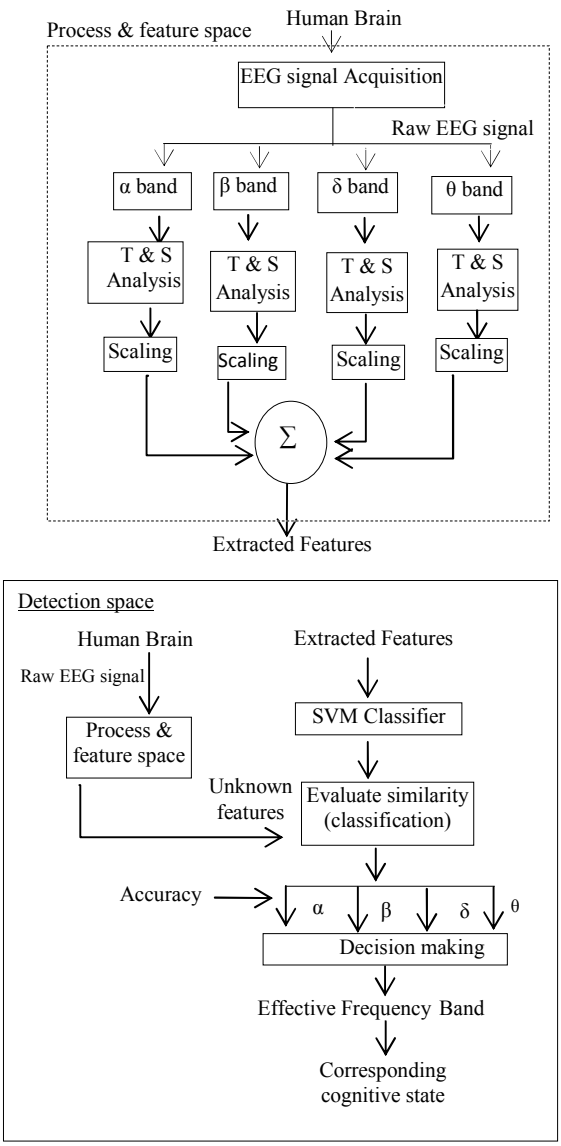

Fig. 2. Proposed approach for cognitive state estimation.

II. EEG SIGNAL RECORDING

In case of mental state evaluation brain signal is most essential so EEG data acquisition plays a significant role in this research. The electrical activity of human brain gets affected at the time of listening music. The electrical activity is measured at the scalp through a set of electrodes which are rich in information about the cognitive activity at different frequency bands of EEG signal.

A. *Music Selection for Cognitive State Estimation*

A lot of works have shown that different music has different physiological effect on human body rhythms and brain. The effect of music on brain functions rate based on subject's choice of like music (slow, medium and fast song) at different languages such that Bangla, English, Hindi. The selected songs have different spectral stimuli depending on their number of bits per second and affect separately on the EEG band waves and changes the signal characteristics. According to the selected salient features it is determined that which state is more affected with the effective frequency band influenced by the different types of selected songs.

Figs. 3(a), 4(a) and 5(a) show the frequency spectrum of soft, medium and fast song and Figs. 3(b), 4(b) and 5(b) show the corresponding brain signals respectively. In this work the Bangla, English and Hindi slow, medium fast and fast songs were played one after another taking a proper interval to evaluate the effect of cognitive activities of brain influenced by these songs. It is observed that the spectral components are higher for fast song than medium and slow depending which the effect of frequency bands for brain signal varies with the cognitive activities of brain.

B. *Subject Selection and Data Acquisition*

The EEG signals were collected in biomedical signal processing laboratory, KUET. The experimental data were collected from 48 numbers of subjects and the subjects were male, and were in good physical and mental conditions and able to react with different types of songs. Their average age was 23 years so that they are sensitive to all the mental activities.

The room was air conditioned and approximately noise free. In Fig. 6 the position of electrode on the scalp is shown for EEG data acquisition in the period of listening music.

III. Signal Analysis and Feature Extraction

The extracted EEG features are considered as the ideal characteristics to identify the variation of brain activities and represent the non-stationary characteristics of EEG signal which are particularly effective for recognition of human cognitive activities while listening different types of music.

A. *Time Domain Feature*

The most effective property of the statistical measures on time domain signal is that they will vary in magnitude with the variations of brain signal but maintains essential element of homogeneity. In this work, six different kinds of time-domain feature such as mean amplitude, median, standard deviation, variance, skewness, and kurtosis have been considered to show the influence of listening music on human brain. The expressions for different statistical features were briefly discussed in [18].

B. *Frequency Domain Feature*

The frequency-domain features used in this paper are based on the power spectrum of each 256 point of EEG samples. Each epoch of the EEG data is processed with Hamming window by zero padding for 256 points of FFT.

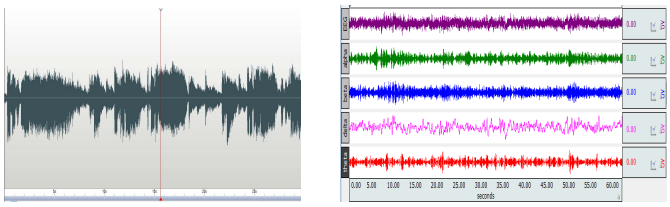

(a) (b)

Fig. 3. (a) Frequency spectrum of English soft song; (b) Corresponding EEG signal for soft song.

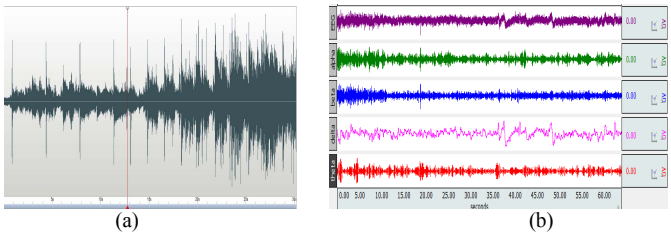

(a) (b)

Fig. 4. (a) Frequency spectrum of English medium song; (b) Corresponding EEG signal for medium song.

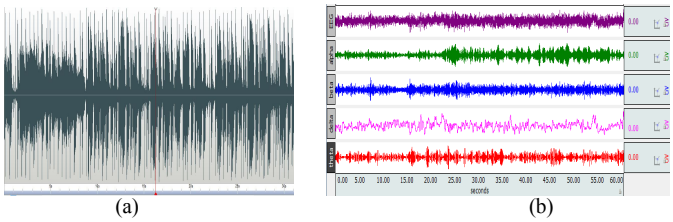

(a) (b)

Fig. 5. (a) Frequency spectrum of English fast song; (b) Corresponding EEG signal for fast song.

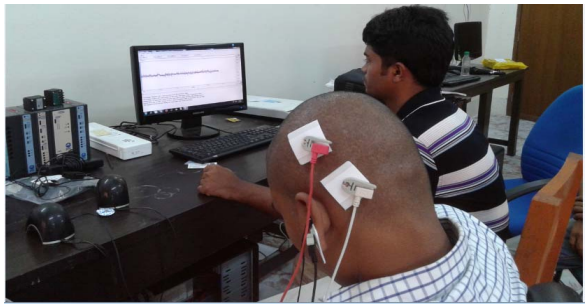

Fig. 6. Signal acquisition at the time of listening different types of music.

The power spectrum of all the sub-epochs is averaged to minimize the artifacts of the collected EEG signals in all sub-windows. Finally, EEG power spectrum is extracted in different channels such as Alpha, Beta, Delta and Theta. Different features for FFT analysis are obtained at alpha, beta, delta and theta component of EEG signal individually to determine the cognitive states influenced by different types of music is given by Eq. (1).

$$X(k)_l = \{X(0), X(1), \ldots X(n-1)\} \tag{1}$$

In Eq. (1), n represents the total number of frequency amplitude components; k represents the harmonic number of frequency components, and l represents alpha or beta or theta or delta. The real value, imaginary value, magnitude, phase angle and power spectral density are the effective features in this analysis.

It is integrated over its entire one-sided frequency domain (0, F) according to FFT analysis:

$$\int_0^F PSD(k)dk = \int_0^F 2\left|X(k)_l\right|^2 /(t_2 - t_1)dk \tag{2}$$

Equation (2) represents the expression of power spectral density in frequency domain where the average power of the signal is in the time range (t_1, t_2).

C. Temporal-Frequency Domain Feature

The discrete wavelet transform (DWT) analyzes the signal at different frequency bands to extract effective energy component by decomposing the signal into a coarse approximation and detail information [16]. In the present paper, the Daubechies4 wavelet function ("db4") is used for extracting features from the EEG signal in time frequency domain because it decomposes the high and low frequency components of EEG signal.

IV. Cognitive State Estimation using Support Vector Machine

In this work, temporal and spectral analysis based selection of effective frequency band of EEG signal for cognitive state estimation is proposed. In our proposed approach statistical and frequency based salient feature extraction are devised in to different EEG bands under the influence of different types of songs for selection of brain activities according to the classification rate of efficient frequency bands and their power spectrum analysis. The steps in effective band selection for the proposed method are given below:

i. The raw EEG signals from several subjects during hearing of different types of music are collected using three electrodes in BIOPAC data acquisition unit which are placed on the scalp.
ii. This preprocessed signal is divided into different EEG frequency bands such as Alpha, Beta, Delta and Theta and the salient global features are extracted from the specific frequency bands.
iii. From the classification rate of effective frequency band wave the pre-specified cognitive states can be determined.

For the evaluation of performance of cognitive states estimation, classification rate of different bands is achieved by using multiclass support vector machine. The human mental states are classified into the defined classes. For example, α = 1, β = 2, δ = 3, θ = 4. In order to perform a more reliable classification process, three stages are implemented. Firstly, The EEG data are prepared in the specified format and scaling is performed if necessary for each subject. Secondly, the data are trained to create a model. Finally, the new input data of another subject are predicted/classified using the model. In case of classifying mental states through SVM, the radial basis function kernel is used and the scaling range was taken -1~3 for statistical features, 0~15 for FFT and -1~1 for DWT.

The MCSVMs require the solution of the following optimization problem: minimize

$$\phi(\omega,\xi) = \frac{1}{2}\sum_{m=1}^{k}\omega_m.\omega_m + C\sum_{i=1}^{l}\sum_{m\neq y}\xi_i^m \tag{3}$$

With constraints

$$(\omega_{y_i}.x_i) + b_{y_i} \geq (\omega_m.x_i) + b_m + 2 - \xi_i^m,$$
$$\xi_i^m \geq 0, i = \{1,2,...,l\}, m \in \{1,...,k\} \mid y_i \tag{4}$$

Where C is the penalty parameter, l is the number of training data, k is the number of classes, y_i is the class of the ith training data ω points perpendicular to the separating hyperplane, b is the offset parameter to increase the margin, \ is set minus which is defined as ($m \in \{1,\ldots, k\}\backslash m \notin y_i$), and ξ is the degree of misclassification of the datum x_i. This gives the decision function:

$$f(x) = arg \max_{m=1,...,k}\left[\omega_m.x + b_m\right] \tag{5}$$

This optimization problem for a dual variable is solved by finding the saddle point of the Lagrangian [17].

$$\begin{aligned} L(\omega,b,\xi,\alpha,\beta) &= \frac{1}{2}\sum_{m=1}^{k}\omega_m.\omega_m + C\sum_{i=1}^{l}\sum_{m=1}^{k}\xi_i^m \\ &- \sum_{i=1}^{l}\sum_{m=1}^{k}\alpha_i^m\left[\left((\omega_{y_i} - \omega_m).x_i\right) + b_{y_i} - b_m - 2 + \xi_i^m\right] - \sum_{i=1}^{l}\sum_{m=1}^{k}\beta_i^m\xi_i^m \end{aligned} \tag{6}$$

With the dummy variables $\alpha_i^{y_i} = 0, \xi_i^{y_i} = 2, \beta_i^{y_i} = 0, i = 1,2,...,l$ and constraints $\beta_i^m \geq 0; \xi_i^m \geq 0; i = 1,2,....,l$

Where, $m \in \{1,2,\ldots, k\}\backslash y_i$ has to be maximized with respect to α and β, and minimized with respect to ω and ξ. Thus the decision function is obtained [8]. In this work the classification rate of different frequency band is obtained by using SVM under the variation of music or sound from which the specified cognitive states effective for the specific frequency bands are determined.

V. Result and Discussion

In this paper, the variations of different frequency bands are determined under the influence of different types of song on brain activity to estimate the cognitive states. The analyzed features and signal characteristics are changed according to the variation of song and their frequency spectrum. For EEG signal, the amplitude of alpha wave changes with the subject's attention to mental task performed.

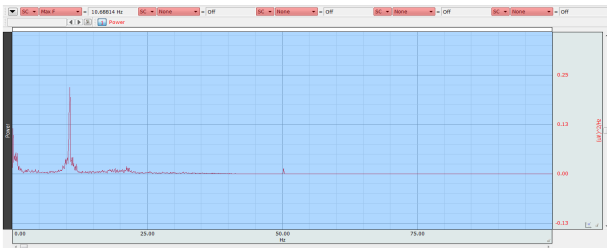

Fig. 7. Power spectral density of EEG signal when subjected to Bangla medium song.

TABLE III. CLASSIFICATION ACCURACY AT DIFFERENT EFFECTIVE BANDS USING SVM FOR BANGLA SONG

Song type	EEG frequency band	Train dataset for SVM	Test dataset for SVM	Classification accuracy
Bangla soft song	Alpha(α)	58	36	64.28%
	Beta(β)	58	35	20%
	Delta(δ)	58	36	36.11%
	Theta(θ)	58	37	86.5%
Bangla medium song	Alpha(α)	62	35	71.18%
	Beta(β)	62	36	3.61%
	Delta(δ)	62	37	23.35%
	Theta(θ)	62	35	23.1%
Bangla fast song	Alpha(α)	56	32	2.5%
	Beta(β)	56	33	97%
	Delta(δ)	56	32	65.68%
	Theta(θ)	56	34	39.47%

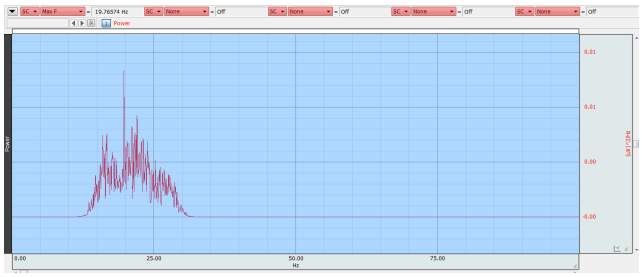

Fig. 8. Power spectral density of EEG signal when subjected to English fast song.

TABLE IV. CLASSIFICATION ACCURACY AT DIFFERENT EFFECTIVE BANDS USING SVM FOR ENGLISH SONG

Song type	EEG frequency band	Train dataset for SVM	Test dataset for SVM	Classification accuracy
English soft song	Alpha(α)	51	36	41%
	Beta(β)	51	35	31.76%
	Delta(δ)	51	36	44.44%
	Theta(θ)	51	37	84.85%
English medium song	Alpha(α)	49	35	85.7%
	Beta(β)	49	36	43.53%
	Delta(δ)	49	37	45.75%
	Theta(θ)	49	35	11.43%
English fast song	Alpha(α)	47	32	5%
	Beta(β)	47	33	88.57%
	Delta(δ)	47	32	54.54%
	Theta(θ)	47	34	31.81%

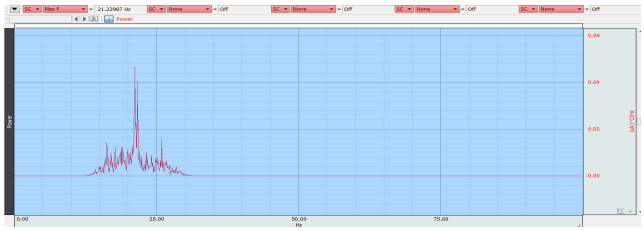

Fig. 9. Power spectral density of EEG signal when subjected to Hindi fast song.

The alpha activity is inversely proportional to concentration of mental activities. The value of alpha is the maximum for relax state and it decreases for the mental task or at stress. Fig. 7 shows the power spectral density of EEG brain wave when listening Bangla medium song. The maximum power occurs at 10.68 Hz which lies within the alpha frequency band. So, alpha band is more effective for medium type of song.

TABLE V. CLASSIFICATION ACCURACY AT DIFFERENT EFFECTIVE BANDS USING SVM FOR HINDI SONG

Song type	EEG frequency band	Train dataset for SVM	Test dataset for SVM	Classification accuracy
Hindi slow song	Alpha(α)	46	36	85.6%
	Beta(β)	46	35	65.1%
	Delta(δ)	46	36	31.25%
	Theta(θ)	46	37	96.37%
Hindi medium fast song	Alpha(α)	63	35	90.32%
	Beta(β)	63	36	3.12%
	Delta(δ)	63	37	53.12%
	Theta(θ)	63	35	80%
Hindi fast song	Alpha(α)	56	32	35.29%
	Beta(β)	56	33	94.11%
	Delta(δ)	56	32	17.14%
	Theta(θ)	56	34	54.11%

Table III shows the train and test dataset for SVM and the classification accuracy of the frequency bands for Bangla song which can detect the effective cognitive states. The classification rate of theta band is higher for Bangla soft song and alpha band is more effective for Bangla medium and fast song and they are 86.5%, 71.18%, and 97% respectively. When human brain is subjected to Bangla soft song the cognitive state was drowsiness or may be called catnap and when medium and fast Bangla song was played the cognitive states indicate relax and tension respectively.

The power spectral density when subjected to English fast song as shown in Fig. 8. It indicates that the maximum power occurs at frequency 19.76 Hz. So in case of English fast song the beta activity is prominent which indicate stress or tension for the subject.

Table IV and Table V shows the classification accuracy of the different effective frequency bands for English song and Hindi song which can detect the effective cognitive states when respective songs were played. In case of English fast, medium and soft song the higher accuracy is found at beta and alpha and theta band which indicate the stress, relax and catnap state respectively. Table V shows that theta and alpha band are more effective for Hindi slow song and medium song and they were

found 96.37% and 90.32% respectively. Hindi fast song shows the effectiveness of beta band which was 94.11%. So from this analysis it is observed that slow song detects the catnap state and medium fast song shows the relax state whereas fast shows the state at stress. So the cognitive state can be evaluated from the larger activity of alpha or beta or theta band.

The maximum power is occurred at frequency 21.22 Hz for Hindi fast song which indicates the beta frequency band as shown in Fig.9. So, the beta activity is more effective for fast song and the high frequency spectrum with fast bit of music leads human mind to stress.

VI. CONCLUSION

This work proposed a framework of cognitive state estimation based on the variations of brain activity with different types of music. The effective time domain and frequency domain features were extracted from spatial and temporal analysis. From the analysis, it was shown that θ-band is more effective for soft song whereas the α-band is effective for medium song and the β-band activity is prominent for Bangla, Hindi and English fast song. The highest classification accuracy for soft song was 96.37% for θ band. For medium and fast song they were 90.32% and 94.11% for α-band and β-band respectively. The α-band activity indicates the positive emotion pleasant or the reduction of mental stress whereas β-band activity shows the effect of mental stress. From this work, it can be concluded that the cognitive states depend on the functional activity of frequency bands while listening different types of songs. In future, cognitive state will be modeled for different types of music.

REFERENCES

[1] B. Geethanjali, K. Adalarasu, and R. Rajsekaran, "Impact of music on brain function during mental task using electroencephalography," *World Academy of Science, Engineering and Technology*, pp. 883-887, 2012.

[2] R. Bhoria, S. Gupta, "A Study of the effect of sound on EEG," *International Journal of Electronics and Computer Science Engineering,* IJECSE, vol. 2, no. 1, pp. 88-99, Dec. 14, 2012.

[3] EG. Schellenberg, T. Nakata, PG. Hunter, S. Tamoto, "Exposure to music and cognitive performance: Tests of children and adults," *Psychology of Music* , vol.35, pp. 5 – 19, 2007.

[4] J. Tanaka, M. Kimura, N. Hosaka, H. Sawaji, K. Sakakura, K. Magatani, "Development of the EEG measurement technique under exercising," *Proceedings of the IEEE Engineering in Medicine and Biology 27th Annual Conference Shanghai*, China, Sept. 2005, pp.1-4.

[5] R. Bhoria, P. Singal, D. Verma, "Analysis of effect of sound levels on EEG," *International Journal of Advanced Technology & Engineering Research (IJATER)*, vol. 2, no. 2, pp. 121-124, March 2012.

[6] H. Asada, Y. Fukuda, S. Tsunoda, M. Yamaguchi, M. Tonoike, "Frontal midline theta rhythms reflect alternative activation of prefrontal cortex and anterior cingulated cortex in humans," *Journal of Neurophysiology*, vol.50, pp. 324 – 328, Oct.1999.

[7] A. J. Lonsdale, AC. North, "Why do we listen to music? A uses and gratifications analysis," *British journal of psychology London England 1953,* vol.1, pp. 108-13, Feb. 2011.

[8] T. Ahmed, M. Islam, and M. Ahmad, "Human emotion modeling based on salient global features of EEG signal," *International Conference on in Advances in Electrical Engineering (ICAEE)*, 2013, pp. 246-251.

[9] G. Gerra, A. Zaimovic, D. Franchini, M. Palladino, G. Giucastro, N. Reali, D. Maestri, R. Caccavari, R. Delsignore, F. Brambilla, "Neuroendocrine responses of healthy volunteers to 'techno-music': relationships with personality traits and emotional state," *International Journal of Psychophysiology*, vol.28, pp. 99-111, Oct.1999.

[10] M. Steriade, "Cellular substrates of brain rhythms," In E. Niedermeyer & F. H. Lopes da Silva (Eds.), Electroencephalography Basic principles, clinical applications, and related fields, 4th Edition, Baltimore: Williams & Wilkins, pp. 28 – 75, 1999.

[11] C. D. Tsang, L. J. Trainor, D. L. Santesso, S. L. Tasker, L. A. Schmidt,"Frontal EEG responses as a function of affective musical features," *Annals of the New York Academy of Sciences*, vol.930, pp. 439 – 442, 2001.

[12] D. Sammler, M. Grigutsch, T. Fritz, S. Koelsch, "Music and emotion: Electrophysiological correlates of the processing of pleasant and unpleasant music," *Journal of Psychophysiology*, vol. 44, no. 2, pp. 293 – 304, 2007.

[13] R. A. Pavlygina, D. S. Sakharov, V. I. Davydov, "Spectral analysis of the human EEG during listening to musical compositions," *Journal of Human Physiology*,vol.30, no.1, pp. 54 – 60, 2004.

[14] N. G. Karthick, A. V. I. Thajudin, P. K. Joseph, "Music and the EEG: A study using nonlinear methods," *International Conference on Biomedical and Pharmaceutical Engineering*, 2006, pp. 424 – 427.

[15] Y. C. Chen, K. W. Wong, D.C. Kuo, T.Y. Liao, D.M. Ke, "Wavelet real time monitoring system: A case study of the musical influence on Electroencephalography," *WSEAS Transactions on Systems*, vol. 7, pp. 56 – 62, 2008.

[16] Schaefer, S. Rebecca, J. V. Rutger, P. Desain, "Music perception and imagery in EEG: Alpha band effects of task and stimulus,"*International Journal of Psychophysiology*, vol. 82, no. 3, pp. 254-259, 2011.

[17] M. Islam, T. Ahmed, M. S. U. Yusuf, and M. Ahmad, "Cognitive state estimation by effective feature extraction and proper channel selection of EEG signal," *Journal of Circuits, Systems, and Computers, World Scientific Publishing Company*, vol. 24, no. 2, pp. 1-24, Feb. 2015.

[18] M. Islam, T. Ahmed, S. S. Mostafa, M. S. U. Yusuf, and M. Ahmad, "Human emotion recognition using frequency & statistical measures of EEG signal," *International Conference on Informatics, Electronics & Vision*, May 2013 pp.1-6.

A Simple and Improved Eye Movement Features Detection Process from Saccadic Samples of Electrooculographic Data

Md. Shazzad Hossain*, Kristie Huda, Sourav Roy, Mohiuddin Ahmad
Department of Electrical and Electronic Engineering (EEE)
Khulna University of Engineering & Technology (KUET)
Khulna-9203, Bangladesh
*E-mail: shazzad2k905@gmail.com

Masud Rana
Department of Electrical and Electronic Engineering (EEE)
Dhaka University of Engineering & Technology (DUET)
Gazipur-1700, Bangladesh

Abstract—**In this manuscript a simple and improved eye movement features detection process is described. As most of human activities involve eyes, eye movement features detection is very important, particularly in ubiquitous computing and smart human computer interfaces. We all are familiar with Eye movement features detection techniques that involves image or video processing. But in this work we concentrated on a relatively new eye movement features detection technique that uses electrostatic potential from eyes, also known as Electrooculography signal. The work includes the detailed signal processing steps necessary to detect the various eye movement features from the raw Electrooculography signal. The detection process is simple and improved compared to previous counterparts. The detection process is user independent and thus free of any calibration problems.**

Keywords—electrooculography, human computer interface, baseline drift removal, eye movement features, automatic threshold determination.

I. INTRODUCTION

Most of the Human Computer Interface (HCI) systems used for rehabilitation purposes today function via bio signals, mostly electrical signals generated from human body referred to as Bio potentials. Bio potentials between any two points in living cell or organism is the result of relative change of concentration of sodium (Na+) and potassium (K+) ions [1]. Bio-potentials like Electromyography (EMG) Electroencephalography (EEG), Electrooculography (EOG) etc. are hot topics in HCI applications in recent years. But bio potentials like Electroencephalogram (EEG) or Electromyogram (EMG) needs complex signal processing and acquiring Electrocardiogram (ECG) 24×7 is not possible always. On the contrary systems based on Electrooculography are fairly easy to design and construct using surface electrodes placed around the eyes realizing EOG a preference over other bio potentials [2].

Apart from its clinical use EOG in recent years have been used in diverse applications. It is used to control devices e.g. computer [3], home appliances [4], wheelchair navigation [5] and to develop gaming consoles [7], [6]. It is also used in applications like activity recognition, analysis of human cognition etc. [5], [8], [9].

Human eye is involved in almost everything he does in his day to day life. So eye can be a potential interfacing component in HCI applications involving eye tracking and eye movement features detection. Eye movement features like eye movement patterns may provide essential cognitive cues which can be detected by analyzing eye movements [9]. There are few methods to track the movements of eye such as Scleral search coil method, Infrared-occulography (IROG), Electro-occulography (EOG), Video-occulography (VOG) etc. [10]. But in recent times EOG based method is becoming the center of eye-based HCI research due to its accuracy, ease of use and economy. This necessitates the need for simple and improved tools for EOG signal processing. This work at hand provides an edge in that regard.

II. BACKGROUNDS

A. The Resting Potential in the Human Eye

Every living cells have potentials across their plasma membranes called a membrane potential. The cytoplasm is charged negative compared to the fluid outside the cell. This discrepancy results from the fact that the distribution of anions and cations on opposite membrane sides is uneven. The membrane potential, varies from about -50 to -200 milli volts (the inside of the cell is charged negative with respect to the outside part. This is indicated by the minus sign.).

When the membrane potential of a cell goes for a long period of time without changing significantly, it is referred to as a resting potential as shown in Fig. 1 [11], [22]. The membrane potential is similar to a power source that controls the flow of all ions across the membrane. As the cell is charged more negatively in the inner part from the outer part, cations flow into the cell and anions out of the cell. This difference in ionic concentration that exists between the inside and outside of this membrane can be related to the diffusion potential – also known as the Nernst Potential. The magnitude of this Nernst potential is determined from the equation [20] below using the ratio of the concentrations of ion on opposite sides of the membrane.

978-1-4673-9257-0/15/$31.00 ©2015

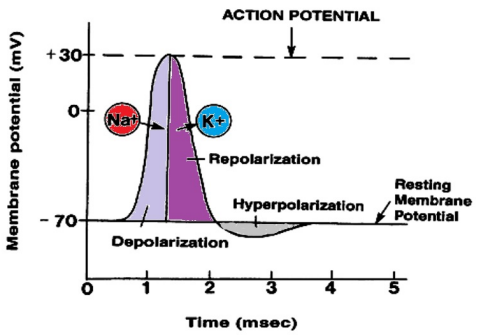

Fig. 1. Resting membrane potential.

$$E_{eq.K^+} = \frac{RT}{zF} ln \frac{[K^+]_{out}}{[K^+]_{in}} \quad (1)$$

Where: $E_{eq.K^+}$ is the equilibrium potential for potassium, R is the universal gas constant, T is the absolute temperature, z is the number of charged ions, F is the Faraday constant, $[K^+]_{out}$ is the concentration of potassium outside the cell, $[K^+]_{in}$ is the concentration of potassium inside the cell.

The eye ball can be regarded as a source of such resting potential, most of which has been attributed to the retina although some research has been done which proves the lens and maybe the cornea also play important roles. This potential known as corneo-retinal potential (CRP) is approximately lined up with the optic axis. Hence it varies with the variation of gaze. As the eyeball changes position the potential at the skin surface around the eye socket also changes. This potential difference can be measured by using surface electrodes placed on the skin around the eyes.

B. Electrooculography

The eye can be modeled as a dipole with cornea as positive pole and retina as negative pole. So the eye can be treated as a constant source of stable cornea-retinal electrostatic potential due to the potential difference between cornea and retina. This difference is attributed to the large presence of charged nerves in the retina with respect to the cornea [12]. The process of measuring the changes in this potential is called Electrooculography. A changing potential due to eye movement can be measured by using bipolar electrodes at opposite sides and a reference electrode. The electrodes are generally placed on the ends of the forehead as shown in Fig. 2 [13]. When the eye moves, the cornea approaches one electrode while the retina approaches the opposite one. Two signal components: EOG_h and EOG_v corresponding to horizontal and vertical movements can be measured [11]. Analyzing the change in these signals the eye movements can be tracked. The EOG signal amplitude varies from 50 to 3500 µV with a frequency range of about DC-100 Hz. Its behavior is practically linear for gaze angles of ±30º and changes approximately 20 µV for each degree of eye movement [7], [14]. EOG signal originates from the resting potential in the human eye.

Fig. 2. Placement of electrodes (Yellow=vertical electrode, Red=horizontal electrode, Black=reference electrode).

III. Eye Movement Features

The eye movement features that are the main concerns in this manuscript are a) Saccades, b) Fixations and c) Blinks.

A. Saccades

Saccades are swift, ballistic eye movements that abruptly change the fixation point. They range in amplitude from the small movements to the larger gaze movements. Saccades can be voluntary, but also can be reflexive whenever the eyes are open, even when fixated on an object. The duration of a saccade is governed by the angular distance the eyes travel during this movement. Typical saccade duration is 0.02 to 0.1 seconds and amplitude of 20 degrees [8], [15].

B. Fixations

Fixations are the rest state of eye between two consecutive saccades when the gaze is held constant on a specific location of the visual scene. The average fixation duration lies between 100 ms and 200 ms [15].

C. Blinks

This is subsequent closing and opening of eyelids. Blinks are of two types: a) reflex blink (in response to something invading in the eye and also as part of scared response) b) involuntary blinks (spontaneous blink controlled by brains blink generator) and b) voluntary blinks (controlled blink) [16]. A typical blink has amplitude of 100 to 400 µV and has duration of about 0.2 to 0.4 seconds. The primary functions of the blinks are to keep the corneal surface from getting dry and to protect the eyes from dirt or other possible damage. This is accomplished by three different kinds of blinks. One is voluntary and two are involuntary. The voluntary blinks are logically the result of the decision to shortly close the eyes. The involuntary blinks are divided in two sub groups. The first contains blink reflexes to protect the eyes from any possible harm and the second contains reflexes to maintain corneal moisture [17]. Fig. 3 shows the various eye movements in the EOG signal.

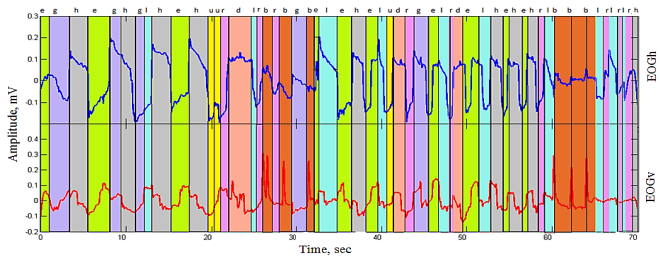

Fig. 3. Various eye movements in EOG signal: ‘r’=right, ‘l’=left, ‘u’=up, ‘d’=down, ‘e’=right-up, ‘f’=right-down, ‘g’=left-up, ‘h’=left-down, ‘b’=blink.

IV. General Detection Process

The general block diagram of the eye movement feature detection process is given below:

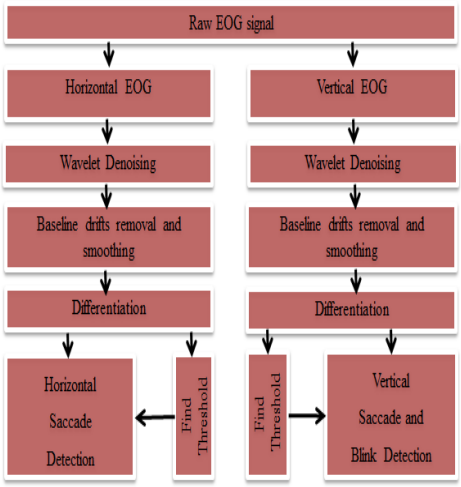

Fig. 4. General block diagram of the detection process.

V. Detailed Detection Process

A. Wavelet Denoising

To remove noise using wavelet thresholds, the wavelet coefficients are thresholded. This removes high frequency components, generally noise. This method does not require any particular assumptions about the bahaviour of the signal, can handle discontinuities and spatial variation in the signal.

In this work signal denoising is accomplished by using universal thresholding method on the wavelet coefficients. The wavelet decomposition of the signal is first found by performing a six level wavelet decomposition on the signal. The wavelet used for this purpose is db4. The denoised signal is found by thresholding the wavelet coefficients. The equation [20] of the wavelet function is given by

$$C[i] = g_0 s[2i] + g_1 s[2i+1] + g_2 s[2i+2] + g_3 s[2i+3] \quad (2)$$

Where $g_0 = h_3$, $g_1 = -h_2$, $g_2 = h_1$, $g_3 = -h_0$ and

$$h_0 = \frac{1+\sqrt{3}}{4\sqrt{2}}, h_1 = \frac{3+\sqrt{3}}{4\sqrt{2}}, h_2 = \frac{3-\sqrt{3}}{4\sqrt{2}}, h_3 = \frac{1-\sqrt{3}}{4\sqrt{2}}$$

The threshold value for the universal threshold method is given by $\sigma=\sqrt{2\log n}$; where n is the number of samples in the signal.

B. Baseline Drift Removal

User concentration is required while using eye movements to control graphical interfaces. Signal extraction for a long time may make the users tired and so it becomes more difficult for users to perform eye movements, this phenomenon is known as 'jitter' [14]. For this reason, users' capacity to control their ocular motor system decreases inversely proportional to tiredness. This event shows drift of signal from baseline. This is called baseline drift defined as the deviation of the signal baseline from a straight line. The drift of the signal from the baseline is modeled by a high degree polynomial which is then subtracted from the original signal to remove the baseline drift. A higher-order Polynomial increases the likelihood of producing an accurate baseline estimate [18]. A polynomial of degree 20 is chosen which models the baseline of the signal most accurately. Much lower and higher degree polynomials give poor results [19].

The polynomial curve fitting method used here uses a kth degree polynomial to model the signal [21]. Suppose the kth degree polynomial is

$$y = a_0 + a_1 x + a_2 x^2 + a_3 x^3 + \cdots + a_k x^k \quad (3)$$

The residual is given by,

$$R^2 = \sum_{i=1}^{n} [y_i - (a_0 + a_1 x_i + a_2 {x_i}^2 + \cdots + a_k {x_i}^k)]^2 \quad (4)$$

should be minimum to obtain least square error.

To obtain the least square error, the unknown coefficients $a_0, a_1, a_2,.., a_k$ must yield zero first derivatives. i.e

$$\frac{\partial R^2}{\partial a_0} = -2\sum_{i=1}^{n}[y - (a_0 + a_1 x + a_2 x^2 + +a_k x^k)] = 0$$

$$\frac{\partial R^2}{\partial a_1} = -2\sum_{i=1}^{n}[y - (a_0 + a_1 x + a_2 x^2 + +a_k x^k)]x = 0$$

$$\vdots$$

$$\frac{\partial R^2}{\partial a_k} = -2\sum_{i=1}^{n}[y - (a_0 + a_1 x + a_2 x^2 + +a_k x^k)]x_k = 0$$

Expanding the above equation we have,

$$\sum_{i=1}^{n} y_i = a_0 \sum_{i=1}^{n} 1 + a_1 \sum_{i=1}^{n} x_i + a_2 \sum_{i=1}^{n} x_i^2 \ldots + a_k \sum_{i=1}^{n} x_i^k$$

$$\sum_{i=1}^{n} x_i y_i = a_0 \sum_{i=1}^{n} x_i + a_1 \sum_{i=1}^{n} x_i^2 + \cdots + a_k \sum_{i=1}^{n} x_i^{k+1}$$

$$\vdots$$

$$\sum_{i=1}^{n} x_i^2 y_i = a_0 \sum_{i=1}^{n} x_i^2 + a_1 \sum_{i=1}^{n} x_i^3 + \cdots + a_k \sum_{i=1}^{n} x_i^{k+2}$$

Solution of these equations gives the value of the coefficients $a_0, a_1, a_2, \ldots, a_k$.

C. Smoothing

The EOG Signal is smoothened by using Savitzky-Golay filter. It is a digital filter which fits a polynomial to the data points according to least square fit and the central point of the fitted polynomial is taken as the new smoothed data point.

For $2M+1$ input sample and N order of polynomial, $\tilde{p}(n)$ is the impulse response design polynomial which can be obtained by following equation [23]

$$\tilde{p}(n) = \sum_{k=0}^{N} \tilde{a}_k n^k - M \le n \le M. \quad (5)$$

Where $\tilde{a}$ is the impulse input, $\tilde{a} = (A^T A)^{-1} A^T d$.

Here $d = [0,0,\ldots.,0,1,0,\ldots,0,0]^T$ is $(2M+1)\times 1$ column vector impulse and A^T is $(N+1)\times(2M+1)$ matrix.

$$A^T = \begin{bmatrix} (-M)^0 \ldots (-1)^0 & 1 & 1^0 \ldots M^0 \\ (-M)^1 \ldots (-1)^1 & 0 & 1^1 \ldots M^1 \\ (-M)^2 \ldots (-1)^2 & 0 & 1^2 \ldots M^2 \\ \vdots \quad\quad \vdots & \vdots & \vdots \quad \vdots \\ (-M)^N \ldots (-1)^N & 0 & 1^N \ldots M^N \end{bmatrix}$$

So, the impulse response of S-G filter is

$$h[-n] = h_{0,n} = \tilde{p}(n). \quad (6)$$

Finally the signal is thresholded to remove high amplitude noise components and very small saccades.

D. Feature Detection

1) Automatic threshold determination

An automatic threshold determination algorithm is adopted which eliminates the need for calibration and thus provides subject independent analysis. The algorithm first finds the local maximas of the derivative of EOG horizontal and vertical components and sorts them in ascending order. Noise usually possesses high amplitude peaks. Large noise peaks are removed by eliminating peaks (starting from high end going towards the low end) above the points where the difference between sequential peaks is less than 0.035mv. This value differentiates the noise peaks from the signal peak. From these peaks the appropriate peaks are selected (depending on the feature being desired) using a universal threshold process. The universal threshold process divides the peaks corresponding to saccades from that of the blinks. Thus blink and saccade thresholds were determined corresponding to EOGh and EOGv. Fig. 5 shows noise peak removal in automatic threshold determination method.

2) Blink detection

Blink features are detected from the vertical EOG signal (EOG_v) where it is characterized by sharp high amplitude peaks of short duration as shown in Fig. 6(a). Blinks are detected from the derivative of EOG_v which characterizes the blinks as a distinct signal feature having two peaks, one positive and one negative with a zero crossing between them as shown in Fig. 6(b). Involuntary eye blinks are eliminated by thresholding the detected blink amplitudes with the blink threshold determined earlier from the automatic threshold determination algorithm. Involuntary eye blinks has smaller amplitudes and smaller duration than voluntary eye blinks which differentiates the intentional blinks from the unintentional ones.

3) Saccade Detection

Saccades corresponding to horizontal and vertical eye movements are detected from the derivative of EOG_h and EOG_v respectively. From the EOG signal characteristics it can be concluded that when the signal amplitude increases then the corresponding eye movement is towards the rightward direction for EOG_h or towards the upward direction for EOG_v. Similarly decreasing amplitude indicates eye movement in opposite directions. So saccades can be detected by simply observing the change in amplitude i.e. by observing the derivative of the signals. The saccadic peaks for horizontal saccades are shown in Fig. 7.

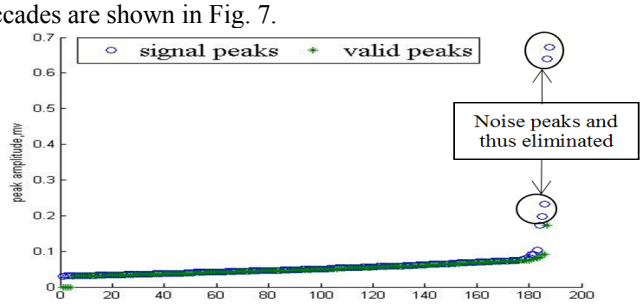

Fig. 5. Noise peak removal in automatic threshold determination.

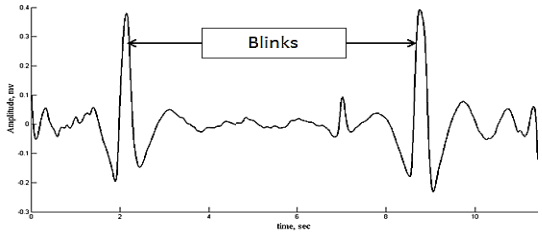

(a)

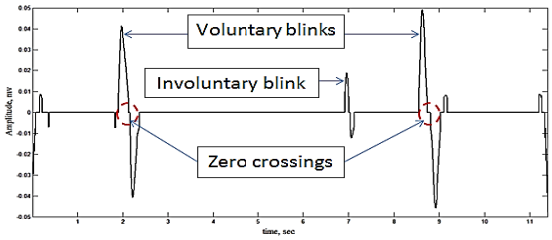

(b)

Fig. 6. (a) Blinks in EOG_v and (b) Voluntary and involuntary blinks.

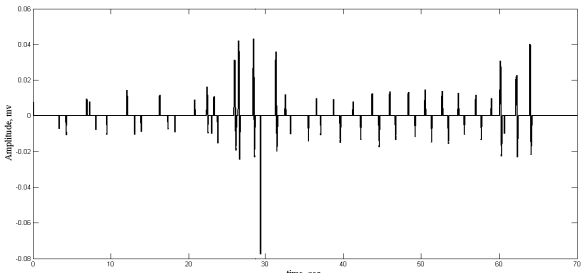

Fig. 7. Saccadic peaks for horizontal saccades.

4) Feature classification

After the features of interest are extracted from both the horizontal and vertical signals, they are classified to find out the unidirectional and oblique saccades and voluntary blinks. Horizontal and vertical saccades are extracted from the derivative of EOG_h and EOG_v respectively. An oblique saccade is found when a horizontal and a vertical saccade occur simultaneously. The blinks are found from the derivative of the EOG_v signal using the zero crossing detection algorithms.

VI. Results

A. Data Acquisition

EOG data were collected in in biomedical signal processing laboratory, Department of BME of EEE Faculty, Khulna University of Engineering & Technology (KUET), Bangladesh. The data acquisition and extracted EOG data for subject S2 is shown in Fig. 8.

The various steps of signal processing are described below for the data from subject S2.

B. Preprocessing of Raw EOG Signal

The raw EOG signal is preprocessed for denoising, baseline drift removal and smoothing to make the signal appropriate for further processing for feature extraction. Fig. 9 shows wavelet denoised EOG signal along with the Raw EOG signal for both the channels.

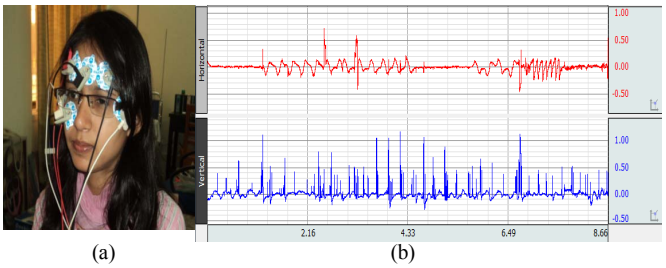

(a) (b)

Fig. 8. (a) Pictorial view of EOG measurement and (b) Measured EOG data for subject S2.

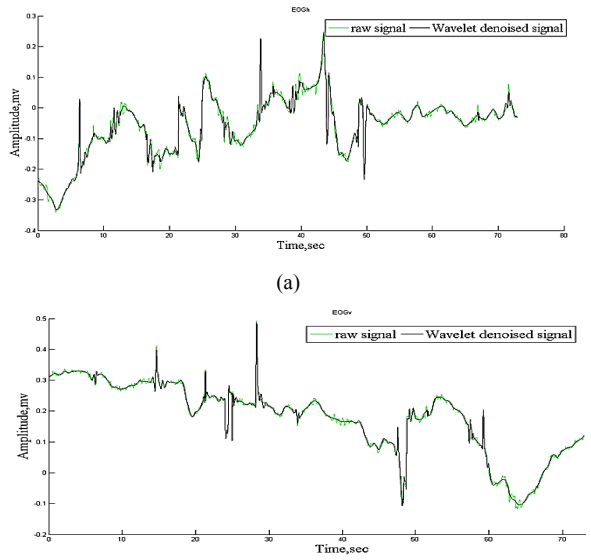

(a)

(b)

Fig. 9. Wavelet denoised EOG signal along with raw EOG signal (a) EOG_h and (b) EOG_v.

The denoised EOG signal is then processed to remove baseline drift using polynomial curve fitting. A polynomial of degree 20 is chosen. The calculated coefficients of the polynomial for the two channels for a particular set of data are given in Table I. The baseline drift removed signal for both channels are shown in Fig. 10.

TABLE I. CALCULATED COEFFICIENTS FOR THE POLYNOMIAL CURVE FITTING FOR BASELINE DRIFT REMOVAL

Signal	Value of Coefficients		
EOG_h	a_0 to a_{18}=0.00	a_{19}= 0.0023	a_{20}=-0.2821
EOG_v	a_0 to a_{18}=0.00	a_{19}= 0.0004	a_{20}=0.3057

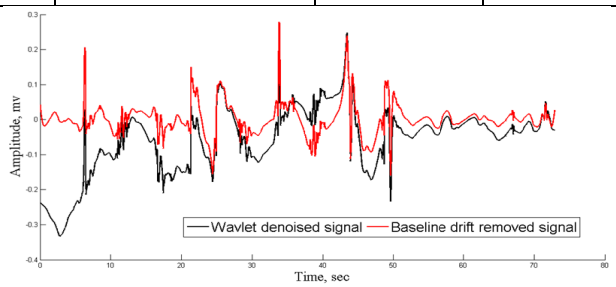

(a)

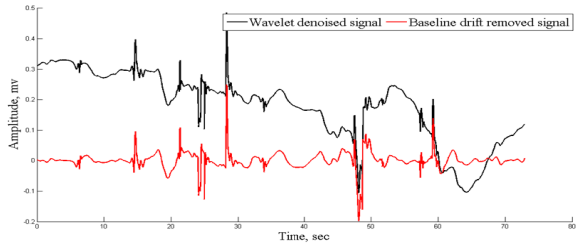

(b)

Fig. 10. Baseline drift removed EOG signal along with wavelet denoised EOG signal (a) EOG_h and (b) EOG_v.

The baseline drift removed signal is then further smoothened by using Savitzky-Golay filter as shown in Fig. 11. The filter uses a fourth degree polynomial with a frame size of 441. The degree and frame size is so chosen by inspection as it gives better results. The thresholds which separate blinks from saccades are calculated from the derivative of EOG signal.

Horizontal threshold=0.031mV; Vertical threshold=0.001 mV

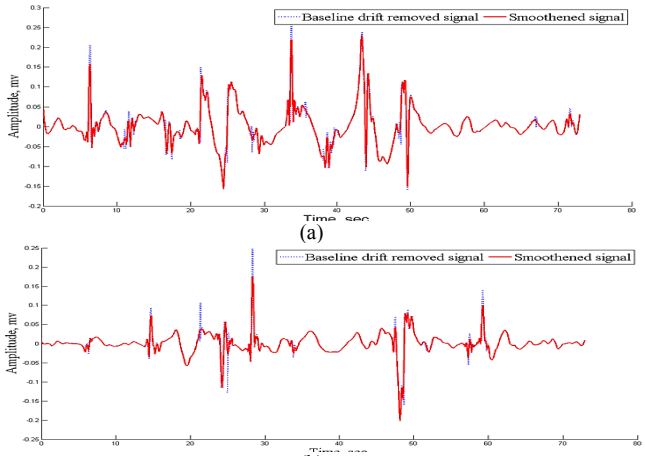

(a)

(b)

Fig. 11. Smoothened EOG signal along with Baseline drift removed EOG signal (a) EOG_h and (b) EOG_v.

C. Extracted Features

Total five eye movement features were extracted namely: Left, Right, Up, Down and Blink. From these the oblique saccades were then found. The detected eye movement features are shown in Fig. 11. The extracted features from a 200 seconds recording for three subjects are shown in Table: II.

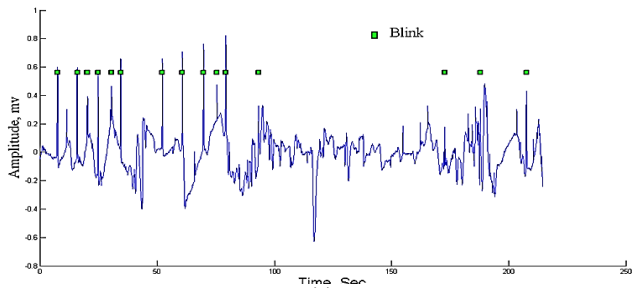

(a)

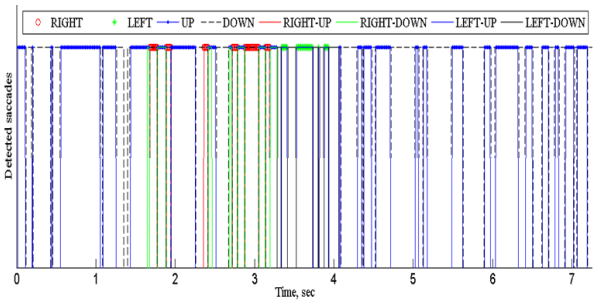

(a)

Fig. 12. Detected eye movement features (a) Blinks and (b) Saccades.

TABLE II. TABLECALCULATED COEFFICIENTS FOR THE POLYNOMIAL CURVE FITTING FOR BASELINE DRIFT REMOVAL

Subjects	Eye Movement Features (Directional movements and blinks)								
	Right	**left**	**Up**	**Down**	**Right-up**	**Right-down**	**Left-up**	**Left-down**	**blinks**
1	32	46	41	33	9	8	15	15	36
2	90	87	88	100	17	22	16	20	12
3	100	90	52	52	21	24	24	22	15

VII. CONCLUSION

In this work a simple and improved EOG signal processing is proposed. The feature detection accuracy of the proposed system in case of blinks and unidirectional saccades was found almost 100% but for oblique saccades accuracy faltered a little bit. The proposed method can be used in practically implementable real-time EOG based applications such as eye based human computer interfaces, human activity recognition, cognitive context measurement and so on.

REFERENCES

[1] N. V. Thakor, "Biopotentials and electrophysiology measurement": the measurement, instrumentation and sensors handbook, Boca Raton, CRC press, 1999.

[2] A. Banerjee, S. Chakraborty, P. Das, S. Datta, A. Konar, D. N. Tibarewala, R. Janarthanan "Single Channel Electrooculogram (EOG) based Interface for Mobility Aid": IEEE Proceedings of 4th International Conference on Intelligent Human Computer Interaction, Kharagpur, India, December 27-29, 2012.

[3] M. S. Hossain, K. Huda, M. Ahmad, "Command the computer with your eye - An electrooculography based approach" 8th International Conference on Software, Knowledge, Information Management and Applications (SKIMA), Dhaka, 18-20 Dec, 2014.

[4] H. Harun, W. Mansor," EOG Signal Detection for Home Appliances Activation ":5th International Colloquium on Signal Processing & Its Applications (CSPA), 2009.

[5] A. A. Haddad, R. Sudirman, C. Omar," Gaze At Desired Destination, and Wheelchair Will Navigate Towards It. New Technique to Guide Wheelchair Motion Based on EOG Signals": First International Conference on Informatics and Computational Intelligence, 2011.

[6] M. R. Kim, G. Yoon," Control Signal from EOG Analysis and Its Application": World Academy of Science, Engineering and Technology, International Journal of Electrical, Electronic Science and Engineering Vol: 7, No: 10, 2013.

[7] A. Bulling, D. Roggen, "Recognition of Visual Memory Recall Processes using Eye Movement Analysis", Proceedings of the 13th international conference on Ubiquitous computing (ubicomp'11), September 17–21, Beijing, China, 2011.

[8] A. Bulling, J. A. Ward, H. Gellersen, G. Tröster,"Eye Movement Analysis for Activity Recognition Using Electrooculography": IEEE transactions on pattern analysis and machine intelligence, vol. 33, no. 4, April 2011.

[9] A. Bulling, C. Weichsel, H. Gellersen," EyeContext: Recognition of High-level Contextual Cues from Human Visual Behaviour": CHI 2013, April 27–May 2, 2013, Paris, France.

[10] H. Singh, J. Singh," Human eye tracking and related issues: a review" International Journal Of Scientific Research (IJSR), 2012.

[11] H. Davison," Physiology of the eye": New York: Pergamon Press, 1990.

[12] Z. Lv, X. Wu, M. Li, C. Zhang, "Implementation of the EOG-based Human Computer Interface System", 2nd International Conference on Bioinformatics and Biomedical Engineering (ICBBE) 2008, Page.2188 – 2191, Shanghai.

[13] W. M. Bukhari W. Daud, Rubita Sudirman, "Time Frequency Analysis of Electrooculograph (EOG) Signal of Eye Movement Potentials Based on Wavelet Energy Distribution": Fifth Asia Modelling Symposium, Kuala Lumpur, 2011.

[14] R. Barea, L. Boquete, S. Ortega, E. López, J.M. Rodríguez-Ascariz,"EOG-based eye movements codification for human computer interaction": Expert Systems with Applications 39 (2012) 2677–2683.

[15] K. G. Rottach, V. E. Das, W. Wohlgemuth, A. Z. Zivotofsky., R. J. Leigh." Properties of Horizontal Saccades Accompanied by Blinks": Neurophysiology, vol.79, page.2985-2902June 1, 1998.

[16] H. Singh, J. Singh,"A review on electrooculography": International Journal of Advanced Engineering Technology (IJAET), Vol:3, Issue:4, Oct-Dec.'2012, pg:115-122.

[17] J. L. Andreassi, "Human Behavior & Physiological Response": Publisher: New York,Lawrence Erlbaum Associates, 5th edition, Published on 31 oct 2006.

[18] M. Kaur, B. Singh, Seema ,"Comparisons of Different Approaches for Removal of Baseline Wander from ECG Signal": 2nd International Conference and workshop on Emerging Trends in Technology (ICWET) 2011.

[19] K. Pettersson, S. Jagadeesan, K. Lukander, A. Henelius, E. Hæggström, K. Müller,"Algorithm for automatic analysis of electro-oculographic data": BioMedical Engineering OnLine 2013, 12:110.

[20] Wikipedia, The Free Encyclopedia. https://en.wikipedia.org/

[21] MATLAB, http://www.mathworks.com/help/

[22] http://sdsu-physics.org/physics180/physics180B/

[23] R. W. Schafer "What Is a Savitzky-Golay Filter?" IEEE Signal Processing Magazine. 07/2011; vol: 28(4), pg: 111-117.

Effects of Elevated Sleeping Postures on Cardiac Functions Analyzing Electrical Bio-impedance and Skin Blood Perfusion

Md. Bashir Uddin
Department of Biomedical Engineering
Khulna University of Engineering & Technology
Khulna-9203, Bangladesh
bas.u.kuet@gmail.com

Shabaz Khan and Mohiuddin Ahmad
Department of Electrical and Electronic Engineering
Khulna University of Engineering & Technology
Khulna-9203, Bangladesh
mohiuddin.ahmad@gmail.com

***Abstract*—This study investigated the effects of elevated sleeping postures on cardiac functions by analyzing electrical bio-impedance and skin blood perfusion in case of normal human subjects. Using different data acquisition units, the electrical bio-impedance based stroke volume and cardiac output were calculated in different elevated sleeping postures. Skin blood perfusion was measured also by laser Doppler flowmetry technique in all elevations to evaluate cardiac activity using frequency domain analysis. At first, data recordings were performed in supine sleeping (0° elevation) then sleeping elevations were changed sequentially from 0° to 15°, 15° to 30° and 30° to 45°. Data were recorded in all mentioned sleeping elevations for every subject. In most of the subjects, the parameters of cardiac functions were found highest in supine sleeping. When sleeping elevations were changed the cardiac functions were also changed in some significant level. Among all elevations except 0°, most significant improvements in cardiac functions were observed in 30° elevation only. It was highly recommended to sleep with an elevation around 30° to get best cardiac functions for those subjects only who prefer to sleep in elevation rather than supine posture.**

Keywords—sleep; elevated sleeping posture; cardiac function; electrical bio-impedance; skin blood perfusion

I. INTRODUCTION

A natural state characterized by the absence consciousness, nearly inactive sensory system of the body, and inhibition of the muscular functions in the body. The sleeping posture is the body configuration assumed by a person during sleep. There are four main sleeping postures with variables of each: left, right, supine and freefall. Some elevated postures are also seen where people prefer to sleep with head or upper body elevated to some angles. These elevated postures aren't commonly seen in our daily life that's why people are not so much aware about these. Many variations are found in sleeping on one's side, some of which are effective in helping to alleviate many sleep disorders such as insomnia and chronic sleep deprivation. The knees slightly upwards towards the chest area are considered as the most comfortable posture of sleep. Some studies have shown the cardiac output to be higher in the supine than in the right or left lateral postures in case of non-pregnant human beings [1]-[2]. Some studies have shown that cardiac output is higher in the left lateral than in the supine or right lateral postures [3], whereas others have concluded no difference in output among these various postures [4]. Cardiac output is higher in the left and right lateral postures than when the animals are in supine posture, shown by some recent studies [5].

Elevated sleeping posture may be considered as an effective way to treat some sleep disorder, although there are limited researches regarding this theme. A study claimed that the elevation resulted in less collapsible airway compared with the supine and the lateral sleeping postures [6] and concluded that in severely affected obstructive sleep apnea (OSA) patients upper body elevation, and to a lesser extent lateral posturing, improved upper airway stability significantly during sleep. In this study, upper airway stability was analyzed for OSA patients but cardiac functions have not been investigated with varying elevation that requires further exploration. Another study performed all-night polysomnography (PSG) while subject lying supine or sitting at a 60-degree angle and found that in the upright position, the frequency of OSA events decreased and gas exchange improved [7]. The above papers have addressed the effects of elevated sleeping for OSA patients only.

Many researchers have done their work on cardiac functions and elevated sleeping postures and the results are conflicting. Most of the research shows that the cardiac output is higher at 30° sleeping angle than other angles but some other research show deviations in results. No research has been conducted to evaluate cardiac functions in different elevated sleeping posture using spectral analysis. Frequency domain analysis hasn't been done to investigate the effects of elevated sleeping on normal human participants. The main goal of this study is to investigate the effects of different elevated sleeping posture (upper body elevated by 0°, 15°, 30°, and 45°) on cardiac functions (cardiac output and cardiac activity). Cardiac output and cardiac activity will be evaluated by analyzing stroke volume and blood perfusion respectively. It is hypothesized that different elevation in sleeping would have different effects on cardiac function and hence affect sleep quality.

978-1-4673-9257-0/15/$31.00 ©2015 IEEE

II. CARDIAC FUNCTIONS

A. Cardiac Output

Cardiac output (CO) is an important parameter to investigate cardiac functions. Cardiac output (CO), the amount of blood pumped by the heart per minute is the multiplication of stroke volume (SV) and heart rate (HR). SV is the amount of blood ejected by the right or left ventricle during a single cardiac cycle. CO can be determined non-invasively by employing electrical bio-impedance measurement techniques. Electrical bio-impedance is simply defined as the characteristic impedance of a volume of tissue and fluid. In case of CO measurement, the corresponding tissue includes the heart and the immediate surrounding volume of the thorax. Blood is the relevant fluid. If the electrical bio-impedance of a volume of tissue and fluid is Z_o (ohms), systolic ejection time is T (seconds), magnitude of the highest impedance change during systole is dZ/dt (ohms/sec) then the expression of SV is noted in (1) where SV is the stroke volume in ml, R is the resistivity of blood in ohms.cm and L is the distance between inner band electrodes in cm. Multiplication of SV and HR is called CO as noted in (2) where CO is the cardiac output in ml/minute and HR is the heart rate in BPM (bits per minute).

$$SV = R \times (L^2/Z_o^2) \times T \times dZ/dt_{(max)} \quad (1)$$

$$CO = SV \times HR \quad (2)$$

B. Cardiac Activity

Cardiac activity is another valuable investigation to find out cardiac functions. Cardiac activity can be demonstrated by Laser Doppler Flowmetry (LDF) and its frequency domain (spectral) analysis. An established and reliable method is LDF for the measurement of blood perfusion. Periodic oscillations in microvascular level are detected by the noninvasive technique of LDF. Five characteristic frequencies have been revealed from human forearm skin using the spectral analysis of LDF signal [8]. In addition to the cardiac and respiratory rhythms around 1 and 0.3 Hz, respectively [9], three frequencies have been detected in the regions around 0.1, 0.04, and 0.01 Hz in human skin [10]. LDF is an inexpensive, noninvasive method of measuring blood perfusion that is the continuous flow of circulating blood on a microscopic level. The working of LDF is the reading of frequency oscillation resulted by Doppler frequency shift of the red blood cells in a peripheral tissue and converts the frequency to an intensity oscillation. The LDF apparatus is composed of a low powered laser light and probe that collects readings and transmits results to an analyzer section. The emitted and reflected light is applied through optical fibers to the recorder of analyzer section. The output of the LDF recording is the flow of red blood cells, defined as the quantity of red blood cells times their velocity, which determines blood perfusion.

Frequency domain analysis of LDF signal is an established way to evaluate cardiac activity [8]-[10]. Fast Fourier transform (FFT) is a frequency based analysis to compute the frequency component of the non-stationary signal. The discrete Fourier transform of the discrete time signal *x(j)* is noted in (3) where, *k* is the harmonic number of frequency components of signal and X_k is the discrete frequency domain at different frequency. The output of a FFT will appear in the graph with magnitude plotted against frequencies. The power spectral density (PSD) is the description of power of the time series data with respect to the corresponding frequency. The expression of PSD can be obtained directly as a function of frequency from the time series data $x_{Sample\ Data}$ as noted in (4) where, *P(f)* has units of power/Hz and T_s is the sampling time period. The output of a PSD will appear in the graph with power plotted against frequencies.

$$X_k = \sum_{j=n_s}^{n_e-1} x(j) e^{-i2\pi\frac{jk}{N}} \quad (3)$$

$$P(f) = \frac{1}{T_s}\left|T_s \sum_{q=0}^{N} x_{Sample\ Data}(q) e^{-i2\pi f q T_s}\right|^2 \quad (4)$$

III. MATERIALS AND METHODS

A. Subject Selection

Several healthy young male subjects were enrolled in this study. All the subjects did not take any medication during the week prior to the study. All the subjects were free from smoking and drinking of alcohol and caffeine containing drinks at least 4 hour prior to the study. No subject was affected by cardiovascular disease or other physiological illness. After being informed about the study design, all the subjects gave their written consent. All the subjects had an initial visit to the experimental laboratory for different required assessments. The age, weight, height, body mass index (BMI) of all subjects is listed in Table I.

B. Experimental Setup and Data Acquisition

The experiment was completed in a silent laboratory room with keeping the temperature nearly constant. Four disposable strip electrodes, lead wire, and CO amplifier were used to record electrical bio-impedance and its derivatives as shown in Fig. 1. The lead was connected to non-invasive CO amplifier through data acquisition unit. Skin blood perfusion measurement on the tip of index finger was performed with fiber-optic based probes connected to LDF amplifier as shown in Fig. 2. Electrocardiogram (ECG) recoding was performed also by using disposable vinyl electrode electrodes, lead set, electrode gel, and data acquisition unit. ECG recording was used find out left ventricular ejection time (T). About 10 minutes were distributed for acclimatization before the data recordings. Data was taken sequentially with 0°, 15°, 30°, and 45° elevation. There was at least 15 minutes time gap between recordings of two successive postures. Electrical bio-impedance and its derivative, blood perfusion, and ECG signal recording for 30° elevated posture is shown in Fig. 3.

C. Processing of Recorded Signal

The recorded signals contained several noises such as 50Hz frequency component. By filtering, this high frequency component was removed. Smoothing technique was also used to find smoothed signal. Mean value smoothing was done here as noted in (5), where "*q*" is the number of points in the window and "*p*" is the sample number [11].

$$x_{Sample\ Data} = \sum_{h=p-q/2}^{h=p-(q-1)/2} x_{Measured\ Data}(h)/q \quad (5)$$

TABLE I. SUBJECT'S SPECIFICATIONS

Parameters	Value (N=4)*
Age (yr)	22±0.0
Weight(Kg)	70.5±2.06
Height (cm)	173.99±1.27
BMI (kg/m^2)	23.41±0.3122

*Values are Mean±Standard Deviation

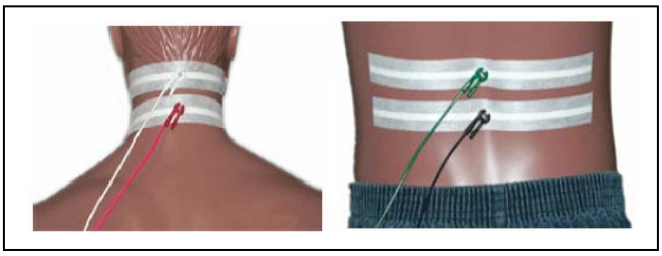

Fig. 1. Pictorial view of electrode placement and lead connection.

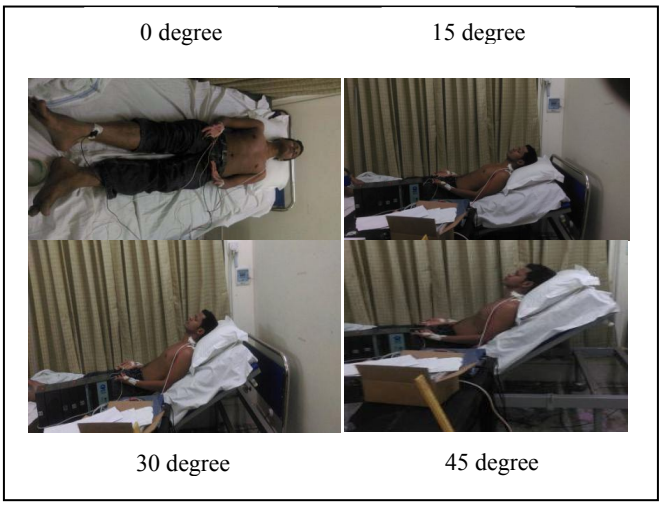

Fig. 2. Pictorial view of different elevated sleeping postures with complete data acquisition setup.

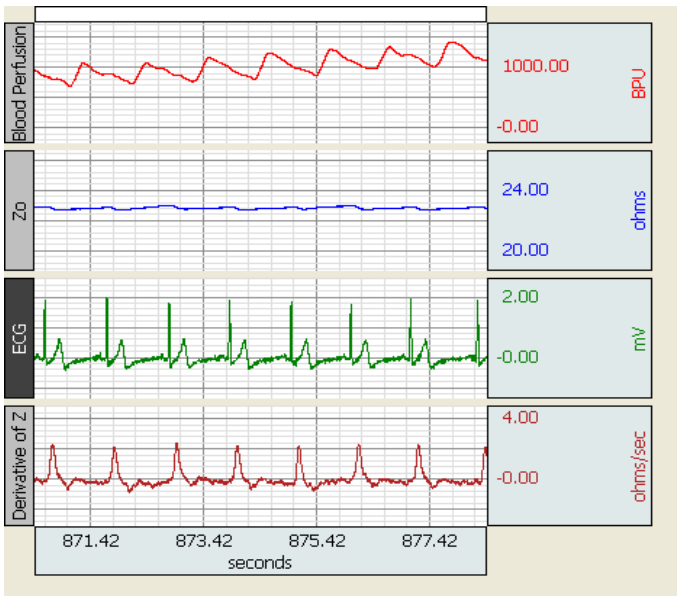

Fig. 3. Recorded signals for 30° sleeping angle.

IV. DATA ANALYSIS

A. Determination of Cardiac Output

The variations in electrical bio-impedance and its derivative, left ventricular ejection time (T), and HR with elevated sleeping postures are listed in Table II for subject 4. These variations are applied to determine SV and CO using (1) and (2) respectively for all sleeping angles. In this calculation, the resistivity of blood (R) is 147 ohms.cm and the length between inner band electrodes (L) is 28cm.

B. Frequency Spectrum Analysis

Cardiac activity can be effectively evaluated by spectral analysis of skin blood perfusion signal within the frequency range 0.6-1.6 Hz. The fast Fourier transform (FFT) and power spectral density (PSD) of skin blood perfusion signal for subject 3 are shown in Fig. 4 and Fig. 5 respectively. The peak magnitude and peak power of FFT and PSD analysis respectively within the frequency range for different sleeping elevations are noted in Table III for subject 2.

C. Statistical Analysis

The statistical analysis of stroke volume and cardiac output for all subjects with different sleeping elevations are shown in Fig. 6 and Fig. 7 respectively. The statistical analysis of spectral components of cardiac activity for all subjects with different sleeping elevations is indicated in Fig. 8 and Fig. 9.

TABLE II. VARIATIONS IN CARDIAC OUTPUT WITH SLEEPING ANGLES

Sleeping Angles	Z_o (ohm)	$dZ/dt_{(max)}$ (ohm/sec)	T (sec)	SV (ml)	HR (bpm)	CO (L/min)
0°	20.24	1.990	.265	148.3	62	9.19
15°	19.52	2.014	.263	160.2	59	9.45
30°	19.02	1.893	.268	161.5	60	9.69
45°	18.61	1.744	.252	146.2	61	8.92

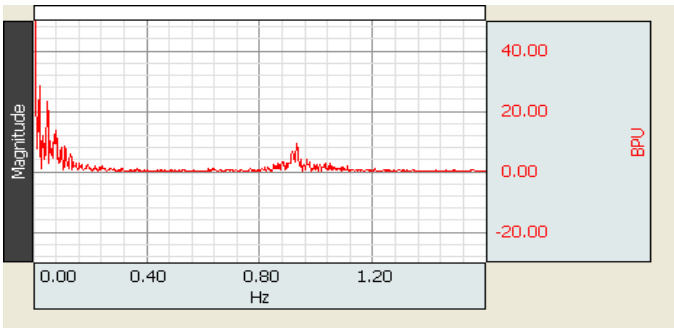

Fig. 4. Fast Fourier transform of skin blood perfusion signal for 30° elevation.

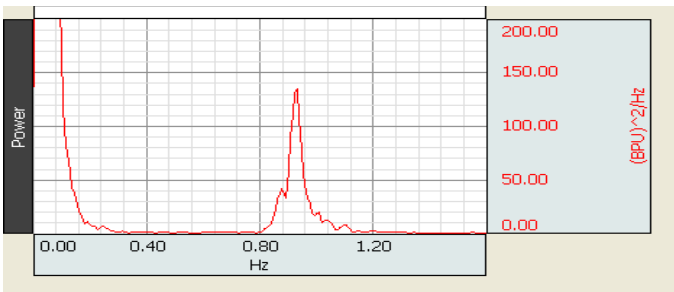

Fig. 5. Power spectral density of skin blood perfusion signal for 30° elevation.

TABLE III. VARIATIONS IN SPECTRAL COMPONENTS OF CARDIAC ACTIVITY

Sleeping Angles	FFT Analysis		PSD Analysis	
	Peak magnitude (BPU)	*f at peak magnitude (Hz)*	*Peak power $(BPU)^2/Hz$*	*f at peak power (Hz)*
0^0	7.236	1.072	81.848	1.076
15^0	4.754	1.029	63.087	1.022
30^0	4.504	1.122	30.090	1.121
45^0	5.054	1.074	31.958	1.106

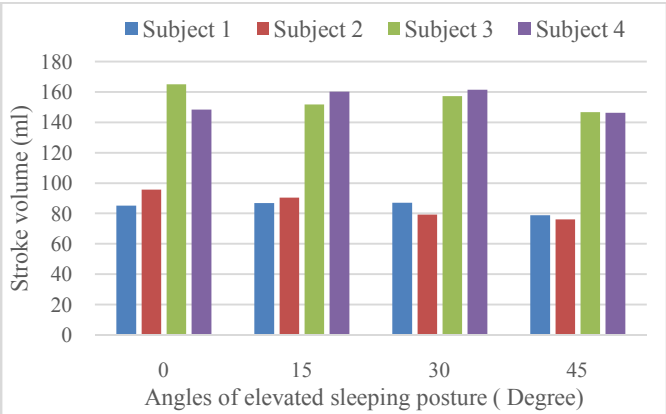

Fig. 6. Variations in SV with sleeping angles.

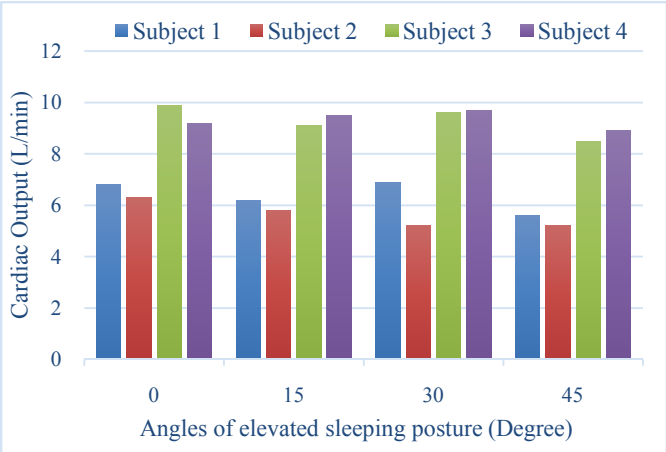

Fig. 7. Variations in CO with sleeping angles.

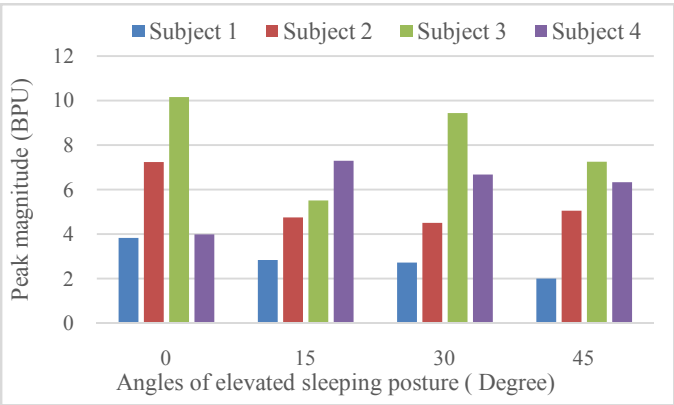

Fig. 8. Variations in peak magnitude of cardiac activity with sleeping angles.

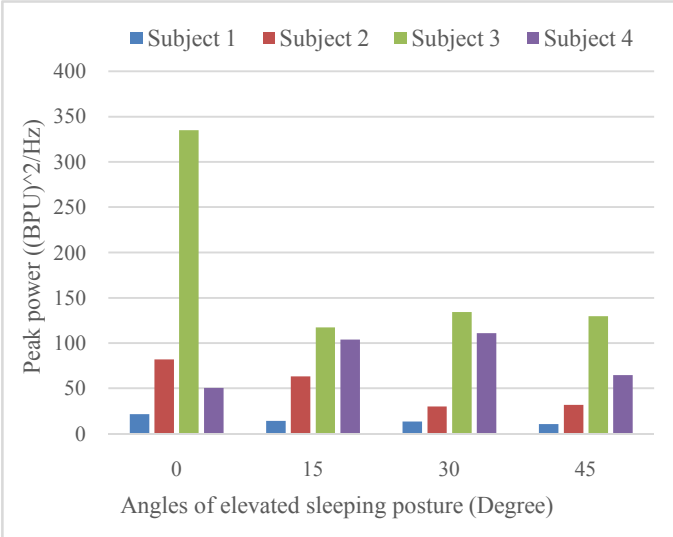

Fig 9. Variations in peak power of cardiac activity with sleeping angles.

V. RESULTS AND DISCUSSIONS

The effects of elevated sleeping postures on cardiac functions can be discussed in two sections- effects on cardiac output and effects on cardiac activity due to elevated postures, as explained below:

Effects of elevated postures on cardiac output: Stroke volume and cardiac output are totally different for different elevated sleeping postures. The highest stroke volume is found 161.5 ml at 30° sleeping angle and the lowest stroke volume is found 146.2 ml at 45° sleeping angle for subject 4. The highest cardiac output is found 9.69 L/min at 30° sleeping angle and the lowest cardiac output is found 8.92 L/min at 45° sleeping angle for the same subject. It is also seen that the highest stroke volume is found at 30° sleeping angle for subject 1 & subject 4 and subject 2 & subject 3 show highest stroke volumes at 0° sleeping angle. Similarly, the highest cardiac output is also found at 30° degree sleeping angle for subject 1 & subject 4 and subject 2 & subject 3 show highest cardiac outputs at 0° sleeping angle.

Effects of elevated postures on cardiac activity: It is found that the peak magnitude of FFT analysis is highest (7.236 BPU) at 1.072 Hz for 0° sleeping angle and lowest (4.504 BPU) at 1.122 Hz for 30° sleeping angle for subject 2. Similarly the peak power of PSD analysis is found highest (81.848 $(BPU)^2/Hz$)) at 1.076 Hz for 0° sleeping angle and lowest (30.090 $(BPU)^2/Hz$)) at 1.121 Hz for 30° sleeping angle for subject 2. The peak magnitude of FFT is found highest for most of the subjects at 0° sleeping angle. Also the peak power of PSD is found highest for most of the subjects at 0° sleeping angle. The significant increment in spectral components of cardiac activity is found at 30° sleeping angle for most of the subjects. The overall result is found by analyzing cardiac parameters such as stroke volume, cardiac output, and spectral components of cardiac activity. The results indicate highest cardiac functions at 0° (supine) sleeping angle. Besides, 30° sleeping angle also results significant increment in cardiac functions.

VI. Conclusions

The effects of different elevated sleeping postures on cardiac functions were investigated in this study by analyzing electrical bio-impedance and skin blood perfusion. Stroke volume, cardiac output and spectral components were analyzed as cardiac functions. Highest cardiac functions were found in supine sleeping (0° elevation) in most of the subjects. More significant increment in cardiac functions was observed in 30° elevation only except 0° elevation. To get best cardiac functions it was recommended to sleep with around 30° elevation in case of elevated sleeping only.

Acknowledgment

This work was partially supported by Higher Education Quality Enhancement Project (HEQEP), UGC, Bangladesh under Sub-project "Postgraduate Research in BME", CP#3472, Department of Biomedical Engineering (BME), Khulna University of Engineering & Technology (KUET), Bangladesh.

References

[1] A. J. Atkins, J. M. Watt, P. Milan, P. Davies, and J. S. Crawford, "The influence of posture upon cardiovascular dynamics throughout pregnancy," Eur J Obstet Gynecol Reprod Biol., vol.12, no. 6, pp. 357-772, December 1981.

[2] B. Newman, C. Derrington, and C. Dore, "Cardiac output and the recumbent position in late pregnancy," Anaesthesia, vol. 38, no. 4, pp. 332-335, April 1983.

[3] G. R. Whitman, D. L. Howaniak, T. S. Verga, "Comparison of cardiac output measurements in 20-degree supine and 20-degree right and left lateral recumbent positions," Heart Lung, vol. 11, pp. 256-257, 1982.

[4] K. Ueland, M. J. Novy, E. N. Peterson, and J. Metcalfe, "Maternal cardiovascular dynamics. IV. The influence of gestational age on the maternal cardiovascular response to posture and exercise," Am J Obstet Gynecol., vol. 104, no. 6, pp. 856-864, July 1969.

[5] S. Nakao, P. C. Come, M. J. Miller, S. Momomura, P. Sahagian, B. J. Ransil, and W. Grossman, "Effects of supine and lateral positions on cardiac output and intracardiac pressures: an experimental study," Circulation, vol. 73 no. 3, pp. 579-585, March 1986.

[6] A. M. Neill, S. M. Angus, D. Sajkov, and R. D. McEvoy, "Effects of sleep posture on upper airway stability in patients with obstructive sleep apnea," Am J Respir Crit Care Med, vol. 155, no. 1, pp. 199-204, 1997.

[7] R. D. McEvoy, D. J. Sharp, and A. T. Thornton, "The effects of posture on obstructive sleep apnea," Am Rev Respir Dis, vol. 133, no. 4, pp. 662-666, 1986.

[8] M. Bracic and A. Stefanovska, "Wavelet based analysis of human blood flow dynamics," Bulletin of Mathematical Biology, vol. 60, pp. 417-433, 1998.

[9] A. Stefanovska, "Self-organization of biological systems influenced by electrical current," Thesis, Faculty of Electrical Engineering, University of Ljubljana, Slovenia, 1992.

[10] A. Stefanovska and P. Kroselj, "Correlation integral and frequency analysis of cardiovascular functions," Open systems & information dynamics, vol. 4, pp. 457-478, 1997.

[11] M. Ahmad, A. Islam, T. T. Khan Munia, M. A. Rashid, and T. M. N. Tunku Mansur, "Physiological signal analysis for cognitive state estimation," Biomedical Engineering: Applications, Basis and Communication, vol. 24, no. 1, pp. 57-69, 2012.

A Novel Dual Purpose Spatial Domain Algorithm for Digital Image Watermarking and Cryptography Using Extended Hamming Code

Sudip Ghosh, Sayandip De
School of VLSI Technology
IIEST, Shibpur
Howrah-711103, India
sudipghosh2005@gmail.com, desayandip@gmail.com

Santi Prasad Maity, Hafizur Rahaman
Department of Information Technology
IIEST, Shibpur
Howrah-711103, India
spmaity@yahoo.com, rahaman_h@yahoo.co.in

Abstract—**The tremendous growth of internet in the recent years has made possible easier copying, manipulation and redistribution of digital media. As a result, the problem of security and copyright violation has greatly increased. To combat this problem, mechanisms like watermarking and cryptography are required. In this paper we have proposed a dual purpose spatial domain robust algorithm for both image cryptography and digital image watermarking where a key is generated using 'Extended Hamming Code' to make the code self-correcting. A comparative study of the proposed algorithm with other spatial domain algorithms in terms of Peak Signal to Noise Ratio (PSNR) and Normalized Correlation (NC) claims better performance in terms of robustness and imperceptibility. Cryptographic performance analysis shows that the algorithm is secure, consistent and fast to perform transmission of binary messages.**

Keywords— Digital Image Watermarking, Cryptography, Extended Hamming Code, Spatial Domain, Binary Watermark.

I. INTRODUCTION

In recent years the tremendous growth of internet has increased illegal transfer, copy, manipulation and redistribution of digital media, thus increasing the problem of copyright violation of digital media like images, audio clips, videos etc. This has highlighted the need for mechanisms like cryptography, steganography and digital watermarking [1].

Cryptography is the process of data hiding in which the contents of the message are protected from the attacker but the existence of the message is known to the attacker [2]. Steganography is the hiding of a message within the communicating data such that the attacker is unaware of the existence of the message. The original purpose of steganographic mechanisms is information hiding without concerning about the robustness.

Digital watermarking is one of the most popular methods to communicate data or message secretly in a host such as an image, audio or video in robust manner [3]. There are two domains of embedding the secret message or watermark into the host: spatial and transform domain. In spatial domain watermarking schemes, watermarks are directly applied by manipulation of intensity values of the pixels. In transform domain watermarking frequency components are manipulated to embed the watermark. Transform domain techniques like DCT, DFT etc. are more robust to attacks compared to spatial domain techniques. Easier implementation, reduced computational complexity and higher capacity has made us adopt the spatial domain watermarking scheme for our algorithm.

This paper proposes a spatial domain dual purpose blind algorithm for cryptography and digital watermarking where the watermark and the cover image are chosen to be binary and grayscale, respectively. The paper is organized with section I as introduction followed by related works in section II. Then the proposed algorithm for watermarking and cryptography has been explained in section III and IV respectively followed by performance analysis and results in section V. Conclusions are given in section VI followed by references.

II. RELATED WORK

A numerous publication exists in the field of security & copyright protection, so all of them cannot be covered in a single survey. So only a few of the popular cryptographic & spatial domain image watermarking methods has been discussed in this review.

Houtan Haddad Larijani et al. [4] presented a new algorithm called "Save Algorithm". Sakthivel. S. M. et al. [3] presented a modification of [4] which is called "PVSA (Pixel Value Search Algorithm)". Both these algorithms perform a pixel by pixel comparison between the host image and watermark and storing the host pixel location in a key in case of a match. Both [4] and [3] achieve high level of imperceptibility as they do not make any change in the host image.

Ben Wang et al. [13] presented a watermarking algorithm based on DWT (Discrete Wavelet Transform), DCT (Discrete Cosine Transform) and SVD (Singular Value Decomposition) which is robust and performs faster embedding and extraction.

Li et al. [7] proposed a robust adaptive blind watermarking scheme with the watermarks encrypted by Fresnel transform and utilizing fuzzy c- means clustering (FCM) technique.

Swaleha Saeed et al. [14] presented an encryption technique using Fisher- Yates Chaotic Shuffling which is consistent, secure and efficient for transmitting grayscale images over insecure networks.

Even though the above algorithms have already been proposed but creating a robust watermarking algorithm with

978-1-4673-9257-0/15/$31.00 ©2015 IEEE

high level of imperceptibility is still a challenging problem. However, our proposed algorithm provides high level of robustness to geometrical, noising, de-noising and image processing attacks along with better PSNR (Peak Signal to Noise Ratio) compared to the above algorithms, thus proving its imperceptibility.

III. Proposed Watermarking Algorithm

The proposed algorithm is a "self-correcting" spatial domain blind algorithm for digital watermarking where corresponding to each watermarked pixel a key is generated as per Extended Hamming Code [6] helping in self-correction. First of all, a grayscale image of size (m x n) is chosen as the host image and a binary image of size (r x c) is chosen as the secret message or watermark such that $m \geq n$. An EX-OR operation is performed between the watermark bit and the 2nd LSB of the host pixel. The result is embedded into the 1st LSB of the host pixel. Corresponding to this modified 1st LSB and the 2nd LSB of the host pixel four parity bits are generated as per Extended Hamming Code [6] (explained in section A). These four parity bits taken together form a 4-bit parity code which is converted to a decimal and stored in a key. The detailed embedding procedure is explained in section B.

A. Extended Hamming Code

Hamming codes are binary linear codes. A (n, k) Hamming code consists of a block length $n=2^r-1$ and a message length of $k=2^r-r-1$ [6] where r is an integer such that $r \geq 2$. Hamming codes can only detect and correct single bit errors. However, Extended Hamming codes are single error correcting and double error detecting (SECDED) codes which are obtained from Hamming codes by adjoining an overall parity check-bit. An (m, k) Extended Hamming code consists of a block length $m=2^r$ and a message length of $k=2^r-r-1$ where $r \geq 2$.

H0	H1	H2	H3	H4	H5	H6	H7
P1	P2	P3	M1	P4	M2	M3	M4

Figure 1. Extended Hamming Code (8,4)

Consider an (8, 4) Extended Hamming code (r = 3) given by H= (H0 H1 H2 H3 H4 H5 H6 H7) which consists of four message bits M= (M1 M2 M3 M4) and four parity bits P= (P1 P2 P3 P4). The arrangement of message and parity bits in Extended Hamming Code is shown in Fig. 1. Usually, a four-bit message code M= (M1 M2 M3 M4) is converted into an (8, 4) Extended Hamming Code by inserting parity bits P= (P1 P2 P3 P4) which are generated as follows:

$$P2= M1 \oplus M2 \oplus M4 \quad (1)$$
$$P3= M1 \oplus M3 \oplus M4 \quad (2)$$
$$P4= M2 \oplus M3 \oplus M4 \quad (3)$$
$$P1= P2 \oplus P3 \oplus M1 \oplus P4 \oplus M2 \oplus M3 \oplus M4 \quad (4)$$

Error Detection and Correction

For error detection and correction, a three-bit error code E= (E1 E2 E3) is generated from the Extended Hamming Code H as follows:

$$E1= H4 \oplus H5 \oplus H6 \oplus H7 \quad (5)$$
$$E2 = H2 \oplus H3 \oplus H6 \oplus H7 \quad (6)$$
$$E3 = H1 \oplus H3 \oplus H5 \oplus H7 \quad (7)$$

The value of E in decimal is obtained and the Eth bit location in H is complemented. If the decimal equivalent of E is 6, then H6 is complemented i.e. H6'= not (H6) to obtain modified H= (H0 H1 H2 H3 H4 H5 H6' H7). All the bits of the newly modified H are EX-ORed to obtain K.

$$K= H0 \oplus H1 \oplus H2 \oplus H3 \oplus H4 \oplus H5 \oplus H6' \oplus H7 \quad (8)$$

Case 1. If K = 0: This means single bit error is present and the error has been corrected by complementing H6.

Case 2. If K=1: This means double bit error is present and the error cannot be corrected.

B. Watermark Embedding

Input: (a) A grayscale image of size (m x n) as the host/cover image. (b) A binary image of size (r x c) is chosen as the watermark. **Output**: (a)A grayscale watermarked image of size (m x n). (b)A key of size (1 x N) where N= r x c.

Step 1. Read the cover image and the watermark image with their corresponding sizes.

$$I= \{x (i, j) \mid 0\leq i \leq m, 0\leq j \leq n, x (i, j) \in \{0, 1, \ldots, 255\}\}. \quad (9)$$
$$W= \{w (u, v) \mid 0\leq u \leq r, 0\leq v \leq c, w (u, v) \in \{0, 1\}\}. \quad (10)$$

Step 2. A key of size (1 x N) is chosen where N= r x c (r denotes row and c denotes column of the watermark image). The size of the watermark image is stored in the first two locations of the key such that key (1 x 1) = r and key (1 x 2) = c.

Step 3. A threshold value is chosen as the visual perception factor of a pixel in such a way that the threshold value and the pixel value are perceptually insignificant. Let the value of the threshold be 200.

Step 4. Count the number of cover pixels having value greater than or equal to threshold.

Step 5. Start with the first pixel of the cover image.

Step 6. Search for a cover image pixel having value greater than or equal to the threshold. Once search is completed store the current pixel location.

Step 7. Convert the obtained cover image pixel into 8-bit binary value. Replace the LSB of the cover image pixel using the following operation.

$$LSB1= LSB2 \oplus w (u, v) \quad (11)$$

where LSB1= LSB in the first bit plane position
LSB2= LSB in the second bit plane position
w (u, v) = watermark pixel

Step 8. With the help of LSB1 and LSB2 form a four-bit message code by padding two zeros in the front such that M= (M1 M2 M3 M4) = (0 0 LSB2 LSB1). As explained in section 3.1.1, obtain the Parity Code P and the Extended Hamming Code H for the message code M. Covert the Parity Code P to decimal and store in the key.

Step 9. Reconvert the modified cover image pixel from binary to decimal and pass the pixel.

Step 10. Recover the stored pixel location as stated in step 6.

Step 11. Repeat steps 6 to 10 for all pixels of the watermark image.

Lemma 1. Watermarking is possible only if N= r x c is less than the count obtained in step 4.

C. Watermark Extraction

Input: (a)A grayscale watermarked image. (b) A key of size (1 x N) where N= r x c where r x c is the dimension of the watermark. **Output**: Binary watermark of size r x c.

In the watermark extraction algorithm, the original cover image or the original watermark is not required. So, the proposed method is blind. However, the key generated during embedding is required to be known for watermark extraction.

Step 1. Read the watermarked image and the key.
Step 2. Read the first two locations of the key to obtain the dimensions of the watermark.
Step 3. Start with the first pixel of the watermarked image.
Step 4. Search for watermarked image pixel having value greater than threshold value and store the corresponding pixel location.
Step 5. Convert the corresponding pixel into 8-bit binary value and extract LSB1 and LSB2. Form a four-bit message code M= (0 0 LSB2 LSB1).
Step 6. Obtain the decimal equivalent of the parity code P from the key. Convert it into four-bit binary value to obtain P= (P1 P2 P3 P4). Combining P and M obtain the Extended Hamming Code H.
Step 7. As explained in section A, check whether single or double bit errors exist in M i.e. in LSB1 and LSB2 and correct them.
Step 8. After correction, the watermark is obtained by the following operation.

$$w(u, v) = LSB1 \oplus LSB2 \qquad (12)$$

Step 9. Extract the stored pixel location (step 4).
Step10. Repeat steps 4 to 9 for the entire dimension of the watermark obtained in step 2.

Lemma 2. The watermark can be extracted only if the key is known.

Lemma 3. This is a self-error correcting algorithm as we are only concerned of errors in LSB1 and LSB2 of watermarked image pixel. So, if by applying Extended Hamming Code, double bit error is detected in M= (0 0 LSB2 LSB1), then both LSB1 and LSB2 are complemented (other 2 bits are always 0, no errors are possible in them). In case of single bit error, Extended Hamming Code will give us the bit position of the erroneous bit and we can easily determine whether error is in LSB1 or LSB2.

IV. PROPOSED CRYPTOGRAPHIC ALGORITHM

Proposed cryptographic algorithm is applicable for symmetric-key systems where a single key or password is known only to the sender and receiver. Encryption and decryption is possible only if the key is known [2]. The message to be encrypted is a binary image of size (r x c) and the key is chosen to be a grayscale image of size equal to that of the binary image i.e. (r x c). The Symmetric-key Cryptographic Model with respect to our proposed algorithm is depicted in Fig. 2.

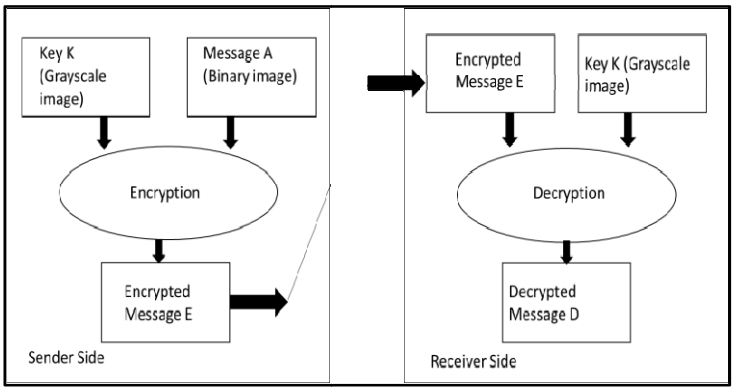

Figure 2. Symmetric-Key Cryptographic Model

D. Encryption

Input: (a) A binary image of size r x c as message A. (b) A grayscale image of size r x c as key K. **Output**: A grayscale encrypted image of size r x c as encrypted message E.

Step 1. Read the message A and the key K. Initialize two matrices B and E each of them having size equal to the message A i.e. r x c.
Step 2. Choose a pixel of the key K, say K (i, j), pixel at ith row and jth column. Convert it into 8-bit binary value. Extract the LSB in the first bit plane position (LSB1) and the LSB in the second bit plane position (LSB2).
Step 3. Choose a pixel of the message A, say A (i, j), pixel at ith row and jth column.
Step 4. Choose a four-bit code M= (M1 M2 M3 M4) such that M1=0, M2=0, M3= LSB2 and M4 = LSB2 $\oplus$ A (i, j).
Step 5. As explained in section A, obtain the Parity Code P and the Extended Hamming Code H for the four-bit code M. Covert the Parity Code P to decimal and store as a modified message pixel in B i.e. B (i, j).
Step 6. Repeat steps 2 to 5 for every set of pixels i and j in the message A and key K. Thus, we get a modified message B.
Step 7. After obtaining B, the final encrypted message E is obtained by performing bitwise EX-OR operation between each pair of pixels in B and K. The operation is shown as follows:

$$E(i, j) = \text{Bitwise EX-OR}(K(i, j), B(i, j)) \qquad (13)$$

where E (i, j) = Pixel in the ith row and jth column of E.
B (i, j) = Pixel in the ith row and jth column of B.
K (i, j) = Pixel in the ith row and jth column of K.

E. Decryption

Input: (a) A grayscale image of size r x c as encrypted message E. (b) A grayscale image of size r x c as key K. **Output**: A binary image of size r x c as decrypted message D.

Step 1. Read the encrypted message E and the key K. Initialize two matrices C and D each of them having size equal to the encrypted message E i.e. r x c.
Step 2. A partially decrypted message C is obtained by performing bitwise EX-OR operation between each pair of

pixels in encrypted message E and Key K. The operation is shown as follows:

$$C(i, j) = \text{Bitwise EX-OR}(K(i, j), E(i, j)) \quad (14)$$

where C (i, j) = Pixel in the ith row and jth column of C.
K (i, j) = Pixel in the ith row and jth column of K.
E (i, j) = Pixel in the ith row and jth column of E.

Step 3. Choose a pixel of the key K, say K (i, j), pixel at ith row and jth column. Convert it into 8-bit binary value. Extract the LSB in the first bit plane position (LSB1) and the LSB in the second bit plane position (LSB2).

Step 4. Choose a pixel of the partially decrypted message C, say C (i, j), pixel at ith row and jth column.

Step 5. Choose a four-bit code M= (M1 M2 M3 M4) such that M1=0, M2=0, M3= LSB2 and M4 = LSB1.

Step 6. Obtain the Parity Code P= (P1 P2 P3 P4) from the last four bits of the partially decrypted message pixel i.e. C (i, j). The Extended Hamming Code H is obtained by combining the four-bit code M and Parity Code P.

Step 7. As explained in section A, check for single bit error that is supposed to exist in M i.e. in LSB1 and LSB2 and correct it.

Step 8. After correction the final decrypted message pixel D (i, j) is obtained by performing EX_OR operation between M3 and M4. The operation is shown as follows:

$$D(i, j) = M3 \oplus M4 \quad (15)$$

where D (i, j) = Pixel in the ith row and jth column of D.
M3= Second LSB in M.
M4= First LSB in M.

Step 9. Repeat steps 3 to 8 for every set of pixels in the partially decrypted message C and the Key K to obtain the final decrypted message D.

Lemma 4. This is a symmetric-key cryptographic system, so the encrypted message can be decrypted only if the key K is known to the receiver.

V. Analysis and Experimental Results

F. For Watermarking Algorithm

The performance of the proposed watermarking algorithm is evaluated by using MATLAB (R2011a) in terms of five metrics- PSNR (Peak Signal to Noise Ratio), MAE (Mean Absolute Error), SSIM (Structural Similarity Index), Quality Index (Q) and Normalized Correlation (NC). Peak Signal to Noise Ratio (PSNR) is the ratio of the maximum signal power to the corrupting noise power. Structural Similarity Index (SSIM) [8] and Normalized Correlation (NC) are the parameters for measuring similarity between two images. Quality Index (Q) [9] measures the distortion of the received image compared to the original image. Mean Absolute Error (MAE) compares two images by providing a qualitative score that describes the degree of fidelity or level of distortion between them [5]. The formula of these metrics is given in Table I. For analysing the effectiveness of our proposed algorithm, we have chosen a variety of grayscale cover images and binary watermarks of different sizes as shown in Fig 3. The imperceptibility of the algorithm is analyzed in Table II by choosing cover images and watermarks of variable sizes. As the size of the watermark increases, the level of imperceptibilty decreases as can be seen in Table II.

TABLE I. Image Performance Metrics

	Formula	Description
PSNR	$MSE = \frac{\sum_{M,N}[I_1(m,n) - I_2(m,n)]^2}{M \times N}$ $PSNR = 10\log_{10}(\frac{255^2}{MSE})$	MSE= Mean Square Error I_1, I_2= The two images under consideration m, n= Rows, Columns of input images. M, N= Size of input images
NC	$NC = \frac{\sum_1^M \sum_1^N I'_{ij} I_{ij}}{\sum_1^M \sum_1^N (I_{ij})^2}$	I= Original Image I'= Extracted Image
MAE	$MAE = \frac{\sum_1^M \sum_1^N \lvert I'_{ij} - I_{ij} \rvert}{M \times N}$	I= Original Image I'= Extracted Image
MSSIM	$MSSIM = \frac{1}{M}\sum_{j=1}^{M} SSIM(x_j, y_j)$ $SSIM = \frac{(\mu_x\mu_y + C_1)(2\sigma_{xy} + C_2)}{(\mu_x^2\mu_y^2 + C_1)(\sigma_x^2 + \sigma_y^2 + C_2)}$	X= Reference Image Y= Distorted Image x_j, y_j= Image contents at jth local window M= No. of local windows
Q	$Q = \frac{4\sigma_{xy}\mu_x\mu_y}{(\sigma_x^2 + \sigma_y^2)(\mu_x^2 + \mu_y^2)}$	x_j, y_j= Image contents at jth local window μ_x, μ_y= Mean Intensity σ_x, σ_y= Standard Deviation

Various kinds of attacks are implemented on the embedded image to check the robustness of the proposed algorithm. The detailed performance of the algorithm to these attacks is shown in Table III. Figure 4 shows the cover image and the watermark chosen for the analysis of robustness.

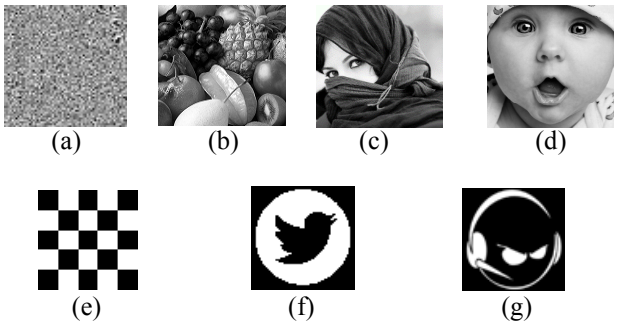

Figure 3. Grayscale Cover Images : (a) Noise (64 x 64) (b) Fruit (128 x 128) (c) Girl (256 x 256) (d) Baby (512 x 512) and Binary Watermark Images : (e) Checkerboard (16 x 16) (f) Bird (32 x 32) (g) Cartoon (64 x 64)

TABLE II. Performance Analysis of Embedded Image with Cover Image

Water mark	Cover Image	PSNR	MSSIM	Q	NC	MAE
Check-erboard	Noise	63.016	0.9999	1.00	0.9999	0.0190
	Fruit	69.668	0.9999	1.00	0.9999	0.0041
	Girl	75.257	0.9998	1.00	1.00	0.0011
	Baby	81.785	1.00	1.00	1.00	0.0002
Bird	Noise	Embedding Not Possible (Lemma 1)				
	Fruit	63.311	0.9999	1.00	0.9999	0.0153
	Girl	69.565	0.9986	1.00	0.9999	0.0039

	Baby	75.335	0.9999	1.00	1.00	0.0012
Carto-on	Noise	Embedding Not Possible (Lemma 1)				
	Fruit	Embedding Not Possible (Lemma 1)				
	Girl	63.549	0.9938	1.00	0.9999	0.0137
	Baby	69.239	0.9997	1.00	0.9999	0.0047

Figure 4. A Particular Case: (a) Chosen Cover Image (256 x 256) (b) Watermarked Image (256 x 256) (c) Chosen Watermark (32 x 32) (c) Extracted Watermarked (32 x 32)

TABLE III. PERFORMANCE ANALYSIS OF EXTRACTED WATERMARK WITH ORIGINAL WATERMARK WHERE CHOSEN WATERMARK IS BIRD IMAGE OF SIZE 32 X 32 AND CHOSEN COVER IMAGE IS GIRL IMAGE OF SIZE 256 X 256

Watermark Attacks	PSNR	MSSIM	Q	NC	MAE
Without Attack	Infinity	1.00	1.00	1.00	0.00
Gaussian Noise	Infinity	1.00	1.00	1.00	0.00
Salt & Pepper Noise	Infinity	1.00	1.00	1.00	0.00
Speckle Noise	Infinity	1.00	1.00	1.00	0.00
Poisson Noise	Infinity	1.00	1.00	1.00	0.00
Blur	Infinity	1.00	1.00	1.00	0.00
Motion Blur	Infinity	1.00	1.00	1.00	0.00
Sharpen	Infinity	1.00	1.00	1.00	0.00
Histogram Equalize	Infinity	1.00	1.00	1.00	0.00
Adaptive Histogram Equalize	Infinity	1.00	1.00	1.00	0.00
Contrast Adjusting	Infinity	1.00	1.00	1.00	0.00
Gamma Correction	Infinity	1.00	1.00	1.00	0.00
Gaussian Filter	Infinity	1.00	1.00	1.00	0.00
Median Filter	Infinity	1.00	1.00	1.00	0.00
Crop (25 %)	Infinity	1.00	1.00	1.00	0.00
Crop (50 %)	Infinity	1.00	1.00	1.00	0.00
Crop (75 %)	55.423	0.5895	0.5746	0.6698	0.1865
Crop (80 %)	52.983	0.2278	0.2698	0.4392	0.3271
Rotation (5°)	Infinity	1.00	1.00	1.00	0.00
Rotation (35°)	Infinity	1.00	1.00	1.00	0.00
Rotation (55°)	Infinity	1.00	1.00	1.00	0.00
Rotation (90°)	Infinity	1.00	1.00	1.00	0.00
Resize (2)	Infinity	1.00	1.00	1.00	0.00
Resize (0.5)	Infinity	1.00	1.00	1.00	0.00
Resize (0.2)	Infinity	1.00	1.00	1.00	0.00
Resize (0.1)	Infinity	1.00	1.00	1.00	0.00
JPEG 10	Infinity	1.00	1.00	1.00	0.00
JPEG 50	Infinity	1.00	1.00	1.00	0.00
JPEG 80	Infinity	1.00	1.00	1.00	0.00

TABLE IV. PARAMETRIC COMPARISION FOR PROPOSED ALGORITHM AND EXISTING ALGORITHMS

Author	Q	PSNR, dB	MSSIM	NC	Capacity* (bits/pixel^2)	MAE
Proposed Algorithm	1.0	81.78	1.0	1.0	$\frac{16 \times 16}{256 \times 256}$	0.0002
Y.-T.Lin et al. [10]	DNS	48.52	DNS*	DNS	$\frac{128}{256 \times 256}$	DNS
Dong Zheng et al. [11]	DNS	42	DNS	DNS	$\frac{8}{512 \times 512}$	DNS
Shijun Xiang et al. [12]	DNS	44.58	DNS	DNS	$\frac{25}{512 \times 512}$	DNS
Ben Wang et al. [13]	DNS	78.23	DNS	DNS	$\frac{32 \times 32}{512 \times 512 \times 8}$	DNS

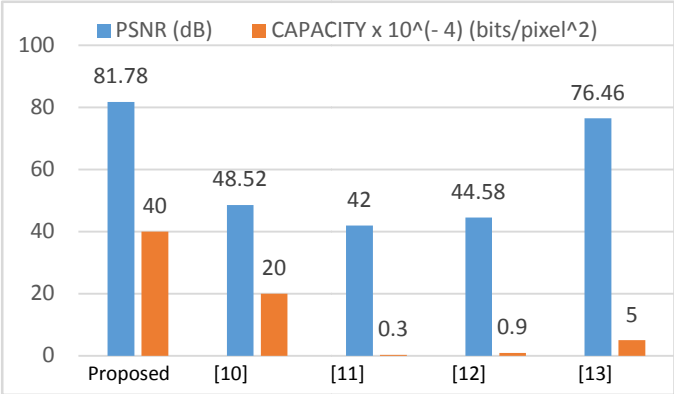

Figure 5. Comparison Statistics for various PSNR and Capacity Value (*capacity is the no. of watermark bits embedded divided by the total no. of pixels in the cover image and *DNS is Data Not Specified)

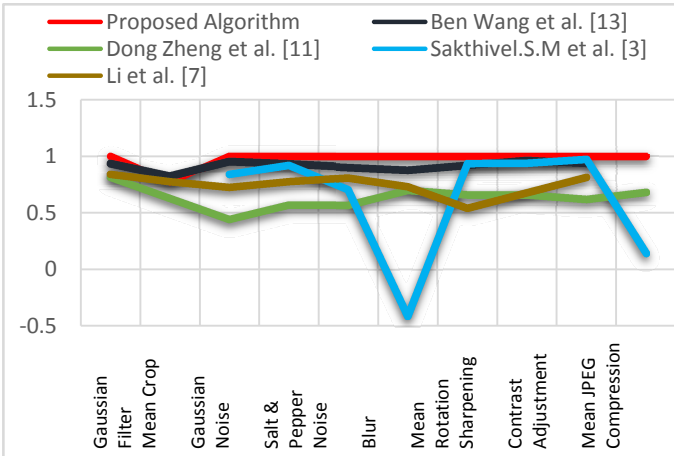

Figure 6. Comparative study of robustness of proposed algorithm with existing algorithms in terms of Normalized Correlation (NC)

A comparative study is done to prove the effectiveness of the proposed algorithm. Table IV and Fig. 5 shows that our algorithm gives a higher degree of imperceptibility by giving the highest PSNR among some of the existing schemes. Also, from Fig. 6 we can conclude that our algorithm is more robust to noise, geometrical, filtering and image processing attacks compared to the schemes proposed by Li et al. [7], Dong Zheng et al. [11], Ben Wang et al. [13] and Sakthivel. S. M et al. [3].

G. For Cryptographic Algorithm

The performance of the proposed cryptographic algorithm is evaluated by using MATLAB (R2014a) and has been implemented on Intel i5 CPU@ 3.20 GHz and 4 GB RAM memory. The grayscale key, original message, obtained encrypted and decrypted message are shown in Table V for two different cases along with the effectiveness in the algorithm for changes in the original key. The performance analysis in terms of various cryptographic parameters like encryption, decryption time [14], Encryption Ratio (*percentage of data that is encrypted with respect to total data) etc. is done in Table VI.

TABLE V. CRYPTOGRAPHIC CASE STUDY SHOWING CHOSEN GRAYSCALE KEY, ORIGINAL MESSAGE, ENCRYPTED MESSAGE AND DECRYPTED MESSAGE

Key Original	Message	Encrypted Message	Decrypted Message with correct key
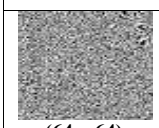 (64 x 64)	(64 x 64)	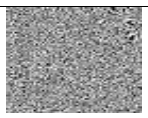 (64 x 64)	(64 x 64)
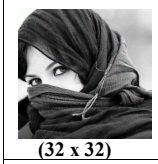 (32 x 32)	(32 x 32)	(32 x 32)	(32 x 32)
Key Original	**Message**	**Decrypted Message with incorrect key (1 pixel modified)**	**Decrypted Message with incorrect key (1 and more than 1 percent of pixels modified)**
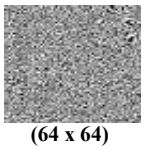 (64 x 64)	(64 x 64)	(64 x 64)	(64 x 64)
(32 x 32)	(32 x 32)	(32 x 32)	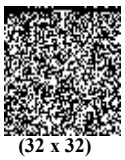 (32 x 32)

TABLE VI. CRYPTOGRAPHIC PERFORMANCE ANALYSIS

Cryptographic Parameters	Case 1 (64x 64) Key	Case 1 (64x 64) Message	Case 2(32 x 32) Key	Case 2(32 x 32) Message	Case 3(16 x 16) Key	Case 3(16 x 16) Message
	Noise	Cartoon	Girl	Bird	Fruit	Checkerboard
Encryption time	1.803 sec		0.4759 sec		0.144 sec	
Decryption time	1.920 sec		0.511 sec		0.158 sec	
Average time	1.861 sec		0.4936 sec		0.151 sec	
Bytes Processed	4608 bytes		1152 bytes		288 bytes	
Data rate	2.42 KB/sec		2.28 KB/sec		1.86 KB/sec	
Encryption Ratio*	100%		100%		100%	
Visual Degradation	PSNR = 4.34 NC = - 0.002 (Lower value preferable)		PSNR = 6.60 NC = - 0.01 (Lower value preferable)		PSNR = 6.42 NC = 0.045 (Lower value preferable)	
Decryption Quality	PSNR = Infinity NC = 1.00		PSNR = Infinity NC = 1.00		PSNR = Infinity NC = 1.00	

VI. CONCLUSION AND FUTURE WORKS

In this paper we have proposed a dual purpose robust algorithm in spatial domain for both digital watermarking and image cryptography. In case of digital watermarking the watermark can be extracted blindly using the watermarked image and the key, hence it finds applications in security and copyrighting purposes. The algorithm gives a higher degree of imperceptibility without sacrificing the robustness. The same algorithm can be used to design a symmetric-key cryptographic system having applications in secure information transferring systems. The hardware implementation of the proposed algorithm will be done in the future.

REFERENCES

[1] W. Bender, D. Gruhl, N. Morimoto and A. Lu, "Techniques for data hiding", *IBM systems Journal*, vol. 35, no 3.4, pp. 313-335,1996.

[2] W. Diffie and S. Landau, *Cryptography*, MIT Press, Edition 1, ISBN 9780262256018, 2007.

[3] J. Sakthivel. S.M. and Dr. Ravi Sankar. A, "A real time watermarking of grayscale images without altering it's content", *International Conference on VLSI-SATA*, Jan 2015, pp. 1 – 6.

[4] R Houtan Haddad Larijani and Gholamali Rezai Rad, " A new spatial domain algorithm for grayscale images watermarking", in *Proceedings of the International Conference on Computer and Communication Engineering*, May 13-15, 2008, pp. 157-161.

[5] Sudip Ghosh, Somsubhra Talapatra, Navonil Chatterjee, Santi P Maity and Hafizur Rahaman, "FPGA based implementation of embedding and decoding architecture for binary watermark by spread spectrum scheme in spatial domain", *Bonfring International Journal of Advances in Image Processing*, vol. 2, no. 4, December 2012.

[6] D. K. Bhattacharrya, S. Nandi' "An efficient class of SEC-DED-AUED codes", *ISPAN '97*, pp. 410-415. doi: 10.1109/ISPAN.1997.645128.

[7] Jianzhong Li, Xiangsu Zhang, Shou Liu, Xuechang Ren, "An adaptive secure watermarking scheme for images in spatial domain using fresnel transform", 1st *IEEE International Conference on Information Science and Engineering* , Dec 2009, pp. 1630- 1633.

[8] Z. Wang, A. C. Bovik, H. R. Sheikh and E. P. Simoncelli, "Image quality assessment: From error measurement to structural similarity" *IEEE Transactions on Image Processing*, vol. 13, no. 1, pp. 600– 612, Jan 2004.

[9] Zhou Wang and Alan C. Bovik, "A Universal Image Quality Index", *IEEE Signal Processing Letters*, vol 9, no. 3, pp. 81- 84, March 2002.

[10] Y.-T. Lin, C.-Y. Huang and G.C. Lee, "Rotation, scaling, and translation resilient watermarking for images", *Image Processing, IET*, vol. 5, no. 4, pp. 328- 340, June 2011.

[11] Dong Zheng, Sha Wang and Jiying Zhao, "RST Invariant Image Watermarking Algorithm with Mathematical Modeling and Analysis of the Watermarking Processes", *IEEE Transactions on Image Processing,* vol. 18, no. 5, pp. 1055- 1068, March 2009.

[12] Shijun Xiang, Hyoung Joong Kim and Jiwu Huang, "Invariant Image Watermarking Based on Statistical Features in the Low-Frequency Domain", *IEEE Transactions on Circuits and Systems for Video Technology,* vol.18, no. 6, pp. 777- 790, June 2008.

[13] Ben Wang, Jinkou Ding, Qiaoyan Wen, Xin Liao and Cuixiang Liu, " An image watermarking algorithm based on DWT DCT and SVD", *IEEE International Conference on IC-NIDC*, November 2009, pp. 1034- 1038.

[14] S. Saeed, M.S. Umar, M.A. Ali, M. Ahmad, " A Gray-Scale Image Encryption Using Fisher-Yates Chaotic Shuffling in Wavelet Domain", *Recent Advances and Innovations in Engineering (ICRAIE)*, May 2014, pp.1-5.

Role of Clinical Engineering to Reduce Patient's Risk Factors in Life Support Ventilator

Md. Anwar Hossain[1], A. K. M. Rahman[2], Md. Rezanur Rahman[3], Md. Rafiqul Islam[4], and Mohiuddin Ahmad[5]
[1]Department of Biomedical Engineering, Khulna University of Engineering & Technology (KUET), Khulna-9203, Bangladesh
[2]Ministry of Fisheries, Government of Bangladesh
[3]Ministry of Health & Family Welfare, Government of Bangladesh
[4, 5]Department of Electrical & Electronic Engineering, KUET, Khulna-9203, Bangladesh
E-mail: anwar.bme@gmail.com, joardrre@gmail.com, mraman@itc.nl, islambit@yahoo.com, mohiuddin.ahmad@gmail.com

Abstract— **The patients who are unable to take breathe normally is taken into life support ventilator, which without clinical engineering professional (CEP) interaction, cannot be kept in safe and functional. The operational characteristics of life support ventilator used in ICU have various risk factors such as, invasively or noninvasively perform diagnostic, therapeutic, corrective or monitoring intervention of the patients. Here we have presented an approach to develop a standard of risk factor management incorporating the role of CEP to mitigate the risks in real-time. For clinical setting and safe operation of ventilator devices, calibration must be ensured in the standard. Development of correlation among doctor, clinical engineer, and nurse is required for proper functioning of the ventilator. A comparison of risk factors is shown with and without CEP and found that the risk factor can be reduced significantly in developed countries with respect to developing countries like Bangladesh. In this study, mathematical model of risk factor reduction is also proposed.**

Keywords—Clinical Engineers, Risk factor, Intensive care, Life support ventillator, Hospital

I. INTRODUCTION

A. The Conceptual Background of the Study

A life support ventilator is an invention of modern medical technology and which is used for the patients who are unable to take breath normally but it has been observed that without clinical engineering interaction, this device could not keep in safe functional mode. An intensive care ventilator is a costly and life support medical device which is used for therapeutic and monitoring purpose of intensive care unit (ICU) patients of hospital.

Medical devices in the hospital such as mechanical ventilators and anesthesia machines have been managed by doctors and nurses throughout the world [1]. In Japan, doctors and nurses have performed the maintenance of mechanical ventilators in the past [2]. With the rapid growth of medical technology, the configuration of ventilator becomes complex due to integration of electrical, electronic and computation technologies. Due to submerge the multi-technology in ICU ventilator, doctors and nurse have felt risky of the use and maintenance of the ventilator in the hospitals [3].

B. Historical Background

The aim of this research is to investigate the effectiveness of maintaining mechanical ventilators by clinical engineers (CEs) using a specialized calibrator in hospitals. It is important to ensure appropriate quality control of mechanical ventilator support. Usually, faulty mechanical ventilators were repaired by the distributor. However, since the late 1990s, clinical engineers (CEs) who have a certificate of completion and have completed established course requirements now perform the maintenance of mechanical ventilators in hospitals. During the 1980s, general-purpose-type mechanical ventilators were in use [4]. Their operating principle was simple, and mechanical ventilators at that time had few circuit boards and/or sensors [5]. These mechanical ventilators were rugged and did not break down easily. Operator error accounted for most of the sudden malfunctions of mechanical ventilators [6, 7].

However, over the last two decades, technological developments have led to significant improvements in the performance of mechanical ventilators [8–11]. Modern critical care mechanical ventilators have circuit structures with numerous CPU boards and sensors [12]. Therefore, these mechanical ventilators have more failure points that increase the likelihood of failure. Blanch reported that spending an immense amount of time and cost could secure the reliability of an apparatus, but it was hard to anticipate the deterioration of mechanical ventilators; their safety and reliability will change significantly as ventilators are used or age [13]. The use of the PTS-2000 calibration analyzer has contributed to the discovery of previously undetected malfunctions in the new generation of high-performance mechanical ventilators. In this way, evaluating ventilation and carrying out in-house repairs has proved to be effective for obviating the chance of renting faulty units. Clinical engineering has decreased medical device failure which exposes patients to potentially harmful risks through proper use of health care technology. The current status of the clinical engineers in Bangladesh is illustrated in [14].

Thus, developed countries have reduced risk factor of ICU patients from ICU ventilators by interfacing the in-house clinical engineering professionals in their hospitals whereas, most of the developing countries such as Bangladesh, Bhutan,

978-1-4673-9257-0/15/$31.00 ©2015 IEEE

Nepal, Myanmar and so many have been maintaining the ICU ventilators through the conventionally short train electrical/mechanical trade diploma engineers on call basis. Instant failure of ventilators could not be repaired by vendor's engineers/ technicians. As a result, harmful situation is continuing for the ICU patients for the developing countries like Bangladesh in the world. From the past and present records, we have been observed that the performance of the use, calibration, software upgrades, preventive maintenance, overhaul of ventilators are very inferior and unsafe for the ICU patients of the developing countries like Bangladesh. Considering the real fact, we have taken it ethically and submit a proposal to reduce the risk factor of the ICU patients of developing countries. We firmly, believe that our research results and recommendations will be able to reduce the present uncountable risk factor of ICU patients from the ventilators. For the convenient of optimum research results, we have selected Bangladesh among the developing countries for a cause study. This research will be helpful for developing countries in world which are similar to Bangladesh.

This paper is organized as follows: Section II discusses the problem concerns. Section III illustrates the proposed methodology. Section IV gives the results and discussions. Recommendations for solving the problem are discussed in section V. Finally, section VI concludes the paper.

II. PROBLEMS CONCERNS

A lot of problems may occur in ICU unit if it is operated without interaction of CEP. Some of the major problems are given below:

- Clinical engineering is a new concept for health care planers of developing countries like Bangladesh although a huge number of medical equipments are being used by the health care services of Bangladesh.
- Health care planers completely could not add this important clinical engineering professionals (CEPs) due lack of their awareness as well as less attention.
- There is no research center /department to catch up the problems.
- Current electro-medical medical engineering department is not updated; as a result, the performance of this department is only 0.34% out of 70%.
- ICU patients are not risk free from life support ventilator as it is not operated following the standard method.

Figures 1(a) and 1(b) show the standard clinical engineering interaction with life support ventilator in ICUs of developed countries like Japan, Germany, etc. In Figure 1(a) shows the procedure of confirming the functionalities of ICU ventilator before it is applied on ICU patients. It is required to check every parameter such as hardware, software, clinical settings before handover the ICUV to the users (ICU doctor, clinical engineering technologists and nurses). Figure 1 (b) shows the activities of a doctor and clinical engineering technologist in ICU.

(a). Examination of ICUV by CEs before use (b). Practical utilization of ICUV in presence of a CE and Doctor

Figure 1. Standard clinical engineering interaction with life support ventilator in ICU.

Figure 2. ICU ventilator without any CE in developing countries.

CEs in developed countries ensure safety and risk of sophisticated modern medical equipments such as ICU ventilators, heart lung machine and so on before using. However, in developing country like Bangladesh has no in-house clinical engineer in any ICU that represents the substandard clinical engineering interaction with life support ventilator. Therefore, ICU patients of developing countries like Bangladesh is not risk free from life support ventilators. We have visited NICVDH, SSMCH and DMCH and not found CEs or CE technologists for ensuring the risk management. Normally ICU specialists and ICU nurses operate the ICU ventilator, however, they do not have enough knowledge about risk management such as low battery level alarm, lees tidal volume alert, leakage current, room temperature , humidity control, wall out let oxygen pressure, leakage of wall out let connectors, ventilator mode change such as CMV,SIMV and spontaneous mode, tidal volume, minute volume, humidity control of Oxygen by humidifier, temperature of humidifier, water changing frequency etc. In this connection, we discuss with ICU doctors, Anesthesiologists, cardiologists and nurses but they are not able to answer according to our queries. We have observed the situations about 7 days and found red alarm in ICU ventilators. The causes which are identified: loose wall out connector, incorrect setting of berating rate alarm, low battery level, patient circuit leakage, low level water in humidity fires, disconnection of humidifier heater, the ratio of inspiration and expiration is not sleeted according to patient weight.

III. PROPOSED METHODOLODY

A. Research Goal

The aim of the research is to reduce the risk factor of the ICU patients from the life support ventilator through the developing inter -professional skilled clinical engineers.

B. Research Design

- Past and presents trends of the failure of ventilator during use for ICU patients.
- Causes of the failures of ventilators.
- Standard operating procedure of ICU ventilators.
- Current operating procedure of ICU ventilator.
- Performance evaluation ICU ventilator with CE and without CEs
- Find out the risk factor of the use, calibration and maintenance of ventilator for ICU patients.

C. *Risk factor reducing method*

Modern medical devices are used in ICU ventilators in which combined knowledge of medical science, mechanical, electrical, electronic and computer are integrated. So, clinical engineering inputs are mandatory for the ICU patients to reduce the risk factor and it is globally recognized. It is therefore very much important to buildup strong correlation among the ICU doctors, CEs and nurses. The risk factor of ICU patients from the ICU ventilators may have a relation and can be expressed as follows:

Suppose the risk factor of ICU patients from the ventilators of hospitals without and with CEs is y_1 and y_2 respectively. If x_1, x_2, and x_3 represent the technical knowledge of skilled medical doctors, nurses, and CEs, then we can express,

$$y_1 = x_1 + x_2 \tag{1}$$

$$y_2 = (x_1 + x_2) + x_3 \tag{2}$$

The parameters x1, x2, and x3 indicate academic and practical score point and denoted in terms of percentage. It is found [14] that for any medical devices the score of CEs=52%= x3, medical doctors= 20% =x1, and Nurses=10% =x2, BMETs=18%=x4. The total score is 100%. Here, we consider only three indicators such as x_1, x_2 & x_3 and total score of the said indicators is 82%.

If R_f denotes the reduce of risk factor, then

$$R_f = y_2 - y_1 \tag{3}$$

Let y_1 is constant for all hospitals and standard and from Eqs. (2) and (3), we can define that $R_f = x_3$.

Values of R_f will reduce the risk factor of ICU patients from ventilators. We will need to reduce value of R_f through introducing CEPs in ICU. We have examined that for 8 bed standard ICU 4 numbers of CEs are mandatory to give the 52% technical input to cover the 24 hours roster duty and remaining 30% technical input will come from ICU doctors and Nurses. So R_f is proportional to x_3 that is CEs. Most of the developing countries like Bangladesh have no in-house clinical engineering department. But only, on call basis vendors or government conventional diploma technicians are maintaining only brake down maintenance. This performance is only average 2% of total 70 % standard requirements.

D. Sample data collection

For data collection and data analysis, we have taken data from developed and developing countries. In this connection, we have reviewed literatures in these fields and we have observed the present trends of Bangladesh.

TABLE I. TABLE FAILURE OF ICU VENTILATOR WITH AND WITOUT CEs IN HOSPITALS OF BANGADESH

Measurement components	A comparison of risk factor due failure of ventilator with respect to standard			
	Standard in developed countries 100 ventilators with CEP [15]	Developing counties like Bangladesh 100 ventilators without CEPs	Responded time in hours	
			Standard In developed countries	Sub-standard in developing countries like Bangladesh
Sensor failure	5	70	2	72
Battery Failure replacement	2	35	1	72
Musk displacement adjustement	1	95	1	2
Humidifer failure recover	2	75	1	8
Valve faileures recover	2	65	1	48
Avearge result	**2.4**	**68**	**1.2**	**40.40**

We have taken data from different hospitals of Bangladesh. We considered 100 ICU ventilators. Accordingly, we have reflected data in Table I and risk factors results are shown in Figure I. From Table I, we have found that the risk factor of ICU patients from ventilators are Bangladesh is very high and more over the responding time to run the ICU ventilators is average very higher than of developed countries. Due to absence of CEPs in hospitals such worth situation has been raised. From Table I, the performance of the ICU ventilators has been calculated. The risk factor of ICU patients from ventilators with and without CEPs for a standard developed country and a developing country like Bangladesh is shown in Fig. 3.

From Fig. 3, we have found that the rsik factors of the ICU ventilatiors are very high due to absence of CEPs. The average value of risk factor of ICU ventilators is about 65% higer in a developing contry than that of a developed country.

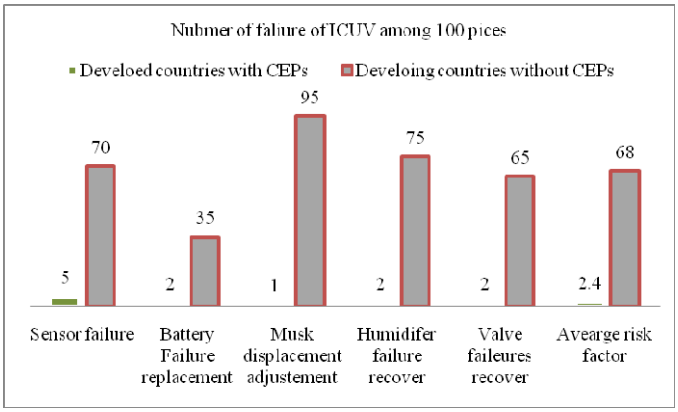

Figure 3. Risk factor of ICU patients from venticular with and without CEPs in developed and developing countries like Bangladesh.

IV. Results and Disscusion

For each ventilator, we evaluated the following parameters: (i) inspiratory flow, (ii) tidal volume, (iii) oxygen concentration, (iv) peak inspiratory pressure (P_{IP}), (v) positive end-expiratory pressure (PEEP), (vi) respiratory rate, and (vii) inspiratory time. ICU ventilators that were out of the acceptable ranges were classified as faulty. Faulty mechanical ventilators were repaired by calibration and replacing sensors and/or circuit boards. The standard parameters said in this section are depend on the category of the patients. In some models compile as machine default settings and some are needed to fix as customize. Here we have shown some data in the below Table II.

TABLE II. PARAMETERS OF ICUV

Parameters of ICU ventilators	**During checking**	**After repair and calibrations**
Inspiratory flow	Abnormal	Normal
tidal volume	Abnormal	Normal
oxygen concentration	Was too high	Normal
Peak inspiratory pressure (P_{IP})	Higher than normal value	Normal
Positive end-expiratory pressure (PEEP)	Was low	Normal
Respiratory rate	30	Normal and set at 16
Inspiratory time	Higher	Normal

We systematically checked mechanical ventilators about 570 times using a PTS-2000 calibrator during the period from January 2007 to December 2014, and there were a total of 100 cases of suspected mechanical ventilator failure. The number of faulty ventilators was 90 for ventilator volume, 39 for oxygen concentration, and 22 for malfunctions. The faulty ventilators needing valve and/or sensor replacement were repaired in-house by CEs. The rare, seriously malfunctioning ventilators (there were a total of 12 cases of circuit board failure) were sent to the distributor for repairing. Regarding response times for valve and/or sensor replacement, in-house repairs were completed immediately. However, if a machine is needed to repair to the distributor, it will take from average 8 hours to 72 hrs but more than 7 days. No ventilators could be run by local vendors within 7 days and charges were found very high which one kind of burden for the patients.

The most important item should be the checking of mechanical ventilators by CEs. CEs are certainly specialists in medical devices, and their involvement in maintaining mechanical ventilators is logical for the hospital, prompt, and most importantly safe. CEs fill an essential role for the safe operation of mechanical ventilators, and, more importantly, the CEs technology provides safe maintenance for many hospitals. From Eqs. (1), (2) and (3), the value of risk factor is found which is R_f = (68–2.4/%) = 65.6%. It means that the ICU patients from ventilators are always carrying about 65.6% risk factor. This is a moral and an emergency issue to reduce the risk factor. Without In-house clinical engineering support, risk factor should not be reduced by current ICU team such as doctors and nurses. To reduce the risk factor of ICU patents from ventilators, some recommendations have been submitted. Subject to the implementation of proposed recommendation, the risk factor will be minimized.

V. Recomedentions

The following standard operating procedure is shown in Table II for reducing the risk factor.

TABLE III. STANDARD OPERATING PROCEDURE TO REDUCE THE RESIK FACTOR

Cause of Risk Factor	Risk Factor Score	Guideline to reduce of risk factor	Responsibility
Product selection	100%	Need based technology selection according to country context	CE, Intensive care unit (ICUN) and ICUIST
Procurement terms	100%	Require consumables for ten years	Quantity depends on patients and hence for ten years a frame work consumables supply contact terms with prices should be determinate by the ICUIST, ICUN.
Oxygen disconcertion	100%	Should be ensured by ICUN.	CE will check
Calibration test	100%	Tools require PST-2000	In-house CE will checked it before use
Distill Water level for humidity and temperature control	100%	Every day ICUN check it according Manuals.	Hospital in House Clinical Engineer (HIHCE)
Oxygen sensor failure	100%	Routine check.	HIHCE
Valves failure	70%	Routine check	HIHCE
Batteries failure	50%	Periodical and predictive.	HIHCE & Vendor Engineers
Air inlet failure	60%	Routine check	HIHCE

Bactria filters	60%	Periodical and predictive.	HIHCE & Vendor Engineers
Electronic boards failure	50%	Preventive and breakdown	HIHCE & Vendor Engineers
Mechanical part failure	35%	Preventive and breakdown	HIHCE & Vendor Engineers.
Patients circuit leakage	58%	Regular check	HICEH and ICUN.

The following recommendations are submitted to reduce the risk factors of ICU patients from ventilator's support during therapeutic.

- It is urgent need to introduced skilled clinical engineers as in-house team for the safety operation, regular calibration, planned preventive maintenance of ICU ventilators in hospitals where ICU supports are available for the patient therapeutic.
- A framework maintenance contract management should be made between local vendors and hospitals to ensure the supply and services within 6 hours for any types of failure or breakdown maintenance. This contract must be made during procurement for the ten years or lifetime of ventilators.
- In-service training for the ICUN, ICUIST should be continue for ensuring better practice of operation and maintenance.
- Continuous monitoring, three-shift CEs are engaged for the safety of patients.
- Equipment enclosure or leakage current must be checked regularly.
- Ventilators self-test should confirm by the qualified CE before and after use of the ventilators.
- Operational software must be customized according to patient's criteria.

VI. CONCLUSION

From the data and results, we have found that the risk factor of ICU patients is very high in hospitals of Bangladesh due lack of proper educated and trained clinical engineers, ICUN and ICUIST. More revenue has been draining out for the new procurement of ICU ventilator since these equipments could not use properly in any hospitals of Bangladesh. As a result, ICU patients are not getting real service. Moreover, due to high risk factors from ICU ventilators, patient's death rate is found high. So ethically and economically, an in-house clinical engineering team is recommended for ensuring the safety aspects from ICU ventilators in the hospitals of Bangladesh as well as developing countries like Bangladesh. We conclude that present risk factor of ICU patents from ventilators could minimize or reduce subject to implementation of our submitted recommendations and proposals.

ACKNOWLEDGMENT

We acknowledged this research work to Ministry of Health & Family Welfare, Government of Bangladesh; Dept. of BME, KUET; NEMEMW & TC, Ministry of Health & Family Welfare, Dhaka, Bangladesh; UGC, HEQEP, CP#3472, KUET; MCH and SPH of Bangladesh.

REFERENCES

[1] S. Chapkowski, N. P. Pucilo, R. D. Cane, B. A. Shapiro, "Impact on ventilator-check time of an in-circuit computerized respiratory monitoring system," Respir Care, vol. 29, pp.144–146, 1984.

[2] A. Hartle, E. Anderson, V. Bythell, L. Gemmell, H. Jones, D. McIvor, A. Pattinson, P. Sim, I. Walke, Association of Anesthetists of Great Britain and Ireland (AAGBI) Checking anaesthetic equipment 2012: Association of Anesthetists of Great Britain and Ireland. Anaesthesia, vol. 67, pp. 660–668, 2012.

[3] J. L. Bourgain, P. Baguenard, J. M. Puizillout, J. C. Ankri, E. Damia, V. Billard, "The breakdown of anesthesia equipment survey," Ann Fr Anesth Reanim, vol. 18, pp. 303–308, 1999.

[4] M. Kawamata, T. Mayumi, M. Miyabe, A. Namiki, "An unusual cause of anesthetic ventilator malfunction," Masui, vol. 41, pp. 1994–1997, 1992.

[5] J. C. M. Richard, R. M. Kacmarek, "ICU mechanical ventilators, technological advances vs. user friendliness: the right picture is worth a thousand numbers," Intensive Care Med, vol. 35, pp. 1662–1663, 2009.

[6] P. B. Blanch, "Mechanical ventilator malfunctions: a descriptive and comparative study of 6 common ventilator brands," Respir Care, vol. 44, pp.1183–1192, 1999.

[7] L. Vignaux, D. Tassaux, P. Jolliet, "Evaluation of the user-friendliness of seven new generation intensive care ventilators, "Intensive Care Med., vol. 35, pp. 1687–1691, 2009.

[8] J. C. Richard, A. Carlucci, L. Breton, N. Langlais, S. Jaber, S. Maggiore, S. Fougère, A. Harf, L. Brochard, "Bench testing of pressure support ventilation with three different generations of ventilators," Intensive Care Med., vol. 28, pp. 1049–1057, 2002.

[9] D. Tassaux, J. B. Michotte, M. Gainnier, P. Gratadour, S. Fonseca, P. Jolliet, "Expiratory trigger setting in pressure support ventilation: from mathematical model to bedside," Crit Care Med., vol. 32, pp. 1844–1850, 2004.

[10] A. W. Thille, A. Lyazidi, J. C. Richard, F. Galia, L. Brochard. A bench study of intensive-care-unit ventilators: new versus old and turbine-based versus compressed gas-based ventilators," Intensive Care Med., vol. 35, pp. 1368–1376, 2009.

[11] A. D. Marchese, D. Chipman, P. de la Oliva, R. M. Kacmarek, "Adult ICU ventilators to provide neonatal ventilation: a lung simulator study," Intensive Care Med., vol. 35, pp. 631–638, 2009.

[12] R. L. Chatburn, "Computer control of mechanical ventilation," Respir Care, vol. 49, pp. 507–517, 2004.

[13] P. B. Blanch, "An evaluation of ventilator reliability: a multivariate, failure time analysis of 5 common ventilator brands," Respir Care, vol. 46, pp. 789–797, 2001.

[14] M. A. Hossain, M. A. Rashid, M. R. Islam, and M. Ahmad, "Current status of skilled clinical engineering in developing countries," Procedia - Social and Behavioral Sciences. vol. 195(2015), pp. 1688-1693, July 2015.

[15] M. A. Hossain, M. R. Rahman, A.K.M. Rahman, M. S. Islam, Azman Hamid, M.A. Rashid, M. H. Rahman Chowdory, B. Gangoloy, M. R. Islam, and M. Ahmad, "Necessity to Produce Clinical Engineering Professional for the Improvement of Present Health Care Management in Developing Countries," ICEHTMC 2015, pp. 173-177, October 21-22, HangZhou, China.

A Mathematical Approach to Determine the Work-done from EMG Analysis

Farzana Khanam[1], Md. Asadur Rahman[2]
[1,2]Department of Biomedical Engineering
Khulna University of Engineering & Technology (KUET)
Khulna-9203, Bangladesh.
farzana0703047@gmail.com[1], bmeasadur@gmail.com[2]

Mohiuddin Ahmad[3]
[3]Department of Electrical and Electronic Engineering
Khulna University of Engineering & Technology (KUET)
Khulna-9203, Bangladesh.
mohiuddin.ahmad@gmail.com[3]

***Abstract*—Electromyography (EMG) measures cumulative action potential by means of voltage from our muscles which means, it is related to work done. As far as we know, there is no exact technique to estimate the mathematical relation between work done and EMG value. In this work, we propose a mathematical relation between work done and EMG signal with proper curve fitting and constant parameter correction. For this purpose, different subjects are chosen for determining work done by lifting different known weight to a defined height and corresponding EMG voltage is measured. Biceps Brachii and Flexor Carpi Radialis muscles are selected for taking EMG values in millivolts. We have considered the mean value from collected sEMG (Surface Electromyography) results for final analysis. From the results, it is observed that EMG voltage maintain almost parabolic relationship with work done. In addition, with that, considering the relationship as exact linear and parabolic, the errors from the measured values are also calculated. The accuracy of our proposed mathematical model is shown numerically.**

Keywords— Surface Electromyography; cumulative action potential; work done; mathematical model; Biceps Brachii.

I. INTRODUCTION

Any human movement is produced by muscular and skeletal systems controlled by the nervous system. Many biomechanical researches have revealed mechanism of the human body dynamics. Some musculoskeletal models of whole body have been developed and reported in a number of investigations [1]. In skeletal muscle, contraction is stimulated by electrical impulses transmitted by the nerves, the motor-neurons (motor nerves) in particular. The electrical potential generated by muscle cells is detected by electromyography (EMG), when these cells are electrically or neurologically activated. EMG is an electro diagnostic medicine technique for evaluating and recording the electrical activity produced by skeletal muscles which allows the measurement of the change in the membrane potential which is transmitted along the fiber [2]. An EMG is the summation of action potentials from the muscle fibers under the electrodes placed on the skin.

Action potential is a short-lasting event in which the electrical membrane potential of a cell rapidly rises and falls. When an action potential is triggered, the membrane potential abruptly shoots upward, often reaching as high as +100 mV. Due to muscle contractions, action potentials are generated which we can measure through EMG analysis. Surface electromyography (sEMG) is a non-invasive technique for measuring the electrical activity of muscle that occurs during muscle contraction and relaxation cycles [3]. Total voltage induction process of action potential analyzed by EMG analysis is given in Fig. 1.

By sEMG analysis, there are a large number of investigations [4]-[7] by several authors. A relation between muscle force and joint moment is analyzed in [5]. Authors in [6], studied the muscle force with EMG and in [7], authors studied muscle force and sEMG where normalized EMG strength versus increment rate of force carried by muscle was calculated. Through sEMG, joint torque estimating model was proposed in [8]. From these research articles, we do not get any information about the relation between work done and cumulative muscle potential. But it is very necessary information to estimate the total work done from a sEMG signal, however as we know so far, there is no such a model to estimate the total work done from the recorded sEMG.

In this paper, we have proposed such an efficient expression that is properly able to estimate the work done or how much calorie burn to complete the work from the sEMG signal. In this proposal, at first we have collected a number of data of known work done and corresponding cumulative sEMG signal in mV. After recording the data, the mean sEMG signal in mV are calculated.

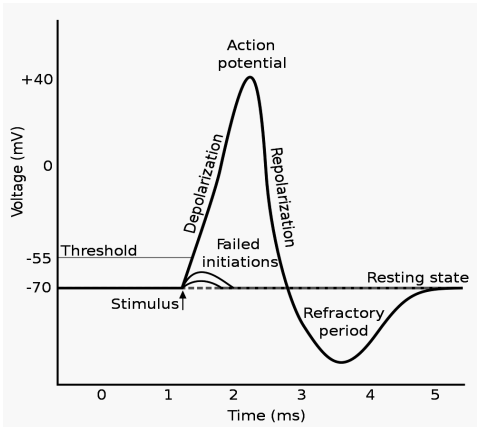

Fig. 1. Voltage induction process in muscle by Action potential.

By this result, we have shown that the cumulative action potential and the corresponding work done obey a linear or a non-linear relationship. By applying linear or parabolic regression, the relationships are established. Furthermore, the procedure to estimate the work done for a specific work from recorded EMG voltage is also presented by mathematical equation.

Amount of work cannot be easily measured in vivo. Therefore, the work done from muscles must be assessed, calculated or mathematically modeled during various amount of work done. By this mathematical modeling, we can differentiate as well as compare various kind of work output in terms of calorie or joule which helps to determine muscle fatigue, muscle work done, identify exercise which burnt calorie more or less to keep our human body fit and sound.

This paper is organized as follows: Section II described the proposed methodology of mathematical analysis and calculation procedure. The total experimental procedure is discussed in section III. Experimental results and respective discussion is presented in section IV. Our total work is concluded in section V.

II. Proposed Methodology

A. Physical Procedure of the Method

The maximum force that a limb is able to apply externally varies with angular position. This is because the geometrical arrangement determines the degree of mechanical advantage. We have chosen two muscles Biceps Brachii (BB) and Flexor Carpi Radialis (FCR) from upper limb of human body. Because, when a weight is lifted by hand; then these two muscles are activated simultaneously which helps to acquire data and electrode placement. In this work, BB was upheld alongside of FCR with angular position 90° approximately as in Fig. 2.

B. Work Done Calculation

There are three key ingredients to work, those are force, displacement, and cause. If the work done is due to force F, the displacement is S and the angular movement with the direction of force is θ, then the amount of work done, W can be equated as,

$$W = F \times S \times \cos\theta \tag{1}$$

According to this proposed procedure, we have done the work by lifting a weight of m kg against gravity from 0 to h meter, then the equation become as,

$$W = m \times g \times h \tag{2}$$

Where, g is the gravitational constant of value $9.81 ms^{-2}$ on earth.

C. Procedure of Acquiring EMG Signal

For the data acquisition of the corresponding study several steps are followed properly. Every step for this study is related to the data acquisition mentioned which is shown in Fig. 3.

Fig. 2. 90^0 angular position between BB and FCR.

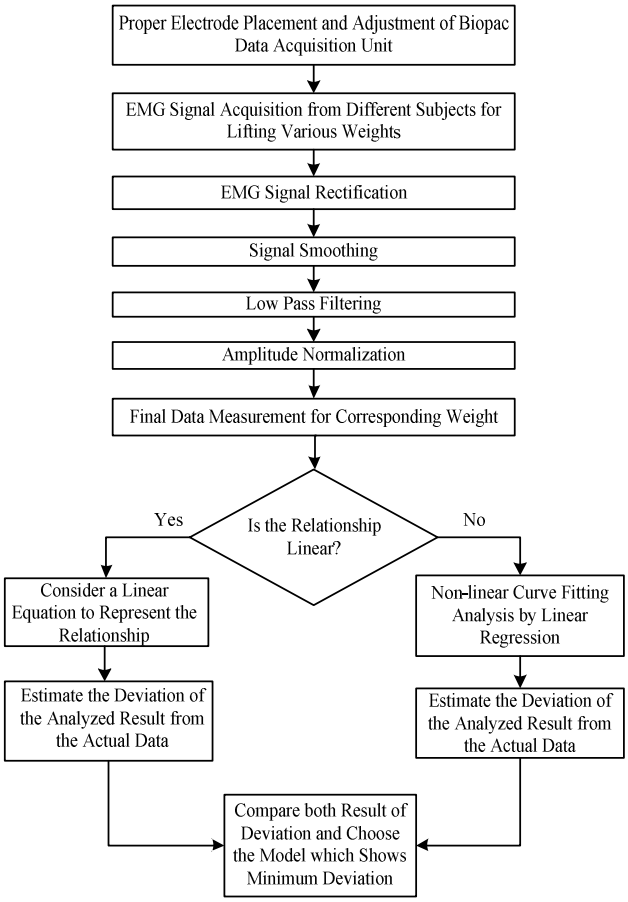

Fig. 3. Flow chart of the proposed data acquisition procedure.

D. Curve Fitting of the Results

If any set of data is nonlinear and can be considered as parabolic, then in generally the set of data can be represented by (3), where the value of the coefficients a, b, and c depends on the shape of the curve.

$$y = a + bx + cx^2 \tag{3}$$

According to least-square fitting, we have to fitted the parabola to the given points (x_1, y_1), (x_2, y_2), …, (x_n, y_n). If the error for the estimated value and measured value is e, then summation of error is $S=\sum e_i^2=(y_i - a - bx_i - cx_i^2)^2$.

By the principle of least square, the value of S is minimum; therefore,

$$\frac{\partial S}{\partial a}=0,\quad \frac{\partial S}{\partial b}=0,\quad \frac{\partial S}{\partial c}=0 \tag{4}$$

By solving (3) and dropping suffix, we have

$$\begin{cases} \sum y = na + b\sum x + c\sum x^2 \\ \sum xy = a\sum x + b\sum x^2 + c\sum x^3 \\ \sum x^2 y = a\sum x^2 + b\sum x^3 + c\sum x^4 \end{cases} \tag{5}$$

Equation (5) is known as normal equations. We can get the values of a, b, and c by solving (5). Putting the value of a, b, and c in (3), we can get the equation of the parabola for best fit [9].

III. Experimental Procedure

A. Data Acquisition Method

As we know, the muscle movement of our body creates action potential. Therefore, different work done produces different action potential according to the amount of work done. There is no direct procedure to estimate such potential to work done relationship. An indirect procedure can be established for estimating this relationship. For example, by performing a known amount of work done we can collect the cumulative action potential or EMG data. To do this, we demonstrate a procedure through some practical step in our laboratory which can be described by the following steps:

Step 1: First of all, we select a height where lifting a weight maintain 90 degree angle between the Biceps Brachii (BB) and Flexor Carpi Radialis (FCR), while the Biceps Brachii will be at the parallel of the body as shown in Fig. 2.

Step 2: We choose some weights to lift which were available in our laboratory. The weights were 0.25, 0.5, 1, 1.5, 2 and 2.5 kg which we can easily lift in the height level from floor to 0.50 meter.

Step 3: The EMG data have been collected from the subjects performing to lift different weights from floor= 0 m to 0.50 meter. In this case, we selected Biceps Brachii muscle of right hand to lift the weights.

Step 4: After collecting the EMG data which resembles the action potential of the BB, we have plotted different curves weight (kg) versus action potential (mV) for male and female subjects respectively.

Step 5: These curves show approximate non-linear parabolic relationship between weight load and EMG data i.e. action potentials. On the basis of the non-linearity, we executed interpolation and extrapolation.

B. Subjects Selection and Laboratory Specifications

The experimental data for this study were collected from 10 subjects among them five are male and five are female subjects (age: 23 ± 5 years, weight: 55±5 kg) with no medical problems. The total experiment is performed in Biomedical Signal Processing Laboratory, Department of BME, Khulna University of Engineering & Technology (KUET), Bangladesh.

C. Apparatus Specification

During data acquisition protocol, the skin was cleaned with abrasive pad and alcohol prep, Lycra swim cap initially. BIOPAC disposable vinyl electrodes (EL503) together with BIOPAC electrode lead set (SS2L) were attached on Biceps Brachii. To press electrodes, 3M Coban Self-adhering Support Wrap were applied against head for improving contact. The electrodes were associated to an EMG data collection system (Biopac Student Lab 3.7 and BIOPAC data acquisition unit) (MP36). For analysing the collected data, Acqknowledge 4.1 software was used. Electrode placement and arrangement along Biceps Brachii of subjects are shown in Fig. 4.

IV. Experimental Results and Discussions

In our work, we have chosen six types of mass such as, 0.25kg, 0.50 kg, 1 kg, 1.5 kg, 2 kg and 2.5 kg. The height is selected as 0.50 meter and it is well known to all that the standard of gravity, g =9.81 ms^{-2}. Therefore, for lifting m kg mass, the amount of work will be W= ($m\times 9.81\times 0.50$) joule or $W/4.2$ calorie (cal) [4.2 joule = 1 calorie]. The EMG signals of some weight lifting from our experiment are shown in Fig. 5. During lifting weights, incrementing weight over 2 kg undergoes in saturated EMG potential. It resembles the fatigue point of that muscle as the experiment is based on BB muscle. In addition, the various weight and corresponding work done is tabulated in Table I.

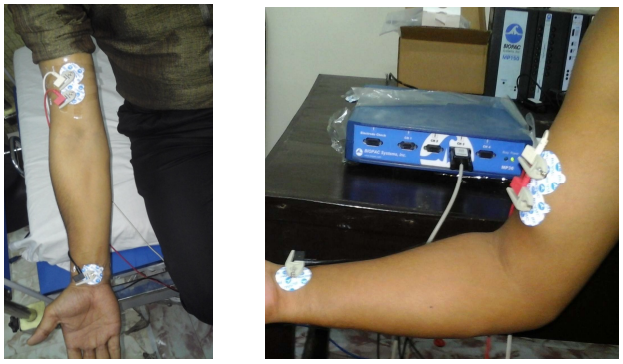

Fig. 4. Electrode placement and lead setting arrangement along Biceps Brachii of subjects.

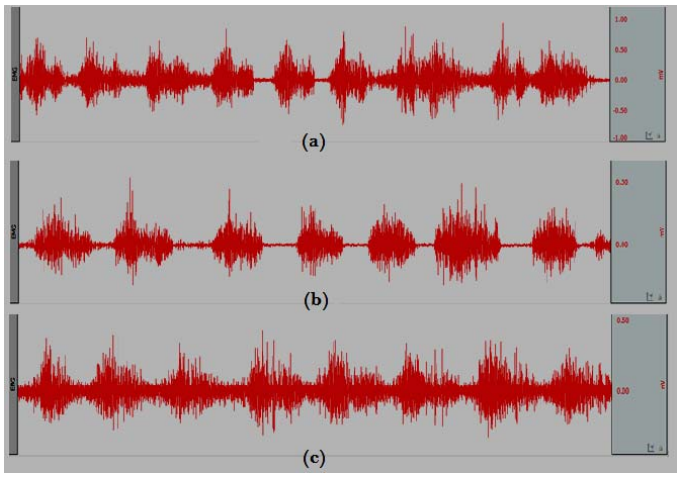

Fig. 5. Sample EMG signal in Acqknowledge 4.1 software- for (a) 2.5 kg, (b) 2 kg, and (c) 1 kg weight lifting.

TABLE I. WORK DONE AND CALORIE BURN FOR DIFFERENT WEIGHTS

SL#	Weight in Kg	Work Done (J)	Calorie (Cal)
1	0.25	1.22625	0.2919
2	0.50	2.4525	0.58392
3	1.00	4.905	1.16785
4	1.50	7.3575	1.751
5	2.00	9.81	2.335
6	2.50	12.2625	2.919

TABLE II. MEASURED ACTION POTENTIAL VALUE FOR DIFFERENT WEIGHTS (MALE)

SL#	Wt. (Kg)	S1 (mV)	S2 (mV)	S3 (mV)	Mean (mV)	St. Dev (mV)
1	0	0.22807	0.20498	0.21182	0.214957	0.011860
2	0.25	0.25574	0.26347	0.24607	0.255093	0.008718
3	0.50	0.37129	0.36925	0.36233	0.367623	0.004696
4	1.0	0.58430	0.57751	0.56895	0.57692	0.007692
5	1.5	0.69906	0.70258	0.68294	0.69486	0.010472
6	2.0	0.78043	0.76568	0.76201	0.769373	0.009750
7	2.5	0.90514	0.88703	0.86878	0.886983	0.018180
Mean Standard Deviation=0.010195 mV						

TABLE III. MEASURED ACTION POTENTIAL VALUE FOR DIFFERENT WEIGHTS (FEMALE)

SL#	Wt. (Kg)	S1 (mV)	S2 (mV)	S3 (mV)	Mean (mV)	St. Dev (mV)
1	0	0.20902	0.21417	0.22402	0.2157367	0.0076217
2	0.25	0.25021	0.26112	0.26951	0.26028	0.0096774
3	0.50	0.37672	0.36931	0.37258	0.37287	0.0037135
4	1.0	0.56912	0.58483	0.57388	0.5759433	0.0080557
5	1.5	0.69112	0.68135	0.68013	0.6842	0.0060239
6	2.0	0.76844	0.77474	0.78018	0.7744533	0.0058752
7	2.5	0.90262	0.89214	0.93426	0.9096733	0.0219280
Mean Standard Deviation=0.008985054 mV						

As shown in Fig. 5, by the use of Acqknowledge software the mean EMG voltage for every subject is acquired and among them; data of 3 male and 3 female are given by Table II and Table III. In these tables, mean and standard deviation of the data are also determined and tabularized. From the data tables, we can observe that an approximately linear relationship exists between work done and action potential or EMG voltage. From this result, we took the mean voltage value from all subject and plot it against work done and shown in Fig. 6.

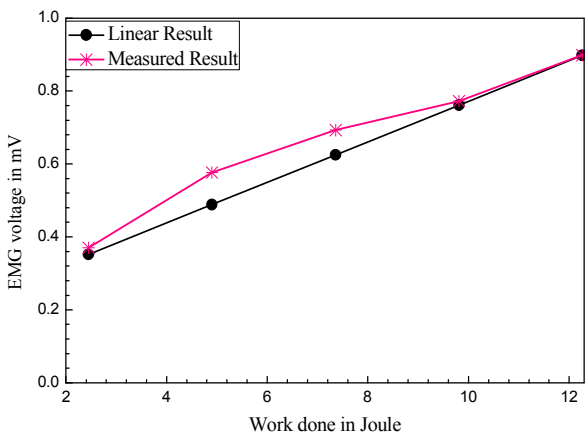

Fig. 6. Deviation of measured and conceptual relationship.

From linear regression analysis the relationship between weight-EMG is given in (6),

$$y_{line} = 0.2111 + 0.05569x \tag{6}$$

From Fig. 6, it is observed that the results, we got through our experiment is not exactly linear. The relation can be considered as approximately parabolic.

Basically, this apparently linear consideration is not correct at all. Therefore to reach the more accuracy of the measure result a nonlinear curve fitting is performed on the measured data. By nonlinear curve fitting the mathematical relationship we get, is given in (7).

$$y = 0.2111 + 0.3842x - 0.0455x^2 \tag{7}$$

The EMG voltage can be evaluated by (7) when the independent variable 'x' is considered as weight. From (7), it is also mentionable that when we consider the lifting weight is zero, then the EMG voltage will be 0.2111 which is exactly as our experimental value. It means that, without lifting any weight, according to our working procedure muscle extract EMG voltage is 0.2111mV. Nevertheless, our target is to relate EMG with work done. Therefore, another mathematical relation is also depicted to relate EMG voltage and work done which is given in (8),

$$Y_2 = 0.2111 + 0.0783i - 0.0019i^2 \tag{8}$$

As a result the actual relationship between work done and EMG voltage can be evaluated from (8) when the independent variable 'i' is considered as the work done in Joule. Furthermore, the EMG voltage from (7) and (8) will be in mV unit. From (7), we have calculated the voltage level of the given work done and their result and error is given in Table IV.

Eventually to prove the accuracy of our result we choose two different weight (0.75 kg and 1.75 kg) and evaluate their corresponding EMG voltage from the Fig. 7 by interpolation. After that, we invite two different subject for the study of the mentioned weight i.e. 0.75 and 1.75 kg from each. The result of the study is given in Table V where it is found that very low level of error exists between our proposed mathematical model and measured result. As the result we get successfully provide strong evidence of the accuracy of our proposed hypothesis on the relation between work done and cumulative action potential (EMG voltage).

TABLE IV. ERROR MEASUREMENT AFTER CONSTANT CORRECTION

SL#	Work done, J	Measured voltage in mV, M	Estimated value in mV, E	Error, |M-E|
1	0	0.21534	0.2111	0.00424
2	2.4525	0.3702465	0.3917	0.02145
3	4.905	0.57643165	0.5494	0.02703
4	7.3575	0.68953	0.6843	0.00523
5	9.81	0.77191315	0.7964	0.02448
6	12.2625	0.89832815	0.8856	0.01272

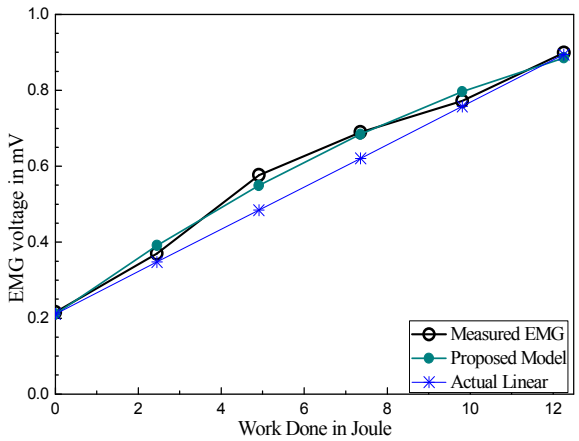

Fig. 7. Impact of proposed mathematical model in error declination.

TABLE V. ACCURACY TESTING OF THE PROPOSED HYPOTHESIS

SL#	Work done in Joule	Measured voltage in mV (Subject 1)	Measured voltage in mV (Subject 2)	EMG voltage from graph	Error
1	3.67875	0.4725	0.4674	0.4734	0.00345
2	8.58375	0.7428	0.7314	0.7432	0.00611

V. CONCLUSIONS

The contribution of this paper is to introduce and develop a new mathematical relationship between performed work and consequent EMG results. In this work, we have explored the cumulative action potential value extracted from EMG signals. All sEMG signals were collected from different male and female healthy subjects through BIOPAC acquisition unit maintaining appropriate experimental protocol. The process of calibration and standardization of EMG signals have been conducted. Then, we have plotted a curve among mean EMG value corresponding weight versus work done deviated from exact parabolic curve. To reduce this difference, we have approached a mathematical model considering all the facts of errors. We have also ensured the accuracy of this equation by putting two random weights with unknown EMG values. The calculated results show negligible errors comparing with measured values. The comparison between measured value and proposed model value will help researchers encounter the perfect method for analyzing EMG signals. Our goal was quite complex to convert a numerical methodology into a direct mathematical relation.

Since, the experiment provides very positive results which encourage us to work to research about the intended combined movements in our future work.

ACKNOWLEDGMENT

This work was supported by Higher Education Quality Enhancement Project (HEQEP), UGC, Bangladesh under Subproject "Postgraduate Research in BME", CP#3472, KUET. This work was also supported by Information and Communication Technology (ICT) Division, Ministry of Post, Telecommunications and Information Technology, Government Peoples Republic of Bangladesh.

REFERENCES

[1] S. L. Delp, F. C. Anderson, P. Loan, A. Habib, C. T. John, E. Guendelman, and D. G. Thelen "Open-source software to create and analyze dynamic simulations of movement," IEEE Trans. on Biomedical Engineeiring, vol. 54, no. 11, pp. 1940-1950, November 2007.

[2] W. C. Mackenzie, The action of muscles: including muscle rest and muscle re-education, New York P.B. Hoeber, 1921 Forgotten Books, 2013.

[3] F. Khanam, S. Islam, M. A. Rahman, and M. Ahmad, "Muscle activity estimation through surface EMG analysis during salat," 2nd International Conf. on Electrical Engineering and Information Communication Technology (ICEEICT), Bangladesh, pp. 1-6, 2015, May 21-23.

[4] M. K. M. Safee, W. A. B. Wan Abas, F. Ibrahim, N. A. Abu Osman, and M. H. R. Salahuddin, "Electromyographic Activity of the Lower Limb Muscles during Salat and Specific Exercises," Journal of Physical Therapy Science, vol. 24, pp. 549-552, July 2012.

[5] T. S. Buchanan, D. G. Lloyd, K. Manal, and T. F. Besier, "Estimation of muscle forces and joint moments using a forward-inverse dynamics model,"Journal of the American College of Sports Medicine, vol. 37, no. 11, pp. 1911–1916, November 2005.

[6] H. U. Kuriki, F. Mí. Azevedo, L. S. Takahashi, E. M. Mello, R. F. N. Filho, and N. Alves, "The relationship between electromyography and muscle force: EMG methods for evaluating muscle and nerve function," Intech Publisher, January, 2012.

[7] G. C. Ray and S. K. Guha, "Relationship between the surface emg and muscular force," Medical & Biological Engineering & Computing, vol. 21, no.5, pp. 576-586, September 1983.

[8] M. H. Jali, T. A. Izzuddin, Z. H. Bohari, H. Sarkawi, M. F. Sulaima, M. F. Baharom, and W. M. Bukhari, "Joint torque estimation model of semg signal forarm rehabilitation device using artificial neural network techniques,"ARPN Journal of Engineering and Applied Sciences, vol. 9, no. 7, July 2014.

[9] P. S. Das, A Textbook Of Engineering Mathematics - III : Transforms and Partial Differential Equations, 5th Edition, India, 2013.

Continuous Heart Rate and Body Temperature Monitoring System using Arduino UNO and Android Device

Md. Asaduzzaman Miah, Mir Hussain Kabir, Md. Siddiqur Rahman Tanveer and M. A. H. Akhand
Dept. of Computer Science and Engineering
Khulna University of Enginnering & Technology
Khulna-9203, Bangladesh

Abstract—**An integrated portable device for continuous heart rate and body temperature monitoring system development is presented in this paper. Heart related diseases are increasing day by day; therefore, an accurate, affordable and portable heart rate and body temperature measuring device is essential for taking action in proper time. Such a device is more essential in a situation where there is no doctor or clinic nearby (e.g., rural area) and patients are unable not recognize their actual condition. The developed system of this study consists of Arduino UNO microcontroller system, transmission system and Android based application. The system gives information of heart rate and body temperature simultaneously acquired on the portable device in real time and shows it through the connected Android application instantly. The developed system is more affordable with low price compared to other developed devices due to use of easy available Arduino UNO and smart phone as Android device. The developed device is shown acceptable outcomes when compared with other measuring devices.**

Keywords—*Arduino UNO, Heart Rate, Body Tempareture, Pulse Detection, Pulse Amplification, Signal Extraction.*

I. INTRODUCTION

Heart rate simply indicates the soundness of our heart. It helps assessing the condition of cardiovascular system [1]. Human's heart pounds to pump oxygen-rich blood to muscles. It carries cell waste products away from tissues [2]. Heart rate varies according to the demand of muscles to absorb oxygen and excrete carbon dioxide changes such thing happen during exercise or sleep [3]-[5]. Normally the heart rate which is calculated for a resting person is about to 70 bpm for adult males and 75 bpm for adult females. A heart rate monitor is simply a device that takes a sample of heartbeats and calculates the heart beats per minute and the information can easily track the current heart condition [6].

On the other hand, body temperature is also a general indication of body condition. Normal human body temperature is (98.6 ° F ± 0.7°F) and it varies activity of the person as well as place of measurement. When a person is too hot, the blood vessels in his/her skin expand to carry the excess heat to his/her skin's surface. And for this reason the person begins to sweat. Then the sweat evaporates and this process helps to cool his/her body. When a person is too cold, his/her blood vessels narrow so that blood flow to his/her skin gets reduced to conserve body heat. As a result he/she starts shivering and it is an involuntary, rapid contraction of the muscles.

Timely measurement of heart rate and body temperature is important for better treatment. In this era of polluted environment, concern regarding human health is top priority than ever before. Everything gets meaningless if one is sick or dead. Now a days, people spend a lot of money to keep sound health. Unfortunately, most of the cases it is found that it is too late to receive proper medical treatment and things are non-invertible. So that unexpected incident happens for being delayed treatment. Since heart rate and body temperature are the most vital notable indexes of the human health, an affordable device to measure such indexes will be helpful for human health. In general, medical equipment is expensive. Moreover, some devices can provide raw medical calculation of data to patients and doctors, but the patients can't always interpret the medical measurement into meaningful diagnosis as they have simple/no medical background. In emergency situation, time should not be wasted. Sometimes continuous assessment is also necessary. Therefore, an automated system for continuous measuring of heart rate and body temperature is very much essential.

In this study, an android assistive integrated heart rate and body temperature measuring embedded system is developed. Since the system provides the information about both heart rate and body temperature through android application, anyone can monitor physical status easily. Moreover, the system may be useful for monitoring condition of vary seek patents from remote place. Rest of the paper explains existing approaches, our system model, system development and finally system performance measurement.

II. EXISTING APPROACHES

There are some existing approaches designed and developed for measuring heart rate. At present, the recent technologies for measuring heart rate are consist of several methods using optical and electrical methods. Casually electrical method provides a bulky strap around one's chest [7]. But the optical method requires no such strap and it can be used more effectively. Low cost heart rate measuring devices were developed using optical technology. In optical method powerful LED and Light Dependent Resister (LDR) are used to sense pulses [8]. The pulse signals are then amplified by an amplifier circuit and filtered through a band pass filter. The amplified and

filtered pulse signals are sent to the microcontroller. The microcontroller checks the analog signals whether they are valid or not comparing with a standard voltage. Microcontroller counts the heart rate and displays the result in a LCD display. There exists another approach where infrared Tx and Rx are used. In that system it senses pulses, amplifies the pulses and filters pulses by a low pass filter. Finally, the pulse signal is sent to a microcontroller [9], [10]. The microcontroller also give output comparing with a reference voltage. Both the approaches give inaccurate result in many cases because analog signal of pulse varies from person to person and the approaches fail to calibrate analog signal of pulses for each person.

M. M. A Hashem *et al.* [8] developed a device which uses infrared technology to measure heart rate and use analog temperature sensor to measure body temperature. This approach can calibrate analog signal of pulses for each person. It uses wireless terminal to send data and wireless receiver to receive the data. The data are then sent to the computer using serial port. Data is then sent to the web server using the internet and can be viewed from anywhere in the web browser. The main drawback of this approach is that it needs a computer to send data to the web server through the internet.

A telemedicine system is presented by N. Navale *et al.* in [11]. In the system, the user carries a hardware device connected with an android application through Bluetooth connection. The device continuously measures the heart rate and body temperature and sends these information to the android application. Android application sends the information to the server and if the user has any problem like heart attack then it sends an emergency message to the patient's doctor and guardians containing the current location of the patient. N. Indumathy, and K. K. Patil [12] developed an android based patient health care monitoring system using several sensors like temperature, heart rate measuring sensor, eye blink detection sensors to detect the current condition of the patient. The system is developed such a way that if patients can't speak or move his hand or body then just blink his/her eyes 5 times then a message send to the caretaker about the current situation of the patient and continuously send the information about heartbeat and body temperature to the server. An android application running in the caretaker phone receive the message and generates voice sound so that caretaker can recognizes the patient's current situation. At the same time, doctor can realize the current situation of the patient accessing the server.

The aim of our study is to develop a device which is interfaced with an Android application so that the heart rate and body temperature are monitored easily. The exiting remote health monitoring system described above are fully dependent on proper communication between the server and client. So it may arise severe condition that server connection gets congested and patient's situation is serious then it creates a problem to recognize the present situation of the patient. For this reason the goal of our project is to design a portable Android assistant heart rate and body temperature monitoring device which is affordable and user friendly, at the same time inexpensive, accurate, and durable.

III. Heart Rate and Body Temperature Monitoring System using Arduino UNO and Android Device

To construct an efficient and affordable device for measuring heart rate and temperature, an infrared Tx and Rx have been used to measure the pulse by measuring the change in blood flow through one of the fingers. A noise filter has been designed to filter out any unwanted noise and interference, due to small movement of finger causes excess noise. A temperature sensor has been used to measure body temperature. The microcontroller of the Arduino UNO board is programmed to count the pulse rate and to measure the body temperature and to send the information to the developed "Heartmate" android application via Bluetooth module. Fig. 1 shows the working diagram of the system and the Fig. 2 represents the functional block diagram of the system. The following sections briefly explains of the system.

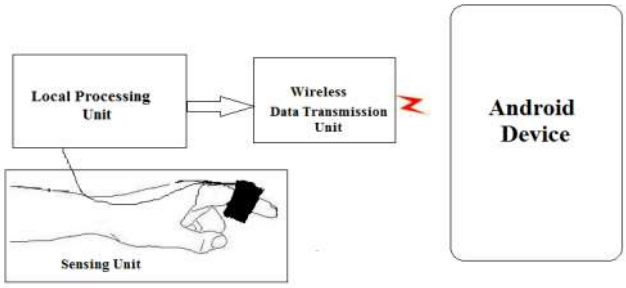

Figure 1. System diagram of the proposed system.

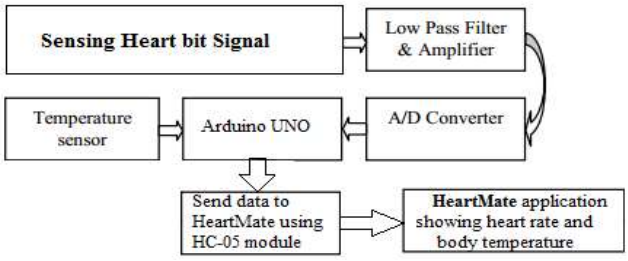

Figure 2. Functional block diagram of the system.

A. Heart Rate and Body Temperature Sensing

With a view to measuring the alteration in blood volume at fingertip with each heartbeat optical sensor has been used to perform this task. The sensor unit consists of an IRTx and IRRx, placed side by side. An infrared light is transmitted by IRTx into the fingertip, and the IRRX senses the portion of the light which is reflected back. The intensity of the reflected light depends upon the blood volume inside the fingertip. As a result each heartbeat slightly alters the amount of reflected infrared light that can be detected by IRRx. Through proper signal conditioning this little change in the amplitude of the reflected light is converted into pulse. The sensor used in this project is TCRT5000 which is a reflective optical sensor that contains both the infrared light emitter and phototransistor placed side by side. They are enclosed inside a leaded package as a result the effect of surrounding visible light is minimum. Connecting the Enable pin to 5V of Arduino will turn the IR emitter LED on and activate the sensor. A fingertip placed over the sensor will act as

a reflector of the incident light. The amount of light reflected back from the fingertip is monitored by the photo transistor. The output (VSENSOR) shows in Fig. 3 from the sensor is a periodic physiological waveform attributed to small variations in the reflected IR light and it is caused by the pulsating tissue blood volume inside the finger.

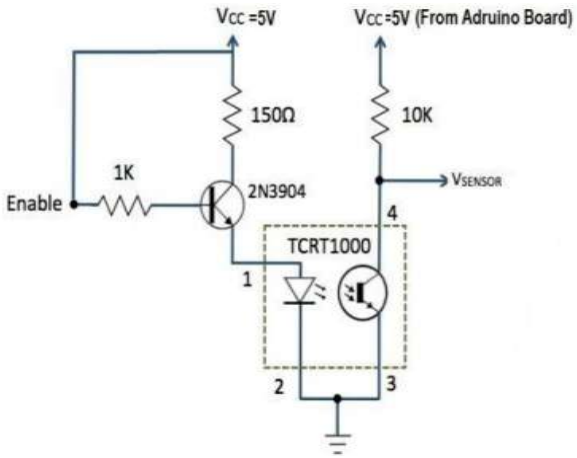

Figure 3. Pulse Detection Circuit

The waveform is synchronous with the heartbeat. This weak signal contains a lot of noise superimposed on the AC signal which is then filtered through a series of signal processing circuits via a Quad OP-AMP LM324N. To get rid of the DC component the signal is first passed through a RC high-pass filter (HPF) showed in Fig. 4. The cut-off frequency of the HPF is set to 0.7 Hz. An active low-pass filter (LPF) which is made of an Op-Amp circuit is on the next stage. The gain and the cut-off frequency of the LPF are set to 101 and 2.34 Hz respectively. As a result the combination of both HPF and LPF helps to remove unnecessary DC signal and high frequency noise which includes 50 Hz mains interference, while amplifying the low amplitude pulse signal (AC component) 101 times. In Fig. 5 shows the further filtering and amplification of the output from the first signal conditioning stage goes to a similar HPF/LPF combination. For this reason the total voltage gain achieved from the two cascaded stages is 101*101 = 10201. The two stages of filtering and amplification converts the input signals to near Transistor–Transistor Logic (TTL) pulses which are synchronous with the heartbeat. A 10K

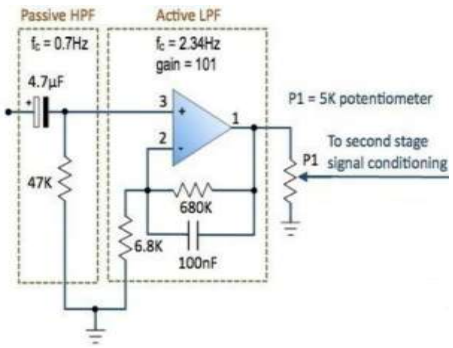

Figure 4. First Stage Signal Conditioning Circuit

potentiometer is placed at the output of the first signal conditioning stage in case the total gain of the two stages is required to be less than 10201. If a heartbeat is detected then an LED connected to the output of the second stage of signal conditioning will blink. The final stage a simple non-inverting buffer is implemented so that output impedance will be lower. While reading the amplified PPG signal through the ADC channel of a microcontroller is used to then it helps much. After that the output is connected to the Digital Pin 8 of Arduino UNO. The diagram shows the configuration of the IR emitter and IR receiver in relation to the finger. They are placed in such a way that the infrared light reflects from the finger to the to the IR receiver.

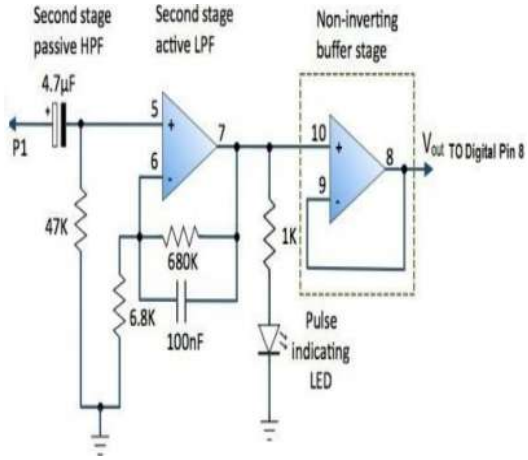

Figure 5. Second Stage Signal Conditioning Circuit

A high frequency noise is caused due to a small movement of finger. For this concern the pulse rate signal filtering is important to block any higher frequency noises present in the signal. Using a low pass filter the desired signal can be extracted from the noisy signal. The equation for cut-off frequency of the low pass filter is represented through eqn. 1.

$$\text{Cut-off Freq.} = 1 / (2\pi\ RC) \quad (1)$$

2.34 Hz is the cut off frequency of the filter which is designed for our system. If it is not amplified then the signal found from the filter circuit which amplitude is in mV level. With a view to understanding and counting pulse rate by the microcontroller it is must to amplify the signal. For this purpose a two stage signal filter and amplifier circuit using LM354 OpAmp is designed. This OpAmp is operated through 5 volts. Gain of each stage of the low pass filter is represented through the eqn. 2.

$$\text{Gain at each stage} = 1 + (R_f / C_f) \quad (2)$$

In the circuit, total gain is 10201. Values of R_f and R_i are 680 KΩ and 6.8 KΩ respectively. The 4.7uF capacitors are connected in series to the inputs of each filter blocks and they must be able to stand some reverse bias. For this purpose they should be non-polarized.

LM35 sensor has been used for measuring body temperature. According to body temperature the sensor outputs an analogue voltage. To reduce output drift due to noise in input voltage a 1uF capacitor is connected across the V_{in} and ground of the sensor. The temperature sensor circuit diagram is shown in Fig. 6.

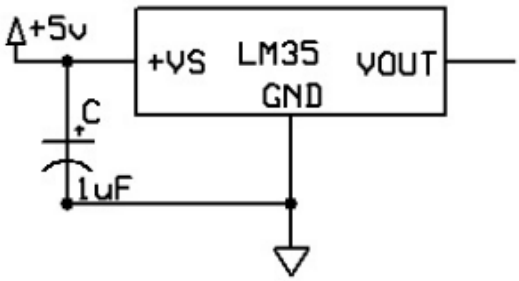

Figure 6. Temperature Sensing Circuit

For basic Centigrade temperature sensor whose rating is (+2˚Cto +150˚C). And its temperature vs. voltage relation is in represented throuh eqn. 3.

$$V_{out} = 0 \text{ mV} + 10.0\text{mV/}^{\circ}\text{C} \quad (3)$$

B. Data Processing through Arduino UNO

In this project we used the Arduino UNO development board which contains ATmega328 microcontroller and the microcontroller is used to calculate the number of heart beats per minute. It also measures the body temperature and sends the calculated values to the android application via HC-05 Bluetooth module. A thread continuously takes the analogue signal of heart condition and body temperature and sends the values to the android application. If the signal voltage is above the threshold voltage, then it is considered as a heartbeat as detected and counts up to 30 beats. A timer counts the time (t30) for 30 beats and calculates heart rate using eqn. 4.The program

$$\text{Beats per minute (BPM)} = 30\times f \quad (4)$$

also takes the analogue voltage output (Vout) of the temperature sensor and measures the body temperature by the following eqn 5 and 6.

$$\text{temp} = \text{temp} \times 0.48828125 \quad (5)$$

$$\text{tempf} = (\text{temp}\times 1.8) + 32 \quad (6)$$

C. Android Application Development to Store and Display

In our system, development of android application, called "Heartmate", is a vital portion. We monitor the heart rate and body temperature through this application. When the heartbeat and body temperature are measured the microcontroller sends the result to the application through the HC-05 Bluetooth module. Instantly the current condition of the patient is displayed in the application interface. So that anyone can easily understand the present situation of the patient and can take immediate action.

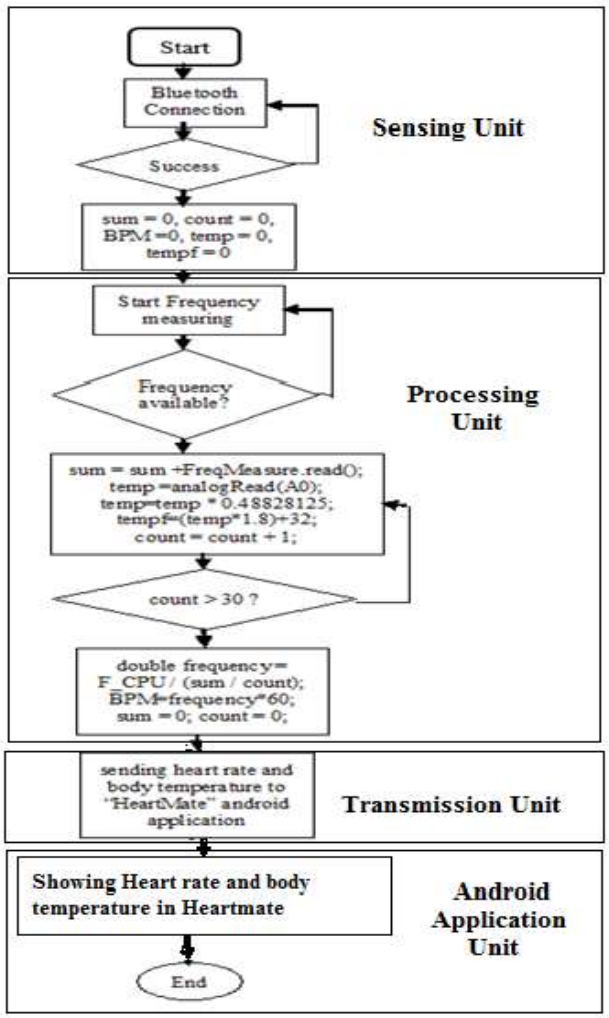

Figure 7. Algorithm for Measuring Heart rate and Body Temperatur

D. System Overview

Fig. 7 shows the system flow chart. At first the system checks the bluetooth connection between the processing unit and microcontroller and the Android device. If the connection is ok then placing the finger in the infrared sensor the microcontroller gets the some analog frequency for corresponding blood flow. Placing the finger infront of the infrared sensor an the receiver gets the transmitted signal from transmitter. After that, using both high pass filter, low pass filter and amplifier circuit shown in Fig. 3 and Fig. 4 the signal is made computable by the microcontroller used in Arduino UNO. The temperature sensor also outputs an analog signal in parallel while the heart beat signal is captured is shown in Fig. 5. For getting good performance 30 values are taken then the average values is considered the appropriate ones. When the signals are digitized by the microcontroller sends the heart rate and body temperature to the android "Heartmate" application through HC-05 Bluetooth module. Through this approach it is now become very easy for continuous heart rate and body temperature monitoring

E. *Significance of the System*

In this system we have tried to implement a low cost heart rate and body temperature monitoring system. We have implemented the system in Android platform since Android devices are available in cheap price. The device is portable and light weight so that it can be carried easily anywhere. Through this system it is possible to monitor the heart rate and body temperature continuously. As a result for those patients for whom it is must to monitor the heart rate and body temperature continuously then in that condition the system can be adopted easily. The system can provide much support to know the present condition of the patient if there is no doctor or clinic nearby.

IV. PERFORMANCE MEASUREMENT

Fig. 8 represents the bread board implementation of heart rate and body temperature measuring hardware module unit of our implemented system. In our implemented system the user has to start the hardware module first then run the *Heartmate* android application. The IR transmitter and receiver are

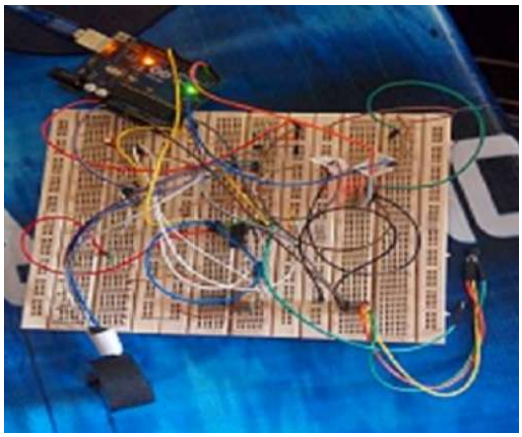

Figure 8. Heart rate and body temperature measuring device bread board implementation.

mounted in a finger ring. Then touching the temperature sensor the module begin to measure both heart rate and body temperature. Fig. 9 shows the measured result in "Heartmate" application.

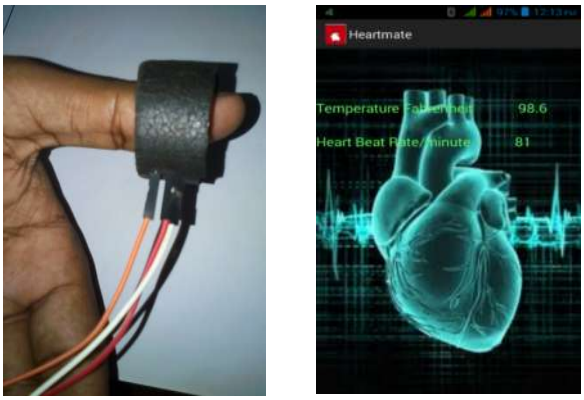

Figure 9. Measuring Heart Rate and Body Tempearture

For performance checking of our system, we measured the heart rate for a person for 20 minutes and the result is shown in the Fig. 10. In this process we measured the heartbeat through Sphygmomanometer which represents the actual measurd heart rate in the Fig. 10. At the same time we measured the heart rate placing our device in the left thumb of the person. Since a little movement of the fingure while measuring heart rate through our system the the analog value for corresponding blood flow is affected by noise. As a result we got some errors in our experimental results. For this reason we got appropriate value at beginning of our experiment then after passing several minutes the result deviated much from the original value. While measuring body temperature we measurd the actual temperature through clinical Thermometer. And along with this we also measured the body temperature with our device. Fig. 11 shows the actual and measured body temperature. We got some varriance in the measured value.

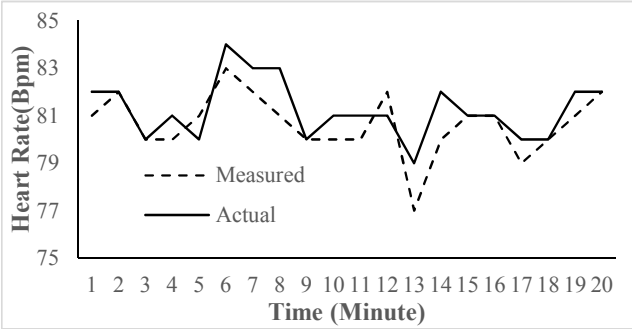

Figure 10. Actual vs. Measured Heart rate measured for 20 minutes

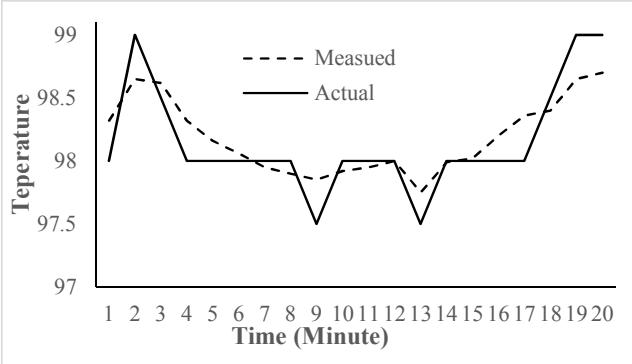

Figure 11. Actual vs. Measured Body Temperature for 20 minutes

V. CONCLUSION

In this paper, we have shown a design of a heart rate and body temperature measuring embedded system. The final outcome of our approach is an android based portable heart rate and body temperature measurement system with a suitable architecture which can be applicable in medical and home appliances in patient health monitoring system. The system has been tested for some valid signal such as heart rate and body temperature. The system gives comparatively better performance than old hand measuring system.

REFERENCES

[1] R. G. Landaeta, O. Casas, and R.P. Areny, "Heart rate detection from plantar bioimpedance measurements", *28th IEEE EMBS Annual International Conference*, USA, 2006, pp. 5113-5116.

[2] How the Heart Works, August 24, 2015 http://www.webmd.com/heart-disease/guide/how-heart-works

[3] Heart Rate During Exercise, August 24, 2015 http://btc.montana.edu/olympics/physiology/cf02.html

[4] Heart Rate Variability During Sleep, August 24, 2015 http://www.livestrong.com/article/134189heart-ratevariability-during-sleep/

[5] Heart Rate Should Slow During Sleep, July 15, 2015 http://www.healthandage.com/your-heart-rate-shouldslow-during-sleep

[6] Heart Rate Monitors, July 17, 2015 http://www.walmart.com/browser/sportsoutdoors/heartmonitors/412541341078104107814 5

[7] Determining Heart Rate from the Electrocardiogram, August 24, 2015 http://www.cvphysiology.com/Arrhythmias/A020.htm

[8] M. M. A. Hashem, R. Shams, Md. A. Kader and A. Sayed, "Design and development of a heart rate measuring device using fingertip," 3rd IEEE International Conference on Computer and Communication Engineering (ICCCE'10), Kuala Lumpur, Malaysia, May 11-12, 2010.

[9] Heart rate measurement from fingertip, August 24, 2015 http://embeddd-lab.com/blog/?p=1671

[10] Wireless Human Health Online Monitor, March 20, 2015 http://people.ece.cornell.edu/land/courses/ece4760/FinalProjects/s2011/xy222_yw437_ha245/xy222_yw437_ha245/index.html

[11] M. Navale, S. Damare, R. Chavan, R. Dube, and S. Patil "Android Based Heart Monitoring and Reporting System", International Journal of Advanced Research in Computer and Communication Engineering Vol. 3, Issue5, May 2014

[12] N. Indumathy and K. K. Patil "Medical Alert System for Remote Health Monitoring Using Sensors and Cloud Computing" International Journal of Research in Engineering and Technology, vol. 3, no. 04, pp. 884-888, 2014.

[13] Pulse oximetry explained, August 24, 2015 http://www.howequipmentworks.com/physics/respi_measurements/oxygen/oximeter/pulse_oximeter.html

A New Approach to Extract Features from ECG Signals

Muhammad Sheikh Sadi, G.M. Mahmudur Rahman, Subroto Debnath, Fahim Feroje Al Jami
Department of Computer Science and Engineering
Khulna University of Engineering & Technology (KUET)
Khulna 9203, Bangladesh
sheikhsadi@gmail.com, dtuhin28@yahoo.com, subroto16.debnath@gmail.com, fahimaljami@gmail.com

Abstract— **Electrocardiogram (ECG) is the record of electrical and muscular movement of the heart over a period of time which is useful for diagnosing many cardiac diseases. Due to the increase in mortality rate associated with cardiac diseases, automatic detection of these diseases is highly required. Hence, feature extraction and de-noising of ECG signals are highly useful in cardiology. This paper describes a novel approach for feature extraction in order to recognize trusty heart rhythm. This method consists of two components: data preprocessing and feature extraction. At pre-processing stage, baseline wander removal and power line inference have been used for removing baseline wander and de-noising the signal respectively. At the second stage, R wave is detected and then Q, S, T and P waves are extracted based on R wave. In this paper, Wavelet transformation is used for power line inference. The experimental studies show that the proposed method provides 96.79% accuracy and 5 features recognition with reduced computational complexity.**

Keywords— ECG, QRS Complex, R Wave, Baseline Wander, De-noising.

I. INTRODUCTION

Elderly population and incessant incidence of Cardio-vascular Diseases (CVD) have put present healthcare methods global under severe strain in terms of the excellence of maintenance supply and its related price [1], [2]. Appropriate disease supervision through uninterrupted monitoring and information fusion of elementary biological signals in lasting CVD patients is observed as the significant mechanism for the fundamental decrease of the cost of CVD care delivery, the improvement of the quality of care/life and the major drop in hospitalizations. The Electrocardiogram (ECG) signal - the key element of a remote CVD observation system - is the process of recording electrical variation of heartbeats of human. These signals can be used to attain clinical diagnosis. The heart's electrical activity can be measured by electrodes which are placed on the patient's limbs and on the surface of the chest. Physicians monitor this activity and its features. The parameters of this feature are: the height and interval of the waves. These parameters are collected from PP interval, RR interval, ST segment, QRS complex, QT segment etc. as shown in Figure 1. This figure presents the simple contour of a fit ECG heartbeat signal with P, Q, R, S, J, T and U.

The features, collected from ECG signals, provide clinical diagnosis of heart rate, rhythm and heart abnormalities. Various diseases like Tachycardia, Bradycardia and abnormal heartbeats etc. can be measured by examining these features of ECG signals.

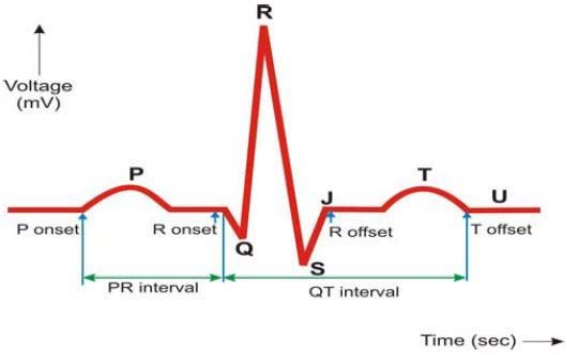

. Figure 1: An ECG Waveform [3]

In general, physicians detect diseases by interpreting those shapes of waves manually. However, this tedious job takes time and may incur additional cost. Also with the change of the parameter's value the diagnosis of disease may change. It is a tough job for a physician to memorize the names of diseases according to the parameters' value. So an automatic artificial intelligence based ECG feature detection and disease detection system is a must to reduce the complexity of interpreting ECG signal.

There are several studies proposed for the analysis of the ECG beats. P.SASIKALA1 and Dr. R.S.D [3] presented retrieval of P wave and T wave in Electrocardiogram by means of Wavelet Transform. *MATLAB* implementation of ECG signal processing was presented by V.Viknesh and P. Ram Prashanth [4]. Gradient-based algorithm and time domain morphology was presented by E.B. Mazomenos et al. [5]. Wavelet transform finds application in ECG beat detection and feature extraction as reported by S.C. Saxena et al. [6]. A wavelet-based ECG delineation was presented by P. Martinez et al. [7]. Also Mahesh used wavelet and Pan- Tompkins algorithm to extract time-frequency features for ECG beat detection system [8]. However, extracting significant and useful features from ECG signal characteristics is still a great

978-1-4673-9257-0/15/$31.00 ©2015 IEEE

challenge for successful implementation of these devices since they need to be fast, simple and computationally efficient.

Motivated by this point, this paper proposes a different computerized ECG feature extraction algorithm that is precisely designed to be effective from a computational view. It entails simpler processing and calculations to extract the features from ECG signals that are to be further used to diagnose the diseases.

The rest of the paper is organized as follows: after reviewing related work in Section II, we describe our algorithm in Section III. Section IV is devoted for the justification of the algorithm, whereas conclusions are drawn in Section V.

II. Related Work

Abdullahi Karaye et al. [2] proposed a robust ECG feature extraction technique suitable for mobile devices. Their technique was to extract samples, between R-R intervals as equivalent R-T interval, using Pan Tompkins algorithm. R-T interval samples were calculated by using discrete wavelet transform. The mean, median, standard deviation, maximum, and minimum coefficient of wavelet were used as a time-frequency domain feature.

Viknesh et al. [4] discussed about MATLAB implementation of ECG signal processing. In their paper they worked on noise filtering and detection of QRS complex using wavelet transform. Their main objective was to reduce noise from an ECG signal and data compression. But they didn't detect other features of ECG Signals.

Mukesh Tiwari et al. [9] proposed a system Feature Extraction of ECG Signal by HHT Algorithm. The HHT algorithm is useful to analyze any nonlinear signal because minor frequency attribute of any signal is produced by HHT algorithm. They used wavelet transform and Huang Hilbert Transform to retrieve the features of ECG signal in regular and irregular condition.

V.K.Srivastava et al. [10], in their paper, used discrete wavelet transform to extract features from ECG signal. They used neuro-fuzzy based approach which was a combined approach of artificial neural networks and fuzzy logic. This approach was used to classify and analyze data. Their accuracy was more than 90% but sensitivity was 60% to 70%.

Coast Doughlas et al. [11] described a method to cardiac arrhythmia investigation by Hidden Markov Models. The Hidden Markov modeling method combines structural and statistical knowledge of the ECG signal in a single parametric model. This technique was also able to detect QRS complex as well as R-R intervals to determine ventricular arrhythmias. The accuracy of the proposed system was 50% to 80%.

Franc Jager [12] developed a new approach to extract which is Kahunen Lo□eve Transform (KLT). It was a powerful approach to the feature extraction. It could provide the clarification if the probability densities of pattern vectors population of a problem domain were unknown. But it was sensitive to noisy pattern of an ECG signal and only gave 80% accuracy.

Naveen Ku. Dewangan et al. [13] made a survey on ECG Signal Feature Extraction and Analysis Techniques. This survey discussed various techniques and transformations of proposed systems for feature extraction and analysis of ECG signals and made a comparison among them.

Zhao et al. [14] offered a feature extraction way by wavelet transform and support vector machines. The proposed system was comprised of three components including data pre-processing, feature extraction and grouping of ECG signals. Wavelet transform was used to determine the coefficients of the transform and autoregressive modeling (AR) was also used to acquire the temporal configurations of ECG waveforms. The support vector machine (SVM) with Gaussian kernel was used to categorize diverse ECG heart regularity. The proposed system gave accuracy of 99.68%, high simplicity and high predictivity.

III. The Proposed Methodology To Extract Features From ECG Signals

With the purpose of extracting information from the ECG signal, the raw ECG signal should be processed. Preprocessing and Feature Extraction as shown in Figure 2.

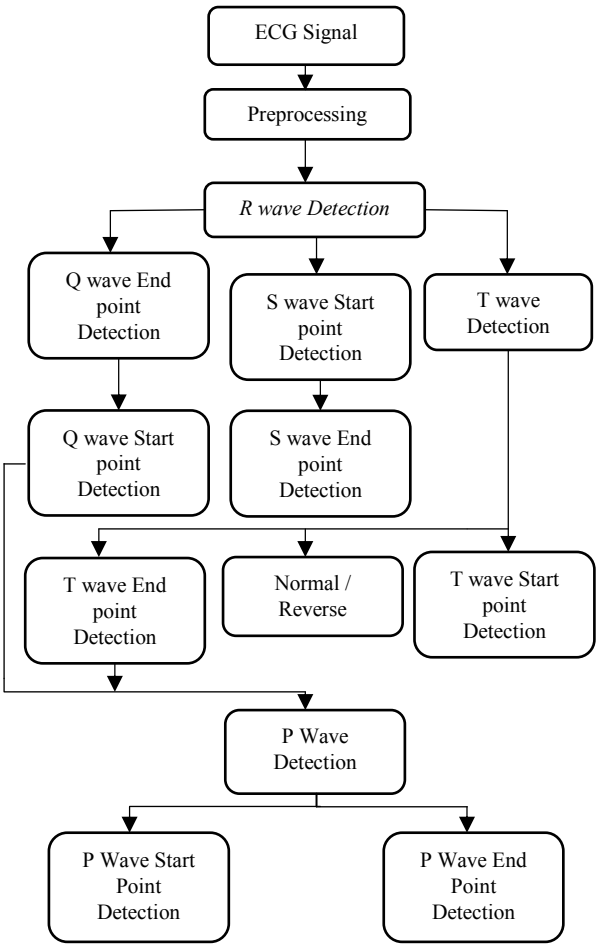

Figure 2: Workflow of ECG Feature Extraction

In our proposed method, the process of ECG signal analysis can be sub-divided into seven sub-processes. These sub-processes are as follows.

1. Data Acquisition
2. Pre-processing
3. R Wave detection
4. Detection of starting point of Q wave and S wave & ending point of S wave
5. T wave Detection
6. P Wave Detection
7. Calculation of Intervals

A. *Data Acquisition*

The heartbeats are recorded simultaneously from patients. For collection of data, we used *BIOPAC Student Inc.* ECG module which can reliably record ECG signals. The *AcqKnowledge* software is used to record ECG data from the module in .acq format then saved it in .mat file format which is *MATLAB* compatible file.

B. *Pre-Processing*

ECG signal comprises of diverse forms of noises that is frequency intrusion, baseline drift, electrode interaction noise, polarization noise, muscle noise, the inner amplifier noise and motorized objects. One of the common problems in ECG signal processing is baseline wander removal and power line inference.

- *Baseline Wander*

Different types of noises are included while an Electrocardiogram signal is recorded. These situations are responsible for an ECG signal to be affected by baseline drift which is difficult to diagnose manually [15]. It is needed to get rid of noise from the signal for proper diagnose. Eliminating the baseline drift of a signal is named as de-trending [15]. According to Vanisree K and Jyothi Singaraju [15], the achieved main ECG signal decomposes into resultant approximation and detail coefficients equal to 8 levels using *Discrete Waveletet Trasformation* where *Dabachies6* (db6) is used in the decomposition as mother wavelet or basis function. The decomposed signal is then restored to obtain main ECG signal components by means of *Inverse Discrete Wavelet Transformation* (IDWT). The recreated approximation and detail coefficients of the signal are A1, A2 . . . ., A8 and D1, D2, … D8 [15]. A1 and D1 have maximum frequencies and A8 and D8 have the lowermost frequencies. As the low frequency components affect the signal for baseline fluctuating, these components must be eliminated to obtain a signal without baseline drift [15].As A8 and D8 have the low frequency components so the De-trended Signal (DS) will be the subtraction between Original Signal, and (A8+D8) [15]. The de-trended ECG signal is shown Figure 3.

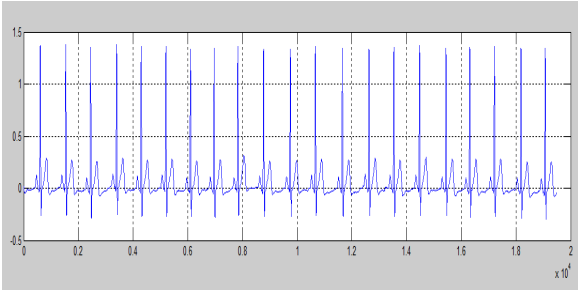

Figure 3: Waveform with Baseline Wander Removed

- *Power Line Inference*

Power line is a known noise source in ECG that is described by 50 or 60 Hz sinusoidal interference [2]. Such noise put forward the investigation and understanding of the ECG further tough, as the explanation of low-amplitude waveforms turn into unpredictable [2]. Precautions have been taken to decrease the outcome of power line inference but still certain extra types of noise may still disturb the feature extraction of ECG. To get rid of the noise, we apply Discrete Wavelet Transform 1d packet. At the beginning, it decomposes the signal into multiple sub-bands then amends each wavelet coefficient using a threshold function. Lastly it recreates the de-noised signal [9]. The signal turn into smoother and the noises vanishes when noises are noticed by high frequency components and lower details are eliminated from the main signal [9].The waveform given by these values is shown in Figure 4.

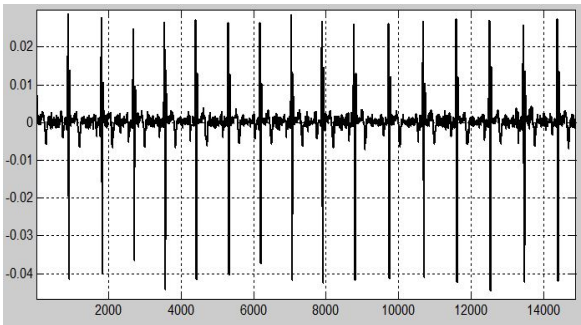

Figure 4: Waveform with Power Line Interference Removed

C. *R Wave Detection*

At first, the length of the de-noised ECG signal is determined which is found from the Wavelet Transformation. As, the height of the R wave can't go lower than the 0.6 times of the maximum height of the R wave [4], the height which is greater or equal to the 0.6 times of the maximum height of the R wave is detected. We increase the counter to 100 ms because the probability of R to R interval in 100ms range is approximately Zero. The pseudo code to detect R wave is shown in Pseudo code-1.

Pseudo code -1

```
Initialize the ECG signal as denoised
Find a=Max(denoised)
Set position counter to 0
Set height counter to 0
Set counter to 1
while counter< length (denoised)
    Set past position to 0
    Set next position to 1
    if denoised[counter]>0.60*a
      while denoised[past position] ≤ denoised[next position]
          Set past position = next position
          Increment next position by 1
      End while
      Increment position counter by 1
      Increment height counter by 1
      Set R_position[position counter]= counter + next position-1
      Set R_height[height counter]= denoised[counter + next
position-1]
      Increment counter by 100
    End if
    Increment counter to 1
End while
     Increment counter by 1
End while
```

- *Detection of start point of R wave*

  In order to determine the start point of R wave in Figure 5, we find the point which is situated before the R_position and where the height of R wave is approximately zero with respect to base line

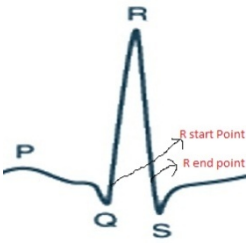

Figure 5: Start Point & End Point of R wave

The pseudo code to detect the start point of R wave is shown in Pseudo code -2.

Pseudo code -2

```
Set the position counter to 0
Set counter to 1
While counter ≤ Total number of R wave
     Set counter_r to 1
     While (height of R position-(height of (R position -
counter_r))) < height of R position
          Increment counter_r by 1
     End while
     Increment the position counter by 1
     position_R_start[position counter]=R position - counter_r
     Increment counter by 1
End while
```

D. Detection of starting point of Q wave & S wave and ending point of S wave

A similar method (pseudo code -2) is used to detect the start point of Q wave & S wave and end point of S wave with a few changes in the arithmetic operations.

E. T wave Detection

To detect T wave, the interval is taken between the end point of S wave and the starting point of next Q wave and then we find the maximum height and the minimum height. The sign of the minimum height is changed and compared with the maximum value. If maximum height is greater than the minimum height then T wave is normal. Else T wave is inverse. The pseudo code to detect of T wave is shown in Pseudo code -3.

Pseudo code -3

```
Find m=total number of R wave
Set T position counter to 0
For counter=1 to m-1
   Set max=0
   Set min=0
   For y=end point of S wave to start point of next Q wave
      Increment y by 1
      T height=denoised[y]
      If T height is greater than 0.0 and max
         max=T height
         T1 position=y
    End If
    If T height is less than 0.0 and min
       min=T height
       T2 position=y
  End For
  min=|min|
  If max>min
     T is normal
     T position[T position counter]= T1 position
  Else
     T is inverse
     T position[T position counter]= T2 position
  End If
  Increment T position counter and counter by 1
End For
```

- *Detection of starting point & ending point of T wave*

  A similar methodology (as shown in Pseudo code -2) is used to identify the starting point and end point of T wave with a few changes in the arithmetic operations.

F. Detection of P wave

In order to identify P wave, the interval is taken between the end point of T wave and the starting point of next Q wave and then we find the position where the height is maximum. A similar method (as shown in Pseudo code -3) is used to detect the position of P wave.

- *Detection of start point & end point of P wave*

A similar method (as shown in Pseudo code -2) is used to detect the starting point and end point of P wave with a few changes in the arithmetic operations.

G. *Calculation of Intervals*

At first, The average time of S wave, Q wave, T wave, QRS complex, R-R interval, Q-T interval and S-T segment are calculated and then compared with a specific S wave, Q wave, T wave, QRS complex, R-R interval, Q-T interval and S-T segment. If the difference between two intervals is greater than 10ms then the specific S wave, Q wave, T wave, QRS complex, R-R interval, Q-T interval and S-T segment are omitted and the average intervals to find the optimum result are re-calculated.

IV. EXPERIMENTAL ANALYSIS

The ECG signals necessary for analysis are gathered from Biomedical Lab, Situated in KUET, Bangladesh, using Biopac System Inc. Two types of ECG signals are used for experiment. One is .mat file and another is tracing paper from Single Channel ECG-901A developed by KADEN Yasen Medical Electronics. This experiment is done on five (Sample 1, Sample 2,…, Sample 5) different people. The samples obtained thus are shown in Figure 6.

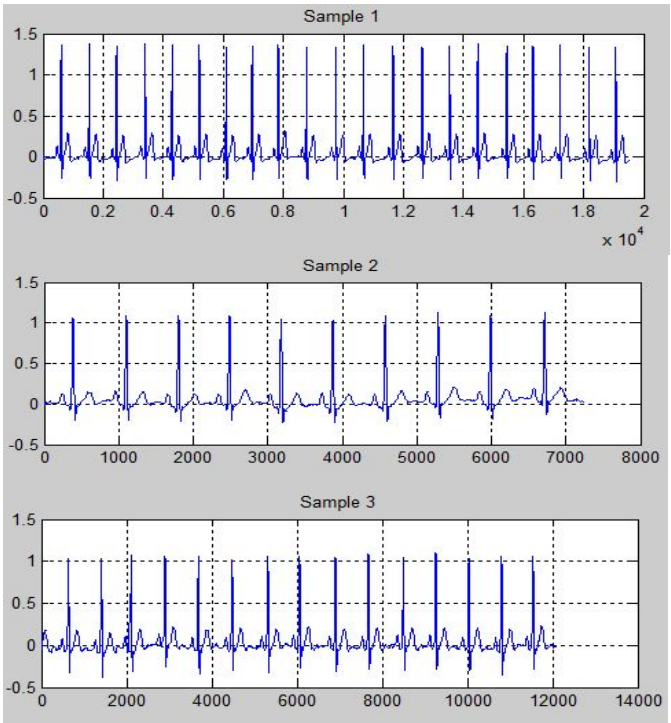

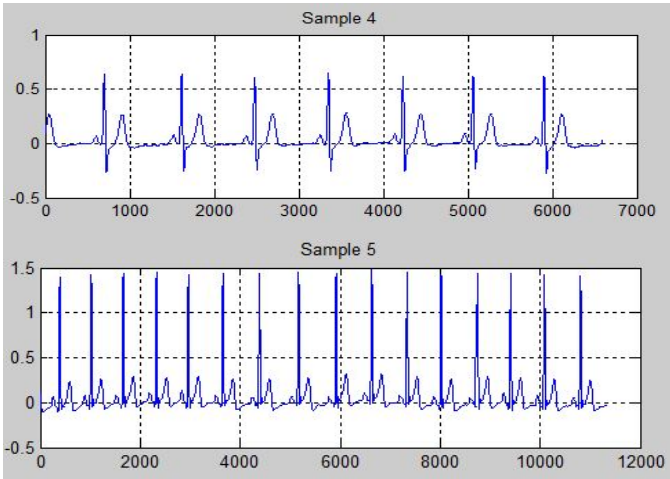

Figure 6: Five Samples from Five people

To assess and calculate the correctness of the proposed process, heart rate, PR interval, P wave, QRS complex, T wave and QT interval are used. The distance between R-R interval is extracted and heart rate is calculated established on the database standards. The info regarding the R Peak and QRS complex acquired is very valuable for ECG Classification, Investigation, Diagnosis, Verification and Documentation performance. The QRS complex is also used for beat detection and the calculation of heart rate using R-R interval estimation. The key benefit of this type of detection is a reduced amount of time consumption for long time ECG signal. The accuracy obtained for the database 96.79% which is a promising result. Table I shows the parameter calculated by using the proposed algorithm and by manually analyzing the ECG signals collected in the tracing paper.

The result of the ECG machine in tracing paper is taken as reference. The accuracy of proposed system is calculated with respect to the result of the ECG machine. The proposed method is experimented over five people. Where the sample 1 provides the accuracy level of 96.71% and the error rate is 3.29%.The proposed method provides an average accuracy level of 95%. Through a simple method we find overall good accuracy to extract the features of ECG signals.

V. CONCLUSIONS

This paper addresses one of the challenging issues in health care services especially for developing countries by proposing a novel feature extraction method. The method used ECG signal data from Biomedical Lab, Situated in KUET, Bangladesh and different filters were designed to reduce unwanted signal like baseline wander and power line interference. Then various features are detected from ECG signal. This proposed algorithm is simple to implement and may sensitive to noisy signal. Thus it is needed to de-noise the signal. Further research can be enhanced to adopt a methodology in order to de-noise the ECG signals.

TABLE I. Feature Detection Performance Comparison

ECG Record	Category	Heart Rate (BPM)	PR Interval (mS)	P Wave (mS)	QRS Complex (mS)	T wave (mS)	QT Interval (mS)	Accuracy
Sample 1	***Tracing Paper Value***	76	106	94	114	139	320	96.71%
	Proposed Algo. Value	75.4	112	98	119	143	328	
Sample 2	***Tracing Paper Value***	74	148	122	104	162	346	96.94%
	Proposed Algo. Value	75	141	119	102	153	338	
Sample 3	***Tracing Paper Value***	82	140	117	107	144	320	98.05%
	Proposed Algo. Value	82.4	138	115	103	141	313	
Sample 4	***Tracing Paper Value***	78	150	122	104	159	342	96.37%
	Proposed Algo. Value	77.4	158	127	109	168	349	
Sample 5	***Tracing Paper Value***	80	150	119	107	173	357	95.88%
	Proposed Algo. Value	80.8	143	112	102	168	348	

REFERENCES

[1] Evangelos B. Mazomenos, Dwaipayan Biswas, Amit Acharyya, Taihai Chen, Koushik Maharatna, James Rosengarten, John Morgan and Nick Curzen, "A Low-Complexity ECG Feature Extraction Algorithm for Mobile Healthcare Applications," *IEEE Journal of Biomedical and Health Informatics,* Vol. 17, No. 2, March 2013.

[2] Sani Saminu, Nalan Özkurt and Ibrahim Abdullahi Karaye, "Wavelet Feature Extraction for ECG Beat Classification," *IEEE 6th International Conference on Adaptive Science & Technology (ICAST)*, 2014.

[3] P.SASIKALA and Dr. R.S.D, "Extraction of P wave and T wave in Electrocardiogram using Wavelet Transform," (*IJCSIT) International Journal of Computer Science and Information Technologies*, Vol. 2 (1) , 489-493, 2011.

[4] V.Viknesh and P. Ram Prashanth, "Matlab implementation of ECG signal processing," *IOSR Journal of VLSI and Signal Processing (IOSR-JVSP)*, Volume 3, Issue 1 (Sep. – Oct. 2013), PP 40-47, e-ISSN: 2319 – 4200, p-ISSN No. : 2319 – 4197

[5] E.B. Mazomenos, T. Chen, A. Acharyya, A. Bhattacharya, J. Rosengarten, K. Maharatna, "A timedomain morphology and gradient based algorithm for ECG feature extraction," *Proceedings of IEEE international conference on industrial technology (ICIT)* ,pp. 117–122, 2012.

[6] S.C. Saxena, V. Kumar, S.T. Hamde, "Feature extraction from ECG signals using wavelet transforms for disease diagnosis," Int J Syst Sci. 33(13):1073–85, 2003.

[7] J.P. Martinez, R. Almeida, S. Olmos, Rocha, A.P., Laguna, P., "A wavelet-based ECG delineation: evaluation of standard databases,*" IEEE Tran Biomed Eng.* 51(4):570–81, 2004.

[8] A.N. Mahesh, "ECG feature extraction using Time-Frequency analysis," *Innovation in Computing Sciences and Software Engineering*, 2014.

[9] Neha Soorma, Jaikaran Singh and Mukesh Tiwari, "Feature Extraction of ECG Signal Using HHT Algorithm," *International Journal of Engineering Trends and Technology (IJETT)* – Volume 8 Number 8- Feb 2014.

[10] V.K.Srivastava and Dr. Devendra Prasad, "Dwt - Based Feature Extraction from ecg Signal," *American Journal of Engineering Research (AJER)*, e-ISSN: 2320-0847 p-ISSN : 2320-0936, Volume-02, Issue-03, pp-44-50.

[11] A. Coast Douglas, Rchard M. Stern, Gerald G. Cano and Stanley A. Briller, "An approach to cardiac arrhythmia analysis using hidden Markov models," IEEE Transaction on Biomed Eng., 37(9): 826-836, 1990.

[12] Franc Jager, "Feature Extraction and Shape Representation of Ambulatory Electrocardiogram Using the Karhunen-Loève Transform," Electrotechnical Review, Ljubljana, Slovenija Elektrotehniˇ ski vestnik, 69(2): 83–89, 2002.

[13] Naveen Ku. Dewangan and S. P. Shukla, "A Survey on ECG Signal Feature Extraction and Analysis Techniques," *International Journal of Innovative Research in Electrical, Electronics, Instrumentation and Control Engineering*, Vol. 3, Issue 6, June 2015.

[14] Qibin Zhao, and Liqing Zhan, "ECG Feature Extraction and Classification Using Wavelet Transform and Support Vector Machines," *International Conference on Neural Networks and Brain*, ICNN&B '05, vol. 2, pp. 1089-1092, 2005.

[15] Vanisree K and Jyothi Singaraju, "Automatic Detection of ECG R-R Interval using Discrete Wavelet Transformation," *International Journal on Computer Science and Engineering (IJCSE)*, Vol. 3 No. 4, ISSN : 0975-339, Apr 2011

Development of Low Cost Wireless Biosignal Acquisition System for ECG EMG and EOG

Md. Asif Ahamed[1*], Md. Asraf-Ul- Ahad[2], Md. Hanif Ali Sohag[1], Mohiuddin Ahmad[1]
[1]Department of Electrical and Electronic Engineering
[2]Department of Conservative Dentistry and Endodontics
[1]Khulna University of Engineering & Technology, Khulna-9203, Bangladesh
[2]Bangabandhu Sheikh Mujib Medical University, Dhaka- 1214, Bangladesh
*E-mail: asif.fx@live.com

***Abstract*— A biosignal is a human body variable that can be measured and monitored continuously and provide information about the health status. Among them well known bioelectrical signals are Electrocardiograph (ECG), Electromyography (EMG), Electroencephalogram (EEG) and Electrooculogram (EOG). Those signals are useful for different applications like disease diagnosis, human machine interface, entertainment. This paper presents a low cost, wireless biosignal acquisition system specialized for ECG, EMG and EOG. In this system, Arduino Uno in used and an application is developed for visualizing and storing the signal in real-time. This application is developed by processing. It stores the signal data in a text file, which can be used in MATLAB for analysis. In this system, biosignal is transferred by Bluetooth serial communication, which ensures safety and reduces noise interference. This system can be used either Windows, Linux, Mac OS and suitable for both laptop and desktop computer.**

Keywords—Biosignal acquisition, ECG, EMG, EOG, Powerline interference

I. INTRODUCTION

Human body generates various different signals. Biosignal can be defined as any signal in living beings that can be continually measured and monitored. It can be both electrical and non-electrical signals. Bioelectrical signals can be sensed by non-invasive method by using skin-surface transducer, which is commonly used for Electrocardiograph (ECG), Electromyography (EMG), Electroencephalogram (EEG) and electrooculogram (EOG) [1]. Both ECG and EOG signals are bipolar low-frequency signal. The normal range of ECG signal is 0.05-100Hz having its amplitude ranges from 10µV to 5mV, whose typical value is 1mV [2]. EOG signal ranges between 15 µV to 200 µV with a frequency range of about 0-30 Hz [3]. Generally the amplitude of the EMG signal ranges from 0-10mV (peak-to-peak) and its frequency ranges from 0- 500Hz [4]. The dominant energy in EMG is being in 50-150Hz [4].

The frequency information of those signal is highly useful for disease diagnosis. Among those signals ECG is very useful for diagnosis especially for heart related diseases and disorders such as, cardiovascular disease, pulmonary disease, sudden cardiac arrest, etc [5]. EMG is used clinically for diagnosis of neurological and neuromuscular problems. Another important application of EMG and EOG is human machine interface and controlling of various devices.

Our research aims to develop a low cost biosignal acquisition system which is affordable for the people of developing and under developed country. In our previous papers, we have developed an ECG data acquisition system and an ECG monitoring system [6,7]. In this research, we have modified the system for acquisition of ECG, EOG and EMG together. This paper presents a prototype biosignal acquisition system, which is portable, battery powered and it includes wireless facility. In this system biosignal is transferred by Bluetooth serial communication and it gives wireless connectivity up to 9 meter. The equipment used in this system consumes low power and this system is battery powered. For this it can be used during load shedding and on those remote areas where electricity have not reached.

This paper is organized as follows: Section II shows the architecture of the system. Section III describes the proposed methodology. Section IV explain the software implementation. Experimental results are illustrated in section V. Finally, section VI concludes the results.

II. SYSTEM ARCHITECHURE

This system consist of three electrodes. Figure 1 shows the

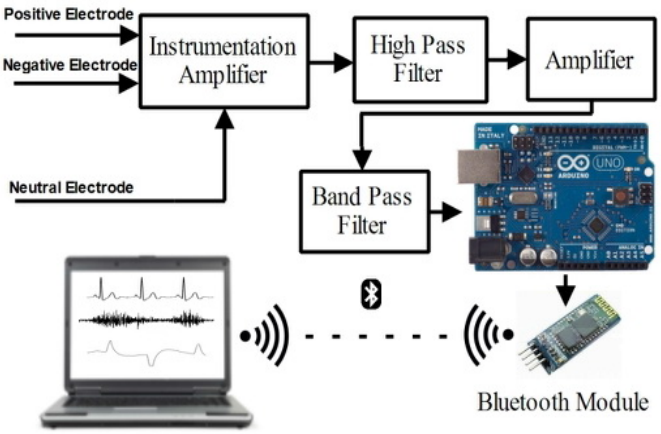

Fig. 1. System Architecture of the Biosignal acquisition system.

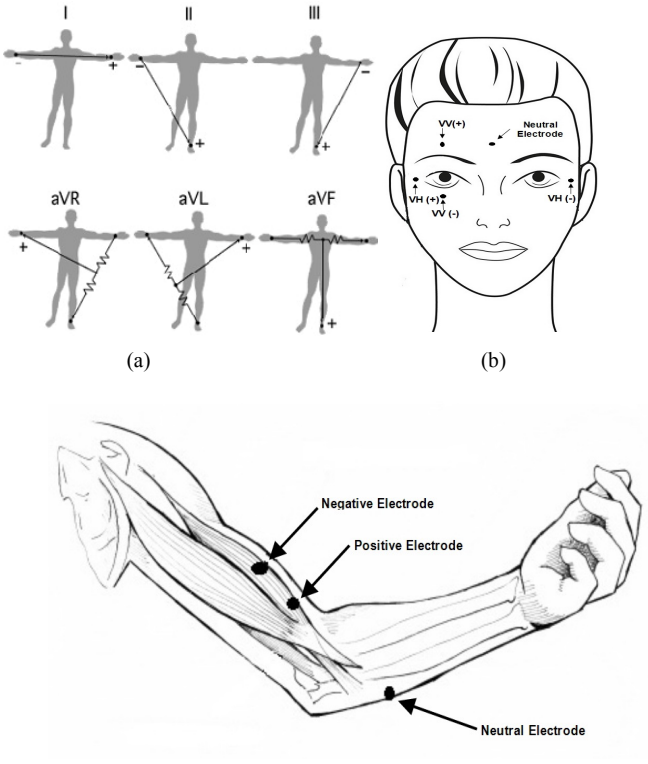

(a) (b)

(c)

Fig. 2. (a) limb leads and augmented limb leads for ECG, (b) Electrode position for horiontal and vrtical eye mvemrnt, (c) Electrode position for biceps EMG.

system architecture of this system. In this system, Arduino Uno is used for analog to digital conversion and signal transmission. By this system ECG can be taken from both limb leads and augmented limb leads. Figure 2 shows the electrode position for ECG, EOG and EMG.

III. Proposed Methodology

The proposed system consists of four units: sensor unit, signal conditioning unit, power supply unit and Microcontroller unit.

A. Sensor Unit

For sensing ECG, EMG and EOG signal, silver chloride electrodes are used. A commercially available disposable electrode named Bio Protech T716 was used, which is shown in figure 4 (b) [8].

B. Signal Conditioning Unit

Signal conditioning unit consist of instrumentation amplifier, op-amp and filter. In the top of figure 3 signal conditioning circuit is shown. In this system, a commercially available low cost instrumentation amplifier AD620 is used, which gives Common-mode rejection ratio (CMRR) greater than 100dB at nearly 1 kHz [9]. Total gain of 840 is achieved by two stage amplification. First stage amplification was done by AD620 and the gain was 13.7. Second stage amplification is done by CA3130 op-amp and the gain of second stage was 51. CA3130 was used as a non-inverting amplifier. To avoid the risk of amplifier saturation two stage amplification is done. Saturation of amplifier generally occurs due to amplification of electrode offset voltages [10]. To set the gain of AD620, a resistor R_g is used and its value was 3kΩ. The gain expression for AD 620 is given in Eq. (1).

$$\text{Gain} = \frac{49.4\ \text{k}\Omega}{R_g} + 1 \tag{1}$$

For removing the low frequency noises first a high pass filter of 0.03 Hz cut off frequency is used after first stage amplification. After second stage amplification, a band pass filter is implemented using a high pass and a low pass filter in cascade. For ECG, EOG and EMG cut off frequency of all high pass filter is 0.03 Hz. For ECG cut off frequency of the low pass filter is 159 Hz. For EMG it is 564 Hz and for EOG it is 15 Hz. Three switches S1, S2 and S3 are used for filtering path selection of the ECG, EOG and EMG signals. All those filters are passive First order filter. General expression for cut off frequency of the filter is given in Eq. (2) [11].

$$F_c = \frac{1}{2\times\pi\times R\times C} \tag{2}$$

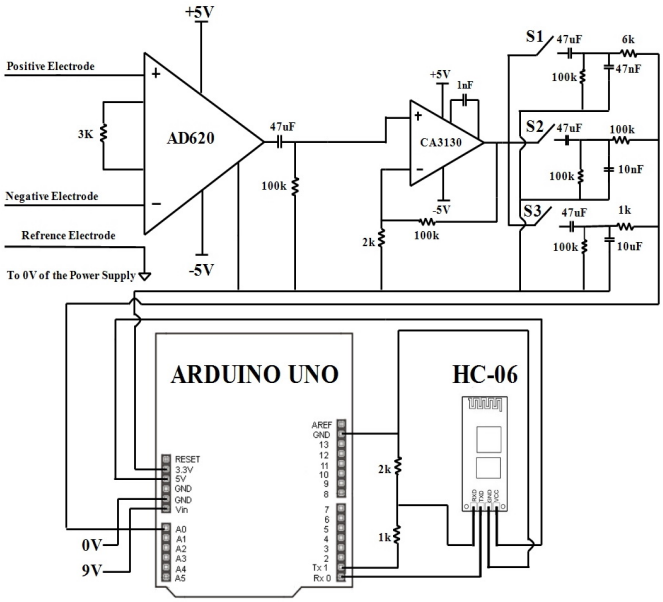

Fig. 3. Circuit diagram of the system.

C. Power Supply Unit

In this system two commercially available 9V disposable Lithium battery is used. A voltage regulator LM7805 is used for safety and short circuit protection. It gives regulated output voltage of ±5V. In this system neutral electrode must connect to the 0V of the dual supply.

D. Microcontroller Unit

This unit consists Arduino Uno board and Bluetooth module HC-06. Arduino UNO board has a 6 channel 10-bit analog to digital converter (ADC) and it returns a linear value from 0 to 1023 corresponding to 0V and +5V respectively [12]. As the ADC works between 0 to 5V, a 3.3V virtual ground is used for making the bipolar signal to unipolar. For serial transmission baud rate is taken as 38400 bps and sampling rate of 1270 samples per second is obtained. A Bluetooth module

HC-06 does signal transmission between Arduino UNO and laptop. Bluetooth module HC-06 has a default baud rate of 9600 bps, which was changed to 38400 bps by a software named putty.

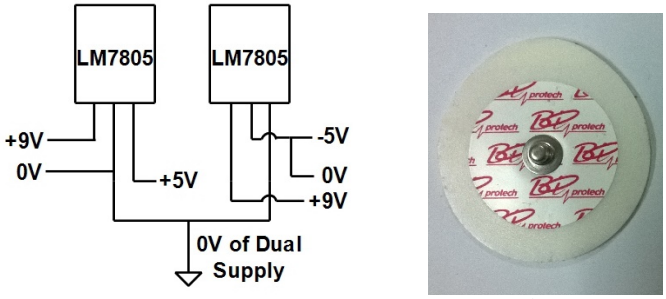

(a) (b)

Fig. 4. (a) Designed ±5V dual power supply. (b) Bio Protech T716 ECG electrode..

IV. Software Implementation

Arduino Uno board has a microcontroller named ATmega328. For programming the microcontroller, integrated development environment provided by the Arduino platform is used. For visualizing and storing the signal an application is developed by Processing. Processing is an open source programming language and integrated development environment (IDE). It builds on the Java language, but uses a simplified syntax and graphics programming model and available for Linux, Mac and Windows operating system. For receiving the signal data serial library of processing is used. In processing line() function is used for visualizing the signal and println() function is used for sorting the signal, which creates a txt file and saves the values received from Arduino ADC [13].

V. Experimental Measurements And Results

Figure 5 shows the experimental measurement performed by us for ECG signal and the prototype biosignal acquisition system.

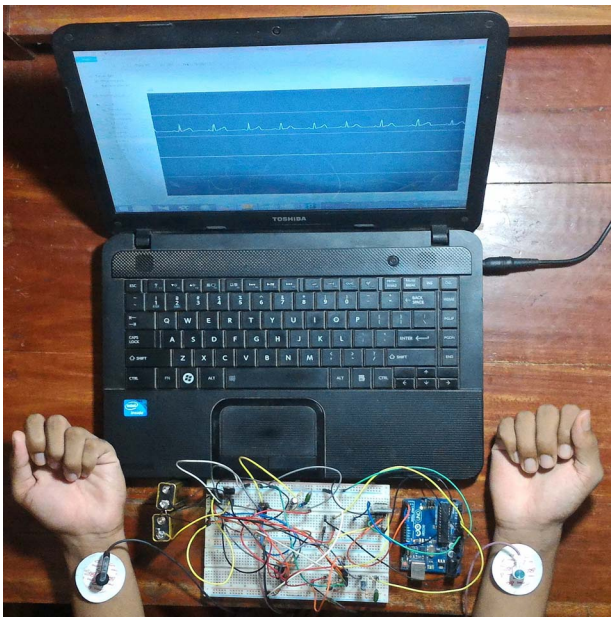

Fig. 5. Experimental measurements performed by us for ECG.

For visualizing and storing the signal a laptop running on Windows 8.1 operating system having Intel B820 processor and 4GB ram was used. ECG, EMG and EOG signals were taken from a boy of 23 years old. The ECG signal was taken in Lead I. In Figure 6, every red line indicates 1V of total 5V and both ECG and EMG signals are above 3V. This is because in this system 3.3V virtual ground is used. Stored ECG, EMG and EOG signals in text file are imported in MATLAB for analysis. MATLAB R2014a is used for analysis.

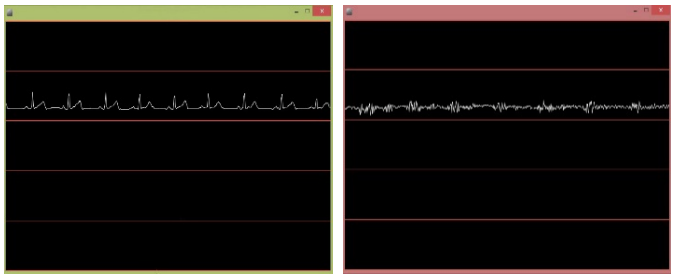

(a) (b)

Fig. 6. Output of the application for (a) ECG and (b) Biceps EMG.

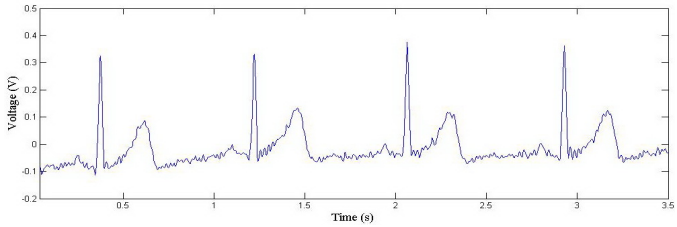

Fig. 7. ECG signal from signal conditionig circuit.

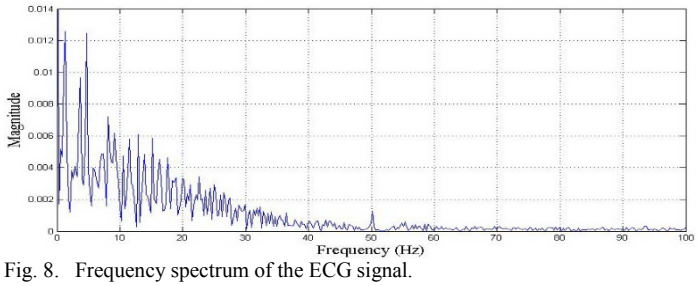

Fig. 8. Frequency spectrum of the ECG signal.

Figure 7 shows the ECG signal from signal conditioning circuit output and this signal is contaminated with power line interference (50Hz). This is because of common-mode voltage produced by the ac mains of 50 Hz frequency with line voltage 220V [14].

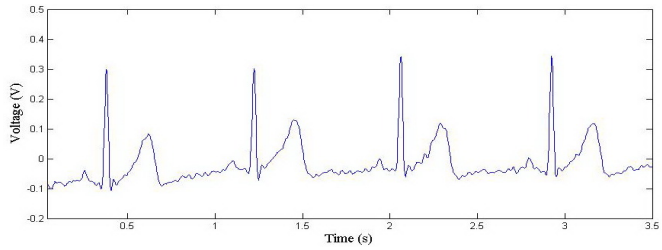

Fig. 9. ECG signal after filtering in MATLAB.

Figure 8 shows the frequency spectrum of the contaminated ECG signal. In this figure, magnitude for 50Hz is 0.001738.

Figure 9 shows the filtered ECG signal. For filtering a Butterworth band pass and an elliptic band stop filter of 50Hz was used. Lower and higher cut off frequency of Butterworth filter was .033Hz and 150 Hz.

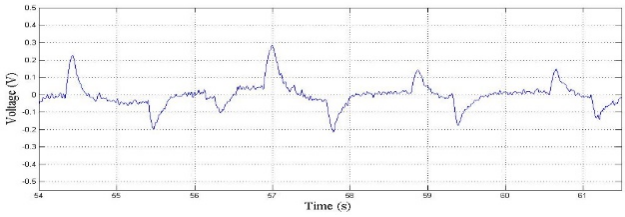

Fig. 10. EOG signal for horizontal eyemovement.

Figure 10 shows the EOG signal for horizontal eye movement. When the eye moves left, a positive peak is found and when the eye moves right, a negative peak is found. In figure 11, the frequency of the EOG signal ranges from 0-10Hz. As a low pass filter of 15 Hz is used, power line interference (50 Hz) does not exist.

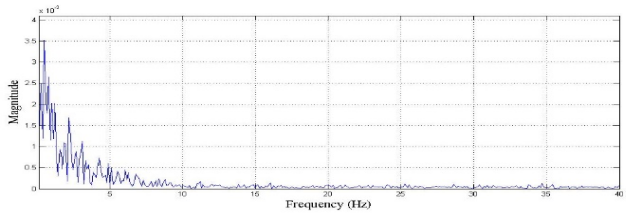

Fig. 11. Frequency spectrum of the EOG signal.

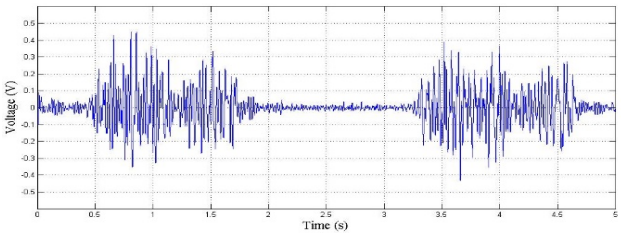

Fig. 12. Biceps EMG signal.

For Biceps EMG signal acquisition electrodes were placed according to figure 2 (c). Figure 12 shows the biceps EMG signal taken from left hand. As the force of the muscle increases the peak of the EMG signal increases. In figure 13 the frequency of the EMG signal ranges from 0-150Hz. There exists a small amount of power line interference same as the ECG signal and the magnitude of 50 Hz is found 0.0015.

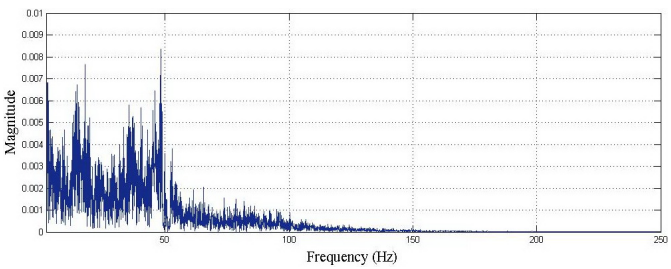

Fig. 13. Frequency spectrum of the EMG signal.

TABLE I. COMPONENT LIST FOR THIS SYSTEM

Component Name	Quantity	Unit Price (USD)	Total Cost (USD)
Arduino UNO	1	9	9
Bluetooth Dongle	1	2	2
Bluetooth Module HC-06	1	6	6
AD620 IA	1	6	6
Resistor and Capacitor	20	0.01	0.2
LM 7805	2	0.15	0.3
CA3130 op-amp	1	0.25	0.25
Electrodes	3	0.09	0.27
9V Battery	2	0.5	1
Total Cost of the system (USD)			25.02

VI. CONCLUSION

The main aim of this research has been fulfilled. We found the desired ECG, EMG and EOG signal and their frequencies in a normal range. In this system we have used simple RC filtering and we have not implemented any analog notch filter of 50Hz. But as the signal conditioning circuit is battery powered and the signal is transferred wirelessly, noise interference in reduced and there exist a very small amount of power line interference (50Hz). This is because of electric field coupling from the nearby power line to the body. The proposed hardware circuit is simple and effective for ECG, EMG and EOG data acquisition. The cost of this system is only USD 25.02. The component used for this system consumes very low power. It takes maximum current of 60mA and it can function up to 22 hours continuously by using two 9V battery.

In future, we will develop the robust biosignal acquisition system with various control supports and protection schemes.

ACKNOWLEDGMENT

This work was partially supported by Higher Education Quality Enhancement Project (HEQEP), UGC, under Sub-project "Postgraduate Research in BME", CP#3472, Bangladesh.

REFERENCES

[1] E. Kaniusas, "Biomedical signals and sensors I: Linking physiological phenomena and biosignals", Springer Science & Business Media, 2012.

[2] A. M. Al-Busaidi and L. Khriji, "Digitally Filtered ECG Signal Using Low-Cost Microcontroller," in International Conference on Control, Decision and Information Technologies (CoDIT), pp. 258-263, 2013.

[3] B. S. M Parameshwari, B. S. Madhurya, and K. U. Rao, "Preparation of papers a cost effective prototype for electrooculogram for effective eye tracking," International Journal of Innovation, Management and Technology , vol. 4, no. 5, pp.494-497, Ocotober 2013.

[4] H. Dong-Mei, Y. Yi, and W. Zheng. "Measurement System for Surface Electromyogram and Handgrip Force Based on LabVIEW", In World Congress on Medical Physics and Biomedical Engineering, Springer Berlin Heidelberg, pp. 67-70, 2009.

[5] M. K Islam, A. N. M. M Haque, G. Tangim, T. Ahammad, and M. R. H. Khondokar, "Study and Analysis of ECG Signal Using MATLAB & LABVIEW as Effective Tools, International Journal of Computer and Electrical Engineering, Vol.4, No.3, pp. 404-408, 2012.

[6] M. A. Ahamed, M. A. Ahad, M. H. A. Sohag, and M. Ahmad. "Development of Low Cost Wireless ECG Data Acquisition System," in

International Conference on Advances in Electrical Engineering (ICAEE), 2015.

[7] M. A. Ahamed, M. K. Hasan, M. S. Alam, "Design and Implementation of Low Cost ECG Monitoring System for the Patient Using Smartphone," in International Conference on Electrical & Electronic Engineering (ICEEE), 2015.

[8] Bio Protech ECG Electrode specification [Online]. Available: http://sanjayintl.com/pdf/ecg_bioprotech.pdf

[9] Datasheet of AD 620 instrumentation amplifier [Online]. Available: http://www.analog.com/media/en/technical-documentation/data-sheets/AD620.pdf

[10] D. Prutchi, M. Norris, "Design and Development of Medical Electronic Instrumentation: A Practical Perspective of the Design, Construction, and Test of Medical Devices," John Wiley & Sons, 2005.

[11] R. Raut and M. N. S. Swamy, "Modern Analog Filter Analysis and Design: A Practical Approach," John Wiley & Sons, 2011.

[12] J. Oxer and H. Blemings, "Practical Arduino: Cool Projects for Open Source Hardware," Apress, 2009.

[13] C. Reas and B. Fry,"Processing: a programming handbook for visual designers and artists", Mit Press, 2007.

[14] A. Brahme,"Comprehensive Biomedical Physics", Newnes, 2014.

An Approach to Convert Conventional Screen into Touch Screen Using Image Processing

Md. Hanif Ali Sohag[1], Mst. Mahmuda Khatun[2], and Mohiuddin Ahmad[3]
[1,3]Department of Electrical & Electronic Engineering
[1,3]Khulna University of Engineering & Technology, Khulna-9203, Bangladesh
[2]Department of English
[2]Northern University Bangladesh, Rajshahi-6204, Bangladesh
E-mail: hanifalisohag@gmail.com, mahmuda.khatun.raj@gmail.com, mohiuddin.ahmad@gmail.com

Abstract— **Touch screen are widely used in the recent electronic devices. In this paper we present a novel and cost-effective webcam based touch screen conversion system for the conventional laptop or desktop using normal LED light. This system converts the normal screen into an interactive touch screen by means of computer vision techniques. In this system the problem of ambient light has been minimized using the brighter LED light which enhances the performance in complex light environments. The position of the bright LED light is easily determined using the scene geometry and camera model. With some further processing of the LED position, the system is capable of calculating the mouse cursor coordinates in the desired laptop or desktop screen to simulate the mouse actions in real time. The user can use the on-screen keyboard for the typing purpose. The system also includes gestures based interaction for playing games and performing additional windows commands easily. The experimental results and practical applications confirmed the effectiveness of the proposed system.**

Keywords— Webcam, LED light, perspective transform, stylus, Image processing.

I. INTRODUCTION

With the growing development of technology, touch screens are becoming more popular in both commercial and personal purposes. Nowadays, Mobile phones, tablets, game machines and control panels cannot be imagined without the touch screens. The human-computer interaction involves interaction between the computer devices and human physical action. The keyboard, mouse, joystick are the main input devices for performing human-computer interaction but without the use of touch technology it is impossible to realize the broad perspective of virtual reality.

E.A. Johnson developed the first capacitive touchscreen at the Royal Radar Establishment which was published in 1965 [1]. In the conventional touch screen technology, the IR emitter and IR transmitter are arranged in such a way that it forms a matrix which indicates the coordinates by getting the block IR position of the touch point[2]. Resistive, capacitive and surface acoustic wave touchscreens are the basic touch screen systems that recognizes a person's touch. The resistive or capacitive touch screen demands the use of special materials such as indium tin oxide to be both transparent and conductive. But the formation of such materials is very expensive and so the cost of the system is gradually increased. Again the amount of material needed for the screen depends on the size of the devices.

For the last decades various types of approaches are developed to find a better solution for the difficulties associated with the resistive or capacitive touch screens. Surface acoustic wave (SAW) technology was proposed in [3] which uses ultrasonic waves. Ultrasonic waves are passed over the screen panel and at the touch point some portion of the wave is absorbed which provides the information about the position of the touch event and sent to the controller for further processing [3]. While resistive, capacitive and surface acoustic wave technology implementation requires a higher cost, optical technique may become unique since it can be used for any flat surface. J.C. Lee demonstrated of such a system using Wiimote [4]. The vision based system using camera and image processing techniques are also implemented which are considered as virtual touchscreen as they require less hardware. Han proposed of a low cost multi-touch sensing system which uses the internal reflection [5].

Another technique is used by Wilson to transform an acrylic plastic to a touchscreen [6]. However, these image processing methods require the cameras and video projector to be placed on the opposite side of the screen from the user which makes it unsuitable for desktop use. In a paper [7], an infrared glove has been used instead of a stylus to interact with the display on an interactive board for collaborative Learning. Shuai Zhang et al. in their paper [8] have presented a method to use an infrared stylus to interact with projected display, using Microsoft's Kinect. Zero-Touch [9] uses the state of art technique to provide the users with comfortable interfacing experience. Another approach is uTouch [10], uses two cameras and skin detection algorithm to get the coordinates of the touch point. But this approach fails as it cannot differ between the skin and background color similar to skin color.

This paper represents a cost-effective and novel approach to convert the normal conventional laptop or desktop screen into an interactive real time touch screen which overcomes all the shortcomings of already proposed techniques. This system is much computationally efficient and cost-effective compared to the available Kinect and Wii based hardware as it requires only an inexpensive webcam and a normal LED light. The webcam can be placed in any direction toward the screen and there is no limitation in size of the

978-1-4673-9257-0/15/$31.00 ©2015 IEEE

device screen. It requires a less amount of time to calibrate and setup is very easy.

II. System Overview

The system is developed to ensure maximum efficiency at minimum hardware requirements which makes it cost effective. It consists of only a webcam, a LED light and a battery. The system doesn't require any other equipment for the human computer interaction. It provides an efficient, natural and real time interaction between the user and normal touch screen device just like the real touch screen device. The LED light acts as a medium of interaction between the user and devices. By tracking the intensity of the LED light when it is touched on the screen the user can easily interact with the normal screen.

Figure 1. Overview of the proposed system

A. Webcam

In this system, we used a low cost webcam which feeds the capture images to the image processing software. It acts as the image source for the image processing algorithms. It captures the bright LED light spot and the software tracks the position of the spot. This system is capable of detecting the LED light in any ambient light condition so the cost of using IR webcam is reduced. With the proposed system, it doesn't require to use any kind of IR light rather the normal LED light can be tracked very efficiently.

B. Stylus

A cool stylus is designed which is used for the interaction with the screen. The stylus contains a red LED light, a push button and a battery. By pressing the push button and pointing the LED to the screen, the touch point is produced on the screen and webcam capture the spot. Then the spot is further processed by image processing algorithm to get the exact coordinate of the spot. The user can easily play interactive games and draw pictures using the stylus. The user can also type text with the stylus by touching the default on screen keyboard.

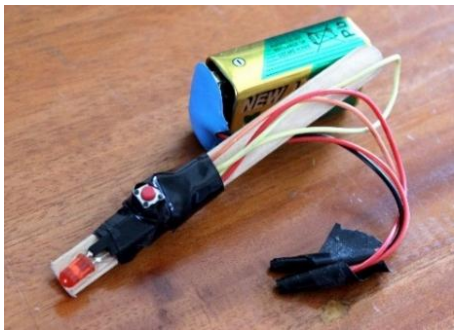

Figure 2. A stylus with normal LED light

III. System Setup And Calibration

The system requires less amount of calibration and is very easy to setup. The webcam is placed in such a position that the whole screen can easily be captured. The camera need not to be straight in front of the screen rather it can be placed at any angle provided the whole screen is visible. After placing the webcam at proper position, the software has to start. After that the calibration process starts. The user has to select the index of the webcam that is placed in front of the screen. Then the system will show the captured images from the webcam whose resolution is 640x480 @ 25fps.

The user will have to click on the four corner points of the screen that is going to be touch screen. There is no limitation of screen size as the user has to choose only the four corner points. The four corner points can be a square, a rectangular, a trapezoid or any kind of tetragonal shape. After getting the required points of the screen proper geometric transformation models are applied to the selected area which results in a desired image of the same aspect ratio of the normal screen.

IV. Proposed Methodology

The system performs the image processing algorithms when it gets the proper selected area of the screen. The area of the screen is selected by clicking the four corner points on the captured image. The overall activity diagram of the proposed system is shown in Fig. 3.

A. Selection of Screen Region

The system requires a certain area of the screen which is going to be touchscreen. So, the user has to select the required area by clicking the four corner points on the captured image from the webcam. The webcam is kept at a proper distance from where the entire screen is visible.

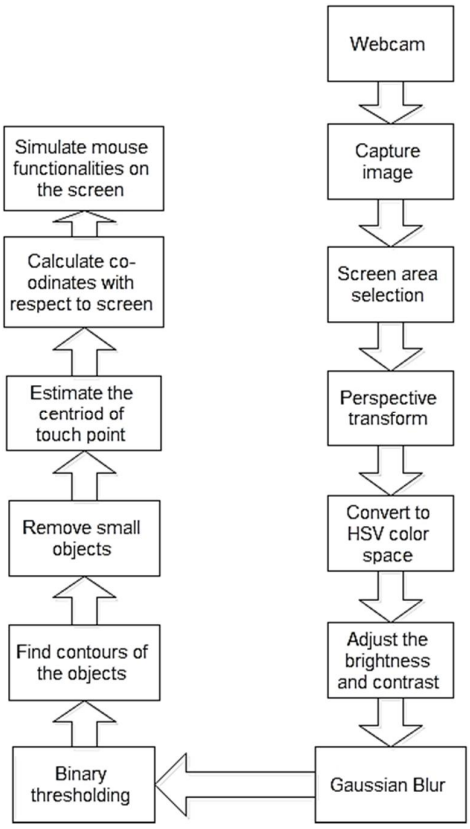

Figure 3. Block diagram of the entire system

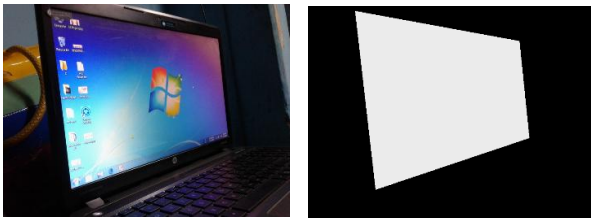

(a) (b)

Figure 4. (a) Capture image by the webcam (b) Selection of the screen region

B. *Perspective Transformation on The Selected Screen*

The selected area of the captured image is not suitable for processing as the webcam is not placed straight to the screen. So, the touch point co-ordinates is different from the real world co-ordinates for the perspective distortion of the image. But for the proper implementation of the system, it needs to establish a relationship between the pixels in the webcam and the pixels in the touch point. So perspective transform algorithm described below is applied to the selected area to overcome the problem. Projective geometry transformation relates the coordinates of a point in a scene to the coordinates of its projection onto an image plane.

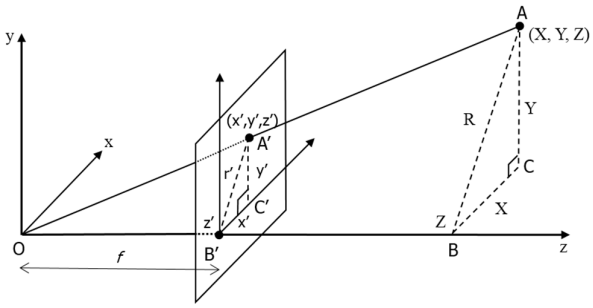

Figure 5. Perspective transformation

From $OA'B'$ and OAB triangles:

$$\frac{f}{Z} = \frac{r'}{R} \tag{1}$$

From $A'B'C'$ and ABC triangles:

$$\frac{x'}{X} = \frac{y'}{Y} = \frac{r'}{R} \tag{2}$$

So, the perspective projection equations:

$$x' = \frac{fX}{Z} \;\; ; \; y' = \frac{Yf}{Z} \;\; ; \; z' = f \tag{3}$$

Within the camera coordinate system the perspective projection of a scene point onto the image plane is described by the above equations. After performing the algorithm, a linear relation between the real screen and the virtual screen is established. The captured image and the transformed image are shown in Fig. 6.

Figure 6. After applying perspective transformation algorithm on the captured image

C. *HSV Conversion*

The captured image by the webcam is a RGB color image which takes longer time to process. As the stylus is using only bright red light as a touch point so there is no need of other color spaces. In order to extract the red light, the captured image is converted to HSV color model which defines a color space in terms of color type, color intensity and color brightness. In our proposed system, we are differentiating the bright red LED by adjusting the HSV values of the image. It provides only the area of the image which contains bright red color ignoring the other component of color.

D. Adjustment of Image and Smoothing

The brightness and contrast of the image is adjusted so that the touch point can easily be differentiated from the background image. For adjusting the contrast and brightness of the capture image the following formula is used:

$$g(x) = \alpha f(x) + \beta \tag{4}$$

The parameters $\alpha > 0$ and β are the gain and bias parameters for controlling the contrast and brightness repectively. Considering $f(x)$ as the source image pixels and $g(x)$ as the output image pixels, the formula can also be written as:

$$g(i,j) = \alpha f(i,j) + \beta \tag{5}$$

where i and j indicates that the pixel is located in the i-th row and j-th column.

E. Smoothing and Thresholding

After proper image adjustments, it is required to reduce the surrounding noises. The use of the Gaussian kernel for smoothing has become extremely popular in image processing application. So, the adjusted image is further smoothed for a better accuracy using a 3×3 Gaussian filter [11]. The Gaussian function (2D) can be expressed as the product of two one-dimensional functions in each coordinate axis.

$$g(x,y) = \frac{1}{2\pi\sigma^2} \cdot e^{-\frac{x^2+y^2}{2\sigma^2}} \tag{6}$$

where x is the distance from the origin in the horizontal axis, y is the distance from the origin in the vertical axis, and σ is the standard deviation of the Gaussian distribution.

After that adaptive threshold is applied to the binary image which provides a clear touch area for further processing.

F. Finding The Point of Touch and Mouse Functionality

The touch area by the stylus can easily be differentiated and tracked due to the fact that the LED light intensity is brighter than the background screen. The contours of the binary image are found using the contour finding algorithm of OpenCV. Around the touch point where the stylus was touched there might be some small noise areas. To eliminate the noise, only the largest contour area is considered as the touch point. The center co-ordinate is then calculated using moments calculation formula. The co-ordinate is mapped to screen co-ordinates to get the exact location of the touch co-ordinate using the following formula:

$$x = \frac{(P_x \times X)}{I_x} \tag{7}$$

$$y = \frac{(P_y \times Y)}{I_y} \tag{8}$$

where (x, y) are screen coordinates, (P_x, P_y) are the touch point coordinates on the processed image, I_x, I_y are the image resolution and X, Y are the screen resolution.

Then the corresponding co-ordinate is passed to windows default mouse events to simulate mouse actions.

Figure 7. The touch point is detected and co-ordinates are calculated

V. Experimental Results

The whole system is implemented by using only a webcam and a LED light. The system works with various ambient light conditions. We implemented the system in daylight and at dark light. But it gives higher accuracy in both conditions. Experiment is made in different ambient light conditions. The light effects are reduced by controlling the contrast and brightness of the captured image. As compared to the IR touch screen system which is affected by the sunlight, this system is more accurate and can simulate mouse events very efficiently.

The image processing is done on a laptop having Intel Core i5 processor 2.60 GHz, 4GB memory running on Windows 7 64 bit Operating system. In our experiment, the display screen of resolution 1024×768 is converted to touch screen with the captured image of resolution 640×480. The HSV values and threshold values are adjusted properly for working with all environment light condition.

We found the average pixel deviation of ± 4 pixels along x axis and deviation of ± 5 pixels along the y axis which can be consider as zero deviation with respect to the entire display screen. The processing time is found to be 19.4ms in normal lighting and 21.9ms in dark lighting as shown in Table I. We found the overall accuracy of 98% in our proposed system as shown in Table II.

TABLE I. Processing Time

Situation	LED detection	Touch Point Detection	Mouse Functionality	Total Time
Natural Lighting	12.1 ms	3.3 ms	4 ms	19.4 ms
Dark Lighting	13.3 ms	4.6 ms	4 ms	21.9 ms

TABLE II. TOUCH POINT DETECTION RESULT

Situation	Pixel Deviation along x Axis for Different Resolution			Pixel Deviation along y Axis for Different Resolution			Average Accuracy
	800×600	*1024×768*	*1366×768*	*800×600*	*1024×768*	*1366×768*	
Natural Lighting	±3	±3	±4	±3	±4	±5	98%
Dark Lighting	±4	±5	±6	±5	±5	±6	

With this system, drawing picture can easily be done shown in Fig. 8. Various kinds of interactive games can easily be played by using this system which is shown in Fig. 10. With the help of the system, typing text is also possible by using the on screen keyboard shown in Fig. 9.

Figure 8. Drawing using the stylus in microsoft paint

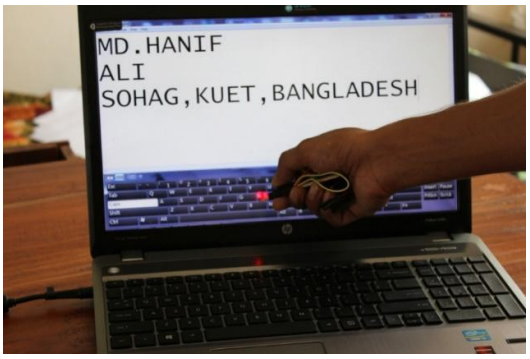

Figure 9. Typing text using input panel on screen keyboard

Figure 10. Playing Angry Birds game on PC

VI. CONCLUSION AND FUTURE WORKS

In this paper, we have designed and implemented a vision-based interactive touch screen computer interaction system using only a webcam and a stylus. The proposed system provides a natural, cost-effective and comfortable human computer interaction interface without use of any complex hardware devices. With respect to the other touch screen techniques this system does not lag efficiency in ambient light condition makes it usable at any time and at anywhere. It requires less time to setup and very easy to use. This system can be used for interactive learning, business and industrial purposes because of its high accuracy and real time response.

We are still developing the system and in our future work, we are planning to improve the feasibility of the system by including multi-touch gesture facility for zoom in, zoom out, scrolling up, scrolling down, and hand writing recognition facility which will make it more fascinating.

REFERENCES

[1] E.A. Johnson, “Touch Display – A novel input/output device for computers”, Electronics Letters, Vol. 1, No. 8, pp. 219-220, 1965.
[2] Touchscreen, http://en.wikipedia.org/wiki/Touch_screen#Infrared.
[3] How stuff works? , How do touch-screen monitors know where you're touching? , August 2011, http://computer.howstuffworks.com/question716.htm
[4] J.C. Lee, “Low-Cost Multi-point Interactive Whiteboards Using the Wiimote” http://johnnylee.net/projects/wii/, last visited Dec. 12, 2013.
[5] J. Han, “Low-cost multi-touch sensing through frustrated total internal reflection”, Proceedings of the 18th annual ACM symposium on User interface software and technology, pp. 115-118, 2005.
[6] A. Wilson, “TouchLight: An Imaging Touch Screen and Display for Gesture-Based Interaction”, 6th International Conference on Multimodal Interfaces, pp. 69-76, 2004.
[7] T. Puckdeepun, J. Jaafar, M. F. Hassan, and F. A. Hussin, “Design of Interactive Board System for Collaborative Learning”, International Symposium in Information Technology (ITSim), pp 1– 5, 2010.
[8] S.Zhang, W. He, Q. Yu, and X. Zheng, “Low-Cost Interactive Whiteboard Using the Kinect”, International Conference on Image Analysis and Signal Processing (IASP), pp. 1– 5, 2012.
[9] J. Moeller and A. Kerne, “ZeroTouch: An Optical Multi-Touch and Free-Air Interaction Architecture”, Proc. CHI, pp. 2165-2174, 2012.
[10] U. Ghufran, “uTouch: A cost effective touch screen solution for gesture based interaction”, ICCMS, 2011.
[11] R.A. Haddad and A.N. Akansu, "A Class of Fast Gaussian Binomial Filters for Speech and Image Processing," IEEE Transactions on Acoustics, Speech and Signal Processing, vol. 39, pp 723-727, March 1991.

A New Sample Preparation Technique for Linear Dilution Gradient with Minimal Sample Utilization and Waste Generation in DMFBs

[1]Pranab Roy, [2]Khokan Mondal, [3]Mayuri Kundu, [4]Hafizur Rahaman
[1,2,3,4] School of VLSI Technology, Indian Institute of Engineering Science and Technology, Shibpur, India
Email – [1]*ronmarine14@yahoo.co.in*, [2]*khokan20@gmail.com*, [3]*kundu.mayuri@gmail.com*, [4]*rahaman_h@yahoo.co.in*

Abstract – Recently, Digital Microfluidic Biochip (DMFB) is developed as a major detection mechanism for biochemical analysis. The technology aims at automation and integration of droplet based microfluidic operation within a miniaturized substrate comprised of 2D planar array of electrodes. Sample preparation remains a major issue for execution of specified bioassay protocols in DMFBs. This requires dilution of samples or formation of mixtures with different targeted concentration factors. Here, we propose new techniques for sample preparation with single source, multiple target concentration having linear dilution gradient for prespecified bioassay execution. The main objective is to i) minimize number of samples as well as reagents for obtaining targeted concentration ii) to employ minimum mixing or dilution operations and thereby optimizing the module utilization and iii) to obtain multiple copies of targeted concentration necessary for fault tolerance and parallel bioassay applications and iv) minimum generation of waste droplets to ensure optimum sample and module utilization.

Keywords: Digital Microfluidics, Bioassay protocols, sample preparation, dilution, concentration factor, module optimization, resource and waste generation

I. Introduction

Microfluidics represents the manipulation and analysis of minute volumes of fluid. Microfluidics in recent years has emerged as a powerful technology for numerous relevant applications in biomedical and biochemical analysis, diagnostics and detection. The fusion of microelectronic and bioanalytical systems has enabled the development of a new class of device known as Lab-on-Chip. Such systems are capable of shrinking an entire laboratory method within a single miniaturized device. The major advantages of such systems are i)less sample and reagent consumption, ii) enhanced heat transfer, iii)faster separation, iv)laminar flow, v)electrokinetic manipulation, vi)low power consumption, vii)parallelization and portability, viii) Improved separation efficiency. Earlier generation of microfluidic biochips were based on continuous fluid flow manipulated through a set of micrometer scale components namely channels, microvalves, micropumps, actuators, sensors and so on [1-2]. Recently, a new generation of device has been emerged as a viable alternative to this continuous flow based design. Such devices termed as Digital Microfluidic Biochip is developed as a new generation of lab-on-chip architecture based upon micro-manipulation of droplets using a programmed external electric field by an individually addressable electrode array. Actuation of droplets can occur through various mechanisms, namely electrowetting on dielectrics, dielectrophoresis, thermo capillary transport and surface acoustic wave transport [3]. Electrowetting on dielectric (EWOD) is currently used as one of the best actuation methods for droplet manipulation in digital microfluidic systems. Electrowetting is a phenomenon where an electric field modifies the wetting behavior of a polarizable or conductive liquid droplet in contact with a hydrophobic, insulated electrode. Actuation is based on the principle of modulating the interfacial tension between a liquid and an electrode coated with a dielectric layer [4]. Droplets are sandwiched between two parallel plates. The bottom plate is the chip surface, which houses the addressable electrode array, and the top is either a continuous ground plate or a passive top plate (Fig.1). The use of unit volume of droplets allows a microfluidic function to be reduced to a set of basic operations. By varying the control voltage pattern in a time-multiplexed manner, all the fluid handling operations can be accomplished at any desired location within the 2D array. Typical fluidic operations on a droplet include dispensing, transport, mixing, splitting, heating, incubation, and sensing [5-8]. DMFBs offer significant flexibility and programmability over their continuous flow counterparts while implementing various assays that mandate high-sensitivity, and low requirement of sample and reagent consumption. Automated and on-chip sample preparation has drawn significant attention in recent years [6]. In sample preparation, producing chemical and bio molecular concentration gradients is of particular interest. Dilution gradients play essential roles in in-vitro analysis of many biochemical phenomena including growth of pathogens and selection of drug concentration. Sample preparation implies formation of a sample with a single or a set of targeted dilution. Here dilution indicates the achievement of a desired concentration factor for preparing the fluid to utilize it in a specified biochemical analysis or detection process. The major step for preparation of a sample with desired concentration factor (with specified accuracy) is to formulate a sequence graph representing the necessary sequence of mixing and splitting using the set of specified samples and available buffers and reagent solutions.

Here, we propose a technique to develop a sequence graph to obtain a targeted set of samples with linear dilution gradients. The major objectives are i) to minimize the number of modules to be used for microfluidic operations namely mixing or splitting, ii) to optimize the process to have minimal number of waste droplets, iii) to use minimal number of samples and reagents and iv) to obtain a set of copies for each target concentration specifically for fault tolerance. The reason is that for obtaining a sample with specific concentration factor, the accuracy might deviate due to faulty mixing or splitting operation, which might require multiple copies of samples with same concentration for additional investigation purpose particularly in cases of preparation errors.

The rest of the work is arranged as follows. Section 2 states the prior contributions regarding sample preparation in DMFBs. Section 3 gives the basic procedures and parameters involved in sample preparation process in DMFBs. Section 4 states the motivation and objectives for the proposed method. Section 5 proposes the algorithm followed by mathematical estimation for the desired resources. Section 6 illustrates a specific example. Section 7 shows the experimental results and comparison with contemporary methods. Section 8 concludes conclusion.

II. Prior Contributions

Major assay operations performed by DMFBs include sample detection, sample pretreatment and sample preparation being integrated within the same device. Dilution is commonly used in biological studies to create a variety of concentrations of the stock solution of samples or reagents by mixing it with buffers on a microfluidic device [9]. Concentrations can be nonlinear or linear and two types of dilution methods can be employed towards generation of the targeted concentration factor, namely serial and linear dilution. In case of linear dilution, the stock solution and its diluents are mixed in different ratios and can create linearly varying concentrations of the stock solution [10]. On the contrary, in serial dilution, a common example of which is the logarithmic method, a solution is repeatedly diluted using the same mixing ratio. Recently, several methods for on chip mixing/dilution control techniques for sample or reagent preparation in DMFBs have been reported in

[11]. First, the dilution control method on DMFBs was proposed in [12], where a dilution algorithm based on binary search strategy has been proposed to determine the sequence of (1:1) mix-split steps. It deals with intermediate droplets and assumes that it is available whenever it is needed. But this technique does not address the waste droplets and storage units. In case of single target sample preparation, BS method has been proposed in [13] considering two or more fluid at any given ratio in (1:1) mixing model. It converts the target concentration into binary representation and scans the bits through right-to-left to decide the mixing and splitting steps. It takes n steps mix-split to complete dilution process with an error of at most $\frac{1}{2^{n+1}}$ in the target concentration factor (CF).

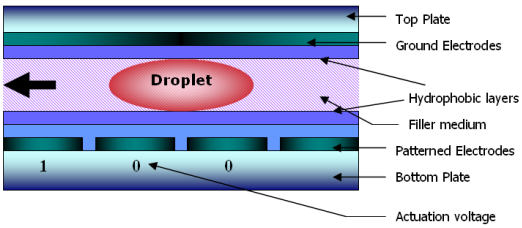

Fig 1. Biochip sectional schematic diagram with 2D array of electrodes

A binary search method has been proposed in 14] to generate a single dilution of sample and reduces the number of waste droplets significantly compared to [13], as the process reuses the intermediate droplets. A reactant minimization algorithm REMIA has been proposed in 15]. This method is based on skewed mixing tree construction. A graph-based optimal reactant minimization algorithm 'GORMA' proposed in [16] is an improved technique which concentrates on minimal reactant usage. It is important to mention that none of the mentioned techniques are capable of producing multiple target concentrations. First, reagent saving mixing algorithm for preparing multiple target concentration has been proposed in [17]. This approach makes a global view of all target concentrations and processes concurrently to generate all target concentrations for the first time.

The algorithm proposed in [15] has been extended in [18] for minimization of reactant usage. Another sample preparation technique known as RSM [19] not only minimizes the consumption of reagents, but also reduces the number of waste droplets and sample preparation time significantly. The work proposed in [16] has been further extended to a waste aware process viz. WARA [20], which states the waste recycling for producing multiple target concentrations. It takes individual mixing tree corresponding to each of multiple targets and reduces waste and increases droplet sharing by combining them. Basic idea of [20] is to mix two non-consecutive CFs that are separated by an odd number of elements of gradient sequence and to produce the median. Though, the above algorithm focuses on generation of multiple target concentration but it consumes huge number of modules. A new algorithm proposed in [21] concentrates on producing random dilutions factors with minimum wastage while it also satisfies the required accuracy in the CF. The algorithm proposed in [22] optimizes cost or increases performance when a certain concentration gradient is required. This algorithm is applied for generation of any arbitrary linear gradient with minimum wastage and also with required accuracy. Recently, a method based on binary de Brujin graph has been proposed in [23] to solve the problem by using Asymmetric travelling salesman problem to get the shortest mix–split sequence while satisfying the given upper bound in concentrations factors.

III. Sample Preparation in DMFB

The primary requirement is to prepare the sample with requisite concentration factor using minimum number of mix split operations and hence with the minimum number of module requirements.

*A. **Preliminaries:***

A few preliminary definitions regarding sample preparation are given below:

Stock solution or Sample: It is the initial sample or reagent volume dispensed into the 2D array for initiating the first step of sample preparation.

Target concentration: It is the final concentration of each stock solution which is the prerequisite to take part in the actual reaction.

Dilution: It is the process of decreasing the concentration of a solute (sample) in solution, usually simply by mixing with more solvents/diluents. The dilution of a solution means to add more solvent/diluents without the addition of more solute/sample. Dilution is commonly used in biological studies to create a variety of concentrations of the stock solution by mixing it with its diluents termed as buffer solution within a microfluidic device.

Linear dilution: The stock solution and the diluent are mixed at different ratios creating linearly varying concentration [10].

Serial dilution: Here a solution is repeatedly diluted using the same mixing ratio. For example, let the mixing ratio is 1:1.So each successive dilution reduces the concentration factor by ½. Hence for n linear dilution, the concentration factor goes down to $\frac{1}{2^n}$.

Thus, the serial dilution method creates discrete nonlinear concentration values of the stock solution [10]. However, in DMFBs, the discrete volumes of sample can only be used and hence, only serial dilution can only be employed to achieve the desired concentration level.

Interpolated Dilution: Two unit volume droplets with CF C_1 and C_2 are taken and after mix-split operation, two droplets with resultant concentration C_r, where $C_r = (C_1+C_2)/2$), are obtained. Both the dilution methods produce concentration factors whose denominators are integral power of two [21].

Concentration factor (CF): We start with a raw sample considering a 100% concentration. CF is defined as the ratio of the initial volume of the sample to the final diluted volume of the sample [14].

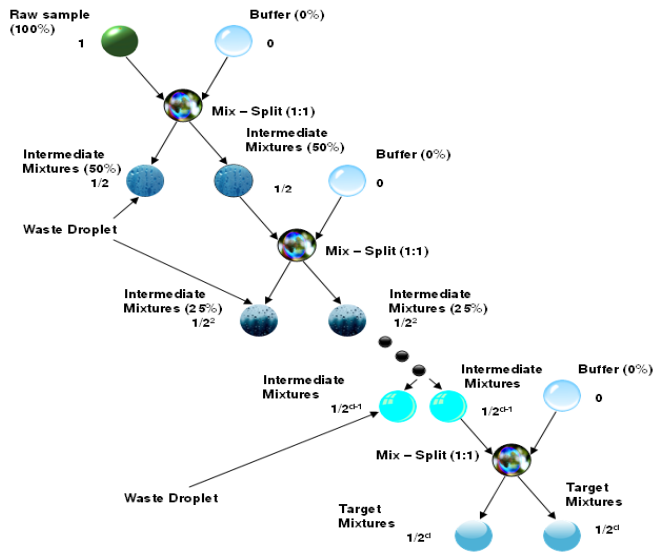

Fig. 2. A sample preparation technique using serial Dilution to achieve a target concentration of $1/2^d$

*B. **Sample preparation process**:*

We consider a preliminary sample preparation process using only serial dilution to achieve a target concentration expressed in powers of 2 as $1/2^d$. We start with a raw sample and buffer solutions together with the given target concentration C_T. Then we carry out a set of serial dilution through mix-split operation to achieve the target concentration C_T. Unlike continuous flow based biochips DMFB manipulates discrete droplets and hence only serial dilution is possible. The dilution strategy defines a mixing tree for serial

mixing that defines the steps involved in achieving the target concentration. Consider Fig. 2, where we start with a raw sample with concentration 100% denoted by '1' and a buffer solution with concentration 0% denoted by '0'. For the first level of dilution with a ratio of 1:1, two resultant mixtures each with concentration 50% denoted by ½ is obtained. Let the target concentration C_T is expressed as $1/2^d$ .This can be achieved through d number of dilution using mixing with buffer of 0% concentration at each step.
The mixing tree or dilution tree as shown in Fig. 2 represents a diagraph which displays the sequence of dilution steps to achieve the target concentration. A dilution tree is a binary tree, where each dilution step represented by a dilution (Mix-Split) node has two children. Each child represents unit volume intermediate droplet, out of which one is utilized for the next dilution step and the other is considered as waste droplet. For the leaf nodes, it is possible to achieve at least two copies of samples with target concentration. Hence, in order to achieve target concentration of $1/2^d$, we require d number of serial dilution steps and each step produces 1 waste droplet with concentration of $1/2^m$ for m^{th} dilution step.

IV. Motivation and Objectives

Biomolecular gradients strongly participate in biological phenomena including those related to cell development, cancer, inflammation, and wound healing. More specifically, the growth, differentiation, and migration of various cell types are governed by biomolecular concentration gradients in vivo [24]. There are different types of dilution profile, one of the common types used for biochemical analysis specifically for drug design is the linear concentration gradient. Here, we attempt to prepare set of sample concentrations with specified linear dilution gradient. The objective is to produce the targeted set of concentration with linear dilution gradient having minimum waste generation, minimum utilization of stock solutions or raw samples (reagents), minimal module or mix-split operation, at least one additional copy for each target concentration to handle fault tolerance and reserve storage for future extension of the specified bioassay.

V. Proposed Technique

A. Problem formulation

General dilution: Given a raw sample with 100% concentration and a buffer with concentration of 0%. A target CF of the sample is to be achieved using minimal number of sequential (m:m) mix-split operations. In our case, we always use m = 1.This is applicable directly for any single dilution gradient.
Obtaining linear dilution gradient: Given a set of linear dilution gradients $L = \left\{ \frac{a}{2^n}, \frac{a+d}{2^n}, \frac{a+2d}{2^n}, \frac{a+3d}{2^n}, \ldots\ldots, \frac{a+kd}{2^n} \right\}$
Hence $|L| = k+1$
Our objective is to obtain all $(k+1)$ number of targeted concentration with minimal number of (1:1) Mix-Split steps and minimal number of waste droplets. Unlike [21], we do not assume sufficient supply of boundary conditions. Instead, we develop a technique to use minimal number of raw samples and reagents directly to generate the sets of output with linear concentration gradient. Let there be p number of raw samples with 100% concentration gradient (denoted by 1). Let the number of Mix/split operations required is x to achieve the given set of $(k+1)$ number of concentration. Let the number of waste droplets produced in the process is w. Our aim is to produce all the $(k+1)$ number of concentration with specified linear dilution gradient such that
i) Each component of the targeted set has at least two copies.
ii) The value of p, x and w is minimal.

B. Proposed Strategy

Forming the base solutions: Let us consider two separate concentrations $\frac{1}{2^p}, \frac{1}{2^m}$ with ($m < p$) are mixed together and the resultant concentration (using interpolated dilution) is given by

$$\frac{1}{2}\left(\frac{2^{p-m}+1}{2^p}\right) = \frac{2^{p-m}+1}{2^{p+1}} = \frac{2^k}{2^{p+1}}$$

Hence any concentration represented by $\frac{x}{2^n}$ can be decomposed in the following manner.

$$\frac{x}{2^n} = \frac{1}{2}\left(\frac{2^{k1}+2^{k2}+2^{k3}+\ldots\ldots 1}{2^{n-1}}\right) \quad \text{(if x is odd)}$$

Where $([n-2]>k1>k2>k3>\ldots>1)$

Or, $\frac{x}{2^n} = \frac{1}{2}\left(\frac{2^{k1}+2^{k2}+2^{k3}+\ldots\ldots+2^{km}}{2^{n-1}}\right)$ (if x is even).

Where $([n-2]>k1>k2>k3>\ldots>km)$

Hence, it may be possible to generate a set of base solutions that can be combined to obtain the desired concentration.
Forming the target concentration: For example let us consider a target dilution for a sample is given as d=92/1024. This can be distributed as d = $\frac{1}{2}\left(\frac{2^6+2^4+2^3+2^2}{2^9}\right)$. The interpolated dilution sequence is given in Fig. 3. This requires only three mix-split operations. Fig. 3 shows a sample preparation technique using interpolated Dilution to achieve a target concentration of 92/1024. Here the base solutions required are

$$\left\langle \frac{2^6}{2^8}, \frac{2^4}{2^8}, \frac{2^3}{2^8}, \frac{2^2}{2^8} \right\rangle \Rightarrow \left\langle \frac{1}{2^2}, \frac{1}{2^4}, \frac{1}{2^5}, \frac{1}{2^6} \right\rangle$$

Each such base solution can be prepared through serial dilutions as shown in Fig.2. However, we need to estimate the number of mix-split operation necessary to achieve the target concentration for a given set of base solutions obtained earlier using serial dilution. Let us assume that m_i represent number of mixers used at stage i and x_i represent the number of intermediate or base solutions exactly taking part in mixing at $(i+1)^{th}$ level. We assume that we start at level 0 where x_0 is the number of base solutions taking part in mix-split operation at level 1. So number of level or stages the mix- splits are to be conducted is given by $l = \lceil \log_2 x_0 \rceil$. For the corresponding levels or mixers until reaching the target concentration, the following is the procedure to determine number of mixers in each level.

$m_i = \frac{x_{i-1}}{2}$ and $x_i = \frac{x_{i-1}}{2}$ if x_{i-1} is even .

Or, $m_i = \frac{x_{i-1}-1}{2}$ and $x_i = \frac{x_{i-1}-1}{2}+1$ if x_{i-1} is odd.

Thus total number of mixing modules to be used is given by

$$M = \sum_{i=1}^{l} m_i + 1 \quad ,$$

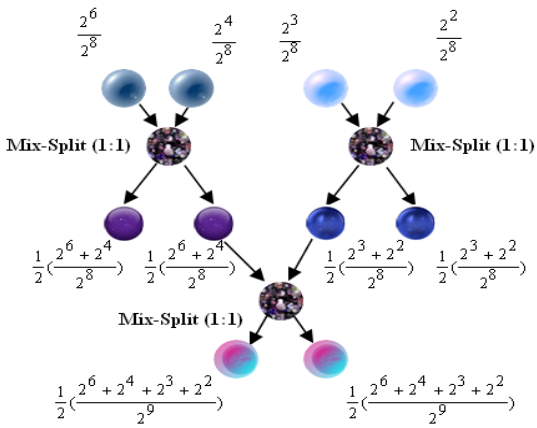

Fig.3. A sample preparation technique using interpolated Dilution

This implies that one additional mixer is used to obtain the final dilution. It has been found that for each mixing module one additional intermediate solution is obtained and is treated as waste

droplet. So for M number of mixers M numbers of waste droplets are generated. However, at level l or at the leaf node of the mixing tree, two copies of the target concentration is obtained. For a given set of base solutions where $x_0 = 10$, the mix-split sequence to reach to the target solution is shown in Fig. 4. It has been found that number of stages is found to be $l = \lceil \log_2 10 \rceil + 1 = 1 + 1 = 5$ (one additional level is necessary for final dilution with buffer solution to achieve two copies of the target solutions), number of mixers = 10, number of buffers = 1 and number of waste droplets = 9 with 2 copies of target solutions. In Fig.4, x_i represents number of base or intermediate solutions at level i, m_i represents number of mixers used at level i, w_i represents number of waste droplets at level i.

Forming the set of linear dilution gradients:

This represents a collection of linearly sequenced concentration factors. It has been found that the set of dilution gradients are arranged in Arithmetic progression. So, additional copies of few of the selected target gradients are first obtained. Thereby, these copies can be mixed together using interpolated dilution to form the arithmetic mean between any two specific target concentrations of the given set. These mean concentrations are termed as derived target concentration. This not only eliminates the effort to separately prepare the base solutions for the derived gradient but also reduces the mix-split operations for the interpolated dilution. This uses the waste droplet solutions obtained at different mixing steps to prepare the additional copies of different target solutions. A similar scheme for preparing intermediate targets is proposed in [21]. The procedure is described below:

Consider any given set of linear dilution gradients

$$L = \left\{ \frac{a}{2^n}, \frac{a+d}{2^n}, \frac{a+2d}{2^n}, \frac{a+3d}{2^n}, \ldots, \frac{a+kd}{2^n} \right\}$$

This set L is first decomposed into p number of secondary sets each containing three concentration elements where each consecutive set has an intersection of one. This implies that element m_3 of set i and element m_1 of set $i+1$ is shared.

If $|L| = k+1$ is odd , $p = (|L|-1)/2$

If $|L| = k+1$ is even, there will be $p+1$ sets where $p = (|L|-2)/2$ sets and the last set contains a single element representing the last target dilution value. We represent the collection of secondary sets as $< s_1, s_2, s_3 \ldots s_p >$, where $s_1 = \{m_{11}, m_{12}, m_{13}\}$, $s_2 = \{m_{21}, m_{22}, m_{23}\} \ldots s_p = \{m_{p1}, m_{p2}, m_{p3}\}$, and $s_i \cap s_{i+1} = m_{i3} = m_{(i+1)1}$, for $1<i<p$

and $m_{i2} = \dfrac{m_{i1} + m_{i3}}{2}$,for $1 \bullet i \bullet p$

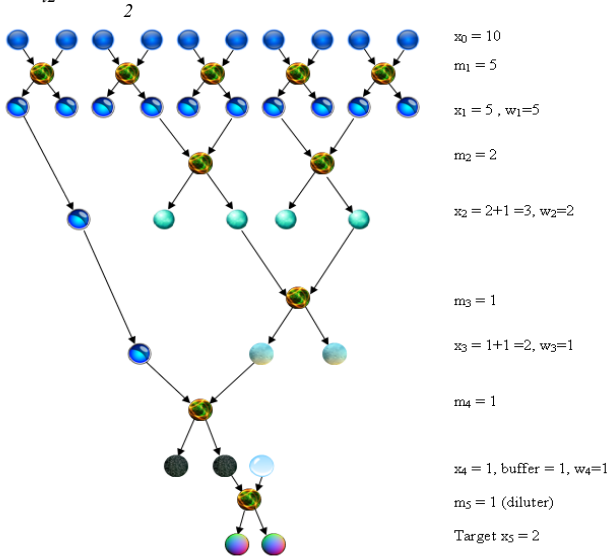

Fig.4. A interpolated dilution example showing the dilution tree starting with $x_0 = 10$ number of base solution.

Hence, for each set s_i ($1<i<p$), three copies of element m_{i3} and for set s_1 and s_p, two copies of m_{11} and m_{p3} are required to obtain the remaining sets of targeted concentrations. Fig. 5 shows the arrangement stated above for a linear dilution gradient with $k=10$. The given set of dilution gradient is

$$L = \left\{ \frac{a}{2^n}, \frac{a+d}{2^n}, \frac{a+2d}{2^n}, \frac{a+3d}{2^n}, \ldots, \frac{a+10d}{2^n} \right\} \text{ and}$$

Number of targeted concentrations $|L| = 11$, number of intersecting sets = 5, Number of initial concentrations derived using vase solutions = 6 and number of derived concentrations = 5; number of interpolated mix-split = 5; number of dilutions = 6. It has also been found that 2 separate sets of targeted concentration can be prepared with each type having two copies.

Table 1 Base solution concentration for the linear dilution gradient

Dilution Gradients	$\frac{1}{2^2}$	$\frac{1}{2^3}$	$\frac{1}{2^4}$	$\frac{1}{2^5}$	$\frac{1}{2^6}$	$\frac{1}{2^9}$
Numbers	1	1	1	2	1	6

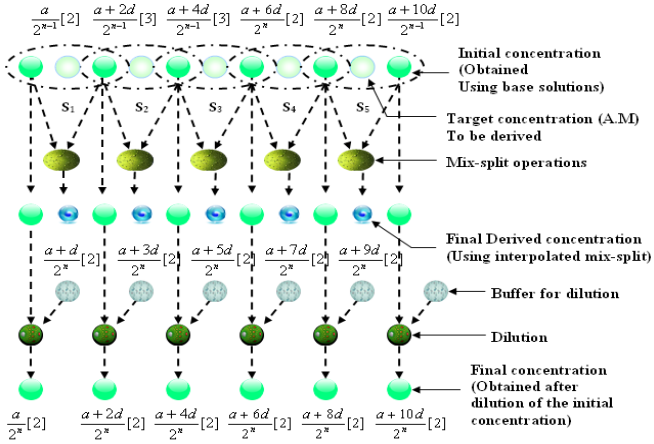

Fig. 5 A method for obtaining specified set of linear dilution gradient using Arithmetic Mean based method. Each concentration is shown with number of copies enclosed with [ ].

C. Proposed Algorithm

Algorithm 1: Linear dilution gradient preparation algorithm

Input: 1.Given set of linear dilution gradient to be obtained

$$L = \left\{ \frac{a}{2^n}, \frac{a+d}{2^n}, \frac{a+2d}{2^n}, \frac{a+3d}{2^n}, \ldots, \frac{a+kd}{2^n} \right\}$$

2. Adequate buffer solutions and estimated stock solutions

Procedure:

1. Decompose the concentration gradient set into a p number of intersecting sets each containing three elements.
2. Identify the initial concentrations to be obtained from base solutions. The number is $C_i = \dfrac{k+2}{2}$, if k is even

   And $C_i = \dfrac{k+1}{2} + 1$ if k is odd
3. Determine the number of copies required for each initial concentration using the technique stated for forming the set of linear dilution gradients in *part B* of this section.
4. Determine the base solutions necessary for each such concentration using the technique stated for *forming the target concentration* in *part B* of this section.
5. Finally prepare all the base solutions necessary as determined in step 4 using the technique stated for *forming the base solutions* (using serial dilution) in *part B* of this section.
6. While forming the base solution take stock of the waste droplets in each serial dilution step and use them for further dilution to obtain multiple copies for different base solutions.
7. Once all the copies of base solutions are obtained use interpolated dilution to prepare the selective initial target concentration(one level before the final dilution using buffer)
8. Derive the final mean derived concentration using arithmetic mean based interpolated dilution technique using reserve

copies of initial target concentrations as mentioned in *forming the linear dilution gradient* in *part B* of this section.

9. Finally the remaining copies of target concentration are subjected to next level of dilution to obtain final level concentration from the initial target concentration.
10. Count the total number of stages required for preparation of the total set and the number of mix split operations
11. Compute the number of remaining waste droplets, number of copies of each element of the target concentration obtained.
12. Compute the total number of stock solutions utilized.

Output: Final set of linear dilution gradient, number of waste droplets, number of modules used and number of stock solutions utilized.

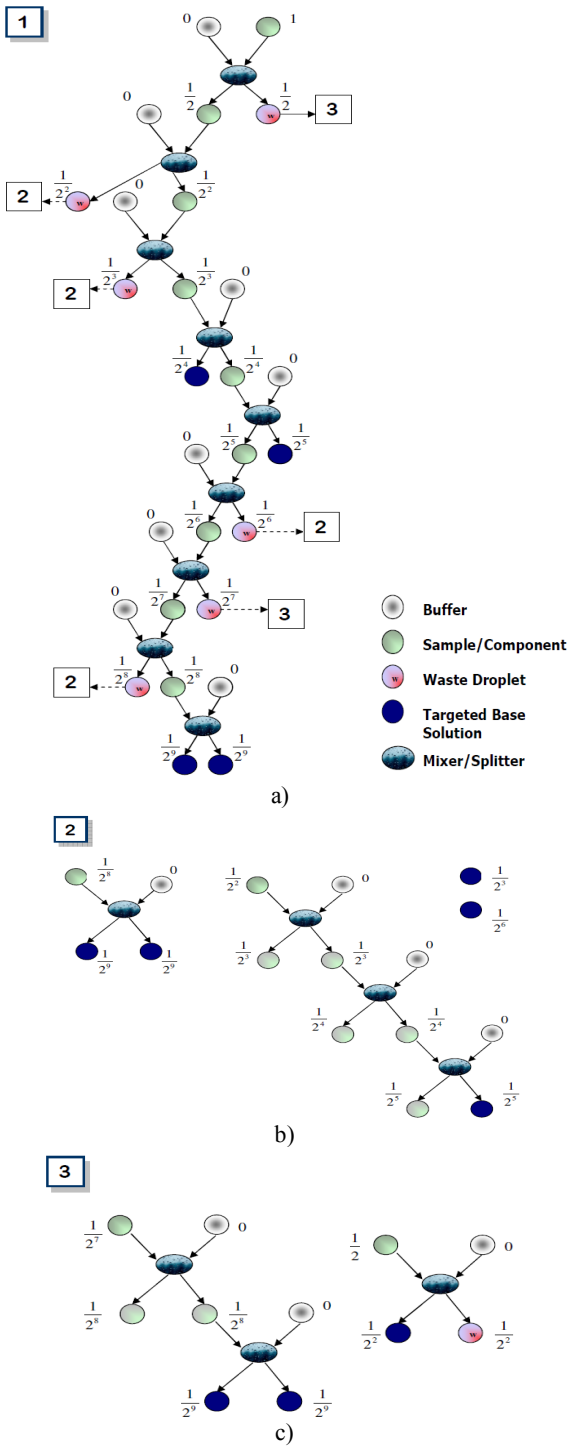

Fig.6. Three step process of preparation of base solution.

VI. Illustrative Example

We consider a set of specified linear dilution gradient (Target Set 1 [22]) given as $L = \langle \frac{50}{2^{10}}, \frac{70}{2^{10}}, \frac{90}{2^{10}}, \frac{110}{2^{10}}, \frac{130}{2^{10}} \rangle$. So initial concentration set $L_i = \langle \frac{50}{2^{10}}, \frac{90}{2^{10}}, \frac{130}{2^{10}} \rangle$, where $p = 3$. Each initial concentration is decomposed into base solutions as follows.

$$\frac{50}{2^{10}} \Rightarrow \frac{2^5+2^4+2}{2^{10}} \Rightarrow \frac{2^5+1}{2^9}, \frac{2^4+1}{2^9} \Rightarrow \frac{1}{2^4}, \frac{1}{2^9}, \frac{1}{2^5}, \frac{1}{2^9} \ldots(1)$$

$$\frac{90}{2^{10}} \Rightarrow \frac{2^6+2^4+2^3+2}{2^{10}} = \frac{2^6+1}{2^9}, \frac{2^4+1}{2^9}, \frac{2^3}{2^9} \Rightarrow \frac{1}{2^3}, \frac{1}{2^9}, \frac{1}{2^5}, \frac{1}{2^9}, \frac{1}{2^6} \ldots(2)$$

$$\frac{130}{2^{10}} \Rightarrow \frac{2^7+2}{2^{10}} \Rightarrow \frac{2^7+1}{2^9}, \frac{1}{2^9} \Rightarrow \frac{1}{2^2}, \frac{1}{2^9}, \frac{1}{2^9} \ldots(3)$$

So number of necessary base solutions for obtaining the linear dilution gradient set is given in table 1. Fig. 6 shows the serial dilution methods for obtaining base solutions necessary. We break the serial dilution methods into three steps. The waste droplets from part 1 are utilized in part 2 and part 3. In the next step, we use interpolated dilution to prepare the initial concentrations. Fig. 7 shows the interpolated dilution using the base solution to prepare initial concentration $L_i = \langle \frac{50}{2^{10}}, \frac{90}{2^{10}}, \frac{130}{2^{10}} \rangle$. Finally, Fig. 8 shows the derived arithmetic mean based interpolated dilution to prepare the derived concentrations gradients $L_d = \langle \frac{70}{2^{10}}, \frac{110}{2^{10}} \rangle$

It has been observed that multiple copies for each concentration gradient have been prepared. In section 4, we have given the detailed description of different linear dilution sets used in target set (Table 3).

VII. Experimental Results

The computed results for the linear dilution set obtained in section VI displaying the sample utilization, waste droplets, number of mix-split inclusive of the base solutions and the number of mix-split operation using only interpolated dilutions are shown in Table 2. The proposed technique is implemented on all the target sets defined in Table 3.The simulation results for all target sets are shown in Table 4. It has been observed that number of samples required while forming the linear dilution sets are reduced considerably and utilization of waste droplets are maximized. Comparison with contemporary works is shown in table 5. Detailed mixing performance for all the target sets as shown in table 4 is represented by a stacked bar graph in Fig. 9. The comparison with contemporary works in terms of number of mix-split operations used and the number of waste droplets generated is shown in Fig.10(a) and 10(b) respectively using clustered column plots.

Table 2. Dilution and mixing details for Target Set 1 [22]

Gradient	Number of Stock solutions used	modules used (additional modules for base solution)	number of copies	number of waste droplets (additional waste for base solutions)	number of base components
$\frac{50}{2^{10}}$	1	5 (+9)	3	2	4
$\frac{70}{2^{10}}$	0	2 (+0)	2	1	2
$\frac{90}{2^{10}}$	0	6 (+4)	2	2(+3)	5
$\frac{110}{2^{10}}$	0	2 (+0)	2	1	2
$\frac{130}{2^{10}}$	0	3 (+3)	2	2(+3)	3
Total	**1**	**18 (+16)**		**8(+6)**	**16**

VIII. Conclusion

In this work, we have proposed sample preparation techniques for obtaining given set of linear dilution gradients. The proposed method involves three steps namely estimation and preparation of base solution, preparation of initial set of gradients and determination of final sets of derived mean gradients. The simulation results for target set involving four sets of linear dilution gradients shows improvement in terms of sample and waste droplet utilization, number of mix-split operations involved. Further it is possible to generate more than one copy of each targeted

concentration value that facilitates verification using the reserve solution in case of faulty dilution while obtaining the targeted dilution. Here we have used linear dilution gradients arranged in arithmetic progression.

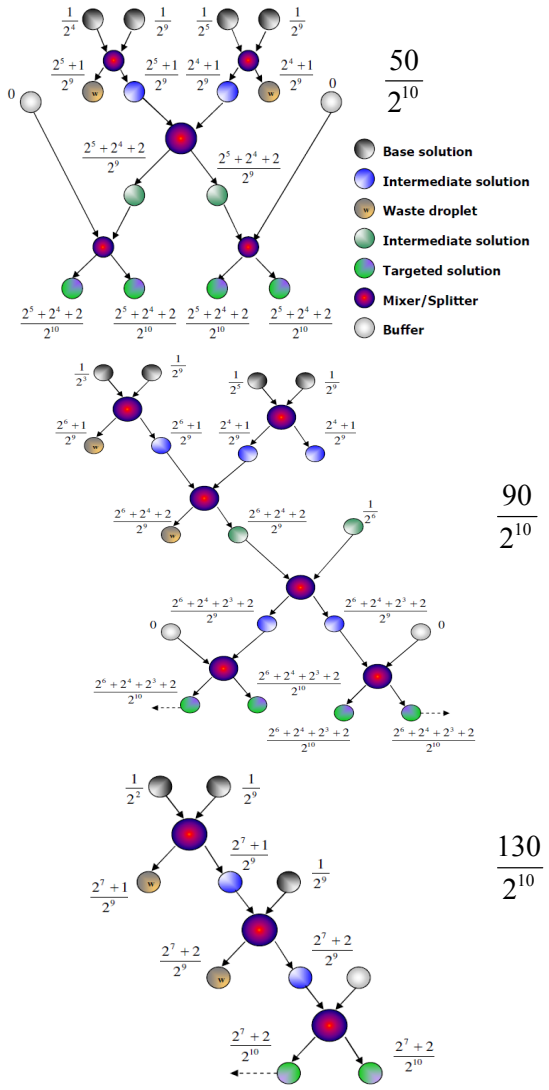

Fig. 7. The interpolated dilution method to prepare initial concentration gradients $L_i = < \frac{50}{2^{10}}, \frac{90}{2^{10}}, \frac{130}{2^{10}} >$

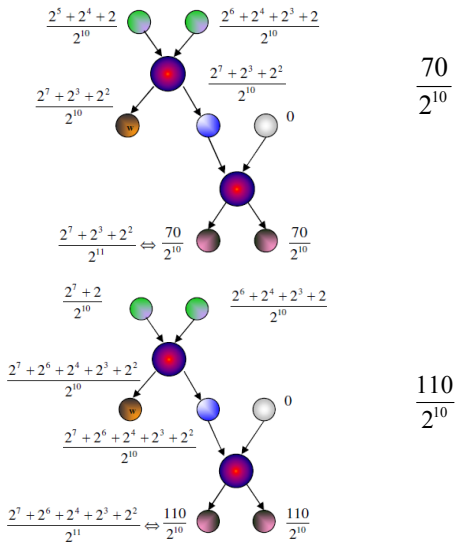

Fig. 8. Final steps using interpolated dilution method to prepare the mean derived concentrations $L_d = \langle \frac{70}{2^{10}}, \frac{110}{2^{10}} \rangle$

Table 3. Target set details [22]

TS name	TS Size	Target set details
TS_1	5	$\langle \frac{50}{2^{10}}, \frac{70}{2^{10}}, \frac{90}{2^{10}}, \frac{110}{2^{10}}, \frac{130}{2^{10}} \rangle$
TS_2	10	$\langle \frac{110}{2^{10}}, \frac{120}{2^{10}}, \frac{130}{2^{10}} \cdots\cdots \frac{200}{2^{10}} \rangle$
TS_3	17	$\langle \frac{20}{2^{10}}, \frac{70}{2^{10}}, \frac{120}{2^{10}} \cdots\cdots \frac{820}{2^{10}} \rangle$
TS_4	20	$\langle \frac{40}{2^{10}}, \frac{70}{2^{10}}, \frac{100}{2^{10}} \cdots\cdots \frac{610}{2^{10}} \rangle$

Table 4. Detailed results for all target sets mentioned in [22]

Target Samples	Mix-split	Additional Mix –split (base Soln.)	Stock samples used	Waste droplets
TS_1	18	16	1	8
TS_2	25	32	5	5
TS_3	55	48	18	7
TS_4	36	50	19	5

Table 5. Comparison of our technique with other methods

TS	Bhattacharjee et al. [22]		Mitra et al. [23]		Hsieh et al.[19]		Huang et al.[18]		Our Technique	
	Mix-Split	Waste	Mix-Split	Waste	Mix-Split	Waste	Mix-Split	Waste	Mix-Split	Waste
TS_1	24	14	33	28	37	28	32	12	18	1
TS_2	40	13	64	54	55	36	64	22	25	5
TS_3	57	12	88	71	82	50	104	39	55	7
TS_4	65	10	108	88	95	58	126	49	36	5

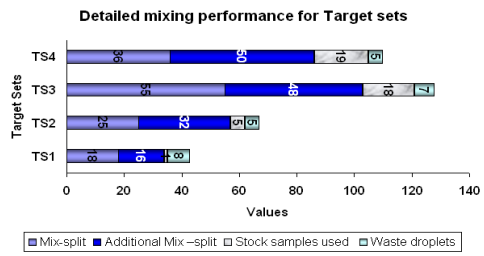

Fig. 9.Stacked bar chart representation of the detailed dilution for obtaining the linear dilution gradient

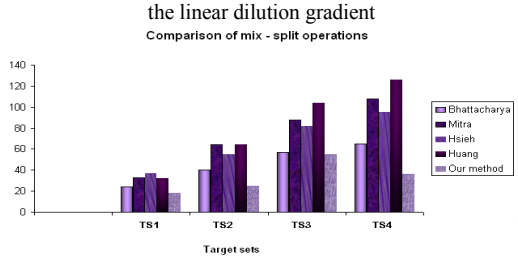

Fig. 10(a) Clustered column chart representation for the number of mix-split comparison of the proposed method to the related works

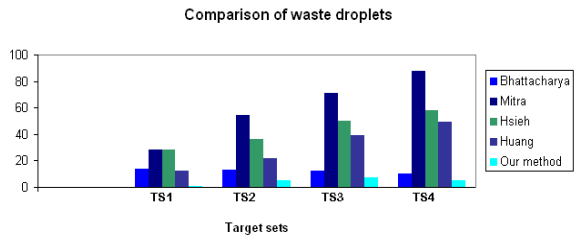

Fig.10(b). Clustered column chart representation for the number of waste droplets generated in comparison of the proposed method to the related works

References

[1] S. Mutlu, F. Svec, C. H. Mastrangelo, J. M. J. Fretcht, and Y. B Gianchandani,"Enhanced electro-osmosis pumping with liquid bridge and field effect flow rectification,"*Proc. IEEE MEMS*, pp. 850–853, Jan. 2004.

[2] T. Thorsen, S. Maerkl, and S. Quake, "Microfluidic large-scale integration," *Science*, vol. 298, no. 5593, pp. 580–584, Oct. 2002.

[3] S.-K. Cho S-K Fan H. Moon H and C-J Kim, "Towards digital microfluidic circuits: creating, transporting, cutting and merging liquid

droplets by electrowetting-based actuation," TechDig MEMS 2002 IEEE Inter Conf on Micro Electro Mechanical Systems pp. 454-61.

[4] M.G. Pollack, R.B. Fair, and A.D. Shenderov, "Electrowetting-based actuation of liquid droplets for microfluidic applications," *Appl. Phys Lett* 77,1725-1727(2000).

[5] F. Su, K. Chakrabarty, and R.B. Fair, "Microfluidics-based biochips: technology issues, implementation platforms, and design automation challenges," IEEE Trans. Computer-Aided Des. Of Integ. Cir. And Sys. 25 211-223 (2006).

[6] R. B. Fair, A. Khlystov, T. D. Tailor, V. Ivanov, R. D. Evans, V. Srinivasan, V. K. Pamula, M. G. Pollack, P. B. Griffin, and J. Zhou, "Chemical and biological applications of digital-microfluidic devices," IEEE Design & Test of Computers, vol. 24, no. 1, pp. 10–24, 2007.

[7] K. Chakrabarty and F. Su. *Digital Microfluidic Biochips - Synthesis, Testing, and Reconfiguration Techniques*. CRC Press, 2007.

[8] Y. Fouillet, D. Jary, C. Chabrol, P. Claustre, and C. Peponnet, "Digital microfluidic design and optimization of classic and new fluidic functions for lab on a chip systems," *Microfluidics and Nanofluidics 2008*, vol.4, pp.159–165.

[9] R. B. Fair, V. Srinivasan,H. Ren,P. Paik,V.K.Pamula, and M.G. Pollack, "Electrowetting-based on-chip sample processing for integrated microfluidics", *IEEE IEDM Tech. Dig.*, 2003, pp. 32.5.1–32.5.4.

[10] A. T. O'Neill and G. M. Walker, "Chapter 18: Linear dilution microfluidicdevices", *Lab-on-a-Chip Technology (Vol.1): Fabrication and Microfluidics. Norfolk, U.K.: Caister Academic Press, Aug. 2009.*

[11] H. Ren, V. Srinivasan, and R. B. Fair, "Design and testing of an interpolating mixing architecture for electrowetting-based droplet-on-chip chemical dilution", *Int. Conf. Solid-State Sensors, Actuators Microsyst. (Tranducers),* 2003, pp. 619–622.

[12] E. J. Griffith, S. Akella, and M. K. Goldberg, "Performance characterization of a reconfigurable planar-array digital microfluidic system," *IEEE TCAD*, vol. 25, no.2, pp. 345–357, Feb. 2006.

[13] W. Thies, J. P. Urbanski, T. Thorsen, and S. Amarasinghe, "Abstraction layers for scalable microfluidic biocomputing", *Nat. Comput.*, vol. 7, no. 2, pp. 255–275, 2008.

[14] S. Roy, B. B. Bhattacharya, and K. Chakrabarty, "Optimization of dilution and mixing of biochemical samples using digital microfluidic biochips" *IEEE TCAD*, vol. 29(11), pp. 1696–1708, Nov. 2010

[15] J.-D. Huang, C.-H. Liu, and T.-W. Chiang, "Reactant minimization during sample preparation on digital microfluidic biochips using skewed mixing trees", *IEEE/ACM ICCAD* 2012, pp. 377–384

[16] T.-W. Chiang, C.-H. Liu, and J.-D. Huang, "Graph-based optimal reactant minimization for sample preparation on digital microfluidic biochips", *IEEE VLSI-DAT*, Taiwan, 2013, pp. 1–4.

[17] Y.-L. Hsieh, T.-Y. Ho, and K. Chakrabarty, "On-chip biochemical sample preparation using digital microfluidics", *Int. Conf. BioCAS*, CA, USA, 2011, pp. 301–304.

[18] J.-D. Huang, C.-H. Liu, and H.-S. Lin, "Reactant and waste minimization in multitarget sample preparation on digital microfluidic biochips", *IEEE TCAD*, vol. 32(10), pp. 1484–1494, 2013.

[19] Y.-L. Hsieh, T.-Y. Ho, and K. Chakrabarty, "A reagent-saving mixing algorithm for preparing multiple-target biochemical samples using digital microfluidics", IEEE TCAD, vol.31 (11), pp. 1656–1669, 2012.

[20] S. Roy, B. B. Bhattacharya, and K. Chakrabarty, "Waste-aware dilution and mixing of biochemical samples with digital microfluidic biochips", *IEEE/ACM DATE* 2011, pp. 1059–1064.

[21] S. Bhattacharjee, A. Banerjee, and B. B. Bhattacharya, "Sample preparation with multiple dilutions on digital microfluidic biochips," *IET Comput. Digit. Tech*., vol. 8(1), pp. 49–58, Jan. 2014.

[22] S. Bhattacharjee, A. Banerjee, T-Yi Ho, K. Chakrabarty, and B. B. Bhattacharya, "Algorithms for Producing Linear Dilution Gradient with Digital Microfluidics", *Emerging Technologies (cs.ET) arXiv:1307.1251*

[23] Debasis Mitra, Sudip Roy, Sukanta Bhattacharjee, Krishnendu Chakrabarty, and Bhargab B. Bhattacharya, "On-Chip Sample Preparation for Multiple Targets Using Digital Microfluidics", *IEEE TCAD*, vol. 33(8), 2014.

[24] T. Kang, J. Han, K. S. Lee,"Concentration gradient generator using a convective diffusive balance", Lab-on-Chip 2008, vol.8, pp.1220 –1222.

Automatic Sleep Stage Classification

Ahnaf Rashik Hassan* and Mohammed Imamul Hassan Bhuiyan
Department of Electrical and Electronic Engineering
Bangladesh University of Engineering and Technology, Dhaka, Bangladesh
Email: *ahnaf.hassan0@gmail.com

***Abstract*—Automated sleep stage classification is essential for alleviating the burden of physicians since a large volume of data have to be analyzed per examination. Most of the existing works in the literature are multichannel based or yield poor classification performance. A single-channel based computerized sleep staging scheme that gives good performance is yet to emerge. In this work, we introduce a novel noise assisted decomposition scheme to perform automatic sleep stage classification from single channel EEG signals. At first, we decompose the EEG signal segments into mode functions using Complete Ensemble Empirical Mode Decomposition with Adaptive Noise (CEEMDAN). Various statistical moment based features are then computed from these mode functions. The effectiveness of statistical moment based features is validated by statistical analysis. In this work, we also introduce Adaptive Boosting for sleep stage classification. Experimental outcomes manifest that the computerized sleep staging scheme propounded herein outperforms the state-of-the-art ones in various cases of interest.**

***Index Terms*—EEG, Sleep Scoring, CEEMDAN, AdaBoost.**

I. Introduction

Sleep staging is traditionally performed by expert scorers based on visual observation of Polysomnographic (PSG) signals which is time-consuming, burdensome, error-prone, and subjective. Automated sleep staging therefore, can eradicate the burden of the physicians, expedite sleep disorder diagnosis, and benefit sleep research. Again, the push toward a wearable, portable yet low-power sleep quality monitoring device necessitates the use of minimum number of channels and reduced computational cost. Most of the existing works, on account of being multichannel or multiple physiological signal based, are unsuitable for device implementation. As a result, automatic sleep scoring based on single channel Electroencephalogram (EEG) is gaining interest in sleep research community.

Various single-channel, multichannel and multiple physiological signal based method have been proposed in the literature for automated sleep staging. Long et al. [1] computed various respiratory amplitude, depth and volume based features from respiratory effort signals and used linear discriminant classifier to perform sleep classification. Zhu et al. [2] generated difference visibility graph (VG) and horizontal VG from single channel EEG signal and extracted nine features from them to classify using support vector machine. Huang et al. [3] used two channel of forehead EEG signals, extracted spectral features by short-time Fourier transform from the signals and performed classification using relevance vector machine. Koch et al. [4] proposed a Latent Dirichlet Allocation topic model based method using four-channel multiple physiological signals (EEG and EOG) for sleep staging. Lajnef et al. [5] employed various features such as linear prediction error energy, variance, skewness, kurtosis, permutation entropy and multi-class support vector machine to perform automatic sleep scoring based on multichannel EEG, EOG and EMG signals. Kayikcioglu et al. [6] proposed an AR coefficient-based feature extraction scheme and utilized partial least squares (PLS) algorithm to classify sleep stages.

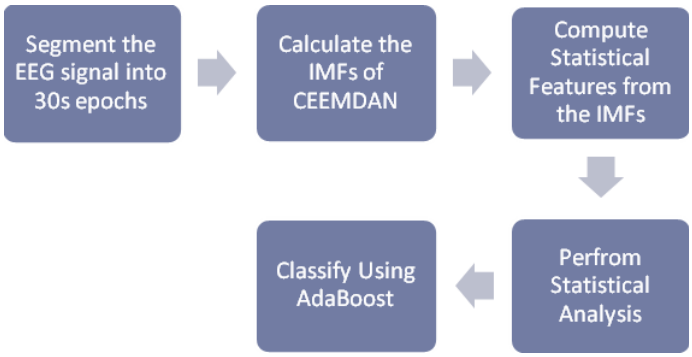

Fig. 1. A schematic outline of the proposed computerized sleep staging method.

In this work, we propound a single channel EEG based sleep scoring algorithm. The outline of our algorithm is presented in Fig. 1. After decomposing the EEG signals into 30s epochs, we further decompose the EEG signal segments into intrinsic mode functions using Complete Ensemble Empirical Mode Decomposition with Adaptive Noise (CEEMDAN). We then extract various statistical features from the intrinsic mode functions. The efficacy of the proposed feature extraction scheme is investigated using statistical analysis. Afterwards, sleep stage classification is performed using an eminent ensemble learning based classification model, namely- Adaptive Boosting (AdaBoost).

II. Materials and Methods

A. Experimental Data

The data-set used for evaluation of the proposed scheme is Physionet's Sleep-EDF data-set which is publicly available [7]. The recordings have been obtained from Caucasian males and females (21 - 35 years old) without any medication. There are eight recordings in two subsets (marked as sc^* and st^*). The first four recordings (sc4002e0, sc4012e0, sc4102e0, sc4112e0) have been acquired in 1989 from ambulatory

978-1-4673-9257-0/15/$31.00 © 2015 IEEE

healthy volunteers during 24 hours in their normal daily life. The last four data recordings (st7022j0, st7052j0, st7121j0, st7132j0) have been obtained in 1994 from subjects who had mild difficulty falling asleep but were otherwise healthy, during a night in the hospital, using a miniature telemetry system [8]. The recordings contain horizontal EOG, Fpz-Cz and Pz-Oz EEG data, each sampled at 100 Hz. It has been suggested in various studies [9] [10] [11] [2] that EEG signal from Pz-Oz channel yields better classification performance than that of the Fpz-Cz channel. So, in the present work Pz-Oz channel EEG signal is used. The sc^* recordings also contain the submental-EMG envelope, oro-nasal airflow, rectal body temperature and an event marker, all sampled at sampling rate of 1 Hz. The st^* recordings contain submental EMG sampled at sampling rate of 100 Hz and an event marker sampled at sampling rate of 1 Hz. Expert scoring of the EEG data is obtained from the same source. Each 30s of EEG data has been scored in accordance with the R&K recommendations [12]. The duration of each epoch is 30s or 3000 data points. Each epoch was scored by expert scorers in one of the eight classes: AWA, S1, S2, S3, S4, REM, MVT (Movement Time) and 'Unscored'. Table I summarizes the number of epochs of different classes that are used in this work. In total, 15,188 EEG epochs are used in this study. This study uses six sleep stages in accordance with R&K standard: AWA, S1-S4 and REM. The 5-state stages of sleep combine S3 and S4 of 6-state as Slow Wave Sleep (SWS) and the 4-state stages combine S1 and S2 of 5-state. The 3-state and 2-state stages of sleep include: AWA, NREM, REM and AWA, Sleep (S1-S4 and REM) respectively.

B. Empirical Mode Decomposition

Empirical Mode Decomposition (EMD) aims to generate highly localized time-frequency estimation of a signal in a data-driven fashion by decomposing it into a finite sum of intrinsic mode functions (IMF) or modes. Each mode must satisfy two conditions [13]:

1) The number of extrema and the number of zero crossings must be the same or differ at most by one.
2) At any point the mean value of the envelope defined by the local maxima and the envelope defined by the local minima is zero.

EMD iteratively decomposes an N-point EEG epoch X into amplitude and frequency modulated oscillatory IMFs using the following steps:

1) Set $h_1 = X$.
2) Identify the local maxima and minima of h_1.

TABLE I
DESCRIPTION OF EPOCHS OF VARIOUS SLEEP STATES USED IN OUR EXPERIMENTS

	AWA	S1	S2	S3	S4	REM	Total
Epochs	8055	604	3621	672	627	1609	15188

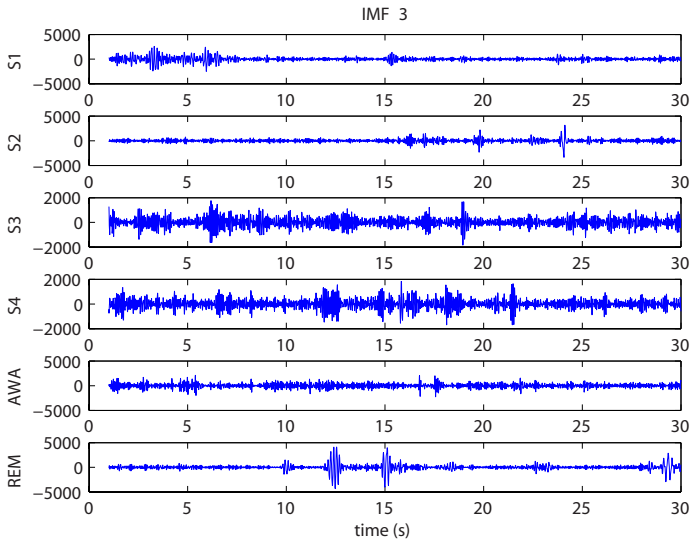

Fig. 2. $\widetilde{IMF}_3$ of CEEMDAN of various sleep stages. Note the variations of the IMFs in different sleep states.

3) Obtain the envelope of local maxima v_{max} and that of local minima v_{min} using cubic spline interpolation.
4) Generate the local mean curve m by generating the upper and lower envelopes:

$$m = \frac{v_{max} + v_{min}}{2} \tag{1}$$

5) Compute h_2 by subtracting the local mean curve from h_1:

$$h_2 = h_1 - m \tag{2}$$

6) Repeat steps 2)-5) until the difference between h_{k+1} and h_k ($SD(k)$) defined as follows reaches a predefined value ϵ.

$$SD(k) = \frac{\|h_{k+1} - h_k\|^2}{\|h_k\|^2} < \epsilon \tag{3}$$

where $\|.\|$ is the Euclidian L2-norm.
7) Set $c_1 = h_k$ as the first mode.
8) Find the residue, $r_1 = x - c_1$. Steps 1)-7) are known as sifting.
9) Substitute X in 1) with r. Repeat steps 1)-7) to find the rest of the IMFs $c_2, c_3, ..., c_L$.

Thus, the input signal can be decomposed into L IMFs until the residue becomes a monotonic function such that further extraction of an IMF is not possible. The input X can be reconstructed from all the IMFs as:

$$X = \sum_{j=1}^{L} c_j + r_L \tag{4}$$

where r_L is the residue of the L-th iteration.

C. Ensemble Empirical Mode Decomposition

A noise-assisted adaptive data analysis based extension of EMD, called EEMD has been proposed in [14] with a view

to eradicating the mode mixing problem. In EEMD, a low-level random noise is added to the input which is decomposed by EMD. The process of implementing EMD on the modified signal is referred as one trial. The trial is repeated I times to obtain the final mode. The steps of EEMD are as follows:

1) Calculate $x^i(n) = x(n) + w^i(n)$ where $w^i(n)$ with $i = 1, 2, ..., I$ represents different realizations of white Gaussian noise.
2) Compute EMD of each of the signals $x^i(n)$ and find the corresponding modes $IMF_k^i(n)$. Here, $k = 1, 2, .., K$ denotes the modes.
3) Find the modes of EEMD method, denoted by $\overline{IMF_k}(n)$ by averaging $IMF_k^i(n)$ as:

$$\overline{IMF_k}(n) = \frac{1}{I}\sum_{i=1}^{I} IMF_k^i(n) \tag{5}$$

$\overline{IMF_k}(n)$ does not necessarily obey the aforementioned conditions required to be an IMF [15].

D. Complete Ensemble Empirical Mode Decomposition with Adaptive Noise

Let us define an operator $E_j(.)$ that produces the j-th mode of EMD. If $w^i(n)$ with $i = 1, 2, ..., I$ are different realizations of white Gaussian noise with zero mean and unit variance and ϵ_0 is the standard deviation of the white Gaussian noise, the CEEMDAN algorithm can be described as follows [16].

1) Calculate $x(n) + \epsilon_0 w^i(n)$.
2) Decompose the above I signals by EMD to obtain their first modes.
3) Compute the first mode $\widetilde{IMF}_1$ of CEEMDAN as:

$$\widetilde{IMF}_1(n) = \frac{1}{I}\sum_{i=1}^{I} IMF_1^i(n) = \overline{IMF_1}(n) \tag{6}$$

4) Find the first residue as:

$$r_1(n) = x(n) - \widetilde{IMF_1}(n) \tag{7}$$

5) Decompose realizations $r_1(n) + \epsilon_1 E_1(w^i(n))$ with $i = 1, 2, ..., I$ up to their first EMD mode. ϵ_k ($k = 1$ for this stage) is the standard deviation of white Gaussian noise of the k-th stage. $\widetilde{IMF}_2(n)$ can be found as:

$$\widetilde{IMF}_2(n) = \frac{1}{I}\sum_{i=1}^{I} E_1(r_1(n) + \epsilon_1 E_1(w^i(n))) \tag{8}$$

6) Compute the k-th residue for $k = 2, 3, ..., K$ as:

$$r_k(n) = r_{k-1}(n) - \widetilde{IMF}_k(n) \tag{9}$$

7) Decompose realizations $r_1(n) + \epsilon_1 E_1(w^i(n))$ with $i = 1, 2, ..., I$ up to their first EMD mode and define the $(k+1)$-th mode as:

$$\widetilde{IMF}_{k+1}(n) = \frac{1}{I}\sum_{i=1}^{I} E_1(r_k(n) + \epsilon_k E_k(w^i(n))) \tag{10}$$

8) Go to step 6 for next k.

Steps 6 to 8 are repeated until the residue becomes a monotonic function such that further extraction of an IMF is not possible. Fig. 2 shows two such IMFs for various sleep stages. If K is the total number of modes and $r_k(n)$ is the final residue, the input $x(n)$ can be reconstructed from all the IMFs as:

$$x(n) = \sum_{k=1}^{K} \widetilde{IMF}_k(n) + r_k(n) \tag{11}$$

E. Motivation of Using CEEMDAN

The use of CEEMDAN in stead of EMD or EEMD in the algorithm propounded herein is motivated by various advantages of CEEMDAN over commonly used signal processing techniques. EMD is data-driven but it suffers from mode mixing problem which causes disparate oscillations in the same mode or similar oscillations in different modes. Despite effectively resolving the mode mixing problem, there are a number of caveats which makes EEMD unsuitable for practical implementation. Decomposing the same signal several times with EEMD can produce different number of modes [17]. If we reconstruct the signal after the application of EEMD, residual noise is obtained [17] [15]. Moreover, EEMD is also computationally expensive. CEEMDAN on the other hand, provides an exact reconstruction of the original signal and a better spectral separation of the modes [15]. The computational cost of CEEMDAN is also lower [17]. These factors motivated the use of CEEMDAN instead of EMD or EEMD in our proposed feature extraction scheme. Also, note that the traditional time-frequency transforms such as wavelet transform based methods' performance is affected by the choice of the best basis function. The best basis function is application-specific and may vary from case to case [15]. On the other hand, CEEMDAN is data-driven and does not require a prior basis function which makes it an attractive choice for processing highly nonlinear and non-stationary signals such as sleep-EEG signals.

F. Statistical Moment Based Features

The features that are used in this work are- mean, variance, skewness and kurtosis. For an N-point $\widetilde{IMF}$, $X = \{x_1, x_2, x_3, .., x_N\}$ mean (μ), variance (σ^2), Skewness (γ) and Kurtosis (κ) can be expressed mathematically as [18]:

$$\mu = \frac{1}{N}\sum_{i=1}^{N} x_i \tag{12}$$

$$\sigma^2 = \frac{1}{N}\sum_{i=1}^{N} (x_i - \mu)^2 \tag{13}$$

$$\gamma = \frac{1}{N}\sum_{i=1}^{N} \left(\frac{x_i - \mu}{\sigma}\right)^3 \tag{14}$$

$$\kappa = \frac{1}{N}\sum_{i=1}^{N} \left(\frac{x_i - \mu}{\sigma}\right)^4 \tag{15}$$

TABLE II
P-VALUES OF THE PROPOSED FEATURES

p-Values of	IMF 1	IMF 2	IMF 3	IMF 4	IMF 5	IMF 6	IMF 7
μ	2.4119e-146	3.3696e-23	7.8781e-90	2.2518e-88	4.5127e-186	8.7108e-132	4.0894e-09
σ^2	5.3247e-47	1.9888e-59	5.7717e-56	5.9530e-55	1.4858e-246	3.9000e-231	6.5459e-220
γ	3.2805e-21	2.2792e-65	9.6112e-87	7.9627e-73	1.1627e-40	4.8087e-34	4.7436e-37
κ	2.4385e-40	2.0876e-111	8.2096e-89	2.7199e-137	9.7257e-32	1.4340e-95	1.1660e-76

G. Statistical Analysis

Statistical hypothesis testing must be performed for the feature selection stage of any classification problem. This ensures that the chosen set of features has discriminatory capability among various classes [19]. Hypothesis testing also helps us ascertain whether the discriminatory capability of the selected set of features is statistically significant or not. To assess whether the values of the features in the six classes differ significantly, we perform a non-parametric Kruskal-Wallis one-way analysis of variance. Unlike its parametric equivalent which is known as one-way analysis of variance (ANOVA), Kruskal-Wallis test does not require an assumption of normal distribution of the data samples [20]. The test is carried out in MATLAB's Statistics Toolbox. The test is performed at 95% confidence level. Hence, a difference is statistically significant if $p < \alpha(= 0.05)$. Table II gives the result of the hypothesis testing and we can see that all of the IMFs features give lower p-values indicating good discriminatory capability among the six sleep states.

H. Adaptive Boosting

Boosting is one of the most eminent ensemble learning algorithms that creates an ensemble of classifiers by resampling the data in a manner such that the most informative training data is provided to each consecutive classifier [21]. Adaptive Boosting (AdaBoost) was pioneered by Freund and Schapire [22]. AdaBoost generates a set of hypotheses such that subsequent hypotheses focus on increasingly difficult instances. Afterwards, it combines them through weighted majority voting of the classes predicted by the individual hypotheses. Each of the hypothesis is generated by training a weak classifier using instances drawn from an iteratively updated distribution of the training data. This distribution update makes sure that instances misclassified by the previous classifier are more likely to be included in the training data of the next classifier. Consequently, consecutive classifiers training data are geared towards increasingly difficult-to-classify instances. This is the essence of AdaBoost learning algorithm. Freund and Schapire also propounded two extensions of AdaBoost [22], namely-AdaBoost.M1 and AdaBoost.M2. AdaBoost.M1 requires that all hypotheses generated by the weak classifiers have a weighted error no greater than 0.5. AdaBoost.M2 which is a multi-class extension of AdaBoost.M1, relaxes the weighted error restriction. Instead, it defines a pseudo-loss which itself is then required to have an error no larger than 0.5. This pseudo-loss measures the goodness of the weak hypotheses. Moreover, the probability of error for random guessing is much higher for multi-class problems ($\frac{C-1}{C}$ for C-class classification problem) than that of binary classification problems. Since the learners are weak, achieving an error of 0.5 becomes harder with the increase of classes. These two factors make AdaBoost.M2 a powerful tool for multi-class classification and motivated its use in the present study. Since, AdaBoost.M2 is a multi-class extension, for two stage classification we use AdaBoost.M1.

Algorithm 1: AdaBoost.M2

Input:

- Sequence of N instances $S = [(x_i, y_i)]$ of C classes with labels $y_i \in \omega$, $\omega = \{\omega_1, \omega_2, ..., \omega_C\}$ and $i = 1, 2, 3, ..., N$.
- Weak learning algorithm **WeakLearn**.
- Integer T specifying the number of iterations.

Let, $B = \{(i, y) : i = 1, 2, ..., N, y \neq y_i\}$

Initialize $D_1(i, y) = 1/|B| for (i, y) \in B$

for $t = 1, 2, 3, ..., T$ **do**

1. Call **WeakLearn**, providing it with distribution D_t.
2. Get back a hypothesis $h_t : X \times Y \rightarrow [0, 1]$.
3. Calculate the pseudo-error ϵ_t of h_T:

$$\epsilon_t = \frac{1}{2} \sum_{(i,y) \in B} D_t(i, y)(1 - h_t(x_i, y_i) + h_t(x_i, y))$$

4. Set $\beta_t = \epsilon_t/(1 - \epsilon_t)$.
5. Update distribution D_t:

$$D_{t+1}(i, y) = \frac{D_t(i, y)}{Z_t} \beta_t^{\frac{1}{2}(1+h_t(x_i,y_i)-h_t(x_i,y))}$$

where is a $Z_t = \sum D_t(i)$ normalization constant chosen so that D_{t+1} becomes a distribution function.

end

Output: The final hypothesis:

$$h_{final}(x) = \arg\max_{y \in Y} \sum_{t=1}^{T} (log \frac{1}{\beta_t}) \times h_t(x, y)$$

AdaBoost.M2 is expounded in Algorithm 1. In Step 1 and 2, the weak classifier denoted by **WeakLearn** is invoked with a distribution D_t and a hypothesis h_t is obtained. We use decision trees as **WeakLearn** in the proposed method. The weak learner's goal then is to minimize the pseudo-loss ϵ_t, as defined in Step 3. The distribution function is updated as shown in Step 5. For a given instance x, the final hypothesis $h_{final}(x)$ outputs the label y that maximizes a weighted average of the weak hypothesis values $h_t(x, y)$. The procedure

TABLE III
DESCRIPTION OF VARIOUS CLASSES

Class	Sleep States
6	AWA, S1, S2, S3, S4, REM
5	AWA, S1, S2, SWS (S3-S4), REM
4	AWA, S1-S2, SWS (S3-S4), REM
3	AWA, NREM (S1-S4), REM
2	AWA, Sleep (REM & NREM)

TABLE IV
PERFORMANCE COMPARISON OF VARIOUS STATE-OF-THE-ART METHODS. ONLY THE HIGHEST ACCURACY VALUES OF EACH METHOD ARE REPORTED

Authors	6-Class	5-Class	4-Class	3-Class	2-Class
Herrera et al. [23]	-	-	69.80%	-	-
Huang et al. [24]	-	-	77.12%	-	-
Berthomier et al. [9]	-	71.2%	74.5%	88.3%	95.4%
Hsu et al. [25]	-	87.20%	-	-	-
Linag et al. [10]	-	83.60%	-	-	-
Hassan et al. [26]	80.34%	82.03%	82.83%	-	-
Ronzhina et al. [11]	76.70%	-	81.42%	88.97%	96.90%
Hassan et al. [27]	85.57%	86.53%	87.49%	89.77%	95.05%
Zhu et al. [2]	**87.50**%	88.90%	89.30%	92.60%	97.90%
Proposed Method	86.89%	**89.52**%	**91.48**%	**93.18**%	**98.29**%

of AdaBoost.M1 is similar to that of Algorithm 1 except for the fact that instead of pseudo-loss, it uses a weighted error defined as:

$$\epsilon_t = \sum_{i:h_t(x_i)\neq y_i} D_t(i) \tag{16}$$

If $\epsilon_t > \frac{1}{2}$ the process halts.

III. RESULTS AND DISCUSSIONS

The configuration of the computer which has been used in our experiments is Intel(R) Core(TM) i5-3470, 3.2 GHz CPU, 4 GB of RAM. MATLAB 2013a is employed to carry out the simulations. In this paper, we consider five cases of sleep stage classification. These classes are described in Table III. The cases listed in Table III are clinically relevant and consistent with the experimental settings with contemporary works in the literature.

The performance of the proposed algorithm is evaluated against state-of-the-art sleep staging algorithms in the literature. To ensure fair comparison, Table IV compares the proposed method's performance to some contemporary works

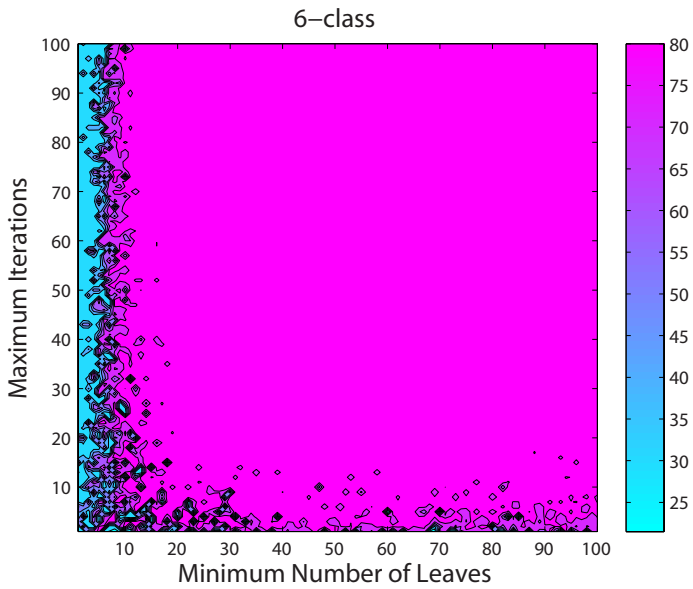

Fig. 3. Variation of accuracy with number of iterations and minimum number of leaves of decision tree. The high levels of accuracy for a wide range of value of these two parameters confirm the robustness of the proposed scheme.

in the literature based on Sleep-EDF data-set. It is evident from Table IV that the proposed method gives superior performance to prior works in the literature. Although the algorithmic performance of our method is slightly low than that of [2], in general, the performance of our method is better as Table IV evinces.

The proposed method's consistent algorithmic performance for various cases of interest already highlights its reliability. Another salient feature of the proposed scheme is that it is robust. This fact is evident from Fig. 3. Fig. 3 presents the variation of accuracy with number of iterations and minimum number of leaves of decision tree. The high levels of accuracy for a wide range of value of these two parameters confirm the robustness of the proposed scheme. In other words, the accuracy values are high not for a few sporadic values of number of decision trees merely. The proposed method's reliability and robustness suggest that this algorithm is suitable for both clinical practice and device implementation.

IV. CONCLUSIONS

In this work, we have introduced a novel signal processing technique, namely- CEEMDAN for sleep stage classification. Experimental results backed by statistical validation clearly indicates that statistical features in the CEEMDAN domain can characterize various stages of sleep quite well. AdaBoost is also implemented for computer-aided sleep scoring. Until now, this is the first time CEEMDAN in conjunction with AdaBoost is employed for sleep staging to the best of our knowledge. The proposed scheme can be extended for other physiological signal classification problems as well. In conclusion, we can anticipate that the proposed sleep staging algorithm will alleviate the onus of the clinicians, speed-up sleep disorder

diagnosis, and can be marked as an important step towards making a sleep quality evaluation device feasible.

REFERENCES

[1] X. Long, J. Foussier, P. Fonseca, R. Haakma, and R. M. Aarts, "Analyzing respiratory effort amplitude for automated sleep stage classification," *Biomedical Signal Processing and Control*, vol. 14, pp. 197 – 205, 2014.

[2] G. Zhu, Y. Li, and P. Wen, "Analysis and classification of sleep stages based on difference visibility graphs from a single channel eeg signal," *Biomedical and Health Informatics, IEEE Journal of*, vol. PP, no. 99, pp. 1–1, 2014.

[3] C.-S. Huang, C.-L. Lin, L.-W. Ko, S.-Y. Liu, T.-P. Su, and C.-T. Lin, "Knowledge-based identification of sleep stages based on two forehead electroencephalogram channels," *Frontiers in Neuroscience*, vol. 8, no. 263, 2014.

[4] H. Koch, J. A. Christensen, R. Frandsen, M. Zoetmulder, L. Arvastson, S. R. Christensen, P. Jennum, and H. B. Sorensen, "Automatic sleep classification using a data-driven topic model reveals latent sleep states," *Journal of Neuroscience Methods*, vol. 235, no. 0, pp. 130 – 137, 2014.

[5] T. Lajnef, S. Chaibi, P. Ruby, P.-E. Aguera, J.-B. Eichenlaub, M. Samet, A. Kachouri, and K. Jerbi, "Learning machines and sleeping brains: Automatic sleep stage classification using decision-tree multi-class support vector machines," *Journal of Neuroscience Methods*, no. 0, pp. –, 2015.

[6] T. Kayikcioglu, M. Maleki, and K. Eroglu, "Fast and accurate pls-based classification of eeg sleep using single channel data," *Expert Systems with Applications*, vol. 42, no. 21, pp. 7825 – 7830, 2015.

[7] B. Kemp, "The sleep-edf database online." [Online]. Available: http://www.physionet.org/physiobank/database/sleep-edf/

[8] B. Kemp, A. Zwinderman, B. Tuk, H. Kamphuisen, and J. Oberye, "Analysis of a sleep-dependent neuronal feedback loop: the slow-wave microcontinuity of the eeg," *Biomedical Engineering, IEEE Transactions on*, vol. 47, no. 9, pp. 1185–1194, Sept 2000.

[9] C. Berthomier, X. Drouot, M. Herman-Stoca, P. Berthomier, J. Prado, D. Bokar-Thire, O. Benoit, J. Mattout, and M.-P. dOrtho, "Automatic analysis of single-channel sleep eeg: Validation in healthy individuals," *Sleep*, vol. 30, no. 11, p. 15871595., Nov 2007.

[10] S.-F. Liang, C.-E. Kuo, Y.-H. Hu, Y.-H. Pan, and Y.-H. Wang, "Automatic stage scoring of single-channel sleep eeg by using multiscale entropy and autoregressive models," *Instrumentation and Measurement, IEEE Transactions on*, vol. 61, no. 6, pp. 1649–1657, June 2012.

[11] M. Ronzhina, O. Janouek, J. Kolrov, M. Novkov, P. Honzk, and I. Provaznk, "Sleep scoring using artificial neural networks," *Sleep Medicine Reviews*, vol. 16, no. 3, pp. 251 – 263, 2012.

[12] A. Rechtschaffen and A. Kales, "Manual of standardized terminology, techniques and scoring systems for sleep stages of human subjects," *U. G. P. Office, Washington DC Public Health Service*, 1968.

[13] A. R. Hassan, "Automatic screening of obstructive sleep apnea from single-lead electrocardiogram," in *Electrical Engineering and Information Communication Technology (ICEEICT), 2015 International Conference on*, May 2015, pp. 1–6.

[14] Z. Wu and N. E. Huang, "Ensemble empirical mode decomposition: a noise assisted data analysis method," *Advances in Adaptive Data Analysis*, vol. 01, no. 01, pp. 1–41, 2009.

[15] A. R. Hassan and M. I. H. Bhuiyan, "Computer-aided sleep staging using complete ensemble empirical mode decomposition with adaptive noise and bootstrap aggregating," *Biomedical Signal Processing and Control*, vol. 24, pp. 1 – 10, 2016.

[16] A. R. Hassan and M. A. Haque, "Epilepsy and seizure detection using statistical features in the complete ensemble empirical mode decomposition domain," in *TENCON 2015, 2015 IEEE Region 10 Conference*, Nov. 2015, pp. 1–6.

[17] M. Torres, M. Colominas, G. Schlotthauer, and P. Flandrin, "A complete ensemble empirical mode decomposition with adaptive noise," in *Acoustics, Speech and Signal Processing (ICASSP), 2011 IEEE International Conference on*, May 2011, pp. 4144–4147.

[18] A. R. Hassan and M. A. Haque, "Computer-aided sleep apnea diagnosis from single-lead electrocardiogram using dual tree complex wavelet transform and spectral features," in *Electrical and Electronic Engineering (ICEEE), 2015 International Conference on*, Nov. 2015, pp. 1–4.

[19] ——, "Computer-aided gastrointestinal hemorrhage detection in wireless capsule endoscopy videos," *Computer Methods and Programs in Biomedicine*, pp. –, 2015.

[20] S. Bashar, A. Hassan, and M. Bhuiyan, "Identification of motor imagery movements from eeg signals using dual tree complex wavelet transform," in *Advances in Computing, Communications and Informatics (ICACCI), 2015 International Conference on*, Aug 2015, pp. 290–296.

[21] A. R. Hassan, "A comparative study of various classifiers for automated sleep apnea screening based on single-lead electrocardiogram," in *Electrical and Electronic Engineering (ICEEE), 2015 International Conference on*, Nov. 2015, pp. 1–4.

[22] Y. Freund and R. E. Schapire, "A decision-theoretic generalization of on-line learning and an application to boosting," *Journal of Computer and System Sciences*, vol. 55, no. 1, pp. 119 – 139, 1997.

[23] L. Herrera, A. Mora, C. Fernandes, D. Migotina, A. Guillen, and A. Rosa, "Symbolic representation of the eeg for sleep stage classification," in *Intelligent Systems Design and Applications (ISDA), 2011 11th International Conference on*, Nov 2011, pp. 253–258.

[24] C.-S. Huang, C.-L. Lin, L.-W. Ko, S.-Y. Liu, T.-P. Sua, and C.-T. Lin, "A hierarchical classification system for sleep stage scoring via forehead eeg signals," in *Computational Intelligence, Cognitive Algorithms, Mind, and Brain (CCMB), 2013 IEEE Symposium on*, April 2013, pp. 1–5.

[25] Y.-L. Hsu, Y.-T. Yang, J.-S. Wang, and C.-Y. Hsu, "Automatic sleep stage recurrent neural classifier using energy features of eeg signals," *Neurocomputing*, vol. 104, no. 0, pp. 105 – 114, 2013.

[26] A. R. Hassan, S. K. Bashar, and M. I. H. Bhuiyan, "Automatic classification of sleep stages from single-channel electroencephalogram," in *India Conference (INDICON), 2015 Annual IEEE*, Dec 2015, pp. 1–6.

[27] A. Hassan, S. Bashar, and M. Bhuiyan, "On the classification of sleep states by means of statistical and spectral features from single channel electroencephalogram," in *Advances in Computing, Communications and Informatics (ICACCI), 2015 International Conference on*, Aug 2015, pp. 2238–2243.

Mitigation of Thermally Induced Crosstalk Noise by Dynamically Adjusting Driver Strength

Md M Rahman, Pankaj Bhowmik and Selahattin Sayil
Department of Electrical Engineering
Lamar University
Beaumont, USA
E-mail: mrahman5@lamar.edu, pbhowmik@lamar.edu, sayil@lamar.edu

Abstract—**The space between interconnects is shrinking and its increasing aspect ratio is causing modern VLSI circuit to be more prone to crosstalk noise. Moreover, modern high-performance CMOS circuits are more power consuming, resulting in the chip experiencing higher temperature. As a consequence of this high temperature, CMOS driver strength reduces which introduces a new reliability concern, thermally induced crosstalk noise, which is addressed in this research work for the very first time in literature. This superimposing with the normal crosstalk can cause the VLSI circuit to fail by toggling the logic or bit flipping. In this paper, our goal is to provide a solution to mitigate the thermally induced crosstalk noise by dynamically adjusting gate voltage to keep driver strength the same despite changing temperature. We propose a temperature sensor that generates the necessary voltage to the gate to keep driver strength constant. Using 10-π modelling for interconnect in 45nm technology, we explore the effect of on-chip temperature gradient on crosstalk noise. Our simulation result demonstrates that the proposed method can successfully mitigate thermally induced crosstalk noise up to 85% in the worst case temperature scenario.**

Keywords—thermally induced crosstalk noise, temperature sensor, temperature insensitivity, crosstalk noise mitigation

I. INTRODUCTION

Due to the advancement of technology and the increasing demand for miniaturizing of smart devices, the semiconductor industry has been trying to shrink the device size and the spaces between interconnects. On the other hand, the width of interconnect cannot be scaled down in similar fashion to keep interconnect resistance low, resulting in increase of its aspect ratio. This diminishing spaces between interconnects and larger aspect ratio increases coupling capacitance between adjacent interconnect lines. As reported in [1], more than 85% of the total interconnect capacitance in 90nm technology and below is due to coupling capacitance. This increasing coupling capacitance and reduced device size combined with today's multi-gigahertz signal on one interconnect adversely effects the signal integrity on the neighboring line through a mechanism called as crosstalk noise. In literature, different techniques have been proposed to reduce crosstalk noise including device sizing [2,3], repeater insertion [4] and shielding method [5,6].

On the other hand, due to the integration of hundreds of million devices in a single chip, the total power consumption and power per unit area have raised unprecedentedly. As the power consumption is converted into heat, which ultimately increases the operating temperature. This high operating temperature adversely affects the circuit performance, such as reliability and robustness. Moreover, the employment of different power management techniques and diverse activities of functional blocks cause the chip to experience non-uniform temperature throughout the whole chip area. This on-chip temperature gradient can be as high as 50°C as reported in [7]. The increased temperature affects both interconnect resistance and strength of interconnect drivers. The interconnect resistance increases as the temperature goes up, because the commonly used interconnect materials, copper and aluminum, both have a positive temperature co-efficient of 0.00401 and 0.004308[8] respectively.

However, the effect of temperature change on buffer is not straightforward, as two important device parameters, carrier mobility and threshold voltage, have conflicting effects on device drain current with the change of temperature. As temperature increases, carrier mobility decreases which causes the device current to go down. On the other hand, increased temperature reduces the device threshold voltage causing device current to increase. Depending on dominant effect in between mobility and threshold voltage, device responds accordingly. If the gate to source voltage is little higher than zero, the change of threshold voltage dominates over the change of mobility and that cause to increase the drain current with temperature rise. On the other hand, at nominal supply voltage, change in carrier mobility dominates over the change of threshold voltage which causes the device current to decrease with increased temperature. As a result of this increased interconnect resistance and decreased buffer driving strength, charge from neighboring aggressor interconnect tends to produce an extra glitch on victim line other than the normal crosstalk, this extra glitch is named as thermally induced crosstalk. Unlike other research works which were concerned with the normal crosstalk, we are first in literature to address this temperature effect on crosstalk. Superimposing this thermally induced crosstalk noise on normal crosstalk can cause the total crosstalk noise to cross the noise margin of the subsequent gate, which ultimately may generate and propagate the wrong value. If this wrong data propagates in the latching window of a storage device e.g. latch, the wrong data will be stored, eventually causing the circuit to fail.

As the thermally induced crosstalk noise results from decreased buffer strength and increased interconnect resistance, to mitigate this noise, we have proposed a buffer that keeps its driving strength constant and compensate for the increased interconnect resistance even if the temperature changes.

978-1-4673-9257-0/15/$31.00 ©2015 IEEE

Several schemes have been proposed to keep driver strength constant in changing temperature situation. In [9], the authors proposed a dynamically adaptive driver that involves designing of temperature sensor with a wave-shaping circuit. The output from the wave-shaping circuit is used to control the gate of extra pMOS and nMOS connected in series with the original buffer which dynamically adjust the buffer current as temperature changes. While this technique achieves good temperature insensitivity, designing the temperature sensor and wave-shaping circuit are complex and extra four devices in the buffer, raise area overhead. In Multi-threshold technique [10], the authors suggested that, by proper interleaving low threshold (lvt), standard threshold (stv) and high threshold (hvt) devices it is possible to achieve temperature insensitivity. As each type device (lvt,stv,hvt) has different temperature dependencies, that entails body bias for individual devices, resulting in overhead to be large. Shakeri and Meindl suggested a variable supply voltage in [11], but requirement of different voltage and routing them all over the chip is a problem. Moreover, the number of level converters required for different sections poses another design bottleneck.

In [12], Wolpert and Ampadu suggested programmable temperature compensation device (PTCD) to keep buffer current constant in variable temperature situation. They proposed an extra nMOS and pMOS device in series with original buffer transistors**.** As suggested in Section [II], both nMOS and pMOS show temperature insensitivity at particular gate voltage (V_{INS}). Wolpert and Ampadu [12] connected gates of these extra devices to V_{INS} to make the buffer strength constant. As nMOS and pMOS have different V_{INS}, two extra voltage levels have to be routed over the whole chip, which consumes costly routing resources. Furthermore, as V_{INS} is far lower than the nominal technology voltages, at this lower gate driving voltage, buffer current is much lower (~44.8% lower than nominal) resulting in degradation of overall speed performance.

In our proposed technique, instead of connecting the gates of these extra devices to a fixed voltage (V_{INS}), we connect gate of nMOS to a voltage closer to nominal voltage and sweep it up as temperature increases and for pMOS, gate is connected to a voltage closer to ground and sweep it down as temperature moves up. For setting these initial voltages and moving it up or down in response to the temperature change, we propose a simple temperature sensor which locally generates these controlling voltages preventing the routing of two voltage level.

The next sections are organized as follows: in section II, temperature dependency of device and crosstalk noise is explained, our proposed method is provided in proposed methodology, section III. Section IV is arranged by crosstalk modeling and simulation result and finally we conclude in section V.

II. TEMPERATURE EFFECT

A. Temperature Effect on Device

The dependency of device drain current (I_D) on temperature can be explained by the alpha power model for short channel MOSFET [13]. I_D mainly depends on three parameters, threshold voltage V_{th}, carrier (electron or hole) mobility μ and saturation velocity in saturation region υ_{sat} [14][15]. According to [14], these dependencies can be expressed as,

$$V_{th}(T) = V_{th}(T_0) - k(T - T_0) \quad (1)$$

$$\mu(T) = \mu(T_0)\,(T_0/T)^m \quad (2)$$

$$\upsilon_{sat}(T) = \upsilon_{sat}(T_0) - h(T - T_0) \quad (3)$$

Here T_0 is the nominal temperature, $V_{th}(T_0)$, $\mu(T_0)$ and $\upsilon_{sat}(T_0)$ are threshold voltage, mobility and the saturation velocity at the nominal temperature, k is temperature coefficient of threshold voltage (~0.8mV.K^{-1}[13]) and m and h are the technology dependent temperature coefficient (is measured as 1.5~1 and 150ms^{-1}.K^{-1} respectively [15]). All these coefficients are positive [14]. That means with the increase of temperature, threshold voltage, mobility of electrons or holes and the saturation velocity (υ_{sat}) change accordingly. The effect of μ, υ_{sat} and V_{th} on drain saturation current (I_D) of the device can be shown as follows [2]

$$I_D(T) = \upsilon_{sat}(T).W.P_s.\,[V_{GS} - V_{th}(T)]^{\alpha}(1+\lambda V_{DS}) \quad (4)$$

Where, W is the device width, Ps is the technology specified constant and λ is the channel length modulation coefficient. From the equation (4), it is evident that decreased υ_{sat} reduces $I_D(T)$ while reduced threshold voltage increases drain current. As at higher supply voltage, the change in mobility and saturation dominates over change in threshold, any increase of temperature tends to decrease I_D. On the other hand, at lower supply voltage, change in V_{th} dominates, resulting in the increase of I_D with the increase in temperature. In between these two regions, there is the supply voltage where the effects of threshold voltage and mobility on drain current are same with different temperature. So I_D will neither increase nor decrease and consequently the device will be temperature insensitive. This supply voltage is called temperature insensitive point (V_{INS}) or zero temperature coefficient (ZTC). As electron and hole have different mobility, pMOS and nMOS have different values of V_{sat} and consequently different V_{INS}. The simulation result for the pMOS and nMOS in 45nm

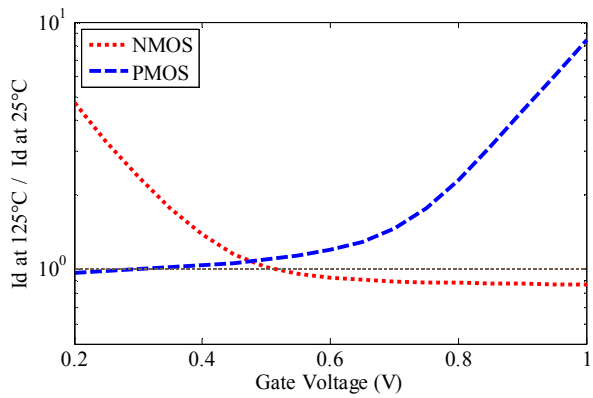

Fig. 1 Drain current dependency of temperature and gate voltage

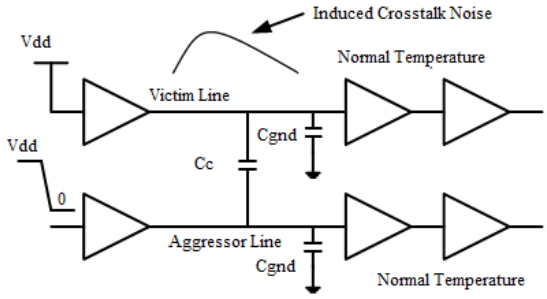

Fig. 2 Normal Crosstalk Noise

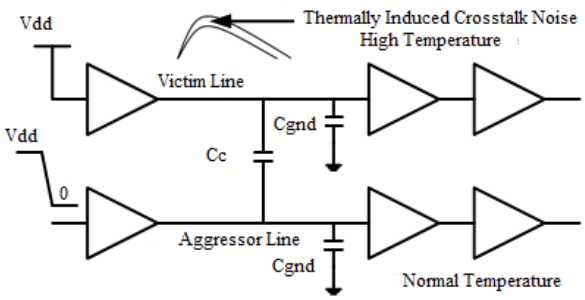

Fig. 3 Thermal Crosstalk

technology is shown in Figure 1. Where x-axis represents gate voltage and y-axis represents the ratio of drain current at 125°C and nominal temperature in logarithmic scale. In Figure 1, at lower V_{GS}, drain current ratio is more than one, indicates drain current increases with increase in temperature and this is called reverse temperature region. On the other hand, at larger V_{GS}, ratio is less than one, exhibits reverse trend in drain current, that is said to be normal temperature region. But, at V_{GS} of 0.520V for nMOS and V_{SG} of 0.680V (V_G is 0.320V) for pMOS, this ratio have a value exactly one, indicating drain current to be independent of temperature change

B. Temperature Effect on Crosstalk noise

The space between interconnect is diminishing and its width is also going down with miniaturization of CMOS circuits. But to keep interconnect resistance low, the thickness cannot be scaled down proportionately, which causes the interconnect thickness to width ratio to increase. The combination of both trends (diminishing wire spacing and increasing thickness to wire ratio) causes more parasitic.

Now, assume that aggressor is at low temperature and the victim is at higher temperature. When aggressor switches, it injects (or drain) charges to (or from) the victim which causes to generate a crosstalk induced glitch on the victim. As the victim is at higher temperature and operating at nominal voltage in Figure 3, its buffers drain current is lower than the drain current it had if it was at normal temperature. So in this case, if the aggressor switches from 0 to VDD, it injects charges to the victim and due to lower drain current victim of buffers lose its capacity to dump the excess charges, and that in turn produces an extra glitch on the victim line, generates coupling between wires. That means the switching in aggressor wire causes an undesirable glitch to its neighboring victim wire. Figure 2 illustrates how a switching aggressor causes to induce crosstalk noise to its neighboring wire (victim). When aggressor switches and victim line does not, there flows a current through the coupling capacitor due to the voltage difference between two side of the capacitor. That means aggressor injects charge to the victim when aggressor switches from Ground to VDD, which produces a positive glitch on the victim. Similarly, when aggressor switches from VDD to Ground, it drains charge from victim, producing a negative glitch. If the glitch (crosstalk noise) crosses the noise margin (VDD/2), then the subsequent logic circuit may capture a wrong value, 1 instead of 0, or 0 instead of 1, which may produce an erroneous value at the output. By increasing victim buffers size, induced crosstalk can reduce thermally induced crosstalk noise. Similarly, if the aggressor switches from VDD to 0 it drains charges from the victim and due to lower drain current of victim buffer it loses the capacity to drain charges from VDD and that in turn generates an extra temperature induced crosstalk glitch which is shown in Figure 3. And that is the reason at higher temperature the crosstalk noise boosted up by certain voltage and sometimes that is enough to cross the noise margin. That motivates us to design a temperature insensitive circuit to nullify the thermally induced crosstalk noise, which has never been noticed before.

III. PROPOSED METHODOLOGY

In this section, the technique to keep driver strength constant is explained concisely and also a new tiny temperature sensor is introduced to maintain driver strength as high as possible and also to keep the strength at constant value with temperature change.

A. Maintaining driver strength

As in (4), by controlling the gate overdrive voltage (VGS-VT) [17] transistor region of operation can be adjusted. In [12], the authors controls this gate overdrive by inserting an extra controlling device as shown in Figure 4 and adjusted its gate to tune V_{GS}. The simulation results, shown in Figure5 and Figure 6, explain how adjusting the gate voltages, temperature insensitivity can be achieved. The Y-axis of these figures represents the drain current ratio of the device at

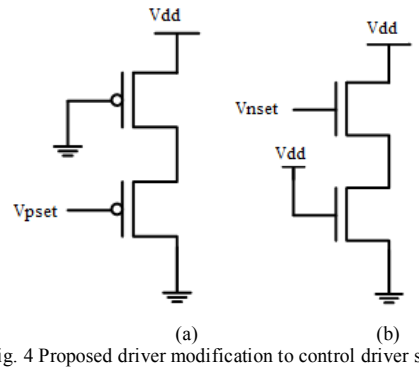

Fig. 4 Proposed driver modification to control driver strength

operating temperature to the drain current at 25°C. At V_{nset} of 1.0V and V_{pset} of 0.0V, this ratio exhibits a negative slope, indicating a decreasing trend in drain current as temperature increases. On the other hand, at V_{nset} of 0.350Vand V_{pset} of 0.700V this ratio has a positive value, which implies increased drain current at higher temperature. For V_{nset} of 0.520V and V_{pset} 0.320V this ratio shows a near zero value, indicating insensitivity to temperature change, and these values of V_{nset} and V_{pset} are referred as temperature insensitive voltage (V_{INS}). In [12], the authors use these values V_{INS} to make the buffer temperature insensitive. But as these V_{INS} are far away from the nominal supply voltage, the device drain current is lower which degrades the speed performance.

In our work, instead of connecting gate to a fixed V_{INS} as in [12], we propose to change the gate controlling voltage with change in temperature as shown in the inset figure of Figure 5 and Figure 6. Drain current decreases with increased temperature, at nominal supply voltage. Sweeping up the gate voltage of nMOS controlling device and sweeping down the gate voltage of pMOS controlling device with temperature rises, allow these devices to flow more current to compensate the reduced drain current at higher temperature. So, by setting V_{nset} at higher value than V_{nINS} and moving it up and also by setting V_{pset} at lower value than $V_{pINS,}$ and moving it down, with increase in temperature, we can make drain current constant of the device. Thus, temperature resilient buffer is achieved. For setting and sweeping the V_{nset} and V_{pset}, we propose a simple temperature sensor that dynamically adjust its generated voltage according to the requirement of controlling devices to keep its drain current constant

B. Proposed Temperature Sensor

Gate-source voltage of a diode-connected MOS transistor biased with a constant current exhibits a temperature dependency [18]. By controlling the drain current and the W/L ratio of the device, sensitivity of the generated gate-source

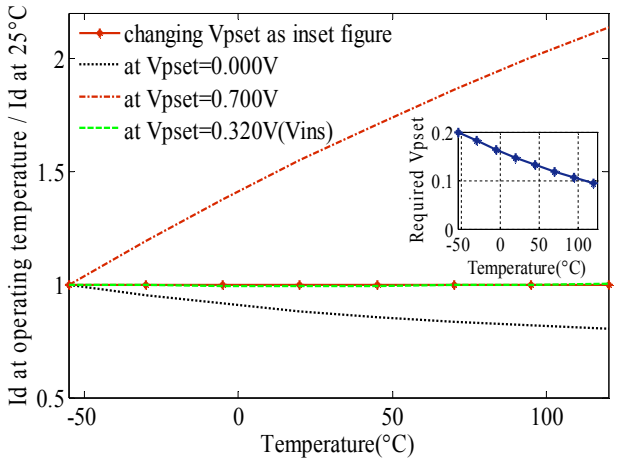

Fig. 5 Controlling temperature sensitivity for pMOS by Vpset

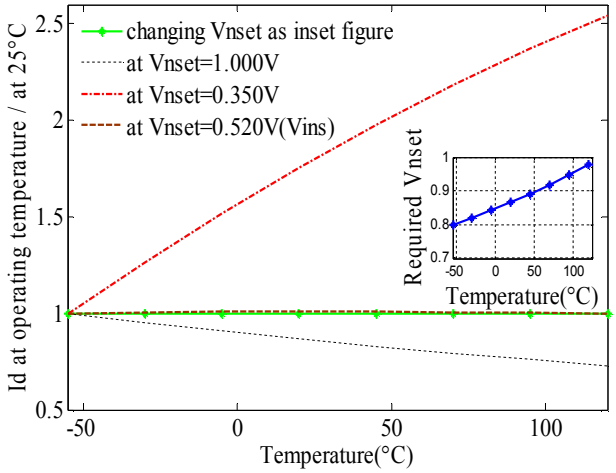

Fig. 6 Controlling temperature sensitivity for nMOS by Vnset

voltage (mV/°C) can be well controlled [17]. In our temperature sensor, resistor R1 forms the reference current and transistor M1 forms the diode connected load. The generated gate source voltage of M1, which is set to have negative sensitivity (-mV/°C), is feed to the pMOS (M2). As the pMOS(M2) drain current increases when its gate voltage is reduced. So combination of R1, M1 and M2 forms a high temperature sensitive current source.

Finally, load resistance R2 converts this current to voltage that generates the required V_{nset}. By adjusting the values of R1, R2, W/L ratio of M1, and width of M2, we set the value of V_{nset} at 25°C as 0.878V with sensitivity of 1.07mV/°C. Similarly, the values R3, R4 and W/L ratio of M3, and width of M4 is adjusted, which give V_{pset} as 0.167V at 25°C with sensitivity of -0.08mV/°C.

IV. CROSSTALK MODELLING AND SIMULATION RESULT

To analyze the temperature effect on crosstalk and to show the effectiveness of our proposed method, we consider two

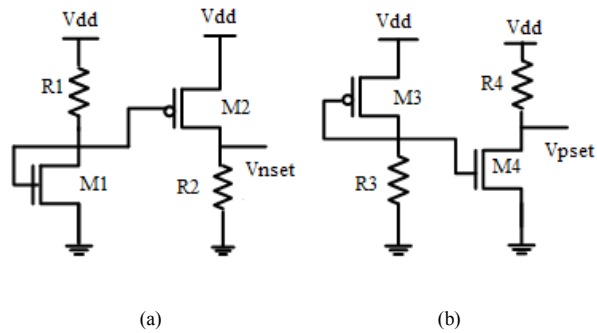

Fig. 7 Proposed temperature sensor to generate (a)Vnset (b)Vpset

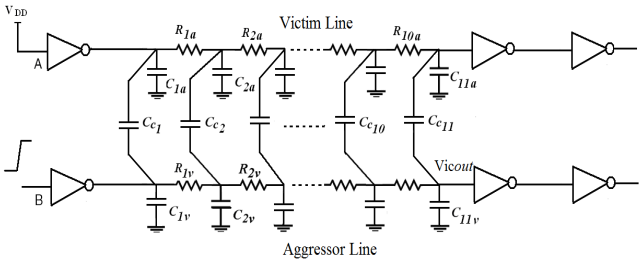

Fig. 8 Simulation setup for crosstalk noise calculation

intermediate wire in 45nm length of 500µm running parallel to each other, with dimension of width and spacing 0.14 µm, thickness is 0.35 µm [19] and modeled 10-π for interconnect [20]. For modeling the driver we have used 45nm technology model card from [19] and also performed our simulation on HSPICE. The value of interconnect resistance, capacitance and mutual capacitance is calculated from [21]. We have used V_{DD} of 1.0v, which is nominal voltage for 45nm technology. Figure 8 Shows the HSPICE implementation of our model.

A. *Crosstalk noise modelling*

To illustrate the effect of temperature on crosstalk, we have applied a step pulse at the input of aggressor buffer and victim driver input is kept at V_{DD} as shown in Figure 8. The voltage glitch that induces at the input of the second buffer in Figure 8 on the victim line, is the crosstalk noise. This crosstalk noise is measured for different driver size and also for two different temperatures (25°C and 125°C) in victim line keeping normal temperature (25°C) at aggressor and the result is shown in Figure 8, which shows that, with the gradual increase in driver size, crosstalk noise increases and also the application of high temperature (125°C) on victim line instigates the crosstalk noise. When aggressor switches, it

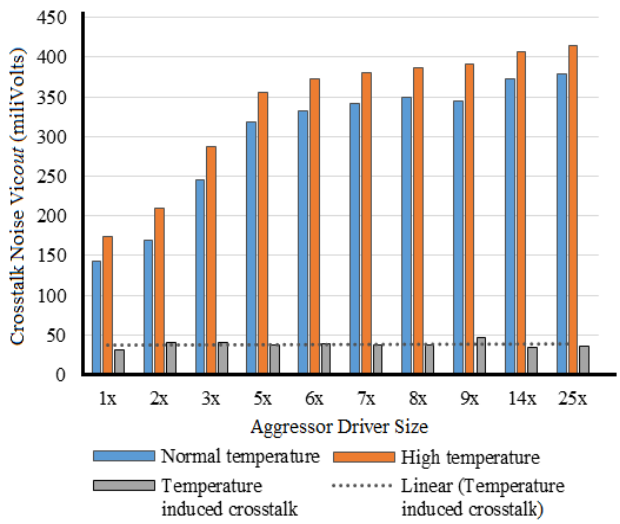

Fig. 9 Comparison of normal crosstalk noise and thermally induced crosstalk noise

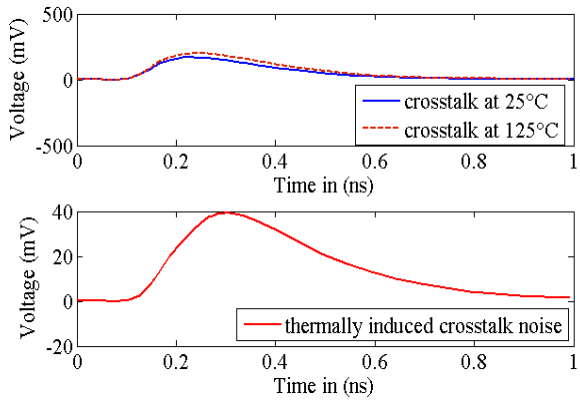

Fig. 10 High temperature and Thermal induced crosstalk at victim m node for 2x aggressor driver size

induces crosstalk noise on victim line, which complicates the normal operation of VLSI circuit. If victim line stays at higher temperature, it gets more susceptible to crosstalk due to its reduced current. As a result, more noise will be induced in high temperature. According to our simulation, thermally induced crosstalk noise remains unchanged with the change of aggressor driver sizing, which is depicted also in Figure 8. As a consequence, thermally induced crosstalk doesn't depend on driver sizing, which is treated to be the most viable approach to mitigate crosstalk noise, i.e. increasing victim driver size, it will reduce crosstalk but thermally induced crosstalk noise will remain undiminished.

B. *Mitigation of thermally Induced Crosstalk*

Figure 10, shows the simulation result for original buffer with 2X driver size for both aggressor and victim, when both the aggressor and victim are at 25°C, the crosstalk induced noise has value of 165mV, but when the victim is at higher temperature at 125°C, due to its reduced driving strength, the induce noise grows to a value of 205mV. This extra 40mV of induced noise is due to the higher temperature at victim line and that is thermally induced crosstalk noise.

Figure 11 shows the result of applying the technique proposed in this work. In our proposed method, both the aggressor and victim is first set at 25°C and V_{nset} and V_{pset} of both the aggressor and victim are connected to 878mV and 147mV respectively. As the victim temperature starts to increase, it starts to loss its capacity to mitigate the imposed extra charge due to switching aggressor. To keep its strength same at higher temperature, V_{nset} is swept up and V_{pset} is swept down. When the victim line is at 125°C, its V_{nset} is set to 985mV and V_{pset} is set to 90mV to maintain same strength as it was at 25°C. The result shows a significant reduction of thermally induced crosstalk noise. By using our technique we can limit it to 6mV whereas it was 40mV for original buffer. So our proposed method can reduce 85% thermally induced crosstalk. This success rate varies for other driver sizes because it actually depends on the temperature sensor's output. Our sensor can't

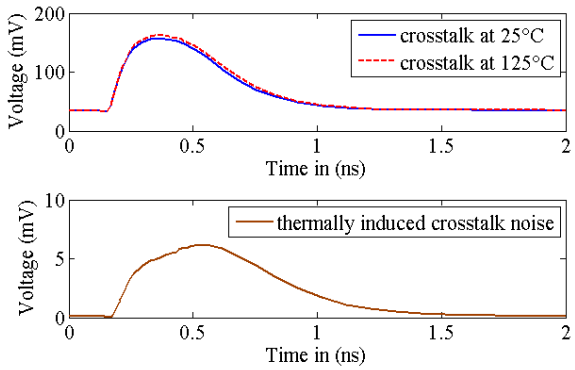

Fig. 11 Mitigation of thermally induced Crosstalk Noise

make exactly the required V_{pset} and V_{nset}. But they give an output which has 5-10% error rate. However, for instance in 3x and 4x driver size, it mitigates 86.5% and 82.9% thermal crosstalk and on an average it mitigates 85% noise successfully.

V. Conclusion

In this proposed method, the effect of on-chip temperature on crosstalk noise, has been encountered in intermediate layer of VLSI interconnect. Simulation has been made using the distributed RC model of interconnect in 45nm technology. We substantiated thermally induced crosstalk as a threat and we can tarnish this threat by controlling the gate voltage and maintaining the driver strength constant with the change of temperature profile at victim line. According to our solution, temperature sensors sense the temperature profile and give the required gate voltage for dynamically adjusting the buffer strength or drain current to a constant value. Our method demonstrates a reduction of 85% of thermally induced crosstalk noise from the victim line. In the future, this same methodology can be applied to reduce the temperature induced clock skew in clock tree for global interconnect.

References

[1] S. Dubey, and J. Jorgenson, "Crosstalk reduction using buffer insertion," in *Proc. IEEE Int. Symp. Electromagnetic compatibility*, Aug. 2002, vol. 2, pp. 639-642.

[2] S. Dubey, and J. Jorgenson, "Crosstalk reduction using buffer insertion," in *Proc. IEEE Int. Symp. Electromagnetic compatibility*, Aug. 2002, vol. 2, pp. 639-642.

[3] I. H. R Jiang, Y. W. Chang and J. Y. Jou, "Crosstalk-driven interconnect optimization by simultaneous gate and wire sizing," *IEEE Trans. Computer-Aided Design of Integrated Circuits and Syst.,* vol. 19, no. 9, pp. 999-1010, Sep. 2000.

[4] C. J. Alpert, A. Devgan, and S. T. Quay, "Buffer insertion for noise and delay optimization," *IEEE Trans. Computer -Aided Design of Integrated Circuits and Syst.*, vol. 18, no. 11, pp. 1633-1645, Nov. 1999.

[5] J. Zhang, and E. G. Friedman, "Crosstalk modeling for coupled RLC interconnects with application to shield insertion," *IEEE Trans. VLSI systems,* vol. 14, no. 6, pp. 641-646, May, 2010.

[6] G. Fattah and N. Masoumi, "Crosstalk in VLSI partially coupled interconnect structures, a comprehensive evaluation," in *Proc. 15th IEEE Workshop Signal Propagation on Interconnects,* May 2011, pp. 15-18.

[7] S. Borkar, T. Karnik, S. Narendra, J. Tschanz, A. Keshavarzi, and V. De, "Parameter variations and impact on circuits and microarchitecture," in *Proc. ACM 40th annual Design Automation Conference*. June, 2003, pp. 338-342.

[8] (2010) Fundamentals of Electrical Engineering and Electronics [Online]. Available at http://www.vias.org/feee/conduct_07.html.

[9] T. Ragheb, A. Ricketts, M. Mondal, S. Kirolos,G. M. Links, V. Narayanan, and Y. Massoud, "Design of thermally robust clock trees using dynamically adaptive clock buffers," *IEEE Trans. Circuits and Systems I,* vol. 56, no. 2, pp. 374-383, Feb. 2009.

[10] A. Calimera, E. Macii, M. Poncino, and R. I. Bahar, "Temperature insensitive synthesis using multi-vt libraries," in *Proc. 18th ACM GreatLakes Symp. VLSI*, May 2008, pp. 5–10.

[11] Q. Chen, M. Meterelliyoz, and K. Roy, "A CMOS thermal sensor and its applications in temperature adaptive design," in *Proc. Int. Symp. Qual. Electron*. Dec. 2006, pp. 243–248.

[12] D. Wolpert and P. Ampadu, "Exploiting programmable temperature compensation devices to manage temperature-induced delay uncertainty," *IEEE Trans. Circuits and Systems I,* vol. 59, no. 4, pp. 735-748, Apr. 2012.

[13] T. Sakurai, "Alpha-power law MOSFET model and its applications to CMOS inverter delay and other formulas," *IEEE Trans. Solid-State Circuits,* vol. *25*, no. 2, pp. 584-594. Apr. 1990.

[14] N. Arora, MOSFET Modeling for VLSI Simulation: Theory And Practice, Singapore: World Scientific, 2007.

[15] A. Calimera, R. Bahar, E. Macii, and M. Poncino, "Temperature-insensitive dual-synthesis for nanometer CMOS technologies under inverse temperature dependence," *IEEE Trans. VLSI,* vol. 18, no. 11, pp. 1608-1620, Oct. 2010.

[16] J. C. Ku, & Y. Ismail," On the scaling of temperature-dependent effects, Computer-Aided Design of Integrated Circuits and Systems," *IEEE Trans. Comput.-Aided Design Integr. Circuits Syst.,* vol 26, no. 10, pp. 1882-1888, Oct. 2007.

[17] R. Kumar and V. Kursun, "Reversed temperature-dependent propagation delay characteristics in nanometer CMOS circuits," *IEEE Trans. Circuits Syst. II Exp. Briefs*, vol. 53, no. 10, pp. 1078-1082, Oct. 2006.

[18] I. M. Filanovsky and S. T. Lim. "Temperature sensor applications of diode-connected MOS transistors." in *Proc. IEEE International Symp. Circuits and Syst.,* May, 2002, pp. II-149

[19] (2008) Predictive Technology Model (PTM). [Online]. Available: http://www.ptm.asu.edu/

[20] S. Sayil, V. K. Boorla and Yeddula, "Modeling Single Event Crosstalk in Nanometer Technologies" *IEEE Trans. Nuclear Science,* vol. 58, no. 5, pp. 2493-2502, Oct. 2011.

[21] K. Sundaresan, and N. R. Mahapatr, "Accurate energy dissipation and thermal modeling for nanometer-scale buses," in *Proc.11th IEEE Int. Symp. High-Performance Computer Archi*. Feb. 2005, pp. 51-60.

Implementation of Multi-Input Dual-Output DC-DC Boost Converter Using Renewable Energy for Hybrid Electric Vehicle

*Tanvir Ahmed, Tushar Kumar Kha,
S.M. Hasanuzzaman, Tafikul Islam, Al Islam
Dept. of Electrical & Electronic Engineering
Bangladesh University of Business & Technology
Dhaka, Bangladesh
*p_piash@yahoo.com

Md Aminul Hoque, Md. Abid Hossain
Dept. of Electrical & Electronic Engineering
Bangladesh University of Engineering & Technology
Dhaka, Bangladesh

Abstract— **In this paper, a systemic approach of multi-input-dual-output boost converter for any hybrid electric vehicle is proposed. This kind of multi-input-dual-output boost converter has immense application in hybridizing the electric vehicle efficiently. It also enables the scope of introducing the use of alternative natural renewable energy as well as the other electric potential energy instead of using the most familiar low efficient fuel used internal combustion engine.**

Keywords— Hybrid Electric Vehicle, Multi-Input-Dual-Output, DC-DC Boost Converter, Natural Renewable Energy, Hybrid Power System

I. INTRODUCTION

Climate change, the consequence of greenhouse effect has become one of the most sensitive issues among the climatologist in today's world. As the population is always on the rise, the uses of fuel, natural resources, and other energy resources are increasing. So the amount of these resources is decreasing in an uncontrolled rate. The main culprit of the greenhouse effect is CO_2, which is emitted from more than 50 percent from the conventional vehicles. Hybrid electric vehicle is familiarized now-a-days as an attractive solution in the traffic system to provide environmental friendly travelling with the uses of clean and renewable energy besides can bring the revolutionary change in the traffic system in modern world [2],[3]. In this kind of vehicle multi-input source is introduced to make the input system more reliable, efficient and environment-friendly. Plugin AC voltage, solar energy, environment-friendly fuel cell and some other regenerative energy sources are used as input and a battery is used bi-directionally for storing extra energy and supplying energy when other sources are not available. To provide a specific voltage level and control of power efficiently between input and output, a multi-level input and output converting system is needed [4]. So, a multi-input-dual-output DC-DC boost converter is proposed and investigated in this paper. In the multi-input process plugin AC voltage is introduced where a rectifier is used to rectify the AC sinusoidal voltage into DC voltage and a DC-DC buck converter is used to get the required voltage that is needed to charge the battery. The process of battery charging and AC-DC conversion is controlled by operational switches and manual push button switches. Then comes fuel cell, one of the modern and promising technologies that uses clean energy and can meet very efficiently the demand of future. As it is very costly, so our focus should be to use it as less as possible.

978-1-4673-9257-0/15/$31.00 ©2015 IEEE

II. WORKING PRINCIPLE

The hybrid electric vehicle is basically a modern type of electric vehicle that is more efficient in fuel consuming, environmental friendly and almost zero percent emission of toxic gas. Hybrid vehicle depends on more than one source as input to provide sufficient voltage efficiently at the output. To sustain the required high peak voltage in output with the variation of the low peak voltage in the input, a multi-input-multi-output DC-DC boost converter is already proposed [1]. In this paper, a new model of multi-level DC-DC boost converter is proposed, where total 4 types of different sources are included as input to provide voltage to the dual-output If "k" is denoted as duty cycle, "R" is denoted as load resistance of operational switch then the average output voltage and output current is given by[12],

$$V_a = \frac{Vs}{1-k} \tag{1}$$

$$\Delta I = \frac{Vsk}{fL} \tag{2}$$

Various kind of hybrid electrical vehicles are available in the market on the basis of their working purpose and they have different types of voltage shown in Table I [6]-[11].

Proposed multi-input dual-output DC-DC boost converter is made of 4 different input sources and 2 different outputs shown in Fig.1. Among them, in plugin AC voltage source AC voltage is rectified into DC voltage by a rectifier that is made of diode D1, D2, D3, and D4. Capacitor C1 reduces the ripple and output DC voltage is found across resistor R1.High peaked DC voltage is converted into 9-volt DC by buck converter made of operational switch Op_Sw1, diode D5, inductor L1, and capacitor C2 in order to charge up the 9-volt DC battery. The converted output is found across the resistor R2.The main function of plugin AC is to just charge up the battery. Then comes fuel cell, a very promising technology that supplies also 9 volts into the circuit as a second input

source. Thirdly comes battery that is charged up dually by solar cell and plugin AC voltage source and after charging up, it supplies the necessary voltage to the circuit. Diode D6 protects the circuit and other sources from the reverse current of the battery. Finally comes the solar cell which produces 9 volt, can simultaneously charge the empty 9-volt battery and also feed the necessary voltage to the running vehicle.

All the inputs need to be boosted up and hence DC-DC boost converter is introduced here [5]. The boost converter boosts to 24 voltage DC and 72 voltage DC from 9-volt DC. The boost converter for 24-volt output is made of operational switch Op_Sw2, Diode D8, Capacitor C3 and inductor L2. The capacitor C3 holds the voltage and helps to boost up the charge, the operational switch controls the duty cycle and diode D7 protects the other parts excluding the boost circuit from the reverse current of the boost converter. The boosted output is found across the resistor R3. Similarly, the boost converter for 72-volt output is made of operational switch Op_Sw3, Diode D10, Capacitor C4 and inductor L3. The capacitor C4 holds the voltage and helps to boost up the charge, the operational switch controls the duty cycle and diode D9 protects the other parts excluding the boost circuit from the reverse current of the boost converter. The boosted output is found across the resistor R4.

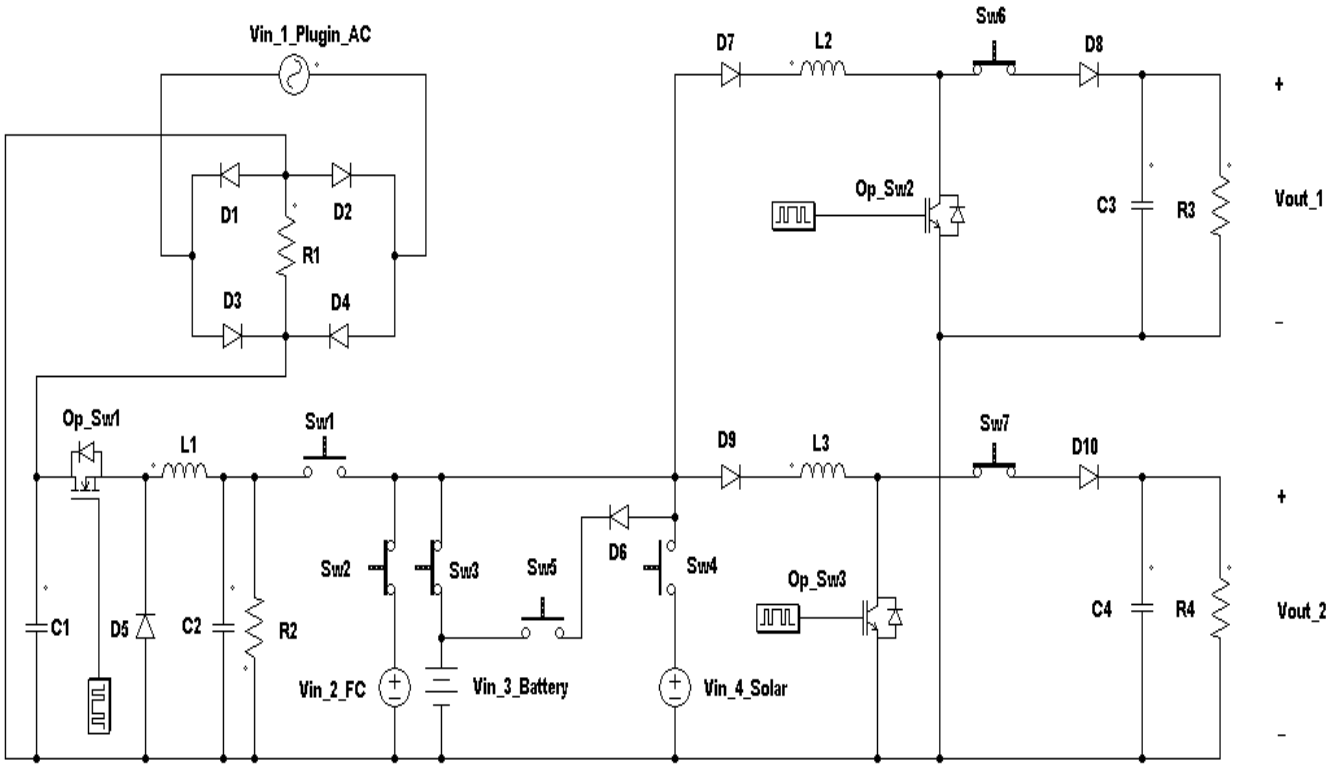

Fig. 1. Multi-input dual-output DC-DC boost converter.

TABLE I. DIFFERENT VEHICLE VOLTAGE

Sl. No	Model/Type	Battery Voltage Range (Volt)
1	Renault Twizy	12 & 400
2	Toyota Pirus PHEV	12 & 650
3	Honda Accord PHEV	12 & 320
4	Mitsubishi Outlander PHEV	12 & 300
5	Tesla Cars	250-425
6	S S Limited	12 & 48
7	Golf Car	12 & 48
8	Street Legal	12 & 48
9	People Mover	12 & 72
10	Off Road Riding or Hunting	12 & 48
11	Industrial or Commercial	12 & 72

III. Operation Mode

The modes are divided mainly into three types- full stop mode, a partial active mode where only 24 voltage is active and finally the fully active mode where both 24 and 72 voltage outputs are active. Various kinds of situations may arise with a hybrid electric vehicle in these modes. Some important situations are described here.

A. Full Stop Mode

This is also known as battery charging mode and here dual outputs are inactive through switch Sw6 and Sw7 and case wise input source switches are ON for charging the battery and also others remain OFF. Battery charging line is ON

through switch Sw5 and diode D6 protects the other elements from battery reverse current.

- Case 1: When electricity, solar and fuel cell are available then the battery is charged by electricity and solar through switch Sw1 and Sw4 and operational switch Op_Sw_1 is in operation for getting charged by electricity. Proposed circuit is shown in Fig. 2.

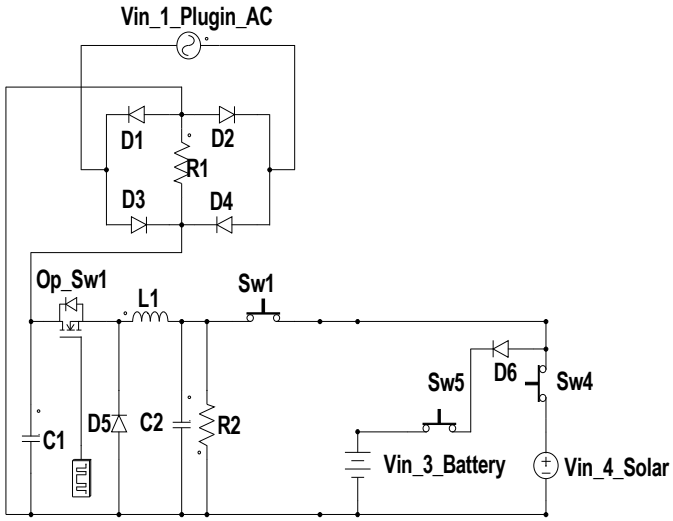

Fig. 2. The battery is getting charged by electricity and solar.

- Case 2: When electricity and fuel cell are available then the battery is just charged up by plugin AC voltage through switch Sw5. Proposed circuit is in Fig. 3.

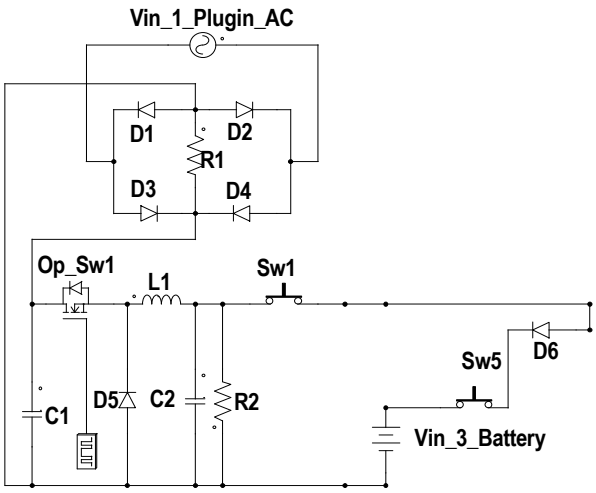

Fig. 3. Battery is charged by electricity.

B. *Partially active Mode (Only 12 V required)*

In this case, only 24-volt output is active through switch Sw6 and operational switch Op_Sw_2 is in operation. Case wise input source switches are on and others remain off. The 24-volt boost up process from 9 volt is achieved by inductor L2, diode D8, capacitor C3. Outputs are found across resistor R3 and diode D7 protect the other elements of the circuit from the reverse current.

- Case 1: When battery, electricity, solar and fuel cell are available then the output is powered by the solar cell through switch Sw4. Proposed circuit is given in Fig. 4.

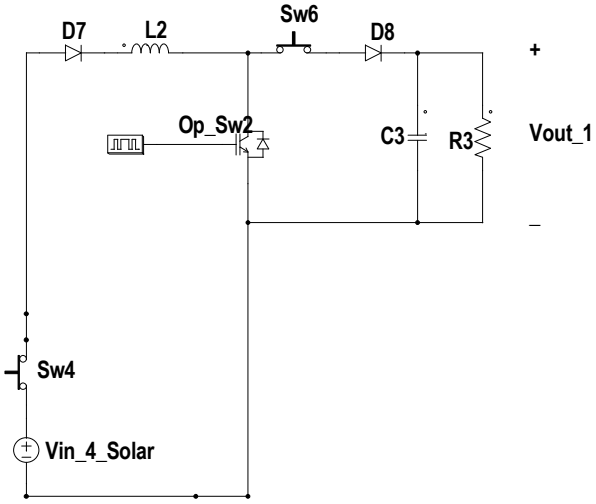

Fig. 4. Output is powered by solar cell.

- Case 2: When battery and fuel cell are available then output is powered by battery through switch Sw3. In this mode, the output 24 volt is powered by battery. Proposed circuit is given in Fig. 5.

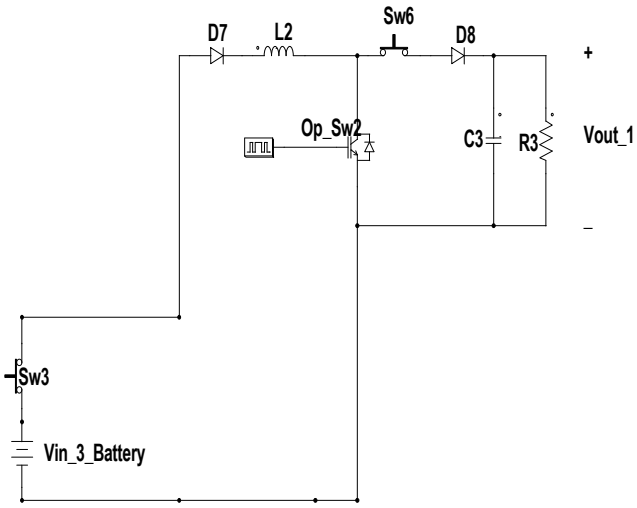

Fig. 5. Output is powered by battery

C. *Fully active Mode*

Dual outputs are active through switches Sw6 and Sw7 in this mode and operational switches Op_Sw_2 and Op_Sw_3 are active, case wise input source switches are on and others remain off. The 24-volt and 72-volt boost up process from 9-volts are achieved respectively by inductor L2, diode D8, capacitor C3 and inductor L3, diode D10, capacitor C4.

Outputs are found across resistor R3 and resistor R4. Diode D7 and diode D8 protect the other elements of the circuit from the reverse current.

- Case 1: When battery, solar and fuel cell are available outputs are powered by solar cell through switch Sw_4. Proposed circuit is given in Fig. 6.

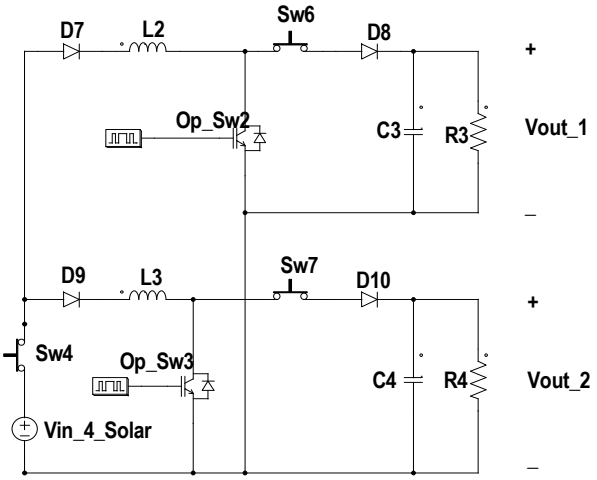

Fig. 6. Outputs are powered by solar cell.

- Case 2: When solar and fuel cell are available and the battery is empty then outputs are powered and battery is charged by the solar cell through switches Sw4 and Sw5. Battery switch Sw5 is off after charging and outputs are powers by solar cell through switch Sw4. Proposed circuit is given in Fig. 7.

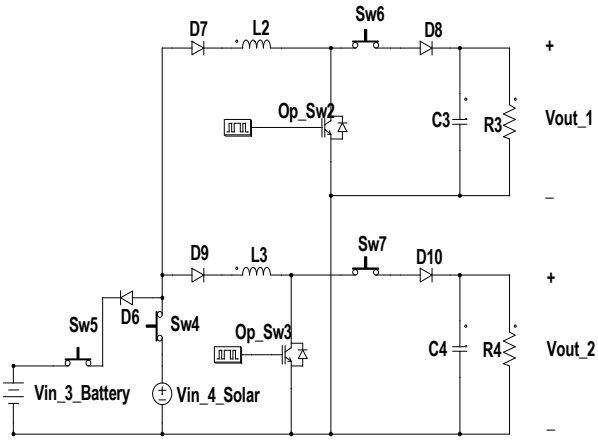

Fig. 7. Outputs and battery are powered by the solar cell.

IV. PERFORMANCE PARAMETER

In order to verify the performance of the proposed converter simulation have been done for the fully active mode with the battery is fully charged and solar and fuel cells are available by PSIM software. The input solar voltage is considered as 9 volt and outputs are desired to be 24 volt and 48 volt. Switches Sw4, Sw6 and Sw7 are active besides operational switches Op_Sw_2 and Op_Sw_3 are in operation mode. The output voltage and current curves are shown in Fig. 8 and data of the performance parameters of both outputs are given in Table II.

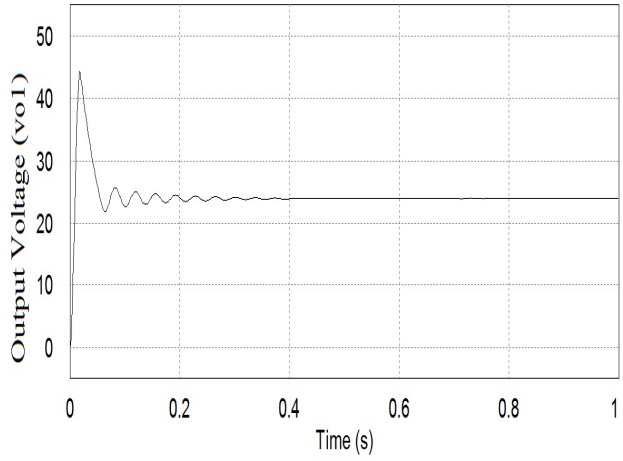

(a)

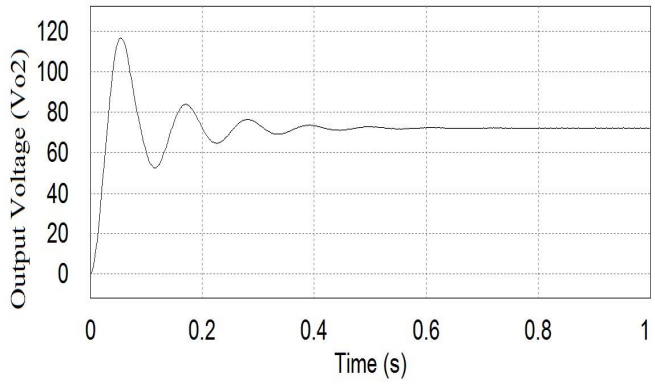

(b)

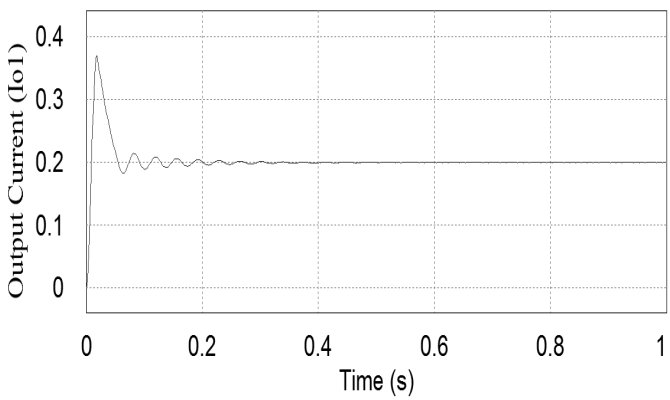

(c)

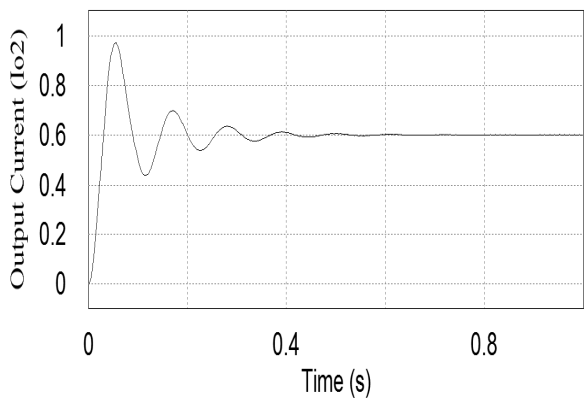

(d)

Fig. 8. Output voltage of converter (a) Vo1 (b) Vo2 and Output Current of the converter (c) Io1 (d) Io2

TABLE II PERFORMANCE PARAMETERS FOR BOTH OUTPUTS.

Performance Parameters	Vo1 (24 Volt)	Vo2 (72 Volt)
Delay time, t_d	6.67 ms	19 ms
Rise time, t_r (10% to 90%of its final value)	6.05 ms	19.85 ms
Peak time, t_p	18 ms	54.89 ms
Settling time, t_s	209 ms	440 ms
Percentage of overshoot, PO%	83.33 %	61.8 %

The transient performance can be significantly improved if concepts of control theory can be applied. For instance, an appropriate PID controller can be designed to decrease the percentage of overshoot as well as other parameters such as rise time, settling time, delay time etc. As far as the final value is concern, the system makes almost zero steady state error.

V. Research Limitation

The improvement of HEV design over conventional vehicle is largely on converter efficiency. To verify the optimal design of vehicle converter circuit, validation using costly prototype is expensive and sometimes impractical. PSIM simulation is a method for fast and systematic investigation of different design options and configurations, including the choice of various types of battery, transmission, fuel cells, renewable fuel sources, etc. as well as their parameters. Therefore, simulation based analysis on vehicle performance is both useful and crucial to the development of new hybrid vehicles. At present, the available vehicle simulation tools cannot support the modeling and analysis of all vehicle design options, rather than focusing on very specific applications. Considerable work is needed to introduce more capable and reliable converter modeling and simulation tools to guide new hybrid vehicle design.

VI. Future Prospects

The research forms the foundation for further studies on the modeling and analysis of advanced hybrid vehicle converter configurations using advanced modeling and simulation tools. The preliminary studies on renewable hybrid power system for elevating power backup system; the three mode hybrid vehicle converter configuration; and the use of PSIM to model complex hybrid vehicle converter design and thus provide promising research directions that deserve further study.

VII. Conclusion

A multi-input-dual-output DC-DC boost converter is proposed for hybridizing the input power source and furthermore can be used in transferring energy between different energy resources such as electricity, fuel cell, solar and energy storage system such as battery in this paper. Battery is used power source and energy storage system dually. This converter also can be used as single input single output converter as well as the multi-input-multi-output DC-DC boost converter. The converter have three main operation mode, full stop mode, partial active mode where 24 voltage is active and fully active mode where both 24 and 72 voltage are active. It is seen that under different conditions when the resources are not available to feed the sufficient voltage in the input, a microcontroller sensor is used and applied here that senses the instant intensity and availability of resources and changes the duty cycle of the operational switches that is made of IGBT to sustain the fixed level output voltage. It could be practically verified but shortage of resources and software older version, it has not possible yet. As it emphasizes the use renewable energy, the proposed circuit can be thought to be more efficient than others in the sense.

VIII. References

[1] Nahavandi A., Hagh M.T., Sharifian M.B.B., Danyali S., "A Nonisolated Multiinput Multioutput DC–DC Boost Converter for Electric Vehicle Applications" Power Electronics, IEEE Transactions vol. 30,Issue no. 4, pp. 1818 - 1835, May.2014

[2] X. Zhang, C. Mi, "Vehicle Power Management", springer, 2011.

[3] M. Ehsani, Y. Gao, A. Emadi, "Modern Electric, Hibrid electric and Fuel Cell vehicle Fundamentals, Theory and Design", second edition, CRC Press, New York, 2010.

[4] T. Bhattacharya, V. S. Giri, K. Mathew and L. Umanand, " Multiphase Bidirectional Flyback Converter Topology for Hybrid Electric Vehicle" IEEE Trans. Industrial Electron, vol. 56, no. 1, pp. 78-83, January. 2009.

[5] Hasaneen, B.M. and Mohammed, A.A.E.; "Design and simulation of DC/DC boost converter", Power System Conference, 2008. MEPCON 2008. 12th International Middle-East

[6] Renault Twizy Electric Vehicle. Available at: http://www.sevcon.com/renault-selects-sevcon-to-provide-controllers-for-twizy.aspx

[7] Toyota Pirus Hybrid Vehicle Dismantling Manual , Available: https://techinfo.toyota.com/techInfoPortal/staticcontent/en/techinfo/html/prelogin/docs/priusphvdisman.pdf

[8] Emergency Response Guide of Honda Accord, Available: https://techinfo.honda.com/rjanisis/logon.asp

[9] Mitsubishi Outlander PHEV 2013 New York International Auto Show, Available:http://media.mitsubishicars.com/releases/b3d9a889-c5c2-4f5b-abca-32c6babfe042

[10] Tesla Motors, Power Control, Available: http://my.teslamotors.com/roadster/technology/power-electronics-module

[11] Star electric Vehicle Website , Available at: http://www.starev.com

[12] Muhammad H. Rashid, "Power Electronics: Circuits Devices and Applications." 3rd edition, Pearson Education, 2007, Chapter 5.

Artificial Neural Network based Soft-Starter for Induction Motor

Tuton Chandra Mallick, Sharith Dhar
Department of Electrical & Electronic Engineering
Premier University
Chittagong, Bangladesh

Jubaer Khan
Department of Electrical & Electronic Engineering
Chittagong University of Engineering & Technology
Chittagong, Bangladesh

Abstract— **the necessity of soft-starter is increasing day by day to reduce the starting current & to maintain the torque smoothly according to the load requirement. Now intelligent soft-starter is developed to improve the performance of conventional starter. This paper focused on the designing of an artificial neural network controlled soft-starter. Back-propagation algorithm is used as learning algorithm in the artificial neural network. Error correcting capability of this learning algorithm makes it more suitable to use in neural network. For comparative performance analysis two different types of back propagation algorithms are used in the neural network learning process. According to condition of learning rate parameter gradient descent with momentum back-propagation algorithm provide better response. A comparative study between conventional starting method (Direct on Line) and proposed soft-starter. Artificial Neural Network controlled soft-starter is able to reduce starting current compared with DOL method & able to accelerate the load at starting period efficiently compared with star-delta starting method.**

Keywords—ANN, Soft-starter, back-propagation etc.

I. INTRODUCTION

In recent years with the development of the industrialization and the need of electrical system for manufacturing processing of the goods are taking more attention for use of efficient & easy controllable equipment. Electrical machine are one of the most common in industries. Induction motor (IM) is replacing the traditional motor like DC or Synchronous motor due to their features like low cost, rigid construction & easy control mechanism in the industrial processing. Controlling their speed, torque & current are taking much more attention in the research and development. Today's Induction motor starting is the most challenging task. The starting process of induction motor effects on the entire power system adversely. Due to the rapid technological progression the application of the power electronic devices & AC drives are increasing day by day. To maintain the power system quality, appropriate starting technique should be used otherwise electrical network fluctuation may be occurred which affects the all running electrical & electronic devices that are connected to the victim power system. During the choice of starting methods some factors need to be considered which are inrush current, torque, voltage dip, acceleration time, frequency dip, robustness, cost, reactive power & starting power factor [1]. There are different types of starting techniques such as Primary resistor, Star-delta, Auto transformer etc. [1]. These starting techniques are not enough to reduce the inrush current [6]. To overcome this problem soft starter becomes useful to start up the motor smoothly. The torque can be adjusted according to the condition of loading [5]. Today it is needed to start motor more smoothly according to the variation of the load in order to avoid unwanted situation. Although soft starter performs better than conventional starting systems to start motor smoothly, it has also some drawbacks that makes it imperfect to the application where smooth starting with different loads is the big concern. To overcome the problems of conventional soft- starter, intelligent soft-starter is being used. The intelligent soft-starter should have the ability to adapt to a new environment & to changes in the current environment, the ability to acquire knowledge from the environment, capacity for reason & abstract thought, ability to evaluate & judge [7]. The features mentioned above makes the soft-starter intelligent to start motor so smoothly with variation of loads that desired response can be achieved without any mechanical hazards.

The big revolution in the control scheme comes with the application of intelligent algorithms in the control system. Soft-starter of an Induction Motor (IM) using Neural Network (NN) based Feedback Estimator can control the inrush current & adjust the firing angle of thyristor for a specified load. This ANN based controller have two inputs (torque & speed) & single output (firing angle) [3]. Soft starting of an induction motor using adaptive neuro-fuzzy inference system reduces the inrush current & vibrations in the output torque. This controller uses artificial neural networks (ANN) & adaptive neuro-fuzzy inference system (ANFIS) based intelligent techniques for the selection of the firing angle of the thyristor of the voltage controller fed induction motor and moreover the speed characteristics is not good enough compare to reference speed [2]. Soft-starting of induction motors using ANN & adaptive neuro-fuzzy inference system uses ANN estimator to adjust the firing angle of thyristors of AC voltage controller under different loading conditions. This soft-starting system eliminates pulsations in the developed torque & controlled inrush current significantly [4].

978-1-4673-9257-0/15/$31.00 ©2015 IEEE

II. NN BASED INTELLIGENT SOFT-STARTER

Our developed system composed of five main parts which are supply unit, thyristor unit, synchronizationunit, syncronized pulse generator & artificial neural network controller. Fig.-1 shows the design flowchart. Six back to back thyristors are fired by a pulse generator. The thyristor unit is placed between the supply and Induction Motor. A synchronization unit gives the information about the supply voltage's phase and frequency according to which thyristors gets fired. The Artificial Neural Network (ANN) Controller gives the gate delay to pulse generator. According to the control signal the power flow to the motor is controlled hence the starting current is reduced. We used artificial neural network based controller that makes the soft-starter intelligent.

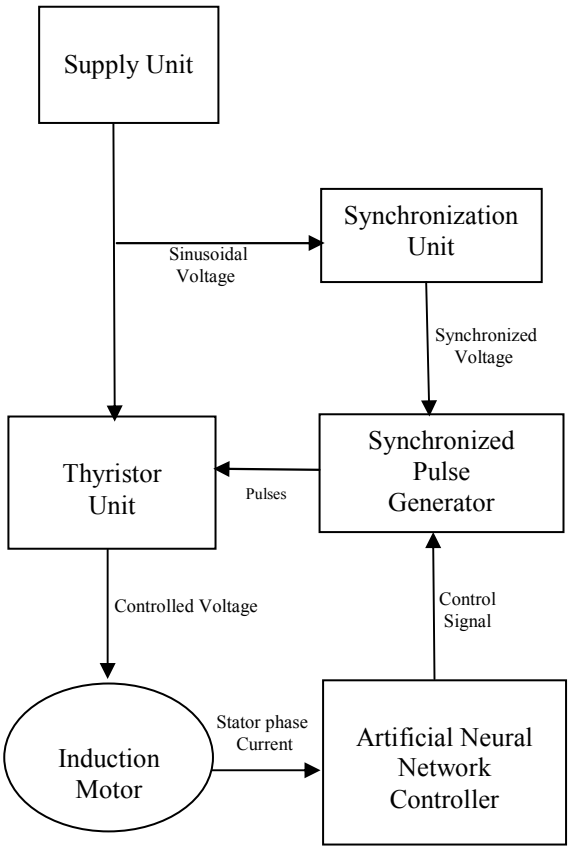

Fig. 1. Functional Representation of the control process.

A. Supply Unit

We used three AC voltage source for three phase supply each have 330V peak amplitude that provide 233V r.m.s phase to neutral voltage. The three phase supply unit is given in figure-2.

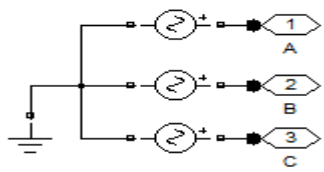

Fig. 2. Simulation model of three phase supply unit.

B. Synchronization Unit

The function of synchronization unit is to provide three line to line synchronization voltages for synchronized pulse generator. These synchronization voltages are made from supply end by building delta loop with using voltage measurement blocks. The output voltages of the

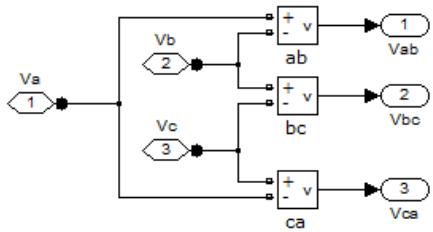

synchronization unit are connected to the six synchronized pulse generator. The simulation model of synchronization unit is shown in figure-3

Fig. 3. Simulation model of synchronization unit

C. Synchronized Pulse Generator

The synchronized pulse generator produces gate pulses for thyristor unit; pulses are generated alpha degree (delay angle) after the increasing zero crossing of the thyristors commutation voltages. The thyristor unit consists of six back to back thyristors shown in Fig.4. We configured our pulse generator to function in double pulsing mode & 60 degrees pulse width. In double pulsing mode, two pulses are provided for each thyristor; after reaching delay angle (alpha degree) the first pulse is sent, then 60 degree later the second pulse is sent.

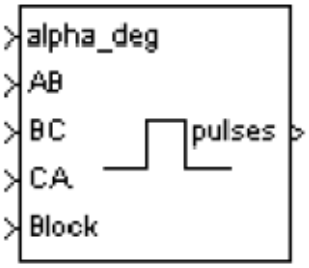

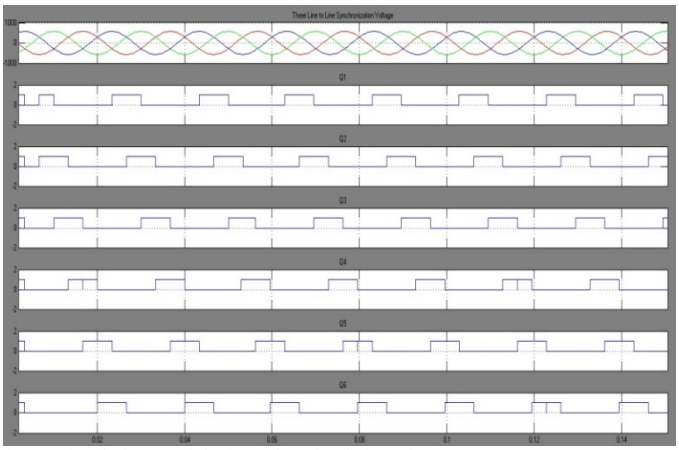

Fig. 4. Simulation model of synchronized six pulse generator
Fig. 5. Generated six gate pulses for 'traingda' training function by the synchronized 6 pulse generator.

It is important to note that, the delay angle (alpha degree) of the pulse generator is supplied from the intelligent controller. The intelligent controller controls the starting voltage & current by providing appropriate delay angle. The simulation model of the six pulse generator is shown in figure-4. Figure-5 shows Generated six gate pulses for 'traingda' training function by the synchronized 6 pulse generator.

D. Thyristors Unit

This unit consists of three pairs of back to back thyristors. Each pair of back to back thyristor is connected in series with single phase supply; other end of back to back thyristor connection is connected in series with motor terminal.

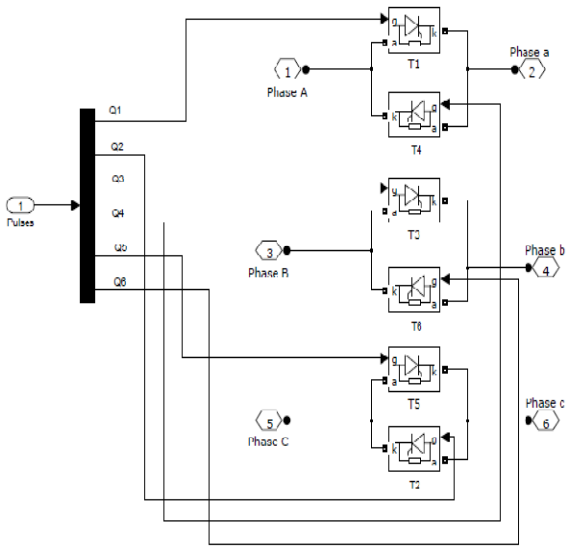

Fig. 6. Simulation model of three pairs of back to back thyristors

Figure-6 shows the back to back connection of six thyristors. The gate pulses of the thyristors are provided by synchronized six pulse generator that describes previous section. The thyristor is a semiconductor (power electronics) device that can be turned on via a gate signal (gate pulses). The series snubber circuit is connected in parallel with each thyristor. The value of snubber resistance (Rs) is set to 500ohm & snubber capacitance (Cs) is set to 250e-9F. Snubber circuit has been used to give a dv/dt protection.

E. Nerural Network Controller

During starting period, intelligent controller provides delay angle of α = 30.06 degree; pulses are generated after zero crossing of the line to line voltages. This delay angle (α = 30.06) is constant for 0 to 0.05 second, then from 0.05 to 0.1 second the delay angle α = 22.35 degree remains constant, α = 21.11 degree is constant for time 0.1 to 0.15 second; α = 25.31 degree is constant for 0.15 to 0.2 second & so on. According to these delay angles, the gate pulses are shifted & according to these gate pulses the thyristors are fired. Figure-7 shows the control signal (delay angel) generated by ANN controller.

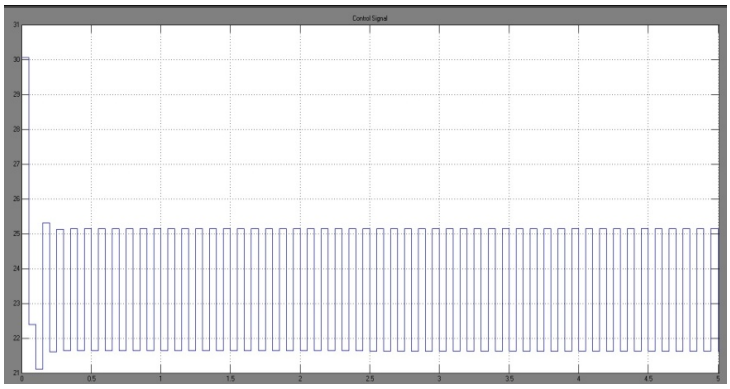

Fig. 7. Control signal (delay angle) generated by NN controller.

III. ARTIFICIAL NEURAL NETWORK

Artificial neural network' formed in a manner based on biological neural network. Basically the artificial neural network is the mathematical model or the computational model consists of artificial neurons where neurons are interconnected in a group. Biological neural network consists of real biological neurons which are connected according to the information supplied through in the nervous system; in the area of neuroscience they are formed groups that perform a particular physiological task. On the other hand, artificial neural network made up of interconnecting artificial neurons which have the properties of biological neurons. In the artificial neural network, information processing is done by the connectionist that approach to computation. Artificial neural network may change its construction external or internal way that flow through the network during learning period. We used 'model reference control' neural network

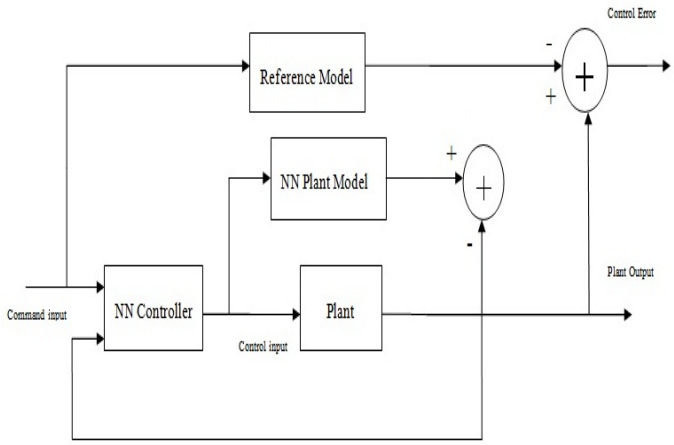

toolbox from MATLAB which act as an artificial neural

Fig. 8. Internal connection between NN controller network & plant model network.

network based controller. The controller structure uses two neural networks one is controller network & other is plant model network. Figure-8 indicates the internal connection between two networks. At first, plant models is identified. Neural network plant model is created on the basis of plant model's input-output characteristics then NN plant model is trained so that it can predict future plant output. In the NN controller, a set of output data is generated for reference model After that the controller is trained such a way that the plant output follows the reference model. On the basis of following characteristic, the NN controller generate control signal which is connected to the soft-starter as 'delay angle'. The NN plant model & NN controller both have three layers; one of them is input layer and other two are hidden layer & output layer. There is an option to select number of neuron to use in the hidden layers. For training artificial neural network plant model, a training function named 'traingda' has been used which is a gradient descent with adaptive learning rate back propagation algorithm that updates weights & bias values according to the gradient descent with adaptive learning rate [8]. For training the controller we used training function 'trainbfgc' (BFGS quasi-Newton back propagation). It is a network training function that updates weight and bias values according to the BFGS quasi-Newton method [8].

IV. SIMULATION

A MATLAB based simulation model has designed to simulate the ANN controlled soft-starter. In this simulation model we used three phase squirrel cage motor; the stator & rotor winding of the motor are connected in wye connection to an internal neutral point. The rating & internal specifications of the induction motor are given below:

Rated voltage	= 230V
Frequency	= 50Hz
Rated speed	= 1430rpm
Rated power	= 4KW
Mechanical Input (Load)	= 10 Nm
Stator resistance	= 1.405 ohm
Stator inductance	= 0.005839H
Rotor resistance	= 1.395 ohm
Rotor inductance	= 0.005839H
Mutual inductance	= 0.1722H
Inertia	= 0.0131 Kg.m²
Pole pairs	= 2

Figure-9 represents simulation model of soft starting method with artificial intelligent controller. Simulation model consists of Synchronization unit provides three line to line synchronization voltages for synchronized pulse generator. These synchronization voltages are made from supply end by building delta loop with using voltage measurement blocks. The output voltages of the synchronization unit are connected to the synchronized pulse generator. The artificial neural network controller provides control signal (delay angle) for the pulse generator. The reference input of the artificial neural network controller is stator phase current of the induction motor. The starting current of the induction motor basically controlled by control signal that produced from artificial neural network controller. Thyristor unit controlled the stator phase voltages according to the gate pulses generated by synchronized pulse generator. The gate pulses are connected to the gate inputs of the corresponding thyristors.

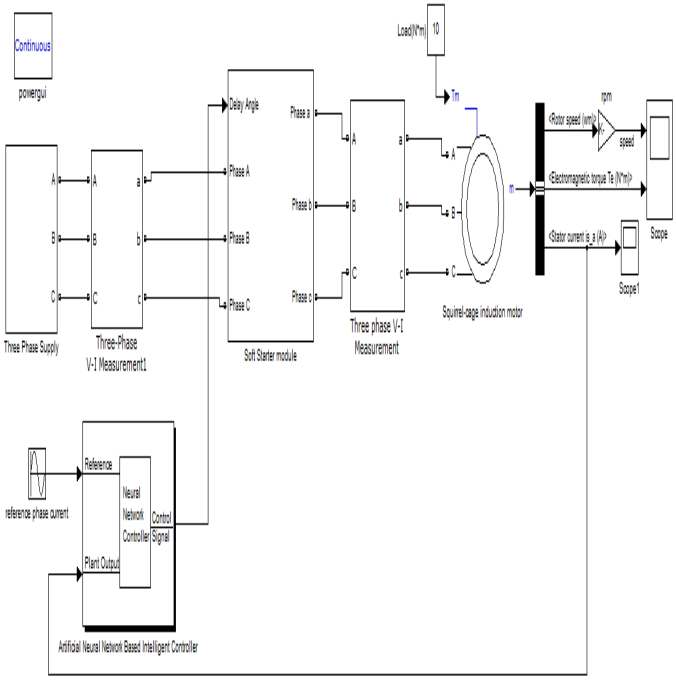

Fig. 9. Simulation model of the soft starting method with artificial neural network controller

V. RESULT & ANALYSIS

For 10 Nm load, the stator phase current of the direct on line (D.O.L) method are shown in fig-10. Fig.10 shows the starting current of DOL method is 81.66A (Peak) & after 0.08 sec. This current reduces to 6.82A (Peak) at running condition. For 'traingda' training function, starting current of soft-starting method is 73.8A (peak) shown in fig-11; that means 7.86A (peak) current is reduced from D.O.L starting current. The current during running condition is 6.8A (peak). The accelerate torque is 124.4 Nm that is enough to accelerate the load during starting condition; the rated speed is reached after 0.15 sec which have been shown in fig-12 and fig-13.

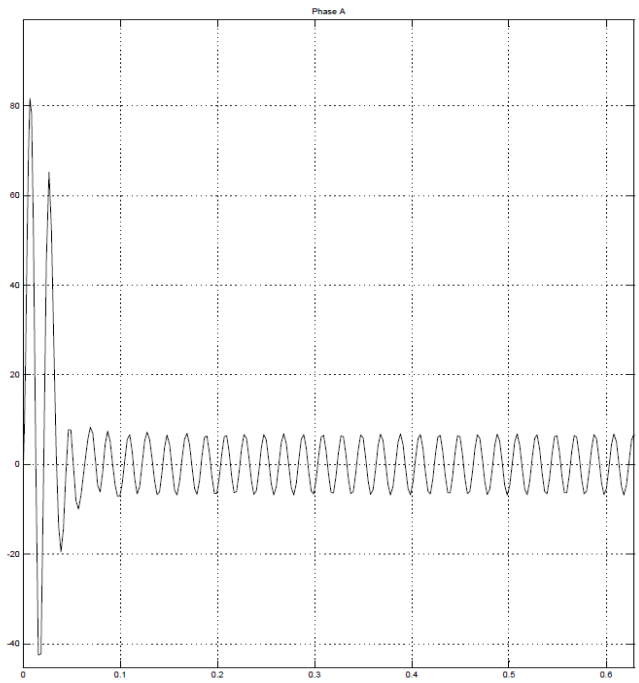

Fig. 10. Stator phase current of direct on line method

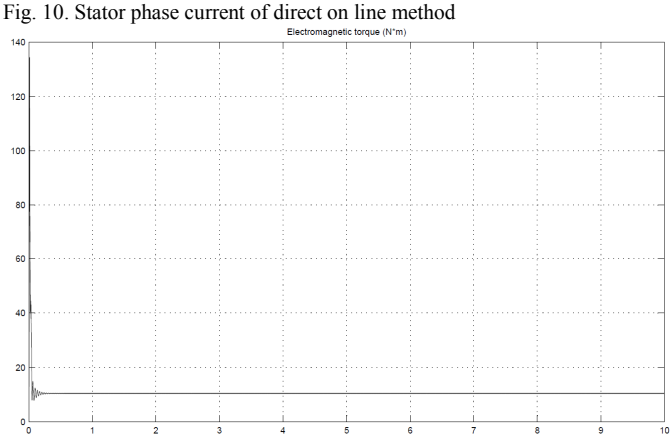

Fig. 12. torque characteristics of intelligent soft-starting method using 'traingda' training function

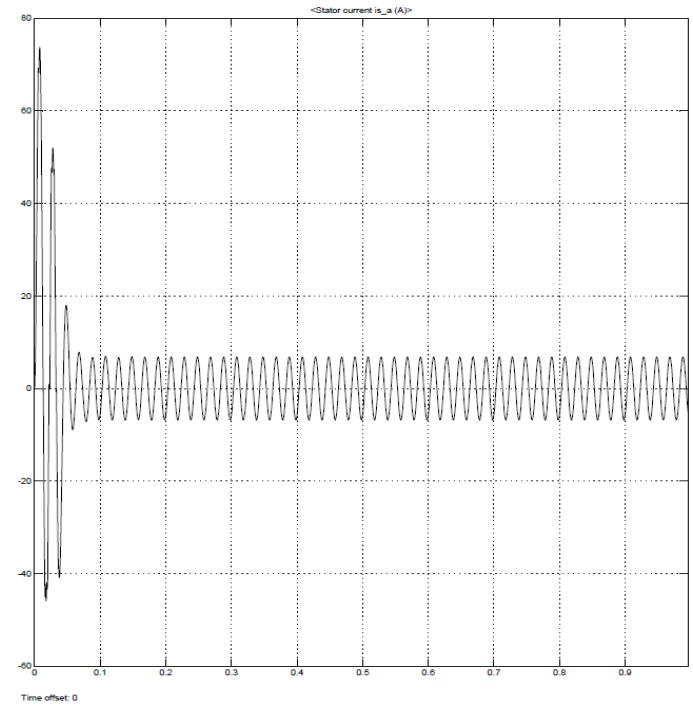

Fig. 11. Stator phase current of intelligent soft-starting method using'traingda' training function

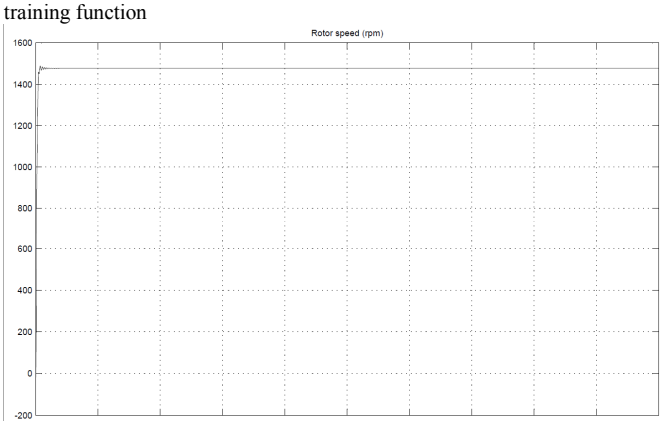

Fig. 13. Speed characteristics of intelligent soft-starting method using 'traingda' training function

.

VI. CONCLUSION

A neural network based soft-starter has been shown in this paper. An improved result has been achieved compare to conventional DOL starter and also with the improved new less starting current an adequate speed-torque goal has been achieved. Here on the simulation only one phase has counted for the simplicity.

REFERENCES

[1] Adam John Wigington, "A Comparison of Induction Motor Starting Methods Being Powered by a Diesel-Generator Set," M.S. thesis, University of Nebraska, Lincoln, Nebraska, July. 2010.

[2] A.R. Kashif and M.A. Saqib, "Soft starting of an Induction Motor Using Neuro-Fuzzy Inference system*" in Proc. IEEE Int. Conf. Electrical Eng. 2007 ,pp.1-5*

[3] M.A. Saqib, A.R. Kashif and Tehzeeb-ul-Hassan, "Soft Starter of an Induction Motor using Neural Network Based Feedback Estimator," *in Proc. IEEE Int. Conf. power Eng., Dec. 2007, pp. 1–5.*

[4] Syed Abdul Rahman Kashif and Muhammad Asghar Saqib, " Soft Starting of Induction Motors using Neuro Fuzzy and Soft Computing*" in Proc. IEEE Int. Conf. Electrical Eng., March. 2008,pp.1-7*

[5] *Soft starter Hand book*, ABB, 2003.

[6] Yuan Youxin Xia Zezhong Wang Yalan Yuan Peigang Peng Wanquan, " A Soft starter of Three Phase Asynchronous Motor *" in Proc. IEEE Int. Conf. power Electronics specialists, 2007,pp.563-567*

[7] Simon Haykin*, Neural Network: A comprehensive foundation*, Pearson Education, 1999

[8] http://www.mathworks.com/

Analysis of Common-Mode Rejection Ratio of a CMOS Differential Amplifier Considering All the Non-idealities

[1]Madiha Amina, [2]Protik Biswas, [3]Aman Ullah, [4]Md. Iqbal Bahar Chowdhury
Department of Electrical and Electronic Engineering
United International University
Dhaka, Bangladesh.
[1]opsara@ymail.com, [2]protik_biswas@yahoo.com, [3]amanullah.en@gmail.com, [4]ibchy@eee.uiu.ac.bd

***Abstract*—This paper attempts an analytical approach to accurately determine common-mode rejection ratio (CMRR) considering the effects of various non-idealities such as the presence of channel length modulation, body effect, finite resistance of the current source, mismatches in transconductances and drain resistances between the two driver MOSFETS of a common source CMOS differential amplifier. This analysis brings to light the hitherto unforeseen dire impacts of these non-idealities put together on CMRR, and hence strongly suggests that these effects should not be, in any ways, ignored from theoretical calculations for CMRR. Moreover, the work would be helpful for researchers in this field to have a better insight on the differential amplifier circuits.**

***Index Terms*—Common-Mode Rejection Ratio, Common Source CMOS Amplifier, Differential Amplifier, Non-idealities.**

LIST OF SYMBOLS

$CMRR$ = Common Mode Rejection Ratio
$A_{V,DM}$ = Differential-mode gain of the differential pair
$A_{V,CM-DM}$ = Common-mode gain of the differential pair
M_1 = 1st one of the two n-channel MOSFETs (on the left hand side of the differential pair)
M_2 = 2nd one of the two n-channel MOSFETs (on the right hand side of the differential pair)
g_{m1} = Transconductance of M_1
g_{m2} = Transconductance of M_2
CLM = Channel Length Modulation
g_{mb1} = Transconductance of M_1 due to body effect
g_{mb2} = Transconductance of M_2 due to body effect
V_{bs1} = Body-to-source voltage in M_1
V_{bs2} = Body-to-source voltage in M_2
R_{D1} = Drain resistance of M_1
R_{D2} = Drain resistance of M_2
r_{01} = Channel resistance of M_1
r_{02} = Channel resistance of M_2
V_{DD} = Supply DC Voltage
V_{in1} = Small AC signal applied to the gate of M_1
V_{in2} = Small AC signal applied to the gate of M_2
V_x = Drain voltage of M_1
V_y = Drain voltage of M_2
V_p = Voltage at the common source of M_1 and M_2
V_{bs1} = Body to source voltage of M_1
V_{bs2} = Body to source voltage of M_2
I_{ss} = Current through the current source
I_x = Current through R_{D1}
I_y = Current through R_{D2}
R_{ss} = Resistance of the current source

I. INTRODUCTION

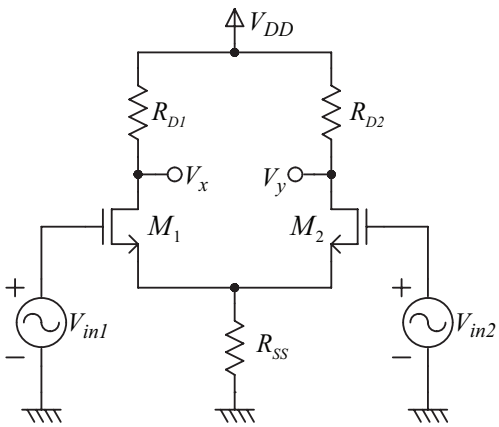

Fig. 1. A common source CMOS differential amplifier made of two similar n-channel MOSFETS

The name Differential Amplifier itself well describes its functionality. The resultant output voltage is simply the difference between the amplified output drain voltages, V_x and V_y, due to the two inputs, V_{in1} and V_{in2}, as shown in Fig. (1). When a differential signal is chosen as input to the differential pair, the unexpected environmental noise, which is very obvious to appear in analog circuits, is cancelled out automatically during the operation [1]. This particular property, besides many others, makes the differential amplifier an important building block in analog circuits. The primary concern while using differential amplifiers is to get a greater

978-1-4673-9257-0/15/$31.00 © 2015 IEEE

amplification of differential-mode input voltages while suppressing the common-mode input voltages. In doing so, the effectiveness of the differential pair in rejecting common-mode interference is termed as CMRR.

A high value of CMRR is expected in regular applications, especially in electro-encephalography where the amplifier is expected to respond to two small anti phase signals. However, the signals may appear in phase with each other with a larger interfering voltage. In that case, CMRR must have a pretty high value, preferably over 90 dB [2]–[5].Until now, several works have been done to improve the performance, especially CMRR, of CMOS differential amplifiers, but comparatively very few works have been focused on the precise mathematical derivation of CMRR [2], [3], [6], [7]. Moreover, the available models do not consider all the non-idealities that affect CMRR and make its nature less deterministic [1], [8].

This work, on the other hand, includes all the non-idealities, which are: the presence of CLM and body effect, finite resistance (R_{ss}) of the current source and mismatches between transconductances (g_m) and drain resistances (R_D) in M_1 and M_2 .

II. Analysis

The following analysis is done considering all the non-idealities mentioned in the previous section, i.e., the presence of CLM for which $r_{01} \neq \infty$ and $r_{02} \neq \infty$, the presence of body effect for which $g_{mb1} \neq 0$ and $g_{mb2} \neq 0$, finite resistance of the current source ($R_{ss} \neq \infty$), mismatch between the transconductances ($g_{m1} \neq g_{m2}$) and mismatch between the drain resistances ($R_{D1} \neq R_{D2}$).

The CMRR of a common source CMOS differential amplifier can be stated as:

$$CMRR = \frac{A_{V,DM}}{A_{V,CM-DM}} \tag{1}$$

A. Differential Mode Gain

For a differential signal input, $A_{V,DM}$ of the differential pair have the following expression:

$$\begin{aligned} A_{V,DM} &= \frac{V_x - V_y}{V_{in1} - V_{in2}} = \frac{V_x - V_y}{2V_{in1}} \\ &= \frac{1}{4}\left[\left(\frac{V_x}{V_{in1}} - \frac{V_y}{V_{in1}}\right) - \left(\frac{V_x}{V_{in2}} - \frac{V_y}{V_{in2}}\right)\right] \end{aligned} \tag{2}$$

where $\frac{V_x}{V_{in1}}$ can be determined with the application of superposition theorem. When V_{in2} is considered to be zero, according to Fig. (2), the effect of V_{in1} on V_x can be shown as:

$$\frac{V_x}{V_{in1}} = -\frac{g_{m1} r_{01} R_{D1}}{(g_{m1} + g_{mb1}) R_{s1} r_{01} + R_{s1} + r_{01} + R_{D1}} \tag{3}$$

where $R_{s1} = R_{s1}\prime \parallel R_{ss}$ and

$$R_{s1}\prime = \frac{1 + \frac{R_{D2}}{r_{02}}}{g_{m2} + g_{mb2} + \frac{1}{r_{02}}}$$

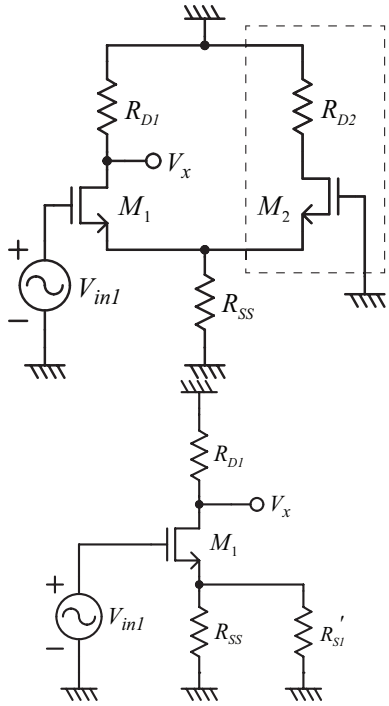

Fig. 2. AC Analysis: Effect of V_{in1} on V_x, where $V_{in2} = 0$

Similarly, the effect of V_{in2} on V_y can be expressed as:

$$\frac{V_y}{V_{in2}} = -\frac{g_{m2} r_{02} R_{D2}}{(g_{m2} + g_{mb2}) R_{s2} r_{02} + R_{s2} + r_{02} + R_{D2}} \tag{4}$$

where $R_{s2} = R_{s2}\prime \parallel R_{ss}$ and

$$R_{s2}\prime = \frac{1 + \frac{R_{D1}}{r_{01}}}{g_{m1} + g_{mb1} + \frac{1}{r_{01}}}$$

According to Fig. (3), the effect of V_{in1} on V_y becomes:

$$\frac{V_y}{V_{in1}} = \frac{V_y}{V_{th1}} \times \frac{V_{th1}}{V_{in1}} \tag{5}$$

where

$$\frac{V_y}{V_{th1}} = \frac{((g_{m2} + g_{mb2}) r_{02} + 1) R_{D2}}{(g_{m2} + g_{mb2}) r_{02} R_{th1} + R_{th1} + r_{02} + R_{D2}} \tag{6}$$

and

$$\frac{V_{th1}}{V_{in1}} = \frac{\left(\frac{1}{g_{mb1}} \parallel r_{01}\right) \parallel R_{ss}}{\frac{1}{g_{m1}} + \left(\frac{1}{g_{mb1}} \parallel r_{01}\right) \parallel R_{ss}} \tag{7}$$

In [Eqn. 6], $R_{th1} = R_{th1}\prime \parallel R_{ss}$ while

$$R_{th1}\prime = \frac{1}{g_{m1}} \parallel \left(\frac{1}{g_{mb1}} \parallel r_{01}\right)$$

In the same way, the effect of V_{in2} on V_x can be expressed as :

$$\frac{V_x}{V_{in2}} = \frac{V_x}{V_{th2}} \times \frac{V_{th2}}{V_{in2}} \tag{8}$$

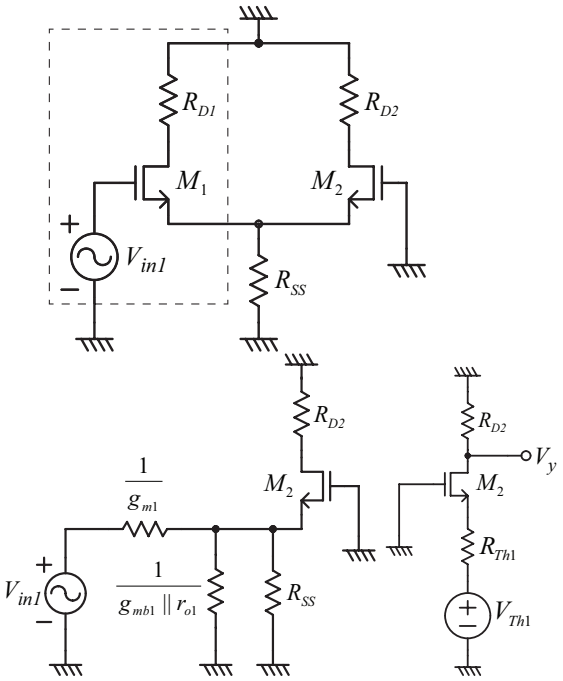

Fig. 3. AC Analysis: The effect of V_{in1} on V_y, where $V_{in2} = 0$

where

$$\frac{V_x}{V_{th2}} = \frac{((g_{m1} + g_{mb1})r_{01} + 1)R_{D1}}{(g_{m1} + g_{mb1})r_{01}R_{th2} + R_{th2} + r_{01} + R_{D1}} \tag{9}$$

and

$$\frac{V_{th2}}{V_{in2}} = \frac{\frac{1}{g_{mb2}} \parallel r_{02} \parallel R_{ss}}{\frac{1}{g_{m2}} + \frac{1}{g_{mb2}} \parallel r_{02} \parallel R_{ss}} \tag{10}$$

In [Eqn. 9], $R_{th2} = R_{th2\prime} \parallel R_{ss}$ while

$$R_{th2\prime} = \frac{1}{g_{m2}} \parallel \left(\frac{1}{g_{mb2}} \parallel r_{02}\right)$$

B. Common Mode-Differential Gain

In the following sections, the symbol δ has been used to show the small changes in the variables just next to it.

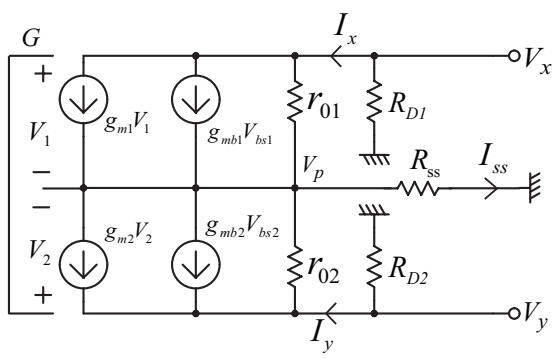

Fig. 4. Small signal equivalent circuit for common-mode input

The common-mode differential gain stated in [Eqn. 1] can be expressed as:

$$\begin{aligned} A_{V,CM-DM} &= \frac{\delta V_x - \delta V_y}{\delta V_{in,cm}} \\ &= (1 - \frac{y}{x}).p + \frac{y}{x}.q \end{aligned} \tag{11}$$

where

$$\begin{aligned} x &= \frac{1}{R_{ss}} + \left(\frac{g_{mb1}r_{01} + 1}{R_{D1} + r_{01}} + \frac{g_{mb2}r_{02} + 1}{R_{D2} + r_{02}}\right) \\ &\quad + \left(\frac{g_{m1}r_{01}}{r_{01} + R_{D1}} + \frac{g_{m2}r_{02}}{r_{02} + R_{D2}}\right) \\ y &= \frac{g_{m1}r_{01}}{r_{01} + R_{D1}} + \frac{g_{m2}r_{02}}{r_{02} + R_{D2}} \\ p &= -g_{m1}R_{D1}\frac{r_{01}}{r_{01} + R_{D1}} + g_{m2}R_{D2}\frac{r_{02}}{r_{02} + R_{D2}} \\ q &= \left(\frac{R_{D2}g_{mb2}r_{02}}{R_{D2} + r_{02}} - \frac{R_{D1}g_{mb1}r_{01}}{R_{D1} + r_{01}}\right) \\ &\quad + \left(\frac{R_{D2}}{R_{D2} + r_{02}} - \frac{R_{D1}}{R_{D1} + r_{01}}\right) \end{aligned}$$

Again, in [Eqn. 11],

$$\delta V_x - \delta V_y = -(\delta I_x R_{d1} - \delta I_y R_{D2}) \tag{12}$$

Now, by applying KCL in Fig. (4), the equation for δI_x is formed like this:

$$\begin{aligned} \delta I_x &= g_{m1}(\delta V_{in,CM} - \delta V_p) + g_{mb1}(-\delta V_p) \\ &+ \frac{\delta V_x - \delta V_p}{r_{01}} \end{aligned} \tag{13}$$

or

$$\begin{aligned} \delta I_x &= g_{m1}(\delta V_{in,CM} - \delta V_p).\frac{r_{01}}{r_{01} + R_{D1}} \\ &- \delta V_p.\frac{g_{mb1}r_{01} + 1}{R_{D1} + r_{01}} \end{aligned} \tag{14}$$

Similarly,

$$\begin{aligned} \delta I_y &= g_{m2}(\delta V_{in,CM} - \delta V_p).\frac{r_{02}}{r_{02} + R_{D2}} \\ &- \delta V_p.\frac{g_{mb2}r_{02} + 1}{R_{D2} + r_{02}} \end{aligned} \tag{15}$$

Putting the values of I_x and $I_y$in [Eqn. 12],

$$\delta V_x - \delta V_y = (\delta V_{in,cm} - \delta V_p).p - \delta V_p.q \tag{16}$$

where

$$\delta V_p = (\delta I_x + \delta I_y)R_{ss} \tag{17}$$

substituting for δI_x and δI_y in [Eqn. 17]:

$$\delta V_p = \frac{y}{x} \cdot \delta V_{in,cm} \tag{18}$$

or

$$\delta V_{in,cm} - \delta V_p = (1 - \frac{y}{x})\delta V_{in,cm} \tag{19}$$

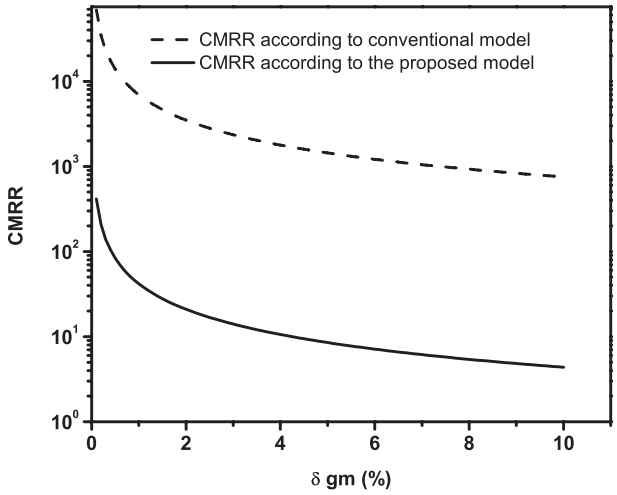

Fig. 5. Response of CMRR to various differences (0%-10%) between g_{m1} and g_{m2} (i.e., δg_m) of M_1 and M_2 respectively.

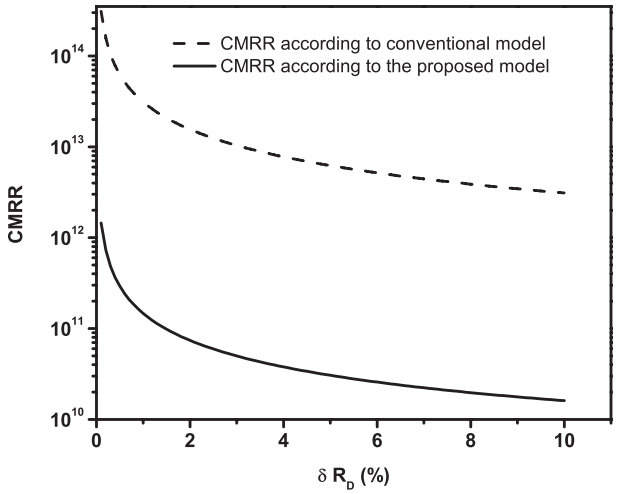

Fig. 6. Response of CMRR to various differences (0%-10%) in R_{D1} and R_{D2} (i.e., δR_D) of M_1 and M_2 respectively.

III. Results and Discussion

The simulation results, shown in Fig. (5)-(6), have been carried out considering standard 0.5μm process. In both cases, the results obtained considering all non-idealities stated here are compared with those that are obtained from equations based on conventional approaches, where the effects of some of the non-idealities have been ignored [1]. Fig. (5) shows how CMRR responds to different levels of mismatches between g_{m1} and g_{m2} (δg_m) according to both conventional (presented by dotted line) and proposed model (presented by solid line). It is clear that CMRR decays, as expected, exponentially with the increased g_m mismatches. This happens, because in common mode operation, difference in g_m causes difference in two branch currents (I_x and I_y), hence introduces difference in voltage drops against R_{D1} and R_{D2}, and finally creates difference between V_x and V_y. As a result, common-mode differential gain, which is unexpected in an ideal case, starts to rise, causing CMRR to decay. In the same way, Fig. (6) shows a similar response of CMRR to the change in δR_D, which is also varied from 0% to 10%.

In both the cases, CMRR based on the model proposed here is much less than that based on conventional model [1]. In fact, the common-mode gain increases as more and more non-idealities are added to the system. The increased common-mode gain causes the CMRR to flag drastically. This phenomenon can be realised from [Eqn. 11]. When any non-idealities such as body effect (g_{mb}), CLM (i.e., finite r_{01} and r_{02}), differences in transconductance (δg_m) and drain resistances (δR_D) are introduced, the quantity 'q' in [Eqn. 11] increases. The increased 'q' causes the common-mode gain ($A_{V,CM-DM}$) to rise and thus CMRR to fall.

IV. Conclusion

A deeper and more practical analytical model for calculating CMRR has been established here. The results are far different from those that are simulated based on conventional theoretical approaches used today. This finding indicates that the calculations for CMRR should not be done ignoring the effects of any of the non-idealities, for in that case, the experimental output would differ too much from the theoretical ones. To get closer to the experimental data, the theorists must always be concerned about the existence of all the non-idealities possible in a CMOS differential amplifier. In this paper, therefore, the authors have tried to establish an analytical model for CMRR calculations where all those non-idealities are incorporated successfully .

References

[1] B. Razavi, "Design of Analog CMOS Integrated Circuits", *McGraw-Hill, 2002.*

[2] A. K. N., S. Bose, A. Gupta, "A High Gain, High CMRR Two-Stage Fully Differential Amplifier Using g_m/I_d technique for Bio-medical Applications", *IEEE Asia Pacific Conference on Postgraduate Research in Microelectronics and Electronics (PrimeAsia)*, pp. 40-45, 2003.

[3] Y. M. Hsiao, M. S. Shiau, K. H. Li, et al., "Design a Bioamplifier with High CMRR", *VLSI Design*, vol. 2013, Article ID 210265, pp. 1-5, Apr. 2013.

[4] Nagel, J. H., "Biopotential amplifiers", *Biomedical engineering hand book, 2nd edition,* Ed. Joseph D. Bron Press LLC, 2000.

[5] K. A. Ng, and P. K. Chan, "A CMOS Analog Front-End IC for Portable EEG/ECG Monitoring Applications", *IEEE Trans. Circuits and Systems*, vol. 52, no. 11, pp. 1-12, Nov. 2005.

[6] J. I. Brown, "Differential Amplifiers That Reject Common-Mode Currents", *IEEE J. Solid-State Circuits*, vol. SC-6, no. 6, pp. 385-391, Dec. 1971.

[7] M. Brotz, and A. Kley, "The common-mode rejection of transistor differential amplifiers", *IEEE Trans. Circuits Theory*, vol. CT-13, pp. 171-175, Dec. 1966.

[8] R. Jiang, H. Tang, and K. Mayaram, "A Simple and Accurate Method for Calculating the Low Frequency Common-Mode Gain in a MOS Differential Amplifier with a Current-Mirror Load", *IEEE Trans. Education*, vol. 43, no. 3, pp. 362-364, Aug. 2000.

Implimentation And Evaluation Of An Efficient Clock Distribution Network For Deep-Submicron Technology

Md. Abdur Rahman*, Md. Mamunur Rahman, Farhadur Arifin
Department of EEE
American International University-Bangladesh
Dhaka, Bangladesh
*nayem.rahmanmdabdur@gmail.com

Abstract—**A differential clock distribution network using current mode logic (CML) buffer and RCL interconnect model for low-skew is presented in this paper. We investigate attenuation and skew of the proposed clock distribution network. An efficient differential CML buffer is used as it is capable of operating with low voltage and high frequency which makes this clock distribution network more advantageous over the conventional models. Different clock distribution networks with clock trees such as H-tree, X-tree and binary tree are designed. Those networks are analyzed by using different technological nodes, such as 22nm, 32nm, 45nm. Due to the high clock frequency, more accurate RCL interconnect model has been explored. According to the analysis, compared to other clock trees, X-tree has less skew of 179ps with large area and the binary tree has a constant delay ratio.**

Keywords—Differential clock distribution network, Differential CML Buffer, RLC interconnect, Deep-submicron technology.

I. INTRODUCTION

Latest integrated circuits are more complex with billions of transistors and run at multi-GHz frequency. Clock frequency has already exceeded 3GHz. This uprising frequency level results more power consumption. A clock distribution network approximately consumes 30%-50% of total power of processor. Besides, when VLSI technology improved and reduced under 65nm, interconnect delay gradually affects the chip performance [1]. At high frequency clocks, it is a challenge to reduce clock skew and clock jitter values. In order to cope with the progressive designs, it is important to propose a new and efficient clock distribution network for modern ICs.

A clock distribution network is a network that distributes the clock signal to the all clock element and the load inside a VLSI system. Clock tree is built with clock tree synthesis tools and it varies routing paths and placement of clock cells and clock buffers. This network is a structure that allows different loads to share the data simultaneously. Synchronous clocking is most widely used mechanism for commercial microprocessors with multi gigahertz clock pulses. The clock arrival time difference between two different levels of signal is called clock skew [2]. Networking of clock distribution system is developing continuously, such as a network with top-down flow, a network with exact equidistant trees and a presented skew balanced diagram. Later on, a model was proposed that balanced the delay using Elmore RC delay model [3]. Some buffer less resonant clock distribution network can also reduce the power consumption of the synchronous system [4].

Late clock signal, early clock signal or any kind of time related issue will limit the maximum clock frequency. Efficient clock distribution networks minimize the clock skew and jitter issue. Clock signals travel a long path operating at high frequency. These signals can be interrupted by different issues. In recent times, many signaling techniques have been proposed which have high-speed data buses with long line lengths and small power consumption [5]. One of the useful and efficient techniques is current mode logic signaling which can be used in the clock distribution network also. The transmitter-receiver pair system of current-mode clock distribution network reduces the fluctuation of delay although there are some parametric variations. In a synchronous VLSI system, clock signal drives thousands of loads. There is a hierarchy in the modeling of clock distribution network, which has three levels, namely global, regional and local as shown in fig. 1. Every level of the original clock signal is regenerated and improved by different buffer [6].

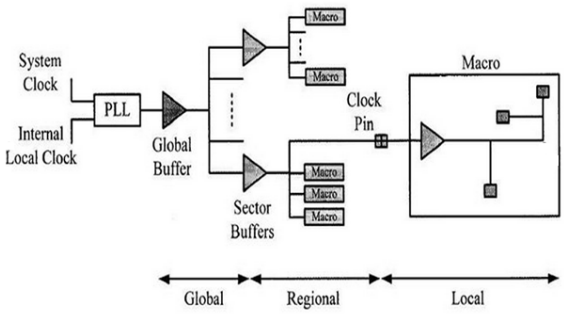

Figure 1. Hierarchy of clock distribution network for a high performance synchoronous VLSI system [6].

978-1-4673-9257-0/15/$31.00 ©2015 IEEE

In this paper, we focused on the local level of the clock distribution network where the clock pin is delivered to the load. We have implemented different clock distribution networks using different clock tree synthesis. Providing uninterrupted clock pulses from the input to the load, we used an efficient differential current mode logic (CML) buffer and a realistic interconnect equivalent model. In our proposed model, a clock pulse is provided to the network and the signal reached the load through transmission lines and buffer as shown in fig. 2 and fig. 3. The block situated at the middle represents the differential CML buffer and the other two sides of the box represent the transmission line. The differential buffer is used as a regenerator of the signal. We analyzed x-tree, H-tree & binary-tree technique and compared the resulting clock pulse on the different nodes, branches in 22nm and 45nm CMOS technologies. The realized model of X-tree has less amount of skew of 178ps which is efficient in case of using a higher number of loads as it has less number of levels.

The entire presentation is divided into four sections. In section I, the importance, present scenario and prospects of the clock distribution network is discussed. Section II discusses the CML buffer and the interconnect structure used in the proposed model. In section III, the simulation results of analysed differential networks with different trees are presented. Finally, the conclusion of this work is discussed in section IV.

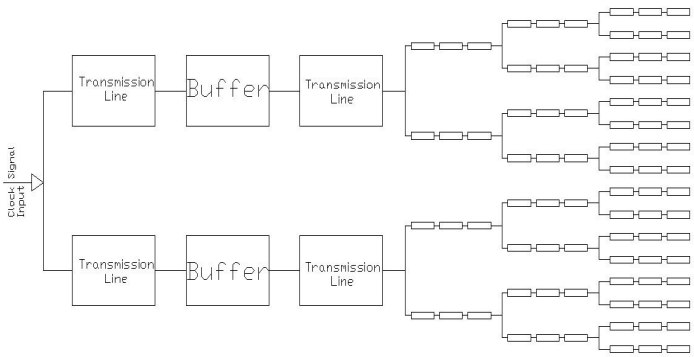

Figure 2. Distribution network with Binary tree configuration.

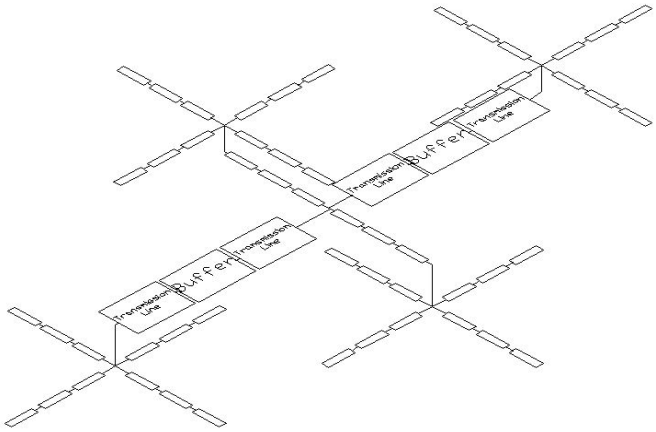

Figure 3. Distribution network with X tree configuration.

II. MODELING OF CLOCK DISTRIBUTION NETWORK

A. Differential CML buffer

As the function of the clock distribution network is to transmit a healthy clock pulse, CMOS buffer plays very important role in this system. It helps to transmit unbiased clock pulses throughout the transmission line and to achieve synchronism in the ICs. The buffer is also used to avoid the effect of load mismatch. At high speed and multi-Giga hertz transmission system, the use of conventional buffer losing advantages and exposing issues. Due to this complicated situation they cannot be used anymore. Difficulties like electromagnetic coupling of single-ended circuits, use of PMOS and its limitation of maximum operating frequency are significant [7]. Differential circuitry reduces power consumption and current mode logic is compatible with low input voltage. Current mode logic with CMOS technology is capable of working in low signal voltage, high operating frequency and low supply voltage [8].

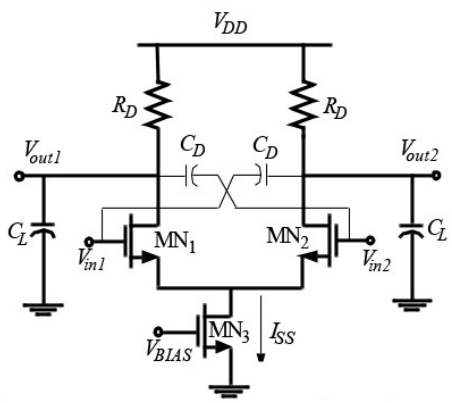

Figure 4. A current mode logic buffer [8].

Buffer is a core part of a clock distribution system. It is the part of a clock distribution system that ensures unbiased clock signal distribution. A differential buffer amplifies between its two inputs and outputs a pair of differential signal. Basic NMOS differential buffer consists of two NMOS transistors.

Variance of maximum and the minimum common mode voltage of NMOS buffer is possible when all the transistors are in the saturation region [8].

In our work we have used differential current mode logic buffer. We used only NMOS to construct the buffer due to some significant drawbacks of PMOS. Buffer parameters used as follows where operating clock frequeny is 1GHz. Table I, table II and table III represent buffer perameters that is used in this work with different technological nodes. Threshold voltage V_{th} =0.18V and V_{dd}=1V where, T_{ox}=1.1nm and R_{dsw}=155 Ω [9].

TABLE I. BUFFER PARAMETER FOR 22NM TECHNOLOGY

Tree Type	*Length (nm)*	*Width(nm)*
Binary Tree	22	33
H-Tree	22	33
X-Tree	22	33

TABLE II. BUFFER PARAMETER FOR 32NM TECHNOLOGY

Tree Type	*Length (nm)*	*Width(nm)*
Binary Tree	32	48
H-Tree	32	48
X-Tree	32	48

TABLE III. BUFFER PARAMETER FOR 45NM TECHNOLOGY

Tree Type	*Length (nm)*	*Width(nm)*
Binary Tree	45	67.5
H-Tree	45	67.5
X-Tree	45	67.5

B. Interconnects

There are some electrical properties of interconnect wires like resistance, capacitance and inductance. Some relation can be presented to drive their values and combine these properties into an electrical model and prepare an equivalent circuit of the total transmission line effect. There are different kinds of models to represent different effects and they can vary with entire circuitry, the type of conductor used in transmission line and physical or geometrical configuration of the lines, different kind of loads and technology. The internal resistance, reactance and capacitance of the wire and some mutual inductance between closely attached lines also play an important role in designing and analyzing the equivalent model [10]. The model parameters of the transmission line are mainly of two types like lumped element model of transmission line and distribution model elements of transmission line.

All wires have some value of resistance. The interconnect resistance changes proportionally with the length (L) of the wire and resistivity (ρ) and inversely with the cross sectional area (A). Resistance of a rectangular conductor can be expressed as:

$$R = (\rho . L) / A \quad (1)$$

Due to, very high frequencies, conductive materials face a phenomenon which is called the skin effect. This effect makes the resistance, frequency dependent.

In our design, we used an interconnect RCL pi model where Cu was used as a metal. The parameters were as follows in table IV [9].

TABLE IV. INTERCONNECT MODELING PARAMETERS

Dimensions	RLC	RLC (/mm)
W = 0.10 um s = 0.10 um l = 100 um t = 0.20 um h = 0.20 um K = 2.2	R = 109.999 Ohm L = 0.14 nH M12 = 0.118 nH M13 = 0.104 nH M14 = 0.096 nH (k12 = 0.842 k13 = 0.742 k14 = 0.685) C_{ground} = 1.9419 fF C_{couple} = 5.3683 fF C_{total} = 14.6204 fF	R = 1099.99 Ohm/mm L = 1.4 nH/mm C_g = 19.419 fF/mm C_c = 53.683 fF/mm C_{total} = 146.204 fF/mm

III. SIMULATION AND RESULTS

The clock pulse output of different clock distribution networks is presented using different nanometer technologies with a differential buffer and transmission line of different parameters. To show the outputs HSPICE software is used which is an analog electronic circuit simulator capable of performing transient, steady state and frequency domain analysis. To analyze the output clock pulse of 1 GHz to 5 GHz frequency level was used as input.

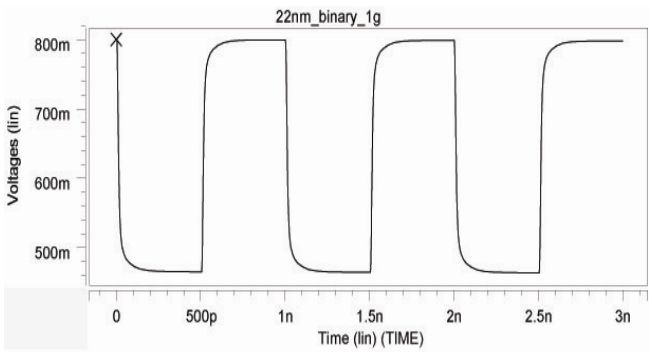

(a)

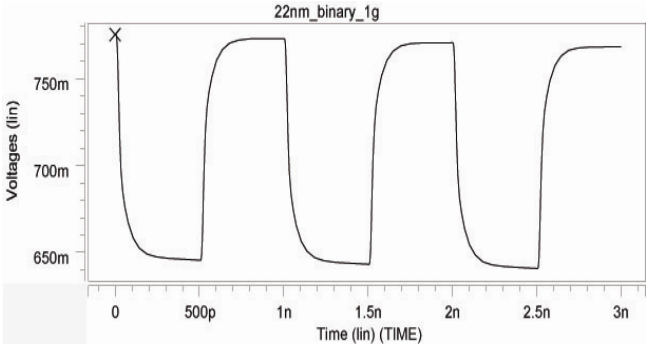

(b)

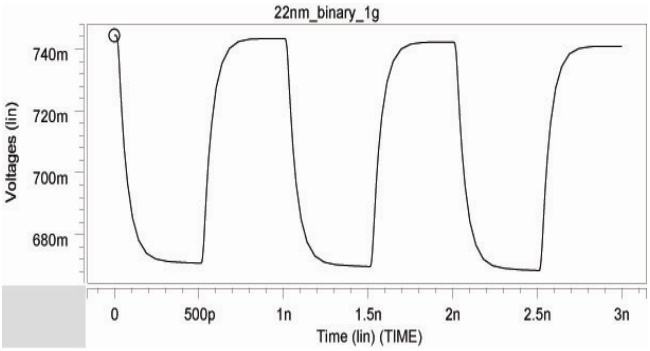

(c)

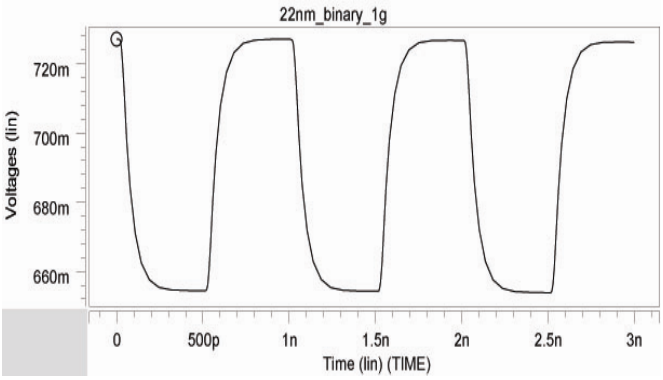

(d)

Figure 5. Waveforms of H-Tree (22nm RLC) at four consicutive levels of a, b, c and d.

Fig. 5 presents the output of H-tree 22nm technology RLC PI model. From the simulated result, it is observed that voltage level of clock pulse decreases with increasing the level. The proposed differential clock distribution network shows voltage differences in different levels of Binary tree, H-tree and X-tree. The buffer is used such that it offers low skew. The fall time and rise time is also varied with different network trees and different nanometer technologies. We measured the skew at different technology and different trees at various frequencies. Higher frequency affects the output signal of the levels. Table V analyses the skew of different levels of different nanometer technologies with different trees at 1GHz frequency.

TABLE V. SKEW AT DIFFERENT LEVELS

Level	**Binary Tree**		**H-Tree**		**X-Tree**	
	22 nm	*45 nm*	*22 nm*	*45 nm*	*22 nm*	*45 nm*
	Skew	Skew	Skew	Skew	Skew	Skew
Level 1	0.179ns	0.176 ns	0.16 ns	0.189ns	0.178ns	0.192ns
Level 2	0.238ns	0.235ns	0.242ns	0.23ns	0.224ns	0.212ns
Level 3	0.236ns	0.3ns	0.3ns	0.29ns	0.21ns	0.22ns
Level 4	0.225ns	0.312ns	0.256ns	0.312ns	0.25ns	0.231ns

IV. CONCLUSION

Different clock distribution networks in nanometer technology with less skew and power dissipation is analyzed. We designed a clock distribution network using H-tree, X-tree and Binary tree technique in this work. We used a low voltage differential CML buffer to ensure an unbiased clock pulse through the whole interconnect line. We designed and analyzed the buffer with different sub nano-CMOS technology like 22nm, 32nm, 45nm, 65nm and 90nm and implemented them in the clock distribution network. From the analysis, we found that without changing the buffer configuration, clock delay is increasing with the reduction of buffer size and technology. We improved the output by changing the buffer size and using a different model parameter. We also analyzed different clock distribution network with different buffer model with the RCL interconnect model.

According to our observation, X-tree is more effective in case of a large number of sequential loads as it has only two levels, but it has different propagation delay on different branches of the network. On the other hand, H-tree propagates the clock signal through four different levels but with almost equal propagation delay. Delay of binary-tree technique increased per branch. We used 1V and 0.8V supply voltage. As we used low power and high speed buffer, our power consumption was much less compared to other conventional design. Frequency was a very crucial element for our simulation. We used 0.5 GHz to 5 GHz clock pulse as our input signal. Our output signal was better at the 1 GHz or less frequency signal, but delay and other effects increased as we increased our clock frequency.

REFERENCES

[1] Tsai, Chia-Chun, Chung-Chieh Kuo, Feng-Tzu Hsu,Lin-Jeng Gu, and Trong-Yen Lee. "X-architecture zero-skew clock tree construction with performance and DFM considerations", 2010 International SoC Design Conference, seoul, 2010, pp. 294 – 297.

[2] Restle, Phillip J., Timothy G. McNamara, David Webber, Peter J. Camporese, Kwok F. Eng, Keith Jenkins, David H. Allen et al. "A clock distribution network for microprocessors.", Solid-State Circuits, IEEE Journal of. Vol. 36, no. 5, pp. 792-799, may, 2001.

[3] Lu, Jingwei, Wing-Kai Chow, and Chiu-Wing Sham. "Fast Power- and Slew-Aware Gated Clock Tree Synthesis", IEEE Transactions on Very Large Scale Integration (VLSI) Systems, vol. 20, no. 11, oct 2012.

[4] Xu, Yi, Shu-ming Chen, Xiang-yuan Liu, and Tao Tang. "Bufferless resonant clocking with low skew and high variation-tolerant", 2011 IEEE 54th International Midwest Symposium on Circuits and Systems (MWSCAS), pp. 1-4, Aug 2011.

[5] Kancharapu, Naveen Kumar, Marshnil Dave, Veerraju Masimukkula, Maryam Shojaei Baghini, and Dinesh Kumar Sharma. "A Low-Power Low-Skew Current-Mode Clock Distribution Network in 90nm CMOS Technology", 2011 IEEE Computer Society Annual Symposium on VLSI, Vol. 36, no. 5, pp. 792-799, 2011.

[6] Houman Zarrabi, Zeljko Zilic, Yvon Savaria and A. J. Al-Khalili. "On the Efficient Design & Synthesis of Differential Clock Distribution Networks", VLSI, Zhongfeng Wang (Ed.), 2010, available online: http://www.intechopen.com/books/vlsi/on-the-efficient-design-amp-synthesis-of-differentialclock-distribution-networks

[7] Restle,P.J; McNamara, T,G webber, D.A; Camporese , P.J; Eng,K.F;Allen, D.H;Rohin, M.J; Quaranta , M.P; Boerstler, D.W; Alpert, C.J; Carter,C.A; Bailey, R.N Petrovick, J.G. Krauter, B.L & McCredie, B.D(2001). A clock distribution network. Vol-36, pp-792-779.

[8] PayamHeydari, "Design Issues in Low-Voltage High-Speed Current-Mode Logic Buffers", IEEE Fourth International Symposium on Quality Electronic Design, 2003, P.p 293 – 298, March 24-26, 2003.

[9] Predictive Technology Model (PTM) available online: http://ptm.asu.edu/

[10] BorivojeNikolic, EE141: Digital Integrated Circuits, chapter 4, page 109, 2001.

Microcontroller Based Self Sustaining Automatic Traffic Light Control Using Speed Breaker

Mrinmoy Dey, Tawhida Akand, Sadeka Sultana and Jahedul Islam

Department of Electrical and Electronic Engineering
Chittagong University of Engineering and Technology
Chittagong-4349, Bangladesh
mrinmoycuet@gmail.com, tawhidacuet@yahoo.com, sadekazinia@yahoo.com, jahedul.islam.2014@ieee.org

Abstract—**Present development of the world is measured by the amount of energy consumption. Energy of today world is generated from conventional energy sources mostly which are decreasing day by day. Moreover, these conventional energy sources causes pollution and responsible for global warming. To solve these problems, researchers are trying frequently to explore new sources of energy which are clean, environment friendly and sustainable. This project is focused on microcontroller based auto traffic light control using energy conversion by speed breaker. In this project based research work, generated voltage depends on spring constant, displacement of rack length, gear ratio, number of gear combination and number of vehicles passing through the speed breaker. In this research work, the automatic traffic light control circuit controls the vehicle flow automatically and saves the working time which is wasted due to the traffic jam.**

Key words— **Microcontroller, Speed breaker, Traffic light.**

I. Introduction

The world is facing a problem of finishing the fuel stored in response of large demand of energy. Consequently, it has become a severe problem to fulfil energy security for next generation. According to various statistics the production of fossil fuel will start to decrease after 2015. To meet the demand of energy new sources of energy are important. So, renewable energy sources are needed to reduce the carbon dioxide emission and meet the future energy crisis. A steady increase in metro-city population, the number of automobiles and cars increases rapidly and metro traffic is growing crowded which leads to the traffic jam problem that severely affect the working time and reduce the efficiency of a person.

The control of traffic is performed by human effort at the circle of road proves to be ineffective due to the fast raise of vehicles and the complexity of road networks. Many researchers are trying to develop efficient traffic control system to reduce the traffic jam that overcomes the time waste in roadside communication. Rotake and Karmore developed an intelligent traffic signal control system using embedded system which consists of high performance, low power AVR_32 microcontroller with 32 kbytes of in-system programmable flash memory and in-built 8-channel, 10-bit ADC which is required to process the IR input from sensor network]1[. R. A. Ganiyu et. al developed a system to control roadside traffic light which was tested by constructing a prototype and showed that it can be used for real life traffic control and training kit to learn about traffic light control system [2]. A project to generate power from speed breaker through rack and ratchet mechanism implemented by A. Padma Rao et. al and tested as a power generation source for lighting the lamps near the speed breakers [3]. Md. Saiful Islam et. al designed a compact power generation unit to show how energy can be produced, stored and through the pressure of vehicles or any kind of pressure as the number of vehicles passing over the speed breaker in roads is increasing day by day [4]. Another project was done by Amanpreet Kaur et. al to harvest power using speed breaker that generated power for the various applications of street lights and traffic signal [5]. Sachin Jaiswal et. al designed intelligent traffic control using IR sensor [6].

In this research work, the proposed system designed for controlling traffic signal in an intelligent way that play vital role to avoid the traffic jam. The power generation system for controlling automatic traffic light has greater flexibility since the displacement of rack length, gear combination, rotation of dynamo, gear ratio and number of rack can be changed.

II. Methodology

A. *Block Diagram*

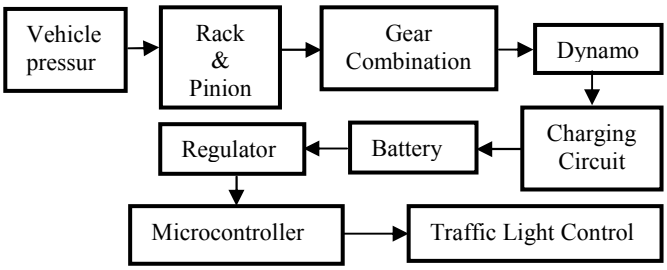

Fig.1: Block diagram

B. *Schematic Design*

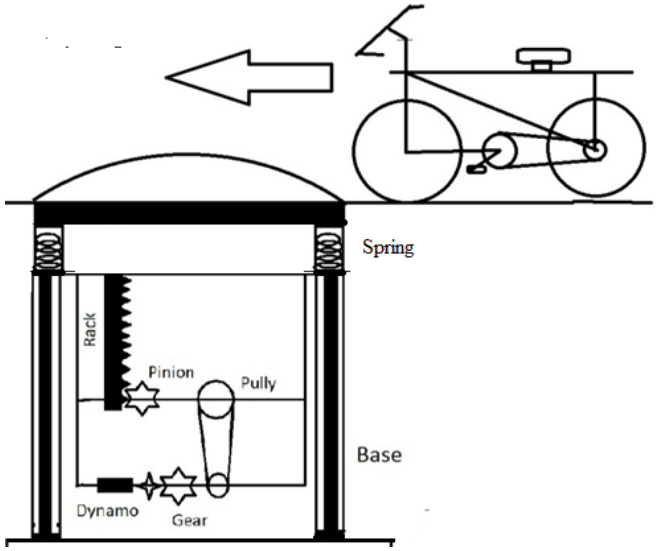

Fig. 2: Mechanical device design

978-1-4673-9257-0/15/$31.00 ©2015 IEEE

When vehicles cross across the speed breaker, it squeezes the spring and moves the rack downward which rotates the pinion, pulley and gear. Then rotary motion produces rotational energy and dynamo is used to convert it into electrical energy. The ratio of small gear and large gear diameter controls the rotation of dynamo.

The expansion of springs takes place and positioning at previous stage when the vehicles cross over the speed breaker. Movement of vehicles on the road is essential to generate continuous power supply from the implemented system. A charging circuit is to charge a 12V battery and the purpose of the regulator is to provide a fixed voltage to the microcontroller that controls the traffic light intelligently as it is programmed.

C. *Flow chart*

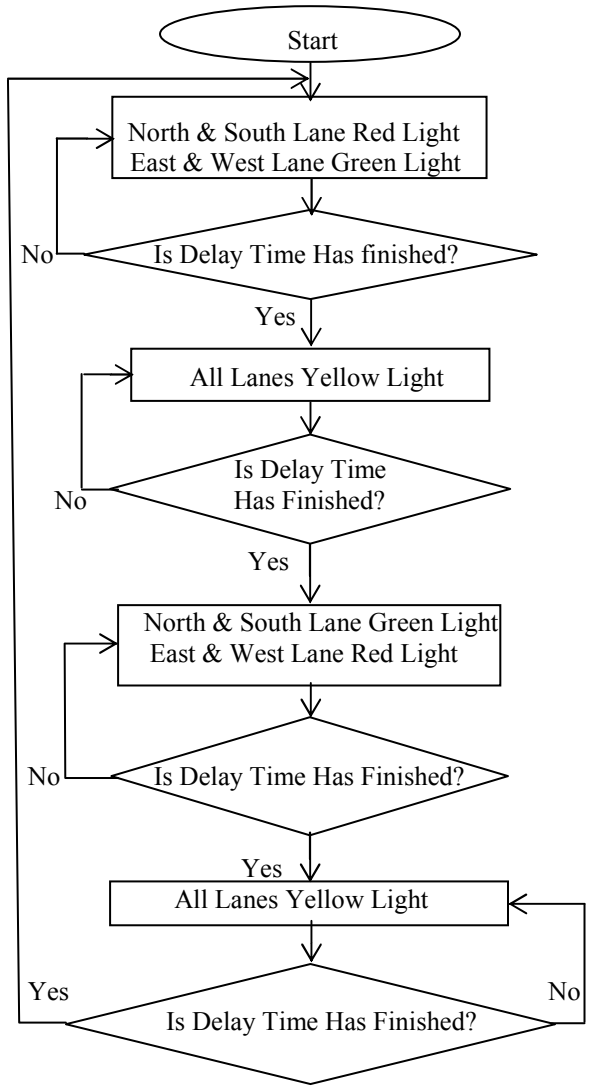

III. System Construction

The following components are used to design an automatic traffic light control system

- Speed Breaker
- Rack and Pinion
- Springs
- Gear
- Belt
- Hole
- Dynamo
- Charging Circuit
- Battery
- Regulator
- Microcontroller
- Traffic Light Control

A. *Speed Breaker*

Speed breaker is used to sustain the pressure of vehicle and event of squeeze happening when vehicle pass through it. It is mainly made of iron and physically looks like curve shaped. A certain time gap should be provided between two vehicles passing time so that the speed breaker can be restored in its original position. If speed breaker cannot restore its original place, there will be no sufficient displacement of rack that causes insufficient generated voltage.

B. *Rack and Pinion*

The circular gear is called pinion and the linear gear is called rack. Force is applied on the linear gear rack which causes pinion rotation. Thus the mechanical force is converted into rotational force. The generated voltage depends on the length of the rack displacement.

C. *Springs*

When vehicle pressurizes on speed breaker, then springs are squeezing although back into normal position on the incident of released pressure. Springs are positioned below the speed breaker.

D. *Gear*

More gear combinations are used to increase the number of rotation. Output voltage increases if gear ratio is more than unity and decreases if gear ratio is less than unity.

E. *Belt*

Belt is tied with the small gear of third gear combination to rotate the dynamo.

F. *Dynamo*

Dynamo uses rotating coils of wire and magnetic fields to convert mechanical rotation into pulsating direct electric current through Faraday's law of induction. A dynamo machine consists of a stationary structure (stator) which provides the constant magnetic field and a set of rotating windings called the armature which turns within the field. The overall mechanical setup is represented by Fig. 3.

Fig. 3: Total mechanical set up

G. *Hole*

A hole is needed to place the setup and the size of hole is same as like the mechanical set up with 4 inch clearance.

H. *Protection*

To protect the setup from extra pressure of soil, humidity, soil temperature, it is covered with polythene which is available, not erosive and cost effective. For better coverage wood box or steel box are used which can tolerate greater pressure and not erosive also.

I. *Charging Circuit*

Charging circuit is used mainly to charge the battery. In this work, lm 317 is a regulator, D1 is a 13 V zener diode and RV1 and R1 are used to set the voltage level. Green and red LED indicate the charging mode and full charged condition of the battery respectively. Red LED is lit on when voltage level is greater than 15 V. The charging circuitis shown in Fig. 6.

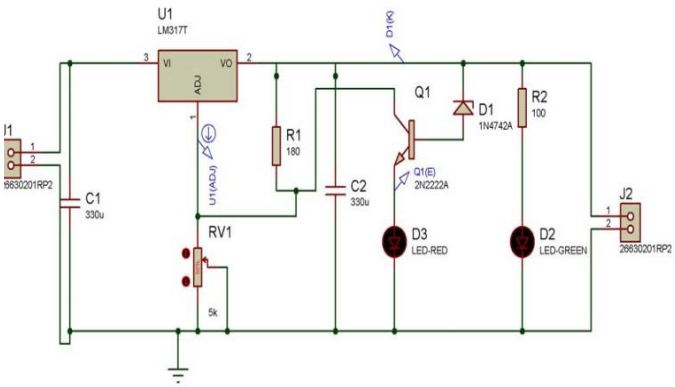

Fig. 4: Charging circuit

J. *Regulator*

A regulator of 5 V is used to power the microcontroller circuit for traffic light control system.

K. *Microcontroller Circuit*

A fixed time delay is used to control the four lane traffic signal. In this research work, microcontroller pic 16F877A is used. RB0, RB1 and RB2 are used to control the traffic signal. The control circuit is shown in Fig. 5.

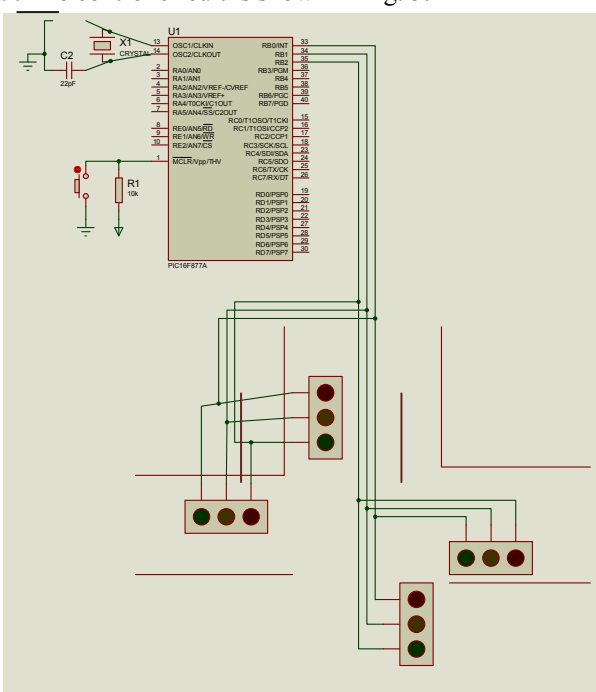

Fig. 5: Control circuit for traffic signal

IV. System Implementation

This system is implemented in Chittagong Collegiate School (CCS) situated in Ice Factory Road, Chittagong 4000, Bangladesh on 3 July, 2015. Implemented system is shown in Fig. 6.

Fig. 6: Implemented system

V. Cost Analysis

To implement the system, used essential components along with respective quantities and cost are given in Table I. The cost of these components may be varied depending on its brand, quality and place.

Equipments	No. of set	Price (BDT)
Rack	1	300
Pinion	1	400
Gear	3	1000
Dynamo	1	2000
Belt	1	60
Chain	1	100
Spring	4	200
Body	1	1000
Microcontroller	1	360
Traffic light		140
Wiring		200
Installation and maintenance cost		1000
Miscellaneous		500
Total Cost		7,260

VI. Result Analysis

A. *Theoretical Analysis:*

Pinion's rotation is expressed by

$$n = \frac{l \times N}{L} \tag{1}$$

Where, n is the number of rotation of the pinion
N is number of rotation of the pinion for total length
l is the displaced length of rack in meter
and L is the total length of rack in meter

In this system, the value of pinion's rotation,

$$n = \frac{1.2 \times 2.1}{20} = 0.1275$$

Generated voltage per rotation is expressed by

$$V_g = n \times R_G \times V_r \tag{2}$$

Where, V_g is the generated voltage per rotation in volt
n is the number of pinion's rotation
R_G is the gear ratio
and V_r is the rated voltage in volt.

The value of generated voltage per rotation

$$V_g = 0.1275 \times 7.2 \times 12 \approx 11$$

Efficiency is expressed by

$$\eta = \frac{V_g \times I}{m \times g \times l} \times 100\% \qquad (3)$$

Where, η is the efficiency of the system
I is the current through the system in mA
m is the mass of the vehicle in kg
g is the gravitational acceleration in ms^{-2}
and l is the displaced length of rack/time

Efficiency measured in this system

$$\eta = \frac{8 \times 60 \times 10^{-3}}{60 \times 9.8 \times 0.0002} \times 100\%$$
$$= 4.085\%$$

B. *Charging Time for Mechanical Device:*

Charging time is expressed by

$$t = \frac{Ah}{I} \qquad (4)$$

Where, t is the time in hour
Ah is the ampere-hour rating of the battery
I is the generated current for 10 mechanical devices

If 10 set of mechanical devices are used, then the charging time of 4.5 Ah 12 V battery is

$$t = \frac{4.5}{0.6} = 7.5 \text{ hours}$$

C. *Experimental Result*

The generated voltage and current flowing through the system are summarized in Table I.

TABLE I: RELATION AMONG VOLTAGE, CURRENT AND NUMBER OF VEHICLES

Observation No.	Number of vehicle passing	Generated Voltage, E_g (volt)	Current, I (mA)
1	1	7.19	8.09
2	1	4.48	6.52
	2	10	5.5
3	1	4.9	8.41
	2	9.07	7.4
	3	13.08	1.03
4	1	7.15	8.09
	2	9.7	3.74
	3	10.77	7.33
	4	16.48	4.8
5	1	8.9	8.04
	2	10.82	8.98
	3	15.88	1.98
	4	17 .76	5.74
	5	19.87	0.89

It is evident from Table I that generated voltage and current flowing through the system are increased with the increase of number of vehicles pass through the speed breaker. Relation between generated voltage and current flowing through the system is shown in Fig. 7.

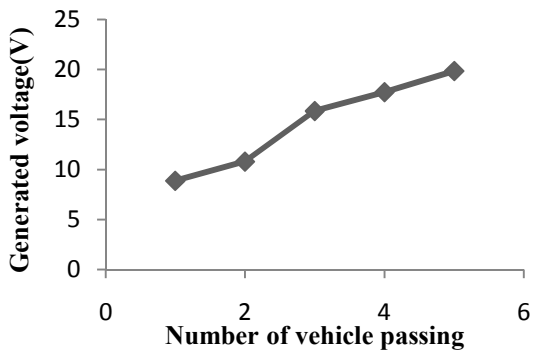

Fig. 7: Relation between generated voltage and number of vehicle passing

D. *Simulation Output*

Simulation output of traffic control system when north and south lane vehicles are stopped, all vehicles are waiting and east and west lane vehicles are stopped are shown in Fig. 8, Fig. 9 and Fig. 10 respectively.

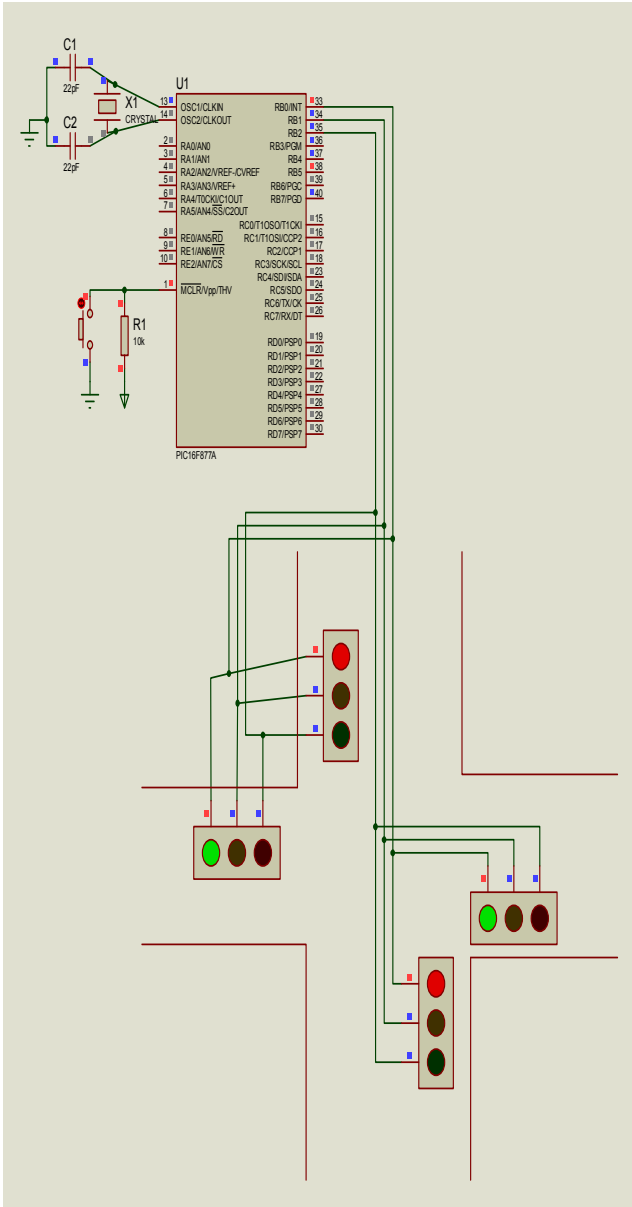

Fig. 8: North and South lane vehicles are stopped. East and west lane vehicles are running

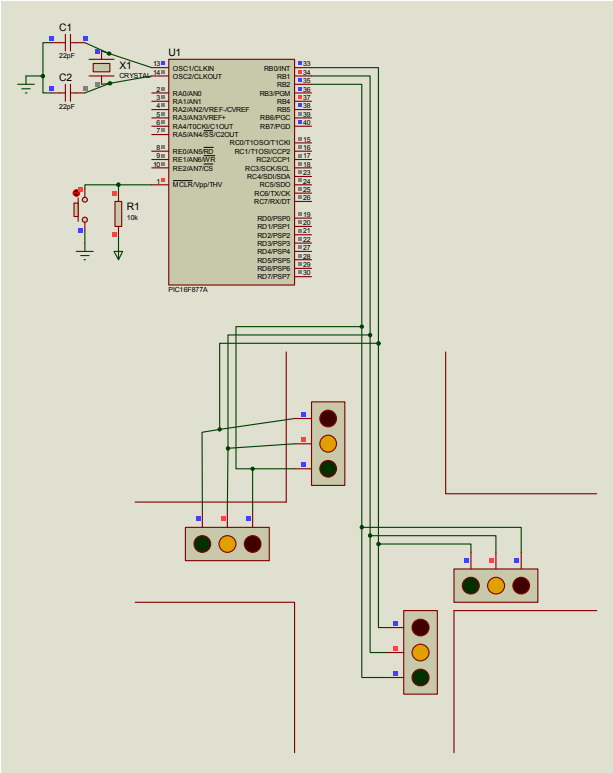

Fig. 9: All vehicles are waiting

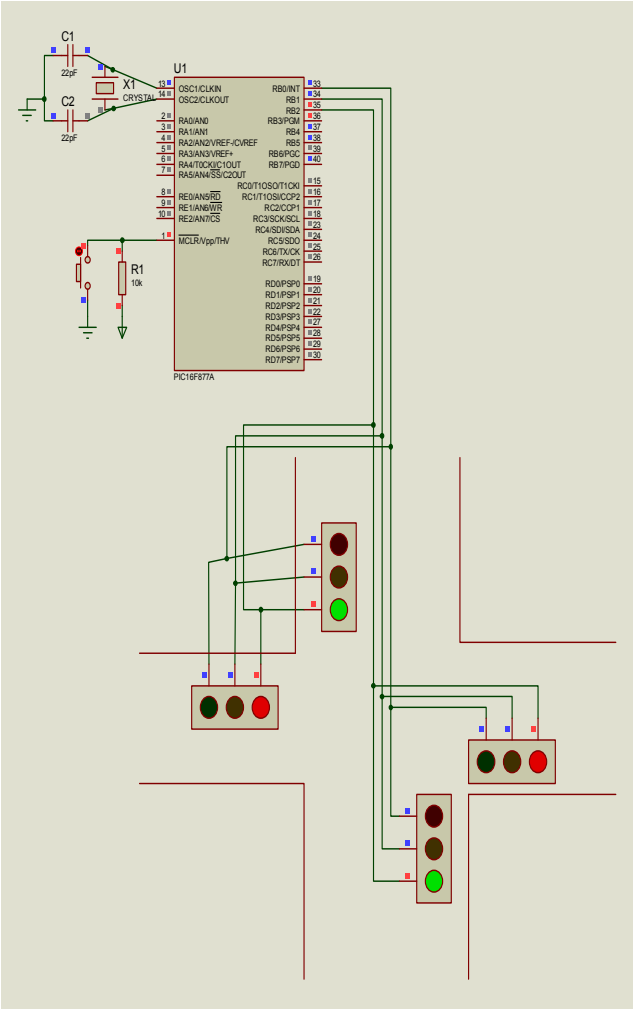

Fig. 10: North and South lane vehicles are running. East and west lane vehicles are stopped.

VII. ADVANTAGES

- Low maintenance cost
- Low installation cost
- Pollution free power generation.
- No manual work necessary during generation.
- No fuel transportation problem.
- Energy available all year round.
- Provide orderly movement of traffic
- Minimize conflicting movement
- Increase traffic handling capacity
- Simplicity

VIII. CONCLUSIONS

The power generation system for controlling automatic traffic light has greater flexibility and the power source of the implemented system is non conventional. Moreover, the way of power generation technique to control the automatic traffic light is clean, cost-effective and safe also. This system not only reduces power crisis and load shedding but also controls the vehicles flow automatically that play important role to avoid the traffic jam which wastes large man-hour in present times. The overall system is environmental friendly and sustainable development is possible by adopt this technique.

ACKNOWLEDGMENT

The authors would like to thank the Department of Electrical & Electronic Engineering (EEE) of Chittagong University of Engineering & Technology (CUET), Chittagong-4349, Bangladesh.

REFERENCES

[1] Dinesh Rotake and Prof. Swapnili Karmore, "Intelligent traffic signal control system using embedded system," *Innovative Systems Design and Engineering,* vol. 3, no. 5, 2012.

[2] R. A. Ganiyu, O. T. Arulogun and O. O. Okediran, "Development of a microcontroller-based traffic light system for road intersection Control," *International Journal of Scientific & Technology Research,* vol. 3, no. 5, May 2014.

[3] A. Padma Rao, A. Kiran Kumar and S. Suresh, "Power Generation from Speed Breaker by Rack and Ratchet Mechanism," *International Journal of Current Engineering and Technology*, sp. no. 2, February 2014.

[4] Md. Saiful Islam, Syed Khalid Rahman and Jakeya Sultana Jyoti, "Generation of Electricity Using Road Transport Pressure," *International Journal of Engineering Science and Innovative Technology (IJESIT),* vol. 2, no. 3, May 2013.

[5] Amanpreet Kaur, Shivansh Kumar Singh, Rajneesh, Parwez, and Shashank, "Power Generation Using Speed Breaker with Auto Street Light," *International Journal of Engineering Science and Innovative Technology (IJESIT),* vol. 2, no. 2, March 2013.

[6] Sachin Jaiswal, Tushar Agarwal, Akanksha Singh, and Lakshita, "Intelligent Traffic Control Unit," *International Journal of Electrical, Electronics and Computer Engineering,* vol.2, no. 2, pp. 66-72, 2013.

Password Protected Multiuser Wireless Electronic Noticing System by GSM with Robust Algorithm

Sayidul Morsalin[1], Abdur Rahman[2]
[1,2,3,4,5]Department of Electrical and Electronic Engineering
[1,2,3,4,5]Chittagong University of Engineering & Technology
Chittagong, Bangladesh
morsalinbd@yahoo.com[1], kakoncuet9@gmail.com[2]

Md Abu Bakar Siddiqe[3], Prattay Saha[4], Md. Reduanul Halim[5]
abubakar.khadachara@yahoo.com[3]
prattayeee08@gmail.com[4], mrh.eee.cuet@gmail.com[5]

Abstract—**This paper elucidates a wireless digital noticing system to provide information in an innovative and smart way. The proposed notice board is a multiuser password-protected SMS-based system fabricated with an LCD. The communication and information transfer between the authentic user and the LCD display unit is done via GSM to ensure remote display facilities, so any notice can be displayed on the electronic board from the user's mobile SMS from distant places. To ensure system flexibility, a multiuser noticing and displaying system has been implemented in the system which can display several notices simultaneously. In addition, the user also can print any notice which is of concern to them. The total system is designed with simple logic with a robust algorithm and fabricated with a PIC midrange microcontroller, LCD, GSM module and other commercially available electronic devices to ensure efficiency and reliability with less cost.**

Keywords-digital notice board; electronic notice; GSM; LCD; microcontroller

I. INTRODUCTION

A notice Board is a place where an authenticated authority can leave public messages to advertise things, announce events or provide information of general concern for any important issue [1]. Traditional analog notice boards are usually made of cork, timber or aluminium, which facilitating the addition and removal of paper messages. But some shortcomings make this analog notice board unpopular in general. Ascribed personnel are always needed to change any notice or originate a new one. Also, multiple people gather, struggle and cluster in front of a single traditional notice board for information in case of any urgent notification [1]. Sometimes malicious intentions of any persons can manipulate, remove or perish paper notices attached in a board, leaving other people uninformed. If the boards are placed in busy places, e.g. near entrances or exit points, then a busy person does not get enough time and scope to access and read all the informations posted on a notice board. It become more problematic when no digital printout is possible. One other disadvantage is that these traditional boards often get dirty, having wear and tear on notices and an unorganized pattern, which make the notice board quite inconvenient for users. There is also an unregulated display of information, difficulty in storage and no efficient reference to pass relevant information. This paper deals with an attempt to efficiently overcome the shortcomings of traditional notice boards. Here a system is developed for a modern electronic notice board using SMS-based wireless technology along with secured password protection to allow efficiently people toaccess a notice at a convenient time. With this systems high officials surely don't need to relay on the peons for the notices to hang over. Whenever or wherever the user is, they can just type what information they want to provide on a cell phone and just press the send button. The message will be sent to the board and displayed. Presently almost all electronic notice boards are designed using a wired system [2]. One of the drawbacks of the design is that the system is inflexible in terms of placement because of the messy wires [2]. Since the proposed system is wireless, this problem is alleviated. This system is user-friendly because authenticated personnel display the message at notice boards situated at different locations through a single SMS from the mobile phone. Thereby it eliminates the wastage of paper and ensures the immediate transfer of information. Information can be displayed page by page and expired notices can be stored in the database for a long time. In addition, people can print out multiple copies of any posted notices. So it can be concluded that the proposed system can used successfully in traditional Schools and Colleges, Waiting Rooms, Company Reception Areas, Factory Production Areas, Hospitals, Public Transport Timetables, Exhibition Centres, Art Galleries, Car Show Rooms, Exhibition etc. without errors and maintenance. The users can read notices posted from anywhere provided that the computer is connected through a local area network (LAN) facility.

II. SYSTEM DESCRIPTION

Figure 1 shows the overall block diagram of the system and shows how an effective and reliable communication between a mobile phone and a microcontroller is established by using a GSM modem. The system consists of two modules; transmitter and receiver. The transmitter module is accessed by a user to place a message through an input module such as a keypad or keyboard. The information then transmitted using RF technology to the receiver. It is then be decoded and displayed on an electronic notice board. The RF wireless communication system operates in the presence of a periodic noise environment, includes first and second wireless devices, each such device having, a source of power, a transceiver

coupled to the power source, and a controller/CPU for controlling the operation of the transceiver .

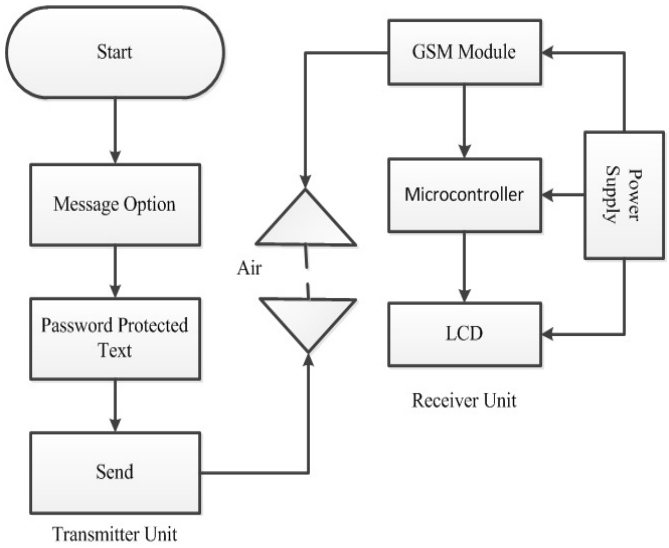

Figure 1. Block diagram of the system

A PIC microcontroller is the heart of the proposed system. The microcontroller is interfaced with GSM modem. A 20×4 Character LCD display is attached to the microcontroller to display messages as notices and notifications. The messages are displayed on the notice board until any new message comes. The new message will trash the old message automatically. Multiple users are authorized to update notices on the electronic notice board by providing password and sending an SMS from their mobile.

III. SYSTEM CIRCUIT DIAGRAM

The overall circuit diagram is depicted in Figure 2. The circuit diagram illustrates interfacing a PIC 16F73 (Peripheral Interface Controller) with GSM module Sim908c, LCD (20×4), 7805, 7812, LM317T voltage regulators, transistor BC547BP act as a power key, and another BC547BP transistor for network lighting. Sim908c is a 60-pin GSM modem; 8 pins 1, 3, 5, 7 are connected to ground and 2, 4, 6, 8 are connected to a 12 volt battery source [3]. Point 13 acts as the power key and is activated generally by a switching mechanism which is to be pressed for at least 1 second. But in our project we made the switching mechanism software based. So a transistor BC547BP along with current limiting resistors 2k, 22k, 47k has been used. When current flows through the base of the transistor then it connects the collector and emitter terminals, which powers the GSM modem [4]. The network light is a red LED, which blinks on the availability of the network. Pin 16 is connected with a voltage-divider circuit of two 47k resistors and then connected to the base of the transistor BC547BP and which turns ON so that the NET-Light blinks [5]. Whether the GSM modem is enabled or not is indicated by a green LED (whether it is on or off), passing through a resistor 47k between pins 20 and 40 of the modem. Microcontroller PIC 16F73 is the central processing unit of this system. A crystal of 20 MHz is used between pins 9 and 10. Pins 17 and 18 pins are used for the data transmit (RXD), data receive (TXD) and for interfacing the data to pins 29, 31 of the GSM module [4]. Pins 25, 26, 27, 28 are the data inputs connected to pins 12, 13 and 14 pin of the LCD display. 23, 24 are EN, RS pins connected to pins 4 and 6 of the LCD display. SIM slots are connected by pins 17, 19, 23 of the GSM modem to pins 6, 5 and 4 pin of the sim card slot. Pin 6 is used for the VDD of the sim and pins and 5 are the reset and clock pins respectively. Pin 21 is the data terminal of the GSM modem and is connected to the I/O port of the sim card and pin 3 is grounded. Pins 1, 4 and 5 are passed through 22k resistors for current limiting. A battery source of 12 volts is passed through a diode so that it gives a protection from polarity mismatch of the loads [6]. If the polarities are mismatched then the diode will not permit the flow of current, saving the instruments. The GSM modem is run by a 3.8 volt battery source and the microcontroller is powered by 5 volts. Voltage regulators 7805 and LM317T are used for this purpose. From a battery source 12 volts is passed through voltage regulator 7805 to generate 5 volts which is connected to port 1 to power up the microcontroller and to the VDD port of the LCD. LM317T gives a steady output of 3.8 volts to power the GSM modem and is connected to the 2, 4, 6, 8 ports of the GSM modem [6, 13]. 10nf and 100 microfarad capacitors are used in the battery source to make the output smooth.

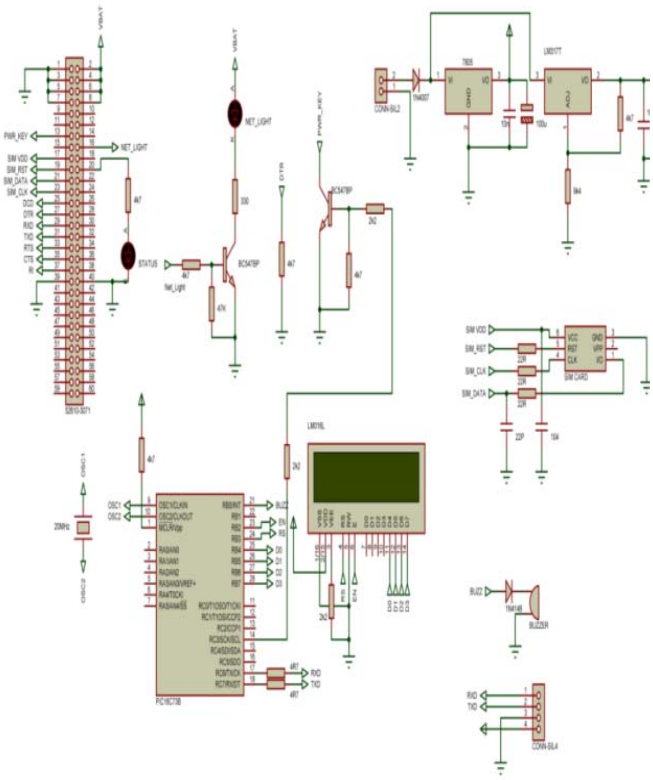

Figure 2. System circuit diagram

IV. HARDWARE DESCRIPTION

To reduce the complexityof the design process, simple algorithms and commercially available devices have been used to implement the system.

A. Central Processing Unit

A PIC 16F73 microcontroller has been chosen as the central microprocessor unit of this system. It is a 28-pin DIP IC [8-9]. It has a Program Memory of 4096 bytes (Single Word Instructions), Data SRAM of 192 bytes, 22 I/O Ports, 11 Interrupt pins, five 8-bit A/D channels, two timers 8 bit, one timer 16 bit, Operating Frequency DC - 20 MHz, FLASH Program Memory 4K (14-bit words) and instruction set of 35 instructions [8]. Basically its low cost and commercial availability make it attractive as the main processing unit. Moreover, all necessary peripherals are already built into it, saving time, space and cost. Sometimes analog circuitary with different control approach [19] can be used for the information processing, however for the simplicity microcontroller is recommended for this system [9].

B. GSM SIM908C Modem

A GSMSIM908C Modem has been used in the system to send messages from an authenticated authority to the main monitoring unit i.e. the notice board. It sends and receives data by wireless so that it can easily communicate from a distance. SIM908 is a new version of the ARM926EJ-S module and it enhances the main frequency performance compared to the previous ARM7 type. Moreover, this advanced module can save power consumption by up to 40% in sleep mode over the current industry average [11]. This modem has an internal GPS system which is integrated with the main circuit. This type of modem offers reliability, performance, efficiency, cost, and space. It occupies less space and weight: about 30*30*3.2 mm and 5.2 grams. It controls by AT commands. Its voltage range for GPRS and GPS is about 3.2- 4.8V and 3.0- 4.5 V respectively, with a very low power consumption. Its operating temperature range is 40~ 85ºC [11, 14].

C. System Power Supply Unit

The power supply of the system is designed specially. The system is run by the main power system which is placed adjacent to the digital notice board. So the system doesn't need costly battery circuitary. A rectifier converters the main supply power to the system operating level. To regulate the voltage, an IC LM 7805 voltage regulator has been used [12-14].

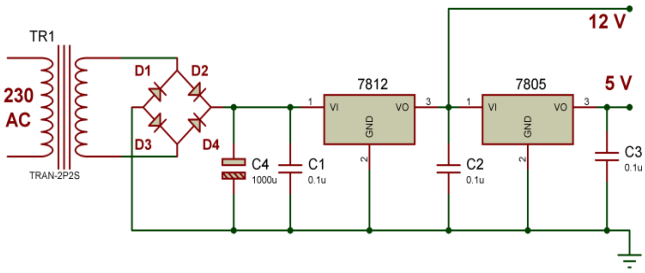

Figure 3. System power supply unit

D. AT Commands for Transmission or Reception of SMS

Basically AT commands are used as the control instructions of the modem. To control the dial-up modem or the GSM/GPRS modem several AT commands are used. The ATO command is used to return to the online data state, ATH is used for hook control, ATA is used for answer, ATD is used to dial. These commands are also supported by the mobile phones [15]. The message or information which is stored to the subscriber identity module (SIM) can be read by appropriate AT commands also. GSM/GPRS modems support some additional AT commands for same purposes side by side the standard AT commands. To read messages or information via the SIM by the computer, mobile phones or GPRS/GSM modem should support two AT commands: +CMGR (this command is used to read information or messages through the PC at a specific location of the storage) and +CMGL (This command is used to list messages, to read messages that have specific status in storage like stored unsent, stored sent, received read, received unread) [15] [18]. The +CMGL AT command is used to cover messages from the storage section. To active short message service (SMS), an authentic SIM should be used in the mobile phone or GPRS/GSM modem, and to connect to the computer [16]. Table 1 shows some AT commands which are used in the system for writing, sending, reading, status checking and others [12].

TABLE I. SOME AT COMMANDS USED IN GSM DATA TRANSFER MODULE OF THE SYSTEM

AT Command	Description
+CMGC	Sending the command
+CMGS	To send message/information
+CMMS	Additional SMS to send
+CMGW	To write message/information
+CMGD	To delete message/information
+CMSS	Send message from storage
+CMGI	Module testing

V. SOFTWARE DESCRIPTION

A flowchart for the software algorithm to implement the system is depicted in Figure 4. High-level programming language in the microcontroller has been used to implement the firmware of the system. "Proton IDE of PIC" compiler facilitate this firmware development by providing useful built-in routines and flexibility in writing code for the microcontroller [15-18]. The reason for using this software as a programmer is that this program is compiled easily and provide instant feedback on syntax errors while writing. This facility provides less hassle and uninterrupted workflow to write the code and compile using the program. This is suitable for all levels of user. The Proton Development Suite allows them to develop code in a brand-new IDE, then compile a BASIC program and view the resulting assembly language commented with its own code. Proteus software has been used for microprocessor simulation, schematic capture and printed-circuit-board (PCB) design. The suite mixes combined-mode

SPICE circuit design, microprocessors models, and animated components which is convenient in the microcontroller-based design process and simulations [16]. It simulates input/output ports, interrupts, timers, USARTs and all other peripherals present on each supported processor and allows creating clinical executable decision support guidelines with little effort. On completion, the HEX file generated from Proton IDE is loaded into the microcontroller.

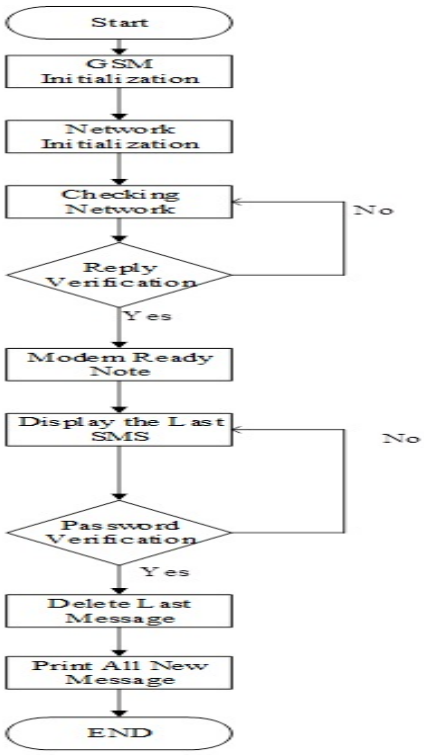

Figure 4. Flow chart of the system

VI. IMPLEMENTED SYSTEM VISUALIZATION

The implemention of the wireless noticing systems is illustrated in Figure 5.

Figure 5. Arrangement of implemented system

When an authenticated person transmits a notice, they should write the password first, then text. The receiver unit receives the SMS and match the password to see whether the person is authenticated or not. If so then there is a display 'Powering Up…. Modem Ready!!' on the LCD which is shown Figure 6.

Figure 6. Initializing the system

The notice to be displayed is always determined and maintained by the assigned authority. For this system a notice of text 'Welcome to the very new technology of messaging. This is first time in C.' is displayed on the LCD, as in Figure 7. The notice can be printed depending upon the viewer inclination.

Figure 7. Notice on LCD display

VII. CONCLUSION

The proposed system works very effectively. Due to password protection, security is maintained strictly which makes it user friendly to officials. Also the viewer can store the notice by printing if they are in hurry. Some additional features can make the system more attractive, for example interfacing an EEPROM with the system can allow it to store more messages at a time and also can give a revive facility at any hazardous condition like power failure or other power problems. The proposed implemented system's alphanumeric LCD can be replaced by a large LED display without changing the cardinal algorithm and design methodology, and can gives more space for noticing, better resolution and a more attractive display.

REFERENCES

[1] Osamor, V. C., Aloba, O. S., & Osamor, I. P., "From wooden to digital notice board (dnb): design and implementation for university administration," International Journal of Electrical & Computer Sciences, 10(2), 79-83, 2010, pp. 79-83

[2] Shruthi, K., Harsha Chawla, and Abhishek Bhaduri. "Smart notice board." Research & Technology in the Coming Decades (CRT 2013), National Conference on Challenges in. IET, 2013.

[3] Villar, N., Van Laerhoven, K., & Gellersen, H., "A physical notice board with digital logic and display." Proceedings of the 2nd European Union symposium on Ambient intelligence. ACM, 2004.

[4] Mishra, P., Pinki, S., and Shivani, G., "SMS based wireless notice board display using gsm mobile." International Journal of Advance Research in Science and Engineering (IJARSE), Vol – 2, No- 10, October, 2013

[5] Azim, M. R. S., Mahmud, K., and Das, C. K., "Automatic train track switching system with computerized control from the central monitoring unit," International Journal of u-and e-Service, Science and Technology, 7(1), 2014, pp. 201-212.

[6] Nayagi, R. P., & Seethalakshmi, R., "Design and Implementation of Digital Notice Board Using Power Line Communication." International Journal of Engineering & Technology (0975-4024) 5.2 (2013).

[7] Bhoyar, Mayur R., Suraj Chavhan, and Vaidehi Jaiswal. "Secure Method of Updating Digital Notice Board Through Sms With Pc Monitoring System."

[8] Mahmud, K., Alam, M. S., and Ghosh, R., "Design of digital thermometer based on PIC16F77A single chip microcontroller," 2013 3rd International Conference on Consumer Electronics, Communications and Networks (CECNet), 20-22 November, 2013, Xianning, China, pp. 246-249.

[9] Mahmud, K., "Neural network based PID control analysis," 2013 IEEE Global High Tech Congress on Electronics (GHTCE), 17-19 November, 2013, Shenzhen, China, pp. 141-145.

[10] Mahmud, K., Alam, M. S., and Jobayer, A., "Design and performance evaluation of PIC16F77A microcontroller based fluid velocity meter," 2013 IEEE Global High Tech Congress on Electronics (GHTCE), 17-19 November, 2013, Shenzhen, China, pp. 21-24.

[11] Gaikwad, A., Tej, K., Manan, L., and Deepak, K., "Wireless Electronic Notice Board." International Journal on Advanced Computer Theory and Engineering (IJACTE), Vol- 2, Issue- 2, 2013

[12] Zohedi, F. N., "Wireless electronic notice board." BSc. diss., Universiti Malaysia Pahang, 2007.

[13] Alam, M. S., Jamil, I. A., Mahmud, K., and Islam, N., "Design and implementation of a RF controlled robotic environmental survey assistant system," 2013 16th International Conference on Computer and Information Technology (ICCIT), 8-10 March, 2014, Khulna, Bangladesh, pp. 438-442.

[14] Morsalin, S., Mahmud, K., Halim, M. R., Saha, P., and Jamil, I. A., "Freighter fuel level detection and overload alarming system with safety notification via GSM," 2014 International Conference on Informatics, Electronics & Vision (ICIEV), 23-24 May, 2014, Dhaka, Bangladesh, pp. 1-5.

[15] Kamdar, F., Malhotra, A., and Mahadik, P., "Display message on notice board using GSM," Advance in Electronic and Electric Engineering, ISSN 2231-1297, Vol- 3, No- 7, 2013

[16] Nivetha S. R, Pujitha. R, Selvaraj, P., and Yashvanthini S. M, "SMS based wireless notice board with monitoring system," International Journal of Advanced Electrical and Electronics Engineering (IJAEEE), Vol- 2, Issue- 3, 2013

[17] Ahmed, M., Sadanand, K. M., and Nasrin, S., "Wireless Electronic Notice Board using GSM Technology." International Journal of Research in Computer Engineering & Electronics 3.6 (2015).

[18] Bashir, A., Qazi, S., Banday, S. A., Nazir, L., & Shah, B. "DTMF based smart notice board system." International Journal of Scientific and Research Publications, Volume- 3, Issue- 11, November 2013

[19] Morsalin, S., Mahmud, K., Mohiuddin, H., Halim, M.R., Saha, P.,"Induction Motor Inter-turn Fault Detection Using Heuristic Noninvasive Approach by Artificial Neural Network with Levenberg Marquardt Algorithm," 2014 International Conference on Informatics, Electronics & Vision (ICIEV), 23-24 May, 2014, Dhaka, Bangladesh, pp. 1-6.

Numerical analysis of O-PCF structure for sensing applications with high relative sensitivity

Kawsar Ahmed, Sayed Asaduzzaman and Md. Faizul Huq Arif
Department of Information and Communication Technology (ICT)
Mawlana Bhashani Science and Technology University (MBSTU)
Santosh, Tangail-1902, Bangladesh

***Abstract*— In this study, micro structured core and cladding based O-PCF has been analyzed by its propagation characteristics. The effects of pitch variation, total power consumption and effective refractive index are investigated on O-PCF. The analyzing process takes place by the full vectorial finite element method (FEM). The analysis O-PCF contains five layers of the air holes in octagonal shape which increases relative sensitivity significantly and decreases confinement loss than the prior structures. Beyond that, the analysis O-PCF can sense the three chemicals water, Ethanol and Benzene at a wide range of wavelength.**

Keywords — Chemical Sensor, Confinement Loss, Evanescent Field, Liquid Sensing, Octagonal Photonic Crystal Fiber (O-PCF) and Sensitivity

I. INTRODUCTION

In recent years, the appealing and versatile application of Photonic Crystal Fiber has aroused the attention of the pioneers and researchers. In PCF, a periodic arrangement of microscopic tiny air holes in the entire fiber contains silicon background with low and high refractive index materials which is a low loss periodic dialectric medium. Propagation of light in PCF using total internal reflection is more superior to the conventional fibers. The two main categories of PCF are index-guiding fibers and photonic band gap (Air guiding) fibers (PBF) bears the difference of effective refractive index between the core and cladding. Nonlinear generation of a UV super continuum and visible in a single transverse mode was the widespread application of PCF which enhanced the potential effectiveness on the conventional optical fiber.

A sophisticated device that converts the light rays into electrical signals which can detect the change and response of ambient condition or can measure the intensity of electromagnetic waves called an optical sensor. A photonic crystal fiber demonstrates its potentiality for sensing applications due to its unique geometrical structure. Physical and biochemical sensor based on sensor measurement parameters has been shown in [1]. PCF can be used for evanescent field sensing where core and cladding region were both microstructure [2]. The light guided in the fiber for producing evanescent field sensing with tight mode confinement possibility was shown in [3]. A Hollow core PCF (HC-PCF) was designed to detect gases as a sensor and the sensitivity was 2.27×10^{-3} dB/ppm with response time 15s [4]. Modified PCF structures with the ring defect at the core were proposed to measure toxic/ flammable gases for safety against the fire, explosion or toxic exposure. Those structures enhance the sensitivity as gas sensor to 13.23 % and reduced confinement loss to 3.77×10^{-6} [5]. W. Jin et al. [6] depict all recent micro and nano-engineered optical fibers for gas detection. Here absorption and photo acoustic spectroscopy based detection schemes were also discussed. A 2-D double hole defect PCF was designed as a refractive index sensor where sensitivity was s=500 nm/RIU [7].

A graphene based birefringent PCF had showed high amplitude sensitivity of 860 RIU^{-1} which was based on Surface Plasmon Resonance [8]. As the application field of photonic crystal fiber is increasing as sensors the PCFs are now used as bio-sensing applications [9], [10]. For sensing temperature and pressure a hollow core was proposed in [11]. In the paper, the sensitivity of the HC-PCF enhanced to 480 nm/RIU at the wavelength λ=1.55 µm. High index material based ring defect was used at the core to enhance the chemical sensing capabilities [12]. The high RIS in media with high thermo optic coefficients causes a noticeable nonlinear behavior in the temperature response of the etched Fiber Bragg Grating (FBG). Thermo optic coefficient (like water, Ethanol and other Hydro carbons) was determined in this article [13]. Fiber loop mirror (FLM) based Ethanol filled two PCF structures were proposed as a temperature sensor where refractive index changes with the applied temperature [14].

The guiding properties (relative sensitivity, confinement loss, Birefringence and dispersion) of the photonic crystal fiber depend much on its geometrical structure. Different researchers form different structures and change the existing structures to enhance the guiding properties. In [15] Y. Hou presents highly birefringent polymer terahertz (THz) fibers where cladding air holes were in honeycomb arrangement and elliptical air holes int the core region. Those structures gained high Birefringence and low confinement loss. To measure the characteristics and enhance the guiding properties different structures at the core region were applied. A THz SPSM PCF including a rectangular array of micro array air holes in the core region which could achieve the SPSM operation with a band of 320 GHz in the THz band near 1 THz at the same time the propagation loss of the guided THz wave was also relatively reduced [16]. Broader bandwidth, low loss and much more flattened dispersion were acquired by porous core photonic band gap fiber [17]. Micro structured core [18] and multicore [19] were applied to acquire the desired guiding properties. Two simple structure PCF was proposed by M. Morshed et al. [20, 21] which shows better sensitivity as gas sensors. The proposed simple structures shows higher sensitivity as a gas sensor as well as it shows lower confinement loss at the same time.

Confinement loss is an important guiding property which increases with the increase of sensitivity of PCF. As increasing the sensitivity and at the meanwhile decreasing the confinement loss is a great challenge. Many works had been performing to reduce confinement loss [22, 23].

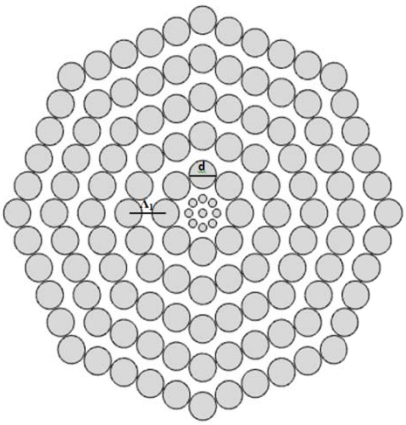

Fig. 1. Cross sectional view of O-PCF.

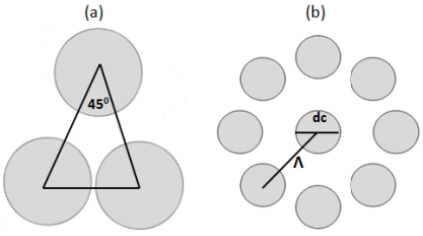

Fig. 2. (a) The unit triangle of PCF (b) The micro-core region

In this paper an octagonal photonic crystal fiber (O-PCF) has been presented which shows better sensitivity and lower confinement loss than the [24, 25]. A numerical analysis was executed on the O-PCF which was proposed [25] by K. Ahmed and M. Morshed. The maximum sensitivity and minimum confinement loss was achieved by pitch value 0.9 µm. But the article [25] did not mention the relationship between wavelength and total power as well as refractive index. This paper is also designed to show those relationships. Now fabrication is a crucial issue for microstructures PCF. Now a day's sol-gel technique has removed the complexity of fabrication of any kind of micro structured optical fiber as well as PCF [26]. So the proposed O-PCF can be easily fabricated using sol-gel technique.

II. Geometries of the Proposed O-PCF

The cross sectional view of the proposed O-PCF has been shown in the Figure 1. The figure clearly depicts the whole geometrical structure of the PCF. The proposed structure of the PCF is in octagonal in shape. So the vertices of the adjoining air holes contain 45^0 angles to form octagonal structure. The pitch between the two layers has been denoted by Λ_1=2.4 µm and the pitch between the two adjacent air holes of same layer has taken 1.80 µm. The diameters of the layers of the supplementary air holes are same for each layer and are denoted by d. The core region contains 8 holes and an air hole at the center. The diameters of the supplementary air holes at the core region is denoted by d_c and the pitch among the supplementary air holes at core is denoted by Λ. The first layer of the supplementary air holes contains 8 air holes and the other layers contain two times more air holes than the premature layer. Various analyst with refractive index like Water (n=1.33), Ethanol (n=1.354) and Benzene (n=1.366) are filled into the supplementary air holes at the core region. Fig. 2 (a) shows the unit triangles of the PCF where the angles are 45^0 and Fig. 2(b) shows the Micro-core region of the proposed O-PCF.

III. Numerical Analysis

Maxwell's equations were applied for analyzing the proposed PCF structure because of its reliability [27]. The Finite Element Method (FEM) has been utilized with a circular perfectly matched boundary layer (PML) to solve Maxwell's equations. Here we investigated and analyzed the sensitivity and the confinement loss of the proposed PCF.

Relative sensitivity coefficient is an important parameter of a PCF to quantify the efficiency of the PCF. Relative sensitivity coefficient measures the interaction between light and the analyte and it can be calculated through the following equation.

$$r = \frac{n_r}{n_{eff}} f \tag{1}$$

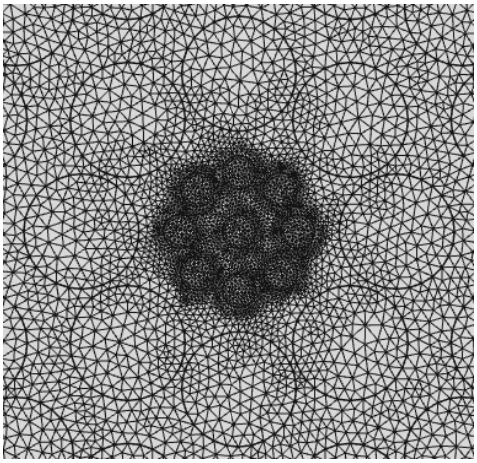

Fig. 3. Finer mesh analysis of O-PCF.

Where, n_r represents the refractive index of sensed material within the air holes and n_{eff} is the modal effective index. f is the percentage energy of holes. For particular fiber mode f can be calculated through the following equation.

$$f = \frac{\int_{sample} Re(E_x H_y - E_y H_x)\, dx\, dy}{\int_{total} Re(E_x H_y - E_y H_x)\, dx\, dy} \times 100 \tag{2}$$

Where, E_x , H_x , E_y , H_y are mode field pattern and calculated by solving Maxwell's equation using finite element method (FEM). E_x and H_x are transverse electric field and magnetic field, E_y and H_y are longitudinal electric field and magnetic field.

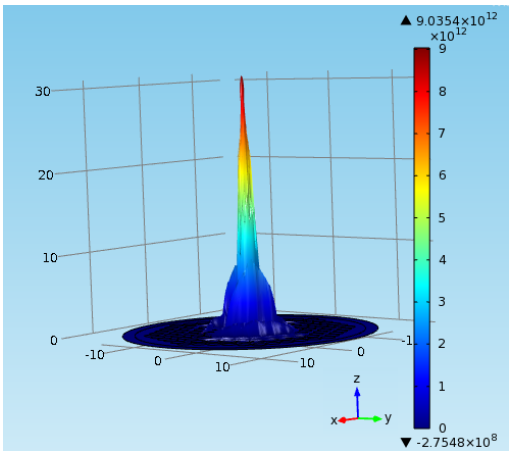

Fig. 4. 3-D view of the modal intensity distribution.

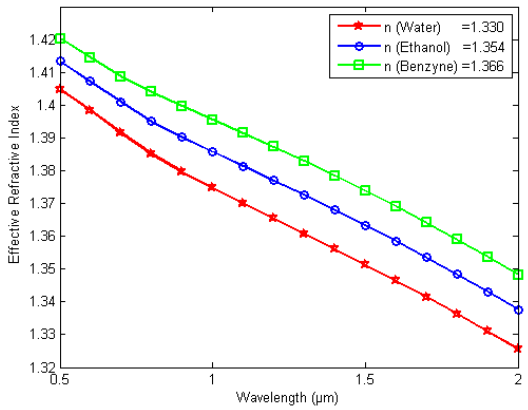

Fig. 5. Comparison of effective refractive index with the wavelength for n=1.330, n=1.354 and n=1.366

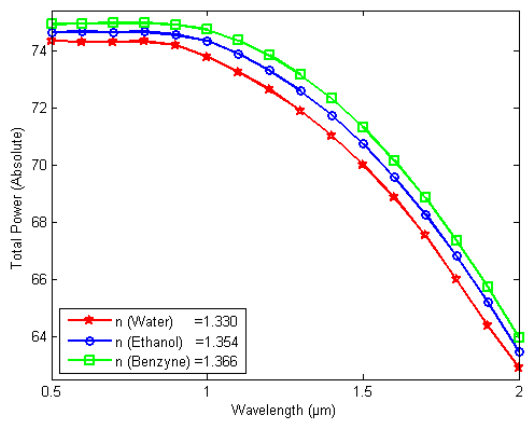

Fig. 6. Comparison of the total power for three different chemicals n= 1.330 (water), n=1.354 (Ethanol) and n=1.366 (Benzene).

A small portion of power loss happens when light energy passes through a PCF. This loss is known as confinement loss of the PCF. Confinement loss L_c (dB/m) can be calculated through the equation (3).

$$L_c = \frac{40\pi.\mathrm{Im}[n_{eff}]\times 10^6}{\lambda.ln(10)} \quad \text{(dB/m)} \qquad (3)$$

Where, $\mathrm{Im}[n_{eff}]$ is the imaginary part of the refractive index and λ is the wavelength of light.

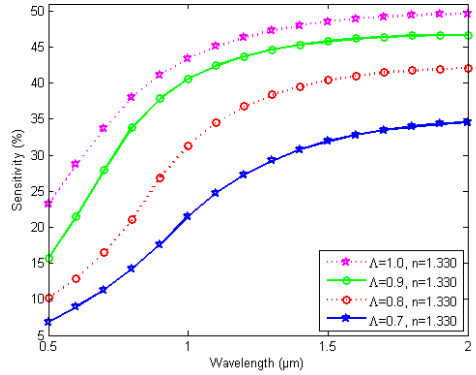

Fig. 7. Comparison of the sensitivity for Λ=1.0, Λ=0.9, Λ=0.8, Λ=0.7 when n=1.330 (water).

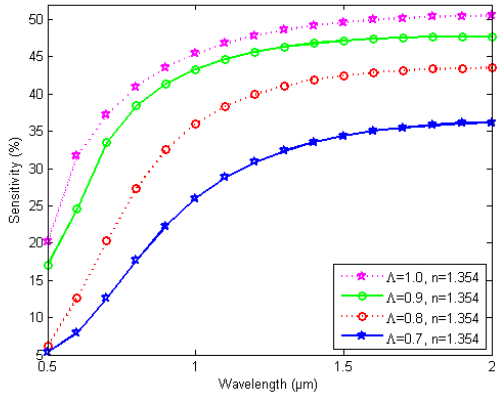

Fig. 8. Comparison of the sensitivity for Λ=1.0 μm, Λ=0.9 μm, Λ=0.8 μm, Λ=0.7 μm when n=1.354 (Ethanol).

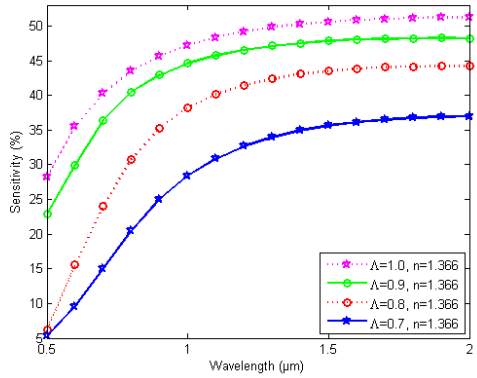

Fig. 9. Comparison of the sensitivity for Λ=1.0 μm, Λ=0.9 μm, Λ=0.8 μm, Λ=0.7 μm when n=1.366 (Benzene).

IV. Results and Analysis

In this section the field profile of fundamental mode, modal intensity distribution and comparison of the prior and proposed PCF has been shown. The comparison of relative sensitivity and confinement loss for three different chemicals

also takes place in this section. Fig. 3 illustrates that mesh analysis of O-PCF structure in finer mode.

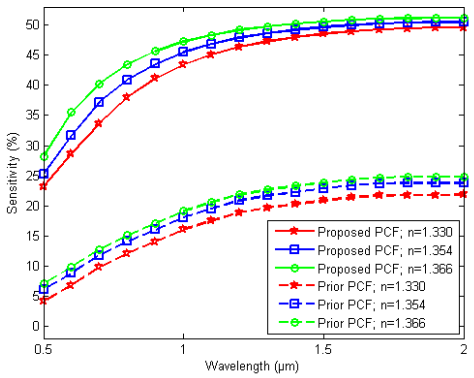

Figure 10. Comparison of the sensitivity of prior and O-PCF

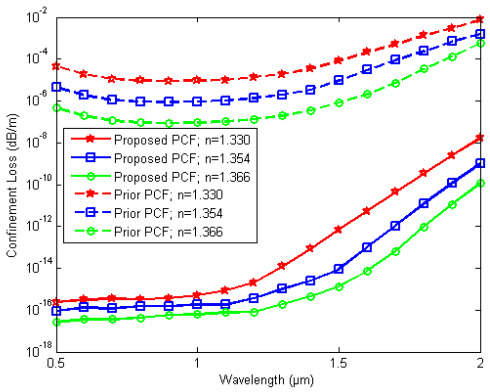

Figure 11. Comparison of the confinement loss of prior and O-PCF

Fig. 4 shows the 3-D view of the modal intensity distribution of the Proposed PCF. The mode has been tightly confined at the core region and is properly distributed along the Z-axis of the figure.

From Fig. 5 it is clear that the effective refractive index linearly decreases with the increase of the wavelength. The lower refractive index based chemical like water (n=1.330) shows higher effective refractive index and higher refractive index based chemicals like Benzene (n=1.366) shows lower effective refractive index.

The total power of a PCF means the power of the holes and the power of the total silica background with perfect matched layer (PML). From the figure it can be describe that the total power of the proposed PCF remains same for the wavelength from 0.5 μm up to 0.9 μm. Then from the wavelength 1 μm the total power decreases linearly according to the wavelength.

Fig. 7, Fig. 8 and Fig. 9 shows the comparison of the sensitivity for the different pitch values are Λ=1.0 μm, Λ=0.9 μm, Λ=0.8 μm and Λ=0.7 μm according to the three different chemicals water (n=1.330), Ethanol (n=1.354) and Benzene (n=1.366). The sensitivity increases with the wavelength and for Λ=1.0 μm the proposed O-PCF shows the higher sensitivity for water (n=1.330), Ethanol (n=1.354) and Benzene (n=1.366).

The proposed O-PCF shows the higher relative sensitivity and lower confinement loss than the previous PCF's better results for three chemicals water (n=1.330), Ethanol (n=1.354) and Benzene (n=1.366) which has been shown in Fig. 10 and Fig. 11. Here Λ_1=2.4 μm, d = 1.75 μm Λ=0.9 μm and dc= 0.514 μm of the proposed O-PCF were constant as the propagation characteristics.

V. Conclusion

In this work a micro core O-PCF has been presented for chemical sensing which shows better sensitivity along with lower confinement loss. The behavior of the proposed PCF has been investigated by changing different geometrical and optical parameters by using three different liquids water, Benzene and Ethanol as analysts. The confinement loss has been decreased and the relative sensitivity of the proposed PCF has also been enhanced almost 2.4 times than the previous PCF for the three chemicals. At the same time our proposed PCF can sense the chemical at a wide range of wavelength from 0.5 μm to 2 μm. The result is simulated using COMSOL Multiphysics 4.2 version. Due to not fabrication of proposed O-PCF the result may be little bit varied after fabrication what is the main drawback of our proposed O-PCF.

Acknowledgment

The authors are grateful who participated to this research.

References

[1] M. Pinto and M. Lopez-Amo, "Photonic crystal fibers for sensing applications," *Journal of Sensors*, vol. 2012, 2012.

[2] C. Cordeiro, M. A. Franco, G. Chesini, E. Barretto, R. Lwin, C. H. Brito Cruz, and M. C. Large, "Microstructured-core optical fibre for evanescent sensing applications," *Optics Express*, vol. 14, no. 26, pp. 13056–13066, 2006.

[3] T. M. Monro, W. Belardi, K. Furusawa, J. C. Baggett, N. G. R. Broderick, and D. J. Richardson, "Sensing with microstructured optical fibres," *Measurement Science and Technology*, vol. 12, no. 7, p. 854, 2001.

[4] X. I. N. Gui, L. Zheng-Ying, H.-H. Wang, J. I. A. He, C.-C. Hu, L.-J. Ma, and others, "Research on Distributed Gas Detection Based on Hollow-core Photonic Crystal Fiber.," *Sensors & Transducers (1726-5479)*, vol. 174, no. 7, 2014.

[5] S. Olyaee, A. Naraghi, and V. Ahmadi, "High sensitivity evanescent-field gas sensor based on modified photonic crystal fiber for gas condensate and air pollution monitoring," *Optik-International Journal for Light and Electron Optics*, vol. 125, no. 1, pp. 596–600, 2014.

[6] W. Jin, H. L. Ho, Y. C. Cao, J. Ju, and L. F. Qi, "Gas detection with micro-and nano-engineered optical fibers," *Optical Fiber Technology*, vol. 19, no. 6, pp. 741–759, 2013.

[7] L. A. Shiramin, R. Kheradmand, and A. Abbasi, "High-sensitive double-hole defect refractive index sensor based on 2-D photonic crystal," *Sensors Journal, IEEE*, vol. 13, no. 5, pp. 1483–1486, 2013.

[8] J. N. Dash and R. Jha, "Graphene-based birefringent photonic crystal fiber sensor using surface plasmon resonance," *Photonics Technology Letters, IEEE*, vol. 26, no. 11, pp. 1092–1095, 2014.

[9] U. S. Dinish, C. Y. Fu, K. S. Soh, B. Ramaswamy, A. Kumar, and M. Olivo, "Highly sensitive SERS detection of cancer proteins in low sample volume using hollow core photonic crystal fiber," *Biosensors and Bioelectronics*, vol. 33, no. 1, pp. 293–298, 2012.

[10] S. M. Shamah and B. T. Cunningham, "Label-free cell-based assays using photonic crystal optical biosensors," *Analyst*, vol. 136, no. 6, pp. 1090–1102, 2011.
[11] S. Padidar, V. Ahmadi, and M. Ebnali-Heidari, "Design of High Sensitive Pressure and Temperature Sensor Using Photonic Crystal Fiber for Downhole Application," *Photonics Journal, IEEE*, vol. 4, no. 5, pp. 1590–1599, 2012.
[12] J. Park, S. Lee, S. Kim, and K. Oh, "Enhancement of chemical sensing capability in a photonic crystal fiber with a hollow high index ring defect at the center," *Optics express*, vol. 19, no. 3, pp. 1921–1929, 2011.
[13] R. C. Kamikawachi, I. Abe, A. S. Paterno, H. J. Kalinowski, M. Muller, J. L. Pinto, and J. L. Fabris, "Determination of thermo-optic coefficient in liquids with fiber Bragg grating refractometer," *Optics Communications*, vol. 281, no. 4, pp. 621–625, 2008.
[14] D. Wu, Y. Zhao, and H. Hu, "Experimental research on FLM temperature sensor with an ethanol-filled photonic crystal fiber," *Sensors and Actuators A: Physical*, vol. 209, pp. 62–67, 2014.
[15] Y. Hou, F. Fan, Z.-W. Jiang, X.-H. Wang, and S.-J. Chang, "Highly birefringent polymer terahertz fiber with honeycomb cladding," *Optik-International Journal for Light and Electron Optics*, vol. 124, no. 17, pp. 3095–3098, 2013.
[16] H. Chen, H. Wang, H. Hou, and D. Chen, "A terahertz single-polarization single-mode photonic crystal fiber with a rectangular array of micro-holes in the core region," *Optics Communications*, vol. 285, no. 18, pp. 3726–3729, 2012.
[17] J. Liang , L. Ren , N. Chen , C. Zhou, "Broadband, low-loss, dispersion flattened porous -core photonic band gap fiber for terahertz (THz)-wav e propagation" , *Optics Communications*, vol. 295, no. 1, pp. 257–261, 2013.
[18] C. Cordeiro, M. A. Franco, G. Chesini, E. Barretto, R. Lwin, C. H. Brito Cruz, and M. C. Large, "Microstructured-core optical fibre for evanescent sensing applications," *Optics Express*, vol. 14, no. 26, pp. 13056–13066, 2006.
[19] B. Li, G. Zhou, C. Xia, H. Liu, and Z. Hou, "Analysis of supermode and structural characteristics of octagonal multicore photonic crystal fiber with large effective mode area and low confinement loss," *Optical Engineering*, vol. 53, no. 5, pp. 056114–056114, 2014.
[20] M. Morshed, M. F. H. Arif, S. Asaduzzaman, and K. Ahmed, "DESIGN AND CHARACTERIZATION OF PHOTONIC CRYSTAL FIBER FOR SENSING APPLICATIONS," *European Scientific Journal*, vol. 11, no. 12, 2015.
[21] M. Morshed, S. Asaduzzaman, M. Arif, F. Huq, and K. Ahmed, "Proposal of simple gas sensor based on micro structure optical fiber," in *Electrical Engineering and Information Communication Technology (ICEEICT), 2015 International Conference on*, 2015, pp. 1–5.
[22] T. P. White, R. C. McPhedran, C. M. de Sterke, L. C. Botten, and M. J. Steel, "Confinement losses in microstructured optical fibers," *Optics Letters*, vol. 26, no. 21, pp. 1660–1662, 2001.
[23] S. Haxha and H. Ademgil, "Novel design of photonic crystal fibres with low confinement losses, nearly zero ultra-flatted chromatic dispersion, negative chromatic dispersion and improved effective mode area," *Optics communications*, vol. 281, no. 2, pp. 278–286, 2008.
[24] H. Ademgil, "Highly sensitive octagonal photonic crystal fiber based sensor," *Optik-International Journal for Light and Electron Optics*, vol. 125, no. 20, pp. 6274–6278, 2014.
[25] K. Ahmed and M. Morshed, "Design and numerical analysis of microstructured-core octagonal photonic crystal fiber for sensing applications," *Sensing and Bio-Sensing Research*, vol. 6, 2015.
[26] R. T. Bise and D. J. Trevor, "Sol-gel derived microstructured fiber: Fabrication and characterization," in *Optical Fiber Communications Conf.(OFC)*, 2005, vol. 3.
[27] F. Brechet, J. Marcou, D. Pagnoux, and P. Roy, "Complete analysis of the characteristics of propagation into photonic crystal fibers, by the finite element method," *Optical Fiber Technology*, vol. 6, no. 2, pp. 181–191, 2000.

Free-Space Optical Communication with m-ary Pulse Position Modulation under Strong Turbulence with Different Type of Receivers

Md. Athaharul Islam* and Ashraful Bari Chowdhury
Department of EEE
Ahsanullah University of Science and Technology
Dhaka, Bangladesh.
*E-mail: a1b2i3r45@gmail.com

***Abstract*—With the exponential increase in demand for high speed precision communication system, free-space optics (FSO) has been proven to be a viable solution to this problem. This relatively new technology has gained popularity because of its wider bandwidth, comparatively greater security and relatively economical configuration. However, in FSO links, due to the atmospheric turbulence which is one of the characterizing elements in the system between the transmitter and the receiver, the magnitude of received signal intensity and also the phase of the received light signal wavers. To diminish fading in FSO systems combination of single or multiple transmitter and receiver are used. Moreover, the efficiency of the FSO systems are enhanced by utilizing the most pertinent modulation technique and channel model, making a suitable compromise between system implementation complexity and overall performance. Taking everything into account, we focus our attention in this paper on m-ary pulse position modulation (PPM) with gamma-gamma atmospheric turbulence model, under strong turbulent condition. Furthermore, APD and PIN photodiodes are used as receiver and a comparison of performance is also been made between them. The overall performance of the system are computed in the form of bit error rate (BER) and the simulation results confirm the analytical findings.**

Keywords*—avalanche photodiode (APD); free-space optics (FSO); gamma-gamma distribution model; m-ary pulse position modulation (PPM); positive intrinsic negative (PIN) photodiode; signal Intensity.

I. INTRODUCTION

Free-space optical communication (FSO) system also known as optical wireless system uses the atmosphere/space between the transmitter and receiver as the propagation medium and the line of sight as the link. It can be used between various platforms such as satellites, ships, aircrafts etc. either stationary or in motion in space and in the atmosphere. Due to its unregulated spectrum, inherent security, high data rate and wider bandwidth, FSO is considered as a supplement to radio frequency (RF) communication [1]. Despite all of its advantages over conventional communication links, because of its propagation medium which cannot be controlled or conditioned, FSO systems are subjected to the consequences of some atmospheric phenomena. The primary challenges associated with free-space optical systems are narrow beam width, transmission signal scattering and scintillation. Because of atmospheric turbulence, intensity of the received signal fluctuates which is known as scintillation [2].

Optimization of the system is achieved by minimizing transmission error rate under both weak and strong atmospheric turbulences and it is done by using combination of single or multiple transmitters and receivers [3], [4]. However, here we specifically consider single transmitter array, in combination with multiple photo detectors (PDs) as multiple receiver arrays. The transmitter and the receiver arrays are positioned in such a way that the fading phenomenon between transmitter–receiver pair is considered statistically independent. Hence, gains through diversity can be accrued from single-input and multiple-output (SIMO) system.

Due to the variable nature of the FSO channel it is very difficult to specifically design the channel with high order accuracy. Despite the difficulty and complexity, several statistical description of the atmospheric channel has been introduced. One of the most commonly used statistical model for the probability of density function (PDF) is log-normal distribution. Although, it is pertinent to the weak atmospheric turbulence [5]. Moreover, with the rise in the strength of turbulence, signal scattering intensifies and consequential aberration from log-normal distribution is manifested in the data. Hence, we consider another statistical model which is gamma-gamma distribution. It has two parameters and the basis of this distribution model is a doubly stochastic theory of scintillation and the assumption of the theory is that both small and large scale irradiance deviations of the transmitted wave are dictated by independent gamma distributions. Moreover, the validity of the gamma–gamma distribution has been proven for both weak and strong atmospheric turbulences [6].

In the receiver arrays, the positive intrinsic negative (PIN) photodiodes and the avalanche photodiodes (APDs) are the most commonly used photodiodes in FSO. PIN photodiode is widely employed because of its low-cost, high mitigation to extensive temperature fluctuations and its inherent capability to operate with cheap small-bias voltage power supply. Moreover, PIN photodiode is comparatively less sensitive than APD. In case of APD, here we use silicon (Si) APD in the system because of its ionization ratio (ς), which has a great dependency on applied electric field across the APD.

978-1-4673-9257-0/15/$31.00 ©2015 IEEE

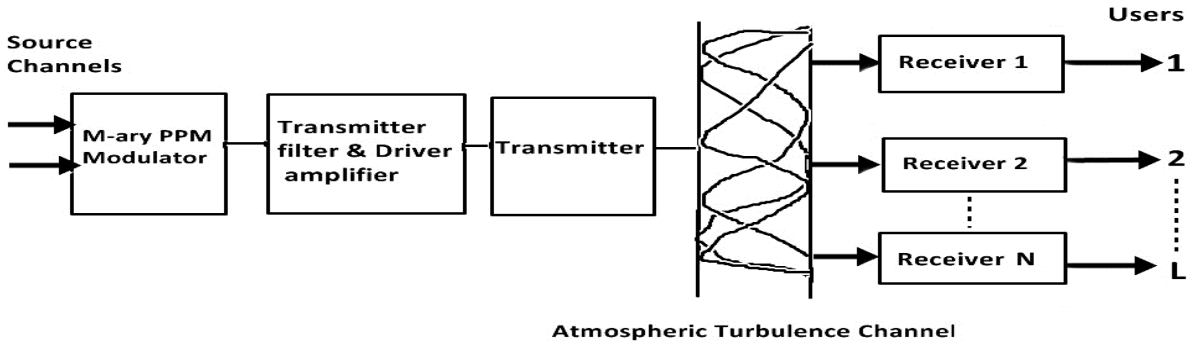

Fig. 1. FSO SIMO system with m-ary PPM under strong atmospheric turbulence.

Furthermore, at low electric fields the values of ionization ratio of APD is at its nadir (in case of Silicon). Moreover, increased power margin provides a more robust communication link than PIN receivers. This allows further reduction in transmitter power and SNR can be increased through the internal gain of APDs. However, APD is expensive and require comparatively higher voltage for operation which limits their practical usage [7], [8], [9]. Out of different modulation techniques, Pulse position modulation (PPM) is among the most commonly used modulation techniques for FSO system. In contrast to other modulation techniques such as on-off keying (OOK), PPM provides several advantages such as better power management efficiency and greater overall performance of the system at the price of a diminished efficiency of bandwidth [10]. Adopting high order m-ary PPM modulation for FSO is shown to enhance the power and bandwidth efficiencies as compared to conventional PPM technique [10], [11].

In the subsequent sections of this paper, we analyze and evaluate the performance of FSO SIMO system with m-ary PPM using two different type of receivers (APD and PIN); in order to make a comparison of performance between them. The overall system performance is computed in the form of bit error rate (BER) assuming the strong atmospheric turbulence is statistically designed with gamma-gamma distribution. The arrangement of the remainder of this paper is- System model is presented in Section II. Then, channel model is depicted in Section III followed by the theoretical analysis in Section IV. After the computation is carried out, results and discussions are carried out in Section V. Lastly, the Section VI consists of the conclusions drawn in this paper.

II. System Model

Block diagram of the model under consideration is illustrated in Fig. 1. The modulation of the source codes has been done with m-ary PPM and the encoding is done by the SIMO encoder and the laser diodes in the transmitter array are modulated by output of this encoder. Then the light passes through gamma-gamma distribution. AWGN due to shot noise and thermal noise, are added at the receiver input. As receiver, we use PIN and APD to convert the light intensity into electrical current. The information of the full channel state is considered to be available at the photo detectors. Let the gain of our considered path be A_{MN} , from M number of sources (for SIMO system, M=1) to N number of detector. In case of m-ary PPM, each transmitted data consists of m number of time slots, thereby transmitting $L=\log_2^m$ bits per data. The transmitted signals are outlined by the waveforms,

$$X = S_m(t) = \begin{cases} 1, & for\ t \in \left(\frac{(m-1)T_s}{L}, \frac{mT_s}{L}\right) \\ 0, & elsewhere \end{cases} \quad (1)$$

The received signal is directed onto the array of photodiodes. Signal at receiver is given by

$$P = P_R \times X \quad (2)$$

Here, P_R represents average power of received signal. X is defined by (1). The conversion of the optical signal to electrical signal at the photodiode is done with responsivity, R. Both shot and thermal noise are described with a zero-mean Gaussian noise. At receiver electrical signal, y is defined as-

$$y = RP + n \quad (3)$$

Here, P represents signal at the receiver and zero-mean Gaussian noise with Rytov variance σ_R^2 is represented by n. Now, the average power of optical signal at the receiver is given by [12].

$$P_R(I) = P_T \eta_T \eta_R G_T G_R \left(\frac{\lambda}{4\pi L}\right)^2 I \quad (4)$$

Here, the average transmitted power is represented by P_T; efficiency of transmitter and of receiver are respectively η_T and η_R; transmitter and receiver gains are respectively G_T and G_R; wavelength under consideration is λ; measured distance between transmitter and receiver is L; state of the channel because of turbulence is I.

III. Channel Model

The complex and variable channel can be precisely calculated if the statistical model under consideration is appropriate for the atmosphere. In order to properly model a FSO system with strong atmospheric turbulence it is essential to characterize the channel through proper probability density functions (PDFs). Several PDFs have been introduced for the intensity deviations at the photo detectors of FSO systems. From all, this paper mainly highlights on the use of gamma-gamma distribution model. This model is mathematically characterized by the Rytov variance σ_R^2.

Gamma-Gamma Distribution:

This model considers two random processes, both of which are independent and the product of them, each with a gamma PDF describes the factorization of irradiance. The probability density function of the deviation in intensity is given by [13],

$$f(I)=\frac{2(\alpha\beta)^{(\alpha+\beta)/2}}{\Gamma(\alpha)\Gamma(\beta)} I^{\frac{(\alpha-\beta)}{2}-1} K_{(\alpha-\beta)}\left(2\sqrt{\alpha\beta I}\right),\ I>0 \quad (5)$$

Here, I (w/m²) represents signal intensity, $\Gamma(.)$ represents gamma function, and $K_{(\alpha-\beta)}$ represents modified Bessel function of second kind and order $\alpha\beta$. α and β represent PDF parameters, defining scintillation and considering, zero-inner scale are defined by [13]

$$\alpha = \frac{1}{\exp\left[\frac{0.49\sigma_R^2}{\left(1+1.11\sigma_R^{12/5}\right)^{7/6}}\right]-1} \quad (6)$$

$$\beta = \frac{1}{\exp\left[\frac{0.51\sigma_R^2}{\left(1+0.69\sigma_R^{12/5}\right)^{5/6}}\right]-1} \quad (7)$$

Here, σ_R^2 is the Rytov variance, which is given by [3].

$$\sigma_R^2 = 1.23 C_n^2 K^{7/6} L^{11/6} \quad (8)$$

Here, C_n^2 represents refractive index structure parameter.

IV. Theoretical Analysis

Here, we consider two cases: m-ary PPM with APD as receiver and also with PIN photodiode as receiver. All cases are discussed for gamma-gamma distribution model. The generalized bit error rate of the system with m-ary PPM under gamma-gamma distribution, P_b^m is derived from [10]

$$P_b^m \le \frac{m}{2} W|X| \sum_{i=-N, i\neq 0}^{N} Q\left\{\frac{IX^2}{\sqrt{F\, IX^2 + K_n}}\right\} \quad (9)$$

Here, m represents level of modulation, I represents signal intensity (Irradiance), W and X respectively represent weight factors and the zeros of the Hermite polynomial, N is the receiver number, K_n represents per slot total noise and is derived from [10],

$$K_n = \frac{[\log_2(m)]2\sigma_R^2}{m(E\{g\}q)^2} + 2FK_b \quad (10)$$

Here, σ_R^2 is Rytov variance, K_b represents average background noise photons per slot, APD average gain is represented by $E\{g\}$ and q represents charge of electron. Considering statistical nature of avalanche multiplication by using McIntyre formula, excess noise factor can be defined as [14],

$$F = \varsigma E\{g\} + (1-\varsigma)\left(2 - \frac{1}{E\{g\}}\right) \quad (11)$$

Here, ς is the ionization factor. Considering $\varsigma < 0.1$ and $E\{g\} > 20$ McIntyre formula in (11) can be shortened with great accuracy and so the noise factor F of APD becomes,

$$F \approx 2 + \varsigma E\{g\} \quad (12)$$

Using the derived value of F from (12) in (9), the bit error rate is calculated for the system with APD photodector. Similarly, the bit error rate is also calculated for the system with PIN photodector by setting the value of both noise factor (F) and gain $(E\{g\})$ to unity in (11).

V. Results and Discussions

After the theoretical analysis propounded in section IV, we calculate the BER for m-ary PPM using SIMO FSO link. The simulation is completed using matlab. Different system elements used for computation are displayed in Table I [5], [10].

TABLE I. Elements Used For Computation

Element Name	Specific Value/ Range of Values
Background noise, K_b	20 photons per bit
Bit rate	2.4 Gbps
Average gain, $E\{g\}$ (for APD)	150
Average gain, $E\{g\}$ (for PIN)	1
Signal Intensity, I	0 to 3 w/m²
Ionization factor, ς	0.028
Length, L	100 m
Load resistance, R_L	50Ω
Modulation level, m	2, 8, 16
No. of receivers, N	5
Rytov variance, σ_R^2	0.7
Temperature, T	300 K
Wavelength, λ	850×10^{-9} m

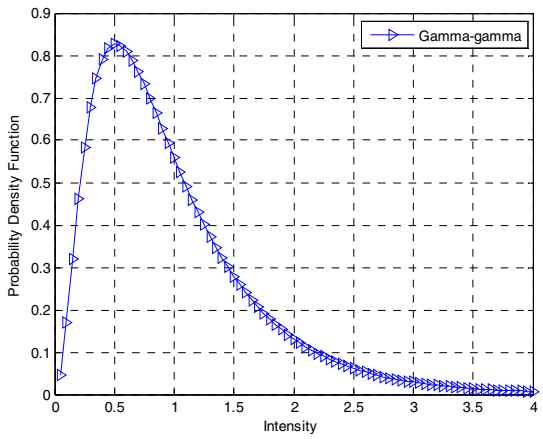

Fig. 2. Plot of PDF vs. Intensity (w/m²) for gamma-gamma distribution.

The plot of Fig. 2 depicts the PDF with respect to intensity for gamma-gamma distribution.

Fig. 3 illustrates the plots of bit error rate vs. Intensity of the system with APD as receiver; in case of m = 2, 8, 16 simultaneously.

Fig. 4 depicts the plots of bit error rate vs. Intensity of the system with PIN photodiode as receiver; in case of m = 2, 8, 16 simultaneously.

Fig. 5 provides an overall comparison of previous plots (Fig. 3 and Fig. 4). From Fig. 5, it is clear that after a certain value of Intensity ($\approx$ 0.25), differences start to emerge in the values of BER in all cases (m = 2, 8, 16) for PIN and APD. Although, regardless of the modulation level (m = 2, 8, 16), the BERs for PIN decrease slowly compared to APD. Hence, significant improvement in performance is noticed for PIN at a greater intensity; whereas in case of APD, BERs decline sharply with increasing intensity for all modulation levels (m=2, 8, 16), implying a significant improvement in performance. Conclusively, considering both APD and PIN

photodiode as receiver with m-ary PPM under strong turbulence it is clear that, APD is better as receiver than PIN photodiode, with m-ary PPM in all cases (m=2, 8, 16).

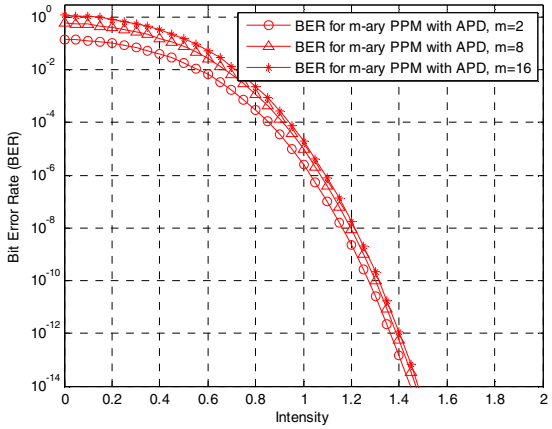

Fig. 3. Plots of BER vs. Intensity (w/m^2) for m-ary PPM with APD receiver.

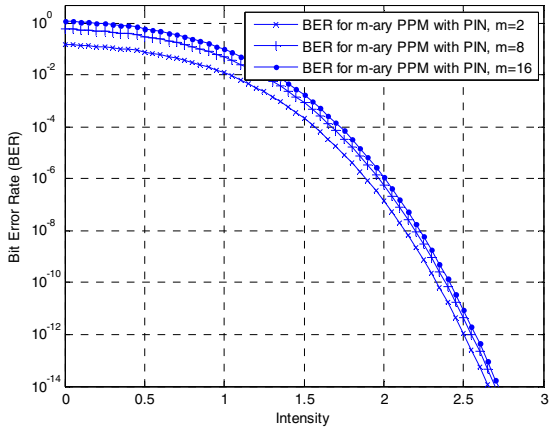

Fig. 4. Plots of BER vs. Intensity (w/m^2) for m-ary PPM with PIN receiver.

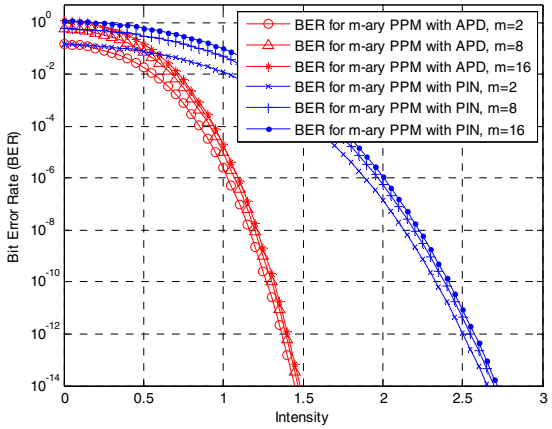

Fig. 5. Plots of BER vs. Intensity (w/m^2) for m-ary PPM with both APD and PIN receivers.

VI. Conclusions

In this paper, we have considered a FSO SIMO system modulated with m-ary PPM and with a strong atmospheric turbulence defined by gamma-gamma distribution using APD and PIN receivers separately. Then a combined comparative evaluation has been made including both cases. The correct expression of the BER is used for the system in both the cases of APD and PIN photodiode in the receiver arrays. By observing the results the following conclusions are made. APD is better than PIN photodiode as receiver with m-ary PPM in the cases of modulation levels, m=2, 8 and 16; due to a better data transmission efficiency is achieved with lower signal intensity. Moreover, due to the same reason considering practical implementations it can be said that, with m-ary pulse position modulated systems, APD is a more cost-efficient solution compared to PIN photodiode.

From the results, we have also concluded that system performance improves with increasing intensity, almost at a similar rate for the considered modulation levels, m=2, 8 and 16 in both APD and PIN photodiode receivers.

References

[1] DAS, S., HENNIGER, H., EPPLE, B., MOORE, C., RABINOVICH, W., SOVA, R., YOUNG, D. Requirements and challenges for tactical free-space lasercomm. In *IEEE Military Communications Conference.* San Diego (USA), 2008, p. 1-10.

[2] L. C. Andrews, R. L. Phillips, C. Y. Hopen, M. A. Al-Habash, "Theory of optical scintillation," J. Opt. Soc. Am. A 16, 1417–1429 (1999).

[3] Wilson S.G., Brands-Pearce M., Cao Q., and Leveque J.J.H.,III, "*Free-Space optical MIMO transmission with Q-ary PPM," IEEE Transactions on Communications,* vol. 53, pp. 1402-1412, 2005

[4] G. Ochse, Optical Detection Theory for Laser Applications. NewYork: Wiley-Interscience, 2002.

[5] Bobby Barua, Mirza Moazzem Hossain, Md. Rezwan Islam, Md. Khairul Bashar, "Performance Evaluation of Different Type of Channel Models in FSO Communication," International Journal of Science and Advanced Technology (ISSN 2221-8386), Volume 1 No 5 July 2011.

[6] M. Uysal, J. T. Li, and M. Yu, "Error rate performance analysis of coded free-space optical links over gamma-gamma atmospheric turbulence channels," *IEEE Transactions on Wireless Communications,* vol. 5, pp. 1229-1233, June 2006.

[7] H. Shaban, S. D. A. E. Aziz, and M. H. Aly, "Probability of error performance of free space optical systems in severe atmospheric turbulence channels," in *10th Mediterranean Microwave Symposium (MMS'2010),* Morphou, Cyprus, Aug. 25–27, 2010, pp. 355–359.

[8] C. Singh, J. John, Y. N. Singh, and K. K. Tripathi, "A review of indoor optical wireless systems," *IETE Technical Review*, vol. 19, no. 1-2, pp. 3–17, Jan.-Apr. 2002.

[9] K. Kiasaleh, "Performance of APD-based, PPM free-space optical communication systems in atmospheric turbulence," *IEEE Transactions on Communications,* vol. 53, no. 9, pp. 1455–1461, Sep. 2005.

[10] M. R. Abaza, N. A. Mohammed, and M. H. Aly, "BER performance of M-ary PPM free-space optical communications with channel fading," in *Proceeding of the 8th International Conference on High Capacity Optical Networks & Enabling Technologies (HONET 2011)*, Riyadh, Saudi Arabia, Dec. 19–21, 2011, pp. 111–115.

[11] J. Yan, Z. Zheng, W. Hu, and A. Xu, "Improved performance of M-ary PPM free-space optical communication systems in atmospheric turbulence due to forward error correction," in *Proceeding of the 10th International Conference on Communication Technology (ICCT)*, Guilin, China, Nov. 27–30, 2006, pp. 1–4.

[12] Hennes HENNIGER, Otakar WILFERT, "An Introduction to Free-space Optical Communications," *IEEE Transactions on RADIOENGINEERING*, vol. 19, no. 2, pp. 203–212, June 2010.

[13] M.A. Al-Habash, L.C. Andrews and R.L. Phillips, *Optical Engineering 40*, pp. 1554-1562 (2001).

[14] McIntyre, R.J., *Multiplication Noise in Uniform Avalanche Diodes, IEEE Transactions on Electron Devices*, ED-13, pp. 164-168 (1966).

Performance Analysis of Large Scale ZigBee Network Design Through Geometric Structure

MD. Jaminul Haque Biddut, Nazrul Islam, Mehedy Hasan Rafsan Jany, Asma Islam Swapna
Department of Information and Communication Technology
Mawlana Bhashani Science and Technology University
Santosh, Tangail-1902, Bangladesh
Email: biddutict@gmail.com, nazrul.islam@mbstu.ac.bd, rafsanjany@outlook.com, asma0swapna@gmail.com

***Abstract*—Wireless Sensor Network (WSN) is a group of the specialized wireless devices which forms a communication infrastructure at a diverse location. IEEE 802.15.4 standard for wireless devices like ZigBee has demonstrated its enormous application as WSN. ZigBee has got popularity for its both small range and wide range coverage. In wide range coverage, a large scale ZigBee network deployment is going ahead. Without proper network structure, a lot of sensor nodes needed for coverage. And also take down the network performance of the large-scale ZigBee network. This study, however, carries a new geometric structure to improve the formation of large scale ZigBee network and its performance. The network simulator Riverbed is used to design and implement a large ZigBee network in geometrical patterns. And also the network performance is analyzed by scrutinizing different network parameters. For real-time communication, free from network path is chosen according to the traffic inside the network. Finally, a deep analysis between two geometric structures - random and octagonal has presented with related parametric aspects. The analysis indicates the new octagonal structure shows significant performance in large scale ZigBee network deployment. This study will create a new opportunity to establish a reliable large-scale ZigBee network.**

Keywords*—WSN, ZigBee Network, Geometrical Network Structure, Performance Analysis, Riverbed.

I. Introduction

ZigBee is a standard wireless sensor device to form a perfectly interoperable sensor network. ZigBee is the standard network protocol base solely conducted under the ZigBee Alliance. IEEE 802.15.4 standard initializes the ZigBee as the standard of the wireless network. IEEE 802.15.4 defines the physical layer under network and application layer of the ZigBee network. ZigBee has superb features such as low cost, low data rate, high security, green power, low power consumption etc. That draws its global value. ZigBee is used in security, pervasive computing, indoor position monitoring, data gathering, industry, home or office automation etc. From consumer electronics to industrial PC peripherals, ZigBee has the ability to control in the various areas of use [1], [2], [3], [4].

ZigBee has three perspective nodes - Coordinator, Router and end devices [1]. Coordinator - works for network intelligence, router connects the path between selected nodes for network establishment. Hence, WSN is the potential aspect between these. Through various optimization processes in Physical and Medium Access Control (MAC) sublayer, IEEE 802.15.4 is designed to achieve an efficient and less power consuming Network [5]. ZigBee's low duty cycle is the counter parameter in the scale of efficiency. The ZigBee network layer, however, uses an altered and on demand default routing system in a large scale ZigBee network called Ad Hoc On-Demand Distance Vector (AODV) [6].

Recent studies in the field of WSN [6], [7], [8] emphasize mainly in Quality of Service (QoS) support for ZigBee network efficiency improvement. This improvement focuses on reliability and performance under heavy energy constraints of the network with respect to QoS performance in the network. Guaranteed Time Slot (GTS) allocation and scheduling algorithm with QoS support routing algorithm applied to large scale WSN [9], [10]. Moreover, Fuzzy logic based smart routing implemented in the ZigBee network [11]. In another study [12], to overcome ZigBee's delay and congestion, a Hybrid Technology Network (HTN) adopted in a large scale network. CSMA/CA mechanism, beacon enabled cluster tree structure implemented to minimize power consumption and to get adequate coverage presented in the article [6]. Furthermore, an enhanced design has adopted with an extra processor connected to the Coordinator by an RS-232 interface presented in the article [13]. Martelli et al. in [14], presented the ZigBee network with CSMA/CA model through stochastic geometry. ZigBee's wireless control system designed in the article [15].

However, all these studies describe the performance enhancement technique of the large scale ZigBee network. All these techniques applied to improve ZigBee's performance in a particular issue rather than the overall network performance. In a broad sense, there is a lacking in large-scale ZigBee network design standards and proper sensor nodes orientation pattern. A perfect network design model may improve efficiency of ZigBee network. A specific network structure analysis and performance evaluation is yet left for large-scale ZigBee network deployment. Hence, this paper emphasizes on geometric structure based network design for a large ZigBee network.

Firstly, the paper represents a performance analysis of different ZigBee network structure layout. This implies, in details, the analysis of random and a specific geometric octagonal structure is considered here, and their prospective performance comparison in terms of global MAC delay, MAC load, End to End delay, Throughput and so forth. Secondly, it accentuates the enhancement could be made in large scale ZigBee automation using the octagonal structured routing. Hence, the main purpose of this paper is to offer a real-time QoS support for a large scale ZigBee network and design it under a specific geometric structure.

The rest of the paper structured in a way where, Section II provides literature reviews with research methodology needed for network design. Section III identifies the problem, simulation study and performance evaluation of ZigBee network. Section IV presents the simulation result with the perspective parametric comparison. Section V concludes the paper with further paths derived from the research findings.

II. Methodology

A literature review has performed to devise the performance of the large-scale Zigbee network design in geometric structure. A deep study has been done to select Octagonal structure among various geometric structures and how to build this large structure with Tree routing. The Octagonal structure having great capability to form a large area coverage network and thus is chosen for constructing the large-scale ZigBee network and analyzing the QoS performance. To analyze the QoS performance of the large-scale Octagonal Zigbee network need a simulation tool which can provide sufficient parameters in different layers of Zigbee network and show precise simulation results. There is variety of simulators like Network Simulator NS-2 and NS-3 [16], OMNET++ [17], Riverbed [18], QualNet [19], Matlab [20] etc. Riverbed modeler, a simulation tool has been used to its user-friendly environment with vast parameters resources and good potential for providing precise results [21]. Riverbed has selected in this simulation study. The Riverbed has installed and configured in an Intel Core i5 based workstation for efficient analysis of ZigBee's different layers.

The different ZigBee protocol layers generate a vast variety of data after simulation. The simulated data from different layers are collected carefully. After analyzing the simulated data, different graphs are plotted. The graphs reflect the effect of ZigBee different network parameters in the large scale ZigBee network and offer competitive measurement for Octagonal versus Random structure.

III. Design and Implementation

This section presents a novel ZigBee network structure has designed with respect to Octagonal structure and randomly node distribution structure. The designed network forms a large-scale ZigBee network. The section also describes the full simulation procedure.

A. Problem Description

ZigBee network is a wireless medium with sensing capability. It constructs a sensor network field in a small area. ZigBee devices have the capability to cover 30-100 m range. ZigBee can able to construct a network with 65,535 devices [21]. The sensor ZigBee end devices are oriented randomly in the small personal area network. To build a large size network just increasing sensor nodes at the end of one sensor node's coverage range in network field [22]. Though extended end devices or routers may provide larger area coverage, it has a great problem with interference with internal and external devices [23], [24], [25]. The problem degrades ZigBee network performance. The randomly oriented sensor nodes sometimes send more application traffic to the Coordinator. Besides, more node density in one portion of the network than other portion that may effect on network performance. Moreover, in the fewer node's portion may arise also coverage problem.

In a broad sense, for setting up a large area ZigBee network to monitor or other sensing tasks in a randomly distributed manner of ZigBee nodes, some obstacles arise and network performance may be hampered.

B. ZigBee Network Planning

Extending the area of the ZigBee network in a random distribution of nodes is an ineffective procedure. To solve the above problem, a novel approach has taken. To set up a large scale ZigBee network, where a lot of ZigBee sensor nodes available and provides a long distance coverage, a geometrical structure based design would be a solution of it.

Various geometric structures exist in the field of networking. Square, Circular. Triangular, Hexagonal etc. are the most common shape in geometrical structure. These structures widely used in the field of network planning and designing context. Different networks have constructed in different shapes. These shape oriented network devices have minimum distance each other as they cover a deterministic distance as its necessity. In ZigBee, end nodes are distributed throughout the entire field.

The octagonal structure has simply eight vertices and connected edges to form an octagon shape. This octagonal structure has a great capability to form a large coverage area network. To set up a large scale ZigBee network based on above solution following sequences is implemented:-

Place all the ZigBee routers in the vertices of Octagonal structure. The ZigBee end devices have to be placed throughout the network centering at routers. All the routers maintain the equal distance from each other as per network area. Coordinator placed at the center of the network field.

Among the routers, end devices and end devices to the router always maintain a similar distance. This creates an opportunity to communicate one device to other devices via intermediary nodes like routers. This helps to Coordinator for processing. This structure runs with the Tree routing method for its high security, robust and reliable routing capability.

In the tree structure, the address of the device in a ZigBee network is assigned by its parent node. The parameter nwkmaxChildren (C_m) represents the largest number of child nodes which can associate with a router or a coordinator. The parameter nwkmaxRouters (R_m) means the number of child nodes which can be a router. The parameter nwkMaxDepth (L_m) decides the most depth in this network. And for this network, different nodes usually have the constant (C_m) and (R_m). Every potential parent is provided with a finite sub-block of the address space, which usually assigned for the network address to its children. Given nwkmaxChildren (C_m), nwkmaxDepth (L_m), and nwkmaxRouters (R_m), to compute the function C_{Skip_d} as the size of the address sub-block distributed by each parent at depth d as follows:

$$C_{Skip_d} = 0, when \;\; R_m = 0.$$

$$\mathrm{C}_{Skip_d} = \frac{1+C_m-R_m-C_m.R_m^{L_m-d-1}}{1-R_m}, when \;\; R_m > 1.$$

$$C_{Skip_d} = 1 + C_m.(L_m - d - 1), when \ \ R_m \neq 1.$$

When C_{Skip_d} of a routing node is 0, it is unable to distribute address for the child node. If C_{Skip_d} of a routing node is greater than 0, the node can accept other nodes as its child nodes and distribute network address for its child nodes. The address of a node which joins in the network firstly is one more than faster node.

Network addresses shall be assigned to the n-th router's child and 1-th end device child at depth $d+1$ in a sequential manner respectively. According to the following equations:

$$A_{d+1,rn} = A_{Parent} + C_{Skip_d}.(n-1) + 1$$

$$A_{d+1,el} = A_{Parent} + C_{Skip_d}.R_m + l$$

Where $1 \leq l \leq R_m$, and A_{Parent} represents the address of the parent. When $1 \leq l \leq (C_m - R_m)$ [26], [27].

This also increases packet delivery ratios. It decreases internal interferences. Furthermore, random orientation of ZigBee nodes and routers in the same network has low packet delivery ratio, increased packet loss etc.

C. Simulation Process

Based on the implementation procedure, popular Riverbed simulator simulates the entire network settings with the Tree routing method. Two scenarios have created as follows- one is randomly distributed nodes architecture called Random structure model (Scenario_1) as depicted in Fig. 1. And another is uniformly distributed nodes that follow the Octagonal structure in Scenario_2 as depicted in Fig. 2. The two scenarios have an equal number of end nodes, routers, and Coordinator. The Tree routing method has to set for both scenarios. Operating frequency, power, simulation time and other used simulation parameters have set for the two scenarios that shown in Table I.

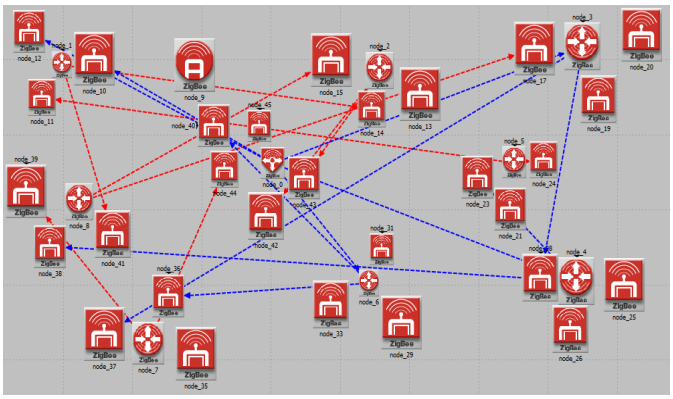

Fig. 1. Routing layout of Random structure model simulation.

IV. Results And Analysis

This section provides a competitive analysis of proposed geometric structure (Octagonal Structure Model) versus random Structure model to design a large scale ZigBee network. The results are gained from Riverbed based discrete event simulation. The graphs are plotted on the basis of analyzing ZigBees different layer parameters (e.g. the end to end delay, packet delivery ratio, MAC delay, MAC load, data dropped threshold and throughput).

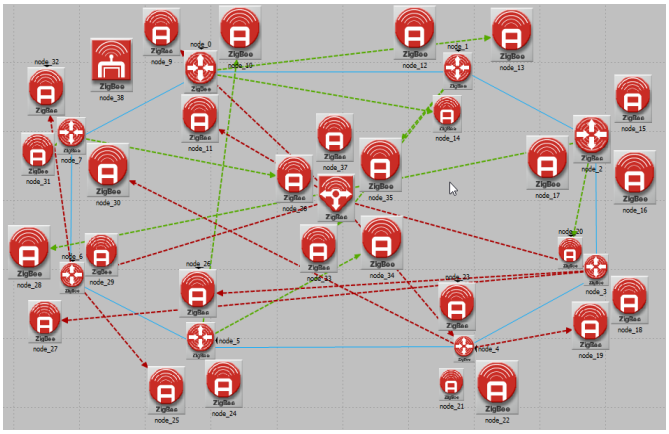

Fig. 2. Routing layout of Octagonal structure model simulation.

TABLE I. ZigBee Network Simulation Parameters Overview

Parameters	Description
ACK status	Enabled
Number of retransmission	5
Frequency Band	2.45 GHz
Data Rate	Auto Calculate
Packet Size	Constant (1024)
Packet interval time	Constant (1,0)
Packet receptionpower threshold	-85
Transmission Power	0.05
Scenario Type	Random and Octagonal
Start Time	Uniform (20,21)
Stop Time	Infinity
Traffic Dimension in Octagonal Model	Routers, End nodes and Coordinator
Traffic Destination in Random Model	Routers, End nodes and Coordinator
No. of Nodes (overall)	39
No. of Coordinator	1
No. of Routers	8
No. of End Devices	30
Network Dimension	500 m *500 m
Simulation Time	600 sec

A. End to End Delay

End-to-End delay or One-way delay is defined as the amount time a packet takes to be transmitted across a network from source to destination. Delay components:-

$$D_{end-end} = N[d_{trans} + d_{prop} + d_{proc}];$$

Where,

$$D_{end-end} = End - to - End \ \ Delay;$$

$$d_{trans} = Transmission \ \ Delay;$$

$$d_{prop} = Propagation \ \ Delay;$$

$$d_{proc} = Processing \ \ Delay;$$

$$N = Number \ \ of \ \ links \ \ (Number \ \ of \ \ routers \ \ + 1)$$

Each router will have its own d_{trans}, d_{prop}, d_{proc} hence this formula hints a rough estimate [28].

End-to-End delay for the global network in Random Structure Model is slightly higher than the Octagonal Structure Model. At the simulation start time, it is in the highest peak and after time being it gradually decreased as shown in Fig. 3.

End-to-End delay in Octagonal Structure is lower for its sequential router and other end device setup. Application traffic

from end devices at the different corner of the network travels in shortest possible time.

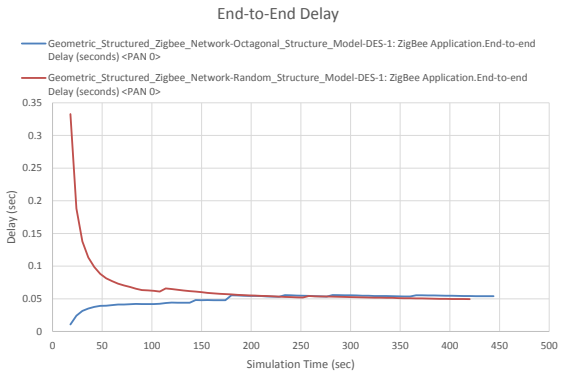

Fig. 3. End to End delay (sec) for global network.

B. Packet Delivery Ratio (PDR)

The packet delivery ratio is considered as one of the vital performance metrics in this research work. It can be calculated as the ratio between the total number of receiving data packets by the sink and the total number of data packets that are sent by all nodes in average [29]. The expression is following:

$$PDR_{avg} = P_{R_{total}} / P_{S_{total}}$$

Where,

$$PDR_{avg} = Average\ \ Packet\ \ Delivery\ \ Ratio$$

$$P_{R_{total}} = Total\ \ Packets\ \ Received\ \ by\ \ the\ \ Sink$$

$$P_{S_{total}} = Total\ \ Packets\ \ Sent\ \ by\ \ all\ \ Nodes$$

Fig. 4 illustrates PDR value for Random Structure Model (Scenario_1), is almost 0.36. In the other word, Coordinator receives in average 36% of data packets successfully.

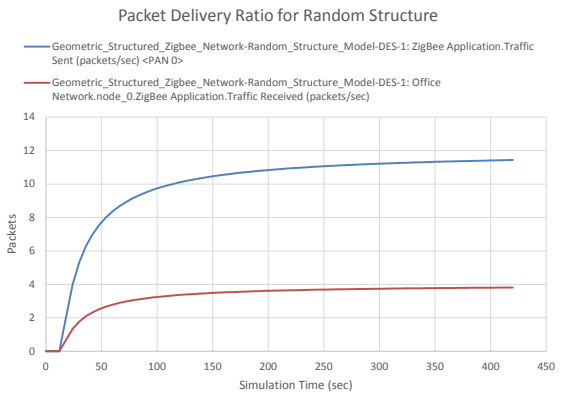

Fig. 4. PDR for Random structure model (Scenario_1).

Fig. 5 illustrates for Octagonal Structure Model (Scenario_2), PDR value is almost 0.50. This represents Coordinator receives in average 50% of data packets successfully.

It shows that in Octagonal Structure model application packets are delivered to destinations or Coordinator at the maximum rate for its end nodes and router set up.

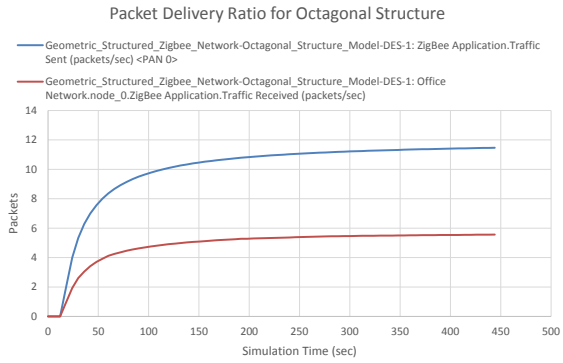

Fig. 5. PDR for Octagonal structure model (Scenario_2).

C. Global MAC Delay

MAC layer delay represents the end to end delays of all packets received through the ZigBee/802.15.4 MACs all WPAN nodes in the network and forwarded to the higher layers. The total queuing and contention delays of the data frames transmitted through all the ZigBee device's 802.15.4 MAC (Medium Access Control). For each frame, this delay is calculated as the duration from a time when it is inserted into the transmission queue, which is arrival time for higher layer data packets and creation time for all other frames types, until the time when the frame is sent to the physical layer for the first time.

Fig. 6 shows at the beginning of the simulation, Coordinator delay for Octagonal Structure Model decreases gradually from 0.09 sec to 0.025 sec. On the contrary, the Coordinator's MAC delay for Random Structure Model increases dramatically 0.01 to 0.135 sec.

MAC delay for the global network is about 2% higher in Random Structure Model than the Octagonal Structure Model.

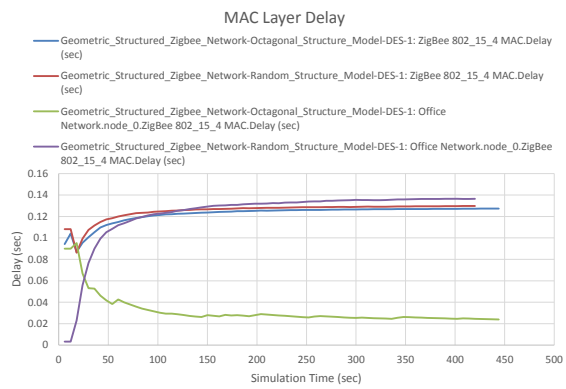

Fig. 6. MAC delay (sec) for global network and Coordinator (node_0).

All the data packets are transferred to the MAC layer for further execution. The delay affects overall network performance. In Octagonal Structure Model, the queue size is smaller and data packets spend less time in queues. Moreover, in Random Structure Model randomly many requests wait in Coordinator queue for execution. Thus, the average MAC delay is always lower in Octagonal Structure Model both for global network and Coordinator (node_0).

D. Global MAC Load

MAC layer load represents the total load (bits/sec) submitted to the ZigBee/802.15.4 MAC by all higher layers in all WPAN nodes of the network.

Fig. 7 describes MAC load for Coordinator is about 1.2% higher and 4% higher for the global network on Random Structure Model than the Octagonal Structure Model respectively.

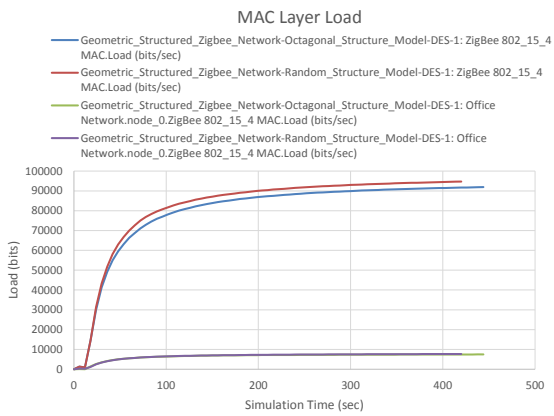

Fig. 7. MAC load (bits/sec) for global network and Coordinator (node_0).

Coordinator processes all the data request from its queue. In Random Structure Model, randomly a lot of requests come in the Coordinator queue from the different corner of the network. It increases Coordinator load as well as the overall network load. On the other hand, in Octagonal Structure Model, routers and Coordinator process request jointly. Though routers also process requests in the Random Structure Model, it is less than the Octagonal Structure Model for its random behavior.

E. Global Data Dropped Retry Threshold

Higher layer data traffic (bits/sec) dropped in the ZigBee 802.15.4 MAC due to consistently failing transmission or retransmissions. This threshold statistic reports the number of the higher layer packets that are dropped because the MAC could not receive any ACKs for the retransmissions of those packets or their fragments, and the packet retry counts reached MACs retry limit or failure to transmit a packet due to channel access failure (reaching the maximum backoff limit). The threshold statistic also reports the outstanding packets in the buffers that are dropped during roaming.

Fig. 8 describes data dropped (bits/sec) for the Coordinator in Random Structure model is increased from the start of the simulation. In Coordinator, more data drops for Random Structure model than Octagonal Structure Model. The data dropped rate is about 6.89% higher in Random Structure Model for the global network than the Octagonal Structure Model as depicted in Fig. 8.

As randomly much requests come to Coordinator queue in Random Structure Model, some data request may be lost in queuing timeout, some are lost Coordinator unavailability, some are lost internal data packet collision and some are lost for lacking coverage of intermediary nodes. Besides, routers, end devices are setup such a way that total network field gets radio coverage. In this way, data requests from the end nodes

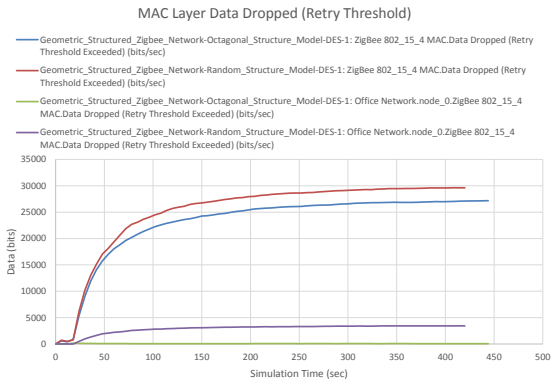

Fig. 8. Data dropped (bits/sec) for global network and Coordinator (node_0).

cannot be lost without coverage and internal interference for using the same intermediary device. Moreover, the data request process in Coordinator queue in a sequential manner and it has less time to process. Thus, data drop rate for queuing timeout has decreased as well as average data dropped rate lower in the Octagonal Structure Model.

F. Throughput

MAC layer throughput represents the total number of bits (bits/sec) forwarded from ZigBee/802.15.4 MAC to the higher layer in all WPAN of the network.

Fig. 9 illustrates MAC layer throughput for Coordinator is 30% higher in Octagonal Structure Model than Random Structure Model. Moreover, it shows that throughput for the global network is 14% higher in Random Structure Model than the Octagonal Structure Model.

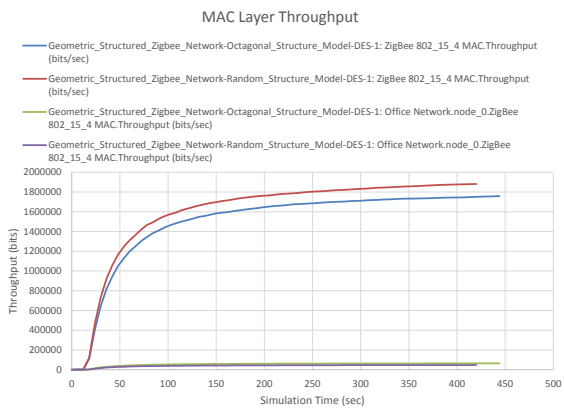

Fig. 9. Throughput (bits/sec) for global network and Coordinator (node_0).

The Coordinator has a higher throughput for Octagonal Structure model for its less data dropped and high packet delivery ratio. But average global network throughput is slightly higher in Random Structure Model for its more packet availability than the Octagonal Structure Model.

Here, different ZigBee layer parameters are analyzed on the basis of various performance measurement metrics. And also observed various characteristics of ZigBee network. To build a large-scale ZigBee network on Octagonal Structure Model shows more efficiency than random orientation. In Octagonal

Structure, all the routers and devices arranged in such a way that it looks like an octagon. This structure covers entire network field and process data request efficiently. Besides, randomly placed end devices and routers have limitations to provide maximum coverage and some routers may idle for its distinct position. That is the main potentiality of the Octagonal structure in large network formation.

V. Conclusions

This paper presents a novel study on ZigBee network design with respect to geometric structure. It deals with new Octagonal structure and Random structure. And it proposes that the newly developed Octagonal structure has higher performance for designing large scale Zigbee network than Random structure. This paper is abundantly supplied with simulation data, graphs and competitive study for corroborating the proposed structure. Almost in all the observations indicate that the Octagonal Structure network performance is going prominent than the Random Structure network. Observations show that End to End delay, MAC delay, MAC load is lower in the Octagonal structure indubitable. The study also shows that about 14% more data packets are received successfully by the coordinator and 6.89% less data dropped in Octagonal structure than Random structure. Throughput is also higher for Coordinator in the Octagonal structured network. The Octagonal Structure Model will be more suitable for large-scale automation for home, office or industry.

In the future, it would be interesting to see mobility management in large-scale for Zigbee network, performance evaluation and analysis for the mobile sensor in the large scale Zigbee network and effects on the environment.

References

[1] "Specification, ZigBee. ZigBee Alliance," http://www. Zigbee.org, [Online; Accessed: 28-Jan-2015].

[2] S.-H. Fang, C.-H. Wang, T.-Y. Huang, C.-H. Yang, and Y.-S. Chen, "An Enhanced ZigBee Indoor Positioning System with an Ensemble Approach," *IEEE Communications Letters*, vol. 16, no. 4, pp. 564–567, 2012.

[3] C. Luo, F. Wu, J. Sun, and C. W. Chen, "Compressive Data Gathering for Large-scale Wireless Sensor Networks," in *Proceedings of the 15th annual international conference on Mobile computing and networking*, Beijing, China, September 2009.

[4] W.-S. Jang, D.-E. Lee, and J.-h. Choi, "Ad-hoc Performance of Wireless Sensor Network for Large Scale Civil and Construction Engineering applications," *Automation in Construction*, vol. 26, pp. 32–45, 2012.

[5] J.-C. Cano and P. Manzoni, "A Performance Comparison of Energy Consumption for Mobile Ad-hoc Network Routing Protocols," in *Proceedings. 8th International Symposium on Modeling, Analysis and Simulation of Computer and Telecommunication Systems*, San Francisco, California, September 2000.

[6] M. Kohvakka, M. Kuorilehto, M. Hännikäinen, and T. D. Hämäläinen, "Performance Analysis of IEEE 802.15.4 and ZigBee for Large-scale Wireless Sensor Network Applications," in *Proceedings of the 3rd ACM international workshop on Performance evaluation of wireless ad hoc, sensor and ubiquitous networks*, Torremolinos, Spain, October 2006.

[7] W. Dong, Y. Liu, Y. He, T. Zhu, and C. Chen, "Measurement and Analysis on the Packet Delivery Performance in a Large-scale Sensor Network," *IEEE/ACM Transactions on Networking*, vol. 22, no. 6, pp. 1952–1963, 2014.

[8] T. R. Burchfield, S. Venkatesan, and D. Weiner, "Maximizing Throughput in ZigBee Wireless Networks through Analysis, Simulations and Implementations," in *Proc. Int. Workshop Localized Algor. Protocols WSNs*, Santa Fe, New Mexico, USA , June 2007.

[9] S. Rao, S. Keshri, D. Gangwar, P. Sundar, and V. Geetha, "A Survey and Comparison of GTS Allocation and Scheduling Algorithms in IEEE 802.15.4 Wireless Sensor Networks," in *IEEE Conference on Information & Communication Technologies (ICT)*, Tamil Nadu, India, April 2013.

[10] C. E. Perkins, E. M. Royer, S. R. Das, and M. K. Marina, "Performance Comparison of Two On-demand Routing Protocols for Ad-hoc Networks," *IEEE Personal Communications*, vol. 8, no. 1, pp. 16–28, 2001.

[11] A. M. Ortiz, T. Olivares, and L. Orozco-Barbosa, "Smart Routing Mechanism for Green ZigBee-based Wireless Sensor Networks," in *IEEE Symposium on Computers and Communications (ISCC)*, Kerkyra (Corfu), Greece, June-July 2011.

[12] P. L. Shrestha, M. Hempel, Y. Qian, H. Sharif, J. Punwani, and M. Stewart, "Performance Modeling of a Multi-tier Multi-hop Hybrid Sensor Network Protocol," in *IEEE Wireless Communications and Networking Conference (WCNC)*, Shanghai, China, April 2013.

[13] L. Yanfei, W. Cheng, Q. Xiaojun, Z. Yunhe, and Y. Chengbo, "An Improved Design of ZigBee Wireless Sensor Network," in *2nd IEEE International Conference on Computer Science and Information Technology*, Beijing, China, August 2009.

[14] F. Martelli, C. Buratti, and R. Verdone, "Modeling Query-Based Wireless CSMA Networks Through Stochastic Geometry," *IEEE Transactions on Vehicular Technology*, vol. 63, no. 6, pp. 2876–2885, 2014.

[15] M. S. Mahmoud, "Wireless Networked Control System Design: An Overview," in *IEEE 23rd International Symposium on Industrial Electronics (ISIE)*, Istanbul, Turkey, June 2014.

[16] "The Network Simulator - NS-2, NS-3," http://www.isi.edu/nsnam/ns/, [Online; Accessed: 20-Jan-2015].

[17] "OMNeT++ : Discrete Event Simulator," https://omnetpp.org/, [Online; Accessed: 15-Dec-2014].

[18] "Riverved," http://www.riverbed.com/, [Online; Accessed: 15-Feb-2015].

[19] "QualNet: Scalable Network Technologies," http://web.scalable-networks.com/content/qualnet/, [Online; Accessed: 15-Feb-2015].

[20] "MATLAB: Simulink," http://mathworks.com/, [Online; Accessed: 20-Feb-2015].

[21] N. Islam, M. J. H. Biddut, A. I. Swapna, and M. H. R. Jany, "A Study on Priority Based ZigBee Network Performance Analysis with Tree Routing Method," *Journal of Computer and Communications*, vol. 3, no. 08, pp. 1–10, 2015.

[22] A. Babaei, P. Agrawal, and B. Jabbari, "Capacity Bounds in Random Wireless Networks," *Journal of Communications and Networks*, vol. 14, no. 1, pp. 1–9, 2012.

[23] C.-J. M. Liang, N. B. Priyantha, J. Liu, and A. Terzis, "Surviving Wi-fi Interference in Low Power ZigBee Networks," in *Proceedings of the 8th ACM Conference on Embedded Networked Sensor Systems*, Zurich, Switzerland, November 2010.

[24] C. Park and T. S. Rappaport, "Short-range Wireless Communications for Next-Generation Networks: UWB, 60 GHz Millimeter-wave WPAN, and ZigBee," *IEEE Wireless Communications*, vol. 14, no. 4, pp. 70–78, 2007.

[25] P. Baronti, P. Pillai, V. W. Chook, S. Chessa, A. Gotta, and Y. F. Hu, "Wireless Sensor Networks: A Survey on the State of the Art and the 802.15.4 and ZigBee Standards," *Computer communications*, vol. 30, no. 7, pp. 1655–1695, 2007.

[26] J. Li, X. Zhu, N. Tang, and J. Sui, "Study on ZigBee Network Architecture and Routing Algorithm," in *2nd International Conference on Signal Processing Systems (ICSPS)*, Dalian, China, July 2010.

[27] T. Kim, S. H. Kim, J. Yang, S.-e. Yoo, and D. Kim, "Neighbor Table Based Shortcut Tree Routing in ZigBee Wireless Networks," *IEEE Transactions on Parallel and Distributed Systems*, vol. 25, no. 3, pp. 706–716, 2014.

[28] A. Kaur, J. Kaur, and G. Singh, "Simulation and Investigation of ZigBee Sensor Network with Mobility Support," in *IEEE International Advance Computing Conference (IACC)*, Gurgaon, India, February 2014.

[29] K. Dong, "Performance and Fairness Enhancement in ZigBee Networks," Ph.D. dissertation, TU Delft, Delft University of Technology, 2011.

A New Mu-Negative Metamaterial

S. S. Islam [1,2], M. R. I. Faruque[1]
Space Science Centre, IPI,
[1]Universiti Kebangsaan Malaysia,
Selangor, Malaysia,
[2]International Islamic University
Chittagong, Bangladesh
sikder_islam@yahoo.co.uk

M. T. Islam
Department of Electrical, Electronic
and Systems Engineering, Universiti
Kebangsaan Malaysia, Malaysia.
titareq@gmail.com

T. Alam
Dept. of CSE,
International Islamic University
Chittagong, Bangladesh
touhid13@yahoo.com

[1]***Abstract*— A new metamaterial with negative permeability is presented in this study. Negative permeability metamaterials are called mu-negative (MNG) metamaterial as well. The transmission co-efficient of this metamaterial shows resonance at a certain frequency in the C-band of microwave frequency range for the z-axis wave propagation. It also exhibits the characteristics of a mu-negative (MNG) metamaterial there. In the basic construction, the unit cell was formed by joining two metal split square resonator by a copper link on FR-4 substrate material. The measured result is presented and it shows good conformity with the simulated result.**

Keywords—C-band; MNG; Metamaterials;

I. INTRODUCTION

Recently, a new type of material usually called "metamaterial'' that are naturally unavailable and show some extraordinary electromagnetic properties. The most interesting property of this material is to exhibit negative permittivity (ε) and permeability (μ) simultaneously, which usually denoted as double negative (DNG) material or negative-refractive index material or backward wave media. A metamaterial may have either epsilon (ε) or mu (μ) negative that is denoted as 'Single Negative (SNG)' metamaterials. The epsilon (ε) negative metamaterial is called ENG. Some metamaterials have negative permeability only. This is often regarded as Mu-negative (MNG) material that has a significant effect on electomagnetic waves like the gyrotropic material. MNG material provides magneto-optic effect that alters the electromagnetic waves by its quasi-static magnetic field. In 1968, Russian scientist Victor Veselago revealed that materials with such properties. These materials' had some different properties that were not naturally found [1]. However, up to 1999 this proposal did not receive too much concern to the researcher as such material is naturally unavailable. Smith *et al.* in 2000 first showed a split ring based such material with double negative property [2].

Depending on these exceptional properties of the metamaterial, various types of designs have been proposed for numerous essential applications; for example ,designing antenna, electromagnetic cloaking, reduction of SAR etc [2-8]. Many metamaterial structure were proposed in the literature although a small number of them are appropriate for C-band (4-8 GHz) [9] microwave spectra as MNG metamaterial [10-15]. For example, Jason C. Soric *et al.* In [11], showed a metamaterial that works in the L-band and exhibit epsilon-near-zero (ENG) characteristics only. In [12], Hayet Benosman *et. al.* presented a metamaterial but it works in K_u-band only. In [13] a new SNG metamaterial was reported but it was applicable for S-band only. In [14] Evren Ekmekçi *et. al.* showed a SNG metamaterial but it works in X-band only.

In this study, we are going to present a new unit cell structure of SNG metamaterial where two split square resonators were linked by a copper strip. The resonant frequency is found for the material in the frequency of 5.13 GHz and the material displays MNG characteristics at that certain frequency.

II. STRUCTURE OF THE UNIT CELL

The Fig. 1 depicts the proposed C-band metamaterial unit cell. The unit cell was formed with two metal (copper) split square resonators. All the copper thickness was kept 0.035mm. The outer length is 10mm with 0.5mm split and the width of each resonator is 1mm. The gap between the two resonators is 1mm and they have been connected to shape an H-like structure by a 1mm wide copper stripe. The unit cell was printed over a 30×30mm^2 FR-4 substrate material having dielectric constant and loss-tangent of 4.3 and 0.025 respectively and the thickness was maintained 1.6 mm.

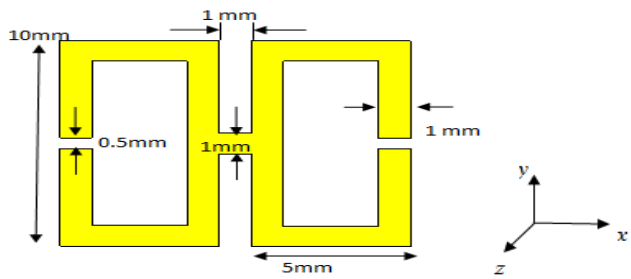

Fig. 1. The basic metamaterial cell structure

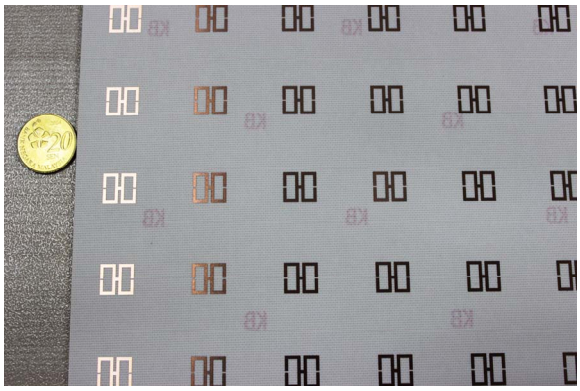

Fig. 2. Fabricated metamaterial prototype on FR-4 substrate material for measurement

III. METHODOLOGY

In this study, the well-known electromagnetic simulation software CST microwave studio was chosen for the S-parameter calculation. The unit cell was placed in such a way that electromagnetic waves pass along the Z-axis and two face-to-face waveguide ports were utilized for it. The perfect electric-magnetic conductor (PEMC) boundary conditions were applied in the consecutive X-and Y-axis. For the range of frequency 2-10 GHz, the simulation was done. The method mentioned in [16] was adopted to extract the effective medium parameters form the complex value of S_{21} and S_{11}.

$$V_1=S_{21}+S_{11} \quad (1)$$

$$V_2=S_{21}-S_{11} \quad (2)$$

$$\mu_r \approx \frac{2}{jk_0 d}\frac{1-V_2}{1+V_2} \quad (3)$$

$$\varepsilon_r \approx \frac{2}{jk_0 d}\frac{1-V_1}{1+V_1} \quad (4)$$

$$\eta = \sqrt{\varepsilon_r \mu_r} \quad (5)$$

where, ε_r is the effective permittivity, μ_r is the effective permeability, 'd' is the thickness of the substrate, k_0 is the wave number and η is the refractive index.

A 240×240 mm^2 prototype of 8×8 unit cell is fabricated for measurement, as shown in Fig. 2. The prototype is then placed between two horn antennas, which are 1.5m apart in the same plane. The vector network analyzer named 'Agilent E8363D' was taken to evaluate the S-parameters. For calibration purpose, measurement without metamaterial and with metamaterial is done. The measurement is done in a semi anechoic chamber environment. The whole measurement setup is shown in Fig. 3.

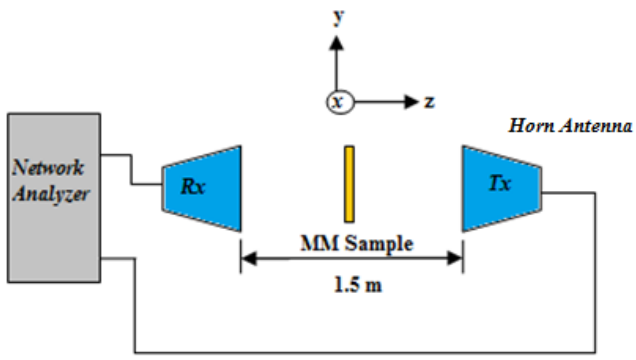

Fig. 3. Measurement set-up

IV. RESULTS AND DISCUSSION

In the Fig. 4, the transmission (S_{21}) parameters for the proposed unit cell are being displayed. It shows that the magnitude of S_{21} shows resonance in the microwave range at the frequency of 5.133 GHz. The measured transmission properties for with and without metamaterial are shown in the Fig. 5 and Fig. 6 respectively. The measured result of the transmission (S_{21}) characteristics agrees well with the simulated result.

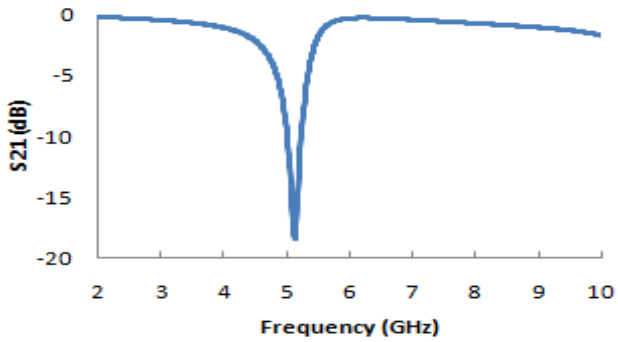

Fig. 4. Simulated magnitude of transmission parameter (S_{21}) in dB

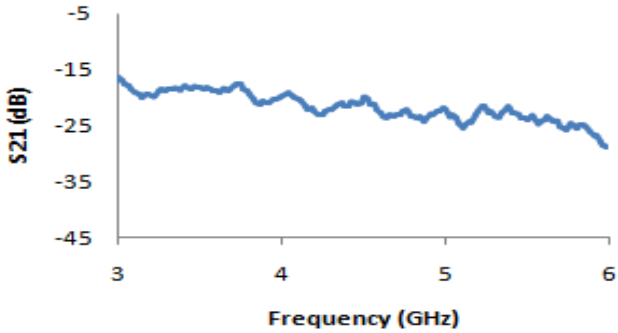

Fig. 5. Measured value of transmission parameter (S_{21}) in dB without metamaterial

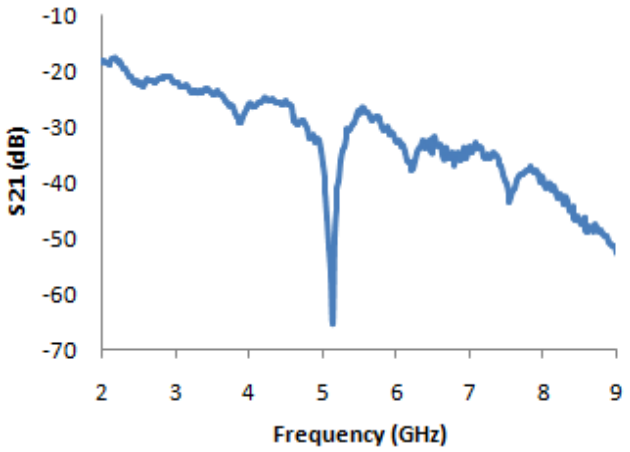

Fig. 6. Measured peak of transmission parameter (S_{21}) with metamaterial

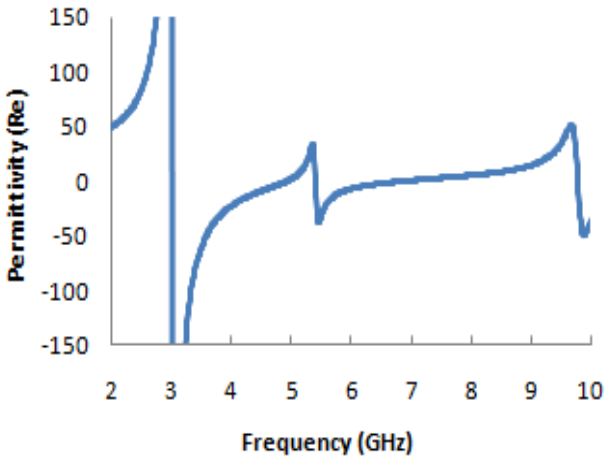

Fig. 7. Magnitude (real) of permittivity (ε)

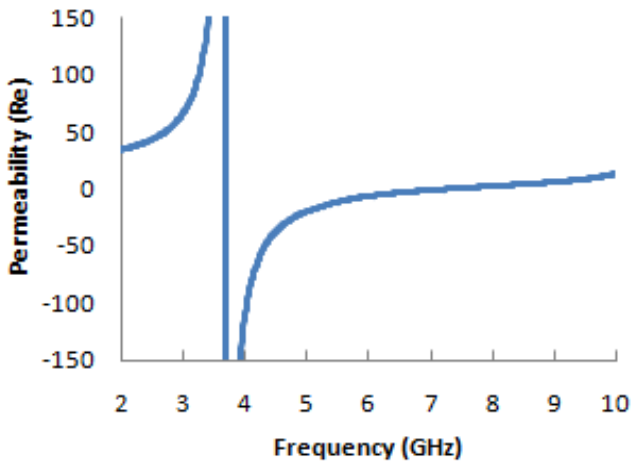

Fig. 8. Magnitude (real) permeability (μ)

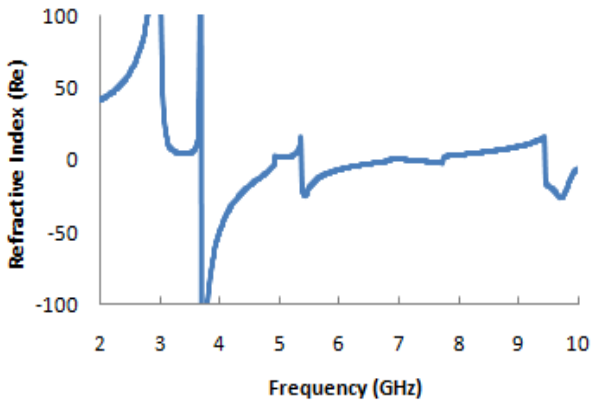

Fig. 9. Magnitude (real) of Refractive Index

The calculated permittivity (ε) as well as permeability (μ) against frequency is seen in Fig. 7 and 8 respectively. In Fig.7 it is seen that at 5.133GHz the permittivity curve displays positive real magnitude of ε = 7.80. Similarly, the Fig. 8 reveals the permeability curve where at the points of resonance frequency of 5.133GHz it has the value of μ = -17.50. Therefore the material can be characterized as a single negative (SNG) material. Here, it is seen that only permeability shows negative magnitude for the proposed structure. That is why, it can be characterized as mu-negative (MNG) metamaterial. The refractive index curve is seen in Fig. 9. It shows the positive real value of η=1.76 at the frequency of 5.133GHz.

V. Conclusion

This paper presents a MNG metamaterial, having resonance frequency at 5.133GHz of the C-Band. Usually, C-band of microwave arena is employed for remote communication like, satellite communications. Therefore, the structure has good applications in the design of antenna for satellite and other similar fields in this range. The simulated and the measured result are compared and they show good conformity as well.

References

[1] V. G. Veselago, "The electrodynamics of substances with simultaneously negative values of ε and μ," Soviet Physics Usp., vol. 10, pp.509–514, 1968.

[2] D. Schurig, J. J. Mock,1 B. J. Justice, S. A. Cummer, J. B. Pendry, A. F. Starr, D. R. Smith, Metamaterial Electromagnetic Cloak at Microwave Frequencies, *Science,* Vol. 314, pp. 977-980, 2006.

[3] M. R. I. Faruque and M. T. Islam, "Novel Design Of Triangular Metamaterial For Electromagnetic Absorption In Human Head," *Progress In Electromagnetics Research*, Vol.PIER 141, pp. 463-478, 2013.

[4] B.I. Wu, W. Wang, J. Pacheco, X. Chen, T. Grzegorczyk and J. A. Kong, A Study Of Using Metamaterials As Antenna Substrate To Enhance Gain, *Progress In Electromagnetics Research*, Vol.PIER 51, pp.295–328, 2005.

[5] S. S. Islam, M. R. I. Faruque, M. T. Islam; A Near Zero Refractive Index Metamaterial for Electromagnetic Invisibility Cloaking Operation; *Materials*, *8*, pp. 4790-4804; 2015; doi: 10.3390/ma8084790

[6] M. R. I. Faruque, M. T. Islam, N. Misran, "Electromagnetic (EM) Absorption Reduction in a Muscle Cube with Metamaterial Attachment," Medical Engineering & Physics (Elsevier), vol. 33, Issue. 5, pp. 646-652, June 2011

[7] Le-Wei Li, Ya-Nan Li,Tat Soon Yeo,Juan R. Mosig, and Olivier J. F. Martin, A broadband and high-gain metamaterial microstrip antenna, Applied Physics Letters **96**, 164101 , 2010

[8] S. S. Islam, M. R. I. Faruque and M. T. Islam; A two-component NZRI metamaterial based rectangular cloak; *AIP Advances*, Vol. 5, pp. 107116:1-9

[9] IEEE standard letter designations for Radar frequency bands, IEEE standard. 521-2002.Available at:https://standards.ieee.org/findstds/standard/521-2002.html (accessed on 22th March 2014)

[10] S. S. Islam, M. R. I. Faruque, M. T. Islam; A new double negative metamaterial for multi-band microwave applications; Applied Physics A, Volume 116, Issue 2, pp 723-733, August **2014**

[11] Jason C. Soric, N. Engheta, S. Maci, and A. Alù, 'Omnidirectional Metamaterial Antennas Based on Near-Zero Channel Matching', IEEE Transactions on Antennas and Propagation, VOL. 61, NO. 1, JANUARY 2013

[12] H. Benosman, N. B. Hacene, Design and Simulation of Double "S" ShapedMetamaterial; IJCSI International Journal of Computer Science Issues, Vol. 9, Issue 2, No 1, March 2012

[13] S. S. Islam, M. R. I. Faruque, M. T. Islam; Design of a New ENG Metamaterial for S-Band Microwave Applications; Journal of Electrical and Electronics Engineering - Vol. 7, Nr. 2, October 2014

[14] E. Ekmekci and G. Turhan-Sayan, "Investigation of effective permittivity and permeability for a novel V-shaped metamaterial using S-parameters,"proceedings od 5th International Conference on Electrical and Electronics Engineering, December 2007, Bursa, Turkey.

[15] S. S. Islam, M. R. I. Faruque, M. T. Islam; Design and Analysis of a New Double Negative Metamaterial; Informacije MIDEM; Vol. 44, No. 3, pp.218 – 223**,** 2014**.**

[16] S. S. Islam, M. R. I. Faruque and M. T. Islam; 'A New Direct Retrieval Method of Refractive Index for Metamaterials', *Current Science*, Vol. 109, No. 2, 2015

Security in Cooperative Spatial Multiplexing System with Zero-Forcing Filtering

D. K. Sarker, M. Z. I. Sarkar and M. S. Anower
Department of Electrical and Electronic Engineering
Rajshahi University of Engineering and Technology
Rajshahi-6204, Bangladesh.
Email: dks_ms@yahoo.com

***Abstract*—This paper is concerned with the analysis of secrecy capacity and secure outage performance of cooperative spatial multiplexing system with the effect of linear equalization. A confidential communication scenario is considered through Rayleigh fading channel in which a number of users communicate with a destination via multiple relays. An eavesdropper observes their communication and tries to decode the confidential information. At first, we derive the exact closed-form expression for the ergodic secrecy capacity with linear equalization in cooperative spatial multiplexing system. Then, we derive the exact closed-form expressions for the secure outage probability and the complementary cumulative distribution function (CCDF) of secrecy capacity to investigate the secure outage performance of the proposed model. Finally, we justify the validity of analytical results comparing with the Monte-Carlo simulation results.**

***Index Terms*—Ergodic secrecy capacity, secure outage probability, zero-forcing filtering.**

I. Introduction

Now a days, the security becomes an important issue in wireless communication networks due to the increase of application area and the mobility of users and network components, because of the fact that the wireless communication networks are frequently used to transmit personal and confidential information and the wireless medium is susceptible to eavesdropping and fraud. Therefore security is a challenging quality of service constraint that must be accounted for the design of wireless communication network. On the other hand, the cooperative spatial multiplexing system significantly increases the spectral efficiency compared to its cooperative diversity while the relays transmit different sub-streams to the destination simultaneously [1].

Recently, Pasolini et al. proposed an analytical framework in [2] for investigating the amount of secret information and derive the intrinsic secrecy content of wide-sense stationary wireless channels in frequency, time and spatial domains. The impact of imperfect channel state information at the transmitters (CSIT) on the achievable diversity gain in a cooperative relay channel with multiple destination antennas is investigated by X. J. Zhang in [3], considering both decode-and-forward (DF) and amplify-and-forward (AF) relaying protocols. They showed that the control of transmit power based on the imperfect CSIT significantly improves the achievable diversity gain. In [4], the performance of open-loop multi-antenna point-to-point links in ad hoc medium access control (MAC) networks is investigated considering spatial multiplexing transmission with linear maximum ratio combining and zero forcing receivers. In [5], X. Tao et al. studied cooperative techniques, such as relay, distributed antennas systems (DAS), multicell coordination, group cell, coordinated multiple point transmission and reception (CoMP), those turn the traditional cellular system into a cooperative system and proposed some joint processing policies to demonstrate the group cell (CoMP) concept. A multiple-input multiple-output (MIMO) cooperative spatial multiplexing system with distributed single antenna relay stations, operated in AF mode is proposed in [6], where the system bit error rate (BER) performance is evaluated by means of a semi-analytic bounding method. In [7], R. Bassily et al. studied the role of cooperative relays to provide and improve secure communication rates through DF and ZF strategies in a full-duplex multiple relay network with an eavesdropper.

In this paper, we analyze the secure outage performance of cooperative spatial multiplexing system over Rayleigh fading channel. At first, we define the secrecy capacity of cooperative spatial multiplexing system so that the eavesdropper is unable to decode information from the main channel (i.e., channel between users and destination) and derive the exact closed-form expressions for the ergodic secrecy capacity. Then, we find the probability density function (PDF) of secrecy capacity and use it to derive the secure outage probability and the CCDF of secrecy capacity. Finally, the analytical results are verified by comparing with Monte-Carlo simulations.

The rest of the this paper is organized as follows: The system model and problem formulation are described in Section II. Section III describes the formulation of ergodic secrecy capacity. In Section IV, the expressions for the secure outage probability and the CCDF of secrecy capacity are stated. Numerical results are shown in Section V. Finally, Section VI provides the concluding remarks of this work.

Notation: We use upper and lower case boldface letters for denoting matrices and vectors respectively. $\mathbf{I}_n$ represents the $n \times n$ identity matrix. The superscript $(\cdot)^\dagger$ stands for the complex conjugate transpose and $[\cdot]^T$ denotes the transpose operation of a vector. A complex Gaussian distribution with mean μ and variance σ^2 is denoted by $\mathcal{C}\tilde{\mathcal{N}}(\mu, \sigma^2)$. $\mathbb{E}[\cdot]$ is the expectation operator and $P_r(\cdot)$ represents the probability. $\Gamma(\cdot)$ and $2F1(\cdot)$ denote the Gamma function and the Gauss

Hypergeometric function, respectively.

II. System Model and Problem Formulation

We consider a secure cooperative spatial multiplexing system in which M sources send confidential information to the destination via K relays as shown in Fig.1. The communication between sources and destination occurs in the presence of an eavesdropper. The sources and relays are equipped with single antenna while the destination and eavesdropper are equipped with n_D and n_E antennas, respectively. All the terminals operate in half duplex mode yielding the communication occurs in a dual-hop transmission. All the propagation channels are considered to be affected by small-scale fading which is modeled as Rayleigh fading.

During the first-hop, the mth source transmits s_m, $(m = 1, \ldots, M)$ to the relays. Therefore, received signal at the kth relay is given by

$$x_k = \sum_{m=1}^{M} g_{m,k} s_m + \mu_k = \mathbf{g}_k \mathbf{s} + \mu_k, \tag{1}$$

where $g_{m,k}$ denotes the channel coefficient between mth source to kth relay and $\mathbf{g}_k = [g_{1,k}\ g_{2,k} \ldots g_{M,k}]$. $\mathbf{s} = [s_1\ s_2 \ldots s_M]^T$ and $\mu_k \sim \tilde{\mathcal{N}}\left(0, \sigma^2\right)$ denotes the background noise of kth relay with mean zero and variance σ^2. During the second hop, all the relays simultaneously transmit their own signals to the destination over the same physical channel and eavesdropper observes their transmission through another physical channel and tries to decode the information. For simplicity, we assume that the gain of each relay is unity and the kth relay transmits its own signal x_k. Let $\mathbf{y}_d$ and $\mathbf{y}_e$ denote the received signals at the destination and eavesdropper,

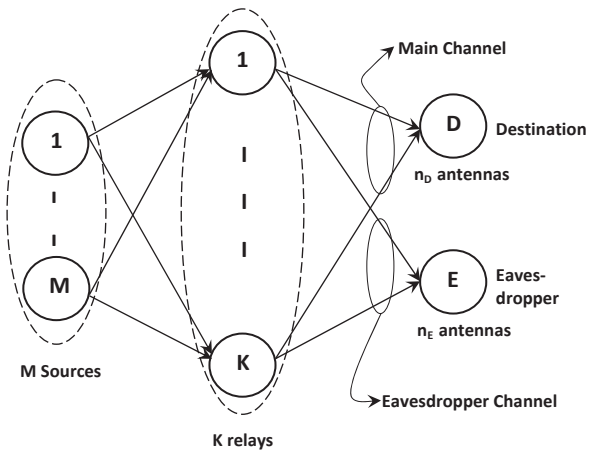

Fig. 1. A Cooperative spatial multiplexing system with M sources, K relays and a destination in the presence of an eavesdropper.

respectively. Then, we have

$$\begin{aligned}\mathbf{y}_d &= \sum_{k=1}^{K} \mathbf{h}_{dk} x_k + \mathbf{n}_d = \sum_{k=1}^{K} \mathbf{h}_{dk} \mathbf{g}_k \mathbf{s} + \sum_{k=1}^{K} \mathbf{h}_{dk} \mu_k + \mathbf{w}_d \\ &= \mathbf{H}_d \mathbf{s} + \mathbf{z}_d, \end{aligned} \tag{2}$$

$$\begin{aligned}\mathbf{y}_e &= \sum_{k=1}^{K} \mathbf{h}_{ek} x_k + \mathbf{n}_e = \sum_{k=1}^{K} \mathbf{h}_{ek} \mathbf{g}_k \mathbf{s} + \sum_{k=1}^{K} \mathbf{h}_{ek} \mu_k + \mathbf{w}_e \\ &= \mathbf{H}_e \mathbf{s} + \mathbf{z}_e, \end{aligned} \tag{3}$$

where $\mathbf{H}_d = [\mathbf{h}_{d1}\mathbf{g}_1\ \mathbf{h}_{d2}\mathbf{g}_2 \ldots \mathbf{h}_{dK}\mathbf{g}_K] \in \mathbb{C}^{n_D \times K}$ and $\mathbf{H}_e = [\mathbf{h}_{e1}\mathbf{g}_1\ \mathbf{h}_{e2}\mathbf{g}_2 \ldots \mathbf{h}_{eK}\mathbf{g}_K] \in \mathbb{C}^{n_E \times K}$ denote the channel coefficients from relays to destination and eavesdropper, respectively. The elements of $\mathbf{H}_d$ and $\mathbf{H}_e$ are the independent complex Gaussian random variables but not identically distributed (i.n.i.d.) due to the separation of relays. $\mathbf{s} \in \mathbb{C}^{K \times 1}$ denotes the transmit signal vector from the relays. $\mathbf{w}_d \sim \mathcal{C}\tilde{\mathcal{N}}\left(0, \sigma^2 \mathbf{I}_{n_D}\right)$ and $\mathbf{w}_e \sim \mathcal{C}\tilde{\mathcal{N}}\left(0, \sigma^2 \mathbf{I}_{n_e}\right)$ denote the additive white Gaussian noises imposed on the destination and eavesdropper, respectively. $\mathbf{z}_d = \sum_{k=1}^{K} \mathbf{h}_{dk}\mu_k + \mathbf{w}_d$ and $\mathbf{z}_e = \sum_{k=1}^{K} \mathbf{h}_{ek}\mu_k + \mathbf{w}_e$ are the $n_D \times 1$ and $n_E \times 1$ complex AWGN vectors which models noises at the receivers of destination and eavesdropper, respectively.

The channel mean power from the relays to destination and eavesdropper are denoted by $\alpha_{m,k,d}$ and $\alpha_{m,k,e}$, respectively. If we apply zero forcing (ZF) filtering matrix to decode the transmitted signal, then the signals can be decoded independently. The post processing SNR of x_k for the destination and eavesdropper channels are given by [1] $\gamma_{m,k,d} = \frac{\gamma_{0,d}}{\left[\left(\mathbf{H}_d^{\dagger}\mathbf{H}_d\right)^{-1}\right]_{kk}}$ and $\gamma_{m,k,e} = \frac{\gamma_{0,e}}{\left[\left(\mathbf{H}_e^{\dagger}\mathbf{H}_e\right)^{-1}\right]_{kk}}$, where $\gamma_{0,d}$ and $\gamma_{0,e}$ are the average SNR per symbol at the destination and eavesdropper channels, respectively. The probability density function (PDF) of $\gamma_{m,k,d}$ and $\gamma_{m,k,e}$ can be expressed as [1]

$$f_{\gamma_{m,k,d}}\left(\gamma_{m,k,d}\right) = \frac{e^{-\frac{\gamma_{m,k,d}}{\gamma_{0,d}\alpha_{m,k,d}}}}{\gamma_{0,d}\alpha_{m,k,d}\vartheta_d!}\left(\frac{\gamma_{m,k,d}}{\gamma_{0,d}\alpha_{m,k,d}}\right)^{\vartheta_d}, \tag{4}$$

$$f_{\gamma_{m,k,e}}\left(\gamma_{m,k,e}\right) = \frac{e^{-\frac{\gamma_{m,k,e}}{\gamma_{0,e}\alpha_{m,k,e}}}}{\gamma_{0,e}\alpha_{m,k,e}\vartheta_e!}\left(\frac{\gamma_{m,k,e}}{\gamma_{0,e}\alpha_{m,k,e}}\right)^{\vartheta_e}, \tag{5}$$

where $\vartheta_d = n_D - K$ and $\vartheta_e = n_E - K$.

III. Ergodic Secrecy Capacity

In this section, at first we deduce the expression of secrecy capacity considering the cooperative spatial multiplexing effect of relays. Then, we derive the closed-form expression for ergodic secrecy capacity.

A. Secrecy Capacity

Since each kth symbol, x_k is detected independently at the destination, capacity at the destination for M users can be expressed from (2) as

$$C_d = \frac{1}{2}\sum_{m=1}^{M}\sum_{k=1}^{K}\log_2\left(1 + \gamma_{m,k,d}\right). \tag{6}$$

Similarly, from (3), the capacity at the eavesdropper can be derived as

$$C_e = \frac{1}{2}\sum_{m=1}^{M}\sum_{k=1}^{K}\log_2\left(1+\gamma_{m,k,e}\right). \tag{7}$$

Hence, the secrecy capacity is given by

$$C_s = \max_{f(x_k)}\left(C_d - C_e\right) = \frac{1}{2}\sum_{m=1}^{M}\sum_{k=1}^{K}\log_2\left(\frac{1+\gamma_{m,k,d}}{1+\gamma_{m,k,e}}\right). \tag{8}$$

B. Ergodic Secrecy Capacity

The ergodic secrecy capacity for cooperative spatial multiplexing system over Rayleigh fading channel can be expressed as

$$\langle C_s\rangle = \frac{1}{2}\sum_{m=1}^{M}\sum_{k=1}^{K}\Big\{\mathbb{E}\left[\log_2(1+\gamma_{m,k,d})\right] - \mathbb{E}\left[\log_2(1+\gamma_{m,k,e})\right]\Big\}. \tag{9}$$

Now, we have

$$\mathbb{E}\left[\log_2(1+\gamma_{m,k,d})\right] = \int_0^\infty \log_2(1+\gamma_{m,k,d}) \times f_{\gamma_{m,k,d}}\left(\gamma_{m,k,d}\right)d\gamma_{m,k,d}. \tag{10}$$

Using (4) into (10) and by applying the result, $\int_0^\infty \ln(1+t)t^{n-1}e^{-at}dt = (n-1)!e^a\sum_i^n \frac{\Gamma(-n+i,a)}{a^i}$ from [8, Appendix B], we obtain

$$\mathbb{E}\left[\log_2(1+\gamma_{m,k,d})\right] = \frac{e^{1/\gamma_{0,d}\alpha_{m,k,d}}}{2\log_e 2} \times\sum_{l=1}^{L}\frac{\Gamma\left(-L+l,\frac{1}{\gamma_{0,d}\alpha_{m,k,d}}\right)}{\left(\gamma_{0,d}\alpha_{m,k,d}\right)^{L-l}}, \tag{11}$$

where $L = \vartheta_d + 1$. Similarly, we can express

$$\mathbb{E}\left[\log_2(1+\gamma_{m,k,e})\right] = \frac{e^{1/\gamma_{0,e}\alpha_{m,k,e}}}{2\log_e 2} \times\sum_{v=1}^{V}\frac{\Gamma\left(-V+v,\frac{1}{\gamma_{0,e}\alpha_{m,k,e}}\right)}{\left(\gamma_{0,e}\alpha_{m,k,e}\right)^{V-v}}, \tag{12}$$

where $V = \vartheta_e + 1$. Substituting (11) and (12) into (9), the closed-form expression for ergodic secrecy capacity is shown in (13) at the bottom of this page.

IV. Outage Performance Analysis

In order to analyze the secure outage performance, at first, we determine the PDF of C_s. Then, it is used to derive the closed-form expressions for the outage probability and the CCDF of secrecy multicast capacity.

A. Probability Density Function of C_s

Here, we find the PDFs of C_d and C_e from the following proposition and then use them to find the PDF of C_s.

Proposition 1: *Let the probability density function of x is denoted by $f(x)$. Then, the probability density function of $C = \log_e(1+\theta x)$ is given by*

$$q(C) = \frac{e^C}{\theta}f\left(\frac{e^C-1}{\theta}\right). \tag{14}$$

Proof: We have, $C = \log_e(1+\theta x)$. The probability density function of the capacity, C can be written as

$$q(C) = \int \delta\left(C - \log_e(1+\theta x)\right)f(x)dx. \tag{15}$$

The following mathematical facts have been used for this proof [9];
i) $\delta\left(f(x)\right) = \sum_l \frac{\delta(x-x_l)}{|\frac{df}{dx}|_{x_l}}$, where x_l are the zeros of $f(x)$, i.e. $f(x_l) = 0$;
ii) $\int_a^b \delta(x-x_1)\delta(x-x_2)dx = \delta(x_1-x_2)$ for $a < x_1, x_2 < b$; and
iii) $\int_U f(x)\delta(x-x_0)dx = \begin{cases} f(x_0), & t_0 \in U \\ 0, & \text{otherwise.}\end{cases}$
Assuming $\kappa = 1+\theta x$, we have $f(\kappa) = C - \log_e\kappa$ and $f^{'}(\kappa) = -\frac{1}{\kappa}$. Now from $f(\kappa) = 0$, $\kappa = e^C$ and $f^{'}(\kappa)|_{\kappa=e^C} = -\frac{1}{e^C}$. Using the above mathematical facts and from equation (15), we have

$$\begin{aligned} q(C) &= \int e^C\delta(1+\theta x - e^C)f(x)dx \\ &= e^C\int\delta\left(\theta\left(x-\frac{e^C-1}{\theta}\right)\right)f(x)dx \\ &= \frac{e^C}{\theta}\int\delta\left(x-\frac{e^C-1}{\theta}\right)f(x)dx \quad \text{Since, } \delta(dx) = \frac{1}{|d|}\delta(x) \\ &= \frac{e^C}{\theta}f\left(\frac{e^C-1}{\theta}\right), \end{aligned}$$

where $\delta(\cdot)$ is a delta function.

Using Proposition 1, $q(C_d)$ and $q(C_e)$ can be determined as

$$q\left(C_d\right) = \frac{e^{C_d}\rho e^{-\rho(e^{C_d}-1)}}{\vartheta_d!\left[\rho(e^{C_d}-1)\right]^{-\vartheta_d}}, \tag{16}$$

$$q\left(C_e\right) = \frac{e^{C_e}\varrho e^{-\varrho(e^{C_e}-1)}}{\vartheta_e!\left[\varrho(e^{C_e}-1)\right]^{-\vartheta_e}}, \tag{17}$$

$$\langle C_s\rangle = \frac{1}{2\log_e 2}\sum_{\eta=1}^{M}\sum_{k=1}^{K}\left[\sum_{l=1}^{L}\frac{\Gamma\left(-L+l,\frac{1}{\gamma_{0,d}\alpha_{m,k,d}}\right)}{e^{-1/\gamma_{0,d}\alpha_{m,k,d}}\left(\gamma_{0,d}\alpha_{m,k,d}\right)^{L-l}} - \sum_{v=1}^{V}\frac{\Gamma\left(-V+v,\frac{1}{\gamma_{0,e}\alpha_{m,k,e}}\right)}{e^{-1/\gamma_{0,e}\alpha_{m,k,e}}\left(\gamma_{0,e}\alpha_{m,k,e}\right)^{V-v}}\right]. \tag{13}$$

where $\rho = (1/\gamma_{0,d}\alpha_{m,k,d})$ and $\varrho = (1/\gamma_{0,e}\alpha_{m,k,e})$. The PDF of C_s can be derived as

$$q(C_s) = q(C_d) * q(C_e) = \int_{-\infty}^{\infty} q(C_s + C_e)\, q(C_e)\, dC_e. \quad (18)$$

From (16), the PDF of $(C_s + C_e)$ can be determined as

$$q(C_s + C_e) = \frac{e^{C_s+C_e}\rho e^{-\rho(e^{C_s+C_e}-1)}}{\vartheta_d!\left[\rho(e^{C_s+C_e}-1)\right]^{-\vartheta_d}}. \quad (19)$$

Substituting (17) and (19) into (18) and performing integration by changing variables and using the identity $\int_0^\infty x^n e^{-bx}dx = n!b^{-n-1}$ of [10, eq. (3.351.3)], we obtain

$$q(C_s) = \frac{\rho^L \varrho^V e^{\rho+\varrho}}{\vartheta_d!\vartheta_e!} \sum_{\kappa=0}^{\vartheta_d} \binom{\vartheta_d}{\kappa} \sum_{\upsilon=0}^{\vartheta_e} \binom{\vartheta_e}{\upsilon} \times (-1)^\nu e^{(\kappa+1)C_s} \left(\rho e^{C_s} + \varrho\right)^{-(\varphi+1)} \varphi!, \quad (20)$$

where $\varphi = (\kappa + \upsilon + 1)$ and $\nu = (\vartheta_d + \vartheta_e - \kappa - \upsilon)$.

B. Secure Outage Probability

The secure outage probability is defined as

$$P_{out}(R_s) = P_r(C_s \le R_s) = \int_0^{R_s} q(C_s)dC_s, \quad (21)$$

where R_s denotes the target secrecy rate. Now substituting (20) into (21), we have

$$P_{out}(R_s) = \frac{\rho^L \varrho^V e^{\rho+\varrho}}{\vartheta_d!\vartheta_e!} \sum_{\kappa=0}^{\vartheta_d} \binom{\vartheta_d}{\kappa} \sum_{\upsilon=0}^{\vartheta_e} \binom{\vartheta_e}{\upsilon} \times \varphi!(-1)^\nu \int_0^{R_s} e^{(\kappa+1)C_s} \left(\rho e^{C_s} + \varrho\right)^{-(\varphi+1)} dC_s. \quad (22)$$

Performing integration the closed-form expression for secure outage probability is shown in (23) at the bottom of this page.

C. CCDF of Secrecy Capacity

The CCDF of secrecy capacity C_s is defined as

$$CCDF_{C_s} = P_r(C_s > R_s) = \int_{R_s}^{\infty} q(C_s)dC_s. \quad (24)$$

Substituting (20) into (24) and performing integration, the closed-form expression for CCDF of C_s is obtained as

$$CCDF_{C_s} = \frac{\rho^L \varrho^V e^{\rho+\varrho}}{\vartheta_d!\vartheta_e!} \sum_{\kappa=0}^{\vartheta_d} \binom{\vartheta_d}{\kappa} \sum_{\upsilon=0}^{\vartheta_e} \binom{\vartheta_e}{\upsilon} \frac{(-1)^\nu \varphi!}{\rho^{(\varphi+1)}} \times \frac{2F1\left(\varphi+1, \upsilon+1, \upsilon+2, -\frac{\varrho e^{-R_s}}{\rho}\right)}{(\upsilon+1)e^{(1+\upsilon)R_s}}. \quad (25)$$

V. Numerical Results

In this section, the theoretical analysis described in sections III and IV is validated by a set of Monte-Carlo simulations. For this purpose, in the simulation environment, at first, we have generated Rayleigh fading channels $\mathbf{H}_d$ and $\mathbf{H}_e$ using Matlab code prepared by the authors using Matlab function 'random'. Secondly, 110000 realizations of the channels have been averaged before using them to calculate secrecy capacity. Thirdly, the 110000 realizations of the calculated secrecy capacity have been averaged to calculate the ergodic secrecy capacity. The similar process has been adopted to find the channels that are used to find the secure outage probability and the CCDF of secrecy capacity. Note that our work is different from [11] in the sense that it deals with the analysis of secrecy capacity and secure outage performance of cooperative spatial multiplexing system with linear equalization.

Fig.2 shows the simulation and analytical results of ergodic secrecy capacity versus average SNR with number of users $M = 2$, relays $K = 6$ and destination antennas $n_D = 7$ to investigate the effect of number of eavesdropper antennas n_E. In order to observe the effect of n_E, three curves are shown for $n_E = 5$ (dot line), $n_E = 6$ (dash-dot line) and $n_E = 7$ (dash line). We observe that, the ergodic secrecy capacity decreases with n_E.

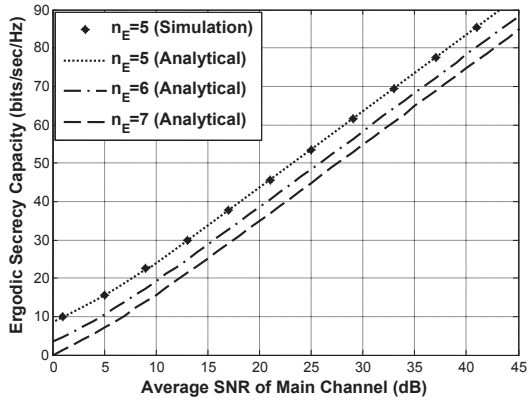

Fig. 2. The simulation and analytical results of ergodic secrecy capacity versus average SNR of main channel for selected values of n_E with $M = 2$, $K = 6$ and $n_D = 7$.

In order to investigate the effect of receive diversity provided by the destination antennas n_D and the effect of spatial multiplexing provided by the relays K, the simulation and analytical results of ergodic secrecy capacity versus average SNR are shown in Fig.3. In order to observe the effect of n_D, two curves are shown for $n_D = 4$ (dash line) and $n_D = 6$ (solid line) with $M = K = n_E = 4$. In order to see the effect of K, two curves are shown for $K = 3$ (dot line) and $K = 4$ (dash-dot line) with $M = 2$, $n_E = 4$ and $n_D = 5$. It is found

$$P_{out}(R_s) = \frac{\rho^L \varrho^V e^{\rho+\varrho}}{\vartheta_d!\vartheta_e!} \sum_{\kappa=0}^{\vartheta_d} \binom{\vartheta_d}{\kappa} \sum_{\upsilon=0}^{\vartheta_e} \binom{\vartheta_e}{\upsilon} \frac{(-1)^\nu \varphi!}{\rho^{(\varphi+1)}} \left[\frac{2F1\left(1, -\upsilon, 2+\kappa-\frac{\rho e^{R_s}}{\varrho}\right)}{e^{-(1+\kappa)R_s}\left(e^{R_s}+\frac{\varrho}{\rho}\right)^{\varphi}\frac{\varrho(1+\kappa)}{\rho}} - \frac{2F1\left(1, -\upsilon, 2+\kappa, -\frac{\rho}{\varrho}\right)}{\left(1+\frac{\varrho}{\rho}\right)^{\varphi}\frac{\varrho(1+\kappa)}{\rho}} \right]. \quad (23)$$

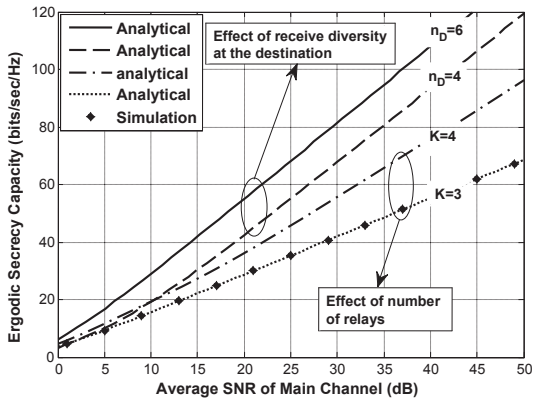

Fig. 3. The simulation and analytical results of ergodic secrecy capacity versus average SNR of main channel showing the effect of receive diversity with $M = K = n_E = 4$ and the effect of number of relays with $M = 2$, $n_E = 4$ and $n_D = 5$.

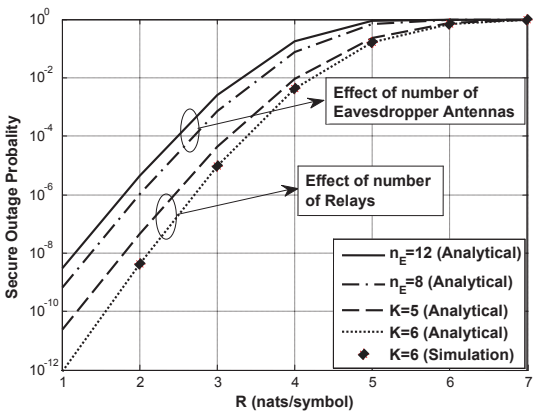

Fig. 4. The simulation and analytical results of secure outage probability versus target secrecy rate R_s showing the effect of K with $n_E = 6$ and $n_D = 12$ and the effect of n_E with $K = 5$ and $n_D = 12$.

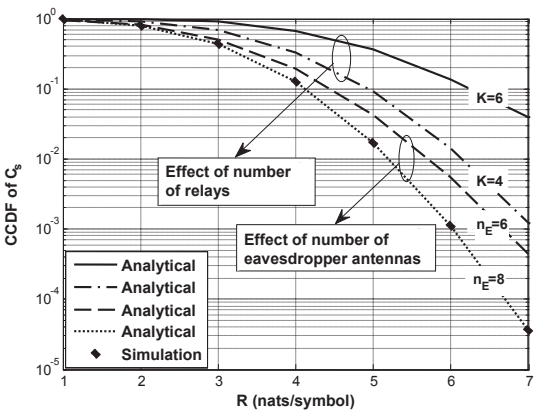

Fig. 5. The simulation and analytical results of complementary cumulative distribution function versus target secrecy rate R_s showing the effect of K with $n_E = 5$ and $n_D = 12$ and the effect of n_E with $K = 4$ and $n_D = 8$.

that, though n_D and K both are the increasing function of ergodic secrecy capacity, but with the increase in average SNR of main channel, the effect of spatial multiplexing provided by K is more significant than the effect of receive diversity provided by n_D.

Fig.4 shows the simulation and analytical results of secure outage probability as a function of target secrecy rate R_s to investigate the effect of K and n_E. In order to investigate the effect of K, two curves are shown for $K = 5$ (dash line) and $K = 6$ (dot line) with $n_E = 6$ and $n_D = 12$. We see that the secure outage probability decreases with K. To observe the effect of n_E, two curves are shown for $n_E = 8$ (dash-dot line) and $n_E = 12$ (solid line) with $K = 5$ and $n_D = 12$. We see that the secure outage probability increases with n_E.

In order to investigate the secure outage performance, we also present the simulation and analytical results of CCDF of secrecy capacity as a function of target secrecy rate R_s in Fig.5 for selected values of K and n_E. In order to observe the effect of K, two curves are shown for $K = 4$ (dash-dot line) and $K = 6$ (solid line) with $n_E = 5$ and $n_D = 12$. We see that the CCDF of secrecy capacity increases with K. To see the effect of n_E, two curves are shown for $n_E = 6$ (dash line) and $n_E = 8$ (dot line) with $K = 4$ and $n_D = 8$. We observe that the CCDF of secrecy capacity decreases with n_E. Moreover, from our observation it is clear that the effect of relays is more significant than the effect of eavesdropper antennas.

VI. Conclusion

In order to investigate the security in a cooperative spatial multiplexing system where a number of relays transmit different sub-streams to the destination antennas simultaneously, the closed-form expressions for the ergodic secrecy capacity, the secure outage probability and the CCDF of secrecy capacity using ZF filtering at the receiver terminal are derived in the Rayleigh fading environment. Based on our observations and from the numerical results, we may conclude that the cooperative spatial multiplexing provided by the relays with ZF filtering enhances spectral efficiency compared to receive diversity which causes an improvement in the ergodic secrecy capacity and decreases the secure outage probability of proposed model significantly.

Acknowledgment

This work is supported by the Research Support and Publication Division of University Grant Commission, Bangladesh.

References

[1] T. Q. Duong and H.-J. Zepernick, "On the ergodic capacity of cooperative spatial multiplexing systems in composite channels," in *Proc. IEEE Radio and Wireless Sympo. (RWS 2009), San Diego, CA*, January 2009, pp. 175–178.

[2] G. Pasolini and D. Dardari, "Secret information of wireless multidimensional Gaussian channels," *IEEE Trans. on Wireless Communications*, vol. 14, no. 6, pp. 3429–3442, February 2015.

[3] X. J. Zhang, Y. Gong, and K. Letaief, "On the diversity gain in cooperative relaying channels with imperfect csit," *IEEE Trans. on Communications*, vol. 58, no. 4, pp. 1273–1279, April 2010.

[4] H. Y. R. Louie, M. R. McKay, and I. B. Collings, "Open-loop spatial multiplexing and diversity communications in ad hoc networks," *IEEE Trans. on Information Theory*, vol. 57, no. 1, pp. 317–344, January 2011.

[5] X. Tao, X. Xu, and Q. Cui, "An overview of cooperative communications," vol. 50, no. 6, pp. 65–71, June 2012.

[6] N. Xie and A. Burr, "Cooperative spatial multiplexing with distributed amplify-and-forward relays," in *Proc. IEEE Int. Sympo. Wireless Commu. Systems (ISWCS), 2012, Paris, France*, August 2012, pp. 616–620.

[7] R. Bassily and S. Ulukus, "Secure communication in multiple relay networks through decode-and-forward strategies," *IEEE Journal of Communications and Networks*, vol. 14, no. 4, pp. 352–363, August 2012.

[8] M.-S. Alouini and A. J. Goldsmith, "Capacity of Rayleigh fading channels under different adaptive transmission and diversity-combining techniques," *IEEE Trans. on Vehicular Technology*, vol. 48, no. 4, pp. 1165–1181, July 1999.

[9] T. Ratnarajah and R. Vaillancourt, "Quadratic forms on complex random matrices and multiple-antenna systems," *IEEE Trans. on Information Theory*, vol. 51, no. 8, pp. 2976–2984, August 2005.

[10] I. S. Gradshteyn and I. M. Ryzhik, *Table of Integrals, Series, and Products*, 7th ed. San Diego, CA: Academic, 2007.

[11] S.-C. Wang and W. Liao, "Cooperative multicasting for wireless scalable video transmissions," *IEEE Trans. on Communications*, vol. 61, no. 9, pp. 3980–3989, Sept. 2013.

Evidence Theory-Based Cooperative Spectrum Sensing in Multi Antenna Cognitive Radio System

Md. Tahidul Islam
Electronic and Telecomm. Engg. Department
International Islamic University Chittagong
Chittagong, Bangladesh
Email: tahidcce@gmail.com

Muhammad Sajjad Khan
School of Electrical Engineering
University of Ulsan
Ulsan, South Korea
Email: sajjad.khan@iiu.edu.pk

Insoo Koo
School of Electrical Engineering
University of Ulsan
Ulsan, South Korea
Email: iskoo@ulsan.ac.kr

***Abstract*—Cooperative spectrum sensing has a great impact to increase the performance for detecting the Primary User (PU) signal over single node sensing. Recent developments in multiple antenna techniques adjoin a new dimension in spectrum sensing. In this paper, we have proposed a multi-antenna based signal detection for multi bands considering cooperative approach with Rayleigh fading channel. In addition to that, data fusion is considered by ordered sequential method where the sequential fusion is performed by Dempster Shafer (DS) theory-based reliability. The significance and efficiency of the proposed method is justified through analysis and simulation. The experimental results demonstrate that the proposed multi-antenna assisted DS-theory based spectrum sensing reduces sensing and reporting time significantly for the cognitive user as compared with the conventional system.**

***Keywords*—cognitive radio, evidence theory, multi-antenna, sequential fusion, spectrum sensing**

I. INTRODUCTION

Cognitive Radios (CRs) [1,2] are being considered as a promising solution that can maximize the utilization of the frequency resources by allowing Cognitive Users (CUs) to access the allocated spectrum bands, which are temporally idle. In traditional single CU, primary signal does not deal with the hidden terminal problem [3], which is occurred due to the multi-path fading and shadowing effects. An outstanding performance can be obtained by cooperative spectrum sensing over single node sensing method [4, 5]. Moreover, the concept of multiple-antenna system has drawn a lot of interest in the CR research, which can mitigate fading, and shadowing effects where multipath is effectively converted into benefit for communication system. Therefore, combination of multiple antennas with multiple user cooperation can provide outstanding performance for detecting the Primary User (PU) signal over conventional system. A number of papers have investigated the application of multiple antennas with energy detection for spectrum sensing from different point of view [6, 7, 8]. Previously, authors of [9, 10] have enlightened in the aspects of cooperative spectrum sensing and decision fusion. To implement conventional cooperative spectrum sensing, each CU makes a local decision and those decisions are reported to a fusion center to give a final decision according to some fusion rules (e.g. OR, AND, Half voting, Majority rule, etc). Unlike the conventional fusion rule, a data fusion scheme based on DS-theory of evidence was first recommend by P. Zeng et. al. where it was shown that the proposed scheme improve detection performance significantly without any prior knowledge of primary user signal [11]. N. T. Nhan et. al. proposed an enhanced DS-theory based fusion scheme for cooperative spectrum sensing [12]. Moreover, an efficient ordered sequential cooperative spectrum sensing method based on DS-theory was proposed in [13]. There are numerous works on the throughput maximization of cognitive radio communication [14-17]. Y. C. Liang et al. proposed sensing throughput tradeoff strategy for cognitive radio network [14]. Again, analysis of throughput for cooperative cognitive radio network was done by R. Muta et. al. [15]. Moreover, C. You et. al. proposed optimization of hard decision based cooperative TV spectrum sensing [16]. And throughput optimization by hard fusion based spectrum sensing was performed by [17]. However, all the papers considered conventional decision fusion rule with single antenna based sensing and yet to increase throughput significantly. In this paper, the impact of multi-antenna based spectrum sensing with energy detection for fading (Rayleigh) channel is analyzed. Moreover, instead of sensing single band, sensing and reporting accross multiple bands together are taken into account. Again, DS theory-based ordered sequential reporting methodology is applied for multiple bands. Based on the simulation result we have shown that the proposed multiple antenna and DS-theory based cooperative spectrum sensing can reduce sensing and reporting time. Moreover, reporting multiple bands in a single time slot instead of single band to FC has a significant reporting time reduction. Thus the proposed scheme has outperformed over traditional cooperative methods for shrinking sensing and reporting time.

The remainder of this paper is organized as follows. In section ii, system model is illustrated. The proposed multiple antenna and DS-theory based cooperative sensing is explained in section iii, and in section iv, proposed multiple-antenna based sensing and detection is illustrated. Moreover, the simulation result is provided in section v. and the conclusion is drawn in last section which is section vi.

II. SYSTEM MODEL

A. Spectrum Sensing

Consider a cognitive radio network with bandwidth $FHertz$ which is divided into total B disjoint small sub bands:

$$F^b = [F_b, F_{b+1}), F = \bigcup_{b=1}^{B} F^b \tag{1}$$

The received signal consists of total B sub bands with the boundaries located at $F_1 < F_2 < .... < F_B$. Therefore, total N_T CU nodes, each having M antennas is assigned to perform spectrum sensing on some sub bands. Moreover, we have considered a fusion center (FC) that has a single antenna. Signals received from the multiple antennas go through the energy detectors and the local decision is made at every CU. The received samples are represented by Y with a sample index n where and $n = 1, 2, ...N$. The local spectrum sensing problem can be formulated as binary hypothesis problem [18]:

$$Y_{i,j}(n) = \begin{cases} \eta_{i,j}(n) : H_0 \\ h_{i,j}s(n) + \eta_{i,j} : H_1 \end{cases} \tag{2}$$

where H_0 and H_1 represent signal absence and signal presence, respectively. $Y_{i,j}(n)$ is the signal from i^{th} CU with j antenna that has N samples where $i = 1, 2, ...N_T$ and $j = 1, 2, ...M$. h_{ij} is fading channel coefficient of the $i'th$ CU at antenna j. If the CU knows nothing about the waveform transmitted by the PUs in a frequency band of interest, energy detection is more suitable for detection[10] since it is only based on the measured energy of the received signal in that band.The principle of energy detection [18] is based on the difference between the energy of PU transmission signal and the noise. In the energy detection process, the energy of the received signal measured in a fixed bandwidth S over an observation time period T. The observed energy of a CU by a single antenna for a single sub-band is denoted by E and defined as: In conventional system, coarse sensing is performed with single antenna but in our proposed system it is performed by multiple antennas. Fine detector is performed with large number of samples to detect the band. In this paper, energy detection is used for fine sensing. In conventional case, fine sensing is performed by single antenna and to obtain one vacant band only. However, in proposed system, fine sensing is performed by multiple antennas and total numbers of vacant bands are dependent on number of CRU to utilize vacant band. If total vacant bands are smaller than number of required bands, the fine detector needs to seek up to last band.

$$E = \sum_{n=1}^{N} |Y(n)|^2 \tag{3}$$

The noise in each sample is a Gaussian random variable with mean zero and variance σ_η^2 and the signal variance σ_y^2. As a result, if PU is absent, $\frac{Y}{\sigma_\eta{}^2}$ follows a central chi-square distribution with N degree of freedom. Otherwise, $\frac{Y}{\sigma_\eta{}^2}$ follows a non-central chi-square distribution with N degree of freedom and a non-centrally parameter N_γ

$$\frac{Y}{\sigma_\eta{}^2} \sim \begin{cases} X_N{}^2, H_0 \\ X_N{}^2(N_\gamma), H_1 \end{cases} \tag{4}$$

where γ is the Signal to Noise Ratio (SNR). By the central limit theorem, the test statistic can be approximated as a Gaussian distribution.

$$\begin{aligned} H_0 :& E \sim Normal(N\sigma_\eta{}^2, 2N\sigma_\eta{}^4) \\ H_1 :& E \sim Normal(N(\sigma_\eta{}^2 + \sigma_y{}^2), 2N(\sigma_\eta{}^4 + \sigma_y{}^4)^2) \end{aligned} \tag{5}$$

The performance of detection is measured by two parameters P_d and P_f . The Rayleigh fading occurs when a signal experiences a Non-Line-of-Sight multipath. Due to Rayleigh fading, the signal amplitude follows a Rayleigh distribution, and the SNR of the PU signal at each CU follows an exponential distribution whose Probability Density Function is given by:

$$f_\gamma(\gamma) = \frac{1}{\gamma} e^{\frac{\gamma}{\hat{\gamma}}}, \gamma > 0 \tag{6}$$

where $\hat{\gamma}$ is the mean SNR value.

B. Frame structure for cooperative spectrum sensing

The cooperative spectrum sensing and detection is the combination of sensing and reporting period. Fig. 1 shows the time frame structure for cooperative spectrum sensing where total Q frames exist. The total frame time T of a frame is divided mainly into two parts: detection time T_d and transmission time $T - T_d$. Further, T_d is consisted of sensing time T_S and reporting time T_R.

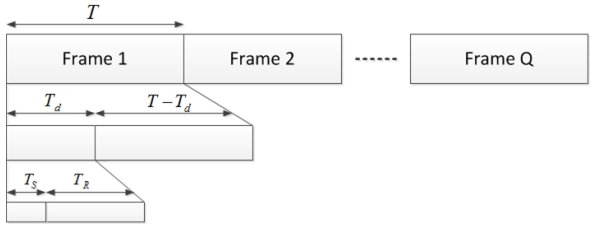

Fig. 1. The Frame structure for Cooperative Cognitive Radio

III. The Proposed Multiple Antenna and DS-Theory Based Cooperative Sensing

The overall process of the proposed scheme is shown in Fig. 2. The total spectrum sensing and decision process consists of three main parts: local sensing in CUs, data fusion to fusion center and final processing for global decision in fusion Center. In local sensing stage the sensing operation is performed by multiple antennas; and multiple sub-bands are sensed together instead of single band. The data of multiple bands are sent to FC in ordered sequential manner for making final decision. Upon obtaining the target detection and false alarm the FC manages to stop reporting for all the CUs.

The details of these operations are provided below:

A. Multiple-antenna based sensing and detection

In this paper, it is assumed that multiple antennas are uncorrelated. Energy of received signal at each antenna is calculated independently and the energy is added to perform detection. Fig. 3 shows multiple antenna signal detection and combining process for a single sub-band. For multiple bands, it is required to minimize processing complexity to reduce time and energy cost. Since the equal gain combining (EGC) method has relative lower complexity order for processing as compared to other methods complexity, in this paper EGC is utilized for signal detection. Pre-detection diversity signal output Y of a CR can be written as:

$$Y_j(n) = g_j[S_j(n) + \eta_j(n)] \tag{7}$$

Where, g_j is the weight factor from antenna $j = 1, 2, ..., M$ and $S_j = h_j s(n)$. For EGC, the branch weights are all set to unity.

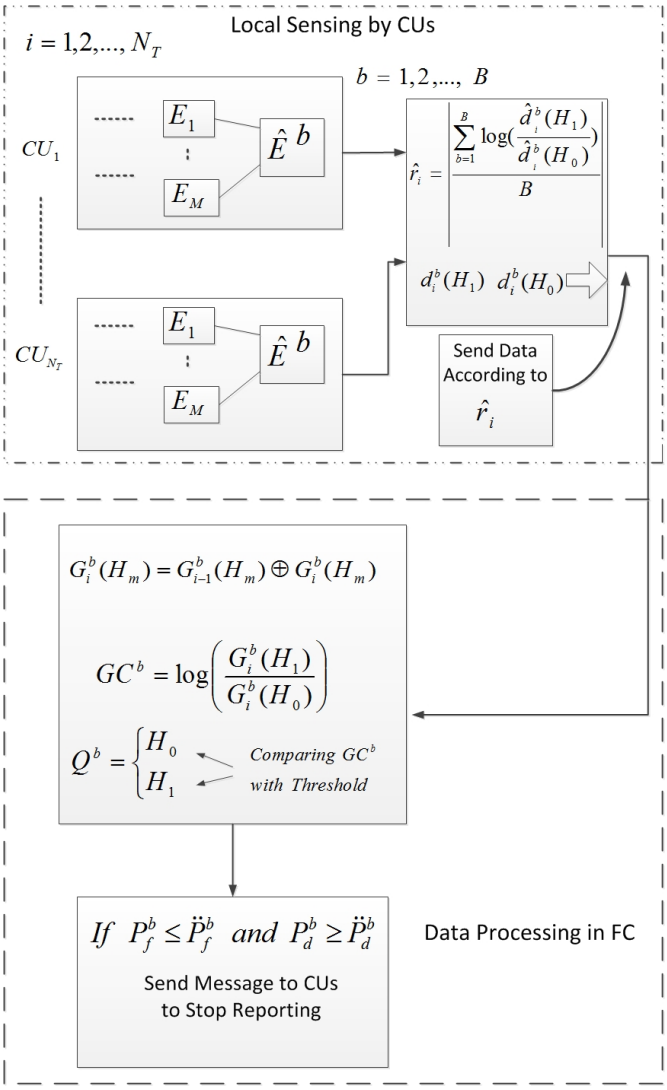

Fig. 2. Overall Structure of Multi-antenna and DS-theory Based Spectrum Sensing

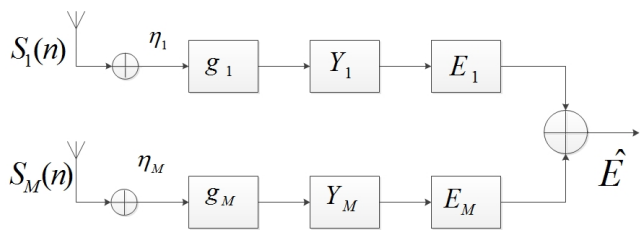

Fig. 3. Block diagram of pre-detection energy combining scheme for multiple antennas

The calculated energy for antenna j becomes:

$$E_j = \sum_{n=1}^{N} |Y_j(n)|^2 \tag{8}$$

However, the total observed energy of the CU by multiple antennas is denoted by $\hat{E}$ and defined as:

$$\hat{E} = \sum_{n=1}^{N} E_j \tag{9}$$

Therefore, for uncorrelated multiple antenna case, H_0 and H_1 hypothesis can be expressed as:

$$\begin{aligned} H_0 &: \hat{E} \sim Normal(MN{\sigma_\eta}^2, 2MN{\sigma_\eta}^4) \\ H_1 &: \hat{E} \sim Normal(MN({\sigma_\eta}^2 + {\sigma_y}^2), 2MN({\sigma_\eta}^4 + {\sigma_y}^4)^2) \end{aligned} \tag{10}$$

B. DS-theory based sequential data fusion for multiple bands

1) Local data and reliability calculation: : The D-S theory of evidence is applied to make final decision of CU's detection, the frame of discernment is defined as: $\{H_0, H_1, \zeta\}$, where ζ is ignorance hypothesis which denotes either hypothesis is true. After sensing time, each CU will estimate its self-assessed decision credibility which is equivalent to Basic Probability Assignment (BPA) for two hypotheses. The BPA function for local hypothesis measurement for every band $b(b = 1, 2, ..., B)$ can be written as a form of the cumulative density function which is found in [12] as follows:

$$\hat{d}_i^b(H_0) = \int_{\hat{E}_i}^{+\infty} exp(\frac{-(Y - \sigma_{ni})^2}{2{\sigma_{ni}}^2})dx \tag{11}$$

$$\hat{d}_i^b(H_1) = \int_{-\infty}^{\hat{E}_i} exp(\frac{-(Y - \sigma_{si})^2}{2{\sigma_{si}}^2})dx \tag{12}$$

$$\hat{d}_i^b(\zeta) = 1 - m_i(H_0) - m_i(H_1) \tag{13}$$

The sensing data reliability r_i of i'th CU for single band $(b = 1)$ can be defined as follows:

$$r_i = \frac{\hat{d}_i^b(H_1)}{\hat{d}_i^b(H_0)} \tag{14}$$

However, the reliability for multiple bands is denoted by $\hat{r_i}$ and calculated as:

$$\hat{r_i} = \frac{\sum_{b=1}^{B} log(\frac{\hat{d}_i^b(H_1)}{\hat{d}_i^b(H_0)})}{B} \tag{15}$$

Each CU transmits the data of all bands in the order of reliability $(\hat{r_i})$ of sensing result to FC where the final decision of every band is made individually based on a sequential test.

2) Reporting and global decision: : In this paper, we have considered reservation reporting method for ordered sequential reporting mechanism and followed the similar parameters of IEEE 802.11. The total reporting time consists of two main parts: reservation period and reporting period which is shown in Fig.4.

Reservation period:
In reservation period, each CU performs a reservation by utilizing a short burst signal according to a selected reservation timeslot in the common control channel. The node that has higher sensing results reliability $(\hat{r_i})$ has higher order in the reservation time and will be allowed to report in a priority

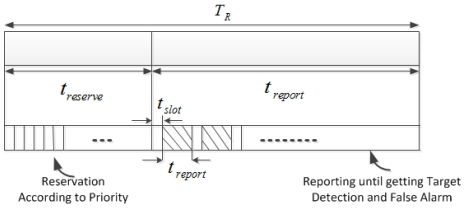

Fig. 4. Reservation reporting method

basis to FC.

Reporting period:

In reporting period, before transmitting the sensing report, the nodes have to listen to a short time for the burst signal from fusion center, which is equivalent to slot time. And a polling period is required to transmit data. Upon making final decision, the FC will perform burst to cancel reporting and decision message is sent to all CUs to stop their reporting. At FC, the BPA is sequentially combined in the order of data arrival for b^{th} band as follows:

$$G_i^b(H_m) = G_{i-1}^b(H_m) \oplus G_i^b(H_m) \tag{16}$$

$m = 0, 1$ and $G_{i-1}^b(H_m)$ and $G_i^b(H_m)$ are $(i-1)^{th}$ and i^{th} global BPA of hypothesis H_m respectively and is defined by DS theory. The global decision credibility ratio of bth band at the ith report is denoted by GC^b and is given as:

$$GC^b = log\frac{G_i^b(H_1)}{G_i^b(H_0)} \tag{17}$$

where GC^b is compared with threshold for final decision. The decision credibility ratio is justified with threshold for making final decision (Q) forbi^{th} band as follows:

$$Q^b = \begin{cases} H_0;\ if\ GC^b(H_m) < -\lambda \\ no\ decision;\ otherwise \\ H_1;\ if\ GC^b(H_m) > \lambda \end{cases} \tag{18}$$

Therefore global probability of false alarm P_f^b and detection P_d^b for the bth band is calculated as follows:

$$P_f^b = Prob(\frac{\hat{H}_1}{H_0}) \tag{19}$$

$$P_d^b = Prob(\frac{\hat{H}_1}{H_1}) \tag{20}$$

Where $\hat{H}_1$ and $\hat{H}_0$ are occupied and null hypothesis respectively detected in the fusion center.

C. Detection time and throughput

The total detection time is divided into two parts: sensing time and reporting time.

1) Sensing time: The total sensing time varies for single (multiple) antenna and bands. Sensing time for single band requires sensing only certain number of sample of a band. And single antenna does not need additional time for combining the signal. Therefore, sensing time for single band by single antenna is as follows:

$$T_S = N_S t_e \tag{21}$$

where N_S is the number of sample and t_e is the time for sensing single bit. Sensing by multiple antennas is performed in parallel way. Thus, it does not need any additional time for sensing by multiple antennas. However, after calculating energy in each antenna, all energies are combined to justify total energy. Thus for multiple antennas, it is needed a very small time for combining energies. Sensing time for single band by multiple antennas:

$$T_S = N_S t_e + t_{comb} \tag{22}$$

where t_{comb} is the time to add energy from multiple antennas. For multiple bands, each band is sensed individually to calculate energy. Therefore, it is required B times of single antenna for B bands. Sensing time for multiple bands by single antenna is:

$$T_S = \sum_{b=1}^{B} N_S t_e \tag{23}$$

Sensing time for multiple bands with multiple antennas becomes:

$$T_S = \sum_{b=1}^{B} N_S t_e + t_{comb} \tag{24}$$

2) Reporting time: All the bands of every CU are reported in a single time slot. In the first phase all the CUs perform reservation for ordered sequential reporting and the reservation time is denoted by $t_{reserve}$. And in the second phase the CU reports to the FC. For single band, every CU sends data of H_0 and H_1 hypothesis in a time slot. Total reporting time for single band with single antenna case is as follows:

$$T_R = N_{T1}(t_r + t_{slot}) + t_{reserve} \tag{25}$$

where N_{T1} is the required number of CU to obtain global target probability of detection and false alarm, t_r and t_{slot} are the reporting time and slot time respectively. For single and multiple bands, reservation time is equal. However, slot time depends on the number of CUs reporting. And since every CU sends multiple bands data of H_0 and H_1 hypothesis in a time slot, the reporting time increases. Total reporting time for multiple band with single antenna case is given by:

$$T_R = N_{T1}(\hat{t_r} + t_{slot}) + t_{reserve} \tag{26}$$

where $\hat{t_r}$ is the reporting time for multiple bands and $\hat{t_r} > t_r$. Reporting time for single band with multiple antennas is:

$$T_R = N_{T2}(t_r + t_{slot}) + t_{reserve} \tag{27}$$

where N_{T2} is the required number of CU to obtain global target probability of detection and false alarm for multiple antennas. Reporting time for multiple band with multiple antennas is given by:

$$T_R = N_{T2}(\hat{t_r} + t_{slot}) + t_{reserve} \tag{28}$$

Therefore, total detection time consists of sensing time and reporting time and can be written as:

$$T_d = T_S + T_R \tag{29}$$

IV. Simulation Result

In order to evaluate the proposed scheme for global detection, the numerical simulation results have been experienced under different conditions, which are shown in Figs.5-9. The general parameters are as following: all the simulations are conducted with the assumption that the presence and absence are equal (0.5). The Bandwidth of each sub-band is $6MHz$. Fig. 5 shows the global false alarm and miss detection for different SNRs $(-14\ to - 10dB)$. Firstly, we have considered a cognitive radio network environment with 100 nodes each of which independently senses the primary user presence and absence by energy detection. The performance shown in Fig.5 is for 10% reporting of total nodes. The comparative performance is shown by single and 4 antennas where every CU performs sensing on single and multiple bands. From the figure it is evident that the global false alarm probability is lower and detection probability is higher in the case of multiple antennas and vice versa for single antenna. Moreover, for multiple bands the probability of false alarm increases and detection decreases due to the decrement of reliability for multiple bands.

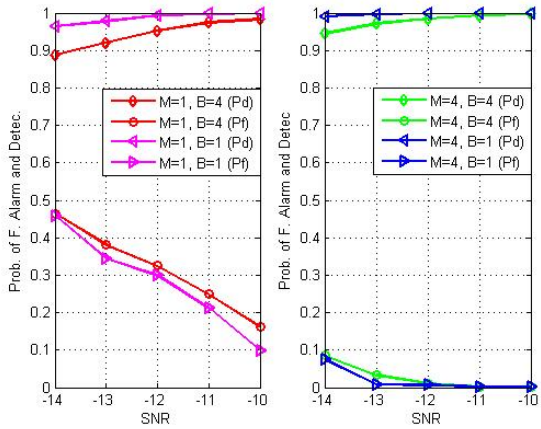

Fig. 5. ROC curve for Prob. of false alarm and detection for different SNRs

The total error probability for different percentage of reporting is plotted in Fig.6. It is assumed that every CU endures $-14\ dB\ SNR$. The total error probability is defined as a combination of the probability of miss detection and false alarm and for B bands it can be written as follows: $\epsilon_{total} = \frac{\sum_{b=1}^{B} P_f^b P(H_0) + (1-P_d^b)P(H_1)}{B}$. From Fig.6, it is observed that total error probability decreases as the number of reporting increases. In addition to that, multiple bands have higher probability of error as compared with single band. Moreover, utilizing 4 antennas has lower error probability as compared with utilizing single antenna. The Fig.7 shows total error probability for different number of samples when total 10% reporting are considered with $SNR\ -14\ dB$. Note that these samples are taken for only single band and for multiple bands the sample is multiple of the number of band. As the number of samples increases, the sensing time will increase and total error probability will be improved due to the cost of longer sensing time.

The required numbers of CUs reporting to obtain target probability of detection and false alarm for different number

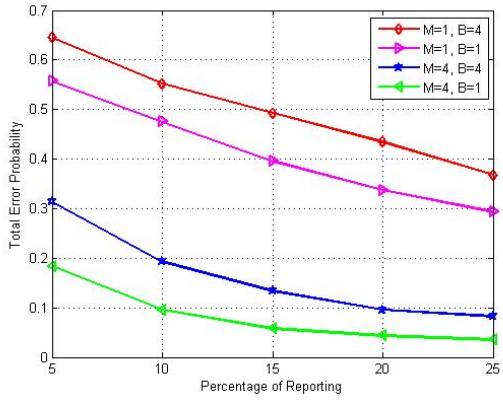

Fig. 6. Total error probability according to the percentage of reporting

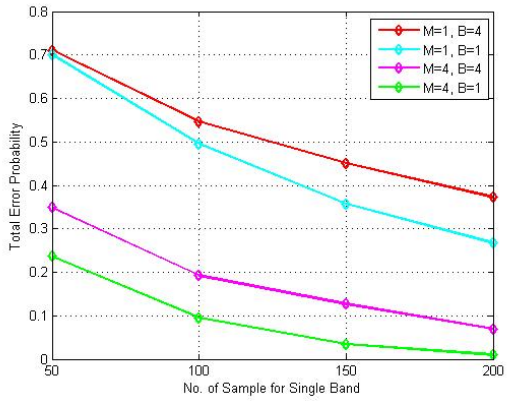

Fig. 7. Total error probability according to the number of samples for single band

of SNRs are observed in the Fig.8. The target probability of detection and false alarm are set as $P_d^b \geq 0.9$ and $P_f^b \leq 0.1$ respectively. From Fig.8, the following observations are obtained: For low SNR, the gap between single and multiple bands for single or multiple antennas are higher. As the SNR decreases, average reliability decreases and the gap becomes larger. For multiple bands $(m = 4)$, single antenna based cognitive radio needs a large number of nodes reporting, compared with CU with multiple antennas. For instance, single antenna-based sensing requires $72,\ 50\ and\ 34$ nodes reporting respectively when SNR is $-14,\ -13\ and\ -12$ respectively. On the other hand, multiple antennas-based sensing requires $12,\ 8\ and\ 4$ nodes reporting to obtain the target probability. The same phenomenon is observed in the case of single and multiple antennas for single band. Additionally, the single band case requires less number of CUs reporting than multiple bands case. Fig. 9 shows the required reporting time to obtain target probability of false alarm and detection for different values of SNRs. The simulation parameters for calculating reporting time are provided in table 1. As depicted in Fig.9, the multiple band and single antenna $(M = 1, B = 4)$ case has the highest reporting time. For single band with single antenna has second higher reporting time but CU with multiple antenna has significantly lower reporting time as compared with CU

TABLE I. THE PARAMETERS FOR CALCULATING REPORTING TIME

Parameters	Values
Slot time: t_{slot}	20 μ sec
Poll time: $t_p = 10 * (t_{slot})$	200 μ sec
Reporting slot interval for single band: $t_r = 3 * t_p$	20 mili sec
Reporting slot interval for multiple band: $t_r = 5 * t_p$	1 mili sec
Reservation time:$t_{reserve} = 5 * N_T * t_{slot}$	6 mili sec

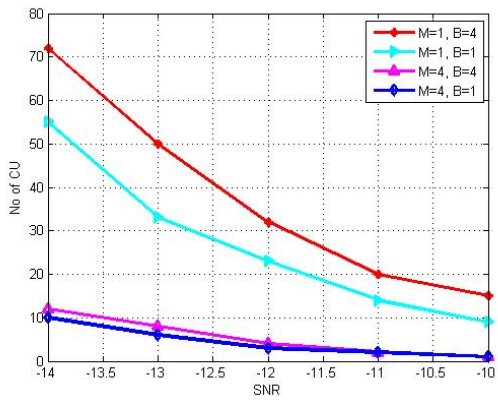

Fig. 8. The required number of CUs to obtain target probability of false alarm and detection according to SNR when 100 samples are taken for each band

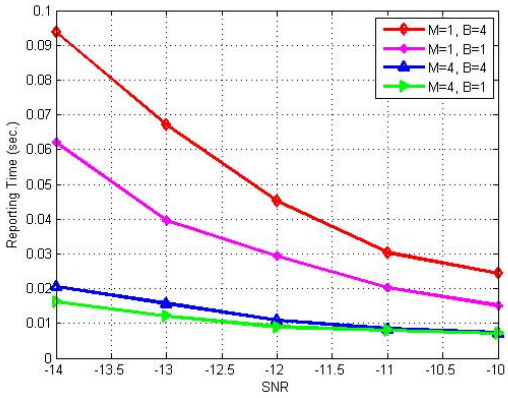

Fig. 9. The required reporting time to obtain target probability of false alarm and detection according to SNR

with single antenna. For instance, the required reporting time is 60 $milli-seconds$ when $SNR = -14dB,\ M = 1\ and\ B = 4$, and the required reporting time is 60 $milli-seconds$ when $SNR = -14dB,\ M = 1\ and\ B = 1$. These reporting times are approximately more than 100 $milli-seconds$ when 3 to 4 times higher than multiple antenna case.

V. CONCLUSION

In this paper, we have proposed a multiple antennas based multi-band cooperative spectrum sensing for cognitive radio network. The ordered sequential reporting is justified with the DS-theory based reliability. The efficiency of relative performance for global sensing is justified in terms of throughput. It has observed that the proposed multiple antennas based multi-band sensing with DS-theory based ordered sequential reporting have higher efficiency over single antenna, single band and traditional reporting method for augmenting the throughput significantly.

REFERENCES

[1] J. Mitola and G. Q. Maguire, Cognitive radios: making software radios more personal, IEEE Personal Commun., vol. 6, no. 4, pp. 13-18, 1999.

[2] S. Haykin, Cognitive radio: brain-empowered wireless communications, IEEE Trans. Commun., vol. 23, no. 2, pp. 201-220, 2005.

[3] D. Cabric, S. Mishra, and R. Brodersen, Implementation issues in spectrum sensing for cognitive radios, in Signals, Systems and Computers, 2004. Conference Record of the 38thAsilomar Conference, vol. 1, pp. 772 776, Nov. 2004.

[4] N. Nguyen-Thanh and I. Koo, An enhanced cooperative spectrum sensing scheme based on evidence theory and reliability source evaluation in cognitive radio context, Communications Letters, IEEE, vol. 13, no. 7, pp. 492 494, July 2009.

[5] G. Ganesan and Y. G. Li, Cooperative spectrum sensing in cognitive radiopart I: two user networks, IEEE Trans. Wireless Commun., vol. 6, pp. 22042213, June 2007.

[6] S. Rodriguez-Parera, V. Ramon, A. Bourdoux, et al. Spectrum Sensing over SIMO Multi-Path Fading Channels based on Energy Detection, Global Telecommunications (GLOBECOM) Conference, IEEE 2008.

[7] A.Salarvan, G.K. Kurt, Multi-Antenna Spectrum Sensing for Cognitive Radio under Rayleigh Channel, IEEE Symposium on Computers and Communications (ISCC), 2012.

[8] Sahai and D. Cabric, Spectrum sensing: fundamental limits and practical challenges," in Proc. IEEE International Symp. New Frontiers Dynamic Spectrum Access Networks (DySPAN), Baltimore, MD, Nov. 2005.

[9] Z. Wei, R.K. Mallik, and K. Ben Letaief, Cooperative spectrum sensing optimization in cognitive radio networks, in Proc. of IEEE Int. Conf. on Communications, pp. 3411-3415, May 2008.

[10] L. Chen, J. Wang, and S. Li, An adaptive cooperative spectrum sensing scheme based on the optimal data fusion rule, 4th Int. Symposium on Wireless Communication Systems, pp. 582-586, Oct. 2007.

[11] Q. Peng, K. Zeng, J. Wang ans S. Li, A distributed spectrum essnsing scheme based on credibility and evidence theory in cognitive radio context, IEEE 17th International Symposium on Personal, Indoor and Mobile Radio Communications, pp.1-5, Sept. 2006.

[12] N. T. Nhan and K. Insoo, An enhanced cooperative spectrum sensing scheme based on evidence theory and reliability source evaluation in cognitive radio, IEEE Communications Letters, vol.13, pp.492-494, 2009.

[13] N. T. Nhan and K. Insoo, An efficient ordered sequential cooperative spectrum sensing scheme based on evidence theory in Cognitive Radio, IEICE Tansactions on Communication. Vol. E93-B, No. 12 Dec 2010.

[14] Ying-Chang Liang, Yonghong Zeng, Edward C.Y. Peh, and Anh Tuan Hoang "Sensing-Throughput Tradeoff for Cognitive Radio Networks" IEEE Trans. on Wireless Communications, Vol.7, No.4 April 2008.

[15] Ryuji Muta, Ryuji Kohno, "Throughput Analysis for Cooperative Sensing in Cognitive Radio Networks" Personal, IEEE 20th International Symposium on Indoor and Mobile Radio Communications, Sept. 2009.

[16] C. You, H. Kwon, and J. Heo, Cooperative TV Spectrum Sensing in Cognitive Radio for Wi-Fi Networks, IEEE Transactions on Consumer Electronics, Vol. 57, No.1, Fe. 2011.

[17] S. Maleki. S. P. Chepuri, G. Leus, Optimization of hard fusion based spectrum sensing for energy-constrained cognitive radio networks, Physical Communication (2012), July 2012.

[18] H. Urkowitz, Energy detection of unknown deterministic signals, Proceedings of the IEEE, vol. 55, no. 4, pp. 523 531, april 1967.

A Metamaterial Based Triangular Cloak

S. S. Islam [1,2], M. R. I. Faruque[1]
Space Science Centre, IPI,
[1]Universiti Kebangsaan Malaysia,
Selangor, Malaysia; EEE,
[2]International Islamic University
Chittagong, Bangladesh
sikder_islam@yahoo.co.uk

Mohammad Tariqul Islam
Department of Electrical, Electronic
and Systems Engineering, Universiti
Kebangsaan Malaysia, Malaysia.
titareq@gmail.com

Touhidul Alam
Dept. of CSE,
International Islamic University
Chittagong, , Bangladesh.
touhid13@yahoo.com

***Abstract*— In this paper, a metamaterial based triangular shaped electromagnetic cloak is presented. The pi-shaped metamaterial shows wideband NZRI (near-zero refractive-index) characteristics in the C-band of microwave spectra. The metamaterial was then utilized in designing a triangular shaped cloak. The cloak hides a metal cylinder electromagnetically where the metamaterial shows NZRI property. At the cloaked frequency, the normalized scattering width (NSW) of the object was reduced to zero. This is a promising design for wideband NZRI characteristics and C-band electromagnetic cloaking operation.**

Keywords—Cloak; C-band; Metamaterials

I. INTRODUCTION

Advances in metamaterial have opened many opportunities to tailor the electromagnetic property of a device. Metamaterial is a naturally unavailable artificially constructed composite material that may have some extraordinary electromagnetic properties, like, negative permittivity, negative permeability, etc. Due to these existing properties, it has applications in many fields like, design of filter, antenna, cloak and so on [1-4].

In the field of invisibility cloak design, metamaterials can play an interesting role. To cloak (hide) an object, electromagnetic waves is manipulated in such a way around an object to be cloaked, that the wave will bend around the object and makes the object hidden to the outside world. For cloaking operation, near zero refractive index (NZRI) metamaterial has good prospect [5]. There are some metamaterials are found in the literature, but very few of them have NZRI property [6-9]. Among the other cloaking methods, 'scattering cancellation' is a one kind of method that had been studied in some of the literature for cloaking operation [10-13]. In this method, an object can be cloaked by reducing the scattering cross section (SCS) of the object, which can be done by metamaterial shell. To cloak an object the SCS should be kept below one [14]. However, most of the cloaking structures were cylindrical or square shape. Moreover, these cloaks were not designed for C-band.

This paper reveals a new metamaterial-based 'triangular-shape' cloak. It operates in the C-band. For numerical analysis, the finite integration technique was adopted. The metamaterial was designed first and then it was applied for building the cloak device. The measured result was presented for metamaterial that agrees well with the numerical result as well.

II. STRUCTURE OF THE UNIT CELL

The Fig.1a shows the proposed metamaterial unit cell structure. The structure has been designed with two complementary copper arms with a little split between them and all of them having a thickness of 0.035mm. The design parameters are, *d=6, g=0.33, h=6, l=8, m=1, n=1.5, p=6.27, q=1, s=0.5* all in mm unit. The design was done on the FR-4 substrate material with dielectric constant 4.2 and loss tangent 0.002 and thickness 1.6mm.

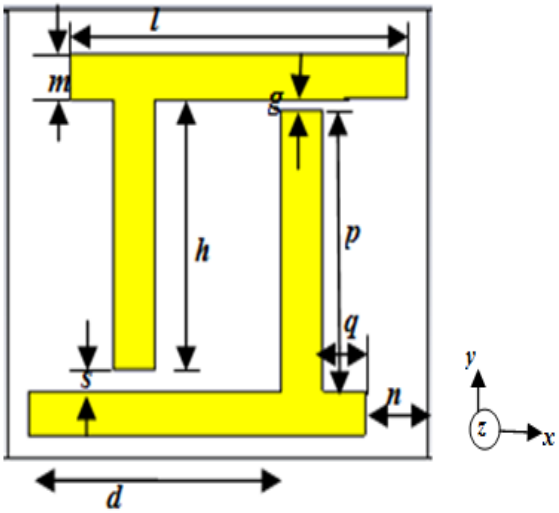

Fig. 1. The proposed unit cell structure

III. METHODOLOGY

For numerical analysis finite integration technique based, software, 'CST Microwave Studio' was adopted. Using two waveguide ports, the electromagnetic wave was propagated in the z-axis of the unit cell and the S-parameters' were calculated. The simulation was done in the frequency range of 5 GHz -9 GHz.

The NRW-method mentioned in [15] was utilized for the calculation of effective medium parameters. The simplified formulae have been given below,

$$V_1 = S_{21} + S_{11} \quad (1)$$

$$V_2 = S_{21} - S_{11} \quad (2)$$

$$\mu_r \approx \frac{2}{jk_0 d} \frac{1 - V_2}{1 + V_2} \quad (3)$$

$$\varepsilon_r \approx \frac{2}{jk_0 d} \frac{1 - V_1}{1 + V_1} \quad (4)$$

$$\eta = \sqrt{\varepsilon_r \mu_r} \quad (5)$$

Where, ε_r is the effective permittivity, μ_r is the effective permeability, 'd' is the thickness of the substrate, k_0 is the wave number and η is the refractive index.

The metamaterial was then used to design a triangular shaped cloak. A cylinder made of aluminium was chosen as object to be cloaked. The transverse electric wave was propagated parallel to the axis of the cylinder through the z-axis of the cloak structure from left to right side to observe the cloaking effect.

IV. Cloak Design

As a part of further work, the metamaterial was applied in designing a triangle-shaped cloak design. For designing the cloak, the wall composed of 2×2 unit cells of the proposed metamaterial was prepared. Three metamaterial walls were prepared and a triangular-shaped cloak was formed. The cloak structure is seen in Fig. 2.

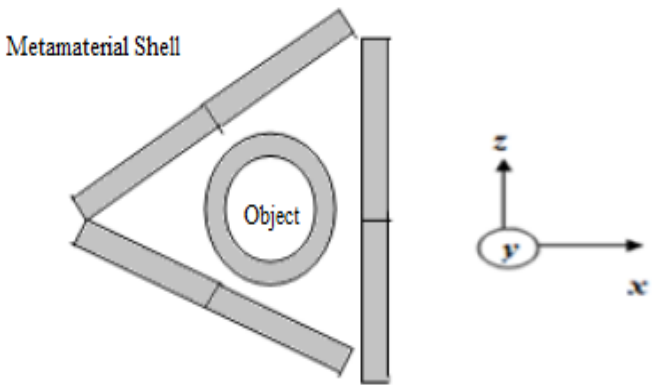

Fig. 2. The proposed cloak structure (top view)

The inner and outer radius of the object is 4mm and 5 mm respectively and the height of the object was kept 20mm.

V. Results and Discussion

The numerical results of S-parameters are presented in Fig.3 for the unit cell. The S-parameters results show one sharp resonance at 8.29 GHz.

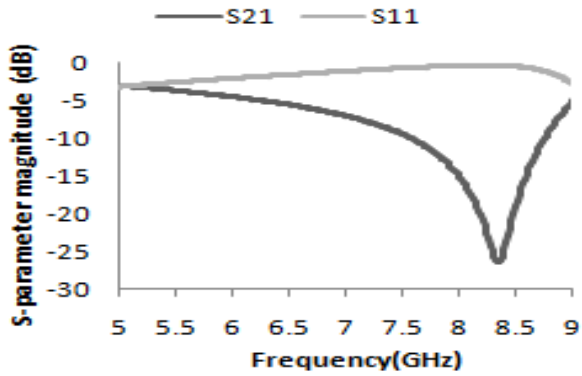

Fig. 3. S-parameter magnitude

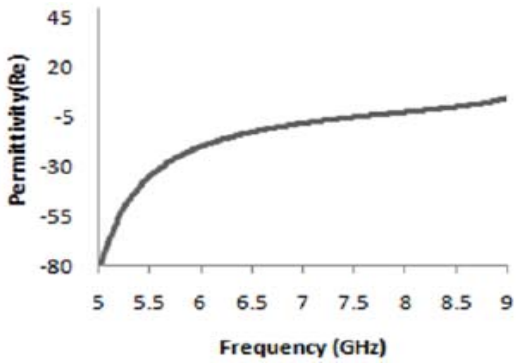

Fig. 4. Numerical real peak of permittivity (ε)

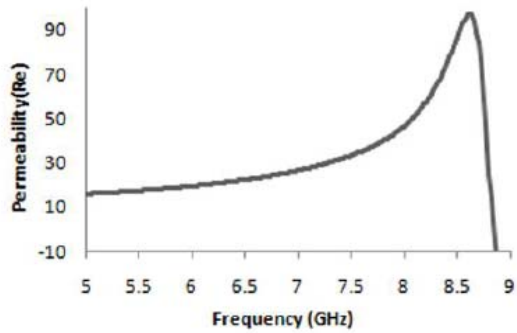

Fig. 5. Numerical real peak of permeability (μ)

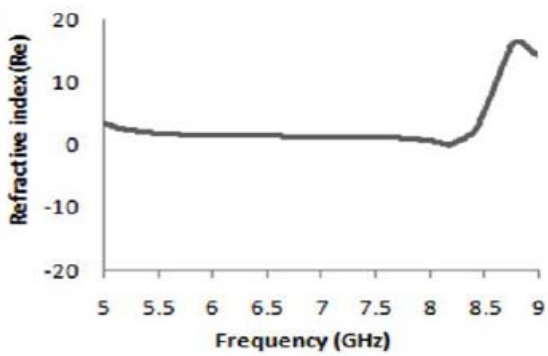

Fig. 6. Real magnitude of refractive index (η) for the unit cell

In Fig. 4 and Fig. 5 the effective permittivity and effective permeability is shown against frequency consecutively. In the Fig. 4 the permittivity curve shows negative magnitude from the 5 GHz to 8.45 GHz. However, in the Fig.5, the permeability curve displays positive peak in the same region. Moreover, at the frequency of 8.29 GHz, the permittivity curve shows negative magnitude and the permeability curve displays positive peak.

In the Fig. 6, the real magnitude of the refractive index curve is shown. It is evident that the refractive index curve displays near-zero refractive index (NZRI) region that is within the frequency range of 5 GHz to 8.40 GHz. The NZRI property has good prospects of designing an invisibility cloak.

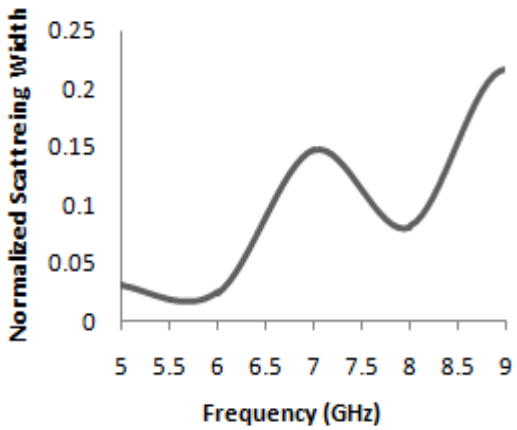

Fig. 7. Numerical value of NSW of the cloaked object

The Fig. 7 reveals the simulated outcome of the NSW of the cloaked object. Normalization of the cloaked object was done with the bare object. It is apparent from the Fig.7 that the scattering width shows the lowest value at 5.67 GHz that is very close to zero. The metamaterial also shows near zero refractive index property there. It depicts that the metallic cylinder is being cloaked at this frequency (5.67 GHz).

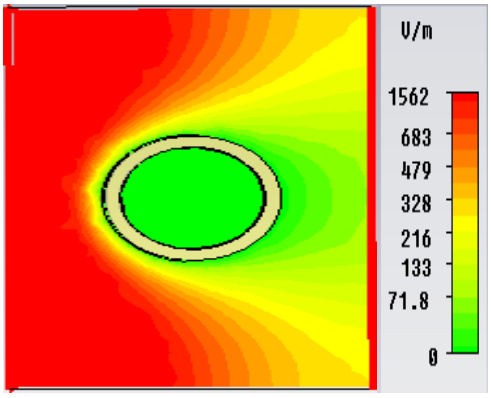

Fig. 8. E-field distribution of bare object for *x-y*-plane (mm) at 5.67 GHz

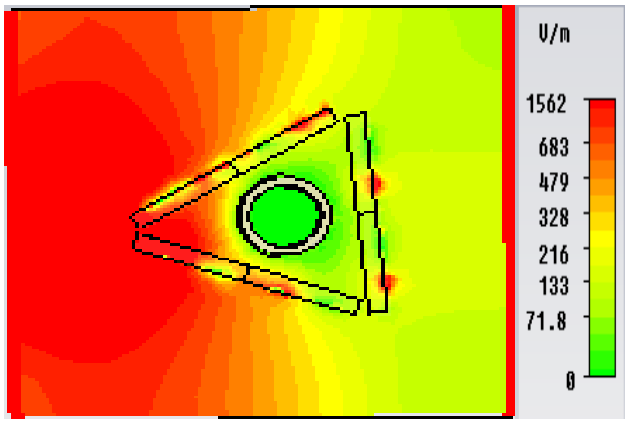

Fig. 9. E-field map in the *x-y*-plane (mm) when the object is covered with the metamaterial at the uncloaked frequency

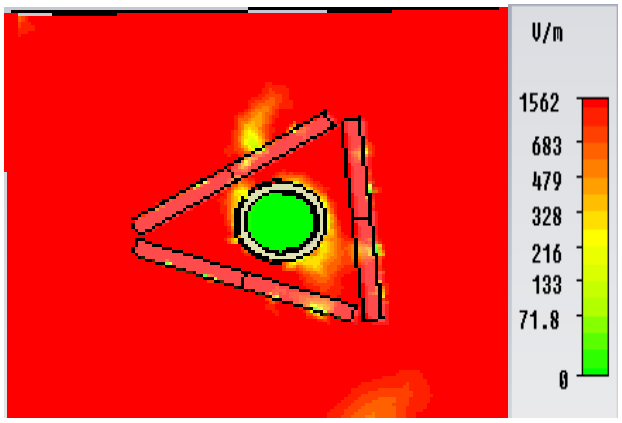

Fig. 10. E-field map in the *x-y*-plane (mm) when the object is covered with the metamaterial at the cloaked frequency (5.67 GHz).

The Fig. 8 shows the field distribution for uncloaked or bare object where some shadow in the forward direction is seen at 5.67 GHz. This shadow refers to the forward scattering of waves from the object. Fig. 9 shows the field distribution of the object at the frequency of uncloaked state. It is clear that the scattering in the forward direction is still present at the right side of the object. However, in the Fig. 10, the object inside the cloak, but at cloaked frequency is presented where the is clear that the forward scattering is completely alleviated and the scattered wave has returned to its original path. Therefore, the existence of the metal cylinder will remain completely undetected at that certain cloaked frequency.

VI. Conclusion

This paper presents a new metamaterial-based electromagnetic cloak that hides a metallic cylinder in a certain frequency of the C - band region. The metamaterial also shows more than 2 GHz NZRI property in the cloak region. Cloaking has good applications in the defense sector,

especially for stealth coating of aircraft or missile. Therefore, the this cloak can be applied in the C-band applications besides other cloaking device.

REFERENCES

[1] M. H. Ullah, M. T. Islam and M. R. I. Faruque, A Near-Zero Refractive Index Meta-Surface Structure for Antenna Performance Improvement; Materials, 6, pp.5058-5068; 2013

[2] M. M. Islam, M. T. Islam, M. Samsuzzaman, M. R. I. Faruque, N. Misran, and M. F. Mansor; A Miniaturized Antenna with Negative Index Metamaterial Based on Modified SRR and CLS Unit Cell for UWB Microwave Imaging Applications. *Materials*,8 pp. 392-407; 2015.

[3] S. S. Islam, M. R. I. Faruque, M. T. Islam; A Near Zero Refractive Index Metamaterial for Electromagnetic Invisibility Cloaking Operation; *Materials*, *8*, pp. 4790-4804; 2015; doi: 10.3390/ma8084790

[4] M. R. I. Faruque, M. T. Islam, N. Misran, "Analysis of Electromagnetic Absorption in the Mobile Phones Using Metamaterials," Electromagnetics Journal (Taylor & Francis Group), Vol. 31, Issue no. 3, pp.215-232, 2011

[5] J. Schilling, The quest for zero refractive index. *Nat. Photon.* **2011**, *5*, 449–451.

[6] S. S. Islam, M. R. I. Faruque, M. T. Islam; A new double negative metamaterial for multi-band microwave applications; Applied Physics A, Volume 116, Issue 2, pp 723-733, August **2014**

[7] S. S. Islam, M. R. I. Faruque, M. T. Islam; Design and Analysis of a New Double Negative Metamaterial; Informacije MIDEM; Vol. 44, No. 3 (2014), 218 – 223

[8] S. S. Islam, M. R. I. Faruque, M. T. Islam; Design of a New ENG Metamaterial for S-Band Microwave Applications; Journal of Electrical and Electronics Engineering - Vol. 7, Nr. 2, October 2014

[9] O. Turkmen, E. Ekmekci, G. Turhan-Sayan; Nested U-ring resonators: a novel multi-band metamaterial design in microwave region; IET Microw. Antennas Propag., Vol. 6, Iss. 10, pp. 1102–1108; 2012

[10] N. Kundtz, D. Gaultney, and D. R. Smith; Scattering cross-section of a transformation optics-based metamaterial cloak; *New Journal of Physics;* 12**;** 043039; 2010

[11] P. Alitalo and C.A. Valagiannopoulos; Demonstration of electromagnetic cloaking of conducting object by the dielectric material cover; Electronics Letters, Vol. 48 No. 17, August 2012

[12] J.C.Soric, P.Y.Chen, A. Kerkf, D.Rainwater, K.Melin, A. Alu, Demonstration of an ultralow profile cloak for scattering suppression of a finite-length rod in free space. *New J. Phys.* **2013**, *15*, 033037.

[13] R.S.Schofield, J.C.Soric, D.Rainwater, A. Kerkhoff, A. Alù, Scattering suppression and wideband tunability of a flexible mantle cloak for finite-length conducting rods. *New J. Phys.* **2014**, *16*, 063063.

[14] X.Wang, F.Chen, E. Semouchkina; Implementation of low scattering microwave cloaking by all-dielectric metamaterials. *IEEE Microw. Wirel. Comp. Lett.* **2013**, *23*, 63–65.

[15] S. S. Islam, M. R. I. Faruque and M. T. Islam; 'A New Direct Retrieval Method of Refractive Index for Metamaterials', *Current Science*, Vol. 109, No. 2, 2015

Implementation of a 1x16 Router Using 2x2 Mach-Zehnder Interferometer Electro-Optic Switch

Rabeya Khatun, Raqibul Hossen, Kazi Tanvir Ahmmed
Department of Applied Physics, Electronics & Communication Engineering
University of Chittagong, Chittagong-4331, Bangladesh
shompa.apece@gmail.com, raqib_saikat@yahoo.com, tanvir@cu.ac.bd

***Abstract*—In optical communication signal router is a novel photonic component used to ensure communication between optical networks. Signal routing has a significant commercial demand in dense wavelength division multiplexing. This paper presents the description of designing a 1x16 signal router using Mach-Zehnder electro-optic Switch operating at 1.55 µm. To design the router we used 2x2 Mach-Zehnder electro-optic switch made by titanium diffused lithium niobate (Ti:$LiNbO_3$) which is used as waveguide medium in designing the desired signal router. Enhanced performance of the switch with reduced insertion loss, excess loss and high extinction ratio was evaluated first and then the router was implemented using that optimized switch. 16 switches were required to implement the router. Optical power can be switched to each of the 16 output ports with the application of applied voltage at each central electrode of the 16 MZI switches. The results are observed using finite difference beam propagation method of OptiBPM12.2 simulation software.**

Keywords—Mach-Zehnder interferometer, Electro-optics switch, Insertion loss (IL), Extinction ratio (ER), Signal router.

I. INTRODUCTION

Mach-Zehnder interferometer is a basic component in photonic lightwave circuit (PLC). It is a classical mirror interferometer which was the most common dual-beam-interferometer for a long time and used in measuring refractive index distributions of transparent objects. It was developed by Mach and Zehnder in 1892 [1]-[2]. Now-a-days it has been used for many applications such as electro-optic switch, modulator, optical sensor, wavelength filters, multiplexers etc [3]-[7]. Directional coupler, Y-shaped splitter, multimode interference coupler etc are used as power splitter and combiner in Mach-Zehnder interferometer [8]-[10]. Electro-optic based 2x2 MZI optical switch using directional coupler requires materials with high nonlinear characteristics such as LiNbO3, KNbO3 etc [11]-[14]. LiNbO3 shows some advantages of having zero residual birefringence, less complexity, high electro-optic coefficient, high speed of operation but it is subjected to polarization sensitivity [8]. Such switches are suitable for time division signal processing and signal routing. Andy W. Brown and Min Xiao demonstrated an all-optical two-port signal router [15]. Ruiqiang Ji experimentally investigated a spatially non-blocking five-port optical router based on micro-ring resonators, which was tuned through the thermo-optics effect and 12.5 Gbps high-speed signal transmission rate was obtained [16]. S. K. Raghuwanshi analytically demonstrated a 1x4 signal router based on 2x2 electro-optic MZI switch and showed the variation in output power due to change in control signal [17]. Santosh Kumar constructed a 1x8 signal router with the application of control signal [18]. As demand for systems with higher capacity is increasing rapidly, so to adapt and to build a large optical cross-connect (OXC) for wide-area communication network and also to provide high-speed interconnections between a no of processors in a parallel, distributed computing system [19], signal router with high configuration is required. In this paper we will demonstrate a 1x16 signal router based on electro-optic effect. Section II represents basics of electro-optic switch, section III shows the construction of 1x16 signal router and section IV shows the simulation results and section V gives a conclusive study.

II. BASICS OF ELECTRO-OPTIC SWITCH

Electro-optic effect is referred to the change in the optical properties of a material with varying electric field. The term includes a number of distinct phenomena, which are, i) the change of the absorption coefficient and ii) the change of the refractive index and permittivity. Second term is referred to Pockels effect i.e. the change in the refractive index which is linearly proportional to the change in electric field. Only certain crystalline solids show the Pockels effect like $LiNbO_3$, $KNbO_3$, $NH_4H_2PO_4$, (ADP), KH_2PO_4 (KDP), $LiTaO_3$ and CdTe etc. The relation of refractive index n with applied electric field E is given below [20].

$$n(E) = n + a_1 E + \frac{1}{2} a_2 E^2 + \cdots \tag{1}$$

The change in refractive index and the resulting change is phase can be calculated by equation 2 and equation 3 [17].

$$\Delta n = (\frac{n^3}{2}) rE \tag{2}$$

$$\Delta\varphi = \frac{2\pi}{\lambda}[(\frac{n^3}{2}) rE] L. \tag{3}$$

L describes substantial length required to obtain certain phase change for directing light into desired path, which is for a 2x2 MZI electro-optic switch 10000 µm and r represents the

978-1-4673-9257-0/15/$31.00 ©2015 IEEE

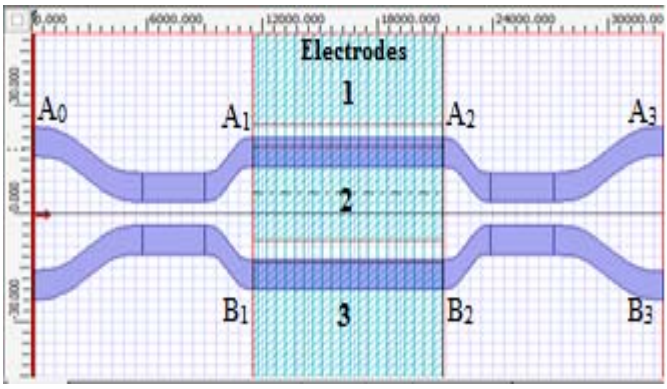

Fig. 1. 2x2 Mach-Zehnder electro-optic switch.

electro-optic coefficient and for $LiNbO_3$, it is 3.66×10^{-10} m/V. Now, if we consider that the voltage difference between two electrodes shown in Fig. 1 is V and d is the distance between the electrodes, then electric field is V/d. So, we can write

$$\Delta\varphi = \frac{2\pi}{\lambda}[(\frac{n^3}{2})\frac{V}{d}r]L. \tag{4}$$

When applied voltage is 0 V, phase change i.e Δφ become zero and with voltage V the phase change Δφ is π. This particular voltage is called V_π and is given by,

$$V_\pi = \frac{\lambda}{n^3}\frac{1}{r}\frac{d}{L}. \tag{5}$$

Now let us find power at output ports of the switch. From Fig. 1 we can see that inputs at first directional coupler i.e to the power splitter denoted as A(Z) and B(Z), which are described by the following equations [21].

$$A(\mathrm{Z}) = \{[\cos(qz) + j\frac{\delta}{q}\sin(qz)]A(0) - j\frac{k}{q}k\sin(qz)B(0)\}\exp(-j\delta_z) \tag{6}$$

$$B(\mathrm{Z}) = \{-j\frac{k}{q}\sin(qz)]A(0) + [\cos(qz) - j\frac{\delta}{q}\sin(qz)]B(0)\}\exp(j\delta_z) \tag{7}$$

Here q represents the number of local peaks of electric field propagating along the x and y-axis directions and given by

$$q = \sqrt{(k^2 + \delta^2)} \tag{8}$$

And also,

$$\delta = 2\pi\left(\frac{l_1 - l_2}{\lambda}\right) \tag{9}$$

In equation 9, l_1 represents the coupling length of the upper waveguide, where l_2 is the coupling length of the lower waveguide and k is the wave number. Let us consider that the case light is launched into the upper waveguide of a MZI. Since both arms have the same waveguide structures; so, δ=0 which results in, $A(0)=A_0$ and B(0)=0. Here the first coupler which functions as power splitter is a 3-dB coupler with kl=π/4, so the light splitting ratios can be written as,

$$A_1 = A_0\cos(kl) = \frac{A_0}{2} \tag{10}$$

$$B_1 = -jA_0\sin(kl) = -j\frac{A_0}{\sqrt{2}} \tag{11}$$

l is the coupling length. After light being traveled through the interferometer arms, the output from these arms A_2 and B_2 will be,

$$A_2 = A_1\exp(-j\beta L) = \frac{A_0}{\sqrt{2}}\exp(-j\beta L) \tag{12}$$

$$B_2 = B_1\exp(-j\beta L + J\varphi) = -j\frac{A_0}{\sqrt{2}}\exp(-j\beta L + j\varphi) \tag{13}$$

L is the length of switching region and φ represents an excess phase shift at the second arm of the interferometer. The second coupler is also a 3-dB coupler where kl=π/4. So, the outputs are given by [20],

$$|A_3|^2 = |A_0|^2.\sin^2(\frac{\varphi}{2}) \tag{14}$$

$$|B_3|^2 = |A_0|^2.\cos^2(\frac{\varphi}{2}) \tag{15}$$

If the voltage applied is 0 V, then φ = 0, the output will be switched to the lower port as $|B_3|^2 \approx |A_0|^2$. With the certain applied voltage for which φ =π, the output will be switched to the upper port as $|A_3|^2 \approx |A_0|^2$. For a 1x16 signal router the same theory is applied, only difference is that 16 control signal is to be varied to launch light to the desired port.

III. Construction of 1x16 Signal Router

To design a 1x16 signal router, 16 individual 2x2 MZI switches are required. No of switches could not be minimized, because it will either increase the width of the device or electrodes will overlap each other. The device then will not function accurately. Titanium diffused lithium niobate waveguide is used to design MZI switch. The switch is made on Z-cut wafer of lithium niobate with air surrounding. It is not more than 33000 μm long and 100 μm wide. The waveguide has a width of 8.0 μm along X-axis. In 3D wafer properties air is defined as coating material with thickness of 2.0 μm and substrate is defined as lithium niobate with a thickness of 10 μm. Three electrodes created on buffer layer with 0.3 μm thickness and refractive index of 1.47. The buffer layer has horizontal and vertical permittivity of the order of 4.

TABLE I. SIMULATION PARAMETERS.

Reference index	Modal
Wavelength	1.55 µm
Polarization	Transverse magnetic (TM)
Mesh-number of points	2000
BPM solver	Paraxial
Engine	Finite Difference
Scheme parameter	0.5
Propagation step	1.3
Boundary condition	Transparent Boundary Condition (TBC)

Thickness of each electrode is 4.0 µm. Both first and third electrodes have a width of 50 µm with zero voltage applied. The second electrode is defined with a width of 26 µm and voltage of 0 V. The separation of 1-2 and 2-3 is 6 µm. Table I shows the list of simulation parameters.

Before constructing 1x16 signal router we optimized the device parameters. Best performance was found for 0.0775 µm titanium strip thickness, 8 µm waveguide width, 9900 µm arm length, 34 µm arm gap, 14.5 µm 3dB coupler gap with outputs at 0 V, 0.000437526 mW and 0.997974 mW and at 8.8 V, 0.997974 mW and 0.000437526 mW for port 1 and 2 respectively. As a result we obtain 33.581 dB extinction ratio and 0.00881 dB insertion loss, 0.0069 dB excess loss for both cross state and bar state [22], where in reference [8] lowest insertion losses were 0.0138 dB and 0.0129 dB & maximum extinction ratios were 30 dB and 29.9 dB for cross sate and bar state respectively obtained with titanium strip thickness of 0.0825 µm. In figure 2,3,4,5,6 simulation results for optimized electro-optic 2x2 MZI switch are shown. Fig. 2 shows refractive index propagation of the optimized device.

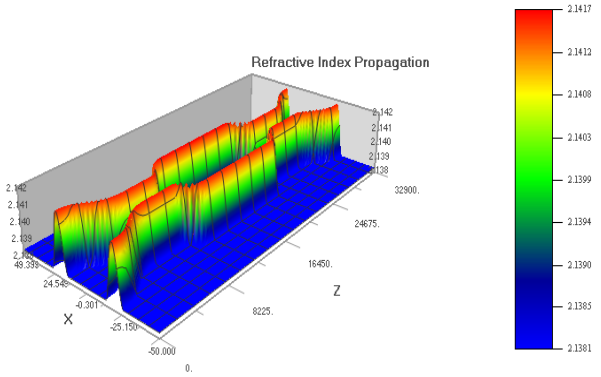

Fig. 2. Refractive index propagation of MZI switch (3D view) .

Optical field propagation for both 0V and 8.8 V are shown in Fig. 3. Fig. 4 ensures that light is switched completely from port 1 to port 2 with the application of applied voltage. It takes 11 iterations to switch light from port 1 to port 2. Fig. 5 represents power in output waveguides for a voltage range of

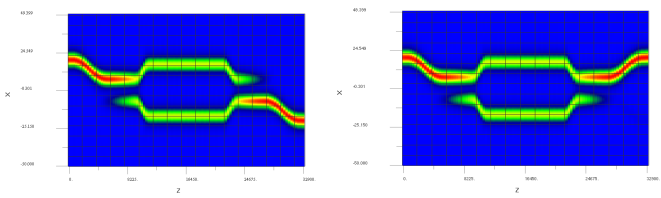

Fig. 3. Optical field propagation at 0 V and 8.8 V respectively.

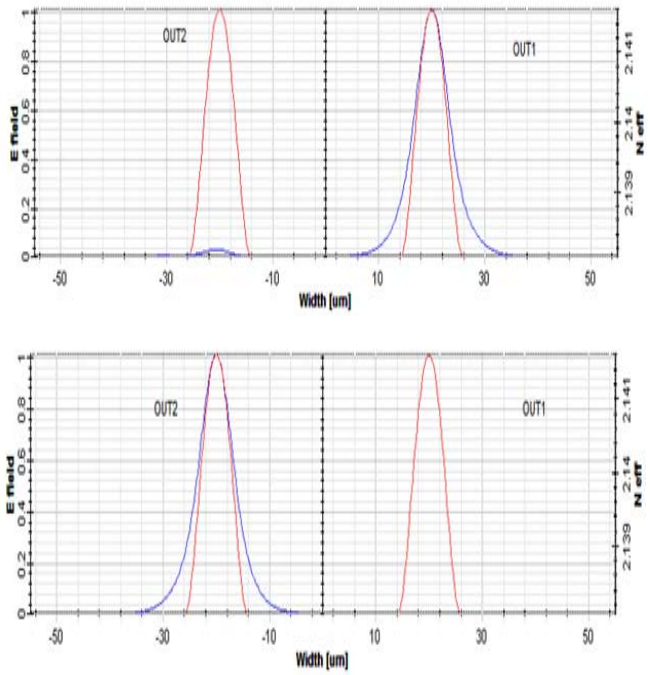

Fig. 4. Electric field at 0V and 8.8 V respectively.

0 V to 8.8 V and from Fig. 6 we can observe power overlap integral characteristics versus distance of propagation of waveguide for both low and high voltage. These results are obtained by running the following visual script,

Const NumIterations = 11

ParamMgr.SetParam “V2”, 0.0

For x= 1 to NumIterations

Param Mgr. Simulate

Param Mgr. Set Param “V2”, 0.8* x

WGMgr.Sleep (50)

Next

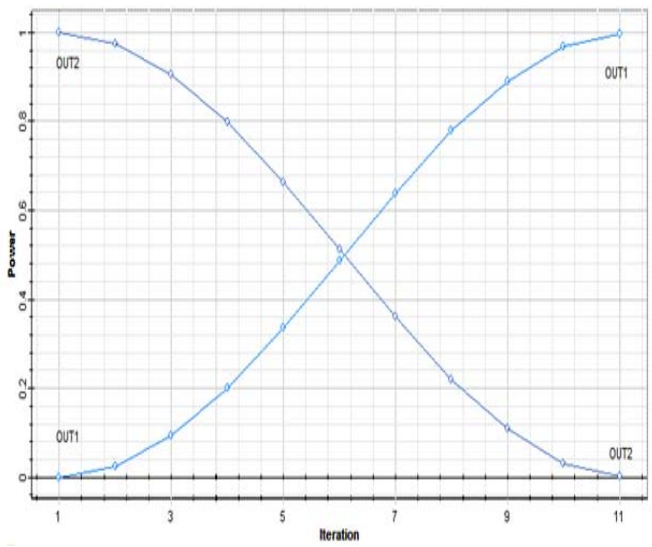

Fig. 5. Power in output waveguides.

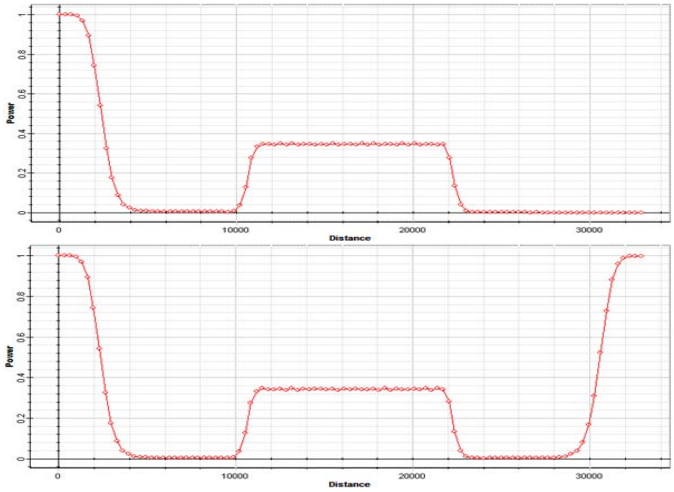

Fig. 6. Power overlap integral at 0V and 8.8 V respectively.

Fig. 7 and Fig. 8 show the layout and refractive index propagation of 1x16 signal router respectively. Central electrode of each switch was positioned 5.5 µm above from the original axis.

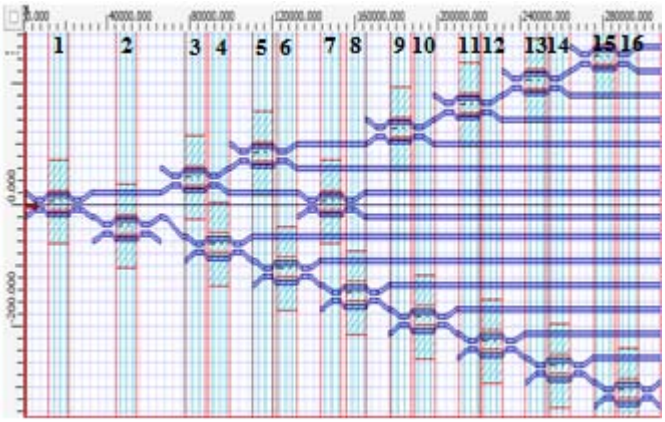

Fig. 7. Layout of 1x16 signal router.

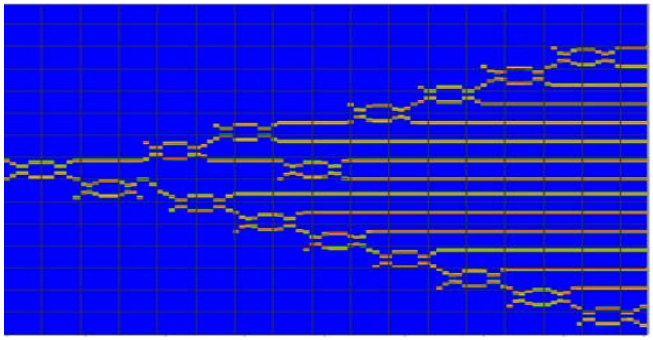

Fig. 8. Refractive index propagation of 1x16 signal router.

MZI switches are numbered as 1, 2, 3 and so on. we assumed the second electrode of each switch as control electrode and they are also numbered similarly as S_1, S_2, S_3 etc.

IV. Simulation Results

Results are observed by OptiBPM software. From Fig. 7 we can see that there are 16 output ports. To switch power into one of these ports particular combination of voltages across the central electrodes of these 16 MZI switch is required. The width of this structure is not more than 700 µm and length is not more than 307600 µm. Table II shows output power at 16 different ports on the basis of control signal S_1, S_2, S_3, S_4, S_5, S_6, S_7, S_8, S_9, S_{10}, S_{11}, S_{12}, S_{13}, S_{14}, S_{15}, S_{16} representing voltages across central electrodes of 16 switch respectively. In table II logic 0 represents 0 V and logic 1 represents 8.8 V and X represents don't care condition. S_1 is kept high to switch upper 8 output ports and with S_1 low lower 8 output ports are to be switched. When S_1 is high output goes to MZI 3, with S_3 kept at 0 V output goes to MZI 5, again with S_5 low output goes to MZI 9, with S_9 low output goes to MZI 11, consequently with S_{11}, S_{13}, S_{15} low output goes to the output port 1. Similarly for each of the combinations shown in table II we can find high output at desired output port. Fig. 9 shows the optical field propagation at different output ports.

TABLE II. Different combinations of control signal of 1x16 signal router.

Output	S_1	S_2	S_3	S_4	S_5	S_6	S_7	S_8	S_9	S_{10}	S_{11}	S_{12}	S_{13}	S_{14}	S_{15}	S_{16}
Port 1	1	X	0	X	0	X	X	X	0	X	0	X	0	X	0	X
Port 2	1	X	0	X	0	X	X	X	0	X	0	X	0	X	1	X
Port 3	1	X	0	X	0	X	X	X	0	X	0	X	1	X	X	X
Port 4	1	X	0	X	0	X	X	X	0	X	1	X	X	X	X	X
Port 5	1	X	0	X	0	X	X	X	1	X	X	X	X	X	X	X
Port 6	1	X	0	X	1	X	X	X	X	X	X	X	X	X	X	X
Port 7	1	X	1	X	X	X	1	X	X	X	X	X	X	X	X	X
Port 8	1	X	1	X	X	X	0	X	X	X	X	X	X	X	X	X
Port 9	0	1	X	1	X	X	X	X	X	X	X	X	X	X	X	X
Port 10	0	1	X	0	X	1	X	X	X	X	X	X	X	X	X	X
Port 11	0	1	X	0	X	0	X	1	X	X	X	X	X	X	X	X
Port 12	0	1	X	0	X	0	X	0	X	1	X	X	X	X	X	X
Port 13	0	1	X	0	X	0	X	0	X	0	X	1	X	X	X	X
Port 14	0	1	X	0	X	0	X	0	X	0	X	0	X	1	X	X
Port 15	0	1	X	0	X	0	X	0	X	0	X	0	X	0	X	1
Port 16	0	1	X	0	X	0	X	0	X	0	X	0	X	0	X	0

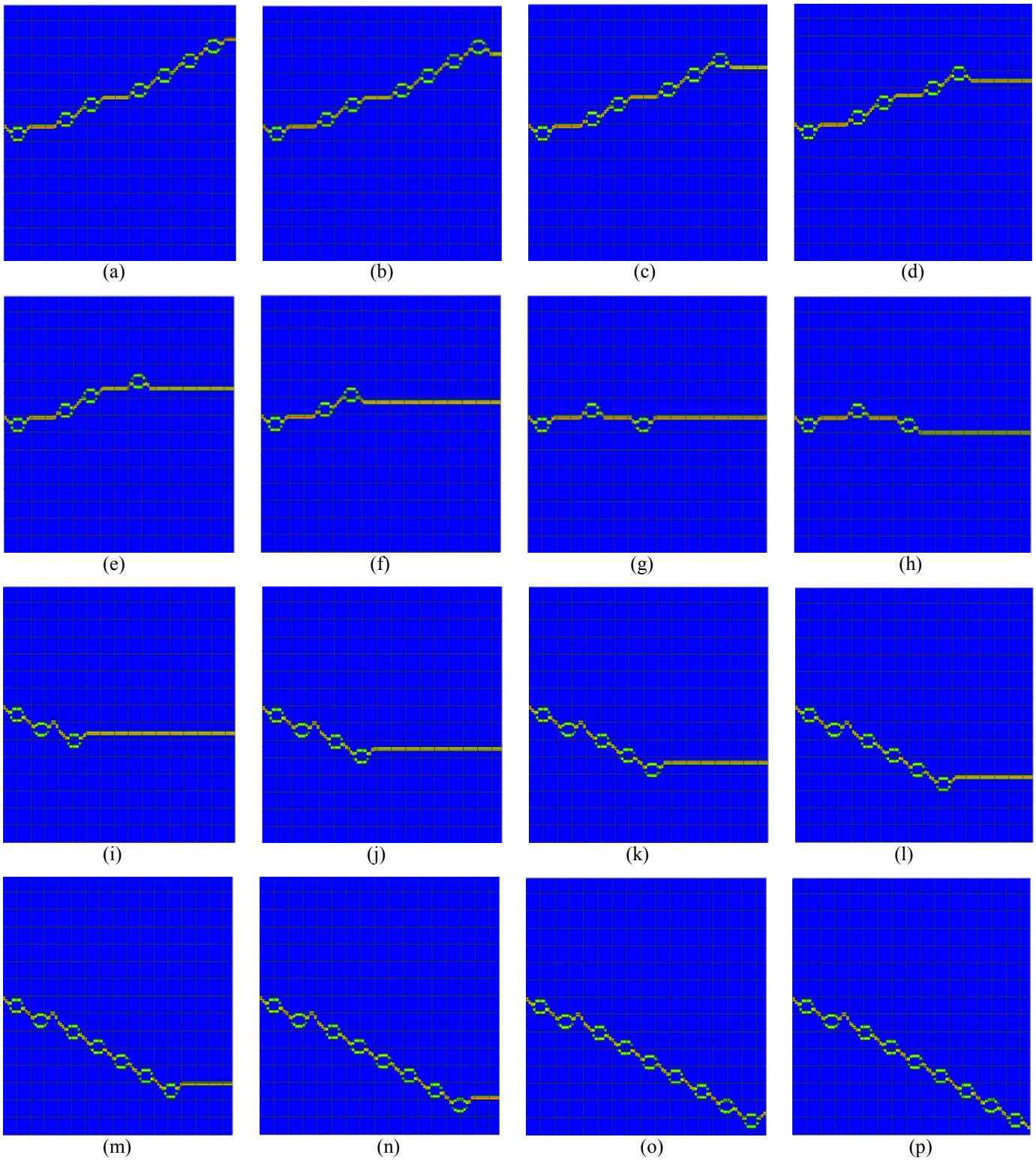

Fig. 9. Optical field propagation at (a) port 1, (b) port 2, (c) port 3, (d) port 4, (e) port 5, (f) port 6, (g) port 7, (h) port 8, (i) port 9, (j) port 10, (k) port 11, (l) port 12, (m) port 13, (n) port 14, (o) port 15, (p) port 16.

V. Conclusion

This paper gives elaborate discussion on a 1x16 signal router. 16, 2x2 electro-optic switches are used in construction, which gives the device a length of 307600 µm and width of 700 µm. At first the fundamental device i.e. MZI switch is optimized and we obtained lowest insertion loss of 0.00881 dB, excess loss of 0.0069 dB and highest extinction ratio of

33.581 dB. Then outputs for different combinations of control signals are observed and we find power being switched to each one of 16 output ports for each combination.

REFERENCES

[1] L. Mach, "Ueber einen Interferenzrefraktor," Z. Instrumentenk, Springer publication ,vol. 12, pp. 89-93, 1892.

[2] L. Zehnder, "Ein neuer Interferenzrefraktor," Z. Instrumentenk, Springer publication, vol. 11, pp. 275-285, 1891.

[3] G. Singh, "Design of 2×2 Optoelectronic Switch Based on MZI and Study the Effect of Electrode Switching Voltages," Journal of World Academy of Science, Engineering and Technology, vol. 39, pp. 401-407, 2008.

[4] D.J. Thomson, F.Y. Gardes, Sheng Liu, H. Porte, L. Zimmermann, J.M. Fedeli, Youfang Hu, M. Nedeljkovic, Xin Yang, P. Petropoulos, G.Z. Mashanovich, "High Performance Mach–Zehnder- Based Silicon Optical Modulators," IEEE Journal of Selected Topics in Quantum Electronics, vol. 19, issue. 6, pp. 85 – 94, November-December 2013.

[5] Xianxin Jiang, Yangqing Chen, Fang Yu, Longhua Tang, Mingyu Li, Jian-Jun He, "High-sensitivity optical biosensor based on cascaded Mach–Zehnder interferometer and ring resonator using Vernier effect," Opt. Lett., vol. 39, issue. 22, pp. 6363-6366, 2014.

[6] E.L. Wooten, R.L. Stone, E.W. Miles, E.M. Bradley, "Rapidly tunable narrowband wavelength filter using $LiNbO_3$ unbalanced Mach-Zehnder interferometers," Journal of Lightwave Technology, vol. 14, no. 11, pp. 2530-2536, November 1996.

[7] T. Mizuochi, T. Kitayama, K. Shimizu, K. Ito, "Interferometric crosstalk-free optical add/drop multiplexer using Mach-Zehnder-based fiber gratings," Journal of Lightwave Technology, vol. 16, issue. 2, pp. 265, 1998.

[8] Nazmi A. Mohammed, Huda S. Abo Elnasr, Moustafa H. Aly, "Performance Evaluation and Enhancement of 2×2 Ti: $LiNbO_3$ MachZehnder Interferometer Switch at 1.3 µm and 1.55 µm," The Open Electrical & Electronic Engineering Journal, vol. 6, pp. 36-49, 2012.

[9] Jing Wang, Minghao Qi, Yi Xuan, Haiyang Huang, Zhen Sheng "Ultrabroadband Silicon-on-Insulator Polarization Beam Splitter Based on Cascaded Mode-Sorting Asymmetric Y-Junctions," IEEE Photonics Journal, vol. 6, no. 6, article #. 2700608, December 2014.

[10] Shaochun Cao, Liping Sun, M. Savoie, "2×2 MMI-MZI GaAs-GaAlAs carrier-injection optical switch," Photonics Society Summer Topical Meeting Series, 2010 IEEE, pp. 207-208, 19-21 July 2010.

[11] Nazmi A. Mohammed , Huda S. Abo Elnasr , Moustafa H. Aly, "Analysis and design of an electro-optic 2 × 2 switch using Ti: $KNbO_3$ as a waveguide based on MZI at 1.3µm," Opt Quant Electron (springer journal), vol. 46, pp. 295–304, 2014.

[12] M. P. Earnshaw, " 8×8 Optical Switch Matrix Using Generalized Mach–Zehnder Interferometers," IEEE Photonics Technology Letters, vol. 15, no. 6, pp. 810-812, 2003.

[13] T. Sasaki, H. Sato, K. Nakatsuhara, T. Nakagami, "Demonstration of switching operation in a symmetric Mach-Zehnder interferometer switch using Si waveguide with a ferro-electric liquid crystal cladding," Conference on Lasers and Electro-Optics-Pacific Rim, pp. 1-2, 26-31 August 2007 .

[14] K. Suzuki, "High-Speed Optical 1×4 Switch Based on Generalized Mach–Zehnder Interferometer With Hybrid Configuration of Silica-Based PLC and Lithium Niobate Phase-Shifter Array," IEEE Photonics Technology Letters, vol. 19, no. 9, pp. 674-676, May 2007.

[15] Andy W. Brown, Min Xiao, "All-optical switching and routing based on an electromagnetically induced absorption grating," Opt. Lett., vol. 30, pp. 699-701, 2005.

[16] Ruiqiang Ji, Lin Yang, Lei Zhang, Yonghui Tian, Jianfeng Ding, Hongtao Chen, Yangyang Lu, Ping Zhou, Weiwei Zhu, "Five-port optical router for photonic networks-on-chip," Opt. Express, vol. 19, issue. 21, pp. 20258-20268, 2011.

[17] S. K. Raghuwanshi, A. Kumar, S. Kumar, "1×4 Signal Router Using 3 Mach-Zhender Interferometers," Opt. Eng., vol. 52, no. 3, pp. 035002, 2013.

[18] Santosh Kumar, Sanjeev Kumar Raghuwanshi, Ajay Kumar, "Implementation of optical switches using Mach–Zehnder interferometer," Optical Engineering, vol. 52, no. 9, pp. 097106, September 2013.

[19] Michael J. O'Mahony, "Future Optical Networks," IEEE Journal Of Lightwave Technology, vol. 24, no. 12, pp. 4684-4696, December 2006.

[20] Bahaa E. A. Saleh, Malvin Carl Teich, "Fundamentals of Photonics," Publisher: John Wiley & Sons, Inc. ISBNs: 0-471-83965-5 (Hardback), 0-471-2-1374-8 (Electronic), pp. 698, 1991.

[21] Katsunari Okamoto, "Fundamentals of Optical Waveguides," Laboratory Ltd Ibaraki: Japan, 2nd ed., pp. 195-196, 2006.

[22] Rabeya Khatun, Kazi Tanvir Ahmmed, A. Zahed Chowdhury, Raqibul Hossen, "Optimization of 2x2 MZI Electro-Optic Switch and Its Application as Logic Gate," 18th International Conference on Computer and Information Technology, 2015, in press.

Enhanced Wi-Fi Direct Power Saving with Power Control for the Mobile Phone

Nam Gon Kim[1,*], Hyun Hak Cho[1], Chang Min Eun[1], and Ok Hyun Jeong
[1]Department of Electronic Engineering, Sogang University, Seoul, Republic of Korea
[*] E-mail: kimngon88@sogang.ac.kr

Abstract— **Wi-Fi Direct, that is a peer-to-peer specification based on IEEE 802.11 standard by Wi-Fi Alliance, defines the role of power saving mechanism. However, it indicates only basic rule and does not specify effective environment and the way of configuration for each parameter. In this paper, we studied the way of the optimizing Power Save Mode (PS Mode) for Wi-Fi Direct in the mobile. To maximize efficient of the PS Mode, we dynamically controlled sleep period each fixed a beacon signal period, called Target Beacon Transmit Time (TBTT) and we adapted power control scheme based on IEEE 802.11. As a result, to schedule sleep period of NoA on the power control has a benefit for the total transmission time and power consumption.**

Keywords—Wireless LAN, Wi-Fi Direct, Power Save Mode (PS Mode), Notice of Absence(NoA) protocol.

I. INTRODUCTION

In the last decade, as a variety of mobile devices including tablet PC and mobile phone have been spread and communication technology has advanced rapidly, the data traffic has increased exponentially. Device-to-device communication, such as Wi-Fi Direct using a wireless LAN has emerged to distribute traffic based on the communication technology of at least 150Mbps speed of 4G. It was not a big issue in the past, because AP is connected to an external power source without mobility. However, recent mobile devices have a high degree of mobility and use simultaneously other wireless communication such as LTE and GPS so it increases load on the mobile phone. In other words, the continuity of battery without any external power source is arising as main issue.

For this purpose, Wi-Fi Alliance has published a new standard called Wi-Fi Direct (Wi-Fi P2P) by making up for a low-speed communication in ad-hoc network and a problem based on infrastructure in conventional wireless LAN based on IEEE 802.11 [2]-[3]. Specially, it describes efficient communication methods by concurrent operation, service discovery and power saving. We studied with a focus on PS Mode because the transfer of data payload occupies a large portion on data transmission.

Wi-Fi Direct defines two way of power saving: the Opportunistic Power Save (OppPS) and the Notice of Absence (NoA) in technical specification. OppPS Protocol is a method of determining the sleep state of Group Owner (GO) whether the clients send the data using the beacon signal. On the contrary, NoA Protocol is a method for determining a transmission timing of the client in accordance with the state of GO through the beacon signal. However, the standard defines only basic transmission Protocol. It is difficult to use the protocols of PS Mode to specify parameter configuration without describing the criteria.

Therefore, we studied how to set up efficiently the parameter of PS Mode utilizing the IEEE 802.11 network and how to optimize PS mode to avoid the ambiguity of configuration without additional overhead. Thereby, we intended to reduce the power consumption of peer-to-peer communication in the mobile environment. In this paper, we have experimented that controlling the sleep period and transmission power level of the Wi-Fi Direct using the channel information for efficient parameter setting.

We tested using the Network Simulator-3 that operates based on the C ++ in Linux OS. We tried the simplest structure with two mobile devices, each GO and Client is connected 1:1 peer-to-peer network. The simulations have been performed by modifying the number of the power level of transmission for power control and the count for NoA parameter. Namely, the simulation has been conducted by changing the sleep period and transmission level each channel state during a fixed TBTT to compare the basic operation of NoA protocol.

The paper is organized as follows. Chapter 2 reviews the background and proposal. It shows that simulation is conducted how to setup the experimental environment in chapter 3. It indicates results of implementation and analysis of performance in chapter 4. Lastly, chapter 5 sets out the conclusions of this paper.

II. BACKGROUND AND PROPOSAL

First, we discuss power save mechanism of IEEE 802.11 and Wi-Fi Direct. Then, we consider the propriety of using the power control for the power saving. Finally, we propose optimizing the Wi-Fi Direct power saving with power control scheme.

978-1-4673-9257-0/15/$31.00 ©2015 IEEE

A. Related work

As specified in the standard [3], a WLAN based on IEEE 802.11 is available a power save mechanism for the power management. It determines the AP with other station to stay in one of the states; idle, awake, or sleep. In IEEE 802.11, the AP on PSM periodically announces state to mobile stations through the Traffic Indication Map (TIM) contained in the beacon frames. The stations wake up periodically to listen to the beacon from the sleep state. Similarly, Wi-Fi Direct also defines two power management protocols [2]. The OppPS protocol is advantageous for burst data transmission when it comes to the power consumption. In contrast, the NoA protocol has profit to transmit dynamic data traffic with the Delivery Traffic Indication Map (DTIM) for power consumption [7].

Another approach about the power management is the power control. Several power/rate adaptation mechanisms have been proposed for multiple rates supported by 802.11 [13]-[14]. For example, Multi-rate adaptation algorithms were proposed to improve throughput performance in ad hoc networks. Another rate control algorithms are developed specifically to extend past algorithms with power control. However, power or rate adaptation algorithms use to minimize interference among neighboring Stations.

In Wi-Fi Direct, only channel 1, 6 and 11 are employed because they have low degree of interference. We need to shift the usage of power adaptation algorithm for its usage to only adjust the power level of RF channel.

B. Proposed method

To increase the efficiency of the NoA protocol, we applied the power control scheme to power saving mechanism. The power control scheme is an efficient scheme to reduce the channel interference caused to use adjacent channels. However, because of using less interference channel in Wi-Fi Direct, we exert the power control scheme to adjust the transmission power level for reducing power consumption. Also, we have to limit the maximum transmission level to mobile environment. The experiments have been performed with Power-controlled Auto Rate Fallback (PARF) algorithm [5] for power control as changing the two factors and optimizing the parameter.

III. Experimental Environment

A. The setup of simulator

We modified the C++ code of Wi-Fi module which had been implemented in ns-3 and we implemented a NoA protocol of Wi-Fi direct communication. Ns-3 contains various models of high-quality validated and is spread over a large community of users and developers [4]. The simulation models a wireless network interface controller based on the IEEE 802.11 standard [3]. The IEEE 802.11 MAC protocol is implemented with several C++ classes on ns-3. We have simulated based on Broadcom's BCM4335 chipset for power model of realistic environments. The results of simulation were verified transmitted packets with Wireshark [6]. Only to analysis the NoA protocol through the data transfer, we simulated without device discovery, service discovery and group formation on Wi-Fi Direct. Also, to analysis the transfer a single MPDU, we simulated an 802.11g. Table 1 indicates the configuration of the power module for Wi-Fi Direct.

For wireless systems, the radio channel is the propagation loss and propagation delay model and ignore real-world effects such as multipath fading and channel capture. First, we have to examine the effects of the number of power level of transmission and the count of NoA parameter. Then, we implemented and experimented dynamic scheduling the sleep period according to the channel state on power control scheme. The available transmission is a minimum 0 dBm and maximum 16 dBm.

TABLE I. The Configuration of Power Module in NS-3

Parameter	Value
Target Chipset	BCM4335, Broadcom
Standard	802.11g / 54Mbps (OFDM)
Input Voltage	3.6V
Sleep Current	0.1mA
Tx Current	76mA

B. The network architecture of experiment

The network structure for the experiment can be seen in Fig 1. Only for two mobile devices, GO and Client is connected 1:1 peer-to-peer network. We confirmed by transmitting a packet for 60 seconds on condition that the respective parameters of NoA were changed. During 60 seconds, the Client is moved 30 meters at the GO where is 5 meters away. It stays during every 15 seconds. After that time, it is placed a new position where is 10 meters away from previous position. In other words, the distance increases 10 meters per 15 seconds. Consequentially, the position of the Client has a different channel conditions respectively. The TBTT for NoA parameter is 10.24ms; the sleep period was a 50% duty cycle. Outputs for power consumption in the simulation showed to watt.

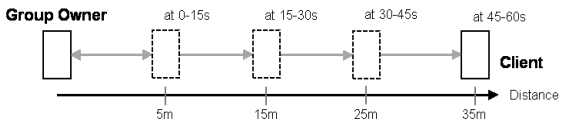

Figure 1. The network structure for the simulation

IV. Analysis of Simulation Result

A. The configuration of NoA parameter

The NoA protocol of PS Mode timing is scheduled by the values of Start time, Interval, Duration and Count. The Start time is the start time of NoA schedule. The Interval indicates the absence time. The Duration is the period of each absence. The Count is the number of absences. GO announces every beacon message to client with these four parameters. GO

978-1-4673-9257-0/15/$31.00 ©2015 IEEE

changes the state at determined time, Client keeps NoA schedule most recently received. The example of operation for P2P GO NoA protocol with power control is shown as Fig 2.

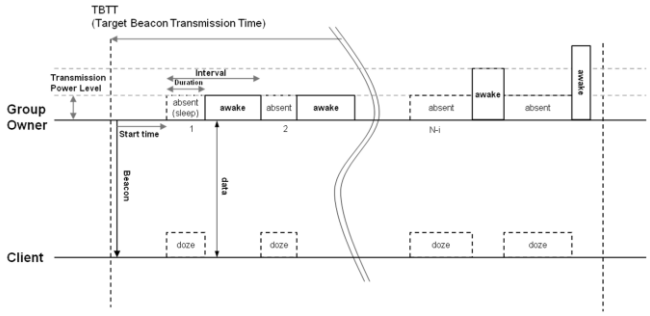

Figure 2. The example of operation for P2P GO NoA protocol with power control

1) *The number of transmission power levels*

First, we have carried out the simulation to verify the effect of power control. When the data is transmitted from WLAN devices, the maximum transmission power is typically 16~20 dBm. To use the adaptation of power control, we configured 16 dBm for maximum powers. The number of transmission power levels available between 0 dBm and 16 dBm and we turned from 4 to 16 sequencely raising 2 degrees. The Count is configured 4. At the rate of awake and sleep, that is duty cycle, is 50%.

2) *The number of count*

Next, it was set equal to a total time of transmitting the data for performance comparison of each experiment. In other words, the total processing time multiplied by the time of interval and count was configured the same one scheduling period of NoA. And by increasing the count from 4 to 12, simulation was performed with maintaining a TBTT. The setup of dividing maximum transmission level is 4. And duty cycle is fixed to 50%.

3) *The optimization of the NoA parameter*

Last, we simulated the proposed optimizing Wi-Fi Direct PS mode with power control. The simulation is conducted by scheduling sleep period and changing transmission power level according to the channel conditions. In the channel condition which is deteriorated in step 4 shown as Fig 1.; Case 1 is that sleep period is fixed the ratio of the awake and sleep time by one-to-one, the 50 percent of duty cycle. Case 2 has the time of scheduling sleep period from 87.5 to 12.5 percent per 15 seconds when the packets are transmitted. In contrast, in Case 3, the packets are transmitted with increasing the duty cycle from 12.5 to 87.5 percent. All of these cases are configured 4 as the number of transmission power level and count.

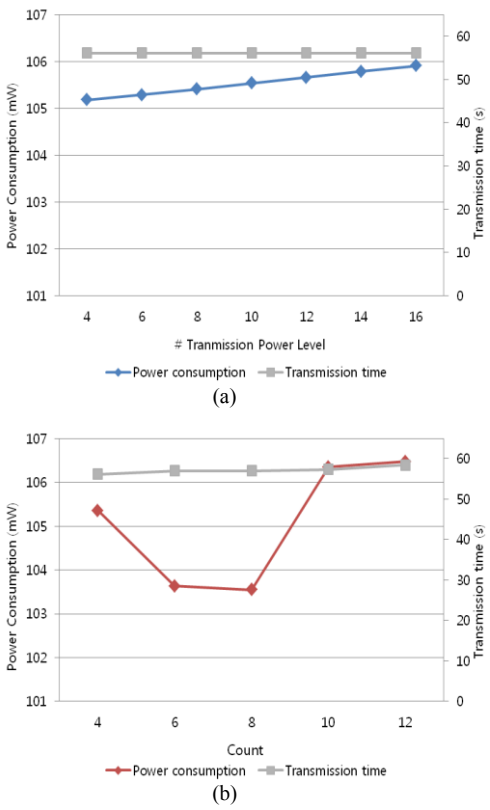

Figure 3. (a) The power consumption with the number of transmission power levels (b) The power consumption with the number of count

B. *The result of simulation*

1) *The number of transmission power levels*

We were tested by varying the number of transmission power level. In 4 to 16 levels, the power consumption was observed that the more the number of transmission power level, the more power consumption is represented. This could be the result of increasing the frequency of performing power adaptation according to the channel state for the more number of power level. The power consumption with changing the number of transmission power levels is shown in Fig 3-(a).

2) *The number of counts*

Fig 3-(b). shows power consumption with the count of NoA. The following are the results of experiments by changing the count of the NoA protocol. As the count is smaller as shown in the graph, power saving effect is larger until 8. For the total transmission time, it also completed a transmission in the first but it was little difference. While the effect of power saving is improved in infrequent scheduling and flat channel cases, it has the disadvantage that it is impossible to change flexibly the parameters due to less frequency of the scheduling in the channel which has large fluctuation. Eventually, the efficiency of NoA power saving as to the count is expected to be influence by the variation rate of channel state.

978-1-4673-9257-0/15/$31.00 ©2015 IEEE

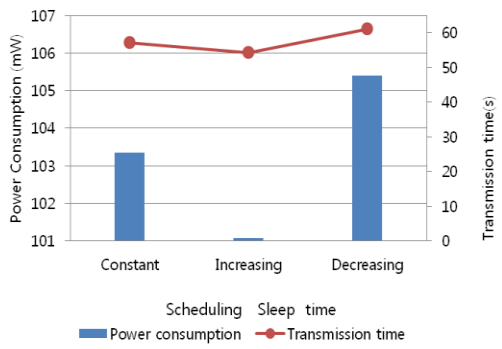

Figure 4. The power consumption in accordance with the way of dynamic scheduling.

3) *The optimization of the NoA parameter*

Finally, It is confirmed that the case 2 (Increasing sleep time) is presented the best performance in terms of the total transmission time and power consumption. Conversely, the result of case3 has the most power consumption and long transmission time. This is because the case 2 was scheduled a way to increase the capability of the transmission with NoA protocol as the transfer consumes less power when a good channel at power adaptation algorithm. As a result, it can be seen that the case 2 of performance is the best way better than 3.34% in the constant case. The power consumption in accordance with the way of dynamic scheduling is shown as Fig 4.

V. CONCLUSION

This paper has mentioned about how to use the Wi-Fi direct based on IEEE 802.11 as it is widely popular in recent years, and prepared to seek how to use a little more effective PS Mode for an increasingly important power issue. In the environment for performing power adaptation scheme according to the channel condition of the Wireless LAN, to use the NoA scheduling protocols in an efficient manner, it is good to scheduling by dividing appropriately according to the number of transmission power level in the environment and reducing the value of count in the maximum flexibility. Above all things, it is that the way to improve the power efficiency using the NoA protocol scheduling is to secure the awake time in good channel and to increase the frequency of the scheduling with the maximum flexibility in poor channel.

ACKNOWLEDGMENT

“This research was supported by the MSIP(Ministry of Science, ICT and Future Planning), Korea, under the C-ITRC(Convergence Information Technology Research Center) (IITP-2015-H8601-15-1004) supervised by the IITP(Institute for Information & communications Technology Promotion)"

REFERENCES

[1] (2015) The Wi-Fi Alliance website. [Online]. Available: http://Wi-fi.org

[2] Wi-Fi Alliance, P2P Technical Group, Wi-Fi Peer-to-Peer (P2P) Technical Specification v1.5, Wi-Fi Alliance, Aug. 2014.

[3] IEEE 802.11-2007 Standard, Wireless LAN Medium Access Control (MAC) and Physical Layer (PHY) Specifications, IEEE std. 802.11, 2012

[4] (2015) The ns-3 simulator website. [Online]. Available: http://www.nsnam.org.

[5] Aditya Akella, Glenn Judd, Srinivasan Seshan, and Peter Steenkiste, “Self-management in chaotic wireless deployments,” in *ACM Int. Conf. Mobicom.*, Jun. 2005, pp. 737–755.

[6] (2015) Wireshark: A Network Protocol Analyzer website. [Online]. Available: http://www.wireshark.org/

[7] D. Camps-Mur, A. Garcia-Saavedra, and P. Serrano, “Device-to-Device Communications with Wi-Fi Direct: Overview and Experimentation,” *IEEE Wireless Communications, vol. 20, no. 3*, pp. 96-104, Jun 2013.

[8] D. Camps-Mur, X. Perez-Costa, S. Sallent-Ribes, “Designing energy efficient access points with Wi-Fi Direct,” *ACM Computer Networks: The International Journal of Computer and Telecommunications Networking, vol. 55*, pp. 2838-2855, Sep 2011.

[9] Shojiro Takeuchi, Kosuke Yamazaki, Kaoru Sezaki, and Yasuhiko Yasuda “An Improved Power Saving Mechanism for MAC Protocol in Ad Hoc Networks,” in *Proc. IEEE int. conf,* Nov 2004. pp. 2791-2796.

[10] ByungGi Lee and SungHyun Choi, *Broadband wireless access and local networks: mobile WiMax and WiFi* , Artech House, 2008

[11] Walke and Bernhard H, *IEEE 802 wireless systems : Protocols, Multi-hop Mesh/Relaying, Performance and Spectrum Coexistence*, John Wiley & Sons, 2007

[12] Perahia, Eldad, Stacey, and Robert, *Next Generation Wireless LANs Throughput, Robustness, and Reliability in 802.11n, 802.11ac*, Cambridge University Press, 2013

[13] B. Sadeghi,V. Kanodia, A. Sabharwal and E. Knightly, “Opportunistic media access for multi-rate Ad Hoc networks”, *in Proc. ACM int. Conf. MobiCom.*, Sep 2002, pp. 24–35.

[14] A. Santhanam and R. Cruz, “*Optimal routing, link scheduling and power control in multi-hop wireless networks*”, in. *Proc. IEEE Int. Conf. Infocom.*, Apr 2003, pp. 702–711.

978-1-4673-9257-0/15/$31.00 ©2015 IEEE

PAPR Reduction of OFDM System Using Condex Matrix Based SLM Method with Low Computational Overhead

Md. Moshiur Rahman*, Muhammad Sajjadur Rahim†, Md. Nur Al Safa Bhuiyan‡ and Sabbir Ahmed§
Department of Information and Communication Engineering
University of Rajshahi, Rajshahi-6205, Bangladesh
Emails:*mintu_apee@yahoo.com, †sajid_ice@ru.ac.bd, ‡safa@ru.ac.bd, §sabbir@ru.ac.bd

***Abstract*—High Peak-to-Average Power Ratio (PAPR) is one of the main drawbacks that may limit practical applications of Orthogonal Frequency Division Multiplexing (OFDM) System. Based on the well known Selective Mapping (SLM) method of PAPR reduction, in this paper, we propose a new phase sequence generation technique from Condex matrix that can achieve better PAPR reduction compared to the generally used Bauml sequence. From the simulation results, we show that our proposed phase sequence achieves 4.0 dB higher PAPR reduction compared to original SLM method and also reduces the computational overhead about 59 percent.**

***Keywords*—OFDM; PAPR; SLM; condex matrix**

I. Introduction

The concept of Orthogonal Frequency Division Multiplexing (OFDM) in terms of parallel data transmission and frequency division multiplexing was first developed in the 50s [1]. It offers a considerable high spectral efficiency, multipath delay spread tolerance, immunity to frequency selective fading and so forth [2]. At present, OFDM is considered as a strong candidate for the next generations of mobile communication systems. However, one significant problem with OFDM systems is that it can give rise to very high values of Peak-to-Average Power Ratio (PAPR). Over the last decade, various techniques to reduce PAPR have been proposed. For example, clipping and filtering, companding and coding, multiple signal representation and so forth [3–5]. The last kind includes Selected Mapping (SLM) and Partial Transmit Sequence methods (PTS) [6, 7]. Clipping and filtering is the simplest technique but it may cause in-band distortion and out-of-band radiation. In-band distortion can not be reduced by filtering and results in performance degradation, while out-of-band radiation reduces the spectral efficiency. The coding technique does not cause distortion or out-of-band radiation, but it lacks spectral efficiency. In SLM scheme, PAPR reduction is achieved by multiplying the independent phase sequences to the original input data and determining the PAPR of each phase sequence and input data combination. The combination with the lowest PAPR is transmitted. Generally Bauml sequence, based on the value set of (± 1,$\pm j$), is used in SLM. In this paper, Condex phase sequence based SLM is proposed to reduce PAPR of OFDM signal. Here, we show that Condex matrix based sequence can be used for improved PAPR reduction capability with less computational overhead.

II. Background

A. OFDM System Model

Let us consider an OFDM system consisting of N sub-carriers in the frequency domain, where vector $X = [X_0, X_1, ..., X_{N-1}]$ denotes the input data blocks. Each symbol in X is used to modulate a sub-carrier, and the input symbol vector is called the input symbol sequence. For N-th sub-carrier, let $f_k, k = 0, 1, ...N-1$. In the OFDM system as the adjacent sub-carriers are orthogonal to each other, let, $f_k = k.\Delta f$, where $\Delta f = 1/(NT)$ and T is the symbol duration. Therefore, the complex baseband representation of the transmitted OFDM signal is given by:

$$x(t) = \frac{1}{\sqrt{N}} \sum_{k=0}^{N-1} X_k e^{j2\pi k t \Delta f}, 0 \leq t \leq NT \tag{1}$$

where $j = \sqrt{-1}$, Δf is the sub-carrier spacing, and NT denotes the useful data block period. If $x = [x_0, x_1, ..., x_{N-1}]$ denotes a discrete time OFDM signal vector, then x corresponds to the Inverse Fast Fourier Transform (IFFT) of X. that is, $x = QX$, where Q is the IFFT matrix.

B. PAPR

In general, PAPR is defined as the ratio between the maximum power and the average power for the envelope of a baseband complex signal during an OFDM symbol period. The PAPR of the OFDM signal $x(t)$ can be written as follows:

$$\text{PAPR} = \frac{\max\limits_{0 \leq t \leq T} |x(t)|^2}{E(|x(t)|^2)} \tag{2}$$

where $E[.]$ is the expectation operator which denotes the average value over the time duration of OFDM symbol. The PAPR reduction techniques are concerned with reducing max $|x(t)|$. In practical situation, the discrete-time signals are mostly used.

In OFDM system, some input sequences would result in higher PAPR than others. For example, an input sequence that requires all such carriers to transmit their maximum amplitudes would certainly result in a high output PAPR. Thus, by limiting the possible input sequences to a smallest sub set, it is possible to obtain output signals with a guaranteed low output PAPR.

Some of the important performance factors that should be considered while judging the performance of a PAPR reduction technique are PAPR reduction capability, spectral spreading, bit error rate, computational complexity, loss of data rate etc. In this paper, we focus on reduction of PAPR as well as computational complexity.

III. SLM TECHNIQUE

In the SLM technique, the transmitter generates a set of sufficiently different candidate data blocks, all representing the same information as the original data block, and selects the most favorable for transmission [6, 8]. A block diagram of the SLM technique is shown in Figure 1. Each data block is multiplied by U different phase sequences, each of length N, $B^{(u)} = [b_{u,0}, b_{u,1}, ...b_{u,N-1}], u = 1, 2, ..., U$, resulting in U modified data blocks. To include the unmodified data block in the set of modified data blocks, we set $B^{(1)}$ as the all-one vector of length N.
Let us denote the modified data block for the u_{th} phase sequence $D^{(u)} = [D_0 b_{u,0}, D_1 b_{u,1}, ...D_{N-1} b_{u,N-1}], u = 1, 2, ..., U$, after applying SLM to X, the multi-carrier signal becomes

$$d_k^{(u)} = \sum_{n=0}^{N-1} D_n.b_{u,n}.exp(\frac{j2\pi kn}{N}) \;\; 0 \leq k \leq N-1. \qquad (3)$$

Among the modified data blocks $D^{(u)}$, the one with the lowest PAPR is selected for transmission. Information about the selected phase sequence need to be transmitted to the receiver as side information. At the receiver, the reverse operation is performed to recover the original data block. For implementation,the SLM technique needs U times IDFT operations, and the number of required side information bits is $log_2 U$ for each data block. This approach is applicable with all types of modulation and any number of subcarriers.

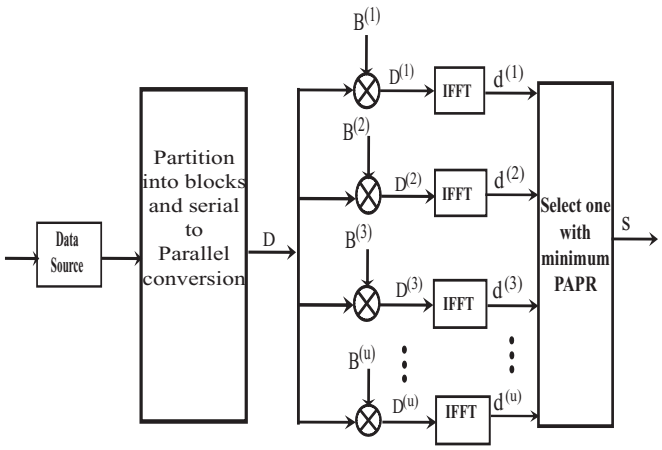

Fig. 1. Block diagram of the SLM technique with U different signal representation and phase weights to produce a minimized PAPR signal

The amount of PAPR reduction for SLM depends on the number of phase sequences U and the design of the phase sequences. There are extensions of SLM technique which does not need explicit information to be sent to the receiver. For further information see the reference [9].

IV. PHASE SEQUENCE GENERATION USING CONDEX MATRIX

PAPR of the OFDM system can be reduced by selecting appropriate phase sequences in the SLM method. In order to do so, in this paper, we have investigated a set of counter-example matrices to condition number estimators [10, 11], and practically have selected the SONEST [11] to generate proper phase sequences for the OFDM system. We term this matrix here as Condex matrix. Using the algorithm as in [11], a Condix matrix (C) of order 4 can be writhen as:

$$C = \begin{bmatrix} 1.0000 & 0.0000 & 0 & 0.0000 \\ 0.0000 & 59.7379 & -10.6796 & -48.0583 \\ 0 & -10.6796 & 2.9417 & 8.7379 \\ 0.0000 & -48.0583 & 8.7379 & 40.3204 \end{bmatrix} \qquad (4)$$

From the above equation $C^{(u)} = [C_0^{(u)}, C_1^{(u)}, .., C_{N-1}^{(u)}]$ can be defined with each row of the normalized Condex matrix C. Each input data block $D = [D_0, D_1, ...D_{N-1}]$ is multiplied with U different phase vectors $C^{(u)}, u = 1, 2, ..., U$ Then, all U subcarrier vectors are transformed into time domain to get the following:

$$d^{(u)} = IDFT\{D^{(u)}\} = IDFT\{D_{(n)}.C_n^{(u)}\} \qquad (5)$$

Finally, the one with the minimum PAPR is selected for transmission.

V. SIMULATION RESULTS

In this section, we show simulation results depicting the comparative performance of SLM technique using Condex and Bauml phase sequence. The simulation parameters are introduce in Table I. Fig. 2 shows the number of symbols that achive minimum PAPR versus Condex phase sequence

TABLE I
SIMULATION PARAMETERS

Number of Sub-carriers (N)	64
Modulation Technique	$BPSK$
Phase Sequences	$Bauml\ and\ Condex\ Matrix$
Length of Phase Sequences	64
Number of OFDM Symbols	$10,000$
Simulation Tool and Version	MATLAB [7.8.0.347 (R2009a)]

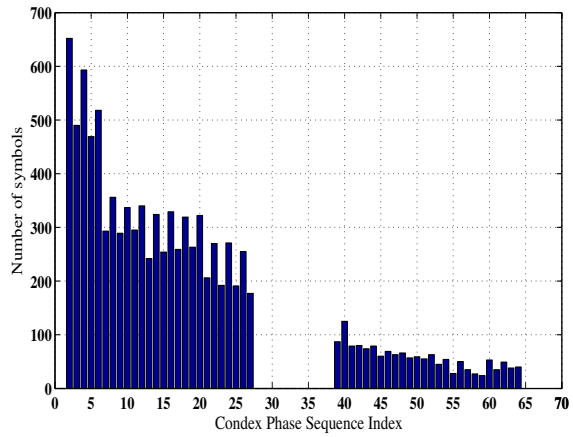

Fig. 2. Complexity diagram for SLM scheme (Condex Phase Sequence) with minimum PAPR

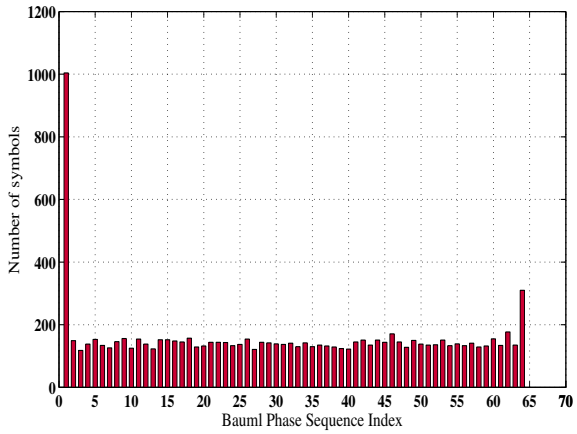

Fig. 3. Complexity diagram for SLM scheme (Bauml Phase Sequence) with minimum PAPR

index, we call this plot as the complexity diagram since it depicts the number of search operations required to achieve a certain level of PAPR. It can be observed from the figure that the highest number of symbols with minimum PAPR can be seen at the phase sequence number 2. With the increasing number of Phase sequence index from 2 to 27, it is also observed that the number of symbols is continuously decreasing. Similar decreasing phenomenon for number of symbols is also seen as we go along from phase sequence number 39 to 64. Moreover, it is observed from the figure that regarding number of symbols, even phase index showed better performance than odd one.

In Fig. 3, we show the number of OFDM symbols with minimum PAPR versus the Bauml phase sequence index. It is observed that about $1,000$ out of total $10,000$ OFDM symbols meet the minimum PAPR requirements at phase sequence index 1 while less than 200 symbols did the same

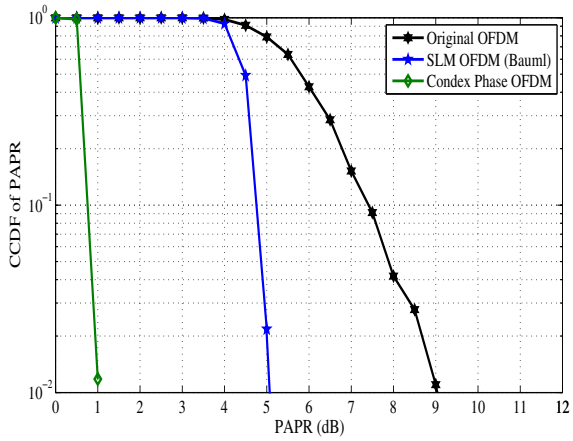

Fig. 4. CCDF vs. PAPR of OFDM Blocks

for index 2 to 63 with the exception of index 64 which has slightly higher number of such symbols.

Now the CCDFs of PAPR for Condex matrix, Bauml phase sequence and original OFDM are plotted against PAPR (dB) in Fig. 4. It shows that for a probability of 10^{-2}, the corresponding PAPRs of Condex matrix, Bauml phase sequence and original OFDM are 1dB, 5.1dB and 9.0dB, respectively.

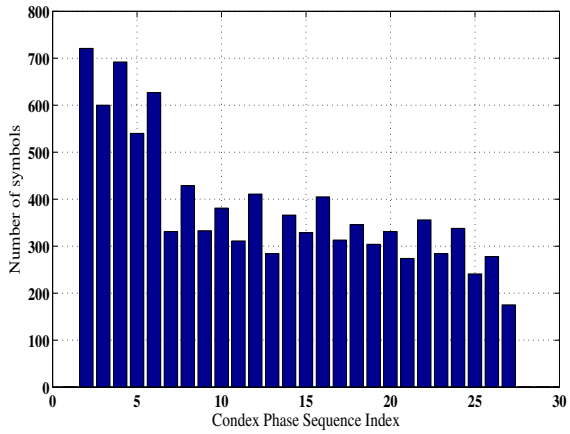

Fig. 5. Complexity diagram for SLM scheme (Condex Sequence from 2 to 27 index) with minimum PAPR

Since Fig. 2 shows that large number of OFDM symbols satisfy minimum PAPR requirement when sequence no. is between 2 to 27, we focused in this region and show the corresponding complexity diagram in Fig. 5. Since total no. of sequence are reduce from 64 to 26, it implies that only 26 numbers of iteration is required to attain almost the same level of PAPR that previously required 64 iterations. It means, a complexity reduction has been reduce by 59%.

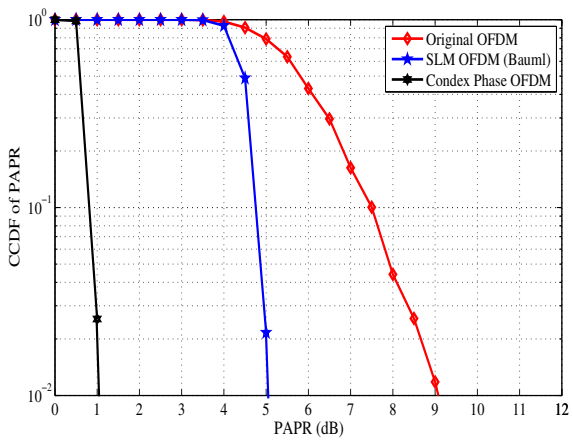

Fig. 6. CCDF vs. PAPR of OFDM Blocks Corresponding to Fig. 5

.

Figure 6 shows the comparative CCDF of PAPR for Condex and Bauml phase sequence based SLM techniques with that of original OFDM. We see for Condex sequence no. 2 to 27 that for a probability of 10^{-2}, the corresponding PAPR of Condex, Bauml and original OFDM are 1.1dB, 5.1dB and 9.0dB, respectively, which means had to sacrifice 0.1dB PAPR compared to Fig. 4.

VI. Conclusion

Large PAPR of transmitted signals may be a main cause of performance degradation of OFDM system. Several techniques have been proposed for PAPR reduction. But most of them cannot achieve simultaneously a large reduction in PAPR with high frequency efficiency, low complexity and good error correction. No specific PAPR reduction technique is the best solution for all multicarrier transmission. It is an important issue to choose the right phase sequence for original SLM method according to the above mentioned requirements. Using this techniques, we showed that it is possible to simultaneously achieve significant reduction in PAPR along with low computational overhead. The PAPR reduction capability was evaluated using MATLAB simulation tool, the results show that the proposed scheme offers better PAPR reduction than other schemes consider here. The simulation results (Figs. 5 and 6) show that the computational complexity can be reduced up to 59% if we sacrifice little 0.1 dB PAPR. In our future work, we have plans of investigating the effects of higher order modulation scheme such as 4-QAM,8-QAM using ours proposed method. This will help to make a comparative study of different modulation scheme from the perspective of PAPR performance.

References

[1] B. Saltzberg, "Performance of an efficient parallel data transmission system," *IEEE Trans. on Commun. Technology, vol. 15, no. 6, pp. 805-813, Dec. 1967.*

[2] Y. Wu and W. Y. Zou, "Orthogonal frequency division multiplexing: a multicarrier modulation scheme," *IEEE Trans. Conf. Elect., vol. 41, no. 3, pp. 392-399, Aug. 1995.*

[3] K. R. Panta and J. Armstrong, "Effect of clipping on the error performance of OFDM in frequency selective fading Channels," *IEEE Trans. Wireless Commun., vol. 3, no. 2, pp. 668-671, March 2004.*

[4] X. Wang, T. T. Tjhung, and C. S. Ng, "Reduction of peak-to-average power ratio of OFDM system using a companding technique," *IEEE Trans. on Broadcast., vol. 45, no. 3, pp. 303-307, Sept. 1999.*

[5] J. A. Davis and J. Jedwab, "Peak-to-mean power control in OFDM, Golay complementary sequence and Reed Muller codes," *IEEE Trans. on Info. Theory, vol. 45, no. 7, pp. 2397-2417, Nov. 1999.*

[6] R. W. Buml, R. F. H. Fisher, and J. B. Huber, "Reducing the peak-to-average power ratio of multicarrier modulation by selected mapping," *IEEE Elect. Letters., vol. 32, no. 22, pp. 2056-2057, Oct. 1996.*

[7] S. H. Muller and J. B. Huber, "OFDM with reduced peak-to-average power ratio by optimum combination of partial transmit sequences," *IEEE Elect. Letters, vo1. 33, no. 5, pp. 368-369, Feb. 1997.*

[8] S. H. Muller and J. B. Huber, "A comparison of peak-power reduction schemes for OFDM," *in Proc. IEEE Global Telecommu. Conference (GLOBECOM), Phoenix, AZ, vol. 1, Nov. 1997, pp. 1-5.*

[9] M. Breiling, S. H. Mller-Weinfurtner, and J. B. Huber, "SLM peak-power reduction without explicit side Information," *IEEE Commun. Letters, vol. 5, no. 6, pp. 239-241, June 2001.*

[10] A. K. Cline and R. K. Rew, "A set of counter-examples to three condition number estimators," *SIAM J. Sci. Stat. Comput., vol. 4, no. 4, pp. 602-611, Dec. 1983.*

[11] N. J. Higham, "FORTRAN codes for estimating the one-norm of a real or complex matrix, with applications to condition estimation," *ACM Trans. on Mathematical Software, vol. 14, no. 4, pp. 381-396, Dec. 1988.*

Energy-Efficient Cellular Communications Powered by Smart Grid Technology

Imtiaz Nasim, Mostafa Zaman Chowdhury, and Md. Syadus Sefat
Department of Electrical and Electronic Engineering
Khulna University of Engineering & Technology, Khulna-9203, Bangladesh
E-mail: imtiaz_nasim@hotmail.com, mzceee@yahoo.com, sefat_235711@yahoo.com

***Abstract*—The energy efficiency aspect of cellular networks is a vital topic of research over the recent days. As energy consumption is on the rise and the price of electricity is increasing very rapidly, necessity to reduce electricity usage in every aspect is becoming much more significant. The power grid infrastructure, from which the cellular networks attain the required electricity for operation is considering a significant change from the traditional electricity grid to the smart grid. The base stations, which are the main candidates for energy consumption in cellular networks, remain in operation even when there are a very few users or no user at all. In this paper, we propose an effective application scenario of the femtocell technology for power saving purpose of cellular networks. Effective deployment of femto-access-points in the required places can reduce the power usage of cellular networks by turning off the redundant base stations. Moreover, the signal to noise plus interference ratio is also enhanced in comparison to the traditional scheme. The base station turn off probability and the energy consumption in the overall network are analyzed. The comparison results show that the proposed energy efficient model can significantly reduce energy consumption and increase the service quality of the cellular users.**

Keywords*— *Smart grid, cellular network, energy consumption, QoS, and femtocell

I. Introduction

The smart grid *(SG)*, also called smart power grid, intelligent grid, intelligrid, future grid or intragrid, is an enhancement of the 20th century power grid. The traditional power grids are normally used to carry power in one way direction only. These power grids generally carry power from a few central generators to a large number of users or consumers. On the other hand, SG creates an automated and distributed advanced energy delivery network by using the two-way flow of electricity. The SG uses modern information technologies and is capable of distributing power in a more efficient way. It also emphasizes on energy saving of the different smart appliances and commodities [1].

Recently, rapidly rising energy price has led to a trend of studying the energy efficiency aspect of communication networks. The cellular operators pay a handsome amount of electricity bill which has become a significant portion of their total expenditure. The CO_2 emissions produced by wireless cellular networks all over the world are equivalent to those from more than 8 million cars. In a typical wireless cellular network, base stations (BSs) consumes 60 − 80% energy of the overall cellular network's energy consumption. Almost 120,000 new base stations are deployed throughout the world every year to provide necessary support to the cellular users [2]. Our survey works suggest that a base station consumes more than 85% of its peak energy even when there is little or no traffic. Therefore, a dynamic operation of the cellular base stations based on the traffic is very much essential for the energy efficient approach of cellular networks. The proposed model in this paper is expected to reduce the energy consumption of cellular networks to a significant level. However, this model is much more applicable for some remote areas where there are a very few cellular users and a base station remains in operation continuously to serve those few users. Using the simulation results, we show that the proposed scheme can save energy of cellular networks and improve the quality of service (QoS) to a certain level.

The rest of this paper is organized as follows. Section II shows the proposed energy efficient model. Section III shows the performance analysis of the proposed scheme. Finally, conclusions are drawn in the last section.

II. Proposed Energy Efficient Model

Suppose a cellular network is powered by smart grid where there is a flow of electricity and communication simultaneously as shown in Fig. 1.

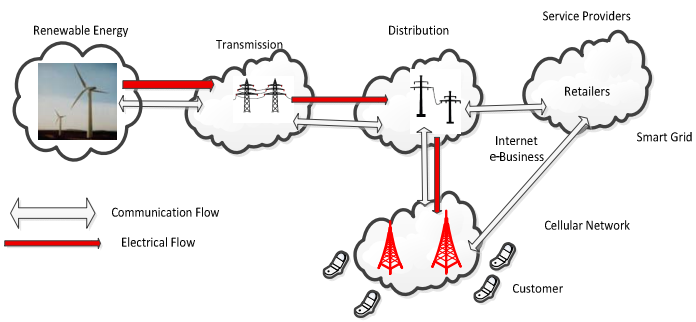

Figure 1. A cellular network powered by the smart grid [2].

978-1-4673-9257-0/15/$31.00 ©2015 IEEE

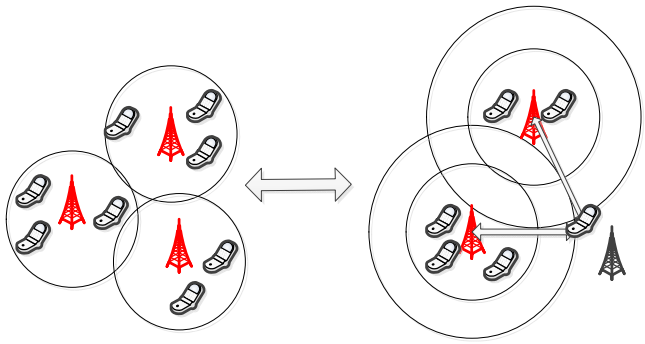

Figure 2. Coverage extension and energy saving with coordinated multipoint (CoMP) [2].

In [2], the authors proposed a model in which the redundant base station is turned off and the users of that network are served by coverage extension of the neighboring base stations using the coordinated multipoint method for energy saving purpose. This model is showed in Fig. 2.

If the redundant base station is turned off as shown in Fig. 2, a decent amount of energy can be saved if the existing user is served by the neighboring base stations. But we propose another model for saving energy of cellular networks using femtocell network which may turn out to be a very promising solution for saving more energy of cellular networks especially in remote areas.

In our proposed model, femto-access-points are installed in some places which have the most probability of carrying a mobile user in the entire cellular network served by a base station. The femto-access-points (FAPs) are low-power, small-size home-placed base stations that enhance the service quality for the indoor mobile users [3]. Fig. 3 shows an example of the proposed energy efficient model. When all the users remain inside the femtocellular coverage region, the macrocellular BS is allowed to turn off. But if any user stays outside the femtocellular coverage, the macrocellular BS must remain in operation to serve that particular user. Periodic checking of user's location and the QoS is tested by the dynamic checking application of the SG. Our purpose is not only saving energy of cellular networks but also to increase the service quality of the existing users. Femto-access-points are ideal for this case as these devices run with very low operating power and at the same time can enhance the QoS to a significant level.

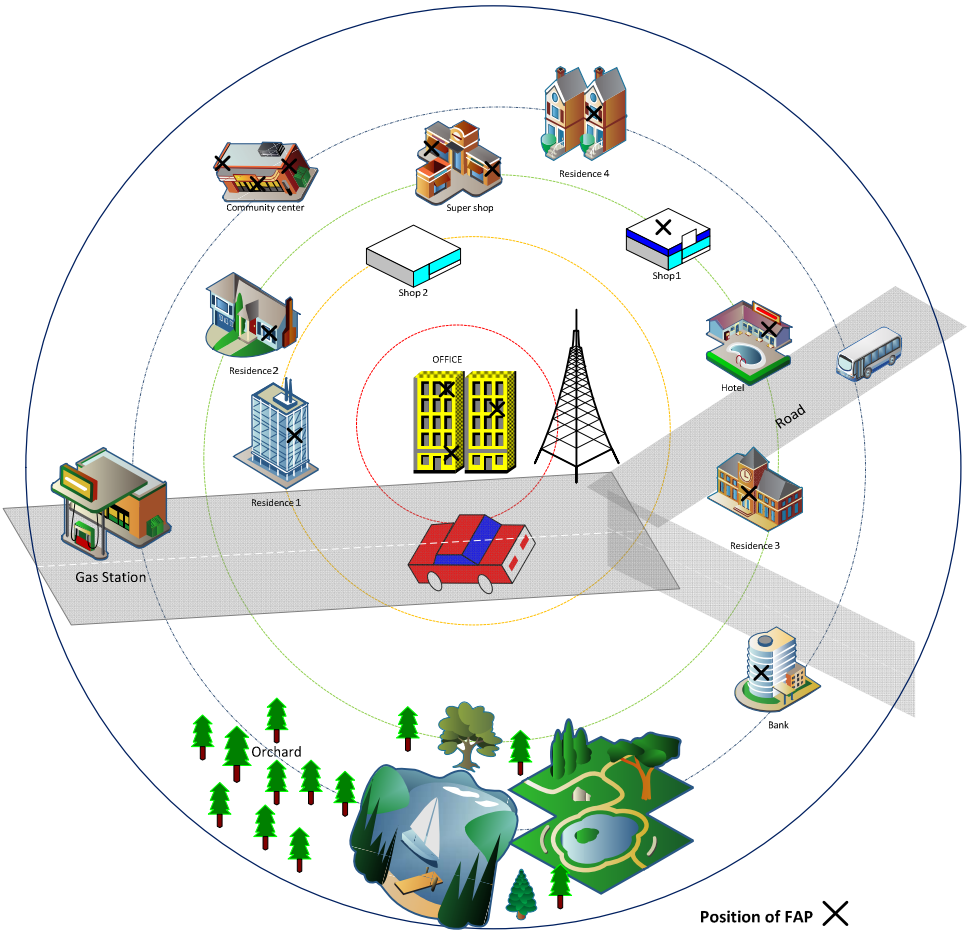

Figure 3. Proposed energy efficient model with femtocell/Macrocell integrated network.

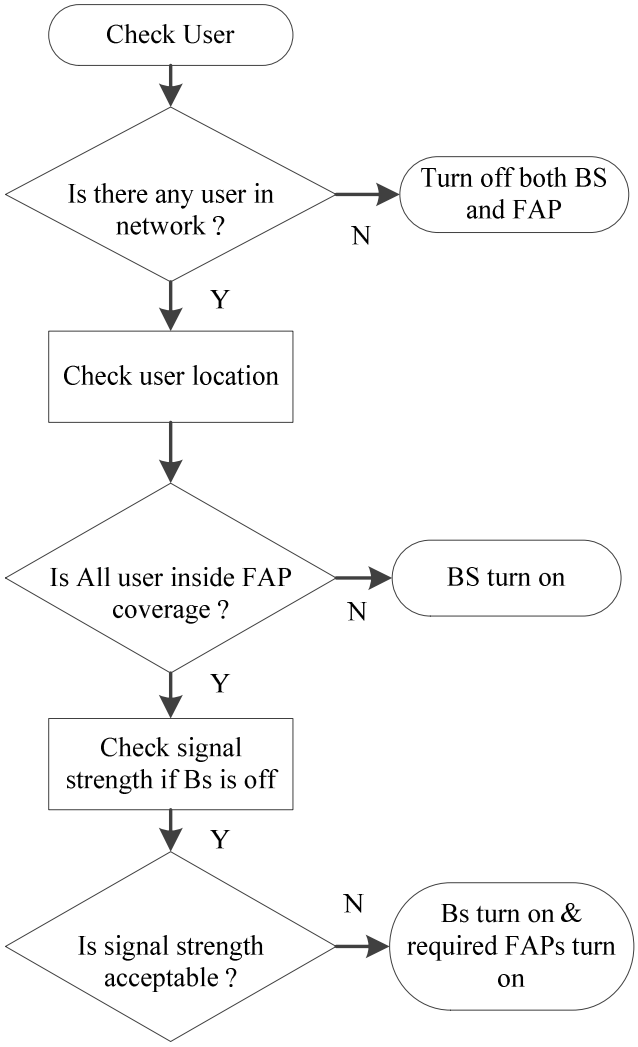

Figure 4. Flow chart showing the condition for the BS to be turned off in the proposed scheme.

Femtocells are small base stations with low transmission power, and with almost all cellular functionalities, but a limited coverage to end users in indoor environments. A femtocell allows service coverage extended to indoor environments, especially where wireless access is limited or unavailable, without expensive deployment cost.

A flow chart is shown in fig. 4 which shows the algorithms of the proposed scheme. The network will first check the existence of a user. If no user exists in the network, both the macrocellular BS and the FAPs will remain off. If any users exist, then the network will search for user's location. When any of the users remain outside the FAP coverage area, the BS will not be allowed to turn off. But, if all users exist inside the femtocellular network, then the network will check the signal strength available for the users if the BS is shut down. The BS will shut down if the signal strength is found within acceptable limit, otherwise; it will remain on in order to provide network support to the existing users. This model requires a periodic checking of the position of each user inside the network. By adopting this process, the macrocellular BS will sometimes remain turned on and sometimes remain turned off.

III. PERFORMANCE ANALYSIS

This section provides the probability analysis performance and the signal quality performance of our proposed model.

A. Probability Analysis

When a redundant BS is shut down and the users of that area are to be served using FAPs, then it is required to analyze the probability of the existence of a user under the femtocell coverage area. If all users are within the femtocell coverage area then the BS may remain shut down and service is provided to the user by the femtocell network, but if any user remains outside the femtocell coverage area, then the BS must be turned on in order to provide service to that user.

For simplicity in calculation, we have divided the total considered area into 4 sub-circles each with a fixed distance from the center point of the main circle. The coverage area of a macrocellular BS is assumed to be 500m. We performed our analysis assuming 15 FAPs in the total coverage area. All the stations considered in the coverage area have a specific factor according to the importance of that station for carrying users. The factors assumed for each station is given in Table I. The coverage area of a FAP is determined by

$$a=4\square r^2$$

where r is the radius of each FAP coverage.

If there exist stations with n number of factors then Let, A_1 is the area under user existence probability factor f_1, A_2 is the area under user existence probability factor f_2, A_3 is the area under user existence probability factor f_3, and A_n is the area under user existence probability factor f_n.

Let the remaining area where no FAPs are installed is A_M with a user existence probability factor of f_M

The probability of a user to exist in the FAP coverage area is given by

$$P=\frac{f_1\sum_{i=1}^{N_1}A_{1i}+f_2\sum_{i=1}^{N_2}A_{2i}+f_3\sum_{i=1}^{N_3}A_{3i}+.....+f_n\sum_{i=1}^{N_n}A_{ni}}{\left(f_1\sum_{i=1}^{N_1}A_{1i}+f_2\sum_{i=1}^{N_2}A_{2i}+f_3\sum_{i=1}^{N_3}A_{3i}+.....+f_n\sum_{i=1}^{N_n}A_{ni}\right)+f_mA_m} \quad (1)$$

where N_1 is the number of places under user existence probability factor f_1, N_2 is the number of places under user existence probability factor f_2, N_3 is the number of places under user existence probability factor f_3, N_n is the number of places under user existence probability factor f_n.

The probability of the BS to be turned off with the number of user can be expressed as

$$p=\left(f_p\right)^n \quad (2)$$

where f_p is the average importance factor considered for the entire region and n is the number of user.

The analysis is performed assuming only 15 FAPs in the considered total area. The performance would be better if more number of FAPs are used. However, FAPs should be installed in the places where there is a big possibility of users to exist. Unplanned deployment of FAPs in the network may result in no significant advantage for saving energy. Table II summarizes the values of the parameters that we used in our analysis.

TABLE I: SUMMARY OF NUMBER OF FAP AND DIFFERENT FACTORS USED IN ANALYSIS

Station Name	No. of FAP	Factor *(f)*
Office	3	1 (=f_1)
Super shop	2	0.8 (=f_2)
Community center	3	0.8 (=f_2)
Residence 1	1	0.7 (=f_3)
Residence 2	1	0.7 (=f_3)
Residence 3	1	0.7 (=f_3)
Residence 4	1	0.7 (=f_3)
Bank	1	1 (=f_1)
Hotel	1	0.7 (=f_3)
Shop 1	1	0.7 (=f_3)
Shop 2	0	0.3 (=f_3)
Remaining free space	0	0.01 (=f_3)

TABLE II: SUMMARY OF THE PARAMETER VALUES USED IN ANALYSIS

Parameter	Value
Carrier frequency	1800 [MHz]
Transmit signal power by the macrocellular BS	1.5 [kW]
Transmitted signal power by a FAP	15 [mW]
Power required for operation of a macrocellular BS	2 [kW]
Power required for operation of a macrocellular BS	8 [W]
Height of a macrocellular BS	100 [m]
Height of a FAP	2 [m]
Distance of the MS from reference FAP	7 [m]
Lpen	20 [dB]
Lsh	8 [dB]
Range of a macrocellular BS	500 [m]
Range of a FAP	15 [m]
Average importance factor, f_p	0.7
Total received noise	$7 * 10^{-7}$ [mW]

The probability of a macrocellular BS to be turned off increases rapidly with the increase of FAPs installed in the considered network. As FAPs are very low power consuming devices, installment of a large number of FAP in the network will still result in less energy consumption compared to that by the BS alone. Fig. 5 shows the comparison of the probability for 3 different number of users existing in the network. As the number of user increases, the probability of the BS to be turned off decreases. So, the BS needs to be turned on when the number of user is more in the network as there will be a probability of at least one user to stay outside the femtocell network region.

Fig. 6 shows the comparison between 3 different cases for BS turn off probability. The energy saving possibility is enhanced if more FAPs are used. If only 5 FAPs are used in the network, the probability of the BS to be turned off is nearly 5% when 5 users exist in the network. But if 25 FAPs are used for the same network, the probability of the BS to be turned off is more than 50% for the same number of user.

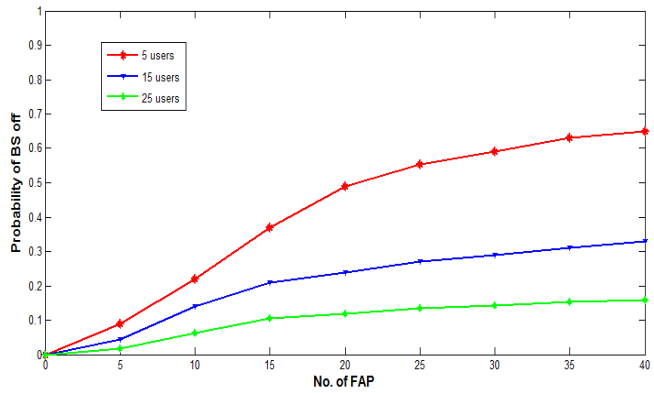

Figure 5. Probability of macrocellular BS to be turned off with increasing FAP for different number of users.

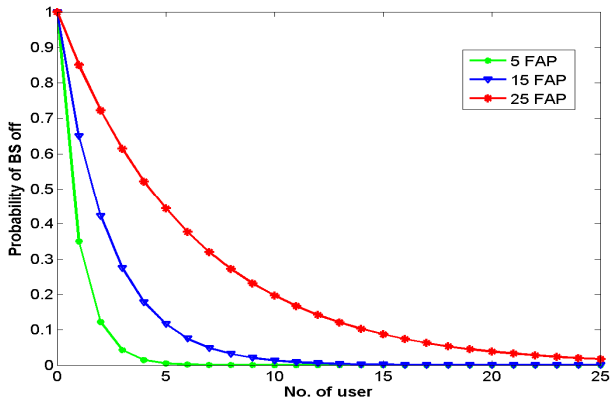

Figure 6. Comparison of macrocellular BS turn off probability with number of user for different cases.

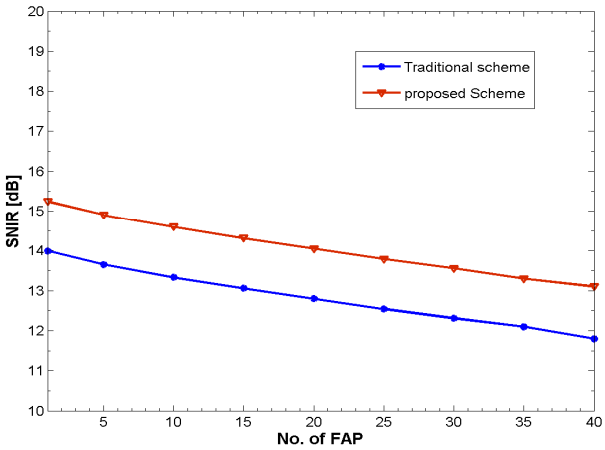

Figure 7. Comparison of *SNIR* levels between the proposed model and the traditional model

B. SNIR Analysis

The propagation model for a macrocell case can be expressed as:

$$L = 36.55 + 26.16\log_{10} f_c - 3.82\log_{10} h_b - a(h_m) + [44.9 - 6.55\log_{10} h_m] \log_{10} d + L_{sh} \quad [dB]$$

$$a(h_m) = 1.1[\log_{10} f_c - 0.7]h_m - (1.56\log_{10} f_c - 0.8) \tag{3}$$

where fc is the center frequency in MHZ, h_b is the height if the macrocellular BS in meter, h_m is the height of the MS in meter, d is the distance between the macrocellular BS and the MS in kilometer, Lsh is the shadowing standard deviation.

The propagation model for a femtocell case can be expressed as [3]:

$$L_f = 20\log_{10} f_c + N\log_{10} d_1 + 4n^2 - 28 \quad [dB] \tag{4}$$

where fc is the center frequency in MHZ of the femtocell, n is the number of walls between the MS and the FAP, and d_1 is the distance between the FAP and the MS in meter.

The received *SNIR* level of a femtocell user in a macrocell/femtocell integrated network can be expressed as:

$$SNIR = \frac{S_0}{I_m + I_f + N} \tag{5}$$

Simulation results show that the proposed model provides better signal-to-noise plus interference level. Fig. 7 demonstrates the comparison of SNIR level between traditional scheme and proposed scheme. The effect of the macrocellular BS and the number of FAPs has been considered here. As the BS will not remain turned on for all the time in the proposed model, there will be a decrease in the average noise level. Thus, the SNIR level is increased in the proposed model according to equation (5).

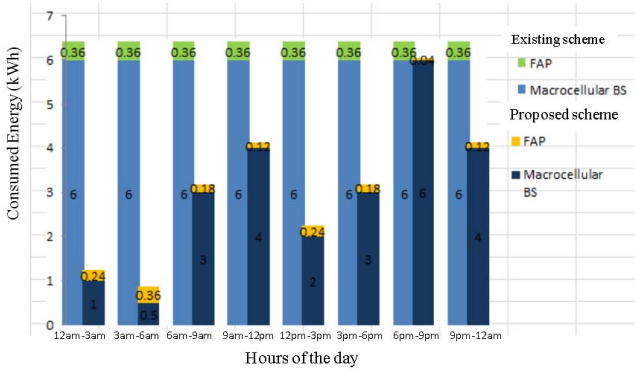

Figure 8. Comparison of energy consumption between the proposed model and traditional model

C. Comparison of Energy Consumption

In our proposed model, the macrocellular BS will only remain shut down if the existing FAP can provide proper service to all the active users. In general, the number of active user becomes low in the middle of the night. So the BS may remain shut down for most of the time during late night. Thus, a large amount of energy can be saved in that period of night. However, the BS may remain turned off even in different times of the day if the FAPs can provide proper service to the existing users in that period of time. The FAPs consume very low energy compared to the macrocellular BS. So using many FAPs can still result in significant energy saving.

If we compare the energy consumption of the cellular network for the traditional model and the proposed model, there is a large amount of energy saved in the proposed model as the main energy consuming element for cellular network i.e., the macrocellular BS remains off for a certain period of time in this model. Fig. 8 shows the comparison of energy consumed between the traditional model and the proposed model. The saving of energy can be increased further by installation of FAPs in required places where there is a great possibility of carrying mobile users. For vehicular environment, the proposed model in [4] is good enough to serve the mobile users.

IV. CONCLUSIONS

Saving of energy in cellular network communication is an important issue as energy prices are increasing day by day. Energy efficiency of the cellular network can be enhanced by the use of femto-access-points. Proper utilization of FAPs can result in improved service quality and reduction in the consumed energy of macrocellular base station. If the base station is allowed to turn off even for a small amount of time, a significant amount of energy can be saved as most of the energy required in the cellular communication is consumed by the base station. Our proposed model can be used extensively for energy saving purpose in cellular communications. Femtocells are a novel wireless networking technology that has several advantages including lower cost, better signal quality, and reduced infrastructure cost. In this paper, we

discussed the advantages of femtocellular network for saving energy of cellular communication networks. The various performance analysis and the comparison results are presented. The simulation results demonstrate that the deployment of femtocells will significantly reduce the consumption of energy of cellular networks.

REFERENCES

[1] X. Fang, S. Misra, X. Guoliang, D. Yang, "Smart Grid — The New and Improved Power Grid: A Survey," *IEEE Communications Surveys & Tutorials*, vol. 14, no. 4, pp. 944,980, Oct. 2012.

[2] B. Shengrong, F. Richard Yu, Y. Cai,and X. P. Liu, "When the Smart Grid Meets Energy-Efficient Communications: Green Wireless Cellular Networks Powered by the Smart Grid," *IEEE Transactions on Wireless Communications,* vol. 11, no. 8, pp. 3014-3017, Aug. 2012.

[3] M.Z. Chowdhury, S. H. Chae andY. M. Jang, "Group Handover Management in Mobile Femtocellular Network Deployment," *International Conference on Ubiquitous and Future Networks (ICUFN),* July 2012.

[4] M.Z. Chowdhury, S. Q. Lee, B. Han Ru, N. Park, Y. M. Jang, "Service Quality Improvement of Mobile Users in Vehicular Environment by Mobile Femtocell Network Deployment," *International Conference on ICT Convergence (ICTC)*, Sept. 2011.

Orientation Dependent Performance of 635nm Vertical Cavity Surface Emitting QW Red Laser

Muhammad Mainul Islam, Md. Shamim Sarker, Md. Mahbub Hasan, Md. Rafiqul Islam
Department of Electrical and Electronic Engineering
Khulna University of Engineering & Technology
Khulna-9203, Bangladesh
E-mail: mainul0803004@gmail.com, sarkershamimbd@gmail.com, hasanimahbub@yahoo.com, islambit@yahoo.com

Abstract— **In this paper, the crystallographic orientation-dependent performances of 635nm red quantum well (QW) laser are numerically studied. The electronic and optical characteristics of the laser are investigated by solving time independent Schrodinger equation using finite difference method. The results are obtained in (001), (101), ((111), (113), and (211) orientations and found that there is a substantial correlation of the peak gain and peak emission wavelength with crystal orientations. The maximum and minimum gains are estimated in (113) and (211) orientations and the peak emission wavelengths are found 640nm and 648nm for the crystal orientations (113) and (211). The orientation dependent energy band dispersion profiles are used to explain the results presented here.**

Keywords— VCSEL, Red laser, QW, Crystal orientation

I. INTRODUCTION

Vertical cavity surface emitting laser (VCSEL) can be used as a high power laser source in medical science, communication and industrial sectors. Red VCSEL was first demonstrated in 1992 (optical pumping) and 1993 (electrical pumping) at Sandia National Laboratories [1], [2] and Chiao Tung University in Taiwan [3]. Recent research demonstrates that lasers at 635nm wavelength are the exact vibration of a healthy living cell and is optimal for healing and most beneficial for stimulating acupuncture points [4]. Red lasers are also used in photodynamic therapy, solid state laser pumping, semiconductor surface inspection, sensor and other applications which led us to concentrate our interest in 635nm red laser [5]-[7].

Generally gallium indium phosphide ($Ga_xIn_{1-x}P$) is used in the active region of the quantum well (QW) material for red laser [8], [9]. In a QW structure energy levels are discretized due to the quantum confinement effect. Lasing occurs due to transition of electrons from the conduction band minima to different valance sub-bands. This transition plays an important role in determining the optical gain and emission wavelength of a laser. To understand the orientation dependent gain and peak emission wavelength characteristics the proposed VCSEL is modeled using time independent Schrodinger equation.

The band structures of QW strongly depend on crystal orientation [10]. Recently, some works [11]-[13] reported on orientation dependent growth techniques and laser performance. The growth of high quality epitaxial layer on (201) GaAs substrate was reported by Woolf et al. [11]. Orientation dependent growth of InGaAs/InP was noticed by Zwinge et al. [12]. Nootzel and Plog grown AlAs/GaAs multi-layered structure on (210) oriented substrate [13]. Metal Organic Chemical Vapor Deposition and Molecular Beam Epitaxy techniques are suitable for the growth of thin, uniform non-(001) crystal orientated QW structure. Although, it is possible to fabricate thin active region on non-(001) oriented substrate, it becomes very difficult to grow thick laser due to structural degradation. Wafer bonding technique is used to avoid this type of structural degradation [14], [15].

In infrared range, orientation dependent performance of InGaSb laser was reported in the past [16]. But in the visible range, orientation dependent characteristics of lasers have not been reported yet. Here, we have studied the performance of a 635nm $Ga_{0.5}In_{0.5}P/(Ga_{0.5}Al_{0.5})_{0.5}In_{0.5}P$ red laser in different crystal orientations. The orientation dependent optical gain and peak emission wavelength are investigated and their characteristics are explained by the energy separation between the conduction and valence band as well as magnitude of momentum matrix elements.

II. BAND GAP ENERGY CALCULATION

The peak emission wavelength of laser mainly depends on the band gap energy of the material used in active region. So, the selection of composition of the semiconductor material used in the active region and barrier layer is very important. In this structure GaInP is used in the active region and AlGaInP is used in the barrier of QW.

The band gap energy of $Ga_xIn_{1-x}P$ is given [17] by-

$$E_{gw}(Ga_xIn_{1-x}P) = E_g(GaP)x + E_g(InP)(1-x) - bx(1-x)$$

where, E_{gw} is the band gap energy of the material used in the QW, x is the mole fraction of Ga and b is the bowing parameter.

978-1-4673-9257-0/15/$31.00 ©2015 IEEE

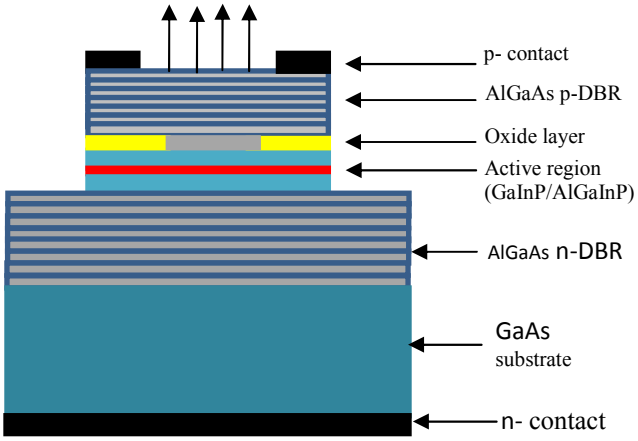

Figure 1. Structure of $Ga_{0.5}In_{0.5}P/(Ga_{0.5}Al_{0.5})_{0.5}In_{0.5}P$ red laser.

Here $(Ga_{0.5}Al_{0.5})_{0.5}In_{0.5}P$ is used in the barrier layer. The bandgap energy of the barrier material is determined using the following relationship [18]

$$E_{gb} = E_{gw}(Ga_x In_{1-x} P) + 0.36$$

III. DEVICE STRUCTURE

"Fig. 1" shows the proposed VCSEL where $Ga_{0.5}In_{0.5}P$ ternary alloy is used in the active layer and $(Ga_{0.5}Al_{0.5})_{0.5}In_{0.5}P$ quaternary alloy in the barrier layer. The QW structure is grown on n+ GaAs substrate. Above the substrate, an n-AlGaAs high reflectivity distributed bragg reflector is grown. Then the active region having a thickness of 8nm is sandwiched between two barrier layers each with a thickness of 10nm. Above the upper AlGaInP barrier layer an oxide aperture is used for current and index confinement. Highly doped contact layers are grown at the top and the bottom of the surface for the formation of ohmic contact.

III. ORIENTATION DEPENDENT GAIN

The optical gain of QW structure by considering the valence band intermixing effect can be expressed [19] by

$$g(E) = \frac{2q^2\hbar}{n\varepsilon_0 c m_0^2 LE} \sum_{n,m} \int_0^\infty \frac{k_t M_{nm}(k_t)(\Gamma/2\pi)}{(E_{cn}(k_t) - E_{kpm}(k_t) - E)^2 + (\Gamma(2\pi)^2} (f_c^n - f_v^m) dk_t \quad (1)$$

where q is the free electron charge, $\hbar$ is the reduced Planck constant, n is the refractive index, ε_0 is the free space dielectric constant, c is the speed of the light, E is the photon energy, M_{nm} is the momentum matrix, $\Gamma = 2\pi\frac{\hbar}{\tau}$ where τ is the relaxation time, f_c^n ***and*** f_v^m are the fermi functions for the conduction and valance bands, E_{cn} *is* n-th conduction subband, E_{vm} is mth valence subband, n and m denote the electron states in the conduction band and heavy/light hole states in the valence band, respectively. The momentum matrix M_{nm} is given by

$$M_{nm}(k_t) = \frac{3}{4}[<\Psi_n | g_m^{(1)}>^2 + \frac{1}{3}<\Psi_n | g_m^{(2)}>^2]M_b^2$$
$$= \frac{3}{4}[\frac{1}{3}<\Psi_n | g_m^{(3)}>^2 + <\Psi_n | g_m^{(4)}>^2]M_b^2 \quad (2)$$

where $M_b^2 = (\frac{m_0}{m_e} - 1)\frac{m_0 E_g(E_g + \Delta)}{6(E_g + (2/3)\Delta)}$ (3)

Here Ψ_n ***and*** $g_m^{(j)}$ are the conduction and valence bands wave function, M_b is the bulk average crystal momentum matrix, m_0 is the free space mass, m_e is the effective mass of electron, Eg is the band gap energy and Δ is the split off valence band energy seperation. In our calculation orientation dependent hole effective mass has not been considered.

The expression of the rotation matrix is as follows

$$O_R = \begin{pmatrix} \cos\theta\cos\phi & -\sin\phi & \sin\theta\cos\phi \\ \cos\theta\sin\phi & \cos\phi & \sin\theta\sin\phi \\ -\sin\theta & 0 & \cos\theta \end{pmatrix} \quad (4)$$

where, $\theta = \tan^{-1}(\frac{\sqrt{h^2+k^2}}{l})$ and $\phi = \tan^{-1}(k/h)$

The Hamiltonian matrix in (hkl) orientation can be calculated by the following equation [20]

$$H^{hkl} = UH^{(001)}U^* \quad (5)$$

where $U = R(\theta)R(\phi)$ (6)

Here, $R(\theta)$ and $R(\phi)$ represent the spinor rotations which transform the (001) orientated valence band Hamiltonian to arbitrary crystal orientated Hamiltonian matrix. The expressions of $R(\theta)$ and $R(\phi)$ can be given by [20]

$$R(\theta) = \begin{pmatrix} \alpha^2 & -\sqrt{3}\alpha^2\zeta & \sqrt{3}\alpha\zeta^2 & \zeta^3 \\ \sqrt{3}\alpha^2\zeta & \alpha^3 - 2\alpha\zeta^2 & -2\alpha^2\zeta + \zeta^3 & \sqrt{3}\alpha\zeta^2 \\ \sqrt{3}\alpha\zeta^2 & 2\alpha^2\zeta - \zeta^3 & \alpha^3 - 2\alpha^2\zeta & -\sqrt{3}\alpha^2\zeta \\ \zeta^3 & \sqrt{3}\alpha\zeta^2 & \sqrt{3}\alpha^2\zeta & \alpha^3 \end{pmatrix} \quad (7)$$

Here $\alpha = \cos\frac{\theta}{2}$ and $\zeta = -\sin\frac{\theta}{2}$

$$R(\phi) = \begin{pmatrix} e^{i(3/2)\phi} & 0 & 0 & 0 \\ 0 & e^{i(1/2)\phi} & 0 & 0 \\ 0 & 0 & e^{-i(1/2)\phi} & 0 \\ 0 & 0 & 0 & e^{-i(3/2)\phi} \end{pmatrix} \quad (8)$$

IV. RESULT AND DISCUSSION

Using "(1)" the gain of the laser is determined at 300k for different crystal orientations. "Fig. 2" shows the orientation dependent optical gain of the laser. It is seen that the peak gain and peak emission wavelength have crystal orientation dependence. The value of the peak gain with its emission wavelength is enlisted in Table I.

TABLE I

Orientation	Peak optical gain (cm^{-1})	Peak emission wavelength (nm)
(001)	1063	640
(101)	1017	644
(111)	1003	646
(113)	1178	642
(211)	847	648

The orientation dependent lasing characteristics of the QW VCSEL can be are described by energy dispersion profiles. To compare the energy separation characteristics, in different sub- bands the dispersion profiles are plotted in "Fig. 3" in the same scale where the valence band dispersion profiles of $Ga_{0.5}In_{0.5}P$/ $(Ga_{0.5}Al_{0.5})_{0.5}In_{0.5}P$ are presented in (001), (101), (111), (113) and (211) orientations. In this figure HH1, HH2 and HH3 indicates first, second and third heavy holes and LH1 is the first light hole bands. Lasing action occurs due to the allowed transition from conduction sub-band C1 to valence sub- bands HH1.

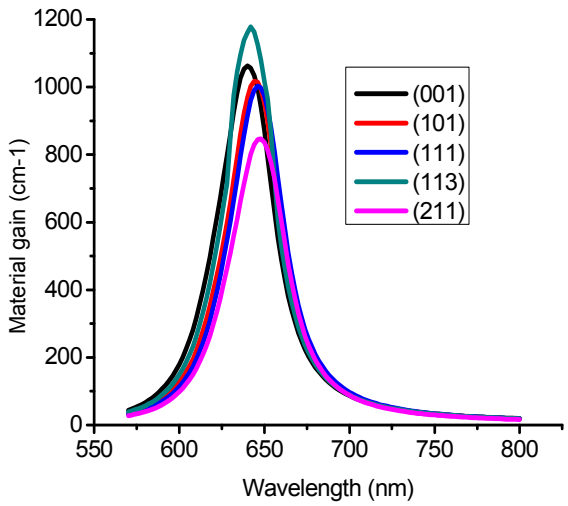

Figure 2. Optical gain spectrum of $Ga_{0.5}In_{0.5}P/(Ga_{0.5}Al_{0.5})_{0.5}In_{0.5}P$ red laser as a function of crystal orientations

Other transitions such as intra-subbands transitions are forbidden because it reduces the gain of the laser. Among the intra-subbands, transition probability is maximum between HH1 and LH1, which is reduced when the energy separation between HH1 and LH1is higher. For higher gain intra-subband transition should be reduced. For a particular orientation, the higher gain can be obtained when the energy separation between HH1 and LH1 becomes higher in the dispersion profiles. Since the energy separation between HH1 and LH1 is maximum and minimum in (113) and (211) orientation, the optical gain of the laser is found to be maximum and minimum in (113) and (211) orientations.

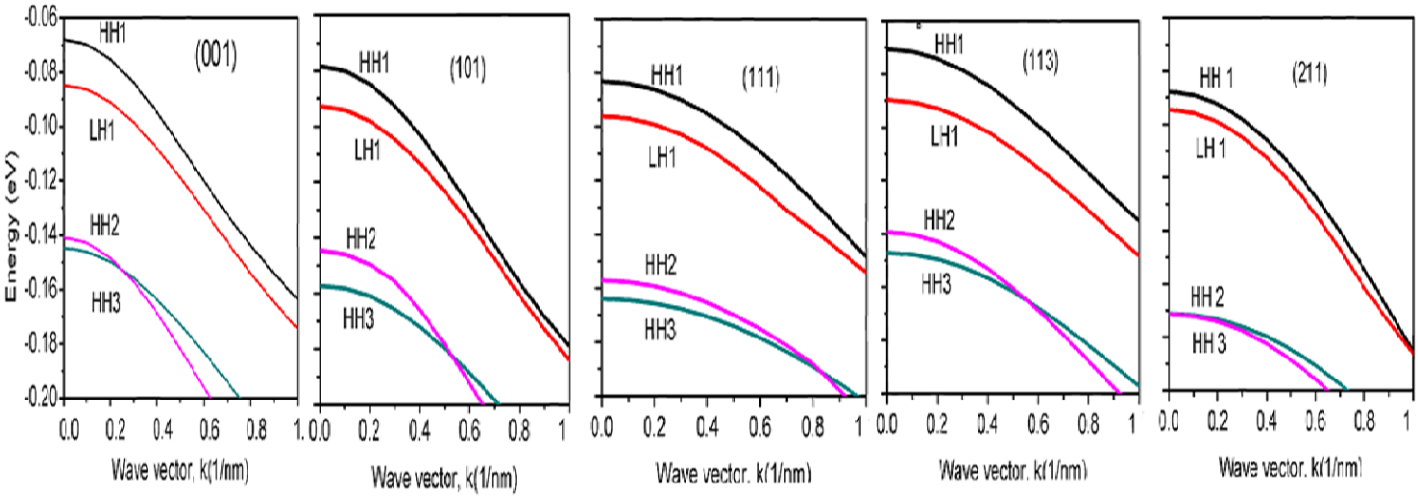

Figure 3. Valence band dispersion profile of $Ga_{0.5}In_{0.5}P$/ $(Ga_{0.5}Al_{0.5})_{0.5}In_{0.5}P$ red laser in different crystal orientation

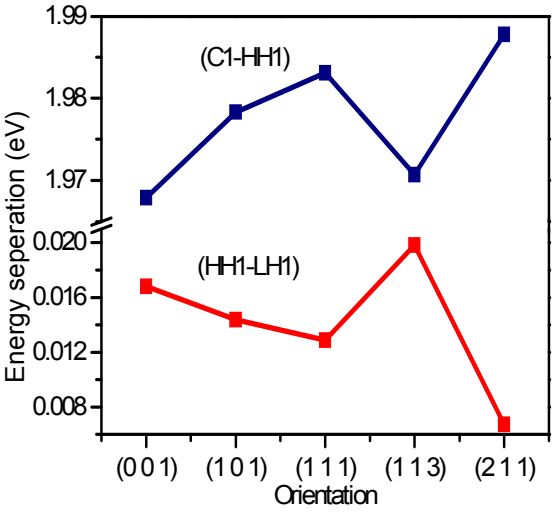

Figure 4. Orientation dependent energy separation between (C1-HH1) and (HH1-LH1)

In order to explain the wavelength dependence of peak emission wavelength the energy separation between the conduction (C1) and heavy hole (HH1) bands is estimated from the energy band dispersion profiles and plotted in "Fig. 3". It is found in Fig. 3 that the energy separation between conduction band minima and valence band maxima changes with crystal orientations. The energy separation between C1-HH1 is found to be 0.0168, 0.01438, 0.01287, 0.01983 and 0.00673 eV corresponds to the orientations (001), (101), (111), (113), and (211), respectively. This clearly explains why the peak emission wavelengths are shifted with crystal orientation. As seen in Fig. 2 the peak emission wavelength changes from 640nm to 648nm for the change in crystal orientation from (001) to (211). That is, laser with tunable characteristic can be obtained by changing the crystal orientation in the material used in active region.

To understand the orientation dependent peak gain of the laser, the energy separation between (HH1-LH1) and momentum matrix elements are further determined. The results are shown in Fig.4 and Fig. 5, respectively. The lower intra band mixing effect is observed in (131) orientation and higher in (211) orientation. Further, the orientation dependent peak gain can be explained by the momentum matrix elements, which depends on the overlapping wave functions of electrons and holes. "Fig. 5" shows that the transition probability is maximum in (113) orientation and minimum in (211) orientations. As a result, higher optical gain is estimated in (113) and lower in (211) orientation.

V. CONCLUSION

The optical gain characteristics of $Ga_{0.5}In_{0.5}P/(Ga_{0.5}Al_{0.5})_{0.5}In_{0.5}P$ 635nm red laser is investigated here in different crystal orientations. The peak gain is found to be

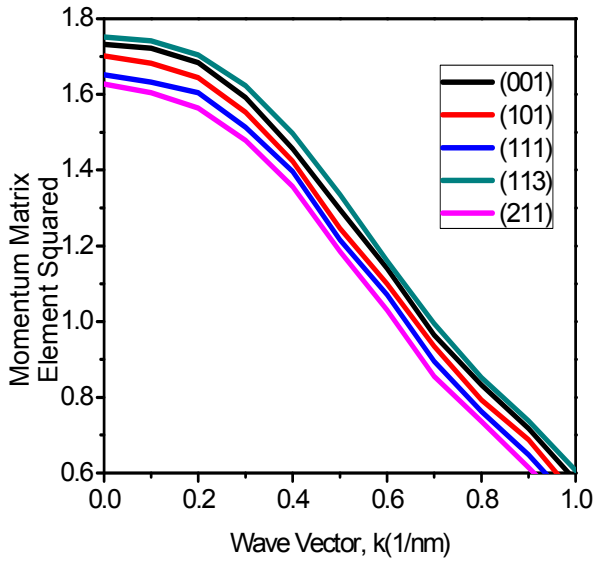

Figure 5. Crystal orientation dependent momentum matrix element squared for C1-HH1 transition

maximum in (113) orientation as the band mixing effect is minimum here. Also, the value of the momentum matrix element for the transition from C1 to HH1 and energy seperation between HH1 and LH1 is found to be higher in (113) orientation in comparison to other orientations. The peak gain is minimum in (211) orientation as the band mixing effect is maximum here. It is also seen that the peak emission wavelength varies from 640nm to 648nm when the orientation changes from (001) to (211). This demonstrates that tunable laser with various optical gains can be realized by changing crystal orientation in the active layer material.

REFERENCES

[1] R. P. Schneider, R. P. Bryan, J. A. Lott and G. R. Olbright , "Visible (657 nm) InGaP/InAlGaP strained quantum well vertical-cavity surface-emitting laser," *Applied Physics Letters*, vol. 60, no. 15, pp. 1830 – 1832, Apr. 1992

[2] R. P. Schneider and J. A. Lott, "Cavity design for improved electrical injection in InAlGaP/AlGaAs visible (639–661 nm) vertical-cavity surface-emitting laser diodes," *Applied Physics Letters*, vol. 63, no. 7, pp. 917 – 919, Sep. 1993

[3] K.F. Huang, K. Tai, C.C. Wu and J.D. Wynn, "Continuous wave visible InGaP/InGaAlP quantum-well surface-emitting laser diodes," *IEEE Trans. Electron Devices*, vol. 40, no. 11, pp. 613-614, Nov. 1993

[4] H. *Solmaz, M. Gülsoy and* Y. Ülgen***, "***635nm diode laser biostimulation on cutaneous wounds***", in*** SPIE Proceedings Vol. 9129***,*** 8 May 2014

[5] I. Charamisinau, G. S. Happawana, G. A. Evans, J. B. Kirk, D. P. Bour, A. Rosen, R. A. Hsi, "High-power semiconductor red laser arrays for use in photodynamic therapy," *IEEE Journal of Selected Topics in Quantum Electronics*, vol. 11, no. 4, pp. 881–891, Jul.-Aug. 2005.

[6] D. W. Hughes and J. R. M. Barr, "Laser diode pumped solid state lasers," *J. Phys. D: Appl. Phys.,* vol. 25, no.4, pp. 563–586, 1992.

[7] E. Alvarado-Mendez,. J. M. Estudillo-Ayala, E. Vargas-Rodriguez, M. E. Sosa-Morales, J. M. Sierra-Hernandez, D. Jauregui-Vazquez, R. Rojas-Laguna." Laser Temperature Sensor Based on a Fiber Bragg

Grating,'' *IEEE Photonics Technology Letters*, vol. 27, no. 11, pp. 1141–1144, Jun. 2015.

[8] C. Kaspari, M. Zorn, M. Weyers and G. Erbert, "Growth parameter optimization of the GaInP/AlGaInP active zone of 635 nm red laser diodes" *Journal of Crystal Growth*, vol. 310, no. 23, pp 5175–5177, Nov. 2008.

[9] C. Z. Kim, J. H. Choi, K. Song, C. S. Shin, C. G. Ko and H. Kim "Optical investigation of GaInP-AlGaInP quantum-well layers for high-power red laser diodes" *Journal of the Korean Physical Society*, Vol: 62, no: 9, pp: 1301-1306, May 2013.

[10] M. Phon, Y. Chung, W. I. Wang, ''Orientation dependence of valence-subband structures in GaAs-$Ga_{1-x}Al_xAs$ quantum-well structures,'' *J. App. Phys.*, vol. 64, no. 9, pp. 4609–4613, Nov. 1988.

[11] D. A. Woolf, J. P. Williams, D. I. Westwood, Z. Sobiesierski, J. E. Aubrey and R. H. Williams, "The homoepitaxial growth of GaAs(111)A and (111)B by molecular beam epitaxy: an investigation of the temperature dependent surface reconstructions and bulk electrical conductivity transitions," *Journal of Crystal Growth* , vol. 127, no. 1, pp. 913-917, Feb. 1993.

[12] G. Zwinge, H.-H. Wehmann, A. Schlachetzkiand and C. C. Hsu, "Orientation-dependent growth of InGaAs/InP for applications in laser-diode arrays", *Applied Physics Letters*, vol. 74, no. 9, Nov. 1993

[13] R. Notzel and K. H. Ploog, "Man-Made Low-Dimensional Solids:. New challenges in Microstructure Materials Science", *Int. J. Mod. Phys.* vol. 7, no. 15, pp. 2743-2778, Jul. 1993.

[14] Y. Okuno, "Investigation on direct bonding of III-V semiconductor wafers with lattice mismatch and orientation mismatch", *Applied Physics Letters*, vol. 68, no. 20, pp. 2855 – 2857, 1996.

[15] Y. Okuno, K. Uomi, M. Aoki, T. Tsuchiya, "Direct wafer bonding of III-V compound semiconductors for free-material and free-orientation integration",*IEEE Journal Quantum Electronics*, vol. 33, no. 6, pp. 959-969, Jun.1997

[16] M.M. Hasan, M.R. Islam, K. Teramoto, ''Crystallographic orientation dependent optical properties of GaInSb mid-infrared quantum well laser,'' *International Journal for Light and Electron Optics*, vol. 3, no. 5, pp. 1566–1575, Sep. 2004.

[17] I. Vurgaftman1, J. R. Meyer1 and L. R. Ram-Mohan, "Band parameters for III–V compound semiconductors and their alloys", *J. App. Phys.*, vol. 89, no. 11, pp. 5815–5876, Jun. 2001.

[18] Weng W. Chow, Stephan W. Koch, *Semiconductor-Laser Fundamentals Physics of the Gain Materials,* Springer-Verlag Berlin Heidelberg New York, 1999

[19] S. L. Chuang, *Physics of Optoelectronic Devices*, Wiley Series in Pure and Applied Optics, 1995

[20] T. Ohtoshi, T. Kuroda, A. Niwa, and S. Tsuji," Dependence of optical gain on crystal orientation in surface-emitting lasers with strained quantum wells", *Applied Physics Letter*, vol. 65, no.15, pp. 1886-1888, Oct.1994.

Wideband Planar Monopole Antenna for LTE, GSM, Bluetooth, WiMAX, DCS, PCS, and GPS Mobile Terminals

Rahinur Rahman, Khaled Mahbub Morshed, Sumyea Sabrin and Md Mostafizur Rahman
Department of Electronics and Communication Engineering
Khulna University of Engineering & Technology, Khulna 9203, Bangladesh
E-mail: rahinur2k11@gmail.com, khaled.morshed@ece.kuet.ac.bd, sweetykuet@gmail.com, mostafiz963@yahoo.com

Abstract—**A simple planar antenna of high gain for long term evolution (LTE), global system for mobile communications (GSM), Bluetooth, worldwide interoperability for microwave access (WiMAX), digital cellular services (DCS), personal communication services (PCS), wireless local area network (WLAN), and global positioning system (GPS) mobile terminals is presented. The antenna has wide -6 dB reflection coefficient bandwidth of 2.17 GHz (1.33 – 3.5 GHz). The antenna has a compact size of 44.9 mm ×35.5 mm × 0.87 mm placed one side of the substrate of dimension 35.5 mm × 75.5 mm. The antenna has high gain of 3.85 dBi at 2.7 GHz, maximum directivity is 5.04 dBi at 2.7 GHz and total efficiency of the antenna varies between 61% and 95% within the wide impedance bandwidth. In addition, the antenna gain and efficiency is almost constant in individual operating band of operation. Dimensions of the antenna are optimized for wide impedance band. Antenna radiation patterns are presented at 1.5, 2, 2.5, and 3 GHz.**

Keywords—Planar monopole antenna, LTE, TDD, FDD, GSM, Bluetooth, WiMAX, DCS, PCS, WLAN, and GPS.

I. INTRODUCTION

Growing demand of data rates accelerate towards next generation wireless mobile communication having wideband antenna installed within hand-held mobile devices [1] – [5] and also required added services support e.g. global positioning system (GPS), worldwide interoperability for microwave access (WiMAX), wireless local area network (WLAN), Bluetooth etc. [6] – [12]. Broadband/wideband antenna not only support these bands but also increases the channel capacity [5] – [8].

Long term evolution (LTE) bands (LTE-1 to LTE-40) can be divided into two major categories based on their dependency like time division duplex (TDD) band and frequency division duplex (FDD) band [13] – [14]. These bands cover three wide bands, lower one from 0.698 GHz to 0.966 GHz, middle band from 1.427 GHz to 2.69 GHz and the higher band from 3.4 GHz to 3.8 GHz [15] – [20]. In parallel of LTE support mobile terminals need to cover GSM bands for voice only [21] – [24].

Smartphones are attractive because of their additive services like GPS (1.559 – 1.61 GHz), Bluetooth (2.4 GHz ISM band), WiMAX in 2.3, 2.5, 3.5 GHz band, WLAN in 2.4 GHz band, digital cellular services (DCS) in the band 1.71 – 1.88 GHz, and personal communication services (PCS) in the band 1.85 – 1.99 GHz together with LTE and global system for mobile communications (GSM) support [1], [5], [34] - [36].

Several antennas has been proposed in the previous years for the use in hand held mobile devices including planar monopole [1], [6], [8], [9], planar inverted-F [5], [7], array antenna, reconfigurable antenna [2] , [3], slot antenna [10]. Also, different feeding technique e.g. multi resonance feed structure [11], hybrid feed [14], different isolation technique [24], dielectric resonator feed [19], and modified ground plane e.g. protruded [17] has been used to achieve multiband operation having limited form factor. Moreover, several antennas have been proposed for WiFi and WiMAX applications where inverted-L load [25] – [29], F-L load [30] – [32] and planar wire antenna [33], leaky wave antennas [37] [38] have been considered for gain enhancement but the size of those antennas are not feasible for hand-held mobile terminal. Most of the proposed antenna for smartphone applications comes with wideband that covers 1.6 GHz to 2.7 GHz and recently one paper has been published that support additional 3.4 – 3.8 GHz band [3].

In this paper, a technique is presented to remove notch exist in current design and using the proposed technique a simple planar wideband antenna is presented for LTE, GSM, Bluetooth, WiMAX, DCS, PCS, and GPS applications. The antenna design strategy are briefly described in Section II. Section III presents the simulation results and the paper ended with a conclusion in Section IV.

II. WIDEBAND ANTENNA DESIGN STRATEGY

The antenna is designed using low cost FR-4 substrate with dielectric constant 4.3 and loss tangent 0.025 in CST Microwave Studio. Thickness of the substrate is 0.8 mm and thickness of copper cladding is 0.035 mm. Fig. 1 shows the design steps in achieving continuous band antenna as a replacement for having a notch. Firstly, the antenna radiating legs are connected to form a loop antenna. Then, two parasitic is placed on the either side of the feeding line to form capacitive effect and finally a capacitor is placed in the right arm of the antenna, shown in Fig. 1(a), 1(b), 1(c), and 1(d), respectively.

978-1-4673-9257-0/15/$31.00 ©2015 IEEE

Fig. 2 present the top view and bottom view of the antenna. For feeding arrangement, coaxial connector is used and the antenna feeding is comes from the bottom of the antenna, shown in Fig. (2). Overall dimension of the substrate is 35.5 mm × 60.5 mm and the antenna radiator dimension is 44.9 mm × 35.5 mm. Dimension of the feeding arrangement is 10.5 mm × 31.4 mm, shown in Fig. 3, also the detailed structure of the antenna presented. Here all values are in mm. The values of the capacitor C is 2 nF and is placed by creating a gap of 1 mm. In our design we have used antenna in [1] as a reference, shown in Fig. 1(a), and we modify the structure to achieve continuous band by following aforementioned procedure/steps.

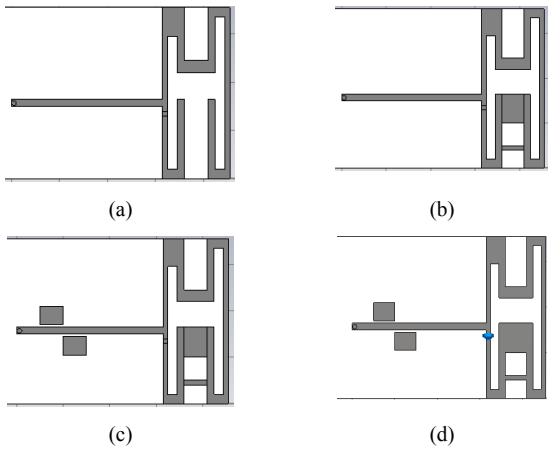

Fig. 1. Antenna design strategy for wideband operation (a) base antenna structure [1], (b) right legs are connected with two radiating elements of size 5 mm × 6.5 mm and 5 mm × 1 mm, (c) two parasitic radiator placed with a gap of 0.5 mm with the 50 Ω feeding line, and (d) final structure with addition of 2 nF capacitor on the right arm of the loop in a 1 mm space.

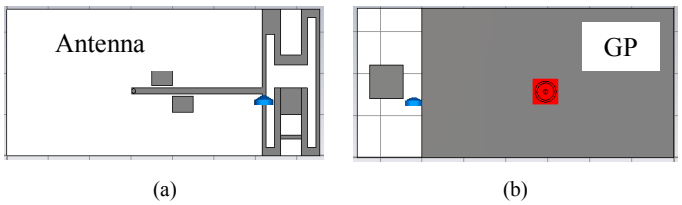

Fig. 2. Structure of the proposed monopole antenna (a) top view and (b) bottom view.

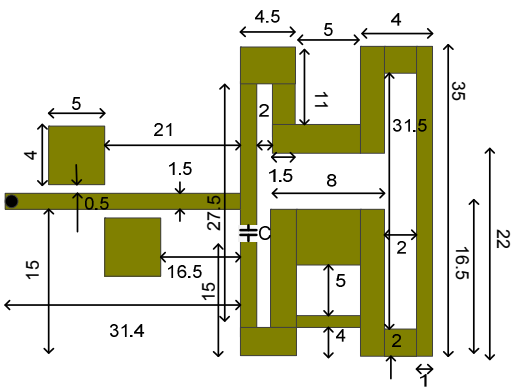

Fig. 3. Detailed geometry of the proposed antenna. Here all values/dimensions are in mm.

III. Resuls and Discussion

The antenna proposed in [1] covers 1.5 to 4.12 GHz with notches around 2.5 GHz and 3.84 GHz, shown in Fig. 4 (line AA). These two notches block the LTE 7 and radio frequency identification bands. Firstly we increase the band of the antenna by connecting two right radiator of U shape using two parallel radiator of dimension 5 mm × 6.5 mm and 5 mm × 1 mm, respectively, shown in Fig. 1(b). These two connected radiator improves the bandwidth but not reduced the notch completely, shown in Fig. 4 (line BB). After that, two parasitic patch of size 4 mm × 5mm is placed with a gap of 0.5 mm from the feeding strip shown in Fig. 1(c). This parasitic patch removes the notch slightly but has no effect on the bandwidth of the antenna, shown in Fig. 4 (line CC). To further reduce the notch at 3.84 GHz, manual impedance matching can be employed. A capacitor of size 2 nF, decided by parametric simulation studied in software, is placed on the right arm of the antenna because this arm giving resonance at that frequency, reduces the notch completely, shown in Fig. 4 (line DD). Here the positioning of the capacitor, 1 mm away from the 50 Ω feeding line.

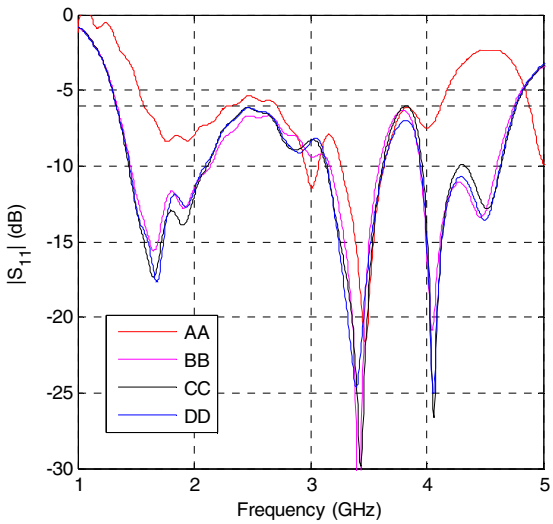

Fig. 4. Reflection coefficient of the proposed antenna for the geometry presented in Fig. (1). Here, return loss corresponds to AA, BB, CC, and DD are for the structure shown in Fig. 1(a), 1(b), 1(c) and 1(d), respectively.

After finalizing the structure, the detailed geometry are presented in Fig. 3 and the simulated reflection coefficient are shown in Fig. 5. The proposed/modified antenna has a wide impedance bandwidth of 3.43 GHz, from 1.33 GHz to 4.76 GHz, with a voltage standing wave ratio (VSWR) 3:1 (-6 dB reflection coefficient or 6 dB return loss). From the figure it can easily be observed that the proposed antenna can provide multi band operation to support GPS, DCS, PCS, WLAN, Bluetooth, WiMAX, and LTE.

Total efficiency of the antenna is varied between 61% and 95%, shown in Fig. 6. Total efficiency is minimum at 3.8 GHz and maximum at 1.6 GHz. Because of the non-symmetric structure the efficiency has significantly changes within the

978-1-4673-9257-0/15/$31.00 ©2015 IEEE

operating bandwidth which leads to the change in gain/realized gain and directivity of the antenna, shown in Fig. 7.

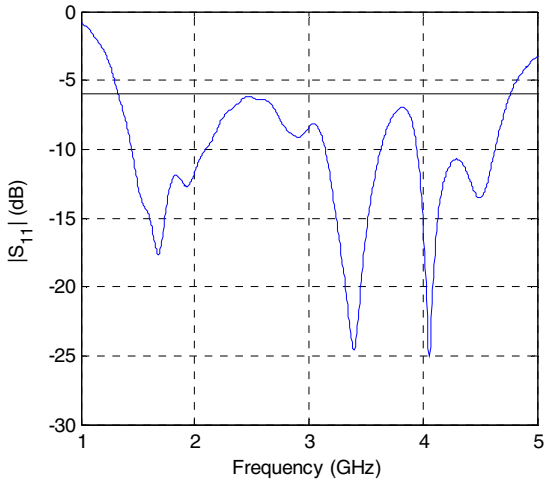

Fig. 5. Reflection coefficient vs frequency of the proposed antenna.

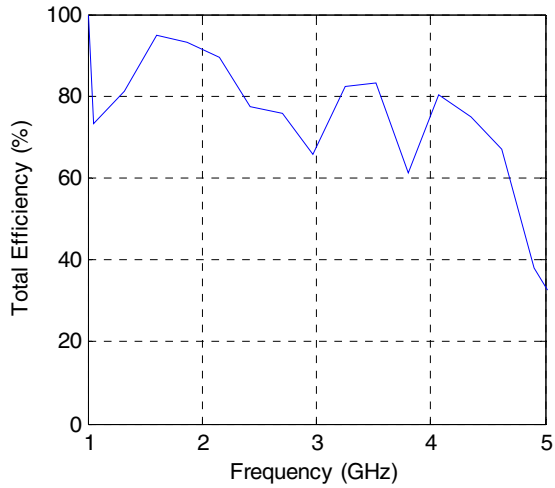

Fig. 6. Total efficiency of the proposed antenna vs frequency.

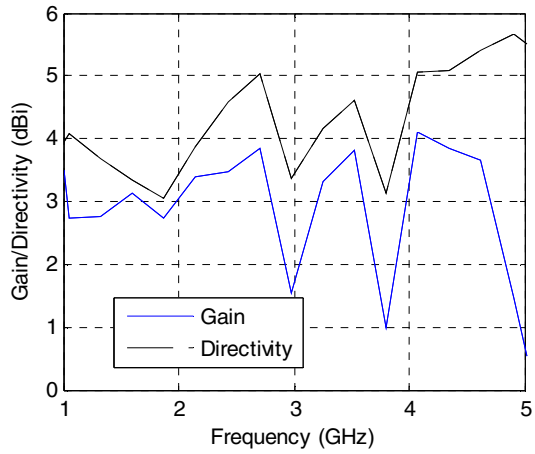

Fig. 7. Gain and directivity of the proposed antenna as a function of frequency.

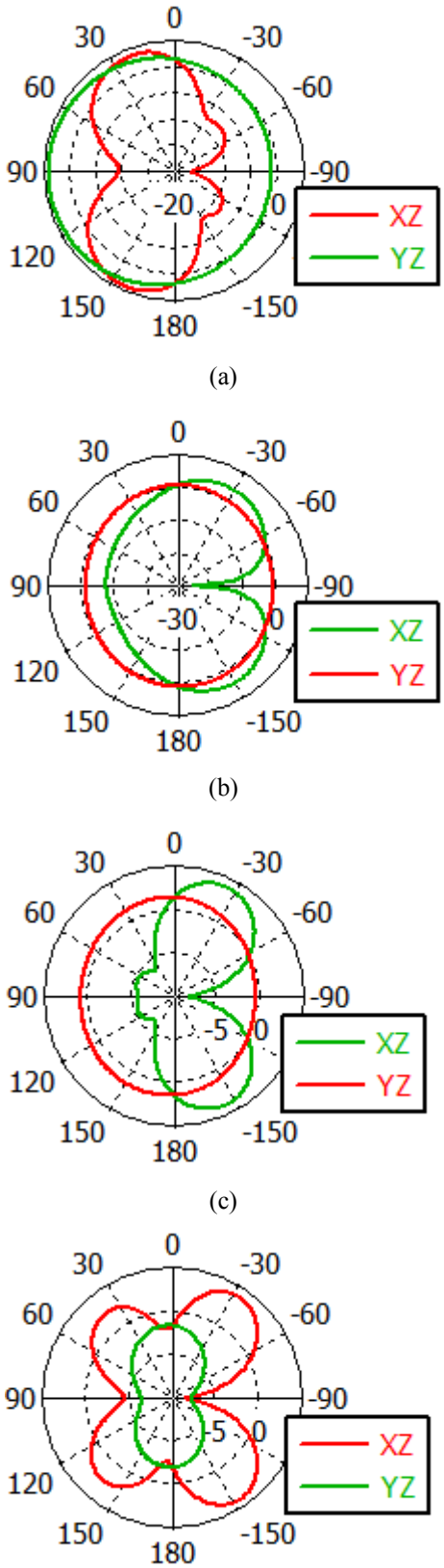

978-1-4673-9257-0/15/$31.00 ©2015 IEEE

(d)

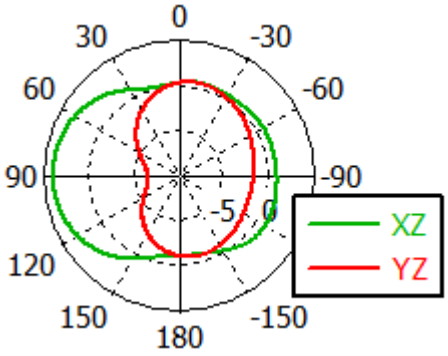

(e)

Fig. 8. Radiation patterns of the proposed antenna at (a) 1.5 GHz, (b) 2 GHz, (c) 2.5 GHz, (d) 3 GHz, and (e) 3.5 GHz.

Realized gain of the antenna is changes from 1.55 dBi (at 2.975 GHz) to 3.85 dBi (at 2.7 GHz) while the directivity of the antenna changes from 3.06 dBi (at 1.875 GHz) to 5.04 dBi (at 2.7 GHz), shown in Fig. 7. However, the gain variation within an individual band is less than 0.5 dB, e.g. < 0.5 dB at GSM 1800, <0.5 dB at ISM band. Directivity is always higher than realized gain which is expected. Realized gain is about 2.3dBi for GPS, DCS, PCS, and WiMAX band, and above 2.5dBi for WLAN, and Bluetooth. The proposed antenna has a directivity of 2.6 – 2.5 dBi for GPS, DCS, PCS band. 2.7 – 4.5 dBi directivity is achieved for WiMAX, WLAN band. The overall directivity of the antenna is above 3.06 dBi for all through the operating frequency

Radiation patterns of the antenna at 1.5, 2, 2.5, 3, and 3.5 GHz are shown in Fig. 8. At frequencies, below 3.5 GHz, this antenna radiation pattern is like planar monopole antenna having radiation almost omnidirectional shown in Fig. 8(a), 8(b), 8(c), 8(d), and 8(e). Though the antenna bandwidth covers till 4.7 6GHz but there are improvement in radiation patterns required to make this antenna useful beyond 3GHz. In obtained results, nulls have been observed on the radiation patterns and these nulls are generated because current are highly condensed along the right and left edges of the antenna loop.

IV. Conclusion

A wideband planar monopole antenna for LTE, GSM, Bluetooth, WiMAX, DCS, PCS, and GPS mobile devices/smartphones was designed. The bandwidth improvement of this antenna has been achieved through adding two parasitic element near the feeding line for capacitive effect and then adding a series capacitor in the loop monopole to maintain the impedance matching at the notch frequency. The simulated return loss, antenna efficiency, directivity and the radiation pattern suggest the potential use of this antenna for wide band operation in mobile devices.

References

[1] Y. –J. Chi, F. –C. Chen, "Compact Printed Hepta-Band Monopole Antenna for Mobile Devices," in *Asia-Pacific Microwave Conference Proceedings (APMC)*, pp.2216 – 2219, 7 – 10 Dec. 2010.

[2] Z. H. Hu, C. T. P. Song, J. Kelly, P. S. Hall, P. Gardner, "Wide Tunable Dual-Band Reconfigurable Antenna," Electronics Letters, vol.45, no.22, pp.1109-1110, Oct. 22, 2009.

[3] K. –L. Wong, Z. –G. Liao, "Passive Reconfigurable Triple-Wideband Antenna for LTE Tablet Computer," *IEEE Transactions on Antennas and Propagation*, vol.63, no.3, pp.901-908, Mar. 2015.

[4] K. –L. Wong, C. -Y. Tsai, "Low-Profile Dual-Wideband Inverted-T Open Slot Antenna for the LTE/WWAN Tablet Computer with a Metallic Frame," *IEEE Transactions on Antennas and Propagation*, vol.63, no.7, pp.2879-2886, Jul. 2015.

[5] K. R. Boyle, P. G. Steeneken, "A Five-Band Reconfigurable PIFA for Mobile Phones," *IEEE Transactions on Antennas and Propagation*, vol.55, no.11, pp.3300-3309, Nov. 2007.

[6] Y. –L. Ban, C. –L. Liu, Z. Chen, J. L. -W. Li, K. Kang, "Small-Size Multiresonant Octaband Antenna for LTE/WWAN Smartphone Applications," *IEEE Antennas and Wireless Propagation Letters*, vol.13, pp.619-622, 2014.

[7] C. –H. Chang, K. –L. Wong, "Printed-PIFA for Penta-Band WWAN Operation in the Mobile Phone," *IEEE Transactions on Antennas and Propagation*, vol.57, no.5, pp.1373-1381, May 2009.

[8] J. -H. Lu; Y. -S. Wang, "Planar Small-Size Eight-Band LTE/WWAN Monopole Antenna for Tablet Computers," *IEEE Transactions on Antennas and Propagation*, vol.62, no.8, pp.4372-4377, Aug. 2014.

[9] T. Zhang, R. L. Li, G. P. Jin, G. Wei, M. M. Tentzeris, "A Novel Multiband Planar Antenna for GSM/UMTS/LTE/Zigbee/RFID Mobile Devices," *IEEE Transactions on Antennas and Propagation*, vol.59, no.11, pp.4209-4214, Nov. 2011.

[10] Y. F. Cao, S. W. Cheung, T. I. Yuk, "A Multiband Slot Antenna for GPS/WiMAX/WLAN Systems," *IEEE Transactions on Antennas and Propagation*, vol.63, no.3, pp.952-958, Mar. 2015.

[11] J. Lee, Y. Liu, H. Kim, "Mobile Antenna Using Multi-Resonance Feed Structure for Wideband Operation," *IEEE Transactions on Antennas and Propagation*, vol.62, no.11, pp.5851-5855, Nov. 2014.

[12] J. –T. Yeh, W. –J. Liao, S. –H. Chang, "Compact Internal Antenna for Handheld Devices with Comprehensive DTV Band Coverage," *IEEE Transactions on Antennas and Propagation*, vol.62, no.8, pp.3998-4007, Aug. 2014.

[13] J. –H. Lu, J. –L. Guo, "Small-Size Octaband Monopole Antenna in an LTE/WWAN Mobile Phone," *IEEE Antennas and Wireless Propagation Letters*, vol.13, no., pp.548-551, 2014.

[14] K. –L. Wong, L. –Y. Chen, "Small-Size LTE/WWAN Tablet Device Antenna with Two Hybrid Feeds," *IEEE Transactions on Antennas and Propagation*, vol.62, no.6, pp.2926-2934, Jun. 2014.

[15] Y. –L. Ban, Y. –F. Qiang, Z. Chen, K. Kang, J. –H. Guo, "A Dual-Loop Antenna Design for Hepta-Band WWAN/LTE Metal-Rimmed Smartphone Applications," *IEEE Transactions on Antennas and Propagation*, vol.63, no.1, pp.48-58, Jan. 2015.

[16] K. –L. Wong, C. –Y. Tsai, "Small-Size Stacked Inverted-F Antenna with Two Hybrid Shorting Strips for the LTE/WWAN Tablet Device," *IEEE Transactions on Antennas and Propagation*, vol.62, no.8, pp.3962-3969, Aug. 2014.

[17] Y. –L. Ban, S. Yang, Z. Chen, K. Kang, J. L. -W. Li, "Decoupled Planar WWAN Antennas with T-Shaped Protruded Ground for Smartphone Applications," *IEEE Antennas and Wireless Propagation Letters*, vol.13, no., pp.483-486, 2014

[18] B. –Y. Park, M. –H. Jeong, S. –O. Park, "A Magneto-Dielectric Handset Antenna for LTE/WWAN/GPS Applications," *IEEE Antennas and Wireless Propagation Letters*, vol.13, no., pp.1482-1485, 2014.

[19] Y. –F. Lin, H. –M. Chen, C. –Y. Lin, Shan-Cheng Pan, "Planar Inverted-L Antenna with a Dielectric Resonator Feed in a Mobile Device," *IEEE Transactions on Antennas and Propagation*, vol.57, no.10, pp.3342-3346, Oct. 2009.

[20] Y. –L. Ban, Z. –X. Chen, Z. Chen, K. Kang, J. L. -W. Li, "Decoupled Hepta-Band Antenna Array for WWAN/LTE Smartphone Applications," *IEEE Antennas and Wireless Propagation Letters*, vol.13, pp.999-1002, 2014.

[21] Y. –L. Ban, Z. X. Chen, Z. Chen, K. Kang, J. L. –W. Li, "Reconfigurable Narrow-Frame Antenna for Heptaband WWAN/LTE

978-1-4673-9257-0/15/$31.00 ©2015 IEEE

Smartphone Applications," IEEE Antennas and Wireless Propagation Letters, vol.13, pp.1365-1368, 2014.

[22] C. –K. Hsu, S. –J. Chung, "Compact Antenna with U-Shaped Open-End Slot Structure for Multi-Band Handset Applications," *IEEE Transactions on Antennas and Propagation*, vol.62, no.2, pp.929-932, Feb. 2014.

[23] J. Lee, Y. Sung, "Heptaband Inverted-F Antenna with Independent Resonance Control for Mobile Handset Applications," *IEEE Antennas and Wireless Propagation Letters*, vol.13, pp.1267-1270, 2014

[24] A. Cihangir, F. Ferrero, G. Jacquemod, P. Brachat, C. Luxey, "Neutralized Coupling Elements for MIMO Operation in 4G Mobile Terminals," *IEEE Antennas and Wireless Propagation Letters*, vol.13, pp.141,144, 2014.

[25] K. M. Morshed, D. K. Karmokar, and M. Talukder, "Numerical and experimental analysis of impedance matched inverted-L and stair inverted-L antenna for 5 GHz WLAN operation," *Journal of Communications*, vol. 5, no. 8, pp. 612–619, Aug. 2010.

[26] K. M. Morshed, D. K. Karmokar, and A. M. Numan-Al-Mobin, "Numerical analysis of impedance matched inverted-L antennas for Wi-Fi operations," in *IEEE International Conference on Computer and Information Technology (ICCIT)*, Dhaka, Bangladesh, Dec. 2009, pp. 691–696.

[27] K. M. Morshed, D. K. Karmokar, and M. M. Rahman, "Dual band two elements inverted-L antenna for 2.3 GHz mobile WiMAX and 5.5 GHz Wi-Fi operations," in *IEEE International Conference on Computer and Information Technology (ICCIT)*, Dhaka, Bangladesh, Dec. 2011, pp. 223–228.

[28] M. A. Hossain, M. R. Basar, and K. M. Morshed, "Ultra-wideband LLI-slit slotted antenna for WLAN, bluetooth and Wi-Fi operations," in *IEEE International Conference on Computer and Information Technology (ICCIT)*, Dhaka, Bangladesh, Dec. 2011, pp. 229–233.

[29] M. R. Basar, M. A. Hossain, M. R. U. Hoque, and K. M. Morshed, "Compact dual L-slit slotted antenna for spacecraft, WLAN, Wi-Fi, and bluetooth application," in *IEEE International Conference on Electrical Computer Engineering (ICECE)*, Dhaka, Bangladesh, Dec. 2012, pp. 706–708.

[30] D. K. Karmokar, K. M. Morshed, M. S. Hossain, and M. N. Mollah, "Wideband low profile double inverted-F antenna for 5.2/5.8 GHz WLAN and 5.5 GHz WiMAX applications," *ACEEE International Journal on Communications*, vol. 2, no. 1, pp. 28–32, Mar. 2011.

[31] D. K. Karmokar, K. M. Morshed, A. M. Numan-Al-Mobin, and A. E. Kabir, "High gain multiband loaded inverted-F antennas for mobile WiMAX,Wi-Fi, bluetooth and WLAN operation," *International Journal of Engineering (IJE)*, vol. 4, no. 3, pp. 219–232, Jul. 2010.

[32] A. A. Talukder, D. K. Karmokar, K. M. Morshed, and M. N. Mollah, "Low profile inverted-F-L antenna for 5.5 GHz WiMAX applications," *ACEEE International Journal on Communications*, vol. 3, no. 1, pp. 15–19, Mar. 2012.

[33] M. J. Hossain, M. A. M. Khan, A. M. Numan-Al-Mobin, and K. M. Morshed, "A simple structured planar wire antenna for wireless communication applications," in *IEEE International Conference on Electrical Computer Engineering (ICECE)*, Dhaka, Bangladesh, Dec. 2012, pp. 709–712.

[34] J. Ilvonen, R. Valkonen, J. Holopainen, V. Viikari, "Design Strategy for 4G Handset Antennas and a Multiband Hybrid Antenna," *IEEE Transactions on Antennas and Propagation*, vol.62, no.4, pp.1918-1927, Apr. 2014.

[35] S. F. Roslan, M. R. Kamarudin, M. Khalily, M. H. Jamaluddin, "An MIMO Rectangular Dielectric Resonator Antenna for 4G Applications," *IEEE Antennas and Wireless Propagation Letters*, vol.13, pp.321-324, 2014.

[36] B. Lee, F. J. Harackiewicz, H. Wi, "Closely Mounted Mobile Handset MIMO Antenna for LTE 13 Band Application," *IEEE Antennas and Wireless Propagation Letters*, vol.13, pp.411-414, 2014.

[37] D. K. Karmokar, K. P. Esselle, "Periodic U-Slot-Loaded Dual-Band Half-Width Microstrip Leaky-Wave Antennas for Forward and Backward Beam Scanning," in *IEEE Trans. Antennas Propag.*, vol.PP, no.99, pp.1-1.

[38] D. K. Karmokar, K. P. Esselle, T. S. Bird, "An Array of Half-Width Microstrip Leaky-Wave Antennas Radiating on Boresight," in *IEEE Antennas Wireless Propag. Letters*, vol.14, no., pp.112-114, 2015.

978-1-4673-9257-0/15/$31.00 ©2015 IEEE

On the Architectures of RF Based Underwater Wireless Sensor Networks for Intruder Detection

[1]Musbiha Binte Wali and [2]Md. Farhad Hossain
Department of Electrical and Electronic Engineering
Bangladesh University of Engineering & Technology (BUET), Dhaka-1000, Bangladesh
Email: [1]musbihabintewali@yahoo.com, [2]mfarhadhossain@eee.buet.ac.bd

***Abstract*- For underwater surveillance and observations, the widely used medium is the acoustic wave based underwater wireless sensor networks (UWSNs). But acoustics in underwater environment face high challenges to meet the necessity for fast transmission rates in different newly emerging underwater operations. Then again, underwater network systems based on radio frequency (RF) have incredible potential for supporting fast information transmission. In light of this, we propose and examine two three dimensional (3D) cluster-based UWSN architectures for identifying intruders in an underwater surveillance area. The proposed architectures comprised of cluster heads (CHs) and sensor nodes (SNs) senses the presence of an intruder inside the surveillance area and then pass the real-time location of the intruder to a coastal base station (BS) via a sink situated at water surface. All the data transfers from SNs to BSs are RF based. The data of the received RF signal strength and the positions of the SNs and CHs are the information used for calculating the intruder's position. For assessing the proposed system architectures' localization capacities in a seawater circumstance, substantial simulations are carried through. Localization precision of the architectures is altogether examined in terms of inaccuracy in distance and direction estimations. Effect of different framework parameters on the performance is likewise interpretatively scrutinized exhibiting noteworthy performance discord between the architectures.**

Keywords–intruder detection; target localization; RF based UWSN; 3D sensor networks; underwater communications

I. Introduction

For enquiring into the resourceful underwater worlds, research on underwater operations conveys great significance as almost seventy five percent of the surface of the planet Earth is covered by water, most part by ocean and seas [1]. While investigating this prodigious area of underwater, UWSN systems have been approved by the analysts as an attainable, minimal effort arrangement [2] as the advances in sensor technologies have made sensor networks utilizable for any kind of circumstances. Objectives of deploying UWSNs include navigations, observation on sea boundaries, mine surveillance, trace and rescue operations, preventing cataclysms, seaward investigations, oceanography and numerous sea-going applications [1]-[2]. In most cases UWSNs use acoustics as transmission media. Notwithstanding, with the increment in the quantity of fast moving submerged vehicles and independent weapons in current times, there is a concern for speedier transmission media like optical or radio frequency (RF), particularly for detection and tracing purposes, as the transmission speed by acoustics is slower than the needed [3]. But then, optical wave is not feasible for major submerged applications as it requires line of sight (LOS) with tight arrangement and clear water in its transmission way [4]. In this way, how to utilize the RF's quick transmission capacity in underwater environment to make real-time high-throughput applications achievable is catching the attention of the related academic group. Numerous long sought aims, for example, real-time localization and transmission, resistance to acoustic clamor, turbidity and pressure slopes; diminished effect on marine life and ability of non-LOS communications can be attained utilizing RF based UWSNs which acoustic based systems cannot [5], [6].

Given this situation, this paper is meant to investigate the designs of submerged surveillance system for localizing unwelcomed objects utilizing RF as transmission coverage. Our broad survey shows that there is progressing investigation on RF communication based underwater intruder localizing systems and this field needs more efforts. Beforehand, a two dimensional (2D) submarine locating procedure utilizing a dispersed sensor system of binary-detection capacity was proposed in [7]. Furthermore, the writers in [8] introduced 2D two disseminated particle filter based object locating and tracing strategies utilizing clustered UWSNs. Then again, submerged 3D target identification and tracking strategies utilizing UWSNs were presented in [9]-[11]. The entry time of the reverberation messages originating from the object is utilized for deciding the distance from the sensor to the object in [9]. At that point trilateration is used to compute target's location. Node's position and the above speed will then be utilized for tracking the submerged target. Nonetheless, all the previously stated works are carried out in light of acoustic network systems. Provided the feasibility of diversified applications of UWSNs proven by the time, further sea trials have been carried out in [12] to introduce EM into the UWSNs with a view to undersea target detection & tracking using EM-acoustic combination.

Therefore, this paper proposes and explores two 3D UWSN architectures for identifying and locating intruders underwater. Each architecture comprises of a cluster-based UWSN formed utilizing sensor nodes (SNs) and cluster heads (CHs), a sink situated at the water surface and an inland base station (BS) with the essential mathematical models for localization. The inspiration of utilizing cluster based UWSNs originates from their powerful topology and the certainty of their inclination in extended system life through effectual energy sparing techniques [13], [14]. Every step in the communications from the SNs to the BS via CHs are proposed to be by means of RF. Intruder locations are computed utilizing the data of received RF signal strength and the positions of SNs and CHs. Performances of the presented architectures are assessed using substantial simulations.

978-1-4673-9257-0/15/$31.00 ©2015 IEEE

Localization precision is analyzed and compared in terms of inaccuracies in both distance and direction approximations. Effect of system size and signal identification threshold on the system perfection is likewise examined.

The remaining of the paper is organized as follows: Section II introduces the general outline of the proposed localization strategies. Then in Section III, Proposed architectures are illustrated in detail. Section IV characterizes new performance metrics and then the simulation results with insightful investigation in Section V. The paper concludes in Section VI by abridging the key findings.

II. Proposed Overall Localization Scheme

The general operation guideline of the proposed submerged intruder identifying and locating strategy is talked about in this segment. The network comprises of two fundamental components, SNs and CHs. Again, every SN involves low power sensor bundle and an omnidirectional RF transmitter. The sensor bundle of every SN uses distinctive standards for detecting an intruder, for example, movement sensor, pressure sensor (as a fast moving intruder will acquaint pressure amid drawing nearer to the system), metal identifier (to guarantee whether the intruder is of metal body) and passive sonar (to be sure whether the approaching intruder has a motor, particularly when submarines are to be recognized). To mention, the proposed architectures are outlined independent of the kind of detecting methods of the SNs. A CH alongside a team of SNs constructs a cluster. Every CH comprises of RF transmitter and recipient. Collecting the neighborhood data from SNs and/or different CHs and sending those to the sink are the duties of a CH.

These SNs and CHs, being organized in a specific position, construct the clusters in 3D underwater space and subsequently develop to the architectures discussed in the segment III. The working rule of the general localization strategy as appeared in Fig. 1 is as follows: Both SNs and CHs typically stay in dormant or rest mode for energy saving. Receiving RF signal strength above than a specific threshold P_{th} either from another CH or from the close-by SNs can just alter the CH's to active mode, while an SN just after sensing an intruder. When an intruder enters the reconnaissance zone, the nearby SNs sense the vicinity of the intruder and alter to active mode. Detecting the vicinity of an intruder, SN transmits its location information utilizing RF signal of power P_{SN} and frequency f_{SN}. After receiving RF signal from SNs, CHs are switched to active mode. These active CHs gather the location data of the SNs and the strength of the received RF signal from the SNs. At that point the necessary pieces of information are sent to the particular CHs of the direct upper layer using RF signal of power P_{CH} and frequency f_{CH} and so on. The data, in this manner, gets to the surface sink from the CHs of the topmost layer. The accumulated data is then transmitted to the inland BS for handling and approximating the location of the object. All the transmissions including SN-CH, CH-CH, CH-surface sink and surface sink-BS are based on RF signal.

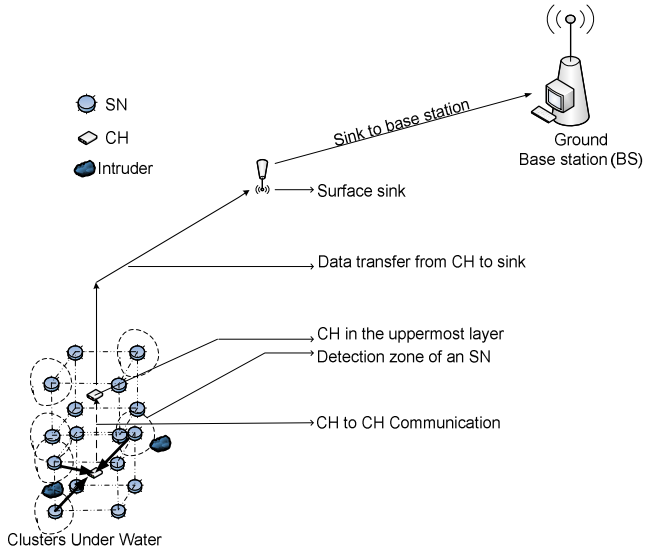

Fig. 1: Overall model of the proposed localization schemes.

III. Proposed UWSN Architectures

Proposed UWSN architectures for recognizing intruders are presented here below. We assume a plane seabed and overlook the versatility of system components. SNs and CHs are organized in 3D space constructing the basic building block as shown in Fig. 2(a). The XY plane of the arrangement is viewed as parallel to the seabed and the Z-axis is considered along the sea depth. The fundamental building block is repeated to build the UWSN covering a reconnaissance region of a cubic area $D_x \times D_y \times D_z$, where D_x, D_y, and D_z are the length of the observation region along the X-, Y-and Z-axes respectively. The evolved UWSN is shown in Fig. 2(b). Based on the localization rule, we now propose two distinct intruder detecting architectures symbolized as A_1 and A_2, which are discussed in detail in following sections.

A. Architecture A_1

In topology A_1, SNs are allocated at each of the eight vertices of a rectangular cuboid of cubic dimension $\Delta_x \times \Delta_y \times \Delta_z$ as illustrated in Fig. 2(a). In this manner, the whole UWSN is constructed by allocating SNs at each Δ_x, Δ_y and Δ_z distance along X-, Y- and Z-axis respectively. Then again, one CH is set at the focal point of every cuboid. Along these lines the distance of a CH from the SNs of its cuboid is equal to $D_{CE} = \frac{1}{2}\sqrt{\Delta_x^2 + \Delta_y^2 + \Delta_z^2}$. The UWSN, in this manner, has eight SNs encompassing every CH and vice versa.

Under A_1, we assume that each CH holds the information about its own position coordinate. As soon as an SN senses an unwelcomed approaching object, it alerts the nearby CHs around by transmitting RF signal. If a CH receives RF signal of power above P_{th} transmitted by the SN, the CH switches to active mode and sends its coordinate to the exact upper layer's

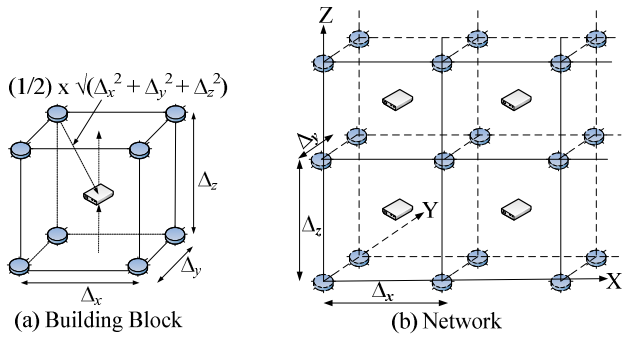

Fig. 2: Topology for architecture A_1 and A_2.

CHs through RF signal. By means of this flow of location data from CHs of one layer to those of the upper layers, the coordinates of the CHs initiating RF signal transmission is consequently known to the BS, which are also the CHs nearer to the target. If the BS receives the location data from N CHs, then the approximated coordinate (x_{est}, y_{est}, z_{est}) of the target is given by

$$x_{est} = \frac{1}{N}\sum_{i=1}^{N} x_i \tag{1}$$

$$y_{est} = \frac{1}{N}\sum_{i=1}^{N} y_i \tag{2}$$

$$z_{est} = \frac{1}{N}\sum_{i=1}^{N} z_i \tag{3}$$

where (x_i, y_i, z_i) is the coordinate of the ith active CH in 3D.

B. Architecture A_2

Architecture A_2 utilizes the same topology of A_2. However, the location approximation principle in A_2 is significantly different than that of in A_1. Architecture A_2 utilizes both the location information of the active CHs (from the CHs nearest to the target) and additionally the power of RF signal a CH received from the SNs. First, similar to A_1, an approximate location (x_{int}, y_{int}, z_{int}) of the target is calculated using (1)-(3). After that, the primarily approximated position of intruder is fine tuned to acquire a new coordinate (x_{est}, y_{est}, z_{est}) by utilizing the information of the received RF power at CHs from the SNs. The equations for this fine tuning are as below

$$x_{est} = \frac{1}{N}\sum_{i=1}^{N} \frac{(P_{max} - P_i)x_{int} - (P_{int} - P_i)x_i}{P_{max} - P_{int}} \tag{4}$$

$$y_{est} = \frac{1}{N}\sum_{i=1}^{N} \frac{(P_{max} - P_i)y_{int} - (P_{int} - P_i)y_i}{P_{max} - P_{int}} \tag{5}$$

$$z_{est} = \frac{1}{N}\sum_{i=1}^{N} \frac{(P_{max} - P_i)z_{int} - (P_{int} - P_i)z_i}{P_{max} - P_{int}} \tag{6}$$

where P_i is the true value of the strength of the RF signal that was received by the ith CH. P_{max} and P_{int} are the strength of the received RF signal at i^{th} CH if the SN were situated at the location of the CH and (x_{int}, y_{int}, z_{int}) respectively. Each of the power values utilized in (4)-(6) are expressed in dBm. Eq. (4)-(6) basically make use of the fact that the received signal strength expressed in dBm diminishes linearly with travelled distance from the transmitter, i.e., the closer the receiver's position to the transmitter, the bigger will be the value of the received power (ignoring all kind of fading).

IV. Performance Metric

For assessing the performance of the proposed intruder localization architectures, performance metrics are defined below, which calcuate the error in location approximation in terms of distance and direction. For doing this, at first the reference point is shifted to the approximated location (x_{est}, y_{est}, z_{est}) of the intruding object as demonstrated in Fig. 3. After this, the original position of an intruding object is re-calculated in spherical coordinate denoted as (r, θ, φ) with respect to the new reference.

A. Error in Distance Estimation

If (x, y, z) is the true position of the intruding object which is our target of localization, then the absolute distance r between the original and the approximated location is hereby assumed as a measure of error. The localization inaccuracy can be given by

$$r = \sqrt{(x_{est} - x)^2 + (y_{est} - y)^2 + (z_{est} - z)^2} \tag{7}$$

Then the normalized mean square error (NMSE) in location approximation defined as the mean of r^2 normalized by the square of the minimum separation between two SNs can be written as

$$NMSE_r = \frac{\sum_{i=1}^{M} r_i^2}{M\left[\min\left(\Delta_x, \Delta_y, \Delta_z\right)\right]^2} \tag{8}$$

where M is the number of Monte-Carlo simulations.

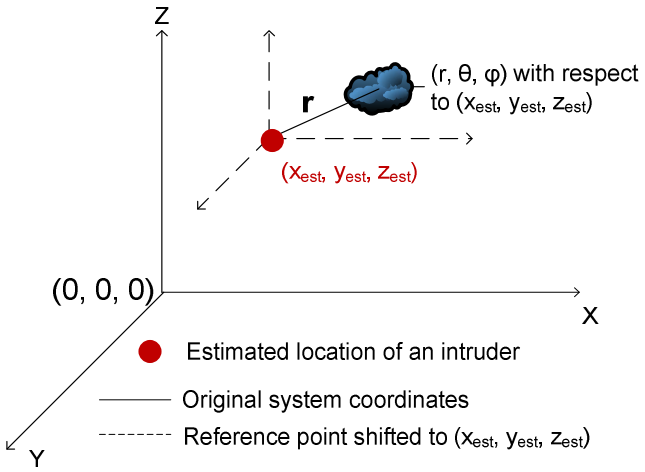

Fig. 3: Shifting of reference point for calculating the errors in localizations.

B. Error in Direction Estimation

The polar angle θ and the azimuthal angle φ of the actual location of an intruder with respect to the approximated location is considered as the measures of error in direction approximation. This can be given by

$$\theta = cos^{-1}\left(\frac{z - z_{est}}{r}\right), -90° \leq \theta \leq 90° \quad (9)$$

$$\varphi = tan^{-1}\left(\frac{y_{est} - y}{x_{est} - x}\right), -180° \leq \varphi \leq 180° \quad (10)$$

V. Simulations, Results and Discussions

A. Simulation Setup

Substantial simulations using MATLAB are implemented for assessing the performance of the proposed target localization topologies. The average results illustrated below are obtained by averaging the results over 1000 individualistic simulations. Without losing the generalized state, a 3D UWSN with measurement $D_x = D_y = D_z$ is assumed. An underwater RF propagation model with a given path-loss $20\times(\log_{10}e)\times 2\pi\times\sqrt{(\sigma \times f \times 10^{-7})}$ dB/m is used, where f is the transmission frequency in Hz and σ is the conductivity of water in S/m [5]. For fresh water, usual value is $\sigma = 0.01$ S/m, but this value is much bigger for seawater due to the increased salinity level dependent on the depth of water and temperature also [5]. Localization performance of the topologies is assessed considering salty water environment using $\sigma = 4$ S/m. Two different frequencies, $f_{SN} = 6$ kHz and $f_{CH} = 3$ kHz, and transmission power $P_{SN} = 100$ mW and $P_{CH} = 1$ W are used. If not otherwise specified, network size $D_x\times D_y\times D_z = 400\times400\times400$ m^3, $\Delta_x = \Delta_y = \Delta_z = 20$ m and the detection threshold $P_{th} = -60$ dBm are used for simulations.

B. Result Analysis

Cumulative distribution functions (CDFs) of the errors in distance and direction approximation are illustrated in Figs. 4(a)-4(c) from which, it is obvious that in spite of the use of same architecture, the better accuracy of A_2 compared to that of A_1 is directly attributed to the further fine-tuning of the initially approximated location using the information of received RF power. This additional feature however may increase the cost, computational complexity and energy consumption in CHs. On the other hand, both the polar and the azimuthal angle errors nearly follow uniform distributions over the same ranges respectively for both the architectures as seen in Figs. 4(b)-(c). The conclusion drawn from Fig. 4(a) is also corroborated by the NMSE plots in Fig. 5.

Performance of the architectures in terms of NMSE in the approximated distance normalized by 20×20 m^2 for three different detection thresholds is illustrated in Figs. 5(a)-(c). Insights identified by observing the figures: *At first*, we observe increasing trends of NMSE of both the architectures with the increase of the length of the sides of the 3D UWSNs. This increase in the length of the sides of the networks implies that keeping the relative positions as well as the number of SNs and CHs unchanged, D_x, D_y and D_z are increased in equal steps leading to increased distances among the nodes in the networks. Consequently, SNs are more distant from the target to be identified, higher distance between the SNs and the corresponding CHs which the SNs have to communicate with and CHs at a higher distance from the upper layer CH can communicate with those in the upper layer leading to decreased accuracy and increased NMSE. Besides, with the

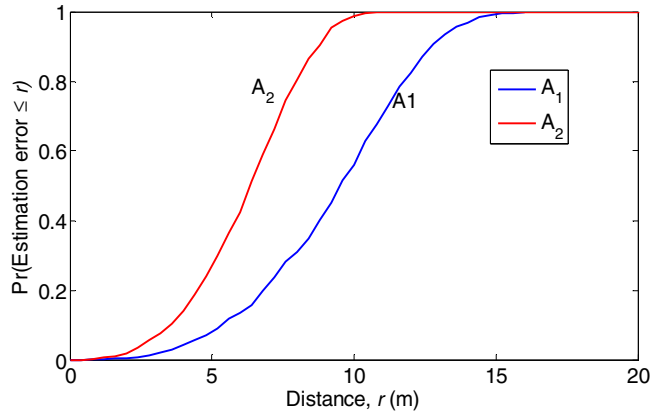

(a) Absolute distance r

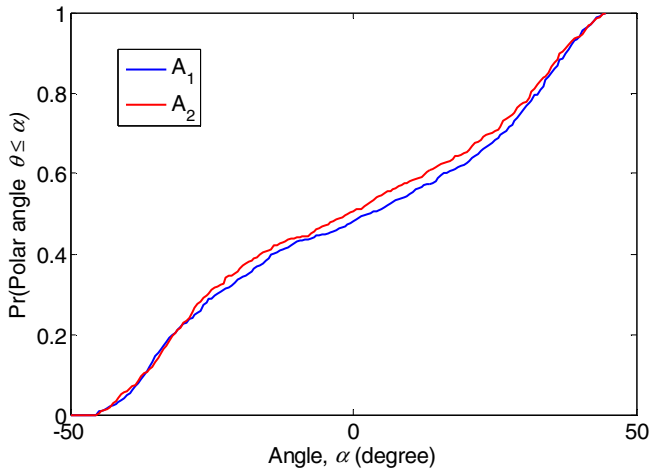

(b) Polar angle θ

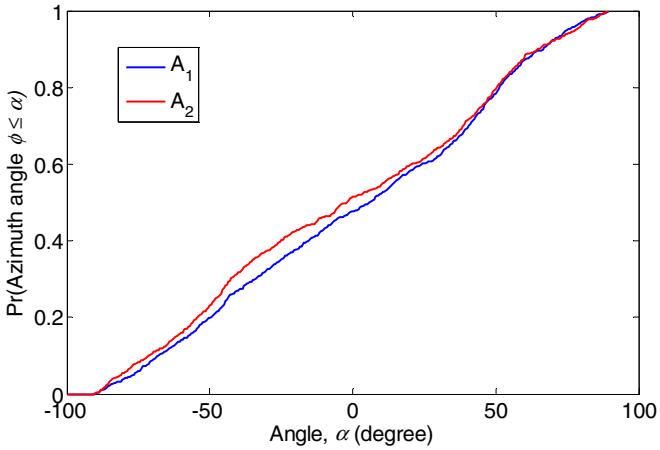

(c) Azimuthal angle φ

Fig. 4: CDF of estimation errors in distance and direction.

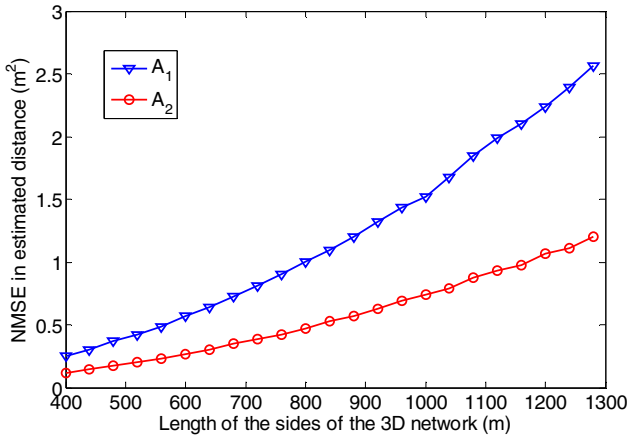

(a) P_{th} = -90 dBm

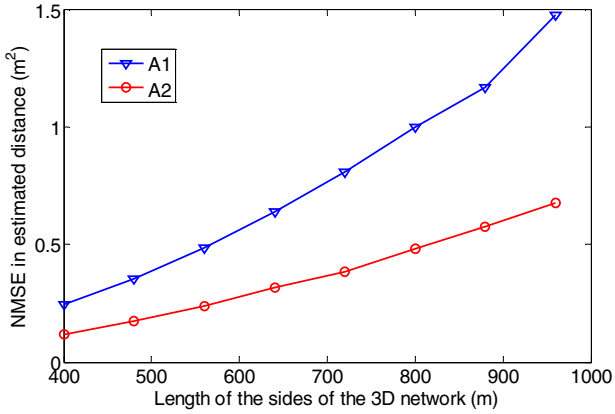

(b) P_{th} = -60 dBm

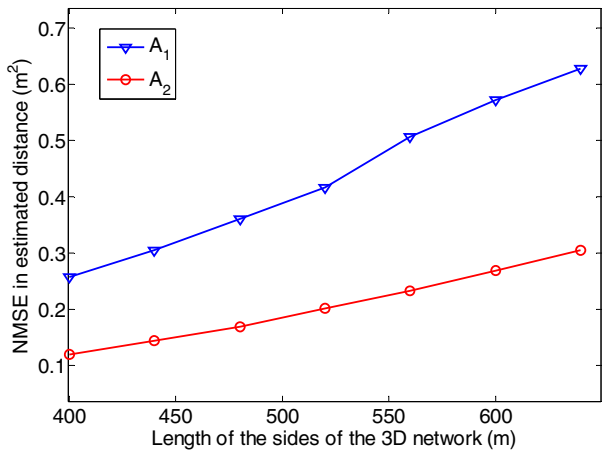

(c) P_{th} = -30 dBm

Fig. 5: NMSE in distance estimation with network length.

increase of detection threshold from -90 dBm to -30 dBm, the maximum network dimension is correspondingly reduced from 1280 m to 640 m. *Secondly*, from the better performance of A_2 compared to that of A_1, we can infer that the utilization of received power information for calculating the intruder location significantly improves the network's localization accuracy.

VI. Conclusion

The propositions of this paper include two different RF based 3D UWSNs architectures for the identification and localization of submerged intruders. The proposed architectures are both same in the topology but different in the method of estimating the location of intruding objects. Localization performance has been assessed in terms of NMSE of estimated distance as well as the polar and the azimuthal angles. Simulation results have illustrated a great effect of network's working rule on the localization performance. It has been recognized that the using of information of received RF signal strength in location approximation can essentially ameliorate the localization correctness. Furthermore, it has been identified that with the increase of the network dimension as well as the RF signal identification threshold, precision of the topologies in identifying intruding objects reduces significantly. Our future work will comprise more complicated network scenario including mobility, shadowing and multi-path fading. The localization capacity will be further upgraded by integrating further supplementary features, such as denoising filters, channel approximation mechanisms and angle-of-arrival (AoA) information.

References

[1] S. Al-Dharrab, M. Uysal and T. M. Duman, "Cooperative Underwater Acoustic Communications," *IEEE Communications Magazine*, vol. 51, no. 7, pp. 146-153, July 2013.

[2] R. Headrick and L. Freitag, "Growth of Underwater Communication Technology in the U.S. Navy," *IEEE Communications Magazine*, vol. 47, no. 1, pp. 80-82, Jan 2009.

[3] J. Partana, J. Kurosea, and B. N. Levinea, "A Survey of Practical Issues in Underwater Networks," *ACM Mobile Computing and Communications Review*, vol. 11, no. 4, pp. 23–33, 2007.

[4] S. Arnon and D. Kedar, "Non-Line-Of-Sight Underwater Optical Wireless Communication Network," *Journal of Optical Society America*, vol. 26, pp. 530–539, Mar 2009.

[5] X. Che, I. Wells, G. Dickers, P. Kear and X. Gong, "Re-evaluation of RF Electromagnetic Communication in Underwater Sensor Networks," *IEEE Communications Magazine*, vol. 48, no. 12, pp. 143-151, Dec 2010.

[6] Palmeiro, A., Martin, M., Crowther, I., Rhodes, M, "Underwater radio frequency communications," *IEEE OCEANS*, Santander, Spain, pp.1-8, June 2011.

[7] S. Zhou and P. Willett, "Submarine Location Estimation via a Network of Detection-only Sensors," *IEEE Transactions on Signal Processing*, vol. 55, no. 6, pp. 3104–3115, June 2007.

[8] Y. Huang, W. Liang, H.-B. Yu, and Y. Xiao, "Target Tracking Based on a Distributed Particle Filter," *Wireless Communications and Mobile Computing*, vol. 8, no. 8, pp. 1023–1033, Oct. 2008.

[9] G. Isbitiren and O. B. Akan, "Three-Dimensional Underwater Target Tracking with Acoustic Sensor Networks," *IEEE Transaction on Vehicular Technology*, vol. 60, no. 8, pp. 3897–3906, Oct. 2011.

[10] Z. Madadi, G. V. Anand and A. B. Premkumar, "3-D Source Localization in Shallow Ocean with Non-Gaussian Noise using a Linear Array of Acoustic Vector Sensors," *Proc. IEEE International Conference on Information Science, Signal*

Processing and their Applications (ISSPA), Montreal, QC, Canada, pp.1353-1358, July 2012.

[11] W. Cheng, A. Y. Teymorian, L. Ma, X. Cheng, X. Lu and Z. Lu, "Underwater Localization in Sparse 3D Acoustic Sensor Networks," *Proc. IEEE International Conference on Computer Communications (INFOCOM)*, Phoenix, AZ, USA, pp. 13-18, Apr 2008.

[12] Dalberg, Lauberts, Lennartsson, Levonen and Persson, "Underwater target tracking by means of acoustic and electromagnetic data fusion", *Proc. IEEE International Conference on Information Fusion*, Florence, Italy, pp.1-7, July 2006.

[13] N. M. A. Latiff, C. C. Tsimenidis and B. S. Sharif, "Energy-Aware Clustering for Wireless Sensor Networks using Particle Swarm Optimization," *Proc. IEEE International Symposium on Personal, Indoor and Mobile Radio Communications (PIMRC), pp.* 1-5, Sep 2007.

[14] M. Younis, M. Youssef, and K. Arisha, "Energy-Aware Management for Cluster-based Sensor Networks," *Computer Networks*, vol. 43, no. 5, pp. 649-668, Dec 2003.

Modelling of Highly Birefringent Dispersion Compensating Circular Photonic Crystal Fiber

Umme Ayesha Siddika[1,*], M. Shaifur Rahman[2]
[1,2]Department of Electrical and Electronic Engineering, Khulna University of Engineering & Technology, Khulna-9203
[*]E-mail: ash.kuet@gmail.com

Abstract— **This paper represents a highly birefringence circular-lattice Photonic Crystal Fiber (PCF) which compensates polarization and chromatic dispersion covering the E to U communication bands (1310–1640 nm). The finite element method (FEM) with perfectly matched layers is applied to investigate the guiding properties of the proposed PCF. From simulation, it is observed that the proposed PCF has dispersion coefficient about -220.9032 to -792.7265 (ps/nm-km) for E to U band. Particularly at the wavelength of 1550 nm the value of dispersion coefficient is found to be -678.1918 (ps/nm-km) and nonlinear coefficient is 56.41 ($W^{-1}Km^{-1}$). Besides that at that particular wavelength (1550 nm), the proposed PCF offers high birefringence which is about 0.0108 with the confinement loss of 0.0582 dB/km.**

Keywords— Chromatic dispersion, Photonic crystal fiber, Finite element method, Fiber birefringence, Confinement loss.

I. INTRODUCTION

In optical fiber communication systems, dispersion limits the maximum transmission distance and the bit rate [1]. Because the optical pulse get broadened due to dispersion while transmitting through the fiber. Thus, the dispersion must be compensated during the long distance optical data transmission system. Generally, a standard single-mode optical fiber have positive dispersion from 10 to 20 ps/(nm.km). To successfully compensate the positive dispersion of SMF over a long distance, short piece of a dispersion compensating fibers (DCFs) having large negative dispersion are widely used and commercially available [2]. Generally, conventional DCF fibers give a high negative dispersion only at a particular wavelength but not over wide band [3]. Photonic crystal fiber (PCF), known as 'holey' fiber, is a micro-structured fiber consisting of air hole arrays that run along the waveguide length of the fiber, which have unique properties that are not realized in standard optical fiber [4, 5].

The PCF is a single material optical fiber which contains microscopic air-holes in a silica background running down the length of the fiber. As a result the entire structure forms silica-air microstructure that causes lower refractive index in the cladding region and higher refractive index in the core [3]. In addition, the index-contrast between the core and cladding increases due to the silica-air microstructure in the cladding which helps to tailor the optical properties of the PCF. Modulating some parameters of the silica-air micro structure, it is possible to tune the dispersion properties of the PCF which helps to specially design the broadband dispersion compensating fiber (DCF).

Several designs of dispersion compensating PCFs (DCPCFs) have been proposed to achieve high negative dispersion as well as a suitable bandwidth for dispersion compensation in [6-16]. Silva et al. proposed a Ge-doped-core PCF using a genetic algorithm shows an average negative dispersion of −212 (ps/nm-km) [6]. But the main drawback of this structure is fabrication difficulties due to the doped core. To obtain a wide compensation bandwidth and a zero ultra-flattened dispersion coefficient, a honeycomb structure PCF has been proposed by Nghiem et al. [7]. A dual core PCF with a highly doped internal core reported by Huttunen et al. [8] which have dispersion coefficient was about −59,000 ps/(nm-km). But, these fibers exhibit more confinement loss and fabrication process more difficult. The PCFs mentioned above have not taken into account about the polarization effect and hence these are less attractive for polarization maintaining applications. To eliminate the effect of polarization mode dispersion, High birefringence property can be easily created by altering the air hole sizes near the core area [9,10] or by distorting the shape of the air holes [11,12]. Highly birefringent photonic crystal fibers are also suitable for various applications including optical device and sensing applications. Recently, Habib et al. proposed a hybrid octagonal structure with dispersion coefficient of −465.5 ps/(nm-km) and birefringence of the order 2.68 × 10−2 [13].But, Due to smaller air holes in the inner PCF, the design is more complex than the previously reported. More recently, Haque et al. proposed a hybrid circular structure with dispersion coefficient of −650 ps/(nm-km) and birefringence of the order 2.1 × 10−2[14]. In spite of attractive birefringence, this hybrid PCF is also difficult to fabricate due to its design complexity and higher no. of rings.

In this paper, we proposed a unique circular photonic crystal fiber with four air-hole rings over a widely used wavelength bands considering the polarization issue. The main advantages of the proposed structure are the design simplicity along with high negative dispersion, high birefringence and attractive nonlinear coefficient which are very crucial for high-bit rate transmission network, nonlinear optics and sensing applications. Simulation results show that it is possible to achieve large negative dispersion of about -220.90 to -792.72 ps/(nm-km) over E to U telecommunication band. At λ=1.55 μm, values of dispersion coefficient, nonlinear coefficient and birefringence are found to be -678.1918 ps/(nm-km), 56.41 (W-1km-1) and 0.0108 respectively.

978-1-4673-9257-0/15/$31.00 ©2015 IEEE

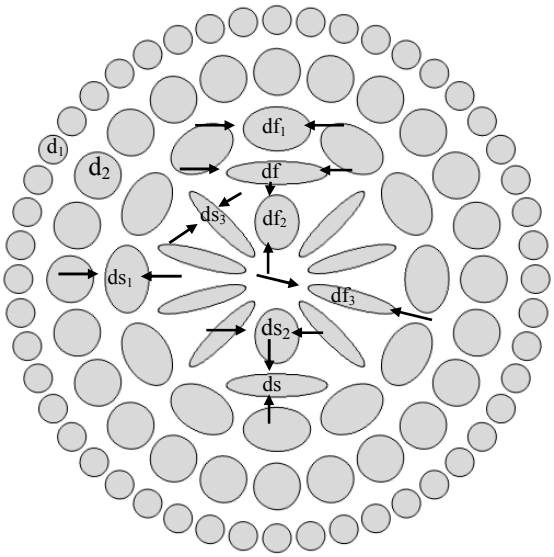

Figure 1. Air hole arrangement of the proposed DC-PCF

II. DESIGN MODEL

Fig.1 represents the air hole arrangement of proposed C-PCF. However, the construction of the CPCF for broadband dispersion compensation is mostly identical with C-PCF with these elliptical air holes which have been used to enhance the dispersion compensating capability. The proposed C-PCF contains only four air-hole rings and the material is taken to be silica which is simplest design respect to other design [6-18].

The 1st and 2nd elliptical air holes of the first ring with diameter in x direction is df and in y direction is ds which are rotated at angles 150and 450 respectively. To break symmetry of 1st ring 3rd elliptical air hole with diameter in x direction is df2 and in y direction is ds2 which is rotated 900 and just above it 4th elliptical air hole is taken which diameter in x direction is ds3 and in y direction is df3.Similarly, 5th, 6th, 7th, 8th, 11th and12th air holes of the 1st ring have diameter in x direction is df and in y direction is ds and these are rotated at angles 1350, 1650, 1950, 2250, 3150 and 3450 respectively where 9th elliptical air hole with diameter in x direction is df2 and in y direction is ds2 which is rotated 2700 and just above it 10th elliptical air hole is taken which diameter in x direction is ds3 and in y direction is df3.Diameter of second ring air holes are in x direction is ds1 and in y direction is df1 and rotated at an angle 300.The diameters of third and fourth air holes are d1 and d2 with rotation angles 150 and 7.50 respectively.

III. ANALYSIS OF MODEL AND OPTICAL CHARACTERISTICS OF PCF

The finite element method (FEM) is very suitable for handling complicated geometry structures of hollow core as well as solid Photonic Crystal Fiber. It is used to calculate chromatic dispersion, birefringence, confinement loss and effective area. The COMSOL 4.2 software is used as simulation tools.

A. Chromatic Dispersion

The performance of PCF directly effects by chromatic dispersion. Because, it affects pulse broadening, phase-matching conditions etc. It also affects to determine bandwidth and power requirements of device in which the fiber will be used. Nowadays, minimization of chromatic dispersion is one of the most challenging issues of optical fiber communication. The chromatic dispersion in ps/(nm-km) is easily calculated from the following equation[14]

$$D(\lambda) = -\frac{\lambda}{c}\frac{d^2\,\mathrm{Re}[n_{eff}]}{d\lambda^2}. \tag{1}$$

Where, $\mathrm{Re}[n_{eff}]$ is the real part of effective refractive index, λ is the wavelength, c is the velocity of light in vacuum.

B. Birefringence

In PCF, the birefringence properties are imperative for eliminating the effect of polarization mode dispersion (PMD) and in stabilizing the operation of optical devices, and can also be used in sensing applications. It can be achieved by creating asymmetric core. The birefringence is defined as a difference between effective refractive indices of two fundamental polarization modes and can be written as [14]

$$B = \left| n_x - n_y \right|. \tag{2}$$

Where, n_x and n_y are the mode indices of the two orthogonal polarization fundamental modes.

C. Confinement loss

Confinement loss is the light confinement ability within the core region. The confinement loss L_c in dB/km is then obtained from the imaginary part of $\lfloor n_{eff} \rfloor$as follows [15]:

$$L_c = \frac{\left(20\times10^6\right)}{\ln(10)} k_0\,\mathrm{Im}[n_{eff}]. \tag{3}$$

Where, $\mathrm{Im}[n_{eff}]$ represents the imaginary part of the wavelength dependent refractive index and $k_0 = 2\pi/\lambda$ is the wave number in the free space.

D. Effective Area

The effective area in μm^2 of the proposed PCF is obtained from [17] and is given by A_{eff} [14] ,

$$A_{eff} = \frac{(\iint |E|^2 dxdy)^2}{\iint |E|^4 dxdy}. \tag{4}$$

Where, E is electric field vector in the medium.

E. Nonlinear Coefficient

The nonlinear coefficient in $W^{-1}Km^{-1}$ can be obtained from the effective area [17] and is given by γ [14],

$$\gamma = \left(\frac{2\pi}{\lambda}\right)\left(\frac{n_2}{A_{eff}}\right) \quad (5)$$

IV. Simulation Result and Discussion

At operating wavelength of 1550 nm, Fig.2 represents the fundamental mode Optical Field distribution of designed C-PCF for both X and Y polarization. According to simulation, it is clearly seen that the optical field for X and Y polarization light is firmly confined into the center core region due to the relatively higher refractive index of the core as compared with the lower refractive index of the cladding region.

Fig.3. shows Chromatic dispersion at X-polarization and Y-polarization. As wavelength is increased, Chromatic dispersion coefficient increases monotonically and at 1550 nm wavelength for X and Y polarization the chromatic dispersion coefficient are found to be -678.1918 ps/(nm-km) and -607.7927 ps/(nm-km) respectively. The X-polarized mode is slightly higher in magnitude than the Y-polarized mode which represents fast axial mode. However, for optimum design parameters the designed fiber shows a very high negative dispersion coefficient of about -220.9032 to -792.7265 ps/(nm-km) over 1310 to 1640 nm bands which reduces the length of DCFs and higher cost.

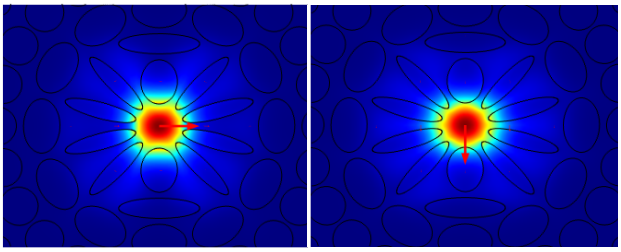

Figure 2. Optical Field distribution of fundamental mode for X and Y polarization at operating wavelength of 1550 nm.

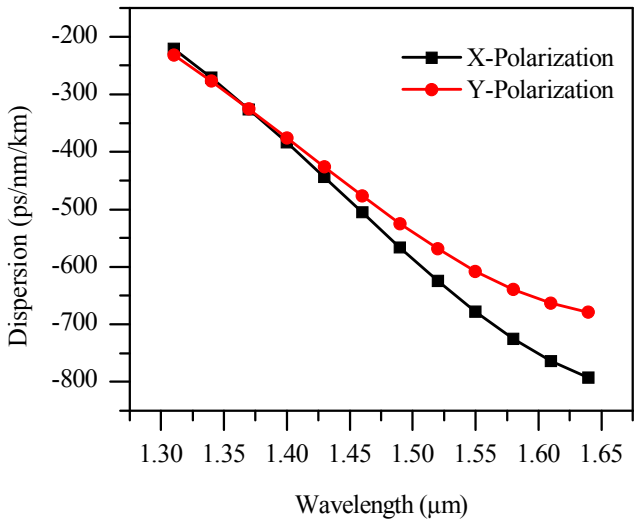

Figure 3. Chromatic dispersion properties of proposed PCF for optimum design parameters.

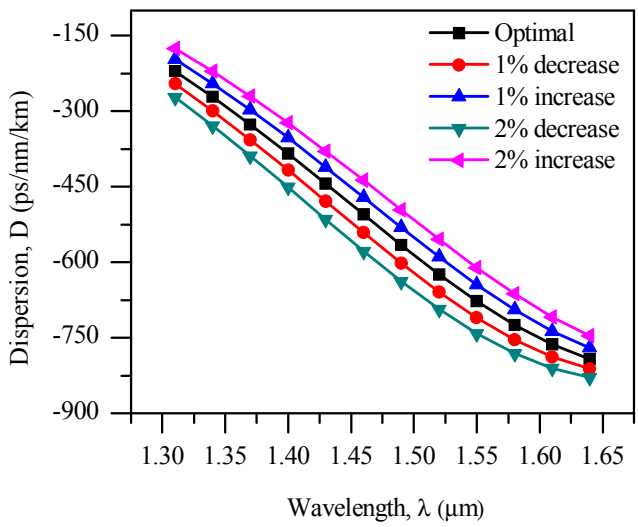

Figure 4. Chromatic dispersion properties of proposed PCF: optimum dispersion and effect of changing pitch.

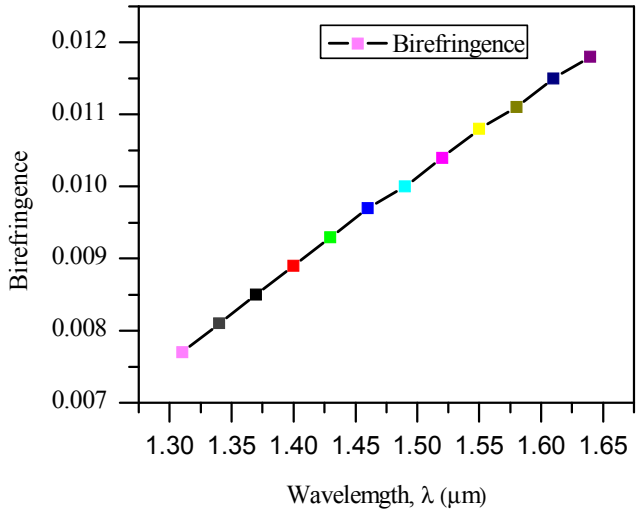

Figure 5. Birefringence properties of proposed PCF for optimum design parameters.

Fig.4 shows the effect of changing pitch on dispersion behavior whereas other parameters remain constant. For wavelength bands 1310-1640 nm, it is seen that the peak value of negative dispersion increases with the decrease of pitch due to greater index difference while the peak value decreases with the increase of pitch. From curve, it is observed that, there is an insignificant effect on dispersion behavior when pitch is varied as ±1% to ±2%.

Fig.5. shows wavelength dependent birefringence of the proposed PCF for optimum parameters. It shows a high birefringence with increase in operating wavelength and at 1550 nm wavelength, the birefringence is about 1.08×10^{-2}. Where the current conventional polarization mode fiber shows

a modal birefringence of about 5×10^{-4} which is 21.6 lower than the proposed PCF.

The effects of changing the pitch on birefringence are shown in Fig.6. Here, it is seen that the birefringence of the proposed PCF increases rapidly with decrease in pitch due to the high index difference between two orthogonal polarization axes while decreases with increase in pitch due to low index difference between the two modes. Simulation result shows that as the pitch varies from +1% to +2% birefringence decreases whereas the pitch varies from -1% to -2% birefringence increases.

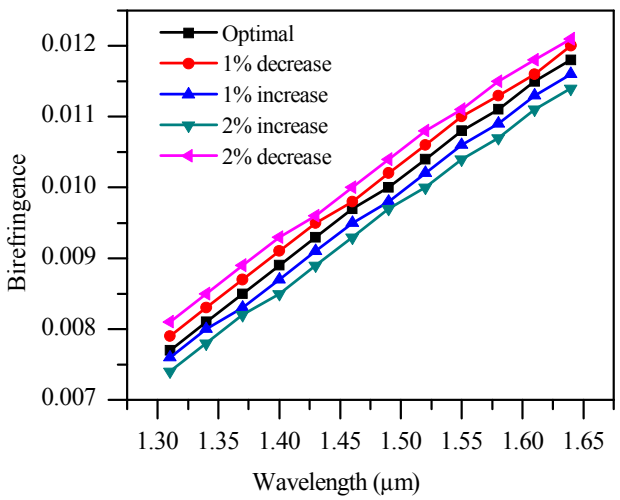

Figure 6. Birefringence of proposed PCF: optimum birefringence and effect of changing pitch

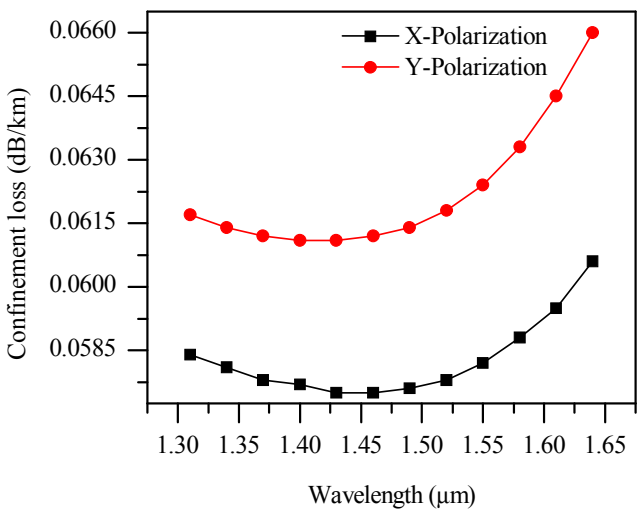

Figure 7. Confinement loss properties of proposed PCF for optimum design parameters.

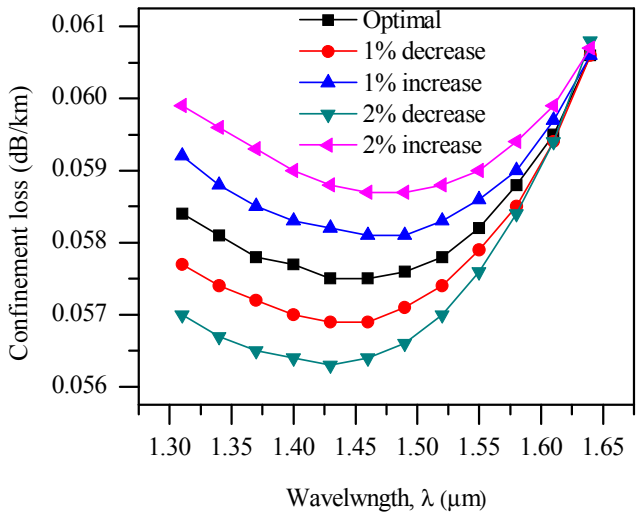

Figure 8. Confinement loss of proposed PCF: optimum confinement loss and effect of changing pitch .

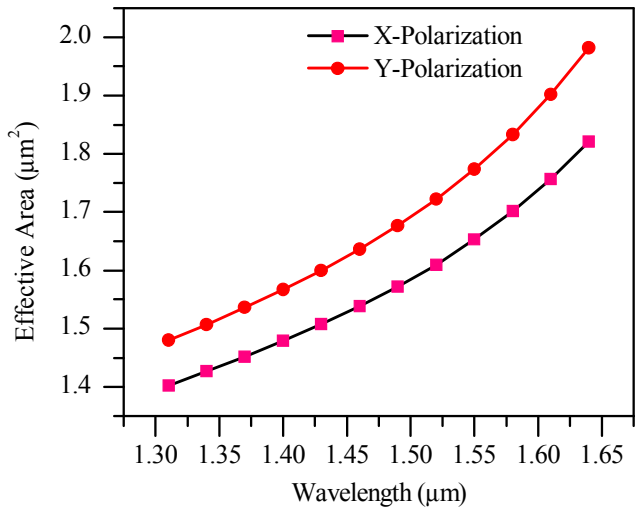

Figure 9. Effective Area of proposed PCF for optimum design parameters.

Fig.7. shows the confinement loss against wavelength for optimum design parameters. From this figure, it is observed that the confinement loss is about 0.0582 and 0.0624 for X-polarization and Y-polarization respectively. It is seen that confinement loss of Y-polarization is greater than X-polarization and increases with increase in wavelength but the value of confinement loss is in limit without causing any leakage.

The effects of changing the pitch on confinement loss are shown in Fig.8. Here, it is seen that the confinement loss of the proposed PCF increases rapidly with increase in pitch while decreases with increase in pitch.

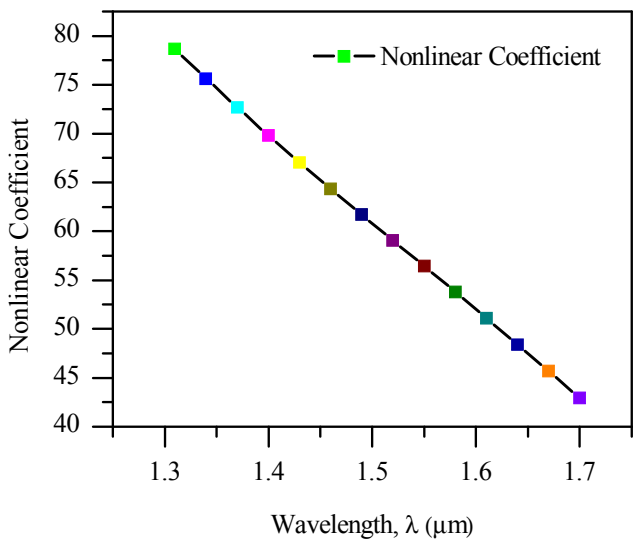

Figure 10. Nonlinear Coefficient of proposed PCF for optimum design parameters.

Simulation result shows that as the pitch varies from +1% to +2% confinement loss increases whereas the pitch varies from -1% to -2% confinement loss decreases.

Simulation result also shows that the effective area of the fiber increases with increase in wavelength as in Fig.9. At 1550 nm wavelength, the value is 1.7735 μm^2 . Due to small effective area, it is expected that the proposed PCF will be insensitive to bending and have low bending loss [15].

Fig. 10 shows nonlinear coefficient for optimum parameters. At 1550 nm, the nonlinear coefficient is found to be 56.41$W^{-1}km^{-1}$.This characteristic is suitable for dispersion compensation and effective in self-phase modulation for switching, pulse-forming, wavelength conversion applications and supercontinuum generation for frequency metrology [16].

"Table 1" shows comparison of the proposed PCF with the other existing design [14, 15]. It shows that proposed PCF is simple in design than others, because it contains only 4 air hole rings. Though, birefringence of proposed PCF is less, negative dispersion and nonlinear coefficient is higher than the other existing design [14,15].

CONCLUSION

A 4 rings Circular lattice PCF with elliptical and circular air holes has been investigated for its large negative dispersion properties as well as high birefringence and low confinement loss. It ensures large negative dispersion and high birefringence which are in the range of -220.9032 to -792.7265 (ps/nm-km) and 0.0077 to 0.0118 respectively at operating wavelengths 1310 nm to 1640 nm. It is expected that the proposed C-PCF will be applicable for broadband dispersion compensation in future optical fiber technology.

TABLE I. COMPARISON BETWEEN PROPOSED PCFS AND OTHER PCF AT 1.55 μm

PCFs	$D(\lambda)$ *ps/(nm.km)*	*Birefringence*	γ *($W^{-1}km^{-1}$)*	*No. of rings*
Ref.[13]	-491.5	3× 10-2	39.53	5
Ref.[14]	-650	2.10× 10-2	45.5	5
Proposed PCF	-678	1.08× 10-2	56.41	4

ACKNOWLEDGMENT

The authors would like to acknowledge the Information and Communication Technology (ICT) Division, Ministry of Posts, Telecommunication and IT, Government of the People's Republic of Bangladesh for their financial support.

REFERENCES

[1] K. Fukuchi, T. Kasamatsu, M. Morie, R. Ohhira, T. Ito, K. Sekiyap. Ogasawara, and T. Ono,"1092-Tb/s {273x40 Gb/s) triple-band/ultra-dense WDM optical-repeatered transmission experiment," in Proc.OFC, Anaheim, CA, Mar. 2001, pp. PD24- 1 -PD24-3.

[2] M. Samiul Habib∗, Redwan Ahmad, M. Selim Habib, S.M.A. Razzak," Design of single polarization single mode dispersion compensating photonic crystal fiber" Optik - Int. J. Light Electron Opt. vol.125, pp.4313-4318, Aug. 2014.

[3] J. Laegsgaard, S.E.Barkoulibori, K. Hougaard, J. Riished, T. T. Larsen, and T. Sorensen, "Dispersion properties of photonic crystal fibers-issues and opportunities," Mater. Res. Soc. Symp. Proc.,vol. 797, 2004.

[4] J. C. Knight, T.A. Birks, P. St. .J Russell, "All-silica single-mode optical fibre with photonic crystal cladding," Optics Letters, vol. 21, pp.1547-1549,1996.

[5] E. Yablonovitch, "Inhibited spontaneous emission in solid state physics and electronics," Phys. Rev. Lett., vol. 58, pp. 2059-2062, 1987.

[6] J. P. da Silva, D. S. Bezerra, V. F. R. Esquerre, I. E. Fonseca, and H. E. H. Figueroa, "Ge-doped defect-core micro-structured fiber design by genetic algorithm for residual dispersion compensation," IEEE Photon. Technol. Lett. 22, pp.1337–1339, 2010.

[7] Nghiem Xuan Tam, Nguyen Xuan Son, Pham Hong Thai Nguyen Hoang Hai , "New Proposal of Chromatic Dispersion Control in Honey Comb Photonic Crystal Fiber for Broadband Communication," IEEE 5th International Conference on Communications on Electronics(ICCE),July 2014, pp.34-39.

[8] A. Huttunen, P. Torma, Optimization of dual-core and microstructure fiber geometries for dispersion compensation and large mode area, Opt. Express vol.13,pp. 627–635,2005.

[9] K. Saitoh, M. Koshiba, Full-vectorial imaginary-distance beam propagation method based on a finite element scheme: application to photonic crystal fibers, IEEE J. Quant. Electron. vol.7 pp.927–933, 2002.

[10] M. A. Islam and M. S. Alam, "Design of a polarization maintaining equiangular spiral photonic crystal fiber for residual dispersion

compensation over E + S + C + L + U wavelength bands,'' IEEE Photon. Technol. Lett. vol.24, pp.930–932,2012.

[11] T. Matsui, K. Nakajima, I. Sankawa, Dispersion compensation over all the telecommunication bands with double-cladding photonic-crystal fiber, J. Light-wave Technol. vol.25 pp.757–762,2007.

[12] S. Haxha and H. Ademgil, ''Novel design of photonic crystal fibres with low confinement losses nearly zero ultra-flatted chromatic dispersion, negative chromatic dispersion and improved effective mode area,'' Optical Communications, vol. 281, no. 2, pp. 278–286, Jan. 2008.

[13] M. Samiul Habib, Redwan Ahmad, M. Selim Habib, and M. Imran Hasan, N. Ahmed, ''Residual dispersion compensation over theS+C+ L +U wavelength bands using highly birefringent octagonal photonic crystal fiber,'' APPLIED OPTICS Vol. 53, No. 14.pp.3057-3062, May 2014.

[14] M. Mejbaul Haquea, M. Shaifur Rahman, M. Selim Habib, M. Samiul Habib, ''A single mode hybrid cladding circular photonic crystal fiber dispersion compensation and sensing applications,'' Photonics and Nanostructures – Fundamentals and Applications Vol. 14, pp.63-70, April 2015.

[15] S. F. Kaijage, Y. Namihira, N. H. Hai, F. Begum, S. M. A. Razzak, T. Kinjo, K. Miayagi, and N. Zou, ''Broadband dispersion compensating octagonal photonic crystal fiber for optical communication applications,'' Japanese Journal of Applied Physics, vol.48, pp. 052401–052408, 2009.

[16] H. Ademgil, S. Haxha, F.A. Malek,''Highly nonlinear bendinginsensitive birefringent photonic crystal fibres,'' Eng. vol.2 pp.608–616, 2010.

[17] M. M. Haque, M. S. Rahman, M. Samiul Habib, M. Selim Habib, S. M. A. Razzak, ''A new circular photonic crystal fiber for effective dispersion compensation over E to L wavelength bands,'' Journal of Microwaves, Optoelectronics and Electromagnetic Applications, Vol. 12, No. 2, pp.281–291, Dec. 2013.

Design and Evaluation of a UWB Wearable Textile Antenna for Body Area Network

Kawshik Shikder*, Farhadur Arifin
Department of Electrical and Electronic Engineering (EEE)
American International University-Bangladesh
Dhaka, Bangladesh
*kawshik_pappu@yahoo.com

***Abstract*—This paper presents a novel Ultra Wide Band (UWB) wearable textile antenna for body area networks. The proposed antenna consists of a hexagonal radiating patch and a partial ground plane. The substrate of the proposed antenna is made of Dacron fabric with permittivity 3. Ultra wide bandwidth is achieved by optimizing the geometry, introducing a square notch in the partial ground plane and introducing novel slot pattern on the radiating patch of the antenna. This novel slot represents the "wireless antenna" icon. The dimension of the proposed antenna substrate is 40×34×1.7 mm^3 and the bandwidth 16.56 GHz starting from 2.6 GHz to 19.16 GHz for return loss less than -10 dB. The gain variation is from 2 dB to 6.35 dB and average total efficiency more than 83%. Maximum power of 17.39 mW may be set as input to the proposed antenna in order to guarantee compliance with the IEEE C95.1-1999 safety standard. The proposed antenna design details and simulated results are presented by Commercial electromagnetic simulation package CST Microwave Studio.**

Keywords—UWB; body area network; wearable textile antenna; patch antenna

I. INTRODUCTION

Wearable textile systems are very promising technology since their demands for navigation, tracking, portable communication, and public safety requirements are increasing rapidly. In recent years, the presence of wearable textile systems expressed the necessity for Wireless Body Area Network (WBAN) system to provide standalone outfit [1]. Antenna is the fundamental part of wearable textile system in WBAN. At present, textile antenna is one of the most impressive and cutting edge research areas of modern era. The textile antenna for wearable applications is actually the bond that integrates cloth into the communication system. These are made from textile materials and placed on body, into clothing or may be worn as a button antenna. Wearable textile antenna is mostly used microstrip patch antenna if textile fabric is used as substrate. However, the main limitation of the traditional microstrip patch antenna is limited bandwidth that restricts its applications. Due to this reason, Ultra Wide Band (UWB) technology is considered to be a favorable choice which provides wider bandwidth.

UWB is a radio technology, used for short-range communication. It occupies a bandwidth of at least 25% of the centre frequency or more than 1.5 GHz unlike the narrower frequency band of the conventional systems. UWB signal uses Orthogonal Frequency Division Multiplexing (OFDM) as the modulation technique to occupy the wide frequency band. The commercial use of frequency bands from 3.1 to 10.6 GHz for UWB systems was approved by the Federal Communications Commission (FCC) in 2002 [2]. UWB offers extremely low radiated power in low/medium data-rate applications based on narrow pulses, thus being very attractive for body worn battery operated devices in wearable computing.

Numerous papers have been published about the design, fabrication and applications of wearable antennas and systems. Previously reported works are based on single frequency band wearable antennas [3] and later dual frequency band wearable antennas [4]. In the recent researches, Wideband and UWB technology is one of the most fascinating choices for WBAN applications. Many of UWB antennas using rigid substrate material [5-6], large in size and small bandwidth [7-10][12-13] have been reported. However, it is quite difficult to obtain large bandwidth with compact size and a very low thickness in case of wearable antennas. In this paper, a novel and compact design of wearable textile antenna is proposed for WBAN applications by merging the UWB technology with wearable textile technology.

This paper is motivated from the above reported papers and presents a novel design of a wearable hexagonal UWB textile antenna. Novelty of this work is – the slotted area of hexagonal patch that represents the "wireless antenna" icon which is unique and also compact in size. The bandwidth of the proposed antenna operates in the wide range, achieving the UWB system requirements.

The outline of this paper is organized as follows. Section II represents a brief description of the wearable antennas. Design of the proposed wearable textile antenna and simulated results are illustrated in Section III & IV respectively. Finally, the conclusions of this research work are presented at the end of this paper in Section V.

II. WEARABLE ANTENNAS

Wearable textile antenna is usually consisted of three different layers which made of two types of material. A metallic conducting patch is on the top of a non-conducting dielectric substrate and a conducting ground plane is beneath the dielectric substrate.

978-1-4673-9257-0/15/$31.00 ©2015 IEEE

A. Non-conducting Material

The most important properties of textile antennas in wearable applications are flexibility to conform to the body, comfort to touch, and softness. Permittivity or Dielectric constant of the antenna substrates has a significant role in antenna designing. Different substrates having different dielectric constants affect the antenna performance in various ways. Textile substrate materials generally have a very low dielectric constant which reduces surface wave losses and improves antenna's bandwidth. Here, hypalon coated Dacron fabric textile material is used as the antenna substrate for dielectric constant is $\varepsilon_r = 3$ while the loss tangent is $\tan\delta = 0.025$. The properties of Dacron fabric include high tensile strength, high resistance to stretching, outstanding electrical property and durability.

B. Conducting Material

In order to build the communication system, an electrically conducting material is required for the radiating patches as well as for the ground plane. However, for the purposes of textile antenna designs, a conducting material needs to satisfy several requirements such as having a low and stable electrical resistance (1 ohm/square) in order to minimize losses, material must be homogeneous over the antenna area, and the variance of the resistance through the material should be small. Therefore, the conducting properties of various materials used in antenna fabrication and packaging play an important role in achieving the desired performance of antenna designs. Based on the above-mentioned facts, Perfect Electric Conductor (PEC) is used in this paper as the conducting materials for the radiating patch (front side) as well as for the ground plane (back side). A 50Ω transmission line is also made with this conducting material.

III. Antenna Design

The proposed antenna consists of a hexagonal patch with slotted area and fed by a microstrip line, and a partial ground plane. The structure of proposed antenna is shown in Fig. 1 (Front view), Fig. 2 (Cross-sectional view), Fig. 3 (Back view) and Fig. 4 (Phantom). Instead of resonance frequency or operating frequency, lower band edge frequency and entire bandwidth become the design considerations for UWB antenna. The lower band edge frequency (f_l) in GHz, has been calculated for UWB antenna according to (1) given below [11]:

$$\text{Lower band edge frequency, } f_l = \frac{c}{\lambda} = \frac{72}{(H + r + T)} \quad (1)$$

where, H is the height of the hexagonal patch in mm, r is the radius of the equivalent cylindrical monopole antenna in mm and T is the gap between ground plane and hexagonal patch in mm.

With reference to configurations in Fig. 1 with side length (L_p), the dimensions of H, r and D_p of the equivalent cylindrical monopole antenna are obtained (by equating their areas) as follows:

$$\text{Radius, } r = \frac{3L_p}{4\pi} \quad (2)$$

$$\text{Height, } H = \sqrt{3}L_p \quad (3)$$

$$\text{Diameter, } Dp = 2L_p \quad (4)$$

By selecting the value of L_p, the following parameters: r, H, D_p and f_l can be computed using (1-4). The dimensions of proposed antenna parameters are provided in Table I and computed parameters value of the proposed antenna are provided in Table II.

TABLE I. Dimensions of The Proposed Antenna Parameters

Parameters		Size (mm)
Substrate	Length	40
	Width	34
	Thickness	1.7
Ground	Length	16
	Width	34
	Thickness	0.5
Patch	Height (H)	20.551
	Side Length (L_p)	11.865
	Thickness	0.5
Feed Line	Length	18
	Width	4.6
	Thickness	0.5

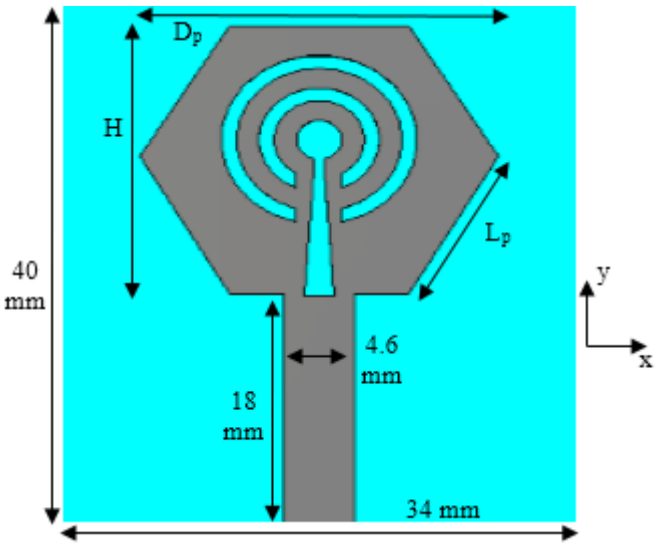

Fig. 1. Geometry of the Proposed Antenna (Front view)

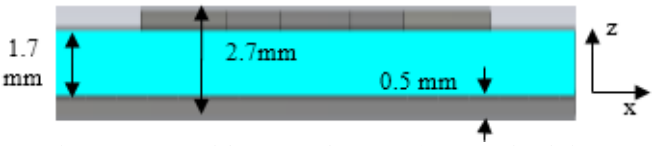

Fig. 2. Geometry of the Proposed Antenna (Cross-sectional view)

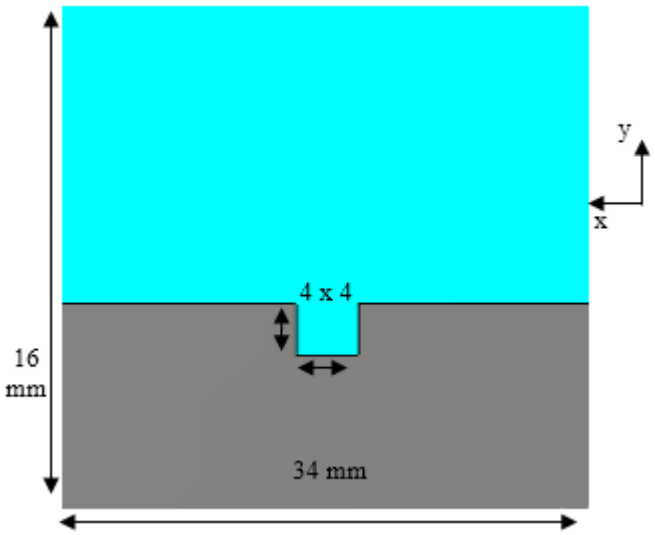

Fig. 3. Geometry of the Proposed Antenna (Back view)

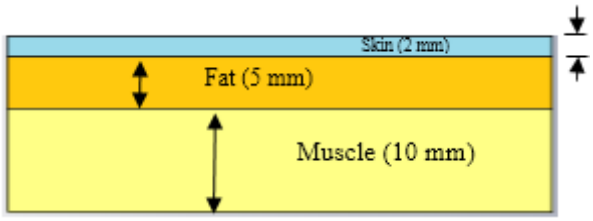

Fig. 4. Human Body Model (Phantom)

TABLE II. COMPUTED PARAMETERS VALUE FOR THE PROPOSED ANTENNA

L_p (mm)	r (mm)	H (mm)	T (mm)	D_p (mm)	f_l (GHz)
11.865	2.833	20.551	1.36	23.73	2.91

In order to enhance the bandwidth, one slotted circle along with a slotted triangle is introduced at the centre and two partial slotted rings are introduced at the top of the slotted triangle of hexagonal radiating patch.

TABLE III. OPTIMIZED VALUES FOR SLOTTED AREA OF PATCH

Parameters		Size (mm)
Radius of slotted circle at center, R_1		1.5
Triangle	Length	11
	Width (W_1, W_2)	0.5, 2
Slotted ring (Middle)	Inner radius, R_2	3
	Outer radius, R_3	4
Slotted ring (Outside)	Inner radius, R_4	5.5
	Outer radius, R_5	6.5
Distance between ring and circle, d		1.5

The overall slotted area of hexagonal patch represents the icon of "wireless antenna" shown in Fig. 1. Optimized values for slotted area of the patch are provided in Table III. Fig. 2 illustrates the cross-sectional view of the proposed antenna which indicates the thickness of different layers. A rectangular notch with size 4×4 mm^2 is also introduced on the top of partial ground plane (Fig. 3) to improve bandwidth of the presented antenna. The proposed antenna is mounted on the body phantom which model is shown in Fig. 4. The distance between antenna and phantom is 1 mm. Hence, it is explicit that the overall dimension of the antenna is quite small as compared to others. Commercial electromagnetic simulation package CST Microwave Studio is used to design the antenna.

IV. RESULTS AND DISCUSSION

This section analyzes the performances of the proposed UWB wearable textile antenna in terms of return loss (S_{11}), radiation patterns, antenna gain and efficiency over frequency, radiation effect on the body.

A. S_{11} Analysis of the Proposed Antenna

The simulated S_{11} plot over frequency of the proposed UWB wearable textile antenna is shown in Fig. 5.

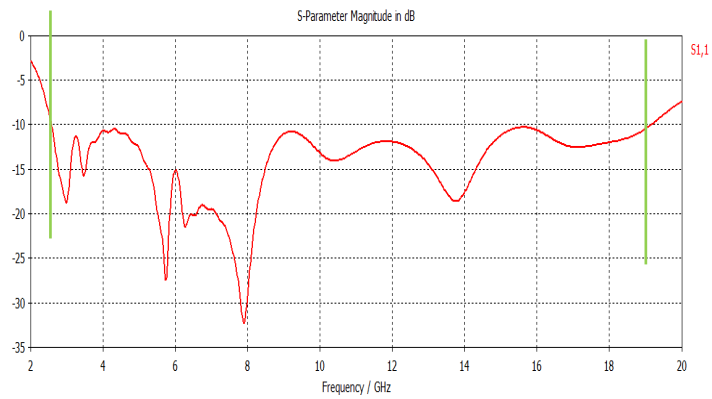

Fig. 5. Simulated S_{11} result

Fig. 5 indicates that the proposed antenna occupies a bandwidth of 16.56 GHz starting from 2.6 GHz to 19.16 GHz for S_{11} less than -10 dB. Lower edge frequency of simulated result is almost equal to the computed value. Hence, a very less number of incident waves reflect back to the source.

B. Radiation Patterns of the Proposed Antenna

The simulated azimuth and elevation radiation patterns at different frequencies of the proposed UWB wearable textile antenna are shown in Fig. 6 and Fig. 7 respectively.

The azimuth radiation patterns of the UWB wearable textile antenna at 3, 5.75, 7.9 and 13.75 GHz have been shown in Fig. 6. Theta (θ) has been set to both 0 and 90 degree for all values of phi (φ) to obtain azimuth radiation pattern. At 3 and 7.9 GHz, it exhibits almost omni-directional radiation pattern. Little deformation of radiation pattern is observed at 5.75 GHz. At 13.75 GHz, it has quite significant distortion from omni-directional pattern.

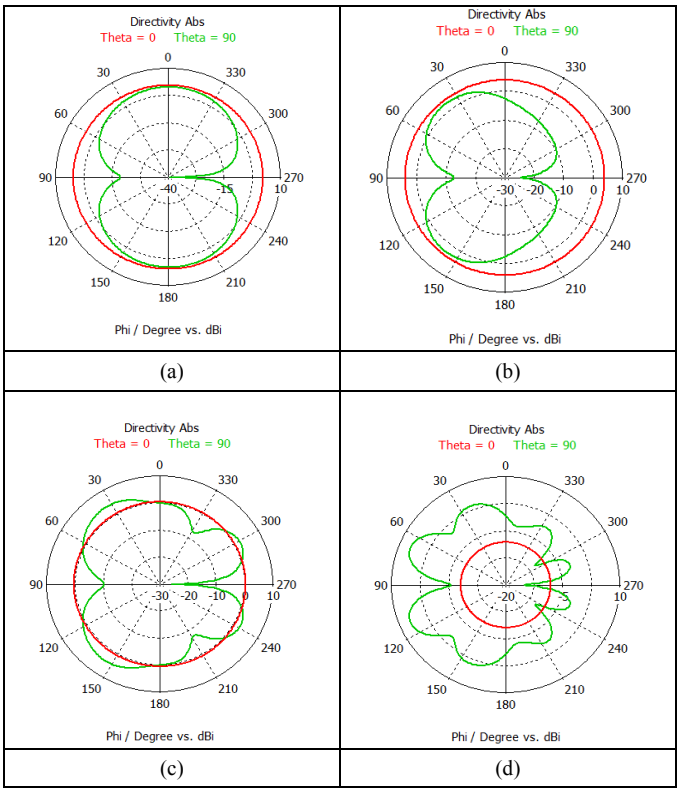

Fig. 6. Azimuth radiation patterns at (a) 3GHz, (b) 5.75 GHz, (c) 7.9 GHz and (d) 13.75 GHz

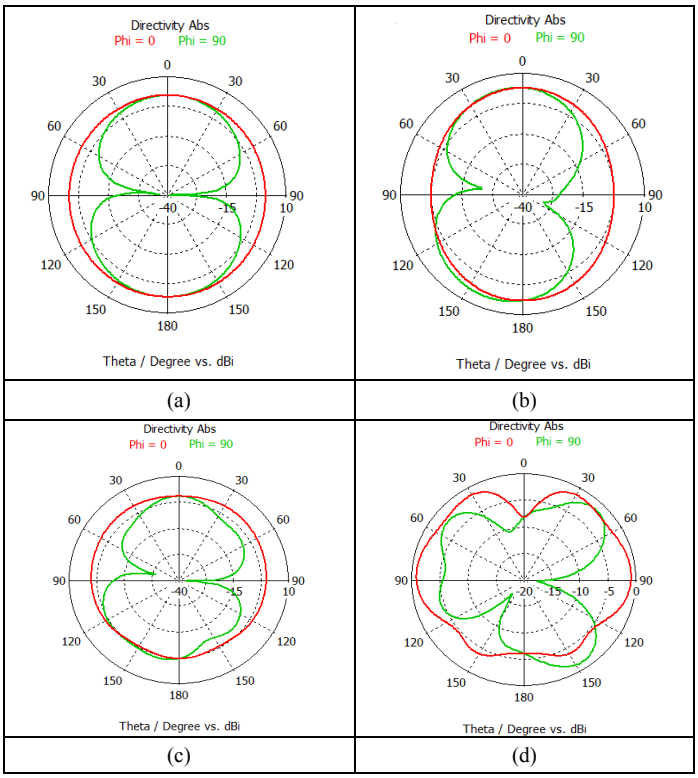

Fig. 7. Elevation radiation patterns at (a) 3GHz, (b) 5.75 GHz, (c) 7.9 GHz and (d) 13.75 GHz

Similarly for elevation pattern, phi (φ) has been set to both 0 and 90 degree for all values of theta (θ). The elevation radiation patterns of the UWB wearable textile antenna at 3, 5.75, 7.9 and 13.75 GHz have been shown in Fig. 7. At 3 and 7.9 GHz, it also exhibits almost omni-directional radiation pattern whereas little deformation of radiation pattern is observed at 5.75 GHz and quite significant distortion from omni-directional pattern observed at 13.75 GHz.

The analysis of Fig. 6 and Fig. 7 shows that the significant deviation of radiation patterns is found at higher frequencies. Furthermore, the data of radiation patterns (i.e.- main lobe magnitude, main lobe direction) of the UWB wearable textile antenna at 3, 5.75, 7.9 and 13.75 GHz have been provided in Table IV.

TABLE IV. DATA OF RADIATION PATTERNS AT DIFFERENT FREQUENCIES

Freq. [GHz]	**Main Lobe Magnitude [dBi] Direction [degree]**	**Theta (θ) [Degree]**		**Phi (φ) [Degree]**	
		0	**90**	**0**	**90**
3	Magnitude	2	1.2	2.8	2.8
	Direction	27	358	180	179
5.75	Magnitude	3.8	2.6	3.8	4.8
	Direction	86	142	180	163
7.9	Magnitude	0.2	4.1	1.2	0.2
	Direction	88	35	38	0
13.75	Magnitude	-8.2	7	-0.9	-1.5
	Direction	44	67	86	146

C. *Antenna Gain and Efficiency Results of the Proposed Antenna*

The variations of gain versus frequency and total efficiency versus frequency of the wearable textile UWB antenna designs are demonstrated in Fig. 8.

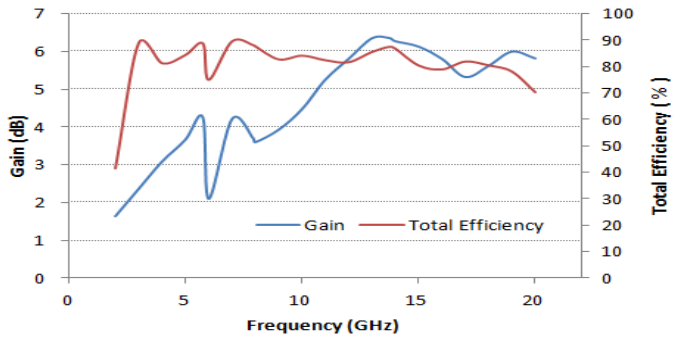

Fig. 8. Simulated Gain and Total Efficiency vs. Frequency

The highest gain and maximum total efficiency is achieved about 6.35 dB at 13.75 GHz and 90% at 7 GHz respectively

whereas the lowest gain and minimum total efficiency achieved almost 2 dB at 6 GHz and 75% at 6 GHz in the entire frequency range 2.6 ~ 19.16 GHz. From Fig. 8, the gain of the antenna varies significantly with changing frequencies while the efficiency varies slightly though it doesn't affect the overall performance. However, the gain variation is from 2 dB to 6.35 dB and average total efficiency more than 83%.

D. Specific Absorption Rate (SAR)

The SAR is a parameter to measure the power deposition in a human body when it is exposed to an electromagnetic field. For a net input power of 0.2 W at frequency 7.9 GHz incident to the antenna, the maximum 1 g averaged (1 g avg.) SAR value is found to be equal to 18.4 W/Kg. Therefore, in order to guarantee conformance with the IEEE C95.1-1999 (1 g avg. SAR ≤ 1.6 W/kg [14]) safety standard, the maximum allowed net input power has to be limited to 17.39 mW.

E. Comparison of the Proposed Antenna with Reported UWB Antennas

Table V shows the comparison of the proposed wearable UWB textile antenna with reported UWB antennas in terms of dimensions and occupied bandwidth.

TABLE V. COMPARISON WITH REPORTED UWB ANTENNAS

Ref. no.	Dimensions	Bandwidth
Proposed Antenna	34 x 40 mm^2	16.56 GHz (2.6–19.16GHz)
Ref. [7]	120 x 130 mm^2	3 GHz (1-4 GHz)
Ref. [8]	30 x 30 mm^2	10.4 GHz (3.6–14 GHz)
Ref. [10]	25 x 10 mm^2	8.2 GHz (3–11.2 GHz)
Ref. [12]	32 x 52 mm^2	10.04 GHz (3.11–13.15 GHz)
Ref. [13]	35 x 35 mm^2	9 GHz (2.8–11.8 GHz)

Comparison shown in Table V reveals the suitability for UWB applications as comparing with reference antennas. The overall performance of the proposed "wireless antenna" icon slotted hexagonal antenna on Dacron fabric material indicates that the drawbacks of reported UWB antennas have improved. Thus, the proposed antenna suits well to demonstrate the UWB characteristics.

V. CONCLUSION

In this paper, a novel UWB wearable textile antenna for body area network is presented. A novel slot pattern on hexagonal radiating patch is introduced that represents "wireless antenna" icon. A square notch in the partial ground plane is also introduced in this design. The proper selection of dimensions, square notch on the partial ground plane and positions of novel slot on the radiating patch strongly affects the antenna to achieve ultra-wide bandwidth. The proposed antenna design provides 16.56 GHz bandwidth ranges from 2.6 to 19.16 GHz with compact size on flexible substrate material. S_{11} characteristics illustrates that it has good impedance matching between antenna and transmission line with all over its occupied bandwidth. The antenna exhibits almost omni-directional radiation pattern but it has quite significant distortion from omni-directional pattern at higher frequencies. The gain of the antenna varies significantly with changing frequencies while the total efficiency varies slightly though it doesn't affect the performance. However, the gain variation of the antenna is from 2 to 6.35 dB and average total efficiency more than 83%. The IEEE C95.1-1999 standard is found to limit the aximum allowable net input power to 17.39 mW. Thereby, conclusion can be drawn that overall performance of the proposed antenna indicates that it is suitable candidate for UWB wearable textile applications. Reducing the size as well as increasing the bandwidth could be focus towards the further improvement of this design.

REFERENCES

[1] T. Zasowski, F. Althaus, M. Stäger, A. Wittneben, and G. Tröster, "UWB for noninvasive wireless body area networks: Channel measurements and results," presented at the IEEE Ultra Wideband Syst. Technol. Conf. (UWBST 2003), Reston, VA, Nov. 2003.

[2] First Report and Order, "Revision of part 15 of the commission's rule regarding ultra-wideband transmission system FCC 02-48", Federal Communications Commission, 2002.

[3] G. A. Conway and William G. Scanlon, "Antennas for over-body-surface communication at 2.45GHz," IEEE Transactions on Antennas and Propagation, vol. 57, no. 4, pp. 844-855, April 2009.

[4] S. Zhu and R. J. Langley, "Dual-Band Wearable Textile Antennas on An EBG Substrate," IEEE Transactions on Antennas and Propagation, Vol. 57, No.4, Apr 2009.

[5] Mai A. R. Osman, "The Investigation of Flannel Fabric Layers", 2010 International Symposium on Antennas and Propagations, Macao, China, 23-26 November 2010.

[6] Y. Chen, S. Yang, S. He, and Z.-P. Nie, "Design and analysis of wideband planar monopole antennas using the multilevel fast multipole algorithm," Progress In Electromagnetics Research B, Vol. 15, 95-112, 2009.

[7] Shuvashis Dey, Nandita Saha and Subrata Biswas. "Design and performance analysis of UWB circular disc monopole textile antenna and bending consequences." The 5th European Conference on Antenna and Propagation, 2011, April 2011, Rome, Italy.

[8] Mahmud MS, Jabri FJJ, Mahjabeen B. "Compact UWB Wearable antenna on leather material for wireless applications," IEEE Antennas and Propagation Society International Symposium (APSURSI). Orlando, FL; July 2013.

[9] M. Klemm and G. Troester, "Textile UWB antennas for wireless body area networks," IEEE Trans. Antennas Propag., Vol. 54, no. 11, pp. 3192-3197, Nov. 2006.

[10] Chahat N., "Design and Characterization of an UWB Wearable Antenna", 2010 Loughborough Antennas and Propagation Conference (LAPC), 2010, pp. 461-464.

[11] Ray, K. P., Tiwary, S. "Ultra Wide Band Printed Hexagonal Monopole Antennas", IET Microwaves, Antennas and Propagation, 2010, vol. 4, no. 4, p. 437-445.

[12] Mondal T, Das S. "UWB printed hexagonal monopole antennas with WLAN band rejection," IEEE Antenna Week (IAW). Kolkata, India; 2011.

[13] Lodi, G. A., R. I. Zafar, and M. Bilal. "A novel goblet shaped patch antenna for ultra wide band applications." *Communication Technology (ICCT), 2010 12th IEEE International Conference on*. IEEE, 2010.

[14] "IEEE standard for safety levels with respect to human exposure to radiofrequency electromagnetic fields, 3 kHz to 300 GHz," IEEE Standard C95.1 (1999).

Effective Modeling of Microstrip Patch Antenna with Circular EBG Structure

Md. Anwarul Quader, Minar Ashiq Tishan, Md. Masud Rana, and Reefat Inum
Department of Electrical and Electronic Engineering
Rajshahi University of Engineering and Technology
E-mail: akshuvo10@gmail.com, tishan150@gmail.com, md.masud.rana@ruet.ac.bd

***Abstract*—In this paper we have presented a rectangular microstrip patch antenna with circular Electromagnetic Band Gap (EBG) structure. The operating frequency of the patch antenna along with EBG structure is 7.3 GHz. All the simulation is done by using Computer Simulation Technology Microwave Studio (CST-MWS). In comparsion with the rectangular EBG structure, improvement has been achieved in the overall antenna return loss by 10.22% bandwidth by 8.89% and gain by 16.84%.**

Keywords— bandwidth; EBG; gain; patch antenna; return loss

I. Introduction

In recent years the microstrip patch antennas have made great progress as they offer more advantages and better prospects compared to other antennas. For example they are lighter in weight, lower in volume, lower in profile and easier to fabricate [1]. However, the main drawbacks of microstrip patch antennas are low bandwidth, low efficiency and relatively large size [2]. In case of the design of a microstrip patch antenna the most important prospect is to increase the inherent narrow bandwidth of antenna and to miniaturize the patch antenna size. The bandwidth of the antenna can be improved by increasing the substrate thickness [3]. Again, in order to minimize the other drawbacks, the substrate, ground plane and the patch of the microstrip patch antennas can be incorporated with different materials and structures. For example DGS [4], two layer Substrate [5] and metamaterials among which using metamaterials is found to be the most suitable approach [6].

Metamaterials are basically artificially engineered materials which exhibit electromagnetic properties that are not found in nature (e.g. negative refractive index and both negative permittivity and negative permeability). In 1967 Veselago discovered the concept of metamaterials [7]. He hypothesized an unknown material that possesses a negative permeability and permittivity in the same frequency range and it shows the abnormal electromagnetic properties when the uniform plane-wave propagation was studied [7]-[9]. As a result, the left-handed material (LHM) has a reverse basic feature of light, such as negative refractive index (NRI) [8]-[9]. Surprisingly, the idea got only little attention until the year 2000 when smith further studied the LHM and realized this material was a periodically-arranged conducting concrete and it shows extraordinary properties [9].

The EBG structures can be categorized as a special type of metamaterial due to their unique band gap features. This unique property has been applied to design antenna systems with better gain and efficiency, lower side-lobes and back-lobe levels by suppressing surface wave modes [2], [10]. The effect of using EBG structure is found to be the reduction of the patch resonant length and the bandwidth as a result of stronger capacitive coupling [2].

Paper [11] proposes a rectangular microstrip patch antenna along with metamaterial structure at a height of 3.2mm from the ground plane, which consists of a Split Ring Resonator (SRR). The paper focuses on increasing the bandwidth of low profile microstrip patch antenna by Double-Negative properties. The aforementioned design has increased the bandwidth by 300MHz.

Similarly paper [12] introduce a bandwidth enhancement of a narrow band rectangular microstrip antenna on square shape (EBG) patch structure. The measured results show better return loss and good impedance matching which resulted in an increase of bandwidth to more than 39.63% after the EBG structure was introduced. Both of these papers, [11] and [12], show improvement in antenna bandwidth. Considering all these articles, the novelty of our work is that we have proposed a more effective EBG structure for the patch antenna which is capable of increasing the antenna bandwidth, return loss as well as the gain of the patch antenna.

II. Design Specification

A. Patch Antenna Design

The Patch Dimension has been calculated using the following equation.

Step-1: Patch width

$$w = \frac{v_0}{2f_r}\sqrt{\frac{2}{\varepsilon_r+1}} \quad (1)$$

Where

978-1-4673-9257-0/15/$31.00 ©2015 IEEE

v_0 = The velocity of light.

ε_r = Dielectric constant of substrate.

Step-2: Effective Dielectric constant of the rectangular microstrip patch antenna.

$$\varepsilon_{eff} = \frac{\varepsilon_r+1}{2} + \frac{\varepsilon_r-1}{2}\left(\frac{1}{\sqrt{1+\frac{12h}{w}}}\right) \quad (2)$$

Step-3: Patch Length

$$L = L_{eff} - 2\Delta L \quad (3)$$

$$L_{eff} = \frac{c}{2f_r\sqrt{\varepsilon_{eff}}} \quad (4)$$

Calculation of Length Extension

$$\Delta L = 0.412h\frac{(\varepsilon_{eff}+0.3)(\frac{w}{h}+0.264)}{(\varepsilon_{eff}-0.258)(\frac{w}{h}+0.8)} \quad (5)$$

Step-4: Inset Feed

$$50 = R_{in}\,(\cos(\frac{\pi}{L}y_0))^2 \quad (6)$$

R_{in}=The input impendence at the leading radiating edge of the patch. While 50 (Ω) is the desired impendence.

Table I

Rectangular Microstrip Patch Antenna Specifications

Parameters Name		Dimensions without EBG (mm)	Optimized Dimension With Circular EBG Shape (mm)
Patch Width	W	14.53	14.53
Patch Length	L	11.53	8.95
Inset Feed	y_0	3.125	3.41
Inset Gap	g	1.901	0.38
Feed Length	L_f	13.202	11.895
Feed Width	W_f	1.901	1.9010
Substrate Width	W_S	31.02	31.0170
Substrate Length	L_S	31.68	25.92
Substrate Thickness	h	0.75	1.03
Resonant Frequency f_c		7.3 GHz	

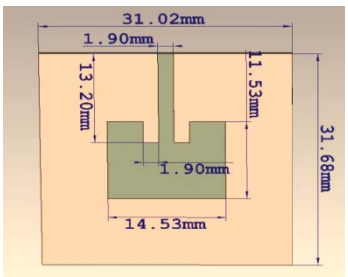

Fig. 1: Patch antenna without EBG.

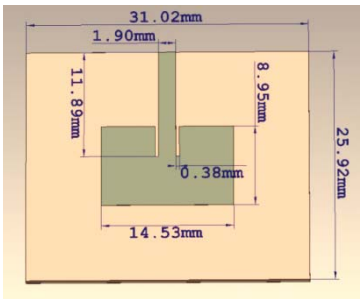

Fig. 2: Patch antenna with EBG

B. EBG Structure Design

Some equations have been adopted with a view to designing the EBG structure. The following equations are as follows for the square EBG structure,

$$L = 0.10\lambda \quad (7)$$

$$D = 0.02\lambda \quad (8)$$

and for the circular shape the radius of the circle is given by,

$$r = 0.10\lambda \quad (9)$$

Table II

DIMENSION OF EBG STRUCTURE

Parameters	Values (mm)
L	4.88
D	2.80
Radius r	2.44

The geometry of EBG structures (both rectangular and circular shapes with proper dimension) is shown in the following figure 3. Rogers R03003 has been chosen as antenna substrate due to flexibility for high frequency application compared to FR4 substrate.

Table III

ROGERS RO3003 SUBSTRATES CHARACTERISTICS

Parameters	Values
Permittivity	3
Permeability	1

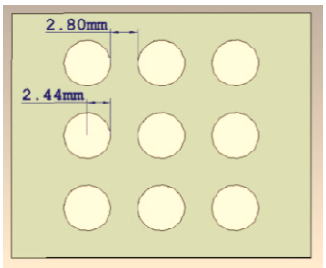

(a)

978-1-4673-9257-0/15/$31.00 ©2015 IEEE

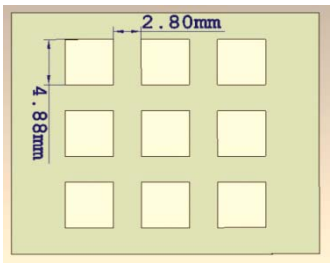

(b)

Fig. 3: (a) Circular EBG structure (b) Rectangular EBG structure.

Nicholson-Ross-Weir (NRW) technique is used as a conversion approach. Both permeability and permittivity is obtained from S-parameter using this approach [13].

III. Simulation Results

Antenna design and simulation are based on CST-MWS 2015 using frequency domain solver. From the simulation the results associated with Bandwidth, Return loss and Gain are discussed in details.

A. Return Loss and Bandwidth

Fig-4(a) shows the return loss plot of patch antenna without EBG and with rectangular EBG. From the following figure we can see that the return loss S_{11} of antenna without EBG is -17.24 dB and the return loss S_{11} of the rectangular EBG patch antenna is -47.598dB. According to fig-4(b) when we have introduced the circular shape of EBG on the ground plane of the antenna the return loss S_{11} has improved from -47.598 dB to -52.519dB.

In case of bandwidth, patch antenna without the EBG structure provides 154.27MHz, with rectangular EBG structure provides 305.48MHz, and with circular EBG structure provides 332.64 MHz.

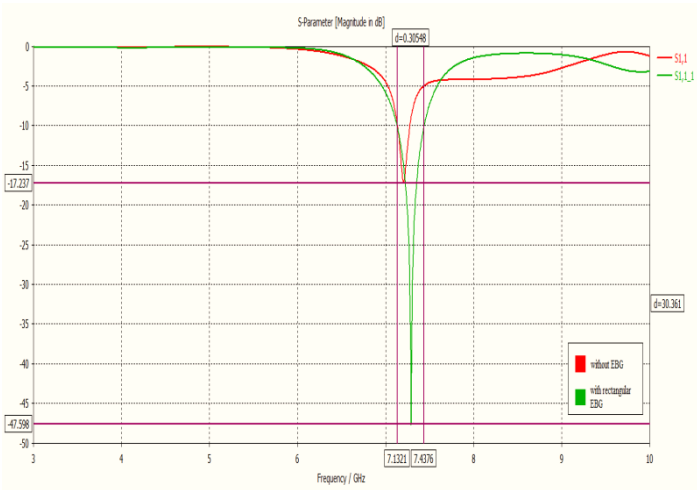

(a)

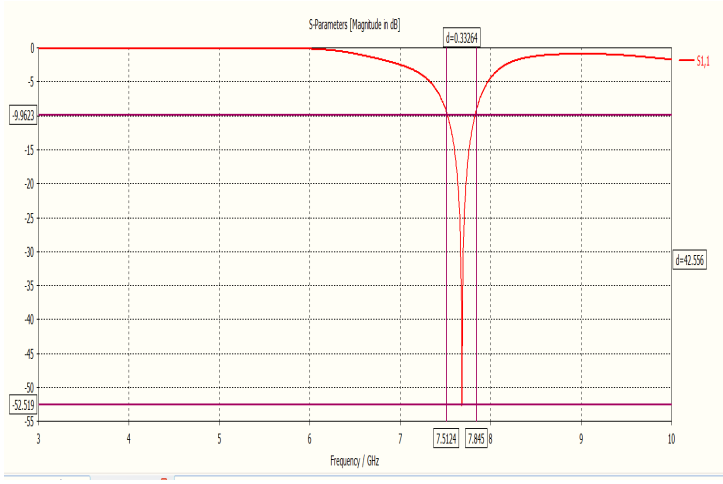

(b)

Fig. 4: (a) Return loss plot of the antenna without EBG and with rectangular EBG. (b) Return loss plot of microstrip patch antenna with Circular EBG structure.

B. Gain

Figure-5 provides 3-D plot of antenna gain for both rectangular and circular EBG structures. Normally the gain of the patch antenna without EBG structure is $7.92dB$. Patch antenna with rectangular EBG provides gain 5.94 dB . For circular EBG the gain improves from 5.94 dB to 6.94 dB.

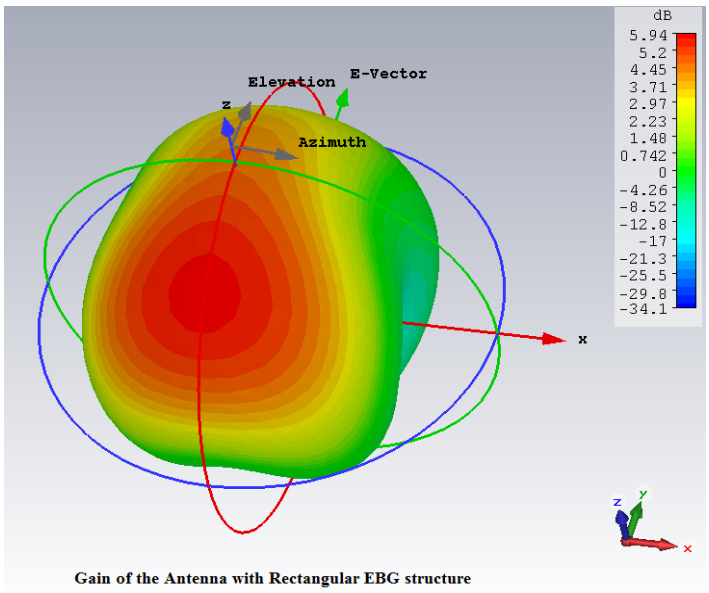

(a)

978-1-4673-9257-0/15/$31.00 ©2015 IEEE

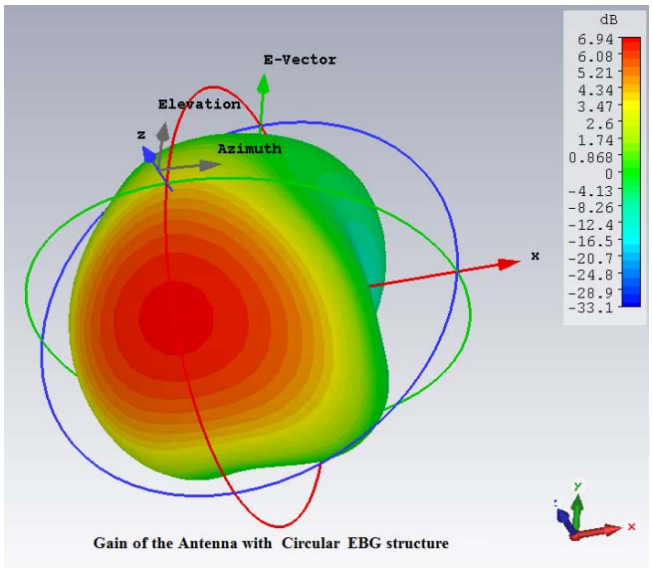

(b)

Fig. 5 (a) 3-D plot of antenna gain in dB for rectangular EBG structure (b) 3-D plot of antenna gain in dB for circular EBG structure.

Table IV
Comparison table between the simulation results

	Patch antenna without EBG	Patch antenna with Rectangular EBG	Patch antenna with Circular EBG	Improvement with respect to rectangular EBG (%)
Return loss	-17.24	-47.647	-52.519	10.22
Bandw -idth	154.27	305.49	332.64	8.89
Gain	7.92	5.94	6.94	16.84

This table represents the comparison between the simulation results in terms of Return loss, Bandwidth and Gain. It is seen that patch antenna with Circular EBG structure produced improved results.

IV. Conclusion

We have simulated the patch antenna with rectangular and circular EBG structures and after the comparison of the simulated results we have found that the EBG structure on the antenna ground plane with the circular shape provides improved results than rectangular EBG structure.

V. Future Work

Though from the simulation it is seen that the antenna bandwidth, return loss and gain have improved significantly with respect to rectangular shape of EBG but in comparison to patch antenna without EBG the gain is comparatively small. Different types of shape can be tried to improve the antenna performance

References

[1] Indrasen Sing, and Dr V. S. Tripathi, "Micro strip Patch Antenna and its Applications: a Survey," *Int. J. Comp. Tech. Appl.,* vol. 2, no. 5, pp. 1595-1599, 2011.

[2] Jing Liang, and H. Y. David Yang, "Microstrip patch antennas on tunable electromagnetic band-gap substrates," *IEEE Transactions on Antennas and Propagation.,* vol. 57, no. 6, pp. 1612-1617, June 2009.

[3] Abdelaziz, Abdelmonem Abdelaziz, "Bandwidth enhansment of microstrip antenna." *Progress In Electromagnetics Research.,* vol. 63, pp. 311-317, 2006.

[4] Amit Sing Bhadouria, Mithilesh Kumar, "Microstrip patch antenna for radiolocation using DGS with improved gain and bandwidth," *IEEE International Conference on Advances in Engineering and Technology Research (ICAETR),* 2014.

[5] Luk, K. M., et al. "Broadband microstrip patch antenna, " *Electronics Letters.,* vol. 34, no. 15, pp. 1442-1443, 1998.

[6] Bae-Ian Wu, W. Wang, J. Pacheco, X. Chen, T. Grzegorczyk, and J. A. Kong, "A study of using metamaterials as antenna substrate to enhance gain," *Progress In Electromagnetics Research,* vol. 51, pp. 295-328, 2005.

[7] M. Lapine, and S. Tretyakov, "Contemporary notes on metamaterials," *IET Microw. Antennas & Propagation.,* vol. 1, no. 1, pp. 3-11, February 2007.

[8] Nader Engheta, and Richard W. Ziolkowski, "A positive future for double-negative metamaterials," *IEEE Transactions on Microwave Theory and Techniques.,* vol. 53, no. 4, pp. 1535-1556, 2005.

[9] LI Le-Wei, YAO Hai-ying, WU Qun, and CHEN Zhi-ning, "Broad-bandwidth and low-loss metamaterials: theory, design and realization," *Journal of Zhejiang University Science A.*, vol. 7, no. 1, pp. 5-23, 2006.

[10] Abedin, M. Faisal, Mohammed Z. Azad, and Mohammod Ali, "Wideband smaller unit-cell planar EBG structures and their application," *IEEE Transactions on Antennas and Propagation,* vol. 56, no. 3, pp. 903-908, 2008.

[11] Ahmad A. Sulaiman, Ahmad S. Nasaruddin, Mohd H. Jusoh, Nor H. Baba, Rabi'atun A. Awang, and Mohd F. Ain, "Bandwidth Enhancement in patch antenna by metamaterial substrate," *European Journal of scientific research.,* vol. 44, no. 3, pp. 493-501, 2010.

[12] Nabilah Ripin, Robi'atun Adayiah Awang, Ahmad Asari Sulaiman, Noor Hasimah Baba, Suhaila Subahir, "Rectangular microstrip patch antenna with EBG structure," *2012 IEEE Student Conference on Research and Development (SCOrED)*, pp. 266-271, 2012.

[13] Kuek, C. Y. "Measurement of dielectric material properties." *Rohde & Schwarz Application Note, RAC0607-0019*, 2006.

978-1-4673-9257-0/15/$31.00 ©2015 IEEE

Observation of Low-pass Performance from Novel Trapezoidal Slotted Dumbbell Shape EBGS

S. M. Shakil Hassan
Department of Electrical and Electronic Engineering
Eastern University, EU
Dhaka, Bangladesh
shakil@easternuni.edu.bd

*Md. Nurunnabi Mollah and Khandkar Raihan Hossain
Department of Electrical and Electronic Engineering
Khulna University of Engineering and Technology, KUET
Khulna, Bangladesh
*nurunnabim12@gmail.com

***Abstract*—A novel modified dumbbell shape electromagnetic bandgap structure (EBGSs), trapezoidal slotted dumbbell shape EBGS, has been introduced. Very wide stopband and improved low-pass performances have been reported for particular designs using them. These designs are compared with conventional dumbbell shape EBGS. Trapezoidal slotted dumbbell pattern has shown very attractive performance with very sharp attenuation and significantly reduced ripple heights in insertion loss curve.**

Keywords—Dumbbel shape EBGS, Electromagnetic bandgap structure, Low-pass filter, Trapezoidal slotted EBGS.

I. INTRODUCTION

It is well known that periodic structures at the beneath of microstrip transmission line (T-line) shows very attractive band rejection property for microwave and millimeter wave frequencies [1]-[3]. Such periodic structures are called as Electromagnetic bandgap (EBG) structures or photonic bandgap (PBG) structures [4]; they are very popular in different types of microwave filter designing due to their unique behavior of rejecting certain frequencies [5]. EBG structures have found potential application in planner microwave devices such as patch antenna, phased array antenna, microwave filters, resonators [6]-[8]. Different kinds of electromagnetic bandgap structures (EBGSs) are proposed by the researchers around the world such as circular and square shapes [9], rectangular shape [10]; dumbbell shape [5], tuning fork shape [11], E-shape [8]. Periodic dumbbell shape EBGS (DS-EBGS) in the ground plane of a microstrip T-line introduces high line inductance and capacitance in microstrip line; therefore, it results wider and compact [11] stopband and low-pass [12], [13] performances. Various patterns of DS-EBGS are being studied e.g. square slotted, rectangular slotted, tapered, hybrid etc. and very promising performances are being explored by researchers [14], [15].

In this paper, we have proposed a modified dumbbell shape pattern where instead of square slots as bigger slots, trapezoids are used to give dumbbell look which is referred as trapezoidal slotted DS-EBG. Performance of this particular pattern has been compared with the same sized DS-EBGS. Another design is observed where we have noticed a wider stopband; but that performance later turned to low-pass when an increased number of EBG element are used.

This work is sponsored by Eastern University, Dhaka, Bangladesh. We are grateful to the organization for providing the financial support.

II. DUMBBELL SHAPE EBG PATTERNS

DS-EBG pattern, basically, consists of two bigger slots and a smaller slot where the smaller slot adjoins the bigger slots. Bigger slots generally are square in shape; but recently rectangular shape is taking over due to significant improvement and variation in the performance. The narrow slot is usually a rectangle. Such dumbbell like shape with square slots are, in fact, conventional DS-EBGS – formerly termed as defected ground structure (DGS) [12].

A. Rectangular Slotted DS-EBGS

In Fig. 1(a), a rectangular slotted DS-EBGS is shown. Various types of performances (i.e. wider stopband, dual-band, multi-band and LPF) of rectangular slotted DS-EBGS have been reported in [14]. In the figure, *b* and *c* are two arms of bigger slot and *g* and *h* are width and length of narrow slot respectively. It is reported that the bigger slots of dumbbell shape EBGS introduce inductance whereas the narrow slot introduces capacitance to the microstrip transmission line shown in Fig. 1(b) [12]-[13].

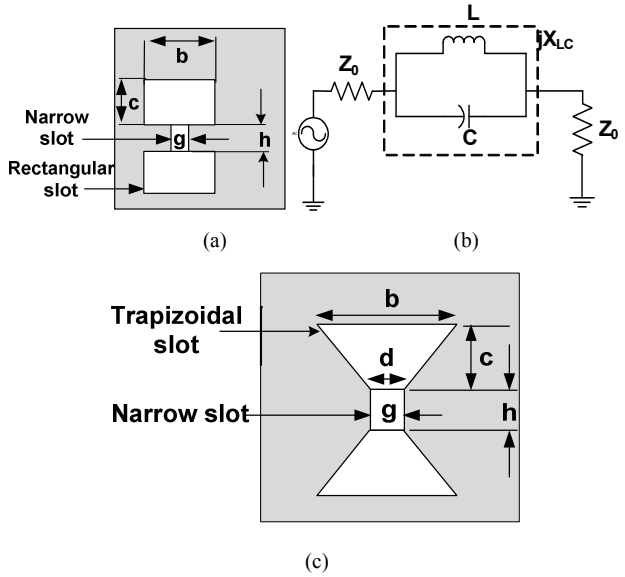

Fig. 1. (a) Conventional dumbbell shape EBGS with rectangular bigger slots, (b) equivalent circuit of conventional dumbbell shape EBGS, (c) trapizoidal slotted DS-EBGS.

978-1-4673-9257-0/15/$31.00 ©2015 IEEE

B. Trapizoidal Slotted DS-EBGS

Figure 1(c) displays a typical trapezoidal slotted DS-EBGS, where *b*, *d* and *c* are the bigger arm, smaller arm and height of the trapezoid respectively. From the figure, it can be seen that instead of square or rectangular slots two trapezoidal slots have been used at both end of the narrow slot. Height and width of the narrow slot is *h* and *g* respectively.

III. EBGS ASSISTED T-LINES

In this paper, we have designed four different designs, where in all the cases the width of the microstrip transmission line is 2.2642mm for maintaining the characteristic impedance (Z_0) 50Ω. Dielectric constant (ε_0) and thickness of the substrate are 2.45 and 31mil (0.7874mm) respectively.

A. Designs 1 : Rectangular Slotted Dumbbell Shape (b=8mm)

In this design, the width (*g*) and length (*h*) of the narrow slot are 2 mm and 1.27mm respectively; therefore, the area of the narrow slot is 2.54mm^2. The dimension of the bigger rectangular slot is b = 8mm and c = 3.987mm respectively; thus, the area of a bigger slot is 31.896 mm^2. Thus the total area (A_{EBG}) of the rectangular slotted DS-EBGS is 66.332mm^2. Inner element spacing (*a*), formally defined as center to center distance between two EBG elements, is 10.4308mm and number of EBGS elements is nine shown in Fig. 2(a).

B. Designs 2 : Trapizoidal Slotted Dumbbell Shape (b=8mm)

This pattern contain trapezoidal slot in place of rectangular slot shown in Fig. 1(c) and the size of the trapezoid is *b* = 8 mm, *d* = 2mm and *c* = 3.987mm; therefore, the area of the trapezoid is 19.94mm^2. The size of the narrow slot is *g* = 2mm and h = 1.27mm, same as the rectangular slotted dumbbell shape design. Thus the total area of an EBG element becomes 42.42mm^2, which is much less than that of design 1. Here, *a* = 10.4308mm too.

C. Designs 3&4: Trapizoidal Slotted DS-EBGS (b=4.622mm)

In this design *b* = 4.622 mm, *d* = 2 mm and *c* = 3.987 mm; the narrow slot: *g* = 2 mm and *h* = 1.27 mm. Thus the total area of an EBG element becomes 28.942 mm2, which is much less than that of design 1 and 2. We have observed the performances of this trapezoidal slotted DS-EBGS for different number of EBG elements at the beneath of T-line where a = *10.4308 mm.*

1) Designs 3 using 5 EBGSs: In this design we get five EBG elements at the beneath of T-line.

2) Designs 4 using 9 EBGSs: In this case the same size of trapezoidal slotted DS-EBGS is used; but the number of EBG element is nine.

IV. S-PARAMETER PERFORMANCES

All the simulations have been performed by using a method of moment (MOM) based software named Zeland IE3D. Simulation results obtained from this EM software have been found in good agreement with the experimented results [8], [11]. We have actually verified the simulated results with experimented results in [5]; however, in this paper we have also confirmed that the simulated result follows theoretical consideration.

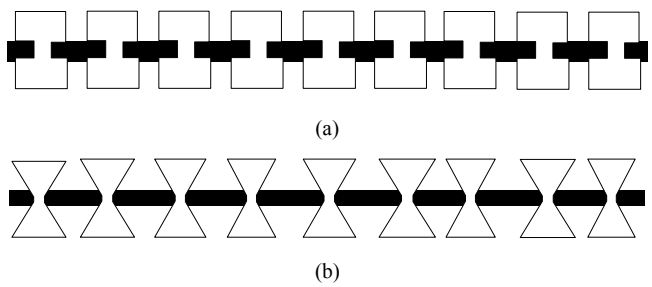

Fig. 2. EBGS assisted microstip T-line having (a) design 1: DS-EBGS with rectangular bigger slots, (b) design 2: trapizoidal slotted DS-EBGS.

In this paper, we performed all the simulations for more than 20 GHz frequency. Results have been discussed in terms of insertion loss (IL), return loss (RL), bandwidth (BW) and maximum ripple heights (RH) at passband from the Scattering parameter (S-parameter) performance of the designs. IL and RL curves are described as S_{21} and S_{11} respectively in the s-parameter performance.

A. S-parameter of rectangular DS-EBGS: Design 1

From the Fig. 3, a bigger stopband is found in Design 1. The stopband started at 4.59 GHz and ended at 17.89 GHz; therefore, the stop bandwidth is 13.3 GHz, which is quite wider than usual. However, passband width is 4.1 GHz and -3dB cut off frequency is observed at 4.13 GHz. Maximum ripple height of IL curve at the passband is -3.32dB.

B. S-parameter of trapezoidal slotted DS-EBGS: Design 2

Though the bigger arm of the trapezoid is identical to the bigger arm of the rectangular slot and height of the trapezoid is

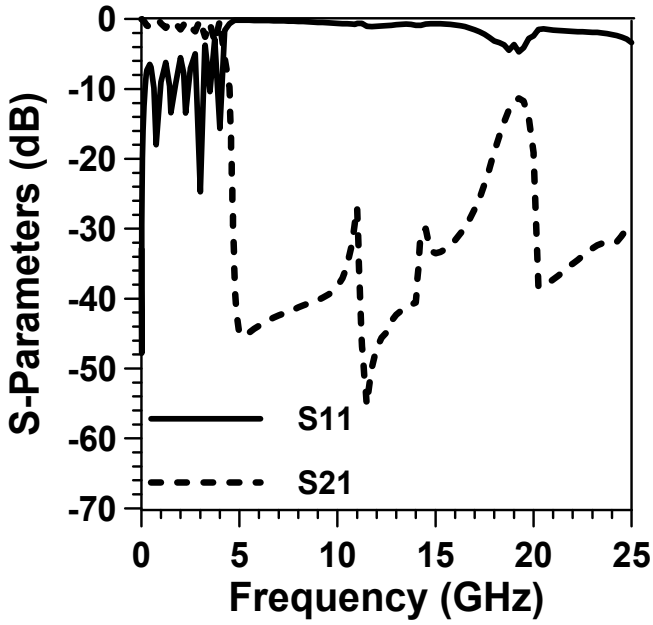

Fig. 3. S-parameter performance of rectangular slotted dumbbell shape EBGS assisted microstrip transmission line (Design 1).

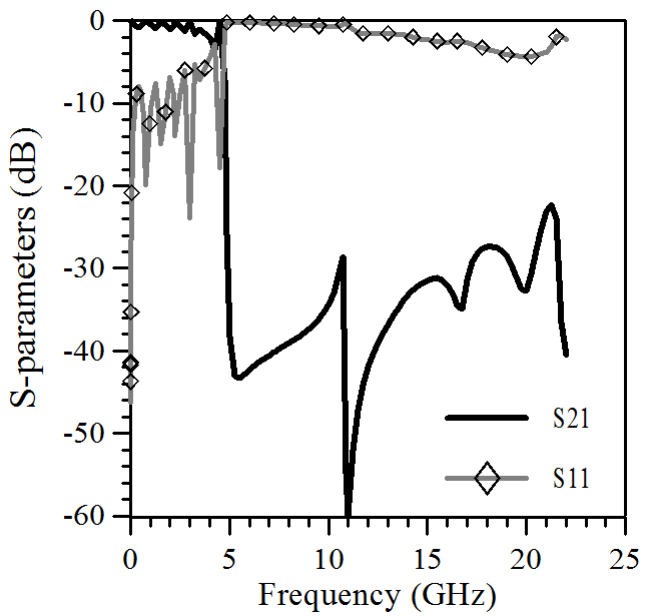

Fig. 4. S-parameter performance of trapizoidal slotted dumbbell shape EBGS assisted design of Design 2.

equal to the other arm of the rectangle, the trapezoidal slot DS-EBGS exhibits a distinguished low-pass performance up to 22 GHz simulation as showed in the Fig. 4. The stopband started from nearly 4.81 GHz. However, passband width is 4.62 GHz and -3dB cut off frequency is observed at 4.60 GHz. Maximum ripple height of IL curve at the passband is -3.33dB. Comparison with the performance of rectangular slotted DS-EBGS is shown in the Table I.

C. Performance of Design 3 & 4

T-line consisting of five trapezoidal slotted DS-EBGSs and nine EBGSs have resulted in a wider stopband and a low-pass performance respectively (shown in Fig. 5). We have observed following performances from this pattern by changing the number of EBGS only.

1) Wider Stopband performance using 5 EBGSs: Band rejection property is started at 5.68 GHz for five EBGS

TABLE I. S-PARAMETER PERFORMANCES OF ALL DESIGNS

Design Title	Different Values of S-parameter				
	Passband at -10dB (GHz)	*-3 dB cutoff frequency (GHz)*	*Stopband at -20dB*	*Max. RH (dB)*	*Total etching area (mm^2)*
Design 1	4.10	4.13	13.3	-3.32	66.332
Design 2	4.62	4.60	LPF started 4.813	-3.33	42.42
Design 3 (5 EBGs)	4.47	5.258	12.984	-1.31	28.942
Design 4 (9 EBGs)	4.20	5.058	LPF started 5.513	-1.94	28.942

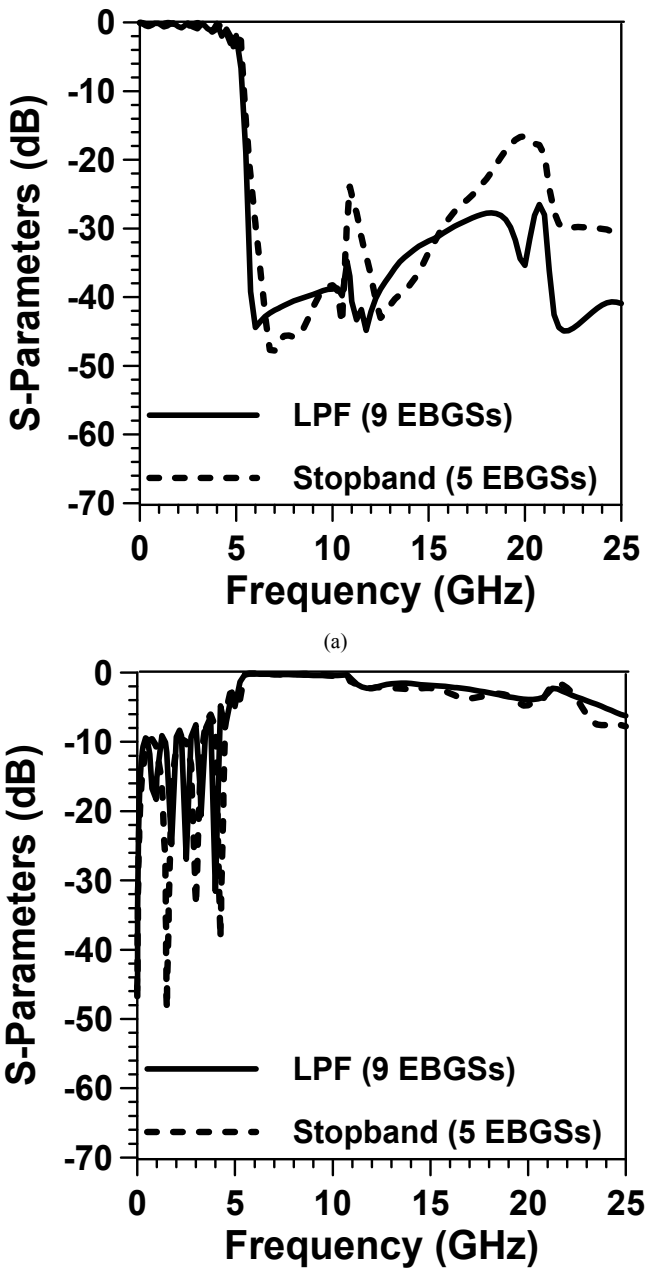

Fig. 5. (a) Insertion loss (S_{21}) curve (b) return loss (S_{11}) curve of trapizoidal slotted DS-EBGS assisted design having five and nine EBGS elements.

assisted design, the stopband width is 12.984 GHz which is larger too. Passband, -3dB cut off frequency and maximum RH at passband for this designs are 4.47 GHz, 5.258 GHz.

2) Low-pass performance utilizing 9 EBGSs: Passband, -3dB cut off frequency and maximum RH at passband for nine EBGSs assisted designs are 4.2 GHz, 5.058 GHz and -1.94 dB respectively. A prominent low-pass performance is observed from this design. Performances are compared in the Table I.

Number of EBGS, basically, has a bearing on the IL curve – the more EBGSs are used the more IL occurs [2]. However,

from the Fig. 5(a), S_{21} curve did not follow the conviction of the other frequencies except near 20 GHz. In essence, the proposed trapezoidal slotted DS-EBG structure performs better band-rejection compared to rectangular slotted DS-EBGS, although etching area is smaller. In contradiction, we know that if the etching area of EBGS (i.e. area of EBGS) is larger, more insertion loss meant to happen. From the earlier discussion, it is obvious that trapezoidal slotted DS-EBGS exhibits quite improved rejection performance.

V. Result Validation

Simulation results are obtained from Zeland IE3D usually are in good congruency with the experimented results [2], [5], [9]. However, to validate the results obtained from this simulation tool a standard 50 Ω T-line without having any EBG element etched at the ground plane has been simulated. Figure 7 shows the performance of this simulation where, it is seen that IL curve (S21) stand along the 0dB line i.e. no insertion loss is observed and return loss remained bellow -20dB; which is theoretically expected performance. Sine, the simulated result followed the theoretical realization; hence it can be considered that all the simulation results we get from the Zeland ie3d simulator will find very well agreement with experimented results.

VI. Conclusion

The design, consisting five trapezoidal slotted DS-EBGS, elements shows well formed wide stopband; in addition to that same trapezoidal slotted DS-EBGS with nine EBGS elements shows distinguished low-pass performance. While compared with rectangular slotted DS-EBGS of same bigger arm and height, it is observed that a trapezoidal slotted DS-EBG pattern has resulted very improved low-pass performance too, whereas the rectangular slotted dumbbell shape EBGS has shown a wider stopband. Therefore, band-rejection property of the proposed design is quite better than that of conventional DS-EBGS. We believe, the proposed pattern will find potential application for such low-pass filter designing soon.

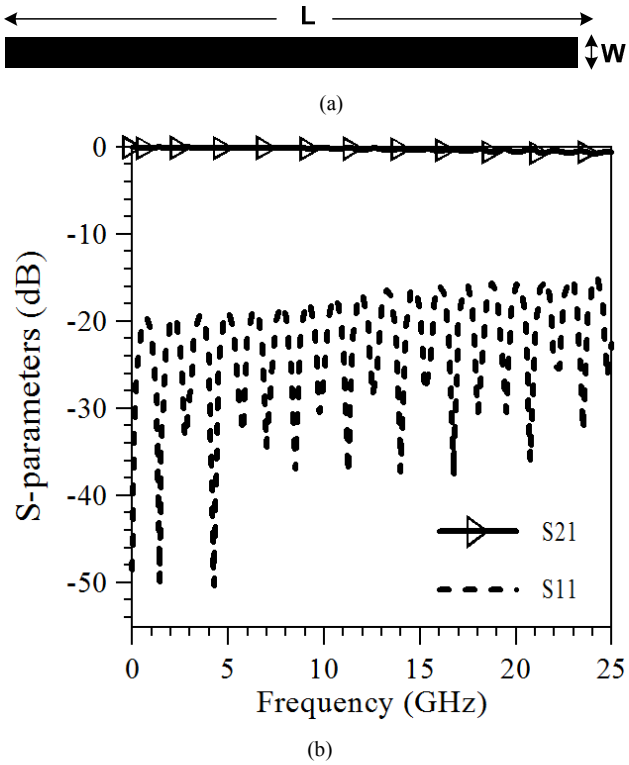

Fig. 6. (a) Standard 50Ω microstrip T-line without any EBGS (b) performance of the standard microstrip T-line.

References

[1] V. Radisic, Y. Qian, R. Coccioli, and T. Itoh, "Novel 2-D photonic bandgap structures for microstrip lines," IEEE Microwave and guided wave lett., vol. 8 no. 2, pp.69-71, Feb. 1998.

[2] Nemai C Karmaker and Mohammad N Mollah, "Potential applications of PBG engineered structures in microwave engineering - part one," Microwave Journal, vol. 47, no. 7, pp. 22-44, July 2004.

[3] S. Y. Huang, and Y. H. Lee, "Tapered dual-plane compact electromagnetic bandgap microstrip filter structures," IEEE Trans. Microw. Theory Techn., vol. 53, no. 9, pp.2656–2664, Sep. 2005.

[4] F. Falcone, T. Lopetegi, and M. Sorolla, "1-D and 2-D photonic bandgap microstrip structures," Microw. Opt. Technol. Lett., vol. 22, no. 6, pp. 411–412, Sep. 1999.

[5] S. M. S. Hassan, S. M. Anayetullah, and M. N. Mollah, "Sinusoidal appearance of nonuniform dumbbell shape EBGSs in microstrip transmission line," in 1st *Int. Conf. on Elect. Inform. and Commun. Technol.*, Khulna, Bangladesh, Feb. 2014, pp. 509-513.

[6] V. Radisic, Y. Qian, and T. Itoh, "Broad-band power amplifier using dielectric photonic bandgap structure," IEEE Microw. Guided Wave Lett., vol. 8, no. 1, pp. 13–14, Jan. 1998.

[7] M. N. Mollah, and N. C. Karmakar, "A compact photonic bandgap assisted phased array antenna," Asia-Pacific Microwave Conf., Korea, Nov. 2003.

[8] S. Y. Huang, and Y. H. Lee, "A compact E-shaped patterned ground structure and its application to tunable bandstop resonator," IEEE Trans. Microw. Theory Techn., vol. 57, no. 3, pp.657–666, Mar. 2009.

[9] N. C. Karmakar, and M. N. Mollah, "Investigation into nonuniform photonic-bandgap microstrip low-pass-filters.," IEEE Trans. Microw. Theory Techn., vol. 51, no. 2, pp.564–572, Feb. 2003.

[10] S. M. S. Hassan, S. M. Anayetullah, M. N. Mollah, K. R. Hossain, M. M. Ahmed, M. A. A. Shufian, and M. M. Hassan, "Realization of low-pass filters from arbitrarily designed nonuniform EBG structures," in 1st *Int. Conf. on Elect. Inform. and Commun. Technol.*, Khulna, Bangladesh, Feb. 2014, pp. 305-310.

[11] L. Yang, M. Fan, F. Chen, J. She, and Z. Feng, "A novel compact electromagnetic-bandgap (EBG) structure and its application for microwave circuits.," IEEE Trans. Microw. Theory Techn., vol. 53, no. 1, pp.183–190, Jan. 2005.

[12] D. Ahn, J.S. Park, C.S. Kim, J. Kim, Y. Qian and T. Itoh, "A design of the lowpass filter using the novel microstrip defected ground structure," *IEEE Trans. On Nicrowave Theory and Techniques*, vol. 49, no. 1, pp. 86-93, 2001.

[13] J. S. Lim, C. S. Kim. D. Ahn, Y. C. Jeong, and S. Nam, "Design of low-pass filters using defected ground structure.," IEEE Trans. Microw. Theory Techn., vol. 53, no. 8, pp.2539–2545, Aug. 2005.

[14] S. M. S. Hassan, M. N. Mollah, M. A. Rashid, N. H. Ramly, and M. Othman, "Dumbbell shape EBGS structure – worth to EBG assisted microwave filter designing," IEEE Asia-Pacific Conf. on Applied Electromagnetics, Malaysia, Dec. 2012.

[15] M. N. Mollah, and N. C. Karmakar, "Compact hybrid defected ground plane," Microw. Opt. Technol. Lett., vol. 44, no. 3, pp.266–270, Feb. 2005.

Receiver Initiated Multi-channel Medium Access Control Protocol for Cognitive Radio Network

Amran Hossain, Sahelee Sultana and Md. Obaidur Rahman
Department of Computer Science and Engineering , Dhaka University of Engineering & Technology(DUET), Gazipur
Gazipur-1700, Bangladesh
amran_duet38@duet.ac.bd, sahelee.cse@gmail.com, orahman@duet.ac.bd

Abstract— **At present Cognitive Radio Network (CRN) is one of the contemporary research area in order to improve efficiency as well as improve spectrum utilization factor of wireless communication. The impression of profitable CRN (i.e., simultaneous presence of primary and secondary users in licensed bands) is increasing popularity in wireless communication research. In fact fixed unlicensed band is used by wireless users in different networks to complete data communication. However, in practical number of wireless users are increasing day by day and guides this limited bandwidth to a saturation state. In CRN as at the absence of primary user, the secondary users access the channels of licensed bands; thereby the Medium Access Control (MAC) protocol for CRN faces many challenges. The challenges include throughput maximization, channel rendezvous amongst the secondary users, minimize delay, and to keep continuing data transmission without interfering the primary users. A large number of sender initiated MAC protocols have been proposed for CRN to solve these challenging issues. However we argue that efficient channel rendezvous in many scenarios still a major concern in accordance with the rest of the mentioned challenges. In this paper, we have come up with a Receiver Initiated Multi-channel (RIM) Medium Access Control (MAC) protocol named as RIM-MAC exploiting the pseudorandom number channel sequence and hopping method for multi-channel rendezvous amongst the secondary users of CRN. This protocol is efficient scheme for channel rendezvous success rate. We have analyzed and implemented our proposed RIM-MAC protocol, and found that it provides better performance in terms of throughput, rendezvous rate and delay.**

Keywords—Cognitive radio, psedurandom number channel sequence, channel rendezvous, primary user, secondary user.

I. INTRODUCTION

Cognitive Radio Network (CRN) gains popularity in the research area because it enables the current fixed spectrum channel assigned by FCC to be utilized by the new users [1]. It is noteworthy that most of the spectrums assigned to television channels, radio channels dividends a huge amount of bandwidth and are kept idle most of the time; whereas wireless network users (i.e., WLAN and Wi-fi users) share a small range of spectrum. In practical, when there are many wireless users at a time, the network gets congested because of the limited number of channels with less bandwidth. Hence, it is predictable that bandwidth would not be sufficient to provide better support for the wireless users in terms of quality of service (QoS), throughput and delay. So, the ultimate solution is to find out some alternative. CRN is one of the possible solutions to overcome this problem. Cognitive radio (CR) is an intelligent transceiver, adaptive and network technology, which can be configured with dynamism property. It has ability to automatically detect free or available channels from wireless spectrum and change its transmission parameters enabling more communications to run concurrently. In point of fact, CRN is structured with both the secondary user (SU) and primary user (PU) in which, SUs consist CR-enabled radios and the PUs whose radios need not be CR-enabled [2]. Cognitive capability means to the ability to sense opportunities in spectrum where and when channels are not employed by PUs [3].

In view of the fact that, the SUs operate separately on dissimilar channels based on availability (i.e., during the absence of primary users), channel rendezvous seems to be the most challenging issue in CRN. Fig. 1, illustrates that nodes *A* and *Y*, *W, C* and *X*, *B* and *Z*; the pairs of SUs opportunistically make channel rendezvous on channel 1, channel 3, and channel 5 respectively, where no PU exists. Note that channel 2 and 4 are occupied by the PUs. Hence, SU do not have any activity on these channels. It is observed that, there are different approaches exist for channel rendezvous between two SUs in CRN. *Firstly,* the *common control channel* (CCC) approach for channel rendezvous [4] creates bottleneck situation on the common control channel.

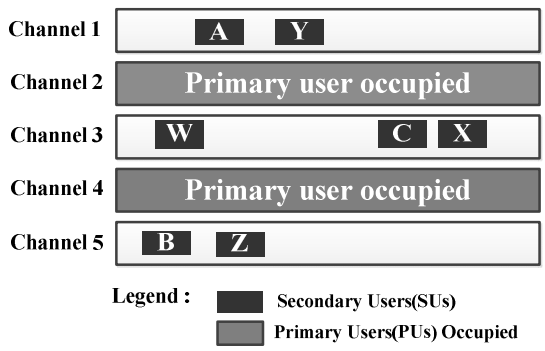

Figure 1: Basic communication manner in CRN

Furthermore, rendezvous scheduling complexity may arise. *Secondly,* the *channel hopping* approach [5-6] can be used by the SUs to discover each other on a channel while hopping different channels. This approach uses *pseudorandom sequence* according to available channel list. When PU is occupied channel(s) gradually, then decrease channel rendezvous rate as well as increase channel rendezvous delay. Conversely, if two SUs follow reciprocally exclusive sequence, still after lots of iterations, those may not succeed in

978-1-4673-9257-0/15/$31.00 ©2015 IEEE

discovering each other [7]. *Finally*, in *synchronization approach* [8], nodes are needed to be synchronized; hence synchronous overhead becomes the main concern for a large network.

Considering the above mentioned limitations on different channel rendezvous approaches, we have motivated to design an efficient channel rendezvous technique using *pseudorandom number channel sequence* for making channel rendezvous between SUs considering all channels.

The rest of the paper is organized as follows: in Section II the background study and problems domains are presented. Section III describes the proposed RIM-MAC protocol design. Analysis and performance evaluation are described in Section IV and V respectively, and Section VI concludes the paper.

II. Related Work and Problem Statement

Till date, a number of MAC protocols have been proposed for CRN to solve the channel rendezvous problem, where the protocols either use any one approach of the followings or make the combinations amongst those; such as- *common control channel approach* [9-12], *channel hopping approach* [6], and *synchronization approach* [8].

A. Common Control Channel Approach

In this approach selects one channel that serves as a rendezvous channel and all the essential control information is exchanged among the SUs on this channel [9-12]. When a SU wishes to communicate with its potential receiver (i.e., another SU), at first it switches to the CCC during *control interval* and attempts to negotiate with its potential receiver using a control packet. When negotiation is complete on CCC, the SU switches to negotiation channel [5] which is available or common to both and then data communication can be accomplished during the *data exchange interval* through available channel. In addition, bottleneck situation may occur in the CCC when multiple nodes negotiate for rendezvous in a single channel.

B. Channel Hopping Approach

In the channel hopping approach [6], each SU generates a pseudorandom sequence using its own available channels. According to predefined hopping sequence SU switches/hops from one channel to another until finds its neighbor. When two SUs meet on a channel which is common between them, they need to exchange the necessary control information as well as complete their data communication. Hence, we conclude that a large number of iterations are required for channel rendezvous using pseudorandom channel hopping sequence as well as, even after lots of iterations; neighbor discovery of SUs may not be successful if SUs follow mutually exclusive pseudorandom sequence [7].

C. Synchronization Approach

In this approach [8] time is divided into N number of equal time slots of fixed duration. Each time slot is dedicated to one channel for control signal exchange. At the end of the network initialization state, all nodes are synchronized and every node has the information about its neighbors and their respective channel sets. To exchange the control signals it chooses one of the channels common between itself and its neighbor during at the beginning of specified time slot. Therefore, nodes are needed to be synchronized; hence, synchronization overhead occurs in this approach and increase the rendezvous delay.

Considering the above mentioned limitations of different channel rendezvous approaches, in this paper we have proposed a RIM-MAC protocol for SUs. The proposed method makes a pseudorandom number channel sequence according to total number of channels for rendezvous among the SUs.

III. Proposed RIM-MAC Protocol Design

A. Protocol Overview

RIM-MAC is a multichannel asynchronous duty-cycling MAC protocol. It does not require nodes to synchronize. It also does not use common control channel behavior. In this protocol design a ***beacon packet*** (i.e., Hello Packet) is considered to exchange all the control information of a SU node. Each SU has a ***prediction state*** (i.e., *initial state*) to learn about receiver's available channel set, *beacon sending time* and *pseudorandom number channel sequence*.

In RIM-MAC protocol, a node avoids choosing channels that are occupied by PU. When a node wakes up on a channel according to pseudorandom number channel sequence to send a beacon, it uses a CCA (Clear Channel Assessment) technique to check and make sure the channel is idle/free before beginning its transmission. If the channel is idle/free, the node sends the beacon and complete data transmission with their potential sender node. If the channel is occupied by PU, the receiver node skips the channel and goes to sleep; and wait on that channel till a cycle time, denoted by T_C (i.e., mentioned later). Additionally, after waiting the nodes switch to next pseudo randomly chosen channel and repeat the CCA technique and beacon sending method.

B. Network Model

Fig. 2 is shown as simple cognitive radio network model. In this model SUs are mentioned as S (i.e., Sender Node) and R (i.e., Receiver Node). We know that in IEEE 802.11b standard protocol uses only 16 channels. SU can occupy any channel among the standard channel list of ISM band. Here, for simple explanation we have assumed only 5 channels. The PUs is mentioned as P_S in sender side and P_R in receiver side respectively.

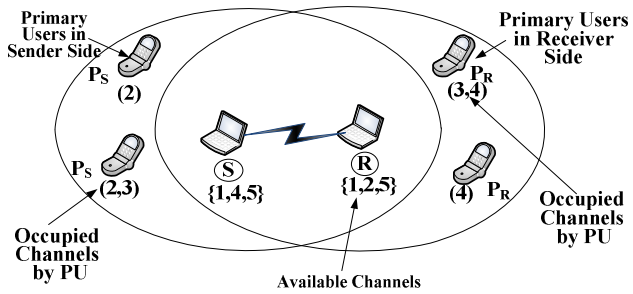

Figure 2: Simple CRN model

In sender range PUs occupied channel(s) are (2, 3) and in receiver range PUs occupied channel(s) are (3, 4). So the available channel(s) set of *S* is {1, 4, 5} and available channel(s) set of *R* is {1, 2, 5}. In the next sections we have used these available channel(s) list for explanation.

C. Protocol Operation

RIM-MAC is a multichannel asynchronous duty-cycling MAC protocol. The design of RIM-MAC is mainly encouraged by the multi-channel EM-MAC [13] protocol for WSN. RIM-MAC protocol operation is categorized into three phases such as-*Network Initialization State, Stable Phase and Adaptive Phase* which are described in the following sections.

1) Network Initialization State

Each SU node equipped with a single radio multi-channel transceiver and can act as a sender or a receiver and maintains a common communication characteristic. Initially it is considered that a node has a packet to send to a receiver but does not have the receiver's ***prediction state*** (i.e., receiver's available channel list, beacon time and pseudorandom number channel sequence). Hence, at the initialization the node having data (i.e., the sender *S*) starts sensing the first available channel of its own pseudorandom number channel sequence. *Firstly*, the sender checks that if the channel is occupied by any PU, it switches to the next channel of pseudorandom number channel sequence; otherwise, it enlists the channel in its available channel list and waits for receiver's beacon on that channel. If the sender does not receive beacon from the receiver during its waiting time interval on that channel, then the sender switch to another channel and so on. After receiving the beacon from the receiver, the sender sets a flag in the header of the data packet sent to the receiver, requesting the receiver to embed its prediction state in the following beacon. Thus, the node gets aware of the receiver's beacon time offset on respective available channels and maintains the same for future data communication. So the receiver beacon should be sufficient to ensure that the receiver will visit the channel at least once during this time. Let T_C be the cycle time interval of a node and the node wakes-up on different channels using the pseudorandom number channel sequence using the T_C cycle time interval. However, if the next channel(s) of the pseudorandom number channel sequence is occupied by the PU the node stays on its current channel and after elapsing appropriate T_C cycle time interval(s) it switches to the next available channel. It should be sufficient to ensure that receiver will visit the available channel at least once during this time. So the maximum waiting time of a sender on a channel would be

$$T_{Wait} = N_{ch} \times T_C \qquad (1)$$

Where, T_C is the cycle time, and N_{ch} is the total number of channels. Fig. 3 illustrates the initialization state of protocol. Based on the *overlapping principle* [14] it is expected that *S* would receive the beacon from *R* and subsequently sends the data packets and complete communication. If the sender does not receive a beacon from the receiver after waiting T_{Wait}, the sender switches to the next channel and repeats the waiting procedure. If the sender is unable to rendezvous with the receiver after waiting on all channels, the sender assume that

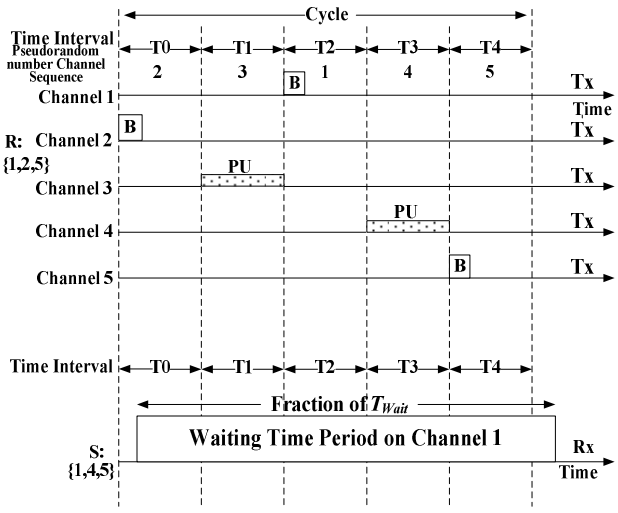

Figure 3: Network initialization state

the receiver is unreachable. In contrast, the same node, when acts as a receiver, then it sends the beacon to its potential sender(s) posterior to the waiting time *(T_{Wait})* for its own receiver's beacon.

2) Stable Phase

Every SU node independently decides and maintains its own pseudorandom number channel sequence switching behavior, wake-up offsets and available channel list. A sender rendezvous with a receiver on a particular channel by predicting the receiver's wake-up channel, wake-up offset and available channels. We denote that a SU *Sender* as node *S* and a SU *Receiver* as node *R*. Fig. 4 illustrates an example of the operation of proposed RIM-MAC, with time progressing from left to right. As RIM-MAC is a receiver initiated multichannel MAC protocol, a receiver node *R* first sends a beacon on an available channel (i.e., no primary user is on that channel) according to its generated pseudorandom number channel sequence. On the contrary, it is assumed that the sender *S* is well aware of receiver's channel sequence, available channel list and beacon time offset on different channels. Hence, the sender *S* proactively remains on the receiver's available channel to receive the beacon from node *R* and consequently sends data to *R*. As shown in Fig. 4, sender *S* has channel {1, 4, 5} as its available channel list. Now receiver *R* first scans the channels according to its pseudorandom number channel sequence. Thus, on a particular time offset/interval receiver *R* sends a beacon *B* to sender *S* and initiates a communication on available channel 2 during cycle time T_C, but on that time sender *S* is not stayed on that channel because channel 2 is occupied by PU for *S*. So *R* does not get any data from sender *S*. Now *R* switches to next channel(s) and so on. Here, channels 3 and 4 are occupied by PU so receiver skips these channels and switches to next channel. The channel 1 is available to *R,* so *R* sends a beacon to sender *S* on this channel. After receiving the beacon *B* from *R*, node *S* sends the data packet *D* to *R*. In reply, *R* sends an acknowledgement beacon *B* to *S* to acknowledge the data packet receipt. Moreover, the acknowledgement beacon *B* works as a request for another data packet to be sent to *R* by *S* or another sender. In the providing example no other data packet is available so *S* and *R*

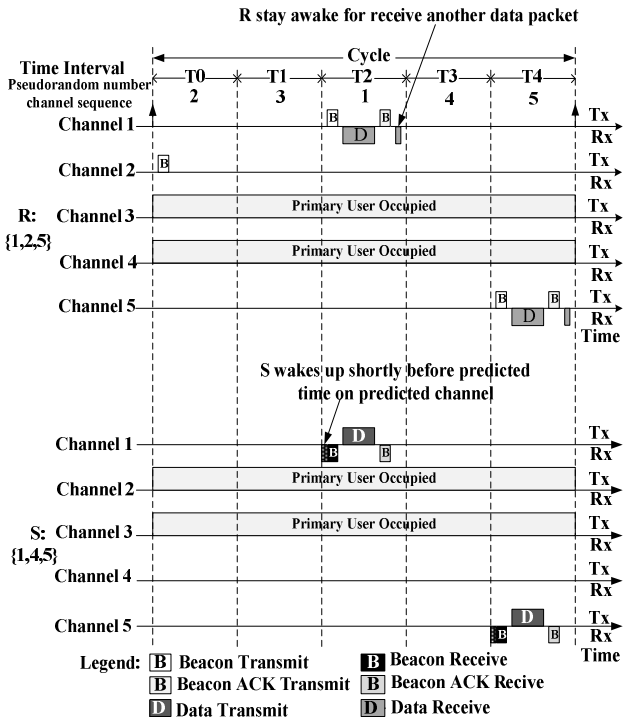

Figure 4: RIM-MAC protocol operation scenario.

quickly go back to sleep. After Cycle time T_C, R wakes up for the second time on another available channel such as 5 and complete data packet transmission with S and so on. Hence, sender S has prediction state of R, so S wakes up shortly before predicted time on predicted channel(s) before data transmission.

3) Adaptive phase

In adaptive phase, we have assumed that after sometimes or next cycle, when available channel list of R is updated with few additional channels due to non-occupation of PUs. In such case, receiver R follows its own pseudorandom number channel sequence for sending beacon in the newly added channel(s). In contrast, it is expected that S will be updated about the changes in available channel list in R through the earlier/later beacons. Thus it can perform data transmission with R in the newly added channel(s). When, available channel list of R is updated with fewer channel(s) due to channel occupation of PUs.

In such case, receiver R follows its own pseudorandom number channel sequence for sending beacon in the available channel(s) only. Here as well S will be updated or presume about the changes in available channel list in R. Thus it can perform data transmission with R in the newly added channel(s). Let, after few seconds previous sender S now acts as a new receiver R, and its available channel(s) list is {1, 4, 5} and its pseudorandom number channel sequence is 31542. Therefore, new receiver R follows its own pseudorandom number channel sequence and completes the data transmission with another sender S according to stable phase. Fig. 5 illustrates new adaptive operation in this case.

IV. Rendezvous Delay Analysis

For channel rendezvous delay analysis, we have considered three cases as follows: worst case rendezvous delay analysis, best case rendezvous delay analysis and average case rendezvous delay analysis.

Case 1: Worst case rendezvous delay analysis

If a sender S has no prediction state of R, then S first waits on an available channel until getting the receiver beacon. Let T_C be the cycle time interval of a node and the node wakes-up on different channels using the pseudorandom number channel sequence using the T_C cycle time interval. However, if the next channel(s) of the pseudorandom number sequence is occupied by the PU the S stays on its current channel and after elapsing appropriate T_C cycle time interval(s) it switches to the next available channel. It should be sufficient to ensure that receiver will visit the available channel at least once during this time. So worst case rendezvous delay would be calculated as follows:

$$T_{Wait}^{Worst} = N_{ch} \times T_C \tag{2}$$

Here, T_C = Cycle time, N_{ch} is the total number of channels.

Case 2: Best case rendezvous delay analysis

In the best case sender S would get the beacon exactly on its first available channel without wait. So the best case rendezvous delay would be calculated as follows:

$$T_{Wait}^{Best} = \delta;\ Where\ \delta \rightarrow 0 \tag{3}$$

Case 3: Average case rendezvous delay analysis

Average case rendezvous delay would be calculated as:

$$T_{Wait}^{Average} = \delta;\ where\ \delta \rightarrow \frac{N_{ch} \times T_C}{2} \tag{4}$$

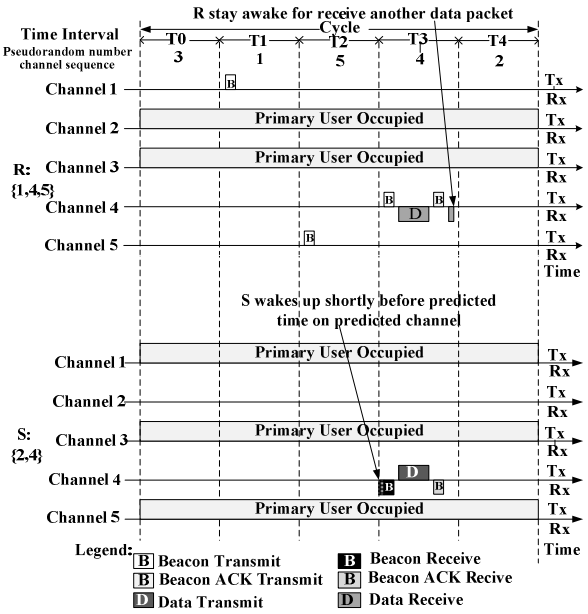

Figure 5: RIM-MAC protocol operation in adaptive phase

V. PERFORMANCE EVALUATION

We have demonstrated the performance evaluation of our proposed RIM-MAC protocol and compare the results with that of a CCC-MAC protocol and SYN-MAC protocol. We have used our own simulation model developed in Java Platform (NetBeans IDE 7.0) and we have implemented our proposed RIM-MAC, CCC-MAC and SYN-MAC protocols and compare the results with among them. In this simulation environment, 10 channels are used for modeling licensed channels for PUs and randomly some of the channels made free/unlicensed and set available to the SUs. Maximum 20 nodes are deployed in 500 x 500 m^2 area to make variation in number of PU and SU. 10 nodes are chosen randomly as the sources and the other 10 nodes as destinations. The transmission range of each node is set to 250*m*. In this simulation, 10 simulation cycles are considered, each having a cycle period of 10 seconds. Hence, total simulation time is 100 seconds. Each data packet is considered to cost 1 Joule for single transmission, which is used to calculate energy consumption of each node. In case of data packet transmission failure, 1 Unit (i.e., Second) is assumed, which is used to calculate delay of each node. In our simulation, for evaluation the performance of Proposed RIM-MAC, SYN-MAC and CCC-MAC, we have considered five performance metrics such as- *Throughput, Rendezvous Success Rate, Rendezvous Delay, Packet Transmission Success Rate,* and *Energy Consumption.*

A. *Throughput Performance*

Fig. 6 shows the aggregated throughput of proposed RIM-MAC with the SYN-MAC and CCC-MAC protocols as the network traffic is increased. The throughput of RIM-MAC is significantly higher than SYN-MAC and CCC-MAC. The main cause for this behavior is that a CCC among all the nodes is not always available and so many times a connection is not established. Hence, due to these failures the throughput is significantly lower in CCC-MAC. In SYN-MAC when nodes are increased, then synchronization overhead is increased so connection problem and problem of message collaboration among the nodes are increased. So throughput is comparatively lower than the RIM-MAC. In RIM-MAC, there is no control signal shared with among all nodes and hence, nodes are communicated any time any available channel(s). Therefore, RIM-MAC has the better throughput from the SYN-MAC and CCC-MAC protocols.

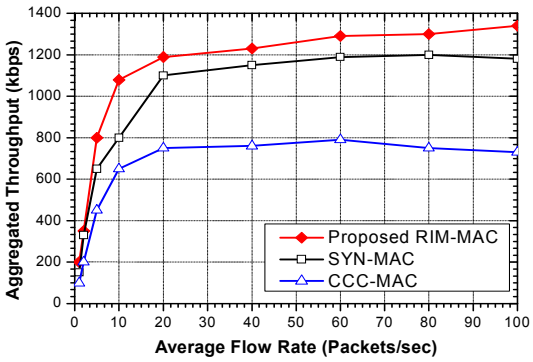

Figure 6: Average throughput Vs flow rate

B. *Rendezvous Success Rate*

Fig. 7 demonstrates the results of rendezvous success rate in percent with respect to simulation time for channel rendezvous. As shown in figure, in 1st cycle, rendezvous success rate among the SUs in RIM-MAC is 100%, in SYN-MAC is 100% and in CCC-MAC is 70%, and so on. After 10th cycle of simulation, it is observed that the rendezvous success rate in RIM-MAC is 60% and steady, and SYN-MAC and CCC-MAC are abrupt. So, it can be concluded that proposed RIM-MAC protocol provides higher rendezvous success rate than the SYN-MAC and CCC-MAC approaches.

C. *Rendezvous Delay Rate*

Fig. 8 demonstrates the outcome of rendezvous delay in second with respect to simulation time for channel rendezvous. As shown in figure, in 1st cycle, rendezvous delay among the SUs in RIM-MAC is 0 (i.e., no delay), in SYN-MAC is 1 and in CCC-MAC is 3, in 2nd cycle; rendezvous delay among the SUs in RIM-MAC is 0 in SYN-MAC is 1 and in CCC-MAC is 4 and so on. Finally at 10th cycle of simulation, it is observed that the rendezvous delay in RIM-MAC is 4 and steady, and SYN-MAC and CCC-MAC are increased. So, it can be concluded that proposed RIM-MAC protocol provides lower rendezvous delay than the SYN-MAC and CCC-MAC approaches.

D. *Packet Transmission Rate*

Fig. 9 exhibits the results of packet transmission success rate in percentage with respect to simulation time. In figure, in 1st cycle, packet transmission rate among the SUs in RIM-MAC is 100%, in SYN-MAC is 90% and in CCC-MAC is 70% and so on. It is also observed that in 10th cycle, the packet

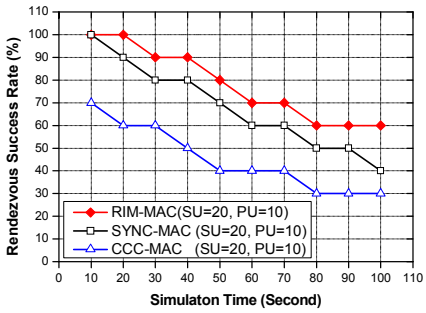

Figure 7: Rendezvous success rate with respect to simulation time

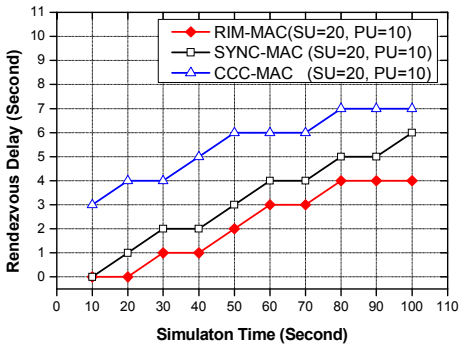

Figure 8: Rendezvous delay with respect to simulation time

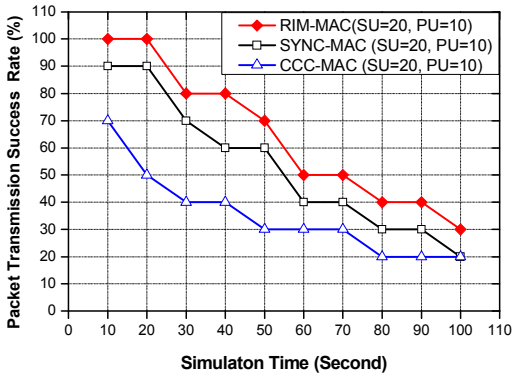

Figure 9: Packet transmission success rate with respect to simulation time

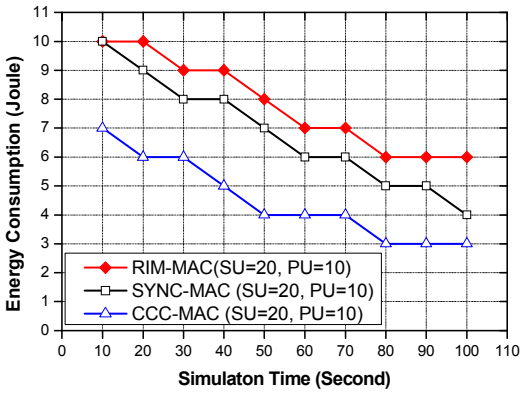

Figure 10: Energy consumption with respect to simulation time

transmission success rate in RIM-MAC is 30%, and 20% in SYN-MAC and CCC-MAC respectively. So we can say that RIM-MAC protocol provides higher packet transmission success rate than the SYN-MAC and CCC-MAC protocols

E. Energy Consumption

Fig. 10 illustrates the outcome of energy consumption in second with respect to simulation time. It is observed in RIM-MAC rendezvous success rate and packet transmission success rate is higher than the SYN-MAC and CCC-MAC which are shown in Fig. 7 and 9 respectively. So it is concluded that the energy consumption in proposed RIM-MAC is higher than the SYN-MAC and CCC-MAC.

VI. CONCLUSION

In this paper we have presented a new CRN MAC protocol and channel rendezvous scheme using pseudorandom number channel sequence based mechanism for SUs considering all the channels of the list. Proposed RIM-MAC protocol algorithm ensures that maximum number of SUs can make channel rendezvous and successfully complete their data transmission with each other. This protocol automatically eliminates the control channel saturation problem and synchronization overhead. In addition, this protocol increases throughput, maximize channel rendezvous success rate, maximize packet transmission rate and reduces delay.

ACKNOWLEDGMENT

This work is supported by the "*Research Development Fund*" of Dhaka University of Engineering & Technology (DUET), Gazipur and Dr. M. O. Rahman is the corresponding author.

REFERENCES

[1] Federal Communications Commission. (2015) The FCC website.[Online]. Available: https://apps.fcc.gov/edocs_public/ attachmatch/ FCC-03-289A1.pdf.

[2] N. Meghanathan, "A survey on the communication protocols and security in cognitive radio networks," *International Journal of Communication Networks and Information security (IJCNIS)*, vol. 5, no. 1, pp.19-38, Apr.2013.

[3] I. F. Akyildiz, W. Y. Lee, M. C. Vuran, and S. Mohanty, "Next generation dynamic spectrum access /cognitive radio wireless networks: a survey," *International Journal* of *Computer Networks (Elsevier)*, vol. 50, no.13, pp. 2127–2159, Sept. 2006.

[4] I.F. Akyildiz, W.Y, Lee, and K. R. Chowdhury, "CRAHNs: cognitive radio ad hoc networks," *International Journal of Ad Hoc Networks(Elsevier)*, vol. 7, no. 5, pp. 810-836, Jan. 2009.

[5] Z. Htike, and C.S. Hong, "Neighbor Discovery for Cognitive Radio Ad Hoc Networks," in *Proc. International conference on Ubiquitous Information Management and Communication (IMCOM),* Kota Kinabalu, Malaysia, Jan. 2013.

[6] L. DaSilva and I. Guerreiro, "Sequence-based rendezvous for dynamic spectrum access," The 3rd IEEE International Conference on New Frontiers in Dynamic Spectrum Access Networks, Chicago, IL, Oct. 2008, pp. 1-7.

[7] M. R. Islam, M.A.E. Shakib, M. A. Rahaman, M. O. Rahman, and A. S. K. Pathan, "A Neighbour Discovery Approach for Cognitive Radio Network Using Tower of Hanoi(ToH) Sequence Based Channel Rendezvous," in *Proc. The 5th International Conference on Information and Communication Technology for The Muslim World (ICT4M)*, Kuching, Nov. 2014, pp.1-6.

[8] Y. R. Kondareddy and P. Agrawal, "Synchronized MAC Protocol for Multi-hop Cognitive Radio Network," *IEEE International Conference on Communications*, May 2008, pp. 3198 - 3202.

[9] X. Zhang and H. Su, "CREAM-MAC: cognitive radio-enabled multichannel MAC protocol over dynamic spectrum access networks," *IEEE Journal of Selected Topics in Signal Processing*, vol. 5, no. 1, pp. 110 – 123, 2011.

[10] C. Cordeiro and K. Challapali, "C-MAC: A cognitive MAC protocol for multi-channel wireless networks," The 2nd *IEEE International Conference on New Frontiers in Dynamic Spectrum Access Networks, DySpan*, Dublin, Apr. 2007, pp. 147–157.

[11] B. F. Lo, "A survey of common control channel design in cognitive radio networks," *International Journal of Physical Communication (Elsevier)*, vol. 4, no. 1, pp. 26–39, Mar. 2011.

[12] K. R. Chowdhury, I. F. Akyildiz, "OFDM-Based Common Control Channel Design for Cognitive Radio Ad Hoc Networks," *IEEE International Journal of Mobile Computing*, vol.10, no.2, pp. 228-238, Feb.2011.

[13] L. Tang, Y. Sun, O. Gurewitz and D. Johnson; "EM-MAC: A Dynamic Multichannel Energy-Efficient MAC Protocol for Wireless Sensor Networks" MobiHoc '*11Proceedings of the Twelfth ACM International Symposium on Mobile Ad Hoc Networking and Computing,* Paris, France, May 2011, Article No. 23.

[14] M. O. Rahman, R. Kamal, C. S. Hong, S. Lee, Deokjai and Y.C. Bang, "A light-weight channel rendezvous Scheduling for Multi-channel Medium Access in Sensor Networks," *International Conference on ICT Convergence (ICTC),* Sept. 2011, pp. 40-45.

Opportunistic System Approach for Capacity Enhancement and Congestion Mitigation in Advanced Wireless Networks

Kazi Nawshad Azam and Mostafa Zaman Chowdhury
Department of Electrical and Electronic Engineering, Khulna University of Engineering & Technology, Bangladesh
E-mail: nawshad_kuet@yahoo.com, mzceee@yahoo.com

Abstract—**Today's technology in communicating among wireless systems are more complicated and sophisticated with more opportunities, services and facilities to its users. As wireless network technology advances so as the challenges associated with it increases to solve some basic problems such as congestion, interference, call admission and service quality control etc. In the macro integrated femtocellular or heterogeneous wireless network the system capacity enhancement in a low congestion environment is a key issue to focus on and to do so a novel approach is proposed in this paper. We propose an opportunistic system approach where intelligent resource reallocation (IRR) scheme is used to create opportunity to its user to be connected in the high capacity advanced wireless network system with reduced congestion. Performance of our proposed scheme is given in this paper where we can see that how capacity and congestion of wireless network are correlated to provide a reliable wireless system.**

Keywords— Opportunistic system, congestion, system capacity, interference, intelligent resource reallocation.

I. INTRODUCTION

Complex wireless technology is today's demand for high traffic in communication channel [1], [2]. There are different ways of resource allocation to provide better reliable network coverage to serve user's demand. In existing technology capacity of a particular communication channel is predefined that is fixed. For this predefined channel capacity user per channel is also fixed. This channel condition makes the system performance poor. System performance poor means low signal strength, high signal-to- noise plus interference ratio (SNIR), high congestion, low throughput, low quality of service for user [3]. These problems origins from different part of the system design considerations such as power control scheme, frequency allocation scheme, and interference mitigation technique etc [4]. All these problems can be reduced in a considerable limit by applying proper intelligent techniques. Cognitive or opportunistic radio system is a way where cognitive user can use dedicated channel in different way but not in the presence of dedicated user in that channel [5].

When interference is low, SNIR is high and hence increased system capacity [6]. Again when number of user is high in a system then interference may increase which in turn create possibility of reducing system capacity. Also when power control and frequency planning are not adequate in the system then it causes high interference effect [7]. Improper frequency allocations also make wastage of valuable resource. So, user suffers from congestion problem in busy areas. This congestion problem causes higher rate of call drops. To reduce call drop problem call admission control is required.

In this paper we focus on reducing congestion problem and also making system capacity dynamic of wireless network by applying intelligent resource reallocation (IRR) scheme where system capacity can be increased in some extent to support extra users according to existing user's resource utilization natures. New frequency allocation is proposed to make dynamic system capacity for both macrocell and femtocell wireless networks which is shown in Fig. 1. They are: (a) available frequency; dedicated frequency use and opportunistic frequency use (left portion of Fig. 1), and (b) reserved frequency; macrocell frequency share and femtocell frequency share (right portion of Fig. 1). To make user equipment (UE) compatible with proposed opportunistic system as shown in Fig. 2(a), existing UE should have extra mode sensing and switching mechanisms installed inside it. So, user equipments (UEs) for both macrocell and femtocell are proposed to be reconfigurable capability such as to use the above mentioned proposed frequency allocation schemes as: full mode resource utilization and reserve mode resource utilization states, respectively as shown in Fig. 2(b) [8]. Some other measurable parameters such as user's mobility/speed threshold, signal strength threshold, and decision threshold are also considered for our analysis. Here, the author's contribution is in the proposed IRR scheme, where system supports extra opportunistic user in a dedicated channel which is not fully occupied by its dedicated users at the same time seamlessly. Rest of this paper is organized as follows: section II provides our proposed opportunistic system approach; system modeling is given in section III, section IV presents the numerical results, and finally conclusions are drawn in the last section.

II. PROPOSED OPPORTUNISTIC SYSTEM APPROACH

A. Opportunity Creation in Proposed IRR Scheme

Proper resource utilization should be guaranteed in order to confirm reliable wireless communication with low cost by providing different intelligent ways which is termed as opportunity creation. Here, we provide intelligent resource reallocation (IRR) scheme which is an opportunity creative

978-1-4673-9257-0/15/$31.00 ©2015 IEEE

scheme by which overall system capacity of advanced heterogeneous wireless network can be increased along with reduced congestion problem. Congestion problem occurs when available system resource is smaller than demanded by users. For instance, let us consider a wireless system where macrocell and femtocell coexists to form advanced wireless network as shown in Fig. 3. From Fig. 3 we can see that, a channel k is allocated to j dedicated user group (UG_{dj}) where $j = 1, 2, \ldots, J$ and $l < J$ in different time slot number, N_{ts} uniformly without prior knowledge about user's actual resource demand as shown in Fig. 2(a) or actual required resource utilization as shown in Fig. 2(b). Now resource utilization occurs by different users according to their type of activities and in this case activities are not same for all users which mean different activities for each user. For this reason with existing fixed resource allocation scheme capacity of wireless network is fixed as shown in Fig. 3. With this fixed capacity of existing system users experiences more congestion problem as shown in Fig. 4, along with high rate of call drop, increased intra- and/or inter-system handover problem. To avoid these problems we proposed IRR scheme among heterogeneous system for users by considering different preliminaries and measurement of different system parameters as shown in Fig. 5.

B. *Capacity Enhancement and Congestion Reduction*

The capacity of a wireless system should be adequate to support extra users without overloading channel, increasing interference level, and higher call drop problems. Call drop rate increases with high rate of user's resource utilization in a fixed or limited capacity wireless system and also which causes high congestion problem. Fig. 6 depicts an intelligent way of resource reallocation technique to make a system with limited capacity into a dynamic capacity. Figure 6 shows that how the capacity of a particular channel in advanced macro integrated femtocellular or heterogeneous wireless network changes from fixed capacity to variable capacity according to user's activity such as actual resource demand and utilization. The natures of activities of different users are different located at the same geographic region that is under the same (only femtocell or macrocell nework) or different network (heterogeneous network) which is serving them. We can also see that each channel is reallocated at different time slots and different hypothesis are allocated for each utilization time slot for UG_{dj} such as hypotheses $H_{01,k}$ is given to first time slot (UG_{d1}), fourth time slot (UG_{d4}) and last time slot (UG_{dJ}) user group over channel k and $k = 1, 2, \ldots, K$. The hypothesis $H_{01,k}$ is indicating that among these three dedicated users group each user's resource utilization state is up to lower threshold limit ($\gamma_{low,k}$). These lower limits is less than 50% of maximum capacity of serving channel k where we can easily create opportunity for new cognitive or opportunistic user groups (UG_{cj}) where $j = 1, 2, \ldots, J$ and $l < J$ at different time slots number, N_{ts} such as UG_{c1}, UG_{c4} and UG_{cJ}. Then UG_{d1}, UG_{d4}, and UG_{dJ} and UG_{c1}, UG_{c4}, and UG_{cJ} user groups get new hypothesis notation from system as hypothesis $H_{11,kNd}$ (fully utilized channel by UG_{dj}) and hypothesis $H_{00,kNc}$ (empty channel available for UG_{cj}),

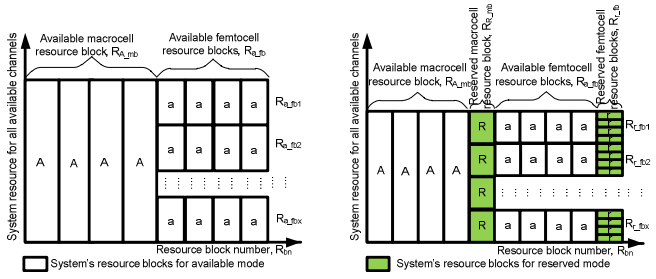

Figure 1. Allocated resource status in a channel for poposed IRR scheme in existing advanced heterogeneous wireless network.

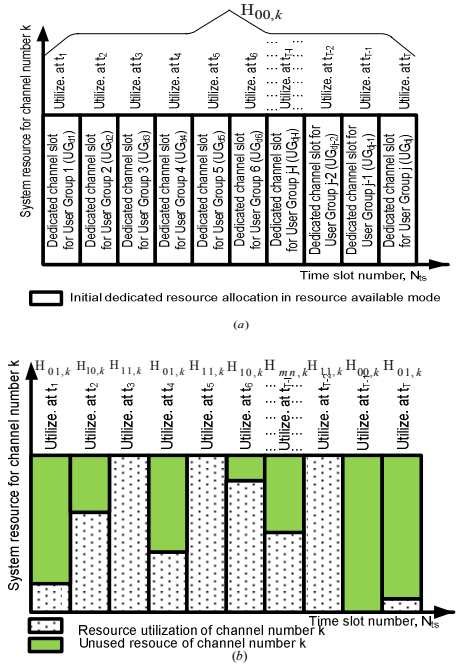

Figure 2. Allocated (a) resource status and (b) resource actual utilization status in a channel for existing advanced heterogeneous wireless network.

respectively. From hypothesis $H_{00,kNc}$, system can allow new opportunistic user to be served and hence capacity is increased. This process is done for each hypothesis except $H_{11,kN}$. Therefore, by comparing between two types of capacity such as without IRR that is fixed system capacity and with IRR that is dynamic system capacity, it is obvious that with proposed IRR scheme the dynamic system capacity serves more users than existing system having fixed capacity. The white area with dashed circle of different femto access points (FAPs) of later scenario indicates resource scarcity. With resource scarcity the new users can not be connected to the system and hence causes call drops, low signal quality and congestion problem for the existing system. With proposed IRR scheme the former scenario shows less congestion for the same number of users causing high user satisfaction in existing system. Resource is reallocated by the system in such a way that each connected users (FAPs with dotted white colored coverage area as shown in Fig. 7) can be served properly and unutilized resources are harvested to reallocate

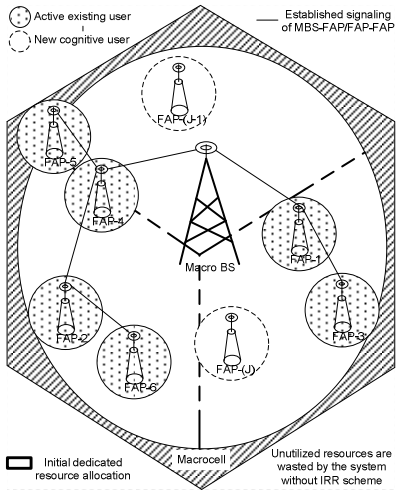

Figure 3. Scenario of capacity problem in existing advanced heterogeneous wireless network.

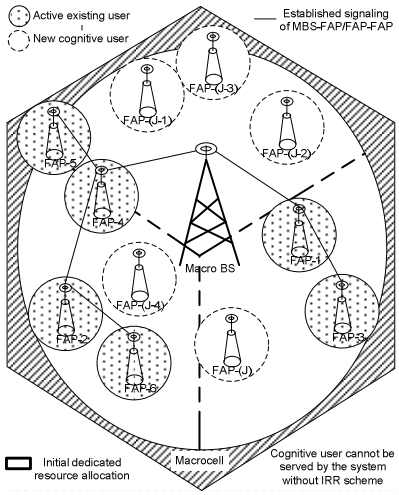

Figure 4. Scenario of congestion in existing advanced heterogeneous wireless network.

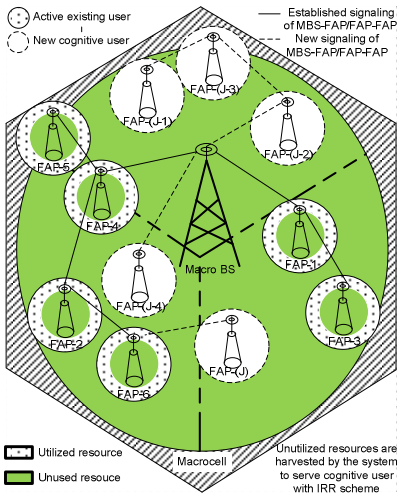

Figure 5. Scenario of resource utilization with IRR scheme in existing advanced heterogeneous wireless network.

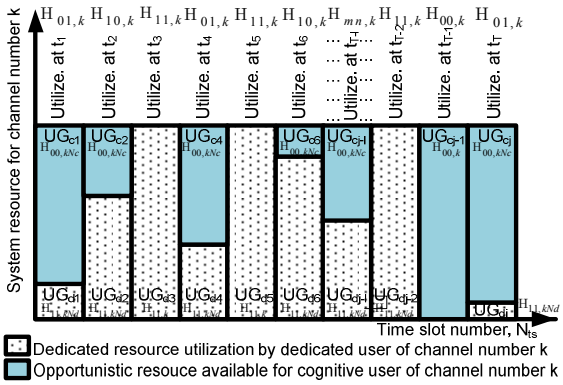

Figure 6. Allocated resource rescheduled status in a channel for poposed IRR scheme in existing advanced heterogeneous wireless network.

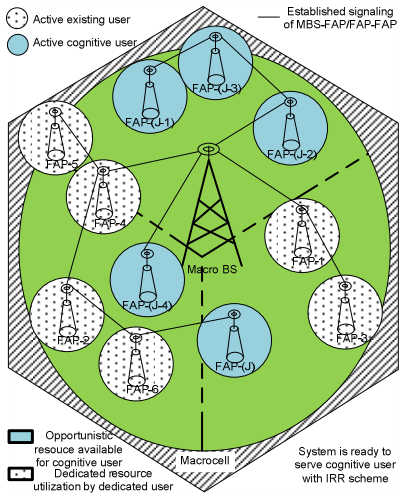

Figure 7. Scenario of IRR scheme with dynamic capacity and reduced congestion in existing advanced heterogeneous wireless network.

them to new users (FAPs with light blue colored coverage area as shown in Fig. 7). As in the network, rate of association of new users increases in a particular area causes congestion problem so, as reverse process (rate of existing user leaving the network) reduces this problem. But there is a predefined minimum resource allotment is required to allow a new user in a network which put limits to minimization of congestion. Therefore, proposed IRR scheme outperforms over existing scheme in minimizing congestion in the advanced heterogeneous wireless network. In proposed IRR scheme, when capacity increases for a certain user groups (causing congestion for existing system), causes less congestion as shown in Fig. 7 problem by opportunity creation by the system itself in an intelligent way.

III. System Modeling

In this section we provide a model of our system with k number of channels. Advanced wireless network system having macro integrated femtocellular that is heterogeneous network is modeled here and details are given in the following:

A. Hypothesis for Opportunistic System Approach

We consider four binary hypotheses to provide coordination among different allocated channels and its user's. These hypotheses are:

$$\mathrm{H}_{00,k} = (\text{"}Full\ Empty\text{"}) = Full\ Opportunity\ (FO)$$

$$\mathrm{H}_{01,k} = (\text{"}Partial\ Occupied\text{"}) = High\ Partial\ Opportunity\ (HPO)$$

$$\mathrm{H}_{10,k} = (\text{"}Partial\ Empty\text{"}) = Less\ \ Partial\ Opportunity\ (LPO)$$

$$\mathrm{H}_{11,k} = (\text{"}Full\ Occupied\text{"}) = No\ Opportunity\ (NO)$$

where 0 (channel utilization absent) and 1 (channel utilization present), respectively gives user channel utilization states over channel k and $k = 1, 2, \ldots, K$.

B. Some Decision Preliminaries

- System monitors environment continuously to identify load flow.
- If system finds any user doing real time activity then system gives this user highest priority of reliability that is not to interrupt.
- If system finds any user doing non real time activity then system gives this user lowest priority of reliability that is tries to interrupt.
- If system manages to create opportunity for new users then reallocation of resources occurs.
- System gives access to new user to avoid congestion by taking proper measurements of user's mobility, required resource demand, resource utilization type, and duration of activity etc.

C. Necessary Mathematical Relations

Decision probability of providing proper hypothesis to a channel during channel resource reallocation is

$$\Pr(\mathrm{H}_{mn,k}) = \frac{1}{4k}\Delta_k \tag{1}$$

where $\Pr(\mathrm{H}_{mn,k})$ is probability of providing proper hypothesis to a channel with subscript notation m (where $m = 0\ or\ 1$) and n (where $n = 0\ or\ 1$), and Δ_k is decision threshold over channel k and $k = 1, 2, \ldots, K$.

Channel resource utilization threshold is

$$Z_{u_j,k} = \begin{cases} \gamma_{0,k}(H_{00,k}) \\ \gamma_{low,k}(H_{01,k}) \\ \gamma_{up,k}(H_{10,k}) \\ \gamma_{max,k}(H_{11,k}) \end{cases} \quad \text{for user u_j, whwre j=1,2,} \ldots \text{,J} \tag{2}$$

where $Z_{u_j,k}$ is channel utilization threshold for user u_j, $j = 1, 2, \ldots, \mathrm{J}$ of channel k and $k = 1, 2, \ldots, K$.

Actual utilized channel capacity is

$$C_{Z,k} = \sum_{k=1}^{K} C_k Z_{u_j,k} \tag{3}$$

where $C_k = W_k \log_2(1 + SNIR_k)$ is actual capacity with channel bandwidth W_k and signal-to-noise plus interference ratio $SNIR_k$ of channel k and $k = 1, 2, \ldots, K$.

Opportunistic utilizable channel capacity is

$$C_{O_Z,k} = \sum_{k=1}^{K} C_k \Pr(\mathrm{H}_{mn,k})(1 - Z_{u_j,k}) = \frac{1}{4k}\sum_{k=1}^{K} C_k \Delta_k (1 - Z_{u_j,k}) \tag{4}$$

where $1 - Z_{u_j,k}$ is channel opportunistic utilizable spaces for user u_j, $j = 1, 2, \ldots, \mathrm{J}$ of channel k and $k = 1, 2, \ldots, K$.

User's satisfaction in resource utilization is

$$S_{u_j,k} = \begin{cases} \sum_{k=1}^{K} s_k Z_{u_j,k}, & \text{for static capacity system} \\ \sum_{k=1}^{K} s_k Z_{u_j,k} + \frac{1}{4k}\sum_{k=1}^{K} s_k \Delta_k (1 - Z_{u_j,k}), & \text{for dynamic capacity system} \end{cases} \quad \text{where } s_k = \begin{cases} 0 \\ 1 \end{cases} \tag{5}$$

where $S_{u_j,k}$ is total user's satisfaction of satisfied user, and s_k is user's level of satisfaction (0 for no satisfaction and 1 for satisfied) per channel for total user u_j, $j = 1, 2, \ldots, \mathrm{J}$ of channel k and $k = 1, 2, \ldots, K$.

Total revenue gain of operator is

$$R_k = \sum_{r=1}^{k} r_{v,k}\left(\sum_{k=1}^{K} C_k (Z_{u_j,k}) + \frac{1}{4k}\sum_{k=1}^{K} C_k \Delta_k (1 - Z_{u_j,k})\right) + r_{f,k} \tag{6}$$

where R_k is revenue earning of operator, r_{vk} rate of variable cost, and r_{fk} rate of fixed cost for contribution of user u_j, $j = 1, 2, \ldots, \mathrm{J}$ of channel k and $k = 1, 2, \ldots, K$.

D. Some Basic Observations of System

- Is it healthy (without any abnormality) system or not?
- Is it fully occupied or not?
- Is there any unused resource exists or not?
- Is there any user that demanding more or less overhead than system can provide or not (near/far-location effect)?

- Is there any user that is only connected without doing any significant activity for a long/predefined/any specified time or not?
- Is there any user that needs to use the system urgently with low/high mobility or not?
- Is there any user that is leaving the system urgently with low/high mobility or not?
- Is congestion exists or not?
- Is congestion exists due to non availability of resources or not?
- Is congestion exists due to uncontrolled traffic flow in a busy area/hot spot or not?
- Is the quality of signal adequate or not?
- Is the rate of user movement inwards or outwards of the system high/low creates congestion or not?
- Is call drop rate is high/low due to congestion or not?
- Is there any unused resource which is already allocated or not?

Finally, system search for unused resources and reallocate it again to enhance overall wireless system capacity as shown in Fig. 7.

IV. NUMERICAL RESULT

Let us, consider a system as shown in Fig. 3 where number of serving channel is k with $k = 1, 2, \ldots, K$.

A. Table and Algorithm

1) Data table for analysis: The conditional values used in the analyses are given in the following table. Different threshold values are also given in the table.

TABLE I. CONDITIONAL VALUES USED IN ANALYSES

Sl. No.	Criteria Details		
	Description	***Lower limit***	***Upper limit***
1	Full opportunity[a], $H_{00,k}$	0.76	1.00
2	High partial opportunity[a], $H_{01,k}$	0.51	0.75
3	Less partial opportunity[a], $H_{10,k}$	0.26	0.50
4	No opportunity[a], $H_{11,k}$	0.00	0.25
5	Number of femto user per FAP, u_j_f	0	5
6	Number of existing FAP, n_{fap}	1	100
7	Number of extra FAP, n_{fape}	1	20
8	Number of existing macro user, u_j_m	0	1000
9	Number of extra macro user, u_j_{me}	0	400
10	Number of channel, k	1	10
11	Decision threshold, Δ_k	0	1
12	Channel utilization threshold, $Z_{u_j,k}$	0.00	0.95

a. Hypothesis selection criteria. (For IRR scheme)

2) Algorithm for hypothesis selection: To select and reshedule the resources, proper hypotheses selection for each channel is required and is given as follows.

a) Step 1: After system power is on, system initialization and basic system parameters reading process is done.

b) Step 2: Check network environment to get information about user, network, and available resouce allocation, utilization, and management.

c) Step 3: Acoording to step 2 select proper frequency selection schem and power control scheme.

d) Step 4: System continuously monitors the network and user's activity to control traffic.

e) Step 5: At initial stage that is when full opportunity is avalable $(\gamma_{0,k})$ for all users then system selects hypothesis $H_{00,k}$ as shown in Fig. 2(a) for channel k and $k = 1, 2, \ldots, K$.

f) Step 6: When user's activity increses in each channel and in a particular channel resource allocation is utilized upto lower threshold limit $(\gamma_{low,k})$ of that channel by the user's of that particular channel then system selects hypothesis $H_{01,k}$ as shown in Fig. 2(b) for channel k and $k = 1, 2, \ldots, K$.

g) Step 7: Again user's activity increses in each channel and in a particular channel resource allocation is utilized upto upper threshold limit $(\gamma_{up,k})$ of that channel by the user's of that particular channel then system selects hypothesis $H_{10,k}$ as shown in Fig. 2(b) for channel k and $k = 1, 2, \ldots, K$.

h) Step 8: Now user's activity increses in each channel and in a particular channel resource allocation is fully utilized up to maximum limit $(\gamma_{\max,k})$ of that channel by the user's of that particular channel then system selects hypothesis $H_{11,k}$ as shown in Fig. 2(b) for channel k and $k = 1, 2, \ldots, K$.

i) Step 9: While system doing this each time, system conditions changes and step 5 to step 8 is repeated according to users activity as shown in Fig. 6. Thus, the capacity of the system changes from static to dynamic to a certain extent according to different criteria.

B. User satisfaction performance comparison

Figure 8 shows that, the capacity of a particular channel in advanced macro integrated femtocellular or heterogeneous wireless network provides better user's satisfaction. For existing system the capacity is static so number of user for a specific channel number k is fixed though that channel is not fully utilized by all the users all the time. For this reason at busy time extra user causes congestion problem. Mean while if that extra user can be served with reserved resource as shown in Fig. 1 (right portion) which is proposed in IRR scheme for the system, then user would suffer less congestion problem which ensures higher user's satisfaction.

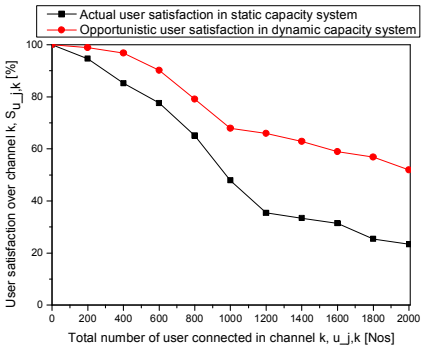

Figure 8. Performance evaluation for user satisfaction versus total number of user connected in both static and dynamic capacity system.

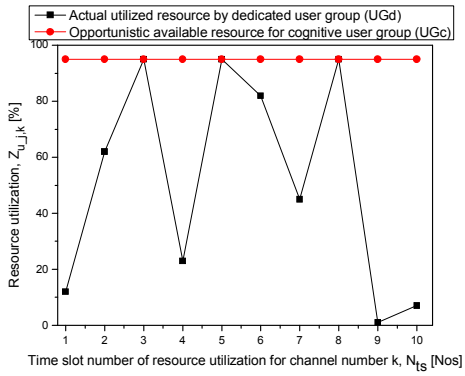

Figure 9. Performance evaluation for resource utilization versus time slot number of resource utilization for channel number k for both static and dynamic capacity system.

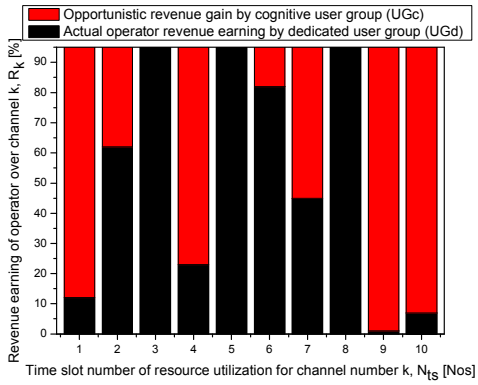

Figure 10. Performance evaluation for revenue earning of operator versus time slot number of resource utilization for channel number k for both static and dynamic capacity system.

C. *Resource utilization and revenue earning of operator performance comparison*

Figure 9 depicts efficient resource utilization for the system with less congestion with proposed IRR scheme than typical fixed resource allocation scheme. When there is less actual resource utilization in existing system then higher the opportunistic resource utilization exists in IRR scheme. We can see from Fig. 9 that for a specific channel number k when user's resource utilization is high, then low possibility of opportunity to reallocate the resource to extra users of that particular channel.

Figure 10 shows a revenue gain of operator when efficient resource utilization occurs for the system with less congestion with proposed IRR scheme than typical fixed resource allocation scheme. When there is less actual resource utilization in existing system then higher the opportunistic resource utilization exists in IRR scheme which in turn provides revenue gain opportunity to system operator. Here, when resource utilization for a specific channel number k is higher then number of user for that channel k is high and hence higher the revenue gain for system operator.

V. CONCLUSIONS

Advanced wireless network is a demanding issue for reliable and high speed communication with low power consumption, and user friendly service. For this reason user satisfaction level need to be consider as an evaluation parameter in both systems that is with existing fixed capacity and with proposed IRR scheme dynamic capacity. The user satisfaction level outperformed in proposed IRR scheme utilized system than existing typical system with increased number of users as shown in performance curve. In near future traffic will increase exponentially more than today so, channel capacity requirement would be higher than today's system. To do so with limited resources best utilization of resource is required. Along with capacity problem, dense traffic in communication channel causes significant congestion. To reduce these capacity and congestion problems together, proposed IRR scheme is a strong candidate to face the challenges associated. Performance of existing fixed capacity system in resource utilization and revenue earning of operator is poor than proposed IRR scheme performance as shown in evaluation line and bar graphs, respectively. Thus, proposed IRR scheme is promising one.

REFERENCES

[1] K. Pahlavan and P. Krishnamurthy, Principles of Wireless Networks, Prentice Hall PTR, New Jersey, 2002.

[2] J. D. Hobby and H. Claussen, "Deployment Options for Femtocells and Their Impact on Existing Macrocellular Networks," *Bell Labs Technical Journal*, vol. 13, no. 4, pp. 145-160, Feb. 2009.

[3] M. Z. Chowdhury, Y. M. Jang, and Z. J. Haas, "Network Evolution and QoS Provisioning for Integrated Femtocell/Macrocell Networks," *International Journal of Wireless & Mobile Networks (IJWMN)*, vol. 2, no. 3, pp. 1-16, Aug. 2010.

[4] Femtoforum, "OFDMA Interference Study: Evaluation Methodology Document," Nov. 2008.

[5] A. Wyglinski, M. Nekovee, and Y. Hou, Cognitive Radio Communications and Networks Principles and Practice, New York: Elsevier, 2010.

[6] K. N. Azam and M. Z. Chowdhury, "Intelligent Interference Management Based on On-Demand Service Connectivity for Femtocellular Networks" in Proceeding of *IEEE International Conference on Informatics, Electronics & Vision (ICIEV)*, May 2013.

[7] M. Z. Chowdhury, Y. M. Jang, and Z. J. Haas, "Cost-Effective Frequency Planning for Capacity Enhancement of Femtocellular Networks," *Wireless Personal Communications*, vol. 60, no.1, pp. 83-104, Sept. 2011.

[8] 3GPP TS 32.500, "Telecommunication Management; Self-Organizing Networks (SON); Concepts and Requirements," Jun. 2011.

A Comparative Analysis of the Characterization Methods for Submicron Silicon Waveguide Propagation Loss

Mohammad Istiaque Reja[1,2,3*], Jobaida Akhtar[1,2,3], Muhammad Nouman Malik[2,3], Md. Jahedul Islam[4], Md Asif Iqbal[3], Shamim Ahmed[2]

[1]Chittagong University of Engineering and Technology, Bangladesh
[2]Scuola Superiore Sant'Anna, Pisa, Italy
[3]Aston Institute of Photonic Technology, Aston University, United Kingdom
[4]University of Sydney, Australia
[*] E-mail: m.istiaquereja@master.sssup.it, rejami@aston.ac.uk

Abstract— **An important parameter in integrated optical device is the propagation loss of the waveguide. Its characterization gives the information of the fabrication quality as well as the information of other passive devices on the chip as it is the basic building block of the passive devices. Although, over the last three decades many methods have been developed, there is not a single standard present yet. This paper presents a comparative analysis of the methods existing from the past as well as methods developed very recently in order to provide a complete picture of the pros and cons of different types of methods and from this comparison the best method is suggested according to the authors opinion. To support the claim, apart from the analytical comparison, this paper also presents a comparison performed with the experimental results between the suggested best method which is recently proposed by Massachusetts Institute of Technology (MIT) researchers based on undercoupled all-pass microring structure and the popular cut-back method.**

Keywords— Integrated optics, Si photonics, waveguide propagation loss, microring reseonator.

I. INTRODUCTION

The most important feature that has made 'Silicon' the ideal and best candidate for next generation of interconnection network on chip requiring large bandwidth is the fact that it is compatible with complementary metal-oxide-semiconductor (CMOS) technology. This property has made it possible to fabricate optoelectronic chip monolithically in a cost-effective way using Silicon-on-insulator (SOI) platform [1].

A natural planar optical waveguide with a refractive index of about 3.5 for Si core and 1.46 for SiO_2 cladding at 1550 nm is provided by SOI structure. Very strong optical confinement in waveguide is possible using this high refractive index difference. This structure also allows to make waveguides with small bend radii and makes silicon the best choice for making the important photonic devices like microring having very low bend radius. Moreover this fact enables to reduce the footprint of the devices and increase the density of the integration [2].An important parameter in integrated silicon photonic devices is the propagation loss of waveguide. So to ascertain the suitability of the silicon waveguides for specific application, it is very essential to characterize the loss properly. Most of the propagation losses in Si nanowire arise mainly due to the sidewall roughness and this roughness is a result of the fabrication process, more specifically lithography and etch process [3]. Typical Roughness value is of the order of 2 nm (having a correlation length of ~40nm), which is a large value for a Si waveguide width of submicron order. So, this high roughness results to a high propagation loss of the order of 2 dB/cm [4].

Also, we know that the quality of all the passive element can be specified by knowing the quality of the silicon waveguide as it is the fundamental building block of a silicon photonic circuit. So, characterizing the waveguide loss not only help us to know the quality of the waveguide in terms of fabrication accuracy but also gives us a hint about the quality of the other passive device on the silicon chip.

There is not a single standard yet for measurement of the waveguide loss [4]. Many methods have been developed over the last three decades for measuring the loss accurately. In this paper the common loss characterization methods which are generally used will be described and their pros and cons will be presented. Also the methods, which researchers have proposed recently will be compared with the existing commonly used methods. From this comparison a conclusion will be drawn to suggest the best method according to the authors opinion. To support the claim, the suggested best method which has been reported in 2013 by the Massachusetts Institute of Technology (MIT) researchers [4] will be explained in a greater detail with some simulation results and its superiority will be assessed experimentally by comparing with an existing popular method.

II. DESCRIPTION OF DIFFERENT TYPES OF LOSS CHARACTERIZATION METHODS

A. Commonly used methods

The methods which are commonly used to measure the waveguide loss can be categorized into four types.

978-1-4673-9257-0/15/$31.00 ©2015 IEEE

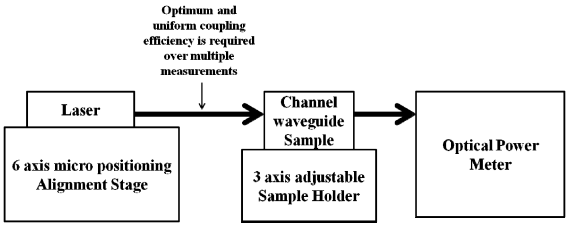

Figure 1. The measurement setup for cut-back method

These are: (i) the cut-back or paper-clip method; (ii) the Fabry-Perot resonance method; (iii) scattered light measurement method and (iv) Sliding prism method [5]. These methods are described briefly in the following subsections.

(i) Cut-back or paper-clip method

This method is based on a very simple concept. A channel waveguide sample of length l_1 is excited by a laser and then output power from the waveguide P_1 is measured. The same procedure is followed for another length l_2 and output power P_2 is measured. Therefore, we can write

$$\frac{P_1}{P_2} = exp^{-\alpha(l_1 - l_2)} \quad (1)$$

Here waveguide propagation loss (α) is in cm^{-1}. Hence, α in dB/cm

$$\alpha = 10\, log_{10}\left(\frac{1}{l_1 - l_2} ln(\frac{P_1}{P_2})\right) \quad (2)$$

However, it is not easy to make waveguides of different lengths maintaining the same quality. So, in order to change the length of the waveguide it is cut after each measurement. After cleaving the waveguide sample the edge of the waveguide facet is polished. A series of measurements are done following this procedure with different sample lengths. The output power is measured by using a optical power meter [5], [6]. The measurement setup is schematically shown in the fig. 1.

In spite of the fact that this method is very fast and simple, the accuracy of this method is poor. Because it is difficult to maintain uniform facet quality and coupling efficiency during every measurement after cutting the waveguide.

(ii) Fabry-Perot (FP) resonance method

This method is based on the concept that a waveguide can be thought of a Fabry-Perot cavity where the two facets can act as mirrors. So, the Fabry-Perot resonances can be used to measure the propagation loss [5].

The waveguide propagation loss α can be written as,

$$\alpha = -\frac{1}{L} ln\left(\frac{1}{R}\frac{\sqrt{I_{max}/I_{min}} - 1}{\sqrt{I_{max}/I_{min}} + 1}\right) \quad (3)$$

where R is the reflectivity of the facet and L is the sample length, I_{max} and I_{min} denotes the maximum and minimum transmission intensity respectively [7].

This method is more accurate than cutback method as it is more repeatable [5] and is independent of the requirement of the input coupling knowledge. But here another problem arises which is the requirement of facet reflectivity estimation and the accuracy of this method mostly depends on the knowledge of facet reflectivity [7]. Moreover, it is necessary to use a stabilized light source to maintain constant input power over Fabry-Perot fringes measurement and a source having narrow line-width.

It has been shown in [8] that, the requirement of the knowledge of facet reflectivity can be eliminated by measuring the transmission and reflection both from FP cavity. But in that case the power from the input facet need to be measured very precisely and carefully. Moreover, both from the input and output sides, similar coupling efficiencies are needed. These requirements are very complex to accomplish in the experimental setup.

So, the problem with the FP resonance method is that the experimental procedure is quite complex here.

(iii) Scattered light measurement method

This method is based on the concept that the scattered light can be measured from the top of the surface along the waveguide length in order to measure the loss [9]. It is assumed in this method that the amount of scattered light will increase with the increase of the propagated light inside the waveguide. An optical fiber can be scanned along the waveguide length in order to collect the light [5]. Though this method is independent of input coupling losses, it can be easily understood that the accuracy of this method is limited by the wafer surface quality [7].

(iv) Sliding prism method

The propagation loss can be measured by using the sliding prism method. This is also a widely used method. This method is based on the concept of measuring the guided power at varying distance from the input coupling region through the use of sliding prism placed at right-angle and thus measuring the propagation loss [10].

An experimental setup for this method is shown in fig. 2 [5]. The slab waveguide sample must be clamped very tightly under the prism. In order to couple the prism with the modes of the waveguide, either the guided mode or the substrate mode, the contact between the prism and the waveguide must be very good. Also dirt free prism must be needed [5].

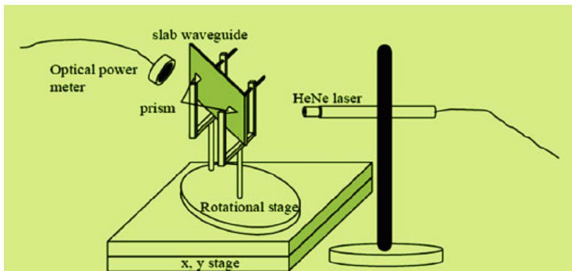

Figure 2. The measurement setup for sliding prism method [5]

The problem with this method is that the requirement of complex mechanical arrangement makes the experimental procedure difficult.

B. *Recently developed methods*

(i) Modified FP method

In conventional FP method, in order to fulfill the necessity of narrow linewidth source, external cavity tunable lasers are used. But it is not easy to stabilize it when wide wavelength region is needed. Moreover this kind of light source is also expensive. So broadband low-coherence source, which has low cost, is desirable.

It has also several other advantages over high coherence tunable lasers such as more stability in comparison to the tunable lasers and it is less prone to reflections. Also it is possible to measure over multiple wavelengths in one single measurement in contrast to the tunable laser [7].

But the issue with the broadband source such as superluminescent diode is, with the change in wavelength the input power also changes which made it difficult for the broadband source to be used in FP method. In [7], Sareh tabi *et al*. proposed a modification in conventional FP method, where they suggest a way of curve fitting in order to solve the issue of power change in broadband light source. So, in this modified method the experimental procedure has been simplified due to the use of broadband superluminescent diode.

This method also suggests a way in order to solve the reflectivity measurement issue, since for accurate measurement, the knowledge of the reflectivity is needed. They have rewritten the equation (3) as

$$-\alpha L = ln\left(\frac{1}{R}\right) + ln\left(\frac{\sqrt{I_{max}/I_{min}} - 1}{\sqrt{I_{max}/I_{min}} + 1}\right) \quad (4)$$

After that, measurement for different length waveguides are done and the value of $ln\left(\frac{\sqrt{I_{max}/I_{min}}-1}{\sqrt{I_{max}/I_{min}}+1}\right)$ is plotted with respect to length L. From this plot, the loss and the reflectivity both can be measured without assuming either of the two. Loss (α) can be found from the slope of the curve and reflectivity (R) can be measured from the intercept.

This method was proposed in 2008. Although this method is not very recent, in comparison to the other methods, proposed long ago, it can be considered as a recent method.

To summarize, this method uses curve fitting approach to solve the power consumption issue in broadband low-coherence source and eliminates the requirement of the narrow linewidth source which is very difficult to stabilize. Also, the reflectivity measurement issue is solved by taking measurement from different length waveguides. So, by solving the problems of conventional FP method, this modified FP method provides very accurate results.

(ii) Method based on undercoupled All-Pass microring structure

This is a very simple method proposed by the Massachusetts Institute of Technology (MIT) researchers in 2013 [4], which can measure the loss very accurately using simple undercoupled microring structure. The loss is measured here by way of fitting the experimental spectrum with the simulated curve generated from the developed all-pass model. The concept of this method is based on the interplay between standing wave modes and traveling ring modes which arise due to back-reflection from edge roughness.

In this method a number of microrings are coupled with a common bus waveguide with different bus to ring gap. All of the rings have radius around 10 micrometer and the radius is varied very slightly in order to have different free spectral ranges. Fig. 3 shows the schematic diagram of the structure.

In fig. 4 the five resonances corresponding to the five rings are shown. It can be seen that the first three rings which do not show any splitting in the resonances represent the overcoupled condition whereas the last two rings showing clear splitting represent undercoupled condition. The microring quality factor degrades very largely in undercoupled condition which results in a splitting in the resonance. This is because the waveguide loss effect is dominant here over the low bus to ring coupling amount. Thus, the effect of loss is very clear and explicit here. So, the ideal condition for precisely measure the waveguide loss is undercoupled condition.

In the fig. 5 the effect of loss change on the overcoupled and undercoupled resonances have been shown and it can be seen that, in the undercoupled spectrum responses are highly sensitive to α as the depth of the split resonances changes very fast with the increase of the loss.

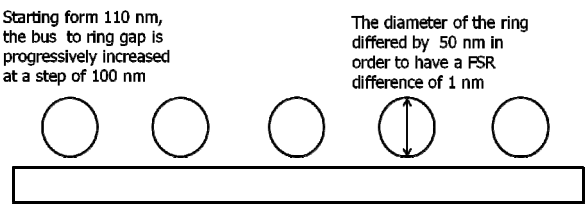

Figure 3. The schematic diagram of the all-pass architecture used in this method

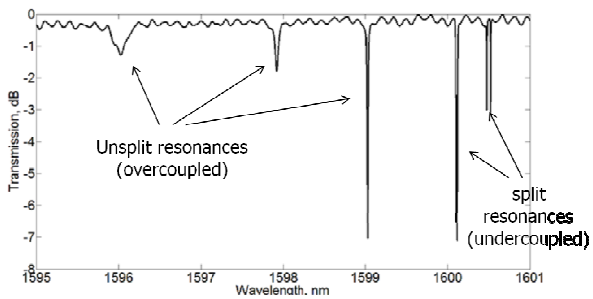

Figure 4. The spectral scan showing the five resonances for the rings having different bus to ring gap.

But, the change of loss does not have a significant effect on the response in overcoupled condition. It has been seen from the simulation results that the more we moves toward the under (over) coupled regime the more (less) sensitive the response becomes with respect to loss.

So, by way of curve fitting, this model propose to measure the waveguide propagation loss in undercoupled condition in order to see the effect of loss more clearly, thus measuring the propagation loss more accurately. Also this model is better from those models which measures the loss by assuming that critical coupling condition is met [11], because spotting the critical coupling condition is extremely difficult and it is highly intolerant [4].

Also, from the model developed it is found that in the undercoupled condition, if the reflection coefficient i.e. the amount of reflected light due to the backscattering increases the separation between the spitted peaks increases as shown in fig.6. This is because, this model considers that each scattering point leads to a backward reflection which is again reflected by the same scattering point after a round trip and thus forms a standing wave. This standing wave interacts with the radiation unaffected by scattering. In summary, the standing wave formation which is due to the intercavity scattering of light is a scenario similar to Fabry Perot (FP) cavity and the propagation of the light radiation which is unaffected by scattering is a scenario similar to travelling wave cavity. The competition between these two cavities determines the presence of the usual transmission dip [4].

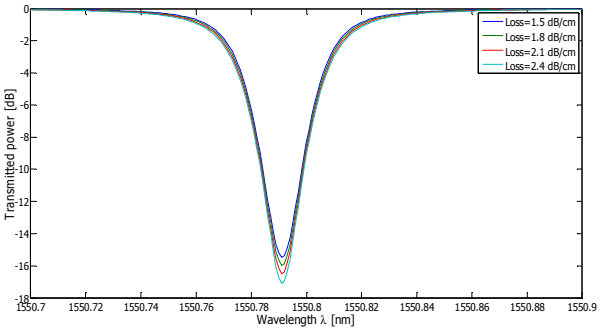

(a)

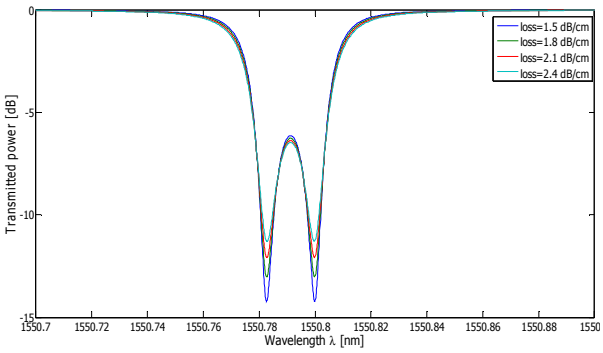

(b)

Figure 5. Effect of loss change in (a) overcoupled and (b) undercoupled condition

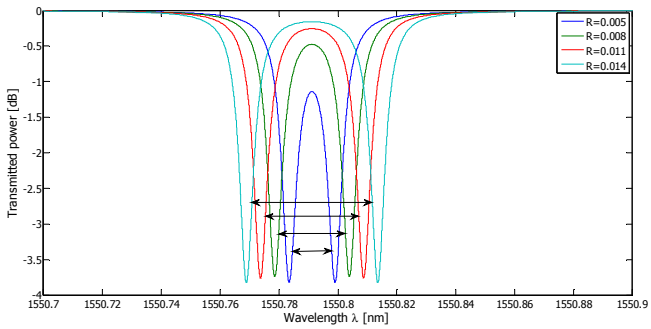

Figure 6. Effect of Reflection coefficient (R) change in undercoupled condition

So, considering all these effects, the simulated spectrum is fitted with the experimental spectrum by changing the value of loss, reflection coefficient and coupling coefficient and finally it gives the value of loss.

The fitting method based on this model is very accurate as seen from a comparison with another model reported in [12] which also assumed the backscattering as the reason for splitting in the resonances. But that model which is based on the concept of double ring filter does not lead to very good fitting in comparison to this model which is based on the competition between FP and travelling wave cavity. Indeed it has been shown in [4], the average loss measured for a number of samples using fitting of this model is 1.7 dB/cm and using the fitting of that double ring based model is 1.1 dB/cm. So, the loss is underestimated.

In summary, the advantage of this method lies on the fact that it is independent of input coupling loss and reflection which leads to very accurate measurement of propagation loss.

III. COMPARATIVE ANALYSIS OF THE METHODS

The popular cut back method, although provides very simple and direct measurement of the loss, has very poor accuracy because of various reasons. Firstly, the quality of the facet changes each time after the cutting. Secondly, The measurements must be performed under optimum input coupling efficiency. Moreover, the coupling efficiency cannot be maintained exactly same for every measurement [13].

In the conventional FP method the requirement of the exact knowledge of facet reflectivity limits the accuracy. Also the need for using stabilized narrow line width sources makes the experimental procedure very difficult.

The sliding prism technique requires extracting light with 100% efficiency. Also, the mechanical arrangement is quite complicated here. A new method, which is a modification of conventional sliding prism technique based on sliding right angle-prism (RP), is proposed in [10] in order to make the operation convenient. This method uses a RP and non sliding isosceles prism (IP) together to get accurate result. But still the method is a bit complex in comparison to other characterization methods.

TABLE I. A COMPARISON OF THE LOSS CHARACTERIZATION METHODS

Comparison parameters	Cut back	Sliding prism	Scattered light measurement	FP resonance	Modified FP	All-pass undercoupled
Input coupling loss dependency	Yes	No	No	No	No	No
Experimental Procedure / Mechanical Arrangement	Simple	Complex	Simple	Complex	Simple	Very simple
Requirement of the estimation of facet reflectivity	No	No	No	Yes	Yes (solved through curve fitting)	No
Curve fitting	No	No	No	No	Yes	Yes
Curve fitting quality	N/A	N/A	N/A	N/A	Very good	Very good
Accuracy	Poor	Poor	Poor	Poor	Good	Good
Reason for the limited accuracy	Requirement of the same facet quality and coupling efficiency over multiple measurements	Requirement of 100% light extraction efficiency	Dependency on the wafer surface quality	Requirement of facet reflectivity knowledge and narrow linewidth stable source	N/A	N/A

The accuracy of the method based on the scattered light measurement depends very strongly on the wafer surface quality.

The modified FP method seems to be very accurate as this method provides the solution of the problems of conventional FP method and may be adopted very widely for loss characterization in future. The experimental procedure has been simplified through the use of curve fitting by using the low coherence broadband source instead of high coherence tunable lasers. This method also provides a way to measure both the reflectivity and loss together without the assumption of the either.

The method based on the undercoupled all-pass microring structure seems to be the best in terms of accuracy and experimental simplicity. This method is totally independent of the input coupling loss and has tolerance to the ring to bus gap choice. This method measures the loss in undercoupled condition where the effect of loss have dominant effect over the bus to ring coupling. So, the loss effect is very explicit here which makes it possible to accurately measure the loss. Moreover, The fitting method, which is based on the concept of the competition between FP cavity and travelling wave cavity, provides very good fitting in contrast to the other fitting model based on double ring cavity.

In table 1 a comparison of different types of methods is presented and it can be said that the best method in terms of simplicity and accuracy is the method based on undercoupled all-pass microring structure.

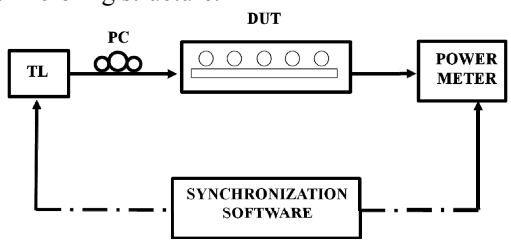

Figure 7. Experimental setup to measure the loss using the method based on all-pass structure

IV. EXPERIMENTAL COMPARISON OF COMMONLY USED 'CUT BACK METHOD' AND METHOD BASED ON 'ALL-PASS UNDERCOUPLED STRUCTURE'

The method based on all-pass undercoupled structure is used to experimentally measure the losses of ten samples. The experimental setup for spectrum measurement is shown in fig. 7. The light from a tunable laser (TL) is coupled into the device under test (DUT) through a polarization controller (PC) that maximizes the coupling efficiency between the fiber and the input grating coupler of the device under test. Then with a synchronized power meter the output spectrum is collected from the 'through' port grating coupler.

By way of fitting the undercoupled resonances taken from all the spectra with the simulated curve, the average loss has been measured as 2.14 dB/cm. The measured loss from the cutback PCM structure is 1.98 dB/cm. So, the loss in the cutback method is underestimated because of its limited accuracy.

V. CONCLUSION

As characterization of loss is an important step to know the quality of the fabrication process many loss measurements methods have been proposed over the last three decades. But still there is not a single standard for this loss characterization. This paper presents a comparative analysis of all types of loss characterization methods in order to provide a complete picture of the advantages and disadvantages of the methods. Widely used loss characterization methods from past are compared with two recently developed methods. From the comparison, the recent method based on undercoupled all-pass microring structure is suggested to be best in terms of simplicity and accuracy. To support this claim an experimental comparison between this method with the popular cut-back method is shown and it is found that the loss is underestimated in cut-back method due to its limited accuracy.

ACKNOWLEDGMENT

The authors would like to thank Scuola Superiore Sant'Anna, Pisa (SSSUP), Italy for providing the laboratory

facility for this work. The authors would also like to acknowledge the support of Institute of Microelectronics (IME), Singapore for the fabrication of PICs that have been used for the loss measurements.

REFERENCES

[1] J. K. Doylend, A. P. Knights, "The evolution of silicon photonics as an enabling technology for optical interconnection," *Laser Photonics Rev*, vol. 6, pp. 504–525, 2012.

[2] T. Hu *et al.,* "Silicon photonic network-on-chip and enabling components," *Science China Technological Sciences*, vol. 56, no. 3, pp. 543-553, March 2013.

[3] M. Williamson and A. Neureuther, "Enhanced, quantitative analysis of resist image contrast upon line edge roughness (LER)" *in Proc. SPIE 5039*, pp. 423–432, 2003.

[4] M. Moresco *et al.,* "Method for characterization of Si waveguide propagation loss" *Optics Express*, vol. 21, no. 5, pp. 5391-5400, 2013.

[5] Tong, Xingcun Colin, *Advanced Materials for Integrated Optical Waveguides*, Springer Series in Advanced Microelectronics, Springer International Publishing Switzerland, 2014, vol. 46.

[6] A. Rickman, G. T. Reed, B. L. Weiss, and F. Namavar, "Low-Loss Planar Optical Waveguides Fabricated in SIMOX Material", *IEEE photonics technology letters,* vol. 4, no. 6, June 1992.

[7] S. Taebi, M. Khorasaninejad, and S. S. Saini, "Modified Fabry-Perot interferometric method for waveguide loss measurement," *Appl. Opt.* vol. 47 no. 35, pp. 6625–6630, 2008.

[8] K. H. Park *et al.*, "Non destructive propagation loss and facet reflectance measurements of GaAs/AlGaAs strip-loaded waveguides" *J. Appl. Phys*., vol. 78, pp.6318–6320, 1995.

[9] Y. Okamura, S. Yoshinaka, and S. Yamamoto, "Measuring mode propagation losses of integrated optical waveguides: a simple method," *Appl. Opt*. vol. 22, pp. 3892–3894, 1983.

[10] J. Wei *et al.*, "Improved method for loss measurements in planar waveguides," *Elsevier Optics and Lasers in Engineering* vol. 45, pp. 419–422, 2007.

[11] T. R. Bourk, M. M. Z. Kharadly, and J. E. Lewis, "Measurement of waveguide attenuation by resonance methods," *Electron. Lett.* Vol. 4, no. 13, pp. 267–268, 1968.

[12] Z. Zhang, M. Dainese, L. Wosinski, and M. Qiu, "Resonance-splitting and enhanced notch depth in SOI ring resonators with mutual mode coupling," *Opt. Express*, vol. 16, no. 7, pp. 4621–4630, 2008.

[13] S. Chen, Q. Yan, Q. Xu, Z. Fan, J. Liu, "Optical waveguide propagation loss measurement using multiple reflections method," *Elsevier Optics Communications*, vol. 256, no.1–3, pp. 68–72, December 2005.

Effect of Complementary Triangular Split Ring Resonator on Microstrip Patch Antenna

Sunanda Roy[1,#], Swadesh Podder[2,*], M. Abdus Samad[1,+]
[1]Khulna University of Engineering & Technology, Bangladesh
[2] Banglalink digital communication ltd, Bangladesh
[#]sunandaroy75@gmail.com, [*]swadesh_ku@live.com, [+]prof.m.a.samad01@gmail.com

Abstract—**In this paper, a new complementary triangular split ring resonator (CTSRR) is proposed and the impact of CTSRR on conventional patch antenna is investigated at 2.44 GHz for WLAN applications. The electromagnetic behavior of CTSRR, as well as their equivalent circuit is developed and explained. The demonstrated theoretical approaches result in a meaningful improvement than in comparison to conventional patch antenna. The parametric studies are completed in this work with the different orientation pattern of CTSRR structure. This is exposed that with the increment of CTSRR on patch, antenna performances improve, but resonance frequency shifts toward lower frequency region.**

Keywords—Complementary triangular split ring resonator (CTSRR), gain, directivity, microstrip patch antenna (MPA), wireless local area network (WLAN).

I. INTRODUCTION

During modern centuries, there is immense evolution in wireless local area network (WLAN) applications. Providing of a quality service for the recently increased demand in WLAN is a core level concern as usually for antenna and communication devices. The WLAN is used in our everyday life applications such as notebooks, mobile phones, routers etc. To meet the daily increasing needs, antennas used in WLAN applications are noteworthy factor. With respect to performance, a low cost feed network with miniaturization in size is also very important to carry out in terms of antenna design. Therefore, microstrip patch antenna (MPA) with compactness, low cost and ease of fabrication is effective for WLAN applications and these are widely presented in books and papers in the last decade [1-3].

The standard microstrip patch antenna has a very low gain, low efficiency, low power handling capacity, narrow bandwidth, simple, and inexpensive to manufacture using modern printed–circuit technology [1]. Many researchers have amended the parameters and modified geometry to produce better performance of the patch antenna considering required applications. These improvements cover several shapes of antennas, addition of special structures, and attachment of RF components or integrated circuits into the patch antenna [2].

Now a day's split ring resonator (SRR) is used to produce the desired magnetic response which influences the applied EM field. Several theoretical and experimental works have been studied by researchers on SRR and their potential applications [4-5].There are many types of split ring resonator design such as edge coupled SRR (EC-SRR) [6],broadside-couple SRR (BC-SRR) [7], nonbianisotropic SRR (NB-SRR) [8] and etc. However, there is a very few work on resonator based patch antenna with conventional substrates. Therefore, proper background understanding of resonator and possible impacts on conventional MPA are indispensable. In this work, a complementary triangular split ring resonator (CTSRR) has been proposed on conventional inset feed patch antenna and effect of the CTSRR on regular MPA has been analyzed from various viewing platform.

II. GEOMETRIC VIEW OF CTSRR

The geometric view of the single unit of complementary triangular split ring resonator is shown in Fig. 1.The outer and inner length of the CTSRR structure is L_{out}= 4.25mm and L_{in}= 3.25mm respectively. The dimension of the resonator gap W_s =0.98mm and the thickness of the triangle T_r =1mm. The distance between two TSRR is 0.66 mm and each dimension is similar to the single unit of CTSRR structure.

For a given resonance frequency (f_r), dielectric constant (ε_r), the design equations for calculating patch width (W) and length (L) of our conventional inset feed rectangular microstrip patch antenna (RMPA) are [9]

$$W=\frac{1}{2f_r\sqrt{\mu_0\varepsilon_0}}\sqrt{\frac{2}{\varepsilon_r+1}}=\frac{c}{2f_r}\sqrt{\frac{2}{\varepsilon_r+1}} \qquad (1)$$

Where, C = free space velocity of light, ε_r =Dielectric constant of substrate, f_r = Resonance Frequency. This width, W makes equal to about half a wavelength. It leads to good radiation efficiencies and acceptable dimensions.

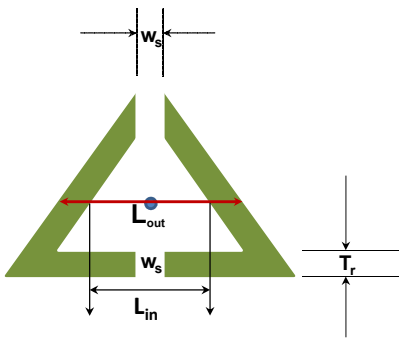

Figure 1. Top view of CTSRR Structure

978-1-4673-9257-0/15/$31.00 ©2015 IEEE

In order to account for the fringing and the wave propagation in the line [10] an effective dielectric constant (ε_{reff}) must be obtained.

$$L_{eff} = \frac{c}{2f_r\sqrt{\varepsilon_{reff}}} \qquad (2)$$

$L_{eff} > L$ .Thus, the resonance condition is

$\beta^{(n)}L_{eff} = n.\frac{\pi}{2}, n = 1, 2, ...$ which depends on L_{eff} , not L.

The effective patch length

$$\frac{\Delta L}{h} = 0.412\frac{(\varepsilon_{erff} + 0.3)(\frac{W}{h} + 0.264)}{(\varepsilon_{erff} - 0.258)(\frac{W}{h} + 0.8)} \qquad (3)$$

Equation (3) shows that the extension of the length ΔL is a function of the ratio $\frac{W}{h}$ and ε_{erff} .

To calculate the effective length, it has been added the length *L* to the extension of the length ΔL.

$$L_{eff} = L + 2\Delta L \qquad (4)$$

The length and width of ground plane L_g and W_g are given as

$$L_g = 6h + L \qquad (5)$$

$$W_g = 6h + L \qquad (6)$$

Where h = substrate height

Substrate height *h* is chosen considering surface wave & spurious radiation minimization for a given dielectric constant such that

$$h \le \frac{c}{4f_r\sqrt{\varepsilon_r - 1}} \qquad (7)$$

After calculating all the data, optimized values (ε_r=2.2, substrate height *h*= 1.5 mm) for patch width and length are *W*= 49.4 mm and *L*= 40 mm. For impedance matching, edge impedance of 50 ohm has been used for all cases and simulation has been done by CST microwave studio.

III. Equivalent Circuit Model: CTSRR Geometry

In Fig. 2(a), the geometrical view of a CTSRR and other dimensions are indicated. The modified structure of CTSRR is newly designed with strip width *c* and spacing g_1 and g_2 between the divided parts of triangle. The equivalent circuit model of the TSRR is presented in Fig. 2(b), which behaves as a resonant cavity modeled by an *LC* circuit. The inductance is due to the gap between the two halves of CTSRR and the capacitance is due to the gaps in the rings itself. The divided pure copper part of triangle contributes a total inductance *L* and C_{g1}, C_{g2} are the gap capacitances due to the triangular splits within the upper and the bottom part respectively. Here, magnetic field H, perpendicular to the plane, allows the creation of gaps capacitance at the opening of the ring.

The electromagnetic properties of CTSRRs have been already analyzed in [11] and [12]. This analysis shows that CTSRRs behave as an *LC* resonator that can be excited by an external magnetic flux and exhibits a strong diamagnetism above their first resonance. CTSRRs also exhibit cross-polarization effects (magneto electric coupling) [12] so that excitation by a properly polarized time-varying external electric field is also possible. This resonant behavior is due to capacitive elements such as gaps and splits, and in turn results in very high positive and negative values of permeability close to f_0 .Therefore, the orientation of the TSRR structure with respect to an electric field may affect the strength of the resonance.

CTSRR can be mainly considered as a resonant magnetic dipole that can be excited by an axial magnetic field [11]. In a more rigorous analysis, the cross-polarization effects in the SRR [11], thus, this element will also exhibit a resonant magnetic polarizability along its y-axis (see Fig. 2 (a)) and, therefore, its main resonance can also be excited by an external magnetic field applied along this direction [13].These features do not affect the intrinsic circuit model of the elements, although they may affect its excitation model.

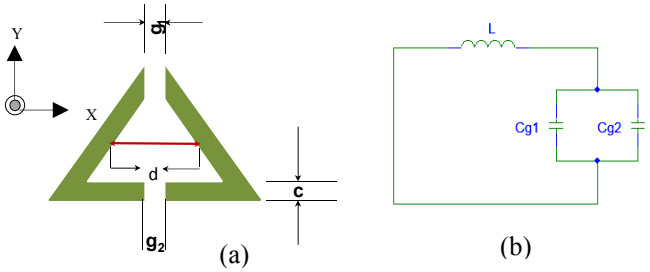

Figure 2. (a) Geometric view of CTSRR, (b) Equivalent circuit of CTSRR

IV. Antenna Design with Complementary Triangular SRR Design

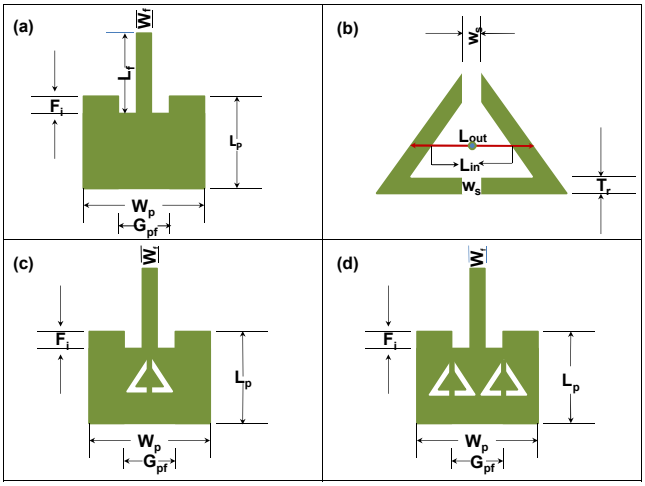

Figure 3. Schematic diagram of (a) Conventional patch antenna, (b) Top view of CTSRR, (c) Antenna with CTSRR, and (d) Antenna with dual CTSRR.

This design is simulated in CST Microwave Studio using a commercially available Roger RT/Duroid 5880 material as substrate with dielectric constant ε_r =2.2 and dielectric loss tangent δ=0.0002. The dimension of the substrate is 50 mm width x 51 mm length. The ground plane is printed in the back side of the substrate with same dimension. A 50Ω port is used to feed power into the radiator. The length of the inset feed (L_f) and the width of the feed line (W_f) for all antennas have been adjusted considering impedance matching. Fig.4 shows the geometrical top view of inset feed patch with different structures. The dimension parameters are shown in following TABLE I.

TABLE I. DIMENSION OF ANTENNA & PROPOSED CTSRR

Geometric Name	Symbol	Dimension (mm)
Resonator outer width	L_{out}	4.25
Resonator inner width	L_{in}	3.25
Thickness of TCR	T_r	1.00
Resonator gap	W_s	0.98
Patch length	L_p	40
Patch wide	W_p	49.4
Substrate length	L_s	52.7
Substrate wide	W_{sb}	50
Feed length	L_f	25.5
Feed wide	W_f	4.85
Slot or Gap of Feed line	G_{pf}	3.5
Substrate height	H	1.5

V. RESULT AND DISCUSSION

In this comparative study it has been studied on the analysis of CTSRR structure on patch antenna design, increment of the number of CTSRR on patch and various orientations of CTSRR structures. The key performance analysis results have been investigated.

The return loss (RL) is a ratio between reflected and transmitted waves at the input of an antenna. In the impedance matching network, better RL is desirable for lower insertion loss, surface wave loss, and spurious radiation loss. From TABLE II, we find that at resonance frequency (f_r), 2.400 GHz, RL of -30.835 dB is obtained for conventional patch antenna and -28.64 dB and -33.39 dB is achieved at f_r of 2.422 GHz and 2.440 GHz for CTSRR and DCTSRR respectively. The RL of patch antennas with various structures are described in Fig. 5. The f_r has been shifted because of fringing effect on MPA due to inclusion of CTSRR. Intersecting point of return loss at - 10 dB line of this design has been evaluated for bandwidth (BW) calculation and for all three antennas obtained BW is almost equal.

For WLAN antenna design the gain and directivity are some other important features need to consider achieving good signal strength for end point user. For conventional antenna gain and directivity of 7.72 dB and 8.09 dBi has been obtained, respectively. Here, proposed resonator structure contains split gaps in opposite ends which store charges and influences radiation pattern on *Z* direction. For 1 CTSRR, gain, and directivity of 7.85 dB, and 8.15 dBi and for 2 TSRR, 7.75 dB and 8.11 dBi has been obtained, individually.

TABLE II. SIMULATED PERFORMANCE OF THE CONVENTIONAL PATCH AND THE OPTIMIZATION DIMENSION OF PATCH ANTENNA

Antenna	Resonance Frequency (f_r) (GHz)	Return Loss(dB)	Gain (dB)	Directivity (dBi)
Normal	2.400	- 30.835	7.72	8.09
1 TSRR	2.422	- 28.864	7.85	8.15
2 TSRR	2.440	- 33.392	7.75	8.11

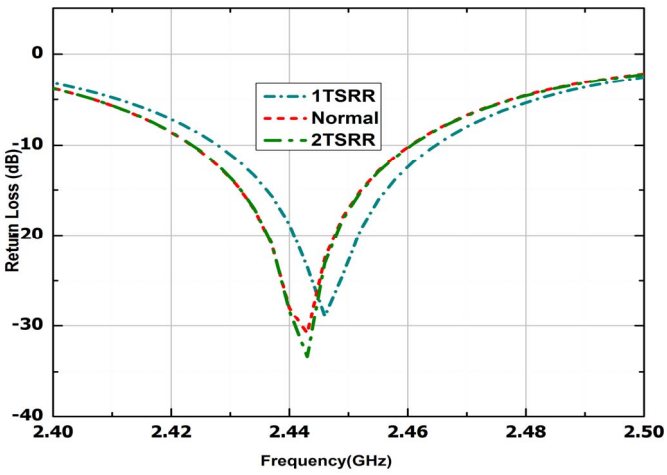

Figure 4. Return loss of normal patch antenna, TSRR & proposed DTSRR.

The radiation pattern is a graphical representation of the relative field strength transmitted from or received by the Antenna, Simply it can be said that the power radiated or received by the Antenna is the function of angular position and radial distribution from the Antenna. In Fig. 6 radiation pattern of the proposed Antenna is revealed. The directivity has been improved by 0.02dBi and radiation efficiency of antenna increase from 91.76% to 94.49%.

From above analysis, we found better RL, optimized gain and directivity for dual CTSRR. So orientation of CTSRR and increment of CTSRR unit cell on conventional patch antenna may have some influence. In this phase of optimization process, antenna performance has been measured with respect to unit cell orientation keeping internal distance equal for all case studies. Fig.7 shows the various orientation of resonant cut triangle of proposed antenna which has been denoted from A to J. All oriented dual CTSRR pattern perform on nearly same resonant frequency. The comparison of return loss among various orientationsis represented in TABLE III and IV. After extensive analysis of data and simulated results among ten oriented patterns from A to J, optimum performance has been obtained by pattern A with 7.75 dB gain and -33.391 dB of return loss while others are inferior than A. These intensive analyses prove that antenna performance also varies with orientation of recommended CTSRR.

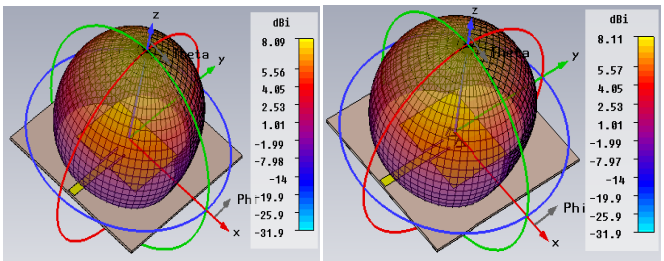

Figure 5. Farfield directivity of Normal and CTSRR Antenna.

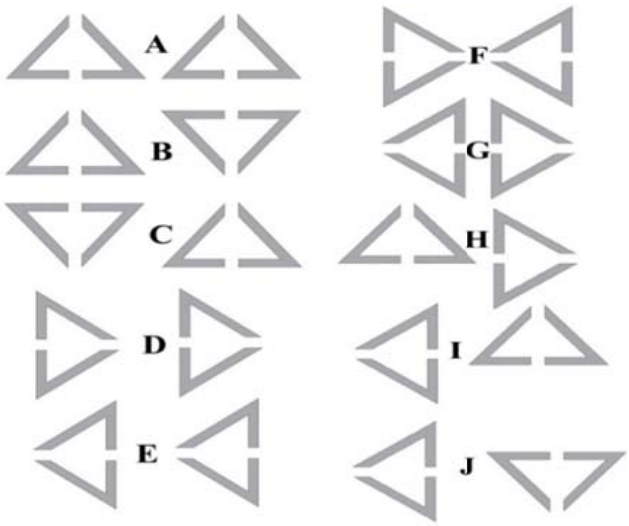

Figure 6. Orientation of dual TSRR Pattern A, B, C, D, E, F, G, H, I and J.

TABLE III. THE RETURN LOSS OF PATCH ANTENNA FOR DIFFERENT DETSRR PATTERN A TO PATTERN E

TSRR Orientation	Resonant frequency, f_r (GHz)	Return loss (dB)	Gain (dB)	Directivity(dBi)
A	2.443	- 33.391	7.75	8.11
B	2.443	- 28.245	7.73	8.10
C	2.443	- 28.175	7.73	8.21
D	2.428	- 23.968	7.39	8.29
E	2.428	-24.727	7.40	8.16

TABLE IV. THE RETURN LOSS OF PATCH ANTENNA FOR DIFFERENT DETSRR PATTERN F TO PATTERN J

TSRR Orientation	Resonant frequency, f_r (GHz)	Return loss (dB)	Gain (dB)	Directivity(dBi)
F	2.428	- 25.449	7.39	8.16
G	2.428	- 24.790	7.41	8.25
H	2.434	- 32.747	7.56	8.27
I	2.437	- 31.636	7.57	8.29
J	2.434	-34.127	7.56	8.28

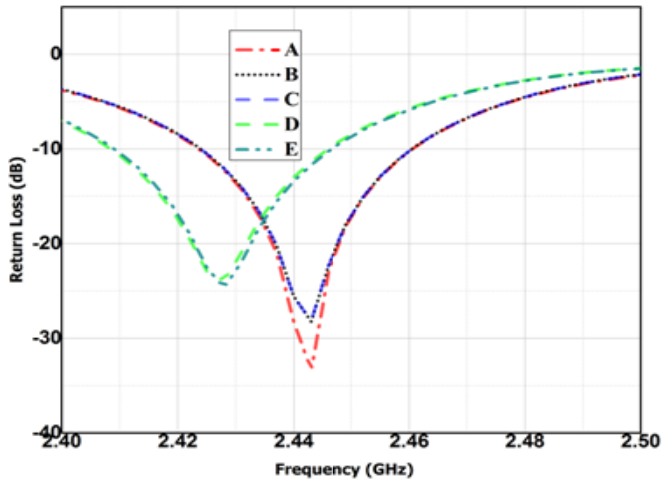

Figure 7. The return loss of patch antenna A to pattern E and pattern F to pattern J.

The directivity is alternative noticeable feature need to consider on WLAN antenna design. The directivity is the capability of an antenna to concentrate energy in a particular direction when transmitting or receiving energy in a specific course. The gain can be linked with directivity using a factor named antenna efficiency. Therefore, the design of MPA with high-directivity is not only essential but also a puzzling assignment. In Fig.10, (a) and (b) represent the Far field gain in polar form and (c) and (d) denotes the Far field directivity pattern from A to J.

In this phase of research our goal is to analysis the performance measurement of WLAN antenna with respect to the increment of CTSRR unit cell. The number of CTSRR addition has been aligned various ways on the patch antenna. TABLE V describes the various antenna parameters with respect to the number of triangular resonators. The variation of return loss in patch antenna with respect to increment of TSRR is expressed in Fig.11.This may be due to addition of capacitive charge concentration across width of MPA. So, incorporation of CTSRR on MPA can be utilized as frequency shifter.

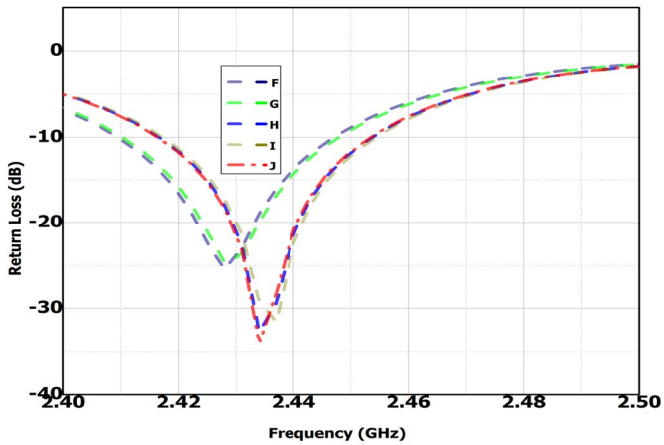

Figure 8. The return loss of patch antenna pattern F to pattern J.

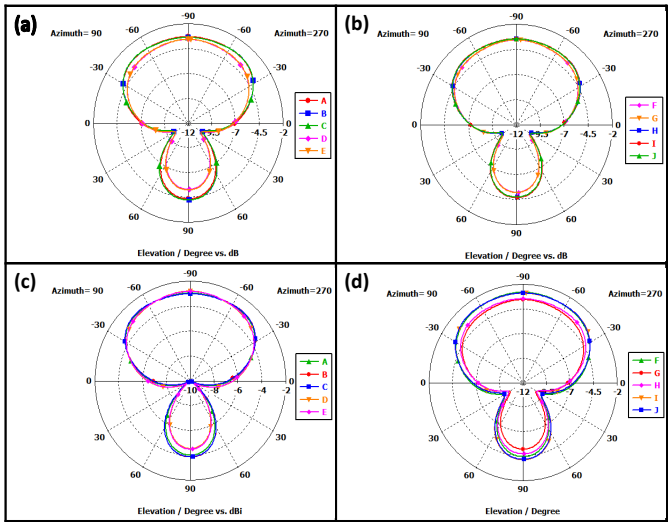

Figure 9. (a) Far field gain from orientation A to pattern E(b) Far field gain from orientation F to pattern J (c) Far field directivity from orientation A to pattern E (d) Far field directivity from orientation F to pattern J.

TABLE V. RETURN LOSS OF PATCH ANTENNA WITH INCREMENT NUMBER OF TSRR ROW WISE ALIGNMENT

Antenna	Resonant frequency, f_r (GHz)	Return loss (dB)	Gain (dB)	Directivity(dBi)
One CTSRR	2.446	- 28.864	7.85	8.29
Two CTSRR	2.443	- 33.391	7.75	8.25
Three CTSRR	2.437	- 36.114	7.31	8.21
Four CTSRR	2.434	- 41.765	7.34	8.30
Five CTSRR	2.434	-35.824	7.33	8.31
Six CTSRR	2.434	-45.386	7.29	8.24

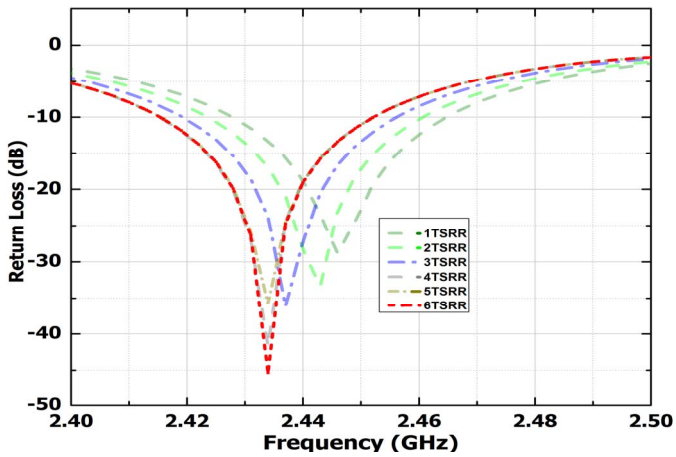

Figure 10. Return loss of patch antenna with respect to increment of TSRR.

From TABLE V, and figure 10, we observe that highest gain is achieved on antenna with one CTSRR and most directivity is achieved on antenna with five CTSRR. But on the other hand, return loss improves with respect to increment of CTSRR on patch and interestingly this shifts to lower frequency region. This may be due to concentration of electron and its impact on electromagnetic field distribution. Therefore, this finding can be indispensable for frequency tunable solution.

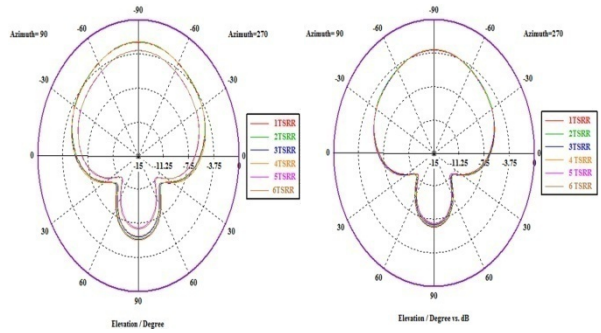

Figure 11. Fairfield gain and directivity of patch antenna with respect to increment of TSRR .

TABLE VI. COMPARISON OF DIFFERENT ANTENNA PARAMETERS WITH RECENT RELATED WORKS

Research, year	SRR structure type	Application SRR	Size (mm)	Frequency (GHz)	Return loss (dB)	Gain (dBi)
Huda, 2008[14]	Square edge-couple SRR with 2 ring gap	Microstrip antenna	9.1 x 9.1	2.4	- 18	7.47
Rahim, 2009[15]	Square edge-couple SRR with 2 ring gap	Microstrip antenna	49 x 17 2	2.7	> - 10	11.08
Jiun-Peng, 2011 [16]	Edge-coupled SRR S	Slot dipole antenna	6 x 6 2	2.49	> - 25 4	4.71
Xiaoyu, 2011[17]	Complementary rectangular edge couple SRR	Folded patch antenna	15 x 7.3	2.36	- 18.4	0.1
Norikman 2013[18]	Rombic Split Ring Resonator	Microstrip antenna	3.93x3.93	2.40	-24.029	6.37

VI. CONCLUSION

The impact of CTSRR on the performance of microstrip patch antenna is theoretically investigated. For various orientation of CTSRR and increment of CTSRR unit cell, the antenna resonates between 2.43 to 2.45 GHz bands. The antenna shows a directional radiation pattern and capacitive charge develops in gap-cut position improves gain and directivity. Numerical study of the effect and physical parameters of CTSRR on antenna has been carried out. Resonance frequency shifts toward the lower frequency region with the increment of CTSRR unit cell. So, proposed design may be helpful for frequency tunable solution. Expected improvement in bandwidth, and impact of gain and directivity with respect to addition of CTSRR on Patch has not been observed flawlessly due to patch antenna feeding technique or perfect impedance matching. Future modified feeding network or designs can be effective to overcome this problem.

REFERENCES

[1] C. A. Balanis, Antenna Theory: Analysis & Design, John Willey & Sons, Inc., 1997.

[2] Y. Qin, S. Gao, A. Sambell, E. Korolkiewicz and M. Elsdon, "Broadband patch antenna with ring slot coupling," *Electronics Letters*, Vol. 40 No. 1, January 2004.

[3] J.R. James, P.S Hall and C. Wood, "Microstrip Antenna Theory and Design",1981.

[4] WZiolkowski, R. W. and E. Heyman,"Wave propagation in mediahaving negative permittivity and permeability,"*Physical Reviewe*," Vol. 64, 56625.1-056625.15, 2001.

[5] RGundogdu, T. F., M. GÄokkavvas, K. Guven, M. Kafesaki,C. M. Soukoulis, and E. Ozbay, "Simulation and micro-fabrication of optically switchable split ring resonators," *Photonics and Nanostructures Fundamental and Applications*, Vol. 5, 106-112, 2007.

[6] TheMajid, H.A., M. Rahim and T.Masri, 2008, "Left Handed Metamaterial Design For Microstrip Antenna Application," *IEEE International RF and Microwave Conference (RFM 2008)*, Kuala Lumpur, Malaysia, pp: 218-221.

[7] Ekmekci, E. and G. Turhan-Sayan, 2011, "Metamaterial Sensor Applications Based on Broadside-couple SRR and V-Shaped Resonator Structures,"*2011 IEEE International Symposium on Antennas and Propagation (APSURI)*, Washington, USA, pp: 1170-1172.

[8] M. Marques, R., R. Medina and E. I. Raffi, 2002, "Role of Bi-anistropy in Negative Permeability and Left-handed Metamaterials," *Physical Review B*, 65(1),pp: 1-6.

[9] Constantine A. Balanis, Antenna *Theory and Design*, John Wiley & Sons, Inc., 1997.

[10] J.R James and P.S. Hall, *Handbook of Microstrip Antennas*, vol. 2, Peter Peregrinus Ltd., London, 1989.

[11] R. Marqués, F. Mesa, J. Martel, and F. Medina, "Comparative analysis of edge- and broadside coupled split ring resonators for metamaterial design Theory and experiment," *IEEE Trans. Antennas Propag.*, vol. 51, no. 10, pp. 2572–2581, Oct. 2003.

[12] R. Marqués, F. Medina, and R. Rafii-El-Idrissi,"Role of bianisotropy in negative permeability and left handed metamaterials," *Phys. Rev. B, Condens. Matter,* vol. 65, pp. 144 441(1)–144 441(6), 2002.

[13] F. Falcone, T. Lopetegi, M. A. G. Laso, J. D. Baena, J. Bonache, M.Beruete, R. Marqués, F. Martín, and M. Sorolla, "Babinet principle applied to metasurface and metamaterial design," *Phys. Rev. Lett.*, vol. 93, pp. 197 401(1)–197 401(4), 2004.

[14] M. Gil, J. Bonache, F. Martin, "Metamaterial Filters: A Review", *Metamaterial*, vol. 2, pp. 186-197, 2008.

[15] M. K. A. Rahim, H. A. Majid, T. Masri, "Microstrip Antenna Incorporated with Left-Handed Metamaterial at 2.7 GHz," *IEEE International Workshop on Antenna Technology (iWAT 2009)*, pp. 1-4, 2009.

[16] C. Jiun-Peng, H. Powen, "A Miniaturized Slot Dipole Antenna Capacitively Fed by a CPW With Split Ring Resonators," *2011 IEEE International Symposium on Antennas and Propagation (APSURSI)*, pp. 779-781, 2011.

[17] C. Xiaoyu, S. Jun, K. Cheolbok, D. E. Senior, Y. Yong-Kyu, "A Compact Self Packaged Patch Antenna with Non-Planar Complimentary Split Ring Resonator Loading," *2011 IEEE International Symposium on Antennas and Propagation (APSURSI)*, pp. 1036 – 1039, 2011.

[18] H. Nornikman, B. H. Ahmad, M. Z. A. Abd Aziz, A. R. Othman,"Effect of Single Complimentary Split Ring Resonator Structure on Microstrip Patch Antenna Design", *IEEE Symposium on Wireless Technology and Applications (ISWTA)*, pp.239-244, September 2013.

A High-Gain Slot-Loaded Microstrip Patch Antenna Fed by a Half-Width Microstrip Line for 5.5 and 5.8 GHz Wi-Fi/WiMAX Applications

Debabrata K. Karmokar*, Khaled M. Morshed†, Md. Selim Hossain*, and Md. Nurunnabi Mollah*
*Department of Electrical & Electronic Engineering
†Department of Electronics & Communication Engineering
Khulna University of Engineering & Technology, Khulna-9203, Bangladesh
E-mail: dkkarmokar@ieee.org; kmm_ece@yahoo.com; selimkueteee@yahoo.com; nurunnabim12@gmail.com

***Abstract*—A new type of antenna is presented in this paper. The main structure is a slot-loaded microstrip patch antenna fed by a half-width microstrip line. Two different types of antenna structure are combined together to make a single element antenna, and the radiation properties of both antennas are utilized in the proposed highly efficient antenna. Radiation from the antenna structure is achieved primarily from the first higher-order microstrip mode. The 10 dB return loss bandwidth of the antenna is 640 MHz (5.41 GHz to 6.05 GHz). The antenna produces a directive beam with a peak gain of 9.1 dBi, and the variation of the gain within the 640 MHz impedance bandwidth is only 1.35 dB.**

***Index Terms*—Microstrip patch antenna, leaky-wave antennas (LWAs), half-width (HW), WiMAX, Wi-Fi.**

I. Introduction

Microstrip-based antennas are attractive due to their planar low-profile configuration, fabrication simplicity, and ease of integration with microwave and millimeter-wave circuits. Low profile antennas for different wireless local area network (WLAN) systems such as wireless fidelity (Wi-Fi) and worldwide interoperability for microwave access (WiMAX) are highly desirable [1]–[3]. Wi-Fi (IEEE 802.11 standard) operates in the 2.4 GHz band (frequency range 2.4–2.5 GHz), and 5 GHz band (frequency ranges are: 5.15–5.35 GHz, 5.47–5.725 GHz, and 5.725–5.875 GHz) [1], [2]. Different standards for WiMAX have been developed by the IEEE 802.16 working group, such as 5.725–5.86 GHz [4].

Different types of antennas have been developed to meet the above mentioned requirements, most of which are patch antennas [1], [4]–[9]. Another attractive research area is microstrip leaky-wave antennas (LWAs) which usually use a microstrip line to achieve radiation. Microstrip LWAs are also planar low profile, and they have inherent beam scanning capabilities [10], [11]. The fundamental mode of a microstrip line does not radiate at lower frequencies because the electric field is strongly bound between the microstrip and the ground plane. The first higher-order mode of a microstrip line produces radiating leaky waves. Microstrip LWAs were proposed in the late 1970s with methods to excite the first higher-order microstrip mode [12]. A half-width microstrip LWA has been developed in [13] which operates in the first higher-order mode. In order to excite a microstrip line in its first higher-order mode a shorting wall was introduced along the center of the microstrip line and hence the width of the line is reduced to half of the original width. The shorting wall allows a microstrip line to excite the first higher-order mode. This antenna is called a half-width microstrip LWA (HW-MLWA). Research has been conducted on HW-MLWAs to steer the antenna beam by sweeping the frequency, or at a fixed frequency [14]–[21].

In this paper a microstrip patch antenna fed by a HW microstrip LWA is presented for 5.5 and 5.8 GHz Wi-Fi and WiMAX applications. Two different antennas, a HW-MLWA and a slot-loaded patch antenna, are cascaded to make a single directive antenna with relatively higher gain.

II. Antenna Configuration

The configuration of the antenna investigated in this paper is shown in Fig. 1. It was designed and analysed using CST Microwave Studio. The antenna is designed to be fabricated on a Rogers RT5880 substrate with a thickness (t) of 1.575 mm, dielectric constant (ε_r) of 2.2, and loss tangent (tan δ) of 0.0009. All the parameters of the antenna were optimized using parameter analysis conducted in CST. The length (L) and width (W) of the substrate and ground plane are 76.5 mm and 40 mm, respectively, i.e. the dimensions of the whole antenna are 76.5 mm $\times$ 40 mm. The complete structure can be divided into three different sections: (i) patch section, (ii) HW-MLWA section, and (iii) feed section.

A. Patch Section

The right section (Fig. 1(a)) of the antenna is the patch section which consists of a rectangular patch. The length (l_p) of the patch is 15 mm whereas the width (W) of the patch is the same as the width of the substrate i.e. 40 mm. A slot with dimensions of 5 mm $\times$ 30 mm ($w_s \times h_s$) is located at the middle of the patch.

978-1-4673-9257-0/15/$31.00 ©2015 IEEE

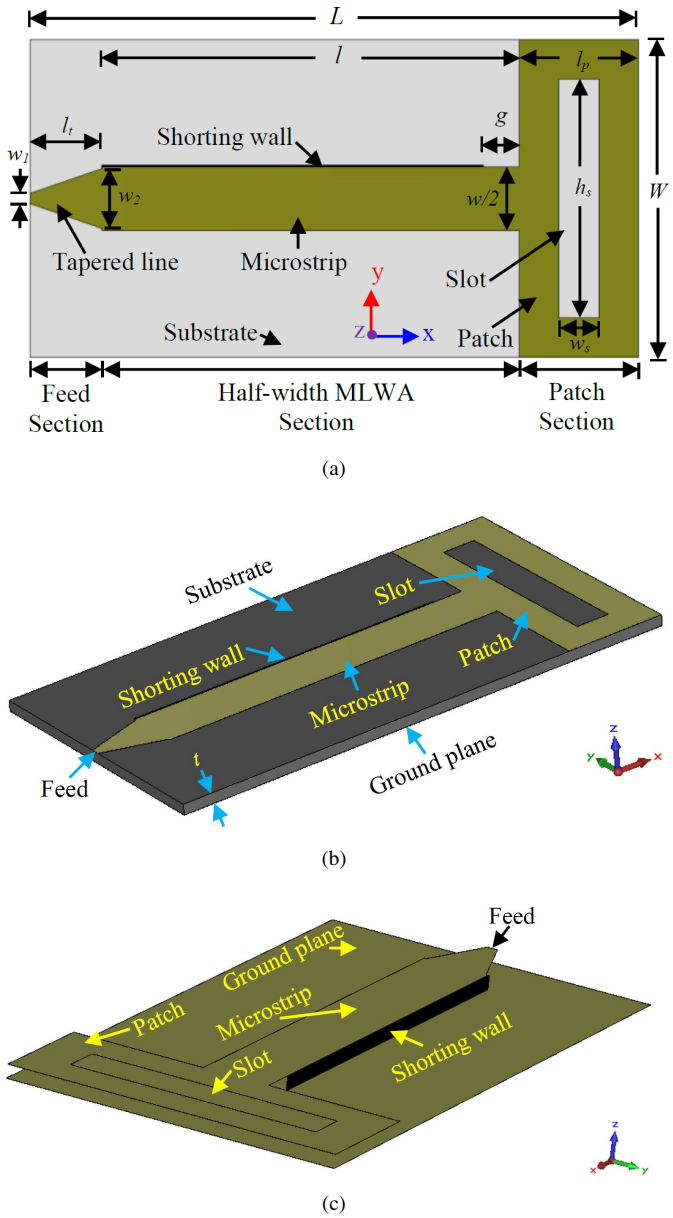

Fig. 1. Proposed microstrip antenna: (a) top view, (b) perspective view, and (c) perspective view (substrate omitted).

B. HW-MLWA Section

The middle section of the structure is the half-width microstrip LWA section, which consists of a HW-MLWA. The length (l) (along x-axis) and width ($w/2$) (along y-axis) of the microstrip line are 52.5 mm and 8 mm, respectively. As discussed earlier, in an implementation of a HW-MLWA, one edge of the microstrip is shorted to the ground plane by a shorting wall [Fig. 1(c)]. A gap (g) is introduced between the patch and the shorting wall [Fig. 1(a)]. The gap improves the impedance matching and allows the wave to propagate towards the patch. The optimum value of the gap (g) was found to be 4.5 mm, from full-wave parametric analysis conducted in CST.

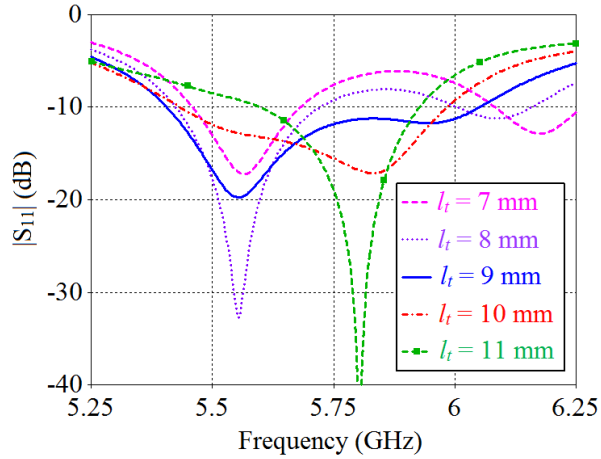

Fig. 2. Variation of reflection coefficient of the antenna in Fig. 1 with the length (l_t) of the tapered line.

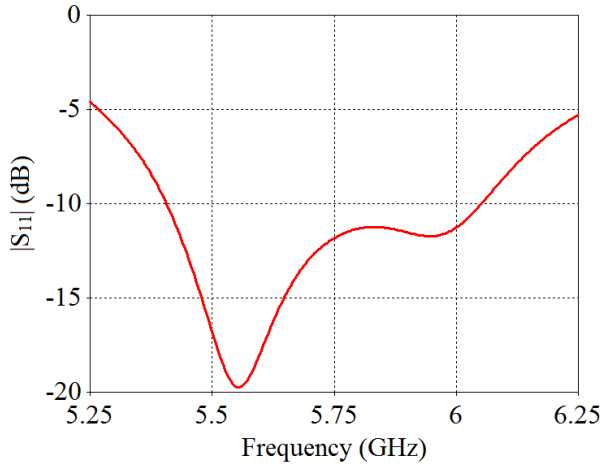

Fig. 3. Predicted $|S_{11}|$ of the antenna in Fig. 1.

C. Feed Section

The third and last section is the feed section, which is at the left side of Fig. 1(a). The antenna is fed from one end through a tapered line. To achieve good impedance matching, the dimensions of the tapered line have been optimized through some parametric studies. The effect of the tapered line length (l_t) on the return loss is depicted in Fig. 2, which shows that the best matching is achieved with l_t = 9 mm. The optimum values of the width (w_1) at the feed end and the width (w_2) at the microstrip end of the tapered line were also determined using similar parametric analysis and found to be 1.3 mm and 7.5 mm, respectively.

III. Results and Discussion

A. Reflection Coefficient

The antenna is excited from the left side by a discrete port in CST as shown in Fig. 1. Fig. 3 represents the input

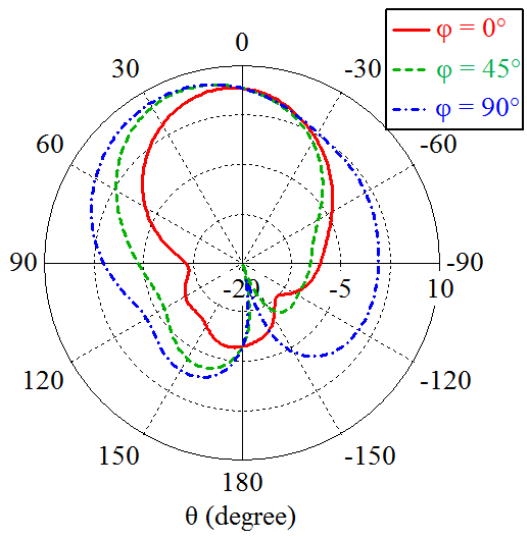

Fig. 4. Predicted radiation pattern cuts on constant-ϕ plane at 5.47 GHz.

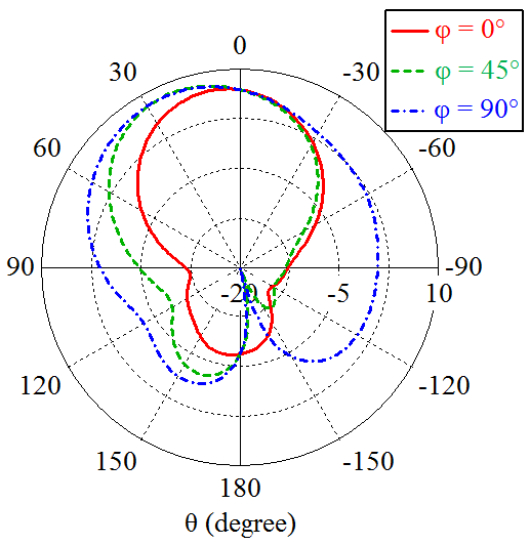

Fig. 5. Predicted radiation pattern cuts on constant-ϕ plane at 5.5 GHz.

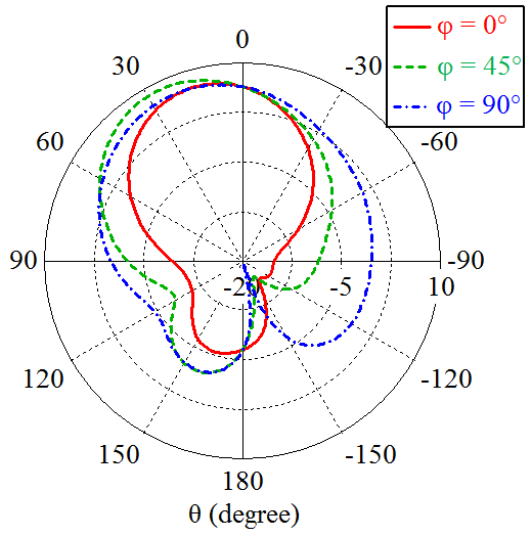

Fig. 6. Predicted radiation pattern cuts on constant-ϕ plane at 5.8 GHz.

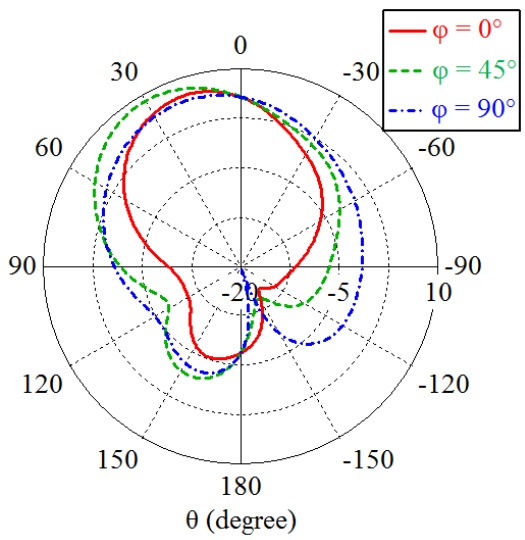

Fig. 7. Predicted radiation pattern cuts on constant-ϕ plane at 5.875 GHz.

reflection coefficient of the antenna in Fig. 1. It can be seen that the antenna has a -10 dB reflection bandwidth from 5.41 to 6.05 GHz.

B. Radiation Pattern

Figs. 4 – 7 show the radiation patterns of the antenna at four different frequencies. In order to represent the antenna beam properly the radiation pattern cuts are taken at three different constant-ϕ planes. The antenna beamwidth is narrow in the ϕ = 0° plane. However, the beamwidth is much wider in the ϕ = 90° plane. At lower frequencies the beam points closer to the boresight (Figs. 4 and 5), where, in this case, the boresight is the z-direction, perpendicular to the plane of the antenna structure. With an increase of frequency the beam in the ϕ = 0° plane shifts slightly towards the x-axis (Figs. 6 and 7). Though the beam in the ϕ = 0° plane changes slightly with frequency, the beam in the ϕ = 90° plane remains almost the same.

C. Surface Current Distribution

Fig. 8 displays the surface current distributions of the antenna at 5.5 and 5.8 GHz. It can be observed that at lower frequencies [Fig. 8(a)] most of the power radiates from a section closer to the feed and less power radiates from the patch. As the frequency increases the power travels further and more power radiates from the patch end as shown in Fig. 8(b).

D. Gain and Directivity

The variation of the directivity and gain of the antenna with frequency are shown in Fig. 9. The peak directivity of

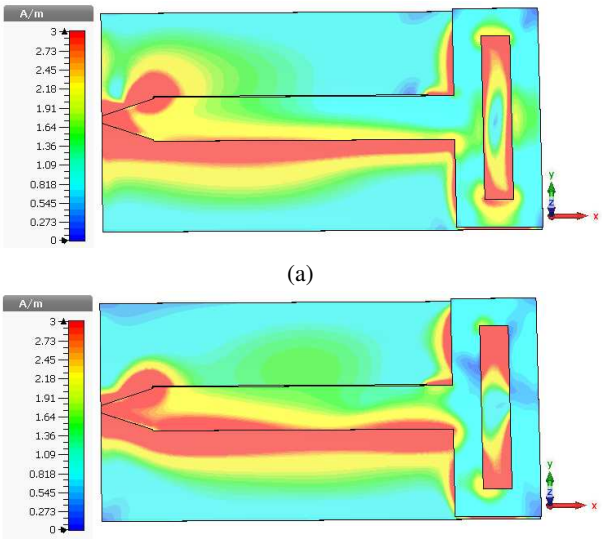

(a)

(b)

Fig. 8. Surface current distribution (amplitude) at: (a) 5.5 GHz and (b) 5.8 GHz.

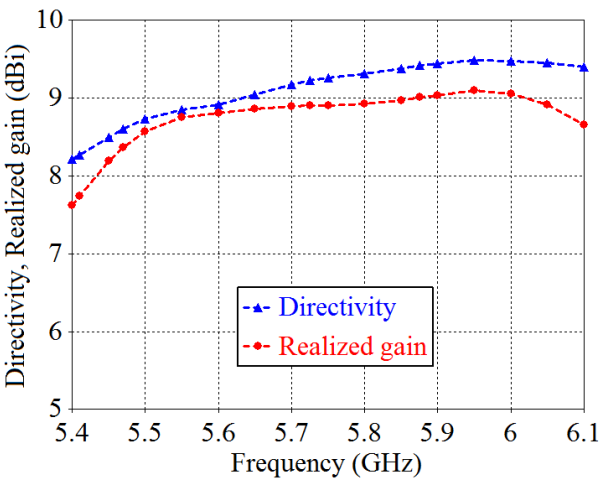

Fig. 9. Predicted directivity and gain of the antenna with frequency.

the antenna within the impedance bandwidth is 9.5 dBi at 5.95 GHz. The directivity is greater than 8.26 dBi within the impedance bandwidth. The peak gain of the antenna is 9.1 dBi at 5.95 GHz, and its variation within the impedance bandwidth is only 1.35 dB. It can be seen that the gain and directivity are low at lower frequencies and increase with frequency. This is due to the short effective aperture at lower frequencies and the long effective aperture at higher frequencies, as described in Section III-C.

E. Antenna Efficiency

Fig. 10 represents the radiation and total efficiencies of the antenna within its operating band. The radiation efficiency of the antenna is more than 98% throughout the operating band. The total efficiency of the antenna is over 84% within the impedance bandwidth and over 90% between 5.42 GHz

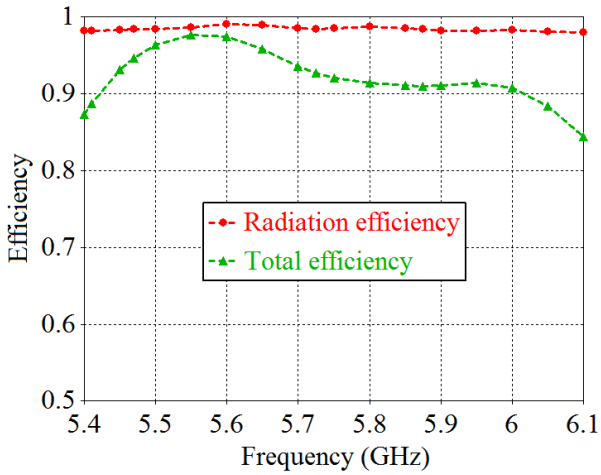

Fig. 10. Predicted radiation and total efficiencies of the antenna with frequency.

TABLE I
GAIN COMPARISON OF DIFFERENT ANTENNAS

Antenna Structure	Antenna Peak Gain
PIFA in [4]	4.4 dBi at 5.75 GHz
Self-complementary antenna in [7]	3.8 dBi in 5.8 GHz band
T-shaped monopole antenna in [8]	≈ 4 dBi in 5.8 GHz band
Printed monopole antenna in [9]	3 dBi between 5 and 6 GHz
Proposed antenna	9.1 dBi between 5.41 and 6.05 GHz

and 6.01 GHz. The total efficiency is very high from 5.47 to 5.66 GHz, almost equal to the radiation efficiencies. Since the total efficiency considers the mismatch losses, so where the return loss is high the deviation between the total and radiation efficiencies is low. For example, at 5.55 GHz the return loss is 19.7 dB ($|S_{11}|$ = -19.7 dB), the radiation efficiency is 98.6% and the total efficiency is 97.7%.

F. Comparison between the Proposed and Reference Antennas

In this subsection a comparison between the proposed and reference antennas is given in terms of antenna gain. The gains of different antennas are listed in Table I together with that of the proposed antenna. It can be seen that the proposed antenna has significantly higher gain than these reference antennas. Some of the antennas have been reported have high gain, e.g. antennas in [2], [3]. However, these antennas use a separate matching network for impedance matching.

IV. CONCLUSION

A slot-loaded patch antenna that is fed by a half-width microstrip LWA is presented in this paper. The proposed antenna is a combination of two different antennas, a LWA and a patch antenna. This antenna is able to produce a directive beam with very high gain. The Impedance bandwidth of the proposed antenna is 640 MHz and its gain is consistent within

its operating band. The predicted peak gain of the antenna is more than 9.1 dBi and its gain is above 7.75 dBi between 5.41 and 6.05 GHz. Moreover, the radiation efficiency of the antenna is above 98% and its total efficiency is over 84% throughout the operating band.

REFERENCES

[1] L. Pazin, N. Telzhensky, and Y. Leviatan, "Multiband flat-plate inverted-F antenna for Wi-Fi/WiMAX operation," *IEEE Antennas and Wireless Propag. Lett.*, vol. 7, pp. 197–200, 2008.

[2] D. K. Karmokar, M. S. Hossain, and M. N. Mollah, "Low-profile impedance matched wideband double inverted-F antenna for WiMAX/Wi-Fi operations in a laptop computer," in *Proc. Int. Conf. Devices and Communications (ICDeCom)*, Feb 2011, pp. 1–5.

[3] K. M. Morshed, D. K. Karmokar, and A. M. Numan-Al-Mobin, "Numerical analysis of impedance matched inverted-L antennas for Wi-Fi operations," in *Proc. 12th Int. Conf. on Computer and Information Tech. (ICCIT)*, 2009, pp. 691–696.

[4] S. Zuo, Y. Yin, Z. Zhang, and W. Wu, "A compact tri-band PIFA antenna for WLAN and WiMAX applications," *Microwave and Optical Technology Letters*, vol. 52, no. 4, pp. 919–922, 2010.

[5] K. M. Morshed, D. K. Karmokar, and M. Talukder, "Numerical and experimental analysis of impedance matched inverted-L and stair inverted-L antenna for 5 GHz WLAN operation," *Journal of Communications*, vol. 5, no. 8, pp. 612–619, Aug. 2010.

[6] D. K. Karmokar and K. M. Morshed, "Analysis of inverted-F and loaded inverted-F antennas for 2.4 GHz ISM band applications," *J. Elect. Eng.*, vol. EE 36, no. II, pp. 4–9, Aug. 2009.

[7] K.-L. Wong, T.-Y. Wu, S.-W. Su, and J.-W. Lai, "Broadband printed quasi-self-complementary antenna for 5.2/5.8 GHz WLAN operation," *Microwave and Optical Tech. Lett.*, vol. 39, no. 6, pp. 495–496, 2003.

[8] S.-W. Su, K.-L. Wong, and H.-T. Chen, "Broadband low-profile printed T-shaped monopole antenna for 5-GHz WLAN operation," *Microwave and Optical Tech. Lett.*, vol. 42, no. 3, pp. 243–245, 2004.

[9] W.-S. Chen, B.-Y. Lee, and P.-Y. Chang, "A compact and small printed monopole antenna for WLAN applications," *Microwave and Optical Technology Letters*, vol. 53, no. 7, pp. 1518–1522, 2011.

[10] D. K. Karmokar, K. P. Esselle, and T. S. Bird, "An array of half-width microstrip leaky-wave antennas radiating on boresight," *IEEE Antennas Wireless Propag. Lett.*, vol. 14, pp. 112–114, 2015.

[11] D. K. Karmokar, D. N. P. Thalakotuna, K. P. Esselle, and M. Heimlich, "Controlling the beam scanning limits of a microstrip leaky-wave antenna," in *Proc. IEEE APSURSI*, July 2013, pp. 1330–1331.

[12] W. Menzel, "A new travelling wave antenna in microstrip," in *Proc. 8th Eur. Microw. Conf.*, Sept. 1978, pp. 302–306.

[13] G. M. Zelinski, G. A. Thiele, M. L. Hastriter, M. J. Havrilla, and A. J. Terzuoli, "Half width leaky wave antennas," *IET Microw., Antennas Propag.*, vol. 1, no. 2, pp. 341–348, Apr. 2007.

[14] D. K. Karmokar and K. P. Esselle, "Periodic U-slot-loaded dual-band half-width microstrip leaky-wave antennas for forward and backward beam scanning," *IEEE Trans. Antennas Propag.* [Online]. Available: http://ieeexplore.ieee.org/

[15] G.-F. Cheng and C.-K. C. Tzuang, "A differentially excited coupled half-width microstrip leaky EH_1 mode antenna," *IEEE Trans. Antennas Propag.*, vol. 61, no. 12, pp. 5885–5892, Dec. 2013.

[16] D. K. Karmokar, D. N. P. Thalakotuna, K. P. Esselle, L. Matekovits, and M. Heimlich, "Reconfigurable half-width microstrip leaky-wave antenna for fixed-frequency beam scanning," in *Proc. 7th Eur. Conf. Antennas Propag.*, April 2013, pp. 1314–1317.

[17] Q. Lai, C. Fumeaux, and W. Hong, "Periodic leaky-wave antennas fed by a modified half-mode substrate integrated waveguide," *IET Microw., Antennas Propag.*, vol. 6, no. 5, pp. 594–601, Apr. 2012.

[18] D. K. Karmokar, K. P. Esselle, and S. G. Hay, "Shifting the fixed-frequency beam scanning range of a leaky-wave antenna by slot loading," in *Proc. IEEE-APS Topical Conf. Antennas and Propag. Wireless Commun.*, 2014, pp. 640–643.

[19] G.-F. Cheng and C.-K. C. Tzuang, "Guided wave structure for dual leaky-mode microstrip antenna design," in *Proc. 6th European Conf. Antennas and Propag. (EUCAP)*, Mar. 2012, pp. 2823–2826.

[20] D. K. Karmokar and K. P. Esselle, "Fixed-frequency leaky-wave antenna for simultaneous forward and backward scanning," in *Proc. IEEE Antennas and Propag. Society Int. Symp. (APSURSI)*, 2014, pp. 1794–1795.

[21] Y. Li, Q. Xue, E. K.-N. Yung, and Y. Long, "The periodic half-width microstrip leaky-wave antenna with a backward to forward scanning capability," *IEEE Trans. Antennas Propag.*, vol. 58, no. 3, pp. 963–966, Mar. 2010.

Aluminium Nitride based Parasitic Strip Patch Antenna for Multiband Wireless Applications

Swadesh Poddar[1,*], Sourav Roy[2, 3], Sunanda Roy[2], Md. Tanvir Hasan[4]
[1]Banglalink Digital Communication Ltd., Bangladesh
[2]Department of Electrical and Electronic Engineering, KUET, Khulna, Bangladesh
[3]Faculty of Electrical and Electronic Engineering, JUST, Jessore, Bangladesh
[4]Faculty of Electrical and Electronic Engineering, AIUB, Dhaka, Bangladesh
[*] E-mail: swadesh_ku@live.com

***Abstract*— A new approach with aluminum nitride (AlN) based parasitic strip wideband patch antenna has been introduced for 2.5 and 5.8 GHz wireless applications. The novelty of the proposed design is inherited in reduction of edges of patch which influences antenna performance. The impedance bandwidth of the antenna is 0.28 GHz for the first resonance, whereas 2.04 GHz for the second resonance with an antenna radiation efficiency of 89.6% and 95.32%, respectively.**

***Keywords*— Patch antenna, parasitic strip, multi-resonant, Aluminum Nitride**

I. INTRODUCTION

In this era of modern communication, prompt expansions in wireless communications have been established in order to meet the growing demand of the end terminal user. The 2.5 GHz and 5.8 GHz ISM bands are very popular for both wireless metropolitan area networks (WMAN) and wireless local area network (WLAN), respectively. Thus a multi-resonant antenna is more desirable for operations of WMAN and WLAN together. To meet the daily snowballing thirst in these operating bands, numerous antenna models with different feeding techniques have been recently anticipated for compact, efficient, and low cost design [1-4]. For an example, planar inverted-F antennas (PIFA) [5-7] are used in multiband operating at 2.5 GHz and 5.8 GHz for wireless applications. The PIFA are normally made of a large ground plane which makes the antenna bulkier. To reduce the dimension of PIFA, the feed probe point has been externally shorted. As a result, this technique leads to a decrease in the bandwidth. Besides numerous designs of fractal antennas using capacitive coupling [8], planar monopoles [4], and planar slot antenna with embedded metal strip [9] have been also suggested. In terms of design methodology, the fractal antennas are more complex, whereas the planar monopole antenna has also a large ground plane. The feeding technique of planar slot antenna is intricate to design. To overcome this problem another multi-resonant antenna, consists of bent strips printed on substrate, has been proposed [10]. However, these types of antennas are complicated in geometry and require long transmission lines [11]. Additionally, a modified feeding network is required to mitigate the difficulties like spurious feed radiation, surface wave loss, and long feed length. Therefore, it is immense important to take in account the issues such as wideband, compactness in size, and multiband for designing an antenna.

Parasitic strips for achieving resonance are well known for designing an antenna. Shorted parasitic element with monopole antenna has been employed for operation in both wideband and dual band [12-13]. Parasitic elements assure the wide banding of an antenna with many resonance frequencies which appear neighboring to the main frequency band. However, to control the resonance frequencies, details understanding of parasitic strip patch antenna are required. In this paper, a modified edge cut parasitic strip antenna for dual band operation with AlN substrate has been introduced. The antenna design; optimization and simulation have been done with Finite Element Method (FEM) based 3D full-wave electromagnetic solver HFSS v15. The antenna is comprised of modified feeding network with 50 Ω port impedance and small ground plane. The resonant frequency of the proposed antenna can be varied by tuning the length of the patch. The reflection coefficient and bandwidth are improved due to changing the width of the patch with edge cuts.

The layout of this proposal is outlined as follows: the details on Antenna evolution, design and geometry are illustrated in section 2. Results and discussions on the return loss, gain and efficiency are presented in section 3. Finally, a conclusion is depicted in section 4.

II. ANTENNA DESIGN

A. Substrate Selection

Growths in the area of III-nitride (GaN, InN, and AlN) semiconductors have been remarkable due to their inherent properties such as wide bandgap, high critical electric field, low intrinsic carrier concentration, high-electron mobility, and high-drift velocity [14]. Those parameters are very promising for high frequency, high power, and high temperature device applications. Among III-nitrides, AlN has a huge prospective to use as a substrate for a patch antenna because of wide bandgap (6.1 eV), low dielectric constant (4.84), and high critical electric field for breakdown (450 kV/cm). These suggest that AlN substrate is advantageous for wideband patch antenna.

B. Antenna Evolution

The antenna is derived and progressed from a conventional T shape parasitic strip antenna depicted in Fig. 1. The reflection coefficient has been presented for all three models.

978-1-4673-9257-0/15/$31.00 ©2015 IEEE

The antenna resonates near 2.5 GHz and 5.8 GHz for all three cases. From the Fig. 1 this is indicated that after the inclusion of edge cut on patch, antenna reflection coefficient and BW has been improved (model 3). Also the patch of proposed antenna has a 4~8% reduction in area in comparison with the patch area illustrated for model 1 and 2 in the Fig. 1. The smaller size of the proposed antenna improves dual band wireless performance. A comparative analysis is shown at table 1.

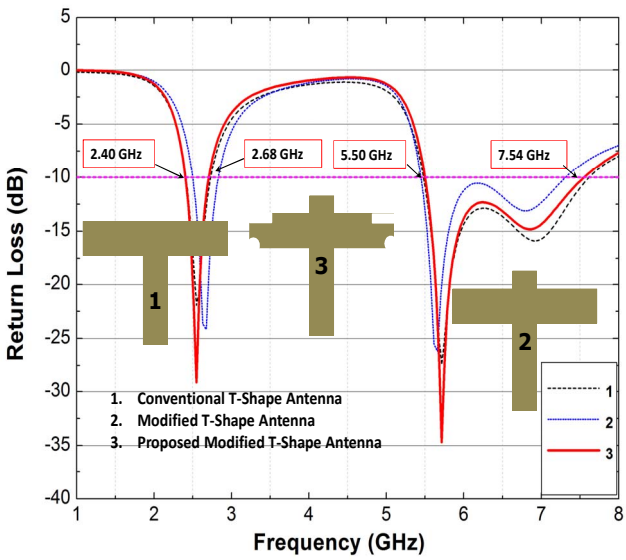

Fig 1: Antenna evolution

Table 1: Comparative analysis of conventional antenna and proposed antenna

Parameter	Conventional Patch	Proposed Antenna
Frequency(f_r)	2.5 GHz	2.5 GHz
Patch Width (W)	Patch Width $W=\frac{1}{2f_r\sqrt{\mu_0\varepsilon_0}}\sqrt{\frac{2}{\varepsilon_r+1}}=\frac{c}{2f_r}\sqrt{\frac{2}{\varepsilon_r+1}}$	
Patch Length (L)	Effective Length, $L_{eff}=\frac{c}{2f_r\sqrt{\varepsilon_{reff}}}$	
Substrate Dimension	L_s= 6h+L W_g = 6h +W	
Dimension	W = 37 mm; L = 29 mm; Height, H= 1.6 mm; L_s= 37 mm; W_s = 46 mm	W = 26.5 mm; L = 4.5 mm; H= 1.6 mm; L_s= 40 mm; W_s = 40 mm
Patch Area	1073 mm^2	156 mm^2
Substrate Area	1702 mm^2	1600 mm^2

C. Design and Geometry

Fig. 2 shows the geometry of our projected antenna. The modified patch shape with finite ground plane is printed on the same side over the AlN substrate of dielectric constant (ϵ_r) 4.84 and height of 1.6 mm. The transmission feed line of 50 Ω is printed on the back side of the substrate. The patch size occupies an overall volume of 6.28 mm^3 printed on a substrate of 40 mm * 40 mm. The physical dimension of the antenna is given in table 2.The width of the feed line W_2 and overlapping extended patch on feed line, D_2-D_1 has been kept fixed considering impedance matching. The edge cut has some advantages as these can control the surface wave loss, spurious radiation loss and reduce the patch size.

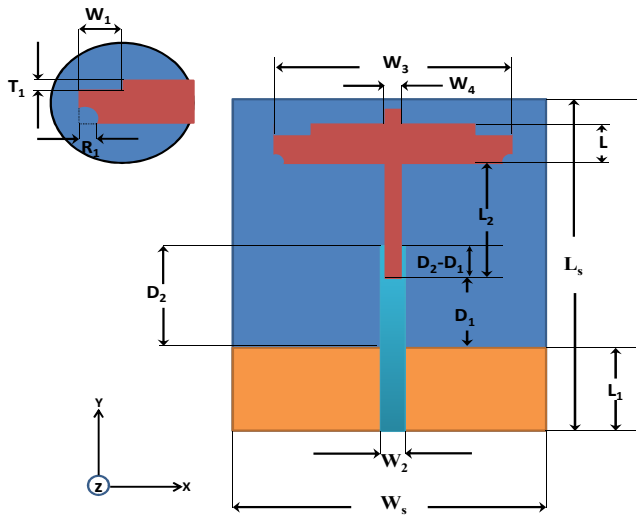

Fig 2: Geometry of the proposed antenna

Table 2: Physical Dimension of Antenna

Geometric Name	Parameter	Dimension (mm)
Substrate Length	L_s	40
Substrate Width	W_s	40
Finite Ground	L_1	12
Feed Width	W_2	3
Feed length	$D_2 + L_1$	21
Patch Length	L	4.5
Extended Patch Width	W_3	26.5
Patch Cut Width	T_1	0.6
Patch Cut Length	W_1	3
Circular Cut Radius	R_1	1.5
Patch Length	W_4	1.95

III. RESULTS AND DISCUSSIONS

A. Return Loss

The return loss (RL) is a factor that is identified as a ratio between reflected and transmitted waves at the input of an antenna. In the impedance equivalent network, improved RL is required for perfect matching. For the proposed antenna,

couple of design parameters that influences the antenna performances is the width W_3, length L, rectangular edge cut W_1, and circular edge cut R_1. The effect of these design parameters on antenna performance can be described from surface current distribution on dual resonant frequencies. In Fig. 3 and 4 the simulated RL with respect to antenna patch width (W_3) and length (L) has been represented.

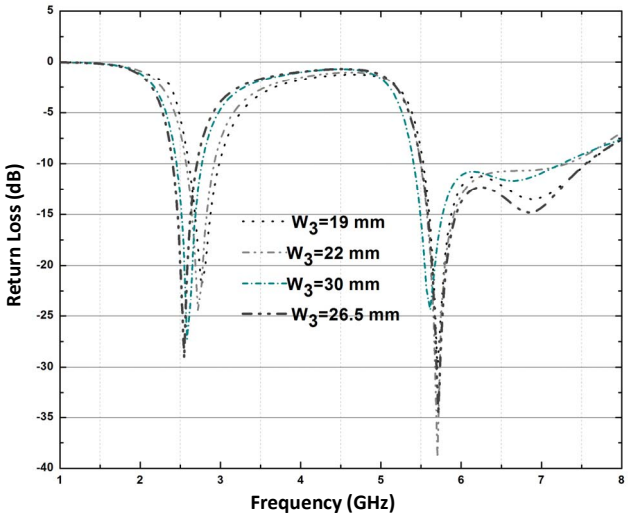

Fig 3: Return loss of antenna with variation of w_3

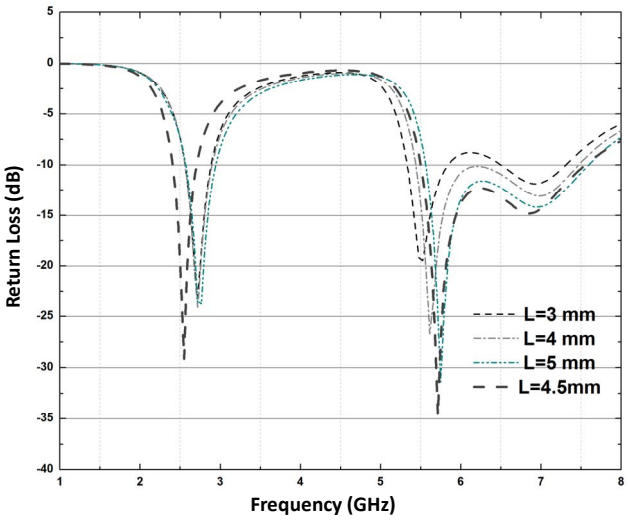

Fig 4: Return loss of antenna with variation of L (w_3=26.5mm)

B. *Electric Field, Surface Current and Polarization:*

A detailed dissemination of the excitation of the patch and the polarization of the antenna can be obtained by investigating field distribution and surface current analysis at resonance frequencies. Fig. 5(a) and 5(b) depicts the E field distribution of dual resonant frequencies near 2.5 GHz and 5.8 GHz. At the fundamental resonant frequency of 2.5 GHz and 5.8 GHz, E-field at the end of the patch is maximum and minimum at center. From Fig. 5, it is observed that E-field changes side according to instantaneous phase of the applied signal and can be denoted for multi-resonant behavior using TM_{nm} mode.

The surface current distributions of the proposed antenna in both of the bands are shown in Fig. 6(a) and 6(b). At lower resonance frequency, 2.5 GHz, the surface current along the patch are parallel with the horizontal component of the antenna whereas at lower portion on finite ground plane, surface current are vertical to horizontal component. On the other hand surface current at 5.8 GHz are parallel to horizontal component on both patch and finite ground plane. Therefore, with the increment of W_3, two resonance frequencies can shift in the lower region and by increasing L, the current path for lower region is lengthen and effects lower resonant frequency whereas higher resonant frequency remain steady. Rectangular and circular edge cut on patch may influence to minimize spurious radiation, surface wave loss, effective dielectric constant (ε_{reff}), influences radiation pattern, and enhances impedance bandwidth.

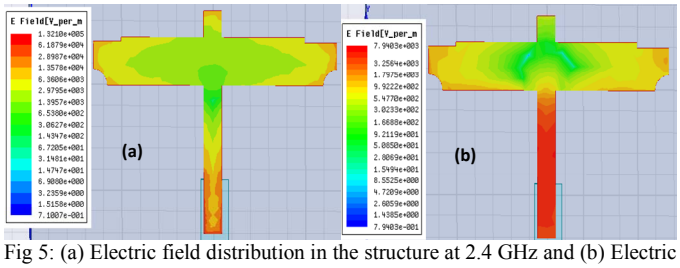

Fig 5: (a) Electric field distribution in the structure at 2.4 GHz and (b) Electric field distribution in the structure at 5.8 GHz

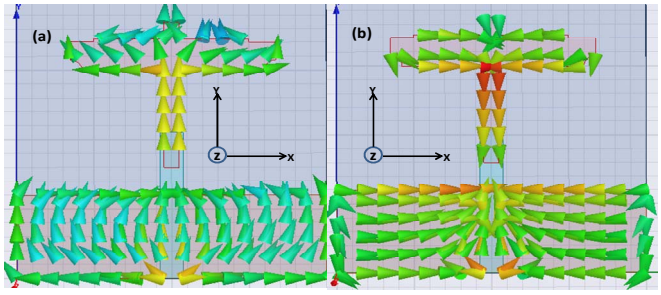

Fig 6:(a) Surface current distribution in the structure at 2.5 GHz and (b) Surface current distributions in the structure at 5.8 GHz

C. *Gain and Efficiency*

Fig. 7 depicts the 3D total gain at two resonant frequencies. The pattern is almost omnidirectional for both the bands. The last adaptive gain is 2.58 dB with peak efficiency of 89.6% at 2.5GHz and 3.69 dB with peak efficiency of 95.32% at 5.8 GHz. Fig. 8 (a) and 8 (b) depict radiation efficiency and peak gain with respect to operating bands. The return loss can be expressed in terms of voltage standing wave ratio (VSWR) which is 1.07 and 1.05 respectively for lower and higher bands. The transmitted and reflected powers are 99.90% and 99.97% for resonance frequency (f_r) of 2.52 GHz and 5.78

GHz with a mismatch loss of 0.003 dB and 0.001 dB [15].

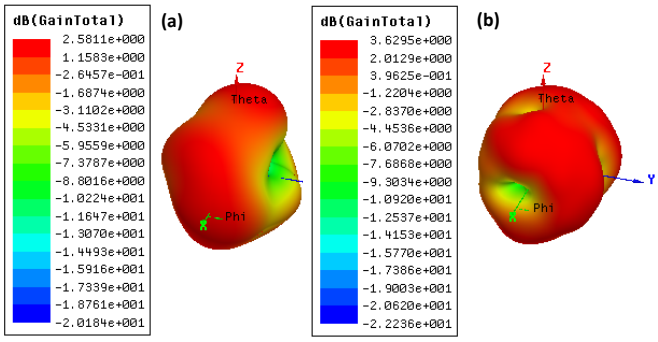

Fig 7: (a) 3D polar plot at 2.5 GHz and (b) 3D polar plot at 5.8 GHz

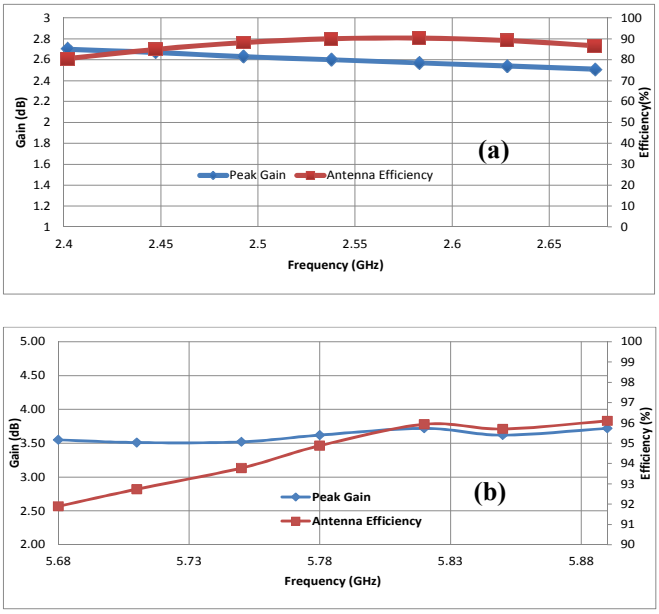

Fig 8: Simulated peak gain and efficiency of the antenna, (a) 2.5 GHz and (b) 5.8 GHz

IV. CONCLUSION

To recapitulate, the impact of modified patch shape on gain and radiation characteristics of multi-resonant wideband patch antenna with a parasitic strip are theoretically investigated to be used in wireless applications using AlN substrate. The proposed antenna model on AlN, featuring high band gap and high electron mobility may influence a significant role on fabrication of practical antenna. The exclusive reduction of ground plane and patch area in comparison with other multi-resonant antennas have been established also. From the simulation results, it has been observed that the antenna resonates at 2.52 GHz and 5.78 GHz with a bandwidth of 0.28 GHz and 2.04 GHz, separately, an impedance BW of 11.67% and 35.17%, respectively. The gain pattern of antenna is almost omnidirectional with radiation efficiency of 89.6% and 95.32% at lower and higher resonant, individually. These results regard that proposed modified patch on AlN with a parasitic strip is a highly potential structure for the wideband antenna for multi-band wireless applications.

REFERENCES

[1] Eldek, A. A., A. Z. Elsherbeni, and C. E. Smith, "Dual wideband square slot antenna with a U-shaped printed tuning stub for personal wireless communication systems," Progress In Electromagnetics Research, PIER 53, 319–333, 2005.

[2] Abdelaziz, A. A., "Bandwidth enhancement of microstrip antenna," Progress In Electromagnetics Research, PIER 63, 311–317, 2006.

[3] Zhao, G., F.-S. Zhang, Y. Song, Z.-B. Weng and Y.-C. Jiao, "Compact ring monopole antenna with double meander lines for 2.4/5 GHz dual-band operation," Progress In Electromagnetics Research, PIER 72, 187–194, 2007.

[4] Lee, E., P. Hall, and P. Gardner, "Novel compact wideband or multi-band planar monopole antenna," IEEE Antennas and Propagation Society International Symposium, 624–627, 2000.

[5] Young Jun Cho, Yong Sun Shin, and Seong-Ook Park, "An Internal PIFA for 2.4/5 GHz WLAN applications," Microwave conference proceedings, APMC, Vol. 4,Suzhou, China, 2005, pp 1-3.

[6] Wenjun Huang, Terence S. P See, Zhi Ning Chen, "2.4/5-GHz Dual-Band PIFA for Portable Devices," APSURSI, Pokane, Washington, USA, 2011, pp- 430-433.

[7] Xingyu Zhang, Jun hong Wang, "A Novel Dual-Band Planar Inverted-F Antenna for WLAN Applications," 8th International Symposium on Antennas, Propagation and EM Theory, 2008 , pp 148-151.

[8] Sindou, M., G. Ablart, and C. Sourdois, "Multiband and wideband properties of printed fractal branched antennas," Electronic Letters, Vol. 35, No. 3, 181–182, Feb. 4, 1999.

[9] Meng-Ju Chiang, Jia-Yi Sze, Guang-Fu Cheng, "A Compact Dual-Band Planar Slot Antenna Incorporating Embedded Metal Strips for WLAN Applications," EuMC, Rome, Italy, 2009, pp 221-224.

[10] Ge, Y., K. P. Esselle, and T. S. Bird, "Small quad-band WLAN antenna," IEEE Antennas and Propagation Society International Symposium, Washington D.C., USA, July 3–8, 2005.

[11] W. Qin,"A novel patch antenna with a t-shaped parasitic strip for 2.4/5.8GHz wlan applications," Journal of Electromagnetic Waves and Appl., Vol. 21, No. 15, 2311–2320, 2007.

[12] C. F. Tseng, C. L. Huang, C. H. Hsu, "Microstrip Fed Monopole Antenna With A Shorted Parasitic Element For Wideband Application," Progress in Electromagnetic Research Letters, Vol. 7, pp 115-125, 2009.

[13] C. Y. Huang, P. Y. Chiu, "Dual-band monopole antenna with shorted parasitic element," Electronics Letters, Vol. 41, No. 21, pp 1154 – 1155, 2005.

[14] Bhuiyan, Ashraful Ghani; Hashimoto, Akihiro; Yamamoto, Akio, "Indium Nitride (InN): A review on growth, characterization and properties", Journal of Applied Physics, Vol. 94, Issue 5, PP 2779-2808, 2003.

[15] Return loss to VSWR conversion table – Marki Microwave, [Online]: http://www.markimicrowave.com/Assets/data/return%20loss%20to%20vswr.pdf

The 1x1 Annular Ring: Bandwidth Enhancement of Microstrip Asymmetric Couple-Line Bandpass Filter with Superior Matching and Lower Insertion Loss

Shakhawat Parvez, * Nazmus Sakib,* Md. Nurunnabi Mollah
Department of EEE, Khulna University of Engineering & Technology
Khulna-9203, Bangladesh
*shakhawat_parvez@yahoo.com,*sakib483@yahoo.com

***Abstract*— Electromagnetic Band Gap (EBG) structures which is an exclusive innovation in modern microwave design arena by reason of their high potential and less intricacy of designing in the microwave and millimeter-wave integrated circuits. This paper examines the relationship between the filling factor (FF) of the annular ring structure on couple-line and capacitive coupling for improving the performance. A number of methods, method of moments (MOM) for numerical analysis and uniform distribution with constant aspect ratio (AR) for designing the circuit are used. In like manner, the parametric comparison has been demonstrated considering selectivity, 3-dB bandwidth (3-dB BW), insertion loss and return loss in the passband. Consequently, not only a very wide passband upto 49% increment but also a return loss upto 65 dB which illustrates great matching are achieved. Although, the insertion loss is less than 0.2 dB in the passband, but the selectivity shrinks with expanding bandwidth. In short, remodelling of the selectivity can be done by appropriately choosing the filling factor for annular ring pattern on the couple-line as well as on the transmission line.**

Keywords—3-dB Bandwidth; Aspect Ratio; Insertion Loss; Selectivity; Return Loss.

I. INTRODUCTION

Recently, Electromagnetic Band Gap structures (EBGs) which is a subset of metamaterials have grown in reputation as a result of less complexity in fabrication, superior efficiency, compact architecture and cooperative integration with microwave and millimeter-wave circuits. In brief, this metamaterials have such exclusive properties which is noteworthy for a single natural crystal [1]. However, the stopband and bandgap property of the structures can be influenced by some sophisticated design parameters. Like element spacing, number of the element on transmission line, aspect ratio and volumetric ratio of the elements, dielectric and radiation losses are the predicament for designing the EBG structures [2]. Furthermore, the efficacy of the wideband system is disturbed by the harmonics transmission which may cause increasing radiation loss. To enhance the performance of the propagation characteristics, a particular factor (namely, slow wave mode propagation) is analysed for achieving the low insertion loss [3]. On the other hand, bandpass filters having wideband, low insertion loss in the passband and wide attenuation in the stopband are the passband and wide attenuation in the stopband are appropriate for microwave system. However, by modifying the coupling coefficient of the couple-line and impedence of the transmission line, not only the pass bandwidths and transmission zeros of the filter can be regulated but also wider stopband and sharp selectivity can be achieved [4]. In addition, to increase the coupling coefficient pair of slots parallel to the microstrip line engraved on the ground plane for attaining wide bandwidth in the passband was reported in [5]. Also, the dielectric and radiation losses can be minimized without the coupling gaps. As a result, low insertion loss in the passband can be obtained with good matching. Moreover, adding two tuning stubs and dual mode characteristics, the performance of the bandpass filter in both passband and stopband can be significantly enhanced [6].

In this exposition, a lower insertion loss, better impedence matching, enhanced bandwidth and wider stopband asymmetric couple-line filter with annular ring EBG structure is proposed. In fact, annular ring structures are used in the four stage couple-line section for better optimization in the coupling coefficient. Besides, in both of the 50Ω transmission line to enhance the pass bandwidth and reduce the radiation losses in the coupled line section higher volumetric ratio element are used. In short, to enhance the 3-dB bandwidth with low insertion loss and large stopband is the individuality of this exposition.

The asymmetric couple-line bandpass filter with annular ring structures has a number of exclusive features, which includes the following:

a. The structure is compact and simple.
b. The optimization in the coupling coefficient has been made in this filter which proves the good matching.
c. The passband provides wide 3-dB bandwidth.
d. The filter has sharp rates of roll-off transfer function.
e. The insertion loss is very low with wider stopband performance.

The whole structure is simulated by method of moments (MOM) based EM software *Zeland IE3D.*

II. DESIGN THEORY

The annular ring pattern is etched on the ground plane of standard 50Ω transmission line with a period "*a*" which is a

978-1-4673-9257-0/15/$31.00 ©2015 IEEE

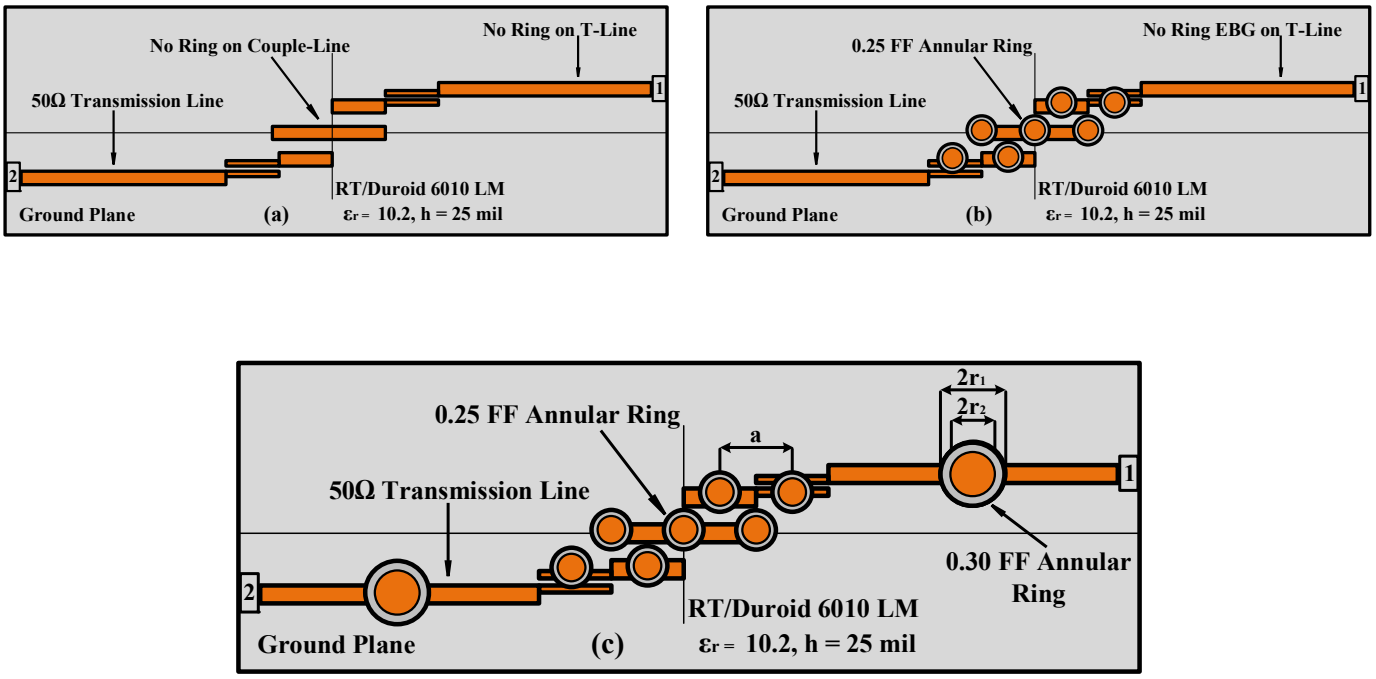

Fig. 1: Schematics of the (a) Published reference model by T. Itoh et al. [3]; (b) Proposed designed couple-line filter with 0.25 FF annular ring on four stage couple line and no EBG ring on transmission line; (c) Proposed designed couple-line filter with 0.25 FF annular ring on four stage couple line and 0.30 FF annular ring on both of the transmission line; where the AR=0.535, period, a=150 mil in 50Ω transmission line etched on the ground plane of the RT/Duroid 6010LM, h=25 mil.

crucial parameter to attain stopband characteristics. Moreover, filling factor of the annular ring patterned EBGs are drafted from the equation:

$$FF = \frac{r_1}{a} \tag{1}$$

Where, Filling Factor (*FF*), outer ring radius (r_1), spacing between two elements (*a*).

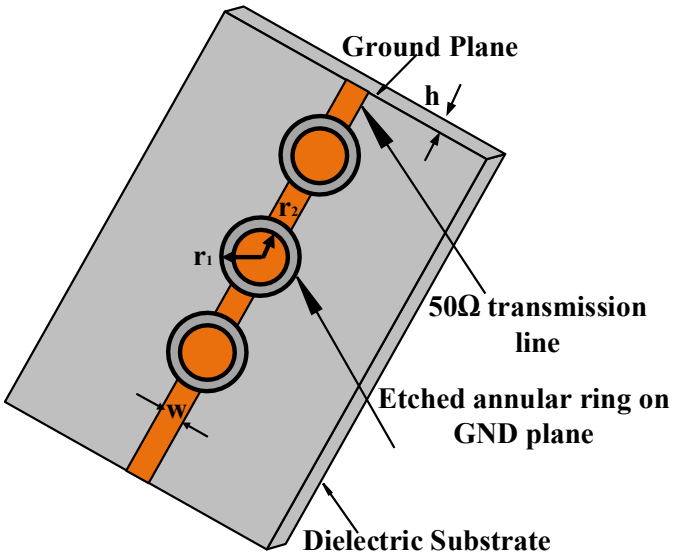

Fig. 2: Three-dimensional (3-D) view of the conventional annular ring architecture on a 50Ω transmission line.

Aspect ratio (AR) of the annular ring may be defined as the ratio of the inner ring radius (r_2) to outer ring radius (r_1) which is an exclusive feature.

$$AR = \frac{r_2}{r_1} \tag{2}$$

The center frequency of the stopband [7] can be calculated using:

$$\beta a = \pi \tag{3}$$

Where, β is the wave number of dielectric slab, *a* is the period of the annular ring pattern.

III. Proposed Structures

The proposed asymmetric couple-line filters were composed on RT/Duroid 6010 LM substrate with dielectric constant of 10.2 and thickness of 25 mil. For good tuning and simulation scope, the annular ring assisted couple-line bandpass filter is simulated by MOM based EM software Zeland IE3D. Outer ring radius r_1 can be developed from the filling factor. Likewise, inner ring radius r_2 would always be determined by aspect ratio. Nevertheless, the aspect ratio kept consistent at 0.535 while the volumetric ratio of ring structure is varied.

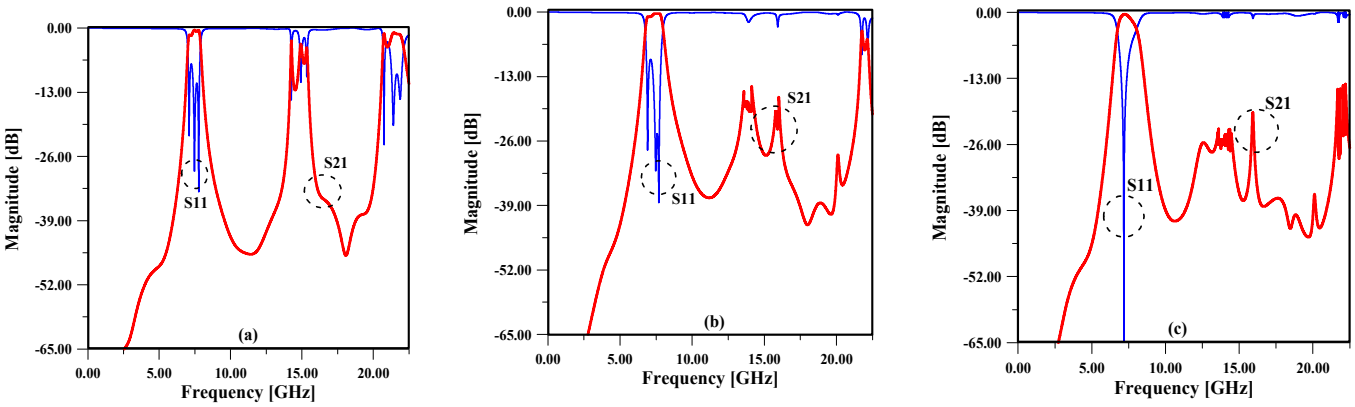

Fig. 3: Simulated frequency response of the (a) Published reference model by T. Itoh et al. [3]; (b) Proposed designed couple-line filter with 0.25 FF annular ring on four stage couple line and no EBG ring on both of the transmission line; (c) Proposed designed couple-line filter with 0.25 FF annular ring on four stage couple line and 0.30 FF annular ring on both of the transmission line; where the AR=0.535, a=150 mil in 50Ω transmission line etched on the ground plane of the RT/Duroid 6010LM, h=25 mil.

A. Design 1 :

As can be seen in Fig. 1(a), the reference asymmetric couple-line bandpass filter have four couple-line segments, lower and upper transmission line. Again, no EBG element on couple-line as well as on both of the 50Ω transmission line. This four stage coupled line filter with 0.5 dB equal ripple response where center frequency is at 7.5 GHz. In Fig. 3(a), at initial passband insertion loss starts from 120 dB. The filter has sharp selectivity of 45.95 dB/GHz and 3-dB cut-off frequency at 7.03 GHz. As the filter is tightly coupled, it results of a very narrow bandwidth. The return loss in the passband is 33.10 dB. But from Fig. 3(a), the filter is influenced by the spurious transmission in the conclusive stopband.

B. Design 2 :

Observing from Fig. 1(b), the proposed asymmetric couple-line bandpass filter have seven annular ring EBG elements with 0.25 FF on four section couple-line. But, like the Fig. 1(a), no annular ring EBG element are etched on both of the 50Ω transmission line. Consequently, for utilizing the ring element on couple line the balance between the capacitive coupling and coupling coefficient is established. In Fig. 3(b), insertion loss starts from 125 dB. As a result of balanced coupling, the 3-dB pass bandwidth has increased which is 1.17 GHz. But the matching in the Fig. 3(b) not increased significantly compare to Fig. 3(a). Likewise, no significant coupling has done as no ring EBG is etched on both of the transmission line which results no significant improve in matching in the passband. Although, the bandwidth is increased, but the selectivity is 34 dB/GHz. As seen from Fig. 3(b), not only the ripple is diminished in the passband but also the spurious transmission in conclusive stopband is also reduced. For further improvement of the overall performance (namely, coupling coefficient) of the asymmetric couple-line bandpass filter, annular ring EBG with certain FF need to be used in the both 50Ω transmission line for better coupling.

C. Design 3 :

As illustrated in Fig. 1(c), the proposed asymmetric couple-line bandpass filter have seven volumetric ratio of 0.25 annular ring EBG element on four segment couple-line like the Fig. 1(b). But, this proposed design has 0.30 FF annular ring EBG element has placed at center on both of the 50Ω transmission line. At first the coupling settled on the four stage couple-line, it also yields the mutual coupling between both of the 50Ω transmission line. Still, the signal gets weaker at the end of the port due to the dielectric and radiation losses as a result of tight coupling. Finally, with a proper volumetric ratio of 0.30 ring structure has placed on the middle for further improvement in the coupling. As seen from Fig. 3(c), insertion loss starts from 134 dB. Furthermore, not only the 3-dB pass bandwidth increased to 1.25 GHz but also the matching in the passband has significantly improved to 65 dB. But, the value of selectivity reduced to 30.81 dB/GHz which is normal compared to the bandwidth. Alternatively, the spurious transmission due to the skin effect in the conclusive stopband is also reduced significantly which results a very large stopband compared to Fig. 3(a) and Fig. 3(b).

IV. RESULTS

As illustrated in Fig. 4, Fig. 5 and Table I, a comparative study has done by virtue of their rigorous parametric analysis (namely, selectivity, return loss S_{11} in the passband, 3-dB bandwidth and percentage enhancement in the bandwidth) with respect to the volumetric ratio. In this section, overall improvement in the efficacy of the couple-line filer will be presented meticulously.

TABLE I

COMPARATIVE STUDY BETWEEN THE PERFORMANCE OF ASYMMETRIC COUPLE-LINE BANDPASS FILTER; *AR=0.535* REMAIN CONSTANT.

EBG on T-Line	Selectivity [dB/GHz]	S_{11}(Passband) [dB]	3-dB BW [GHz]	BW Enhancement [%]
Ref. [3]	45.95	33.10	0.84	N/A
No EBG	34.00	38.50	1.17	39.39
0.30 FF	30.81	65.00	1.25	48.81

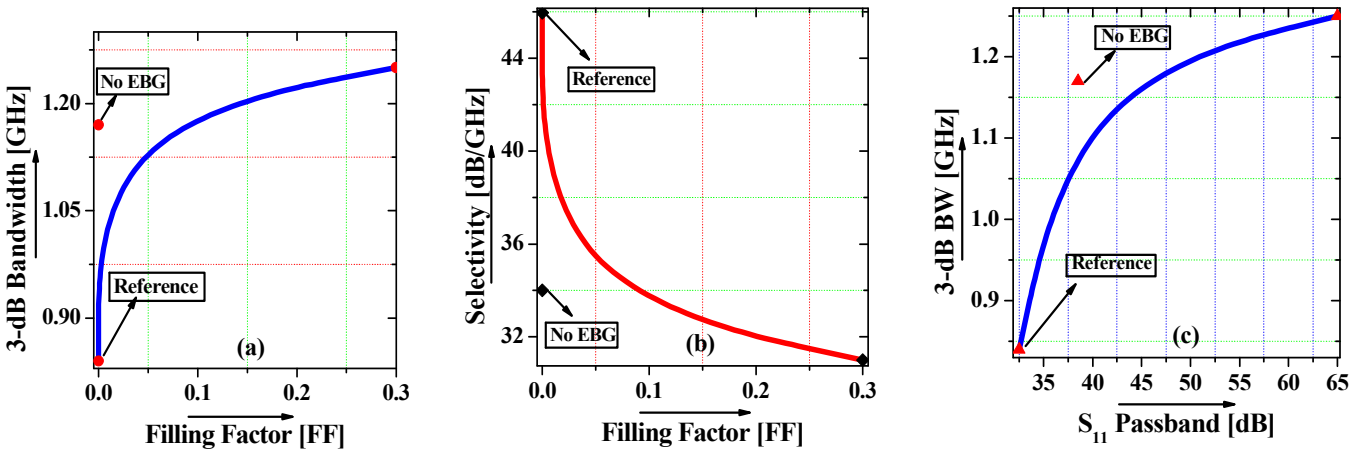

Fig. 4: Comparative study between the Published reference model by T. Itoh et al. [3], Proposed designed couple-line filter with 0.25 FF annular ring on four stage couple line and no EBG and 0.30 FF annular ring on both of the transmission line representing (a) FF vs. 3-dB BW; (b) FF vs. Selectivity; (c) return loss in the passband vs. 3-dB BW; where the AR=0.535, a=150 mil in 50Ω transmission line etched on the ground plane of the RT/Duroid 6010LM, h=25 mil.

A. Bandwidth Enhancement :

In this article, one of the most significant findings is 3-dB bandwidth enhancement with respect to the filling factor. As can be seen in Fig. 4(a) and Table I, reference filter is about less than 0.90 GHz while the proposed structure with no EBG in transmission line has 1.17 GHz and 0.30 FF EBG on transmission line has 1.25 GHz respectively. As the filter is tightly coupled, so the radiation loss due to skin effect will be more. Likewise, adding EBG on transmission line has equally distributed the capacitive coupling throughout the total transmission line. The consequence of that is, enhancement in the 3-dB bandwidth with a uniform and healthy coupling. The value of the curve increases gradually with a proper pattern. In Fig. 4(a), the curve is parabolic which shows a saturation in the coupling.

B. Shrinkage in Selectivity :

As can be seen in Fig. 4(b), the curve is decreasing exponentially which is noteworthy. The reference has the selectivity of 45.95 dB/GHz with a narrow bandwidth and no proper EBG pattern either on the couple-line or on the 50Ω transmission line. Nevertheless, involvement of the annular ring pattern on the couple-line in Fig. 1(b) and on both of the couple-line and on the T-line in Fig. 1(c), selectivity immediately falls off from 45.95 to 34 and 30.81 dB/GHz respectively. In conclusion, as the width of the passband rises, low selectivity occurs.

C. Improvement of Matching :

As illustrated in Fig. 4(c) and Table I, in the passband of the reference filter return loss is about 33.10 dB as a result of the non-uniform tight coupling between the couple-lines. At first, inclusion of the 0.25 FF ring pattern on couple-line improve the coupling balance at small-scale. Furthermore, inclusion of 0.30 FF ring with already placed 0.25 FF ring pattern on couple-line

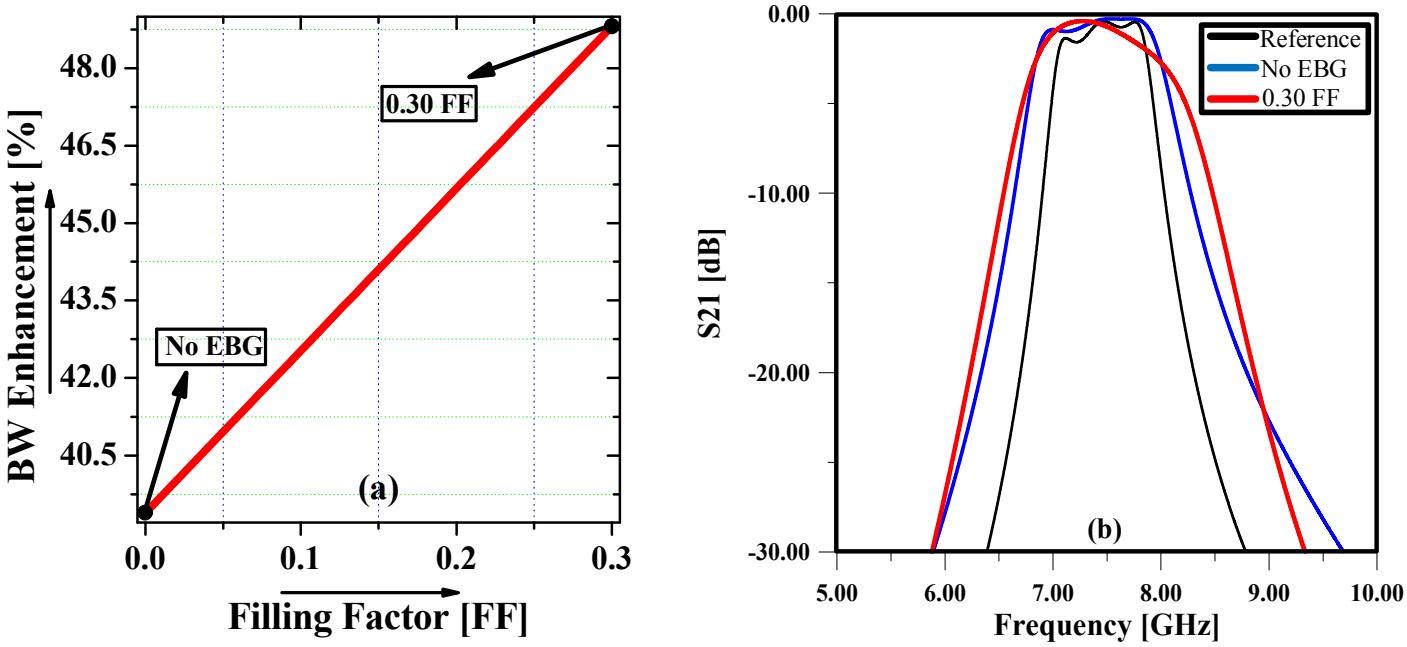

Fig. 5: Graphical representation of the (a) FF vs. percentage (%) of bandwidth enhancement; (b) frequency vs. insertion loss in the passband, black line-reference, blue line-no EBG on T-line, red line- 0.30 FF on T-Line; where the AR=0.535, a=150 mil remain constant.

a drastically improved matching in the passband of 65 dB can be observed in Fig. 4(c). From the Fig. 4(c), it can be observed that coupling is distributed consistently along the lower and upper transmission line.

D. Percentage of Bandwidth Enhancement :

As observed from Fig. 5(a) and Table I, the straight line which has very sharp tangent exhibits the percentage advancement of the bandwidth. From Fig. 5(a), the design with no EBG pattern on transmission line has increment of 39.39% and the pattern with 0.30 FF ring EBG on transmission line has 48.81%.

E. Low Insertion Loss :

Observing the Fig. 5(b), both insertion losses of the proposed circuits are improved significantly over the reference one. Furthermore, reference one bandwidth is bit narrower than both of the proposed designs. Likewise, at the tip of the passband in the reference model, ripple is present. With the increment of the filling factor, the ripple was no more with very smooth frequency response in the passband.

V. Conclusions

In this paper, the equal length asymmetric couple-line with annular ring patterns that can be utilized to effectively comprehend the bandpass filter is demonstrated. Furthermore, to certify the design method two examples of microstrip annular ring patterns on transmission line is established. In the illustrated cases, the 3-dB bandwidth increases by 39.39% and 48.81% respectively. Likewise, by properly placing the annular ring patterns on the couple-line section, sharp selectivity and more efficient passband can be obtained. On the other hand, appropriately selecting the volumetric ratio on both lower and upper transmission line, the matching and spurious transmission can be further improved. Alternatively, polynomial distribution with ring architecture can play a vital role for further improvement of overall efficacy of the couple-line filter.

References

[1] Fan Yang, Yahya Rahmat-Samii, *Electromagnetic Band Gap Structures in Antenna Engineering*. Cambridge CB2 8RU, UK: Cambridge University Press, 2009.

[2] Dal Ahn et al., "A Design of the Low-Pass Filter Using the Novel Microstrip Defected Ground Structure," in *IEEE Trans. Microwave Theory Tech,* vol. 49, no. 1, pp.86-93, Jan. 2001.

[3] F. R. Yang, K. P. Ma, Y. Qian and T. Itoh," A Uniplanar Compact Photonic-Bandgap (UC-PBG) Structure and Its Applications for Microwave Circuits," in *IEEE Trans. Microwave Theory Tech,* vol. 47, no. 8, pp.1509-1514, Aug. 1999.

[4] W. J. Feng, W. Q. Che, Y. M. Chang, S. Y. Shi and Q. Xue," High Selectivity Fifth-Order Wideband Bandpass Filters With Multiple Transmission Zeros Based on Transversal Signal-Interaction Concepts," in *IEEE Trans. Microwave Theory Tech,* vol. 61, no. 1, pp.89-97, January. 2013.

[5] M. K. Mandal, S. Sanyal," Compact Wideband Bandpass Filter," in *IEEE Microwave and Wireless Components Lett.* vol. 16, no. 1, pp.46-48, Jan. 2006.

[6] L. H. Hsieh, K. Chang," Compact, Low Insertion-Loss, Sharp-Rejection, and Wide-Band Microstrip Bandpass Filters," in *IEEE Trans. Microwave Theory Tech,* vol. 53, no. 4, pp.1241-1246, April. 2003.

[7] Nemai Chandra Karmakar, Mohammad Nurunnabi Mollah, "Investigations Into Nonuniform Photonic-Bandgap Microstripline Low-Pass Filters," IEEE Trans. Microwave Theory Tech., vol.51, no.2, pp.564-572, Feb.2003.

Dumbbell Annular Ring with Circular Patterned Microstrip Low-Pass Filter with Higher Selectivity, Wider Stopband and Lower Insertion Loss

Shakhawat Parvez, * Nazmus Sakib,* Md. Nurunnabi Mollah
Department of EEE, Khulna University of Engineering & Technology
Khulna-9203, Bangladesh
*shakhawat_parvez@yahoo.com,*sakib483@yahoo.com

***Abstract*— Electromagnetic Band Gap Structures (EBGs) have been developed to improve the efficiency of microwave and millimeter-wave devices, grown into most prominent framework by virtue of their unique electromagnetic and electrical properties. This article inspects the relationship between the operating performances of the low pass filter with the different EBG pattern. In this article, two high selectivity, wide stopband low pass filters (LPF) etched on ground plane with Tschebycheff polynomial distribution are proposed. A number of methods, method of moments (MOM) for numerical analysis and Tschebycheff polynomial distribution for designing the circuit are used. Moreover, to increase the stopband bandwidth of the new filters, a hybrid structure is used. The filter using ten dumbbell annular ring (DAR) patterns has improved selectivity of 47.19%, great matching upto 80 dB, negligible insertion loss less than 0.2 dB and two rejections in the stopband within 6.25 GHz, 12.97 GHz. In brief, this high selectivity, compact, wide stopband low pass filters were designed to alleviate the problem of low selectivity and small stopband bandwidth in microwave communication.**

Keywords—Low Pass Filters; Tschebycheff Polynomial Distribution; Selectivity; Dumbbell Annular Ring, Insertion Loss.

I. INTRODUCTION

In recent times, Electromagnetic Band Gap structures (EBGs) which is a subset of metamaterials have grown in reputation considering some periodic patterned, quite extraordinary and sophisticated properties. However, such high level properties is infrequent for a single natural material [1]. In microwave sector, EBGs display wider bandpass, steeper and deeper band rejection properties. In this present day, EBG assisted microstrip filters are frequently playing a role in modern microwave and RF engineering. To minimize the spurious transmission and register the compactness of circuits, numerous active and passive microwave and millimeter wave devices have been fabricated. However, due to the predicament of the modeling, utilizing an EBG structure for the fabrication of these components. Such as the element spacing, operating frequency, width, height of the substrate, thickness, irregularity of the surface, volumetric ratio of the EBG element, pattern of the elements which have influence on bandpass and band rejection properties. In addition, other complication in EBG circuit due to the radiation from aperiodic etching with no proper formulation as a result of the inappropriate selection of dielectric substrate [2].

978-1-4673-9257-0/15/$31.00 ©2015 IEEE

In this paper, applying Tschebycheff polynomial distribution with dumbbell annular ring (DAR) patterned EBG structures inscribe on the ground plane of a microwave transmission line is proposed. On the whole, microwave assisted low pass filter return loss, insertion loss and selectivity enhanced performance where Tschebycheff polynomial distribution are employed to fabricate the filter. Moreover, two new sharp selectivity, wide stopband low pass filter based on hybrid pattern (namely, only DAR and DAR with interleaved circular) concepts, is the novelty of the paper. Developing wider, deeper stopband and suppressing ripples in the passband are great features of the Tschebycheff polynomial. A unique measure of the Tschebycheff polynomial the side lobe level (SLL) is exploited to manage the width of stopband insertion loss, the depth of passband return loss, ripples in both passband and stopband, selectivity. Consequently, with the Tschebycheff distribution ripple, width and depth of the stop bandwidth can be mitigated with the improvement of selectivity of the transfer function at cut-off frequency [3].

The proposed low pass filter utilizing the Tschebycheff polynomial distribution with the novel Hybrid structure not only has some specific ground of originality but also has some unique features, which includes the following:

a. The stopband is greater than 12 GHz which is very wide than that of a traditional low pass filter.
b. Two architectures will be fabricated according to the Tschebycheff polynomial distribution.
c. The ripple is less than 0.2 dB and significant improvement in matching in the passband.
d. The rates of roll-off transfer function is very sharp.
e. The return loss in the stopband is negligible.

All the structures are simulated by method of moments (MOM) based EM software *Zeland IE3D*.

II. DESIGN THEORY OF STRUCTURES AND POLYNOMIAL DISTRIBUTION

Tschebycheff polynomial has a convenient characteristic of equal ripple characteristic which is observed for a selective side lobe level (SLL). The Tschebycheff excitation coefficient are determined by the SLL. The recurrence formula [4] for Tschebycheff polynomial:

$$T_m(z)=2zT_{m-1}(z)-T_{m-2}(z) \quad (1)$$

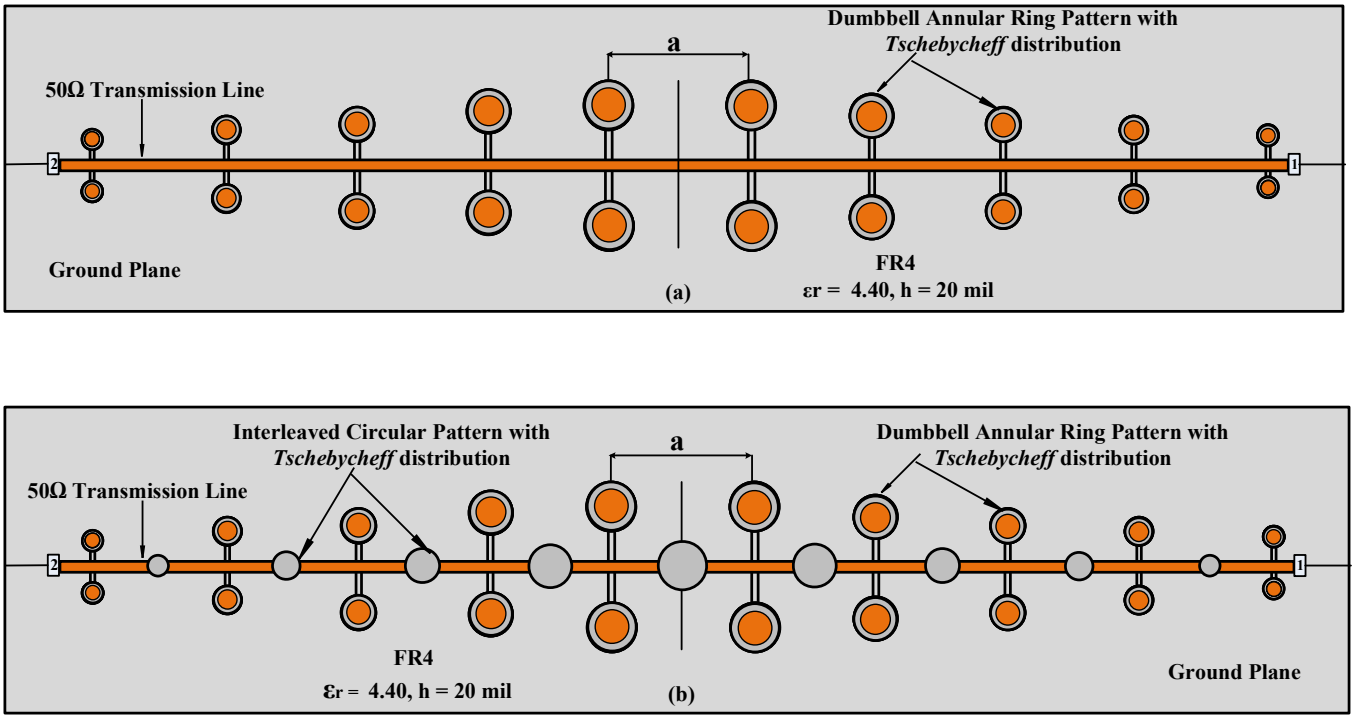

Fig. 1: Schematics of the (a) Proposed designed dumbbell annular ring assisted low pass filter on transmission line; (b) Proposed designed low pass filter with dumbbell annular ring with interleaved circular (Hybrid) pattern on the transmission line; where the AR=0.535, FF=0.25, period, a=320 mil in 50Ω transmission line etched on the ground plane of the FR4 substrate, h=20 mil.

Every polynomial can be evaluated using:

$$T_m(z)=\cos[m\cos^{-1}(z)];\ -1 \le z \le +1 \qquad (2)$$

$$T_m(z)=\cosh[m\cosh^{-1}(z)];\ z\langle -1,\ z\rangle +1 \qquad (3)$$

As major to minor lobe ratio for 25 dB, the amplitude of coefficient will be:

$$0.40\ 0.51\ 0.72\ 0.90\ 1\ 1\ 0.90\ 0.72\ 0.51\ 0.40$$

The volumetric ratio of each circular element will be:

$$FF=\frac{r}{a} \qquad (4)$$

Where, Filling Factor (*FF*), radius of each element (*r*), spacing between two elements (*a*).

On the ground plane, the ring pattern is placed into the standard 50Ω transmission line with period "*a*" which is a influential parameter for achieving sharp selectivity and wider stopband. However, the filling factor for annular ring will be:

$$FF=\frac{r_1}{a} \qquad (5)$$

Where, outer ring radius (r_1). The ratio of the inner ring radius (r_2) to outer ring radius (r_1) is called Aspect ratio (AR).

$$AR=\frac{r_2}{r_1} \qquad (6)$$

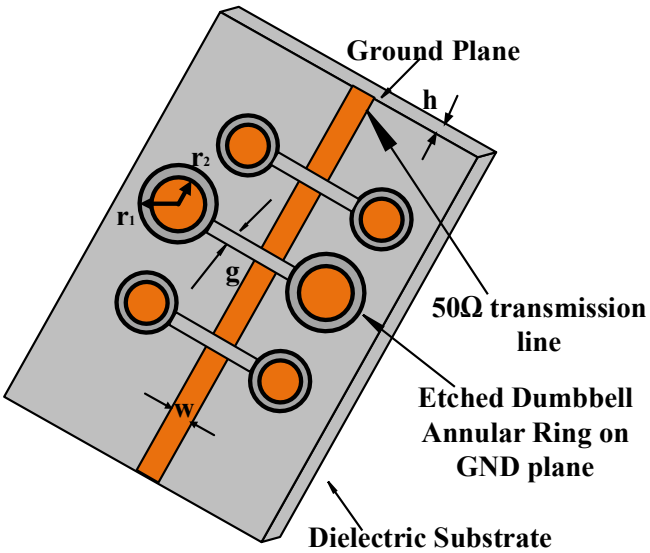

Fig. 2: Three-dimensional (3-D) view of the conventional dumbbell annular ring structure with Tschebycheff distribution etched on a ground plane on a 50Ω transmission line, grey- etched portion, colour-copper portion; where, w and g are the width of the transmission line and arm of the dumbbell annular ring respectively.

The center frequency of the stopband can be calculated using:

$$\beta a=\pi \qquad (7)$$

Where, β is the wave number of dielectric slab, a is the period of the annular ring pattern.

TABLE I

COMPARATIVE STUDY BETWEEN THE PERFORMANCE OF THE PROPOSED DUMBBELL ANNULAR RING ASSISTED LOW-PASS FILTER; *AR=0.535, FF=0.25* REMAIN CONSTANT, PERIOD, 320 MIL WILL VARY ACCORDING TO THE TSCHEBYCHEFF POLYNOMIAL.

Structures	Selectivity [dB/GHz]	Stopband isolation S_{21max} [dB]	f_0 [GHz]	20-dB IL BW [GHz]	10-dB RL BW [GHz]	3-dB Cut-Off Frequency [GHz]	Frequency Deviation %	1st Null & Peak [dB] Null	Peak
Only DAR	89.47	80.00	9.82	6.25	4.55	4.46	-1.80	59.2	17.60
DAR with Circular	130.77	78.60	9.81	12.97	4.98	4.90	-1.90	64.6	13.20

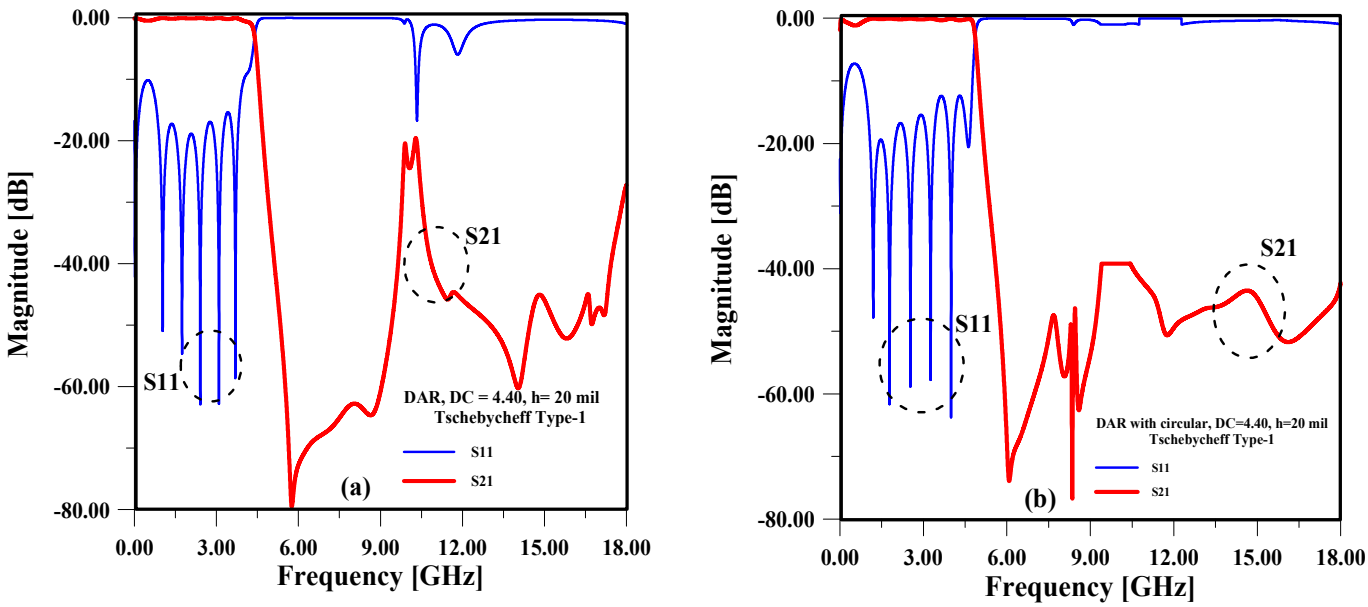

Fig. 3: Simulated frequency response of the (a) Proposed designed dumbbell annular ring assisted low pass filter on transmission line; (b) Proposed designed low pass filter with dumbbell annular ring with interleaved circular (Hybrid) pattern on the transmission line; where the AR=0.535, FF=0.25, period, a=320 mil in 50Ω transmission line etched on the ground plane of the FR4= 4.40 substrate, h=20 mil; AR = 0.535 remain constant throughout the analysis.

III. PROPOSED DESIGN STRUCTURES

The dumbbell annular ring (DAR) structured low-pass filters were constructed on FR4 substrate with dielectric constant of 4.40 and thickness of 20 mil. For simulation purpose and great tuning, the couple-line filter is simulated by EM software Zeland IE3D. Outer ring radius r_1 which derives from filling factor and inner ring radius r_2 which can be obtained from aspect ratio, this both factor are kept consistent at 0.25 and 0.535 respectively throughout the analysis. Likewise, 25-dB Side lobe level with ten amplitude coefficient will determine the dimension for each of the dumbbell annular ring (DAR) as well as the capacitive coupling between them. Besides, Tschebycheff polynomial distribution are applied with center frequency at 10GHz. Selectivity, 20-dB IL BW and 10-dB RL BW, this three significant parameters will be taken account to find out the structure for the low pass filter with the best, reliable and remarkable efficacy.

A. Only Dumbbell Annular Ring (DAR) structure on T-Line:

As can be seen from Fig. 1(a), the proposed filter have ten dumbbell annular ring (DAR) EBG elements with 0.25 FF, arm width and height of the structure are 113 and 10 mil respectively. But, like the Fig. 1(b), no other (namely, circular) pattern EBG element are etched on the 50Ω transmission line. However, by the Tschebycheff polynomial for 25-dB SLL not only the dimension of the DAR will vary but also spacing between each DAR will also fluctuate accordingly. As a result, spacing between two DAR will increase with Tschebycheff distribution However, the coupling between each element is strong which results in sharp selectivity. Although the structure is symmetric, but the capacitive coupling between each of the dumbbell annular ring are unbalanced and weak in compare with Fig. 1(b). To improve the overall coupling and bandgap properties, circular patterned EBG structures is utilized in between the DAR in Fig. 1(b).

TABLE II
PERFORMANCE COMPARISON BETWEEN DIFFERENT LPF

Filter Structures	Selectivity [dB/GHz]	Stopband isolation S_{21max} [dB]	Ripple Height [dB]
Ref. [3]	20.92	61.50	< 0.5
Ref. [5]	6.29	68.00	< 5
Ref. [6]	24.28	65.30	2
Only DAR	89.47	80.00	< 0.2
DAR with Circular	130.77	78.60	< 0.2

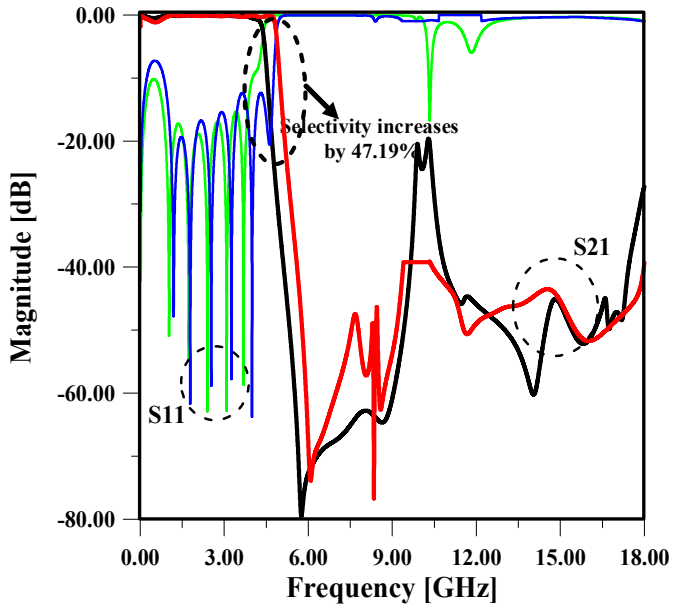

Fig. 4: Comparative study between two proposed low pass filters with Tschebycheff polynomial distribution; where, green-only DAR (S_{11}), black-only DAR(S_{21}); blue-DAR with circular (S_{11}), red- DAR with circular (S_{21}).

B. Dumbbell Annular Ring (DAR) with circular structure on T-Line:

As illustrated in Fig. 1(b), the proposed DAR assisted low pass filter have ten dumbbell annular ring EBG elements with 0.25 FF, arm width and height of the structure are 113 and 10 mil respectively. Likewise, nine circular patterns with the same volumetric ratio as annular ring, this EBG element with Tschebycheff distribution and same spacing between them like DAR are etched on the 50Ω transmission line. Moreover, in this design the dimension of DAR will also fluctuate in agreement with 25-dB SLL Tschebycheff polynomial. Consequently, the coupling between the patterns become stronger and balanced than design 1. Besides, the ripple in the stopband also diminishes with high rates of roll-off transfer function. Likewise, this hybrid design also prevails with very wide stopband with increased selectivity. In brief, DAR with circular pattern yields a unique combination, which constitutes more attractive bandgap properties in EBG structure.

IV. RESULTS

Modeling the low pass filters (LPF) by Tschebycheff polynomial distribution with hybrid patterns to realize the performance of the LPF is examined. As can be seen from Fig. 3(a), Fig. 3(b) and Table-I, it is found that, in Tschebycheff distribution with FR4 substrate for structure with only DAR and DAR with circular exhibit selectivity, 20-dB IL and 10-dB RL bandwidth of 89.47 dB/GHz, 6.25 GHz, 4.55 GHz and 130.77 dB/GHz, 12.97 GHz, 4.98 GHz respectively. However, FR4 is a lossy substrate at high frequency [7]. Nevertheless, the structure-1 displays negligible insertion loss in the passband with ripple less than 0.2 dB, great selectivity, well impedence matching upto 60 dB and very wide stop bandwidth upto 6.5 GHz. Besides, the structure-2 reveals very wide return loss bandwidth upto 5 GHz with ripple not greater than 0.2 dB, excellent matching, sharper roll-off and wider stop bandwidth upto 13 GHz. Although, in design-2, modeling is robust because of circular pattern are etched between the DAR on 50Ω transmission line. Also, the arm length of the annular ring fluctuates according to the Tschebycheff polynomial. Similarly, annular ring has a unique feature namely, aspect ratio which is equivalent of variable capacitance, so in design-2 exhibits profound performance than design-1. Observing the Table-I, design-2 has more stable passband performance with increase in 10-dB RL bandwidth as well as 3-dB cut-off frequency. At 11 GHz, design-1 exhibits poor performance in the stopband. With stronger coupling in design-2, this disturbance due to spurious transmission is alleviated. Consequently, the width and depth of the stopband increases. Besides, the maximum isolation of the stopband in design-1 is greater than design-2 with 1.75% increment. The width of the stopband has been expanded 107.52% in design-2 than design-1. As illustrated in Fig. 4, the selectivity in design-2 is sharper than design-1 with amount of 47.19%. Furthermore, from the observation of comparative study in Table II, performance of different low pass filters, it is appreciated that roll-off rates has been improved significantly with a minimum amount of 2.67 times by the proposed two structures. Moreover, the depth of the stopband is upto 80 dB and passband ripples is quite negligible. In conclusion, only DAR and DAR with circular patterns reveal more superior passband and stopband performance with Tschebycheff distribution respectively.

V. CONCLUSIONS

A new hybrid, wide stopband, low insertion loss and high selectivity microstrip low pass filter has been demonstrated. A low pass filter with hybrid structure namely, dumbbell annular ring (DAR) and circular is introduced. A new design was developed to increase not only the rate of roll-off transfer function but also the width of the stopband. However, with the hybrid design forming more stable capacitive coupling, the dielectric and radiation losses are reduced significantly. The consequence of that is, negligible

ripple in the passband with superior matching. The new low pass filters were designed to alleviate the low selectivity and small stop bandwidth in microwave communication.

REFERENCES

[1] Fan Yang, Yahya Rahmat-Samii, *Electromagnetic Band Gap Structures in Antenna Engineering*. Cambridge CB2 8RU, UK: Cambridge University Press, 2009.

[2] Dal Ahn et al., "A Design of the Low-Pass Filter Using the Novel Microstrip Defected Ground Structure," IEEE Trans. Microwave Theory Tech, vol. 49, no. 1, pp.86-93, Jan. 2001.

[3] N. C. Karmakar, M. N. Mollah, "Investigations Into Nonuniform Photonic-Bandgap Microstripline Low-Pass Filters," IEEE Trans. Microwave Theory Tech., vol.51, no.2, pp.564-572, Feb.2003.

[4] C.A. Balanis, *Antenna Theory Analysis and Design*, 2 ed. New York: Wiley, 1997.

[5] S. Parvez et al., "Investigation on EBG Structures: A Critical Analysis to optimize the performance of Asymmetric Couple-Line Bandpass Filter," in Int. Conf. on Software, Knowledge, Inform. Manage. and Applicat., Dhaka, Bangladesh, 2014, pp. 1-7.

[6] G. M. Rafiquzzaman et al., "A New to Design Microstrip Low Pass Filter Using Novel Defected Ground Structure," in Int. Conf. on Elect. and Comput. Eng., Dhaka, Bangladesh, 2014, pp. 568-571.

[7] John Conrod, "Understanding When To Use FR4 or High Frequency Laminates," Rogers Corp., Roosevelt Avenue, Chandler, AZ. Rep. 26-30, Sept. 2011.

Design & Simulation of Ultra-Flattened Dispersion Large Mode Area and Low Splice Loss Photonic Crystal Fiber

Md. Rakib Hasan
Department of Electrical and Electronic Engineering
Rajshahi University of Engineering & Technology, RUET
Rajshahi-6204, Bangladesh
sumon.ruet09@gmail.com

Md. Selim Hossain
Department of Electrical and Electronic Engineering
Rajshahi University of Engineering & Technology, RUET
Rajshahi-6204, Bangladesh
Dr.S.Hossain@ieee.org

***Abstract*— This paper presents dispersion flattened (DF) large mode area (LMA) fiber design based on single cladding structure using finite element method (FEM) with perfectly matched layer (PML) boundary. The modal properties of the PCFs are investigated due to change in cladding parameters. To improve these properties of PCF our proposed design has obtained satisfactory results especially for flattened dispersion, effective area and splice loss. It has been shown that proposed PCFs can obtain very low dispersion variation 0.3537 ps/(nm.km) along 1300nm to 1700nm wavelength, with both a large effective area more than 82 μm^2 and splice loss of 0.0040 dB in 1550nm wavelength. As the properties obtained from simulation are suitable for the C+L+U communication bands, our proposed design can be used within these bands with better performance.**

Keywords*— Photonic crystal fibers; ultra-flattened dispersion; large effective mode area; nonlinear coefficient; splice loss;

I. Introduction

Photonic crystal fiber (PCF) [1] has received increasing attention because of its novel optical characteristics [2]. Fiber-optic communication system has brought revolution in the telecommunication industry. It is advantageous in comparison with other communication system [3]. PCFs are characterized by numerous cladding air holes arranged in an orderly manner over the whole fiber length [4]. As there are several parameters to tailor in a PCF, it can be utilized to obtain very useful properties like flat negative dispersion [5], large mode effective area [6], very high or very low nonlinearity [7], splice loss [5] and low bending loss [5]. By modulating the parameters of holey cladding, the above properties can be controlled [7]. Because of high attenuation of these types of fibers, PCFs are still under investigation as high-speed optical transmission media but recently, the attenuation level has been lowered to the order 0.28 dB/km at the 1550 nm wavelength [8]. This has encouraged the researchers to rethink the applicability of PCFs in signal transmission and modern fabrication technology is giving momentum to such thinking.

Optical transmission systems require PCFs with large effective mode area is required not only to support broadband optical transmission but also to minimize the coupling losses to standard single mode fibers (SMFs) [7]. To design large mode-area (LMA) fibers, it is desired that fibers should remain single-mode (SM) to ensure the high beam quality, which is measured through beam quality factor $M2$ (<1.2) for diffraction limited operation [9]. Again, in communications systems dispersion-flattened fiber (DFF) is very effective for optical data transmission over the broadband wavelength range [10]. For example, in wavelength division multiplexing communication systems it is essential to maintain a uniform response in different wavelength channels. This is strictly achieved by ensuring ultra-flattened dispersion characteristics of fibers [7]. Splice loss and nonlinearity are other important key factors for designing PCF. When connecting two fibers using splicing technique, geometrical misalignments occurs that leads to losses known as splice loss. Controlling the splice loss of the fiber, it will be of great use in fiber to the home (FTTH) application [11]. The nonlinearity of a fiber depends on effective area and it is inversely proportional to the effective area of the fiber. There are so many literatures dealing with large mode effective area with flattened dispersion [2,7], [12-14]. Some of which even warrant low splice loss [7], [11] as well. There are only a few papers dealing with PCFs having LMA, dispersion-flattened characteristics, low splice loss and nonlinearity at the same time.

Pourmahayabadi *et al*. [13] have proposed such an LMA PCF in 2009. They have theoretically achieved dispersion variation 1.75 ps/(nm.km) in 1.53μm to 1.57 μm wavelength but their effective area is only 20.0535 μm^2. Razzak *et al*. [7] have proposed another MOF LMA PCF design in 2010. They have theoretically achieved effective area of more than 150 μm^2 with dispersion variation 0.6 ps/(nm.km) in 1.4μm to 1.7μm wavelength and a splice loss of 0.19 dB. The PCF proposed in [7] and [13] have not mentioned about nonlinearity of their designs.

In this paper, we propose a two layer cladding PCF characterized by a common pitch and three different air-hole dimensions. The whole work aims at designing and numerical simulating the large mode effective area, flattened dispersion, low splice loss and low nonlinearity photonic crystal fiber. PCFs with such novel properties are suitable for telecom applications.

II. Numerical Analysis

The key propagation properties of the PCF are evaluated using Finite Element Method (FEM). The FEM directly solves the Maxwell equations to best approximate the value of the effective refractive index [15-16]. A commercial full-vector

978-1-4673-9257-0/15/$31.00 ©2015 IEEE

finite-element software (COMSOL) has used for both the modal and loss analyses. To allow accurate evaluation of the insertion losses, anisotropic perfectly matched layer has included in the finite-element model. We have also used Sellmeier equation to evaluate the refractive index of silica. Following equations are used to evaluate dispersion D, effective area A_{eff}, nonlinear coefficient γ and splice loss L_s. The main concern of this paper is to obtain ultra flattened and low dispersion variation, large effective area, low nonlinearity and low splice loss. The dispersion D with respect to λ is given by

$$\text{Dispersion, } D(\lambda) = -\frac{\lambda}{c}\frac{d^2}{d\lambda^2} R_e[n_{eff}] \quad (1)$$

Here, $D(\lambda)$ is in ps/(nm km) and $Re[n_{eff}]$ is the real part of the effective refractive index n_{eff}. The material dispersion is directly included in the FEM calculation. The effective area A_{eff} is given by

$$\text{Effective area, } A_{eff} = \frac{\left(\int_{-\infty}^{\infty}\int_{-\infty}^{\infty}|E|^2\,dxdy\right)^2}{\int_{-\infty}^{\infty}\int_{-\infty}^{\infty}|E|^4\,dxdy} \quad (2)$$

Where, E is the electric field distribution and A_{eff} is in μm^2. The study of A_{eff} is, thus, an important starting point in understanding of the nonlinear phenomena in PCFs.

$$\text{Nonlinear coefficient, } \gamma = \left(\frac{2\pi n_2}{A_{eff}\lambda}\right)\times 10^3 \quad (3)$$

Where, n_2 is the nonlinear refractive index for silica. The nonlinear coefficient is inversely proportional to the effective mode area. The splice loss can be obtain from the following:

$$\text{Splice loss, } L_s = -20\log_{10}\frac{2w_{SMF}w_{PCF}}{w_{SMF}^2 + w_{PCF}^2} \quad (4)$$

Where, w_{SMF} and w_{PCF} are the (Mode Field Diameter) MFDs of the (Single Mode Fiber) SMFs and the PCFs, respectively.

III. Geometry of The MAC-PCF Design

We have proposed two hexagonal geometrical designed PCFs and both are arranged 8 air hole rings in the cladding region with silica background.

A. MAC-PCF-1

Fig. 1 shows our proposed MAC (Multiple Air holes Core) -PCF-1 design. The design has two layer cladding is composed of a common air-hole pitch, Λ_1. It has three different air-hole diameters d_c, d_1 and d_2, where d_c is less than d_1 and d_2 is greater than d_1. Dimension of the first ring is lowered down to flatter the dispersion characteristics and air-holes of inner rings are chosen smaller to achieve larger mode area. Moreover, five air holes having diameter d_c are placed in the core to obtain large effective area using smaller pitch. The pitch among five air holes is in the core by the relation (Λ_1*0.5). The air hole diameter of 1st four rings is d_1 and 2nd four rings are d_2.

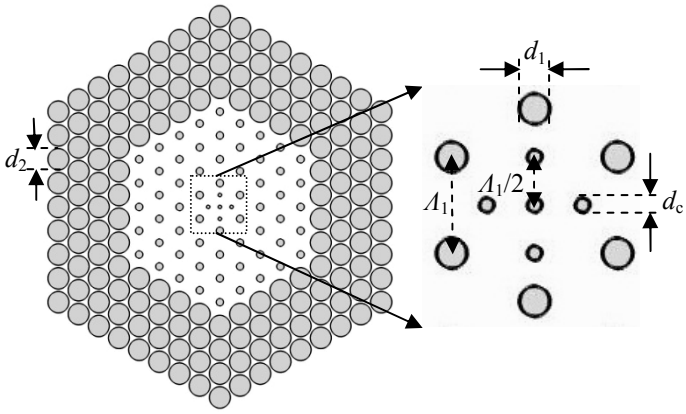

Fig. 1. Design of MAC-PCF-1.

B. MAC-PCF-2

Fig. 2 shows our another proposed MAC (Multiple Air holes core)- PCF-2 design. The design has also two layer cladding is composed of a common air-hole pitch, Λ_2. It has three different air-hole diameters d_c, d_1 and d_2, where d_c is less than d_1 and d_2 is greater than d_1. Like previous design, five air holes having diameter d_c are placed in the core to obtain large effective area using smaller pitch. The pitch among five air holes is in the core by the relation (Λ_2*0.5). In MAC-PCF-2 design diameter of all the air holes is kept d_1 except 5th ring having air hole diameter d_2 in fig. 2. As a result we have obtained almost same effective area and more flattened dispersion curve but using lower pitch in Fig. 1 than Fig. 2.

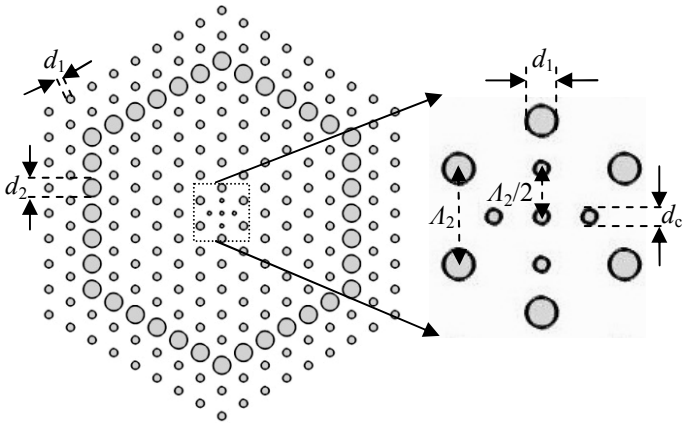

Fig. 2. Design of MAC-PCF-2.

IV. Simulation Results

Fig. 3 shows the optical field distribution for both x and y polarization at 1550 nm wavelength of MAC-PCF-1 and MAC-PCF-2. It is seen that the optical field is well confined to the outer side of the core due to the presence of air holes in the core region which increases the effective area.

Fig.4 shows the wavelength dependence of dispersion variation of the proposed two designs for y-polarized mode respectively with optimum design parameters. In MAC-PCF-1, we set pitch, Λ as 3μm, d_c=0.225 μm and d_1=0.5025 μm, d_2 = 1.35 μm. But in MAC-PCF-2, we set pitch, Λ as 2.5μm, d_c=0.1875 μm and d_1=0.39375 μm, d_2 = 0.875 μm. In Fig. 3,

MAC-PCF-1 shows almost flattened dispersion for y-polarization from 1500 nm to 1700 nm wavelength but MAC-PCF-2 shows more flattened dispersion than MAC-PCF-1 for y-polarization from 1300 nm to 1650 nm wavelength.

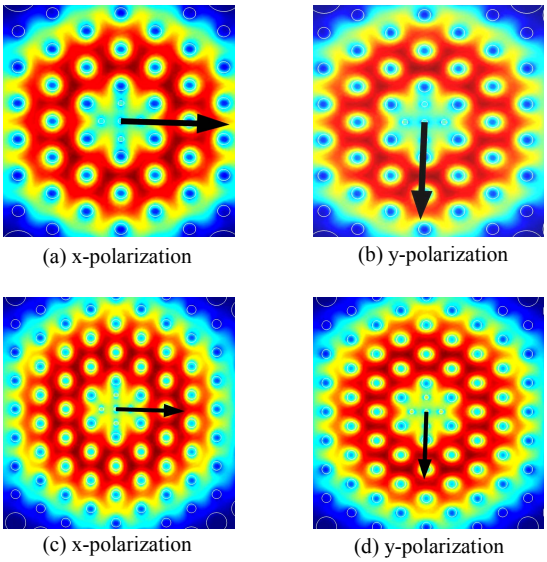

Fig. 3. Optical field distribution at 1550 nm wavelength of MAC-PCF-1 (a) &(b) and MAC-PCF-2 (c) & (d)

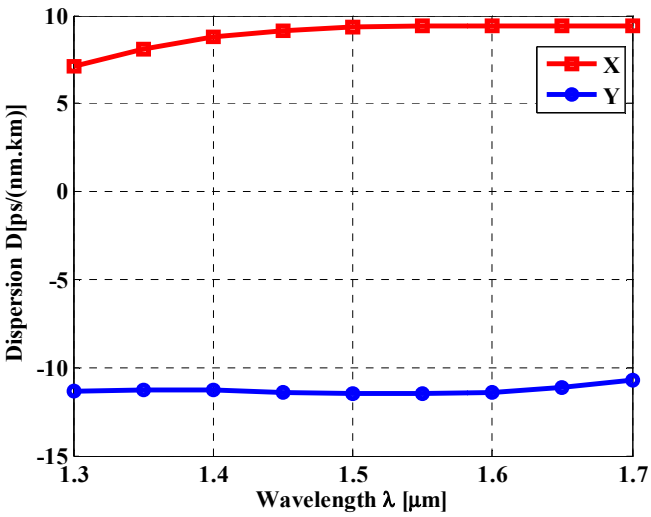

Fig. 4. Dispersion for optimum parameters of MAC-PCF-1 and MAC-PCF-2.

Fig 5(a) and 5(b) show the Effect on dispersion of pitch *Λ* variation in MAC-PCF-1 and MAC-PCF-2. The MAC-PCF-1 and MAC-PCF-2 show dispersion variation of 2.32 and 0.3537 ps/(nm.km) respectively from 1300 nm to 1650 nm wavelength.

The effective area or simply the effective area is the area where the beam intensity drops to 13.5% of the maximum value and the diameter of which is called the mode field diameter (MFD). Fig. 6 shows wavelength dependence of effective area of MAC-PCF-1 and MAC-PCF-2. We have obtained 82.88 μm^2 in MAC-PCF-1 and 83.45 μm^2 in MAC-PCF-2 at 1550 nm wavelength which is very high compared to that of conventional fiber. The PCFs with flattened dispersion and relatively high effective area would be useful to support broadband optical transmission and also in wavelength division multiplexing systems. Fig 7(a) and 7(b) also show the effect on effective area of pitch *Λ* variation in MAC-PCF-1 and MAC-PCF-2.

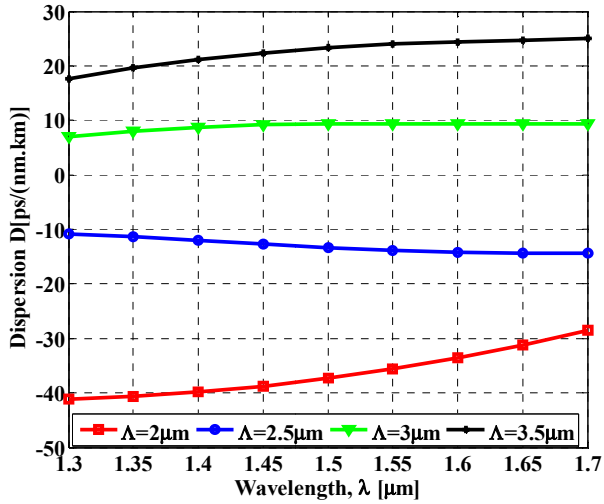

Fig. 5(a). Effect of dispersion of pitch *Λ* variation in MAC-PCF-1.

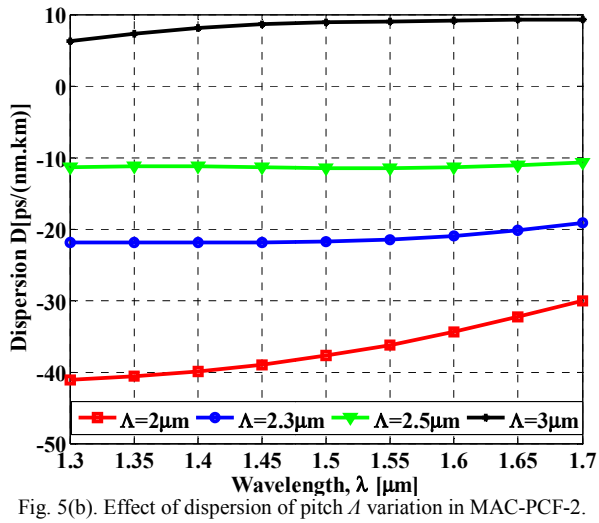

Fig. 5(b). Effect of dispersion of pitch *Λ* variation in MAC-PCF-2.

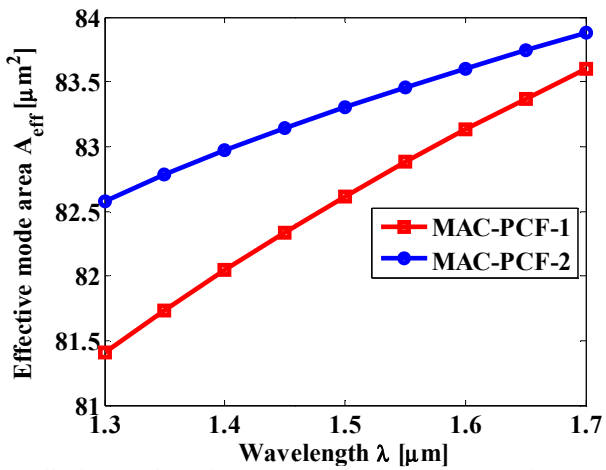

Fig. 6. Effective area for optimum parameters of MAC-PCF-1 and MAC-PCF-2.

One can observe from Fig. 5(a) & 5(b) and Fig. 7(a) & 7(b) that the flattened dispersion curve cannot be obtained for large effective area.

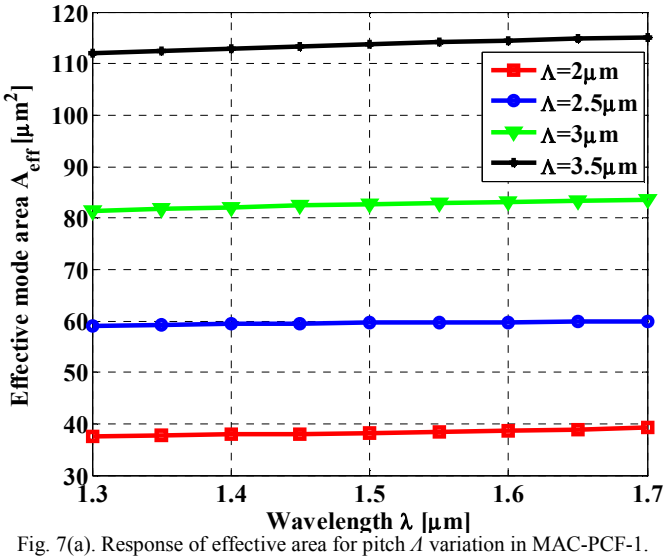

Fig. 7(a). Response of effective area for pitch *Λ* variation in MAC-PCF-1.

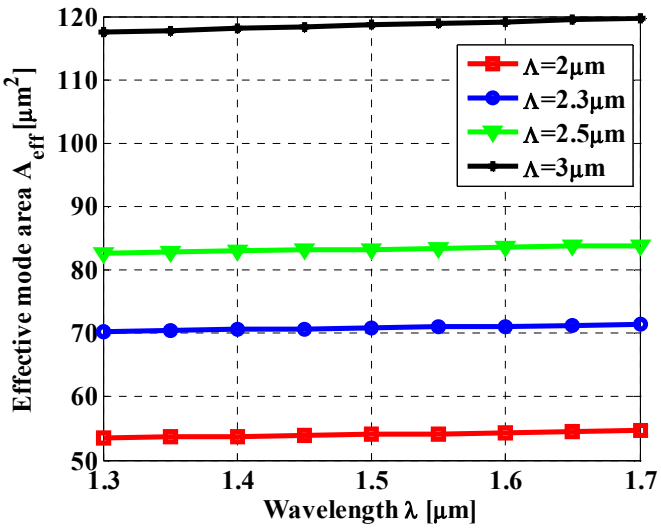

Fig. 7(b). Response of effective area for pitch *Λ* variation in MAC-PCF-2.

The nonlinear coefficient of PCFs depends on the value of the nonlinear refractive index and the effective area of the PCF. A lower value of the effective area gives a higher nonlinear coefficient and vice-versa as the value of n_2 is constant for silica PCFs. One can see from Fig.8 the MAC-PCF-2 has very low nonlinear coefficient than MAC-PCF-1. The MAC-PCF-2 design shows maximum effective area at wavelength 1550 nm than MAC-PCF-1.

The splice loss is a very important design consideration for single mode fibers. When coupling two similar fibers or a PCF with a single mode fiber (SMF) using the splicing techniques, a mismatch occurs due to the dissimilar MFD or geometrical misalignments during the fusion process that leads losses known as the splice loss. We have obtained 0.0031 dB in MAC-PCF-1 and 0.0040 dB in MAC-PCF-2 at 1550 nm wavelength in Fig. 9. By controlling the splice loss of the fiber, it will be of great use in these telecommunication applications.

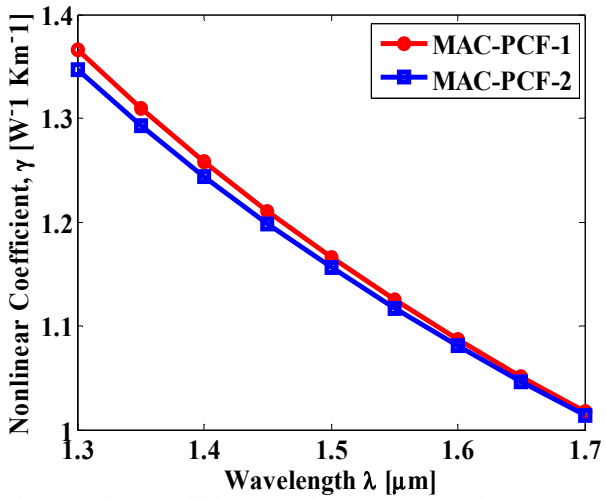

Fig. 8. Nonlinear coefficient for optimum parameters of MAC-PCF-1 and MAC-PCF-2.

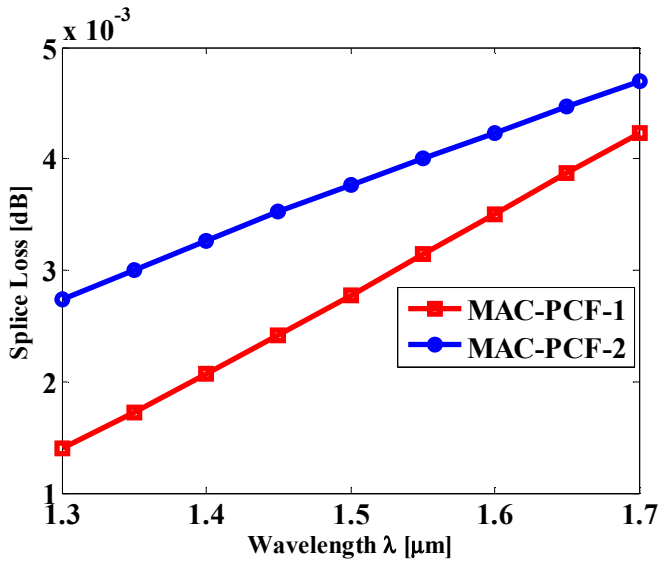

Fig.9. Splice loss for optimum parameters of MAC-PCF-1 and MAC-PCF-2.

V. COMPARATIVE STUDY

Finally a comparison is given in table I between properties of the designed PCFs and existing PCFs. It is clear from table that the four-ring photonic crystal fiber (PCF) structure addressed in [12] has low variation in dispersion curve over the telecommunication band but area is too low. Our proposed designs are better than four-ring (PCF) structure [12]. Our effective area is not so high than DF-PCF [2] but they mention about their dispersion variation only for 1.53μm to 1.57 μm and high splice loss. The large effective mode area microstructure optical fiber [7] has better effective area than ours but the splice losses of our designs are better than the microstructure optical fiber [7]. At the last though the large mode area (PCF) [13] has low dispersion variation but their area is poor and there is nothing about splice loss.

TABLE I. COMPARISON OF PROPOSED PCF DESIGN WITH THE EXISTING PCF.

PCFs	effective area in μm^2	D(Λ) ps/(nm.km)	Dispersion variation ps/(nm.km)	Splice loss dB
Ref [2]	80	4.7	<0.8 in 1.53μm to 1.57 μm	1.6
Ref [7]	122	-27.2	0.6 in 1.4μm to 1.7μm	0.19
Ref [12]	13.2	-	±0.25 in 1.295μm to 1.725 μm	-
Ref [13]	20.05	38.4	1.75 in 1.53μm to 1.57 μm	-
MAC-PCF-1	**82.88**	**9.18**	**2.32 in 1.3μm to 1.7 μm**	**0.0031**
MAC-PCF-2	**83.45**	**-11.50**	**0.3537 in 1.3μm to 1.7 μm**	**0.0040**

VI. CONCLUSION

In this paper, light guiding properties of PCF have been investigated based on FEM method with PML boundary for telecommunication and wavelength-division multiplexed (WDM) communication systems. The design of air hole(s) in the core of PCF which carrying flattened dispersion in the telecommunication band is investigated. This design offers large mode area with low splice loss. This fiber is easy to fabricate due to its hexagonal design. The proposed MAC-PCF-2 offers very low dispersion variation 0.3537 ps/(nm.km) for 1300nm to 1700nm wavelength and MAC-PCF-1 offers very low splice loss of 0.0031dB in 1550nm wavelength. So both PCFs can be used for specific applications.

REFERENCENS

[1] J. C. Knight, "Photonic crystal fibers," Nature 424, pp. 847-851, 2003.

[2] T. Matsui, J. Zhou, K. Nakajima and I. Sankawa, "Dispersion-flattened Photonic Crystal Fiber with Large Effective area and Low Confinement Loss," Journal of Lightwave Technology, Vol. 23, No. 12, pp. 4178-4183, Dec 2005.

[3] J. Broeng, D. Mogilevstev, S. E. Barkou, and A. Bjarklev, "Photonic crystal fibers: A new class of optical waveguides," Optical Fiber Technology, vol. 5, pp. 305–330, 1999.

[4] M. A. Islam, M. S. Alam, "Bend-insensitive single mode photonic crystal fiber with ultra large effective area for dual applications," Optical Engineering, Vol. 52(5), pp. 050501-1–050501-3, May 2013.

[5] P. Russell, "Photonic crystal fibers," Science 299(5605), 358 – 362(2003).

[6] M. Napierała, E. B. Pawlik, T. Nasilowski, P. Mergo, F. Berghmans, H.Thienpont, "Photonic Crystal Fiber With Large Mode Area and Characteristic Bending Properties," IEEE Photonics Technology Letters, Vol. 24, No. 16, August 15, 2012.

[7] S. M. A. Razzak, Y. Namihira, "Theoretical design of a large effective mode area microstructure optical fiber," Optica Applicata, Vol. XL, No. 3, 2010.

[8] Z. Jian, K. Tajima, K. Nakajima, K. Kurokawa, C. Fukai, T. Matsui, I. Sankawa, "Progress on low loss photonic crystal fibers," Optical Fiber Technology 11 (2), pp. 101–110, 2005.

[9] G. Thavasi Raja and S. Kumar Varshney, "Extremely Large Mode-Area Bent Hybrid Leakage Channel Fibers for Lasing Applications," IEEE Journal of selected topics in Quantum Electronics, Vol. 20, No. 5, September/October 2014.

[10] T. Okuno, H. Hatayama, K. Soma, T. Sasaki, M. Onishi, and M. Shigematsu, "Negative dispersion-flattened fiber suitable for 10 Gb/s directly-modulated signal transmission in whole telecommunication band," Electronics Letters, vol. 40, no. 12, pp. 723–724, Jun. 2004

[11] S. Priyambada, Dr. D. K. Singh, "Analysis of Effective Area and Splicing Loss Behavior of Square and Hexagonal Phtonic Crystal Fiber," International Journal of Scientific and Research Publications, Volume 3, Issue 5, May 2013

[12] T. Wu, C. Chao, "A novel ultra flattened dispersion photonic crystal fiber," IEEE Photonics Technology Letters, vol. 17, pp. 67-69, 2005.

[13] M. Pourmahayabadi and S. M. Nejad, "Design of a Large Mode Area Photonic Crystal Fiber with Flattened Dispersion and Low Confinement Loss," 17th Iranian Conference on Electrical Engineering 2009, Iran University of Science and Technology, Tehran, Iran, Electronics, vol.1, 12-14 May, 2009.

[14] S. M. A. Razzak, Y. Namihira and F. Begum, "Ultra-flattened dispersion photonic crystal fiber," Electronics Letters, Vol. 43, No. 11, 24th May 2007.

[15] M. Koshiba, "Full vector analysis of photonic crystal fibers using the finite element method," IEICE Trans. Electron, vol. E85-c, no. 4, pp. 881–888, Apr. 2002

[16] S. M. A. Razzak, Y. Namihira, M. A. G. Khan, F. Begum, and S. Kaijage, "Chromatic dispersion properties of a Decagonal Photonic crystal fiber", Information and communication Technology, pp. 159-162, 2007.

[17] G. Agrawal, Nonlinear Fiber Optics, 3rd Edition, Academic Press, 2001, pp. 5–10.

Outage Capacity Analysis of Cluster-based Forwarding Scheme for Body Area Network using Nano-electromagnetic Communication

Fariha Afsana* , M. R. Ahmed†, S. A. Mamun ‡ and M. S. Kaiser §
Institute of Information Technology*‡§
Jahangirnagar University, Dhaka-1342, Bangladesh
Military Technological College, Muscat, Oman†
Email: afsana.fariha@gmail.com*, rais80@yahoo.com†, {sam‡, kaiser§}@juniv.edu

***Abstract*—The emergence of nano-electromagnetic communication becomes appealing for potential applications in nano-scale Body Area Network (BAN). In this work a new energy aware communication model for nano-electromagnetic communication in Terahertz (THz) Band is developed based on clustering scheme for the performance improvement of BAN. The proposed conceptual network model is used to determine channel capacity. A closed-form expression for outage probability is also derived. The approach is extended to determine outage capacity for maintaining a constant rate with a specified outage probability. Simulation shows that in term of outage capacity, proposed scheme outperforms the random forwarding scheme.**

***Index Terms*—Nanotechnology, Body Area Network, Cluster, Terahertz, Outage Capacity.**

I. Introduction

Nanotechnology emerges as a promising paradigm to manupulate matter at a subatomic or nanometer level. At this level, the most basic functional unit is nano-machine which is capable of performing tasks like computing, storing, sensing or actuation. Typically such nano-machines are integrated devices around 10-100 μm^2 in size. Based on applications, multitudes of different nano-devices are used [1]. Interconnected nano-machines form nano network and execute collaborative tasks in a distributed manner. Existing electronic devices are scaled down from micro to nano domain in top-down approach. In bottom-up approach, molecular components are used to realize nano-machines. The bio-hybrid approach develops nano-machine by using biological elements as patterns to be replicated with systhesized component.

In recent years, the breadth of potential applications have been expanded tremendously with the advancement of nanotechnology. First, in the biomedical domain, nanomaterials are currently used in human body to monitor glucose, sodium and cholesterol, i.e. , in health monitoring, to support immune system, drug delivery system, to detect presence of infectious agents or to identify specific types of cancer [2]. Another domain is responsible for revealing the complexity of the induced defense signaling networks of plants by deploying molecular and genomic tools, controlling biodiversity, assisting biodegradation [3]. Again, in military and defense applications, nanotechnology can be deployed in advanced nuclear, biological and chemical (NBC) defenses and sophisticated damage detection systems for surveillance etc. Finally, in industrial domain, nanomaterials can be used for self-cleaning anti-microbial textiles, manufacturing processes and quality control procedures [1][4].

To be used in multiple nano-scenarios, classical communication paradigms need to undergo a profound revision. Based on the used transmission medium, different communication techniques - acoustic, nanomechanical, molecular and electromagnetic (EM) communication paradigms are proposed in literature [5]. At nano level, acoustic communication implies the integration of ultra-sonic transducers in nanomachines and transmission of information through acoustic energy such as pressure variations [1]. Nanomechanical communication is modeled by transmitting information through hard junctions between transmitter and receiver. In molecular communication, molecules with encoded information move as carriers from transmitter nanomachine to receiver nanomachine in a bio-inspired fashion. In EM communication, novel nanomaterial based components are used to modulate and demodulate electromagnetic waves. In acoustic communication, radio frequency transceivers and acoustic transducers represent a major barrier in integration at nanoscale because of their size. The nanomechanical communication holds the drawback by requiring physical direct contact between transmitter and receiver nanomachines. Most promising approaches for nanotechnology are therefore molecular and EM communication.

Recent advancements in Terahertz (0.06 - 10 THz) Band communication has opened the door to a new generation of nano-electromagnetic communication. Network, operating in THz Band promises new solutions for vast areas of applications such as health monitoring, military biochemical weapons monitoring, agricultural plant monitoring etc. As many molecules have resonance frequencies within the THz band, THz radiation may exploit the advantage of penetration of many opaque materials and the high selectivity, enabling their detection when they are present [6].

Health care is one of the fundamental right and thus it gets more attention for the researchers to developed energy efficient, low cost, simple, scalable e-Health solution. Espe-

978-1-4673-9257-0/15/$31.00©2015 IEEE

cially due to population aging, health care has to be made affordable in the future.With the increasing demands in body-area applications, current candidate systems have difficulties in performing consumer electronic device functions and health care application at the same time. Personal health monitoring is increasingly important to detail changes of our health status. A new emerging paradigm is the use of body area network of nano sensors based on THz Band in health care application. It is important to understand the limits of EM power exposure that human body can sustain without any crucial biological damages.

An energy efficient forwarding scheme at nano level is proposed in this paper to improve the performance of body area network so that it can facilitate e-Health application. The remainder of the paper is organized as follows. Related works on existing scheme is presented in section II. System model is presented in section III. Section IV and V includes channel behaviour model and simulation results respectively. And finally the work is concluded in section VI.

II. Literature Review

It is imperative to develop new and efficient communication and networking techniques to overcome unique challenges and requirements of nanonetworks.

Interconnecting nanoscale communication networks to the wider internet extends the Internet of Things to the Internet of Nano Things (IoNT). A reference architecture of IoNT was introduced in [7]. THz Band was considered for nano electromagnetic communication. Again, major research challenges in terms of channel modeling, information modulation and protocols for nanonetworks were highlighted from the communication and information theoretic perspective. For intrabody disease detection, a wireless nanosensor network at nanoscale was proposed in [8] as an application of IoNT. From the energy efficient point of view, proposed hexagonal cell based nanosensor network was analyzed for data transmission efficiency exploiting the hybrid, direct and multi-hop methods. A new energy efficient clustering of sensor nodes in ad hoc sensor networks was presented in [9] which guaranteed the fairly uniform cluster head distribution across the network.

Electromagnetic (EM) communications among nano-devices over the THz Band was focused in [10] with a view to developing a physical channel model. Developed propagation model was used to investigate signal path loss, molecular absorption noise and channel capacity of EM network.

In [11], Wireless Nano Sensor Network (WNSN) based on electromagnetic communication in THz Band was used to develop a new routing algorithm along with an efficient MAC protocol for communication. Focusing the attention on a WNSN operating in a health monitoring scenario, network behaviour was investigated. [12] is another approach where a new communication scheme for electromagnetic WNSNs was presented to evaluate the performance in terms of information capacity for single user case as well as aggregated network capacity for multi user case. In [13], performance of multi-hop links were analyzed and SER and outage probability were approximated based on end-to-end signal-to-noise ratio (SNR).

To better characterize the performance of channel, [14] is another approach where outage capacity was maximized over cut-off fading states for wireless channels. Authors assumed that both transmitter and receiver had full channel state information (CSI).

III. System Model

A. Assumptions and network Modeling

We assume that a network of nano sensor nodes are implanted on human body to construct a body area network. We assume that all nodes are constrained in energy. The proposed system architecture is shown in fig. 1.

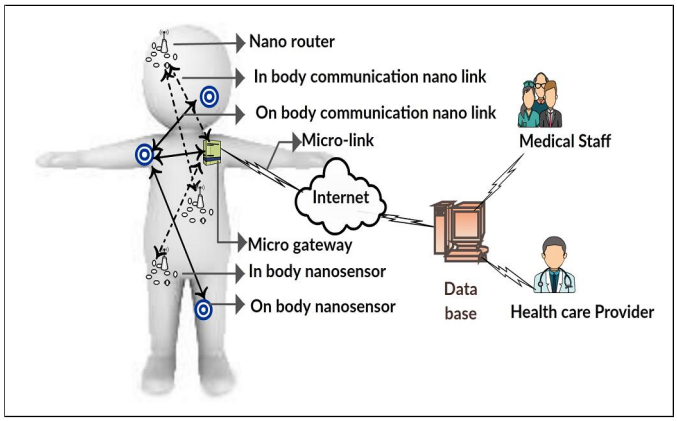

Fig. 1. A possible Scenario

The communication is considered to take place from inside of the body to the outside of the body through nano sensor nodes. Nano routers deployed in in-body communication to aggregate information coming from in-body nano sensors. Micro-gateway a wireless interface connection nano sensors to internet is used to collect data and forward them to the health care provider and medical staff.

B. Cluster Composition:

Clusters are formed to maintain efficient connectivity among deployed nano sensors. The proposed technique uses residual energy, denoted by $E_{residual}$, and packet forward ratio, denoted by PFR, to choose the cluster coordinator, CC. At first $E_{residual}$ of n nano sensors will be checked and among them m nodes having greater $E_{residual}$ from a certain threshold value will be selected as participants in cluster constellation. From m nano sensors the node with X_{max} will be selected as CC, where

$$X_i = \frac{1}{2}\left\{\frac{PFR_i}{PFR_{max}} + \frac{E_{residual_i}}{E_{max}}\right\} \qquad i = 1, 2, \cdots m. \quad (1)$$

Elected CC will broadcast short range advertisement message to remaining $(m-1)$ nano nodes. Active nano sensors having higher $RSSI$ will send join request to elected CC and register them as cluster member, CM. Similar process will be continued among rest of the nodes to form clusters. Re-clustering will be done periodically for distributing load

uniformly among all nodes. Fig. 2 is the cluster-based scenario of our proposed scheme.

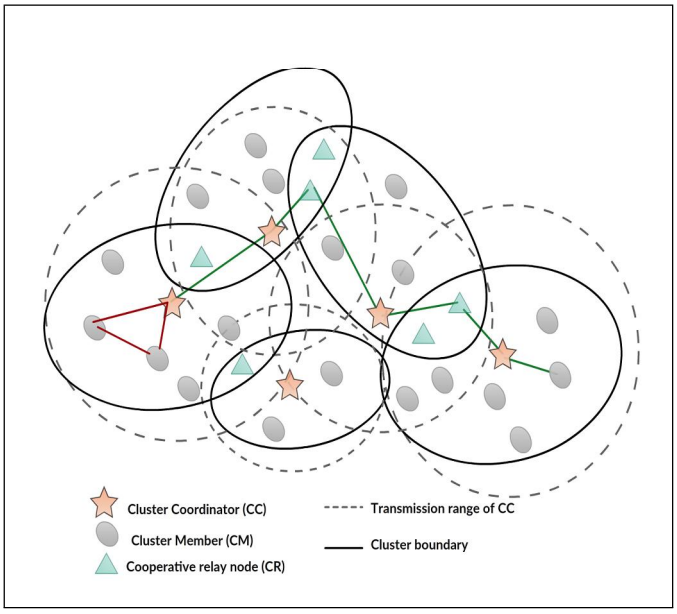

Fig. 2. A possible cluster-based Scenario

C. Communication Framework:

Communication framework is consisting of intra-cluster and inter cluster communication. Intra-cluster communication involves CC and CMs in communication. Energy efficiency is taken as a measure of extent to conduct communication. We assume that $E(d_{ik})$, $E(d_{ij})$ and $E(d_{jk})$ denote energy bit consumption through direct link ik, via link ij and jk respectively(figure 2). If equation (2) is satisfied, then data will transmitted directly to CC. Otherwise CM will use single-hop to reach CC.

$$\exists(d_{ij}, d_{jk})\{E(d_{ij}) + E(d_{jk})\} > E(d_{ik}), \tag{2}$$

where d_{ij} is distance between node i and j.

Cluster coordinators of different clusters conduct inter cluster communication. Cooperative relay nodes (CR) act as cluster gateways to conduct communication when CCs are out of transmission range of one another and operate under decode-and-forward (DF) cooperative strategy [15]. Flow chart of communication framework is depicted in fig. 3.

IV. Channel behavior Model

Nano-electromagnetic communication through human tissue suffers from frequency selective path loss and several attenuation due to shadowing and molecular absorption.

The absorption loss, A_m, is attenuation due to the molecular absorption. The type of molecular composition of the medium and concentration make it vary from medium to medium. A_m can be derived from Beer-Lambert law as [10]:

$$A_m(f, d_{i,j}) = \frac{1}{\tau} = e^{K(f)d_{i,j}}. \tag{3}$$

Here $K(f)$ stands for molecular absorption coefficient, f is frequency, τ is the transmittance of medium and $d_{i,j}$ is the distance between nanosensor i and j.

As our considered medium human body, the value of $K(f)$ for human body,$K(f)_{HB}$ is calculated as weighted average of different absorption coefficients of water molecules spreading over it in [16].

While propagating through human tissues, the expanded wave experiences attenuation named spreading loss, denoted by A_s [17].

$$A_s(f, d_{i,j}) = \left(\frac{4\pi f d_{i,j}}{c}\right)^2. \tag{4}$$

Here, c stands for speed of light in vacuum.

In THz band, transmission range of nano devices is limited due to large spreading loss. Shadowing occurs during transmission of signal between transmitter and receiver. Considering transmitted power, P_t from source, the received power, P_r at destination due to shadowing can be written as,

$$P_r(i,j) = P_t(i) G d_{i,j}^{-\eta} X_{i,j}, \tag{5}$$

where,

$X_{i,j}$	=	$10^{\frac{\xi_{i,j}}{10}}$ which represents log-normal random process representing the effect of shadowing,
$\xi_{i,j}$	=	Normal distributed random variable with zero mean and standard deviation σ
G	=	Constant representing the mean value of received power at distance $d_{i,j}$ from transmitter
η	=	Path loss exponent

Total received power in dB at destination due to molecular absorption, spreading and shadowing can be written as,

$$P_{total}(i,j) = P_r(i,j) - A_m(f, d_{i,j}) - A_s(f, d_{i,j}) \tag{6}$$

The interference power, P_I, can be expressed as,

$$P_I(k,j) = \sum_{k\epsilon(n:n\backslash i)} P_r(k,j) - A_m(f, d_{k,j}) - A_s(f, d_{k,j}) \tag{7}$$

If Signal to interference plus noise ration (SINR) of j hops are denoted by $\gamma_1, \gamma_2, \cdots, \gamma_j$ respectively, then γ_j can be computed from (8).

$$\gamma_j = \frac{P_{total}(i,j)}{P_I(k,j) + N(f, d_{k,j})}. \tag{8}$$

Here $N(f, d_{k,j})$ is Additive White Gaussian Noise.

Path loss due to shadowing in molecular level follows log-normal distribution. So, γ_j follows log-normal distribution under log normal shadowing .The probability density function (PDF) of γ_j is then given by

$$f_{\gamma_j}(\gamma) = \frac{1}{\gamma_j}\frac{\varepsilon}{\sigma\sqrt{2\pi}} exp - \left[\frac{(10\log_{10} - \mu)^2}{2\sigma^2}\right]. \tag{9}$$

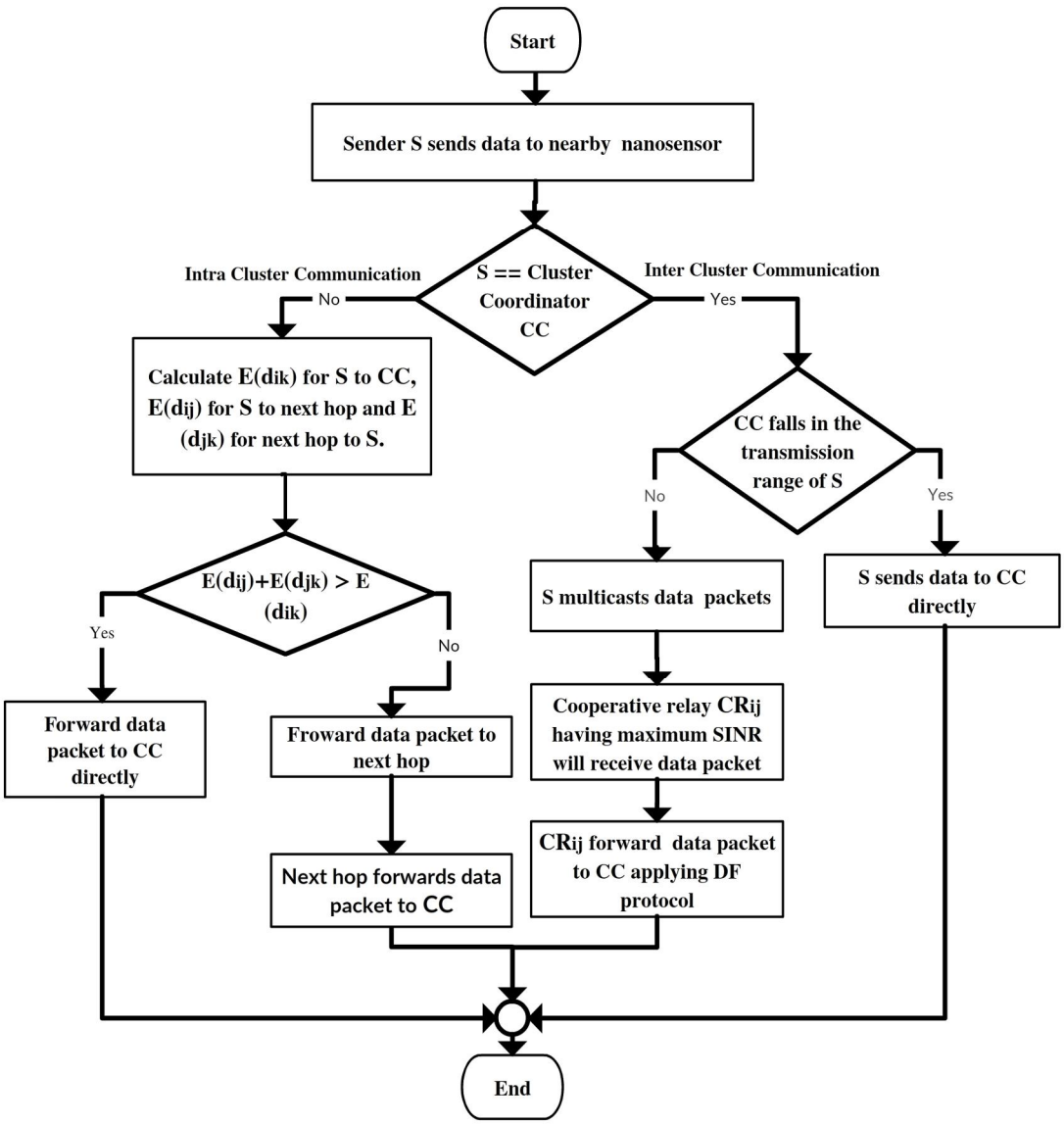

Fig. 3. A flow chart of Communication Framework

The probability that system can be in outage, denoted by P_{out}, is designed based on a certain specified threshold γ_{th} and can be expressed as [18]:

$$\begin{aligned} P_{out} &= Pr(\gamma_j < \gamma_{th}) \\ &= \int_0^{\gamma_{th}} f_{\gamma_j}(\gamma) d\gamma_j \\ &= \int_0^{\gamma_{th}} \left[\frac{1}{\gamma_j} \frac{\varepsilon}{\sigma\sqrt{2\pi}} exp - \frac{(10\log_{10}\gamma_j - \mu)^2}{2\sigma^2} \right] d\gamma_j \\ &= \int_0^{\gamma_{th}} \left[\frac{1}{\gamma_j} \frac{\varepsilon}{\sigma\sqrt{2\pi}} exp - \frac{1}{2}\Big(\frac{10\log_{10}\gamma_j - \mu}{\sigma}\Big)^2 \right] d\gamma_j \\ &= \frac{a\varepsilon}{\sigma} \times \left[1 - \frac{1}{2} erfc\Big(\frac{a\ln\gamma_{th} - b}{\sqrt{2}}\Big) \right] \end{aligned}$$

$$\text{where, } a = \frac{10\log_{10} e}{\sigma} \quad \text{and} \quad b = \frac{\mu}{\sigma}.$$

Here, (10) characterises cumulative density function (CDF) of γ_j.

It is shown in [10] that, a summation of capacity of each narrow sub-channel states THz channel capacity. Given PDF, $f_{\gamma_j}(\gamma)$, of γ_j, the capacity of channel, denoted by C, can be obtained from

$$C = \int_0^{\infty} B\log_2(1+\gamma_j) f_{\gamma_j}(\gamma) d\gamma_j \quad b/s. \tag{10}$$

Where, B is the bandwidth of each sub-channel.

Outage capacity determines the constant data rate in non-outage fading states subject to a given P_{out} and it can be

defined as:

$$C(P_{out}) = B\log_2(1+\gamma_j)(1-P_{out}). \quad (11)$$

V. Simulation Results

The performance evaluation of proposed cluster based forwarding scheme for Body Area Network using nano-electromagnetic communication is investigated in this section. The joint effects of path loss and shadowing have been considered for the simulation. In this paper, the Monte Carlo simulations have been performed for outage capacity analysis. Fig. 4 shows the BPSK and QPSK constrained outage capacity

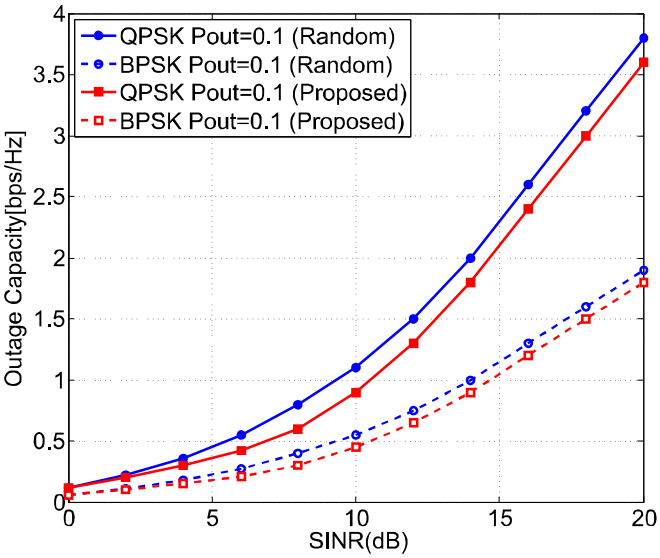

Fig. 4. Outage capacities for BPSK and QPSK

as a function of SINR in dB with 10% outage probability. For the given P_{out}, fig. 4 shows that, with BPSK values $C_{(p_{out})}$ is approximately $1.9bps/Hz$ and for QPSK it increases to $4bps/Hz$. In both cases, the proposed scheme outperforms random scheme.

Fig. 5 shows the performance comparison of outage capacity values obtained from the proposed expression and from Monte Carlo simulation. For simulating, outage capacity is considered as a function SINR for different values of outage probability. The results show that the proposed energy efficient cluster based forwarding scheme outperforms the random forwarding scheme.

VI. Conclusion

This work has proposed an energy efficient routing scheme for THz based nano-scale communication with a view to improving the performance of BAN. Link SINR has been calculated based on joint impact of shadowing, molecular absorption attenuation and spreading loss. Outage probability and outage capacity have been considered as performance metric for proposed scheme. Simulation results show that proposed scheme outperforms random forwarding scheme.

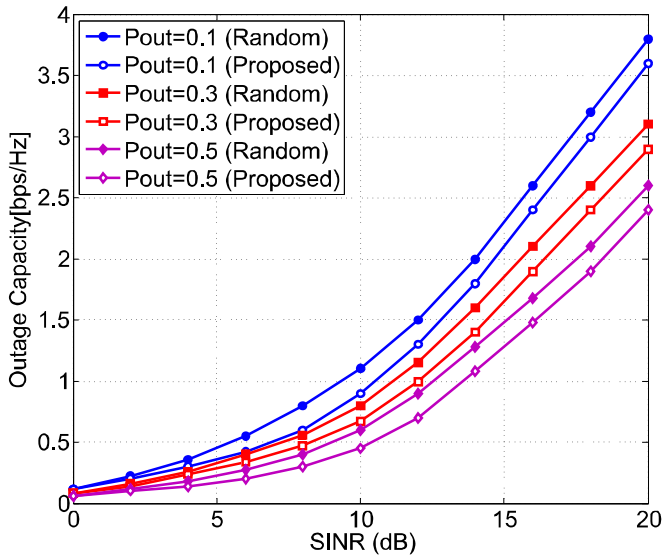

Fig. 5. Performance of random vs. proposed scheme

References

[1] I. F. Akyildiz, F. Brunetti, and C. Blázquez, "Nanonetworks: A new communication paradigm," *Comput. Netw.*, vol. 52, pp. 2260–2279, Aug. 2008.

[2] F. Dressler and F. Kargl, "Towards security in nano-communication: Challenges and opportunities," *Nano Communication Networks*, vol. 3, no. 3, pp. 151–160, 2012.

[3] S. Pudasaini, S. Shin, and K. S. Kwak, "Robust modulation technique for diffusion-based molecular communication in nanonetworks," *Computer science, Cornell University library*, pp. 1–4, Jan. 2014.

[4] N. Rikhtegar and M. Keshtgary, "Article: A brief survey on molecular and electromagnetic communications in nano-networks," *International Journal of Computer Applications*, vol. 79, pp. 16–28, October 2013.

[5] I. F. Akyildiz, J. M. Jornet, and C. Han, "Terahertz band: Next frontier for wireless communications," *Physical Communication*, vol. 12, pp. 16–32, 2014.

[6] A. Moldovan, M. Ruder, I. Akyildiz, and W. Gerstacker, "Los and nlos channel modeling for terahertz wireless communication with scattered rays," *Globecom Workshops (GC Wkshps), 2014*, pp. 388–392, Dec 2014.

[7] I. F. Akyildiz and J. M. Jornet, "The internet of nano-things," *Wireless Commun.*, vol. 17, pp. 58–63, Dec. 2010.

[8] Lee, S. Jin, et al. "Design of Wireless Nanosensor Networks for Intra-body Application," International Journal of Distributed Sensor Networks, 2015.

[9] O. Younis, S. Fahmy, "Distributed Clustering in Ad-hoc Sensor Networks: A Hybrid, Energy-Efficient Approach",Proceedings of IEEE INFOCOM, pp. 1-12, 2004.

[10] J. Jornet and I. Akyildiz, "Channel modeling and capacity analysis for electromagnetic wireless nanonetworks in the terahertz band," *Wireless Communications, IEEE Transactions on*, vol. 10, pp. 3211–3221, October 2011.

[11] G. piro, L. A. Grieco, et. al., "Nano-Sim: simulating electromagnetic-basednanonetworks in the Network Simulator 3", Proceedings of the 6th International ICST Conference on Simulation Tools and Techniques, pp. 203-210, 2013.

[12] J. M. Jornet and I. F. Akyildiz, "Information Capacity of Pulse-based Wireless Nanosensor Networks," in Proc. of the 8th Annual IEEE Communications Society Conference on Sensor, Mesh and Ad Hoc Communications and Networks (SECON), Salt Lake City, Utah, USA, June 2011.

[13] J. Cao, L. Yang, and Z. Zhong, "Performance of Multihop Wireless Links over Generalized-K Fading Channels," Vehicular Technology Conference Fall (VTC 2010-Fall), vol. 62, pp.1-5, Sept. 2010.

[14] A. Behruzifar, A. Falahati, "Maximizing Outage Capacity in Rayleigh Fading Channel ", International Journal of Computer Science and Artificial Intelligence, pp. 1-3, vol-2(1), 2012.

[15] A. Khina, Y. Kochman, G. Wornell, "Decode-and-Forward for the Gaussian Relay Channel via Standard AWGN Coding and Decoding", IEEE Information Theory Workshop, 2012.

[16] Javed, I. T., and Naqvi, I. H.," Frequency band selection and channel modeling for WNSN applications using simplenano," In Communications (ICC), 2013 IEEE International Conference , pp. 5732-5736, June 2013.

[17] K. e. e. Yang, "Terahertz communication in human skin tissues at the nano-scale for healthcare applications," *RF and Wireless Technologies for Biomedical and Healthcare Applications (IMWS-Bio), 2014 IEEE MTT-S International Microwave Workshop Series*, pp. 1–3, Dec. 2014.

[18] F. Afsana, N. Z. Zenia et al, "Multi-priority and trusted multi-path selection algorithm for ad-hoc network,"2014 International Conference on Electrical Engineering and Information & Communication Technology (ICEEICT), pp. 1-6, April 2014.

Graphene nanoribbon based Antenna For Terahertz Band Communication

Sakib Adnan[1],Md.Osman Goni[2]
Department Of Electronics & communication Engineering
Khulna University of Engineering & Technology, Khulna 9203, Bangladesh
{sakibadnan7[1], osmanhku[1]}@gmail.com

***Abstract*—Nanotechnology has enabled the use of nano-sized devices for various purposes i.e. biological, industrial, and military and especially in communication field. By using graphene the antennas can be implemented in nano scale. And the miniature antennas would work more efficiently then the conventional antennas. The miniature device can transmit data in terabyte scale. Conventional antennas would require very high frequency which is quite unfeasible. But the slower movement of electrons in graphene would enable the grapheme nano antennas to operate at a feasible frequency.[1][2].In this paper we designed, Graphene nano ribbon based antenna that would operate in terahertz band and investigatedits radiation characteristics in the 2.45-2.98 THz band. The proposed antennas are also compared with the conventional antennas operating in terahertz band. The antenna is simulated by using the finite element method based simulator -CST (computer simulation technology).**

Keywords—Nanoantennas,Graphene,nanoribbon,Terahertz band ,Patch antenna.

I. INTRODUCTION

Communication among the nano scale devices is an unsolved challenge.The main obstacle to solve this problem is that when we do the miniaturization of conventional antennas that would require very high radiating frequency. This is unfeasible because the power of the nano scale devices are very low[1].Again miniaturization process of transceiver at these very high frequencies is still an unsolved problem. Moreover, intrinsic material properties of common metals remain unknown at the nano scale [7][9]. The use of nanomaterial to fabricate miniature antennas can help to overcome these limitations[2][8]. Due to micro cracks, the metallic antennas can't transmit properly in the terhertz band. And for that reason graphenenano ribbon based antennas are more efficient than the metallic antennas in nano scale. In graphene, the carrier mobility is mainly limited by the acoustic phonon scattering of the graphene lattice and it is referred to as the intrinsic carrier mobility. Graphene offers a new approach to THz communications because of its ability to support the propagation of Surface- Plasmon Polariton (SPP) waves in the terahertz frequency band[17][18] .In this paper we discuss about the designing process of the GNR based antennas and the radiation characteristics of these antennas in terahertz band.

II. NANO ANTENNAS

Nano systems cannot be accomplished by simply decreasing the length of these metal antennas mainly because that could enforce the use of extremely high resonant frequencies within the optical array. The possibility regarding nano networks could be affected in the event that this approach ended up used because of:

• The very low limited power used in this Nano systems.

• The low electron mobility in metals where Nano scale structure are considered.

These problems occur at nano transceivers to operate at such a high frequency [4].

III. GRAPHENE BASED NANO-ANTENNA THEORY

Graphene is the building material of carbon nano tubes (1991) and grapheme nano ribbons (2004)[3].

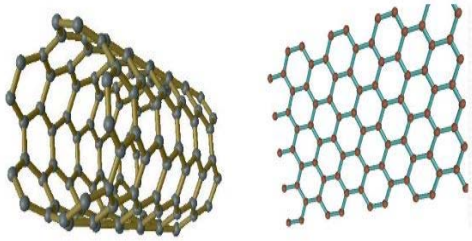

Figure 1. Carbon Nano tube (left), graphene Nano ribbon (right)

The two main important theories that are important for graphene based Nano antenna. First one is that nano patch antennas can be manufactured by graphene. And the second one is that there are several quantum effects that alter the propagation of electromagnetic waves in grapheme[3].

Initial resonant frequency along with the feedback resistance connected with graphene-based nano-patch and nano-dipole antennas acquired seeing that perform on the antenna size, edge geometry and strength[5]. Some sort of GNR can be used for any nano-patch antenna the 2-D antenna whilst CNT employed for the nano-dipole antenna virtually the 1-D antenna. New atomically accurate types will be achievable in the near future[6].

IV. ANTENNA DESIGN EQUATION AND SIMULATION TOOL

A. Microstrip Rectengular Patch antenna at 2.6 THz:

To simulate the graphene based antenna we at first design a micro strip patch antenna has resonant frequency of 2.6THz.

978-1-4673-9257-0/15/$31.00 ©2015 IEEE

The length and width of the antenna depends on the following equations [10] given below:

Antenna length and widthfor rectangular patch antenna,

$$L = \frac{c}{2f_r}\left(\frac{1}{\sqrt{\varepsilon}}\right) \quad (1)$$

Where, f_r=resonance frequency

The width of the patch antenna,

$$W = \frac{c}{2f_r}\sqrt{\frac{1}{\varepsilon+1}} \quad (2)$$

The design specification we followed to design the patch antenna is given below:

From eq. (1) and (2) by putting, frequency f_r =2.6 THz, permittivity, ε =2.3 and c=3×10^8 m/s we get, length, L= 11µm and width, W =14.76µm approximately. The rest of the measurement parameters are found from Figure.2they are given below at Table. I.

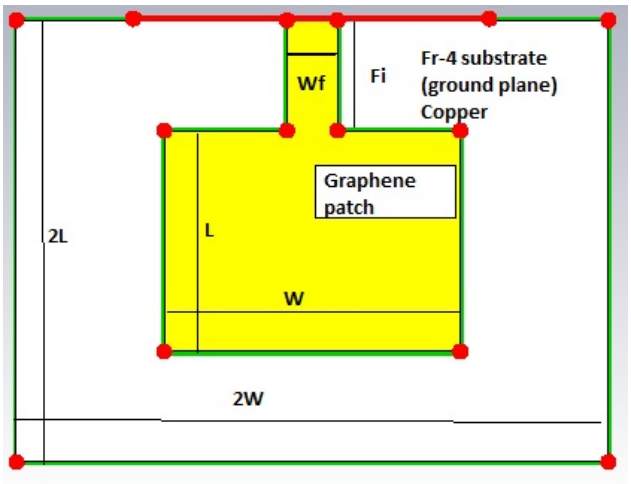

Figure 2.The model followed for designing rectangular patch antenna

B. Circular patch antenna at 2.6 THz

Circular patch antenna consists of a single circular metallic patch. But here we used graphene patch instead. The radius of the patch can be calculated from the empirical formula [10]

Patch radius

$$a = \frac{F}{\sqrt{\{1+\frac{2\times h}{\pi\varepsilon F}[\ln(\frac{\pi F}{2h})+1.7726]\}}} \quad (3)$$

Where h is the thickness, ε is the dielectric constant of the substrate material and F is related by the following equation:

$$F = \frac{8.791\times10^9}{f_r\sqrt{\varepsilon_r}} \quad (4)$$

Here a circular shapedmicro strip patch antenna is designed at resonant frequency of 2.6 THz. The proposed antenna is constructed using single circular patch of radius 11.26 □m.The proposed antenna shape is shown in Figure.3. Thesubstrate of thickness 1.305µm is used on which the structure is mounted. Dielectric constant is chosen 2.3 while the loss tangent is 0.025.The opposite side of the substrate contains the copper plate that act as the reflecting ground plane. The graphene is used as the radiating material. The thickness of both the radiator and ground plane are 0.0489 µm.The substrate we used is square of dimension 29.34 µm.Co-axial feed is used to excite the antenna.

C. Simulation tool

There are different types of simulation tool. But the most important problem is that the graphene simulator which work on mainly on the theory of Density functional theory, Classical potentials, or Extended Huckle theory they are not electromagnetic field solver. So we focus on the EM field solver tools or antenna simulation tools. These tools actually analysis high frequency devices. But the disadvantage of these types of simulator is this type of simulator does not have any model for graphene [3].

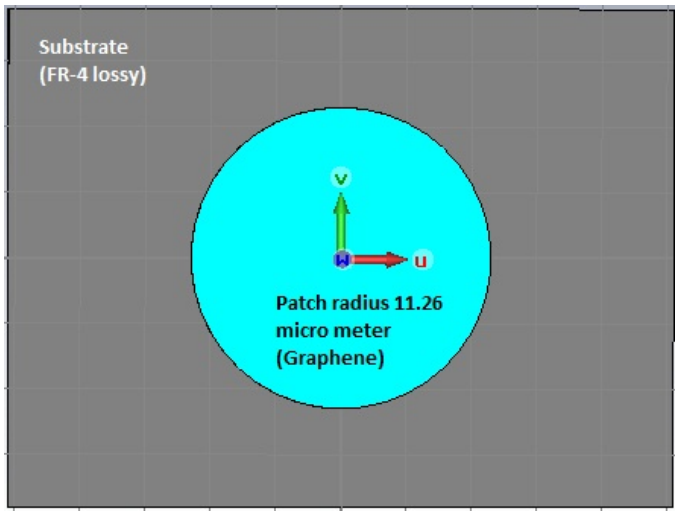

Figure 3.The model followed for designing micro strip circular patch antenna

D. Designing Graphene material for Graphene patch

Because of the absent of graphene model we followed two models to design and simulate graphene based nano antenna on this type of simulator. The models are complex permittivity model which accounts for intraband and interband transitions of electrons [11].And the second model is Drude approximation which only accounts for intraband transitions of electrons [12]. So for using graphene patch antenna we have at first designed graphene material. First, we considered the complex conductivity model by using the numerical values. CST simulates the structures which have length, width and thickness. But graphene is an one atom thick material. So for simulating graphene based antennas we make the thickness of the structures close to zero. [3].

E. Antenna design(Rectengular Patch)

The graphene nano ribbon based microstrip patch antenna is designed which has dimension in order of few micrometers. Conventionally the micro strip patch antenna consists of a

radiating patch where graphene is used as the material by editing the conductive and dispersion parameters of the drude material. The patch and the ground plane is separated by a thin dielectric substrate. We used the rectangular shape of the patch for ease in the analysis procedure. As indicated in Fig.2, the graphene nano ribbon is used as the patch where the patch thickness is much smaller than the wavelength. The radiating patch and ground plane is separated by a 1.305 µm thin substrate.

TABLE I. GNR BASED TERAHERTZ RECTANGULAR PATCH ANTENNA DESIGN PARAMETER[16]

Parameter	Description of the parameters		
	Symbol	***Value***	***Unit***
Patch length & width	L×W	11×14.76	μm^2
Resonant frequency	F	2.6	THz
Substrate length,width and thickness	2×(L×W×h)	2×(11×14.76×1.305)	μm^3
Dielectric constant	ε_r	2.3	-

The circular patch and the ground plane isalso separated by a thin dielectric substrate. We used the circular patch for comparing the performance characteristics with the rectangular patch antenna. Also the shape of the patch gives ease in the analysis procedure. As indicated in Figure. 3, the graphene nano ribbon is used as the patch where the patch thickness is much smaller than the wavelength. The radiating patch and ground plane is also separated by a 1.305 µm thin substrate.

TABLE II. GNR BASED TERAHERTZ CIRCULAR PATCH ANTENNA DESIGN PARAMETER[16]

Parameter	Description of the parameters		
	Symbol	***Value***	***Unit***
Patch area	$A=\pi r^2$	$\pi\times11.26^2$	μm^2
Resonant frequency	F	2.6	THz
Substrate length,width and thickness	2×(A×h)	$2\times\pi\times11.26^2\times1.305$)	μm^3
Dielectric constant	ε_r	2.3	-

V. SIMULATION AND EXPERIMENTAL RESULT

A. Simulation Results

The designed antenna is resonant at 2.6THz. The excitation signal is supplied by a 50Ω source. The simulation results mainly consist of the return loss, the directivity, and gain and radiation pattern of the patch antenna.

B. Return Loss,gain and Voltage standing wave ratio

The proposed rectangular patch antenna is designed and its radiation characteristics are investigated in the band of 2.45-2.98 THz, using the CST simulation tool. We have measured the return loss (S_{11}) and the voltage standing wave ratio for the patch antenna from Figure.4 & Figure5 it can be observed that the return loss at the resonant frequency is -15.179 dB and the voltage standing wave ratio at the resonant frequency is 1.421.

The proposed circular patch antenna is designed and its radiation characteristics are investigated in the band of 2.45-2.98 THz, using the CST simulation tool

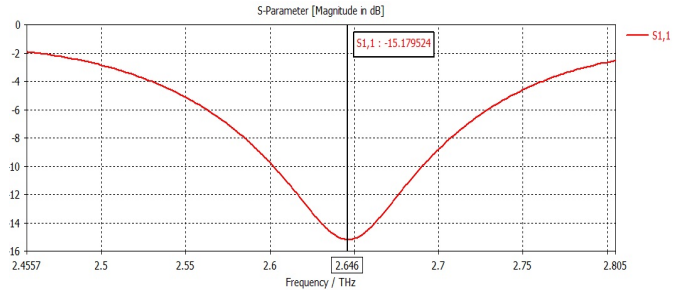

Figure 4.Return Loss for rectangular patch antenna

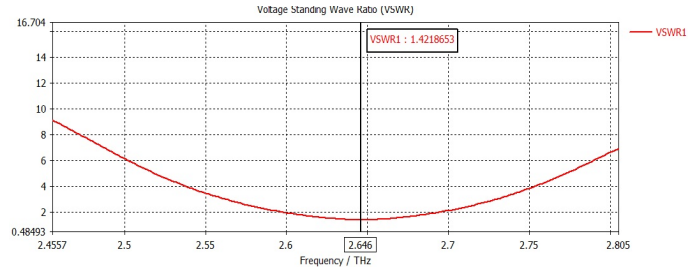

Figure 5.Voltage standing wave ratio for rectangular patch antenna

We have measured the return loss (S_{11}) and the voltage standing wave ratio for the patch antenna. From Figure.6 and Figure.7 can be observed that the return loss at the resonant frequency is -14.82 dB and the voltage standing wave ratio at the resonant frequency is 1.64.

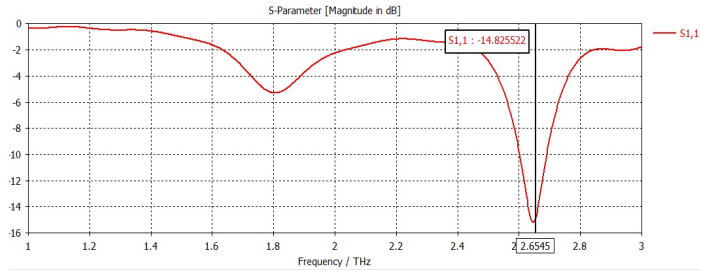

Figure 6.Return loss for circular patch antenna

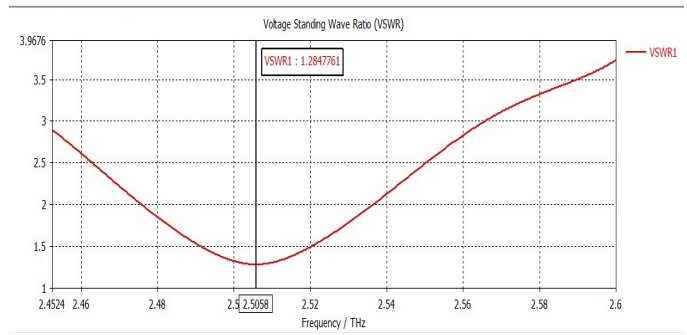

Figure 7.Voltage Standing wave ratio for circular patch antenna

The E and H planes far-field radiation patterns of the proposed rectangular and circular antennas in the range of 2.515 THz are visualized in Figure 8(a)-(b) and 9(a)-(b). The E-plane radiation plot demonstrates that the antenna has least back flap radiation in the craved band. So better front to back projection proportion is accomplished, and examined in Table III. It is seen from Figure.10, GNR based rectangular patch antenna has yielded a farfield increase of 19.8dB and the

circular patch has yielded a farfield addition of 34.3dB at 2.6 THz.

The Gain for the circular and rectangular patch antenna are shown in Figure. 10 (a)-(b) in the polar radiation pattern. For observing the gain we used linear scaling in the far field plot.

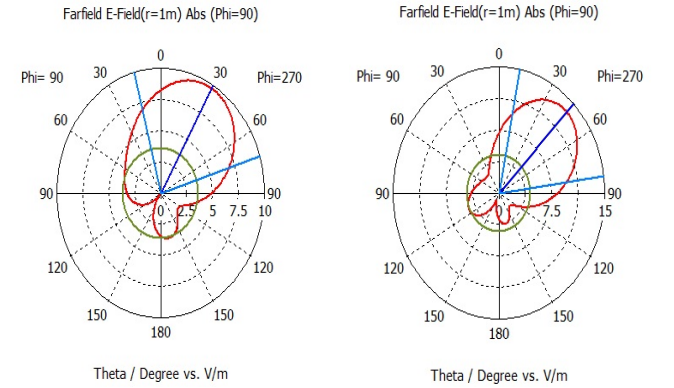

(a) (b)

Figure 8.E-plane (solid line) far field radiation patterns of the proposed antenna (a) Rectangular patch antenna (b) circular patch antenna

The visualization of far field gain as 3D radiation patterns of the proposed rectangular and circular patch antenna are shown in Figure 11(a) and 11(b) respectively.

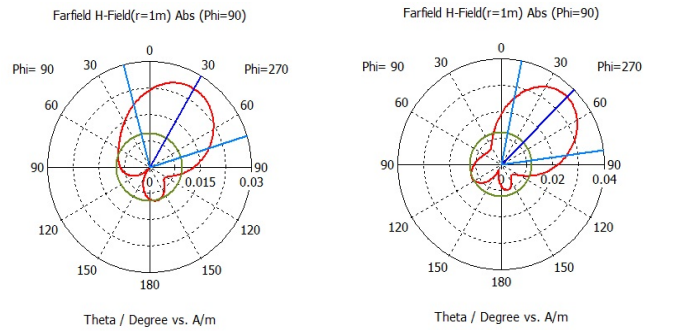

(a) (b)

Figure 9.H-plane (solid line) far field radiation patterns of the proposed antenna (a) Rectangular patch antenna (b) circular patch antenna

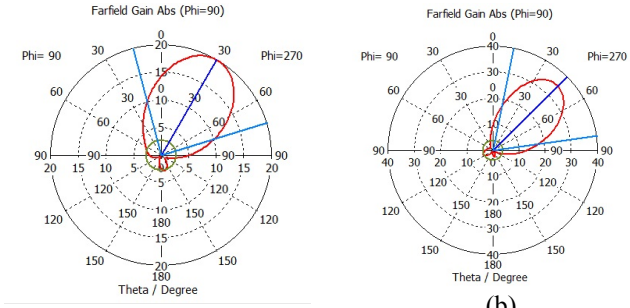

(a) (b)

Figure 10.Farfield gain (solid line) patterns of the proposed antenna (a) Rectangular patch antenna (b) circular patch antenna

The radiation qualities of the proposed antenna are contrasted and that of the already reported graphene based and ordinary antennas working in terahertz band is compressed in Table III. The proposed GNR based patch antenna is not optically transparent. So this outcome will utilize graphene based patch antenna to be utilized as a part of future THz band correspondence framework.

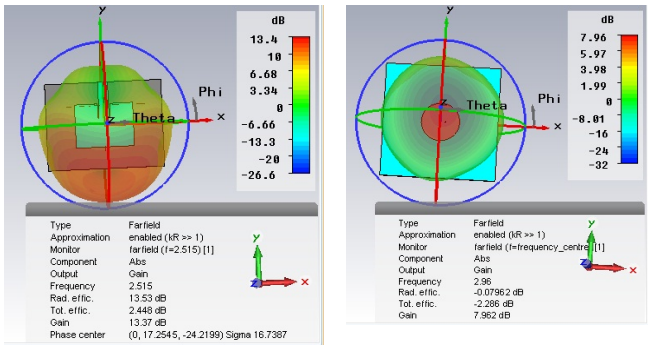

(a) (b)

Figure 11.3D radiation patterns of the proposed antenna (a) Rectangular patch antenna (b) circular patch antenna

TABLE III. PERFORMANCE COMPARISON OF THE GNR BASED ANTENNA WITH THE EXISTING ANTENNASIN THE CONTEXT OF RADIATION CHARACTERISTICS.

Parameter	GNR based antennas			Conventional antenna	
	Proposed antenna	*[16]*	*[13]*	*[14]*	*[15]*
Resonant Frequency(THz)	2.6	0.750	0.800	1.425	2.15
Gain(dB)	13.4(rectengular),7.96(circular)	5.09	-	1.65	4.97
Directivity(dB)	10.74(rectengular),9.76(circular)	5.71	0	-	-
Front To back Lobe ratio	78.3(rectangular),73.31(circular)	70.27	-	-	-

VI. CONCLUSION

In this paper, the radiation attributes of grapheme nanoribbon based nano scale strip rectangular and circular patch antenna have been explored in the 2.45-2.98 THz band. Graphene nanoribbon based terahertz patch antenna is reproduced by utilizing the finite component system based test system CST. The proposed antenna has appeared to create the top increase of 13.4dB for rectangular patch and 7.96dB for circular patch at 2.515 THz .The antenna has likewise the most astounding directivity in the desired band. The design parameters of the proposed rectangular and circular patch antenna is listed in Table I and Table II, and the proposed antenna is compared contrasted with the already reported graphene based antennas,

furthermore with ordinary patch antennas in Table III. It shows that although we used a higher resonant frequency for our proposed antenna, the gain, directivity and front to back lobe ratio have improved significantly.

REFERENCES

[1] I. F. Akyildiz and J. M. Jornet, “Electromagnetic wireless nanosensornetworks,” Nano Commun. Netw. (Elsevier) J., vol. 1, no. 1, pp. 3–19,Mar. 2010

[2] I. F. Akyildiz and J. M. Jornet,."Graphene-based Plasmonic Nano-Antenna for Terahertz Band Communication in Nanonetworks"IEEE journal

[3] Simulation of Graphene-based Nano-antennas,Nanonetworking center in catalunya ap@ac.upc.edu

[4] Z. L. Wang, “Towards self-powered nanosystems: From nanogenerators to nanopiezotronics,” Advanced Functional Materials, vol. 18, no. 22, pp. 3553–3567, 2008.

[5] A. Geim and K. Novoselov, “The rise of graphene,” Nature materials, vol. 6, no. 3, pp. 183–91, Mar. 2007.

[6] Ivan S. Maksymov , Arthur R. Davoyan , Andrey E. Miroshnichenko , Constantin Simovski ,Pavel Belov,Yuri S. Kivshar, "Multifrequency tapered plasmonic nanoantennas", Optics Communications 285 (2012) 821–824.

[7] S.P. Lacour, D. Chan, Y. Wagner, T. Li, Z. Suo, Mechanisms of reversible stretch-ability of thin metal films on elastomeric substrates, Appl. Phys. Lett. 88 (2006)204103)

[8] J. E. Burke, “Analytical study of tunable bilayered-graphene dipole antenna,” Army Armament Research, Development and Engineering Center, Dover, NJ, USA, Tech. Rep., Mar. 2011

[9] P. Burke, S. Li, and Z. Yu, “Quantitative theory of nanowire and nanotube antenna performance,” IEEE Trans. Nanotechnol., vol. 5, no. 4, pp. 314–334, July 2006

[10] Constantine A. Balanis; Antenna Theory, Analysis and Design, John Wiley & Sons Inc. 2ndedition. 1997.

[11] Gusynin, V. P., Sharapov, S. G., and Carbotte, J. P., “AC conductivity of graphene: from tight-binding model to 2+1-dimensional quantum electrodynamics,” International Journal of Modern Physics B, vol. 21, pp. 4611, 2007.

[12] Hanson, G., “Dyadic Green's Functions for an Anisotropic, Non-Local Model of Biased Graphene,” IEEE Transactions on Antennas and Propagation, vol. 56, pp. 747-757, 2008.

[13] M. Tamagnone, G.-D. Juan Sebastian, J.R. Mosig, P.-C. Julien, Reconfigurable ter-ahertz plasmonic antenna concept using a graphene stack, Appl. Phys. Lett. 101(2012) 214102.

[14] A.N.Z. Rashed, H.A. Sharshar, Optical microstrip patch antennas design andanalysis, Optik 124 (2013) 4331–4335.

[15] S. Anand, D. Sriram Kumar, R.J. Wu, M. Chavali, Analysis and design of opti-cally transparent antenna on photonic band gap structures, Optik 125 (2014)2835–2839.

[16] S. Ananda,D. Sriram Kumara, Ren Jang Wub, Murthy Chavalica' Graphene nanoribbon based terahertz antenna on polyimide substrate.'Optik 125 (2014) 5546–5549

[17] G. W. Hanson, Journal of Applied Physics103, 064302 (2008).

[18] .M. Jablan, H. Buljan, and M. Solja˘ci´c, Phys. Rev. B80, 245435 (2009).

Optimization of Indium Gallium Nitride Quantum Dots for Absorbing Light from Solar Spectra

Sadia Sultana
Department of APECE
University of Chittagong
Chittagong, Bangladesh
Sadiasultana012@gmail.com

Md. Shah Alam
Department of APECE
University of Chittagong
Chittagong, Bangladesh
Shah.alam@cu.ac.bd

***Abstract*— Use of renewable energy is the key to produce electricity from limited resources. Solar cells appear as promising candidates for this purpose. Research on third generation quantum dot solar cells have drawn much attention. Solar cells made of wide bandgap materials that utilize quantum dots have the potentials for being ideal solar cells of future. Quantum dots have a tunable bandgap, so they can be designed to absorb light from the entire solar spectra. Proper tuning of the quantum dots in the absorber layer is the key factor for absorbing solar photons. Here we have optimized Indium Gallium Nitride quantum dots for absorbing photons from most of the solar spectra. It covers the entire range of visible light along with a significant portion from ultraviolet (UV) and Infrared (IR) light . In this theoretical approach, the bandgap of Indium Gallium Nitride and the radii of the quantum dots were varied throughout the simulation. At an optimal mole fraction of Indium & Gallium, we tuned the quantum dots to absorb wavelengths from 142 nm to 1565 nm.**

Keywords—Quantum dots; tuning; intermediate band solar cells; solar spectra; Brus Equation.

I. INTRODUCTION

In solar cells, atomic level conversion of light into electricity takes place in two steps- 1) Atoms of solar cells get hit by the photons and absorb the energy transferred from the photon 2) This absorbed energy is used to free electrons. These free electrons produce electric current when they are driven in an orderly way. Light is absorbed by a semiconductor material producing an electron-hole pair known as exciton. This pair is separated by an internal electric field. It results in flow of electrons and holes. This is how and electric current is produced. In case of conventional silicon based solar cells the efficiency is limited to 30%. They have limited operation range because they can work within a limited range of solar spectra that includes visible light only. Photons only with energies higher than the bandgap of the material can free electrons and contribute to current. Those with lower energies cannot contribute to produce electricity [1], [2]. Solar spectra consists of 3 to 5% Ultraviolet (wavelength < 400 nm) , 42 to 43% Visible (400-700 nm) and 52 to 55% Infrared (wavelength > 700) light (Fig. 1) . So if the Infrared (IR) and Ultraviolet (UV) range are also utilized for energy harvesting, more of the solar energy will come into use. A solution to this problem is the intermediate band (IB) solar cell. Intermediate bands are formed by addition of a narrow band of states in the middle of the band gap of a photovoltaic material .

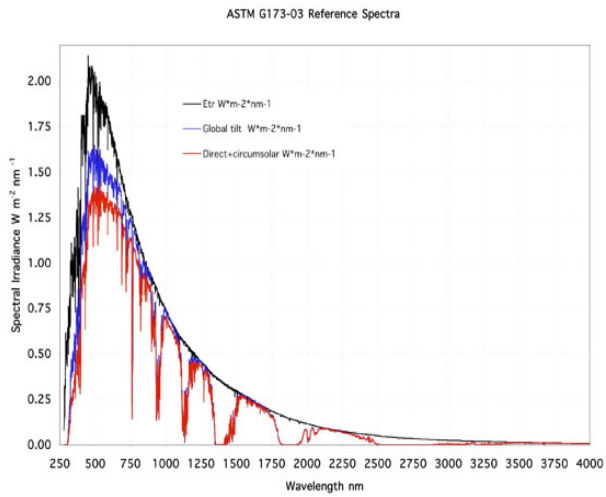

Fig. 1. AM 1.5 solar spectra [22], [23]

Electrons can jump from valence band to intermediate band being excited by a low energy photon, then jump to conduction band by another low energy photon. Thus photons with lower energies are also utilized. This can be achieved by insertion of Quantum dots as the absorbing material into the bulk semiconductor. These are nano sized particles where carriers in the semiconductor are confined by potential barriers . Quantum dot solar cells promise conversion efficiency upto 86% by using multiple junctions . Quantum dots have a tunable bandgap depending on their size. So QD (Quantum Dot) solar cells can be designed to work in any part of the solar spectra. This lets the whole spectra to be utilized [3]-[10] . Gallium Nitride (GaN) based solar cells with Indium Gallium Nitride (InGaN) quantum dots are promising candidates for ideal wide spectrum solar cells. Indium Gallium Nitride itself has a tunable bandgap which is determined by the mole fraction of Indium and Gallium present in the alloy. It can be varied from 0.7 eV to 3.42 eV corresponding to a wide range in solar spectra. This feature of InGaN along with flexible bandgap of

978-1-4673-9257-0/15/$31.00 ©2015 IEEE

quantum dots provide an excellent scope for tuning InGaN quantum dots to any desired wavelength region [11]-[14]. At a particular mole fraction of constituent elements, the radii of the embedded quantum dots in the different layers of the intrinsic region can be varied in such a way that dots in different layers absorb different wavelengths (Fig. 2).

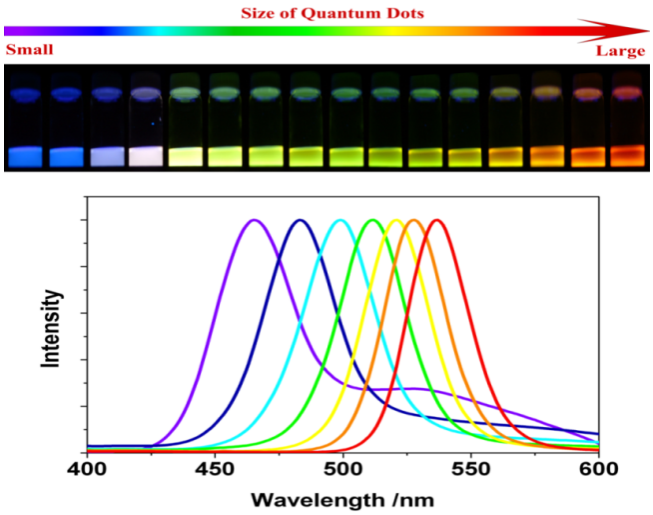

Fig. 2. Change in wavelength of quantum dots with change in size [24]

In that case, photons with energies corresponding to the quantum dots' bandgap energies will be absorbed by that layer. For designing such an efficient wide spectrum QD solar cell, the optimum bandgap of the dot material and also the required confinement radii must be known. This needs specific study on these criteria. Researchers have varied the size of Zinc Oxide (ZnO), Cadmium Selenide (CdSe), Zinc Sulphide (ZnS) and Gallium Arsenide (GaAs) QDs and calculated the resulting bandgap, emitted wavelength etc. using Brus equation which match pretty well with experimental data [15]-[18] . But no specific study on optimizing InGaN quantum dots to match the solar spectra has been reported in literature. We have varied the mole fraction of Indium (In) and Gallium (Ga) and calculated the effective bandgap of Indium Gallium Nitride. Then using the Brus equation and we have varied the size of QDs at an optimal mole fraction to absorb specific wavelength from 142 nm to 1565 nm. It covers the range of existing wavelengths of solar spectra starting from 280 nm to 1565 nm. This covers the whole range of UV and visible light from AM 1.5 solar spectra and a significant portion of IR region [23].

II. Theoretical Framework

Being a ternary compound, the bandgap of InGaN depends on the mole fractions of the constituent elements. Bandgap energy of the quantum dots depends on the effective mass of excited electrons and holes as well as the size of the dot. Absorbed wavelength can be found from the relationship between energy and wavelength (i.e. E=hc/λ). So a number of factors need to be considered to reach the optimum condition.

A. Bandgap of InGaN as a function of mole fraction

The bandgap of InGaN varies with the mole fraction of Indium (In) and Gallium (Ga) in the alloy as well as temperature. If X be the In doping relative to Ga, E_{InN} is the bandgap of Indium Nitride (InN), E_{GaN} is the bandgap of Gallium Nitride (GaN) , b is the bowing parameter of $In_xGa_{1-x}N$, then the bandgap of the alloy is given as-

$$E_{g,InGaN}(X) = XE_{InN} + (1-X)E_{GaN} - bX(1-X) \qquad (1)$$

By varying X in (1), the bandgap of InGaN can be adjusted to any desired value within 0.7 to 3.42 eV [19].

B. Brus Equation

L. E. Brus in 1984 first developed an equation for size dependence of lowest excited electronic state in case of small semiconductor crystallites [15] . With some moderations, the equation named after him is written as-

$$E(QD) = E_g(bulk) + \frac{h^2}{8R^2}\left(\frac{1}{m_e^*} + \frac{1}{m_h^*}\right) - \frac{1.786e^2}{4\pi\varepsilon_0\varepsilon_r R^2} \qquad (2)$$

Where E(QD) is the bandgap energy of quantum dot, the first term in right hand side of the equation represents the bandgap energy of bulk semiconductor, ε_0 is the permittivity of vacuum, ε_r is the relative permittivity of the semiconductor, m_e^* is the effective mass of excited electron, m_h^* is the effective mass of excited hole, R is the radius of spherical quantum dot. The second additive term in the right hand side, is dependent on inverse of square of the radius. It accounts for the additive energy due to quantum confinement. The third term in the right hand side is due to the coulombic interaction energy of exciton and is negligible for materials with high dielectric constants [16], [17]. So the overall Brus Equation to be used in this work is-

$$E(QD) = E_g(bulk) + \frac{h^2}{8R^2}\left(\frac{1}{m_e^*} + \frac{1}{m_h^*}\right) \qquad (3)$$

Varying R in (3) at a certain mole fraction, quantum dots can be tuned to absorb any specific wavelength. Quantum dot confinement region must be smaller than or comparable to their De Broglie wavelength or to the Bohr radius of excitons .

C. Calculation of electron and hole effective mass

As can be seen from (3), electron effective mass m_e^* plays an important role in determining the bandgap of the QD. It changes with varying mole fraction. Effective mass of electron in *InGaN* can be calculated using the following equation which utilizes the interpolation formula[20] , [21] –

$$m_{e,InGaN} = m_{e,GaN} + X(m_{e,InN} - m_{e,GaN}) \qquad (4)$$

The value of hole effective mass can be calculated in same way using the equation below-

$$m_{h,InGaN} = m_{h,GaN} + X(m_{h,InN} - m_{h,GaN}) \quad (5)$$

D. Condition for varying Quantum dot radius:

For the confinement effects to be prominent, the radius of the quantum dot must be kept less than the exciton Bohr radius of the quantum dot material [3]. The exciton Bohr radius of a semiconductor material can be calculated as-

$$a_B = \frac{4\pi\varepsilon_0\varepsilon_R\hbar^2}{m_{eff}q^2} \quad (6)$$

Where m_{eff} is the effective mass of the electron-hole pair, q is the charge of a carrier. If the radius of the dots exceed the exciton Bohr radius of the material, the quantum confinement effects will not hold any more and Bandgap energy of the quantum dots will not practically resemble the Brus equation. Exciton Bohr radius for InGaN is very small, it can be as small as 3 nm for less indium concentration [25] . If indium content is increased in the alloy, the exciton Bohr radius increases like 7 nm for indium concentration, X=0.75 [26]

III. PARAMETERS AND SIMULATION

Value of InN, GaN bandgap, bowing parameter of InGaN have been adapted from [12] . Interpolation formula has been used where necessary. The values of the basic parameters used in the simulation have been listed in Table I. Here, m_0 is the rest mass of an electron.

TABLE I. PARAMETER VALUES

Parameter name	Value
Bandgap of InN at 300K	0.7 eV
Bandgap of GaN (wurtzite) at 300K	3.42 eV
Bowing parameter for InGaN alloy	1.43
Electron effective mass of GaN, $m_{e,GaN}$	0.2 m_0
Hole effective mass of GaN, $m_{h,GaN}$	1.25 m_0
Electron effective mass of InN, $m_{e,InN}$	0.05 m_0
Hole effective mass of InN, $m_{h,InN}$	0.6 m_0

MATLAB version 7.10.0499 (R2010a) has been used as the simulation software throughout this work.

IV. RESULTS AND DISCUSSIONS

At first, the possible bandgaps for InGaN were calculated by varying the mole fraction of Indium, X . As can be seen from Fig. 3., it could be tuned from 3.37 eV for X = 0.01 to 0.713 eV for X = 0.99. As the mole fraction of Indium increases, the bandgap of InGaN tends to decrease because of low bandgap of InN [19].

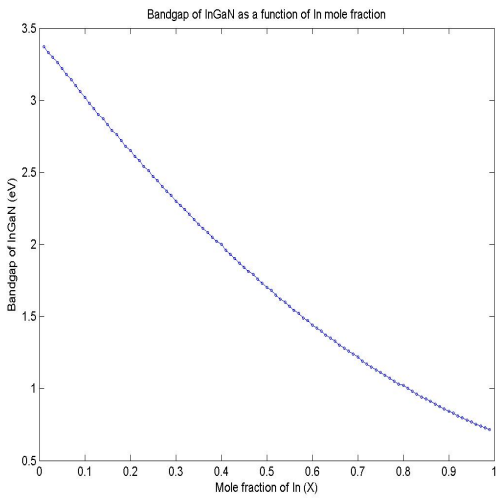

Fig. 3. Bandgap of InGaN with changing mole fraction of In

By calculating the exciton Bohr radius for various mole fraction of the constituents, it was found that as the Indium concentration in the alloy increases, exciton Bohr radius of InGan alloy increases too. Fig. 4 shows that, for X = 0.01, calculated exciton Bohr radius was 2.77 nm. The exciton Bohr radius reached its highest value of 10.75 nm for X = 0.99. This is the optimal mole fraction where the radius of the quantum dots can be varied over a wide range to cover the whole spectra. With this value of X, calculated bandgap of InGaN alloy was 0.713 eV.

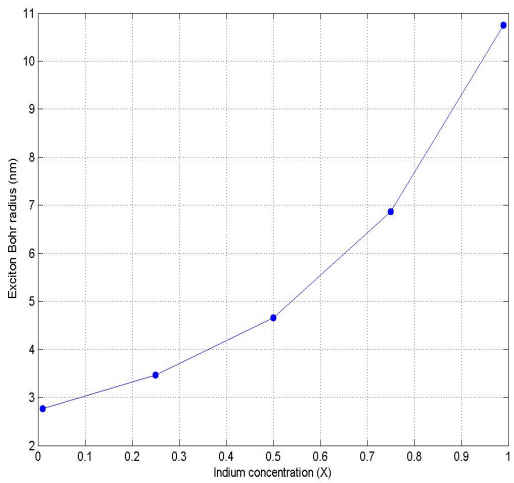

Fig. 4. Exciton Bohr radius of InGaN alloy at different In concentration

The optimum bandgap is chosen such that varying the dot size only gives an absorption range that covers as much portion as possible from UV, visible and Infrared region . For tuning the dots to absorb UV light with Indium composition X = 0.99, radius of the dots were varied from 1 nm to 1.83 nm. It gave an absorption range starting from 142 nm wavelength to 400 nm as shown in Fig. 5.

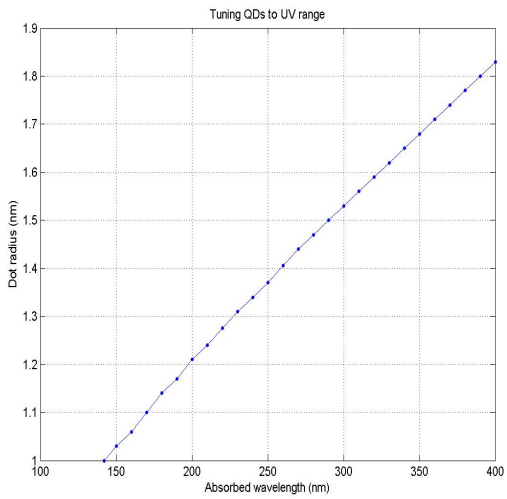

Fig. 5. Dot radius versus absorbed wavelength plot for UV region

By varying the dot radius from 1.83 nm to 2.75 nm, wavelengths from 400 to 700 nm can be absorbed which covers the whole visible range. This is shown in Fig. 6. If the dot radii are further increased, and varied from 2.75 nm to 10.05 nm, it gives an absorption range from 700 nm to 1565 nm in the Infrared region as shown in Fig. 7. Observations show that as the In mole fraction in the alloy is increased, the bandgap of the alloy gets lower. To design quantum dots for absorbing higher energy photons Indium concentration in the alloy must be reduced .

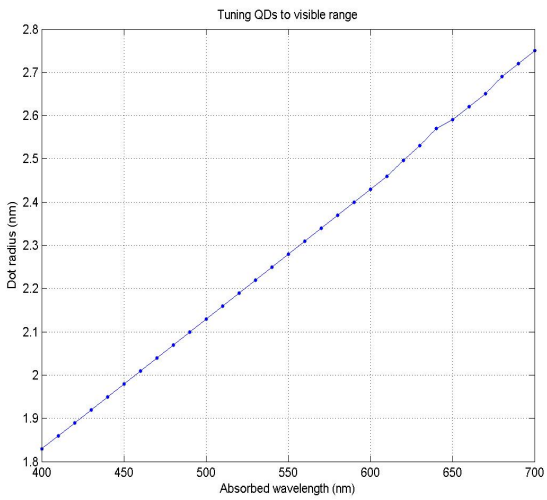

Fig. 6. Dot radius versus absorbed wavelength plot for visible region

Another thing apparent from the observation is that, smaller quantum dots with greater energy gap are able to absorb shorter wavelength photons which contain much energy. As the quantum dot radius is increased and their size gets bigger, the confinement strength gets reduced. That is why larger quantum dots have smaller bandgap energies. These quantum dots absorb photons with larger wavelengths and less energy.

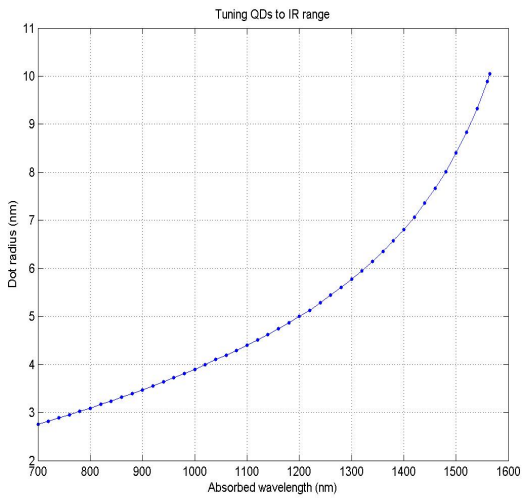

Fig. 7. Dot radius versus absorbed wavelength plot for IR region

The optimum bandgap for tuning InGaN quantum dots was found to be 0.713 eV with Indium composition X = 0.99. If the dot radius is varied from 1 nm to 10.05 nm, they can absorb wavelengths starting from 142 nm to 1565 nm which covers the whole UV and visible range along with significant portion of Infrared region of AM 1.5 solar spectra as can be seen from Fig. 8.

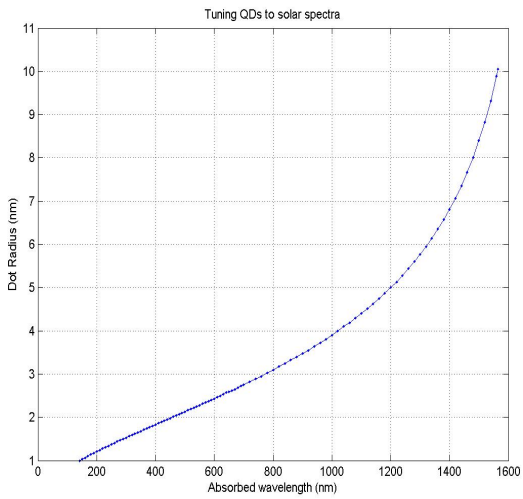

Fig. 8. Dot radius and absorption range with X = 0.99

V. CONCLUSION

InGaN quantum dots have a wide range of tunable bandgap and absorption spectra. This feature can be used to absorb almost any wavelength within the AM 1.5 solar spectra. InGaN quantum dots can be used to design an efficient wide spectrum solar cell. Solar photons over a wide range of wavelengths will be absorbed and utilized. Future work may include the investigation of the confinement effects for different shapes of InGaN quantum dots like pyramid, hexagonal, cubic etc. Effects of changing shape on the absorption spectra should also be studied.

ACKNOWLEDGMENT

We gratefully acknowledge support for this work provided by ICT Fellowship 2014-2015 under the Information and Communication Technology Division, Government of the People's Republic of Bangladesh.

REFERENCES

[1] Geoffrey A. Landis , Philip Jenkins, David Scheiman, Rayan Rafaelle, "Extended temperature solar cell technology development," in *Proc. AIAA 2nd International Energy Conversion Engineering Conference*, 2004, pp. 1-7 .

[2] International Renewable Energy Agency (irena) white paper on "Solar Photovoltaics," volume 1: power sector, 2012, pp. 1-45.

[3] Charles P. Poole Jr. and Frank J. owens, "*Introduction to nanotechnology*," Published by John Wiley & Sons, Inc., Hoboken, New Jersey (2003), pp. 226-234.

[4] A.J. Nozik, "Quantum dot solar cells," *Physica E* 14 (2002) , pp. 115-120.

[5] Dr. Dennis J. Flood, "Solar cells and quantum dots – a white paper," Natcore Technology Inc.

[6] Mohammad A. Halim, "Harnessing sun's energy with Quantum dots based next generation solar cells," in journal *Nanomaterials*, 2013, 3, issn: 2079-4991 , pp. 22-47.

[7] Brown A., Green M. , "Detailed balance limit for the series constrained two terminal tandem solar cell," *Physica E* 14 (2002), pg. : 96-100.

[8] A Luque, A Marti, A Nozik, "Solar cells based on quantum dots," *MRS bulletin*, 2007, 32:236-241.

[9] Ayman Rizk, Kazi Islam and Ammar Nayfeh , "Modeling of InAs/GaAs Quantum Dot Solar Cells," in *Proc.* 2013 *European Modelling Symposium,* 2013 issn : 978-1-4799-2578-0/13 , pp. 677-680.

[10] Boqun Dong, Christopher G. Bailey, Andrei Afanasev, Mona Zaghloul, "Modeling and Simulation of InAs/GaAs Quantum Dot Solar Cells In SILVACO TCAD," in *Proc. 40th IEEE Photovoltaic Specialists Conf.* , 2014, issn: 978-1-4799-4398-2/14 , pp. 476-478.

[11] Joshua J. Williams, April M. Jeffries, Laura Ding, Srikanth Gangam, Kunal Ghosh, Todd L. Williamson, Mariana I. Bertoni and Christiana B. Honsberg,"Structural and Optical Investigations of GaN-Si Interface for a Heterojunction Solar Cell," in *Proc. 40th IEEE Photovoltaic Specialists Conf.* , 2014, issn: 978-1-4799-4398-2/14, pp. 841-843.

[12] G.F. Brown, J.W.AgerIII, W.Walukiewicz, J. Wu, "Finite element simulations of compositionally graded InGaN solar cells," in Solar Energy Materials & SolarCells 94(2010) , Elsevier, doi:10.1016/j.solmat.2009.11.010, pp. 478-483.

[13] Nicolas Cavassilas, Fabienne Michelini and Marc Bescond, "Transport modeling of InGaN/GaN multiple quantum well solar cells," in *Proc. 40th IEEE Photovoltaic Specialists Conf.* , 2014, issn: 978-1-4799-4398-2/14, pp. 2875 – 2877.

[14] Kuang-Chung Wang, and Yuh-Renn Wu, "Transition Rate in the InGaN Quantum Dot Intermediate-Band Solar Cell," in *Proc. 38th IEEE Photovoltaic Specialists Conf.* , *2012*, issn: 978-1-4673-0066-7/12, pp. 822-825.

[15] L. E. Brus, "Electron-electron and electron-hole interactions in small semiconductor crystallites: The size dependence of the lowest excited electronic state," *J. Chem, Phys.* 80 (9), 1 May 1984, under copyright of AIP, pp. 4403-4409.

[16] Chukwuocha, E.O, Onyeaju, M.C, "Effect of Quantum Confinement on The Wavelength of CdSe, ZnS And GaAs Quantum Dots (Qds)," *International Journal of Scientific & Technology Research*, issue 7 , August 2012, issn: 2277-8616, pp. 21-24.

[17] Changiz Vatankhah, Ali Ebadi, "Quantum Size Effects on Effective Mass and Band gap of Semiconductor Quantum Dots," *Research Journal of Recent Sciences*, issn: 2277-2502 , Vol. 2(1), January (2013), pp. 21-24.

[18] Anusorn Kongkanand, Kevin Tvrdy, Kensuke Takechi, Masaru Kuno, and Prashant V. Kamat, "Quantum Dot Solar Cells. Tuning Photoresponse through Size and Shape Control of CdSe−TiO2 Architecture," *Journal of the American Chemical Society*, 2008, 130 (12), 4007-4015 DOI: 10.1021/ja0782706, pp. 908-918.

[19] R. R. Pelá et al. , "Accurate band gaps of AlGaN, InGaN, and AlInN alloys calculations based on LDA-1/2 approach", *Applied Physics Letters*, 98, 151907 (2011).

[20] Jasdeep Anand, Alexander Buccheri, Michael Gorley, Iain Weaver, "P2_12 InGaN quantum-well width w.r.t λ", *Journal of Special Topics*, Vol. 8, no 1, November 16, 2009.

[21] Ursula M. E. Christmas, A. D. Andreev, and D. A. Faux, "Calculation of electric field and optical transitions in InGaN/GaN quantum wells," *Journal of Applied Physics*, **98**, pp. 073522-1 – 073522-12. (2005)

[22] *American Society for Testing and Materials (ASTM) Terrestrial Reference Spectra for Photovoltaic Performance Evaluation*, ASTM G-173-03.

[23] Reference Solar Spectral Irradiance: Air Mass 1.5 [Online]. Available: http://rredc.nrel.gov/solar/spectra/am1.5/ (date accessed : 27-8-2015)

[24] Debasis Bera , Lei Qian, Teng-Kuan Tseng and Paul H. Holloway, "Quantum Dots and Their Multimodal Applications: A Review," in journal *Materials,* 3, pp. 2260-2345; doi:10.3390/ma3042260, 2010 .

[25] S. Amloy et al. , "Dynamic Characteristics of the exciton and the biexciton in a single InGaN quantum dot," in *Applied Physics Letters*, 101, 061910 (2012).

[26] Giovanni Giannoccaro, T. Muciaccia, Vittorio M N Passaro. "Evaluation of the Absorption Spectrum in Quantum Dots for Efficient Solar Cells," in *Proc. Fotonica AEIT Italian conference on Photonics Technologies*, 2014, pp. 1-4.

Analysis of Carrier Injection and Recombination in Modified ITO Based Organic Light Emitting Diode Using Numerical Simulation

Riku Chowdhury
Electrical & Electronic Engineering
FSET, USTC
Chittagong, Bangladesh
eeeriku@gmail.com

Md. Rashedul Haq
Electrical & Electronic Engineering
FSET, USTC
Chittagong, Bangladesh
rasahaq_17@yahoo.com

Md. Sarwar Uddin Chowdhury
Electrical & Electronic Engineering
CUET,
Chittagong, Bangladesh
sarwarcuet@gmail.com

Sukanta Paul
Computer Science & Engineering
CUET,
Chittagong, Bangladesh
skpaulustc@gmail.com

***Abstract*— Using numerical simulation, the performance of organic light emitting diode (OLED) based on modified indium tin oxide (ITO) has been investigated. The effects of ITO surface modification in energy barrier reduction at anode side which increase charge carrier injection, transport and recombination have been explained quantitatively. Calculated current balance factor from simulation results also confirmed the efficiency enhancement of bilayer OLED by the ITO work function modification technique.**

Keywords*— *indium tin oxide (ITO); hole current density; numerical simulation; current balance factor; carrier recombination

I. INTRODUCTION

As an optoelectronic device, OLED has been covered most of the area in the field of lighting and displays technologies over other existing lighting sources like light emitting diodes (LEDs) and liquid crystal displays (LCDs) because of their low turn on voltage, low input power, fast turn on response time, wide viewing angle (~180^0), thin and light weight, low cost, non-toxic materials and emitting light spectrum near to sun [1, 2]. After the demonstration of first bi-layer OLED by C. W. Tang and S. A. Vanslyke group in 1987 [3], the research on modification of OLED structures has been expanded dramatically. As a result, graded and mixed host based devices have been modeled and fabricated to improve the OLED lifetime and efficiency limitations [2, 4, 5]. However, these structures based devices increased complexity during fabrication. To overcome device fabrication complexity and increase charge injection rate into the device for improve device performance, ITO work function modification by O_2 and Cl_2 plasma treatment [6], post annealing treatments, adding buffer layer [7, 8] and UV-ozone treatments [9] are the most efficient and effective processes. Since, ITO commonly used as anode in most optoelectronic devices especially in OLEDs, hence device performance can be enhanced significantly using these ITO surface modification process which reduce the energy barrier for carriers to cross the ITO/organic interface [8].

H.-W. Lu, C.-W. Huang, P.-C. Kao, S.-Y. Chu, and Y.-D. Juang. [7] recently reported a work function modification technique of ITO by soaking in 1 wt%, 5 wt% and 10 wt% concentration of caesium fluoride (CsF) solution where the work function of ITO modified from normal work function of 4.78 eV to 4.95 eV, 5.01 eV and 5.11 eV correspondingly. They tried to explain the effects of ITO surface modification on the ITO/CsF/NPB/Alq_3/LiF/Al based bilayer OLED performance by analysis the current density- luminance - voltage (J-L-V) characteristic curves and surface morphology. However, that works unable to explain how ITO surface modification effects on the internal carrier distribution, electric field and recombination of device those are key factors for device modeling.

Motivating from this point, the effects of ITO surface modification on device J-L-V and efficiency have been explained through this numerical simulation in terms of charge carrier distribution, hole current density and carriers recombination. Moreover, the calculation of current balance factor which is proportional to the experimental quantum efficiency, able to justify this modified ITO based OLED performance. By the systematic study of the device performance of OLED, it is possible to explain some effects qualitatively. But, without numerical simulation, it is difficult to explain these effects quantitatively [10]. Numerical simulation is more viable to get any analytical results directly from the OLEDs where complicated working process and several interfaces are involved [11]. Therefore, this work led by numerical simulation which treated as powerful method to retrieve detailed information such as the charge carrier injection, distribution of electric field and recombination those are difficult to measure directly through experiments, investigate the underlying device mechanism and their amplitude which can affect the device performance.

II. ELECTRICAL MODEL

To analysis the effect of ITO work function modification on the underlying physics and performance of bi-layer OLED,

drift-diffusion electrical model has been implemented using a numerical simulator called 'SETFOS' (Semiconducting Thin Film Optics Simulation Software). Poisson equations and continuity equations as presented in "(1)," and "(2)," correspondingly considered in that electrical model to solve the electric field distribution and time evaluation of the system.

$$\frac{dE}{dx} = \frac{q}{\varepsilon\varepsilon_0}(p-n) \tag{1}$$

$$\frac{dn}{dt} = \frac{dJ_n}{qdx} - R - T \tag{2}$$

where, E is the electric field inside the OLED, q the elementary charge, □ the dielectric permittivity of the organic materials, □$_0$ the dielectric constant, p and n are the hole density and the electron density respectively, J_n the electron current density, R the recombination rate and T the trapping rate for free carriers. The carrier density distribution can be obtained by solving the drift and diffusion equation based on the Langevin recombination (R) process those are calculated using "(3)," and "(4)," respectively. The conventional electric filed dependent 'Poole-Frenkel mobility (PFM)' model as expressed in "(5)," applied for carrier mobility calculation in the device. The current balance factor (b) in "(6)," used to measure the device quantum efficiency [12] which is defined as the recombination current with the total current density.

$$J_n = qp\mu_n E + qD_n \frac{dn}{dx} \tag{3}$$

$$R = \frac{q}{\varepsilon\varepsilon_0}(\mu_p + \mu_n) \tag{4}$$

$$\mu(E) = \mu_0 \exp(\gamma * \sqrt{E}) \tag{5}$$

$$b = \frac{\int_0^L qR(x)dx}{J_T} \tag{6}$$

Here, μ_p and μ_n are the hole and electron mobility respectively, D_n the diffusion constant, $\mu(E)$ is the charge carrier mobility under electric field (E), μ_0 is the mobility under zero electric field, γ is the Poole-Frenkel field dependent factor, J_T is the total current density and L is the total device thickness.

III. Device Structure And Input Prameters For Simulation

The OLED structure as shown in "Fig. 1," used for simulation where the HOMO and LUMO levels of NPB (Alq_3) are 5.4 eV (5.7 eV) and 2.3 eV (3.0 eV) and the work function of LiF/Al is 3.0 eV [4, 7]. Before, surface modification, the usual work function of ITO is 4.78 eV which is modified after soaking in different concentration of CsF solution. The work functions of modified ITO become 4.95 eV (1 wt% CsF solution), 5.01 eV (5 wt% CsF solution) and 5.11 eV (10 wt% CsF solution). The work functions of ITO and organic materials parameters obtained from the UV- photoelectron spectrometer [7] and time of flight (TOF) measurement [13, 14] correspondingly, used as input during simulation. Considering the normal work function based ITO as reference, the effects of modified ITO work function using different concentrations of CsF solutions on hole injection efficiency, carrier recombination rates and current balance factor have been analyzed in the next section.

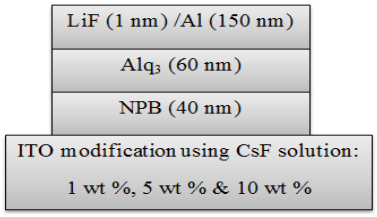

Fig. 1. Modified ITO based OLED Structure

IV. Results and Discussions

A. J-L-V Characteristics and Efficiencies

Figure 2 shows the current density-voltage (J-V) and the luminance-voltage (L-V) characteristics curves of four OLEDs where one OLED based on unmodified ITO as reference and others OLEDs based on modified ITO by CsF solution. 1 wt%, 5 wt% and 10 wt% solutions of CsF improved the work function of ITO from normal value of 4.78 eV to 4.95 eV, 5.01 eV and 5.11 eV respectively. These work function improvement of ITO increased the hole injection rate by which the J-L-V curves influenced significantly. At a constant operating voltage of 6 V (Fig. 2(a)), the current density of OLEDs based on reference, 1 wt%, 5 wt% and 10 wt% CsF solutions are 46 mA/cm^2, 356 mA/cm^2, 751 mA/cm^2 and 928 mA/cm^2. On the other side, at 500 cd/m^2 (Fig. 2(b)), the operation voltage of reference, 1 wt%, 5 wt% and 10 wt% CsF solutions based OLEDs are 6.9 V, 4.7 V, 3.7 V and 3.3 V correspondingly. 10 wt% CsF solution based OLED shows the highest current density and luminance due to higher hole injection rate which also result of higher efficiency as evidence as presented in Fig 2(c). The improved values of electroluminescence (EL.) efficiency, γ (power efficiency, η) of modified ITO based OLEDs by 1 wt%, 5 wt% and 10 wt% CsF solutions are 4.79 cd/A (4.68 lm/W), 5.28 cd/A (5.38 lm/W) and 5.39 cd/A (5.89 lm/W) over without ITO modification based OLED where the value of EL. efficiency (power efficiency) is 4.4 cd/A (4.52 lm/W). These significant performance improvements of OLEDs using ITO surface modification by CsF solutions can be visualized and explained form the carrier distribution and recombination profiles.

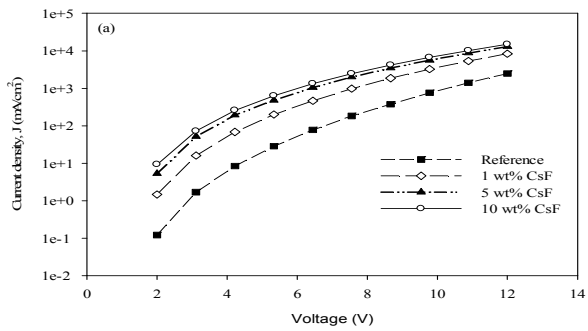

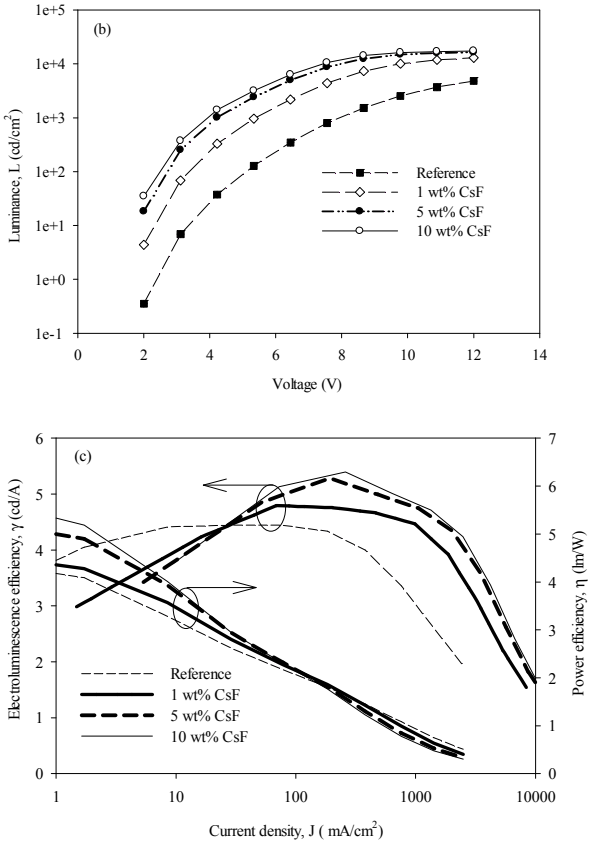

Fig. 2. Characteristics curves of OLEDs in terms of (a) Current density-Voltage, (b) Luminance-Voltage and (c) Electroluminescence and Power Efficiency-Current density

B. *Effects of ITO surface modication on current balance and recombination*

From the carrier concentration profile as shown in Fig. 3 (a), it is observed that at operation voltage of 6 V, the hole density increased around 1, 1.7 and 2 orders due to ITO surface modification by 1 wt%, 5wt% and 10 wt% CsF solutions respectively, when the interfacial energy barrier between ITO (4.95 eV, 5.01 eV and 5.11 eV) and NPB (HUMO=5.4 eV) reduced from 0.62 eV (in unmodified condition (4.78 eV)) to 0.45 eV, 0.39 eV and 0.29 eV correspondingly. Therefore, these significant reduction of interfacial energy barrier increased the hole current density in the NPB layer (Fig. 3(b)) around 5, 9 and 11 times which linked to increase the total current density of the modified ITO based OLEDs over unmodified ITO based OLED. Moreover, the electric field distribution along the device as shown in Fig. 4(a) increased steadily from anode/NPB interface to NPB/Alq_3 interface due to this CsF solution based ITO surface modification technique which harmoniously influenced the recombination rate at that organic layers interface. The highest calculated values of current balance factor in Fig. 4(b) of modified ITO based OLEDs with 1 wt%, 5wt% and 10 wt% CsF solutions are 0.68, 0.77 and 0.90 respectively where ITO surface modification based OLEDs reached steady state position before unmodified ITO based OLED (0.61).

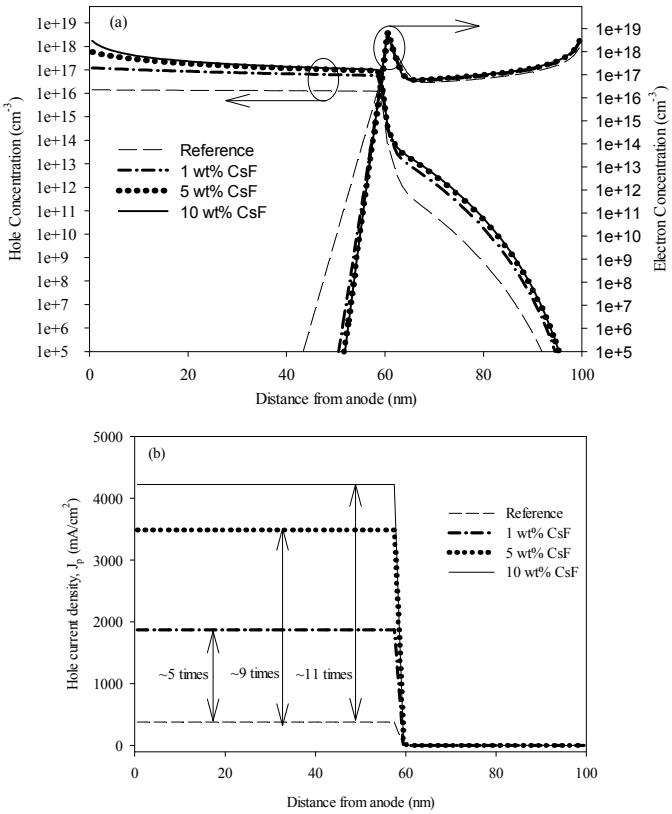

Fig. 3. (a) Carriers concentration profile and (b) Hole current density in treated and untreated ITO based OLEDs at 6V.

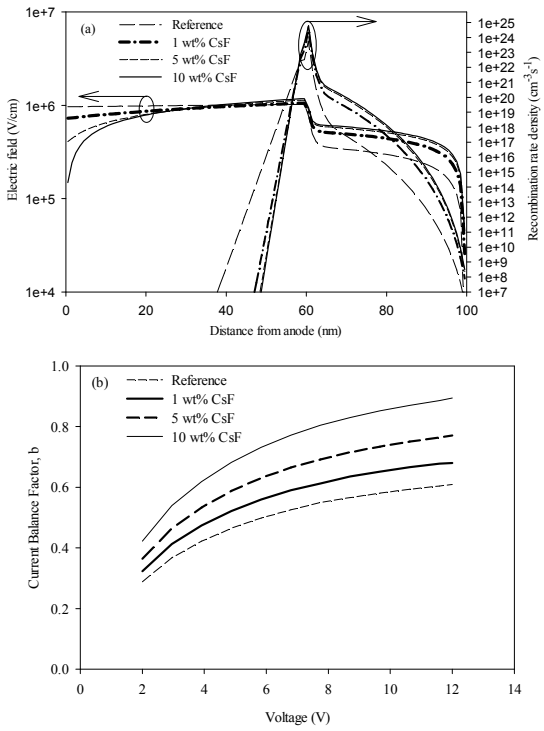

Fig. 4. (a) Distribution of Electric field and Recombination zone at 6V and (b) Current Balance Factor for treated and untreated ITO based OLED

C. Discussions

Through this numerical simulation, the influence of CsF solution on ITO work function modification and device performance have been explained from the hole current density, recombination rate and current balance factor. Due to the ITO surface modification by ITO soaking in 1 wt%, 5wt% and 10 wt% CsF solutions, the energy barrier at anode/organic interface reduced by 0.17 eV, 0.23 eV and 0.33 eV respectively from the original value (0.62 eV) and hence increased the hole injection rate. Therefore, the device EL. efficiency and power efficiency correspondingly improved by 1.08, 1.20 and 1.23 times, and 1.03, 1.19 and 1.30 times. Due to this CsF solution based ITO surface modification technique, a summary of performance improvements of all modified devices in terms of their efficiencies and CBF have been presented in TABLE I. Around 1.5 times improvement (10 wt% CsF solution) in current balance factor over normal condition also confirmed the improvement of device quantum efficiency.

TABLE I. COMPARISON OF OLEDS PERFORMANCES WITH AND WITHOUT ITO MODIFICATION.

Work function of ITO	**Simulation Results (Experimental Results [7])**					
	Max. EL. Efficiency, γ (cd/A)	***Max. Power efficiency, η (lm/W)***	**CBF**	**Improvement over unmodified ITO based OLED**		
				γ (cd/A)	**η (lm/W)**	**CBF**
4.78 eV (Reference)	*4.4 (2.81)*	*4.52 (1.47)*	*0.61*	-	-	-
4.95 eV (1 wt% CsF Sol.)	*4.79 (2.85)*	4.68 (1.51)	0.68	1.08 (1.01)	1.03 (1.02)	1.11
5.01 eV (5 wt% CsF Sol.)	*5.28 (2.62)*	5.38 (1.37)	0.77	1.2 (0.93)	1.19 (0.93)	1.26
5.11 eV (10 wt% CsF Sol.)	5.39 (3.0)	5.89 (1.58)	0.90	1.23 (1.06)	1.3 (1.08)	1.47

V. CONCLUSIONS

The effects of CsF solution based ITO surface modification technique on OLED performance have been analyzed from the 'SETFOS' based numerical simulation results. Due to ITO surface modification with 10 wt% CsF solution, the energy barrier for hole injection reduced more than 2 times (from 0.69 eV to 0.29 eV) which significantly increased hole injection rate at anode, accumulation of holes and recombination at the NPB/Alq_3 interface. Therefore, both EL. and power efficiencies increased around 1.23 and 1.30 times respectively. The value of current balance factor also improved from 0.61 to 0.90 (around 1.5 times) which is proportional to the experimental quantum efficiency. Moreover, the quantitative results of OLEDs performances by this numerical simulation comparable with experimental results [7].

REFERENCES

[1] N. C. Erickson and R. J. Holmes, "Highly efficient, single-layer organic light-emitting devices based on a graded-composition emissive layer," *Appl. Phys. Lett.*, vol. 97, no. 8, p. 083308, 2010.

[2] D. Ma, C. S. Lee, S. T. Lee, and L. S. Hung, "Improved efficiency by a graded emissive region in organic light-emitting diodes," *Appl. Phys. Lett.*, vol. 80, no. 19, p. 3641, 2002.

[3] C. W. Tang and S. a. VanSlyke, "Organic electroluminescent diodes," *Appl. Phys. Lett.*, vol. 51, no. 12, p. 913, 1987.

[4] C.-H. Hsiao, Y.-H. Chen, T.-C. Lin, C.-C. Hsiao, and J.-H. Lee, "Recombination zone in mixed-host organic light-emitting devices," *Appl. Phys. Lett.*, vol. 89, no. 16, p. 163511, 2006.

[5] C. Riku, Y. Y. Kee, T. S. Ong, S. S. Yap, and T. Y. Tou, "Simulation of mixed-host emitting layer based organic light emitting diodes," in *AIP Conference Proceding*, vol. 1657, no. 1, p. 070002, 2015.

[6] X. A. Cao and Y. Q. Zhang, "Performance enhancement of organic light-emitting diodes by chlorine plasma treatment of indium tin oxide," *Appl. Phys. Lett.*, vol. 100, no. 18, p. 183304, May 2012.

[7] H.-W. Lu, C.-W. Huang, P.-C. Kao, S.-Y. Chu, and Y.-D. Juang, "Effects of ITO Electrode Modification Using CsF Solution on Performance of Organic Light-Emitting Diodes," *ECS J. Solid State Sci. Technol.*, vol. 4, no. 3, pp. R54–R59, Jan. 2015.

[8] T. J. Whitcher, K. H. Yeoh, Y. B. C. Ng, N. A. Talik, C. L. Chua, K. L. Woon, N. Chanlek, H. Nakajima, T. Saisopa, P. Songsiriritthigul, S. Oswald, and B. K. Yap, "Enhancement of the work function of indium tin oxide by surface modification using caesium fluoride," *J. Phys. D. Appl. Phys.*, vol. 46, no. 47, p. 475102, Nov. 2013.

[9] P.-R. Huang, Y. He, C. Cao, and Z.-H. Lu, "The origin of the high work function of chlorinated indium tin oxide," *NPG Asia Mater.*, vol. 5, no. 8, p. e57, Aug. 2013.

[10] E. Knapp and B. Ruhstaller, "Numerical analysis of steady-state and transient charge transport in organic semiconductor devices," *Opt. Quantum Electron.*, vol. 42, no. 11–13, pp. 667–677, Feb. 2011.

[11] H. Wang, K. P. Klubek, and C. W. Tang, "Current efficiency in organic light-emitting diodes with a hole-injection layer," *Appl. Phys. Lett.*, vol. 93, no. 9, p. 093306, 2008.

[12] J. C. Scott, S. Karg, and S. A. Carter, "Bipolar charge and current distributions in organic light-emitting diodes," *J. Appl. Phys.*, vol. 82, no. 3, p. 1454, Aug. 1997.

[13] R. G. Kepler, P. M. Beeson, S. J. Jacobs, R. A. Anderson, M. B. Sinclair, V. S. Valencia, and P. A. Cahill, "Electron and hole mobility in tris(8-hydroxyquinolinolato-N1,O8) aluminum," *Appl. Phys. Lett.*, vol. 66, no. 26, p. 3618, Jun. 1995.

[14] S.-W. Liu, J.-H. Lee, C.-C. Lee, C.-T. Chen, and J.-K. Wang, "Charge carrier mobility of mixed-layer organic light-emitting diodes," *Appl. Phys. Lett.*, vol. 91, no. 14, p. 142106, 2007.

Study on the Prospects of Sb_2Te_3 Back Surface Field in ZnCdS/ZnCdTe Thin Film Solar Cell

Md. Muin Uddin[1], M. S. Hossain[1,3], and N. Amin[2,3]
[1]Department of Electrical & Electronic Engineering (Dhaka University of Engineering & Technology, Bangladesh)
[2]Department of Electrical, Electronic and Systems Engineering (University Kebangsaan Malaysia, Malaysia)
[3]Solar Energy Research Institute (University Kebangsaan Malaysia, Malaysia)
[*] E-mail:sharafat57@mail.com

Abstract—**This paper numerically explores the possibility of high efficiency, ultrathin and stable ZnCdTe (CZT) polycrystalline solar cell using well accepted simulator AMPS-1D. The base line structure of the ZnCdTe cell (Glass/ITO/CdS/ZnCdTe/Back Contact) was the beginning point of this work and further this base line structure was modified to achieve ultrathin, higher efficiency and stable solar cell. In modified structure, CdS window layer has been replaced by a wide band gap material $Zn_xCd_{1-x}S$ which increase the spectral response in the blue region as well as $Zn_xCd_{1-x}S$ window layer was reduced to the extreme limit with insertion of a suitable buffer layer of ZnO in between ITO and window layer to check forward leakage current of ultrathin window layer. To lessen the back surface recombination loss and barrier height at back contact another extra layer (BSF p-Sb_2Te_3) has been inserted in between p-ZnCdTe layer and back contact (BC). Then the thickness of the window layer and absorber layer of the modified structure has been optimized. The modified structure with back surface field (BSF) layer (Glass/ ITO/ZnO/$Zn_xCd_{1-x}S$/$Zn_xCd_{1-x}Te$/Sb_2Te_3/BC) shows the highest efficiency of 23.17% (*Jsc*=33.50 mA/cm^2, *FF*=0.77% and *Voc*= 0.98V). Finally the temperature effect on cell parameters was investigated and the overall temperature coefficient (TC) of the proposed cell is found to be 0.085%.**

Keywords—TFSC, CZT solar cell, ZnCdS, Photovolatic, BSF.

I. INTRODUCTION

Polycrystalline thin film solar cells such as Cu(InGa)Se_2 (CIGS), $CuInSe_2$ (CIS) and CdTe compound semiconductors are important for global application because of their high efficiency, long term stable performance and prospective for low cost production. Because of the high absorption coefficient (~10^5 cm^{-1}) a thin layer of ~2 μm is enough to absorb the useful part of the spectrum [1]. Highest recorded efficiency of 19.2% for CIGS [2] and 16.5% for CdTe [3] solar cell has been achieved. However there are rooms to improve the thin film solar cell (TFSC) performance by reformed cell design and using simple deposition technique to increase any one of cell performance parameters.

. Materials with high energy conversion efficiency have attracted substantial attention in the recent year. In this regards semiconductors having band gaps in the visible region of the electromagnetic spectrum are of commercial interest due to their valuable application in optoelectronic devices [4]. Silicon (Si) and germanium (Ge) are simplest and conventional semiconductors used in these devices but the problem with these semiconductors are their brittle nature as well as fixed and indirect band gap. CdTe is a direct band gap semiconductor with a fixed 1.45 eV band gap which is not good enough to involve wide range of energy from near infrared to near-ultraviolet. That's why the best replacement of these semiconductors in terms of efficiency and operating temperature is CZT due to its wide band gaps and high absorption rate at room temperature. In this work, a new TFSC structure is planned, where Zinc Cadmium Sulfide ($Zn_xCd_{1-x}S$) was used as window layer and Zinc Cadmium Telluride ($Zn_xCd_{1-x}Te$) was used as absorber layer with an extra benefit of variable band gap. As the spectral region sensitivity of the material depends on its band gap which depends on the controlled composition x in $Zn_xCd_{1-x}S$ and $Zn_xCd_{1-x}Te$, hence the value of x is varied symmetrically in the range $0<x<1$ to involve wide range of energy from near infrared to near ultraviolet [4]. In consideration to fabrication challenges, simulation results and resistivity of $Zn_xCd_{1-x}S$ film, in this work x=0.1 [5] is selected which showed low resistivity and high conversion efficiency in comparison to other value of x. The band gap E_g=1.57 eV is selected for ZnCdTe because it is in the range of optimum band gap. Moreover this band gap of $Zn_xCd_{1-x}Te$ can be obtained practically using the composition of x=0.1 in $Zn_xCd_{1-x}Te$ [6]. In the following text, $Zn_xCd_{1-x}S$ window layer and $Zn_xCd_{1-x}Te$ absorber layer has been written to $Zn_{0.1}Cd_{0.9}S$ and $Zn_{0.1}Cd_{0.9}Te$ respectively.

Now a day's one of the main goal of solar cell research is using a lesser amount of semiconductor material by making the cell thinner. Thinning will not only save material but also decrease layer deposition time as well as the energy requirement of production. All of these aspects will decrease the production cost of cell. In this work to reduce the cell thickness, modified cell structure (Glass/ITO/ ZnO/$Zn_xCd_{1-x}S$/$Zn_xCd_{1-x}Te$/Sb_2Te_3/BC) has been proposed and optimized the cell thickness without compromising the cell performance using Sb_2Te_3 BSF. Eventually, the modified CZT cell was investigated and achieved the maximum efficiency of 23.17% (*Jsc*=33.50 mA/cm^2, *FF*=0.77% and *Voc*= 0.98V).

978-1-4673-9257-0/15/$31.00 ©2015 IEEE

II. Device Design And Simulation

Thin film solar cell can be grown in both substrate or superstrate configuration, but the uppermost efficiency is achieved in the superstrate configuration [1]. In this work superstrate configuration is used and the usual superstrate structure of baseline CdS/ZnCdTe solar cell and modified ZnCdS/ZnCdTe solar cell is shown in Fig. 1. It is apparent from Fig. 1(a) that in the baseline structure of CZT solar cells, SnO_2 with 500 nm thickness is used as TCO or front contact, CdS with 100 nm thickness is used as window layer and ZnCdTe with 4000 nm thickness is used as absorber layer. It is also clear from Fig. 1(b) that the modified structure has an additional layer (ZnO) in the middle of TCO and n-$Zn_{0.1}Cd_{0.9}S$ layer to achieve ultrathin $Zn_{0.1}Cd_{0.9}S$ layer and another extra layer (BSF p-Sb_2Te_3) in between p-$Zn_{0.1}Cd_{0.9}Te$ layer and back contact. The key purposes of the BSF are to shrink the back surface recombination loss and to reduce the barrier height at BC. The specific BSF material selected to investigate in this work is Antimony Telluride (Sb_2Te_3).

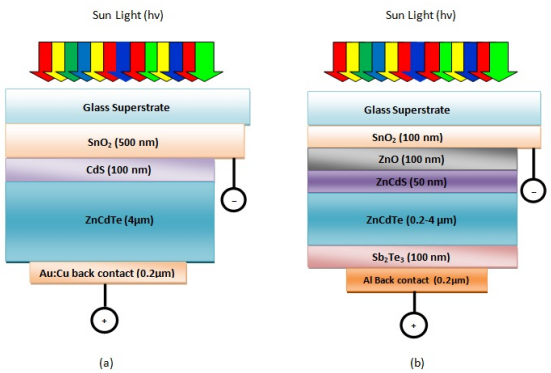

Figure 1. Schematic view of the CZT solar cell (a) baseline structure (b) proposed modified structure.

In this study, AMPS 1D [7] was used to explore the CZT baseline solar cell and modified structured solar cell for achieving ZnCdTe and ZnCdS layer with higher conversion efficiency. This simulation program has been developed to simulate faithfully the electrical characteristics of thin film heterojunction solar cell. That's why the four basic layers that have been emphasized in this modeling are the buffer layer (ZnO), n-$Zn_{0.1}Cd_{0.9}S$ window layer, p-$Zn_{0.1}Cd_{0.9}Te$ absorber layer and Sb_2Te_3 BSF layer. Table 1 displays the material parameters used in this work, which were selected based on literature values, theory or in some case, reasonable guesstimates. In this analysis, $Zn_{0.1}Cd_{0.9}Te$ absorber layer thickness has been varied from 0.2 µm to 4.0 µm and $Zn_{0.1}Cd_{0.9}S$ window layer thickness has been varied from 25 nm to 200nm by kept all other parameters at fixed value as stated in table 1 aiming to get efficient and thinner CZT solar cell.

III. Results And Discussions

A. Analysis of Baseline CZT Cell Structure

The baseline structure of CZT solar cell has shown in Fig. 1(a). The performance parameters of the baseline structure of CZT solar cell are: efficiency, η=21.63%; short circuit current density, Jsc=33.7mA/cm^2; open circuit voltage, Voc=0.96 V and fill factor, FF=0.73%. The thickness of the baseline structure cell was 4600nm. Further modifications have done to increase the cell performance as well as reduce the cell thickness to achieve an ultrathin solar cell. In the modified structure (Fig. 1(b)) of CZT cell, the window layer CdS was replaced by a wide band gap alloy ZnCdS which provide a more transparent window layer. As a result the spectral response at blue region and photocurrent generation has been increased. It is clear from the Fig. 2 that, the quantum efficiency of 50 nm thick ZnCdS shows better quantum efficiency than 100 nm thick CdS window layer. Lessening of ZnCdS thickness causes pinhole, which was reduced by insertion of 100 nm thick n-ZnO buffer layer in between TCO and n-ZnCdS window layer. Another layer has been introduced in modified structure which is called BSF to overcome rollover effect, to reduce the loss due to minority carrier recombination at back contact as well as to improve the stability of the cell at high operating temperature. All these modifications turn into increment of cell efficiency (21.63% to 23.17%). The J-V characteristics curve of the baseline structure and modified structure of CZT cell has shown in Fig. 3.

Table I. Materials properties used in AMPS-1D simulation

Typical cell properties		
Parameters	**Front contact**	**Back contact**
Φ_b [eV]	Φ_{bn} = 0.05	Φ_{bp} = 1.0 (Cu) and 0.1 (Sb_2Te_3)
S_e [cm/s]	1×10^7	1×10^7
S_h [cm/s]	1×10^7	1×10^7
R_f [I]	0.01	0.99 (Al) and 0.99 (Cu_2Te)

Layer properties				
Parameter	**ZnO**	**$Zn_xCd_{1-x}S$ (x=0.1)**	**p-$Zn_xCd_{1-x}Te$ (x=0.1)**	**p-Sb_2Te_3**
W (µm)	0.1	0.05-0.2	0.2- 4.0	0.5
$\varepsilon/\varepsilon_0$	9.0	9.3	9.5	55
μ_e (cm^2/Vs)	100	95	250	1094
μ_p (cm^2/Vs)	25	35	70	320
n, p (cm^{-3})	10^{19}	2.5×10^{16}	5×10^{14}	7.5×10^{21}
Eg (eV)	3.0	2.55	1.57	0.30
N_c (cm^{-3})	2.0×10^{18}	2.1×10^{18}	1.5×10^{17}	7.5×10^{17}
N_v (cm^{-3})	1.5×10^{19}	1.7×10^{19}	1.8×10^{19}	1.5×10^{19}
χ (eV)	4.35	4.44	4.20	4.15

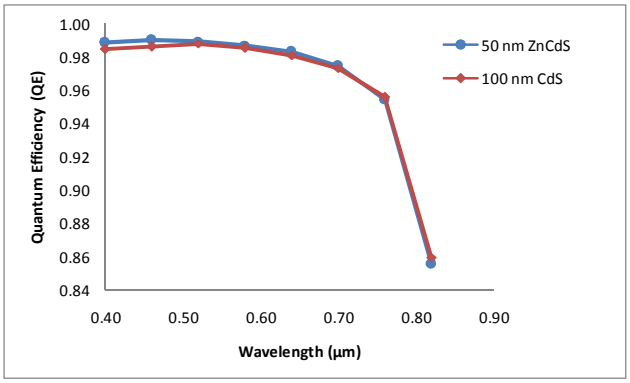

Figure 2. Spectral responses of ZnCdS and CdS window layer.

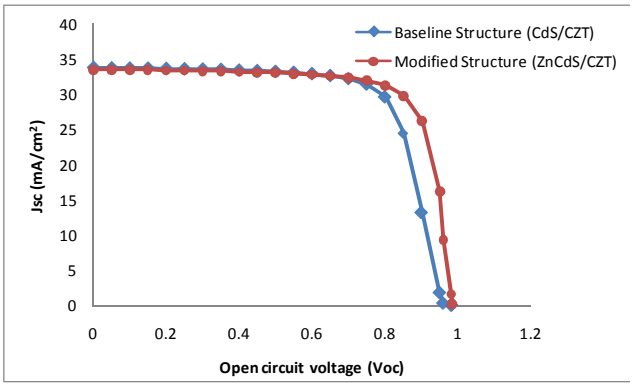

Figure 3. J-V characteristics curve of baseline and modified CZT solar cell.

Table II. Comparison of performance parameters between baseline case and modified cell

Performance parameters	Baseline case structure of CZT cell	Modified structure of CZT cell
η (%)	21.63	23.17
FF (%)	0.73	0.77
Jsc (mA/Cm^2)	33.71	33.50
Voc (V)	0.96	0.98

B. *Optimization of window and absorber layerthickness*

In this part, $Zn_{0.1}Cd_{0.9}S$ window layer thickness and $Zn_{0.1}Cd_{0.9}Te$ absorber layer thickness are optimized to form an ultrathin solar cell without affecting the cell performance. The thickness of window layer is changed from 25 nm to 200 nm.

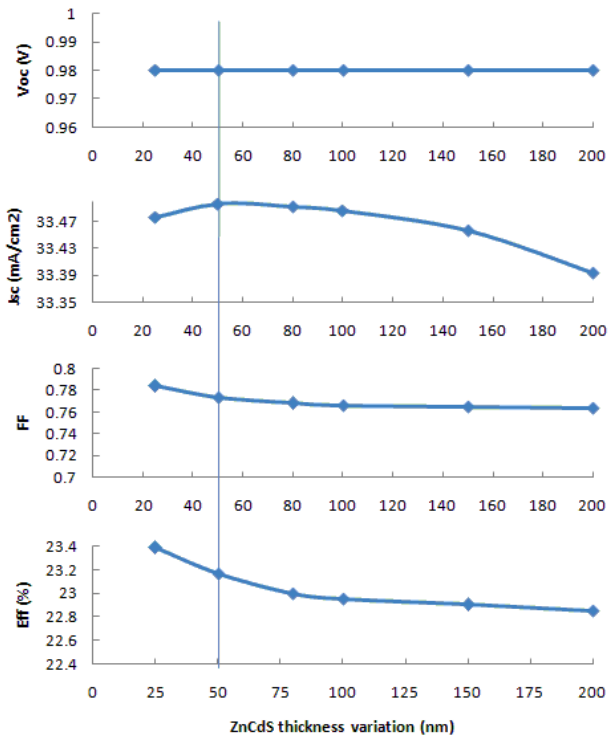

Figure 4. Effect of ZnCdS window layer thickness on cell performance parameters.

Fig. 4 shows the effect of window layer thickness variation on cell performance parameters. It is investigated that by decreasing the thickness of window layer the cell efficiency (η), current density (*Jsc)* and fill factor (*FF*) has been increased. Efficiency is increased due to increase of *Jsc* and *Jsc* is increased due to the use of wide band gap window layer as well as insertion of additional layers of ZnO and Sb_2Te_3. ZnO reduced the pinhole creation in ZnCdS layer and prevent forward leakage current. Whereas BSF layer reduced the loss due to minority carrier recombination at back contact as well as improved the stability of the cell at high operating temperature. However, by decreasing the thickness of window layer *FF* is increased a bit, because thinner window layer decreases overall cell resistance. But there is no change in *Voc* due to reduction of window layer thickness. The thickness of window layer is reduced from 200nm to 25nm and as a result the efficiency increases from 22.85% to 23.38%. Still to date it is impractical to fabricate good quality devices with ZnCdS film thickness below 50nm. Consequently the optimum thickness of window layer has been set to 50nm with conversion efficiency 23.17%.

In this work the thickness of absorber layer is varied from 0.2 µm to 4.0 µm. The effect of thickness variation of $Zn_{0.1}Cd_{0.9}Te$ absorber layer has shown in Fig. 5. It is evident from Fig. 5 that, efficiency almost follows the short circuit current trend. It can be seen that by decreasing the absorber layer thickness from 4.0 µm to 1.0µm the magnitude of *Jsc* decreases slightly. But *Jsc* decreases rapidly with the change of thickness from 1.0µm to 0.2µm. This is because of less absorption of light photon by reduced absorber layer thickness. That's why the efficiency decreases with lessening of absorber layer thickness because of the shrinking of *Jsc*. The increase of CZT layer thickness causes big area of p-n junction as the main

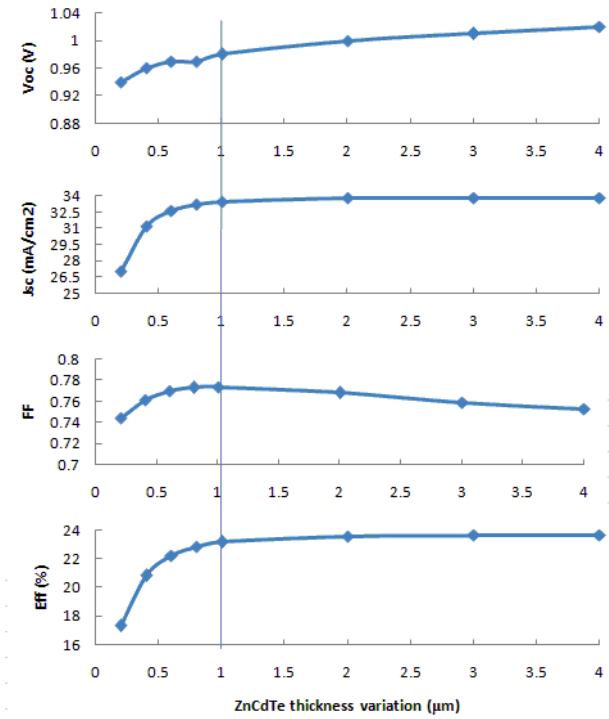

Figure 5. Effect of $Zn_{0.1}Cd_{0.9}Te$ absorber layer thickness on cell performance parameters.

part of p-n junction is formed in CZT layer. It is evident from Fig. 5 that by changing absorber layer thickness *Voc* increases gradually due to the increment of layer series resistance. On the other hand *FF* is increased with the reduction of absorber layer thickness. It is also noticed from Fig. 6 that the cell output parameters gradually decrease from 4.0µm to 1.0µm thick ZnCdTe layer. Where, all performance parameters decrease dramatically with the thinning of absorber layer thickness from 1.0µm to 0.2µm. It was also investigated that in this work the thickness of absorber layer is reduced from 4.0µm to 0.2µm and as a result the efficiency changes from 23.67% to 17.33%. Though efficiency decreases a little bit (only 0.5%) for thickness reduction from 4.0µm to 1.0µm, thus 1.0µm thick absorber layer is proposed for modified CZT cell with a little sacrifice of efficiency but grater saving of absorber layer material ($Zn_{0.1}Cd_{0.9}Te$).

C. *Effect of temperature on cell performance*

To investigate the temperature effect on cell performance of modified cell, temperature is changed from 25°C to 100°C. Temperature effect on different performance parameters has been shown in the Fig. 6. With the increment of temperature from 25°C the cell efficiency and *FF* has slightly increased up to 50°C after then it started to decrease for further temperature increment. As temperature rises, the band gap of semiconductor decreases and *Voc* decreases with a temperature dependency factor q/kT. Solar cells therefore have a negative temperature coefficient of *Voc* (β). That's why *Voc* decreases with the increase of temperature. On the other hand, as temperature rises the band gap of semiconductor shrinks meaning more incident energy is absorbed because a greater percentage of the incident light has enough energy to increase

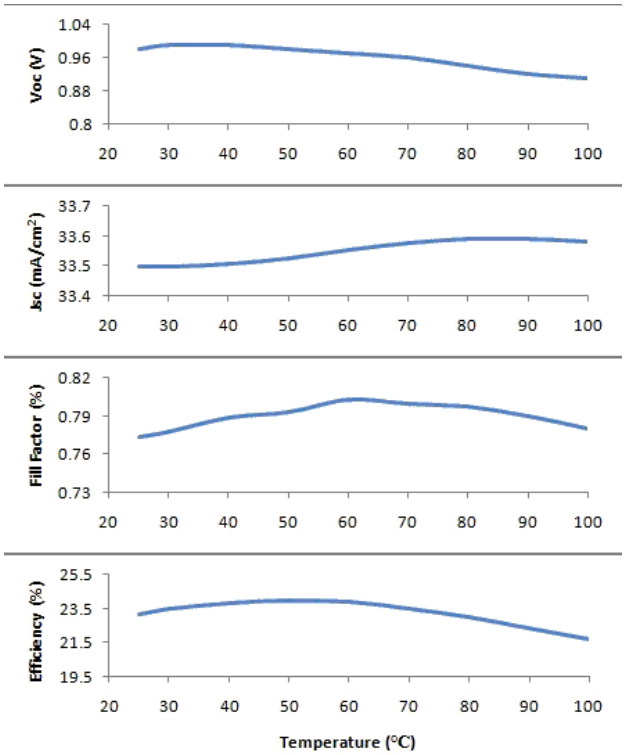

Figure 6. Effect of temperature on cell performance parameter of modified CZT cell.

charge carriers from the valance band to the conduction band. In effect, a larger photocurrent results; thus, *Isc* increases for a given insulation and solar cells have a positive temperature coefficient of *Isc* (α). Thus *Jsc* increases with the increment of temperature which is clear from the Fig. 6. The efficiency of the proposed cell at T=25°C is 23.17%, and when temperature is increased to T=50°C the efficiency become 23.83% and finally 21.68% is obtained at T=100°C. The overall temperature coefficient (TC) of the proposed cell is found 0.085% which means that this cell has good stability at higher temperature.

IV. Conclusion

From this numerical analysis it has been substantiated that the proposed modified CZT solar cell structure became thinner (1350 nm) than the reference CZT solar cell structure thickness (4600 nm) using Sb_2Te_3 BSF. It is clearly apparent that almost 70% less material will be used in this modified solar cell structure which was one of the main targets of this study. On the other hand the proposed solar cell performance has been risen (η=23.17%, *Jsc*=33.50%mA/cm^2, *Voc*=0.98V and *FF*=0.77%) due to few authentic effective modifications in the starting baseline structure. As well as the proposed cell also shows better stability (TC=0.085%) with Sb_2Te_3 BSF at high operating temperature. Thus this study clearly brings out a good prospect of the ZnCdS/ZnCdTe solar cells using Sb_2Te_3 BSF.

References

[1] A. Romeo, M. Terheggen, D. Abou-Ras, D. L. Batzner, F-J Haug, M. Kalin, D. Rudmann and A. N. Tiwari, "Development of Thin Film Cu(In,Ga)Se_2 and CdTe Solar Cell," *Progress in photovoltaics: Research and Application.*, Vol. 12, pp. 93-11, 2004.

[2] Ramanathan K, Contreras MA, Perkins CL, Asher S, Hasoon FS, Keane J, Young D, Romero M, Metzger W, Noufi R, Ward J, Duda A, "Properties of 19.% efficiency ZnO/CdS/Cu(In, Ga)Se_2 thin-film solar cell," *Progress in photovoltaics: Research and Application.*, Vol. 11, pp. 225-230, 1999.

[3] Wu X, Kane JC, Dhere RG, DeHart C, Albin DS, Duda A, Gessert TA, Asher S, Levi DH, Sheldon P, "16.5% Efficiency CdS/CdTe polycrystalline thin-film solar cell," *in Proc. 17th European Photovoltaic solar energy Conf. Munich*, 2002, pp. 995-1000.

[4] Imad Khan, H.A. Rahnamaye Aliabad, Waqar Ahmad, Zahid Ali, Iftikhar Ahmad, "First principle optoelectronic studies of visible light sensitive CZT," *Superlattices and Microstructures.*, vol. 63, pp. 91–99, Sep. 2013.

[5] M. S. Hossain, M.M Aliyu, M. A. Matin, M. A. Islam, K.Sopian, M. R. Karim and N. Amin, "prospect of $Zn_xCd_{1-x}S$ window layer in CdTe thin-film solar cell from numerical analysis ," *Int. Conf. on the development in renewable energy technology, Dhaka.*, vol. 2, pp. 04–08, Jan. 2012.

[6] T.E. Schlesinger, J. E. Toney, H. Yoon, E. Y. Lee, B. A. Brunett, L. Franks and R. B. James, "Cadmium zink telluride and its use as a numerical radiation detector materials," *Materr. Sci. Eng.* Vol. 32, no. 4-5, pp. 103-189, Apr. 2001.

[7] S. Degrave, M. Burgelman, and P. Nollet, "Modeling of polycrystalline thin-film solar cells: new feature in scaps version 2.3," *in Proc. World Conf. on Photovoltaic Energy Conversion,* May 2003, pp. 487-49

Study on Crystal Orientation-dependent Hole Effective mass in III-V Semiconductors

Sourav Roy[1, 2,*], Utpal Bhowmik[1], Md. Rafiqul Islam[1], Md. Mahbub Hasan[1]
[1]Department of Electrical and Electronic Engineering, KUET, Khulna, Bangladesh
[2]Faculty of Electrical and Electronic Engineering, JUST, Jessore, Bangladesh
[*] E-mail: souravroy2k9@gmail.com

***Abstract*— A numerical approach is presented to calculate crystal orientation-dependent effective mass of heavy hole, light hole and spin-orbit split-off hole of III-V semiconductors (GaAs, InAs, InP, GaSb, and InSb etc.) at Gamma-point by envelope approximation using *k.p* method. Unitary transformation is used to modify the wave vector and eight-band k.p Hamiltonian is applied in conventional (100) crystal orientation. The simulation is carried out for conventional crystal orientations (100), (110) and (111) as well as non-conventional orientations (113), (131) and (201). It is found that there is a substantial correlation between the effective mass and the crystal orientation. The results obtained from conventional crystal orientations are compared with that of estimated by well-established PBE, HSE and MBJLDA methods and found to have within good agreement. This indicates that the proposed technique can be applied to evaluate effective mass in arbitrary orientation of III-V semiconductors. It is also found that (113) orientation possesses lowest effective mass than other orientations. The outcome of this paper would be a boost to design high-speed optoelectronic devices with improved performance by introducing non-100 oriented epitaxial layers.**

Keywords*— *Crystal orientation, Effective mass, Tensor rotation, k.p method, III-V semiconductors

I. INTRODUCTION

The zinc-blende (ZB) III-V semiconductors have received considerable attention in the last decades due to its unique characteristics such as high electron mobility and superior carrier saturation velocity [1]. Consequently, its application scope broadens up to the operation in the active region of different optoelectronic devices [2-4]. Recently, it has become apparent that energy band dispersion profile of III-V materials is strongly co-related with crystal orientations. High performance optoelectronic devices can be realized in non-conventional orientation having favorable band structure [5-6].

Modern fabrication techniques such as molecular beam epitaxy (MBE) and metal-organic chemical vapor deposition (MOCVD) enables the growth of non-(100)-orientated crystal structure. High quality epitaxial layer on (201)-oriented GaAs substrate using MBE was cited by Woolf et al. [7]. In another research work, Nötzel and Ploog reported AlAs/GaAs multilayered structures on (210)-oriented substrate [8]. The orientation-dependent emission profile of InGaSb as well as InGaAs lasers were studied and found that non-(100) oriented laser structures show excellent performance with orientation-dependent tunable characteristics [9]. In another study, Ahmed and Debbichi showed that InAsN/GaSb quantum well laser diode in (110) and (111) orientation had better optoelectronic properties than the habitual (100) growth direction [10]. Oshima et al. reported orientation dependent features of recessed gate InGaAs/AlGaAs HEMT [11]. In a separate research, Lee and Zucca showed crystal orientation effect on planer InGaAs Schottky barrier field effect transistors [12].

To explore and explain the orientation-dependent performance of III-V semiconductor based electronic and optoelectronic devices, it is very much essential to know the orientation-dependent effective mass. Extensive researches have already been carried out experimentally and theoretically to calculate effective mass of heavy hole and light hole, paying particular attention to their fundamental properties and band topologies. The band structures and effective mass of ZB III-V semiconductor are studied using the Perdew, Burke and Ernzerhof (PBE) method, the Heyd, Scuseria, and Ernzerhof hybrid functional (HSE) method, and modified Becke-Johnson combined with the local-density approximation (MBJLDA) [13]. In these studies, the masses were evaluated numerically by fitting the calculated dispersion curves around the Γ-point along the directions (100), (110) and (111). However, these methods require an extensive fitting to experimental data, which are often scarce and possibly inaccurate. Moreover, for arbitrary crystal orientation such as, (113), (131) and (201) etc., considerable uncertainty still exists for the above mentioned methods due to unavailability of experimental effective masses [13-18].

In this paper, a general mathematical model based on tensor rotation technique is developed to determine effective mass of heavy hole (HH), light hole(LH) and spin-orbit split off hole(SH) in arbitrary (hkl) crystal orientation for ZB III-V semiconductor (GaAs, InAs, GaSb, InSb, InP) at Γ-point. The electronic band structure is calculated using an eight-band ***k.p*** Hamiltonian including spin-orbit coupling which enables us to have a good model for the non-parabolic dispersion of topmost valence band. Tensor rotation technique is used to modify wave vector and Hamiltonian for conventional (100) crystal orientation. The conduction and valence band wave functions and Eigen energies are evaluated using the finite difference method. The average heavy hole, light hole and spin-orbit split-off hole masses are obtained by exploring the orientation dependent parameters and addressing the energy separation from conduction band to heavy hole and light hole valence bands over all possible directions of wave vector. To confirm the validity of the results obtained from the proposed model, they are compared with the experimental and simulation

978-1-4673-9257-0/15/$31.00 ©2015 IEEE

results reported in previous studies for (100), (110) and (111) orientations.

The layout of this proposal is outlined as follows: the theoretical details to calculate electronic band structure and valence band effective masses of the ZB III-V semiconductor are illustrated in section 2. Results and discussions on the valence band structure in arbitrary orientation, Hole effective masses, and optical gain are presented in section 3. Finally, a conclusion is depicted in section 4.

II. THEORY

A. The k.p Method of Band-Structure Calculation near Γ-point

The electronic band structure is solved in envelope approximation using eight-band $\boldsymbol{k}\cdot\boldsymbol{p}$ Hamiltonian, H_0. The Kane's 8×8 Hamiltonian matrix can be asserted by [19]:

$$H\psi_h(z) = E\psi_h \tag{1}$$

The components of the Hamiltonian matrix are:

$$H_0=\begin{bmatrix} A & 0 & V^* & 0 & \sqrt{3}V & -\sqrt{2}U & -U & \sqrt{2}V^* \\ 0 & A & -\sqrt{2}U & -\sqrt{3}V^* & 0 & -V & \sqrt{2}V & U \\ V & -\sqrt{2}U & -P+Q & -S^* & R & 0 & \sqrt{\frac{3}{2}}S & -\sqrt{2}Q \\ 0 & -\sqrt{3}V & -S & -P-Q & 0 & R & -\sqrt{2}R & \frac{1}{\sqrt{2}}S \\ \sqrt{3}V^* & 0 & R^* & S & -P+Q & S^* & \frac{1}{\sqrt{2}}S^* & \sqrt{2}R^* \\ -\sqrt{2}U & -V^* & 0 & R^* & S & -P+Q & \sqrt{2}Q & \sqrt{\frac{3}{2}}S^* \\ -U & \sqrt{2}V^* & \sqrt{\frac{3}{2}}S^* & -\sqrt{2}R^* & \frac{1}{\sqrt{2}}S & \sqrt{2}Q & -P-\Delta & 0 \\ \sqrt{2}V & U & -\sqrt{2}Q & \frac{1}{\sqrt{2}}S^* & \sqrt{2}R & \sqrt{\frac{3}{2}}S & 0 & -P-\Delta \end{bmatrix} \tag{2}$$

The wave function $\Psi_h(z)$ can be given by:

$$\Psi_h(z) = \begin{bmatrix} \Phi_{1/2,1/2}(z) \\ \Phi_{1/2,-1/2}(z) \\ \Phi_{3/2,1/2}(z) \\ \Phi_{3/2,-1/2}(z) \\ \Phi_{3/2,3/2}(z) \\ \Phi_{3/2,-3/2}(z) \\ \Phi_{1/2,1/2}(z) \\ \Phi_{1/2,-1/2}(z) \end{bmatrix} = \begin{bmatrix} g^{(1)}(z) \\ g^{(2)}(z) \\ g^{(2)}(z) \\ g^{(4)}(z) \\ g^{(5)}(z) \\ g^{(6)}(z) \\ g^{(7)}(z) \\ g^{(8)}(z) \end{bmatrix} \tag{3}$$

where, ϕ_{j,m_j} or $g^{(j)}$ is the conduction and valence band wave function component and E is the energy of conduction band and three valence bands.

The matrix elements are [19]:

$$A=E_c-\frac{\hbar^2}{2m_0}(k_x^2+k_y^2+k_z^2) \tag{4}$$

$$P=-E_v-\gamma_1\frac{\hbar^2}{2m_0}(k_x^2+k_y^2+k_z^2) \tag{5}$$

$$Q=-\gamma_2\frac{\hbar^2}{2m_0}(k_x^2+k_y^2+k_z^2) \tag{6}$$

$$R=\sqrt{3}\frac{\hbar^2}{2m_0}[\gamma_2(k_x^2-k_y^2)-2i\gamma_3k_xk_y] \tag{7}$$

$$S=-\sqrt{3}\gamma_3\frac{\hbar^2}{2m_0}k_z(k_x-ik_y) \tag{9}$$

$$U=\frac{-i}{\sqrt{3}}p_0k_z \tag{10}$$

$$V=\frac{-i}{\sqrt{6}}P_0(k_x-ik_y) \tag{11}$$

P_0 is the coupling between the conduction and valence bands, E_c and E_v are the (unstrained) conduction and valence band energies respectively, and Δ is the spin orbit splitting. The γ_i's are modified Luttinger parameters.

The energy dispersion profile along (100) orientation is calculated as a function of k for the 8-band $\boldsymbol{k.p}$ theory by diagonalizing the Hamiltonian using finite difference scheme.

B. Crystal orientation dependent Energy Band

As the conduction band wave function does not change exclusively with crystal orientation, here we are interested about the modification in the valence band Hamiltonian matrix owing to crystal orientations. If the working region is grown on arbitrary crystal orientation, the wave vectors on (100) crystal can be attained by the subsequent formula [20]:

$$\begin{pmatrix} k_1 \\ k_2 \\ k_3 \end{pmatrix} = O_R \begin{pmatrix} k_x \\ k_y \\ k_z \end{pmatrix} \tag{12}$$

where, k_x, k_y, k_z are the wave vectors along (hkl) direction. The expression of the rotation matrix is as follows [21]:

$$O_R = \begin{pmatrix} cos\theta cos\emptyset & -sin\emptyset & sin\theta cos\emptyset \\ cos\theta sin\emptyset & cos\emptyset & sin\theta sin\emptyset \\ -sin\theta & 0 & cos\theta \end{pmatrix} \tag{13}$$

where, $\theta = \tan^{-1}\left(\frac{\sqrt{(h^2+k^2)}}{l}\right)$ and $\phi = \tan^{-1}(k/h)$

Practicing the wave vector in the (100) crystal orientation, the Hamiltonian matrix for (100) crystal orientation can be calculated using eqn. (2). Then the Hamiltonian matrix in (hkl) orientation can be obtained by [22]:

$$H^{hkl} = U H^{(100)} U^* \tag{14}$$

where, $U = R(\theta)R(\phi)$

In this equalization, $R(\theta)$ and $R(\phi)$ are symbolized as rotations which transform the (100) orientated valence band Hamiltonian to arbitrary crystal orientated Hamiltonian matrix. The argument of $R(\theta)$ and $R(\phi)$ can be defined by [21]:

$$R(\theta)=\begin{pmatrix} \alpha^2 & -\sqrt{3}\alpha^2\zeta & \sqrt{3}\alpha\zeta^2 & \zeta^3 \\ \sqrt{3}\alpha^2\zeta & \alpha^3-2\alpha\zeta^2 & -2\alpha^2\zeta+\zeta^3 & \sqrt{3}\alpha\zeta^2 \\ \sqrt{3}\alpha\zeta^2 & 2\alpha^2\zeta-\zeta^3 & \alpha^3-2\alpha^2\zeta & -\sqrt{3}\alpha^2\zeta \\ \zeta^3 & \sqrt{3}\alpha\zeta^2 & \sqrt{3}\alpha^2\zeta & \alpha^3 \end{pmatrix} \tag{15}$$

$$\alpha = \cos\frac{\theta}{2} \text{ and } \zeta = -\sin\frac{\theta}{2}$$

$$R(\phi) = \begin{pmatrix} e^{i(3/2)\phi} & 0 & 0 & 0 \\ 0 & e^{i(1/2)\phi} & 0 & 0 \\ 0 & 0 & e^{-i(1/2)\phi} & 0 \\ 0 & 0 & 0 & e^{-i(3/2)\phi} \end{pmatrix} \tag{16}$$

C. *Crystal orientation dependent Effective Mass:*

A general mathematical model based on tensor rotation technique is proposed to determine average heavy hole (m^*_{hh}), light hole (m^*_{lh}) and spin-orbit split off hole (m^*_{so}) effective masses for Zinc blende III-V semiconductors in arbitrary (*hkl*) crystal orientations over all possible directions of wave vector k considering the wrapped spheres of valence band energy surface figured out by 8×8 k.p Hamiltonian. The formulations can be given by [23]:

$$(1/m^*_{hh}) = \frac{-2A + 2B(1+ 2C^2/15B^2)}{\hbar^2} \quad (17)$$

$$(1/m^*_{lh}) = \frac{-2A - 2B(1+ 2C^2/15B^2)}{\hbar^2} \quad (18)$$

$$(1/m^*_{so}) = 1-(2/3)\left(\frac{M^2}{m_0(E_0+\Delta_0)} + \frac{2N^2}{m_0(E_0+\Delta_0)}\right) \quad (19)$$

The constants A, B, C (in units of $\hbar^2/2m$) are related to momentum matrix element between conduction band and valence band and energy band gaps and can be given by [23]:

$$\frac{2m_0}{\hbar^2}A = 1-\frac{2}{3}\left[\left(\frac{M^2}{m_0E_0}\right) + \left(\frac{2N^2}{m_0E_0'}\right)\right] \quad (20)$$

$$\frac{2m_0}{\hbar^2}B = \frac{2}{3}\left[\left(\frac{-M^2}{m_0E_0}\right) + \left(\frac{2N^2}{m_0E_0'}\right)\right] \quad (21)$$

$$\left(\frac{2m_0}{\hbar^2}C\right)^2 = \frac{16M^2N^2}{3m_0E_0m_0E_0'} \quad (22)$$

E_0= energy separation between conduction and heavy hole band
E'_0 = energy separation between conduction and light hole band
Δ_0= Spin-orbit splitting of valence band

M and N is the orientation dependent wave vector that can be given by [23]:

$$M=\left(\frac{\hbar^2\gamma_1}{2m_0}\right)(k_x^2+k_y^2+k_z^2) \quad (23)$$

$$N=\left(\frac{\hbar^2\gamma_2}{2m_0}\right)(k_x^2+k_y^2 - 2k_z^2) \quad (24)$$

Since change in crystal orientation changes the splitting between valence bands; knowing the energy separation E_0 and E'_0 and orientation dependent M and N parameters, Valence band effective masses in any arbitrary (hkl) orientation can be calculated.

III. RESULTS AND DISCUSSIONS

Following the mathematical model presented in section II, effective mass of heavy hole, light hole and spin-orbit split-off hole of ZB III-V semiconductors (GaAs, InAs, InP, GaSb, InSb etc.) at Γ-point for arbitrary (hkl) crystal orientation are determined. The simulation is carried out in MATLAB environment at room temperature. The valence band dispersion profiles of GaAs are evaluated in (100), (110), (111) and (113) orientations and shown in Fig. 1(a)-(d) respectively. To compare the orientation-dependent band dispersion profiles, the figures are plotted as a function of wave vector in the same scale. It is demonstrated that, for nonzero value of k (wave vector in the plain direction), the increasing conduction and spin-orbit split off band coupling gives rise to strong non-parabolicities in the valence band structure at (111) and (113) orientations. For (113) orientation, larger energy spacing between heavy hole and light hole is found so hole effective mass may reduce. From Fig. 1, it is demonstrated that crystal orientation exclusively changes the topmost valence band curvature which explains effective mass has an orientation-dependent characteristic.

The effective mass of heavy hole, light hole and spin-orbit split-off hole is determined from eqns. (17-19).The related parameters are extracted from the orientation-dependent band dispersion profiles. The results estimated from the proposed technique are listed in Table I for (100), (110) and (111) orientations at the Γ-point.To confirm our results; they are compared with the results obtained from the well-established

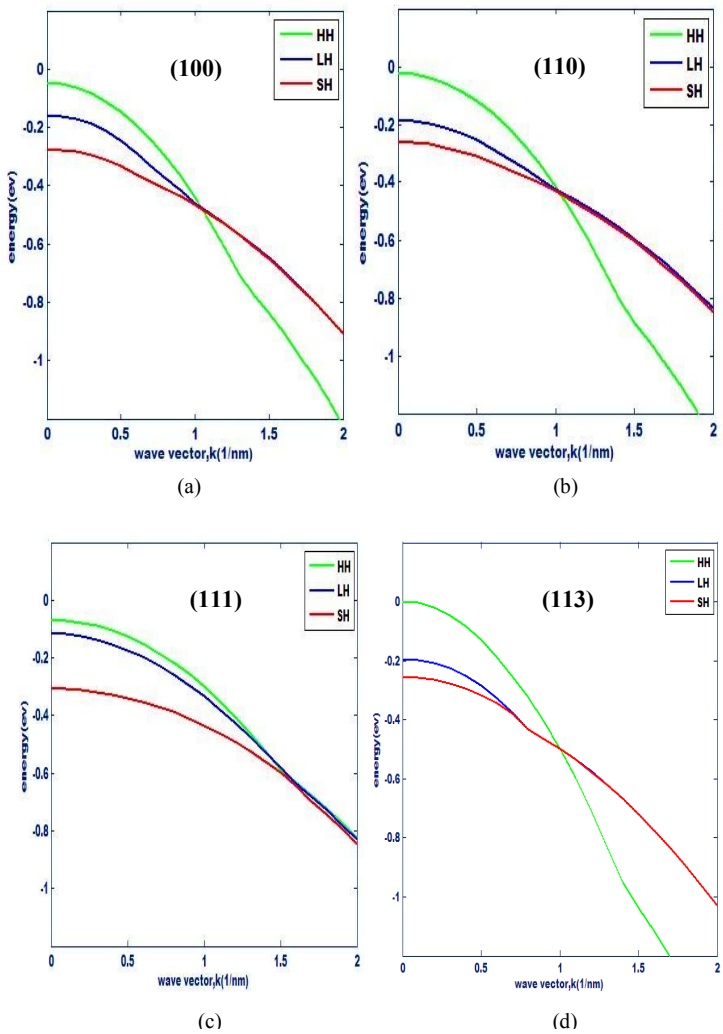

Fig. 1: Valence band dispersion profiles of (a) (100), (b) (110), (c) (111), and (d) (113) - oriented GaAs

PBE, HSE and MBJLDA methods. It is noted here that, in previous studies, the masses were evaluated numerically by fitting the calculated dispersion curves around the Γ-point for the conventional directions (100), (110), and (111) [Ref. 18]. It is seen from Table I that there is a good agreement between our results and the results obtained from the well-established methods. Fig. 2 demonstrates the correlation of heavy hole effective mass of GaAs obtained from well-established HSE, PBE, MBJLDA methods and our proposed formulations along (100), (110) and (111) orientations. It is observed that from our proposed formulations, effective mass of heavy hole of GaAs along (100), (110) and (111) orientations is found to be $0.345m_0$, $0.528\ m_0$, $0.823\ m_0$ whereas, from HSE method, they are found to be $0.3257m_0$, $0.5571\ m_0$ and $0.7299\ m_0$ which shows a reasonable agreement. From this motivation, we calculated effective mass of these materials along arbitrary (hkl) crystal orientations such as (113), (131) and (201) etc. The results are listed in Table II. From Table I and II, it can be seen that lowest heavy hole effective mass for GaAs, InAs and InSb is found in (113) orientation. So it is quite visible that the smallest effective masses in (113) orientation leads to have high performance (113)-oriented optoelectronic devices than the habitual crystal growth orientations like (100) and (111).

TABLE I: Heavy hole, light hole and split-off hole effective masses in (100), (110) and (111) orientations

Material	Method	$m^*_{heavy-hole}/m_0$			$m^*_{light-hole}/m_0$			$m^*_{split-off\ hole}/m_0$
		Crystal orientation			Crystal orientation			Crystal orientation
		(100)	(110)	(111)	(100)	(110)	(111)	(100)
InP	PBE [a]	0.4562	0.7570	0.9703	0.0723	0.0681	0.0667	0.139
	MBJLDA [a]	0.5071	0.8405	1.075	0.1410	0.1270	0.1230	0.230
	HSE [a]	0.4970	0.8032	1.0101	0.1172	0.1075	0.1047	0.212
	Expt. [a]	0.307	0.885	0.682	0.14	0.111	0.118	0.210
	Proposed model	0.425	0.853	0.754	0.118	0.108	0.105	0.200
InAs	MBJLDA[a]	0.4291	0.4494	0.9341	0.0439	0.0422	0.0416	0.133
	HSE [a]	0.3378	0.6042	0.8196	0.0332	0.0319	0.0314	0.112
	Expt. [a]	0.26	0.513	0.729	0.027	0.026	0.0259	0.140
	Proposed model	0.327	0.627	0.835	0.033	0.032	0.031	0.120
InSb	MBJLDA[a]	0.3012	0.4854	0.6097	0.0242	0.0235	0.0233	0.150
	HSE [a]	0.2590	0.4405	0.5747	0.0181	0.0176	0.0175	0.129
	Expt. [a]	0.26	0.435	0.454	0.0154	0.0148	0.014	0.110
	Proposed model	0.250	0.415	0.574	0.018	0.016	0.0175	0.130
GaAs	PBE [a]	0.3367	0.5649	0.7299	0.0362	0.0347	0.0342	0.108
	MBJLDA[a]	0.3861	0.6622	0.8695	0.1112	0.0993	0.0958	0.210
	HSE [a]	0.3257	0.5571	0.7299	0.0831	0.0756	0.0732	0.166
	Expt. [a]	0.4	0.643	0.91	0.088	0.081	0.085	0.172
	Proposed model	0.345	0.528	0.823	0.085	0.076	0.073	0.165
GaSb	MBJLDA[a]	0.2785	0.4705	0.6211	0.0536	0.0550	0.0536	0.175
	HSE [a]	0.2457	0.4184	0.5464	0.0469	0.0434	0.0424	0.143
	Expt. [a]	0.22	0.422	0.714	0.045	0.040	0.039	0.120
	Proposed model	0.234	0.209	0.526	0.047	0.022	0.042	0.150

[a]Reference 18.

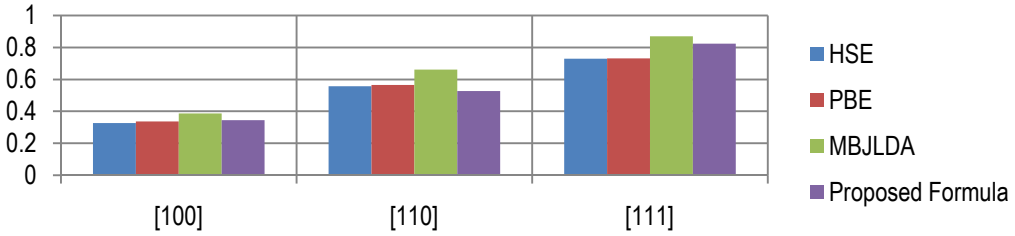

Fig. 2: Comparison between heavy hole effective mass obtained from HSE, PBE, MBJLDA methods and proposed method. The masses are calculated for GaAs along (100), (110) and (111) crystal orientations

TABLE II: Heavy hole, light hole and split-off hole effective masses evaluated by proposed method for GaAs along arbitrary (hkl) orientation

Material	Heavy hole mass(m^*_{hh}/m_0)			Light hole mass(m^*_{lh}/m_0)			Split-off hole mass(m^*_{so}/m_0)		
	(113)	(131)	(201)	(113)	(131)	(201)	(113)	(131)	(201)
GaAs	0.289	0.651	0.837	0.083	0.068	0.056	0.242	0.473	0.621
InAs	0.314	0.507	0.573	0.028	0.040	0.019	0.128	0.327	0.198
InP	0.921	0.723	0.489	0.110	0.103	0.113	0.564	0.670	0.429
GaSb	0.580	0.457	0.352	0.037	0.051	0.034	0.211	0.391	0.283
InSb	0.252	0.593	0.561	0.012	0.022	0.027	0.168	0.428	0.351

IV. CONCLUSION

A general mathematical model based on tensor rotation technique is proposed to understand the impact of crystal orientation on valence band effective masses of ZB III-V semiconductors at the Γ-point. The theoretical results depict that the curvature of topmost heavy hole and light hole bands changes exclusively with crystal orientation. Addressing the splitting between energy bands and exploring the orientation dependent parameters over all possible directions of wave vector, the average heavy hole, light hole and spin-orbit split-off hole masses are obtained which show that lowest effective masses are obtained in (113) orientation for GaAs, InAs and InSb crystals. However, this results are not consistent for GaSb and InP materials and also for light hole and split off hole masses. This simulation results demonstrate that our proposed formulations will be a boost for the fabrication of novel optoelectronic devices along other crystallographic orientations than the conventional [100] or [111] growth direction.

REFERENCES

[1] Kruse P W 1970 Semiconductors and Semimetals, vol. 5 ed. R. K Willardson and A C Bee (New York: Academic) pp. 15-70

[2] C. B. Geller, W. Wolf, S. Picozzi, A. Continenza, R. Asahi, W. Mannstadt, A. J. Freeman, and E. Wimmer, Appl. Phys. Lett. 79, 368 (2001).

[3] Brown, E R, Soderstrom J R, Parker C D, Mahoney L J,Molvar K,Mand McGill, Appl. Phys. Lett. 58, 2291(1991)

[4] S. Nakamura and G. Fasol, The Blue Laser Diode (Springer, Berlin, 1997), p. 7.

[5] H.W.A.M Rompa, M.F.H Schuurmans, and F. Williams, Phys. Rev. Lett. 52,675(1984)

[6] M. Phon, Y. Chung, W.I. Wang, Orientation dependence of valence-subband structures in GaAs–$Ga_{1-x}Al_xAs$ quantum well structures, J. Appl. Phys. 64 (1988) 4609–4613.

[7] D.A. Woolf, J.P. Williams, D.I. Westwood, Z. Sobiesierski, J.E. Aubrey, R.H. Williams, The homoepitaxial growth of non-axis GaAs(1 1 1)A, (1 1 1)B and (2 0 1) compared with GaAs(1 0 0): doping and growth temperature studies, J. Cryst. Growth 127 (2002) 913–917.

[8] R. Notzel, K.H. Ploog, Man-made low-dimensional solids: new challenges in microstructure material science, Int. J. Mod. Phys. B7 (1993) 2743–2778.

[9] M.M. Hasan, M.R. Islam, Strain-dependent optical properties of mid-infrared GaInSb/GaInAlSb quantum well laser, International Conference on Computer and Communication Engineering (ICCCE 2010), 11–13, May 2010, KualaLumpur, Malaysia, 2010, ISBN 978-1-4244-6234-6, IEEE Catalog Number:CFP10390-CDR.

[10] A ben Ahmed, S Ridne and H Bouchriha, Orientation dependence of optoelectronic properties of InAsN/GaSb quantum well laser diodes, Semicond. Sci. Technol. **28** (2013) 065006 (10pp)

[11] T. Oshima, M. Yoshida, S. Picozzi, A. Continenza, R. Asahi, W. Mannstadt, M. Tsunotani, and T. Kimura, Orientation Dependent Characteristics of Recessed-Gate InGaAs/AlGaAs HEMTs, Appl. Phys. Lett. 79, 368 (2001).

[12] P. Lee, R. Zucca, B. Welch, Orientation effect on planer InGaAs schottky barrier FET, Appl. Phys. Lett. 37, 311 (1988).

[13] J. E. Peralta, J. Heyd, G. E. Scuseria, and R. L. Martin, Phys. Rev. B 74, 073101 ,2006.

[14] J. Paier, M. Marsman, K. Hummer, G. Kresse, I. C. Gerber, and J. G. Ángán, J. Chem. Phys. 124, 154709 ,2006.

[15] J. Paier, M. Marsman, K. Hummer, G. Kresse, I. C. Gerber, and J. G. Ángán, J. Chem. Phys. 125, 249901,2006.

[16] V. Krukau, O. A. Vydrov, A. F. Izmaylov, and G. E. Scuseria, J. Chem. Phys. 125, 224106 , 2006.

[17] Dragica Vasileska, Tutorial for semiconductor band structure calculation, Arizona State University, Tempe, AZ

[18] Kim et al., Towards efficient band structure and effective mass calculations for III-V direct band-gap semiconductors, PHYSICAL REVIEW B 82, 205212 (2010)

[19] Craig Pryor, Eight-band calculations of strained InAs/GaAs quantum dots compared with one, four, and six-band approximations, Physical Review B, 03/1998

[20] T. Ohtoshi, T. Kuroda, A. Niwa, S. Tsuji, Dependence of optical gain on crystal orientation in surface-emitting lasers with strained quantum wells, Appl. Phys. Lett. 65 (1994) 1886–1889.

[21] Md. Mahbub Hasan, M.R. Islam, Crystal orientation-dependent optical properties of mid-infrared GaInSb/GaInAlSb quantum well laser, International Conference on Computer and Communication Engineering (ICCCE 10), 05/2010

[22] Semiconductors, edited by O. Madelung, M. Schilz, and H. Weiss, Landolt-B¨ornstein, Numerical Data and Functional Relations in Science and Technology Vol. 17 (Springer-Verlag, New York, 1982).

[23] I. Vurgaftman, J. R. Meyer, and L. R. Ram-Mohan, J. Appl.Phys. 89, 5815 (2001).

Realistic Edge Shape Effects on the Vibrational Properties of Graphene Nanoribbons

Md. Sherajul Islam, Ashraful G. Bhuiyan
Department of Electrical & Electronic Engineering
Khulna University of Engineering & Technology
Khulna, Bangladesh
sheraj_ruet@yahoo.com

Akihiro Hashimoto
Department of Electrical & Electronic Engineering
University of Fukui
Fukui, Japan
hasimoto@fuee.u-fukui.ac.jp

***Abstract*—Graphene nanoribbons (GNRs) are predicted to be essential components in future graphene nanoelectronics. Recent studies show that atomic scale edge structures of GNRs consist of armchair and zigzag edges with some other defects. Here we probe systematically the details of the phonon properties of GNRs with realistic edge structures combining the armchair and zigzag edges along with some vacancies using the forced vibrational method. We have calculated the phonon density of states (PDOSs) and typical mode patterns of GNRs considering the effects of the mixture of the different directional armchair edge and zigzag edge with some vacancy type defects. We find that in-plane longitudinal and transverse optical (LO) and (TO) mode phonons of realistic edge shaped GNR are non-degenerate and shifted down with the decrease of ribbon width. The PDOS at low frequency region changes significantly for the realistic edge structures. We observe a strongly localized eigenmodes of in-plane transverse optical phonon (iTO) near the armchair edges and defect sites which are conceptually very good agreement with the Raman D peak comes from the armchair edges or the defects of GNRs activated by the iTO phonons.**

Keywords—Graphene nanoribbons, realistic edge strucures, phonon density of states, vacancy defects, strong localization.

I. INTRODUCTION

High expectations are set for graphene electronics [1] due to its incomparable properties. However, the electronic applications are crippled by the absence of energy band gap in the pristine graphene. If graphene sheet is patterned into a narrow ribbon, it opens a band gap by quantum confinement [2]-[6]. It is envisaged that the large band gap opening in the nanoribbons depend on the nature of the edge structures and their orientations. The edge geometry is the preeminent parameter which determines the electronic properties of the nanoribbons. For example, localized states appear at the edge with energies close to the Fermi level [7]-[8] in the graphene nanoribbons with zigzag edges. In contrast, edge states are away for ribbons with armchair edges. It has been suggested that armchair edges give rise to intervalley backscattering, which is suppressed at zigzag edges [9]. The research of the edge dependent fundamental and application oriented properties are thus of indispensable prerequisite for tomorrow's graphene-based electronics.

Recent studies [10]-[11] on edge structures of graphene nanoribbons (GNRs) perceive that although the edge may be mainly armchair or zigzag at the microscopic scale, it is not perfect armchair or zigzag at the atomic scale, but a mix of them with some other defects. It is also believed that the armchair edge of GNRs act as a crystalline defects. As electrons and phonons are strongly coupled in graphene related materials, the electron transports of GNRs strongly depend on the nature of edge-phonon modes in addition to the roughness of the ribbon edge [12]-[13]. Because of the scattering by disorders, phonons have the finite lifetime and localization length, which is one of the main contributions to the natural line width of the Raman spectra, the widely used tool for the investigation of graphene related system. We thus require a detailed understanding of the effects of various types of edges, their orientation, and the defects on the phonon modes which noticeably change the electron transport properties.

Over the last few years, many approaches have been employed to estimate the vibrational properties of graphene nanoribbons including force constant fittings [14]-[15], density functional theory [16]-[17] and the first-principles calculations [18]-[19]. In contrast to the intensive research on the ribbons with perfect edges, there is no studies on the vibrational properties of GNRs having realistic edge structures. The disordered edges of GNRs may induce the symmetry breakdown of elemental topological arrangements [12], which generate more complex lattice structures. Therefore, the dynamical matrix technique needs enormous computational resources. These long computational times and convergence problems in the dynamical matrix calculations restrict the systems of interest to benchmark molecules. Nonetheless, a considerably larger scale model is essential for an in-depth understanding of vibrational properties of disordered atomic structures. It is thus indispensible to develop a reliable model to observe the phonon modes of GNRs with realistic edge structures directly.

In this work, we explore systematically the details of the phonon properties of GNRs consist of realistic edge structures combining the armchair and zigzag edge with some vacancy defects. We have estimated the phonon density of states (PDOSs) of GNRs considering the effects of the mixture of the various directional armchair and zigzag edges with some

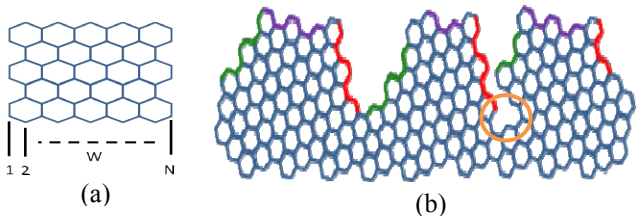

Figure 1. Graphene nanoribbons with (a) perfect armchair edge on both sides(b) realistic edge combining the armchair and ziga edges along with some point defects. The dimer and red lines indicate the ribbon width and different directional armchair edges, respectively. Orange circle shows the vacancy defects.

vacancy type defects. For all calculations, we employed the forced vibrational method [20], which is based on the mechanical resonance to extract the vibrational eigenmodes for very complex and large disordered systems by numerical simulation. Due to the defects, the phonon modes lie outside of the allowed frequency range of the pristine crystal. These are called localized modes as the mode energy is concentrated near the defect site. Since localization virtually immobilizes phonons and makes them non-conducting, these phonons lose their nature as heat carriers. In spite of graphene related systems have the excellent thermal conductance, disordered regions may interrupt the crystallinity and impede the flow of thermal energy. To study the localized eigenmodes, typical mode pattern of GNRs considering different directional real edges and defects has also been calculated. Here, we mainly concentrate on the K-point of the in-plane optical mode phonons as they have significant effects on the Raman spectra of GNRs.

II. Computational Details

All the calculations in this work were carried out using the forced vibrational (FV) method introduced by Williams and Maris [20]. The FV method is an efficient scheme for computing spectral densities, eigenvalues and eigenvectors of complex and large disordered physical systems. The algorithm utilizes a principle of Hamilton mechanics: a linear lattice dynamical system driven by a periodic external force of certain frequency will respond with large amplitudes in those eigenmodes close to this frequency. Specifically, the eigenvalue analysis is reduced to solve the time development of the equations of motion in the presence of an external periodic force. In general, the equation of motion of the system consists of N atoms which are coupled together with linear springs, with the scalar displacement of the lth mass, $u_l(t)$ is:

$$M_l \ddot{u}_l(t) + \sum_{l'} \phi_{ll'} u_{l'}(t) = 0 \qquad (1)$$

For time t > 0, a random force $F_l = F_0\sqrt{M_l}\cos(\varphi_l)\cos(\Omega t)$ is applied to each atom l at rest. Where, F_0 is a constant amplitude, the phase φ_l and Ω are a random variable with respect to the site number l and a frequency of the external force, respectively. Thus, for large times the periodic external force excites only those modes whose frequency is close to Ω. When we average all possible values of φ_l and use the orthonormality of the eigenvectors, the averaged total energy of the system after time T becomes:

$$\langle E(\Omega,T)\rangle \approx \frac{\pi t F_0^2}{8}\sum_{\lambda}\delta[(\omega_\lambda - \Omega) = \frac{\pi t F_0^2 N g(\Omega)}{8} \qquad (2)$$

where $g(\Omega)$ is the phonon density of states (PDOS). Thus:

$$g(\Omega) = \frac{8\langle E(\Omega,T)\rangle}{\pi t F_0^2 N} \qquad (3)$$

In order to obtain the PDOS, our task is to compute the averaged total energy $\langle E(\Omega,T)\rangle$. Moreover, the mode patterns can also be obtained by applying iteratively the external periodic force proportional to the displacements of atoms at each step. The calculations start with the GNRs having perfect armchair edges on both side. Following the previous convention [12]-[13], the GNRs with armchair shaped edges on both sides are classified by the number of dimer lines (N) across the ribbon width W. The structural model of GNRs with perfect armchair edge and realistic edge combining the armchair and zigzag edge along with some point defects is shown in Fig. 1a and 1b, respectively. The maximum width of up to 4 nm (~32 AGNR), while the length is about 120 nm long in the total of 17,474 atoms are considered. The simulations are performed under the free boundary conditions (FBCs). Only interactions up to the fourth nearest neighbor atoms are used and the force constant tensor between two carbon atoms is taken from Jishi et al. [21]. For atoms near an edge, only the force constant of actual atoms is included in the calculation under the FBC.

III. Results and Discussions

Fig. 2 shows the width dependent PDOSs of pure armchair GNRs in comparison with that of the GNRs consist of realistic edges combining the armchair and zigzag edges along with some vacancy type defects. There are more fine structures (peaks) in PDOS curves for the wider GNRs, and the PDOS approaches that of infinite graphene sheet with the increase of

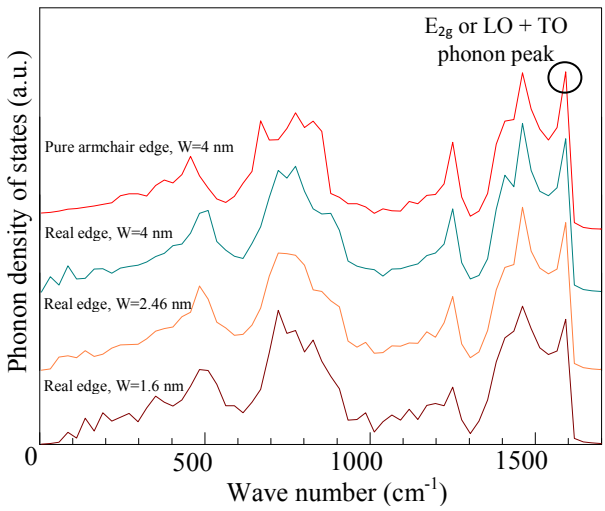

Figure 2. Width dependent phonon density of states of GNRs with realistic edge structures.

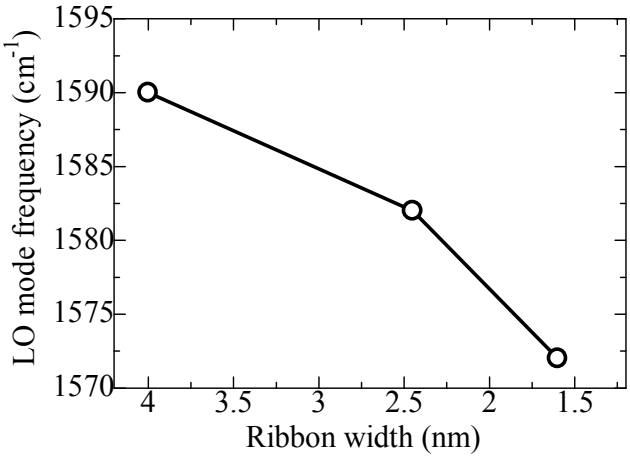

Figure 3. Longitudinal optical mode phonon as a function of ribbon width for the realistic edge structures of GNRs.

the GNR width of about 4 nm. The simulation results reveal that the PDOS of GNR with realistic edge shapes are distorted, non-degenerate and softened with the decrease of ribbon width. Generally, a group of six Γ point phonon modes are observed for GNRs. The physical origin of the G peak (around 1590 cm^{-1}) of Raman spectra comes from the scattering of a doublydegenerate longitudinal optical (LO) and transverse optical (TO) phonon at the Brillouin zone center. It is found that the Γ point of the LO and TO mode phonons of realistic edge shaped GNR are non-degenerate and shifted down with the decrease of ribbon width. The other noteworthy characteristic of the PDOS is the vanishing of fine structure (peaks) at high frequency region, while some fine peaks appear at low frequency region with the decrease of ribbon width as shown in Fig. 2. The shift of the PDOS towards the low frequency region may be induced by the increase of the numbers of the unsaturated C atom with some dangling bonds because the increase of the unsaturated C atoms in the ribbons cause to decrease of the density of high frequency modes.

In armchair graphene nanoribbons (AGNRs), only the LO phonon modes are Raman active, and the G band Raman spectra near the edge shows a down shift of the LO mode. Due to the conical shape of the energy spectrum, momentum conservation notifies that a direct electron–hole pair can couple to the Γ point LO phonon modes, thus shows a down shift of the LO mode [13]. Nevertheless, the TO phonon modes are decoupled from electron–hole pairs. Consequently, the frequency of the TO mode remains same as the original Γ point (LO and TO mode) frequencies of infinite graphene sheet [13]. These effects indicate that the LO phonon mode has the significant contribution to the electron transport in comparison with the TO phonon mode. We have extracted the LO phonon frequencies for various width of GNRs having realistic edge shapes. As can be seen from Fig. 3, the LO frequencies of the nanoribbons are shifted down. It is envisaged that the disorder edges incite the phonon non-degeneracy and move down the LO phonon frequency. The force constant tensors of carbon atoms at the disordered edges are less than that of the pure graphene nanoribbons. Therefore, the phonon frequency decreases compared with that of the ribbon with perfect edges.

The calculated typical mode pattern for the realistic edge structure of GNR is shown in Fig. 4. Here, each circle denotes an atom, and the color denotes the displacement. We mainly focus on the K point of the in plane optical modes (iTO branch) phonon of the eigenmodes due to the dominant effect of these modes on the large D band features of the Raman spectra, especially for defective states of the sample. Due to the defects, the phonons propagations are constrained into a particular region. We observe a strongly localized eigenmodes near the armchair edges and defect sites which are conceptually very good agreement with the Raman D peak comes from the armchair edges or the defects of crystals. These strongly localized states originate from the resonant vibration of the randomly arranged atoms in the disordered edges. In spite of showing the localized vibration of the mode patterns, the centers of the localized modes are not in the same places for different time development. To take out the eigenmodes, a random force has been applied to the each atom of the systems. It is thus expected that the centers of the localized modes are traveled with the each time development. However, in all time development, the centers of the localized modes stay asymmetrically near the armchair edges or the vacancies.

IV. Conclusion

In conclusions, the effect of realistic edge structures on the vibrational properties of graphene nanoribbons has been studied systematically. The forced vibrational method which is

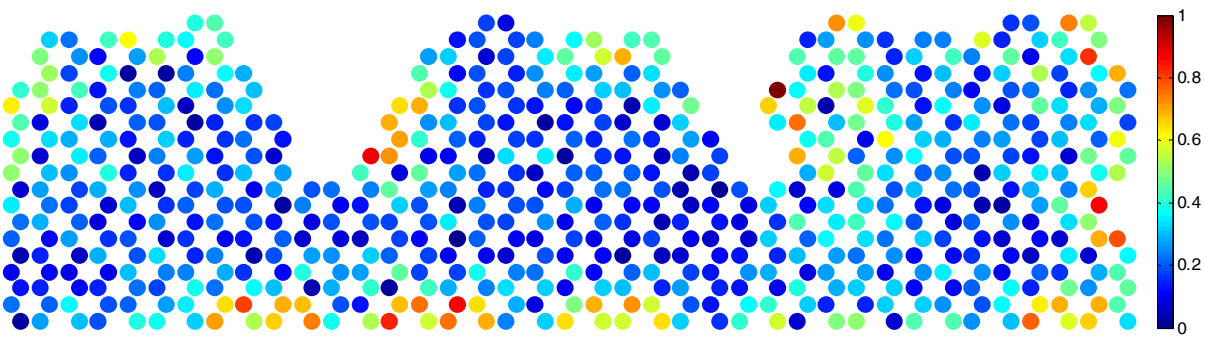

Figure 4. Typical mode pattern for in-plane transverse optical mode phonons of GNRs at 1355 cm^{-1}.

based on the mechanical response to extract the pure vibrational eigenmodes has been employed to perform the numerical experiment. We have calculated the phonon density of states (PDOSs) and typical mode patterns of GNRs considering the effects of the mixture of the different directional armchair and zigzag edges with some vacancy type defects. Our results show that the vibrational properties strongly depend on the realistic edge structures and the width of the ribbons. The PDOSs at low frequency region change significantly for the realistic edge structures. We observe a strongly localized eigenmodes of k-point iTO mode phonon near the armchair edges and defect sites which are conceptually very good agreement with the Raman D peak comes from the armchair edges or the defects of GNRs induced by the iTO mode phonon. These analyses are important not only in fundamental science, but also in advanced nanoelectronics, where the non-ideal realistic edges of GNRs affect the electronic properties significantly.

REFERENCES

[1] C. Berger, Z. Song, T. Li, X. Li, A.Y. Ogbazghi, and R. Feng et al., "Ultrathin Epitaxial Graphite: 2D Electron Gas Properties and a Route toward Graphene-based Nanoelectronics," J. Phys. Chem. B, vol. 108, pp.19912-19916, December 2004.

[2] C. Tao, L. Jiao, O.V. Yazyev, Y. Chen, J. Feng, and X. Zhang et al., "Spatially resolving edge states of chiral graphene nanoribbons," Nat. Phys., vol. 7, pp. 616-620, May 2011.

[3] Z. Chen, Y.M. Lin, M.J. Rooks, and P. Avouris, "Graphene nanoribbon electronics," Physica E, vol. 40, pp. 228-232, December 2007.

[4] M.Y. Han, B. Ozyilmaz, Y. Zhang, and P. Kim, "Energy band-gap engineering of graphene nanoribbons," Phys. Rev. Lett., vol. 98, pp. 206805, May 2007.

[5] J. Cai, P. Ruffieux, R. Jaafar, M. Bieri, T. Braun, S. Blankenburg et al., "Atomically precise bottom-up fabrication of graphene nanoribbons," Nature, vol. 466, pp. 470-473, July 2010.

[6] Y.Y. Li, M.X. Chen, M. Weinert, and L. Li, "Direct experimental determination of onset of electron-electron interactions in gap opening of zigzag graphene nanoribbons," Nat. Commun., vol. 5, pp. 4311, July 2014.

[7] M. Fujita, K. Wakabayashi, K. Nakada, and K. Kusakabe, "Peculiar Localized State at Zigzag Graphite Edge," J. Phys. Soc. Japan, vol. 65, pp. 1920-1923, July 1996.

[8] K. Wakabayashi, M. Fujita, H. Ajiki, and M. Sigrist, "Electronic and magnetic properties of nanographite ribbons," Phys. Rev. B, vol. 59, pp. 8271-8282, March 1999.

[9] L.G. Cancado, M.A. Pimenta, B.R.A. Neves, M.S.S. Dantas, and A. Jorio, "Influence of the Atomic Structure on the Raman Spectra of Graphite Edges," Phys. Rev. Lett., vol. 93, pp. 247401, December 2004.

[10] Md. Sherajul Islam, D. Tamakawa, S. Tanaka, T. Makino, and A. Hashimoto, "Polarized microscopic laser Raman scattering spectroscopy for edge structure of epitaxial graphene and localized vibrational mode," Carbon, vol. 77, pp. 1073-1081, October 2014.

[11] Md. Sherajul Islam, A.G. Bhuiyan, S. Tanaka, and A. Hashimoto, "Polarized micro Raman scattering spectroscopy for curved edges of epitaxial graphene," Appl. Phys. Lett., vol. 105, pp. 243103, December 2014.

[12] Md. Sherajul Islam, S. Tanaka, and A. Hashimoto, "Effect of vacancy defects on phonon properties of hydrogen passivated graphene nanoribbons," Carbon, vol. 80, pp. 146-154, December 2014.

[13] Md. Sherajul Islam, K. Ushida , S. Tanaka, and A. Hashimoto, "Numerical analysis on vacancy induced vibrational properties of graphene nanoribbons," Comput. Mat. Sci., vol. 79, pp. 356-361, November 2013.

[14] F. Mazzamuto, J. Saint-Martin, A. Valentin, C. Chassat, P. Dollfus, "Edge shape effect on vibrational modes in graphene nanoribbons: A numerical study," J. Appl. Phys., vol. 422, pp. 064516, March 2011.

[15] M. Xia, Y. Song, S. Zhang, "Specific heat of graphene nanoribbons," Phys. Lett. A, vol. 375, pp. 3726–3730, October 2011.

[16] Y. Yamakita, K. Ohno, "Phonon dispersion and vibronic coupling in carbon nanoribbons," J. Phys.: Conf. Ser., vol. 185, pp. 012055, October 2009.

[17] M. Vandescuren, P. Hermet, V. Meunier, L. Henrard, Ph. Lambin, "Theoretical study of the vibrational edge modes in graphene nanoribbons," Phys. Rev. B, vol. 78, pp. 195401, November 2008.

[18] R. Gillen, M. Mohr, C. Thomsen, J. Maultzsch, "Vibrational properties of graphene nanoribbons by first-principles calculations," Phys. Rev. B, vol. 80, pp. 155418, October 2009.

[19] Z.W. Tan, J.S. Wang and C.K. Gan, Nano Lett., "First-Principles Study of Heat Transport Properties of Graphene Nanoribbons," Nano Lett., vol. 11, pp. 214-219, January 2011.

[20] M.L. Williams, H.J. Maris, "Numerical study of phonon localization in disordered systems," Phys. Rev. B, vol. 31, pp. 4508-4515, April 1985.

[21] R.A. Jishi, L. Venkataraman, M.S. Dresselhaus, G. Dresselhaus, "Phonon modes in carbon nanotubules," Chem. Phys. Lett., vol. 209, pp. 77–82, January 1993.

Modeling of Crosstalk Induced Overshoot/Undershoot Effects in Multilayer Graphene Nanoribbon Interconnects

Manodipan Sahoo and Hafizur Rahaman
Department of Information Technology, Indian Institute of Engineering Science and Technology,
Shibpur, Howrah-711103, India
E-mail: manodipansahoo@gmail.com, rahaman_h@it.iiests.ac.in

***Abstract*—Crosstalk induced overshoot/undershoot effects in Multilayer Graphene Nano Ribbon interconnects (MLGNRs) are investigated using ABCD parameter matrix approach for intermediate level interconnects at 8 nm technology node. The worst case crosstalk induced peak overshoot voltage for perfectly specular doped multilayer zigzag GNR interconnects is comparable to that of copper interconnects. It is observed that the performance of neutral GNR interconnects is better than that of its doped counterpart in terms of peak crosstalk induced overshoot voltage. But from the perspective of effective electric field across the gate oxide, the multilayer doped GNR interconnects outperform neutral ones and copper interconnects for all the cases. Finally, our analysis has shown that from the gate oxide reliability perspective, the perfectly specular doped multilayer zigzag GNR interconnects are significantly advantageous to copper interconnects for future generation Integrated circuit technology.**

Keywords*—Crosstalk ; Overshoot/Undershoot ; Graphene Nano Ribbon (GNR) ; Interconnects ; ABCD parameter ; Specular ; Neutral ; Gate oxide reliability ; Integrated circuit.

I. Introduction

The ever increasing circuit complexity led by Moore's law with the continuous scaling of CMOS technology has made the role of interconnects in nanometer technology nodes very prominent. However conventional copper wires face tremendous challenges of the nanometer technology where the requirement is of reliable high speed wires with minimal crosstalk effects. Graphene has been regarded as a suitable material for nanometer technology [1], [2] because of its tolerance to higher maximum current density, lower resistivity and lower capacitive effects compared to copper at nanometer dimensions [2]. Moreover, compared to multi-walled carbon nanotubes (MWCNT), Graphene is suitable for its simpler fabrication processes, better material control and reproducibility. Recently, a CMOS Ring oscillator with graphene interconnects is fabricated to operate at a frequency of 1.3 GHz [3].

Xu et. al. have studied the performance of GNR interconnect in [5]. Naeemi and Meindl has proposed a physics based circuit model for GNR interconnect in [4]. Crosstalk effects in MLGR interconnects have been studied in [7], [8], [6]. In all these works, the crosstalk induced effects are analyzed using SPICE simulations. However Simulation tools like SPICE is computationally expensive at the full-chip level [9]. Therefore, a non-SPICE based model is necessary for analyzing crosstalk effects in dense high performance ICs. The ABCD parameter matrix based model has been proposed for analyzing crosstalk induced effects in SWCNT bundle interconnects [10], MWCNT bundle interconnects [11] and MLGNR interconnects [12]. In this work, ABCD parameter based model is used to analyze crosstalk induced overshoot/undershoot effects in multilayer neutral and doped zigzag GNR interconnects of various specularity at 8 nm technology node. The impact of overshoot/undershoot on the gate oxide reliability is also estimated. It is found that 100 μm long, doped perfectly specular MLGNR interconnects have gate oxide failure rate (AFR) of three orders lesser than copper interconnects for 8 nm technology node.

The paper is presented in the following sequence. Section II presents the equivalent RLC model for multilayer GNR interconnects. Section III discusses the proposed ABCD parameter matrix based approach in details. Section IV describes how crosstalk induced overshoot/undershoot impacts the gate oxide reliability of CMOS devices. Section V presents simulation results. Finally the conclusions are drawn in Section VI.

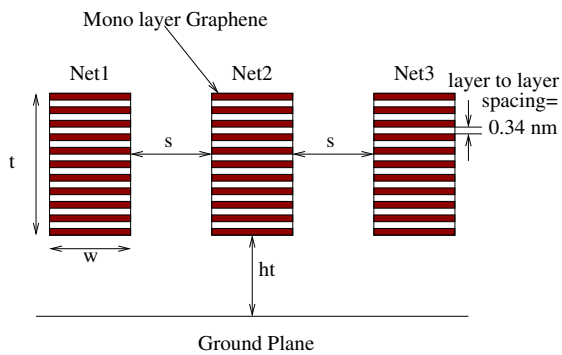

Fig. 1: Multilayer GNR structure.

II. Electrical modeling of multilayer GNR interconnects

The carbon atoms are arranged in a honeycomb structure in graphene. Graphene shhet is regarded as either armchair or

This work is partially supported by the DIT, Government of West Bengal, India under VLSI Design Project.

978-1-4673-9257-0/15/$31.00 ©2015 IEEE

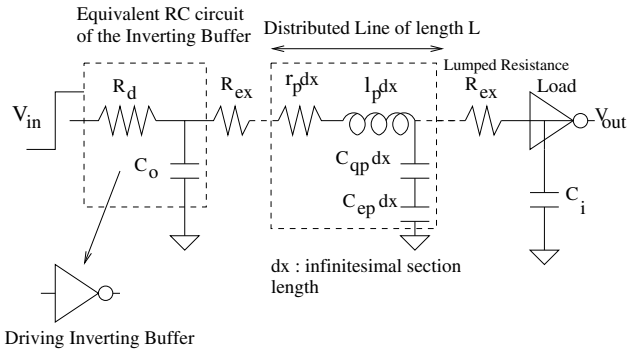

Fig. 2: Equivalent RLC model of a typical multilayer GNR interconnect system.

zigzag based on the arrangement of carbon atoms. Chirality differs the conductive property in zigzag and armchair GNR. For interconnect applications, zigzag GNR is proposed due to its metallic property. Multi-layer zigzag GNR structure is utilized in modeling the nanoscale interconnects here because of the low conductivity of the mono layer GNR interconnects. Fig. 1 shows a typical MLGNR interconnect structure [5]. The interconnect dimensions are represented as t (thickness), w(width), ht(height from ground plane), and s(spacing between the interconnects) and δ (= 0.34 nm) (spacing between each graphene layer known as the Van der Waal's gap). The interconnect dimensions have been considered according to latest ITRS-2013 data [1] as shown in Table I. The number of graphene layers is given by,

$$N_{layer} = 1 + \lfloor \frac{t}{\delta} \rfloor \tag{1}$$

Fig. 2 depicts the equivalent RLC model of a typical MLGNR interconnect system. In the figure, L is the interconnect length, R_{ex} is the lumped resistance (i.e., consists of GNR-electrode contact resistance(R_C) and quantum resistance(R_Q), $R_{ex} = (R_C + R_Q)/2$), r_p is per unit length (p.u.l) distributed resistance, l_p is p.u.l self inductance (consists of kinetic inductance, L_k and self inductance, L_s), C_{qp} is p.u.l quantum capacitance, C_{ep} is p.u.l electrostatic ground capacitance. The quantum resistance is defined as [5],

$$R_Q = \frac{\frac{h}{2q^2}}{N_{ch}N_{layer}} = \frac{12.94K\Omega}{N_{ch}N_{layer}} \tag{2}$$

where, N_{ch} is the number of conducting channels (modes) in one layer, N_{layer} is the number of GNR layers, h is the Plancks constant (=6.626×10^{-34} J.s), and q is the electronic charge (=1.6×10^{-19} C). The number of conducting channels in mono-layer graphene (i.e., N_{ch}) is given by [5],

$$N_{ch} = \sum_{j=1}^{n_C} \left[1 + e^{\frac{(E_{j,n} - E_F)}{K_B T}} \right]^{-1} + \sum_{j=1}^{n_V} \left[1 + e^{\frac{(E_{j,h} + E_F)}{K_B T}} \right]^{-1} \tag{3}$$

where, j (=1, 2, 3, ...) is a positive integer, E_F is Fermi energy, K_B is the Boltzmann constant, T is absolute temperature, and n_C and n_V are the number of conduction and valence subbands, respectively. $E_{j,n}$ and $E_{j,h}$ are the energies of electron and hole in j^{th} subband as given by [4],

$$E_j = \frac{h\nu_F}{2w} |j + \frac{1}{2}| \tag{4}$$

TABLE I: Global-level Interconnect Parameters (ITRS-2013)

Parameters \ Year	2024	2027
DRAM1/2 pitch(nm) (contacted)	11.0	8.4
MPU/ASIC Metal1 1/2 pitch(nm) (contacted)	11.3	8.0
MPU Physical gate length (nm)	7.39	5.62
No. of Metal levels	15	16
Wiring pitch (nm)	23	16
	34	24
Wiring height to width ratio	2.1	2.2
	2.34	2.4
A/R (Via)	1.9	1.9
	1.5	1.5
Effective Resistivity ($\mu\Omega$-cm)	8.75	10.81
	7.04	8.50
V_{DD} (Volt)	0.69	0.65
V_{th} (Volt)	0.233	0.265
Equivalent Oxide thickness (EOT) (nm)	0.49	0.43
Effective dielectric constant (k_{eff})	1.88-2.28	1.65-2.09
Average dielectric constant (k_{avg}) of the interlevel dielectric	2.08	1.87

TABLE II: RC parameters of the inverting buffer for various technology nodes

Parameters \ Technology node	11 nm	8 nm
R_d (in KΩ)	42.1	65.8
C_o (in fF)	0.012	0.007
C_i (in fF)	0.036	0.021

where, j(=1, 2, 3, ...) is an integer. The p.u.l resistance (r_p) of the MLGNR interconnect is calculated according to the method explained in [5].

The per unit length quantum capacitance (C_{qp}) is expressed as ,

$$C_{qp} = N_{ch}N_{layer}\frac{4q^2}{h\nu_F} = N_{ch}N_{layer} \times 193.18aF/\mu m \tag{5}$$

where, ν_F is the Fermi velocity = 8×10^5 m/s for GNR [4]. The per unit length kinetic inductance(L_k) is expressed as [5],

$$L_k = \frac{\frac{h}{4q^2\nu_F}}{N_{ch}N_{layer}} = \frac{8.0884}{N_{ch}N_{layer}} nH/\mu m \tag{6}$$

The self inductance (L_s) and electrostatic capacitance (C_{ep}) of GNR are assumed to be same as that of Cu with equal dimensions [5]. The total p.u.l inductance of the MLGNR interconnect is expressed as $l_p \approx (L_k + L_s)$. Inverting buffers are used to implement both the driver and load. The load capacitance, C_i in Fig. 2, denotes the gate capacitance of the load inverting buffer. The parameters of the buffers are R_d(equivalent switching resistance), C_o(equivalent diffusion capacitance) and C_i(equivalent gate capacitance). The RC parameters (i.e., R_d, C_o and C_i) for the driver/load buffer at 8 nm technology node are calculated from ITRS-2013 roadmap [1] as shown in Table II. The analytical equations used to calculate distributed RLC parameters of copper interconnect are taken from [13].

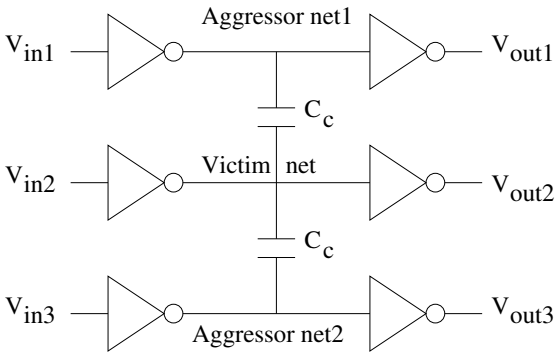

Fig. 3: How the overshoot/undershoot effects occur through coupling capacitance?

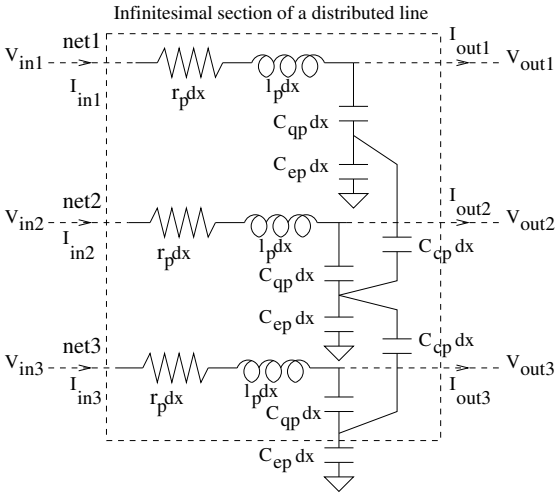

Fig. 4: Infinitesimal section of an identically coupled three conductor multilayer GNR interconnect system.

III. Modeling of Crosstalk induced overshoot/undershoot effects

Fig. 3 shows how coupling capacitance induces overshoot and undershoot in victim net. With victim net at logic high level if aggressor nets(net1 and net2) switch from logic low to high then overshoot occurs in the victim net. Whereas, for victim net kept at logic low level if both the aggressor nets switch from logic high to low then undershoot occurs.

An efficient computational model for crosstalk induced overshoot/undershoot analysis in identically coupled multilayer doped GNR interconnect systems is presented. In our proposed methodology first, we develop an analytical expression for the crosstalk induced overshoot/undershoot in Laplace domain. Then we adopt the inverse Laplace transform to find out its time-domain response. Our methodology is as accurate as SPICE but computationally much faster [10], [11]. The proposed methodology is illustrated as follows.

A. ABCD parameter based approach

An infinitesimal lumped RLC section of an identically coupled multilayer doped GNR interconnect system is shown in Fig. 4. The Kirchhoff equation for an infinitesimally small segment of these three identically coupled interconnects is given by the following equation [14],

$$\phi_{in} = P\phi_{out} \tag{7}$$

where,

$$\phi_{in} = [V_{in1}, V_{in2}, V_{in3}, I_{in1}, I_{in2}, I_{in3}]^T \tag{8}$$

$$\phi_{out} = [V_{out1}, V_{out2}, V_{out3}, I_{out1}, I_{out2}, I_{out3}]^T \tag{9}$$

and, matrix P is shown in (12). The matrix P may be diagonalized as $P = VWV^{-1}$, where,

$$V = \begin{bmatrix} Z_1 & -Z_1 & Z_2 & -Z_2 & -Z_3 & Z_3 \\ Z_1 & -Z_1 & -2Z_2 & 2Z_2 & 0 & 0 \\ Z_1 & -Z_1 & Z_2 & -Z_2 & Z_3 & -Z_3 \\ 1 & 1 & 1 & 1 & -1 & -1 \\ 1 & 1 & -2 & -2 & 0 & 0 \\ 1 & 1 & 1 & 1 & 1 & 1 \end{bmatrix} \tag{10}$$

and, W is a diagonal matrix as shown in (13). Here, dx is the length of the infinitesimal line and θ_1, θ_2 and θ_3 are the propagation constants of the decoupled interconnects. Z_1, Z_2 and Z_3 are the characteristic impedances of the decoupled interconnects. These parameters are defined as: $dx = L/n$, $\theta_1 = \sqrt{s(\alpha.C_{qp})(r_p + sl_p)}$, $\theta_2 = \sqrt{s(\beta.C_{qp})(r_p + sl_p)}$, $\theta_3 = \sqrt{s(\gamma.C_{qp})(r_p + sl_p)}$, $Z_1 = \sqrt{\frac{(r_p+sl_p)}{s(\alpha.C_{qp})}}$, $Z_2 = \sqrt{\frac{(r_p+sl_p)}{s(\beta.C_{qp})}}$ and $Z_3 = \sqrt{\frac{(r_p+sl_p)}{s(\gamma.C_{qp})}}$. Here, n is the number of infinitesimal sections. Other parameters are defined as, $\alpha = (1-2g-h)$, $\beta = (1+g-h)$ and $\gamma = (1+2f-g-h)$, where, $f = \frac{a^2}{ab^2+b^3-2a^2b}$, $g = \frac{ab}{ab^2+b^3-2a^2b}$ and $h = \frac{b^2}{ab^2+b^3-2a^2b}$ with $a = \frac{C_{cp}}{C_{qp}}$ and $b = \frac{C_{ep}+C_{qp}+C_{cp}}{C_{qp}}$. Using, $P^n = (VWV^{-1})^n = (VW^nV^{-1})$ and the identity, $\lim_{n\to+\infty}(1+\frac{x}{n})^n \to e^x$, P^n can be written as shown in (14), where, $ta = \cosh(L\theta_1)$, $tb = \cosh(L\theta_2)$, $tc = \cosh(L\theta_3)$, $td = \sinh(L\theta_1)$, $te = \sinh(L\theta_2)$,and $tf = \sinh(L\theta_3)$. Here, P_{dr} and P_{dc} are the ABCD matrices of the driving buffer, P_{Rf} is the ABCD matrix representation of the lumped resistance R_{ex} and P_{load} is that of the capacitive load. The final Kirchoff equation for the coupled interconnects can be written as,

$$\Phi_i = P_{dr}P_{dc}P_{R_{ex}}P^nP_{R_{ex}}P_{load}\Phi_o \tag{11}$$

By solving (11), the final output voltages V_{o1}(s), V_{o2}(s) and V_{o3}(s) can be represented in terms of the inputs V_{i1}(s), V_{i2}(s) and V_{i3}(s) in matrix form as shown in (15). The exact expressions of H_1(s), H_2(s) and H_3(s) in (15) are shown in (16), (17) and (18) respectively where, $A = (1 + sR_dC_o)$ and, $B = (R_d + AR_{ex})$. H_1(s), H_2(s) and H_3(s) are the transfer functions of the decoupled interconnects. Here, The transfer function for the crosstalk induced overshoot/undershoot evaluation in the victim net will be denoted as H(s) throughout the paper. H(s) can be derived from (15) for different evaluation conditions (i.e., crosstalk induced overshoot/undershoot). We consider a fifth-order Padé expansion for approximating hyperbolic functions in (16), (17) and (18) with high degree of accuracy [15]. So the transfer function H(s) will be of the form as follows [given in (19)] after the Padé expansion.

$$H(s) = \frac{1}{1 + sb_1 + s^2b_2 + s^3b_3 + s^4b_4 + s^5b_5 + s^5b_5 + s^6b_6 + s^7b_7} \tag{19}$$

where, the coefficients are shown below,

$$b_1 = \frac{L^2r_pC}{2} + R_d(C_o + C_i) + 2R_{ex}C_i + (R_d + R_{ex})LC + LC_ir_p \tag{20}$$

$$\begin{aligned} b_2 = {} & 2R_{ex}R_dC_oC_i + \frac{L^2l_pC}{2} + C_iLl_p + \frac{C_iL^3r_p^2C}{6} + \frac{L^4r_p^2C^2}{24} \\ & \frac{L^2r_pC(R_dC_o + R_dC_i + 2R_{ex}C_i)}{2} + \frac{(R_d + R_{ex})r_pL^3C^2}{6} + \\ & LR_{ex}C(R_dC_o + R_dC_i + 2R_{ex}C_i) + LC_iR_dC_or_p \end{aligned} \tag{21}$$

$$P = \begin{bmatrix} 1 & 0 & 0 & (r_p + sl_p)dx & 0 & 0 \\ 0 & 1 & 0 & 0 & (r_p + sl_p)dx & 0 \\ 0 & 0 & 1 & 0 & 0 & (r_p + sl_p)dx \\ sC_{qp}(1-(g+h-f))dx & -sC_{qp}.g.dx & -sC_{qp}.f.dx & 1 & 0 & 0 \\ -sC_{qp}.g.dx & sC_{qp}(1-h)dx & -sC_{qp}.g.dx & 0 & 1 & 0 \\ -sC_{qp}.f.dx & -sC_{qp}.g.dx & sC_{qp}(1-(g+h-f))dx & 0 & 0 & 1 \end{bmatrix} \tag{12}$$

$$W = \begin{bmatrix} (1+\theta_1 dx) & 0 & 0 & 0 & 0 & 0 \\ 0 & (1-\theta_1 dx) & 0 & 0 & 0 & 0 \\ 0 & 0 & (1+\theta_2 dx) & 0 & 0 & 0 \\ 0 & 0 & 0 & (1-\theta_2 dx) & 0 & 0 \\ 0 & 0 & 0 & 0 & (1+\theta_3 dx) & 0 \\ 0 & 0 & 0 & 0 & 0 & (1-\theta_3 dx) \end{bmatrix} \tag{13}$$

$$P^n = \begin{bmatrix} (\frac{ta}{3}+\frac{tb}{6}+\frac{tc}{2}) & (\frac{ta}{3}-\frac{tb}{3}) & (\frac{ta}{3}+\frac{tb}{6}-\frac{tc}{2}) & (\frac{td.Z1}{3}+\frac{te.Z2}{6}+\frac{tf.Z3}{2}) & (\frac{td.Z1}{3}-\frac{te.Z2}{3}) & (\frac{td.Z1}{3}+\frac{te.Z2}{6}-\frac{tf.Z3}{2}) \\ (\frac{ta}{3}-\frac{tb}{3}) & (\frac{ta}{3}+\frac{2tb}{3}) & (\frac{ta}{3}-\frac{tb}{3}) & (\frac{td.Z1}{3}-\frac{te.Z2}{6}) & (\frac{td.Z1}{3}+\frac{2te.Z2}{3}) & (\frac{td.Z1}{3}-\frac{te.Z2}{3}) \\ (\frac{ta}{3}+\frac{tb}{6}-\frac{tc}{2}) & (\frac{ta}{3}-\frac{tb}{3}) & (\frac{ta}{3}+\frac{tb}{6}+\frac{tc}{2}) & (\frac{td.Z1}{3}+\frac{te.Z2}{6}-\frac{tf.Z3}{2}) & (\frac{td.Z1}{3}-\frac{te.Z2}{3}) & (\frac{td.Z1}{3}+\frac{te.Z2}{6}+\frac{tf.Z3}{2}) \\ (\frac{td}{3Z1}+\frac{te}{6Z2}+\frac{tf}{2Z3}) & (\frac{td}{3Z1}-\frac{te}{3Z2}) & (\frac{td}{3Z1}+\frac{te}{6Z2}-\frac{tf}{2Z3}) & (\frac{ta}{3}+\frac{tb}{6}+\frac{tc}{2}) & (\frac{ta}{3}-\frac{tb}{3}) & (\frac{ta}{3}+\frac{tb}{6}-\frac{tc}{2}) \\ (\frac{td}{3Z1}-\frac{te}{3Z2}) & (\frac{td}{3Z1}+\frac{2te}{3Z2}) & (\frac{td}{3Z1}-\frac{te}{3Z2}) & (\frac{ta}{3}-\frac{tb}{3}) & (\frac{ta}{3}+\frac{2tb}{3}) & (\frac{ta}{3}-\frac{tb}{3}) \\ (\frac{td}{3Z1}+\frac{te}{6Z2}-\frac{tf}{2Z3}) & (\frac{td}{3Z1}-\frac{te}{3Z2}) & (\frac{td}{3Z1}+\frac{te}{6Z2}+\frac{tf}{2Z3}) & (\frac{ta}{3}+\frac{tb}{6}-\frac{tc}{2}) & (\frac{ta}{3}-\frac{tb}{3}) & (\frac{ta}{3}+\frac{tb}{6}+\frac{tc}{2}) \end{bmatrix} \tag{14}$$

$$\begin{bmatrix} V_{o1}(s) \\ V_{o2}(s) \\ V_{o3}(s) \end{bmatrix} = \begin{bmatrix} (\frac{1}{3}H_1(s)+\frac{1}{6}H_2(s)+\frac{1}{2}H_3(s)) & \frac{1}{3}(H_1(s)-H_2(s)) & (\frac{1}{3}H_1(s)+\frac{1}{6}H_2(s)-\frac{1}{2}H_3(s)) \\ \frac{1}{3}(H_1(s)-H_2(s)) & (\frac{1}{3}H_1(s)+\frac{2}{3}H_2(s)) & \frac{1}{3}(H_1(s)-H_2(s)) \\ (\frac{1}{3}H_1(s)+\frac{1}{6}H_2(s)-\frac{1}{2}H_3(s)) & \frac{1}{3}(H_1(s)-H_2(s)) & (\frac{1}{3}H_1(s)+\frac{1}{6}H_2(s)+\frac{1}{2}H_3(s)) \end{bmatrix} \begin{bmatrix} V_{i1}(s) \\ V_{i2}(s) \\ V_{i3}(s) \end{bmatrix} \tag{15}$$

$$H_1(s) = \frac{1}{(A(1+sC_iR_{ex})+sC_iB)\cosh(\theta_1 L)+(\frac{B}{Z_1}(1+sC_iR_{ex})+AsC_iZ_1)\sinh(\theta_1 L)} \tag{16}$$

$$H_2(s) = \frac{1}{(A(1+sC_iR_{ex})+sC_iB)\cosh(\theta_2 L)+(\frac{B}{Z_2}(1+sC_iR_{ex})+AsC_iZ_2)\sinh(\theta_2 L)} \tag{17}$$

$$H_3(s) = \frac{1}{(A(1+sC_iR_{ex})+sC_iB)\cosh(\theta_3 L)+(\frac{B}{Z_3}(1+sC_iR_{ex})+AsC_iZ_3)\sinh(\theta_3 L)} \tag{18}$$

$$\begin{aligned} b_3 = {} & \frac{L^2 l_p C(R_dC_o+R_dC_i+2R_{ex}C_i)}{2} + Cr_pL^2R_dR_{ex}C_oC_i + \\ & \frac{C^2r_pl_pL^4}{12} + l_pLC_iR_dC_o + \frac{C^2r_p^2L^4(R_dC_o+R_dC_i+2R_{ex}C_i)}{24} \\ & + CLC_iR_{ex}^2R_dC_o + \frac{C^2r_pL^3R_{ex}(R_dC_o+R_dC_i+R_{ex}C_i)}{6} + \\ & \frac{Cr_p^2L^3R_{ex}C_iC_o}{6} + \frac{Cr_pl_pC_iL^3}{6} + \Big(\frac{Cl_pL^3}{6}+\frac{C^2r_p^2L^5}{120}\Big) \\ & (C(R_d+R_{ex})+r_pC_i) \end{aligned} \tag{22}$$

$$\begin{aligned} b_4 = {} & Cl_pL^2R_dR_{ex}C_oC_i + \frac{C^2l_p^2L^4}{24} + \frac{C^2r_p^2L^4(R_dC_oR_{ex}C_i)}{12} + \\ & \frac{C^2r_pl_pL^4(R_dC_o+R_dC_i+2R_{ex}C_i)}{12} + \frac{Cr_pl_pC_iL^3R_dC_o}{6} + \\ & \frac{C^2r_pC_iL^3(R_dC_oR_{ex}^2)}{6} + \frac{C^2r_pl_pL^5}{60}(C(R_d+R_{ex})+rC_i) + \\ & \Big(\frac{Cl_pL^3}{6}+\frac{C^2r_p^2L^5}{120}\Big)(CR_{ex}R_dC_o+CR_{ex}C_i(R_d+R_{ex})+ \\ & r_pC_iR_dC_o+l_pC_i) \end{aligned} \tag{23}$$

$$\begin{aligned} b_5 = {} & \frac{C^2l_p^2L^4}{24}(R_dC_o+R_dC_i+2R_{ex}C_i) + \Big(\frac{Cl_pL^3}{6}+\frac{C^2r_p^2L^5}{120}\Big) \\ & (CR_{ex}^2C_iR_dC_o+l_pC_iR_dC_o) + \frac{C^2l_p^2L^5}{120}(C(R_d+R_{ex})+rC_i) + \\ & \frac{C^2r_pl_pL^4(R_dC_oR_{ex}C_i)}{6}(CR_{ex}R_dC_o+CR_{ex}C_i(R_d+R_{ex})+ \\ & r_pC_iR_dC_o+l_pC_i) + \frac{C^2r_pl_pL^5}{60} \end{aligned} \tag{24}$$

$$\begin{aligned} b_6 = {} & \frac{C^2l_p^2L^4(R_dC_oR_{ex}C_i)}{12} + \frac{C^2r_pl_pL^5}{60}(CR_{ex}^2C_iR_dC_o+ \\ & l_pC_iR_dC_o) + \frac{C^2l_p^2L^5}{120}(CR_{ex}R_dC_o+CR_{ex}C_i(R_d+R_{ex})+ \\ & r_pC_iR_dC_o+l_pC_i) \end{aligned} \tag{25}$$

$$b_7 = \frac{C^2l_p^2L^5}{120}(CR_{ex}^2C_iR_dC_o+l_pC_iR_dC_o) \tag{26}$$

Similarly, H_2(s) and H_3(s) can be represented in a form as given in (19). The parameter C in the coefficients b_1 to b_7 varies according to the transfer function of the decoupled interconnect and it is represented as αC_{qp}, βC_{qp} and γC_{qp} in $H_1(s)$, $H_2(s)$ and $H_3(s)$ respectively. The other parameters correspond to the distributed parameters of the copper interconnect, length of the interconnect, driver and load RC parameters.

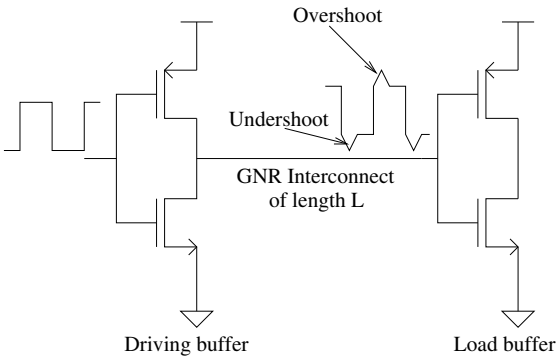

Fig. 5: Crosstalk induced overshoot/undershoot effects.

IV. Gate oxide reliability of CMOS devices

Fig. 5 depicts how overshoot stresses the NMOS gate oxide and undershoot stresses the PMOS gate oxide. As understood from the figure that, gate oxides of MOS transistors are operated under pulsed conditions. Thus the gate oxide faces an ac electric field. However, to estimate the impact of this electric stress on the oxide, an effective electric field is defined as follows [16],

$$E_{avg} = \frac{1}{\psi}\ln\Big[\frac{1}{T}\int_0^T e^{\psi E_{ins}(t)}dt\Big] \tag{27}$$

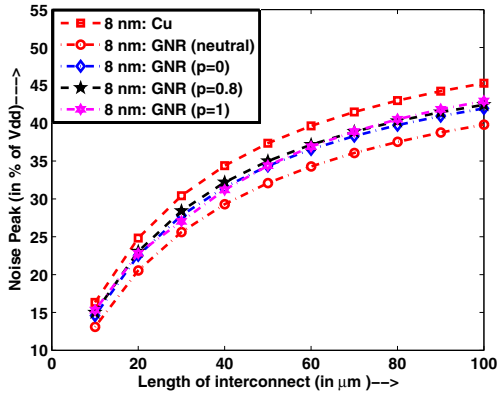

Fig. 6: Comparison of crosstalk induced peak overshoot voltage at 8 nm node

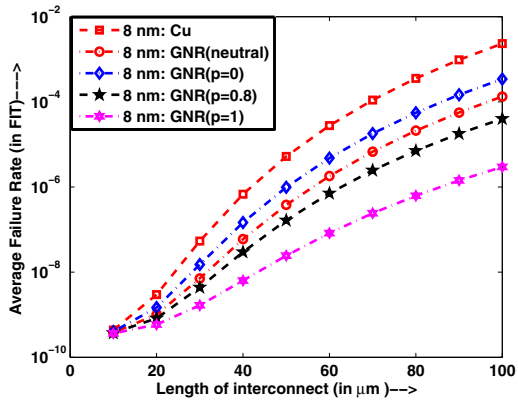

Fig. 8: Comparison of average failure rate of MOS gate oxide at 8 nm node.

where, ψ is the field acceleration factor. In [17], it is shown that the impact of the overshoot/undershoot induced electric field can be estimated by calculating the average failure rate (AFR) of the MOS gate oxides. Information about failure rates of gate oxides is already gathered under various electric stress conditions (i.e., varying oxide thickness, applied gate voltage etc.) using a reference oxide area and reference temperature. The AFR [16] of a MOS device having gate oxide area A is then expressed as below,

$$AFR = \frac{AFR_{const}}{A_{const}} A e^{\psi W_S (E_{avg} - E_{const})} \tag{28}$$

where, AFR_{const} is the reference failure rate, A_{const} is the reference area of the sample used for calculating reference failure rate, W_S is the Weibull slope, E_{avg} is the effective electric field across the gate oxide, and E_{const} is the reference electric field. Using (28), we calculate the AFR of the MOS devices. For this purpose, we consider parameters such that the failure rate of a chip operating at nominal voltage is 10 FIT, assuming one billion transistors in a chip.

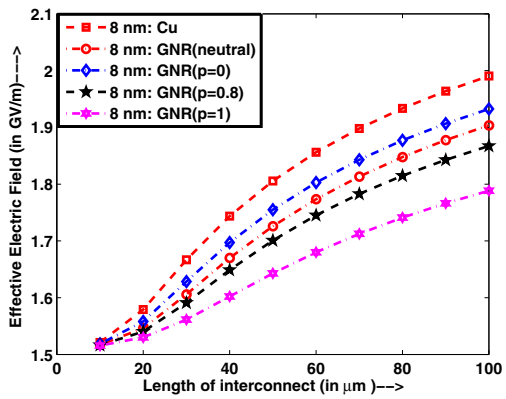

Fig. 7: Comparison of effective electric field across the gate oxide at 8 nm node.

V. Simulation Results

The proposed analytical model is implemented in MATLAB 7.1 running on standard desktop with 1.6 GHz Intel Core 2 Duo processor with 2.5 GB memory. The crosstalk induced overshoot values are calculated for different RLC values of the intermediate level multilayer GNR interconnect at 8 nm technology node with length ranging from 10 μm to 100 μm. Driving and load inverter buffer sizes are chosen as 50 times the minimum sized buffer. The individual GNR layer-electrode contact resistance is considered as 100 KΩ. Fermi levels are set as 0 eV and 0.3 eV respectively for neutral and doped GNR interconnects [5]. Perfectly specular (i.e., $p = 1.0$) GNR edges are assumed for neutral zz-GNR, whereas specularity index (i.e., p) is varied from completely diffusive edges ($p = 0.0$) to completely specular edges ($p = 1.0$) for AsF_5 intercalation doped zz-GNR interconnects [5]. Further Mean free path (i.e., λ) is considered here as 419 nm and 1.03 μm for neutral and AsF_5 doped MLGNR interconnects respectively [5].

A. Analysis of crosstalk induced overshoot effects

Fig. 6 delineates the worst case peak crosstalk induced overshoot for copper and GNR interconnects of various specularity viz. $p = 0.0, 0.8$ and 1.0 for both the technology nodes. It is a fact that the peak crosstalk induced overshoot voltage depends upon the coupling ratio (C.R.) where, C.R.=$\frac{C_{cp}L}{SC_i + C_{cp}L + C_{ep}L}$. At smaller interconnect lengths, due to smaller coupling ratio, peak overshoot is dependent upon the time constant of the interconnect system. Copper interconnects induce the maximum overshoot amongst all. While the perfectly specular GNR interconnects induce the maximum overshoot amongst the GNR counterparts (i.e., of various specularity) due to its least time constant. Being of larger time constant, the neutral GNR interconnect induces the least amount of overshoot.

B. Analysis of gate oxide reliability

Fig. 7 depicts the effective electric field produced because of this excess electric field over the gate oxide. As observed from the figure, copper interconnect again is the victim of producing maximum electric field across the gate oxide irrespective of technology nodes. Interestingly though doped perfectly specular MLGNR interconnect induces higher overshoot but produces the least effective electric field in both the technology nodes with others producing electric field in between. The reason behind this is that because of its least

time constant amongst all, it induces least amount of overshoot area (i.e., $\frac{1}{2} \times overshoot\ peak \times overshoot\ width$). Finally, Average failure rate (AFR) is plotted in Fig. 8. As observed from (28) that effective electric field is the marker for how reliable will be the interconnect and this is quantified through Average failure rate (AFR). It is seen that 100 μm long, doped perfectly specular MLGNR interconnects have an AFR of three orders smaller than copper interconnects for 8 nm technology node respectively. Further it is inferred from the figure that with higher interconnect length AFR increases, which can also be intuitively understood.

VI. Conclusions

In this work, an ABCD parameter matrix based model for crosstalk induced overshoot/undershoot has been proposed for multilayer Graphene Nano Ribbon interconnects for intermediate level interconnects at 8 nm node. The worst case crosstalk induced peak overshoot/undershoot voltages have been derived for both neutral and doped zigzag MLGNR interconnects and compared to those of conventional copper interconnects. The worst case crosstalk induced peak overshoot voltage for near specular, doped multilayer zigzag GNR interconnects is comparable to that of copper interconnects. It has been observed that the performance of neutral MLGNR interconnects is better than that of its doped counterpart with respect to peak crosstalk induced overshoot, but from the perspective of effective electric field across the gate oxide, doped MLGNR interconnects outperform neutral ones and copper interconnects for all the cases. Finally, our analysis has shown that from the gate oxide reliability perspective, perfectly specular, doped multilayer zigzag GNR interconnects are significantly advantagious compared to copper interconnects for future IC technology generations.

References

[1] International Technology Roadmap for Semiconductors (ITRS-2013) Reports, [Online]. Available: http://www.itrs.net/reports.html.

[2] A. Naeemi and J.D. Meindl., "Performance Benchmarking for Graphene Nanoribbon, Carbon Nanotube, and Cu Interconnects", *IITC 2008*, pp. 183–185.

[3] X. Chen et. al., "High-speed Graphene Interconnects Monolithically Integrated with CMOS Ring Oscillators Operating at 1.3 GHz", *IEEE IEDM*, 2009, pp. 1-4.

[4] A. Naeemi and, J. D. Meindl, "Compact Physics- Based Circuit Models for Graphene Nanoribbon Interconnects," *IEEE Trans. on Electron Devices*, vol. 56, no. 9, pp. 1822-1833, Sep. 2009.

[5] C. Xu, H. Li and, K. Banerjee, "Modeling, Analysis, and Design of Graphene Nano-Ribbon Interconnects," *IEEE Trans. on Electron Devices*, vol. 56, no. 8, pp. 1567-1578, Aug. 2009.

[6] D. Das and, H. Rahaman, "Crosstalk and Gate Oxide Reliability Analysis in Graphene Nanoribbon Interconnects", 2nd *International Symposium on Electronic System Design (ISED)*, Dec. 2011, pp. 182-187.

[7] W.-S. Zhao and, W.-Y. Yin, "Signal Integrity Analysis of Graphene Nano-Ribbon (GNR) Interconnects", *IEEE Electrical Design of Advanced Packaging and Systems Symposium (EDAPS)*, pp. 227–230, 2012.

[8] W. -S. Zhao and W. -Y. Yin, "Comparative Study on Multilayer Graphene Nanoribbon (MLGNR) Interconnects", *IEEE Trans. on Electromagnetic Compatibility*, vol. 56, no. 3, pp. 638–645, June 2014.

[9] Y. Eo et. al., "Generalized travelingwave- based waveform approximation technique for the efficient signal integrity verification technique of multicoupled transmission lines," *IEEE TCAD*, vol. 21, no. 12, pp. 1489-1497, Dec. 2002.

[10] M. Sahoo, P. Ghosal and, H. Rahaman, "An ABCD parameter based Modeling and Analysis of Crosstalk Induced Effects in Single-Walled Carbon Nanotube Bundle Interconnects", *IEEE ASQED*, Aug. 2013, pp. 264–273.

[11] M. Sahoo, P. Ghosal and, H. Rahaman, "An ABCD Parameter Based Modeling and Analysis of Crosstalk Induced Effects in Multiwalled Carbon Nanotube Bundle Interconnects", *IEEE* 27th *International Conference on VLSI Design*, pp. 433–438, Jan. 2014, .

[12] M. Sahoo and H. Rahaman, "An ABCD Parameter Based Modeling and Analysis of Crosstalk Induced Effects in Multilayer Graphene Nano Ribbon Interconnects", *IEEE ISCAS*, pp. 1138–1142, June 2014,.

[13] Predictive Technology Model [Online]. Available: http://ptm.asu.edu/.

[14] J. Zhang and E. G. Friedman, "Decoupling Technique and Crosstalk Analysis for Coupled RLC Interconnects",*IEEE ISCAS*, pp. 521–524, 2004.

[15] K. Banerjee and A. Mehrotra, "Analysis of On-Chip Inductance Effects for Distributed RLC Interconnects", *IEEE TCAD*, vol. 21, pp. 904-915, Aug. 2002.

[16] W. R. Hunter, "The statistical dependence of oxide failure rates on Vdd and, tox variations, with applications to process design, circuit design, and end use," *Proc. IEEE* 37th *Annu. Int. Rel. Phys. Symp.*, 1999, pp. 72-81.

[17] N. S. Nagaraj, W. R. Hunter, P. Balsara, and C. Cantrell, "The impact of inductance on transients affecting gate oxide reliability," *Proc.* 18th *Int. Conf. VLSI Design*, pp. 709-713, Jan. 2005.

Analytical Drain Current Model for Graphene Metal-Oxide semiconductor Field-Effect Transistor

Sudipta Bardhan
School of VLSI Technology
IIEST
Howrah, India
sudipta.bardhan15@gmail.com

Manodipan Sahoo and Hafizur Rahaman
dept. of Information Technology
IIEST
Howrah, India
manodipansahoo@gmail.com
rahaman_h@yahoo.co.in

***Abstract*— A physics based analytical model for double gate metal oxide semiconductor graphene field effect transistor (GFET) has been presented. We have derived the expression of drain to source current using the general physics of conventional silicon MOSFET. The explicit expression of drain current is very simple and few fitting parameters have been considered to obtain the I-V characteristics. This model is also applicable for top gated GFET. Results using our analytical model show very good agreement with the experimental results and result using NANOHUB tool. This model can be integrated in circuit simulation tools.**

Keywords-graphene, field effect transistor, model, fitting parameters.

I. INTRODUCTION

GRAPHENE is a promising material for high performance RF and analog electronics [1]-[3] for next generation. It has got excellent electrical properties such as high carrier mobility (2×10^5 cm^2/V.s) at room temperature [4] and high saturation velocity (6.3×10^7 cm/s) which is six times higher than silicon [5]. Due to absence of bandgap, the ON/OFF current ratio is very small, so there are certain limitations for digital application but for analog or RF application, researchers have focused on zero bandgap graphene material where high ON/OFF current ratio is not required. Device designers have shown the figure of merit of RF devices in Gigahertz range for gapless large area graphene channel MOSFET. The cutoff frequencies as high as 427 GHz have been presented in [6].

The schematic of the GFET structure is shown in Fig. 1. The double gate transistor is considered here, where top gate oxide is hafnium oxide and back gate oxide is silicon oxide. The back gate oxide has been deposited on doped silicon. Thus device models need to be developed to gauge the applicability of G-FETs for various applications as sensors, VLSI interconnects or devices.

978-1-4673-9257-0/15/$31.00©2015 IEEE

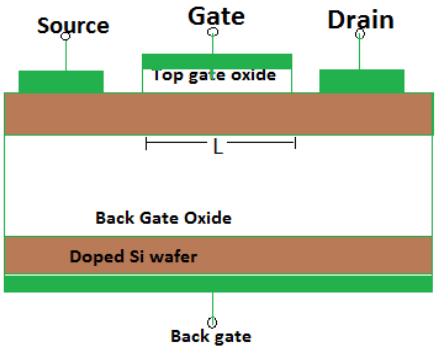

Figure 1. Schematic of GFET

Different types of models may be categorized either as physical model or empirical model. Physical model of GFET has already been developed previously [7-10] based on device physics. Empirical or semi empirical models are mostly acceptable for implementation on standard EDA tools because they achieve moderate accuracy with far lesser computational burden than very accurate physical centric models. Most of the physical models focus on the first principle based calculation of band structure, tunneling effect and carrier transport. GFETs with gapless, large area graphene channel are modeled using a quasi analytical approach in [11]. Another compact physical model for GFET has been presented in [12],[18]. Conventional MOSFET models [13]-[15] form the basis of this model. The models are only validated with experimental data for long channel GFETs ($L_G > 1\mu$m) [18]. Drift diffusion based model [16] has been used here to obtain explicit drain current model. Virtual source model [17] has been utilized for obtaining the I-V characteristics. In previously developed models, the expression of drain to source current is a function of channel potential making it more complicated than our model where, drain current expression is directly related to front gate, back gate & drain bias with few fitting parameters. The model I-V behaviors show very good agreement with experimental and simulation results.

The drain to source current expression is valid for both double and single gate technology. For positive or negative gate biases the drain current can be determined very easily, so this model is highly applicable for circuit simulation using standard EDA tools.

The paper is organized as follows. Section II discusses, about the model description of GFET. Section III discusses establishment of the drain to source current equation with the fitting parameters. The analytical results of I-V characteristics of model have been compared with the experimental and simulation results, for the same GFET configuration, and values of fitting parameters have been discussed in section IV. Finally the conclusions are drawn in section V.

II. GFET MODEL

The large area graphene channel [18] has been deposited on a thick SiO_2 layer that is grown on a heavily doped silicon wafer. The source and drain electrodes are contacting the graphene channel. The SiO_2 layer forms back gate oxide capacitance and silicon acts as a back gate. The conductivity type of the channel can be changed by applying constant back gate voltage. The top gate oxide is HfO_2 form top gate capacitance which controls the carrier charge density.

The drain current I_D of a conventional field effect transistor can be expressed as

$$I_{DS} = -q\rho_{CH}(x)v(x).W$$
$$= -q\rho_{CH}[V(x)]v[V(x)].W \quad (1)$$

where q = charge of electron.

$\rho_{CH}(x)$ = carrier density in the channel at position x

$v(x)$ = carrier drift velocity.

W = gate width

Channel sheet density and saturation velocity is function of x. The local potential $V(x)$ exist across the channel from source to drain so right hand side of equation is substituted by $V(x)$ at the position of x. Now channel sheet density and saturation velocity is function of $V(x)$.

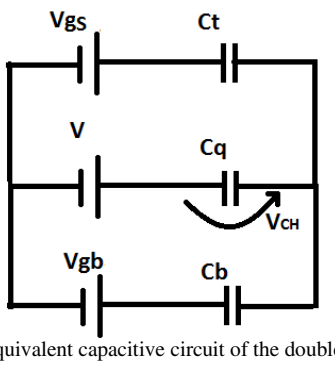

Figure 2. Equivalent capacitive circuit of the double gate GFET.

The concept of the electrostatic of dual gate GFET can be understood from equivalent capacitive circuit from figure.2. The top gate oxide and bottom oxide capacitance are Ct and Cb respectively and the quantum capacitance is Cq. The channel potential V_{CH} is the voltage drop across quantum capacitace Cq.

Here, we have considered the quantum capacitance directly depends on gate bias and drain bias. The expression of quantum capacitance is [19].

$$Cq = \left(e^2/\sqrt{\pi}v_F\hbar\right)\begin{pmatrix}\rho_{CH0}{}^2 + ([Cb(Vgb - Vgb0) + \\ Ct(Vgs - Vgs0)]/q)^2\end{pmatrix}^{1/4} \quad (2)$$

where v_F = Fermi velocity

ρ_{CH0} = residual carrier sheet density

Here, Ct=top gate capacitance, Cb= back gate capacitance. Vgs and Vgb are top gate and back gate bias respectively. Vgs0 and Vbs0 are top gate voltage and back gate voltage at Dirac point. In Dirac point the charge carrier density is minimum. This is similar to the flat band voltages in conventional silicon MOSFET.

Applying Kirchhoff's circuit law in fig.2 we get the following relation

$$V_{CH} = (Vgs - V(x))\alpha + (Vgb - V(x))\beta \quad (3)$$

where $Vgs = Vgstop - Vgs0$

$Vgb = Vgback - Vgb0$

$$\alpha = \frac{Ct}{Ct + Cb + \frac{1}{2}Cq} \quad \text{and} \quad \beta = \frac{Cb}{Ct + Cb + \frac{1}{2}Cq}$$

The α and β is treated as fitting parameter depends on top gate, back gate, and quantum capacitances used to adjust the channel potential. The voltage drop across the graphene channel is $V(x)$ which is zero at source end at x=0 and equal to drain source voltage Vds at the drain end at x=L.

The calculation of the approximate value of graphene sheet charge carrier density is defined as the [11], [20]

$$Q_{CH} = q\rho_{CH} = -\int CqV_{CH} = -\frac{1}{2}CqV_{CH} \quad (4)$$

As we consider here parallel plate capacitor, so Q_{CH} not equal not equal to $-CqV_{CH}$ but half of it. From equation (4) we get the carrier sheet density as

$$q\rho_{CH} = \theta V_{CH} \quad (5)$$

where $\theta = -(Cq/2)$

Here, θ is considered as fitting parameter, used to control the carrier sheet density in the channel region.

III. DRAIN CURRENT MODEL

The carrier velocity v=$v(x)$ has been defined in (1) is important parameter to derive the drain current expression. The steady state velocity field characteristics of graphene have been shown by Monte carlo simulations which is a soft saturation [20] that can be approximated by the expression,

$$v = \frac{\mu E}{1 + \mu E/v_{sat}} \quad (6)$$

where E = electric field

μ = low field carrier density

v_{sat} = saturation velocity

Remote interfacial phonon scattering [21] is important phenomena and the saturation velocity is affected by this

scattering. Two surface optical phonons of SiO_2 are involved in this process. With considerable accuracy, the process can be described by only one phonon with an effective energy $\hbar$. Saturation velocity depends on the effective energy and also on sheet carrier density(ρ_{CH}) and the expression is given below,

$$v_{sat} = \frac{\phi}{\sqrt{\pi \rho_{CH}}} \tag{7}$$

where, ϕ=phonon energy

Applying $E = -\frac{dV(x)}{dx}$ and combining (6) & (7) the drain current becomes,

$$Id = -q\rho_{CH} \frac{\mu\left(-\frac{dV}{dx}\right)}{1+\mu\frac{(-dV/dx)}{v_{sat}}} W \tag{8}$$

The left hand side of (8) is integrated w.r.t device length using boundary conditions x=0 to x=L and right hand side w.r.t V from V=0 at x=0 to V=V_{DS} at x=L. The resulting expression for drain current is,

$$Id = \frac{q\mu W \int_0^{Vds} \rho_{CH}\, dV}{L - \mu \int_0^{Vds} \frac{1}{v_{sat}} dV} \tag{9}$$

Integrating (9) using V as a integral variable, the explicit expression for Ids can be finally obtained,

$$Ids = \frac{\mu W \theta}{Leff}[(\alpha Vgs - \beta Vgb)Vds - (\alpha+\beta)(Vds^2/2)] \tag{10}$$

where,

$$Leff = L - \left(\frac{2}{3}\sqrt{\frac{\pi}{q}}\right)\cdot\left(\frac{\mu\sqrt{\theta}}{(\alpha+\beta)\,\phi}\right)\left[\begin{array}{l}((\alpha Vgs - \beta Vgb) - (\alpha+\beta)Vds)^{3/2} \\ -(\alpha Vgs - \beta Vgb)^{3/2}\end{array}\right]$$

IV. Result And Discussion

To compare with the experimental I/V characteristics, the voltage drop at source and drain region has to be considered. The relationship between external drain voltage $Vdsext$ and the internal drain voltage Vds is given by the corresponding equation,

$$Vds = Vdsext\left(1 - \frac{Ids}{\zeta}\right) \tag{11}$$

where $Vdsext$=External applied drain voltage

$$\zeta = \frac{Vdsext}{(Rs + R_D)}$$

Rs = Source resistance

and R_D = Drain resistance

The parameter ζ is treated as a fitting parameter which depends on external applied drain voltage and source and drain resistance.

To verify the model validity, we have benchmarked the resulting current voltage characteristics with experimental results. The model has been tested against two different experimental environments. First test (TEST A in Table I) parameters have been extracted from Meric et.al [18] and second and third test (TEST B and TEST C in Table I) parameters from Kedzierski et. al [19].

Fig. 3 shows the plot of I-V characteristics of GFET (TEST A parameters are considered) . The experimental [18] value of mobility(μ) is 550 $cm^2/V.s$, source and drain resistance value is Rs=700Ω and R_D=700Ω respectively. A good agreement between experiment and our model (as expressed in (10)) is obtained with μ=600 $cm^2/V.s$, Rs=800Ω and R_D=800Ω. So for best fit, the mobility value of 9%, source and drain resistance of 14% higher than experimental value have been chosen. The fitting parameters have been used to derive the final expression of drain current in our model. The values of the parameters are, α=0.2, β=0.004, θ= - 0.02, and ζ=-0.0025.

In the second experiment [19], the design of GFET is different, only top gate technology has been used. Fig. 4 (TEST B parameters are considered) displays the plot of output characteristics. For the best fit with the experiment, the mobility of holes and electrons agree with experiment, only resistance values Rs=400Ω and R_D=400Ω, have been considered which is 33% higher than measured value. The fitting parameters are, α=0.3, β=0,θ= - 0.01, and ζ= - 0.003.

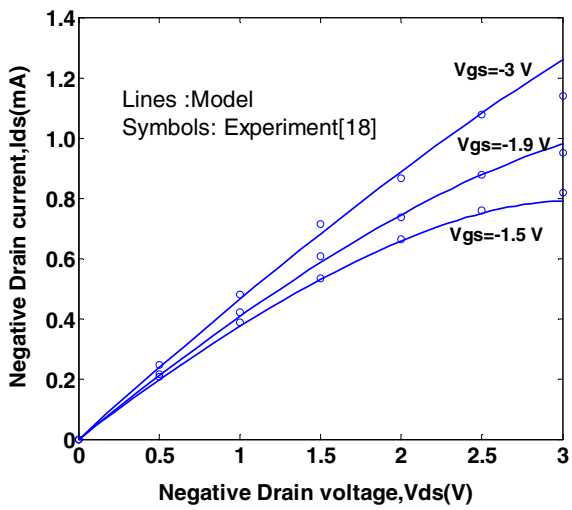

Fig. 3. Drain current as a function of drain source voltage for Vgs =-1.5V,-1.9V, and -3V, (from bottom to top) with α=0.2, β=0.004, θ= - 0.02, and ζ=-0.0025.

TABLE I. DIMENSIONS AND PARAMETERS OF THE MODELED GFET

MODEL PARAMETERS	TEST A	TEST B	TEST C	TEST D	TEST E
Channel Length, L (μm)	1	10	10	1	0.6/2
Channel Width, W (μm)	2.1	5	5	1	1
Top gate oxide Thickness, $t_{ox\text{-}top}$ (nm)	15	40	40	8/12	8
Back gate Oxide Thickness, $t_{ox\text{-}back}$ (nm)	285	…	…	300	300
Flat band voltage at top gate,Vgs0 (V)	1.45	0.85	0.65	0	0
Flat band voltage at back gate,Vbs0 (V)	2.7	…	…	…	…
Residual charge density, ρ_{CH0} (cm^{-2})	5×10^{12}	1×10^{12}	1×10^{12}	0	0
Source Resistance , Rs (Ω)	800	400	400	1	1
Drain Resistance , R_D (Ω)	800	400	400	1	1
Electron Mobility, μ_n (cm^2/V.s)	600	6500	1500	3000	3000
Hole Mobility, μ_h (cm^2/V.s)	600	6500	1500	3000	3000
Phonon energy, $\hbar$ (meV)	55	99	99	78	78
External back gate voltage (V)	-40	…	…	…	…

The plot in fig. 5 (TEST C parameters are considered) shows the transfer characteristics for two different drain biases *Vdsext*=0.1*V*, and *Vdsext*=1*V* respectively. The graph matches with the experiment taking all previously values for output characteristics, only *Vgs0*=0.65*V* have taken for final tuning with the fitting parameters α=0.2, β=0, θ= - 0.01, and ζ=-0.002.

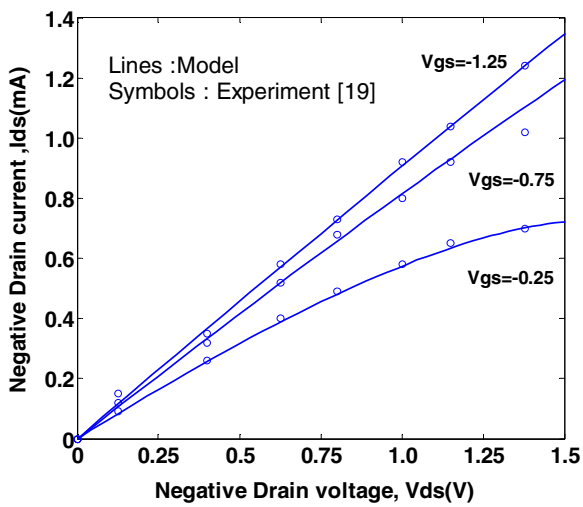

Fig. 4. Drain current as a function of drain source voltage for Vgs =-0.25V, -0.75V, and -1.25V (from bottom to top) with α=0.3, β=0,θ= - 0.01, and ζ= - 0.003.

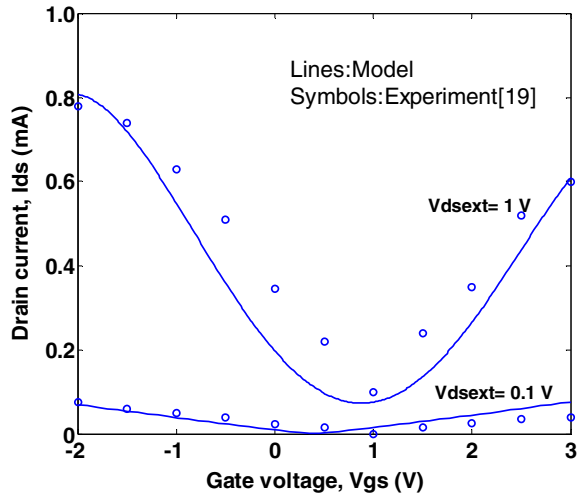

Fig. 5. Drain current as a function of gate source voltage for Vdsext= 0.1V and Vdsext= 1V with α=0.2, β=0, θ= - 0.01, and ζ=-0.002.

Finally, we have verified our model, against a known simulation tool, GFET tool from nanoHUB. In this simulation tool, the drift diffusion transport mechanism has been used to obtain the output characteristics. The dielectric material is silicon dioxide for both top gate and back gate oxide. Graphene mobility is characterized as a function of carrier density at temperature from 300 K to 500 K.

The model has been tested in two different conditions. For the first test (TEST D in Table I), channel length and width are kept fixed and top gate oxide thickness is varied. The parameters used in simulation are mentioned in Table I. Fig. 6 shows the output characteristics with this test setup.

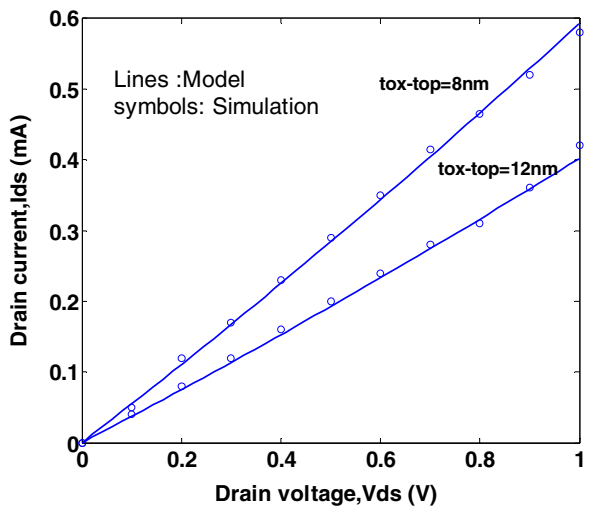

Fig. 6. Drain current of the GFETs with different top gate oxide thickness, tox-top =8nm with α=0.08, β=0,θ= - 0.02, and ζ= - 0.50 and tox-top =8nm with α=0.07, β=0,θ= - 0.01, and ζ= - 0.50 for Vgs = 0.6 V.

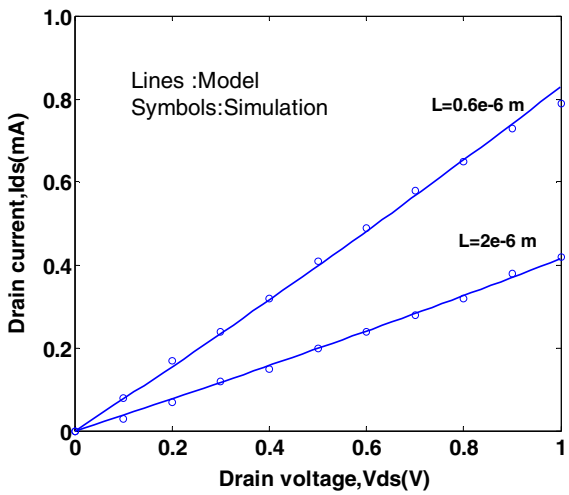

Fig. 7. Drain current of the GFETs with different channel length, L =0.6μm with α=0.08, β=0, θ= - 0.02, and ζ= - 0.50 and L =2μm with α=0.07, β=0,θ= - 0.01, and ζ= - 0.5 for Vgs = 0.6 V.

In the second test (TEST E in Table I), the channel length of GFET has been varied, for fixed channel width and top gate oxide thickness. Simulation parameters are shown in Table I. Fig. 7 shows the output characteristics with this test setup.

V. Conclusion

We have presented a compact drain current model of GFET, based on conventional transport equation for large channel area GFET, with double gate bias configuration. From saturation velocity and channel carrier density, we have determined the explicit closed form expression of drain current, using few fitting parameters. The analytical expression of drain to source current is very simple. Results using our model match very well for both experimental and simulation results and also it is valid from long channel regime (L=10μm) to short channel (L=600nm) regime. The circuit design engineers use the drain current and drain voltage characteristics to simulate different circuits. The GFET model in this paper is suitable for circuit simulation tools.

References

[1] L. Liao and X. Duan, "Graphene for radio frequency electronics," Mater.Today, vol. 15, pp. 328–338, Oct. 2012.

[2] F. Schwierz, "Graphene transistors: Status, prospects, and problems," *Proc. IEEE*, vol. 101, no. 7, pp. 1567–1584, Jul. 2013.

[3] K. S. Novoselov, V. I. Fal'ko, L. Colombo, P. R. Gellert, M. G. Schwab, and K. Kim, "A roadmap for graphene," Nature, vol. 490, no. 7419, pp. 192–200, Oct. 2012.

[4] A. S. Mayorov, R. V. Gorbachev, S. V. Morozov, L. Britnell, R. Jalil, L. A. Ponomarenko, P. Blake, K. S. Novoselov, A. K. Geim, and F. Guinea,"Micrometer-scale ballistic transport in encapsulated grapheme at Room temperature," *Nano. Lett.*, vol. 11, pp. 2396–2399, May 2011.

[5] V. E. Dorgan, M.-H. Bae, and E. Pop, "Mobility and saturation velocity in graphene on SiO2 ," *Appl. Phys. Lett.*, vol. 97, no. 8, pp. 082112-1–082112-3, Aug. 2010.

[6] R. Cheng, J. Bai, L. Liao, H. Zhou, Y. Chen, L. Liu, Y.-C. Lin, S. Jiang, Y. Huang, and X. Duan, "High-frequency self-aligned grapheme transistors with transferred gate stacks," *Proc. Nat. Acad. Sci. U.S.A.*, vol. 109,no. 29, pp. 11 588–11 592, Jun. 2012.

[7] M. Cheli, G. Fiori, and G. Iannaccone, "A semianalytical model of bilayer graphene field effect transistor," *IEEE Trans. Electron Devices*, vol. 56,no. 12, pp. 2979–2986, Dec. 2009.

[8] S. Thiele and F. Schwierz, "Modeling of the steady state characteristics of large-area graphene field-effect transistors," *J. Appl. Phys.*, vol. 110, no. 3, pp. 034506-1–034506-7, Aug. 2011.

[9] J. G. Champlain, "A first principles theoretical examination of graphene- based field effect transistors," *J. Appl. Phys.*, vol. 109, no. 8, pp. 084515-1–084515-19, Apr. 2011.

[10] S. O. Koswatta, A. Valdes-Garcia, M. B. Steiner, L. Yu-Ming Lin, and P. Avouris, "Ultimate RF performance potential of carbon electronics," *IEEE Trans. Microw. Theory Tech.*, vol. 59, no. 10, pp. 2739–2750, Oct.2011

[11] S. A. Thiele, J. A. Schaefer, and F. Schwierz, "Modeling of graphene metal–oxide–semiconductor field-effect transistors with gapless large area graphene channels," *J. Appl. Phys.*, vol. 107, no. 9, pp. 094505-1–094505-8, May 2010.

[12] K. L. Shepard, I. Meric, and P. Kim, "Characterization and modeling of graphene field-effect devices," in *Proc. IEEE/ACM ICCAD*, 2008, pp. 406–411.

[13] J. Brews, "A charge-sheet model of the MOSFET," *Solid State Electron.*,vol. 21, no. 2, pp. 345–355, Feb. 1978.

[14] A. B. Bhattacharyya, *Compact MOSFET Models for VLSI Design*. Piscataway, NJ: Wiley-IEEE Press, 2009.

[15] S. M. Sze and K. K. Ng, *Physics of Semiconductor Devices*, 3rd ed. Hoboken, NJ: Wiley, 2009, ch. 6.

[16] D. Jiménez and O. Moldovan, "Explicit drain-current model of

graphene field-effect transistors targeting analog and radio-frequency applications," *IEEE Trans. Electron Devices*, vol. 58, no. 11, pp. 4049–4052,Nov. 2011.

[17] H. Wang, A. Hsu, J. Kong, D. A. Antoniadis, and T. Palacios, "Compact virtual-source current-voltage model for top- and back-gated graphene field-effect transistors," *IEEE Trans. Electron Devices*, vol. 58, no. 5,pp. 1523–1533, May 2011.

[18] I. Meric, "Current saturation in zero-bandgap, top-gated graphene Field effect transistors," *Nature Nanotechnol.*, vol. 3, pp. 654–659, Nov. 2008.

[19] J. Kedzierski, P.-L. Hsu, A. Reina, J. Kong, P. Healey, P. Wyatt, and C. Keast, "Graphene-on-insulator transistors made using C on Ni chemical-vapor deposition," *IEEE Electron Device Lett.*, vol. 30, no. 7, pp. 745–747, Jul. 2009.

[20] T. Fang, A. Konar, H. Xing, and D. Jena, Appl. Phys. Lett. **91**, 092109 (2007).

[21] J.-H. Chen, C. Jang, S. Xiao, M. Ishigami, and M. S. Fuhrer, Nat. Nanotechnol.**3**, 206 (2008).

An Approach to Determine Bandgap Energy in Graphene under Shear Strain Condition

Md. Delwar Hossain*, Abu Bakkar Siddiq+, Md.Shamim Sarker$, Muhammad Mainul Islam&, Md. Rafiqul Islam#
Department of Electrical and Electronic Engineering,
Khulna University of Engineering & Technology,
Khulna-9203, Bangladesh
E-mail: *delwarhossain3035@gmail.com, + eeealin@gmail.com, $sarkershamimbd@gmail.com, &mainul0803004@gmail.com
mri@eee.kuet.ac.bd

Abstract— **A simple analytical approach is presented to investigate the energy band structure of graphene under the application of shear strain. The strain-induced deformation in the unit cell in terms of the angle between two unit vectors is taken into consideration in the framework of nearest neighbor tight binding model. The proposed approach is applied to evaluate the energy band gap in graphene structure under shear strained condition. The results obtained from the proposed approach are compared with those of reported by DFT calculation and they are found to be in good agreement. This demonstrates that the proposed approach can be applied to calculate the band gap energy in shear strained graphene.**

Keywords— Graphene, shear strain, tight binding model, analytical approach, band structure.

I. INTRODUCTION

Graphene [1] is a name given to a flat single layer of carbon atoms tightly bonded into a two dimensional (2D) honeycomb lattice and is a fundamental building block for graphitic materials of all other dimensionalities [2]. Graphene is considered to be the strongest material ever [3]. As the graphene has excellent electronic structure [4]-[6] and transport property [7], researchers are having great interest in graphene. Since graphene is very thin having excellent electronic properties, it may be used in future logic devices to face the challenge of Gordon Moore's law, that is, the number of logic components per integrated circuit would double every 2 years. But the main problem with graphene is its zero band gap[1,8], which reveals that it cannot be used in logic circuits as well as other electronic applications. Scientists are working to find out the way to open the energy gap in graphene. Different methods have been proposed to create band gap in graphene, such as using quantum confinement effect in graphene nanoribbon (GNR) [9]-[11], applying external electric fields, introducing symmetry breaking of regular hexagonal structure[13],[14], by the process of doping [15]-[17], and by the process of external strain [18],[19]. To calculate the band gap in strained graphene, several techniques were applied [18-20] such as first principal calculation, tight binding model, K.P method, density function theory (DFT) etc. Most of them are performed by numerical simulation techniques which have huge computational complexity and hence needs high capacity super computer [18]. Some analytical works have also been done on strained graphene and GNR using tight binding approximation which mainly focuses on the strength of strain and spin polarization interaction [19]. In a recent study [20], we have reported an analytical approach to calculate strain-dependent energy band gap in uniaxially strained graphene. In this study a simple analytical approach is presented to determine the energy dispersion of graphene under the application of shear strain. In the proposed technique strain-induced unit cell deformation is incorporated in the framework of tight binding model. Using the proposed approach the band gap is determined for different values of shear strains. The results obtained from the proposed technique are compared with the results published by the DFT [19] and found to be in good agreement.

II.PROPOSED APPROACH

In symmetrically strained graphene, the band structure remained unchanged just like unstrained graphene. To introduce band gap in graphene structure asymmetrical strain (shear /uniaxial) could be applied that breaks the symmetry in the lattice structure. This leads to localize the delocalized electron and hence to create band gap in the graphene. The strain-induced lattice structure deformation under the application of shear strain along with unstrained lattice structure is shown in Fig. 1.

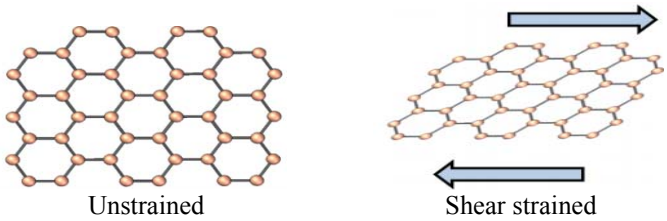

Figure 1. Unstrained and shear strained graphene structure [21].

978-1-4673-9257-0/15/$31.00 ©2015 IEEE

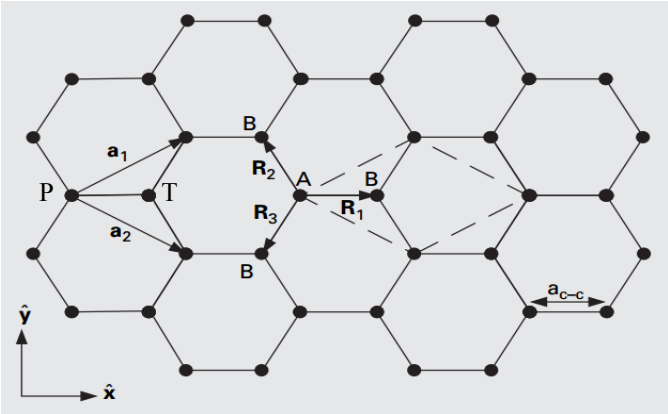

Figure 2. The honeycomb lattice of graphene. The primitive unit cell is the equilateral parallelogram (dashed lines) with a basis of two atoms denoted by A and B.

In our study, we have used the nearest neighbor tight binding model. Here the type-A atom in the graphene lattice is bonded with three of its nearest neighbors of type-B atoms as shown in fig. 2, where the primitive unit cell is also shown by dashed line. In unstrained graphene the angle between the unit vectors $\mathbf{a_1}$ and $\mathbf{a_2}$ is 60^0, which with respect to a unit vector and the reference line PT is 30^0. However, under the application of shear strain the unit cell will be deformed. As a result, the angle between the unit vectors $\mathbf{a_1}$ and $\mathbf{a_2}$ will be changed. A typical deformation of unit cell due to shear strain is shown in Fig. 3, where α and β are the angles between the line PT and unit vectors $\mathbf{a_1}$ and $\mathbf{a_2}$, respectively.

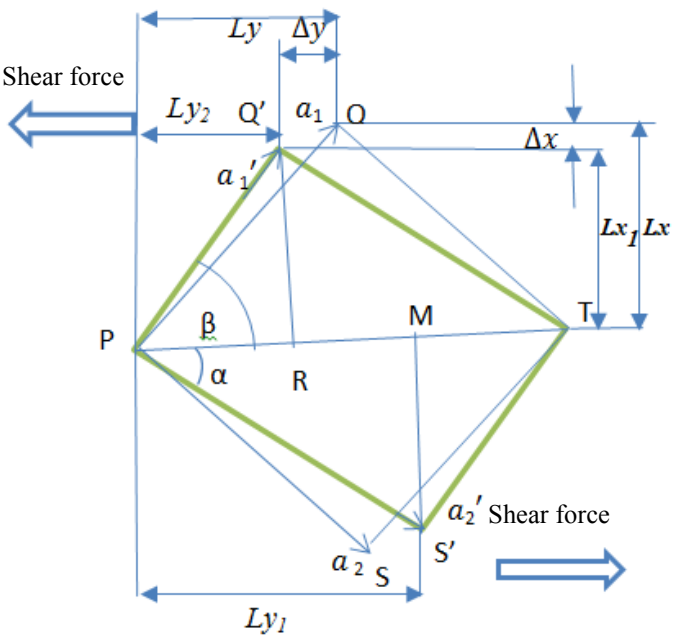

Figure 3. The un-deformed and shear strain-induced deformed primitive unit cells with their primitive unit vectors.

When shear strain is applied the points Q and S is shifted to points Q' and S' due to unit cell deformation, assuming that the points P and T are fixed as seen in Fig. 3. Using trigonometric relationship in $\Delta PQ'R$ the angle β can be expressed by

$$\beta=\tan^{-1}\frac{L_{x1}}{L_{y2}}=\tan^{-1}\frac{L_x-\Delta x}{L_y-\Delta y} \quad (1)$$

where $\Delta x = L_x - L_{x1}$ and $\Delta y = L_y - L_{y2}$. Δx and Δy represent the deformation in the primitive unit vectors due to shear strain.

Similarly from $\Delta PMS'$,

$$\alpha=\tan^{-1}\frac{L_{x1}}{L_{y1}}=\tan^{-1}\frac{L_x-\Delta x}{L_y+\Delta y} \quad (2)$$

Due to the strain-induced deformation of primitive unit cell the vectors $\boldsymbol{a_1}'$ and $\boldsymbol{a_2}'$ become

$$\boldsymbol{a_1}' = [a_1'\cos(\beta), a_1'\sin(\beta)],$$
$$\boldsymbol{a_2}' = [a_2'\cos(\alpha), -a_2'\sin(\alpha)] \quad (3)$$

Here a_1' and a_2' represent magnitude of the vectors. It is found in "Fig. 2" that there are three nearest neighboring atoms. The separation of these atoms can be represented by three vectors $\boldsymbol{R_1}$, $\boldsymbol{R_2}$, and $\boldsymbol{R_3}$.

$$\boldsymbol{R_1} = (\tfrac{2}{3}a_1'\cos\beta, 0) = \tfrac{2}{3}a_1'\cos\beta\,\mathbf{x} \quad (4)$$

$$\boldsymbol{R_2} = -\boldsymbol{a_2}' + \boldsymbol{R_1} = \left(\tfrac{2}{3}a_1'\cos\beta - a_2'\cos\alpha\right)\mathbf{x} + a_2'\sin\alpha\,\mathbf{y} \quad (5)$$

and $\boldsymbol{R_3} = -\boldsymbol{a_1}' + \boldsymbol{R_2}$

$$\boldsymbol{R_3} = \left(-\frac{1}{3}a_1'\cos\beta - a_2'\cos\alpha\right)\mathbf{x} + (a_2'\sin\alpha - a_1'\sin\beta)\,\mathbf{y} \quad (6)$$

From tight-binding energy dispersion model the formula of energy dispersion can be given by

$$E(k) = \pm\sqrt{H_{AB}(k)H_{AB}^*(k)} \quad (7)$$

where $H_{AB}(k)$ is the Hamiltonian matrix. For unstrained graphene the Hamiltonian matrix element reduces to a sum of three terms:

$$H_{AB(k)} = \gamma e^{-ikR_1} + \gamma e^{-ikR_2} + \gamma e^{-ikR_3} \quad (8)$$

When shear strain is applied " (8)" becomes

$$H_{AB(k)} = \gamma_1 e^{-ikR_1} + \gamma_2 e^{-ikR_2} + \gamma_3 e^{-ikR_3} \quad (9)$$

and its conjugate is

$$H^*_{AB(k)} = \gamma_1 e^{ikR_1} + \gamma_2 e^{ikR_2} + \gamma_3 e^{ikR_3} \quad (10)$$

Here γ is a fitting parameter which is often called the nearest neighbor overlap energy. In unstrained graphene, $\gamma_1 = \gamma_2 = \gamma_3 = \gamma = -2.8\, eV$[22]. When shear strain is applied, the change of three bond length with three nearest neighbor become different. As a result, the values of γ_1, γ_2, and γ_3 become different [22]. Now

$$H_{AB}(k)H^*_{AB}(k) = (\gamma_1 e^{-ikR_1} + \gamma_2 e^{-ikR_2} + \gamma_3 e^{-ikR_3}) * (\gamma_1 e^{ikR_1} + \gamma_2 e^{ikR_2} + \gamma_3 e^{ikR_3}) \quad (11)$$

Putting the value of $\boldsymbol{R_1}$, $\boldsymbol{R_2}$, $\boldsymbol{R_3}$ and $\boldsymbol{K} = k_x\boldsymbol{x} + k_y\boldsymbol{y}$ and after some mathematical manipulation we get

$$\mathrm{H}_{AB}(k)H^*_{AB}(k) = \gamma_1^2 + \gamma_2^2 + \gamma_3^2 + 2\gamma_1\gamma_2 c_1 + 2\gamma_2\gamma_3 c_2 + 2\gamma_3\gamma_1 c_3 \quad (12)$$

where $c_1 = \cos[-a_2^{'}\cos\alpha k_x + a_2^{'}\sin\alpha k_y]$

$$c_2 = \cos[-\, a_1^{'}\cos\beta\, \mathrm{k_x} - a_1^{'}\sin\beta\, \mathrm{k_y}] \quad (13)$$

$$c_3 = \cos[(a_1^{'}\cos\beta + a_2^{'}\cos\alpha)\mathrm{k_x} + (a_1^{'}\sin\beta - a_2^{'}\sin\alpha)k_y)]$$

Substituting "(12)" into "(7)" we have

$$E(k) = \pm\sqrt{\gamma_1^2 + \gamma_2^2 + \gamma_3^2 + 2\gamma_1\gamma_2 c_1 + 2\gamma_2\gamma_3 c_2 + 2\gamma_3\gamma_1 c_3} \quad (14)$$

This is the generalized equation for the energy dispersion relation of graphene under shear strain condition.

III.RESULTS AND DISCUSSION

We have studied the electronic band structure of shear strained graphene. Application of shear strain leads to create bandgap. The strain-induced deformation of unit cell causes change in angles (α and β) between vectors ($a_1^{'}$ and $a_2^{'}$) and reference line PT asymmetrically. These angular changes are taken as parameters to calculate the band structure of graphene under shear strained condition. Using "(1)" and "(2)" values of α and β are evaluated 29.66^0, 29.01^0, 27.75^0, 26.93^0 and 30.29^0, 30.99^0, 32.25^0, and 33.07^0 respectively, for the change in strain values 0.48% , 1.86% , 4.17%, and 5.58%. Using "(13)" the band gap energies are estimated

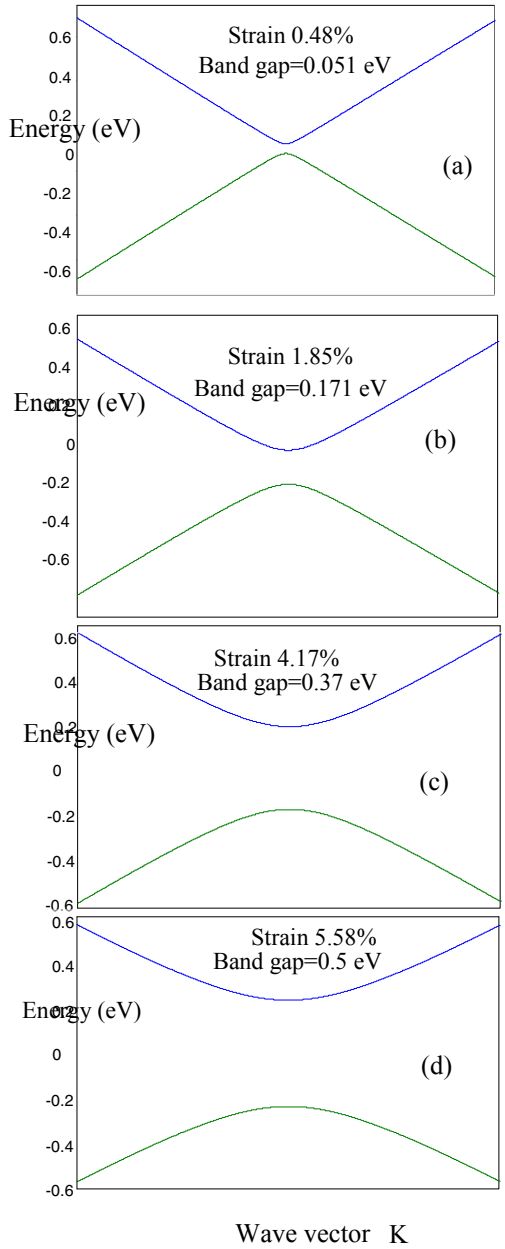

Figure 4. Bandgap opening under the application of shear strain (a) 0.48 % (b) 1.85 %(c) 4.17 %, and (d) 5.58% strain

and are found to be 0.051, 0.171, 0.37 and 0.50 eV for the corresponding percentage of strain. Due to the application of shear strain the symmetry of the regular hexagonal structure is broken, as a result, energy bangap created in shear strained graphene. The results are shown in Fig. 4 (a), (b), (c), and (d). To observe the results clearly, the dispersion profiles are extended near the K-point of the Brillouin zone.

IV. CONFIRMATION OF THE PROPOSED TECHNIQUE

In order to confirm the proposed analytical approach, the results obtained from the present study is compared with the previously published results. A comparison is shown in Table 1. It is found that the results obtained from the proposed technique agree with the results evaluated from DFT calculation, upto the 5.6 percents of applied strain [19]. This demonstrates that the proposed technique can be applied to determine the bandgap in shear strained graphene structure.

TABLE I. COMPARISON OF SHEAR STRAIN-DEPENDENT ENERGY GAPS OBTAINED FROM THE PROPOSED TECHNIQUE AND DFT CALVULATION [19]

L_{x1} (nm)	L_{y1} (nm)	L_{y2} (nm)	DFT (eV)	Proposed approach (eV)
0.12397	0.21769	0.21219	0.0489	0.051
0.12559	0.22650	0.20902	0.196	0.171
0.12673	0.23340	0.20680	0.287	0.252
0.12803	0.24029	0.20489	0.401	0.321
0.12845	0.24414	0.20359	0.435	0.37
0.13045	0.25680	0.20034	0.583	0.5

V. CONCLUSION

In this study, a simple analytical approach is proposed to evaluate the energy dispersion in shear strained graphene on the basis of nearest neighbor tight binding model. The strain-dependent change in the angle between the two primitive vectors of a unit cell of graphene is taken into consideration. It is found that the angles between two primitive vectors with respect to a reference change asymmetrically due to shear strain. It is found that with the increase in strain the energy band gap increases and it is evaluated to be 0.5 eV for the value of strain 5.58%. Finally, to confirm the proposed technique our results are compared with those of reported by DFT calculation and found to be in good agreement.

REFERENCES

[1] K.S. Novoselov, A.K. Geim, S.V. Morozov, D. Jiang, Y. Zhang, S.V. Dubonos, I.V. Grigorieva and A.A. Firsov ‘’electric field effect in atomically thin carbon film’’, Science 306, 666 (2004).

[2] H.-S. Philip Wong and Deji Akinwande,’’Carbon Nanotube and Graphene Device Physics’’, (pub: 2011).

[3] C. Lee, X. Wei, J. W. Kysar, and J.Hone, Science.321, 385(2008).

[4] M. Y. Han, B. zyilmaz, Y. B. Zhang, and P. Kim, Phys. Rev. Lett.98,206805 (2007).

[5] L. Yang, C. H. Park, Y. W. Son, M. L. Cohen, and S. G.Louie, Phys. Rev. Lett. 99, 186801 (2007).

[6] P. Shemella, Y. Zhang, M.Mailman, P. M. Ajayan, and S.K. Nayak, Appl. Phys. Lett.91, 042101(2007).

[7] Z.Y. Li, H.Y. Qian, J. Wu, B. L. Gu, and W. Duan, Phys. Rev. Lett. 100,206802 (2008).

[8] K.S. Novoselov, D. Jiang, F.Schedin, T.J. Bhoot, V.V. Khot-kevich, S.V. Morozov and A.K Geim, Proc.Natl.Acad. Sci. U.S.A. 102,10451 (2005)

[9] M.Y. Han, B. Ozylmaz, Y. Zhang, and P. Kim, “Energy band gap engineering of grapheme nanoribbons,” Phys. Rev. Lett. ,vol. 98, no. 20, P. 206805, May 2007.

[10] Y. W. Son, M. L. Cohen, and S. G. Louie, “Energy gaps in graphene nanoribbons,” Phys. Rev. Lett., vol. 97, no. 21, p. 216803, Nov. 2006.

[11] JIANG Lianjun, XIONG Cuixiu , HUANG Li , ZHOU Guanghui , “ The Gap Opening and Threshold of Graphene by Shear Strain “, Journal of Materials and Applications (2013)

[12] T. Ohta, A. Bostwick, T. Seyller, K. Horn, and E. Rotenberg, “Controlling the electronic structure of bilayer graphene,” Science, vol. 313, no. 5789, pp. 951–954, Aug. 2006.

[13] Y. Zhang, T.-T. Tang, C. Girit, Z. Hao, M. C. Martin, A. Zettl, M. F. Crommie, Y. R. Shen, and F. Wang, “Direct observation of a widely tunable bandgap in bilayer graphene,” Nature, vol. 459, no. 7248, pp.820–823, Jun. 2009.

[14] Jun Ito, Jun Nakamura, and Akiko Natori, “Semiconducting nature of the oxygen-adsorbed graphene sheet,” Journal of applied phys. 103,113712 (2008).

[15] Paolo Marconcini, Gianluca Fiori, Alessandro Ferretti, Giuseppe Iannaccone, and Massimo Macucci,“Numerical analysis of transport properties ofboron-doped graphene FETs”.

[16] Zhipping Xu and Kun Xue,“Engeneering graphene by oxidation: a first principle study,” Nanotechnology21 (2010) 045704

[17] Gui Gui, Jin Li, and Jianxin Zhong ‘Band structure engineering of graphene by strain: First-principles calculations’, PHYSICAL REVIEWB 78, 075435 2008.

[18] V.J. Surya, K. Iyakutti, H. Mizuseki, and Y. Kawazoe, “Tuning electronic structure of Graphene: A first-principle calculation,” IEEE Trans. Nanotechnology, vol.11, No.3,pp.534-541, May 2012.

[19] Yang Li, Xiaowei Jiang, Zhongfan Liu, Zhirong Liu, “Strain Effects in Graphene and Graphene Nanoribbon: The underlying mechanism,”Nano Res (2010) 3: 545–556.

[20] M. S. Sarker , M. M Islam, Md. R Islam, ‘’An Analytical Approach to Study Energy Band Structure in Strained Graphene’’,2013.

[21] Anderson Smith, Dr. Max Lemme, Prof. Mikael Östling, “Strain Effects on Electrical Properties of Suspended Graphene” October, 2010.

[22] JIANG Lianjun, XIONG Cuixiu, HUANG Li, ZHOU Guanghui, “The Gap Opening and Threshold of Graphene by Shear Strain” Journal of Materials and Applications 2:1 (2013).Trans. Nanotechnology, vol.11, No.3,pp.534-541, May 2012

Modeling and Performance Analysis of Multilayer Zigzag Graphene Nanoribbon (zz-MLGNR) Interconnect for VLSI Application

Monjurul Feeroz Meem*, Abdullah Ash-Saki and Dr. A. B. M Harun-Ur Rashid
Department of Electrical and Electronic Engineering, Bangladesh University of Engineering and Technology, Dhaka, Bangladesh
* E-mail: monjurul_bueteee@yahoo.com

***Abstract*—Based on equivalent single conductor (ESC) model, an appropriate RLC equivalent circuit model for multi layer zigzag graphene nanoribbon (zz-MLGNR) interconnect is presented. The values of different circuit parameters (i.e resistance, inductance and capacitance) are calculated. The impact of various interconnect parameters (e.g., dimension of interconnect, number of GNR layers, Fermi energy) on the circuit parameters are discussed. The per unit length resistance of zz-MLGNR interconnect is compared with other interconnect materials [e.g., copper (Cu), tungsten (W) and carbon nanotubes (CNTs)]. The analysis revealed that zz-MLGNR can offer lower resistance than Cu, W and even single-walled carbon nanotubes (SWCNs). Time delay of zz-MLGNR interconnect is analyzed using the RLC equivalent circuit model and it is shown that intercalation-doped zz-MLGNR can outperform Cu.**

Keywords—GNR interconnect, multilayer graphene nanoribbon (MLGNR), interconnect delay.

I. INTRODUCTION

To keep up with the Moore's law both transistor and interconnect dimensions are scaled down rapidly. The continuing exponential reduction in feature size on electronic chips, leads to ever larger number of faster devices at lower cost per device. The decrease in minimum feature size of devices has led to a proportional decrease in interconnect cross-sectional area and pitch, as a consequence the delay associated with the transistors, gate delay, has continuously decreased with decrease in minimum feature size, while the delay associated with interconnect, the parasitic resistance, capacitance and inductance delay has increased significantly. International Technology Roadmap for Semiconductors (ITRS) [1] has pointed out that, due to this scaling down, traditional semiconductor material, silicon (Si) and interconnect material, copper (Cu) are reaching their threshold limit, so the industry is in search for viable alternatives; and carbon based materials are the protagonist in this endeavour.

Graphene, an atomic layer of carbon atoms arranged in a two dimensional (2D) honeycomb lattice, has recently emerged as a potential candidate for nanoelectronics due to its promising electronic properties [2]. The high mobility and carrier velocity in graphene promises ballistic devices with high switching speeds. The fabrication of the first field-effect graphene-based transistor [3], led to an explosion of interest in the electronic properties of graphene. Nowadays, graphene is considered to be a viable alternative to Si and Cu [4]. If graphene sheet is patterned into narrow strips then it is called graphene nano-ribbon (GNR). GNR can conduct much larger current densities than Cu, due to its strong sp^2 hybridize bonds and absence of severe reliability problems that plague Cu, particularly for future interconnect geometries [3, 5-8]. Thermal conductivity of GNR is much larger than Cu [9-11]. Moreover, compared to Cu, GNR has larger carrier mean free path (MFP), which leads to larger electrical conductance [12-14]. Physically graphene can be metallic or semiconducting according to its chirality. For example zigzag edge GNR (zz-GNR) is always metallic, while armchair-GNR (ac-GNR) can exhibit both semiconducting and metallic behaviour depending on the number of carbon atom along its width [15]. The potential performance of GNR transistors has been studied in several publications, and it has been projected that such transistors can potentially outperform Silicon transistors because of the large carrier mobility and the better electrostatic control of gate on channel [16, 17]. GNR interconnects can potentially be used as intracell interconnects linking GNR transistors in a seamless fashion [3, 18, 19] or in a multilevel interconnect network like conventional interconnects [20]. The former would reduce the number of metal-to-graphene connections and, therefore, would improve the circuit performance by eliminating some contact and quantum resistances. Although the maximum current-carrying density up to *108 A/cm*^{2} (*~100* times of Cu) was reported, current density of SLGNR is limited by its 2D atomically-thin geometry, sensitivity to ambient, poor noise tolerance, and conductance degradation due to edge-related effects [21, 22]. 3D nano-carbon, or vertically stacked multilayer graphene (MLGNR), can potentially be employed to address this challenge, yielding an ultra conductive material system as shown in Fig. 1. Multilayer graphene has received significant amount of theoretical and experimental attentions in recent years [23]. The in-plane conductivity of graphite can be several tens of magnitude by intercalation doping, which involves an insertion of one dopent layer between each pair of graphene layers [24]. Intercalation doping can increase the carrier density due to increased layer spacing [25].

In this paper we have presented a RLC equivalent circuit model for multi layer zigzag graphene nano-ribbon (zz-MLGNR) based on equivalent single conductor (ESC) model [26]. Per unit length resistance, capacitance and inductance of zz-MLGNR are calculated using the proposed model. The effect of interconnect width, number of layers and Fermi energ-

978-1-4673-9257-0/15/$31.00 ©2015 IEEE

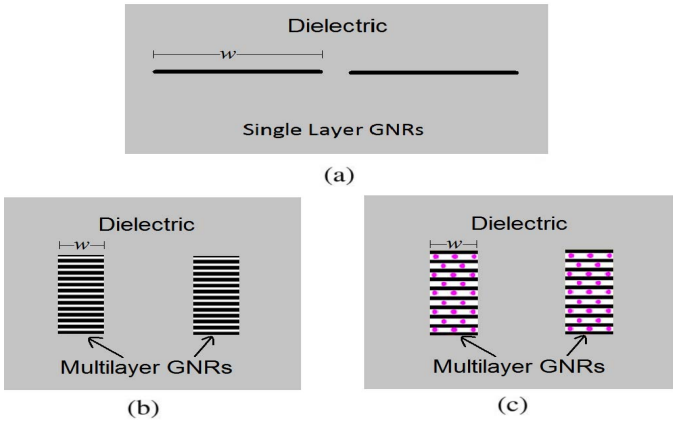

Figure 1. Schematic view of (a) monolayer GNR, (b) neutral multi layer GNR, (c) intercalation-doped multilayer GNR.

y on different parameters are discussed. Resistance of zz-MLGNR is benchmarked against other traditional interconnect materials. Finally 50 percent delay of zz-MLGNR interconnect is calculated and benchmarked against Cu.

II. CIRCUIT MODELING

Let's consider a N layer zz-MLGNR interconnect of length L, width w ($w << L$), thickness t as shown in Fig. 2(a). The per unit length equivalent circuit of zz-SLGNR is shown in Fig. 2(a). In Fig. 2(a), R_Q is the quantum resistance which is expressed as [27]

$$R_Q = h/2e^2 N_{ch} \approx 12.9\ k\Omega/N_{ch} \quad (1)$$

Where h is Plank's constant and N_{ch} is the number of conduction channel, which is a function of GNR width w, chirality, temperature and Fermi energy. N_{ch} is calculated by [28]

$$N_{ch} = \Sigma 1/[1+exp((E-E_F)/k_BT)] + \Sigma 1-1/[1+exp((E-E_F)/k_BT)] \quad (2)$$

Magnetic inductance (L_M) and electrostatic capacitance (C_E) are determined by the geometry and the materials surrounding the interconnects. Kinetic inductance (L_K) represents the kinetic energy of the electrons and because of small density of states in GNR, its value is substantially larger than the magnetic inductance [29]. Unlike magnetic inductance, kinetic inductance has no mutual component and its value decreases linearly with increase in N_{ch} ($8\ nH/\mu m/N_{ch}$) [30]. Quantum capacitance is also the consequence of small density of states and increases linearly with N_{ch} ($200\ N_{ch}\ aF\ /\mu m$). The scattering resistance per unit length is represented by r which can be expressed as $r = R_Q / l_D$. Here l_D the mean free path which is around $1\mu m$ in graphene [31]. zz-MLGNR can be considered as a arrangement of N zz-SLGNR, Fig. 2(b) shows the per unit length equivalent circuit of MLGNR, and the multiconductor transmission line (MTL) representation of it is shown in Fig. 2(c), here R_c is terminal contact resistance, L_m is magnetic inductance and C_m is mutual capacitance. In order to reduce the computational effort of the complex MTL approach, zz-MLGNR can be analyzed using an equivalent single conductor (ESC) model [32]. The ESC model is represented in Fig. 3(a). R_{ESC} can be calculated by,

$$R_{ESC} = h/2e^2\ N_{ch}\ N\ l_D \quad (3)$$

L_{ESC} and C_{ESC} are calculated from Fig. 3(b) and Fig. 3(c) respectively.

III. RESULTS AND DISCUSSIONS

In the process of modelling zz-MGNR interconnect various physical properties were investigated. Fig. 2(a) shows the schemata of the considered structure. The number of conduction channel (N_{ch}) is obtained using closed from expression Eq. 1 and plotted versus width for different Fermi energy in Fig. 4. Increasing width and Fermi energy populates more subbands and therefore, increases the number of conduction channel. Knowing the number of conduction channel the per unit length resistance of zz-MLGNR are calculated from ESC model and plotted versus width for different number of layers and Fermi energy in Fig. 5. For reference, the per unit length resistance of Cu and W wires with unity aspect ratio and monolayer single walled nanotube (SWCNT) interconnect with random chiralitiy are also plotted. The analysis reveals that the per unit length resistance of neut-

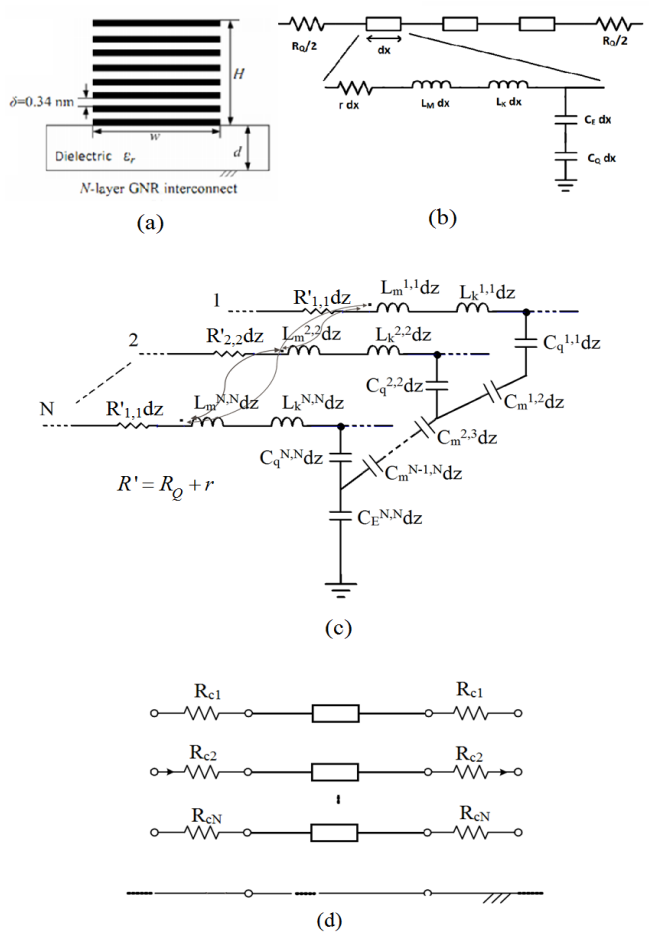

Figure 2. (a) Geometry of a N layer zz-MLGNR along with, (b) per unit length equivalent circuit model of zz-SLGNR, (c) per unit length equivalent circuit model of zz-MLGNR and (d) multiconductor representation of zz-MLGNR including terminal resistance.

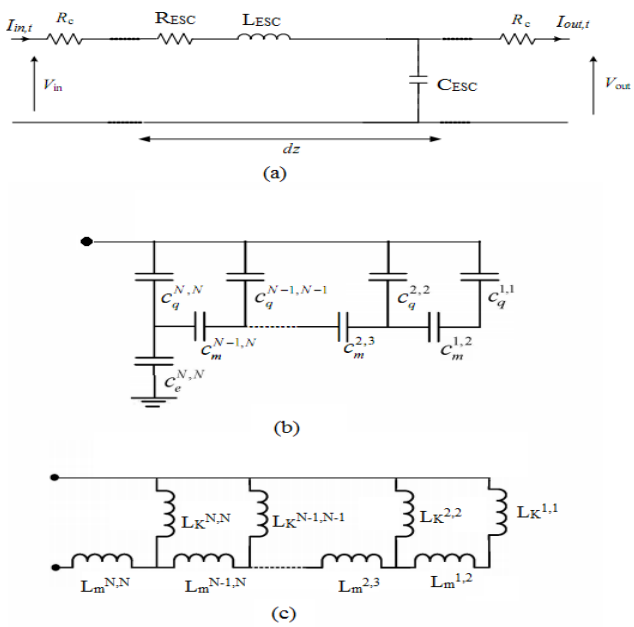

Figure 3. (a) ESC circuit of an MLGNR interconnect and per unit length equivalent network for (b) capacitance; (c) inductance.

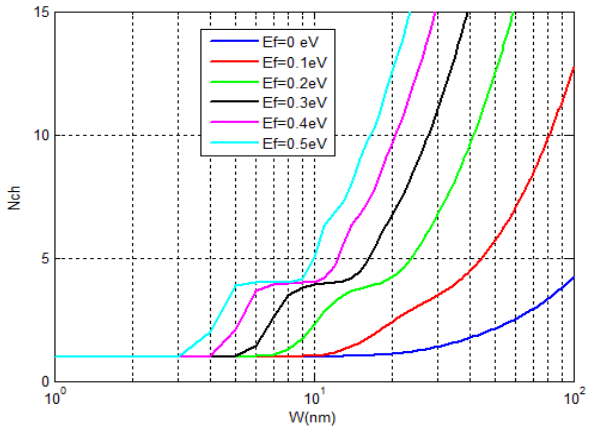

Figure 4. Number of conduction channel (N_{ch}) versus width for different Fermi energy is shown.

ral (E_F = 0) zz-MLGNR is higher that Cu and SWCNT. But at higher Fermi energy it can offer significantly less per unit length resistance than both Cu and SWCNT. The per unit length capacitance of zz-MLGNR is calculated using the ESC model and plotted. Fig. 6 (a) shows the per unit length capacitance as a function of width and Fig. 6 (b) shows the per unit length capacitance as a function of layer number for both *14nm* and *22nm* technology nodes. Fig. 6 reveals that, capacitance increases with increase in width but shows little variation due to change in Fermi energy or number of GNR layers. This is because, all the components of C_{ESC} i.e C_Q, C_m and C_E increases with width but among them only C_Q changes with Fermi energy and whose value is much-much larger than C_m or C_E.

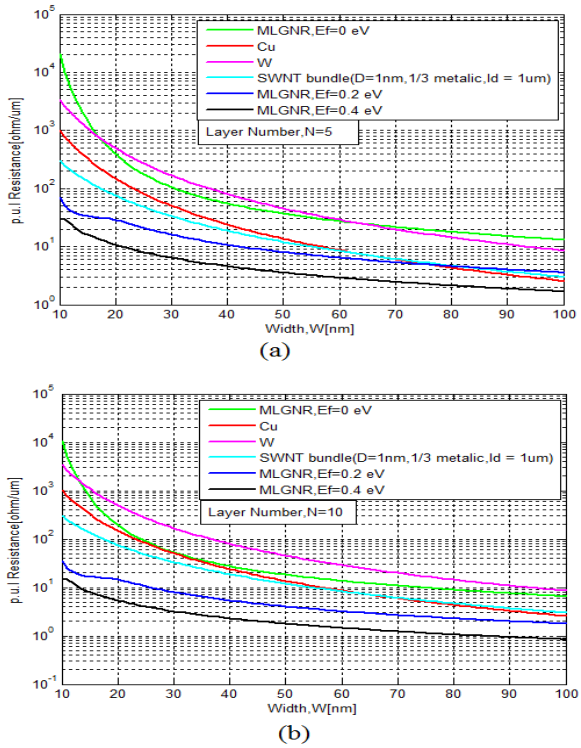

Figure 5. Per unit length resistance of zz-MLGNR shown for (a) 5 layers and, (b) 10 layers. Per unit length resistance of Cu, Wires with unit aspect ratio and monolayer SWNT (D = 1nm) with random chirality is also shown for comparison.

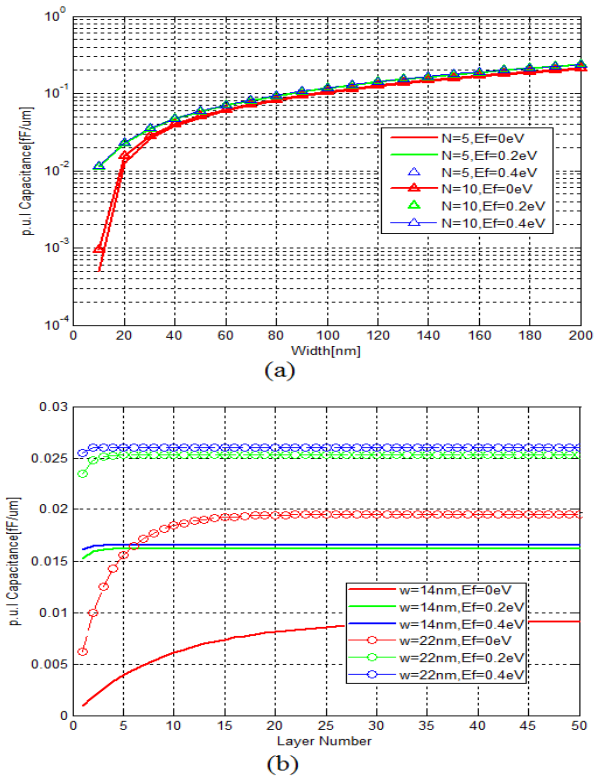

Figure 6. Per unit length capacitance of zz-MLGNR as (a) function of width (b) function of number of GNR layer.

Fig. 7 shows the per unit length inductance as a function of width and number of GNR layer . L_k decreases with increase in width, Fermi energy and number of GNR layer and L_m decreases with increase in GNR width, so the total inductance decreases with increase in width, Fermi energy and number of layers.

For delay calculation a driver-GNR interconnect as shown in Fig. 8 is studied. Based on the proposed RLC model, simulations were implemented using HSPICE. The driver equivalent resistance and capacitance are obtained from the ITRS [1]. Fig. 9 shows the 50% delay of zz-MLGNR of width *14nm* consisting of 10 layers with respect to Cu interconnect of same dimension. It is evident from Fig. 9 that the performance of neutral zz-MLGNR is much worse than Cu but it can outperform Cu when its Fermi energy is raised at 0.6 eV, which can be achieved by intercalation doping [33].

IV. Conclusion

We have developed an RLC equivalent circuit for zz-MLGNR based on ESC model. We have investigated all the lumped elements in zz-MLGNR based on the proposed model and compared with that of Cu, W and SWCNT interconnect. The analysis revealed that, zz-MLGNR can provide lower per unit length resistance than Cu, W and SWCNT it also offers lower per unit length capacitance but in the expense of higher inductance. We have analyzed interconnect delay of zz-MLGNR using the proposed RLC equivalent circuit. It is concluded that the performance of zz-MLGNR can match or become better than Cu only if it is intercalation doped.

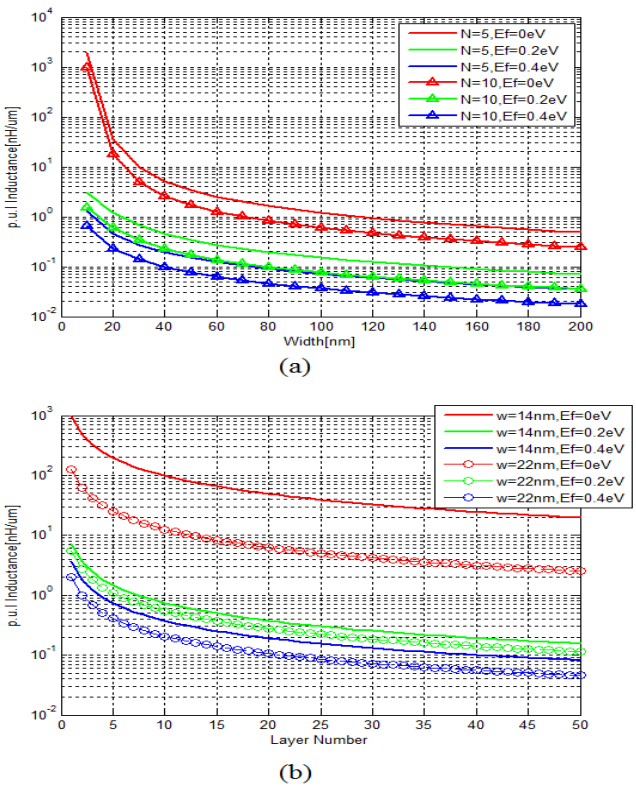

Figure 7. Per unit length inductance of zz-MLGNR as (a) function of width and, (b) as a function of number of GNR layer.

Figure 8. Configuration of the driver-GNR interconnect-load system.

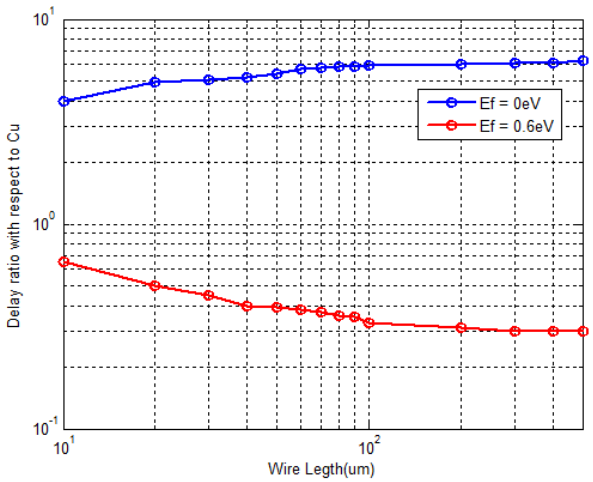

Figure 9. 50% Time delay of zz-MLGNR(layer number, $N = 10$) for 14 nm technology node with respect to the Cu interconnect delay of same dimension is shown.

References

[1] [Online]. Available: http://www.itrs.net/

[2] A. H. Castro Neto, F. Guinea, N.R. Peres, K.S. Novoselov, A.K. Geim, "The electronic properties of graphene", *Rev. Mod. Phys.*, vol. 81, pp.109-162, 2009.

[3] K. S. Novoselov *et. al.*, "Electric Field-Effect in atomically thin carbon films", *Science* vol. 306, pp. 666-669, 2004.

[4] F. Schwierz, "Graphene transistors", *Nat. Nanotechnol.*, vol. 5, pp. 487- 496, 2010.

[5] N. Srivastava and K. Banerjee, "Interconnect challenges for nanoscale electronic circuits," *TMS J. Mater.*, vol. 56, no. 10, pp. 30–31, Oct. 2004.

[6] N. Srivastava, H. Li, F. Kreupl, and K. Banerjee, "On the applicability of single-walled carbon nanotubes as VLSI interconnects," *IEEE Trans. Nanotechnol.*, vol. 8, no. 7, 2009.

[7] M. Radosavljević, J. Lefebvre, and A. T. Johnson, "High-field electrical transport and breakdown in bundles of single-wall carbon nanotubes," *Phys. Rev. B, Condens. Matter*, vol. 64, no. 24, p. 241 307, Dec. 2001.

[8] B. Q. Wei, R. Vajtai, and P. M. Ajayan, "Reliability and current carrying capacity of carbon nanotubes," *Appl. Phys. Lett.*, vol. 79, no. 8, pp. 1172–1174, Aug. 2001.

[9] J. Hone, M. Whitney, C. Piskoti, and A. Zettl, "Thermal conductivity of single-walled carbon nanotubes," *Phys. Rev. B, Condens. Matter*, vol. 59, no. 4, pp. R2 514–R2 516, Jan. 1999.

[10] P. Kim, L. Shi, A. Majumdar, and P. L. McEuen, "Thermal transport measurements of individual multiwalled carbon nanotubes," *Phys. Rev. Lett.*, vol. 87, no. 21, p. 215 502, Oct. 2001.

[11] A. A. Balandin, S. Ghosh, W. Bao, I. Calizo, D. Teweldebrhan, F. Miao, and C. N. Lau, "Superior thermal conductivity of single-layer graphene," *Nano Lett.*, vol. 8, no. 3, pp. 902–907, Mar. 2008.

[12] P. L. McEuen, M. S. Fuhrer, and H. Park, "Single-walled carbon nan-otube electronics," *IEEE Trans. Nanotechnol.*, vol. 1, no. 1, pp. 78–85, Mar. 2002.

[13] H. J. Li,W. G. Lu, J. J. Li, X. D. Bai, and C. Z. Gu, "Multichannel ballistic transport in multiwall carbon nanotubes," *Phys. Rev. Lett*., vol. 95, no. 8, p. 086 601, Aug. 2005.

[14] K. I. Bolotin, K. J. Sikes, J. Hone, H. L. Stormer, and P. Kim, "Temperature dependent transport in suspended graphene," *Phys. Rev. Lett*., vol. 101, no. 9, p. 096 802, Aug. 2008.

[15] D. A. Areshkin, D. Gunlycke, and C. T. White, "Ballistic transport in graphene nanostrips in the presence of disorder: Importance of edge effects," *Nano Lett*., vol. 7, no. 1, pp. 204–210, Jan. 2007.

[16] Y. Ouyang, Y. Yoon, J. K. Fodor, and J. Guo, "Comparison of performance limits for carbon nanoribbon and carbon nanotube transistors," *Applied Physics Letters*, vol. 89, no. 20, pp. −, 2006. [Online]. Available: http://scitation.aip.org/content/aip/journal/apl/89/20/10.1063/1.2387876

[17] G. Liang, N. Neophytou, D. Nikonov, and M. LUNDSTROM, "Performance projections for ballistic graphene nanoribbon field-effect transistors," *Electron Devices, IEEE Transactions on*, vol. 54, no. 4, pp. 677−682, April 2007

[18] R. Van Noorden, "Moving towards a graphene world," *Nature*, vol. 442, no.7100, pp. 228−229, 2006.

[19] C. Berger, Z. Song, X. Li, X. Wu, N. Brown, C. Naud, D. Mayou, T. Li, J. Hass, A. N. Marchenkov *et al*., "Electronic confinement and coherence in patterned epitaxial graphene," *Science*, vol. 312, no. 5777, pp. 1191−1196,2006.

[20] A. Naeemi and J. Meindl, "Performance benchmarking for graphene nanoribbon, carbon nanotube, and cu interconnects," in *Interconnect Technology Conference, 2008. IITC 2008. International*, June 2008, pp. 183−185.

[21] T. Yu, E.-K. Lee, B. Briggs, B. Nagabhirava, and B. Yu, "Bilayer graphene system: current-induced reliability limit," Electron Device Letters, IEEE, vol. 31, no. 10, pp. 1155−1157, 2010.

[22] R. Murali, Y. Yang, K. Brenner, T. Beck, and J. D. Meindl, "Breakdown current density of graphene nanoribbons," *Applied Physics Letters*, vol. 94, no. 24, p. 243114, 2009.

[23] Y. Sui and J. Appenzeller, "Screening and interlayer coupling in multilayer graphene field-effect transistors," *Nano letters*, vol. 9, no. 8, pp. 2973−2977,2009.

[24] M. S. Dresselhaus and G. Dresselhaus, "Intercalation compounds of graphite," *Adv. Phys*., vol. 51, no. 1, pp. 1–186, Jan. 2002.

[25] J. E. Fischer and T. E. Thompson, "Graphite intercalation compounds," *Phys. Today*, vol. 31, no. 7, pp. 36−45, Jul. 1978.

[26] M, S, Sarto and A. Tamburrano, "Comparative analysis of TL models for multilayer graphene nanoribbon and multi wall carbon nanotube interconnects," *int, Symp. EMC*, 2010, pp, 212−217.

[27] S. Datta, *Quantum transport: atom to transistor*. Cambridge University Press, 2005.

[28] D. K. Ferry and S. M. Goodnick, *Transport in Nanostructures*. Cambridge, U.K.: Cambridge Univ. Press, 1997.

[29] P. J. Burke, "Luttinger liquid theory as a model of the gigahertz electrical properties of carbon nanotubes," *IEEE Trans. Nanotechnol*., vol. 1, no. 3, pp. 129–144, Sep. 2002.

[30] A. Naeemi and J. D. Meindl, "Design and performance modeling for single-walled carbon nanotubes as local, semiglobal, and global inter connects in gigascale integrated systems," *IEEE Trans. Electron Devices*, vol. 54, no. 1, pp. 26–37, Jan. 2007.

[31] C. Berger, Z. Song, T. Li, X. Li, A. Y. Ogbazghi, R. Feng, Z. Dai, A. N. Marchenkov, E. H. Conrad, P. N. First, and W. A. de Heer, "Ultrathin epitaxial graphite: 2D electron gas properties and a route to- ward graphene-based nanoelectronics," *J. Phys. Chem. B*, vol. 108, no. 52, pp. 19 912–19 916, Dec. 2004.

[32] M. S. Sarto and A. Tamburrano, "Electromagnetic analysis of radio-frequency signal propagation along SWCN bundles", *Int. Symp. IEEE-NANO 2006*, Cincinnati, USA, July 2006.

[33] J. Shioya, H. Matsubara, and S. Murakami, "Properties of AsF_5-intercalated vapor-grown graphite," *Synth. Met*., vol. 14, no. 1/2, pp. 113–123, Mar. 1986.

Study of the Variation of Resistivity, Permeability and Curie Temperature of Rare Earth Metal Yttrium (Y) Substitution on $Ni_{0.60}Zn_{0.40-x}Y_x Fe_2O_4$ (x=0.05, 0.10, 0.15) Ferrites

M. A. Hossain
Department of Physics
Khulna University of Engineering & Technology (KUET), Khulna-9203, Bangladesh
E-mail :litonalam.bd@gmail.com
M. N. I. Khan
Materials Science Division
Atomic Energy Center
Dhaka-1000, Bangladesh
S. S. Sikder
Khulna University of Engineering & Technology (KUET), Khulna-9203, Bangladesh

***Abstract*—**In this research work, ferrites with compositions of $Ni_{0.60}Zn_{0.40-x}Re_xFe2O4$ where x=0.05, 0.10, 0.15 were prepared by double sintering ceramic technique. The samples were pre sintered at 1000^0 C for 4 hours in air and sintered at 1250^0 C for 3 hours. The influence of Yttrium (Y) substitution on various properties of Ni-Zn ferrites have been studied in this work. Investigations were carried out by the measurements of AC resistivity, Permeability and Curie temperature of the sample. AC resistivity shows the nature of the semiconductor of the samples. The initial magnetic permeability remains constant from low frequency to 10 MHz thenceforth sharply fall to very low values at higher frequencies and again remain constant onward to Zn deficient of Ni -Zn ferrites with substituting of Y. At T = T_c the sharp directress of permeability indicates the samples are good homogeneity.

Keywords— Permeability, Curie temperature, Rare Earth metal and Sintering etc.

Introduction

Iron and its alloys were used as magnetic materials in order to serve the need of the electrical industry at the beginning of the industrialization. With the advent of higher frequencies, the standard techniques of reducing eddy current losses, using lamination or iron powder cores, were no longer efficient or cost effective. S. Hilpert in Germany in 1909, first reported this realization stimulated a renewed interest in "Magnetic Insulators". By 1945 Snoek had laid down the basic fundamentals of the physics and technology of practical ferrite materials [1]. In 1948, the Neel theory of ferromagnetic provided the theoretical understanding of this type of magnetic material. Soft ferrites polycrystalline prepared from metal oxides are magnetic semi conductors and have made important role, both technological and theoretical to the development of electronics. These soft ferrites still remain the best magnetic materials and cannot replaced by any other magnetic materials with respect to their very high frequency application because they are inexpensive, more stable, easily manufactured [2].The most important progress were made in ferromagnetism in the field of magnetic oxides (ferromagnetic). The progress of high frequency ferrites was initiated by the work done by J. L. Snoek [3], who found that connected with excellent properties in the high frequency range, Mn-Zn and Ni-Zn ferrites provide a family of magnetic materials helpful for radio and TV sets as well carrier telephony as cores of inductors transformer and so forth. The most well-liked combination are Ni-Zn [4], Ni-Cu-Zn [5-7], Mg-Zn [8] and Mg-Cu-Zn [9] a ferrites. Ferrite crystallizes with two magnetic sub-lattices i.e. tetrahedral (A) site and Octahedral (B) site based on Neel's model. Magnetic and electrical properties of ferrites are strongly dependant on distribution of cation in A and B sites and their valance state [10]. The properties of Ni-Zn ferrites can be modified by substitutions them with different metals ions such as Co^{2+},Mg^{2+},Mn^{2+},Cu^{2+}etc. The addition of rare earth metal in Ni-Zn ferrite composition is known to play a crucial role in increasing the sintering density and lowering the sintering temperature. Various additives such as V_2O_5, Bi_2O_3, PbO, MoO_3, WO_3, E_2O_3 P_2O_5, La_2O_3, W_2O_3, LiO etc. having low melting point, facilitated to reduce the sintering temperature of these oxides materials due to liquid phase either due to the melting of the additives or due to the eutectic liquid phase formation between the additives and the ferrite. Amount of liquid phase increase with increasing amount of sintering aids which results in increased densification. However excessive amount of sintering additives' will deteriorate electromagnetic properties of the ferrite. So, optimum content of sintering aids is necessary to achieve good sinter ability as well as better electromagnetic properties. Till now researches have not yet been able to formulate a rigid set of rules for ferrites about a single property. Among these La_2O_3,Y_2O_3 and E_2O_3 were the most effective sintering for Ni-Zn ferrite the systematic research is still necessary for effects has been under taken to prepare Ni-Zn ferrite doped with La_2O_3,Y_2O_3 and Eu_2O_3. Scientists still continue their efforts to find out optimum parameters of ferrites, like high saturation magnetization, high permeability, high resistivity, etc. In the present research work we prepared $Ni_{0.60}Zn_{0.40-x}Y_x$ Fe_2O_4 (x=0.05, 0.10, 0.15) Ferrites. We studied the variation of electrical resistivity and magnetic permeability in both temperature and frequency dependent cases.

EXPERIMENTAL

Double Sintering Ceramic Technique: In this method, the required composition is usually prepared form the appropriate amount of raw mineral oxides or carbonates by crushing, grinding and milling. The most common type of grind is the ball grind but instead of ball grind we performed it by hand grind. Grind can be carried out in a wet medium to increase the degree of mixing. The solid state inter-diffusion between

the raw materials play crucial role in this method. Normally, solids do not react at room temperature over normal time scales. Hence it is necessary to heat them at higher temperatures for the diffusion length $(2Dt)^{1/2}$ to exceed the particle size, where t is the firing time , and D is the diffusion constant for the fast-diffusing species. At temperature above 1000^0C, the grind powders are then calcined in air or oxygen. For some time, this process is continued until the mixture is converted into the correct crystalline phase. These powders are again crushed into fine powders. Using hydrostatic pressure the tablet and ring shaped samples are prepared from these fine powders. Pre sintering is carried out at temperature 1000^0C for (3) three hours and sintering at the temperature 1250^0 C for (4) four hours. The general solid state reaction leading to a ferrite MFe_2O_4 may be represented as

$$MO + Fe_2O_3 \rightarrow MeFe_2O_4$$ where M is the divalent ions.

Table of 20 gm compositional details of $Ni_{0.6}Zn_{0.4-x}La_xFe_2O_4$ [x = 0.05, 0.10, 0.15] ferrites

Content,x	NiO	ZnO	La_2O_3	Fe_2O_4
0.05	3.756	2.387	0.473	13.384
0.10	3.731	2.033	0.940	13.296
0.15	3.707	1.683	1.401	13.209

A flow chart of preparation of sample is presented below

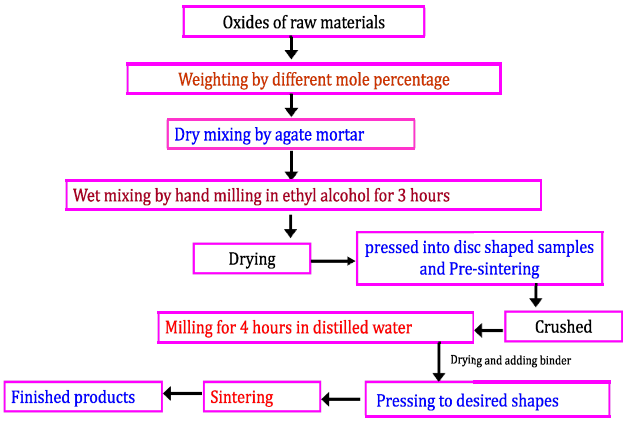

As a whole the preparation procedure generally represents:

- A mixture of materials was prepared with the cations in the ratio corresponding to that in the final product.
- Pre sintering the mixture at temperature 1000^0C to form ferrite.
- Converting the raw ferrite into powder and pressing the powder using hydrostatic pressure into the required shapes.
- Sintering at 1250^0C to produce a highly densified product.

Results and discussion

Table-1 Resistivity at room temperature of Ni0.60 $Zn_{0.40-x}$ $La_xFe_2O_4$ ferrites

Content,x	Resistivity at room temperature(30^0C)
0.05	7.562
0.10	13.112
0.15	129.08

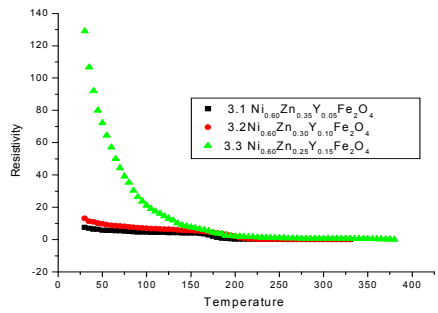

Figure-1: Temperature dependence of resistivity, as a function of Temperature of $Ni_{0.60}$ $Zn_{0.35}$ $Y_{0.05}$ Fe_2 O_4, $Ni_{0.60}$ $Zn_{0.30}$ $Y_{0.10}$ Fe_2 O_4, and $Ni_{0.60}$ $Zn_{0.25}$ $Y_{0.15}$ Fe_2 O_4, sintered at 1250^0C

In figure -1 the rectangular black sign indicates the sample $Ni_{0.60}$ $Zn_{0.35}$ $Y_{0.05}$ Fe_2 O_4.The curve of sample $Ni_{0.60}$ $Zn_{0.35}$ $Y_{0.05}$ Fe_2 O_4 shows that with increasing the temperature from room temperature the resistivity decreasing up to 180^0C. After that with increasing the temperature the resistivity becomes constant and almost temperature independent. In figure-1 the circle shaped red sign indicates $Ni_{0.60}$ $Zn_{0.30}$ $Y_{0.10}$ Fe_2 O_4 which indicates that with increasing the temperature the resistivity decreasing up to 185^0 C and becomes constant and almost temperature independent onward. In figure-1 triangular green sign indicates sample $Ni_{0.60}$ $Zn_{0.25}$ $Y_{0.15}$ Fe_2 O_4 which shows that with increasing temperature the resistivity decreasing gradually and after 190^0C becomes almost temperature independent. All the samples show the nature of the semiconductor.

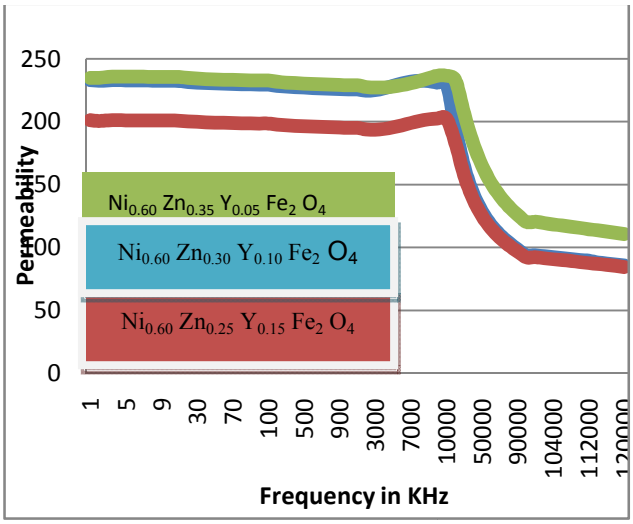

Figure-2: The real part of the permeability dependant on frequency of $Ni_{0.60}$ $Zn_{0.35}$ $Y_{0.05}$ Fe_2 O_4, $Ni_{0.60}$ $Zn_{0.30}$ $Y_{0.10}$ Fe_2 O_4, and $Ni_{0.60}$ $Zn_{0.25}$ $Y_{0.15}$ Fe_2 O_4, sintered at 1250^0C

Figure-2 describes the change of permeability with the change of frequency. For sample $Ni_{0.60}$ $Zn_{0.35}$ $Y_{0.05}$ Fe_2 O_4, $Ni_{0.60}$ $Zn_{0.30}$ $Y_{0.10}$ Fe_2 O_4, and $Ni_{0.60}$ $Zn_{0.25}$ $Y_{0.15}$ Fe_2 $O_4Ni_{0.60}Zn_{0.35}La_{0.05}Fe_2O_4$ it is seen that the initial permeability is as same as up to a very high frequency 10 MHz i.e., initial permeability is constant up to 10 MHz thenceforth the initial permeability sharply decreases up to 100MHz after that it remains constant on wards. At high frequency greater than 100 M the permeability becomes frequency independent.

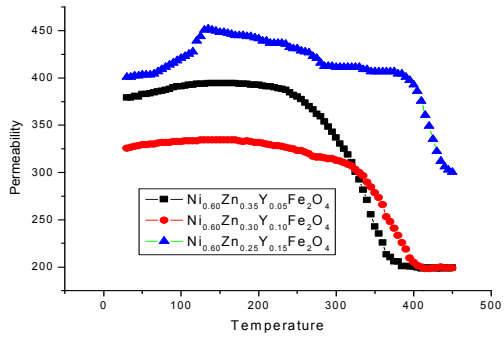

Figure-3: The real part of the permeability dependant on temperature of $Ni_{0.60}$ $Zn_{0.35}$ $Y_{0.05}$ Fe_2 O_4, $Ni_{0.60}$ $Zn_{0.30}$ $Y_{0.10}$ Fe_2 O_4, and $Ni_{0.60}$ $Zn_{0.25}$ $Y_{0.15}$ Fe_2 O_4, sintered at 1250^0C

Table-1 Data of Curie temperature (T_C) ($Ni_{0.60}$ $Zn_{0.40-x}$ $Y_xFe_2O_4$)

Zn- deficient content , x	$T_s = 1250^0$C
	T_c^{0C}
2.1 $Ni_{0.60}Zn_{0.35}Y_{0.05}Fe_2O_4$	340
2.2 $Ni_{0.60}Zn_{0.30}Y_{0.010}$ Fe_2O_4	355
2.3 $Ni_{0.60}Zn_{0.25}Y_{0.15}Fe_2O_4$	395

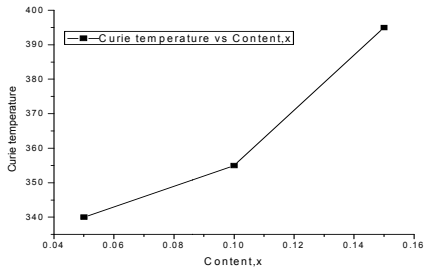

Figure-4: Curie temperature dependence of the content, as a function of Temperature of $Ni_{0.60}$ $Zn_{0.35}$ $Y_{0.05}$ Fe_2 O_4, $Ni_{0.60}$ $Zn_{0.30}$ $Y_{0.10}$ Fe_2 O_4, and $Ni_{0.60}$ $Zn_{0.25}$ $Y_{0.15}$ Fe_2 O_4, sintered at 1250^0C

Figure-4 shows the variation of Curie temperature, T_c with contents. Curie temperature gradually increases with increasing the contents mainly depends upon the strength of A-B exchange interaction.

Conclusion

Effect of electrical and magnetic properties of $Ni_{0.60}Zn_{0.40-x}Y_x$ Fe_2O_4 has studied thoroughly on the Yttrium (Y) substitution where x = 0.05, 0.10, 0.15. Temperature dependence resistivity was measured to identify the nature of the samples. Initially resistivity decreases gradually at lower temperature region and with further increasing the resistivity decreases sharply and at higher temperatures region it becomes almost independent of temperature. Initial permeability dependant on frequency was studied to fathom the frequency response initial permeability. Temperature dependence permeability has been used to measure the Curie temperature of $Ni_{0.60}Zn_{0.40-x}$ Y_x Fe_2 O_4 (x=0.05, 0.10, 0.15) Ferrites. Curie temperature of Ni-Zn ferrite increases with the decrease in Zn-content. There is much scope for further research in controlling the magnetic characteristics by changing composition and heat treatment certain important parameters like temperature dependence magnetization, anisotropy and magnetostriction can be study in detail for a better understanding of micro structure properties of the samples.

Acknowledgements

One of the authors (M. A. Hossain) is thankful to Khulna University of Engineering & Technology (KUET), Khulna, Bangladesh for the financial support. The authors are also grateful to the Materials Science Division of Atomic Energy Centre, Dhaka (AECD), Bangladesh. for allowing their facilities to prepare the samples and to utilize the laboratory facilities for various measurements. Financial support from International Program in Physical Science (IPPS), Uppsala University, Sweden for this work is highly acknowledged.

REFERENCES

[1] R. F. louh, T.G. Reynolds and R.C. Buchanan," Ceramic Materials for Electronics", 3rd edition, edited by R.C. Buchanan, Marcel Dekker Inc. 2004

[2] J. Kulikowski;1"Soft magnetic ferrites development of stagnation"; J. Magn. Magn. Matter; Vol. 41 p.56-62, 1984

[3] J. L. Snoek; "New development of Ferromagnetic Materials"; Elsevier Publ. Co. N.Y. 1984

[4] T. T. Ahmed, I. Z Rahman and S. A. M. Tofial; " Effect of Copper in distribution on the magnetization of nano scaled Ni-Zn ferrites". J. Magn. Magn. Matter; Vol. 272-276, pp. 2250-

2252, 2004
[5] Z. H. Khan, M. Mahbubur Rahman, S. S. Sikder, M. A. Hakim, D. K. Saha; "Complex Permeability of Fe deficient Ni-Cu-Zn ferrites"; Journal of Alloys and Compounds, 584, 208-215, 2013
[6] S. H. Seo and J. H. Oh; " Effect of MoO3 Addition of Sinterial behaviors and Magnetic properties of Ni-Cu-Zn Ferrite for Multilayer Chip inductors"; IEE Transctions on Magnetics, Vol. 35, No.5, 1999
[7] Kin O. Low, Frank R. Sale; " Electromagnetic properties of gel-derived Ni-Cu-Zn ferrites"; J. Magn. Magn. Mater. 246, pp.30-35, 2002
[8] M.A Hakim, M. Manjurul Haque, M. Huq, Sk. Manjura Hoque and P. Norbblad; "Reentrant Spin Glass Behavior of Diluted Mg-Zn Ferrites"; CP 1003, Magnetic Materials International Conference on Magnetic Materials, AIP. P-295, ICMM-2007
[9] M. Manjurul Huq and M. Huq and M.A. Hakim ;" Thermal hysteresis of Permeability and Transport properties of Mn Substituted Mg-Cu-Zn ferrites"; Journal of Physics D: Applied Physics, Vol.41, 055007, pp.1-10, 2008
[10] M. Manjurul Haque, M. Huq and M.A. Hakim; "Influence of CuO and Sintering Temperature on the microstructure and magnetic properties of Mg-Cu-Zn ferrites"; J. Magn. Magn. Mater . Vol. 320, pp.2792-2799, 2008.

Large Signal Performance of Graphene-FET Considering Contact Resistance

Md. Askarul Haque*; Md. Rasidul Islam; Md. Nur Kutubul Alam; Md. Rafiqul Islam;
Department of Electrical and Electronic Engineering
Khulna University of Engineering & Technology, Khulna-9203, Bangladesh
Email: shajibeeekuet@gmail.com*, ronyrasidul@gmail.com

Abstract—**Effect of source/drain contact resistance on the DC characteristics of large area Graphene Field Effect Transistor (GFET) is reported here. As graphene has been identified as a potential candidate for replacing silicon based devices, their performance has been thoroughly investigated. In practical devices, the contact resistance at the interface of channel and Source/Drain (S/D) contact is inevitable; therefore a compact model is proposed taking them into account. In the simulation, Ti, Au, Pt and Ni are considered as contact metals. The result shows the DC characteristics of GFET greatly depends on the contact resistance. Drain current reduces with increasing contact resistance and saturation in the current voltage characteristics disappears at high value of the contact resistance.**

Keywords- Graphene; GFET; Contact Resistance; DC characteristics; Compact modeling

I. INTRODUCTION

In order to sustain Moore's law, the size of silicon (Si) based field effect a transistor has been being reduced for last four decades. As they reached at 22 nm node, they are almost at their physical limit [1, 2]. Enhanced short channel effects (SCEs) as well as diminutive control of gate over the channel leads severe performance variation from the intended design [3]. To solve this problem, Si needs to be replaced from the channel with some material having superior transport properties. One of the most promising materials is graphene mainly due to its wide spread availability as well as low cost along with its excellent physical and electronic transport properties. The sp^2 bonded carbon atoms organized in hexagonal lattice format makes graphene 200 times stronger than steel. The enhanced elastic constant further leads to better thermal conductivity. For electron transport, graphene offers carrier mobility at the range of 3000 cm²/Vs to 27000cm²/Vs [4] [5]. However, the only problem is the semi-metal band structure, i.e. graphene possesses no band gap that forbids its application in logic devices. Nevertheless, its outstanding transport properties have led to many comprehensive studies on the applicability in various fields such as nanoelectronics and high frequency electronics [6], energy storage and conversion [7], field emission display [8], transparent conductors [9] and so on.

However, most of the studies are done for ideal graphene based devices. In real devices, when a channel material is connected with contact, it forms an inherent resistance at the channel-contact interface. In this study, we report the large signal model of GFET and a simple mathematical expressions to analysis the DC characteristics in presence of contact resistance. The basic model given in [10] is modified under the postulates given in [11]. And they are done by adding the effect of contact resistance (R_C) of graphene-metal contact. The values of R_C vary from a few hundred to a few thousand Ω-μm, and depends on the metal used, fabrication procedure, gate bias and measurement conditions [12]. A gate-dependent nickel-graphene contact resistance of 500 Ω μm has been reported at 300 K [13]. For a titanium–graphene system, an R_C of less than 250 Ω μm has been reported at liquid helium temperatures, and an R_C of greater than 1,000 Ω μm at 300 K [13]. These experimental values are used in the elucidation of our proposed model.

II. LARGE SIGNAL MODEL NEGLECTING R_C

Large signal model of graphene FET (GFET) is shown in Fig. 1. It consists of drain, source, graphene channel and an insulated top gate. The effect of R_C between drain/source and graphene has been neglected in this section.

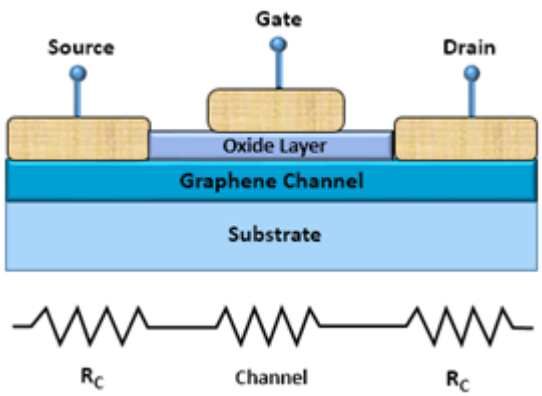

Fig. 1: Schematic diagram of graphene field effect transistor (GFET), and equivalent circuit including the contact resistance.

978-1-4673-9257-0/15/$31.00 ©2015 IEEE

A. Drain Current Modeling

The expression of drain current of top gated GFET is [10, 11]-

$$I_D = \mu W \frac{\int_0^{V_D}(|Q_{net}| + n_{puddle})dV}{L + \mu|\int_0^{V_D}\frac{1}{v_{SAT}}dV|} \quad (1)$$

Where μ is the carrier mobility, W is the width of the graphene sheet, L is the channel length, and V_{SAT} is the saturation velocity in the graphene layer, Q_{net} is the net mobile charge, e is electron charge and n_{puddle} is the residual carrier density which is induced by spatial in homogeneity within the graphene layer. It is given as [14]-

$$n_{puddle} = \frac{\Delta^2}{\pi\hbar^2 v_f^2}$$

Δ represents the spatial in homogeneity of the electrostatic potential, $\hbar$ is the reduced Planck constant, and v_f is the Fermi velocity. Equation (1) can be written as:

$$I_D = \frac{Num_1 + Num_2}{Den} \quad (2)$$

where,

$$Num_1 = \frac{\mu W}{4\beta}\int_0^{V_D}\left[-C_T + \sqrt{C_T^2 + 4\beta|C_T(V_{eff} - V) + eN_f|}\right]^2 dV \quad (3)$$

Here the factor $\beta = \frac{e^3}{\pi\hbar^2 v_f^2}$. C_T is the top oxide capacitance, V is the potential variation along the channel due to drain voltage V_D and N_f is a term that accounts for the net acceptor/donor concentration. The effective gate-source overdrive voltage, $V_{eff} = V_G + V_{TH,0}$. Where V_G is top gate voltage and $V_{TH,0} = eN_f/C_T$ is zero bias threshold voltage for GFET devices. Equation (3) contains integration of absolute function. It can be expanded as followed:

$$Num_{1\,(V_{eff} \geq V_D)} = -\frac{\mu W}{\beta^2 C_T}\left[\frac{-\beta C_T^3 V_D}{2} + \frac{\beta^2 C_T^2}{2}\left\{(V_{eff} - V_D)^2 - V_{eff}^2\right\} + \frac{C_T}{12}(C_T^2 + 4\beta C_T V_{eff})^{3/2} - \frac{C_T}{12}\left(C_T^2 + 4\beta C_T(V_{eff} - V_D)\right)^{3/2}\right] \quad (4)$$

$$Num_{1\,(V_{eff} < V_D)} = -\frac{\mu W}{\beta^2 C_T}\left[\frac{\beta C_T^3 V_D}{2} - \frac{\beta^2 C_T^2}{2}\left\{(V_{eff} - V_D)^2 + V_{eff}^2\right\} + \frac{C_T}{12}(C_T^2 + 4\beta C_T V_{eff})^{3/2} + \frac{C_T}{12}\left(C_T^2 - 4\beta C_T(V_{eff} - V_D)\right)^{3/2}\right]$$

The second term of numerator is given by:

$$Num_2 = \mu W \int_0^{V_D} en_{puddle} dV = \mu W e n_{puddle} V_D \quad (5)$$

The denominator in equation (2) can be expressed as:

$$Den = L + \mu\left|\int_0^{V_D}\frac{1}{v_{SAT}}dV\right| \quad (6)$$

This can be simplified assuming an average V_{SAT} given by [10]:

$$v_{SAT,AV} = \frac{\omega}{\sqrt{\pi\frac{|Q_{net,AV}|}{e} + n_{puddle}}} \quad (7)$$

Where ω is obtained from the surface phonon energy of the substrate ħω and $Q_{net,AV}$ is the average charge [10] given by:

$$Q_{net,AV} = \frac{1}{4\beta}\left[-C_T + \sqrt{C_T^2 + 4\beta\left|C_T\left(V_G - \frac{V_D}{2}\right)\right|}\right]^2 \quad (8)$$

The model is simulated in MATLAB using numerical parameters given in table-1. Fig. 2 shows the simulated I_d-V_D characteristics considering no contact resistance.

TABLE I

Symbol	Description	Value
μ	Mobility	$7000\ cm^2V^{-1}s^{-1}$
C_{TOP}	Top oxide capacitance	$3.6 \times 10^{-3}\ \mu Fcm^{-2}$
Δ	Spatial inhomogeneity	8.65×10^{-21}meV
e	Charge of electron	1.6×10^{-19}C
$\hbar$	Reduced plank constant	1.055×10^{-34}J/s
ω	Angular frequency	$8.5 \times 10^{13}\ s^{-1}$
L	Channel length	1μm
v_f	Fermi velocity	$960000\ cm^{-1}$
W	Channel width	$1\ \mu$m

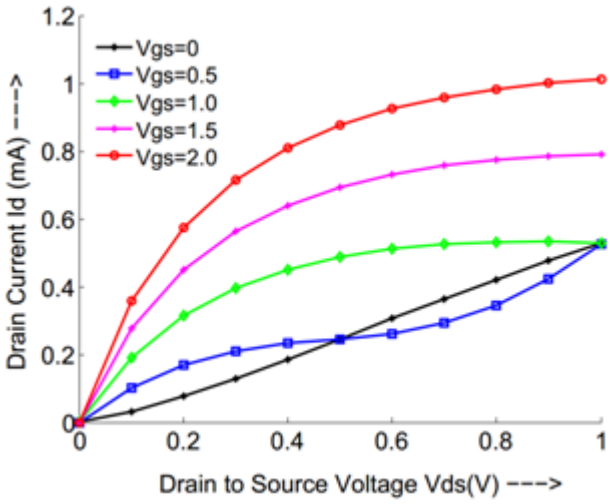

Fig. 2: I_D-V_D characteristics of large area GFET when no contact resistance is taken into account.

B. Transfer Characteristics

The voltage in gate terminal creates electric field in graphene channel that changes or controls the conductivity of the graphene channel. It also controls the number of electrons that can pass through the channel. From the equation (1), it is clear that the I_D is proportional to the polynomial of gate voltage V_G. It is seen in the I_D-V_G characteristics in Fig. 3 that both for positive and negative gate bias, the drain current is positive. Also note that drain current of GFET never goes to zero, it becomes minimum at certain gate bias called the "Dirac point". Left to the Dirac point, current is carried by hole and right to that point, it is carried by electron. That also means the Dirac point distinguishes the point of bipolar conduction.

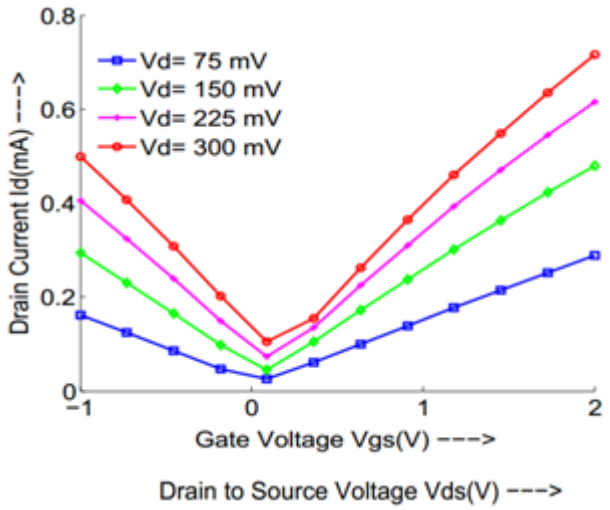

Fig. 3: I_D-V_G characteristics of large area GFET when no contact resistance is taken into account.

III. GFET MODEL CONSIDERING R_C

For a complete model of GFET, the contact resistances R_C cannot be neglected where R_C is in the order of few hundred ohms. The contact length of 0.5 μm is considered. The complete model is shown in Fig. 4.

A. Effect of R_C on Drain Current

When voltage is applied between drain to source (V_D), a portion of it drops across each R_C. In that case, the V_D is given as-

$$V_D = V_{Ch} + 2I_D R_c \qquad (9)$$

The limit used in the integrals in equation (1) is the potential extremes at the channel region. That is why when contact resistance is added, they must be modified as follows:

$$I_D = \mu W \frac{\int_{I_D R_C}^{V_D - I_D R_C} (|Q_{net}| + n_{puddle}) dV}{L + \mu \left| \int_{I_D R_C}^{V_D - I_D R_C} \frac{1}{v_{SAT}} dV \right|} \qquad (10)$$

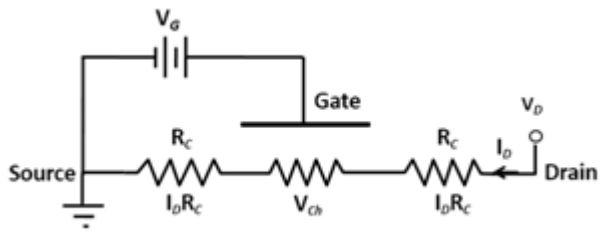

Fig. 4: The complete GFET model with the voltage drops in channel and in contact resistances.

The further calculations are same as described in section II. The equation (10) is a polynomial of drain current I_D and it cannot be solved directly. That is why it is solved by numerical root finding methods. From several available techniques, Bisection method is used here.

The simulation results of $I_D - V_D$ characteristics for different R_C are shown in Fig. 5. It is observed that the I_D decreases with the increase of R_C. Also the saturation regions of $I_D - V_D$ characteristics disappears for the higher values of R_C.

B. Effect of R_C on Transfer Characteristics

The transfer characteristics with the contact resistance can be simulated in the same way explained in preceding section, and are shown in Fig. 6. It is observed that at zero contact resistance (R_C=0), the I_D–V_G curves are linear before and after Dirac point. This linearity disappears and I_D–V_G curves get saturated for higher values R_C. However, no change in position of Dirac points is observed.

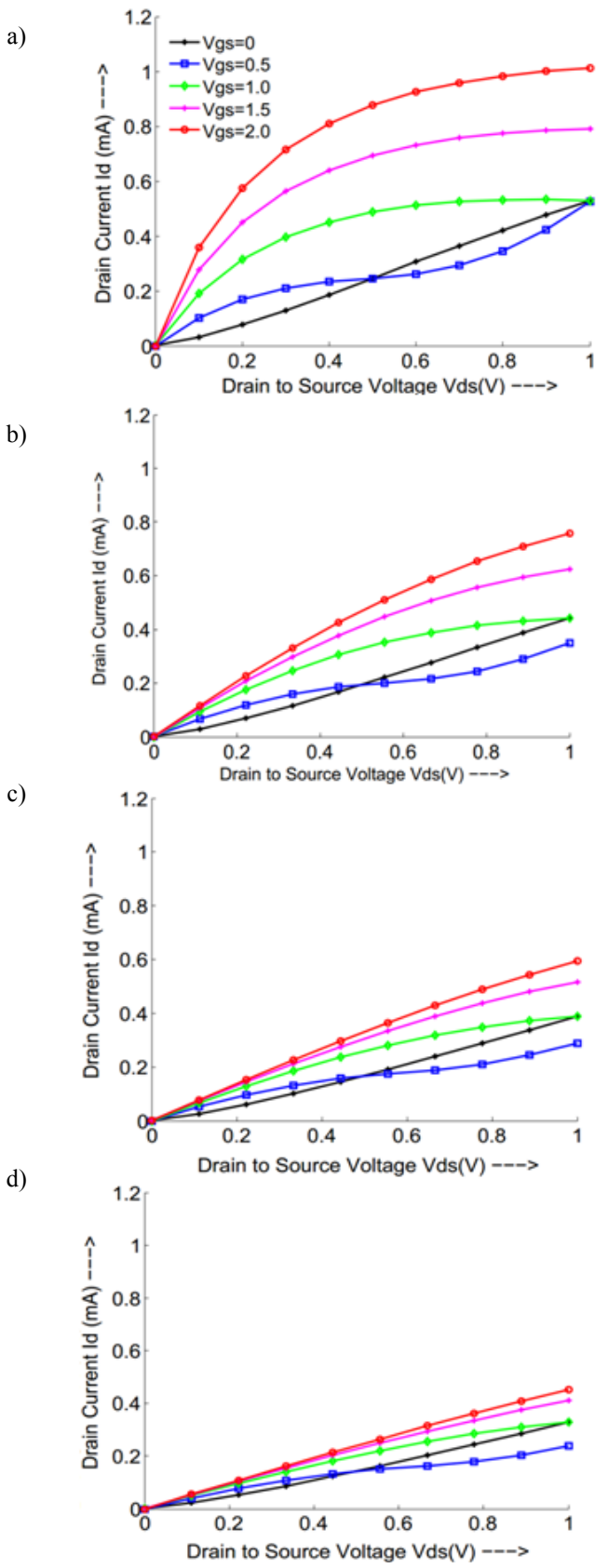

Fig. 5. The effect contact resistance R_C on I_D–V_D characteristics of GFET. (a) without R_C; (b) with R_C = 300 Ω; (c) with R_C = 600 Ω; (d) with R_C = 900 Ω

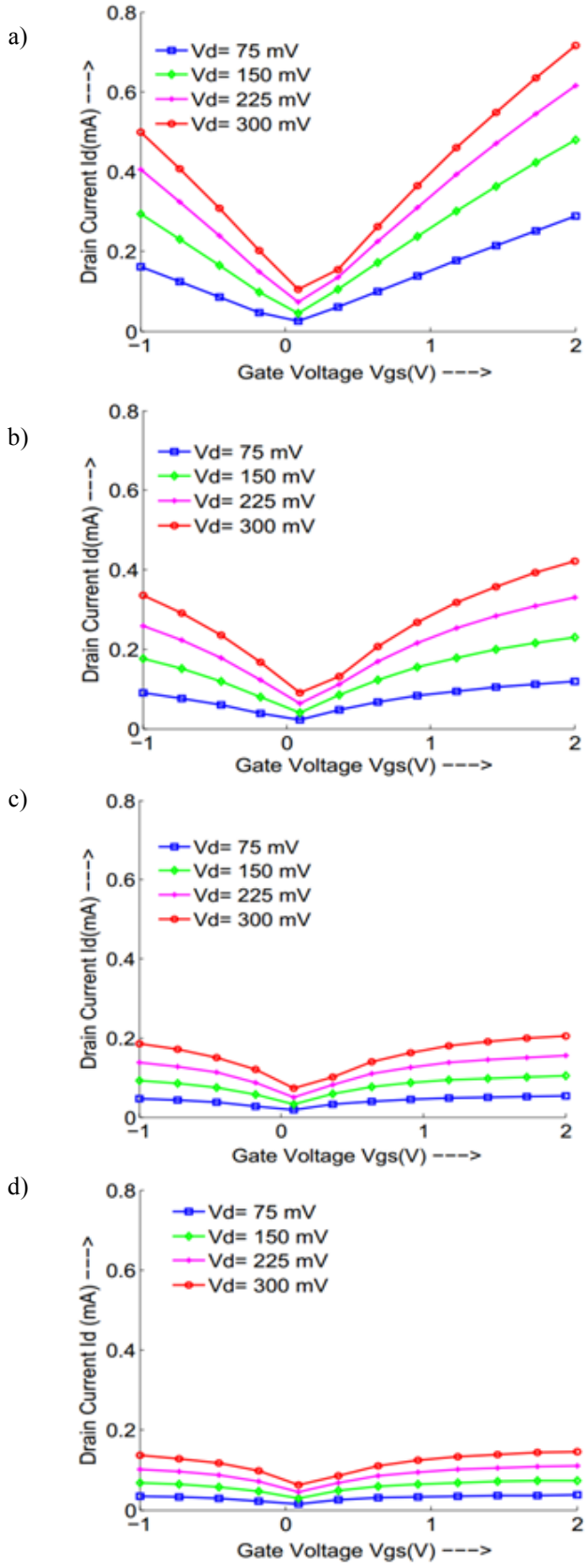

Fig. 6. The effect contact resistance R_C on I_D–V_G characteristics of GFET. (a) without R_C; (b) with R_C = 300 Ω; (c) with R_C = 600 Ω; (d) with R_C = 900 Ω

IV. CONCLUSION

In this research, we present a compact model for large signal characteristics for top-gated graphene FET with no band-gap engineering of the graphene channel. Because of zero band-gap, GFET cannot be used as logic device, but it can be used in RF (Radio Frequency) applications. Taking into account the contact resistance, an analytical expression is provided for the drain current I_D which is a polynomial function of all relevant parameters. Simulation result shows that the contact resistance has a significant effect on the $I_D - V_D$ and transfer characteristics. When contact resistance is neglected, the saturation region $I_D - V_D$ is flat enough to make the device compatible for analogue application. However, with increasing resistance, I_D decreases significantly and When R_C increases, the voltage drops in drain and source terminals increases. So for a fixed value of drain voltageV_D, the channel potential decreases. The expression of I_D is a very complex function of V_D, V_G and R_C. So it is difficult to explain the disappearance of saturation region.

References:

[1] Isabelle Ferain, Cynthia A. Colinge, and Jean-Pierre, "Multigate transistors as the future of classical metal-oxide-semiconductor field-effect transistors," Nature, vol. 479, pp. 310-316, November 2011.

[2] Farzin Assad, Zhibin Ren, Dragcia Vasileska, Supriyo Datta, and Mark Lundstrom, "On the Performance Limit for Si MOSFETs: A Theoretical Study," IEEE Trans. Electron Devices, vol. 47, no. 1, pp. 232-240, January 2000.

[3] Honghui SUN, Liang FANG, Yao WANG, Yaqing CHI, Rulin LIU "A Low Contact Resistance Graphene Field Effect Transistor with Single-Layer-Channel and Multi-Layer-Contact" Nanoscale Architectures (NANOARCH), 2014 IEEE/ACM International Symposium on, pp. 139 144,2014.

[4] K. S. Novoselov, A. K. Geim, S. V. Morozov, D. Jiang, Y. Zhang, S. V. Dubonos, I. V. Grigorieva, andA. A. Firsov, "Electric Field Effect in Atomically Thin Carbon Films", Science, Vol. 306, pp. 666-669,October 2004.

[5] C.Berger, Z. Song, X. Li, X. Wu, N. Brown, C. Naud, D. Mayou, T. Li, J. Hass, A. N. Marchenkov, E. H. Conrad, P. N. First, and W. A. de Heer, "Electronic Confinement and Coherence in Patterned Epitaxial Graphene", Science, vol. 312, pp. 1191-1196, April 2006.

[6] Yanqing Wu, Keith A. Jenkins, Alberto Valdes-Garcia, Damon B. Farmer, Yu Zhu, Ageeth A. Bol, Christos Dimitrakopoulos, Wenjuan Zhu, Fengnian Xia, Phaedon Avouris*, and Yu-Ming Lin, "State-of-the-Art Graphene High-Frequency Electronics", Nano Letters, Vol. 12 No. 6, pp 3062–3067, 2012.

[7] Rinaldo Raccichini et. al. "The role of graphene for electrochemical energy storage", Nature Materials, Vol. 14, pp. 271-279, 2015.

[8] Cheng-Kuang Huang et. al. "Well-aligned graphene arrays for field emission displays", Applied Physics Letters, Vol. 98, pp. 3104-3, 2011.

[9] Jonathan K. Wassei, Richard B. Kaner, "Graphene, a promising transparent conductor", Materialstoday, Vol. 13, issue 3, pp. 52-59, 2010.

[10] S. Fregonese, M. Magallo, C. Maneux, H. Happy, and T. Zimmer,"Scalable Electrical Compact Modelling for Graphene FET Transistors,"IEEE Trans. on Nanotechnology, vol. 12, no. 4, pp. 539–546, 2013.

[11] Rodriguez, Saul, Sam Vaziri, Anderson Smith, Sebastien Fregonese, Mikael Ostling, Max C. Lemme, and Ana Rusu. "A comprehensive graphene FET model for circuit design." arXiv preprint arXiv:1310.1940 (2013)

[12] Fengnian Xia, Vasili Perebeinos, Yu-ming Lin, Yanqing Wu and Phaedon Avouris, "The origins and limits of metal–graphene junction resistance", Nature Nanotechnology, Vol. 6, pp. 179-184, 2011.

[13] Nagashio, K., Nishimura, T., Kita, K. & Toriumi, A. Metal/graphene contact as aperformance killer of ultra-high mobility graphene—analysis of intrinsicmobility and contact resistance. IEEE International Electron Devices MeetingIEDM.2009.5424297, Baltimore, Maryland (2009).

[14] W. Zhu, V. Perebeinos, M. Freitag, et P. Avouris, "Carrier scattering, motilities, and electrostatic potential in monolayer, bi-layer, and tri-layer graphene," *Physical Review B*, vol. 80, p. 235402, Dec. 2009.

Efficient design of thermal management by graphene heat spreader in embedded system

S.M.Rafi-Ul-Islam
Department of Electrical and Electronic Engineering
Bangladesh University of Engineering and Technology
Dhaka, Bangladesh
E-mail:rafiulislam89@gmail.com

Samia Subrina
Department of Electrical and Electronic Engineering
Bangladesh University of Engineering and Technology
Dhaka, Bangladesh
E-mail:ssubrina@gmail.com

***Abstract*— In this paper, a thermal model of an embedded system consisting of MOSFET, MESFET and HFET is presented in nano-electronic system by using FEM (Finite Element Method) . This model is used to analyze the thermal effects of an embedded system and to solve the associated thermal problems by using graphene heat spreader on different positions of the embedded system. This paper also suggests the best position of graphene heat spreader to ensure maximum reduction of temperature of the electronic devices. As high temperature sets a limit to the reliability of the devices, such modeling is very useful for the optimization of an embedded system to guarantee a longer lifespan and a better reliability.**

Keywords*— *Graphene, Heat Spreader, Embedded System, Thermal Management.

I. INTRODUCTION

Self-heating is a severe problem for the high-power related electronic, optoelectronic and photonic embedded devices [1]–[3]. Average temperature rise and non-uniform distribution of dissipated power in embedded systems consist of MOSFETs, MESFETs and HFETs individually or combination of these transistors, leading to the emergence of hotspots nears the device channels. These hotspots bring about degradation of the drain current, gain and output power, and can cause thermal breakdown [4]–[6]. Furthermore, the down-scaling of devices and higher circuit speeds lead to further increase in heat generation, power densities and temperature rise [7-8]. Temperature rise to an abrupt level also causes an increase in gate-leakage current and results in a poor reliability [9]. Various thermal management solutions, for example, conventional heat spreaders (HS) like Copper or Aluminum results poor improvement in thermal management for FET devices. To overcome these shortcomings, a newly invented material named Graphene, the 2-D allotrope of carbon atoms arranged in hexagonal pattern with superior thermal conductivity, ranging from 3000-5300 W/m.K at room temperature can be a potential candidate. It has very high electron mobility as well as very low resistivity. It also provides lower thermal contact resistance due to its flat geometry. The heat propagates in a lateral direction within the graphene plane that increases the area of the heat dissipation, increases the removal of heat flux from hot spots, reduces temperature and thus high heat flux thermal management becomes more efficient [10] .

In this work we carry out two dimensional thermal modeling in order to study the effect of graphene heat spreaders in thermal management of an embedded system.

II. MODEL FOR HEAT CONDUCTION

To find out the best position for adding graphene heat spreader, we simulated the embedded system with Graphene heat spreader (a) at the drain region of every FET devices (b) at only two drain terminals of the whole embedded system (c) at the junction of GaAs and SiC substrate region.

The simulated embedded system consists of 5 FET devices with a separation of 5μm between two consecutive FET transistors (cf. Fig. 1).

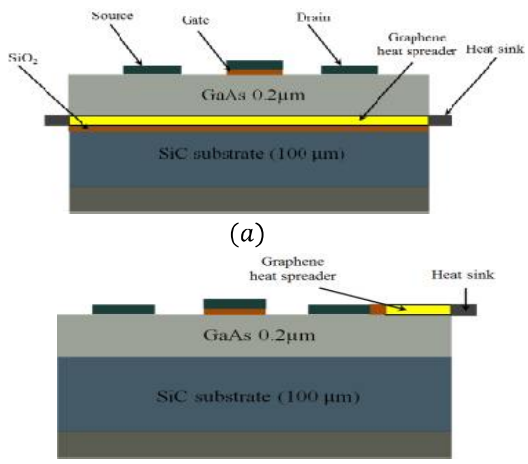

Fig. 1 Heat removal technique using graphene heat spreader (a) when graphene HS is connected to the substrate level and (b) when graphene HS is connected to the drain region. (One of the five FETs of the embedded system is shown in the figure.)

978-1-4673-9257-0/15/$31.00 ©2015 IEEE

The whole device width is 26μm. For MOSFET and MESFET, the thicknesses of SiC substrate, epitaxial GaAs film and graphene heat spreader are 100μm, and 0.2μm , and 1nm, respectively while their thermal conductivities are 490W/m.K, 46W/m.K and 2000W/m.K, respectively for different embedded systems simulated here [11-12]. A SiO_2 is used as an insulator with a thermal conductivity of 1.4 W/m.K and thickness of 10nm. For AlGaAs/GaAs HFETs, the thickness of SiC substrate, GaAs, AlGaAs and SiO_2 layers were 100μm, 192nm, 8nm and 10nm, respectively. Their corresponding thermal conductivities at the room temperature are taken from the literature to be 350W/mK, 160W/mK, 120W/mK and 1.4W/mK, respectively [13]-[15].

The whole simulation is carried out with FEM (Finite Element Method) using COMSOL software [16]. A conventional heat sink is attached to the device structure at the bottom. A graphene heat spreader, when used, is connected- at first case, at drain region of each FET devices; in the second case, at the drain region of the two terminal FET devices only; and in the third case, at GaAs and SiC layer for heat escaping. The heat spreader is insulated from the drain terminal by a thin SiO_2 layer. In our proposed device structure the size of the graphene layer is in micrometer range which is much larger than phonon mean free path of graphene (775 nm). Hence in our work, the thermal transport is considered to be diffusive and does not reveal any edge dependence[17]-[20].

In this paper, the thermal profiles have been simulated by using the Fourier's law expressed as:

$$-\nabla \cdot (k\,\nabla T) = Q \qquad (1)$$

and the Ohm's law given by:

$$J = \sigma E + J_e \qquad (2)$$

Here Q is the heat source, defined as the heat energy generated within a unit volume per unit time, T is the absolute temperature and k is the thermal conductivity of material, J is the current density, σ is electrical conductivity and E is the electric field. The operator $\nabla = \partial/\partial x + \partial/\partial y + \partial/\partial z$. The bottom surface of the substrate and the far end of the graphene heat spreader were kept at a constant temperature T = 300 K. The external boundaries were considered to be adiabatic and given by $\nabla \cdot (k\,\nabla T) = 0$ i.e. the temperature gradient across the boundary is zero. All the heat sinks were considered to be held at a constant room temperature and were described as $T = T_0$, where T_0 = 300K. The external surfaces were modeled as insulated from the environment.

III. Simulation and Results

Thermal issue is more critical in embedded systems and we get a clear picture of this phenomenon from the simulation results shown in Fig. 2. The maximum temperature in integrated chip is very high without the heat spreader. By using graphene heat spreader,maximum temperature is reduced by a significant amount.

An embedded system is energized by a drain voltage and an electric current. Maximum heat is generated in the channel region. The hot spot temperature was obtained using 2D simulation, using COMSOL multiphysics software. With the graphene heat spreader, heat generated from the hot spot can be propagated to a larger area, and dissipated by natural convection, thus a temperature drop of the embedded system's hot spot was observed. The reduced hot spot temperature suggests improved temperature uniformity across the chips and enhanced performance and lifetime for electronic devices.

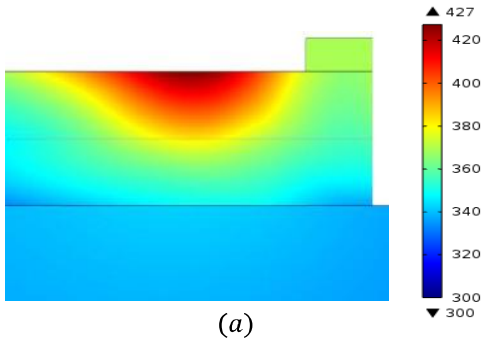

(a)

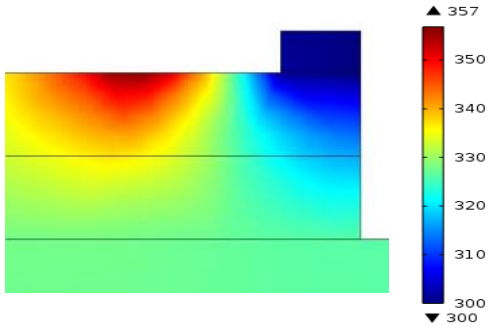

(b)

Fig.2. Temperature distribution in simulated 2-D embedded MOSFET system (a) without and (b) with graphene heat spreaders attached to the side heat sinks. (Zoomed view of one of the five MOSFETs).

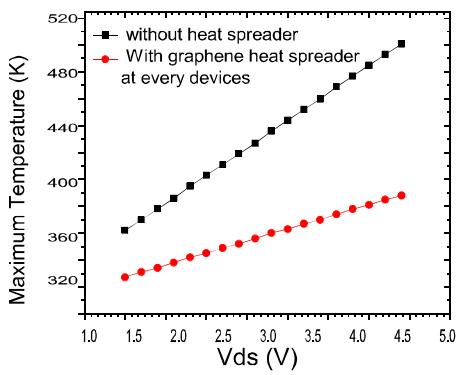

(a)

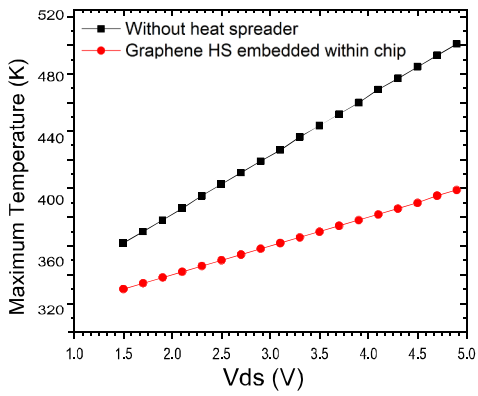

(b)

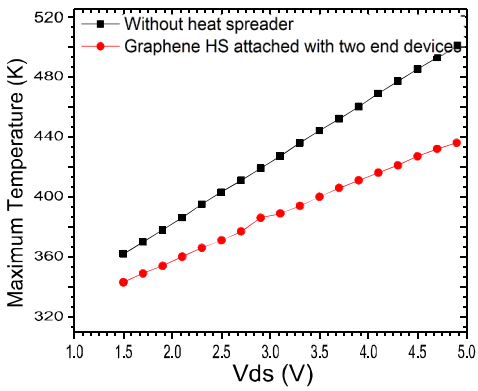

(c)

Fig.3. Temperature profile for a MOSFET embedded system with Graphene HS (red colored line) (a) at drain region of each MOSFET, (b) at SiC substrate level in another words as embedded within chip and (c) only at two MOSFETs located at the ending terminals of the embedded system. All the figures compared with respect to same system having no heat spreader (black colored line).

Fig. 3(a) represents the temperature effects on a MOSFET embedded system when no heat spreader is used (black colored line) and with graphene heat spreaders used at the end of drain terminals of each device (red colored line). We observed that graphene HS reduces temperature of the embedded system by a great extent. Fig. 3(b) and Fig. 3(c) represent the temperature effects on a MOSFET embedded system without any heat spreader and with graphene heat spreaders used at substrate levels and only at the end of two Terminal devices, respectively.

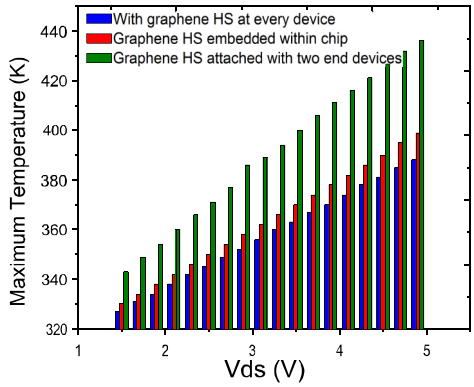

Fig.4. Comparison among three different positions of the graphene HS for the MOSFET embedded system.

Fig. 4 represents the comparison among thermal improvement of a MOSFET embedded system when graphene heat spreaders connected at different positions of the system. As it is clear from the graph that, graphene HS, if connected to each drain terminals of the system, gives the best improvement in devices; and when graphene HS is connected only at two endmost terminal devices, it gives poor result; and moderate thermal improvement occurs when graphene HS is connected at substrate level. For instance, for a given gate voltage $V_{gs} = 1.5V$ and drain voltage $V_{ds} = 3.0V$, maximum temperatures of the MOSFET embedded device are 427K, 357K, 362K and 389K in case of without heat spreader, graphene HS at every device, graphene HS at the substrate level and graphene HS at only two terminal devices, respectively.

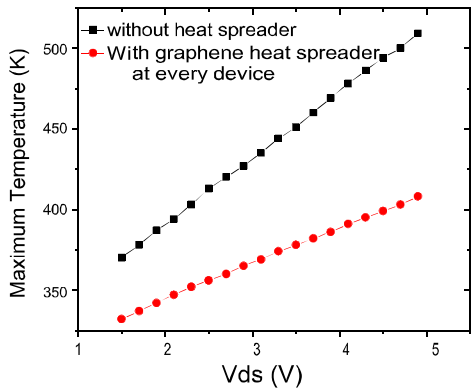

(a)

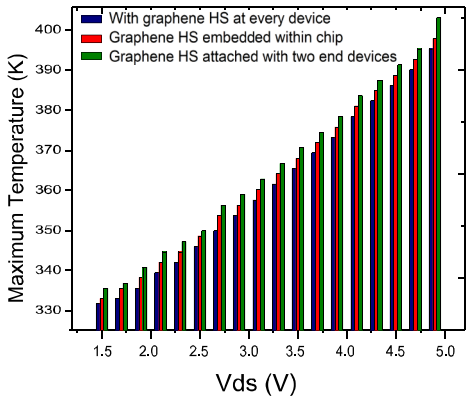

(b)

Fig.5.Temperature profile for a MESFET embedded system with graphene HS (red colored line) (a) at drain region of each MESFET, of the embedded system. The figure is compared to same system having no heat spreader. (b) Comparison among three different positions of the graphene HS.

Fig. 5(a) demonstrates the thermal improvement of a MESFET embedded system when graphene heat spreader is incorporated to device terminals with respect to without heat spreader. As it is clear form the figure that with the increment of drain to source voltage, thermal improvement is quite significant with graphene HS.

Fig. 5(b) compares the thermal improvements for different drain to source voltages for incorporation of graphene HS at different positions of the embedded system. When graphene heat spreaders are connected to the drain region of the each MESFET of the system, it gives the best result in terms of temperature reduction as well as increasing of system lifetime, while graphene HS embedded within the chip, in another words at substrate level gives a satisfactory thermal improvement and graphene HS at only terminal most two MESFET of the system gives least improvement among three possible ways of heat escaping as demonstrated here.

For a given gate voltage $V_{gs} = 1.5V$ and drain voltage $V_{ds} = 3.0V$, temperature improvements of the MESFET embedded device are 66K, 63K and 59K with respect to without HS and when graphene HS at every device, graphene HS at substrate level and HS at only two terminal devices is used to the system respectively.

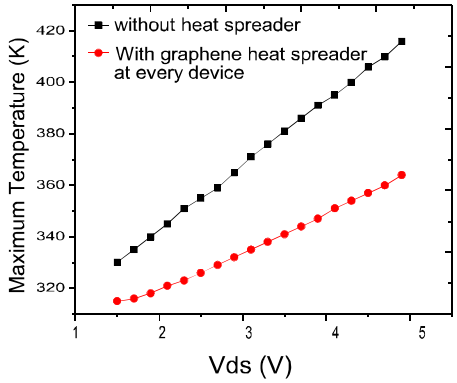

(a)

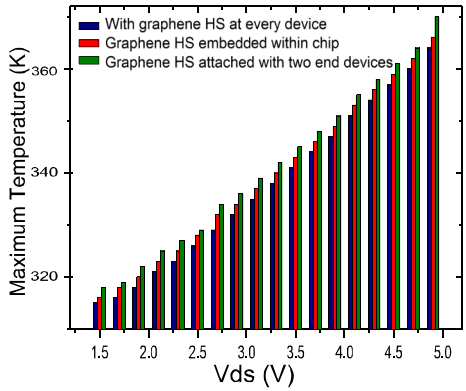

(b)

Fig.6.Temperature profile for a HFET embedded system with Graphene HS (red colored line) (a) at drain region of each HFET, of the embedded system, with the results being compared with that having no heat spreader(black colored line). (b) Comparison among three different positions of the graphene HS

As for a HFET embedded system, using of graphene heat spreader gives an outstanding thermal improvement with respect to using no heat spreader, depicted in Fig. 6(a). The maximum temperatures of the system are 371K and 335K for without heat spreader and for the case of using heat spreader respectively, at $V_{gs} = 1.5V$ and $V_{ds} = 3.0V$. Fig. 6(b) reveals the best option for incorporating of graphene heat spreader to the embedded system. It shows that graphene HS at the end of each HFET gives the best improvement and HS at only two end devices of embedded HFET system gives the least thermal improvement among three possible paths for heat escaping.

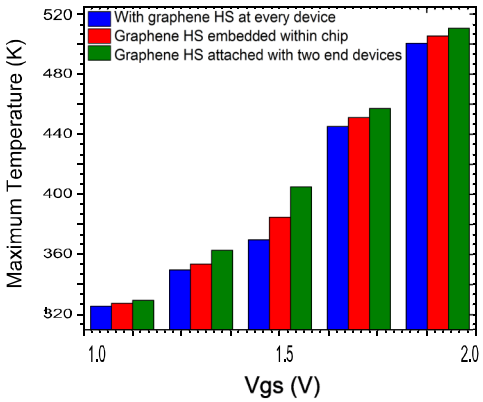

Fig.7.Temperature profile for an embedded system with Graphene HS at different positions of the MOSFET embedded system with the variation of gate to source voltage.

Fig. 7 shows the temperature variation of an embedded system with the variation of gate to source voltage. It is clear from the graph that graphene heat spreader connected at every device reduces the maximum temperature of the system to a significant amount.

IV. CONCLUSION

We carried out a feasible study of the use of graphene as the material for lateral heat spreading in embedded chips. Although our results show that the amalgamation of graphene or FLG (few layer graphene) at the drain terminal of each FET devices gives the best thermal improvement,this is a less feasible solution for fabrication perspectives. Graphene heat spreader embedded within chip,in another words graphene HS at the interface of the insulating and the substrate layer can lead to substantial reduction in temperature of the hot spots which is very close to the thermal improvement for HS connected to each device with more feasible fabrication process.Graphene HS only at the end of two endmost FET devices carried out the poorest result among these three possible positions of incorporation of graphene a HS at embedded FET devices. Hence we suggest embedded graphene heat spreader as the most pragmatic and convenient means of improving thermal issues of FET devices. The efficiency of the hot spot removal with graphene depends on the specifics of the device structure, geometry, and position of the heat spreader. The obtained results can lead to a new type of possibility of thermal management of nano-electronic circuits.

REFERENCES

[1] Trew, R. J., Green, D. S. & Shealy, J. B. AlGaN/GaN HFET reliability. *IEEE Microw. Mag.* **10,** 116–127, 2009.

[2] Kuzmik, J. *et al.* Self-heating phenomena in high-power III-N transistors and new thermal characterization methods developed within EU project TARGET. *Int. J. Microwave and Wireless Tech.* **1,** 153–160, 2009.

[3] Green, D. S. *et al.* GaN HEMT thermal behavior and implications for reliability testing and analysis. *Phys. Stat. Sol. (c)* **5,** 2026–2029, 2008.

[4] P. G. Mautry and J. Trager, "Investigation of self-heating in VLSI and ULSI MOSFET's," *Proc. 1990 IEEE Conf Microelectronic Test Structures,* 221-226, Mar. 1990.

[5] L. I. McDaid, S. Hall, W. Eccleston, and I. C. Alderman, "Monitoring the temperature rise in SOI transistors by measurement of leakage current," *Proc. 1991 IEEE Int. SOI Conf,* 28-29, Oct. 1991..

[6] L. T. Su, J. E. Chung, D. A. Antoniadis, K. E. Goodson, and M. I. Flik, "Measurement and modeling of self-heating in SOI MOSFETs," *IEEE Trans. Electron Devices,* 41, 69-75, Jan. 1994.

[7] E. Pop, S. Sinha and K. E. Goodson, "Heat generation and transport in nanometer scale transistors," *Proc. of IEEE,* 94, Aug. 2006.

[8] C. Fenigna, Y. Yang, E. Sangiorgi and A. G. O' Neill, "Analysis of self-heating effects in ultrathin-body SOI MOSFETs," *IEEE Trans. Electron Devices,* 55, 233-244, 2008.

[9] P. G. Mautry and J. Trager, "Investigation of self-heating in VLSI and ULSI MOSFET's," Proc. 1990 IEEE Conf Microelectronic Test Structures, 221-226, Mar. 1990.

[10] D. L. Nika, S. Ghosh, E. P. Pokatilov, and A. A. Balandin, "Lattice thermal conductivity of graphene flakes: Comparison with bulk graphite," *Appl. Phys. Lett.* 202-203, 2009.

[11] M. Shamsa, P. M. Solomon, K. A. Jenkins, A. A. Balandin, W. Haensch, "Investigation of thermal crosstalk between SOI FETs by the subthreshold sensing technique," *IEEE Trans. Electron Devices, 55, 1733-1740, Jul. 2008.*

[12] S.Subrina,D Kotchetkov, and A.A.Balandin, "Heat removal in Silicon-on-Insulator Integrated circuits with graphene heat spreaders,". *IEEE Elec. Dev.* 30.12.2009,pp.1281-1283.

[13] Liu, W. L. & Balandin, A. A. Thermal conduction in AlGaN alloys and thin films. *J. Appl. Phys.* **97,** 073710 , 2005.

[14] Balandin, A. A. *et al.* Low flicker-noise GaN/A1GaN heterostructure fieldeffect transistors for microwave communications. *IEEE Trans. Microwave Theory & Tech.* **47,** 1413–1417,1999.

[15] Sheppard, S. T. *et al.* High-power microwave GaN/AlGaN HEMT's on semiinsulating silicon carbide substrates. *IEEE Elec. Dev. Lett.* **20,** 161–163,1999.

[16] [Online].Available: http:// www.comsol.com

[17] W Balandin, A. A. et al. Superior thermal conductivity of single-layer grapheme. *Nano Lett.* 8, 902–907,2008.

[18] S. Ghosh, I. Calizo, D. Teweldebrhan, E. P. Pokatilov, D. L. Nika, A. A. Balandin, W. Bao, F. Miao, and C. N. Lau, "Extremely high thermal conductivity of graphene: Prospects for thermal management applications in nanoelectronics," *Appl. Phys. Lett.*, 92, 151911, Apr. 2008.

[19] D. L. Nika, E. P. Pokatilov, A. S. Askerov and A. A. Balandin, "Phonon thermal conduction in graphene: Role of Umklapp and edge roughness scattering," *Phys. Rev. B* 79, 155413, Apr. 2009.

[20] S. V. Morozov, K. S. Novoselov, M. I. Katsnelson, F. Schedin,D. C. Elias, J. A. Jaszczak, and A. K. Geim, "Giant intrinsic carrier mobilities in graphene," *Phys. Rev. Lett.*,100, 016602, Jan. 2008.

Analytical Approach of J-V Characteristics of CdTe Based Thin Film Solar Cells Including Voltage and Space Dependent Electric Field in the Absorber Layer

[1]Protik Biswas, [2]Abdullah Sakib Hasan, [3]Ashiq Been Rahim, [4]Aman Ullah, [5]Md. Iqbal Bahar Chowdhury
Department of Electrical and Electronics Engineering (EEE)
United International University
Dhaka, Bangladesh
[1]protik_biswas@yahoo.com, [2]ovi_uiu05@yahoo.com, [3]real619@hotmail.com, [4]amanullah.en@gmail.com, [5]ibchy@eee.uiu.ac.bd

***Abstract*—This work reports on development of an optimized analytical model to investigate the current-voltage (J-V) characteristics of a lightly doped CdTe-based thin film solar cell considering voltage-space dependency of electric field in the absorber region. Following the theory of perturbation, the intractable mathematical equations have been solved analytically. Finally, changes in J-V characteristics curve are observed in various conditions such as effect of stress, life time of holes and electrons and varying series resistance. The proposed model is proven to be helpful in giving better physical insight of Cds/CdTe solar cell.**

Keywords— CdS/CdTe Solar Cell, J-V Characteristics, non-uniform electric field , Perturbation Theory, stress effect.

I. INTRODUCTION

Thin-film CdS/CdTe solar cells fabricated on glass substrates have been recognised as one of the most potential candidates for the development of cost-effective and reliable solar cells in large-scale photovoltaic applications. The documented experimental efficiency of these cells is about 16%–17% and the consequent theoretical values are more than 28% [1]. The advantages of using CdTe include high absorption capability for being a direct bandgap material and the simplicity of device processing [2]. It can be deposited on glass typically a few micrometers deep as absorber layer with a very thin layer of CdS (0.1µm) in the emitter side [2], [3]. In Cds/CdTe solar cells, higher percentage of incident light is absorbed in first few micrometers of lightly doped CdTe layer. The photo-generated carriers in this region are collected by the voltage-dependent electric field [4]–[6].

A number of numerical as well as analytical models [4] – [7] have been introduced in the literature to model the current-voltage (J-V) characteristics of Cds/CdTe solar cells. All these models used a lot of fitting parameters. Anjan *et al*. [8] and Mannan *et al*. [9] developed their models with minimum number of fitting parameters. In [8] electric field is considered as uniform throughout the absorber layer, whereas the same is considered as space-dependent in [9]. Both models used the voltage-dependency of the electric field; but these models used numerical iterations to model the J_L-V_L characteristics, although they deduced the photo-generation current analytically. Later Haque *et al*. [10] derived the J_L-V_L characteristics analytically using the concept of perturbation method. But this model considered the electric field in the absorber layer as constant.

This work focuses on developing a model that removes the abovementioned limitations. In the proposed model, the electric field across absorber layer is considered nonuniform. Furthermore, the theory of perturbation has been applied in order to solve the intractable major differential equations which are proven to be more time effective and acceptable than that of typical lengthy iteration methods. The variations of J-V characteristics under different parameters, i.e., before and after stress, life time of holes and electrons and series resistance have been analysed.

II. ANALYSIS

The load current density (J_L) against the load voltage (V_L) of any solar cell including the effect of series resistance can be expressed as

$$J_L(V_L) = -J_{ph}(V_L) + J_0(V_L)(e^{\frac{V_L - J_L R_s}{nV_T}} - 1) \quad (1)$$

Where, J_{ph} is the photogenerated current density, J_0 is the dark saturation current density, n is the ideality factor and V_T is the thermal voltage. Since the band-gap of CdS (E_g = 2.42 eV) is comparatively higher than that of CdTe (E_g = 1.5 eV), the dark saturation current at the emitter region caused by diffusion is negligible and hence, is dominated by the recombination process in the absorber region. In [9], the expression for J_0 is given as

978-1-4673-9257-0/15/$31.00 ©2015 IEEE

$$J_0(V_L) = \frac{qn_iW_a}{2\sqrt{\tau_n\tau_p}} \quad (2)$$

where, q is the electronic charge, n_i is the intrinsic carrier concentration and τ_n and τ_p are the lifetimes of electron and hole respectively for CdTe, and W_a is the width of the absorber layer .

The photogenerated current can be obtained by adding the average electron current density ($J_{n,avg}$) and average hole current density ($J_{p,avg}$) in the absorber layer and can be expressed as

$$J_{ph} = J_{n,avg} + J_{p,avg} \quad (3)$$

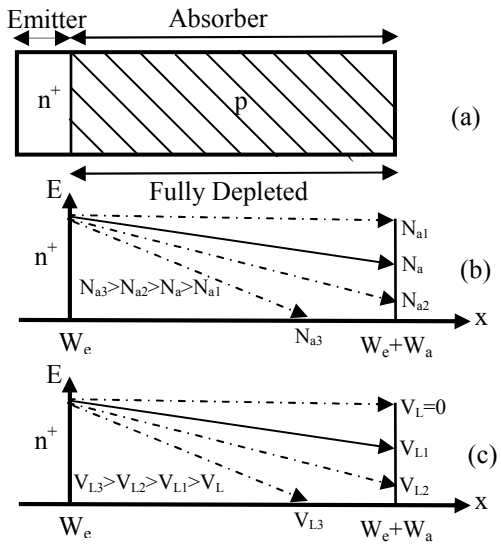

Fig. 1. Electric Field (E) Profile

where, $J_{n,avg}$ and $J_{p,avg}$ can be calculated according to [8], [9] as

$$J_{n,avg} = \frac{1}{W_a}\int_0^{W_a} J_n(x)dx \quad (4)$$

$$J_{p,avg} = \frac{1}{W_a}\int_0^{W_a} J_p(x)dx \quad (5)$$

where, $J_n(x)$ and $J_p(x)$ stands for electron current density and hole current density respectively. The basic equations needed to deduce the $J_n(x)$ and $J_p(x)$ are as follows

$$J_n(x) = qn(x)\mu_n E(x) \quad (6)$$

$$J_p(x) = qp(x)\mu_p E(x) \quad (7)$$

$$\frac{dJ_n(x)}{dx} = \frac{qn(x)}{\tau_n} - q\alpha(\lambda)G_0(\lambda)e^{-\alpha(\lambda)x} \quad (8)$$

$$\frac{dJ_p(x)}{dx} = -\frac{qp(x)}{\tau_p} + q\alpha(\lambda)G_0(\lambda)e^{-\alpha(\lambda)x} \quad (9)$$

Where, n(x) and p(x) is electron and hole density, E(x) for electric field at any point x in Fig. (1), μ_n and μ_p represents electron and hole mobility, α for wavelength-dependent absorption coefficient of the material and G_0 for the optical generation rate given by

$$G_0(\lambda) = (1 - R(\lambda))\frac{\lambda I_0(\lambda)}{hc} \quad (10)$$

Where, h is Planck's constant, c is the velocity of light, $I_0(\lambda)$ is the intensity of light, $R(\lambda)$ is the reflection coefficient and λ is the wavelength of the incident light.

In the thin film hetero-junction structure of CdS/CdTe-based solar cell deposited on the glass substrate, the base (CdTe) region is lightly doped. So, the entire absorber layer will be depleted. For intrinsic or very lightly doped absorber, the electric field can be considered as constant. Previous analysts [2-5] have used this approximation in their analytical approach; but in practical cases for a little increase in the absorber doping results in a linearly-decreasing electric field. However, the electric field in the depletion region close to the emitter side is considered negligible due to its very narrow width. If the absorber layer is fully depleted under short circuit condition, then increase in the absorber doping level [Fig. 1(b)] or in the load voltage [Fig. 1(c)] decreases the field at the right of the absorber layer. Since the electric field is linear throughout the absorber layer and non-zero at the edge, solving Poisson's Equation this field can be calculated as [9]

$$E(x) = \frac{V_{bi} - (V_L - J_L R_S)}{W_a} + \frac{qN_a}{\varepsilon}\left(x - \frac{W_a}{2}\right) \quad (11a)$$

where, ε is the permittivity of absorber material (CdTe), W_a is the absorber width which is equal to the metallurgical base width and V_{bi} is the built-in voltage across the absorber layer. However, if the absorber doping level or the load voltage is further increased, the depletion edge moves towards the left. Hence, the depletion width is no longer equal to the base width and the electric field becomes zero before the base edge. Under this situation, the expression for the electric field can be expressed as found in the standard text books [11]:

$$E(x) = \frac{qN_a}{\varepsilon}(x - W_a) \quad (11b)$$

Combining (6), (8) and (7), (9) gives the first order differential equations of n(x) and p(x) in the absorber layer as

$$\frac{dn}{dx} + \left[\frac{1}{E(x)}\frac{dE}{dx} - \frac{1}{\tau_n\mu_n E(x)}\right]n(x) = -\frac{\alpha(\lambda)G_0(\lambda)}{\mu_n E(x)}e^{-\alpha x} \quad (12)$$

$$\frac{dp}{dx}+\left[\frac{1}{E(x)}\frac{dE}{dx}+\frac{1}{\tau_p\mu_p E(x)}\right]p(x)=\frac{\alpha(\lambda)G_0(\lambda)}{\mu_p E(x)}e^{-\alpha x} \quad (13)$$

Since electrons and holes are swept out by the electric field from the absorber layer in the opposite direction, it can be assumed that $p(W_e) \approx 0$ and $n(W_e+W_a) \approx 0$. Using these boundary conditions, the solutions for the electron and hole concentration can be obtained as

$$n(x)=\frac{\alpha(\lambda)G_0(\lambda)}{\mu_n IF_n(x)}\int_{W_e+x}^{W_e+W_a} e^{-(\alpha+f_n(x))}dx \quad (14)$$

$$p(x)=\frac{\alpha(\lambda)G_0(\lambda)}{\mu_p IF_p(x)}\int_{W_e}^{W_e+x} e^{-(\alpha+f_p(x))}dx \quad (15)$$

where, $IF_n(x)=Ee^{-f_n(x)}$, $IF_p(x)=Ee^{-f_p(x)}$,

$$f_n(x)=\int\frac{dx}{\mu_n\tau_n E(x)},\ f_p(x)=\int\frac{dx}{\mu_p\tau_p E(x)}$$

Now putting the values of n(x) and p(x) from (14) and (15) to (6) and (7) gives the electron and hole current densities as

$$J_n(x)=qG_0(\lambda)\alpha(\lambda)e^{f_n(x)}\int_{W_e+x}^{W_e+W_a} e^{-(\alpha+f_n(x))}dx \quad (16)$$

$$J_p(x)=qG_0(\lambda)\alpha(\lambda)e^{f_p(x)}\int_{W_e}^{W_e+x} e^{-(\alpha+f_p(x))}dx \quad (17)$$

Putting the value of Jn(x) and Jp(x) at (4) and (5), $Jn,_{avg}$ and $Jp,_{avg}$ can be solved.

From (1) it is observed that the load current (J_L) at any load voltage (V_L) can only be determined using numerical methods due to the presence of unknown J_L on both sides. However, using the concept of the perturbation theory this J_L can be determined analytically. According to this theory, if J_L at any V_L is known then, the same at $V_L+\delta V_L$ can be determined using this value, provided that $\delta V_L \rightarrow 0$. Proceeding in the same manner, currents at $V_L+2\delta V_L$, $V_L+3\delta V_L$ …….. can be determined from the current values at $V_L+\delta V_L$, $V_L+2\delta V_L$ …… respectively. Photo-generated current calculated without considering R_s can be used as the initial guess of this process.

III. Results and Discussions

Simulation results based on the proposed model are presented and discussed in this section. The incident photon flux is the air mass (AM) 1.5 global spectrum, which is obtained from the ASTM G-173-03 standard [12]. The absorption coefficients for CdS and CdTe are obtained from the absorption curves in Ref. [13]. The thickness of CdS and CdTe layers are 0.1 and 3.5 µm respectively.

The current-voltage (J_L-V_L) characteristics curve simulated using the proposed model has been shown in Fig. (2). It is noteworthy that the open circuit voltage (0.84 v) and the short circuit current density (17.82 mA-cm^{-2}) obtained in the proposed model are in well agreement with that obtained in the work of Hegedus *et al.* (Fig. 9 of [7]), for R_s = 1.2 Ω cm^2 and n =1.7 and J_0=8×10^{-8} mA-cm^{-2}.

Fig. (3) shows the nature of J_L and V_L with respect to different values of series resistance, R_s. It is observed from the simulation result that though both J_L and V_L decrease slightly in the middle region with the increase in R_s, neither J_{sc} nor V_{oc} changes due to change in R_s.

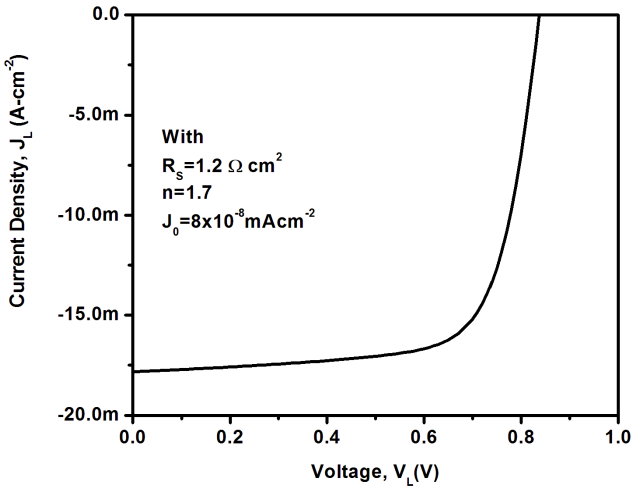

Fig. 2. J_L-V_L Characteristics of the proposed model

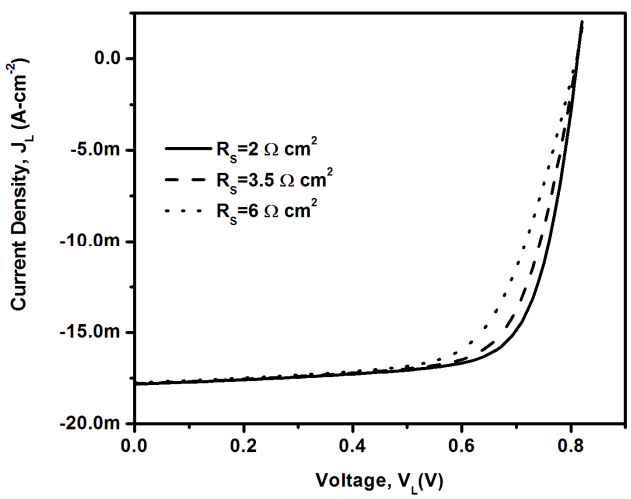

Fig. 3. J_L-V_L characteristics curve under the variation of series resistance (R_s)

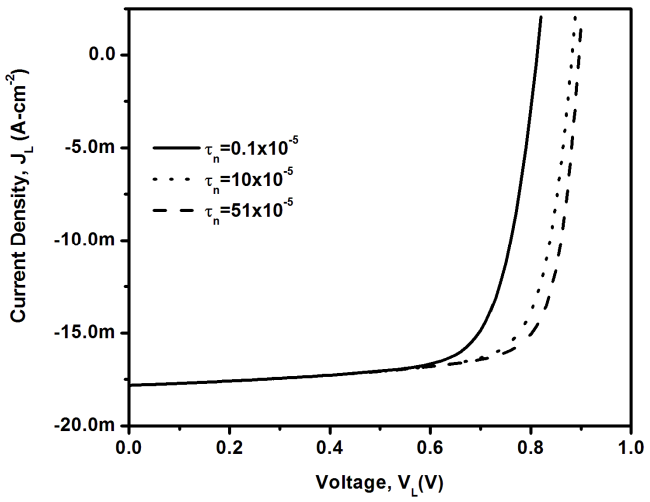

Fig. 4. J_L-V_L characteristics curve against the variation of electron lifetime (τ_n).

J_L-V_L curves have been shown for different lifetimes of electrons (τ_n) in [Fig. (4)] and of holes(τ_p) in [Fig. (5)]. It is found that J_L increases with the increase in any of τ_n or τ_p. This is quite normal, but interestingly, variation in τ_p has a noticeably greater impact on current than that in τ_n has. This phenomenon is quite logical. In fact, most of the photons are absorbed near the emitter side of the n-p junction. Since the fully depleted p-region is much longer than the n-region, it can be argued that the most of the absorption and hence the generation of electron-hole pairs is occurred in a region, which is more distant from bottom contact than from the top contact [Fig. (1)]. The built in electric field then drives the electrons towards the top and the holes towards the bottom of the cell. The holes have to travel a longer way than the electrons do before leaving the cell, holes experience more recombination than the electrons. Hence, the impact of change in τ_p is greater than that in τ_n on J_L.

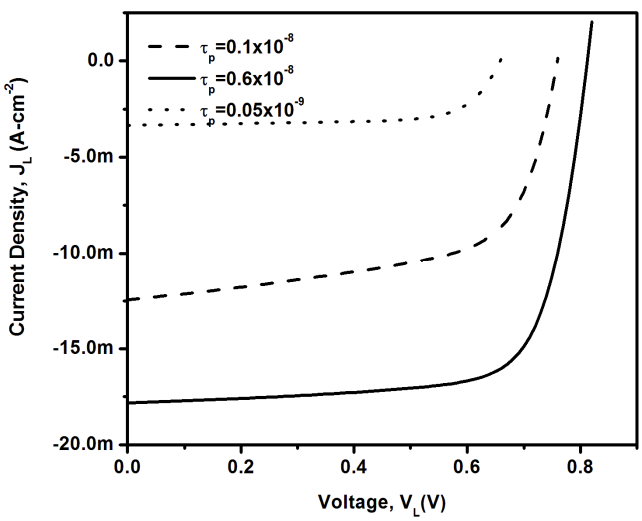

Fig. 5. J_L-V_L characteristics curve against the variation of hole lifetime (τ_p)

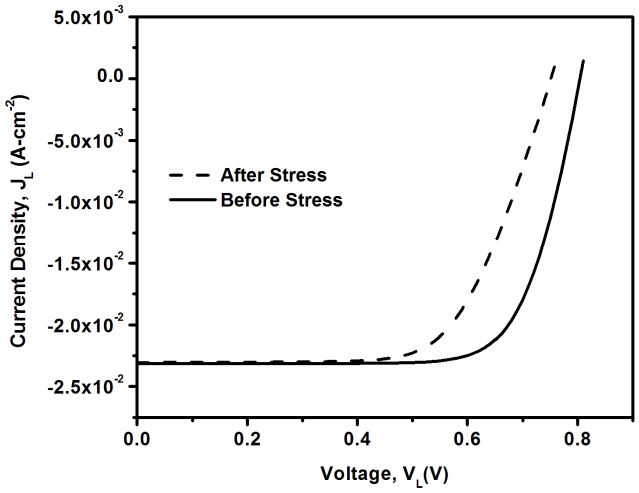

Fig. 6. J_L-V_L characteristics curve before and after applying stress.

Fig. (6) shows the behavior of J_L and V_L of CdTe based solar cell of 7 μm thick CdTe layer and with a Cu/Ni bilayer contact (15 nm/50 nm) of before and after stress, as mentioned in [6], to observe the degradation effects of contact materials over time. The cell was stressed by keeping it at 85^0 C in dry air under 100% sun illumination and open circuit condition for 15 days. Simulation has been done for n=1.66, R_s= 2.4 Ω cm^2 and J_0=1.5×10^{-10} mA cm^{-2} before stress while for n=1.58, R_s= 5.1 Ω cm^2 and J_0=2×10^{-10} mA cm^{-2} after stress. The results i.e., J_{sc} (before stress 23.16 mA cm^{-2} and after stress 23.06 mA cm^{-2}) and V_{oc} (before stress 0.8 v and after stress 0.75 v) has a good agreement with those stated in [6]. The increased value in R_s and J_0 reflects the increased recombination due to degradation, which results in a decreased value in V_{oc}.

IV. Conclusion

The current-voltage characteristics including the series resistance of a CdS/CdTe-based thin film solar cell deposited on the glass substrate have been analytically modeled and analyzed using perturbation theory. The proposed model assimilates both the voltage and the space dependency of the electric field in the absorber region. The model is able to include the stress effects due to contact, explains the more sensitivity of the solar cell to the hole transport than to the electron transport and shows the effects of series resistance. Consequently, the proposed model will be helpful for the better understanding of the physics of the thin-film solar cells.

V. References

[1] T. Aramoto, *et al*, "16.0% Efficient Thin-Film CdS/CdTe Solar Cells" *Jpn. J Appl. Phys*., vol. 36, no. 10, pp. 6304-6307, 1997.

[2] G. C. Morris and S. K. Das, "Some fabrication procedures for electrodeposited CdTe solar cells," *International Journal of Solar Energy*, vol. 12, no. 1–4, pp.95–108, 1992.

[3] S. Ikegami, "CdS/CdTe solar cells by the screen-printing-sintering technique:Fabrication, photovoltaic properties and applications," *Solar Cells*, vol. 23, no. 1-2, pp. 89–105, 1988.

[4] J. Nelson, *The Physics of Solar Cells*, Imperial College Press, Chap. 8, 2003

[5] S. Hegedus, "Current-Voltage Analysis of a-Si and a-SiGe Solar Cells including Voltage-dependent Photocurrent Collection," *Prog. in Photovoltaics: Research and Applications*, vol. 5, pp. 151–168, 1997.

[6] C. Thompson, D. Desai, and S. Hegedus, "Voltage Dependent Photocurrent Collection in CdTe/CdS Solar Cells," *Prog. in Photovoltaics: Research and Applications*, vol. 15, pp. 587–602, 2007.

[7] S. S. Hegedus and W. N. Shafarman, "Thin-Film Solar Cells: Device Measurements and Analysis," *Prog. in Photovoltaics: Research and Applications*, vol. 12, pp. 155–176, 2004.

[8] M. S. Anjan and M. Z. Kabir, "Modeling of Current-Volatge characteristics of CdS/CdTe Solar Cells," *Phys. Stat. Solidi A,* vol. 208, pp; 1813–1816, 2011.

[9] M. A. Mannan, M. S. Anjan and M. Z. Kabir, "Modeling of Current-Voltage Characteristics of Thin Film Solar Cells," *Solid-State Electron*, vol. 63, pp. 49–54, 2011.

[10] M. M. Haque, M. M. Rahman and M. I. B. Chowdhury, "Current-Voltage Characteristics of CdS/CdTe Thin Film Solar Cells: An Analytical Approach," *Proceedings of 2014 3rd International Conference on Non-Conventional Energy (ICDRET 2014)*, pp. 1-4, May 29-31, 2014, Dhaka, Bangladesh.

[11] J. Wilson and J.F.B. Hawkes, *Optoelectronics-An introduction,* 2nd ed., Englewood Cliffs, NJ, Prentice Hall, 1989, pp. 483

[12] NREL,http://rredc.nrel.gov/solarspectra/am1.5/ASTMG173/ASTMG173.html.

[13] M. Burgelman in: J. Poortmans and V. Arkhipov (Editors.), Thin film Solar Cells: Fabrication, Characterization and applications, Wiley & Sons, Chap. 7, 2006

.

Effect of Dislocation Density on the Performance of InGaN-Based MJ Solar Cell:Analytical Approach

Ibne Sabid, Md. Soyaeb Hasan, Md. Fahim-Al-Fattah and Md. Rafiqul Islam
Dept. of Electrical and Electronic Engineering (EEE)
Khulna University of Engineering & Technology (KUET),
Khulna-9203, Bangladesh
ibnesabid.10@gmail.com

Ibrahim Mustafa Mehedi
Dept. of Electrical and Computer Engineering (ECE)
King Abdulaziz University (KAU),
Jeddah, Saudi Arabia
imehedi@kau.edu.sa

***Abstract*—In this study the effect of dislocation density on the performance of InGaN based multi junction solar cell has been calculated analytically. It is found that dislocation density adversely affects the open circuit voltage, short circuit current density and conversion efficiency of a solar cell. Efficiency is found to be improved with the increase in the number of junction (24.4-43.56% for single-six junction solar cells) while considering no dislocation. Whereas it is found that the efficiency is affected when dislocation density (10^{01}-10^{13}m^{-2}) is incorporated for analyzing the performances of either single junction (24.47-8.25%) or multi junction solar cell (43.56-15.25% for six junctions). The effect of dislocation density on minority carrier life time is also been anticipated in this study.**

Keywords— Dislocation density, Multi Junction (MJ), Minority carrier diffusion length, Recombination center

I. INTRODUCTION

The ternary InGaN alloy, a direct band gap material can cover most parts of solar spectrum owing to its tunable bandgap (0.64-3.4eV) [1]. It has some unique properties such as high mobility, high absorption coefficients, and low effective mass of carriers which make it promising especially in photovoltaic (PV) applications [2]-[5]. Since single junction (SJ) InGaN solar cell is not able to convert full spectrum to electrical energy, MJ solar cell is being studied widely all over the world during the last few years. However this approach has some challenges. One of the most critical issues is the higher density of threading dislocations (TD) prevailing in III-nitrides epilayers at levels of ~1×10^{9}cm^{-2} [6]. It is found that a large lattice and thermal expansion coefficient mismatches exist between the layer and substrate. These introduce higher dislocations which lead to the degradation of material quality and consequently the performance of its constituent devices [7]–[9]. For InGaN single junction solar cell the edge, screw, and mixed type misfit dislocations are found [10]. A higher density of TDs incorporates in InGaN based MJ solar cell during hetero-epitaxial growth due to higher lattice mismatch. These dislocations emerge as scattering centers and mid bandgap states, which act as recombination centers and decrease the minority carrier lifetime.

Exploration is going on the improvement of the performances of InGaN based MJ solar cells. In available theoretical works that have been performed for analyzing InGaN solar cells, there is no such work showing the effect of dislocation density on the performances. InGaN based high efficient MJ solar cell has been projected in the literatures without considering the effect dislocation density [11]-[13]. Efficiency of InGaN-based solar cell is found to be 24.24% and 43.56% for single and six junctions respectively [11]. Theoretical investigation on InGaN/InGaN/Si three-junction tandem cell has also been performed without dislocation [13]. Moreover, literatures reviews show the discrepancy between the theoretical and practical performances of InGaN-based solar cell. In this study, dislocation density has been attributed for this disparity in projected and practical performances for InGaN-based MJ solar cell. The impacts of dislocation density, minority carrier diffusion length, and surface recombination velocity on the performance parameters of InGaN based MJ solar cells have been simulated analytically.

II. MODELING

Dislocations play a dominant role in determining the electrical and PV characteristics of thin-film InGaN based SJ and MJ solar cells acting as recombination centers. The recombination losses at dislocations which reduce short-circuit current and enhance excess leakage current is the predominant loss mechanism in thin-film InGaN solar cells. The transport of minority carrier to the dislocation can be found from one dimensional continuity equation solved by Yamaguchi and Amano [14].

$$\frac{\partial n}{\partial x} = \frac{D\partial^2 n}{\partial^2 x} \tag{1}$$

Using the following boundary conditions

$$n = 0 \text{ at } x = 0$$

$$\text{and } \frac{\partial n}{\partial x} = 0 \text{ at } x = X_c = 1/(\pi N_{dis})$$

Where n is the excess minority carrier concentration, X_c is the unit cell radius, and N_{dis} is the dislocation density. With these conditions the continuity equation can be satisfied for:

$$n = n_0 e^{-t/\tau} \sin\left(\frac{x\pi}{2x_c}\right) \tag{2}$$

978-1-4673-9257-0/15/$31.00 ©2015 IEEE

Here n_0 is the equilibrium concentration of minority carrier and τ is the minority carrier lifetime. This solution includes only the first order sine function that gives a best case result for the effective diffusion length approach. By combining (1) and (2), the minority carrier diffusion length limited by recombination at the dislocations is found to be:

$$\frac{1}{L_{dis}^2} = \frac{\pi^3 N_{dis}}{4} \tag{3}$$

With a reciprocal rule the effective minority carrier diffusion length as follows.

$$\frac{1}{L_{eff}^2} = \frac{1}{L_0^2} + \frac{1}{L_{dis}^2} \tag{4}$$

Here L_0 is the minority carrier diffusion length where dislocations are not present. The short circuit current density (J_{SC}) has been calculated from one dimensional steady state continuity equation for electron in p-type and hole in n-type semiconductor. The J_{SC} being dependent on minority carrier diffusion length has been calculated for different dislocation densities. Efficiency calculation includes the total number of photons in solar spectrum per unit area per unit time and band gap is selected in each junction so that equal number of photon can be absorbed. The bottom junction band gap energy is optimized and the other junction's band gap energy is chosen accordingly. When a light of wavelength λ is incident on semiconductor the generation rate of electron hole pairs (EHPs) at a distance x' from the semiconductor surface is given by [15]:

$$G(\lambda, x') = \alpha(\lambda) F(\lambda)[1 - R(\lambda)] e^{[-\alpha(\lambda)x']} \tag{5}$$

Where, $\alpha(\lambda)$ is the absorption coefficient, $F(\lambda)$ the number of incident photons/cm^2/s per unit bandwidth and $R(\lambda)$ is the fraction of these photons reflected from the surface.

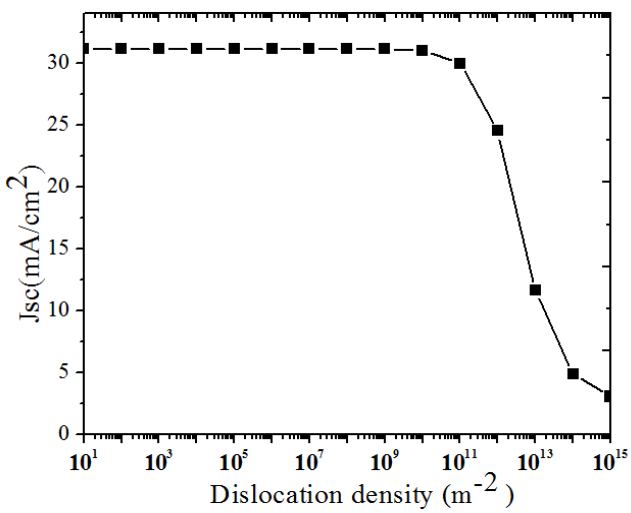

Figure 1. Dependence of short circuit current density (J_{sc}) on dislocation density.

One dimensional steady-state continuity equations for holes in n-type semiconductors under low injection condition are:

$$G_p - \frac{p_n - p_{no}}{\tau_p} + \frac{1}{q}\frac{dJ_p}{dx'} = 0 \tag{6}$$

The current density equation for hole can be expressed as:

$$J_p = q\mu_p p_n \xi - qD_p \frac{dp_n}{dx'} \tag{7}$$

Here, D_p = Diffusion coefficient for p-type. Combining the equation (5), (6) and (7) yields the expression:

$$D_p \frac{d^2 p_n}{dx'^2} + \alpha F(1-R) e^{(-\alpha x')} - \frac{p_n - p_{no}}{\tau_p} = 0 \tag{8}$$

Solving the equation (8) and using two boundary conditions at the surface, $x' = 0$ and at the edge of the depletion region $x' = x_j$ the resultant hole density can be calculated. The resultant photocurrent density due to hole collected at the depletion region, J_p has been calculated. Similarly electron photocurrent density collected at the depletion edge, J_n is evaluated. Total photocurrent density at a given wavelength:

$$J(\lambda) = J_p(\lambda) + J_n(\lambda) + J_{dr}(\lambda) \tag{9}$$

The efficiency expression is given by:

$$\eta = \frac{J_{ph} V_{oc} FF}{\Phi_0} \tag{10}$$

Finally open circuit voltage and efficiency have been calculated at a fill factor FF=0.85 and the incident irradiance Φ_0 = 96.366 mW/cm^2 [16].

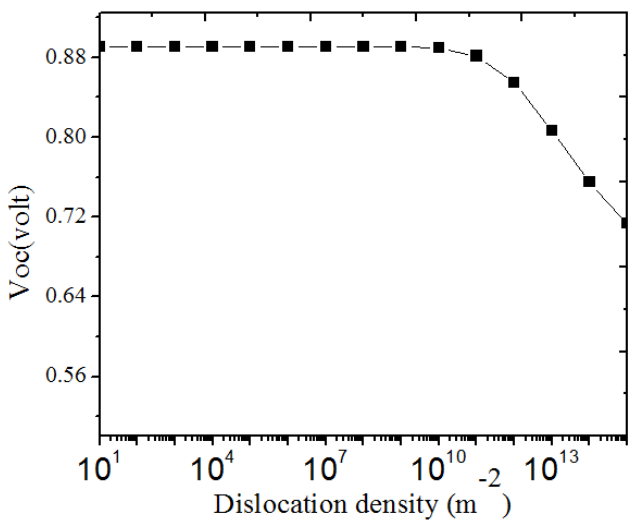

Figure 2. Dependence of open circuit voltage (V_{oc}) on dislocation density.

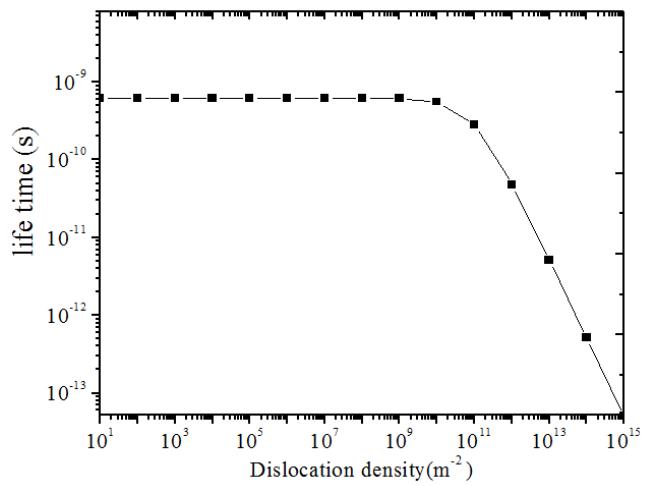

Figure 3. Change of minority carrier lifetime with the variation of dislocation density in $In_{0.51}Ga_{0.49}N$ single junction solar cell.

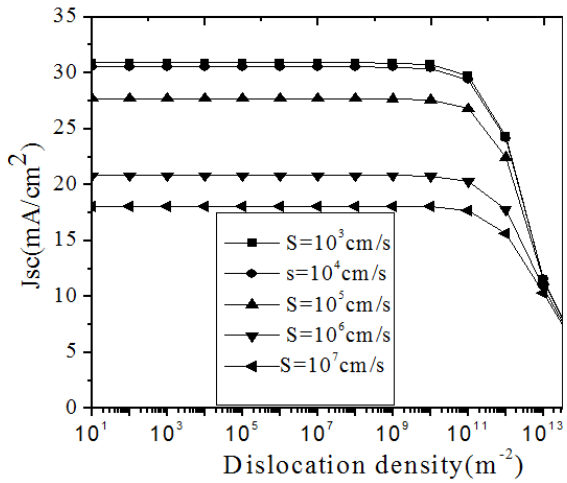

Figure 4. Variation of short circuit current density (J_{sc}) with the change of dislocation density at different values of surface recombination velocity.

III. Result and Discussion

A. Performance evaluation for Single Junction Solar Cell

Fig. 1 depicts the short circuit current density (J_{SC}) at different dislocation densities. The J_{SC} falls significantly above the dislocation density $10^{11}m^{-2}$. Fig. 2 shows that the V_{oc} decreases gradually with the increase of dislocation density above $10^{11}m^{-3}$. The V_{oc} decreases from 0.887v to 0.67v with the increase of dislocation density from 10^{01} to 10^{15} m^{-2} for a fix value of recombination velocity S=10^3cm/s in a single junction solar cell considering band gap 1.38862eV. The optimized value of band gap is 1.38862 eV when we choose x=0.514. The variation of the minority carrier lifetime with the dislocation density in above n on p-$In_xGa_{1-x}N$ solar cell is depicted in Fig. 3. The minority carrier lifetime of electrons in p-$In_{0.51}Ga_{0.49}N$ base layer is 6.25E-10s when the dislocation density is lower than 10^8 m^{-2} and starts to decrease rapidly to 10^{-13}s as the dislocation density increases above 10^9m^{-2}. Since minority carrier life time is important parameter to determine the performances of solar cell, it should be increased in order to enhance the performances. The calculated value of J_{sc} at different dislocation densities with different values of surface recombination velocity (S) are illustrated in Fig. 4. The J_{sc} decreases as the recombination velocity increases for a same set of dislocation densities. All the values of J_{sc} were plotted at finite value of S. The J_{sc} of solar cell is significantly lowered by increasing S. The S generally increases with increasing dislocation density.

The S of direct band gap semiconductor, such as GaAs, InP, GaN, InN etc. is very high. Change in efficiency is observed when the S increases at a constant dislocation density. The change in efficiency with change in S is shown in Fig. 5. A negligible variation in efficiency is observed for S when it is bellow 10^4cm/sec and efficiency falls as S increases above 10^4cm/sec. Efficiency is an important parameter to

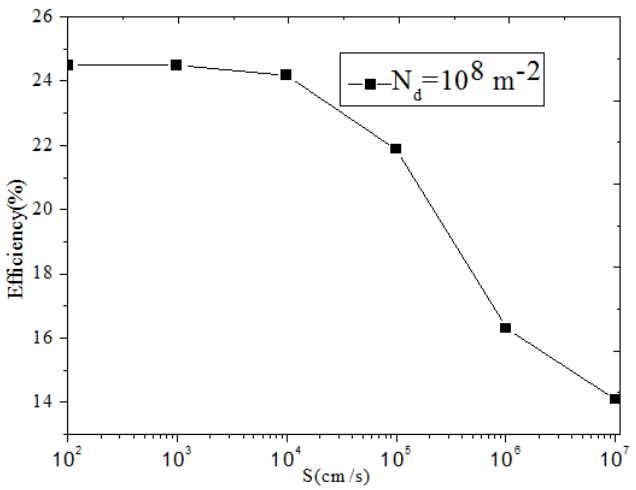

Figure 5. Dependence of efficiency on recombination velocity at a fixed value of dislocation density.

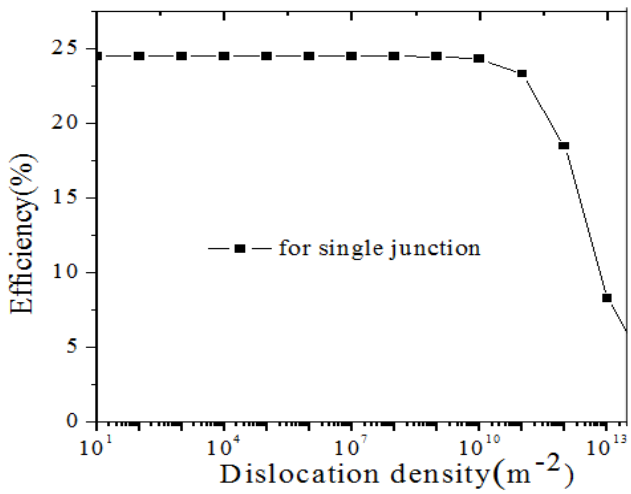

Figure 6. Dependence of efficiency on dislocation density (N_d) at a fixed value of recombination velocity, S=10^3 cm/s

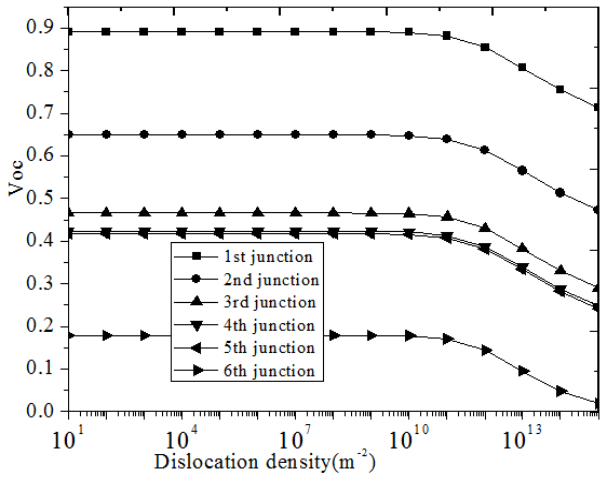

Figure 7. Change in open circuit voltage with dislocation density for individual junction.

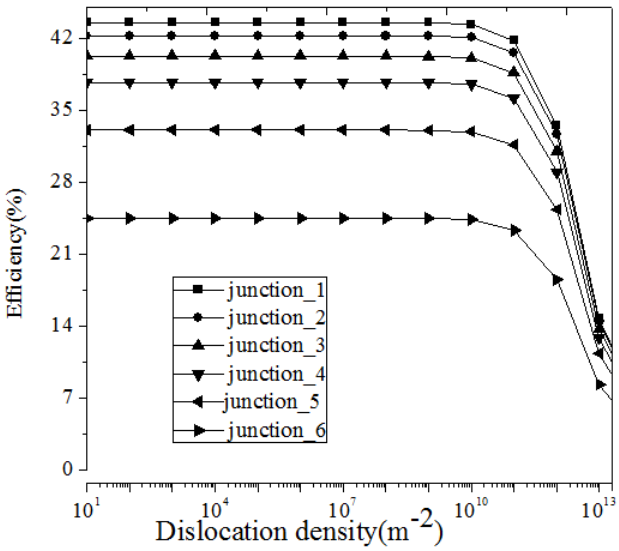

Figure 9. Dependence of Efficiency on dislocation density up to six junctions.

investigate the performances of solar cells. The efficiency of InGaN based SJ solar cell decreases as the dislocation density increases depicted in Fig. 6. There is a marginal change in cell efficiency when the dislocation density increases from 10^{10} to $10^{13}m^{-2}$ at a fixed surface recombination velocity. The efficiency remains nearly constant up to $10^{10}m^{-2}$ at a fix value of surface recombination velocity which is good agreement with [11]**.** result for SJ solar cell. There is a rapid decrease in efficiency when the dislocation density goes above $10^{10}m^{-2}$.

B. Performance evaluation for MJ

The effect of dislocation on V_{oc} for individual junction is represented in Fig. 7. The optimum band gap energies are taken as 1.381eV, 1.15eV, 0.974eV, 0.938eV, 0.938eV, 0.7eV respectively for single-to-six junctions. The open circuit voltage is found to be 0.894 V and 0.18 V, respectively for the

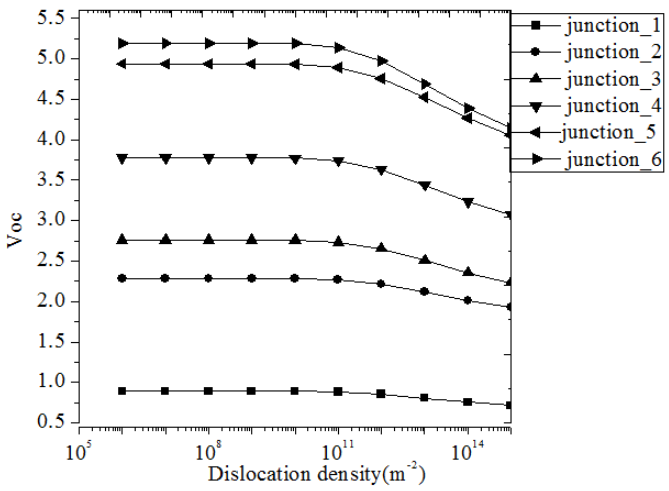

Figure 8. Open circuit voltage up to six junctions with the variation dislocation density.

1st and 6th junction individually at dislocation density below $10^{10}m^{-2}$. The variation of V_{oc} with respect to dislocation density is shown in Fig. 8. The V_{oc} is plotted as the summation of individual junction. Fig. 9 shows the efficiency of InGaN based MJ solar cell up to six junctions at different dislocation density. From the figure it is evident that the efficiency remains nearly constant up to dislocation density $10^{10}m^{-2}$. The efficiency falls dramatically above the dislocation density 10^{11} m^{-2}. The efficiency is found to be varied 24.47% to 8.25% for single junction and 43.56% to 15.25% for six junctions with the increase in dislocation density from 10^{01} to $10^{13}m^{-2}$.

It is found from the simulation results that for InGaN based MJ solar cell, the overall efficiency degradation starts to occur when dislocation density is greater than $10^{10}m^{-2}$. It is evident that the edge, screw, and mixed type misfit dislocations are found to be occurred 4.69×10^{10}, 4.53×10^{9}, and $4.03\times10^{11}cm^{-2}$ in InGaN [10], [17]. Hence, if we want fabricate InGaN-based high efficient MJ solar cell we should go through the steps that can reduce the dislocation density.

IV. CONCLUSION

The effects of dislocation density on the performance of InGaN based solar cell have been investigated analytically. It is found that higher dislocation density has negative impact on the performance of either SJ or MJ solar cells. It is seen that due to higher dislocation density, surface recombination velocity increases which results in fall in efficiency. The outcomes of our simulation depicts that the performance parameters are intensely affected when dislocation density is above $10^{11}m^{-2}$ and remains approximately persistent bellow this value. Furthermore, in comparison with previous simulation based investigations without considering the dislocation density, it is informed that the calculated efficiency is somewhat lower for each junction.

REFERENCES

[1] A. Bhuiyan, K. Sugita, A. Hashimoto, and A. Yamamoto, "InGaN Solar Cells: Present State of the Art and Important Challenges," in *Photovoltaics, IEEE Journal of* , vol.2, no.3, pp.276-293, July 2012.

[2] E. Matioli, C. Neufeld, M. Iza, S. C. Cruz, A. A. Al-heji, X. Chen, "High internal and external quantum efficiency InGaN/GaN solar cells". *Applied Physics Letters*, vol. 98, no. 2, pp. 021102-3, Jan. 2011.

[3] R. Dahal, B. Pantha, J. Li, J. Y. Lin, and H. X. Jiang. "InGaN/GaN multiple quantum well solar cells with long operating wavelengths." *Applied Physics Letters,* vol. 94, no. 6, pp. 063505-3, Feb. 2009.

[4] O. Jani, I. Ferguson, C. Honsberg, and S. Kurtz. "Design and characterization of GaN/ InGaN solar cells." *Applied Physics Letters,* vol. 91, no. 13, pp. 132117-3, Sep. 2007.

[5] Ji-Hong, Zhu, Wang Liang-Ji, Z. Shu-Ming, W. Hui, Z. De-Gang, Z. Jian-Jun, L. Zong-Shun, J. De-Sheng, and Y. Hui. "Simulation of the light extraction efficiency of nanostructure light-emitting diodes." *Chinese Physics B,* vol. 20, no. 7, pp. 077804-4, Nov. 2011.

[6] M. M. Song, Z. Wu, Y. Fang, R. Xiang, Y. Sun, H. Wang, C. Yu, H. Xiong, J. Dai, and C. Chen. "Improved photovoltaic performance of InGaN single junction solar cells by using n-on-p type device structure." *Journal of optoelectronics and advanced materials,* vol. 12, no. 7, pp. 1452 – 145, July 2010.

[7] H. K. Cho, J. Y. Lee, K. S. Kim, G.M. Yang, "Formation of misfit dislocations and stacking faults in high indium content $In_xGa_{1-x}N$ layers grown by metal organic chemical vapor deposition". *J. Korean Phys*. vol. 39, no., pp.165-169, Dec-2001.

[8] H. Wang, D. S. Jiang, U. Jahn, J. J Zhu, D.G. Zhao, Z.S. Liu, "Investigation on the strain relaxation of InGaN layer and its effects on the InGaN structural and optical properties". *Physica B: Condensed Matter*, vol. 405, no. , pp. 4668–4672, Nov. 2010

[9] H. K. Cho, G. M. Yang, "Generation of misfit dislocations in high indium content InGaN layer grown on GaN". *J. Crystal Growth,* vol. 243, no. 1, pp. 124–128, Aug. 2002.

[10] M. A. Hossain, M. R. Islam, M. K. Hossain, A. Hashimoto, and A. Yamamoto. "Dislocation reduction in heteroepitaxial $In_xGa_{1-x}N$ using step-graded interlayer for future solar cells." *Materials for Renewable and Sustainable Energy,* vol. 3, no. 1, pp. 1-14, March. 2014.

[11] M. R. Islam, M. A. Rayhan, M. E. Hossain, A. G. Bhuiyan, M. R. Islam, A. Yamamoto, "Projected Performance of $In_xGa_{1-x}N$-Based Multijunction Solar Cells," in *Electrical and Computer Engineering, 2006. ICECE '06. International Conference on* , vol., no., pp.241-244, 19-21, Dec. 2006.

[12] A. Yamamoto, M. R. Islam, T. T. Kang, and A. Hashimoto. "Recent advances in InN-based solar cells: status and challenges in InGaN and InAlN solar cells." *physica status solidi (c)* vo. 7, no. 5, pp. 1309-1316, March. 2010.

[13] L. Hsu, and W. Walukiewicz. "Modeling of InGaN/Si tandem solar cells."*Journal of Applied Physics,* vol. 104, no. 2, pp. 024507-3, Jul. 2008.

[14] M. Yamaguchi, A. Yamamoto, and Y. Itoh, "Effect of dislocations on the efficiency of thin-film GaAs solar cells on Si substrates", *J. Appl. Phys.*, vol. 59, pp. 1751-1753, Nov. 1986.

[15] Sze, Simon M., and Kwok K. Ng. *Physics of semiconductor devices*. John Wiley & Sons, 2006.

[16] U. K. Mishra, Y. F. Wu, B. P. Keller, S. Keller, and Denbaars, S. P. (1998). GaN microwave electronics. *Microwave Theory and Techniques, IEEE Transactions on*, vol. *46*, no. 6, pp. 756-761.

[17] M. R. Islam, Y. Ohmura, A. Hashimoto, A. Yamamoto, K. Kinoshita, and Y. Koji. "“Step-graded interlayers” for the improvement of MOVPE $In_xGa_{1-x}N$ (x~ 0.4) epi-layer quality." *physica status solidi (c)*, vol.7, no. 7-8, pp. 2097-2100, Nov. 2010.

Effects of Photon Recycling on the Properties of p+ n GaAs Solar Cell

Sadi Mohammad[1*], Md.Injammaul Islam Chowdhury[1], Md. Sherajul Islam[1] and Ashraful Ghani Bhuiyan[1]
[1] Khulna University of Engineering & Technology, Bangladesh
[*] E-mail: sadi_mohammad@yahoo.com
[1]

Abstract— **The main drawback of currently used photovoltaic cell is it's low conversion efficiency. Among the single junction solar cells, cells with GaAs material offers the maximum efficiency.For direct bangap material like GaAs photon recycling is an exciting approch.Benefication to solar cell properties due to photon recyling(PR) has been speculatively and carefully investigated in a p+ n structure of GaAs. In this study all the concentration has been made on the effect of PR that enhance the functioning of the cell. This study is also focused on the effect of architechtural and substantial parameters reliance on the magnitude of PR effect. For the PR effect short circuit current density, open circuit voltage of the cell is found to be increased which in turns increases the efficiency. PR is largely effected by high surface recombination velocity, emitter thickness, doping density.**

Keywords—Solar cell, Photon Recyling (PR), GaAs, p+n strcuture, Surface recombination velocity (SRV), Doping Density, Emitter thickness.

I. INTRODUCTION

Energy is major concept of economic development. World need more energy to provide the growing population with increase standard of living. Fossils fuels such as, oil, gas etc. are the major sources of energy and contribute to a bigger portion of world's energy supply. There are other source of energy, known as renewable energy source, fulfill a small portion of world's energy demand. It's importance is increasing and it is expected that it will become more important in future. The common renewable energy sources are biomass, geothermal, wind, solar etc. Among these sources solar energy is very important because it does not require any fuel cost and it is plentiful in nature. Most importantly, solar technologies are environmental friendly. Solar cell does not produce any environmental waste during it's operation and no noise is produced, if produced it is very small.

With respect to other available energy sources,the efficiency of solar cell is coparatively low. Besides the cost of solar energy is more than the conventional energy. There are many factors which affect the cost of solar energy. The cost of solar cell can be reduced by improving the performance of solar cells. Among the performance parameters, the efficiency of solar cell is very important. There are many approaches to increase the efficiency. Although most of them provide high efficiency but their fabrication process and control is much difficult and costly. An important role in the cost minimization is played by single junction cell. It's fabrication is comparatively less difficult and it provides higher efficiency with minimum cost. Among all the single junction solar cell GaAs offers maximum efficiency.

Among all the exciting approch to increase the efficieny of solar cell photon recyling is an encouraging step.The efficiency of semiconductor solar cell is dependent on minority carrier parameters.The efficiency is high if the minority carrier charge density can be increased. Minority carrier charge density is dependent on photon recycling and increased due to photon recycling in direct bandgap semiconductors.During the radiative recombination process re-absorption of photons emitted is referred to as photon recycling(PR).PR utilizes the photon emitted during the recombination of electron with hole. It minimizes the loss due to recombination. Minimization of the loss due to recombination is a contribution to the increase of efficiency. As a consequence of this process new electron–hole pairs are generated and the minority carrier charge density increases. One of the main factors that contribute to the improvement of efficiency of solar cell is short circuit current. Short circuit current increases with the increase of minority carrier charge density. So utilization of recycled photon is the best way to improve the efficiency of solar cell. As GaAs is a direct bandgap semiconductor, band-band recombination with accompanying photon emission and subsequent photon reabsorption at another location in the cell may occur [3]. Previously many scientists explored the effect of PR in the improvement of cell.Very recently Alexandre et al. has shown the current–voltage characteristics of the cells [11].This model is founded on Shockley–Read–Hall lifetimes based on internal quantum efficiency measurement.Gilt edge design of the cell has been done for the variation of base thickness and Shockley–Read–Hall lifetime using reflector. It is shown in the paper that the doping concentration is insignificant in the enhancement of open circuit voltage. Some other factors of a solar cell that have on authority in the improvement of efficiency is not considered in their model. The other factors that can grease the efficiency is considered in this paper like the surface recombination velocity, emitter thickness and the doping concentration.

978-1-4673-9257-0/15/$31. 00 ©2015 IEEE

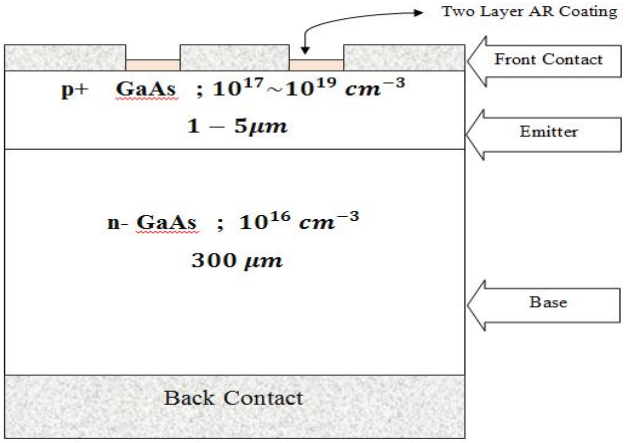

Figure 1: Structure of the p+ n solar cell used

II. MATHEMATICAL EXPRESSION FOR PHOTON RECYLING MODEL

To model PR effects, a number of different approaches have been made. Hypothesis was proposed by Asbeck regarding radiative lifetime multiplication factor to explain lifetime measurements in GaAs. Due to PR effect additional generation of minority carrier has incorporated. In order to enumerate the one dimensional photon recycling generation rate the basic formulation of Kuriyama et al. has been used in this paper. The cell model of fig.1 has been used. At first applying the boundary condition distribution of excess minority carrier density, without photon recycling is found. There will be a short circuit current density. As there are two layers in solar cell, emitter and base. Short circuit current is generated in each layer and also within the depletion region. The total short circuit current is the sum of the contribution from the emitter, base and depletion region. This will be

$$J_{sc} = J_{psc} + J_{nsc} + J_{dr} \quad \ldots\ldots\ldots\ldots\ldots\ldots\ldots\ldots\ldots\ldots\ldots\ldots(1)$$

Where,

Short circuit current due to holes collected at the depletion edge

$$J_{psc} = q(1-R_o)F\frac{\alpha_0^2 L_p^2}{\alpha_0^2 L_p^2 - 1}\left\{\frac{1+{\xi_p}/{\alpha_0 L_p}}{\cosh\left({x_j}/{L_p}\right)+\xi_p \sinh\left({x_j}/{L_p}\right)}\right\} \quad \ldots\ldots..(2)$$

Short circuit current due to electrons collected at the depletion edge

$$J_{nsc} = q(1-R_o)F\frac{\alpha_0^2 L_n^2}{\alpha_0^2 L_n^2 - 1}\left\{\frac{1+{\xi_n}/{\alpha_0 L_n}}{\cosh\left({x_j+w}/{L_p}\right)+\xi_n \sinh\left({x_j+w}/{L_n}\right)}\right\}\ldots(3)$$

Short circuit current generation takes place within the depletion region.

$$J_{dr} = qF(1-R)\exp(-\alpha x_j)\left[1-\exp(-\alpha W)\right] \quad \ldots\ldots\ldots..(4)$$

Where, τ is minority carrier lifetime, α_o is absorption coefficient of the excitation light, R_o is reflectivity, F is photon flux density, d is thickness of emitter and L is the diffusion length of minority carrier. ξ is the normalized surface recombination velocity defined by $\xi = {SL}/{D}$, S is surface recombination velocity and D is the diffusion constant. W is the width of depletion region.

Now during recombination a new photon will be emitted. From a certain point within the cell a photon will be emitted. By absorbing the photon energy a new pair of electron-hole will generate. Thus increase the minority carrier density. Including the photon recycling process the expression for short circuit current density will be:

$$J_{t,sc} = J_{pr} + J_{sc} \quad \ldots\ldots\ldots\ldots\ldots\ldots\ldots\ldots\ldots\ldots\ldots\ldots(5)$$

Where,

$$J_{pr} = J_{pr,psc} + J_{pr,nsc} + J_{dr,pr} \quad \ldots\ldots\ldots\ldots\ldots\ldots\ldots\ldots\ldots\ldots\ldots..(6)$$

From the hole density distribution the resulting hole short circuit current density due to photon recycling at the depletion edge is,

$$J_{pr,psc} = q\frac{1}{\cosh\left({x_j}/{L_p}\right)+\xi_p \sinh\left({x_j}/{L_p}\right)}\left\{\int_0^{x_j} g_{pr,k}(\xi_p)\cosh\left({\xi_p}/{L_p}\right)d\,\xi_p + \int_0^{x_j} g_{pr,k}(\xi_p)\sinh\left({\xi_p}/{L_p}\right)d\,\xi_p\right\} \quad \ldots\ldots\ldots(7)$$

The short circuit current due to electrons by photon recycling collected at the depletion edge is,

$$J_{pr,nsc} = q\frac{1}{\cosh\left({x_j+w}/{L_p}\right)+\xi_n \sinh\left({x_j+w}/{L_n}\right)}\left\{\int_0^{x_j+W} g_{pr,k}(\xi_n)\cosh\left({\xi_n}/{L_n}\right)d\,\xi_n + \int_0^{x_{j+W}} g_{pr,k}(\xi_n)\sinh\left({\xi_n}/{L_n}\right)d\,\xi_n\right\} \quad \ldots\ldots\ldots..(8)$$

The short circuit current density due to photon recycling in the depletion region is as follows:

$$J_{dr,pr} = q\int_{x_j}^{x_j+W} g_k(z)dz \ldots\ldots\ldots\ldots\ldots\ldots\ldots\ldots\ldots\ldots\ldots(9)$$

From the value of diode saturation current J_0 and short circuit current the value of open circuit voltage can be calculated. The open circuit voltage due to photon recycling, $V_{t,oc}$ will be,

$$V_{t,oc} = \frac{kT}{q}\ln\left(\frac{J_{t,sc}}{J_o}+1\right) \quad \ldots\ldots\ldots\ldots\ldots\ldots\ldots\ldots\ldots\ldots..(10)$$

In order to determine the efficiency fill factor is to be calculated. It is known that fill factor,

$$V_m J_m = FF \times V_{t,oc} \times J_{t,sc} \ldots\ldots\ldots\ldots\ldots\ldots\ldots\ldots\ldots\ldots..(11)$$

Efficiency of the cell due to photon recycling,

$$\eta = \frac{FF \times V_{t,oc} \times J_{t,sc}}{P_{in}} \quad \ldots\ldots\ldots\ldots\ldots\ldots\ldots\ldots\ldots\ldots\ldots.....(12)$$

III. SIMULATION RESULTS

Photon recycling takes place within the cell. It's performance will obviously rely on the structural and material parameter of the cell. Moreover recombination are dependent on the material of the cell, doping level and the structure. So this factor will have influence upon the magnitude of photon recycling effects. In the following section graphical representation of the dependence of photon recycling on different parameters will be shown.

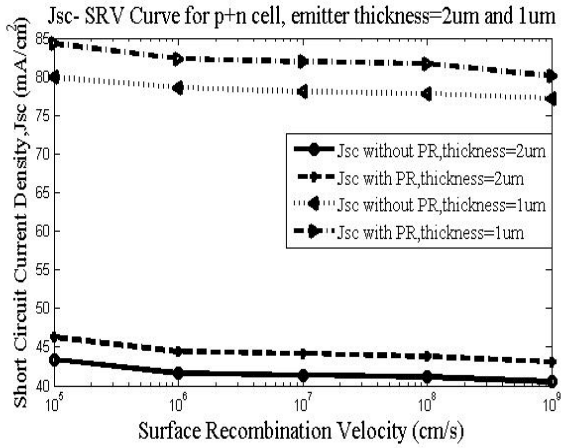

Figure 2. J_{sc}– SRV curve for p+ n cell at emitter thickness,2μm and 1μm

A. *Varying the surface recombination velocity :*

Fig 2 shows the variation of the short circuit current density with the surface recombination velocity. Two different cases has been considered. One is for emitter thickness of 1μm and the other one is for 2μm.In both the cases due to PR effect the short circuit current density has increased. But it has been found out that when the emitter thickness is reduced the PR effect increases. So one can come to conclusion that the lower the emitter thickness higher will be the PR effect. Due to increase in minority carrier density the increase in current density is observed. As the current density is increased, the open circuit voltage and the efficiency of the cell is increased in turns, shown in fig.3 and fig.4. Average increase of efficiency is 10.9% for emitter thickness of 2μm and for emitter thickness of 1μm this is 5.7%.The average increase in the two cases is different but overall increase of efficiency is higher for emitter with lower thickness. This may be due to the fact that the diffusion length of the minority carrier remain almost constant for different emitter thickness. At lower thickness the contribution of minority carrier density is more than at higher thickness.

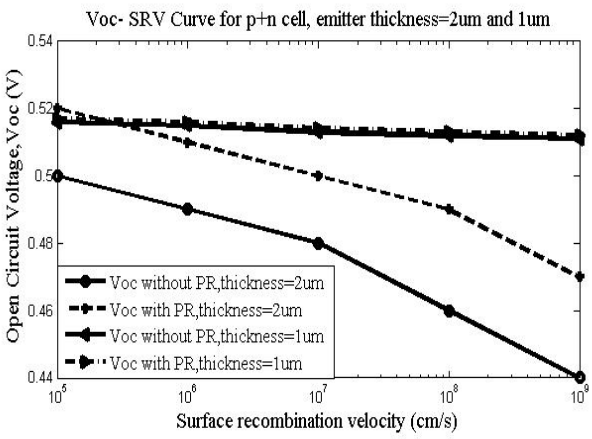

Figure 3. V_{oc}– SRV curve for p+ n cell at emitter thickness2μm and 1μm

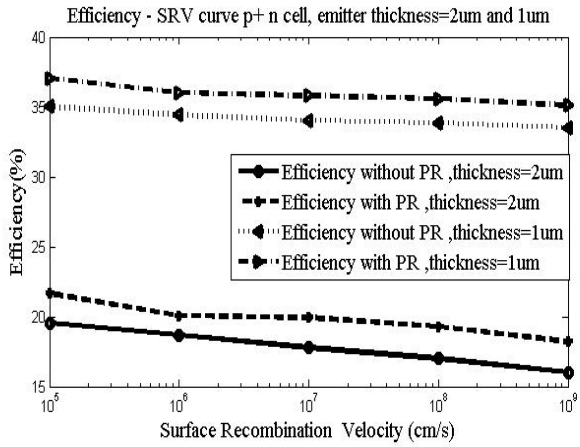

Figure 4. Efficiency– SRV curve for p+ n cell at emitter thickness 2μm and 1μm

B. *Varying the emitter thcikness :*

In the second case emitter thickness is varied taking two surface recombination velocity fixed .From fig.5 it can be easily said that the PR effect is largely dependent on the thickness of emitter. PR effect increases the short circuit current density but short circuit current density goes on decreasing with the increase of emitter thickness. At large surface recombination velocity the effect is lower. As because at higher surface recombination velocity recombination take place quickly. So the photon with minimum energy required for the generation of electron-hole pair do not emit. As the short circuit current density goes on decreasing so does the open circuit voltage and the efficiency of the cell decreases, shown in fig 6. and fig 7. The average increase of efficiency for surface recombination velocity of $10^5\ cm/s$ is 17%. On the other hand for surface recombination velocity of $10^7\ cm/s$ increase of efficiency is 15%.

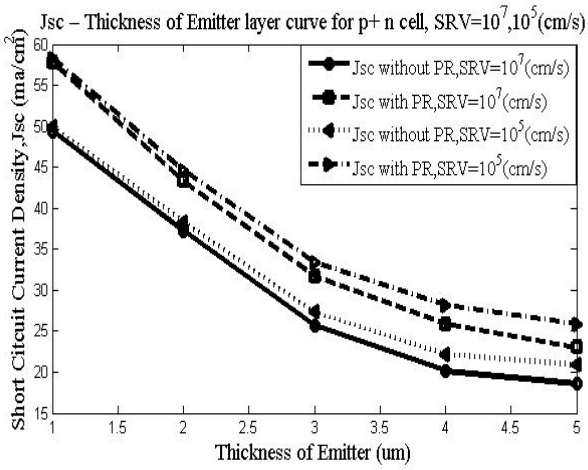

Figure 5. J_{sc}– thickness of emitter curve for p+ n cell at SRV, 10^7 cm/s and 10^5 cm/s

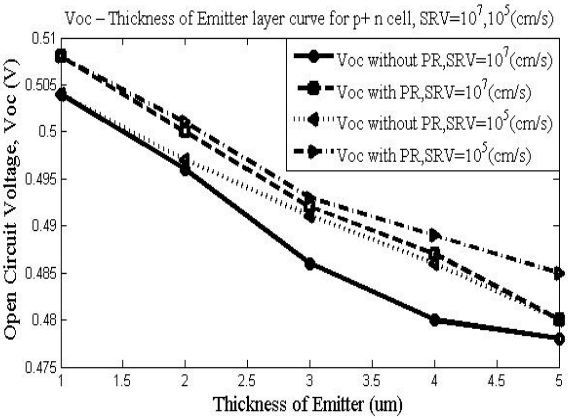

Figure 6. V_{oc}– thickness of emitter curve for p+ n cell at SRV, 10^7 cm/s and 10^5 cm/s

C. *Varying the doping density :*

In the third case keeping the surface recombination velocity and thickness of emitter constant, the doping density of the emitter is varied. From fig 8. it is clear that with the increase of doping density the short circuit density goes on decreasing. But the PR effect increases the current density for all the doping densities. As the short circuit density increases due to PR effect, the open circuit voltage and the efficiency of the cell also increases. Difference of efficiency is observed for with and without PR. At higher doping density the PR effect is more. Because the probability of radiative recombination increases with the increases of doping density .So minority carrier density in the p+ base decreases. The average increase of efficiency is 12% due to PR effect due to increase of doping density.

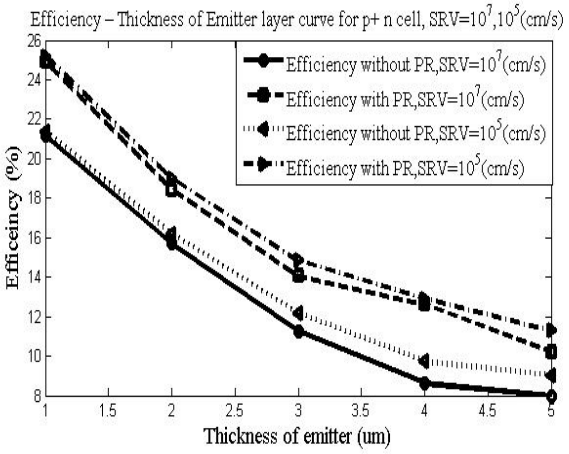

Figure 7. Efficiency– thickness of emitter curve for p+ n cell at SRV, 10^7 cm/s and 10^5 cm/s

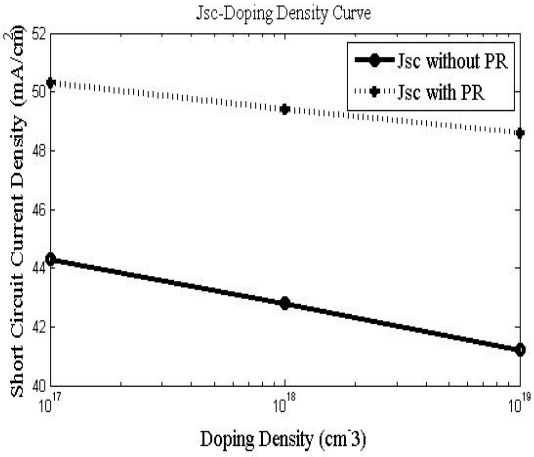

Figure 8. J_{sc}– Doping density of emitter curve

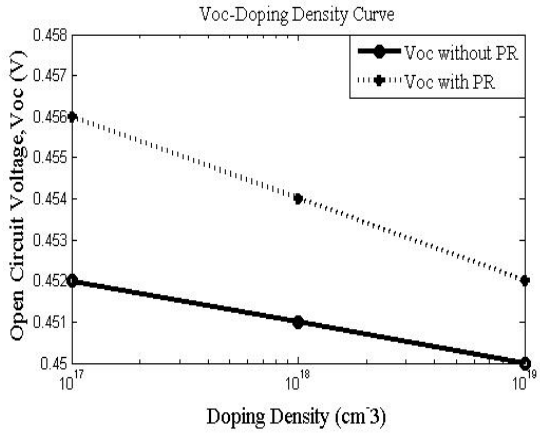

Figure 9. V_{oc}– Doping density of emitter curve for p+ n cell

IV CONCLUSION

In order to find out the prominent factors for PR in GaAS solar cell structures, research has been done on p+ n cell using the method schemed by Kuriyama et al. PR effect is actuated by thickness of emitter , surface recombination velocity and

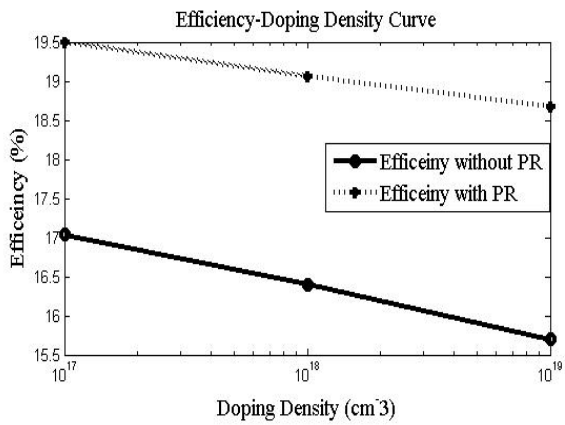

Figure 10. Efficiency– Doping density of emitter curve for p+ n cell

doping density of p+ emitter. Effect of base n-layer is negligible on PR effect. Among the three dominant factor thickness effects the PR more. The lower the thickness the better will be the efficiency of the cell. PR effect accelerate the cell performance in the positive direction. While designing a cell with PR different factors must be taken into consideration.

REFERENCES

[1] Sadao Adachi, "III-V Binary Semiconductors," in *Optical Constants of Crystalline and Amorphous Semiconductors*, Japan, Springer Science + Business Media., LLC, 1950,ch *B*, sec *B12*, pp. *213-226.*

[2] Green ,Martin A. "Efficiency Limits ,Losses and measurement," in *Solar cells*, USA, Prentice Hall, INC,1982,ch 5, pp. *85-98*.

[3] K. Ahrenkiel, S. Lundstrom, "Radiative Transitions in GaAs and Other III-V Compounds, minority carriers in III-V semiconductors physics and applications," in *Semiconductors and semimetals*, Academic Press, New York, 1993, ch *1,2*, pp. *22,119*.

[4] T. Kuriyama ,T. Kamaiya and H. Yanai, "Effect of photon recycling on Diffusion length and internal quantum efficiency of $Al_xGa_{1-x}As-GaAs$,"Japan, *J. appl. Phys* , 1977, 16,*465-477*

[5] P. Asbeck, "Self-absorption effects on the radiative lifetime in GaAs-GaAlAs double heterostructures," America, *J. appl. Phys* , 1977, 48 ,*420-822*

[6] Ph. Renaud, F. Raymond, B. Bensaïd, and C. Vèrié, "Influence of photon recycling on lifetime and diffusion coefficient in GaAs," America, *J. appl. Phys,*1992*,* 71 (4),*1907-1913*

[7] S. M. Durbin and J. L. Gray. "Numerical modeling of photon recycling in high efficiency GaAs solar cells," *Proc. 22nd IEEE Photovoltaic conf,*Las Vegas, NV. Oct. 1991. *188.*

[8] S. M. Durbin and J. L. Gray, "Numerical Modeling of Photon Recycling in Solar Cells" *IEEE Trans. on Electron Devices* , Vol. 41, No. 2, February 1994.

[9]A. Yamamoto, M. Kurizuka, Md. M. Murshid, M. Ohkubo, A. Hashimoto, "Material and structural parameter dependencies of photon recycling effects in conventional n +- p InP solar cell," *Elsevier Science B.V*, Solar Energy Materials and Solar Cells, 50, 1998,*259-264*

[10]A. Yamamoto, M. Kurizuka, Md. M. Murshid, and A. Hashimoto, "A Comparative Study on Photon Recycling effects in N+P and P+-N Inp Solar Cells with Bragg Reflector," *26th PVSC,IEEE*,1997,*903-906*

[11] Alexandre W. Walker, Oliver Hohn, Daniel Neves Micha, Benedikt Blasi, Andreas W. Bett, and Frank Dimroth, "Impact of Photon Recycling on GaAs Solar Cell Designs," *IEEE Journal of photovoltaics*, VOL. 5, NO. 6, November 2015

[12] P. Ender. "Photon recycling in double hetero structure," *Physica Status Solidi R.* 1986, vol. 1.37. p. *701*.

[13] W. P. Dumke. "Spontaneous radiative recombination in semiconductors," *Physical Rev* **,** 1957, vol. 105. p. *139*.

Studying The Impacts of Cyber-attacks On Smart Grid

Tanzim Meraj, Shaela Sharmin, Asif Mahmud

Dept. of EEE, Ahsanullah University of Science & Technology
141 & 142, Love Rd, Dhaka 1208, Bangladesh
tanzim.austianz83@gmail.com, shaela.ritu@gmail.com, asifmahmud24790@gmail.com

***Abstract*—This paper investigates the smart grid infrastructure with an upgradation of existing electricity networks and advanced information and communication technologies (ICT), intelligent devices & system. Considering the energy utilities play an increasingly important role in our daily life, smart grid technology introduces new security challenges that must be addressed. This paper has focused on the implementation of smart grid architecture to develop a real time situation and study the impacts of cyber-attacks on its communication infrastructure. A micro grid structure with particular generation and distribution specification along with its relevant communication infrastructure is designed to analyze the security challenges. The studies are performed based on a digital computer simulation approach using Power Factory 14.1. Some dynamic system events are formulated linking the change in different system parameters and effects of these changes are examined on the smart grid generation and distribution network.**

Keywords— Smart grid, communication infrastructure, microgrid, cyber attacks, generation power, power system, load demand, frequency respsonse, control center, system frequency.

I. INTRODUCTION

Smart grid is an electricity supply network which is based on a digital technology. It uses a two way digital communication to establish a communication path between the supplier and consumers. This allows the smart grid system to monitor, analysis and control the efficiency, cost, reliability and the sustainability of the production and distribution of electricity [1]. As this next generation power grid strongly depends on digital technology, it is vulnerable to different types of security issues. In recent time different research have been conducted to explore and solve the security issues and challenges of smart grid network. The concept of smart grid consists of its infrastructure, components, framework etc. The infrastructure of smart grid mainly consists of two major systems; the management system and the protection system. The management system provides advanced management and control services such as improving energy efficiency, demand profile, utility, cost and emission, based on the infrastructure by using optimization, machine learning, and game theory. The protection system provides advanced grid reliability analysis, failure protection as well as security and privacy protection services. The security of the smart grid infrastructure is very crucial to ensure uninterrupted and reliable power supply to the users during emergency situations. As this communication infrastructure highly depends on information and cyber technologies, it is highly vulnerable to cyber interruption and which can cause failure of any critical power system component and eventually lead to devastating physical impacts [2], [3]. In order to protect this infrastructure from any kind of security threats and to maintain stable and reliable power supply operations, the power grid must be modernized and incorporated with special features like advanced metering and monitoring system, advanced electricity generation and distribution, dedicated devices and software, highly secured control center etc. Another effective way of developing the security issues of smart grid is to divide a large power grid system into several microgrid structures. A microgrid system consists of interconnected set of electricity sources and loads that fall under a common control center. Microgrid system has the ability to separate and isolate itself from the utility grid manually or automatically using a switch during any kind of disturbances faultlessly with little or no disruption to the loads within the microgrid. After islanding, a microgrid remains operational in a self-directed mode and functions as an island. After the separation, a microgrid is permitted to reconnect with the utility grid only when the restoration of the main system and the microgrid is achieved. System voltages and frequencies must be either returned to normal range or maintain in a normal range for a reasonable period of time to achieve the grid restoration. The foremost objective of this paper is to identify the growing threats of cyber based attacks on nation's electrical grid and other critical infrastructure and also analyzing the changes in the real time data in different parts of the system after various faults, analyzing the fault conditions and monitors the values of these fault conditions with the help of a graph based simulation. This paper is based on a specific microgrid test system and a specific simulation tool has been used to run and analyze the test system.

II. SMART GRID COMPONENTS

A. Power System Components

Electrical power system is now one of the most effective components of the infrastructure on which modern society depends. They are used to deliver electrical energy to

978-1-4673-9257-0/15/$31.00 ©2015IEEE

industrial, residential and commercial consumers to meet the increasing demand [4]. Main components of modern electric power system are consists of: power stations, bulk generators, transformers, conductors, reactors, power utility equipments, capacitors, electronics and general load [5].

B. Communication Components

It is essential to digitize communication systems on power line in order to provide secure, profitable, reliable, proficient, environmental friendly power grid system. Communication components that are crucial for next generation power grid are: incorporated communications, measurement and sensing, advanced power devices, highly developed control methods and highly improved appliances.

C. Advanced Communication Components

The smart grid's behavior can be determined by using advanced components. These next generation power system devices will apply the latest research in materials, superconductivity, power storage, power electronics and microelectronics. Some advanced components regarding power electronics devices are dynamic volt amp reactive (DVAR), unified power flow controller (UPFC), distribution static compensator (DSTATCOM), static VAR compensator (SVC), medium voltage static voltage regulator (MV SVR), solid state transfer switch and AC/DC inverter [6].

III. CYBER SECURITY OF SMART GRID

Implementation of cyber security system and protection of a smart grid system from any sort of cyber threats or cyber intrusion has become much challenging nowadays. As the communication infrastructure of smart grid greatly depends on digital technologies, it has several vulnerabilities. These vulnerabilities can easily allow a cyber hacker to break into a network, gain access to the control center, spread malware to affect software and alter load conditions to destabilize the grid in unpredictable ways [7]. Developed cyber security strategies are required to eliminate these types of rapidly evolving threats and also to give flexibility to the manufacturers, utilities, and grid operators so that they can respond quickly and decisively during any kind of emergency situations. The basic concept of smart protection is to ensure first that the power grid has the ability to monitor, analysis, control and communication capabilities to the national electricity delivery system. Smart protection of power grid is also needed in order to maximize the output of the system and to reduce energy consumption. The reliability, security, and efficiency of the electrical grid is improved by the smart grid technologies which can be automatically adjusted by intelligent devices connected to the system and changing conditions to prevent blackouts and increase the capacity. Seven major features must be applied in a smart grid to make it self-aware and self-protective from any kind of cyber-attacks:

- Ensure customer security by protecting consumer's private information, activities and devices.
- Provide maximum security to power generation and distribution areas which may be targeted as attack entry points.
- Enable new and upgraded devices, products, technologies and services in order to fight against new types of cyber incursions.
- Maintain power quality to ensure reliable and stable electricity supply to the consumers.
- Optimize the intelligent devices which can increase the operating efficiency of the power grid.
- Implement a security system which can anticipate and respond quickly to any kind of system disturbances in a self healing manner.
- Operate resiliently against physical and kinds of natural disasters [8].

A cyber attacker can penetrate a smart grid using variety of attacks which can be classified into three categories; component wise, protocol wise and topology wise. Component wise cyber attack targets the field components and protocol wise cyber attack targets the communication protocol while topology wise cyber attack targets the topology of the smartgrid. Some other types of attacks are discussed below;

A. Spreading Malware

Malware can be developed by an attacker and spread to infect and corrupt different software which can damage smart meters or company servers. Malware can also be used to replace or add any function to a device or a system to send wrong information to the control center.

B. Exploiting The Control System Network

Activities are recorded by the control system network then mirror the logs into the business network. If the database management systems are not properly secured, a cyber hacker can easily gain access to the business database exploiting the control system network.

C. Compromising Communication Equipment

Some of the communication equipments such as multiplexers or sensors can be compromised by an attacker by injecting false information into these devices such as wrong data, false tripping information and fake emergency event causing direct damage to these devices.

D. Traffic Analysis and Network Protocol

Internet protocol (IP) and transmission control protocol (TCP)/IP stacks are used by the smart grid system which can be subjected to denial of service attacks (DoS). If these vulnerabilities are exploited by a cyber hacker then it can cause delay, block, or corruption of information transmission. A hacker can monitor the network traffic and can also obtain sensitive information by doing this.

IV. RESULTS AND ANALYSIS

A. Test System and Simulation Tool

The system shown in Fig. 1. is composed of a 13.8-kV, three-feeder distribution subsystem which is connected to a large network through a 69-kV radial line. The 13.8-kV substation busbar is radially connected to the main grid through the substation transformer and a 69-kV line. The network at the end of the 69-kV line is represented by a 69-kV, 100-MVA short-circuit capacity bus. A combination of linear and nonlinear loads of Load 1, Load 2, Load 3, Load 4 and Load 5 are supplied through three radial feeders of the subsystem. The system also includes two distributed energy resources (DER), i.e., DER1(3.5 MVA) and DER2 (3.5 MVA) on feeders F3 and F1 respectively. DER2 is a synchronous rotating machine equipped with excitation and governor control systems. DER1 utilizes a voltage-sourced converter (VSC) as the interface medium between its source and the power system. It also represents a dispatchable source with adequate capacity to meet the real/reactive power commands, within pre-specified limits. Such a dispatchable source may also include energy storage interfaced at the converter DC bus. DER1 also provides control on its output of real and reactive power components independently.

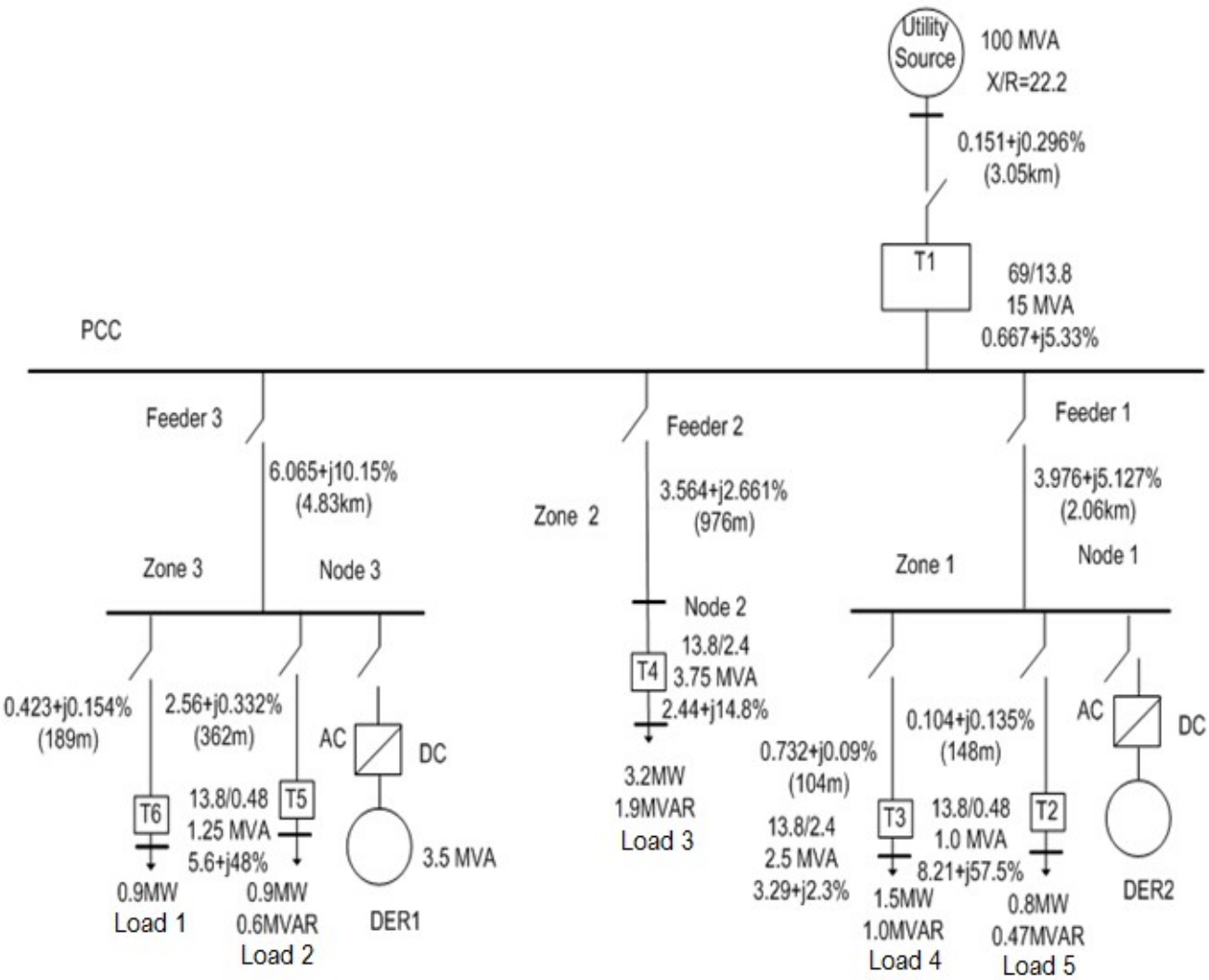

Fig. 1. Single-line diagram of the studysystem

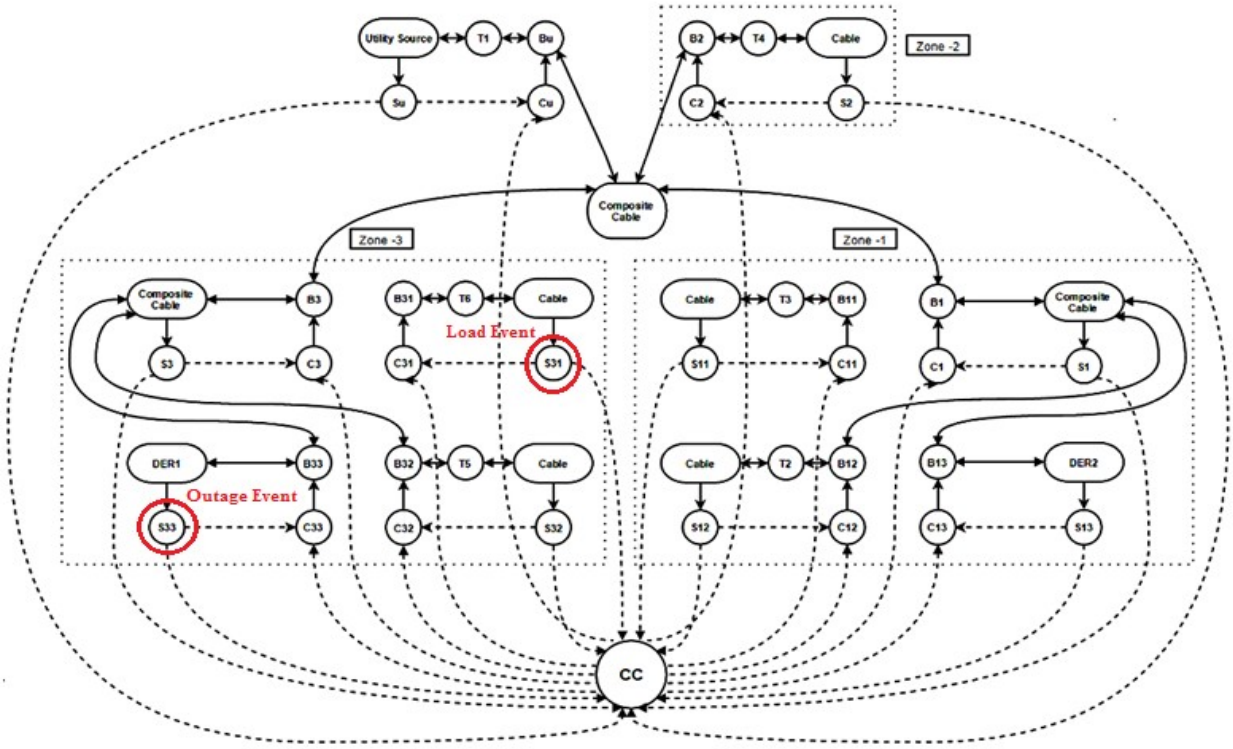

Fig. 2. Electrical and cyber graphs for system of Fig. 1. in islanding mode. Nodes are comprised of DERs, circuit breakers *Bi*, cables, transformers *T* of the electrical network and sensors *si* and actuator controls *ci* of the cyber network.

B. Simulation Results

Here the results are presented in pertaining to the graph and dynamic systems modeling of cause-effect relationships of a cyber-attack on the test system as proposed in [9]. A graph-theoretic formulation of distributed control is well-suited to this smart-grid representation. Using DigSILENT Power Factory 14.1 two types of simulation events are performed for this system; the single load event and the outage event. The utility source of this test system has a generation capacity of 3.17 MW and 3.04 MVAR. Load shedding or tripping off of generator will be occurred if an individual or the combined load demand exceeds generation. The impacts of cyber-attack on smart grid can be observed by creating events on different components of the system. The system frequency is 50Hz and the threshold value for generator under-frequency is set at 48Hz (4%); that means when the system frequency drops under 48Hz, the generator will be tripped out. Preliminary results can also be found in [9].

1) *Single Load Event*

The generator of this test system serves five general loads of different rating. If the load demand on a system suddenly increases the generation limit, this will cause frequency drop to the system and eventually the generator may trip out as the generation is not compatible with the increased demand which may apparently increase load demand on several sections of the system. Intentional load events are performed here in order to differentiate the before and after effect of increasing load demand on the system. For single load event Load 1 has been targeted where real power and reactive power are increased.

Load 1 has the rating of 0.9MW. In the simulation at 0s the load is assumed to come on along with all other loads in the system. The cyber-attack is applied at the time 1.2 sec on the sensor element by adding a load event which increases the load demand to 200% of its initial active power value and 50% of its initial reactive power value and the simulation has been performed for 400 seconds. If load demand increases suddenly, the system frequency drops from 50Hz as showed in Fig. 3. to 47.736 Hz at t=191.092 sec and after that it becomes constant as showed in Fig. 4. The under frequency relay is tripped after sensing the frequency drop in the system (at 4% mismatch of the nominal value). In normal condition when no event has taken place i.e. system is running smoothly, total generated power equals to the total load demand. If this situation remains the same, no load shedding or generator trip will take place. But the scenario changes when sudden increase on load demand takes place. This sudden change can be performed by cyber attack which has become a very common issue nowadays.

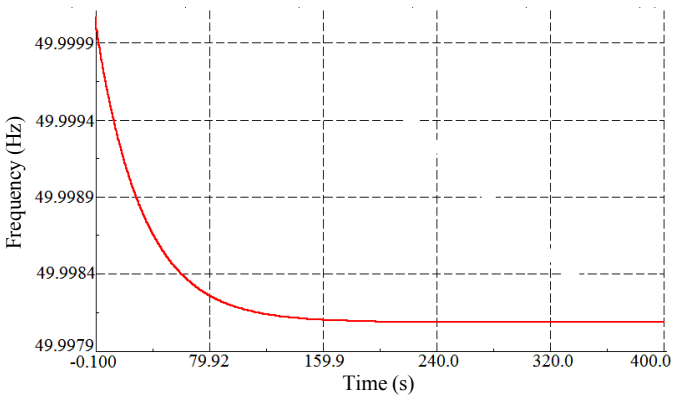

Fig. 3. The overall system frequency before any type load event taking place

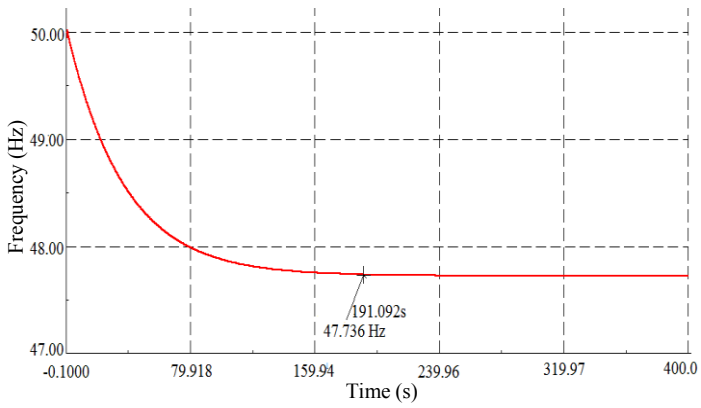

Fig. 4. Frequency plot for the sudden increase on load demand when Load 1 is increased

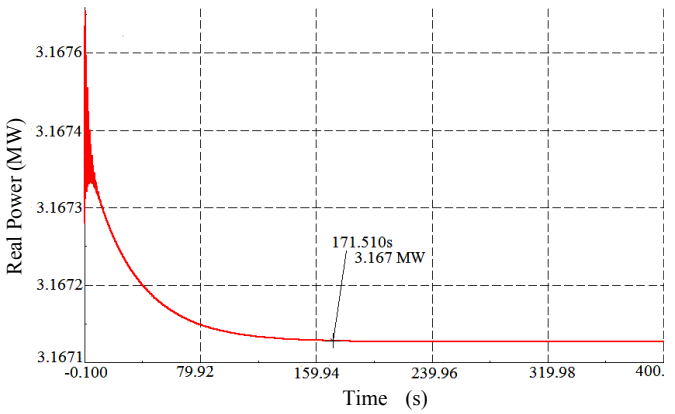

Fig. 5. Total power generation in the external grid before load event.

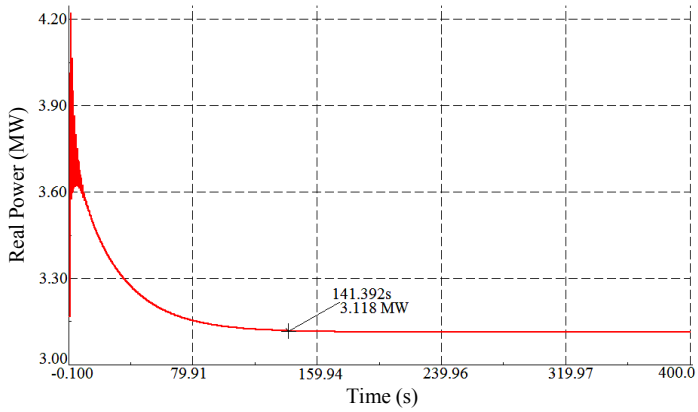

Fig. 6. The power generation at the external grid after load event takes place on Load 1

If any sensor gets wrong information due to the attacks, it may influence the control center to make a wrong decision as shown in Fig. 2 which represents an electrical cyber graph for system of Fig. 1 [6]. In case of single load event where Load 1 is suddenly increased by cyber attacks, sensor S31 is targeted. Control center, cc communicates all control signals at a particular time. For this general load, control signal C31 denotes whether a particular breaker B31 is open or close. Control center, cc collects information through sensor S31 and employs some algorithm to ideally avoid an unexpected situation if some unusual incidents occurs which make the system frequency unstable. When an attack is superimposed, sensor S31 is misinformed and this sensed information is collected by control center. It then performs necessary algorithms and makes quick decision for the whole system. If the sensed information shows that the load demand exceeds the generation power, system frequency will fall from its nominal value. An engine powered generator has a device on it named governor. In order to maintain speed it looks at the speed of the generator and controls the fuel going to the engine. The engine starts to slow down as the load increases. By increasing fuel, the governor keeps it from drifting too far out. If the requirement for electrical power is larger than what the engine can deliver, the governor can't make the engine put out more horse power that it's capable of. Then it slows down and can't maintain the frequency. If the frequency goes too slow, by using control signals the load management sheds one or more loads to avoid frequency deviation by opening their corresponding switches. In large interconnected system if this happens, sometimes we may experience cascading blackout.

2) *Outage Event*

For outage event two individual attempts have been performed, where two different system elements i.e. synchronous generator (DER1) and Load 1 of the test system have taken out of service separately in order to observe the after effect on the system frequency. For both case simulation has run for 400 seconds and elements have taken out of service from the system at t=1s. In order to take DER1 out of service, its corresponding sensor S33 becomes point to object. Fig. 7. displays the frequency response of the system after DER1 is taken out of service. This frequency plot asserts that system frequency falls from 50Hz to 43.65Hz at t=204.45s and after that it becomes constant. When DER1 is targeted by cyber-attack, corresponding sensor S33 senses the sudden change. At any time t, for a switch i, the control center, cc communicates with all control signal $C_i(t)$ where $C_i(t) = 0$ indicates open switch and $C_i(t) = 1$ indicates close switch. When sensor S33 is misinformed due to attack, corresponding

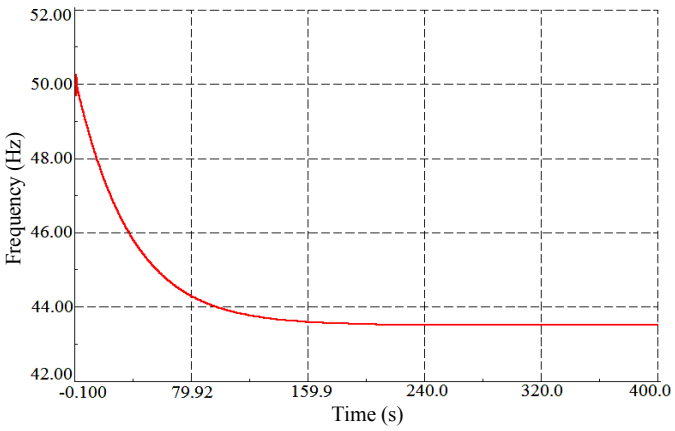

Fig. 7. Frequency plot for synchronous generator(DER1)

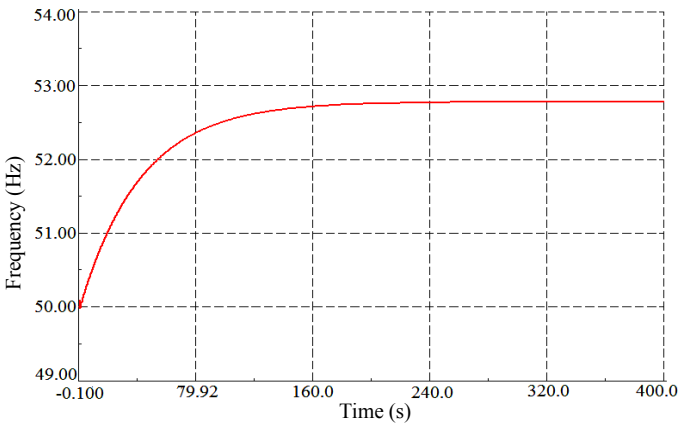

Fig. 6: Frequency plot for Load 1

control signal C33 helps control center, cc to collect this information so that it can perform necessary algorithm to make a quick decision for the whole system. DER1 is a dispatchable source of 3.5MVA rated power with adequate capacity to meet the real/reactive power demands. Due to its outage generation power will be less than total demand and consequently system frequency will fall. As the system frequency falls from its nominal value, load management sheds one or more loads by opening corresponding switches or in extreme condition it may cause system black out. Load1 has been intentionally taken out of service on the next attempt. Likely before, corresponding sensor of this load S31 is misinformed as shown in Fig. 2. This information is collected by control center, cc via control signal C31 and by performing some necessary algorithm a very fast decision is made. The frequency plot due to outage of Load 1 is shown in Fig. 8. System frequency rises from 50Hz to 52.76Hz at t= 255.41s as load demand decreases due to outage of Load 1. Studies showed that electrical equipment designed for any rated frequency may damage if they run above that rated frequency and to solve this problem some backup loads can be reserved so that system frequency remains constant.

V. CONCLUSION

A smart grid is an advanced power grid system that carries out the ever growing electricity demand in a reliable and sustainable manner. It is built on a modern communication infrastructure and adjusted to make the integration of all kinds of power utilities easier. Compared to current grid infrastructures, smart grid infrastructures adds significant complexity including security issues. As a result this increased complexity will require more effort to understand the system and will also provide numerous opportunities for the cyber hackers to exploit it. From the perspective of the defender, more complex systems require more effort to analyze and defend the system. Current approaches to secure cyber infrastructures are: techniques for key management, secure communication, secure code execution, intrusion detection systems, etc. These approaches model the malicious behaviors as components failures, fake information, false inputs and noises. Then analyzing their effects it will design counter measures to defend the attacks. However, the simulation world is modeled with estimation whereas the physical world is more complex, which can result in a deviation of any model to the reality. Therefore, theoretic approaches are mostly based on approximations compared to the physical world's unpredictability. As discussed in this paper, smart grid system demands additional security requirements, such as continuity of power delivery and accuracy of dynamic events. Such requirements are closely related to the models and states of the system, which are difficult to represent only by cyber security. Therefore, both cyber security and theory based security are essential to securing smart grid systems, offering exciting research challenges for many years to come.

ACKNOWLEDGEMENT

We would like to show our deepest gratitude to our respected and honorable supervisor Dr. Tareq Aziz, Associate Professor, Department of EEE, Ahsanullah University of Science and Technology for his unbounded guidance, encouragement, inspiration and valuable assistance in completion of this work.

REFERENCES

[1] DOE's Office of Electricity Delivery and Energy Reliability, ''The Smart Grid: An Introduction,'' 2009.

[2] Xu Li, X.Liang and X.Shen, ''Securing smart grid: cyber attacks, counter measures, and challenges,'' *IEEE Communications Society*, vol. 50, no. 8, 2012.

[3] Eric B.Rice, Anas AlMajali, ''Mitigating the risk of cyber attack on smart grid system,''*Conference on System Engineering Research*,2014.

[4] IEC-TC 57, "Communication networks and systems in substations- Part 1: Introduction and overview," *IEC Standard IEC/TR 61850-1*, 2003.

[5] Electronics lab, available at: http://www.powerelectricalblog.com

[6] Smart grid advanced components available at: https://www.smartgrid.gov/sites/default/files/pdfs/appendix_b3_advanced_components.pdf

[7] D.Wei, Y. Lu, M. Jafari, P.M. Skare, and K. Rohde, "Protecting smart grid automation systems against cyberattacks," *IEEETransactions on Smart Grid*, vol. 2, no. 4, pp. 782–795, 2011.

[8] Kundur.D., Feng.X., Mashayekh.S., Liu.S., Zourntos.T and Butler-Purry K.L, 'Towards modelling the impact of cyber attacks on a smart grid', *Int. J. Security and Networks*, Texas A&M University, USA, 2011.

[9] Tanzim Meraj, Sharmin Jahan, Shaela Sharmin, Rabeya Habiba and Asif Mahmud, ''Studying the impacts of cyber attack on a smart grid, *BSc. Thesis, Dept of EEE*, Ahsanullah University of Science and Technology, 2015.

Production of Transportation fuel from Municipal Solid waste.

Md. Alauddin[1]
Department of Mechanical Engineering
Rajshahi University of Engineering and Technology
RUET, Rajshahi, Bangladesh
alauddin102006@gmail.com

Shimul Barua[3]
Department of Mechanical Engineering
Rajshahi University of Engineering and Technology
RUET, Rajshahi, Bangladesh
shimulbarua.ruet@gmail.com

Md. Jiyaul Kabir[2]
Department of Mechanical Engineering
Rajshahi University of Engineering and Technology
RUET, Rajshahi, Bangladesh
zia.ruet10@gmail.com

Md. Abdul Mannan Akanda[4]
Department of Mechanical Engineering
Rajshahi University of Engineering and Technology
RUET, Rajshahi, Bangladesh
mannandinner@gmail.com

A.K.M. Enamul Hoque[5]
Department of Mechanical Engineering
Rajshahi University of Engineering and Technology
RUET, Rajshahi, Bangladesh
shovo.ruet102021@gmail.com

Abstract*— The energy is running out with the increase of demand of people in the world day by day. So accomplish this crisis alternative energy source can be weapon of this demand. In our project "from biogas to methane i.e. vehicle gas" can be a substitutive way to minimize this assertion. The target of this paper to produce biogas from saturated organic waste for example cow dung and pig slurries, food wastes i.e. municipal solid waste (MSW). To use as vehicle fuel, it has to be updated. In biogas contain CH_4, CO_2 and lean amount of H_2S. CO_2 is detrimental for our environment and atmosphere and H_2S have corrosive in nature. For better quality of fuel, the percentage of CH_4 have to be increased which is our main aim. By reducing CO_2 from the biogas, it is possible to increase the calorific value of the fuel and this fuel less emissive than that of fossil fuel i.e. diesel, petrol. On the other hand sources of fossil fuel are very limited in our country and it is not environmentally friendly, it causes greenhouse effect in the atmosphere. But by using biofuel, greenhouse effect is less than the fossil fuel and it is less costly and production is easy and improves local air quality compared to the other fuel. This paper is focused on preparation of available biogas production technology. This paper is going to disclose how the biogas is converted into transportation fuel to save the environment and atmosphere and to make the world green.

Keywords*— *Municipal solid waste; Biogas plant; Biogas; Impurities removals; Compress natural gas.

I. INTRODUCTION

Energy sources are decreasing gradually with the enhancement of assertion. Municipal solid waste is another form of Biomass. With fast socio economic and industrial development, the municipal solid waste increases rapidly in recent years. We have to look over alternative energy source to fulfill our challenge. Biomass is one of the major sources in present world. Every year about 140 billion metric ton of biomass is generated all over the universe [1]. Landfill gas which is produced from biomass contains about 36% to 44% carbon dioxide, 45% to 55% Methane, 17% to 19% Nitrogen, 2% or nil Oxygen, saturated with moister and H_2S is about 25ppmv to 1,000 ppmv+ [2].

Biogas is produced form biomass. Biomass recovers from residual stalks, straw, leaves, roots, husk, nut, seed shells, waste wood and animal husbandry waste. By using biofuel greenhouse effect is 21% less than the fossil fuel.

Now-a-days, Vehicle fuel is one of the important issues in present world. In this paper we are focusing about conversion

Fig. 1. Integrated Waste management of municipal solid waste

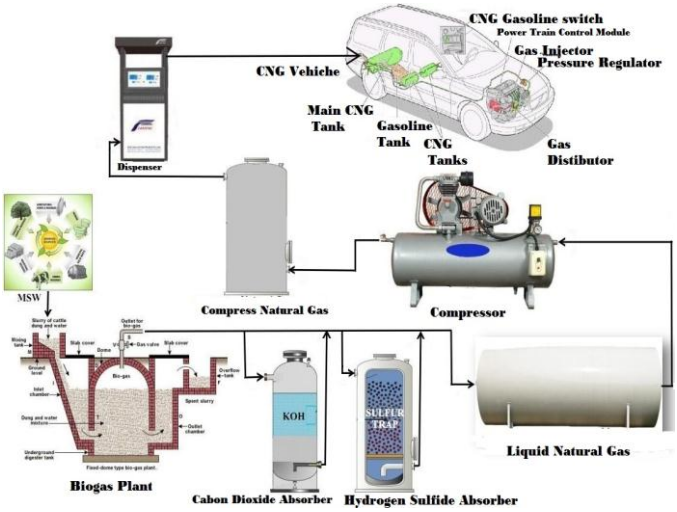

Fig. 2. Schematic view of municipal Solid waste to vehicle fuel.

from biogas to vehicle fuel. Landfill Gas can be produced from this biomass by proper utilization and it can be used in house hold works, industrial purposes. In our country, maximum vehicle are confined on fossil fuel for example Diesel, Petrol, Natural gas and Furnace oil. Diesel and Petrol is costly and not environmental friendly. It also more and emissive which is responsible for greenhouse effect and environmental pollution. Besides The Natural gas is more environmental friendly but resource of it is very limited in our country. Those resources are gradually diminished and it is a very threat full for our next generations.

By removing of carbon dioxide from landfill gas it can be used as vehicle fuel which impacts a major effect in our country. By using converted landfill gas, we can reduce extraction of natural source. After converting Landfill Gas into vehicle fuel that means it will be converted into compressed natural gas.

Volume fraction of biogas produced by controlled anaerobic digestion produces Bio-Compressed Natural Gas and there Methane (CH_4) contains 95.0% or more, Carbon dioxide (CO_2) contains 2.5% or less, Water (H_2O) contains 4 mg/ Nm^3 or less, Hydrogen sulfide (H_2S) contains 5 mg/Nm3 or less, Oxygen (O_2) contains 100 ppm or less, Hydrogen (H_2) contains 6% or less, Nitrogen (N_2) is no more [3]. This Compressed natural gas is usable for vehicle fuel.

There are different methods of managing MSW. The Integrated Waste Management (IWM) technique developed by the EPA is one such methodology in which use of different practices is made to safely and effectively handle the solid waste.

II. LITERATURE REVIEW

In ancient cities, wastes were thrown into streets and roadways, where they were left to accumulate. At that time, a system for waste removal began to evolve in Greece and in the Greek-dominated cities of the eastern Mediterranean. Disposal methods were very crude, involving open pits located just outside the city walls. As populations increased, efforts were made to transport waste farther out from the cities. In 1714 at first the city in England was found the waste management system. Toward the end of the 18th century in America, municipal collection of garbage was begun in Boston, New york city and Philadelphia [4].

The U.S Environmental Protection Agency (EPA) encourages consumers to reuse and recycle these valuable products to keep them out of the waste stream [5]. With this in mind, waste management has partnered with several companies, like LG Electronics, to recycle electronics for reprocessing [6].

There are large quantities of the biomass available in Bangladesh. Huge amount of Landfill Gas is produced from biomass by removing of CO_2 and H_2S from Landfill Gas, Landfill gas is composed of a mixture of hundreds of different gases. By volume, landfill gas typically contains 45% to 60% methane and 40% to 60% carbon dioxide. Landfill gas also includes small amounts of nitrogen, oxygen, ammonia, sulfides, hydrogen, carbon monoxide, and non-methane organic compounds (NMOCs) such as trichloroethylene, benzene, and vinyl chloride. Landfill gas produced by Bacterial decomposition, volatilization and Chemical reactions [8]. It can be easily converted into Liquid natural gas(LNG) and finally compress LNG will converted into CNG which can be used vehicle fuel.

A work on solid waste management was found that the management system and energy recovery system does not work for proper management of solid wastes because of financial resources, institutional weakness, improper selection of technology, transportation systems and disposal options, public's lack of concern towards environmental cleanliness and sanitation have made this service unsatisfactory. Wrong attitudes and perceptions of the people about sanitation issues contributed to solid waste management problems of the respective City Corporations.

III. METHODOLOGY

By bacterial decomposition of organic material contained in municipal solid waste (MSW), Landfill gas (LFG) is produced. Some factors influence the quantities of gas that a MSW landfill produces are organic compounds in the waste, and the moisture content and temperature of the waste. Temperature and moisture levels are influenced by the surrounding climate.

Landfills often accept waste over period of 20 to 30 year and large scale Landfill gas is produced by Bacterial decomposition. Natural process of bacterial decomposition of landfill waste consists of four sequential stages.

First stage: At the beginning of the first stage of decomposition, aerobic bacteria which live only in the presence of oxygen, consumes oxygen while breaking down the long molecular chains of complex carbohydrates, proteins, and lipids that comprise organic waste. The primary byproduct of this process is CO_2. In this stage, depending on the presence of oxygen, decomposition can last for days or months.

Second stage: After introducing oxygen in the landfill Gangrene starts. Bacteria is converted into compounds created by aerobic bacteria into acetic, lactic, and formic acids and alcohols such as methanol and ethanol by using an anaerobic process. The landfill becomes highly acidic. The gaseous byproducts of these processes are CO_2 and H_2.

Third stage: Initialization of decomposition depends on the consumption of organic acids produced in second stage by the certain types of anaerobic bacteria. Hence production of the landfill gas becomes more neutral environment in which methane-producing bacteria begin to establish themselves.

Fourth stage: Mortification starts in this stage, when both the production rates and the composition of landfill gas remain relatively constant. In this stage landfill gas usually contains approximately 45% to 60% CH_4 by volume, 40% to 60% CO_2 and 2% to 9% other gases for examples sulfides.

Gas is produced at a stable rate about 20 years. If greater amounts of organics are present in the waste, such as at a landfill receiving higher than average amounts of domestic animal waste [8].

The raw gas contains several impurities like water, dust, H_2S, CO_2, siloxanes, Hydrocarbons, NH_3, oxygen and several other elements that must be removed in order to reach certain standards of quality [14]. From Biogas plant firstly collect Landfill gas and burnt off in a controlled manner (flaring) in order to destroy pollutants. While flaring LFG will largely mitigate the negative effects of these emissions, the strategy can also be seen as a lost opportunity for converting the gas into a useable form of energy. LFG can be used for many energy recovery projects [7].

A. Removal of water: Possible impact of water is corrosion in compressors, gas storage, tanks and engines due to reaction with H_2S, CO_2 and NH_3 to the acid. Untreated or raw biogas is usually saturated with water and the absolute water quantity depends on the temperature (according to chemical equilibrium) and water is removed by Physical separation of condensed water or chemical drying [8].

B. Hydrogen sulfide (H_2S): It is a foul odor of rotten eggs colorless, very poisonous, flammable gas with the characteristic. It is removed by two ways [9]

i. Removal of H_2S during digestion:

$$2H_2S+O_2 \rightarrow 2S+2H_2O$$

$$2Fe^{2+}+3S^{2-} \rightarrow 2FeS+S$$

$$Fe^{2+}+S^{2-} \rightarrow FeS$$

ii. Removal of H_2S after digestion:

$$Fe_2O_3+3H_2S \rightarrow Fe_2S_3 + 3H_2O$$

$$2Fe(OH)_3+3H_2S \rightarrow Fe_2S_3 + 6H_2O$$

C. Carbon dioxide (CO_2) Removal: At the contemporary there are several alternative technologies which are adopted for CO_2 removal from gases. Many of them encouraged by the recent interests of segregation of CO_2 from power plant flue gases for the aspect of CO_2 sequestration. Various sophisticated commercial CO_2 removal technologies have been in use for several decades to produce CO_2 catherses for processed food for example soft drinks, for natural gas purification and for tertiary oil recovery. However, at the present time various researches are going on for the removal of CO_2 from gas, which is applicable to begin upgrading. CO_2 removal by using potassium carbonate solutions is now obsolete technology which were mixed with other chemicals to facilitate the process. For CO_2 catharses from the gas, recent proposed process uses refrigeration. However these process are highly sophisticated, precise researches are need to improve the process. Though there are some process of CO_2 removal, the entire world searching for "game changing" technologies for CO_2 removals from power plant and industrial emissions.

Potassium hydroxide (30 % w/v) to absorb CO_2 and cuprous chloride in hydrochloric acid to absorb CO [9]. Potassium hydroxide' solution (250g KOH in 500mL of boiled distilled water), and it absorbs only CO_2. A hydrocarbon is burnt with excess air. The Orsat analysis of the flue gas shows 10.81% CO_2, 3.78% O_2 and 85.40 N_2. Calculate the atomic ratio of C:H in the hydrocarbon and the % excess air [10].

A thin film membrane used which only allows particular molecules to pass through it and allowed molecules will affect the conductivity of the thermocouple system which send signal proportional to the chemical molecules. Based on chemical absorption principle, typical flue gas analyzers measures the quality of CO_2. On depending absorption factor of this components their bulb component, when flue gas is passed through the bulb, components are separated that helps to know the volume drop from initial flue gas volume. By absorption, water vapors in the flue gas removed on solid $CaCl_2$ and then passed a pipettes. The sequence should start from CO_2, if the reagent in the analyzer is KOH in the absorption solution. To absorb, gas then passed into KOH solution pipette to form K_2CO_3 by the following reaction.

$$2KOH+CO_2 \leftrightarrow K_2CO_3 + H_2O \text{ at ambient conditions [11]}$$

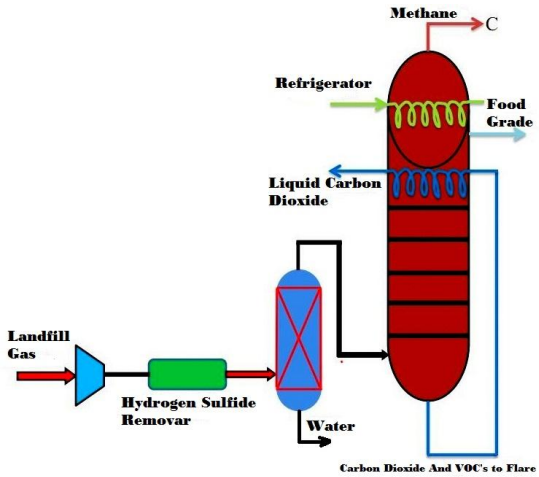

Fig. 3. Schematic view of Removal of CO2 from biogas.

TABLE. 1. TIME OF BIODEGRADABLE [12]

Item	Time to Degrade	Item	Time to Degrade
Paper towel	2-4 weeks	Normal paper	1-2 weeks
Newspaper	6 weeks	Ply wood	1-3 years
Cardboard box	2 months	Wool gloves	1 year
Apple core	2 months	Cotton gloves	1-5 months
Waxed milk carton	3 months	Photo-degradable beverage holder	6 months

TABLE 2. CONSTRUCTION COST ACCORDING TO SIZE [13].

Size (m3)	Operational hours per day	Cow dung requirement per day (kg)	Poultry litter requirement per day (kg)	Approximate construction cost (BDT)
1.6	3-4	43	23	26,000
2.0	4-5	54	28	32,000
2.4	5-6	65	34	36,000
3.2	7-8	87	45	43,000
4.8	10-12	130	68	52,000

IV. ECONOMIC ASPECTS IN BANGLADESH

The diagram depicts that, in the year of 2005, no of biogas plant was 30 and in the year of 2008 no of biogas plant was 4621. This shows within a short time establishment of biogas plant increased rapidly. In the year 2014 no of established biogas plant is 30291. From this diagram it is clear within a difference of 10 years, about 30,000 biogas plant established in Bangladesh. This also indicates that adeptness of biogas plant is increasing and it can be forecast that about 1,00000 biogas plant will be established in the next decade. Thus dependency on biomass will be increased rapidly in the upcoming decades and this introduced method will be fruitfull to compensate this energy demand specifically in transportation sector.

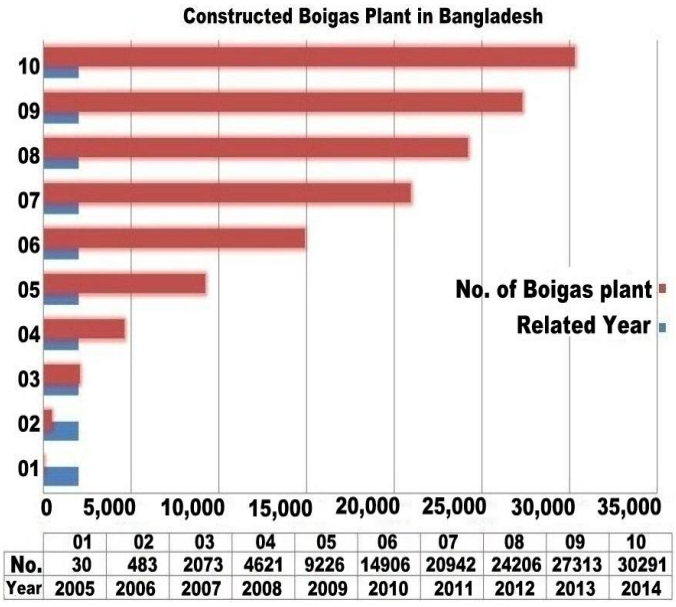

Fig. 4. Biogas plant Construction in Bangladesh previous ten years [14].

V. CONCLUSION

We are extracting energy for different purpose. Now-a-days the diesel, petrol, natural gas are used to appease our pretention. But those energy sources are tethered and diminishing day after day by the increasing amount demand. So to minimize this problem bio-fuel may be an effective source. In our under developing country bio-fuel can play a vital role in our transportation system. Because of less cost it would be popular and most useable fuel in our country. The environmental pollution occurs for food wastes, paper wastes and different organic elements. By using this pollutant elements the environment pollution is reduce considerably and by proper utilization of this toxic element bio-fuel can be produce which affix our energy source and become environmental friendly and greenhouse effect free. For under developing country, the municipal waste, food wastes is available compare to another source and it create pollution negatively. So by constructing dustbin where maximum amount of food wastes ,municipal wastes produce such as hospital where organic wastes can be found, food industry and maximum amount of biomass can be found from dairy farm, poultry farm . By using of this wastes bio-fuel can be produced that will mitigate pollution and will construct green world. If a biogas plant is set-up in every municipal area and all biomass is gathered in biogas plant. Large amount of biogas is produced form each area and it can be converted into CNG to use in vehicle. By this process we can decrease the pressure on natural gas and environment will be pollution free.

REFERENCES

[1] Converting agricultural waste into resource published by UNEP.

[2] "Landfill Gas to CNG 101 Basics of LFG Conversion to B-CNG and B-CNG Utilization" Jeffrey L. Pierce, P.E. Senior Vice President and Steve Hamilton Vice President SCS Energy Long Beach, California.

[3] World Journal of Social Sciences Vol. 2. No. 7. November 2012 Issue. Pp. 174 – 181 Biogas Technology for a Sustainable Energy: The Case of Poultry Farm in Bangladesh Rumana Rashid 1, Mohd. Hamdan Bin Ahmed2, Md. Sayem Khan 3

[4] http://www.Historical background of solid-waste management, early waste disposal, Wikipedia the encyclopedia, visits the page on 12/18/14.

[5] "Reusing and Donating Electronics". Environmental Protection Agency. In 2010-08-20.

[6] "BRIEF: Recycling at State Fair Park". TMCnet.com In 2010-08-18.It can be easily converted into Liquid natural gas(LNG) and finally compress LNG will converted into Compress natural gas which can use vehicle fuel.

[7] ATSDR - Landfill Gas Primer - Chapter 2 Landfill Gas Basics.

[8] Orsat Gas Analysis Experiment (internet source)

[9] Flue Gas Analysis by Orsat Apparatus.pdf (internet source)

[10] http://www.gshakti.org/index.php?option=com_content&view=article&id=177&Itemid=134

[11] http://www.gshakti.org/index.php?option=com_content&view=category&layout=blog&id=54& Itemid=78

[12] http://cmore.soest.hawaii.edu/cruises/super/biodegradation.htm

[13] http://www.gshakti.org/index.php?option=com_content&view=article&id=177&Itemid=134

[14] http://www.gshakti.org/index.php?option=com_content&view=category&layout=blog&id=54& Itemid=78

Simulation and Analysis of Battery Performance of a Solar Car Using a Model Implemented in SIMULINK

Abdullah Al Mahmud[1], Asif Zaman[2], Imran Bin Jafar[3], Mosaddequr Rahman[4]

School of Engineering and Computer Science, BRAC University
66 Mohakhali C/A, Dhaka-1212, Bangladesh

[1]mahmud.abdullah@bracu.ac.bd, [2]asifzaman007@gmail.com, [3]imranjafar@bracu.ac.bd, [4]mosaddeq@bracu.ac.bd

Abstract— **Battery performance of a proposed solar car has been investigated under different road conditions while the car makes a trip in one of the longest routes in Dhaka city, using a model developed in Matlab Simulink. A significant reduction in energy consumption is observed when the car runs at lower speed, which is attributed to lower air drag at lower speed. Energy consumption further reduces with the increase in number of stoppages. Thus the solar/electric car will be an ideal mode of transport for a city like Dhaka, where traffic congestion is a daily occurrence.**

Keywords— **Solar car, SIMULINK, Batteries, Battery modelling, State of charge.**

I. INTRODUCTION

In Dhaka city, a major mode of transportation for daily office commuters is fuel driven cars. However, emissions from such cars pose serious environmental and health hazards, especially during office hours when cars are caught in traffic congestion causing more and more toxic emissions. Solar powered clean cars can be of great advantage to the public and environment and can go a long way to alleviate this problem. On these premises, a solar powered light-weight economically affordable clean car for the daily office commuters of Dhaka city was proposed in [1] which is able to run on solar power alone during sunny days of summer and spring, and with complementary charging of the batteries from other sources during winter and under overcast sky.

Batteries are an indispensable and critical part of the electric drive system of a solar car. A healthy battery will ensure a longer battery life and a safe driving of the car. Further, unlike fuel driven car, there is no rapid recharging system for solar car. Therefore, it is imperative to have a prior understanding of how the battery will perform on the road under different road conditions. With this objective, this paper aims to investigate the battery performance while the car is making a trip from home to office in Dhaka city, considering one of the longest trips, Uttara to Motijheel, which is about 18 km long, under different traffic conditions.

Performance analysis is carried out using a model developed in Simulink assuming the batteries to be fully charged. The simulation has been conducted using the specifications of the solar car that is being built in the Robotics Workshop of BRAC University [2]. In this study, the discharge characteristics, mainly the variation in the state of charge (SOC) and the terminal voltage (V_t) of the battery with travel distance and time under different traffic conditions are observed and analysed. Role of the solar panels is excluded from the study as the purpose of this paper is solely to study the battery performance. Effects of temperature and aging have been ignored in the analysis. In the subsequent sections, sections II and III, models used for the battery, charge controller and the motor power are described, followed by their implementation in Simulink. Section IV provides the simulation results on the battery performance under different road conditions. Finally section V concludes the findings of this work.

II. MODELING OF SOLAR CAR

Fig. 1 shows the block diagram of the electric drive system of the solar car consisting of solar panels charging the battery through the charge controller. Charge controller also controls dissipation of energy to the motor to ensure healthy battery life. Following subsections discuss the modelling of different modules of the electric drive system, except the PV panel.

A. *Modelling of Battery*

The model used for battery is based on Thévenin battery model [3]. In Thévenin battery model (Fig. 2), the resistance R_0 and capacitance C_0 between electrodes and electrolyte of the battery is considered along with the series resistance R_S. V_{OC} is the open circuit voltage and I_L is the load current. Experiments on battery suggest that the voltage drop, V_d across R_0 or C_0 is almost constant for a particular SOC [4]. All the three parameters namely V_{OC}, R_S and V_d in Fig. 2 are functions of SOC.

The load current, I_L for a load which draws out power P can be calculated as,

$$I_L = \frac{(V_{OC} - V_d) - \sqrt{(V_{OC} - V_d)^2 - 4R_S P}}{2R_S} \quad (1)$$

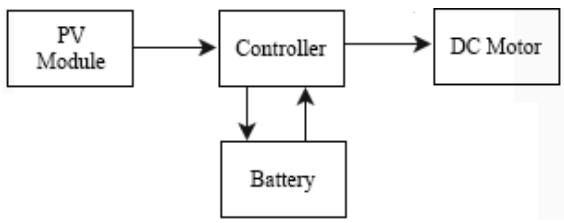

Fig. 1 Block diagram of electric drive system of solar car

978-1-4673-9257-0/15/$31.00 ©2015 IEEE

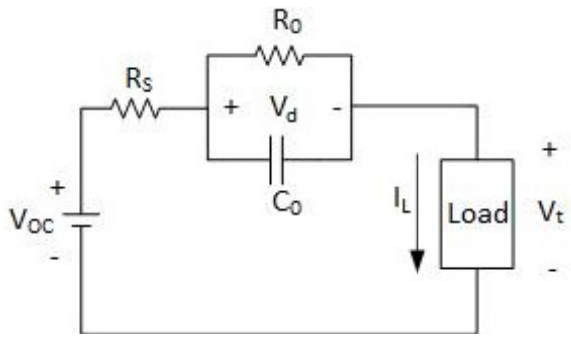

Fig. 2 Thévenin battery model

Once the current is known, the terminal voltage V_t can be determined using (2).

$$V_t = V_{OC} - I_L R_S - V_d \tag{2}$$

The total charge dissipated from battery for time t is calculated using (3).

$$Q_{dis} = I_L \mathrm{t} \tag{3}$$

In case, battery is being charged by I_{CH} current, the overall current flowing out of the battery is reduced to $(I_L - I_{CH})$.

The SOC of the battery after supplying P power for t seconds is calculated as,

$$SOC(new) = SOC(old) - \frac{Q_{dis}}{C} \tag{4}$$

where C is the capacity of the battery.

With this new SOC, V_{OC}, R_S and V_d are re-evaluated according to the following relations which were determined experimentally in [5].

$$V_{OC} = 1.4667SOC - 11.0233 \tag{5}$$

$$V_d = 0.086SOC - 0.011 \tag{6}$$

$$R_S = -0.0531SOC + 0.066 \tag{7}$$

Then the algorithm recurs with the calculation of I_L until SOC gets low enough for the process to cease.

B. *Power Calculation of DC Motor*

A motor draws out power from battery to give the solar car a driving force. The total drive force to make the vehicle move or keep it moving can be estimated by adding together individual force components that arise from different physical effects.

The major three forces are the rolling resistance force F_R, aerodynamic drag force F_D and the force of acceleration F_A. Summing up them, total driving force, F_T is obtained as [6].

$$F_T = F_R + F_D + F_A \tag{8}$$

The rolling resistance force, the frictional force that resists the motion when a vehicle rolls on a surface, is given by,

$$F_R = \mu_R mg \tag{9}$$

where μ_R is the coefficient of rolling resistance, m is the mass of the car and g is the gravitational acceleration.

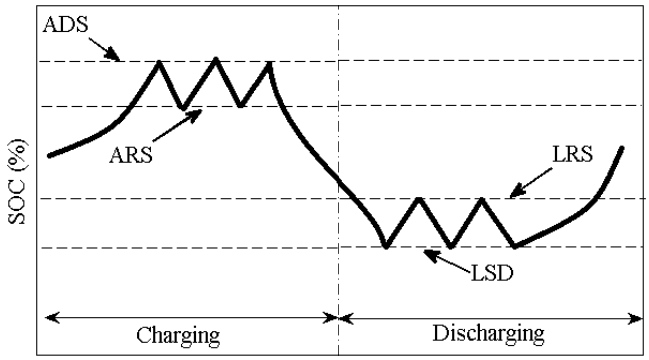

Fig. 3 Charge Controller set points

Aerodynamic drag force is the force exerted by the air against the movement of the car and is given by,

$$F_D = \frac{1}{2} C_D \rho A_{CROSS} v^2 \tag{10}$$

where ρ is the air mass density, A_{CROSS} is the cross sectional area of the car, v is the velocity of the vehicle, and C_D is the coefficient of aerodynamic drag force.

The force of acceleration is given by,

$$F_A = ma \tag{11}$$

where a is the acceleration and is accounted for when the car is accelerating. When the car moves at constant speed, the force of acceleration is zero.

If the car is running at velocity v then the power exerted by the shaft of the motor can be expressed as,

$$P_T = F_T v \tag{12}$$

If the efficiency of the motor is η_m, the power to be supplied by the battery to the motor is given by,

$$P = \frac{P_T}{\eta_m} v \tag{13}$$

C. *Mechanism of charge controller*

There are four set points in a charge controller, two to avoid overcharge and two for overdischarge as in [7]. The maximum SOC the batteries are allowed to reach and above which solar panels are disconnected from the battery is array disconnect SOC (ADS). Then the battery may discharge to a SOC level low enough to start charging again; the level is array reconnect SOC (ARS). Similarly, the load is disconnected at the minimum SOC, namely low SOC load disconnect (LSD), after which more discharging may damage the battery. Then the battery may charge for some time, the SOC rises and the load is connected again at a level of load reconnect SOC (LRS). The points are depicted in Fig. 3.

III. Implementation in Simulink

The implementation of the aforementioned models of battery, motor power and charge controller are described in the following subsections.

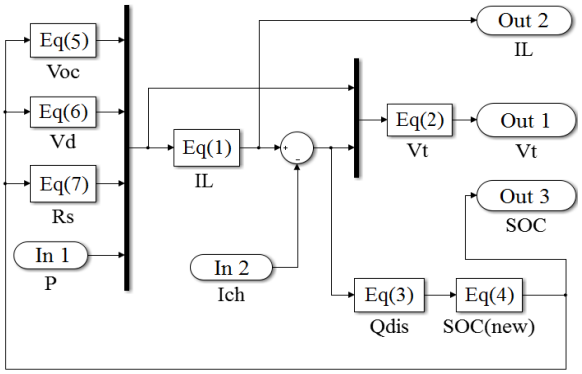

Fig. 4 Implementation of Battery model in SIMULINK

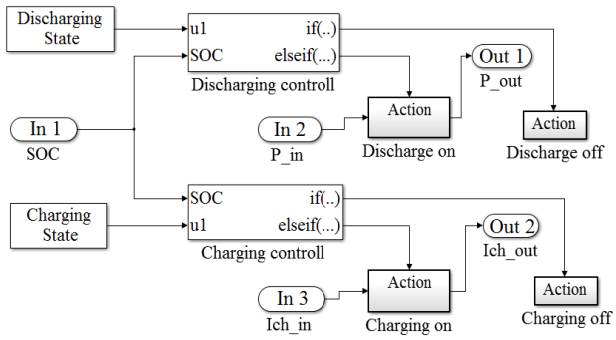

Fig. 5 Implementation of charge controller model in SIMULINK

A. *Implementation of Battery Model*

Fig. 4 shows the battery model in Simulink where the power required P and charging current I_{CH} are the inputs to battery. It calculates I_L, V_t and SOC after dissipating power for a certain time and gives out as outputs. Eq(1), Eq(2) etc. labelled in the diagram refer to the corresponding equation numbers in this paper. The time interval after which the model calculates dissipated charge and records a new SOC can be fixed by the mask parameter dialog box along with the nominal capacity of the battery, initial state of charge, temperature and number of batteries in series.

B. *Implementing Load Block in SIMULINK*

The Simulink block of Load, named 'Load' in Fig. 6, takes inputs of variable velocity on different time frames and some invariants related to the car e.g. its weight, frontal area. If the car moves at velocity v_1 kilometer per hour (kph) for t_1 minutes, comes to a halt and rests for t_1^r minutes, and then starts again at v_2 kph at which it runs for another t_2 minutes, the input format is $v = [v_1 \quad 0 \quad v_2]$ and $t = [t_1 \quad t_1^r \quad t_2]$. Time t_1 consists of the time at which the car accelerates from static position to reach v_1, the time it runs at constant v_1 kph, and fall time when the car decelerates to halt. The inputs are transferred to a MATLAB program which gives a timeseries variable P using the equations (8) to (13). The signal building block of load has some presets e.g. Busy road, Highway, Empty road etc. to select easily or the users may produce one according to their concern.

C. *Implementation of Charge Controller*

Fig. 5 implements the charge controller in SIMULINK. There are two 'if' blocks in the diagram; upper one is controlling the discharging state and lower one the charging state. If the SOC goes below the given level to turn off discharging, and the discharging process is not switched off yet, the upper if block commands the Discharge off block to disconnect the load. On the other hand, if the SOC is high enough to turn on discharging, the same if block triggers Discharge on action block to connect the load and deliver input power to the output. Same mechanism applies for the charging state controller 'if' block except, this time, the input charging current flows to output when charging is turned on.

D. *Combining the Components*

All the components portrayed in earlier sections are packed inside subsystems and combined together to build a complete model of vehicle as in Fig. 6. As mentioned earlier, the concern here studying discharging characteristics, and hence charging current is considered zero. All data found by the simulation are transfered to the MATLAB workspace to plot and analyze the results.

IV. RESULTS AND DISCUSSIONS

An itinerary is assumed for a Dhaka city dweller from his home to office, which is 18 km long. For the sake of convenience, it is assumed that the person leaves his home in the morning with his car fully charged and reaches his office by driving 10% of the distance at 10 kilometer per hour (kph) and rest of the road either 30 kph or 60 kph depending on the road condition. In the afternoon, he returns by the same route with same speed characteristics.

Fig. 7 shows the plots of power required P, SOC and V_t with respect to time as the car travels at different velocities from its origin to destination. The top most plot shows the different velocities of the car during its trip which starts with 10 kph at its origin covering 5% of the distance, goes at after that for 15% of the road, then goes at 60 kph for 60% of the road, after which it goes at 30 kph and 10 kph for the rest of

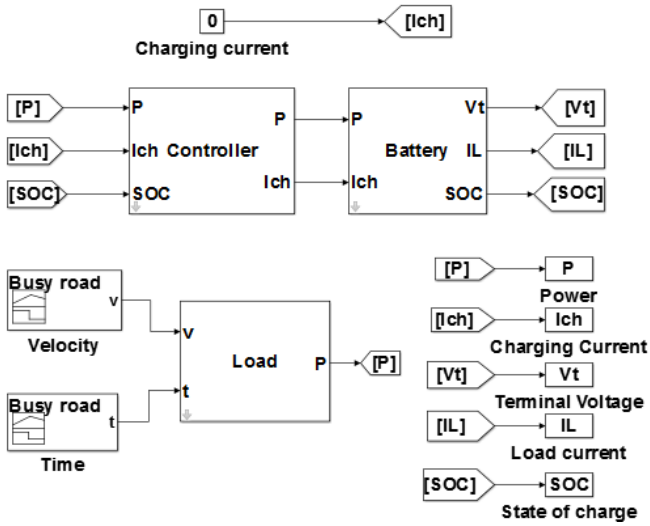

Fig. 6 The Model of the solar car combining all individual components

TABLE I
PROPERTIES OF SOLAR CAR

Components	Parameters	Value
Battery [5]	Capacity of the Battery, C (AH)	40
	Number of Batteries in Series	5
Vehicle Platform [1]	Mass of the car, m (kg)	500
	Maximum velocity, v_{max} (kph)	60
	Time to get max. velocity, t_{max} (min)	1.5
	Frontal Area, A_{CROSS} (m^2)	1.1
Environment [6]	Coeff. of Rolling Resistance, μ_R	0.01
	Coeff. of Aerodynamic drag force, C_D	0.035
	Air Density, ρ (kg/m^3)	1.2

15% and 5% of the road, respectively, before it reaches the destination. For the sake of simplicity we assumed a constant acceleration with which the car reaches the maximum speed from its rest position and a constant deceleration with which it comes to a halt from its maximum speed. For higher speed higher acceleration and deceleration are assumed than those at lower speed. The required power increases gradually with the increase in car speed as can be seen from the power plot below the velocity plot in Fig. 7. The power drops abruptly whenever the velocity reaches target speed because as the driver releases the accelerator, force of acceleration becomes zero requiring less power to drive. SOC plot shows gradual decrease in SOC with a faster drop when the car runs at the peak speed of 60 kph.

Fig. 8 shows how the SOC varies when the car travels at the top speed of 60 kph for different lengths of the road. As can be seen from this figure, SOC drops to almost 67% when the car runs 90% of the road at the top speed, indicating about 33% consumption of battery charge at this speed. However, SOC drops to only 81% when the car runs only 30% of the road at the top speed with 60% at half the top speed and the rest 10% at 10 kph, indicating more that 40% reduction in energy consumption at this slower speed. The higher energy requirement at higher speed is due to the higher aerodynamic drag force which increases as the square of the velocity according to (10). Energy requirement is further reduced if the trip is accompanied with frequent breaks (topmost plot in Fig. 8) during heavy traffic congestion which is a common phenomenon in the city of Dhaka.

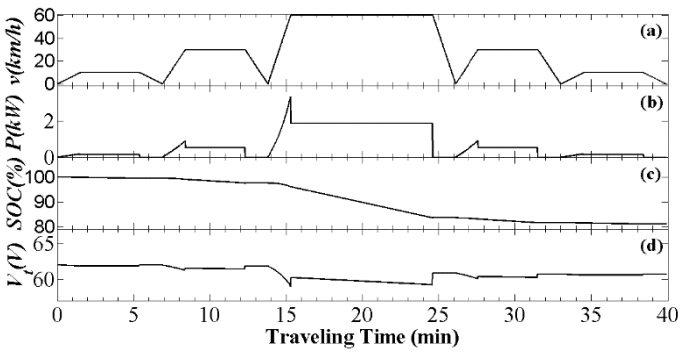

Fig. 7 Variation in (a) car speed, (b) motor power, (c) SOC, and (d) terminal voltage, V_t of the battery during one full trip as the car travels from origin to its destination.

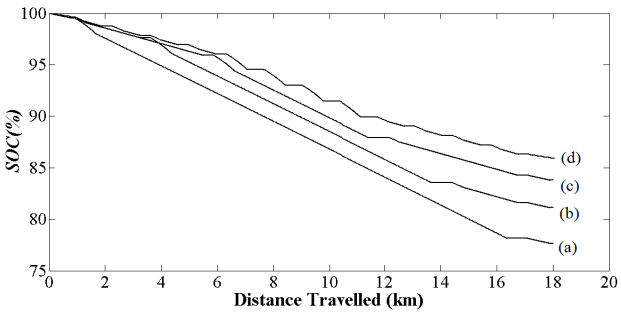

Fig. 8 Variation in SOC with the car traveling (a) 90%, (b) 60%, and (c) 30% of the road at the top speed. Plot (d) is that for 30% with 20 number of stoppages.

Consumption of less energy at slower speed will be an added advantage of the solar car over the fuel driven cars which consume more fuel at slower speed to cover the same distance due to inefficient burning of the fuel.

V. CONCLUSION

Battery performance of a propsed solar car has been investigated while the car makes a trip from home to workplace of an office commuter under different road conditions, using a model developed in Matlab Simulink. It has been observed that energy requirement decreases significantly when the car runs at a slower speed due to lower air drag force at lower velocity. Thus for a city like Dhaka, where traffic congestion is a daily occurrence, solar/electric car will be a perfect mode of transportation as it is not only emission free but also consumes less energy under heavy traffic congestion, unlike the fuel driven cars which consumes more energy and emit more toxic gases under such condition. A detailed performance study of the proposed solar car under different traffic and weather conditions that also includes the solar panels is currently under way.

REFERENCES

[1] S. Ahmed, A. H. Zenan and M. M. Rahman, "A two-seater light-weight solar powered clean car: Preliminary design and economic analysis," in *3rd Int. Conf. on the Develop. in Renewable Energy Technology (ICDRET), 2014*, May 2014.

[2] T. M. A. Khan, S. Rahman, M. K. Afgani and K. E. Fahim, Solar car, Dhaka: BRAC University, 2014 [Online]. Available:http://dspace.bracu.ac.bd/bitstream/handle/10361/3228/09221020.pdf?sequence=1

[3] H. L. Chan and D. Sutanto, "A new battery model for use with battery energy storage systems and electric vehicles power systems," *IEEE Trans. Energy Convers.,* vol. 1, pp. 470-475, January 2000.

[4] R. Carter, A. Cruden, P. J. Hall and A. S. Zaher, "An improved Lead-Acid battery pack model for use in power simulations of electric vehicles,"," *IEEE Trans. Energy Convers.,* vol. 27, no. 1, pp. 21 - 28, 2012.

[5] R. Tariq, S. Sabbir and S. Afrin, Dynamic electrical model of sealed Lead-Acid battery for EV simulation, Dhaka: BRAC University, 2014.

[6] S. Leitman and B. Brant, Build Your Own Electric Vehicle, Third Edition, McGraw Hill Professional, 2013.

[7] J. P. Dunlop, "Batteries and charge control in stand-alone photovoltaic systems fundamentals and application," Florida Solar Energy Center, Cocoa, 1997.

Enhancement of Device Performance with Optimized Absorber Layer in CIGS Solar Cell

Sharmin Aktar Chowdhury, Md. Shah Alam
Department of Applied Physics, Electronics & Communication Engineering
University of Chittagong
Chittagong-4331, Bangladesh
Sharmin_apece1291@yahoo.com, shah.alam@cu.ac.bd

***Abstract*— Numerical simulation of CIGS solar cell has been carried out in this study to investigate the performance of the solar cell with different band-gap and thickness of the absorber layer. In this paper, we also introduce the effect of Ga content on solar cell material parameters. The aim of this work is to check the device performance like open circuit voltage, short circuit current density, fill-factor and efficiency with the change of thickness and band-gap of the absorber layer. It is shown that, by optimizing the CIGS absorber layer it is possible to achieve an AM 1.5G conversion efficiency of greater than 22% which is an increased value than presently reported.**

Keywords—CIGS, band-gap, thickness, Solarcell, simulation.

I. INTRODUCTION

A solar cell is a form of photoelectric cell which generates electrical power by the photovoltaic effect. It is done by converting the sunlight into electricity directly [1]-[2]. Photovoltaic industry has grown rapidly in the last several years. Now, worldwide total installed capacity of photovoltaic reached at least 178 GW at a cost less than $1/W till date. The total output power is now greater than 200 billion kWh, which represents 1 percent demand of worldwide electricity [3]-[4]. So it is strongly desirable to raise the power conversion efficiency while reducing the costs also. It is predicted that the installation rate will grow at a double digit of 16-25 percent and in the range of 55-57 GW at the end of 2015.

Thin film PV cell is a second generation solar cell which uses <1% of the expensive raw materials compared to other wafer based solar cell. So significant price drop can be gain by per watt peak capacity. It is made on a substrate like glass, plastic or metal by depositing one or more thin layer or thin film of photovoltaic material on it [5]. Thin film solar cells are commercially used in several technologies like CdTe, CIGS, and amorphous Si etc. Thin film PV technology is for more than 90% based on silicon as source material and these are low-cost alternatives [6]. Again, CIGS is one of the most promising I-III-VI_2 chalcopyrite photovoltaic materials for thin film solar cell technology [7]. These are highly attractive because of their tunable band-gap, radiation hardness and excellent outdoor stability on the earth. Copper Indium Gallium Deselenide ($Cu(IN_{1-x}Ga_x)se_2$) based solar cell exhibits superior conductivity and higher efficiencies due to native defects [8]-[9]. Recently, CIGS solar cell efficiency has been claimed a record value of 21.7% [10]. CIGS is a compound semiconductor material which has a high absorption coefficient of more than 10^5/cm for 1.5eV band-gap. CIGS solar cell has the advantage of presenting a thin active layer due to direct band-gap of the material. Much information is available in the literature regarding single-junction CIGS solar cell. To improve the overall performance of the solar cell, increasing the open circuit voltage V_{OC} and fill-factor (FF) is highly desirable. Because increased open-circuit voltage (V_{OC}) minimizes the interconnection losses in the manufacture of cell modules. [11]. The optical band-gap of CIGS increases with the use of Gallium which finally increases the open-circuit voltage (V_{OC}) and lowers costs as compared to pure CIS. Again, Cu deficiency increases the majority carrier concentration by increasing the number of Cu vacancies. Because when the films are Cu deficient, its surface layer form an ordered defect compound (OVC) by forming a p-n homo-junction at the interface [12]. To reach the band-gap of 1.5ev which is ideal for a single junction CIGS, a [Ga/(Ga+In)] of 0.7 is optimal. But device performance drops off when the ratio exceeds 0.3 [13].

In this study, we tried to optimize the band-gap as well as the thickness of the absorber layer and enhanced the solar cell device performance.

II. SIMULATION METHODOLOGY

A. Cell Structure

The structure of the studied solar cell based on Copper Indium Gallium Deselenide (CIGS) consists of the following layers: Soda lime glass substrate (SLG) of about 1-3mm thickness which has shown a substantial increase in open-circuit voltage (V_{OC}), Molybdenum back contact generally deposited by sputtering which reflects most unabsorbed light back into the CIGS absorber, a p-type CIGS absorber layer and n-type CdS buffer layer deposited on top of the absorber layer. Next the buffer layer is overlaid with a thin, intrinsic ZnO layer (i-ZnO) which is capped by Al doped ZnO window layer. The Al doped ZnO serves as a transparent conductive oxide to collect and move electrons out of the cell [14]-[15]. The schematic diagram for a typical ZnO/CdS/CIGS solar cell structure is illustrated in Fig 1.

978-1-4673-9257-0/15/$31.00 ©2015 IEEE

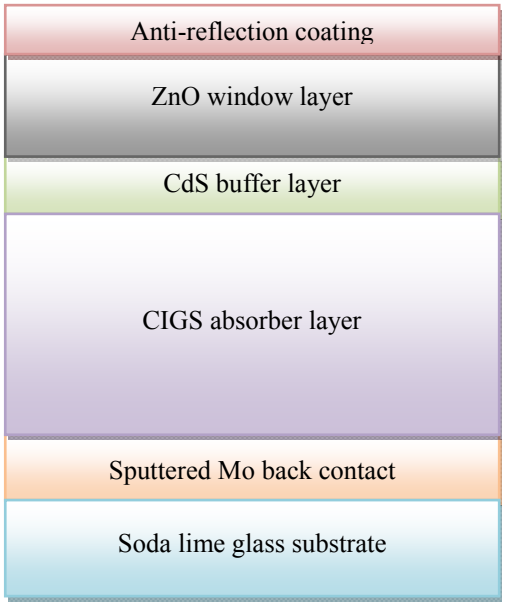

Fig. 1. CIGS solar cell structure used for the simulation

B. Numerical Simulation

In our present work, numerical simulation of CIGS thin film solar cell has been investigated by using the latest version 3.3.0.1 of SCAPS i.e. Solar Cell Capacitance Simulator. This is a 1D solar cell simulation program which developed in the University of Gent at the department of EIS, allows the definition of thin film solar cell devices stacks of layers with a large set of parameters [16]-[17]. SCAPS is originally developed for devices or the solar cell structures specially CdTe and $CuInSe_2$ family [18]. The objective of the numerical method is to test the device performance without fabrication, for analysis of the effect of material parameters variations and finally determining optimal values for the best solar cell performance. SCAPS solves the fundamental solar cell equations like Poisson's equation, the continuity equation for electrons and the continuity equation for hole in one-dimension and in steady-state condition. Generally, Poisson's equation for semiconductor device is [19]

$$\frac{\partial}{\partial x}\varepsilon(x)\frac{\partial}{\partial x}\psi(x)=q\left(p(x)-n(x)+N_D-N_A+\rho_{def}\right) \quad (1)$$

Where, n, p are the concentrations of free electrons and holes, n_t, p_t are the concentration of trapped electrons and holes, N_D, N_A are the concentrations of the ionized donors and acceptors, ε is the dielectric permittivity of semiconductor, q is the electron charge and ψ is the electrostatic potential. Here, the drift-diffusion approach is used as a function of device length, x.

Again, the continuity equation in steady state conditions for electrons and holes are:

$$\frac{1}{q}\frac{d}{dx}J_n=R_n(x)-G(x) \quad (2)$$

$$\frac{1}{q}\frac{d}{dx}J_p=G(x)-R_p(x) \quad (3)$$

Where, q is the electron charge, J_n and J_p are the electrons and holes current density, R_n and R_p are the electrons and hole recombination velocities and G is the optical generation rate.

The photocurrent which flows in opposite direction to the dark current I_D is the maximum current when the voltage across the solar cell is absolutely zero. It is caused by the generation and collection of light generated carriers. I-V characteristics of a p-n junction solar cell under illumination can be expressed as:

$$I=I_{ph}-I_{01}\left(qV/k_BT-1\right) \quad (4)$$

Where, I_{01} is the saturation current and I_{ph} is the photocurrent.

At V=0, short-circuit current is equal to the photo-generated current [20] i.e.

$$I_{sc}=I_{ph} \quad (5)$$

For removing the dependence of the solar cell area, it is usually defined short-circuit current I_{SC} as the short circuit current density J_{SC}. The equation for the short-circuit current density J_{SC} for the solar cell with perfectly passivated surface and uniform generation is as follows [21]:

$$J_{sc}=qG\left(L_n+L_p\right) \quad (6)$$

Again, open-circuit voltage V_{OC} is the maximum voltage available through the solar cell when the current is absolutely zero. Open-circuit voltage can be expressed as:

$$V_{oc}=V_T\ln\left[\frac{I_{sc}}{I_{01}}+1\right] \quad (7)$$

Where, V_T is the thermal voltage and is equal to K_BT/q. the open-circuit voltage can be increased either by increasing substrate doping density or increasing the minority carrier lifetime in the solar cell. High shot-circuit current density J_{SC} is very desirable because it can also enhance the open-circuit voltage V_{OC}, hence we can get an enhanced performance of the device. Typical values of open-circuit voltage V_{OC} ranges from 0.5 to 0.7V [20]-[21].

The fill-factor of the solar cell is the parameter in which in conjunction both the operating points corresponding to I_{SC} and V_{OC} determines the maximum power output from a solar cell. It is a measure of the squareness of the I-V characteristics and is expressed as:

$$F.F.=\frac{P_m}{V_{oc}I_{sc}} \quad (8)$$

Where, P_m is the maximum power output of the p-n junction solar cell and is equal to V_mI_m. Fill-factor depends on the series and shunt resistances and the diode ideality factors. For solar cell, fill-factor is always less than 1 [1], [20], [22].

The ratio between the output electrical power at the maximum power point on the I-V curve to the input electrical power is called the efficiency of the solar cell and is defined as:

$$\eta = \left(\frac{P_{out}(\max)}{P_{in}} \right)\% \qquad (9)$$

Where, P_{in} is the input power from the sunlight, P_{max} is the maximum power output and is equal to $V_{OC}I_{SC}FF$ and η is the solar cell efficiency [20], [21].

III. SIMULATION PARAMETERS

For the calculation of device performance, we need to know the values of the parameters. In this work, we used three layers for the simulation. These are: 1) p-type CIGS absorber layer, 2) n-type CdS buffer layer and 3) ZnO window layer. Here, the surface recombination velocities were set at 10^7 cm/s for both electrons and holes. The AM 1.5G solar spectrum is used and the temperature is set at 300k for this numerical simulation.

The CIGS absorber layer has adjustable band-gap by tuning ratio [12]. Here, band-gap of the CIGS absorber layer was varied from 1.04 to 1.69eV as the Ga content varied from x=0 to x=1, according to the equation:

$$E(x) = 1.02 + 0.67x + 0.11x(x-1) \qquad (10)$$

This band-gap alteration ability makes them perfect candidates for high performance thin film device [23]. Varying the ratio in material affects various parameters in the absorber such as band-gap, optical absorption and defect concentration which influence the solar cell performance. In our simulation, solar cell performance was examined by varying the absorber layer thickness and band-gap and keeping all other parameters at a fixed value.

TABLE I gives the summary of different layer parameters used in this paper.

TABLE I. MATERIAL PARAMETER VALUES FOR THE SIMULATION

Properties	p-CIGS	n-CdS	i-ZnO
W(μm)	variable	0.050	0.200
E_G(eV)	variable	2.4	3.3
X(eV)	4.5	4.2	4.45
Dielectric Permitivity	13.6	10	9
N_C(cm^{-3})	2.200E+18	2.200E+18	3.100E+18
N_V(cm^{-3})	1.800E+19	1.800E+19	1.800E+19
V_n(cm/s)	1.000E+7	1.000E+7	1.000E+7
V_p(cm/s)	1.000E+7	1.000E+7	1.000E+7
μ_n(cm^2/V-S)	100	100	100
μ_p(cm^2/V-S)	25	25	25

IV. RESULT AND DISCUSSION

A. *Effect of absorber layer band-gap:*

The resulting performance parameters are determined by using current-density voltage characteristics.

The simulation results of the solar performance corresponding to different band-gap of the absorber layer are given in TABLE II.

TABLE II. SIMULATED RESULT FOR VARYING BAND-GAP

Eg(eV)	V_{OC}(V)	J_{SC}(mA/cm^2)	FF(%)	η(%)
1.02	0.53	33.15	79.14	13.99
1.05	0.56	33.05	79.67	14.81
1.1	0.61	32.99	80.59	16.25
1.2	0.71	33.0	82.03	19.22
1.3	0.81	33.04	82.52	22.18
1.4	1.27	33.06	57.35	24.05
1.5	1.40	33.07	52.43	24.24
1.67	1.40	33.07	52.31	24.25

From our simulation it is originated that, the efficiency of solar cell increases with the increase of band-gap of the absorber layer. As the band-gap of CIGS absorber layer varied from 1.02 to 1.5eV, the solar cell efficiency increased from 13.99 to 24.24% and the open-circuit voltage (V_{OC}) is also increased from 0.53 to 1.40V as the recombination current falls. It is mainly depends on the saturation current I_o. Further increase in CIGS band-gap has no significant effect on these parameters. Again, it has very little effect on short-circuit current density (J_{SC}).

However, band-gap of the CIGS absorber layer affects the fill-factor of the cell. As the band-gap increased beyond 1.3eV, fill factor decreased sharply. Because increased Ga content causes higher recombination rate and lower carrier lifetime, for which recombination in SCR may overweight the recombination outside of this region. So, ideality factor in accordance with the FF will be decreased due to defect in SCR. This is a key parameter in evaluating solar cell performance. Solar cell with a high fill factor is very desirable, because small amount of the current is dissipated by internal losses [13].

Fig 2 shows the effect of band-gap variation on the performance of CIGS solar cell.

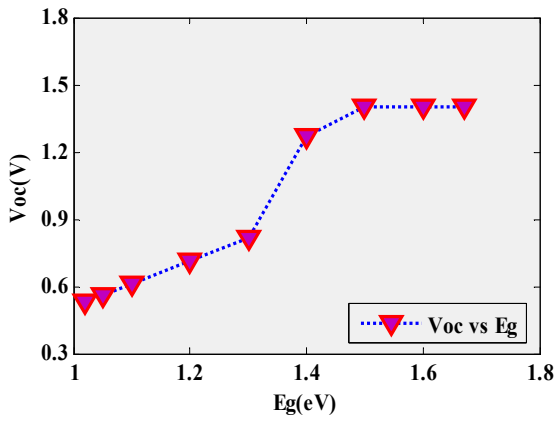

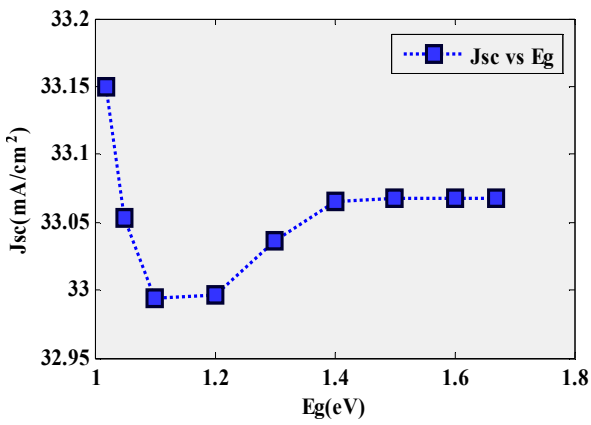

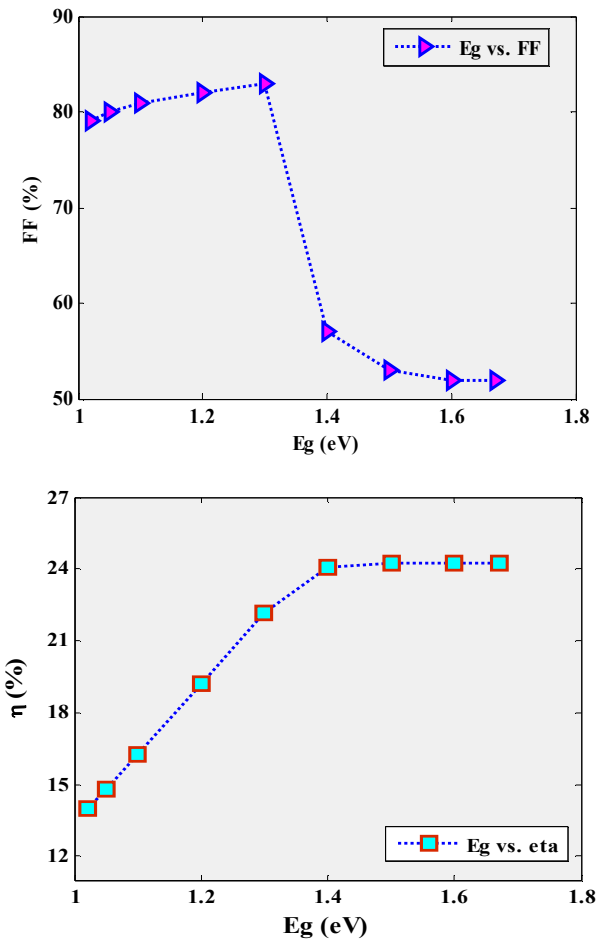

Fig. 2. Band-gap effect on solar cell performance

The trade of among these phenomena is that, an optimum band-gap of 1.3eV is proposed in which the device have a high fill factor without sacrificing its V_{OC} or J_{SC}. The result yields a maximum efficiency of 22.18%.

B. *Effect of absorber layer thickness:*

CIGS solar cell has an absorption which is more than 10 times better than for crystalline silicon. Hence, it is possible to make a solar cell which is very thin compared to well known silicon solar cell. Various researches have reported the impact of the thickness of CIGS absorber layer on solar cell performance parameters. In our simulation, CIGS layer thickness was varied from 0.3µm to 3µm, where the band-gap was kept in the optimum value at 1.3eV and all other layer parameters were kept the same as before. The simulation results for varying thickness of the absorber layer are given in TABLE III.

TABLE III. SIMULATED RESULT FOR VARYING THICKNESS

W(µm)	V_{OC}(V)	J_{SC}(mA/cm^2)	FF(%)	η(%)
0.3	0.69	26.14	69.09	12.54
0.5	0.75	27.30	77.65	15.93
0.7	0.77	28.94	79.70	17.75
0.9	0.78	30.10	80.81	18.99
1.1	0.79	30.94	81.58	19.90
1.5	0.80	32.11	82.43	21.16
2.0	0.81	33.04	82.52	22.18
2.5	0.83	33.66	82.22	22.86
3	0.84	34.10	81.80	23.35

Fig 3 shows the effect of thickness variation on the performance of solar cell.

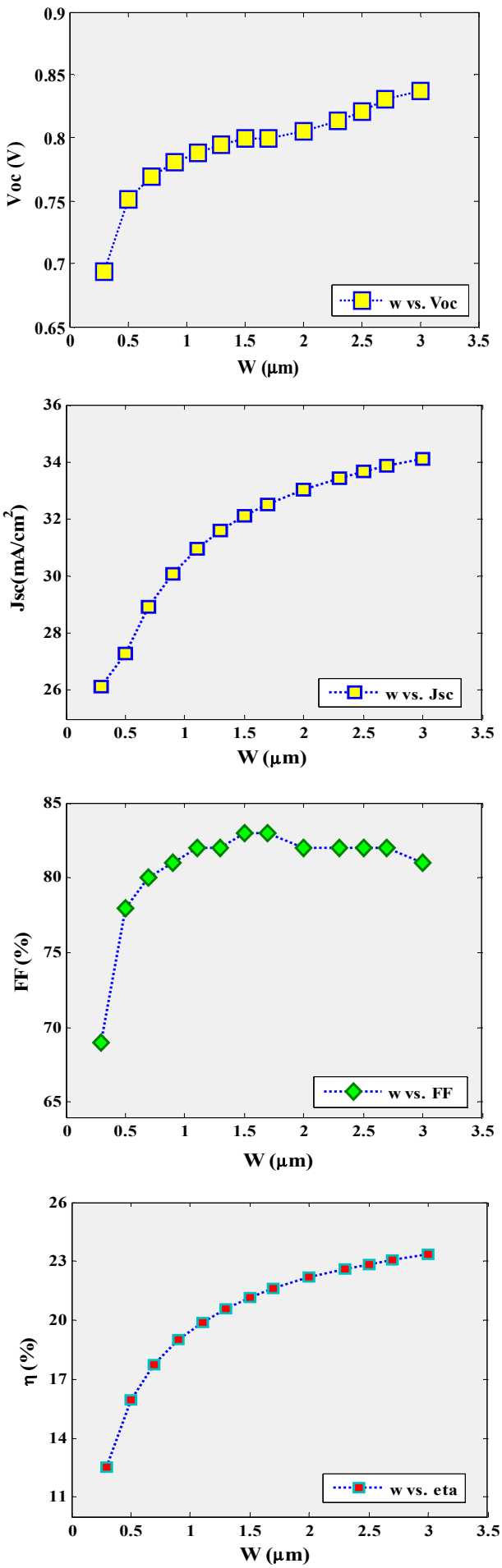

Fig. 3 Thickness effect on solar cell performance

Based on the simulated result it is seen that, device performance was considerably influenced by the absorber layer thickness. The J-V curve reveals that as the thickness of the absorber layer CIGS increases from 0.3 to 2µm, V_{OC} increases from 0.69 to 0.81V due to decreased recombination probability of photon-generated carriers. Again, when the thickness of CIGS increases beyond 2µm, V_{OC} increases very slowly.

Again, in the case of $J_{SC,}$ it follows the same trend with the increasing thickness of the absorber layer. As in fig, Fill-factor increases with the thickness from 0.3 to 2µm and after this it decreases slowly. So, we considered the optimum value of the CIGS absorber layer at 2µm in which the efficiency was 22.18%.

V. CONCLUSION

In this study, numerical optimization has been performed by adjusting parameters like thickness and band-gap of the absorber layer CIGS and it is shown that this parameters has crucial effect on solar cell performance. Simulation results exhibit that, increased solar cell efficiency is obtained by increasing the thickness and band-gap. Other performance parameters like V_{OC}, J_{SC} and FF is also enhanced by optimizing CIGS absorber layer thickness at 2µm. In the case of band-gap it is seen that, after 1.3eV fill-factor drops significantly. So we `optimized the band-gap of the absorber layer at 1.3eV and it is demonstrated that a maximum efficiency of 22.18% can be obtained by CIGS solar cell, where the presently reported best efficiency is 21.7%.

REFERENCES

[1] Antonio Luque, Steven Hegedus, "Handbook of Photovoltaic Science & Engineering," page 3, ISBN 0-471-49196-9, 2003

[2] Pearce, Joshua, "Photovoltaic - A path to Sustainable Future," Vol. 34, No. 7, pp. 663-674,2002

[3] David Feldman, Galen Barbose, Robert Margolis, Ted James, Carolyn Davidson, et al. "Photovoltaic System Pricing Trends - Historical, Recent and Near Term Projection," 2014 edition, NREL

[4] Snapshot of Global PV System 1992-2014, IEA, International Energy Agency, 2015

[5] Vincent Dusastre, Jean-Marie Tarascon, Michael Gratzel, "Materials for Sustainable Energy", ISBN-13:978-981-4317-64-1, 2011

[6] Van Swaaij, Smets, A.H.M Zeman, "Thin Film Si Technology for Highly Efficient Solar Cell," IEEE Bipolar/BiCMOSCircuits and technology meeting (BTCM) , page 1-7, ISSN: 1088-9299, 2012.

[7] Shogo Ishizuka, M. Lorelle Mansfield, Clay DeHart, et al. "Rapid Fabrication of $Cu(In,Ga)Se_2$ Thin Films by the Two-Step Selenization Process," 38th IEEE Photovoltaic specialist conference (PVSC), vol. 2, page 1-7, 2012

[8] K. Ramanathan, M. A. Contreras, C. L. Perkins, S. Asher, F. S. Hasoon, et al. "Properties of 19.2% efficiency $ZnO/CdS/CuInGaSe_2$ thin-film solar cells," Prog in Photovooltaic: Research and Application, vol.11, issue 4, 2003

[9] G F Novikov, E V Rabenok, M J Jeng, L B Chang, "The study loss kinetics of current carriers in copper-indium-gallium selenide by microwave photoconductivity method," Journal of Renewable and Sustainable Energy, vol. 4, issue 1, 2012

[10] M. A. Green, Keith Emery , Yoshihiro Hishikawa , Wilhelm Warta and D. Ewan Dunlop, "Solar Cell Efficiciency tables(version 46)", Progess in Photovoltaics: Research and Applications, Volume 23, Issue 7, June 2015

[11] Wan Fucheng, Tang Fuling, Xue Hongtao, Lu Wenjiang, Feng Yudong, et al., "Effects of defect states on the performance of CuInGaSe2 solar cells", Journal of Semiconductors, Vol. 35, No. 2, February 2014

[12] O. Lundberg, M. Edoff, and L. Stolt, "The effect of Ga-Grading in CIGS thin film solar cells," Thin Solid Films 480-481, PP. 520-525, 2004

[13] I. Repins, B. Egaas, J. Scharf, et al., "Characterization of 19.9% Efficient CIGS Absorbers," 33rd IEEE Photovoltaic Specialists Conference, 2008

[14] P. Udai Singh, Surya Patra,"Progress in Polycrystalline Thin-Film $Cu(In,Ga)Se_2$ Solar Cells" International Journal of Photoenergy, article ID 468147, 2010

[15] M. Buegelman, P. Nollet, S. Degrave, "Modelling polycrystalline semiconductor solar cell," Thin Solid films, vol. 361, pp. 527-532, 2000

[16] M. Burgelman and J. Marlein, "Analysis of graded band gap solar cells with SCAPS", Proceedings of the 23rdEuropean Photovoltaic Solar Energy Conference, p.2151-2155, 2008

[17] J. Vercharaegen, M. Burgelman, "Numerical modelling of intra-band tunneling for heterojunction dolar cell in SCAPS," Thin Solid Films 515: 6276–6279, Elsevier, 2007

[18] A. Niemegeers and M. Burgelman, "Numerical modelling of ac-characteristics of CdTe and CIS solar cells," Proc. 25nd IEEE Photovoltaic Specialists Conference, pp. 901-904, 1996

[19] S.M. Sze., K. N. G. Kwok , "Physics of semiconductor device," 3rd edition, New York: John Wiley & Sons Press, ISBN-13:978=0471-14323-9, 2007

[20] Yoshihiro Hamakawa, "Thin film Solar Cell: Next generation Photovoltaics & Its Applications," ISBN-3-540-43954-5, Springer, 2004

[21] S. Sheng Li., "Semiconductor Physical Electronics", Page 334-335, ISBN-13:978-1-4612-7635-7,1993

[22] Stephen J Fonash, "Solar Cell Device Physics", 2nd edition, ISBN 978-0-12-374774-7, Elsivier, 2012

[23] Antonino Parisi, Recardo pernice, et al., "Graded Carrier Concentration Absorber Profile for High Efficiency CIGS Solar Cells," International Journal of Photoenergy, article ID 410549, 9pages, 2015

A New Prediction Model for Solar Irradiance using Ant Colony Optimization and Neural Network

Md. Shahid Iqbal[1, *], Md. Monirul Kabir[2], H.M. Imran Hassan[3], Md. Janibul Alam Soeb[4], Md. Ataullah Mishkat[5], and Vobes Ray[6]

[1, 3, 4, 5, 6] Department of EEE, Mymensingh Engineering College, Bangladesh

[2] Department of EEE, Dhaka University of Engineering & Technology, Bangladesh

[*] Email: shahidiqbal_05@yahoo.com

Abstract—**In this paper, a new prediction model for solar irradiance has been proposed using ant colony optimization (ACO) and neural network (NN), called as ACOSIP. In ACOSIP, the most salient climatological features are selected in order to enhance the solar irradiance prediction (SIP) accuracy. To implement such idea, ACO search technique utilizes the advantages of the combined activities of the features by considering the correlation information among the features and the outcome of NN. Thus, ACOSIP introduces the wrapper and filter approaches in its feature selection process. To make an effective ACO search, two sets of new rules have been designed for pheromone update and heuristic information measurement. To evaluate the performance of ACOSIP, 12 solar irradiance data samples in between the year of 2000-2013 were collected from Bangladesh Meteorological Department (BMD). Experimental results show that ACOSIP can select six most salient features easily with increasing the prediction accuracy, which are longitude, latitude, day light hour, max temp., min temp., and humidity. In addition, the averaged prediction accuracy of ACOSIP for 35 stations of BMD in testing case is 99.74% including the MAPE of 0.26%. The proposed ACOSIP also represents high correlation of 99.93% in between the actual and forecasted data.**

Keywords—Solar radiation forecasting, Artificial neural network, Ant colony optimization and Feature selection .

I. INTRODUCTION

Solar energy research is based on solar radiation data, but is not available for most of the sites due to non-availability of solar radiation measuring equipments at the meteorological stations. Therefore, it is essential to predict solar radiation for a location using several climatic variables. Furthermore, the application of solar energy among the different types of renewable energy sources has more attentions nowadays throughout the whole world that might be increasing in the following days.

A number of works has already been published in the literature related to modeling and prediction of solar radiation for various solar energy applications [1]. Analytic formula [3], numeric simulation or statistical approaches [4] are developed two or three decades before to predict solar irradiance. But, these prediction models resulted in large errors. To overcome these limitations, NN-based models [3-9] has been introduced in the recent years for predicting the solar irradiance.

Mohandas proposed a model in [5] where solar irradiance data was collected from different 41 stations in Saudi Arabia to train the NN for finding the irradiance prediction accuracy. The incorporated input variables are latitiude, longitude, altitude and sunshine duration. The results for the testing stations are within 16.4%. In [6], NN-based model used 12 various Indian weather stations with different climatic conditions. The results of RMSE in NN model is in between 0.0486-3.562 for Indian region. On the other hand, S. Rahman's proposed model [7] used data for Abha city of Saudi Arabia in NN training where the result of MAPE is 4.49%. S. Quaiyum proposes a SIP model [8] for Bangladesh obtained the result of MSE is 0.29%. Hasni proposes a SIP model [9] for south-western region of Algeria where the MAPE obtained is 2.9971%. In [3], Kalogirou has reviewed the use of NN in the applications of renewable energy systems. In addition, Mellit [4] has shown NN for sizing of PV systems.

According to the afore-mentioned proposed models for predicting the solar irradiance, it has been observed that, NN-based models cannot perform well in predicting the solar radiation using all the available features. The reason is that, the performance of NN always degrades if some irrelevant features exist in the available feature set [10]. Therefore, selecting those irrelevant features from the original set is a crucial work in the NN-based SIP process. In this regard, Will tries in [11] to select climatic variables for 14 weather stations in North Argentina using niching genetic algorithm.

However, in this paper, an ACO-based SIP model has been proposed to select the most relevant features to increase the prediction performance of NN. ACO here incorporates two techniques in its weight update rules, which are wrapper and filter approaches.

The remainder of this paper is organized as follows. ACOSIP are broadly discussed in Section 2. Simulation results, comparison to other methods, are reported in Section 3. Short conclusions with few remarks are given in Section 4.

II. PROPOSED ACOSIP MODEL

To determine the best climatological features in increasing the solar irradiance accuracy, ACOSIP uses hybrid ACO based search technique. Furthermore, to obtain a small subset of salient features, the ants are guided at its traversal period upon the feature space. For comprehensibility, the proposed ACOSIP model can be discussed by the flowchart shown in Fig. 1, which is described as follows:

i) Let D is a given data set with n distinct features. Initialize the pheromone trails τ and the heuristic information η of all n features by giving equal values to τ and η.

ii) Measure the correlation data of individual n features using correlation measurement scheme. The reason is to select more distinct features by ants. Thus, the ants are guided to select the features which are less correlated among the original features.

iii) Motivate the ants to choose location information (i.e., latitude and longitude) at each iterations.

iv) Generate a set of artificial A ants equivalent to n, i.e. $A = n$.

v) Subset size, s is determined prior to SC for each of the A ants. By using the conventional probabilistic transition rule [13] for selecting features with which to construct the subsets as follows:

$$P_i^A(t) = \begin{cases} \dfrac{[\tau_i(t)]^\alpha [\eta_i(t)]^\beta}{\sum_{u \in j^A} [\tau_u(t)]^\alpha [\eta_u(t)]^\beta} & if \;\; i \in j^A \\ 0 & otherwise \end{cases} \quad (1)$$

where j^A is the set of effective features, τ_i and η_i are the pheromone and heuristic values for the feature i (i= 1, 2,…..,n). The relative importance of the pheromone value and heuristic information is decided by α and β. Eq. (1) shows random behavior in subset construction initially, since the initial value of τ and η for all individual features are equal.

vi) After completion of subset construction by all ants, then system move forward, on the other hand system will back to Step 4.

vii) The subsets $R^A(t)$ is evaluated and measure the performance using MAPE $M(R^A(t))$. Here, $R^A(t)$ refers to the effective sets constructed by A ants at iteration t.

Step 8) The $R^l(t)$ (local best subset) among all $R^A(t)$ and the R^g (global best subset) among all $R^l(t)$ is selected with the searching methodogy. Here, t = 1, 2,3,…….,I where I is a number of iterations.

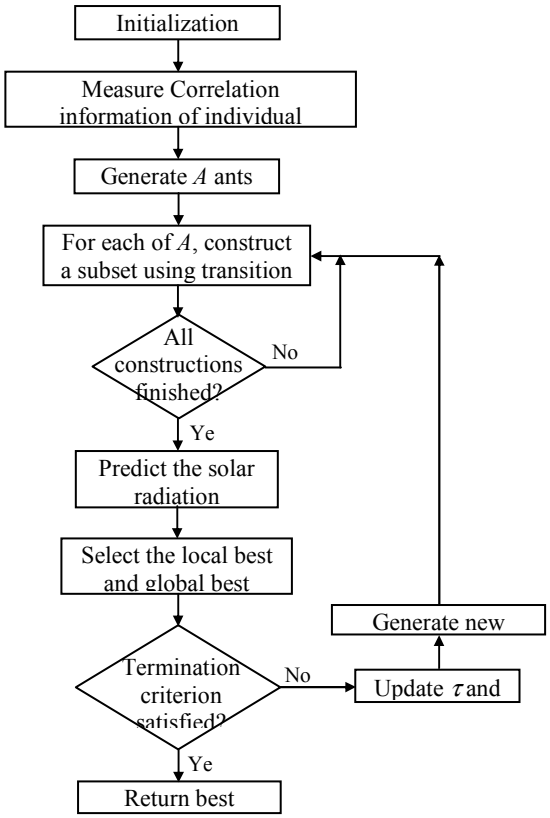

Figure 1. Flowchart of ACOSIP

Step 9) Check whether $R^l(t)$ attains a predefined SIP performance, or the algorithm execution reaches an iterative limit I_{th} and then terminate the selection process. Note that, at iteration I_{th} the model cannot find anymore variation in R^g. Otherwise continue the FS and save the evaluation results of all local best subsets, $M(R^l(t))$ for further use.

Step 10) The values of τ and η for all the features will be updated according to the rules of pheromone update and heuristic value measurement, respectively.

Step 11) A new set of artificial A ants will be generated and proceed the scheme similarly.

Clearly, the idea behind ACOSIP is straightforward, which used ACOFS algorithm to guide the ants in bounded region (between 3 to 6) of search space and providing mixed technique to the ants search. To select the distinct features which is helpful for effective learning of NN, a correlation information measurement procedure has been integrated, so performed only once throughout the FS process.

III. HYBRID SEARCH PROCESS

In ACOSIP, a hybrid search technique has been introduced that is composed by wrapper and feature approaches. These

approaches are embedded in the newly designed two sets of rules, which are pheromone update and heuristic value. Note that, these both rules are involved with correlation information measurement of individual features, which are further described as follows:

A. Pheromone Update Rule

On basis of random and probabilistic phenomena, a set of two pheromone update rules are introduced from the original one mentioned in [10] as follows:

Random case: The rule presenting in Eq. 2 is selected from [10], in which case second term is divided by f_i. The features are selected to construct subsets randomly according to their experiences. This enhances the exploration capability of ants. The rule has been accepted as follows:

$$\tau_i(t+1) = (1-\rho)\tau_i(t) + \frac{1}{f_i}\sum_{A=1}^{n}\Delta\tau_i^A(t) + e\Delta\tau_i^g(t) \tag{2}$$

$$\Delta\tau_i^A(t) = \begin{cases} M(R^A(t)) & if\ i \in R^A(t) \\ 0 & otherwise \end{cases},$$

$$\Delta\tau_i^g(t) = \begin{cases} M(R^l(t)) & if\ i \in R^l(t) \\ 0 & otherwise \end{cases}$$

Here, i refers to the number of feature (i = 1, 2,……n),and f_i is the count for the specific selected feature i in the current iteration. $\Delta\tau_i^A(t)$ is the value of pheromone taken by the local update for feature i, which is included in $R^k(t)$ at iteration t. Similarly, the global update, $\Delta\tau_i^g(t)$,is the value of pheromone for feature i that is included in $R^l(t)$. Finally, ρ and e are the pheromone decay value and elitist parameter, respectively.

Probabilistic case: Eq. (3) shows the updated pheromone rule (probabilistic case).

$$\tau_i(t+1) = (1-\rho)\tau_i(t) + \sum_{A=1}^{n}\Delta\tau_i^A(t) + e\Delta\tau_i^g(t) \tag{3}$$

$$\Delta\tau_i^A(t) = \begin{cases} M(R^k(t)) \times C_i & if\ i \in R^A(t) \\ 0 & otherwise \end{cases},$$

$$\Delta\tau_i^g(t) = \begin{cases} M(R^l(t)) \times C_i & if\ i \in R^l(t) \\ 0 & otherwise \end{cases}$$

Here, feature I is renown by the global update. The $\Delta\tau^g$ is provided only to those features that are actually efficient, because, global update has an important part in selecting the effective features in ACOSIP.

B. Heuristic Value Measurement

In this paper, we propose a set of new heuristic value estimation rule depending on two basic phenomena in SC. To describe the attractiveness for each features heuristic value, η, is important. So, to overcome the greediness η, is therefore necessary [12], and finally an effective solution may be appeared.

Random case: In the initial stage, the ants are involved to construct the feature subsets randomly, and the heuristic value of all features i can be estimated as follows:

$$\eta_i = \frac{1}{f_i}\sum_{A=1}^{n} M(R^A(t))(1+\phi e^{-\frac{|R^A(t)|}{n}})$$
$$if\ i \in R^A(t) \tag{4}$$

Probabilistic case: In the following iterations, after constructing subsets on the basis of the probabilistic behavior, the following formula is used to estimate η for all features i:

$$\eta_i = f_i\varphi_i\sum_{A=1}^{n} M_a(S^k(t))C_i(1+\phi e^{-\frac{|S^k(t)|}{n}})$$
$$if\ i \in S^k(t) \tag{5}$$

In these two rules, φ_I refer to the count of a particular selected feature I from previous iterations to the current iteration, except for the initial iteration. C_i refers to the correlation value for feature i. The aim of including C_i is based on the following two factors:(a) to select the more distinct features during SCs, and (b) enhancing the robustness of learning model. Thus, best features may be selected in the SC for different iterations, thus of course enhancing the prediction accuracy of the ACOSIP.

C. Correlation Value Measurement

In order to measure relationship between the climatological features which are used as the input pattern in ANN and to choose distinct features correlation information (CI) is important and useful statistics. To reduce the effect of features to each other and to increase the learning power of ANN we need more uncorrelated features set in training purpose. This information is providing to heuristic information measurement η of all individual features. In this work, Pearson product-moment correlation coefficient is used. The correlation coefficient, r_{ij} between two features, i and j is,

$$r_{ij} = \frac{\sum_p (x_i - \bar{x}_i)(y_j - \bar{y}_j)}{\sqrt{\sum_p (x_i - \bar{x}_i)^2}\sqrt{\sum_p (y_j - \bar{y}_j)^2}} \tag{6}$$

The correlation coefficient is computed for all possible combinations of features then ACOSIP computes the correlation of each feature. The correlation, Cor_i, of any feature i is

$$Cor_i = \frac{\sum_{j=1}^{n}|r_{ij}|}{n-1} \qquad i \neq j \tag{7}$$

where n is the number of features used. Then to find the uncorrelated features we use C_i, which is

$$C_i = 1 - Cor_i \tag{8}$$

IV. DATA COLLECTION

The significance of ACOSIP has been evaluated in this section on twelve well known climatological features as longitude (Ln), latitude (Lt), elevation (ev), year (y), month (m), station constant (sc), day light hour (DL), relative humidity(Rh), maximum temperature (Mat), minimum temperature (Mit), rainfall(Rf) and wind speed (Ws), and the solar radiation data is used as the target. These features have been used in many of solar radiation prediction models using ANN. In this study we use 14 years (2000 - 2013) monthly averaged data, for 35 stations, which are collected from Bangladesh Meteorological Department (BMD), Weather office.

V. METHODOLOGY

To verify the effectiveness of ACOSIP for FS and RP, a number of experiments have been carried out on ACOSIP. To justify the FS and RP task suitability in ACOSIP, one basic step need to be considered, namely, giving values for user-specified parameters such as $\eta, \tau, \alpha, \beta, \rho$ and ϕ, which are common for the all datasets. These parameters have been chosen after some runs. To achieve a level of balance between exploitation and exploration proper selection of the values of parameters is helpful of ants to select feasible features.

VI. EXPERIMENTAL RESULTS

The effectiveness of ACOSIP model is verified by a succession of experiments. To prove the strength of the proposed model 35 ACOSIP models have been designed for 35 stations and then results are being averaged to show the global strength of the model – shown in Table 1. As Table 1, the avg. results of PA and MAPE for 35 stations are 99.60 % (training), 99.49% (testing) and 0.42% (training), 0.49 (testing), respectively validated the ACOSIP structures for predicting solar irradiance.

TABLE I. AVERAGED PERFORMANCE RESULTS OF 35 MODEL OF ACOSIP

Local Investigated Data					
DATA	**Avg. PA (%)**	**Avg. MAPE (%)**	**Avg. RMSE (%)**	**Avg. MSE (%)**	**Avg. R (%)**
Training	99.60	0.42	0.244	0.077	99.81
Testing	99.49	0.49	0.289	0.104	99.72

TABLE II. PERFORMANCE RESULTS FOR WELL PERFORMED STATIONS

Station Names	**DATA**	**Avg. PA (%)**	**Avg. MAPE (%)**	**Avg. RMSE (%)**	**Avg. MSE (%)**
Chittagong	Training	99.79	0.21	0.0366	0.00135
	Testing	99.67	0.33	0.0576	0.00332
Dhaka	Training	99.86	0.14	0.0244	0.00059
	Testing	99.74	0.26	0.0454	0.00206
Khulna	Training	99.76	0.24	0.0419	0.00175
	Testing	99.66	0.34	0.0593	0.00352

Table 2 shows the results for different ACOSIP model of each station. The model of Dhaka region found to be best among the 35 models.

The effectiveness of FS algorithm and the prediction ability of ANN have been ascertained using the data for Dhaka region. In this respect the 15 independent runs for ACOSIP model for Dhaka have been performed and then averaged the results – shown in Table 3.

As Table 3, the PA and MAPE for training and testing case are 99.84%, 0.16% and 99.70%, 0.3%, respectively.

And as the value of R is higher (99.90%), so it can be easily understood that the ACOSIP model has stronger prediction capability.

Table 4 depicts the positive effect of feature selection strategy. PA is 99.74% with selected features.

Determination of the best solution in ACOSIP can be seen in Fig. 2, it can be showed that, the PAs varied with the size of those subsets and for the performances of the local best subsets.

The PAs were maximized in various points, but the best solution was selected (indicated by circle) by considering the reduced size subset.

How the selection of salient features in different iterations progresses in ACOSIP, Fig. 3 and Fig. 4 shows the scenario of such information for a single run.

We can see that, features 1, 2, 12, 7, 8 and 4received maximum values of τ and η so these features have a higher priority of selection.

Ultimately, a successful evaluation function NN model is used to find high- quality solutions for ACOSIP in prediction. As training process progresses and converges to a certain limit up to 40 epochs (Fig. 5(a)). However, the training is terminated, because at this instant validation error increases due to over training (Fig. 5(b)).

At the termination epoch we also observed that the number of hidden neuron is 3. Table 5 shows the correlation information that the selected features are highly uncorrelated.

TABLE III. PERFORMANCE OF ACOSIP MODEL AND RESULTS WERE AVERAGED OVER 15 INDEPENDENT RUNS.

Local Investigated Data For Dhaka Region For 15 Independent Run					
DATA	Avg. PA (%)	Avg. MAPE (%)	Avg. RMSE (%)	Avg. MSE (%)	Avg. R (%)
Training	99.84	0.16	0.027941	0.000781	99.90
Testing	99.70	0.3	0.052889	0.002745	99.82

TABLE IV. PERFORMANCE (AVERAGED) OF ACOSIP MODEL FOR FEATURE SELECTION OVER 15 INDEPENDENT RUNS.

Avg. Result for all features				Avg. Result for selected features			
N	SD	PA (%)	SD	ns	SD	PA (%)	SD
12	0.00	95.5	1.12	6.13	0.82	99.74	0.40

TABLE V. CORRELATION INFORMATION (CI) OF SELECTED FEATURES

Features	Ln.	Lt.	DL	Rh	Mat	Mit
Correlation	4.8	5.91	5.83	7.6	5.96	8.96
Less Correlated	95.2	95.09	90.17	92.4	94.04	91.04

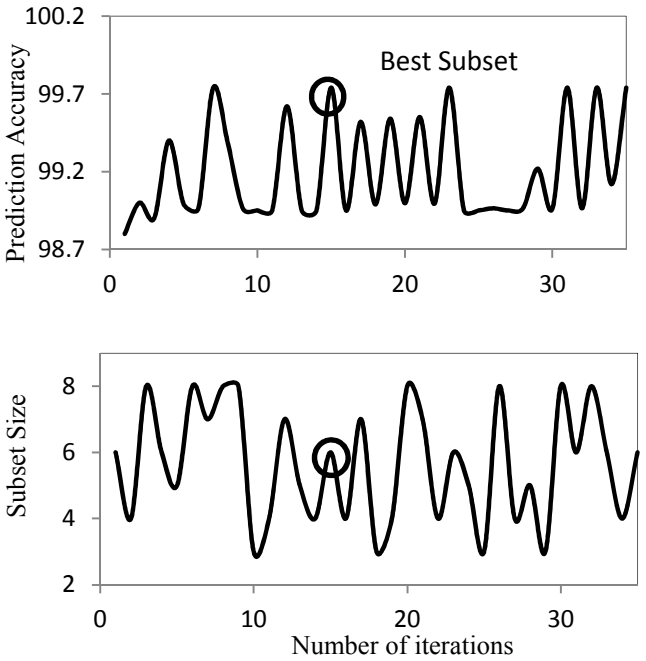

Figure 2. Finding best subset of the features for a single run.

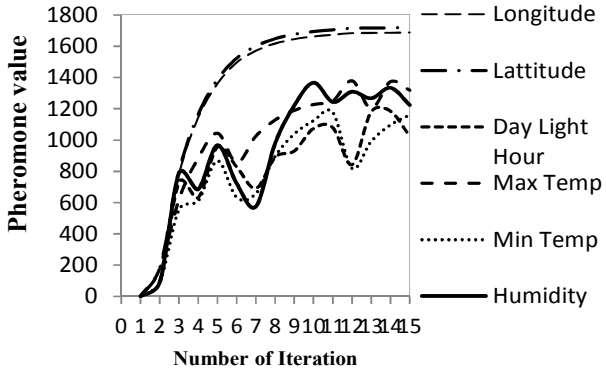

Figure 3: Distribution of pheromone level in different iterations for a single run.

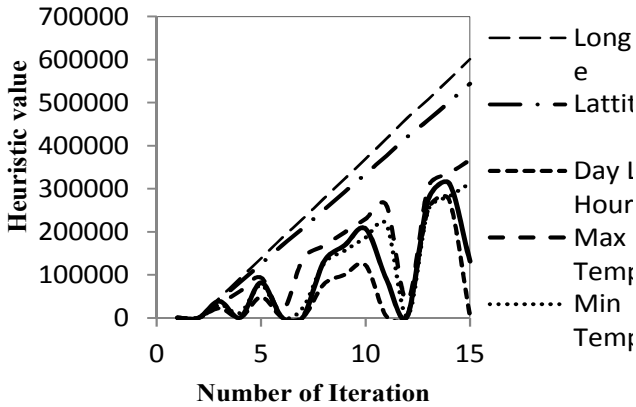

Figure 4: Distribution of heuristic level in different iterations for a single run.

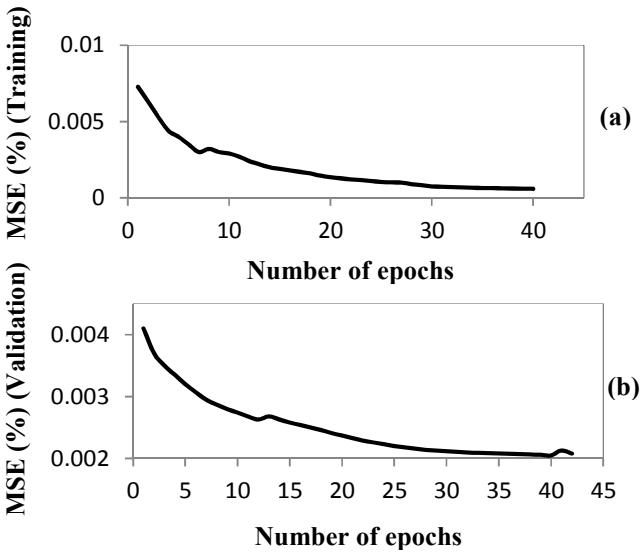

Figure 5. Training process to evaluate the constructed subsets by ants: (a) training error, (b) validation error.

It can be seen from Fig. 6 that the high correlation is present between actual and predicted data.

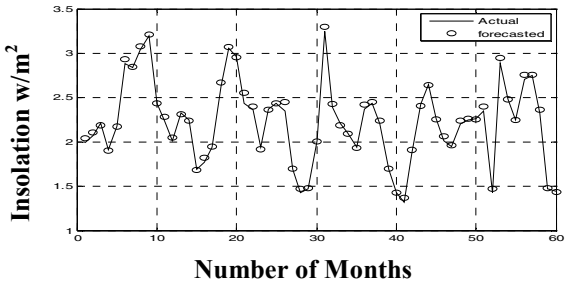

Figure 6. Actual and predicted insolation curve

VII. COMPARISON WITH OTHER WORKS.

Theoretically, a huge amount of attempts have been carried out in designing solar radiation prediction models. The proposed model is quite different from those discussed in [3 – 9], where the prediction models use the features, based on knowledge or availability with no attempts to search the best feature subset. From Table 6 it can be seen that, the proposed ACOSIP perform better with feature selection strategy.

TABLE VI. COMPARISON WITH OTHER WORKS

Name of Authors	MSE (%)	PA (%)	MAPE (%)
Proposed Model	0.000598	99.86	0.14
Amit Kumar Yadav [6]	0.0024		0.2783
Shafiqur Rahman [7]			4.49
Salman Quaiyum [8]	0.29		

VIII. CONCLUSION

This work represents a new model (ACOSIP) for predicting solar irradiance using ACO and NN. In ACOSIP, the most salient climatological features are selected in order to improve SIP accuracy. To facilitate the activity of ACOSIP, two sets of new rules have been designed for pheromone update and heuristic value measurement, where the correlation information technique and the outcome of NN are embedded. Experiment results show that, ACOSIP performs well in 12 solar radiation data samples collected from BMD, where it selected six most salient features easily with better prediction accuracy. The selected features are longitude, latitude, day light hour, max temp., min temp., and humidity. Furthermore, the averaged prediction accuracy of ACOSIP for 35 stations of BMD in testing case is 99.74% including the MAPE of 0.26% (Table 2). The proposed ACOSIP also represents high correlation of 99.93% (Table 1) in between the actual and forecasted data. On the other hand, the results of the low standard deviations of prediction accuracies exhibit the robustness of this model. Comparison results presented in Table 6 show that, ACOSIP can perform well comparing to other existing models. Thus, it can be said that, the proposed ACOSIP model may have capability to select the relevant features and to predict solar radiation at any location in the world, provided that the proper data from the locations are available.

REFERENCES

[1] EPIA Renewable Energy House, "European Photovoltaic Industry Association (EPIA): Market Report 2011," Belgium, 2012. Available online:http://www.epia.org/publications/ epiapublications.html (accessed on 22 November 2011).

[2] European Commission Joint Research Centre, "Solar Cell Production and Market Implementation of Photovoltaics: PV Status Report,"*Publications Office of the European Union*, Italy, 2011. Available online: http://ie.jrc.ec.europa.eu (accessed on 22 November 2011).

[3] S. A. Kalogirou, "Artificial neural networks in renewable energy systems applications: a review,"*Renewable and Sustainable Energy Review*, vol. 5(4), pp. 373-401, 2001.

[4] A. Mellit, S. A. Kalogirou, L. Hontoria, and S. Shaari, "Artificial intelligence techniques for sizing photovoltaic systems: a review," *Renewable and Sustainable Energy Reviews*, vol. 13, pp. 406-19, 2009.

[5] M. Mohandas, S. Rehman, and T.O. Halawani, "Estimation of global solar radiation using artificial neural networks,"*Renew Energy*, vol. 14, pp. 179-184, 1998.

[6] A.K. Yadav, S.S. Chandel, "Artificial Neural Network based Prediction of Solar Radiation for Indian Stations,"*International Journal of Computer Applications*, vol. 50, 2012.

[7] S. Rahman, M. Mohandes, "Artificial neural network estimation of global solar radiation using air temperature and relative humidity,"*Energy Policy*, vol. 36, pp. 571 – 576, 2008.

[8] S. Quaiyum, S. Rahman, "Application of Artificial Neural Network in Forecasting Solar Irradiance and Sizing of Photovoltaic Cell for Standalone Systems in Bangladesh,"*Int. Journal of Comp. App.*, vol. 32, pp. 51-56, 2011.

[9] A. Hasni, A. Sehli, B. Draoui, A. Bassou, and B. Amieur, "Estimating global solar radiation using artificial neural network and climate data in the south- western region of Algeria,"*EnergyProcedia*, vol. 18, pp. 531-7, 2012.

[10] M.M. Kabir, M. Shahjahan, and K. Murase, "A new hybrid ant colony optimization algorithm for feature selection,"*Expert Systems with Applications*, vol. 39, pp. 3747–3763, 2012.

[11] A. Will, J. Bustos, M. Bocco, J. Gotaya,andC. Lamelas,"On the use of niching genetic algorithms for variable selection in solar radiation estimation,"*Renewable Energy*, vol. 5, pp. 168-76, 2011.

[12] L. Ke, Z. Feng, and Z. Ren, "An efficient ant colony optimization approach to attribute reduction in rough set theory,"*Pattern Recognition Letters*, vol. 29, pp. 1351-1357, 2008.

[13] M. Dorigo, C. Blum, "Ant colony optimization theory: A survey,"*Theoretical Computer Science*, pp. 243-278, 2005.

[14] M.L. Gambardella, M. Dorigo, "Ant-Q: A reinforcement learning approach to the TSP,"*Proceedings of the 12th international conference on machine learning*, 1995, pp. 252-260

Power Distribution Scheme Using Smart Meter, Perspective Bangladesh

Md. Noor Hossain[1*], Jannatul Ferdous [2], Md. Farhan Fuad[3], K. M. Ahsan-uz-Zaman [4] and Abdul Wahed [5]
[1, 2, 3,4] Dept. of EEE, Mymensingh Engineering College, Mymensingh, Bangladesh
[5] Faculty, Dept. of EEE, Mymensingh Engineering College, Mymensingh, Bangladesh
[*] E-mail: noor_mec@yahoo.com

***Abstract*—Smart meter, the core part of smart grid system, is becoming an active field of research for its immense potential in efficient power distribution and load management. It is expected to have potential applications in Bangladesh as well. Efforts are already underway from distribution companies to introduce intelligence in the meter system. This paper proposes several smart meter assisted economic energy consumption schemes for consumers and power outage reduction scheme for distribution utility companies that will enhance the quality of service. Necessary analyses have been included to verify the proposed schemes. Real-life electric power demand and supply data from various substations under Dhaka Electric Supply Company (DESCO) have been used to validate the power outage reduction scheme. Results show that the schemes provide economic benefit to the consumer and an effective load management strategy for distribution companies. Operating issues related to the proposed schemes have also been detailed to highlight the practicality of the proposed schemes**

Keywords-Smart meters, power management, power outage reduction, implementation factors)

I. INTRODUCTION

Smart grid is being increasingly seen as an efficient and effective power transmission and distribution system. Smart meters at customer premises represent the core part of the intelligence and automatic control system of smart grid infrastructure [1]-[2]. Smart meters present themselves as enablers for cost-effective energy management strategies for consumers and power distribution companies [3]-[4]. An estimated 62% Bangladeshi people is connected to the electric grid. The electricity supply is not reliable and peak demand cannot be met. In the rural areas, where more than 70% of the population lives, only about 30% of them have access to electricity supply [5]. In the context of energy scenario in Bangladesh where there is a large deficit between energy generation and demand, smart meters offer the potential of providing economic usage of energy for customers and smart management of distribution system so as to minimize the impact of the energy deficit [6]. Dhaka Electric Supply Company (DESCO) in an attempt to introduce intelligent metering keeping in line with smart meter concept conducted a pilot project to introduce prepaid meters with limited feature for residential customers. Extension of such approaches will form the future of electric power distribution and consumption strategies by relying on smart meters with advanced algorithms and reliable two-way communications between the meter and the central control located at the distribution center. With increase in energy tariff coupled with energy deficit, customers will look for avenues to reduce their electricity expenses while expecting a good quality of service from the distribution companies. With a smart meter installed at the customer premise, customers can avail various options to optimize electricity usage and minimize energy expense.

This paper proposes several energy management strategies that are applicable at customer and distributor end. This includes keeping the monthly bill within a pre-set limit and being notified of tariff slabs as energy is being consumed. The proposed techniques further include energy consumption within the assigned load limit or sanctioned load. Additionally, it is possible through implementation of the proposed techniques to alleviate the existing power outage crisis and to provide uninterrupted power at a useful level. It may be worthwhile to draw differences with research that address smart meter applications at customer premises [3]-[4] and [6]. The cited research focuses on actual hardware details of a household smart meter, wider range demand side management or configuration of appliances to match the peak-hour in demand. In contrast, the research presented in this paper provides an in-depth analysis of load management scheme and addresses the practical issues that arise from such schemes. Moreover, the proposed schemes have the potential of mutually reinforcing the efficacy of load management technique. Recorded data of supply and demand over time from DESCO has been used to analyze the performance of the proposed power outage reduction scheme [7]. It is expected that the research presented in this paper will provide a practical direction for technically and economically feasible deployment.

The organization of the paper is as follows. Section II presents smart meter enabled smart electricity consumption management for customers. Section III proposes power outage reduction scheme while Section IV addresses practical issues related to the proposed management schemes. Section V touches upon the communications infrastructure to support the proposed schemes followed by concluding remarks.

II. SMART METER FOR ECONOMIC ENERGY USAGE

Consumers can regulate his/her energy usage through smart meter based usage management: (A) Fixed budget for electric bill. (B) Electricity cost management according to price slabs, and (C) Sanctioned load monitoring. These are described in details in the following subsections.

A. Fixed budget for electric bill

A smart meter can be used to help the consumer plan a monthly budget for electricity usage. The consumer will give his/her allocated budget as an input to the meter and the meter will calculate the available energy units based on the existing tariff rate. Based on the available units, the meter will calculate the daily average allowed unit. For each day, the meter will determine the consumed energy units for that day and raise an alarm if that consumed energy is higher than the average value. Thus, the consumer will be informed of his/her daily status on consumed energy units and will adjust the energy consumption for the remaining days of the month so that the total consumed energy is within the allotted budget set at the beginning of the month. An example of variation of daily consumed energy is shown in Figure 1 along with the meter computed the average daily energy unit. Here it is assumed that the allocated budget allows 570 units (i.e., kW-Hr) of energy for a given month and the resulting per day allowable energy use is about 18.8 units. Thus, whenever the consumed load exceeds the preset average value, the smart meter will raise an alarm and generate a message about exceeding the average and the remaining allowable energy units. The customer then lowers the energy consumption below the allowable daily limit.

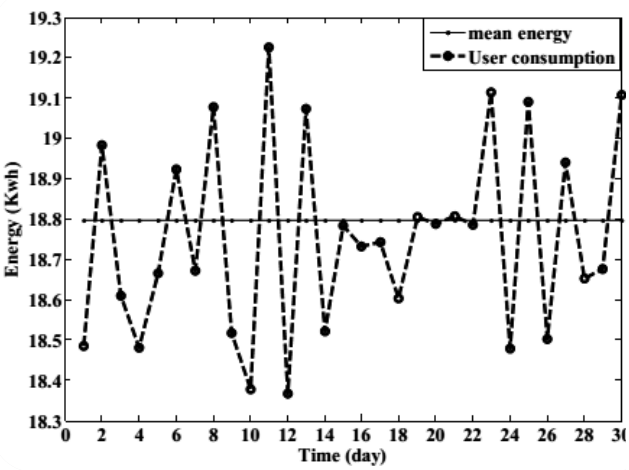

Figure 1: Energy consumption pattern following fixed budget plan.

Figure 2 shows the cumulative energy consumption from the budgeted limit (straight line representing mean energy) and from smart meter assisted user regulated scheme. The plots reveal that the proposed scheme enables the user to closely approximate the preset limit and to keep within the budget.

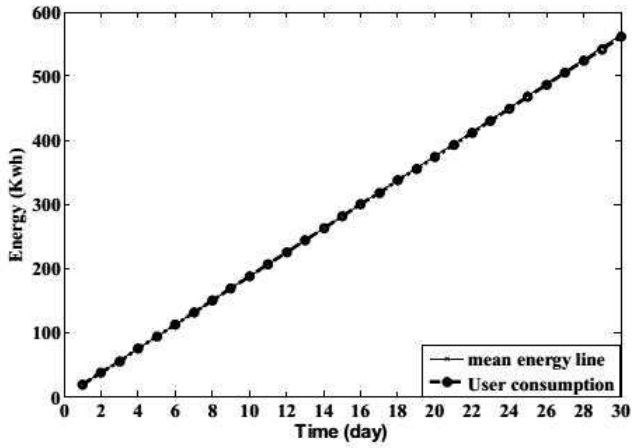

Figure 2: Allocated and daily energy consumption lines for a month.

B. Electricity cost management according to price slabs

The Dhaka electric supply company (DESCO) has implemented new tariff rates from 01 September 2012 in accordance with Bangladesh Energy Regulatory Commission (BERC) [7]. Figure 3 shows only the residential component of the tariff structure. This tariff rate is flat throughput the day irrespective of the peak demand hours.

TABLE 1: PRICE SLABS FOR RESIDENTIAL AREA IN BANGLADESH [5]

Category	Per unit Rate (BDT)
Life Line : From 1 to 50 units	3.33
First Step : From 1 to 75 units	3.53
Second Step : From 76 to 200 units	5.01
Third Step : From 201 to 300 units	5.19
Fourth Step: From 301 to 400 units	5.42
Fifth Step: From 401 to 600 units	8.51
Sixth Step: Above 600 units	9.93

As per this tariff structure, the consumer pays increasingly higher tariff as his energy consumption increases and crosses over to the higher price slabs. A smart meter can help customers become more energy-conscious as it can alert them when the energy consumption is approaching the slab with the next higher tariff rate. This will help the customers to keep the energy consumption within an affordable limit. Various algorithms can be devised to keep track of the energy consumption, the related total cost and to implement the user control (manual or automatic).

C. Sanctioned load monitoring

The customers of power distribution companies are assigned various levels of allowable sanctioned loads based on their demands whenever they subscribe to a particular company. The sanctioned load implies a tacit agreement that customer will not cross the sanctioned load. However, there is no

provision for monitoring operating customer loads and penalty for exceeding the sanctioned load. Only recently, DESCO is deploying energy meters on a small scale with instantaneous load monitoring capability and applying penalty in case of exceeding the limit. That monitoring scheme turns off the meter should there be a first-time violation of sanctioned load and the user can turn on the meter. If the violation occurs second time, the user is still allowed to turn the meter on; however, with the next violation, the meter turns off and cannot be turned on except from official intervention along with a penalty. A better and more customer-friendly approach can be adopted where the meter will alert the consumer whenever the current load limit is within a certain percentage of the sanctioned load (e.g., within 5% or if the operating load is around 950W when the sanctioned load is 1kW). Thus, with this alert in mind, the consumer will plan his energy consumption and prioritize appliances so that overall load is kept below the sanctioned load. For the case when the operating load does exceed the sanctioned limit, then the smart meter will turn off and will not turn back on until the operating load is reduced below the sanctioned load limit.

D. Operational Aspects

Hardware implementation of smart meter based energy management is an important operational aspect [8]. The proposed schemes (A-C) can be implemented through a smart meter, user interface and supporting communication system installed within consumer premises. For tracking energy consumption cost management (schemes A, B), a smart meter can be programmed to monitor daily usage and generate alert messages and alarms as needed. For implementing sanctioned load monitoring (C), the smart meter can play the role of load monitoring and generating alert messages and alarms. However, for consumer responses to the alerts and alarms, some additional features can be provided through indoor short range communication link between the smart meter and the appliances that can be controlled by the smart meter. It can be safely assumed that high-wattage appliances have major impact on operating load, pushing energy cost into higher price slabs. Thus, if the electrical outlets for these appliances are fitted with switches or relays (smart switches) controlled by smart meters through Zigbee based communication links, the operation of these devices can be controlled as per requirements from sanctioned load settings and tariff structures. For example, if the consumer would like to turn on a high-power appliance, he/she will press the smart switch and the smart switch will request the smart meter to enable it. The smart meter will monitor the parameter settings for a particular application (i.e., sanctioned load monitoring or energy cost reduction), will issue a command accordingly to the smart switch. For sanctioned load monitoring, the smart meter will not enable the smart switch till the load is reduced below the sanctioned limit. For energy cost reduction, the smart meter will disable the switch when an alert condition is encountered; however, the user can press the smart switch second time that will enable that switch and turn on the appliance.

III. POWER OUTAGE REDUCTION

There is an acute shortage of electricity production at the national level in Bangladesh and the gap between production and demand has to be compensated by power outage. In the metropolitan areas, the power outage is usually scheduled by the electricity distribution companies where an alternating hourly pattern of availability of electricity and power outage (termed load shedding) is maintained. The outage scenarios in rural areas is even worse as generated electricity is mainly channeled to city and industry areas giving less priority to rural areas. A typical hourly pattern for electricity supply, demand and the resulting amount of load shedding for a specific zone (Dhanmondi zone under DESCO) is shown in Figure 4. From the figure it can be seen that the demand is higher than the supply throughout the day with the peak demand occurring at 5 pm onwards. The peak amount of load shedding is somewhat higher than 15 MW while the peak available supply is about 22 MW.

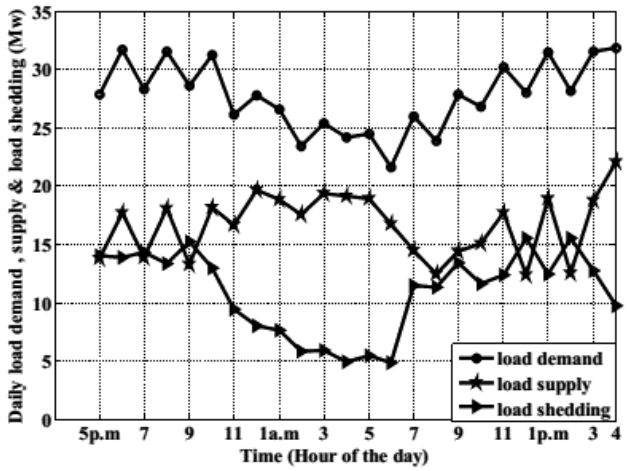

Figure 3: Load demand, supply and load shedding patterns of Dhanmondi zone in a metropolitan city Dhaka [1]

A. Proposed load management scheme

As per the current practice of load shedding, the 11 KV feeders coming out of a substation are selectively switched off in a pre-determined schedule. Thus, a group of consumers belonging to a set of feeders faces power outage in specific one hour duration while in the next hour the feeders are switched on. Thus, there is an hourly "on-off" pattern for available electricity to the consumers. The consumers usually respond to power outages by installing IPS for home use and diesel generators for high-rise residential apartments and offices and educational institutes.

Smart meters in combination with appropriate control mechanism at the distribution substation side can enable an alternative strategy where electricity can be made available to the consumers throughout the day albeit at a reduced level. The distribution companies will predict the load demand D(t) at a given time t for a given day and will

estimate a "load meet" factor *LM(t)*based on the available electricity supply S(t) allotted to it from the national grid as follows.

$$LM(t) = \frac{S(t)}{D(t)} \quad (1)$$

The central control system at the distribution substation will then relay this value to the smart meters for individual consumers and instruct the smart meters to reduce to a level as per the computed value of LM (t). A plot of LM (t) for the hourly patterns of demand and supply from figure 3 is shown in Figure 4.

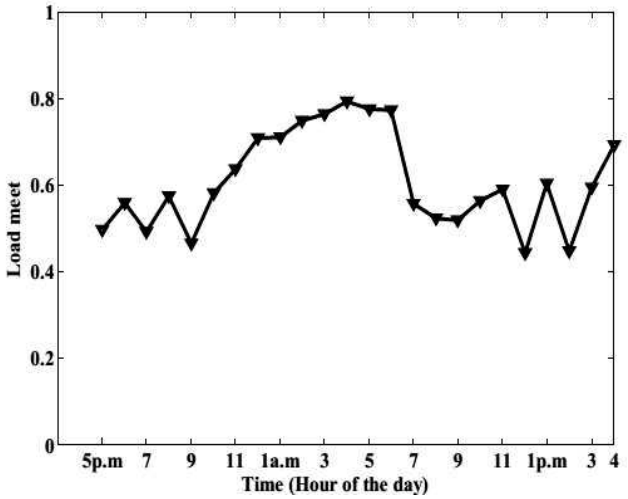

Figure 4: Variation of load meet factor with the period of time in a day.

It is instructive to compare the proposed scheme of offering energy all the time at a reduced level with the existing "on-off" hourly pattern of electricity supply.

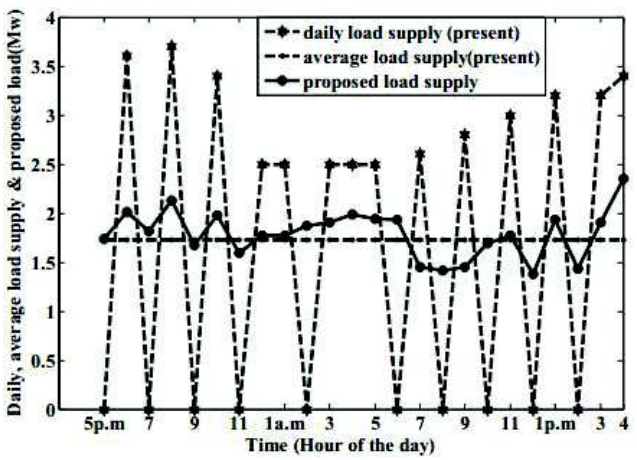

Figure 5: Existing power supply scheme and the proposed outage management scheme.

Figure 5 shows the hourly pattern of existing load shedding for a given day at a given feeder at the Dhanmondi zone for DESCO. The figure shows that except for midnight to early morning load shedding occurs regularly at alternating hours. The average available load from this load shedding approach is also shown as a straight line. The proposed load management scheme offers uninterrupted electricity supply at a reduced level of 1.5 to 2.4 MW. It can be seen that the proposed load management scheme behavior is relatively stable and is close to the average load supply from the existing load shedding technique. This shows that the proposed outage management scheme provides average energy supply to the customers that is similar to that from the present on-off scheme while maintaining continuity of service.

The different feeders of the same substation (Dhanmondi zone, DESCO) can also be studied for their allowable load variation throughout the day. The temporal patterns for the allowable load for the individual feeders for the same substation are shown in Figure 7. It can be seen that the variations are correlated depicting common residential customer energy consumption pattern. The variation in peak load supply can be attributed to individual feeder capacity.

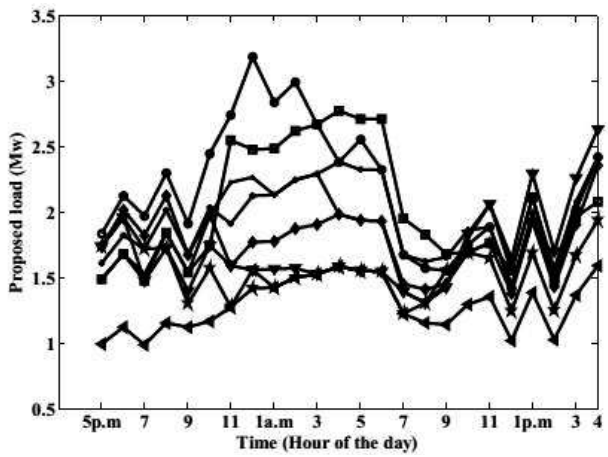

Figure 6: Variation of proposed load across different feeders of the same substation.

Let be the supplied load in a $d_1(t)$, $d_2(t)$, ⋯⋯ $d_N(t)$ substation and be the load demand of substation where N is the total number of feeders in that substation. Then total load-meet factor for a given substation can be expressed as

$$LM(t) = \frac{\sum_{n=1}^{N} P_n(t)}{\sum_{n=1}^{N} d_n(t)} \quad (2)$$

Load-meet actors for different substations (Shyamoli, Dhanmondi and Paribagh) have been computed from data available from DESCO web page. Figure 8 shows the variation of LM(t) for these substations. The plots in Figure 8 reveal that there is a strong correlation of the patterns across the substations. Thus, load distribution at different substations will follow the general pattern from applying the proposed power outage management scheme.

IV. Important Implementation Factors

The proposed load management schemes aim at more efficient and economic electricity consumption for customers. Additionally, it offers the distribution companies to provide uninterrupted electricity supply to their customers. One issue may arise and needs to be addressed is that the uninterrupted service occurs at lower load level. The main effects of that are:

- Individual consumers will need to lower their load level below the sanctioned load. Thus, the consumer needs to plan electricity appliances usage to be within the assigned load level. Thus, for a consumer with 1kW sanctioned load, he/she may be allowed minimum of 450W (45% load meet value in Figure 5) and maximum of 800W (80% load meet level in Figure 5). This can be accommodated by using more efficient electric appliances coupled with smart usage strategy implemented through smart meter.
- The availability of uninterrupted electricity will lead customers to do away with IPS and battery charging system. The charging of battery during "on" period in the current load shedding scheme can put significant burden on the available supply. Generally batteries designated for use with IPS tend to have shorter charging period by consuming higher current. For example, a 100AH battery at 12 volt can be designed to be completely charged in 3 hours; this implies that with a charging current of 100AH/3H 33 A,, the IPS system will consume 33 12 = 396 WH within the „on" time of 1 hour of the period. This can constitute a significant impact on the customer load and contribute to increase in demand during peak load.
- For high-rise apartment systems, the supply to lift/elevator and water motor can be left out of the proposed reduction scheme. Since the motors for these heavy electric devices cannot be operated at a reduced supply, the smart meters connected to these devices will be allowed to operate at their rated required capacity. This will reduce the operating expenses of the residents by excluding generators.
- Hospitals and emergency services can be left out of proposed load reduction scheme. Alternately, they can be guaranteed certain amount of supply throughout the day and difference between this supply and requirement can be compensated by installing generators.
- Since monitoring of sanctioned load does not take place currently, there is more energy consumption than the allowable limit from the consumer's side placing an increasing demand on the system. The proposed load management scheme offers monitoring of sanctioned load, and it is expected that this will bring down the demand on the distribution system with more energy aware consumers.
- These proposed load management schemes will also drive entrepreneurs to offer green energy solutions at customer premises or at the distribution centers. With additional energy from non-conventional renewable sources, the load management scheme will become more efficient and consumer friendly.

V. Communication Links for the Proposed Schemes

The proposed schemes will need a reliable two-way communications link between the smart meter and central substation [9] and between the smart meter and home appliances for automatic control. The communication link to support power outage management can be implemented via wireless or wired infrastructure. For wireless implementations, modems are needed at the smart meters to set up the link, a local concentrator to aggregate the data from multiple smart meters and relays to channelize the data to the central substation. Since the data rate is expected to low to support the scheme, the link can be designed to be small bandwidth systems. The wireless system can also be implemented through a mobile operator where data and control information can be communicated via mobile operator network so that the overall design can be made relatively simple [10]. As an alternative to the wireless systems, wired communication links can be established that will use the existing power distribution lines from the distribution substation to customer premises. This can be implemented using broadband over power lines (BPL) or power line communication (PLC) techniques [11]. Devices that are needed in this case are PLC modems at customer premises, extractor to concentrate the incoming signals, repeaters to keep the signal strength at a satisfactory level and injectors. Except for the cost of these additional devices, the PLC based implementation is expected to be economic since the existing power line network can be used as the communication infrastructure. As for energy consumption regulation at customer end (schemes A-C), customer response to smart meter alerts and alarms can be either manual or automatic. For scheme A and B, the customer can respond to alerts by planning energy consumption on his own without the need for any smart device. For scheme C, smart switches can be used for heavy load appliances to respond to alarms. In this case, low to moderate data rate links based on Zigbee systems will be sufficient for automatic control of the appliances.

VI. Conclusions

The research presented in this paper focuses on smart meter assisted energy consumption management for consumers and load management for distribution companies. Necessary analysis has been presented to verify the schemes. Analyses reveal that the proposed schemes have the potential to benefit the consumer and also assist distribution companies to provide a better quality of energy supply. The practical operational issues that can result from the proposed load outage reduction scheme have been discussed in details. The existing communications network in Bangladesh is adequate to support the proposed schemes. Thus, the proposed schemes can bring the much needed benefits and quality of electric energy supply and can be implemented through off-the-shelf components using the existing communication infrastructure.

ACKNOWLEDGMENT

The authors are grateful to Md. Faruk Hossain, Assistant Engineer, 70 MW Peaking Power plant, Bera, Pabna, for his thoughtful comment on power distribution and load shedding scheme.

REFERENCES

[1] J. Zheng ; Gao, D.W. ; Li Lin, "Smart Meters in Smart Grid: An Overview", IEEE Green Technologies Conference, 2013, Page(s): 57 – 64.

[2] Marron, L.; Osorio, X.; Llano, A. ; Arzuaga, A. ; Sendin, A., "Low voltage feeder identification for smart grids with standard narrowband PLC smart meters", 17th IEEE International Symposium on Power Line Communications and Its Applications (ISPLC), 2013, Page(s): 120 - 125.

[3] Barbato, A. ; Dipt. di Elettron. e Inf., Politec. di Milano, Milan, Italy ; Capone, A. ; Rodolfi, M. ; Tagliaferri, D., "Forecasting the usage of household appliances through power meter sensors for demand management in the smart grid"Smart Grid Communications 2011 , pp: 404 – 409

[4] Di Leo, G. ; Landi, M. ; Paciello, V. ; Pietrosanto, A. "Smart metering for demand side management", IEEE Instrumentation and Measurement Technology Conference, 2012 , pp: 1798 – 1803

[5] S. I. Khan, and Md. F. Rabbi, "An Innovative Financing Mechanism: Creating Access to Renewable Energy for Rural People of Bangladesh". Global Conference on Rural Energy Access, Addis Ababa, Ethiopia, December 4-6, 2013.

[6] GMA E. Rahman, K. I. Ahmed, R. Mostafa, and M. F. Khan,"A Novel Smart Metering System for Loss Reduction and Efficient Load Management in the Power Distribution Sector of Bangladesh,"ICAEE 2013, December 19-21, 2013

[7] https://www.desco.org.bd/index.php?page=tariff-rate

[8] M. Kuzlu, M. Pipattanasomporn, and S. Rahman, "Hardware Demonstration of a Home Energy Management System for Demand Response Applications," IEEE Tr. on Smart Grid, VOL. 3, NO. 4, DECEMBER 2012, pp. 1704-1711

[9] Y. Yan, Y. Qian, H. Sharif, and D. Tipper, "A Survey on Smart Grid Communication Infrastructures: Motivations, Requirements and Challenges" IEEE Communications Surveys and Tutorials, vol. 15, no. 1, pp. 5–20, 2012.

[10] M. M. Abdullah andB. Dwolatzky, "Smart Demand-Side Energy Management Based onCellular Technology - A way towards Smart GridTechnologies in Africa and Low Budget Economies", IEEE AFRICON 2009, 23 - 25 September 2009.

[11] S. Galli, A. Scaglione and Z. Wang, "For the Grid and Through the Grid: The Role of Power Line Communications in the Smart Grid" Proceedings of the IEEE Vol. 99, No. 6, June 2011, pp.998-1027.

Efficient PV Array Modelling by Analyzing PV System(cell/module/array) Based on MATLAB

Abu Naim Rakib Ahmed, Khalid Nowaz, Jarin Tasnim, and Nashrah Afroze
Department of Electrical and Electronic Engineering
Khulna University of Engineering & Technology (KUET), Khulna-9203, Bangladesh
E-mail: naimkuet05@gmail.com

***Abstract*—The increasing energy demand has enhanced the use of renewable energy as the source of fossil fuel cannot meet up this demand. The photovoltaic cell converts sunlight to electricity without any pollutant emission. A complete analysis on Photo Voltaic system is required to get the maximum output. But because of some external and internal factors, the generation of maximum output power is disrupted. Shading, temperature, irradiance as external factors and series and parallel resistance as internal factors change the maximum power point of a Photo Voltaic system. In this research, the generalized model for Photo Voltaic system was implemented in MATLAB interface. According to the change of the values of irradiance, shading, temperature, series and parallel resistance. The I-V and P-V characteristics are analyzed for the best case. On the basis of the analysis, effective Photo Voltaic system is built which gives approximately 5000W output by using the best values for the above mentioned factors. The proposed system is built to serve the purpose of an industry.**

Keywords—Irradiation; temperature; shading effect; bypass diode; maximum power point.

I. INTRODUCTION

The excessive demand for energy as a result of the industrial development and rapid population growth has lead to the necessity for alternative energy. The dwindling fossil fuel reserve has emphasized on this quest for alternative energy. Renewable energy is a great contribution to meet up the energy crisis. Solar energy is one of the candidates which has replaced fossil fuel by 20% to 25% over the past 20 years [1]. The use of solar power is growing at a rate of 60%. With no pollutant emission, low cost, availability, research in this topic has gained popularity. Bangladesh is also heading towards the use of solar energy in mass level in order to balance the insufficient supply of energy. In this country the duration of sunshine is 3 to 11 hours daily and the solar irradiation varies from 3.8 KWh/m^2/day to 6.4KWh/m^2/day. So there is high potential to implement solar system in the country. As a result Bangladesh Government has a target of 650 MW electricity generations by 2020. All this causes lead to the proper implementation of PV system with great performance.

The efficiency of PV system can be improved by variation of temperature, solar irradiance, shading [2, 3]. Series and parallel resistance are another factors that influence the losses.Previously some researchers gave importance on generalized PV model without considering partial shading [4].Again Partial shading [5] or MPPT [6, 5] was main focus of other authors. While the series resistance R_s and the parallel resistance R_p are discussed in others [7, 8, 9].

The focus of the paper is to develop an effective and complete PV system to manipulate important factors (shading, irradiance, temperature) and investigate a Simulink model with best values of them.

In section II, formation of a PV array is elaborated. Section III consists of the analysis of effect of irradiance, shading and temperature on cell, module and array respectively. The effect of parallel and series resistance on cell are also explained here. Section IV gives a short discussion on the analysis of section III.

II. STEP TOWARDS PV ARRAY

A. Operating Mechanism

The smallest unit of PV array is the PV cell. In a semiconductor material, electron in the valance band excites when it is irradiated and the energy of the photon exceeds the band gap energy of the material creating a hole. The n-type region gets rich of electrons and p-type region of holes because of the depletion region. This leads to a photo generated current flow if the PV cell is connected to an external circuit as shown in Fig. 1.

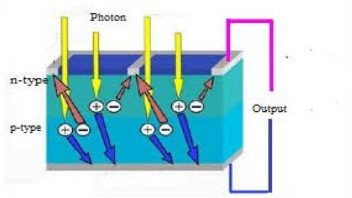

Figure 1. Process of producing photo-generated current and voltage.

B. Equivalent model of a PV cell

An equivalent model is developed to simulate a PV cell which contains a current source representing the photo generated current I_L with a diode connected in parallel can replace a PV cell. The p-n junction is represented by the diode. The external behaviour of the model is represented by a resistance in parallel named Rp and in series named Rs as shown in Fig. 2.

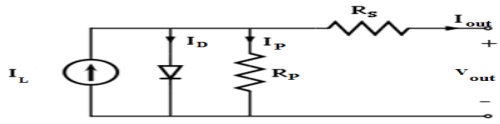

Figure 2. Equivalent model of a PV cell.

978-1-4673-9257-0/15/$31.00 ©2015 IEEE

The output voltage and current equations of a PV cell for this model are given below.

$$I_{out} = I_L - I_0(e^{\frac{qV_d}{mkT}} - 1) - \frac{V_d}{R_p} \quad (1)$$

$$V_{out} = V_d - I_{out}R_s \quad (2)$$

Here, output current is represented by (1) and output voltage by (2). In this equations above I_{out} is the output current, I_L is the photo generated current, R_s is the series resistance, R_p is the parallel resistance, I_0 is the Reverse saturation current is the electron charge (1.602 X 10^{-19}C), m is the diode ideality factor (for an ideal diode its 1), k is the Boltzmann constant (1.38 X 10^{-23}J/°K), T is the Temperature, V_d is p-n junction diode voltage. The output current is dependent on the series and parallel resistance, short circuit current and open circuit voltage, irradiation and reverse saturation current. Newton-Raphson method is very useful for solving non-linear equation which depends on numerical approximation. So V_d can be calculated by using Newton-Raphson method by using the best values of R_p and R_s randomly. The numerical process is done following the given flow chart in Fig. 3.

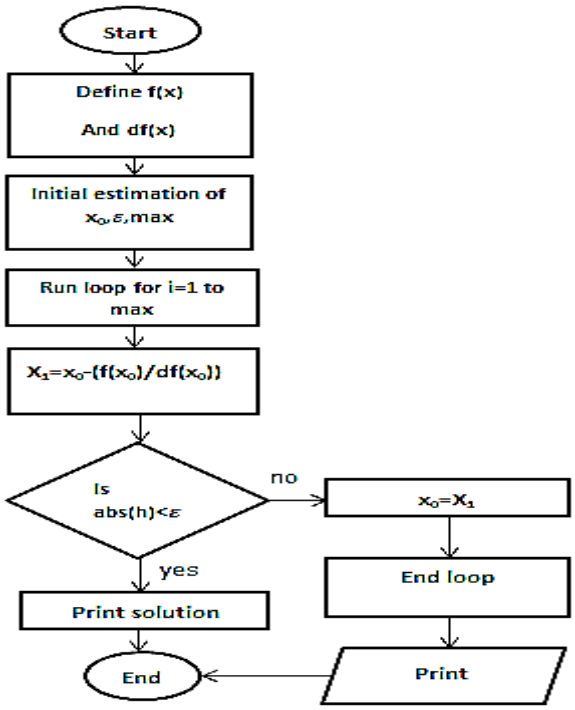

Figure 3. Algorithm of Newton-Raphson method.

C. Construction of PV module and array

To increase the total amount of voltage, PV cells are connected in series. A PV module is formed by connecting 28 to 36 PV cells as shown in Fig. 4. The total voltage is equal to the summation of the individual voltages. A PV array fulfills a desired amount of voltage as in Fig. 5 by connecting the modules in series and parallel forms. Each series branch in array is called a string.[15].

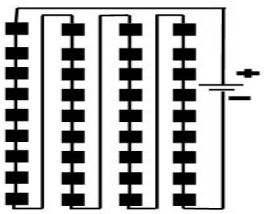

Figure 4. PV module scheme

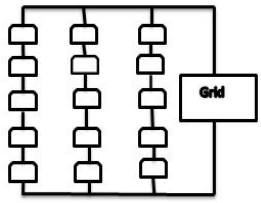

Figure 5. PV array diagram.

III. SIMULATION AND ANALYSIS

A. Cell analysis

1)Effect of series and shunt resistance on single PV cell: The performance of a cell is determined by the accuracy of series and parallel resistance. The two types of losses in the equivalent model of PV cell are leakage current loss and the losses of the semiconductor. These losses are to be minimized. Fill factor known as curve factor is the ratio of maximum power and the product of short circuit current and open circuit voltage. A large fill factor is expected.It usually ranges from 0.5 to 0.88[14-16].

$$F.F. = \frac{P_{max}}{V_{oc}.I_{sc}} = \frac{V_{max}.I_{max}}{V_{oc}.I_{sc}} \quad (3)$$

A method by which the values of R_s and R_p can be determined is using (4).

$$R_p = \frac{V_{out} + I_{out}.R_s}{I_L - I_{out} - I_0[e^{\frac{q(V_{out}+I.R_s)}{mkT}} - 1]} \quad (4)$$

Best values of R_s and R_p were assumed in order to analyze the effect of resistance. The value of V_d was estimated by using (1) and (2) on the basis of taking initial value zero. The algorithm of Newton-Raphson method used for this purpose is as Fig.3. For the required analysis, in the first case parallel resistance is taken approximately 6 Ω and series resistance is given as 0 Ω. In the second case, Rp and Rs are given as 6 Ω and 0.006 Ω respectively. In the third case, the value of R_p is made 0.06 Ω keeping R_s 0.006 Ω. The short circuit current increases but power decreases as series resistance and also parallel resistance increases as shown in Fig.6 and Fig.7. The fill factor also increases in this case.

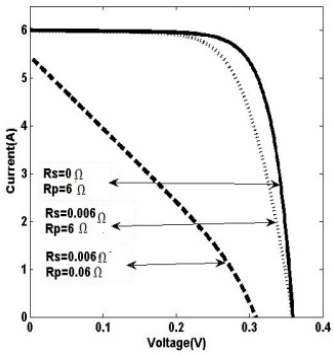

Figure 6. The influence of series and parallel resistance on I-V curve for a cell.

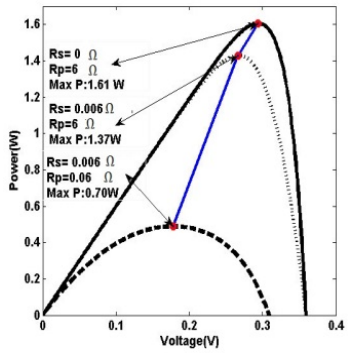

Figure 7. The influence of series and parallel resistance on P-V curve for a cell.

2)Effect of temperature on single PV cell: The reverse saturation current depends on temperature [14,15]. The performance of the PV cell is highly dependent on temperature variation. The reverse saturation current decreases with increasing temperature as from (1).

$$I_L = I_L(T_1) + K_0(T - T_1) \tag{5}$$

$$K_0 = \frac{I_{sc}(T_2) - I_{sc}(T_1)}{T_2 - T_1} \tag{6}$$

$$I_0 = I_0(T_1) \times \left(\frac{T}{T_1}\right)^{3/n} \times e^{\frac{qV_d T_1}{nk\left(\frac{1}{T} - \frac{1}{T_1}\right)}} \tag{7}$$

$$I_0(T_1) = \frac{I_{sc}(T_1)}{e^{\frac{qV_{oc}(T_1)}{nkT_1}} - 1} \tag{8}$$

The relation between photo generated current of T_1 and T can be expressed by (5). MATLAB was used to implement these equations. T is 25°C and T_1 is 75°C. The ratio of difference between short circuit current at T_1 and T_2 and the difference between the corresponding temperatures is K_0. I_0 is the reverse saturation current.

Concerning the temperature variation in Bangladesh, the variation is observed at 15°C, 25°C and 35°C and thus I-V and P-V characteristics curves are drawn as in Fig.8 and 9. These curves match with the ideal characteristics. At fixed irradiation=1000W/m^2, the reverse saturation current decreases with increasing operating temperature and so the open circuit voltage decreases but the short circuit current increases slightly.

With increasing temperature, the current increases but it cannot minimize the effect of decreasing short circuit voltage. As a result as temperature increases, MPPT seems to decrease. As shown in Fig.9, the maximum power point shifts up-ward. The MPPT was calculated 1.68W, 1.46W and 1.16W respectively at 15°C, 25°C and 35°C by MATLAB simulation. It is better to keep the temperature low. For the PV system described in this paper, temperature is chosen 25°C.

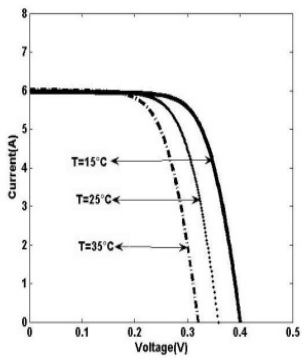

Figure 8. The influence of temperature on I-V curve for a cell.

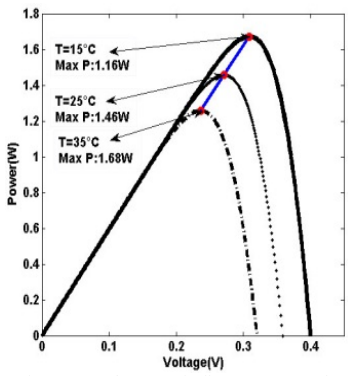

Figure 9. The influence of temperature on P-V curve for a cell.

*3)Effect of different solar irradiation on single PV cell:*Irradiation is an important effect to analyze. As it causes photo generated current to flow and at high irradiation [13, 14, 15].

$$I_L(T_1) = I_{sc}(T_1, G_{nom}) \times \frac{G}{G_{nom}} \tag{9}$$

The equation of photo generated current is given above where $I_L(T_1)$ is the photo generated current at $T_1$where T_1 is 25°C, G is the irradiance of 1000W/m^2 and G_{nom} is the irradiance which was varied. I_L is the photo generated current at 25°C and I_{sc} is the short-circuit current at 25°Cand at 1000W/m^2.

I-V and P-V curves are found by using equation (9) in MATLAB. The irradiances are taken as 1000 W/m^2, 1500 W/m^2, 2000 W/m^2. As irradiation increases, current is produced as seen in Figs. 10 and 11 which increases the open circuit voltage. This occurs because photo generated current increases at high solar irradiation. The power also increases as 0.89W, 1.38W, 1.86W shifting the maximum power point upward. So irradiance is kept at 1000 W/m^2 throughout.

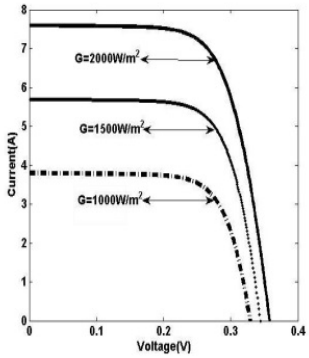

Figure 10. The influence of irradiance on I-V curve for a cell.

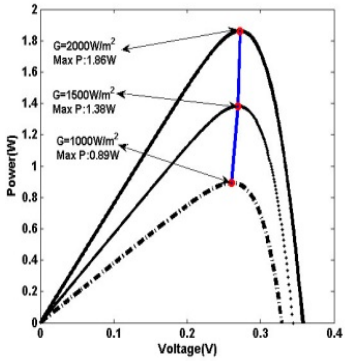

Figure 11. The influence of irradiance on P-V curve for a cell.

B. Module Analysis

By connecting 36 PV cells in series, PV module is constructed for better and accurate result. So total voltage is multiplied cell number times but the current remains constant. The cell number may be varied.

1) Effect of shading on PV module: When uneven shading is taken into account, I-V and P-V curves are slightly different. Because the heat produced by the shading effect affects the module. Shaded cells act as load. It draws current from fully illuminated cell and reduces the output power significantly. The operations are carried out on the basis of the following equations:

$$I_c = (1 - p_i)I_L - I_0\left(e^{\frac{qV_{di}}{mkT}} - 1\right) - \frac{V_{di}}{R_p} \tag{10}$$

$$V_{ci} = V_{di} - I_c.R_s \tag{11}$$

$$V_s = V_{c1} + V_{c2} + ... + V_{c(n-1)} + V_{cn} \tag{12}$$

Here, V_{di} and V_{ci} are the p-n junction diode voltages and output voltages of the *i*th PV cell, I_L is the full sun photo generated current and pi is the shading factor of the ith cell. By varying the p_i, the shading effects are taken as 0%, 40% and 80% for uneven shading.

More power is consumed and the terminal voltage is also changed when the charge carriers of the un-shaded cell flow through the shunt resistance of the shaded cell. To make the electrons flow through the shaded cells, more voltage is consumed and so the terminal voltage decreases during each kind of shading but the short circuit current remains constant. The output power decreases with the increasing shading factor because current is constant and terminal voltage decreases. During 0% shading, output power is maximum. The output maximum powers obtained are 45.68W, 50.38W and 52.54W for 80%, 40%and 0% shading respectively by simulating the equations in MATLAB. The characteristics are shown in Figs. 12 and 13.

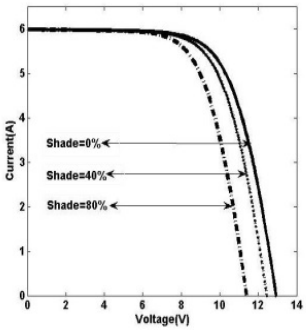

Figure 12. The influence of shading on I-V curve for a module.

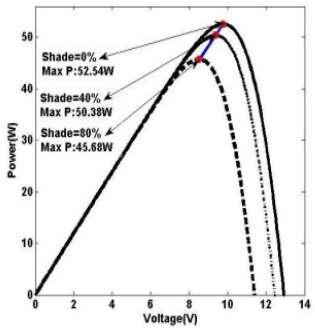

Figure 13. The influence of shading on P-V curve for a module.

2) Effect of Bypass Diode on PV Module: Bypass diode is connected in parallel with PV cells in opposite direction to reduce the impact of shading analyzed previously. Normally a bypass diode is connected in parallel with the series PV cells as in Fig**.** 14. This creates a bypass way for the current generated in the other unshaded cell [13]. The equations used for simulation are given below:

$$I_{ci} = (1 - p_{ij})I_L - I_0(e^{\frac{qV_{di}j}{mkT}} - 1) - \frac{V_{dij}}{R_p} \quad (13)$$

$$V_{pdi} = V_{ci1} + V_{ci2} + ... + V_{ci(n-1)} + V_{ciL} \quad (14)$$

$$V_{cij} = V_{dij} - I_{ci}.R_s \quad (15)$$

$$I_s = I_{ci} + I_0(e^{-qV_{pdi}/mkT} - 1) \quad (16)$$

$$V_s = V_{pd1} + V_{pd2} + ... + V_{pd(m-1)} + V_{pdM} \quad (17)$$

Here, V_{dij} and V_{cij} are p-n junction diode voltage and PV cell output voltages of the *j*th PV cell within the *i*th bypass diode group, p_{ij} stands for the shading factor relevant to the full sun condition for the *j*th PV cell within the *i*th bypass diode group, I_{ci} is the output current of the series PV cells within the *i*th bypass diode group, and V_{dpi} represents the voltage applied to the *i*th bypass diode. i is the number diode and j is the number of cell and L=N/M is the number of PV cell group where one bypass diode is connected.

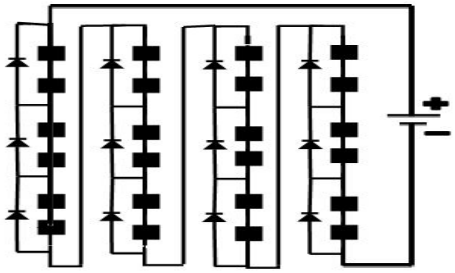

Figure 14. PV array diagram where 3 series branches, containing 6 PV modules, are connected in parallel to complete the array.

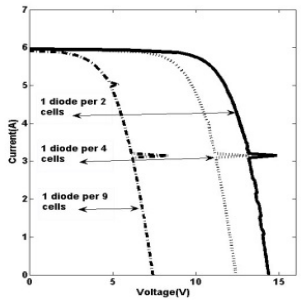

Figure 15. The influence of bypass diodes on I-V curve for a module.

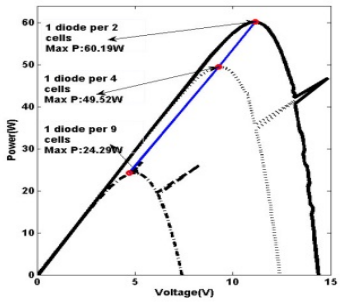

Figure 16. The influence of bypass diodes on P-V curve for a module.

From Fig**.**16**,** the less the PV cells are under one bypass diode, the less is the power consumption as seen from simulation. Because the shaded power absorption is reduced in this case and so bypass diode is added for 2, 4 and 9 PV cells respectively. The open circuit voltage increases with the maximum output power increase when less PV cells are under one bypass diode as in Fig. 15. Maximum output power obtained are 24.29 W, 49.52 W and 60.19 W when 9, 4 and 2 PV cells respectively are connected under one bypass diode. While adding one diode with each 4 PV cells maximum output power is 49.13 W. This output is increased at 60.19 W in case of reducing PV cells to 2.So better output can be produced by reducing the number of cells under one diode.

3) Effect of temperature and irradiance on PV module: The effect of temperature on the output current, voltage and power of PV module matches with that on PV cells. As voltage decreases, the power decreases with the increase of temperature. Short circuit current is constant and the simulation is done according to section III. The maximum powers are 60.33W, 52.55 W and 45.32W for the above temperatures respectively. The I-V and P-V curves with the variation of temperature are shown in Figs.17 and 18. [13,14,15] when irradiance is kept constant at 1000W/m^2.

Greater irradiance gives better results in case of PV module. This is verified by simulation as done in section III using Equation (9). The irradiance is changed as 1000W/m^2, 1500W/m^2 and 2000W/m^2 while both the short circuit current and open circuit voltage increases as in Fig. 19. The cause of increasing photogenerated current is same as explained in

section III. The maximum power point shifts upward as 32.9W, 49.91W, 66.41W.

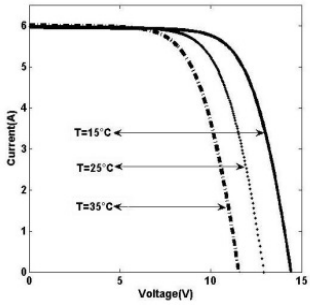

Figure 17. The influence of temperature on I-V curve for a module.

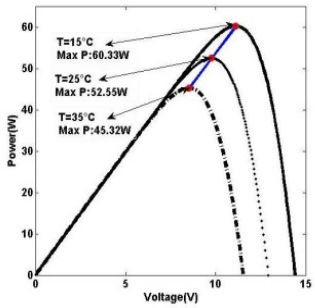

Figure 18. The influence of temperature on P-V curve for a module.

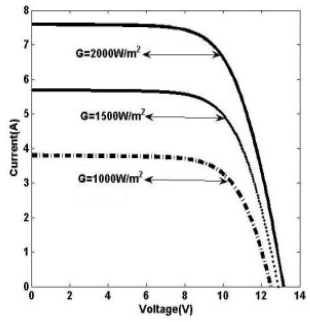

Figure 19. The influence of irradiance on I-V curve for a module.

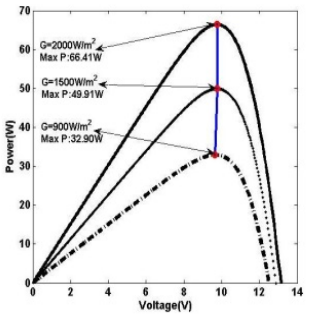

Figure 20. The influence of irradiance on P-V curve for a module.

C. Array Analysis

PV array and module shows similar characteristics.3 strings are connected in parallel consisting of 6 modules to design a 1KW PV system in the array.

*1) Effect of shading and bypass diode on PV array:*Maximum power is obtained for shading of PV array when shading is 0%. For increased shading, the output powers are 945.8 W, 906.91W and 822.24 W respectively at 0%, 40%, 80% as in Fig. 22. As seen in Fig. 21 the open circuit voltage decreases and this can be improved by using bypass diode as in Fig. 24. Power increases as 0.35 KW, 0.81 KW and 1.01 KW for 9,4 and 2 PV cells respectively under each bypass diode. By reducing the cell number by half under one bypass diode, the maximum power increases from 0.81 KW to 1.01 KW as shown in Fig. 24.

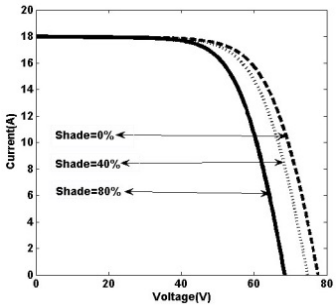

Figure 21. The influence of shading on I-V curve for an array.

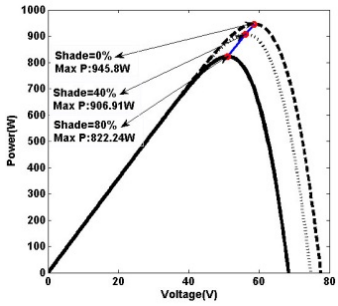

Figure 22. The influence of shading on P-V curve for an array.

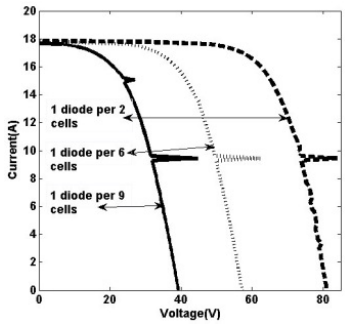

Figure 23. The influence of bypass diodes on I-V curve for an array.

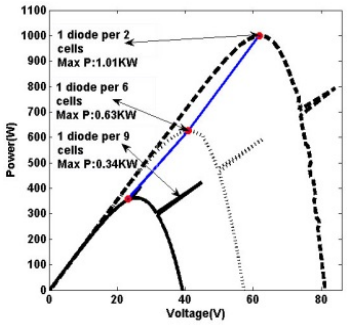

Figure 24. The influence of bypass diodes on P-V curve for an array.

*2) Effect of temperature and irradiance on PV array:*The maximum output powers are 1.09 KW, 0.95 KW and 0.82 KW for 15°C, 25°C, 35°C are obtained by simulating the equations of section III in MATLAB. This is shown in Fig. 26. With the increase in temperature, the open circuit voltage decreases as shown in Fig. 25. The theory used here matches with section III. The irradiances are considered as 2000W/m^2, 1500W/m^{2}and 1000W/m^2 for convenience and the corresponding output powers are 1.19 KW, 0.9 KW and 0.59 KW obtained from MATLAB simulation. These effects are well understood from the curves in Fig. 27 and 28.

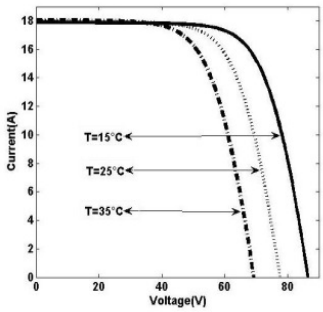

Figure 25. The influence of temperature on I-V curve for an array.

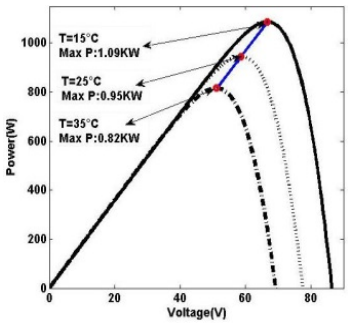

Figure 26. The influence of temperature on P-V curve for an array.

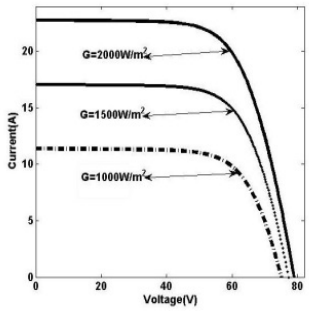

Figure 27. The influence of irradiance on I-V curve for an array.

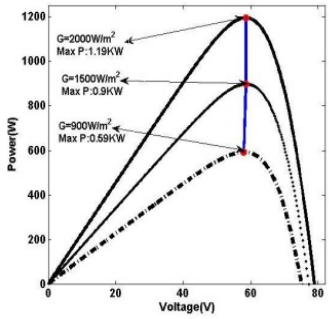

Figure 28. The influence of irradiance on P-V curve for an array.

3) Simulink Model of an array: A Simulink model is built to get around 5000 watt output power from a PV array. Built in PV cell of MATLAB was used in this purpose. A PV module of 20 PV cell is taken. It generates 250 W. And 1 string is prepared taking 4 modules in series. 2 such strings are

connected in parallel. The output is taken at solar irradiance of 1000W/m^{2}at 25°C. The Simulink model is shown in Fig.29.

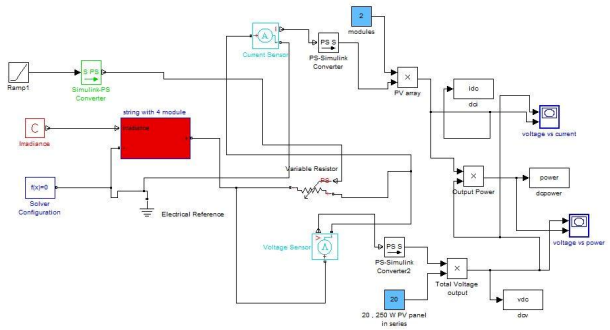

Figure 29. Simulink model for almost 1KW maximum power output.

After developing the Simulink model, the graphs are obtained as shown in Fig. 30 and Fig. 31. Analyzing the graphs it is seen that maximum output power is obtained as 5.05 KW. Under this condition V_{out} is 1129 volt and I_{out} is 5.87 Amp. R_s of 0.006Ω and R_p of 6 Ω are used. For developing the Simulink model, solar irradiation of 1000 W/m^2 and temperature of 25°c is considered.

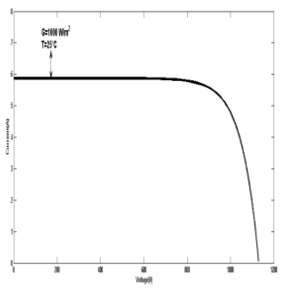

Figure 30. I-V characteristics curve for the Simulink model.

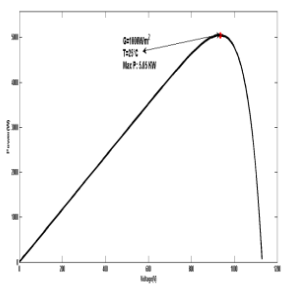

Figure 31. P-V characteristics curve for the Simulink model.

A table showing all the Electrical characteristic data of the Simulink model is as following:

TABLE I. ELETRICAL CHARACTERISTICS DATA OF THE SIMULINK MODEL

Electrical Characteristics	Values
Maximum Power	5.05 K Watt
Voltage at Maximum Power	931.2 Volt
Current at Maximum Power	5.41 Amp
Open Circuit Voltage	1129 Volt
Short Circuit Current	5.87 Amp
Series Resistance	0.006 Ω
Parallel Resistance	6 Ω
Fill Factor	0.76

IV. CONCLUSION

In the preceding sections, simulation in MATLAB was done to analyze the behavior of PV cell completely, module and array. With a view to this, different influencing factors such as temperature, irradiance, shading, series and parallel resistance are varied to observe the change in the output power. And thus the methods of improving the output performance are mentioned. All the analyses are done using the best values in MATLAB. Along with the above works, a solar panel with an output of 5 KW is designed. This work can further be used to get the maximum output from a solar panel eliminating the effects of various internal and external factors. The analyses done in the paper may be expanded in hardware side too for further study, implementation and improvements.

REFERENCES

[1] T. Salmi,M. Bouzguenda,A. Gastli,& A. Masmoudi. Matlab/simulink based modeling of photovoltaic cell. *International Journal of Renewable Energy Research (IJRER)*, *2*(2), 213-218,2012.

[2] H. Patel, V. Agarwal, MATLAB-based modeling to study the effects of partial shading on PV array characteristics, IEEE Transactions on Energy Conversion 23,302-310,2008.

[3] K. Ishaque, Z. Salam, H. Taheri, Accurate MATLAB simulink PV system simulator based on a two-diode model, Journal of Power Electronics 11, 179-187,2011.

[4] H.L. Tsai, C.S. Tu, Y.J. Su, Development of generalized photovoltaic model using MATLAB/SIMULINK, in: Proceedings of the World Congress on Engineering and Computer Science, San Francisco, USA, 2008

[5] O. Wasynczuk, Dynamic behavior of a class of photovoltaic power systems, IEEE Transactions on Power Apparatus and Systems 102 , 3031-3037,1983.

[6] C.C. Hua, C.M. Shen, Study of maximum power tracking techniques and control of dc-dc converters for photovoltaic power system, in: Proceedings of 29th Annual IEEE Power Electronics Specialists Conf., Fukuoka, 1998, pp. 86-93.

[7] Walker, Geoff. Evaluating MPPT converter topologies using a matlab PV model. Aust. J. Electr. Electron. Eng. 21,2001.

[8] A. Bouzid,R. Chenni,T. Kerbache, M. Makhlouf, A Detailed Modeling Method for Photovoltaic Cells Energy. Elsevier,2005.

[9] F. Bryan , Simulation of grid-tied building integrated photovoltaic systems. MS thesis. Solar Energy Laboratory, University of Wisconsin, Madison,1999.

[10] Townsend, T.U., Method For Estimating The Long-Term Performance Of Direct-Coupled Photovoltaic Systems. M.S. Thesis, Mechanical Engineering, U. Of Wisconsin-Madison,1989.

[11] B. Alsayid,J. Jallad. Modeling and simulation of photovoltaic cells/modules/arrays. Int. J. Res. Rev. Comput. Sci. (IJRRCS) 2 ,2001.

[12] A. Chouder,L. Rahmani,N. Sadaoui,S. Silvestre. Modeling and simulation of a grid connected PV system based on the evaluation of main PV module parameters. Simul. Model. Pract. Theory 20, 46–58,2012.

[13] H.Zheng. SOLAR PHOTOVOLTAIC ENERGY GENERATION AND CONVERSION—FROM DEVICES TO GRID INTEGRATION (Doctoral dissertation, The University of Alabama TUSCALOOSA), 2013.

[14] I. Yahyaoui,M. Ammous&F. Tadeo . Algorithm for Optimum Sizing of a Photovoltaic Water Pumping System. *International Journal of Computer Applications*, *111*(6), 21-28,2015.

[15] Elias, B. H., AlSadoon, S. H., & Abdulgafar, S. A. Modeling and Simulation of Photovoltaic Module Considering an Ideal Solar Cell.

[16] A. Blorfan, Flieller, D., Wira, P., Sturtzer, G., & Merckle, J. A new approach for modeling the Photovoltaic Cell using Orcad comparing with the Model done in Matlab. *International Review on Modelling and Simulations*, *3*(5), 948-954,2010.

Replacing Diesel Irrigation Pumps with Solar Photovoltaic Pumps for Sustainable Irrigation in Bangladesh: A Feasibility Study with HOMER

Md. Nazmul Islam Sarkar*, Anwarul Islam Sifat, Nazmul Rahim and S. M. Shamim Reza
Institute of Energy, University of Dhaka
Mokarram Hossain Bigyan Bhaban, Doel Chattar, Dhaka 1000, Bangladesh
* Corresponding author email: sarkarmni@gmail.com

***Abstract*—As a tropical country Bangladesh receives a substantial amount of solar insolation suitable for PV application. Being an agricultural economy, the irrigation need is increasing day by day. Use of diesel run pumping system is neither cost effective nor environment friendly. Even though 47.8% of the total irrigation pumps are diesel run which emits a huge amount of CO2 and other toxic gases. In this paper a typical year round irrigation load has been modelled and used to analyze the feasibility of replacing diesel irrigation pumps with solar PV powered motor-pump systems in HOMER. It was found that stand alone operation of diesel powered pumps are not at all cost effective. PV powered pumps are more feasible than a hybrid PV-Diesel Generator-Battery powered pump systems if it has a larger storage tank. If storage tank is not available then excess electricity fraction rises up to 84% which can be used in residential needs or can be used in other agricultural needs.**

***Keywords*—Feasibility of solar irrigation; Sustainable irrigation; Photovoltaic pumping; Green farming; Green energy.**

I. Introduction

Agriculture is the vital component of the economy of Bangladesh in terms of GDP share and also lifestyle. The rural economy contributes 60% of the GDP [1] which mostly comes from the agricultural sector. Irrigation is an essential component of this agriculture. Proper irrigation at proper time increases the yield of crop significantly. Due to climate change and intensive agricultural practices of changing crops and cropping patterns the demand for irrigation water increased a lot [1]. Besides this, expansion of High Yielding Variety (HYV) rice cultivation increased the need for groundwater irrigation which is 73% of the total irrigation need [2]. To lower the cost of energy (COE) and increase the renewable fraction in the energy basket we have to use renewable solutions like solar photovoltaic energy, wind energy or other type of renewable energy in the irrigation sector as well.

A design and analysis of low cost solar water pump for irrigation in rural Bangladesh was done by researchers of Bangladesh University of Engineering & Technology [16]. Some researchers have also studied the prospect of hybrid solar irrigation system in Bangladesh [17]. Practical set up of solar irrigation pump system was done by various groups from industry and local people. Direct coupling of pump with solar panel for sustainable irrigation is also investigated by Bangladesh University of Engineering & Technology [18]. Application of photovoltaic array for water pumping as an alternative to diesel engines is investigated by various researchers of the world [12-15, 19-20].

In this work, a pre-feasibility study was done to see the optimal condition to replace the diesel powered irrigation pumps with solar PV powered motor-pumps in Bangladesh.

II. Present Irrigation Scenario of Bangladesh

Presently, in 2013-14 there were around 1630866 unit irrigation pumps in operation among which 96% are Shallow Tube Well (STW) and 2% Deep Tube Wells (DTW) and 2% Low Lift Pumps (LLP) [3]. The average elevation of Bangladesh from sea level is very low and static head of surface water is less than 20-30 m in most of the places [3]. Figure 1 shows the present ground water depth in different areas of Bangladesh.

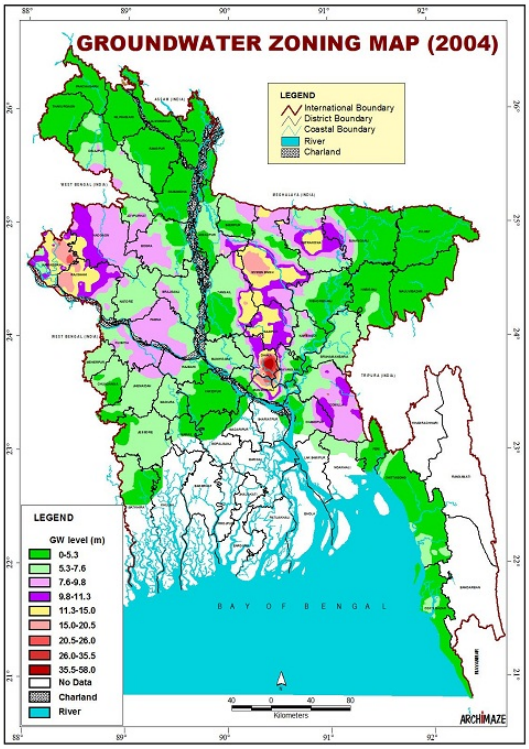

Fig. 1. Groundwater zoning map of Bangladesh [4].

978-1-4673-9257-0/15/$31.00 ©2015 IEEE

Because of this low ground water depth STWs are most popular in irrigation systems of Bangladesh. Figure 2 illustrates the irrigation pump units in 2012-13 and 2013-14 and their fuel mix. Number of irrigation pump units increased 58.8% in 2013-14 than that of 2012-13 and the number of electricity run units were very small in numbers in 2012-13 but in 2013-14 it increased 5 times. The reason behind this is governments declaration of low price of electricity for irrigation (2.51 BDT/unit) and high demand for irrigation water [5]. Whereas number of diesel run units decreased only 8% in 2013-14. From this scenario it is clear that the demand for irrigation water will increase significantly in the next upcoming years and satisfying this stepper demand with grid electricity will be quite impossible. As diesel run pumps cannot be a sustainable solution of this problem we need to find renewable sources to satisfy this demand as well as to replace the diesel run machines to ensure a sustainable irrigation system for future Bangladesh.

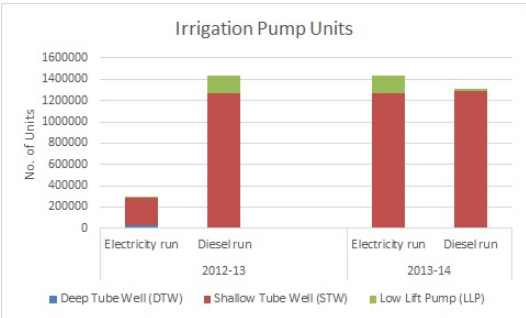

Fig. 2. Distribution of irrigation pump units according to their fuel consumption [3].

III. Characteristics of Solar PV powered motor-pumps

To calculate the working water head of the pump Koner [13] has given the following formula :

$$h = K_1(w^p)^2 - K_2(w_0 - w^p)^2 \tag{1}$$

where,
h: working water head, (m), w_p: pumping speed $(rads^{-1})$
K_1: voltage dependent water head constant, $m(rads^{-1})^{-2}$
K_2: flow rate dependent water head constant, $m(rads^{-1})^{-2}$
w_0: the speed of motor-pump system at no-flow condition, $(rads^{-1})$

The relation of water discharge to water head of the pump was given by Braunstein and Kornfield [14] as:

$$Q = K_3(h_0 - h)^{1/2} = K_3K_2^{0.5}(w_0 - w^p) \tag{2}$$

where,
Q: flow rate of a pump (ls^{-1}),
h_0: water head of a pump at no-flow condition, (m),
K_3: flow speed constant, $(ls^{-1}m^{-0.5})$
The speed-torque relationship is given as:

$$T^p = K_4(w^p)^2 \tag{3}$$

where,
T^p: pump torque, (Nm), K_4: flow-water head constant of a pump, $(ls^{-1}m^{-1/2})$
The equations for DC series motor was deduced by Hsiao and Blevins [15] as follows:

$$V^m = MI^m w^m + I^m R_t \tag{4}$$

$$T^m = M(I^m)^2 \tag{5}$$

$$M = M_0(w^m/(w_0^m)) \tag{6}$$

where,
V^m: motor terminal voltage, (V),
M_0: motor constant, (NmA^{-2})
I^m: armature current of a motor, (A)
w^m: motor shaft speed, $(rads^{-1})$
R_t: Field coil and armature resistances of motor, (ω)

Finally, the efficiency of the motor pump is given by Kolhe, Joshi, and Kothari [12] as:

$$\eta_{mp} = \frac{\rho g Q H}{VI} \tag{7}$$

and the overall efficiency as:

$$\eta = \eta_e \eta_{mp} \tag{8}$$

where,
η_e: PV array efficiency, Q: flow rate, (m^3s^{-1})
H: head of water, (m), g: constant of gravity $(9.81ms^{-2})$
ρ: density of water, (kgm^{-3})

IV. Availability of Solar Energy and Precipitation in Bangladesh

The requirement of irrigation for crops depends on mostly two factors- amount of rainfall and solar insolation. Bangladesh receives most of its rainfall (around 90%) in the monsoon from June to September [6] as shown in fig. 3. In the other months due to lack of rainfall crop production is hampered. So we need to irrigate the crops from surface water in those months.

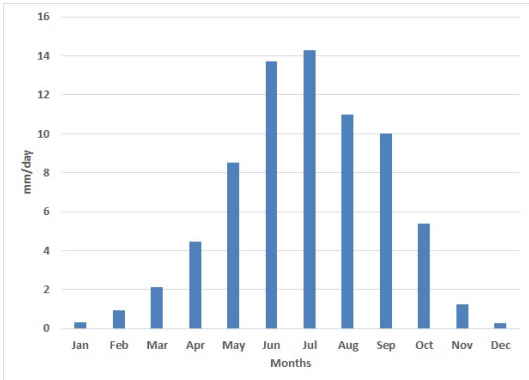

Fig. 3. Monthly Averaged Yearly Precipitation: 22 years average (1983-2005) [7].

On the other hand solar insolation level is pretty high from 4-5 kWh/day around the year [7] which ensures the potential

of solar power harvesting for irrigation in Bangladesh. In fig. 4 the 22 years average of monthly averaged daily solar insolation and clearness index is shown. The effectiveness of solar powered irrigation pump mostly depends on the solar radiation received and thus Bangladesh is a very suitable place for solar irrigation. Besides this, we can use a storage tank to harvest rain water.

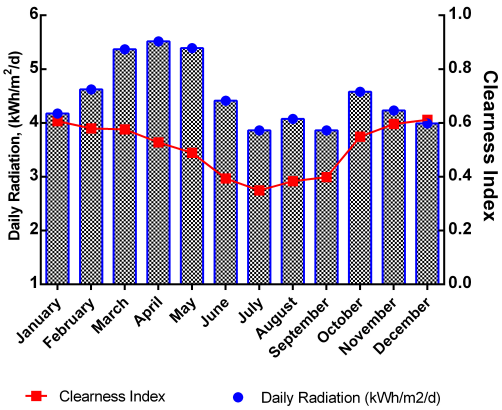

Fig. 4. Monthly averaged daily solar insolation with superimposed clearness index [7].

V. Modeling the Irrigation Pump System in HOMER

HOMER is a micropower optimization and simulation software developed by National Renewable Energy Laboratory (NREL), USA. The word HOMER came from the abbreviation of "Home Energy". It simulates the operation of a system by calculating energy balance equations for 8,760 hours in a year and compares the solutions with different possible configuration and finds the best possible and economically suitable solution [8].

As irrigation water requirement is not a primary load and can be deferred for a later time the load was modelled as a deferrable DC load in HOMER. The deferrable load, PV arrays and a battery element was connected in the DC bus, and a diesel powered AC generator was added in the AC bus coupled with a converter to power the DC bus. The schematic diagram is shown in fig. 5.

A. Modeling the deferrable load

Irrigation for crops can be delayed for 1-3 days without any disturbance in the production process [4]. Therefore we have assumed our load to be a deferrable load. A deferrable load is an electrical load that must be met within some time period, but the exact timing is not important [9]. Loads are normally classified as deferrable because they have some storage associated with them. In irrigation system we can use a storage tank, pond or canals as the storage system for the deferrable load.

Three different crops were taken to find the average water requirement per hectare land. The average water need was calculated as shown in the table 1 [10].

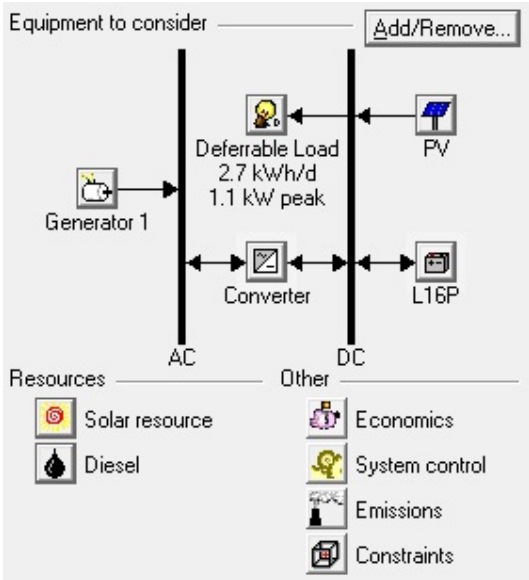

Fig. 5. Schematic diagram of the simulation in HOMER

TABLE I
Average monthly water need for crops

Name of the crops	Required Water Volume (m3/hectare)	Average (m3/hectare/year)	Average (l/hectare/month)
Rice	850		
Wheat	700	750	62500
Cotton	700		

A typical 1.1 kW solar pump has a flow rate of 55 LPM with 20m water head [11]. So, at rated power the solar pump can lift 3300 lit/hour. Ten hectares of sample land was taken to irrigate per day and therefore taking these values and the amount of precipitation approximate values of monthly averaged daily water pumping load was calculated as shown in table 2.

As the time of rainfall over the year is uncertain so 0.5 kWh/day load was added for supplementary irrigation need during May September. Figure 6 shows the daily load profile of our deferrable load.

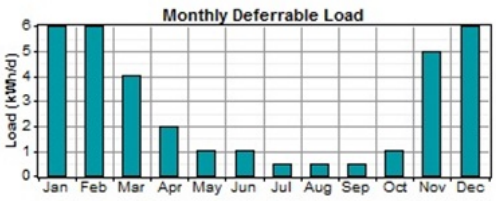

Fig. 6. Monthly average daily deferrable water pumping load modeled for HOMER.

B. Other input parameters

The present market condition was analyzed to find the current prices of PV arrays, diesel generator set, converter and batteries. Table 3 lists the other input values given in HOMER.

TABLE II
CALCULATION OF MONTHLY AVERAGED DAILY WATER NEED AND ENERGY REQUIREMENT.

Month	Average water requirement (l/hectare/month)	Rainfall (l/hectare/month)	Average irrigation requirement (l/hectare/month)	Average irrigation requirement (l/10hectare/day)	Average Energy need, kWh/day
Jan	62500	300	59500	19833.33	6.01
Feb	62500	9200	53300	17766.66	5.38
Mar	62500	21300	41200	13733.33	4.16
Apr	62500	44400	18100	603.33	0.18
May	62500	85100	-22600	-7533.33	0
Jun	62500	137000	-74500	-24833.3	0
Jul	62500	143000	-80500	-26833.3	0
Aug	62500	110000	-47500	-15833.3	0
Sep	62500	100000	-37500	-12500	0
Oct	62500	53800	8700	2900	0.87
Nov	62500	12500	50000	16666.66	5.05
Dec	62500	2800	59700	19900	6.03

TABLE III
DIFFERENT INPUT VALUES OF DIFFERENT COMPONENTS

Name of the Component	Cost ($/kW)	Replacement Cost ($/kW)	Operation & Maintenance Cost	Sizes to consider
PV array	1000	900	$ 0 (/year)	0,1-10 kW
Diesel Generator	600	500	$ 0.05 (/hr)	0,1,2,4,6,8 kW
Converter	500	400	$ 50 (/year)	0,2,4,6,8 kW
Trojan L16P Battery	300 (per piece)	200 (per piece)	$ 30 (/year)	0,2,4,6,8

C. Sensitivity Variables

A sensitivity analysis can be performed by HOMER by entering multiple values for a particular input variable. An input variable for which multiple values are specified is called a sensitivity variable [9]. HOMER repeats its optimization process for each value of that variable and lets you see how the results are affected.

As we want to see the feasibility of replacing diesel generator with PV powered motor-pump system several sensitivity variables was used to find the best possible solutions. Table 4 lists all the sensitivity variables used in HOMER.

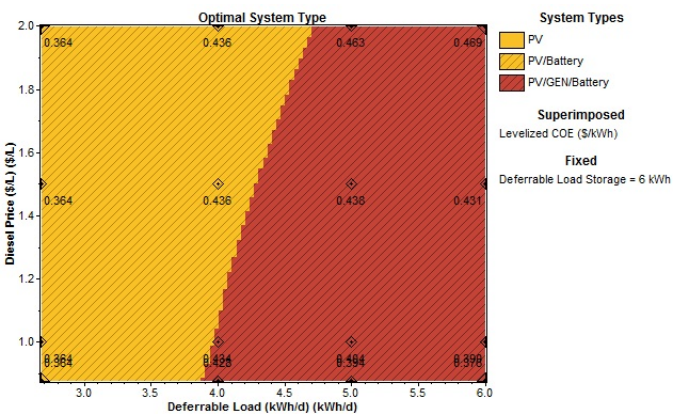

Fig. 8. Effect of diesel price.

VI. ANALYSIS AND RESULTS

After doing the analysis HOMER gives the optimal system type graph superimposed with levelized Cost of Energy (COE)

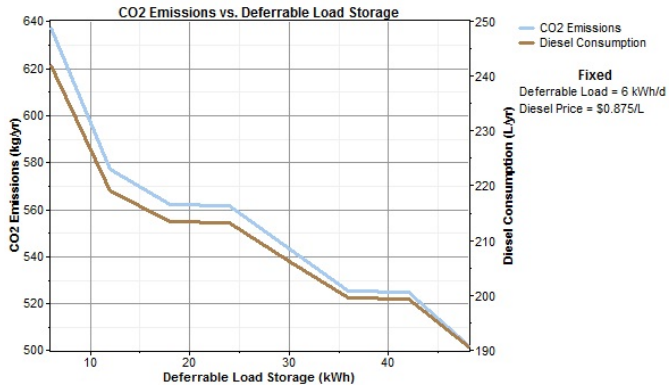

Fig. 9. CO_2 emission vs. deferrable load storage.

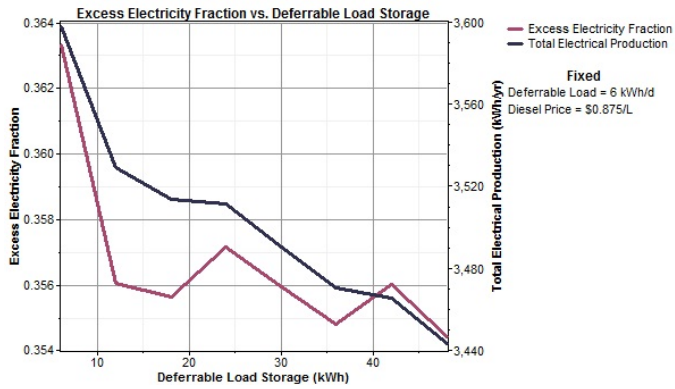

Fig. 10. Excess electricity fraction Vs. Deferrable load storage.

TABLE IV
SENSITIVITY VARIABLES

Sensitivity Variable	Input Values	Reason why this sensitivity variable was used
Deferrable Load (kWh/day)	2.67 (scaled annual average), 4, 5, 6	To find the optimum system with variable load.
Deferrable Load Storage Capacity (kW)	6, 12, 18, 24, 30, 36, 42, 48	To see how water storage capacity affects the output of the system
Diesel Price ($)	0.875 (present cost), 1, 1.5, 2	To find optimum system with a higher diesel price.

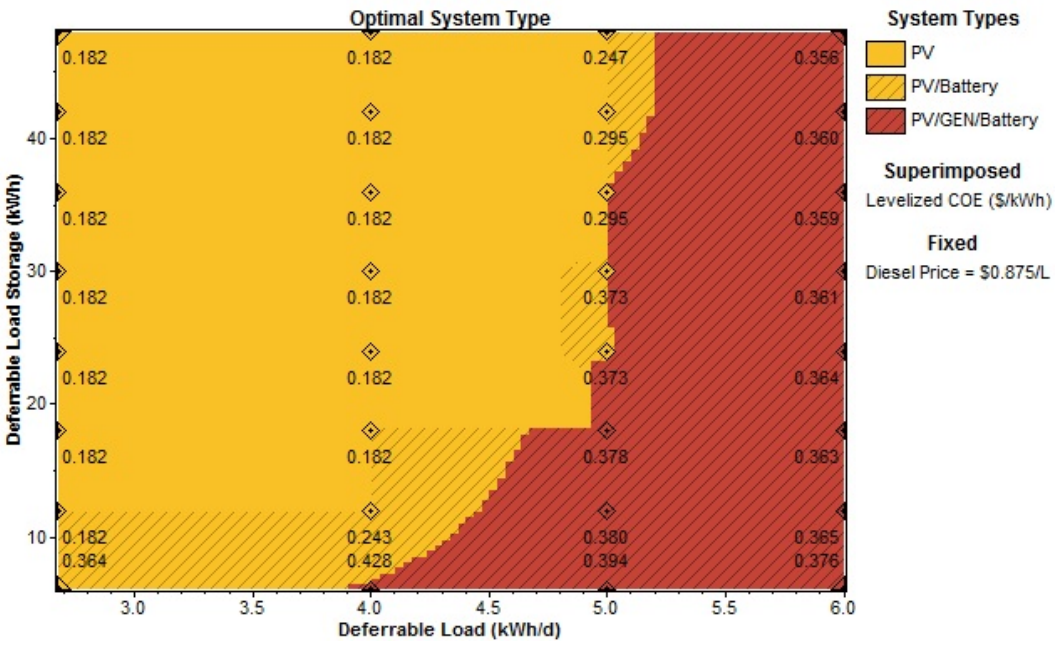

Fig. 7. Optimal system type superimposed with Levelized COE.

as shown in fig. 7. It is evident that PV has the most dominant portion in the graph. With low deferrable load storage PV needs battery backup but with high storage PV itself is sufficient. The levelized COE is as low as $0.182 with PV in operation. Interestingly using only diesel generator is not at all feasible as there is no portion of the graph with only generator shown.

By changing the axis in HOMER we can also find the graph of optimal system type with variable diesel price as shown in fig. 8. It is evident that as the diesel price increases PV becomes more feasible.

Using the line graph option fig. 9 10 shows the CO2 emissions and excess electricity fraction with the change of deferrable load storage. It is very clear from the graph that if there is low deferrable load storage which is water storage tank in our case, there will be a frequent need for diesel generator operation. PV arrays need solar insolation which is not a continuous source of energy and therefore use of a larger storage tank is important. With a larger storage tank added in the pump system will give higher system stability with lower possible COE.

Besides this, lower storage capacity will increase the excess electricity fraction significantly which can be as high as 83.2% of the total production. To lower this excess electricity fraction either we have to use larger storage tank or we can supply this excess electricity to local consumers or can run other agricultural equipment.

VII. CONCLUSIONS

From the above analysis the following conclusions can be made:

01. Stand-alone operation of diesel generator for irrigation purposes is not at all feasible in Bangladesh. So, diesel generators should be replaced with PV powered motor-pump systems as soon as possible.

02. Use of a larger water storage tank is very important. CO2 emissions and excess electricity fractions can be lowered to 0% if a larger storage tank is used.

03. If a larger storage tank is not available then the excess electricity can be supplied to the local consumers or can be used in other agricultural energy need.

ACKNOWLEDGMENT

We would like to express our gratitude to Institute of Energy, University of Dhaka for aiding with technical support. We would also like to thank Bangladesh Meteorological Department (BMD), Bangladesh Agricultural Development Corporation (BADC), Bangladesh Agricultural Research Council (BARC), and Dhaka Electric Supply Company Limited (DESCO) for their data and support.

REFERENCES

[1] M. A. H. Chowdhury, M. S. Hassan, "Handbook of Agricultural Technology", BARC, 2013.

[2] S. G. Hussain, A. Iqbal, "Research priorities in Bangladesh agriculture", BARC Feb 2011.

[3] (2015) Bangladesh Agricultural Development Corporation (BADC) website. [Online]. Available: http://www.badc.gov.bd/

[4] (2015) Bangladesh Agricultural Research Council website. [Online]. Available: http://www.barc.gov.bd/

[5] (2015) Dhaka Electric Supply Company Limited (DESCO) website. [Online]. Available: https://www.desco.org.bd/

[6] (2015) Bangladesh Meteorological Department (BMD) website.[Online]. Available: http://www.bmd.gov.bd/?/home/

[7] (2015) NASA data. [Online]. Available: http://eosweb.larc.nasa.gov/sse/

[8] T. Lambert, P. Gilman, P. Lilienthal, "Micropower system modelling with HOMER", NREL.

[9] HOMER software help index (Version 2.68beta).

[10] M. T. Khan, S. Sarkar, S. Hossain, A. U. Ahmed, and B. B. Pathik, "The Feasibility Study of Solar Irrigation: Economical Comparison between Diesel and Photovoltaic Water Pumping Systems for Different Crops", International Conference on Electrical Information and Communication Technology (EICT), 2013.

[11] (2015) Lorentz Pump System data sheet. [Online]. Available: http://www.lorentz.de/(accessed on 10 July 2015).

[12] M. Kolhe, J. C. Joshi, and D. P. Kothari, "Performance Analysis of a Directly Coupled Photovoltaic Water-Pumping System", IEEE Trans. Energy Conversion, vol. 19, no. 3, pp. 613-618, September 2004.

[13] P.K. Koner, "Optimization techniques for a photovoltaic water pumping system", Renewable Energy, Vol. 6, No. 1, pp. 53-62, 1995.

[14] A. Braunstein and A. Kornfield, "Analysis of solar powered electric water pump", Solar Energy, vol. 27, no.3, pp. 235-240, 1981.

[15] Y. R. Hsiao and B. A. Blevins, "Direct coupling of photovoltaic power source to water pumping system". Solar Energy, Vol. 32, No. 4, pp. 489-498, 1984.

[16] S. I. Khan, M. M. R. Sarkar, and M. Q. Islam, "Design and alalysis of a low cost solar water pump for irrigation in Bangladesh", Journal of Mechanical Engineering, Vol. ME 43, No. 2, December 2013.

[17] M. A. Hasnat, M. N. Hasan, and N. Hoque, "A brief study of the prospect of hybrid solar irrigation system in Bangladesh", International Conference on Mechanical, Industrial and Energy Engineering 2014, 25-26 December, 2014, Khulna, Bangladesh.

[18] S. M. S. Reza, and M. N. I. Sarkar, "Design and Performance Analysis of a Directly-Coupled Solar Photovoltaic Irrigation Pump System at Gaibandha, Bangladesh", 3rd International Conference on Green Energy & Technology (ICGET) 2015, 11-12 September, 2015, Dhaka, Bangladesh.

[19] M. Al-Smairan, "Application of photovoltaic array for pumping water as an alternative to diesel engines in Jordan Badia, Tall Hassan station: Case study", Renewable and Sustainable Energy Reviews, Vol. 16, (2012), pp. 45004507.

[20] J.K. Kaldellis, G.C. Spyropoulos, K.A. Kavadias, and I.P. Koronaki, "Experimental validation of autonomous PV-based water pumping system optimum sizing", Renewable Energy, Vol. 34, (2009), pp. 11061113.

Cost Analysis of Rural Distribution Systems with Three Phase and Single Phase Tap Lines

S. K. Roy
Department of Electrical and Electronic Engineering
Khulna University of Engineering and Technology
Khulna-9203, Bangladesh
Email: engrsanjib2010@gmail.com

N. K. Roy
Department of Electrical and Electronic Engineering
Khulna University of Engineering and Technology
Khulna-9203, Bangladesh
Email: nkroy@eee.kuet.ac.bd

***Abstract*—Rural Distribution Systems (RDSs) are expanding abruptly day by day. With this continuous expansion, the distribution loss is increasing deliberately as a coherent parameter. Constructing single phase HT (high tension) line, it becomes more alarming with respect to loss as well as system management. This paper highlights the advantages of three phase tap lines for the reduction in line loss compared to single phase. A cost analysis is carried out by designing all HT lines of RDSs with three phase taps instead of single phase taps and the obtained result is compared with the single phase tap line. Then, an optimum length of single phase tap line is determined using simplex method for linear programming considering the cost of three phase tap line as a standard. The results show that more area can be electrified using three phase tap lines compared to the single phase tap line with the same cost.**

Keywords—cost analysis; power loss; rural distribution system (RDS); single and three phase tap line; simplex method.

I. INTRODUCTION

The primary objective of a distribution power system design is to deliver reliable power to the remotest consumer with maximum efficiency and minimum cost [1]-[3]. As consumer, so load, is increasing, to meet the objective it is essential to think about the restructuring of power distribution systems [4]-[9].

Bangladesh Rural Electrification Board (BREB), among all the Electricity Distribution Utility of Bangladesh, is the largest having 2,70,000 Km of distribution line with 1,22,00,000 nos. of different category consumers purchasing 18,80,000 MWhr energy per month. The average sales per month is 16,10,000 MWhr to the consumers. Therefore, 2,70,000 MWhr of energy waste as system loss [10], which is 12.92% of the total purchased energy. This loss includes mostly technical loss, as well as minor non-technical loss. One of the important factors to increase technical loss is the design standards and considerations for the construction of HT (High Tension) and also LT (Low Tension) lines adopted so far.

As it is known that from the very beginning BREB follows the standard to construct three phase backbone distribution HT lines of 11 kV voltage with both three phase and single HT taps of 11 kV and 6.35 kV voltage, respectively and both three phase and single phase LT lines of 0.415 kV and 0.23 kV voltage, respectively. Single phase HT and LT lines are taken into consideration considering the lower construction cost for rural people. If we construct a single phase line, we do not have any option to construct other than single phase line until it is renovated or converted. When we start with a few span of single phase line, due to Area Coverage Rural Electrification (ACRE) [11], it becomes a line of fifty spans, even hundred-fifty spans, of single phase line, which ultimately creates operational problem, unbalance system and at the same time increases line loss, consequently system loss.

It is obvious that for the same load, line loss is lesser for a three phase system than that of a single phase [11]. However, the line construction and maintenance cost in a three phase system is higher than that of a single phase system. With the practical hazard for operation management, system management, and loss management, a narrow thinking was started-'Are single phase distribution lines cost effective with all respect?' To be clear from a misty thinking, this research has conducted over both single phase and three phase lines considering line loss, construction and maintenance cost for their whole life, which is normally considered as 30 years for a rural distribution line.

Traditional tapping lines of BREB are single phase which produce an unbalance system due to the loading in phases individually and it is not expected from system management and economical viewpoints. Therefore, three phase power distribution systems may be the right choice for their superior power carrying capability at a reduced cost. However, it needs a rigorous investigation before implementing three phase taps to avoid unnecessary cost.

In this paper, a RDS is designed with single phase and three phase taps for a comparative analysis. Moreover, an Excel Solver [12, 13] is used to calculate the optimum length of the single phase tap lines which determines the area coverage by tap lines in the RDS. The system is optimized using simplex algorithm for linear programming (LP). In the next of this paper, following topics are discussed: Why three phase?, losses in power distribution system, costs considered, Excel solver algorithm, case study and conclusion.

978-1-4673-9257-0/15/$31.00 ©2015 IEEE

II. WHY THREE PHASE?

A three phase line generates three individual "waves" of power which joins three alternating waves of the same frequency, each 120 degrees out of phase with each other. The power in a three phase power supply never goes down to zero, but in single-phase the power goes down to zero 3 times for every cycle as shown in Fig.1. Thus, in a three phase power supply, the power delivered is constant [14]. To fulfill the requirement of balance system and to avoid neutral **c**urrent in grounded Y-connected line, which incur additional loss, three phase lines are better choice for transmitting power.

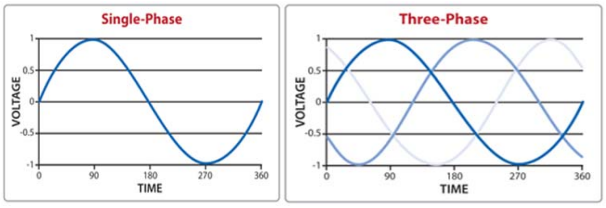

Fig.1. Single phase and three phase wave shape [14].

III. LOSSES IN POWER DISTRIBUTION SYSTEM

Losses in power distribution system is a term which may express as the difference between the total power received by a 11 kV feeder and total power delivered to the individual consumer. If P_R is the power received and P_D is the total power delivered to the consumer connected to this feeder; then power loss P_{loss} will be [11]

$$P_{loss} = P_R - P_D \quad (1)$$

A. Categorization of Losses:

The power distribution losses are commonly classified into two categories: 1) technical loss and 2) non-technical Loss.

1) Technical Losses: Technical losses are internal to the distribution power system and occur in the equipment installed in that system. In RDS, it occurs for the power dissipation in the lines (HT/LT), distribution transformers, junctions and joints, service drops, etc. [15].

2) Non-Technical Losses: Non-technical losses occur due to actions external to the power system, which includes primarily of electricity theft, not running meters and errors in accounting and record-keeping [15].

B. Mathematical Representation of Technical Losses:

In a system, technical loss means the power losses incurred by the physical properties of components connected to it. The power loss, P_{loss} (kWh) is proportional to the total line resistance (R_T) of the conductor and the square of the current (I) flows through that portion of line in Amps [11].

So, power loss is [11]

$$P_{loss} \text{ /Month} = (I^2 \text{ x } R_T \text{ x LsF x Total Hour})/1000 \text{ kWh} \quad (2)$$

where, R_T = No. of phase x R_p x line length in Km
R_p= Resistance per phase per Km of line.
Ls.F. = Loss Factor
= 0.85*(Load factor)^2+0.15*(Load factor) (3)

Load factor is defined as the ratio of average power delivered to the peak load of a certain period. The value of load factor for a 11 kV feeder of the RDS varies between 40% to 60%.

IV. COSTS CONSIDERED

Rural Distribution lines are constructed by both wooden poles and SPC (Spun Pre-stressed Concrete) poles with wooden cross-arms, GI hardware and ACSR (Aluminum Conductor Steel Reinforced) conductors. Taken geographical condition into account, the life of constructed distribution lines is considered to be almost 30 years.

In this paper, to optimize the design cost, following costs are considered [15]:

1) Cost of technical loss unit: The total cost for technical loss is calculated multiplying the technical loss unit (kWh) by per unit rate (Tk.), which occurs for whole of the life if the line is under energized condition.

2) Cost of distribition line construction: The costs for construction of distribution lines include material costs and labour costs, which occur once in its life.

3) Cost of maintenance: The maintenance cost of lines is to maintain the line in working condition which includes reparing, ROW (Right of Way) clearing, etc. This cost also occurs over whole life of the line until it becomes idle.

V. EXCEL SOLVER AS OPTIMIZATION TOOL

The Microsoft Excel Solver is very popular and the most widely used general purpose optimization tool. The Microsoft Excel Solver combines the functions of a graphical user interface (GUI), an algebraic modeling language like general algebraic modeling system (GAMS) or a mathematical programming language (AMPL), and optimizers for linear, nonlinear, and integer programs [12, 13].

The flowchart of the proposed methodology is shown in Fig. 2. The algorithm is described below.

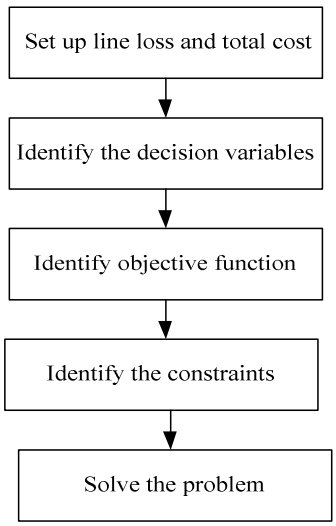

Fig. 2. Flowchart of the proposed methodology.

• *Data set up:* The first step of the proposed method is to set up distribution line loss data and total cost which includes line loss cost, construction cost and maintenance cost of the line.

• *Decision variables:* The decisions of the problem are represented as decision variables. The length of single phase tap is considered here as a decision variable.

• *Objective function:* The objective of the problem is to minimize the total cost incurred by line loss, construction and maintenance cost. For this purpose, the target value is set up which is the difference between the cost of three phase and single phase tap line.

• *Constraints:* The limitations or requirements of the problem are expressed as inequalities or equations in decision variables. The upper and lower limit of the considered tap line is specified as constraints.

The Excel Solver builds a representation of the model suitable for an optimizer by extracting the optimization problem from the spreadsheet formulas. For a linear programming (LP) problem, the focus of this model representation is the LP coefficient matrix, which in general terms, is the Jacobian matrix of partial derivatives of the problem functions (objective and constraints) with respect to the decision variables. For a linear problem, the matrix entries are constant and only need to be evaluated once at the start of the optimization [13].

The Excel Solver uses finite differences and supports all of Excel's built-in functions as well as user-written functions. In calculating finite differences, the [*i,j*]-th element of the Jacobian matrix is approximated by the formula [13].

$$\frac{|f_i(x+\delta e_j)-f_i(x)}{\delta} \quad \text{where } \delta = eps\,|1+x_j| \qquad (4)$$

The solver perform linearity test after it had obtained a solution using the simplex method. It uses these solution values x^* and the initial values x^0 for the variables, to check that the objective and each constraint function $f_i(x)$ until satisfied the following condition [13].

$$|f_i(x^*)-(f_i(x^0)+\nabla f_i(x^0)(x^*-x^0))| \le tol \qquad (5)$$

where $\nabla f_i(x^0)$ is the function gradient and ≥ is the precision value in the solver options dialog box with a default value of 10^{-6}.

The Solver results dialog box is displayed whenever the solver stops and allows the user to keep the solution or restore the original values of the variable cells to generate one or more reports.

VI. CASE STUDY

Let us consider a distribution line feeding from a sub-station, which we shall call as three phase back bone line. Line to line voltage of the backbone line is 11 kV. The line is constructed by # 4/0 ACSR conductor. The feeder backbone line distributes 1.6 MW load. We observe in the next study what will happen, what is the effect on system loss if tap lines from the backbone are constructed single phase and three phase.

A. *When All Taps are Single Phase:*

Consider 10 Km of backbone line for loss calculation. Current feeding at starting point for R-phase is 110 Amps, Y-phase is 85 Amps & B-phase is 75 Amps. For single phase tap the system is unbalance at the starting. A phase balancing is critical for this type of long and loaded single phase tap.

Here in R-phase there are two single phase tap. First tap is 5 Km and second tap is 10 Km apart from the starting point. First tap carries 30 Amps current, second tap carries 60 Amps. In Y-phase there are also two single phase tap. First tap is 3 Km and second tap is 8 Km apart from the starting point. Here, first tap carries 30 Amps current, second tap carries 45 Amps. In B-phase there are two single phase tap. First tap is 4 Km and second tap is 9 Km apart from starting point. First tap bears 30 Amps current, second tap carries 36 Amps. The connection and currents are shown in Fig. 2 given below:

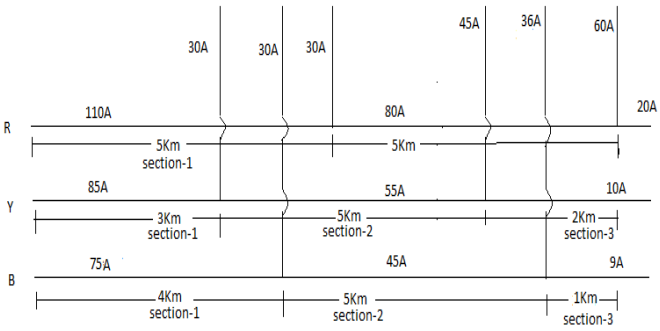

Fig. 2. Three phase system with single phase tap

For simplicity we consider load factor=0.5 for all over the line. Also, consider all tap lines (single phase & three phase) are constructed by #3 ACSR bare conductor. Resistance per Km per phase of #4/0 ACSR & #3 ACSR is R_p & R_t , value of which is 0.3522 Ohm & 1.3946 Ohm, respectively.

So, loss factor = 0.85*(Load factor)^2+0.15*(Load factor)
= 0.85*(0.5)^2+0.15*(0.5)
= 0.2875

Sample loss calculation for Section-1, Tap-1 is given below:

R-phase, Section-1:

Line Length : 5 Km
Current thru the section , I_1 : 110 Amps
Line Conductor : # 4/0

So, P_{loss} /Month = (I_1^2 x R_T x L.F x Total Hour)/1000 KWh
Here, R_T = 1 x 0.3522 x 5 Ohm=1.761 Ohm
P_{loss} /Month = [(110)^2 x 1.761 x 0.2875x720)]/1000 KWh
= 4410.77 KWh

R-phase, Tap-1:

Line Length : 5 Km
Current thru the section , I_{rt1} : 30 Amps
Line Conductor : # 3 ACSR

So, P_{loss} /Month = (I_{rt1}^2 x R_T x L.F x Total Hour)/1000 KWh
Here, R_T = 1 x 1.3946 x 5 Ohm=6.973 Ohm
P_{loss} /Month = [(30)^2 x 6.973x0.2875x720)]/1000 KWh
= 1299.07 KWh

Calculation for other sections and taps have summarized in Table I considering construction cost of three phase line of #4/0 ACSR per Km is Tk. 13,00,000, single phase line of #3 ACSR per Km is Tk. 9,00,000.

B. *When All Taps are Three Phase:*

Consider the same 10 Km of backbone line. Total load flowing through the phases was (110+85+75) = 270 Amps. So, the average load per phase is 90 amps. If all the taps or minimum the long and loaded taps are three phase, then we can get balance system, which was not easily possible for the single phase system. So, we can consider in this case, per phase current is equal and the value is 90 amps.

TABLE I. THREE PHASE LINE WITH SINGLE PHASE TAP

	A	B	C	D	E	F	G	H	I	J
1	Table 1 Three Phase Line With Single Phase Tap									
2										
3	Sl no.	Load, Amp	Resistance	Length, km	Loss per month, kwh	Loss in whole life, KWh	Loss in whole life, Tk	Cost for Line Construction/ Km, TK	Total Cost for Line Construction, TK	Maintenance cost in whole life, Tk
4	1	110	0.3522	5.00	4410.78	1587879.61	9527277.67	1300000	6500000	140000.00
5	2	30	1.3946	5.00	1299.07	467665.16	2805990.98	900000	4500000	105000.00
6	3	80	0.3522	5.00	2332.97	839870.21	5039221.25	1300000	6500000	140000.00
7	4	60	1.3946	15.00	15588.84	5611981.97	33671891.81	900000	13500000	315000.00
8	5	85	0.3522	3.00	1580.22	568880.84	3413285.02	0	0	0.00
9	6	30	1.3946	5.00	1299.07	467665.16	2805990.98	900000	4500000	105000.00
10	7	55	0.3522	5.00	1102.69	396969.90	2381819.42	0	0	0.00
11	8	45	1.3946	12.00	7014.98	2525391.89	15152351.31	900000	10800000	252000.00
12	9	10	0.3522	2.00	14.58	5249.19	31495.13	0	0	0.00
13	10	75	0.3522	4.00	1640.37	590533.74	3543202.44	0	0	0.00
14	11	30	1.3946	10.00	2598.14	935330.33	5611981.97	900000	9000000	210000.00
15	12	45	0.3522	5.00	738.17	265740.18	1594441.10	0	0	0.00
16	13	36	1.3946	7.00	2618.92	942812.97	5656877.82	900000	6300000	147000.00
17	14	9	0.3522	1.00	5.91	2125.92	12755.53	0	0	0.00
18					42244.71	15208097.07	91248582.44		61600000.00	1414000.00
19									Total cost,1-0	154262582.44

For the first, we consider the tap which was connected in Y-phase in the single phase tapping. The load was 30 amps. If the tap was constructed in three phase, we can get balanced load of 10 Amps per phase. With the same consideration, second tap which is 4 Km apart from the starting point, carries 10 Amps per phase. Thirdly, the tap is 5 km apart from starting point and carries balanced load of 10 amps per phase. Fourth tap which is 8 Km apart from starting point, carries balanced load of 15 amps per phase. For fifth and sixth tap which are apart 9 Km & 10 km from the starting point and carries balanced load of 12 Amps & 20 Amps per phase. The connection and currents are shown in Fig. 3 given next.

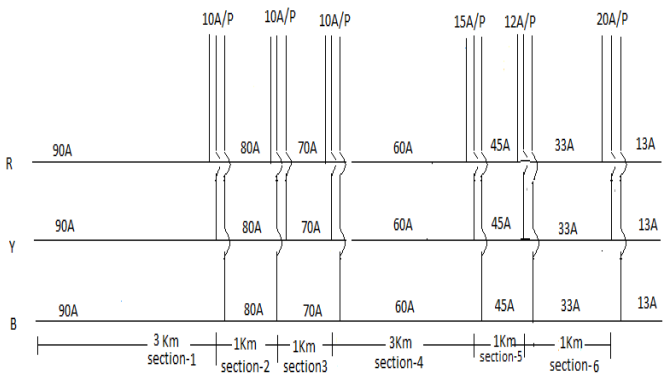

Fig. 3. Three phase system with three phase tap.

Sample loss calculation for Section-1, Tap-1 is given below:

Section-1:

Line Length : 3 Km
Current thru the section , I_{r1} : 90 Amps
Line Conductor : # 4/0

So, P_{loss} /Month = $(I_1^2 \times R_T \times L.F \times \text{Total Hour})/1000$ kWh
Here, R_T = 3 x 0.3522 x 5 Ohm=5.283 Ohm
P_{loss} /Month = $[(90)^2 \times 5.283 \times 0.2875 \times 720)]/1000$ KWh
= 5314.80 kWh

Tap-1:

Line Length : 5 Km
Current thru the section , I_{t1} : 10 Amps
Line Conductor : # 3 ACSR

So, P_{loss} /Month = $(I_{t1}^2 \times R_T \times L.F \times \text{Total Hour})/1000$ kWh
Here, R_T = 3 x 1.2673 x 5 Ohm=19.0095 Ohm
P_{loss} /Month = $[(10)^2 \times 19.0095 \times 0.2875 \times 720)]/1000$ kWh
= 393.50 kWh

Calculation for other sections and taps have summarized in Table II given below.

TABLE II. THREE PHASE LINE WITH THREE PHASE TAP

	A	B	C	D	E	F	G	H	I	J
1	Table 2 Cost for Three Phase Line with Three Phase Tap									
2										
3	Sl no.	load, amps	resistance	length, km	Loss per month, KWh	Loss in whole life, KWh	Loss in whole life, Tk	Cost for Line Construction/ Km, TK	Total Cost for Line Construction, TK	Maintenance cost in whole life, Tk
4	1	90	0.3522	3	5314.80	1913329.32	11479975.91	1300000	3900000	84000.00
5	2	10	1.2673	5	393.50	141658.79	849952.76	1200000	6000000	140000.00
6	3	80	0.3522	1	1399.78	503922.12	3023532.75	1300000	1300000	28000.00
7	4	10	1.2673	10	786.99	283317.59	1699905.53	1200000	12000000	280000.00
8	5	70	0.3522	1	1071.71	385815.38	2314892.26	1300000	1300000	28000.00
9	6	10	1.2673	5	393.50	141658.79	849952.76	1200000	6000000	140000.00
10	7	60	0.3522	3	2362.13	850368.59	5102211.51	1300000	3900000	84000.00
11	8	15	1.2673	12	2124.88	764957.49	4589744.93	1200000	14400000	336000.00
12	9	45	0.3522	1	442.90	159444.11	956664.66	1300000	1300000	28000.00
13	10	12	1.2673	7	793.29	285584.13	1713504.77	1200000	8400000	196000.00
14	11	33	0.3522	1	238.18	85745.50	514472.99	1300000	1300000	28000.00
15	12	20	1.2673	15	4721.96	1699905.53	10199433.17	1200000	18000000	420000.00
16					20043.63	7215707.33	43294244.00		77800000.00	1792000.00
17									Total cost,3-Ø	122886244.00

Analyzing two costs mentioned in Table I and Table II, it is clear that the cost for three phase line with single phase tap is higher than that of all three phase tap. However, another objective of this paper is to compare the area covered by the three phase tap and single phase tape considering the cost of Table II as standard.

If the cost of single phase line becomes same as that of three phase line i.e. cost difference reduced to '0' (zero), then that will be the optimal design with single phase. This can be done by Excel Solver Program. To obtain objective function, the target cell (J22) is set as '0' and this zero may be achieved by changing the length of single phase line i.e. cell no. D5, D7, D9, D11, D14, D16 assuming the constraints of this cell value not below zero i.e. no negative value is allowed. Maximum value is set as the exact length of single phase line. Table III shows the optimized length of single phase tap line in Column D.

TABLE III. DIFFERENCE MINIMIZES TO ZERO BY EXCEL SOLVER

	A	B	C	D	E	F	G	H	I	J
1	Table 1 Three Phase Line With Single Phase Tap									
2										
3	Sl no.	Load, Amp	Resistance	Length, km	Loss per month, kwh	Loss in whole life, KWh	Loss in whole life, Tk	Cost for Line Construction/ Km, TK	Total Cost for Line Construction, TK	Maintenance cost in whole life, Tk
4	1	110	0.3522	5.00	4410.78	1587879.61	9527277.67	1300000	6500000	140000.00
5	2	30	1.3946	3.09	803.29	289183.57	1735101.44	900000	2782602.121	64927.38
6	3	80	0.3522	5.00	2332.97	839870.21	5039221.25	1300000	6500000	140000.00
7	4	60	1.3946	10.92	11353.12	4087123.26	24522739.55	900000	9831849.835	229409.83
8	5	85	0.3522	3.00	1580.22	568880.84	3413285.02	0	0	0.00
9	6	30	1.3946	3.09	803.29	289183.57	1735101.44	900000	2782602.121	64927.38
10	7	55	0.3522	5.00	1102.69	396969.90	2381819.42	0	0	0.00
11	8	45	1.3946	9.19	5371.52	1933746.03	11602476.15	900000	8269788.62	192961.73
12	9	10	0.3522	2.00	14.58	5249.19	31495.13	0	0	0.00
13	10	75	0.3522	4.00	1640.37	590533.74	3543202.44	0	0	0.00
14	11	30	1.3946	8.09	2102.36	756848.74	4541092.42	900000	7282602.121	169927.38
15	12	45	0.3522	5.00	738.17	265740.18	1594441.10	0	0	0.00
16	13	36	1.3946	4.77	1786.06	642982.26	3857893.58	900000	4296491.865	100251.48
17	14	9	0.3522	1.00	5.91	2125.92	12755.53	0	0	0.00
18					34045.33	12256317.02	73537902.13		48245936.68	1102405.19
19									Total cost,1-Ø	122886244.00
20									Total cost,3-Ø	122886244.00
21										
22									Difference	0.00

Figure 4 shows the original and optimized lengths of the single phase tap lines from which it can be seen that lengths of all the single phase taps are reduced after optimization. These results signify that single phase taps will cover less area compared to three phase tap lines. Thus, three phase taps are cost effective for covering the whole area of the considered RDS.

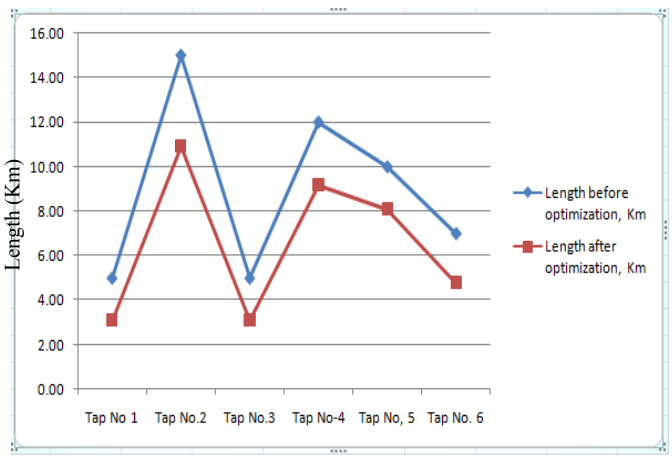

Fig. 4. Length of single phase tap before and after optimization.

VII. CONCLUSION

This paper concentrates on the analysis of the RDS with different tap lines and verifies the effectiveness of three phase tap line over single phase. An optimization model for single phase taps is developed considering the cost of all three phase taps as a standard. It is found that three phase taps provide the cost effective solution to reach all the consumers in terms of length of the considered distribution network. Therefore, to keep the door open for further expansion of reliable distribution line cost effectively, which is the main objective of the area coverage rural electrification, this paper may be an initiator of future days' design. Ultimately, this may contribute in the process of overall national development by electrifying more rural area.

REFERENCE

[1] D. Zhang, Z. Fu, and L. Zhang, "Joint optimization for power loss reduction in distribution systems," IEEE Trans. on Power Systems, vol. 23 , no. 1, pp. 161-169, 2008.

[2] T.T. Erbato and T. Hartkopf, "Smarter micro grid for energy solution to rural Ethiopia," IEEE PES Innovative Smart Grid Technologies (ISGT), pp. 1-7, 16-20 Jan. 2012.

[3] S.M. Abdelkader, "Characterization of transmission losses", IEEE Trans. on Power Systems, vol. 26, no. 1, February 2011.

[4] I. Hussain and A.K. Roy, "A new heuristic approach for optimal reconfiguration of distribution systems for improvement of power delivery efficiency through loss reduction," International Conference on Advances in Engineering, Science and Management (ICAESM), pp. 571-576, 30-31 March 2012.

[5] Joon-Ho Choi and Jae-Chul Kim, "Network reconfiguration at the power distribution system with dispersed generations for loss reduction," IEEE Power Engineering Society Winter Meeting, pp. 2363 – 2367, 23-27 Jan. 2000.

[6] R.J. Sarfi, M.M.A. Salama, and A.Y. Chikhani, "Distribution system reconfiguration for loss reduction: a new algorithm based on a set of quantified heuristic rules," Canadian Conference on Electrical and Computer Engineering, 25-28 Sep 1994.

[7] D. Shirmohammadi and H.W. Hong, "Reconfiguration of electric distribution networks for resistive losses reduction," IEEE Trans. Power Delivery, vol. 4, no. 2, pp. 1402–1498, Apr. 1989.

[8] M.W. Siti, D.V. Nicolae, A.A. Jimoh,and A. Ukil ,"Reconfiguration and load balancing in the LV and MV distribution networks for optimal performance," IEEE Trans. on Power Delivery, vol. 22, no. 4, pp. 2534 – 2540, Oct 2007.

[9] C. Cavelluccil and C. Lyra, "Minimization of energy losses in electric power distribution systems by intelligent search strategies," International Trans. in Operational Research, vol. 4, no. 1, pp. 23-33, Jan 1997.

[10] Bangladesh Rural Electrification Board, MIS Report June 2015, www.reb.gov.bd

[11] Engineering and Staking Manual, BREB Instruction No. 100-21.

[12] Frontline Systems Inc. 1994, Solver User Guide: Premium, Quadratic, and Large-Scale LP Solvers.

[13] D. Fylstra, L. Lasdon, J. Watson and A. Waren, "Design and use of the Microsoft Excel solver", INTERFACES, vol. 28, no. 5, Sept-Oct 1998, pp. 29-55.

[14] http://www.tripplite.com/products/single-vs3-phase, accessed on 3 Sept. 2015.

[15] S. Ghosh, "Loss reduction and efficiency improvement: a critical appraisal of power distribution sector in India," International Journal of Modern Engineering Research, vol. 2, no. 5, Sep-Oct. 2012, pp.3292-3297.

Investigation of THD on a 12-Pulse HVDC Transmission Network and Mitigation of Harmonic Currents Using Passive Filters

Sanjib Kumar Nandi, Ridown Rashid Riadh, Md. Siddikur Rahman

American International University-Bangladesh, Dhaka, Bangladesh

sanjib.eee.aiub@gmail.com, rashidridown@gmail.com, rahman.siddikur286@gmail.com

Abstract— **Due to the different types of conversion purposes lots of harmonic creates in DC operated power system. Our goal is to minimize the harmonics at a certain level. The main focus of this research is to explain the effects of harmonics in a 12-pulse High Voltage Direct Current (HVDC) transmission network and take corresponding steps to reduce those effects. It includes harmonic reduction technique to improve the power quality of the HVDC transmission system. This paper also explains how harmonic distortion in HVDC network is one of the important problems associated with power quality and creates several disturbances to the overall power system. In this paper, simulation results were developed on the basis of bus no 1 and 2 of an ideal HVDC transmission Link where there are a lot of harmonics created primarily both in voltage and current due to the presence of Transformer, Converter Devices and Nonlinear Loads. After using passive filter, this harmonic level will be minimized at a certain point which is explained in details on this paper with practical justification.**

Keywords—Harmonics, Total Harmonic Distortion (THD), Transmission network, HVDC Transmission, Passive Filter, Harmonic Reduction

I. INTRODUCTION

In a High voltage direct current (HVDC) system, from the transmitting station AC voltage is being converted into DC voltage with the help of a rectifier and then DC power is transmitted through the transmission line. After that at the receiving station DC power is being reconverted into AC power through an inverter and the power is supplied in the system [1]. When compared to the AC transmission, it is robust against a disturbance and improves a dynamic characteristic of AC power system and lowers the short circuit capacity as voltage, current and transmission power in the DC transmission can rapidly be controlled [1, 2]. But due to various conversion purposes and the rapid uses of nonlinear loads & power electronic devices the harmonic current distortion of the DC transmission system is a highly concerned issue.

In power system design and operation, controlling and eliminating such harmonics have been a great concern for the power engineers. Therefore, in power system planning, control, and operation the HVDC power system harmonic analysis is essential [3]. Harmonic Studies are also important in respect to avoid damages due to excessive harmonic currents in transformers and capacitor banks, to ensure that due to excessive harmonic voltage distortion sensitive electronic equipment will not malfunction and to satisfy the utility's voltage and current harmonic distortion requirements.

Previously, researches have been conducted research on load behavior and harmonic contribution in various sectors of HVDC power system. For instance Capacitor behavior on harmonic distortion is investigated [2]. HVDC Transmission Systems and HVDC Power System Harmonic Analysis were discussed in [3, 4, 5 and 6]. Harmonic characteristics of new HVDC transmission system based on new converter transformer were analyzed in [7]. Harmonic reduction methods using active filters for HVDC networks were introduced in [8, 9]. Different control topologies of the HVDC network have been further developed in [15, 16 and 17].

This paper represents the results of a simulation study of Passive filter on a 12 pulse HVDC (High Voltage Direct Current) Transmission network using a system design in SimPowerSystems tools of Matlab. The objective of the study is to investigate the performance of the system's harmonic contents with and without the presence of Passive Filters. This paper is organized as follows: Section II presents a brief overview of sources of harmonics on HVDC Transmission network and their effects on the overall Power System. A brief introduction to Passive filter technique for harmonic reduction used in this study has been presented in section III. Simulation results along with the influence in harmonic contents with the appearance of Passive filters have been discussed in section IV. Some discussions and explanations of the findings have also been provided finally in section V conclude the work highlighting the major contributions.

II. HARMONICS ON 12-PULSE HVDC TRANSMISSION NETWORK

Among all power transmission systems, HVDC utilized direct current (DC) for high voltage bulk transmission of electrical power contrary to the more common alternating current (AC) systems [3, 10]. A constitutional task occurred in an HVDC system when the conversion of electrical current from AC to DC (rectifier) and from DC to AC (inverter) at the transmitting end and the receiving end respectively.

978-1-4673-9257-0/15/$31.00 ©2015 IEEE

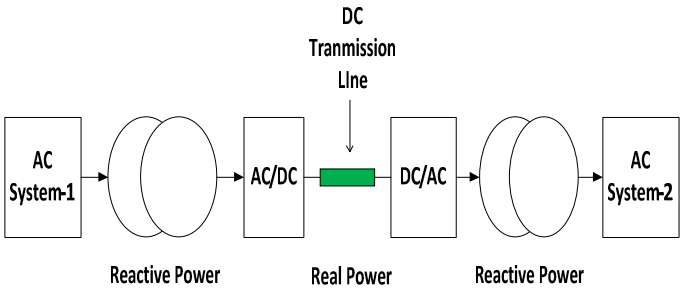

Figure.1: Simple mono polar HVDC Transmission System

HVDC transmission may be performed in two ways, mono polar and bi-polar. Mono-polar HVDC transmits power in one way whether bi-polar HVDC can transmit power in a bi - directional path.

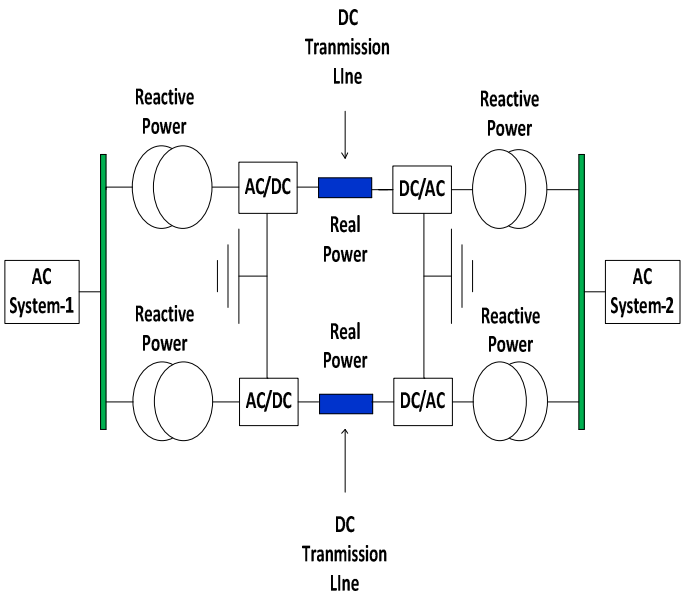

Figure.2: Bipolar HVDC Transmission system

The performance of HVDC power system is being affected by the harmonics created by the higher use of non-linear devices. Due to the presence of solid state drives or electric furnaces and capacitor banks in the HVDC power system, harmonics are generated frequently. Just as high blood pressure can cause stress and serious problems in the human body, high levels of harmonic distortion could result in problems for the utility's transmission system, the plant's distribution system, as well as the equipment under that transmission system. Most familiarize sources of HVDC harmonics and their effects are described in details below.

A. Sources of HVDC Harmonics

Since electrical signal is scrutinized, matter of harmonic is considered also. Harmonic is defined as the content of the signal whose frequency is an intrinsic multiple of the radical system frequency assembled by the generators. In HVDC power system, harmonics are assembled by some system elements which have non-linear characteristics, such as transformers, generators, power converters and electrical machines [11, 12 and 13]. Specifically, converters are the considerable sources of harmonic in an HVDC network during a steady state operation and engender harmonics on both AC and DC sides of their valve groups. The valve operation in converters of a 12 pulse HVDC link changed the original shape of voltage and current in a steady state condition, as a result of system harmonics. In HVDC power system, the interaction of primary currents and characteristic harmonic in non-linear components assembles sum as well as the difference in frequencies. The secondary voltage harmonics to the primary three phase voltage waves fetch the voltage zeros from the zeros of the primary waves unescorted and these fetches of zeros cause asymmetrical firings of the valves and non-characteristic AC harmonics are engendered.

Transformers are other acceptable source of harmonics, and this harmonics are incorporated with their design and operation. Besides, throughout the large disturbances transformers can substantially increase their contribution of harmonic and the transfer current accommodated both odd and even harmonics in an unbalanced condition. Generators such as electric machines are another acceptable source of harmonics also in HVDC power systems because of their economical as well as practical design. A machine has not operated in the saturation region if the magnetic flux of a machine has a perfectly sinusoidal distribution around the air gap. In machines, the magnetic saturation can also be contributed to the generation of harmonics like as transformers [3].

B. Effects of Harmonics

In HVDC system, harmonics reduced the efficiency of power generation and transmission. They lower the efficiency of power utilization and damage the insulation of system components also. If the system has high harmonic contents, the plant malfunction can be occurred after that the harmonics are entering the ark network and the DC line may result in the overheating of generators and capacitors, the interference with communication circuits and the instability of the system controls. The unwanted signal induced by a power system on a communication circuit degrades the transmission quality of the communication signals [11]. Harmonic resonances genesis excessive currents and over voltages which dramatically increase the losses of system devices and even can damage them. Effects of HVDC power system harmonics have been seen in rotating machines, which introduced losses [14]. The pierce of harmonics in a network cause additional network losses due to the increase of the effective values of current. Harmonic currents increased the harmonic voltage drops across circuit impedances. When the electric power is transmitted by cables, harmonic voltages increased dielectric stress in proportion to their crest voltages. The high dielectric stress shortens the useful life of the cables. The harmonics also have effects on the corona. The corona starting and extinction levels depend on peak-to-peak voltages, which are affected by

978-1-4673-9257-0/15/$31.00 ©2015 IEEE

harmonics. These types of scenario are seen in converter stations.

III. PASSIVE FILTER TECHNIQUES FOR HVDC HARMONICS REDUCTION

Due to the commutating process of the converter bridge, several characteristic and non-characteristic harmonics are generated on the 12-pulse HVDC transmission system [7].There are many ways to reduce harmonics in HVDC power system. Such as- using phase controlled thyristor rectifier, using larger DC or AC inductor, using Tuned single or multiple arm passive filter, External active filter etc. To maintain the power quality of an HVDC transmission system Active and passive filters is essential [9]. Filtering is currently the most common method used for limiting the effects of harmonics to the rest of the system [8]. Filters typically consist of Tuned Series L-C circuits and its impedance is negligible with respect to the rest of the transmission network [14].

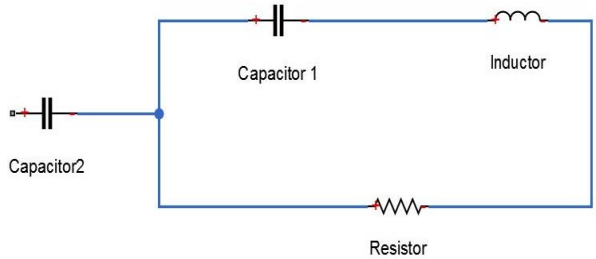

Figure.3: Basic representation of C-type high pass passive filter

Passive filters consist of resistors, inductors and capacitors. They are not expensive and are often used to restrict the harmonic currents from entering the power system thereby minimizing the effect of harmonics. Also, the passive filters are kept close to the source of harmonic generated loads. Doing so, in reducing the harmonic effect the passive filters produce better results. The passive filters create a resonance frequency in order to reduce the harmonic effect. This resonance frequency is kept away from the harmonic distortion of the nonlinear loads.

IV. DESIGN AND SIMULATION RESULTS

The peak demand of Bangladesh is of the order of 4200-5500 MW and the peak deficit is about 1000-1500 M [14]. The HVDC interconnection between the electrical grids of India and Bangladesh would facilitate transfer of 500 MW Power in either direction [14]. This section deals with the design and implementation of a Software Based system where SimPowerSystems tools of Matlab were used as the simulation tool. The proposed Simulink model consists of several parts. The block representation, including the overall system is shown in Figure 4 below.

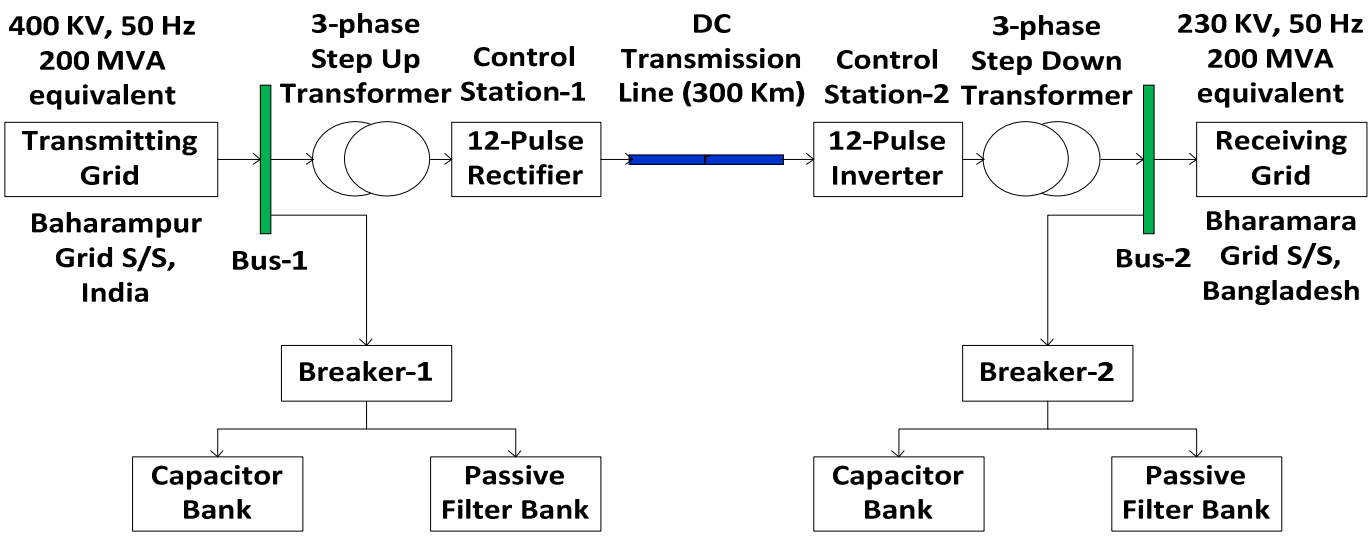

Figure.4: Test System

In the above HVDC system design in figure 4, 500 MW Power is transmitted from a 400 KV network to a 230 KV network. Both the network has a power rating of 200 MVA and frequency of 50 Hz. The converter is connected to the system with a 200 MVA Three-Phase transformer (three windings). The rectifier and the inverter are 12-pulse converters using two 6-pulse thyristor bridges, are interconnected in series through a 300 km distributed parameter line and two 30 mH smoothing reactors. Two three-phase Circuit Breakers (CB-1 & CB-2) are separately used to connect the filters set on the AC bus. The filter sets connected to Bus-1on the transmitting grid through Circuit Breaker-1 are made of the following components - one

978-1-4673-9257-0/15/$31.00 ©2015 IEEE

capacitor banks of 75 Mvar, 3x75 Mvar tuned low pass filters for removing the lower order harmonic (11th, 12th and 13th) and one 75 Mvar high pass damped filter for higher order (24th) harmonic reduction using the three-phase harmonic filter modeling. The total Mvar rating of the filter sets connected to Bus-2 is then 455 Mvar. The filter sets connected to Bus-2 on Load side through Circuit Breaker-2 are made of the following components - one capacitor banks of 91 Mvar, 3x91 Mvar tuned low pass filters for removing the lower order harmonic (11th, 12th and 13th) and one 91 Mvar high pass damped filter for higher order (24th) harmonic reduction using the three-phase harmonic filter modeling. The total Mvar rating of the filter sets connected to Bus-2 is then 455 Mvar.

From the design, four parameters Vabc_B1, Iabc_B1, Vabc_B2 and Iabc_B2 and their corresponding harmonic components (both voltage harmonics and current harmonics) has been observed for three phases. With the help of SimPowerSystems under SimScape division in Matlab results of THD have been measured for with and without passive filter connections. Simulations have been carried out with two different conditions. Condition 1 calculates the existing THD of the 12-pulse HVDC transmission network without any filter in the system. Condition 2 represents the improved THD value of the HVDC network after adding passive filters into. The results of this design and implementation considering phase sequence A are described briefly for a better comparison scenario.

Condition-1: When both the Breakers were open (Without Passive Filter)

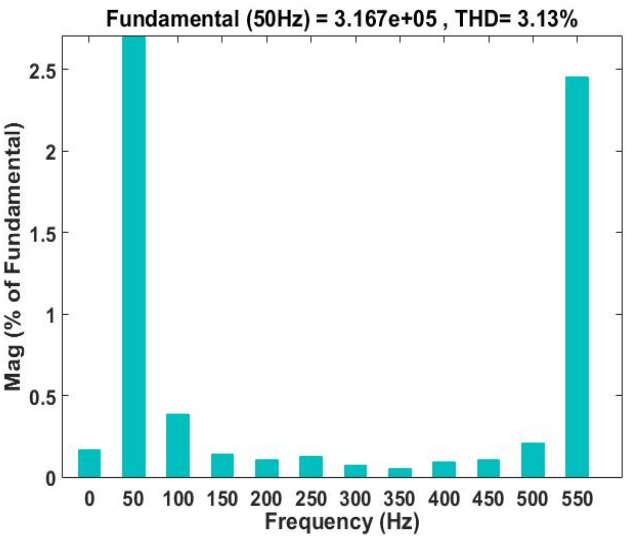

Figure.5: Voltage Harmonics (THD_V) – At Phase A of Bus 1.

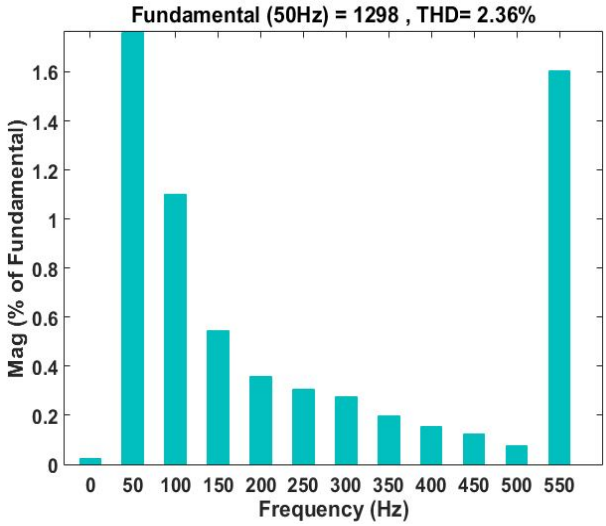

Figure.6: Current Harmonics (THD_I) – At Phase A of Bus 1.

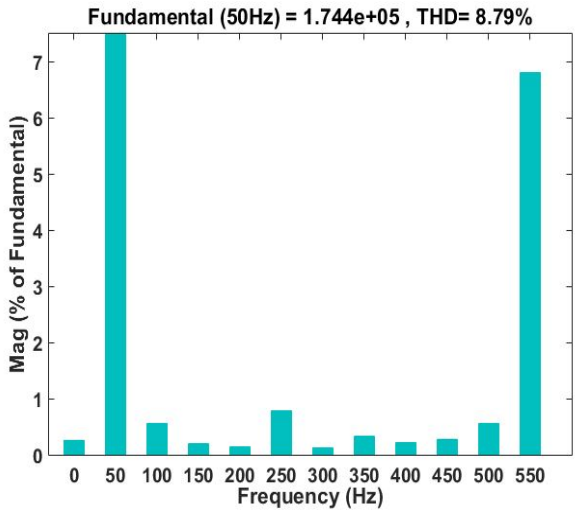

Figure.7: Voltage Harmonics (THD_V) – At Phase A of Bus 2.

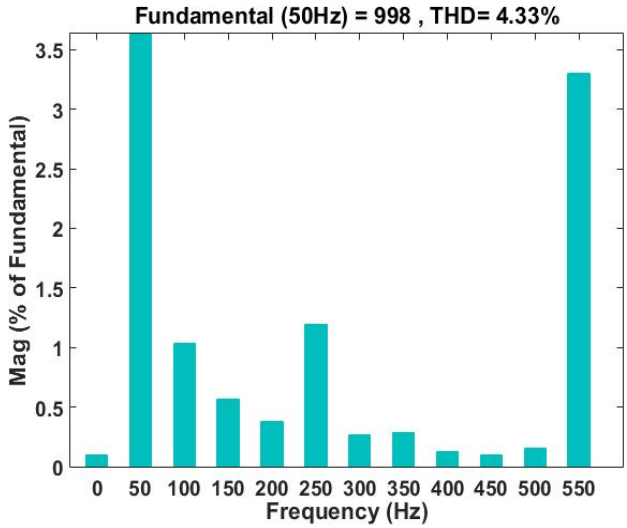

Figure.8: Current Harmonics (THD_I) –At Phase A of Bus 2.

978-1-4673-9257-0/15/$31.00 ©2015 IEEE

In the above figures (5, 6, 7, 8), THD of the system without harmonic filter has been demonstrated and found that design's THD is much higher without harmonic filter installation. At fundamental frequency, the Voltage (THD_V) & Current (THD_I) harmonic distortion level at Bus-1(phase A) are 3.13% and 2.36% respectively. And at Bus-2 (phase A), Voltage (THD_V) & Current (THD_I) harmonic distortion level are 8.79% and 4.33% respectively. That's why a second case study was performed by designing passive harmonic filter on the HVDC transmission network to examine the performance of the system and harmonic distortion level.

Condition-2: When both the Breakers were closed (With Passive Filter)

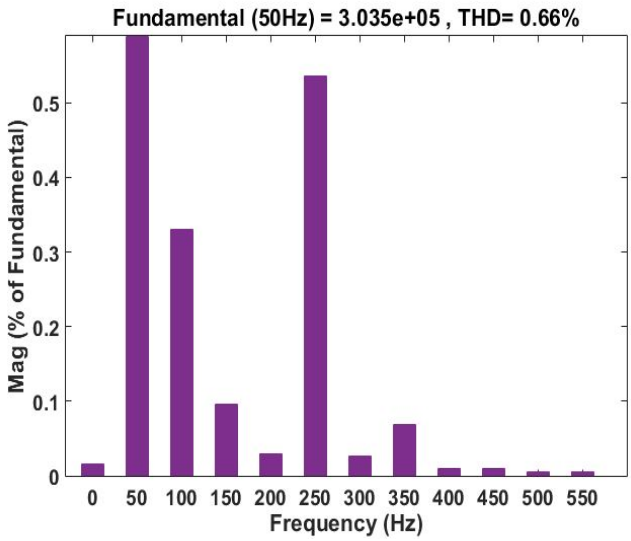

Figure.9: Voltage Harmonics (THD_V) – At Phase A of Bus 1.

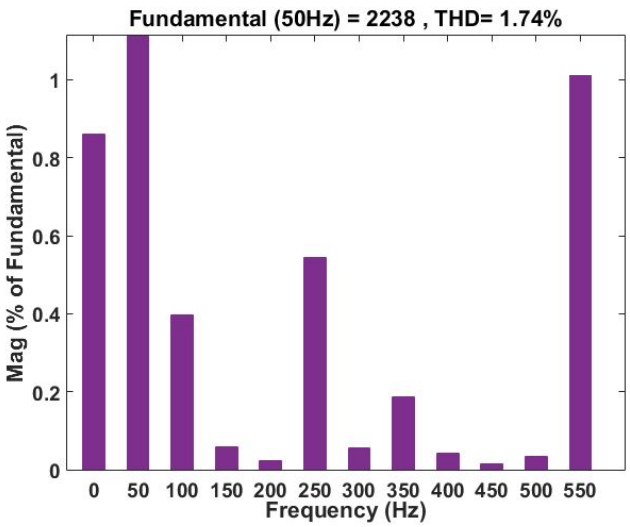

Figure.10: Current Harmonics (THD_I) – At Phase A of Bus 1.

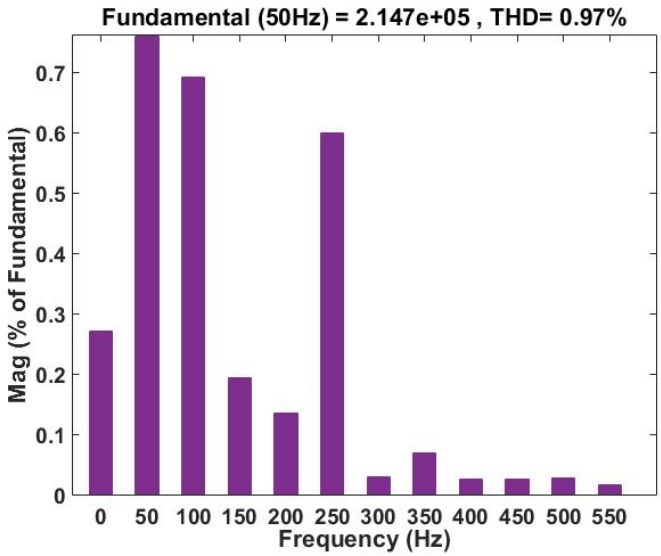

Figure.11: Voltage Harmonics (THD_V) – At Phase A of Bus 2.

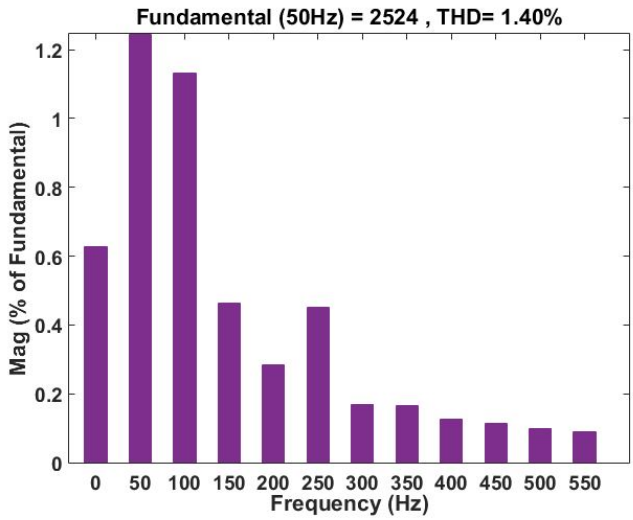

Figure.12: Current Harmonics (THD_I) – At Phase A of Bus 2.

In the above figures (9, 10, 11, 12), THD of the system with passive harmonic filter has been demonstrated. At fundamental frequency, the Voltage (THD_V) & Current (THD_I) harmonic distortion level at Bus-1(phase A), are 0.66% and 1.74% respectively. And at Bus-2 (phase A), Voltage (THD_V) & Current (THD_I) harmonic distortion level are 0.97% and 1.40% respectively. All the findings of the proposed design and simulation results of two different conditions are tabulated in Table-1.

The above results are about time domain simulation. The findings of the above discussions are demonstrated in the table below.

978-1-4673-9257-0/15/$31.00 ©2015 IEEE

Table.1: Value of THD for fundamental component of 50Hz with and without passive filter

Bus No.	Phase	THD(%) without passive filter		THD(%) with passive filter	
		Voltage	Current	Voltage	Current
1	A	3.13	2.36	0.66	1.74
2	A	8.79	4.33	0.97	1.40

From the above comparison, the harmonic limit is under the IEEE std. 519 after using the passive harmonic filter. The observation was that the harmonic filters almost eliminate the harmonics generated by the converter.

V. CONCLUSION

When large amounts of power are to be transmitted for long distances, HVDC is considered an economically beneficial because of their low electrical losses. But the impact of harmonics in HVDC network might be detrimental and redundant to both loads and grid. With the use of Passive harmonic filters are ways of mitigating the effects of such. To determine harmonic distortion levels and filtering requirements harmonic studies with passive filter on the HVDC transmission network were performed. Designing proper implementation with the help of the Simscape division of Matlab was performed with practical system and data's. This study determines if harmonic voltages and currents are at acceptable levels. An evaluation of the harmonic voltage and current limits is completed to determine the effectiveness of the proposed filter installation. The founding's of this work concludes that Harmonic analysis with passive harmonic filter is a very important discussion on the modern day's power system which reduces excessive current flow on the non-linear load. The application of Passive harmonic filters will significantly alter the frequency response of the power system. After completing the task, it will be minimize the wasteful impact of unnecessary power conversion, which saves more energy in the system. With the rapid conversion of AC to DC system more and more filters will be required to keep the harmonic limits within the acceptable range. So in future, further studies can be performed for improved implementation based on this research work.

VI. REFERENCES

[1] Ghijselen, Jozef, Wouter R. Ryckaert, and Jan Melkebeek. *"Required load behaviour for power quality improvement."* In Power Engineering Society Summer Meeting, 2002 IEEE, vol. 2, pp. 998-1003. IEEE, 2002.

[2] Herrera, Reyes S., Patricio Salmerón, and Salvador P. Litrán. *"Assessment of Harmonic Distortion Sources in Power Networks with Capacitor Banks."*

[3] Louie, K. W., P. Wilson, R. W. Wachal, A. Wang, and P. Buchanan. *"HVDC power system harmonic analysis in the time and frequency domains."* In Power System Technology, 2006. PowerCon 2006. International Conference on, pp. 1-8. IEEE, 2006.

[4] Zidi, S. A., S. Hadjeri, and M. K. Fellah. *"Regular paper Dynamic Performance of an HVDC Link."* J. Electrical Systems 1, no. 3 (2005): 15-23.

[5] Rudervall, Roberto, J. P. Charpentier, and Raghuveer Sharma. *"High voltage direct current (HVDC) transmission systems technology review paper."* Energy week 2000.

[6] Kure, Hans Magnus, Carl Olav Larsson, Tore Skottvoll Lefstad, Leif Arne Müller, and Øyvind August Rui. *"HVDC Transmission–Skagerrak 4."* Group 9: 2.

[7] Luo, Longfu, Yong Li, Kazuo Nakamura, Gerhard Krost, Ji Li, Jiazhu Xu, and Fusheng Liu. *"Harmonic characteristics of new HVDC transmission system based on new converter transformer."* In Electric Utility Deregulation and Restructuring and Power Technologies, 2008. DRPT 2008. Third International Conference on, pp. 1868-1872. IEEE, 2008.

[8] *"Harmonic reduction methods",* Eaton Corporation, Printed in USA, Publication No. AP04014001E / Z12198 April 2012, Eaton Corporation

[9] Islam, F. R., and H. R. Pota. *"Virtual active filters for HVDC networks using V2G technology."* International Journal of Electrical Power & Energy Systems54 (2014): 399-407.

[10] Arrillaga, J., and D. A. Bradley. "P S Bodger,*"Power system harmonics."* A Wiley-Interscience Publication, Norwich (1985).

[11] Louie, K. W., P. Wilson, R. A. Rivas, A. Wang, and P. Buchanan. *"Discussion on power system harmonic analysis in the frequency domain."* In Transmission & Distribution Conference and Exposition: Latin America, 2006. TDC'06. IEEE/PES, pp. 1-6. IEEE, 2006.

[12] M D Singh and K B Kanchandani, *"Power Electronics",* Second Edition, Tata McGraw Hill Education Private Limited

[13] Okba, Mohamed H., Mohamed H. Saied, M. Z. Mostafa, and T. M. Abdel-Moneim. *"Harmonics in HVDC Links, part II—Effects and reduction techniques."* In IECON 2012-38th Annual Conference on IEEE Industrial Electronics Society. 2012.

[14] Data Collected from PGCB (Power Grid Company of Bangladesh Ltd.) and POWERGRID, India.

[15] Karlsson, Per, and Jörgen Svensson. *"DC bus voltage control for a distributed power system."* Power Electronics, IEEE Transactions on 18, no. 6 (2003): 1405-1412.

[16] Roy, Rajib Baran, and Md Ruhul Amin. *"Analysis of Proposed Controlling Topology of the HVDC link between Bangladesh and India."* In Strategic Technology (IFOST), 2014 9th International Forum on, pp. 390-395. IEEE, 2014.

[17] Flourentzou, Nikolas, Vassilios G. Agelidis, and Georgios D. Demetriades. *"VSC-based HVDC power transmission systems: An overview."* Power Electronics, IEEE Transactions on 24, no. 3 (2009): 592-602.

978-1-4673-9257-0/15/$31.00 ©2015 IEEE

Harmonic Analysis on LVDC Distribution System and Passive Filter Techniques for Harmonic Reduction

Sanjib Kumar Nandi, Md. Siddikur Rahman, Ridown Rashid Riadh

American International University-Bangladesh, Dhaka, Bangladesh

sanjib.eee.aiub@gmail.com, rahman.siddikur286@gmail.com, rashidridown@gmail.com

Abstract— **Usages of DC power instead of AC power on the secondary distribution system creates a lot of harmonics. Our goal is to eliminate the harmonics onto the system and due to the limited specification of filter it has not been possible to reduce all the harmonics in the secondary distribution system. But we must be more focused to achieve this goal, because large shares of household loads are turning into DC in recent years. If this trend continues, the impact of harmonics on customer end will reach a level which might be detrimental and redundant to both loads and grid. The main objective of this research is to explain the effects of harmonics on the low voltage direct current (LVDC) distribution system and measure the harmonic content present in the network and proposed a recovery method by inserting filter. Due to additional non-linear loads on the LVDC distribution system, a sufficient amount of harmonics will be created. To solve this issue, use of passive harmonic filter is recommended for the DC operated secondary distribution system. After using a passive filter into the LVDC network, the system harmonics are being reduced into the acceptable limits and almost eliminate the harmonics generated by the converter and nonlinear loads.**

Keywords—Harmonics, Total Harmonic Distortion (THD), DC Power, LVDC Distribution System, Passive Filter, Harmonic Reduction

I. INTRODUCTION

Among all the existing network technologies, LVDC system is one of the emanating technology renovations for Smart Grid application to the distribution of electricity and a highly interesting challenge [1]. The salient purposes beyond this development of the LVDC network is to enhance the power quality and furnish security experienced by the end users of the electricity for ameliorating the distribution economy [1]. This pledge flexible and robust coupling point for small scale generation and evolve infrastructure for interactive and intelligent distribution network [1, 2]. The distribution transformer is one of the key parts of LVDC system [3]. The nonlinear nature of the load has generated harmonic currents which may cause problems in the power system and overheating transformers. Nonlinear loads have generated harmonic currents which are flown from the load towards the power source, following the least impedance paths [4].

Modern electrical system consists of a vast amount of nonlinear loads which causes disturbances in DC current. Commercial buildings often have a large amount of nonlinear electronic loads such as lighting, computers, monitors and adjustable-speed drives for air conditioning. Due to this huge presence of nonlinear loads, electromagnetic-compatibility and power quality problems may occur [5]. For which power system suffers from unfavorable consequences and may damage electrical equipment's. IEEE Standard 519-1992 specifies limits for each harmonic up to the 35th and limits the total harmonic distortion (THD) to 5% [6]. EN 50160 limits the THD to 8% and the unbalance to 2% [7].

This problem can require special consideration to serve non-linear loads with a reduce amount of harmonic distortion. Using various techniques power distribution system's Harmonic distortion might be restrained [2]. Previously, researches have been conducted on load behavior and harmonic contribution in various sectors of the power system. For instance, The LVDC power distribution network concept is presented [8]. Harmonic analysis and DC operated electrical system with distributed resources for recovery from the effects of harmonics and closely relevant criteria have been proposed in [9, 10, 11 and 12]. The LVDC distribution system concept has been developed in [13]. Passive filter installation for reducing harmonic in single phase motor, varying load has been introduced in [4].

Analysis of harmonics and measuring simulation based results is helpful for preparing data based efficient models of the LVDC distribution system. Investigation of harmonic content present in low voltage direct current (LVDC) power distribution network has been demonstrated in this article. This paper mainly focuses on the effects of the increase amount of harmonics in a LVDC distribution network and possible solution to overcome. The primary objective is to measure harmonic contents on the LVDC distribution system. And the secondary objective of this work is using an active harmonic filter to improve the system performance of the LVDC distribution system. For investigation, simulation environment at SimPowerSystems tool of Matlab Simulink is used. The organization of the paper is set as: in Section II, a brief overview of LVDC distribution network was introduced. Sources of harmonics in LVDC network and their effects in distribution feeders have been discussed in section III. A brief introduction to Passive filter technique for harmonic reduction used in this study has been presented in section IV. Simulation

978-1-4673-9257-0/15/$31.00 ©2015 IEEE

results along with the influence in harmonic contents of LVDC system with the appearance of Passive filters have been discussed in section V. Some discussions and explanations of the findings have also been provided finally in section VI conclude the work highlighting the major contributions.

II. LVDC DISTRIBUTION SYSTEM

The LVDC distribution system is an advanced revolution in the field of electricity distribution. Recently, power electronic constituents have developed in the way of economic and technological, which enabled to apply power electronics in LV network. A basic conviction of LVDC distribution system concentrated at the DC/AC interface focused on implementation of customer-end inverter [13]. The LVDC distribution system builds of power electronic converters and DC link between the converters. A LVDC distribution system can have different types of topologies that the AC/DC conversion can be placed at various locations [14].

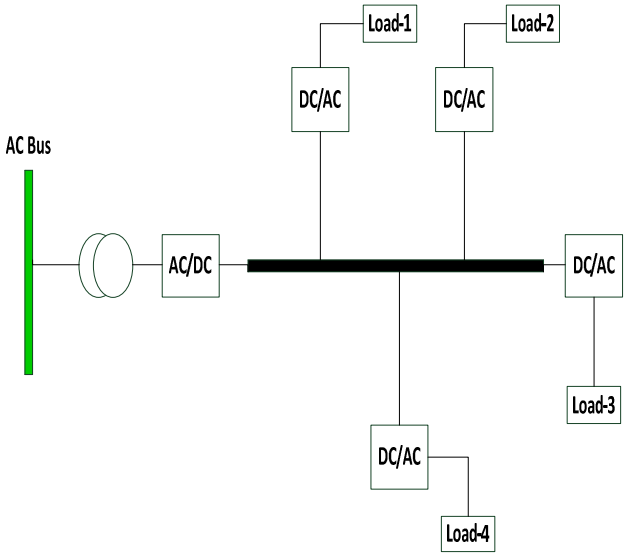

Figure.1: Simple LVDC Distribution system

LVDC system consists of a distribution transformer, a DC link, a rectifier, DC/AC inverter units, customer loads and filters [15]. In LVDC distribution system, DC connection is used to avoid the need to build a medium voltage branch line as well as traditional low voltage AC grid to furnish electricity to a group of low power customers [16, 17]. In LVDC distribution grid, DC grid is powered by a front-end rectifier. The front-end rectifier includes of two 6-pulse thyristor bridges. Thyristor bridges are powered by phase shifting transformer with two secondary windings to form a 12-pulse rectifier. The customer-end inverters loaded the DC system. The bipolar DC power distribution network serves as the power supplier of the inverters. Both single phase and three phase inverters can be used to energize the consumer end AC network. Due to high ±750 VDC voltage used in the LVDC network, inverters are generally connected in between the zero pole and plus or minus DC pole. Customer's coupling point can also be located in the DC side in some special cases [18].

III. HARMONICS ON LVDC DISTRIBUTION NETWORK

Using a DC distribution system makes it easier to incorporate more local energy storage and sources. To connect an energy source with a DC system only the voltage has to be controlled, as opposed to the AC system where voltage magnitude, frequency and phase must be matched [9]. An indispensable deliberation when estimating the smash of harmonics is their effect on power system constituent and loads [16]. Higher consumption of reactive power causes more system losses and malfunction the protection of the power system [5]. The current harmonics found in the grid components may sustain impairments in distinct devices which are fastened to the same grid [16].

The converters used in the LVDC distribution system produce flexible harmonic contents. The distortion of voltages and currents can cause extra losses in system components [17]. Generally, industrial electronic devices and nonlinear loads are the considerable source of harmonic generation. When sinusoidal voltage is applied to a nonlinear load, then the resulting current is distorted. So, non-linear loads are the leading source of harmonic distortion in power system. Modern personal computer's power supply is a familiar example of nonlinear load. It's switching action results in distortion of the current waveform [19]. With the increase use of PV grid integration also causes harmonics problem inside the power system [20].

Distribution transformer is one of the vital constituents of LVDC system. Harmonic load currents consequence heating inside and cause eddy current losses in transformer. The escalated depletions due to harmonic distortion can seed excessive depletions as well, hence the anomalous temperature rise. The assessment of iron depletions and copper depletions of transformers is the prime in particular for transformers feeding nonlinear loads [16].

Whenever there is a large number of a nonlinear load, more harmonics are observed in the LVDC distribution system. Harmonic currents which are engendered by nonlinear loads are flown from the load toward the power source, shadowed the ways of minimal impedance. Due to greater percentage of harmonics many more unnatural situation may occur such as - overheating of electrical distribution system wiring, transformer overheating which shortened transformer service life, false circuit breaker tripping, power factor correction capacitor failure etc. [21] The likelihood of experiencing problems increases with the increase of harmonic levels. In Rising temperature and creating Skin Effect harmonic is an important factor. Both the electrical distribution systems and equipment have consequences due to heating effect. Problems in neutral conductors, unpredictable operation of relays and breakers, presence of distinct magnetic fields near transformers and switchgear etc. are also the outcomes of harmonics. Harmonics may also results in electronic instrument's reading errors, false instruction, excessive line loss, thermal loading of motors, malfunction of transformers, generators, electronics equipment like computers, air conditioning systems, PLCs, remote monitoring systems etc.

978-1-4673-9257-0/15/$31.00 ©2015 IEEE

IV. HARMONICS REDUCTION BY PASSIVE FILTER

A lot of harmonics are generated on the LVDC distribution system due to different types of conversion process and nonlinear loads. There are many ways to reduce LVDC power system harmonics. Such as- using phase controlled thyristor rectifier, using larger DC or AC inductor, using Tuned single or multiple arm passive filter, External active filter etc. To maintain the power quality of an LVDC distribution system Active and passive filters is essential. Filtering is currently the most common method used for limiting the effects of harmonics to the rest of the system. Filters typically consist of Tuned Series L-C circuits and its impedance is negligible with respect to the rest of the distribution network. Passive filters are used to restrict the harmonic currents by providing a low impedance path to enter the power system. Resistors, inductors and capacitors are the main components for designing of the passive harmonic filters [22]. A basic structure of a Passive Shunt Filter with Load connection has been shown in figure.2.

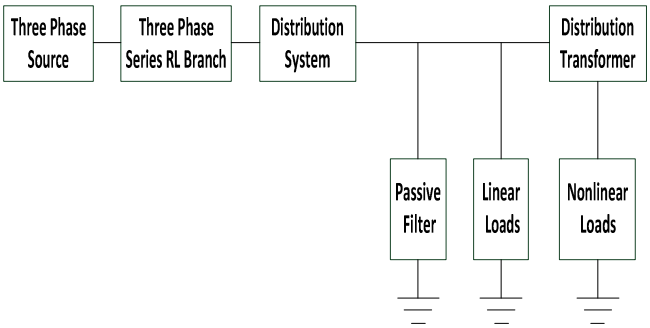

Figure.2: Passive Shunt Filter with Load connection

By using Passive filter as a harmonic reduction technique, power quality of the distribution network can be improved [4, 23]. Passive harmonic filter reduces harmonics which are existed due to nonlinear loads in the power system by injecting equal current or voltage distortion [4]. Passive filters are not expensive and often used to restrict the harmonic currents from entering the power system thereby minimizing the effect of harmonics. Also, the passive filters are kept close to the source of harmonic generated loads. Doing so, in reducing the harmonic effect the passive filters produce better results. The passive filters create a resonance frequency in order to reduce the harmonic effect [4]. This resonance frequency is kept away from the harmonic distortion of the nonlinear loads.

V. SIMULATION RESULTS

When designing a system, several things need to be addressed in order to observe the Impact of increased share of DC load. LVDC grid requires 1500 VDC Medium-voltage fretwork and 20 KV voltages have to be laid down by a transformer to low AC voltage like 1 KV in power distribution. When ripple voltage is not more than 10 % of the nominal voltage, is to be known as DC voltage, but the real scenario of the ripple voltage has considerably underneath the margin of losses in DC cables. For analyses of a bipolar LVDC network ± 750 VDC distribution systems is considered. The proposed Simulink model block diagram representation is shown in Figure 3 below that presents the overall system where a simple LVDC system is designed.

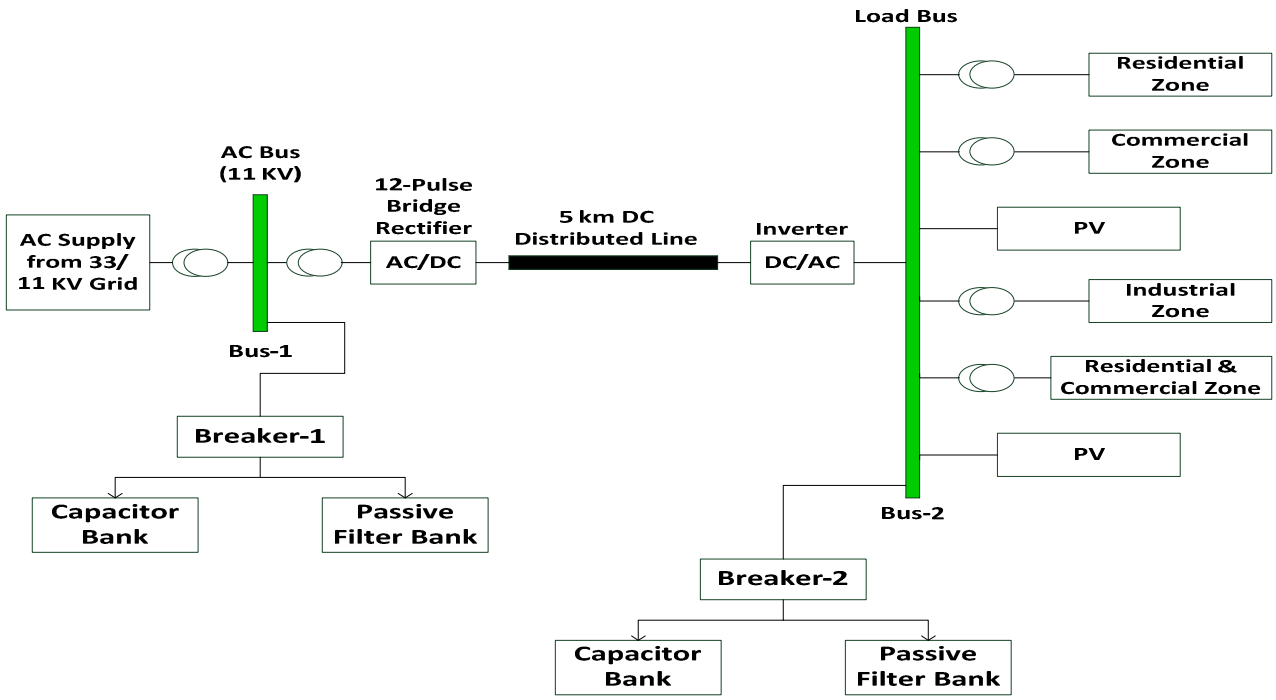

Figure.3: Test System

978-1-4673-9257-0/15/$31.00 ©2015 IEEE

The Simulink model consists of a LVDC distribution system along with Passive Harmonic Filters connected to the adjacent AC Bus. It is important to get familiarized with the components needed to observe the impact of increased share of DC loads. The components used for observing the impact of increased share of DC loads are Three-Phase Source, Series RLC Branch, Three-Phase Transformer, 12 pulse Thyristor controlled bridge rectifier, inverter, linear and nonlinear loads and Three-Phase Harmonic Filter. Designing and implementing of this Software Based system is followed by the implementation using SimPowerSystems Tool of Matlab. The Harmonic Filter uses a Phase Locked Loop to generate a reference sinusoidal source current which is in phase and has the same RMS gain as the load current.

A 5 km DC interconnection is used to transmit power from an 11 KV, 50 Hz distribution Grid to load side. The converter is connected to the system with Three-Phase transformer windings. The rectifier is a 12-pulse converter using two 6-pulse thyristor bridges. An inverter bridge is used in the load side for DC/AC conversion which is interconnected in series through a 5 km distributed parameter line. Six individual feeders carrying on different types of loads (both linear and nonlinear) are connected to Bus-2 through individual transformer. Here, along with residential, commercial and industrial loads, Photovoltaic (PV) was also inserted to have a better scenario. 8 MW load in residential feeder, 2.5 MW load in Commercial feeder, 4.5 MW load in (Residential + Commercial) feeder, 5 MW load on Industrial feeder and 2 MW load in each PV individually were considered and connected to the system. Total load connected to the LVDC network was amounted to be 24 MW. Two Passive filters were connected to Bus 1 and 2 The filter sets are made of the following four components – one capacitor banks of 91 Mvar, one C-type high-pass filter of 150 Mvar, two single-tuned filter of 2x150 Mvar for reduction of odd harmonics, one high-pass damped filter of 150 Mvar modeled using the three-phase harmonic filter. The total Mvar rating of the filters set was 455 Mvar at individual Bus. A three-phase circuit breaker was used with each filter block to connect the filters set on the AC bus separately.

The most important part of this design was to observe the impact increased share of DC load. From the design, four parameters Vabc_B1, Iabc_B1, Vabc_B2 and Iabc_B2 and their corresponding harmonic components (both voltage harmonics and current harmonics) has been observed for three phases. With the help of SimPowerSystems under SimScape division in Matlab results of THD have been measured for with and without passive filter connections. Simulations have been carried out with two different conditions. Condition 1 calculates the existing THD of the LVDC distribution network without any filter in the system. Condition 2 represents the improved THD value of the LVDC network after adding passive filters into it. The results of this design and implementation considering phase sequence C of each Bus are described briefly for a better comparison scenario.

<u>Condition-1:</u> When both the breakers were open (without Passive filter)

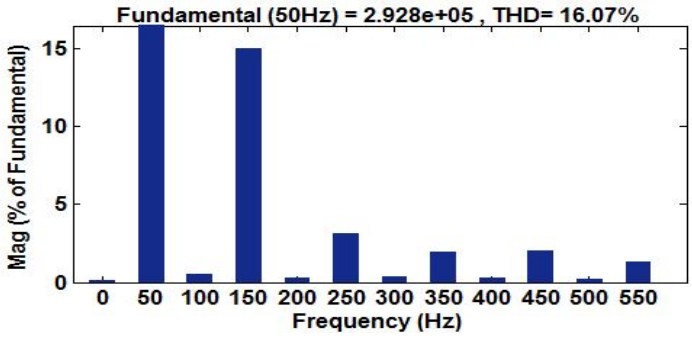

Figure.4: Voltage Harmonics (THD_V) – At Phase C of Bus 1.

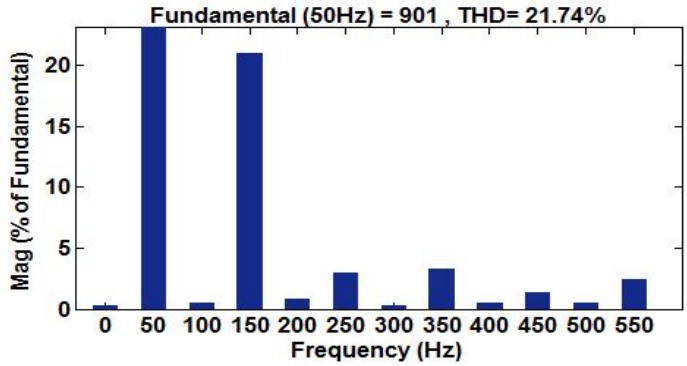

Figure.5: Current Harmonics (THD_I) – At Phase C of Bus 1.

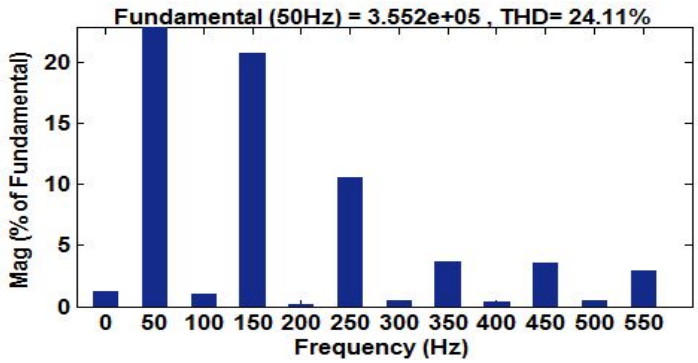

Figure.6: Voltage Harmonics (THD_V) – At Phase C of Bus 2.

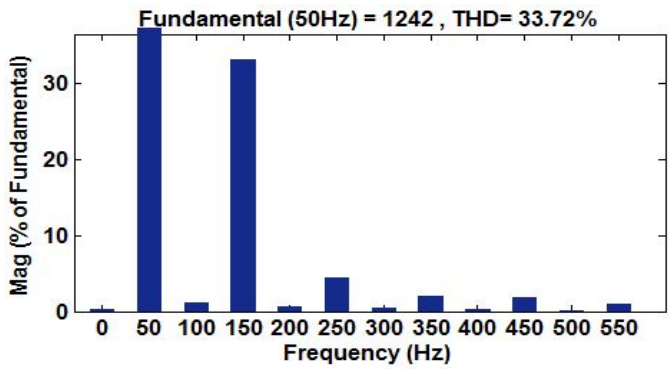

Figure.7: Current Harmonics (THD_I) –At Phase C of Bus 2.

978-1-4673-9257-0/15/$31.00 ©2015 IEEE

In the above figures (4, 5, 6, 7), THD of the system without harmonic filter has been demonstrated. It has been found that design's THD is much higher without harmonic filter installation. At fundamental frequency, the Voltage (THD_V) & Current (THD_I) harmonic distortion level at Bus-1(phase C) were 16.07% and 21.74% respectively. And at Bus-2 (phase C), Voltage (THD_V) & Current (THD_I) harmonic distortion level were 24.11% and 33.72% respectively. That's why a second case study was performed by designing passive harmonic filter on the LVDC distribution network to examine the performance of the system and harmonic distortion level.

<u>Condition-2:</u> When both the breakers were closed (with Passive filter)

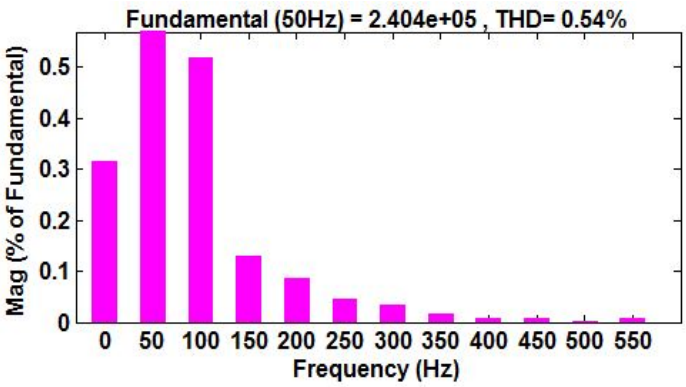

Figure.8: Voltage Harmonics (THD_V) – At Phase C of Bus 1.

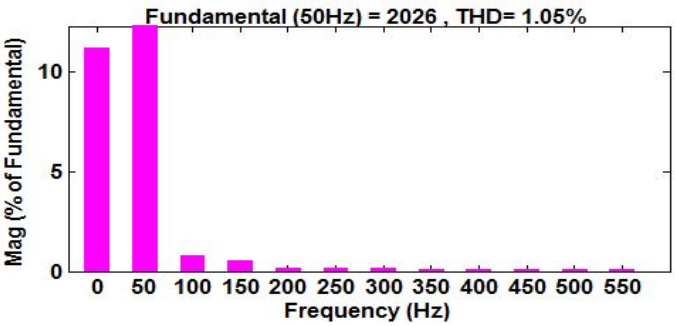

Figure.9: Current Harmonics (THD_I) – At Phase C of Bus 1.

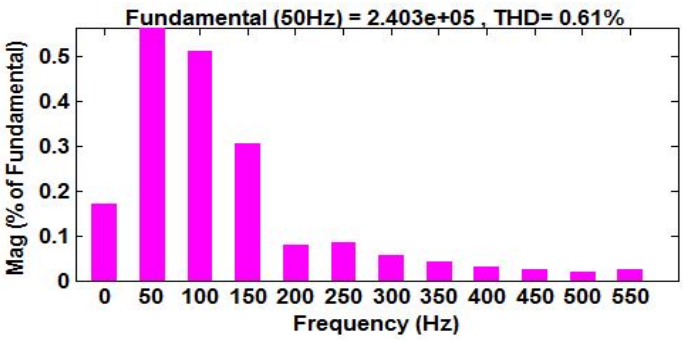

Figure.10: Voltage Harmonics (THD_V) – At Phase C of Bus 2.

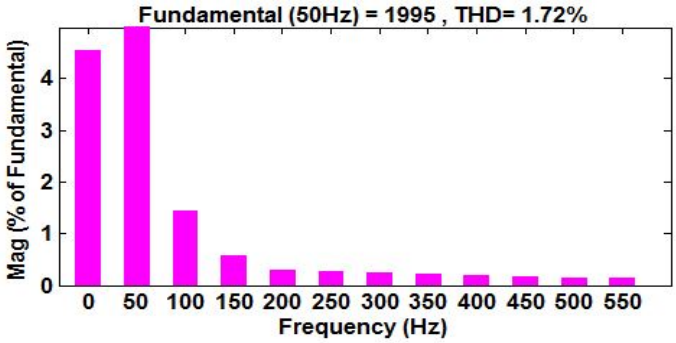

Figure.11: Current Harmonics (THD_I) – At Phase C of Bus 2.

In the above figures (8, 9, 10, 11), THD of the system with passive harmonic filter has been demonstrated. At fundamental frequency, the Voltage (THD_V) & Current (THD_I) harmonic distortion level at Bus-1 (phase C) were 0.54% and 1.05% respectively. And at Bus-2 (phase C), Voltage (THD_V) & Current (THD_I) harmonic distortion level were 0.61% and 1.72% respectively. All the findings of the proposed design and simulation results of two different conditions are tabulated in Table-1.

Table.1: Value of THD for fundamental component of 50Hz with and without passive filter

Bus No.	Phase	THD(%) without passive filter		THD(%) with passive filter	
		Voltage	Current	Voltage	Current
1	C	16.07	21.74	0.54	1.05
2	C	24.11	33.72	0.61	1.72

Analyzing from the First Furrier Transform (FFT) tool of the PowerGui the finding is that the passive harmonic filter reduces the THD of the voltage and current injected into the system.

VI. CONCLUSION

In this work, the wasteful impact of unnecessary power conversion was sought for and recognizes that negative impact of increasing the amount of nonlinear loads. It creates lots of harmonic if the DC power distribution system is used instead of an AC power distribution system. The investigation into power quality and analyzing the harmonics of a LVDC distribution system is performed using Matlab simulation environment. The simulation results are compared by verifications with measurements and practical examples. The effect of system reconfiguration on DC network and transformer harmonic content is determined. The simulated LVDC network with passive harmonic filter is meeting voltage and current harmonic distortion limits of IEEE std. 519. As the amounts of nonlinear loads are increasing day by day throughout the power system, efficient filter designing are required instantly to overcome from the effects of harmonics. The achieved models and results of this paper will be useful in the dimensioning LVDC distribution network components and system designing. This work will be highly applicable on the

978-1-4673-9257-0/15/$31.00 ©2015 IEEE

sight of rural area and different kind of office, bank and where solar panel should be used. After using the proposed filtering, it will be minimize the wasteful impact of unnecessary power conversions, which saves more energy in the system. In future work, using DC power and measurement of maximum tolerable range of DC load integration with the variation of nonlinear load up to which harmonics are tolerable in the secondary distribution system based further analysis can be developed.

VII. REFERENCES

[1] P. Nuutinen. *"Implementing a laboratory development platform for an LVDC distribution system",* 2011 IEEE International Conference on Smart Grid Communications (SmartGridComm), 10/2011

[2] Nasr, Abdulhakim. *"Harmonics analysis of a wind energy conversion system with a permanent magnet synchronous generator",* 2015.

[3] Ghijselen, Jozef, Wouter R Ryckaert, and Jan Melkebeek. *"Required load behaviour for power quality improvement."* In Power Engineering Society Summer Meeting, 2002 IEEE, vol. 2, pp. 998-1003. IEEE, 2002.

[4] Khan, M. Shuja. *"Implementation of a Passive Tune Filter to Reduce Harmonics in Single Phase Induction Motor with Varying Load",* International Journal of Engineering & Technology/20771185, 20110601

[5] Sannino, Ambra, Giovanna Postiglione, and Math HJ Bollen. *"Feasibility of a DC network for commercial facilities."* Industry Applications, IEEE Transactions on 39, no. 5 (2003): 1499-1507.

[6] Horowitz, Noah. *"Power supplies: a hidden opportunity for energy savings."* Natural Resources Defense Council, Tech. Rep (2002).

[7] IEEE Std. 519-1992, IEEE Recommended Practices and Requirements for Harmonic Control in Electrical Power Systems, New York, 1992.

[8] Kaipia, Tero, Janne Karppanen, Aleksi Mattsson, Andrey Lana, Pasi Nuutinen, Pasi Peltoniemi, Pekka Salonen et al. *"A system engineering approach to low voltage DC distribution."* (2013): 1292-1292.

[9] Rekola, Jenni. *"DC distribution and power electronics applications in smart grid."* (2012).

[10] Salomonsson, Daniel, and Ambra Sannino. *"Low-voltage DC distribution system for commercial power systems with sensitive electronic loads."* Power Delivery, IEEE Transactions on 22, no. 3 (2007): 1620-1627.

[11] Brenna, Morris, Enrico Tironi, and Giovanni Ubezio. *"Proposal of a local dc distribution network with distributed energy resources."* In Harmonics and Quality of Power, 2004. 11th International Conference on, pp. 397-402. IEEE, 2004.

[12] Karlsson, per, *"DC distributed power systems-Analysis, design and control for a renewable energy system".* Lund University, 2002.

[13] Louis Hapeshis, P. E., and D. Square. *"Power System Harmonic Mitigation for Water and Wastewater Treatment Plants."*

[14] Zavalani, Orion, Myrteza Braneshi, Aida Spahiu, and Luela Prifti. *"Potentials of power electronics in LV electricity distribution systems in Albania",* Proceedings of 14th International Power Electronics and Motion Control Conference EPE-PEMC 2010, 2010.

[15] Hur, Don, and Ross Baldick. *"An Economic Analysis of Potential Cost Savings from the Use of Low Voltage DC (LVDC) Distribution Network",* Journal of Electrical Engineering and Technology, 2014.

[16] Salonen, Pasi, Tero Kaipia, Pasi Nuutinen, Pasi Peltoniemi, and Jarmo Partanen. *"An LVDC distribution system concept."* In Nordic Workshop on Power and Industrial Electronics (NORPIE/2008), June 9-11, 2008, Espoo, Finland. Helsinki University of Technology, 2008.

[17] Kaipia, Tero, Pasi Peltoniemi, Jukka Lassila, Pasi Salonen, and Jarmo Partanen. *"Impact of low voltage DC system on reliability of electricity distribution."* In Electricity Distribution-Part 1, 2009. CIRED 2009. 20th International Conference and Exhibition on, pp. 1-4. IET, 2009.

[18] Khramov, Alexey. *"Converter supply transformer for LVDC distribution system."* (2009).

[19] M D Singh and K B Kanchandani, *"Power Electronics",* Second Edition, Tata McGraw Hill Education Private Limited

[20] Li, H., and Z. Wang. *"An Integrated Three-port Bidirectional DC-DC Converter for PV Application on DC Distribution System",* IEEE Transactions on Power Electronics, 2012.

[21] Shwehdi, M.H.. *"Harmonics Effect in Industrial and University Environments",* Power Quality Harmonics Analysis and Real Measurements Data, 2011.

[22] Kaipia, Tero, Pasi Salonen, Jukka Lassila, and Jarmo Partanen. *"Possibilities of the low voltage DC distribution systems."* In Nordac, Nordic Distribution and Asset Management Conference, pp. 1-10. 2006.

[23] Singh, S, G Bhuvaneswari, and B Singh. *"Power quality improvement in switched mode power supplies using two stage DC-DC converter",* International Journal of Engineering Science and Technology, 2012.

978-1-4673-9257-0/15/$31.00 ©2015 IEEE

An Accurate and Efficient Solar Tracking System Using Image Processing and LDR Sensor

Md. Hanif Ali Sohag[1], Md. Mahmudul Hasan[2], Mst. Mahmuda Khatun[3], and Mohiuddin Ahmad[4]
[1,2,4]Department of Electrical & Electronic Engineering
[1,2,4]Khulna University of Engineering & Technology, Khulna-9203, Bangladesh.
[3]Department of English
[3]Northern University Bangladesh, Rajshahi-6204, Bangladesh.
E-mail: hanifalisohag@gmail.com, mubin.eee.kuet@gmail.com, mahmuda.khatun.raj@gmail.com, mohiuddin.ahmad@gmail.com

Abstract— **The use of renewable energy resources is increasing for the purpose of producing electricity in modern world due to lack of non-renewable sources. As solar panels are becoming more popular day by day, it is a crying need to maximize the solar panel efficiency. The efficiency of solar panels can be increased to a great extent if the solar panels continuously rotate in the direction of sun. Microcontroller and an arrangement of LDR sensors can be used for the purpose of tracking the sun. But the system is less efficient because of the low sensitivity and disturbance of light dependent resistors. In this paper, a methodology of an automatic solar tracker is proposed by means of both sensors and image processing simultaneously. The mechanism of solar tracking was implemented by the use of an image processing software which combines the effect of sensors and processed image of sun and controls the solar panel accordingly. The methodology is a combination of hardware and software which can be used to control hundreds of solar panels in a solar power plant with more accuracy. It can be concluded that the proposed system is more accurate and efficient than the conventional solar tracking systems which can optimize the power requirement.**

Keywords—Photovoltaic cell, Solar tracker, Light dependent resistor, Microcontroller, Servomotor.

I. INTRODUCTION

While thinking about the development of a nation, the prime factor comes to mind is 'energy'. Huge amount of nonrenewable energy is extracted, distributed, converted and consumed in the global society daily. Almost 85% of energy production depends on fossil fuels. The resources of the fossil fuels are limited and their usage results in global warming because it can be a threat for human being by the emission of greenhouse gases. If we want to provide a sustainable power production and safe world to the future generation, we have to utilize the growing demand for energy from renewable sources like solar energy. Renewable energy sources are considered to be the best sources of energy which means no harm to global environment. Solar energy is a renewable resource which is clean, economical, and less polluted compared to other resources and energy [1].

Photovoltaic module is one of the efficient sources by which solar energy is converted in the form of electricity. Different semiconductor materials are used to make a solar panel. If Si is used to make solar panel, it becomes approximately 24.5% efficient [2]. Solar panel engrosses the energy from the sun and the energy can be stored in the battery which can be used for different purposes. Solar tracker is a system by which a solar panel can actually follow the sun to increase the power [3]. The main objective of this system is to develop a standard model of solar tracking system which consists of image processing using C++ programming language and sensor simultaneously. Thus it can increase the efficiency of solar panel at a great extent compared with the conventional systems.

The paper is organized as follows: Section II describes the photovoltaic technology and methods to improve efficiency of solar panel. Section III illustrates the proposed system. The hardware implementation is described in section IV. The methodology and developed prototype are briefly described in section V and VI respectively. The experimental result and discussion is described in section VII. Finally, section VIII concludes the paper.

II. PHOTOVOLTAIC TECHNOLOGY AND IMPROVING EFFICIENCY OF SOLAR PANEL

Researchers are trying to develop various methods whereby maximum power can be obtained from the solar panel. Maximum power point is the point where the maximum power from the system can be obtained by tracking that point during the sunshine hours. Fig. 1 represents the short circuit current versus voltage and power versus voltage characteristics of a photovoltaic cell [4].

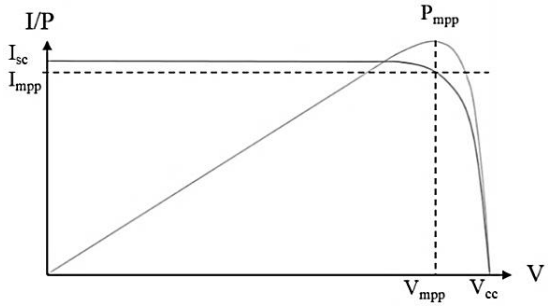

Figure 1. I_{sc}-V and P-V characteristics of solar cell

Researchers developed many Maximum power point tracking (MPPT) algorithms to maximize the output power from solar panel [5]. A solar tracker can increase the efficiency of the

978-1-4673-9257-0/15/$31.00 ©2015 IEEE

solar panel by tracking the sun. This mechanism can increase the power output of solar panel 30% to 60% than the fixed solar panel system [6]. Researchers developed different solar tracking algorithms recently [7, 9].

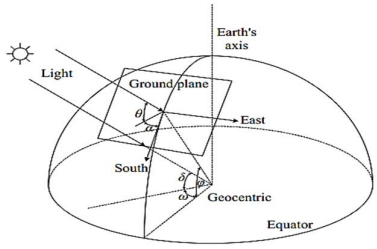

Figure 2. Geometric model of solar position

The sun trajectory tracking mode can work normally till the panel's azimuth and elevation angle change in accordance with the current solar azimuth and elevation angle [10]. From astrophysical knowledge, the solar azimuth and elevation angle at any given time can be calculated [11] [12].

The solar azimuth α and the elevation angle θ can be calculated using (1) and (2):

$$sin\theta = sin\varphi sin\delta + cos\varphi\ cos\delta\ cosw \quad (1)$$

$$sin\alpha = \frac{cos\delta\ sinw}{cos\theta} \quad (2)$$

Where, φ indicates the latitude angle, δ indicates the declination angle, ω indicates solar hour angle. The meanings of the parameters used are presented in Fig. 2 [10].

The declination angle δ and the solar hour angle ω can be calculated using (3) (Cooper Equation) and (4) [11].

$$\delta = 23.45° sin\frac{360°(284+d)}{365} \quad (3)$$

$$\omega = (h + E) \times 15 + \psi - 300° \quad (4)$$

In (3) and (4), h signifies the Beijing time, E indicates jet lag, ψ indicates the local longitude, d indicates the date, for example, d=2 stands for January 2nd, d=364 stands for December 30th [12]. Let, solar position is (α_t, θ_t) at t. Now, after interval T, the position changes to $(\alpha_{t+T}, \theta_{t+T})$. During this time, the variation of solar position can be expressed by $\Delta\alpha=\alpha_{t+T}-\alpha_t$, $\Delta\theta=\theta_{t+T}-\theta_t$.Let the panel has been aligned at t, if it is still aligned from t to T, the panel should rotate Δα in the horizontal direction and Δθ in the vertical direction respectively. In this way, sun trajectory can be explored.

III. Proposed System

The block diagram of the proposed system is presented in Fig. 3. The LDR sensor first takes the solar panel to a desired position. Then image processing is applied to track the sun coordinate. The servo motors are adjusted such that the canter of sun is always at the middle of the scaled camera window. By the iterative method it frequently checks the position of the sun and thus adjusts it to that particular position. The combined effect of LDR sensors and image processing operates simultaneously which gives better performance and efficiency.

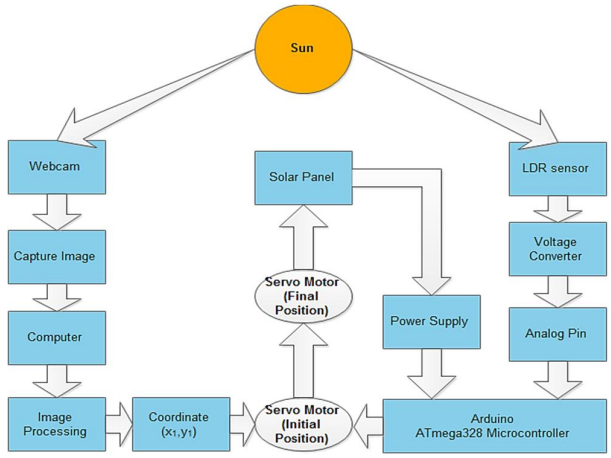

Figure 3. Block diagram of the system

IV. Hardware Design

The hardware consists of an Arduino UNO, two servo motors and four LDR sensors. The LDR sensors sense the sun light and the Arduino UNO takes decision to whether to rotate the vertical servo or horizontal servo motor. The circuit diagram of the system is shown in Fig. 4.

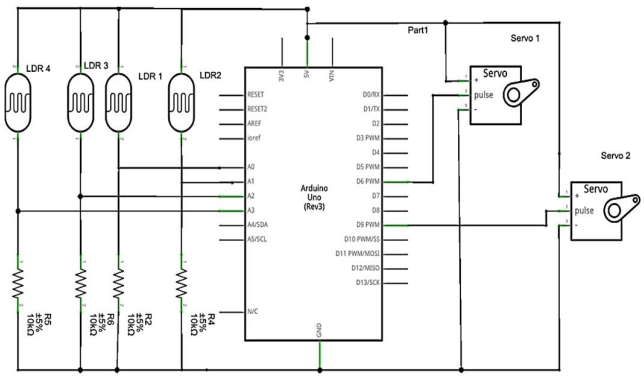

Figure 4. Circuit diagram of the system

V. Methodology

The sun is tracked in two stages- using the sensitivity of LDRs and then the adjustment of camera in new position by shifting the origin. Firstly, LDR sensors with the shadow arrangement compares the intensities fall on them and thus adjust the solar panel at an initial position. If the solar panel is out of track or in the opposite direction of sun it is adjusted towards the direction of sun. Secondly, the webcam mounted on the solar panel captures image of the sun and the computer processes the image using image processing algorithm. A new co-ordinate point is calculated by the described process and the two servo motors are controlled such that the sun remains at the center point of the captured image. The two steps occurred repeatedly and position of the sun is tracked accurately by the webcam.

A. Solar Tracking Using LDR Sensor

The resistivity of photo resistor decreases when the intensity of incident light increases. In the dark, an LDR can have a high

resistance like few mega ohms (MΩ). In the light, it can have very low resistance like a few hundred ohms. When we apply a constant voltage across the LDR and the intensity of light is increased, the current starts increasing. There are four LDRs in the proposed system as shown in Fig. 5. The resistivity of the LDRs will vary according to the intensity of light fall on them. LDR sensors are light sensitive. So, we arranged the LDRs in the proposed system in such a position that when the incident light is on the LDRs of one side (east), the LDRs of other side (west) are shaded. When it is afternoon and the sun goes towards the west, gradually the light intensity on the LDRs of the west will be high and the east LDRs will be in the shaded portion.

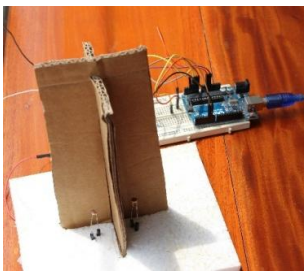

Figure 5. Shadow effect on LDRs

B. Image Processing

The proposed system represents the steps of estimating sun co-ordinates by using image processing. The steps involved in tracking the sun are given in Fig. 6.

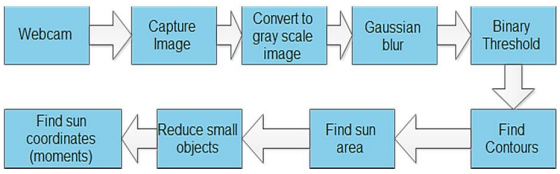

Figure 6. Image processing steps

1) Gray scale conversion and filtering: The captured image consists of the bright sun and blue sky. The processing of image is done in gray scale by extracting the luminescence plane from the RGB plane. Then Gaussian filter is used for the noise reduction of the captured image. The gray scale image is shown in Fig. 7.

Figure 7. Gray scale image with bright sun image

2) Sun detection: In order to extract the bright sun spot, binary thresholding technique is applied on the filtered image. Due to having cloud around the sun, there are some smaller objects detected in the image. Finding the largest contours, the smaller objects are removed. This situation is shown in Fig. 8 (a) and Fig. 8 (b).

(a) (b)

Figure 8. (a) After binary threshold, (b) Estimating the largest area

3) Sun tracking and co-ordinate estimation: After proper segmentation of the blob, the co-ordinates of the sun are estimated by using the centroid formula for irregular objects. The center position of the image is also calculated. Sun co-ordinate point is compared with the image center co-ordinate as shown in Fig. 9 for proper controlling of the servomotors.

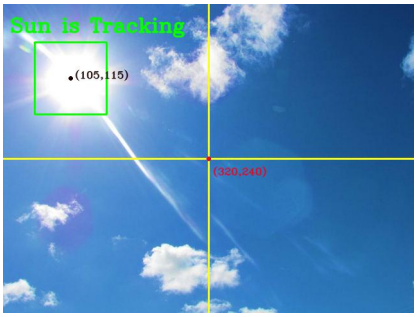

Figure 9. Sun co-ordinates calculation

C. Axis Transformation

1) Transformaton of origin with respect to change of axis: If the origin $O(x_0, y_0)$is shifted at $O'(x_1, y_1)$but the direction of axes remain unchanged, then in the transformed coordinate the origin to be shifted by $(x_1 - x_0)$distance in the x direction and $(y_1 - y_0)$distance in the y direction. The axis transformation is shown on Fig. 10.

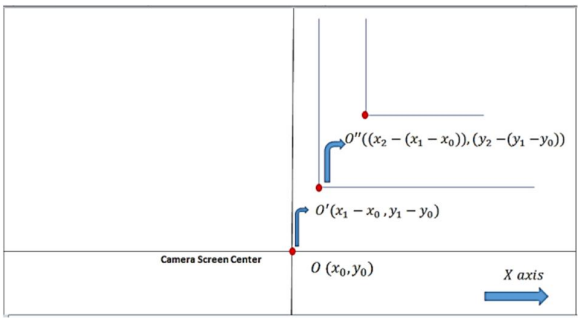

Figure 10. Transformation of origin

2) Adjustment of the solar panel position by tracking the cordinates of the sun: The webcam captures the images of the

sun and the coordinates of the sun is calculated. Now, the initial camera screen center point is adjusted such that the sun always remains at the center point which is shown in Fig. 11. Then proper transformation formulas are used to get the distance from the initial origin point to the sun coordinates. The two servo motors are controlled to get the proper position.

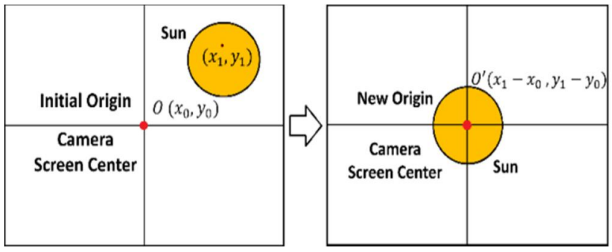

(a) (b)

Figure 11. Camera position control (a) camera detect sun at (x_1, y_1) point (b) camera screen center is shifted to that point

VI. Developed Prototype

The hardware for LDR based solar tracking system consists of an Arduino UNO, two servo motors and four LDR sensors. The LDR sensors are arranged such that the shadow effect works on them. The image processing based solar tracking system consists of a webcam and a personal computer. The system was tested on a core i5 2.60 GHz processor, 4GB memory running on Windows 7, 64-bit Operating system. The webcam installed on the solar panel had a resolution of 2 mega pixels. The developed prototype for real time sun tracking is shown in Fig. 12.

(a)

(b)

Figure 12. Developed Prototype (a) solar panel with webcam (b) LDR arrangement with Arduino and image processing using PC

VII. Experimental Results and Discussion

In this proposed system we used a mono crystalline BX-5W solar panel. The technical specifications were rated power of 5W, 17.4V rated voltage and 0.29A rated current. The open circuit voltage was V_{oc} =21.6V and short circuit current was I_{sc} =0.32A. The normal operating cell temperature of solar panel was45 ℃. The experimental data was recorded in Khulna University of Engineering & Technology (KUET) campus, Khulna-9203, Bangladesh at different times of the day. The experimental data is shown in Table 1.

While working using fixed solar panel, we found the maximum short circuit current of 0.2420A and maximum open circuit voltage of 19.170V at 1pm. Then the experiment was done using same solar panel and with the LDR based solar tracking system. In this case we found the maximum short circuit current of 0.2443A and maximum open circuit voltage of 20.016V at 12pm. Finally, the solar tracking system was implemented using both LDR arrangement and using webcam. In this case, we found the maximum short circuit current of 0.2497A at 2pm and maximum open circuit voltage of 20.456V at 11am. The short circuit current versus the day time was plotted in Fig. 13. The open circuit voltage versus the day time curve is shown in Fig. 14. The power versus the day time curve was plotted in Fig. 15.

This literature describes a novel system of solar tracking mechanism which repeatedly uses LDR sensors and image processing to track the sun. The image processing was done in C++ using OpenCV library. This mechanism is more efficient than the previous solar tracking mechanisms. From the power versus day time curve in Fig. 15, the maximum power was 4.89W at 12pm when we used only LDR sensors in the solar tracker. The maximum power was found to be of 4.96W at 12pm when we used the LDR sensors and webcam simultaneously. Of course the LDR based solar tracking system power curve was above the fixed system. So, it was better than the fixed solar panel system. But the LDR arrangement and webcam based solar tracking system was more efficient during morning and evening but it was quite difficult for the LDR arrangement alone. It was because of the low intensity of the sun light during this period. This system is much preferable compared with the conventional systems.

The sun can be tracked solely by either using Image processing of sun or using LDR sensors. When the LDR sensors are inactive or disabled or become obsolete, the solar tracker can track the sun using image processing spontaneously. On the other hand, if the webcam becomes obsolete or a fault occurs to it, the solar panel can easily operate using the sensitivity of LDRs. After the sun sets, the power supply to the system is disconnected and the system again operates in the next morning.

TABLE I. DATA OBTAINED FOR DIFFERENT SOLAR SYSTEM

Day Time	Fixed Panel			Solar Tracker using LDR			Solar Tracker using LDR and Image Processing		
	Isc (A)	*Voc (V)*	*Pout (W)*	*Isc (A)*	*Voc (V)*	*Pout (W)*	*Isc (A)*	*Voc (V)*	*Pout (W)*
7:00 AM	0.0586	15.674	0.91826	0.0718	17.113	1.229	0.0782	17.316	1.3536
8:00 AM	0.0882	15.791	1.393	0.0988	17.674	1.747	0.1228	18.861	2.316
9:00 AM	0.1167	16.341	1.908	0.1394	18.142	2.530	0.1436	19.012	2.729
10:00 AM	0.1363	18.025	2.457	0.1534	18.423	2.827	0.1725	19.889	3.430
11:00 AM	0.1616	18.342	2.965	0.1852	19.073	3.533	0.2021	20.456	4.134
12:00 PM	0.2401	19.042	4.572	0.2443	20.016	4.891	0.2460	20.161	4.962
1:00 PM	0.2420	19.170	4.642	0.2441	19.432	4.752	0.2446	19.742	4.831
2:00 PM	0.2135	18.026	3.849	0.2358	18.329	4.323	0.2497	19.021	4.753
3:00 PM	0.1724	15.977	2.754	0.1885	17.307	3.263	0.2018	18.892	3.812
4:00 PM	0.0636	15.322	0.975	0.0728	17.023	1.239	0.0934	18.723	1.748
5:00 PM	0.0542	14.136	0.766	0.0673	16.453	1.107	0.0734	17.674	1.297

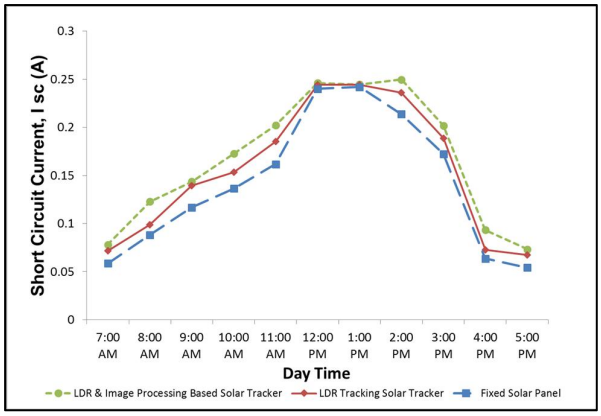

Figure 13. I_{sc}vs Day time for different solar panel system

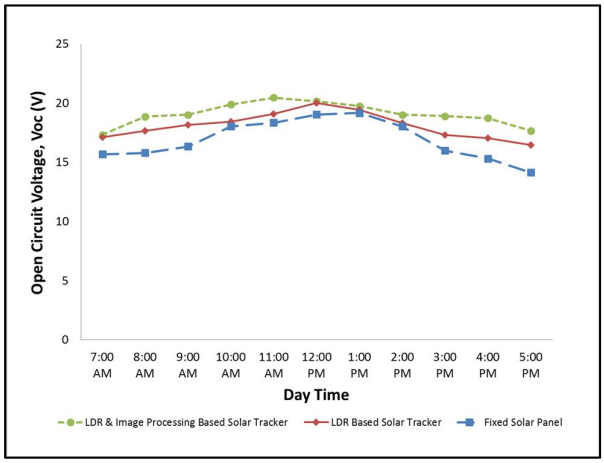

Figure 14. V_{oc} vs Day time for different solar panel system

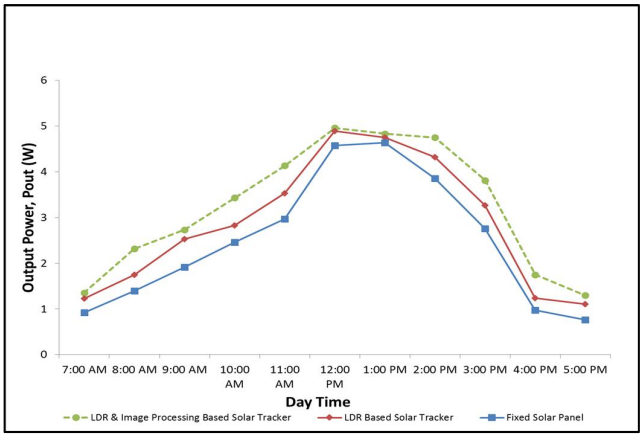

Figure 15. P_{out} vs Day time for different solar panel system

VIII. CONCLUSION

To conclude, it can be said that the proposed system increased the efficiency of the solar panel by tracking the sun in appropriate direction. The mechanism can be more effective if more LDR sensors are used and every solar panel in a particular area has a webcam. But for minimizing cost, thousands or hundreds of solar panel can track the sun using a single arrangement of LDR and a single webcam. The greater the resolution of the camera the better will be the performance of the solar tracking system. Thousands of solar panel can be operated by using this mechanism in the solar power plant. PLC can be used for the controlling purpose of thousands of solar panels. The more cameras be used; the efficiency of solar trackers will be more high. For minimizing cost, Raspberry Pi can be used instead of computer. The motors and microcontroller can be fed through the power produced by the solar panel itself. After all, we can say that the proposed system can optimize the power requirement by tracking the sun more appropriately.

REFERENCES

[1] A. Zahedi, "Energy, People, Environment, Development of an integrated renewable energy and energy storage system, an uninterruptible power supply for people and for better environment," Int'l Conf. on Systems, Man, and Cybernetics, 1994. 'Humans, Information and Technology', vol. 3, pp. 2692-2695, 1994.

[2] M. A. Green, “Clean Electricity from Photovoltaics,” Ed. Mary D. Archer and R. Hill, Series on Photo conversion of Solar Energy, vol.1, Imperial College Press, UK.
[3] D. Appleyard, “Solar Trackers: Facing the Sun,” Renewable Energy World Magazine, UK: Ralph Boon, June 1, 2009.
[4] M. T. A. Khan, S.M. S. Tanzil, R. Rahman, and S M S. Alam, “Design and Construction of an Automatic Solar Tracking System,” 6th International Conference on Electrical and Computer Engineering, Dhaka, Bangladesh, December 18-20, 2010.
[5] C. Hua and C. Shen, “Comparative study of peak power tracking techniques for solar storage system,’’ Applied Power Electronics Conference and Exposition, vol. 2, pp. 679-685, February 15-19, 1998.
[6] A. K. Saxena and V. Dutta, “A versatile microprocessor based controller for solar tracking,’’ Photovoltaic Specialists Conference, vol. 2, pp. 1105-1109, 1990.
[7] B. Koyuncu and K. Balasubramanian, “A microprocessor controlled automatic sun tracker,’’ IEEE Transactions on Consumer Electronics, vol. 37, no. 4, pp. 913-917, 1991.
[8] O. Bingol, A. Altinta, and Y. Oner, “Microcontroller based solar tracking system and its implementation,” Journal of Engineering Sciences, vol. 12, pp. 243–248, 2006.
[9] M. F. Khan and R. L. Ali, “Automatic sun tracking system,” All Pakistan Engineering Conference, Islamabad, Pakistan, 2005.
[10] H. Peng , T. Du, and W. G, “Application Design of A Sun-Tracking System,” 25th Chinese Control and Decision conference(CCDC) , 2013
[11] S. Wang, W. Gao, and S.Huang, “Research on the mixed two-axes sun tracker,” Renewable Energy Resources, vol.25, no.6, pp.10-13, 2007.
[12] J. Xiu, “GA based T-S type model of switched reluctance motor,” Micromotors, vol.42, no.3, pp.27-31, 2009.

Effect of Different Solar Radiation on the Efficiency of $GaInP_2/GaAs/Ge$ based MultiJunction Solar Cell

Syed Nazmus Sakib
Syeda Puspita Mouri
and Zannatul Ferdous
Dept. of Electrical, Electronic &
Communication Engineering
MIST, Dhaka, Bangladesh
Email:s.nazmus.sakib@ieee.org

Abu Kowsar
Institute of Fuel Research and Development
Bangladesh Council of Scientific
and Industrial Research

M. Shamim Kaiser
Institute of Information Technology
Jahangirnagar University
Savar, Bangladesh
Email:mskaiser@juniv.edu

***Abstract*—This paper represents the effect of solar radiance on the efficiency of GaInP$_2$/GaAs/Ge based multi junction solar cell. Solar radiation changes with the different wavelength and air mass. With the change in the irradiance data, the theoretical efficiency of the multi junction solar cell changes. The whole calculation is based on a modified version of spectral p-n junction solar cell model. The three sub layers are lattice matched and connected in series so that optical transparency and maximum current conductivity through the top and bottom cell can be produced. Short circuit current density, open circuit voltage, maximum current density, maximum power, fill factor and efficiency change with the variation of irradiance for the different air mass. For the simplicity of calculation, there are some assumptions which are necessary. The analysis is done under one sun condition. The J-V curves is also plotted for different layers under different air mass condition.**

***Index Terms*—multijunction solar cell, efficiency, air mass, current density, irradiance**

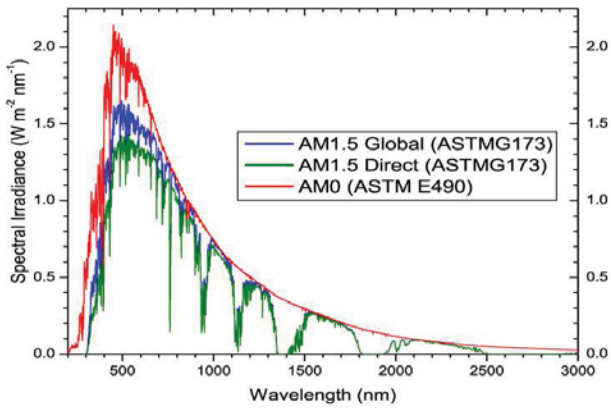

Fig. 1. Spectral irradiance for the different AM

I. Introduction

Power crisis has been one of the most significant issues all over the world. Scientists and researchers have been working relentlessly to find a solution for this problem. Most of them are doing their work on renewable energy. Because the amount of energy that can be generated from coal, gas or any other petroleum materials is limited. So scientists are more encouraged to work on the renewable energy sources for its unlimited availability. Among all the renewable energy sources, solar energy has got more popularity than all the others. Many works have been done to increase the efficiency of the solar cell.

Single junction solar cell was first introduced. But the efficiency of this solar cell is very low because the maximum efficiency depends on the incident spectrum [1]. The reason working behind that is, there is a good amount of solar spectrum remains unabsorbed due to the single junction. As the absorption is done by only one layer, the energy of the photon greater than the band gap cannot be absorbed by the single junction.

The researchers then developed an idea of converting different parts of solar spectrum that will be incident to the cell. This idea was considered since 1995 [2] [3]. So to reduce the losses and to increase the efficiency of solar cell, multi junction solar cell is introduced. With the innovation of multi junction solar cell, different solar spectrum now can be absorbed by the different layer of the multi junction solar cell. So the losses are reduced that results in increasing the efficiency.

In the figure: 1, it is clearly seen the solar spectra for different air mass [4]. From the figure it is seen that in multi junction solar cell it is possible to absorb most portions of solar radiation by choosing the band gap of different layers.

For the calculations of different parameters of solar cell, many scientists have given different models. First modern silicon solar cell with efficiency of 6 % has been developed in Bell Laboratory in 1954 [5]. In 1961,William Shockley and Hans Queisser reported the maximum theoretical efficiency of 33.7% for a single junction solar cell [6]. Spectral p-n junction model was published both for single junction cell and tandem

978-1-4673-9257-0/15/$31.00 ©2015 IEEE

cell for infinity thickness cell that is the thickness absorbed all incident irradiance equal or greater than thecorresponding band gap of the material [7]. Considering the thickness and modifying the reversesaturation current density equation, a theoretical model for tandem solar cell was reported [8].

For different value of air mass (AM) condition such as AM0,AM 1.5D and AM 1.5G the efficiency of $GaInP_2$/$GaAs$/Ge based multijunction solar cell has been calculated in this paper.

In this paper, section II depicts the discussion about solar cell and renewable energy, section III describes the multi junction solar cell model parameters, section IV gives the idea about the assumptions that are made for the calculations as well as the optoelectronic parameters of the different layer materials, section V shows the results for three air mass conditions and then the paper is concluded in the next section.

II. Solar Cell

Renewable energy is derived from naturally regenerative sources like solar, wind, geothermal or hydroelectric actions. Among these sources the demand of solar energy is increasing rapidly for its feasibility in developing countries. A solar cell is an electrical device by which light energy can be converted into electricity. The electrical characteristics of this photoelectric cell vary due to the different intensity of light [9]. There are various types of solar cells. Single crystalline i.e. monosilicon solar cell having commercial efficiency of about 22% is mostly used in integrated circuits and processing units of computers.

Thin film solar cells have semitransparent nature with lower efficiency of about 12-20%.The third generation PV cell or Organic PV cell are used for light absorption or electrical charge transport [10]. Single junction solar cells usually have lower efficiency. Increasing short circuit current density by better light trapping the efficiency can be improved for single junction solar cells [11].

III. Multijunction Solar Cell Model

Single junction solar cells have lower efficiency. Increasing the efficiency of PV cell is the main motto of current generation that is why multi junction solar cell is introduced into modern technology. Multijunction solar cells are constructed by connecting two or more p-n junction layers in series. Multijunction solar cells can generate power over a larger spectrum of sunlight having a higher efficiency than single junction solar cells. The lattice of the materials must be matched with each other to produce the same current in the different layers of multijunction solar cell. Thus the design for this kind of solar cell becomes complex with an increasing cost [12].The efficiency can be increased due to the reduction of top cell thickness. Cells with low surface recombination velocities can also help to increase open circuit voltage, resulting in higher efficiency [1]. The irradiance changes with the change in air mass coefficient. Thus the efficiency can be varied by using different air mass coefficient (AM).

The short circuit current density J_sc can be calculated by using irradiance data [13].

$$J_{sc} = eF \tag{1}$$

Where, F is the photon flux and e is the charge of an electron. Again,

$$F = \frac{\lambda I}{hc} \tag{2}$$

Where, is the wavelength, I is the irradiance, h is the Planck's constant and c is the speed of light.

The reverse saturation current density can be expressed as [1] [7] [8],

$$J_0 = e\sqrt{\frac{D_e}{\tau_e}}\frac{n_i^2}{N_A}\left(\frac{S_e\sqrt{\frac{\tau_e}{D_e}}\cosh\left(\frac{x_p}{\sqrt{D_e\tau_e}}\right)+\sinh\left(\frac{x_p}{\sqrt{D_e\tau_e}}\right)}{S_e\sqrt{\frac{\tau_e}{D_e}}\sinh\left(\frac{x_p}{\sqrt{D_e\tau_e}}\right)+\cosh\left(\frac{x_p}{\sqrt{D_e\tau_e}}\right)}\right) + e\sqrt{\frac{D_h}{\tau_h}}\frac{n_i^2}{N_D}\left(\frac{S_h\sqrt{\frac{\tau_h}{D_h}}\cosh\left(\frac{x_n}{\sqrt{D_h\tau_h}}\right)+\sinh\left(\frac{x_n}{\sqrt{D_h\tau_h}}\right)}{S_h\sqrt{\frac{\tau_h}{D_h}}\sinh\left(\frac{x_n}{\sqrt{D_h\tau_h}}\right)+\cosh\left(\frac{x_n}{\sqrt{D_h\tau_h}}\right)}\right) \tag{3}$$

Where, D_e and D_h are the diffusion current constant for electron and hole respectively. $N_A$is acceptor concentration, N_D is donor concentration, S_e and S_h are the surface recombination for electron and hole respectively, n_i is the intrinsic carrier concentration, τ_e is the minority carrier lifetime for electron and τ_h is the minority carrier lifetime for hole, x_p and x_n are the thickness of p-layer and n-layer respectively.

For the ease of calculation the above equation can be simplified as,

$$J_0 = eS_e\frac{n_i^2}{N_A} + eS_h\frac{n_i^2}{N_D} \tag{4}$$

The diffusion constants can be calculated from the Einstein Relationship,

$$D_e = kT\frac{\mu_e}{e}$$
$$D_h = kT\frac{\mu_h}{e}$$

Where, k is the Boltzmann's constant, μ_e is the electron mobility and μ_h is the hole mobility. The equation for minority carrier lifetime for electron and hole are:

$$\tau_e = \frac{1}{\frac{1}{\tau_{SRH}} + BN_D}$$
$$\tau_h = \frac{1}{\frac{1}{\tau_{SRH}} + BN_D}$$

B is the direct band-band recombination coefficient and is the Shockley-Read-Hall lifetime. The surface recombination velocities for electron and hole can be written as:

$$S_e = \sqrt{\frac{D_e}{\tau_e}}$$
$$S_h = \sqrt{\frac{D_h}{\tau_h}}$$

The intrinsic carrier concentration can be calculated from:

$$n_i^2 = 4M_cM_v\left(\frac{2\pi kT}{h^2}\right)^3 (m_e^* m_h^*)^{\frac{3}{2}} \exp\frac{-E_g}{kT}$$

Where, M_c and M_v are the densities of states in the conduction and valance band, T is the temperature, E_g is the energy gap of the material, $^*_e$ and m_h^* are the effective mass of electrons and holes respectively, M_c and M_v are the number of equivalent minima in the conduction and valance band. The open circuit voltage can be expressed as:

$$V_{oc} = \left(\frac{kT}{e}\right)\ln\left(\left(\frac{J_{sc}}{J_0}\right)+1\right) \tag{5}$$

The maximum voltage is:

$$V_m = V_{oc} - \frac{1}{\beta}\ln(1+\beta V_m)$$

Maximum current density is:

$$J_m = J_{sc}\left(1 - \frac{1}{\beta V_m}\right)$$

The final equation for the efficiency of the solar cell is:

$$\eta = \frac{V_{oc}J_{sc}F.F.}{P_{in}} \times 100\%$$

Where, P_{in} is the input power and F.F. is the fill factor

IV. ASSUMPTIONS AND PARAMETERS

The parameters that are required for calculation of different layers of the semiconductor materials are considered at the temperature of 298K. The input power densities for AM0 is 1353 W/m^2 and for AM1.5G is 1000 W/m^2 and for AM1.5D is 900 W/m^2 [14] [15] [16]. It is also assumed that there are no losses regarding reflection, grid coverage and series resistance. All the calculations are done using the modified versions of standard equations that is the modified version of spectral p-n junction model [1] [8]. The value of irradiance data is gathered from the data provided by ASTM [17].

It has been considered that, there is no carrier generation or recombination in the space charge region, neutral region operates at low injection condition and electric field in neutral region is negligible and photon recycling effects are also negligible.

The optoelectronic parameters are collected for 298K temperature [18] [19] for the different materials used for the three layers.Taking the values of different parameters from the table I, the calculations are done for the various equations that are mentioned in the previous section. The three materials that are chosen for the different layers are lattice matched.

TABLE I
OPTOELECTRONIC PARAMETERS [18] [19]

Parameter	$GaInP_2$	$GaAs$	Ge
Band Gap,(E_g) eV	1.9	1.42	0.67
wavelength,(λ) nm	654.28	875	1775
No of Equivalent Minima in Conduction Band (M_c)	1	1	1
No of Equivalent Maxima in Conduction Band (M_v)	3	1	1
electron mobility (η_e) m^2/Vs	0.4	0.2322	0.39
hole mobility (η_h) m^2/Vs	0.02	0.02	0.19
m_c^*/m_e	0.155	0.067	1.64
m_h^*/m_h	0.460	0.473	0.28
Shockley-Read-Hall Lifetime(T_{SRH}) s	10^{-5}	10^{-5}	10^{-5}
Direct band-band recombination co-efficient(B) s^1m^3	7.5×10^{-16}	7.5×10^{-16}	7.5×10^{-16}
Acceptor Concentration (N_A) m^{-3}	1×10^{23}	9×10^{23}	1×10^{23}
Donor Concentration (N_D) m^{-3}	2×10^{24}	7.8×10^{23}	2×10^{24}
Thickness of p-layer(X_p) m	1×10^{-07}	1×10^{-07}	1×10^{-07}
Thickness of n-layer(X_n) m	2.08×10^{-07}	3×10^{-07}	4×10^{-07}
Lattice constant (a) m	5.660×10^{-10}	5.659×10^{-10}	5.646×10^{-10}

Most of the parameters are dependent on the temperature. So if the temperature is changed, the values of these parameters will change. The thickness of the p layer is kept same for the each layer whereas the thickness for the m layer is different for the three layers of the multi junction solar cell.

V. RESULTS

Using the different equations mentioned in section III the following calculations are done. MATLAB is used for the calculations of the different parameters.

In table II the variations of short circuit current density and the open circuit voltage of the three layers for different air mass condition is shown.

Table III depicts the variations in overall current density, total open circuit voltage, maximum voltage, maximum current density, fill factor and efficiency of the solar cell for different solar radiation spectrum for different air mass.

The total leakage current density vs the open circuit voltage for each multi junction solar cell under different air mass solar radiation spectrum is plotted in the graph.

Figure:2 shows the J-V characteristic for solar radiation spectrum under AM0 condition, figure: 3 shows the J-V

TABLE II
COMPARISON OF DIFFERENT LAYERS

Parameters	AM0	AM 1.5 G	AM 1.5D
Top Layer $GaInP_2$			
Short circuit current density(J_{sc1}), A/m^2	828.9520	744.89	674.0564
Open circuit voltage(V_{oc1}), V	1.4387	1.4300	1.4334
Mid Layer $GaAs$			
Short circuit current density(J_{sc2}), A/m^2	658.5420	652.39	623.859
Open circuit voltage(V_{oc2}), V	1.0418	1.0415	1.0404
Bottom Layer Ge			
Short circuit current density(J_{sc3}), A/m^2	251.3022	163.9747	160.1052
Open circuit voltage(V_{oc3}), V	0.1325	0.1216	0.1210

TABLE III
COMPARISON OF THE TOTAL CELL PARAMETER

Parameters	AM0	AM 1.5 G	AM 1.5D
Short circuit current density(J_{sc}), A/m^2	251.3022	163.9747	160.1052
Total open circuit voltage(V_{oc}), V	2.6129	2.5991	2.5947
Maximum voltage (V_m), V	2.4939	2.4802	2.4759
Maximum current density (J_m), A/m^2	248.7122	162.2754	158.4431
Fill Factor (F.F.)	0.9446	0.9444	0.9443
Power input (P_{in}) , W/m^2	1353	1000	900
Efficiency (η), %	45.8441	40.2482	43.5879

characteristic for solar radiation spectrum under AM1.5D condition & figure: 4 shows the J-V characteristic for solar radiation spectrum under AM1.5G condition.

The total leakage current density is different for different layer and also for different solar radiation spectrum. The reason behind this is the short circuit density is dependent on the irradiance. The value of irradiance varies for the different wavelength. The wavelength is different for different band gap as well as for different layers for absorption. So as the value of irradiance is varying so does the total leakage current density.

For AM0 condition, the value of irradiance data [20] is higher than that of the AM1.5G and AM1.5D.because AM0 is suitable condition for space where the solar radiation is much more than the earth surface. The data that is used is generated by the American Society for Testing and materials (ASTM). It is one of the most accurate and recognized data for multi junction solar cell which is developed by counting one year average weather of United States of America [14]. Efficiency

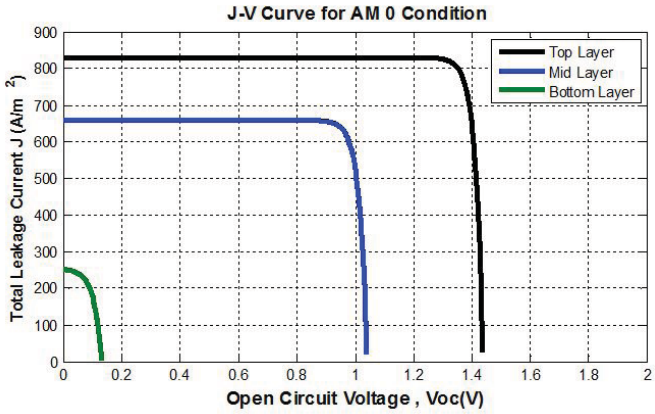

Fig. 2. J-V characteristic for AM0

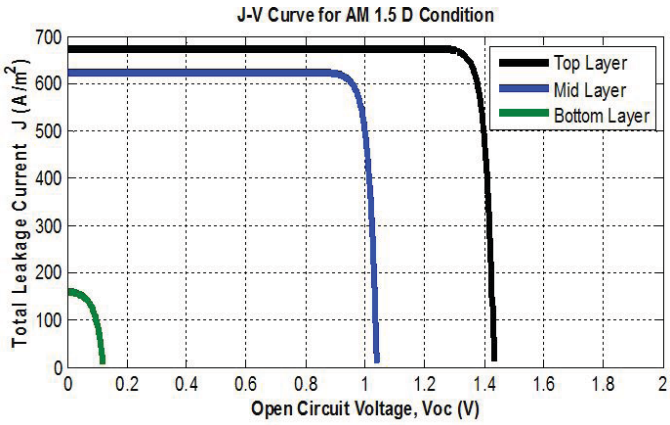

Fig. 3. J-V characteristic for AM1.5D

for AM1.5D is greater than the efficiency for AM1.5G because sunlight hit the solar cell directly in case of AM1.5D and for AM1.5G sunlight hit the solar cell after diffusion.

In the above figures, it is clearly seen that the total leakage current density remains same for a certain increment of open circuit voltage. But after a certain voltage the current density falls. By finding a maximum current and voltage and

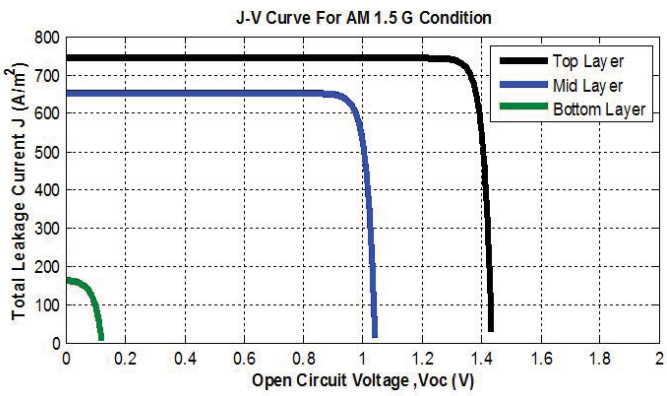

Fig. 4. J-V characteristic for AM1.5G

multiplying them maximum power can found for the solar cell.

In each solar cell, the minimum leakage current is flowing from the bottom layer. So the total cell current density will be the value of the bottom cell current density. So to increase the cell efficiency, the increase of leakage of current density in the bottom cell is necessary.

This characteristic may change in the practical scenario as there are losses. Conditions like carrier recombination in the space charge region, operating injection condition of neutral region, the amount of electric field in the neutral region, effects of photon recycling can cause decrement to the leakage current density and open circuit voltage leads to the reduction in the maximum power resulting in reducing the overall efficiency.

VI. Conclusion

The paper represents the variations in efficiency of GaInP2/GaAs/Ge based multijunction solar cell in different AM conditions such as AM0 , AM1.5D & AM 1.5G. Parameters such as short circuit current density, open circuit voltage also vary in each of the three layers considering change in AM condition. Maximum current density ,maximum voltage & total leakage current for the cell shows a significant change for diverse air mass values. For the three layer solar cell, the minimum current density is found in the bottom cell and it is the current density for the solar cell. As the junctions are connected in series, the open circuit voltage rises as the total open circuit voltage is the summation of three layers open circuit voltages.

References

[1] A. Kowsar, M. S. Islam, K. R. Mehzabeen and Z. H. Mahmood, *Study on the Efficiency of the $GaInP_2$/GaAs/Ge Multijunction Solar Cell*, Proc. of International Conference on Environmental Aspects of Bangladesh (ICEAB10), Japan, Sept. 2010

[2] D. Trivich and P. A. Flinn, *Maximum efficiency of solar energyconversion by quantum processes* , Solar Energy Research, F. Daniels, J. A. Duffie, Eds. Madison, WI: Univ. of Wisconsin Press, 1955, p. 143

[3] E. D. Jackson, Areas for improvement of the semiconductor solarenergy converter, Trans. Intern. Con. *Use of Solar EnergyThe Scientific Basis*, vol. V, p. 122, 1955.

[4] ASTM G-173-03 (International standard ISO 9845-1, 1992)

[5] D. M. Chapin, C. S. Fuller, and G. L. Pearson, *A new silicon p- n junction photocell for converting solar radiation into electricalpower*, Journal of Applied Physics, 25, 1954, 676677..

[6] William Shockley and Hans J. Queisser, *Detailed Balance Limit of Efficiency of p-n Junction Solar*, Journal of Applied Physics, 32, 1961, 510-519

[7] E. M. Nell and A. M. Barnett, *The spectral p-n junction model for tandem solar-cell design*, IEEE Transaction on Electron Devices,Ed-34, No. 2, 1987, 257-266.

[8] S. R. Kurtz, P. Faine, J. M. Olson, *Modeling of two-junction, series-connected tandem solar cells using top-cell thickness as anadjustable parameter*, Journal of Applied Physics, 68 (4), 1990, 1890 1895

[9] L.A. Coldren and S.W. Corzine, *"Diode Lasers and Photonic Integrated Circuits"* ,Wiley Interscience, 1995.

[10] F. Meillaud, A. Shah, C. Droz, E. Vallat-Sauvain, C. Miazza, *Efficiency limits for single-junction and tandem solar cells*, Institute of Microtechnology (IMT), University of Neuchtel, A.-L Breguet 2, 2000 Neuchtel, Switzerlan.

[11] *Solar Tech-USA* http://www.solartech-usa.com/types-of-solar-cells.

[12] Andrew Bates, Sherif Michael, *The Design and Optimization of an Advanced Four Junction Solar Cell*, Naval Postgraduate School, Monterey, California, 93955

[13] R. Hulstrom, R. Bird and C. Riordan, *Spectral solar irradiance datasets for selected terrestrial condition*, solar cells 15(1985) 365 391

[14] ASTM Standard G173, *Standard Tables for Reference Solar Spectral Irradiance:Direct Normal and Hemispherial on 37o Tilled Surface,* , Amer. Society for Testing Matls. West Conshochen PA, USA 2007.

[15] K. W. Mitchell, *High efficiency concentrator solar cells,*, Conf., of 15th IEEE Photovoltaic specialists con., pp . 142-146, 1981.

[16] Abu Kowsar, Abdullah Yousuf Imam, Mashudur Rahaman, Muhammad ShahriarBashar, Md. Saidul Islam, Sumona Islam, Nowrin Akter Surovi, Zahid Hasan Mahmood, *IOSR Journal of Applied Physics (IOSR-JAP)* Issue 6 Ver. IV (Nov.-Dec. 2014), PP 13-17.

[17] ASTM G173-03 Reference Spectra Derived from SMARTS v. 2.9.2

[18] Hamza Bennacer, Smail Berrah, Abdelkader Boukortt, Mohamed Issam Ziane *Electronic and optical properties of $GaInX_2$ (X= As, P) from first principles study*, Indian Journal of pure & Applied Physics, Vol. 53, March 2015, pp. 181-189.

[19] *Physics of Semicoductor Devices* 3rd Edition by S . M. Sze and Kwok K. Ng, Copyright 2007, John Wiley & Sons, Inc

[20] *Solar Spectra: Air Mass Zero* 2000 ASTM Standard Extraterrestrial Spectrum Reference E-490-00

Multi-agent System Modeling For Managing Limited Distributed Generation of Microgrid

Mirajul Islam, Abu Md. Safiul Alam and C. K. Das
Department of Electrical and Electronic Engineering
Chittagong University of Engineering and Technology
Chittagong-4349, Bangladesh
mirajul.islam075@gmail.com, foisal52cuet@yahoo.com, choton46@gmail.com

***Abstract*— This paper focuses on operation of small scale renewable plants so that the energy produced can be utilized to its highest potential. Energy crisis being one of the main problems is leading the researchers to find fossil fuel replacement which is eventually renewable energy. In most cases, renewable energy is unpredictable as they rely on the nature. Besides, in developing countries it is discouraged to install renewable technology due to their random nature. In order to design a reliable microgrid where renewable resources contribute to its grid power supply, multi-agent system has been incorporated to add intelligence to the system. The various loads to be fed are divided according to importance. The proposed concept also allows sharing of load among utility supply and renewable sources during normal operation.**

***Index Terms*—microgrid, intelligent, multi-agent system, limited renewable resource**

I. INTRODUCTION

Microgrid may be the eventual answer to the present energy crisis that is growing steadily in our world. Implementation of microgrid increases reliability in power distribution system. The utilization of renewable energy in a microgrid though may be a great challenge, this is where the assistance of another system is required which will act as the brain for the microgrid. The multi-agent system (MAS) technology is quite attractive in this respect as it provides a touch of intelligence to the system. There has been significant research on MAS technology in the recent times. MAS use multiple software agents to complete a collective task by dividing and distributing the task among the agents. Renewable energy resources like solar PV, wind turbine etc. contributes a lot to the distributed energy resources (DER) of the microgrid. These renewable energy sources being unpredictable and not always reliable, it becomes a great challenge to utilize them to their highest potential. Hence a system is needed that can adapt to the dynamic behavior of the sources.

Designing agent architecture for microgrid is a complex task. Several studies have been conducted in this field are noteworthy. The research on Intelligent Distributed Autonomous Power System (IDAPS) [1] has discussed on developing architecture for an intelligent system which works in co-ordination with different agents for managing customer owned units in the distribution network. Another research on securing critical loads in a PV-based microgrid with multi-agent system [2] was conducted which basically focused on the design and implementation of a multi-agent system through simulation. There were further discussions on securing critical loads during grid failure. Practical implementation of a multi-agent system was somewhat achieved in [3]. The research concentrated on building hardware modules for the agents. A research on optimization of solar panel output for microgrid based on multi-agent system has been conducted in [4]. Detailed research on scheduling of distributed generation is discussed in [5]. Some more application of MAS in microgrid have been deliberated in [6]-[8].

The sole purpose of this research is to develop a control mechanism for required agents so that they can respond to the changes in the scenario and act accordingly. It is also intended that the power generated from the renewable sources be wisely utilized in order to reduce power consumption from the utility grid supply. In order to make the research as reliable as possible the load profiles for the microgrid is based on the load of Chittagong University of Engineering & Technology (CUET), Chittagong, Bangladesh.

II. OVERVIEW

The first task was to analyze the electrical loading in different feeders of CUET. The microgrid was designed according to the data acquired from the analysis of the loads. The units comprising the DER of the microgrid were selected. This was followed by choosing of different agents that are responsible for managing the DER output. At last model architecture was developed using the agents.

III. LOAD ANALYSIS

A. Collection of data

The data was collected from CUET substation on an hourly basis for a month. There are in total 11 feeders in this educational facility that provides electricity to various loads.

B. Determination of peak load

The data collected was later processed to a load profile of a single day by taking into count the average loadings of working

978-1-4673-9257-0/15/$31.00 ©2015 IEEE

days in the institution. The list of feeders and their peak loads are given in table I.

TABLE I. ESTIMATED PEAK LOAD FOR EACH FEEDER

Feeders	Details	Daily power consumption (kW)	Estimated Peak loads(KW)
Feeder 0	12 floor engineering building, auditorium, Ansar camp	447	50
Feeder 1	Electrical & Mechanical Engineering building Mechanical Engineering Workshop	319	45
Feeder 2	teachers & officer's quarters	1052	70
Feeder 3	Civil & CSE building	510	50
Feeder 4	Vice Chancellor's Bungalow	172	13
Feeder 5	Sufia Kamal Hall	276	18
Feeder 6	Pump , IRP	546	40
Feeder 7	Shaheed Tareq Huda Hall, Shaheed Mohammad shah Hall and Dr. Qudrate Khuda Hall	1169	72
Feeder 8	Pre-engineering building, VC office, library	781	75
Feeder 9	Staff quarter	509	28
Feeder 10	Bangabandhu Hall, canteen, Bank, Mosque, PME Building	414	35

C. *Load curve*

Each feeder was analyzed in order to get a daily load curve that gives an idea on the load behavior of the grid. The load curve gives better prediction on what the demand will be and measures can be taken accordingly.

For simplicity the load curve of all the feeders united is shown in Fig. 1.

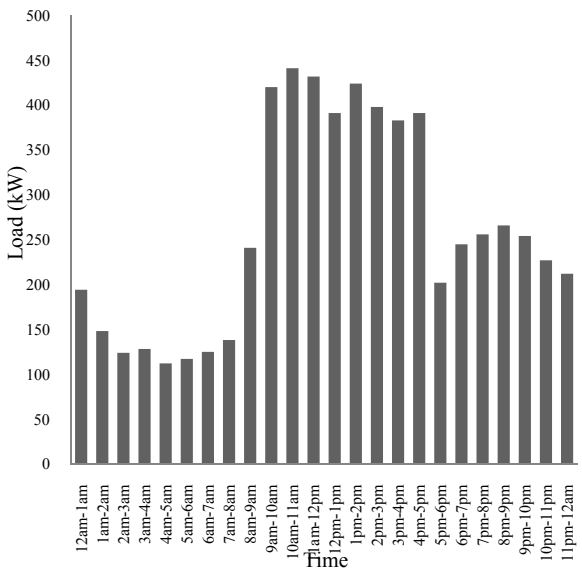

Figure 1. Load curve of the whole system for a single day

From the load curve in Fig. 1 we can observe the electrical activities for a whole day.

IV. MICROGRID MODELING

The microgrid that is intended to design has two parts, the physical part and the virtual part. The virtual part will be discussed later. The distribution system is divided into two parts, (i) utility grid and (ii) DER grid. Considering each feeder as a subsystem that consists of the load, we have 11 subsystems. These subsystems will be powered by utility grid supply and the DER sources. The DER sources include a PV panel and a diesel generator. The different parts of the microgrid are briefly discussed below.

A. *Utility Grid*

Two lines have merged, one from Madunaghat substation and the other from Chandraghona substation supplying 33kV line to the CUET substation.

B. *The subsystems*

The 33kV line is further stepped down to 11kV and then again to 380V. This line is fed to all the feeders. As mentioned earlier, different feeders are considered as subsystems that will denote the loads. The subsystems are further divided into critical and non-critical loads. The selection of critical load depends on the type of load that is to be supplied. Critical loads for residential purpose will differ from that in a class room.

C. *The DER grid*

For efficient distribution of energy, DER grid has been designed to operate isolated from the utility grid. For this research, it is vital fact as the alternative sources which we selected are not able to fully sustain all the critical loads during outage or fault.

The DER grid as mentioned earlier is powered by a PV module and a diesel generator as discussed below:

1) PV module: We assume that a 50kW solar PV panel provided with a battery is existent in our system.

2) Diesel generator: A diesel generator of 67.5kVA is being used for our model.

Each subsystem is provided supply from the DER grid. Another important fact for the diesel generator is that it will only be activated during 'emergency' protocol. The 'emergency' protocol is a manual override during which the diesel generator will be allowed to supply power. The schematic diagram of the whole system is shown in Fig. 2.

V. SELECTION OF CRITICAL LOAD

Selection of critical load is very important for our microgrid design. Critical loads may vary from subsystem to subsystem. At optimum condition, a total of 50 + 67.5 = 117.5 kW (considering power factor unity) can be generated. Owing to the fact that there are several unavoidable losses, the sum is multiplied by a factor of 0.9 which leads to getable power of 105.75kW. Hence while selecting critical loads each subsystem

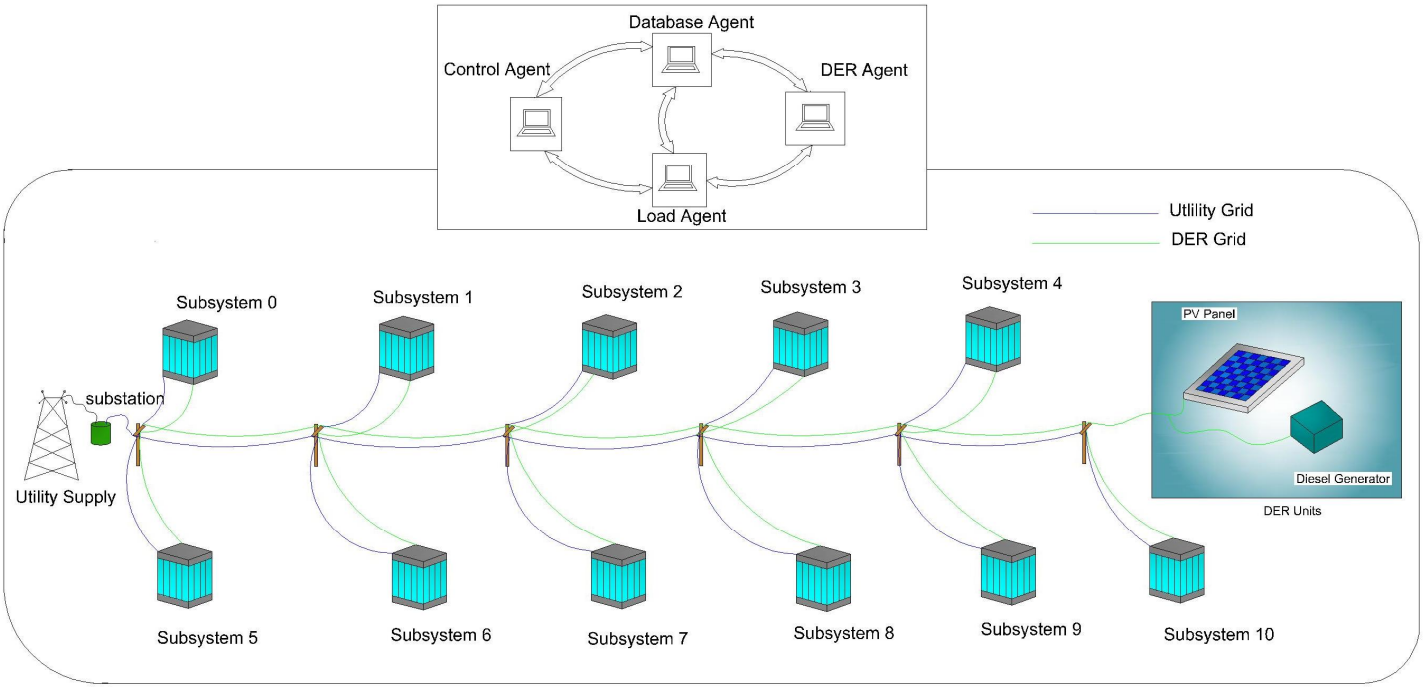

Figure 2. Schematic diagram of the Microgrid in collaboration of MAS

will be assigned a specific amount of loads to gain supply. The selection of load was done according to the need of the subsystem. The allocation of critical loads for each substation is given in table II.

TABLE II. CRITICAL LOAD ALLOCATION

Subsystem	Types of load	Allocated load in kW
0	light, fan, multimedia projectors	12.5
1	light, fan, multimedia projectors, computer	11.5
2	light, fan	18
3	light, fan, multimedia projectors, computer	13
4	light, fan	4
5	light, fan	4.5
6	pump, street lamps	10
7	light, fan	15
8	light, fan, computers	20
9	light, fan	8
10	light, fan , computers	9
	Total	**125.5**

From the table, we observe that a total of 125.5 kW load has been assigned and our total getable power is 105.75 kW. Moreover, the diesel generator is not intended to be used until dire need arises. Hence, distributing the 50 kW PV output among the loads is our main objective.

VI. MULTI-AGENT ARCHITECTURE

According to the requirements of our microgrid the agents are to be selected. The agents must be well defined in order to complete their assigned tasks.

A. Selection of agents

Four agents are required to achieve the goal that has been set. They are,

1) Control Agent: Control agent acts as the actuator of the decisions that are taken. It controls all circuit breakers (CB).

2) Load Agent: Load agent monitors the voltage and frequency of the different subsystem. It sends power request during fault or outages.

3) DER Agent: DER agent monitors the output from the various DER sources. It also checks fuel inventory for diesel generator.

4) Database Agent: Database agent stores data in the form of log.

B. Assign task to the agents

In order to function the agents properly, primarily their tasks and goals have to be set. The tasks are discussed as follows

1) Islanding: This the task performed by the database agent when fault occurs in the utility grid. The other agents are informed about the fault. During islanding the internal grid system is isolated from utility grid.

2) Load shed: This task is performed by the control agent. During islanding all the non-critical loads are shed by invoking this task

3) Emergency: The database agent responds to this task and broadcasts if emergency protocol has been activated

4) Check DER output: The DER agent performs this task by continuously monitoring the output of various DER sources.

5) Check inventory: The DER agent monitors the fuel inventory for diesel generator through this task.

6) Check demand: The load agent checks the voltage and current of various loads through this task.

7) CB open/close: This task is performed by the control agent. Through this task, command signal are sent to the circuit breakers to open or close.

8) Check priority: Priority is a floating number assigned to each subsystem from 0-1. Higher the value the greater the priority.

C. Agent Collaboration

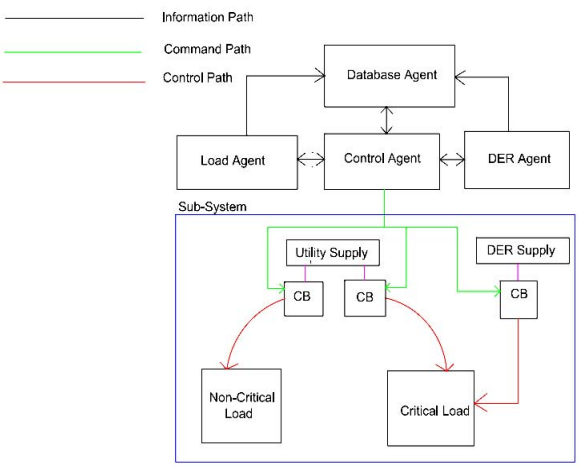

Figure 3. Agent Collaboration

Analogy of a single substation is shown in the Fig. 3. The load agent and the DER agent constantly update the database. The control agent checks for any fault or emergency and acts accordingly. Control agent also controls the circuit breakers that provide power to the loads.

D. Agent Algorithm

The main objective of the agents is to distribute the power output from the DER grid as efficiently as possible. The flow diagram of the control algorithm is shown in Fig. 4.

Suppose an outage occurs, so the grid algorithm will be objected to restore power in the DER grid. At first the subsystem with highest priority is chosen. The output power of the PV panel and the demand of the subsystem are checked. If the demand is less than or equal to the output, circuit breaker to the critical load is closed. If the demand is greater, although being of higher priority the subsystem is ignored. Then the process is repeated for the next priorities until all the subsystem are checked. The system will check if emergency protocol is activated. If not then the system remain as it is until the priority changes or PV output changes.

Next, if there is emergency then the fuel inventory are checked. If there are sufficient supplies, the generator will start. Subsystems those which were ignored will be checked again. If the demand and output match then the critical circuit breaker will close or the system will stay as it is until the priority changes or there is short of supplies.

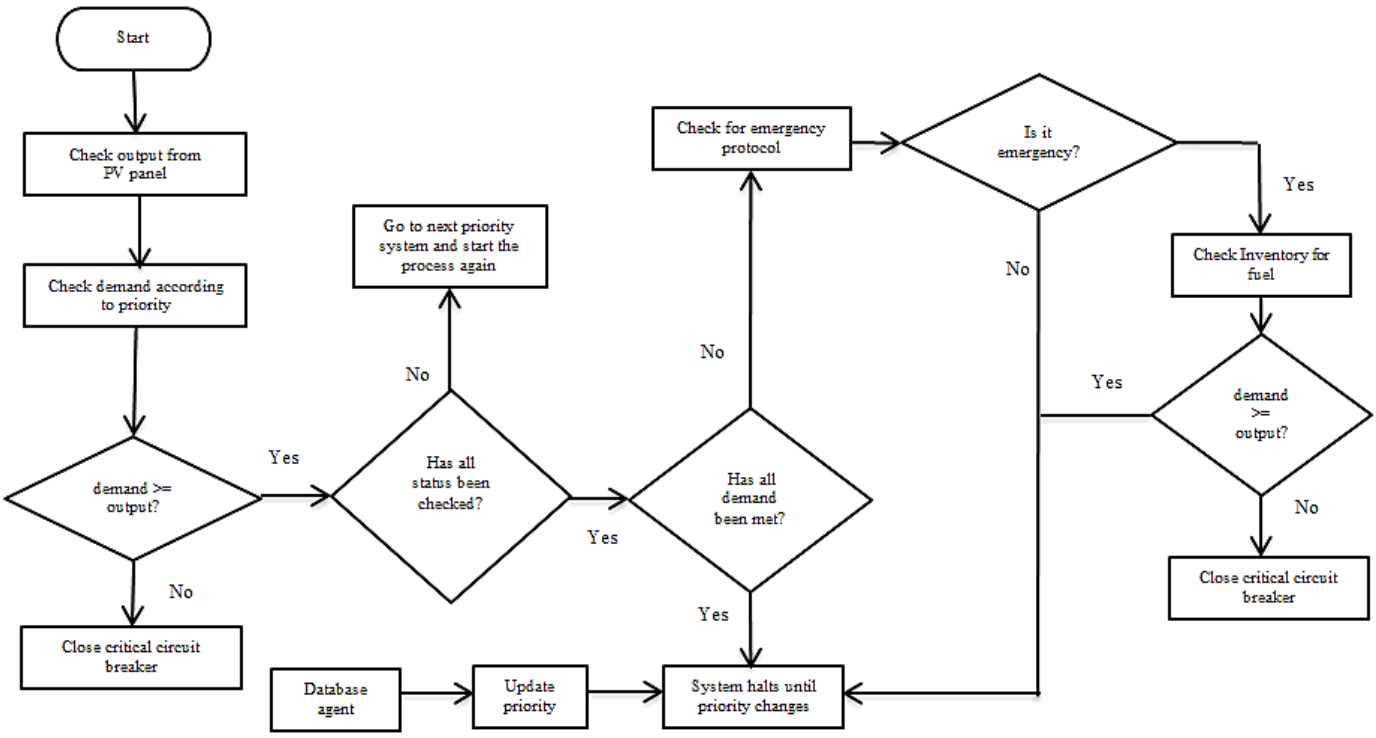

Figure 4. Control analogy for distribution of DER output during outage, fault or load sharing

VII. MICROGRID FEATURES

The designed microgrid has two noteworthy features as discussed below:

A. Islanding Mode

The islanding mode is a very important feature of the microgrid. It protects the microgrid from external fault by isolating it. This feature helps in prevention of blackout, brownout or any other utility grid faults affecting the system.

B. Load Sharing Mode

The designed microgrid not only restores power during outages but also reduces load on utility supply whenever the PV panel is producing enough. The load is at its peak during 9am to 4pm. During this time the PV panel also produces sufficient power. So the critical load which can be sustained by the PV supply are disconnected from the main grid and instead powered by the DER grid. The reduction in power consumption can be shown in Fig. 5.

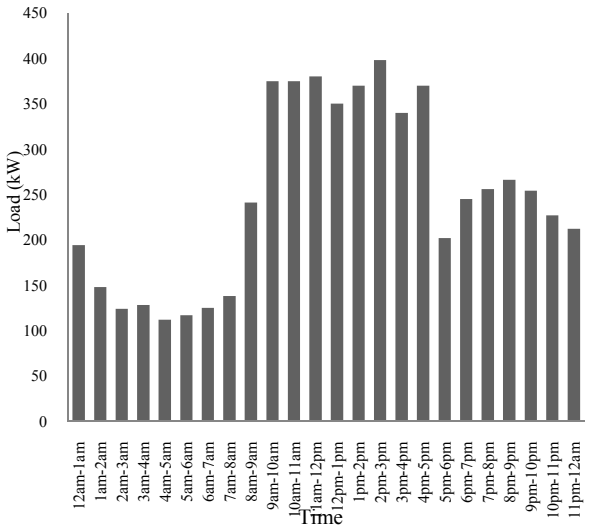

Figure 5. Load curve of the whole system while load sharing

It can be observed that the peak power demand has reduced to 360kW which was around 400kW initially.

VIII. SYSTEM REALIZATION

Multi-agent system realization has been shown in various research works. Some published researches on realization of the system have been mentioned in [9]-[12]. Although system realization is beyond the scope of this research, but a brief process is discussed as follows.

In most of the cases, the microgrid is simulated using MATLAB/Simulink. The loads, sources and other components are available in the library. The agents are developed using agent building toolkit such as JADE [13] and Zeus [14]. The physical system i.e. the microgrid developed in Simulink and the virtual system which are the agents are connected over a TCP/IP connection. The TCP/IP protocol allows computer of different sizes and operating system to communicate with each other [15]. Then a third party software [16] is used to establish the link. The agents communicate among themselves in various ways. For ZEUS based agent architecture, message is exchanged among the agents as a means of communication [2]. In case of IP based network, the agents are placed at single server [12] where they can communicate among themselves easily.

The physical system can be implemented in several ways. In this research, different grid for utility supply and DER supply has been used. The one line diagram of a single system is shown in Fig. 6. The other subsystems also have a similar arrangement. The critical load circuit breakers, non-critical load circuit breakers and the DER control circuit breakers are controlled by the agents while the LV circuit breakeris dependant on fault conditions.

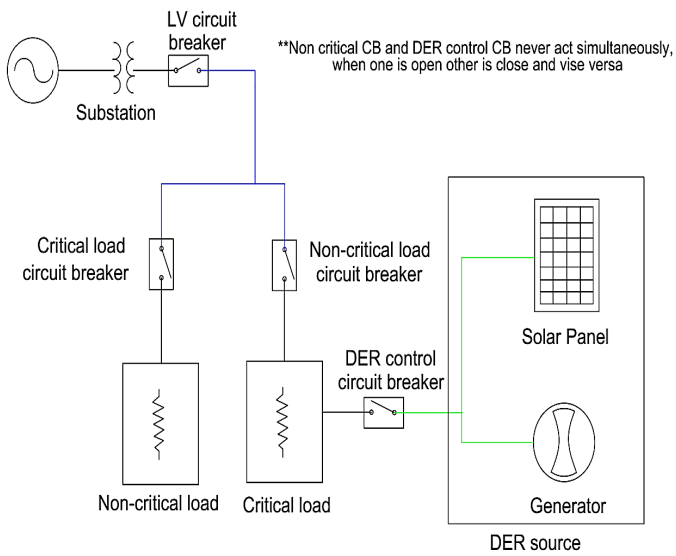

Figure 6. One line diagram of a single subsystem

IX. RESULT AND DISCUSSION

The load analysis revealed that most of the electrical activities are around 9 am to 5pm when the peak load is about 400 kW. For supplying a critical load of 125.5 kW a collective distributed generation of 105 kW is available. In order to distribute the power generated by the PV panel and the generator, the algorithm proposed earlier for scheduling the distributed generation is quite important. Some test conditions are applied to the algorithm and the results are tabulated in table III & table IV.

The four agents as defined earlier are able to function properly to achieve the goal of proper distribution of limited distributed generation. This gives a lot of option and alternative to make an efficient scheduling for distributed generation. Even when there is no sunlight the grid can be supplied by the

generator without taking the machine to overload conditions. If any unit is added or is unavailable the agents will act accordingly to maintain power supply.

Two cases have been shown for visualization of the effectiveness of the algorithm. In the first case only, a PV output of 50 kW is incorporated as shown in table III. In the second case, a combined output of which the PV output of 30 kW and the generator supply of 67.5 kW is considered. For both cases, the priority orders are set as depicted in table III and table IV.

TABLE III. SCHEDULING WHEN PV OUTPUT IS 50 KW AND GENERATOR IS OFF

Sub-system	Priority order	Critical load in kW	State of DER control CB	Power supplied by		
				Grid	PV	Gener-ator
0	1	12.5	closed		✓	
1	2	11.5	closed		✓	
2	3	18	closed		✓	
3	4	13	open	-	-	-
4	5	4	closed		✓	
5	6	4.5	open	-	-	-
6	7	10	open	-	-	-
7	8	15	open	-	-	-
8	9	20	open	-	-	-
9	10	8	open	-	-	-
10	11	9	open	-	-	-
Demand fulfilled by PV				**45.5 kW**		
Demand fulfilled by generator				**0 kW**		

TABLE IV. SCHEDULING WHEN PV OUTPUT IS 30 KW AND GENERATOR IS ON (67.5 KW)

Subs-ystem	Priority order	Critical load in kW	State of DER control CB	Power supplied by		
				Grid	PV	Gener-ator
0	1	12.5	closed		✓	
1	2	11.5	closed		✓	
2	3	18	closed			✓
3	4	13	closed			✓
4	5	4	closed		✓	
5	6	4.5	closed			✓
6	7	10	closed			✓
7	8	15	closed			✓
8	9	20	open	-	-	-
9	10	8	open	-	-	-
10	11	9	open	-	-	-
Demand fulfilled by PV				**28 kW**		
Demand fulfilled by generator				**60.5 kW**		

Power consumption can be reduced up to 10% when running on load sharing mode.

X. CONCLUSION

In this research, a microgrid model is designed for adapting to limited DER supply. The multi-agent architecture is also developed which incorporated with the microgrid helps to develop an autonomous system which is able to adapt to the dynamic behavior of the renewable energy sources. The control algorithm ensured that the system is a reliable and efficient. Successful implementation of small scale renewable power plants will encourage the initiative of making larger plants. Besides, the system is also able to deal with faults and outages and take necessary actions.

Automation of electrification in case of microgrid opens up a lot of scope in research. Meshing up two or three microgrids and sharing power among them is also possible. Hence, a market can be created where power will be the currency. Agent behavior and performance can be greatly enhanced by the use of neural network and fuzzy logic.

REFERENCES

[1] S. Rahman, M. Pipattanasomporn and Y. Teklu, "Intelligent Distributed Autonomous Power Systems (IDAPS)", in *Proc. of the IEEE PES Annual General Meeting,* Tampa, Florida, Jun. 2007, pp. 8.

[2] M. Pipattanasomporn, H. Feroze and S. Rahman, "Securing critical loads in a PV-based microgrid with a multi-agent system", in *Proc. Elsevier B.V.,Renewable Energy*, v.39, no.1,pp. 166-174, Mar. 2012

[3] Il-Yop Chung, Cheol-HeeYoo and Sang-Jin Oh, "Distributed Intelligent Microgrid Control Using Multi-Agent Systems", Engineering, vol 5, Jan. 2013, pp:1-6.

[4] L. Rajua, S. Sankar and R. S. Milton "Distributed Optimization of Solar Micro-grid using Multi Agent Reinforcement Learning*",in Proc. Elsvier B. V. Procedia Computer Science*, v 46, 2015, pp 231-239

[5] Y.S. Foo Eddy, H.B. Gooi and S.X Chen., "Multi-Agent System for Distributed Management of Microgrids", in *Proc. Power Systems, IEEE Transactions* on , vol.30, no.1, Jan. 2015, pp.24,34.

[6] P. Oliveira, T. Pinto, I. Praca, Z. Vale, and H. Morais, "Intelligent micro grid management using a multi-agent approach," in *PowerTech (POWERTECH), IEEE Grenoble*, 2013, pp. 1–6.

[7] D.H. Moore, J.M Murray, F.P. Maturana, T Wendel, "Agent-based control of a DC MicroGrid" in *2013 IEEE Energytech*, Cleveland 2013, pp. 1–6.

[8] F. Ibarra Hernandez , C. A. Canesin , R. Zamora , F. Martina , and A. K. Srivastava , " Energy management and control for islanded microgrid using multi-agents," in *North American Power Symposium (NAPS)*, 22–24 September 2013, pp. 1, 6.

[9] M. Pipattanasomporn, H. Feroze, S. Rahman, "Multi-Agent Systems in a Distributed Smart Grid: Design and Implementation," *Proc. IEEEIPES 2009 Power Systems Conference and Exposition*, Mar. 2009, pp. 1-8.

[10] T. Logenthiran, D. Srinivasan, and D. Wong, "Multi-agent coordination for DER in MicroGrid," in *Proc. IEEE Int. Conf. Sustainable Energy Technologies*, Singapore, 2008, pp. 77–82.

[11] E. Kremers, J. Gonzalez de Durana and O. Barambones "Multi-agent modeling for the simulation of a simple smart microgrid" *Energy Conversion and Management*, Nov. 2013, vol. 75, pp. 643-650.

[12] T. Li, Z. Xiao, M. Huang and J. Yu "Control System Simulation of Microgrid Based on IP and Multi-Agent*", International Conference on Information, Networking and Automation (ICINA)*, Kunming, Oct. 2010, vol. 1, pp. 235-239.

[13] Zeus agent development toolkit [Online]. Available: http://labs.bt.com/projects/agents/zeus/. (23rd Mar. 2015)

[14] JADE agent development toolkit [Online]. Available: http://jade.tilab.com. (23rd Mar. 2015)

[15] W. Richard Stevens, *TCP/IP Illustrated Volume 1*, the Protocols, pp. 15.

[16] Zimmermann W. IOlib e Hardware Input/Output Library for Matlab and Simulink [Online]. Available, http://www.it.hs-esslingen.de/wzimmerma/software/index_uk.html; April 2011. Retrieved.

Renewable Energy Based Hybrid Power System: the Best Way to Keep the World Pollution Free from GHG

Md. Nurunnabi
Department of Electrical and Electronic Engineering
Khulna University of Engineering and Technology
Khulna-9203, Bangladesh
Email: nurnabi32@yahoo.com

N. K. Roy
Department of Electrical and Electronic Engineering
Khulna University of Engineering and Technology
Khulna-9203, Bangladesh
Email: nkroy@eee.kuet.ac.bd

***Abstract*—Current power generation scenarios all over the world are not climate friendly as the generation systems are mainly dependent on fossil fuels that produce greenhouse gas (GHG) which contributes to global warming. This paper conducts a feasibility analysis to explore the potentialities of green energy at Kuakata in Bangladesh. The considered renewable energies for investigation are solar and wind. Initially, a hybrid model has been designed with varying the contribution of renewable resources for the considered coastal region of Bangladesh using Hybrid Optimization Model for Electric Renewable (HOMER) software. This model explores a suitable design for mini-grid by varying the capacity of wind and solar units. Also, a comparison has been carried out for different models on the basis of GHG emission. The simulation results show that the proposed grid-PV-wind hybrid power system model with 76% renewable fraction is most suitable, economical and eco-friendly for the considered region.**

Keywords—greenhouse gas (GHG); grid; HOMER; hybrid power system; solar; wind.

I. Introduction

Renewable energy (RE) can play an important role in reducing global warming and high cost of energy [1]. Every sector of modern civilization is dependent on energy which comes from various energy sources such as nuclear energy and fossil fuel (coal, oil and natural gas). The combustion of these energy sources emits huge amount of greenhouse gases (GHG) such as carbon dioxide, sulfur dioxide, nitrogen dioxide that harm the atmosphere and health of the population [2]. Recently, hybrid power systems using RE are becoming popular due to their potential benefits on environment [3].

Presently, the power demand of Bangladesh is about 10,000 MW and it is increasing day by day. As natural gas is used for about 80% energy generation, Bangladesh is responsible for a large amount of GHG emission [4]. Moreover, the present reserve of fuel used for power generation would be depleted by a decade [5]. Therefore, an alternative way of energy generation in Bangladesh is very urgent. RE sources are considered as the best way to meet the energy demand as they are clean and environmental friendly [6].

Although RE sources such as wind and solar have several advantages, a solar or wind generator in a stand-alone system cannot supply the load continuously due to their intermittent nature [7]. As load demands are always changing with time, the changes in solar or wind energy generation do not always match with the time distribution of load [8]. Therefore, there is a need of additional battery storage or other components for providing continuous power supply to the consumer. It has been investigated that a hybrid PV/Wind/battery system is a reliable source of electricity [9]. However, due to the high cost of battery energy storage, a stand-alone system is very expensive [10]. Therefore, it is important to find a suitable combination of different RE sources to maximize the benefit.

Therefore, the main objective of this paper is to quantify the amount of GHG gas emissions from different system models. The economic and environmental feasibility of grid connected proposed model is analyzed. The potential of PV and wind energy is also investigated in the considered region (Kuakata, Bangladesh) and finally, the contribution of renewable energy is determined to get the optimum performance.

The rest of the paper is organized as follows. Section II describes the system description. Methodology is given in Section III. Simulation models are provided in Section IV and results are evaluated in Section V. Finally, conclusions are drawn in Section VI.

II. System Description

In this paper, a number of hybrid power system models with different percentage of renewable energy contribution have been designed to evaluate and determine the cost of different models. GHG emissions from each model are also determined. The analysis is conducted using HOMER software. The HOMER simulation software needs some input data to evaluate the optimization results for different combinations which are described in the next section [11].

978-1-4673-9257-0/15/$31.00 ©2015 IEEE

A. Electricity Demand in Considered Region

The region considered in this paper is Kuakata situated in Patuakhali district in Bangladesh. In this study, after collecting data for load calculation, we assumed that 200 families consumed average 6.6 kWh/d/family, 50 shops consumed 2.5 kWh/d/shop, 15 tourist hotels that consumed 25 kWh/d/hotel, 300 battery run auto rickshaw consumed about 9.66 kWh/d/rickshaw, the total load for the whole area is 4820.87 kWh per day with a peak load of 794.66 kW. The load is grouped in two parts, one is load 1 which consists of houses, shops and hotels loads; another is load 2 which consists of battery run auto rickshaws. The daily average load profile for two types of load is shown in Fig. 1 and Fig. 2, respectively in which 17:00 to 23:00 h time period has been observed as peak demand for domestic load and 23.00 to 06.00 h for charging of the battery of auto rickshaw. The peak value of demand requirement determines the size of the system.

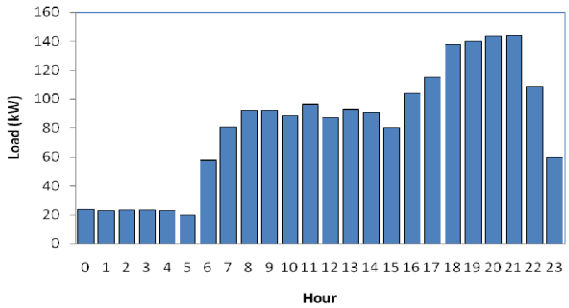

Fig. 1. Daily household load profile.

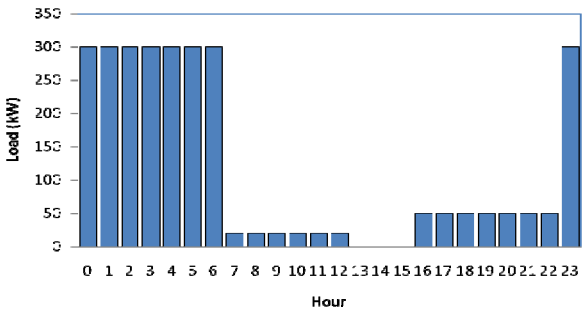

Fig. 2. Daily load profile for auto rickshaw charging.

B. Energy Sources in Kuakata

The coastal area of Bangladesh is suitable for the production of electricity as there is strong wind flow coming from Indian Ocean. This wind blows over Bangladesh form March to September. According to the meteorological department of Bangladesh, monthly average wind speed is observed 3 m/s to 8.3 m/s [12]. The wind speed is high during March to September and other months of a year (October to February) wind speed remains quite low. The peak wind speed occurs during the month of April and May [8]. Fig. 3 shows the monthly average wind speed around the year at Kuakata. Monthly average solar radiation is obtained from NASA surface meteorology and solar energy database and it is shown in Fig. 4. As used in HOMER software, the latitude and longitude of Potuakhali district are 21°49.3´N and 90°7.39´E, respectively. The annual average solar radiation is estimated to be 4.76 kWh/m^2/day [11].

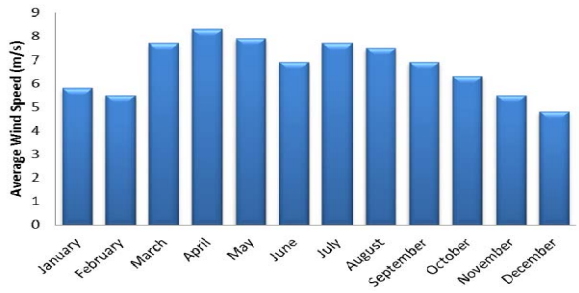

Fig. 3. Monthly average daily wind speed.

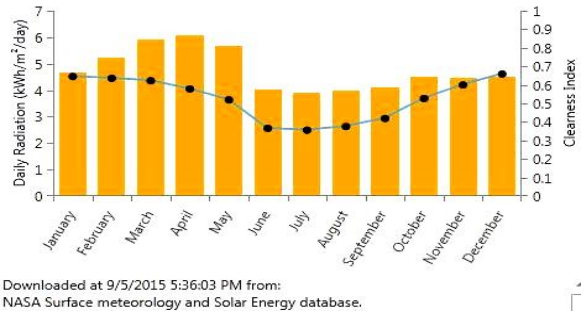

Fig. 4. Monthly average daily solar radiation and clearness index..

III. Methodology

A. HOMER Software

HOMER software is developed by the National Renewable Energy Laboratory (NREL) [13] in the United States (USA). It is generally used for the design and analysis of hybrid power system. In this paper, electrical load, solar radiation and wind speed data, and component details and cost are provided as input information to HOMER.

B. Cost Analysis Procedure by HOMER[2,11,13]

1) Net present cost (NPC): NPC means the present value of al component (operating and maintenance cost) that isinstalled in the plant, minus the present value of all the revenues that it earns over the plant life-span [2,11].

2) Total annualized cost: The total net present cost in a year is called the total annualized cost. It expressed as [2,11]:

$$C_{yr,total} = CRF\ (i, R_{plant\text{-}life}).\ C_{NPC,total}$$

where $C_{NPC,total}$, i, CRF, and $R_{plant\text{-}life}$ represents the total net present cost in dollar, the annual real interest rate, capital recovery factor and the plant life-time in year, respectively.

3) Capital recovery factor (CRF): It is a ratio which is needed to calculate the present value of a series of equal yearly cash flows. It can be expressed as [2,11]:

$$CRF(i,n) = \frac{i \times (1+i)^n}{(1+i)^{n-1}}$$

where, n = number of years and

i = the real interest rate in a year

4) Annual real interest rate: It is the discount rate which is used to convert between one-time costs and yearly costs. It is calculates as follows [2,11].

$$i = \frac{i' - F}{1+F}$$

where, i, i' and F is the real interest rate, nominal interest rate, and annual inflation rate, respectively.

5) Cost of energy (COE): It is defined as the mean value of cost per kWh of useful electrical energy produced by the plant. It is expressed as the ratio of electricity production cost in a year to the total electrical load served by the system. The electricity production cost includes plant installation cost and operation and maintenance cost. Total electrical loads are divided into AC primary load and DC primary load. It is calculated by the following equation [2,11].

$$COE = \frac{C_{yr,total}}{AC_{load} + DC_{load}}$$

where, $C_{yr,total}$ AC_{load} and DC_{load} is the total annualized cost, AC primary load and DC primary load, respectively.

IV. SYSTEM DESIGN

The components are chosen from HOMER to perform the simulation. Fig. 5 shows the grid connected hybrid power system design using HOMER which consists of PV array, wind generator, converter, load, and grid connection.

In order to estimate the system performance under different situations, HOMER simulates the result of the above two arrangements at the same area and same load based on different criteria such as the estimated installation cost, replacement cost, operation and maintenance cost, interest, and cost of energy.

The major components of the different models designed here are wind turbine, PV, battery bank, and a power converter. For economic analysis, the following values are used.

A. PV Array:

In this paper, the initial installation cost of PV arrays is assumed as $3000 per kW and the operation and maintenance cost is zero.

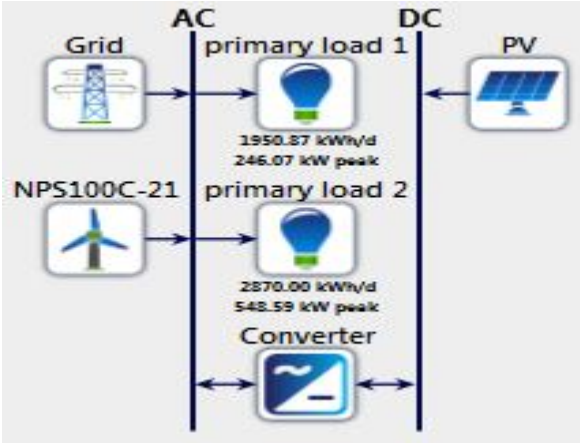

Fig. 5. Grid connected hybrid power system design using HOMER

B. Wind Turbine:

For this study, average wind velocity at 50 m height is 6.73 m/s in Kuakata. It varies from 3 to 8.3 m/s. Here, nine Northern Power NPS100C-21,100 kW wind turbines are used [11]. The wind turbine power output characteristic is shown in Fig. 6. The capital costs are $320000 and also operation and maintenance cost are $2500/yr.

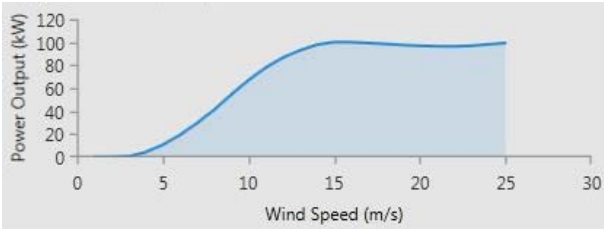

Fig. 6. Wind turbine power curve [11].

C. Power Converter:

In this paper, the capital cost for a 1 kW converter is $300, replacement cost is $300 and operation and maintenance cost practically zero.

D. Battery Bank:

The name of the battery bank is CELLCUBE®FB10-40, manufactured by Gildemeister, with a capacity of 40 kWh, life time 876000 kWh. A battery bank is only used for a stand-alone system design.

E. Grid:

In grid connected design, a grid is used as a backup power component or excess power absorber. The grid supplies power when there is not enough RE power to meet the load demand and grid consumes power when an excessive power is available.

V. SIMULATION RESULTS

The simulation results are described below.

A. Economic Impact

Table I shows the optimization results for the hybrid power system model with different share of renewable energies. For grid connected system, the minimum cost of energy (COE) obtained from the result is $0.0891 whereas for off-grid system it is $0.1588375. Figures 7 and 8 show the COE and NPC values as a function of the number of PV units. It can be observed that the COE and NPC values of the system are increased with the increase in the capacity of PV unit. Also, with the increase of PV capacity, the capital cost of the system is increased. On the other hand, figures 9 and 10 show the graphs of COE and NPC values as a function of the number of wind turbines, respectively from which it can be noticed that COE and NPC values decrease with the increase in the number of wind turbines. It can be also seen that the values of COE and NPC vary from $0.1617027/kWh to $0.0891009/kWh and 5.370379 million dollar to 3.669484 million dollar, respectively. In this paper, size of the plant is considered as 1 MW for which 76% renewable fraction gives the feasible solution. It has to be mentioned that by increasing the size of hybrid power plant the percentage of renewable share can be increased.

TABLE I. SIMULATION RESULT FOR FINDING OPTIMAL DESIGN

Type of the system	PV (kW)	No. of Wind turbine	Battery Bank	COE ($)	NPC ($ million)	Renewable Fraction (%)	CO_2 emission (Tons/yr)
Grid connected	900	1	0	0.1617027	5.370379	52%	269.0764
Grid connected	800	2	0	0.1501716	5.075439	57%	169.8644
Grid connected	700	3	0	0.1403417	4.817061	61%	85.23243
Grid connected	600	4	0	0.1306933	4.583252	65%	1.258075
Grid connected	500	5	0	0.1216871	4.367301	68%	-76.02873
Grid connected	400	6	0	0.1125443	4.16875	70%	-161.3187
Grid connected	300	7	0	0.1040462	3.985773	72%	-245.622
Grid connected	200	8	0	0.0962585	3.818419	74%	-328.4017
Grid connected	100	9	0	0.0891009	3.669484	76%	-410.4542
Off Grid	100	9	8000	0.1588375	3613144	100%	0
Only Grid	0	0	0	0.2000003	4549493	0	1112.077

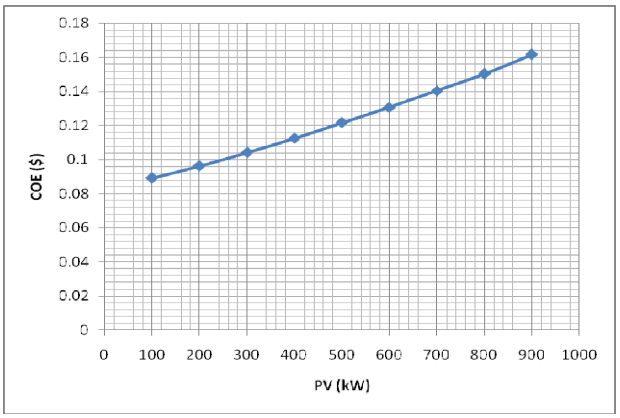

Fig. 7. The COE vs. PV capacity.

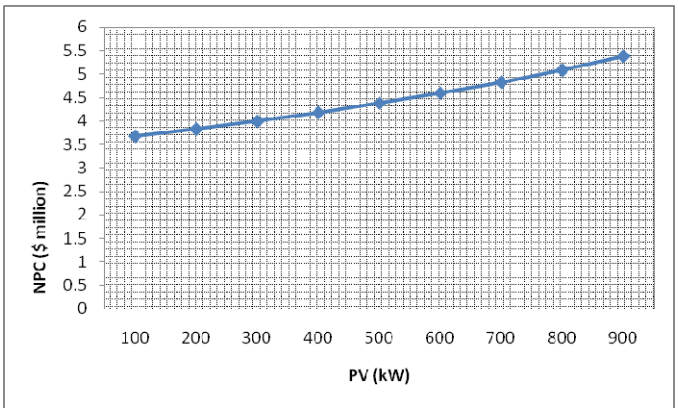

Fig. 8. The NPC vs. PV capacity.

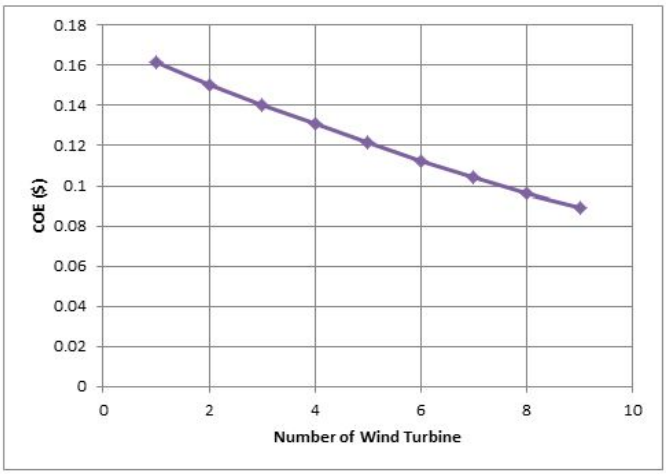

Fig. 9. The COE vs. the number of wind turbines.

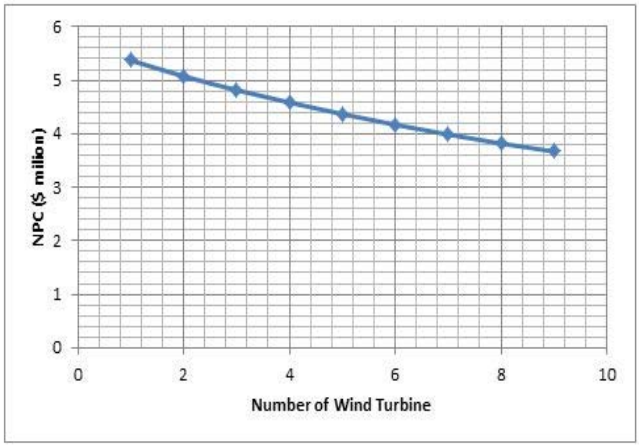

Fig. 10. The NPC vs. the number of wind turbines.

B. *Environmental Impact*

The CO_2 emission with the various contribution of renewable energy is shown in Fig. 11 from which it can be investigated that the emission decreases as the contribution from renewable energy increases. The share of renewable energy can be increased by increasing the number of wind turbines as there is an abundant of wind energy in the considered area compared to solar radiation. The result (Table I) shows that only grid-connected system emitted 11,12077 kg CO_2 per year while wind-PV-grid connected system emitted -410454.2 kg CO_2 per year. Here, the negative CO_2 emission is observed for 76% and some other renewable fraction rate because this system sells more power than it purchases from the grid as it has an excess of electricity. Figure 12 shows the monthly average electric production of various components for 76% renewable fraction rate where the major contribution is coming from wind turbine.

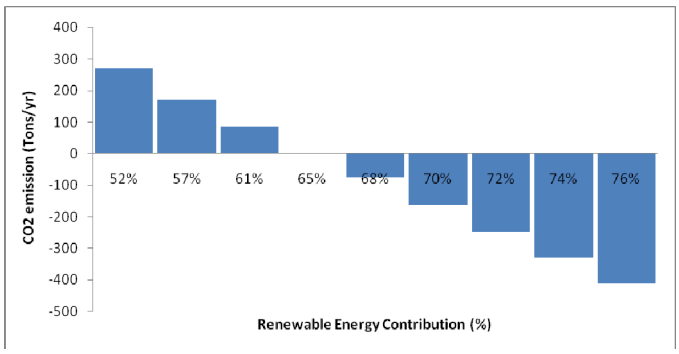

Fig. 11. The CO_2 emission against the various contribution of renewable energy.

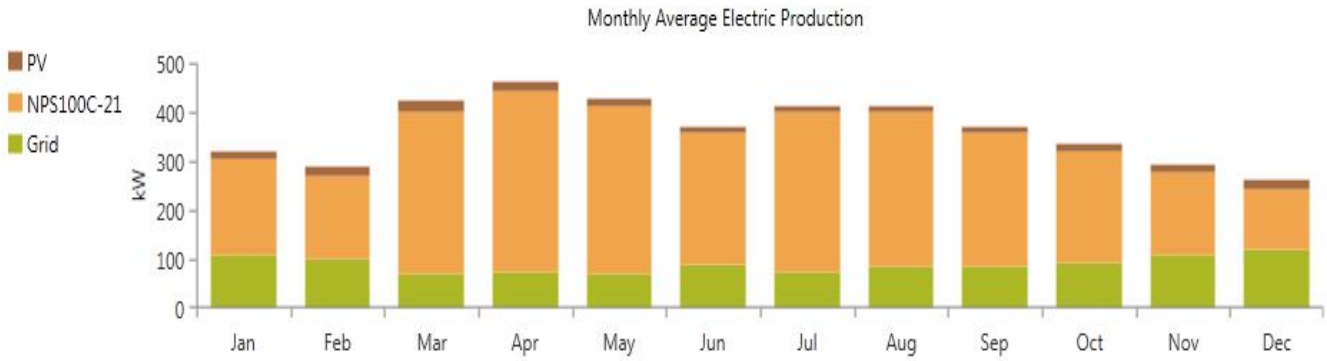

Fig. 12. Monthly average electricity production for final model (renewable fraction 76%)

VI. CONCLUSION

From the analysis it can be concluded that proper utilization of renewable energy reduces an enormous amount of GHG emission in the atmosphere. It is found that the proposed hybrid model with 76% renewable fraction is most suitable, economical and eco-friendly than the other models. It can be concluded that although hybrid model with 100% renewable fraction (off-grid) emits zero kg GHG, it is not always cost effective. The excess output power of the off-grid system goes unused. On the other hand, the proposed grid connected hybrid system does not require an extra battery bank in normal operating condition and excess power that is produced by renewable energy are added to the grid, thereby reducing the total emission.

REFERENCES

[1] A. Rohani, K. Mazlumi, and H. Kord, "Modeling of a hybrid power system for economic analysis and environmental impact in HOMER," 18th Iranian conference on Electrical Engineering (ICEE), 2010, pp.819-823, 11-13 May 2011.

[2] H. Rezzouk and A. Mellit, "Feasibility study and sensitivity analysis of a stand-alone photovoltaic–diesel–battery hybrid energy system in the north of Algeria," Renewable and Sustainable Energy Reviews, vol. 43, pp. 1134–1150, 2015.

[3] G.M Shafiullah, M.T.O Amanullah, A.B.M. Shawkat Ali, Dennis Jarvis, and Peter Wolfs, "Prospects of renewable energy - a feasibility study in the Australian context" Renewable and Sustainable Energy Reviews, vol. 39, no. 1, pp. 183-197, 2012.

[4] *http://www.bpdb.gov.bd/bpdb/index.php* (accessed on 15 July 2015)

[5] P. Mazumder, M.H. Jamil, C.K. Das, and M.A. Matin, "Hybrid energy optimization: an ultimate solution to the power crisis of St. Martin Island, Bangladesh" 9th International Forum on Strategic Technology (IFOST), pp.363-368, 21-23 Oct. 2014.

[6] M.S. Nagan and C.W. Tan, "Assessment of economic viability for PV/wind/diesel hybrid energy system in southern Peninsular Malaysia," Renewable and Sustainable Energy Reviews, vol. 16, no. 1, pp. 634–647, January 2012.

[7] S.K. Pawar, Y.V. Aaher, A.C. Chaudhari, and Y.B. Jadhav, "Modeling and simulation of hybrid solar-wind-grid power generation system for electrification," International Conference on Advances in Engineering and Technology (ICAET), pp.1-6, 2-3 May 2014.

[8] A. Zubair, A.A. Tanvir, and M. M. Hasan, "Optimal planning of standalone solar-wind-deesel hybrid energy system for a coastal area of Bangladesh," International Journal Of Electrical And Computer Engineering (IJECE), vol. 2, no. 6, pp. 731-738, 2012.

[9] S. Liu, Z. Wu, X. Dou, and B. Zhao,"Optimal configuration of hybrid solar-wind distributed generation capacity in a grid-connected microgrid" IEEE PES Innovative Smart Grid Technologies (ISGT), pp. 1-6, 24-27 Feb. 2013.

[10] B. Roy, A.K. Basu, and S. Paul, "Techno-economic feasibility analysis of a grid connected solar photovoltaic power system for a residential load" First International Conference on Automation, Control, Energy and Systems (ACES), pp. 1-5, 1-2 Feb. 2014.

[11] Getting Started Guide for HOMER Version 3.3.1; ⟨https://www.homerenergy. com⟩.

[12] *www.bmd.gov.bd* (accessed on 20 July 2015)

[13] *www.nrel.gov/homer* (accessed on 18 July 2015)

Damping of Power System Oscillations using STATCOM

Mehedi Hassan
Department of Electrical and Electronic Engineering
Jessore University of Science and Technology
Jessor-7408, Bangladesh
Email: mhj24.jsr@gmail.com

N. K. Roy
Department of Electrical and Electronic Engineering
Khulna University of Engineering and Technology
Khulna-9203, Bangladesh
Email: nkroy@eee.kuet.ac.bd

***Abstract*—This paper investigates the damping performance of power systems through eigenvalue analysis. The analysis is conducted on an IEEE 14-bus test system. The maximum loading limits of the load buses are determined using continuation power flow method and a static synchronous compensator (STATCOM) is installed as an objective to increase the system loadability. Then, the dominant modes and associated states that affect the damping of the system are identified and an oscillation damping controller is designed. The result shows that the proposed damping controller equipped with STATCOM can improve the damping performance of the system significantly.**

Keywords—damping performance; eigenvalue; synchronous generator; static voltage stability; STATCOM.

I. Introduction

Power system is a large interconnected complex network. The main challenges that power system engineers are facing around the world is related to stability [1]-[3]. Reactive power support is a vital issue to improve a power system's performance.

In order to improve the stability of power systems, a static synchronous compensator (STATCOM) is increasingly popular [4, 5]. A STATCOM can dynamically support/absorb the reactive power to/from the power network and hence improves the system voltage profile and angle stability [6]. It can also enhance the overall stability of a power system if it is equipped with some more supplementary control signals.

The effect of different loads and voltage compensation using voltage source converter based STATCOM is presented in [7] which shows that, in some cases, it is hard to maintain the load angle close to unity. Time-domain analysis of a system with and without STATCOM is investigated in [8] for different types of faults in which inadequately damped oscillations are observed under certain critical conditions.

The disturbance in power system is mainly due to the connection/disconnection of large loads, faults, and loss of excitation in the generator [9]. The occurrence of contingencies in power system can cause poorly damped or even unstable oscillations which must be damped to ensure reliable power supply.

A STATCOM is usually used for voltage regulation. However, to achieve satisfactory performance, a proper and efficient control system should be designed for this device. Therefore, the aim of this paper is to investigate the damping performance of power systems through linear and nonlinear simulations. To improve the damping of the oscillatory mode of the system a supplementary controller for STATCOM is designed.

The rest of the paper is organized as follows. The description of the system is given in Section II, static and dynamic analysis is given in Section III and conclusions are given in Section IV.

II. System Description

A single line diagram of the IEEE 14-bus test system considered in this paper is shown in Fig. 1 [10]. It consists of two synchronous generators with IEEE type-1 exciters and three synchronous compensators. All the loads are considered as constant impedance loads and mechanical inputs to the generators are assumed to be constant. A sixth order model of the synchronous generator is used for the analysis. The test system data is given in Appendix.

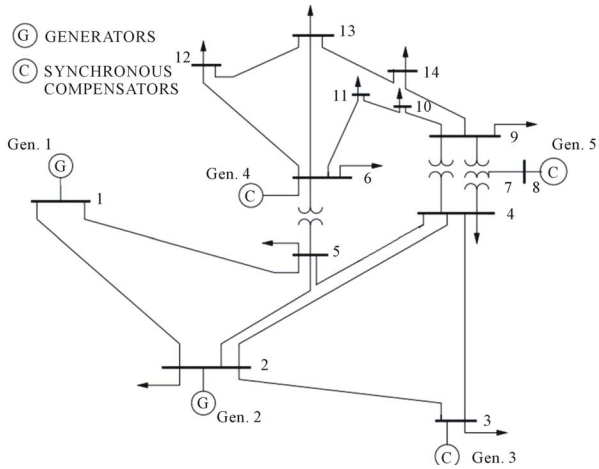

Fig. 1. IEEE 14-bus test system [10].

978-1-4673-9257-0/15/$31.00 ©2015 IEEE

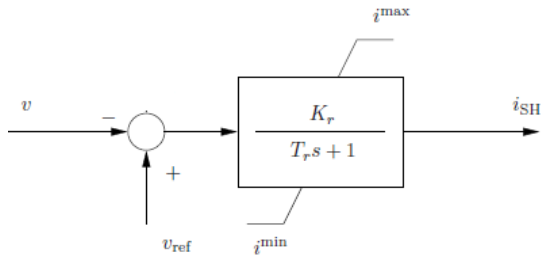

Fig. 2. Block diagram of STATCOM [10].

A STATCOM is used as a Flexible AC Transmission System (FACTS) device in this analysis. Figure 2 shows the block diagram of a STATCOM where v is the measured voltage at the connected bus, v_{ref} is the reference voltage, i^{max} and i^{min} is the maximum and minimum current, respectively, i_{SH} is the total injected current at the connected bus, K_r and T_r is the regulator gain and time constant, respectively. A STATCOM is equipped with a power oscillation damping (POD) controller as shown in Fig. 3 which contains gain, wash-out and compensator blocks.

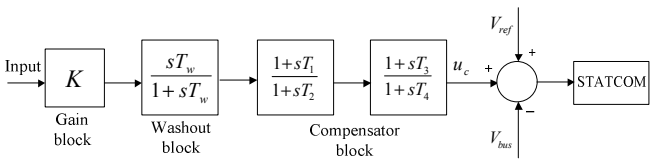

Fig. 3. STATCOM with POD controller

III. Static and Dynamic Analysis

A load flow study for the considered test system is conducted using Newton-Raphson method [11]. To analyze the static voltage stability generally real power-voltage (P-V) or reactive power-voltage (Q-V) curves are used which determine the maximum loading limit of a system [1, 12]. Here, P-V curve has been produced by using a series of power flow solutions (continuation power flow) using power system analysis toolbox (PSAT) in MATLAB environment for different load levels.

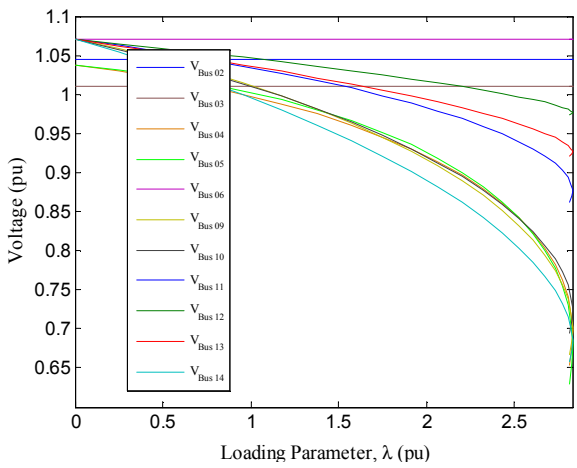

Fig. 4. Loading parameter-voltage curve under base case.

The variations in load bus voltages with the loading factor are obtained and plotted in Fig. 4 from which it can be observed that us-14 is the weakest bus of this network. In this paper, a STATCOM is installed at bus-14 to enhance the static voltage stability of the system.

Next, to understand the inherent dynamics of the system, the test system is linearized and eigenvalues are calculated without STATCOM connection. It is found that the system has a pair of eigenvalue at -0.04654±8.1151 which is the critical mode of this system. Table I shows the participation factors of the dominant states associated with this mode, where e1q_Syn_1 and vf_Exc_1 represents the quadrature axis voltage of synchronous machine 1 and voltage of the exciter 1, respectively; delta_Syn_1 and omega_Syn_1 represents the angle and speed of the generator 1, respectively. This mode has a damping ratio of 0.57%. It is known that the minimum damping requirements for reliable operation of power system is 5%.

TABLE I. Critical Mode of the Considered System

Critical mode	Dominant States and participation factor	Damping ratio (%)
-0.04654±8.1151	e1q_Syn_1=0.22377, vf_Exc_1=0.17139 delta_Syn_1=0.04332,omega_Syn_1=0.04332	0.57

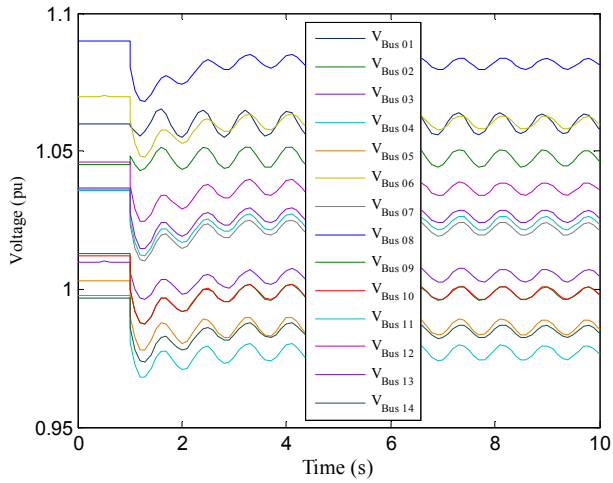

Fig. 5. Bus voltages of IEEE 14-bus test system under disturbance.

To test the dynamic performance of the system, the line between bus 2 and bus 4 is disconnected at 1s. Figure 5 shows the bus voltage profile of the system from which it can be seen that the system suffers from low frequency oscillations. The real power of the sysnchronous generator is shown in Fig. 6. In this analysis, mechanical input to the generator is kept constant. It can be seen from Fig. 6 that the system has large oscillations in its output power.

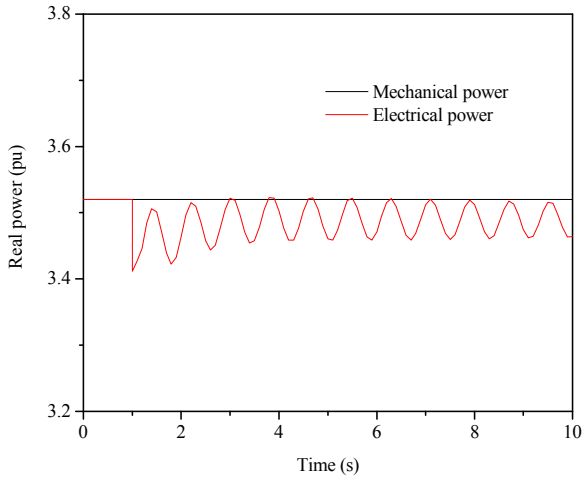

Fig. 6. Mechanical input power and electrical output power of synchronous generator 1.

To solve the above problems, a STATCOM is connected and a POD controller is equipped with it based on the line active power measurement from bus 1. The transfer function of the POD controller is given below [13].

$$H(s) = K\frac{sT_w}{sT_w+1}\left[\frac{sT_{ld}+1}{sT_{\lg}+1}\right]^{m_c} \quad (1)$$

$$\varphi_{comp} = 180^0 - \arg(R_i) \quad (2)$$

$$\alpha_c = \frac{T_{ld}}{T_{\lg}} = \frac{1-\sin(\frac{\varphi_{comp}}{m_c})}{1+\sin(\frac{\varphi_{comp}}{m_c})} \quad (3)$$

$$T_{\lg} = \frac{1}{\omega_i\sqrt{\alpha_c}}, \quad T_{ld} = \alpha_c T_{\lg} \quad (4)$$

where, the phase angle φ_{comp} shows the compensation angle needs to move the eigenvalue direct to the left parallel with the real axis. T_w, T_{ld} and $T_{\lg}$ are the time constant of the wash-out, lead and lag block, respectively, $\arg(R_i)$ is the phase angle of the residue R_i, ω_i, m_c and K is the frequency of the mode of oscillation in rad/s., number of compensation stages and the controller gain, respectively. In this paper, number of compensation stages are 2.

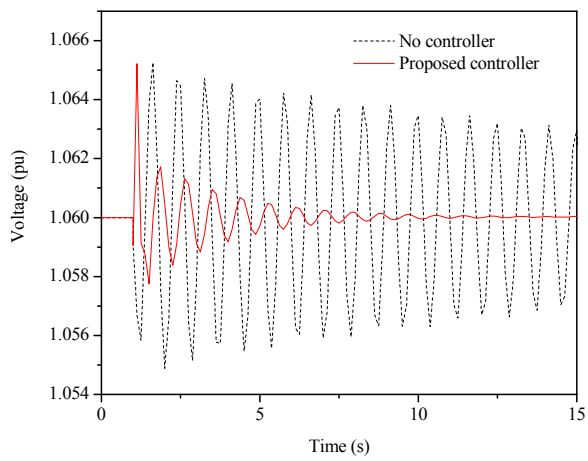

Fig. 7. Bus 1 voltage.

The voltage profile of the test system at bus 1 with and without the proposed controller is shown in Fig. 7 from which it can be clearly observed that the proposed control scheme damps the oscillations quickly. The dominant eigenvalue of the system with the proposed controller is -0.6402±7.6527 with a damping ratio 8.3% which is greater than the minimum limit (5%).

IV. Conclusion

This article investigates the stability improvement problem of a power system considering a STATCOM. The small-signal stability assessment of IEEE 14-bus test system is conducted. It is found that the system has low frequency oscillations with reduced damping. As the weakest bus requires highest reactive power, a STATCOM is connected at the weakest bus of the network. Although a STATCOM improves the static voltage stability of the system, it is not always suitable for damping the oscillatory mode of the system. Therefore, a supplementary controller is designed using the real power deviation as input signal. The result shows that the proposed controller can enhance the damping performance of the system. Thus, this paper proves that an auxiliary control law can be applied to existing devices to enhance the dynamic performance of the system. Determining the optimum size of a STATCOM through static and dynamic analysis is the future aim of this work.

APPENDIX

The line and load data of IEEE 14-bus test system is given in Table II and Table III, respectively [14].

TABLE II. LINE DATA OF IEEE 14-BUS TEST SYSTEM

From bus - To bus	Line charging (pu)	Tap ratio	Resistance, (pu)	Reactance, (pu)
1-2	0.0528	1	0.01938	0.05917
1-5	0.0492	1	0.05403	0.22304
2-3	0.0438	1	0.04699	0.19797
2-4	0.0374	1	0.05811	0.17632
2-5	0.034	1	0.05695	0.17388
3-4	0.0346	1	0.06701	0.17103
4-5	0.0128	1	0.01335	0.04211
4-7	0.00	0.978	0.00	0.20912
4-9	0.00	0.969	0.00	0.55618
5-6	0.00	0.932	0.00	0.25202
6-11	0.00	1	0.09498	0.1989
6-12	0.00	1	0.12291	0.25581
6-13	0.00	1	0.06615	0.13027
7-8	0.00	1	0.00	0.17615
7-9	0.00	1	0.00	0.11001
9-10	0.00	1	0.03181	0.08450
9-14	0.00	1	0.12711	0.27038
10-11	0.00	1	0.08205	0.19207
12-13	0.00	1	0.22092	0.19988
13-14	0.00	1	0.17093	0.34802

TABLE III. LOAD DATA OF IEEE 14-BUS TEST SYSTEM

Bus no.	P_{load} (pu)	Q_{load} (pu)
1	0.00	0.00
2	0.2170	0.1270
3	0.9420	0.1900
4	0.4780	0.00
5	0.0760	0.0160
6	0.1120	0.0750
7	0.00	0.00
8	0.00	0.00
9	0.2950	0.1660
10	0.0900	0.0580
11	0.0350	0.0180
12	0.0610	0.0160
13	0.1350	0.0580
14	0.1490	0.0500

REFERENCES

[1] P. Kundur, Power system stability and control. McGraw-Hill, New York, 1994.

[2] T. Zabaiou, L.-A. Dessaint, and I. Kamwa, “Preventive control approach for voltage stability improvement using voltage stability constrained optimal power flow based on static line voltage stability indices,” IET Generation, Transmission & Distribution, vol. 8, pp. 924 – 934, 2014.

[3] B. H. Lee and K.Y. Lee, “Dynamic and static voltage stability enhancement of power systems,” IEEE Trans. on Power Systems, vol. 8, pp. 231 – 238, 2002.

[4] P.C. Thomas, “Placement of STATCOM in a wind integrated power system with storage for improving the loadability of the system,” 7th International Conference on Intelligent Systems and Control (ISCO), pp. 31 – 35, 4-5 Jan. 2013.

[5] J. Lakkireddy, “Steady state voltage stability enhancement using shunt and series FACTS devices,” Clemson University Power Systems Conference (PSC), 10-13 March 2015.

[6] M. R. S. Tirtashi, A. Rohani, and R. Noroozian, "PSS and STATCOM controller design for damping power system oscillations using fuzzy control strategies," 18th Iranian Conference on Electrical Engineering (ICEE), pp.901-906, 11-13 May 2010.

[7] H.S. Dalvi, and V.K. Chandrakar, "Voltage improvement using STATCOM for prototype hardware model, using synchronous and induction type generator," 3rd International Conference on Emerging Trends in Engineering and Technology (ICETET), pp.413-417, 19-21 Nov. 2010.

[8] S. P. Teeuwsen, "STATCOM with optimized POD controller for efficient inter-area oscillation damping," IEEE Power and Energy Society General Meeting (PES), pp.1-5, 21-25 July 2013.

[9] S. Vishwakarma, R. K. Tripathi, "Transient energy dissipation and damping improvement using STATCOM & SSSC," International Conference on Power, Control and Embedded Systems (ICPCES), pp.1-4, Nov. 29 2010-Dec. 1 2010.

[10] F. Milano, “Power System Analysis Toolbox (PSAT) documentation” version 2.1.6.

[11] E. Balagurusamy, Numerical methods, Tata Mc-Graw-Hill, New Delhi, 1999.

[12] N.K. Roy, H.R. Pota and A. Anwar, “A new approach for wind and solar type DG placement in power distribution networks to enhance systems stability," IEEE Power Engineering and Optimization Conference (PEOCO), pp. 296-301, 6-7 June 2012.

[13] R. Sadikovic, P. Korba, and G. Andersson, "Application of FACTS devices for damping of power system oscillations," IEEE Russia Power Tech, pp.1-6, 27-30 June 2005.

[14] S.K.M. Kodsi and C.A. Cañizares, “Modeling and simulation of IEEE 14 bus system with FACTS controllers,” Technical Report no. 2003−3,https://ece.uwaterloo.ca/~ccanizar/papers/IEEEBenchmarkTFreport.pdf.

Automatic Gender Identification System for Bengali Speech

Md. Shahriar Rahman*, Md. Fasihul Kabir†, Khandaker Abdullah-Al-Mamun‡ and Mohammad Nurul Huda§
Department of Computer Science and Engineering, United International University, Dhaka, Bangladesh
*tiloknet@gmail.com, †aboutrafi@gmail.com, ‡mamun@cse.uiu.ac.bd, §mnh@cse.uiu.ac.bd

***Abstract*—This paper describes a set of features along with different classifiers for gender (male, female) identification. Gender identification is the problem to detect the gender of the speaker of the audio content. The proposed method in this study comprises three stages: i) Corpus construction, iii) Input Feature Vector Construction and iii) Identification using a classifier. In this connection, we have constructed a medium scale Bengali speech corpus from The Bengali Daily Newspaper Prothom Alo. The total number of male/female speakers and spoken sentences are eighty and eight thousand, respectively, where the training and test corpus is selected by the 10-fold cross validation. From the experiments it is observed that the accuracies using the most of the classifiers are 100% on audio content duration size 0.7 minutes to 8.4 minutes.**

***Keywords*—Gender identification; Logistic Regression; K-Nearest Neighbor; Decision Tree, Support Vector Machine; Ridge Classifier**

I. Introduction

In modern multimedia information retrieval systems, gender identification has several potential applications. It can be used in audio or video content indexing, gender based classifiers can improve the accuracy of speech recognition [1] and speech coders [2] system. Moreover it can be used in forensic investigations.

In this study, we have proposed a method for gender identification that consists of corpus construction, input feature vector construction, and identification using a classifier. Here, a medium scale Bengali speech corpus is constructed from The Bengali Daily Newspaper Prothom Alo. The originality of this research for Bengali is special features (Energy, Envelope, LPC, etc; in total we used 27 features) extraction from an input speech and use of machine learning tools for this identification. The training and test corpus is selected by the 10-fold cross validation from the eight thousand spoken sentences uttered by eighty male and female speakers. From the experiments it is observed that the accuracies using the most of the classifiers are 100%.

II. Related Works

Gender Recognition based several types of research work have been done for decades. The system described in [3] introduced a new gender identification method using Bootstrapping on audio classification. This paper shows good performance (more than 90%) for Naive Bayes, Decision Trees (C4.5), k-Nearest Neighbors, Logistic regression, Neural Network and Support Vector Machine Classifiers. Content based multimedia indexing using Piecewise Gaussian Modeling with mixture of neural networks was presented in [4]. With one second audio segments, the classification accuracy was 90% regardless of any language and channel of the speech. A system is proposed in [5] where audio classification using multimedia indexing on audio channel having more than 90% accuracy. In [6] a support vector machine (SVM) based gender identification is applied on discriminative weight training. By SVM consisting of optimally weighted mel-frequency cepstral coefficient (MFCC) which is based on minimum classification error (MCE) method, generates a gender decision rule. It outperformed another method mentioned in [7] and has the accuracy almost 100%. Gender Identification based on pitch is proposed in [8], where two stages classifier using Gaussian Mixture Model (GMM) is created to ensure low complexity and high accuracy. Following this method we can get more than 95%. Most of the above described previous works were performed using foreign language (not used Bengali Corpus). But unfortunately for Bengali language, we cannot see much example. The method described in [9] proposed a gender identification method for Bengali consisting of a front end and a back end system. Feature extraction is done using Fast Fourier Transform (FFT) in front end and in back end, a gender model is created using a classifier which produces poor performance around 80%.

III. Methodology

A. Corpus Construction

Different sentences from the Bengali newspaper Prothom Alo uttered by male and female speakers of different regions of Bangladesh are collected. All of the speakers are Bangladeshi nationals and native speakers of Bangla. The age of the speakers ranges from 20 to 40 years. We have chosen the speakers from a wide area of Bangladesh: Dhaka (central region), Comilla Noakhali (East region), Rajshahi (West region), Dinajpur Rangpur (North-West region), Khulna (South-West region), Mymensingh and Sylhet (North-East region). On the other hand, though all of them speak in standard Bangla, they are not free from their regional accent.

Recording was done in a quiet room located at United International University (UIU), Dhaka, Bangladesh. A desktop was used to record the voices using a head mounted close-talking microphone. We record the voice in a place, where ceiling fan and air conditioner were switched on and some low level street or corridor noise could be heard.

978-1-4673-9257-0/15/$31.00 ©2015 IEEE

Jet Audio 7.1.1.3101 software was used to record the voices. The speech was sampled at 16 kHz and quantized to 16 bit stereo coding without any compression and no filter is used on the recorded voice. Duration of the speech files are between 0.7 minutes and 8.4 minutes.

The development of data sets is given as follows.

Data Set-I (D1): This data set consists of 3000 sentences uttered by 30 male speakers (each speaker by 100 sentences). The data is sampled at 16 kHz.

Data Set-II (D2): This data set consists of 3000 sentences uttered by 30 female speakers (each speaker by 100 sentences). The data is sampled at 16 kHz.

Data Set-III (D3): This data set consists of 1000 sentences uttered by 10 male speakers (each speaker by 100 sentences). These sentences are different from D1 data set. The data is sampled at 16kHz.

Data Set-IV (D4): This data set consists of 1000 sentences uttered by 10 female speakers (each speaker by 100 sentences). These sentences are different from D2 data set. The data is sampled at 16 kHz

B. Input Feature Vector Construction

a feature vector is an n-dimensional vector of numerical features that represent some object. In machine learning and pattern recognition, a feature is an individual measurable property of a phenomenon being observed [10]. Choosing informative, discriminating and independent features is a crucial step for effective algorithms in pattern classification. In our experiment we used two steps to construct our feature vector. In first step, we extracted the features from the audio files and in the second step, we normalize the features using different statistical formulas.

1) Feature Extraction: Feature extraction is an essential pre-processing step to pattern recognition and machine learning problems. We extracted time, frequency, coefficient domain features using yaafe - audio features extraction [11]. Followed is the description of each of the features we extracted using the tool:

1) **Amplitude Modulation** [12] is a form of modulation used for radio transmissions for broadcasting and two way radio communication applications. We have used 200 Decimation factor to compute envelope, 32768 output frames size, 16384 steps between consecutive frames are used to calculate the Amplitude Modulation.
2) **Auto Correlation** is used to compare a signal with a time-delayed version of itself. Here, 49 auto correlation coefficients are used. To calculate it we used 1024 output frames size, 512 step between consecutive frames.
3) **Complex Domain Onset Detection** [13] is computed onset detection using a complex domain spectral flux method. Hanning method is used weighting window to apply before FFT, output frames size equals to 1024 and step between consecutive frames equals to 512 is used to calculate the value.
4) **Energy** [14] is computed as root mean square of an audio Frame. We have used output frames size equals to 1024 and step between consecutive frames equals to 512, to calculate the Energy.
5) **Envelope**, extract amplitude envelope using Hilbert transform, low-pass filtering and decimation. Decimation factor equals to 200, output frames size equals to 32768 and step between consecutive frames equals to 16384 is used to calculate the Envelope.
6) **Envelope Shape Statistics** is centroid, spread, skewness and kurtosis of each frames amplitude envelope. Same parameters in calculation of Envelope are used to calculate Envelope Shape Statistics.
7) **Frames** are segment in input signal. Same parameters in calculation of Energy are used to calculate Frames.
8) The **LPC** [15], [16] coefficients are a short-time measure of the speech signal, which describe the signal as the output of an all-pole filter. The first 2 orders of LPC parameters are chosen.
9) **Loudness** [17], [18] coefficients are the energy in each Bark band, normalized by the overall sum.
10) **MFCC** [16] calculation includes discrete Fourier transform of audio frames, followed by filtering by a triangular bandpass filter bank, logarithmic scaling and discrete cosine transform. Here, 13 MFCCs are used.
11) **Magnitude Spectrum** is computed using an analysis window (Hanning or Hamming), or not.
12) **Mel-Spectrum** [19] computes the Mel-frequencies spectrum.
13) **OBSI** [20] or Octave band signal intensity is calculated using a triangular octave filter bank.
14) **OBSIR** computes log of OBSI ratio between consecutive octaves.
15) **Perceptual Sharpness** [17] computes the sharpness of Loudness coefficients.
16) **Perceptual Spread** [17] computes the spread of Loudness coefficients.
17) **Spectral Crest Factor Per Band** computes spectral crest factor per log-spaced band of $1/4$ octave.
18) **Spectral Decrease** [17] computes spectral decrease.
19) **Spectral Flatness** computes global spectral flatness using the ratio between geometric and arithmetic mean.
20) **Spectral Flatness per Band** computes spectral flatness per log-spaced band of $1/4$ octave, as proposed in MPEG7 standard.
21) **Spectral Flux** computes flux of spectrum between consecutive frames.
22) **Spectral Roll off** [21] is the frequency so that 99% of the energy is contained below.
23) **Spectral Shape Statistics** [17] computes shape statistics of Magnitude Spectrum.
24) **Spectral Slope** [17] is computed by linear regression of the spectral amplitude.
25) **Spectral Variation** [17] is the normalized correlation of spectrum between consecutive frames.
26) **Temporal Shape Statistics** computes shape statistics of signal frames.
27) **ZCR** [16] or a zero-crossing is said to occur if successive samples have different signs. The zero-crossing ratio is the number of the time-domain zero-

crossings and total number of samples in a frame. To calculate the value we have kept Minimal distance between consecutive autocorrelation peaks equals to 5, number of autocorrelation peaks equals to 3, number of frames to integrate together equals to 60 and number of frames to skip between two integration equals to 30.

2) Feature Normalization: Feature Normalization is a method used to standardize the range of independent variables or features of data. To normalize the features data we have used mean, variance or standard deviation of the each feature data.

C. Identification Using a Classifier

In this phase we design a classifier using different machine learning approaches [22] and use that classifier to identify gender. Fig-1 describes how we design the classifier and use the classifier to identify gender using unlabeled audio content.

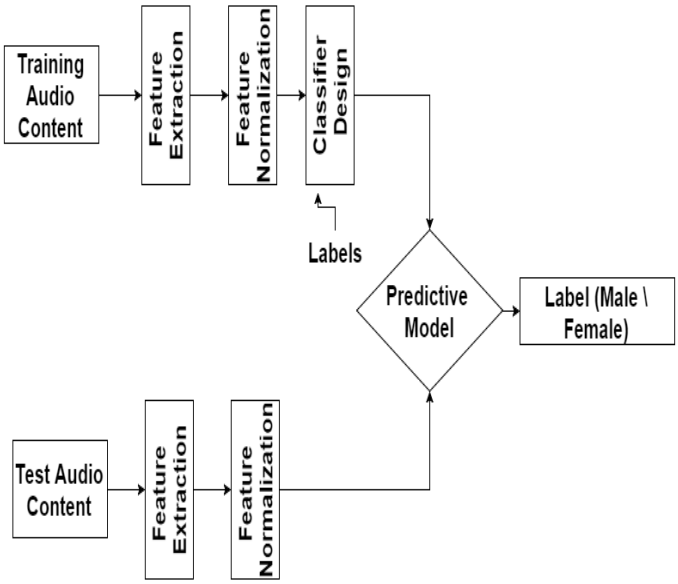

Fig. 1: Gender Identification Using Designed Classifier

Followed we describe about the experimental setup we have used to design our gender identification classifier.

- **Logistic Regression:** [23] For experiment we have used tolerance for stopping criteria=0.0001, C=1.0 and maximum number of iteration is fixed to 100. One vs Rest concept has been used for multi-class classification.
- **Decision Tree:** [24] We have used Gini impurity [25] function to measure the quality of a split, two as minimum number of samples required to split an internal node and one as minimum number of samples required to be at a leaf node.
- **K-Nearest Neighbors (KNN):** [26] For our experimental setup, we used Ball Tree [27] algorithm to compute the nearest neighbors, five as number of neighbors, leaf size = 30, Minkowski is used as the distance metric to use for the tree, where power parameter=2 is used for the Minkowski metric.
- **Ridge Regression Classifier:** [28] For our experimental setup we have used $\alpha = 1.0$ and $tol = 0.001$.
- **Support Vector Machine (SVM):** [29] For our experimental setup we have used, $C = 1.0$, $tol = 0.0001$, max iteration=1000, penalty='l2' and Linear function as kernel function. One vs rest [30] method is used to work for multi-class classification.

IV. Experimental Results

For our experiment we have used the corpus in two different manner: **CS1:** Considering eight thousand speech file and applied 10-fold cross validation and **CS2:** Considering 80 speakers and applied 10-fold cross selection. Moreover we have used three different statistical formula Mean (MN), Variance (VE) or Standard Deviation (SD) to normalize the feature obtain from the feature extraction phase. Therefore, in total we have setup six experiments in this connection: EXP-I)CS1 + MN, EXP-II)CS1 + VE, EXP-III)CS1 + SD, EXP-IV)CS2 + MN, EXP-V)CS2 + VE, EXP-VI)CS2 + SD.

To evaluate our experiments we used Precision (P), Recall (R) and F1-Score(FS) [31].

$$precision = \frac{tp}{tp + fp} \tag{1}$$

$$recall = \frac{tp}{tp + fn} \tag{2}$$

$$f1 - score = 2\frac{precision * recall}{precision + recall} \tag{3}$$

Where, tp equals to true positive, fp equals to false positive and fn equals to false negative.

Here, Table-I, Table-II, Table-III, Table-IV, Table-V and Table-VI show the results of our six experimental setups. From the tables we can observe that KNN gives the best performance for all the six experimental setup and gives a recall equals to 1.0.

Table-I shows result of experimental setup **EXP-I**, where we considered eight thousand speech files and applied 10-fold cross validation(CS1) and Mean(MN) as statistical formula to normalize the extracted features. We got the best recall value for Logistic Regression, KNN and SVM. From the table we can see that, F1-Score is almost same for every classifier.

TABLE I: Result of EXP-I

Classifier	P	R	FS
Logistic Regression	0.999	1.0	0.999
Decision Tree	0.999	0.999	0.999
KNN	0.999	1.0	0.999
Ridge	1.0	0.999	0.999
SVM	0.999	1.0	0.999

Table-II expresses data of experiment setup **EXP-II**, where we considered eight thousand speech files and applied 10-fold

cross selection (CS1). Here we use Variance (VE) as statistical formula to normalize the extracted features and got best recall value for decision tree and KNN classifier which is also same if consider Precision and F1-Score value.

TABLE II: Result of EXP-II

Classifier	P	R	FS
Logistic Regression	0.999	0.999	0.999
Decision Tree	1.0	1.0	1.0
KNN	1.0	1.0	1.0
Ridge	0.969	0.985	0.977
SVM	0.999	0.999	0.999

Table-III demonstrates the consequence of the experiment setup **EXP-III**, where we considered eight thousand speech files and applied 10-fold cross validation (CS1) and Standard Deviation (SD) statistical formula to normalize the extracted features. We got best result for Logistical Regression, Decision Tree and SVM classifier in basis of Recall values.

TABLE III: Result of EXP-III

Classifier	P	R	FS
Logistic Regression	0.999	1.0	0.999
Decision Tree	1.0	1.0	1.0
KNN	1.0	1.0	1.0
Ridge	0.999	0.998	0.999
SVM	0.999	1.0	0.999

Table-IV shows the result of experimental setup EXP-IV. In this setup we consider 80 speakers and applied 10-fold cross selection (CS2) and used Mean (MN) statistical formula to normalize the feature obtained from the feature extraction phase, we got the result that except Ridge classifier, the recall value for every classifier is 1.0.

TABLE IV: Result of EXP-IV

Classifier	P	R	FS
Logistic Regression	0.999	1.0	0.999
Decision Tree	0.999	1.0	0.999
KNN	0.999	1.0	0.999
Ridge	1.0	0.999	0.999
SVM	0.999	1.0	0.999

In Table-V, we mentioned the results of experimental setup EXP-V. Where we considered 80 speakers and applied 10-fold cross section (CS2) and to normalize the extracted feature, we have used Variance. Here we got the best recall value for Decision Tree and KNN classifier.

TABLE V: Result of EXP-V

Classifier	P	R	FS
Logistic Regression	0.999	0.999	0.999
Decision Tree	1.0	1.0	1.0
KNN	1.0	1.0	1.0
Ridge	0.965	0.983	0.973
SVM	0.999	0.997	0.998

Table-VI describes the result of the experiment step up EXP-VI, where we considered 80 speakers and applied 10-fold cross section (CS2) and to normalize the extracted features we have used Standard Deviation (SD) statistical formula. We got best recall value for Logistic Regression, Decision Tree, KNN and SVM classifier.

TABLE VI: Result of EXP-VI

Classifier	P	R	FS
Logistic Regression	0.999	1.0	0.999
Decision Tree	1.0	1.0	1.0
KNN	1.0	1.0	1.0
Ridge	0.999	0.997	0.998
SVM	0.999	1.0	0.999

V. Discussions

In this connection we setup six experiments using our media Bengali speech corpus and for each setup we incorporate five machine learning approaches. Among these experimental setups EXP-IV gives the best performance in terms of recall score and KNN gives the best result among five classification algorithms we used for all the six setups with recall score equals to 1.0.

In this experiment, we were able to produce higher accuracy rate as both the training data and test data are almost know because Data set D1 and D2 is built using the same hundred lines and on the other hand Data set D3 and D4 is built using the same hundred lines. Though we used 10-fold cross validation to split our corpus, the input sentences of audio files are nearly same. Moreover, the age range of the speakers is between 20 to 40 years which may tend to give wrong label for speaker age out of the range. In future we would like to add more speakers of different age groups and also use unique sentences to develop our corpus. In spite of this issue, our experiment is able to identify gender from noisy audio content and also from small size of audio content as we used audio content of duration from 0.7 seconds to 8.4 seconds.

In this paper, we only consider two genders male and female. Third Gender (Transgender) sample is not provided in corpus nor we test with this type of voice. In future we would like to extend our experiments with third gender.

VI. Conclusion

This study has proposed a system for gender identification. The paper concludes the following:

- This study incorporates special features with respect to [9]. These features are Energy, Envelope, LPC, etc.
- This study embeds the machine learning tools, which were not in [9].
- In our method accuracy (recall value) is approximately 100%, but corresponding value of [9] is 80% only.

The author would like to do further experiments for male, female and Trans Gender in near future. Also try to add speaker count and age identification of the speakers.

References

[1] W. Abdulla, N. Kasabov, and D.-N. Zealand, "Improving speech recognition performance through gender separation," *changes*, vol. 9, p. 10, 2001.

[2] I. Potamitis, N. Fakotakis, and G. Kokkinakis, "Gender-dependent and speaker-dependent speech enhancement," in *Acoustics, Speech, and Signal Processing (ICASSP), 2002 IEEE International Conference on*, vol. 1. IEEE, 2002, pp. I–249.

[3] G. Tzanetakis, "Audio-based gender identification using bootstrapping," in *Communications, Computers and signal Processing, 2005. PACRIM. 2005 IEEE Pacific Rim Conference on*. IEEE, 2005, pp. 432–433.

[4] H. Harb and L. Chen, "Voice-based gender identification in multimedia applications," *Journal of intelligent information systems*, vol. 24, no. 2-3, pp. 179–198, 2005.

[5] ——, "A general audio classifier based on human perception motivated model," *Multimedia Tools and Applications*, vol. 34, no. 3, pp. 375–395, 2007.

[6] S.-I. Kang and J.-H. Chang, "Discriminative weight training-based optimally weighted mfcc for gender identification," *IEICE Electronics Express*, vol. 6, no. 19, pp. 1374–1379, 2009.

[7] L. Kye-Hwan, K. Sang-Ick, K. Deok-Hwan, and J.-H. Chang, "A support vector machine-based gender identification using speech signal," *IEICE transactions on communications*, vol. 91, no. 10, pp. 3326–3329, 2008.

[8] Y. Hu, D. Wu, and A. Nucci, "Pitch-based gender identification with two-stage classification," *Security and Communication Networks*, vol. 5, no. 2, pp. 211–225, 2012.

[9] M. S. Ali, M. S. Islam, and M. A. Hossain, "Gender recognition system using speech signal."

[10] C. M. Bishop, *Pattern recognition and machine learning*. springer, 2006.

[11] B. Mathieu, S. Essid, T. Fillon, J. Prado, and G. Richard, "Yaafe, an easy to use and efficient audio feature extraction software." in *ISMIR*, 2010, pp. 441–446.

[12] A. Eronen *et al.*, "Automatic musical instrument recognition," *Mémoire de DEA, Tempere University of Technology*, p. 178, 2001.

[13] C. Duxbury, J. P. Bello, M. Davies, M. Sandler *et al.*, "Complex domain onset detection for musical signals," in *Proc. Digital Audio Effects Workshop (DAFx)*, no. 1, 2003, pp. 6–9.

[14] Y. Konig and N. Morgan, "Gdnn: a gender-dependent neural network for continuous speech recognition," in *Neural Networks, 1992. IJCNN., International Joint Conference on*, vol. 2, Jun 1992, pp. 332–337 vol.2.

[15] J. Makhoul, "Linear prediction: A tutorial review," *Proceedings of the IEEE*, vol. 63, no. 4, pp. 561–580, 1975.

[16] M. Liu, C. Wan, and L. Wang, "Content-based audio classification and retrieval using a fuzzy logic system: towards multimedia search engines," *Soft Computing*, vol. 6, no. 5, pp. 357–364, 2002.

[17] G. Peeters, "{A large set of audio features for sound description (similarity and classification) in the CUIDADO project}," 2004.

[18] B. C. Moore, B. R. Glasberg, and T. Baer, "A model for the prediction of thresholds, loudness, and partial loudness," *Journal of the Audio Engineering Society*, vol. 45, no. 4, pp. 224–240, 1997.

[19] S. B. Davis and P. Mermelstein, "Comparison of parametric representations for monosyllabic word recognition in continuously spoken sentences," in *Readings in speech recognition*. Morgan Kaufmann Publishers Inc., 1990, pp. 65–74.

[20] S. Essid, "Classification automatique des signaux audio-fréquences: reconnaissance des instruments de musique," Ph.D. dissertation, Université Pierre et Marie Curie-Paris VI, 2005.

[21] E. Scheirer and M. Slaney, "Construction and evaluation of a robust multifeature speech/music discriminator," in *Acoustics, Speech, and Signal Processing, 1997. ICASSP-97., 1997 IEEE International Conference on*, vol. 2. IEEE, 1997, pp. 1331–1334.

[22] F. Kabir, S. Siddique, M. Kotwal, and M. Huda, "Bangla text document categorization using stochastic gradient descent (sgd) classifier," in *Cognitive Computing and Information Processing (CCIP), 2015 International Conference on*, March 2015, pp. 1–4.

[23] D. G. Kleinbaum and M. Klein, *Analysis of Matched Data Using Logistic Regression*. Springer, 2010.

[24] M. A. Friedl and C. E. Brodley, "Decision tree classification of land cover from remotely sensed data," *Remote sensing of environment*, vol. 61, no. 3, pp. 399–409, 1997.

[25] L. Breiman, "Technical note: Some properties of splitting criteria," *Machine Learning*, vol. 24, no. 1, pp. 41–47, 1996.

[26] W. Henley and D. J. Hand, "A k-nearest-neighbour classifier for assessing consumer credit risk," *The Statistician*, pp. 77–95, 1996.

[27] A. M. Kibriya and E. Frank, "An empirical comparison of exact nearest neighbour algorithms," in *Knowledge Discovery in Databases: PKDD 2007*. Springer, 2007, pp. 140–151.

[28] N. R. Draper, H. Smith, and E. Pownell, *Applied regression analysis*. Wiley New York, 1966, vol. 3.

[29] N. Cristianini and J. Shawe-Taylor, *An introduction to support vector machines and other kernel-based learning methods*. Cambridge university press, 2000.

[30] J. Weston, C. Watkins *et al.*, "Support vector machines for multi-class pattern recognition." in *ESANN*, vol. 99, 1999, pp. 219–224.

[31] D. M. Powers, "Evaluation: from precision, recall and f-measure to roc, informedness, markedness and correlation," 2011.

A Support Vector Regression Model for Forecasting Rainfall

Nasimul Hasan[1], Nayan Chandra Nath[1], Risul Islam Rasel[2]
Department of Computer Science and Engineering
International Islamic University Chittagong, Bangladesh
Email: nasimul_hsn@yahoo.com[1],nayanctg143@gmail.com[1],rasel.kmutnb@gmail.com[2]

Abstract— Rainfall prediction is a very important part of weather forecasting. In countries like Bangladesh; which has several seasons a year, rainfall prediction is really a key factor for many sectors. Rainfall data is a time series data and it changes time to time as climate and season changes. Moreover, rainfall depends on several factors as flow of wind, humidity etc., it is very challenging to make a hundred percent perfect prediction. This paper exhibits a robust rainfall prediction technique in view of the recent rainfall data of Bangladesh utilizing Support Vector Regression (SVR), a relapse methodology of Support Vector Machine (SVR). The collected raw data wasn't prepared for using as input of algorithm, thus it had been pre processed manually to suit into the algorithm, then fed to the algorithm. The evaluation results of the study conducted on the data shows that the projected technique performs higher than the conventional frameworks in term of accuracy and process running time. The proposed approach yielded the utmost prediction of 99.92%

Keywords— Rainfall prediction; timeseries data; windowing operator; sliding window validation; Support Vector Regression;

I. INTRODUCTION

Weather (especially rainfall) has a great influence over cultivation, flood and some other sectors, The cultivation of corps relies mostly on rainfall here and it is important to predict how much rainfall may happen in an upcoming season. A perfect rainfall prediction can help us to take decision what to cultivate and what to not. Since many other things such as drought, tourism, transportation, construction etc. also sometimes depends on rainfall; a good prediction can help to take decisions regarding these sectors. From ancient time people are trying to find the pattern of weather and predict weather for their well-being. From the very beginning of science and technology, weather prediction is a very interesting sector of study. Forecasting rainfall is a tough task due to the complication of the physics and different variable which cause rainfall [1]. It is actually a very noisy and deterministically disordered natural event. Some very important factors as monsoon, wind, moisture, heat, rotation of earth etc. plays a very strong role on the rainfall issue.

A lot of intelligent techniques as Artificial Neural have been used to predict rainfall. Among them Artificial Neural Network (ANN) is a commonly used technique to produce a good prediction [2] [3] [4]. Frequent study shows that ANN can work way better than different regression, MA and EMA. ANN frequently displays conflicting and unpredictable execution on boisterous data [5]. Support Vector Machine (SVM) is a supervised classification and regression algorithm. An SVM model represents the samples as point spaces. It is mainly based of decision plane concept. It separates objects with different class by a visible gap as much as possible between the classes. SVM can perform both linear and non-linear classification with super efficiency. Kesheng Lu and Lingzhi Wang [6] showed in their research that Support Vector Machine can perform an efficient rainfall prediction with a low error rate. Their model can produce almost 99% accurate prediction. A. Mellit, A. Massi Pavan & M. Benghanem [7] developed a SVM model which can produce up to 99% accurate prediction for different models. At the point when utilizing SVM, the fundamental issue is defied: how to pick the appropriate kernel and how to set the best kernel function. The best possible parameters setting can enhance the SVM relapse exactness. Diverse kernel capacity and distinctive parameter settings can bring about huge contrasts in execution. However, there are no investigative strategies on the other hand solid heuristics that can direct the client in selecting a fitting part capacity and great parameter values [6].

In this study, different kernel functions of Support Vector Machine (SVM) and a data preprocessing technique windowing is combined to predict rainfall. Three different models- Total rainfall prediction, maximum rainfall prediction and average rainfall prediction with three different sub models, for 1day ahead, 7 day ahead and 10 day ahead prediction are proposed here for a better rainfall prediction technique.

II. METHODOLOGY

ε-insensitive loss function was introduced by Vapnik and then SVM was developed to solve regression problems as well. The process is known as Support Vector Regression (SVR). SVR has an excellent performance regarding the perfection of solving non-linear regression.

Support Vector Regression: Almost all principals of SVM classification are followed by Support Vector Regression (SVR). As the output is real number and there are unlimited possibilities. To handle this problem, a limitation to the tolerance (epsilon) is set to the SVM which would have effectively asked for from the problem. It minimizes $\|\omega\|^2$ to reduce the model complexity. Here ξ_i and ξ_i^* are slack variables and i= 1, …, n to calculate the difference of training data outside $\varepsilon -$ sensitive zone [8] [9].

Minimize:

978-1-4673-9257-0/15/$31.00 ©2015 IEEE

$$\frac{1}{2}\|\omega\|^2 + C\sum_{i=1}^{n}(\xi_i + \xi_i^*) \quad (1)$$

Subject to:

$$\begin{cases} y_i - f(x_{i,\omega}) \leq \in + \xi_i^* \\ f(x_{i,\omega}) - y_i \leq \in + \xi_\iota \\ \xi_\iota, \xi_i^* \geq 1, \dots, \mathrm{n} \end{cases} \quad (2)$$

The optimization problem can lead to the dual problem and the solution is:

$$f(x) = \sum_{i=1}^{n_{sv}}(\alpha_i - \alpha_i^*)K(x_i, x) \quad (3)$$

Subject to, $0 \leq \alpha_i^* \leq C, 0 \leq \alpha_i \leq C$

Here, n_{sv} denotes the number of Support Vector (SVs).

Kernel Functions:

$$K(x_i, x_j) = \begin{Bmatrix} X_i, X_j & \text{Linear} \\ (\gamma X_i \cdot X_j + C)^d & \text{Polynomial} \\ exp\left(-\gamma|X_i - X_j|^2\right) & \text{RBF} \\ \tan h\,(\gamma X_i \cdot X_j) + C & Sigmoid \end{Bmatrix} \quad (4)$$

Here, $K(X_i, X_j) = \emptyset(X_i, X_j)$ and γ is the adjustable parameter.

A. Time series data:

Rainfall data is time series data. Time series data is a set of values of something where the intervals of the value are listed in such a way that the time period between each attribute is exactly same.

B. Moving Average:

A Moving Average (rolling average or running average) is an estimation to analyze data points by making a progression of midpoints of distinctive subsets of the full data set.

$$\text{MA} = \frac{x_1 + x_2 + \cdots + x_n}{n} \quad (5)$$

Here, $x_1 + x_2 + \cdots + x_n$ are the average values of the monthly rainfall and n is the total number of observation. Moving average of 7 days was considered for all attributes taken as labels in this study

C. Windowing operator:

Windowing operator is an exclusive operator which can perform better for time series prediction. It converts series sample data into single valued data. The series data must be given as Example Set. The parameter "series representation" defines how the series data is represented by the Example Set.

III. Evaluation Process

A. RMSE

Root Mean Square Error is a well-known and commonly used evaluation process for regression models.

$$\text{RMSE} = \sqrt{\frac{\sum_{i=1}^{n}(yt - \widehat{yt})^2}{n}} \quad (6)$$

Here, yt is the original value of a point for a given time period *t*, *n* is the total number of fitted points, and $\widehat{yt}$ is the fitted forecast value for the time period *t*.

B. MAE

Mean Average Error (MAE) is an widely used evaluation formula. Mean Absolute Error (MAE) measures how far predicted values are away from observed values.

$$\text{MAE} = \frac{\sum_{i=1}^{N}|x_i - \hat{x}_j|}{N} \quad (7)$$

Here, x_i is the actual observations time series, is the estimated or forecasted time series, SAE is the sum of the absolute errors (or deviations), N is the number of non-missing data points

IV. Experiment Design

A. Research Data:

6 years Rainfall data (2008-2014) of Chittagong, Bangladesh from the Meteorological Department, Bangladesh were collected to perform experiment and evaluation this study. Here we took only the data of March to October of each year as basically in this period rainfall occurs here normally. Three different models for forecasting maximum, total r and average rainfall were built with the same data. 80% of the data were considered as training data and the rest 20% as testing data. Six attributes, Date, total, avg., max, min, MA included both the training and test data. The 'Date' attribute was selected as id for all three models and another attribute ('max' for maximum rainfall prediction, 'avg.' for average rainfall prediction and 'total' for total rainfall prediction) was chosen as label. Figure 1 shows the actual rainfall (2008-2014)

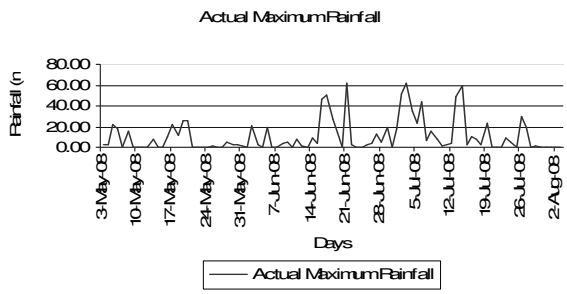

Figure1. Actual Rainfall of Chittagong (Total, 2008-2014)

B. Model construction and analysis:

This step starts with the preprocessing step of data. At the very first Moving Average (MA) technique was applied on the data set. Then windowing operator was used so that it can convert series data to universal dataset and feed the learning process [10]. As learning technique we used Support Vector Regression (SVR). The model structure includes two vital stages, training and testing. Both the stages are continuous process as the main objective of the study was to build a efficient model for rainfall forecasting.

Training and testing stages are mentioned below.

1*) Training stage:*

The training stage starts with the retrieving of data from the repository. The data were processed before entering this stage. After this, the role of the attributes in the dataset was assigned. Then one of the attributes (Date) was selected as the id and another as the label. The selection of label was different for three different models. The next step was to set the windowing operator. The parameters of windowing operator were set and then windowing was performed. A special and efficient validation 'Sliding Window Validation' was performed for validation. Afterwards, the main process was fed and the parameters of the Support Vector Regression. Then the model was set to run.

2) Testing stage:

In this phase the testing data were retrieved from the repository and the role of the attributes of the data was set and then the id and label were selected as done in the training stage. Like the training stage, the parameters of windowing operator were set and run and then the main process was fed. The performance was compared finally.

V. EXPERIMENT RESULT

A. Windowing operator analysis:

At this point we used windowing operator to the time series data to convert it into generic data. Table I shows the windowing operators parameter settings used in this study.

TABLE I. WINDOWING OPERATOR ANALYSIS

Model		Horizon	Window size	Step Size
Total	1 day	1	2	1
	7 day	7	2	1
	10 day	10	2	1
Maximum	1 day	1	3	1
	7 day	7	2	1
	10 day	10	2	1
Average	1 day	1	2	1
	7 day	7	2	1
	10 day	10	2	1

B. Support Vector kernel Analysis:

The parameters selecting of Support Vector Regression is a very crucial and important part. The perfection of prediction depends on best setting of parameters. So that, the parameters were chosen carefully and a log was kept to find the best parameter set. Table II shows the parameter settings for Support vector used in this study. Here, C is the constant of complexity and G is the value of kernel gamma.

TABLE II. SUPPORT VECTOR KERNEL ANALYSIS

Model	Days	Kernel Type	degree	C	G	∈	∈ +	∈ -
Total	1	Anova	1	2000	1	1	1	1
	7		1	1000	1	1	1	1
	10		1	1000	1	1	1	1
Max	1		1	400	1	1	1	1
	7		1	700	1	1	1	1
	10		1	1000	1	1	1	1
Average	1		1	1000	1	1	1	1
	7		1	1000	1	1	1	1
	10		1	1000	1	1	1	1

C. Sliding window validation:

As the validation process for this study sliding window validation was used. It is a special validation for series data. It takes a certain window for training and another window for testing. The window then moves to another window and determine the average of all estimation. The parameter "cumulative training" shows if every single previous sample ought to be utilized for preparing (rather than just the present window) [11]. Table III shows the parameter properties of Sliding Window validation and Table IV shows the result of the study.

TABLE III. SLIDING WINDOW VALIDATION

Model		Training Window Width	Training Window step	Test Window width	Horizon
Total	1	2	1	2	1
	7	2	1	2	7
	10	2	1	2	10
Max	1	2	1	2	1
	7	2	1	2	7
	10	2	1	2	10
Avg	1	2	1	2	1
	7	2	1	2	7
	10	2	1	2	10

TABLE IV. RESULT FOR 1 DAY AHEAD PREDICTION

	Date	Actual Rainfall	Predicted Rainfall 1 day
Total	4-Jul-12	0.1	0.19
	5-Jul-12	2.5	1.76
	6-Jul-12	0.0	0.74
	7-Jul-12	1.6	1.17

	Date	Actual Rainfall	Predicted Rainfall 1 day
Maximum	4-Jul-12	0.1	0.85
	5-Jul-12	2	1.26
	6-Jul-12	0	1.04
	7-Jul-12	1	1.11
Average	4-Jul-12	0.0125	0.76
	5-Jul-12	0.3125	0.76
	6-Jul-12	0	0.68
	7-Jul-12	0.2	0.81

TABLE V. RESULT FOR 7 DAY AHEAD PREDICTION

	Date	Actual Rainfall	Predicted Rainfall 7day
Total	10-Jul-12	6.8	1.81
	11-Jul-12	4.6	6.97
	12-Jul-12	78	107.79
	13-Jul-12	115	30.54
Maximum	10-Jul-12	6	1.47
	11-Jul-12	4.6	1.90
	12-Jul-12	53.8	5.48
	13-Jul-12	106	1.52
Average	10-Jul-12	0.85	1.17
	11-Jul-12	0.575	0.06
	12-Jul-12	9.75	14.49
	13-Jul-12	14.375	5.72

TABLE VI. RESULT FOR 10 DAY AHEAD PREDICTION

	Date	Actual Rainfall	Predicted Rainfall 10 day
Total	13-Jul-12	115	28.65
	14-Jul-12	66.2	7.83
	15-Jul-12	44.1	1.41
	16-Jul-12	5	2.41
Maximum	13-Jul-12	106	14.10
	14-Jul-12	40	0.38
	15-Jul-12	16	2.63
	16-Jul-12	4	2.91
Average	13-Jul-12	14.375	10.74
	14-Jul-12	8.275	2.93
	15-Jul-12	5.5125	0.51
	16-Jul-12	0.625	1.88

D. *Error calculation:*

The error calculated from the actual rainfall value and the predicted rainfall value from the Support Vector Regression model proposed in this study.

TABLE VII. ERROR CALCULATION

Model		RMSE	MAE
Total	1 day	18.60	0.08
	7 day	24.95	4.99
	10 day	24.97	86.35
Maximum	1 day	11.39	0.75
	7 day	15.99	4.53
	10 day	14.26	91.90
Average	1 day	2.85	0.45
	7 day	3.30	0.31
	10 day	3.54	3.63

E. *Graphical Representation of the study:*

Two different models- Maximum rainfall prediction and Total rainfall prediction are proposed here with 1 day ahead, 7 day ahead and 10 day ahead models for each. Figure 2, Figure 3, Figure 4, Figure 5, Figure 6, Figure 7, Figure 8, Figure 9 and Figure 10 shows the difference between the actual value of rainfall (mm) and the predicted value of rainfall (mm).

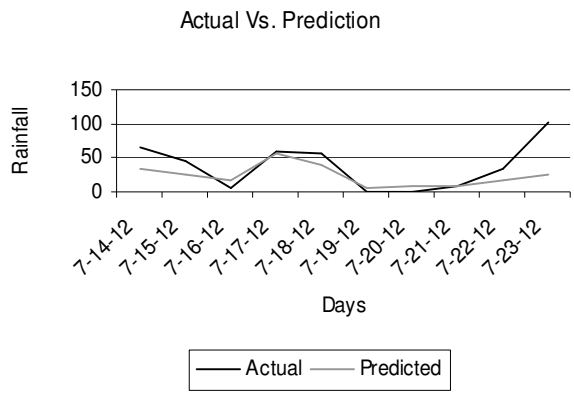

Fig 2 . Actual Vs. Prediction (Total, 1 day Ahead)

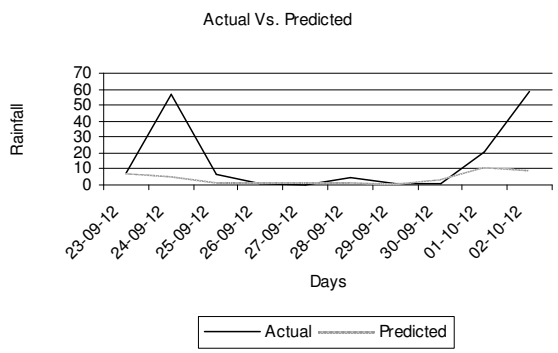

Fig 3. Actual Vs. Prediction (Total, 7 day Ahead)

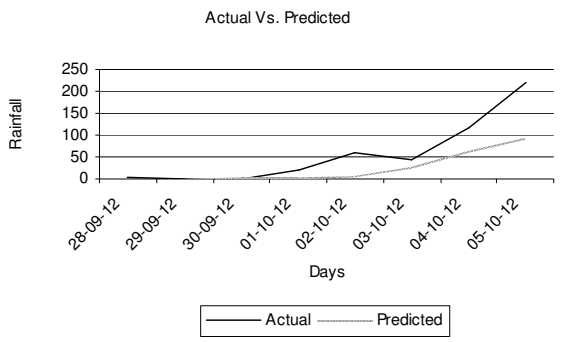

Fig 4. Actual Vs. Prediction (Total, 10 day Ahead)

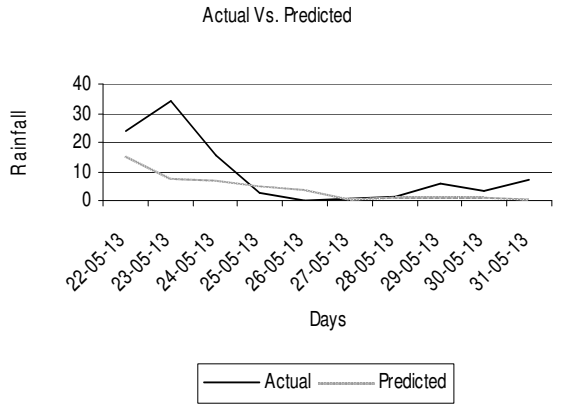

Fig 5. Actual Vs. Prediction (Max, 1 day Ahead)

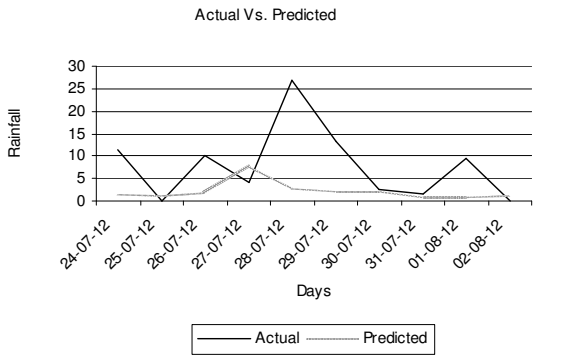

Fig 6. Actual Vs. Prediction (Max, 7 day Ahead)

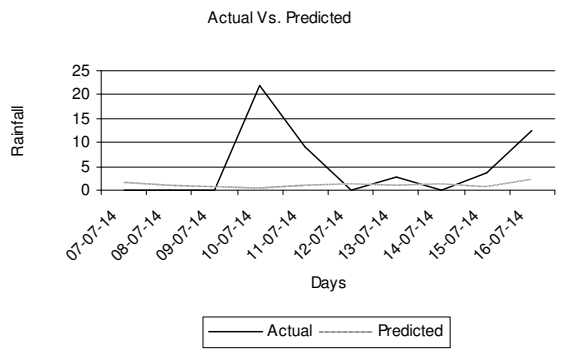

Fig 7. Actual Vs. Prediction (Max, 10 day ahead)

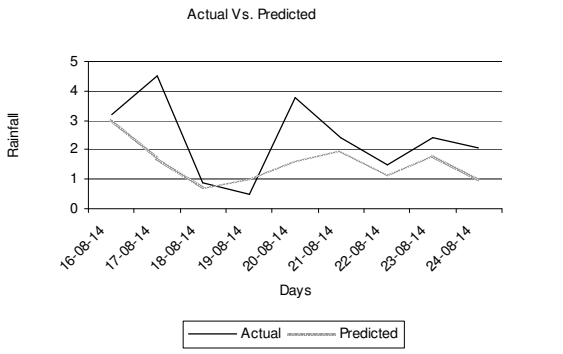

Fig 8. Actual Vs. Prediction (Average, 1 day ahead)

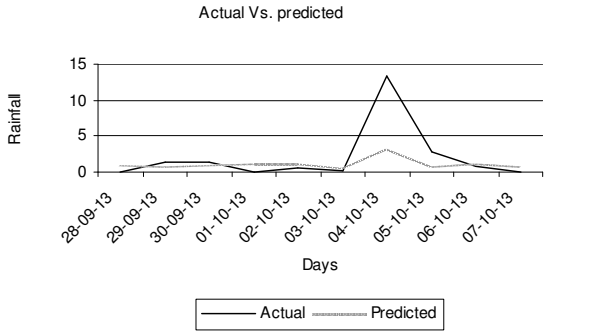

Fig 9 Actual Vs. Prediction (Average, 7 day ahead)

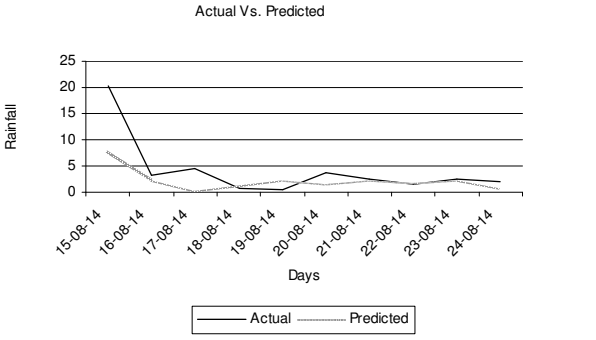

Fig 10. Actual Vs. Prediction (Average, 10 day ahead)

VI. CONCLUSION

A. Discussion

This paper presents a robust rainfall prediction technique using Support Vector Regression. The result of the experiment done with the data of Chittagong, Bangladesh shows that the proposed model can forecast more accurately in comparison with the regular technique used. The proposed model can predict better than any model before one day. The 7 days ahead model also performs very well than conventional processes.

B. Limitation and Future Work

Only Moving Average and Windowing operator were used as data preprocessing step in this study. The data was taken for only Chittagong area of Bangladesh. In future more data preprocessing steps and different algorithms will be used. Data from other stations of different countries and area will be used to get a universal model.

REFERENCES

[1] Lihua Xiong, K. M. Connor, "An empirical method to improve the prediction limits of the GLUE methodology in rainfall– runoff modeling," Journal of Hydrology, Vol. 349, pp: 115–124, 2008.

[2] Jiansheng Wu; Liangyong Huang; Xiaoming Pan, "A Novel Bayesian Additive Regression Trees Ensemble Model Based on Linear Regression and Nonlinear Regression for Torrential Rain Forecasting," in Computational Science and Optimization (CSO), 2010 Third International Joint Conference on , vol.2, no., pp.466-470, 28-31 May 2010

[3] Jiansheng Wu, "A novel nonparametric regression ensemble for rainfall forecasting using particle swarm optimization technique coupled with artificial neural network," Lecture Note Computer Science, Vol. 5553, No. 3, pp: 49–58, Springer- Verlag Berlin Heidelberg, 2009.

[4] G. F. Lin and L. H. Chen, "Application of an artificial neural network to typhoon rainfall forecasting," Hydrological Processes,Vol. 19, pp. 1825–1837, 2005.

[5] W. C. Hong, "Rainfall forecasting by technological machine learning models," Applied Mathematics and Computation, Vol. 200, pp: 41–57, 2008.

[6] Kesheng Lu; Lingzhi Wang, "A Novel Nonlinear Combination Model Based on Support Vector Machine for Rainfall Prediction," in Computational Sciences and Optimization (CSO), 2011 Fourth International Joint Conference on , vol., no., pp.1343-1346, 15-19 April 2011

[7] A. Mellit, A. Massi Pavan, M. Benghanem, "Least squares support vector machine for short-term prediction of meteorological time series" in Theoretical and Applied Climatology, Volume 111, Issue 1-2 , pp 297-307

[8] Lucas, K., Lai, C., James, N., Liu, K.: Stock Forecasting Using Support Vector Machine. In: Proceedings of the Ninth International Conference on Machine Learning and Cybernetics, pp. 1607–1614 (2010)

[9] Debasish, B., Srimanta, P., Dipak, C.P.: "Support Vector Regression. Neural Information Processing"– Letters and Reviews 11(10), 203–224 (2007)

[10] R.I.Rasel, Nasrin Sultana, P.Meesad (in press), "An Efficient Modelling Approach for Forecasting Financial Time Series Data Using Support Vector Regression and Windowing operators", In: International Journal of Computational Intelligence Studies, 2015

[11] F.R.EngLucas, K., Lai, C., James, N., Liu, K.: Stock Forecasting Using Support Vector Machine. In: Proceedings of the Ninth International Conference on Machine Learning and Cybernetics,pp. 1607–1614 (2010).

Enhancing Software Development Process Using Automated Adaptation of Object Ensembles

Md. Emran, Humaun Kabir, Ziaur Rahman, Nazrul Islam

Department of Information and Communication Technology

Mawlana Bhashani Science and Technology University

Santosh, Tangail-1902, Bangladesh

Email: emranict08@gmail.com, humaunkabirmstu10@gmail.com, zia@iut-dhaka.edu, nazrul.islam@mbstu.ac.bd

***Abstract*— Software development has been changing rapidly. This development process can be influenced through changing developer friendly approaches. We can save time consumption and accelerate the development process if we can automatically guide programmer during software development. There are some approaches that recommended relevant code snippets and API-items to the developer. Some approaches apply general code, searching techniques and some approaches use an online based repository mining strategies. But it gets quite difficult to help programmers when they need particular type conversion problems. More specifically when they want to adapt existing interfaces according to their expectation. One of the familiar triumph to guide developers in such situation is adapting collections and arrays through automated adaptation of object ensembles. But how does it help to a novice developer in real time software development that is not explicitly specified? In this paper, we have developed a system that works as a plugin-tool integrated with a particular Data Mining Integrated environment (DMIE) to recommend relevant interface while they seek for a type conversion situation. We have a mined repository of respective adapter classes and related APIs from where developer, search their query and get their result using the relevant transformer classes. The system that recommends developers titled automated objective ensembles (AOE plugin). From the investigation as we have ever made, we can see that our approach much better than some of the existing approaches.**

***Keywords*—Adaptation of Object Ensembles, Source Repository, Software Developing Process, Data Mining Integrated Environment.**

I. INTRODUCTION

The Software development process can be enriched by using many processes. Many guidelines are given which influence software development process, especially in the coding stage. Reusing previously completed software repository to enhance the development process is a common phenomenon in the field of Mining Software Repository (MSR). If developers get suggestions in e.g. API recommendations, object usage pattern, class structure or code snippets from the existing projects they might be benefited a lot what they eventually expect while coding. Some of the approaches have integrated web based code, searching in their customized tool like MAC [1] and MAPO [2] before mining the code source abstractions. Although MAC and MAPO are server dependent or online based, by which they are not flexible for a developer. Automated Adaptation of Object Ensembles (AOE) shows a process of adapting the collection frameworks and Arrays, but it is not clear view how to use it as a plug-in tool.

In software development there are different ways available to guide software developers during the development period. A programmer can use programming code in a software system easily by using an automated adaptation of object ensembles. By this process user can find out required data easily. We have used an AOE Plug-in by which a software developer can complete a code in a short time. It takes less time compared to existing approaches. The existing approaches like simply using the Integrated Development Environment (IDE) like Net Beans [3], IntellijIdea [4], and Eclipse [5], is vulnerable to flaws and it is unable to provide us the required interfaces. In essence, it consumes developers' valuable times. We have investigated between the conventional ways and our AOE plug-in approach to evaluate the efficiency of our proposed tool. The study shows that it is able to accelerate the developer's performance and facilitate less time consuming with decreasing code flaws and errors.

Although in MAC [1], MAPO [2], AOE [6]and many others code repository had several limitations such as server dependent searching, either database based or Internet based where data is not preprocessed according to rules of data mining so these are not friendly for a developer. In our methodology we try to show our repository plugin as an offline repository that is filed based instead of a database and it has special source abstraction technique. Adapter classes are the key point in our approach. In AOE the result depends on the resource of the repository of adapter classes. Recently, a number of works are available to guide developers in the field of software engineering. All we have seen is that our approach is comparatively easier to handle than other existing approaches.

The paper is so far structured in the followings: Section II background and related works of this study. Section III shows that full design and proposed approach. The detailed results and evaluation of this paper is presented in Section IV. Section V concludes with the set of observation and future work of this research.

II. BACKGROUNDS AND RELATED WORKS

As the software development process can be influenced by using many techniques, so many researchers try to provide a flexible way that can influence the software development process. Need not to say that previously completed software repository technique enhance the development process is a common framework in the field of mining software repository. The developers can be benefited by following the provided suggestions from various recommendations like API recommendations, object usage pattern, class structure or code snippets from the existing projects. Some of the approaches have integrated web based code, searching in their customized tool like MAC [1] and MAPO [2] before mining the code source abstractions.

There are some processes by which a software system is established by code reusing. But in our approach we use a repository of adapter classes and a tool which adapt this code. By using this AOE plug-in which integrates with the IDE, the user can find the required data type easily. There are some existing efforts such as adapting collection and array by using Automated Adaption of Object (AOE)[6]. Some approaches like Code reusing in MAPO [2], better user recommendation using enhancing software development repository, Scenario Based API Recommendation System [7] and others are also used to accelerate the software development process. As we have proposed that if there have been adapter tools [8] which adapt the given interfaces it will be more helpful for the programmers to find the required interfaces. Mining API Usages from Open Source Repositories (MAPO) [2], [3] was one of the first and MAC [1] was one of the updated triumphs to mine API usage pattern. Other recent works called Enhancing Software Development Process (ESDP) [9] where the developers are highly guided by recommendations from a mined repository is also one of our referral works.

One of the best concepts of test-driven reuse showed by Reiss [10] common test-cases issued as input for a component search engine in [11]. Nevertheless, there exist some problems such as license problem and dependency problem. When the user changes the parameter types, then it might need an even more propagated deep adjustment of type changes. The formal and rule-based language is proposed by Kell [12] that was named Cake for automated wrapper generations. The designing used to define interface relations; transformation object structures are possible by applying these rules. We introduced that transformation should happen automatically but it is most overhead for a developer writing mapping rules, basically for an unknown complex object. It overcame Nita and Notkin [13] by providing an approach which concerned with adapting programs to alternative APIs. When the variations among the APIs are small its schema considers not-straightforward structural respect as out of scope, which is the main challenge, is providing transformation. The work showed by Hummel [14] is depending on the Identity Map Pattern from Fowler [15] and identifies the answer about the problems of the Gang of Four adapter pattern. The approach is integrated into another work by Hummel and Atkinson [14] that supplies relaxed-signature matching for primitive data types.

Recently there have done many works to enhance the software development process. There have applied many tools such as adapter generation tool [6]. In this way a user can find the required method easily. As a result a user can save time and solve any problem easily. The software development process is an easy task for a developer.

In the approach we try to overcome the limitations of existing repository tools. We try to provide as an offline repository tool that are file based instead of a database that has special source abstraction. Adapter and transformer classes are the key point in our approach.

III. PROPOSED APPROACH

In our approach we have developed a plug-in tool that is able to guide software development through suggesting interfaces by using the respective adapter classes. The tool is completely written in java and is executable as a standalone application. It can work with IDE like Net beans [3] and Eclipse [5] as they have the software extensibility.

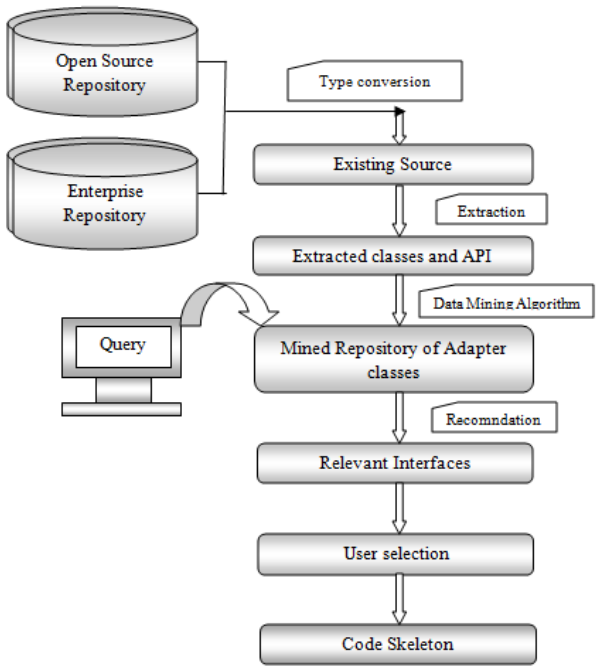

Fig. 1. Automated Object Ensembles (AOE) plugin Framework

Open Source Repository (OSR) is an online software code repository. In this repository many projects problem solving codes are stored. When a programmer stays in online and gets any programming problem, then the programmer can search in this repository for required code. OSP is an Internet based repository. In many software companies, there are stored many projects. It is called the Enterprise Repository.

In repository, there are stored a large number of programs. Many unusual code lines are staying in programs. We take the

only important line for a program. By using type conversion we build up Existing Source where projects are stored without unusual code lines. Programming code is stored in Existing Sources. We extract classes of API from these projects which exist in Existing Sources.

Data Mining Algorithm is used to build up a mined repository of Adapter classes. When a programmer searches any classes, the required classes are shown at first. Then we will find related classes. Programmers, search their needed query in the mined repository of Adapter Classes. Then we get relevant interfaces with the help of a transformer and recommendation interfaces. The user selects the required interfaces and gets code skeleton.

Now a day, there has various tools to increase the optimizing capability in software development field; adapter generation tool is one of them. To overcome mismatches on the signature level a good way is to add an adapter that controls message forwarding from one interface to the other. The adapters allow classes to work together that could not otherwise because of incompatible interfaces. It can also be familiar as a "Wrapper" which wraps the incompatible class into the adapter class, where adapter adapt any types of object, method and interface that helps in the programming fields. There exist projects available the newly integrated ability to transform arrays and collections, which can be executed for verifying the adaptation capabilities. This idea is to describe by Hummel [11], where able to generate a random Array List and a sorted Vector instance the helper class Generator is used. When a client uses an automated adapter class that depends on the interfaces that are provided by collection frameworks then the client needs help to use any plugin.

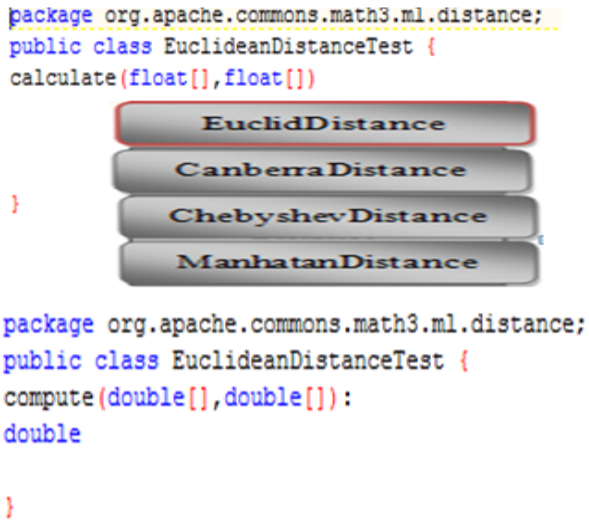

Fig. 2. Adaptation testing overview

For example, when a programmer writes their code in the IDE like as Net Beans they must write the full code to reach the required result, But when they use AOE plug-in by pressing the right button, then the programmer will be guided by the several adapter classes that are shown in the fig. 2., which is remarked by red color box is chosen. Suppose coder write ,calculate (float [], float []) then AOE plaguing suggest Euclid Distance adoptee adapt that generate in D. Seffert and O. Hummel [7] where adapter depends on transformer that transform provided instance to require instance and vice versa. Suppose a client requires a specific data types, then its search in the adapter fields after matching needed data types client can choose any of them. By finishing the process of adaptation successfully the modified test case was executed here using the final adapter instead of the adapter directly. Nevertheless, test case executed full filly the adapter's transformation capability was verified. For example, in the test case the compute method of the selected class from *org.apache.commons.math3.ml.distance* package is tested. That takes as an input two vectors, showed by an array of type double each, and calculates the distance between them. The distance should be zero, if the same vector is provided as the first and second parameter such as in this example. The public double computes (double [], double []) is the interface of the compute method.

```
package org.apache.commons.math3.ml.distance;
public class EuclideanDistanceTest {
final DistanceMeasure distance = new EuclideanDistance();
public void testZero() {
final double [] a = {0, 1, -2, 3.4, 5, -6.7, 89};
Assert.assertEquals(0, distance. compute(a, a), 0d);
```

The array of type double was replaced with a Link List<Float> after the verification of the original test case executed successfully, where the expected name of the method was changed from compute to calculate. The test case is changed to public void double calculate (Linked List<Float>) for the require interfacing. The adapter generator overcome a parameter type and the method name mismatch, namely from Linked List<Float> on double [] and calculate in a computer.

Imagine a client requires one method within two parameters, but there exist more than two parameters in a similar method in the tool then adaptation process solves this complexity. In this paper, we want to describe how easily use collection frameworks as a plug-in tool in software development fields. The collection framework refers the way of implementing interfaces with the help of several classes that are considered as a supported plaguing tool.

We have seen in the approaches [2] [MAPO] that they have used a code search engine to find the desired item following a search query given by a particular client. Like MAPO this paper also enhances the automated adaptation of object ensembles as a repository tool. In this approach the require source may online or offline repository that contain various

kinds of tools. Eventually, the approaches are not only suggesting an adapter class, but also provide its related code implementation to reach the desired goal of a software developer. It works automatically when a client type any code during programing according to their require data types or interfaces. In order to consider the existing paper [6] that shows how to generate an adapter with the help of transforms that can able to solve the matching problems of complex data types. In fig.2. There have given a snapshot of the adapter generation tool. On other existing paper there have no idea about the plugin. But in our paper, we want to use plugin for a user.

A plugin is a software component that adds a specific feature to an existing once. When an application supports plug-in, it enables customization. In our paper we want to provide an adapter plug-in by which any client can complete a task more easily than existing processes. When a client wants to find classes or interfaces, there have given some adapter class options. From these options which is chosen then it finds out the required data by using adapter plug-in.

```
package result;
import java.util.WeakHashMap;

public calss Matrix{

private adaptees Rechteck adaptee;
private static WeakHashMap<adaptees.Rechteck,Matrix>Map=

public Matrix (int param0,int param1,String param2){
    adaptee=new adaptees.Rechteck (param0,param1,param2);
    map.put(adaptee,this);
    }
private Matrix(adaptees.Rechteck adaptee){
    this.adaptee=adaptee;
    map.put(adapte,this);
        }
public adaptees Reckteck getAdaptee(){
    return adaptee;
    }
}
```

Fig. 3. A snapshot 1 of Adapter generation tool (AOE)

IV. Evaluation

There have given a guideline for a programmer to enhance the software development process. An automated adaptation of object ensembles is a process by which any software developer can find the required data easily. There have given some comparison by which we will understand which process is better than another.

a. Environmental setup

In this development process, there have used a repository of adapter classes. How much healthier this repository the development process is more easy. If our adapter class repository is enriched, a user can find the required interfaces in a short time and easily. There have given same adapter class name such as:

SL	Adapter Classes	Line of Code (LOC)
A	EuclidDistance	17
B	CanberraDistance	11
C	ChebyshevDistance	15
D	ManhattanDistance	14
E	OnewayAnova	16

There used an adapter generation tool. Some object oriented language is used. There needs an adapter by which adaptation code is plagued with user. There have given an adapter generation tool such as adaptation tool.zip [6].

b. Time complexity

Time is an important thing when a program is solved. By which a program is solved quickly this process is better than other. When a programmer solves a program in IDE (Net Beans, eclipse) there have needed some times such as 40sec.

TABLE I. TIME COMPLEXITY

Task	IDE with AOE plug-in(no of solved problem)	NetBeans(no of solved problem)
T1	60 sec	120 sec
T2	130 sec	200 sec
T3	150 sec	310 sec
T4	120 sec	360 sec
T5	140 sec	400 sec

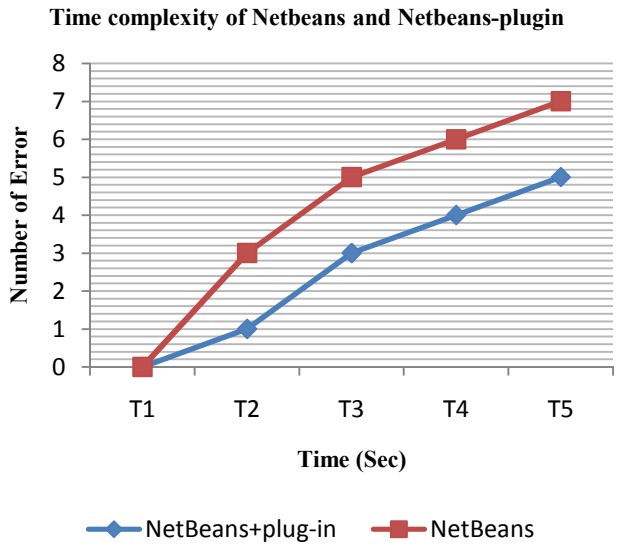

Fig. 4. Time complexity between NetBeans and NetBeans+plug-in

But the same programmer solves this same problem in net beans, but there have plugged-in AOE. As a result, we see that at this time the programmer can solve this problem in 0.20sec. When AOE is plugged-in, they have saved 20sec. There have given a table of how much program is solved without AOE plugged-in and within AOE plugged-in.

c. *Error Vulnerability*

In TABLE II we see that after the total time in IDE with plague-in there have found 13 errors, but at the same time problem solving only in IDE there have found out 21 errors.

TABLE II. Error possibility

Time	NetBeans+plug-in	NeatBeans
T1	0	0
T2	1	3
T3	3	5
T4	4	6
T5	5	7
Total error	=13	=21

As a result, we understand that when the plugin is used error rate is low. So this process is better than another.

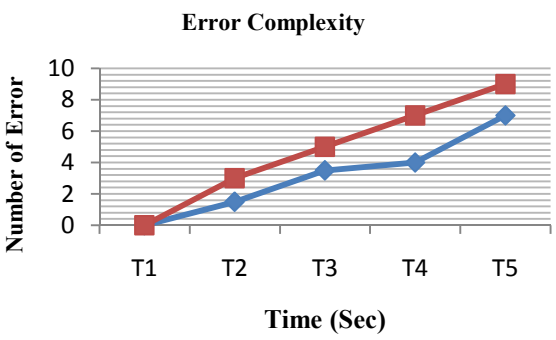

Fig. 5. Error comparison between net beans and NetBeans+plug-in

d. *Thread of the evaluation*

Everything has a limitation. There has some limitation of evaluation. This guideline for software development process is more effective. The evaluation is observed at the same time and same experiment. Such as

a. By having more AOE adapter classes in the repository a user finds more accurate data.

b. A program is evaluated by the same user.

c. It is a lengthy process to plug in a user in an adapter class repository.

d. A user cannot find the mining data.

The results observed in the empirical study may not be applicable to the programming tasks other than those considered in the study, being a threat to the external validity. If the tasks mentioned out there in the study change the results may also be changed. Before we start our evaluation the team members are well trained. The receiving capacity of team members may vary. So the learning curve of these numbers may affect the results.

Within many problems this guideline for a programmer is more effective to develop software process. By this process a user can find any data very quickly. It will keep an important role to enhance the software development process.

V. CONCLUSION

The AOE plug-in approach is more enriched than any other Existing approaches. The approach is able to find out any required data easily and there have needed less time than any other approach. A user finds a data in adapter classes than the AOE plug-in give the required data to the client. The process which we have provided in this paper is different from any other existing process. That is able to enhance the SDP recently.

This paper provided a guideline by which a user can get the required data easily and it is comfortable to use. But these data are not mined. In Future there have used data mining algorithm and find out mined data to enhance software development process.

REFERENCES

[1] Hsu, Sheng-Kuei, and Shi-Jen Lin. "MACs: Mining API code snippets for code reuse." *Expert Systems with Applications* 38.6, p. 7291-7301, 2011.

[2] Xie, Tao, and Jian Pei. "MAPO: Mining API usages from open source repositories." *Proceedings of the 2006 international workshop on Mining software repositories*. ACM, p. 54-57, 2006.

[3] NetBeans plug-in(2015),Retrieved from: https:// www.plugins.netbeans./ [Accessed June 28, 2015]

[4] Jet Brain, (2015), Retrieved from: https:// www.jetbrains.com/idea/[Accessed" June 25, 2015]

[5] Genuitec,(2015),Retrievedfrom:http://www.genuitec.com/myeclips

[6] Seiffert, Dominic, and Oliver Hummel. "Adapting Collections and Arrays: Another Step towards the Automated Adaptation of Object Ensembles." *Software Reuse for Dynamic Systems in the Cloud and Beyond.* Springer, pp. 348-363, 2014

[7] Shahnewaz, "A Scenerio based API recommendation system using syntax and semantics of client source code". Master's Thesis, Department of CSE, Islamic University of Technology, OIC, Gazipur-1704, Bangladesh. April, 2014

[8] http: // oliverhummel. com / adaptation / tool.zip [Accessed July 29, 2015]

[9] Rahman, Z., Hasan, K., "*Enhancing Software Development using Data Mining Integrated Environment*," Master's Thesis of Islamic University of Technology, Dhaka, pp. 1-75, June 2012.

[10] Reiss, S.P.: Semantics-based code search. *In: IEEE 31st International Conference on Software Engineering, ICSE* 2009, pp. 243–253 (2009)

[11] Hummel, O., Janjic, W.: Test-Driven Reuse: Key to Improving Precision of search Engins for Software Reuse. *In: Finding Source Code on the Web for Remix and Reuse*, pp. 227–250. Springer(2013)

[12] Kell, S.: Component adaptation and assembly using interface relations. *In: Proceedings of the ACM International Conference on ObjectOriented Programming Systems Languagesand Application*, OOPSLA 2010, pp. 322-340 , 2010.

[13] Nita, M., Notkin, D.: Using twinning to adapt programs to alternative apis. In: Proceedings of the *32nd ACM/IEEE International* Conference on Software Engineering, ICSE 2010, vol. 1, pp. 205–214 ,2010

[14] Hummel, O., & Atkinson, C. "Automated creation and assessment of component adapters with the test cases*" In Comonent-Based Software Engineering* (pp. 166-181). Springer Berlin Heidelberg.

[15] Janjic, W., Atkinson, C.: Leveraging software search and reuse with automated software adaptation. *In: 2012 ICSE Workshop on Search Driven Development - Users, Infrastructure, Tools and Evaluation*, pp. 23-26 , 2012

A Modified Fuzzy Relational Clustering Approach for Sentence-Level Text

Sikder Tahsin Al-Amin, Mahade Hasan, and M. M. A. Hashem
Department of Computer Science and Engineering
Khulna University of Engineering and Technology
Khulna-9203, Bangladesh
E-mail: stahsin.cse@gmail.com, mahade047@gmail.com, mma.hashem@outlook.com

Abstract— **This paper proposes a fuzzy relational clustering (FRC) to find similar sentences from a set of sentences as well as group them in clusters. For finding similar sentences here FRC used both word-to-word and order similarity. For word-to-word similarity FRC used Jiang and Conrath similarity measure (JnC) with the help of WordNet database. Order similarity is calculated from joint word set. As a sentence may relate to more than one theme so FRC used a fuzzy clustering approach. Here FRC used FRECCA algorithm for the sentence clustering purpose. The algorithm works on Expectation-Maximization where importance of a sentence is expressed by PageRank score which is treated as likelihood. The PageRank scores and mixing coefficients are initialized with Uniform Random Number generation technique. Applying this method on a quotation dataset of different classes we found that it is capable of identifying and grouping similar sentences in a cluster. FRC is also applied on a news article dataset and found admirable results.**

Keywords—Fuzzy Clustering, Sentence Similarity, Relational Data.

I. INTRODUCTION

The amount of data being generated and stored is growing exponentially which presents new opportunities and challenges for unlock the information embedded within this data. Modern field of data mining can be used to extract important knowledge from data [1]. This method only emphasizes on text data. FRC used pre-processed text data of quotes. This method can be further used on pre-processed text data from emails, newspapers, websites, online blogs etc. One of the applications is that, on a certain day many newspapers are published. There are some news articles that are printed in all or most of them but are not written in the same format or language nevertheless the idea of the news is similar. So the main objective is to find similarity between the sentences residing in the news article.

Several works have been done on fuzzy clustering. First one was Relational Fuzzy c-means by Hathaway et al [2]. Then ARCA and K-Medoids [3],[4] was also proposed. But these algorithms had some limitations. In Relational Fuzzy C-means distance between data points couldn't be measured although it could operate on relational data. If the size of data set increased by high number, it causes the ARCA algorithm to fail. K-Medoids were affected by poor initialization which is done randomly.

A sentence is likely to be related to more than one theme or topic present within a document. However, because most sentence similarity measures do not represent sentences in a common metric space, a bag-of-words [5] approach or conventional fuzzy clustering approaches based on prototypes or mixtures of Gaussians are generally not applicable to sentence clustering [6].

Hence there is a need of fuzzy clustering algorithm that operates on relational input data. Relational data are in the form of a square matrix of pairwise similarities between data objects. FRC finds similarities between sentences and puts them into a cluster by calculating the cluster membership values. As the approach is fuzzy, a sentence may reside in more than one cluster with some amount of membership value. The sum of the membership values of a sentence in all clusters is 1. A sentence is considered to be in a cluster for which the corresponding membership value is largest.

This paper has improved the 'Measuring Sentence Similarity' method. The sentence similarity method measures similarity between two sentences based on both Word-to-Word similarity and Order similarity. Word-to-Word similarity measures the similarity between two words with the help of a lexical database known as WordNet [7]. On the other hand Order similarity measures the positioning of a word in a sentence.

The proposed method Sentence-Clustering based on FRC (SBFRC) has improved the 'Initialization' step of the algorithm. The FRECCA algorithm initializes the membership values and PageRank values using simple random number generation technique. FRC implemented 'Uniform Random Number' generation technique.

The rest of the paper is organized as follows. Section 2 summarizes some related works. Section 3 describes the methodology of SBFRC. Section 4 illustrates the experimental studies. Finally Section 5 concludes the paper.

II. RELATED WORKS

Hathaway et al.'s Relational Fuzzy c-Means (RFCM) algorithm [2] is considered as the first successful fuzzy clustering algorithm. Although RFCM operates on relational

978-1-4673-9257-0/15/$31.00 ©2015 IEEE

data input, it does not the express the relation by this data to be Euclidean.

Though having success, the Euclidean requirement in RFCM was considered limited, and various alternatives have been proposed. For instance, the ARCA algorithm [8] uses an attribute-based representation. A limitation of this method is the high dimensionality. It causes by representing objects in terms of their similarity with all other objects.

K-Medoid family is popular in clustering algorithms. Fuzzy versions of k-Medoids have also been introduced. Like k-Means, k-Medoids are also highly sensitive to the initial selection of centroids which is done randomly. And often requires running the algorithm several times from different random initializations.

Many spectral clustering algorithms that can be applied to sentence clustering by Zha [9], and Wang et al. [10]. They have recently applied a closely related nonnegative matrix factorization [11] technique to sentence clustering in the context of multi-document summarization.

Our proposed approach Sentence-Clustering based on FRC (SBFRC) is based on a fuzzy relational clustering algorithm which is known as FRECCA algorithm [6]. Here, Cluster Membership values for each node represent the degree or extent to which the object or a sentence belongs to each of the respective clusters, and mixing coefficients represent the probability of an object being in a cluster [6].

III. SENTENCE-CLUSTERING BASED ON FRC (SBFRC)

To overcome the shortcomings of the above approaches, SBFRC has proposed in this paper that can group similar sentences together in a cluster. It contains several steps which are described as follows. Fig. 1 is the flowchart of the steps of SBFRC.

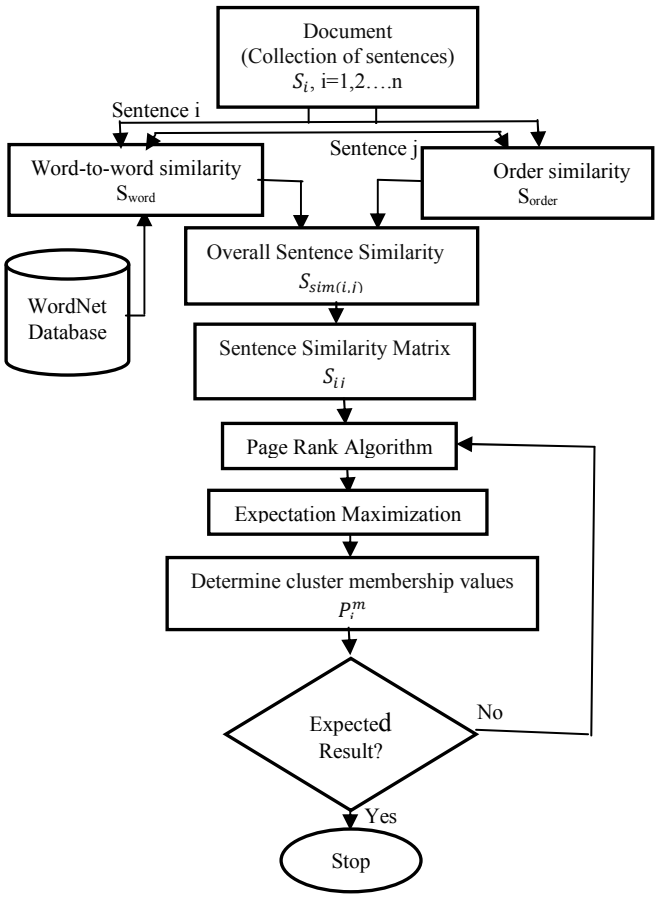

Fig. 1. Flow chart of SBFRC

Step 1: The input set is produced by pre-processing a text document. The sentences are extracted from a paragraph and the numbers of sentences are determined.

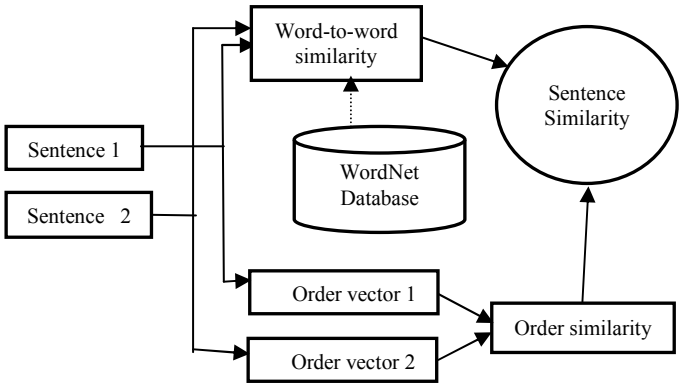

Fig. 2. Measuring Sentence Similarity

Step 2: Second step of SBFRC is to word-to-word similarity measure. Sentence similarity measures play an important role in text-related research. Existing methods for measuring sentence similarity have been adopted from approaches used for long text documents. These methods process sentences in a very high-dimensional space and are consequently inefficient and are not adaptable to some application domains. [12]

The proposed sentence similarity method derives similarity between two sentences using both word-to-word similarity and order similarity. A text is considered to be a sequence of words. The words, along with their combination structure, make a specific meaning.

Unlike existing methods, the proposed method calculates both word-to-word similarity and order similarity to compute final sentence similarity.

For word-to-word similarity the method used knowledge based measures, the WordNet [7] based measure due to Jiang and Conrath[13].

The Jiang-Conrath measure is based on the idea that the degree to which two words are similar is proportional to the amount of information they share. The similarity between words w1 and w2 is defined as equation 1:

$$Sim_{j\&c}(w1,w2) = \frac{1}{IC(w1)+IC(w2)-2*IC(LCS(w1,w2))} \quad (1)$$

Where , $LCS(w1,w2)$ is the word that is the deepest common ancestor of word w1 and w2, $IC(w)$ is the information content of word w, and defined as $IC(w) = -logP(w)$, where $logP(w)$ is the probability that word w appears in a large corpus [12].

Step 3: Third of SBFRC is to measure order similarity. For each sentence, a raw semantic vector is derived [12]. An order similarity is calculated using the two order vectors.

Step 4: The fourth step is to calculate the overall similarity as showed in Fig 2. Word-to-word similarity represents the lexical similarity. On the other hand, word order similarity provides information about the relationship between words: which words come before or after other words. Then, the overall sentence similarity is derived by combining word-to-word similarity and order similarity. And the similarity value is stored in the similarity matrix in respective position.

Overall sentence similarity is calculated using the equation 2 [12]-

$$S_{sim(s1,s2)} = r * S_{word} + (1 - r) * S_{order} \quad (2)$$

Where r <=1 decides the relative contributions of word-to-word and word order information to the overall similarity computation [12]. Since word-to-word similarity is more important and plays a vital role to overall sentence similarity, r should be a value greater than 0.5.

Step 5: Fifth step is to form the similarity matrix. The similarity method is applied between all possible pairs of sentences. After calculating similarity values between all the sentences in a document, the similarity values are stored in a matrix. If there are N sentences in a document then the matrix S_{sim} which size is NxN.

Step 6: Sixth step is to applying the PageRank algorithm [14],[15]. Unlike Gaussian mixture models, which use a likelihood function parameterized by the means and covariances of the mixture components, this method uses the PageRank score of an object within a cluster as a measure of its centrality to that cluster. These PageRank values are then treated as likelihoods. PageRank values are calculated using the equation no. 3:

$$PR_i^m = (1 - d) + d * \sum_{j=1}^{N} w_{ji}^m \left(\frac{PR_j^m}{\sum_{k=1}^{N} w_{jk}^m}\right) \quad (3)$$

Here, PR_i^m is the pagerank score of object i in cluster m. W_{ij}^m is the weight between objects i and j in cluster m calculated previously. And d is the damping factor. The damping factor d that appears in the PageRank calculation affects the fuzziness of the clustering, but generally does not affect the number of clusters, provided that the value is above approximately 0.8. In general, the higher the value of d, the harder is the clustering, with cluster membership values being close to either zero or one. We have used a value of 0.85.

After PageRank scores are calculated, these are treated as likelihoods and then they are used to calculate cluster membership values. Cluster membership values are obtained using the equation 4:

$$P_i^m = \frac{\pi_m * l_i^m}{\sum_{j=1}^{C} \pi_j * l_i^j} \quad (4)$$

Where, π_m is the mixing coefficient for cluster m. And l_i^m is the likelihoods for object i in cluster m which is obtained from the PageRank values. Membership values are normalized so that membership for an object sums to 1 for all clusters [6].

Step 7: Seventh step is the Expectation-Maximization (EM) step. Here there are two steps. The E-step calculates the membership values for each cluster. For each pair of sentences in a cluster weight is calculated using values from similarity matrix and membership values. That is –

$$W_{ij}^m = S_{ij} * P_i^m * P_j^m \quad (5)$$

In equation no. 5, W_{ij}^m is the weight between sentences i and j in cluster m. S_{ij} is the similarity between sentences i and j derived from Sentence similarity matrix. And P_i^m and P_j^m are the respective membership values of sentences i and j in cluster m [6]. With the help of this step once the PageRank scores are calculated they are treated as likelihoods and cluster membership values are calculated afterwards.

In the M-step the membership values are updated until convergence. It actually updates the mixing coefficients based on membership values. The value of mixing coefficient for each sentence in a cluster is same. As in the equation no. 6.

$$\pi_m = \frac{1}{N} \sum_{i=1}^{N} P_i^m \quad (6)$$

Where, π_m is the mixing coefficient for cluster m, P_i^m is the membership values calculated in expectation step and N is the total number of sentences.

Step 8: The eighth and last step is to find the convergence point for the clusters. The convergence is achieved when the membership of the sentences in the clusters is not updating anymore or the difference between the previous values is very little.

IV. Experimental Analysis

A. Experimental Setup

SBFRC has been development under the environment on Intel core i5-2.30 GHz processor with 4.0 GBytes of RAM running on windows 7 operating system. Here SBFRC has been developed in Java. WordNet database has been used while measuring word-to-word similarity. The quotation dataset on Table 1 [16] and news article dataset on Table 3 [6] are partial of the full dataset.

Table 1: Quotation dataset

Knowledge Class
1. Our knowledge can only be finite, while our ignorance must necessarily be infinite. 2. Everybody gets so much common information all day long that they lose their common sense. ……
Marriage Class
11. A husband is what is left of a lover, after the nerve has been extracted. 12. Marriage has many pains, but celibacy has no pleasures. ….
Nature Class
21. I have called this principle by which each slight variation if useful is preserved by the term natural selection. 22. Nature is reckless of the individual. When she has points to carry, she carries them. ….
Peace Class
31. There is no such thing as inner peace there is only nervousness and death. 32. Once you hear the details of victory, it is hard to distinguish it from a defeat. …..
Food Class
41. Food is an important part of a balanced diet. 42. To eat well in England you should have breakfast three times a day. …..

Experimental Results and Comparisons

Table 2 shows the results of applying our method, ARCA, Spectral Clustering, and k-Medoids algorithms to the quotations data set and evaluating using the external measures.

Our method requires that an initial number of clusters must be specified. This number was varied from 3 to 8, running 50 trials for each case, each trial commencing from a different random initialization of membership values. In each case the same affinity matrix was used, with pairwise similarities calculated as described before. However, only three unique clustering were found, each containing a different number of clusters, which ranged from four to seven.

Table 2: Evaluation of quotation dataset

No. of Cluster	Purity	Entropy	Rand	F-Measure
		SBFRC		
4	.350	**.550**	**.750**	**.450**
5	.400	**.500**	**.795**	.400
6	.400	**.445**	.765	**.480**
7	.400	.550	.770	.340
		ARCA		
4	.543	.646	.710	.391
5	.622	.515	.786	.459
6	.680	.451	.815	.462
7	.678	.444	.817	.427
		Spectral Clust.		
4	.641	.572	.715	.440
5	.652	.508	.785	.477
6	.690	.475	.800	.444
7	.699	.429	.809	.431
		K-Medoids		
4	.560	.605	.691	.392
5	.600	.569	.733	.433
6	.720	.457	.779	.459
7	.740	.425	.805	.461

To demonstrate how the algorithm may perform in more general use in activities related to text mining, the system is also applied to clustering sentences from a news article.
Table 3 shows the sentences from an article about President Barak Obama's presidency.

Table 3: News article dataset

News Articles
1. President Barak Obama on Tuesday championed nuclear energy expansion as the latest way that feuding parties can move beyond the broken politics …… 12. That mission however remains in doubt … 15. In Saginaw Biden insisted the stimulus is working even as he acknowledged it's going to take us a while to get us out of this ditch ….. 27. It includes more direct and rapid response to criticism more events at which the president speaks directly to the public without the filter of the media 28. The intended narrative is one in which Obama hears people's frustrations and is working directly to end them. 29. There is a little doubt the public is angry. 30. A CBS news poll in early February found eighty one percent saying it's time to elect new people to congress

The result from the news article dataset is shown below-

Table 4: Results of News Article dataset

Sentences
3,5,6,9,10,13,14,15,16,17,19,21,24
2,7,12,18,20,22,25,26,27,28,29
1,8,23,30

B. Discussions

The performance measure techniques (Purity, Entropy [17], Rand, F-measure [18]) evaluated our method. The algorithm is run 50 times for the quotation dataset and chosen the best results from it. Since the method is unsupervised, there is no fixed output. As the four performance measures are not always consistent as to which algorithm achieves best performance for a given number of clusters, boldface indication of the value corresponding to SBFRC for which the measure is a maximum. For example, for the Rand Index corresponding to Cluster No =5, our method achieves a value of 0.795, which is greater than that achieved by the other algorithms (0.786, 0.785, and 0.733), and for cluster No. = 6, the proposed method achieves the value of entropy .445 whereas other method has higher value than it (0.451, 0.475 and 0.457) hence these values are represented in boldface. It can be seen from the table that when the number of clusters is 5, the algorithm performs well than when cluster number is 5 or 6 as measured by all five external cluster evaluation criteria.
The result achieved from the news article dataset, it is observed that in 1st cluster, sentence 15 has the highest PageRank score. So the sentence 15 would go in cluster 1. The sentences 3, 5, 6, 9, 10, 13, 14, 16, 17, 19, 21, 24 are also in cluster 1. There PageRank score in close to the PageRank of sentence 15. These sentences are of similar meaning. For 2nd cluster sentence 27 has highest PageRank. Closer to this are the sentences 2, 7, 12, 18, 20, 22, 25, 26, 28, 29. And most of them are similar as they are of negative sense (criticism, angry, frustration).

V. CONCLUSION

An obvious potential application of the algorithm is to document classification and summarization. Like any other clustering algorithm, the performance of this method will ultimately depend on the quality of the input set, and as for the sentence clustering the performance can be improved with better sentence similarity measures. As the cluster number is provided initially the algorithm appears to be able to converge to an appropriate number of clusters. The idea can be expanded to the development of a hierarchical fuzzy relational clustering algorithm as well as the proposed method can also be applied to a cloud trust system to measure its performance by analyzing user feedback comments.

REFERENCES

[1] Gary M. Weiss & Brian D. Davison, "To appear in the Handbook of Technology Management", H. Bidgoli (Ed.), John Wiley and Sons, 2010.

[2] R.J. Hathaway, J.W. Devenport, and J.C. Bezdek, "Relational Dual of the C-Means Clustering Algorithms," Pattern Recognition, vol. 22, no. 2, pp. 205-212, 1989.

[3] R. Krishnapuram, A. Joshi, and Y. Liyu, "A Fuzzy Relative of the k-Medoids Algorithm with Application to Web Document and Snippet Clustering,"Proc. IEEE Fuzzy Systems Conf.,pp. 1281-1286, 1999.

[4] T. Geweniger, D. Zu¨hlke, B. Hammer, and T. Villmann, "Median Fuzzy C-Means for Clustering Dissimilarity Data,"Neurocomputing, vol. 73, nos. 7-9, pp. 1109-1116, 2010.

[5] Wikipedia: the Free Encyclopedia. Wikimedia Foundation Inc. Updated 26 August 2015. 16.19 UTC. Encyclopedia online. Available from https://en.wikipedia.org/wiki/Bag-of-words_model. Accessed on 2 September 2015.

[6] Skabar, A. and Abdalgader, K. "Clustering Sentence-Level Text Using a Novel Fuzzy Relational Clustering Algorithm", IEEE transactions on knowledge and data engineering, vol. 25, no. 1, 2013.

[7] C. Fellbaum, WordNet: An Electronic Lexical Database. MIT Press, 1998.

[8] P. Corsini, F. Lazzerini, and F. Marcelloni, "A New Fuzzy Relational Clustering Algorithm Based on the Fuzzy C-Means Algorithm," Soft Computing, vol. 9, pp. 439-447, 2005.

[9] H. Zha, "Generic Summarization and Keyphrase Extraction Using Mutual Reinforcement Principle and Sentence Clustering," Proc. 25th Ann. Int'l ACM SIGIR Conf. Research and Development in Information Retrieval, pp. 113-120, 2002.

[10] D. Wang, T. Li, S. Zhu, and C. Ding, "Multi-Document Summarization via Sentence-Level Semantic Analysis and Symmetric Matrix Factorization," Proc. 31st Ann. Int'l ACM SIGIR Conf. Research and Development in Information Retrieval, pp. 307-314, 2008.

[11] D. Lee and H. Seung, "Algorithms for Non-Negative Matrix Factorization," Advances in Neural Information Processing Systems, vol. 13, pp. 556-562, 2001.

[12] Y. Li, D. McLean, Z.A. Bandar, J.D. O'Shea, and K. Crockett, "Sentence Similarity Based on Semantic Nets and CorpusStatistics," IEEE Trans. Knowledge and Data Eng., vol. 8, no. 8, pp. 1138-1150, Aug. 2006.

[13] J.J. Jiang and D.W. Conrath, "Semantic Similarity Based on Corpus Statistics and Lexical Taxonomy,"Proc. 10th Int'l Conf. Research in Computational Linguistics,pp. 19-33, 1997.

[14] S. Brin and L. Page, "The Anatomy of a Large-Scale Hypertextual Web Search Engine," Computer Networks and ISDN Systems, vol. 30, pp. 107-117, 1998.

[15] [5] Wikipedia: the Free Encyclopedia. Wikimedia Foundation Inc. Updated 30 August 2015. 7.27 UTC. Encyclopedia online. Available from http://en.wikipedia.org/wiki/PageRank, accessed on 02 September, 2015.

[16] http://www.famousquotesandauthors.com,2012, accessed on 30 August, 2014.

[17] Wikipedia: the Free Encyclopedia. Wikimedia Foundation Inc. Updated 1 September 2015. 8.20 UTC. Encyclopedia online. Available from http://en.wikipedia.org/wiki/Entropy_(information_theory), accessed on 02 September, 2015.

[18] Wikipedia: the Free Encyclopedia. Wikimedia Foundation Inc. Updated 27 July 2015. 11.13 UTC. Encyclopedia online. Available from http://en.wikipedia.org/wiki/Precision_and_recall#F-measure, accessed on 02 September, 2015.

Performance Analysis for Detection of Breast Cancer Biomarker HER2 using a Double Gate FET Nano Biosensor

Mohsin Sajjad
Department of Electrical & Electronic Engineering
Bangladesh University of Engineering & Technology
Dhaka, Bangladesh
md.mohsinsajjad@gmail.com

Md. Raqibull Hasan and Arif Abdullah Samy
Department of Electrical & Electronic Engineering
Primeasia University
Dhaka, Bangladesh
rakib0803011@gmail.com

***Abstract*— This paper addresses the performance of a double gate field effect transistor (FET) based nano biosensor in detecting human epidermal growth factor receptor 2 (HER2) which is a key biomarker for detecting breast cancer. At first dimensions of different parameters of a double gate FET were set in order to enhance sensitivity. Then various parameters of HER2 protein were calculated. Various nano biosensor characteristics in terms of settling time, selectivity and sensitivity were simulated. The results demonstrate that the designed nano biosensor has significant prospects of detecting the target.**

Keywords*— *diffussion; hydrophobic; potentiometric; sensitivity.

I. Introduction

In the present world, breast cancer is one the most invasive cancers. It accounts for 16% of all female cancers and 22.9% of invasive cancers in women. 18.2% of all cancer deaths worldwide, including both males and females, are from breast cancer. Research suggests that breast cancers can be divided in four molecular subtypes according to hormone receptor expression (HR±) and/or epithelial cell of origin (luminal or basal). There are two HR+ breast cancers (Luminal A and Luminal B) and two HR- cancers (human epidermal growth factor receptor 2 (HER2)-enriched and basal-like) [1-2]. Gene-expression profiling is not currently standard clinical practice, but, for nearly a decade, testing for joint HR/HER2 status has been a routine part of treatment planning [3]. Breast cancers with HER2 gene amplification or HER2 protein overexpression are called HER2-positive in the pathology report. HER2-positive breast cancers tend to grow faster and are more likely to spread and come back compared to HER2-negative breast cancers [4].

The small size, improved solubility and multifunctionality of nanoelectronics have opened many new research avenues for scientists. Though a lot of research activity has been involved in developing biosensors for various purposes the time has come to bring this technology to the forefront and make it commercially available. Biological signaling mechanism categorizes the types of biosensors. These types are potentiometric detection, amperometric detection, mass detection etc. In this paper a potentiometric detection system is analyzed. Potentiometric biosensors are generally based on ion-selective electrodes (ISE) and ion-sensitive field effect transistors (ISFET) [5-6]. To detect biomolecules, however, ISFET should be immersed and operated in the electrolyte solution to immobilize biomolecules. Thus, it has been pointed out that biosensors based on ISFET showed unreliable operational behaviors, such as drift and hysteresis [7-8]. To overcome these problems a double gate FET biosensor is presented. A Si channel FET is straddled by double gates is demonstrated. The separated double gates allow independent voltage control for channel potential which allows to beat the fundamental Nernst limit and improve sensitivity [9].

II. Modeling of Biosensor

Figure 1 shows the proposed design of a Double Gate Field Effect Transistor based nano biosensor (DGFET). The channel is made of Si. The FET channel is doped with p-type material as our experimental biomarker contains positive charge when acidic solution is used [10]. The front or reference gate is submersed in the solution. It is to be noted that the electrode used in this FET must be faradic electrode. The solution (pH<7) may create an insulator on non-faradic electrode surface which will affect the charge flow.

There are two dielectrics. Top dielectric is the receptor surface. This surface needs to be hydro phobic surface. If hydro phobic surface is not used the surface will not be able to hold on the sample solution. Hydrophobic surface will create a spherical structure of the solution which will help to capture maximum target molecules. Below the drain and source there is a second dielectric whose oxide thickness is much bigger than the front oxide one in order to increase sensitivity. This phenomena will be discussed later. The response time required for minimum number of analyte molecules to be captured to activate the sensor is called the settling time. There is a fundamental limitation for settling time (t_s) for each sensor which is given by the following equation.

$$\rho_0 = N_s * t_s^{-(\frac{3-D_F}{2})} \quad (1)$$

N_s is the minimum number of analyte molecules to activate the sensor which depends on transduction process and ρ_0 is the density of analyte. D_F is the fractal dimension of the surface which is equal to 2 for this sensor.

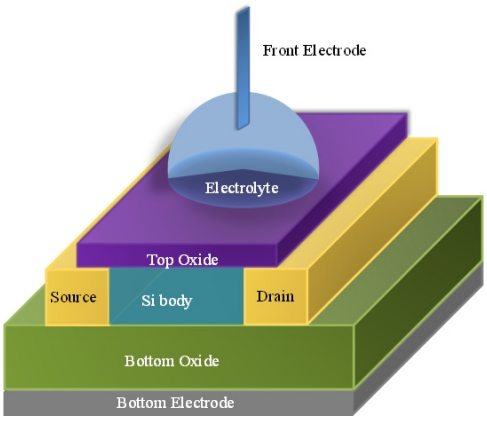

Fig. 1. Structure of DGFET biosensor.

$$N(t) = C_{D(t)}\rho_0 t \quad (2)$$

$$C_{D(t)} = \frac{D}{\sqrt{2Dt}} \quad (3)$$

The number of captured molecules ($N(t)$) in a given time can be calculated from the transient response of biosensor. $C_{D(t)}$ is the diffusion coefficient dependent capacitance. The sensitivity of the biosensor is defined by several ways. In this paper we have worked with the drain current and showed its response. The change in drain current (I_D) with respect to initial current (I_D) is normally called sensitivity (S).

$$S = \frac{\Delta I_D}{I_D} \quad (4)$$

$$S(t) = c_1 \ln(\rho_0) + c_2 \frac{(3-D_F)\ln(t)}{2} - c_3 \ln(I_0) + c_4 \quad (5)$$

c_1, c_2, c_3, c_4 are constants. Several experimental results have shown that sensitivity is non-linear, time dependent and depends on several aspects of the mechanism.

This sensitivity has logarithmic response to density of analyte. Sensitivity is further increased logarithmically with time but decreases logarithmically as we increase the buffer ion concentration. This complex response indicates that all of the parameters should be carefully chosen to design a successful biosensor [11]. One of the fundamental problems of the biosensor is the screening. For screening the salt concentration is generally about 100mM which is very high comparatively when we try to detect biomolecules at a range of µM to nM. From equation (5) we can easily understand how high salt concentration can reduce the sensitivity. There are several ways to beat the screening effect. One of the ways is amplification. This is why double gate is used. The drain current can be amplified by the bottom gate. Top gate and bottom gate produce two drain currents $I_{D,top}$ and $I_{D,bot}$ respectively.

$$I_{D,top} = \mu_1 C_{tox}(\frac{W}{L})V_{DS}V_{G,top} \quad (6)$$

$$I_{D,bot} = \mu_1 C_{box}(\frac{W}{L})V_{DS}V_{G,bot} \quad (7)$$

μ_1 is the carrier mobility, W and L are the channel width and length respectively. $V_{DS}$is the drain to source voltage. C_{tox} and C_{box} are the top and bottom dielectric capacitance respectively. $V_{G,top}$ and $V_{G,bot}$ are two gate voltages. Total drain current (I_D) is denoted by,

$$I_D = \frac{C_{tox}+C_{box}}{C_{tox}+C_{box}+C_{DL}}\nu \quad (8)$$

Q_{MOS} is the deposited charge on FET, ν is the charge velocity and Φ is the extra potential. Equation (8) shows that the total drain current (I_D) on FET operating in accumulation mode is dependent on top oxide capacitance (C_{tox}), bottom oxide capacitance (C_{box}) and capacitance associated with Debye length (C_{DL}). As capacitance is inversely proportional to thickness of oxide layer, in order to increase the sensitivity the bottom oxide thickness is made much bigger than the top oxide thickness. This phenomena helps to beat the Nernst Limit.

The biosensor needs to address two selectivity issues mainly. First one is the binding to wrong molecule. There will be a lot of parasite molecules in the analyte solution. Before the sensing process Polymerase Chain Reaction (PCR) can be used to amplify the number of target biomolecules. The second problem is binding in the empty space. The biosensor surface needs to be hydrophobic and the receptor density should be as much as possible. The signal-to-noise ratio (SNR) of the biosensor can be found by equation (11).

$$SNR = \frac{\sigma_T k_T \rho_T}{\sigma_p k_p \rho_p}\frac{r_T^2}{r_p^2}\frac{\theta}{\theta_{r,p}^{\infty}-\theta} \quad (11)$$

σ_T/σ_p denotes the signal transduction scheme. For example, it could be the ratio of electrostatic charge of the target and the parasitic molecule for electrical detection, or the ratio of the thickness of the target molecular layer to the parasitic molecule etc. k_T and k_p are the association constants of target and parasite molecules. ρ_T and ρ_p are the density of target and parasite molecules respectively. r_T and r_p are the radius surface coverage of each target and parasite molecules respectively. θ is the surface coverage for all target molecules. $\theta_{r,p}^{\infty}$ is the asymptotic surface coverage for a DRSA consisting of receptor conjugation followed by parasitic conjugation. As θ is directly proportional to the receptor density (N_0), the SNR is rapidly increased with higher receptor density [12].

III. HER2 Biomarker

HER2 overexpression and amplification has been linked to augmented cell proliferation, cell motility, tumor invasiveness, accelerated angiogenesis and reduced apoptosis. HER2 positive breast cancers are considered in the "intermediate or high histologic grade," absent of estrogen and progesterone receptors, while including positive lymph node metastases [13-14]. The structure of HER2 can be found in protein data bank. The accepted FASTA sequence of HER2 is given below [15]:

DIQMTQSPSS LSASVGDRVT ITCRASQDVN
TAVAWYQQKP GKAPKLLIYS ASFLYSGVPS
RFSGSRSGTD FTLTISSLQP EDFATYYCQQ
HYTTPPTFGQ GTKVEIKRTV AAPSVFIFPP
SDEQLKSGTA SVVCLLNNFY PREAKVQWKV
DNALQSGNSQ ESVTEQDSKD STYSLSSTLT
LSKADYEKHK VYACEVTHQG LSSPVTKSFN RGEC

The total number of sequence in 214 and the protein weighs 23.45 kilo Daltons. As the charge of the protein will be transduced into signal and the protein charge is associated with the pH of the solution. The pH vs charge relationship is

calculated using protein data bank calculator and is represented in figure 2. The isoelectric point (*pI*) is calculated using Henderson-Hasselbalch equation. The *pI* is found to be 7.70 approximately. This denotes that when pH level is below 7.70 then the protein contains positive charge and vice versa.

IV. Simulation and Results

The modelled DGFET has length and width of 1μm. The bottom oxide is taken 10 times thicker than the top oxide. The channel is a Si body having width of 40nm where the doping concentration is 1e19cm^{-2}**.** The sensor surface is assumed to be highly sticky. So the association and dissociation constant value are taken to be 3e06 and 1 respectively. The protein diffusion coefficient is associated with its size. The diffusion coefficient value for the selected protein is 1.11e06 cm^{2}s^{-1}. The experiment incubation time is set to 180min and temperature is set at 27^{0}C. The receptor density is 1e12 cm^{-2}.

The DGFET response over HER2 was simulated in online biosensor lab from nanohub.org. Figure 3 demonstrates the settling time changing with analyte concentration. The settling time is described in equation (1). It is also to be noted that the settling time increases with the minimum number of captured molecules is increased. But increment of settling time tends to saturate when higher no of molecules to be captured.

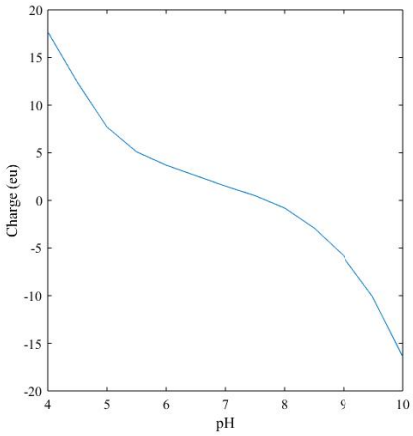

Fig. 2. HER2 charge at different pH level.

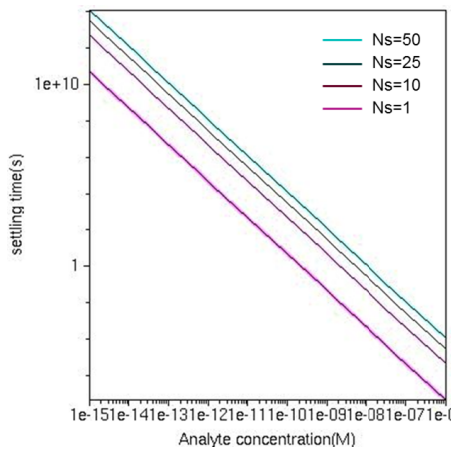

Fig. 3. Effect of analyte concentration on settling time.

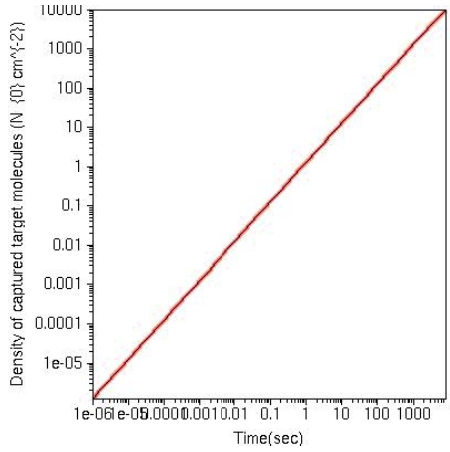

Fig. 4. Time dependency of density of captured molecules.

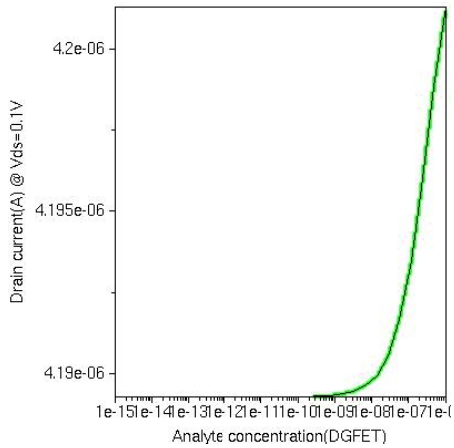

Fig. 5. Drain current response at different analyte concentrations.

The time dependent capture of target molecules is shown in figure 4. The starting time is accounted to be 1e-06sec. it is found that after 1000sec a significant density of captured molecules can be achieved. The sensitivity is assessed by the response in drain current of the FET. Figure 5 depicts the drain current response. A very insignificant response is found when analyte concentration is less than 1nM. The current increases exponentially with analyte concentration. But when the back gate voltage is introduced the response is amplified. From equation (5) we can understand that for a lower buffer ion concentration the drain current is increased with time. But at high concentration due to negative logarithmic effect the increment of current tends to saturate which is shown in figure 6. This is called the screening problem of biomolecule detection where high salt concentration is necessary. This effect can be reduced by using high frequency descreening.

The charge of the biomolecule varies with the pH. With the increase of pH the charge tend to change from positive to negative. So the drain current is also reduced for solution having high pH. Figure 7 clearly indicates that the solution should be acidic and pH level is set to 4 for the biosensor operation. For checking the selectivity it is assumed that the size of the parasite molecules is half of the target molecules. The concentration of parasite molecules is set to be 1μM which is higher than the target molecule concentration of 1nM and 1fM. The maximum surface coverage is 0.54. From figure 8 it

is indicated that SNR increases with the receptor density and if a target molecule is to be detected at 1fM range then the receptor density should be higher. But in reality it is very difficult to achieve receptor density much more than 1e12 cm^{-2}.

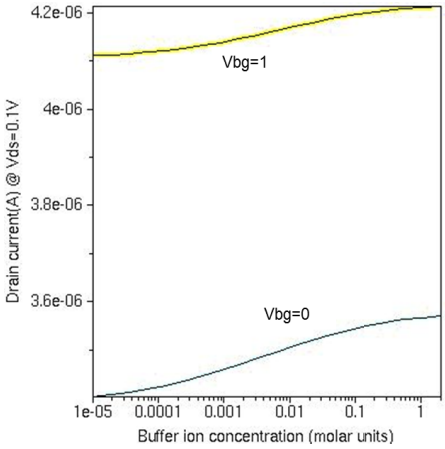

Fig. 6. The effect of buffer ion concentration on drain current.

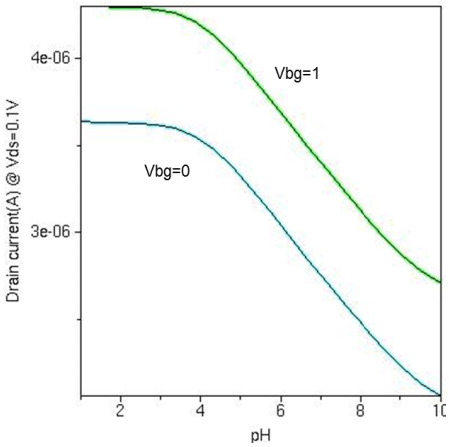

Fig. 7. The change in drain current over pH level.

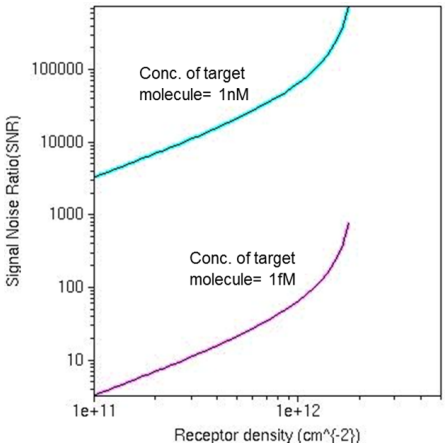

Fig. 8. SNR vs receptor density.

V. Conclusion

The simulated settling time and SNR results clearly indicate that it is possible to detect HER2 biomarker at a minimum concentration of 1nM. The biosensor sensitivity can also be enhanced by back voltage and increased buffer ion concentration. Another way of detection of target molecule can be done by varying the pH level of the solution and checking the difference in drain current. The DGFET biosensor model discussed above for detecting HER2 exhibits satisfactory performance. But several aspects like binding energy of the biomolecule or screening problem should be carefully examined in terms of fabrication of the sensor.

References

[1] W.F. Anderson, P.S. Rosenberg, A. Prat, C.M. Perou and M.E. Sherman, "How many etiological subtypes of breast cancer: two, three, four, or more?," J Natl Cancer Inst, vol. 106, August 2014.

[2] W.F. Anderson, S. Luo and N. Chatterjee, "Human epidermal growth factor receptor-2 and estrogen receptor expression, a demonstration project using the residual tissue repository of the Surveillance, Epidemiology, and End Results (SEER) program," Breast Cancer Res Treat, vol. 113, pp. 189–196, 2009.

[3] W.F. Anderson, P.S. Rosenberg and H.A. Katki, "Tracking and evaluating molecular tumor markers with cancer registry data: HER2 and breast cancer," J Natl Cancer Inst, vol. 106, May 2014.

[4] A.W. Kurian, K. Fish, S.J. Shema and C.A. Clarke, "Lifetime risks of specific breast cancer subtypes among women in four racial/ethnic groups," Breast Cancer Res., vol. 12, 2010.

[5] D.R. Thevenot, K. Toth, R.A. Durst and G.S. Wilson, "Electrochemical biosensors: recommended definitions and classification," Biosensors & Bioelectronics., vol.16, pp.121–131, 2001.

[6] J. Ding and W. Qin, "Potentiometric sensing of nuclease activities and oxidative damage of single stranded DNA using a polycation-sensitive membrane electrode," Biosensors and Bioelectronics., vol. 47, pp. 559–565, 2013.

[7] C. G. Jakobson, M. Feinsod and Y. Nemirovsky, "Low frequency noise and drift in ion sensitive field effect transistors," Sens. Actuators B Chem., vol. 68, no. 1–3, pp. 134–139, Aug. 2000.

[8] J. C. Chou and C. N. Hsiao, "The hysteresis and drift effect of hydrogenated amorphous silicon for ISFET," Sens. Actuators B Chem., vol. 66, no. 1–3, pp. 181–183, Jul. 2000.

[9] O. Knopfmacher, et al., "Nernst Limit in Dual-Gated Si-Nanowire FET Sensors,"Nano lett., vol. 10, pp. 2268–2274, 2010.

[10] Nair, R. Pradeep and A.A. Muhammad, "Design considerations of silicon nanowire biosensors." Electron Devices, IEEE Transactions, vol. 54, Issue 12, pp. 3400-3408, 2007.

[11] Baumgartner and Stefan, "Predictive simulations and optimization of nanowire field-effect PSA sensors including screening," Nanotechnology, vol. 24, no. 22, pp. 225-503, 2013.

[12] Nair, R. Pradeep and A.A. Muhammad, "Theory of"Selectivity of label-free nanobiosensors: A geometro-physical perspective." Journal of applied physics, vol. 107, no.6, pp. 064701-064701, 2010.

[13] N.E. Hynes, H.A. Lane, "ERBB receptors and cancer: The complexity of targeted inhibitors," Nat. Reviews Cancer, vol. 5, pp. 341-354, May 2005.

[14] A.W. Burgess, H.S. Cho, C. Eigenbrot, K.M. Ferguson and S. Yokoyama, "An open-and-shut case? Recent insights into the activation of EGF/ErbB receptors," Molecular cell, vol. 12, pp. 541-552, Sep. 2003.

[15] H.S. Cho, et al., "Structure of the extracellular region of HER2 alone and in complex with the Herceptin," Fab. Nature, vol. 421, pp. 256-260, 2003.

Helping Software Developers through Offline Repository Based API Searching in Data Mining Integrated Environment

Md. Ratul Uddin Ashraf[*], Anujoy Das[*], Ziaur Rahman[*], Ali Newaz Bahar[*], Husne Ara Rubaiyeat[γ]

[*] *Department of Information and Communication Technology,* [γ]*Department of Computer Science*

[*] *Mawlana Bhashani Science and Technology University, Tangail-1902,* [γ]*National University, Gazipur-1704*

Mail: ratulshourov01@gmail.com, anujoydas@gmail.com, zia@iut-dhaka.edu, bahar_mitdu@yahoo.com, rubaiyeat@yahoo.com

***Abstract*—Software development is getting changed so rapidly. It will be highly benefited if we can accelerate software development process by guiding developers. Appropriate guidelines and accurate recommendations to developers during development process can reduce software development expenses, as well as can save valuable times of developers. There are a number of approaches to speed up the software development process. It can be done through code assistance tools that help developers by recommending relevant items from searching particular repository of Application Programming Interface (API). Some approaches are based on online searching that have some drawbacks due to request and response latency as it has to deal with the extra-large files in a server. Developers generally uses previously completed resources as well as libraries or frameworks to generate relevant snippets which are supplied by the referral repository of APIs. Developers find it hard to choose the appropriate methods as there are thousands of methods in which some are not properly documented. In this paper we have proposed a concept and its respective framework to guide developers that suggests relevant API methods from an offline mined repository. From the investigation we made, we can say that our approach works much better than some of the existing approaches.**

Keywords—Application Programming Inteface (API), Offline Repository, ORBAS, Data Mining Integrated Environment (DMIE).

I. INTRODUCTION

Software development processes for a system is basically done by writing a program based on specific design specification. Nowadays it can be done by using various techniques. To do this development process developers in the software industries generally creates new methods or modifies existing ones or reuses previously defined methods. One of the processes to develop software is the reuse of existing libraries and frameworks. Developers can be highly benefited if they get appropriate guidelines and accurate recommendations. It can decrease development cost and can save valuable time. Application Programming Interface (API) is a process to search relevant items from an existing repository. This process is widely used all over the world. Some approaches of these API search processes are based on online searching. Developers usually searches for API usage pattern using online repositories provided by different tools.

General code search engines often deals with the extra-large files. These extra-large files often contain a large number of API methods. Developers find it very difficult to choose the appropriate API methods to use as there are also duplicate methods. The API methods returned by the search engines are not mined so relevant data cannot be displayed. As the database of the search engines contains a large amount of data; it takes a long time to find appropriate methods. The online search processes for API methods are fully dependent on the server; as it is fully internet based it takes more time to generate the entire API methods thus making it a time consuming process. Normal API library or framework written in object oriented languages and it contains a huge number of methods and classes. If the API methods and classes do not have the meaningful name sometimes even experienced programmers often face a lot of problems. The API methods returned by the search engines are not often well documented. Developers find it challenging to use the most effective and appropriate methods.

To solve these problems we have proposed ORBAS (Offline Repository Based API Searching) thatis an offline repository that contains various API attributes. ORBAS mines API pattern usage methods from the innovative sequences of API in source code. The mined patterns contain less redundant patterns so that the developers cannot find the similar patterns repeatedly. The high coverage usage of API methods should be returned by the patterns to ensure a beneficial achievement to the developers.

In this paper we first plan to make a query in the repository for searching methods. Then the repository returns the associated source files of the matched inquiries. After that there is a code analyzer which extracts API methods from the source files. In the paper we have propose PMD [1] source code analyzer which extracts the API methods from the source code even if the source code is not compilable. The methods are then clustered into groups for mining. Then mining is implemented on the clusters to produce frequent closed sequence. We propose the BIDE [2] algorithm for mining frequently closed API usage patterns. We have again used a clustering technique in the frequent closed sequences. Thus two-step clustering techniques are implemented before and after the BIDE algorithm to produce more accurate usage patterns. Finally the closed API usage clusters are then produced and the related API usage methods are

recommended to the developers. We have come to see that after following this approach ours are more efficient than some of the exiting approach to guide developers for getting API usage patterns.

II. Background and Related works

There exist a number of API usage pattern search theories or tools to find out useful API patterns from source code. Some of these are MAPO[3], MAC[4], ESDP[5], Hipikat[6], ParseWeb[7] etc. Often this search tools are based on online code search repositories such as Koders[8] and Google code search[9]. These code search engines generally evaluate code snippets containing keywords of API methods. Strathcoma[12] is a code snippet recommender, which finds out a set of code snippets by matching the structure of the codes. MAPO is a tool which mines API usage patterns and uses mined patterns for recommending code snippets. MAPO mines API usage pattern which have sequential information among the method calls. But the sequences patterns are not clustered in MAPO. ParseWeb accepts queries from the programmer and generates code samples based on the object type of the source and destination. UP-miner is also a mining tool for mining closed sequences returned from the API methods. It uses two-step clustering technique to find out frequently closed sequences. But it does not use a code analyzer to extract source files from the given result provided by search engines based the programmer query.

Unlike many related works, we have developed ORBAS based on the mining algorithm to mine API methods and a two-step clustering technique to produce frequently closed sequences. As our process searches an offline repository we aim to make it a time consuming procedure.

III. Framework

To mine API usage patterns from an offline based repository we have developed a framework based on the mining and clustering of frequent closed sequences acquired from the source files which are resulted from the query performed in the repository. There are five major components in the framework: an offline repository, a code analyzer, sequence miner, sequence cluster and recommender.The implementation of ORBAS framework is given here. The total procedure works as illustrated in Fig. 1.

Step-1: In the ORBAS framework there is an offline repository in which programmer performs a query.

Step-2: A set of source code is returned from which the code analyzer extracts API methods.

Step-3: A two-step clustering technique is performed before and after mining API sequences.

Step-4: The best API usage cluster is produced and the required methods are recommended to the programmers.

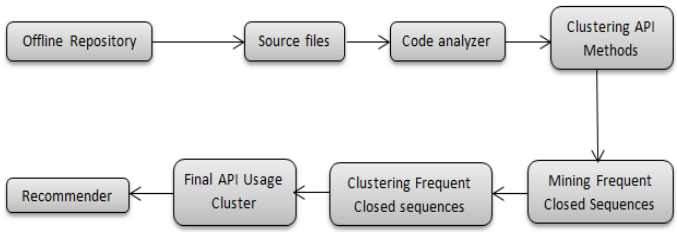

Fig. 1.An overview of ORBAS framework.

IV. Working Approach

A. *Offline repository:*

We have developed an offline repository in which different API methods are being inserted. The repository is organized by using a XML document to store API methods. The repository consists of sections such as search, update and delete. In the search section API methods can be searched by providing the method name. The update section makes necessary steps to add a new API method in the repository. It provides the insertion of methods. The delete section can remove API methods from the repository.

B. *Source files:*

As our framework is based on offline repository so the source files are collected directly from the repository based on the query implemented in the repositories. The repository provides the API methods which matches the input query. If the input method matches with the API methods stored in the repository, the complete source files of the methods are returned by the query.

C. *Code analyzer:*

Code analyzer helps us to extract the API methods from the source files. PMD [1] is a source code analyzer which does not need compilable source files for extracting API methods. PMD search outs common programming flaws like unused variables, empty catch blocks, unnecessary object creations etc. The code analyzer extracts a list of methods for each source files. This is done by collecting class name and full package name for each method. Based on the receiver object name we track the field declarations and local declarations to know the class name of the method calls. For the case of the classes which are exported in the import statement; we keep tracks of import statements to get the full package name of these classes.

D. *Clustering API methods:*

The method sequences returned by the source code analyzer can be two types. One is the frequently used API patterns which have large threshold support and another is less frequently used patterns which has minimum threshold. Clustering technique increases the chance of less frequently used sequence patterns to mine out before mining the frequently closed sequence. *SeqSim* [10] is an n-gram based technique which computes the similarity of two different sequences.

The set G(X) is defined as the n-gram set for a sequence $S(s_1 s_2 \ldots s_n)$ as a collection of unigrams, bi-grams, … , n-gram of *S*:

$(S) = \{s_1, s_2 \ldots, s_n, s_1s_2, s_2s_3 \ldots, s_{n-1}s_n, \ldots, s_1s_2..s_{n-1}, s_2s_3..s_{n-1}s_n, s_1s_2..s_{n-1}s_n\}$

Two situations are considered to evaluate a similarity between two sequences:

i) Sequences are similar if they both equally have a large number of API methods between their representative n-gram sets.

ii) Sequences are similar if they both equally have common subsequences.

If two sequences are s_1 and s_2 then the similarities are:

$$\text{SeqSim}(s_1, s_2) = \frac{\sum i \text{ Weight } (gi\cap)}{\sum i \text{ Weight } (giU)}$$

Where $g^i_\cap$ € $G_\cap = G(s_1) \cap G(s_2)$, g^i_U€ $G_U = G(s_1) \text{ U } G(s_2)$, weight $(g^i_\cap)$ is equal to the length of $g^i_\cap$.

As an example, given s_1 = abc and s_2 = cab, then we will have

$G_\cap$ = {a,b,c,ab}, G_U = {a,b,c,ab,bc,ca,abc,cab} andWeight(ab) = 1, Weight(ab) = 2, SeqSim(s_1,s_2) = 0.33 .

Based on the result of SeqSim, we cluster the API sequences. The remoteness of two clusters is considered as the highest value of remoteness between a pair of items in these two clusters.

E. Mining frequent closed sequence:

BIDE algorithm [11] is used to recognize the frequent API usages for mining frequent closed sequences. A sequence s_1 is a sub-sequence of s_2 and s_2 is a super-sequence of s_1 when s_1 is contained in s_2 and s is a frequent sequence. As there are no appropriate super sequences of s with the same support then s is a frequent sequence in a set of sequence if sup(s) ≥ min_sup. Sup(s) is called the support of sequence which is derived by the ratio of the sequences that are super sequences of s in the sequence set. Min_sup is the minimum threshold support [2].To prepare the frequent closed sequences for the cluster, BIDE algorithm is applied to each cluster originated from the procedure described in the previous section. For example, let us assume there are three sequences is a cluster which are xy, xyz, xyt. If the minimum threshold support is 0.5, BIDE algorithm gives the result of frequent closed sequences xy, where other sequence mining algorithms will provide the result x, y and xy. If xy is frequent then it can be easily noted that x and y will also be frequent. Thus x and y does not need to be enlisted. BIDE algorithm provides the sequences in which there are subsequences of similar support.

F. Clustering frequent closed sequences:

The API method sequences that are clustered using the proposed SeqSim technique in previous section; can be of two types. One is the sequences which are not similar to each other and another is the sequences which are similar. The sequences that are not similar are partitions into clusters. But the sequences that are similar can produce redundancy in the final API usage patterns. To solve this problem, another clustering is performed for the similar sequences. In this process the resulting clusters are considered as usage patterns. For example, we consider two frequent closed sequence xyz and zy which are mined from two distinct clusters. These two sequences are grouped together and shown as xyz after performing the clustering technique. The total number of superfluous sequences can also be removed using the technique. By applying the SeqSim technique; we can measure similarities between two frequent closed sequences.

G. Recommender:

After performing the clustering techniques the frequent closed sequences are produced and the results are shown to the programmers. The programmers can bypass the process of checking code sequences one by one as the recommender returns the mined patterns as an index of sequences. The best API patterns are shown on the top of the index thus providing the programmers a suggestion to select which one is to be used.

V. EVALUATION

A. Environmental Setup:

The implementation of our work requires the usage of severe environmental setups. ORBAS, MAPO and Koders are used as search engine. To produce a graph based result we have implemented our result data in MATLAB. The system platforms in which we developed our framework contain core-i5 processor (2.30 GHz), RAM of 4GB and 3G network.

B. Time Response Evaluation:

Our work in ORBAS is compared to the existing MAPO and Koders search engine for evaluating time response. For example we have consideredWebRequest.create as sequence 1, then we have considered another sequence HTTPWebRequest.getResponse as sequence 2 for both Table I and Table II and so on. By inputting these sequences we generate an output based on the time response of the search tools which is shown in Table I.

TABLE I. TIME RESPONSE EVALUATION

Squ. No.	API Name	MAPO[3]	Koders[8]	ORBAS
1	WebRequest.create	5	7	3
2	HTTPWebRequest. getResponse	7	9	2
3	HTTPWebRequest.create	6	7	4
4	SQLConnection.open	3	5	1
5	SQLDatabase.read	4	6	2
6	SQLConnection.close	2	5	1
7	SQLCommand. parametersAdd	4	8	2
8	SQLDataAdapter.Bill	5	7	1
9	HTTPResponse.setContent	6	5	3
10	HTTPResponse.write	7	5	3

Fig. 2 shows the graphical representation of the response time from the data of Table I. The graph shows result analysis of the time response evaluation of API sequences among ORBAS, MAPO and Koders. The graph is designed in MATLAB by inserting the values of Table I. From the graph it is clear that the time responses for each method are lesser in ORBAS than MAPO and Koders.

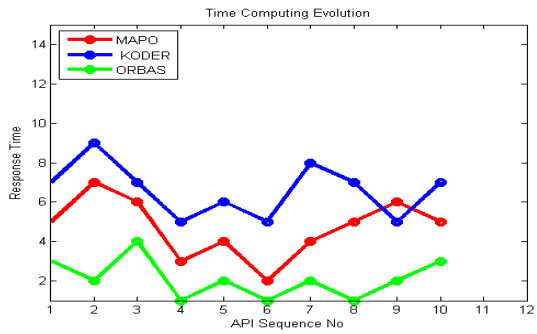

Fig. 2. Response time with different API sequences.

C. Performance Evaluation:

By inputting the sequences into different search engines we have evaluated the performance. Table II shows the performance evaluation based on the methods returned by each search tools. It is shown that ORBAS returns a few number of effective and useful methods compared to MAPO and Koders.

TABLE II. PERFORMANCE EVALUATION

Squ. no.	API Name	MAPO [3]	Koders [8]	ORBAS
1	WebRequest.create	71	110	8
2	HTTPWebRequest.Get Response	58	95	7
3	HTTPWebRequest.cre ate	22	55	4
4	SQLConnection.open	94	105	12
5	SQLDataReader.Read	67	82	10
6	SQLConnection.close	44	50	2
7	SQLCommad.paramet ersAdd	56	70	8
8	SQLDataAdapter.Bill	19	25	3
9	HTTPResponse.setcon tent	8	14	2
10	HTTPResponse.write	5	9	1

Fig. 3 shows the graphical representation of the number of methods returned by per API sequence. The graph shows the result analysis of the number of methods returned for ORBAS, MAPO and Koders. The graph is designed in MATLAB by inserting the data of Table II. It is clear from the graph that ORBAS returns a few but useful API methods than MAPO and Koders.

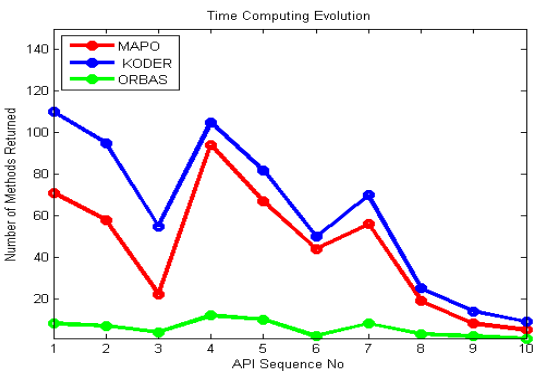

Fig. 3.Methods return from different API sequences.

VI. CONCLUSION AND FUTURE WORK

With a view to helping developers to understand API usages and client code more nicely we have developed a framework called ORBAS which is a supporting tool for mining API usages from anoffline repository. Our experimental results show that ORBAS generates useful API pattern than the existing tools. In future we will try to focus on automatic code generation based on the returned API patterns. Then these automatic generated codes can easily be inserted into developer's code. Our framework ORBAS may require some more data mining techniques. We further need to investigate to confirm whether the selected technique is the best or not. For the purpose of mining API usage patterns we plan to apply other clustering techniques such as k-means clustering. We also have a plan to apply other partial order miner in the mining stage. We plan to include other features such as class structure for clustering. We plan to find out the weights and thresholds value. We will concern other approach and technique and compare with our current process. In our working procedure we do not see the quality of the mined pattern directly. Usually most libraries do not provide usage pattern, there islacking in the field of the usage pattern. We must concern to experiment the quality of the usage pattern. Our framework approach must be applicable to many other object oriented languages. We will try to adapt our supporting tool in other large-scale databases. In our approach we have extracted API usages only for the API client code. In the future we will try to extract to the client code and the implementation code both.

REFERENCES

[1] 'PMD', GitHub. [Online]. Available: https://pmd.github.io/ [Accessed: 4-Sep-2015].

[2] J.Wang and J. Han. "BIDE: efficient mining of frequent closed sequences," In Proc. ICDE 2004, pp. 79.

[3] H. Zhong, T. Xie, L. Zhang, J. Pei, H. Mei. "MAPO: mining and recommending API usage patterns," In Proc. ECOOP 2009, pp. 318-343.

[4] SK. Hsu and SJ. Lin. "MACs: Mining API code snippets for code resuse," Elsvier 2011.

[5] Z. Rahman and K. Hasan. "Enhancing Software Development Process using Data Mining Integrated Environment," Masters Thesis of Islamic University of Technology, 16-80, 2015,

[6] A. Michail. "Data mining library reuse patterns usinggeneralized association rules," In Proc. 22nd InternationalConference on Software Engineering, pages 167–176, 2000.

[7] S.Thummalapenta, T. Xie. "PARSEWeb: a programmer assistant for reusing open source code on the web," In Proc. ASE 2007.

[8] 'Koders source code search engine', [Online]. https://www.blackducksoftware.com/news/releases/2009-09-09 [Accessed: 4-Sep-2015].

[9] 'Google code search', [Online].https://code.google.com/p/chromium/codesearch [Accessed: 4-Sep-2015].

[10] J. Wang, Y. Dang, H Zhang, K. Chen, T.Xie. "Mining Succinct and High-Coverage API Usage Patterns From Source Code," In conference on Mining-dl.acm.org, 2013.

[11] P.L. Buse and W. Weimer. "Synthesizing API Usage Examples," In Proc. ICSE, pp 782-792, 2012.

[12] R.Holmes and G. C. Murphy. "Using structural context to recommend source code examples," In Proc. ICSE, 2005.

An Experimental Study of Stylometry in Bangla Literature

Prapti Das, Rishmita Tasmim, Sabir Ismail
Department of Computer Science and Engineering
Shahjalal University of Science & Technology
Sylhet-3114, Bangladesh.
prapti.das.06@gmail.com, rishmita.sustcse015@gmail.com,sabir-cse@sust.edu

Abstract— **Every writer has a different style of writing of their own. By analyzing various kinds of features we can identify and specify some characteristics in a writer's writing which is known as stylogenetics. In this paper we gathered Bangla blogs written by four different Bangladeshi writers. Using machine learning methods we tried to identify special Stylometry features in their writing style. We analyzed various features in their writings, for example, percentage of unique words, word length, sentence length, and frequency of some parts of speech, number of suffix, frequency of first word, second word, second last word and last word of a sentence, counting average number of question marks per document, frequency of word by its position in a sentence etc. We gathered statistical data from analyzing those features and tried to find the variance among these writers using the statistical data.**

Keywords— stylogenetics, stylometry, machine learning, unique word, word length, sentence length, parts of speech

I. INTRODUCTION

Now-a-days language technology has reached to a different level of art. This enables the systematic study of the variation of linguistic properties in texts like author detection, find time period of the author, genre of writing, gender of the author etc. In short it helps to detect the characteristic and personality of the author.

Stylogenetics is clustering-based stylistic analysis of literary corpora [1]. It is a way of analyzing written texts to learn about the writer. Some features are often included unconsciously by the writer, for example gender, age, geographic location of the writer, personality characteristics, etc. A writer may use two specific consecutive words most frequently, may start and end a sentence with specific parts of speech, may write using a specific tense most of the time etc. These are some of the features that can be used to identify a writer.

Stylogenetics helps to detect who is the actual author of a specific writing and may assist in identifying fraudulent writing or in cases where multiple authors claim the ownership of a particular writing. Stylogenetics will analyze the writing and find a specific pattern or characteristic of that writing. Through which we can detect the original author.

Stylogenetics is a new area of research in the field of Bangla literature. Researchers in the past have worked with English literature, particularly with worked famous English writers like Shakespeare, Jane Austen, Charles Dickens etc.

However, there has not been any analysis on Bengali writers. There are many talented and skillful writers in our country and we often find interesting style and pattern in their writings. By analyzing their writing we can distinguish among the characteristics and features of individual writers.

Bangla is our mother tongue and Bangla literature is very rich and famous all around the world, which prompted us to initiate the first stylogenetics research in this area.

In this paper we investigated on the writings of four different Bangladeshi writers namely AH, EZ, MZI, SS (Due to Copyright Protection original name of the writers are not used in this paper).The reason behind choosing these four specific writers is the availability and popularity of their writings. We collected the blogs in a random way. A writer may write on a wide range of topics, for example, political issues, educational infrastructure, economical development, critics/novel etc. In this paper, we tried to identify the specific topic used most frequently by a writer.

Through our analysis we found some features that proved to be important to detect an author. But we did not find any absolute way of author detection. So our end-goal is to find a way which can identify an author perfectly.

The methodology we propose is to work with features like unique words used by an author, word length, sentence length which means number of words used in a sentence, number of parts of speech like conjunction and pronoun, number of question mark etc. There are several other possible features, for example, use of punctuations, use of stop words, use of simple/complex/compound sentences etc, which we plan to incorporate into our study in the future. Since in Bangla literature lexical and morphological analyzer is not rich, we could not work with some small details yet.

II. RELATED WORKS

Stylogenetics is the statistical analysis of variations in literary style between one writer or genre and another. Stylogenetics analyzes written texts to learn about the author. In various papers they worked with different features for the purpose of analysis.

Ramyaa et. al. [6] investigated some features like type-

token ratio, mean word length, mean sentence length, standard deviation of sentence length, mean paragraph length, number of commas, question marks, exclamation marks per thousand tokens.

Daelemans et. al [1] adopted a methodology from topic detection research, which included more complex features than the simple lexical features suggested by traditional approaches. They used authors or group of authors as a prediction of class, with clustering methods to indicate the differences and similarities between authors.

On the basis of the stylistic genome of authors, they tried to cluster them into closely related and meaningful groups. They also reported on experiments with a literary corpus of five million words consisting of representative samples of female and male authors.

III. OUR METHODOLOGY

We collected around 50 blogs each written by four different Bangladeshi writers for this study. The features we used and the detail experimental setup are described below.

A. Features Used :

1) Word frequency:

Word frequency means how many times a word was used in a writers writing. We counted frequency of both one word and two consecutive words. This is used as a feature to find the most frequent words used by a writer.

2) Word length:

The distributions of words of different length have been used as a feature. We calculated the frequency of words of different length.

3) Sentence length:

The number of words present in a sentence is used as a feature.

4) Type-token ratio:

The type-token ratio is *N/V*, where *V* is representing the size of the vocabulary of the sample, and *N* is representing the number of unique words. It is a measure indicating the vocabulary richness of an author.

5) Distribution of parts-of-speech:

Syntax-based features are not under the conscious control of the author and therefore it is considered as a feature. We mainly calculated the number of conjunction and pronoun in the texts.

6) Position specific word frequency:

We counted the frequency of words in first, second, last, second last and other random positions.

7) Writer specific unique words:

We created a list of words for each writer containing words which are mainly used by that particular writer. If another writer uses any of those words more than five times, then those words were not be considered as a unique word for that specific writer.

8) Previous and following words of a unique word:

We collected the previous and following words in a sentence for every unique word used by a writer.

9) Frequency of words related with "আমি", "করা","পারা" :

When we considered the word "আমি" we selected words like, আমি, আমরা, আমার, আমাদের etc. For "করা" we selected করা, করর, কররনা etc. And for "পারা" we selected পারা, পারর, পাররনা, etc.

B. Experimental Study:

1) Calculating Word Frequency:

A writer may frequently use some specific words and by calculating frequency of those words we can rank them as words most frequently used by a writer.

2) Frequency of one word:

We have implemented a program using java programming language to calculate the frequency of every word. Fig. 1 shows the words most frequently used by the four writers.

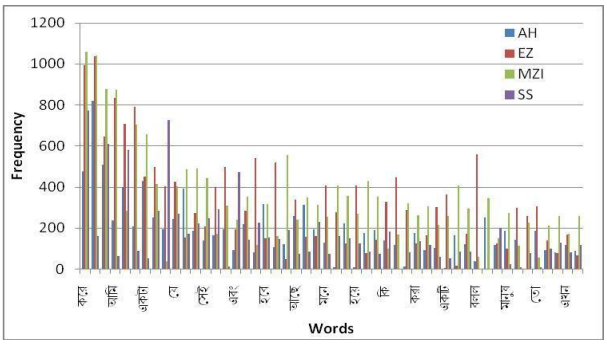

Figure 1. One word frequency of four writers.

As shown in Fig. 1 the words 'বলল' were most frequently used by EZ compared to other writers. So we can say that this can be used as a significant feature in case of EZ.

3) Frequency of two consecutive words:

Writers often use two specific words consecutively. We counted the frequency of two consecutive words using another program implemented in java similar to the program used above. Fig. 2 shows the most frequent two consecutive words used by the four writers.

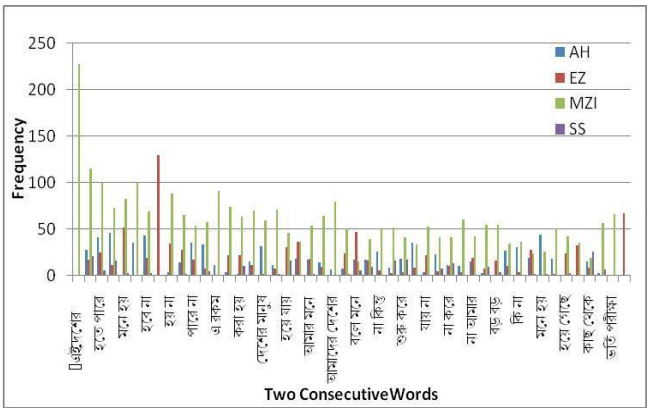

Figure 2. Two consecutive word frequency of four writers.

As shown in Fig. 2 the pair 'এই দেশের' were used in a higher

frequency by MZI than the others. The similar differences are shown in case of other writers.

4) Word Length:

Longer words are traditionally associated with more formal style, whereas shorter words are a typical feature of informal spoken language. Shorter words are also a feature of the modern day writes.

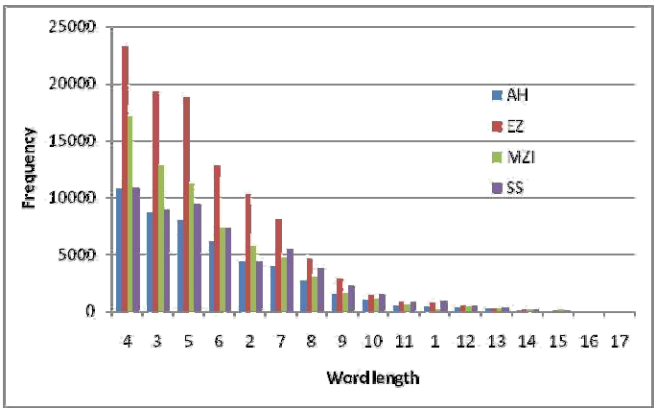

Figure 3. Frequency of words with different lengths.

As shown in Fig. 3 all the writers prefer to use shorter words more frequently than longer words most noticeably the writer EZ.

5) Sentence Length:

While shorter sentences are more indicative of spoken language, longer sentences indicate formal writing. Fig. 4 shows the usage of shorter sentences in a high frequency in case of all four writers.

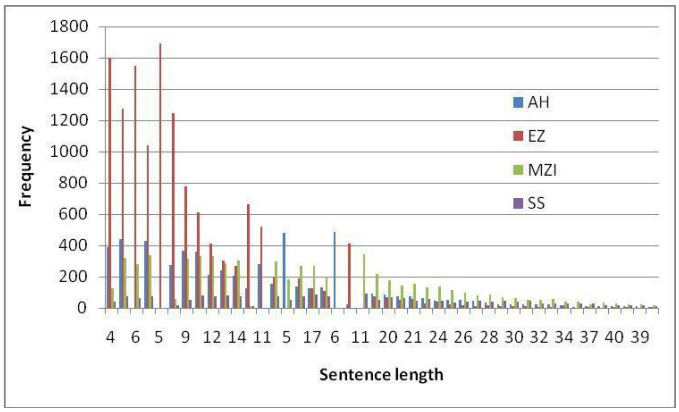

Figure 4. Frequency of sentences with different length.

As shown in Fig. 4 shorter sentences were used most frequently by EZ, while longer sentences were used in a higher frequency in case of MZI.

6) Type-token ratio**:**

The ratio of number of unique words and total number of words present in a document.

$$\text{Type-token ratio} = N/V, \qquad (1)$$

Here, N= number of unique words, V= Total words

Type-token ratio helps to find the richness of the vocabulary of a text. The writer that has the larger ratio has a richer vocabulary. Fig. 5 shows a pie-chart of the type-token ratio of all four writers.

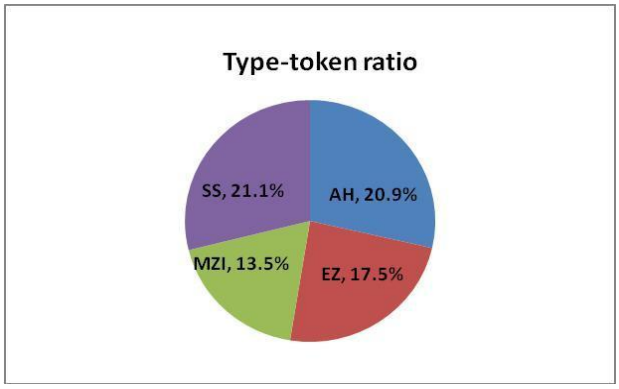

Figure 5. Type-token ratio of four writers.

The pie-chart above shows that SS and AH has higher type-token ratio compared to MZI and EZ. SS has highest type-token ratio, while MZI has the lowest ratio.

7) Distribution of parts-of-speech**:**

As part of identifying the distribution of parts-of-speech, we calculated the number of "conjunction" and "pronoun" in the documents.

Frequency of conjunction indicate continuity in someone's writing. On the other hand frequency of pronoun is indicative of particular pattern or style in writing.

Fig. 6 below shows the comparison of average number of conjunction and pronoun used per document by each writer.

It shows that average number of pronoun used by AH is higher than the others and in case of average number of conjunction is higher for EZ.

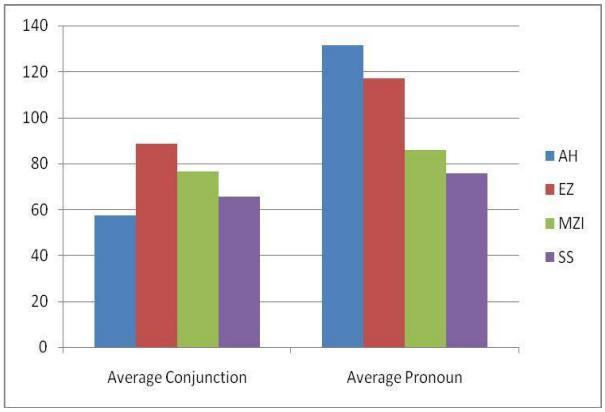

Figure 6. Average number of "Conjunction" & "Pronoun" per document.

8) Position wise word frequency:

Same words can be used in a different position in a sentence by different writers.

9) Writer wise unique words:

These words are especially used by one particular writer. These can be considered as recognizable words for a writer, which indicates the type or category of the text. In our analysis we found some recognizable words of three of the four writers.

In case of EZ, the "Recognizable words" are using different "Names."

Fig. 7 shows the frequency of recognizable words used by EZ comparing to other three writers.

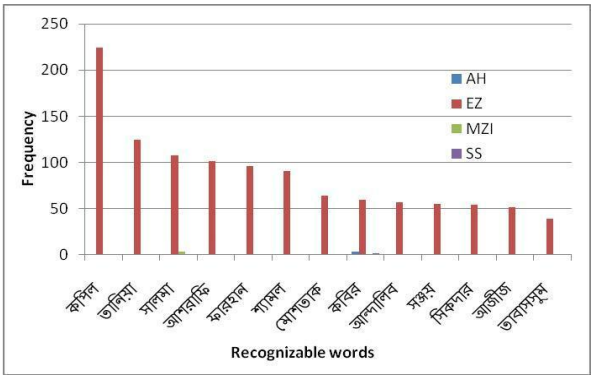

Figure 7. Comparison of "Recognizable words" used by EZ with others.

In case of MZI, the recognizable words are "Educational Words".

Fig. 8 shows the frequency of "Recognizable words" used by MZI comparing to other three writers.

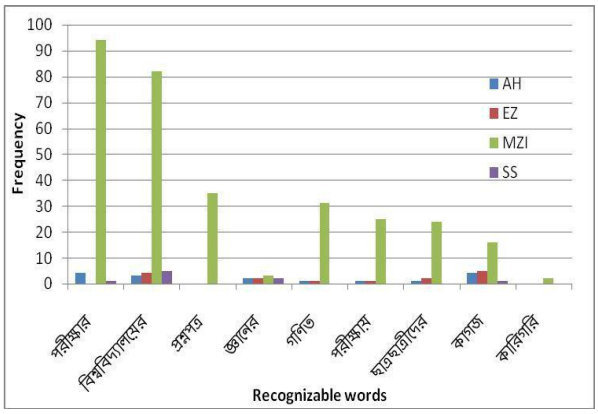

Figure 8. Comparison of "Recognizable words" used by MZI with others.

In case of SS the "Recognizable words" are "Political Words".

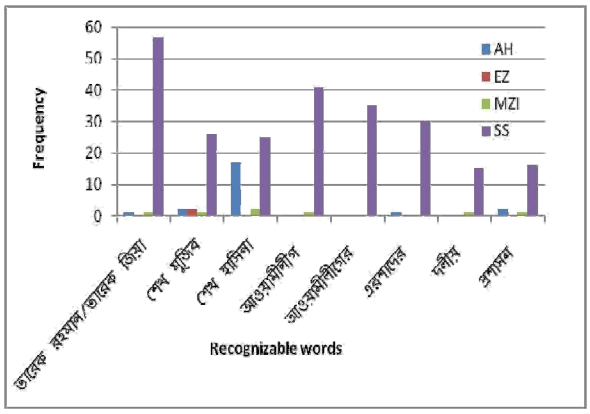

Figure 9. Comparison of "Recognizable words" used by SS with others.

10) Previous and Following words of a unique word:

There might be several words that are used frequently by all four writers. But analyzing the previous and following we can find some difference which could be an important feature.

11) Frequency of words related with "আমি", "করা", "পারা":

If the usage of words related with "আমি" is high in someone's writing, it can indicate that he is more likely to write in first person.

Fig. 10 shows the comparison of using words related with "আমি", "করা", "পারা" among four writers.

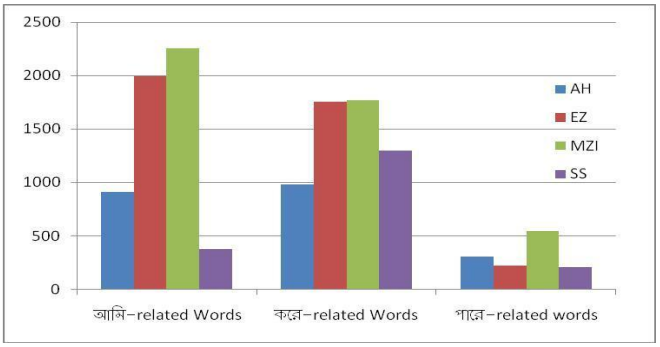

Figure 10. Usage of words related with "আমি", "করা" and "পারা".

We collected training data from these feature analysis. Then we compared the data with some random test data using statistical and machine learning approaches.

A. Standard Deviation:

It is a measure that is used to quantify the amount of variation or dispersion of a set of data values.

We counted the average number of conjunction per document for each writer from our training data. We did the same for test data. Then we calculated the standard deviation between a test data and each of the four writers' training data, e.g. we have test_data_1 and training data of four writers- AH, EZ, MZI and SS. If test_data_1 has the lowest standard deviation with training data of EZ, this indicates that test_data_1 might be the writing of EZ. Fig. 11 shows the standard deviation between test data and training data for average number of conjunction.

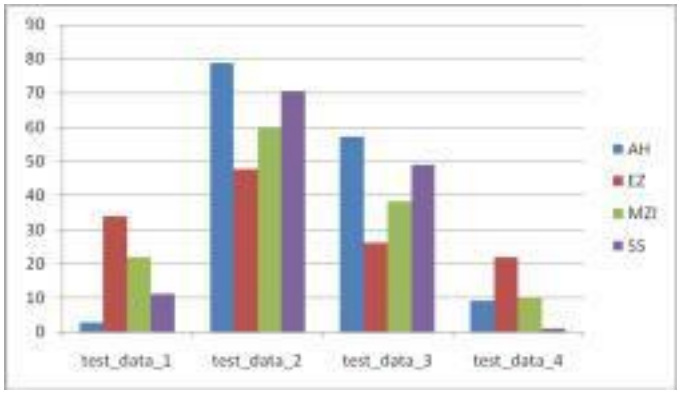

Figure 11. Standard Deviation between "Test data" & "Training data" for average number of "Conjunction".

We applied the same approach for average number of Pronoun.

Fig. 12 shows the standard deviation between test data and training data for average number of pronoun.

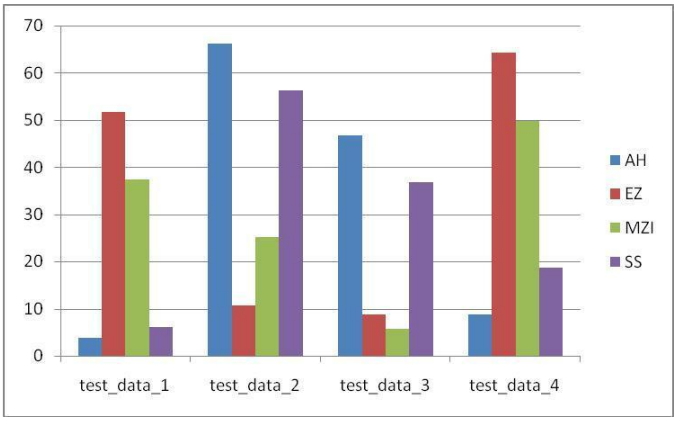

Figure 12. Standard Deviation between "Test data" & "Training data" for average number of "Pronoun".

B. Jaccard Similarity:

Jaccard Similarity is used to find similarity between two data sets. We applied this method for the feature writer wise unique word. We created a vector space model for the training data of unique words of each of the four writers and also for test data. Then we calculated the Jaccard similarity between test and training data, e.g. if test_data_1 has highest similarity value with AH, it indicates test_data_1 is most likely to be written by AH. Fig. 13 shows the Jaccard Similarity between test data and training data for writer wise unique words.

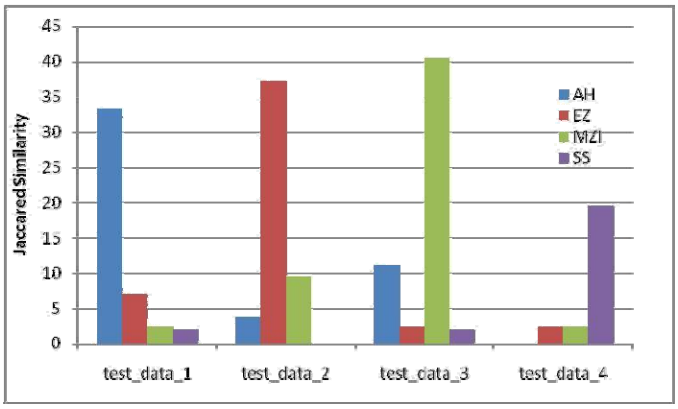

Figure 13. Jaccard Similarity between test data and training data for writer wise unique words.

IV. CONCLUSION

Stylogenetics provides an interesting venue for motivating and demonstrating many standard multivariate statistical techniques. This can be very useful for exploring and analyzing literary data. This paper attempts to recognize different authors based on their style of writing. As our first approach in this paper we analyzed twelve features according to the style of Bangla literature. Both standard deviation and Jaccard similarity can be one of the approaches to find some significant Stylometric features of a writer.

There have been no previous works on Stylometry for Bangla literature. Machine learning methods like Cosine similarity or Clustering can also be used to find some Stylometric features of a writer.

Stylogenetics is quite a new topic in the field of science and literature, especially Bangla literature. We hope our work will inspire others to work with Bangla literature in future.

REFERENCES

[1] Kim Luyckx,Walter Daelemans and Edward Vanhoutte, "Stylogenetics: Clustering-based stylistic analysis of literary corpora" , University of Antwerp Faculty of Arts Universiteitsplein 1, B-2610 Antwerp, Belgium.

[2] Roger Peng and Nicolas Hengartner, "Quantitative Analysis of Literary Styles", The American Statistician 56.3 (2002), 175-185.

[3] Michael Brennan and Rachel Greenstad," Practical Attacks Against Authorship Recognition Techniques", Dept. of Computer Science, Drexel University, 3175 JFK Blvd Room 140 Philadelphia, PA 19104.

[4] David. I. Holmes, "A Stylometric Analysis of Mormon Scripture and Related Texts", Journal of the Royal Statistical Society. Series A (Statistics in Society), Vol. 155, No. 1,(1992), 91-120.

[5] Holmes, David I, "The Analysis of Literary Style: A Review," Journal of the Royal Statistical Society, Series A (General), (1985), 328-341.

[6] Ramyaa, Congzhou He, Khaled Rasheed, "Using Machine Learning Techniques for Stylometry", Artificial Intelligence Center, Proceedings of International Conference on Machine Learning, 2004.

[7] Jan Rygl, "Automatic Adaptation of Author's Stylometric Features to Document Types", Text, Speech and Dialogue, Springer International Publishing, 2014, 53-61.

[8] Bangla Blog, http://blog.priyo.com/blogs, Last accesses: 11th May, 2015.

[9] Bangla Blog, http://www.somewhereinblog.net/blog, Last accesses: 11th May, 2015

[10] Bangla Blog, https://shadashidhekothaarchive.wordpress.com, Last accesses: 11th May, 2015.

Designing an Empirical Framework to Measure the Level of Interest of Human

Mizanur Rahman, Minakshi Debnath, ShylaSarmin, Lamia Alam, Safayet Arefin, and Mohammed Moshiul Hoque
Chittagong University of Engineering & Technology (CUET), Bangladesh
* E-mail: mmoshiulh@gmail.com

Abstract— **Human–robot interaction (HRI) is an interdisciplinary research field aimed at improving the interaction between human beings and robots. For effective and prolonged interaction, both interacting partners need to be identified the focus of attention of each other. In other words, need to tracks or determine the each other interest and their level of interest. Interaction between a human and a robot may influence by the proximity and angle between them. In this paper, we proposed a computer vision framework for robots that will determine the level of interest of its human partner in two-party setting. We have used the distance and angle parameters to determine the level of interest in several categories: high, medium, low, and so on. The level of interest information can be used as an indicator of people's willingness to engage in an interaction with a robot. The proposed framework uses depth and visual information, provided by a Kinect sensor. Experimental results show that the system is functioning quite well to measure level of interest of the human with a reasonable accuracy.**

Keywords*—— *Human robot interaction, level of interest, human detection, interest classification, evaluation.

I. INTRODUCTION

Interest may be defined as the cognitive process of selectively concentrating on one thing of the environment while ignoring or giving lower concentration to the other things. Determining someone's interest is the pre-requisite in any human-human and human-robot interactions. Determining human's interest and its level considered also as one of the important features for a social robot. Though human behavior is complex, it is need to be structured along individual and social lines [1]. In order to interact with the human in an uncontrolled environment, the robotic system should able to interpret, predict and respond to the human behaviors appropriately [2]. Thus, to behave in a socially acceptable manner, the robot should be capable of performing a lot of social and cognitive functions [3].

Due to the increased introduction of robots in the human world such as home, offices, shopping mall and so on, the robots are still stumbling to adjust with the social behavior of the human which can be solved by detection of level of interest. For example, considering the scenario of a service robot in a shopping mall where the robot needs to deal with plenty of customers. In that case, the robot needs to understand who is asking for service from it and has to be aware about who is trying to draw its attention. Again, the robot has to serve the customer on a priority basis (i.e. physical positioning of customers in the queue, who comes earlier). In different cases, the robot is required to have the ability to analyze the level of attention of human. Communication between a human and a robot may take several forms, but these forms are largely influenced by whether the human and the robot are in close proximity to each other or not. It also depends on their angular position. Thus, interest can be considered as a function of distance and angle. Depending on the functions, the level of interest varies from high to low. The level of interest can be measured in terms of physical and physiological parameters. In order to measure the level of interest, we consider two parameters: (i) distance between the human and the robot and (ii) angle between the human and the robot (with respect to the camera position of the robot and the line of sight of the human). In this work, we propose an empirical framework to measure the level of interest of human in terms of two parameters that can lead robots with the necessary capability to initiate an interaction episode in a more natural and social manners. After measuring the level of interest of the interacting human, the robot is able to display appropriate behaviors to him/her who are willing to interact with it.

II. RELATED WORK

There are lots of research activities have been conducted on designing several social capabilities of robots such as eye contact [4, 5], joint attention [6, 7], and attention control [8, 9]. However, still there are plenty issues remained unsolved related to developing the social capabilities of robots. In this paper, we focus such one of the important issue: measuring level of attention of human. Miguel et al. [10] estimated the level of attention by analyzing looking response toward the robot. Their system was able to detect the persons in its vicinity by using the stereo system and fuzzy logic is used to define a possibility of interest for the detected persons to interact with the robot. An attention system is proposed by Alcalde et al. [11] for robot-human interaction. This system uses depth and visual information, provided by a Kinect sensor to detect a user when s/he is requiring attention and predict the objects that are suitable for interaction. An approach is presented in [12] for a mobile robot to detect the level of attention of a human (i.e., null, partial, and total) in first-person interactions. Das et al. [13] proposed an attention control mechanism for social robots that attracts and controls the attention of a target person depending on his/her current attentional focus. Their system detects the interest or willingness of the target person to interact with it.

Most of the previous work used expensive color cameras and evaluated only in laboratory conditions. The proposed system uses a comparatively cheaper sensor (i.e., Kinect) that will work in non-laboratory conditions too. The IR color sensor of Kinect will produces better results. Moreover, the most of

the previous works dealt only with analytical dimensions rather than making a system. We propose an empirical framework which can estimate the level of interest of human with better accuracy.

III. PROPOSED FRAMEWORK

Although there are various parameters can be used to measure the level of interest of interacting partner, in this work, we considered two important parameters regarding the detection of human interest visually. First one is the distance between the human and the robot's camera and second one is the angle between the camera and the human. Level of interest of human can be measured by observing these parameters in real environment. We consider depth information by Kinect in this context to estimate the physical distance and angle between the human and the robot's camera.

Initial position of the human head is determined based on the depth image. Positioning is updated frame by frame according to the depth data which results in tracking the human. Distance and angle from the Kinect to the human is then measured by the system. Finally, the level of interest is determined based on the predefined rules. Fig. 1 illustrates the schematic demonstration of the proposed framework.

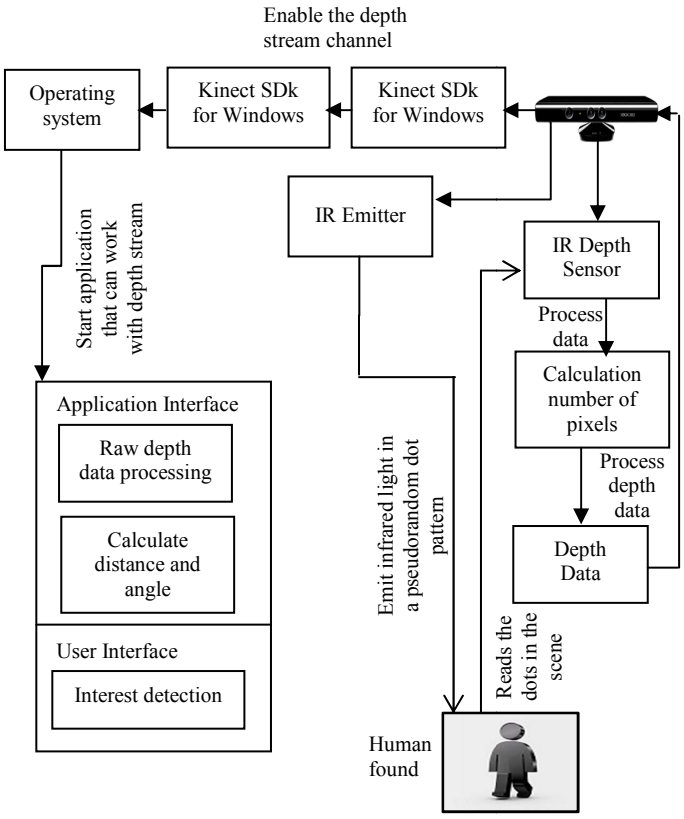

Figure.1: Proposed framework to measure the level of interest.

A. Capturing Depth Data

The infrared (IR) emitter and infrared (IR) depth sensors of Kinnect are used to capture the depth information of human. Kinnect produces a depth image of the human in front of it. The IR emitter and the IR depth sensor are used a combined function to obtain the X, Y and Z co-ordinate values on specific point of the detected human. We considered the head part of the human body to detect the human in our current implementation.

B. Identification of Human and Tracking

We use a model based method for human detection from depth images. Here, human is detected using depth information obtained by Kinect using a 2-stage head detection process, which includes a 2D edge detector and a 3D shape detector. Fig. 2 shows the overview of the human detection process.

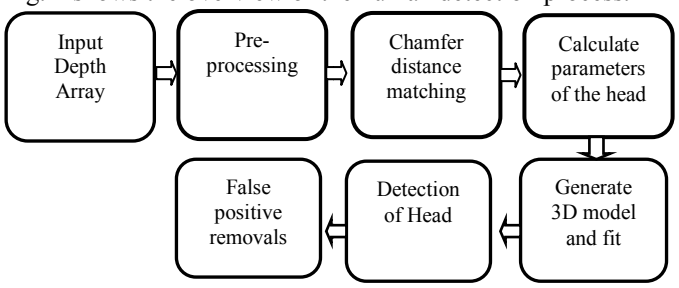

Figure 2: Overview of Human Detection Process

2D chamfer for distance matching algorithm is used. It scans across the whole image and gives the possible regions that may contain people. We examine each of these regions using a 3D head model. We extract the parameters of the head from the depth array and use the parameter to build a 3D head model. Then we match the 3D model against all the detected regions to make a final estimation. From the detection result of 2D chamfer matching, we can get the depth of the head like object from the depth array. In order to generate virtual 3D model of sphere (i.e. head), the only parameter that is required is radius of the sphere has conducted a regression test that have arrived at a cubic equation that gives the relationship between the depth value and the approximate height of head [10]. The cubic equation that fits the geometrical height of the head is computed as Eq. 1.

$$-y = -1.3835\times10^{-9}x^3 + 1.8435\times10^{-5}x^2 - 0.09140x + 189.38 \quad (1)$$

By equation Eq. (1), we calculate the standard height of the head in this depth. Then search for the head within a certain range that is defined by the standard height of the head by the Eq. (2).

$$R = 1.33\,\frac{h}{2} \quad (2)$$

Here, h is the height of the head, R is the search radius. Now, convert the height from millimeter into pixel unit as the matching works pixel by pixel.

$$Radius\ (pixel) = \left(\frac{1}{1.3}\right) \times Radius\ (\text{mm}) \quad (3)$$

Then we fit the model onto the regions detected from previous steps. We extract a circular region with radius R around the detect center and normalize its depth using Eq. (4).

$$En = \sum |\,\text{normalized_real_depth}\ (i,j) - \text{ideal_depth}\ (i,j)\,|^2 \quad (4)$$

We used a threshold value to decide the region is actually a head or not and remove the false positives. If the matching value is within the threshold, then we say the head is detected that in turns means there is a human.

Tracking algorithm is worked based on the movements of the human's head. This Kinect-based head tracking system uses user-specific 3D face template to track head pose. Head movement prediction is used to provide initialization result for ICP tracking, depending on whether or not the previous tracking results are available. The work flow of the human head tracking process is presented in a flowchart [Fig. 3].

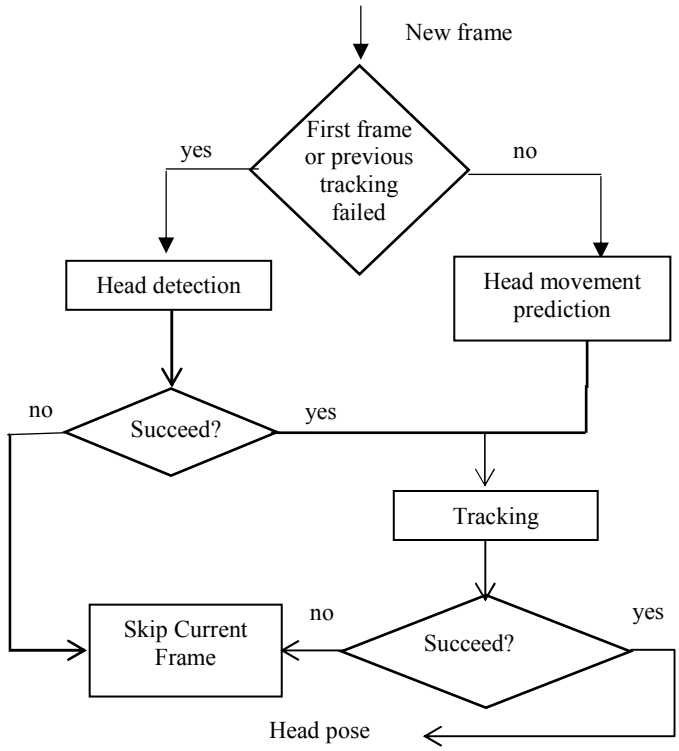

Figure 3: Workflow of the Human Head Tracking System.

Human can be detected either while s/he standing or sitting and facing the Kinect. However, sideways poses could prove to be difficult to be detected because of parts of the human are not visible to the camera.

C. Depth Information Processing

Kinect for windows device is connected to a general purpose PC with an USB cable. When there is a need to capture depth data, the Kinect is turned on and all of its sensors are initiated. Then IR emitter constantly emits infrared light in a random dot pattern over everything in front of it. IR depth sensor that reads the dots in the scene, processes the data, and sends the depth information from which they were reflected.

D. Measuring the Level of Interest Human

Interest can be considered as a function of two parameters distance (D) and angle (θ), $LI(H) = f(D,\theta)$, Where, LI (H) is the level of interest of human, D is the distance between the human and the Kinect sensor, and θ is the angle between the human and the Kinect respectively. Level of interest depends on the distance and varies inversely. Lower distance indicates the higher level of interest and vice-versa. Similarly, interest depends on the angle too. If we consider these two parameters together, then we can calculate interest from the rules below,

$$LI(H) = f(D,\theta)$$

$$LI = \frac{1}{(D+\theta)}; \quad when\ \theta > 0 \tag{5}$$

Here, D is the distance and θ is the angle between the human and Kinect. From the Eq. (5), level of interest is determined with respect to D and θ and varies inversely with them. We classify the level of interests in terms of ten categories based on the measurements of LI. The classification rules of level of interest level are illustrated in Table I.

TABLE I. CLASSIFICATION OF LEVEL OF INTEREST (LI)

Level of Interest (LI)	Classification
If (I = 0)	No Interest
If (I > 0 && I< 10)	Minimum Interest (MNI)
If (I >=10 && I< 20)	Very Low Interest (VLI)
If (I >=20 && I< 30)	Low Interest (LWI)
If (I >=30 && I< 40)	Lower Medium Interest(LMI)
If (4 >=40 && I< 50)	Medium Interest (MDI)
If (I >=50 && I< 60)	Higher Medium Interest (HMI)
If (I >=60 && I< 70)	High Interest (HGI)
If (I >=70 && I< 80)	Very High Interest (VHI)
If (I >=80 && I< 100)	Maximum Interest (MXI)

E. Measuring Parameters (D and θ):

After getting the depth stream data as a succession of the depth image frame the Kinect sensor returns raw depth with 16-bit grey scale format then we can measure distance. Behind the scenes the Kinect sensor runs a series of algorithms on the captured data to give more than an image, which tells how far each pixel in that frame is. Hence the depth pixel contains the distance between the Kinect device and the human in front of the device, in meters. Here we consider the head position of the human, so we measure the distance of the head of the human from the Kinect. The joint positions (here only head) are measured by three coordinates (X, Y, and Z). After getting these coordinate values, finally we calculate the distance between the Kinect and the detected human. The distance between two points (x_1, y_1, z_1) and (x_2, y_2, z_2) in 3-dimensional space can be determined by the Eq. 6.

$$d = \sqrt{\{(x_2 - x_1)^2 + (y_2 - y_1)^2 + (z_2 - z_1)^2\}} \tag{6}$$

Here, we assume that the sensor is in the origin point and another point is the position of the head of the detected human. Then we calculate the angle between Kinect and the human. We consider the angle to the respect of the line of sight of Kinect. In this set up line of sight is the straight line through the sensor. Here x axis is the line of sight and the negative value of θ indicates left side of the human. We use Eq. (7) to calculate the angle (θ).

$$\theta = \tan^{-1}(a/b) \tag{7}$$

Where, a indicates the value along X axis of the head position of human and b indicates the value along Z axis of the head position of the human.

IV. Evaluation Results

In order to evaluate the proposed framework, we have performed several trials in different environments. In each trails, we varied the distance as well as angle to estimate the level of interest. In one trial, a participant is asked at a time to interact with the framework and instructed to move forward and backward to change the distance. The participant also instructed to change their position for varying angle. We have calculated the level of interest of the participant in terms of distance only, angle only, and combined distance and angle respectively.

A. Output of the system

We experiment and analyze the system with different human as input in different real-world environments. We found significant results for most of the cases. We consider the level of interest in three criteria (i.e. IL against distance, angle and distance plus angle) for proper evaluation. A graphical interface is also represented to observe the variation of the interest level over time and to comprehend the significance of distance and angle both for measuring the interest level [Fig. 4].

Figure 4: Graphical User Interface of the System

In Fig. 4, a detected human is seen in the graphical interface of the application, this human stands from Kinect at 1.59 meter distance, and her angle from Kinect is -1.34 degrees. That means, from the equation (3) the level of interest of the participant with respect to distance and angle is 47.38%, which is Medium Interest (MI) according to the table 1.

B. Quantative Analysis of Level of Interest Measurement

To evaluate the level of interest, we have followed a three steps evaluation method. Firstly, we have taken the level of interest (LI) against a single parameter (i.e. distance). Secondly, the level of interest measured against another single parameter (i.e. angle). Finally, the level of interest will measured by combing distance and angles both parameters. We find significant changes among the outcomes that worked with combined parameter than that of single parameter.

Table II shows the summary of the analysis. We considered 10 interaction cases at different positions. Interest level based on single parameter and interest level based on both parameters together is compared. If we consider the first case of the table, here we can see the human in front of Kinect standing at 1.98 meter distance and her angle is 0.01 radian from the Kinect sensor. Therefore, we found that her level of interest is 30.9% which indicates category of Lower Medium. Fig. 5 illustrates this fact.

TABLE II. Measurement of Level of Interest (IL) with Distance, Angle and Combined Distance with Angle.

Case No.	Distance only (D) (m)	Level of interest	Angle only (θ) (rad)	Level of interest	Level of interest (D+θ)
1	1.98	50%	0.01	50%	30.9%
2	2.27	44%	0.07	14.28%	20.72%
3	0.97	100%	0.03	33%	100%
4	0.23	100%	0.16	6.25%	58.23%
5	1.37	73%	0.06	16.66%	9.34%
6	2.2	58%	0.21	4.76%	18.27%
7	2.43	39%	0 .45	2.22%	11.43%
8	1.73	41%	0.5	2%	38.7%
9	1.1	80%	0.04	34%	82.94%
10	4.55	Out of Social Distance	0.39	2.1%	No interest

Figure. 5: Graphical User Interface for case 1. In that case, the distance is 1.98 m, angle is 0.01 (rad), level of interest is 30.9%, and interest category is low medium.

Fig. 6 shows the graphical representation of Interest with respect to D, θ and both of them (D+θ). This Fig. indicates that the level of interest measurement varies both on the parameters D and θ. For example, if the distance is small but the angle is large (i.e., the human is attending the opposite side of the camera), the level of attention can be considered as very low. On the other hand, if the distance is large but the angle is small, then the level of interert can be consideded as the high. Thus, it is better to consider both parameters. In this work, we have proposed to combine the both distance and angle parameters for determining the level of interest of the human partner. Fig. 6 indicates that the level of interest changes

moderately while using combined distance and angle parameters than that of the individual parameter (distance or angle).

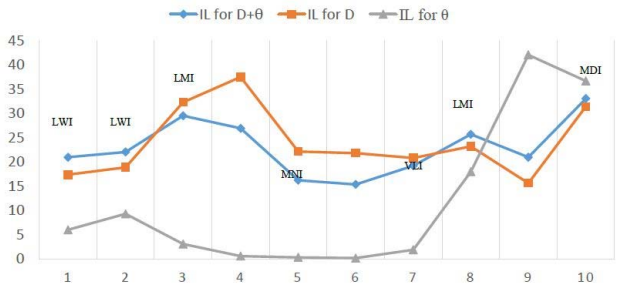

Figure. 6: Graphical representation of level of interest based on D, θ and (D+θ) parameters.

V. CONCLUSION

Measurement of level of interest of human can play a significant role in natural human-robot interaction. In this work, we presented a framework which can primarily measure the level of interest of human based on the distance between the human and camera and angle between them. The system also detects and tracks human as a pre-requisite of the interest measurement. As we worked with depth data rather than that of RGB image processing, performance is quite improved overcoming the environmental effects. Image based processing requires complex algorithm and computational costs. We used simpler algorithm for dealing with depth data. The system was evaluated in different environments with different participants and results reveal that it is able to measure the level of interest of the human with a reasonable accuracy. The proposed system is limited only two parameters. However, more parameters may include such as face area, sound source, attention span, and so on that will enhance the effectiveness of the proposed framework. The system may also extend for estimating the level of interest of multi-person scenario.

REFERENCES

[1] S. Lang, and G. Sagerer, "Multi-modal anchoring for human robot interaction", Robotics and Autonomous Systems, vol. 43, no. 2-3, pp. 133–147, 2003.

[2] B. Walker., P. Caroline, D.S. William, "Using depth information to improve face detection, Proc. of the 6th International Conference on Human-Robot Interaction; Lausanne, pp. 119-120, Switzerland, 2011.

[3] D. Das, Y. Kobayashi, and Y. Kuno, "Attracting attention and establishing a communication channel based on the level of visual focus of attention", in IEEE/RSJ International Conference on Intelligent Robots and Systems (IROS), pp. 2194-2201, Japan, 2013.

[4] D. Das, G. M. Rashed, Y. Kobayashi, and Y. Kuno "Supporting human-robot interaction based on the level of visual focus of attention", IEEE Trans. On Human Machine Systems, pp. 1-12, no. 99, 2015.

[5] D. Miyauchi, A. Nakamura and Y. Kuno, "Bidirectional eye contact for human-robot communication", IEICE Trans. Info. Syst. 88-D, pp. 2509-2516, 2005.

[6] P. Michalowski, S. Sabanovic, and R. Simmons, "A spatial model of engagement for a social robot", Proc. *IEEE International Workshop on Advanced Motion Control*, Istanbul, Turkey, pp. 762-767, 2006.

[7] K. Hosoda, H. Sumioka, A. Morita, and M. Asada. Acquisition of human-robot joint attention through real-time natural interaction. In *IEEE/RSJ International Conference on Intelligent Robots and Systems*, pp. 2867–2872, USA, 2004.

[8] M. M. Hoque, T. Onoki, Y. Kobayashi and Y. Kuno, Effect of robot's gaze behaviors for attracting and controlling human attention, Adv. Robo. vol. 27, pp. 813-829, 2013.

[9] G. S. and V. Hafner "Evaluating the effect of saliency detection and attention manipulation in human-robot interaction", in International Journal of Social Robotics, vol. 4, pp.123-139, 2012.

[10] G. Miguel and A. Gonz´alez, "A fuzzy system for visual detection of interest in human-robot interaction," [online], Available: http://www.researchgate, 2008.

[11] F. J. Alcalde, I. varea, and J. M. G´omez, "Active attention for human robot interaction using visual and depth information," Workshop of Physical Agents, 2012.

[12] L. C. Gonzalez-Garcia, L. A. Torres-Mendez, J. Martinez, J. Sattar and J. J. Little, "Are you talking to me? Detecting attention in first-person interactions, Proc. 17th International Conference on Advanced Cognitive Technologies and Applications, pp. 137-142, 2015.

[13] D. Das, M. M. Hoque, Y. Kobayashi, and Y. Kuno, Attention control sysetm considering the target person's attention level, 8th ACM/IEEE International Conference on Human Robot Interaction, pp. 111-112, 2013.

BQAS: A Bilingual Question Answering System

Sanjidul Hoque
Department of CSE,
CUET, Bangladesh
Email: sanjid133@gmail.com

Mohammad Shamsul Arefin
Department of CSE,
CUET, Bangladesh
Email: sarefin_406@yahoo.com

Mohammed Moshiul Hoque
Department of CSE,
CUET, Bangladesh
Email: moshiulh@yahoo.com

***Abstract*—In this paper, we present a bilingual question answering system, BQAS that can generate questions and provide their answers from electronic Bangla and English documents. The system first performs the analysis of the contents of the documents to generate questions based on user provided query. It then generates answers of the questions. The system has been evaluated with real documents. We have found that our system can generate questions and related answers up to a satisfactory level from the documents of two different languages as well as from the documents of the same language.**

***Index Terms*—Bilingual systems, keywords extraction, query execution, clustering.**

I. INTRODUCTION

Question Answering System is system where it produces an amount of questions from one or several documents and justifies users answer. It is one of the popular topics in natural language processing and one of the best ways to retrieve information from the documents. It is very helpful for those students who want to justify his / her learning through putting answer of generated questions.

There are many existing question answering systems. Most of them are unilingual in nature and none of them considers the generation of questions and answers considering the documents of Bangla and English. Considering this fact, in this paper, we develop a bilingual question answering system known as BQAS that can generate questions and their related answers considering the documents of Bangla and English. We implement the system considering users' provided queries and domain information. At first, the system extracts keywords from the documents those are related to the user query. Here, we consider postfix statistics to determine the root words. Then, digit and keyword based questions are generated from those documents. Our translation system then translates those generated questions and stores those questions into the database. A number of questions are shown to the user's screen in users selected language. Later on the system provides the answers of the generated questions.

Our main goal is to generate fact-based questions from the documents of Bangla and English. The importance of the generated is measured in two steps. In the first steps, we identify whether the question is asking something about the topic or something that is very closely related to the topic. For this purpose, we use Latent Dirichlet Allocation (LDA) [1] to identify the sub-topics in the given body of texts and apply the Extended String Subsequence Kernel (ESSK) [1] to calculate their similarity with the questions. In the second step, we judge the syntactic correctness of each generated question. We rank the questions by considering their topic relevance and syntactic correctness scores.The contribution of this paper can be summarized as follows:

The remainder of this paper is organized as follows. Section II provides a brief review of related work. In section III, we detail the computation framework of our proposed approach. Section IV presents the experimental results. Finally, we conclude and sketch future research directions in Section V.

II. RELATED WORK

The idea of automatically generating questions from sentences has been proposed and implemented as early as 1976. Recently question generation has got immense attention from the researchers and hence different methods have been proposed to accomplish the task in different relevant fields.

There are some question answering systems thats operate in English only. Such as, Plamondon et al. [1] developed a system where the question must be asked in English, the document collection is in English and the answer extraction is performed in English. Kaur et al. [2] described a system that first collects the corpus of data or paragraph from encyclopedia to make the questions and find the exact answer. Filho et al. [3] developed a system where they tried to classify the questions in only 4 types ("who", "where", "when" and "how many" questions). Hitomi et al. [4] concerned with a type of infant bilingualism in which children have been regularly exposed to two languages from birth as a result of each of their parent's speaking a different language. Their system produces only negative question in both Japanese and English language and judge the user's response.

Xu et al. [5] focused on the methods for question generation and answer judgement as well as the game implementation. Here they worked with Chinese and English statements. A cross-language question answering system is developed by Plamondon et al. [6]. Here they develop a system that receives questions in English language and show the answer in English for English document collection. They also transformed the system into a bilingual system to allow French speakers to ask their questions in French and get answer in French as well, but using an English document collection.

GistSumm [7] is an automatic summarizer based on a simple extractive method, called gist-based method. QUASAR [8] is

978-1-4673-9257-0/15/$31.00 ©2015 IEEE

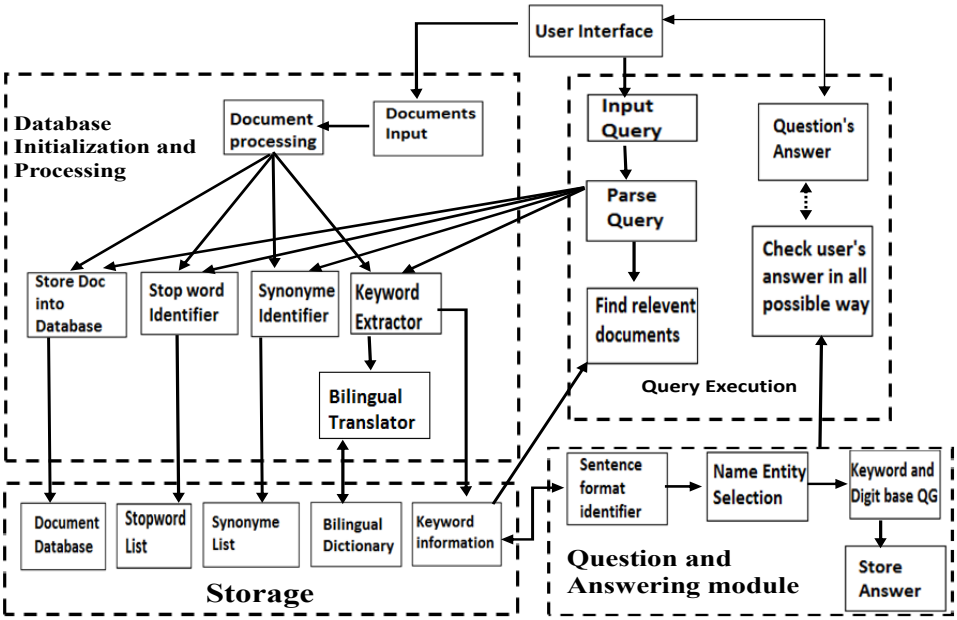

Fig. 1. System architecture of the proposed system

a QA system based on the JIRS1 Passage Retrieval engine, which has been fine-tuned for the QA task, whereas most QA systems use classical PR methods.

A few Banglaa and English question answering system also developed. Haque et al. [9] developed a question answering system based on transliteration and table look-up as an interface for the medical domain. The system is in no way a complete QA system; however, it gives a basis to implement a complete QA system for Bangla. The implementation involves questions from the medical domain only. They also consider only simple questions (wh-question).

There are about 220 million native and 250 million total Bangla language speakers. But there are a few works on Bengali language. So, working with Bangla language is most significant. Besides, Bangla and English question answering system helps students to make their learning more effective.

Considering this fact, in this paper we propose a framework for generating questions and corresponding answers considering the documents of two different languages: Bangla and English.

III. System Architecture and Design

The system architecture of Bilingual Question Answering System comprises four basic modules: Database initialization and processing module, storage module, question and answering module and query execution module. The function of database initialization and processing module is to set up the database from a set of documents for information retrieval. Storage module store all related information to the database. Question and answering module is for generating question and analyzing the answer and query execution module performs all information retrieval queries. The architecture of the proposed system is shown in shown in Fig. 1.

Algorithm: *Documents_storing*

Input: Documents

Require: Store the documents.

1. **begin**
2. create a table named document having the field DocID, Doc Title, No of word
3. Initialize the counter variable is 1
4. While the counter variable is less than the no of total document
5. Insert the file name and counter into the table
6. Increment the counter variable
7. **End**

Fig. 2. Algorithm for storing documents into database

A. Database Initialization and Processing Module

The database initialization and processing module consists of sub-modules: store documents into database, stop word identification, synonym identification, keyword extraction. The relationships among the sub-modules are also shown in the Fig. 1. The document database is created with document ID, document title and total word into the document. Algorithm for storing documents is given in Fig. 2.

There are some words which do not make any significant change in absence of them. Those words are called stop word. Our current step is to remove those words from the documents. There are a lot of stop words in English language such as: a, about, above, across, after, afterwards, again, against, all, back, be, became, because, become, becomes, becoming, been, before, by, call, can, cannot, can't, due, during, each, eg, etc. There are also a lot of stop words in Bengali as well. A list of English stopwords and Bangla stopwords are enlisted and stored into the database, which are used in the process of stopwords elimination by the system. Algorithm for stopwords removal is given in Fig.3.

```
Algorithm: Stop_word_elimination
Input: List of words.
Require: Delete the unnecessary word.
begin
for each word do
    search the stop word list
  if word is found then
      remove the word from sentence
  else
      do nothing
  end if
end for
End
```

Fig. 3. Algorithm for stopwords elimination

```
Algorithm: Keyword_Extraction
Input: sentences and list of words.
Require: Find the keyword.
begin
for each independent word do
    initialize a 2D matrix with value=0;
end for
count=0;
for each independent word do
    if word match with the sentence's word then
        count++;
    else
        Do nothing;
    put the counted value in corresponding index;
  end if
end for
Determine the maximum value
    define the keyword;
End
```

Fig. 4. Algorithm for keywords extraction

Synonym identification sub-module performs the identification of synonyms from the documents. A words having the same meaning as another in the same language is called the synonym of that word. It is very much important to manage the synonyms efficiently. Because if the synonyms having same meaning are not treated as same words, there will be a great degradation of system's accuracy.

Keywords are used for different purposes. They are used to determine those documents which are related to the domain information. Keywords are also used to generate questions. Each keyword is stored into the database by its ID and name. Keyword extractor sub-module extracts the keywords from the documents with the help of algorithm of Fig. 4.

B. Storage Module

The storage module handles the storage of the document and important information for retrieval purposes. The stop lists are stored into the database. Synonyms are stored into the database accordingly. A bilingual dictionary is also stored for translation purposes. For further calculation keywords are necessary so keywords are also stored into the database.

C. Question and Answering module

It is the main module of our system. Here questions are generated and corresponding answers are also retrieved. There are several sub-modules: Sentence format identification, Name entity identification, Keyword and Digit based question generation and the storage of answer.

1) Sentence Format Identification: It is our first step to generate questions. Fist, we have to identify the sentence structure. If the sentence is simple then it is ready to generate question. For complex and compound sentences we convert them to simple sentences for making questions generation task easier.

2) Name Entity Selection: We use our database information to determine a name entity in the document. We use some general purpose rules to create some basic questions related to name.

3) Digit and keyword based question generation: Digits in documents play significant roles for generating questions. It is easy to generate questions by replacing the digits with a question word shown in Table I. We also consider keywords to generate the questions.

TABLE I
QUESTION TEMPLATE

English Question	Bangla Question word	Arguments
Who	কে	Person
Where	কোথায়	Place
When	কখন	Time
What	কি	Object
Which	কোনটি	Object
How	কিভাবে	Process
Why	কেন	Cause

D. Query Execution

The sub-modules are: Input query, parse query, find relevant document, user's answer, and find all possible answer. At first user input a domain name on which he/she wants to generate question. After taking the domain name as input from user our system needs to parse the domain name. Then using a clustering algorithm (such as cosine similarities) our system finds the relevant documents which are used for generating question. While answering a question our system needed to check the all possible solution for that question and match with the user's answer.

E. Documents Categorization

The similarity between domain and documents can be calculated by the cosine similarity. If the the cosine similarity -1 between the vectors of two documents means that the documents are exactly opposite, 1 means exactly same, 0 usually indicates independent documents, and in-between values indicates intermediate similarity or dissimilarity. For text matching, the attribute vectors are usually the term frequency vectors of the documents. In our situation, the cosine similarity range from 0 to 1. Based on the similarity measures, we short the documents in descending order of similarity with the query information. Then, we choose the documents those have the similarity scores grater than a defined threshold for considering question generation. Fig. 5 shows the algorithm of this approach.

```
Algorithm: Document_Categorization
Input: domain name and keyword list
Require: select the desired documents.
1.  begin
2.  for each keyword do
3.      Calculate the cosine similarity.
4.  end for
5.  if similarity_ value >= threshold do
6.      select the document for generating question
7.  else
8.      do nothing;
9.  end if
10. end for
```

Fig. 5. Algorithm for documents categorization

```
Algorithm: Duplicate_question_elimination
Input: List of generated questions.
Require: Delete the duplicate questions.
1.  begin
2.  for each question do
3.      search the question database
4.      if question is found more than one then
5.          remove the duplicate question
6.      else
7.          do nothing
8.      end if
9.  end for
```

Fig. 6. Algorithm for duplicate questions elimination

F. Duplicate Question Elimination

The system may generate same question from different documents. So, we need to remove the duplicate questions. The algorithm for duplicate questions elimination is given in Fig. 6. As our system first generates question from each document separately and store them in the database, we can easily eliminate duplicate questions by searching the database. While we insert a question into our question database, we first check whether the question is already in the database or not. If any question from our database matches with our newly generated question then the system does not insert it into our question database. Otherwise, the system inserts the question into the database.

G. Bilingual Translation

Algorithm for translation is given in Fig. 7. Generally Bangla sentence structure is different from English sentence structure. A simple Bangla sentence structure is "Subject + Object + Verb" while in English it is "Subject + Verb + Object". At first using bilingual dictionary, we have to find the translated word and feature of each word. Then by using word's feature we have to determine the sentence structure. After that we have to place those translated word in corresponding sentence structure.

H. Answer Judging

When users insert the answer for each question we have to check the answer whether it is right or wrong. There are many ways to answer a question correctly. An answer to a wh-question "How many versions of the Internet Protocol (IP)?" can be "two", "2", "2 versions" etc. The system needs to accept all these possible answers, and at the same time reject incorrect answers. Algorithm in Fig. 8 is used by our system for this purpose.

```
Algorithm: Bilingual_Translation
Input: Sentence
Require: Translated sentence.
1.  begin
2.  for each word in the sentence do
3.      search the word into the dictionary
4.      if found then
5.          Store into an array
6.      else
7.          do nothing
8.      end if
9.  end for
10. for each rule do
11.     if sentence matches with a rule do
12.         Apply translation rule to translate.
13.     else
14.         do nothing;
15.     end if
16. end for
17. End
```

Fig. 7. Algorithm for bilingual translation

```
Algorithm: Answer_Judging
Input: user's answer and answer database
Require: result.
1.  begin
2.  for each word in the answer do
3.      search the word into the database
4.      if match partially then
5.          calculate the percentage of matching
6.      else
7.          do nothing
8.      end if
9.  end for
10. set correct=0;
11. set wrong=0;
12.     if matching percentage>=70% do
13.         .increment correct value'
14.     else
15.         increment wrong value;
16.     end if
17. show the result
18. End
```

Fig. 8. Algorithm for answer judging

IV. Implementations and Experiments

In this section, we provide the implementation procedure and performance analysis of our developed system.

A. Experimental Setup

The developed Bilingual Question Answering System has been implemented on a machine having the windows 7, 2.50 Core i3-4100 processor with 4GB RAM. The system has been developed in JAVA in the front end and SQLite manager is used in the back end for storing related data to complete this project. For coding we have used NetBeans IDE.

For experimental purpose, we consider total twenty three Bangla and English documents of different domains. Table II shows the document name, domain name and number of containing words on those documents.

B. Implementation

Fig. 9 shows the generated questions with user provided answers in Bangla. Fig. 10 shows the accuracy of user's answers by comparing it with system generated answers. Here,

TABLE II
LIST OF THE DOCUMENTS FOR EXPERIMENTS

Doc_name	Domain	No_of_words
bangladesh.doc	Bangladesh	227
bangladesh_english.doc	Bangladesh	319
Bangladesh_education.doc	Bangladesh	275
bangladesh_government_bangla.doc	Bangladesh	179
bangladesh_government2_bangla.doc	Bangladesh	302
Economics.doc	Bangladesh	413
computerbng2.doc	Computer	175
computeren2.doc	Computer	413
computer_bangla.doc	Computer	255
computer_english.doc	Computer	242
bangladesh_histroy2_bangla.doc	Independence day	415
bangladesh_histroy3_bangla.doc	Independence day	335
independence_bangla.doc	Independence day	687
inter_english.doc	Internet	554
interneten2.doc	Internet	253
Interneten3.doc	Internet	602
interneteng.doc	Internet	413
internet_bangla.doc	Internet	97
IP_english.doc	IP address	284
ip_english2.doc	IP address	260
Ip2bangla.doc	IP address	315
Ip3bangla.doc	IP address	497
urlbangla.doc	IP address	228

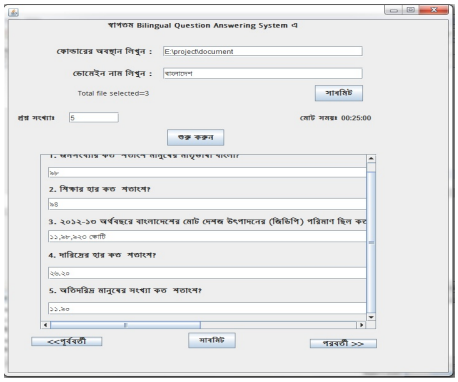

Fig. 9. Question with user's answer

for generating questions and answers for Bangladesh domain it considers eight documents out of twenty three documents.

Table III shows the number of retrieve documents considering by the system under different domains.

C. Performance Evaluation

We have evaluated the performance of our proposed system with respect to documents of Table II. For the experimental evaluation, we have generated questions and answers by our system and compared them with human generated questions and answers.

Our first experiment shows a comparison about question generation with respect to different domain information. Fig. 11 shows the result. From the graph of Fig. 11, we can find that human always generates more question than our system. This is because Human can generate a line of text in different way.

In our next experiment, we show top-10 questions generated by our system and by the human. Table IV and Table V show the results in Bangla and English, respectively. From

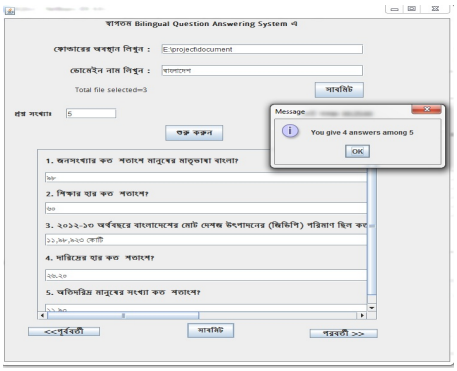

Fig. 10. User's score

TABLE III
DOMAIN SPECIFIC DOCUMENTS INFORMATION

Domain information	Total found documents	Documents
Bangladesh	8	bangladesh.doc, bangladesh_english.doc, Bangladesh_education.doc, bangladesh_government_bangla.doc, bangladesh_government2_bangla.doc, Economics.doc, bangladesh_histroy2_bangla.doc, bangladesh_histroy3_bangla.doc
Independence day	4	independence_bangla.doc, bangladesh_histroy2_bangla.doc, bangladesh_histroy3_bangla.doc, bangladesh_government_bangla.doc,
Computer	6	computer_bangla.doc, computer_english.doc, inter_english.doc, internet_bangla.doc, computerbng2.doc, computeren2.doc
Internet	7	inter_english.doc, internet_bangla.doc, IP_english.doc, ip_english2.doc, interneten2.doc, Interneten3.doc, interneteng.doc
IP address	5	IP_english.doc, ip_english2.doc, Ip2bangla.doc, Ip3bangla.doc,Urlbangla.doc

the tables, we can find that our system can generate questions almost as accurate as the human. This is due to small domain size.

Our next experiment shows the accuracy in translation. The result is shown in Table VI. From Table VI we can see that our system can perform translation of the questions in the desired language upto a satisfactory level.

For each generated question our system produce answers. When user put answer for a corresponding question our system try to check produce all sorts of possibility to check the

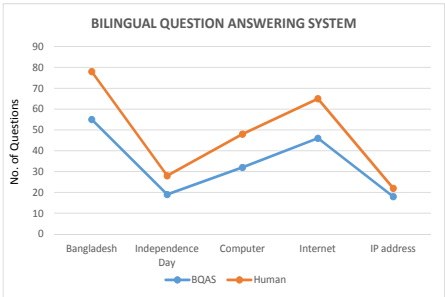

Fig. 11. Comparative question generation performance

TABLE IV
TOP 10 QUESTIONS GENERATED IN BANGLA BY HUMAN AND BQAS

Rank	Top 10 Questions generated by Human	Top 10 Questions generated by BQAS
1	আয়তন হিসেবে বাংলাদেশ বিশ্বে কত তম?	বাংলাদেশ বিশ্বে কত তম আয়তন?
2	বাংলাদেশের আয়তন কত ?	জনসংখ্যার কত শতাংশ মানুষের মাতৃভাষা বাংলা?
3	জনসংখ্যার কত শতাংশ মানুষের মাতৃভাষা বাংলা?	শিক্ষার হার কত শতাংশ?
4	২০১২-১৩ অর্থবছরে বাংলাদেশের মোট দেশজ উৎপাদনের (জিডিপি) পরিমাণ ছিল কত টাকা?	২০১২-১৩ অর্থবছরে বাংলাদেশের মোট দেশজ উৎপাদনের (জিডিপি) পরিমাণ ছিল কত টাকা?
5	শিক্ষার হার কত শতাংশ?	দারিদ্রের হার কত শতাংশ?
6	দারিদ্রের হার কত শতাংশ?	অতিদরিদ্র মানুষের সংখ্যা কত শতাংশ?
7	বাংলাদেশের সংবিধান কত খ্রিস্টাব্দে প্রণীত হয়?	বার্ষিক দারিদ্র হ্রাসের হার কত শতাংশ?
8	২০১১ খ্রিস্টাব্দ পর্যন্ত সর্বমোট কত টি সংশোধনী আনা হয়েছে?	২০১১ খ্রিস্টাব্দ পর্যন্ত সর্বমোট কত টি সংশোধনী আনা হয়েছে?
9	বার্ষিক দারিদ্র হ্রাসের হার কত শতাংশ?	মহিলাদের জন্য কত টি সংরক্ষিত আসন আছে?
10	মহিলাদের জন্য কত টি সংরক্ষিত আসন আছে?	বাংলাদেশ কত টি প্রশাসনিক বিভাগে বিভক্ত?

TABLE V
TOP 10 QUESTIONS GENERATED IN BANGLA BY HUMAN AND BQAS

Rank	Top 10 Questions generated by Human	Top 10 Questions generated by BQAS
1	What is the position of Bangladesh in the world in terms of area?	What is the position of Bangladesh in the world in terms of area?
2	what is the area of Bangladesh?	What percentage of population people mother tongue Bengali?
3	What percentage of population people's mother tongue is Bengali?	What percentage of literacy rate?
4	What is the total production amount of Bangladesh in 2012-2013 economic year?	
5	What is the percentage of literacy rate?	What percentage of poverty rate?
6	What is the percentage of poverty rate?	What percentage of extremely poor people number?
7	When did the constitution of Bangladesh applied?	What percentage of poverty reduction rate?
8	How many amendments brought in up to2011?	How many amendments brought in up to2011?
9	What percentage of poverty reduction rate?	How many reserved seat for women?
10	How many reserved seat for women?	How many administrative division separate in Bangladesh?

correctness. Table VII shows the result. From Table VII we can find that our system can judge the answers upto a satisfactory level.

V. CONCLUSION

In this paper, we provided a framework for bilingual question answering system. We have implemented the system with Bangla and English electronic documents. Form the experimental evaluation, we found that the developed system can generate questions and answers efficiently. Although in this paper, we have considered documents of two different languages, it can incorporate other language easily.

In this work, we considered an in-house database of documents and it is necessary to scan a document before it is considered in the system. In future, we hope to develop a system that can efficiently generate questions and answers from the documents of the Internet without scanning them in the system.

TABLE VI
QUESTION TRANSLATION INFORMATION

Domain name	No. of Bangla doc	No. of English doc	No. of generated question in Bangla	No. of generated question in English	Total No. of correct translated question
Bangladesh	6	2	37	18	44
Independence Day	3	1	12	7	13
Computer	4	2	21	11	19
Internet	4	3	29	17	31
IP address	3	2	11	7	11

TABLE VII
ANSWER JUDGING ACCURACY

No.	Domain Name	No. of Generated Questions	Total correct answer	Total incorrect answer	Answer not found	Correctness %
1	Bangladesh	55	48	5	2	87.24%
2	Independence day	19	14	4	1	73%
3	Computer	32	24	6	2	75%
4	Internet	46	32	10	4	69.57%
5	IP address	18	12	2	4	66.67%

REFERENCES

[1] L. Plamondon, G. Lapalme, L. Kosseim, "The QUANTUM question answering system at TREC-11", *In Proceedings of the Eleventh Text Retrieval Conference*, Gaithersburg, Maryland (2002)

[2] H. Kaur, R Kumari, "Novel scoring system for identify accurate answers for factoid questions", *In International Journal of Science and Research (IJSR)*, 2013.

[3] P.P.B. Filho, V.R. de Uzeda, T.A.S. Pardo, M.D.G.V. Nunes, "Using a text summarization system for monolingual question answering", *NcleoInterinstitucional de LingsticaComputacional (NILC)Instituto de CitnciasMatemticas e de Computao - Universidade de So Paulo*, CP 668, 13.560-970 So Carlos-SP, Brasil, 2003.

[4] N. Hitomi, "A Japanese-English bilingual child's system of answering negative questions", *In Proc. of Japan Journal of Multilingualismand Multiculturalism*, vol.1,no.1, pp. 28-37.

[5] Y. Xu, A. Goldie, S. Seneff, "Automatic question generation and answer judging: a QA game for language learning", *Spoken Language Systems Group, MIT Computer Science and Artificial Intelligence Laboratory*, United States, 2009.

[6] L. Plamondon, G. Foster, "Quantum, a French/English cross-language question answering system", *in In Proc. of Cross Language Evaluation Forum*, 2003.

[7] C. Amaral, H. Figueira, A. Martins, A. Mendes, P. Mendes, C. Pinto, "Priberams question answering system for Portuguese", CLEF 2005.

[8] J. Soriano, D. Buscaldi, E. Asensi, P. Rosso, E. Arnal, "QUASAR: The question answering system of the universidad politecnica de Valencia", LNCS 4022, pp. 439-448, CLEF 2006.

[9] N. Haque, M. Rosner, "A prototype framework for a Bangla question answering system using translation based on transliteration and table look-up as an interface for the medical domain", *Masters Thesis*, University of Malta Gertjan Van Noord, 2010.